

Coastal Sediments '07



Volume 1

ASCE

Edited by
Nicholas C. Kraus
Julie Dean Rosati

An Institute of The American Society of Civil Engineers

COASTAL SEDIMENTS '07

VOLUME ONE

PROCEEDINGS OF THE SIXTH INTERNATIONAL SYMPOSIUM ON COASTAL ENGINEERING AND SCIENCE OF COASTAL SEDIMENT PROCESSES

May 13–17, 2007
New Orleans, Louisiana

SPONSORED BY
Coasts, Oceans, Ports, and Rivers Institute (COPRI)
of the American Society of Civil Engineers

IN COOPERATION WITH
American Shore and Beach Preservation Association
Dept. of Oceanography and Coastal Science, Louisiana State University
Geological Society of America
International Association of Geomorphologists
International Union of Geological Sciences
U.S. Army Corps of Engineers, Coastal Inlets Research Program
U.S. Geological Survey, Coastal and Marine Geology Program

EDITED BY
Nicholas C. Kraus
Julie Dean Rosati

Published by the American Society of Civil Engineers

Library of Congress Cataloging-in Publication Data

International Symposium on Coastal Engineering and Science of Coastal Sediment Processes (6th : 2007 : New Orleans, La.)
Coastal sediments '07 : proceedings of the sixth International Symposium on Coastal Engineering and Science of Coastal Sediment Processes, May 13–17, 2007, New Orleans, Louisiana / sponsored by Coasts, Oceans, Ports, and Rivers Institute (COPRI) of the American Society of Civil Engineers in cooperation with American Shore and Beach Preservation Association ... [et al.] ; edited by Nicholas C. Kraus, Julie Dean Rosati.
p. cm.
Includes bibliographical references and index.
ISBN-13: 978-0-7844-0926-8
ISBN-10: 0-7844-0926-9
1. Coast changes--Congresses. 2. Coastal sediments--Congresses. I. Kraus, Nicholas C. II. Rosati, Julie Dean. III. Coasts, Oceans, Ports and Rivers Institute (American Society of Civil Engineers) IV. Title.

GB450.2.I58 2007
627'.58--dc22 2007009073

American Society of Civil Engineers
1801 Alexander Bell Drive
Reston, Virginia, 20191-4400

www.pubs.asce.org

Any statements expressed in these materials are those of the individual authors and do not necessarily represent the views of ASCE, which takes no responsibility for any statement made herein. No reference made in this publication to any specific method, product, process, or service constitutes or implies an endorsement, recommendation, or warranty thereof by ASCE. The materials are for general information only and do not represent a standard of ASCE, nor are they intended as a reference in purchase specifications, contracts, regulations, statutes, or any other legal document. ASCE makes no representation or warranty of any kind, whether express or implied, concerning the accuracy, completeness, suitability, or utility of any information, apparatus, product, or process discussed in this publication, and assumes no liability therefore. This information should not be used without first securing competent advice with respect to its suitability for any general or specific application. Anyone utilizing this information assumes all liability arising from such use, including but not limited to infringement of any patent or patents.

ASCE and American Society of Civil Engineers—Registered in U.S. Patent and Trademark Office.

Photocopies and reprints.
You can obtain instant permission to photocopy ASCE publications by using ASCE's online permission service (www.pubs.asce.org/authors/RightslinkWelcomePage.html). Requests for 100 copies or more should be submitted to the Reprints Department, Publications Division, ASCE, (address above); email: permissions@asce.org. A reprint order form can be found at www.pubs.asce.org/authors/reprints.html.

Photo Credit.
Top: East Island, Isle Dernieres, Louisiana, October 20, 1990. Bottom: Belle Pass and Port of Fouchon, Louisiana, November 3, 1989. *Images Courtesy USGS*

Copyright © 2007 by the American Society of Civil Engineers. All Rights Reserved.
ISBN 13: 978-0-7844-0926-8
ISBN 10: 0-7844-0926-9
Manufactured in the United States of America.

Foreword

The COASTAL SEDIMENTS '07 conference was organized as a technical specialty conference devoted to the physical aspects of sediment processes and morphology change in the coastal and inlet environment. Following previous conferences in the Coastal Sediments series that were held in 1977, 1987, 1991, 1999, and 2003, COASTAL SEDIMENTS'07 celebrated 30 years of the Coastal Sediments series and promoted exchange of information and views among specialists in the fields of coastal engineering, geology, oceanography, and related disciplines. The theme of COASTAL SEDIMENTS '07 was "Coastal Engineering and Science in Cascading Spatial and Temporal Scales," which established the trend of thinking and approach of the conference, as well as determined in part the composition of the papers that were presented. This theme was chosen to stimulate research devoted to the various scales of processes and their interactions at which coastal engineers and scientists must work in developing knowledge and capabilities to assist society in managing the coast under present and future conditions. Emphasis was on papers that recognize and relate to coastal morphology change of long-term consequence.

The COASTAL SEDIMENTS '07 conference returned to the site of the 1987 conference, New Orleans, Louisiana, because of the extraordinary morphologic change along the coasts of Louisiana, Mississippi, and Texas, caused by Hurricanes Katrina and Rita that struck in August and September, respectively, of 2005. In addition to the recent hurricanes, this coast is experiencing long-term natural and anthropogenic change including rapid and differential subsidence, severe reduction in renewable sediment supply, deltaic adjustment of fine-grained material, and oil and gas exploration and extraction. The theme is intended to generate papers and discussion of coastal sediment processes from the micro-scale to the regional scale at which integrated coastal design and management must be accomplished. Participants were given an overview of recent hurricane damage within the context of the long-term morphologic change in Louisiana in the Keynote Address delivered by Mr. James R. (Randy) Hanchey, Deputy Secretary of the Louisiana Department of Natural Resources.

Professor Leo van Rijn of Delft Hydraulics and the University of Utrecht, The Netherlands, accepted the 2007 Coastal Award at the Conference Awards Luncheon on May 16th. Starting in 2001, the Coastal Award has been presented every 2 years alternately at the Coastal Dynamics conference and the Coastal Sediments conference through coordination between the organizing committees of these two technical specialty conferences. The Organizing Committee of Coastal Sediments '07 joins conference participants and the extended research community in celebrating Professor van Rijn's research contributions that have greatly influenced engineers and geologists working in the areas of coastal sediment transport and morphology change.

These *Proceedings* volumes are the permanent record of the conference, containing the latest thinking and progress of the world's leading scientists and

engineers in the areas of coastal sediment transport and morphology change. The contents are a valuable source of information on coastal sediment and morphology processes ranging from basic research to case studies and lessons learned. The papers contained herein provide the most recent results and ideas in a wide range of approaches and viewpoints not assembled elsewhere in both quality and breadth. The *Proceedings* were produced in hard copy in two volumes in black and white and also provided to conference participants as a CD ROM with searchable index of PDF files in color. All papers are available to the public in PDF format via the ASCE Research Library at www.ascelibrary.org.

Three-hundred fifty abstracts were submitted to the Conference Steering Committee. On average, each abstract received five reviews, and 225 submissions were invited for development into full papers and presentation over 3 days of technical sessions. The 197 papers appearing in these Proceedings originated from approximately 24 countries, demonstrating the international scope of COASTAL SEDIMENTS '07. Each paper included in these *Proceedings* received positive peer review. Each paper is eligible for discussion in the *Journal of Waterway, Port, Coastal and Ocean Engineering* and can be nominated for ASCE awards.

The Steering Committee of COASTAL SEDIMENTS '07 gratefully acknowledges the assistance of many individuals, both known and anonymous, in the 2 years of preparations by an all-volunteer committee. Numerous individuals assisted the Steering Committee in review of abstracts and final papers. The efforts of the following persons are acknowledged: Matthew Arsenault, U.S. Geological Survey (USGS); Mark Byrnes, Applied Coastal Research and Engineering, Inc.; Duncan FitzGerald, Boston University; Guy Gelfenbaum, USGS; Cheryl Hapke, USGS; John Headland, Moffatt & Nichol; Todd Holland, Naval Research Laboratory; Peter Howd, USGS; Bruce Jaffe, USGS; Magnus Larson, University of Lund; Jeffrey List, USGS; Randy Parkinson, Coastal and Environmental Geological Consulting; Robert Morton, USGS; James O'Connell, Woods Hole Oceanographic Institution; Lisa Robbins, USGS; Vladimir Shepsis, Coast and Harbor Engineering; Donald Stauble, U.S. Army Corps of Engineers; Marcel Stive, Delft Hydraulics; Hilary Stockdon; USGS; and Curt Storlazzi, USGS.

We also thank the session moderators for agreeing to lend their time and experience to run the conference smoothly and productively. We are indebted to the tour leaders and their organizations for arranging and conducting memorable and stimulating technical trips. The "Geology of the Louisiana Coastal Zone: Implications for Coastal Management and Restoration" tour was led by Mark Kulp, University of New Orleans (UNO); Mike Miner, UNO; Duncan FitzGerald, Boston University; and Ioannis Giorgiou, UNO. The "Wax Lake-Atchafalaya Delta Complex Sedimentation, Stratigraphy" tour was led by Harry Roberts, Louisiana State University. Finally, we thank Lucy King of ASCE for assisting and often leading in conference logistics; Donna Dickert of ASCE for accurately producing the Proceedings; and Lesa Rair and Chris Hanson of COPRI for assisting with conference arrangements, including exhibitors and sponsors.

We also would like to thank our exhibitors and sponsors for Coastal Sediments 2007 for their support:

Sponsors

Applied Coastal and Research Engineering Inc.
Coastal Engineering Consultants, Inc.
Coast & Harbor Engineering
Great Lakes Dredge & Dock Co.
NortekUSA
Olsen Associates, Inc.
Weeks Marine, Inc.

Exhibitors

American Vibracore Services, Inc.
COPRI
Frontier Surveying Co.
Louisiana Dept. of Natural Resources
Moffatt & Nichol
N.S. Nettles & Associates, Inc.
NortekUSA
SonTek/YSI
Taylor Engineering, Inc.
Teledyne RD Instruments
Tensar Earth Technologies, Inc.
U.S. Army Corps of Engineers, Coastal Inlets Research Program
U.S. Army Corps of Engineers, Navigations Systems Research Program
U.S. Army Corps of Engineers, Regional Sediment Management Program
U.S. Geologic Survey, Coastal and Marine Geology Program
University of New Orleans
URS Corporation
Weeks Marine, Inc.

To everyone who participated, we thank you for contributing to this remarkable conference that is precious to all of us.

Conference Steering Committee

Nicholas C. Kraus
Conference Co-Chair
U.S. Army Engineer
Research and Development Center

Hans Hanson
University of Lund, Sweden

Julie Dean Rosati
U.S. Army Engineer
Research and Development Center

S. Jeffress Williams
U.S. Geological Survey,
Coastal and Marine Geology Program

William G. McDougal
Conference Co-Chair
University of Florida

Luke Le Bas
Coastal Engineering Division,
Louisiana Department of
Natural Resources

Ping Wang
University of South Florida

Harley S. Winer
U.S. Army Corps of Engineers,
New Orleans District

Contents

Volume One

Sediment Transport Fundamentals I

Wave-Related Transport and Nearshore Morphology 1
Leo van Rijn, Gerben Ruessink, Bart Grasmeijer, Jebbe van der Werf, and Jan Ribberink

Closed Form Solution for Threshold Velocity for Initiation of Sediment Motion under Waves 15
Hans Hanson and Benoît Camenen

Influence of Velocity Moments on Sand Bar Movement During CROSSTEX 28
Gregory Guannel, H. Tuba Özkan-Haller, Merrick C. Haller, and James T. Kirby

Development of a New Practical Model for Sand Transport Induced by Non-Breaking Waves and Currents 42
Jebbe J. van der Werf, Jan S. Ribberink, and Tom O'Donoghue

A Total Load Formula for the Nearshore 56
Benoît Camenen and Magnus Larson

Sediment Transport Fundamentals II

Longshore Sand Transport Rate Measurements Using Small-Scale Physical Models 68
Roshan Suminda Ranasinghe and Shinji Sato

Pressure-Induced Subsurface Sediment Transport in the Surf Zone 82
Ole Secher Madsen and William McKinney Durham

Tracking Sediment Particles under Wave-Current Coexisting Field 96
Yoshimitsu Tajima, Masayuki Kozuka, Masahito Tsuru, Toshimasa Ishii, Takeharu Sakagami, Kazuo Momose, Nobuo Mimura, and Ole S. Madsen

Sediment Transport in Response to Wave Groups Generated by High-Speed Vessels 110
Philip D. Osborne, Neil J. MacDonald, and Shaun Parkinson

Sediment Transport Fundamentals III

Flume Experiments under Cat-Scan to Measure Internal Sedimentological Parameter During Sediment Transport 124
Stéphane Montreuil and Bernard F. Long

The Effects of Bed Slope and Wave Skewness on Sediment Transport and Morphology 137
D. J. R. Walstra, L. C. van Rijn, M. van Ormondt, C. Briére, and A. M. Talmon

Sediment Transport off Northeast Florida Outside the Surf Zone during Hurricanes 151
Michael Krecic, Christopher Bender, and Kristen Odroniec

Longshore Transport

Geomorphic and Sedimentologic Evidence for Net Littoral Drift—A Review 165
Terry Healy

Cross-Shore Variation of Predominant Longshore Sediment Transport Rate 179
Yoshiaki Kuriyama and Hikari Sakamoto

Longshore Sand Transport Calculated by Time-Dependent Shear Stress 193
Ernest R. Smith and Nicholas C. Kraus

Sediment Budget of the Danube Delta Coastal Zone 207
Sebastian Dan, Marcel Stive, Dirk Jan Walstra, and François Sabatier

Field Measurements and Modeling of Longshore Sediment Transport 221
J. J. Williams, L. S. Esteves, M. A. Lisniowski, and H. L. S. Perotto

Sediment Transport Fundamentals IV

Infragravity Waves in Mobile-Bed Laboratory Experiments 235
Florent Grasso, Hervé Michallet, and Eric Barthélemy

Large-Scale Laboratory Modeling of Suspended Sand Concentration Fluctuations under Irregular Waves 248
Joachim Grüne, Ruben Kos'yan, Hocine Oumeraci, Igor Podymov, Reinold Schmidt-Koppenhagen, and Chris E. Vincent

Change in Longitudinal Profile Using Sand of Mixed Grain Size in Large Wave Tank and its Numerical Simulation 259
Massaya Fukuhama, Takaaki Uda, Masumi Serizawa, and Toshinori Ishikawa

Probabilistic-Deterministic Modelling of Swash Zone Morphology 272
T. E. Baldock, P. Kim Son, P. Manoonvoravong, M. P. Barnes, and J. M. Alsina

Modelling Sheet Flow Sediment Transport Using Convolution Integrals 286
P. Guard, I. Teakle, P. Nielsen, and T. Baldock

Shoreline Change Modeling

A Middle-Term Evolution Model for Beaches 300
Soledad Requejo, Raul Medina, and Mauricio Gonzalez

Model for Predicting Beach Changes on Coast with Sand of Mixed Grain Size Based on Bagnold's Concept 314
Masumi Serizawa, Takaaki Uda, Toshiro San-nami, Kou Furuike, Toshinori Ishikawa, and Takayuki Kumada

A Circulation Modeling Approach for Evaluating the Conditions for Shoreline Instabilities 327
Jeffrey H. List and Andrew D. Ashton

An Alternative Explanation for the Shape of 'Log-Spiral' Bays 341
Ryan Littlewood, A. Brad Murray, and Andrew D. Ashton

The Response of Spit Shapes to Wave-Angle Climates 351
Andrew D. Ashton, A. Brad Murray, and Ryan Littlewood

Observed Shoreline Change

Historical Shoreline Changes and Morphodynamics of Parramore Island, Virginia (1852-2006) 364
Trent M. Richardson and Randolph A. McBride

Temporal and Spatial Scales of Profile and Planform Adjustment on a Nourished Beach 378
Nicole A. Elko and Ping Wang

Shoreline Response to Dike Failure at Grand Marais Harbor, Lake Superior, Michigan 392
Rachel R. Roblin, Mohammad Dibajnia, Robert B. Nairn, and James P. Selegean

Successful Beach Modelling, Monitoring and Management for a Large LNG Facility 406
Jonathan A. Kemp, Tom C. Coates, Richard Head, and Jenny S. Harcourt

Gravel Coasts I

The Design of Stable and Aesthetic Beach Fills: Learning from Nature 420
Paul D. Komar

Variation in the Organization of Gravel-Dominated Coastal Systems: Evidence from Nova Scotia and Southern England 434
Julian D. Orford and Simon C. Jennings

Profile Dynamics and Particle Tracer Mobility of a Cobble Berm Constructed on the Oregon Coast 449
Jonathan C. Allan and Roger Hart

Mixed Sediment Beach Processes: Kachemak Bay, Alaska 463
Peter Ruggiero, Peter N. Adams, and Jonathan A. Warrick

Mixed Sand and Gravel Beach Design and Construction for Habitat Restoration 477
David Simpson, Michael Wray, John Houghton, and John Klekotka

Gravel Coasts II

Influence of Changing Management Regimes on the Morphodynamic Response of a Mixed Gravel and Sand Barrier Beach 492
Andrew P. Bradbury and Julian D. Orford

The Influence of Groundwater on Profile Evolution of Fine and Coarse Sand Beaches 506
Diane P. Horn, Tom E. Baldock, and Ling Li

Effects of Permeability on the Performance of Mixed Sand-Gravel Beaches 520
Kaiming She, Louise Trim, Diane Horn, and Paul Canning

Cross-shore and Longshore Transport of Tracer Pebbles on a Macrotidal Mixed Sediment Beach, Somme Estuary, France 531
J. Curoy, U. Dornbusch, C. A. Moses, D. A. Robinson, and R. B. G. Williams

Why Are Shingle Beaches Replacing Sandy Beaches? (Coastal Zone of NW Portugal) 545
Helena Granja and Eduardo Loureiro

Gravel Coasts III

Field Measurements of Shore Conditions to Assess Bulkhead Effects in Thurston County, South Puget Sound 561
Susan P. Tonkin, Tim Abbe, José Carrasquero, and Steve Morrison

Coral-Gravel Storm Ridges: Examples from the Tropical Pacific and Caribbean 572
Bruce M. Richmond and Robert A. Morton

Field Observations of Step Dynamics on a Macrotidal Gravel Beach 584
Daniel Buscombe, Martin J. Austin, and Gerhard Masselink

Large-Scale Scour of the Sea Floor and the Effect of Natural Armouring Processes, Land Reclamation Maasvlakte 2, Port of Rotterdam 598
Sander Boer, Edwin Elias, Stefan Aarninkhof, Dano Roelvink, and Tiedo Vellinga

Dunes and Profiles

Dune Erosion Prediction Methods Incorporating Effects of Wave Periods 612
Marcel R. A. van Gent, E. Martijn Coeveld, Hans de Vroeg, and Jan van de Graaff

Reevaluation of Equilibrium Beach Profile Scale Parameter 626
Zhanxian Wang and Robert G. Dean

Shoreface Response to Sediment Deficit 633
G. M. Kaminsky, M. A. Ferland, P. J. Cowell, H. R. Mortiz, and P. Ruggiero

Louisiana Coast

The Challenges of Restoring Louisiana Barrier Islands: From Design through Construction 647
Gordon G. Thomson, Greg M. Grandy, and Rachel Sweeney

Field Observations of Wave-Current-Sediments Dynamics, Atchafalaya Shelf, Louisiana, USA 661
Sergio Jaramillo, Alex Sheremet, and Mead Allison

Investigation of Morphosedimentary Processes on a Schematic Louisiana Barrier Island Using Process-Based Numerical Modeling 671
T. Campbell, B. de Sonneville, L. Benedet, D. J. W. Walstra, and C. W. Finkl

Restoration-Quality Sand from Ship Shoal, Louisiana: Geotechnical Investigation for Sand on a Drowned Barrier Island 685
Syed M. Khalil, Charles W. Finkl, Jeff Andrews, and Christopher P. Knotts

Mississippi River Sand for Barrier Island Restoration in Louisiana: Geophysical and Geotechnical Investigations for Sand Mining 699
Jeffrey L. Andrews, Syed M. Khalil, Charles W. Finkl, and Lindino Benedet

Mississippi River Delta

Re-Engineering the Mississippi River as a Sediment Delivery System 712
Harley S. Winer

Sediment Flux and Fate in the Mississippi River Diversion at West Bay: Observation Study 722
T. Mitchell Andrus and Samuel J. Bentley

Initial Morphologic and Stratigraphic Delta Evolution Related to Buoyant River Plumes 736
Joep E. A. Storms, Marcel J. F. Stive, Dano (J.) A. Roelvink, and Dirk Jan Walstra

Physical and Numerical Modeling of River and Sediment Diversions in the Lower Mississippi River Delta 749
Clinton S. Willson, Nathan Dill, William Barlett, Samantha Danchuk, and Ryan Waldron

A Geomorphic Process-Response Model for Chenier-Plain Evolution in Southwestern Louisiana, USA 762
Randolph A. McBride, Matthew J. Taylor, and Mark R. Byrnes

Marshes and Wetlands

Sediment Analysis for Habitat Restoration: Adaptation of Open-Coast Beach Nourishment Principles 776
Daniel J. Heilman, Joel T. Darnell, and M. Cameron Perry

Subsurface Exploration and Containment Dike Design Criteria for Coastal Louisiana Marsh Restoration 785
Russ Joffrion, Michael Poff, and Mitch Andrus

Ice Raft Formation, Dispersion and Sedimentation on New England Salt Marshes 798
Brittina A. Argow, Zoe J. Hughes, and Duncan M. FitzGerald

Effects of Large Scale Morphological Changes to a Back-Bay System 814
Lee L. Weishar, Theodore Keon, and Donald K. Stauble

Volume Two

Deltas and River Mouths

Morphodynamic Feedbacks on Deltaic Coasts: Lessons from the Wave-Dominated Danube Delta 828
Liviu Giosan

Coastal and River Mouth Morphology Change in Sri Lanka Due to 2004 Indian Ocean Tsunami 842
Hitoshi Tanaka, Kazuo Ishino, Bandara Nawarathna, Hajime Nakagawa, and Shinichiro Yano

Holocene Evolution of the Merrimack Embayment, Northern Massachusetts, Interpreted from Shallow Seismic Stratigraphy **856**
Christopher J. Hein, Duncan M. FitzGerald, and Walter A. Barnhardt

The Use of Historic Topography for the Characterization of Time-Dependent Geomorphic Change and Sediment Delivery **867**
David A. Jaffe

Impact of Hurricanes Katrina and Lili on the Inner Shelf of the Mississippi-Atchafalaya Delta **882**
Mead A. Allison, Timothy M. Dellapenna, Miguel A. Goñi, and Alex Sheremet

Storms I

Coastal-Change Impacts during Hurricane Katrina: An Overview **888**
Asbury Sallenger, C. Wayne Wright, and Jeff Lillycrop

Modeling Dune Response Using Measured and Equilibrium Bathymetric Profiles **897**
Laura A. Fauver, David M. Thompson, and Asbury H. Sallenger

Sediment Transport along the Southwestern Louisiana Shoreline: Impact from Hurricane Rita, 2005 ..... **911**
Walter S. Guidroz, Gregory W. Stone, and Dane Dartez

Heterogeneity and Dynamics on a Shoal during Spring-Winter Storm Season, South-Central Louisana, USA **921**
Daijiro Kobashi, Felix Jose, and Gregory W. Stone

Winter Storm and Tropical Cyclone Impacts on the Short-Term Evolution of Beaches and Barriers along the Northeastern Gulf of Mexico **935**
Gregory W. Stone, Baozhu Liu, and Felix Jose

Storms II

Impact of a Major Storm on Sediment Exchanges between the Dunes, Beach, and Nearshore **951**
Aart Kroon, Susanne Quartel, and Troels Aagaard

Storm Patterns and Climatic Trends Based on Water Level Fluctuations: Duck, North Carolina, USA **963**
Joan Pope

Hindcasting Potential Hurricane Impacts on Rapidly Changing Barrier Islands **976**
Hilary F. Stockdon, David M. Thompson, and Asbury H. Sallenger, Jr.

EOF Analysis of Morphological Response to Hurricane Ivan **986**
Chris Houser, Stuart Hamilton, Klaus Meyer-Arendt, and Jonathan Oravetz

Storm Surge and Sediment Process Owing to Hurricane Isidore in Terminos Lagoon, Campeche **996**
Juan C. Espinal, Paulo Salles. A de A, and Diana K. Moran

Tsunami I

Tsunami Damage Estimation in Consideration of Beach Transformation and Dike Failure 1008
Fuminori Kato, Masaya Fukuhama, Hiroyuki Fujii, and Toshimitsu Takagi

Beach Morphology at Banda Aceh, Indonesia in Response to the Tsunami on 26 December 2004 1019
Ella Meilianda, C. Marjolein Dohmen-Janssen, Ben H. P. Maathuis, Suzanne J. M. H. Hulscher, and Jan P.M. Mulder

Dune Morphology as an Indicator of Paleotsunamis 1033
James R. Goff

Sedimentological Characteristics of Regional-Scale Washover Deposits Caused by Hurricane Ivan 1047
Mark H. Horwitz and Ping Wang

Tsunami II

Impacts of the 2004 Indian Ocean Tsunami on the Southwest Coasts of Sri Lanka 1061
Robert A. Morton, James R. Goff, and Scott L. Nichol

Reconstructing Tsunami Run-Up from Sedimentary Characteristics—A Simple Mathematical Model 1075
Richard L. Soulsby, David E. Smith, and Alan Ruffman

Numerical Study of Tsunami Run-Up over Erodible Sand Dunes 1089
Takenori Shimozono, Shinji Sato, and Yoshimitsu Tajima

Predicted Sedimentary Record of Reflected Bores 1103
Bretwood Higman, Guy Gelfenbaum, Patrick Lynett, Andrew Moore, and Bruce Jaffe

Tsunami Inundation and Sediment Transport in Vicinity of Coastal Mangrove Forest 1117
Guy Gelfenbaum, Deepak Vatvani, Bruce Jaffe, and Frank Dekker

Sea Level Rise I

From Transgression to Regression: Coastal Evolution near The Hague, The Netherlands, around 5000 Years BP 1129
Ad J. F. van der Spek, Jelmer Cleveringa, and Sytze van Heteren

Changing Orientation of Ocean-Facing Bluffs on a Transgressive Coast, Cape Cod, Massachusetts 1142
Graham S. Giese and Mark B. Adams

Modeling Barrier Island Response to Sea-Level Rise in the Outer Banks, North Carolina 1153
Laura J. Moore, Jeffrey H. List, S. Jeffress Williams, and David Stolper

1880 to 2005 Morphological Evolution of a Transgressive Tidal Inlet, Little Pass Timbalier, Louisiana 1165
Michael D. Miner, Duncan M. FitzGerald, and Mark A. Kulp

Sea Level Rise II

Impacts of Rising Sea Level to Backbarrier Wetlands, Tidal Inlets, and Barrier Islands: Barataria Coast, Louisiana 1179
Duncan FitzGerald, Mark Kulp, Zoe Hughes, Ioannis Georgiou, Michael Miner, Shea Penland, and Nick Howes

Modeling Future Coastal Wetland Transition Induced by Relative Sea-Level Rise 1193
James C. Gibeaut

Morphological Interactions within UK Estuaries: A Preliminary Analysis of Critical Rates of Sea-Level Rise 1200
Kate Rossington, Robert J. Nicholls, and Michiel A. F. Knaapen

Variable Shoreline Responses to Sea-Level Rise and Climate Change 1214
A. Brad Murray, Lisa Valvo, Jordan Slott, Andrew Ashton, and Tom Crowley

Model Scenarios of Shoreline Change at Kaanapali Beach, Maui, Hawaii: Seasonal and Extreme Events 1227
Sean Vitousek, Charles H. Fletcher, Mark A. Merrifield, Geno Pawlak, and Curt D. Storlazzi

Wind-Blown Sand

Aeolian Processes, Coastal Dunes, and the *Coastal Engineering Manual*, Part III, Chapter 4—"Wind-Blown Sediment Transport" 1241
Frank Hopf and Douglas J. Sherman

Distribution of Horizontal Distance Traveled by Saltating Sand Grains in Air 1255
Shintaro Hotta, Susumu Kubota, and Nagatomo Nakamura

Beach Stabilization Works Against Wind Blown Sand on Beaches: Experiences from Japan 1269
Susumu Kubota, Souichi Harikai, and Shintaro Hotta

Coastal Dunefield Evolution in Conditions of Limited Sediment Availability: Natural and Anthropogenic Controls on the Corralejo Dunes 1283
Herminia I. Valdemoro, José A. Jiménez, Ignacio Alonso, Paloma Lorente, and Manuel Rodriguez-Herrerias

Coastal Inlets I

Hydrodynamic and Morphologic Modeling at Sebastian Inlet, FL 1297
Gary A. Zarillo and Florian G. A. Brehin

Erosion and Channel Migration at the Shoalwater Bay Reservation, Willapa Bay, Washington 1311
Andrew Morang, David J. Mark, and Jane M. Smith

Sediment Management Plan Development for the St. Lucie Inlet, Martin County, Florida 1326
John Ramsey, Trey Ruthven, Kevin Kremkau, and Kathy Fitzpatrick

Sand Bypassing Restores Natural Processes to Assateague Island, Maryland 1340
Courtney A. Schupp, Gregory P. Bass, and William G. Grosskopf

Morphological Responses to Jetty Construction at Tidal Inlet: Lake Saroma, Japan 1354
Kentaro Hayashi, Koji Hashimoto, Takayuki Sasaki, Akihiro Honma, and Seizo Matsura

Coastal Inlets II

Morphodynamics of Texel Inlet, The Netherlands 1363
Edwin P. L. Elias and Marcel J. F. Stive

Sedimentation Patterns in a Stabilized Migratory Inlet, Blind Pass, Florida 1377
Ping Wang, David K. Tidwell, Tanya M. Beck, and Nicholas C. Kraus

Approaches to Understanding Multiple-Inlet Stability 1391
William C. Seabergh

Engineering Guidelines for the Siting of Sand Bypassing Discharges 1405
Douglass W. Mann

Shoreline Implications of Flood-Tide Delta Morphodynamics. The Case of Port Stephens (SE Australia) 1417
Ana Vila-Concejo, Andrew D. Short, Michael G. Hughes, and Roshanka Ranasinghe

Mud Coasts I

Using Simple Semi-Empirical Models for Integrated Assessment of Scenarios for a Navigation Channel. The Case of the Port of Ostend, Belgium 1431
Toon Verwaest

Sediment Processes and Mangrove-Habitat Expansion on a Rapidly-Prograding Muddy Coast, New Zealand 1441
Andrew Swales, Samuel J. Bentley, Catherine Lovelock, and Robert G. Bell

The Influence of Mud on the Inner Shelf, Shoreface, Beach, and Surf Zone Morphodynamics—Cassino, Southern Brazil 1455
Lauro J. Calliari, K. Todd Holland, Pedro S. Pereira, Rafael M. C. Guedes, and Renato E. Santo

The Hurricane Katrina Storm Surge in Mississippi 1466
Alan W. Niedoroda, Lyle Hatchett, Himangshu Das, Andrew Cox, Robert Weaver, Stephen Baig, and Shabbar Saifee

Texas Inlets

Coastal Inlets of Texas, USA 1475
Nicholas C. Kraus

Cedar Bayou—Inlet Dynamics and Engineering 1489
Vladimir Shepsis and Joshua Carter

Navigation Improvements, Mouth of the Colorado River, Texas 1502
Ronnie G. Barcak, Nicholas C. Kraus, Lihwa Lin, Ernest R. Smith, Daniel J. Heilman, and Robert C. Thomas

Long-Term Inlet Stability of a Multiple Inlet System, Pass Cavallo, Texas **1515**
Brian K. Batten, Nicholas C. Kraus, and Lihwa Lin

Morphologic Response to a New Inlet, Packery Channel, Corpus Christi, Texas **1529**
Deidre D. Williams, Nicholas C. Kraus, and Carl M. Anderson

Coastal Inlets III

Evolution of a Relocated Tidal Inlet: Mason Inlet, NC **1543**
John M. Welsh and William J. Cleary

Present Hydrodynamics of Ancão Inlet, 10 Years after its Relocation **1557**
André Pacheco, Ana Vila-Concejo, Oscar Ferreira, and Alveirinho Dias

The Influence of Tidal Prism and Vegetation on Tidal Channel Morphology: Implications for Marsh Stability **1571**
Matthew L. Kirwan and A. Brad Murray

Natural and Anthropogenic Influences on the Morphodynamics of Big Sarasota Pass, Florida **1582**
Richard A. Davis, Ping Wang, and Tanya Beck

Morphological Behavior of Seasonal Closure of Tidal Inlets **1589**
Tran Thanh Tung, Marcel J. F. Stive, Jan van de Graaff, and Dirk-Jan R. Walstra

Estuaries

The National Academies Report on Mitigating Shore Erosion along Sheltered Coasts **1601**
Jeff Benoit and Susan Roberts

Field Measurement and Modeling of Scour Pit Dynamics in a Sandy Estuary **1609**
A. G. Davies and J. M. Brown

Projection of Topographic Change of an Estuary Terrace by Horizontal 2-D Simulation Model, Considering Grain Size **1623**
Toshimitsu Takagi, Go Asano, Takushi Inukai, and Masaya Fukuhama

Examining the Contribution of Sediment Stratification to the Evolution of Seabed Morphology **1635**
S. Falchetti, D. C. Conley, and M. Brocchini

From River Basin to Barrier Reef: Pathways of Coastal Sediments **1647**
Piet Hoekstra, Ton Hoitink, Frans Buschman, Ayi Tarya, and Gert van den Bergh

Mud Coasts II

Wave Evolution on Fluid Mud Bottom **1660**
Kevin Hall and Ali Oveisy

A Fine Sediment Transport Modeling Framework and its Application to Fluid Mud Processes **1669**
Tian-Jian Hsu and Minwoo Son

Field Measurement of Fine Sediment Transport Process around Navigation Channel 1678
Yasuyuki Nakagawa and Hideo Matsumoto

Time Dependent Mud Fluidization and Irregular Wave Transformation on Muddy Profiles 1690
Mohsen Soltanpour, S. Abbas Haghshenas, and Tomoya Shibayama

Volume Three

Regional Processes I

Regional Beach/Cliff System Dynamics along the California Coast 1696
Cheryl J. Hapke and Dave Reid

Factors Influencing the Long-Term Stability of the Carbonate Sand Beaches of Mauritius 1708
Michael J. Risk, Robert B. Nairn, and Mark O. Kolberg

Evolution of Erosion Hot Spots on a Barrier Island: Fire Island, New York 1722
Kathryn Seaver, Frank Buonaiuto, and Henry Bokuniewicz

Tropical Mixed Wave/Tide Dominated Barrier-Spit System: A Case Study from NE Brazil 1731
Helenice Vital, Francisco Santos Neto, Jose S. Placido Junior, and Venerando E. Amaro

Regional Shoreline and Beach Changes in the Santa Barbara Sandshed 1740
David L. Revell and Gary B. Griggs

Regional Processes II

Engineering Activities Influencing Historical Sediment Transport Pathways at the Columbia River Mouth, WA/OR 1754
Mark R. Byrnes, Sarah F. Griffee, and Hans R. Moritz

Implementing Regional Sediment Management to Sustain Navigation at an Energetic Tidal Inlet 1768
Hans R. Moritz, Guy R. Gelfenbaum, George M. Kaminsky, Peter Ruggiero, Joan Oltman-Shay, and Doris J. McKillip

Decadal Evolution of Shoreface Geometry in South Carolina, USA 1787
B. M. Reynolds, P. A. Wren, and P. T. Gayes

Improving Statistical Validity in Calculating Erosion Hazards from Historical Shorelines 1799
Ayesha S. Genz, L. Neil Frazer, and Charles H. Fletcher

Linking Coastal Evolution and Super Storm Dune Erosion Forecasts 1813
L. M. van der Burgh, K. M. Wijnberg, S. J. M. H. Hulscher, J. P. M. Mulder, and M. van Koningsveld

LIDAR and ARGUS

***CHARTS*-Enabled Data Fusion for Coastal Zone Characterization** 1827
Jennifer M. Wozencraft, Christopher L. Macon, and W. Jeff Lillycrop

Using Topographic LIDAR Data to Delineate the North Carolina Shoreline 1837
Patrick W. Limber, Jeffrey H. List, Jeffrey D. Warren, Amy S. Farris, and Kathryn M. Weber

Exploring Rippled Scour Depressions Offshore Huntington Beach, CA 1851
Eleyne L. Phillips, Curt D. Storlazzi, Peter Dartnell, and Brian D. Edwards

A Study of Intertidal Bar Dynamics Using the Argus Video System 1865
Amaia Ruiz de Alegria Arzaburu, Suzana Ilic, and Yohama Gunawardena

Depth of Closure Derived from Airborne Laser Bathymetry 1877
William Robertson V, Keqi Zhang, and Dean Whitman

Remote Sensing

Assessing Nearshore Bar Movements during Storms Using Time-Averaged X-Band Radar Images 1886
Luciana S. Esteves, Jon J. Williams, and Paul S. Bell

Longshore Migration of Coastal Features Observed with X-Band Radar 1900
Satoshi Takewaka, El Sayed Galal, Ryosuke Matsumoto, and Shinya Sasakura

Detailed 3-D Models of New Zealand Barrier Stratigraphy Provide Insight into Coastal Evolution in Various Spatial and Temporal Settings 1910
Amy J. Dougherty and Scott L. Nichol

Swash Zone

A Formula for Longshore Sediment Transport in the Swash 1924
Magnus Larson, Ty V. Wamsley

Importance of the Swash Longshore Sediment Transport in Morphodynamic Models 1938
Yasuyuki Baba and Benoît Camenen

Direct Bed Shear Stress Measurements in Bore-Driven Swash and Swash Interactions 1947
Matthew P. Barnes and Tom E. Baldock

Limits of Beach and Dune Erosion in Response to Wave Runup Elucidated from SUPERTANK 1961
Tiffany M. Roberts, Ping Wang, and Nicholas C. Kraus

Interaction of Dune Face and Swash Zone 1975
Jaap S. M. van Thiel de Vries, Linden B. Clarke, Stefan G. J. Aarninkhof, E. Matrijn Coeveld, Rob A. Holman, Meg L. Palmsten, Ad J. H. M. Reniers, Marcel J. F. Stive, and Wim S. J. Uijttewaal

Barrier Island Breaching

Critical Width of Barrier Islands and Implications for Engineering Design 1988
Julie Dean Rosati and Gregory W. Stone

Barrier Island Vulnerability to Breaching: A Case Study on Dauphin Island, Alabama 2002
Mark Hansen and Asbury H. Sallenger

Morphologic Modeling of Multiple Barrier Island Breaches for Regional Application 2011
Kenneth J. Connell, Magnus Larson, and Nicholas C. Kraus

Breach Stability and Growth Analysis Using a Morphological Model 2025
Santiago R. Alfageme, Masood Khondker, and Rafael Canizares

Spatial Distribution of Cross-Shore Sediment Transport Rate for Berm Formation and Erosion 2037
Takayuki Suzuki, Maiko Takeuchi, Naoki Tomoda, Satomi Yamaguchi, and Yoshiaki Kuriyama

Overwash and Washover

Sediment Transport Patterns During Overwash 2049
Ana Matias, Ana Vila-Concejo, Óscar Ferreira, Brad Morris, and João A. Dias

Characterization and Modeling of Washover Fans 2061
Chantal Donnelly and Asbury H. Sallenger

Experimental Study of Overwash 2074
Billy L. Edge, Young Hyun Park, and Margery Overton

Backbarrier Evolution and Complete Overwash Occurrence 2084
Ana R. Carrasco, Óscar Ferreira, Ana Matias, and João A. Dias

Sand Bars, Beach Cusps

Geomorphic Features Shaped by Crossing Waves 2097
Robert B. Nairn and Mohammad Dibajnia

Observation and Modeling of Crescentic Bars in Barcelona Embayed Beaches 2111
F. Ribas, R. Garnier, E. Ojeda, A. Falqués, J. Guillén, and D. Calvete

Mesoscale Behaviour of Longshore Bars—Net Onshore or Net Offshore Migration 2124
Troels Aagaard and Aart Kroon

Morphological Characteristics of Rip Current Embayments on the Oregon Coast 2137
Matthew M. Dalon, Merrick Haller, and Jonathan Allan

Geologic Framework of the Long Bay Inner Shelf: Implications for Coastal Evolution in South Carolina 2151
Walter Barnhardt, Jane Denny, Wayne Baldwin, William Schwab, Robert Morton, Paul Gayes, and Neal Driscoll

Sand Waves and Channels

A Relic Sand Wave Field in a Tidal Channel 2164
Shelley J. Whitmeyer and Duncan FitzGerald

Geometric and Statistical Characteristics of Bed Forms in the Lower Mississippi River 2177
K. Kheiashy, J. McCorquodale, I. Georgiou, and E. Meselhe

Bathymetric Evolution of a Sandy Bed under Transient Progressive Waves **2191**
Blake J. Landry and Marcelo H. García

Analysis of Sebastian Inlet, FL, Morphologic Changes Using Complex Empirical Orthogonal Functions (CEOF) **2199**
Florian G. A. Brehin, Jo-Ann Rosario-Llantin, and Gary A. Zarillo

Investigating Ship Induced Scour in a Confined Shipping Channel **2213**
David Taylor, Kevin Hall, and Neil MacDonald

Beach Nourishment

Evolution of Grain-Size Distribution on Bogue Banks: Implications for Selection of Borrow Material **2229**
Timothy W. Kana

New Findings in Equilibrium Grain Size Distribution **2242**
Jordi Galofre, Raúl Medina, Gabriela Medellin, and César Vidal

Determination of Overfill Factor for Offshore Sand in Barrier Island Restoration on the Louisiana Coast **2254**
Daniel L. Bolinger, Dominic Izzo, and Edward J. Schmeltz

Broward County Beach Demonstration Project: From Beers to Beaches **2265**
Christopher Makowski, Gordon Thomson, Peter Foye, and Stephen Higgins

Beach Nourishment Evolution in the Cancún Beach, Quintana Roo, México **2279**
Diana K. Morán, Paulo Salles, A de A, José C. Sánchez, and Juan C. Espinal

Case Studies

Geomorphic Response and Elements of Sediment Budget at St. Joseph Harbor, Southeast Lake Michigan **2292**
Mohammad Dibajnia, Robert B. Nairn, and James P. Selegean

Chesapeake Bay: Headland Control Systems Performance Including Hurricane Isabel **2306**
C. Scott Hardaway, Jr. and James R. Gunn

Coastal Protection against Wind-Wave Induced Erosion Using Soft and Porous Structures: A Case Study at Lake Biel, Switzerland **2321**
Selim M. Sayah and Stephan Mai

Physical Processes Study of Goldsmith Inlet, New York **2331**
Michael J. Morgan and Nicholas C. Kraus

Dredging

Design of Navigation Channel Deepening Works Using a Morphological Model in Barranquilla, Columbia **2345**
Rafael Cañizares, Santiago Alfageme, and Tucker Mahoney

Beach Renourishment through Spoil Disposal Downdrift of a Dredged Entrance Channel **2358**
Kyle C. Spiers and Terry R. Healy

Desktop Methodology for Estimating Maintenance Dredging Requirements for Widened and Deepened Navigation Channels 2372
Larry A. Wise and Oleg Mouraenko

A Mass-Balance, Control-Volume Approach for Estimating Vertical Sediment Flux and Settling Velocity within Dredge Plumes 2382
S. Jarrell Smith and Carl T. Friedrichs

What Does "Physical Regeneration" of Marine Aggregate Dredging Sites Mean? 2394
Markus Diesing

Beach Nourishment and Structures

Performance of Beach Fill and Nearshore Breakwaters at East Ocean View Beach, Norfolk, VA 2402
Peter Elkan, Laural Krynock, Nicole Vanderbeke, James White, and Lee Rosenberg

Assessing Fill Compatibility through Project Performance Evaluation 2418
Donald K. Stauble

Coastal Structure Design for Shore Protection and Sand Retention: Practical Aspects 2432
John R. Headland, Santiago Alfageme, Eric Smith, and Peter Kotulak

Quantitative Evaluation of Controlling Effect of Headland on Longshore Sand Transport Using Model for Predicting Changes in Contour Lines and Grain Size 2446
Takayuki Kumada, Takaaki Uda, and Masumi Serizawa

Evaluation of Controlling Effect of Sand Transport by Detached Breakwaters Built on Dynamically Stable Beach 2460
Takaaki Uda, Masumi Serizawa, and Toshinori Ishikawa

Seafloor Mapping

Geologic Characterization of Offshore of Shelf Areas Using usSEABED for GIS Mapping, Modeling Processes and Assessing Marine Sand and Gravel Resources 2473
S. Jeffress Williams, James D. Bliss, Matthew A. Arsenault, Chris J. Jenkins, and John A. Goff

USGS Advances in Integrated, High-Resolution Sea-Floor Mapping: Inner Continental Shelf to Estuaries 2487
Jane F. Denny, William C. Schwab, David C. Twichell, Thomas F. O'Brien, William W. Danforth, David S. Foster, Emile Bergeron, Charles W. Worley, Barry J. Irwin, Bradford Butman, Page C. Valentine, Wayne E. Baldwin, Robert A. Morton, E. Robert Thieler, David R. Nichols, and Brian D. Andrews

A Rapid Compatibility Analysis of Potential Offshore Sand Sources for Beaches of the Santa Barbara Littoral Cell 2501
Neomi Mustain, Gary Griggs, and Patrick L. Barnard

Presence of Beach-Compatible Sediments in Offshore Borrows: New Challenges and Trade Offs in Developing Codifications **2515**
Charles W. Finkl, Jeffrey L. Andrews, and Lindino Benedet

Indexes

Subject Index **I-1**

Author Index **I-5**

WAVE-RELATED TRANSPORT AND NEARSHORE MORPHOLOGY

Leo van Rijn[1], Gerben Ruessink[1], Bart Grasmeijer[1],
Jebbe van der Werf[2], Jan Ribberink[2]

1. Department of Physical Geography, University of Utrecht. The Netherlands.
   leo.vanrijn@wldelft.nl; g.ruessink@geo.uu.nl; b.grasmeijer@alkyon.nl
2 Department of Civil Engineering, University of Twente. The Netherlands.
   j.j.vanderwerf@ctw.utwente.nl; j.s.ribberink@ctw.utwente.nl

Abstract: This paper discusses the simulation of nearshore bar migration using the CROSMOR profile model. Two sediment transport formulations have been used : the method of Van Rijn (2006) and that of Van der Werf (2006). The model has been applied to two large-scale laboratory experiments in the Delta flume of Delft Hydraulics. Both transport models can represent the trends observed in the laboratory experiments.

INTRODUCTION

As surface gravity waves arrive at the shore from deep water, they transfrom primarily owing to shoaling, refraction, breaking, and non-linear wave interactions. These interactions cause dramatic transformations of the wave shape. From deep into intermediate waterdepths, the initially symmetric, nearly sinusoidal profiles develop into profiles with sharp crests and broad, flat troughs. This horizontal aymmetry is known as skewness. Into shallower water, the waves ultimately transform into pitched-forward, sawtooth profiles, known as (vertical) asymmetry, which have zero-skewness. Field studies, like those of Doering and Bowen (1995), have indicated that near-bed velocity skewness and asymmetry can be parameterized reasonably well with the local Ursell number, suggesting that wave non-linearity is determined locally, and does not depend on, for instance, beach slope. The mechanism for the wave shape transformation is nonlinear, near-reasonant triad interactions, involving the energy transfer from two primary waves with frequencies ω_1 and ω_2 to a secondary wave with frequency $\omega_1 + \omega_2$. This secondary wave is phase locked to the primary waves, initially with a phase difference of 0 degrees to result in a skewed wave profile, increasing to -90 degrees for a sawtooth wave.

The local non-linearity of the near-bed orbital motion is important to sediment transport. The recognition that skewed waves may induce onshore transport because of the much larger onshore than offshore velocities already dates back to the 19th century. The relevance of asymmetric waves to onshore transport (e.g., Hoefel and Elgar, 2003) is still under considerable debate (e.g., Henderson et al., 2004; Hsu et al., 2006). However, the notion that wave non-linearity leads to onshore transport only may be too simple. Fundamentally different physical processes determine sand transport rates above plane and rippled sand beds in oscillatory flow. Above plane beds, momentum transfer and associated sediment dynamics occurs primarily by turbulent diffusion. In contrast, in the bottom part of the boundary layer above rippled beds, momentum transfer and the associated sediment dynamics are dominated by coherent periodic vortex structures; above this, in a layer of thickness of about 1-2 ripple heights, the coherent motions break down and are replaced by random turbulence. The effect of this is that sand is entrained into suspension to considerably greater heights above rippled beds than above plane beds. In addition, the phase of sand pick-up from the bottom during the wave-cycle is also significantly different above rippled beds, with pick-up being linked to the phase of vortex shedding. This has potentially important consequences for the net sand transport rate beneath asymmetrical waves, which can be in the negative ('offshore') direction despite the larger positive ('onshore') orbital velocities (Van der Werf, 2006).
The aim of the present paper is to present preliminary work on the influence of bedforms, wave shape and phase-lags on wave-induced suspended sediment transport. Existing engineering transport formulations for wave-induced suspended sediment transport, like those of Houwman and Ruessink (1996), are reviewed and adjusted to incorporate phenomena like phase lags. We then incorporate the various formulations in the CROSMOR profile model and apply it to the prediction of sandbar migration in two large-scale laboratory tests. The CROSMOR model has been described earlier by the first author. Papers on the CROSMOR-model can be downloaded from www.leovanrijn-sediment.com.

CROSS-SHORE TRANSPORT PROCESSES

In recent years, many full-scale oscillatory flow tunnel experiments have been carried out in order to increase the insight of the complex nature of cross-shore sediment transport and to obtain reliable data for validation and further development of various types of models. One of the advantages of those type of experiments is that net sediment transport rates can be measured accurately. Figure 1 shows measured net sediment transport rates as a function of the mobility number $\psi=2(u_{rms})^2/((s-1)gd_{50})$, with u_{rms} =the root-mean-square orbital velocity, s=the relative sediment density, g =the acceleration due to gravity and d_{50} =the median grain-size (Van der Werf, 2006). The orbital flow was regular asymmetric with larger positive (‘onshore’) velocities and smaller negative (‘offshore’) velocities and the degree of flow asymmetry was similar across the experiments.
This figure shows that the net sediment transport rate is alternately negative (‘offshore-directed’) and positive (‘onshore-directed’), depending on presence or absence of ripples and the grain-size. For mobility numbers smaller than 100, the bed is covered with two-dimensional ripples. On the lee-side of these ripples vortices are generated, which are

ejected at times of flow reversal. As a consequence, there exists strong phase differences between the peak concentrations and peak velocities. Van der Werf (2006) shows that this results in negative net wave-induced sediment transport when suspension is dominant.

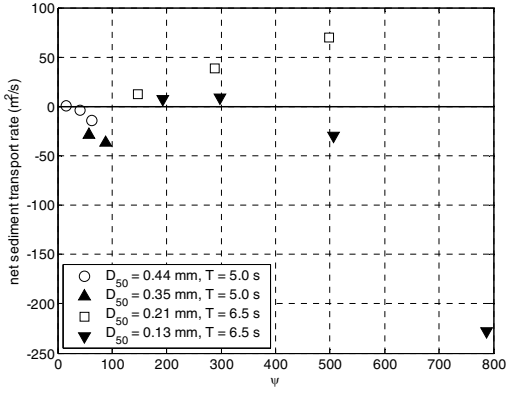

Fig. 1. Net sediment transport rates as function of mobility parameter

For larger mobility numbers, the ripples are washed out, the bed becomes plane again and the sheet-flow regime is entered. Sediment is transported in a thin layer of a few centimetres thick close to the bed. Experimental results show that net sediment transport rates mostly are in the 'onshore' direction in the sheet-flow regime, because the sediment responds almost instantaneously to the flow. However, phase lags between velocity and concentration (delayed pick-up and settling) become also important in the sheet-flow regime for finer sediments. When phase lags are important, the net sediment transport in oscillatory flow cannot be modelled in a quasi-steady way, and better agreement with the observed transport data may be obtained with the semi-unsteady transport model of Dohmen-Janssen (1999). Grasmeijer (2002) has found that the net wave-related suspended transport under irregular waves over a rippled bed in a large-scale laboratory flume (Delta flume of Delft Hydraulics) and at a field site (Egmond beach, The Netherlands) always is onshore-directed.

Figure 2 shows the schematic behaviour of the net sediment transport rate as a function of the Shields mobility parameter (θ') with: $\theta' = \tau'_{b,w}/((\rho_s-\rho_w)gd_{50})$; $\tau'_{b,w}$ = *wave-related bed shear stress*. In the ripple regime the net sand transport under low waves (mobility parameter $\theta'<1$) may become negative (in offshore direction) depending on the shape and dimensions of the ripples and the type of oscillatory flow (regular of irregular wave motion), (Van der Werf, 2006). For mobility parameters approaching 1 ($\theta' \cong 1$) the ripples will be washed out (sheet flow regime) and the net transport rate will become positive again. For very large mobility parameters ($\theta' \cong 5$ to 10) the net transport rate may become very small again due to the generation of phase lags between velocity and concentrations in the sheet flow layer (U_w=1.3 m/s, T=4 s and d_{50}=0.13 mm, see Dohmen-Janssen, 1999). Accurate modelling of wave-induced cross-shore transport and

nearshore morphology using a profile model thus requires an accurate modelling of the shape of the near-bed orbital flow and the bed form regime.

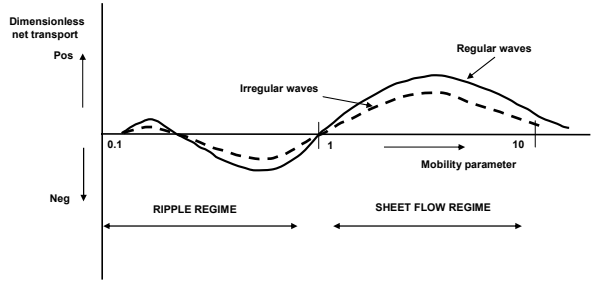

Fig. 2. Schematic behaviour of net sand transport rates (dimensionless) as function of grain-related mobility parameter

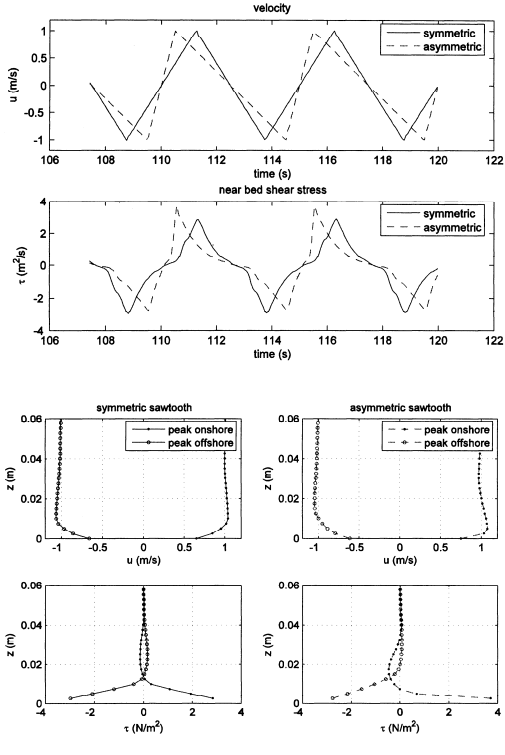

Fig. 3. Peak onshore and offshore velocities and bed-shear stresses in the case of symmetric and asymmetric saw-tooth waves

MODELLING OF BED-SHEAR STRESSES IN ASYMMETRIC WAVE MOTION

The peak orbital velocities in the CROSMOR model are computed by using the method of Isobe-Horikawa (1982), as modified by Grasmeijer (2002). This method can represent the skewness effect, but not the asymmetry effect under forward-leaning waves. In sinusoidal wave motion over a flat bed the instantaneous bed-shear stress is described as:

$$\tau'_{b,t}=0.5\ \rho_w f'_w\ |U_{w,t}|\ U_{w,t} \tag{1}$$

with: f'_w=grain-related wave friction factor, $U_{w,t}$=instantaneous orbital velocity at edge of wave boundary layer.

Basically, a detailed boundary layer model is required to compute the bed-shear stresses in strongly, asymmetric wave motion (saw-tooth waves). Figure 3 shows the bed-shear stresses in symmetric and asymmetric saw-tooth waves (strong forward leaning waves in asymmetric wave motion, U_{max}=1 m/s, T=5 s, $k_s=2.5d_{50}$) based on results from a boundary layer model including k-ε based turbulent shear stresses (Grasmeijer, 2004). It can be seen that the peak bed-shear stress increases by about 10% to 15% in asymmetric wave motion (second panel from top).

Nielsen (1992) has suggested a method to compute the instantaneous bed-shear stress under skewed wave motion including enhanced acceleration effects in asymmetric waves. This method includes the phase lead (φ_τ) of the bed-shear stress compared with the free-stream velocity.

The method of Nielsen (1992) for turbulent flow conditions reads, as:

$$\tau'_{b,t}=0.5\rho_w f'_w\ |[\cos(\varphi_\tau)\ (U_{w,t})+\omega^{-1}\sin(\varphi_\tau)(dU_w/dt)]|/[\cos(\varphi_\tau)(U_{w,t})+\omega^{-1}\sin(\varphi_\tau)(dU_w/dt)] \tag{2}$$

The time derivative can be evaluated as: $dU_w/dt= (U_{w,t+\Delta t} - U_{w,t-\Delta t})/(2\Delta t)$. In the case of a simple sinusoidal wave motion, Equation (2) yields a simple sinusoidal bed-shear stress shifted forward by the phase angle φ_τ. In the case of asymmetric wave motion the bed-shear stresses are enhanced during times of acceleration. For waves with saw-tooth type of asymmetry this leads to a dominant onshore shear stress and hence net onshore transport. This enhancement of the bed-shear stress from higher harmonics expresses the physical fact that high-frequency waves have thinner boundary layers and hence larger shear stresses. Wijetunge and Sleath (1998) have made velocity measurements using LDA in oscillatory flow in a wave tunnel to determine the phase lead effects. The phase lead of τ_{max} (with respect to free-stream velocity) is found to be about 45° just above the non-moving bed and about 30° at y=0 (initial bed) and about zero at 10 mm above the bed (near top of sheet flow layer).

The method of Nielsen (1992) has been used to compute the bed-shear stress under asymmetric waves described by $U=U_1\cos(\omega t)+U_2\cos(2\omega t)$. The data of an experiment of Ribberink et al. (2000) have been used as input data: U_{max}=1.45 m/s, U_{min}=-0.7 m/s, T=9 s, d_{50}=0.21 mm, d_{90}=0.32 mm, $q_{b,net}$=108 10^{-6} m^2/s=0.29 kg/s/m. Figure 4 shows the instantaneous free-stream velocity and the dimensionless mobility (Shields) parameter

$\theta' = \tau'_{b,t}/((\rho_s-\rho_w)gd_{50})$ with $\tau'_{b,t}$ based on Equation (2) without phase lag and with phase lag. The friction factor is taken as f'_w=0.01. Computed results are shown for phase leads of 0, 10°, 25° and 40° degrees (Figure 4). The curves are shifted forward for phase lags (leads) of 10°, 25° and 40° degrees. The peak bed-shear stress increases with increasing phase lag. Using a simple bed-load transport formula, Nielsen and Callaghan (2003) show that the inclusion of the acceleration effects leads to a much better agreement of the computed net sand transport rate with measured values for a large-scale wave flume experiment. Wave-related streaming effects were found to be much less important. Herein, it is assumed that the method of Nielsen (1992) yields sufficiently accurate results of the instantaneous bed-shear stress in asymmetric wave motion.

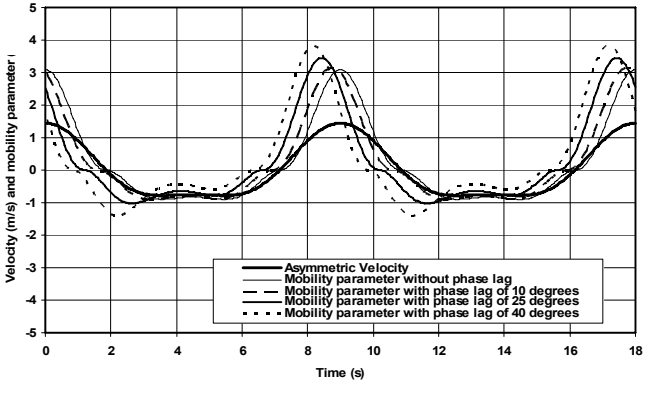

Fig. 4. Velocity and mobility (Shields) parameter as function of time; asymmetric velocity

BED FORM REGIME

As the value and direction of the net sediment transport is strongly related to the type of bed forms (ripples or flat bed), it is necessary to predict the type of bed forms and their effective bed roughness. Van Rijn (2006, 2007) has proposed a method to predict the effective bed roughness (k_s) of the bed forms in combined current and wave conditions.

CROSS-SHORE BED-LOAD TRANSPORT

It is assumed that the instantaneous bed-load transport rate (kg/s/m) is related to the instantaneous bed-shear stress, which is based on the instantaneous velocity vector (including both wave-related and current-related components) defined at a small height above the bed. The formula applied, reads as:

$$q_b = \gamma \rho_s d_{50} D_*^{-0.3} [\tau'_{b,cw}/\rho]^{0.5} [(\tau'_{b,cw} - \tau_{b,cr})/\tau_{b,cr}]^{\eta} \quad (3)$$

in which: $\tau'_{b,cw}$= instantaneous grain-related bed-shear stress due to both currents and waves= $0.5\,\rho f'_{cw} (U_{\delta,cw})^2$; $U_{\delta,cw}$= instantaneous velocity due to currents and waves at edge of wave boundary layer; f'_{cw} = grain friction coefficient due to currents and waves= $\alpha\beta f'_c + (1-\alpha) f'_w$; f'_c = current-related grain friction coefficient, f'_w = wave-

related grain friction coefficient, α= coefficient related to relative strenght of wave and current motion, β= coefficient related to vertical structure of velocity profile, $\tau_{b,cr}$= critical bed-shear stress according to Shields, ρ_s= sediment density, ρ= fluid density, d_{50} = particle size, D_* = dimensionless particle size, γ= coefficient= 0.5, η= exponent= 1 (based on calibration by using measured data, see Van Rijn, 2006).
The net bed-load transport rate can be obtained by time-averaging (over the wave period T) of the instantaneous transport rate using a bed-load transport formula for steady flow (quasi-steady approach), as follows: $q_b = (1/T) \int q_{b,t}\, dt$ with $q_{b,t}$ = F(instantaneous hydrodynamic and sediment transport parameters).
Equation (3) is based on the assumption that the sediment particles respond instantaneously (quasi-steady) to the oscillatory fluid motion near the bed. The net transport rate will always be in the direction of the largest peak orbital velocity. This assumption is reasonably valid for the sheet flow regime with sediment particles larger than about 0.2 mm. According to Dohmen-Janssen (1999), the phase-lag effects can be very well represented by the parameter $P=\delta_s\omega/w_s$ with δ_s= thickness of sheet flow layer (order of 0.01 m), $\omega=2\pi/T$=angular frequency, T= wave period. Phase-lag effects are important for fine sediment, large peak orbital velocities and small wave periods (P>0.5). Dohmen-Janssen (1999) proposed to correct the bed-load transport rates based on quasi-steady expressions, using a correction factor dependent on the P-parameter. Thus: $q_{b,net}= r\, q_{b,net,\ steady}$ with $r=F(p)$=correction factor between 0 and 1, $q_{b,net,\ steady}$=net bed-load transport according to quasi-steady expression. Using this approach, the net bed-load transport rate will be reduced but the net transport rate can not be against the direction of the largest peak velocity, which may occur over a rippled bed.

CROSS-SHORE SUSPENDED LOAD TRANSPORT

Two methods to compute the cross-shore transport rates are herein explored on their ability to represent the cross-shore transport in a cross-shore profile model. (CROSMOR). Both models can deal with negative oscillatory suspended transport rates due to the presence of rippled beds.

Method of Houwman and Ruessink (1996)

The wave-related suspended transport can also be estimated by the approach introduced by Houwman and Ruessink (1996).
The wave-related suspended transport at level z is given by:

$$q_{s,w,z}=(1/T)\ {}_o\int^T <U_w C_w> \tag{4a}$$

Using: $C_w=k_1 / U_w^3 /$, it follows that:

$$q_{s,w,z}=(1/T)\ {}_o\int^T [k_1 U_w / U_w^3 /dt] \tag{4b}$$

Using: $U_w=U_{on}\, sin(\omega t)$ with $\omega=2\pi/T$ for $0<t<0.5T$ and $U_w=U_{off}\, sin(\omega t)$ for $0.5T<t<T$, the time-averaged concentration is given by:

$$c_z=(k_1/(0.5T))\ {}_o\int^{0.5T} / U_{on}^3 / sin^3(\omega t)dt + (k_1/(0.5T))\ {}_{0.5T}\int^T / U_{off}^3 / sin^3(\omega t)dt=$$

$$=k_1(2/T)\,[U^3_{on}+U^3_{off}]\ {}_o\int^{0.5T} \left|\sin^3(\omega t)\right| dt \tag{4c}$$

The k_1-coefficient of Equation (4c) is substituted in Equation (4b), resulting in:

$$q_{s,w,z}=(1/T)\ c\ {}_o\int^{T} [A^{-1}][U_w \left|U_w^{\,3}\right| dt] \tag{4d}$$

with: $A= (2/T)\,[U^3_{on}+U^3_{off}]\ {}_o\int^{0.5T} \left|\sin^3(\omega t)\right| dt$
This yields:

$$q_{s,w,z}=\gamma\,[(U^4_{on}-U^4_{off})/(U^3_{on}+U^3_{off})]\ c \tag{4e}$$

with: $\gamma=I_3/I_4;\ I_3=(1/T)\ {}_o\int^{0.5T} \sin^4(\omega t)dt;\ I_3=(2/T)\ {}_o\int^{0.5T} \left|\sin^3(\omega t)\right| dt$; the γ-value is $9\pi/64\cong0.44$.

The total wave-related suspended transport component in the near-bed region can be estimated, as follows:

$$q_{s,w} = \gamma f_P\,[(U_{on})^4-(U_{off})^4]/[(U_{on})^3+(U_{off})^3]\ \int c\ dz \tag{5a}$$

with: $U_{on}=U_{\delta,f}$= near-bed peak orbital velocity in onshore direction (in wave direction) and $U_{off}=U_{\delta,b}$= near-bed peak orbital velocity in offshore direction (against wave direction), c= time-averaged concentration (integrated over the wave boundary layer) and γ= coefficient, f_P= function to include phase lag effects. Grasmeijer (2002) has determined the γ-coefficient by fitting of Equation (5a) to the measured wave-related transport rates, yielding values in the range of 0.1 to 0.2
As phase lag effects are related to the wave conditions, sand size and bed geometry (ripples), the f_p-function is supposed to be a complicated function of these parameters (yielding negative values for very fine sand).

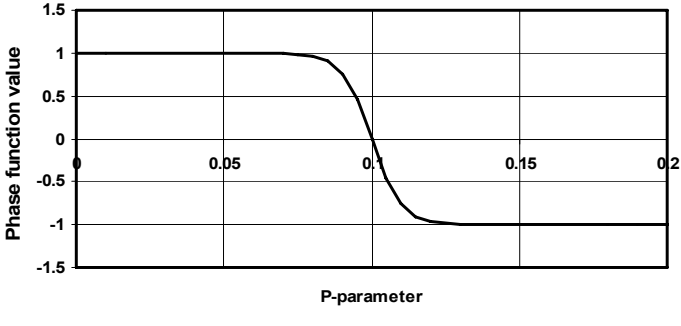

Fig. 5. Phase function of wave-related suspended transport

Assuming that the net suspended transport in onshore or in offshore direction is of the same order of magnitude (maximum values are about +0.02 or -0.02 kg/m/s), the phase

function is herein assumed to vary between +1 (fully onshore-directed) and -1 (fully offshore-directed). The phase function is tentatively described by (see Figure 5):

$$f_P = -\tanh[100(P-P_{cr})] \quad (5b)$$

with: $P=k_{s,w,r}/(w_s T_p)$, $k_{s,w,r}$=wave-related bed roughness height (estimate of ripple height), w_s= settling velocity of bed material, T_p=peak wave period, P_{cr}=0.1, yielding onshore transport for $P<P_{cr}$ and offshore transport for $P>P_{cr}$.
Simulation of the wave-related suspended transport according to Equation (5) requires computation of the time-averaged sand concentration profile and integration of the time-averaged sand concentration profile in vertical direction. Herein, the integration is taken over a near-bed layer with a thickness equal to about 10 times the thickness of the wave boundary layer (about 0.25 to 0.5 m), assuming that the suspended sand concentrations above this layer are not much effected by the high-frequency wave motion with periods in the range of T= 5 to 10 s. This assumption is satisfied if the fall time of a suspended sand particle over a distance of 0.25 to 0.5 m is much larger than the wave period ($T_{fall}= 0.5/w_s$ yielding about 25 s for d= 0.2 mm with w_s= 0.02 m/s). Furthermore, the data of the Deltaflume (Grasmeijer, 2002) show that most of the wave-related suspended transport occurs in the near-bed layer with a thickness of about 0.5 m (10 to 20 times the ripple height).

Method of van der Werf (2006)
Using a large amount of net transport data from oscillatory flow tunnel experiments, Van der Werf (2006) has developed a relatively simple model for net transport (mainly suspended sediments) in oscillatory flow over a rippled bed following the ideas of Dibajnia and Watanabe (1992). It is based on the division of the wave motion into an onshore and an offshore directed half wave-cycle. The net transport is the sum of both onshore and offshore quantities, as follows:

$$q_t = 6.75\,[Y/|Y|][|Y|^{0.64}][(s-1)g(d_{50})^3]^{0.5} \quad (6a)$$
$$Y = [U_c\,T_c\{(\Omega_{c1})^3+(\Omega_{t2})^3\} - U_t\,T_t\{(\Omega_{t1})^3+(\Omega_{c2})^3\}]/[(U_c+U_t)T] \quad (6b)$$

with:
q_t= net sand transport (m^2/s)
$P_w=\Delta_r/d_{50}$=vortex suspension parameter
$P_{w,cr}$=35
Δ_r=ripple height (measured or predicted); herein $k_{s,w,r}=\Delta_r$
$f'_w = exp(-6+5.2(A_w/2.5d_{50})^{-0.19})$=grain-related friction factor
A_w= orbital excursion amplitude
U_c= representative peak wave crest velocity (onshore-directed, positive value)
U_t= representative peak wave trough velocity (offshore-directed, positive value)
T_c= duration of wave crest phase
T_t=duration of wave trough phase
$T = T_c + T_t$=wave period
if $P_w \le P_{w,cr}$

$\Omega_{c1}=0.5\, f'_w\, (U_c)^2/((s-1)gd_{50})$=onshore-entrained and onshore-directed transport
$\Omega_{c2}=0$
$\Omega_{t1}=0.5\, f'_w\, (U_t)^2/((s-1)gd_{50})$= offshore-entrained and offshore-directed transport
$\Omega_{t2}=0$
if $P_w>P_{w,cr}$
$\Omega_{c1}=(P_w/P_{w,cr})0.5\, f'_w\, (U_c)^2/((s-1)gd_{50})$=onshore-entrained and onshore-directed tr.
$\Omega_{c2}=((P_w-P_{w,cr})/P_w)\ 0.5\, f'_w\, (U_c)^2/((s-1)gd_{50})$=onshore-entrained and offshore-directed
$\Omega_{t1}=(P_w/P_{w,cr})0.5\, f'_w\, (U_t)^2/((s-1)gd_{50})$= onshore-entrained and onshore-directed tr.
$\Omega_{t2}=((P_w-P_{w,cr})/P_w)\ 0.5\, f'_w\, (U_t)^2/((s-1)gd_{50})$=offshore-entrained and onshore-directed

The model has been developed for wave-only flows and is valid in the rippled bed regime only. Currently, a new practical model for net sand transport induced by non-breaking waves and currents is being developed within the SANTOSS research project (see the Coastal Sediments 2007 paper by Van der Werf et al.).

If P_w is larger than $P_{w,cr}$, the total amount of entrained sediment during a wave cycle should be divided in two parts: one part transported as bed load and near-bed suspended load during the same half wave cycle and a second part transported as suspended load (in the opposite direction) during the next half cycle. Net transport rates become negative (offshore-directed) when more sand is transported during the offshore half cycle than during the onshore half cycle. This occurs when P_w is approximately twice as large as $P_{w,cr}$. If P_w is smaller than $P_{w,cr}$, there is no sediment interaction between the two half wave cycles, transport takes place only very close to the bed, entrained and transported in the direction of the peak velocity.

Cross-shore morphology

Two tests from the LIP experiments (Sánchez-Arcilla, 1995) have been used to study the effect of wave-related transport on the nearshore morphology using the process-based CROSMOR profile model. Test1B simulates a storm condition with a breaker bar in the surf zone moving in offshore direction (offshore event). Test 1C simulates a typical swell condition (post-storm) with a breaker bar in the surf zone moving in onshore direction (onshore event). The bed material consists of sand with d_{10}=150, d_{50}=200, d_{90}=400 μm. The offshore water depth (h_o) to still water level is 4.1 m in all tests. The model is run in standard mode with all cross-shore wave, flow and sand transport processes included (Van Rijn 2006, 2007). The effect of the wave-induced fluid acceleration in asymmetric waves on the bed-shear stress and hence on the bed-load transport has been included. The computed wave-related net sand transport rates (due to wave asymmetry) are found to be in onshore direction, when the phase lag effects on sand transport processes are excluded. The wave-breaking induced undertow causes offshore-directed sand transport rates. Bed level changes depend on the gradients of the balance of these two transport components.

Test1B

Figure 6A,B shows the measured and computed wave heights, undertow velocities and peak orbital velocities for Test 1B. Computed wave heights are rather good. The

computed undertow velocites are in good agreement with the measured values with exception in the region close to the waterline. Computed peak orbital velocites are in good agreement with measured values. Measured data in the region close to the waterline are not available.

Figures 7A,B show the measured and computed bed levels after 18 hours using the transport method of Van Rijn. The generation and migration of the outward breaker bar is simulated rather well for Test 1B. When only the undertow transport component is taken into account, the simulated bar is in its most outward position (Fig. 7A). Conversely, when only the onshore wave-related transport components are taken into account, the simulated bar is in its most inward position (Fig. 7A). The observed bar behaviour is slightly better simulated if the acceleration effects based on the method of Nielsen are included (Figure 7B). Fluid acceleration effects do not seem to be very important for breaking wave conditions, because wave velocity skewness is suppressed in breaking wave conditions. Inclusion of phase lag effects has not much influence on the computed bed levels. The model also predicts an inner bar with sand eroded from the beach for Test 1B; the measured bed profile does not show this behaviour. Thus, the physics close to the shore are not simulated properly. Both the undertow velocity and the wave asymmetry have to be improved significantly.

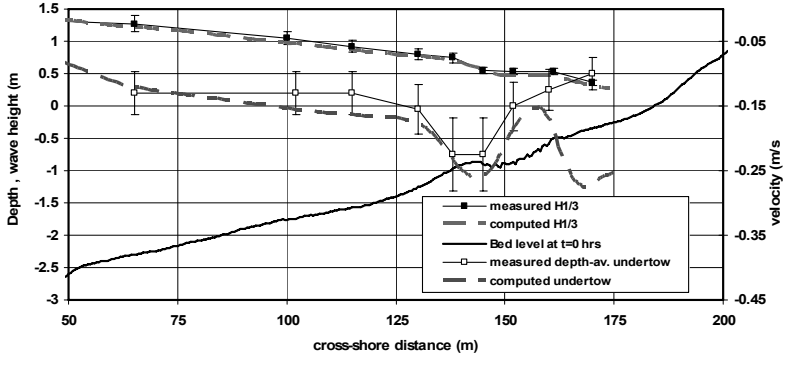

Fig. 6A. Measured and computed wave height and undertow for Test 1B

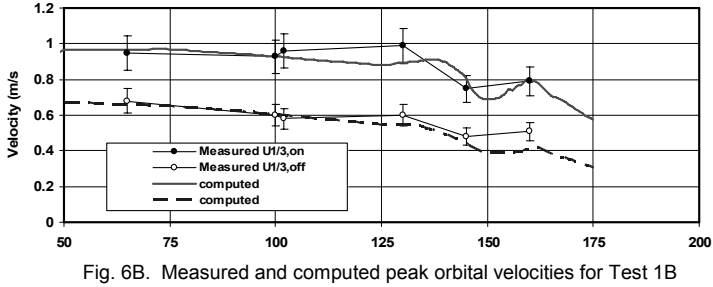

Fig. 6B. Measured and computed peak orbital velocities for Test 1B

Figure 7C shows measured and computed bed levels using the transport method of Van

der Werf (Equation 6). This method yields transport values of the right order of magnitude, but it can not yet simulate the undertow transport component. The offshore bar migration is much too small excluding the undertow transport component and much too large including the undertow transport component (based on the Van Rijn method).

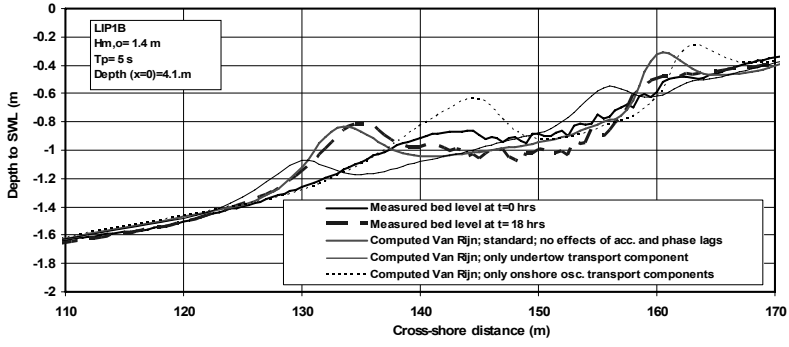

Fig. 7A. Measured and computed bed levels for Test 1B; method Van Rijn

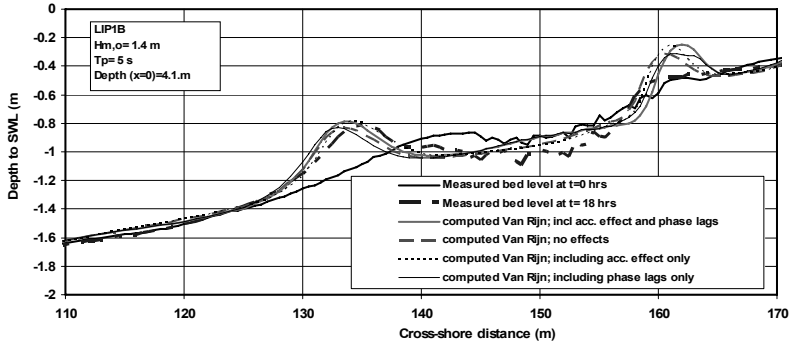

Fig. 7B. Measured and computed bed levels for Test 1B; method Van Rijn

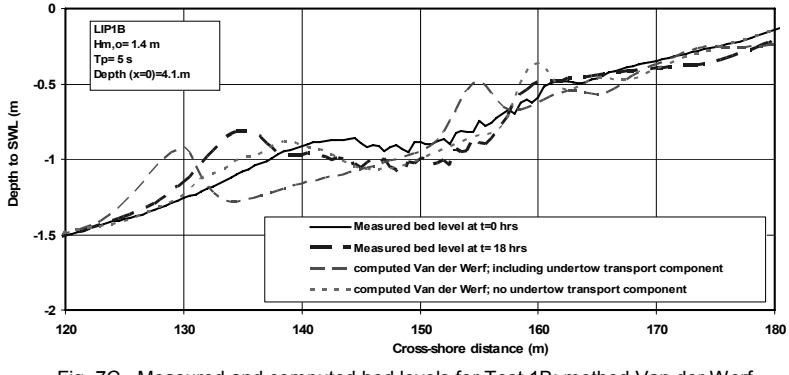

Fig. 7C. Measured and computed bed levels for Test 1B; method Van der Werf

Test 1C

Figure 8 shows that the standard model of Van Rijn also yields onshore bar migration, but the onshore migration is much too small. Inclusion of the acceleration effect on the bed-load transport improves the prediction. Inclusion of phase lag effects has almost no effect, which means that phase function predicts onshore-directed suspended load transport in agreement with the observed onshore bar migration. Probably, the observed bed ripples are not steep enough (under irregular waves) to generate strong vortex motions with phase lags between sediment concentration and orbital velocity and hence offshore-directed transport. The transport method of Van der Werf (Equation 6) produces similar trends (not shown) as for Test 1B; the transport rates are of the right order of magnitude. The bar moves onshore neglecting the undertow transport component, but it moves offshore including the undertow transport component.

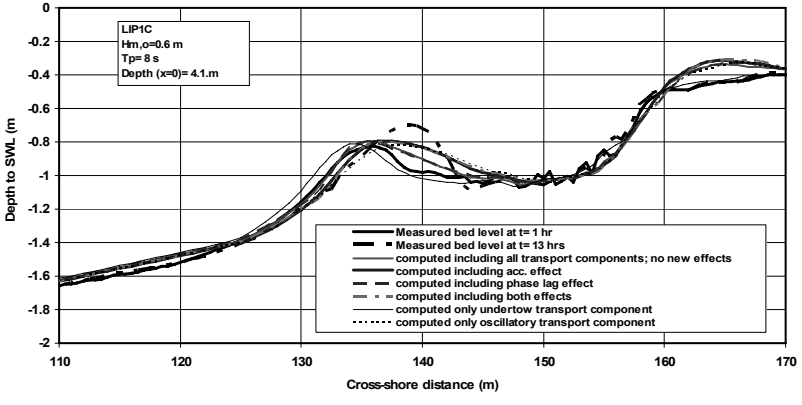

Fig. 8. Measured and computed bed levels for Test 1C; method Van Rijn

CONCLUSIONS

Summarizing, the model runs show that the sediment transport model of Van Rijn can simulate the qualitative aspects of the outer surf zone dynamics reasonably well. Fluid acceleration effects on bed-shear stress and hence on sand transport appear to be important for low wave conditions, but not for storm conditions (breaking waves). It is most important to model the onshore-directed wave asymmetry transport and the offshore-directed transport by the undertow correctly. Phase lag effects influencing the wave-related transport do not seem to be very important under irregular waves over a sand bed of about 0.2 mm. Future work will be focussed on improvement of the wave skewness and asymmetry close to the shore. The transport model of Van der Werf (2006) can represent the trends observed in the laboratory experiments. However, the validity of this model is limited to wave-only flows over rippled beds. Currently, the model is being extended to also cover the flat-bed/sheet-flow regime and to include the current-related related transport.

REFERENCES

Dibajnia M., and Watanabe, W. 1992. Sheet-flow under non-linear waves and currents. Proc. 23rd ICCE, Venice, Italy, pp. 2015-2025.

Doering, J.C. and A.J. Bowen, 1995. Parameterization of orbital velocity asymmetries of shoaling and breaking waves using bispectral analysis. Coastal Eng., 26, 15-33.

Dohmen-Janssen, C.M., 1999. Grain size influence on sediment transport in oscillatory sheet flow: phase lags and mobile-bed effects. Doctoral Thesis, Delft University of Technology, Delft, The Netherlands, 246 pp.

Grasmeijer, B.T., 2002. Process-based cross-shore modelling of barrred beaches. Doctoral Thesis, Dep. of Physical Geography, Univ. Utrecht, The Netherlands.

Grasmeijer, B.T., 2004. Personal communication.

Henderson, S.M., J.S. Allen, and P.A. Newberger, 2004. Nearshore sandbar migration predicted by an eddy-diffusive boundary layer model. Journal of Geophysical Research, 109, C06024, doi:10.1029/2003JC002137.

Hoefel, F. and S. Elgar, 2003. Wave-Induced Sediment Transport and Sandbar Migration. Science, 299, 1885-1887.

Houwman, K.T. and Ruessink, B.G., 1996. Sediment transport in the vicinity of the shoreface nourishment of Terschelling. University of Utrecht, The Netherlands.

Hsu, T.J., S. Elgar and R.T. Guza, 2006. Wave-induced sediment transport and onshore sandbar migration. Coastal Engineering, 53, 817-824.

Isobe, M. and Horikawa, K., 1982. Study on water particle velocities of shoaling and breaking waves. Coastal Engineering in Japan, Vol. 25.

Nielsen, P., 1992. Coastal Bottom Boundary Layers and Sediment Transport. Advanced series on Ocean Engineering, volume 4. World Scientific, Singapore, 324 p.

Nielsen, P. and Callaghan, D.P., 2003. Shear stress and sediment transport calculations for sheet flow under waves. Coastal Engineering, Vol. 47, p. 347-354.

Ribberink, J.S., 1998. Bed-load transport for steady flows and unsteady oscillatory flows. Coastal Eng., Vol. 34, No. 1-2, p. 59-82.

Ribberink, J.S., Dohmen-Janssen, C.M., Hanes, D.M., McLean, S.R. and Vincent, C., 2000. Near-bed transport mechanisms under waves; a large-scale flume experiment. 27th ICCE, Sydney, Australia.

Sánchez-Arcilla, A. et al., 1994. The Delta Flume experiment 1993. Proc. Coastal Dynamics, UPC, Barcelona, p. 488-502

Van der Werf, J.J., 2006. Sand transport over rippled beds in oscillatory flow. Doctoral Thesis, Department of Civil Engineering, University of Twente, The Netherlands.

Van der Werf, J.J., Ribberink, J.S. and O'Donoghue, T. Development of a new practical model for sand transport induced by non-breaking waves and currents. Paper presented at Coastal Sediments 2007.

Van Rijn, L.C., 2006. Principles of sediment transport in rivers, estuaries and coastal seas. Part 2 Supplement/Update. Aqua Publications (www.aquapublications.nl)

Van Rijn, L.C., 2007. A unified view of sediment transport by currents and waves; Parts 1 to 4. Accepted by Journal of Hydraulic Engineering, ASCE (in Press)

Wijetunge, J.J. and Sleath, J.F.A., 1998. Effects of sediment transport on bed friction and turbulence. Journal of Waterway, Port, Coastal and Ocean Engineering, Vol. 124, No. 4, p. 172-178.

CLOSED FORM SOLUTION FOR THRESHOLD VELOCITY FOR INITIATION OF SEDIMENT MOTION UNDER WAVES

Hans Hanson[1] and Benoît Camenen[2]

1. Dept. of Water Resources Engineering, Lund University, Box 118, S-22100 Lund, SWEDEN, Hans.Hanson@tvrl.lth.se.
2. Cemagref Lyon, 3 bis quai Chauveau, CP 220, 69336 Lyon cedex 09, FRANCE, camenen@lyon.cemagref.fr.

Abstract: The present paper presents a rational expression for the initiation of motion for non-cohesive sediment under rough turbulent wave conditions. Previously proposed relationships for the initiation of motion are examined as well as laboratory measurements corresponding to fully rough turbulent boundary layers (which is normally the case under prototype conditions). By combining the modified Shields criterion as proposed by Bagnold (1963) with the wave friction factor, f_w, from Jonsson (1966), an easily applied criterion for the threshold velocity for incipient motion under rough turbulent conditions. The new relationship is formulated as $U_{w,cr} = 4\sqrt{\varphi_{cr}}\left[1.1\ \log_{10}\left(\sqrt{\varphi_{cr}T}/(\pi d_{50})\right) - 0.08\right]^{1/0.9}$. Predictions with the new criterion are shown to be in good agreement with measurements over the full range of typically encountered engineering conditions.

INTRODUCTION

The threshold of sediment motion is of central concern in calculating littoral transport under wave action. Based on experimental data in steady current, Shields (1936) proposed a critical value for the bottom shear stress as a function of the grain Reynolds number $\Re_* = u_* d_{50}/\nu$ where $u_* = \sqrt{\tau/\rho}$ is the friction velocity, τ is the bottom shear stress, ρ is the fluid density, ν the kinematic viscosity of the fluid, and d_{50} is the median grain size. He proposed to use a dimensionless shear stress to characterize the threshold value for the sediment transport. This dimensionless shear stress is nowadays well-known as the Shields parameter:

$$\theta_{i,cr} = \frac{f_i U_i^2}{2(s-1)gd_{50}} \tag{1}$$

where the subscript i may be replaced by c (current related terms) or w (wave related terms), f is the friction factor, U is the horizontal near-bottom velocity, $s = \rho_s/\rho$ is the relative density of the sediment, and g the acceleration due to gravity. He found, using steady current data (*c.f.* Fig. 1), that the critical Shields parameter varies from 0.04 to 0.07 depending on the particular Reynolds number.

For practical applications, the Shields relationship is, however, inconvenient as the critical shear velocity appears on both sides. For this reason, many authors (Valembois 1960; Madsen and Grant 1976; van Rijn 1984; Soulsby 1997) proposed relationships between the critical Shields parameter and the dimensionless grain size $d_* = (g(s-1)/\nu^2)^{1/3} d_{50}$ (see Fig. 1). A simple algebraic expression that fits Shields' curve closely was proposed by Soulsby and Whitehouse (1997):

$$\theta_{c,cr} = \frac{0.24}{d_*} + 0.055\left[1 - \exp\left(-0.02 d_*\right)\right] \tag{2}$$

However, using more recent data, Soulsby (1997) observed much smaller values for $\theta_{c,cr}$ when $d_* < 2$. He thus proposed a modification of Eq. 2(Fig. 1):

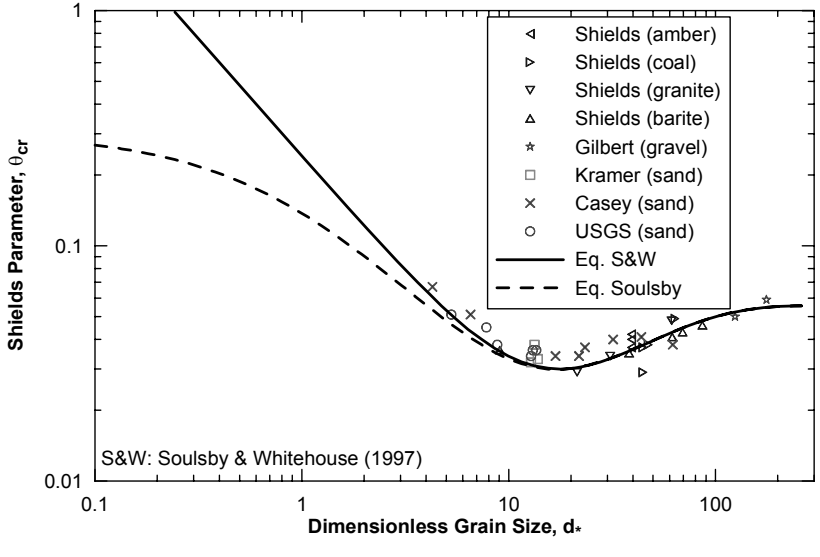

Fig. 1. Critical Shields parameter as a function of the dimensionless grain size for steady current data (data from Brownlie 1981).

$$\theta_{c,cr} = \frac{0.30}{1+1.2d_*} + 0.055\left[1-\exp\left(-0.02d_*\right)\right] \tag{3}$$

It is, however, difficult to define the exact threshold of sediment transport from the incipient motion regime where a few particles on the bed surface are seen to be moving and the general surface motion which corresponds to a well-defined and reproducible transition from occasional motion to general motion of the uppermost particles (Chan *et al.* 1972).

Many authors (van Rijn 1984; Soulsby 1997) also assumed that the results for steady currents can be extended to waves, and combined waves and currents using the maximum value of the Shields parameter over a wave cycle. However, large uncertainties about the critical Shields parameter seem to occur in the case of waves as the estimation of the wave-related friction coefficient strongly affects the results. As Camenen and Larson (2005) pointed out, the estimation of the critical Shields parameter has a significant influence on the bed load flux for low regimes. It is, thus, fundamental to provide better estimation of the threshold velocity and the critical Shields parameter for the inception of movement. The main objective of this study is to derive a closed form solution for the threshold velocity for initiation of sediment motion under oscillatory water waves that has a reasonable accuracy and that is easy to use.

ESTIMATION OF THE CRITICAL VELOCITY FOR THE INITIATION OF SEDIMENT MOVEMENT

Background

A large number of studies (mostly in laboratory) and empirical relationships concerning the threshold velocity for sediment motion have been presented in the literature. For example, Madsen and Grant (1976) demonstrated that the critical Shields parameter together with the non-dimensional parameter $S_* = \sqrt{(s-1)gd_{50}^3}/(4\nu)$, give a good description of reanalyzed older experimental data, provided that the boundary shear stress is related to the wave friction factor, f_w, as presented in Jonsson (1966). Like the ordinary Shields curve, this modified version is somewhat difficult to use in a practical situation. Here, the Shields parameter is based on the maximum value of the boundary shear stress during one wave period. Komar and Miller (1975) and Komar (1976) found, also using the results of Jonsson (1966), that the threshold condition is well described by:

$$\frac{U_{w,cr}^2}{(s-1)gd_{50}} = \alpha\left(\frac{2A_{w,cr}}{d_{50}}\right)^{\beta} \tag{4}$$

where $U_{w,cr}$ is the maximum near-bottom horizontal velocity and $A_{w,cr}$ is the water particle horizontal amplitude at the bottom according to linear wave theory. For grain sizes smaller than 0.5 mm, $\alpha = 0.21$ and $\beta = 0.5$, respectively; and for grain sizes greater than 0.5 mm the coefficient values are set to $\alpha = 0.68\pi$ and $\beta = 0.25$, respectively. These

two expressions are comprehensive and easy to use. There is, however, a discrepancy between the two expressions in the region of small wave periods and grain diameters around 0.5 mm. According to the authors themselves, the diagram should not be used in this area. Thus, it is not valid for waves and sediment typical for a large number of beaches around the world. Hallermeier (1980) proposed a very simple criterion where the threshold velocity only depends on sediment diameter and density according to:

$$U_{w,cr} = \sqrt{8(s-1)gd_{50}} \tag{5}$$

In the present study it will be shown, after comparison with experimental data, that this relationship is too simplistic. In conclusion, for the determination of threshold conditions for initiation of sediment motion, there seems to be a choice between more "accurate" curves which are somewhat complicated to use and more convenient curves which are not valid under typical field conditions.

Chan *et al.* (1972) investigated the effect of the kinematic viscosity (no significant influence found) and the relative particle density on the inception of the sediment transport (general movement of the upper layer). Using their own experimental data with various particles characteristics and fluid densities, they proposed the following empirical relationship, where T is the wave period:

$$U_{w,cr} = 0.37\left(\frac{2\pi}{T}\right)^{-0.5}\left[(s-1)g\right]^{0.75} d_{50}^{0.25} \tag{6}$$

Proposed threshold relationship

Employing the classical definition of the wave friction factor, f_w, according to $\tau_{w,cr} = 0.5 f_w U_{w,cr}^2$ together with the definition of the Shields parameter, $\theta_{w,cr}$ (cf. Eq. 1), we can derive:

$$f_w U_{w,cr}^2 = 2\theta_{w,cr}(s-1)gd_{50} \equiv \varphi_{cr} \tag{7}$$

In the rough turbulent case, the wave friction factor, f_w, is independent of the wave Reynold's number and related to the relative roughness k_s/A_w only (Jonsson 1966) as

$$\left(\frac{1}{4\sqrt{f_w}}\right) + \log_{10}\left(\frac{1}{4\sqrt{f_w}}\right) = \log_{10}\left(\frac{A_w}{k_s}\right) - 0.08 \tag{8}$$

where k_s is the Nikuradse roughness height. It is difficult to estimate k_s for a rippled and duned bottom, but for a plane horizontal bottom of non-cohesive material, it may be taken as $k_s = 2d_{50}$ (Yalin 1977). It should be noted however that Eq. 8 is not applicable for small values of A_w/k_s. In order to better fit the data (see below), the original formulation of (Jonsson 1966) is slightly modified in this study according to:

$$\left(\frac{1}{4\sqrt{f_w}}\right)^{0.9} + \log_{10}\left(\frac{1}{4\sqrt{f_w}}\right)^{1.1} = \log_{10}\left(\frac{A_w}{k_s}\right)^{1.1} - 0.08 \tag{9}$$

With $A_w = U_w T/(2\pi)$, Eq. (9) may be combined with Eq. (7) to yield a closed form solution of the critical threshold velocity as:

$$U_{w,cr} = 4\sqrt{\varphi_{cr}}\left[1.1\,\log_{10}\left(\frac{\sqrt{\varphi_{cr} T}}{\pi d_{50}}\right) - 0.08\right]^{1/0.9} \tag{10}$$

In order to evaluate this proposed Eq. (10), comparisons need to be made against experimental results. These will be made in three stages as the threshold velocity depends on the determination of the critical Shields parameter value as well as the wave friction factor.

COMPARISON AGAINST EXPERIMENTAL DATA

Wave Friction Factor

For the wave friction factor, Eq. (9) is plotted against the available data together with the proposed formulations of Jonsson (1966), Swart (1974), and Nielsen (1992) in Fig. 2. As seen from Table 1 (where *e.g.* $P_{1.2}$ means percentage of calculated values within a factor of 1.2 from the measurements) Eq. (9) and the Nielsen (1992) relationship appear to yield the best results among the studied formulas.

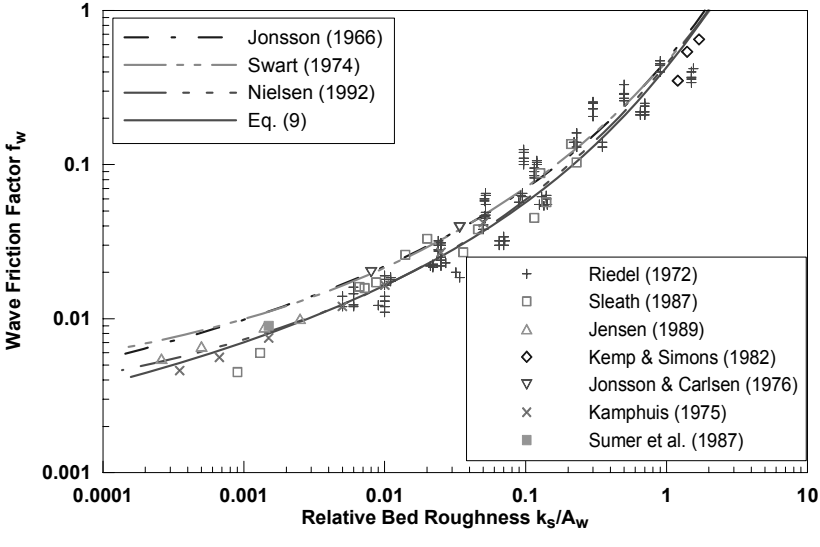

Fig. 2. Proposed relationships and measured values for the wave friction factor in the rough turbulent regime.

Table 1. Calculated measures of accuracy (%) of the calculated wave friction factor.			
	$P_{1.2}$	$P_{1.5}$	P_2
Jonsson (1966)	39	74	98
Swart (1974)	35	74	98
Nielsen (1992)	42	83	98
Eq. (9)	44	83	98

Critical Shields Parameter

As previously discussed, the Shields criterion may be extended to define the threshold of sediment motion under oscillatory water waves. Fig. 3 shows threshold data under waves together with the proposed expressions for a steady current (Eqs. 2 and 3). It is obvious that the data do not support the lines derived from the original Shields curve. Based on this result, two new expressions for the critical Shields parameter are proposed here. As opposed to the previous estimation based on steady current, it seems that $\theta_{w,cr}$ is not increasing with smaller values of d_* when $d_* < 10$ or for larger values of d_* when $d_* >100$. Also, it seems that larger values of $\theta_{w,cr}$ are observed for larger values of d_* under waves compared to the results for steady currents. As a straight-forward approach, a representative value on the critical Shields parameter of $\theta_{w,cr} = 0.07$ (based on a best fit) independent of grain size is suggested (dash-dot line in Fig. 3). One would suspect, however, that the critical Shields parameter for the inception of movement should be a function of the dimensionless grain size (*cf.* Eq. 5). For this reason, a simple relationship dependent on grain size (full line in Fig. 3) is also proposed for testing against the data:

$$\theta_{w,cr} = 0.08\left[1 - \exp\left(-15/d_* - 0.02d_*\right)\right] \tag{11}$$

Table 2 examines the accuracy of the predictions within specified limits for the different relationships together with the average value and standard deviation of the difference $\Delta U_{w,cr} = U_{w,cr,c} - U_{w,cr,m}$ where $U_{w,cr,c}$ and $U_{w,cr,m}$. are the calculated and measured values of the critical Shield parameter values, respectively. The *P*-values are a direct measure of the accuracy of the predictive relationship. A small avg($\Delta U_{w,cr}$) value indicates that the predicted values are evenly spread on either sides of the correct value while a small std($\Delta U_{w,cr}$) value indicates that the predicted values are close together. None of these two latter values are, however, a direct measure of accuracy.

Table 2. Calculated measures of accuracy (%) and spreading of the calculated critical Shields parameter.					
	$P_{1.2}$	$P_{1.5}$	P_2	avg($\Delta U_{w,cr}$)	std($\Delta U_{w,cr}$)
Soulsby & Whitehouse (1997)	19	51	86	-0.0200	0.0152
Soulsby (1997)	19	49	82	-0.0208	0.0159
$\theta_{w,cr} = 0.07$	34	73	94	0.0114	0.0171
Eq. (11)	56	88	99	0.0045	0.0137

As seen from Table 2, Eq. (11) significantly improves the results compared to the other relationships. This equation is quite similar in its form to that of Eq. (2) (Soulsby and Whitehouse 1997) except that it does not grow for smaller values of d_*. The minimum

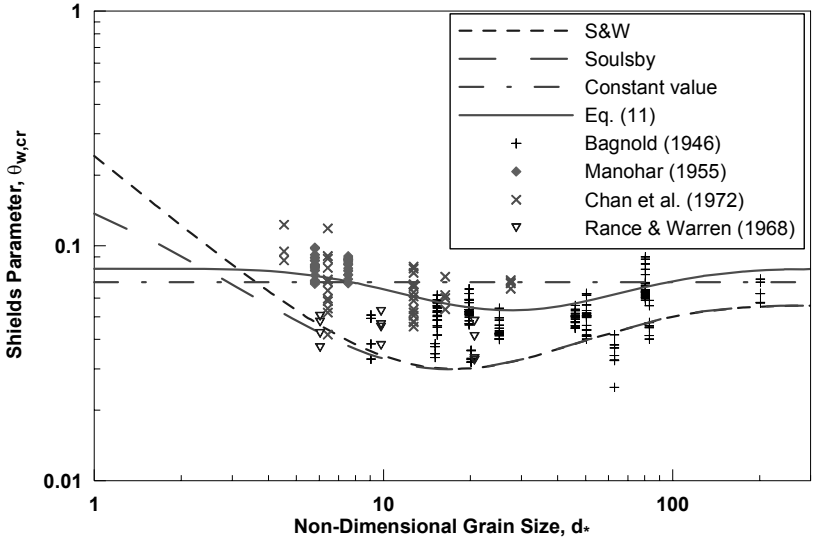

Figure 3: Critical Shields parameter as a function of the dimensionless grain size under oscillatory water waves.

value for $\theta_{w,cr}$ is also observed for a larger d_* ($d_{*,min}$ = 40 instead of 20 looking at the Shields study). Soulsby (1997) suggested that the average rather than the peak bed shear stress may be used in case of waves (and wave and current interaction). Using Eq. (3), this would, however, lead to an underestimation of the results for the critical Shields parameter prediction The results for the fixed Shields parameter value is doing surprisingly well, much better that Soulsby and Whitehouse (1997) or Soulsby (1997). While the constant value has no dependency on grain size, the other two seem to be too sensitive to the grain size. It appears, thus, that the results for a steady current cannot so easily be extended to situations involving waves.

Critical Velocity for Initiation of Motion

In order to compare Eq. (10) with experimental results, portions of the data from Bagnold (1946), Manohar (1955) and Rance and Warren (1968), corresponding to fully rough turbulent conditions, as well as the data from Chan *et al*. (1972) were examined. Measured values of the incipient velocities $U_{w,cr,m}$ are compared to those given by Eq. (10) $U_{w,cr,c}$, where Shields parameter is given as a constant and by Eq. (11), respectively (*cf*. Tab. 3). In addition, the proposed solution is compared to those of Chan *et al.* (1972), Komar and Miller (1975), and Hallermeier (1980), respectively. Statistically, the proposed Eq. (10) using a fixed Shields parameter doing somewhat better than that of Komar and Miller and significantly better than that of Chan *et al*. or Hallermeier. Eq. (10) in combination with a varying Shields parameter according to Eq. (11) is not strong on the $P_{1.2}$ level but doing much better on the other two levels.

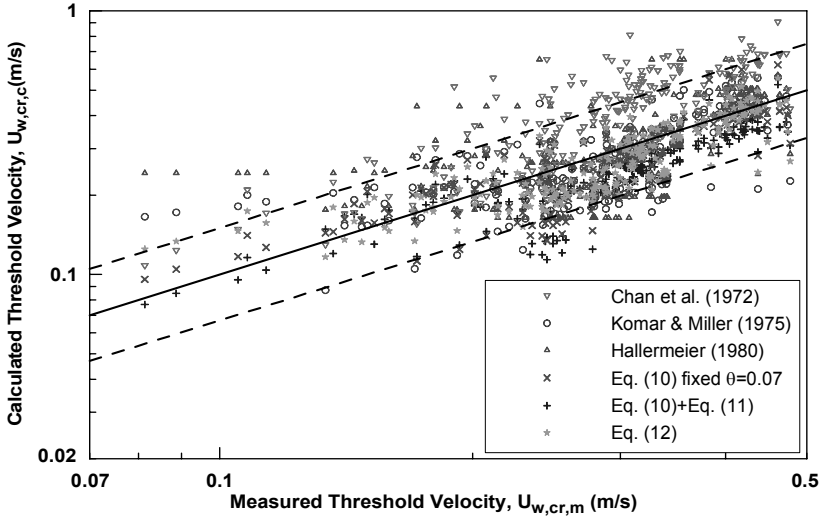

Figure 4: Calculated vs. measured threshold velocities for the initiation of motion under oscillatory water waves. Solid line indicates calculated value = measured value. Dashed lines indicate values within a factor of 1.5.

Following the work by Chan *et al*. (1972) and Hallermeier (1980) but using all the available data, a simple empirical function for the threshold velocity is proposed (see Eq. (12) in Fig. 4 and Table 3):

$$U_{w,cr} = 0.5\sqrt{\left[(s-1)g\right]^{1.25} d_{50}^{0.75} T^{0.5}} \tag{12}$$

The comparison against the experimental data shows that Eq. (12) yields better results than even Eq. (10) with a fixed Shields parameter. Also, it yields much better results compared to the other formulas.

Table 3. Calculated measures of accuracy (%)and spreading of the calculated threshold velocity for initiation of motion under oscillatory water waves.

	$P_{1.2}$	$P_{1.5}$	P_2	avg($\Delta U_{w,cr}$)	std($\Delta U_{w,cr}$)
Chan et al. (1972)	28	62	95	0.126	0.107
Komar & Miller (1975)	62	84	99	-0.010	0.067
Hallermeier (1980)	50	76	95	0.021	0.097
Eq. (10) fixed θ= 0.07	65	91	100	-0.024	0.052
Eq. (10) + Eq. (11)	45	93	98	-0.050	0.046
Eq. (12)	62	97	100	-0.020	0.049

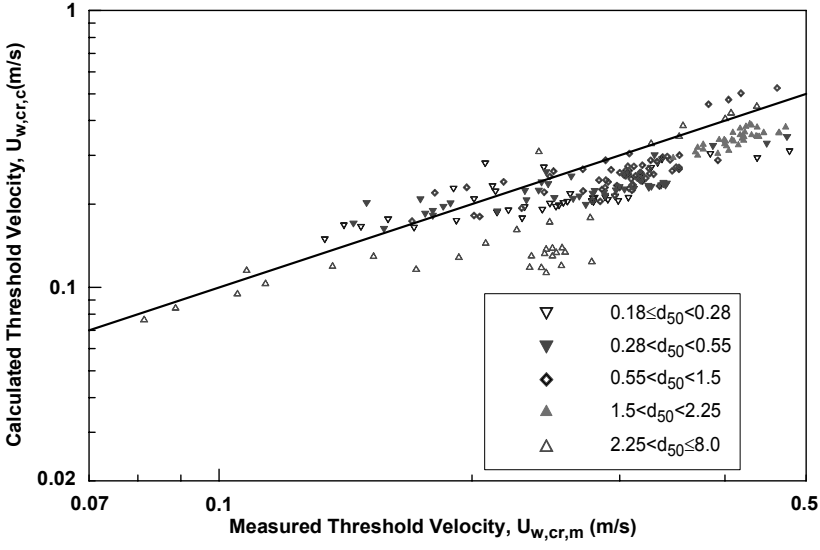

Fig. 5. Estimation of the threshold velocity; comparison between Eqs. (13)-(15) and experimental data. The straight line indicates calculated value = measured value.

Recommended Relationships

From these results it would be tempting to recommend Eq. (12). However, as the threshold velocity and the critical Shields parameter are linked it seems more appropriate to use a coherent set of $\theta_{w,cr}$ and $U_{w,cr,m}$ that both are in reasonable agreement with data. Thus, this study leads to the recommendation to use Eq. (11) for $\theta_{w,cr}$ and then use Eq. (10) in combination with Eq. (11) to calculate $U_{w,cr,m}$, *i.e.*

$$\theta_{w,cr} = 0.08\left[1-\exp\left(-15/d_* - 0.02d_*\right)\right] \tag{13}$$

$$U_{w,cr} = 4\sqrt{\varphi_{cr}}\left[1.1\,\log_{10}\left(\frac{\sqrt{\varphi_{cr}T}}{\pi d_{50}}\right)-0.08\right]^{1/0.9} \tag{14}$$

with

$$\varphi_{cr} = 2\theta_{w,cr}\left(s-1\right)gd_{50} \tag{15}$$

In Fig. 5, the threshold velocity $U_{w,cr}$, estimated from Eqs. (13)-(15) is compared to experimental measurements. It shows the very good correlation between the theory and the data. It seems, however, that the predictions are slightly underestimated for all grain sizes, especially for the coarser particles.

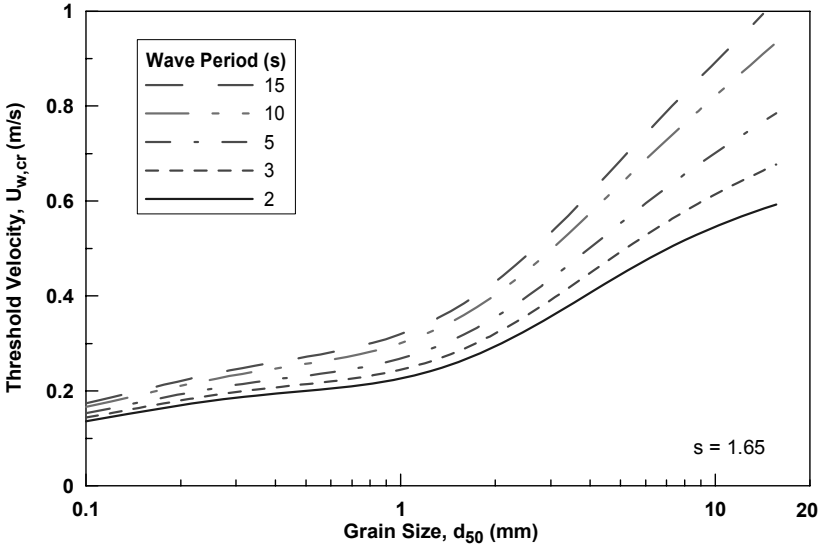

Fig. 6. Proposed near-bottom velocities for initiation of motion under rough, turbulent oscillatory water waves.

Having gained confidence in Eq. (14) it is now possible to draw proposed "design curves" for the threshold velocity for initiation of motion as shown in Fig. 6. For smaller grain sizes, the influence of wave period is less pronounced than for coarser sediments.

Critical Wave Height for Initiation of Motion

With the critical bottom velocity determined by Eq. (10), the corresponding critical wave height H_{cr} at a particular depth h_{cr} may be calculated according to linear wave theory as:

$$H_{cr} = \frac{U_{w,cr}T}{\pi}\sinh\left(\frac{2\pi h_{cr}}{L}\right) \tag{13}$$

where L = wave length at depth h_{cr}. This relation is displayed in non-dimensional form in Fig.7. Inversely, this relationship may be solved for the water depth h_{cr} out to which sediment will move under a specific wave condition to yield:

$$h_{cr} = \frac{L}{2\pi}\ln\left(\frac{\pi H_{cr}}{U_{w,cr}T} + \sqrt{\left(\frac{\pi H_{cr}}{U_{w,cr}T}\right)^2 + 1}\right) \tag{14}$$

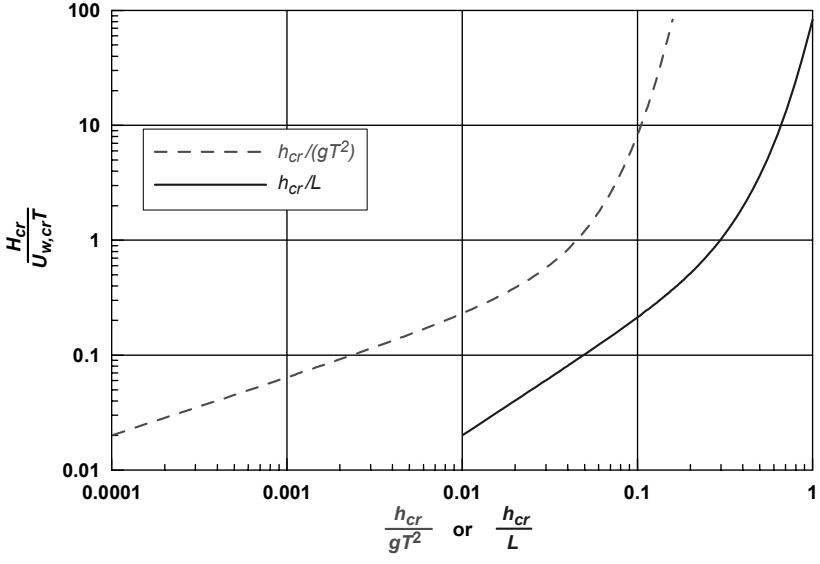

Fig. 7. Non-dimensional wave height $H_c/(U_{w,cr}T)$ versus non-dimensional water depth $h_c/(gT^2)$for the initiation of motion under rough, turbulent oscillatory water waves.

CONCLUSIONS

A study of the threshold velocity and critical Shields parameter has been undertaken for rough oscillatory flows. New relationships were proposed for the estimation of the critical Shields parameter as well as the threshold velocity for initiation of sedment motion under waves (Eqs. 13-15). The expression for the threshold velocity is an easy to use criterion for practical evaluation of sediment threshold conditions under rough, turbulent field wave conditions. The proposed relation has no ambiguity for any applicable grain size or wave period.

The proposed relationship for the threshold velocity has a tendency to underpredict measured threshold velocities, especially for coarser grain sizes. These discrepancies are mainly caused by factors inherent in this simplified derivation but also due to the difficulties in identifying the threshold situation in the laboratory. However, threshold velocities in nature are expected, as a result of sloping and rippled bottom, to be lower than those measured for plane horizontal bottom in the laboratory.

ACKNOWLEDGMENT

This work was conducted under the Inlet Modeling System Work Unit of the Coastal Inlets Research Program, U.S. Army Corps of Engineers, and partly sponsored by the Japanese Society for the Promotion of Science.

REFERENCES

Bagnold, R. (1963). “An approach of marine sedimentation,” in '*The Sea*', Vol. 3, M.N. Hill, Interscience, New York, 507-528.

Brownlie, W.R. (1981). "Compilation of alluvial channel data: laboratory and field," Technical Report KH-R-43B, California Institute of Technology, Passadena, CA, U.S.A.

Camenen, B. and Larson, M. (2005). “A bedload sediment transport formula for the nearshore,” *Estuarine, Coastal and Shelf Science,* 63, 249-260.

Chan, K., Baird, M., and Round, G.(1972). “Behaviour of beds of dense particles in a horizontally oscillating liquid,” *Proc. Royal Society of London,* A(330), 537-559.

Hallermeier, R. (1980). “Sand motion initation by water waves: two asymptotes,” *J. Waterways Harbors Division* 106(WW3), 299-318.

Jensen, B.J. (1989) "Experimental Investigation of Turbulent Oscillatory Boundary Layers," *Series Paper 45*, Inst. of Hydrodynamic and Hydraulic Engineering (ISVA), Technical University, Denmark.

Jonsson, I. (1966). “Wave boundary layers and friction factors,” *Proc. 10th Int. Conf. Coastal Eng.*, ASCE, 127-148.

Jonsson, I.G. and Carlsen, N.A. (1976). "Experimental and Theoretical Investigations in an Oscillatory Turbulent Boundary Layer," *J. Hydraulic Research*, (14), 45-60.

Kamphuis, J.W. (1975). "Friction Factors Under Oscillatory Waves," *J. Waterways, Harbors and Coastal Engineering Div*., ASCE, (101), 135-144.

Kemp, P.H. and Simons, R.R. (1982). "The Interaction Between Waves and a Turbulent Current: Wave Propagating with the Current," ," *J. Fluid Mechanics*, (116), 227-250.

Komar, P. (1976) “*Beach processes and sedimentation*,” Prentice-Hall, INC., Englewood Cliffs, New Jersey. 429 pp.

Komar, P. and Miller, M. (1975). ”On the comparison of the threshold of sediment motion under waves and unidirectional currents with a discussion of the practical evaluation of the threshold,” *J. Sedimentary Petrology*, 45(2), 362-367.

Madsen, O. and Grant,W. (1976). “Sediment transport in the coastal environment,” Technical Report 209, M.I.T., Cambridge, Massachusetts, USA.

Manohar, M. (1955). “Mechanics of bottom sediment movement due to wave action,” Technical Memo 75, Beach Erosion Board, U.S. Army Corps of Engineers, Washington, D.C.

Nielsen, P. (1992). “Coastal bottom boundary layers and sediment transport,” *Vol. 4 of Advanced Series on Ocean Engineering*, World Scientific Publication.

Rance, P. and Warren, N.(1968). “The threshold of movement of coarse material in oscillatory flow,” *Proc. 11th Int. Conf. Coastal Eng.*, ASCE, 487-491.

Riedel, H.P. (1972). "Direct Measurements of Bed Shear Stress under Waves," Ph.D. Thesis, Dept. of Civil Engineering, Queen's University, Kingston, Ontario, Canada.

Shields, A. (1936). “Anwendung der Änlichkeits-Mechanik und der Turbulenzforschung auf die Geschiebe-bewegung,“ Preussische Versuchsanstalt für Wasserbau und Schiffbau, 26. Berlin.

Soulsby, R. (1997). “*Dynamics of marine sands, a manual for practical applications,”* Thomas Telford, ISBN 0-7277-2584, H.R. Wallingford, UK.

Soulsby, R. and Whitehouse, R. (1997). "Threshold of sediment motion in coastal environment," *Proc. Pacific Coasts and Ports '97 Conf*', University of Canterbury, Christchurch, New Zealand, 149-154.

Sumer, B.M., Jensen, B.L., and Fredsoe, J. (1987), "Turbulence in oscillatory boundary layers." In: Comte-Bellot G. and Mathieu, Eds., *Advances in Turbulence*, Springer, New York, pp. 556–567.

Swart, D. H. (1974) "Offshore Sediment transport and Equilibrium Beach Profiles," *Delft Hydr. Lab. Publ*., No. 131, 302 pp.

Sleath, J.F.A. (1987). "Turbulent Oscillatory Flow over Rough Beds," *J. Fluid Mechanics*, (182), 369-409.

Valembois, J. (1960), Etude sur modèle du transport littoral –conditions de similitude," *Proc. 7th Int. Conf. Coastal Eng.*, Vol. 1, ASCE, 315-325.

van Rijn, L. (1984), "Sediment transport ,part I: Bedload transport," *J. Hydraulic Division,* 110(10), 1431-1456.

Yalin, M. (1977). "*Mechanics of Sediment Transport*," Pergamon Press, Oxford. 2nd edition.

INFLUENCE OF VELOCITY MOMENTS ON SAND BAR MOVEMENT DURING CROSSTEX

Gregory Guannel[1], H. Tuba Özkan-Haller[2], Merrick C. Haller[1], James T. Kirby[3]

1. Department of Civil, Constr., and Env. Engineering, Oregon State University, Corvallis, OR 97331 USA; guannelg@engr.orst.edu, hallerm@engr.orst.edu.
2. College of Oceanic and Atmospheric Sciences, Oregon State University, Corvallis OR 97331 USA; ozkan@coas.oregonstate.edu.
3. Center for Applied Coastal Research, University of Delaware, Newark, DE 19716 USA; kirby@udel.edu.

Abstract: During the 2005 CROSSTEX laboratory experiments, a series of bar generation and degeneration events and repeated cycles of offshore and onshore transport were documented. These changes were driven by regular modifications to the specified incident wave field. Based on collected bathymetric data we first assessed the spatial and temporal movement of two sand bars. We used hydrodynamic and video data to relate the movement of these bars to the occurrence of wave breaking and the magnitudes of undertow, velocity skewness and acceleration skewness. This analysis indicates that undertow currents generated the first sand bar through offshore-directed transport. The second bar was formed by onshore transport, with the first bar serving as the likely sediment source. On the other hand, onshore migration and degeneration of both sand bars correlated well with acceleration skewness.

INTRODUCTION

Many investigations in the recent past have focused on identifying processes responsible for cross-shore sediment movement and sand bar migration in the surf. It is now widely accepted that undertow currents move sediment offshore (Thornton and Humiston, 1996; Gallagher et al., 1998; Elgar et al., 2001) and are responsible for the formation of sand bars. On the other hand, processes responsible for onshore sediment movement are more difficult to pinpoint, although recent efforts indicate that acceleration skewness and other factors, such as drift velocity, boundary layer

streaming, pressure gradients, or plug flow might play significant roles (e.g. Hoefel and Elgar, 2003; Henderson et al., 2004, Foster et al., 2006).

Experimental data is required in order to evaluate the relative importance of the various transport processes. However, while there is currently a wealth of data involving offshore bar migration events, there is relatively little concerning onshore migration. To fill that gap, the CROSSTEX (CROss-Shore Sediment Transport EXperiment) experiment was conducted at the O. H. Hinsdale Wave Research Laboratory (HWRL) at Oregon State University.

Four different teams of investigators were involved in CROSSTEX, each focusing on different processes, such as the evolution of sand ripples, turbulence, sand bar migration and swash zone processes. The present authors were principally involved in the sand bar migration portion of these experiments, which will be discussed in further detail in the remainder of this paper.

In the following sections, we will first describe the set-up and implementation of the experiment. Then we will describe the spatial and temporal evolution of the bars, and relate the evolution to the measured velocity moments. Finally, we will investigate correlations between the spatial and temporal evolutions of two of these bars with variables such as wave breaking, the undertow strength, velocity skewness, and acceleration skewness.

EXPERIMENTS AND BED RESPONSE

Experimental set-up

CROSSTEX took place in the HWRL's 104m-long Large Wave Flume (LWF; see Figure 1) from June to September 2005. This flume was selected because its dimensions are ideal to conduct most experiments at near prototype scale. For these experiments the LWF was filled with well sorted, fine to medium sand mined from Florence, Oregon, with a median grain size D_{50}=0.22mm, and a standard deviation of σ_Φ=0.3. Prior to our experiments, the bed profile was adjusted to an average slope of 1V:20H through wave action.

The LWF is equipped with a flap wavemaker that can generate regular and irregular waves, a mobile cart with a vertically moving frame where various instruments can be mounted, as well as a Multiple Transducer Array (MTA) to conduct bathymetric surveys. The coordinate origin is located on top of the east wall of the tank and aligned with the wave paddle. Consequently, in all tables and figures presented in this paper, X is onshore positive and Z is positive up.

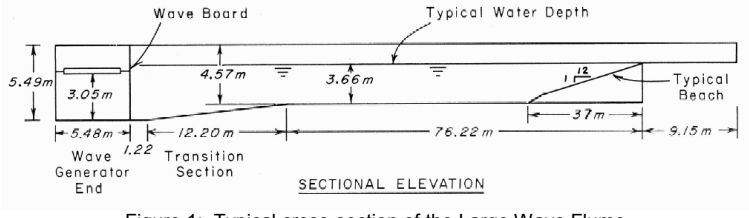

Figure 1: Typical cross-section of the Large Wave Flume

The cross-shore evolution of water surface elevation was measured with twelve resistance-type wave gauges mounted along the walls of the flume. Eight wall-mounted Vectrino Acoustic Doppler Velocimeters (ADVs) and Optical Backscatter Sensors (OBSs) were also deployed in order to observe the near-bottom hydrodynamics and sediment concentrations, as depicted in Figure 2 and in Table 1.

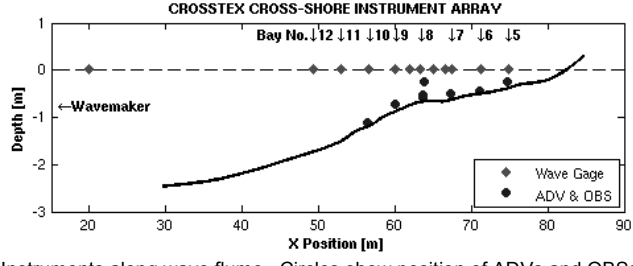

Figure 2: Instruments along wave flume. Circles show position of ADVs and OBSs, and diamonds show position of wave gages.

Table 1: Position of Wall Mounted ADVs and OBSs

Bay		5	6	7	8			9	10
X [m]	ADV	75	71	67	64	64	64	60	56
	OBS	75	71	67	64	64	64	60	56
Dist. Abv Bed [cm]		10	2	7	9	5	42	9	4

In addition to wall-mounted instruments, one wave gauge, eight ADVs, four Electromagnetic Current Meters (EMCMs), seven OBS, and twenty Fiber-Optic Backscatter Sensors (FOBSs) were also placed on the cart's mobile frame. Typical elevations of the cart instruments during deployments are presented in Figure 3.

Cart instruments were deployed at different cross-shore locations during different runs, and lowered before each wave run so that the lowermost ADVs would capture velocity fluctuations at one centimeter above the bed, and the lowermost FOBS sensor would sit one centimeter inside the fixed bed. Finally, three ARGUS cameras (Holman, et al., 1993) were installed above the LWF and are used here to evaluate percent wave breaking at various cross-shore locations.

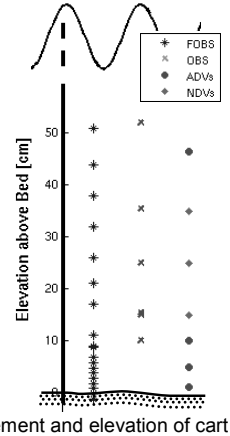

Figure 3: Typical arrangement and elevation of cart mounted instruments.

Experimental conditions

The objectives of the experiment were to first generate an offshore breaker bar and then to move that bar onshore. Consequently, the generated wave field (TMA spectrum) was modified as the experiment progressed. At the beginning, relatively high energy waves were generated to move sediment offshore. Once an offshore bar was generated, wave height and period were adjusted to create conditions conducive to onshore bar movement (see Table 2). Regular bathymetric surveys were performed to verify that designed waves were indeed causing the bar(s) to move in the intended direction.

Table 2: Consecutive Wave Conditions during Experiment

Wave Height [m]	Wave Period [s]	Wave Time [min]
0.60	4.0	210
0.30 – 0.32	8.0	675
0.55 – 0.35	3.5	135
0.40 – 0.32	5.5	330
0.320 – 0.175	3.5	795

The experiment involved approximately 36.5 hours of wave action (36.5 wave hours), and consisted of several fifteen minutes runs (or 15 wave minutes). This length was determined based the limitations of the data acquisition system, and to limit effects of seiching.

Bed evolution

Three main stages of bed evolution were identified during the course of the experiment:

1. Generation of an offshore bar (Figure 4a), during the first 210 minutes of waves.
2. Recession of the offshore bar and growth of a "middle bar" (Figure 4b), from wave time 210 to 900 minutes.
3. Recession of middle bar and smoothing of profile (Figure 4c), from wave time 900 to 2200 minutes.

It is worth mentioning that we also observed the rapid formation and decay of a nearshore terrace/bar very close to shore, while the middle bar was still evolving. Also, we observed the formation of mega-ripples (Figure 4b, final profile) between the middle bar and the nearshore terrace, or bar. We will not evaluate the dynamics of these bedforms in this paper.

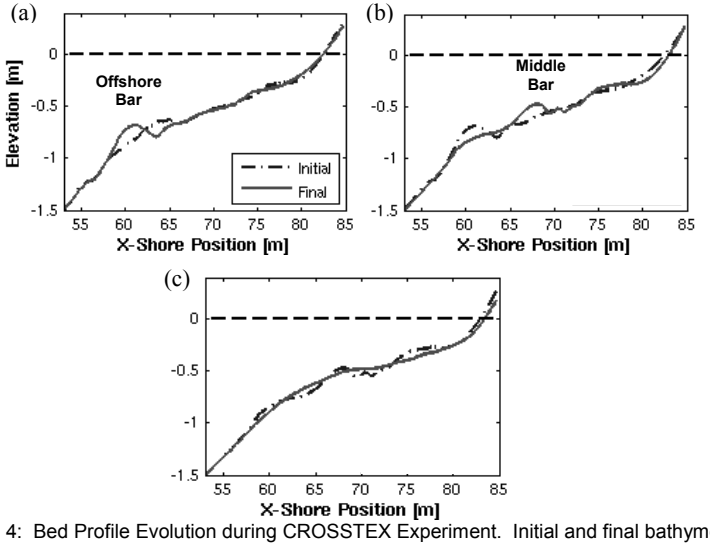

Figure 4: Bed Profile Evolution during CROSSTEX Experiment. Initial and final bathymetries are shown by the dashed and solid lines, respectively.

In conclusion, during this experiment we were able to generate three sand bars and other bedforms by varying wave conditions in the tank. Furthermore, we collected detailed bathymetric, hydrodynamic and sediment concentration data at various locations throughout the tests. These data will enable us to better evaluate wave conditions and processes responsible for cross-shore sediment movement. In the remainder of this paper, we will focus on the life cycle of the offshore and middle bars.

WAVE CONDITIONS AND SAND BAR GENERATION/DEGENERATION

In order to characterize the morphologic response to the range of wave fields generated in the LWF, we identified several representative parameters for the offshore and middle sand bars, as defined in Figure 5, and tracked their evolution

through time. These parameters were bar height and position, and bar half-width. Together, these parameters provide a good, general representation of the spatial and temporal evolution of the two bars.

As mentioned earlier, undertow and acceleration skewness have been recognized as cross-shore velocity moments that correlate well with cross-shore migration of sand bars. So, in order to assess their role in the evolution of the sand bars, we will relate these quantities, as well as amount of breaking, to the temporal and spatial characteristics of the bars. Some of the hypotheses drawn from this analysis will be confirmed by looking at sediment flux values, which provide information about sediment sources and pathways.

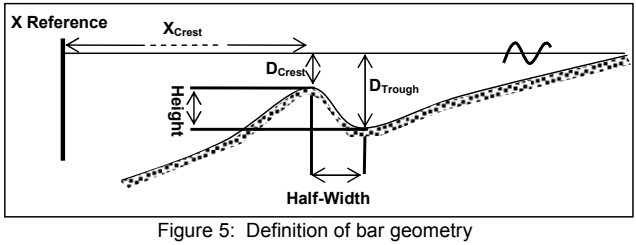

Figure 5: Definition of bar geometry

Spatial and Temporal Evolution of Sand Bars

Using the computed bathymetric data, we first plotted bar height versus cross-shore position for the two bars (Figure 6). These figures show that the bars take different paths during generation when their heights start to increase and during degeneration, when height decreases; initial and final position during this cycle are close, but not identical.

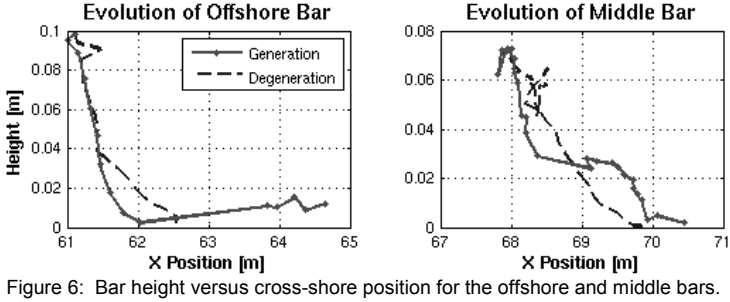

Figure 6: Bar height versus cross-shore position for the offshore and middle bars.

We also plotted bar height and position as a function of time for both sand bars, as shown in the third and fourth panels of Figure 7. In this figure, we also show percent of wave breaking (color bars, second panel) computed from the Argus videos that were collected during 23 runs. We do not have data for the other runs, so most of the color bars are separated by white space.

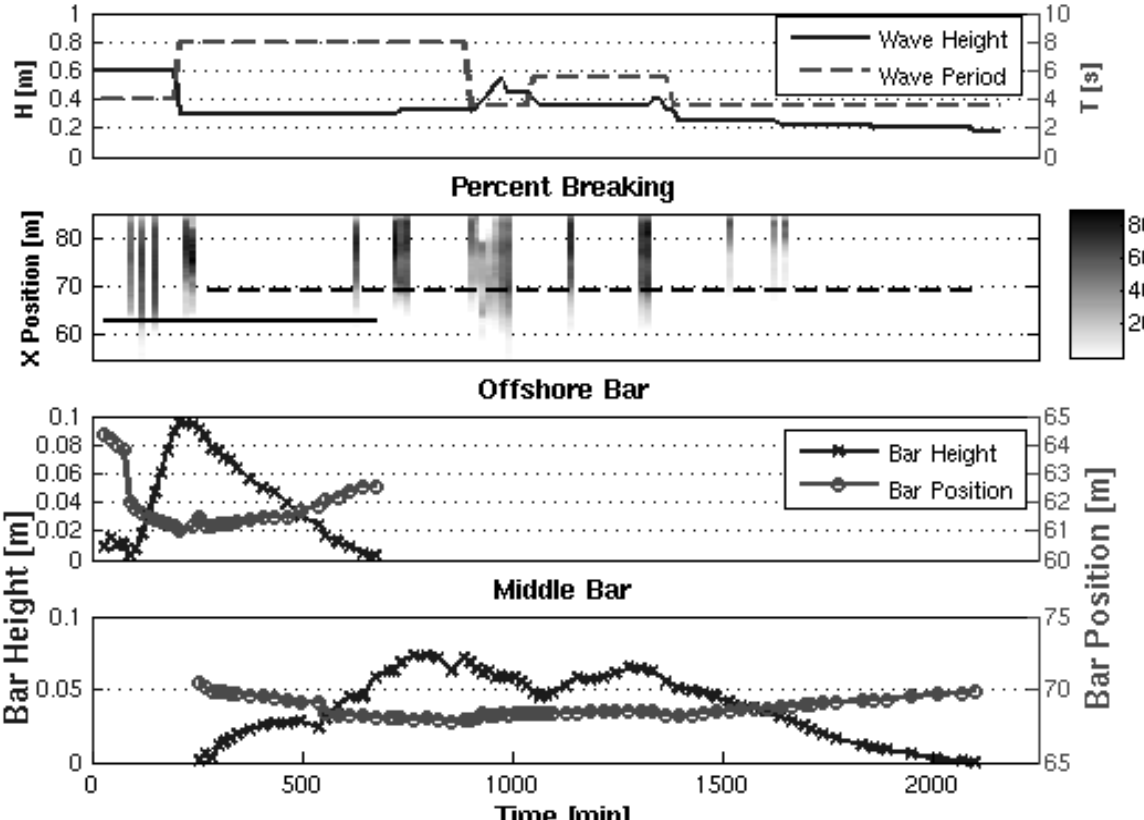

Figure 7: Spatial and Temporal evolution of the offshore and middle bars. Generated wave field is shown in top panel, and percent of wave breaking for 23 discrete runs by the color bars in 2nd panel, where solid and dashed line show average position of the offshore and middle bars, respectively. Third and fourth panel show bar height (solid line with crosses) and position (solid line with circles).

At the beginning of the experiment, under the attack of fairly high, energetic waves (Figure 7, top panel), sediment moved offshore and started to accumulate at approximately x = 64m to form an offshore bar (Figure 7, third panel). This bar continued to move offshore at a speed of approximately 1 cm/min as it grew in height, until wave conditions changed at wave time 210 min. During that period, approximately 40 percent of the waves were breaking on the offshore bar, and approximately 70 percent of the waves were breaking just shoreward of it (Figure 7, second panel).

Almost immediately after the change in wave field, offshore bar height started to decrease as the bar moved onshore at a speed of approximately 0.3 cm/min. Simultaneously, the middle bar started to form. Similarly to the offshore bar, its height increased as it moved offshore (Figure 7, third and fourth panels), but its speed was approximately 0.3 cm/min. The middle bar generation, which will be referred as Phase I in the remainder of this paper, continued until wave conditions were changed, at around wave time 900 min. During this period, between 30 and 40 percent of the waves were breaking on top of the middle bar. In contrast, approximately less than five percent of the waves were breaking on top of the offshore bar, which continued to degenerate.

Successive changes in wave conditions, between wave time 900 and 1350 min, resulted in changes in middle bar height (slight decrease during Phase II and slight increase during Phase III), while it continued to move very slowly onshore. Reduction in wave height and period at wave time 1350 min led to the final decay and onshore migration of the middle bar (Phase IV). During this phase, less than five percent of the waves were breaking on top of the bar, and the bar moved onshore at a speed of approximately 0.1 cm/min, which is smaller than the onshore migration speed of the offshore bar.

The information gathered from these figures along with bar half-width data (not shown), describe the bars temporal and spatial evolution. Both bars were generated when wave breaking was moderate above their crest, and as they moved offshore, they grew higher and wider. After changes in wave conditions, the bars decayed and moved onshore, while getting shorter and narrower, with almost no wave breaking on them. The two sand bars are very dynamic, responded quite rapidly to changes in the wave field, and are probably interdependent.

Moreover, we expect undertow currents to be associated with the principal mechanisms of bar formation, but play a weaker role in bar decay. Other processes, such as the ones correlated with acceleration skewness, are expected to become more predominant during bar degenration. The relationship between velocity moments and sand bars temporal and spatial evolution will be analyzed in more detail in the next section.

Influence of Velocity moments

To compute values of undertow, acceleration skewness and velocity skewness, and to evaluate their influence on the evolution of the bars, we used records of wall instruments located immediately shoreward and offshore of the bars. These records have been band-passed to remove turbulence and seiching signals.

During offshore bar generation, Figure 8, undertow and velocity skewness values were relatively high shoreward of the bar, while acceleration skewness was relatively modest. Furthermore, while gradients of undertow and acceleration skewness seemed to be fairly strong on top of the bar, there was no significant change in velocity skewness in that region.

During offshore bar degeneration, overall undertow and velocity skewness values decreased, while acceleration skewness values shoreward of the bar increased. Again, gradients in undertow and acceleration skewness seemed to be strong near the bar, while velocity skewness did not vary much. Also, it is interesting to note that while acceleration skewness values were higher offshore of the bar during the generation phase, they became larger shoreward of the bar during the bar degeneration.

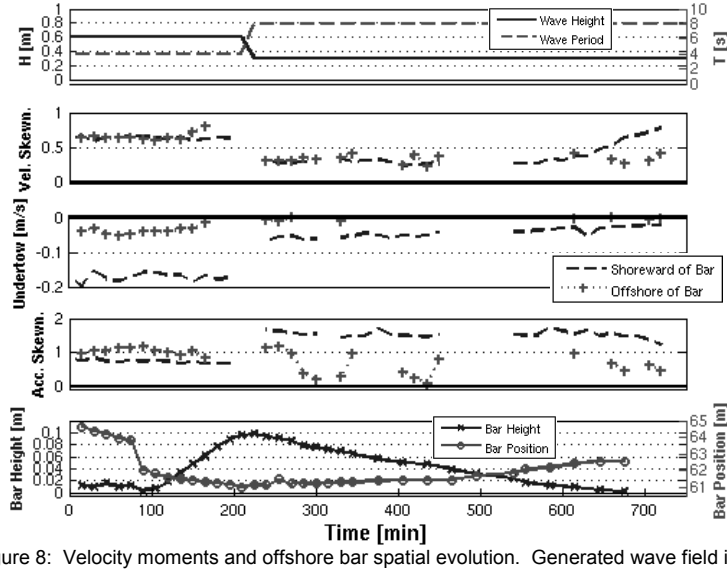

Figure 8: Velocity moments and offshore bar spatial evolution. Generated wave field is shown in top panel, velocity skewness, undertow and acceleration skewness shoreward (dashed lines) and offshore of the bar (dotted lines with crosses) in 2nd, 3rd, 4th panels, and bar height (solid line with crosses) and position (solid line with circles) in bottom panel.

Another way to look at the influence of wave moments on the evolution of the offshore bar is presented in the left panel of Figure 9, where undertow values

measured during generation and degeneration phases are plotted as a function of acceleration skewness. This figure, combined with the information presented in previous figures, show that the bar generated during strong undertow conditions, but degenerated in the presence of very weak undertow and strong accelerations skewness.

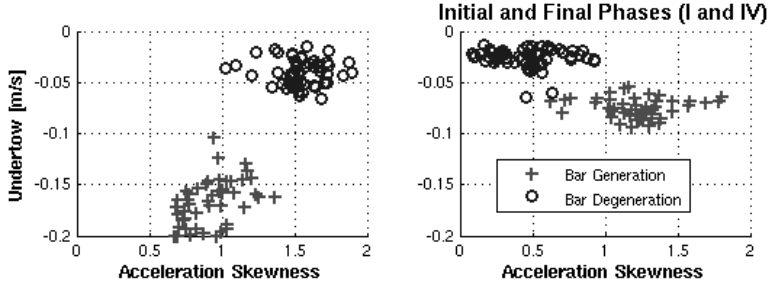

Figure 9: Undertow current versus acceleration skewness values during offshore (left panel) and middle (right panel) bar generation (crosses) and degeneration (circles).

A similar analysis was conducted for the middle bar, as shown in Figure 10. During middle bar initial generation, Phase I, values of velocity skewness offshore and shoreward of the bar decreased, compared to values it had from the beginning of the experiment to wave time 210 min. On the other hand, gradients of that moment increased. Undertow strength shoreward of the bar remained stable, but it decreased from values it had before wave time 210 min. Gradients of undertow decreased also during that period. Finally, acceleration skewness values on either side of the bar decreased during that period. The reduction of that moment was stronger offshore than shoreward of the bar.

During Phases II and III, strength of the undertow near the bar did not change much, velocity and acceleration skewness varied. However, as mentioned earlier, these are intermediate states in the evolution of the middle bar, and we will not evaluate influence of moments on Phases II and III any further.

During the bar final degeneration, Phase IV, velocity skewness values decreased, and undertow current is almost null, and both have almost zero gradient over the bar. On the other hand, acceleration skewness values decreased, although its gradient is still significant on top of the bar.

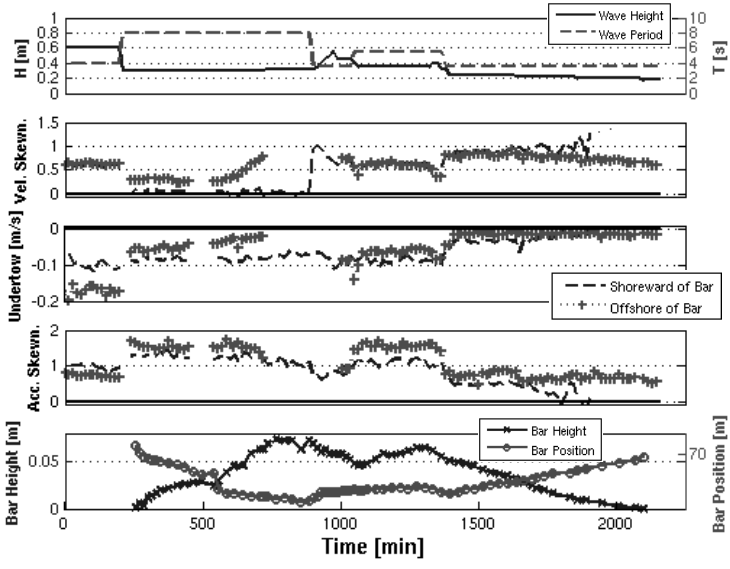

Figure 10: Velocity moments and middle bar spatial evolution. Generated wave field is shown in top panel, velocity skewness, undertow and acceleration skewness shoreward (dashed lines) and offshore of the bar (dotted lines with crosses) in 2nd, 3rd, 4th panels, and bar height (solid line with crosses) and position (solid line with circles) in bottom panel.

When we combined information presented in the previous figure with the distribution of undertow versus acceleration skewness values (right panel of Figure 9), we see that the middle bar formed when undertow currents were approximately 50 percent lower than what they were during generation of the offshore bar. Also, acceleration skewness values during that period were 50 percent higher than what they were during generation of the offshore bar. This situation suggests that the middle bar was not undertow-formed, which is characteristic of most sand bars (such as the offshore bar). On the other hand, because gradients of acceleration skewness were moderate over the middle bar during that bedform degeneration, but undertow currents were almost non-existent, it is likely that processes related to this moment were responsible for the decay of that bar.

In summary, the information presented in these figures indicates that 1. velocity skewness did not seem to be a major factor in the life cycle of either bedforms; 2. undertow currents were probably responsible for the offshore bar growth, but might have been only been partially responsible for the formation of the middle bar. Other processes, probably correlated with acceleration skewness, might have been more prevalent.

It is likely that processes correlated with acceleration skewness led to the degeneration of both bars, but that the value of that moment played a role in the

onshore migration speed of both bars: the offshore bar moved onshore quicker than the middle bar probably because acceleration skewness was higher in one case than the other. One way to assess some of these hypotheses is to compute sediment flux values Q and evaluate the origin of sediments that led to the generation of these bars.

Sediment Flux Calculation

Sediment fluxes that led to the generation of the offshore and middle bars (Figures 11) were computed from the integration of the difference between pre- and post-sandbar generation bed profiles. In this figure, negative flux means offshore sediment transport, while negative flux signifies onshore movement.

Analysis of the left panel of Figure 11 shows that the offshore bar was mostly generated by the offshore movement of a fair amount of sediments, and to a lesser extent by sediment that moved from offshore regions. Most of the sediments that moved offshore seem to originate to regions less than five meters shoreward of the bar.

Based on results of previous sections, we can infer that most sediment that moved offshore was mobilized and moved by undertow currents. Offshore of the bar, because undertow currents were weak, wave processes (possibly acceleration skewness) became predominant and moved some sediment onshore. Sediments accumulated at the final bar location due to the confluence of erosive (i.e. undertow driven) and accretive (i.e. acceleration skewness driven) processes.

If we now look at the middle bar (Figure 11, right panel), it appears that most of the sediments that led to its formation moved onshore from the offshore bar that was degenerating. This movement of sediment, probably driven by acceleration skewness related processes, seemed to have continued beyond the location of the middle bar, but at a lower rate. The change in flux intensity near the trough of the middle bar suggests that onshore sediment movement shoreward of the bar was probably slowed by other processes, such as the undertow.

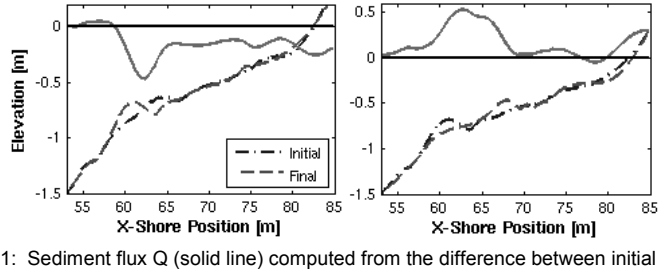

Figure 11: Sediment flux Q (solid line) computed from the difference between initial (dashed dotted line) and final (dashed line) profiles during generation of offshore (left panel), and middle bars (right panel). Offshore sediment movement corresponds to a negative Q.

CONCLUSIONS

During this portion of the CROSSTEX experiment, the generation and degeneration of an offshore and a middle bar was studied in a controlled environment. The analysis of the temporal and spatial evolution of these bars showed that they were quite responsive to changes in wave conditions, interdependent, and sensitive to velocity moments.

Our analysis indicates that the offshore bar was formed by the action of undertow currents, caused by intense wave breaking. On the other hand, the middle bar appears to have been formed by the onshore movement of sediments originating from the offshore bar. Undertow currents and acceleration skewness played a role in this movement, but their relative importance is different from what occurred during the life cycle of the offshore bar. Finally, the degeneration of these bars is correlated with weaker undertow currents, higher acceleration skewness, and almost non-existent breaking. What separates them is their rate of decay, which is probably dictated by the value of acceleration skewness.

In conclusion, the two sand bars were probably formed by different processes, but were extremely interdependent. In a sense they might even represent the same bedform that evolved in different ways because of the ever changing balance between processes that drive cross-shore sediment movement. These processes are correlated with moments such as undertow and acceleration skewness, but their exact nature, and the way they mobilize sediment particles and move them has yet to be determined. This is especially true for acceleration skewness related processes. Further analysis of the data that was collected might shed a light on the role of that moment.

ACKNOWLEDGEMENTS

We wish to thank all the faculty and staff of the O.H. Hinsdale Wave Research Laboratory for their time and support during the experimental phase of CROSSTEX. The O.H. Hinsdale Wave Research Laboratory is partially supported by the George E. Brown Jr. Network for Earthquake Engineering Simulation (NEES) Consortium Incorporated contract OMSA v.3.1 through their National Science Foundation Cooperative Agreement CMS-0402490. Some of the instrumentation used in this project was purchased under National Science Foundation NSF-0429219. Also, we would like to thank Patricio Catalan for his help in computing percent of wave breaking from the Argus videos. Finally, we would like to thank our sponsors for this study, NSF Grant OCE-0351297 and OCE-0351153, and Sea Grant grant NA16RG1039.

REFERENCES

Elgar, S., E. Gallagher, and Guza, R. T. (2001). "Nearshore sand bar migration", *Journal of Geophysical Research*, 106(C6), 11,623-11,627.

Foster D. L., Bowen, A. J., Holman, R. A., Natoo, P. (2006). “Field evidence of

pressure gradient induced incipient motion", *Journal of Geophysical Research*, 111 (C5).

Gallagher E.L., Elgar S., and Guza R.T. (1998). "Observations of sand bar evolution on a natural beach," *Journal of Geophysical Research*, 103 (C2), 3203-3215.

Henderson S.M., Allen J.S., and Newberger P.A. (2004). "Nearshore sandbar migration predicted by an eddy-diffusive boundary layer model," *Journal of Geophysical Research* 109 (C6).

Hoefel, F., and Elgar, S. (2003). "Wave-induced sediment transport and sandbar migration," *Science*, 299, 1885-1887.

Holman, R. A., Sallenger, J.A.H., Lippmann, T. C., and Haines, J. W. (1993). "The application of video image processing to the study of nearshore processes", *Oceanography*, 6, 78-85.

Thornton, E. B., Humiston, R. T., and Birkemeier, W. A. (1996). "Bar/trough generation on a natural beach," *Journal of Geophysical Research* 101 (C5), 12,097-12,110.

DEVELOPMENT OF A NEW PRACTICAL MODEL FOR SAND TRANSPORT INDUCED BY NON-BREAKING WAVES AND CURRENTS

Jebbe J. van der Werf[1], Jan S. Ribberink[2], Tom O'Donoghue[3]

1. Water Engineering and Management, University of Twente, P.O. Box 217, 7500 AE Enschede, The Netherlands. J.J.vanderWerf@utwente.nl.
2. Water Engineering and Management, University of Twente, P.O. Box 217, 7500 AE Enschede, The Netherlands. J.S.Ribberink@utwente.nl.
3. University of Aberdeen, Department of Engineering, King's College, Aberdeen, AB24 3UE, Scotland. T.O'Donoghue@eng.abdn.ac.uk.

Abstract: A new practical model for net sand transport induced by non-breaking waves and currents is being developed within the SANTOSS research project. Phase I of model development is reported here. In comparison with existing models, the main improvement is the description of the wave-related transport. More specifically, phase lag effects in the sheet-flow and ripple regime – which potentially have a large effect on the net transport – are accounted for in a parameterized way. The santoss model is calibrated against a large set of data from oscillatory flow tunnel experiments covering a wide range of flow and sand conditions. The new model is seen to perform better than existing practical transport models, and is applicable to a larger range of conditions.

INTRODUCTION

In recent years a substantial body of field- and laboratory-based research has been devoted to measuring sand transport processes induced by waves and currents, and predictive models for the net (wave-averaged) sand transport have been developed. In broad terms, the models can be classified as practical or research models. Research models represent many of the detailed physical processes involved in sand transport by waves and currents, and resolve the vertical and sometimes also the horizontal structure of the time-dependent (intra-wave) velocity and sand concentration fields. Such models are complex, require long computation times and are therefore generally not implemented in coastal morphological models. Practical models require short

computation times and can be implemented easily in coastal morphological models. However, they do not resolve the spatial and temporal structure of the velocity and sand concentration fields. Existing practical and research models to predict the net sand transport induced by waves and currents still have considerable shortcomings (see e.g. Davies et al., 2002).

This paper describes the development of a new practical model to predict the net sand transport in coastal waters. This model has been developed within the Dutch/UK research project SANTOSS (Sand Transport in Oscillatory Flows in the Sheet-flow Regime). Hence, the new model is called the santoss model hereafter.

The santoss model is being developed using the santoss database of experimental data. The database contains a large amount of net sand transport data from full-scale, non-breaking wave and non-breaking wave plus collinear current experiments (see Schretlen and Van der Werf, 2006). We use the net transport data from oscillatory flow tunnel experiments with uniform sediments, flow periods $T \geq 3$ s, and orbital flow asymmetries $R = \hat{u}_c / (\hat{u}_c + \hat{u}_t) \leq 0.7$, where $\hat{u}_c$ and $\hat{u}_t$ are the peak crest and peak trough orbital velocity respectively.

Table 1 presents an overview of the data used for the model development. The bedform regime (ripples or sheet-flow), the flow type (W: wave-alone; W+C: wave+current), and the experimental facilities (AOFT: Aberdeen Oscillatory Flow Tunnel; LOWT: Large Oscillating Water Tunnel; TUWT: Tokyo University Water Tunnel) are distinguished. Furthermore, the range of median grain size, D_{50}, is shown.

Table 1. Overview of the data used for the development of the santoss model. W: wave-alone experiments; W+C: wave-current experiments. AOFT: Aberdeen oscillatory flow tunnel; LOWT: large oscillating water tunnel; TUWT: Tokyo university water tunnel.

Bedform regime	Flow type	Facility	No.	D_{50} (mm)
Ripples	W	AOFT	23	0.22-0.44
		LOWT	16	0.21-0.35
		TUWT	0	-
	W+C	AOFT	0	-
		LOWT	1	0.35
		TUWT	0	-
Sheet-flow	W	AOFT	8	0.13-0.46
		LOWT	26	0.13-0.34
		TUWT	26	0.20-0.74
	W+C	AOFT	0	-
		LOWT	36	0.13-0.32
		TUWT	24	0.20

Figure 1 presents an overview of the hydraulic conditions covered by the data, based on the oscillatory flow period T and the wave mobility number given by:

$$\psi_w = \frac{\hat{u}^2}{\Delta g D_{50}} \tag{1}$$

where Δ is the relative density of sediment and g is acceleration due to gravity. Relative net current strength is given by $< u_b > / \hat{u}$, where $< u_b >$ is the net current strength at z = 0.15 m and $\hat{u}$ is the characteristic orbital velocity amplitude.

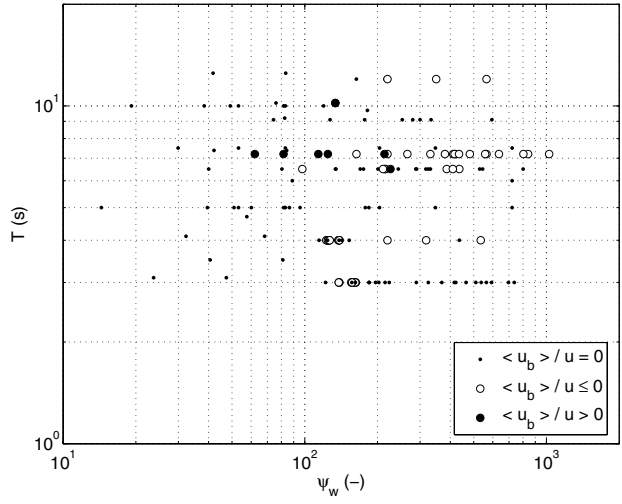

Figure 1. Overview of the data used for the model development in terms of the wave mobility number ψ_w, the flow period T, and the relative net current strength $< u_b > / \hat{u}$.

This figure shows that the net transport data simultaneously cover a wide range of full-scale flow periods ($T \approx 3 - 10$ s) and wave mobility numbers ($\psi_w \approx 40 - 700$). For $\psi_w >\approx$ 100 there is also a reasonable amount of net transport data in which $< u_b > / \hat{u} \leq 0.5$. There is a limited amount of net transport data from experiments with relatively strong net currents ($< u_b > / \hat{u} > 0.5$). In general, the experimental conditions can be characterized as wave-dominated.

The paper is organized as follows. Section 2 describes the state-of-the-art of practical sand transport modeling. In the next section the santoss model is presented, calibrated and compared with existing practical sand transport models. The conclusions are presented in Section 4.

STATE-OF-THE-ART FOR PRACTICAL SAND TRANSPORT MODELING

There are three types of practical sand transport models: 1) time-averaged models, 2) quasi-steady models, and 3) semi-unsteady models. Time-averaged models were the first models to be developed to derive the sand transport rate under waves and currents. The sand transport rate is described at a time scale much longer than the wave period using

the wave-averaged values of velocity and concentration. A widely-used time-averaged transport formula was developed by Bijker (1971), which describes the current-related transport (suspended load and bedload) with waves acting as stirring agent. In time-averaged models, the total net transport is always in the direction of the mean current and the wave-related transport component is not taken into account.

Quasi-steady models (e.g. Bailard, 1981; Van Rijn, 1993; Ribberink, 1998) consider the sand transport on an intra-wave scale, i.e. a time-scale much shorter than the wave period. These are based on the assumption of quasi-steadiness: the instantaneous sand transport is related to the instantaneous flow velocity or bed shear stress, as if the flow is steady at each phase during the wave-cycle. In this way the wave-related sand transport is implicitly included. The assumption of quasi-steadiness only holds for conditions where the response time of sand particles is short relative to the wave period. In other words, the pick-up and settling of sand particles must take place in a much shorter time than the wave period. This does not happen in the case of fine sand sheet-flow conditions (Dohmen-Janssen, 1999, O'Donoghue and Wright, 2004a) and rippled bed conditions (see Van der Werf, 2006). In these cases the phase lag between velocity and concentration can become so large than the net sand transport induced by asymmetric oscillatory flows (e.g. second-order Stokes) is offshore-directed (negative), i.e. against the orbital flow asymmetry. This is illustrated in Figure 2 which shows net transport data from wave-alone experiments with $T \geq 4$ s as a function of the wave mobility number.

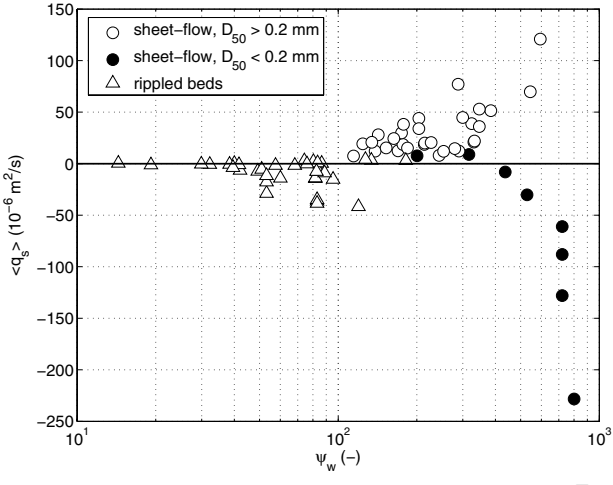

Figure 2. Net sand transport rate data from wave-alone experiments with $T \geq 4$ s as a function of the wave mobility number.

Quasi-steady models fail to predict the net transport correctly under conditions where phase lags are important. Semi-unsteady models account for these phase lag effects in a parameterized way. Existing semi-unsteady models are either mainly based on sheet-

flow data (e.g. Dibajnia & Watanabe, 1996; Camenen and Larson, 2006, Silva et al, 2006) or on ripple data (e.g. Nielsen, 1988; Van der Werf et al., 2006). Furthermore, these models are generally constrained to wave-alone cases. There does not exist a practical sand transport model capable of predicting net transport induced by non-breaking waves and currents including the phase lag effects in both the rippled bed and plane bed/sheet-flow regime.

NEW PRACTICAL SAND TRANSPORT MODEL

In comparison with existing sand transport models for the coastal environment, the main improvements of the santoss model lie in the description of the wave-related transport. The model will account for (i) phase lag effects in the sheet-flow and rippled bed regime (ii) surface wave effects and (iii) acceleration skewness effects. Model development is taking place in two phases. Phase 1 development is primarily based on existing knowledge (model concepts), making use of existing oscillatory flow tunnel experimental data. Surface wave and acceleration effects are not considered in Phase 1. Phase 2 development will incorporate new knowledge on surface wave and acceleration effects based on new experiments carried out during the course of the SANTOSS research project. This paper discusses the first phase of model development.

Velocities

The near-bed velocity vector at reference level $z = \delta$ above the bed due to the combined wave-current motion is defined as follows (see Figure 3):

$$\vec{u}_b(t) = \langle \vec{u}_b \rangle + \vec{u}_{b,osc}(t) \tag{2}$$

where $< \vec{u}_b >$ is the current velocity vector at $z = \delta$ and $\vec{u}_{b,osc}(t)$ the free-stream orbital velocity vector. Therefore, δ should be outside the wave boundary layer. We have taken $\delta = 0.15$ m.

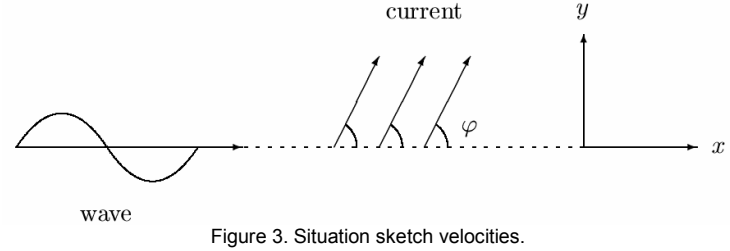

Figure 3. Situation sketch velocities.

The maximum velocity (under the wave crest, *c*) and the minimum velocity (under the wave trough, *t*) are defined as follows:

$$\vec{u}_{b,c} = \left\{ \hat{u}_c + \langle u_b \rangle \cos\varphi, \langle u_b \rangle \sin\varphi \right\} \tag{3}$$

$$\vec{u}_{b,t} = \left\{ \langle u_b \rangle \cos\varphi - \hat{u}_t, \langle u_b \rangle \sin\varphi \right\} \tag{4}$$

Irregular oscillatory flows are treated as regular oscillatory flows using $\hat{u}_c = u_{1/3,on}$, $\hat{u}_t = u_{1/3,off}$ and $T = T_p$, where $u_{1/3,on}$ is the mean of the highest one-third onshore orbital velocity peaks, $u_{1/3,off}$ the mean of the highest one-third offshore orbital velocity peaks, and T_p the spectral peak period. The degree of orbital flow asymmetry in the case of irregular oscillatory flows is defined by:

$$R = \frac{u_{1/3,on}}{u_{1/3,on} + u_{1/3,off}} \tag{5}$$

In cases where the orbital velocity amplitude under the wave crest, $\hat{u}_c$, and under the wave trough, $\hat{u}_t$, are not known, they are computed from the root-mean-square orbital velocity, $\tilde{u}_{rms}$, and the degree of flow asymmetry, R, as follows (assuming a second-order Stokes velocity function):

$$u_1 = \sqrt{\frac{\tilde{u}_{rms}^2}{(2R-1)^2 + 1}} \tag{6}$$

$$u_2 = (2R-1)u_1 \tag{7}$$

$$\hat{u}_c = u_1 + u_2 \tag{8}$$

$$\hat{u}_t = u_1 - u_2 \tag{9}$$

The characteristic orbital velocity amplitude, $\hat{u}$, is given by:

$$\hat{u} = \sqrt{0.5\hat{u}_c^2 + 0.5\hat{u}_t^2} \tag{10}$$

Bed shear stress

We use the method of Ribberink (1998) to calculate the bed shear stress due to the waves and currents. The wave-related Shields parameter under the wave crest and trough are computed using:

$$\left|\tilde{\theta}_{b,c}\right| = \frac{f_w \hat{u}_c^2}{2\Delta g D_{50}} \tag{11}$$

$$\left|\tilde{\theta}_{b,t}\right| = \frac{f_w \hat{u}_t^2}{2\Delta g D_{50}} \tag{12}$$

where the wave friction factor, f_w, is computed using the formula of Swart (1974).

Following Madsen and Grant (1976), the combined wave-current friction factor is calculated as a linear combination of the wave friction factor and the current friction factor:

$$f_{cw} = \alpha f_c + (1-\alpha) f_w \tag{13}$$

$$\alpha = \frac{\langle u_b \rangle}{\langle u_b \rangle + \hat{u}} \tag{14}$$

where f_c is the current friction factor computed assuming a logarithmic net current profile. The wave crest and trough Shields parameters for the wave-current condition are then:

$$|\theta_{b,c}| = \frac{f_{cw}|u_{b,c}|^2}{2\Delta g D_{50}} \tag{15}$$

$$|\theta_{b,t}| = \frac{f_{cw}|u_{b,t}|^2}{2\Delta g D_{50}} \tag{16}$$

The wave and current roughness height include additional roughness related to the sheet-flow layer in the following way:

$$k_{sc} = \max\left\{3D_{90}, D_{50}\left[1 + 6\left(\langle|\theta|\rangle - 1\right)\right]\right\} \tag{17}$$

$$k_{sw} = \max\left\{D_{50}, D_{50}\left[1 + 6\left(\langle|\theta|\rangle - 1\right)\right]\right\} \tag{18}$$

where $\langle|\theta|\rangle$ is the time-averaged absolute Shields parameter.

Transport contributions

Following an approach as proposed by Dibajnia and Watanabe (1992), we assume that there are four contributions to the sand transport:

$$\Omega_i = \begin{cases} \left(|\theta_{b,i}| - \theta_{cr}\right)^n & \text{if } P_i \le P_{cr} \\ \dfrac{P_{cr}}{P_i}\left(|\theta_{b,i}| - \theta_{cr}\right)^n & \text{if } P_i > P_{cr} \end{cases} \tag{19}$$

$$\Omega_i' = \begin{cases} 0 & \text{if } P_i \le P_{cr} \\ \dfrac{(P_i - P_{cr})}{P_i}\left(|\theta_{b,i}| - \theta_{cr}\right)^n & \text{if } P_i > P_{cr} \end{cases} \tag{20}$$

where $i = c$ (wave crest) or t (wave trough). Ω_c represents the amount of sand that is entrained and transported when the x-component of the velocity vector is positive; Ω_c' represents the amount of sand that is entrained when the x-component of the velocity vector is positive and is transported when the x-component of the velocity vector is negative; Ω_t represents the amount of sand that is entrained and transported when the x-component of the velocity vector is negative; Ω_c' represents the amount of sand that is entrained when the x-component of the velocity vector is negative and is transported

when the *x*-component of the velocity vector is positive. The critical bed shear stress, θ_{cr}, is computed using the formula of Soulsby (1997). Of course $\Omega_i = \Omega_i^{'} = 0$ if $|\theta_{b,i}| \leq \theta_{cr}$.

We take the phase lags in the ripple and sheet-flow regime into account through phase lag parameter *P*, following Dibajnia and Watanabe (1992), Dohmen-Janssen (1999) and Van der Werf et al. (2006):

$$P_c = \frac{\alpha_r \eta}{35 D_{50}} + \frac{\alpha_s \delta_{s,c}}{w_s T_c} \tag{21}$$

$$P_t = \frac{\alpha_r \eta}{35 D_{50}} + \frac{\alpha_s \delta_{s,t}}{w_s T_t} \tag{22}$$

where η is the ripple height, $\delta_{s,c}$ and $\delta_{s,t}$ are the sheet-flow layer thicknesses under the wave crest and trough computed using the formula of Dohmen-Janssen (1999), w_s the fall velocity of suspended sand computed using the formula of Soulsby (1997) and α_r and α_s are fit parameters. The critical phase lag parameter, P_{cr}, has a value of 1. T_c and T_t are the times during which the *x*-component of the velocity is positive (*c*) and negative (*t*), respectively. In what follows, we use the a priori knowledge on the bedform regime (rippled bed or flat bed) and the measured ripple height as input.

The net sediment transport is then computed as follows:

$$\vec{\Phi}_c = \left(\Omega_c + \Omega_t^{'}\right) \frac{\vec{u}_{b,c}}{|u_{b,c}|} \tag{23}$$

$$\vec{\Phi}_t = \left(\Omega_t + \Omega_c^{'}\right) \frac{\vec{u}_{b,t}}{|u_{b,t}|} \tag{24}$$

$$\left\langle \vec{\Phi} \right\rangle = \frac{\left\langle \vec{q}_s \right\rangle}{\sqrt{\Delta g D_{50}^3}} = \frac{m}{T}\left(T_c \vec{\Phi}_c + T_t \vec{\Phi}_t\right) \tag{25}$$

where it is assumed that the transport contributions Ω_c and $\Omega_t^{'}$ are in the direction of the velocity vector $\vec{u}_{b,c}$, and the transport contributions Ω_t and $\Omega_c^{'}$ are in the direction of the velocity vector $\vec{u}_{b,t}$. *m* and *n* are calibration factors.

Calibration

There are four fit parameters: i) phase lag parameter α_s for the plane bed/sheet-flow regime, ii) phase lag parameter α_r for the ripple regime, iii) proportionality coefficient *m*, and iv) power law of the excess Shields parameter *n*. *m* and *n* have the same value in the ripple and sheet-flow regime. *n* is set equal to 1.5 following for example Nielsen (1992) and Soulsby and Damgaard (2005).

In the calibration procedure the coefficient of determination r^2 is optimized. In our case, r^2 represents the quality of fitting a straight line with zero intercept to the measured and predicted net transport values. The calibration procedure is as follows. (i) Tune α_s to find highest r^2 for sheet-flow experiments. (ii) Tune α_r to find highest r^2 for ripple regime experiments. It is necessary that α_s is tuned first, since α_s also affects the net transport rates predicted for rippled bed cases. (iii) Tune m to find highest r^2 for the combined sheet-flow and ripple regime data.

The calibration procedure resulted in the following parameter values: $\alpha_s = 3.3$, $\alpha_r = 0.89$ and $m = 4.2$. Figure 4 shows a comparison between all measured transport rates contained in the santoss database (160 cases) and the transport rates predicted by the santoss model with these parameter settings.

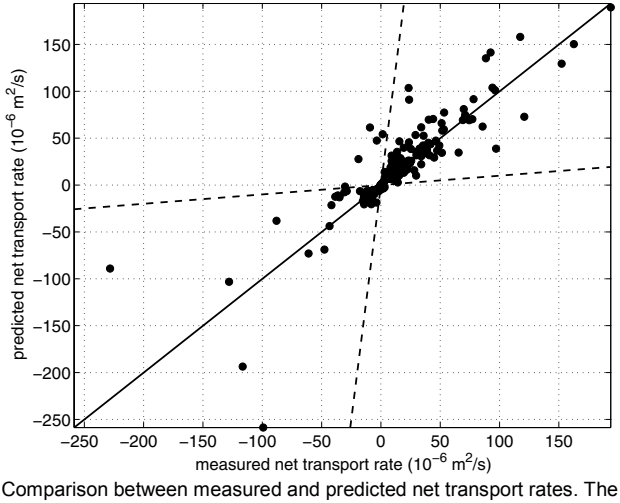

Figure 4. Comparison between measured and predicted net transport rates. The solid line denoted perfect agreement, the dashed lines a factor 10 difference.

The new practical sand transport model shows good agreement with the data. In 71% of the cases it predicts the net transport within a factor 2, in 88% of the cases within a factor 5, and in 91% of the cases within a factor 10.

Comparison with other practical sand transport models

In this section we compare the new model with the practical transport models of Dibajnia and Watanabe (1996) (DW96), Camenen and Larson (2006) (CL06), and Silva et al. (2006) (S06). There is substantial overlap in the data that are used to calibrate these four models.

The data set consisting of 160 different net transport measurements (see Table 1) is randomly divided into two: the first half is used for calibration of the santoss model and

the second part is used for the intercomparison of the DW96, CL06, S06, and the santoss model. In this way, the data sets used for calibration and validation are (at least to a certain extent) independent. This procedure is repeated 100 times. For all 100 times, the santoss model predicts the largest number of cases within a factor 2, 5 and 10. Therefore, we conclude that the santoss model is better capable of predicting the net sand transport rates for this large data set covering a wide range of flow and sand conditions than existing transport models.

It is important that a sand transport model is able to predict the correct behavior of net sand transport as function of important flow and sand parameters. Figures 5-8 show example comparisons between the measured and predicted behavior of the net sand transport as a function of the median grain size D_{50}, flow period T, net current strength $\langle u_b \rangle$, and the root-mean-square orbital velocity $\tilde{u}_{rms}$. Measured data are selected such that only one variable varies and the others are constant or nearly constant. The following coding is used: ia: irregular asymmetric orbital flow; ra: regular asymmetric orbital flow; fb: flat beds; rb: rippled beds. DIB1992 denotes Dibajnia and Watanabe (1992); ODO2004 O'Donoghue and Wright (2004b); RIB1994 Ribberink and Al-Salem (1994); VEA2007 Van der Werf et al. (in press).

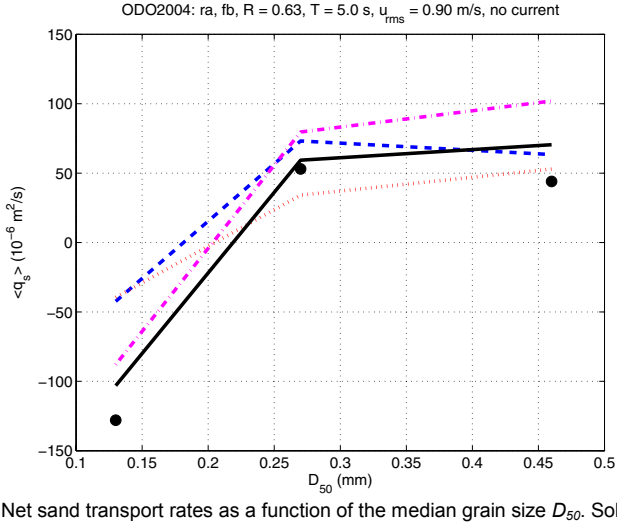

Figure 5. Net sand transport rates as a function of the median grain size D_{50}. Solid circles: measured; dashed line: DW96 model; dotted line: CL06 model; dashed-dotted line: S06 model; solid line: santoss model.

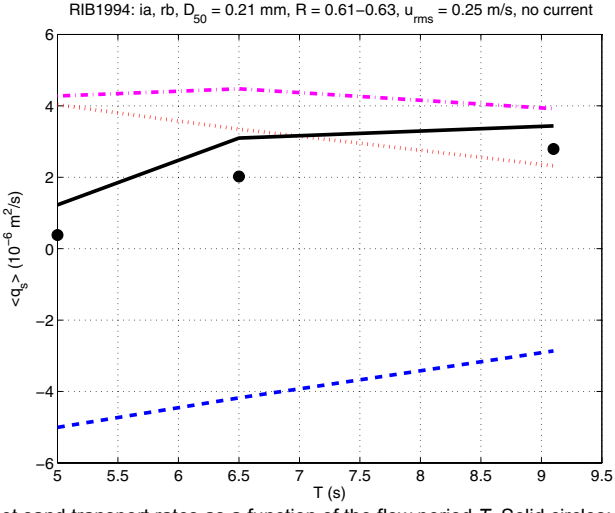

Figure 6. Net sand transport rates as a function of the flow period *T*. Solid circles: measured; dashed line: DW96 model; dotted line: CL06 model; dashed-dotted line: S06 model; solid line: santoss model.

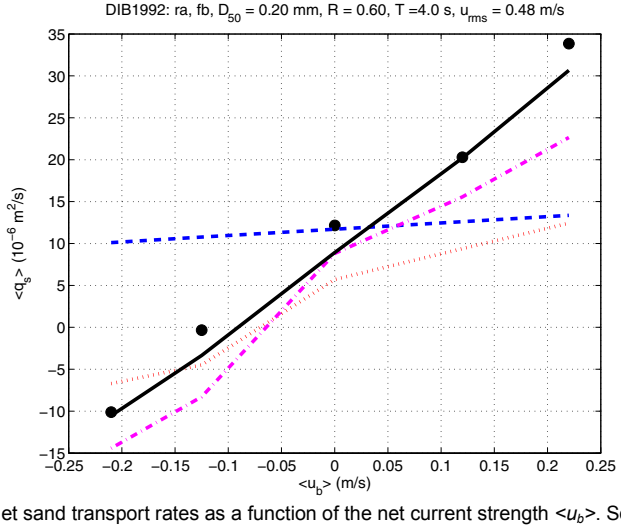

Figure 7. Net sand transport rates as a function of the net current strength $<u_b>$. Solid circles: measured; dashed line: DW96 model; dotted line: CL06 model; dashed-dotted line: S06 model; solid line: santoss model.

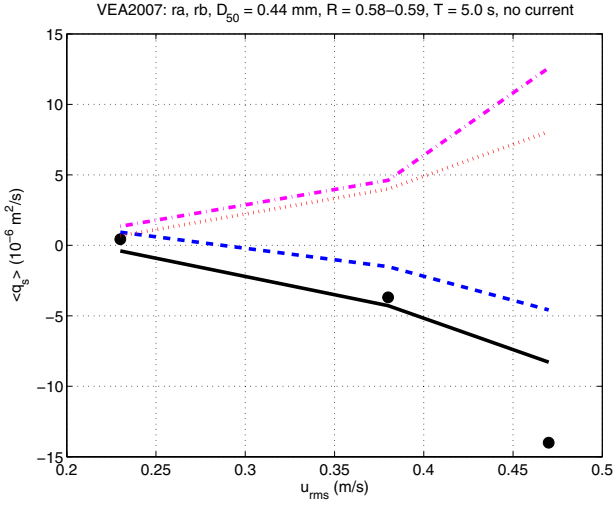

Figure 8. Net sand transport rates as a function of the root-mean-square orbital velocity $\widetilde{u}_{rms}$. Solid circles: measured; dashed line: DW96 model; dotted line: CL06 model; dashed-dotted line: S06 model; solid line: santoss model.

The following observations are made from Figures 5 to 8 and from a large number of similar plots:

- The CL06 and S06 models are (mainly) developed for plane bed, sheet-flow conditions and cannot correctly predict the offshore-directed net transport rates observed in the ripple regime.
- All of the models are able to predict the measured change from onshore to offshore net transport for decreasing grain size in the sheet-flow regime.
- In the rippled bed experiments of RIB1994, net transport decreases with flow period, but stays onshore-directed. Only the santoss model is able to pick up this behavior.
- The influence of the net current on the net transport is well-predicted by the S06 and the santoss models. The DW96 model and, to a lesser extent, the CL06 model underpredict this influence.

CONCLUSIONS

A new practical model for net sand transport induced by non-breaking waves and currents is being developed within the SANTOSS research project. Phase I of model development is reported here.

The main improvements compared to previous practical sand transport models lie in the description of the wave-related sand transport, particularly for cases where phase lag effects are important. The model can deal with regular and irregular oscillatory flows, wave-alone and combined wave and collinear current cases, and flat beds and rippled

beds. Model development uses a large dataset compiled from existing oscillatory flow tunnel experiments involving uniform sediments. The net transport data cover a wide range of full-scale flow periods and wave mobility numbers. In general, the experimental conditions are wave-dominated.

The Phase 1 santoss model has been compared with the semi-unsteady transport models of Dibajnia and Watanabe (1996), Camenen and Larson (2006) and Silva et al. (2006). The santoss model proves to be best capable of predicting both the absolute values of the net sand transport and the behavior of the net sand transport as functions of the median grain size, flow period, root-mean-square orbital velocity and net current strength. Furthermore, the new model is applicable to a larger range of conditions.

Surface wave and acceleration skewness effects will be included in the Phase 2 development of the santoss sand transport model, using new data and insights from new large-scale tunnel and wave flume experiments carried out as part of the SANTOSS project.

ACKNOWLEDGEMENTS

This work has been carried out within the project SANTOSS ('Sand Transport in Oscillatory flows in the Sheet-flow regime') funded by the UK's EPSRC (GR/T28089/01) and the Dutch research organization STW (TCB.6586).

REFERENCES

Bailard, A.A. (1981). An energetics total-load sediment transport model for a plane sloping beach, *J. Geophys. Res.* 86 (C11), 10938-10954.

Bijker, E.W. (1971). Longshore transport computations *J. Waterway, Port, Coast., Ocean Eng.* 97, 687-701.

Camenen, B., and Larson, M. (2006). Phase-lag effects in sheet flow transport, *Coast. Eng.* 53, 531-542.

Davies, A.G., Van Rijn, L.C., Damgaard, J.S., Van de Graaff, J., and Ribberink, J.S. (2002). Intercomparison of research and practical sand transport models, *Coast. Eng.* 46, 1-23.

Dohmen-Janssen, C.M. (1999). *Grain size influence on sediment transport in oscillatory sheet flow. Phase lag and mobile-bed effects*, Ph.D. thesis, University of Twente, The Netherlands.

Dibajnia M., and Watanabe, W. (1992). Sheet-flow under non-linear waves and currents, *Proc. 23rd ICCE*, Venice, Italy, pp. 2015-2025.

Dibajnia, M., and Watanabe, A. (1996). A transport rate formula for mixed sands, *Proc. 25th ICCE*, Orlando, USA, pp. 3791-3804.

Madsen, O.S., and Grant, W.D. (1976). *Sediment transport in the coastal environment*, Technical Report 209, Massachusetts Inst. of Tech., USA.

Nielsen, P. (1988). Three simple models of wave sediment transport, *Coast. Eng.* 12, 43-62.

O'Donoghue, T. and Wright, S. (2004a). Concentrations in oscillatory sheet flow for well sorted and graded sands, *Coast. Eng*. 50, 117-138.

O'Donoghue, T., and Wright, S. (2004b). Flow tunnel measurements of velocities and sand fluxes in oscillatory sheet flow for well-sorted and graded sands, *Coast. Eng.* 51, 1163-1184.

Ribberink, J.S., and Al-Salem, A.A. (1994). Sand transport in oscillatory boundary layers in case of rippled beds and sheet flow, *J. Geophys. Res.* 99(C6), 12707-12727.

Ribberink, J.S. (1998). Bed-load transport for steady flows and unsteady oscillatory flows, *Coast. Eng.* 34, 59-82.

Schretlen, J.L.M., and Van der Werf, J.J. (2006). *SANTOSS Database. Existing data from experiments in oscillatory flow tunnels and large wave flumes*, Report SANTOSS_UT_IR1, University of Twente, The Netherlands.

Silva, P.A. da, Temperville, A., and Santoss, F.S. (2006). Sand transport under combined current and wave conditions: A semi-unsteady, practical model, *Coast. Eng.* 53, 897-913.

Soulsby, R.L. (1997). *Dynamics of marine sands*, Telford, London, UK.

Soulsby, R.L., and Damgaard, J.S. (2005). Bedload sediment transport in coastal waters, *Coast. Eng.* 52, 673-689.

Swart, D.H. (1974). *Offshore sand transport and equilibrium beach profiles*, Delft Hydraulics Publication 131, Delft Hydraulics, The Netherlands.

Van der Werf, J.J. (2006). *Sand transport over rippled beds in oscillatory flow*, Ph.D. thesis, University of Twente, The Netherlands.

Van der Werf, J.J., Ribberink, J.S., O'Donoghue, T, and Doucette, J.S. (2006). Modelling and measurement of sand transport processes over full-scale ripples in oscillatory flows, *Coast. Eng.* 53, 657-673.

Van der Werf, J.J., Doucette, J.S., O'Donoghue, T, and Ribberink, J.S. (in press). Detailed measurements of velocities and suspended sand concentrations over full-scale ripples in regular oscillatory flow, *accepted for publication in J. Geophys. Res. Earth Surface*.

Van Rijn, L.C. (1993). *Principles of sediment transport in rivers, estuaries, and coastal seas*, Aqua Publications, Amsterdam, The Netherlands.

A TOTAL LOAD FORMULA FOR THE NEARSHORE

Benoit Camenen[1] and Magnus Larson[2]

1. Cemagref, 11 bis, quai Chauveau, CP220 F69336 Lyon Cedex 09, France. benoit.camenen@lyon.cemagref.fr
2. Department of Water Resources Engineering, Lund University, Box 118, S22100 Lund, Sweden. magnus.larson@tvr.lth.se

Abstract: A total load sediment transport formula based on recent studies on the bed load and suspended load transport for the nearshore is presented . Phase-lag in the sheet-flow layer or due to ripples, as well as acceleration effects, is included in the formula. A sensitivity analysis is performed to better qualify and quantify the current-related and wave-related sediment transport. It appeared that the prediction of the ripple characteristics is fundamental for a proper estimation of the suspended load in the direction of the waves. For the longshore sediment transport where the current-related total load prevails, the formulas are not as sensitive to ripples.

INTRODUCTION

Accurate prediction of sediment transport rates is an important element in morphological studies for the coastal environment. Most of the existing formulas used in numerical models compute current-related sediment transport only. This component of the sediment transport generally prevails in the longshore direction. However, in the cross-shore direction the waves do not only increase the quantity of sediment available for transport, but they also strongly affect the direction of the sediment transport (Dibajnia and Watanabe, 1992; Ribberink and Al Salem, 1994; Van der Werf and Riberink, 2004). First, asymmetric waves induce onshore wave-related sediment transport. Second, phase-lag in the sediment suspension (which occurs in case of ripples or sheet flow) may reduce the total net sediment transport and even induce a net transport opposite to the wave direction. Ribberink and Al Salem (1994) showed that, assuming the velocity ($u(z)$) and concentration ($c(z)$) equal to a constant part ($\overline{u}(z)$ and $\overline{c}(z)$) and a fluctuating part ($\widetilde{u}(z)$ and $\widetilde{c}(z)$), the net sediment transport rate ($q_{s,net}$) may be written

as the sum of a current-related sediment transport and a wave-related sediment transport according to:

$$q_{s,net} = \int_0^h \bar{u}(z)\bar{c}(z)dz + \int_0^h \tilde{u}(z)\tilde{c}(z)dz \tag{1}$$

where h is the water depth and z a vertical coordinate. Both components of the sediment transport may be significant in the nearshore zone.

A TOTAL LOAD FORMULA

Camenen and Larson (2005a, b; 2006a, b; 2007) proposed a bed load and suspended load formula for the nearshore calibrated with a large amount of data from both laboratory and field measurements, described in the following.

Bed load sediment transport

The bed load transport (q_{sb}) is expressed as follows (Camenen and Larson, 2005a, 2006a):

$$\begin{cases} \dfrac{q_{sb,w}}{\sqrt{(s-1)gd_{50}^{\ 3}}} = a_w \sqrt{\theta_{cw,net}}\,\theta_{cw,m} \exp\left(-b\dfrac{\theta_{cr}}{\theta_{cw}}\right) \\ \dfrac{q_{sb,n}}{\sqrt{(s-1)gd_{50}^{\ 3}}} = a_n \sqrt{\theta_{cn}}\,\theta_{cw,m} \exp\left(-b\dfrac{\theta_{cr}}{\theta_{cw}}\right) \end{cases} \tag{2}$$

where the subscripts w and n correspond, respectively, to the wave direction and the direction normal to the wave direction, s (= ρ_s/ρ) is the relative density between sediment (ρ_s) and water (ρ), g the acceleration due to gravity, d_{50} the median grain size, a_w, a_n and b are empirical coefficients, $\theta_{cw,m}$ and θ_{cw} the mean and maximum Shields parameters due to wave-current interaction, θ_{cn} the current-related Shields parameter in the direction normal to the wave direction, and θ_{cr} the critical Shields parameter for the inception of transport. The net Shields parameter $\theta_{cw,net}$ in Eq. 2 is given by:

$$\theta_{cw,net} = (1-\alpha_{pl,b})\theta_{cw,on} + (1+\alpha_{pl,b})\theta_{cw,off} \tag{3}$$

where $\theta_{cw,on}$ and $\theta_{cw,off}$ are the mean values of the instantaneous Shields parameter over the two half periods T_{wc} and T_{wt} ($T_w = T_{wc} + T_{wt}$, in which T_w is the wave period; *cf.* Fig. 1, where φ is the angle between the wave and the current directions), and $\alpha_{pl,b}$ a coefficient for the phase-lag effects (Camenen and Larson 2006a). The Shields parameter is defined by $\theta_{cw,i} = 1/2 f_{cw} U_{cw,j}^{\ 2} / \left((s-1)gd_{50}\right)$ with f_{cw} being the friction coefficient taking into account wave and current interaction. Madsen and Grant (1976) suggested that f_{cw} could be obtained as a linear combination of f_c and f_w ($f_{cw} = X_v f_c + (1-X_v) f_w$ with $X_v = |U_c| / \left(|U_c| + U_w\right)$ and U_c being the steady current

velocity and U_w the wave orbital velocity amplitude). A constant value on the friction coefficient over the wave period was also assumed when calculating the Shields parameter. Drake and Calantoni (2001), Nielsen (2002, 2006), Antunes Do Carmo *et al.* (2003), and Watanabe and Sato (2004) showed that in general the wave friction coefficient depends also on the acceleration of the fluid near the bottom and thus may strongly influence the direction of the sediment transport in the wave direction. This effect will be discussed later.

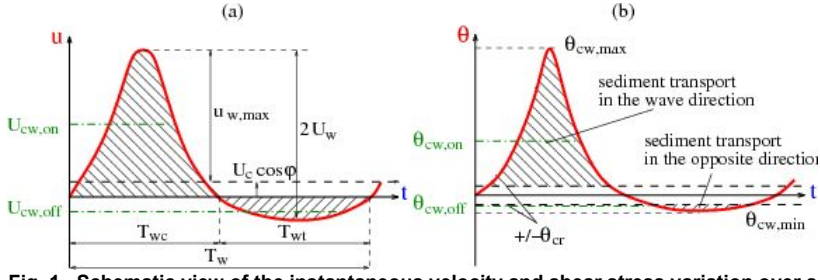

Fig. 1. Schematic view of the instantaneous velocity and shear stress variation over a wave period and in the direction of the waves

Phase-lag effects in the sheet flow layer were included through the coefficient $\alpha_{pl,b} = \alpha_{b,onshore} - \alpha_{b,offshore}$ (Camenen and Larson, 2006a) with:

$$\alpha_{b,i} = \frac{\nu^{0.25} U_{wj}^{0.5}}{W_s T_j^{0.75}} \exp\left[-\left(\frac{U_{w,crsf}}{U_{wj}} \right)^2 \right] \tag{4}$$

where ν is the kinematic viscosity of water, $U_{w,crsf}$ the critical velocity for the inception of sheet flow, and the subscript j should be replaced either by *onshore* or *offshore*.

Suspended load sediment transport

The suspended sediment load (q_{ss}) may be obtained from (Camenen *et al.*, 2005b; Camenen and Larson 2006b, 2007):

$$\begin{cases} q_{ss,w} = U_{cw,net} \dfrac{c_R \varepsilon}{W_s} \left[1 - \exp\left(-\dfrac{W_s h}{\varepsilon} \right) \right] \\ q_{ss,n} = U_c \sin\varphi \dfrac{c_R \varepsilon}{W_s} \left[1 - \exp\left(-\dfrac{W_s h}{\varepsilon} \right) \right] \end{cases} \tag{5}$$

where c_R is the reference concentration at the bottom, W_s the sediment fall speed, ε the sediment diffusivity, and $U_{cw,net}$ the net mean current ($U_{cw,net} = U_c$ for a steady current).

The bed reference concentration is written as follows based on the analysis of a large data set on sediment concentration profiles (see Camenen *et al*., 2005; Camenen and Larson, 2007):

$$c_R = 3.510^{-3} \exp(-0.3 d_*) \theta_{cw,m} \exp\left(-4.5 \frac{\theta_{cr}}{\theta_{cw}}\right) \tag{6}$$

where $d_* = \sqrt[3]{(s-1)g/\nu^2}\, d_{50}$ is the dimensionless grain size. The sediment diffusivity was related to the total energy dissipation, in which the energy dissipation from wave breaking (D_b) and from bottom friction due to current (D_c) and waves (D_w) were added:

$$\varepsilon = \left(\frac{k_c{}^3 D_c + k_w{}^3 D_w + k_b{}^3 D_b}{\rho}\right)^{1/3} h \tag{7}$$

where k_b, k_c and k_w are coefficients with $k_b = 0.01$ corresponding to an efficiency coefficient related to dissipation due to wave breaking, whereas k_c and k_w are associated with the Schmidt number. Assuming the Rouse parabolic profile to be a correct approximation of the vertical sediment diffusivity, its mean value over the depth may be written as follows, for a steady current or non-breaking waves, respectively:

$$\varepsilon_{c/w} = k_{c/w}\left(\frac{D_{c/w}}{\rho}\right)^{1/3} h = \frac{C_w \sigma_{c/w}}{6} \kappa u_{*c/w} h \tag{8}$$

where $\sigma_{c/w}$ is the Schmidt number or the ratio between the vertical eddy diffusivity of the particles ε_v and the vertical eddy viscosity ν_v, $u_{*,c/w}$ is the shear velocity due to current or waves only, respectively, κ von Karman's constant, and $C_w = 1$ in case of current or $C_w = 2/\pi$ in case of waves (this coefficient results from a time-average assuming a sinusoidal wave). Based on the analysis of experimental data, the following expressions were developed for the Schmidt numbers $\sigma_{c/w}$:

$$\sigma_{c/w} = \begin{cases} A_1 + A_2 \sin^2\left(\dfrac{\pi}{2}\dfrac{W_s}{u_{*,cw}}\right) & if\ \dfrac{W_s}{u_{*,cw}} \le 1 \\ 1 + (A_1 + A_2 - 1)\sin^2\left(\dfrac{\pi}{2}\dfrac{u_{*,cw}}{W_s}\right) & if\ \dfrac{W_s}{u_{*,cw}} > 1 \end{cases} \tag{9}$$

where $A_1 = 0.4$ and $A_2 = 3.5$ in case of a steady current only, and $A_1 = 0.15$ and $A_2 = 1.5$ in case of waves only. For wave-current interaction, a weighted value is used for the Schmidt number, $\sigma_{cw} = X_t \sigma_c + (1 - X_t)\sigma_w$ with $X_t = \theta_c / (\theta_c + \theta_w)$ and θ_c being the current Shields parameter and θ_w the wave Shields parameter.

The net current $U_{cw,net}$ is defined in a similar way to the net Shields parameter $\theta_{cw,net}$ in order to take into account a possible sediment transport due to wave asymmetry, as well as phase-lag in the suspended concentration due to ripple effects (Van der Werf and Ribberink, 2004; Camenen and Larson, 2006):

$$U_{cw,net} = (1-\alpha_{pl,s})U_{cw,on} + (1+\alpha_{pl,s})U_{cw,off} \tag{10}$$

where $\alpha_{pl,s}$ is the coefficient describing phase-lag effects on the suspended load and $U_{cw,j}$ is the root-mean-square value of the velocity (wave plus current) over the half period T_{wj} (*cf.* Fig.1), where the subscript j should be replaced either by on (onshore) or off (offshore). In the same way as for the bed load formula, phase-lag effects in the suspended load due the ripples were included through the coefficient $\alpha_{pl,s} = \alpha_{s,onshore} - \alpha_{s,offshore}$ (Camenen and Larson, 2006b) with:

$$\alpha_{s,i} = 0.7\left(\frac{U_{cw,i}}{W_s}\right)^{0.5}\left(\frac{H_r}{T_{wi}W_s}\right)^{0.25}\exp\left[-0.25\left(\frac{P_{WR,cr}}{P_{WR}}\right)^4\right] \tag{11}$$

where $P_{WR} = H_r / d_{50}$ (H_r is the ripple height) is the vortex suspension parameter proposed by Van der Werf and Ribberink (2004) to predict the direction of the net sediment transport. The critical value is reached for approximately $P_{WR} = 100$.

APPLICATION OF FORMULA

Transport by steady current and waves

The proposed formula (Eqs. 2 to 11) was compared to a large set of experimental data with prevailing bed load or suspended load for both field and laboratory measurements, with current only or with waves and current combined (Camenen and Larson, 2005a, b, 2006a, b, 2007). It generally yields the best results with respect to other relationships found in the literature when compared to the compiled data set (*cf.* Tab.1 and previous papers for the description of the data sets). As shown in Tab.1 where the prediction (in %) of the sediment transport within a factor two is presented, an improvement of the results was obtained using Eqs. 2 and 5, especially for the bed load cases and when phase-lag effects start to prevail. For the suspended load, a slightly larger dispersion of the results was observed, but the prediction results were still better for most of the cases. The proposed formula should thus improve the prediction of sediment transport rate in both the longshore and cross-shore directions.

Table 1. Prediction (in %) of total load transport rate within a factor of 2 for different regimes (B: bed load; S: suspended load; C: current; CW: wave and current; SF: sheet flow; and PL: phase-lag)

Authors	B-C	B-CW	SF	S-C	S-CW	S-PL
Bailard (1981)	31	48	45	33	19	1
Dibajnia & Watanabe (1992)	30	38	42	42	22	15
Eq. 2 and 5	78	57	53	37	43	46

Longshore sediment transport

The longshore sediment transport is in general current-related, and the waves act primarily as a stirring agent. As observed by Bayram *et al.* (2001), most of the existing formulas yield similar predictive results, *i.e.*, a cross-shore distribution of the longshore sediment transport that is closely related to the cross-shore distribution of the longshore current. The main difference concerns the magnitude of the sediment transport rate, which may be adjusted trough calibration coefficients. A remaining difficulty to describe in the surf zone is that the total sediment transport is often underestimated on the bar, where the waves break, whereas it is often overestimated in the following trough where the breaking waves change to bores. Also, the longshore sediment transport in the swash zone is often neglected although many observations (Wang *et al.*, 2002; *cf.* also Fig.2) have shown that the magnitude of the longshore sediment transport in the swash might be of the same order as magnitude (or even larger than) the longshore sediment transport over the longshore bar. Baba and Camenen (2007) proposed a simple hydrodynamic model for the swash zone to be able to use the formula presented in this paper. Results of comparison between predictions by the present formula (denoted as the Lund-CIRP formula) and measurements from an experimental case presented by Wang *et al*. (2002) are shown in Fig. 2.

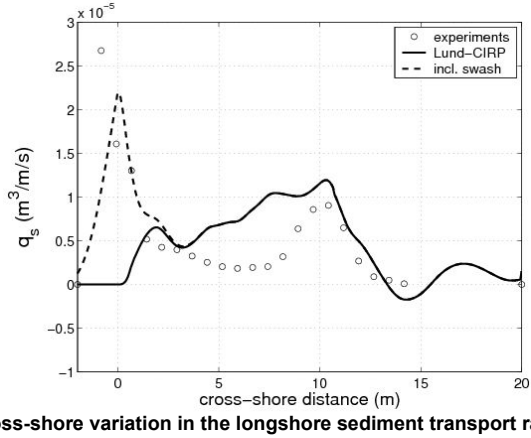

Fig. 2. Cross-shore variation in the longshore sediment transport rate from an experimental case by Wang *et al.* (2002; case 6 with plunging waves)

IMPORTANCE OF WAVE-RELATED TRANSPORT IN CROSS-SHORE DIRECTION

In the cross-shore direction, the current-related sediment transport induces a net transport towards the offshore only (in the direction of the undertow). Including the wave-related sediment transport allows for a possible transport in the onshore direction due to wave asymmetry. However, a complex interaction is obtained that is highly dependent on the bed regime. In case of ripples (offshore zone), the suspended load is prevailing and may be directed offshore due to phase-lag effects, even for strongly

asymmetric waves. In a similar manner, in the case of sheet flow (surf zone), the bed load often prevails and it may also be directed offshore due to the phase-lag effects. As a result the total net sediment transport rate along a cross-shore profile may change direction several times and thus induce a multiple bar system. As all these regimes are highly sensitive to ripple predictions and bed shear stress estimates, significant uncertainties in the calculations are expected.

In order to investigate the sensitivity of the formula in the nearshore, a simple model for the hydrodynamics was developed for a cross-shore line based on Larson and Kraus (2002). It includes the wave evolution and asymmetry (Dibajnia *et al.*, 2001), longshore and cross-shore (mean undertow) depth-averaged currents, bed form characteristics (Van Rijn, 1993; or Soulsby and Whitehouse, 2005; assuming wave ripples prevail), induced current and wave-related bed shear stresses, and total sediment load. In Fig.3, results of the hydrodynamic and sediment transport models are presented for a barred beach and estimates of the total load including (d) or not (c) the phase-lag effects, using the Van Rijn formulas (1993) for the ripple characteristics. The roughness height in presence of ripples was calculated with the Kim (2004) formula.

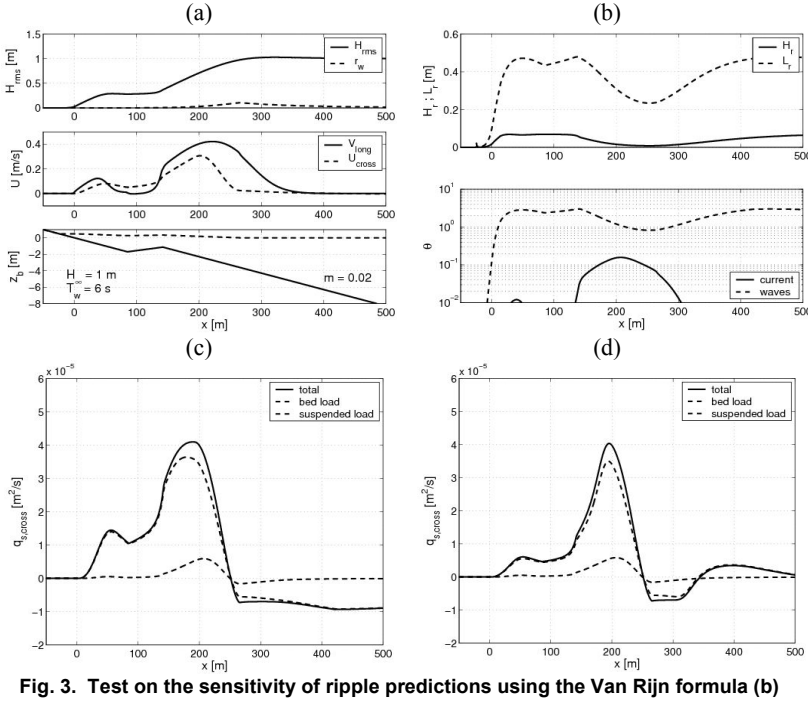

Fig. 3. Test on the sensitivity of ripple predictions using the Van Rijn formula (b) and the induced total load formula with (d) and without (c) the phase-lag effects for typical beach and hydrodynamic conditions (a)

When no phase-lag effects are included, the sediment transport is controlled by the balance between the undertow (which leads to offshore sediment transport) and the wave asymmetry (which leads to onshore sediment transport). If the undertow effects prevail in the surf zone, the wave asymmetry prevails in the offshore zone (cf. Fig.3(c)). A second observation is that the suspended load dominates over the bed load everywhere on a cross-shore line, even in the zone where the ripples are washed out. Fig.3(c) and (d) show how significant the influence of the phase-lag is on the suspended load. Two phenomena occur: First, a reduction of the total sediment flux is observed in the surf zone. Some phase-lag effects are observed since the offshore velocity is larger than the onshore velocity (because of the undertow). This phenomenon may, however, be unrealistic and only an artifact of Eq.11 which allows negative values on $\alpha_{pl,s}$. Second, strong phase-lag occurs in the offshore zone due to the ripples which leads to an opposite direction for the net sediment transport compared to the case when no phase-lag effects are included.

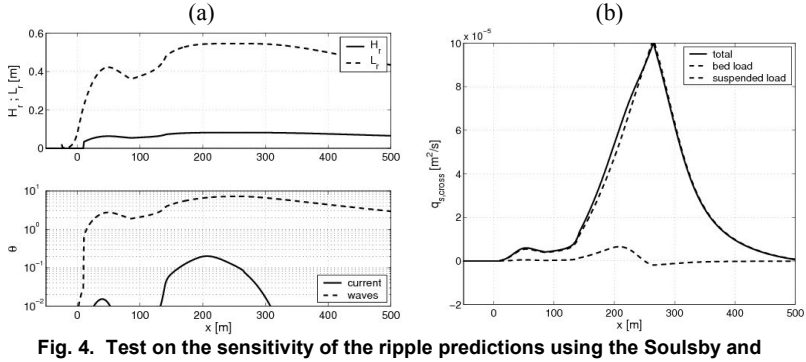

Fig. 4. Test on the sensitivity of the ripple predictions using the Soulsby and Whitehouse formula (a) and the induced total load formula with the phase-lag effects (b) for the same conditions as in Fig.3.

Using the Soulsby and Whitehouse (2005) formulas for the prediction of the ripple characteristics, the results are similar as for the Van Rijn (1993) formula, if the phase-lag effects are not included. However, the presence of ripples on the bar as predicted by the Soulsby and Whitehouse (2005) formula seems unrealistic and induces larger values for the Shields parameter and the suspended load over the bar (cf. Fig. 4(a)). When the phase-lag effects are included, since the Soulsby and Whitehouse formula predicts larger ripple heights on the seaward side of the bar, the phase-lag effects on the suspended load is also stronger. The direction of the net sediment transport is now offshore everywhere on the cross-shore profile. Thus, it seems that the estimate of the ripple characteristics strongly affects the prediction of the net suspended load (and then total load), especially when phase-lag effects are included. The predictors for the ripples characteristics over the domain have to be carefully chosen. Estimation of ripple washout appears to be one of the key issues to improve the prediction of sediment transport in the cross-shore direction.

IMPROVEMENT AND APPLICATION OF FORMULA IN INNER SURF ZONE AND SWASH ZONE

Because of the wave transformation in the surf zone, the wave change to a bore which induces a different velocity profile in the inner surf zone and swash zone (saw-tooth shaped). The asymmetry in the amplitude of the onshore and offshore parts of the velocity may be negligible ($r_w = 0$), but an asymmetry appears in the acceleration profile due the saw-tooth shaped velocity profile (cf. Fig. 5). This asymmetry may be defined with the coefficient $R_{ac} = T_{cu} / T_{cd}$ (for relatively simple wave velocity profile where $r_w = 0$, $R_{at} = T_{tu} / T_{td} = R_{ac}$). On the contrary to T_{wc} and T_{wt}, T_{cu}, T_{cd} T_{tu}, and T_{td} are not function of the steady current U_c and $T_{cu} + T_{cd} + T_{tu} + T_{td} = T_w$. In that sense, the proposed definition slightly differs from the definition proposed by Watanabe and Sato (2004). Watanabe and Sato (2004) observed that an increase in the acceleration asymmetry yields an increase in the suspension at the maximum velocity. They attributed this effect to an increase in the effective near-bed velocity. To treat this problem, Nielsen (2002, 2006) introduced a phase shift between the free stream velocity and the bed shear stress at the peak frequency. This so called "time domain filter method" yields an increase in the instantaneous bottom shear stress for the accelerated part of the flow.

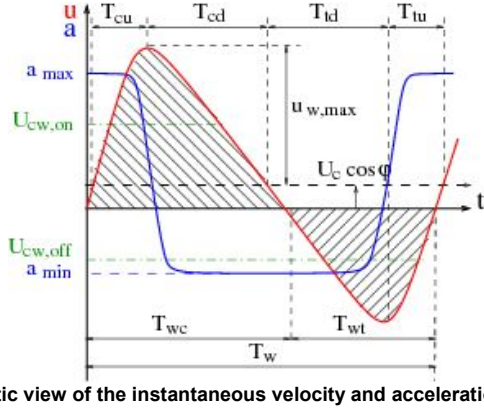

Fig. 5. Schematic view of the instantaneous velocity and acceleration variation for a bore over a wave period and in the direction of the waves

To introduce the effects of the acceleration asymmetry in the bed load formula (Eq. 2), the friction coefficient for wave-current interaction f_{cw} (used for the calculation of the mean shear stress $\theta_{cw,on}$ and $\theta_{cw,off}$) may be modified, assuming that f_{cw} is time-dependent. This modification relies on the assumption that an accelerated flow combined with an increasing velocity yields an increase in the instantaneous friction coefficient (compared to its time-averaged value); an accelerated flow combined with an decreasing velocity yields a decrease in the instantaneous friction coefficient. Eq.3 is thus rewritten:

$$\theta_{cw,net} = (1-\alpha_{pl,b})(1+\alpha_a)\theta_{cw,on} + (1+\alpha_{pl,b})(1-\alpha_a)\theta_{cw,off} \tag{12}$$

where α_a is a coefficient that is a function of R_{ac}. Using the data provided by Watanabe and Sato (2004), the following relationship is proposed:

$$\alpha_a = \frac{1-R_{ac}}{1+R_{ac}} \tag{13}$$

In Fig. 6 is a comparison between the predicted and measured values presented using Eqs.12 and 13 and the experimental data by Watanabe and Sato (2004). About 65% of the data are correctly predicted within a factor two allowed. Even if α_a may also be a function of the medium grain size and the wave period, Eq.13 already yields improved results.

As observed by Nielsen (2006), such an approach requires wave-by-wave analysis for irregular waves which is not very convenient for a simple nearshore model. As a first approximation, a constant value for R_{ac} may be employed also for the case of irregular waves.

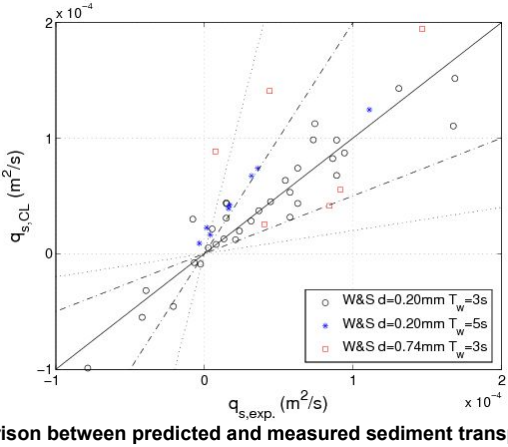

Fig. 6. Comparison between predicted and measured sediment transport rate using Eqs. 2, 12 and 13, and the experimental data from Watanabe and Sato (2004), which illustrates the influence of the acceleration asymmetry

In the same manner as Dibania *et al.* (2001) proposed an empirical relationship for the wave asymmetry across the surf zone (based on a large experimental data set), there is a need of a relationship to estimate the acceleration asymmetry across the surf zone and the swash zone. This latter quantity may be estimated using experimental data and numerical Boussinesq-type wave models.

CONCLUSIONS

A total load sediment transport formula is presented based on recent studies on the bed load and suspended load transports for the nearshore. Phase-lag in the sheet-flow layer or due to ripples, as well as acceleration effects, is included in the formula. This total load formula yields the best results among the studied formulas using a large data set of laboratory and field measurements for various regimes where bed load or suspended load prevails and with possible phase-lag effects in the sheet-flow layer or over the ripples. The formula also appeared to be applicable in the swash zone thanks to a simple hydrodynamic model.

A sensitivity analysis was performed to better qualify and quantify the current-related and wave-related sediment transport. It appeared that the prediction of the ripple characteristics (and the phase-lag effects over the ripples) is fundamental for a proper estimation of the suspended load in the direction of the waves. The ripple washout criterion may be one of the key issues. For the longshore sediment transport where the current-related total load prevails, the formulas are not as sensitive. Some improvement may be made for the effects of the breaking waves and rollers on the suspension.

Finally, the formula was improved to include the effects of a possible acceleration asymmetry in the wave velocity profile. The formula yields correct results compared to the experimental data by Watanabe and Sato (2004). There is however a need of a simple model to estimate the acceleration asymmetry across the surf zone and the swash zone.

ACKNOWLEDGEMENTS

This work was in part conducted under the Inlet Modeling SystemWork Unit of the Coastal Inlets Research Program, U.S. Army Corps of Engineers, and the Japanese Society for the Promotion of Science.

REFERENCES

Antunes Do Carmo, J., Temperville, A. and Seabra-Santos, F. (2003), "Bottom friction and time-dependent shear stress for wave-current interaction", *J. Hydraulic Research* 41(1), 27-37.

Baba, Y. and Camenen, B. (2007), "Importance of the swash longshore sediment transport in morphodynamic models", in *Proc. Coastal Sediments'07*, ASCE, New Orleans, Louisiana, USA.

Bailard J.A. (1981), "An energetic total load sediment transport model for a plane sloping beach" *J. Geophysical Research* 86(C11), 10938-10954.

Bayram A., Larson, M., Miller, H.C., and Kraus N.C. (2001), "Cross-shore distribution of longshore sediment transport: comparison between predictive formulas and field measurements" *Coastal Engineering* 44, 79-99.

Camenen, B. and Larson, M., (2005a). "A bedload sediment transport formula for the nearshore" *Estuarine, Coastal and Shelf Sciences* 63, 249-260.

Camenen, B., Larson, M. and Yamashita, T. (2005b), "A suspended load formula for the nearshore", in *Proc. 52nd Japanese Coastal Eng. Conf.*, JSCE, Aomori, Japan, pp. 381-385. (in Japanese).

Camenen, B. and Larson, M., (2006a). "Phase-lag effects in sheet flow transport" *Coastal Engineering* 53, 531-542.

Camenen, B. and Larson, M., (2006b). "A suspended load formula over rippled bed" Proc. 30th Int. Conf. Coastal Eng., ASCE, San Diego, California, USA.

Camenen, B. and Larson, M., (2007). "A suspended load sediment transport formula for the nearshore" accepted in *J. Coastal Research*.

Dibajnia, M. and Watanabe, A. (1992)"Sheet flow under nonlinear waves and currents" in *Proc. 23rd Int. Conf. Coastal Eng.*, ASCE, Venice, Italy, 2015-2029

Dibajnia, M., Moriya T. and Watanabe, A. (2001) "A representative wave model for estimation of nearshore local transport rate" *Coastal Engineering Journal* 43(1), 1-38

Drake, T. and Calantoni, J. (2001), "Discrete particle model for sheet flow sediment transport in the nearshore", *J. Geophysical Research* 106(C9), 19859-19868.

Kim H. (2004) "Effective form roughness of ripples for waves" *J. Coastal Research* 20(3), 731-738

Larson, M. and Kraus, N.C., (2002). *"NMLONG: Numerical Model for Simulating Longshore Current; Report 2: wave-current interaction, roller modeling, and validation of model enhancements",* CHETR-02-22, Coastal and Hydraulics Laboratory, U.S. Army Corps of Engineers, Vicksburg, Mississippi, USA

Madsen, O. and Grant, W. (1976), Sediment transport in the coastal environment, Technical Report 209, M.I.T., Cambridge, Massassuchetts, USA.

Nielsen P. (2002) "Shear stress and sediment transport calculations for swash zone modeling" *Coastal Engineering* 45, 53-60

Nielsen P. (2006) "Sheet flow sediment transport under waves with acceleration skewness and boundary layer streaming" accepted in *Coastal Engineering*

Ribberink, J. and Al Salem, A. (1994), "Sediment transport in oscillatory boundary layers in cases of rippled beds and sheet flow" *J. Geophysical Research* 99(C6), 707-727.

Soulsby R.L., and Whitehouse R.J.S.W. (2005) "*Prediction of ripple properties in shelf seas: Mark 1, Predictor*", TR 150, Wallingford, UK

Van der Werf J. and Ribberink, J. (2004), "Wave induced sediment transport processes in the ripple regime", in *Proc. 29th Int. Conf. Coastal Eng.*, ASCE, Lisbon, Portugal, 1741-1753.

Van Rin, L.C. (1993), "*Principles of sediment transport in rivers, estuaries and coastal seas*", Aqua Publication, The Netherlands

Wang P., Ebersole B.A. and Smith E.R. (2002) "*Longshore sand transport - Initial results from large-scale sediment transport facility*", CHETN-II-46, Coastal and Hydraulics Laboratory, U.S. Army Corps of Engineers, Vicksburg, Mississippi, USA

Watanabe A. and Sato, S. (2004), "A sheet-flow transport rate formula for asymmetric, forward-leaning waves and current", in *Proc. 29th Int. Conf. Coastal Eng.*, ASCE, Lisbon, Portugal, 17031-1714.

LONGSHORE SAND TRANSPORT RATE MEASUREMENTS USING SMALL-SCALE PHYSICAL MODELS

Roshan Suminda Ranasinghe[1] and Shinji Sato[2]

1. Doctoral student, Department of Civil Engineering, 7-3-1, Hongo, Bunkyo-ku, The University of Tokyo, Tokyo, 113-8656, Japan.
   sumindar@coastal.t.u-tokyo.ac.jp
2. Professor, Department of Civil Engineering, 7-3-1, Hongo, Bunkyo-ku, The University of Tokyo, Tokyo, 113-8656, Japan.
   sato@coastal.t.u-tokyo.ac.jp

Abstract: Small-scale laboratory experiments were conducted to investigate the total and the cross-shore distribution of longshore sand transport rate on long straight beaches of uniform grain size under monochromatic waves. An efficient trap system was introduced to collect the sediments transported alongshore. Substantial peak in the distribution of longshore sand transport rate was observed in the swash zone, in addition to the peak at the breaker zone under relatively strong plunging breakers. The cross-shore distribution of longshore sand transport rate was found to be dependent on the profile of the beach and the period of the waves, which controlled the breaker type.

INTRODUCTION

The breaking waves in nearshore combined with various nearshore currents transport beach sediments. Under certain conditions, it is only a local rearrangement of sediments in cross-shore direction, *e.g*., normal and storm beach profiles. The sand transport, which is found to occur parallel to the coast within the surf zone is defined as longshore sand transport. Cross-shore gradient of the longshore momentum flux generated by wave breaking process sets up longshore current and considered to be the major driving force of the longshore sand transport (hereafter LST).

If the LST rate is uniform in the longshore direction, the beach should become stable and fall into dynamic equilibrium state, i.e., beach profile will not change, while sediments

are still transported in longshore direction; hence any variation of LST rate could be a major factor, which governs erosion or accretion along a coast. In this sense, it is essential to obtain a better understanding of LST process in both qualitative and quantitative terms for most of the coastal engineering applications such as shoreline evolution behind structures, dredging of navigation channels etc. Not only the prediction of total transport rate but also its cross-shore distribution is desired to describe the morphological change in the vicinity of coastal structures and shoreline response behind them accurately.

The primary objective of this study is to investigate the sensitivity of beach profile and incident wave period to cross-shore structure of LST rate and to describe sediment movement mechanism on beaches, where the bed load dominates the suspended load.

EXPERIMENTAL METHODS

Experimental set-up

Experiments were performed in a wave basin with dimensions 11m x 6.5m x 0.3m using obliquely incident monochromatic waves. The wave basin was equipped with wave paddles capable of generating multi-directional random waves. The system could be run with the "reflection absorption mode" that was designed to cancel reflection from the wave generating boards. To minimize wave reflection from the downdrift end boundary of the wave basin, a "sponge layer" with 0.5m in width was provided as sketched in Fig. 1 (not drawn to scale).

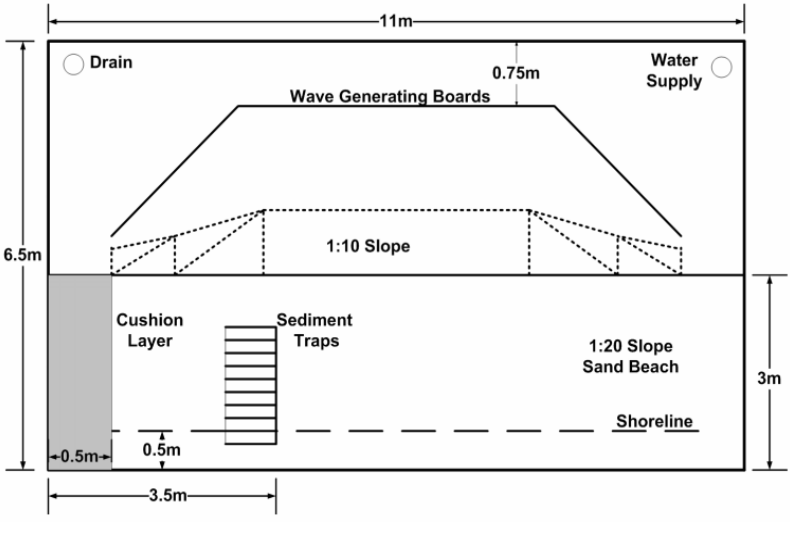

Fig. 1 Wave basin set-up

Each experiment was divided into three 15-minute segments. During the first segment, waves were generated without any measurement being taken, to allow the beach to reach a stable profile. Then wave heights and current velocities were measured during next two segments, respectively. No sand recharge was carried out during the experiments as no significant alongshore variation in the beach profile was observed during these experiments.

Beach profile preparation

To obtain the rate of LST and its cross-shore distribution accurately, it was necessary to maintain straight and parallel depth contours throughout the model beach, as beaches having three-dimensionality tend to change nearshore waves and longshore currents, and subsequently sediment transport.

Material used in the experiments was well-sorted fine quartz sand of $D_{50} = 0.2$ mm. The area of 10m x 3m was filled with sand to an average depth of 4cm over the 1/20 uniform slope. The beach slope was 1/20 for the entire area except for the foreshore portion of swash motion, which was kept at 1/7.5. The height of the berm was selected so that the maximum excursion of wave run-up in the swash zone would not reach the highest elevation of the berm. It was desirable to introduce a 2-D berm artificially to the beach, in order to avoid three-dimensional evolution of topography. On the other hand, it was also necessary to reduce the time for the beach to reach a realistic profile (concave shape). The foreshore slope (1:7.5) was evaluated after several tests for 2-3 hours of wave action starting with an initial plane beach of 1:20 slope (preliminary movable bed experiments).

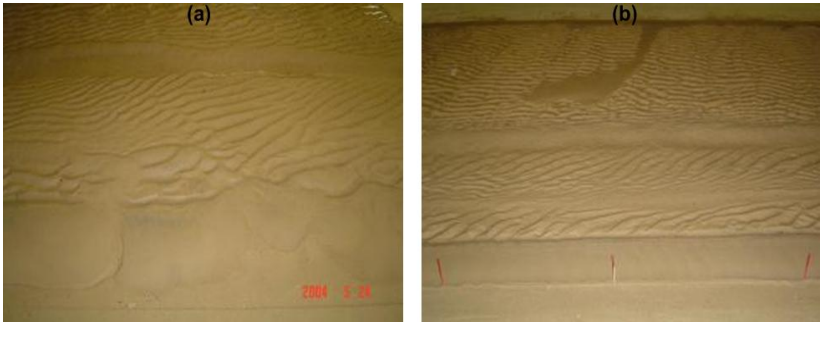

Fig. 2 Resulted bottom topography (a) without an initial berm after 2 hours (3-Dimensional beach) (b) with an initial berm behind the foreshore portion after 45 minutes.

Wave height and longshore current velocity measurements

Wave heights were recorded using capacitance type wave gauges (two gauges were mounted on the bridge with 25cm interval in the alongshore direction) and the cross-shore distribution of longshore current was measured using electromagnetic current meters (EMC). The current meter was located at one third of the water depth from the

bottom, which was near the elevation of the depth-averaged current velocity in the case of a logarithmic velocity profile.

Wave direction at the breaking point was estimated from the phase lag between the two wave gauges and compared with that obtained using EMC meter, in which wave direction was determined from linear regression of cross-shore water particle velocity vs. longshore water particle velocity plot.

Sediment collection

It was important to introduce a reliable technique to measure the cross-shore distribution of LST rate. Three standard techniques are used worldwide in field namely, sand tracers, long and short time impoundments and streamer traps. However, a buried type of trap system was found to be the only feasible technique to serve this purpose, having evaluated the available laboratory conditions and resources. The best geometry and the structure of the trap were determined through a laborious trial and error method.

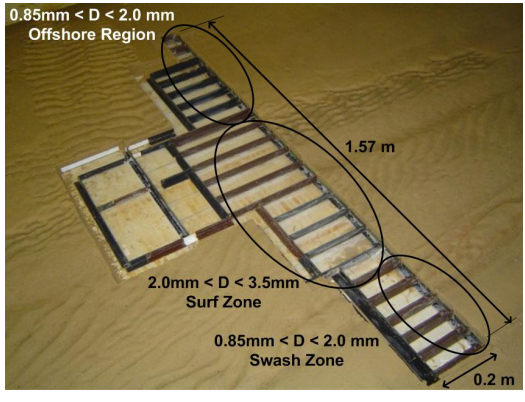

Fig. 3 Buried type of trap system.

The trap system (see Fig. 3) was installed in the centre of the wave basin, as it was impossible to keep it at the furthest point of downdrift side, due to the boundary effect of the wave basin. The boundary between the trap and the sand bed was found to be highly sensitive to the sand movement. If the trap boundary was higher than the sand bed level, it would underestimate sand volume due to the obstruction caused by the boundary. It could even divert the current offshore and at the same time caused scour at the boundary. On the other hand, if the trap boundary was lower than the bed level, it might over-predict sand movement. Therefore, the rigid boundary of the trap had to be lower than the lowest level of the sand bed, while the remaining portion was covered with a flexible material.

First, the trap was emptied prior to sediment collection. The offshore portion of the trap was then filled with a coarser material (0.85mm< D_{50} <2.0mm) to eliminate any over-

prediction due to orbital motion of sand particles. Here the minimum diameter of the coarser material needed to be larger than the maximum diameter of the fine sand. Sediment of similar size (0.85mm< D_{50} <2.0mm) was used within the trap situated in the swash zone, as swash motion was highly sensitive to the sediment size due to the relatively smaller scale fluid motion there. The remaining area of the trap was covered with an aluminum mesh to allow sufficient space for the sand to get collected and was leveled with a much coarser material of mean diameter (2.0mm< D_{50} <3.5mm), leaving sufficient space for the sand to be trapped without being bypassed over the trap. Materials inside each trap cell were sieved and fine sand was separated from coarse sand after the action of waves over a known sampling period. This fine sand was then dried and weighed to calculate the sand transport rate.

Repeatability of test results

It was necessary to reproduce the results under the same wave condition to confirm the reliability of sand transport rate measurements. Fig. 4 shows the average beach profile and cross-shore distribution of LST rate for wave condition SW4E (see Table 1) in two different tests. Only minor differences could be observed in average beach profiles and sand transport rates confirming the repeatability of the tests and the reliability of the buried trap system for sediment collection.

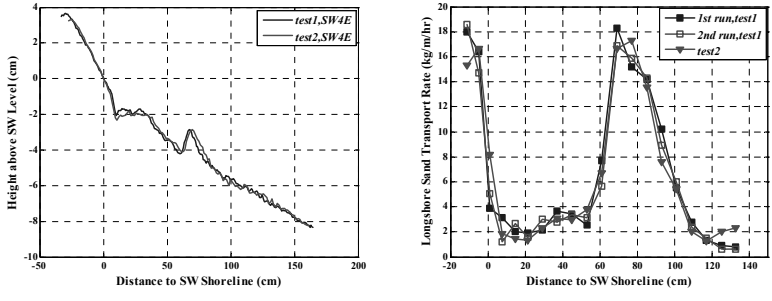

Fig. 4 Repeatability of test results.

RESULTS & DISCUSSION

Introduction

In LST, sand grains are set in motion mainly by wave action and carried by longshore current. Despite many research outputs are available on total LST rate, only few are reliable on the cross-shore distribution. In this study, monochromatic incident waves were used to obtain LST rates and its distributions for different wave conditions (see Table 1, in which wave conditions with subscript *board* stands for the condition at wave generating boards, *b* for breaking condition and 0 for deepwater condition). Each test was conducted with a water depth of 0.24m at the wave generating boards. In the present

study, bottom slope at the breaking point (m_b) is defined as the slope between the breaker line and the still water shoreline.

Wave height distribution and the average beach profile associated with all the tests are shown in Fig. 5, where SW1E, SW2E, SW4E, SW7E, SW8E were conducted on barred concave beach profiles with steep foreshore slope and SW4U on uniform beach profile of 1/18 slope.

Table 1. Longshore Sand Transport Experiment Wave Conditions

Experiment		SW1E	SW2E	SW4E	SW4U	SW7E	SW8E
Wave Height (cm)	H_{board}	3.8	3.4	3.4	3.4	3.4	4.0
	H_0	4.2	3.7	3.6	3.6	3.7	4.3
	H_b	5.4	5.0	5.6	5.7	4.8	6.6
Wave Period (s)	T	1.0	1.0	1.25	1.25	1.0	1.25
Water Depth (m)	h	0.24	0.24	0.24	0.24	0.24	0.24
Wave Angle (deg)	θ_{board}	20	15	20	20	30	16
	θ_b	13.4	6.7	11.8	13.1	15.0	9.9
Breaker Index	γ_b	0.83	0.98	0.98	1.00	0.99	1.02
Breaker Slope	m_b	0.054	0.054	0.057	0.055	0.053	0.055
Surf Similarity Parameter	ξ_0	0.33	0.35	0.47	0.45	0.34	0.41
	ξ_b	0.29	0.30	0.38	0.36	0.30	0.33
Breaker Type		WPL	WPL	PL	PL	WPL	PL

* WPL – Weakly Plunging; PL – Plunging.

In test cases SW1E, SW2E and SW7E, wave breaking was weakly plunging as it could be seen by the formation of mild bars. At the incipient breaking point, energy dissipation was found to be less dynamic. However, secondary wave breaking occurred in the mid surf zone particularly in SW1E and SW2E, creating prominent intermediate bars. In SW4E, SW4U and SW8E, waves broke by plunging as evident by the formation of substantial alongshore bars and troughs (except SW4U). In addition, bar type formations were observed in the mid surf zone in all cases, which resulted by the induced mass transport cells under partial standing waves (significant wave reflection was observed in all the tests, which led to node/anti-node phenomenon across the surf zone, see Fig 6).

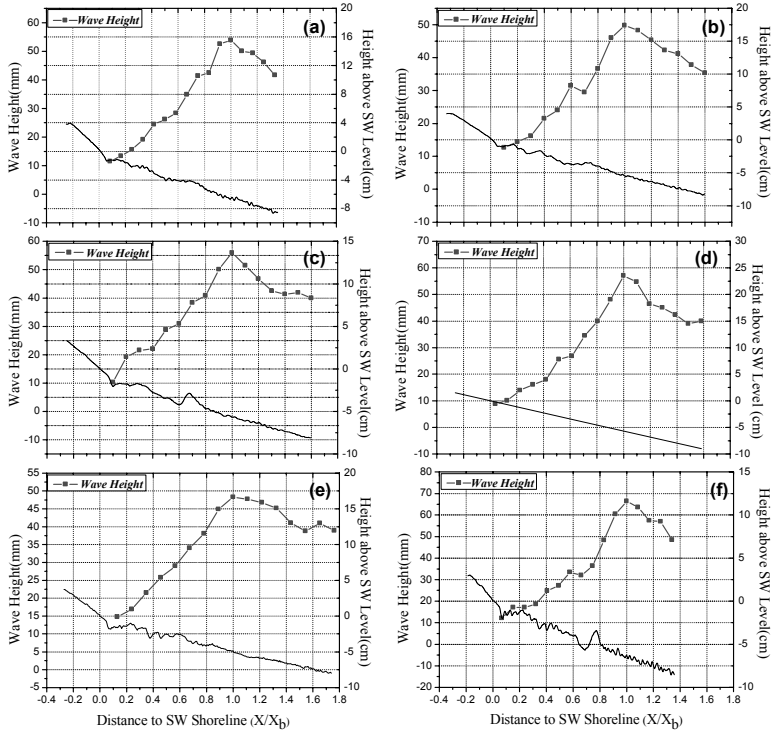

Fig. 5 Wave height distribution and the beach profile across the surf zone associated with (a) SW1E (b) SW2E (c) SW4E (d) SW4U (e) SW7E (f) SW8E

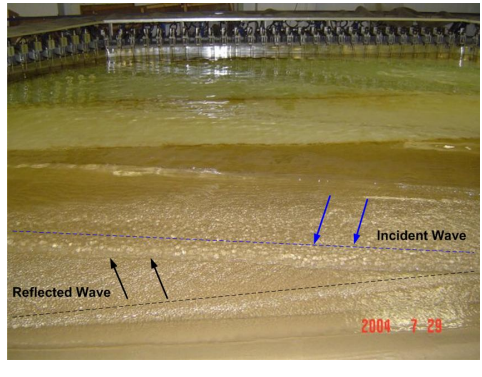

Fig. 6 Wave reflection from the steep foreshore

Cross-shore distribution of longshore sand transport rate

The cross-shore distributions of longshore current velocity for all the tests except SW8E (unexpected error occurred during the measurement of longshore current) are shown in Fig. 7. Interestingly peaks were observed just shoreward of the incipient breaker point bars in all the tests and prominent secondary peaks were observed shoreward of intermediate bars in SW1E and SW2E.

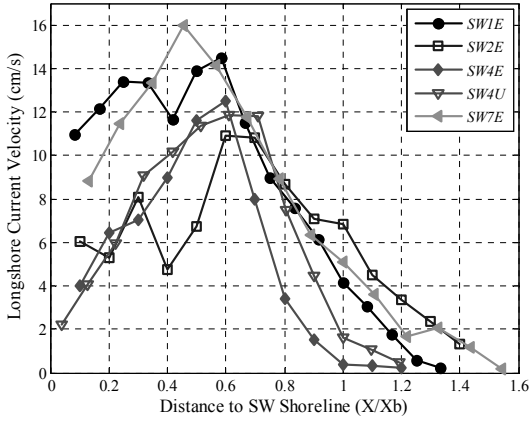

Fig. 7 Cross-shore distributions of longshore current velocity

Generally, the cross-shore gradient of the radiation stress and that of the longshore momentum flux due to the surface roller are thought to be the driving forces of the longshore current. The energy of the wave motion is first transferred to the surface roller energy, and then the energy is dissipated. Accordingly, the peak of the cross-shore gradient of the momentum flux due to the surface roller is located shoreward of the peak of the gradient of the radiation stress. As a result, when the cross-shore gradient of the momentum flux due to the surface roller is comparable to that of the radiation stress, the peak of the longshore current velocity is shifted shoreward. However, Reniers and Battjes (1997) suggested that surface roller effect can at most cause a relatively minor shift of the longshore current velocity maximum away from the bar crest. Further they concluded that longshore inhomogeneities in the bathymetry and wave field might result in longshore pressure gradients, which leads to this shoreward shift of longshore current velocity peak (Putrevu et al., 1995).

The cross-shore distribution of measured LST rates for all the tests are shown in Fig. 8. At incipient breaking, a substantial peak in the distribution of LST rate was found for SW4E, SW4U and SW8E, which were the plunging breaker wave cases. The turbulence associated with the plunging waves (due to the curl of water) penetrated deep into the water column, impacted the bed, and caused sand to be suspended and transported by the longshore current. In SW1E, SW2E and SW7E, the main breaker type was found to be

weakly plunging and some turbulence associated with this breaking caused relatively small peaks in the cross-shore distribution of LST rate at the incipient breaking.

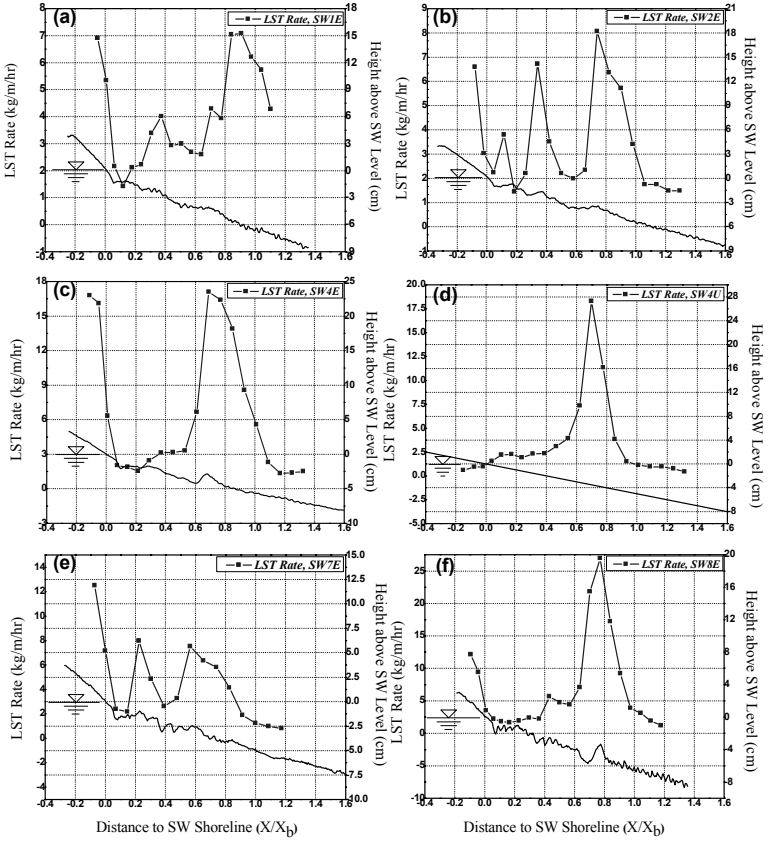

Fig. 8 Cross-shore distribution of longshore sand transport rate in cases (a) SW1E (b) SW2E (c) SW4E (d) SW4U (e) SW7E (f) SW8E

It is often believed that the sediment flux in mid surf zone is mainly controlled by the water depth; hence, wave height is the dominant parameter over wave period. In that sense, if a gradual decay of wave height is observed, less sediment flux can be expected in mid surf zone. However due to the secondary breaking, peaks were found in the cross-shore distribution of LST rate in mid surf zone for SW1E and SW2E (peak just shoreward of the peak at incipient breaking) and the secondary peaks in the longshore current velocity distribution complimented them. In addition, another peak of LST rate was found offshoreward of the peak in swash zone for SW2E and SW7E, apparently at

the bar (which formed under partial standing waves) due to the sediment mobility at the bar (anti-node) and low water depth. It is interesting to note that, substantial peak in the distribution of LST rate was observed at the swash zone (the region where run-up & run-down of waves are observed) in all the cases except SW4U.

No significant difference was observed in the wave height and longshore current distributions between SW4E (concave beach profile with steep foreshore slope) and SW4U (uniform beach slope). However prominent differences were noticed in the longshore sand transport distribution at the swash zone and the breaker zone. Substantial peak in the LST rate distribution was not observed in SW4U compared to SW4E at swash zone. This was mainly due to the mild foreshore slope in SW4U. Peak of the distribution in LST rate around the breaker point for SW4U was found to be slightly higher than that of SW4E, possibly due to the intensive cross-shore sand transport at the plunging point until it reached some near equilibrium to a bar and trough formation. On the other hand, the peak of the LST rate distribution of SW4E was found to be broader (offshoreward of breaker zone peak) than that of SW4U due to the difference of bed forms, as the suspended sediments over ripple bed, which were carried by longshore current, enhanced the sand transport rate in SW4E.

Total longshore sand transport rate

The total LST rates (dry mass rate) were calculated by summing up the sediment fluxes measured in all the trap cells and are listed in Table 2.

Table 2 Measured and Computed LST Rates

	SW1E	SW2E	SW4E	SW4U	SW7E	SW8E
Measured total LST rate (kg/hr)	5.98	5.00	9.66	5.36	5.34	10.96
Calculated total LST rate (kg/hr) by Kamphuis (1991) formula (dry mass rate)	22.38	14.46	30.66	34.89	17.74	37.06

Among the numerous formulae for predicting longshore sediment transport (derived using energetic, force balance or dimensional analysis method), the one derived by Kamphuis (1991) was used to compare the results obtained in the present study. This formula was developed after extensive model studies and has been applicable to prototype sandy beaches (see Fig. 9).

The Kamphuis (1991) formula in dimensionless form is expressed as follows:

$$\left(\frac{Q_u}{\rho H_{sb}^3 / T_p}\right) = 1.3x10^{-3}\left(\frac{H_{sb}}{L_{op}}\right)^{-1.25} m_b^{0.75}\left(\frac{H_{sb}}{D_{50}}\right)^{0.25} \sin^{0.6}(2\alpha_b) \qquad (1)$$

where Q_u is the underwater mass of transported sand, ρ is the density of fluid, H_{sb} is

the significant breaking wave height, T_p is the peak wave period, D_{50} is the median grain diameter, m_b is the beach slope at wave breaking, and θ_b is the breaking wave angle.

Wang et al. (2002) carried out large-scale laboratory experiments at CHL, US Army Corps of Engineers, Vicksberg, USA, to investigate the effect of breaker type on longshore sand transport rate with equilibrium beach concept (concave shape). The average deep-water wave height was around 0.2m and mean diameter of the sand used was 0.15mm. In their study, the final equilibrium beach profiles were obtained with the initial preparation of 1:5.5 slope for foreshore and 1:27 slope for surf zone. These results also showed that the Kamphuis (1991) formula provided consistent and fairly accurate predictions for the total rate of longshore sand transport under different wave conditions (see Fig. 9).

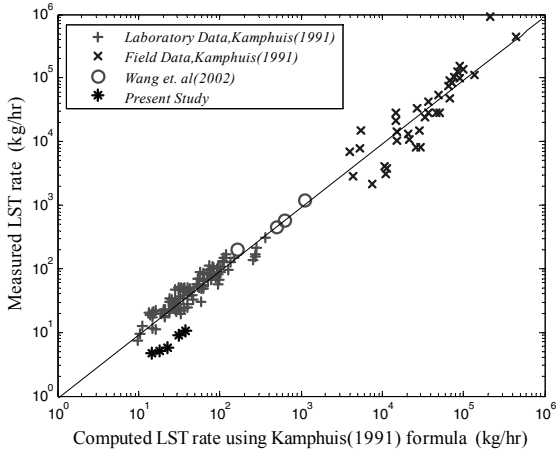

Fig. 9 Comparison of measured LST rates with Kamphuis(1991) formula

Generally, beach profile in field conditions exhibits remarkably concave shape under equilibrium conditions, which can be expressed by Dean (1977) model; i.e. $h(y) = Ay^{2/3}$, in which $h(y)$ is the water depth at a distance y offshore, A is a function of sediment size, D_{50}. Dean proposed a simple relationship between A and fall velocity, $w_f (= f(D_{50}))$.

$$A = 0.5 w_f^{0.44} \tag{2}$$

where A has the dimensions of $\mathrm{m}^{1/3}$ and w_f is in m/s, in which,

$$w_f = \left[(\rho_s/\rho - 1)g\right]^{0.7} \frac{D_{50}^{1.1}}{6\nu^{0.4}} \quad \text{for} \quad 0.13x10^{-3} \le D_{50} \le 1.6x10^{-3} \text{ m} \tag{3}$$

and for coarser material

$$w_f = 1.05\left[(\rho_s/\rho - 1)gD_{50}\right]^{0.5} \quad \text{for} \quad 1.6x10^{-3} \le D_{50} \le 8.0x10^{-3} \text{ m} \tag{4}$$

where ρ_s is the density of sediments, ρ is the density of fluid in kg/m^3, g is the gravitational acceleration in m/s^2 and ν is the kinematic viscosity of fluid in m^2/s.

At the same time, it is essential to describe the beach slopes with respect to the mobility number (H_b / D_{50}), as an equilibrium beach profile occurs when constructive and destructive forces acting on seabed are balanced. In that sense, if a beach is not fully modeled (wave height and periods are modeled but not the sand grain size) in the laboratory, the model beach will have a steeper slope than the prototype beach.

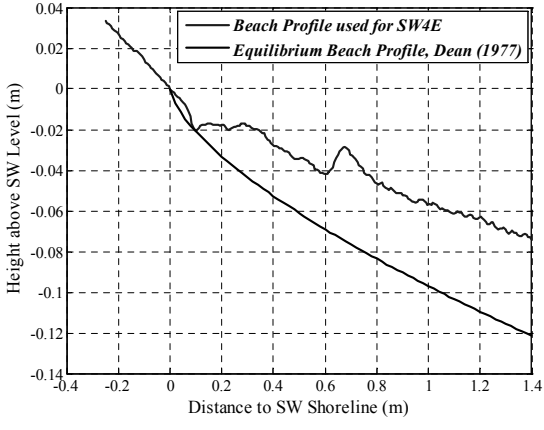

Fig. 10 Comparison of beach profiles used in present experiments.

As Kamphuis (1991) experiments were also carried out under small-scale laboratory conditions (slightly larger scale than the present study), his experiments certainly suffered the scale effect. However average beach slope was around 1:10 at equilibrium under the given wave conditions due to small H_b / D_{50} value. The direct scale effect (not scaling the sediment size) decreased the sand transport rate, while the increase in beach slope (the smaller the ratio H_b / D_{50}, the steeper the beach slope) increased the sand transport rate, *e.g.*, spilling breaker condition in the field might become plunging breaker in a model beach (given that the sediments were not scaled) under laboratory conditions; hence leading to the increase in sand transport rate due to change in breaker

type as the energy dissipation through wave breaking is concentrated over a much narrower region. The other important consequence of this narrow, energetic breaker zone was that the swash zone had been of similar width to the surf zone and accordingly the sediment transport within swash zone was more significant. Moreover, in those steep model beaches refraction of waves could have easily been incomplete, making the waves to arrive at the beach face with a considerable angle. Kamphuis (1991) showed that under these conditions, scale effect for sand transport rate appeared to be small, since the effects of distorted beach slope and grain size tended to cancel. Kamphuis also investigated the applicability of Eq. (1) to beaches with coarse-grains by comparing its predictions with the experimental results of Van Hijum and Pilarczyk (1982). He found that his formula over-predicted their results by a factor 2-5, concluding that this was to be expected, since gravel beaches will absorb substantial wave energy by percolation and the motion of the larger grains is much closer to the critical mobility numbers. Neither of these factors was included in his dimensional analysis leading to Eq. (1).

Kamphuis (1991) experiments were conducted in a slightly larger scale than the present experiments and the suspended load was found to be 0.7 times the bed load on average. However in physical models of present study (which can be considered as representative scaled models to coarse-grained beaches, irrespective of the beach slope and hydraulic conductivity) bed load was found to be more dominant over suspended load due to the relatively low stresses exerted, where in certain portions of the mid surf zone, the sand transport rate was found to be as low as 2 kg/m/hr. On the other hand, as it is evident from Fig. 10, longshore sediment transport rates were not measured on equilibrium beach slopes (the beach slopes were milder than the equilibrium beach slopes for the given wave condition and sediment size) in the present experiments, hence no substantial increase in sand transport rate was expected due to the effect of beach slope. This incompatibility in equilibrium beach slope further increased the difference between the measured sand transport rates and those predicted using Kamphuis (1991) formula (see Fig. 9).

CONCLUSION

A series of laboratory experiments were performed to investigate the cross-shore distribution of longshore sand transport rate under different wave conditions. An improved buried-type trap system was developed to measure the cross-shore distribution of longshore sediment transport.

The total LST rate and its distribution were found to be dependent on wave period and beach profile. Significant amounts of sand transport were measured for all the cases in the swash zone. Under relatively strong plunging breaker conditions substantial peaks were observed at the plunging point and swash zone. The dynamic behavior of the plunging breakers stirred the sand to be suspended and carried by longshore current at the plunging point. High energy of the run-up and run-down process in long period waves made the difference in the distribution of LST rate at swash zone compared to relatively short period waves. Alongshore bars were observed in mid surf zone for all the tests. Secondary breaking or induced mass transport cells under partially standing waves

or a combination of those two was found to be the reason for the formations of intermediate bars. Interestingly peaks in the cross-shore distribution of LST rate were noticed apparently at these bars including the one at the main breaking point.

Kamphuis (1991) formula overpredicted total LST rates obtained from these small-scale physical models as the critical shear parameters were not included in the dimensional analysis leading to his expression (the motion of sediment grains was much closer to critical mobility numbers in the present experiments). On the other hand, beach slopes were not modeled to match the equilibrium under the wave condition and the sediment size used in present experiments; hence, surf zone was found to be relatively broader and less energetic, which is inconsistent with Kamphuis (1991) experiments. This resulted less sediment suspension in both surf zone and swash zone, which further increased the difference between measured and predicted LST rates by Kamphuis (1991) formula.

Despite the shortcomings of scale effect, data from physical model tests conducted here can be utilized to calibrate and validate formulae for predicting total longshore sand transport rate and its distribution, particularly for coarse-grained beaches.

REFERENCES

Bayram, A., Larson, M., Millar, H.C., Kraus, N.C. (2001). Cross-shore distribution of longshore sediment transport; comparison between predictive formulas and field measurements. *Coastal Engineering,* 44: 79-99.

Dean, R.G. (1977). Equilibrium beach profiles: US Atlantic and Gulf coasts. *Ocean Engineering Report No. 12,* Department of Civil Engineering, University of Delaware, Newark, DE.

Kamphuis, J.W. (1991a). Alongshore sediment transport rate. *Journal of Waterways, Port, Coastal and Ocean Engineering,* ASCE, 117(6): 624-641.

Kamphuis, J.W. (1991b). Alongshore sediment transport rate distribution. *Coastal Sediments '91,* ASCE, Seattle, Washington, USA, pp. 170-183.

Kamphuis, J.W., (2002). Alongshore sediment transport of sand. *Proceedings, 28th International Conference on Coastal Engineering*, ASCE, Cardiff, Wales, pp. 31-45.

Reniers, A.J.H.M, Battjes, J.A. (1997). A laboratory study of longshore currents over barred and non-barred beaches. *Coastal Engineering,* 30: 1-22.

Van Hijum, E., Pilarczyk, K.W. (1982). Equilibrium profile and longshore sand transport of coarse material under regular and irregular wave attack. Delft Hydraulic Laboratory, Netherlands, Publication no. 174.

Van Wellen, E., Chadwick, A.J., Mason, T. (2000). A review and assessment of longshore sediment transport equations for coarse-grained beaches. *Coastal Engineering,* 40: 243-275.

Wang, P., E.R. Smith and B.A. Ebersole. (2002). Large-scale laboratory measurements of longshore sediment transport under spilling and plunging conditions, *Journal of Coastal Research,* (18) 1: 118-135.

Putrevu, U.J., Shay, O., Svendsen, I.A. (1995). Effect of longshore non-uniformities on longshore current predictions. *Journal of Geophysics Research,* (100): 16119-16130.

PRESSURE-INDUCED SUBSURFACE SEDIMENT TRANSPORT IN THE SURF ZONE

Ole Secher Madsen and William McKinney Durham

Ralph M. Parsons Laboratory, Department of Civil & Environmental Engineering
Massachusetts Institute of Technology, Cambridge, MA 02139-4307
osm@mit.edu and durham@mit.edu

Abstract: The horizontal pressure gradient associated with the steep front of forward-leaning breaking waves is transmitted into the porous bottom to depths far exceeding the depth of the shear-stress-induced surficial transport sheet flow layer. The horizontal pressure gradient induces a flow within the bed which exerts a seepage force on the soil-skeleton. If sufficiently large the seepage force will cause a failure of the soil matrix and displace subsurface sediment grains, i.e. result in a subsurface sediment transport. This paper investigates the pressure-induced subsurface transport mechanism experimentally by photographically recording the displacement profile of subsurface lightweight sediment grains during passage of the steep front of breaking waves. A simple theoretical model for the dynamic response of subsurface sediments in failure is developed and provides predicted displacement profiles in reasonable agreement with measurements. The potential importance of the subsurface sediment transport mechanism is discussed.

INTRODUCTION

The pressure distribution on the bottom underneath forward-leaning near-breaking or broken waves is transmitted into the porous bed, where it induces a flow. This pressure-induced porous media flow extends to depths into the bed scaled by the horizontal scale of the pressure distribution and exerts a seepage force on the sediment grains within the bed. The horizontal component of this seepage force is related to the horizontal pressure gradient of the pressure distribution on the bottom and is therefore particularly pronounced under the steep front of a forward-leaning breaking wave and may, if sufficiently large, cause a soil-mechanics-type failure of the bed. This mechanism of a

pressure-induced subsurface failure during passage of breaking waves was first identified by Madsen (1974) who, based on a simple model akin to models used for the prediction of slope stability in geotechnical engineering, hypothesized that this failure mechanism could explain the burial of tracer particles to considerable depths below the sediment-fluid interface in the surf zone. He argued, however, that this failure mechanism would have an insignificant effect on sediment transport rates in the surf zone because it would merely reduce the critical shear stress for initiation of motion from τ_{cr} to 0 with τ_{cr} reasonably expected to be far smaller than the bottom shear stress, τ_b, under breaking waves, i.e. $\tau_b - \tau_{cr} \approx \tau_b$, and hence an insignificant effect on surficial shear-stress-induced sheet flow transport.

Drake and Calantoni (2001) developed a sophisticated granular flow model for the bottom-shear-stress-induced surficial sediment transport, referred to as sheet flow transport, under forward-leaning breaking waves. They found that inclusion of a forcing term related to the pressure gradient under the steep front of a breaking wave had a pronounced effect on the surficial sediment transport rates predicted by their model. Following their lead, Hoefel and Elgar (2003) subsequently succeeded in predicting on-shore bar migration by including a pressure gradient transport term in their empirical sediment transport formulation.

The renewed interest in pressure-gradient-associated sediment transport processes in the surf zone and the delicate balance between on- and off-shore transport rates for equilibrium beach profile predictions, prompted us to revisit the subsurface pressure-induced failure mechanism and its potential contribution to sediment transport rates in the surf zone. This time, however, a more extensive experimental investigation is carried out, as described in the first section of this paper. Also, the simple soil mechanics subsurface failure analysis, presented by Madsen (1974), is extended to include the dynamic response of the subsurface sediment in failure. This model is described in the subsequent section and affords an approximate prediction of the displacement of subsurface sediment grains caused by the passage of the steep front of a forward-leaning breaking wave. Finally, we show that the simple approximate model is capable of predicting experimentally observed displacements reasonably well; and we conclude with a discussion of the potential importance of the subsurface pressure-gradient-induced sediment transport rate relative to the shear-stress-induced surficial sheet flow transport rate in the surf zone. The reader interested in more details of this study than the page-limitation allows us to present here, is referred to Durham (2007).

EXPERIMENTAL INVESTIGATION

Experiments were conducted in the 30m-long, 0.9m-deep and 0.76m-wide wave flume in the J. Robert Gunther Environmental Fluid Mechanics Laboratory in the Ralph M. Parsons Laboratory. The wave flume is equipped with a programmable piston-type wave maker and has a 1 on 10 sloping absorber beach. An instrument carriage runs along the length of the flume on rails that are mounted on top of the frames that support the flume's glass sidewalls.

The Experimental Set-up

The experimental set-up, show in Figure 1, consists of a horizontal shelf made of marine plywood that forms a "false bottom" 25 cm above the actual flume bottom. Waves climb a 1 on 6 sloping ramp and enter the shelf where breaking is triggered. The breaking wave travels over the first section of the shelf before it enters the test section, which consists of a 10cm-wide, 100cm-long and 15cm-deep Lucite tray installed into the false bottom along the centerline of the flume. To prevent lateral loss of sediment during experiments the tray is covered by gauze, and to allow determination of longitudinal transport, sediment collection bags are installed at each end of the tray.

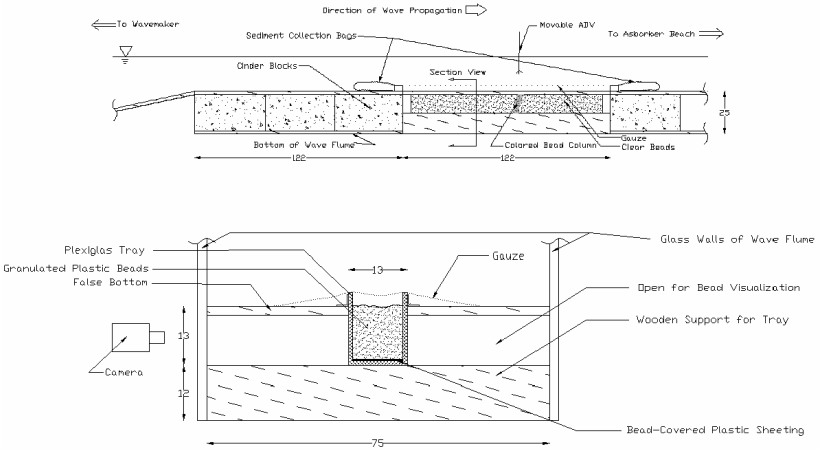

Fig. 1. Experimental Set-up (all dimensions in cm)

The Lucite tray protrudes below the false bottom and contains the sediment, making the sediment bed directly observable through the flume's glass sidewalls. The subsurface movement of a ~2cm-long column of colored sediment inserted in the sediment bed, at the midpoint of the test section, is recorded photographically using a Canon PowerShot S230 digital camera for both stills and video (with a frame rate of 15 frames per second). From the videos, shot during passage of a breaking wave, frame by frame analysis determines when the sediment column starts to move, when it reaches its maximum forward deflection, and when it comes to rest after the wave has passed. Since we are recording the displacement of the column of colored beads along the sidewalls of the Lucite tray, we cut a slice along the centerline of the Lucite tray, by inserting a thin Lucite sheet into the bed, to see if the observed displacements along the sidewall were representative of the displacements over the entire width of the column of colored beads. As evidenced by the still photos shown in Figure 2, we have in this manner verified the validity of our experimental procedure for the determination of subsurface, pressure-gradient-induced movements of a sediment bed.

Since the experimental conditions simulate two-dimensional conditions, the smooth sidewalls of the Lucite tray allow a near-frictionless movement of the sediment grains in contact with the sidewalls, i.e. reproduce two-dimensional conditions. The bottom of the Lucite tray is covered by sediment grains glued to the surface of a thin plastic sheet. Preliminary experiments showed that the entire sediment bed would slide along the bottom when this was left smooth. With the roughened bottom, the near-bottom sediments in the Lucite tray remained immobile during the experiments (see Figure 2).

The initial "top" of the column of colored sediments coincides with initial sediment fluid interface and is covered from view by the false plywood bottom. However, after passage of several waves a sharp interface between the top of the column of colored sediments, now covered by plain sediment, is clearly visible (Figure 2(b) and (c)). Thus, as conjectured previously in the Abstract, the pressure-gradient-induced subsurface transport, represented by the displacement of the column of colored sediments, extends to much greater depth within the bed than the thickness of the sheer-stress-induced surficial sheet flow, which is responsible for the shaving off of the top portion of the column of colored sediments.

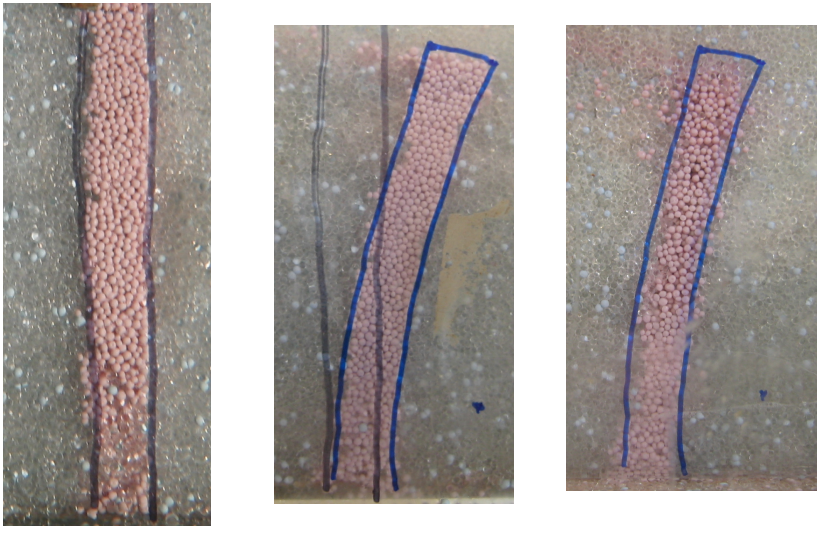

(a) (b) (c)

Fig. 2. Still Photos of the Colored Sediment Column Inserted in the Sediment Bed. (a) Before; (b) After waves (along sidewall); (c) After waves (along centerline)

The Sediment

Madsen (1974) showed that pressure-induced bed failure would occur if the bottom pressure gradient exceeded a critical value given by

$$\left|\frac{\partial p}{\partial x}\right|_{crit} = \left(\rho_s(1-n) - \rho(1-n)\right) g \tan\varphi = \left(\rho_b - \rho\right) g \tan\varphi \qquad (1)$$

where ρ_s and ρ are the sediment and fluid densities, respectively, n is the porosity, g is gravity, φ is the internal friction angle of the sediment which is assumed cohesionless, and ρ_b is the density of the saturated bed. To maximize the subsurface pressure-gradient-inducing displacements and make these detectable in our small scale laboratory experiments, a light-weight "sediment", Polyethylene Terephthalate (PET), was chosen. The relevant physical characteristics of this sediment were determined to be: diameter = d = 1.1 ± 0.1 mm, density = ρ_s = 1.27 ± 0.01 g/cm^3, porosity = n = 0.37 ± 0.02, so ρ_b = 1.17 ± 0.01 g/cm^3 and angle of internal friction φ = 34°.8 ± 1° and 39°.2 ± 1°.1 for loosely and densely packed deposits, respectively. The characteristics of the colored PET beads were determined to be essentially identical to those listed above, and a surfactant (Windex) was added to the water to prevent the beads from sticking together.

The Waves

To maximize our ability to stop the experiment after any number of waves, the experiments were performed programming the wave maker to generate solitary waves. The near-bottom orbital velocity as the breaking waves pass over the test section was measured with a Sontek ADV system sampling at a rate of 25Hz. Assuming the breaking waves to be of near-permanent form, i.e. taking $\partial/\partial t \cong -c\partial/\partial x$ with c denoting the phase velocity of the wave, the smoothed time-series of near-bottom horizontal velocity, $u(t)$, provides an estimate of the associated bottom pressure gradient, since we have

$$-\frac{\partial p}{\partial x} = \rho\left(\frac{\partial u}{\partial t} + u\frac{\partial u}{\partial x}\right) \cong \rho\frac{\partial u}{\partial t}\left(1 - \frac{u}{c}\right) \qquad (2)$$

Furthermore, by replacing $-\partial p/\partial x$ by $c^{-1}\partial p/\partial t$, (2) may be integrated to obtain the temporal bottom pressure variation $p(t)$ from which the spatial variation of the bottom pressure, $p(x)$, is obtained by replacing t by $-x/c$. Figure 3 shows the smoothed record of the measured near-bottom horizontal velocity $u(t)$ and the corresponding temporal variation of bottom pressure and pressure gradient obtained from (2) by ensemble averaging 10 wave realizations. For the phase velocity we took c = 1.5 m/s, the average of the measured speed of the crest (1.6 m/s) and the predicted phase velocity for our solitary wave (1.4 m/s). It is noted that the maximum experimental pressure gradient shown in Figure 3, ~180 dynes/cm, exceeds the critical pressure gradients predicted from (1), 116 dynes/cm and 136 dynes/cm for φ = 34.°8 and 39.°2, respectively. Thus, bed failure should occur and, as evidenced by the photos in Figure 2, it obviously did.

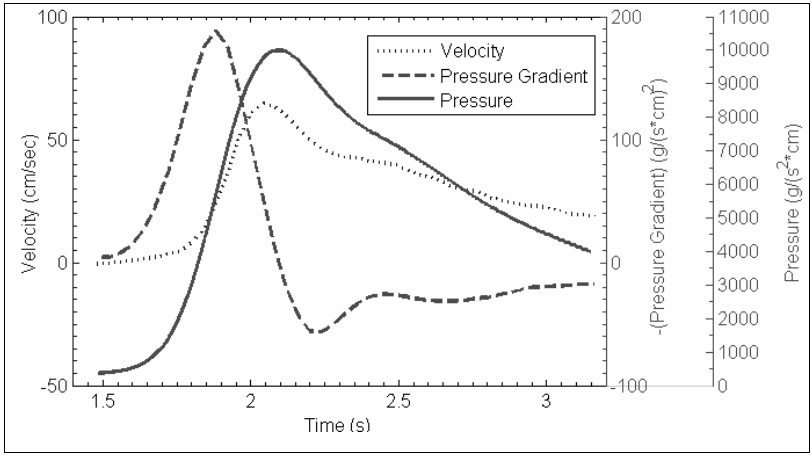

Fig. 3. Experimental Wave Characteristics.

THEORETICAL MODEL

The theoretical model is based on the principles adopted by Madsen (1974), i.e. pressure-induced subsurface failure is assumed to take place along circular arcs, slip circles, as shown in Figure 4.

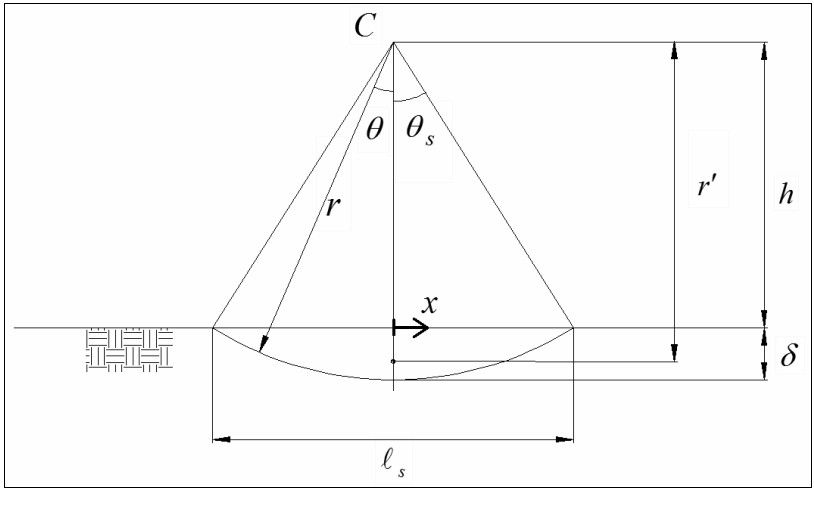

Fig. 4. Slip Circle Characteristics

From Madsen's (1974) analysis of effective stresses along the slip circle, it follows that

the maximum moment around the slip circle's center, C, due to shear stresses corresponding to failure along the slip circle (the "stabilizing" moment) is approximately

$$M_s = 2(\rho_b - \rho)gr^3 \sin\theta_s (1 - \theta_s \cot\theta_s)\tan\varphi \tag{3}$$

where the slip circle's radius = $r = h + \delta$, h being the distance of C above the bottom and δ the maximum depth of the slip circle below the bottom, and the angle

$$\theta_s = Arc\cos\left(\frac{h}{r}\right) \tag{4}$$

The length of the bottom segment within the slip circle is

$$l_s = \frac{2\delta \sin\theta_s}{1 - \cos\theta_s} \tag{5}$$

and it is over this distance, l_s, that the wave-associated bottom pressure acts and produces a moment around C as the bottom pressure distribution $p(x)$ translates past l_s at speed c. This moment, the "driving" moment, is a function of time and is given by

$$M_d(t) = \int_{-l_s/2}^{l_s/2} p(x)x\,dx = \int_{t+l_s/2c}^{t-l_s/2c} p(t')(ct')c\,dt' \tag{6}$$

with $p(t)$ as show in Figure 3.

Madsen (1974) determined the characteristics of the limiting slip circle by equating the maximum driving moment obtained from (6) for a specified value of $l_s = l_{smax}$ to the stabilizing moment given by (3), Madsen (1974, Eq. (15)). Here we obtain $l_{smax} = c\Delta t$ where Δt, the time interval during which the pressure gradient exceeds its critical value given by (1), is obtained from Figure 3. With this value of $l_s = l_{smax}$ balancing M_{dmax} and M_s produces the limiting slip circle along which the sediment just reaches failure at the instant when $M_d(t) = M_{dmaz}$. With all slip circles being concentric, for kinematic reasons, any slip circle contained within the limiting slip circle will experience failure for some short period during passage of the pressure distribution associated with the breaking wave.

Figure 5 shows the temporal variation of M_d, the driving moment, and the corresponding value of the maximum realizable stabilizing moment, M_s, for slip circles identified by their depth of penetration into the bed, δ, relative to that of the limiting slip circle, δ_{smax}.

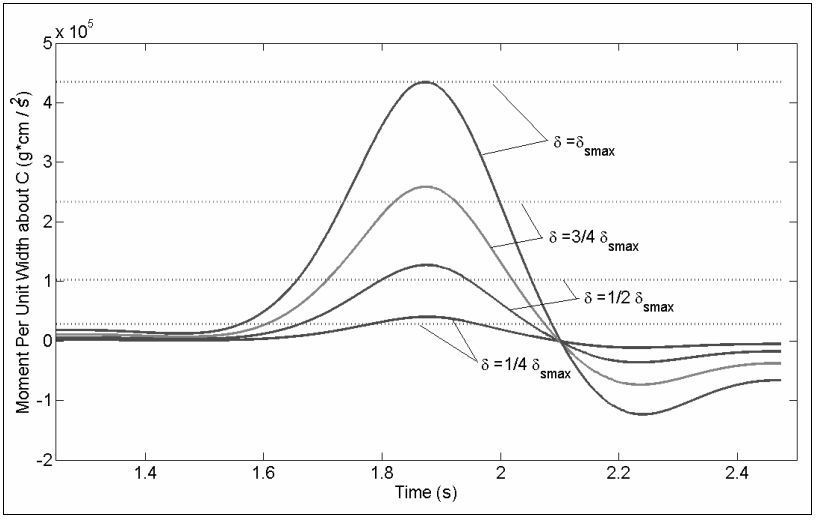

Fig. 5. Temporal Variation of Driving Moments (full lines) and Corresponding Stabilizing Moments (dotted lines) for Different Slip Circles

For the time interval during which $M_d > M_s$ for a particular slip circle, no static moment balance is possible and the bed material above the slip circle responds by rotating around C. As a simple approximate model for the dynamic response of the bed material above a slip circle when $M_d > M_s$ we take

$$I\frac{d^2\theta}{dt^2} + mgr'\theta = M_d(t) - M_s \tag{7}$$

where I is the radial moment of inertia of the bed material above the slip circle of radius r around C

$$I = \frac{r^4}{4}\left(2\theta_s - \sin 2\theta_s + \frac{2}{3}\sin 2\theta_s \sin^2\theta_s\right)\rho_b \tag{8}$$

The mass of the bed material above the slip circle is

$$m = \frac{r^2}{2}(2\theta_s - \sin 2\theta_s)\rho_b \tag{9}$$

and the distance from its center of gravity to C is

$$r' = \frac{4}{3}\frac{\sin^3\theta_s}{2\theta_s - \sin 2\theta_s} r \tag{10}$$

Finally, θ is the rotation angle around C of the material above the slip circle.

With $M_d(t)$ and M_s given for a particular slip circle of radius r, (7) may be solved subject to the initial condition of $\theta = d\theta/dt = 0$ at $t = 0$, and the computation proceeds until $d\theta/dt$ changes sign, i.e. $d\theta/dt = 0$ or $\theta = \theta_{max}$, signifying a change in the sense of rotation and hence a sudden change in the sign of M_s, which always must act in the direction opposite the sense of rotation of the material above. Having solved (7) for a particular value of r, the horizontal displacements of the subsurface sediment a distance of $\delta = r - h$ below the bottom is obtained from

$$\xi = r\theta \le \xi_{\max} = r\theta_{\max} \tag{11}$$

The salient features of this simple model are conceptualized by its graphical representation in Figure 6.

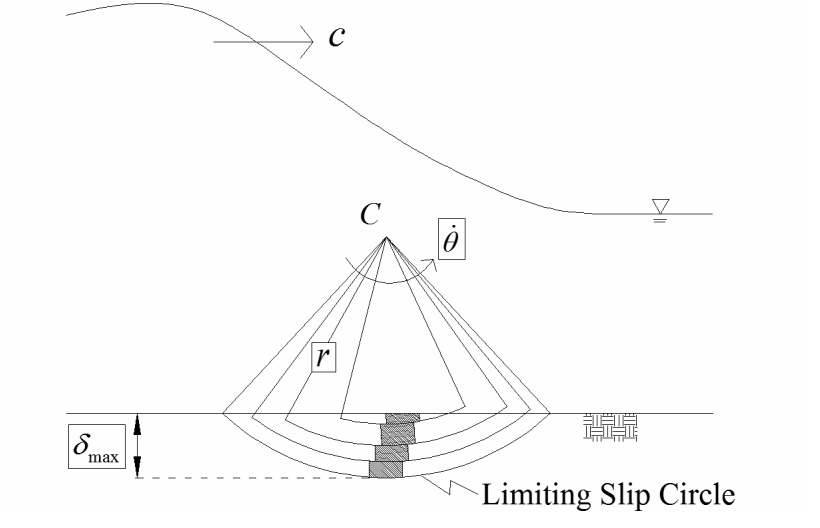

Fig. 6. Conceptual Illustration of the Theoretical Model of Subsurface Sediment Displacements during Failure

RESULTS

From the frame by frame analysis of the videos shot during passage of the steep front face of a forward-leaning breaking wave the displacements of subsurface sediment grains

during the period of pronounced bottom pressure gradients are obtained. Ensemble averaged subsurface displacement profiles (from four realizations) are plotted in Figure 7 as a function of number of waves that have passed over an initial "deposited" bed. A striking reduction in the magnitude of the displacement with number of waves is noticed. We conjecture that this reduction is associated with a strengthening of the bed as this is being reworked by the preceding waves, e.g. causing initially weak spots within the soil matrix to become stronger by rearranging individual grains into more stable configurations.

Also shown in Figure 7 are the predicted displacement profiles afforded by our simple theoretical model for the pressure-induced subsurface failure mechanism. The predicted results are shown for various friction angles, φ, which is the only "free parameter" in our model. It is clearly demonstrated that our model predicts a dramatic decrease in displacement as φ, i.e. the strength of the bed material, increases. This lends credence to our conjecture that the observed dramatic decrease in displacements with number of waves is associated with the accumulated reworking and strengthening of the bed material caused by previous waves.

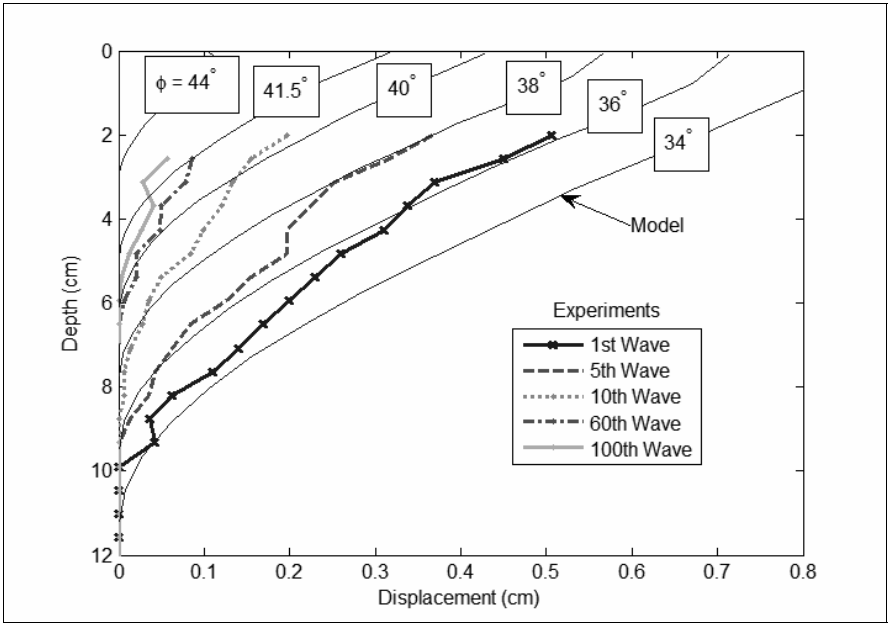

Fig. 7. Subsurface Displacement Profiles Caused by the Passage of the Steep Front Face of a Breaking Solitary Wave

It is particularly encouraging that the predicted displacement profiles are in reasonable

agreement with observations for values of the friction angle φ corresponding to those obtained for our sediment, i.e. $\varphi = 34.°8 \pm 1°$ for loosely packed sediments corresponding to passage of the first wave and $\varphi = 39.°2 \pm 1.°1$ for densely packed sediments corresponding to heavily reworked bed conditions.

A Reality Check

Before getting carried away by the apparent success of our simple model's ability to predict the observed subsurface displacement profiles in Figure 7, it must be emphasized that the observed displacement profiles shown in Figure 7 correspond to the forward subsurface displacements associated with the steep front, i.e. the large pressure gradient peak seen in Figure 3, of the breaking solitary wave passing overhead. Once this pressure gradient "pulse" has passed, the pressure gradient changes sign and drops to values well below the critical value of ~120 dynes/cm^2 predicted by (1). Thus, our simple model would predict that there should be no subsurface failure and hence no backward displacement after the crest of the breaking wave has passed.

But the experiments do not corroborate this prediction! In fact, following the strong forward displacement observed during passage of the steep wave front, the column of colored sediment rebounds, i.e. moves backwards, despite the negligible magnitude of the pressure gradient and comes to rest at a position suggesting the permanent displacement caused by the passage of the entire solitary wave to be but a mere fraction (of the order of one fifth) of the displacement experienced during the passage of the steep front, i.e. the observed displacement shown in Figure 7.

A clue to why this rebound takes place may be found in Figure 2(b) which shows the column of colored beads after the passage of several (~50) solitary waves. Clearly the column, while displaced, is still intact, i.e. individual beads have not been sliding across each other but stayed in contact with their neighbors throughout the experiment. Thus, an actual failure, in the soil mechanics sense, of the subsurface sediments really has not taken place during passage of a breaking wave overhead. If we stipulate that a relative displacement of $\Delta\xi > d$ between adjacent horizontal "layers" of thickness ~d signifies bed failure, since this would allow adjacent sediment grains to change neighbor, we may express a "failure" condition as $\left|\partial\xi/\partial z\right| > 1$, where z is the vertical coordinate. From the displacement profiles shown in Figure 7 we see that $\partial\xi_{max}/\partial z \leq\sim 0.1$ which supports our conclusion of "no real failure" reached from inspection of the still photos is Figure 2. This need to an angular displacement to exceed a critical value in order for actual failure to take place, appears related to the critical shear condition for irreversibility and the appearance of chaos mentioned by Gollub and Pine (2006).

Thus, the strong pressure gradient under the steep front of the wave has forced the column to deflect in the forward direction but not sufficiently to cause an actual failure. After passage of the wave front the column is left in an unstable state and rebounds in a nearly elastic manner once the force that caused its original deflection is removed. The integrity of the column of colored beads, as it appears along the sidewall of the Lucite tray in Figure 2(b), is somewhat broken up in the middle of the Lucite tray (Figure 2(c)).

However, the mixing of beads in the center of the tray may well have been caused by the insertion of the Lucite sheets into the bed during preparation of the center cut.

CONCLUSIONS

Experiments that demonstrate conclusively the existence of a subsurface sediment transport mode under breaking waves were conducted. A simple theoretical model based on soil mechanics principles for failure along slip circles was developed and was capable of predicting, with some success, the observed subsurface displacements caused by the passage of the pressure gradient "pulse" associated with the steep front of a forward-leaning breaking wave. However, the theoretical model did not predict the observed rebound of the subsurface sediments after passage of the crest of the breaking wave. This flaw is believed to be associated with the fact that an actual failure, in the soil mechanics sense, did not take place within the subsurface sediments. Nevertheless, we are confident that the observed (and predicted) subsurface displacements are pressure-gradient-induced. Since a large pressure gradient in the fluid corresponds to large fluid accelerations, this subsurface sediment transport mechanism is indirectly evidence of one of potentially many effects of fluid accelerations in sediment transport processes in the surf zone.

This leaves the all-important question of the importance of this subsurface sediment transport mode relative to the conventional surficial sheet flow transport mode to be answered. To shed some light on this issue, the total sediment transport rate in our experiments was measured by using the ADV system as a bottom profiler. After passage of two solitary waves over an initially plane bed the bottom elevation change (divided by 2 to obtain the value corresponding to passage of a single wave) was measured at 1 cm intervals along three transects for the entire 100cm-length of the Lucite flume. Denoting the measured bottom elevation change associated with passage of a single solitary wave by $\zeta(x)$, the sediment continuity equation

$$q_T(x) = q_{T0} - (1-n)\int_0^x \zeta(x)dx \qquad (12)$$

can be used to obtain the total sediment volume transport q_T [cm^3 of sediment per cm width of the tray per solitary wave] by using the amount of sediment captured by the upwave collection bag to determine q_{T0}, the transport at $x = 0$.

The results from ensemble averaging three such experiments for $q_T(x)$ are shown in Figure 8 including the standard deviations of $q_T(x)$. As one would expect $q_{T0} \approx 0$, since the orbital velocity of a solitary wave is purely positive, and q_T increases from $x = 0$ until it reaches a near-constant value of $q_T \approx 3.0$ cm^3/cm for $x > \approx 40$ cm, which is approximately the value of the excursion, $\int_0^\infty u(t)dt$, for our wave. It is noticed that the predicted transport at the end of the tray is in (remarkably) good agreement with the transport inferred from the sediment volume captured in the down-wave collection bag

at x = 100 cm (indicated by a tick-mark in Figure 8). Thus, we have confidence in our estimate of the total, i.e. surficial as well as subsurface, sediment volume transport per solitary wave being 3.0 cm^3/cm.

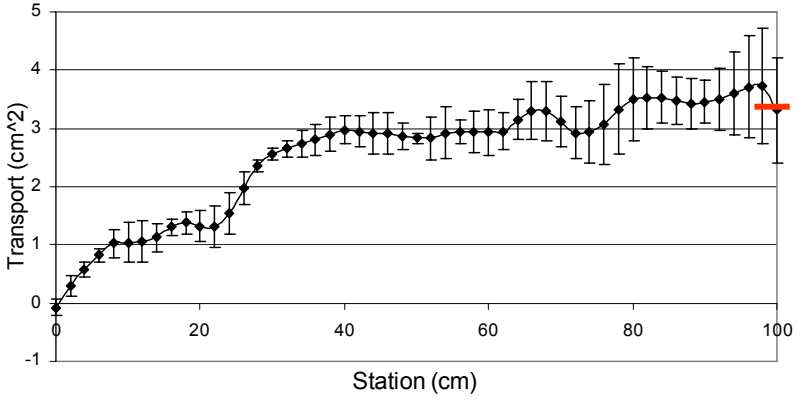

Fig. 8. Measured Total Sediment Volume Transport per Solitary Wave along the Test Section

For comparison, the subsurface sediment transport rate, inferred from the forward displacements during passage of the steep front of the breaking solitary wave (Figure 7), amounts to ~1.3 cm^3/cm for the first and ~0.1 cm^3/cm for the 100th wave. Given the fact that the net subsurface transport rate, i.e. accounting for the "rebound", is lower than the values obtained from Figure 7, by a factor of ~5, it would appear that the subsurface transport rate is at most ~10% of the total. However, this estimate of the relative importance of surficial and subsurface transport rates is obtained for a solitary wave. For a periodic wave the forward velocity (and surficial transport) is followed by a backward velocity (and surficial transport), i.e. a net transport that is a potentially small difference between the forward and backward transport. In contrast, the subsurface transport is exclusively associated with the passage of the steep front of the breaking wave and this should not be significantly different for periodic and solitary waves. We therefore need further experiments involving periodic waves and including the effect of bottom slope, as well as investigations of the behavior of denser sediments (natural sands) during repeated wave-loading, in order to make a final conclusion regarding the potential significance of the contribution of the subsurface sediment transport mechanisms to the total net cross-shore sediment transport rate in the surf zone.

ACKNOWLEDGEMENTS

The support of the Office of Navel Research, Coastal Geosciences Program under Grant Number: N00014-6-1-0318 is gratefully acknowledged as is the assistance of Ms. Lizzie Lundgren who, as a UROP student, conducted some of the experiments and tirelessly analyzed videos, frame by frame, to obtain displacement profiles.

REFERENCES

Drake, T.G. and Calantoni, J. (2001), "Discrete particle model for sheet flow sediment transport in the nearshore". *J. Geophys. Res., 106*, 19,859-19,868.

Durham, W. M. (2007), "The effect of fluid acceleration on sediment transport in the surf zone", SM Thesis, Department of Civil and Environmental Engineering, MIT, Cambridge, MA 02139., 184p.

Gollub, J. and Pine, D. (2006), "Microscopic irreversibility and chaos", in August Issue of *Physics Today*.

Hoefel, F., and Elgar, S. (2003), "Wave-induced sediment transport and sandbar migration", *Science, 299,* 1885-1887.

Madsen, O.S. (1974), "Stability of a sand bed under breaking waves", in *Proceedings of the 14th International Conference on Coastal Engineering*, ASCE, Reston, Va. 2: 776-794 [also R.M. Parsons Laboratory, Report No. 182, Department of Civil Engineering, MIT, March 1974, 75p.].

TRACKING SEDIMENT PARTICLES UNDER WAVE-CURRENT COEXISTING FIELD

Yoshimitsu Tajima[1], Masayuki Kozuka[2], Masahito Tsuru[2], Toshimasa Ishii[3], Takeharu Sakagami[4], Kazuo Momose[4], Nobuo Mimura[5], Ole S. Madsen[6]

1. Department of Civil Engineering, The University of Tokyo, Hongo 7-3-1, Bunkyo, Tokyo 113-8656, Japan. yoshitaji@coastal.t.u-tokyo.ac.jp.
2. Penta-Ocean Construction Co., Ltd., Koraku 2-2-8, Bunkyo, Tokyo, Japan.
3. Tokyo Electric Power Service Co., Ltd., Higashi-Ueno 3-3-3, Taito, Tokyo, Japan.
4. The Japan Atomic Power Company, Mitoshiro 1-1, Chiyoda, Tokyo, Japan.
5. Department of Urban and Civil Engineering, Ibaraki University, Nakanarusawa 4-12-1, hitachi, Ibaraki, Japan.
6. R.M. Parsons Laboratory, Massachusetts Institute of Technology, 77 Massachusetts Ave., Cambridge, MA 02139, USA.

Abstract: Predictive skills to track the discharged sand grains are essential to design optimum sand-recycling system. This paper develops a new numerical model which focuses on the movement of a group of sand grains discharged at arbitrary locations in the near-shore area. While particles in a group of discharged sands may be transported with the group, spatial distribution of the group may be dispersed due to certain random effects such as near-bottom turbulence and wave motions. The present model follows the concept of existing process-based bedload sediment transport model to represent the former "mean" movement of sand particles. In addition, the model introduces random walk theory to account for the latter dispersive characteristics of discharged sand grains. The model shows excellent predictive skills of both mean and dispersive movement of dyed sand grains observed in the newly performed field survey.

INTRODUCTION

Sand-recycling or sand-bypassing system, which artificially transports sand from certain deposited area to the other eroded area, is one of environmentally sustainable, and thus preferable, sand-controlling systems that have relatively low impacts on

coastal environments. In order to propose the optimum design of such systems, predictive skills of the movement of discharged sand is essentially important. A field sand-tracking survey using dyed sand grains as a tracer is often applied to capture the feature of sediment movement around the possible dumping site of collected sand. However, the longer the observation period and the wider the spatial distributions of deposited sand grains, such field survey may become less reliable because the number of tracer particles in the sampled sands decreases.

As complement of such sand-tracking field survey, a numerical model, which traces Lagrangian movement of single sand grain, is often applied in Japan. Since these models focus on the movement of single sand particle, however, the model does not account for the features based on the movement of multiple sand grains, e.g., sediment transport rate and dispersive characteristics of discharged sand grains. These features are of great importance to determine the most effective sand-dumping locations and volumes in the actual sand-recycling project. For instance, dispersive feature of a certain group of sand grains is necessary to estimate how much sand grains out of initial total volume of dumped sand grains are transported to the target site where one aims to deposit these sand grains. Dispersive feature of sand grains are also important for us to examine the model validity by directly comparing the predicted sand distributions with field sand-tracking survey observations. The goal of this study is therefore to develop a new numerical model which is capable of predicting these features which are readily applicable to design the optimum sand-recycling or sand-bypassing systems. The newly developed model should accommodate various predictions such as volume of total sand grains in motion, mean movement of representative sand grains, and the dispersive characteristics of the group of dumped sand grains.

In this paper, we first develop a new numerical model which tracks certain groups of sand grains deposited on the sea bed. We then outline newly performed field survey, in which we monitored spatial distributions of tracer particles of dyed sand. Finally, we apply the developed model to the present field survey conditions and examine the model applicability by comparing predicted and measured spatial distributions of tracer particles.

NUMERICAL MODEL DEVELOPMENT

In this section, we develop a new numerical model to track a group of discharged sand grains. The model should account for both mean and dispersive movement of multiple sand grains. Sand-dumping site may be arbitrarily selected on a sea bed with various geometry where periodic or random waves and wave-induced near-shore mean currents may coexist.

Model Outline

Fig. 1 shows the flowchart of the present model. In the figure, $\mathbf{x}_i^t$ is a position vector of i-th sand particle (i=1,2, ... N) at time, t ($t=\Delta t, 2\Delta t, \ldots T_{end}$), and z_i^t is a depth of the same sand particle located below the sand bed surface at the initial dumping location.

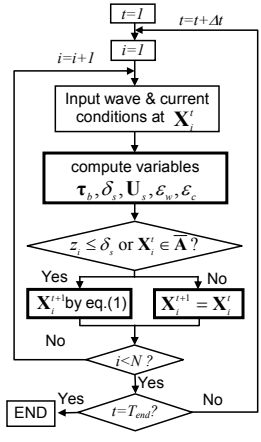

Fig. 1. Flow chart of the present model

As shown in the flowchart, the model consists of two iteration loops that proceed with time and number of particles, respectively, i.e., the model computes position vectors of different N sand grains at every time step, t. The same procedure is iterated until the time, t, reaches the designed computation time, T_{end}. In each iteration time step, the model first determines wave and current conditions at locations of each sand grain, $\mathbf{X}_i^t$. Based on the local wave and current conditions, the model determines following variables that govern the movement of sand grains: τ_b, bottom shear stress; δ_s, thickness of the moving sand grains layer; U_s, mean velocity of the moving sand grains; and ε_w and ε_c, dispersion coefficients of moving sand grains due to wave motion and mean current, respectively. In the present model, we applied energy balance equations to compute wave field with incident wave conditions specified from the measured wave data. Near-shore mean current field is then computed by non-linear shallow water equation with radiation stress determined from the computed wave field.

If the depth of the computing sand grain below the bed surface, z_i^t, is smaller than δ_s, then the model computes a new location of the sand grain, $\mathbf{X}_i^{t+\Delta t}$, by following equation.

$$\mathbf{X}_i^{t+\Delta t} = \mathbf{X}_i^t + \mathbf{U}_s \Delta t + \mathbf{R} \tag{1}$$

Here, $\mathbf{R}$ is a horizontal vector of random walk step for time step, Δt. Note that z_i^t decreases as the other surface sand grains are washed out and the remaining sand grains located in the deeper portion at the initial dumping site eventually begin to move. In this manner, the model accounts for the instantaneous volume of moving sand grains. Note that the present model applied this procedure only at the initial sand dumping site based on the assumption that sand grains remain on the surface once they are initiated to move. Computation of the movement of multiple sand

grains in (1) enables the model to estimate dispersive characteristics of discharged sand. The total number of sand grains, N, do not need to be the actual number of sand grains but should be sufficiently large so that the computed results well represent the dispersive feature of discharged sands. Determinations of all these variables are discussed in the following sections.

Velocity of Moving Sand Grains

Based on the number of field sand-tracking survey (e.g., Komar and Inman, 1970), Nadaoka et al. (1981) proposed that the time-averaged velocity of the moving sand grains, $\mathbf{U_s}$, under wave and current coexisting field is proportional to the depth-averaged mean current velocity, $\mathbf{U_c}$, and the ratio of these velocities, $|\mathbf{U_s}|/|\mathbf{U_c}|$, is about one or two percents. While this empirical relationship is simple, it does not account for various physical processes such as influence of waves, sizes and density of sand grains and the local bottom geography conditions. The present model introduces Madsen's (1991) bedload sediment transport model to determine the velocity of moving sand grains. Since Madsen's (1991) bedload sediment transport model is based on the physical mechanisms of the movement of sand grains, the model can accommodate various physical phenomena stated above.

Assuming that the near-bottom current velocity, u_{cr}, is just large enough to initiate the movement of sand particle at bottom, Madsen (1991) expressed the force balance equation on this single sand particle as

$$\frac{1}{2}\rho C_{DS} a_s u_{cr}^2 = (s-1)\rho g v_s (\cos\beta \tan\phi_s + \sin\beta) \tag{2}$$

Here ρ is density of the surrounding sea water, C_{DS} is a drag coefficient of static sand particle, a_s is surface area of the particle, $s=\rho_s/\rho$ with ρ_s, the density of the particle, v_s is a volume of the particle, g is gravity, $\tan\beta$ is a bottom slope in the current flow direction and ϕ_s is a friction angle of static sand grain. Critical current velocity to initiate the movement of a sand particle is thus expressed as

$$\frac{u_{cr}^2}{(s-1)g(v_s/a_s)} = \frac{2}{C_{DS}} \tan\phi_s \cos\beta \left(1 + \frac{\tan\beta}{\tan\phi_s}\right) \tag{3}$$

When the arbitrary current velocity, u_f, is greater than this critical velocity, u_{cr}, and the sand particle is moving in the direction of the current velocity with speed, u_s, the force balance equation acting on this moving particle is expressed as

$$\frac{1}{2}\rho C_{DM} S_s (u_f - u_s)^2 = (s-1)\rho g v_s (\cos\beta \tan\phi_m + \sin\beta) \tag{4}$$

with C_{DM}, a drag coefficient and ϕ_m, a friction angle of moving sand grain. Representing (4), difference of u_f and u_s is expressed in a similar form of (3) as

$$\frac{(u_f - u_s)^2}{(s-1)g(v_s/a_s)} = \frac{2}{C_{DM}} \tan\phi_m \cos\beta \left(1 + \frac{\tan\beta}{\tan\phi_m}\right) \tag{5}$$

From (3) and (5), relationship among current and moving sand grain velocities are expressed as

$$u_s = u_f - \beta_s u_{cr0} \tag{6}$$

Here u_{cr0} is the critical velocity on a horizontal plane bed, obtained by substituting β=0 in (3), and β_s is a coefficient which accounts for the influence of the bottom slope. Note that (6) is valid only when $u_f > \beta_s u_{cr0}$ and u_s=0 otherwise. If one takes $C_{DM} \sim C_{DS}$ and $\tan\phi_m / \tan\phi_s \sim 0.5$, β_s is derived from (3) and (5) as

$$\beta_s^2 = \frac{1}{2}\cos\beta\left(1+\frac{\tan\beta}{\tan\phi_m}\right) \tag{7}$$

From equations (6) and (7), the velocity of moving sand grain is expressed as functions of current velocity around the grain, critical current velocity, and the bottom slope in the direction of current flow. If one applies law of the wall, u_f, the fluid velocity at $z=z_d$, elevation of a particle from the bottom, is determined as

$$u_f = \alpha u_{*b} \qquad \alpha = \frac{1}{\kappa}\ln\frac{z_d}{z_0} \tag{8}$$

Here $u_{*b} = \sqrt{\tau_b / \rho}$ is shear velocity at the bottom with bottom shear stress, τ_b, κ(=0.4) is von Karman's constant and $z_0 = k_N$ /30 with k_N, Nikuradse's (1933) equivalent bottom roughness which is of the order of bottom sediment diameter, d. The value of α in (8) is explicitly determined as functions of k_N and z_d. For example, if one takes $k_N = d$ and $z_d = 0.8d$, equation (8) leads $\alpha \sim 8$. Taking similar procedure to (8), the critical fluid velocity, u_{cr0} is also expressed in terms of critical shear velocity, $u_{*cr} = \sqrt{\tau_{cr} / \rho}$ as

$$u_{cr0} \sim \alpha\, u_{*cr} \tag{9}$$

Substituting (9) and (10) into (6), instantaneous velocity of the moving particle, u_s, is determined as functions of bottom shear velocity,

$$u_s = \alpha\left(u_{*b} - \beta_s u_{*cr}\right) \tag{10}$$

Note again that (10) is valid only when $u_{*b} > \beta_s u_{*cr}$ and u_s=0 otherwise.

Moving Sand Layer Thickness and Bedload Sediment Transport Rate

As shown in the field sand-tracking survey discussed in the later section, a certain fraction of dyed sand grains tends to stay where they were initially placed for a certain period of time. This feature may be simply because some of these dyed sand grains were placed below the bed surface and thus did not "feel" the shear force due to near-bottom current velocity. The similar feature should occur in the actual sand recycling project especially when a relatively large amount of recycled sand is dumped in a relatively small area and thus the thickness of the dumped sand is relatively large. In this sense, it is important for the model to capture this time-difference of the initial movement of each sand grain. The model accounts for this feature by introducing the concept of the thickness of moving sand layer based on Madsen's (1991) conceptual bedload sediment transport model. By applying Madsen's bedload sediment transport mode to determine both velocity and thickness of the moving sand grains, we can ensure that the instantaneous sand volumes which moves away from the initial sand discharged area are also consistent with the well-known bedload sediment transport rate.

Following Madsen (1991), thickness of the moving sand layer, δ_s, is derived from the horizontal force balance equation for entire moving sand grains. Since the sand grain does not move just below the lower boundary of the moving sand grain layer, the shear stress acting on this boundary should be the critical shear stress, τ_{cr}. Taking V_s to be a total volume of sand moving across unit width, horizontal force balance equation acting on all the moving sand grains leads

$$\tau_b - \tau_{cr} = \rho(s-1)gV_s \cos\beta(\tan\phi_m - \tan\beta) \tag{11}$$

Taking a porosity of the moving sand as n, thickness of the moving sand layer, δ_s, is obtained from (11) as

$$\begin{aligned}\delta_s = \frac{V_s}{1-n} &= \frac{\tau_b - \tau_{cr}}{(1-n)\rho(s-1)g\cos\beta(\tan\phi_m - \tan\beta)} \\ &= \frac{(\psi_b - \psi_{cr})d}{(1-n)\cos\beta(\tan\phi_m - \tan\beta)}\end{aligned} \tag{12}$$

where $\psi = |\tau| / \rho(s-1)gd$ is Shields number with subscripts b and cr corresponding to the values based on bottom shear stress and critical shear stress, respectively. Finally, the product of (10) and (12) yields following Madsen's (1991) conceptual bedload sediment transport model with effect of the bottom slope,

$$q_{SB} = u_s V = u_s \delta_s (1-n) = \frac{8(u_{*b} - \beta_s u_{*cr})(\psi_b - \psi_{cr})d}{\cos\beta(\tan\phi_m - \tan\beta)} \tag{13}$$

Here α=8 was applied in (10). According to Madsen (1991), the bed load sediment transport rate obtained from (13) agrees with well-known Meyer-Peter and Muller's (1948) (referred as MPM hereafter) bedload formula within an error of around 10% on the horizontal bed (β=0). It should again be stressed that (13) is applicable only when $u_{*b} > \beta_s u_{*cr}$ and $\psi_b > \psi_{cr}$ and q_{SB}=0 otherwise.

Model Extension to Actual Field Problems

In this section, we extend the present model to actual field problems, in which waves and mean current may coexist and the sandy movable bed may form ripples or sheet flow. Especially in the near-shore area, where we put more focus on as sand recycling site, wave-induced near-shore mean current and waves coexist and relatively intensive wave orbital velocity often causes sheet flow bed conditions. Wave-current coexisting field yields time-varying bottom shear stress and sheet flow bed, which has larger equivalent bottom roughness, increases the sediment transport rates.

According to Wilson (1987), MPM bedload sediment transport formula yields reasonable sediment transport rate even on the sheet flow bed if one were to apply the total shear stress on the movable bed, i.e., the shear stress based on the movable bed roughness. The present model therefore applies the following Herrmann and Madsen's (2006) sheet flow bed roughness to determine the bottom shear stress. Using obtained total bottom shear stress, the model then determines the bedload sediment transport rate from (13), which is known to yield nearly the same sediment transport rate as MPM formula.

$$k_N = [2 + 4.5(\psi_b - \psi_{cr})]d \tag{14}$$

If the local Shields number, ψ_b, nears the critical Shields number, ψ_{cr}, i.e., there is no sand grains moving on the surface, equation (14) becomes $k_N=2d$, which is equivalent to well-known Jonson's friction model on a fixed sandy bed. In this study, therefore, we simply apply (14) to determine the equivalent bottom roughness whether or not the bed forms sheet flow conditions.

Applying Madsen's (1994) bottom boundary layer model under wave-current coexisting field, instantaneous bottom shear stress vector, $\boldsymbol{\tau}_\mathbf{b}$, is expressed as

$$\boldsymbol{\tau}_\mathbf{b} = \boldsymbol{\tau}_\mathbf{c} + \frac{f_{cw}}{2} u_{wm} \mathbf{u}_\mathbf{w}(t) \tag{15}$$

Here, $\boldsymbol{\tau}_\mathbf{c}$ is a bottom shear stress vector due to mean current velocity, f_{cw} is a friction factor, and $\mathbf{u}_\mathbf{w}(t)$ and u_{wm} are wave orbital velocity vector and its amplitude, respectively. Bedload sediment transport rate under wave-current coexisting field with sheet flow bed condition is thus determined by

$$\mathbf{q}_\mathbf{SB} = \frac{8\left(|\boldsymbol{\tau}_\mathbf{b}| / \rho u_{*m} - \beta_s u_{*cr}\right)(\psi_b - \psi_{cr})d}{\cos\beta(\tan\phi_m + \tan\beta)} \frac{\boldsymbol{\tau}_\mathbf{b}}{|\boldsymbol{\tau}_\mathbf{b}|} \tag{16}$$

Note that β is also a function of time because the flow direction varies with time and equation (16) is applicable only when $u_{*b} > \beta_s u_{*cr}$ and $\psi_b > \psi_{cr}$ as stated before.

On the sheet flow bed, the fraction of moving particle velocity, $\mathbf{u}_\mathbf{s}$, and thickness of the moving particles, δ_s, may be different because the different structures of movable bed roughness should affect the flow velocity near the bottom. In order to ensure that the present model yields the same bedload sediment transport rate as Madsen's (1991) model even on the sheet flow bed, we first assume that following relationship among $\mathbf{U}_\mathbf{s}$, δ_s and bedload sediment transport rate, $\mathbf{q}_\mathbf{SB}$, obtained by (16) holds.

$$\mathbf{q}_\mathbf{SB} = \mathbf{u}_\mathbf{s} V_s = \mathbf{u}_\mathbf{s} \delta_s (1 - n) \tag{17}$$

Based on this assumption, the present model first determine $\mathbf{u}_\mathbf{s}$ on arbitrary movable bed conditions and then inversely estimate δ_s from (16) and (17) with obtained $\mathbf{u}_\mathbf{s}$. As discussed previously, $\mathbf{u}_\mathbf{s}$ can be determined from (6) as functions of the fluid velocity vector around the sand grain, $\mathbf{u}_\mathbf{f}$. Following Madsen's (1994) wave-current bottom boundary layer model, the instantaneous current velocity, $\mathbf{u}_\mathbf{f}$, near the bottom, $z=z_d$, is expressed as

$$\mathbf{u}_\mathbf{f} = \frac{\boldsymbol{\tau}_\mathbf{b}}{\rho \kappa u_{*m}} \ln \frac{z_d}{z_0} = \alpha \frac{\boldsymbol{\tau}_\mathbf{b}}{\rho u_{*m}} \tag{18}$$

Here, u_{*m} is a maximum shear velocity under wave-current coexisting field and it should be stressed that (18) is valid only when z_d is below the outer-edge of wave-current bottom boundary layer thickness, δ_{cw}. As seen in (18), the value of α and corresponding $|\mathbf{u}_\mathbf{f}|$ decrease as the movable bed roughness, k_N, and thus $z_0=k_N/30$ increase. This feature is consistent with Wilson's (1987) experimental study in which he suggested that a part of the total shear stress on a sheet flow bed balances with friction forces among moving sediment particles and thus the current velocity within the sheet flow layer should be smaller than the current velocity on the fixed bed with

the equivalent bottom roughness of the order of sediment diameter, d. Based on a number of experimental data, Wilson (1987) proposed the current velocity in the sheet flow layer in the following form.

$$u_f = \frac{2u_{*b}}{\kappa}\sqrt{\frac{z}{\delta_{sf}}} \tag{19}$$

Here, δ_{sf} is thickness of the sheet flow layer. Averaging (19) over the sheet flow layer thickness, δ_{sf}, we obtain the "layer-averaged" flow velocity within the sheet flow layer. Under the steady current, i.e., $u_{*m} = u_{*b} = \sqrt{|\boldsymbol{\tau}_b|/\rho}$, equation (18) corresponds to this average flow velocity within the sheet flow layer if one takes α~3.3. To obtain α=3.3, equation (18) requires z_d/k_N to be around 0.12, which seems somewhat reasonable since the sheet flow roughness is about the order of magnitude greater than the sand diameter. Following these discussions, we simply estimate $\mathbf{u_f}$ from (18) with equivalent bottom roughness obtained by (14). This enables us to have smoothly varying α as functions of movable bed roughness. The instantaneous velocity of the moving sand grain, $\mathbf{u_s}$, is then obtained by the following vector form of (10).

$$\mathbf{u}_s = \max\left\{0,\ \alpha\left(\left|\frac{\boldsymbol{\tau}_b}{\rho u_{*m}}\right| - \beta_s u_{*cr0}\right)\right\}\frac{\boldsymbol{\tau}_b}{|\boldsymbol{\tau}_b|} \tag{20}$$

Thickness of the moving sand grain layer, δ_s, is then determined by substituting above $\mathbf{u_s}$ into (17) as

$$\delta_s = \frac{8(\psi_b - \psi_{cr})d}{\alpha(1-n)\cos\beta(1+\tan\beta/\tan\phi_m)} \tag{21}$$

Since the shear stress varies with time due to wave motion, δ_s and $\mathbf{u_s}$ should also vary with time. For computational efficiency, the model applies the mean velocity and thickness of the moving sand grain, $\mathbf{U_s}$ and $<\delta_s>$, which are obtained by time-averaging (20) and (21) over one wave period, respectively.

Fig. 2 shows $|\mathbf{U_s}|/|\mathbf{U_c}|$ predicted by the present model as functions of $|\mathbf{U_c}|/u_{wm}$ and ψ_w/ψ_{cr} with ψ_w, maximum Shields parameter under wave orbital velocity. As seen in the figure, predicted $|\mathbf{U_s}|/|\mathbf{U_c}|$ falls within the range of 0.01 to 0.05 and these predictions are surely consistent with the empirical relationship, $|\mathbf{U_s}|/|\mathbf{U_c}|$~O($10^{-2}$), proposed by Nadaoka et al. (1981). In contrast to this empirical relationship that assumed $|\mathbf{U_s}|/|\mathbf{U_c}|$ to be uniform, the present model shows that $|\mathbf{U_s}|/|\mathbf{U_c}|$ increases as $|\mathbf{U_c}|/u_{wm}$ or ψ_w/ψ_{cr} increases. If $|\mathbf{U_c}|/u_{wm}$ increases, the relative intensity of the wave-induced turbulence decreases and hence the relative magnitude of the mean shear current velocity becomes larger. If ψ_w/ψ_{cr} increases, the influence of critical shear stress decreases and thus $|\mathbf{U_s}|/|\mathbf{U_c}|$ should increase. The present model reasonably explains these phenomena.

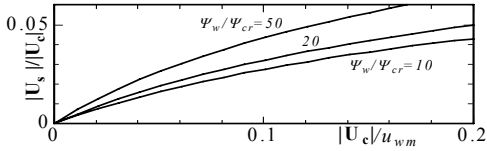

Fig. 2. $|\mathbf{U}_s|/|\mathbf{U}_c|$ as functions of $|\mathbf{U}_c|/u_{wm}$ and ψ_w/ψ_{cr}.

Modeling Dispersive Characteristics Based on Random Walk Theory

As seen in equation (1), the present model accounts for dispersive characteristics of the group of discharged sand grains by introducing the concept of random walk theory. In the field sand-tracking survey of dyed sand grains, as is introduced in the following section, we found that sand particles are more dispersed in the wave-propagation direction rather than the other direction. In order to represent this anisotropic dispersion feature, the model introduces anisotropic dispersion coefficients to determine horizontal random walk step vector, **R**.

The present model applies two different dispersion coefficients, ε_w, and ε_c, i.e., the dispersion due to wave motion acting in the wave-propagation direction and the dispersion due to mean current acting in the mean current flow direction, respectively. Applying the random walk theory, relationship between random walk step vector for computation time step, Δt, is expressed by

$$\mathbf{R} = c_w \mathbf{r_w} \sqrt{2\varepsilon_w \Delta t} + c_c \mathbf{r_c} \sqrt{2\varepsilon_c \Delta t} \tag{22}$$

Here, $\mathbf{r_w}$ and $\mathbf{r_c}$ are unit vectors in wave-propagation and mean current flow directions, respectively, and coefficients c_w and c_c are 1 or -1 whose sign changes randomly with every computational iteration. Finally, the dispersion coefficients may be determined as near-bottom turbulent eddy diffusivity due to the bottom shear stress, i.e.,

$$(\varepsilon_w,\ \varepsilon_c) = \kappa l (u_{*wm},\ u_{*c}) \tag{23}$$

In (23), l is length scale of the near-bottom turbulence, κ (=0.4) is von Karman's constant, and u_{*wm} and u_{*c} are components of bottom shear velocity due to wave orbital velocity and mean current flow, respectively. The length scale l may be δ_s or the bottom boundary layer thickness δ_{cw}. If one assumes that the characteristic velocity and mixing length may be scaled by velocity of the moving particle, U_{sw}, and the excursion amplitude of the sediment particle grain, $A_{bms}=U_{sw}\omega$, the dispersion coefficient due to wave, ε_w, may be determined as

$$\varepsilon_w = \lambda U_{sw} A_{bms} \tag{24}$$

with λ, proportional constant. In this study, we apply these dispersion coefficients and compare the predicted results with the newly conducted field survey results.

FIELD SAND-TRACKING SURVEY

In order to capture the movement of the discharged sand grains, we newly conducted field sand-tracking survey using dyed fluorescent sand grains on the Pacific Coast of

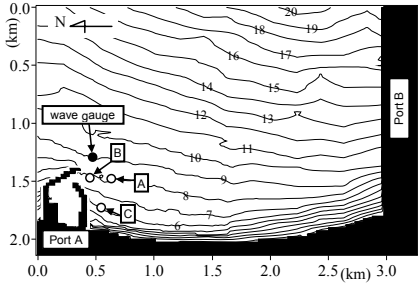

Fig. 3 Geometry of the field survey area and locations of sand-dumping point.

Japan. Fig. 3 shows geography of the field survey site with three different locations where we dumped sand particles dyed with different fluorescent paints. As seen in the figure, the survey site has about 2.5km-long sandy pocket beach between Ports A and B. In the middle of this sandy beach, the shoreline has been severely deteriorated. The beach has well-sorted quarts sand grains with median diameters , d=0.13 mm. The yearly-averaged significant wave height and wave period are 1.1m and 8.6s, respectively, at water depth in the offshore deep water area of this site. About 90% of waves are incident from ENE, E or ESE and dominant wave direction changes with seasons, i.e., most waves are incident from ENE to E in winter and waves from E to ESE are predominant in summer. During the survey, we had measured time-varying wave and current conditions at h=9m as shown in Fig. 3.

At each dumping location A, B and C, we placed around 0.63m^3 of dyed sand grains with diameter of 0.13mm on November 8th, 2004. This volume of sand placed at each point is estimated to be around 6.8×10^{10} sand grains. We then sampled bottom surface sand at 65 different sampling points 40 days after the placement of dyed sand grains. The volume and the surface area of the sampled sand at each sampling point were 300cm^3 and 120cm^2, respectively. These 65 sampling points around the dumping site were selected at grid points of 50m×50m square mesh in the on-offshore and along shore directions. From each of these 65 sand samples, we counted the number of dyed sand grains which were located within unit surface area, A=120cm^2.

MODEL APPLICATION

In order to investigate predictive skills of the present model, we applied the model to the present field sand-tracking survey conditions and compared predicted and sampled spatial distribution of dyed sand grains. Based on the actual wave data measured at the offshore of the survey site, we specified the incident wave conditions for every 12 hours during the entire field survey. These incident waves were determined so that the wave conditions represent the time-average of measured wave energy and radiation stress during each 12-hour period. In the numerical model, we first computed spatial distributions of wave and current conditions for every 12 hours and used the computed results to specify the local wave and current conditions where

and when the computing sand particle is located. We set the number of total sand grains to be N=10^5 at each of three sand-dumping sites, A, B and C. Since the actual number of placed dyed sand grains at each site is about 6.8×10^{10}, each of imaginary particle in the numerical computation represents about 6.8×10^5 of actual dyed sand grains, which correspond to the volume of about 6.3cm^3 of sand. Considering the fact that our focus is to capture the movement of a group of sand grains whose volume is of the order of cubic meters, the total number of N=10^5 seems sufficiently large to capture the features of our focus. Finally, the predicted number of sand particles at each sampling area was multiplied by 6.8×10^5 to estimate the actual number of dyed sand grains. In this manner, we can examine the quantitative predictive skills of the model by simply comparing the spatial distributions of measured and predicted number of dyed sand particles.

Fig. 4 compares observed and predicted significant wave heights, wave directions, near-shore mean current components in the eastward and northward directions at the wave gauge near the harbor mouth of Port A. The data are shown as functions of time during the entire period of the field sand-tracking survey. Note that the incident wave conditions used in the numerical model are not obtained from these measured data but are specified from the other wave gauge installed in the offshore area. Reasonable agreement between measured and predicted wave conditions at this wave gauge near the harbor mouth thus supports the validity of the present computation method. The near-bottom mean current velocity was measured by the electromagnetic flow meter attached on the same wave gauge, which was installed on the sea bed of still water depth, h=9m. Although the measured near-bottom current velocity is relatively small and may not be the suitable data to test the model, predicted near-bottom mean current velocities reasonably agreed with the observed data.

Fig. 5 compares predicted and measured spatial distributions of the number of tracer sand grains, K, sampled from the unit sampling area of 120cm^2. The comparison is when the dyed sand grains were placed at dumping site, A. Note that the numbers, K, in these figures are expressed in logarithmic numbers, i.e., $\log_{10}K$. The first three

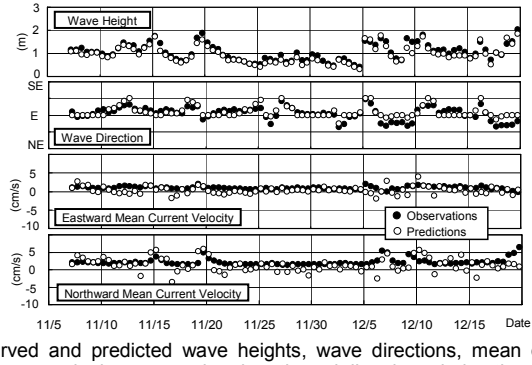

Fig. 4 Observed and predicted wave heights, wave directions, mean current velocity components in the eastward and northward directions during the survey period.

computed results compare different predictions when we applied the following three different dispersion coefficients, respectively: (i) both ε_w and ε_c determined by (20) with turbulent length scale represented by moving sand layer thickness, i.e., $l=\delta_s$; (ii) the same definitions as (i) except the turbulent length scale represented by wave-current bottom boundary thickness, i.e., $l=\delta_{cw}$; and (iii) ε_c identical to (ii) and ε_w determined by (21) with λ=0.4. While these length scales change with the wave and current conditions, the thickness of moving sand layer, δ_s, is generally greater than δ, the thickness of wave-current bottom boundary layer. For example on November 19th 2006, when we observed relatively large waves, H_s=1.87m at point B with h=8m, these layer thicknesses were estimated as δ_s=0.38mm, and δ_{cw}=3.1cm, respectively. As seen in the figures, predictions with dispersion coefficients (i) apparently underestimate the dispersive characteristics of the sand grains. While predictions with dispersion coefficients (ii) significantly improve the predictive skills of the dispersive characteristics, the predictions with dispersion coefficients (iii) showed the best agreement with the observed data. These comparisons clearly suggest that dispersions due to wave motions is greater than the one based on the turbulence caused by the bottom shear stress.

The computed result (iv) shown in Fig. 5 is the prediction when the model applied the same dispersion coefficients as (iii) but $\mathbf{U_s}$, were determined by the simple

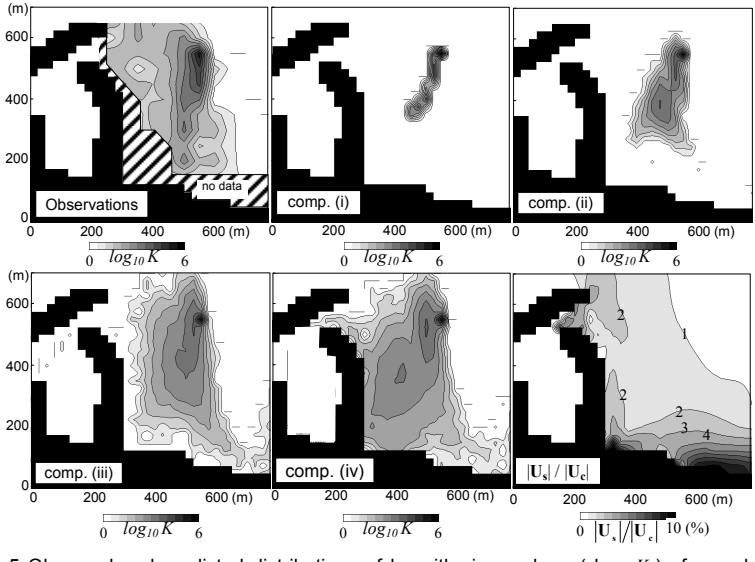

Fig. 5 Observed and predicted distributions of logarithmic numbers ($\log_{10}K$) of sampled dyed sand grains dumped at station A. The first three computations are the results with different dispersion coefficients. The forth computation result is the same as (iii) except $\mathbf{U_s}$ replaced by $\mathbf{U_s}$=0.01$\mathbf{U_c}$. The last figure shows $|\mathbf{U_s}|/|\mathbf{U_c}|$ predicted by the present model with incident wave conditions on Nov. 19th.

empirical formula, $\mathbf{U_s}=0.01\mathbf{U_c}$. For comparisons, Fig. 5 also shows $|\mathbf{U_s}|/|\mathbf{U_c}|$ estimated by the present model with incident wave conditions on November 19th. As seen in this figure, predicted $|\mathbf{U_s}|/|\mathbf{U_c}|$ falls into the range of one or two percents in deeper water where dyed sand grains were initially placed but it increases up to around 5 percents as the wave shoals near the surf zone where both wave-induced current velocity and near-bottom wave orbital velocity become larger. Comparing computed results (iii) and (iv), the present model (iii) predicts more sand transported in the longshore southward direction (rightward direction in the figure) due to the relatively large $|\mathbf{U_s}|$ in the near-shore area and thus predicts less sand grains left around Port A. This feature clearly improves the predictive skills of the spatial distribution of sand grains and thus somehow supports the validity of the present model which accounts for the varying $|\mathbf{U_s}|/|\mathbf{U_c}|$ based on Madsen's (1991) process-based bedload sediment transport model.

Fig. 6 shows the similar comparisons to Fig. 5 but for cases when dyed sand grains were placed at different locations, B and C, respectively. As seen in these observed spatial distributions of dyed sand grains, characteristics of sand grains movement are remarkably dependent upon the initial sand-dumping locations. Locations A and B, for example, are located nearly on the same water depth and at the same distance from the shoreline but B is about 200m away from A in the longshore direction toward the harbor mouth. Due to this alongshore difference of the initial dumping location, sand grains placed at B appears to have less movement than those at A and tend to stay around the harbor mouth. The present model reasonably captures this

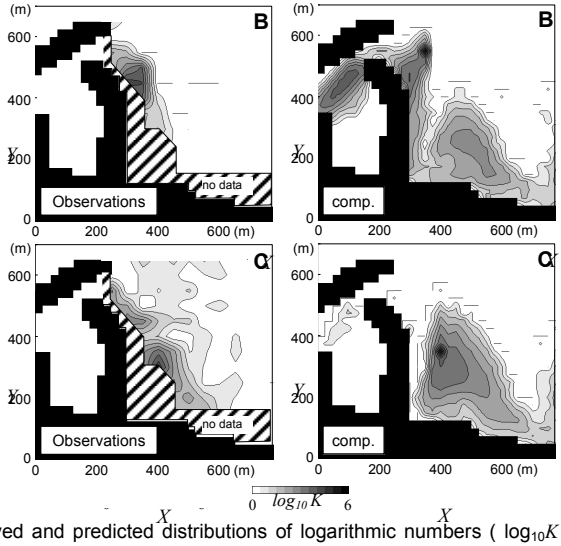

Fig. 6 Observed and predicted distributions of logarithmic numbers ($\log_{10}K$) of sampled dyed sand grains dumped at station B and C.

feature, i.e., the model surely represented that most of dyed sand placed at B stayed around the harbor mouth and had less dispersion compared to the one located at A. In the model predictions for B, certain amount sand grains are also deposited in relatively shallow area whose peak is around X=500m and Y=300m. Due to the lack of field data in this area where the water depth was too shallow to sample the bottom sand, model verification in the shallow water including the surf zone is left as future research. Dumping site C is located in the shallower area and, as seen in the figure, less sand is left at the initial dumping site compared with the other two cases. Although the number of sand grains left at C was over-predicted, the model successfully represented the overall spatial distributions of dyed sand grains along the coast.

CONCLUSION

A numerical model to track the movement of certain specific groups of discharged sand grains was newly developed. The model accommodates predictions of movement of group sand grains due to sediment transport processes as well as the dispersive characteristics of the discharged sand group. Introducing the same concept as Madsen's (1991) process-based bedload sediment transport model, the present model determined the velocity and layer-thickness of moving sand particles, whose product is consistent with Madsedn's (1991) bedload sediment transport rate. Introducing random walk concept, the model also accounts for the dispersive effects. The present model showed excellent predictive skills of the movement of dyed sand grains observed in the newly performed field survey.

REFERENCES

Herrmann, J. M. and Madsen O. S. (2007) "Effect of stratification due to suspended sediment on velocity and concentration distribution in turbulent flows." J. of Geoph. Res. (in press).

Komar, P.D. and Inman, D.L. (1970) "Longshore sand transport on beaches." J. of Geoph. Res., vol.75, No. 30, pp.5914-5927.

Madsen, O.S. (1991) "Mechanics of cohesionless sediment transport in coastal waters." Proc. of Coastal Sediments '91, vol.1, pp.15-27.

Madsen, O.S. (1994) "Spectral wave-current bottom boundary layer flows." Proc. 24th ICCE, pp.384-398.

Meyer-Peter, E. and Muller, R. (1948) "Formulas for bed-load transport." Proc. 2nd Cong. of Int. Assoc. for Hydr. Struc. Res., pp.39-64.

Nadaoka, K., Tanaka, N. and Katoh, K. (1981) "Field observation of local sand movements in the surf zone using fluorescent sand tracer." Report of the Port and Harbour Resarch Institute, vol.20, No.2, pp.75-126.

Nikuradse, J. (1933) "Stromungsgsetze in glatten und rauhen rohren." VDI Forschungsheft 361.

Wilson, K. C. (1987) "Analysis of bed-load motion at high shear stress." J. of Hydraulic Eng., 113(1), pp.97-103.

SEDIMENT TRANSPORT IN RESPONSE TO WAVE GROUPS GENERATED BY HIGH-SPEED VESSELS

Philip D. Osborne[1], Neil J. MacDonald[2], and Shaun Parkinson[3]

1. Pacific International Engineering, PLLC, 123 Second Ave. South, P.O. Box 1599, Edmonds, WA, 98020, USA. philo@piengr.com
2. Pacific International Engineering, Corp, 260 Centrum Blvd., Ste 220, Ottawa, Ontario, Canada, K1E 3P4 neilm@piengr.com
3. Idaho Power Company, P.O. Box 70, Boise, ID, 83707, USA, sparkinson@idahopower.com

Abstract: Suspended sediment transport dynamics occurring at relatively short time scales under super-critical wave groups created by moving high speed vessels are investigated by means of field measurements and the application of numerical models. Examples are provided from a variety of different environments, including predominately sandy beaches in low energy estuarine and fluvial settings. Model simulations combining the hydrodynamics of the wakes with steady currents and a sand transport model provide results that are largely consistent with field measurements and observations of the suspended load fraction. Wakes re-suspend sand in the nearshore that would otherwise be immobile and move it incrementally offshore and alongshore, eventually into deeper water where stronger ambient flows (tidal or fluvial) can transport the sediment. Super-critical wakes from high speed vessels have a tendency to cause offshore transport of sand-sized sediment leading to beach flattening while their sub-critical counterparts often lead to beach steepening.

INTRODUCTION

Wave-induced erosion associated with ship traffic in confined waterways has been widely reported including locations in San Francisco Bay, California, Puget Sound, Washington, Georgia Strait, British Columbia, Saint Lawrence River, Quebec, Waitemata Harbor and Marlborough Sounds, New Zealand, Loch Ryan, Scotland and Kattegatt, Denmark (see review by Parnell and Kofoed-Hansen, 2001). Because of their size and speed, many commercial and recreational vessels are capable of producing

sizable wakes that can be damaging to the adjacent shoreline and dangerous to other craft. Unfortunately, there is little design information and few unified design tools are available to scientists and engineers needing to predict the sediment transport and associated morphological effects on shorelines resulting from vessel wakes. This paper examines the details of the fluid and suspended sand dynamics that occur at medium (hours) and short (seconds) time scales on beaches with a range of grain sizes (sand-pebble) present in response to super-critical wave groups created by moving high speed vessels. Examples are provided from Snake River, Idaho and Auckland, NZ. The purpose is to gain insight into the differing modes of transport for coarse- and fine-grained sediments under wakes produced by high speed vessels.

SUPER-CRITICAL AND SUB-CRITICAL WAKES

A vessel wake observed at the shoreline in a coastal, estuarine, or fluvial environment occurs as a sequence or group of waves. The characteristics of the wave group observed at the shoreline depend on a large number of variables related to the moving vessel including position, heading, and distance from shore, speed, hull geometry, trim and displacement, as well as the properties of the ambient water body including depth contours, presence of currents, or wind waves. The term *super-critical* is sometimes used to describe high-speed vessels while the term *sub-critical* is used to describe displacement vessels traveling at slow speed. Super-critical refers to the state where the vessel is moving faster than the speed at which a wave of the same length can travel in that depth of water. The super-critical condition depends on the speed of the vessel and the depth of the water. The wake produced by a super-critical vessel is different from that produced by a vessel moving at sub-critical speed (see Osborne et al., 2006 for examples). In the latter case, the wake produced has both diverging and transverse components. The transverse component is monochromatic and its wavelength is determined from the linkage between the speed of the vessel and the celerity of the wake for the given depth of water. Whereas the spectrum of a super-critical wake shows peaks in energy at a number of frequencies and the wake passing a point shows a steady decline in wave period through time.

Figure 1a illustrates the classical wake pattern generated by a sub-critical vessel. The wake is composed of two types of waves; diverging wakes that move away from the vessel at an angle of 35.27^{o} and transverse wakes that move in the vessel's direction. Both types of wakes theoretically exist only within a cone set at 19.47^{o} from the vessel. This pattern, first described mathematically by Lord Kelvin in 1887, can be derived from simple geometry. The wavelength and speed of the wake can be found from linear wave theory. As the vessel speed increases, so does the celerity of the wake. A point will be reached where the vessel is moving faster than its transverse wake and this part of the wake is shed. From this point on (i.e. if the vessel maintains a speed equal to or greater than this speed and the depth remains the same or decreases) the wake will assume a new form; the super-critical wake pattern is composed only of diverging wakes (Figure 1b). The super-critical wakes cannot exist as free gravity waves in a classical Kelvin wake pattern. Super-critical vessels produce a wake pattern in which the period of the waves appears, to a stationary observer, to decrease in an approximately exponential manner.

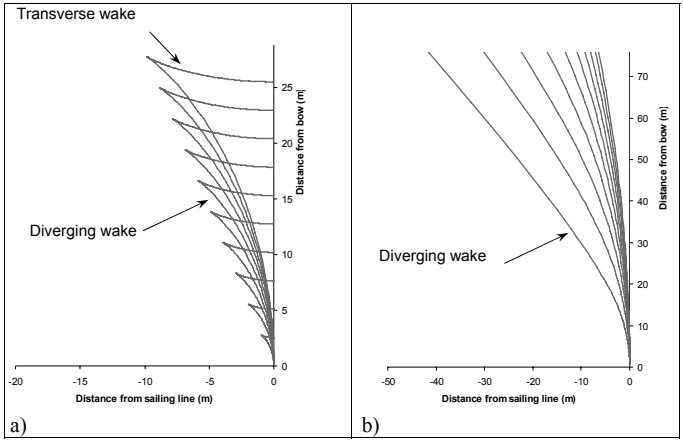

Figure 1. Wake patterns: a) sub-critical vessel; and b) super-critical vessel

METHODS

The approach in this paper involves a combination of detailed and direct field measurements and numerical modeling of the relevant processes. Field measurements were obtained from three different environments:

- a mixed sand and gravel beach exposed to wind waves, wakes from both conventional and high speed commercial and recreational vessels, and strong tidal currents in Puget Sound, Washington (see Osborne et al., in press),
- sand and gravel bars exposed to wakes from jetboats and river flows in the Hells Canyon Reach of Snake River, Idaho and
- a sandy foreshore exposed to wakes and wind waves in the Waitemata Harbor Auckland, NZ.

The approach to modeling is demonstrated with examples from a sand bar in the Snake River, Idaho.

Field Measurements

Field measurements collected and analyzed for this paper include time series of wakes and water surface elevations measured with pressure sensors or capacitance wires, 3D orbital velocities measured with Acoustic Doppler Velocimeter (ADV), and suspended sand concentrations (*ssc*) measured with Optical Backscatter Sensors (OBS). The ADV was integrated with other sensors as part a Sontek HYDRA system (Figure 2).

The sediment dynamic response under wakes and ambient conditions was determined by direct visual observation of sediment motion and recording of *ssc* time series with OBS. Calibration of the OBS to determine *ssc* was achieved using local sediment in a laboratory calibration facility following typical procedures for sandy sediments.

Wakes from a variety of different high speed vessels including recreational jet boats, conventional catamarans, and foil-assisted catamarans are considered. Measured wake time series were analyzed to compute wake wave characteristics using zero-crossing analysis and spectral analysis methods. The measurements allow validation of numerical models, but also provide valuable insights on processes occurring under boat wakes that lead to improvements in modeling.

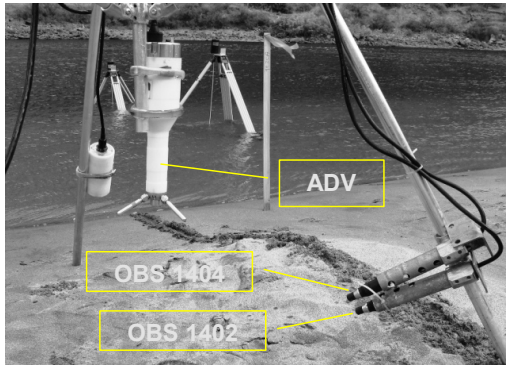

Figure 2. Sontek HYDRA system consisting of ADV and 2 OBS

Numerical modeling

Computer model application in the study includes tidal and river circulation models, wind wave models, a new wake prediction model for high speed vessels, and a Lagrangian sediment transport model. The approach to modeling is demonstrated in this paper with an example from the Fish Trap sand bar in the Snake River, Idaho. The general approach of the modeling exercise is as follows:

- Computer modeling with the Lagrangian Super critical Vessel (LSV) model, an enhanced 2D wake prediction model (MacDonald, 2005), is used to predict the spatially- and temporally-varying wake train produced by a powerboat as it passes a sand bar.
- The wake data is combined with flow data from a large-scale hydrodynamic model (MIKE 21C, IPC) of the river to predict the potential sediment transport caused by this single boat passage (i.e. the sediment put into suspension).
- A medium-term particle tracking simulation (48 hours) is performed with a Lagrangian Particle Tracking Model (PTM, MacDonald et al., 2006) to determine the transport of this sediment. This stage is performed with and without subsequent boat passes. PTM is used to simulate the pattern and magnitude of net sediment transport on the sand bars under the combined influence of boat wakes and river flows.

- An assessment of the fate (i.e. the percentage of material no longer in the vicinity of the sand bar) is made for both the river-only and river plus powerboat simulations to identify the impact of boating on the movement of sediment at the sand bar.

The preceding bullets identify an approach for the quantitative determination of the impact of boating on a select mass of sediments – those put into suspension by the first boat passage in the 48 hour period. The purpose of the modeling is to develop quantitative estimates of the relative role of boat wakes and river flows in causing mobilization of sediment on sand bars with the possibility of developing preliminary estimates of the potential for net transport from the bars. The approach does not consider the fate of any new sediment put into suspension by subsequent wake events, but there is no reason to believe that these new sediments would behave in a different manner. As well, the approach does not consider delivery of fine sediments to the sand bar by the river during high-flow events.

To better account for wave action, especially wave breaking in the nearshore, a new potential sediment transport equation developed by Camenen and Larsen (in press) was added to PTM. The Camenen and Larsen formula is a total load (i.e. bed load and suspended load) potential transport formula. The total transport rate is given by:

$$q_t = \frac{u_* a}{g(\rho_s - \rho)} \frac{\tau_{cw}}{\left(1 + \tan\beta \big/ \tan\Phi_m\right)} \exp\left(-b\frac{\tau_{cr}}{\tau_{cw}}\right)\left[1 + K_T \frac{h}{d_{50}} \frac{U_c}{u_* w} \sqrt[3]{D_t \big/ \rho}\right]$$

where q_t is the volumetric, depth-integrated sediment transport rate [units of m^2/s], θ_{cr} is the critical Shields parameter, w is the sediment fall velocity, τ_c is the current-induced shear stress, τ_{wc} is the combined wave-current shear stress, ρ is the fluid density, ρ_s is the sediment density, g is gravitational acceleration, β is the bed slope, Φ_m is the moving friction angle (≈30°), D_t is the total energy dissipation, d_{50} is the median grain size, U_c is the current speed, $u_* = \sqrt{\tau_c/\rho}$ and:

$$K_T = \frac{2\gamma_o c_B k_d}{a\pi\theta_{cr}}$$

The coefficients in the above equations are a=12, b=4.5, c_B=0.65 and γ_o=2×10^{-5}.

RESULTS

Offshore mean flow during super-critical wakes

Analysis of a large number of velocity records from several locations reveals that as well as introducing an oscillatory component to the nearshore current, the super-critical boat wakes also modify the local steady current by producing an offshore-directed flow. Figure 3 shows a plot of time-averaged nearshore east and north velocity components, V_E and V_N respectively, measured during wake and no-wake intervals at Fish Trap Bar on the Snake River. The shoreline in this case runs approximately north-south and is on the west river bank; therefore positive V_E indicates an offshore directed flow. In general, the

mean flows during the wakes are more easterly and larger than during the no-wake intervals. This pattern of enhanced offshore flow was consistent at all locations.

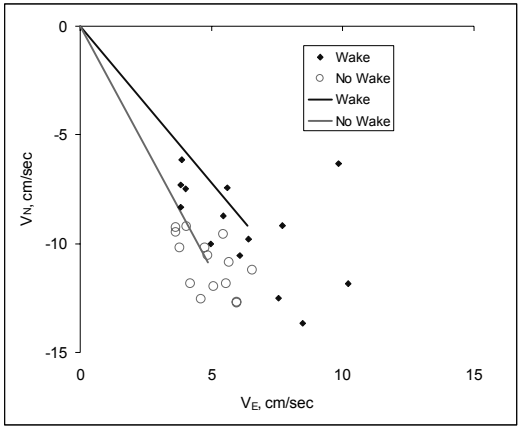

Figure 3. Time-averaged nearshore velocity components (V_E, V_N) measured during wake and no-wake intervals at Fish Trap Bar on the Snake River

The offshore-directed flow has not been previously documented in the context of vessel wakes though it appears to be analogous to a group-forced second-order flow and set-up driven undertow (e.g. Longuet-Higgins and Stewart, 1962, 1964; Doering, 1988). Figure 4 shows a time series of instantaneous near bed wave normal velocity, V_x, measured during a boat wake at Fish Trap Bar. Also shown in Figure 4 is the time variation of the velocities averaged over two to three wave periods (10 sec), $V_{x\text{-}Avg}$. A relatively simple undertow model Grasmeijer and Ruessink (2003) was found to be in good agreement with the measured flows.

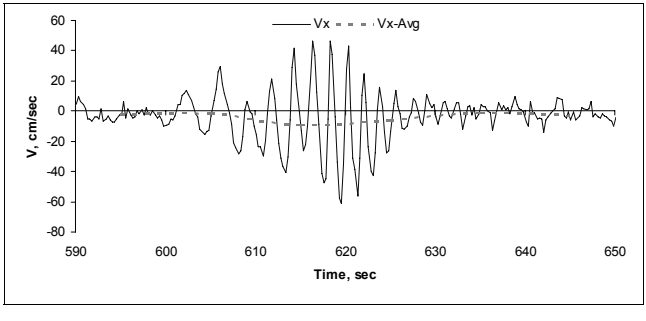

Figure 4. Instantaneous V_x under a wake and 10-sec average velocity, $V_{x\text{-}avg}$, measured at Fish Trap Bar, Snake River

Suspension of sand by super-critical wakes

Figure 5 provides examples of time series of V_x and *ssc* measured during the passage of super-critical wakes produced by different vessels over a variety of different substrates. The relevant conditions are summarized in Table 1. The V_x velocities were determined by rotation of the V_N and V_E velocities such that V_x is the principle component of flow and V_x is positive under the wave crests (approximately onshore in each case); V_y is the secondary flow and is orthogonal to V_x. Peak to peak velocities of +/- 0.40-1.0 m/sec occur under the largest waves in the wakes. The wakes produced by QuickCat result in maximum velocities which are approximately a factor of two larger than those observed in Snake River and correspondingly larger *ssc*. The wave-induced velocities in the wake train are distinctly asymmetric (nonlinear) with short, sharp-peaks under the crests and broader flatter troughs. The high velocities under the wave crests produce the largest peaks in *ssc*. The peaks in *ssc* are relatively low under the long period waves during the first half of the wake, whereas, large peaks in *ssc* occur during the higher, shorter-period waves in the middle of the wake. In most cases *ssc* remains elevated for several waves following the peak velocities.

Table 1. Summary of vessel operating conditions for selected super-critical wakes

Location	*Vessel Name*	*Date*	*TPass*	*Speed (knots)*	*Fr (depth)*	*Fr (length)*	*Distance (m)*	*Boat Length (m)*
Torpedo Bay, Auckland	*QuickCat*	1995-08-02	12:10	26	1.10	0.77	~1 km	33.4
Tin Shed, Snake River	*Hells Canyon Dream*	2005-08-27	11:59	24.5	2.32	1.10	86.0	13.41
Salt Creek, Snake River	*Happy Hour*	2005-08-28	15:50	33.2	1.82	1.65	106.0	10.97

To illustrate the relationships between wave forcing and near-bed sediment suspension on a wave-by-wave basis, phase diagrams of wave-averaged *ssc* as a function of wave-by-wave estimates of the skin friction Shields parameter (θ'_w) are shown in Figure 6 for each of the consecutive waves in the wake trains shown in Figure 5. Waves were identified by zero up-crossing analysis of time-series of V_x. Wave-by-wave estimates of θ'_w are based on U_{sig} (the average of the highest 1/3 velocity measurements under the crest of the wave), and the median sediment diameter representative of the local sediments. Measured *ssc* was averaged through each wave period.

A distinct counter-clockwise hysteresis is apparent in the phase diagrams (Figure 6). All of the phase diagrams exhibit a region of low and steady *ssc* through the first several waves while θ'_w increases well above the threshold for motion and for suspension. As θ'_w approaches a maximum under the largest waves in the wake train, *ssc* increases rapidly. The maximum *ssc* is reached during the wave following the maximum θ'_w and

then begins to decline. Despite a decline in both *ssc* and θ'_w following the maximum *ssc*, the *ssc* is significantly higher while θ'_w is decreasing after the peak than that measured under waves with similar values of θ'_w during the increase before the peak. The pattern is more pronounced at higher elevations above the bed (compare green line with blue line in Figure 6 b,c) indicating a significant temporal phase lag in *ssc* with elevation.

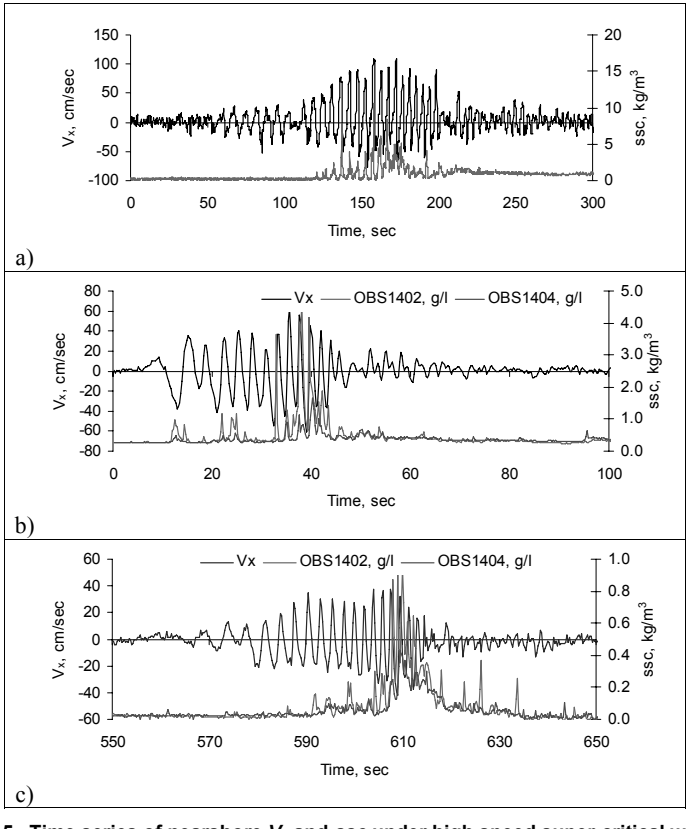

Figure 5. Time series of nearshore V_x and *ssc* under high speed super-critical wakes: a) Torpedo Bay, Auckland, *QuickCat*; b) Tin Shed Bar, Snake River, *Hells Canyon Dream*; c) Salt Creek Bar, Snake River, *Happy Hour*

Simulation of sediment transport by combined wakes and currents

The sediment modeling methodology used in the present work consists of a multi-stage approach:

- development of a detailed daily wake climate using the LSV wake model;
- development of a 48-hour flow hydrograph using MIKE 21C data;

- application of the PTM model to predict the sediment put into suspension on a typical boat passage;
- application of the PTM model to predict the transport of the sediment for a 48-hour period, and;
- analysis of the sediment fate to determine percentage retention/loss of sediment caused by the boat wakes.

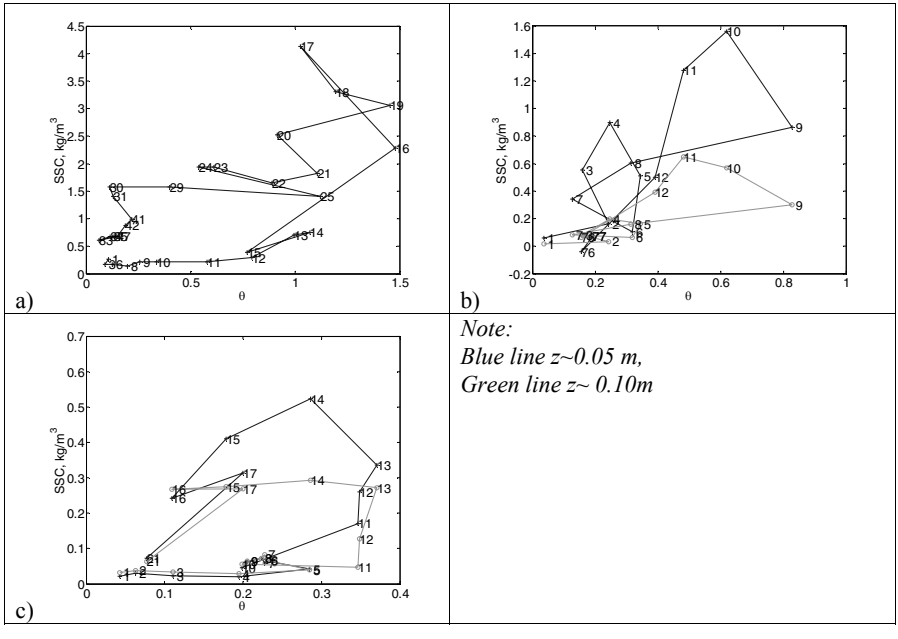

Figure 6. Phase diagrams of wave-by-wave θ'_w and *ssc* during high speed super-critical wakes: a) Torpedo Bay, Auckland, *QuickCat*; b) Tin Shed Bar, Snake River, *Hells Canyon Dream*; c) Salt Creek Bar, Snake River, *Happy Hour*

The LSV model was calibrated for two powerboats, a 26-ft workboat and a 44-ft tour boat, using wake data collected at Fish Trap Bar on the Snake River (Figures 7 and 8). A wave climate for the site was constructed from the number of boat passes measured and by running the LSV model a total of four times at each site (2 boats × 2 directions). Data manipulation programs were used to convert the LSV data into individual standard wave time series files. A wake time series for the 48-hour period was constructed by distributing the appropriate number of wake events, between the hours of 06:00 and 18:00 of each day. The periods between were taken as river-only periods.

A flow time series file for Fish Trap Bar was developed in an analogous manner to that of wake climate. Recorded discharges were used to estimate local discharges at the sand

bar site. Instantaneous hourly flows were interpolated from steady-state MIKE 21C results (5,000 cfs, 10,000 cfs, 20,000 cfs, 30,000 cfs, 50,000 cfs, 75,000 cfs, and 100,000 cfs). The discharge hydrograph for the Fish Trap bar site from 8-27-2005 to 8-29-2005 is shown in Figure 9; time is represented in hours since start of the simulation. Also shown in Figure 9 are the periods of boating activity.

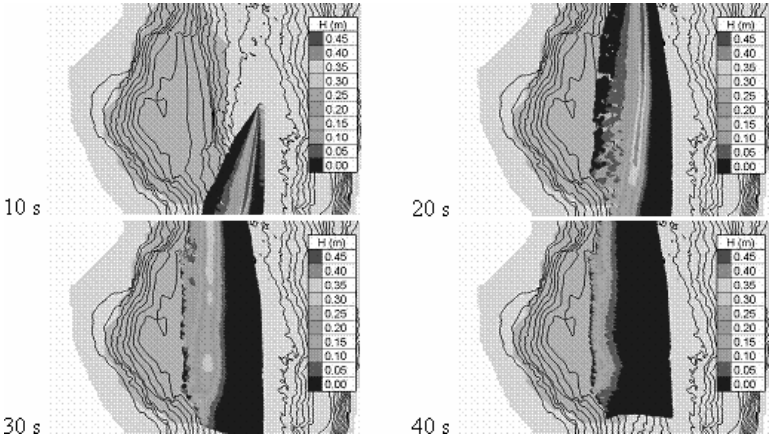

Figure 7. Time sequence of wake height at Fish Trap Bar on the Snake River produced by a 44-ft tour boat at 25 knots headed downstream

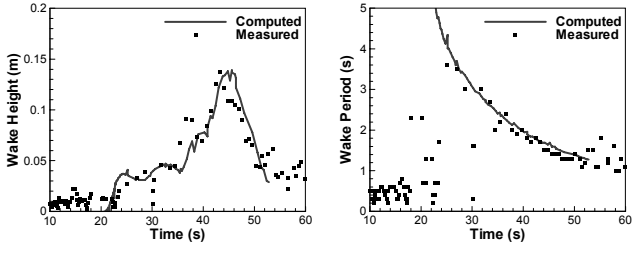

Figure 8. Comparison of measured and computed wake height (left) and period (right) for a 26.ft workboat headed downstream at Fish Trap Bar

The potential sediment transport rate predicted by the Camenen and Larson total load sediment transport formula was calibrated using optical backscatter *ssc* data collected at the study site. The calibration procedure involved operating PTM for a single boat passage and computing the instantaneous sediment load (i.e. the mass of sediment in the water column per unit area). Calibration of the model was obtained by adjusting the value of k_d in the Camenen and Larson formula until the measured and computed values

of the sediment load in the water column agreed. A value of k_d =0.015 was found to provide the best calibration. This value falls within the range of values suggested by Camenen and Larson.

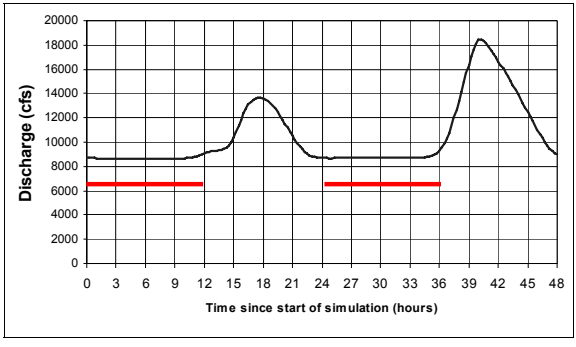

Figure 9. Discharge hydrograph at Fish Trap Bar over 48 hour simulation period. Red bars indicate periods of boating activity

In order to compare the measured results with the computed, they must first be time-averaged and depth-integrated. A two-second time-averaging window was used. Depth integration was performed using an assumed two-part concentration distribution. The concentration was assumed to be uniform over the lower 4 cm and to vary in a parabolic fashion above that point to the surface. Using this distribution a time series of the total suspended sediment load, M is computed (expressed in kg/m^2). Figure 10 shows the generally good agreement obtained between the estimated mass load of sediment in suspension based on field measurements at the study site and that predicted from the preliminary PTM run. The model tends to overpredict the suspended load in the early part of the wake and underpredict it later in the wake; this reflects the "wave group-induced" hysteresis observed in the measurements which is not accounted for in the sediment transport formula (Figure 6).

The results of the PTM simulation for the 48-hour period are presented in Figure 11. A general pattern of movement was observed in the results:

- boat wakes caused bed material to be brought into suspension;
- while in suspension, the ambient river currents and small wake-induced undertow caused a small, but important advection of the suspended material;
- the alongshore and offshore directed advection caused by multiple boat passages (35 on the first day and 23 on the second) and the river flow moved the material into deeper water, and;
- the larger discharge during the evening hours transported the material away from the site. This can be observed in the results at hours 18 and 39.

The general pattern of movement described above was observed at each of the sand bar sites studied on the Snake River. The river flows alone are not sufficient to

mobilize sand sized material in the nearshore zone. Boat wakes do put material into suspension. While in suspension, river flows and the wake-induced undertow gradually move the material along and across the nearshore zone. Often the material was moved into deeper water, where it was later removed when larger flows occurred.

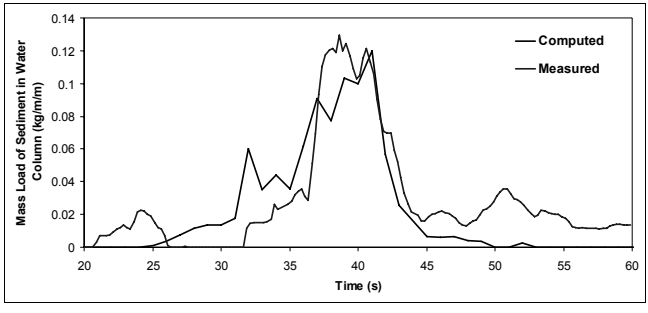

Figure 10. Comparison of measured and computed sediment load in the water column per unit bed area

CONCLUSION

Analysis of a large number of velocity records from several sites reveals that as well as introducing an oscillatory component to the nearshore current, the boat wakes also modify the local steady current by producing an offshore-directed flow. The offshore-directed flow has not been previously documented in the context of vessel wakes though it appears to be analogous to a group-forced second-order flow and set-up driven undertow. A relatively simple undertow model Grasmeijer and Ruessink (2003) is found to be in good agreement with the measured flow.

Suspended load and bedload modes appear to respond differently to waves of varying frequency in a super-critical wake group sequence. Osborne et al. (in press) describe how the longer period motions at the start of a super-critical boat wake result in net offshore transport of gravel and cobble on mixed beaches in Puget Sound. In this paper, the time varying suspension patterns under super-critical wakes are shown to exhibit properties similar to the suspension patterns under conventional wave groups produced by ocean waves (e.g. Villard et al., 2000). The *ssc* remains elevated for a number of waves following the peak velocities under the higher frequency waves in a wake group resulting in a hysteresis between the maximum wave component of bed shear stress and the ssc.

Model simulations combining the hydrodynamics of super-critical wakes with steady currents and a sand transport model provide results that are consistent with the field measurements and observations of the suspended load fraction. The wakes re-suspend sand in the nearshore that would otherwise be immobile. The sand is transported both alongshore and offshore incrementally away from the shoreline eventually reaching deeper water where stronger ambient flows can transport the sediment.

Although the model incorporates some of the elements of the wake induced mean flows, the approach does not fully account for the wave group-induced hysteresis on the suspended sediment load or the differential effects of wave frequency and shape (nonlinearity) effects on the suspended load and bedload. More work is also needed to model the tendency for offshore transport of sand, gravel, and cobble-sized sediment on mixed sediment beaches under super-critical wakes, that leads to beach flattening, while their sub-critical counterparts often lead to beach steepening.

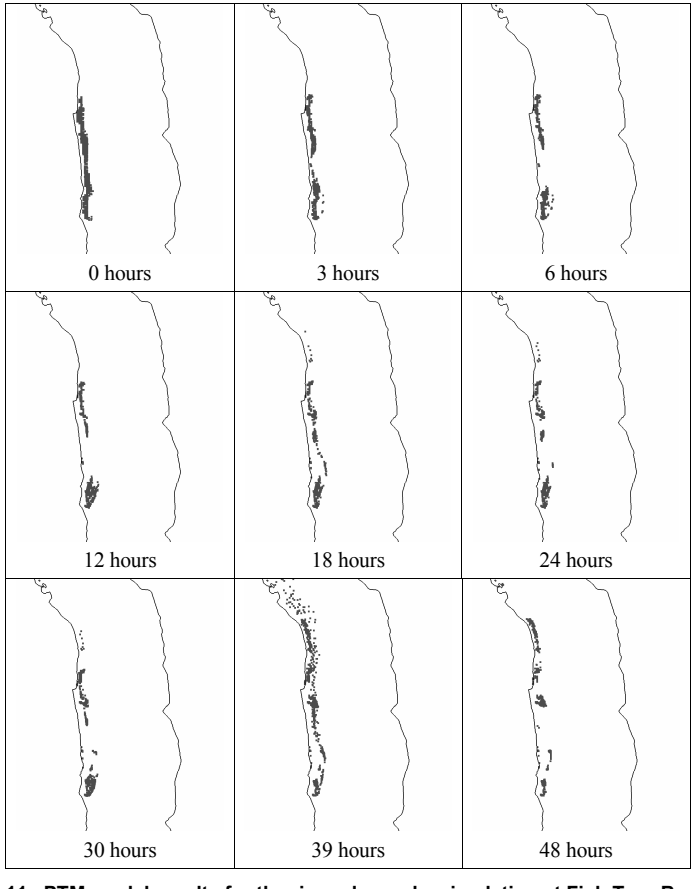

Figure 11. PTM model results for the river plus wake simulation at Fish Trap Bar

ACKNOWLEDGEMENTS

This work would not have been possible without the cooperation and assistance of many people: past and present PI Engineering staff assisted with data collection and

processing; the waterfront property owners of Rich Passage continue to provide access to beaches, and the vessel operators have provided the wakes and vessel performance information. Their contributions are gratefully acknowledged. The development of LSV was funded by a federal grant program administered by the Federal Transportation Administration (FTA-WA-26-7007-2005), designed to support research and investigations of emerging transportation systems. Idaho Power Company (IPC) funded the studies on the Snake River; IPC staff also assisted with data collection and kindly granted permission to publish the results.

REFERENCES

Camenen, B. and Larson, M. (in press) "General sediment transport formula for waves and current." Coastal Engineering (submitted 2006).

Doering, J.R.C. (1988) Wave-wave interactions in the nearshore. Ph.D thesis, Department of Oceanography, Dalhousie University, Halifax, NS, 139p.

Grasmeijer, B.T. and Ruessink, B.G. (2003). Modeling of waves and currents in the nearshore parametric vs. probabilistic approach. Coastal Engineering, 49: 185-207.

Longuet-Higgins, M.S. and Stewart, R.W. (1962) Radiation stress and mass transport in gravity waves, with application to surf-beats. Journal of Fluid Mechanics, 13: 481-504.

Longuet-Higgins, M.S. and Stewart, R.W. (1964) Radiation stress in water waves: a physical discussion with applications. Deep Sea Research, 11: 529-562.

MacDonald, N.J., 2005. Super-Critical Vessel Modeling. In: Proceedings, Canadian Coastal Conference 2005, Halifax, on CDROM.

MacDonald, N. J., M. H. Davies, A. Z. Zundel, J. D. Howlett, Z. Demirbilek, J. Z. Gailani, T. C. Lackey, and S. J. Smith. 2006. PTM: Particle tracking model, report 1: model theory, implementation, and example applications. Technical Report ERDC/CHL TR-06-20. Vicksburg, MS: U.S. Army Engineer Waterways Experiment Station, Hydraulics Laboratory.

Osborne, P.D. MacDonald, N.J. and Reynolds, W.J. (in press) Response of mixed sediment beaches to wake wash from passenger only fast ferries: Rich Passage, Washington. Proc. 30th International Conference on Coastal Engineering, San Diego, CA, ASCE, Sept 2006.

Parnell KE and Kofoed-Hansen H. 2001. Wakes from large high-speed ferries in confined coastal waters: Management approaches with examples from New Zealand and Denmark, Coastal Management 29(3), 217-237

Villard, P.V., P.D. Osborne, C.E. Vincent. 2000. Influence of wave groups on SSC patterns over vortex ripples. Continental Shelf Research. 20 (17): 2391-2410.

FLUME EXPERIMENTS UNDER CAT-SCAN TO MEASURE INTERNAL SEDIMENTOLOGICAL PARAMETER DURING SEDIMENT TRANSPORT

Stéphane Montreuil[1], Bernard F. Long[2]

1. Université du Québec, INRS-ETE, 490, de la Couronne, Québec (Qc), Canada G1K 9A9. stephane_montreuil@inrs-ete.uquebec.ca
2. Université du Québec, INRS-ETE, 490, de la Couronne, Québec (Qc), Canada G1K 9A9. blong@inrs-ete.uquebec.ca

Abstract: X-Ray computed tomography (CAT scanning) has enabled the measurement of the relative density of sand ripples inside the sediment column during ripple migration. A sand ripple produced by stationary flow inside a vertical water tunnel reveals different internal density stratification on CAT-scan profiles. CAT-scan measurements provide a very precise integrated measurement of sediment transport inside the sand ripple, both at the water-sediment interface and in the water column. Results give the total sediment transport (suspended load column concentration and bed load) and illustrate the contribution of each type of sediment transport and their relative magnitude along sand ripples.

INTRODUCTION

The density of a sediment bed provides information on the different phases of the genesis of the internal architecture of sand ripples. The aim of this study is to analyze the evolution of the relative density of a sand ripple during its migration under a stationary flow regime inside a vertical sediment water tunnel on the way to determine the sand ripple characteristics under sediment transport.

Computed axial tomography (CAT) scanning, originally a medical technique which has been adapted to many uses in geosciences (Duliu 1999, Ketcham and Carlson 2001, Mees *et al.* 2003), may be used to measure the relative density of materials such as that of sand layers in sedimentological studies. Density values measured vary from -1024 to +3071 Hounsfield units (HU; Kak and Slaney 1999). Air and water values are respectively -1000 HU and 0 HU (Ketcham and Carlson 2001). For this study, as a first approximation, the conversion factor between density measurements in HU and g/cm³ is considered to be given by

$$Value\ in\ \frac{g}{cm^3} \cong \frac{(Value\ in\ HU + 1024)}{1000} \quad (1)$$

The scanographic research facility at Quebec City dedicated to non-medical use with applications in civil engineering and sedimentology fields, is built around a Siemens Somatom Volume Access CAT-Scan, (Fig. 1).



Fig. 1 CAT-scan facility and the vertical sediment water tunnel. The vertical sediment water flume (VSWF) is fixed on the examination table and the CAT-scan gantry moves along the flume on four parallel rails

The flume used in this study designed by Teeter and Pankow (1989) is 3048 mm long and 1219 mm height. The inner rectangular section 152 mm by 304 mm passes trough the mobile gantry of the CAT scanner. The lower part of the tunnel is filled with a 30 mm thick layer of C-109 Ottawa sand (0,37 mm in grain size with a 1,56 g/cm³ bulk dry density). The flow regime is adjusted by an electrical motor and controlled by a Doppler flow meter (Controltron 1010N). For more details of this apparatus see Montreuil (2006). In this experiment the voxel chosen is 0,391 mm by 0,602 mm and in each slice 512 profiles has been produced.

DEFINITIONS

The internal variation of layer densities in sand ripples agrees with the simple sand ripple model of Reineck and Singh (1975). But some terminology must be defined. The succinct approach of this terminology and the knowledge of the answer is presented in Long and Montreuil (in prep). A typical curve (Fig. 2) of the sediment column density variation is given by the vertical profile 149 of 512, located at H of the stoss-side of a sand ripple. On these profiles different sediment transport layers of the sand ripple body are defined as:

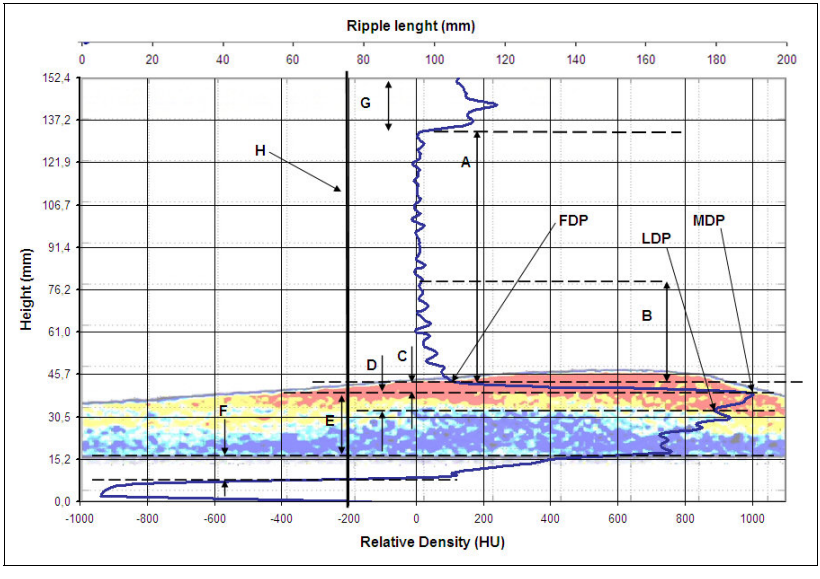

Fig. 2 Density profile, CAT-scan image of a sand ripple and definition of the different transport zone

- The water column (A) includes a free sediment water zone and, in B, the suspended transport zone (STZ). In this STZ, the variations of density over zero indicate the intensity of the sediment transported concentration in the water column. The STZ is separated from the lower unit by the frontier density point (FDP). This point corresponds to the passage between STZ and BTZ.

- The upper part of the solid sediment column (C) called the upper bedload transport zone (UBTZ) is limited at the top by the FDP and at the base by maximum density point (MDP). In this UBTZ, water penetrates more intensely between sediment grains during transport, but friction exists between the grains. This varies from a maximum value when the water concentration is at its minimum and the limit of the friction when the sediments leaves the bedload transport zone and passes into the suspended

load transport zone. After a period of time a new significant point appears close or distant to the maximum density point: the inflection density point (IDP). This point is due probably to the variation of the mechanical characteristics between grains during traction.

- This zone (D) corresponds to the middle bedload transport zone (MBTZ) and is limited at its top by the MDP and at its base by lower density point (LDP). This latter point corresponds to the passage between the MBTZ and the lower bedload transport zone (LBTZ). The thickness of this zone varies along the surface of the ripples. It attains its maximum value on the lee-side of the ripple when the avalanching process is active.

- The zone E. This zone corresponds to the lower bedload transport zone (LBTZ) and is limited at its top by the LDP. This point corresponds to an erosional transition due to the passage of the transgressive bedload transport layer over the discrete transport layer. It is a temporarily inactive transport zone, however it is included as part of the transport zone because it correspond to the upper part of the foreset laminae developed on the lee-side of the ripple. Below this sequence, the inactive transport zone corresponds to the sediment layer not affected by the passage of the sand ripple nor disturbed by the gyres in front of the lee-side.

- The bottom of acrylic flume F and the access port of the flume G were not analyzed.

RESULTS

In this paper, the evolution of the density from the base of the stoss-side of a sand ripple until the end of the lee-side of the ripple is presented. At the beginning of the experiment, the relative density of the dry sand bed was 1,57 g/cm³ (550 HU). Filling with water at 24°C increased the surface density of the sand to 1,91 g/cm³ (890 HU) by the replacement of air by water. Compaction of the sediment column is however not significant.

When the current is over the threshold limit for sediment transport, it was decided, by convention, that the upper limit of the suspended transport zone starts when the water density is greater than 1,02 g/cm³ (0 HU); the lower limit is taken as the density profile frontier point (Tab. 1), located at the intersection of the STZ and the UBTZ. During 3D CAT-scan measurements, the vertical flume creates some artifacts (e.g. beam hardening) near the acrylic wall. The fluid also generates eddy cell wall effects. For this reason, the effective measurement area is reduced from 152 mm by 304mm to 137,3 mm by 284,8 mm.

Table 1. Density of the Frontier point

Figure number	4			5				6			7		
Profile number	451	475	501	11	135	271	375	229	275	325	397	431	355
Frontier Point	0,97	1,09	0,97	1,15	1,09	1,07	1,05	1,02	1,02	1,05	1,06	0,96	1,01

All measurements are in g/cm³

Surface Density of the Sand Ripple

During ripple migration (flow = 25 cm/s), the surface density (Fig. 3) of the reworked layer increases from the beginning to the upper part of the stoss-side of the ripple (1,59 g/cm³ or 570 HU to 2,32 g/cm³ or 1300 HU). This relates to a decrease of the surface erosion of lower sediment layers (old prograding lee-side layers) due to a decrease in the backflow intensity and an increase thickness of the stoss-side laminae (Reineck and Singh 1975) with increasing pressure.

This phenomenon has been described from a sedimentological point of view by Reineck and Singh (1975) and from a hydrodynamic point of view by Middelton and Southard (1977). The evolution of the maximum density, measured on the surface of the sand ripple (Fig. 3), shows increasing density from 2,00 g/cm³ (975 HU) at the bottom of the stoss-side to a maximum of 2,32 g/cm³ (1297 HU) at a new point call maximumpoint located at profile 217 (Fig. 5). Past the maximumpoint, the density decreases to 1,87 g/cm³ (862 HU) at the brinkpoint (Fig. 3). Between the brinkpoint and the toepoint the density increases again to 2,09 g/cm³ (1062 HU) and decreases past the toepoint to 1,89 g/cm³ (864 HU).

The fluctuations noted along the stoss-side are probably related to micro turbulence due to extraction (passage) of transported grains from the bedload layer to the suspended load layer. Turbulence increases in intensity along the stoss-side and has its maximum amplitude just before the maximum density point. After this point the amplitude of the turbulences decreases in intensity.

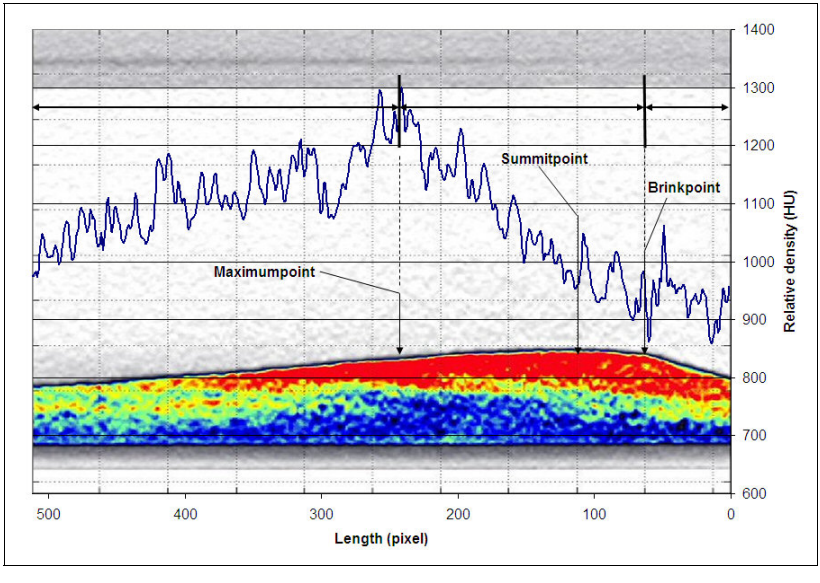

Fig. 3 Maximum surface density and CAT-scan image of the sand ripple (1 pixel = 0,391 mm for a ripple of 200 mm of length)

Lower Stoss-side of the Sand Ripple

To illustrate the evolution of the variations in the vertical density profile the most significant example of each specific zone is illustrated. For the lower stoss-side zone three profiles are presented: profiles 451, 475 and 501 (Fig. 4).

On the density profile 451, the STZ extends 16 mm over two vortexes. The negative HU density zone 1,08 g/cm³ (-56 HU) located at the base of the STZ indicates the presence of captive air inside a vortex, just over the UBTZ. Profile 475, slightly higher on the stoss-side, shows the presence of three vortices but a reduction in vortex intensity. On profile 501 only two vortexes are present and a smooth transition appears between STZ and UBTZ.

Inside the bedload transport zone, profile 451 presents a inflection density point (IDP) where the density of the lower part of the UBTZ passes from 1,80 g/cm³ to 1,97 g/cm³ (774 HU to 949 HU) in 5,4 mm. This limit indicates a deeper penetration of water inside the UBTZ, and consequently the thickness of the limited consolidation zone of the sediments. On profiles 475 and 501, the density of MDTZ increases from1,97 g/cm³ to 2,11 g/cm³, (945 HU to 1087 HU**).** The LBTZ remain similar on the two profiles with a density near 1,97 g/cm³ (950 HU), because sediments are not transported at this level.

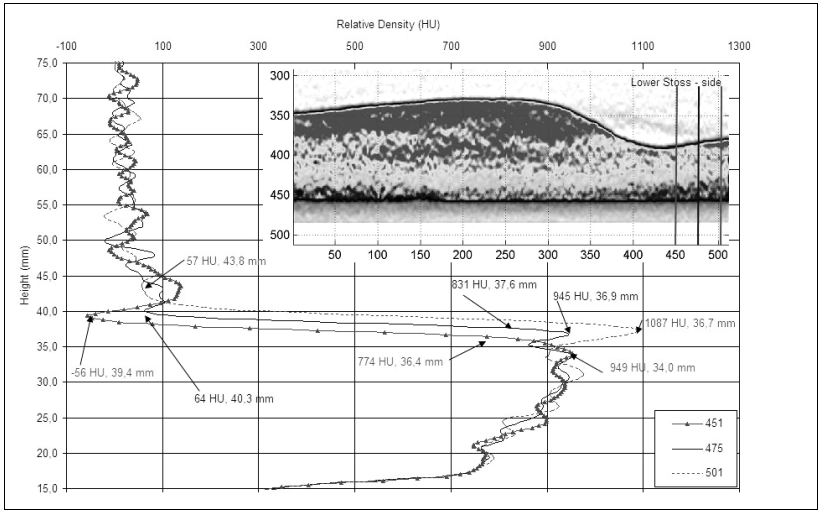

Fig. 4 Profiles of the lower stoss-side and CT-scan image of the sand ripple

Evolution along the Stoss-side of the Sand Ripple

Four profiles have been selected to represent this part of the ripple (profiles 11, 135, 271, and 375; Fig. 5). This selection of profiles presents the evolution of density profiles along the stoss-side. Profile 11, located at the base of the stoss-side (just after the lower part described above) indicates a large suspended sediment transport 19,7 mm thick increasing near the surface of the UBTZ to 1,15 g/cm³ (123 HU) at the interface STZ and UBTZ. Four small pulses appear on the profile.

The profile 135 presents similar results to that of profile 11, with a maximum peak concentration of 1,11 g/cm³ (90 HU) and an extension of the suspended zone of 11 mm with four peaks. On the profile 271, this maximum concentration increases to 1,18 g/cm³ (1152 HU), but the suspended zone is only 15,7 mm thick (This point will be discussed later.) On the summitpoint, the STZ is minimal (14,9 mm thick) and the density is only 0,99 g/cm³ (-32 HU). This value indicates the presence of vortices or eddies.

At the limit of the UBTZ, the frontier density point (FDP) on the density slope changes along the stoss-side. On profile 11, the break on the slope varies from 1,87 to 1,91 g/cm³ (844 HU to 883 HU), within 2,73 mm. On the profile 135, the intensity of the inflection density point (IDP) varies from 2,03 to 1,95 g/cm³ (1002 to 924 HU), within 2,34 mm, and on the profile 271, the slope of the UBTZ is continuous. The profile 375 gives a MDTZ of 6,64 mm and a density of 2,04 g/cm³ (1011 HU).

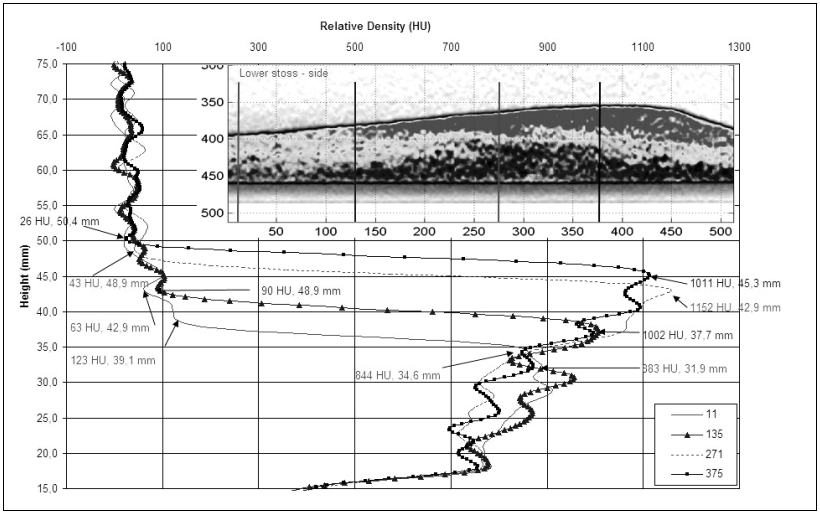

Fig. 5 Density profile along the stoss-side and a CT-scan image of the sand ripple

Summit of the Sand Ripple

Along the summit of the sand ripple, three profiles have been analyzed (profiles 229. 275 and 325; Fig. 6). At the summitpoint, the STZ presents the same aspect for all the profiles 205, 229 and 275 with density of 1,02 g/cm³ (-1 HU) on a thin layer. For the profile 325, located on the upper side of the lee-side, the STZ increases in concentration by 1,05 g/cm³ (23 HU) at the interface STZ and UBTZ.

On the UBTZ, the profiles 205 and 229 remains similar but the density is reduced from 2,16 to 2,13 g/cm³ (1133 HU to 1095 HU). Past the summitpoint, the density of the UBTZ presents an inflection density point (profile 275) where avalanching begins. The thickness of the area affected by avalanching increases on profile 325 and the density decreases to 2,04 g/cm³ (1012 HU).

On the LBTZ, profile 325, the density is reduced to 1,91 g/cm³ (884 HU) indicating the presence of an air bubble trapped inside the bedload zone. A series of prograding layers is observed on the density profiles. As demonstrated by Crémer and al (2002), each prograding layer is represented by a sinusoidal signal corresponding at the geneses of the layer. During an avalanching phase at the beginning of the processes sediment arrives in high concentration and non-compaction or grain organization appears. The signature of this episode is a lower concentration signal. Progressively sediments arrive in a more gentle process and grains are more ordered; the resulting signature of this phenomenon is an increasing of the density signal.

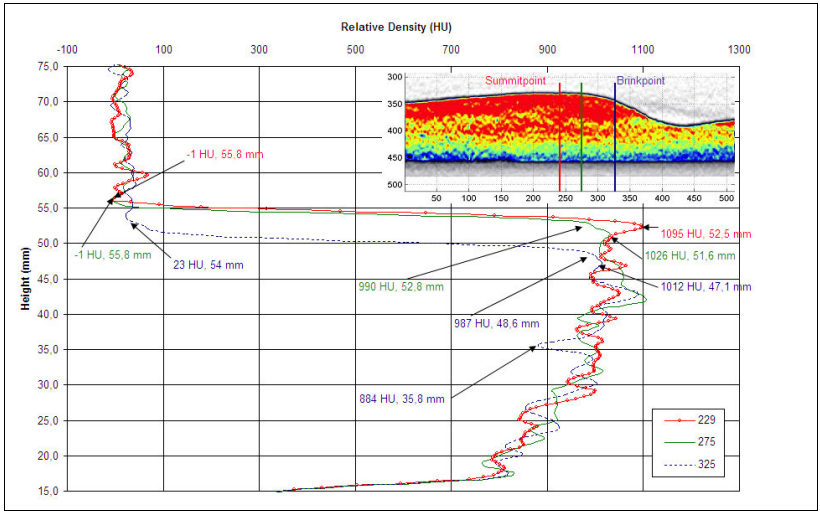

Fig. 6 Density profile over the summit of the sand ripple and a CAT-scan image

Lee Side of the Sand Ripple

Along the lee-side, four profiles located successively at the brinkpoint (profile 325, fig. 6), at the mid distance between the brinkpoint and the toepoint (profile 355, Fig. 7), at the toepoint (profile 397, Fig. 7), and at the troughpoint (profile 431, Fig. 7), have been analyzed. On the upper part of the lee-side on profile 325, the frontier point value increased in comparison to the frontier point located at the summitpoint (profile 275). The concentration varies from 1,02 versus 1,05 g/cm³ (-1 versus 23 HU). Also the vortex zone begins here but it is only discerned on profile 397 (Fig. 7) where the vortex zone is well developed, indicating suspended sediment transport and a vortex zone with a density variation of 1,18 g/cm³ (152 HU). At the toepoint, the high intensity vortex attains a density of 0,96 g/cm³ (-67 HU) and at the troughpoint the vortex intensity is 1,01 g/cm³ (-12 HU), but the thickness of STZ increases from 14,2 mm to 15,1 mm. The IDP present on each profile of the lee-side increases along the avalanching zone to the depositional zone.

The maximum density of the UBTZ on the profiles 325 (fig. 6), 355 (fig. 7) and 431 (Fig. 7) respectively presents a IDP with a MDTZ of 2,04 g/cm³ and 2,07 g/cm³ (1012 and 1044 HU). The profile 355 (Fig. 7) located at middle distance between the toepoint and the troughpoint has a MDTZ with a thickness of 7,1 mm. The profile 431 (Fig. 7) located at the troughpoint, presents a MDTZ of 2,00 g/cm³ (981 HU) and a inflection in the slope from 37,6 mm to 35,2 mm for a thick of 2,4 mm. The troughpoint presents a MDTZ of 1,99 g/cm³ (966 HU) and no inflection in slope.
The LBTZ of profiles 355 and 397 show similarities; the inflection in the slope of profile 397 is present on the LBTZ of the profile 355, indicating previous formation of the foreset laminae.

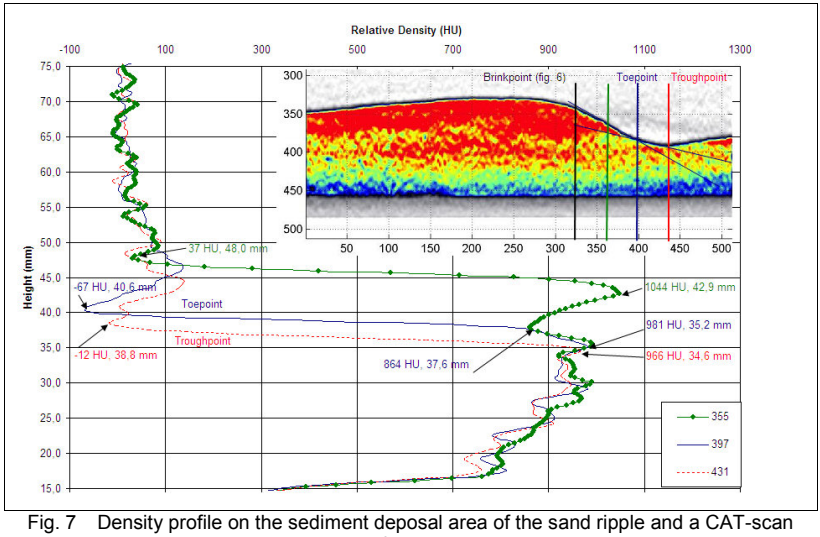

Fig. 7 Density profile on the sediment deposal area of the sand ripple and a CAT-scan image

Evolution of the STZ and UBTZ along the Sand Ripple

Along the sand ripple, the thickness of the STZ of the lower stoss-side lies between 3,4 mm and 5,7 mm (Tab. 2). Its thickness fluctuates on the summit of the sand ripple, increasing from 3,3 mm to 6,9 mm. Approaching the lee-side, the STZ increase rapidly to value near 15 mm.

The thickness of UBTZ of the lower stoss-side lies between 14,3 mm and 16,4 mm. The thickness along the stoss-side decrease until the summit of the sand ripple is approached. Its increases again past the summitpoint, on the lee-side from 10 mm to 25 mm, and decreases to 17,9 mm after the troughpoint.

Table 2. Thickness of the STZ and UBTZ for each profile

Figure number	4			5				6			7		
Profile number	451	475	501	11	135	271	375	229	275	325	397	431	355
STZ thickness*	5.4	3.4	5.7	11	11.2	6	5.1	3.3	4.2	6.9	15.4	14.2	15.1
UBTZ thickness*	16	16.4	14.3	19.7	16	15.7	14.9	10	9.8	15.5	20	25.6	17.9

* All measurements are in millimeters

DISCUSSION

The sedimentological characteristics of Reineck and Singh (1975) provide the basis for the characterisation of sediment transport zones. During this experiment, several zones along the ripple surface have been distinguished from CAT-scan density variations. Four zones have been defined in vertical sections: the STZ, the UBTZ, the MDTZ and the LBTZ. The passage between the STZ and the UBTZ is continuous and is determined by a frontier point on the curve of vertical density concentration. The density related to this frontier point changes along the surface of the ripple. Such changes are probably due to the intensity of the turbulence at the surface of the ripple.

Lower Stoss-side of the Sand Ripple

The top of the STZ (Fig. 4) is created by shear flow over the sediment bed. The concentration of the suspended sediment along the STZ is very great and the thickness of this zone varies from 14,3 mm to 16 mm. The curve in the profile at the transition between STZ and UBTZ indicates the presence of significant vortices which decrease in intensity when rising along the stoss-side. A large quantity of sediment is present in the STZ. To quantify sediment transport, it is essential to use a PIV system. Planned future use of PIV will confirm the exact masses of sediment in suspension in the STZ and on the UBTZ.

The UBTZ located between the lower limit of the STZ and the upper limit of the MDTZ is a transition zone in the bedload transport mechanism. At this stage, water penetrates more and more inside the sediment matrix and has transformed the traction movement of the MDTZ to a pseudo-traction movement where the cohesion between grains decreases dramatically to reach the limit of the cohesion between two grains (frontier density point on the curve). The increasing density of the material in the MDTZ (Fig. 4) indicates a consolidation of the sediment when raising the stoss-side of the sand ripple.

Slope Inflection
The inflection in the slope (profile 451, Fig. 4) indicates deeper penetration of water inside the UBTZ.

Evolution along the Stoss-side of the Sand Ripple
Along the stoss-side, the thickness of the STZ (Fig. 5) is reduced and the size of the UBTZ increased. This co-evolution indicates a change of sediment transport mechanism: suspended sediment transport decrease in intensity in favor of bedload sediment transport. On profile 374, located at the summitpoint of the ripple, the thickness of the MDTZ is maximal (6,64 mm) and this MDTZ passes across the total set of laminae and shows the variation of the architecture of one isolated lamina.
In the STZ and UBTZ, the density profiles distribution is not uniform. Close to the summitpoint the turbulence level is reduced. The STZ gets thinner from the lower stoss-side to the summitpoint.

Maximumpoint
The major parts of the ripples present a point of maximum density (peak). The positions of this maximumpoint vary along the ripple in function of the ripple's form and the flow velocity. The profile 271 (Fig. 5) presents a maximum surface density and MDTZ of 2,18 g/cm³ (1152 HU). This maximumpoint is located on the stoss-side of the sand ripple and represent the maximum pressure of the water column over the bedload (Middleton and Southard 1977).

Summit of the Sand Ripple
The size of the STZ increases past the summit of the sand ripple and simultaneously the gravitational depositional processes begins (profile 275, Fig. 6). The form of the UBTZ indicates avalanching processes and the creation of foreset laminae. The density of MDP is reduced from 2,16 to 2,04 g/cm³ (1133 HU to 1012 HU).

Lee Side of the Sand Ripple
The lower part of the lee-side presents a reduction of STZ (Fig. 6 and Fig. 7). This is related to the form of the sand ripple and by the amplitude of eddies. The reduction of the STZ could also be caused by air trapped inside eddies. The thickness of the STZ is not constant along the deposition zone. During the formation of the foreset laminae, sediments leave the water column and are trapped inside the foreset laminae in formation.
The presence of the UBTZ and the inflection in the slope phenomena are significant of bedload transport. The density of the toepoint is 1,09 g/cm³ (67 HU) due to the high intensity of the vortex over a UBTZ and create the foreset laminae with a large bedload sediment movement indicated by the inflection in the slope.
The UBTZ of the brinkpoint profile presents a inflection in slope indicating a MDTZ of 1044 HU (2,07 g/cm³) and the presence of avalanching processes.
The profile 431 (Fig. 8) with a break in the slope of 3,13 mm indicates deposition of sediment transported by avalanching phenomena.

The troughpoint presents a MDTZ of 1,99 g/cm³ (966 HU) but no inflection in slope, indicating a depositional (avalanching) process with the presence of a vortex over UBTZ indicating the approach of erosional process.

CONCLUSION

In conclusion, the use of Computed axial tomography provides a new perspective for the study of bed forms by providing a means of internal examination of sand ripples. The density variation model obtained during the migration under a stationary flow regime reveals the architecture of the internal part of the ripple and the action of the different phases of sediment transport inside the sand ripple.

The sedimentologique characteristic of Reineck and Singh (1975) gives the base vocabulary for the elaboration of the characteristics of sediments transport zones.

This preliminary work opens the possibility for characterization of sediment transport in 3D. In vertical profiles of the sand ripple, four zones were defined: the STZ, the UBTZ, the MDTZ and the LBTZ. The passage between the STZ and the UBTZ is continuous and is determined by a frontier density point on the curve of vertical density concentration. The density related to this frontier point changes along the surface of the ripple. This is probably due to the intensity of the turbulence at the ripple surface. The MDTZ thickness is determined by the inflection in the slope how indicates an activity in the lower part of the UBTZ. The different stages of transport have been measured successfully for a single grain size and flow velocity.

For the first time, the X-ray gives a look inside the sand ripple without interference on the middle.

X-ray densities define a field between 0 and 4,10 g/cm³ (-1024 and 3071 HU) at 0.001 g/cm³ resolution (with 90% confidence at 0,002 g/cm³) with an image size of 512 by 512 densimetrics value. In the near future, a new CAT-scan to be installed in the Québec scanning laboratory will provide a resolution of 1024 by 1024 for the same span and the possibility for modification of the span for a high density range. PIV techniques will also be used to compute suspended load and bedload sediment transport volumes.

REFERENCES

Crémer J.F., Long B.F., Desrosiers G., de Montety L., and Locat J. (2002). "Application de la scanographie à l'étude de la densité des sédiments et à la caractérisation des structures sédimentaires: exemple des sédiments déposés dans la rivière Saguenay (Québec, Canada) après la crue de juillet 1996". Vol 96. Numéro 2. (2002) p. 440-450.

Duliu, O.G. (1999). "Computer axial tomography in geosciences: an overview". Earth-Science Reviews 48, 265–281.

Kak A. C. and Slaney M. (1999). "Principles of computerized tomographic imaging", IEEE PRESS, New York, 329 pp.

Ketcham R.A. and Carlson W.D. (2001). "Acquisition, optimization and interpretation of X-ray computed tomographic imagery: applications to the geosciences", *Computers & Geosciences* 27 (2001) p. 381– 400.

Long B.F. and Montreuil S. (in prep for Sedimentology). "New classification of the different part of the sediment transport zone".

Mees, F. Swennen, R. Van Geet, M. and Jacobs, P. (2003). "Applications of X-ray computed Tomography in the Geosciences". Geological Society of London Special Publication 215.

Middleton G.V. and Southard J. B. (1977). "Mechanics of sediment movement", "S.E.P.M. Short Course Number 3", Binghamton.

Montreuil S. (2006). "Évolution densimétrique des structures de rides en déplacement sous un courant stationnaire mesuré sous scanographe dans un canal en boucle verticale". MSc Thesis, INRS-ETE, Québec. 121 pp., (unpub.).

Reineck H.-E. and Singh I.B. (1975). "Depositional Sedimentary Environments", Springer study edition, New York, 439 pp.

Teeter Allen M. and Pankow Walter (1989). "Deposition and erosion testing on the composite dredged material sediment sample from New Bedford harbour, Massachusetts", Technical report HL-89-11, US Army Corps of Engineers, Washington, 61 pp.

THE EFFECTS OF BED SLOPE AND WAVE SKEWNESS ON SEDIMENT TRANSPORT AND MORPHOLOGY

D.J.R. Walstra[1,2], L.C. van Rijn[1,3], M. van Ormondt[1], C. Brière[1], A.M. Talmon[1,4]

1. WL | Delft Hydraulics, P.O. Box 177, 2600 MH Delft, The Netherlands, Dirkjan.Walstra@wldelft.nl, Leo.vanRijn@wldelft.nl, Maarten.vanOrmondt@wldelft.nl, Christophe.Briere@wldelft.nl, Arno.Talmon@wldelft.nl
2. Delft University of Technology, Faculty of Civil Engineering and Geosciences, P.O. Box 5048, 2600 GA Delft, The Netherlands.
3. Utrecht University Department of Physical Geography, Faculty of Geosciences, P.O. Box 80.115, 3508 TC Utrecht, Netherlands.
4. Delft University of Technology, Faculty of Mechanical, Maritime and Materials Engineering, Mekelweg 2, 2628 CD Delft, The Netherlands.

Abstract: The potential relevance of wave skewness and sloping beds on morphodynamic predictions is investigated. Based on a comparison with measurements it was shown that the phase lag is potentially important for modeling nearshore bar dynamics as it influences the suspended wave related transports (magnitude and direction). Velocity skewness results in a phase shift between the orbital motion and the instantaneous bed shear stress increasing onshore bed load transport. It was seen that its influence is relatively small but does affect bar migration and helps to predict the observed asymmetric bar shape. The bed slope affecting the initiation of motion and sediment bed-load transport magnitude and direction are investigated by comparing scour hole predictions. The initiation of motion, which is also included on the suspended transports, only has an effect for somewhat steeper slopes. The modifications of bed-load direction and magnitude significantly affect the horizontal and vertical scour hole equilibrium dimensions.

INTRODUCTION

As part of the implementation of the TR2004 transport formulations (Van Rijn, 2006a,b) in the Delft3D-Online model (Lesser et al., 2004) a number of additional processes were included or updated. Here we are focusing on processes of which the relative importance in morphodynamic simulations is not well known. The investigated processes are the phase lag effects on the wave related suspended transport, the role of orbital velocity skewness on the bed shear stress and the effect of sloping beds on bed-load and suspended sediment transport. First, a brief description of the considered processes is given, followed by a limited number of morphodyamic simulations to illustrate their potential relevance. Finally, some concluding remarks and recommendations for further research are given.

PHASE LAG EFFECTS

The wave-induced suspended transports are based on an intra-wave approach, which consists of a parameterized description of the instantaneous response of the suspended sand concentration to the near-bed orbital wave motion (Houwman and Ruessink, 1996):

$$q_{s,w} = \lambda f_p \left(\frac{U_{on}^4 - U_{off}^4}{U_{on}^3 + U_{off}^3} \right) \int_a^{3\delta_s} c\,dz \qquad (1)$$

in which U_{on} is the near-bed peak orbital velocity in onshore direction (in wave direction), U_{off} is the near-bed peak orbital velocity in offshore direction, c the vertical distribution of the time-averaged sediment concentration, λ is a coefficient (0.1), δ_s is the thickness of the wave boundary layer, an extension of the original formulation is the function (f_p) which represents the phase-lag effects.

Phase lag effects may occur when sediment is stirred up and does not respond directly to the orbital wave motion as it takes time to fall back to the bed (Dohmen-Janssen, 1999). The phase lag can result in a decreased transport of sediment in the wave direction or can, in cases of fine sediment and relative short wave periods, result in sediment being transported against the wave propagation direction. Van Rijn (2006b) accounted for this phase-lag effect by including a f_p-phase function ($-1 < f_p < 1$) which depends on the bed characteristics (form roughness, grain size) and the strength of the asymmetric wave motion:

$$f_p = -\tanh\left[100\left(P - P_{cr}\right)\right] \qquad (2)$$

with $P = \dfrac{k_s}{w_s T_p}$, in which k_s is the wave-related bed roughness height, w_s is the settling velocity, T_p is the peak wave period, and P_{cr} is the critical phase lag number which is set to 0.1.

WAVE SKEWNESS

Nielsen (1992, 2002, 2006) and Nielsen and Callaghan (2003) have shown that fluid accelerations in strongly asymmetric wave motion lead to an increase and phase lead of the bed-shear stresses. This is partly due to the presence of boundary layer streaming and

partly to the saw-tooth asymmetry, i.e. the front of the waves being steeper than the back. Moreover, Watanabe and Sato (2004) have shown that the fluid acceleration effects on the bed shear stresses leads to a small net transport in the case of forward leaning waves, even if the peak onshore and offshore orbital velocities are equal, because of the more abrupt acceleration under the steep front. More abrupt accelerations are associated with thinner boundary layers and greater pressure gradients for a given velocity magnitude.

Nielsen and Callaghan (2003) proposed a simple method to deal with these processes, by expressing the transport rate in terms of an instantaneous Shields parameter rather than in terms of a free stream velocity, and accounting for both streaming and accelerations in the Shields parameter calculations. The instantaneous bed-shear stress under asymmetric wave motion including enhanced acceleration effects in saw-tooth waves reads as:

$$\tau_{b,t}^{'} = 0.5\rho_w f_w^{'} \left| u_{w,t}\cos\xi_\tau + \frac{1}{\omega}\frac{du_{w,t}}{dt}\sin\xi_\tau \right| \left(u_{w,t}\cos\xi_\tau + \frac{1}{\omega}\frac{du_{w,t}}{dt}\sin\xi_\tau \right) \quad (3)$$

in which ρ_w is the fluid density, $f_w^{'}$ is the grain-related wave friction factor, $u_{w,t}$ the instantaneous orbital velocity at the edge of the wave boundary layer, ω is the angular wave frequency and ξ_τ is the phase lead.

Consequently the instantaneous bed shear stress values shifts forward and the peak bed-shear stress increases with the phase lead-value, leading to an increase of the onshore net transport. Based on comparison with the Watanabe and Sato (2004) experiments, Nielsen (2006) recommends using a phase lead-value of 51°. However, the range of the optimal values is relatively large for considered experiments (average values for ξ_τ in the range of 40° to 62°). Here we are driving the Nielsen and Callaghan (2003) model with a velocity signal derived from a non-linear wave model based on Isobe and Horikawa (1982) which only describes velocity skewness. Acceleration skewness which is associated with saw-tooth waves (or pitched-forward waves) is not accounted for.

BED SLOPE EFFECTS

Most transport formulas are only valid for (nearly) horizontal beds (bed slope=tan $\beta \leq 10^{-3}$ (positive values of β refer to down sloping beds). Based on the results of experimental work, it appears that the bed slope may affect the transport rate in three ways:

1. the bed slope will influence the local near-bed flow velocity (hydrodynamic effect not considered here);
2. the bed slope will change the threshold conditions for initiation of motion;
3. the bed slope may change the transport rate and/or direction, once the sediment is in motion.

Here we will discuss expressions dealing with the initiation of motion and the change of transport rate and/or direction and how they are implemented in Delft3D.

Threshold conditions

Dey (2001, 2003) studied the critical bed-shear stress on both longitudinal and transverse

(lateral) bed slopes. Experiments were conducted in two different, transparent (perspex) semi-circular ducts for three sizes (600, 940 and 1350 μm with angles of repose of 32°, 34° and 35°) of uniform sediments. Based on these experiments Dey (2003) derived a rather complicated expression to describe the critical bed-shear stress along combined longitudinal and transverse bed slopes, which reads as:

$$\frac{\tau_{b,cr}}{\tau_{b,cr,o}} = a\left(-b + \left(b^2 + c\right)^{0.5}\right) \tag{4}$$

with $a = \left(\left(1 - \eta \tan\phi\right)\tan\phi\right)^{-1}$, $b = \sin\beta + \eta\left(\tan\phi\right)^2\left(\left(\cos\phi\right)^2 - \left(\sin\phi\right)^2\right)^{0.5}$, $c = \left(1 - \left(\eta\tan\phi\right)^2\right)\left(\left(\cos\phi\tan\phi\right)^2 - \left(\sin\phi\tan\phi\right)^2 - \left(\sin\beta\right)^2 - \left(\sin\gamma\right)^2\right)$, η is the ratio of lift and drag forces on a particle, $\tau_{b,cr}$ is the critical bed-shear stress, $\tau_{b,cr,o}$ is the critical bed-shear stress along the horizontal bed, β is the longitudinal slope angle (positive values refer to down sloping beds), γ is the lateral (transverse) slope angle and ϕ is the angle of repose.

Assuming a horizontal bed in normal to the flow direction ($\gamma = \eta = 0$), Eq. (4) reduces to the Schoklitsch equation. When assuming a horizontal bed in longitudinal direction ($\beta = \eta = 0$) Eq. (4) reduces to the Leitner equation (see e.g. Van Rijn, 1993). Dey showed that Eq. (4) is in reasonable agreement with his experimental values. However, it significantly over-predicts the critical bed shear stress for relatively large longitudinal adverse slopes. Here we are using an empirical expression proposed by Dey (2001) which was modified slightly to improve the agreement with measured data (see Fig. 1):

$$\frac{\tau_{b,cr}}{\tau_{b,cr,o}} = \left(1 - \frac{\tan\beta}{\tan\phi}\right)^{0.75}\left(1 - \frac{\tan\gamma}{\tan\phi}\right)^{0.37} \tag{5}$$

The instantaneous bed load transport due to the combined action of waves and currents is based on Van Rijn (2006a) and reads in simplified form:

$$S_{b,t} = A\left(\frac{\tau_{b,cw,t}}{\rho_w}\right)^{0.5}\left(\frac{\tau_{b,cw,t} - \tau_{b,cr}}{\tau_{b,cr}}\right) \tag{6}$$

in which A is a factor (see Van Rijn; 2006a), $\tau_{b,cw,t}$ is the instantaneous grain-related bed-shear stress due to both currents and waves.

From Eq. **Error! Reference source not found.**(6) it becomes clear that the threshold condition, Eq. (5), will result in a linear scaling of the bed load transports.

The modification of the critical bed shear is also applied on the reference concentration, c_a, (Van Rijn, 2006b):

$$c_a = B\left(\frac{\overline{\tau}_{b,cw} - \tau_{b,cr}}{\tau_{b,cr}}\right)^{1..5} \tag{7}$$

in which B is a factor (see Van Rijn, 2006b), $\overline{\tau}_{b,cw}$ is the time-averaged effective bed-shear stress and $\tau_{b,cr}$ is the critical bed-shear stress according to Shields including the

modification of the threshold condition according to Eq. (5).

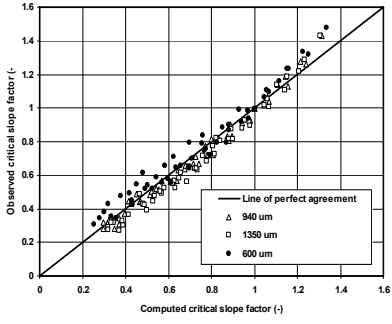

Fig. 1 Observed and computed critical slope factor for combined longitudinal and transverse bed slopes based on Eq. (5) modified expression of Dey (2001).

Bed load transport on sloping beds

Two methods are considered which describe the transverse transports on a sloping bed. The first method, originating from Van Bendegom (1947), determines the angle of the transverse transports based on the forces acting on a particle along a sloping bottom. The second method (Ikeda, 1988) is based on the equation of motion and results in a correction of the transport magnitude. Both transverse correction methods are combined with longitudinal corrections which are mentioned for completeness sake, but are not the focus of this paper.

Direction based transverse transport correction

Van Bendegom (1947) gives the following expression for the direction of sediment moving on a sloping bed:

$$\tan\alpha = \frac{S_{b,n}}{S_{b,s}} = \frac{\sin\delta - \dfrac{1}{f(\theta)}\tan\gamma}{\cos\delta - \dfrac{1}{f(\theta)}\tan\beta} \tag{8}$$

in which $S_{b,n}$ and $S_{b,s}$ are the bed load transports in transverse and longitudinal direction respectively, $f(\theta)$ is a transverse bed-slope coefficient, being a function of the shields number, θ; z_b is the bed elevation, x and y are the horizontal coordinates, δ is the angle of the flow near the bed.

Ignoring the longitudinal bed slope effects ($\delta = 0$ and $\tan\beta = 0$) reduces Eq. (8) to:

$$\tan\alpha = -\frac{1}{f(\theta)}\tan\gamma \tag{9}$$

Talmon (1992) and Talmon et al. (1995) studied the direction of sediment transport (bed load and suspended load) on transverse alluvial bed-slopes based on Eq. (9). Laboratory experiments with transverse bed slopes in a straight flume were performed. Various sand sizes were used (d_{50} of 90, 160 and 790 μm). Suspended load transport was dominant in

the tests with the finer sediments (90 and 160 μm). The initial bed was placed under a transverse slope in the (straight) flume. The bed level difference between the left and right sides of the bed in the flume was observed to be smoothed out (leveled) by the flow as a function of time by transverse sediment transport processes. The observed bed development in the experiments with coarse sand (790 μm) can be represented quite well by a relatively simple mathematical model for the transverse sediment transport processes, in which the *f(θ)*-coefficient is represented as (Koch and Flokstra, 1981):

$$f(\theta) = 1.7\theta^{0.5} \tag{10}$$

In the modeling of the bed slope effects in the presence of suspended load transport, it was assumed that only the bed-load transport part of the sediment transport is affected by the transverse sloping bed. In the experiments with fine sediment (90 and 160 μm) the *f(θ)*-values derived from the experimental results are significantly lower (a factor 1.4 for 90 μm sand to 3.5 for 160 μm sand) than the values predicted by Eq. (10). Considering measured data and numerical simulation results of both natural rivers and laboratory flumes, Talmon et al. (1995) have found a distinct influence of the bed forms which differ in both situations (scale effects, particle size and flow depth). This effect can be expressed through the relative particle size (d_{50}/h) as:

$$f\left(\theta, \frac{d_{50}}{h}\right) = 9\left(\frac{d_{50}}{h}\right)^{0.3} \theta^{0.5} \tag{11}$$

This expression suggests that, at the same θ, the transverse slope effect (i.e. *1/f(θ)*) on the bed load transport particles is stronger (smaller *f(θ)*) in situations with finer sediment (dominant suspended load transport) than with dominant bed-load transport, as found in the laboratory experiments with 790 μm. However, the transverse slope effect may also be acting on the suspended particles (at least those close to the bed). This latter approach yields a larger effect in the case of dominant suspended load transport. Talmon (1992) has also studied the morphological behavior of river bends in the case of dominant suspended load transport (>50%). His mathematical model was formulated in terms of the depth-averaged equations using an asymptotic approximation to represent the horizontal and vertical adjustment of the depth-averaged sediment concentration to changing flow conditions (Galappatti-method). Experiments in a curved laboratory flume have been conducted to provide verification data for the mathematical model. The effect of transverse bed slopes is assumed to act on the bed load transport fraction only. Using this approach, the transverse bed slopes are under-predicted by the model. This suggests that either the *f(θ)*-value acting on the bed load transport fraction is too small or it should also be applied to the suspended load particles.

The approaches described by Eqs. (10) and (11) are combined with a longitudinal slope effect based on Koch and Flokstra (1981) which reads:

$$\alpha_s = 1 + \varepsilon_s \tan\beta \tag{12}$$

in which ε_s is a user-specified tuning parameter (default value: 0.05)

Talmon (1992) used this parameter in various comparisons with experiments and used values for ε_s in the range of 0.15 to 0.3.

Magnitude based transverse transport correction

An alternative approach is based on the equation of motion of a particle moving over a sloping bed, suggested by Ikeda (1988) for transverse sloping beds:

$$\alpha_n = \varepsilon_n \left(\frac{\tau_{b,cr}}{\tau_b} \right)^{0.5} \tan\gamma \tag{13}$$

in which ε_n is a user-specified tuning parameter (default value: 1.5, range between 1.5 and 3).

Lesser et al. (2004) used Ikeda (1988) to model the morphological development (dominant bed load transport; sediment of 450 μm; mean velocity of 0.4 m/s) of a river bend in a laboratory flume. Good results were obtained by using ε=2.

The Ikeda (1988) method is combined with the Bagnold (1956) approach for longitudinal sloping beds:

$$\alpha_s = 1 + \varepsilon_s \left(\frac{\tan\phi}{\cos\left(\tan^{-1}\beta\right)\left(\tan\phi - \tan\beta\right)} - 1 \right) \tag{14}$$

in which ε_s is a user-specified tuning parameters (default value: 1).

Implementation in Delft3D

Both methods to account for sloping beds (van Bendegom and Ikeda) in the bed load transport are included in Delft3D. In both methods first the *magnitude* of the transport is determined or modified by applying the longitudinal bed slope correction factor, next the *direction* of the transport is modified by applying the transverse bed slope correction factor. However, due to the way how the bed slope adjustment factors have been derived, the implementations in Delft3D differ slightly for both methods. The description given here is based on a vectoral description of transports in the horizontal plane.

For the Ikeda/Bagnold method the implementation is based on:

$$\begin{aligned} S'_{b,x} &= \alpha_s S_{b,s} \cos\alpha - S_{b,n} \sin\alpha \\ S'_{b,y} &= \alpha_s S_{b,s} \sin\alpha + S_{b,n} \cos\alpha \end{aligned} \tag{15}$$

in which $S'_{b,x}$ and $S'_{b,y}$ are the adjusted bed-load transport components based on the unadjusted transports $S_{b,s\ or\ n}$ and α_s is determined according to Eq. (14).

By using $S_{b,n} = \alpha_n |S_b|$, $\sin\alpha = \frac{S_{b,y}}{|S_b|}$ and $\cos\alpha = \frac{S_{b,x}}{|S_b|}$, Eq. (15) can be written as:

$$\begin{aligned} S'_{b,x} &= \alpha_s S_{b,x} - \alpha_n \alpha_s S_{b,y} \\ S'_{b,y} &= \alpha_s S_{b,y} + \alpha_n \alpha_s S_{b,x} \end{aligned} \tag{16}$$

For the van Bendegom based methods the bed slope factors are taken into account by

first adjusting the magnitude of the bed load transport:

$$S_b^{'} = \alpha_s S_b \tag{17}$$

with α_s according to Eq.(12).

The adjusted transport is subsequently decomposed by using:

$$S_{b,x}^{'} = S_b^{'}\left(\frac{\alpha_{n,x}}{\left(\left(\alpha_{n,x}\right)^2+\left(\alpha_{n,y}\right)^2\right)^{0.5}}\right) \; and \; S_{b,y}^{'} = S_b^{'}\left(\frac{\alpha_{n,y}}{\left(\left(\alpha_{n,x}\right)^2+\left(\alpha_{n,y}\right)^2\right)^{0.5}}\right) \tag{18}$$

where $\alpha_{n,x}$ and $\alpha_{n,y}$ are the decomposed transverse bed slope factors:

$$\alpha_{n,x} = f(\theta)\frac{S_{b,x}}{S_b}+\frac{dz_b}{dx} \; and \; \alpha_{n,y} = f(\theta)\frac{S_{b,y}}{S_b}+\frac{dz_b}{dy} \tag{19}$$

with $f(\theta)$ being determined according to Eqs. (10) or (11), note that in the above equation the unadjusted transports are used.

MORPHODYNAMIC APPLICATIONS

The aim of this section is to illustrate the relevance of the discussed modifications rather than claiming to provide a comprehensive overview. The selected test cases have the characteristics for which the discussed extensions are potentially important. The phase lag and wave skewness are investigated for the LIP11D experiments carried out in WL | Delft Hydraulics' Delta flume (Arcilla et al., 1994). Using a water depth of 4.1 m, the length of the constructed bottom profile was approximately 180 m. Here both the erosive (Test 1B: H_{m0} = 1.4 m, T_p = 5 s) and accretive (Test 1C: H_{m0} = 0.6 m, T_p = 8 s) test are considered. The predicted and measured profile development are compared after 18 (Test 1B) and 13 hours (Test 1C), with a focus on the bar at x=138 m.

Phase lag effects

Three runs were carried out: f_p was determined using Eq. (2) and setting it to -1 and +1, representing its maximum offshore and onshore limits. The profile developments are compared in Fig. 2 for both tests. It is clear that the wave suspended transport is able to change the direction of the bar migration. The value for f_p according to Eq. (2) is close to +1 which correctly predicts the shoreward or seaward bar migration. However, for Test 1B the λ was set to 0.03 (compared to 0.1 for Test 1C) in Eq. (1).

Wave skewness

A sensitivity analysis was performed by varying the phase lead, ξ_τ, in the range of [0°, 10°, 25°, 40°, 51°]. The results are shown in Fig. 3, from which is becomes apparent that ξ_τ only results in a visible influence when it is 25° or larger. The higher ξ_τ-values enhance the bed-shear stress, increasing of the onshore net transport. The best agreement is obtained for the ξ_τ ranging from 25° to 40°. The observed onshore bar migration which is accompanied with enhanced asymmetry bar shape is qualitatively reproduced by the model using the higher ξ_τ-values for Test 1C. Furthermore, ξ_τ mainly affects the bar regions. The inner bars that are predicted in both tests are not realistic and are mainly

due to the applied relatively simple orbital motion model which does not account for the fact that waves evolve from peaked waves (shoaling) to asymmetric pitched-forward shapes with steep front faces after breaking (Hoefel and Elgar, 2003). This essentially results in a transition from velocity skewness to acceleration skewness being dominant. This is also relevant for the phase lag results discussed in the previous section.

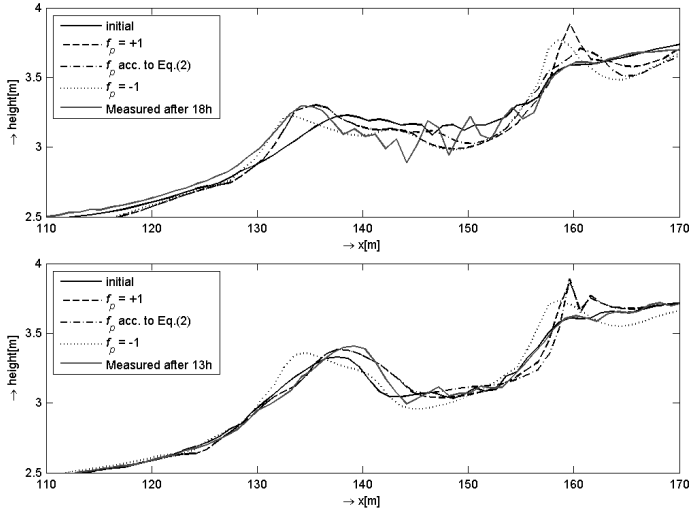

Fig. 2 Profile development induced by various settings of the f_p phase-factor for LIP11D Test 1B (top) and Test 1C (bottom).

Bed slope effects

To illustrate the influence of the discussed slope corrections, transverse and longitudinal transports are compared as a function of the shields parameter for a horizontal bed and two transverse bed slopes ($\tan\gamma = 0.05$ and $\tan\gamma = 0.2$) at 5 m water depth and d_{50} is 0.2 mm. Only transverse bed slopes are considered (i.e. horizontal longitudinal bed). Furthermore, their influence is investigated by comparing the morphodynamic predictions for a schematic case in which, due to current contraction, a scour hole develops.

First the modification of the initiation of motion (Dey, 2001) is investigated by comparing the resulting transports including and excluding Dey (2001) in combination with Ikeda (1988). The transverse bed-load transports are shown in Fig. 4, from which it can be seen that Dey (2001) results in an overall transport increase for the large slope case (compare the blue and the dashed-black lines). For the mild slope Dey (2001) has no visible influence (compare red and solid-black lines). Similar trends are visible for the longitudinal transports shown in Fig. 5.

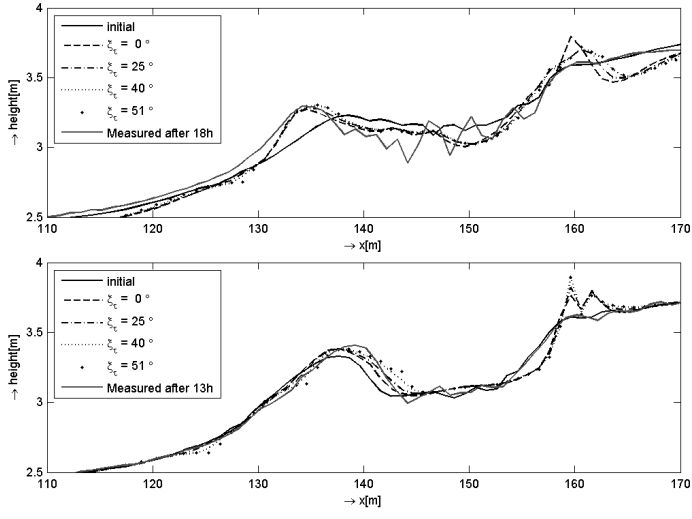

Fig. 3 Profile development induced by various settings of the phase lead for LIP11D Test 1B (top) and Test 1C (bottom).

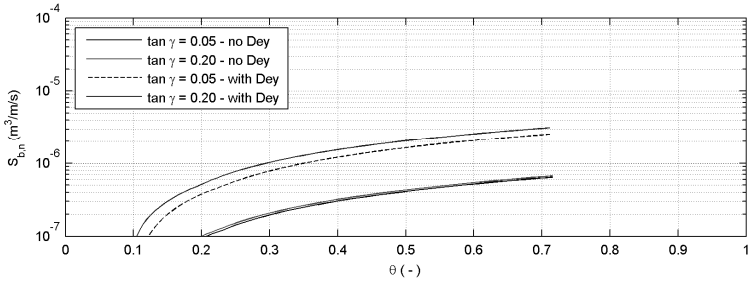

Fig. 4 Transverse bed-load transport as a function of the shields parameter for various transverse sloping beds.

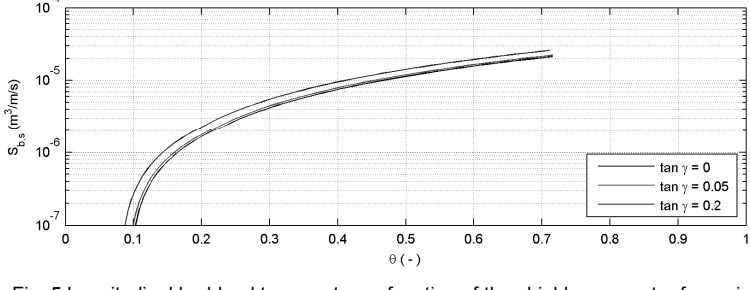

Fig. 5 Longitudinal bed-load transport as a function of the shields parameter for various transverse sloping beds.

The effects on the longitudinal suspended transport are shown in Fig. 6. As could be expected the same trend is found again. However, these results also indicate the potential relevance for including slope effects in the suspended transports. This could especially be the case for areas where suspended sediment is dominant (e.g. ebb tidal deltas and estuaries). Although this approach requires further justification and validation, experimental data (Talmon, 1992) seem to justify this method.

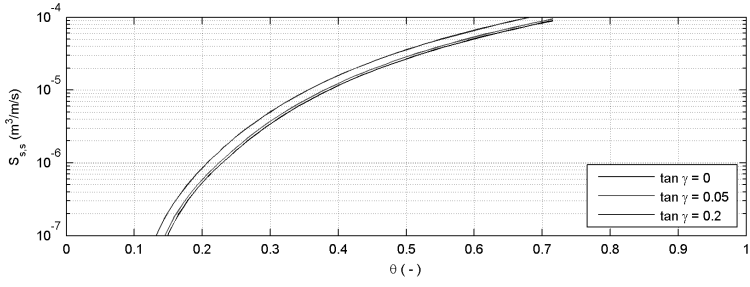

Fig. 6 Longitudinal suspended transport as a function of the shields parameter for various transverse sloping beds.

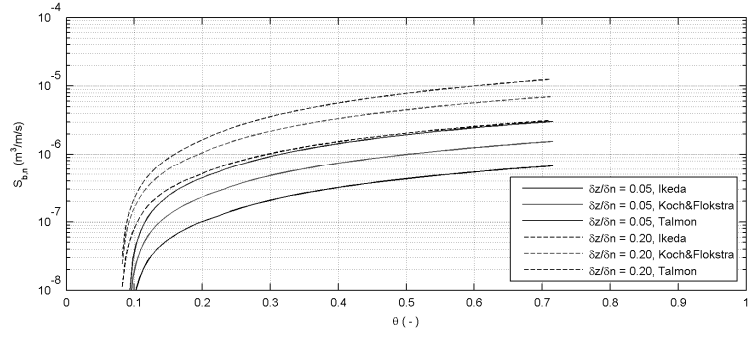

Fig. 7 Transverse bed-load transport as a function of the shields parameter for various transverse sloping bed correction methods.

The transverse bed slope correction methods are compared for the same transverse bed slopes in Fig. 7. The differences between the mild and steep slope transports are of the same order as the differences between the three bed slope correction factors. The behavior of the formulations is very similar, which is somewhat surprising for Ikeda (1988). It was expected for Koch and Flokstra (1981) and Talmon et al. (1995) as they are based on the same approach.

The morphodynamic effects of the different bed slope formulations are investigated by comparing the predictions of a scour hole which is in (near) equilibrium state. The computational grid of the model is 100 m long and 20 m wide with a grid spacing of 1 m in both directions (see Fig. 8) and has an initial uniform water depth of 5 m. Two 4 m

long groynes perpendicular to the flow are situated at x = 20 m from the upstream boundary. A stationary current of 0.5 m/s is imposed at the upstream (left) boundary. Flow contraction results in an initial increase of current velocities up to 0.9 m/s in between the two groynes. The morphodynamic simulations are carried out with the sediment transport relations of Van Rijn (2006a,b) applying a uniform grain size of 0.2 mm. The simulations cover a 100 day period which is sufficiently long to obtain a bathymetry in approximate equilibrium. Three combinations of bed slope formulations are considered, the influence of the initiation of motion (Dey, 2001) is compared in combination with Ikeda (1988) and Talmon et al. (1995) including Dey (2001).

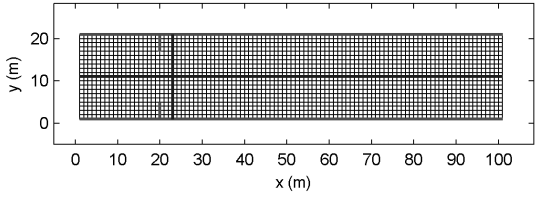

Fig. 8 Grid schematisation including groynes (red) and output transects (blue).

Due to the increased current velocities, a scour hole develops with a depth in the range 6.5 m to 7.2 m depending on the applied bed slope correction formulation as can be seen in Fig. 9. The predicted transverse profiles show a marked difference. Especially the difference between Ikeda (1988) and Talmon et al. (1995) is relatively large.

CONCLUSIONS

The wave-related suspended transport contribution is usually directed in the wave propagation direction, but may, depending on local wave and ripple characteristics, change sign. This transport can be of great importance when modeling morphodynamics in the surf zone, as it can alter the bar migration direction. However, the f_p-phase lag function was not tested extensively and will require further research to assess the robustness of the suggested approach.

Application of the Nielsen and Callaghan (2003) model to account for velocity acceleration in the bed shear stress showed that its effect is relatively small for the considered cases. However, the qualitative trends in bar shape improved with this expression. The best agreement between the model and the observations is obtained for a phase angle, ξ_τ, ranging from 25° to 40°. Including acceleration skewness in the orbital velocity signal may improve predictions in the inner (or saturated) surf zone as acceleration skewness tends to be dominant compared to the velocities skewness in this region. This will not only influence the bed-load transports, but may also affect the wave-related suspended transport.

The applied bed slope effects show the expected trends, but the differences between the considered transverse bed slope correction factors is relatively large and results in distinctly different equilibrium bathymetries for the considered case. In combination

with recently acquired data on 250 and 960 μm sand, Talmon and Wiesemann (2006) focused on the mechanical balance of moving bed-load particles. In that approach the shear stress-to-the-grains θ' is the governing variable, instead of θ. Further research will include this new data and the suggested alternative approach. The inclusion of the initiation of motion in both the bed-load and suspended load transport seems conceptually correct, but requires further research. This is emphasized in view of its importance in the predicted equilibrium bathymetries.

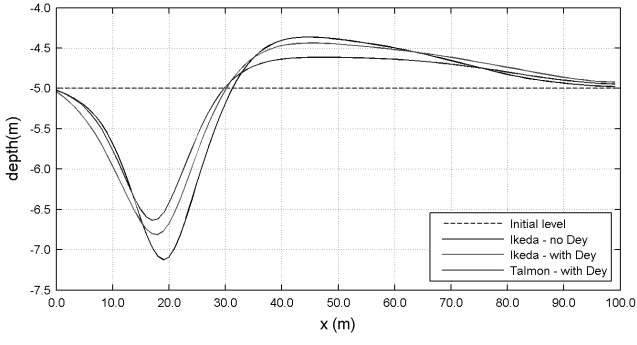

Fig. 9 Resulting longitudinal bottom profiles (y = 10 m) after 100 days.

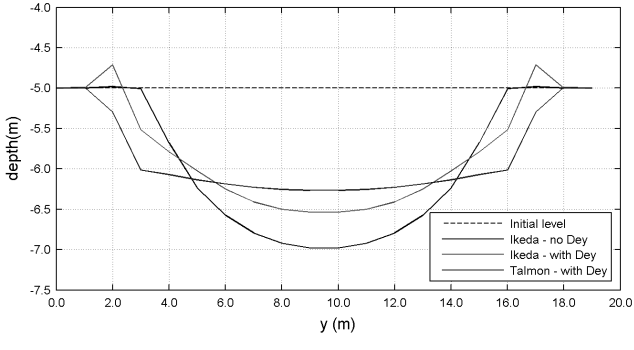

Fig. 10 Resulting transverse bottom profiles (x = 23 m) after 100 days.

REFERENCES

Arcilla, A.S., J.A. Roelvink, B.A. O'Connor and J.A. Jimenez, 1994. The Delta flume '93 experiment, Proc. Int. Coastal Dynamics Conference, Barcelona, pp. 488-502.

Bagnold, R.A., 1956. The Flow of Cohesionless Grains in Fluids. Proc. Royal Soc. Philos. Trans., London, Vol. 249.

Dey, S., 2001. Experimental study on incipient motion of sediment particles on generalized sloping fluvial beds. Int. Journal of Sediment Research, Vol.16, No. 3, p. 391-398

Dey, S., 2003. Threshold of sediment motion on combined transverse and longitudinal sloping beds. Journal of Hydraulic Research, Vol. 41, No. 4, p. 405-415.

Dohmen-Janssen, M., 1999. Grain size influence on sediment transport in oscillatory sheet flow. Doctoral Thesis. Delft University of Technology, Delft, The Netherlands.

Hoefel, F., and S. Elgar, 2003. Wave-induced sediment transport and sandbar migration, 781 Science, 299, 1885–1887.

Ikeda, S., 1982. Lateral Bed-Load Transport on Side Slopes. Journal Hydraulics Division, ASCE, Vol. 108, No. 11.

Ikeda, S., 1988. Lateral Bed Load Transport on Side Slopes. In: Civil Engineering Practice 2, Technomic Publishing Company, USA.

Isobe, M. and Horikawa, K., 1982. Study on water particle velocities of shoaling and breaking waves. Coastal Eng. in Japan, 25, pp. 109−123.

Koch, F.G. and Flokstra, C., 1981. Bed level computations for curved alluvial channels. 19th IAHR congress, Vol. 2, New Delhi, India.

Lesser, G.R., Roelvink, J.A., Van Kester, J.A.T.M. and Stelling, G.S., 2004. Development and validation of a three-dimensional morphological model. Coastal Engineering, Vol. 51, p. 883-915.

Nielsen, P., 2002. Shear stress and sediment transport calculations for swash zone modeling. Coast Eng. 45, 53-60.

Nielsen, P., 2006. Sheet flow sediment transport under waves with acceleration skewness and boundary layer streaming. Coast. Eng. 53, 749-758.

Nielsen, P. and Callaghan, D.P., 2003. Shear stress and sediment transport calculations for sheet flow under waves. Coast. Eng. 47, 347-354.

Talmon, A.M., 1992. Bed topography of river bends with suspended sediment transport. Doctoral Thesis. Delft University of Technology, Delft, The Netherlands.

Talmon, A.M., Van Mierlo, M.C.L.M. and Struiksma, N., 1995. Laboratory measurements of the direction of sediment transport on transverse alluvial-bed slopes. Journal of Hydraulic Research, Vol. 33, No. 4, p. 495-517.

Talmon, A.M. and J.-U. Wiesemann, 2006, Influence of grain size on the direction of bed-load transport on transverse sloping beds, Int. Conf. on Scour and Erosion ICSE2006, Amsterdam.

Van Bendegom, L., 1947. Enige beschouwingen over riviermorfologie en rivierverbetering. De Ingenieur, Vol. 59, No. 4, p. 1-11.

Van Rijn, L.C., 1993. Principles of sediment transport in rivers, estuaries and coastal seas. Aqua Publications, The Netherlands (www.aquapublications.nl).

Van Rijn, L.C., 2006a. A unified view of sediment transport by currents and waves, part 1: initiation of motion, bed roughness and bed load transport. Accepted for publication in Journal of Hydr. Engineering.

Van Rijn, L.C., 2006b. A unified view of sediment transport by currents and waves, part 2: suspended transport. Accepted for publication in Journal of Hydr. Engineering.

Watanabe, A., Sato, S., 2004. A sheet flow transport rate formula asymmetric forward leaning waves and currents. Proc. 29th ICCE, Lisbon, World Scientific, pp. 1703–1714.

SEDIMENT TRANSPORT OFF NORTHEAST FLORIDA OUTSIDE THE SURF ZONE DURING HURRICANES

Michael Krecic[1], Christopher Bender[2], Kristen Odroniec[3]

1. Taylor Engineering, Inc. 9000 Cypress Green Dr, Jacksonville, FL, 32256, USA. mkrecic@taylorengineering.com.
2. Taylor Engineering, Inc. 9000 Cypress Green Dr, Jacksonville, FL, 32256, USA. cbender@taylorengineering.com.
3. Taylor Engineering, Inc. 9000 Cypress Green Dr, Jacksonville, FL, 32256, USA. kodroniec@taylorengineering.com.

Abstract: The highly active Atlantic Ocean hurricane seasons of 2004 and 2005 produced unique morphological changes outside of the surf zone. This paper focuses on two northeast Florida areas — St. Johns County and Volusia County. These morphological changes, as determined by bathymetric surveys, revealed net sediment accretion in greater than 30-foot water depths after the 2004 storms just offshore of the St. Johns County Shore Protection Project and net sediment erosion on sand shoals located in 60-foot water depths, about seven miles offshore of Volusia County after the 2005 storms. Analyses of beach profiles and borrow area survey data revealed significant sediment transport at large depths, greater than those associated with typical wave conditions. Application of depth of closure and near bottom velocity methods showed wave conditions in 2004 and 2005 capable of sediment transport at these large depths.

INTRODUCTION

Many beach fill projects exist around the state of Florida. Project permit requirements include nearshore beach profile monitoring to assess project performance. Issuance of permits require offshore borrow surveys to quantify the availability of beach compatible sand for proposed beach nourishment projects. The highly active Atlantic Ocean hurricane seasons of 2004 and 2005 produced unique morphological changes outside of the surf zone. The availability of the above types of surveys provides an opportunity to assess sediment transport as a result of the active storm seasons. This paper focuses on

two northeast Florida areas — St. Johns County and Volusia County.

ST. JOHNS COUNTY ANALYSIS

Background

St. Johns County lies in northeast Florida about 35 miles south of the Florida/Georgia border. The initial nourishment (referred to as the 2003 project) of the St. Johns County Shore Protection Project (SPP), completed in January 2003, extended approximately 2.9 miles (mi) from approximately 600 feet (ft) north of Florida Department of Environmental Protection (FDEP) monument R-137A (approximately 2.7 mi south of St. Augustine Inlet in Anastasia State Park) south to approximately 600 ft south of FDEP monument R-151 in the City of St. Augustine Beach in St. Johns County, Florida. The State of Florida, piggybacking the federal nourishment project, extended the beach nourishment project approximately 0.9 mi north into Anastasia State Park to FDEP monument T-132. The first renourishment (referred to as the 2005 project) also extended approximately 2.9 mi from monument R-137A to R-151. The 2004 hurricane season forced an expedited schedule of the renourishment project — backed with emergency remediation money appropriated from the U.S. Congress.

Tropical storm Bonnie, a strong northeast storm, and four hurricanes (Charley, Frances, Ivan, and Jeanne) affected the State of Florida during the six-week period from August 12 through September 26, 2004. Each of these significant storms adversely affected the SPP. The occurrence of storms in rapid succession caused erosion and damages beyond those expected from an isolated, individual storm because recovery of nearshore material lost from previous storms did not occur before subsequent storms.

2004 Hurricane Season

Figure 1 contains wave and wind data generated by the National Oceanic and Atmospheric Administration's (NOAA) GFDL and WAVEWATCH III models for location 29.75°N, 81.0°W, offshore of the SPP (USACE, 2005). Wind speeds correspond to outlying winds a few miles from the hurricane's center. National Weather Service estimates of "sustained winds" or "maximum sustained winds" — which refer to eyewall wind speeds recorded by aircraft reconnaissance — will exceed the wind speed values in Figure 1. The following paragraphs provide details for each of the major storms that affected St. Johns County in 2004 — information compiled from FDEP (2004a, b, c) and USACE (2005).

Tropical Storm Bonnie: Tropical Storm Bonnie made landfall near Apalachicola in western Florida at 1200 Eastern Daylight Time (EDT) on August 12th with sustained winds near 50 miles per hour (mph). The storm moved northeast across Florida and caused slightly increased wave heights and wind speeds in the SPP.

Hurricane Charley: Hurricane Charley made landfall at 1700 EDT on August 13th on the southwest coast of Florida just north of Captiva Island in Lee County. A Category 4 hurricane at landfall, Charley contained maximum sustained winds estimated at 145 mph with a storm surge estimated at over 10 ft (FDEP, 2004a). Hurricane Charley featured a

tight radius which allowed the storm to maintain hurricane force winds along a north-northeast trajectory across central Florida (USACE, 2005). Still of hurricane intensity, Hurricane Charley exited the east coast of Florida near Daytona Beach in Volusia County at 0200 EDT on August 14th with maximum sustained winds near 85 mph and higher gusts. Hurricane force winds extended outward up to 25 mi from Charley's center and tropical storm force winds extended outward up to 85 mi. As Hurricane Charley exited the state on August 14th, approximately 50 mi south of the project site. Offshore waves peaked at seven feet with winds reaching 28 knots.

Hurricane Frances: At 0100 EDT on September 5th Hurricane Frances made landfall in northern Martin County on Florida's east coast. A Category 2 storm at landfall, Hurricane Frances had maximum sustained winds near 105 mph and higher gusts. Hurricane force winds extended outward up to 85 mi from the storms' center and tropical storm force winds extended outward up to 200 mi. High waves also affected much of Florida's east coast for a relatively long duration — affecting much of central and south Florida for up to 30 hours — because of the storm's slow pace. As Hurricane Frances made landfall on September 5th, the NOAA Crescent Beach, FL water level station (29°46.1' N, 81°15.5' W) recorded a level of 4.5 ft-National Geodetic Vertical Datum (NGVD), which approaches the 10-year storm water level (combination of astronomical tide and storm surge) return period of 4.8 ft for the St. Johns County project area (USACE, 1990; as referenced in USACE, 2005). Offshore wave heights, peaking at 19.7 ft, approached 15 ft for 33 hours. This peak height falls between the 2-year return period wave height of 18.8 ft and the 5-year height of 21.5 ft (Brooks and Brandon, 1995; as referenced in USACE, 2005). Average wind speeds (peaking at 44 knots) during this time exceeded 25 knots for 54 hours. Hurricane Frances became a tropical storm as the storm continued west-northwest across the Florida peninsula.

Hurricane Ivan: Near 0300 EDT on September 16th Hurricane Ivan made landfall as a Category 3 hurricane in Baldwin County, AL (just west of the Florida Panhandle region). Maximum sustained winds equaled 130 mph and NOAA recorded storm surge elevations of five feet. Wave heights reached 53 ft as recorded by NOAA buoy 42040 (located 62 nautical miles south of Dauphin Island, AL, in 780 ft of water). Hurricane Ivan maintained southerly wave heights near five feet in St John's County.

Unnamed Nor'easter: One week before Hurricane Jeanne's landfall, a strong nor'easter affected Florida's east coast with waves in excess of 10 ft in St. Johns County. During this storm, wave heights remained above eight feet (peaking at 12.4 ft) for nearly three days. Wind speeds reached 25 knots and exceeded 20 knots for nearly 39 hours. Combined tide and storm surge arriving just ahead of the nor'easter reached 4.6 ft-NGVD — approaching a 10-year storm surge event. The extended duration — nearly four days — of high wave and water level conditions caused significant erosion to the SPP.

Hurricane Jeanne: Hurricane Jeanne made landfall at 0000 EDT on September 26th as a Category 3 storm on Florida's east coast in northern Martin County. Maximum sustained

winds equaled 120 mph with storm surge estimates near levels experienced during Hurricane Frances (8-10 ft). The landfall location, near Stuart, nearly matched the landfall location of Hurricane Frances only 20 days earlier. The National Hurricane Center reported that the landfall points came an unprecedented 2 mi apart. Tropical storm force winds extended outward up to 175 mi from the storm's center. Offshore wave heights peaked at 17 ft (and remained above 15 ft for 21 hours) as Hurricane Jeanne augmented waves created by the nor'easter. Offshore wind speeds during this time reached 35 knots and exceeded 28 knots for 39 hours. A Crescent Beach water level station near the SPP measured a maximum water level of 4.9 ft-NGVD; this water level corresponds to a 10-year storm surge event.

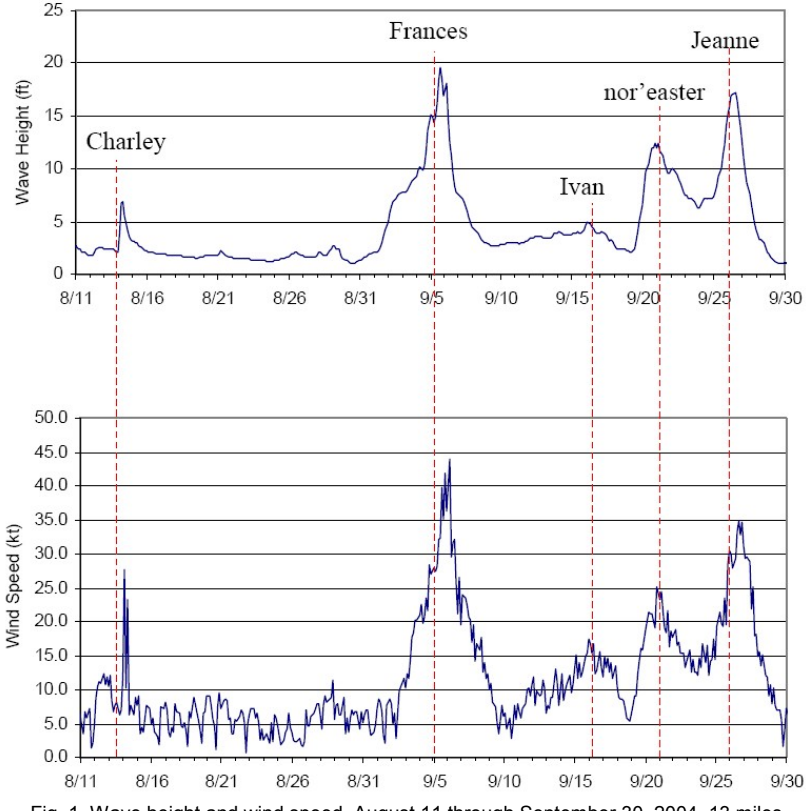

Fig. 1. Wave height and wind speed, August 11 through September 30, 2004, 13 miles offshore of Crescent Beach, St. Johns County, FL; 29.75° N, 81.0° W (USACE, 2005)

Nearshore Data Analysis

Regular monitoring of beach profile surveys in the St. Johns County SPP tracked the beach response to, and recovery after, the 2004 hurricane season. Analysis of the survey

data allows insights into the project performance and sediment dynamics offshore of the surf zone related to the major storms of 2004. This section describes major features of the survey data from pre-hurricanes 2004 to spring 2006. An analysis of wave data from 2002 to 2005 allows estimation of the depth of closure variability offshore of the SPP. Notably, bathymetric changes offshore of the survey extents hamper the analysis of the sediment transport pathways.

A comparison of 2004 pre-hurricanes to 2004 post-hurricanes survey data indicates the impact of the 2004 hurricane season on the SPP. This analysis represents conditions from 36 days before Hurricane Francis to 36 days following Hurricane Jeanne. The intensive forces of the hurricanes affected the beaches tremendously. All profiles in the SPP show erosion above -10 ft and accretion below -10 ft. Unless otherwise stated, all elevations in this section refer to the North American Vertical Datum (NAVD) vertical reference. The beach profile evolution at R-148 demonstrates the dramatic offshore accretion with a large shoal forming below -15 ft (Figure 2). However, longshore sediment transport also contributed to the erosion during the hurricanes. Across the nearshore profile, the fill placement eroded while both North and South control areas accreted — evidence of lateral transport.

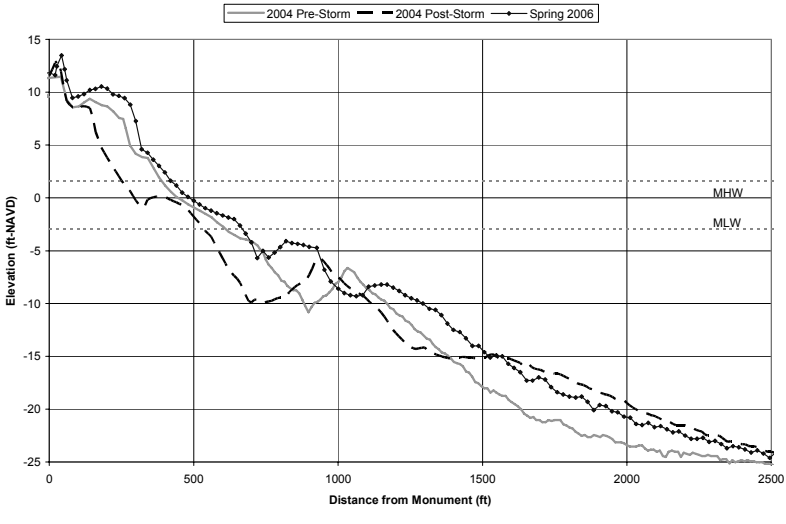

Fig. 2. Survey data for FDEP Monument R-148 in St. Johns County for 2004 pre- and post-hurricane and spring 2006 conditions

The 2004 post-hurricanes to 2005 pre-fill comparison provides an example of the beaches' natural recovery from episodic hurricane events. This analysis represents conditions 190 days following the 2004 post-hurricanes survey. Notably, several winter

storms in late 2004 and early 2005 affected the SPP. In the SPP, erosion continues both above and below MHW following the 2004 hurricane season and winter 2004/05 storms.

To replace sediment lost from recent storms, a beach nourishment project completed in the fall of 2005 placed approximately 2.8 million cy of material in the St. Johns County SPP area (Taylor Engineering, 2006). Comparison of 2005 post-fill to Spring 2006 surveys offers insight on the effect of six months of regular beach processes on beach volumes. This analysis indicates the manner in which beach fill redistributes naturally over time. The SPP eroded above MHW and accreted below MHW, resulting in a net beach volume gain. Erosion onshore and accretion offshore represent normal behavior subsequent to a nourishment project as beach fill diffuses offshore. The few profiles showing net erosion from dune to -20 ft occur at R-142 (St. Augustine Pier) and R-140 to R-141 (just north of the pier) and R-143T to R-143A (just south of the pier). Previous studies have demonstrated increased erosion near R-142, a known erosional hotspot.

Table 1 presents volume changes in the SPP across four nearshore compartments — dune to MHW, MHW to -10 ft, -10 ft to -20 ft, and -20 ft to -30 ft. The table indicates large volume changes below -10 ft, especially below -20 ft. Notably, many surveys did not extend to -30 ft and in these cases the profile analysis terminated at the end of the shortest survey or 3,000 ft from the control monument. The 2004 pre- to post-hurricanes comparison indicates over 1.3 million cy of accretion in the project area between -20 ft and -30 ft. The volume losses above -10 ft do not offset this volume gain. Assuming that longshore processes do not contribute the majority of the excess material requires movement of material from offshore to produce the large accretion below -20 ft. The 2004 post-hurricanes to 2005 pre-project and 2005 pre- to post-project time intervals in Table 1 suggest erosion below -20 ft. The 2005 post-project to spring 2006 analysis indicates accretion between -20 ft and -30 ft.

Table 1. Nearshore Volume Changes between Recent Surveys in the St. Johns County SPP

	2004 Pre-Hurricanes to 2004 Post-Hurricanes	2004 Post-Hurricanes to 2005 Pre-Project	2005 Pre-Project to 2005 Post-Project	2005 Post-Project to Spring 2006
	Volume Change (cy)			
Dune to MHW	-483,900	-72,500	956,000	-31,400
MHW to -10 ft-NAVD	-571,400	-167,400	1,399,700	12,500
-10 ft to -20 ft-NAVD	697,100	-277,500	474,800	244,500
-20 ft to -30 ft-NAVD	1,343,400	-381,500	-355,500	338,300
Dune to -30 ft-NAVD	985,200	-898,900	2,475,000	563,900
Most surveys do not reach -30 ft-NAVD				

The depth of closure represents the theoretical offshore depth beyond which sediment transport does not occur. Under normal conditions, the depth of closure provides a convenient offshore extent for the volume calculations with all volume change landward of that point. Profiles that do not converge in the offshore region cause difficulty for volume change calculations as erosion or accretion extends offshore of the available data. Analysis of wave data offshore of the St. Johns County SPP allows insight into wave-

induced sediment motion outside of the surf zone. The National Data Buoy Center (NDBC) buoy 41012 (30.0 N 80.6 W) contains wave and meteorological information offshore of the SPP from 2002 to 2005.

The Hallermeier (1978, 1981) and Birkemeier (1985) methods allow estimation of the depth of closure (h_c) offshore of the St. Johns County SPP. Hallermeier defined conditions for sediment motion for relatively rare conditions — effective wave height (H_e) and period (T_e) conditions exceeded only 12 hours per year.

$$h_c = 2.28H_e - 68.5\left(\frac{H_e^2}{gT_e^2}\right) \quad (1)$$

Birkemeier (1985) applied high-quality field measurements from the USACE Field Research Facility at Duck, NC to evaluate Hallermeier's relationship. Birkemeier developed a simplified expression for h_c based on the effective wave height.

$$h_c = 1.57H_e \quad (2)$$

Kraus et al. (1998) contains examples and a reference that demonstrate the Hallermeier formulation produce more conservative estimates of h_c than the Birkemeier formulation.

Application of linear wave theory shoaled the NDBC data (2002 to 2005) from the buoy location (~160 ft depth) to a depth of 35 ft. Sorting of the wave data and application of the Hallermeier and Birkemeier methods calculated the depth of closure for each year from 2002 to 2005. Table 2 presents the results of the depth of closure analysis. In all instances (and by an average of almost six feet), the Hallermeier method produces larger h_c values than the Birkemeier method.

Table 2 indicates that the depth of closure varies significantly from year to year with a depth of closure in 2004 that approaches 38 ft with the method of Hallermeier. The 2004 depth of closure nearly doubles the 2002 estimate. Closer analysis of the 2004 wave data revealed, as expected, Hurricanes Frances and Jeanne produced the wave events responsible for the large depth of closure in 2004.

Table 2. Depth of Closure Estimates for St. Johns County SPP with Hallermeier and Birkemeier Methods and NDBC Data

	Depth of Closure--h_c (ft-MLW)	
	Wave Height Transformed to 35 ft depth	
	Hallermeier CEM (III-3-9)	Birkemeier CEM (III-3-12)
2002	17.3	13.8
2003	28.1	20.7
2004	34.9	28.0
2005	27.9	22.1

The values in Table 2 confirm the 2004 hurricane season contained wave events capable of moving sediment at depths greater than typical closure values. Lack of survey data

offshore of -30 ft removes the possibility to evaluate bathymetric changes near the estimated depth of closure. This situation demonstrates that — to capture sediment transport limits in extreme events — survey operations need to extend seaward of typical transport limits.

VOLUSIA COUNTY ANALYSIS

Background

Volusia County lies in northeast Florida about 95 miles from the Florida/Georgia border. As part of an ongoing beach and dune restoration permitting, engineering, and design project for approximately 5.5 mi of beach, Volusia County identified many candidate sand shoals about 5 to 15 mi offshore during a reconnaissance-level study, which consisted of a literature review and bathymetric survey (collected in November 2004). Further refinement of the borrow areas needed for the proposed beach and dune restoration project focused on two sand shoals (B11-3 and B12-1) about 5 to 7 mi offshore in about 60-ft water depths. Note that borrow area B12-1 lies just seaward of borrow area B11-3. Boundaries for the proposed B11-3 borrow area run about 3,000 ft and 6,000 ft in the shore-normal and shore-parallel directions (413 acres). Boundaries for the proposed B12-1 borrow area run about 4,000 ft and 6,000 ft in the shore-normal and shore-parallel directions (551 acres). The long axes of both borrow areas primarily orient along the north-south axis with the greatest shoal relief features primarily orienting along the northeast-southwest axis (Figure 3). Based on the plans & specs-level sand search investigation, Coastal Technology Corporation (2006) analyzed the borrow areas' sediment size characteristics of several vibracores with the B11-3 and B12-1. Mean grain size diameters ranged from 0.21 to 0.22 mm. The median grain sizes equal 0.19 and 0.20 mm for B11-3 and B12-1.

Another bathymetric survey (collected in December 2005), performed as part of the refined work, revealed altered shoal bathymetries (Figure 4). Negative (red) contours indicate areas of erosion and positive (green) contours indicate areas of accretion. Local relief changes showed erosive and accretive patterns on the order of five feet. Over the entire survey extents, the shoal gained 468,000 cy near borrow B11-3. Near borrow area B12-1, the shoal lost 952,000 cy over the entire survey extents. Because of the relative proximity of borrow areas, some of the sand may have moved eroded from near borrow area B12-1 and deposited near borrow area B11-3. The passage of five tropical events (Katrina, Rita, Ophelia, Tammy, and Wilma) and several nor'easters between the two surveys may have affected shoal relief.

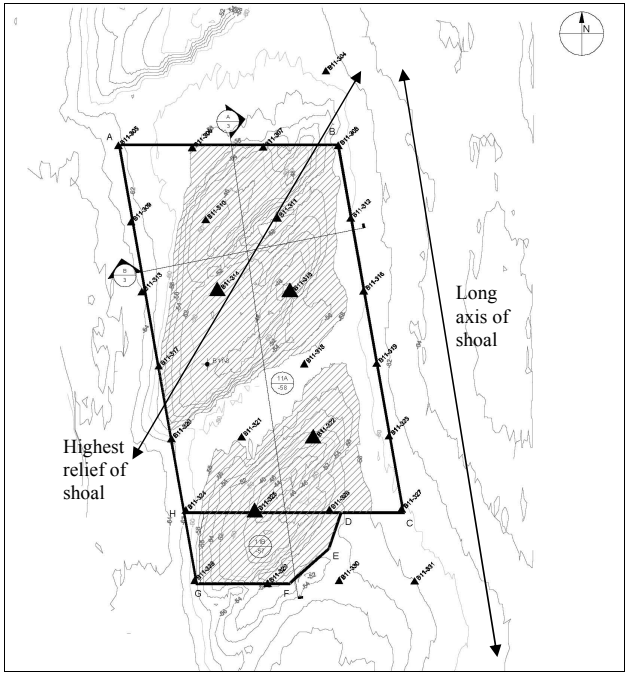

Fig. 3. December 2005 conditions at borrow area B11-3

2005 Storm Season

Several nor'easters and tropical events occurred near Volusia County in 2005. Nor'easters generally form quickly and last about two to three days but may last longer (7 to 10 days). During these storms, northeasterly winds blowing across the Atlantic Ocean over a large fetch (hundreds of miles) produce wind setup and large waves that affect the area. Severe storms occurred in 1925, 1932, 1947, 1956, 1958, 1960, 1962, 1964 – 1966, 1969, 1972 – 1975, 1981, 1984, 1986, 1987, 1989, and 1992 – 1995 (USACE, 1991; USACE, 1982; Taylor and Yáñez, 1994). Taylor Engineering (2003) reports from 1956 – 1975 and 1981 – 1995, the area averaged about 5 – 6 storms per year. From 1976 – 1980, an especially stormy period, the study area averaged 12 storms per year.

Annual frequencies of events reaching tropical storm or hurricane strength vary widely from year to year. The main tropical hurricane season runs from June through November with significant hurricane activity occurring between August and October. NOAA provides historical hurricane data via the Internet. Presented on annual maps, the data include hurricane track, maximum winds, and central pressure. Taylor Engineering (2003) supplemented this information with data from a hurricane database (Pesek, 1991), which includes hurricane forward velocity. On average, tropical storms or hurricanes pass near the area about once every three years.

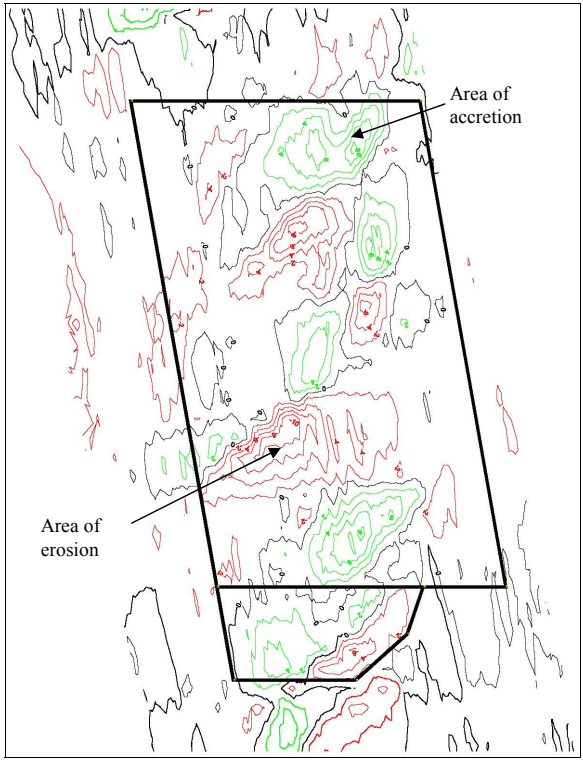

Fig. 4. Comparison of borrow area B11-3 survey data for November 2004 and December 2005 conditions

The NDBC buoy 41009 (28.50 N 80.17 W), about 20 nautical miles east of Cape Canaveral, Florida, contains wave and meteorological information during 2005. Application of linear wave theory shoaled the NDBC data from the buoy location (~136 ft depth) to a depth of 60 ft. Following methodologies presented in Goda (1988, 2000), a peak-over-threshold extreme wave analysis identified storms and their associated largest waves and return periods. In addition to the five tropical events, this analysis revealed nine nor'easter storms. The number of nor'easters and hurricanes exceeded the historical averages.

Six nor'easters occurred in January and February 2005. The maximum wave heights and associated wave periods ranged from about 9 to 14 ft and 6.3 to 13.8 seconds (sec); the storm durations, ranged from two to eight days. Another nor'easter occurred in April and lasted about five days. The maximum wave height and associated wave period equaled about 15 ft and 12.9 sec. Two more nor'easters occurred in November and early

December. These storms produced maximum wave heights of 10 and 15 ft and associated wave periods of 10 and 8.3 sec. The November storm lasted 10 days and the December storm lasted four days.

Five tropical events also passed near the area. These events included Hurricane Katrina (August 25, 2005; Category 1), Ophelia (September 6 to 9, 2005; Tropical Storm, Category 1), Tropical Storm Tammy (October 5 to 6, 2005), and Hurricane Wilma (October 24, 2005; Category 3). The maximum wave heights and associated wave periods ranged from 9 to 19 ft and 6.7 to 10 sec. Storm durations varied from 2 to 11 days. Note Hurricane Wilma produced the largest wave condition but had the shortest duration of the five tropical events. Ophelia had the longest duration. Wind speeds for the tropical events ranged from 25 (Ophelia) to 110 knots (Wilma) at the NDBC buoy.

Offshore Data Analysis

Employing the Willis-Ackers-White method, based on the Ackers and White (1973) method for unidirectional flow and modified by Willis (1979) for waves, can quantify the potential for sediment transport outside of the surf zone. Ackers and White developed their method to calculate total sediment load, including both bed and suspended loads, in unidirectional flow over an alluvial bed. This technique, based on a transport power approach whereby the work exerted to move sediment equals the product of the power available to move sediment and the efficiency of the system, includes a criterion for the inception of sediment motion. Willis defines the threshold of movement criterion due to waves only as

$$F_{grc}^2 = \frac{\left(\frac{0.23}{\sqrt{D_{gr}}} + 0.14\right)^2}{0.04141 D_{gr} + 0.20354} \tag{3}$$

where F_{grc} = the critical mobility number and D_{gr} = the dimensionless grain diameter defined as

$$D_{gr} = \left(\frac{\gamma_s}{\gamma}\frac{gD^3}{\nu}\right)^{\frac{1}{3}} \tag{4}$$

where γ= the specific weight of seawater, γ_s = the specific weight of the sediment, γ= the specific weight of seawater, g = the acceleration due to gravity, D = the sand grain diameter, ν = the kinematic viscosity of water (1.4×10^{-5} square feet per second). Given the wave conditions and sediment characteristics, one calculates D_{gr} from Eq. 4, estimates the bottom shear stress from empirical friction coefficient data from Jonsson (1966; as cited in Willis, 1979) and determines the Ackers and White mobility number, defined as

$$F_{gr}^2 = \left(\frac{u_{*fg}^n u_{*cg}^{1-n}}{\sqrt{gD\left(\frac{\gamma_s}{\gamma} - 1\right)}} \right) \quad (5)$$

where F_{gr} = the Ackers and White mobility number, u_{*fg} and u_{*cg} = shear velocities for material moved as suspended and bed load, and n = an empirical coefficient. If the mobility number at a particular location and depth falls above the critical value, then sediment transport at that depth may occur.

The method defines sediment load as

$$X = C\left(\frac{F_{gr}}{F_{grc}} - 1\right)^m \frac{\rho_s}{\rho}\frac{D}{d}\left(\frac{\rho^{\frac{1}{2}} P_{fg}}{\tau_{fg}^{\frac{3}{2}}}\right)^n \left(\frac{P_{cg}}{\tau_{cg} V}\right)^{1-n} \quad (6)$$

where X = the sediment load, ρ = the seawater density (64 pound per cubic foot), d = the water depth, P = the power per unit area available to move sediment, τ = bottom shear stress, and V = mass transport velocity due to waves (from linear wave theory). The subscripts, *fg* and *cg*, denote fine grains and coarse grains. Multiplying Eq. 6 by the appropriate values yields the sediment transport at a point in units of cy/s/ft.

Analysis of offshore wave data near the borrow areas allows insight into wave-induced sediment motion outside of the surf zone. Based on application of the Willis-Ackers-White method, Ophelia and Tammy generated the most transport (Table 3). Calculated transport rates also revealed that two nor'easters (January No.1 and November) may have contributed to observed bathymetric changes. Relative to Ophelia, Tammy and the two nor'easters generated 5, 16, and 54% less transport.

For comparison purposes, Table 3 also shows the relative rank of the maximum wave heights and storm durations to assess if any trends exist between these characteristics and sediment transport. Although weak, sediment transport and duration ranks showed better correlation than did sediment transport and maximum storm wave heights. This means that storms with longer durations may lead to more sediment transport.

The December 2005 borrow area survey indicates significant sediment movement in the Volusia County project borrow areas compared to November 2004 conditions. The bathymetric changes observed suggest completion of a pre-project survey to obtain existing sediment quantities and locations in the borrow areas.

Table 3. Sediment Transport Estimates Derived from Willis-Ackers-White Method and NDBC Data

Number	Name	WAW transport (cy/s/ft)	Max H (ft)	Rank Transport	% Difference from Rank 1 Transport	Rank Max H	Rank Duration
1	Jan No.1	3.57E-03	13.7	4	-54%	6	4
2	Jan No.2	1.05E-03	9.5	14	-426%	11	9
3	Jan No.3	1.19E-03	10.6	10	-363%	9	9
4	Feb No.1	2.88E-03	13.8	6	-91%	5	3
5	Feb No.2	1.17E-03	8.8	12	-373%	13	14
6	Feb No.3	1.07E-03	8.9	13	-413%	12	11
7	Apr	2.60E-03	14.9	8	-112%	3	6
8	Katrina	1.17E-03	8.6	11	-372%	14	12
9	Ophelia	5.51E-03	13.3	1	0%	7	1
10	Rita	2.29E-03	10.7	9	-140%	8	7
11	Tammy	5.27E-03	15.2	2	-5%	2	5
12	Wilma	2.63E-03	18.8	7	-110%	1	13
13	Nov	4.74E-03	9.8	3	-16%	10	2
14	Dec	2.89E-03	14.9	5	-91%	3	8

CONCLUSION

The highly active Atlantic Ocean hurricane seasons of 2004 and 2005 produced unique morphological changes outside of the surf zone. Bathymetric surveys revealed net sediment accretion in greater than 30-ft water depths after the 2004 storms just offshore of the St. Johns County Shore Protection Project and net sediment erosion on sand shoals located in 60-ft water depths, about five to seven miles offshore of Volusia County after the 2005 storms. Analyses of beach profiles and borrow area survey data revealed significant sediment transport at large depths, greater than those associated with typical wave conditions. Application of depth of closure and near bottom velocity methods showed wave conditions in 2004 and 2005 capable of sediment transport at these large depths.

REFERENCES

Ackers, P. and White, W.R. (1973). "Sediment transport: new approach and analysis," *Journal of Hydraulics Division* 99(HY11), 2041-2060.

Birkemeier, W. A. (1985). "Field data on seaward limit of profile change," *Journal of Waterway, Port, Coastal, and Ocean Engineering* 111(3), 598-602.

Coastal Technology Corporation. (2006). "Volusia County Sand Search – Geotechnical Investigations, Plans & Specs Level Offshore Sand Search Investigation, South Peninsula," Geotechnical report prepared by Coastal Technology Corporation for Volusia County, FL, March 2006.

Goda, Y. (1988). "On the methodology of selecting design wave height," Proceedings, 21st International Conference on Coastal Engineering, American Society of Civil Engineers, 3213- 3226.

Goda, Y. (2000). *Random Seas and Design of Maritime Structures*. World Scientific, River Edge, NJ.

Florida Department of Environmental Protection (FDEP). (2004a). "Hurricane Charley, Post-storm Beach Conditions and Coastal Impact Report with Recommendations for Recovery and Modifications of Beach Management Strategies," Division of Water Resource Management, Bureau of Beaches and Coastal Systems.

FDEP. (2004b). "Hurricane Frances and Hurricane Jeanne, Post-storm Beach Conditions and Coastal Impact Report with Recommendations for Recovery and Modifications of Beach Management Strategies;" Division of Water Resource Management, Bureau of Beaches and Coastal Systems.

FDEP. (2004c). "Hurricane Ivan, Beach and Dune Erosion and Structural Damage Assessment and Post-Storm Recovery Plan for the Panhandle Coast of Florida," Division of Water Resource Management, Bureau of Beaches and Coastal Systems.

Hallermeier, R. J. (1978). "Uses for a calculated limit depth to beach erosion," Proceedings, 16th Coastal Engineering Conference, American Society of Civil Engineers, 1493- 1512.

Hallermeier, R. J. (1981). "A profile zonation for seasonal sand beaches from wave climate," *Coastal Engineering* 4, 253-277.

Kraus, N. C., Larson, M, and Wise, R. A. (1998). "Depth of closure in beach-fill design," Coastal Engineering Technical Note CETN-II-40, U.S. Army Engineer Waterways Experiment Station, Coastal and Hydraulics Laboratory, Vicksburg, MS.

Pesek, T. 1991. STORM Hurricane Tracking Software. Utopia Software.

Taylor Engineering, Inc. (2003). "Volusia County Erosion Assessment Study for Shorelines South of Ponce DeLeon Inlet to Canaveral National Seashore," Engineering report prepared by Taylor Engineering for Volusia County, FL, December 2003.

Taylor Engineering, Inc. (2006). "St. Johns County Shore Protection Project 2005 Monitoring Report," Engineering report prepared by Taylor Engineering for St. Johns County, FL, June 2006.

Taylor, R.B. and Yanez, M.A. 1994. *Ponce DeLeon Inlet Management Plan.* Taylor Engineering, Inc. Jacksonville, FL.

United States Army Corps of Engineers (USACE). (1982). *Section 14 Study, Bethune Beach, Volusia County, Florida.* Jacksonville District, Jacksonville, FL.

USACE. (1991). *Daytona Beach Shores, Florida, Shore Protection Study Reconnaissance Report.* Jacksonville District, Jacksonville, FL.

USACE. (2005). "Project Information Report, Rehabilitation Effort for the Ft. Pierce, Florida, Hurricane/Shore Protection Project," U.S. Army Corps of Engineers, Jacksonville District. Jacksonville, FL.

Willis.D.H. (1979). "Sediment Load under Waves and Currents," National Research Council Canada, Ottawa, Canada.

GEOMORPHIC AND SEDIMENTOLOGIC EVIDENCE FOR NET LITTORAL DRIFT – A REVIEW

Terry Healy
Coastal Marine Group, Dept of Earth and Ocean Sciences,
University of Waikato, New Zealand
trh@waikato.ac.nz

Abstract: Some 24 different indicators of the net littoral or alongshore drift are identified. Most of these relate to the geomorphic and sedimentologic properties of the littoral system, but also include deductions from wind data and wave properties. Not all indicators can be accorded equal confidence as definitive indicators.

INTRODUCTION

For many of the worlds' coastlines the net direction of wave generated alongshore sediment transport, the "littoral drift", is well known, but along some coastal sectors the evidence is not always so clear, for example, in cases of large coastal compartments. Komar (1998) illustrates 6 schematic cases representing the net direction of the littoral drift (Figure 1). Basically 5 of these are variations of sediment impoundment by structures such as groynes, jetties, or breakwaters, and natural structures such as headlands, and the other is long term migration of large tidal inlets or river mouths. However, there are numerous additional geomorphic and sedimentologic indicators of the direction of the net littoral drift. In this paper some 24 separate littoral drift direction indicators are recognised, not all of which can be regarded with the same confidence as definitive indicators.

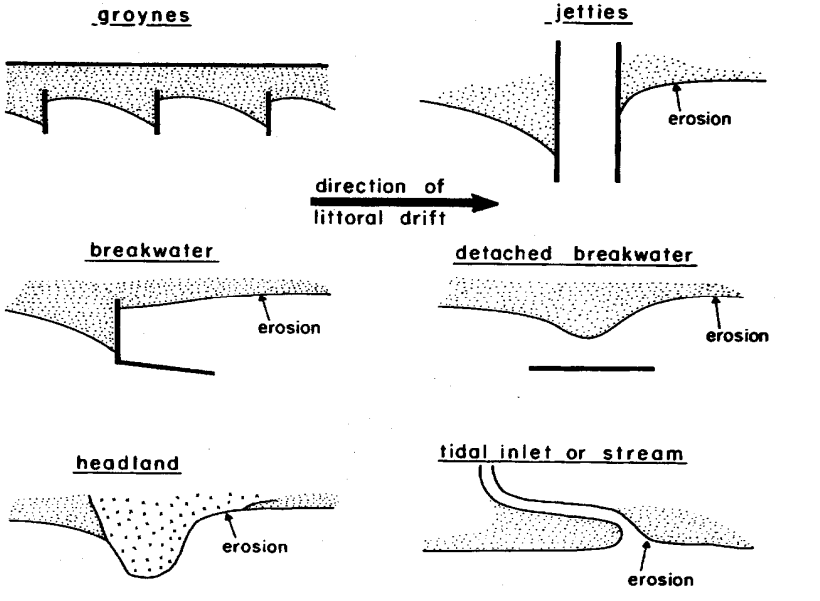

Figure 1. Geomorphic indicators of net littoral drift (From P.D. Komar (1998): *Beach Processes and Sedimentation 2nd Edition)* With permission.

SOME FUNDAMENTAL DEFINITIONS

Waves and currents in the nearshore wave shoaling zone interact to produce transport of sediment on the sea floor which may be onshore–offshore (diabathic) transfer or alongshore (parabathic). "*Littoral or longshore drift*" is the term given to the alongshore transport of material from the nearshore sea floor under the combined action of waves and currents (Muir-Wood 1969; Kidson 1982).

It is axiomatic that alongshore transport or littoral drift on a sandy coastline is primarily wave driven. Waves approaching from one direction, imperfectly refracting and breaking at an angle to the shoreline, will drive sediment in the breaking wave zone alongshore, but at other times waves breaking from the opposing direction will drive sediment in the opposite direction. There is thus a large difference between the ***total*** littoral drift up and down the beach (the sum total of wave generated drift from all of the directions of wave approach up and down the beach on an annual basis) and the ***net*** littoral drift (the difference between the total drift toward one direction along the beach compared to the total drift in the opposing direction).

The net longshore transport rate "*refers to the summation of the amounts of sediment passing a given point during a certain amount of time, usually a year, with a positive quantity applied to transport in one direction, and a negative quantity in the opposite direction. Zero net transport refers to an equilibrium position of a beach where the*

amount of material eroded is balanced by the amount supplied" (Herbich and Handy 1982).

The littoral drift along sandy beaches is considered as comprising two parts, namely, transport in the breaking wave (surf) zone, and transport in the swash zone along the beach face (Komar 1976). Most sediment transport occurs in the surf zone where "*due to the turbulence of the breaking and surging waves, large volumes of sediment are placed in suspension or rolled along the bed in the surf zone*" (Silvester 1974).

LITTORAL CURRENTS AND SEDIMENT TRANSPORT

The fundamental reason that particles comprising the beach sediments move alongshore relates to the physical forcing processes, which when of sufficient magnitude, generate bottom shear stresses that move the individual sediment particles. Mechanisms for generating the shear stresses include the orbital motion beneath the passage of a wave, or from turbulence in the broken wave bore. These processes induce uplift so that the sediment particles are moved along the bottom or become suspended into the water body, at which point they may be transported by any superimposed current.

At least four types of littoral zone current are important for driving sediment transport on beaches, *viz*.: (i) longshore currents, (ii) wave bore currents, (iii) rip currents, and (iv) undertow, downwelling and upwelling currents. In addition, tidal currents interacting with waves may be important in restricted locations such as tidal inlets.

Longshore Currents

These are the most important for driving the alongshore sediment transport or littoral drift that may involve hundreds of kilometers of sediment displacement along the coast. Basically longshore currents are generated when breaking waves are not fully refracted and break at an angle to the alignment of the beach face When there is perfect refraction the wave breaks simultaneously at all points along the beach; and there is no longshore current generated. It is now generally accepted that the generation of longshore currents results from forces associated with the breaking wave on a sloping beach, and in particular the radiation stress, a momentum flux associated with the breaking waves. The radiation stress has two components, onshore (S_{xx}) and alongshore (S_{yy}). When waves approach the coast at an angle with respect to the shoreline, the combined radiation stress is given by:

$$S_{xy} = En \sin\alpha \cos\alpha \qquad (1)$$

where E is the wave energy density {= ⅛ρgH^2 where H is the wave height, ρ is the sea water density}, n is the ratio of the wave group and phase velocities (1 in the surf zone), and α is the angle between the breaking wave crests and the shoreline alignment. As explained by Komar (1998), when the waves approach the shoreline obliquely, S_{xy} is the longshore directed (y component) of the radiation stress that is moving towards the shoreline (in the x direction directly onshore). The 'thrust" that actually drives the longshore current is derived from the dissipation of S_{xy} in the

nearshore surf zone, being a maximum at the breaker zone and decreasing to 0 at the shoreline. Komar (1998) notes that the longshore current is proportional to the parameter $u_m \sin\alpha_b \cos\alpha_b$ (where u_m is the maximum bottom orbital velocity, and α_b is the angle of the wave front with the shoreline at the point of breaking). Komar and Inman (1970) obtained a relationship for the longshore current, V_ℓ, measured at the mid-surf position half way between the breaker zone and the shoreline – the zone of maximum current across the width of the surf zone:

$$V_\ell = 2.7\, u_m \sin\alpha_b \cos\alpha_b \qquad (2)$$

where α_b. is the angle of the breaking wave relative to the beach alignment. When dealing with wave spectra, the relationship of the longshore current to the significant height at breaking, $H_{bs,}$ is given approximately (Komar 1998) as

$$V_\ell = 1.0 \sqrt{gH_{bs}} \quad \sin\alpha_b \cos\alpha_b \qquad (3)$$

From the above it is evident that the prime driver of the longshore current is the breaking wave, and that other factors, such as beach slope, appear to have little influence on the strength of the longshore current.

Wave Bore Currents.

Upon breaking, the oscillatory property of the wave is largely lost and the energy transformed into a wave of mass translation, known as a bore. A wave bore presents as an abrupt change in water height with the front of the advancing bore a mass of white water foaming fluid turbulence as it propagates across the surf zone at about half the speed of the swell wave prior to breaking, and finally runs up the beach face as swash. As the spent wave recedes and runs down the beach face as backwash, it recreates a reduced wave form moving back to the surf zone, inducing a vortex at the base of the beach face where the backwash meets the incoming bore. This vortex can be important in localized erosion of the sediment bed at the base of the beach face.

Rip Currents

When the shoaling waves break with their crests effectively parallel to the shoreline, the currents generated take the form of a cell circulation, the most obvious part of which is the rip current. These strong, spatially restricted, currents flow seaward to beyond the surf zone. Rip currents occur where there are systematic longshore variations in the height of the breaking waves: larger waves have associated larger wave set-up from radiation stress (an excess flow of momentum) in the onshore direction which is converted to localised generation of longshore currents, which in turn feed the rip currents. In simple terms the longshore currents flow “downhill” from alternating areas of greater wave heights and set up to areas of lower waves and set-up where the converging longshore currents turn seaward as rip currents (Komar 1998; Aagaard and Masselink, 1999). Such conditions tend to be more frequently associated with a steeper or “reflective” morphodynamic beach face.

Downwelling (undertow) and Upwelling Currents.

The mass of water carried shoreward by breaking waves and wave bores may be compensated for by a seaward return flow known sometimes as “undertow”. Komar (1998) notes that laboratory and field measurements tend to confirm theoretical

analyses of a net landward flow of water in the wave crests with a compensating return flow beneath the wave troughs. Typically superimposed on this theoretical mechanism is the effect of wind stress on the water surface. Onshore winds significantly enhance the shoreward flow of water as wind stress set-up, and therefore enhance the seaward bottom return flow (down-welling). Conversely offshore winds carry surface water offshore and induce set-down in the surf zone, for which there is a compensatory shoreward bottom return flow (up-welling). Both mechanisms are important for the understanding of both diabathic and parabathic sediment transport as part of the littoral drift system.

Tidal Currents.
Tidal currents normally play no essential role in transporting littoral sediment transport on the open coast long beaches. However they are important at tidal inlets and harbour entrances, (and arguably major large scale topographic constrictions such as the English Channel and large re-entrant embayments such as Hangzhou Bay in China). Here they may sequester sediment transported in the wave generated nearshore littoral drift and transport the sediment into the tidal inlet. Typically the tidal currents accelerate as they converge toward the tidal inlet on the flooding tide and decelerate upon the passing through the inlet. The acceleration generates intense turbulence and large scale bedforms toward the inlet gorge. The converse is true for the ebbing tidal condition.

SEDIMENT TRANSPORT IN THE LITTORAL ZONE

As is evident from the discussion above, the prime driver of the littoral drift along sandy shorelines is the wave generated longshore currents due to obliquely breaking waves. The major driver of the sediment transport is the directed wave power (i.e. wave energy x time in a given direction). The alongshore component of wave power, or wave energy flux in the longshore direction, P_ℓ , is given by:

$$P_\ell = (ECn)_b \sin\alpha_b \cos\alpha_b \quad (4)$$

where $(ECn)_b$ is the wave energy flux at the breaker zone, and α_b is the wave breaker angle. Here $(Ecn)_b$ is the wave power or wave energy flux per wave crest length, and is converted to a unit shoreline quantity by inclusion of the $\cos\alpha_b$, while the longshore component assumed to be available for transporting sediment in the longshore direction derives from $\sin\alpha_b$.

The sand transport rate may be expressed either as a volume transport rate, Q_ℓ, or more usually as an immersed weight transport rate, I_ℓ, given by:

$$I_\ell = (\rho_s - \rho) g\, a\, Q_\ell \quad (5)$$

where ρ_s is the sediment and ρ the water density, and a is a pore space factor (normally taken as 0.6), such that $a\, Q_\ell$ represents the volume of solid sand. The use of I_ℓ is based upon the Bagnold (1963) sediment transport model, and it possesses the same units as P_ℓ so that the relationship becomes:

$$I_\ell = K\, P_\ell \quad (6)$$

where K is a dimensionless proportionality coefficient. Based upon plotting of considerable field data, K ~ 0.7 (Komar 1998) when wave energy calculations are based upon root mean square wave heights for H_{bs}. Note that these equations are based upon empirical data of variable quality from various sand beaches. Komar (1998, p.401 and following pages), in a wide ranging discussion concludes that the dependence of the longshore sediment transport rate on environmental factors such as grain size, beach slope, and wave steepness remains poorly established and requires further research.

Table 1 presents a selection of littoral sediment transport formulae commonly used in the past few decades, and specifically lists the parameters used in each. While most use the obvious parameters of breaking wave height (H_b), breaking wave celerity (C), breaking wave angle (α_b), sediment grain size diameter (D), wave steepness and beach slope, and bottom roughness (both form drag and skin friction) are rarely included.

Table 1. Various Formulae for Longshore Transport/Littoral Drift

Name	Date	Paramaters
Longshore Sediment Transport		
Kalinske - Krijlink formula	1952	$D, g, S_b, V_l, \mu, \rho, \rho_s$
Inman and Bagnold	1963, 1966	$\rho, g, H_b, C_b, \alpha_b$
Inman and Frautschy	1966	$\rho, g, H_b, C_b, \alpha_b$
Bijker formula	1967	$D, g, S_b, \rho, \rho_s, t_c$
Longue - Higgins	1970	$\rho, g, H_b, C_b, \alpha_b$
Komar and Inman	1970	$\rho, g, H_b, C_b, \alpha_b, V_l, \mu_m$
Komar	1977	α_b, V_l, μ_m
Tsuchiya and Yasuda	1978	V_l, D, ρ
Kraus et al.	1982	$\alpha_b, \rho, g, H_b, C_b, V_l, \mu_o$
CERC - formula (SPM)	1984	$H_b, n, C_b, \alpha_b, \rho, g$
Schoones and Theron	1994	ρ, H, g, α_b
Suspension load transport		
Watts	1953	ρ, H_b, g, C_b, V_l
Dean's model	1973	$D, g, \omega, \rho, \rho_s$
Fairchild	1973	ρ, H_b, g, C_b, V_l

Komar and Miller	**1973**	**H_b, h, ρ, g, D, μ_t, L, T**
Brenninkmeyer	**1975**	**β, α_b, V_l, μ_m**
t_c - bed shear stress		μ_o - orbital velocity
α_b - breaker angle		μ_m - maximum bottom orbital velocity
β - bed slope		ρ, ρ_s - water and sand densities
V_l - average longshore current		C_b - wave-celerity at the breaker line
H_b - breaker height		h - water depth
L, T - wave length and period		D - sediment grain size diameter (median)
n - wave number at breaker line (~1)		ω - sediment fall velocity
S_b - bed load transport		μ - so-called " ripple factor"

Sediment Transport from Broken Wave Bores

The intense turbulence in the broken wave bore picks up sediment from the lower beach and transports it up the beach face as swash. As the swash loses momentum these particles become deposited. At the maximum point of wave run up the momentum is spent, some water percolates into the beach sand, which is highly porous, and subsequently the spent wave recedes down the beach face, gathering speed and discharge, at which time many surface particles are re-entrained and transported back toward the surf zone.

When waves break obliquely to the alignment of the beach the swash run-up tends also to travel obliquely up the beach face. Likewise the return swash run-down often continues an oblique pathway rather than normal to the beach profile. In this way particles are transported along the beach face as a component of the overall littoral drift.

Sediment Transport in Rip currents

The cellular circulation associated with rip currents generates its own morphodynamics. Rip currents tend to occur mainly with fully refracted waves, especially on reflective beach morphodynamic states, and under such conditions the overall longshore sediment transport is minimal. In general it can be concluded that rip currents redistribute sediment across, and even seawards of the broad surf zone, but it is not clear that they otherwise impact on the overall magnitude of net littoral drift. However, the onshore component of the cellular circulation assists with the shoreward drift of the nearshore sediment.

Diabathic or Cross Shore Sediment Transport

Sediment transport does not only occur within the breaking wave zone in the along shore direction, but also in given circumstances in an onshore-offshore direction, i.e. as diabathic transport. Sediment may be transported offshore from the beach face by steep waves, often in storms, and replaced on the beach face at times of long waves with low steepness.

But it is being increasingly recognised that onshore or offshore wind stress effects inducing mean water level set-up or set-down at the shoreline markedly enhances cross shore sediment transfer. In principle the stress created by the wind blowing over the water surface, say onshore, generates a wind forced surface water current in the wind direction. This causes a set-up at the coast above water level. For reasons of continuity, a bottom return flow, or down-welling current is generated. Sediment that is uplifted into suspension by the normal oscillatory movements from wave orbital motions, and turbulence generated by passing waves, is acted upon by the downwelling current as it falls back to the sea floor. In this way the downwelling current transports sediment offshore, and this is thought to be the dominant process across the lower shoreface (Cowell et al. 1999). Niederoda et al. (1985) review work in which downwelling velocities of 60 cm/s were measured, but more commonly the downwelling veolocites are around 8-15 cm /s.

Conversely, for offshore winds, the offshore directed wind stress causes surface water from the shoreline to be removed offshore, causing a set-down at the shoreline, and a compensatory bottom return flow, or upwelling current in the onshore direction. In addition onshore transport of sand is assisted by effects of long wave asymmetry, which induces onshore-directed bottom water mass transfer for Stokesian type waves under fair-weather conditions. Under these conditions sediments from the inner shelf and shore face move onshore and even on to the beach[1].

It is evident that maximum diabathic sediment transfer occurs with constant strong onshore or offshore winds, associated with high waves of long period waves, e.g. T ~ 14s, for these long period waves have greater bottom orbital velocities, and therefore induce greater sediment movement at a given depth.

Wind driven, sometimes termed “Ekman”, currents can drive diabathic sediment transport on the shelf, but depending upon wind direction may also generate parabathic (shore parallel) sediment transport along the shelf and obliquely over the shelf. This phenomenon has been well researched in New Zealand’s Bay of Plenty in relation to monitoring of sandy dredge spoil dispersion off Tauranga (Harms, 1989, Healy, Harms and de Lange 1991, Mathews 1995) and also the very detailed work by Bradshaw et al. (1989, 1994) off the Waihi Beach shelf and north along the Coromandel shelf. These studies showed that parabathic (along shelf and presumably obliquely-across-shelf) sediment transport occurs seawards of the surf zone driven by winds and also tidal shelf currents which are exclusive of tidal inlet effects. In particular, side scan sonar mapping off Tauranga (Harms 1989; Healy et al. 1991) and

over the inner shelf off Waihi Beach demonstrated zones of coarse grained ripples, normally referred to as megaripples (Black and Healy 1988) which are identified as scour zones. For the Bay of Plenty shelf these scour zones are frequently being overridden by sheets of fine sand moving toward the northwest. However the rates and volumes of sediment moving over the inner shelf are not known and this is necessary future research for a better understanding of the Bay of Plenty beach systems.

Viewed in relation to instantaneous deterministic processes, sediment transport on the shoreface – inner shelf is the result of time dependent advection of sediments by residual currents. For the most part the sediment flux involves agitation by waves, with other flows responsible for the net drift of the sediments.

INDICATORS OF NET LITTORAL DRIFT

Multiple lines of geomorphic and sedimentologic evidence exist, usually several in combination, which point to the direction of net littoral drift. Some of these are illustrated in Komar (1998, Figure 1).

(i) ***Sand impoundment by artificial structures, and down-drift erosion***. Structures such as "jetties", breakwaters and groynes can provide some of the clearest evidence of the net direction of littoral drift. While beach groynes may be relatively small structures and be subject to seasonal drift reversals, large jetties extending across the surf zone interrupt the net drift in the surf zone, and the resultant pattern of sediment trapped reflects the long term sediment transport direction. In such cases there is impoundment of sand from the up-drift, and compensatory erosion down-drift of the structure.

(ii) ***Sand impoundment by natural headlands, and down-drift erosion***, is the analogue in nature, of the blockage by jetties. Sometimes this feature is difficult to distinguish because of the topographic irregularity of the headland acting as a groyne in nature. For the New Zealand case where there are often headlands adjacent to a tidal inlet system, the down-drift erosion occurs on the barrier spit or island

(iii) ***Offset of sand salient impoundment due to offshore structures*** such as detached breakwaters. Typically in the lee of detached breakwaters a sand salient occurs. Where refraction patterns around the offshore structure are dominant over littoral drift, a symmetrical shaped salient occurs. However on a net littoral drift beach, the sand salient acts as a partial barrier to the littoral drift, resulting in a wider beach up-drift and a narrower, tending to eroded, beach down-drift. The salient apex becomes offset, with a longer tail in the down-drift direction.

(iv) ***Offset natural salients or cuspate forelands in the lee of islands***. Long wave refraction patterns around natural islands induce the formation of cuspate

forelands, and where a littoral drift is superimposed, the salient becomes offset with a longer flank or tail in the direction of net littoral drift.

(v) ***Alongshore increase in width of subaerial beach and dune height***. This condition indicates an increase in sand budget availability in the alongshore direction with an increase in sediment budget. Such a situation occurs up-drift of a major interruption to the littoral drift, and there may often be a change toward a more reflective morphodynamic beach state with increase in sand availability.

(vi) ***Alongshore increase in the width and number of the nearshore beach bars***. The beach bar may act as a reservoir of sediment in the beach system, depending upon the controlling morphodynamic conditions. Occurrence of multiple bars indicates a sediment surplus in the beach system. A trend alongshore from lack of a bar , to vestigial bar, to well formed bar, to multiple bars is indicative of a trend of increasing sediment budget as a result of the littoral drift. Examples occur on the eastern Baltic coast of Lituania and Latvia with an increase in bar size Klaipeda to the foreland peninsula at Mazirbe, and also in Port Phillip Bay (Australia) from Martha Point to Rosebud.

(vii) ***Alongshore decrease in width of subaerial beach and dune height***. This condition occurs where there is a decrease in beach sand availability in the net longshore direction. This may be induced by a major interruption to the littoral drift, for example, sediment starvation from a structure, a dredging operation, or loss offshore to a submarine canyon. The beach morphodynamic state trends toward a dissipative condition. Usually this geomorphic trend occurs over relatively short distances.

(viii) ***Deflection of sizeable river mouths.*** The long term action of wave resultant power from a dominant direction provides sediment from up-drift forcing the river mouth to migrate in the direction of the net littoral drift.

(ix) ***Maintenance of river mouth locational stability by retaining structures.*** Often rivers on a littoral drift coast are maintained in position by moles or a groyne in the down-drift side.

(x) ***Deflection of small streams crossing the beach, and cutting out the frontal dunes.*** Small streams crossing the beach are also influenced by the beach wave processes and driven in the direction of the littoral drift. During storm wave events with elevated water levels from storm surge and set-ups, often accompanied by heavy rainfall events increasing the stream discharge, at high tide especially the streams are diverted and cut out the adjacent frontal dunes. Drainage culverts discharging on the beach may behave similarly. The asymmetry of the embayment in the frontal dunes adjacent to the stream indicates the net direction of the littoral drift.

(xi) ***Deflection of a large stable tidal inlet gorge and tidal discharge jet crossing an ebb tidal delta***. At tidally dominated large tidal inlets with marked ebb tidal delta, more sediment arrives from the net up-drift direction. This typically moves along the ebb tidal delta terminal lobe and over the shoals, forcing sediment into the main tidal discharge channel. This causes the channel and the main discharge jet to be deflected in the direction of the net littoral drift.

(xii) ***Sand deposition on a consistent side of a major tidal inlet navigation channe requiring dredging***. As noted above, along littoral drift coasts sediment migrating in the net littoral drift may frequently spill into a navigation channel of a tidal inlet, requiring dredging. More deposition will be evident on the 'up drift' channel side of the net drift direction.

(xiii) ***Asymmetrical ebb tidal delta from up-drift deposition..*** The deep inlet channel of large tidal inlets acts as a partial barrier to the littoral drift, and thus sediment arriving from the up-drift direction tends to accumulate on the up-drift side resulting in larger and shallower shoals on the up-drift side of the ebb-tidal delta.

(xiv) ***Erosion on the up-drift extremity of a barrier island, (or barrier spit) and***. This arises because the up-drift tidal inlet acting as a partial barrier to the littoral drift, thus promoting down-drift erosion on the adjacent downdrift barrier system and accretion on the downdrift corner. The accretion may take the form of a re-curved spit.

(xv) ***Sand accumulation and extension on the down drift distal end of a barrier island.*** Likewise on the down-drift end of the barrier island there is sand accumulation, which due to the inlet may evolve as a re-curved spit into the inlet.

(xvi) ***Growth of a spit in the direction of littoral drift***. The formation of a spit usually indicates the direction net longshore transport, towards the end of the spit, and causes it to become distended in the direction of littoral drift. Note however that on occasions counter-net drift spits can develop.

(xvii) ***Evolution of sequential re-curved frontal dunes on a prograding spit***. A series of dune ridges on a barrier spit which show sequential re-curving and longshore growth at the distal end of the spit, is a classic indicator of net littoral drift over the time of evolution of the spit. In such a situation the innermost dunes are the older, and wave refraction around the tip of the spit causes the frontal dune to evolve around the re-curved shoreline towards a bay or an inlet. As sediment accumulation and progradation progresses the more recent dunes accrete seawards and also progressively alongshore as the spit grows, creating a sequence of re-curved dune ridges toward the distal end of the spit.

(xviii) ***Alignment of parabolic dune axis and frontal dune blowouts behind the beach.*** Parabolic and dune blowout axis alignment is a function of the resultant of winds of sufficient strength to move sand grains. Thus in environments where local coastal winds influence the littoral drift (from generation of local wind forced waves as distinct from distantly generated swell waves) the axis alignment of the parabolic dunes relative to the shoreline alignment may indicate the direction of net littoral drift, at least the local wind generated waves.

(xix) ***Resultant direction of alongshore wave power (ECn)***. Long term data recorded from a continuous recording directional wave height and period instrument, such as an S4 or similar, deployed beyond but close to the surf zone, provides evidence of the net littoral drift based upon the direction of the wave power (ECn) resultant. A wave power resultant for locally generated wind waves may also be constructed from a wind rose based upon long term wind records.

(xx) ***Mineral species tracing alongshore from an input source.*** Beach sand samples demonstrating alongshore trends of the concentrations of a specific mineral or component sediment type from an identifiable input source such as a river or industry, may indicate the direction of net littoral drift. Samples are typically collected from the beach berm on the basis that this is the most energetic part of the beach face where sorting processes are maximised. Mineral tracing is especially pertinent if there is one exclusive source of a specific mineral, and one input point – e.g. a specific river or erosion of a particular cliff. Concentration trends of a specific heavy mineral, or ratio of minerals typically produce consistent interpretations of longshore drift directions.

(xxi) ***Alongshore trends in beach sediment Mean Grain Size (Mz).*** Alongshore progressive variation in mean grain size can indicate the direction of the net littoral drift. This is particularly evident for gravel sized beach sediments and is based upon larger particles possessing a greater fall velocity. Typically one assumes that a reduction in Mz indicates the direction of the littoral drift, but for sand sized particles this is only true for beach sediments that are near spherical and of closely uniform particle density, such as quartz. Where the beach sands consist of heterogeneous grain size, density and possibly angularity, the opposite occurs. That is the larger more angular lighter particles are transported in preference, so that the trend is for increasing Mz sand size in the direction of net littoral drift.

(xxii) ***Alongshore trends in beach sediment Sorting Parameter.*** Typically for beach sediments of uniform density the direction of net littoral drift is indicated by an improvement in the sorting, i.e. a narrower size range. This feature is most apparent for sediments sampled from the beach berm crest.

(xxiii) ***Alongshore trends in beach sediment particle shape.*** Particularly for gravel beach sediments, the gravels at source will possess a greater angularity. Alongshore in the net drift direction the particles become more rounded and spherical. For gravels the discoidal clasts travel preferentially along the beach face, and thus measures of dioscoidal clasts also can indicate the net littoral drift direction.

(xxiv) ***Alongshore trends in particle "rollabilty".*** Rollability is the ability of a particle to move under the action of waves. Thus an along shore trend from less rollable to more rollable particles indicated the direction of the net littoral drift.

DISCUSSION: CONCLUSIONS AND ENIGMAS FROM LITTORAL DRIFT INDICATORS

Not all of the above indicators possess equal confidence as indicators of littoral drift. Some such, as a sequence of distal recurved prograding frontal dune ridges on a Holocene barrier spit, are indisputable evidence of the direction of net littoral drift; as the spit has evolved each sequential dune ridge has been moved further in the direction of net littoral drift. However, not all indicators are so incontrovertible, and we have more confidence in some of the indicators than others. For example, the directional alignment of a spit, while often indicating littoral drift does not universally do so. For example the spits on the strong littoral drift, but microtidal coast of southeast Australia are counter to the direction of the net littoral drift.

Likewise, typically groynes act to capture the sand from the net updrift direction and cause sand starvation leading to erosion downdrift. They are therefore a good indicator of the net direction of the littoral drift. However if the groynes are short and do not extend across most of the beach, during periods of drift reversal the opposite effect may be seen, so that instantaneously the drift net drift direction may appear to come from the wrong direction. For the case of headlands, especially when associated with tidal inlets, the sand entrapment may not be so clear cut as an artificial groyne constructed across the littoral pathway.

Of these indicators there is strongest confidence for sequential re-curved frontal dunes on barrier spits, sediment impoundment by headlands and large groynes, breaking wave directional power based upon long term wave records, migration of large river mouths, and deflection of large ebb tidal jets. There is only weak confidence in the indicators that are based upon beach sediment textural data alone, upon spit direction alone, or upon parabolic dune axes.

Occasionally paradoxes of the net littoral drift directions occur, such as spits aligned counter to the direction of the regional drift (as on the southeast Australian coast), spits aligned in opposite directions either side of a headland or tombolo (as at Orbithello, Italy), or counter drift sediment transport pathways induced by eddy currents, as may occur at large tidal inlets. Ideally establishment of the net regional littoral drift direction should be based upon several lines of evidence which are

consistent, and where net drift hypotheses are tested by numerical simulation of wave induced sediment transport based upon long term wave data.

REFERENCES

Aagaard, T., and G. Masselink, 1999. The surf zone, *in* A.D. Short (ed.) *Handbook of Beach and Shoreface Morphodynamics*. John Wiley and Sons, Chichester, pp. 72 – 118.

Bagnold, R.A., 1963. Mechanism of marine sedimentation, in M.N. Hill (ed.) *The Sea,* Vol 3, Wiley, New York, pp. 507 -528.

Black, K.P. and T.R. Healy, 1988: Formation of ripple bands in a wave convergence zone. *Journal of Sedimentary Petrology,* 58(2), 195-207.

Bradshaw, B., Healy, T.R., Dell, P.M., and Bolstad, W.M.,1991. Inner shelf dynamics on a storm dominated coast, East Coromandel, New Zealand. *Journal of Coastal Research,* 7(1), 11-30.

Bradshaw, B.E., Healy, T., Nelson, C.S., Dell, P.M., and de Lange, W., 1994. Holocene sediment lithofacies on a storm dominated, back-arc shelf margin: the east Coromandel coast, New Zealand. *Marine Geology* 119, 75-78.

Cowell, P.J., D.J.Hanslow and J.F. Meleo, 1999. The Shoreface, *in* A.D. Short (ed.) *Handbook of Beach and Shoreface Morphodynamics*. John Wiley and Sons, Chichester, pp. 39-71

Healy, T., Harms, C., & De Lange,W., 1991: Dredge spoil and inner shelf investigations off Tauranga Harbour, Bay of Plenty, New Zealand. *Coastal Sediments '91*, A.S.C.E., pp. 2037-2051.

Herbich, J.B., and J.P. Handy, 1982. Longshore transport rate, *in* M.L. Schwartz (ed.) *Encyclopedia of Beaches and Coastal Environments*, Hutchinson Ross, Stroudsberg, pp.266 – 267.

Kidson, C., 1982. Sediment transport, *in* M.L. Schwartz (ed.) *Encyclopedia of Beaches and Coastal Environments*, Hutchinson Ross, Stroudsberg, pp. 743 – 748.

Komar, P.D., 1998. *Beach processes and Sedimentation 2nd Edition,* Prentice-Hall, New Jersey, 544 p.

Komar P.D., and D. Inman, 1970. Longshore sand transport on beaches. *Journal of Geophysical Research*, 75(30), 5514-5527.

Niederoda, A. W., D.J. Swift, and T. S. Hopkins, 1985. The Shoreface. In R. A. Davis. (ed.) *Coastal Sedimentary Environments*, Springer Verlag, New York, pp.533-624.

CROSS-SHORE VARIATION OF PREDOMINANT LONGSHORE SEDIMENT TRANSPORT RATE

Yoshiaki Kuriyama[1], Hikari Sakamoto[2]

1. Littoral Drift Division, Port and Airport Research Institute, Nagase 3-1-1, Yokosuka, Kanagawa 239-0826, Japan. kuriyama@pari.go.jp
2. Praia Co., Ltd., Hisamoto 3-3-15, Aioi-Sonpo Bldg., Takatsu-ku, Kawasaki, Kanagawa 213-0011, Japan. sakamoto@praia.co.jp

Abstract: The cross-shore variation of long-term average longshore sediment transport rate was examined on the basis of longshore sediment transport rates at the Hasaki coast in Japan for 15 years estimated using a one-dimensional numerical model of longshore current velocity. The model was calibrated with longshore current velocities measured once a day at about 50-m intervals along a 427-meter-long pier at the study site for the same period. Numerical simulations showed that the average longshore sediment transport rate was northward near the shore, but southward away from the shore, where the seaward distance from the shore is larger than 150 m.

INTRODUCTION

The predominant longshore sediment transport rates, which are the transport rates averaged over long-term periods, cause long-term morphological changes, and hence understanding the predominant longshore sediment transport is essential for sediment budget analysis and for effective coastal zone management.

The direction of the predominant longshore sediment transport near the shore can be detected from the long-term shoreline changes around coastal structures because the predominant longshore sediment transport induces accumulation on the updrift side of a coastal structure and erosion on the downdrift side. However, because of the lack of field data and numerical simulation results of longshore sediment transport rate away from the shore over long-term periods, the cross-shore variation of the long-term average longshore sediment transport rate is poorly understood although Sato

(1996) has suggested on the basis of longshore current field data that on the Kanazawa coast of Japan, the direction of the long-term average longshore sediment transport offshore may be the opposite to that near the shore.

The objective of this study was to investigate the cross-shore variation of long-term average longshore sediment transport rate using a one-dimensional numerical model developed for the estimation of longshore current velocity. We calibrated the model with longshore current velocities measured along a 427-meter-long pier for 15 years. Using this model, we estimated the cross-shore variations of the longshore sediment transport rate for the 15 years and obtained the cross-shore variation of the long-term average longshore sediment transport rate.

FIELD MEASUREMENT OF LONGSHORE CURRENT VELOCITY

Field measurements of longshore current velocity were conducted once a day from 1987 to 2001 at intervals of about 50 m along a 427-meter-long pier of the Hazaki Oceanographical Research Station (HORS), located on the Hasaki coast of Japan facing the Pacific Ocean (Figure 1).

Nearshore current velocities 1 m below the water surface were measured with a spherical float that had a diameter of 0.2 m and was connected with an identification buoy by a 1-meter-long rope (Figure 2). The float attached to a 30-m-long line was released from the pier, and the time for full extension of the line was measured with a stopwatch (Figure 2). The current velocity was calculated from the time and the length of the line. The transport direction of the float due to the nearshore current was observed with a protractor. At each measurement point, currents were measured three times and the averaged value was used for the analysis.

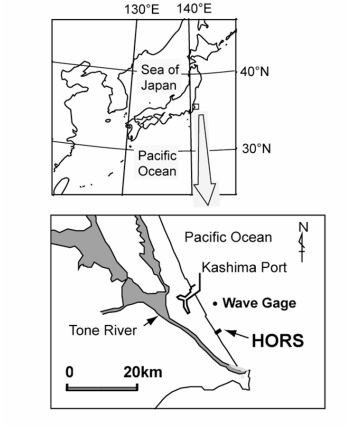

Fig. 1. Locations of the study site and offshore wave gage.

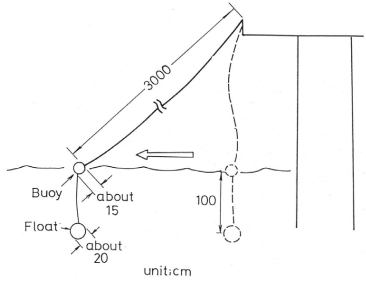

Fig. 2. Float for the measurement of longshore current velocity.

The validity of this measurement method was confirmed with longshore current velocities 1 m below the water surface simultaneously measured with the present method and an electro-magnetic current meter (Kuriyama and Ozaki 1993; Kuriyama 1995). The relationship between the time-averaged longshore current velocities measured with the float U_{FLOAT} and those measured with the current meter U (Figure 3) showed a very strong correlation with only a small influence of the wind. The correlation coefficient r was 0.97, and the standard deviation was 0.086 m/s. The relationship between them was expressed as

$$U = 0.81 U_{FLOAT}. \quad (1)$$

In the following analysis, the values of U were used.

The measurement points were located where the seaward distance relative to the reference point, located close to the entrance of the pier, was 115, 145, 190, 245, 280, 330 and 380 m. Each position along the pier is referred to as the seaward distance and designated as "P." For example, P115m denotes a position 115 m seaward from the reference point.

Besides the longshore current velocities, the beach profiles along the pier were measured at 5-m intervals every day, except for weekends and holidays, with a 5-kg lead from the pier, and with a level and a staff shoreward of the pier. Moreover, the bathymetry near HORS was surveyed once or twice a year in an area 600 m wide in the alongshore direction and about 700 m long in the cross-shore direction. The median sediment diameter along the profile is 0.18 mm and remains almost uniform along the profile (Katoh and Yanagishima 1995). Based on the datum level at Hasaki (Tokyo Peil -0.687 m), the high, mean and low water levels are 1.252 m, 0.651 m, and -0.196 m, respectively.

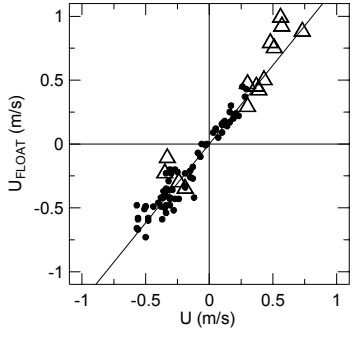

Fig. 3. Relationship between the longshore current velocities measured with the electro-magnetic current meter U and those with the float U_{FLOAT}. Open triangles represent data obtained when the absolute value of the wind velocity exceeded 8 m/s.

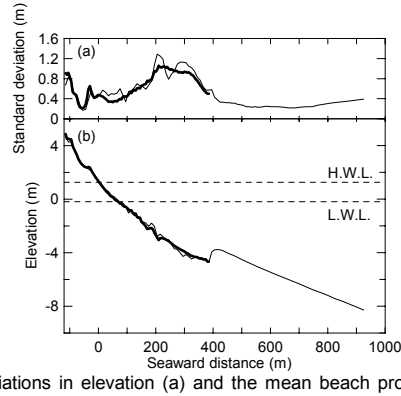

Fig. 4. Standard deviations in elevation (a) and the mean beach profiles (b) based on the daily profile measurements along the HORS pier (thick lines) and yearly bathymetry surveys around HORS (thin lines) (Kuriyama 2002). The elevation is based on the Hasaki datum level.

The averaged beach profiles show that the beach slope during the measurement period decreased gradually in the offshore direction (Figure 4). It was about 1/40 near the shoreline, about 1/100 at P300m and about 1/120 seaward of the tip of the pier. In the region between P200m and P400m, longshore bars emerged, migrated seaward and decayed. Although local scours were observed in trough regions and the discontinuity of the averaged beach profile at P400m was probably caused by these local scours, the locations and elevations of bar crests and the locations of toughs were almost uniform alongshore (Kuriyama 2002).

Deepwater waves were measured at a water depth of about 24 m with an ultrasonic wave gage for 20 minutes every 2 hours (Figure 1). Wave angles were visually observed at the tip of the pier once a day. However, because the time interval and the accuracy of the visual observation were not thought to be sufficient as input data for numerical simulations of longshore sediment transport rate, the offshore wave angles every 2 hours were estimated using the WAM model, a third generation wave prediction model (e.g., Hashimoto et al. 2000). Wind angles and velocities were measured at the tip of the pier for 10 minutes every hour.

The coordinate system used in this study is shown in Figure 5. The positive direction for the longshore current velocity and sediment transport rate was defined as being southward. The wave and wind angles were defined relative to the shoreward direction and were positive in the counterclockwise one.

The seasonal change of the deepwater wave height was large from January to March and from September to October, but small from June to August (Figure 6 (a)). On the other hand, the wave period was almost constant at 8 s (b). Waves mainly came from the north in December to February, and from the south in May to August (c).

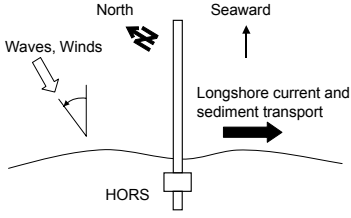

Fig. 5. The coordinate system at HORS.

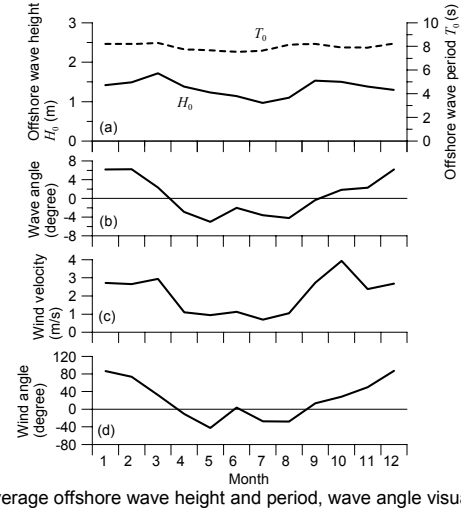

Fig. 6. Monthly average offshore wave height and period, wave angle visually observed at the tip of the HORS pier, and wind velocity and angle.

Strong winds came from the north in October to February, whereas weak winds came from the south in May to August (d). Compared with the seasonal changes, yearly changes were small.

NUMERICAL SIMULATION OF LONGSHORE CURRENT VELOCITY

The 1-D numerical model of longshore current velocity developed by Kuriyama and Nakatsukasa (2000) was utilized to estimate the longshore sediment transport rate. Although it was calibrated with longshore current velocities obtained in the field including HORS, the model was modified and recalibrated with the longshore current data obtained for 15 years from 1987 to 2001 at HORS. The model consists of a wave transformation model and a longshore current model, and adopts a wave-by-wave approach, in which wave heights and longshore current velocities are calculated for individual waves.

Wave Transformation Model

The wave transformation model is based on the model developed by Kuriyama (1996), which calculates the shoaling, breaking and reforming of individual waves. The shoaling of a wave was estimated using the shoaling coefficient proposed by Shuto (1974) with consideration for wave nonlinearity.

The criterion on wave breaking was based on a formula proposed by Seyama and Kimura (1988), who modified Goda's formula (1970). In the formula, the wave height-water depth ratio at wave breaking is expressed as a function of beach slope, offshore wavelength and water depth at wave breaking.

Energy dissipation of the organized wave motion in the surf zone, which is the source of the energy of the surface roller, was estimated with a periodic bore model used by Thornton and Guza (1983). The model is expressed by

$$\frac{\partial E_w C_g}{\partial y} = \frac{1}{4}\rho_w g \frac{1}{T}\frac{(BH)^3}{h}, \tag{2}$$

where E_w is the energy of the organized wave motion ($=\rho_w g H^2/8$), C_g is the group velocity, y is the seaward distance, ρ_w is the sea water density, g is the acceleration of gravity, T is the wave period, H is the wave height, h is the water depth, and B is a dimensionless coefficient determining the amount of energy dissipation. Kuriyama and Ozaki (1996) examined coefficient B with the experimental data of Seyama and Kimura (1988), and proposed the following formula:

$$B = C_B\{1.6 - 0.12\ln(H_0 / L_0) + 0.28\ln(\tan\beta)\}, \tag{3}$$

where C_B is a dimensionless coefficient, H_0 is the offshore wave height, L_0 is the offshore wavelength and $\tan\beta$ is the beach slope.

The location of wave reforming, where the wave energy dissipation stops and a broken wave returns to the unbroken wave, was judged from the wave height-water depth ratio. Based on field data obtained by Kuriyama and Ozaki (1996), the wave height-water depth ratio at the wave reforming point was set at 0.35.

With a significant wave height and a period set at an offshore boundary, a time series of water surface elevation for 10 minutes having the JONSWAP type spectrum at the offshore boundary was numerically simulated. The peak enhancement factor γ was set at 3.3. Next, with the zero-down crossing method, the time series was divided into individual waves, which were used in the calculation.

The incident directions of individual waves at the offshore boundary were determined with the given principal wave direction, the directional spreading function of the Mitsuyasu type and the spreading parameter estimated using the method of Goda and

Suzuki (1975). When the spreading parameter exceeded 100, the individual waves were treated as uni-directional waves.

Longshore Current Model

The time- and depth-averaged longshore current velocity of an individual wave U_{ind} was estimated on the basis of the balance among the bottom friction F_x, the lateral mixing force L_x, the gradient of the radiation stress R_x, the wind stress W_x, and the gradient of the momentum flux due to the surface roller M_x. The balance is expressed by

$$F_x - L_x + R_x + W_x + M_x = 0. \tag{4}$$

The bottom friction was estimated with the following equation proposed by Nishimura (1988).

$$\begin{aligned} &F_x = \frac{C_f}{h}(W + \frac{w_b}{W}^2 \sin^2\theta)U_{ind}, \\ &W = \left(\sqrt{U_{ind}^2 + w_b^2 + 2U_{ind}w_b\sin\theta} + \sqrt{U_{ind}^2 + w_b^2 - 2U_{ind}w_b\sin\theta}\right)/2, \\ &w_b = 2\nu_m/\pi, \nu_m = \pi H/(T\sinh(2\pi h/L)), \end{aligned} \tag{5}$$

where C_f is a friction coefficient, θ is the wave angle and L is the wavelength. Although Kuriyama and Nakatsukasa (2000) showed that numerical simulations with a constant C_f of 0.005 fitted well with the measurements, we expressed C_f as a function of water depth. The modification of the model will be given in the **Modification of the Model** section.

The lateral mixing term L_x was estimated on the basis of the energy dissipation of organized wave motion and the surface roller. In the estimation of the radiation stress term R_x, the small amplitude theory was used.

The wind stress was estimated using

$$W_x = C_d \rho_a W^2 \sin\theta_w. \tag{6}$$

where C_d is a nondimensional coefficient, ρ_a is the air density, W is the wind velocity and θ_w is the wind angle. The coefficient C_d was set at 0.0022, which was estimated on the basis of the data obtained at the tip of the pier when the wave height was small and the bottom friction F_x was assumed to be balanced with the wind stress W_x (Kuriyama and Yanagishima 2006).

The gradient of the momentum flux M_x is expressed by

$$M_x = \frac{1}{\rho_w h}\left(\frac{\partial M_r}{\partial y}\right), \quad M_r = -\frac{1}{3}\rho_w C^2 \frac{A_r}{L}\cos\theta \sin\theta, \tag{7}$$

where M_r is the momentum flux due to the surface roller having a triangle-shaped distribution of time-averaged velocity, in which the velocities at the tip and bottom of the roller are celerity, C, and 0, respectively, (Kuriyama and Nakatsukasa 2000). The value of A_r is the area of the roller.

Kuriyama and Nakatsukasa (2000) proposed the triangle-shaped velocity distribution in the roller because the cross-shore velocity of the roller is thought to change gradually from the top to the wave trough level owing to large eddies reported by Nadaoka et al. (1989), which have shoreward velocity near the surface and seaward velocity near the wave trough.

The area of the surface roller A_r was estimated on the basis of the assumptions given below.

(a) The area of the surface roller is basically assumed to be proportional to the square of the wave height. The area A_{r1} is estimated with a dimensionless coefficient C_A from

$$A_{r1} = C_A H^2. \tag{8}$$

(b) The energy of the surface roller, however, should not exceed the energy transferred from the organized wave motion. The roller area therefore is determined not to exceed the roller area A_{r2} estimated without energy dissipation of the surface roller from the following equation.

$$\begin{aligned} &\frac{\partial (E_w C_g)}{\partial y} + \frac{\partial (W_r C)}{\partial y} = 0, \\ &W_r = \frac{1}{8}\rho_w C^2 \frac{A_{r2}}{L}, \end{aligned} \tag{9}$$

where W_r is the energy of the roller having the triangle-shaped distribution of the time-averaged velocity above the wave trough level.

As for C_A, Kuriyama and Nakatsukasa (2000) showed that numerical simulations with C_A expressed as Eq. (10), which is a function of the surf similarity parameter at the wave breaking position, agreed with longshore current velocities in the field.

$$\begin{aligned} &C_A = 17.0 \log \xi_b + 24.7, \\ &\xi_b = \tan\beta / (H_{1/3,b} / L_{1/3,0})^{1/2}, \end{aligned} \tag{10}$$

where $H_{1/3,b}$ is the significant wave height at the wave breaking position and $L_{1/3,0}$ is the offshore wavelength corresponding to the significant wave period. The value of $H_{1/3,b}$ was defined as a local maximum of the significant wave height.

Modification of the Model

Kuriyama and Nakatsukasa (2000) used a constant C_f of 0.005 to estimate longshore current velocity and showed that estimated longshore current velocities agreed well with the measured values on barred beaches. However, because Garcez Faria et al. (1998) showed that the friction coefficient is not constant in the cross-shore direction, we assumed that C_f would be a function of the water depth as shown by Garcez Faria et al. (1998). It is expressed by

$$C_f = 0.011\left(\frac{k_a}{h}\right)^{\alpha}, \tag{11}$$

where k_a is the apparent bed roughness length scale and α is a coefficient. Although k_a varies according to the bottom and wave conditions (e.g., Garcez Faria et al. 1998), we assumed it to be constant as done by Ruessink et al. (2001). The values of k_a and α were determined so that the overall error between the predicted and measured longshore current velocities defined by Eq. 12 would be minimal.

$$\varepsilon = \sqrt{\frac{\sum\left(U_{mes} - U_{pred}\right)^2}{N}}, \tag{12}$$

where ε is the error, U_{mes} and U_{perd} are longshore current velocities measured and predicted, and N is the data number.

In addition to k_a and α, because the accuracy of the offshore wave angle estimated by the method of Hashimoto et al. (2000) had not been confirmed, we adjusted the estimated offshore wave angles by shifting them with an angle θ_a and minimizing the overall error.

The best parameters were k_a = 1.09 m, α = 1.4 and θ_a = -3 degrees. The correlations between the predicted and measured values at P115m and P380m are shown in Figures 7 (a) and (b). The overall error estimated with Eq. 12 is 0.22 m/s and the error at each measurement point ranged from 0.17 to 0.26 m/s.

Figure 8 shows the cross-shore variations of the estimated and measured longshore current velocities averaged for 15 years. The measured one was based on the values measured once a day, and the estimated one on the longshore current velocities predicted every 2 hours. The beach profile seaward of P445m used in the estimation was the mean beach profile shown in Figure 2. The profiles shoreward of P385m every 2 hours were temporarily interpolated with the ones measured once a day along

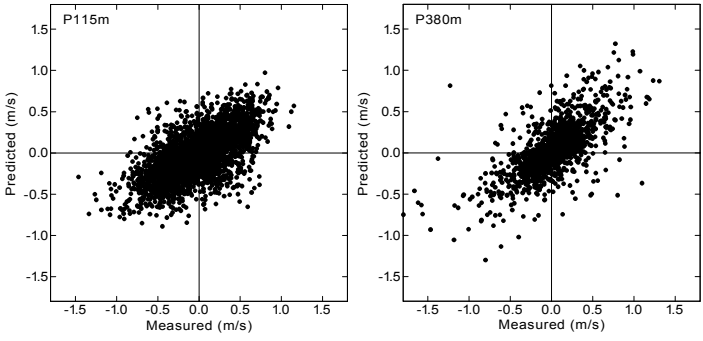

Fig. 7. Comparisons between measured and predicted longshore current velocities at P115m (left) and P380m (right).

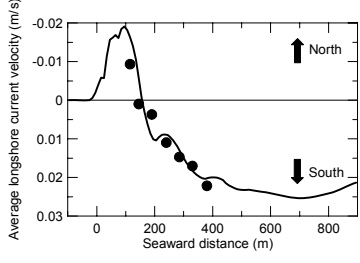

Fig. 8. Cross-shore variations of long-term average longshore current velocities measured (solid circles) and predicted (solid line).

the pier, and the profiles between P385m and P445m were spatially interpolated with the elevations at P385m and P445m. The coefficient C_B in Eq. 4 was set at 0.95 as in Kuriyama and Yanagishima (2006). The grid interval was 10 m, and the seaward boundary was set at P925m, where the elevation of the beach profile is -8.28 m and waves seldom break.

The average value of the predicted longshore current velocity agreed well with that of the measured one, which is northward near the shore and southward away from the shore. The cross-shore variation of the long-term average longshore current velocity was formed owing to the difference between the wave and wind conditions when the northward and southward currents developed (Kuriyama and Yanagishima 2006). When the northward current developed, the deepwater wave height was relatively small and the frequency of the wind from the north was almost equal to that from the south. As a result, the northward current developed only near the shore and decayed outside the narrow surf zone. On the other hand, when the southward current

developed, the deepwater wave height was relatively large and the wind from the north was predominant, which resulted in the southward current developing not only in the wide surf zone but also outside the surf zone. The superposition of the two cross-shore variations produced the cross-shore variation of the long-term average longshore current velocity with a northward velocity near the shore and a southward velocity away from the shore.

ESTIMATION OF LONGSHORE SEDIMENT TRANSPORT RATE

The longshore sediment transport rates Q were estimated using Eq. 13, which is based on Watanabe's formula (1992).

$$\begin{aligned} Q &= A(\tau_b - \tau_{cr})U/(\rho_w g), \\ \tau_b &= \rho_w h F_x, \\ \tau_{cr} &= (\rho_s - \rho_w) g d \psi_{cr}, \end{aligned} \tag{13}$$

where A is a nondimensional coefficient, τ_b is the bottom shear stress, F_x is the bottom friction expressed by Eq. 5, τ_{cr} is the critical shear stress for incipient motion, U is the time-averaged longshore current velocity, ρ_s is the sediment density, d is the sediment diameter and ψ_{cr} is the critical Shields parameter for incipient motion. The sediment diameter was set at 0.2 mm. The value of A was set at 2.0 according to Watanabe (1992), and ψ_{cr} was 0.06 according to Madsen and Grant (1976) and Tsuchiya (1986).

To estimate the longshore sediment transport rates for the 15 years, the longshore current velocities were estimated every 2 hours with the simulation model of longshore current velocity. Next, using Eq. 14, the longshore sediment transport rates were estimated every 2 hours.

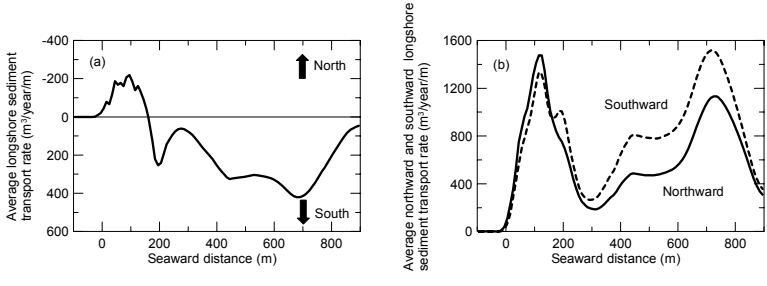

Fig. 9. (a) Cross-shore variation of the average longshore sediment transport rate. (b) Cross-shore variations of the absolute values of the northward and southward average longshore sediment transport rates.

The cross-shore variation of the average longshore sediment transport rate and those of the absolute values of the average northward and southward longshore sediment transport rates are shown in Figure 9. The average northward and southward longshore sediment transport rates at a certain point are defined as the average values of the sediment transport rates when the northward and southward sediment transports developed at the point, respectively. As suggested by the cross-shore variation of the average longshore current velocity (Figure 8), the average longshore sediment transport rate is northward near the shore, and southward away from the shore, seaward of P165m.

DISCUSSION

Sato and Tanaka (1966) analyzed bathymetry data from the shore to a water depth of about 7 m around breakwaters and groins constructed about 10 km north of the study site, and showed that the northward and southward gross longshore sediment transport rates are about 600,000 m^3/year. The integrated values of the average northward and southward longshore sediment transport rates (Figure 9 (b)) from the shore to a water depth of about 7 m, where the seaward distance is 735 m, are 469,000 and 596,000 m^3/year, respectively. These values are consistent with those reported by Sato and Tanaka (1966).

The northward direction of the average longshore sediment transport rate near the shore is identical to that of the predominant longshore sediment transport on the Hasaki coast derived from the shoreline changes (e.g., Tanaka et al. 1980). Thus, these results show that the estimated longshore sediment transport rates were reasonable.

Although the southward average sediment transport away from the shore is not supported by direct evidence, it is most likely to occur because the long-term average longshore current velocity is southward away from the shore (Figure 8). However, the southward average longshore sediment transport rate integrated from P165m to P735m is about 149,000 m^3/year and much larger than the northward one near the shore, 22,000 m^3/year. Further quantitative investigation on the southward average sediment transport rate away from the shore is required.

The finding that the direction of the average longshore sediment transport offshore can be opposite to that near the shore indicates that careful consideration should be given to bathymetry changes around a large-scale port or coastal structure induced by the average longshore sediment transport not only near the shore but also away from the shore.

CONCLUSION

We conducted numerical simulations of the cross-shore variation of longshore sediment transport rate for 15 years using a 1-D model for longshore current velocity in order to investigate the cross-shore variation of the long-term average longshore sediment transport rate. The model was calibrated with longshore current velocity

data obtained with a float once a day at about 50-m intervals along a 427-meter-long pier at the study site for the same period. The accuracy of the measurement method was confirmed with longshore current velocities simultaneously measured with the float and an electro-magnetic current meter.

The simulation results show that the average longshore sediment transport was northward near the shore, but southward away from the shore, where the seaward distance from the shore is larger than 150 m. The direction of the average longshore sediment transport near the shore is identical to that of the predominant longshore sediment transport derived from shoreline changes, and the estimated gross longshore sediment transport rates from the shore to a water depth of about 7 m are consistent with the values shown by a previous study. These results indicate that the estimated longshore sediment transport rates are reasonable. Our findings show the need to consider bathymetry changes near large-scale ports or coastal structures both near and away from the shore because sediment transport movements can occur in opposite directions.

ACKNOWLEDGEMENTS

The offshore data were provided by the Kashima Port Construction Office of the Ministry of Land, Infrastructure and Transport and the Marine Information Division of the Port and Airport Research Institute. We thank all the staff members at HORS, who conducted the field measurements.

REFERENCES

Garcez-Faria, A.F., Thornton, E.B., Stanton, T.P., Soares, C.V. and Lippmann, T.C. (1998). "Vertical profiles of longshore currents and related bed shear stress and bottom roughness," *Journal Geophysical Research* 103(C2), 3217-3232.

Goda, Y. (1970). "A synthesis of breaker indices," *Trans. Japan Soc. Civil Engrs.*, 2(2), 227-230.

Goda, Y. and Suzuki, Y. (1975). "Computation of refraction and diffraction of sea waves with Mitsuyasu's directional spectrum," Tech. Note Port and Harbour Research Institute, No.230, 45p. (in Japanese)

Hashimoto, N., Kawaguchi, K., Maki, T. and Nagai, T. (2000). "A comparison of WAM and MRI based on observed directional wave spectra," *Hydrodynamics IV*, pp.587-592.

Katoh, K. and Yanagishima, S. (1995). "Changes of sand grain distribution in the surf zone," *Proceedings Coastal Dynamics '95*, pp.639-650.

Kuriyama, Y. and Ozaki, Y. (1993). "Longshore current distribution on a bar-trough beach -Field measurements at HORF and numerical model-," Rep. Port and Harbour Research Institute 32(3), pp.3- 37.

Kuriyama, Y. (1995). "Longshore current on a bar-tough beach –Field investigation and verification of numerical models," *Bulletin Permanent International Association of Navigation Congresses* 86, pp.79-94.

Kuriyama, Y. (1996). "Models of wave height and fraction of breaking waves on a barred beach," *Proceedings 25th International Conference on Coastal*

Engineering, pp.247-260.
Kuriyama, Y. and Ozaki, Y. (1996). "Wave height and fraction of breaking waves on a bar-trough beach-Field measurements at HORS and modeling-," Rep. Port and Harbour Research Institute 35(1), pp.1-38.
Kuriyama, Y. and Nakatsukasa, T. (2000). "A one-dimensional model for undertow and longshore current on a barred beach," *Coastal Engineering* 40, 39-58.
Kuriyama, Y. (2002). "Medium-term bar behavior and associated sediment transport at Hasaki, Japan," *Journal Geophysical Research* 107(C9), 3132, doi:10.1029/2001JC000899.
Kuriyama, Y. and Yanagishima, S. (2006). "Cross-shore variation of long-term average longshore current velocity at HORS," Rep. Port and Airport Research Institute 45(4), 15- 30.
Madsen, O.S. and Grant, W.D. (1976). "Quantitative description of sediment transport by waves," *Proceedings 15th International Conference on Coastal Engineering*, pp.1093-1112.
Nadaoka, K., Hino, M. and Koyano, Y. (1989). "Structure of the turbulent flow field under breaking waves in the surf zone," *Journal Fluid Mechanics* 204, 359-387.
Nishimura, H. (1988). "Computation of nearshore current," *Nearshore Dynamics and Coastal Process –Theory, Measurements and Predictive Models-* (edited by Horikawa, K.), pp.271-291.
Ruessink, B.G., Miles, J.R., Feddersen, F., Guza, R.T. and Elgar, S. (2001). "Modeling the alongshore current on barred beaches," *Journal Geophysical Research* 106(C10), 22451-22463.
Sato, S. and Tanaka, N. (1966). "Field investigation on sand drift at Port Kashima facing the Pacific Ocean," *Proceedings 10th International Conference on Coastal Engineering*, pp.595-614.
Sato, S. (1996). "Effects of winds and breaking waves on large-scale coastal currents developed by winter storms in Japan Sea," *Coastal Engineering in Japan* 39(2), 129-144.
Seyama, A. and Kimura, A. (1988). "The measured properties of irregular wave breaking and wave height change after breaking on the slope," *Proceedings 21st International Conference on Coastal Engineering*, pp.419-432.
Shuto, N. (1974). "Nonlinear long waves in a channel of variable section," *Coastal Engineering in Japan* 17, 1-12.
Tanaka, N., Osanai H. and Ezozuka Y. (1980). "Characteristics of sandy beaches in Japan," Tech. Note Port and Harbour Research Institute, No. 356, 67p. (in Japanese)
Thornton, E.B. and Guza, R.T. (1983). "Transformation of wave height distribution," *Journal Geophysical Research* 88(C10), 5925-5938.
Tsuchiya, Y. (1986). "Law of sediment transport on beaches," Lecture Notes on the 22nd Summer Seminar on Hydraulics, pp.B-4-1-B-4-22. (in Japanese)
Watanabe, A. (1992). "Total rate and distribution of longshore sand transport," *Proceedings 23rd International Conference on Coastal Engineering*, pp.2528-2541.

LONGSHORE SAND TRANSPORT CALCULATED BY TIME-DEPENDENT SHEAR STRESS

Ernest R. Smith[1] and Nicholas C. Kraus[1]

1. U.S. Army Engineer Research and Development Center, Coastal and Hydraulics Laboratory, 3909 Halls Ferry Road, Vicksburg, MS 39180-6199, USA. Ernest.R.Smith@erdc.usace.army.mil; Nicholas.C.Kraus@erdc.usace.army.mil.

Abstract: Based on longshore sand transport experiments performed in a large basin, measured sand transport rates obtained for spilling and plunging waves are compared to the Bodge and Dean (1987) and Watanabe (1992) distributed load formulas, representative of typical formulas applied in engineering practice. Neither formula estimates the measurements satisfactorily. The Bodge and Dean formula is sensitive to changes in energy flux and does not include threshold shear. The Watanabe formula includes critical shear, but transport estimates are made from time-averaged values of bottom shear stress, which did not exceed critical shear stress at most cross-shore locations. A new transport formula is introduced based on time-dependent shear stress calculated from the total velocity that includes the wave orbital velocity. The new formula gives reasonable estimates for both spilling and plunging breaker types. A conclusion is that it is essential to represent the time-dependent, or fluctuating, component of fluid motion in predictive equations of the longshore sand transport rate.

INTRODUCTION

Many studies have been conducted to relate longshore sand transport rates to wave and current processes for developing predictive capability in terms of variables that are relatively easy to measure or hindcast. Total, or bulk, load transport refers to the total amount of sand transported along the coast in the surf zone. Distributed transport refers to the cross-shore distribution of longshore transport with a varying local rate across the surf zone. Despite the many studies that have been performed worldwide to develop accurate estimates for the longshore sand transport rate, there are limitations for quantitative applications. The purpose of this paper is to compare the existing distributed

load models of Bodge and Dean (1987) and Watanabe (1992) to high quality mid-scale laboratory data, and to introduce a new distributed load model based on the time-dependent shear stress that more reliably reproduces the measurements.

LABORATORY EXPERIMENTS

Mid-scale laboratory experiments were performed to measure the longshore sand transport and nearshore hydrodynamics in a controlled environment. Mid-scale denotes wave and current conditions that commonly occur on coasts such as the Gulf of Mexico and the Great Lakes. "Midscale" contrasts with much smaller wave heights and shorter wave periods typically generated in three-dimensional laboratory basin facilities. For example, mid-scale wave height and period might be on order of 0.25 m and 3 sec, respectively, as opposed to small-scale laboratory conditions on the order of 0.1 m and 1 sec. Because wave energy is proportional to the square of wave height and energy flux to the 5/2 power of wave height, more than doubling the wave height capable in mid-scale experiments as compared to traditional small-scale laboratory experiments greatly increases mean energy and associated turbulence in the surf zone. Longer wave period increases the extent of the area considered as shallow water.

Numerous laboratory and field studies have found that suspended sand concentration at the breaker line is strongly influenced by breaker type. Sand concentrations measured under plunging breakers are significantly greater than concentrations measured under spilling breakers of similar wave height (Kana 1977; Wang et al. 2002). Because longshore sand flux is the product of sand concentration and longshore current velocity, greater concentration would result in greater sand transport given similar longshore current velocity. The laboratory experiments were designed to include both spilling and plunging breaker types.

LSTF Facility and Experiment Design

The Longshore Sediment Transport Facility (LSTF) is a large-scale laboratory facility capable of simulating conditions comparable to low-wave energy coasts. The sand beach consists of 150 m^3 of fine quartz sand having a mean diameter d_{50} of 0.15 mm. An external recirculation system can maintain a steady and uniform wave-generated longshore current along the beach to minimize boundary effects. The LSTF includes instruments to measure water surface elevation, 3-D current velocity, and sand concentration simultaneously at several cross-shore locations. Wave gauges and acoustic Doppler velocimeters (ADV's) are mounted on a movable bridge that can be positioned at any location along the shore. Twenty sand traps at the downstream boundary of the model are instrumented with load cells to weigh trapped sand and are used to measure total cross-shore distribution of the total longshore sand transport rate generated under obliquely incident waves. Hamilton et al. (2001) discuss LSTF features and capabilities.

Four irregular wave signals with relatively broad spectral shape representative of sea conditions were generated in these LSTF tests. They were designed to obtain and compare transport rates for different breaker types through varying incident wave height and period. Four conditions generated in the LSTF are listed in Table 1, where H_{mo} is

energy-based significant wave height measured near the wave generators, H_{mob} is wave height at breaking, T_p is peak wave period, h is water depth at the wave generators, θ_b is incident wave angle at the generators, and m is the average slope of the beach from the breaker line to the shoreline. The wave conditions can be grouped by energy level. Tests 1 and 3 had similar incident wave height and are referred to as higher energy conditions, and Tests 5 and 6 are referred to as lower energy conditions. Each test was conducted with an h = 0.9 m and θ = 10 deg at the wave generators.

Table 1. LSTF test wave conditions

Test Number	Breaker Type	H_{mo} m	H_{mob} m	T_p sec	h m	θ_b deg
1	Spilling	0.25	0.26	1.5	0.9	6.5
3	Plunging	0.23	0.27	3.0	0.9	6.4
5	Spilling	0.16	0.18	1.5	0.9	6.7
6	Plunging	0.19	0.21	3.0	0.9	6.4

LSTF Results

The cross-shore distribution of wave height of each test is shown in Fig. 1. Test 3 and Test 6 waves shoaled prior to breaking and decreased in height sharply directly shoreward of breaking, typical of plunging waves. Test 1, a spilling case, also showed a sharp decrease in height directly shoreward of breaking. Test 1 had a surf similarity parameter on the upper end of spilling waves, 0.34 (Smith and Kraus 1991), and some plunging waves were observed within the time series; however, waves were observed to break predominately by spilling. Wave height in Test 5 decayed through the surf zone, typical of spilling breakers.

Measured longshore sand flux is plotted as a function of cross-shore location in Fig. 2. Three distinct zones of transport are evident; the incipient breaking zone, inner surf zone, and swash zone. At incipient breaking, a substantial peak in transport occurs for the plunging-waves (Tests 3 and 6), but is not observed in the spilling-waves (Tests 1 and 5). Shoreward of breaking, in the inner surf, wave energy is saturated, and wave height is strongly controlled by depth, independent of wave period. Fig. 2 implies that longshore sand flux in the inner surf zone is dominated by wave height, independent of period. A peak in transport occurs in the swash zone for all tests. For waves having similar incident wave height, but different period, i.e., Tests 1 and 3, and Tests 5 and 6, swash zone transport is much greater for the longer period tests. This result is consistent with elevation of wave runup (Hunt 1959), in which runup is directly proportional to wave period.

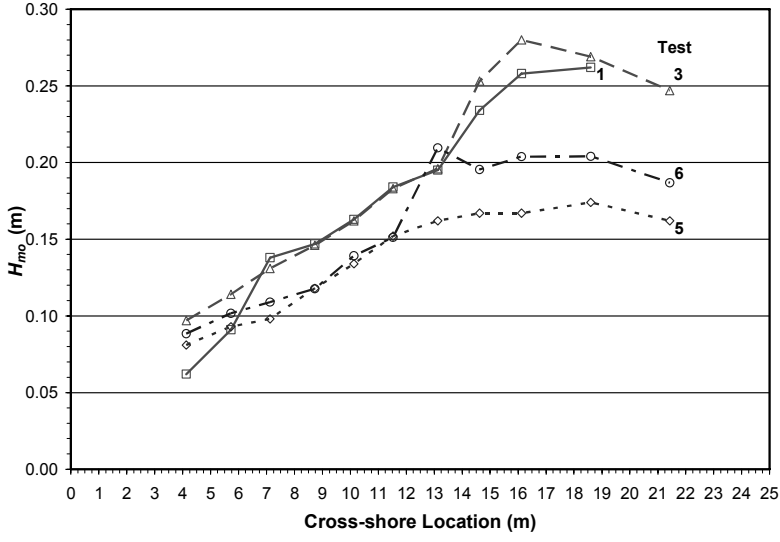

Fig. 1. Cross-shore distribution of measured wave height

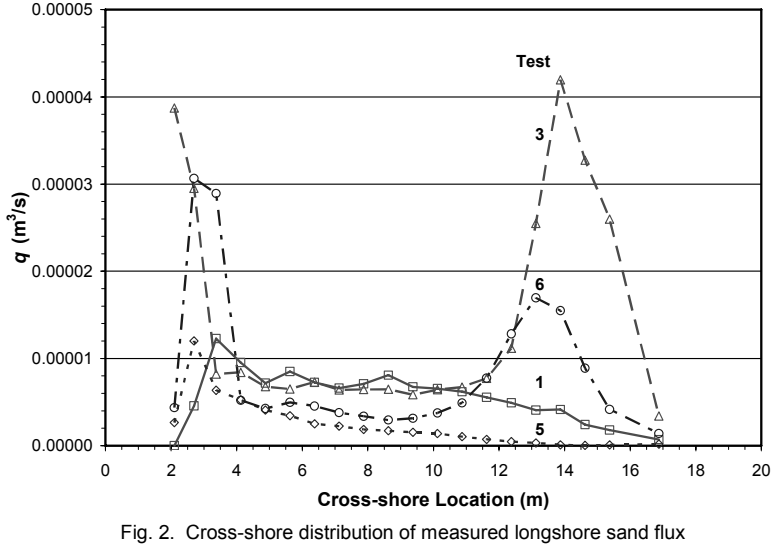

Fig. 2. Cross-shore distribution of measured longshore sand flux

COMPARISON OF LSTF DATA TO SELECTED PREDICTIVE FORMULAS

Smith et al. (2006) compared LSTF results to distributed load formulas of Bodge and Dean (1987) (B&D) and Watanabe (1992), summarized here. B&D examined forms of energetics and stress models and developed several alternative formulas based on laboratory experiments and short-term impoundment of sand under moderate wave conditions in the field. The recommended equation from their study, which predicts longshore transport based on wave energy dissipation and is valid only inside the surf zone where wave energy is expected to dissipate by depth-limited breaking, is given as:

$$i_y = \frac{k_q}{h}\frac{\partial F}{\partial x} V \left[\frac{dh}{dx}\right]^r \tag{1}$$

where i_y is the local immersed weight sand transport rate (force/time) per unit offshore length, k_q is a dimensional coefficient found equal to 0.057 sec for laboratory data and 0.48 sec for field data, h is local water depth, x is cross-shore position, F is average wave energy flux per unit surface area, V is the mean local longshore current, and r is a dimensionless constant, where $r = 0.5$ gave the best agreement with the B&D data set. However, Bodge (1989) stated that scaling effects in the B&D movable-bed laboratory experiments may have exaggerated the apparent relationship between local transport and bottom slope, and that r may equal 0, eliminating the last factor of Eq. 1. In shallow water, average wave energy flux per unit surface area in linear wave theory is the product of wave energy per unit surface area, E, and wave group celerity, C_g:

$$F = EC_g = \left(\frac{\rho g H^2}{8}\right)\sqrt{gh} \tag{2}$$

where ρ is fluid density, g is acceleration due to gravity, and H is local wave height.

Fig. 3 shows that the B&D formula follows the general trend of the Test 1 measurements and predictions vary greatly for the spilling wave condition. Test 3 measurements were underestimated and no transport is calculated in the trough of the breakpoint bar, because dh/dx is negative. The model is based on energy dissipated and will not predict transport where no dissipation theoretically occurs, i.e., regions of increasing wave height or increasing depth, such as from a bar crest to bar trough. Wave gauges were not located in the swash zone, so transport estimates in the swash zone could not be made.

The B&D formula with $r = 0$ is compared to the LSTF measurements in Fig. 4. The B&D formula significantly over-predicts Test 1 measurements. Dropping the slope term produced a transport estimate near the Test 3 breakpoint, but the model greatly over-predicted transport shoreward of breaking. Estimates can be improved by adjusting k_q, but a different coefficient would be required to give optimal results for each breaker type.

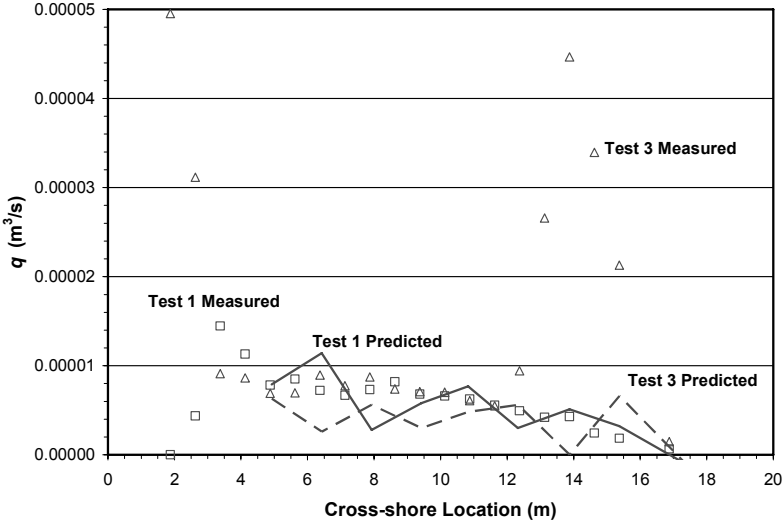

Fig. 3. Bodge and Dean (1987) estimates compared to Test 1 and Test 3 (r = 0.5)

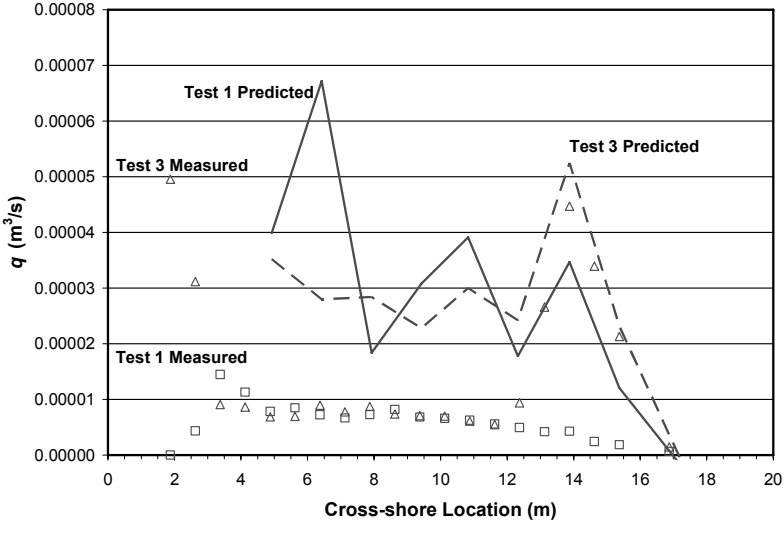

Fig. 4. Bodge and Dean (1987) estimates compared to Test 1 and Test 3 (r = 0)

Watanabe (1992) (W92) proposed a Meyer-Peter and Muller-type equation to calculate longshore sand transport as combined bed and suspended load of the form:

$$q_y = A\left[\frac{(\tau - \tau_{cr})V}{\rho g}\right] \tag{3}$$

where τ_{cr} is the critical shear stress for inception of sediment motion, and A is an empirical coefficient approximately equal to 2 for irregular waves. The magnitude of the total bottom shear stress under waves and currents is represented here as:

$$\tau = \frac{\rho c_f}{2}\sqrt{U^4 + V^4} \tag{4}$$

in which c_f is the bottom friction coefficient for combined waves and quasi-steady current and was calculated as in Buttolph et al. (2006), and U and V are the mean cross-shore and longshore velocities, respectively. Critical shear stress is calculated as:

$$\tau_{cr} = (\rho_s - \rho_w) g d_{50} \theta_{cr} \tag{5}$$

where ρ_s is the density of the sediment, d_{50} is expressed in meters, and θ_{cr} is the critical Shields parameter for sediment motion, taken to be 0.05 for 0.15-mm diameter sand.

The difference in shear stresses in Eq. 3 can be interpreted as representing a stirring function, and the velocity term represents a transport function. This formula has received wide-spread application for its simplicity, while incorporating several physical processes.

The W92 formula is applied to the LSTF Tests 1 and 3 (Fig. 5). Transport is not predicted at several cross-shore locations for both the plunging and spilling breaker conditions because the time-averaged bottom shear stress did not exceed the critical shear at those locations. The formula fails for low-wave conditions because it only estimates transport where the time-averaged bottom shear stress exceeds the critical shear, true for virtually all the smaller wave test locations (Tests 5 and 6).

The two predictive formulas evaluated did not perform well in comparisons to high-quality LSTF data. The B&D model either greatly underestimated the transport at the plunging wave breakpoint or over estimated the spilling wave case, depending on whether the slope term was included. The formula was sensitive to changes in energy flux, and it does not include threshold shear or differentiate between breaker types. The W92 formula includes threshold shear, but estimates longshore sand transport from only the time-averaged values of current. The time-averaged bottom shear stress exceeded critical shear stress at only a few cross-shore locations in the laboratory. Additionally, breaker type is not represented, nor is the wave orbital velocity in the surf zone. These results motivated examination of sand transport mechanics from a more basic approach.

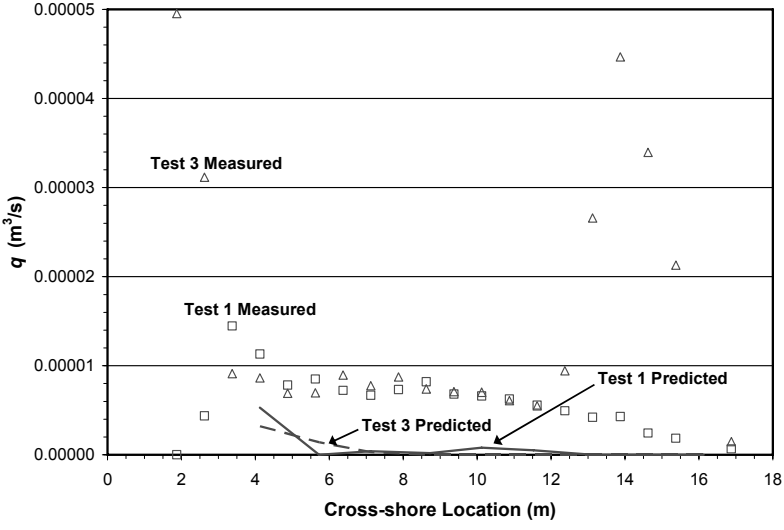

Fig. 5. Watanabe (1992) estimates compared to Test 1 and Test 3

PREDICTIVE FORMULA BASED ON TIME-DEPENDENT SHEAR STRESS

Madsen (1991) states that any model of sediment response to fluid forces that relies on the mean turbulent flow characteristics is limited to being conceptual. The necessity of including the fluctuating component of fluid motion was motivated by the findings of Madsen and Grant (1976), who noted that a sediment grain at point of incipient motion reacts to the fluctuations rather than to the mean value of the entraining force. Kraus et al. (1988) demonstrate that trends in prediction of the local longshore sand transport rate in the surf zone is improved by including the dissipation of waves and standard deviation in the longshore current velocity, both of which represent variations in fluid motion.

The shear stress, including the fluctuating component together with the mean value, can be calculated from the wave orbital velocity measured with the ADV's installed in the LSTF. The total cross-shore component of velocity is written:

$$u(t) = U + u'(t) \tag{6}$$

where U is the time-mean of $u(t)$, and $u'(t)$ is the fluctuating component that includes wave orbital velocity and turbulence. Similarly, the total longshore current velocity can be written as:

$$v(t) = V + v'(t) \tag{7}$$

where V is the time mean of $v(t)$, and $v'(t)$ is the fluctuating component and is typically small compared to V. The total shear stress exerted by the water on the sand bottom is:

$$\vec{\tau}(t) = \hat{x}\,\tau_x + \hat{y}\,\tau_y \tag{8}$$

the magnitude of which is:

$$\tau(t) = \sqrt{\tau_x(t)^2 + \tau_y(t)^2} = \frac{\rho_w c_f}{2}\sqrt{u(t)^4 + v(t)^4} \tag{9}$$

The time series of τ was calculated via Eq. 9 for Test 1, spilling waves at four ADV's having cross-shore locations X = 18.6, 13.1, 8.7, and 4.1 m (Fig. 6). At the most offshore ADV (X = 18.6 m), shear stress sometimes exceeded τ_{cr}, but often did not (Fig. 6a). This result indicates that the sand in the LSTF for this location was only occasionally mobilized for transport, so the transport rate is expected to be small. The magnitudes of total shear stress were much greater at ADV's located at X = 13.1 m and X = 8.7 m (Figs. 6b and 6c, respectively), and transport rates are expected to be greater at these cross-shore locations. Fig. 6d shows that shear stress magnitudes decrease at the most onshore ADV located at X = 4.1 m, but τ_{cr} was exceeded more frequently, i.e., sand was mobilized for transport more frequently at the most onshore ADV than at the other locations shown. The greater mobilization calculated correlates to the cross-shore distribution of sand transport rate observed for this case (Fig. 2).

The original W92 formula (Eq. 3) includes only the mean shear stress and predicted no transport at many LSTF cross-shore locations because the shear stress based on mean velocity did not exceed the critical shear (Fig. 5). In contrast, Fig. 6 shows that the total velocity components, which include the fluctuating components u' and v', produce a shear stress that frequently exceeds the critical shear. Therefore, accounting for the fluctuating component is essential for reproducing longshore sand transport under different types of breaking waves for smaller wave conditions.

Several transport formulas were investigated in this study based on the concept of:

$$q(t) = ST(t) \times TR(t) \tag{10}$$

where $q(t)$ is the time-dependent transport rate per unit length perpendicular to the transport, ST is a stirring function that mobilizes the sand, and TR is a transporting function that moves the sediment (Kraus and Horikawa 1990).

Equation 10 must be averaged over the time record, with the average taken of the full expression, although the averages of each factor on the right-hand side may be of interest in examining the physical processes of sand stirring and transport. A new formula was developed based on the time-mean of longshore sand transport rate:

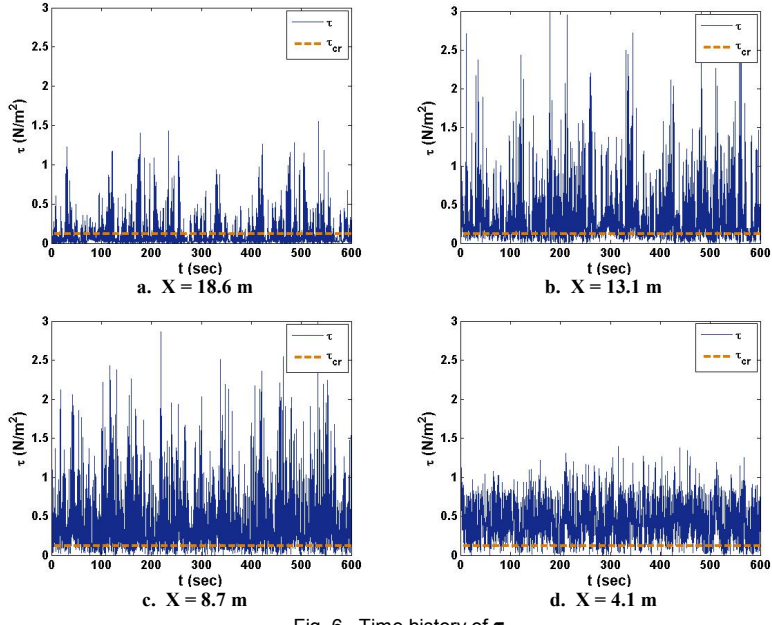

Fig. 6. Time history of **τ**

$$q_y = K\left\langle \left(ST(t) - \tau_{cr}\right)\left(TR_y(t)\right)\right\rangle \tag{11}$$

where K is an empirical parameter that may involve several dimensional quantities, depending on the stirring function $ST(t)$ and transporting function $TR_y(t)$, and <-> represents the time-average operation.

The stirring function $ST(t)$ is the time-average of τ:

$$\langle ST\rangle = \langle \tau(t)\rangle = \frac{1}{N}\sum_{1}^{N}\tau(t) \tag{12}$$

where N is the number of calculation points. For calculating the longshore transport rate, the transporting function $TR_y(t)$ is $v(t)$, Eq. 7, and the time-average is V.

It was observed during the LSTF plunging wave experiments that sand remained in suspension at the trough of the break-point bar for the duration of the tests. The plunging waves distributed sand through the water column, and sand entrained in the upper water column had a greater distance to settle to the bed, requiring a time interval longer than several wave periods. Subsequent waves would redistribute the suspended sand through

the water column. Therefore, sand entrained into the water column by a single plunging wave would continue to be transported during several subsequent waves. An additional term to account for events that cause sand to be suspended through the water column and increase the transport rate near the break point of plunging waves is included in the model. This suspension term $s(t)$ is as defined as:

$$s(t) = \left(u'(t)^2 + v'(t)^2 \right)^k \tag{13}$$

where k is an empirical exponent set to 2 based on numerical comparison to the LSTF data.

The new predictive longshore sand transport rate formula based on time-dependent shear stress is then given as:

$$\begin{gathered} q_y(t) = \left(f_b K \left(\tau(t) - \tau_{cr} \right) + f_s s(t) \right) V \quad \text{for } \tau(t) > \tau_{cr} \\ \text{and} \\ q_y(t) = 0 \quad \text{for } \tau(t) < \tau_{cr} \end{gathered} \tag{14}$$

where $f_b = 10$ and $f_s = 0.014$ are empirical coefficients determined by comparisons to the LSTF results. The time-averaged transport rate over the record was calculated by:

$$q_y = \frac{1}{N} \sum_{1}^{N} q_y(t) \tag{15}$$

Estimates of Test 1 longshore sand transport rates were improved using the time dependent formula (Eq. 15), as shown in Fig. 7. The equation modeled the trend and general magnitude of measured transport rates. Transport rates for Test 3 also are estimated well, especially near breaking and in the surf zone onshore of X = 6 m.

The time-dependent formula was compared to the smaller waves of Test 5 and Test 6 (Fig. 8). Estimates followed the trend of the measured distribution, although slightly high, and were good onshore of X = 6 m. Estimates with Test 6 conditions gave good agreement with measurements. Eq. 15 predicts a peak in transport near breaking with Test 6 waves, although lower than measured, and estimates surf zone transport rates well.

The same values of the empirical coefficients were used for all LSTF test conditions. Eq. 15 estimated the trend and magnitude of cross-shore distributed longshore sand transport rates for both spilling and plunging breakers. Although ADV's were not present throughout the swash zone, the formula presented is capable of estimating swash zone transport if the swash zone hydrodynamics are available for input.

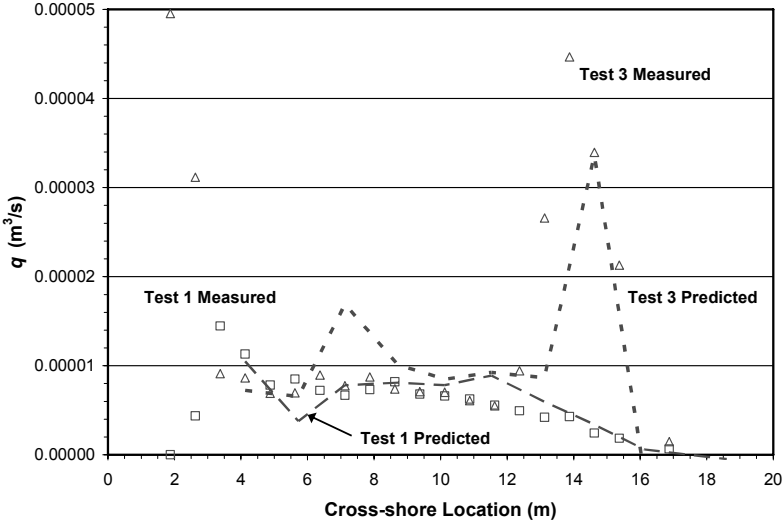

Fig. 7. Estimated transport rate from time-dependent shear stress model, Tests 1 and 3

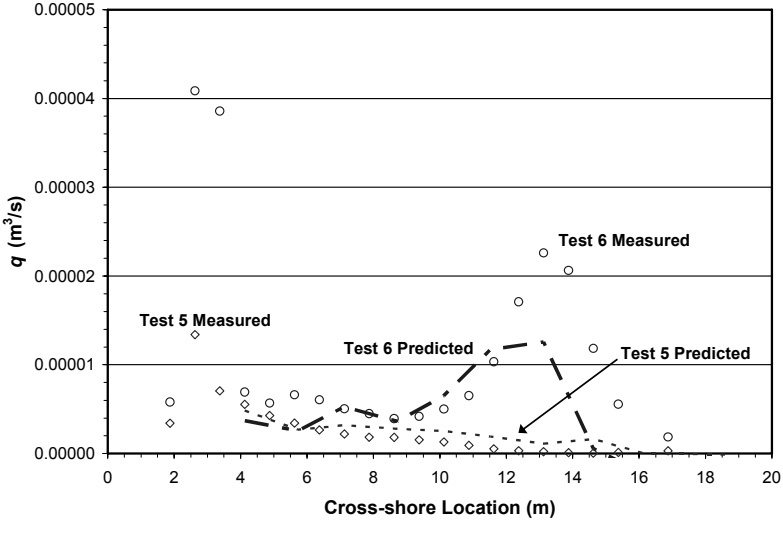

Fig. 8. Estimated transport rate from time-dependent shear stress model, Tests 5 and 6

CONCLUDING DISCUSSION

A key finding of the present study is that it is essential to include the fluctuating component of the wave orbital velocity in predictive sand transport rate equations for the surf zone. Bottom shear stress calculated from the mean velocity rarely exceeds the critical shear for sand motion for small waves or for sediment with a large grain size. Figure 5 illustrates that the original Watanabe (1992) equation, which is based on mean bottom shear stress, predicts zero sand transport for several of the LSTF cross-shore locations. Also, mean values of the longshore current and cross-shore current do not contain significant information on the wave breaking process, which determine in great part the intensity and vertical extent of fluctuations produced. Therefore, it is concluded that the fluctuating component of shear stress must be included in future hydrodynamic simulations aimed at providing forcing for calculating longshore sand transport.

Additionally, breaker type was found to be a central variable in the amount of sand transport that occurs at a location, which agrees with the findings of Kana 1977 and Wang et al. 2002. Plunging breakers produce greater turbulence throughout the water column whereas turbulence associated with spilling breakers remains near the surface in the bore. Mean values of the longshore and cross-shore current do not provide information on the wave breaking process, which determines the amount of turbulence produced.

A new formula was developed that yielded improved estimates of longshore sand transport and includes the fluctuating component of wave orbital velocity. For engineering purposes, the fluctuating component can be related to the mean wave orbital velocity, which is a function of wave height and period. As a result, an accurate wave transformation model is necessary to give reliable estimates of distributed longshore sand transport rates. Comparison of the new predictive transport formula and field measurements is underway, the results are so far favorable.

ACKNOWLEDGEMENTS

The authors wish to acknowledge William Halford, David Daily, and Tim Nisley who provided technical support during the experiments. Data collection presented in this paper was supported by the Navigation System Research Program, U.S. Army Corps of Engineers (USACE). Writing of this paper was supported by the Coastal Inlets Research Program, USACE. Permission to publish this information was granted by Headquarters, USACE.

REFERENCES

Bodge, K.R. (1989). "A literature review of the distribution of longshore sediment transport across the surf zone," *J. Coastal Res.* 5(2), 307-328.

Bodge, K.R., and Dean, R.G. (1987). "Short-term impoundment of longshore transport," *Proc. Coastal Sediments '87*, 468-483.

Buttolph, A.M., Reed, C.W., Kraus, N.C., Ono, N., Larson, M., Camenen, B., Hansen, H., Wamsley, T.V., and Zundel, A.K. (2006). "Two-dimensional depth-averaged circulation model CMS-M2D: Version 3.0, Report 2, sediment transport and morphology change," ERDC/CHL-TR-06-9, U.S. Army Engineer Research and Development Center, Vicksburg, MS.

Hamilton, D.G., Ebersole, B.A., Smith, E.R., and Wang, P. (2001). "Development of a large-scale laboratory facility for sediment transport study." TR ERDC/CHL TR-01-22, U.S. Army Engineer Waterways Experiment Station, Vicksburg, MS.

Hunt, I.A. (1959). "Design of seawalls and breakwaters." *J. Waterways and Harbors Division*, ASCE, 85(WW3), 123-152.

Kana, T.K. (1977). "Suspended sediment transport at Price Inlet, S.C.," *Proc. Coastal Sediments '77*, 366-382.

Kraus, N.C., Gingerich, K.J., and Rosati, J.D. (1988). "Toward an improved empirical formula for longshore sand transport." *Proc. 21st Coastal Eng. Conf.*, ASCE, 1183-1196.

Kraus, N.C., and Horikawa, K. (1990). "Nearshore sediment transport." in *The sea, ocean engineering science*, part B, B. LeMehaute and D.M. Hanes (eds.), John Wiley and Sons, 775-813.

Madsen, O.S. (1991). "Mechanics of cohesionless sediment transport in coastal waters," *Proc. Coastal Sediments '91*, 15-27.

Madsen, O.S., and Grant, W.D. (1976). "Quantitative description of sediment transport by waves." *Proc. 15th Coastal Eng. Conf.*, ASCE, 1093-1112.

Smith, E.R., and Kraus, N.C. (1991). "Laboratory study of breaking waves on bars and artificial reefs." *J. Waterway, Port, Coastal and Ocean Eng.*, 117(4), 307-325.

Smith, E.R., Zhang, J., and Wang, P. (2006). "Longshore sediment transport research performed in a large-scale basin," *Proc. First Int'l Conf. on Application of Physical Modelling to Port and Coastal Protection*, in press.

Wang, P., Smith, E.R., and Ebersole, B.A. (2002). "Large-scale laboratory measurements of longshore sediment transport under spilling and plunging breakers," *J. Coastal Res.*, 18, 118-135.

Watanabe, A. (1992). "Total rate and distribution of longshore sand transport." *Proc. 23rd Coastal Eng. Conf.,* ASCE, 2528-2541.

SEDIMENT BUDGET OF THE DANUBE DELTA COASTAL ZONE

Sebastian Dan[1], Marcel Stive[2], Dirk Jan Walstra[3] and François Sabatier[4]

1. Delft University of Technology, Faculty of Civil Engineering and Geosciences, 2600 GA, Delft, The Netherlands; S.Dan@tudelft.nl
2. Delft University of Technology, Faculty of Civil Engineering and Geosciences, 2600 GA, Delft, The Netherlands; M.J.F.Stive@tudelft.nl
3. WL Delft Hydraulics, Marine and Coastal Management, P.O. Box 177, 2600 MH, Delft, The Netherlands; Dirkjan.Walstra@wldelft.nl
4. CEREGE, Europole de l'Arbois, BP80, 13545 Aix en Provence Cedex, France Sabatier@cerege.fr

Abstract: Reservoirs, dams and barrages regulating the discharges of the Danube river, cut-offs of meanders and the jetties at Sulina mouth have disrupted the natural discharge and circulation of sediment on the coastal zone of Danube Delta. The aim of our research is to quantify the alongshore sediment transport and use this as a prime input to construct a sediment budget. Based on regional wind (1991 - 2000) data and a nearshore state-of-the-art wave model a morphologically representative wave climate along the representative depth contours of the Danube Delta was determined. This forms the basic input for a one-line model approach deriving the alongshore sediment transport and resulting coastline changes. The closure depth was computed and used, along with alongshore sediment transport gradients, to obtain the sediment budget.

1. INTRODUCTION

In modern times, especially the XX century, deltas all over the world were subject to a strong human pressure due to industrialization, Danube Delta being one of these. The circulation of the sediments in its coastal zone was disturbed by human activities such as the prolongation of the Sulina jetties into the sea, decreasing the amount of the sediment reaching the coast due to the damming upstream on the river (Panin 1997; Giosan et al. 1999; Ungureanu et al. 2000; Stanica 2003).

To assess the present day status of the coastal zone in front of the Danube Delta we especially need information on the nearshore wave energy distribution and sediment circulation. Several steps were necessary in order to reach our objectives: the wave

climate, the closure depth, the longshore transport and the sediment budget. These steps will be described and discussed further in this paper.

2. GEOGRAPHICAL SETTING AND DESCRIPTION OF THE STUDY AREA

The Danube River starts its course in the Schwartzwald Mountains in Germany and ends, after 2,857 km, in Romania forming the Danube Delta. This delta is situated the Northwestern part of the Black Sea, between 44°25' and 45°30' Northern latitude and between 28°45' and 29°46' Eastern longitude. The Danube River discharges into Black Sea through three arms (from north to south): Kilia, which transports approximately 52% of the water discharge, Sulina, the major waterway, 20% and Sfantu Gheorghe, 24.5%, the rest of the water being discharged through Razelm-Sinoe lagoon system (Stanica 2003). The distribution of the discharge of the sediments is slightly different: Kilia - approximately 54.5%, Sulina - 6%, Sfantu Gheorghe - 22%, the rest being deposited in the Danube Delta (Stanica 2003).
Southward from the Sf. Gheorghe Branch the Razim-Sinoe lagoon system is situated. Our study zone is bordered by the Sulina jetties northward and Portita inlet southward (figure 1).

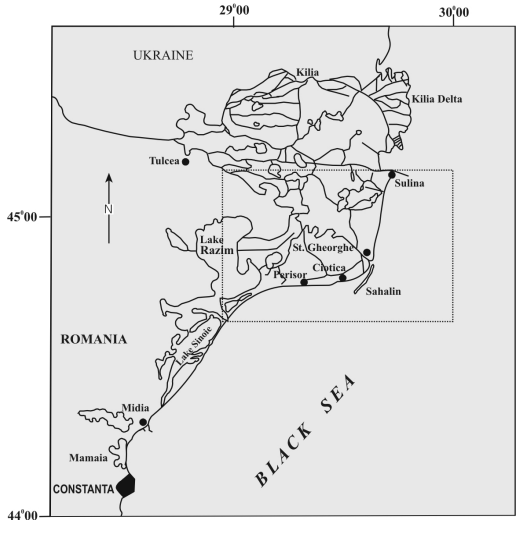

Fig.1 Location of the study zone (dotted lined box).

The human interventions disrupted the natural equilibrium of the coastal zone of the Danube Delta. Among these interventions, two induced major changes: the barrages build along the Danube River and its tributaries, and the Sulina jetties. After the building of two barrages Iron Gates I (943km from the Black Sea) in 1970 and Iron Gates II dam (864 km) in 1983, the sediment discharge decreased with 35% to 50% compared to the mean value of the pre-barrage sediment discharge regime (Panin

1996). The Sulina jetties construction started in 1858 as part of the plan transforming Sulina branch into a navigational channel. Today, the jetties extend 8 km into the Black Sea. The structure, acting like a barrage, blocks the alongshore drift from secondary delta Kilia towards south completely, resulting in the clogging of the Musura Bay and causing "beach starvation" downdrift.
An important role in the historical evolution of the coastal zone of the Danube Delta is played by the changes of mean sea level. The tide regime in the study area has average amplitudes of 7 – 11 cm (Bondar et al. 1973). The relative sea level rise consists of eustatic sea level rise, estimated for the past century at about 1.3 mm/year (Malciu 2000), and natural subsidence, with average values of 1.5 – 1.8 mm/year (Panin 1999).

3. WAVE CLIMATE

The first step in our approach was to obtain a reliable nearshore wave climate. The wave data available in Romania are based on visual observation and the records are not continuous, with blackouts occurring especially during extreme events, which are the most important for coastal changes. Therefore, we took the decision to construct the wave climate from the wind measurements, which we consider more reliable and which are more complete.

Wind data available cover a 10 years period (1991 - 2000) from Sulina (Danube Delta) meteorological station and from 2002 recorded simultaneously at Sulina and the Gloria Oil Rig (offshore). Records were taken four times per day containing speed (m/s) and direction (nautical convention, 16 directions). At Sulina the records were made at a height of 10 m above the mean sea level, but at Gloria Oil Rig at 36 m height. The Sulina meteorological station is situated at the landward end of the Sulina jetties which extend the channel into the sea. Therefore, the station can be considered, as located, on the shoreline. First correction needed was to transform the wind speed of the Gloria data set to a wind speed at the standard elevation of 10 m above the mean sea level ($U_{10} \approx U_{36}/1.2$) (Shore Protection Manual 1984).
The important question was whether the Sulina station is representative for the offshore wind conditions. To answer this a comparison was made between the Sulina 2002 data set and the Gloria 2002 data set (situated offshore). It turned out that almost 70% of the records were similar, which can be considered a good correlation.

A second correction was to apply a land vicinity correction. An empirical method was used, obtained from a study of winds in the Great Lakes area, USA, (Shore Protection Manual 1984), resulting in a dimensionless coefficient of 1.2 as a multiplication factor for the recorded wind speed. Then, the data were split in the 16 directions for each set. For the wind directions, which are crossing land, the corrected data correlate better with those from Gloria. For the directions crossing only water the correlation is better for uncorrected data. Nevertheless, the directions starting from WSW to NNW, clockwise, were not taken in account for wave computations because these only cross land and generate offshore directed waves only.

For the computation of the wave climate using the state-of-the-art wave model SWAN (Simulating WAve Nearshore) (Booij 1999) two kind of data were used as input: a bathymetric map and wind records. The bathymetric survey was carried out in 1995 by GeoEcoMar Bucharest and covers an area between the Sulina jetties in the North and Portita inlet in the South. It covers, also, a range of water depths from the shoreline (East) to 30 – 55 m offshore (West).

Based on the spatial extent of the storm systems in the northwestern part of the Black Sea (Ginzburg et al. 2002) the fetch was chosen to be 100 km from Sahalin Island towards North, West and South. Each directional and speed class corresponds to two runs of the model, one for the large grid and one for the small one. After elimination of the wind directions which are crossing only land (from W to NNW) and the smallest wind speeds (below 5 m/s), considering their insignificant weight in the wave climate, the number of wind conditions that remained was 66. The next step was to simulate the generation and propagation of the waves for each wind direction and speed class. Because the simulation area was rather large the first computation is coarse (2 km each cell). The second computation was a so-called nested grid containing only the littoral area with a finer resolution of computation (200 m each cell). The obtained results were considered representative for one year, being, in fact, an average of the ten years of wind records (Dan et al. 2006).

4. CLOSURE DEPTH

In previous studies on the circulation of sediment in the Danube Delta coastal zone (Giosan et al. 1999) the closure depth was estimated between 6 and 12 m water depth. Since there are no systematic measurements of the submerged beach profile in the studied zone, we have employed the method proposed by Sabatier et al. (2004) to determine the closure depth.

The method is based on a characteristic extreme wave condition which occurs at least 12 hours per year. In our case, the larger waves were produced by winds from N, NE and SW at wind speeds of 40, 28 and 30 m/s, respectively. We took in account ten years of wind records at Sulina, the same used as a base for computing the wave climate. The next step in the procedure was to choose an arbitrary closure depth offshore for the first computation based on Hallermeier's formula (Hallermeier 1980). These depths range between 16 and 20 m. The locations and depths were chosen to be as much as possible representative for the local wave climate. After applying this procedure again a new closure depth resulted. Then, the formula was applied at this new closure depth, obtaining the final value. The resulting values ranged from 5 m depth at Portita area (point 1), 6 m close to Sulina jetties (point 32) to 8.5 in the central part of the Sahalin island (point 19) (point locations in figure 3). The values of the closure depth obtained using the method of Sabatier et al. (2004) proved, in our case, to be heavily dependent on the depths choose to start the computation. Another concern was the relative small values of the closure depth taking in account the extreme wave conditions use for the computation.

Therefore, we decided to use the original method proposed by Hallermeier (1980) in order to check the obtained values. Based on laboratory experiments with regular

waves Hallermeier (1980) determined the transition between motion and no motion as:

$$\frac{A}{D} = \left(\frac{8(s-1)g}{\omega^2 D} \right)^{0.5} \quad (1)$$

where A is the wave excursion, D the diameter of the spherical grains, s is the relative density (ρ_s / ρ), g the acceleration of gravity, and ω is the angular frequency ($2\pi/T$). The density of the sediments ρ_s=2,65 $\cdot 10^3$ kg/m^3, density of the water ρ=1 $\cdot 10^3$ kg/m^3, g=9,81 m/s^2 and the grain size D=0.16 mm were used for the computation. The wave height and period were extracted from the wave climate for every location. We keep the same rule of the list 12 hours per year of extreme wave condition. Waves generated by winds from North at 40 m/s and from South-West at 30 m/s were used for this second method. The locations chosen to extract the wave data coincides with the locations of the 25 profiles used in UNIBEST CL+ longshore sediment transport computation. In table 1 the values for each location are listed.

Table 1 - The closure depth computed using Hallermeier formula. The italic values were determined by the south-west waves and the normal values by the north waves. For location of the profiles see figure 3.

Profile	Closure Depth (m)	Profile	Closure Depth (m)	Profile	Closure depth (m)
Profile 1	*6.9*	Profile 10	10.5	*Profile 19*	*5.1*
Profile 2	*6.8*	Profile 11	11.6	*Profile 20*	*5.0*
Profile 3	6.7	Profile 12	10.8	*Profile 21*	*5.3*
Profile 4	8.4	*Profile 13*	*9.0*	*Profile 22*	*5.6*
Profile 5	8.7	*Profile 14*	*8.0*	*Profile 23*	*5.6*
Profile 6	8.4	*Profile 15*	*5.9*	*Profile 24*	*6.4*
Profile 7	9.6	*Profile 16*	*5.5*	*Profile 25*	*6.6*
Profile 8	9.4	*Profile 17*	*5.6*		
Profile 9	10.0	*Profile 18*	*5.4*		

The computed values for closure depth vary strongly along the studied area. The smallest values occur in the northern and southern parts. This is due to the sheltering of these areas against northern direction waves. The maximum values are reached in the front of Sahalin spit island due to the full exposure to both the main wave directions: northern and southern. This large range of closure depth proves that for an accurate sediment transport computation over a large zone a single (or averaged) value of the closure depth cannot be used.

5. ALONGSHORE SEDIMENT TRANSPORT CAPACITY

The alongshore sediment transport capacity was obtained using the coastline model UNIBEST CL+ (UNiform Beach Sediment Transport Coast Line) (Szmytkiewicz et al. 2000) to obtain a continuous and precise alongshore transport capacity. We use 25 profiles (for location see Figure 3) to compute the sediment transport capacity along the coastal zone between Sulina jetties (north) and Portita (south). The profiles are located where local information is specified. Each of these profiles was placed in

locations considered representative and each of these used a different cross-shore profile determined from the bathymetric map. The closure depths from Table 1 were used. At the offshore extremity of every profile a local wave climate was extracted from the wave climate file. The formulas used for the sediment transport computation were CERC (Shore Protection Manual 1984) and Bijker (Bijker 1971).
The general direction of the alongshore sediment transport, on Sulina – Sfantu Gheorghe segment, is from north to south. An exception from this rule is the sector between the Sulina jetties and profile 1 where the transport is towards north. Because of the influence of the jetties the waves from northern directions have small heights the waves from eastern and southern directions induce the alongshore current here, reversing the general direction. Downdrift, to the Sfantu Gheorghe mouth the alongshore transport is oriented towards south and it is continuously increasing. Between profile 2 and profile 4 the transport is increasing with a very steep gradient, suggesting intense erosion. The next sector (profile 4 - profile 9) is keeping the same trend, but with a milder gradient.

Around the Sf. Gheorghe mouth (profile 9 - profile 11) the transport gradient gets very mild showing almost the same values at the beginning and the end of the sector. Nevertheless, this is the sector where the maximum amplitude of the longshore sediment transport from the whole studied area, is reached, 1,080,000 m^3/yr, according to the CERC formula and 775,000 m^3/yr, according to the Bijker formula. This is also the location where, to this maximal transported sediment quantity is added the contribution of the Sf. Gheorghe branch. By adding this contribution, 350,000 - 500,000 m3/yr (Panin, 1997), a total of 1,200,000 - 1,500,000 m^3 sandy sediment is entering in the Sahalin domain each year.

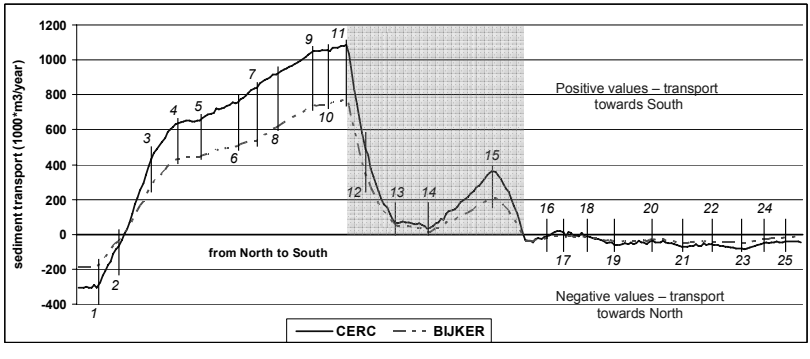

Fig. 2. The alongshore sediment transport capacity computed with UNIBEST CL+. The gray rectangle contains the sediment transport in the Sahalin spit island domain. For location of the profiles see figure 3.

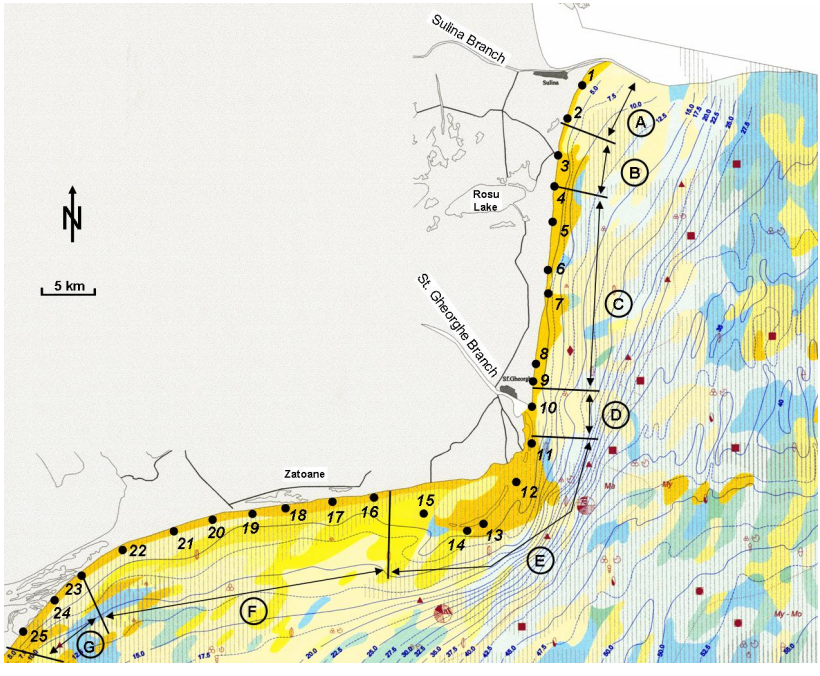

Fig. 3. The location of the profiles used in computation (black dots). Capital letters in circles are the sectors used to compute the sediment budget.

Immediately after the shoreline orientation is changing (profile 11), the transport is decreasing with a strong gradient reaching almost zero at the end of the island domain (profile 16). In front of the Sahalin spit island the wave climate is the strongest from the whole area, both predominant winds sectors (northern and south-western) exerting wave action there. The longshore transport gradient is suggesting here an intense accretion along the island. However, the measurements show an erosion of the island on the eastern side simultaneously with migration towards mainland and elongation in the southern end (Panin, 1998; Giosan et al., 1999). The processes which control the erosion/accretion here are more complex than a coastline model can handle. A special discussion will be paid to this region in the sediment budget chapter.
Around profile 15 a new peak is reached in the sediment transport. Sand is eroded from the end of the spit and, probably "pushed" into the golf, formed between the island and the mainland, by the waves from south and south-west directions.

The sector between profile 16 and profile 25 is characterized by a low sediment transport from south-west toward north-east, the maximum being 55,000 - 85,000 m^3/yr (profile 23). This sector, with a mild slope of the submerged beach, is

controlled by the waves from southern direction, which attack the shores at low incidence angles, explaining the rather small values of the sediment transport.

6. THE SEDIMENT BUDGET

The sediment budget was computed taking into account the longshore sediment transport, closure depth and additional sources of sediment as delivered by Sf. Gheorghe branch. Starting from the northern boundary we describe 9 sectors (figure 3) defined according to the longshore transport gradients and morphological particularities of the coastal zone. The erosion/accretion values are expressed with a minimum (corresponding to Bijker formula) and a maximum value (corresponding to CERC formula). The whole coastal zone can be split into three sections, corresponding with the characteristics of the sediment budget.

Section Sulina - Sfantu Gheorghe

This section is delimited northward by the Sulina jetties. Since these jetties extend into the sea for some 8 km, up to a depth of 7-8 m, we assume there is no sediment input from the northern boundary. Next to the jetties, southward, (sector A) the average advance of the shoreline is ranging, according to our calculation, from 4.5 to 7.5 m/yr. This sector has been described (Panin, 1996; Stanica 2003) as the place where due to the jetties an eddy-like current is forming, reversing the normal direction of the longshore drift. The same authors mention a mean annual shoreline advancement rate ranging between 8 and 10 m. In sector B the largest erosion rate of the whole study area is computed, from 9 to 13 m/yr. From literature, the observed erosion rate here is 6 - 11 m/yr (Panin, 1996; Stanica, 2003). In figure 4, shoreline positions are plotted at different times. In the periods 1952 - 1985 and 1960 - 1985 the average erosion rate is 11 m/yr. This segment is corresponding to the segment profile 30 - profile 26 where, according to our computation, the erosion rate is 5 - 7 m/yr.

The erosion rates decrease in sector C at 2 - 2.5 m/yr reaching values of 0.5 m/yr in the sector D. Sector D coincides with the segment described (Ungureanu at al., 1996; Stanica, 2003) as stable.

Sahalin spit island

The domain of Sahalin island is corresponding to the sectors E in figure 3 and the associated sediment transport is contained in a gray rectangle in figure 2. Here, the longshore transport is just one of the factors controlling the evolution of the island, but other processes, like overwash, migration towards the mainland and the continuous elongation to south-west (Panin, 1999; Giosan et al., 1999) are also important. Although, our computation suggests accretion, according to the same authors the eastern side of the island is strongly eroding. In the Sahalin domain the sand input has two main contributors: the longshore transport which brings here 775,000 - 1,080,000 m^3/yr and the input from Sf. Gheorghe arm which is 350,000 - 500,000 m3/yr.

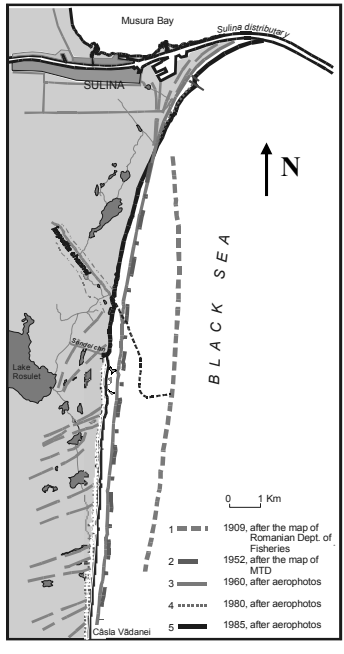

Fig. 4. The evolution of the coastline of the Danube Delta Front in the Sulina - Sfantu Gheorghe section during the last century (modified after Panin, 1996).

Observing the evolution of Sahalin island, the obvious conclusion is that much of the sand brought by the river and the longshore transport is deposited at the southern tip of the island. From figure 5 it can be noticed that the length of the island is increasing with a rate of 85 - 100 m/yr. Obviously, not only the emerged part of the islands is growing, but also the submerged associated domain, both landward and seaward are moving towards south-west with the previous mentioned rate. Based on the evolution of the island in the last decades, the assumption was made that the active domain is confined by the 3 m depth isobaths northward (the largest depth from the bay) and the 8 m depth isobaths southward (the closure depth in that area).

The cross-section chosen for quantification is shown in figure 6. The general direction for the elongation of the island is towards south-west, but the tip of the island is moving toward west, so the cross-section is oriented almost north – south. The result is a surprisingly well match between the sediment entering in the system (1.2 - 1.5 million m^3/yr) and the deposited sediment (1.25 - 1.4 million m^3/yr).
The erosion of the island on the eastern side of the island is, most probably, caused by overwash. This same process explains an important part the accumulation of sediments in the Sahalin bay.

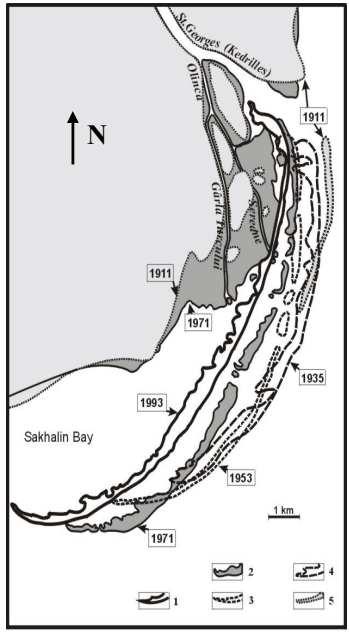

Fig. 5. Evolution of the modern St. George Delta and Sakhalin barrier island (modified after Giosan et al., 1999) 1: coastline in 1993; 2: coastline in 1971; 3: coastline in 1953; 4: coastline in 1935; 5: coastline in 1911.

The sediment accumulated behind the island (Sahalin Bay) has three main sources. The first source is the Sf. Gheorghe arm (with its sub-branches Garla Turcului and Seredne - figure 5). Due to the sheltered environment the grain size of the sediment settled here is, in major proportion, finer than sand (Panin 1998). The second source is the overwash. The overwash processes are stimulated by the elevation of the island which is rather low especially in the central and southern parts (1.5 - 2 m) and the steep slope of the submerged domain eastward. Finally, the third source is "felt" during the storms from southern direction when the sediment (accumulated between profiles 15 and 16 in our computation) is reworked by the waves and transported into the gulf.

The explanation that we propose for the evolution of the Sahalin spit island is taking in account the fact that longshore sediment transport is just one of the factors involved in this process. Observing the evolution of the island (figure 5) it can be noticed that the length of the island is growing constantly since it is formed, so erosion produced by the longshore transport is not responsible for the continuous migration toward land of the island. A significant erosion of the island due to the longshore transport will lead, eventually, to the disappearance of the island, since there is no accumulation on the landwards side of the island. The only process that can be hold responsible for this migration is the overwash. However, the longshore

transport and the Sfantu Gheorghe branch sediment input are the main source for continuous elongation towards south-west of the island.

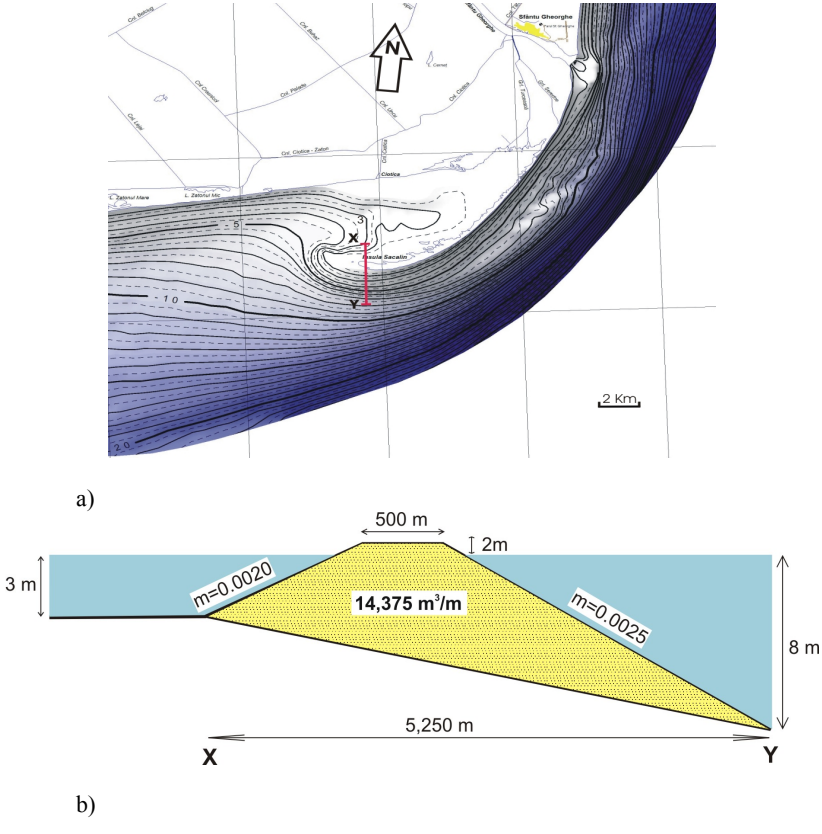

Fig. 6. The cross section used to compute the volume of sand accreting every year in the southern part of the Sahalin island; a) location; b) cross section, m is the slope (not to scale).

A strong argument for this is the good correlation between the quantity of sediment brought into island domain by the longshore drift and the river with the quantity stored every year at the southern tip of the island domain.

The longshore transport gradients in the figure 2 (gray rectangle), especially between profiles 11 and 14 show an ideal situation, since we computed the net alongshore transport capacity. The longshore current from northern direction is having an important source of sediment to erode (area between profiles 2 and 11), but the longshore drift caused by the southern waves is virtually unsaturated with sediments

when it is reaching the Sahalin island. Then, it starts to erode, but very soon (between profiles 12 and 13) the longshore drift loses its transport capacity due to the change in the coastal orientation. When the direction of the longshore drift is changing again (to northern direction) the sediment moved previously by the southern drift along with a new quantity brought by the river and northern drift is transported and deposited at the southern tip of the island. The explanation for the accumulation of the sediment in this area is the fact that the northern longshore drift is losing the transport capacity due to the change of the shoreline orientation (profiles 12 - 14).
The sediment transport between profiles 14 and 16 (figure 2) is not reliable in terms of quantity since UNIBEST CL+ was not designed to model spit islands. However, the trend of the sediment transport seems realistically, since this zone is one of the sediment sources for the clogging of the Sahalin bay.

Section Sahalin - Portita inlet
There are two sectors here: F, with a rate of erosion of 0.4 m/yr and G, with a rate of accretion of 0.6 m/yr. The area corresponding to the eastern half of the sector H and the sector I is described to be erosive, but the western half of the sector H the shoreline is, on average, stable (Panin, 1998). The erosion rate described for eastern half of the H sector is big (10 m/yr) (Panin, 1998), but it seems to be rather a local feature since the neighboring sectors are stable.

7. Discussion and conclusions

The sediment circulation in the studied area is mainly controlled by two wave directions sectors: one from north to north east and the other one from south to south west. However, waves from the northern directions occur more frequently and are associated with larger energy.

The most "energetic" area is the Sahalin spit island domain, in correspondence with the computed closure depths (up to 11.6 m), but also with the maximum quantity of sand transported by the longshore current. The two important factors contributing to this are the full exposure of the western side of the island to both important wave directions (northern and southern) and the rather steep slope of the submerged beach.

The majority of the computed erosion and accretion matches very well with the direct observations. An exception is the position of the shoreline in 1909 from figure 4. According to this map an average erosion rate for the Garla Imputita - Casla Vadanei was over 30 m/yr, three times larger than the computed one. A possible explanation could be the flooding of a large part of the aerial beach, a situation which often occurs in low lying sediment starved coastal zones.

The Sahalin spit island domain is able to store large quantities of sediment, brought by the longshore current and Sfantu Gheorghe branch, through the continuous elongation towards south-west. Cross-shore processes like overwash are responsible for the movement of the island towards the mainland by erosion at the more exposed side, the eastern one, and accumulating on the western side in the quieter

environment of Sahalin Bay. In the case of the elongation of the Sahalin spit we were able to quantify the volumes of sediment moved, but for the Sahalin bay only qualitative explanations were given. In order to quantify also here the volumes of sediment more measurements are required, especially on overwash processes and the input of the fine sediment into the bay through Garla Turcului and Seredne branches. Nevertheless the authors do not exclude the hypothesis that some of the sediment is lost from the system being carried to larger depths than the closure depth. Further, to the south west, longshore transport plays a more important role in the shoreline evolution. According to our computations the net transport is towards south and of small amplitudes. This is not matching with all the descriptions of the area. A possible explanation is the link with the moment when the observations were made. For example, the Perisor - Periteasca (between profiles 8 and 12 in figure 3) is described by Panin (1996), as stable, but with back and forth movements, depending on the energy level of the considered year. Since the data used for derivation of the wave climate and, subsequently, the longshore transport cover ten years (1991 - 2000) we conclude that, over all, a good match was achieved between the computation and the measurements.

6. Acknowledgements

The authors would like to thank to Nicolae Panin, Adrian Stanica and Radu Dimitriu from National Institute of Marine Geology and Geoecology – GeoEcoMar, Romania for supporting the study with valuable data and useful observation. The computation was made during the doctoral fellowship in the frame of *European Centre of Excellence for Environmental and Geo-ecological Studies on River – Delta – Sea Systems in Europe: case study River Danube, its Delta, Black Sea System",* Project number EVK3-2002-00503, European Commission - FP5.

References

Bijker, E.W. (1971). "Longshore transport computations", *Proc. ASCE, Journal of the Waterways, Harbors and Coastal Engineering Division*, WW4, November 1971.

Bondar, C., Roventa V., State I. (1973) "La Mer Noire dans la zone du littoral roumain Monographie hydrologique." Bucharest, Romania.

Bondar, C., Popa, A., Stanica, A. (2000) "Hydrologic, sedimentologic and morphologic processes in the Sulina mouth area" *Proceedings of the "IUG / Comission of the Coastal Zones*" Conference "the Delta's state of the art", p. 19 – 25.

Booij N., Ris R. C. and Holthuijsen L. H. (1999) "A third-generation wave model for coastal regions; 1. Model description and validation", *Journal of Geophysical Research*, Vol. 104, No. C4, p. 7649–7666.

Dan S., Stive, M., van der Westhuysen, A., Walstra, D. J. (2006) "Wave Climate and Sediment Transport on the Coastal Zone of the Danube Delta", *Proceedings Advances in Civil Engineering*, Istanbul, 2006. CD ROM ISBN 975-461-416-4, 10 p.

Ginsburg, A. I., Kostianoy G. K., Nezlin, N. P., Solovieev D. M., Stanichny S. V. (2002) "Anticyclonic Eddies in Northwestern Black Sea", *Journal of Marine Systems* 32, p. 91 - 106.

Giosan, L., Bokuniewicz, H., Panin, N., and Postolache, I. (1999) "Longshore Sediment Transport Pattern Along the Romanian Danube Delta Coast", *Journal of Coastal Research*, 15, (4), pp. 859-871.

Hallermeier, R.J. (1980) "Sand motion initiation by water waves; two asymptotes" Proc. ASCE 106 (WW6), 299–318.

Malciu, V. (2000) "Implications of Accelerated Sea-Level Rise (ASLR) for Romania", *Proceeding of SURVAS Expert Workshop on European Vulnerability and Adaptation to impacts of Accelerated Sea-Level Rise* (ASLR), Hamburg, Germany, pp. 23-24.

Panin, N., (1996). "Impact of global changes on geo-environmental and coastal zone state of the Black Sea", *GEO – ECO – MARINA*, vol. 1, pp. 7-23, Bucharest, Romania.

Panin, N., (1997). "On the geomorphologic and the geologic evolution of the River Danube – Black Sea interaction zone", *GEO – ECO – MARINA*, vol. 2, p. 31-40, Bucharest, Romania.

Panin, N., (1998)., "Danube Delta: Geology, Sedimentology, Evolution" *Association des Sedimentologistes Francais*, Paris.

Panin N., (1999)., Global changes, sea level rise and the Danube Delta: risks and responses, *GEO-ECO-MARINA*, pp. 19-29, vol. 4, Bucharest, Romania.

Sabatier F., Stive M. and Pons F., (2004) "Longshore variation of depth of closure on a micro-tidal wave-dominated coast", International Conference of Coastal Engineering 2004, American Society of Civil Engineering, Lisboa, 2329-2339.

Stănică, A., (2003) "Evolutia geodinamica a litoralului romanesc in sectorul Sulina – Sf. Gheorghe si posibilitati de predictie", *Biblioteca Universitatii Bucuresti, Facultatea de Geologie si Geofizica*, Bucharest (unpublished Ph. D. Thesys, in Romanian).

Szmytkiewicz, M., Biegowski, J., Kaczmarek, L. M., Okrój, T., Ostrowski, R., Pruszak Z., Różyńsky G., Skaja M. (2000) "Coastline changes nearby harbour structures: comparative analysis of one-line models versus field data", *Coastal Engineering,* Volume 40, Issue 2, p. 119-139.

U.S. Army Coastal Engineering Research Center, Department of the Army, Corps of Engineers, 1984. "Shore Protection Manual" U.S. Govt. Printing Office,Washington, DC, USA, vols. 1 and 2.

Ungureanu, Gh., Stănică, A., Gaiță, C., Danielescu–Chirlomez, C., (1996) "Shoreline and beach morphology seasonal variations in the Sf. Gheorghe area (Danube Delta) - a pilot study", *Anuarul Institutului Geologic al României*, Volume 69, Suppl. 1, Bucharest, pp. 197 - 200.

Ungureanu, Gh., Stănică, A. (2000) "Impact of human activities on the evolution of the Romanian Black Sea beaches", *Lakes & Reservoirs: Research and Management*, volume 5, pp. 111-115.

FIELD MEASUREMENTS AND MODELLING OF LONGSHORE SEDIMENT TRANSPORT

J. J.Williams[1], L. S. Esteves[1], M. A. Lisniowski[2] & H. L. S. Perotto[2]

1. School of Geography, University of Plymouth, Plymouth PL4 8AA, United Kingdom. jon.j.williams@plymouth.ac.uk luciana.esteves@plymouth.ac.uk
2. Laboratório de Oceanografia Geológica/FURG, Campus Carreiros, CP 474, Rio Grande, RS 96201-900 Brasil. alineoceano@gmail.com heitor_perotto@)pop.com.br.

Abstract: Measurements of suspended sediment concentration profiles, *C-Profiles*, and hydrodynamic conditions were obtained in the surf zone on a barred beach composed of fine sand using streamer traps. A simple model was used to estimate the total longshore sediment flux. *C-Profiles* predicted for wave-current conditions were found to compare favorably with the field data. In some cases the cross-shore distribution of LST exhibited two peaks associated with wave shoaling and breaking over the bars. Comparisons between present results and predictions from well-known longshore transport formula and a formulae for sediment transport in combined wave-current conditions generally show good agreement. The results indicates that sediment transport processes in the surf zone are not markedly different from those operating in unidirectional and combined wave-current flows under non-breaking wave conditions. The work contributes to the body of published field data by documenting the rates and cross-shore distribution of LST at a previously unstudied field site.

INTRODUCTION

The quantification of hydrodynamic conditions and sediment flux in the surf zone is required in a range of practical engineering applications (e.g. beach nourishment, design of offshore breakwaters and other coastal defence structures). In this zone, sediment is mobilised primarily by oscillatory wave-induced flows. If the wave angle relative to the shoreline is less than 90° sediment is transported by a longshore wave-induced current. Sediment can be also transported onshore and offshore by the combined action of

asymmetric wave-induced flows, undertow and infragravity waves which together give rise to the formation of a range of familiar beach features. Here we focus only on longshore sediment transport (LST) and exclude swash processes.

The measurement of LST in the field presents many challenges. In the surf zone, air bubbles preclude the use of the acoustic instruments and optical techniques are better suited to fine sediments. Furthermore, instruments designed for work in deeper water are relatively delicate and unable to withstand breaking wave conditions. Methods employed in the past to measure LST include interception and tracer techniques. However, there are considerable discrepancies between measured and predicted LST and much of the available field data is subject to considerable errors (Greer and Madsen, 1979).

This paper makes use of time-averaged vertical suspended sediment concentration profiles, *C-Profiles*, measured across the surf zone using streamer traps. The most suitable method for prediction of the measured *C-Profiles* based on available hydrodynamic information is identified. A semi-empirical modeling approach based on well-established formulae is then used to calculate the rate of LST. By necessity, the model makes a number of simplifying assumptions about wave transformation across the surf zone, bedform morphology and the cross-shore profile of the longshore current. Where possible the model is validated with field data. Cross-shore variability in LST and its relationship to surf zone morphology are examined and comparisons are made between predicted LST from the present model with LST predicted by other well-known approaches.

FIELD SITE, EQUIPMENT AND MEASUREMENTS

The measurements of LST were obtained at Cassino, Rio Grande do Sul, Brazil (Fig. 1) on a very long, open ocean dissipative beach composed of fine sand. The site has a mean semidiurnal tidal range $O(0.5$ m) and waves typically have mean annual significant height (H_s) of 1.4 m and peak period (T_p) of 7 s to 9 s. Samples of suspended sediment transported by the longshore current were obtained at a range of heights above the bed using streamer traps (STs, Fig. 1a). These followed the design of Kraus (1987) and comprise a series of 10 nets made from polyester monofilament sieve cloth with a mesh size of 63 μm arranged in an equally spaced vertical array on a steel sampling frame. On the ST, nets are held open to the flow using a metal frame 9 cm high and 14.5 cm wide. Beach profiles and frame locations were measured using a total station. ST frames were deployed to face into the longshore current in the surf zone by two operators standing clear of the trap openings. Surficial bed sediment samples were also obtained at the deployment site and STs were removed after a sampling period of 10 minutes (Fig. 1b). Ripples were observed to be locally present but were not measured.

The local longshore current speed, U_L, was measured in two ways: by timing a drogue float between two fixed points 200 m apart, equidistant from a given ST location and at the same offshore location; and by tracking approximately neutrally buoyant floats using a mm wave radar (*c.f.* Bell et al., 2004). The average wave height H, the average breaking wave height, H_b, and wave period, T, for approximately 150 incident waves

were estimated visually. The wave approach angle relative to the shoreline in the breaker zone, α, was measured using a compass bearing or measured directly from the radar images.

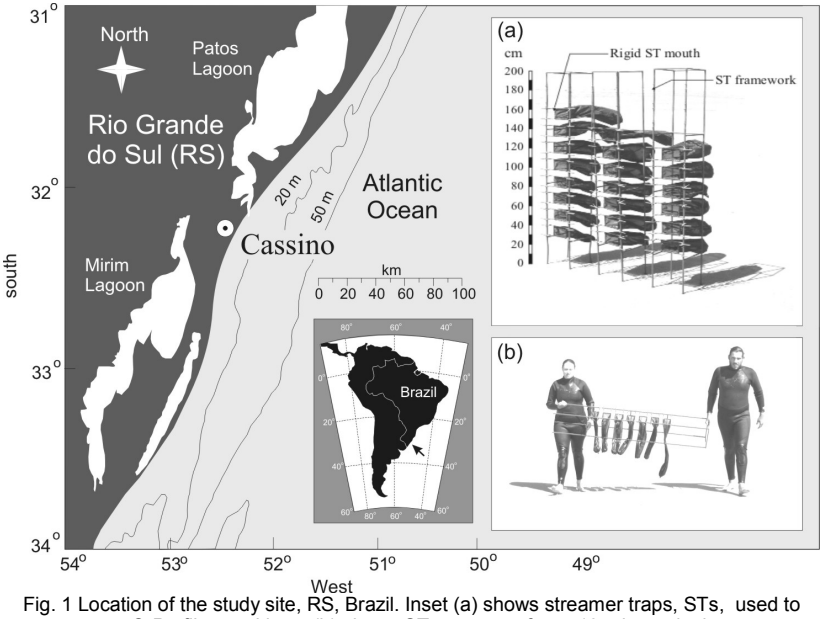

Fig. 1 Location of the study site, RS, Brazil. Inset (a) shows streamer traps, STs, used to measure *C-Profiles*; and inset (b) shows ST recovery after a 10 minute deployment.

Field measurements were undertaken at Cassino on 7/12/2004, 12/3/2005, 27-28/5/2005 and 23/10/2005. Although **all** ST data have been used to study *C-Profiles*, here for brevity we only present modelling results from **three** experiments on 12/3/2005, 28/5/2005 and 23/10/2004, hereafter referred to as Case 1, 2 and 3, respectively. These studies span the range of conditions pertaining during the other experiments. The measured beach profiles and ST locations are shown in Fig. 2 and the measured hydrodynamic conditions are summarized in Table 1. During May and June 2005, further useful data related to the cross-shore distribution of wave height and longshore currents were obtained[1]. By choosing periods when hydrodynamic and meteorological conditions were closely similar to those pertaining during the ST campaigns it was possible to approximate cross-shore profiles of wave height, $H(x)$ and longshore current speed, $U_L(x)$ for modeling studies of Cases 1 to 3.

DATA ANALYSIS

Hydrodynamic measurements obtained by individual observers were cross-checked for

1 These data were obtained from an array of shore-normal instruments (PUV) deployed as part of an experiment examining wave attenuation by offshore mud deposits, (Williams et al., 2007).

consistency. The analysis of data from PUV sensors to quantify $H(x)$ and $U_L(x)$ profiles

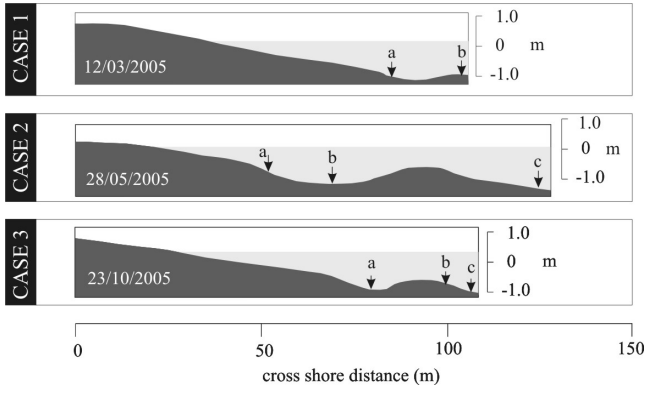

Fig. 2 Measured cross-shore beach profiles and ST locations for Cases 1 to 3.

Case	Test No.	Date	U_L (m/s)	H (m)	T (s)	α (deg)
	Cas1A	07/12/2004		0.5	6	20 to 30
	Cas1B	07/12/2004	0.45			
	Cas1C	07/12/2004	0.32			
1	Cas2A	12/03/2005	0.39	0.5	12	10 to 20
	Cas2B	12/03/2005	0.38	0.5	12	10 to 20
	Cas3A	12/03/2005	0.24	0.3	6 to 8	10 to 20
	Cas3B	12/03/2005	0.26	0.4		6.6 to 8.2
	Cas3C	12/03/2005	0.10	0.5		8.3
	Cas3D	12/03/2005				
	Cas4A	27/05/2005	0.66	0.5	8	5 to 8
	Cas4B	27/05/2005				
	Cas4C	27/05/2005				
	Cas5A	28/05/2005	0.26	0.7	8 to 9	2 to 4
2	Cas5B	28/05/2005	0.33	0.7	8 to 9	2 to 4
	Cas5C	28/05/2005	0.33	0.7	8 to 9	2 to 4
	Cas6A	23/10/2005	0.43	0.8	7	10
3	Cas6B	23/10/2005	0.47	0.8	7	10
	Cas6C	23/10/2005	0.47	0.8	7	10

Table 1. Measured hydrodynamic conditions during ST measurement campaigns at Cassino, RS, Brazil. (Gaps indicate where measurements were not made as conditions were not observed to change). Modelling test cases 1, 2 and 3 are identified here.

is reported in Williams et al, (2007). In the laboratory, ST and surficial bed sediment samples were washed from the nets and oven dried at 110°C before being weighed, sieved at 0.25 phi intervals and analysed for $CaCo_3$ content. Since ST data are an integrated measure of the total suspended sediment flux at a given height above the bed, $M(z)$, determination of the *C-profile* requires knowledge of the vertical longshore current profile. In the absence of current profile data it is necessary here to assume that in water

depth, h, in the range $0h < z < 0.5h$, the vertical current profile takes a logarithmic form (Wang et al., 2002) defined as

$$U_L(z) = \frac{U_*}{\kappa} ln\left(\frac{z}{z_o}\right) \quad (1)$$

where $U_L(z)$ is the measured longshore current speed at height z above the bed, U_* is the bed friction velocity, κ is von Kármáns constant (0.4) and z_o is the total bed roughness (see below). U_* is defined in terms of the skin friction bed shear stress τ_c as $\sqrt{\tau_c/\rho}$ where $\tau_c = \rho Cd U^2$, ρ is the fluid density (1023 kg/m^3 for sea water and salinity of 35ppt), and the drag coefficient, Cd, is given by

$$Cd = \left[\frac{\kappa}{1 + ln(z_0/h)}\right]^2 . \quad (2)$$

For $z > 0.5h$, $U_L(z)$ is assumed to be constant with depth up to the water surface. This type of vertical velocity profile is a reasonable approximation to longshore current profiles measured in the laboratory (e.g. Wang et al., 2002) and in the field (e.g. Garcez Faria et al., 1998). The suspended sediment concentration in g/l, C, was then computed at each sampling height using $C(z) = M(z)/[U_L(z)$ x 0.145 x 0.09 x 600].

MODELLING

The modeling outlined here is used to predict the total LST across the width of the surf zone. In the model, cross-shore distributions of U_L and H (Williams et al., 2007) are imposed on the measured bathymetry and wave period is held constant. A measured cross-shore gradient in D_{50} ranging from 0.18 mm at the shoreline to 0.1 mm at the seaward boundary defines the bed sediments. Although suspended sediment grain size variations with height were measured (Esteves et al., 2007), these are not included in the present model. Interactions between the waves and the longshore current, the resulting bedforms and resuspension and transport of sediments is then simulated at 2 m intervals across the surf zone using some well-know approaches outline below. Each model simulation point along the cross-shore profiles is hereafter referred to as a node.

Sediments

The physical and dynamic properties of the sediments, expressed as settling velocity and entrainment threshold, determine the sediments response to hydrodynamic forcing and are critical parameters governing sediment behavior irrespective of the transport mode. Here the threshold bed shear stress, τ_{crit}, for incipient grain motion is given by $\tau_{crit} = \theta_{crit} g(\rho_s - \rho) D_{50}$ where the critical Shields parameter, θ_{crit}, is defined by the dimensionless grain size parameter D_* so that

$$\theta_{crit} = \frac{0.3}{1 + 1.2D_*} + 0.055\left[1 - exp(-0.02D_*)\right] \quad (3)$$

and $$D_* = \left[\frac{g(s-1)}{\nu^2}\right]^{1/3} D_{50} \quad (4)$$

(Soulsby, 1997). Here s is the ratio of grain to fluid density (ρ_s/ρ) and ν is the kinematic viscosity of the water. Here we use: $g = 9.81$ m^2/s, ρ_s for quartz grains = 2650 kg/m^3 and $\nu = 1.36 \times 10^{-6}$ m^2/s. Estimates of the settling velocity of grains in suspension was calculated using the optimised formula

$$w_s = \frac{\nu}{D_{50S}}\left[\left(10.36^2 + 1.049 D_{*S}^3\right)^{1/2} - 10.36\right] \quad (5)$$

(Soulsby, 1997), where D_{50s} is the **measured** suspended sediment grain diameter (Esteves et al, 2007) and D_{*s} is the D_* values for that sediment. The threshold depth-mean current speed, U_{crit}, for $D_* > 0.1$ is given by Soulsby (1992)

$$U_{crit} = 7\left(\frac{h}{D_{50}}\right)^{1/7}\left[g(s-1)D_{50}\theta_{crit}\right]^{1/2} \quad (6)$$

Bed roughness

Establishing accurately the hydrodynamic roughness of the bed is pivotal in all approaches to estimating bed shear stresses and associated cohesive sediment responses. In the surf zone, where there may be bedforms and active sediment transport, the total bed roughness, z_0, has three components: roughness due to the bed sediments, z_{0G}, defined a $D_{50}/12$, roughness due bedforms (form drag), z_{0R}; and roughness due to sediment transport, z_{0Q}. z_{0R} can be defined as

$$z_{0R} = \Theta\frac{\eta^2}{\lambda} \quad (7)$$

(Soulsby, 1992),where Θ is a scaling parameter in the range 0.3 to 3.0 and λ and η are the wavelength and height of bed ripples, respectively. A widely used equation for z_{0Q} that does not require knowledge of z_0 is *a priori* is $z_{0Q} = 0.00533 U_w^{2.25}$ (Raudkivi, 1990), where U_w is the wave orbital velocity (see below). Thus

$$z_o = z_{0G} + z_{0R} + z_{0Q} = \frac{D_{50}}{12} + \Theta\frac{\eta^2}{\lambda} + 0.00533 U_w^{2.25} \quad . \quad (8)$$

Although the cross-shore distribution of D_{50} was measured, Eq. 8 still relies on estimates of bed morphology coming either from existing equations that predict the dimensions of bedforms or from field observations of bedforms in the surf zone. Since it was not possible in the study to measure bedforms, and surf zone roughness in weak to moderate wave conditions is likely to be dominated by wave-generated bedforms, estimates of η and λ were obtained using the approach of Grant & Madsen (1982) as detailed in Appendix 1.

Waves

Analysis of cross-shore wave properties was undertaken primarily to obtain estimates of the wave-induced bed shear stresses required by formulae given below. Although wave shoaling and breaking processes in the surf zone are highly non-linear and complex Deigaard et al. (1991) show that wave induced stresses under breaking and shoaling waves are not **on average** significantly different from unbroken waves and thus application of conventional approaches to estimation of wave-induced bed shear stresses are possible. Using the appropriate $H(x)$ distribution, estimates of $U_w(x)$, were obtained

at model nodes using Deans stream function wave theory (Dean et al., 1983)[2]. Estimates of the peak wave-induced bed shear stress, $\hat{\tau}_{ws}(x)$, were then obtained using $\hat{\tau}_{ws} = 0.5 f_w U_w^2$, where the wave friction factor, f_w, is defined in terms of the relative roughness, r, by Swart (1974) as $f_w = 0.3$ for $r \leq 1.57$ and $f_w = 0.00251 exp\left(5.21 r^{-0.19}\right)$ for $r > 1.57$. Here $r = A_o / k_s$ where A_o is the orbital amplitude of the waves ($U_w T / 2\pi$). For rough turbulent, flat bed conditions, the Nikuradse equivalent sand grain roughness, k_s, is given by $2.5D_{50}$ and $\hat{\tau}_{ws}$ relates to the **skin friction only**. However, in cases where ripples are present on the bed, and sediment is transported as bedload, k_s is defined by the **total bed roughness** z_0 so that $k_s = 30z_0$ (see below).

Longshore currents

Estimates of the longshore current-related bed shear stress profile, $\tau_C(x)$, are required at locations across the surf zone in order to estimate the combined W+C shear stress responsible for mobilization, suspension and transport of sediment. Although longshore currents were only measured at a few locations during the experiments and very few supporting field data exist related to the spatial or temporal characteristics of U_T, most studies indicate that that the cross-shore distribution of U_T is approximately parabolic and vertical velocity distribution conforms to a logarithmic law (Wang et al., 2002; Reniers and Battjes, 1997). Both these characteristics were confirmed by the cross-shore PUV array and by drogue floats (Williams et al., 2007). These measurements showed that in the case of purely wave-driven longshore currents, the maximum current velocities occur close to areas where wave breaking is most intense (Reniers and Battjes, 1997). Estimates of the τ_C were obtained using $\tau_c = \rho C d \hat{U}_L$, where Cd is the total drag coefficient and $\hat{U}_L$ is the depth-mean longshore currents velocity.

W+C interactions and *C-Profiles*

In order to estimate the total suspended load carried by the longshore current it is essential to model *C-Profiles* at all cross-shore locations accurately. In the surf zone, where longshore currents can exceed 0.5 m/s, it is unclear if the characteristics of the *C-profile* are controlled by the current, by the waves or by a combination of the two. Following investigation of *C-Profiles* predictors for current-only, wave-only and combined wave-current, W+C, conditions, the simple single layer model proposed by Williams et al., (1997) was found to give good agreement with *C-Profiles* measured by the STs and was relatively easy to implement in the model. This takes the form

$$\overline{C}(z) = \overline{C}(a)\left(\frac{z + L\alpha_{wc}}{a + L\alpha_{wc}}\right)^{-\alpha_{wc}} \qquad (9)$$

where $\overline{C}(a)$ is the reference $\overline{C}$ value at height a, L is a vertical length-scale parameterising the vortex ejection process in oscillatory flow over ripples, and α_{wc} is a Rouse-type parameter = $w_s / \kappa(U_{*mean} + U_{*max})$. Here the time-averaged W+C shear velocity, U_{*mean}, defines an apparent sediment mixing coefficient and is used to parameterise the quasi-periodic vortex ejection process over ripples and the peak W+C

[2] Matlab routines from http://faculty.gg.uwyo.edu/DSF

shear velocity, U_{*max}, is analogous to the standard turbulent diffusion mechanism. Here we use the algebraic approximation to the W+C model of Fredøe (1984) from Soulsby et al., (1993) to estimate U_{*max} and U_{*mean} at cross-shore nodes. Estimate of *C(a)* were obtained using

$$C_a = \rho_s \left[\frac{0.331(\theta_s - 0.045)^{1.75}}{1 + 0.720(\theta_s - 0.045)^{1.75}} \right] \quad (10)$$

where θ_S is the skin-friction Shields parameter (Zyserman and Fredsøe, 1994). Following Nielsen, (1992) L is defined by the ripple height, η, and grain settling velocity w_s as

$$L = 0.075 \frac{U_w}{w_s} \eta \quad for \quad \frac{U_w}{w_s} < 18 \quad (11), \qquad \text{and } L = 1.4\eta \quad for \quad \frac{U_w}{w_s} < 18 \quad (12)$$

Bedload and total load transport in W+C conditions

Since we have no absolute measure of LST from the present site, it is useful to compare results from the present model with established predictive formulae. Most formulae used to quantify LST make simple assumptions regarding hydrodynamics and sediment processes, and do not consider factors such as barred topography and/or the cross-shore sediment exchanges. The CERC formula is used widely to predict the LST rate Q and is believed in ideal conditions to have an accuracy of ± 30% to 50%. The CERC formula states

$$Q_{CERC} = \frac{K}{16(s-1)(1-p)} \sqrt{\frac{g}{\xi}} H_b^{2.5} \sin(2\alpha) \quad (13)$$

where Q_{CERC} is the volumetric LST rate (m^3/s) integrated across the width of the surf zone, K is the CERC coefficient, p is the sediment porosity (0.32) and ξ is a wave breaker index (0.78). Here we use the expression $K = 1.4\,exp^{(-2.5 D_{50})}$ from Komar (1988). The Kamphuis (1991) LST formula includes the influence of T, beach slope, m, and D_{50} in the form

$$Q_{K91} = 7.9x10^{-4} \left(\frac{1}{(1-p)} \right) \left(\frac{g}{2\pi} \right) H_b^2 T^{1.5} m^{0.75} D_{50}^{-0.25} \sin^{0.6}(2\alpha) \quad (14)$$

A method designed specifically for estimating sediment transport in W+C conditions is given by Soulsby (1997). It applies **only** to rippled beds and in conditions where $U_w < U_L$ and is expressed as

$$Q = A_s U \left[\left(U^2 + \frac{\xi}{Cd_6} . U_w \right)^{0.5} - U_{crit} \right]^{2.4} \left(1 - 1.6 \tan\phi \right) \quad (15)$$

where ξ is an empirical coefficient (= 0.018), Cd_6 is the recommended drag coefficient for a rippled bed (z_0 = 6 mm). The coefficient A_s is defined as $A_{ss} + A_{sb}$, where

$$A_{sb} = \frac{0.005h(D_{50}/h)^{1.2}}{[gD_{50}(S-1)]^{1.2}} \quad (16)$$

for bedload, and for suspended load.

$$A_{ss} = \frac{0.012 D_{50} D_*^{-0.6}}{\left[g D_{50} (S-1) \right]^{1.2}} \tag{17}$$

RESULTS AND DISCUSSION

All measured *C-Profiles* are shown in Fig. 3. Profiles have been grouped based on the shape of the illustrated best-fit line into concave, convex and irregular profiles. In all cases, concave profiles predominate with convex and irregular profiles being associated with location on top of and just landward of an offshore bar, respectively.

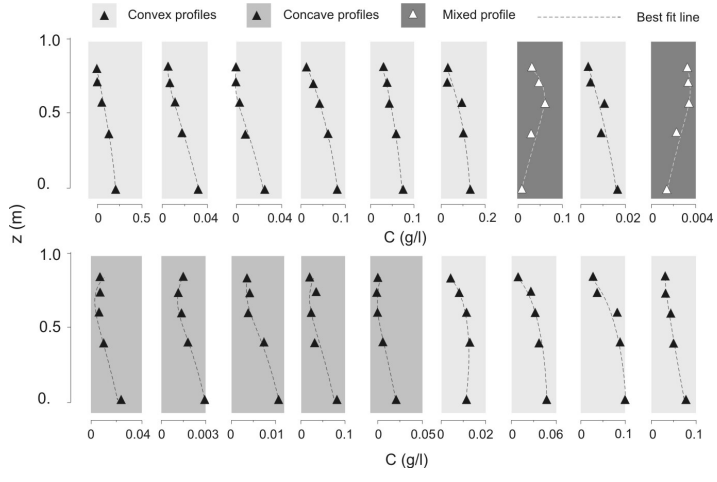

Fig. 3. All *C-Profiles* measured by STs in Cases 1 to 3 with a best-fit line

The shape of *C-Profiles* in Fig. 3 exhibit a good degree of consistency at locations across the surf zone. The principal exceptions to this concern *C-Profiles* measured inshore from the main region of breaking waves in the deepest locations between the shore and the first bar. Here *C-Profiles* show sediment concentrations initially increasing from the bed to approximately 0.5 m and thereafter declining in the expected way. It is thought that at these locations, sediment entrained by breaking waves over the bars is swept into the trough region where wave resuspension is less effective, and where the longshore current is only competent to transport sediment already in suspension. A combination of suppressed sediment entrainment at the bed and the periodic supply of suspended material from above may have resulted in these distorted *C-Profiles*. The exact mechanism remains the subject of further investigation.

A comparison shown in Fig. 4 between all measured *C-Profiles* and *C-Profiles* predicted by Eq. 9 in the range 0.1 m < z < 1 m generally shows good agreement (typically, R^2 = 0.85 or better). Here ST values exhibiting the largest degree of scatter are shown using gray squares. These data values show no systematic trend and are thought to reflect both

the inherent inaccuracy of the ST sampling devices and natural variability of suspended sediment behavior in the surf zone. A reduction in predicted C values by around 4 orders of magnitude between Ca and C at $z = 0.5$ m is typical. Although there is no independent way of verifying the validity of predicted Ca values, the reduction of C with z is predicted independently of the measured *C-Profiles* and thus support the view that predicted Ca values are realistic. As expected from results in Fig. 3, Fig. 4 shows also that some measured *C-Profiles* do not conform to expected behavior. If this was attributable simply to measurement errors, one would expect such profiles to be found at locations other than in the tough behind the inner bar. This is not the case and thus their properties must be considered if a more refined analysis of cross-shore suspended sediment distributions is to be attempted.

The selected model results for cases 1 to 3 in Fig. 5 depict a complicated, but consistent picture of suspended sediment in the surf zone. $H(x)$, $U_L(x)$ and $U_W(x)$ distributions in Fig. 5b shows some modulation of these parameters due to the barred topography of the surf zone (Fig. 5a). Taking into account the various hydrodynamic roughness components described above, including predicted bedforms shown in Fig. 5d, the resulting cross-shore distributions of U_{*mean} and U_{*max} in W+C conditions are shown in Fig. 5c. The bottom 3 panels (Fig. 5e) show predicted $Q(x)$ from the present model and $Q_T(x)$, $Q_S(x)$ and $Q_B(x)$ derived from Eq. 15. In general there is broad agreement between the present model $Q_T(x)$ and $Q_S(x)$. Predictions indicate that $Q_B(x)$ makes only a relatively small contribution to $Q_T(x)$. This might be expected in the present conditions where the longshore current in not greatly in excess of the entrainment threshold, and sediment dynamics are dominated by wave resuspension. Both Case 1 and 3 exhibit similar characteristics with maximum LST predicted between the inner trough and the swash zone, thus reflecting surf zone bathymetry.

In Case 2, wave conditions allowed ST measurements to be obtained at a greater distance from the shoreline. In this case the influence of the second bar is evident and gives rise to two peaks in LST rate, both in the zone displaced shoreward from the outer and inner bar trough regions. In Case 2 we also see less agreement between $Q(x)$ from the present model and $Q_T(x)$ and $Q_S(x)$ predicted by Eq. 15. Reductions in predicted η values correspond to higher shear stresses over the bars and lead to a predicted reduction in bed roughness at suspended sediment. In contrast Eq. 15 utilizes a constant drag coefficient and thus remains unresponsive to possible changes in bed roughness associated with changing hydrodynamic conditions. In this case, peak $Q_T(x)$ and $Q_S(x)$ are correlated with the approximate cross-shore location of maximum U_w and U_L values. The small second peaks in Q_T and Q_S values close to the shore are thought to be an artifact of the imposed $H(x)$ and $U_L(X)$ profiles.

Fig. 6 shows measured and predicted *C-Profiles* from the locations indicated on three upper panels in Fig. 5. Good agreement is shown in all cases supporting the view that the present model is providing reliable predictions of the sediment concentration field across the surf zone.

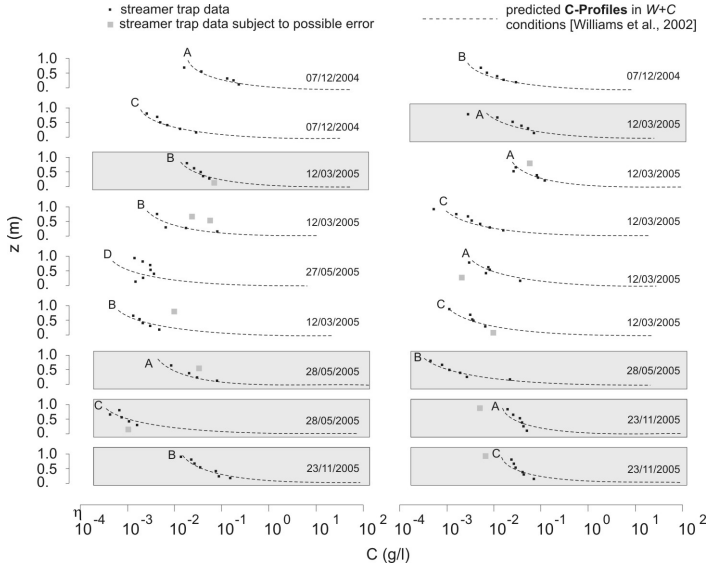

Fig. 4 Comparisons between measured and predicted *C-Profiles* (Eq. 9) for all measured ST profiles. Test cases 1 to 3 are highlighted in gray.

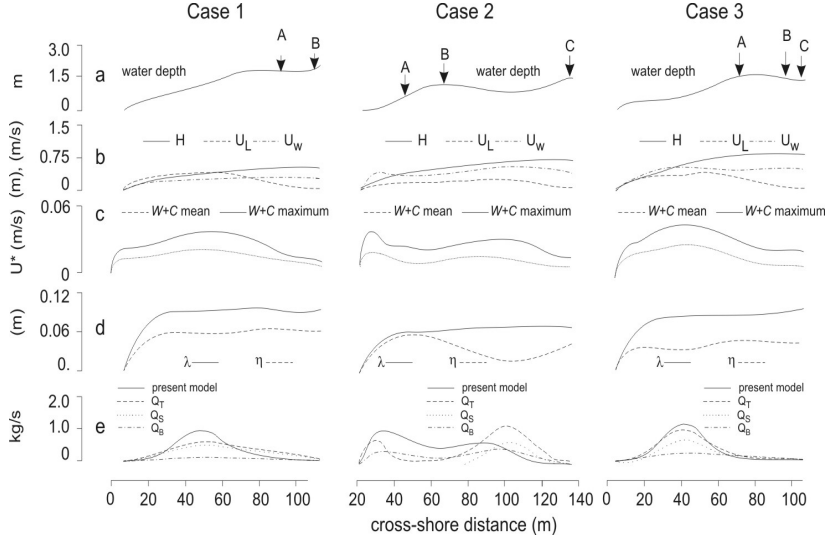

Fig. 5 Predicted ripples morphology, $Q_T(x)$, $Q_S(x)$ and $Q_B(x)$ values and associated hydrodynamic forcing across the surf zone for test cases 1 to 3.

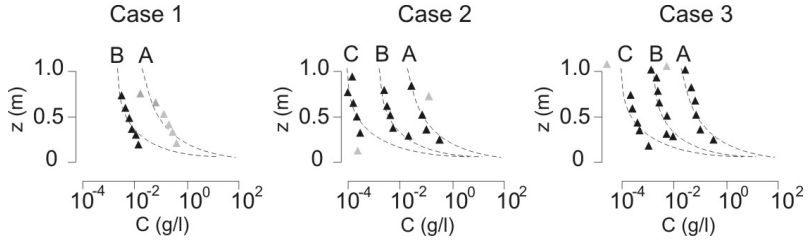

Fig. 6 Measured and predicted *C-Profiles* across the surf zone for test cases 1 to 3.

Table 2. Predicted LST rates across the surf zone for Cases 1 to 3, Cassino, RS, Brazil

Case	Date	CERC	K_{91}	Q_T	Q_S	Q_B	$Q_{Present}$
1	12/03/2005	11.09	11.55	12.50	10.49	2.01	10.19
2	28/05/2005	5.11	5.06	4.09	0.93	3.16	4.83
3	23/10/2005	26.03	10.98	13.55	8.64	4.91	12.69

Table 2 summarises predicted values of the total flux, Q_T, from the CERC, Kamphius (1991) and Soulsby (1997) formulae, and from the present model. It shows also the integrated values for Qs and QB predicted by the Soulsby (1997) formula. The largest discrepancy (a factor of approximately two) is found between CERC and present model predictions for case 3.

CONCLUSIONS

New measurements of *C-Profiles* have been obtained across a barred surf zone and add to the body of published field data pertaining to longshore sediment transport. The ability of the present model to predict with reasonable accuracy *C-Profiles* at a number of different cross-shore locations has been verified with field data. Although shear velocity values and bedform dimension obtained from imposed hydrodynamic gradients across the model domain are at best approximations and may not be accurate across the whole model domain, the use of more advanced approaches cannot be supported by the present sparse field data. Although not presented in the paper, model sensitivity studies showed that predicted *C-Profiles* and estimates of the total LST were very sensitive to subtle changes in bed roughness.

The present model is based on formulae primarily developed for wave-only, uni-directional flows or weakly interacting W+C situations. It is therefore interesting to find that even in the complex hydrodynamics of the surf zone, the relationships they define between the applied bed shear stress and sediment mobility remain reasonably robust and the predicted rate of sediment transported across the width of the surf zone by a longshore current is in fair agreement with some well-established bulk formulae. With this in mind it may now be possible with further refinements to investigate the temporal and spatial behavior of LST and thereby improve our present ability to predict accurately LST over extended periods of time.

ACKNOWLEDGEMENTS

The authors gratefully acknowledge the help of Raphael Pinotti in the field work and the technicians Neuza and Glória from the Laboratório de Oceanografia Geológica (LOG/FURG) for their assistance with the sieving of samples.

REFERENCES

Bell P. S., Williams J. J., Clark S., Morris B. D. and Vila-Concejo A. (2004). "Nested Radar Systems for Remote Coastal Observations", *J. Coastal Res*., Special Issue 39, 5pp, (in press).

Dean R. G., Berek E. P., Gable C. G. and Seymour R. J. (1983). "Longshore sediment transport determined by an efficient trap". *Proc. 18th Coastal Eng. Conf.*, ASCE, 954-967.

Deigaard, R., Justesen, P., and Fredsøe, J. (1991). "Modeling of Undertow by a One equation Turbulence Model", *Coastal. Engineering*, 15, 431-458.

Esteves, L. S., Williams, J. J., Lisniowski, M. A. & Perotto, H. (2007). "Measured cross-shore and vertical variations in grain size, sorting and composition in suspended sediments transported alongshore". *International Coastal Symposium*, April 16-20, 2007. Queensland, Australia. Publication in a special issue of *Journal of Coastal Research* (in press).

Fredsøe J. (1984). "Turbulent boundary layer in wave-current motion". *J. Hydraul. Eng*., ASCE, 110, 1103-1120.

Garcez Faria A. F., Thornton E. B., Stanton T. P., Soares C. V. and Lippmann T. C. (1998). "Vertical profiles of longshore currents and related bed shear stress and bottom roughness." *J. Geophys. Res*, 103, C2, 3217–3232.

Grant, W. D. & Madsen O. S., (1982). "Movable bed roughness in unsteady oscillatory flow". *J. Geophys. Res*., 87, 469-481.

Greer M. N. and Madsen O. S. (1979). "Longshore sediment transport data: a review". *Proc. 16th Coastal Eng*. Conf., ASCE, 1563-1576.

Kamphuis, J. W. (1991). "Alongshore sediment transport rate", *J.Waterways, Port, Coastal and Ocean Eng*., ASCE, 117(6), 624-641.

Komar, P.D. (1988). "Environmental Controls on Littoral Sand Transport", *21st Int. Coastal Engr. Conf.*, *ASCE,* pp 1238-1252.

Kraus N. C. (1987). "Application of portable traps for obtaining point measurements of sediment transport rates in the surf zone". *J. of Coastal Research*, 3(2), 139 -151

Nielsen P. (1992). "*Coastal bottom boundary layer and sediment transport"*. World Scientific Publishing Co., River Edge, N.J., USA.

Raudkivi, A. J. (1990). "*Loose boundary hydraulics"*, 3rd edition, Pergamon Press, Oxford.

Reniers A. J. H. M. & Battjes J. A. (1997). "A laboratory study of longshore currents over barred and non-barred beaches", *Coastal Engineering*, 30(1-2), 1-21

Soulsby R. L., Hamm L., Klopman G., Myrhaug D., Simons R. R. & Thomas G. P. (1993). "Wave-current interaction within and outside the bottom boundary layer". *Coastal Engineering*, 21, 41-69.

Soulsby R. L. (1997). "*Dynamics of marine sands"*, Thomas Telford Publications, 249pp.

Swart D. H. (1974) "Offshore sediment transport and equilibrium beach profiles". *Delft Hydraulic Lab Publication,* No. 131.

Wang P., Ebersole B. A., Smith E. R and Johnson B. D. (2002). "Temporal and spatial variations of surf-zone currents and suspended sediment concentration", *Coastal Engineering*, 46, 175–211.

Williams J. J., Rose C. P., Thorne P. D., O'Connor B. A., Humphery J. D., Hardcastle P. J., Moores S. P., Cooke J. A. and Wilson D. J., (1999). "Field observations and predictions of bed shear stresses and vertical suspended sediment concentration profiles in wave-current conditions". *Cont. Shelf Res*, 19(4), 507-536.

Williams J. J., Esteves, L. S., Thornton, E. B. & Plant, N., (2007). "Relationships between cross-shore wave transformation, longshore currents, and suspended sediments in the surf zone on a barred beach". *J. Geophysical Research*, in preparation.

Zyserman J. A. and Fredsøe J. (1994). "Data analysis of bed concentration of sediment". *J. Hydraul. Eng*., 120 (9), 1021-1042.

Appendix 1
Calculation of bedforms.

In the Grant and Madsen (1982) approach for wave Shields parameter, θ_w , values $\leq \theta_{crit}$

$$\eta = \lambda = 0.$$

For $\theta_w < \theta_{crit} \leq \theta_B$

$$\eta = 0.22(\theta_w/\theta_{crit})^{-0.16} A$$

$$\lambda = \eta / \left[0.16(\theta_w/\theta_{crit})^{-0.04}\right], \text{ and}$$

for $\theta_w > \theta_B$

$$\eta = 0.48\left(D_*^{1.5}/4\right)^{0.8}(\theta_w/\theta_{crit})^{-1.5} A$$

$$\lambda = \eta / \left[0.28\left(D_*^{1.5}/4\right)^{0.6}(\theta_w/\theta_{crit})^{-1.0}\right]$$

Here the ripple scaling shields parameter, $\theta_B = 1.8\theta_{crit}\left(D_*^{1.5}/4\right)^{0.6}$.

INFRAGRAVITY WAVES IN MOBILE-BED LABORATORY EXPERIMENTS

Florent Grasso, Hervé Michallet, Eric Barthélemy

Laboratoire des Ecoulements Géophysiques et Industriels (CNRS – UJF – INPG),
BP53, 38041 Grenoble Cedex 9, France.
florent.grasso@hmg.inpg.fr.
herve.michallet@hmg.inpg.fr.
eric.barthelemy@hmg.inpg.fr.

Abstract: Experiments were carried out in a flume 36 m long and 55 cm wide equipped with a piston wave generator. The sloping bottom consists of a loose material of low density (1.19 kg L^{-1}) with a median diameter d_{50}=0.6 mm in order that Shields and Rouse numbers are of the same magnitude as those of natural environments. Irregular waves are generated according to a JONSWAP spectrum. The waves are measured along the flume and bottom profiles are recorded in between repeated wave sequences. The infragravity modes amplitudes along the flumeare obtained for different wave climates. The correlation between the incident short wave envelope and the infragravity waves clearly indicates that the latter is the consequence of both a break point and a bound long wave release mechanisms.

INTRODUCTION

Field measurements indicate that waves in the infragravity range play a role on beach morphology. The generation of such long period waves can be explained by two different mechanisms. On one hand the breaking is thought to release bound long waves due to wave grouping (Longuet-Higgins & Stewart, 1962). On the other hand wave grouping produces a break point and set-up oscillation that acts as a piston at the wave group period (Symonds *et al.*, 1982). In both cases these incident long period waves reflect on the beach face, interfere with the incident waves to produce long period standing waves known as surf-beats.

Recently, Wang *et al.* (2002) performed velocity and concentration measurements over a beach that was shaped by breaking irregular waves in laboratory flume. A similar topography was obtained in a wave flume and allowed turbulent measurements in the surf zone suspension by Hurther *et al*. (2007). They also observed sediment suspension

concentrations fluctuations at the frequency of a free standing wave. Such laboratory experiments in wave tanks with beaches made of loose material are rare (Dette *et al.*, 2002). Most experimental studies were performed with a rigid bottom topography. Janssen *et al*. (2003) evaluated the long waves generation for a mild slope topography (1:70) molded in sand with a smooth concrete surface. They concluded that the mechanism of bound wave release is dominant. Baldock and Huntley (2002) and Baldock *et al*. (2004) observed breaking forced waves for a steeper uniform slope (1:10) and a barred beach profile. Moreover, the maximum long wave radiation occurs when the mean breakpoint closely coincides with a nodal point of the free standing long wave. The aim of the present paper is to investigate the characteristics of such surf-beats in small-scale mobile bed experiments. We will evaluate their relation to the bottom profile under controlled conditions. More specifically we will compare surf-beat characteristics for a beach at equilibrium and a barred beach in evolution.

EXPERIMENTAL SET-UP

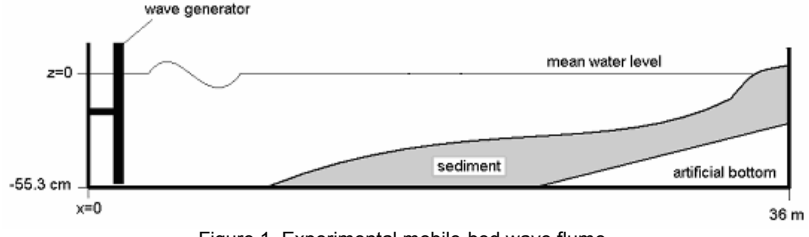

Figure 1. Experimental mobile-bed wave flume.

Our experiments were carried out in a flume 36 m long and 55 cm wide equipped with a piston wave generator (Figure 1). The still water depth is 55.3 cm. The mean overall slope is approximately 1:40. The sloping bottom consists of a loose material of low density (1.19 g cm^{-3}) with a median diameter d_{50}=0.6 mm. In the experiments, the Froude number, the Shields number in the shoaling part and the Rouse number in the breaking zone (ratio of turbulent agitation to the settling velocity of the sediment) are of the same magnitude as those of natural environments. Time and length scales are roughly 1/3 and 1/10. Irregular waves are generated according to a JONSWAP spectrum (peak enhancement factor γ=3.3). For each simulation, we check that these waves conform to the expected spectrum and that they follow a Rayleigh distribution at 2 m downstream of the wave maker. Twelve wave gages mounted on trolleys measure instantaneous water elevations. Records are at least 30 mn long in order to achieve statistical convergence. Bottom profiles are recorded in between wave series.

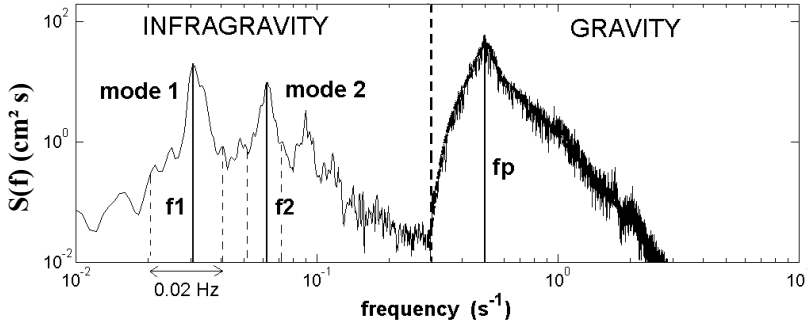

Figure 2. Surface elevation energy spectrum at x=2 m in the flume on the equilibrium beach plotted in Figure 3d (–). Wave parameters: H_{rms0}=7.5 cm, f_p=0.5 Hz, h_0=55.3 cm. First infragravity frequency peak f_1=0.03 Hz.

Spectral estimates *S(f)* were obtained from Fourier transforms of five 50% overlapping data segments, each comprising 32768 points sampled at 50 Hz. A wave spectrum measured at x = 2 m is plotted in Figure 2. Frequencies above $3/5\times f_p$, correspond to the generated JONSWAP spectrum and fall in the "gravity" domain. The generation of low frequency waves – resulting of gravity waves breaking – is clearly visible in the spectral power density below $3/5\times f_p$ (this is the "infragravity" domain). A closer inspection of the low frequency range shows a broad peak at a frequency f_1 around 0.03 Hz. The first harmonic (f_2) of this peak is also clearly visible. The amplitude of the long wave motion associated with both frequencies is evaluated by estimating the energy contained in finite frequency bands of 0.02 Hz centred on peak frequencies. We choose a 0.02 Hz band cutting in order to include the main energy part of the considered peaks.

LONG WAVES STRUCTURE

Comparison for equilibrium profile, transient profile and theory

A wave climate characterized by its peak frequency (f_p=0.5 Hz) and the root mean square wave height at 2 m downstream the wave maker (H_{rms0}=7.1 cm) was run for several tens of hours. Evolutions of H_{rms} and infragravity modes amplitudes (H_{ig}) along the flume are plotted in Figure 3 for two different bottom profiles. These (plotted in Figure 3d) correspond to two different stages. One is a transient stage characterized by a bar that travels onshore at about 1 m/h. This profile shows interesting similarity with the rigid bottom profile in the experiments of Baldock *et al*. (2004). The other profile is at equilibrium in the sense that it changes very little (at plotting precision) over several hours. Note that the barred profile data is more scattered than the equilibrium profile data. The bottom changes between two sets of measurements are not entirely negligible in this case.

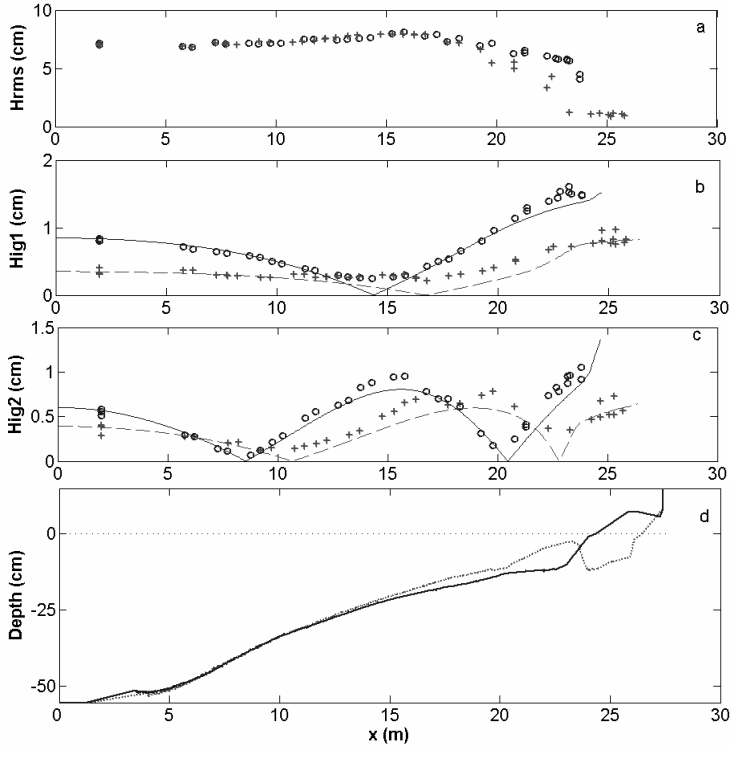

Figure 3. Wave and bottom characteristics along the flume axis for equilibrium profile (o) and transient profile (+): a) root mean square wave height, b) First mode infragravity wave amplitude, c) Second mode infragravity wave amplitude and d) equilibrium bottom profile (–) and transient bottom profile (--).

The infragravity wave energy is plotted in terms of significant amplitude in Figure 3b-c. The first mode amplitude (H_{ig1}) is maximum at the berm, minimum close to x=15 m and large again close to the wave maker. This indicates that a low frequency standing wave with a node somewhere around x=15 m is generated in the flume. Despite the fact that the equilibrium profile is far from being a plane beach, the Wilson formula for a uninodal seiche in a rectangular flume with a plane beach reported by Dean and Dalrymple (1984, p.149) gives a very good estimate of f_1 (*i.e.* 0.03 Hz). In addition, the data are compared with an analytical solution for small amplitude free standing long wave of the linearized Saint-Venant equations (plotted in Figure 3b-c as a solid line for equilibrium profile and a dashed line for the transient profile). The solution yields the modes frequencies, the nodal structure and normalized amplitudes. The overall agreement of the nodal structure is good and the peak frequencies are remarkably well

predicted (*i.e.* f_1=0.031 Hz and f_2=0.063 Hz for the equilibrium profile and f_1=0.024 Hz and f_2=0.047 Hz for the transient profile).

We note on Figure 3b-c that the infragravity significant amplitudes are clearly more important for the equilibrium bottom profile. This difference may be firstly explained by the steep bar of the transient bottom profile, causing a partial waves reflection and decreasing the resonance phenomenon along the flume. . Besides, we note an important decrease of H_{rms} in Figure 3a for the transient profile (+), it corresponds to a large dissipation. Nevertheless this energy is not transferred in the infragravity domain. Figure 4 shows the mean set-up measured for the equilibrium and transient profiles. The waves breaking localised on the bar seems to enhance the time-varying breakpoint mechanism and reinforce the set-up. The energy contained in the set-up could be dissipated through an enhanced undertow current. We emphasize that those observations are only possible in our special configuration of mobile-bed experiments.

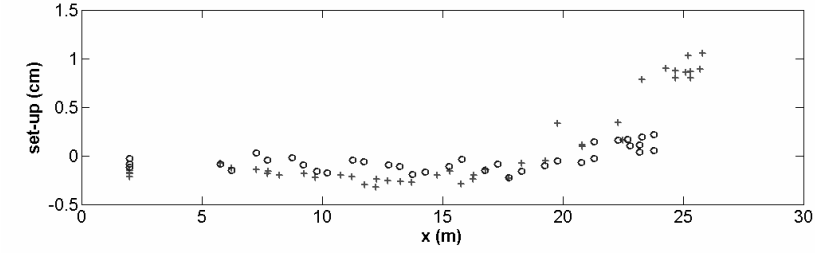

Figure 4. Mean water level along the flume axis for equilibrium profile (o) and transient profile (+) plotted in Figure 3d.

Our results in the barred case exhibit the same features, in terms of long waves amplitudes and node positions, as the results of Baldock *et al*. (2004). Their experiments were performed on a rigid bottom with a barred shape. The generated waves are similar (H_{rms0}=5 cm; 7.5 cm and 10 cm, for f_p=0.6 Hz) to our case, but the mean slope (1:10) is steeper than our transient profile mean slope (1:35). By changing the incoming wave amplitude, they might conclude that a maximum long wave radiation occurs when the mean breakpoint closely coincides with the nodal point of the long wave. In our experiments, the long waves are more energetic on the equilibrium bottom profile for which the breaking point and first mode node position are a few meters apart.

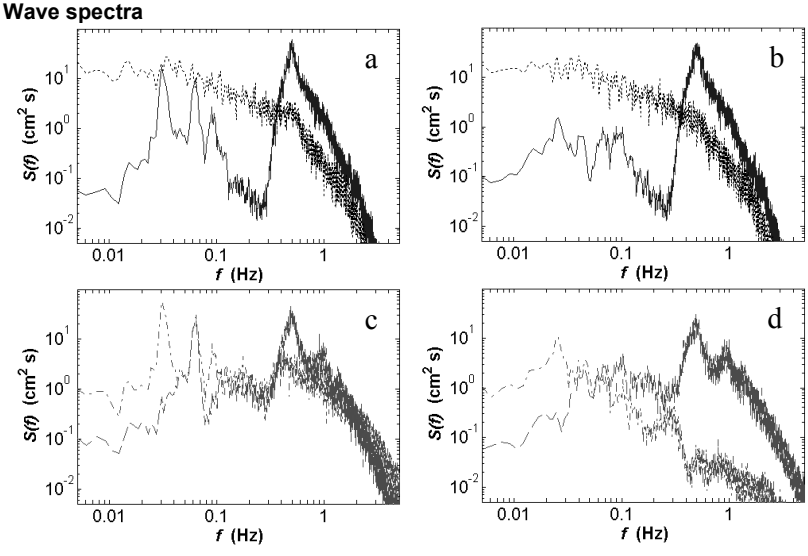

Figure 5. Total wave energy spectra at x = 2 m (—), x = 15.3 m (– –), x = 23.3 m (- . -) and spectrum of the short wave envelope at x = 2 m (.....); for an equilibrium bottom profile (a,c); for a transient bottom profile (b,d).

Surface elevation energy spectra for the two different topographies are plotted in Figure 5.They are presented for three positions along the flume that correspond to the deep region, the breaking region and close to shoreline. The location of the breaking region (maximum of H_{rms} in Figure 3a) is close to the node of the first mode (Figure 3b) and the anti-node of the second mode (Figure 3c). The spectra confirm that the energy in the infragravity domain is a lot larger and the peaks more clearly defined in the case of the equilibrium profile. In the case of the transient profile, we may note that the energy in the gravity domain is very low close to shoreline. Indeed, the short waves have dissipated almost all their energy passing the bar, as indicated by the estimate of H_{rms} for x>23 m in Figure 3a.

In addition, the spectrum of the short wave envelope, obtained via a Hilbert transform of the measured surface elevation data, is plotted in dotted line in Figure 5a,b. This does not account for real energy in surface elevation but as energy possibly contained in the wave packets that could be released in the breaking region. It is important to emphasize that there is no dominant frequency in the wave grouping. This confirms that the frequency peaks of the infragravity waves depend on the beach profile only.

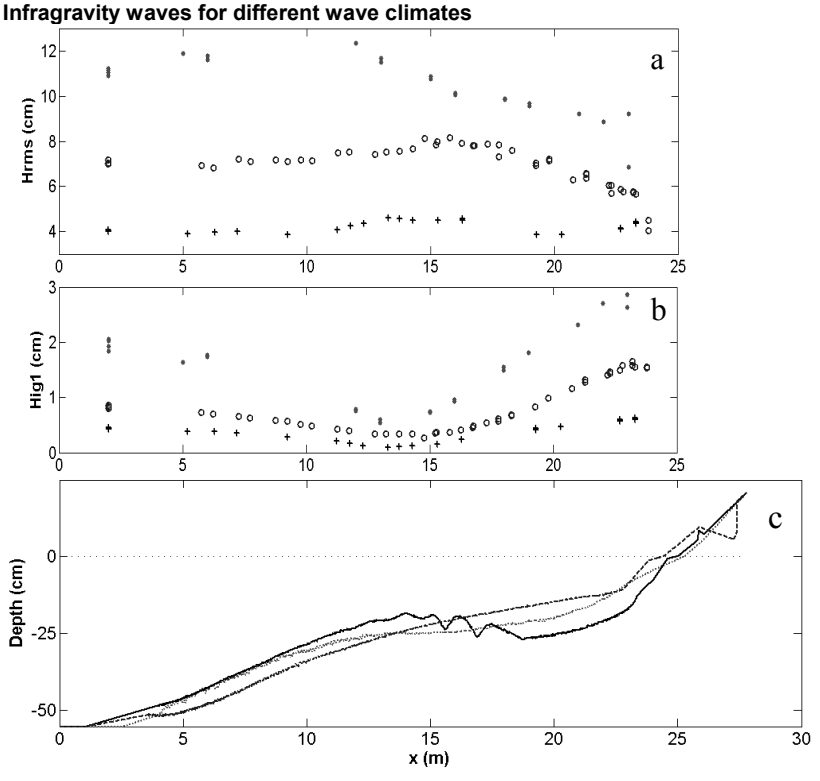

Figure 6. a) Root mean square wave height, b) First mode infragravity wave amplitude and c) bottom profile, for different wave climate: (• ; ...) H_{rms}=11.1 cm, f_p=0.33 Hz; (o ; --) H_{rms}=7.1 cm, f_p=0.5 Hz and (+ ; —) H_{rms}=4 cm, f_p=0.5 Hz.

Different wave climates were generated (varying H_{rms} and peak frequency f_p), that reproduce storms, mild summer climates and very gentle climates. The Figure 6 synthesises the H_{rms} and H_{ig1} data for these three different climates. We note that incident short waves have a direct influence on the long waves amplitude. H_{ig1} is clearly more important for the storm type of climate (•). The maximum of the H_{rms} corresponds to the beginning of the wave breaking location and its decrease is linked to the wave energy dissipation. We observe in Figure 6 a clear distinction between break point positions of the different climates: 12 m for H_{rms}=11.1 cm (.); 16 m for H_{rms}=7.1 cm (o) and 24 m for H_{rms}=4 cm (+). In contrast, the first mode infragravity node position is almost the same in the three cases (13-14 m). Note that the bottom profiles corresponding to the three wave climates are similar in term of length (from the wave-maker to the shoreline) (Figure 6c). We can conclude that the long wave structure mainly depends on the beach morphology rather on the generated wave characteristics.

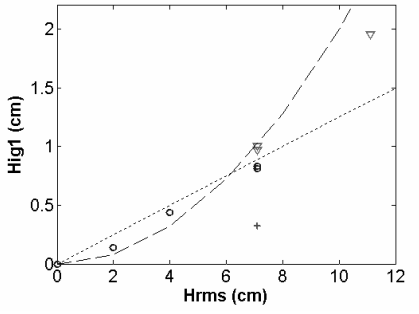

Figure 7. First mode infragravity wave amplitude versus root mean square wave height for different wave climates. (o) equilibrium bottom profile; (▽) quasi-equilibrium bottom profile; (+) transient bottom profile. Linear approximation (…) and quadratic approximation (--).

The first mode infragravity wave amplitudes for different wave climates are plotted on Figure 7 and classified in three categories that depend on the corresponding bottom profile evolution speed. This is estimated by the vertical evolution of the bottom profile ($z(x)$), averaged along the flume, during a time lap ($\Delta t = t_{i+1} - t_i$):

$$V = \frac{\int_{i=1}^{L_{flume}} |z_{i+1} - z_i| dx}{L_{flume} \times \Delta t}. \quad (1)$$

We define that an evolution speed V less than 1.5 mm/h corresponds to an "equilibrium" bottom profile (o); V between 1.5 mm/h and 4 mm/ h is related to a "quasi-equilibrium" (▽) and a "transient" bottom profile is for an evolution speed V larger than 4 mm/h (+). We note again that for a same wave climate (H_{rms}=7.1 cm) the value of H_{ig1} is twice smaller for a transient bottom profile (the cross in Figure 8) compared to equilibrium conditions. The dependency of H_{ig1} to H_{rms} should characterize the long wave generation mechanism. A quadratic relation would correspond to the bound waves release, whereas a linear relation would characterize the break point oscillation mechanism (Baldock & Huntley, 2002). According to the experiments performed by Baldock *et al.* (2004) on a barred rigid bottom (slope 1:10), long waves are shown to be linearly dependent on the incident short wave amplitude both offshore and shoreward of the breakpoint at all frequencies. In our case, the number of different wave climates simulated is too weak to determine a clear tendency in Figure 7

LONG WAVE MOTION CORRELATION WITH THE SHORT WAVE ENVELOPE

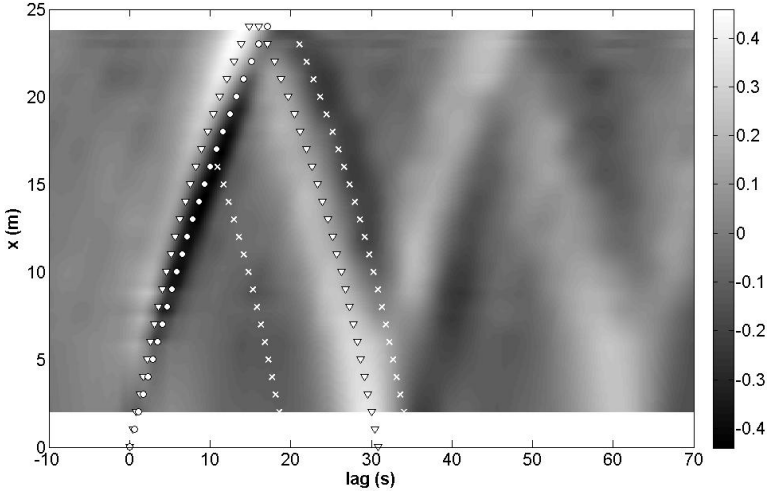

Figure 8. Cross-correlation between the infragravity waves and the short wave envelope at x=2 m, equilibrium bottom profile. Group celerity (for f_p=0.5 Hz): (o); phase celerity (= $\sqrt{gh}$) for positive correlation (▽) and negative correlation (x).

Figure 8 shows the cross-correlation between the short wave envelope in the constant depth region of the flume (x=2 m) and the total low pass filtered surface motion (f<0.3 Hz) along the flume axis. The high spatial resolution of the experimental data allows, using an interpolation function, a presentation of the sequence of correlation functions as quasi-continuous in space. A black ridge corresponds to a negative correlation and a white ridge represents a positive correlation. There is a negative correlation for lags close to zero at x=2 m. This corresponds to the locally forced incident bound long wave, which is out of phase with the short wave envelope (Longuet-Higgins & Stewart, 1962). This black ridge matches the phase-plane trajectory at the group celerity (represented by circular markers on Figure 8). The lag is increasing and the correlation becomes stronger further shoreward as the bound wave amplitude increases due to the shoaling of the short wave and represents a larger proportion of the total long wave energy (at $\tau\approx$10 s and x=15 m). This bound wave is released during breaking and still negatively correlated to the wave envelope at lags $\tau\approx$18 s at x=2 m and $\tau\approx$20 s at x=23 m. The free waves resulting of the bound wave released move to the phase celerity, which is equal to $\sqrt{gh}$ in shallow water (cross markers). We may discern a light black ridge under the white crosses which may correspond to the free wave released close to x=15 m at $\tau\approx$10 s, moving offshore to reach x=2 m at $\tau\approx$18 s.

On the other hand, a positive correlation is present for $\tau \approx 2$ s at x=5 m. It may correspond to a dynamic set-up generated by the breaking of the larger wave packets. The correlation becomes very strong at the shoreline ($\tau \approx 13$ s). We notice that the triangle markers (celerity $\sqrt{gh}$) match the white ridge from $\tau \approx 2$ s to $\tau \approx 16$ s. This is in agreement with Symonds *et al.* (1982) who showed that the long waves generated by breakpoint oscillations propagate freely at the phase celerity. The position and intensity representations of long waves peaks can be distorted due to the overlapping between the long wave resulting of breakpoint oscillations (positive correlation) and the bound long wave released (negative correlation).

Next, the long waves are reflected and propagate offshore (from x=24.5 m to 0) as seen on the correlation signature: a white ridge from $\tau \approx 17$ s to 31 s; and a black ridge from $\tau \approx 21$ s to 35 s. According to the theory, the reflected long waves travel at the phase celerity (plotted with triangle and cross markers). At larger lags, both negative and positive correlation peaks are still present but damped. This indicates that the long waves reflect on both ends of the flume but are not amplified. We recall that Janssen *et al*. (2003) concluded that the bound wave release in their mild slopes laboratory experiments (~1:70) was dominant, while Baldock *et al*. (2004) observed breaking point forced waves for stronger slopes (~1:10). Both mechanisms are clearly observed in our case of an equilibrium beach profile (~1:45).

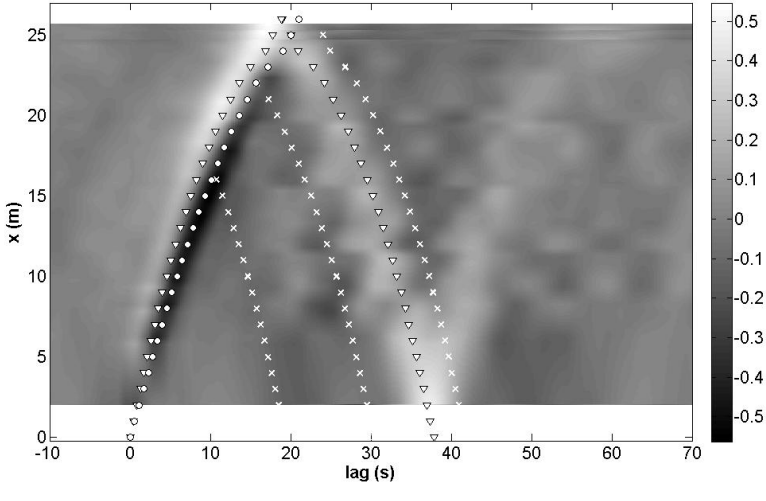

Figure 9. Cross-correlation between the infragravity waves and the short wave envelope at x=2 m, transient bottom profile. Group celerity (for f_p=0.5 Hz): (o); phase celerity (= $\sqrt{gh}$) for positive correlation (▽) and negative correlation (x).

For the transient bottom profile, the correlation picture shown in Figure 9 is in marked contrast. After reflection the correlation peaks have weaker values and we note a quicker and greater damping compared to the equilibrium case. The bound long wave signature (black ridge) is seen from $\tau \approx 0$ s at x=2 m to $\tau \approx 18$ s at x=23 m but not really at the shoreline (x=25.8 m). It may be due to reflection and dissipation of long waves over the bar positioned at x=23 m. We notice again that the bound long wave travels at the group celerity (circular markers).

Clearly, the dynamic set-up induces again a positive correlation (white ridge) evolving at phase celerity (triangle markers), starting for $\tau \approx 2$ s at x=5 m and becoming stronger close to $\tau \approx 18$ s at x=25.8 m. The break point mechanism is apparently dominant for this topography that is closer to Baldock *et al*. (2004)'s experiments. We also note that the bound long wave releases a free wave offshore at nearly $\tau \approx 12$ s and x=15 m (light black ridge under cross markers). We observe two negative correlations (under cross markers): from $\tau \approx 17$ s at x=23 m to $\tau \approx 30$ s at x=2 m; and from $\tau \approx 22$ s at x=25 m to $\tau \approx 38$ s at x=10 m. Those correspond to released bound long waves, partially reflected by the bar (x=23 m) and the berm (x=25.8 m). This probably leads to the weak correlation for larger time lags ($\tau > 60$ s). Bound wave release and breakpoint forcing do not reinforce the generation of the infragravity waves as for the equilibrium beach profile.

BEGINNING OF THE WAVE SEQUENCE

The presence of significant infragravity waves spectral peaks at the shoreline does not necessarily imply resonant amplification. The generated wave packets are not necessarily in phase with the radiated long waves since the incident short wave groups do not have a dominant frequency (as shown by the short waves envelope spectra in Figure 5). In that sense, seiching is not really stationary in the flume. To illustrate this point, we plot in Figure 10 the beginning of the wave sequence. In Figure 10a, the short wave packets in the deep region are visible. They induce a modulation of the mean level close to shoreline. Resulting low frequency motions are shown in Figure 10d. The main period of about 32 s, corresponding to f_1, is sometimes observed. For instance, at x=23.8 m, the peak for $t \approx 34$ s is enhanced for $t \approx 66$ s. In that case, a large waves packet has arrived in the breaking region in phase with the return of the generated long wave. This is not a general feature. The signature of a long wave is generally not seen after a couple of flume travel lengths. The main period of 32 s is not visible in the infragravity wave signal corresponding to the deep region for $t > 130$ s in Figure 10d. In that sense, we do not notice any amplification in the long wave generation process.

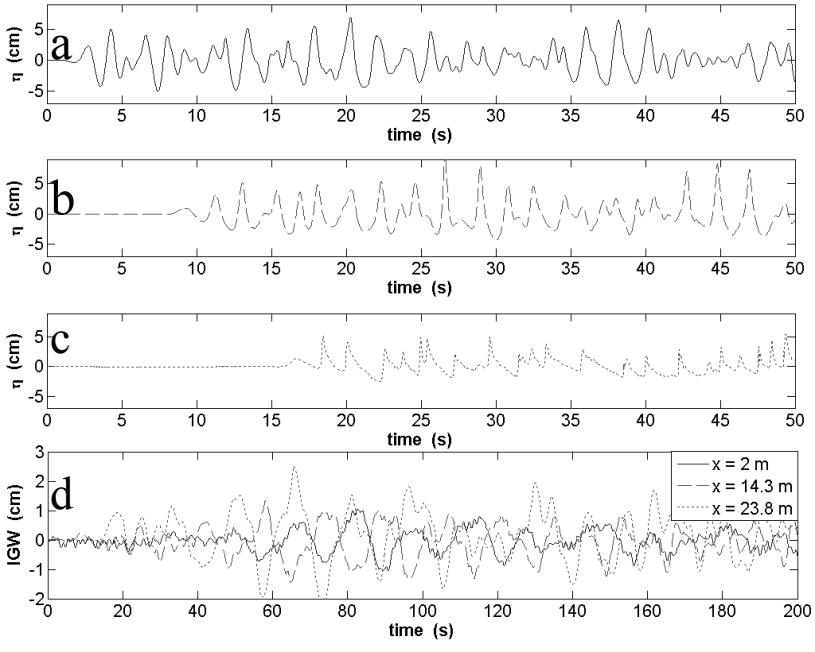

Figure 10. Surface elevation in the deep (a), breaking (b), shoreline (c) regions; and infragravity waves (d) for the equilibrium bottom profile.

CONCLUSION

The experiments show that the long wave structure strongly depends on the beach morphology rather than on the generated short wave characteristics. The nodal structure of the infragravity waves is determined by the beach shape that is, mainly the distance between the wave-maker and the shoreline.

Increasing the incoming wave amplitude increases the long wave amplitude but too few experiments were conducted for precisely determining a dependency in between linear and quadratic.

The experiments of Baldock et al. (2004) and Janssen et al. (2003) indicate that the breakpoint oscillation mechanism is prevailing and could be the result of a steep beach slope (~1:10), while the bound wave release mechanism could be dominant for a weak beach slope (~1:70). In our case, the loose bottom has a beach slope of about 1:40 and both mechanisms are clearly observed as shown by the correlation between the short waves envelope and the long waves.

The infragravity waves are more energetic on the equilibrium bottom profile compared to the transient barred profile. It is suggested that the beach topography evolves as to reinforce both the bound long wave release and the dynamic set-up generation.

ACKNOWLEDGEMENTS

This work has been partially funded by the CNRS-INSU PATOM and LITEAU II. The technical support of J.-M. Barnoud is gratefully acknowledged.

REFERENCES

BALDOCK, T.E.; O'HARE, T.J. and HUNTLEY, D.A., 2004. Long wave forcing on a barred beach, *J. Fluid Mech.*, 503, 321-343.

BALDOCK, T.E. and HUNTLEY, D.A., 2002. Long wave forcing by the breaking of random gravity waves on a beach, *Proc. R. Soc. Lond.*, A 458, 2177-2201.

DEAN, R.G. and DALRYMPLE, R.A., 1984. *Water Wave Mechanics for Engineers and Scientists*, World Scientific.

DETTE, H.H.; LARSON, M.; MURPHY, J.; NEWE, J.; PETERS, K.; RENIERS, A. and STEETZEL, H., 2002. Application of prototype flume tests for beach nourishment. *Coastal Eng.*, 47, 137–177.

HURTHER, D.; MICHALLET, H. and GONDRAN, X., 2007. Turbulent measurements in the surf zone suspension. *Journal of Coastal Research*, submitted.

JANSSEN, T.T.; BATTJES, J.A. and VAN DONGEREN, A.R., 2003. Observation of long waves induced by short wave groups, *J. Geophys. Res.,* 108, 3252-3264.

LONGUET-HIGGINS, M.S. and STEWART, R.W., 1962. Radiation stress and mass transport in gravity waves, with application to 'surf-beats', *J. Fluid Mech.*, 13, 481-504.

SYMONDS, G.; HUNTLEY, D.A. and BOWEN, A.J., 1982. Two dimensional surf beat: long wave generation by a time-varying break point, *J. Geophys. Res.*, 87(C1), 492-498.

WANG, P.; EBERSOLE, B.A.; SMITH, E.R. and JOHNSON, B.D., 2002. Temporal and spatial variations of surf-zone currents and suspended sediment concentration, *Coastal Eng.,* 46, 175-211.

LARGE-SCALE LABORATORY MODELING OF SUSPENDED SAND CONCENTRATION FLUCTUATIONS UNDER IRREGULAR WAVES

Joachim Grüne[1], Ruben Kos'yan[2], Hocine Oumeraci[3], Igor Podymov[4], Reinold Schmidt-Koppenhagen[5], Chris E. Vincent[6]

1. Coastal Research Centre FZK, Merkurstrasse 11, 30419 Hannover. Germany, gruene@fzk.uni-hannover.de
2. The Southern Branch of the P.P.Shirshov Institute of Oceanology, Russian Academy of Sciences. Gelendzhik-7, 353467 Russia. kosyan@coastdyn.ru
3. Coastal Research Centre FZK, Merkurstrasse 11, 30419 Hannover. Germany, office@fzk.uni-hannover.de
4. The Southern Branch of the P.P.Shirshov Institute of Oceanology, Russian Academy of Sciences. Gelendzhik-7, 353467 Russia. podymov@coastdyn.ru
5. Coastal Research Centre FZK, Merkurstrasse 11, 30419 Hannover. Germany, sk@fzk.uni-hannover.de
6. School of Environmental Sciences, University of East Anglia, Norwich NR4 7TJ, U.K. c.vincent@uea.ac.uk

Abstract: The paper describes large-scale laboratory experiments performed with simultaneous measurements of suspended sand concentrations, free surface elevations and three-component velocities (including turbulent fluctuations) at several levels above the sea bed. The data from these experiments are used to develop a more correct description of the contribution of vertical velocity to the convective sand flux and the relationships between fluctuations of turbulent kinetic energy and wave energy dissipation for the estimation of local sand suspending and advection to the temporal variation of suspended sediment concentration.

INTRODUCTION

In traditional models only the time averaged characteristics of water circulation, sediment and pollutant transport processes are considered, without taking into account the group structure of waves, their transformation within the coastal zone and contribution of phase shifts between sediments and the fluid at different frequencies of an irregular wave spectrum. Some advances have been achieved as a result of field research in the last years, which show that the group structure of waves and infragravity waves have considerable influence upon the sediment transport in the

zone of the wave transformation and breaking. Such investigations need to be continued with the emphasis on precise laboratory experiment using a broad range of parameters.

The hypothesis is that a physical model of temporal-spatial fluctuations of sand suspension and transport is possible on the basis of the mechanisms of convective suspension, determination of phase and amplitude ratios between the suspended sediment concentration (SSC), turbulent kinetic energy (TKE) and losses of wave energy due to wave breaking, allowing the estimation of the contribution of local convection, diffusion and advection of sediments to form the concentration field over rippled and plane beds.

Existing data allow neither the correct discrimination of the contribution of vertical velocity to the convective sand flux nor the relationships between fluctuations of turbulent kinetic energy and wave energy dissipation, to the estimation of local sand suspending and advection to the temporal variations of SSC (Kos'yan et al, 2001). Therefore in 2006 new large-scale laboratory experiments ("Hannover-2006") were performed in the LARGE WAVE CHANNEL (GWK) of the Coastal Research Centre (FZK) in Hannover. Simultaneous measurements of SSC, free surface elevations and three-component velocities (including turbulent fluctuations) were carried out at several levels above the sea bed.

LARGE – SCALE EXPERIMENTS

The physical simulation of dynamic processes in the coastal zone at prototype scale is extremely important to keep the similarity of both hydrodynamic and lithodynamic processes. The LARGE WAVE CHANNEL (GWK) of the Coastal Research Centre (FZK) in Hannover has a total length of 303 m, a width of 5 m, a total depth of 7 m and the maximum water depth is 5 m. For the experiments a sand bed was installed (Fig. 1). The wave generator is absorption controlled and allows waves up to 2 m depending of the local water depth along the channel. The measuring equipment used for the experiments consists of:

- Wave gauges (resistance wire type) for measurement of surface elevation along the wave channel (Fig.1)
- Optical turbidimeters for measurement of suspended sediment concentration at 4 different levels above the sea bottom (Fig. 2A);
- 3-component acoustic velocity sensors (type Vector) for measurement of wave induced currents at 2 different levels above sea bottom (Fig. 2 B);
- Sediment accumulators at different levels (Fig. 2E)

The analog sensor signals were sampled by a parallel 80-channel analog-to-digital converter (ADC) with a frequency of 40 Hz and recorded on a computer. A sample and hold modus guaranteed synchronization of all measured signals.

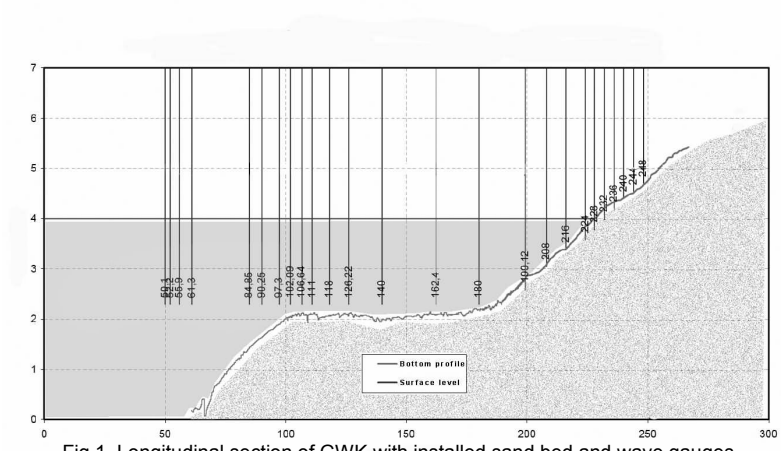

Fig.1. Longitudinal section of GWK with installed sand bed and wave gauges



Fig. 2. Installed turbidimeters, velocity sensors (Nortek-Vector) and sediment accumulators (left hand photo). Positioning of turbidimeters (upper right photo) and velocity sensors (Nortek-Vector) (lower right photo)

Two main test series were performed with respect to the simulated wave spectra:

- Irregular waves with spectra characteristics occurring at the Black Sea
- Irregular waves with artificial spectra where the peak periods were kept constant (Tp = 5 s) and the significant wave heights and spectral steepnesses were changed consecutively (H_{sig} = 0.9 to1.1m, wave spectrum steepness index γ =1.0 to 10.0).

RESULTS

In the following some first results from the ongoing analysis are described. In Fig. 3 examples of synchronously recorded time histories for some sensor signals are plotted. The time histories in Fig. 3 show the suspended sediment concentration fluctuations measured at distances of 7, 15, 25 and 40cm above sea bottom (1 – 4), the surface elevation H (5) and the wave induced velocities, where v_x is the horizontal cross-shore component (6) and v_y the vertical component (7).

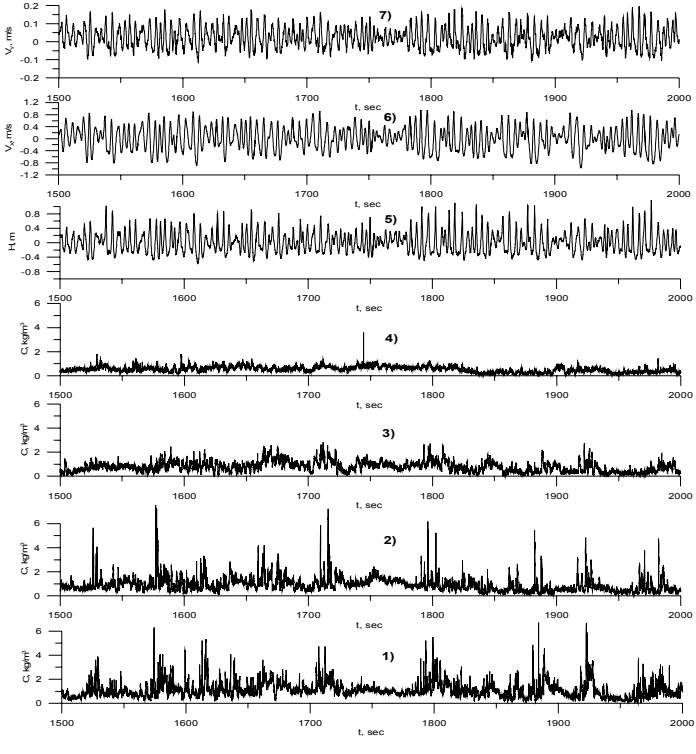

Fig. 3. Fragments of the recorded suspended sediment concentration fluctuations (turbidimeters 1-4 from 7, 15, 25, 40cm above sea bottom), the synchronous free surface elevation H (5) and the water velocities from the Vector sensor, where v_x is the cross-shore (6) and v_y the vertical component (7) of velocity.

The shapes of vertical profiles of suspended sediment concentration (some examples are shown in Fig. 4) vary quickly with time and deviate significantly from the mean values of suspended sediment concentration. When analyzing high-frequency fluctuations of vertical profile of suspended sediment concentration, several characteristic types of vertical concentration distribution were found as plotted in Fig. 5.

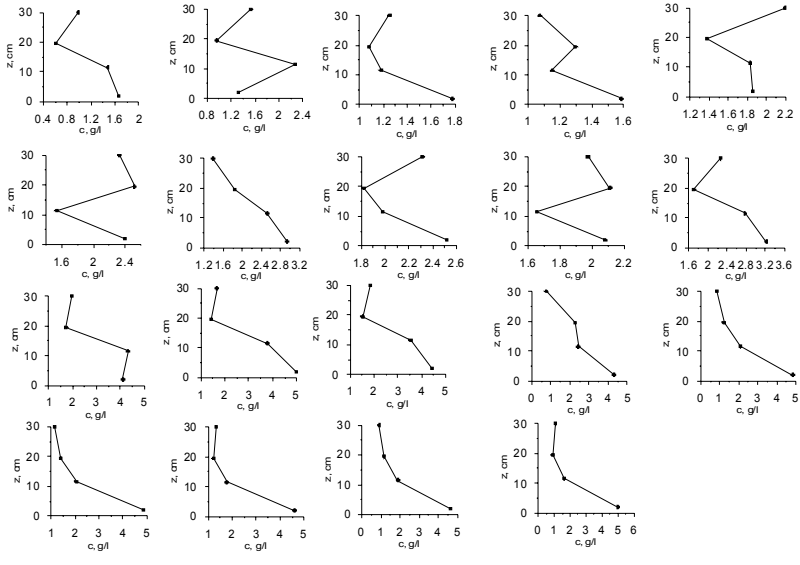

Fig. 4. High-frequency fluctuations of vertical profiles of suspended sediment concentration, each analyzed for a one second time segment from the time histories.

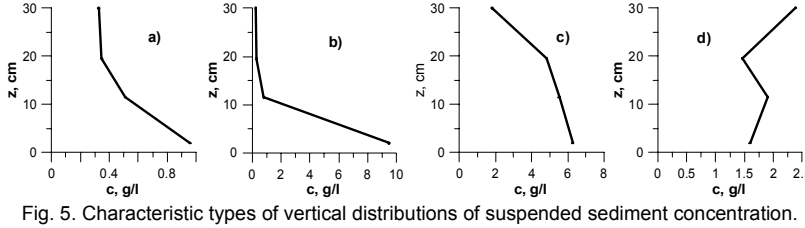

Fig. 5. Characteristic types of vertical distributions of suspended sediment concentration.

In general a vertical profile close to a logarithmic curve (Fig. 5a) is present under small waves between groups of large waves, when wave induced velocities are small and diffusion processes prevail in the formation of suspended sediment field. In the second case (Fig. 5b) high values of suspended sediment concentration are observed at the level of 4 cm over sea bed. They decrease sharply towards the surface. The

concentration gradient decreases by ~1g/l per cm in vertical height. Suspended sand is restricted to near-bottom layer and does not penetrate into higher layers. A third type of vertical concentration distribution (Fig. 5c) is observed during the passage of large waves or during wave collapse when the vertical profile is nearly linear. Sand suspended from the bottom can rise to heights of several tens of centimetres above the bottom with maximum vertical gradients of concentration 20-30 cm above the bottom.

Another type of vertical distribution is an irregular profile (Fig. 5d). Concentration of suspended sediment further away from the bottom layer may be higher than near to the bottom. Alternation of layers with high and low values of suspended sediment concentration is typical. Such vertical profiles of concentration prevail after the passage of high waves when a cloud of suspended sand separates from the bottom, is transported by the flow and gradually disperses and settles. In Fig. 6 a cloud of suspended sediments of about one second duration is shown between 307 and 308 on the time axis, which occurs under the wave trough at the distance of 15 cm from sea bed. At this moment there is no sand suspension from the bottom. Advection processes play a major role in formation of such a vertical distribution of sediments.

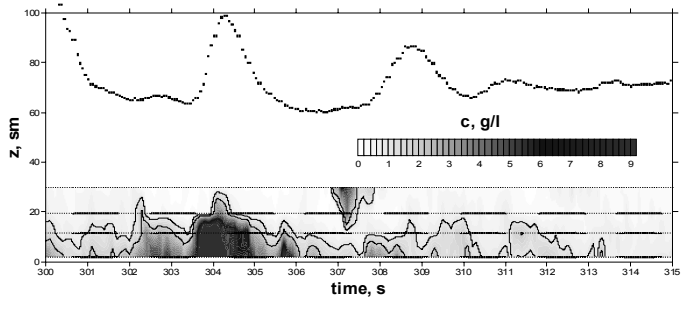

Fig.6. Chronogram of temporal fluctuations of the field of suspended sediment concentration and surface elevation

The analyzed data show that fluctuations of vertical distribution of suspended sediment concentration near the bottom is initiated by individual waves particularly under crests where water velocity is rather high. Penetration of clouds of suspended sand into the water column is not connected statistically with the passage of individual waves. In this case hydro-dynamical processes at the frequency of group waves and features of a group wave structure are determining factors. Thus, high-frequency fluctuations of the vertical distribution of suspended sediment concentration is determined both by the parameters of individual waves and by low-frequency characteristics of the waves. The fluctuations of the vertical profiles of SSC described in detail in Kos'yan et al. (2007).

A model of the fluctuations of suspended sand concentration above a flat bottom under waves with pronounced group structure was constructed and checked against the results of our laboratory experiments "HANNOVER-2006" and those of

"SISTEX'99" (Ribberink et al., 2000). Series of synchronous recording of suspended sediment concentration, components of water velocity and elevation of free surface of waves with group structure were selected for modeling and verification of the model. The model is based on one-dimensional diffusion equation for suspended sediment concentration

$$\frac{\partial C}{\partial t} = w_s \cdot \frac{\partial C}{\partial z} + \frac{\partial}{\partial z}\left(\varepsilon_s \cdot \frac{\partial C}{\partial z}\right) \tag{1}$$

where C(z,t) is suspended sediment concentration, ε_s is a coefficient of turbulent diffusion of suspended particles, w_s is settling velocity, t is time and z is the vertical coordinate.

According to this equation a change of concentration in time at any horizon from the bottom is defined by the change of balance of suspended sediment flow in vertical direction owing to the particle settling (the first term on the right hand side of equation 1) and due to the suspended sediment flux from the bottom (the second term on the right hand side).

At the free water surface suspended sediment flow is considered to be equal to zero:

$$\varepsilon_s \cdot \frac{\partial C}{\partial z} + w_s \cdot C = 0 \tag{2}$$

Near the bottom suspended sediment concentration is described by:

$$C(0,t)=A\ p(t), \tag{3}$$

where p(t) is a function of local ejection of suspended sediment (pick-up function). When individual waves are passing, sediment suspension takes place not during the whole period, but as a quick ejection of a cloud of suspended sediment. The analysis of field data has shown that only one ejection happens during the phase of decrease from maximum to zero of the horizontal component of velocity. This fact is taken into consideration by coefficient A, that changes within $0 \le A \le 1$, and is equal to 1 during the suspension phase and is zero at other times. It applies to both single waves and to group of waves in terms of their envelope.

The results of measurements of the velocity profile, the elevation of the level and suspended sediment concentration under waves with a pronounced group structure were taken as input data. The convective sediment flux is described by formula based on the field and laboratory data. The sediment entrainment from the bottom is represented by a pick-up function that takes into account the phase shift between the suspended sand concentration and the flow velocity.

Mean parameters of the waves, necessary for calculation, were found from the spectral characteristics of waves. An even grid pitch in depth and in time, was used for calculation with $\Delta z = 0.005$ m and $\Delta t = 0.228$ s.

Fig 7 shows a comparison of concentration chronograms calculated using the model, with those measured at 5.5 cm from the bottom. Discrepancy in absolute values of the concentration peaks obtained by experiment and model can be explained by the fact that the model assumes a constant granulometric composition of suspended sediment in vertical direction and median diameter of suspended particles. This effects the particle settling velocity. In the course of our experiments it was confirmed that median diameter of suspended particles becomes smaller when moving away from the bottom, and consequently the value of settling velocity decreases. This fact will be taken into account in the future modelling. Six regions of suspension are clearly seen in Fig. 7, corresponding to the passage of groups of waves (labelled 1-6 in Fig. 7).

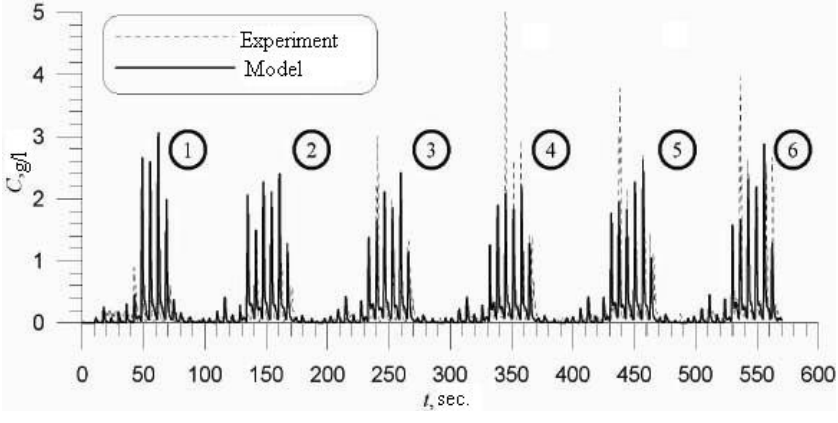

Fig.7. Comparison of concentration chronograms calculated on the model with those measured at 5.5 cm above sea bottom

The results obtained demonstrate a rather high coherence between modelled and observed suspended sand both at low frequencies and frequencies of the maximum of spectral density. This modelled time series of suspended sediment concentration agrees statistically with the experimental one so we can conclude that the model has been successfully elaborated for calculation of the fluctuations of suspended sediment concentration above a flat bottom under the influence of groups of waves. It takes into account the influence of group structure of waves and phases of individual waves upon the sediment suspension which is very important for modelling of fluctuations of suspended sediment concentration. The model demonstrates very well all qualitative peculiarities of sediment suspension in these given conditions. The predicted and measured concentrations coincide satisfactorily in time. The peaks coincide with the inflexion points on the vertical profile of velocity in the bottom boundary layer. This model is described more fully in Kos'yan et al, (2006).

Real processes of sediment suspension are more complex than the mechanisms which are put into the model. The present model of suspension of bottom sediments will be improved as a result of further observations from both experimental and theoretical investigations.

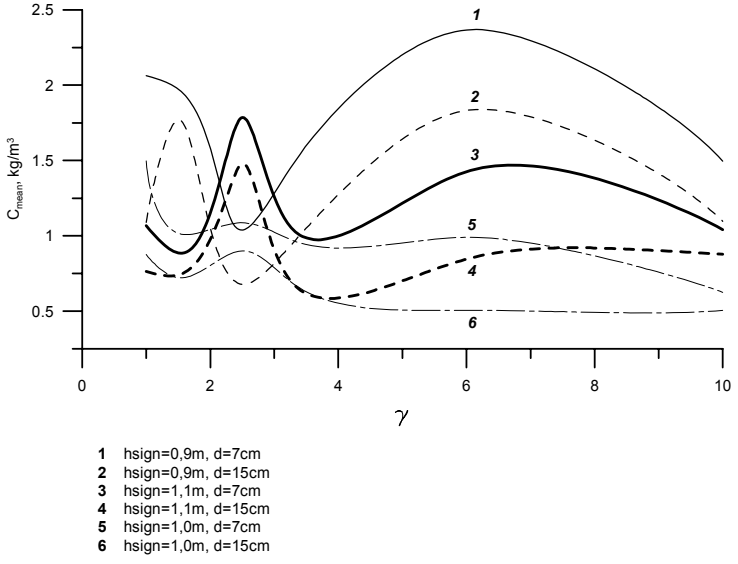

Fig. 8. Dependence of time averaged concentrations at two horizons (7 and 15 cm from sea bottom) for three significant waves heights (H_{sig} = 0.9, 1.0 and 1.1m) on spectral steepness.

One of the tasks of these experiments was to identify any dependence between values of suspended sediment concentration and the form of wave spectrum. Fig. 8 shows the dependence of averaged concentrations at two horizons (7 and 15 cm from the bottom) for three values of significant waves height (H_{sig}= 0.9, 1.0 and 1.1m) on spectral steepness. Fig. 9 shows spectra of suspended sediment concentration for different steepness (γ), and wave heights at the distance 7cm from the bottom.

From the figures it is seen that the form of wave spectrum greatly influences on the SSC values. With the same wave parameters the spectral steepness can alter the concentration by 2.5 times. There are some peaks of SSC values which occur at different steepnesses. Spectra of suspended sediment concentration also greatly depend on the wave spectra steepness. To explain and formulate any dependence we have to have many more new data.

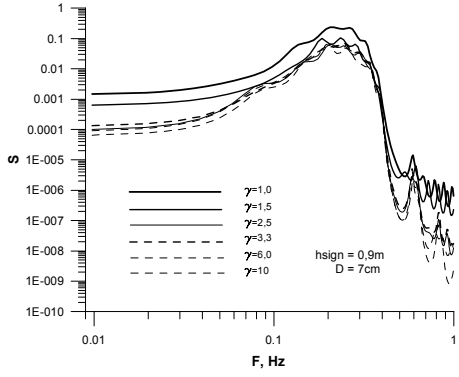

A

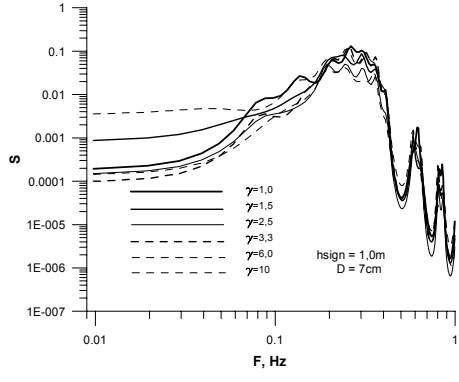

B

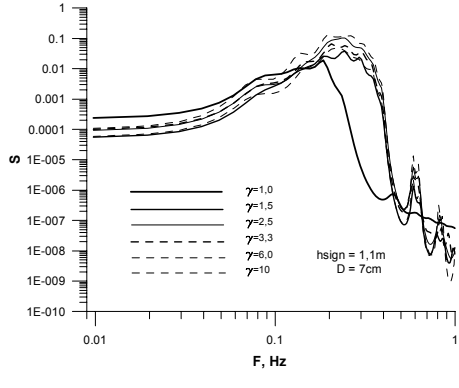

C

Fig. 9. Spectra of suspended sediment concentration for different steepnesses (γ), and wave heights at 7cm above sea bottom. (A: H_{sig} = 0,9 m, B: H_{sig} = 1,0 m, C: H_{sig} = 1,1 m)

CONCLUSION

A series of investigations were conducted in the Large Wave Channel (GWK) of the Coastal Research Centre (FZK) in Hannover which afforded an opportunity to model storm dynamic processes in the coastal zone at almost full-scale. This is most important because it turns out not to be possible to simultaneously similarity of hydrodynamic and lithodynamic processes under any scale of modelling. A data bank of unique experiments, modelling processes of an intensive storm was collected during a short experiment period. The analysis of this data bank gave the possibility of significantly advancing our understanding of storm dynamics and sediment flux in the coastal zone.

In the first stage of analysis of these observations we a) investigated the high-frequency fluctuations of the vertical profile of suspended sediment concentration; b) construct a model of which predicted the fluctuations of suspended sand concentration above a flat sandy bottom under waves with pronounced group structure and c) determined the dependence between values of suspended sediment concentration and the form of wave spectrum.

REFERENCES

Kos'yan, R.D., Krylenko, M.V., Vincent, C.E. (2007). "Fluctuations of instantaneous vertical distribution of suspended sediment in the surf zone," *Proc. of the 30th Intern. Conference on Coastal Engineering,* San Diego. ASCE (in press)

Kos'yan, R., Kunz, H., Kuznetsov, S., Pykhov, N., Podymov, I., Vorobyev, P. (2001). "Physical regularities of suspended sand concentration and transport under irregular waves based on field data," *Die Küste 64*, pp. 161-200.

Kos'yan, R.D., Vincent, C.E., Divinsky, B.V., Krylenko, M.V. (2006). "Modelling of fluctuations of suspended sediment concentration above the flat bottom under waves with pronounced group structure," *Bulletin of the Southern scientific centre of the Russian Academy of sciences. 2(4)*, pp. 53-59. (in Russian)

Ribberink, J.S., Dohmen-Janssen, C.M., Hanes, D.M., McLean, S.R., Taylor, J.A., Vincent, C.E. (2000). "Near-bed sand transport mechanisms under waves: large-scale flume experiments (Sistex'99)," *Proc. of the 26th International Conference on Coastal Engineering,"* Sydney. ASCE, pp. 3263-3276

CHANGE IN LONGITUDINAL PROFILE USING SAND OF MIXED GRAIN SIZE IN LARGE WAVE TANK AND ITS NUMERICAL SIMULATION

Masaya FUKUHAMA[1], Takaaki UDA[2], Masumi SERIZAWA[3] and Toshinori ISHIKAWA[4]

1. Head, Coast Division, National Institute for Land and Infrastructure Management, Ministry of Land, Infrastructure and Transport, Asahi 1, Tsukuba, Ibaraki 305-0804, Japan. fukuhama-m92fc@nilim.go.jp.
2. Dr. Eng., Executive Director, Public Works Research Center, 1-6-4 Taito, Taito, Tokyo 110-0016, Japan. uda@pwrc.or.jp.
3. Coastal Engineering Laboratory Co., Ltd., 1-22-301 Wakaba, Shinjuku, Tokyo 160-0011, Japan. coastseri@nifty.com.
4. Public Works Research Center, 1-6-4 Taito, Taito, Tokyo 110-0016, Japan. ishikawa@pwrc.or.jp.

Abstract: A contour-line-change model considering the sorting effect of grain size was applied to the prediction of the changes in longitudinal profile of a model beach composed of sand of mixed grain size. The results were compared with the experimental results using a large wave tank. The experimental results that sand of mixed grain size is sorted into fine and coarse sand, and that coarse sand is transported shoreward, forming a berm, whereas fine sand sinks into a zone deeper than the depth of closure h_c were accurately reproduced by the numerical simulation. Furthermore, the result that the formation of the berm is rapid, whereas seabed changes in the offshore zone are slow, was also reproduced by the numerical model. The results of the calculation of changes in the content rate indicated that an increase in the volume of coarse sand contributes to the shoreline advance as a result of berm formation, whereas an increase in the volume of fine sand accelerates the outflow of fine sand into a zone deeper than h_c.

INTRODUCTION

When a model beach composed of fine sand is created in a relatively small-scale wave tank and waves are generated, the model beach deforms because of wave

action, resulting in changes similar to that of beach deformation observed on real coasts. This phenomenon has been recognized for a long time, and on the basis of the results of model experiments, a method predicting shoreline recession and advance by introducing a parameter C depending on wave characteristics and grain size has been proposed (for example, Horikawa, 1985).

This method has been extensively used in Japan, but its applicability to real coasts is still questionable. The most important issue is that the dynamic similitude of sand transport has not yet been established, and therefore, the relationship between the phenomena observed in experiments and those observed on real coasts is obscure. To reduce the difficulty to some extent, experiments using a large-scale wave tank have been carried out in recent years, but the mechanisms of the phenomena have not yet been clarified. In solving the problem, studies on the mechanism with which a longitudinal profile tends to approach a stable form are required with respect to changes in longitudinal profile. Furthermore, movable-bed experiments using sand of mixed grain size in a large wave tank have also been carried out, but the interpretation of the phenomena is still insufficient (Meguro *et al*., 2005).

Uda *et al*. (2004) developed a model for predicting changes in beach topography and grain size of seabed materials. In their model, equilibrium slopes for each grain size and the mixing of bed materials in a mixing layer were assumed, and they successfully explained the selective movement of coarse and fine sand. However, the physical evaluation of the model was insufficient. In this study, we aim to investigate the applicability of this model to experiments using sand of mixed grain size, in which the changes in longitudinal profile and cross-shore distribution of the grain size are investigated in detail in a large wave tank.

EXPERIMENT USING LARGE WAVE TANK AND SAND OF MIXED GRAIN SIZE

A movable bed experiment using sand of mixed grain size, which ranges widely from medium sand to silt, was carried out using a 135-m-long, 2-m-wide and 5-m deep wave tank to study the formative processes of an equilibrium beach and grain size distribution (Meguro *et al*., 2005). The median diameter of grain size used was d_{50} =0.62 mm and the initial uniform slope was 1/20. Regular waves with a height of 0.6 m and a period of 3.5 s were generated for 78 hours.

Figure 1 shows the change in longitudinal profile and the cross-shore distribution of d_{50} on the seabed. A flat seabed was formed by erosion at a depth of h_c=1.3 m on the initial uniform slope, and a steep foreshore of slope 1/6 was formed. The flat seabed in the vicinity of the depth h_c was covered with fine sand, whereas coarse sand selectively accumulated on the foreshore. From these facts, it is clear that sand of mixed grain size undergoes a sorting effect by wave action, with coarse sand deposited on the foreshore, forming a berm with a steep slope, and fine sand transported offshore and deposited to form a gentle slope on the offshore bed.

Figure 2 shows the cumulative grain size distributions on the foreshore at x=0.4 m and on the offshore bed at x=30.4 m. The grains in the foreshore and offshore zones are clearly separated into the grains larger and smaller than 1 mm, respectively. On the basis of this result, hereafter we simply refer to grains smaller than 1 mm, as 'fine sand', and larger than 1 mm as 'coarse sand'.

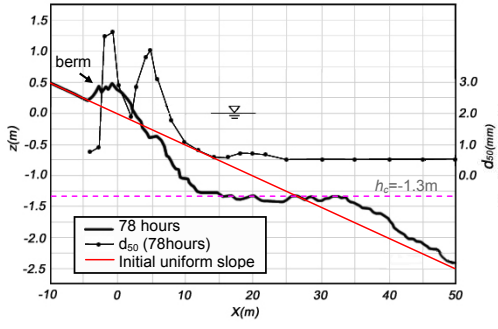

Fig. 1. Change in longitudinal profile and cross-shore distribution of d_{50} in experiment using large wave tank based on work of Meguro *et al.* (2005)

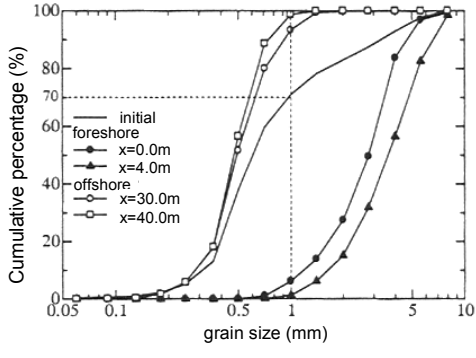

Fig. 2. Cumulative grain size distributions on foreshore at x=0.4 m and on offshore bed at x=30.4 m in experiment

SUMMARY OF EXPERIMENTAL RESULTS

(1) Erosion occurred only in a zone shallower than h_c=1.3 m, which is equal to the depth of closure.

(2) Coarse sand was transported shoreward, forming a 0.5-m-high berm and a foreshore of slope 1/6.

(3) The volume of coarse sand contained in the erosion zone is limited, and the development of a berm depends on this volume of coarse sand. Although the berm

height depends on wave characteristics, a minimum volume of coarse sand is required for the development of a berm.
(4) Fine sand was transported to a zone deeper than h_c, and a slope of 1/10, which was larger than the initial slope, was formed on the offshore bed.
(5) After a berm developed sufficiently, the beach profile became stable, because the grain size on the foreshore matched the slope. The offshore flat bed in the vicinity of h_c also became stable because further erosion did not occur, resulting in the cessation of the offshore discharge of fine sand. Thus, the equilibrium condition is only assumed to result, when a berm develops sufficiently.

NUMERICAL MODEL

A result of a contour-line-change model considering the effect of the change in grain size of seabed materials proposed by Uda *et al*. (2004) was compared with the results of the above-mentioned experiment using sand of mixed grain size. This model can predict not only the beach changes, but also grain-size changes due to the difference in the sorting effect corresponding to grain size.

The fundamental concept was described in Uda *et al*. (2004), but the comparison between the experimental results of the change in longitudinal profile in a wave tank and the numerical model has not yet carried out, requiring the verification of the applicability of the numerical model by physical experiments. In this study, beach changes caused by only cross-shore sand transport are reproduced by the numerical simulation, neglecting the action of longshore sand transport, because the changes in longitudinal profile were obtained in the previously described wave flume test.

The fundamental equations of the simulation are the cross-shore sand transport equations of Eqs. (1)-(3), the mass conservation equations for each grain size of Eqs. (4) and (5), and Eqs. (6) and (7), which calculate the content rate of each grain size.

Cross-shore sand transport

$$q_z^{(k)} = \mu^{(k)} \cdot \varepsilon_z(z) \cdot K_z^{(k)} \cdot (EC_g)_b \sin\overline{\beta} \cdot \left(\frac{\cot\beta}{\cot\beta_c^{(k)}} - 1 \right) \tag{1}$$

$$K_z^{(k)} = \frac{\gamma \cdot A}{\sqrt{d^{(k)}}} \tag{2}$$

$$\varepsilon_z(z) = \begin{cases} = \dfrac{2}{h_c^3}\left(\dfrac{h_c}{2} - z \right)(z + h_c)^2 \quad .....(-h_c \le z \le h_R) \\ = 0 \quad .....(z < -h_c \ , h_R < z) \end{cases} \tag{3}$$

Mass conservation for each grain size

$$\frac{\partial y^{(k)}}{\partial t} = -\frac{\partial q_z^{(k)}}{\partial z} \qquad (k = 1, 2, \cdots, N) \tag{4}$$

$$\frac{\partial Y}{\partial t} = \sum_{k=1}^{N} \frac{\partial y^{(k)}}{\partial t} \tag{5}$$

Change in content rate of each grain size

$$\frac{\partial \mu^{(k)}}{\partial t} = \frac{1}{B}\left\{\frac{\partial y^{(k)}}{\partial t} - \frac{\partial Y}{\partial t}\cdot \mu^{(k)}\right\} \quad (k = 1, 2, \cdots, N) \quad \text{for erosion} \tag{6}$$

$$\frac{\partial \mu^{(k)}}{\partial t} = \frac{1}{B}\left\{\frac{\partial y^{(k)}}{\partial t} - \frac{\partial Y}{\partial t}\cdot \mu_B^{(k)}\right\} \quad (k = 1, 2, \cdots, N) \quad \text{for accretion} \tag{7}$$

Here, N is the number of grain sizes, and k is the number of each grain size (k=1, 2$\cdots$, N), $\mu^{(k)}$ (k=1, 2,$\cdots$, N) is the content rate of grain size k in the exchange layer of sand. z is the depth, t is the time, Y is the location of a specific contour line, and $(EC_g)_b$ is the wave energy flux at breaking point. $\beta_c^{(k)}$ is the equilibrium beach slope angle corresponding to each grain size, $\overline{\beta}$ is the average beach slope angle between the berm height h_R and the depth of closure h_c, and β is the beach slope angle at each contour line. $\varepsilon_z(z)$ is the depth distribution of the cross-shore sand transport given by Eq. (3) (Uda and Kawano, 1996) and $q_z^{(k)}$(k=1, 2,$\cdots$, N) is the cross-shore sand transport of each grain size. $d^{(k)}$ is the grain size (mm), $K_z^{(k)}$ is the coefficient of the cross-shore sand transport for each grain size, and γ is the ratio between the coefficients of sand transport, which expresses the mobility of cross-shore sand transport compared with longshore sand transport. B is the thickness of the exchange layer, and is assumed to be 3% of the breaker height, after Kraus (1985). A is a coefficient that depends on the physical conditions of the beach, and α_{bs} is the angle between the wave-crest line at the breaking point and the contour lines (in this study, α_{bs} = 0). $\mu_B^{(k)}$ is the content rate shoreward of the exchange layer, which is the content rate before the beach changes.

The cross-shore sand transport of each grain size q_z is calculated first, using Eqs. (1)-(3), and then the change in the contour lines is calculated by solving the continuity equation of sand given by Eqs. (4) and (5). Furthermore, the change in content rate in the exchange layer is calculated using Eqs. (6) and (7). The same procedure is recurrently carried out to predict both beach changes and time change in content rate in the exchange layer.

The sinking of sand in a zone deeper than the depth of closure due to gravity and the formation of a scarp on the shore face were predicted using the method proposed by Uda *et al*. (2004). The seabed slope of fine sand in a zone deeper than h_c was assumed to be the value obtained experimentally, considering that the sand movement was due to the effect of gravity. The numerical simulation was carried out by the explicit finite difference method using staggered meshes.

For the calculation condition, the number of grain sizes is assumed to be 2, since the sorting of grains occurred at a critical grain size of 1 mm in the experiment, and two grain sizes of $d^{(1)}$=0.45 mm and $d^{(2)}$=3 mm, which typically represent fine and coarse sand, respectively, are selected. These grain sizes were determined on the basis of the cumulative grain size distribution of the sand of mixed grain sizes used in the experiment, so that $d^{(1)}$ and $d^{(2)}$ are approximately equal to d_{50} calculated from the entire samples of fine and coarse sand, respectively, and so that the mean grain size of the entire sample d_m used in the experiment becomes equal to 1.21 mm.

The initial content rate of sand was assumed to be $\mu^{(1)}$=0.7 for fine sand and $\mu^{(2)}$=0.3 for coarse sand, the same condition as in the experiment. The initial beach profile is given a uniform slope of 1/20, and h_R and h_c are set as h_R=0.5 m and h_c=1.3 m, on the basis of the experimental results.

For the equilibrium slopes, the gentle seabed slope composed of fine sand in the offshore zone and the steep seabed slope composed of coarse sand are given as $tan\beta_c^{(1)}$=1/100 and $tan\beta_c^{(2)}$=1/6, respectively, referring to the experimental results. The width of the exchange layer B is given by the thickness of the exchange layer divided by the slope. Since the experiment had large scale, the thickness is given by 0.02 m, which is 3% of the breaker height (H_b =0.75 m), based on the results obtained from the field observation by Kraus (1985), and B is set to be 0.4 m, dividing the exchange-layer thickness by the initial slope of 1/20.

The critical slope of sinking for sand of each grain size is separately given for on land and on the seabed, similar to that in Uda *et al*. (2004). In this study, the sinking of fine sand into the zone deeper than h_c is considered to be caused by the effect of gravity and is given by a slope of 1/10, which occurred in the experiment. In the other zone, the critical slopes are set to be 1/2 and 1/3 on the land and seabed, respectively, as in Uda *et al*. (2004).

The coefficient of sediment transport A, which defines the rate of beach change, was determined as A=0.2 by a trail calculation, so that the numerical simulation can reproduce the development of a berm in 20 hours as in the case of the experiment, assuming γ =1 in Eq. (2) for simplicity, since longshore sand transport is not related to the phenomenon. For the depth distribution of cross-shore sand transport, the same depth distribution of longshore sand transport as that in Eq. (3) given by Uda and Kawano (1996) was assumed. For the wave condition, the time-averaged breaker height of the observation results, H_b=0.75 m was given. Other calculation conditions such as mesh size and time step are shown in **Table 1**.

Table 1. Calculation conditions

Cases	Reproduction: $\mu^{(1)}$=0.7 and $\mu^{(2)}$=0.3 Prediction: Case 1: $\mu^{(1)}$=0.1 and $\mu^{(2)}$=0.9 Case 2: $\mu^{(1)}$=0.3 and $\mu^{(2)}$=0.7 Case 3: $\mu^{(1)}$=0.5 and $\mu^{(2)}$=0.5 Case 4: $\mu^{(1)}$=0.9 and $\mu^{(2)}$=0.1
Initial topography	Uniform slope of tanβ=1/20
Grain size	Number of grain sizes: N=2 Fine sand: $d^{(1)}$=0.45 mm Coarse sand: $d^{(2)}$=3 mm Initial content rate: $\mu^{(1)}$=0.7 and $\mu^{(2)}$=0.3
Width of exchange layer	B=0.4 m
Wave conditions	Breaker height: H_b=0.75 m (H_0=0.6 m, T=3.5 s) Breaker angle: α_{bs}=0 deg. Tide level: mean sea level
Depth of closure	h_c=1.3 m
Berm height	h_R=0.5 m
Coefficients of sand transport	A=0.2 and γ =1.0
Depth distribution of sand transport rate	Cubic equation given by Uda and Kawano (1996)
Equilibrium slope	$tan\beta_c^{(1)}$ =1/100 (fine sand) $tan\beta_c^{(2)}$ =1/6 (coarse sand)
Critical slope	Fine sand: 1/2 on land and 1/10 on seabed Coarse sand: 1/2 on land and 1/3 on seabed
Calculation domain	z=+1.0 m to -3.0 m
Mesh size	Δz=0.1 m
Time interval	Δt=0.01 h
Total time of calculation	t=200 h (20,000 steps)
Boundary conditions	q_z=0 at landward and offshore boundaries
Calculation method	Explicit finite difference method

RESULTS OF NUMERICAL SIMULATION

4.1 Case of initial content rates of fine and coarse sand : $\mu^{(1)}$=0.7 and $\mu^{(2)}$=0.3

First, numerical simulation was carried out in the case with the same conditions as that of the experiment. **Figure 3** shows the change with time of the longitudinal profile when the content rates of fine and coarse sand are $\mu^{(1)}$=0.7 and $\mu^{(2)}$=0.3, respectively. Erosion starts from a shallow zone in the vicinity of the shoreline, and part of the sand is transported landward forming a berm on the foreshore. Sand is also transported offshore, forming a small hump in the offshore zone.

Figure 4 shows a comparison between the measured and the predicted longitudinal profiles after wave action. The results are in a good agreement in terms of the formation of a berm, the flat offshore sea bottom and offshore deposition of sand. Furthermore, it is realized from **Fig. 3** that the formation of the berm is relatively rapid compared with the change in the offshore topography in establishing a stable condition.

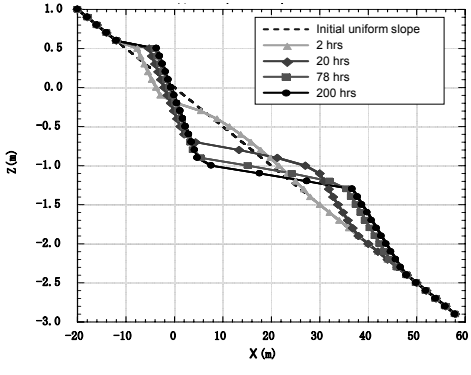

Fig. 3. Change with time of longitudinal profile in case that content rates of fine and coarse sand are $\mu^{(1)}$=0.7 and $\mu^{(2)}$=0.3, respectively

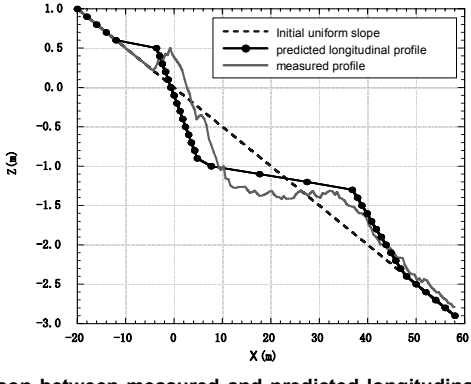

Fig. 4. Comparison between measured and predicted longitudinal profiles after wave action

Figures 5(a) and **5(b)** show the cross-shore distributions of the content rates $\mu^{(1)}$ and $\mu^{(2)}$ corresponding to the profile changes shown in **Fig. 3**. The foreshore materials become only coarse sand ($\mu^{(1)}$=0, $\mu^{(2)}$=1.0), whereas the offshore seabed with a gentle slope becomes covered with only fine sand ($\mu^{(1)}$=1.0, $\mu^{(2)}$=0). **Figure 6** shows the cross-shore distribution of the mean grain size. The grain size is large at 3.0 mm on the steep slope of the foreshore and on the berm, whereas on the offshore seabed it becomes as small as 0.5 mm. These results correspond well to the cross-shore distribution of d_{50} as shown in **Fig. 1**.

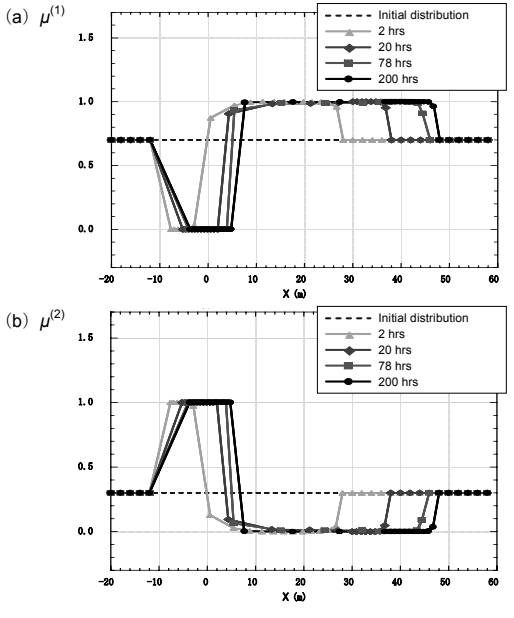

Fig. 5. Cross-shore distribution of content rate $\mu^{(1)}$ and $\mu^{(2)}$ of fine and coarse sand, respectively

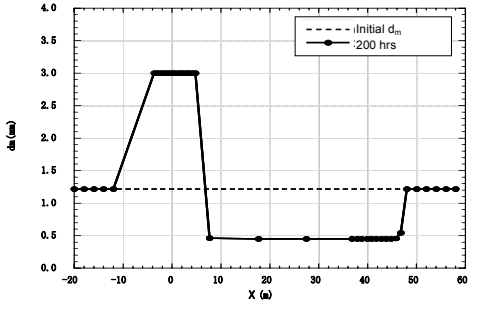

Fig. 6. Cross-shore distribution of mean grain size

In conclusion, the changes in longitudinal profile in the experiment were accurately reproduced in the numerical model, taking into account the five findings described in the 'summary of experimental results' section. It was found that fine and coarse sand are sorted on model beaches composed of sand of mixed grain size, and that coarse sand is transported shoreward, whereas fine sand is transported offshore, finally approaching the equilibrium slope corresponding to each grain size.

4.2 Case of initial content rates of fine and coarse sand : $\mu^{(1)}$=0.3 and $\mu^{(2)}$=0.7

In the experiment, the changes in longitudinal profile were investigated in the case that the initial content rates of fine and coarse sand are inversely $\mu^{(1)}$=0.3 and $\mu^{(2)}$=0.7, respectively, to investigate the effect of the difference in the initial content rates on the final, stable profile. **Figure 7** shows the results.

As a result of the increase in the content rate of coarse sand, sand volume transported shoreward increased compared with the case as shown in **Fig. 3**, and a berm predominantly developed. In contrast, a smaller volume of sand was transported offshore. **Figures 8(a)** and **8(b)** show the change with time of the content rates of fine and coarse sand $\mu^{(1)}$ and $\mu^{(2)}$ in the same manner as shown in **Figs. 5(a)** and **5(b)**. The distributions of $\mu^{(1)}$ and $\mu^{(2)}$ are similar to each other, but shoreward sand movement predominated as a result of the increase in the content rate of coarse sand, and therefore, beach changes became active in a relatively shallow zone.

4.3 Change in initial content rate and equilibrium profile

Figure 9 shows the final, stable profiles in the cases that the initial content rates ($\mu^{(1)}$, $\mu^{(2)}$) are altered to (0.9, 0.1), (0.5, 0.5), (0.3, 0.7) and (0.1, 0.9), as well as the result of the reproduction case with the content rates (0.7, 0.3). The berm develops more with the increase in content rate of coarse sand, $\mu^{(2)}$. In contrast, the berm develops less with the increase in content rate of fine sand, $\mu^{(1)}$, and offshore sand transport becomes dominant, accelerating the deposition of fine sand in the offshore zone.

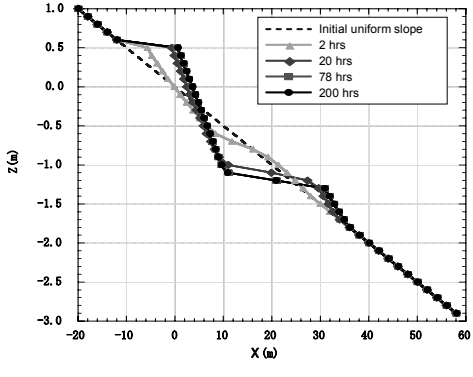

Fig. 7. Predicted changes in longitudinal profile when content rates $\mu^{(1)}$ and $\mu^{(2)}$ are 0.3 and 0.7, respectively

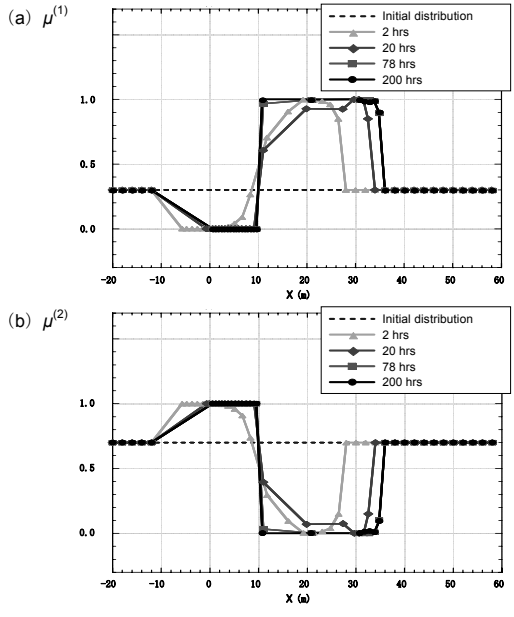

Fig. 8. Change with time of content rate of fine and coarse sand $\mu^{(1)}$ and $\mu^{(2)}$

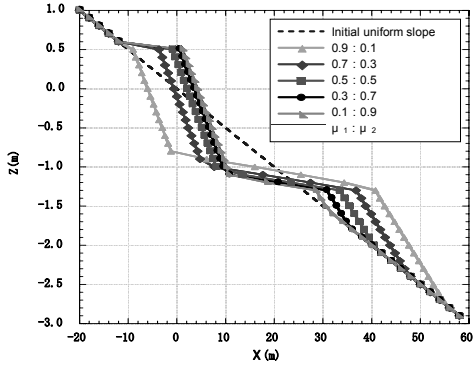

Fig. 9. Final, stable profiles in cases that initial content rates ($\mu^{(1)}$, $\mu^{(2)}$) are altered to (0.9, 0.1), (0.5, 0.5), (0.3, 0.7) and (0.1, 0.9), as well as result of reproduction case with content rates (0.7, 0.3)

Thus, the grain size has a decisive effect on the changes in longitudinal profile. On a beach composed of only fine sand, offshore sand transport from the initial stage never converges and an equilibrium profile cannot ever be attained. The equilibrium

profile in the wave flume experiment is formed only when sufficient volume of coarse sand is available to cover the foreshore and to form a berm.

CONCLUDING REMARKS

The present model accurately reproduced the characteristics that sand of mixed grain size undergoes a sorting effect, coarse sand is transported shoreward to form a berm and fine sand is transported offshore to a zone deeper than h_c. The formation of a berm is very rapid, whereas the time scale of change for the offshore topography to approach a stable condition by the movement of fine sand is much longer. From the calculations when the content rate of coarse sand increases, the foreshore becomes wide owing to the formation of a berm, and it contributes to the shoreline advance. In contrast, with an increase in the content rate of fine sand, the outflow of sand toward a zone deeper than h_c increases.

There are cases that the volume of coarse sand, which accumulates near the shoreline forming a berm with a steep slope, is limited, depending on the initial content rate of sand. This condition often occurs in beach nourishment rather than in natural beach processes. In such a case, the sand used for nourishment is transported offshoreward and a stable profile cannot ever be attained. This means that we must be very careful in selecting the grain size of sand for beach nourishment.

In addition, the most important parameter in determining changes in longitudinal profile is the equilibrium slope, which depends on the grain size. Since the changes in longitudinal profile depend on the combination of the equilibrium slope and the content rate of sand, the parameter such as the shoreline position has less physical meaning.

Since this study focused on reproducing the experimental results using a large wave tank, various parameters of this study must be reconsidered in the application to other experimental results and field data. In particular, in the application to field data, the berm height, depth of closure and equilibrium slope of each grain size of each coast must be determined on the basis of bathymetric survey data and the depth distribution of grain size of the seabed materials. In addition, in the contour-line-change model, in principle, the contour line is defined only as single-valued function of the ground elevation, and therefore, the bar-trough topography is difficult to express because of the necessity of multiple contour lines. In this area, future studies are required.

Finally, a movable-bed experiment using a large wave tank was realized in this study, and a model for predicting the longitudinal profile using sand of mixed grain size was successfully developed. This model will become a useful tool for predicting beach changes during beach nourishment using sand of mixed grain size, because the remaining rate of nourished sand in a shoreline zone corresponds to the grain size.

REFERENCES

Horikawa, K. ed. (1985). Nearshore dynamics and coastal processes, University of Tokyo Press, Tokyo, p. 522.

Kraus, N. C. (1985). Field experiments on vertical mixing of sand in the surf zone, J. Sedimentary Petrology, Vol. 55, pp. 3-14.

Meguro, S., K. Yamamoto and K. Fukuhama (2005). Formation process of equilibrium beach responding grain size of beach nourishment, Annual Jour. Coastal Eng. JSCE, Vol. 52, pp. 501-505. (in Japanese)

Uda, T. and S. Kawano (1996). Development of contour line change model to predict beach changes, Proc. JSCE, No. 539/II-35, pp. 121-139. (in Japanese)

Uda, T., T. Kumada and M. Serizawa (2004). Predictive model of change in longitudinal profile in beach nourishment using sand of mixed grain size, Proc. 29th ICCE, pp. 3378-3390.

PROBABILISTIC-DETERMINISTIC MODELLING OF SWASH ZONE MORPHOLOGY

T. E. Baldock, P. Kim Son, P. Manoonvoravong, M. P. Barnes and J.M. Alsina

Coastal Engineering Research Centre,
University of Queensland,
St Lucia, QLD, 4072, Australia.
t.baldock@uq.edu.au; pkimson@uq.edu.au; mpanut@uq.edu.au;
mbarnes@uq.edu.au; josealsina@uq.edu.au

Abstract: A probabilistic-deterministic model for swash zone sediment transport is presented and applied to predict cross-shore beach profile change under random waves. For accretionary conditions, inclusion of a random wave approach is essential for accurate representation of berm building processes. The model provides good estimates of beach volume changes for small scale laboratory experiments and sediment overwash volumes on a natural beach. Future modeling improvements are discussed, notably the inclusion of pre-suspended sediment, sediment pickup and long wave influences. Field and laboratory data show that sediment is advected into the swash zone from much further offshore than predicted by the classical swash solution, which increases uprush suspended sediment flux. Conversely, backwash suspended sediment flux may be limited by hindered pickup which may occur when the thickness of the backwash sheet flow layer becomes large relative to the flow depth.

INTRODUCTION

Despite recent advances in both analytical (Pritchard and Hogg, 2005) and numerical modelling (e.g. Kobayashi and Johnson, 2001; Karambas, 2006), predictions of morphological evolution in the swash zone remains a challenge, particularly over longer time-scales. As a result, few or no broad scale parametric-deterministic models attempt to model sediment transport in the swash zone. This paper addresses this point and presents a framework for including the influence of random wave runup and sediment transport in deterministic, parametric or empirical hydro-morphodynamic models (e.g.

COSMOS (Nairn, 1990), SBEACH, DELFT3-D, MIKE21 etc.). As a result of the intermittent nature of the swash flow, an event-based model is developed, as opposed to a time-averaged model. The model is compared to laboratory data for both eroding and accreting beaches. Other applications of the model are also discussed, including swash overwash, for which an event-based modeling process is also more appropriate than a time-averaged approach.

The basis for model presented here was reported by Holmes and Baldock (1997). The original approach utilised, and was embedded within a version of the COSMOS profile model developed by Nairn (1990) at Imperial College, UK. At that time, Holmes and Baldock had reservations about the sediment transport routines in the swash model, notably the application of the Bagnold Energetics approach and the use of an equilibrium beach face concept as a predictive tool, and the model was not published further. However, validation of the Energetics approach for swash transport by Masselink and Hughes (1998) and the adoption of Shields type u^3 models by Nielsen (2002) and Pritchard and Hogg (2005) addresses some of these concerns. In addition, further validation of the original swash hydrodynamics model (Baldock and Holmes, 1997) by Hughes and Baldock (2004) and its application to calculate swash overtopping and sediment overwash suggested that revisiting and updating the model would be beneficial.

Section 2 of this paper outlines the original model, together with the revisions and updates based on recent international swash research. Section 3 describes the laboratory setup and wave conditions. Model-data comparisons for beach profile evolution are given in section 4, together with some results of applying the model to field conditions and sediment deposition on the crest of beach berms. A critical evaluation of the model is presented in section 5, together with a discussion of where recent advances could be incorporated. In addition, a caveat concerning the use of representative monochromatic wave conditions to simulate random wave conditions is discussed on the basis of experiments illustrating the influence of surf beat and wave groups on beach profile evolution. Final conclusions follow.

MODEL FORMULATION

Surf zone and swash zone hydrodynamics

The hydrodynamics within the model are predicted using a cross-shore wave transformation model formulated on a full Rayleigh probability density function for the nearshore wave heights and by abandoning the usual depth limitation (Baldock et al., 1998). This model was extensively tested and calibrated by Ruessink et al. (2003) for a wide range of field data. This wave transformation model provides the bore height at the run-down position for subsequent use in the swash hydrodynamics module. The surf zone wave heights govern the remainder of the surf hydrodynamics used in the original ANPM.

The intermittent nature of the swash flow means that the parametric time-averaging approach adopted for the surf zone is inappropriate. For example, a representative

monochromatic wave may provide a good description of the wave energy and sediment stirring in the surf zone, but will under-estimate the maximum run-up under random wave conditions. In the simplest case, this may result in no predicted overtopping or sediment overwash when in reality it would occur. Further, the smoothing effect of the random wave run-up is ignored. However, adopting the parametric approach offshore and in the surf zone prohibits the use of full numerical solutions (e.g. Kobayashi et al., 1989; Masselink and Li, 2001) for the swash. The swash hydrodynamics are calculated using the swash model of Baldock and Holmes (1997), recently extended and applied to field conditions by Hughes and Baldock (2004) and Hughes et al. (2007). The input to the model is the height of the incident bore at the seaward limit of the swash zone, available from the cross-shore wave transformation routine, and a friction coefficient, which can be calculated internally if necessary following Hughes (1995).

Swash zone sediment transport

Holmes and Baldock (1997) adopted an Energetics approach for the swash sediment transport model, following the Energetics approach (e.g. Bagnold, 1966) utilised elsewhere within the ANPM. However, the Energetics approach has some inconsistencies which have not been closely examined. For example, the efficiency factor for the bed load transport rate is usually assumed to be of order 0.1 (Bagnold, 1966; Nairn, 1990). However, for shallow water, Bagnold (1966) suggests that the overall bed load efficiency may approach 0.3, a result of the boundary transport efficiency approaching 1. Consequently, since the power available for suspended load transport depends on the power expended transporting the bed load (Bagnold, 1966), there must be also a corresponding change in the suspended load efficiency factor. In addition, the predicted net transport was always offshore as a result of the predicted flow asymmetry in the swash zone (Baldock and Holmes, 1997). While Holmes and Baldock (1997) found that the Energetics approach gave reasonable results, the model has since been revised to use a Shields type model (e.g. Nielsen, 1992; 2002) in order to adress the first two concerns.

To address the problem of achieving net shoreward transport with negatively skewed asymmetric swash flows, Holmes and Baldock (1997) adopted Turner's (1995) equilibrium beach face concept, where the direction of the net transport on the beach face is determined by whether the beach face gradient is greater or smaller than an equilibrium value. In more recent work, it has been shown that the uprush transports a greater sediment load for a given free stream velocity, or is twice as "efficient" (e.g. Masselink and Hughes, 1998). A number of reasons have been given for this, including infiltration/exfiltration effects (e.g. Turner and Masselink 1998; Masselink and Li, 2001) and flow acceleration (Nielsen, 2002; Puleo et al., 2003), but neither have been conclusively demonstrated. Pre-suspended sediment advected from the inner surf zone (e.g. Pritchard and Hogg, 2005) is potentially a very important contribution to net sediment fluxes and has been incorporated within a parametric framework (Alsina et al., 2005). Nevertheless, correct *a priori* prediction of the direction of sediment transport probably remains beyond the state of the art. Therefore, at present, the model retains the

equilibrium beach face concept. Possible future improvements to overcome this issue are discussed later below.

The sediment transport model is a standard sheet flow Shields model (Nielsen, 1992) where Q is:

$$Q = \Phi d\sqrt{(s-1)gd} \tag{1}$$

with

$$\Phi = C(\theta - 0.05)\sqrt{\theta} \tag{2}$$

and

$$\theta = \frac{1/2\, f_w u|u|}{(s-1)gd} \tag{3}$$

where d is the median grain diameter, s is the specific gravity of the sediment, u is the free stream horizontal velocity, f_w is the wave friction factor and C is an empirical transport coefficient. Here, C= 8 for θ<1 and C=12 for $\theta \geq 1$, which are recommended values (Nielsen, 1992). A standard expression for f_w is (Nielsen, 1992; 2002):

$$f_w = \exp\left[5.5\left(\frac{2d_{50}}{A_{rms}}\right)^{0.2} - 6.3\right] \tag{4}$$

where A_{rms} is based on the free stream velocity variance and the swash frequency $\omega=2\pi/T_s$.

$$A_{rms} = \frac{\sqrt{2}}{\omega}\sqrt{Var\{u(t)\}} \tag{5}$$

A_{rms} and f_w therefore vary across the swash zone. Nielsen (2002) modified (3) for the case where a significant positive local temporal flow acceleration or landward directed pressure gradient occurs. Puleo et al. (2003) proposed that these conditions may occur during uprush and to a lesser extent during the backwash. However, Baldock and Hughes (2006) present field data that indicates that this is not the case, and that the local and total fluid acceleration in the swash is nearly always directed seaward. Consequently, the original formulation is retained.

In the model, (4) and (5) vary across the swash zone, depending on the velocity variance any fixed position. The bed slope was also accounted for by modifying the Shields parameter according to

$$\theta_s = \theta\left(1 - \frac{\tan\beta}{\tan\phi}\right)\cos\beta \tag{6}$$

where ϕ is the friction angle ($\tan\phi$=0.63). The values of f_w are in the range $0.02<f_w<0.05$ of local swash friction factors inferred by Cox et al. (2000) and Raubenheimer et al. (2004). For application to a beach profile model, the net transport per swash, Q_{net}, is determined following Turner (1995) as

$$Q_{net} = Q\frac{\tan\beta_{eq} - \tan\beta}{\tan\beta_{eq} + \tan\beta} \tag{7}$$

where β is the local beach slope and β_{eq} is the user-defined global equilibrium beach slope in the swash zone. (7) therefore controls both the magnitude and direction of the net transport. The choice of β_{eq} is discussed below. Q_{net} may be time-averaged, or retained as a discrete transport volume, depending on the overall modeling framework.

Probabilistic modeling

Application of the model with monochromatic waves leads to an under-estimation of the extent of morphological change for both accretionary and erosive conditions (see section 3 below). Consequently, Holmes and Baldock (1997) adopted a probabilistic-deterministic approach, which has since been utilised to model sediment overwashing natural beach berms. Bore heights in the inner surf zone are well described by a Rayleigh distribution (Baldock et al., 1998), which is consistent with Rayleigh distributed run-up under random waves (e.g. Nielsen and Hanslow, 1991). In the model, the total transport is determined for a series of Rayleigh distributed bore heights, H_b, ranging from H_{bmin} to H_{bmax}, with the net transport at any location weighted by the respective probability of occurrence for that bore height. Hence,

$$Q_{total} = \int_{Hb\min}^{Hb\max} Q_{net}\, p\left(\frac{H_b}{H_{brms}}\right) d\left(\frac{H_b}{H_{brms}}\right) \tag{8}$$

where

$$p\left(\frac{H_b}{H_{brms}}\right) = 2\frac{H_b}{H_{brms}}\exp\left[-\left(\frac{H_b}{H_{brms}}\right)^2\right] \tag{9}$$

H_{brms} is the rms bore height at the run-down position determined by the surf zone wave transformation model. For steep beaches, the maximum run-down below the MWL (setup) intersection with the beach was estimated to be about $0.3R$, where R is the runup obtained from Hunt's (1959) formula. The mean seaward boundary of the swash is assumed to be the MWL (setup) intersection with the beach face. Here, H_{bmin} was set to $H_{brms}/5$, with $H_{bmax}=2.4H_{brms}$, but a finer representation of the wave height distribution could be used. For overtopping and overwash calculations, the runup elevation, z_P,

exceeded by any fraction, P, of the N incident waves can be estimated from Nielsen and Hanslow (1991) as:

$$z_P = R\sqrt{-\ln(P)} \tag{10}$$

Hence, both the number of overwashes and the beach freeboard varies with tide level and wave conditions. Overtopping and overwash is summed for a series of Rayleigh distributed runup events, with P varied from 0.05-0.95 in steps of 0.1, corresponding to runup elevations exceeded by each decile of the incident waves (i.e. z_{95}, z_{85}, …z_5). A finer distribution of runup events (e.g., 1% intervals) can also be adopted.

EXPERIMENTAL SETUP

In 1995-1997 mobile bed experiments were carried out in the large wave flume in the Civil Engineering Department at Imperial College (figure 1). A flat bottom-hinged wave paddle was used to generate regular or random waves up to frequencies of 2Hz, with simultaneous absorption of short waves reflected from the far end of the flume. A slope (β) of gradient 0.05 starts 32m from the paddle, rising to 0.1 in the surf and swash zones. The last 6m of the flume are subdivided into three sections, providing two working sections of width 0.9m and a central section for access to instrumentation. Within the swash zone, fixed and mobile beds of sediment (d_{50}=0.5mm; d_{50}=1.5mm, thickness 0.1m) were used to investigate frictional effects on run-up and beach profile evolution. Further description of the experimental setup is given by Baldock and Holmes (1997). Three sets of Jonswap random wave conditions were used for each sediment size, but only the case with the largest waves is discussed here. Each run started with an initially plane beach, with profile measurements at 30min, 60min, 120min, 240 and 360min run times. Profile measurements were made with a simple drop stick, with accuracy ±1mm in the vertical and ±1cm horizontally. The fine sand beach evolved to a longshore bar-trough system with erosion in the swash zone, whereas the coarse sand beach evolved with the formation of a large swash berm and onshore transport in the surf zone. Both beaches extended sufficiently far landward and seaward to minimise any influence of insufficient sediment supply at the boundaries.

Table 1. Wave conditions

Case	Wave period (s)	H_{rmso} (m)	Offshore wave steepness	Surf similarity, ζ
J1	1.5	90	0.033	.55
J2	1.5	74	0.027	.61
J3	1.0	46	0.031	.57

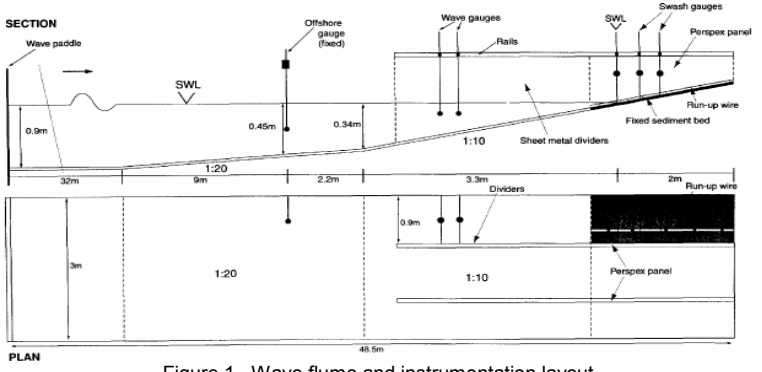

Figure 1. Wave flume and instrumentation layout.

RESULTS

Figures 2a-d illustrates the profile evolution over 360 minutes for both the fine and coarse sand for case J1, indicating a gradual evolution toward equilibrium.

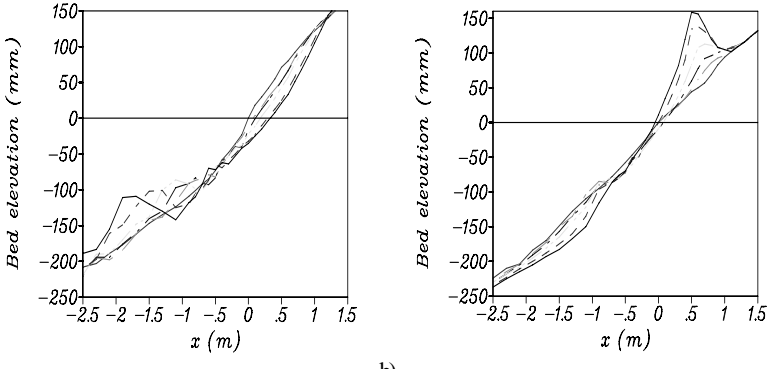

Figure 2. Beach profile at t=0 (red) 30 (green), 60 (blue), 120 (yellow), 240 (magenta) and 360 (black) minutes for fine and coarse sand beaches. a) fine, J1; b) coarse, J1.

Model-data comparisons for t=240min are illustrated in figure 3. The model is run for identical input parameters in both cases, with the exception of grain size and that the suspended load efficiency is set to zero for the coarse sand case and the user-defined equilibrium slope is different. The hydrodynamic and morphodynamic time-step is 6 minutes, but the incident "deep water" wave conditions are constant. For the fine sand, the best fit was obtained with an equilibrium slope of tanβ=0.12. This corresponds closely with the gradient of the model beach at the SWL at all time steps. The optimum

equilibrium gradient for the coarse sand beach was tanβ=0.45, which corresponds to the maximum gradient observed on the model beaches, in this instance in the middle of the seaward face of the swash berm. For the eroding beach, the model results do not differ significantly between the monochromatic and probabilistic approaches, except at the very upper limit of the swash. This is a result of only weak transport in the upper swash, the dominant effect of the offshore bar in controlling the beach morphology at later times and profile smoothing. In contrast, for the accretionary event, it is very important to account for the variable runup in order to predict both the berm position and the total berm volume (figure 3b).

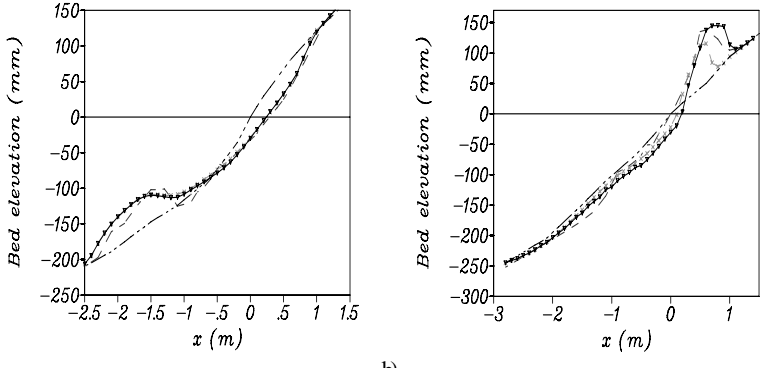

a) b)

Figure 3. Model-data comparisons for a) eroding beach and b) accreting beach. —·· — Initial profile; — — measured profile —∇—, probabilistic model, —×—, monochromatic model. Case J1..

Cumulative eroded/accreted volumes within the swash zone (above the SWL intersection on the beach face) are compared with the model predictions at the different time intervals in figure 4. In conjunction with the equilibrium model, the swash sediment transport routine appears to provide good overall description of the variation in beach face sediment volume. Note that in both cases the trend to morphological equilibrium is quite slow, and may not in fact occur at all for the accreting beach, where the (constant) incident wave conditions continually drive sediment onshore.

The probabilistic approach has also been adopted to calculate swash sediment transport overwashing beach berms, the first step in developing a deterministic parametric model for berm growth. In this case, field data was obtained during sub-aerial berm growth following closure of a coastal lagoon entrance at Belongil Beach, NSW, Australia (see Weir et al., 2005 for details). Overwash volumes were obtained from survey data and compared to sediment transport rates calculated at the berm crest using the probabilistic model. The wave run-up was determined using Hunt's (1954) formula and offshore wave conditions, from which the bore height in the hydrodynamics model is determined. In addition, a constant friction factor was used in Eq. (3). Cumulative overwash volumes

compare well with measured volumes (figure 5) for friction factors in the range f_w=0.024-0.3, which are in the middle of the range suggested by field measurements (e.g. Raubenheimer et al., 2004).

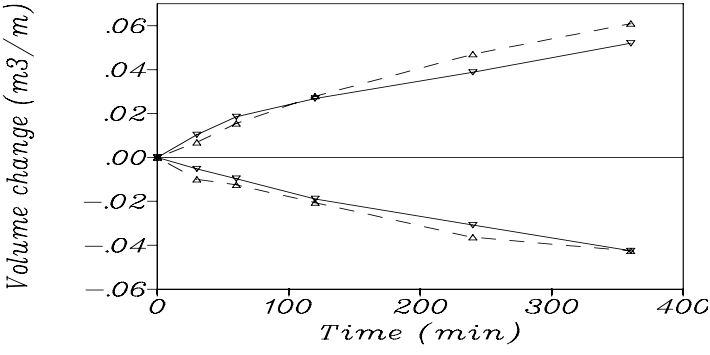

Figure 4. Measured and predicted volumetric change above SWL, case J1.
— Δ — measured; —∇—, probabilistic model.

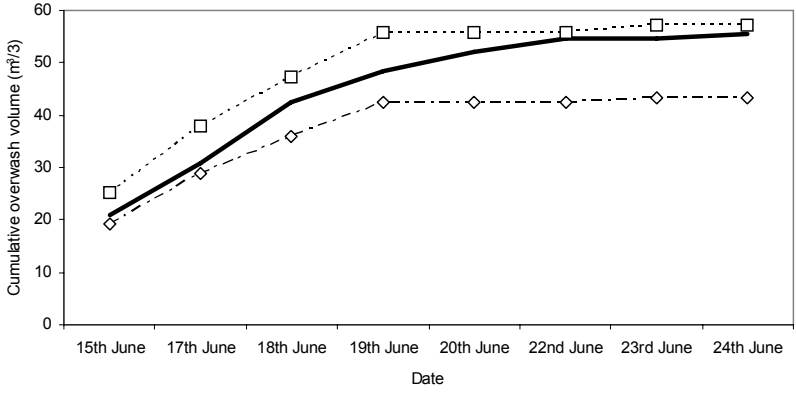

Figure 5. Modelled versus measured cumulative sediment overwash volume at Belongil Creek. Variable truncation point and Rayleigh distributed runup.
Thick line, measured; ≈ predicted - f_w=0.03; ∈ predicted - f_w=0.024.

DISCUSSION

While the model works well for predicting overtopping flows, i.e. uprush transport only, it is not yet a good predictive tool for beach morphology, since the equilibrium slope is required as input to the model. In some respects this is not a major shortcoming, since

many models require calibration or ad hoc fitting, and the equilibrium slope may be a parameter that can be robustly defined for particular beaches or grain sizes. However, the model also neglects some sediment transport dynamics that are likely to play an important role, at least in the lower swash zone. Firstly, the advection of pre-suspended sediment is not considered. The Lagrangian model proposed by Pritchard and Hogg (2005) and Alsina et al. (2005) is promising, but the present hydrodynamic routine is not particularly efficient and does not allow for morphological-hydrodynamic feedback.

The importance of pre-suspended sediment on reflective sand beaches is illustrated in figure 6, which shows a significant sediment load in the inner surf zone just prior to bore collapse. How much sediment enters the swash zone then depends on from how far offshore sediment is advected across the swash boundary following bore collapse (figure 7). The classical swash solution predicts that this distance is very small, $1/16^{th}$ of the run-up length (see Pritchard and Hogg, 2005). However, field and laboratory measurements suggest the advection length is approximately $1/4$-$1/3^{rd}$ of the runup length (figure 8). Consequently, sediment can be advected into the swash from further offshore and the total sediment flux into the swash zone is much greater for a given concentration of pre-suspended sediment. Correct representation of this flux will again require a probabilistic approach, with the flux for different bore heights similarly weighted according to the probability of that bore height occurring.

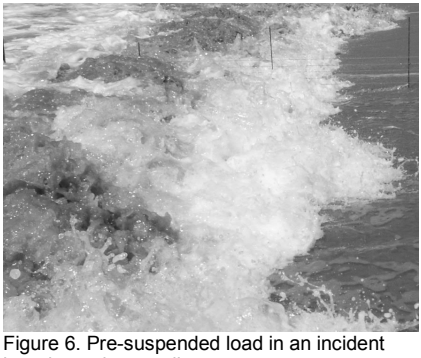

Figure 6. Pre-suspended load in an incident bore just prior to collapse.

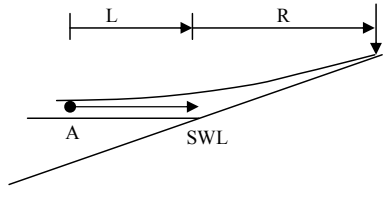

Figure 7. Definition sketch of advection ratio, L/R. Particle at A at time of bore collapse just crosses the SWL during uprush.

An unresolved issue remains the prediction of the net sediment transport in the swash zone, together with the correct cross-shore variation of the net transport (Q(x)). The latter controls the morphological change. The gradients in the net transport rate are therefore very important. However, particularly for accreting beaches, u^3 type models perform poorly in this respect. For example, the important solutions of Pritchard and Hogg (2005) show that quasi-equilibrium u^3 models with maximum asymmetry at the SWL result in maximum morphological change close to the SWL (their figure 12).

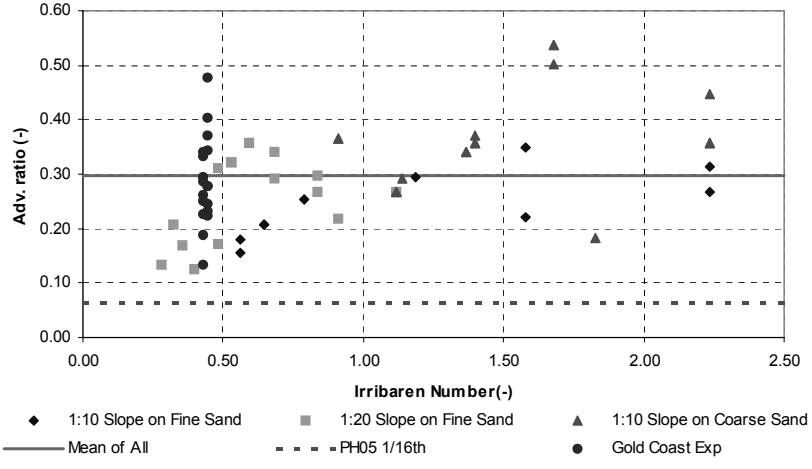

Figure 8. Advection ratio for monochromatic laboratory waves and random waves on a natural beach. After Kudo (1995).

While this is perhaps realistic for net erosion in the swash zone, it is unrealistic for net accretion. However, in the absence of tide, experimental data show that maximum accretion (the berm crest) tends to occur in the mid-upper swash (figure 9a). This requires that Q(x) is initially a downward convex function, with an inflexion point at the berm crest position (figure 9b). For a quasi-intantaneous transport model ($q \propto f(u^n)$), inviscid swash solutions give Q(x) as a monotonic concave function decreasing shoreward, resulting in morphological change that also shows a monotonic concave shape, again decreasing shoreward. Increasing the concentration of the pre-suspended load entering the swash does not change the predicted pattern if a simple suspended load settling model is used in the uprush (see Pritchard and Hogg, 2005). However, a downward convex pattern in Q(x) is possible if an advection-diffusion model is adopted, even for a quasi-intantaneous transport model, provided that the suspended load is the dominant transport mode (see Alsina et al., 2005). Data from Hughes et al. (2007) indicates that during the uprush sediment is maintained in suspension across a large region of the runup zone, well above the mid-swash position, which is consistent with significant morphological change in the upper swash.

Hughes et al. (2007) also note that the concentration in the latter stages of the backwash is lower than might be expected on the basis of the high flow velocity. A possible explanation for the latter may be "hindered pickup" at high bed load transport rates. During the backwash, the concentrated thin sheet flow layer may reduce the relative effectiveness of turbulent bursts in picking up sediment from the immobile bed, in comparison to pickup at lower transport regimes.

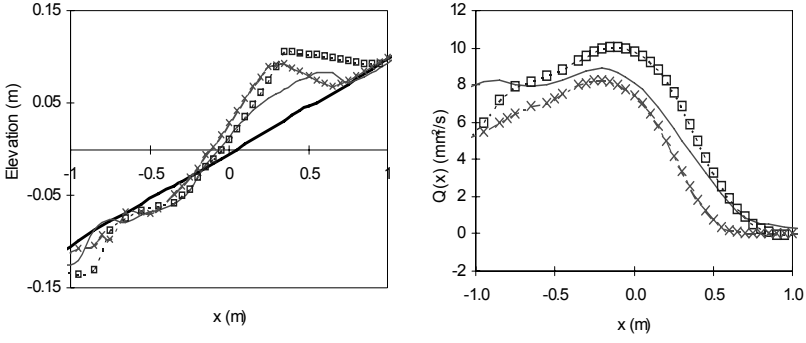

a) b)

Figure 9. Profile evolution and sediment transport rates in the inner surf and swash zone. — ·×· — monochromatic wave; —— monochromatic wave with small amplitude long wave; – –□– – monochromatic wave with large amplitude long wave.

An alternative view of this hindered pickup of suspended sediment can be developed from the Energetics approach. Bagnold (1966) suggested that the bed load efficiency factor, e_c, increases as the flow depth reduces in comparison to the thickness of the moving granular layer. In the backwash, the depth is reducing while the thickness of the mobile layer is increasing, so an increase in e_c may be important. The total bed load efficiency factor, e_b, also increases. An increase in e_c consequently reduces the power available to maintain a suspended load. Indeed, Bagnold (1966) suggests e_c may approach unity. If that was the case, little fluid power would remain available for suspended sediment transport.

Finally, the parametric approach involves the fundamental assumption that a representative H_{rms} wave height can provide a sufficient description of the nearshore processes, with wave grouping and surf beat effects neglected. Limited work has considered the role of surf beat in modifying nearshore wave heights and how long waves may alter sediment transport rates outside the surf zone. Nairn (1990) and Roelvink (1993) investigated the influence of surf beat on beach morphology, but few specific experiments have been reported. Baldock et al. (2007) compare beach profile response for a monochromatic wave and bichromatic wave with the same mean surface variance (energy) and the same mean wave period. The beach profile response was in complete contrast, accretion versus erosion, respectively. Further work is ongoing to determine if this is a direct result of wave grouping or the influence of long waves. For the latter, Baldock et al. (2007) found that free surf beat (free long waves in the presence of monochromatic short waves) generally promoted a trend toward a more reflective beach state, and was particularly important in controlling the morphology in the upper swash zone (see figure 9 above). Including both long wave effects and swash-swash interactions in parametric models requires further work, but is also likely to require a probabilistic approach.

CONCLUSIONS

A probabilistic framework has been presented to include random wave runup and swash sediment transport in parametric swash sediment transport models. Runup elevations and swash hydrodynamics are based on established parametric models. Sediment transport calculations are based on well-established total load transport formula. The magnitude and relative weighting of the swash transport are obtained for a random wave field by assuming Rayleigh distributed runup and nearshore bore heights. The model provides good estimates of uprush sediment transport over a natural beach berm. The model is incorporated within a beach profile model, but is not yet a full predictive tool as a result of the difficulties in predicting net transport in the swash zone. An equilibrium type approach is therefore adopted, with reasonable success. The inclusion of pre-suspended sediment and long waves in these form of models is also discussed.

ACKNOWLEDGEMENTS

The present swash model is embedded within the original COSMOS model developed by Rob Nairn at Imperial College in 1990. The authors gratefully acknowledge the continued use of that model.

REFERENCES

Alsina, J. M., Baldock, T. E., Hughes, M. G., Weir, F. and Sierra, J. P., (2005). Sediment transport numerical modelling in the swash zone. Proc. Coastal Dynamics, April 2005, Barcelona, ASCE.

Bagnold, R.A., (1966). An approach to the sediment transport problem from general physics. Geological Survey Professional paper 422-I. 37pp.

Baldock T. E. and Holmes P., (1997). Swash hydrodynamics on a steep beach. Proc. Coastal Dynamics'97, Plymouth, ASCE, 784-793.

Baldock, T. E., Holmes, P., Bunker, S. and Van Weert, P., (1998). Cross-shore hydrodynamics within an unsaturated surf zone. Coastal Engineering, 34, 173-196.

Baldock, T. E., and Hughes, M. G., (2006). Field observations of instantaneous water slopes and horizontal pressure gradients in the swash zone. Continental Shelf Research, 26, 574-588.

Baldock, T.E., P. Manoonvoravong and P. Kim Son, (2007). Beach face morphology and surf beat sediment transport in the surf and swash zones. Submitted to J. Coastal Res.

Cox, D. T., W. A. Hobensack, and A. Sukumaran, (2000), Bottom stress in the inner surf and swash zone, in Coastal Engineering: Proc. 27th Int. Conf. Coastal Engineering, Sydney, Am. Soc. of Civ. Eng., Reston, Va.

Holmes, P. and Baldock, T.E., (1997). Numerical and physical modeling of beach profile evolution. EPSRC Final report. Imperial College, UK, unpublished.

Hughes M. G., (1995). Friction factors for wave uprush. J. Coastal Res., 13, 1089-1098.

Hughes, M. G. and Baldock, T. E., (2004). Eulerian flow velocities in the swash zone: field data and model predictions. J. Geophys. Res., 109, C08009.

Hughes, M.G., Aagaard, T., Baldock, T. E., (2007). Suspended Sediment in the Swash Zone: Heuristic Analysis of the Spatial and Temporal Variation in Concentration. J.

Coastal Res., in press.
Hunt, I. A., (1959). Design of seawalls and breakwaters. Proc. Amer. Soc. Civ. Eng., 85, 123-152.
Karambas, T.V., (2006). Prediction of sediment transport in the swash-zone by using a nonlinear wave model. Continental Shelf Research 26 (2006) 599–609
Kobayashi, N., DeSilva, G. S. and Watson, K. D., (1989). Wave transformation and swash oscillation on gentle and steep slopes. J. Geophys. Res., 94, 951-966.
Kobayashi, N., Johnson, B.D., (2001). Sand suspension, storage, advection, and settling in surf and swash zones. Journal of Geophysical Research 106 (C5), 9363–9376.
Kudo, A. (1995). The advection of fluid particles into the swash zone. Research thesis report, Div. Civil Engineering, University of Queensland.
Masselink G. and Hughes M.G, (1998). Field investigation of sediment transport in the swash zone. Continental Shelf Research, 18, 1179-1199.
Masselink, G., Li, L., (2001). The role of swash infiltration in determining the beachface gradient: a numerical study. Mar. Geol. 176, 139– 156.
Nairn, R. B., (1990). Prediction of cross-shore transport and beach profile evolution. Ph.D Thesis, Imperial College, UK.
Nielsen P., (1992). Coastal bottom boundary layers and sediment transport, Advanced series on ocean engineering, World Scientific, Singapore, 4. 324.
Nielsen, P., (2002). Shear stress and sediment transport calculations for swash zone modelling, Coastal Eng., 45, 53-60.
Nielsen, P. and Hanslow, D. J., (1991). Wave runup distributions on natural beaches. J. Coastal Research, 7, (4), 1139-1152.
Pritchard, D. and Hogg., A. J., (2005). On the transport of suspended sediment by a swash event on a plane beach. Coastal Engineering, 52, 1-23.
Puleo, J. A., Beach, R. A., Holman, R. A. and Allen J. S., (2000). Swash zone sediment suspension and transport and the importance of bore induced turbulence. J. Geophys. Res., C7, 105, 17021-17044.
Puleo, J.A., K.T. Holland, N.G. Plant, D.N. Slinn, and D.M. Hanes, (2003). Fluid acceleration effects on suspended sediment transport in the swash zone, *J. Geophys. Res., 108*, 3350, doi:10.1029/2003JC001943.
Raubenheimer, B., S. Elgar, and R.T. Guza, (2004). Observations of swash zone velocities: a note on friction coefficients. J. Geophys. Res., 109, C01027.
Roelvink, J.A., (1993). Surf Beat and Its Effect on Cross-Shore Profiles. Ph.D Thesis, DUT, 116p.
Ruessink, B.G., D.J.R. Walstra and H.N. Southgate, (2003). Calibration and verification of a parametric wave model on barred beaches. Coastal Engineering, 48, 139-149.
Turner, I. L., (1995). Simulating the influence of groundwater seepage on sediment transported by the sweep of the swash zone across macro-tidal beaches. *Mar. Geol*., 125, 153-174.
Turner, I.L. and G. Masselink, (1998). Swash infiltration-exfiltration and sediment transport. Journal of Geophysical Research, 103(C13), 30,813-30,824.
Weir, F.M., Baldock, T.E., Hughes, M.G., (2005). Berm development and lagoon closure on a gently sloping beach. Proc. Coastal Dynamics '05, ASCE.

MODELLING SHEET FLOW SEDIMENT TRANSPORT USING CONVOLUTION INTEGRALS

P. Guard[1], I. Teakle[2], P. Nielsen[1], T.Baldock[1]

1. Coastal Engineering Research Centre, Division of Civil Engineering, University of Queensland, St Lucia, Qld 4072, Australia. p.guard@uq.edu.au.
2. WBM Pty Ltd, PO Box 203, Spring Hill, Qld 4004, Australia. iateakle@wbmpl.com.au

Abstract: Existing simple, practical models used to predict the transport rate of cohesionless sediment in the sheet flow regime have obvious shortcomings. They generally relate the transport rate directly to the velocity just outside the boundary layer or to an estimate of the instantaneous bed shear stress. Such models neglect important unsteady flow effects such as phase lags between the flow forcing and the bed shear stress and between the bed shear stress and the transport rate. Most also fail to account for the influence of the acceleration time history on the magnitude of the bed shear stress. In this paper a new simple, practical model is developed that aims to provide similar prediction accuracy as more complex process-based models without the computational expense. Convolution integrals are employed to obtain solutions for the governing differential equations in the time domain while accounting for the important unsteady flow effects.

INTRODUCTION

Simple, practical models for sheet flow sediment transport in the coastal environment have evolved from those developed for steady flows in riverine environments. The simplest of these express the transport rate as a function of the near-bed orbital velocity (e.g. Bailard, 1981; Ribberink, 1998). Such models operate under the assumption that the transport rate responds instantaneously to changes in the near-bed wave induced velocity (i.e. that the process is quasi-steady). However, in the coastal environment this assumption is often invalid due to the unsteady and non-uniform nature of the hydrodynamics. Within the wave boundary layer substantial phase differences may exist between the free stream velocity and bed shear stress, and between bed shear stress and sediment transport rate. Also, for a given free stream velocity, the bed shear stress depends on the time taken to accelerate to that velocity. Models that relate the transport rate directly to the near-bed velocity do not account for these unsteady flow effects.

Sediment transport models at an intermediate level of complexity express the instantaneous transport rate as a function of an estimated bed shear stress or Shields parameter. The calculation of the Shields parameter $\theta(t)$ in an oscillating flow generally requires the use of a boundary-layer model. Simple formulae that attempt to bring in the influence of acceleration on the magnitude and phase of the bed shear stress have been proposed. Nielsen (2006) developed a model of this type that accounts for both acceleration skewness and boundary layer streaming present under real waves. However, such models fail to account for suspension hysteresis, where the amount of mobilised sediment depends on the past history of $\theta(t)$, which is important for finer sands and shorter wave periods.

At a higher level of complexity, process-based models have been developed that solve the continuity and momentum equations for both the fluid and sediment phases down into the mobile bed (e.g. Hsu, 2002; Teakle, 2006). These 1DV models resolve the instantaneous velocity and concentration profiles, which enables calculation of both instantaneous and net sediment flux. However, at present these models are too computationally expensive for practical use in engineering applications.

There is therefore a need for simple, practical sediment transport models that include sufficient physics to account for unsteady flow effects and suspension hysteresis. Teakle (2006) proposed a model framework based on the use of convolution integrals. This approach allows solution of the governing differential equations in the time domain for an arbitrary forcing function. This idea is developed further in this paper and the model is parameterised using results from a detailed two phase process-based model developed by Teakle (2006). The objective is to predict the net transport rate with a similar accuracy to the more detailed process-based model without the computational expense.

MODEL DESCRIPTION

A flowchart outlining the model structure is presented in Figure 1. The near-bed velocity time series is the primary input for the model. The instantaneous bed shear stress (and non-dimensional Shields parameter) is estimated by solving the linearised boundary layer equations in the time domain using a convolution integral technique. The Shields parameter is used as the driver for a pickup function. Assuming a particular sediment entrainment mechanism, solutions for the vertical sediment distribution were presented by Nielsen (1992). These solutions are used as the basis for a convolution integral formulation that calculates the vertically integrated amount of mobilised sediment. Finally, the instantaneous sediment transport rate q_s is determined by multiplying the amount of mobilised sediment by an effective transport velocity. The effective transport velocity is estimated by another convolution integral formulation.

The formulae used in the model were parameterised using results from a detailed process-based model developed by Teakle (2006). This model has achieved success in representing much of the important physics in mobile bed boundary layers. The process-based model was used for the parameterisation because laboratory measurements of sheet flow velocity and concentration profiles are limited in detail and accuracy. The process-based model results can be analysed to reveal the instantaneous value of the important terms in the momentum and mass balances at any phase of the flow.

Overall model performance was assessed by comparing the net transport rates predicted by the model to the measured net transport rates in 104 test cases from European and Japanese oscillatory flow tunnel and wave flume experiments (Dohmen-Janssen et al., 2002; O'Donoghue and Wright, 2004; Ribberink and Al-Salem, 1995; Ribberink and Chen, 1993; Ribberink et al., 2000; Watanabe and Sato, 2004). The experimental parameters of the test cases are shown in Table 1. The Japanese data is from tunnel experiments with velocity time-series representing forward-leaning "saw-tooth" wave profiles with non-zero acceleration skewness. The wave shape was characterised by

$$\beta = 1 - T_{cu} / T_c = T_{cd} / T_c \qquad (1)$$

as illustrated in Figure 2. Three of the test cases (W&S test 28, Ribberink B8 and Aberdeen LS915) are used to illustrate examples of the model output in this paper.

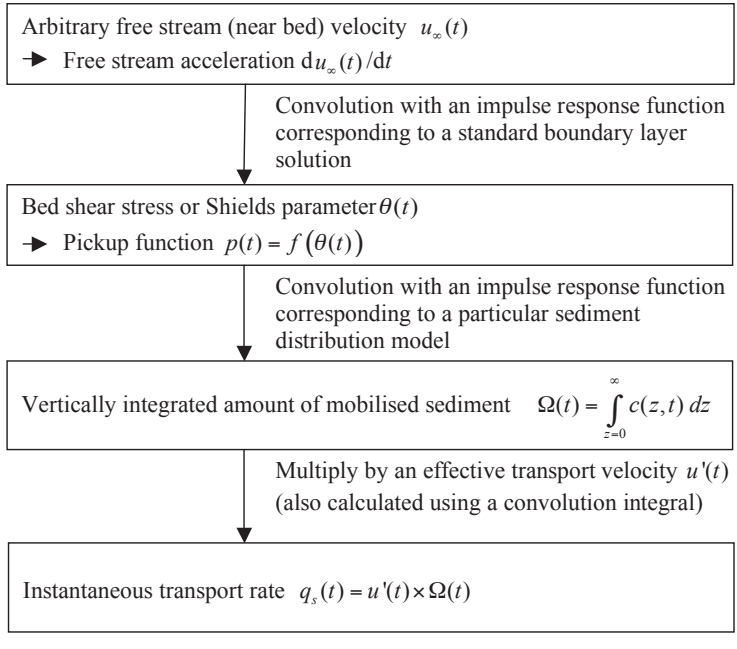

Figure 1: Model flowchart

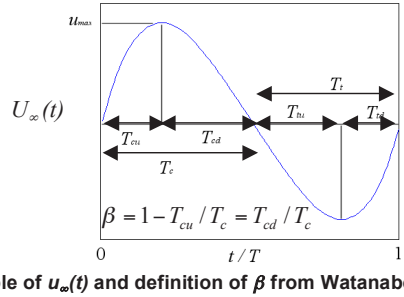

Figure 2: Example of $u_\infty(t)$ and definition of β from Watanabe and Sato (2004)

Table 1: Laboratory test cases used to assess overall model performance

Data from LOWT, AOFT, Hannover wave flume(*)

Test	T [s]	d_{50} [mm]	U_1 [m/s]	U_0 [m/s]	U_2 [m/s]	q_s [m^2/s]
H2	7.2	0.13	0.68	0.23	0	18.8
H3	7.2	0.13	0.93	0.24	0	34.9
H4	7.2	0.13	1.09	0.25	0	40.0
H5	7.2	0.13	1.3	0.24	0	51.7
H6	7.2	0.13	1.47	0.24	0	65.5
H7	7.2	0.13	0.49	0.42	0	15.6
H8	7.2	0.13	0.67	0.43	0	47.4
H9	7.2	0.13	0.94	0.43	0	85.7
H24	4.0	0.13	0.68	0.24	0	12.8
H44	4.0	0.13	1.06	0.25	0	9.0
H212	12.0	0.13	0.68	0.23	0	19.9
H412	12.0	0.13	1.09	0.24	0	97.1
D11	6.5	0.13	0.795	0.02	0.185	9.0
D14	6.5	0.13	0.635	0.02	0.138	7.6
D12	6.5	0.13	1.27	0.06	0.268	-228.3
D13	6.5	0.13	1.03	0.04	0.229	-30.2
I1	7.2	0.32	1.47	0.26	0	94.0
I2	7.2	0.32	1.7	0.25	0	152.3
I3	7.2	0.32	0.65	0.42	0	23.6
I4	7.2	0.32	0.92	0.42	0	53.3
I5	7.2	0.32	1.5	0.45	0	193.7
J1	7.2	0.21	1.06	0.24	0	46.3
J2	7.2	0.21	1.28	0.25	0	74.4
E2	7.2	0.21	1.47	0.23	0	111.8
J3	7.2	0.21	0.46	0.41	0	9.0
J4	7.2	0.21	0.65	0.41	0	25.3
E4	7.2	0.21	0.95	0.44	0	84.4
J5	4.0	0.21	1.04	0.24	0	29.2
J6	12.0	0.21	1.09	0.23	0	49.2
C1	6.5	0.2	0.845	0.00	0.24	20.0
C2	9.1	0.2	0.865	0.00	0.23	28.0
B6	9.1	0.21	0.91	-0.024	0.229	12.0
B7	6.5	0.21	0.73	0.048	0.177	12.4
B8	6.5	0.21	1.01	0.038	0.267	38.9
B9	6.5	0.21	1.29	0.030	0.400	69.8
B10	9.1	0.21	0.75	0.020	0.195	18.6
B11	9.1	0.21	0.97	0.022	0.258	44.8
B12	9.1	0.21	1.37	0.029	0.351	120.9
B13	6.5	0.21	1.05	0.010	0.140	21.0
B14	9.1	0.21	1.06	-0.06	0.199	22.0
B15	5.0	0.21	0.76	0.030	0.190	15.2
B16	12.0	0.21	0.83	0.005	0.195	20.0
MA5010	5	0.28	1.19	0	0.31	52.6
MA7515	7.5	0.28	1.19	0	0.31	35.9
CA5010	5	0.51	1.19	0	0.31	44.1
CA7515	7.5	0.51	1.19	0	0.31	33.8
LA406	4	0.15	1.01	0	0.262	-8.1
FA5010	5	0.15	1.19	0	0.31	-128.0
LA612	6	0.15	1.19	0	0.31	-61.0
FA5015	7.5	0.15	1.19	0	0.31	-88.3
Me*	9.2	0.25	0.96	-0.05	0.413	105.0
Mf*	9.1	0.25	0.93	-0.04	0.371	75.0
Mh*	6.5	0.25	0.88	-0.04	0.230	42.0
Mi*	6.4	0.25	0.84	-0.05	0.176	35.0

Data from Watanabe and Sato (2004)

Test	d_{50} [mm]	T [s]	U_1 [m/s]	U_0 [m/s]	β [-]	q_s [m^2/s]
1	0.2	3	1.06	0	0.547	27
2	0.2	3	1.3	0	0.68	153
3	0.2	3	1.25	0	0.6	80.3
4	0.2	3	1.48	0	0.68	161
5	0.2	3	1.1	0	0.68	78.2
6	0.2	3	1.42	0	0.547	64.4
7	0.2	3	1.43	0	0.6	123.4
8	0.2	3	1.07	0	0.6	50.6
9	0.2	3	1.24	0	0.547	50.6
10	0.2	3	0.71	0	0.547	4.1
11	0.2	3	0.74	0	0.6	7.4
12	0.2	3	0.74	0	0.68	17.9
13	0.2	3	0.88	0	0.547	11
14	0.2	3	0.88	0	0.6	20.7
15	0.2	3	0.92	0	0.68	50.6
16	0.74	3	1.06	0	0.547	39.5
17	0.74	3	1.07	0	0.6	85.9
18	0.74	3	1.1	0	0.68	90.7
19	0.74	3	1.42	0	0.547	6.6
20	0.74	3	1.43	0	0.6	43.5
21	0.74	3	1.48	0	0.68	149.8
22	0.2	5	0.86	0	0.68	4.7
23	0.2	5	0.86	0	0.6	3.4
24	0.2	5	0.86	0	0.547	-3.05
25	0.2	5	1.45	0	0.68	149.8
26	0.2	5	1.44	0	0.6	97.4
27	0.2	5	1.44	0	0.547	27.8
28	0.2	5	1.27	0	0.68	77.4
29	0.2	5	1.26	0	0.6	31.6
30	0.2	5	1.26	0	0.547	14.2
31	0.2	5	1.09	0	0.68	32.5
32	0.2	5	1.09	0	0.6	14.9
33	0.2	5	1.09	0	0.547	1.4
34	0.2	3	1.25	-0.2	0.547	-18.6
35	0.2	3	1.25	-0.2	0.6	-6.75
36	0.2	3	1.25	-0.2	0.68	55.4
37	0.2	3	1.07	-0.2	0.547	-36.7
38	0.2	3	1.07	-0.2	0.6	-2.1
39	0.2	3	1.07	-0.2	0.68	33
40	0.2	3	1.43	-0.2	0.547	-38.3
41	0.2	3	1.43	-0.2	0.6	42.53
42	0.2	3	1.43	-0.2	0.68	80.07
43	0.2	3	1.6	-0.2	0.547	-74.3
44	0.2	3	1.25	-0.1	0.547	4.64
45	0.2	3	1.25	-0.1	0.6	48
46	0.2	3	1.25	-0.1	0.68	82.9
47	0.2	3	1.07	-0.1	0.547	-5.9
48	0.2	3	1.07	-0.1	0.6	12.8
49	0.2	3	1.07	-0.1	0.68	39.6
50	0.2	3	1.43	-0.1	0.547	13.1
51	0.2	3	1.43	-0.1	0.6	65.5
52	0.2	3	1.43	-0.1	0.68	147.9

Bed Shear Stress

The equation of motion within the boundary layer (assuming horizontal uniformity) is

$$\rho \frac{\partial u}{\partial t} = -\frac{\partial P}{\partial x} + \frac{\partial \tau}{\partial z} \tag{2}$$

where u is the horizontal velocity, P is pressure and τ is shear stress. With the assumption of hydrostatic pressure and adopting the Boussinesq eddy viscosity assumption describing the turbulent diffusion of momentum, equation (2) becomes

$$\frac{\partial u}{\partial t} = \frac{\partial u_\infty}{\partial t} + \nu_t \frac{\partial^2 u}{\partial z^2} \tag{3}$$

For the simplest case of constant and uniform eddy viscosity, the velocity profile and bed shear stress for a simple harmonic driver $u_\infty(t) = \mathrm{Re}\left\{Ae^{i\omega t}\right\}$ are given by

$$u(z,t) = \mathrm{Re}\left\{ A\omega \left(1 - e^{-(1+i)\frac{z}{\sqrt{2\nu_t/\omega}}} \right) e^{i\omega t} \right\} \tag{4}$$

$$\tau(0,t) = \mathrm{Re}\left\{ \rho(1+i)\sqrt{\frac{\nu_t \omega}{2}} A\omega e^{i\omega t} \right\} \tag{5}$$

Nielsen (1992) found that a constant, uniform eddy viscosity is a reasonable assumption for flows in the natural roughness range.

The frequency response function for the bed shear stress from input $\frac{\partial u_\infty}{\partial t}$ is then

$$F(\omega) = \rho(1-i)\sqrt{\frac{\nu_t}{2\omega}} \tag{6}$$

The bed shear stress for arbitrary $u_\infty(t)$ can be found by obtaining the Fourier transform of $\frac{\partial u_\infty}{\partial t}$, multiplying by the frequency response function (6), and obtaining the inverse Fourier transform of the result. Alternatively, the equivalent calculation can be carried out in the time domain by convolution of $\frac{\partial u_\infty}{\partial t}$ with an appropriate impulse response function $f(t)$:

$$\tau(0,t) = \int_{t'=0}^{t} f(t-t') \frac{\partial u_\infty}{\partial t'} dt' \tag{7}$$

The impulse response function is found by inverse Fourier transform of the frequency response function. The appropriate convolution integral for calculation of bed shear stress based on the free stream acceleration time series is

$$\tau(0,t) = \rho\sqrt{\frac{\nu_t}{\pi}} \int_{t'=0}^{t} \frac{\frac{\partial u_\infty}{\partial t'}}{\sqrt{t-t'}} dt' \tag{8}$$

This is a useful expression for the estimation of bed shear stress based on the history of the free stream acceleration. Past values of the free stream acceleration are weighted according to the time elapsed. In practice the integral may be used in discrete form and the limit truncated (typically to within a few wave periods), since the magnitude of the impulse response function decays as (t-t') increases.

A convolution integral formula for the calculation of $\tau(0,t)$ can also be derived where the eddy viscosity is a function of distance from the bed. For an eddy viscosity prescribed by

$$\nu_t(z) = C_1\, u_* z^p \tag{9}$$

where C_1 is a dimensional constant, u_* a representative friction velocity and power $0 \le p < 1$, Liu (2006) showed that the leading-order expression for the bed shear stress is

$$\tau(0,t) = C_2 \frac{(1-q)^{2q-1}}{\Gamma(q)} \int_{t'=0}^{t} \frac{\frac{\partial u_\infty}{\partial t'}}{(t-t')^q} dt' \quad \text{where} \quad q = \frac{1-p}{2-p} \tag{10}$$

In terms of Liu's scaling parameters, the dimensional C_2 constant is

$$C_2 = \rho \sqrt{\nu_t(z_0) A^{2q-1} g^{0.5-q} h^{0.5-q}} \tag{11}$$

where A is a horizontal length scale (here taken to be the typical near-bed orbital amplitude), and h is depth. Replacing Liu's velocity scale $\sqrt{gh}$ by $A\omega$ and adopting Nielsen's (1992) empirical expression for the eddy viscosity at the bed $\nu_t(z_0) \sim rA\omega$ where r is the bed roughness, we obtain

$$\tau(0,t) = C_3 \rho \sqrt{rA}\, \omega^{1-q} \int_{t'=0}^{t} \frac{\frac{\partial u_\infty}{\partial t'}}{(t-t')^q} dt' \tag{12}$$

The solution for constant, uniform eddy viscosity is recovered for q=1/2, p=0.
The convolution technique is only useful for the prediction of the bed shear stress due to unsteady components of the forcing signal. In the derivation of (10) the velocity was assumed to be zero at time t=0 and therefore any bed shear stress due to a mean component of the velocity signal must be considered separately. Various ways of incorporating the steady component of the forcing were trialled, and it was found that

$$\tau(0,t) = C_4 \rho \sqrt{rA}\, \omega \left(\int_{t'=0}^{t} \frac{\frac{\partial u_\infty}{\partial t'}}{(t-t')^q \omega^q} dt' + C_5 U_0 \right) \tag{13}$$

performed well with C_5=0.35, where U_0 is the steady component of the forcing. This can be rationalised by considering that the two terms in the bracket on the right hand side of equation (13) have units of velocity, and the appropriate scaling is provided by the terms outside the brackets. A C_4 value of 0.043 was found to lead to successful predictions for the magnitude of maximum shear stress at the initial bed level compared to the process-based model. A value of q=1/8 was found to accurately predict the phase of the maximum shear stress. Considerable uncertainty surrounds the appropriate value for an equivalent roughness height r for mobile beds. A value of $100d_{50}$ was used in this parameterisation based on energy dissipation data (see Nielsen, 1992 p.155). The Shields parameter is

$$\theta(t) = \frac{\tau(0,t)}{\rho(s-1)g d_{50}} \tag{14}$$

For each of the test cases considered, the results from equations (13) and (14) were compared to the Teakle (2006) process-based model results for the total shear stress at the initial bed level. Examples of the predictions of the two models for the three sample test cases are shown in Figure 3.

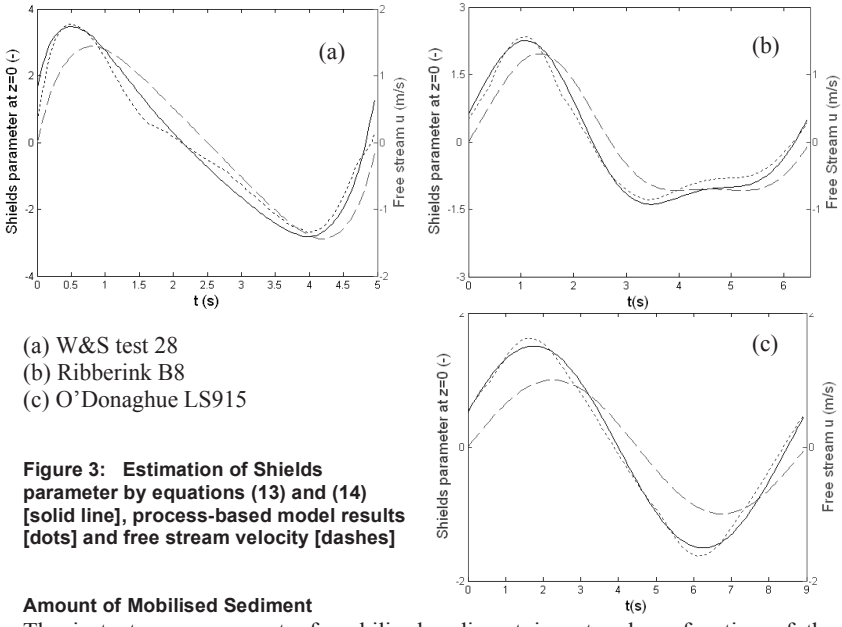

(a) W&S test 28
(b) Ribberink B8
(c) O'Donaghue LS915

Figure 3: Estimation of Shields parameter by equations (13) and (14) [solid line], process-based model results [dots] and free stream velocity [dashes]

Amount of Mobilised Sediment

The instantaneous amount of mobilised sediment is not only a function of the instantaneous value of the bed shear stress but also its immediate past values, since sediment will remain entrained in the flow for some time once it has been picked up. Nielsen and Callaghan (2003) found that for fine sands with $d_{50} < 0.2$mm and wave periods $T < 6$s, phase lags between bed shear stress and the amount of mobilized sediment become important. The use of a convolution integral is an obvious way to bring in the influence of the history of $\theta(t)$.

For a horizontally uniform situation, the sediment conservation equation can be written as a balance between a gravitational settling flux $-w_0 c$ and an upward flux q_z:

$$\frac{\partial c}{\partial t} = w_0 \frac{\partial c}{\partial z} - \frac{\partial q_z}{\partial z} \tag{15}$$

Nielsen (1992) presented two alternative solutions to this equation based on whether the upward flux is due to turbulent convection or diffusion. In each case a pickup function prescribed on the bottom boundary is used to drive the model. For an arbitrary pickup function $p(t)$, Fourier analysis can be used to calculate the overall concentration profile $c(z,t)$ by linear superposition of each harmonic component. The alternative is to use a convolution integral, which enables solution in the time domain. The Shields parameter is used as the driver in a pickup function $p(t)$. The amount of entrained sediment is then

$$\Omega(t) = \int_{z=0}^{\infty} c(z,t)\, dz = \int_{t'=0}^{t} p\left(t'\right) f\left(t - t'\right) dt' \tag{16}$$

where $f(t)$ is an appropriate impulse response function corresponding to the vertically integrated sediment distribution model.

For the convective model with an exponentially decaying distribution function $e^{-\frac{z}{L_c}}$, the impulse response function for the total amount of sediment entrained based on input *p(t)* is (Teakle, 2006):

$$f_C(t) = \frac{w_c}{w_0 + w_c} e^{-\frac{w_0 w_c}{L_c(w_0 + w_c)}t} \tag{17}$$

where L_c is a convective distribution length scale and w_c is a vertical convection velocity. For the diffusive model with constant, uniform sediment diffusivity K_s, the impulse response function is (Teakle, 2006):

$$f_D(t) = \left(1 + \frac{\zeta}{2}\right) - \left(1 + \frac{\zeta}{2}\right) \mathrm{erf}\left(\frac{\sqrt{\zeta}}{2}\right) - \sqrt{\frac{\zeta}{\pi}} e^{-\frac{\zeta}{4}} \tag{18}$$

where

$$\zeta = \frac{w_0^2 t}{K_s} \tag{19}$$

The form of the pickup function needed in the new model framework was determined by back-calculation using Fourier analysis of the Teakle (2006) process-based model results. The required pickup function was found to be of the form

$$p(t) = C_6 w_0 \left|\theta(t) - 0.05\right| \tag{20}$$

where dimensionless coefficient C_6 was found to be approximately 0.1. This expression resembles the pickup function recommended by Nielsen (1992) p.226 except that the Shields parameter is raised to a power of 1 instead of 1.5. A comparison of the pickup function back-calculated from the Teakle (2006) model and from equation (20) for the example test cases is shown in Figure 4. The pickup is seen to occur ahead of the free stream velocity and has a greater magnitude where the free stream acceleration is greater.

The amount of sediment entrained in the flow is calculated using equations (16) and either (17) or (18). Here, an example is given for the diffusive model with constant, uniform sediment diffusivity K_s. The sediment diffusivity K_s was empirically parameterised by analysing results from the process-based model. The following expression was found to perform well:

$$K_s = C_7 \, g \frac{r^{1.5}}{A^{0.5}\omega} \tag{21}$$

where C_7=0.005. The inverse relationship with ω is interesting, since we might have expected the sediment diffusivity to decrease with increasing wave period, as does the eddy viscosity $\nu_t \sim rA\omega$. However, Nielsen (1992) noted on the basis of flume data that the sediment diffusivity needs to be an increasing function of w_0/u_*, which may account for the form of equation (21). In addition, analysis of sheet flow experimental data by Dohmen-Janssen (1999) revealed that the sediment diffusivity derived from the time-averaged concentration profiles increased with increasing period.

Examples of the model output compared to the process-based model results are shown in Figure 5. More sediment is mobilised where the acceleration magnitude is greater.

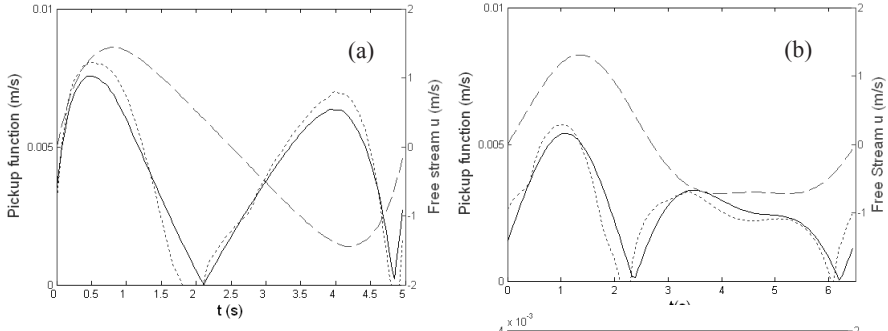

(a) W&S test 28
(b) Ribberink B8
(c) O'Donaghue LS915

Figure 4: Pickup function by equation (20) [solid line], back-calculated pickup function from the process-based model [dots] and free stream velocity [dashes]

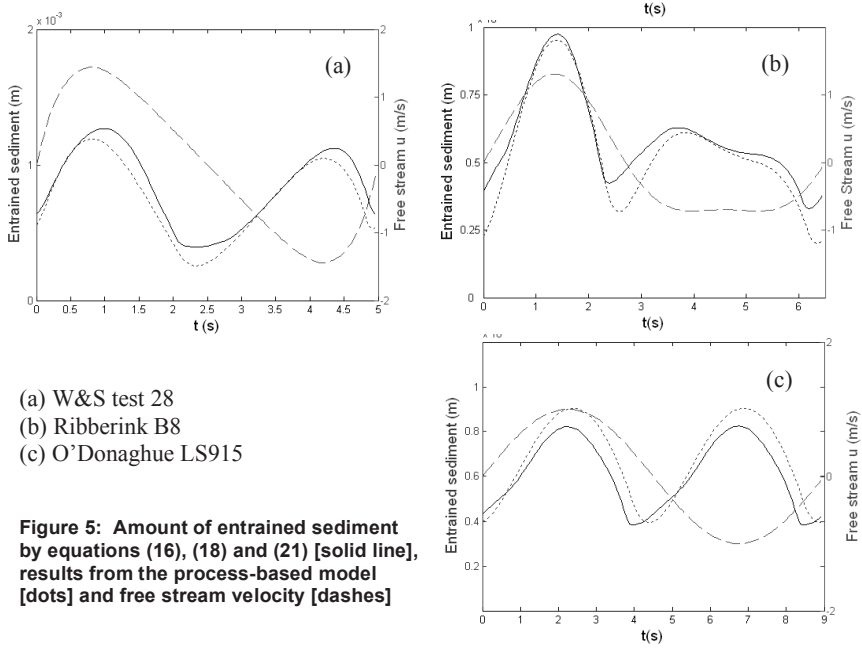

(a) W&S test 28
(b) Ribberink B8
(c) O'Donaghue LS915

Figure 5: Amount of entrained sediment by equations (16), (18) and (21) [solid line], results from the process-based model [dots] and free stream velocity [dashes]

The Effective Transport Velocity

The effective transport velocity was also parameterised by analysing the results of the process-based model. The target effective transport velocity was found by dividing the instantaneous horizontal sediment flux from the process-based model results by the vertically integrated amount of entrained sediment:

$$u'(t)_{\text{target}} = \frac{\int_{z=z_0}^{\infty} c(z,t)\,u_s(z,t)\,dz}{\int_{z=0}^{\infty} c(z,t)\,dz} \tag{22}$$

where z_0 is the instantaneous bed elevation. It was found that for the majority of the test cases considered, the phase and magnitude of the effective transport velocity was accurately predicted by

$$u'(t) = C_6 \frac{A^{0.7}}{r^{0.2} g^{0.5}} \omega^{1-q} \int_0^t \frac{\dfrac{\partial u}{\partial t'}}{(t-t')^q}\,dt' \tag{23}$$

with q=1/8 and C_6=1.16. Examples of the equation (23) results compared to the process-based model are shown in Figure 6. The effective transport velocity is in phase with the bed friction velocity and is enhanced where the acceleration is greater.

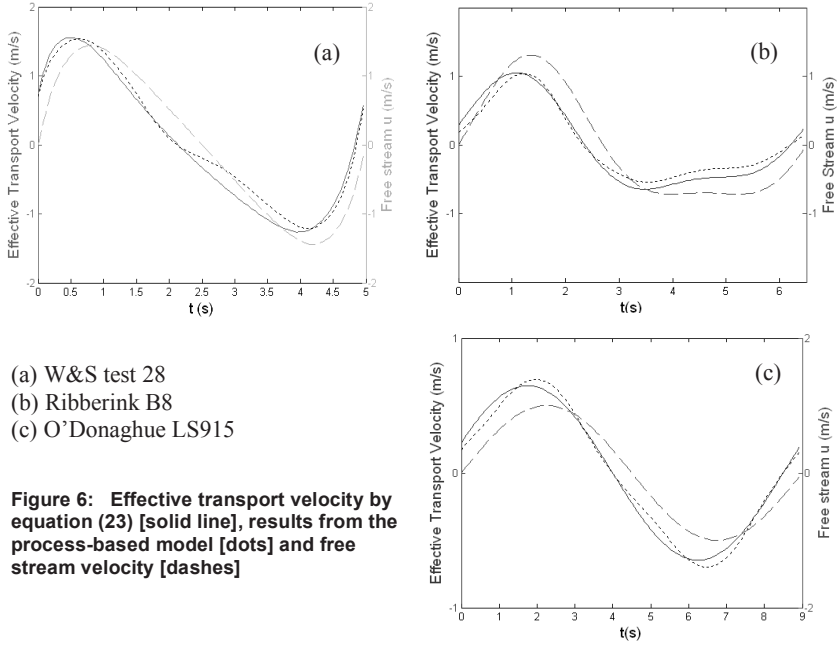

(a) W&S test 28
(b) Ribberink B8
(c) O'Donaghue LS915

Figure 6: Effective transport velocity by equation (23) [solid line], results from the process-based model [dots] and free stream velocity [dashes]

The Instantaneous Transport Rate

The instantaneous transport rate is found by multiplying the instantaneous amount of entrained sediment from (16) by the effective transport velocity from (23).

$$q_s(t) = \Omega(t)u'(t) \tag{24}$$

An example of results from (24) compared to the process-based model results is shown in Figure 7. It is clear that the magnitude of the onshore transport is enhanced by acceleration effects.

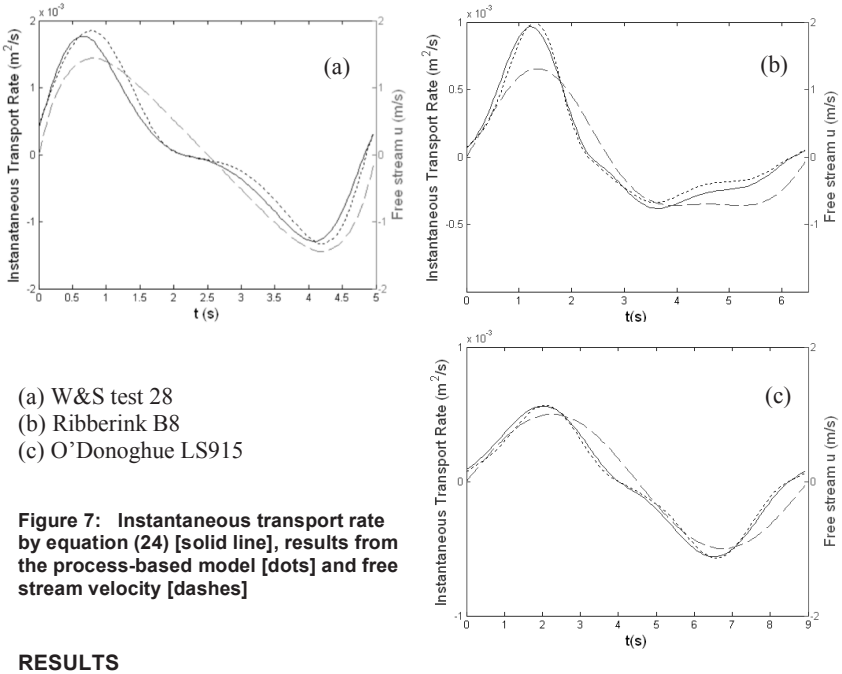

(a) W&S test 28
(b) Ribberink B8
(c) O'Donoghue LS915

Figure 7: Instantaneous transport rate by equation (24) [solid line], results from the process-based model [dots] and free stream velocity [dashes]

RESULTS

The fully parameterised model was run for the 104 test cases listed in Table 1. The net sediment transport predictions of three simple models compared to the measured net transport rates are plotted in Figure 8.

The first model is the simplest, based on a net transport rate directly proportional to the mean of the velocity cubed and ($q_s \sim \overline{u^3}$). Note the poor performance, particularly for the Watanabe and Sato tests where positive net transport was observed for $\overline{u^3} \le 0$.

The second model presented is that of Nielsen (2006) calibrated with a phase angle $\phi_\tau = 47°$. The inclusion of acceleration effects is seen to produce a considerable improvement in model prediction skill compared to the velocity moment model, since the sum of squares of normalised errors is considerably reduced.

The third model presented is the current convolution integral formulation. Note that the agreement is generally within a factor of 2, which is considered to be good performance for a relatively simple model. The sum of squares of normalised errors was further reduced compared to the Nielsen model, demonstrating improved model prediction skill. An area for future improvement is grain size dependence, since the model performance was poorer for the coarser sediment (d_{50}>0.5mm) and finer sediment (d_{50}<0.15mm).

(a) Velocity moment model $q_s \sim \overline{u^3}$

$$\sum \left(\frac{q_{\text{model}} - q_{\text{meas}}}{q_{\text{meas}}} \right)^2 = 25$$

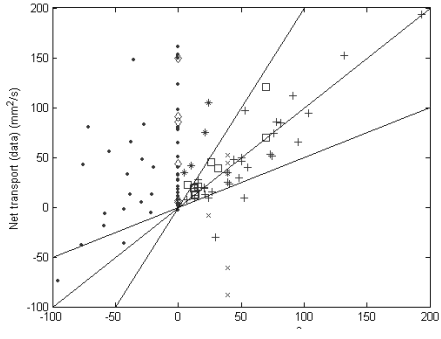

(b) Calibrated Nielsen (2006) model with $\phi_\tau = 47°$

$$\sum \left(\frac{q_{\text{model}} - q_{\text{meas}}}{q_{\text{meas}}} \right)^2 = 13$$

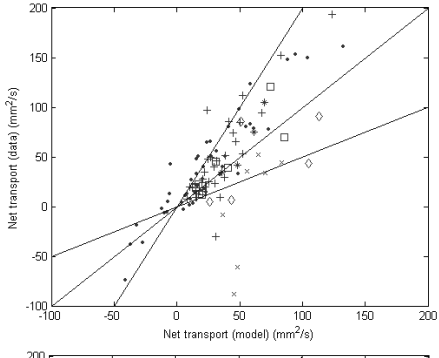

(c) New convolution integral model

$$\sum \left(\frac{q_{\text{model}} - q_{\text{meas}}}{q_{\text{meas}}} \right)^2 = 9$$

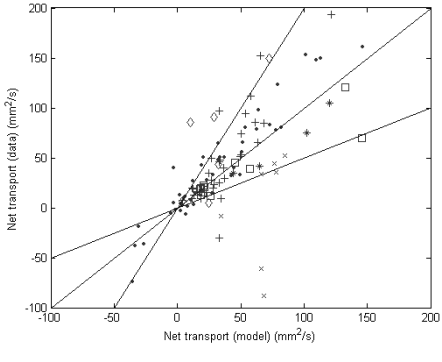

Figure 8: Model results for the net transport rate compared to laboratory data. Watanabe and Sato (0.2mm sand, dots; 0.74mm sand, diamonds), Ribberink and coworkers (Series B, squares; Others, plusses), O'Donoghue and Wright (crosses). The lines indicate a factor 2 difference between model results and data

DISCUSSION

Employing the detailed process-based model of Teakle (2006) to parameterise the new model is justified by the good performance of the new model in predicting net transport rates from tunnel experiments. Although improvements have been made in the measurement of instantaneous velocity and concentration profiles in laboratory experiments, the data is still not of sufficient quality or quantity to effectively enable model parameterisation directly from the measurements.

The effects of acceleration on the bed shear stress and hence the pickup of sediment have been captured by the adopted convolution integral formulation equation (12). The direct action of the pressure gradient on sediment grains may also become important for lightweight sediments and coarse particles, as noted by Sleath (1999). This effect could be included in the model by an extra term in the pickup function related directly to the instantaneous free stream acceleration.

The phenomenon of secondary entrainment of sediment at flow reversal may also be treated by modifying the pickup function. Inclusion of this effect would improve the convolution model performance shown in Figure 8, particularly where $d_{50} < 0.2$ mm.

Suspension hysteresis is particularly important where substantial amounts of sediment remain in suspension through flow reversal, reducing the net transport rate. The use of a convolution integral to solve the sediment conservation equation automatically includes such effects.

Real wave effects such as the boundary layer streaming identified by Longuet-Higgins (1957) can be easily accommodated in the model by addition of a steady component to the equation for the effective transport velocity. The offshore-directed streaming that occurs in wave tunnels simulating 2nd-order Stokes waves (due to the asymmetry of turbulence production) may be treated in a similar manner. Consideration of this process would improve the convolution model performance for many of the outliers in Figure 8.

It is hoped that the model can be extended to other sediment transport regimes such as rippled beds by modifying the form of the pickup function.

Application of the model to a horizontally non-uniform situation, e.g. the swash zone, would in general require a Lagrangian implementation since the convective terms have been neglected in the governing equations.

CONCLUSION

The simple model framework presented in this paper predicts instantaneous sediment transport rates based on simple flow parameters in a computationally efficient manner. Sufficient physics is included to represent the most important boundary layer processes, including phase lags between the flow forcing and the bed shear stress, and between the bed shear stress and the sediment transport rate. Further work will improve the model performance for fine sands ($d_{50} < 0.2$mm) and extend the model to other sediment transport regimes and non-horizontally uniform flows.

ACKNOWLEDGEMENTS

The authors gratefully acknowledge support from the Australian Research Council in the form of an APA scholarship for PG.

REFERENCES

Bailard, J.A., 1981. An energetics total load sediment transport model for a plane sloping beach. J. Geophys. Res., 86(C11): 10,938-10,954.

Dohmen-Janssen, C.M., 1999. Grain size influence on sediment transport in oscillatory sheet flow: phase lags and mobile bed effects. PhD Thesis, Delft University of Technology, 246 pp.

Dohmen-Janssen, C.M., Kroekenstoel, D.F., Hassan, W.N. and Ribberink, J.S., 2002. Phase lags in oscillatory sheet flow: experiments and bed load modelling. Coastal Engineering, 46(1): 61-87.

Hsu, T.J., 2002. A two-phase flow approach for sediment transport. . PhD Thesis, Cornell.

Liu, P.L.-F., 2006. Turbulent boundary-layer effects on transient wave propagation in shallow water. Proc Roy Soc London A, 462: 3481-3491.

Longuet-Higgins, M.S., 1957. The mechanics of the boundary layer near the bottom in a progressive wave, Proc 6th Int Conf Coastal Eng. ASCE, Miami, pp. 184-193.

Nielsen, P., 1992. Coastal bottom boundary layers and sediment transport. Advanced series on ocean engineering, v 4. World Scientific, Singapore, 324 pp.

Nielsen, P., 2006. Sheet flow sediment transport under waves with acceleration skewness and boundary layer streaming. Coastal Engineering, 53(9): 749-758.

Nielsen, P. and Callaghan, D.P., 2003. Shear stress and sediment transport calculations for sheet flow under waves. Coastal Engineering, 47(3): 347-354.

O'Donoghue, T. and Wright, S., 2004. Flow tunnel measurements of velocities and sand flux in oscillatory sheet flow for well-sorted and graded sands. Coastal Engineering, 51(11-12): 1163-1184.

Ribberink, J.S., 1998. Bed-load transport for steady flows and unsteady oscillatory flows. Coastal Engineering, 34(1-2): 59-82.

Ribberink, J.S. and Al-Salem, A.A., 1995. Sheet flow and suspension of sand in oscillatory boundary layers. Coastal Engineering, 25(3-4): 205-225.

Ribberink, J.S. and Chen, Z.W., 1993. Sediment transport of fine sand under asymmetric oscillatory flow, Report H840, Part VII, Delft Hydraulics.

Ribberink, J.S., Dohmen-Janssen, C.M., Hanes, D.M., McLean, S.R. and Vincent, C., 2000. Near-Bed Sand Transport Mechanisms Under Waves A Large-Scale Flume Experiment (Sistex 99), Proc 27th Int Conf Coastal Eng. ASCE, Sydney, pp. 3263-3276.

Sleath, J.F.A., 1999. Conditions for plug formation in oscillatory flow. Continental Shelf Research, 19: 1643-1664.

Teakle, I., 2006. Coastal boundary layer and sediment transport modelling. PhD Thesis, University of Queensland.

Watanabe, A. and Sato, S., 2004. A sheet flow sediment transport formula for asymmetric, forward-leaning waves and currents, Proc 29th Int Conf Coastal Eng. ASCE, Lisbon, pp. 1703-1714.

A MIDDLE-TERM EVOLUTION MODEL FOR BEACHES

Soledad Requejo[1], Raul Medina[2], Mauricio Gonzalez[3]

1. Ocean and Coastal Research Group, University of Cantabria, Avda. de los Castros s/n. 39005 Santander, Spain. requejos@unican.es.
2. Ocean and Coastal Research Group, University of Cantabria, Avda. de los Castros s/n. 39005 Santander, Spain. medinar@unican.es.
3. Ocean and Coastal Research Group, University of Cantabria, Avda. de los Castros s/n. 39005 Santander, Spain. gonzalere@unican.es.

Abstract: A new middle-long term beach evolution model is proposed. This model is based on an analytically integrated sediment conservation equation (without assuming any hypothesis regarding the beach profile) and on a beach profile evolution model. The sediment conservation equation provides the long-shore sediment contributions and the beach profile evolution model combines the cross-shore sediment redistribution associated to seasonal process with this long-shore supplies. The model achieves the prediction of the shoreline position and the profile shape along a beach, from middle to long term scale. Furthermore, in this beach profile evolution model, the definition of the complete profile is incorporated (breaking zone, transition zone, exterior zone and geological zone). The proposed middle-long term beach evolution model has been applied in some test cases and it has also been compared to similar models showing a good capability to predict beach evolution in plan form and profile.

INTRODUCTION

As beach erosion problems have become serious in many countries, necessary measures against erosion are being considered. In this context, the capability to predict beach evolution due to changes in natural conditions or caused by human activities is needed and the development of some tools to predict beach evolution (specifically to determine the shoreline evolution) is required.

Processes involved in beach evolution are complex, occurring at different scales and being three dimensional (3D). At present there is no model to be used in the complete scale range, from the short-term (hours) to the long-term (decades). Therefore, beach evolution models for different temporal and spatial scales are necessary. Beach evolution models can be classified depending on different aspects, perhaps one of the most prominent aspects is the temporal scale (short term: hours-days, middle term: days-years, long term: years-decades). According to the temporal scale, these models can be classified in: short-term, middle-term and long-term beach evolution models. Short-term beach evolution models are usually used for small scales (storms, hours to days). These models require a detailed data base for the calibration, validation and sensibility analysis. However, these models provide reasonably good capability to predict beach hydrodynamic and morphology on this short time scale.

Long-term beach evolution models are applied to predict beach morphology for long scales (years to decades). The classical long-term beach evolution model is the "*one-line model*" or "*shoreline model*" (e.g. GENESIS model, Hanson and Kraus 1989 and ONELINE model, Dabees and Kamphuis 1998). In this type of models, beach evolution is represented by means of the shoreline evolution, which can be well predicted based on a previous calibration and validation of the model with local data. Beach profile variation is negated and the cross-shore transport is not taken into account either. Thus, seasonal shoreline changes (summer-winter variations) and shoreline changes associated to storm events, cannot be predicted by using this type of models. Some process-based morphodynamic models applied to long-term scales have been developed in the last decades. However, as expressed by De Vriend et al. (1993), these kinds of models are not the best approach of long-term modelling. Since the natural system is nonlinear, and the validity of long-term model predictions does not follow straightforwardly from model's validity at the hydrodynamic time scale.

Middle-term beach evolution models try to predict the plan and profile variability presented by a beach in a seasonal cycle (summer-winter). The evaluation of the phenomena that occurs in this time scale presents serious difficulties given that their scale is too great to be able to use process models (wave to wave), and yet is too small to assume that it has reached an equilibrium in certain phenomena (De Vriend et al. 1993). *S*everal models have been developed trying to introduce the beach profile variation to the "*one-line models*". Three different models can be recognized: "*one-line models with a cross-shore transport term",* "*N-line models*" and "*hybrid models*". In "*one-line models with a cross-shore transport term*", a cross-shore transport term is introduced into the simplified sediment conservation equation used by "*one-line models*". However, the beach profile variation is not considered. "*N-line models*" can be defined as several "*one-line models*" connected by cross-shore transport (e.g. INLINE model, Hanson and Larson 2000 and NLINE model, Dabees and Kamphuis 2000). However, the expressions available to calculate this transport are not very reliable and by using the cross-shore transport the involved physical process is not taken into account. Furthermore, "*N-line models*", compared to the "*one-line models*", need longer computer time. Finally, "*hybrid models*" link a "*one-line model*" and a "*beach profile evolution model*". There

are different "*hybrid models*", as for example: 3DBEACH model (Larson et al. 1990), in which the GENESIS model (one-line model) is connected to the SBEACH evolution model (cross-shore model), 3D-SHORE model (Shimizu et al. 1996) and LITLINE module in the LITPACK package (DHI 2001). These kinds of models can be a tool for the middle-term. However, there are important limitations, regarding its calibration (several hydrodynamic and sediment transport parameters) and a high consuming computer time. The limitations for these kinds of models are also more critical in order to predict the combined middle-long term scales.

In this work, a behaviour-oriented beach profile evolution model in the same line as the 3DBEACH is considered the most adequate model to develop a tool for the middle-long term. Thus, following this approach, in this paper a new middle-long term beach evolution model is proposed, which is based on an analytically integrated sediment conservation equation (without assuming any hypothesis regarding the beach profile) and on a beach profile evolution model. The model is able to predict the shoreline position and the profile shape along a beach, in the middle to long term scale. It also incorporates the definition of the extended beach profile (breaking zone, transition zone, exterior zone and geological zone), which is not a process-based model, reducing the computer effort in the long-term.

INTEGRATED SEDIMENT CONSERVATION EQUATION

As most of the classical long-term beach evolution models use a simplified sediment conservation equation, in order to propose a middle-long term beach evolution model, the general sediment conservation equation has to be derived, without assuming any hypothesis regarding the beach profile.

Following Abbott and Price (1994), the sediment conservation equation is determined by using Eq. (1), indicating that the temporal variation of the sediment concentration is due to advection, diffusion and potential sources/sinks.

$$\frac{\partial c}{\partial t}+\frac{\partial}{\partial x}\left(cu_{sed}\right)+\frac{\partial}{\partial y}\left(cv_{sed}\right)+\frac{\partial}{\partial z}\left(cw_{sed}\right)=\frac{\partial}{\partial x}\left(\varepsilon_x\frac{\partial c}{\partial x}\right)+\frac{\partial}{\partial y}\left(\varepsilon_y\frac{\partial c}{\partial y}\right)+\frac{\partial}{\partial z}\left(\varepsilon_z\frac{\partial c}{\partial z}\right)+FS \quad (1)$$

where c = the sediment concentration (kg/m^3); t = time (s); (x, y, z) = spatial coordinates (m), with x the longshore coordinate, y the cross-shore coordinate and z the vertical coordinate (positive upward); $(u_{sed}, v_{sed}, w_{sed})$ = sediment velocity components (m/s); $(\varepsilon_x, \varepsilon_y, \varepsilon_z)$ = diffusion coefficient components (m^2/s) and FS = sediment concentration per unit time due to potential sources/sinks (kg/m^3/s).

In order to get the corresponding equation in two dimensions, Eq. (1) is integrated in vertical and cross-shore coordinates. In the vertical coordinate it is integrated between the bottom position (z_b) and the water surface position (z_η), in the cross-shore coordinate, it is integrated between the shoreline position (y_s) and a time-independent offshore limit position (y_e). The following considerations are taken into account: the bottom sediment

velocity is null, the cinematic condition in the water surface is introduced, the diffusive mass flux perpendicular to the contour is null on the bottom and also on the water surface, the total sediment (sand) concentration along the water column does not change over time and the bottom sediment concentration is uniform along the spatial coordinates x and y. After that, Eq. (2) is obtained.

$$\frac{\partial A_y}{\partial t} + \frac{\partial Q_x}{\partial x} + q_{x_{y_s}} \frac{\partial y_s}{\partial x} - q_{y_{y_s}} = q_{FS} \tag{2}$$

where A_y = the transversal section (m^2) between the bottom elevation and the z axis and from the y_s limit to the y_e limit and is defined by Eq. (3); Q_x = the total longshore sediment transport (m^3/s) integrated between the y_s limit and the y_e limit and is defined by Eq. (4); $q_{x\,ys}$ = the longshore transport (m^2/s) in the shoreline position; $q_{y\,ys}$ = the cross-shore transport in the shoreline position (m^2/s) and q_{FS} the sediment supply or sediment loss (m^2/s) due to potential sources/sinks expressed by Eq. (5). In Eq. (4) and Eq. (5) ρ_s= the sediment density (kg/m^3) and p = the porosity (non-dimensional).

$$A_y = \int_{y_s}^{y_e} z_b dy \tag{3}$$

$$Q_x = \int_{y_s}^{y_e} q_x dy = \frac{\int_{z_b}^{z_n} \left(cu_{sed} - \varepsilon_x \frac{\partial c}{\partial x} \right) dz}{\rho_s (1-p)} \tag{4}$$

$$q_{FS} = \int_{y_s}^{y_e} \left(\frac{1}{\rho_s (1-p)} \int_{z_b}^{z_n} FS dz \right) dy \tag{5}$$

However, A_y and Q_x only have physical meaning if the "x, y" components correspond to the "longshore, cross-shore" components regarding the beach profile. This is why working with a similar equation but set in these local coordinates (x_l, y_l) is recommended. Following O'Rourke and LeBlond (1972), if the curvature radius of the beach is large compared to the surf zone, then Eq. (2) can be represented in local coordinates by using Eq. (6).

$$\frac{\partial A}{\partial t} + \frac{\partial Q_{x_l}}{\partial x_l} - q_{y_{l\,y_{ls}}} = q_{FS} \tag{6}$$

where A = the transversal section of the beach profile (m^2) between the bottom elevation and the z axis and from the y_{ls} limit to the y_{le} limit and the remaining terms have the same meaning as in Eq. (2) but referring to the local coordinates, that is, x_l = longshore

component regarding to the beach profile and y_l = cross-shore component regarding to the beach profile.

Eq. (6) only has information of the sediment variation in the studied area in terms of the temporal variation of the transversal section. Notice that to determine the temporal variation of the shoreline position the dependence between the temporal variation of the transversal section and the temporal variation of the shoreline position must be introduced. Furthermore, as the sediment conservation equation only indicates the temporal variation of the transversal section, even when providing this dependence, the temporal variation of the shoreline position not associated to variations of the transversal section could not be determined at all. The latter variation is usually associated to sediment redistribution along the profile by cross-shore transport, which can generate shoreline position changes without transversal section modifications and it is especially important in the middle-term. That is the case of the seasonal variations of the shoreline position (summer-winter).

Therefore, in order to predict shoreline position in the middle-long term a beach profile evolution model is necessary. This model evolves taking into account the temporal variation of the transversal section imposed by the general conservation equation derived previously (long-shore sediment contributions) combined with cross-shore sediment redistribution associated to middle term forces.

EXTENDED BEACH PROFILE MODEL

Traditionally, the beach profile has been defined taking into account only the breaking-zone (e.g. Dean 1987; Gonzalez et al. 1999), other authors have included a transition zone associated to the shoaling zone (Medina et al. 2000). The beach profile model proposed in this work has been denominated extended beach profile, because it includes different cross-shore zones: breaking zone, transition zone, exterior zone and geological zone (see figure 1).

Extended beach profile zones

The complete beach profile is composed of the following zones: breaking zone, transition zone, exterior zone and geological zone. These zones can be observed in figure 1 and are described next:

Breaking zone. The breaking zone is assumed to be in equilibrium with the incident wave conditions. This zone goes from the high tide level to the breaking point of the low tide level, h_{rt}.

Transition zone. The transition zone is extended from the breaking point of the low tide level (h_{rt}) to the local exterior depth of the low tide level, $h_{e\,loc}$. To calculate this depth, an expression is going to be proposed later.

Exterior zone. The exterior zone is the beach profile zone which remains unchangeable between two successive moments. This zone goes from the local exterior depth of the

low tide level ($h_{e\ loc}$) to the exterior or geological depth of the low tide level, h_e. This exterior limit is time-independent and an expression to estimate this depth will be proposed later.

Geological zone. The geological zone is defined in deeper waters from the exterior geological depth (h_e).

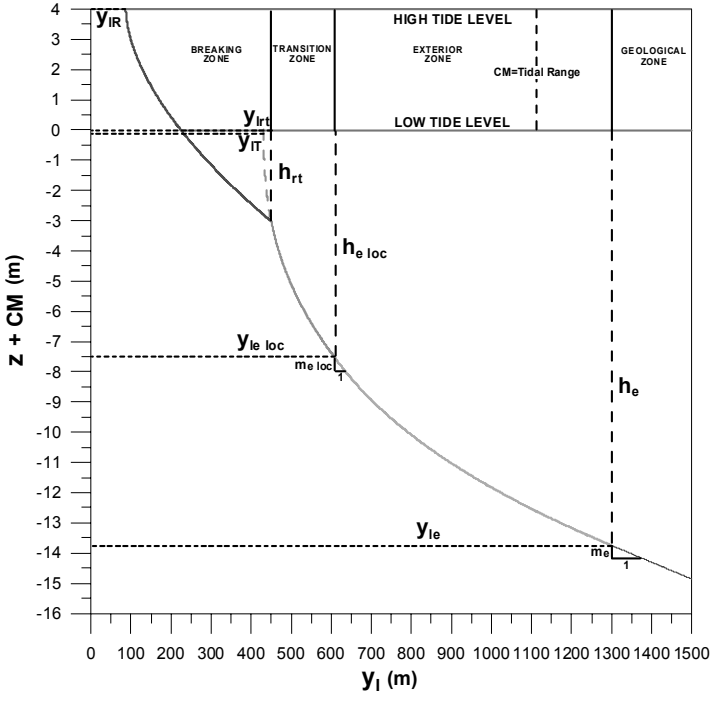

Fig. 1. Zones of the complete beach profile

In figure 1, the vertical z axis begins in the high tide level and is positive above this level. *CM* is the tidal range. Notice that the horizontal axis y_l represents the local axis, but the origin is displaced from the shoreline position.

Extended beach profile formulation

In the following expressions, which are going to be proposed to define every zone along the beach profile, the water depth h (h_R for the breaking zone and h_T for the transition zone) is defined as beginning in the high tide level (as the z axis) and is positive below this level (just the opposed to the z axis). The horizontal cross-shore axis y_l represents the local axis, but the origin is displaced from the shoreline position.

Breaking zone profile. As the breaking zone is assumed to be in equilibrium with the incident wave conditions, any of the formulations existing in the literature for the equilibrium beach profile existing in the literature can be applied to define the profile for this zone. Following, beach profiles similar to Vellinga (1984), Dean (1987), Boon and Green (1989) or Larson et al. (1999), a potential expression is used, as it is indicated in Eq. (7).

$$h_R = A_R \left(y_l - y_{lR} \right)^{m_R} \Rightarrow y_{lR} \le y_l \le y_{lrt} \quad 0 \le h_R \le h_{rt} + CM \tag{7}$$

In Eq. (7) the origin of the potential expression is located in the high tide level, A_R is the shape parameter, m_R is the exponent of the potential expression and y_{lR} is the origin position of the potential expression regarding the origin of the local axis y_l. Therefore, y_{lR} is the shoreline position.

Transition zone profile. This beach profile zone is in constant evolution and is the transition between the breaking zone and the exterior zone. In order to define this profile, a potential expression is also used, as it is presented in Eq. (8).

$$h_T = B_T \left(y_l - y_{lT} \right)^{m_T} + CM \Rightarrow y_{lrt} < y_l \le y_{le\,loc} \quad h_{rt} + CM < h_T \le h_{e\,loc} + CM \tag{8}$$

In Eq. (8) the origin of the potential expression is located in the low tide level. B_T is the shape parameter, m_T is the exponent of the potential expression and y_{lT} is the origin position of the potential expression regarding to the origin of the local axis y_l.

Exterior zone profile. The profile in this zone has to be defined initially at time (t=0) for the evolution model. From this moment on, this zone is automatically determined as the zone which remains unchanging between two successive moments. The definition of this initial profile can be established directly using the real profile or, similarly as in the previous zones, by using a potential expression.

MIDDLE-LONG TERM EVOLUTION MODEL

The proposed middle-long term beach evolution model is based on the analytically integrated sediment conservation equation (without assuming any hypothesis regarding the beach profile) and on a beach profile evolution model. The temporal variation of the transversal section (forced by the long-shore sediment contributions) is imposed by the conservation equation in local coordinates integrated to the exterior limit (time-independent offshore limit) and which was established in Eq. (6). On the other hand, the beach profile evolution model combines the cross-shore sediment redistribution associated to the seasonal processes with this long-shore constributions. The model achieves to predict the shoreline position and the profile shape along a beach, from middle to long term scale.

Model formulation and initial conditions

In order to establish the temporal evolution of the model, the same terminology utilized in the previous section will be used to define the different zones of the beach profile, and a new temporal coefficient will be added to the parameters associated to the beach profile zones, indicating the time at any time step as (1 for t_1) or the time at the next time step as (2 for t_2). The parameters A_R, y_{lR}, m_R, h_{rt}, B_T, y_{lT}, m_T and $h_{e\,loc}$ will be input data for the initial time (t=0) in the evolution model. The parameters A_{R1}, m_{R1}, h_{rt1} and $h_{e\,loc1}$ will be always input data at time t_1. Therefore, the unknown parameters which define the shoreline position and the shape of the profile in the transition zone at the next time step (y_{lR2}, B_{T2}, y_{lT2} and m_{T2}) will be found by matching at the interfaces, as follows.

1. *Continuity of the beach profile in the breaking point* (y_{lrt2}, h_{rt2}). This point belongs to the breaking zone and to the transition zone (see figure 1).

2. *Continuity of the beach profile in the point with associated depth* $h_{e\,loc2}$ ($y_{le\,loc2}$, $h_{e\,loc2}$). This point belongs to the transition zone and to the exterior zone (see figure 1).

3. *Continuity of the beach slope* $m_{e\,loc2}$ *in the point with associated depth* $h_{e\,loc2}$ ($y_{le\,loc2}$, $h_{e\,loc2}$). This is the second condition that the exterior zone imposes on the transition zone.

4. *Sediment conservation* imposed by Eq. (6) on the beach profile evolution model.

Finally, using the previous four conditions, the four unknown parameters y_{lR2}, B_{T2}, y_{lT2} and m_{T2} are obtained. Notice that y_{lR2} is just the shoreline position.

Input parameters determination

Local waves are the forcing dynamic on the system. These waves keep the information regarding the middle term (seasonal) and long term (yearly) variations. Local waves define at each time step and beach location, the sediment longshore flux (Q_{x1}) and the water depth limits h_{rt}, h_{eloc}.

The sediment longshore transport can be calculated applying an expression similar to the Osaza and Brampton (1980) formulation, which includes the transport associated to the wave incident obliquity and the longshore wave height gradients (e.g. Hanson and Kraus 1989; Dabees and Kamphuis 1998).

The expression proposed by Bernabeu et al. (2003) can be used to determine the breaking point of the low tide level, h_{rt}.

The expressions proposed by Requejo (2005) can be utilized to calculate the local exterior depth of the low tide level ($h_{e\,loc}$).

The exterior or geological limit of the low tide level is imposed by the peculiar geology of every particular place. However, a tentative expression to determine the depth h_e associated to this limit was found by Requejo (2005).

APPLICATION CASES

In order to illustrate the advantages of using the proposed model, two comparison examples are going to be presented. The first case is a situation with no temporal variation of the transversal section of the beach profile associated to the longshore sediment transport. The second case is a situation with temporal variation of the transversal section of the beach profile associated to longshore variation of the longshore sediment transport.

Case 1

This case is a rectilinear coast of 1200 m. Boundary conditions correspond to null longshore sediment transport in both contours. Waves reach the coast perpendicularly and the temporal sequence of the significant wave heights are the following: 4 m, 3.5 m, 6 m, 5 m, 5.5 m and 6.5 m. This is a typical case of temporal variation of the shoreline position due to variable wave height, as occurs with the easonal variations of the shoreline position (summer-winter) or middle term variations.

In the proposed model for defining the different zones of the beach profile, the following considerations have been taken into account:

In the *breaking zone*, a potential expression with an exponent value of 2/3 (Dean´s profile) and a shape parameter established with Dean´s formulation (see Dean 1987) for a grain size of 0.0002 m has been used (A_R=0.0975 $m^{1/3}$).

In the *transition zone* a potential expression has also been considered. To calculate $h_{e\,loc}$ depth, expressions proposed by Requejo (2005) have been utilized.

In the *exterior zone*, the exterior geological limit has been defined by a horizontal distance of 1300 m and an exterior or geological depth of 14 m. Additionally, to defining the initial exterior zone, in this limit the beach slope has been determined (m_e=0.006) and the initial transition zone has been extended to a horizontal distance of 650 m. The tidal range (CM) has been established at 2 m.

On the other hand, in classical one-line models, the beach is defined by a unique profile. To define this profile, a potential expression with an exponent value of 2/3 (Dean´s profile) and a shape parameter A_d, established to balance the cross-shore sediment mass, has been used (A_d=0.133 $m^{1/3}$). To be consistent with the values for the sum of the exterior or geological depth (h_e=14 m) and the tidal range (CM=2 m) used in the proposed model, in the classical one-line model the value for the sum of the berm height D_B and the depth of closure D_C is assumed to be the same ($D_B + D_C$=16 m).

In this example, as the wave incidence is normal and there is no longshore variation of the wave height, there is no longshore variation of the longshore sediment transport. Consequently, the temporal variation of the transversal section of the beach profile is null. As classical one-line models can only predict temporal variation of the shoreline

position associated to longshore variations of the longshore sediment transport, in these types of models the shoreline position remains invariable, as it is depicted in figure 2. For this situation the proposed model is especially valuable because this model is not only able to predict temporal variations of the shoreline position related to temporal variations of the transversal section but also is capable to determine the temporal variation of the shoreline position associated to sediment redistribution due to cross-shore transport, as in the present case. Additionally, the estimated shoreline position using the proposed model is represented in figure 2.

For this example, the beach profile evolution is depicted using the proposed model in figure 3. In this figure the beach profile is also presented for classical one-line models, in this case the beach profile is invariable. Therefore, Dean´s profile is extended from the invariable shoreline position.

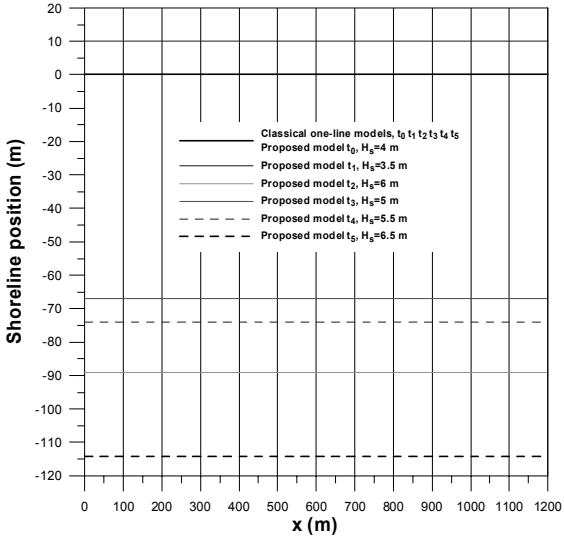

Fig. 2. Plan view of the shoreline position determined with the proposed model and with classical one-line models for Case 1.

Case 2

This case is a rectilinear coast of 1200 m. Boundary conditions correspond to two infinitely long jetties, which is equivalent to the sediment longshore transport is null in both contours. In this case wave conditions are constant, deep water wave conditions are: 3 m for the significant wave height, 10 s for the peak period and 10 degrees for the incidence angle.

This example is the opposite of the previous one because the temporal variation of the shoreline position is associated to the longshore variation of the sediment longshore

transport due to the oblique incidence of waves. In consequence, temporal variation of the transversal section of the beach profile is generated.

Both models, the proposed model and the classical one-line model, have been executed using the following parameters: 25 cells to define the shoreline position, 50 m for the cell width, 12 hours for the execution time interval. To calculate the sediment longshore transport the formula proposed by Ozasa and Brampton (1989) has been used.

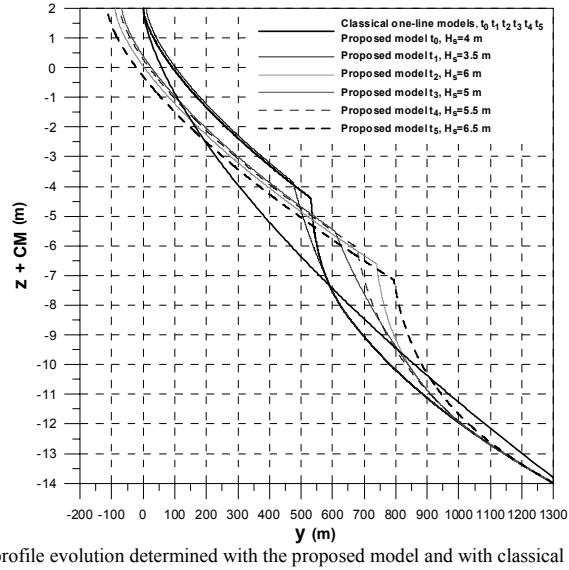

Fig. 3. Beach profile evolution determined with the proposed model and with classical one-line models for Case 1.

Regarding the specific parameters of the model, in the proposed model for defining the different zones of the beach profile, the following considerations have been taken into account:

In the *breaking zone*, a potential expression with an exponent value of 2/3 (Dean´s profile) and a shape parameter established with Dean´s formulation (see Dean 1987) for a grain size of 0.0003 m has been used (A_R=0.119 $m^{1/3}$).

In the *transition zone* a potential expression has also been considered. To calculate $h_{e\,loc}$ depth, expressions proposed by Requejo (2005) have been utilized.
In the *exterior zone*, the exterior or geological limit has been defined by a horizontal distance of 1300 m and an exterior or geological depth of 13.75 m. Additionally, to define the initial exterior zone, in the previous limit the beach slope has been determined (m_e=0.00555) and the initial transition zone has been extended to a horizontal distance of 650 m. The tidal range (*CM*) has been established at 4 m.

On the other hand, in classical one-line models the beach is defined by a unique profile. To define this profile, a potential expression with an exponent value of 2/3 (Dean´s profile) and a shape parameter A_d established with Dean´s formulation (see Dean, 1987) for a grain size of 0.0003 m has been used (A_d=0.119 $m^{1/3}$). To be consistent with the values for the sum of the exterior or geological depth (h_e=13.75 m) and the tidal range (CM=4 m) used in the proposed model, in the classical one-line model the value for the sum of the berm height D_B and the depth of closure D_C is assumed to be the same (D_B + D_C=17.75 m). However, a different value for the sum of the berm height and the depth of closure in the classical one-line model would change the temporal scales of the shoreline evolution. Additionally, in an ordinary case using classical one-line models the beach profile is extended to a smaller depth.

In figure 4 the shoreline evolution determined with both models are presented. For this case, to attain the equilibrium shoreline position in the classical one-line model 105 days are required. Otherwise, in the proposed model 42 days are needed. Therefore, the temporal scales of the beach evolution are different comparing both models.

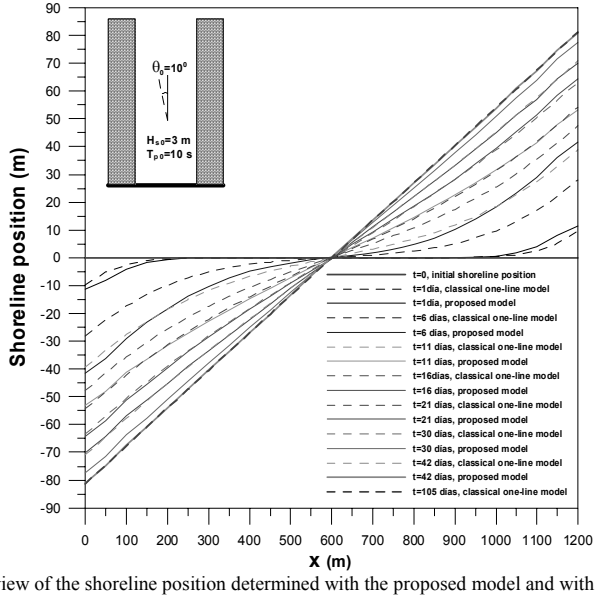

Fig. 4. Plan view of the shoreline position determined with the proposed model and with classical one-line models for Case 2.

CONCLUSIONS

A new middle-long term beach evolution model has been proposed. This model has been established based on an analytically integrated sediment conservation equation (without assuming any hypothesis regarding the beach profile) and on a beach profile evolution

model. The model is able to predict the shoreline position and the profile shape along a beach, from middle to long term scales.

The sediment conservation equation only has information of the sediment variation in the studied area in terms of the temporal variation of the transversal section. However, in order to determine the temporal variation of the shoreline position, the introduction of the temporal variation of the cross-shore profile is required.

The temporal variation of the transversal section (forced by the long-shore sediment contributions) is imposed by the conservation equation integrated to the exterior limit (time-independent offshore limit). On the other hand, the beach profile evolution model combines the cross-shore sediment redistribution associated to seasonal processes with the long-shore contributions.

Traditionally, the beach profile has been defined taking into account only the breaking-zone, other authors have included a transition zone associated to the shoaling zone (Medina et al. 2000). The beach profile model proposed in this work has been denominated extended beach profile, because it includes different cross-shore zones: breaking zone, transition zone, exterior zone and geological zone.

Finally, the advantages of using the proposed model compared to classical one-line models have been determined. A more thorough field validation is also necessary. However, in this work a lack of high quality field measurements of hydrodynamics, sediment samples, shorelines and cross-shore profiles in beaches, at an appropriated time and space scale taking into account seasonal changes throughout several years has been identified.

ACKNOWLEDGEMENTS

M. Gonzalez gratefully acknowledges the financial support provided by the Spanish "Comisión Interministerial de Ciencia y Tecnología" (CICYT) under research grant REN2003-9640/MAR and the Spanish Ministerio de Educación y Ciencia under the Program for mobility of professors in foreign centers.

REFERENCES

Abbott, M.B., and Price, W.A. (1994). "Coastal, Estuarial and Harbour Engineers' Reference Book". M. B. Abbott y W. A. Price (Eds.). Chapman & Hall. Londres. 736 pp.

Bernabeu, A., Medina, R., and Vidal, C. (2003). A morphological model of the beach profile integrating wave and tidal influences. Marine Geology. Vol. 197, 2003. Elsevier. 95-116.

Boon, J.D., and Green, M.O. (1989). "Caribbean Beach Face Slopes and Beach Equilibrium Modes". Proc. 21st Coastal Engineering Conference, ASCE, pp. 1618-1630.

Dabees, M.A., and Kamphuis, J.W. (1998). "Oneline, a numerical model for shoreline change". Proc. 26th Coastal Engineering Conference, ASCE, pp. 2668-2681.

Dabees, M.A., and Kamphuis, J.W. (2000). "Nline: efficient modelling of 3-D beach change". Proc. 27th Coastal Engineering Conference, ASCE, pp. 2700-2713.

Dean, R.G. (1987). "Coastal sediment processes: Toward engineering solutions". Proc. Coastal Sediments'87, ASCE, pp. 1-24.

De Vriend, H.J., Capobianco, M., Chesher, T., de Swart, H.E., Latteux, B., and Stive, M.J.F. (1993). "Approaches to long-term modelling of coastal morphology: a review". Coastal Engineering, vol. 21, pp. 225– 269.

DHI, Danish Hydraulic Institute (2001). LITPACK "Coastline evolution, User's Guide and Reference Manual". Lingby, Dinamarca.

González, M., Medina, R., and Losada, M.A. (1999). "Equilibrium beach profile model for perched beaches". Coastal Engineering, Vol. 36, pp 343-357.

Hanson, H., and Kraus, N.C. (1989). "Genesis: Generalized Model for Simulating Shoreline Change". Technical Report CERC-89-19, Report 2 of a Series, Workbook and User's Manual. US Army Corps of Engineers, Waterways Experiment Station, Vicksburg, MS, USA.

Hanson, H., and Larson, M. (2000). "Simulating Shoreline Evolution Using a New Type of N-line Model". Proc. 27th Coastal Engineering Conference, ASCE, pp. 2808-2821.

Larson, M., Kraus, N.C., and Hanson, H. (1990). "Decoupled numerical model of three-dimensional beach range". Proc. 22nd Coastal Engineering Conference, ASCE, pp. 2173-2185.

Larson, M., Kraus, N., and Wise, R.A. (1999). "Equilibrium beach profile under breaking and non-breaking waves". Coastal Engineering, Elsevier, Vol. 36, pp. 59-85.

Medina R., Bernabeu A.M., Vidal C., and Gonzalez M. (2000). "Relationship between beach morphodynamics and equilibrium profiles". Proc. 27th Itnl. Coastal Engineering Conference. ASCE, Vol. 3, p.p. 2589 –260.

O'Rourke, J.C., and Leblond, P.H. (1972). "Longshore currents in a semicircular bay". Journal of Geophysical Research, Vol 77, pp. 444-452.

Osaza, H., and Brampton, A.H. (1980). "Mathematical modelling of beaches backed by seawalls". Coastal Engineering, 4.1: 47-64.

Requejo, S. (2005). "Análisis y mejoras en la evaluación de diversos términos de los modelos de evolución de playas en escalas de medio plazo", Ph.D Thesis in spanish, University of Cantabria, Spain.

Shimizu, T., Kumagai, T., and Watanabe, A. (1996). "Improved 3-D beach evolution model coupled with the shoreline model (3D-Shore)". Proc. 25th Coastal Engineering Conference, ASCE, pp. 2843-2856.

Vellinga, P. (1984). "A Tentative Description of a Universal Erosion Profile for Sandy Beaches and Rock Beaches". Coastal Engineering, Elsevier, Vol. 8, Nº2, pp. 177-188.

MODEL FOR PREDICTING BEACH CHANGES ON COAST WITH SAND OF MIXED GRAIN SIZE BASED ON BAGNOLD'S CONCEPT

Masumi Serizawa[1], Takaaki Uda[2], Toshiro San-nami[1], Kou Furuike[1], Toshinori Ishikawa[3] and Takayuki Kumada[4]

1. Coastal Engineering Laboratory Co., Ltd., 1-22-301 Wakaba, Shinjuku, Tokyo 160-0011, Japan. coastseri@nifty.com
2. Dr. Eng., Executive Director, Public Works Research Center, 1-6-4 Taito, Taito, Tokyo 110-0016, Japan. uda@pwrc.or.jp
3. Research Engineer, Public Works Research Center, 1-6-4 Taito, Taito, Tokyo 110-0016, Japan. ishikawa@pwrc.or.jp
4. PhD., Laboratory of Aquatic Science Consultant Co., Ltd., 1-14-1 Kami-ikedai, Ota, Tokyo 145-0064, Japan. kumada@lasc.co.jp

Abstract: Returning to the starting point of Bagnold's basic study, sand transport equations were derived. A model for predicting beach changes by applying the concept of the equilibrium slope introduced by Inman and Bagnold (1963) and the energetics approach of Bagnold (1963) was developed. As a result, the physical rationality of the predictive model was enhanced compared with the original model. Typical beach changes caused by the obstruction of longshore sand transport and associated changes in grain size could be predicted. This becomes a practical tool for predicting three-dimensional beach changes on coasts composed of sand of mixed grain size.

INTRODUCTION

Artificial alteration of coasts not only gives rise to beach changes, but also often affects the ecosystem in the shallow zone of the sea through changes in the grain size of seabed materials. Because of this, several models for predicting not only beach changes, but also quantitative changes in seabed materials, or grain size, have been developed in recent years. Uda *et al*. (2004) and Kumada *et al*. (2006) have developed models for predicting both beach changes and grain size changes, applying the contour-line-change model (Serizawa *et al*., 2003). Although the applicability of these models to real cases is high, the sand transport equations used have been derived not

by a theoretically rigorous method but rather by an intuitive method. In this study, we return to the starting point of Bagnold's study and sand transport equations are derived. A model for predicting beach changes by applying the concept of the equilibrium slope introduced by Inman and Bagnold (1963) and the energetics approach of Bagnold (1963) is developed.

PREDICTIVE MODEL

Sand Transport Equation Based on Bagnold's Concept

The fluid motion near the seabed due to waves is oscillatory, changing the direction alternately shoreward and seaward, and a sand particle moves back and forth in the cross-shore direction. Inman and Bagnold (1963) derived their fundamental equations on the basis of energy conservation, using the sand transport equation explicitly including the seabed slope (Bagnold, 1963), and assuming that sand transport in a wave field is the sum of the components caused by shoreward flow during the motion of incoming waves and seaward flow during the motion of outgoing waves. In this study, in accordance with this concept, a simple equation of sand transport flux is derived first, using only the wave conditions at the breaking point for the sediment of a single grain size (Serizawa *et al.*, 2006).

Consider Cartesian coordinates (x, y), and that the elevation at a point Z (x, y, t) is a variable to be solved. Assume that waves are obliquely incident on a coast with a uniform slope of $\tan\beta$. Sand transport in a wave field is assumed to be the sum of the components caused by shoreward flow during the motion of incoming waves and seaward flow during the motion of outgoing waves as suggested by Inman and Bagnold (1963), and the sand transport equation for a unidirectional steady flow introduced by Bagnold (1963) is applied to each component.

Assuming that $\tan\beta$ is infinitesimal, that the flow causes a sand particle to move in the direction of flow and that gravity causes the downslope action, then the sand transport flux of a unidirectional flow is expressed by Eq. (1) as a linear approximation in terms of $\tan\beta$ (Bagnold, 1963; Bailard and Inman, 1981). The first term represents the action produced by the flow and the second term represents the downslope action due to gravity. The sign of the coefficients a_0 and a_1 is always positive.

$$\vec{q_u} = a_0 \vec{e_u} - a_1 \nabla Z \qquad (a_0 > 0, \quad a_1 > 0) \tag{1}$$

Here, $\vec{e_u}$ is the unit vector in the direction of the flow, $\nabla Z = (\partial Z/\partial x, \partial Z/\partial y)$ is the gradient vector of Z, the direction and magnitude of which give shoreward normal to the contour line and $\tan\beta$, respectively. Assume that the sand transport caused by shoreward and seaward flow during the motion of incoming and outgoing waves is expressed by Eq. (1), when the sand transport is averaged over a period. Then, the net sand transport flux due to waves is expressed as Eq. (2) by the summation of the components due to incoming and outgoing waves as shown in Eqs. (3) and (4), respectively. The sign of the coefficients a_0^+, a_0^-, a_1^+ and a_1^- is always positive.

$$\vec{q} = \vec{q^+} + \vec{q^-} \tag{2}$$

$$\vec{q^+} = a_0^+ \vec{e_w^+} - a_1^+ \nabla Z \quad \left(a_0^+ > 0,\ a_1^+ > 0\right) \tag{3}$$

$$\vec{q^-} = a_0^- \vec{e_w^-} - a_1^- \nabla Z \quad \left(a_0^- > 0,\ a_1^- > 0\right) \tag{4}$$

Here, the superscripts + and – show the values corresponding to incoming and outgoing waves, respectively, and $\vec{e_w^+}$ and $\vec{e_w^-}$ are the unit vectors in the directions of shoreward and seaward flow of waves, respectively. Modifying Eq. (2) under the assumption that the directions of waves propagating shoreward and seaward are exactly opposite, as given by Eq. (5), defining the slope satisfying zero net on-offshore sand transport when waves are incident from the direction normal to the shoreline as the equilibrium slope, $\tan\beta_c$ (Eq. (6)), and defining the coefficient A by Eq. (7), sand transport flux can be written as Eq. (8).

$$\vec{e_w^-} = -\vec{e_w^+} \tag{5}$$

$$\tan\beta_c = \left(\frac{a_0^+ - a_0^-}{a_1^+ + a_1^-}\right) \tag{6}$$

$$A = \left(a_1^+ + a_1^-\right) \tag{7}$$

$$\vec{q} = A\left[\tan\beta_c \vec{e_w} - \nabla Z\right] \tag{8}$$

Applying the energetics approach (Bagnold, 1963), in which a part of the dissipating wave energy is used for the work of sand transport and the rate of sand transport is related to the dissipation of wave energy, and assuming that the coefficient A in Eq. (8) is proportional to the wave energy dissipation rate Φ, then total longshore sand transport rate is obtained by integrating the longshore component of Eq. (8) over the depth. This has the same form as the CERC formula of Eq. (9) (Komar and Inman, 1970), and the coefficient A is determined by Eq. (10) from the equivalence of both results. Finally, the sand transport flux due to waves can be written as Eq. (12).

$$Q_s = C_0 K_1 \left(EC_g\right)_b \cos\alpha_b \sin\alpha_b \tag{9}$$

$$A = C_0 \frac{K_1 \Phi}{\tan\beta_c} \tag{10}$$

$$C_0 = \frac{1}{(\rho_s - \rho)g(1-p)} \tag{11}$$

$$\vec{q} = C_0 \frac{K_1 \Phi}{\tan\beta_c}\left[\tan\beta_c \vec{e_w} - \nabla Z\right] \tag{12}$$

Here, $\vec{e_w} = \vec{e_w^+}$ is the unit vector in the wave direction, θ_w, K_1 is the coefficient of

longshore sand transport, a_b is the angle between the wave direction at the breaking point and the direction normal to the contour line, C_0 is the coefficient through which the sand transport rate, expressed by the immersed weight, is related to the volumetric sand transport rate, ρ_s and ρ are the sand and water densities, respectively, g is the acceleration due to gravity, and p is the porosity of the sand.

The equilibrium slope defined by Eq. (6) is equal to the slope for which cross-shore sand transport reduces to zero, when waves are incident from the direction normal to the shoreline, as deduced from Eq. (12). This represents the balance between upslope flow asymmetry and the downslope component of gravity (Inman and Bagnold, 1963; Bowen, 1980; Bailard and Inman, 1981 and Bailard, 1981). Equation (12) has the characteristics that cross-shore sand transport diminishes when waves are incident from the direction normal to the shoreline and the local slope is equal to the equilibrium slope. Shoreward transport is generated when the local slope is smaller than the equilibrium slope, and vice versa.

A sandy beach approaches a statically stable condition, only if the contour lines at each point are orthogonal to the wave direction and the local slope at each point is in agreement with the equilibrium slope. Sand transport is generated if there is a discrepancy from the equilibrium state. These characteristics are the same as those of the contour-line-change model proposed by Serizawa *et al.* (2003).

For a numerical simulation, it is necessary to formulate Φ. In this study, the energy dissipation ratio Φ is simply evaluated by the energy flux of waves at the breaking point, as is the case in the ordinary contour-line-change model (Serizawa *et al.*, 2003), considering the ease of practical use.

Assume that the beach changes occur in a depth zone between the depth of closure $-h_c$ and the berm height h_R corresponding to the wave run-up height. Assuming that Φ is given by the wave energy flux at the breaking point divided by the cross-shore distance between two points, the elevations of which are equal to $Z = -h_c$ and $Z = h_R$, and introducing the depth distribution of the intensity of sand transport $\varepsilon(Z)$, the coefficient A in Eq. (10) can be expressed by the energy flux at the breaking point $(EC_g)_b$. Sand transport flux can thus be written as Eq. (13), which is the fundamental sand transport equation for predicting beach changes on a coast composed of sand of a single grain size.

$$\vec{q} = \frac{G}{\tan\beta_c}\left[\tan\beta_c \vec{e_w} - \nabla Z\right] \tag{13}$$

$$G = C_0 K_1 \varepsilon(Z)\left(EC_g\right)_b \cos^2\alpha_b \tan\beta_c \tag{14}$$

Here, $\varepsilon(Z)$ is defined so that the integral over the depth between $Z = -h_c$ and h_R is equal to 1, and in this study, the depth distribution of longshore sand transport given by Uda *et al.* (1996) is used in the same manner as that of the ordinary contour-line-change

model. In the numerical simulation, the mean beach slope of the coast before the construction of artificial structures is given as the equilibrium slope when considering the long-term prediction of beach changes; the same as in the model of Serizawa *et al.* (2003).

Model for Predicting Beach Changes on Coast Composed of Sand of Mixed Grain Size

A model for predicting not only beach changes, but also grain size changes on a coast composed of sand of mixed grain size was developed by expanding Eq. (13) to include the effect of mixed grain size (N grain sizes) based on the same method as that used by Uda *et al.* (2004) and Kuroiwa *et al.* (2006).

N is set to be the number of grain sizes, and introducing the concept of the exchange layer in the same manner as Hirano (1971), the volume content rate $\mu^{(k)}$ of each grain size $d^{(k)}$ (k=1, 2, $\cdots\cdots$, N) in the exchange layer is added to the variable to be solved. The sand transport for each grain size is expressed by Eqs. (15) and (16), obtained when Eqs. (13) and (14) are multiplied by the content rate to evaluate the distribution of the energy dissipation of waves, and the equilibrium slope for each grain size is introduced.

$$\vec{q}^{(k)} = \frac{G^{(k)}}{\tan\beta_c^{(k)}}\left[\tan\beta_c^{(k)}\vec{e}_w - \nabla Z\right] \quad (k=1,2,\cdots,N) \tag{15}$$

$$G^{(k)} = \mu^{(k)} \cdot C_0 K_1^{(k)} \varepsilon(Z)\left(EC_g\right)_b \cos^2\alpha_b \tan\overline{\beta} \quad (k=1,2,\cdots,N) \tag{16}$$

The coefficient of sand transport for each grain size is assumed to be inversely proportional to the square root of the grain size after Kamphuis *et al.* (1986), as Eq. (17), and in the same manner as assumed by Kumada *et al.* (2006). Beach changes are expressed by Eq. (19) as the summation of components for each grain size obtained from the continuity equation, Eq. (18), for each grain size. Finally, the content rate is calculated from the continuity equation for each content rate in the exchange layer as Eq. (20).

$$K_1^{(k)} = \frac{A_1}{\sqrt{d^{(k)}}} \quad (k=1,2,\cdots,N) \tag{17}$$

$$\frac{\partial Z^{(k)}}{\partial t} = -\nabla\cdot\vec{q}^{(k)} \quad (k=1,2,\cdots,N) \tag{18}$$

$$\frac{\partial Z}{\partial t} = \sum_{k=1}^{N}\frac{\partial Z^{(k)}}{\partial t} \tag{19}$$

$$\frac{\partial \mu^{(k)}}{\partial t} = \begin{cases} \dfrac{1}{B_h}\left(\dfrac{\partial Z^{(k)}}{\partial t} - \mu^{(k)}\dfrac{\partial Z}{\partial t}\right) & \dfrac{\partial Z}{\partial t} \geq 0 \\ \dfrac{1}{B_h}\left(\dfrac{\partial Z^{(k)}}{\partial t} - \mu_B^{(k)}\dfrac{\partial Z}{\partial t}\right) & \dfrac{\partial Z}{\partial t} < 0 \end{cases} \quad (k=1,2,\cdots,N) \tag{20}$$

Here, N is the number of grain sizes, B_h is the thickness of the exchange layer, $\mu^{(k)}$ is the volume content rate of each grain size in the exchange layer, $\mu_B^{(k)}$ is the volume content rate in the layer underneath the exchange layer, $\tan\beta_c^{(k)}$ is the equilibrium slope for each grain size, $K_1^{(k)}$ is the coefficient of longshore sand transport rate for each grain size, $\tan\overline{\beta}$ is the mean slope between $Z = -h_c$ and h_R, and A_1 is a constant depending on the deformation process of the coast. In addition, the unit of grain size $d^{(k)}$ is mm. For B_h, Hirano (1971) chose the maximum grain size, which Kraus (1985) determined to be 3% of the breaker height on the basis of field observation. In this study, B_h was selected to be the larger of the values determined by these two methods, and in this case, was given by the maximum grain size.

Numerical simulation was carried out using in staggered meshes on the x-y plane. The sand transport flux for each grain size is calculated from Eqs. (15)-(17). The mass continuity equations of Eqs. (18) and (19) are solved using an explicit finite difference method to obtain the beach changes. The change in the content rate in the exchange layer is calculated from Eq. (20). These procedures are repeated recursively, and beach changes and the change in content rate are obtained.

For the boundary conditions, sand transport is set to be 0 along the outer boundaries of the calculation domain and along the boundaries of structures. Methods considering the sinking of sand due to gravity in a zone deeper than h_c and on land, the evaluation of the wave field in the wave-shelter zone of the offshore breakwaters, and the extra term to include additional longshore sand transport developed by Ozasa and Brampton (1980) are omitted here (Serizawa *et al.*, 2006).

RESULTS

Beach Changes between Groins under Oblique Wave Incidence

The model was applied to the experimental results of beach changes between groins under oblique wave incidence using sand of mixed grain size by Kumada *et al.* (2003). In their experiment, a 4-m-wide movable bed with a uniform slope of 1/10 using sand of mixed grain size was produced in a wave tank, and waves were obliquely incident to the initial shoreline making a breaker angle of 10 degrees to cause longshore sand transport. Groins were placed at both ends of the wave tank. Regular waves with an equivalent wave height of 4 cm and wave period of 0.8 s were generated.

The bed material used in the experiment was a mixture of two types of sand, the median diameters of which were 0.2 mm and 2 mm, with a volume ratio of 1:1. For the calculation conditions, the beach material is assumed to be composed of sand with two grain sizes of 0.2 mm and 2 mm, and the initial content rate is given by 50 %. The breaker height and angle are given by constant values which are determined by an average of the measured values in the longshore direction. The width of the exchange layer is assumed to 2 mm, equal to the maximum grain size. **Table 1** shows the calculation conditions.

Table 1. Calculation Conditions

Structural condition	Groins	Detached breakwaters
Initial seabed slope	1/10	1/10
Number of grain sizes N Grain size d Initial volume content rate μ Equilibrium slope $\tan\beta_c$	N=2 $d^{(1)}$=0.2 mm, $\mu^{(1)}$=0.5 and $\tan\beta_c$=1/10 $d^{(1)}$=2 mm, $\mu^{(1)}$=0.5 and $\tan\beta_c$=1/10	N=4 $d^{(1)}$=0.1 mm, $\mu^{(1)}$=0.25 and $\tan\beta_c$=1/20 $d^{(1)}$=0.2 mm, $\mu^{(1)}$=0.25 and $\tan\beta_c$=1/20 $d^{(1)}$=0.3 mm, $\mu^{(1)}$=0.25 and $\tan\beta_c$=1/5 $d^{(1)}$=0.4 mm, $\mu^{(1)}$=0.25 and $\tan\beta_c$=1/5
Thickness of exchange layer B_h	2 mm	0.4 mm
Breaker height H_b and breaker angle α_b	H_b=3.6 cm and α_b=6.3°	H_b=5.2 cm and α_b=10°
Depth of closure h_c and berm height h_R	h_c=6 cm and h_R=2 cm	h_c=11 cm and h_R=5 cm
Critical slope	1/2	1/2
Coefficient A_1	0.5	0.1
Ratio of coefficients of littoral drift K_2/K_1	0	1.62
Mesh size $\Delta x = \Delta y$	0.1 m	0.1 m
Time step Δt	0.0002 hr	0.0001 hr
Total time t	10 hrs	2 hrs
Boundary conditions	$q_x = 0$ at both ends	$q_x = 0$ at both ends

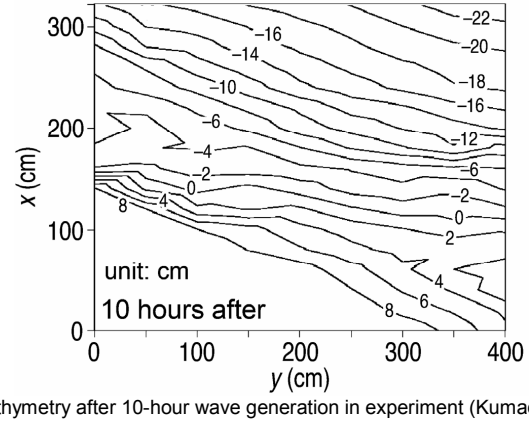

Figure 1. Bathymetry after 10-hour wave generation in experiment (Kumada *et al.*, 2003)

Figure 1 shows the bathymetry obtained after 10 hours of wave action. The initial parallel contours were deformed by obliquely incident waves. Sand was mainly transported downcoast by the longshore sand transport, accumulating on the updrift side of the groin. **Figure 2** shows the calculated bathymetry corresponding to **Fig. 1**. In

the eroded zone, a gentle slope was formed owing to erosion in the zone shallower than h_c = 6 cm, whereas in the accretion zone, sand was deposited forming a flat foreshore on land as well as the formation of a steep slope in the zone deeper than h_c due to the sinking of sand. These results are in agreement with those of the experiment.

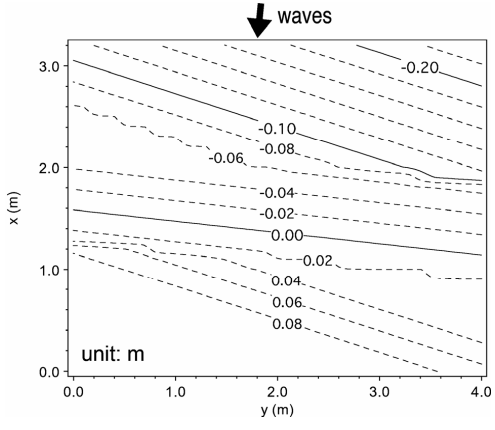

Figure 2. Calculated bathymetry under oblique wave incidence

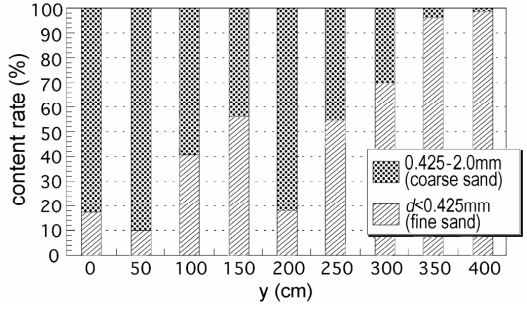

Figure 3. Content rates of coarse and fine sand in experiment (Kumada *et al*., 2003)

Figure 3 shows the longshore distribution of the measured composition of the grain size of bed materials on the shoreline after the beach changes. This figure clearly shows the occurrence of predominant longshore sorting due to longshore sand transport, which is often observed on coasts; in the erosion zone, the content rate of coarse sand increases with the removal of fine sand, whereas fine sand selectively removed from the erosion zone accumulates in the accretion zone.

Figure 4 shows the results of the calculation corresponding to **Fig. 3**, and shows the plane distribution of mean grain size with the initial shoreline and the shoreline after the beach changes. Furthermore, **Fig. 5** shows the predicted composition of the grain size of bed materials along the shoreline after the beach changes. The sorting due to longshore sand transport resulting in coarse sand being left behind in the erosion zone and fine sand selectively accumulating was accurately predicted by the numerical simulation.

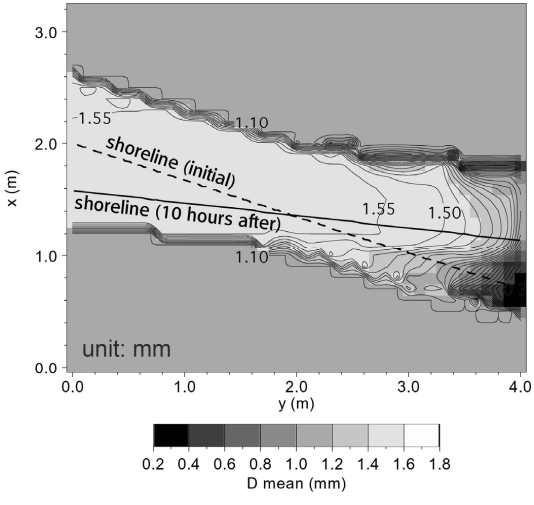

Figure 4. Calculated distribution of mean grain size under oblique wave incidence

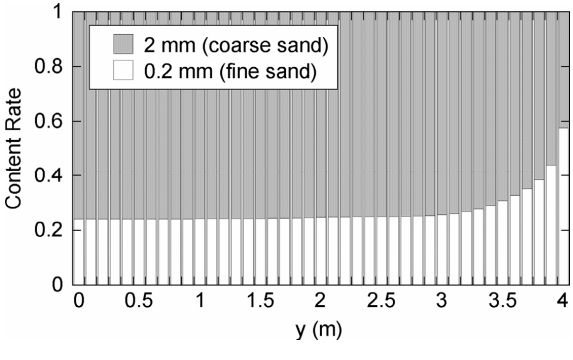

Figure 5. Calculated content rates of coarse and fine sand

Application to Prediction of Beach Changes around Detached Breakwaters

Consider the case when detached breakwaters are built for coastal protection. Uda *et al.* (1987) carried out a movable-bed experiment using a plane wave tank to investigate beach changes around three detached breakwaters subjected to obliquely incident waves. The initial topography in the experiment was a straight beach with a uniform slope of 1/10, and for the wave conditions, the incident wave height was $H_0 = 3$ cm and the breaker angle was 10 degrees. In the experiment, the median diameter of sand used was $d_{50} = 0.28$ mm, but strictly speaking, it was composed of grains of mixed size. In the calculation, a mixture of sand composed of sand of grain sizes 0.1, 0.2, 0.3 and 0.4 mm with the same content rate and the same initial median diameter was assumed. The sorting effect was investigated using this mixture of sand. Assuming that sand of 0.1 and 0.2 mm grain size has an equilibrium slope of 1/20 and sand of 0.3 and 0.4 mm grain size has an equilibrium slope of 1/5 on the basis of the experimental results, the sorting effect of sand was investigated in the model, with the assumption of the width of the exchange layer being 0.4 mm.

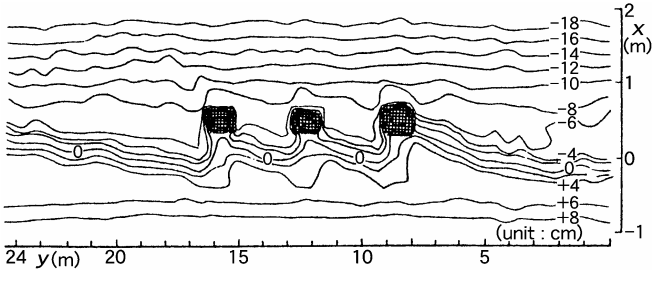

Figure 6. Bathymetry after constructing detached breakwaters in experiment (Uda *et al.*, 1987).

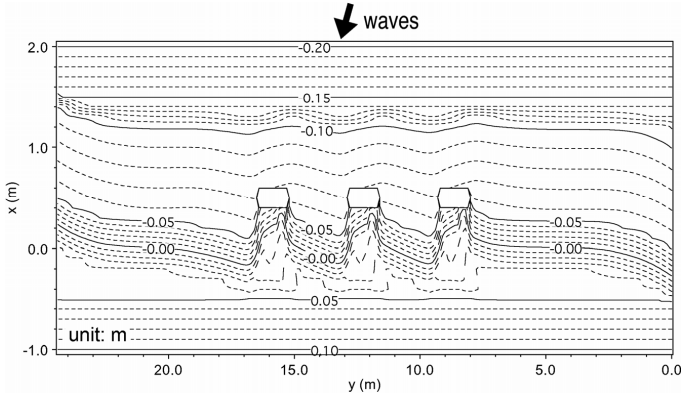

Figure 7. Calculated bathymetry after constructing detached breakwaters

Figures 6 and **7** show the measured and predicted beach topography after 2 hours of wave action when detached breakwaters were installed on the seabed with parallel contours. The calculated results accurately explain the results obtained in the experiment, such as the formation of a salient behind the detached breakwaters, the formation of a steep foreshore slope, a relatively gentle slope off the shoreline and the meandering of contours off the detached breakwaters.

Figure 8 shows the calculated distribution of the mean grain size. Although the direct comparison of predicted values with the experiment is difficult because of the lack of experimental data, the sorting of grain size due to cross-shore sand transport, often observed in real cases, was accurately predicted; coarse sand accumulated in the vicinity of the shoreline and fine sand was transported offshore. Furthermore, the fact that fine sand accumulated behind the detached breakwaters was accurately predicted.

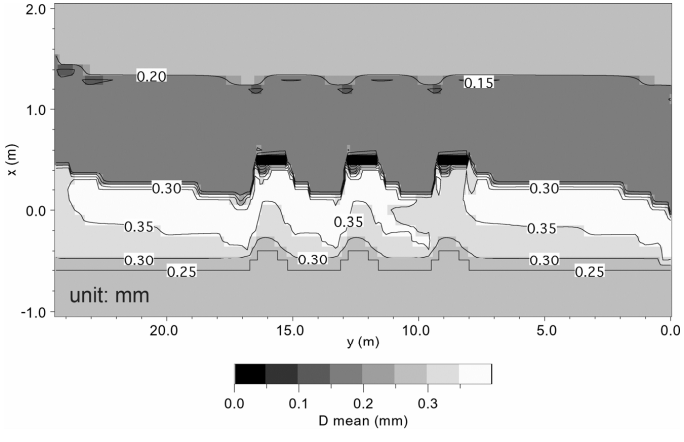

Figure 8. Calculated mean grain size after constructing detached breakwaters

CONCLUSION

Simple equations for evaluating sand transport flux under a wave field were derived based on Bagnold's concept, and a new model for predicting not only beach changes but also grain size changes was developed. As a result of this study, the physical rationality of the predictive model was enhanced compared with those of the models of Uda *et al.* (2004) and Kumada *et al.* (2006). Many examples of typical beach changes caused by the obstruction of longshore sand transport and the changes in grain size described by Uda (2004) are capable of being predicted by the model. Finally, a practical tool for predicting three-dimensional beach changes on coasts composed of sand of mixed grain size was developed.

REFERENCES

Bailard, J. A. (1981). An energetics total load sediment transport model for a plane sloping beach, *J. of Geophys. Res*., Vol. 86, C11, pp. 10938-10954.

Bailard, J. A. and Inman, D. L. (1981). An energetics bedload model for a plane sloping beach: Local transport, *J. of Geophys. Res*., Vol. 86, C3, pp. 2035-2043.

Bagnold, R. A. (1963). Mechanics of Marine Sedimentation, in *The Sea*, M. N. Hill (ed.), Vol. 3, pp. 507-528, New York, Wiley.

Bowen, A. J. (1980). Simple models for nearshore sedimentation; beach profiles and longshore bars, in *The Coastline of Canada*, The Geological Survey of Canada, S. B. McCann, (ed.), Paper 80-10, pp. 1-11.

Hirano, M. (1971). River bed degradation with armoring, *Proc. of JSCE*, Vol. 195, pp. 55-65. (in Japanese)

Inman, D. L. and Bagnold , R. A. (1963). Littoral Processes, in *The Sea*, M. N. Hill, (ed.), Vol. 3, pp. 529-533, New York, Wiley.

Kamphuis, J. W., Davies, M. H., Narim, R. B. and Sayao, O. J. (1986). Calculation of littoral sand transport rate, *Coastal Eng*., Vol. 10, pp. 1-12.

Komar, P. D. and Inman, D. L. (1970). Longshore sand transport on beaches, *J. of Geophys. Res*., Vol. 75, No. 30, pp. 5914-5927.

Kraus, N. C. (1985). Field experiments on vertical mixing sand in the surf zone, *J. Sedimentary Petrology*, Vol. 55, pp. 3-14.

Kumada, T., Kobayashi, A., Sakai, K., Shibazaki, M., Uda, T. and Serizawa, M. (2003). Experiment and computation of three-dimensional sorting of sand of mixed grain size on coast with dominant longshore sand transport, *Proc. of Civil Engineering in the Ocean*, JSCE, Vol. 19, pp. 905-910. (in Japanese)

Kumada, T., Uda, T. and Serizawa, M. (2006). Model for predicting composition changes of grain size of bed materials, *Proc. 30th ICCE*, ASCE, (in press).

Kuroiwa, M., Kuchiishi, T., Matsubara, Y. and Noda, H. (2006). A quasi three-dimensional coastal area model with shoreline changes for mixed-size sands, *Proc. 30th Int. Conf. on Coastal Eng*. (in press).

Ozasa, H. and Brampton, A. H. (1980). Mathematical modeling of beaches backed by seawalls, *Coastal Eng*., Vol. 4, pp. 47-64.

Serizawa, M., Uda, T., San-nami, T., Furuike, K. and Kumada, T. (2003). Improvement of contour line change model in terms of stabilization mechanism of longitudinal profile, *Coastal Sediments '03*, pp. 1-15.

Serizawa, M., Uda, T., San-nami, T. and Furuike, K. (2006). Three dimensional model for predicting beach changes based on Bagnold's concept, *Proc. 30th ICCE*, ASCE, (in press).

Uda, T., Omata, A. and Yamamoto, K. (1987). Report of experiment on control of longshore sand transport, *Technical Memo. of PRWI*, No. 2507, p. 39. (in Japanese)

Uda, T., Yamamoto, Y., Itabashi, N. and Yamaji, K. (1996). Field observation of movement of sand body due to waves and verification of its mechanism by numerical model, *Proc. 25th ICCE*, pp. 137-150.

Uda, T., Kumada, T. and Serizawa, M. (2004). Predictive model of change in longitudinal profile in beach nourishment using sand of mixed grain size, *Proc. 29th ICCE*, ASCE, pp. 3378-3390.

Uda T. (2004). *Beach Erosion in Japan and Measures*, Sankaido Press, Tokyo, p. 304. (in Japanese)

A CIRCULATION MODELING APPROACH FOR EVALUATING THE CONDITIONS FOR SHORELINE INSTABILITIES

Jeffrey H. List[1] and Andrew D. Ashton[1,2]

1. U. S. Geological Survey, 384 Woods Hole Rd., Woods Hole, MA, 02543, jlist@usgs.gov
2. Woods Hole Oceanographic Institution., MS #22, 360 Woods Hole Rd., Woods Hole, MA 02543, aashton@whoi.edu

Abstract: Analytical models predict the growth (instability) of shoreline salients when deep-water waves approach the coast from highly oblique angles, contrary to classical shoreline change models in which shoreline salients can only dissipate. Using the process-based wave, circulation, and sediment transport model Delft3D, we test this prediction for simulated bathymetric and wave characteristics approximating the open-ocean conditions at Duck, North Carolina. We consider two cases: a uniform coast with a varying wave approach angle, and a bathymetry with coastal salients and a single high-angle boundary wave condition. Incident wave conditions include a swell case with no wind and a wind-wave case with active local wave regeneration by wind. The uniform-coast tests predict transport maxima at oblique wave angles for both wave cases, indicating the potential for shoreline instabilities, similar to the analytical models. However, the critical angle for instability is much higher in the wind-wave case. Our tests with coastal salients agree with previous findings that a minimum salient length scale may be required for the instability effect to be active. Here, a salient with a longshore scale of 4 km results in transport divergence (erosion; no instability) at the salient crest while an 8 km salient results in transport convergence (accretion; instability) at the crest.

INTRODUCTION

Since the initial formulation by Pelnard-Considere (1956), the most common approach for modeling shoreline evolution has been the "one-line model," in which shoreline change is related to gradients in longshore transport through a continuity equation. Typically, longshore transport is found using empirical equations relating wave

characteristics at the breakpoint to the total longshore transport in the surf zone. In the U.S. coastal engineering community, a frequently-used model that employs this approach is GENESIS (Hansen and Kraus, 1989), a one-line model that utilizes the "CERC formula" (Komar and Inman, 1970; Rosati et al., 2002) for longshore transport.

Ashton et al. (2001), in an innovative application of the one-line approach, predict that when waves approach the coast from high angles (i.e., highly-oblique or non-normal wave incidence), the diffusive, coast-smoothing, nature of the Pelnard-Considere equation can be reversed, resulting in the growth of coastal salients (referred to as "negative diffusion"). Although breaking wave angles are generally much lower than the critical angle for the instability effect (45° in the CERC formula), Ashton et al. (2001) demonstrate that due to the energy-spreading effect of waves refracting towards the coast, only the deep-water wave angle needs to exceed a critical angle (about 42°) for shoreline instabilities to occur. Using a simple cellular modeling approach and Snell's law for wave transformation over shore-parallel contours, Ashton et al., (2001), Ashton and Murray (2006a), and Ashton and Murray (2006b) simulate many realistic-appearing coastal morphologies that spontaneously grow from small, random perturbations to a uniform coast.

Falqués and Calvete (2005) explored potential limits to the shoreline instability effect using a linear stability analysis and an analytical wave transformation model, and suggest that under certain conditions even very high-angle waves will not result in the growth of coastal salients. In general, they found that the longshore wavelength of the coastal undulations, the depth to which undulations are reflected in bathymetric contours, and the incident wave period control the degree to which the shoreline experiences instabilities. In a similar stability analysis, Uguccioni et al. (in press) employ a simple flow and sediment transport model to assess the effect of flow convective terms on shoreline stability, showing that this has only a moderate impact on the preferred wavelength and growth rate of the instabilities.

In all previous modeling and analytical work on the shoreline instability problem, many simplifying assumptions have been employed, especially in the transformation of wave characteristics from deep water to the surf zone (e.g., limiting wave transformation processes to Snell's law over parallel contours). Our objective here is to employ a much less simplified process-based model to evaluate the potential for shoreline instabilities in a situation approximating an open-ocean beach. We use the circulation and sediment transport model Delft3D (Lesser et al., 2004) in conjunction with the wave model SWAN (Booij et al., 1999) in test cases designed to roughly approximate the bathymetric and wave conditions for a moderate storm on a U.S. east coast beach at Duck, North Carolina. We first evaluate the potential for the instability effect using an (effectively) infinite uniform coast, in which only the deep-water incident wave angle is varied. We then place coastal salients of varying longshore scales on the coast, and apply waves with angles high enough to be within the instability range as indicated by the uniform-coast tests. We derive longshore sediment transport gradients through both the CERC equation and the cross-shore integration of Delft3D-predicted longshore transport through the surf

zone. The patterns of transport convergences and divergences relative to the salient morphology are used to asses the potential for the instability effect. Morphological evolution is not simulated here.

METHODOLOGY

Bathymetric Grids

We use two types of simplified bathymetries for our Delft3D model runs: a uniform coast with a longshore-uniform cross-shore profile, and a coast with salients constructed by superimposing a 3D Gaussian surface on the uniform-coast bathymetry.

The uniform-coast bathymetry consists of a composite plane beach profile, scaled roughly after the coastal profile from the beach to the shelf slope at Duck, North Carolina, at the U.S. Army Corps of Engineers Field Research Facility. Plane beach segments (and their slopes; depth maxima) include the beach/nearshore (0.0125; 8 m), the shoreface (0.004; 17 m), the shelf (0.00003; 40 m), and the shelf slope (0.006; 100 m). While this coastal profile has the advantage of simplicity of bottom grid construction, the slope discontinuities between plane segments produce some minor discontinuities in the model results presented below; for future work it would be advantageous to employ a more smoothly varying profile.

The objective for our uniform-coast model runs was to investigate the effect of variations in incoming wave direction through all angles relevant for generating longshore flow and sediment transport, from normally incident (wave crests 0° relative to the shoreline) to coast following (wave crests 90° relative to the shoreline). Such a range of wave directions presents a significant challenge for applying any wave model (including SWAN) due to the specification of the wave conditions on the "lateral" boundaries (Fig. 1), which encompass depths ranging from dry land to deep water. Although iterative methods exist for establishing such boundary conditions, we follow a simple approach of nesting the wave model, starting with a regional grid that covers an area sufficiently large that lateral boundary effects are absent where boundary conditions are provided to a nested wave grid. Our tests show that this procedure was effective even for waves propagating directly alongshore. An example is given in Fig. 1, in which predicted wave heights near the up-wave lateral boundary are highly affected by boundary effects, yet become uniform in the region of the nested wave grid.

For each uniform-coast model run, three rectilinear grids were constructed over the coastal profile described above. The regional wave grid (Fig. 1) has longshore by cross-shore dimensions of 300,000 by 90,000 m, grid spacings of 2,000 by 500 m, and extends to 100 m water depth. The nested wave grid (Fig. 1) has dimensions of 8,000 by 3,000 m, spacings of 80 m by 20 m, and extends to 16.5 m depth. The grid used for Delft3D circulation and sediment transport is identical to the nested wave grid, except that the longshore dimension is reduced to 6,400 m so that flows are unaffected by boundary problems in the nested wave grid (which still exist despite receiving their boundary conditions from the regional wave grid).

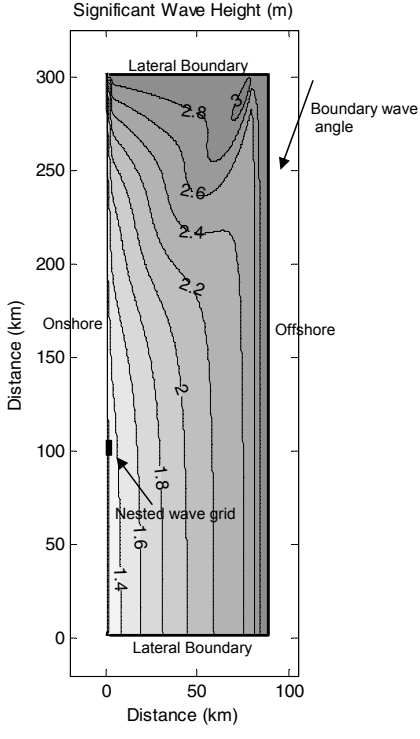

Figure 1. Regional and nested wave grid domains used in the uniform-coast tests. Contours shows the significant wave height for the swell wave case with the angle of incidence on the lateral and offshore boundaries set to 70° relative to normal incidence.

Model grids for the coastal salient tests were constructed similarly, except that the nested wave and flow grids had to be significantly expanded to accommodate the non-uniform bathymetry. The nested wave grid has dimensions of 32,000 by 13,000 m and spacings of 200 m by 50 m. The circulation grid has dimensions of 20,000 m by 13,000 m, and spacings of 100 m by 25 m. Both extend to a water depth of 20 m. Although a curvilinear, coast-following grid with variable spacing (finer closer to shore) would be more efficient and likely provide less noisy results for these tests, our need to construct bathymetric grids for coastal salients at many scales dictated the use of a rectilinear grid for this exploratory work. Coastal salients varying between 1 and 8 km in length were constructed by adding a 3D Gaussian surface to the composite-plane surface used in the

uniform-coast tests. The salient length scale is defined as the distance encompassing 95% of the Gaussian height distribution. The water depth to which bathymetric contours are perturbed by the salient depends on the salient length scale. For our 1 km salient depth contours are modified to a depth of about 2 m, while for the 8 km bump this depth is about 16 m.

All grids for Delft3D flow computations were constructed with one vertical layer, providing flow predictions in a vertically-averaged or 2DH mode.

Delft3D Model Runs

Waves, currents, and sediment transport were simulated by the Delft3D modeling system (Lesser et al., 2004), version 3.25.02. Delft3D employs the wave model SWAN (Booij et al., 1999), a spectral wave action-balance model accounting for the modification of waves by currents. In the mode applied here, SWAN simulations include the effects of refraction (both bathymetry and current-related), depth-induced breaking, dissipation due to bed friction, and the local regeneration by wind (for tests in which wind is present). Two wave conditions were applied uniformly to the lateral and offshore boundaries of the regional wave grid (Fig. 1): swell waves with significant wave height H_s=3.0, peak period T_p=10.0 seconds, directional spread 10°, and no wind; and a wind-wave case with H_s=3.0, T_p=7.0 seconds, directional spread 20°, and a steady, uniform wind of 15 m/s in the same direction as the boundary waves. These conditions roughly approximate moderate storm conditions on the North Carolina coast. It is important to note that the "wind wave" cases examined by Falqués and Calvete (2005) and Ashton and Murray (2006a) included no local regeneration of waves by wind.

For the uniform-coast tests, the boundary wave crest angle relative to the shoreline angle was varied in 5° increments from -5° to 100° (Fig. 2), where 0° is normally incident and 90° is directly alongshore. For the coastal salient tests, boundary wave directions were chosen to maximize the potential for the instability effect.

The Delft3D flow model is driven by gradients in wave-induced radiation stresses which are computed by the SWAN model. In our tests, flows are driven only by wave forces, neglecting tides, density stratification, wind, or other processes that could also generate flows in the coastal zone. Lateral flow boundaries are of the Neumann type (Roelvink and Walstra, 2004), which prescribes a water level gradient at the boundary. The offshore boundary has a fixed, still water level condition. We used the default Delft3D sediment grain size of 0.20 mm, as only patterns of transport gradients, not absolute magnitudes of transport, are relevant here and any grain size that would produce mainly suspended sediment transport would give essentially the same results. Bedload and suspended load sediment transport were predicted using the default Delft3D transport formulations of van Rijn (1993).

The flow model and wave model interact through flow requests for updated wave information every 30 minutes, with the flow model providing fields of sea-surface elevations and depth-averaged currents to the wave model. After each wave model

update, the flow model continues for 30 minutes (model time) using an unchanging field of wave forcing. Because we employ steady wave boundary conditions, the wave/flow solution reaches a steady-state solution after about 17 hours of model time (in the absence of morphological evolution). Only results from the final, steady-state solution are of interest here.

The sensitively of model results was tested in response to many, but far from all, combinations of free model parameters in the flow component of Delft3D. It is believed that the results presented here are qualitatively robust to reasonable ranges of free model parameters, but the possibility that certain combinations of parameters would give substantially different results cannot be discounted.

Longshore Transport and Transport Gradients

We derive longshore transport gradients for our test cases using two methods, both of which utilize the same Delft3D model runs. First, we apply the empirical CERC equation (Komar and Inman, 1970; Rosati et al., 2002) employing SWAN-modeled wave characteristics at the breakpoint. Second we directly use Delft3D predictions of longshore sediment transport within the surf zone.

The CERC equation (also known in similar forms as the Scripps or Komar equations) predicts the volumetric longshore sediment transport rate, Q_x, as

$$Q_x = K_1 a_1 H_b^{5/2} \sin(2\phi_b) \qquad (1)$$

where K_1 is an empirical coefficient (set to 0.6 here), H_b is the root mean square wave height (H_{rms}) at the breakpoint, ϕ_b is the relative angle between the shoreline and the wave crest angle at the breakpoint, and

$$a_1 = \frac{1}{16\left(\frac{\rho_s}{\rho} - 1\right)(1-p)}$$

where ρ_s is the density of sand, ρ is the density of water, and p is the sand porosity. In some studies, including the shoreline instability analysis of Falqués and Calvete (2005), a less tested "second CERC term," accounting for the effects of beach slope and longshore gradients in wave height (Ozasa and Brampton, 1980) is added to Eqn. 1. For our tests, this term's contribution is an order of magnitude less than predicted by Eqn. 1, and is therefore neglected.

We extract H_b and ϕ_b from the nested SWAN wave model output through the procedure described by List et al. (in press). In brief, H_b and ϕ_b are derived independently at each longshore grid node where the breaking wave height to depth ratio, γ_{rms}, equals 0.3.

Note that this γ_{rms} is much lower than typically employed for identifying the breakpoint in applications of the CERC equation in which monochromatic wave models are used (SWAN is a spectral model). Sensitivity tests demonstrated that varying γ_{rms} from 0.2 to 0.4 had no qualitative affect on the results presented here. For the uniform beach tests, ϕ_b is simply the wave crest angle because the shoreline orientation is constant. For the coastal salient tests, ϕ_b is found as the difference between the wave crest angle and the angle of the shoreline defined at the still water level of the flow model (z=0).

Delft3D calculates sediment transport at grid node locations, and can optionally evolve the seabed morphology by translating the gradients in sediment transport between grid nodes into vertical seabed changes. However, in order to obtain estimates of the longshore transport comparable to what is obtained through the CERC approach, we adopt a method for extracting the cross-shore integrated longshore transport from the Delft3D output similar to the approach of Haas and Hanes (2004), with no morphologic evolution permitted. At each longshore location, we integrate the predicted longshore component of the total (suspended and bedload) transport from the shoreline to the offshore extent of the grid to give a Delft3D-predicted Q_x comparable to Q_x in Eqn. 1. No attempt was made to limit the integration to the seaward limit of the surf zone, because minimal flow velocities and transport beyond the surf zone make this unnecessary. Because we are only considering the longshore component of the predicted sediment transport, the influence of cross-shore transport, and associated gradients, are not considered here. Our sign convention is that positive Q_x represents transport towards the right when facing offshore.

For the uniform-coast tests, we derive longshore transport at one representative location away from boundary disturbances. We extract longshore transport as a function of distance along the coast for the salient tests, but only use the component of transport in the alongshore direction of the rectilinear grid, i.e., we do not find the component of transport parallel to the changing orientation of the salient shoreline. We find the longshore transport gradient as $\partial Q_x / \partial x$, also using the rectilinear grid for the alongshore distance, x, thereby removing the problem associated with the curving coastline. A negative $\partial Q_x / \partial x$ indicates transport divergence and a positive $\partial Q_x / \partial x$ indicates transport convergence, assumed to indicate the potential for shoreline erosion and accretion, respectively. (For example, a negative transport gradient within any segment of coast indicates that more sediment is leaving that segment than entering it, indicating that that segment of coast would be erosional.)

RESULTS

Uniform-coast Tests

H_b, ϕ_b, and Q_x for both the CERC and Delft3D approaches are shown for the swell wave tests in Fig. 2 as a function of the wave crest angle specified on the lateral and offshore boundaries of the regional wave grid. All curves are very similar to results obtained

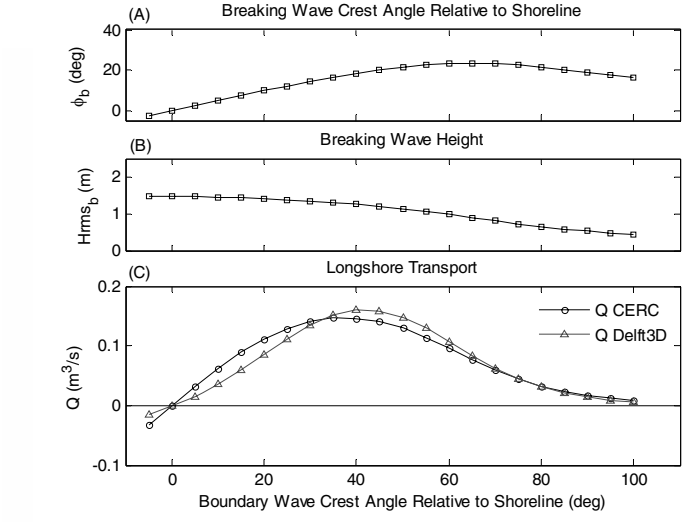

Figure 2. Uniform coast, swell wave tests: (A) breaking wave angle, (B) breaking wave height, (C) longshore transport as a function of wave angle specified at the lateral and offshore boundaries of the regional wave grid.

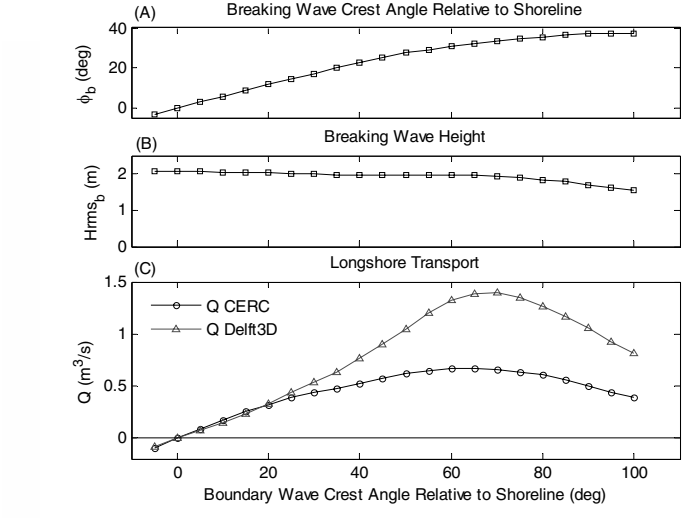

Figure 3. Uniform coast, wind-wave case: (A) breaking wave angle, (B) breaking wave height, (C) longshore transport as a function of wave angle specified at the later and offshore boundaries of the regional wave grid.

through analytical approaches (Falqués, 2003; Ashton and Murray, 2006a), confirming that although the wave crest angle at the breakpoint is always less than the 45° critical angle required for shoreline instabilities in the CERC equation, a Q_x maximum at a boundary wave crest angle of about 40° results from the reduction in wave height at higher angles due to higher refractive spreading. Shoreline instabilities would therefore be expected for these bathymetric and wave conditions when the deep-water wave angle exceeds approximately 40°, very close to the value predicted by Ashton et al. (2001).

Comparable information is shown in Fig. 3 for the wind-wave test case. Although a maximum in transport is still present, the critical boundary angle is shifted to about 65°, indicating that shoreline instabilities would only occur for very high deep water wave angles. The reason for this shift can be understood from the curve for H_b—the refraction-induced decrease in wave height is less strong at higher angles than for the swell case, presumably because of wave energy re-generation by local wind across the shelf and shoreface. In addition, because the wave height diminishes less with increasing deep-water wave angle, ϕ_b does not reduce at high boundary angles as in the swell case where smaller breaking waves are located in shallower water where waves have refracted more towards the coast.

Note that in both wave cases, Q_x does not reduce to zero at 90° (waves traveling directly alongshore), as would be expected from the CERC formula. This is due to the wave directional distribution in the SWAN model, set to 10° in the swell case and 20° in the wind-wave case. The effect is especially pronounced for the wind-wave case, with substantial longshore transport remaining for cases with offshore-directed winds.

Although secondary to the objectives of this paper, the comparison between the CERC-derived and Delft3D-derived Q_x is also of interest. We made no attempt to calibrate either method for a better match, and the close correspondence between the two approaches in Fig. 2 is probably fortuitous, as reflected in the much poorer correspondence in Fig. 3. No explanation for this difference between the swell case and wind-wave case is immediately evident, although the two methods agree on the important aspect of Figs. 2 and 3—the location of the Q_x maxima.

Coastal Salient Tests

The tests in Figs. 2 and 3 indicate the potential for shoreline instabilities occurring within the framework of a process-based model, but it is unclear if these results, based on a uniform coast with parallel bathymetric contours as assumed in the original model of Ashton et al. (2001), would apply to a non-uniform coast in which coastal salients have finite length scales. Falqués and Calvete (2005) address this issue with an analytical approach using a linear stability analysis, predicting that a minimum longshore length scale may be required for instability depending on the bathymetry and wave conditions. We test this result in a more natural situation here by adding coastal salients with finite amplitudes to the uniform bathymetry and evaluating the longshore transport gradients

under high wave angle conditions. A positive transport gradient (convergence) at the salient crest would indicate salient accretion (the instability or negative diffusion effect), while a negative transport gradient (divergence) at the salient crest would indicate salient erosion (diffusion). A gradient pattern of divergence (erosion) on the updrift side of the salient and convergence (accretion) on the downdrift side would indicate salient translation in the downdrift direction.

Coastal salients were constructed with longshore scales of 1, 2, 4, and 8 km for tests under both the swell and wind-wave conditions. The uniform-coast results of Figs. 2 and 3 were used to identify the wave angles with the highest potential for the instability effect. While all angles above the Q_x maxima have this potential, the steepest part of the curve is associated with the highest "negative diffusion," or tendency for the diffusional nature of the Pelnard-Considere formulation to be reversed (Ashton and Murray, 2006a). For the swell wave case we chose 70° and for the wind-wave case we chose 80° (although tests with similar wave angles gave very similar results).

All our salient tests indicate salient translation downdrift, as indicated by the transport gradient curves for both the CERC and Delft3D approaches. Examples are given in Figs. 4 and 5 for our swell and wind-waves tests with 4 and 8 km salients. This result is contrary to some previous shoreline modeling studies which required an arbitrary advection term to the shoreline diffusion equation to produce salient translation (e.g., Thevenot and Kraus, 1995).

However, the transport gradient patterns shown in Figs. 4 and 5 do not indicate pure translation, since the transport gradients at the salient crests (10 km) are not equal to zero. There is a clear tendency for divergence (negative gradient) at the salient crest in the 4 km case (Figs. 4DEF and 5DEF) to shift to convergence (positive gradient) at the crest in the 8 km case (Figs. 4ABC and 5ABC). This can also be seen in the longshore transport curves, with the peak transport appearing downdrift of the salient crest in the 4 km case and updrift in the 8 km case. These results suggest that as the salient scale increases from 4 to 8 km, the shoreline diffusion shifts from positive to negative and coastal salients become more likely to grow rather than being smoothed out.

For comparison, we add the curve "CERC-recast" to Figs. 4 and 5, representing the transport and transport gradients derived using the deep-water wave transformation approach of Ashton et al. (2001). For this approach the transport convergence is nearly centered on the salient crest for both the 4 and 8 km cases, indicating salient growth without translation.

A possible explanation for the difference between our 4 and 8 km salient tests, as well as the difference between the CERC/Delft3D and the CERC-recast results, is the limited water depth to which the salient-perturbed contours extend (about 10 m for the 4 km salient and 16 m for the 8 km salient). An examination of the wave angle field shows that the 4 km salient contours do not extend offshore into the zone where

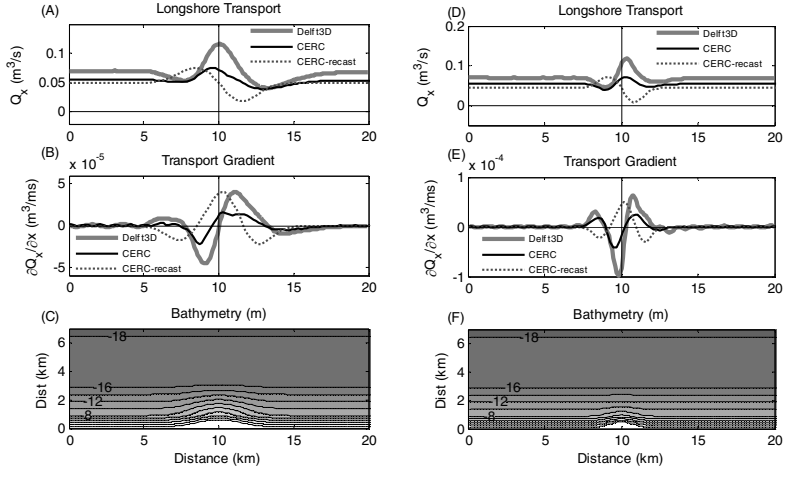

Figure 4. Swell wave case: (A,D) longshore transport (smoothed), (B,E) longshore transport gradient, and (C,F) salient bathymetry for 8 km (A,B,C) and 4 km (D,E,F) salients. The boundary wave crest angle is 70° relative to the overall coastal trend. The sign conventions for panels (A,B,D,E) are explained in the text. The magnitudes of the CERC-recast curves are scaled to match the D3D curves.

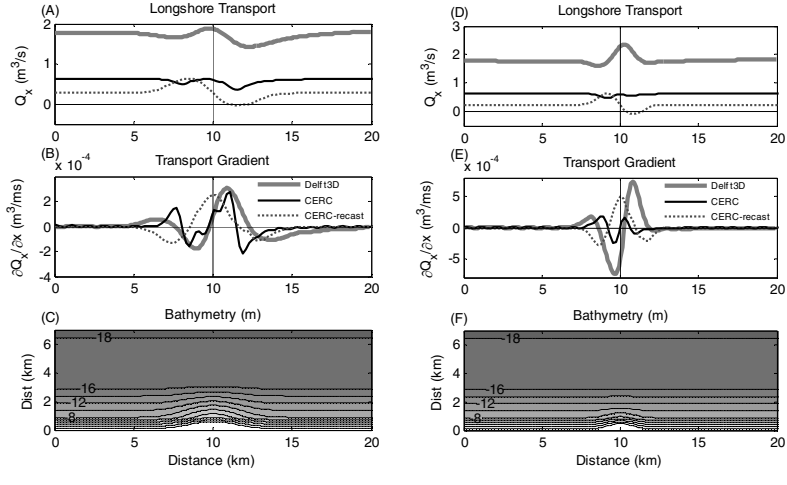

Figure 5. Wind-wave case: (A,D) longshore transport (smoothed), (B,E) longshore transport gradient, and (C,F) salient bathymetry for 8 km (A,B,C) and 4 km (D,E,F) salients. The boundary wave crest angle is 80° relative to the overall coastal trend. See Fig. 4 for more information.

wave angles exceed the critical angle for instability (>40° for the swell wave case, Fig. 2; and >65° for the wind-wave case, Fig. 3). If waves have already refracted below the critical angle before reaching the salient contours, it seems unlikely that any instability effect is possible. For the 8 km salient, swell wave case, the salient-perturbed contours extend a limited distance into the zone of high angle waves, suggesting that the instability mechanism could be active for this case. For the 8 km salient, wind-wave case, the salient-perturbed contours still don't extend into the zone of high wave angles, but it is possible that the very high angle criterion for instability (>65°) determined from the uniform-coast test does not really apply for the wind-wave case. More research is needed to examine the processes by which an increase in salient scale shifts the transport gradients patterns toward salient growth.

The close correspondence between the CERC and Delft3D transport gradients in these tests is noteworthy. This contrasts with the results of List et al. (in press), in which the CERC and Delft3D transport gradients diverged greatly in the case of shoreface pits disconnected from the shoreline. It is apparent that when bathymetric irregularities reflect the shoreline shape, the two approaches give much more similar results.

CONCLUSIONS AND DISCUSSION

We apply a process-based model for evaluating the conditions for shoreline instabilities induced by high angle waves under bathymetric and wave conditions roughly approximating the open-ocean coast at Duck, North Carolina. Tests with a uniform coast indicate the potential for the instability effect for both swell and wind-wave cases, although the critical wave angle required for instability in the wind-wave case was much higher due to the local regeneration of wave energy which balances the energy lost due to refractive spreading.

Tests with high wave angles and coastal salients at a range of scales from 1-8 km suggest a minimum alongshore length scale necessary to initiate the instability effect. While all tests indicate salient translation downdrift, the longshore transport gradients also indicate a shift from salient erosion at the 4 km salient scale to salient accretion at the 8 km scale. This contrasts with the transport gradients found through the approach of Ashton et al. (2001), for which salient growth is predicted independent of scale. The linear stability analysis of Falqués and Calvete (2005), however, also suggests the existence of a minimum salient scale for shoreline instability.

We must add the caveat that in this work we only derive static patterns of transport gradients—we do not simulate shoreline or morphological evolution including feedback between the evolving morphology and the transport gradients. It is possible that given such evolution, the morphological outcome might be very different from the initial transport gradient patterns we present here.

Our results suggest that small-amplitude, random perturbations to an otherwise straight coast might not grow and self-organize into larger scales under the open-ocean

conditions we approximate in our high wave angle tests. Even if such random perturbations contained length scales large enough for the instability effect to operate (apparently larger than 4 km in our tests), the transport gradients associated with these perturbations would be exceedingly small (small differences in longshore transport divided by large distance). On natural coasts, near-ubiquitous shelf and shoreface irregularities which are not associated with shoreline shape might generate much higher magnitude gradients in longshore transport and therefore control the initial shoreline evolution. However, if shoreline features generated in this manner (or through other processes such as geologic framework controls) were of the necessary length scale, the instability effect could then assume control of the subsequent coastal evolution. An example could be the large-scale "Carolina Capes"of the Southeast U.S., identified as a potential long-term result the instability effect (Ashton et al., 2001; Ashton and Murray, 2006b).

ACKNOWLEDGEMENTS

Amy Farris is thanked for writing parts of the post-processing code for analyzing model output. Giles Lesser and Jacco Groeneweg are thanked for expert training in the use of the Delft3D modeling system and SWAN, respectively. Bert Jagers is thanked for modifications to Delft3D needed to conduct the model runs presented here. Edwin Elias is thanked for support in the operation and application of Delft3D for coastal change studies. Guy Gelfenbaum and Chris Sherwood of the USGS are thanked for their efforts to make Delft3D available to all researchers in the USGS. Use of the Delft3D modeling system does not imply endorsement by the USGS. Peter Ruggiero and Chris Sherwood are thanked for reviewing this paper, resulting in substantial improvement.

REFERENCES

Ashton, A., Murray, A. B., and Arnault, O., 2001. Formation of coastline features by large-scale instabilities induced by high-angle waves. Nature, 414: 296-300.

Ashton A. D. and A. B. Murray, 2006a. High-angle wave instability and emergent shoreline shapes: 1. Modeling of sand waves, flying spits, and capes. Journal of Geophysical Research, 111, F04011, doi:10.1029/2005JF000422.

Ashton A. D. and A. B. Murray, 2006b. High-angle wave instability and emergent shoreline shapes: 2. Wave climate analysis and comparisons to nature. Journal of Geophysical Research, 111, F04012, doi:10.1029/2005JF000423.

Booij, N., Ris, R. C., and L.H. Holthuijsen, 1999. A third generation model for coastal regions. Part I: Model description and validation. Journal of Geophysical Research, 104: 7649-7666.

Falques, A., 2003. On the diffusivity in coastline dynamics. Geophysical Research Letters, 30, 2119, doi:10.1029/2003GL017760:

Falques, A. and Calvete, D., 2005. Large-scale dynamics of sandy coastlines: diffusivity and instability. Journal of Geophysical Research, 110, C03007, doi:10.1029/2004JC002587.

Haas, K. A. and Hanes, D. M., 2004. Process based modeling of total longshore sediment transport. Journal of Coastal Research, 20: 853-861.

Hanson, H., and Kraus, N.C., 1989. GENESIS: generalized model for simulating

shoreline change. U.S. Army Corps of Engineers, Coastal Engineering Research Center CERC-89-19, 185 pp.

Komar, P. D. and Inman, D. L., 1970. Longshore sand transport on beaches. Journal of Geophysical Research, 75: 5514-5527.

Lesser, G. R., Roelvink, J. A., and van Kester, J. A. T. M. and Stelling G. S., 2004. Development and validation of a three-dimensional morphological model. Coastal Engineering, 51: 883-915.

List, J. H., Hanes, D. M., and Ruggiero, P., in press. Predicting longshore gradients in longshore transport: comparing the CERC formula to Delft3D. Proceed. 30th International Conference on Coastal Engineering, San Diego, California.

Ozasa, H. and Brampton, A. H., 1980. Mathematical modeling of beaches backed by seawalls. Coastal Engineering, 4: 47-63.

Pelnard-Considere, R., 1956. Essai de theorie de l'Evolution des Formes de Rivage en Plages de Sable et de Galets. 4th Journees de l'Hydraulique, Les Energies de la Mer, Question III (Report No. 1): 289-298.

Roelvink, D. J. A. and Walstra, D., 2004. Keeping it simple by using complex models. Proceed. 6th International Conference on Hydroscience and Engineering, Brisbane, Australia, http://kfki.baw.de/fileadmin/conferences/ICHE/2004-Brisbane/Home.pdf (ISBN 0-937099-12-0).

Rosati, J. D., Walton, T. L., and Bodge, K., 2002. Longshore sediment transport. In: D. B. King (Editor), Coastal Engineering Manual, Part II, Coastal Sediment Processes, Chapter II-2. U.S. Army Corps of Engineers, Washington, D.C.

Thevenot, M. M. and Kraus, N. C., 1995. Longshore sand waves at Southhampton Beach, New York: observation and numerical simulation of their movement. Marine Geology, 126: 249-269.

Uguccioni, L., Deigaard, R., and Fredsoe, J. , in press. Instability of a coastline with very oblique wave incidence. Proceed. 30th International Conference on Coastal Engineering, San Diego, California.

van Rijn, L. C., 1993. Principles of Sediment Transport in Rivers. Aqua Pubblications, Amsterdam, The Netherlands.

AN ALTERNATIVE EXPLANATION FOR THE SHAPE OF 'LOG-SPIRAL' BAYS

Ryan Littlewood[1], A. Brad Murray[2], Andrew D. Ashton[3]

1. Division of Earth and Ocean Sciences, Nicholas School of the Environment and Earth Sciences; Duke University, P.O. Box 93844, Durham, NC 27708-3844, USA. ryan.littlewood@duke.edu.
2. Division of Earth and Ocean Sciences, Nicholas School of the Environment and Earth Sciences; Center for Nonlinear and Complex Systems; Duke University, P.O. Box 90227, Durham, NC 27708, USA. abmurray@duke.edu.
3. Woods Hole Oceanographic Institution, Woods Hole, MA 02543-1050, USA. aashton@whoi.edu.

Abstract: We present a simple numerical model capable of producing distinctive scalloped bays of a form found when a sandy coastline extends downdrift of a rocky headland. The shape of such bays can often be approximated by a log-spiral—a curve for which the radius of curvature increases logarithmically with distance from the headland or 'pinning point.' A considerable body of work has been published attributing this shape to the pattern of refraction and/or diffraction created as waves approaching from a dominant direction interact with the pinning point. Here, we present a fundamentally different explanation for these shapes. We use an existing one-line numerical model of wave-driven alongshore transport which includes shoaling and refraction over contours assumed to parallel local shoreline orientations. Rather than assuming a single wave angle, it generates new waves repeatedly according to an input wave climate. It does not include refraction or diffraction around the pinning point; thus, the log-spiral-like shape evolves as simply as a result of alongshore transport driven by a distribution of deep-water wave approach angles.

INTRODUCTION

When a sandy coast extends downdrift of a relatively inerodible rocky headland, a scalloped bay often forms. Such forms have been given many names, including headland-bay beaches, crenulate bays, hook-shaped bay beaches, half-heart-shaped beaches, and zetaform beaches (e.g. Yasso 1965, Finkelstein 1982. Yasso, the first to claim that the planform shape of these features tended to approach a logarithmic spiral, was responsible for another name, logarithmic- or log-spiral bays.

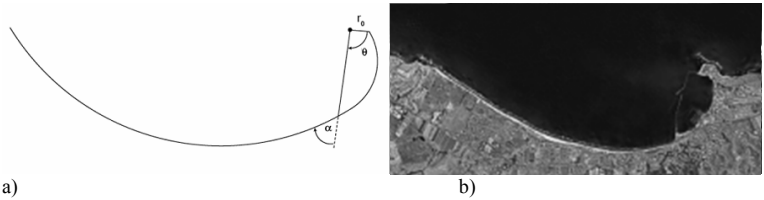

a) b)

Fig 1 a) Logarithmic spiral, given by $r = r_0 e^{\cot(\square)}$. b) Half Moon Bay, California (Yasso 1965) (Image courtesy of NASA).

Log spirals (Fig. 1), first described by Descartes, are curves having the property that a line drawn from the center to any point on the curve cuts a constant angle α. The radius of curvature of a log spiral increases logarithmically with the distance along the curve, and the width of successive whorls increases geometrically. Log spirals are found in nature in many other contexts, including the arrangement of seeds in a sunflower or pine cone and, famously, the coiled shell of the chambered nautilus.

It is generally thought that these bays erode according to alongshore-transport gradients controlled by the influence of the upwind headland, or pinning point, on the angle of waves reaching the beach. In this conceptual model, it is the pattern of refraction and/or diffraction created as waves approaching from a dominant direction interact with the headland which produces a bay decreasing in curvature away from the pinning point at the center of the spiral (e.g. Yasso 1965, LeBlond, 1979, Lavalle and Lakhan 1996, Moreno and Kraus 1999).

Several authors have predicted that refraction and/or diffraction ought to produce bays of this general form. The logarithmic spiral is an elegant hypothesis, although Komar and others (Phillips, 1985) argue that the theoretical ideal shape is less important than more general descriptors such as a downdrift decrease in curvature. Headland-bay beaches have been fit to other curves, sometimes more successfully than to logarithmic spirals (e.g. Moreno and Kraus 1999), but no mechanisms are generally accepted for these correspondences.

A prediction of the logarithmic-spiral model conceptual model is that the bay will reach

equilibrium once the orientation of the shoreline parallels the refracted wave crests approaching from the dominant direction, leading to a zero-alongshore-flux equilibrium configuration (Leblond 1979, Klein et al. 2003).

We here present modeling results that suggest a fundamentally different explanation for these coastline features. Using a simple one-line numerical coastline model, we generate headland-bay beaches that owe their existence not to the shape of diffracted or refracted wave crests, but to the presence of waves of many deep-water approach angles, not only one dominant angle. Shoreline protuberances such as a headland shadow downwind areas from some wave-approach angles, and any local wave climate is thus a nonlocal function of the nearby shoreline shape (Ashton and Murray, 2006a and 2006b).

METHODS

Numerical Model Overview

The modeling framework used has been described previously (Ashton et al. 2001, Ashton and Murray 2006a). The family of models described briefly here, including a version adapted to include the interactions between shoreline lithology and mobile sediment (Valvo, et al., 2006), features the random selection of a daily deep-water wave angle from a probability distribution function; it is therefore not necessary to assume one dominant wave approach angle.

These models fall in the class of 'one-line' models (Larson, et al. 1987, Komar 1998) of coastal evolution. They assume that over the time scales under consideration (years to decades and longer) the shoreface profile may be considered to be constant as the coastline position translates seaward or landward. One line of beach cells is therefore sufficient to specify the location of the shoreline.

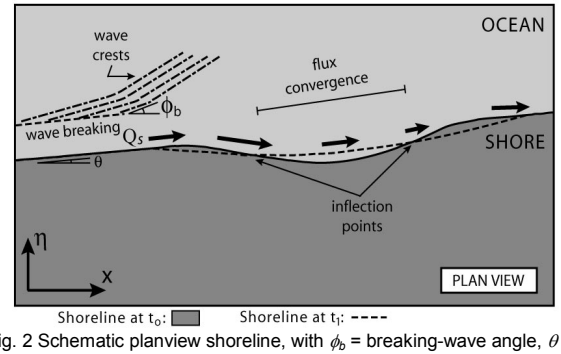

Fig. 2 Schematic planview shoreline, with ϕ_b = breaking-wave angle, θ = local shoreline angle. For low-angle wave climates, divergences from a straight coastline are smoothed away. (from Valvo et al., 2006)

Wave-driven alongshore transport can be related to deep-water wave approach angle relative to the global shoreline orientation with the commonly used CERC equation (Komar, 1998):

$$Q_s = KH_b^{5/2}\sin(\phi_b-\theta)\cos(\phi_b-\theta), \quad (1)$$

where H_b is breaking-wave height, ϕ_b is breaking-wave angle, θ is local shoreline angle relative to the global shoreline orientation, and K is an empirical constant. On a sandy coastline, alongshore gradients in the sediment flux, Q_s, tend to cause changes in the shoreline position, η (Fig. 2), and shoreline change for each cell is determined by the following mass-conservation equation:

$$\partial\eta/\partial t = -(1/D)\partial Q_s/\partial x, \quad (2)$$

where η represents shoreline position and D is the depth to which erosion and accumulation extend. It must be noted that simplified model physics and geometry preclude its application to phenomena at scales less than kilometers and years. Also, the large number of simplifying assumptions make this modeling framework inappropriate for the simulation of any given real coastline; rather, its aim is to explore the causes of poorly-understood phenomena that may arise from even such simplified representations of coastal processes.

The CERC equation predicts a maximum in alongshore sediment transport for deepwater wave-approach angles of about 45°, a prediction with important consequences for shoreline evolution. When deep-water wave angles below this maximum dominate in a wave climate (Ashton and Murray 2006b), diffusive conditions prevail, and planview shoreline features are reduced in amplitude. However, recent work (Ashton et al. 2001; Falques et al. 2005; Ashton and Murray 2006a) has revealed that, given a wave climate dominated by wave angles greater than approximately 45°, diffusivity actually becomes negative, resulting in an instability in planview shoreline shape: alongshore flux converges across the crest of a shoreline perturbation, causing accretion. As planview perturbations grow, regular shoreline features including spits and large capes tend to form (Ashton et al., 2001). In this paper, we consider only low-angle-dominated wave climates that tend to produce smooth coastlines.

Model Algorithm

The model domain consists of a two-dimensional grid of cells representing a planform coast. Shoreline cells are partly filled with water and partly with land; a coastline is defined at the interface. During a model run, deep-water waves are generated repeatedly from a probability distribution function representing a global deep-water wave climate. The input wave climate is parameterized with two variables, one representing the proportion of waves from the right side of the domain (the "asymmetry") and the other specifying the percentage of waves that are high-angle. Wave refraction and shoaling are calculated assuming shore-parallel contours, and breaking wave height and angle are used to calculate the alongshore sediment flux, Q_s, leaving each cell from Equation 1.

Equation 2 determines the erosion or accretion or she shoreline based on sediment-flux gradients.

Adaptation for Rocky Coasts

Initial investigations with this model focused on sandy coastlines, but work by Valvo et al. (2006) included the effect of underlying lithology (the 'geological framework'): in this version, land may consist of mobile sediment or of rock. We use this version of the model in some experiments reported below. Rock weathers into mobile sediment according to an exponential-decay function of the form $W = W_0 e^{-xd}$, where W is the weathering rate in m/yr, x is the amount of sediment cover in meters (Fig. 2), d is a decay constant, and W_0 is a coefficient representing the maximum weathering rate, that for bare rock. This simple parameterization is roughly consistent with observations of terrestrial bedrock weathering (Heimsath et al. 1997) and is appropriate given the lack of empirical data on shoreface weathering and the model's exploratory (Murray, 2003) goals.

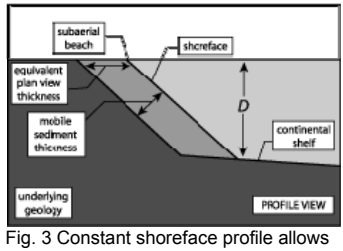

Fig. 3 Constant shoreface profile allows planview thickness to act as proxy for sediment cover (from Valvo et al., 2006)

The thickness of the sediment layer separating bedrock from water is used as a proxy for the degree to which the rock is protected from weathering (Fig. 3); it may be interpreted as representing the frequency with which bedrock is covered by shifting sediment. This simplification represents the assumption that if the time scales being modeled (years and longer) are great enough, intermittent sediment coverage may be reduced to a time-averaged parameter. The variable x is therefore a somewhat abstract quantity representing the ability of sediment cover to impede weathering.

Further, rock composition can vary spatially; this quantity specifies the proportion of the material that weathers into fine sediment (e.g. silt and clay) and will therefore be lost to the nearshore system when a unit of rock is weathered to mobile sediment.

Finally, a feature of the model we add here is the ability to specify sinks, locations on the shoreline that capture all sediment flux. These allow representation of rocky headlands that have steep and deep flanks, and which therefore act to remove sediment delivered by alongshore transport from the nearshore system. This model includes three ways for sediment to be lost from the system—sinks, the removal of weathered rock as fine-

grained sediment, and a globally imposed erosion rate representing sea level rise. Each can be toggled on and off.

Initial Conditions

We explored a range of initial conditions. The initial shoreline configuration consists of a stretch of beach with blocks of inerodible rock at the updrift and downdrift ends. The dry land behind the beach was either set to be rock or mobile sediment. Model experiments reported here involve an asymmetrical wave climate that will produce net sediment transport toward one end of the coast. The wave climate is also dominated by low-angle waves, and thus tends to smooth the shoreline shape.

RESULTS

Necessary conditions for the formation of a scalloped bay include: 1) the predominantly low-angle and asymmetric wave climate; and 2) some mechanism for sediment loss—sinks at the headlands, loss of fine-grained sediment, or simply a globally imposed erosion rate. The equilibrium bay shape was not markedly sensitive to the mechanism of sediment loss.

Figure 4 shows a time series of a sample model run that produced a hook-shaped bay. Near the updrift end of the model domain, an inerodible headland is associated with a sink that removes any sediment transported onto the headland. Downdrift of the pinning point (headland), the lack of sediment influx produces a divergence of sediment flux and therefore erosion; an indentation forms downdrift of the headland, and as more sediment moves downdrift and is not replaced, the indentation becomes a growing bay. As the bay deepens, any location on its coast is increasingly shadowed by the opposite side, and so local wave climates resemble the global deep-water wave climate less and less.

Figure 5 comes from the first years of the same model run and shows that the bay does not acquire an obviously spiraled shape until it has undercut the headland to a sufficient degree to become recurved. At the downdrift end of the new bay, the growing spiral-like shape has an inflection point as its angle approaches that of the undisturbed flat coastline. The bay continues to grow until the downdrift end is intercepted by an inerodible headland, which acts to trap the bay by removing the high-erosion inflection point. After this, the bay approaches a steady state, equilibrium shape. By contrast, Fig. 6 presents a new bay which is not yet influenced by the presence of the downdrift headland.

Figure 7 shows a model experiment in which rock progressively weathers into mobile sediment. As long as the maximum weathering rate exceeds the rate at which sediment transport removes material locally, the presence of rock near the surface does not alter the model behavior. The loss of fine-grained material upon weathering, however, removes the necessity to impose sediment sinks at the headlands.

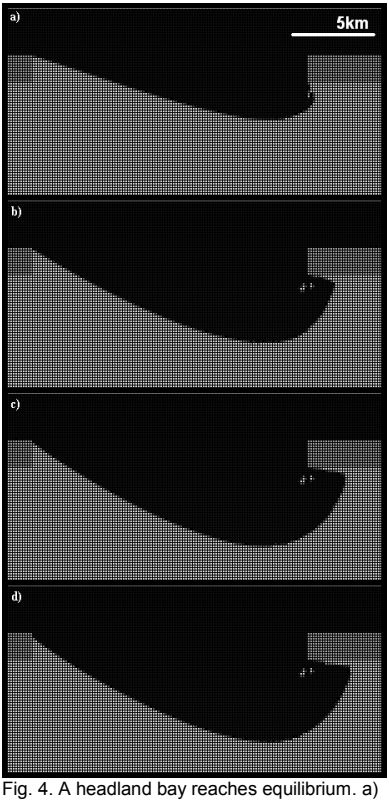

Fig. 4. A headland bay reaches equilibrium. a) t=200yrs. b) t=400yrs. c) t=800yrs. t=1600yrs.

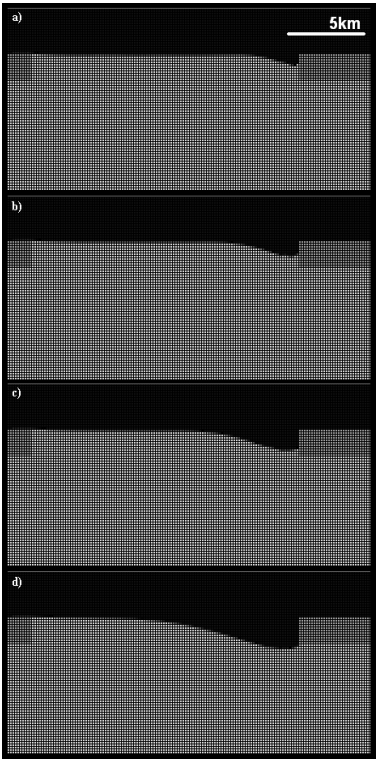

Fig. 5 The origin of the bay. a) t=2yrs. b) t=4yrs. c) t=8rs. d) t=16yrs

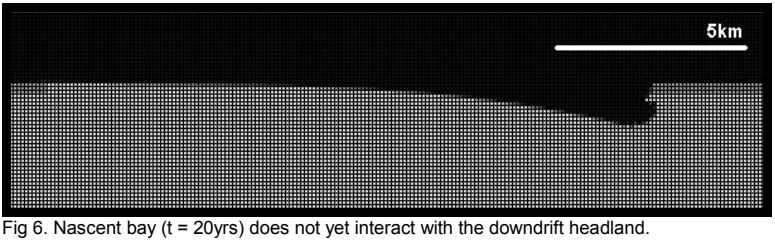

Fig 6. Nascent bay (t = 20yrs) does not yet interact with the downdrift headland.

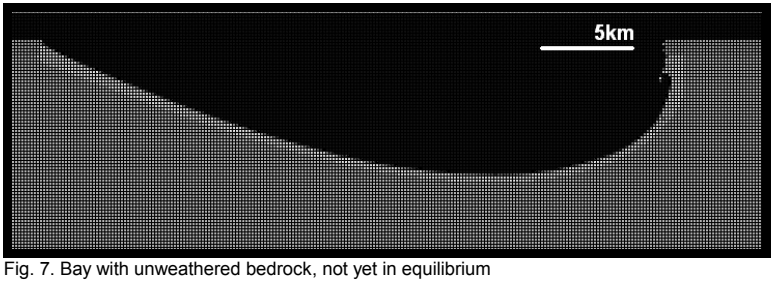

Fig. 7. Bay with unweathered bedrock, not yet in equilibrium

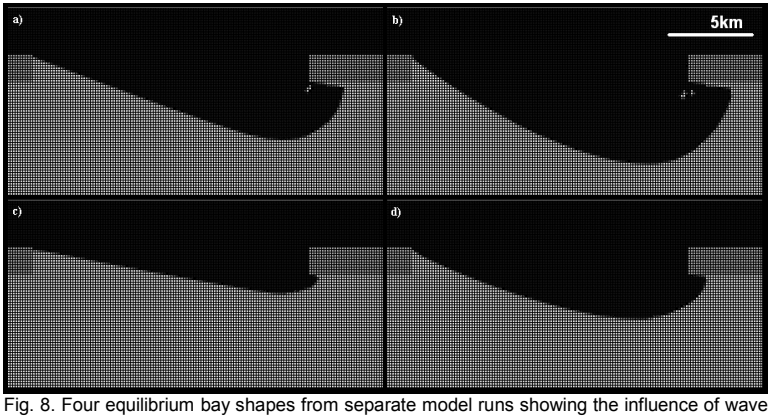

Fig. 8. Four equilibrium bay shapes from separate model runs showing the influence of wave climate. a) Asymmetry = 0.15, Low-angle proportion = 0.9. b) Asymmetry = 0. 15, Low-angle proportion = 0.6. c) Asymmetry = 0.35, Low-angle proportion = 0.9. d) Asymmetry 0.35, Low-angle proportion 0.6.

In Fig. 8, four equilibrium bays are shown. Different combinations of wave diffusivity and asymmetry affect the angle (α) of the spiral; a more-diffusive wave climate with a higher proportion of low-angle waves produces a flatter beach, and a greater proportion of waves from the right produces a deeper beach.

DISCUSSION

These initial modeling results suggest a mechanism for the formation of spiral-like bays that differs significantly from the conventional perception that they reflect patterns of refraction and diffraction of wave energy. In our model, it is the fact that waves come from many directions rather than a single one, combined with simple wave shadowing, that leads to the emergence of the bay shape. As the bay shape evolves, local wave climates change through shoreline reorientation and increasing wave shadowing. The shape ceases to evolve when local wave climates produce no net sediment flux and

therefore no shoreline change.

The evolution of the bay from growing indentation to equilibrium shape highlights the significance of the downdrift lithology: in these model results, a downdrift headland is not necessary for spiral bays to exist, as some previous authors have claimed (Finkelstein 1989), but it is required if the bay is to reach a steady state; if it does not impinge upon and become trapped by a headland, the downdrift end will erode indefinitely. The growing bay tends to evolve into a shape in which net sediment transport is locally minimized, but this is never possible at the inflection point. Only when the inflection point becomes coincident with an inerodible headland is the bay's progress halted. When the shoreline orientation adjacent to the downdrift headland approaches that for which no net sediment transport occurs, because of the deepening of the bay, the bay ceases to deepen, and a steady state results in which net sediment fluxes everywhere approach 0.

Some questions have been raised about the influence of underlying lithology on the morphology of headland-bay beaches. In the model, the presence of rock is not relevant if it weathers fast enough that erosion is controlled only by sediment-transport processes and not by weathering rates. If stretches of the coast are occasionally left bare of sediment, however, erosion will slow locally, limited by the rate at which new sediment is formed, and the bay's evolution will correspondingly be affected. In the long term, however, sediment flux divergences continue to expose the underlying rock to weathering until the bay achieves the shape that features no net sediment flux everywhere. After this, weathering produces a progressively thickening mantle of mobile sediment, and the weathering rate asymptotically approaches 0. Thus, the process of converting rock to sediment does not affect the long-term equilibrium shape.

CONCLUSION

Previous authors have outlined what may well be a sufficient explanation for the existence of spiral-like bays. Based on this initial work, it is not possible to claim that the mechanism proposed here is more likely to be the principal mechanism, particularly because the model used is intentionally simplified. However, because of the good agreement of our model with observed headland-bay morphology, it seems quite possible that the existing explanation is not necessary. If that is the case, the key interactions causing the basic log-spiral-like shape are very different than those commonly assumed. Future, more detailed modeling will be required to evaluate the relative importance of simple alongshore transport, treated as a function of local shoreline orientation, and the wave patterns caused by refraction and/or diffraction around a headland.

REFERENCES

Ashton, A, and Murray, A. B. (2006a). "High-angle wave instability and emergent shoreline shapes: 1. Modeling of capes, flying spits and sandwaves," *Journal of Geophysical Research*, **111**, F04011, doi:10.1029/2005JF000422.

Ashton, A, and Murray, A. B. (2006b). "High-angle wave instability and emergent shoreline shapes: 2. Wave-climate analysis and comparisons to nature," *J. Geophys. Res*, **111**, F04011, doi:10.1029/2005JF000423.

Ashton, A., Murray, A. B., and Arnoult, O. (2001). "Formation of coastline features by large-scale instabilities induced by high-angle waves." *Nature* **414**, 296-300.

Falqués, A., Calvete, D. (2005). "Large scale dynamics of sandy coastlines." Diffusivity and instability, *J. Geophys. Res*. **110**, C03007, doi:10.1029/2004JC002587.

Finkelstein, K. F. (1981). "Morphological variations and sediment transport in crenulate-bay beaches, Kodiak Island, Alaska," *Mar. Geol*. 47, 261-281.

Heimsath, A. M., Dietrich, W. E., Nishiizumi, K., and Finkel, R. C. (1997). "The soil production function and landscape equilibrium," *Nature*. *388*, 358– 361.

Klein, A., Vargas, A., Raabe, A., and Hsu J. (2003). "Visual assessment of bayed beach stability with computer software," *Computers and Geosciences* **29**, 1249-1257.

Komar, P. D. (1998). *"Beach Processes and Sedimentation, Second Ed.,"* Prentice Hall, 544 p.

Larson, M., Hanson H., and Kraus N. C. (1987). "Analytical solutions of the one-line model of shoreline change," *Tech. Rep. CERC-87-15*, U.S. Army Waterw. Exp. Stn., Vicksburg, Miss.

Lavalle, P. D. and Lakhan, V.C. (1997). "A spatial-temporal analysis of the development of a log-spiral shaped embayment," *Earth Surface Processes and Landforms* **22**, 657-667.

LeBlond, P. H. (1979). "An explanation of the logarithmic spiral plan shape of headland-bay beaches," *Journal of Sedimentary Petrology* **49** (4), 1093–1100.

Moreno, L. J. and Kraus, N. C. (1999). "Equilibrium shape of headland-bay beaches for engineering design," *Proc. Coastal Sediments* 1999, ASCE, 860-875.

Murray, A. B. (2003). "Contrasting the goals, strategies, and predictions associated with simplified numerical models and detailed simulations." In: R.M. Iverson and P.R. Wilcock (Editors), *Prediction in Geomorphology*. AGU Geophys. Monogr., pp. 151-165.

Phillips, J. D. (1985). "Headland-bay beaches revisited: an example from Sandy Hook, New Jersey," *Mar. Geol.* **65**, 21-31.

Valvo, L., Murray, A. B., and Ashton, A. (2006). "How does underlying geology affect coastline change? An initial modeling investigation," *J. Geophys. Res.* **111**, F02025, doi:10.1029/2005JF000340.

Yasso W. E. (1965). "Plan geometry of headland-bay beaches," *J. Geol.* **73**, 702-714.

THE RESPONSE OF SPIT SHAPES TO WAVE-ANGLE CLIMATES

Andrew D. Ashton[1,2], A. Brad Murray[3], and Ryan Littlewood[3]

1. Woods Hole Oceanographic Institution, Geology and Geophysics Department, MS #22, Woods Hole, MA, 02543, USA; aashton@whoi.edu.
2. U. S. Geological Survey, 384 Woods Hole Rd., Woods Hole, MA, 02543.
3. Division of Earth and Ocean Sciences, Nicholas School of the Environment and Earth Sciences; Center for Nonlinear and Complex Systems, Duke University, Durham, NC, USA; abmurray@duke.edu.

Abstract: We investigate spit formation and evolution in light of the high-wave-angle instability in shoreline shape arising from a maximizing angle for wave-driven alongshore sediment transport. Single spits emerge in a simple one-contour line numerical model that evolves the coast using morphodynamic feedbacks and a 'climate' of waves approaching the shore from variable directions. Analysis of sediment transport and shoreline stability metrics illustrate how spits can be generated, demonstrating how waves from all angles can play a role in spit formation and evolution. Simulations suggest that regardless of whether high- or low-angle waves dominate relative to the general shoreline trend, as spits extend offshore, they tend to orient themselves such that most of their coast barely experiences low-angle waves and alongshore sediment transport to the spit end is maximized. This 'graded' spit shape minimizes gradients in sediment flux, while the recurve at the spit end experiences larger gradients and a region of high-angle instability. Examining hindcast wave data, similar trends are seen along the natural example of Long Point, Lake Erie, Canada.

INTRODUCTION

Discussion of the presence and the morphological importance of a maximizing angle for alongshore sediment transport is not new (e.g. Bruun 1954; Grijm 1960, 1964); however, interest in the importance of this maximum has recently been reinvigorated by studies of a high-wave-angle instability in shoreline shape (Ashton et al. 2001; Falqués and Calvete 2005). Numerical simulations have demonstrated how 'high-angle' waves, with angles

between deep-water wave crests and the shore greater than this transport-maximizing angle, could cause the self-organization of a coast into quasi-periodic fields of flying spits, cuspate spits, and capes. Although many such series of capes and flying spits can be found in nature, frequently spits are found alone and in regions dominated by low-angle waves. Here, we extend recent developments in the understanding of shoreline evolution (Ashton and Murray 2006a) to study how the maximum in alongshore sediment transport affects the evolution of single spits. Using newly developed wave climate metrics (Ashton and Murray 2006b), numerical modeling results and comparisons with nature suggest that the transport maximum plays an important role in determining the orientation of spits.

BACKGROUND

Fed by an updrift source of littoral sediment, spits represent one of the most common depositional clastic coastal landforms. As the downdrift end of a spit is by definition untethered, primary driving forces, particularly alongshore sediment transport, help determine spit shape and orientation. Sometimes spits are considered to grow in the direction of the alongshore current; unfortunately, drift direction alone cannot be used to explain spit orientation as the alongshore current is by definition shore-parallel. Spits also recurve, or trend back towards the shore—even the high-energy, seaward-facing side of a spit faces many directions, experiencing waves from a variety of deep-water directions.

Spit Orientation

Bruun (1954), from quantitative and laboratory investigations, was one of the first to suggest that a maximizing angle for alongshore sediment may determine the angle of spit accumulation. Grijm (1960; 1964) theoretically explored the shoreline shapes that could result from waves approaching from any one angle greater or less than a suggested maximizing transport angle of 45º (not specifying whether this is a breaking or deeper-water angle). Zenkovich (1967) also studied the influence of wave angle on spit shapes, suggesting that for high-angle waves, spits should grow offshore at an angle of 45º to the shoreline trend.

More recently, Kraus (1999) developed a simple analytic mode of spit extension, although this model does not account for shoreline reorientation. Petersen et al. (2001) present a one-contour-line analytical model for spit accretion for an assumed ‘equilibrium’ spit shape, again emphasizing the importance of a maximizing angle in evolution. Results suggest that more detailed hydrodynamic models are required to give rise to recurved spit ends. Further laboratory experiments, similar to those of Bruun (1954), investigate the growth of a spit subjected to waves from a single high angle (Petersen et al. 2002). These investigations follow the research history of investigating the issue of spit orientation in terms of waves approaching from only one direction.

Other research, particularly studies focusing on the evolution of periglacial environments, suggests a distinction between ‘swash-aligned’ and ‘drift-aligned’ spits (Forbes et al. 1995). According to this distinction, ‘drift-aligned’ coasts tend to

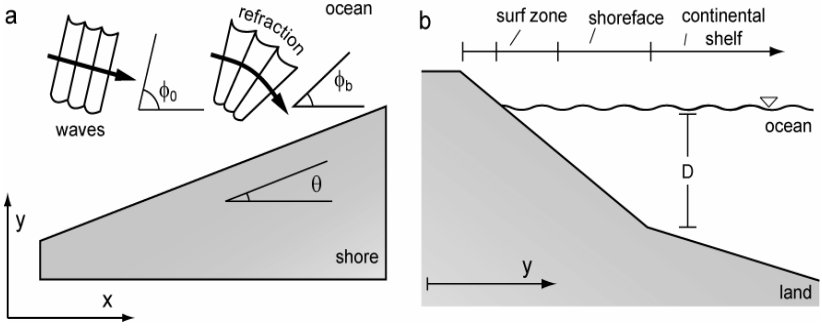

Fig. 1. a) Plan-view domain. b) Cross-shore profile.

experience waves with oblique approach, with strong gradients in wave heights and angles, whereas wave approach tends to be shore-normal for 'swash-aligned' coasts (Orford et al. 1991). The results of numerical modeling experiments presented below raise the question of whether a process distinction must be evoked to explain these different modes of shoreline behavior.

Shoreline Instability

Because wave refraction changes both wave angle and height, common breaking-wave formulations for alongshore sediment transport, such as the CERC formula (Komar 1971), cannot be used to properly understand gradients in alongshore sediment transport along an undulating coast (Ashton and Murray 2006a; 2006b). Instead, a deeper water reference frame is required. The CERC formula can be recast for fully deepwater waves assuming refraction over shore-parallel contours,

$$Q_s = KT^{1/5} H_0^{12/5} \cos^{6/5}(\phi_0 - \theta)\sin(\phi_0 - \theta), \quad (1)$$

where Q_s is the alongshore sediment flux (m^3/s deposited volume), K typically equals ~0.34 $m^{3/5}s^{-6/5}$, T is the wave period (s), H_0 is the root-mean-squared deep-water wave height (m), and $(\phi_0 - \theta)$ is the relative wave angle (Fig. 1). This formula exhibits a maximum for a relative deep-water angle of 42° (Fig. 2a). Recasting the CERC formula for non-breaking waves suggests that the shoreline instability can frequently occur, and does not require that waves break at uncommonly large angles (as previously thought).

The standard one-contour-line approach (Pelnard-Consideré 1956), where local surf-zone gradients in Q_s are assumed to be spread over a shoreface of depth D (Fig. 1b), yields a diffusion-like equation for the plan-view evolution of the shoreline,

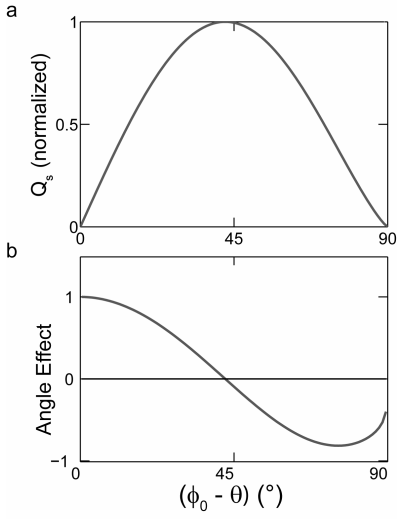

Fig. 2. a) Normalized alongshore sediment transport vs. deep-water angle.
b) The 'angle effect' upon diffusivity vs. deep-water angle.

$$\frac{\partial y}{\partial t} = -\mu \frac{\partial^2 y}{\partial x^2}. \tag{2}$$

For (1), the deep-water CERC formula, the diffusivity, μ (m/s^2), varies with the angle of wave approach,

$$\mu = \frac{K}{D} T^{1/5} H_0^{12/5} \left\{ \cos^{1/5}(\phi_0 - \theta) \left[\left(\frac{6}{5} \right) \sin^2(\phi_0 - \theta) - \cos^2(\phi_0 - \theta) \right] \right\}, \tag{3}$$

The term in the brackets {} represents the wave-angle dependence of the diffusivity. Fig. 2b shows a negative diffusivity for high-angle waves, representing the shoreline instability which causes perturbations to an otherwise straight coast to grow.

Recent research using more realistic treatments of wave refraction suggest that the growth of slight shoreline protuberances is damped at smaller alongshore scales (Falqués and Calvete 2005; List and Ashton 2007). However, the importance of the maximizing angle for Q_s extends far beyond initial instability. For example, simple analysis suggests that waves approaching from a single high angle will cause a finite-amplitude shoreline protuberance to eventually develop into an off-shore extending flying spit with an erosional updrift flank (Ashton and Murray 2006a). Numerical modeling shows that over

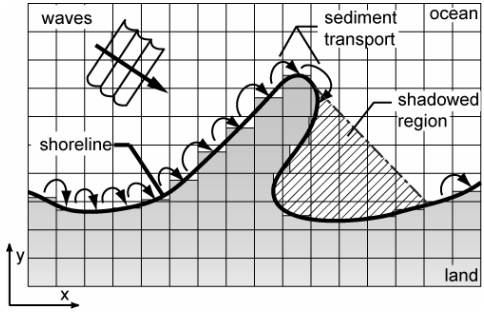

Fig. 3. Plan view model schematic

time, morphodynamic feedbacks and finite-amplitude effects occurring well beyond initial instability play increasingly important roles in high-wave-angle shoreline evolution; these effects, for example, can lead to emergent behaviors, such as the self-organization of alongshore sandwaves, flying spits, and capes (Ashton and Murray 2006a).

As terminal portions of littoral cells, spits elongate because of the gross alongshore delivery of sediment to the spit end (per (1)). Updrift of this point, evolution of the shoreline shape remains controlled by gradients in alongshore sediment transport (per (3)). Interestingly, the CERC formula predicts that such gradients in sediment transport are minimized when transport is at a maximum (diffusivity = 0 at the transport-maximizing angle, Fig. 2), suggesting that the waves that control spit elongation may be unimportant in the evolution of the spit shape, relative to other waves in the climate. Correspondingly, waves important in the evolution of the spit shape will not transport much sediment towards the spit end (large diffusivity when transport is small, Fig. 2). Therefore, it is unlikely that spit evolution can be sufficiently understood using waves approaching from just one presumed 'dominant' angle.

METHODS

Here we apply a previously developed numerical model that evolves the plan-view shape of the shoreline in response to gradients in alongshore sediment transport. Wave climate metrics, used to determine the long-term net, directional alongshore sediment transport and the long-term coastal stability are computed along the shore.

Numerical Modeling

Similar to other common 'one-contour-line' models (Hanson and Kraus 1989), we have developed a model evolving the shape of the shoreline due to gradients of alongshore sediment transport within the surf zone (assuming that the shoreface maintains a constant shape (Fig. 1b)). Discretizing the CERC formula, (1), the model contains a numerically stable solution scheme for the case of high-angle waves, and can accommodate a shoreline that becomes arbitrarily sinuous, even doubling back on itself (Fig. 3) (Ashton et al. 2001; Ashton and Murray 2006a). To simulate spit growth, the model contains a simplified representation of barrier overwash. Overwash is assumed to occur whenever a

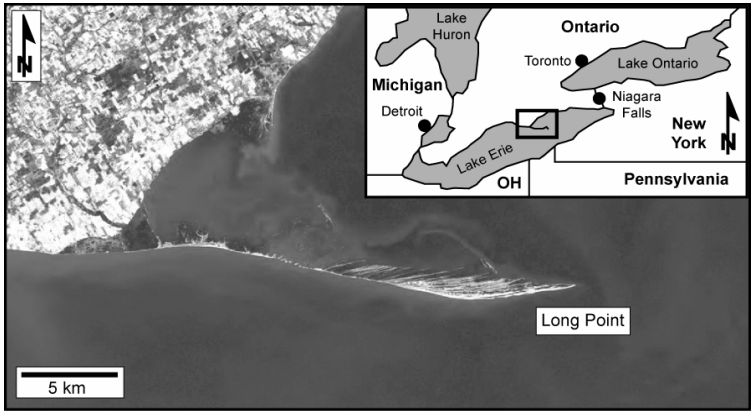

Fig. 4. Long Point, Lake Erie, Canada. Data are available from USGS/EROS (figure from Ashton and Murray 2006b).

barrier is below a minimum critical width (Leatherman 1979), and it will widen a barrier whenever backbarrier depths are less than the shoreface depth (Jiménez and Sánchez-Arcilla). Waves (with $H_0 = 2$ m, $T = 8$ s) approach from a new angle every day, with a direction selected from a probability distribution function determined by U, the fraction of unstable, high-angle waves, and A, the asymmetry, defined as the fraction of waves approaching from the left, looking offshore. Computations assume that all wave refraction occurs over shore-parallel contours.

Wave Climate Metrics

At a shore of a given orientation, the contributions to alongshore sediment transport from a long-term wave climate can be summed, leading to $Q_{S,net}$, the net alongshore sediment transport. Similarly, every approaching wave contributes to the evolution of the coastline, either diffusively or anti-diffusively. A dimensionless 'instability index', Γ, assesses the competition between diffusion and anti-diffusion,

$$\Gamma = \frac{\sum_{i=1}^{n} \mu_i \Delta t_i}{\sum_{i=1}^{n} |\mu_i| \Delta t_i}, \tag{4}$$

for each data point i, and data interval Δt. This normalized index, which represents the 'competition' between high- and low-angle waves, ranges between 1 for a wholly low-angle climate and –1 for a wholly high-angle climate. A Γ of zero would mean that a wave climate is on the verge of instability—low- and high-angle waves balance each other out. (Ashton and Murray 2006b)

RESULTS

First, the model and metrics will be used to build upon research into the effects of high-angle waves by studying in detail a single 'flying' spit, or 'ness'. Further simulations investigate spit growth in wave climates dominated by low-angle waves, and how spit reattachment to the mainland can result in dramatic shoreline reorientation.

Natural 'Flying' Spit: Long Point

Long Point is a large flying spit along the Canadian shore of Lake Erie (Figure 4). WIS hindcast covering 1956-1987 from Lake Erie WIS station 33 shows that the predominant westerly winds blowing along the long axis of the elongate lake result in a high-angle-dominated wave climate along the north and south shores of Lake Erie (Great Lakes WIS hindcast can be found at ftp://ftp.erdc.usace.army.mil/pub/PERM/wisftp/). Although there are other high-wave-angle features along these shores, such as Point Pelee, Rondeau Point, and Presque Isle, they are far from Long Point. This spit, which appears to have formed over the Holocene, is not part of an alongshore chain, likely because it began as a large glacial moraine perturbing to the shoreline trend (Coakley 1992).

Wave climate computations show although local wave climates are unstable at either end of Long Point, the spit is oriented such that the main stretch of the shore is marginally stable (Figure 5). Alongshore sediment transport is dominantly to the left (looking offshore), but it is slightly reduced along the middle of the spit, and maximized at the updrift and downdrift regions where the wave climate becomes unstable. Interestingly, another type of feature associated with high-angle waves, alongshore sand waves, appear along same portions of the spit that experience unstable wave climates (further discussed by Ashton and Murray (2006b)).

Modeled Single 'Flying' Spit

To determine if alongshore sediment transport and the high-angle instability can give rise to a feature similar to Long Point, the numerical model was run using a single initial shoreline protuberance added to an otherwise straight coast. Like the natural case, waves were high-angle ($U = 0.6$) and asymmetric (with more waves approaching from the right, looking offshore, $A = 0.2$). Not only does the simulated flying spit eventually attain a shape that generally resembles Long Point, perhaps more significantly, there are similar trends in wave metrics (Fig. 6). The simulated flying spit has reoriented itself such that the main stretch of the spit experiences predominantly low-angle waves, whereas predominantly high-angle waves affect the proximal and distal spit ends.

Modeled Headland-Extending Spits

As a corollary to the high-angle spit evolution, another simulation investigates how spits extend offshore even if the local wave climate is dominated by low-angle waves. Beginning with a large rectangular protuberance, waves that are regionally low-angle ($U = 0.2$) with an asymmetry (net drift to the right, looking offshore, $A = 0.7$) lead to the extension of spits in both the updrift and the downdrift direction (Fig. 7). As a result of the asymmetry in the wave climate, the spits attain different orientations on either side of the hump. In both cases the direction of spit growth is not parallel to the initial shoreline orientation.

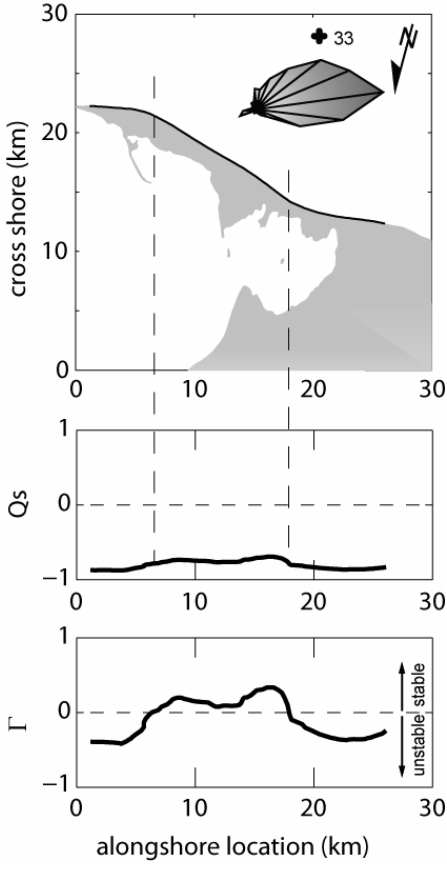

Figure 5. Long Pont rotated 195° clockwise, showing a) shoreline with b) relative Q_s and c) Γ along the shore. Inset rose of 'wave energy' and location of WIS station 33.

After the spits have extended offshore, wave climate metrics indicate that although the coast along most of the spit experiences a predominantly stable wave climate, there is a transition to instability at the end of the spit. For both spits, the transition to instability corresponds to the location of the maximum in net Q_s. This suggests that the instability and the maximizing angle for sediment transport play key roles in the orientation of the spit ends. Interestingly, spits extend in what would be described as a dynamically 'equilibrium' form even though the updrift shore is not dominated by high-angle waves as suggested by Petersen et al. (2001). Note that although for the updrift (left) spit, the maximum in Q_s and the transition to instability occurs at the spit end, for the downdrift

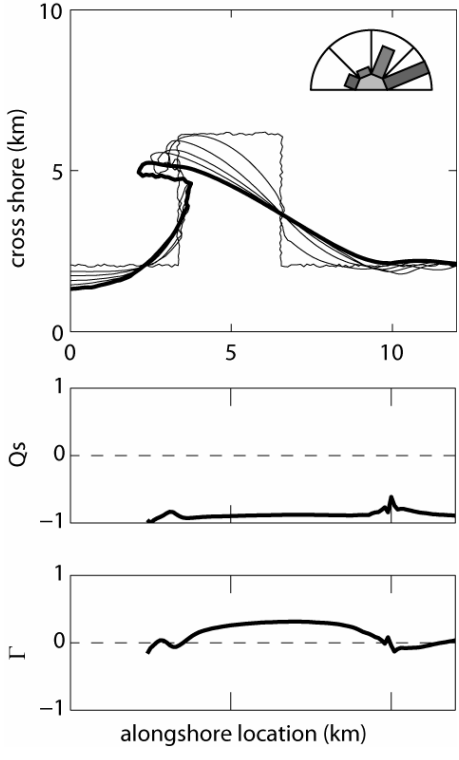

Figure 6. Simulated high-angle spit showing a) shoreline (analyzed shoreline in dark line with b) relative Q_s and c) Γ along the shore. Inset of PDF of wave-approach angle.

(right) spit, the Q_s maximum and instability transition occur updrift of the spit end. This effect is likely due to the wave 'climate' used to simulate shoreline evolution, such behavior would not be predicted by a one-contour-line model using only a single wave approach angle (Petersen et al. 2001).

As the spits continue to extend offshore, they eventually intersect the mainland coast (Fig. 8). After this intersection, shoreline orientation dramatically changes; new behavior occurs after the spit connects to the down drift beach. As the spit end extends offshore, the coastal changes at the spit end are controlled by the rate of sediment delivery, the alongshore flux to the tip. However, once the spit reconnects with the coast, sediment can be transported in both directions—like the rest of the coast, shoreline evolution is now controlled by gradients in alongshore sediment flux, not by the magnitude of flux.

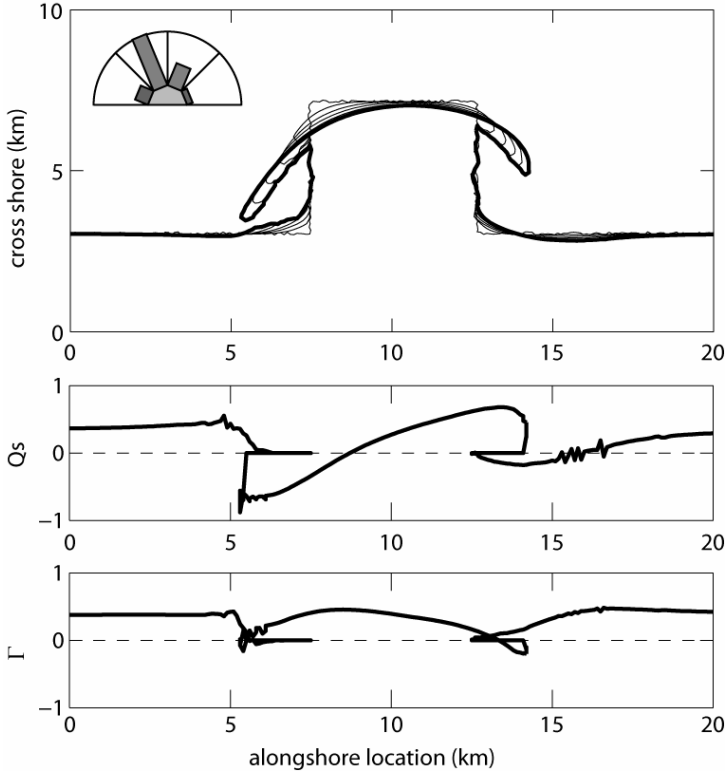

Fig.7. Low-angle spit simulation results showing a) shoreline (analyzed shoreline in dark line) with b) relative Q_s and c) Γ along the shore. Inset of PDF of wave-approach angle.

Because of the generally stable, diffusive wave climate, the simulated shore continues to smooth over time, eventually eliminating the initial hump.

DISCUSSION AND CONCLUSIONS

Although the exploratory model here appears to capture many essential elements of spit evolution, more attention should be paid to the controls upon the accretion rate of the spit end. For instance, if a spit is accreting into water significantly deeper than the shoreface depth, spit growth will be slowed dramatically, which would have a strong effect on spit shapes and orientation (the current numerical model assumes accretion onto a constant depth seabed). Also, the simple one-line approach assumes that a section of coast corresponds to a shoreface segment of the same alongshore width. Where the coastline curvature is extreme, such as at spit ends, this assumption breaks down, as a segment of the shore will correspond with a 'wedge' of shoreface of increasing width offshore.

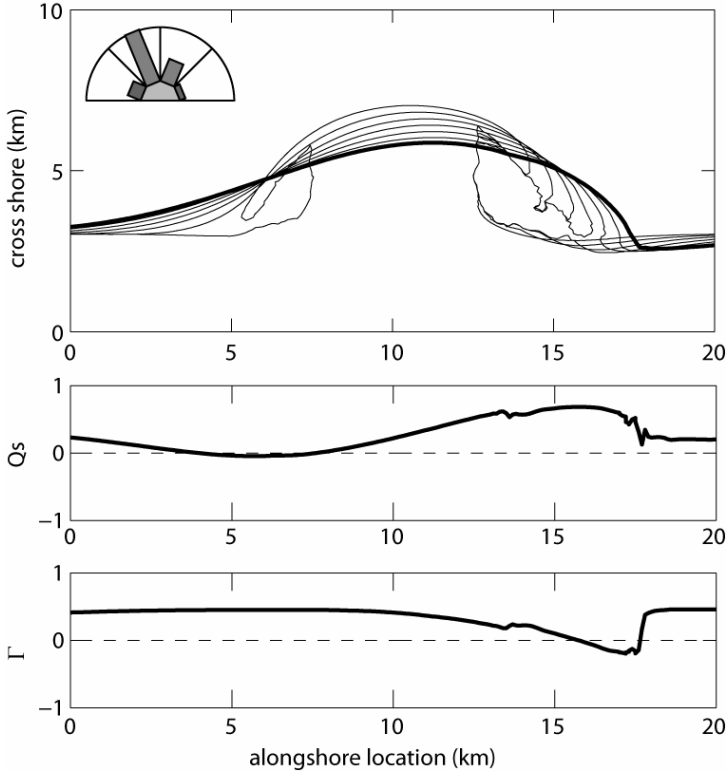

Fig.8. Low-angle spit simulation results showing a) shoreline (analyzed shoreline in dark line) with b) relative Q_s and c) Γ along the shore. Inset of PDF of wave-approach angle.

Rigorously studying spit-end phenomena would require a more spatially explicit model—a break from the one-contour-line approach. Although more explicit models may improve the numerical accuracy of simulations, they would likely be driven mainly by the same processes and feedbacks operating in the existing model.

We have studied shoreline evolution using a one-contour-line model, using sediment transport and stability metrics to better understand how spits can orient themselves in response to wave climates. In both high- and low-angle climates, simulations evolve a smooth spit shape, and along its flank: 1) gradients in net sediment flux are very low; 2) net alongshore sediment flux tends to be maximized; and 3) the effective local diffusivities are small but positive (stable). These three characteristics are intertwined. Net sediment flux for a given wave climate should be maximized when the shoreline orientation produces an effective diffusivity of 0 (Fig. 2). When the effective diffusivity

becomes small, shoreline curvatures do not produce strong gradients in alongshore flux—the shoreline will evolve slowly and its shape will persist. Although continued spit extension (caused by sediment delivery to the spit end) prevents a true static steady state from developing, evolution of the spit shape itself will be slow. In short, the orientation that produces the maximum sediment flux (for a give wave climate) along the flank dictates general spit orientation in this model. Trends along the Long Point coast are consistent with these model suggestions. (Future work should include more comparisons of the modeled wave climate trends with those found along natural coasts.)

These results present a unified model for spit extension, suggesting that distinctions such as 'drift-' and 'swash-aligned' may not be of fundamental importance. The results shown in Fig. 7 show that along a single coastline stretch, areas that would be called swash aligned (experiencing little to no net transport) grade into areas that would be called drift aligned (experiencing the maximum transport possible for the local wave climate). Fig. 8 further demonstrates that even in the same wave climate, alongshore sediment transport alone can result in a coast with spits to trend towards an orientation dramatically different than that of an open coast. These preliminary investigations suggest that the maximizing angle for alongshore sediment transport, combined with boundary conditions, may explain many observed spit behaviors.

ACKNOWLEDGEMENTS

We wish to acknowledge the contributions of Liviu Giosan to this research. Portions of this research were funded by WHOI and the USGS through the WHOI Postdoctoral Scholar program, the Andrew W. Mellon Foundation, and NSF grants DEB-05-07987 and EAR-04-44792.

REFERENCES

Ashton, A., A. B. Murray, and Arnoult, O. (2001). "Formation of coastline features by large-scale instabilities induced by high-angle waves." *Nature* 414: 296-300.

Ashton, A. and A. B. Murray (2006a). "High-angle wave instability and emergent shoreline shapes: 1. Modeling of sand waves, flying spits, and capes." *Journal of Geophysical Research-Earth Surface* 111(F04011): doi:10.1029/2005JF000422.

Ashton, A. and A. B. Murray (2006b). "High-angle wave instability and emergent shoreline shapes: 2. Wave climate analysis and comparisons to nature." *Journal of Geophysical Research-Earth Surface* 111(F04012): doi:10.1029/2005JF000423.

Bruun, P. (1954). Forms of equilibrium of coasts with a littoral drift. *Coastal Stability*. Copenhagen, Atelier Electra**:** 5-22.

Coakley, J. P. (1992). Holocene transgression and coastal-landform evolution in northeastern Lake Erie, Canada. *Quaternary Coasts of the United States: Marine and Lacustrine Systems*. C. H. I. Fletcher and J. Wehmiller. SEPM Special Publication No. 48**:** 415-426.

Falqués, A. and D. Calvete (2005). "Large-scale dynamics of sandy coastlines: Diffusivity and instability." *Journal of Geophysical Research-Oceans* 110, C03007, doi:10.1029/2004JC002587.

Forbes, D. L., J. D. Orford, R.W.G. Carter, J. Shaw, and S.C. Jennings (1995).

"Morphodynamic evolution, self-organisation, and instability of coarse-clastic barriers on paraglacial coasts." *Marine Geology* 126(1-4): 63-85.

Grijm, W. (1960). "Theoretical forms of shorelines." *Proceedings of the 7th Coastal Engineering Conference*: 197-202.

Grijm, W. (1964). "Theoretical forms of shorelines." *Proceedings of the 9th Coastal Engineering Conference*: 219-235.

Hanson, H. and N. C. Kraus (1989). *GENESIS: Generalized Model for Simulating Shoreline Change, Report 1: Technical Reference*. Vickburg, MS, U.S. Army Eng. Waterways Experiment Station, Coastal Eng. Res. Cent.

Jiménez, J. and A. Sánchez-Arcilla (2004). "A long-term (decadal scale) evolution model for microtidal barrier systems." *Coastal Engineering* 51(8-9): 749-764.

Komar, P. D. (1971). "The mechanics of sand transport on beaches." *J. Geophys. Res.* 76(3): 713-721.

Kraus, N. C. (1999). *Analytical model of spit evolution at inlets*. Coastal Sediments '99, Long Island, ASCE.

Leatherman, S. P. (1979). "Migration of Assateague Island, Maryland, by inlet and overwash processes." *Geology*(7): 104-107.

List, J. H. and A. D. Ashton (2007). *A circulation modeling approach for evaluating the conditions for shoreline instabilities*. Coastal Sediments '07, New Orleans, ASCE.

Orford, J. D., R. W. G. Carter, and Jennings, S.C. (1991). "Coarse clastic barrier environments: Evolution and implications for quaternary sea level interpretation." *Quaternary International* 9: 87-104.

Pelnard-Consideré, R. (1956). "Essai de theorie de l'evolution des formes de rivage en plages de sable et de galets." *4th Journees de l'Hydraulique, Les Energies de la Mer* III(1): 289-298.

Petersen, D., R. Deigaard, and J. Fredsøe, (2001). *Shape and size of sandy spits*. 4th Conference on Coastal Dynamics, Lund, Sweden, ASCE.

Petersen, D., R. Deigaard, J. Fredsøe, and N. Drønen (2002). *Morphological development of coasts a very oblique wave incidence*. 28th International Conference on Coastal Engineering, Cardiff, Wales, ASCE.

Zenkovich, V. P. (1967). *Processes of coastal development* Edinburgh, London, Oliver & Boyd.

HISTORICAL SHORELINE CHANGES AND MORPHODYNAMICS OF PARRAMORE ISLAND, VIRGINIA (1852–2006)

Trent M. Richardson[1] and Randolph A. McBride[2]

1. Patton Harris Rust & Associates, 14532 Lee Road, Chantilly, VA 20151, USA. trent.richardson@phra.com
2. Geology Program, Dept. of Environmental Science & Policy, George Mason University, 3055 David King Hall, Fairfax, VA, 22030, USA. rmcbride@gmu.edu

Abstract: Using National Ocean Service topographic sheets and global positioning system shoreline position surveys, historical shoreline changes of Parramore Island, Virginia, are quantified between 1852 and 2006 to address long- and short-term trends in shoreline movement. Quantitative analyses of twelve high water line (shoreline) positions indicate the shoreline is retreating at increasing rates in the short term (decadal) when compared with long-term trends (centennial). In particular, the behavior of the outer shoreline changed from clockwise rotational instability to sustained retreat. Parramore's entire outer shoreline (Cells 3, 4, and 5) experienced a retreat rate of -3.6 m/yr over the long term (1852-2006) and -8.8 m/yr over the short term (1998-2006). The short-term rate changes indicate that the processes controlling shoreline trends, e.g., overwash to the south and inlet dynamics to the north, have intensified and/or changed relative to the long-term.

INTRODUCTION

Shoreline mapping and change studies that utilize geospatial data sets and technology have the ability to map coastal landforms and quantify shoreline processes at various spatial and temporal scales (e.g., Fenster and Dolan, 1993; Byrnes et al., 1995; McBride and Byrnes 1997; Morton et al., 2005). Barrier islands are dynamic geomorphic features, and studies of these coastal environments are hampered by the limited availability and inaccuracy of most historical data sources (Anders and Byrnes, 1991; Crowell et al., 1991; Byrnes et al., 2003; Leatherman, 2003; Boak and Turner, 2005). However, advancements in geospatial technology have surpassed conventional surveying methods in their ability to observe accurately, quickly, and affordably coastal features such as barrier islands. Specifically, the capacity to study

coastal changes was improved by the development of geographic information systems (GIS) and global positioning systems (GPS). In addition, aerial photography and satellite imagery inventories continue to expand and provide a rich source of geospatial data.

In recent years, the open-ocean shoreline of Parramore Island has retreated at a rapid rate as indicated by numerous qualitative factors, such as massive tree die-offs along interior dune ridges, numerous fallen trees across the foreshore, outcropping of relict marsh along the beachface, and exposure of an historical shipwreck on the beach. This study seeks to determine and compare long-term versus short-term change rates for a highly dynamic barrier island located within the Virginia Coast Reserve. In particular, we identify the magnitude and direction of shoreline migration trends, short-term reversals in those trends or rate increases, and investigate the causes of the observed trends. In turn, this approach provides a morphodynamic analysis of Parramore Island.

STUDY AREA

Parramore Island is an undeveloped, mixed-energy, tide-dominated barrier island located mid-way along the Virginia Eastern Shore of the Delmarva Peninsula (Figure 1). Parramore is the largest island of the Virginia Coast Reserve, which constitutes one of the longest stretches of coastal wilderness remaining along the U.S. Atlantic coast. With a mean spring tidal range of 1.7 m and an average significant wave height of ~0.6 m, the island has a classic ‘‘drumstick-shape’’ with large ebb-tidal deltas characterizing the tidal inlets at either end (McBride, 1999). Net longshore sediment transport is to the south. Parramore Island’s outer shoreline is about 12.7 km in length and may be segmented into three geomorphic zones: 1) the high-profile, inlet-influenced northern end; 2) the north-central segment characterized by the truncation of high-profile, tree-lined beach ridges; and 3) the southern portion, which is a low-profile, washover-dominated barrier and barrier spit (Figure 2). Wachapreague Inlet and Cedar Island are to the north and Quinby Inlet and Hog Island are to the south.

DATASETS & METHODS

NOS T-Sheets

Data sets used to reconstruct historical shoreline positions are National Ocean Service (NOS) topographic sheets (T-sheets) from 1852, 1871, 1910, 1914, 1942, and 1959/1962. The shoreline indicator on a T-sheet is typically the mean high water (MHW) line, which is equivalent to the high water line (HWL) as discussed by Leatherman (2003). Thus, the HWL enables the use of the longest possible record of shoreline position (~150 years) for determining change rates as opposed to any other shoreline indicator (Moore, 2000; Honeycutt et al., 2001; Pajak and Leatherman, 2002; Graham et al., 2003; Leatherman, 2003; Boak and Turner, 2005).

GPS Shoreline Position Surveys

GPS shoreline position surveys are a rapid, low-cost, large-scale, and highly accurate means to map a shoreline. The accuracy of a survey depends on the knowledge and competency of the instrument operator, the choice of HWL used in the field, and



Fig. 1. Parramore Island is located along the southern Delmarva Peninsula.

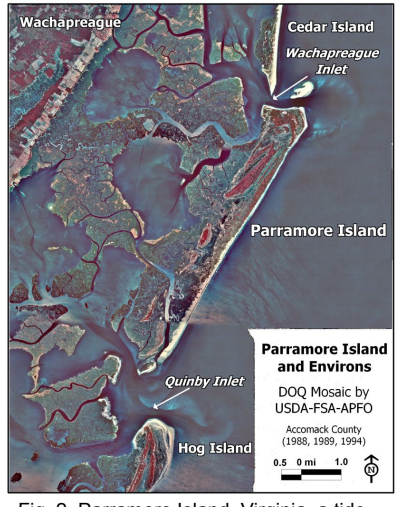

Fig. 2. Parramore Island, Virginia, a tide-dominated barrier island (image provided by the USDA Aerial Photography Field Office).

differential correction techniques. However, Pajak and Leatherman (2002) concluded that identifying a shoreline with GPS was more accurate than using aerial photography to delineate specific shoreline features. Our study uses seven GPS shoreline position surveys (Table 1) that were collected between 1998 and 2006 by visibly identifying the berm crest or the base of active dune scarps through on-the-ground beach surveys (i.e., walking). The GPS shorelines were differentially corrected through a post-processing procedure that used a Continuously Operating Reference Station (CORS) at the Virginia Institute of Marine Science (VIMS) facility in Wachapreague, Virginia, located about 7 km from Parramore Island. The 1998 and 1999 surveys utilized a CORS located in Dover, Delaware (178 km) because a base station was not installed yet at VIMS during these GPS shoreline surveys.

Shoreline Change Studies

The approach that we used to study coastal change requires comparing the areal position of shoreline positions through time. The proxy typically used to measure changes in shoreline position is the HWL. The GPS shoreline surveys map the position of the berm crest to delineate the HWL position. Transects are plotted perpendicular to the shoreline at 50-m intervals to measure and calculate the magnitude and rates of change. We used an ArcGIS software extension, the Digital Shoreline Analysis System (DSAS), to obtain both end point rates (EPR) and linear regression rates (LRR) at each transect (Thieler et al., 2005). The magnitude and rates of shoreline position change are evaluated to assess long- and short-term responses to natural coastal processes for the periods from 1852 to 2006 and from 1998 to 2006. Negative and positive signs indicate retreat and advance, respectively.

Table 1: Summary of Shoreline Data Sets for Study Area

NOS T-Sheets:	Shoreline Name	Date	Scale	Accuracy	RMS
	T-00512 (Va10a02)	1/1/1852	1:10000	8.9 m	x
	T-01200 (Va10b01a)	4/1/1871	1:10000	8.9 m	8.9 m
	T-03095 (Ec10D02)	1/1/1910	1:10000	8.4 m	8.7 m
	T-08440 (raster)	6/1/1942	1:20000	10.2 m	9.1 m
	T-11681 (Ph5907)	10/13/1959 & 4/28/1962	1:10000	6.1 m	8.6 m
GPS Surveys:	Shoreline Name	Date	Scale	Accuracy	RMS
	McBride 98	7/30/1998	1:1	3.5 m	8.0 m
	McBride 99	4/30/1999 & 5/1/1999	1:1	3.5 m	7.6 m
	McBride 00A	5/26/2000	1:1	3.5 m	7.2 m
	McBride 00B	10/6/2000	1:1	3.5 m	6.9 m
	McBride 02	4/26/2002	1:1	3.5 m	6.6 m
	McBride 05	5/12/2005	1:1	3.5 m	6.4 m
	Richardson 06	4/28/2006	1:1	3.5 m	6.2 m

* Accuracies based on Anders and Byrnes (1991), Byrnes et al. (1991), Crowell et al. (1991) and Byrnes et al. (1995).

** RMS = cumulative maximum root-mean-square potential error for the long-term shoreline change data analysis.

We segmented Parramore Island into five separate shoreline change cells based on differences among geomorphic characteristics and shoreline orientation: 1) the bayside, inlet-influenced shoreline; 2) the inlet throat shoreline; 3) the seaward, inlet-influenced shoreline; 4) the north-central, open-ocean shoreline; and 5) the southern, washover-dominated shoreline (Figure 3). An overlay of all shorelines revealed several areas of intersection that correlated to inherent morphodynamics. A linear mean of shoreline cells was then calculated to determine the orientations of the individual baselines used in the analysis. In places, the excessively dynamic and changing shoreline orientations caused us to create several sub-cells and associated baselines within larger cells: (1) the seaward, inlet-influenced shoreline (Cell 3) and (2) the southern, washover-dominated shoreline (Cell 5) (Figure 3).

RESULTS

Cell 1: Bayside, Inlet-Influenced Shoreline

Table 2 is a quantitative summary of the long- and short-term rates and magnitude of change for the bayside, inlet-influenced shoreline (Cell 1). The results demonstrate Cell 1 has retreated at a consistent pace over the long term with LRRs ranging from -0.6 m/yr between 1852 and 1942 to -0.7 m/yr between 1852 and 2006. In addition, the shoreline within this cell experienced only -129.9 m of total retreat for the entire period of record. Short-term results in Table 2 show a slightly higher retreat rate when compared to long-term trends. The shoreline retreated -1.5 m/yr for the period 05/1999 to 04/2006. The results also show that the Cell 1 shoreline has retreated at a slower rate when compared to the other shoreline cells (i.e., Tables 3, 4, 5, and 6).

Cell 2: Inlet Throat Shoreline

Cell 2, the inlet-throat shoreline, displays little variation in average change rates over

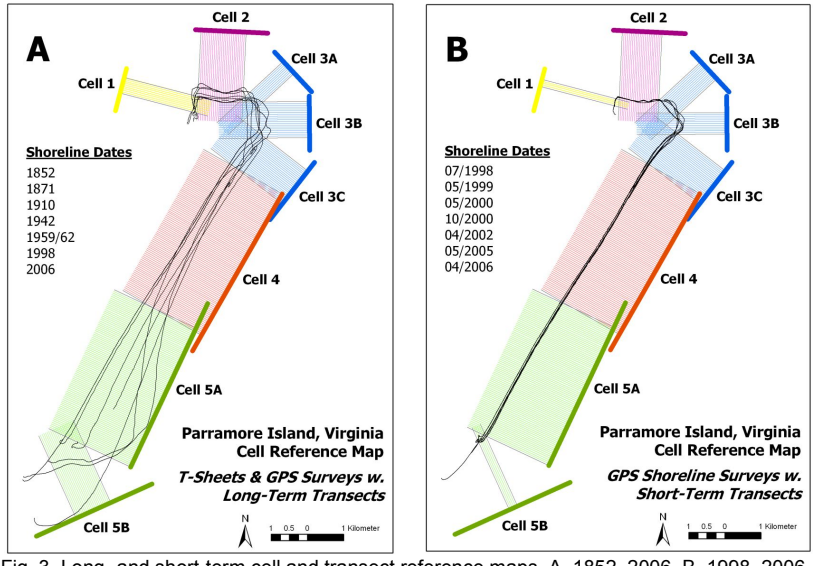

Fig. 3. Long- and short-term cell and transect reference maps. A. 1852–2006. B. 1998–2006. (*Baseline position, length, and orientation are identical for the two periods).

the long term but ranges from advance to retreat in the short term. The long-term LRR from 1852 to 1910 shows minor retreat at -0.3 m/yr, whereas rates for the periods 1852–1962, 1852–1998, and 1852–2006 are similar at -2.1 m/yr. In addition, the LRRs are supported by high R-squared measurements that demonstrate the strength of the linear relationship between shoreline position and time and explain the total variation in the data. The increase in the retreat rate may have occurred during the 1910–1942 timeframe as evidenced by the highest recorded EPR measurement of -4.5 m/yr from 1910 to 1942. The short-term LRR for Cell 2 is -3.5 m/yr (07/1998–04/2006) with an R-squared value of 0.65. Figure 4 clearly demonstrates the minimal spatial variability among rates within the Cell 2 shoreline over the long term as indicated by the LRRs. Essentially, the shoreline in this cell has migrated linearly through time and consistently in space. However, the graph also reflects short-term retreat along the eastern segment of the Cell 2 shoreline.

Cell 3: Seaward, Inlet-Influenced Shoreline

Table 4 shows that considerable temporal and spatial variations existed in shoreline trends for the seaward, inlet-influenced shoreline within Cell 3. Cell 3 is strongly influenced by tidal inlet processes (i.e., ebb-tidal delta of Wachapreague Inlet). The dynamics of the ebb-tidal delta produce substantial swings in shoreline position because of wave refraction, a local reversal in longshore sediment transport, and seasonal onshore/offshore sediment transport. The long-term LRR ranges from 3.7 m/yr between 1852 and 1910 to 0.8 m/yr between 1852 and 2006. However, the R-squared values decrease progressively from 0.70 to 0.36 for the same timeframes and

Table 2: CELL 1 Long-Term and Short-Term Rates and Magnitude of Shoreline Change

1852 to

	1871	1910	1942	1962	1998	2006
EPR	-2.0	x	-0.7	-0.8	x	-0.8
LRR	x	x	-0.6	-0.6	x	-0.7
R2	x	x	0.73	0.61	x	0.75
MAG	-38.9	x	-66.0	-83.0	x	-129.9
SLG	476.7	x	465.2	801.5	x	540.4

07/98 to

	05/99	05/00	10/00	04/02	05/05	04/06
EPR	x	x	x	x	x	x
LRR	x	x	x	x	x	x
R2	x	x	x	x	x	x
MAG	x	x	x	x	x	x
SLG	x	230.4	205.9	x	209.2	207.0

1871 to

	1910	1942	1962	1998	2006
EPR	x	-0.4	-0.5	x	-0.7
LRR	x	x	-0.5	x	-0.6
R2	x	x	0.60	x	0.61
MAG	x	-27.1	-44.0	x	-91.0

05/99 to

	05/00	10/00	04/02	05/05	04/06
EPR	-7.2	-3.4	x	-2.1	-1.7
LRR	x	-4.3	x	-1.8	-1.5
R2	x	0.69	x	0.72	0.72
MAG	-7.8	-4.9	x	-12.9	-11.9

1910 to

	1942	1962	1998	2006
EPR	x	x	x	x
LRR	x	x	x	x
R2	x	x	x	x
MAG	x	x	x	x

05/00 to

	10/00	04/02	05/05	04/06
EPR	4.2	x	-1.2	-0.8
LRR	x	x	-1.4	-1.1
R2	x	x	0.68	0.61
MAG	1.5	x	-6.1	-4.5

1942 to

	1962	1998	2006
EPR	-0.9	x	-1.0
LRR	x	x	-1.0
R2	x	x	0.67
MAG	-17.0	x	-63.9

10/00 to

	04/02	05/05	04/06
EPR	x	-1.7	-1.1
LRR	x	x	-1.3
R2	x	x	0.83
MAG	x	-7.6	-6.0

1962 to

	1998	2006
EPR	x	-1.1
LRR	x	x
R2	x	x
MAG	x	-46.9

04/02 to

	05/05	04/06
EPR	x	x
LRR	x	x
R2	x	x
MAG	x	x

1998 to

	2006
EPR	x
LRR	x
R2	x
MAG	x

05/05 to

	04/06
EPR	1.7
LRR	x
R2	x
MAG	1.6

** EPR = End Point Rate (m/yr), LRR = Linear Regression Rate (m/yr), R2 = R-Squared of LRR, MAG = Magnitude of Change (m), and SLG = Shoreline Length (m).

x = shoreline survey for cell does not exist or at least three shorelines required to generate a LRR.

this reduces the confidence in using the measurement for prediction. Results from the short-term analysis show that Cell 3 is undergoing rapid retreat, but the degree of retreat is moderated through time with the inclusion of additional shorelines. Specifically, the LRR decreases progressively from -43.1 m/yr between 07/1998 and 05/2000 to -7.1 m/yr between 07/1998 and 04/2006. However, the modest R-squared numbers for both the long- and short-term rates show that Cell 3 undergoes variation in shoreline movement that the linear regression cannot explain. This phenomenon could result from nonlinear shoreline migration over time. Figure 5 demonstrates the

Table 3: CELL 2 Long-Term and Short-Term Rates and Magnitude of Shoreline Change

1852 to

	1871	1910	1942	1962	1998	2006
EPR	2.3	-0.1	-1.7	-1.9	-1.7	-1.8
LRR	x	-0.3	-1.7	-2.1	-2.1	-2.1
R2	x	0.49	0.65	0.80	0.87	0.89
MAG	43.7	-5.8	-152.6	-208.1	-248.8	-272.2
SLG	1346.8	1313.9	1266.9	1666.7	1238.9	1343.1

07/98 to

	05/99	05/00	10/00	04/02	05/05	04/06
EPR	-5.8	2.4	-0.1	x	-3.3	-3.1
LRR	x	2.8	1.5	x	-3.4	-3.5
R2	x	0.34	0.27	x	0.59	0.65
MAG	-4.4	4.4	-0.2	x	-22.3	-23.9
SLG	1140.0	1144.2	1162.6	x	1128.9	1127.7

1871 to

	1910	1942	1962	1998	2006
EPR	-1.3	-2.8	-2.8	-2.3	-2.3
LRR	x	-2.7	-2.9	-2.5	-2.4
R2	x	0.85	0.92	0.93	0.94
MAG	-49.5	-196.3	-251.8	-288.1	-311.4

05/99 to

	05/00	10/00	04/02	05/05	04/06
EPR	8.2	2.9	x	-3.0	-2.8
LRR	x	4.1	x	-3.8	-3.8
R2	x	0.44	x	0.68	0.65
MAG	8.7	4.1	x	-17.9	-19.5

1910 to

	1942	1962	1998	2006
EPR	-4.5	-3.9	-2.8	-2.8
LRR	x	-3.9	-2.8	-2.6
R2	x	0.98	0.90	0.91
MAG	-146.8	-202.3	-246.7	-270.0

05/00 to

	10/00	04/02	05/05	04/06
EPR	-12.7	x	-5.4	-4.8
LRR	x	x	-5.1	-4.8
R2	x	x	0.82	0.80
MAG	-4.6	x	-26.7	-28.3

1942 to

	1962	1998	2006
EPR	-2.8	-1.7	-1.9
LRR	x	-1.7	-1.7
R2	x	0.91	0.93
MAG	-55.5	-97.1	-120.5

10/00 to

	04/02	05/05	04/06
EPR	x	-4.8	-4.3
LRR	x	x	-4.4
R2	x	x	0.75
MAG	x	-22.0	-23.7

1962 to

	1998	2006
EPR	-1.2	-1.5
LRR	x	-1.4
R2	x	0.92
MAG	-43.8	-67.1

04/02 to

	05/05	04/06
EPR	x	x
LRR	x	x
R2	x	x
MAG	x	x

1998 to

	2006
EPR	-3.0
LRR	x
R2	x
MAG	-23.3

05/05 to

	04/06
EPR	-1.7
LRR	x
R2	x
MAG	-1.6

** EPR = End Point Rate (m/yr), LRR = Linear Regression Rate (m/yr), R2 = R-Squared of LRR, MAG = Magnitude of Change (m), and SLG = Shoreline Length (m).

spatial consistency of the long-term rates, whereas the short-term data reveal the spatial and temporal variability of shoreline change associated with a tidal inlet.

Cell 4: North-Central, Open-Ocean, Outer Shoreline

Table 5 summarizes the changes of the north-central, open-ocean, outer shoreline that exhibited the highest rates of shoreline advance and near-stability over the long term. However, the interior of the island within Cell 4 is currently experiencing massive tree die-offs along relict dune ridges and numerous large loblolly pines have fallen onto the foreshore. This field evidence validates both long- and short-term results

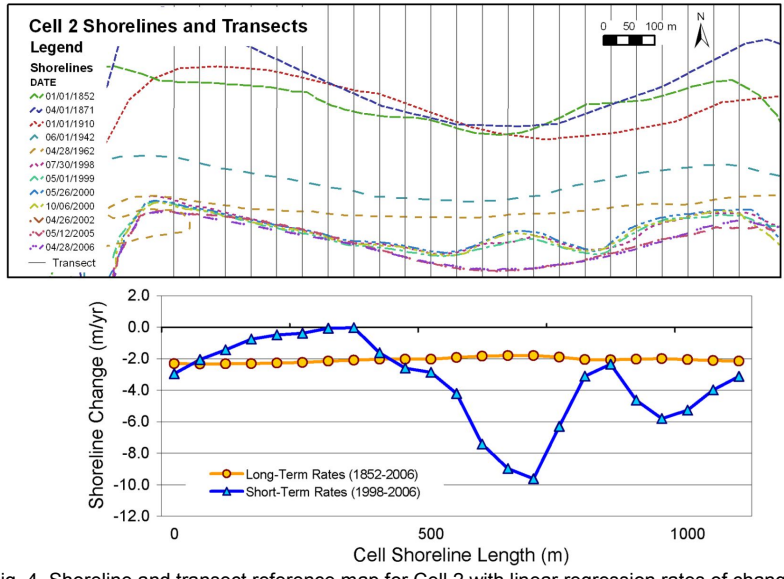

Fig. 4. Shoreline and transect reference map for Cell 2 with linear regression rates of change plotted below.

which demonstrate a switch from advance to retreat over the long term from 5.8 m/yr (1852–1910) to -1.1 m/yr (1852–2006) and an increasing retreat rate in the short term (-4.9 m/yr between 07/1998 and 05/2000 to -7.4 m/yr between 07/1998 and 04/2006). The ever-larger LRRs and associated R-squared values demonstrate the strength of the linear relationship between shoreline position and time and total variation in the data for the different periods of record—specifically, -2.9 m/yr and 0.57, respectively, for the period 1871–2006 to -4.9 m/yr and 0.83 for the period 1910–2006 to -6.7 and 1.00 for both the 1942–2006 and 1962–2006 timeframes. The short-term results also show an increase in the retreat rate. The LRRs for the short-term data illustrate accelerating retreat rates with high R-squared values extending from -7.6 m/yr and 0.82, respectively, for the period 05/1999–04/2006 to -12.9 m/yr and 0.95 for the period 04/2002–04/2006. Figure 6 portrays the smooth retreat rates over the long term and an overall increase with variability in retreat over the short term. Figure 6 also exhibits the increasing retreat rate along the southern segment of Cell 4.

Cell 5: Southern, Washover-Dominated, Outer Shoreline

Table 6 represents the change rates for the southern, washover-dominated, outer shoreline that is characterized by large magnitudes of change and high retreat rates because of extensive overwash processes. In fact, the magnitude of change includes more than a kilometer of landward movement (-1059.0 m between 1852 and 2006). The LRRs for Cell 5 are the highest retreat rates for any cell and the associated R-squared values are also high. Specifically, the long-term values range from -8.4 m/yr and 0.81, respectively, between 1852 and 2006 to -10.6 m/yr and 1.00 between 1962 and 2006. The short-term values range from -10.3 m/yr and 0.91, respectively,

Table 4: CELL 3 Long-Term and Short-Term Rates and Magnitude of Shoreline Change

1852 to

	1871	1910	1942	1962	1998	2006
EPR	7.9	4.0	3.6	3.3	1.3	0.8
LRR	x	3.7	3.3	3.1	1.6	0.8
R2	x	0.70	0.72	0.64	0.42	0.36
MAG	151.7	233.3	328.6	365.2	191.1	121.0
SLG	2978.2	2472.9	2579.0	2911.0	2595.5	2474.5

07/98 to

	05/99	05/00	10/00	04/02	05/05	04/06
EPR	-57.5	-43.8	-35.4	x	-13.3	-10.2
LRR	x	-43.1	-36.2	x	-9.8	-7.1
R2	x	0.75	0.69	x	0.49	0.55
MAG	-43.3	-79.9	-77.4	x	-90.1	-78.6
SLG	2477.4	2443.2	2496.6	x	2457.9	2493.9

1871 to

	1910	1942	1962	1998	2006
EPR	2.1	2.5	2.3	0.3	-0.2
LRR	x	2.5	2.4	0.7	-0.1
R2	x	0.64	0.56	0.37	0.35
MAG	81.7	177.0	213.6	39.5	-30.7

05/99 to

	05/00	10/00	04/02	05/05	04/06
EPR	-34.1	-23.7	x	-7.7	-5.0
LRR	x	-26.1	x	-5.2	-3.6
R2	x	0.79	x	0.54	0.62
MAG	-36.6	-34.0	x	-46.7	-35.3

1910 to

	1942	1962	1998	2006
EPR	2.9	2.5	-0.5	-1.2
LRR	x	2.6	-0.4	-1.3
R2	x	0.55	0.31	0.36
MAG	95.3	131.9	-42.2	-112.4

05/00 to

	10/00	04/02	05/05	04/06
EPR	7.0	x	-2.0	0.2
LRR	x	x	-2.3	-1.1
R2	x	x	0.84	0.83
MAG	2.5	x	-10.1	1.3

1942 to

	1962	1998	2006
EPR	1.8	-2.4	-3.2
LRR	x	-2.7	-3.5
R2	x	0.63	0.59
MAG	36.6	-137.5	-207.6

10/00 to

	04/02	05/05	04/06
EPR	x	-2.8	-0.2
LRR	x	-8.3	-1.7
R2	x	0.39	0.84
MAG	x	-12.7	-1.3

1962 to

	1998	2006
EPR	-4.8	-5.6
LRR	x	-5.3
R2	x	0.86
MAG	-174.1	-244.3

04/02 to

	05/05	04/06
EPR	-11.4	-2.7
LRR	x	-7.9
R2	x	0.38
MAG	-34.6	-23.2

1998 to

	2006
EPR	-9.1
LRR	x
R2	x
MAG	-70.2

05/05 to

	04/06
EPR	11.9
LRR	x
R2	x
MAG	11.4

** EPR = End Point Rate (m/yr), LRR = Linear Regression Rate (m/yr), R2 = R-Squared of LRR, MAG = Magnitude of Change (m), and SLG = Shoreline Length (m).

for the period 07/1998–04/2006 and -13.8 m/yr and 0.94 for the period 04/2002–04/2006. Figure 7 demonstrates the change rate is not spatially uniform along Cell 5. Specifically, the shoreline change rates increase three-fold from north to south over the long term. The short-term rate also increases to the south, but this trend is less pronounced when compared to the long-term values.

DISCUSSION AND CONCLUSIONS

The bayside shoreline (Cell 1) retreated at the slowest rate of all shoreline segments because of its protection from open-ocean processes. However, the bayside shoreline

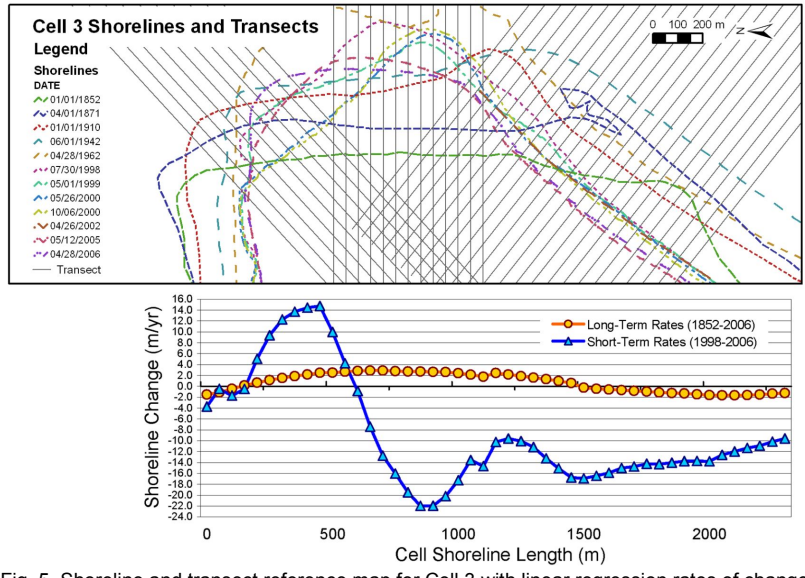

Fig. 5. Shoreline and transect reference map for Cell 3 with linear regression rates of change plotted below. (**90° transects are correlated to the graph, whereas angled transects require interpretation.)

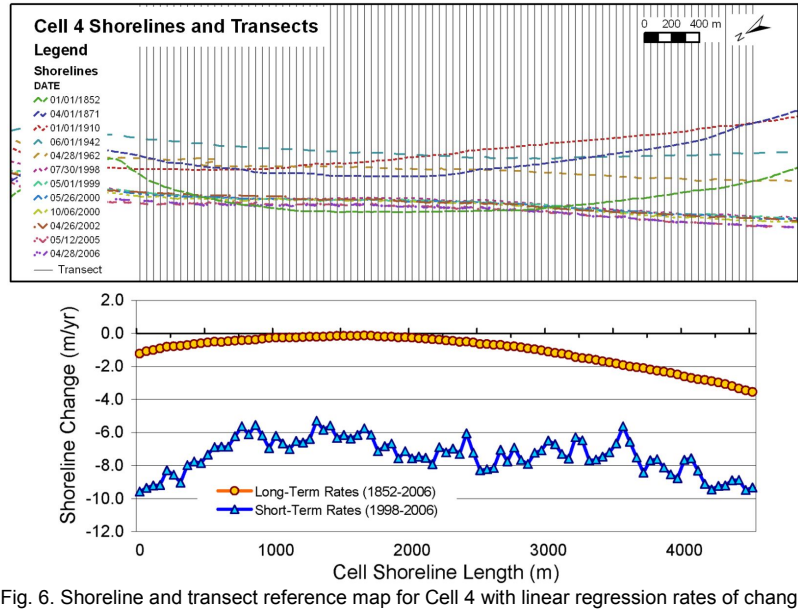

Fig. 6. Shoreline and transect reference map for Cell 4 with linear regression rates of change plotted below.

Table 5: CELL 4 Long-Term and Short-Term Rates and Magnitude of Shoreline Change

1852 to

	1871	1910	1942	1962	1998	2006
EPR	15.3	6.4	4.1	2.2	0.0	-0.4
LRR	x	5.8	3.5	1.9	-0.2	-1.1
R2	x	0.71	0.60	0.37	0.06	0.12
MAG	295.3	373.0	367.2	237.8	-3.9	-59.8
SLG	4551.5	4521.2	4520.3	4809.3	4545.8	4788.9

07/98 to

	05/99	05/00	10/00	04/02	05/05	04/06
EPR	-8.2	-5.0	-9.0	-2.0	-7.9	-7.2
LRR	x	-4.9	-7.6	-2.4	-7.1	-7.4
R2	x	0.68	0.68	0.36	0.74	0.84
MAG	-6.2	-9.2	-19.8	-7.4	-53.9	-56.0
SLG	4605.1	4618.8	4702.0	4670.2	4783.5	4788.9

1871 to

	1910	1942	1962	1998	2006
EPR	2.0	1.0	-0.6	-2.3	-2.6
LRR	x	1.0	-0.4	-2.3	-2.9
R2	x	0.51	0.31	0.41	0.57
MAG	77.7	71.9	-57.5	-299.2	-355.2

05/99 to

	05/00	10/00	04/02	05/05	04/06
EPR	-2.8	-9.5	-0.4	-7.9	-7.1
LRR	x	-8.0	-0.4	-7.4	-7.6
R2	x	0.61	0.35	0.72	0.82
MAG	-3.0	-13.6	-1.2	-47.7	-49.8

1910 to

	1942	1962	1998	2006
EPR	-0.2	-2.6	-4.3	-4.5
LRR	x	-2.4	-4.4	-4.9
R2	x	0.57	0.75	0.83
MAG	-5.8	-135.2	-376.9	-432.8

05/00 to

	10/00	04/02	05/05	04/06
EPR	-29.2	0.9	-9.0	-7.9
LRR	x	3.0	-8.2	-8.2
R2	x	0.39	0.73	0.82
MAG	-10.6	1.8	-44.8	-46.8

1942 to

	1962	1998	2006
EPR	-6.5	-6.6	-6.7
LRR	x	-6.6	-6.7
R2	x	0.99	1.00
MAG	-129.4	-371.1	-427.0

10/00 to

	04/02	05/05	04/06
EPR	8.0	-7.4	-6.5
LRR	x	-8.5	-8.4
R2	x	0.70	0.79
MAG	12.4	-34.1	-36.2

1962 to

	1998	2006
EPR	-6.7	-6.8
LRR	x	-6.7
R2	x	1.00
MAG	-241.7	-297.6

04/02 to

	05/05	04/06
EPR	-15.3	-12.1
LRR	x	-12.9
R2	x	0.95
MAG	-46.5	-48.6

1998 to

	2006
EPR	-7.2
LRR	x
R2	x
MAG	-56.0

05/05 to

	04/06
EPR	-2.1
LRR	x
R2	x
MAG	-2.0

** EPR = End Point Rate (m/yr), LRR = Linear Regression Rate (m/yr), R2 = R-Squared of LRR, MAG = Magnitude of Change (m), and SLG = Shoreline Length (m).

experienced a two-fold increase in its retreat rate from -0.7 m/yr (1852–2006) to -1.5 m/yr (05/1999–04/2006). The inlet-influenced shoreline (Cell 2) migrated more slowly than the open-ocean shoreline segments. Wachapreague Inlet migrated south at -2.1 m/yr (1852–2006) but increased its southern migration rate to -3.5 m/yr from 07/1998 to 04/2006. The seaward, inlet-influenced shoreline (Cell 3) is the only shoreline to show long-term advance at 0.8 m/yr (1852–2006), but the short-term rates reveal a high retreat rate at -7.1 m/yr (07/1998–04/2006). The long- and short-term trends of advance nearest the inlet demonstrate the role of swash bar attachment on mixed-energy barrier islands (Figure 5). However, the reversal to high retreat rates

Table 6: CELL 5 Long-Term and Short-Term Rates and Magnitude of Shoreline Change

1852 to

	1871	1910	1942	1962	1998	2006
EPR	15.8	4.6	-2.1	-5.4	-6.7	-6.9
LRR	x	3.8	-3.4	-6.3	-7.9	-8.4
R2	x	0.43	0.28	0.56	0.74	0.81
MAG	303.9	268.4	-190.5	-590.3	-974.9	-1059.0
SLG	6161.3	6179.0	3062.5	5036.5	4837.6	5148.4

07/98 to

	05/99	05/00	10/00	04/02	05/05	04/06
EPR	-15.6	-12.6	-17.3	-7.8	-11.8	-10.4
LRR	x	-12.5	-15.7	-8.5	-10.8	-10.3
R2	x	0.87	0.86	0.58	0.86	0.91
MAG	-11.8	-23.1	-37.8	-28.9	-80.1	-80.6
SLG	4680.5	4854.3	4718.0	4510.6	4597.9	4571.3

1871 to

	1910	1942	1962	1998	2006
EPR	-0.9	-8.8	-10.0	-10.2	-10.2
LRR	x	-8.7	-10.1	-10.6	-10.8
R2	x	0.95	0.90	0.95	0.96
MAG	-35.6	-622.9	-915.2	-1299.8	-1383.8

05/99 to

	05/00	10/00	04/02	05/05	04/06
EPR	-10.6	-18.1	-5.8	-11.3	-9.8
LRR	x	-16.4	-5.8	-10.5	-10.0
R2	x	0.78	0.35	0.83	0.89
MAG	-11.3	-26.0	-17.1	-68.3	-68.9

1910 to

	1942	1962	1998	2006
EPR	-10.1	-13.3	-12.2	-12.1
LRR	x	x	-12.3	-12.1
R2	x	x	1.00	1.00
MAG	-328.5	-696.7	-1081.3	-1165.3

05/00 to

	10/00	04/02	05/05	04/06
EPR	-40.3	-2.7	-11.5	-9.7
LRR	x	-0.5	-10.4	-9.9
R2	x	0.24	0.80	0.86
MAG	-14.7	-5.8	-57.0	-57.5

1942 to

	1962	1998	2006
EPR	-13.6	-10.9	-10.7
LRR	x	-10.8	-10.5
R2	x	0.99	0.99
MAG	-269.8	-614.2	-686.6

10/00 to

	04/02	05/05	04/06
EPR	5.7	-9.2	-7.7
LRR	x	-10.3	-9.7
R2	x	0.75	0.83
MAG	8.9	-42.3	-42.9

1962 to

	1998	2006
EPR	-10.6	-10.7
LRR	x	-10.6
R2	x	1.00
MAG	-384.6	-468.6

04/02 to

	05/05	04/06
EPR	-16.8	-13.0
LRR	x	-13.8
R2	x	0.94
MAG	-51.2	-51.7

1998 to

	2006
EPR	-10.9
LRR	x
R2	x
MAG	-84.0

05/05 to

	04/06
EPR	-0.6
LRR	x
R2	x
MAG	-0.6

** EPR = End Point Rate (m/yr), LRR = Linear Regression Rate (m/yr), R2 = R-Squared of LRR, MAG = Magnitude of Change (m), and SLG = Shoreline Length (m).

beginning approximately 700 m south of the inlet (-22.0 m; -8.6 m on average) may indicate the control of shorter-term inlet dynamics, such as ebb-tidal delta breaching, outer channel shifting or sediment supply changes on the adjacent shorelines. The north-central, open ocean shoreline (Cell 4) exhibited moderate advance rates during a portion of its past (3.5 m/yr from 1852 to 1942 and 1.0 m/yr from 1871 to 1942), but the shoreline segment still demonstrated a relatively small long-term retreat rate at -1.1 m/yr (1852–2006). However, this reach experienced a higher retreat rate over the short term at -7.4 m/yr (07/1998–04/2006). This short- term result may help explain the extensive tree die-offs along interior relict dune ridges and the large

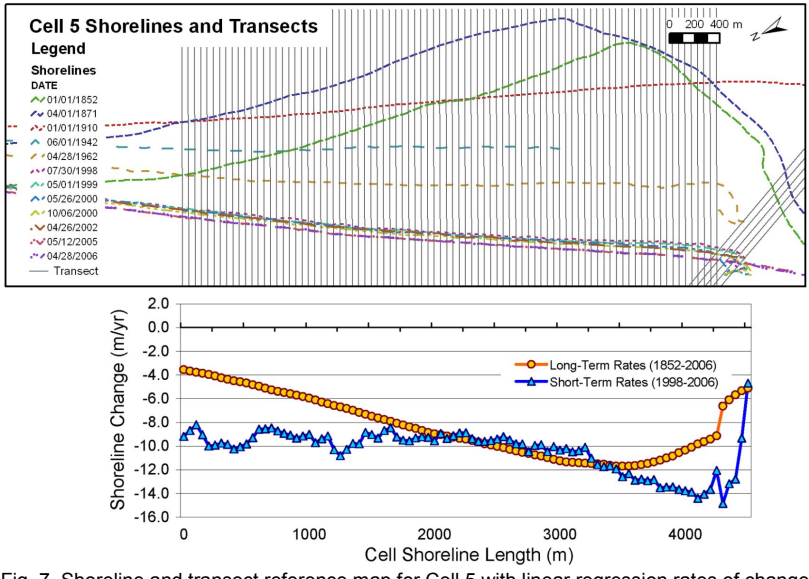

Fig. 7. Shoreline and transect reference map for Cell 5 with linear regression rates of change plotted below. (**90° transects are correlated to the graph, whereas angled transects require interpretation.)

number of fallen trees across the foreshore. Moreover, the parabolic shape of the spatial distribution of the retreat rates (Figure 6) may reveal the location of an inlet-influenced node and the southern-most extent of inlet-influenced processes. The southern, washover-dominated reach (Cell 5) experienced the highest retreat rates among all the shoreline segments with more than 1 km in net shoreline movement. The retreat rate along this reach increased from -8.4 m/yr (1852–2006) in the long term to -10.3 m/yr (07/1998–04/2006) over the short term.

Along the entire outer shoreline (Cells 3, 4, and 5), results indicate that shoreline behavior of Parramore Island has evolved from clockwise rotational instability over the long term as described by Leatherman et al. (1982) to continuous rapid retreat over the short term. Specifically, Parramore's outer shoreline (Cells 3, 4, & 5) experienced a retreat rate of -3.6 m/yr over the long term (1852-2006) and -8.8 m/yr over the short term (1998-2006). We conclude that Parramore Island has undergone a fundamental adjustment in its pattern of shoreline movement. Additional analyses are needed to determine why these shoreline changes are occurring so rapidly and to determine if the change patterns along Parramore Island exist along other barrier islands of the Virginia Coast Reserve and elsewhere.

ACKNOWLEDGEMENTS

The authors would like to thank Dr. Michael S. Fenster (Randolph Macon College) for critically reviewing the manuscript and offering his insightful remarks.

REFERENCES

Anders, F.J., and Byrnes, M.R. (1991). "Accuracy of shoreline change rates as determined from maps and aerial photographs," *Shore and Beach*, 59(1), 17-26.

Boak, E.H. and Turner, I.L. (2005). "Shoreline Definition and Detection: A Review," *Journal of Coastal Research,* 21(4), 688-703.

Byrnes, M.R., Crowell, M., and Fowler, C. (2003). "Shoreline Mapping and Change Analysis: Technical Considerations and Management Implications—Preface," *Journal of Coastal Research,* SPEC. ISS., 38, 1-4.

Byrnes, M.R. McBride, R.A., Tao, Q., and Duvic, L. (1995). "Historical Shoreline Dynamics Along the Chenier Plain of Southwestern Louisiana," *Gulf Coast Association of Geological Societies Transactions,* 45, 113-122.

Byrnes, M.R., McBride, R.A., and Hiland, M.W. (1991). "Accuracy Standards and Development of a National Shoreline Change Data Base," *Proceedings Coastal Sediments '91*, American Society of Civil Engineers, New York, NY, 1027-1042.

Crowell, M., Leatherman, S.P., and Buckley, M.K. (1991). "Historical shoreline change: error analysis and mapping accuracy," *Journal of Coastal Research,* 7(3), 839-852.

Fenster, M.S. and Dolan, R. (1993). "Historical Shoreline Trends Along the Outer Banks, North Carolina: Processes and Responses," *Journal of Coastal Research*, 9(1), 172-188.

Graham, D., Sault, M., and Bailey, J. (2003). "National Ocean Service Shoreline—Past, Present, and Future," *Journal of Coastal Research*, SPEC. ISS., 38, 14-32.

Honeycutt, M.G., Crowell, M., and Douglas, B.C. (2001). "Shoreline-position forecasting: Impact of storms, rate-calculation methodologies, and temporal scales," *Journal of Coastal Research*, 17(3), 721-730.

Leatherman, S.P. (2003). "Shoreline Change Mapping and Management Along the U.S. East Coast," *Journal of Coastal Research,* SPEC. ISS., 38, 5-13.

Leatherman, S.P., Rice, T.E., and Goldsmith, V. (1982). "Virginia Barrier Island Configuration: A Reappraisal," *Science*, 215, 285-287.

McBride, R.A. (1999). "Spatial and temporal distribution of historical and active tidal inlets: Delmarva Peninsula and New Jersey, USA," In: N.C. Kraus and W.G. McDougal (eds.), *Coastal Sediments '99*. American Society of Civil Engineers, Reston, VA, 2, 1505–1521.

McBride, R.A. and Byrnes, M.R. (1997). "Regional variations in shore response along barrier island systems of the Mississippi River delta plain: Historical change and future prediction," *Journal of Coastal Research*, 13(3), 628–655.

Moore, L.J. (2000). "Shoreline Mapping Techniques," *Journal of Coastal Research*, 16(1), 111-124.

Morton, R.A, Miller, T., and Moore, L. (2005). "Historical Shoreline Changes Along the US Gulf of Mexico: A Summary of Recent Shoreline Comparisons and Analyses," *Journal of Coastal Research*, 21(4), 704-709.

Pajak, M.J. and Leatherman, S. (2002). "The high water line as shoreline indicator," *Journal of Coastal Research*, 18(2), 329-337.

Thieler, E.R. Himmelstoss, E.A., Zichichi, J.L., and Miller, T.L. (2005). "The Digital Shoreline Analysis System (DSAS) version 3.0 , an ArcGIS Extension for Calculating Historic Shoreline Change," *U.S. Geological Survey Open-file Report 2005-1304,* USGS Coastal and Marine Geology Program, Woods Hole, MA.

TEMPORAL AND SPATIAL SCALES OF PROFILE AND PLANFORM ADJUSTMENT ON A NOURISHED BEACH

Nicole A. Elko[1] and Ping Wang[2]

1. Department of Environmental Management, Pinellas County, 512 S. Ft. Harrison Ave., Clearwater, FL 33756, nelko@pinellascounty.org

2. Department of Geology, University of South Florida, 4202 E. Fowler Ave., Tampa, FL 33620, pwang@cas.usf.edu

Abstract: Weekly beach profiles, shoreline surveys, and nearshore wave measurements were collected before, during, and immediately after construction of the 1100-m Upham Beach nourishment project on the low-energy, west coast of Florida. Substantial planform diffusion occurred prior to construction completion via formation of a spit extending from the widest portion of the fill. Longshore spreading occurred abruptly, as opposed to gradual adjustment predicted by long-term models. Profile equilibration also occurred rapidly due to the passage of three hurricanes. Nine days after nourishment, Hurricane Frances generated high wave conditions (H_{sig} = 1.7 m) for this region, reducing the steep post-nourishment beach slope from 0.078 to 0.036, nearly the equilibrium slope (0.034). Hurricanes Ivan and Jeanne, which were nearly as energetic, resulted in much less slope change. This study indicated that profile equilibration was an event-driven process, contradicting the concept of long-term equilibration.

INTRODUCTION

This study examines two types of coastal change: gradual and episodic. Gradual change involves processes occurring over time causing a response. Cascading time scales, for example from the century to the daily scale, imply gradual change on various spatial scales. Another type of "temporal scale" that does not fit into the cascade is an event. A similar morphologic response may occur due to gradual change over time or it might occur relatively instantaneously as the result of an event. The magnitude of these event-driven changes will govern their spatial extent. It is

crucial to understand both types of change, gradual and episodic, because distinct processes drive changes at these different time scales.

Beach nourishment provides an excellent opportunity for the study of intensified sediment transport gradients and associated morphologic changes in a natural setting. Generally speaking, a beach nourishment project is a large nearshore perturbation that eventually equilibrates with the surrounding system via longshore and cross-shore sediment transport (Dean 1983). These forcing mechanisms influence the evolution of beach nourishment projects through planform adjustment, i.e. longshore spreading, and cross-shore evolution, i.e. profile equilibration (Fig. 1).

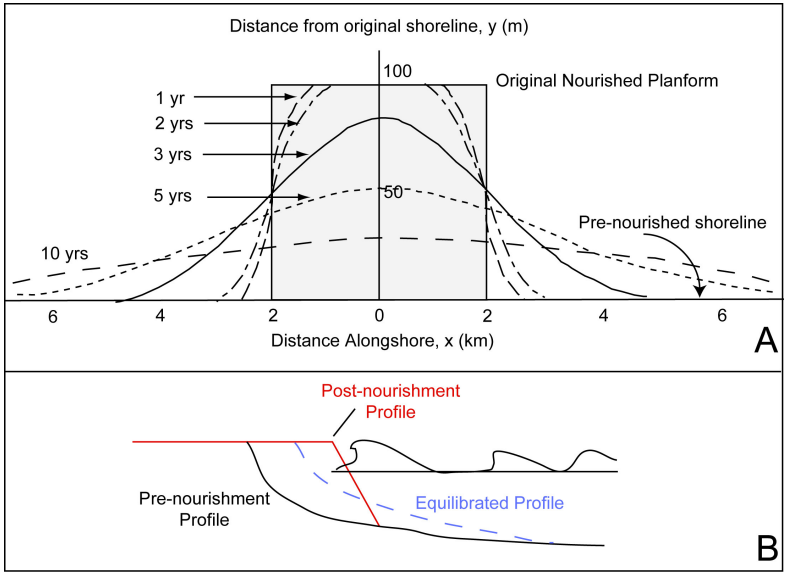

Fig. 1. Beach nourishment project evolution: A) planform adjustment via longshore transport; B) profile equilibration via cross-shore transport (modified from Dean (2002)).

One-line models that predict the long-term planform evolution of nourishment projects (Dean 1983; 1996; Hanson and Kraus 1989) have been developed from the Pelnard-Considére (1956) diffusion equation. Fig. 1A is a schematic of the gradual diffusion over time predicted by the long-term models. During the diffusion process, the post-nourishment shoreline perturbation is smoothed by incoming wave energy that drives longshore transport. The beach fill gradually diffuses from a rectangular planform to a bell-shaped curve that spreads out to a straight shoreline eventually over time (Fig. 1A). This generalization represents long-term and large-scale diffusion; therefore, immediate post-nourishment evolution at the end transitions may not be adequately described. Quantifying short-term, local project adjustment, such

as transport gradients at end transitions, is essential in improving the present state-of-the-art predictive capabilities.

Profile equilibration refers to the reduction of a steep nourished profile to a gentler characteristic, or equilibrium, profile (Fig. 1B). The equilibrium profile form that is frequently estimated with the simple model of Brunn (1954) and Dean (1991)

$$h = Ax^{2/3} \tag{1}$$

is dependent on sediment grain size. In Eq. (1), h is the water depth relative to mean sea level, x is the horizontal distance from the shoreline, and A is a scale parameter correlated with grain size (D). The A value can be determined graphically from Moore (1982), or according to Dean (1987).

Nourished beaches are typically constructed with sediment that differs from the grain size of the natural beach. Nourished beaches are also constructed on steeper slopes than natural profiles. During profile equilibration, most of the fill volume remains within the project area landward of the closure depth, and is redistributed across the profile. The dry beach width is usually reduced during this process (Fig. 1B). Profile equilibration is thought to continue for several years after nourishment (Browder and Dean 2000); however, design guidance for profile equilibration time is limited (Dean and Campbell 1999). Presently, no cross-shore sediment transport models accurately predict time scales of profile equilibration (Dean 2002).

This study analyzes detailed monitoring data collected before, during, and immediately after beach nourishment. The objective is to quantify and predict the immediate profile and planform response of nourishment. Specifically, the time scales and energy levels associated with initial project adjustment are examined.

Study Area

The project area, Upham Beach, is located on the west coast of Florida in southern Pinellas County (Fig. 3). This is a low-energy coastal system with annual average breaking wave heights of 0.3 m (Tanner 1960) and a mean tidal range of about 0.8 m (NOAA 2004). During the 2004 hurricane season, four strong hurricanes made landfall in Florida (Fig. 3). All four hurricanes affected the west-central Florida coast.

Upham Beach is located at the north end of the barrier island of Long Key, and is bordered on the north by Blind Pass. In this region, net annual littoral drift is from north to south (Davis 1994). Upham Beach is sediment starved due to the combined effect of sediment trapping by the Blind Pass jetties, a minimal ebb shoal, and periodic dredging of the inlet. Thus, sediment bypassing around Blind Pass to Upham Beach has been largely eliminated (Davis 1989; CPE 1992). The only sediment supplied to Upham Beach is through beach nourishment.

Prior to the 2004 project, Upham Beach had been nourished six times in 1975, 1980, 1986, 1991, 1996, and 2000. Based on results from the 1996 project, half of the plan area erodes in approximately one year (Elko et al. 2005). Longshore currents transport the nourished material to the downdrift beaches; thus, Upham Beach serves as a "feeder beach" for the rest of Long Key (USACE 1999). A feeder beach is a nourishment project where material is introduced at the updrift end of the area intended to receive fill.

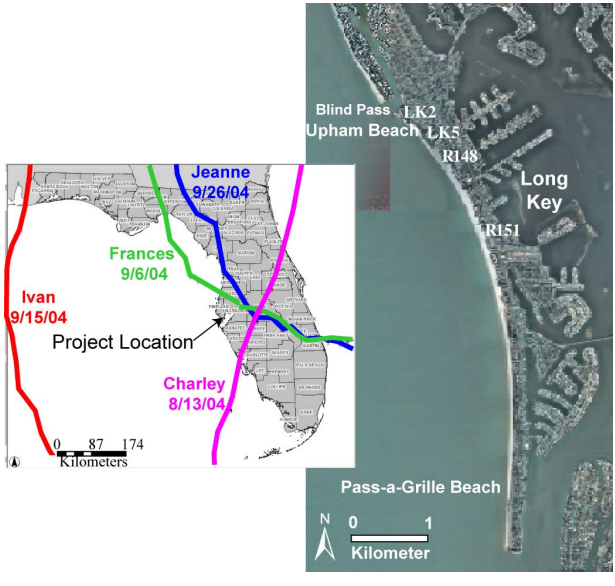

Fig. 2. Study area and the tracks of the four hurricanes that impacted Florida in 2004.

2004 Nourishment Project

The 2004 Upham Beach nourishment project had a total project length of 1100 m, a total volume of 294,000 m^3, and a design berm elevation (B) of 1.8 m. The 2004 project was designed with three distinct segments (Fig. 3): 1) the wide north segment, from Blind Pass to LK3A, 2) the central segment, from LK3A to LK5A, and 3) the south segment, from LK5A to R148, which was nourished for the first time in 2004. The nourishment volume density ranged from 95 m^3/m in the south segment to 360 m^3/m in the north segment. The fill was designed with two transitions: 1) the large transition in the central segment of fill that reduced the berm width from 140 m to 40 m over 260 m, and 2) the slight transition at the south end which tied in with the natural berm width of about 40 m.

Fill placement began on Upham Beach on July 28, 2004 (Table 1). Fill was placed from south to north (Fig. 3) in the opposite direction of net littoral drift. Due to the

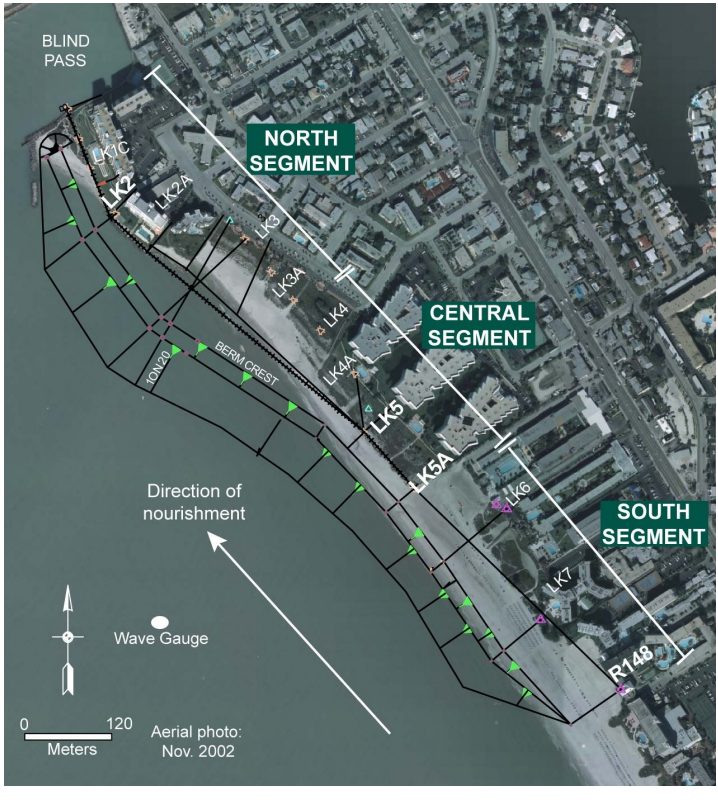

Fig. 3. The planform design template of the 2004 Upham Beach nourishment project.

passage of four hurricanes in August and September 2004, during and shortly after the completion of the project, a large amount of sediment eroded rapidly from the design template. A repair nourishment, authorized for Upham Beach following the storms (Elko 2005), was completed on October 28, 2004. This renourishment repaired a section from Blind Pass to LK4 (Fig. 3) to the original design template.

Table 1. Construction Schedule for the 2004 Upham Beach Nourishment Project.

Segment	Completion date (2004)	Completion to the passage of Hurricane Frances on September 5, 2004 (days)
South	July 22	45
Central	July 28	39
North	August 27	9
Repair	October 28	n/a

METHODOLOGY

A rigorous field-monitoring program was initiated prior to construction of the 2004 nourishment project. Beach profiles, offshore bathymetry, and offshore waves were measured from June to October 2004. Wading profiles, which are typically surveyed to approximately -1.5 m, were extended to capture nearshore changes and measure profile equilibration. The beach profile surveys extended offshore nearly to the depth of closure, which is approximately -3 m in southern Pinellas County (Wang and Davis 1999). These wading beach-profile surveys followed level-and-transit procedures using an electronic total survey station.

Thirteen surveys of the 21 profile lines were conducted during this field effort. Weekly beach profiles were surveyed before, during, and immediately after nourishment until October 1, 2004. The pre-construction beach survey was conducted on June 6, 2004, and the post-construction surveys were conducted at different times along different segments (Table 1). A PUV directional wave gauge was deployed about 600 m offshore of the center of the Upham Beach nourishment project in approximately 4 m of water (Fig. 3).

RESULTS

On August 13, Hurricane Charley made landfall approximately 110 km south of the project area (Fig. 2). Charley generated maximum wave periods (T_p) of about 8.3 s and significant wave heights (H_{sig}) of up to 0.92 m at the project area (Fig. 4). Following the passage of Charley, calm conditions that are commonly observed in the Gulf of Mexico prevailed. Hurricanes Frances, Ivan, and Jeanne made landfall on September 5, 15, and 26, respectively. Hurricane Frances passed by the project area nine days after nourishment was complete. Hurricanes Frances and Jeanne passed by the project area within 50 and 80 km, respectively. These storms generated steep storm waves with maximum wave heights of H_{sig} = 1.7 m (Fig. 4), roughly six times the annual average wave height along this low-energy coast. Waves generated by Hurricane Ivan (max: H_{sig}= 1.0 m, T_p = 15.9 s) approached the project area as a well-organized swell.

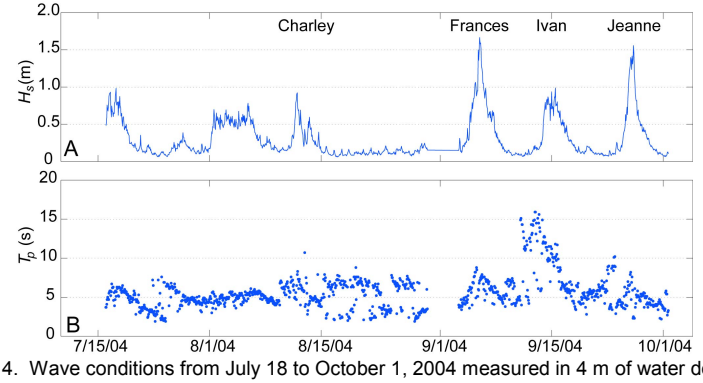

Fig. 4. Wave conditions from July 18 to October 1, 2004 measured in 4 m of water depth.

The mean sediment grain size of the fill material (D_F) was 0.51 mm. The fill material was similar but slightly coarser than the native sand (D_N = 0.45 mm) with the exception of the section from LK3 to LK5 (Fig. 3). The nourishment sediment grain sizes ranged from 0.3 to 0.9 mm. The use of relatively coarser sediments between LK3 and LK5 (mean D_F = 0.6 mm) was expected to improve nourishment performance in this rapidly eroding area.

PLANFORM ADJUSTMENT

During the 40 days between completion of nourishment in the central and south segments and the passage of Hurricane Frances, the beach in these segments prograded. Sediment that eroded from the north segment was deposited in the nearshore and intertidal zones (Fig. 5B and C). In the downdrift region, offshore sand bars accumulated sediment and migrated onshore (Fig. 5D).

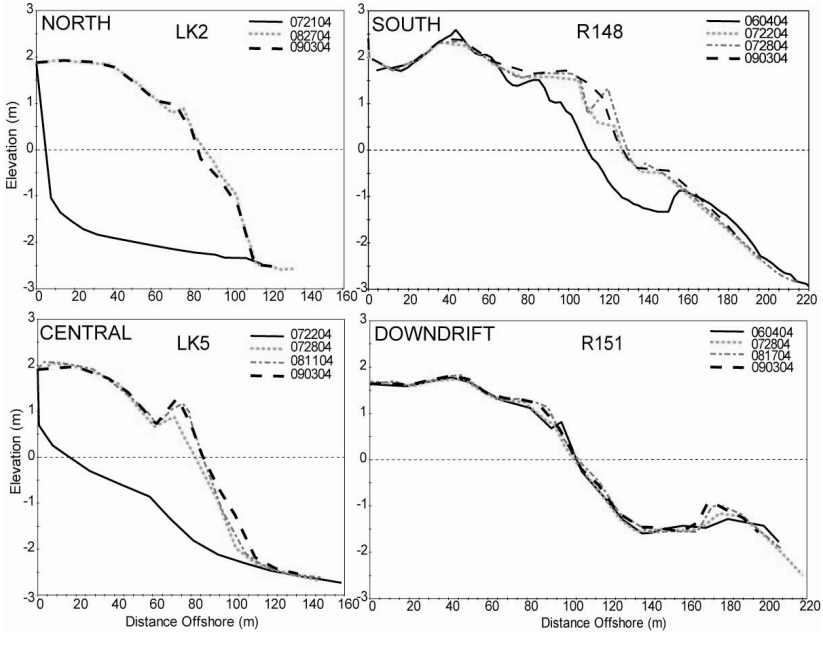

Fig. 5. Profile response after nourishment from the four project segments. See Fig. 2 for profile locations.

Deposition in the central segment was first measured on August 11, about two weeks after nourishment was complete in this segment. Weekly survey data indicated the formation of a large inter- to supra-tidal sediment body in this segment, resembling a spit spreading from the transition of the wide north segment of the planform. Systematic documentation of the formation of this "diffusion spit" is available in

Elko and Wang (2007). Coarse nourished grain size and local wave, tide, and weather conditions combined to promote spit formation. Post-nourishment spit formation is a common occurrence on the west coast of Florida. Diffusion is initiated immediately following nourishment, abruptly reducing the large shoreline orientation change at the end transitions. This immediate planform evolution does not adhere to the generalized model of Fig. 1A.

PROFILE EQUILIBRATION

Profile shape and slope were relatively constant until the passage of Hurricane Frances on September 5, 2004 resulted in remarkable beach profile changes.

Profile-shape adjustment

Beach profile changes resulting from the passage of Hurricane Frances differed in the three nourished segments. The same four profiles from Fig. 5 (except LK5A replaces LK5) are displayed in Fig. 6 to illustrate these changes.

North Segment In the north segment, beach profiles maintained a steep post-construction slope for nine days until the passage of Hurricane Frances on September 5 (Fig. 5A). The newly constructed, wide, north segment of Upham Beach lost over 25 m of shoreline during the week of Frances' passage (Fig. 6A). Net cross-shore transport, e.g., offshore transport and formation of sand bars, as is typical during storms, did not occur. The profile-shape change was largely caused by net longshore transport, resulting in substantial volume loss (60 m^3/m) over the entire profile. This segment typically exhibits a monotonic beach profile, unlike the other segments that contain a nearshore bar. The extreme seaward-advanced position of this segment and the large gradients in longshore transport appear to preclude bar formation.

Central/south Segments Nourishment was completed earlier in the central and south segments than in the north segment (Table 1). Here, the steep post-construction slope persisted for up to 40 days after nourishment (Fig. 5B and C). During this time, the passage of Hurricane Charley generated a brief 0.9 m swell (Fig. 4), but did not induce sufficient cross-shore sediment transport to reduce the beach slope. Due to the passage of Frances, net offshore transport resulted in deposition on the nearshore sand bars (Fig. 6B and C). As compared to the north segment, little berm erosion took place in these segments. In fact, along the central segment, up to 8 m of berm progradation was measured (Fig. 6B), apparently benefiting from the longshore sand supply from the north segment and dispersion of the diffusion spit, which was destroyed by the passage of Frances.

Overall, the morphologic changes within the fill area caused by Frances resulted in reduction of the steep post-nourishment slope. Downdrift of the fill, the sand bar migrated offshore in response to the passage of Hurricane Frances. Otherwise, the profile, which was likely already in an equilibrium form, changed little (Fig. 6D).

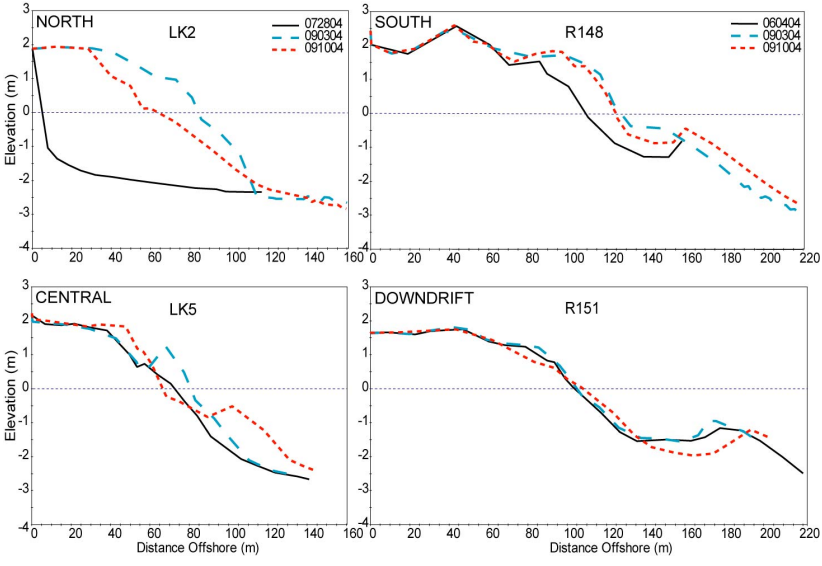

Fig. 6. Beach-profile changes induced by Hurricane Frances for the four segments of the project. See Fig. 2 for profile locations.

Beach slope

To further quantify this apparent rapid profile equilibration, beach slope (γ) was calculated for all of the 106 measured and equilibrium profiles. Beach slope was determined via linear regression from mean high water (MHW = 0.12 m) to the toe of fill (-2.5 m). The limit of this calculation extends seaward of the bar. Although not capable of representing the details of slope variations along the profile, the linear-regression slope represents the beach slope trend from the shoreline to the toe of fill.

The "measured equilibrium" beach slope was estimated from the slope of the pre-nourishment beach profiles, assuming the beach was in equilibrium before nourishment. Pre-nourishment profiles are typically used to represent the natural beach slope, unless scour in front of a seawall has occurred. The "calculated equilibrium" beach slope was estimated based on profiles calculated with Eq. (1).

Overall, the mean slope of the calculated equilibrium profiles (γ_{eq}) was 0.034 and the mean slope (γ_m) of the pre-nourishment profiles (measured equilibrium) was 0.025 (Table 2). The slightly gentler measured slope (γ_m) is influenced by the presence of a nearshore sand bar as discussed in the following sections.

When construction of the project was complete on August 27, the overall mean slope (γ_m) was 0.078 (Table 2), indicating a steep post-nourishment slope, as expected.

Nine days later, due to the passage of Hurricanes Frances, this γ_m was dramatically reduced to 0.036, or less than half of the post-construction slope. The γ_m decreased further due to the passage of Hurricanes Ivan and Jeanne, from 0.036 to 0.028; however, the slope reduction was much less than that induced by Frances. In fact, Hurricane Jeanne generated similar wave conditions to those generated by Frances (Fig. 4). The magnitude of beach change caused by these two events was quite different, with much more change induced by Frances.

Table 2. Calculated Beach Slope (γ) during the Study Period in 2004.

	Calc. Equilib. (γ_{eq})	Pre-nourish (Jun 4)	Post-constr. (Jul 22-Aug 27)	Post-Frances (Sep 10)	Post-Jeanne (Oct 1)	Repair post-constr. (Oct 29)	Winter (Dec 13)
North	0.033	0.026*	0.102	0.046	0.035	0.064	0.034
Central	0.032	0.023	0.075	0.035	0.027	0.055	0.031
South	0.037	0.026	0.041	0.023	0.020		
Mean (γ_m)	**0.034**	**0.025**	**0.078**	**0.036**	**0.028**	**0.063**	**0.033**

* Pre-nourishment slope of LK2 and LK2A was omitted from this calculation due to scour in front of the seawall.

North Segment When fill was placed in the north segment, a 1:20 (0.05) slope was constructed to about -1 m, within the range of the construction equipment. Pre-nourishment profiles were exceptionally steep due to scour in front of the seawall at LK2 and LK2A. Below -1 m (Fig. 5A), the fill settled at a slope of about 1:7 (0.14) resulting in an exceptionally steep post-construction γ_m of 0.102 for the north segment (Table 2). The impact of Hurricane Frances resulted in a sharp drop of γ_m from 0.102 to 0.046 (Fig. 7A). The post-Jeanne slope of 0.035 was similar to the equilibrium slope of 0.033.

Central/south Segments In the central segment of fill, the γ_m was relatively constant at 0.075 for about 40 days after nourishment was complete on July 28 until the passage of Frances on September 5, 2004 (Fig. 7B). The formation of the diffusion spit (Elko and Wang, 2007) and the resulting berm accretion are responsible for the slight increase of γ_m during this period of relatively calm weather. Similar to the north segment, a sharp decrease of γ_m, from 0.075 to 0.035, was measured following the passage of Hurricane Frances.

Fill was mainly placed between the berm and bar in the south segment (Fig. 5C). Consequently, the post-nourishment profile was not as steep (Fig. 7C) as in the north and central segments. The post-nourishment γ_m was constant at 0.041 for about 45 days, followed by a drop to 0.023 induced by the passage of Hurricane Frances. The slope decrease was not as dramatic as in the other segments due to the gentler post-nourishment (or pre-storm) γ_m. In both segments, the storms served to reduce γ_m to approximately the pre-nourishment slope.

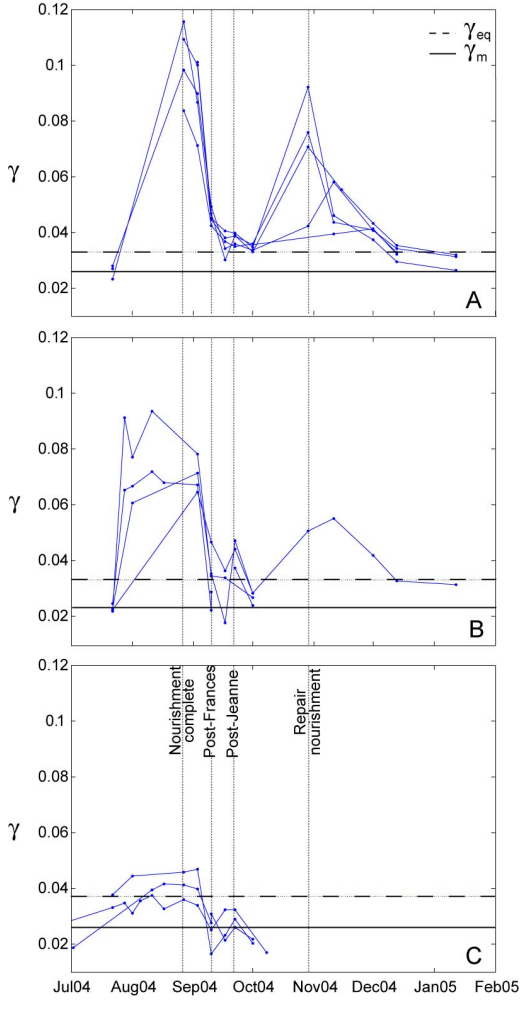

Fig. 7. Time series of measured beach slopes for 12 surveyed profiles. The calculated and measured equilibrium slopes are shown as dashed and solid horizontal lines, respectively.

Rapid Equilibration

The profile shape change shown in Fig. 6 indicates that profile equilibration was controlled by high-energy wave events. The steep nourished profile was flattened by the single event of the passage of Hurricane Frances, reducing the overall beach slope

to nearly the pre-nourishment slope. Based on this morphologic response and the calculated beach slopes (Table 2), it is reasonable to conclude that profile equilibration was largely complete by October 1, 2004, 35 days after nourishment was complete.

Rapid equilibration due to high-energy events is also supported by cross-shore profile adjustment during the winter season following the repair nourishment. When the repair nourishment was complete on October 28, 2004, the measured γ_m for the renourished profiles increased to 0.064 in the northern segment and 0.055 in the central segment (Table 2, Fig. 7). Within six weeks, γ_m decreased to 0.034 in the northern segment and 0.031 in the central segment, once again approaching the equilibrium slope. Several energetic cold fronts, capable of generating waves exceeding 1.2 m, impacted the study area during this time. Rapid slope reduction following the repair nourishment was apparently a result of these cold front events. This suggests that the event-driven equilibration that occurred following the initial nourishment was not simply an anomalous result influenced by the passage of three strong hurricanes. Event-driven profile equilibration also occurred during the winter.

This study documented rapid beach profile equilibration as a result of high-energy events following nourishment on two separate occasions. This result differs from the general understanding, which suggests that profile equilibration continues for several years after nourishment (Dean and Campbell 1999; Browder and Dean 2000; Dean 2002). The present study suggests that profile equilibration can be an event-driven process rather than a process that occurs gradually as the project evolves. The rate of equilibration may be a function of energy rather than time.

In addition, storm conditions may be required for profile equilibration to occur on a nourished beach, particularly in the offshore portion of the profile. Transport to the depth of closure is initiated during energetic conditions (e.g., Hallermeier 1981). For sediment redistribution from a steep post-construction slope to a gentler slope that is relatively constant from the shoreline to the depth of closure, high-energy conditions are necessary. In the case of Upham Beach, transport to a depth of 2.5 to 3 m was induced during the passage of Hurricanes Frances and Jeanne during the month following nourishment.

The duration between the completion of nourishment and the first high-energy event to impact the project area is likely an important factor governing the time scale of profile equilibration. The exponential decay model of Fig. 1A may not apply. This suggests that profile equilibration time is unpredictable. Rapid initial profile evolution toward dynamic equilibrium was also measured in both medium- and large-scale laboratory experiments (Wang et al., 2003; Wang and Kraus, 2005). Profile equilibration should be considered complete once the slope is reduced to near the equilibrium slope. Profile equilibration should demonstrate a clear trend of profile-shape changes (e.g., decreasing beach slope) and should not be confused with dynamic variations in profile shape without a distinctive trend.

CONCLUSION

A wide nourished planform, large gradients in longshore transport, and the impact of severe storms following nourishment were all complicating factors in analyzing profile and planform adjustment with the data presented in this study. However, it is clear that planform adjustment began immediately after nourishment and that the relatively high-energy wave events following both the initial and repair nourishments resulted in profile equilibration. Both profile and planform adjustment can occur rapidly given the appropriate site conditions and energy levels. Substantial planform diffusion occurred prior to construction completion via formation of a spit extending from the widest portion of the fill. Longshore spreading was initiated abruptly, as opposed to gradual adjustment predicted by long-term models.

Based on individual profile-shape analysis and calculated beach slopes, the steep post-nourishment slope equilibrated nearly to the equilibrium slope within weeks of construction. This equilibration was largely dominated by one high-energy event, Hurricane Frances. Subsequent storms completed the equilibration process. Profile equilibration may be an event-driven process rather than a process that occurs gradually as the project evolves. The duration between nourishment and the passage of the first high-energy event appears to be an important, yet unpredictable, factor controlling the time scale of profile equilibration.

ACKNOWLEDGEMENTS

We would like to thank the Pinellas County Board of County Commissioners for funding and encouraging this research. We would like to thank our surveyors, Dave Tidwell, Craig Tolliver, and Andy McManus, who performed the weekly field work.

REFERENCES

Browder, A.E. and Dean, R.G. (2000). "Monitoring and comparison to predictive models of the Perdido Key beach nourishment project, Florida, USA," *Coastal Engineering*, 39 (2-4), 173-191.

Brunn, P. (1954). "Coast erosion and the development of beach profiles," Technical Memo No. 44, U.S. Army Corps of Engineers Beach Erosion Control Board.

Coastal Planning and Engineering (1992). "*Blind Pass Inlet Management Plan*," Boca Raton, FL: Coastal Planning and Engineering, Inc., 69 p.

Davis, R.A., Jr. (1989). "Management of drumstick barrier islands," *Proceedings of the 6th Symposium on Coastal and Ocean Mgmt.*, Charleston, SC, ASCE, 16p.

Davis, R. A., Jr. (1994). "Barriers of the Florida Gulf Peninsula," In: Davis, R. A., Jr. (ed), *Geology of Holocene Barrier Island Systems*, Springer-Verlag, 167-206.

Dean, R. G. (1983). "Principles of beach nourishment," In: Komar, P.D. (ed), *CRC Handbook of Coastal Processes*, Boca Raton: CRC Press, pp. 217-232.

Dean, R.G. (1987). "Coastal sediment processes: Toward engineering solutions," *Proceedings Coastal Sediments*: ASCE, 1-24.

Dean, R. G. (1991). "Equilibrium beach profiles: characteristics and applications," *Journal of Coastal Research*, 7(1), 53-84.

Dean, R. G. (1996). "Beach nourishment performance: planform considerations," *Shore and Beach*, 64, 36-39.

Dean, R.G. (2002). "Beach Nourishment, Theory and Practice," *Advanced Series on Ocean Engineering - Volume 18*. Singapore: World Scientific, 399 p.

Dean, R.G. and Campbell, T.J. (1999). "Recommended beach nourishment guidelines for the state of Florida and unresolved and related issues," FDEP Workshop on Beach Nourishment. Gainesville, FL, 10 p.

Elko, N.A., (2005). "Management of a Beach Nourishment Project during the 2004 Hurricane Season," *Shore and Beach*, 73(2&3), 49-54.

Elko, N.A., Holman, R.A., and Gelfenbaum, G. (2005). "Quantifying the rapid evolution of a nourishment project with video imagery," *Journal of Coastal Research*, 21(4), 633-645.

Elko, N.A. and Wang P. (2007). "Immediate profile and planform evolution of a beach nourishment project with hurricane influences," *Coastal Engineering*, 54(1), 49-66.

Hallermeier, R.J. (1981). "A profile zonation for seasonal sand beaches from wave climate," *Coastal Engineering*, 4(3), 253-277.

Hanson, H., and Kraus, N. C. (1989). "GENESIS: Generalized model for simulating shoreline change, Report 1: Technical reference," Tech. Rep. CERC-89-19, U.S. Army Engineer Waterways Experiment Station, Coastal Engineering. Research Center, Vicksburg, MS.

Moore, B. (1982). "Beach profile evolution in response to changes in water level and wave height," M.S. Thesis, Dept. of Civil Engineering, University of Delaware.

NOAA (2004). "*Tides Online*," National Oceanic and Atmospheric Administration, National Ocean Service (NOS). http://tidesonline.nos.noaa.gov/.

Pelnard-Considére, R. (1956). "Essai de théorie de l'évolution des formes de rivage en plages de sables et de galets," *4ème Journées de l'Hydraulique, les Engergies de la mer*, Question III, rapport 1, Société Hydrotechnique de France, 289-298.

Tanner, W.F. (1960). "Florida coastal classification," *Trans Gulf Coast Assoc. Geol. Society*, 10, 259-266.

U.S. Army Corps of Engineers (1999). "Pinellas County, Florida, Beach Erosion Control Project, Design Memorandum, Long Key (Upham Beach Park) Segment," Jacksonville, Florida: U.S. Army Corps of Engineers Publication, 52 p.

Wang, P., and Davis, R.A., Jr. (1999). "Depth of closure and the equilibrium beach profile: A case study from Sand Key, west-central Florida," *Shore and Beach*, 67(2), 33-42.

Wang, P., Ebersole, B.A., and Smith, E.R. (2003). "Beach profile evolution under plunging and spilling breakers," *Journal of Waterway, Port, Coastal and Ocean Engineering*, ASCE, 129(1), 41-46.

Wang, P. and Kraus, N.C. (2005). "Beach profile equilibrium and patterns of wave decay and energy dissipation across the surf zone elucidated in a large-scale laboratory experiment," *Journal of Coastal Research*, 21, 522-534.

SHORELINE RESPONSE TO DIKE FAILURE AT GRAND MARAIS HARBOR, LAKE SUPERIOR, MICHIGAN

Rachel R. Roblin[1], Mohammad Dibajnia[2], Robert B. Nairn[3], James P. Selegean[4]

1. Baird & Associates, 627 Lyons Lane, Suite 200, Oakville, Ontario, L6J 5Z7, Canada. rroblin@baird.com.
2. Baird & Associates, 627 Lyons Lane, Suite 200, Oakville, Ontario, L6J 5Z7, Canada. mdibajnia@baird.com.
3. Baird & Associates, 627 Lyons Lane, Suite 200, Oakville, Ontario, L6J 5Z7, Canada. rnairn@baird.com.
4. U.S. Army Corps of Engineers, 477 Michigan Avenue, Detroit, MI 48226, USA. James.P.Selegean@lre02.usace.army.mil.

Abstract: This paper summarizes the main findings from the investigations that were conducted, including GIS comparison of historic air photos, an 18-year wave hindcast, longshore sediment transport calculations, and extensive 2DH numerical modeling of hydrodynamics and sediment transport at Grand Marais Harbor. A sediment budget is presented based on geomorphic assessment and numerical modeling results. Future shoreline positions are also predicted.

INTRODUCTION

Grand Marais Harbor is located along the southern shore of Lake Superior, approximately 115 km east of Marquette, MI. The harbor was initially formed by three structures, consisting of two jetties and a pile dike breakwater, all of which were built in the late 1800s (see Figure 1). The jetties fix the opening to the harbor and the pile dike provided sheltered water for vessels in addition to retaining the prevailing west to east longshore sediment transport from the Grand Sable Dunes. The pile dike breakwater was placed approximately 85 degrees clockwise from centerline of the east jetty. It extended from the existing east jetty for approximately 1,740 m. The construction was of timber batter and soldier piles filled with stone. Since 1943, the breakwater has received no maintenance and has deteriorated to the point where little, if any, portion of the structure remains. The last remaining portions of the structure were destroyed in the mid-1970s during the same storm in which the ship known as the Edmund Fitzgerald sank in Lake

Superior. Consequently, Grand Marais Harbor has experienced substantial infilling and the available space with sufficient depth suitable for recreational and commercial vessels has significantly reduced. A breakwater oriented at an angle of 55 degrees to the shore has been proposed to prevent further migration of sediments into the West Bay.

In the present study, several investigations, including GIS comparison of historic air photos, 18-year wave hindcast, longshore sediment transport calculations, and extensive 2DH numerical modeling of hydrodynamics and sediment transport around the harbor were conducted. The analysis was aimed at establishing a sediment budget, evaluation of the morphodynamics at the area since the demise of the pile dike structure, and prediction of future morphology for different scenarios including a "do nothing" approach and structural alternatives.



Fig. 1. Grand Marais Harbor area

SITE DESCRIPTION

A general introduction to the Grand Marais Harbor area is given in Figure 1. Superior Beach is a fillet beach west of the harbor and consists of sand, pebbles and cobbles near the shore with a backbeach area consisting of embryo dunes and more mature dunes further inshore, both with vegetation (beach grass). The west end of this beach is covered by lots of pebbles and cobbles backed by vegetated low dunes. Town Beach is a sandy beach spanning the west end of the bay and backed by vegetation and beach grass. There are no pebbles or cobbles visible on this beach indicating that this is a deposition zone at the west end of the bay where only sand particles can reach.

The north shoreline of the West Bay area features vegetation right up to the water's edge owing to the sheltering from waves. Along the southwest shore of West Bay the shoreline is accreting in both lakeward and westward directions and the mouth of Carpenter Creek is shifting towards the west. Large waves due to NE storms reach this point from time to time and a beach scarp is visible.

Lonesome Beach is located between Lonesome Point bluffs (on the east of East Bay) and the Sucker River mouth. The east end of this beach is mature and features a relatively high beach berm, cobbles, beach grass, shrubs and driftwood. The central part of this beach features lots of pebbles and cobbles with little vegetation. This is currently the most visited nesting area for Piping Plovers in Grand Marais. As the west part of Lonesome Beach grows in the form of a low spit, the distal end of this split forces the migration of the Sucker River mouth toward the west. The west end of Lonesome Beach is sandy and low with no pebbles or cobbles and gets overwashed during storms.

South Beach is located between the Sucker River mouth and the Carpenter Creek area. It is mostly sandy and backed by rather high dunes with beach grass, all indications of a dynamic accretional environment with landward wind-blown transport. The Sucker River is cutting through the east end of this beach as it migrates westward.

GEOMORPHIC ASSESSMENT

Shoreline Comparison

A series of historic aerial photographs from 1939, 1953, 1974, 1983, 1992, 1993 and 1999, a USGS DRG map of 1967 and a satellite image of 2004 were used for GIS analysis and shoreline comparisons (see Figure 2). The timber pile breakwater failed sometime between 1939 and 1953, explaining the erosion of the barrier beach into small remnant islands by 1953. Comparison of the 1939 and 1953 shorelines indicates that the Superior Beach had reached its capacity by 1939, allowing any incoming sediment to bypass the harbor (and fill the channel or reach the downdrift shores). Extension of the west jetty in the 1960's resulted in further trapping of sediment by the new jetty and the subsequent growth of the Superior Beach to its present size. Comparison of the 1953 and 1999 shorelines indicates an infilling rate of 40,000 to 50,000 m^3/year. Comparison of the 1999 and 2004 shorelines indicates little change in the size of this beach and therefore, the Superior Beach has almost reached its capacity again. Sediment currently bypasses the jetties to the downdrift shores. Both the 1999 air photo and the 2004 satellite image show a bypassing path connecting the west jetty tip to the shoreline in the west vicinity of the Lonesome Point.

The monthly mean water level in Lake Superior at the time of the 1939, 1953, 1971, 1974, 1983, 1992 and 1993 photos were at comparable levels but were low (183.2 m) for the 1999 and 2004 photos. Therefore, the 1999 and 2004 shorelines are in slightly lakeward positions relative to other historic shorelines. Sand accumulation near the west

jetty between 1999 and 2004 is partly because of lower water levels in this period and shoreline developments at this area likely have slowed down.

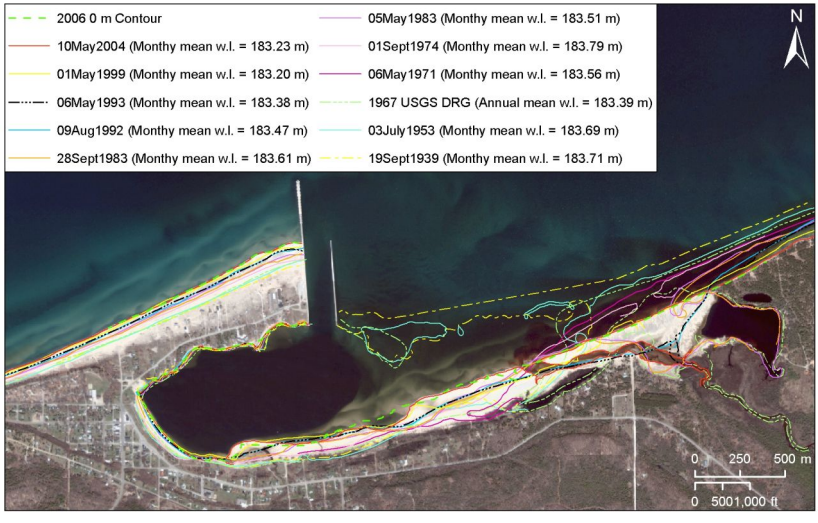

Fig. 2. Grand Marais area shoreline change between 1939 and 2006

On the east side of the harbor, the demise of the pile dike resulted in redistribution of the beach sediment, which it used to hold, towards inside the West Bay. GIS analysis of the visible edge of the underwater sand from the aerial photographs and satellite image shows how this redistribution has occurred. The lines are shown in Figure 3 and represent the changing position of the steep slope defining the boundary between deep (12 to15 m) and shallow (2 to 4 m) water that is no longer safely navigable. Beach sediments have in general moved towards the south to fill the old harbor basin. By 1999 the eastern half of the harbor basin was completely filled in.

With the ongoing infilling of the basin, more and more sediment could reach the south shores of the bay and from there alongshore to the west. Gull Island was also submerged into the basin while moving to the south and its existence closer to the shoreline caused the creation of a salient by 1999. Disappearance of this island and other remnants of the pile breakwater left the inner harbor more exposed to N and NE wave attacks. With burial of the east harbor basin, sediment is now encroaching to the west to fill the remaining part of the basin, the navigation channel of the harbor and southwest shores of the West Bay.

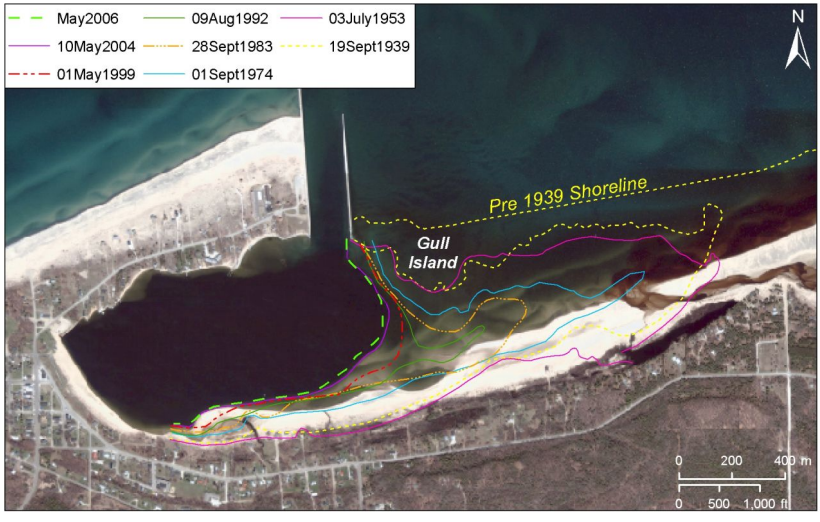

Fig. 3. Harbor basin change between 1939 and 2006

Comparison of the vegetation lines to the east of Sucker River and the East Bay indicates ongoing erosion of the bluffs in this area. The average bluff erosion rate in the area immediately east of Lonesome point was 3.6 m/year between 1939 and 1953, 2.6 m/year between 1953 and 1983 and 3.7 m/year between 1983 and 2004. Assuming that the bluffs are 100% made of sand and gravel, desktop calculations indicate that the bluffs over a 3 to 4 km reach east of Lonesome point could roughly provide up to 110,000 m^3/year of sand and gravel to the littoral system. Waves from north and northeast directions then transport part of this volume towards the west where it is trapped in the Grand Marais Bay area.

Figure 4 shows the geomorphic response of the Lonesome Point - Sucker River mouth zone. The river mouth was located at its most westerly location from 1939 (at that time emptying in the protected East Bay inshore of the timber pile breakwater) through 1953 and later from 1967 to 1971. In 1967 a small spit had extended across the mouth towards the east as a result of local eastward sand transport. Through a combination of the blockage of the mouth, erosion of the narrow barrier between East Bay and the lake, and the high lake levels of 1973, the river mouth switched its position back towards the east, as seen in the 1974 river mouth position. The 1974 condition consisted of a flooded estuary area inshore of an outer barrier beach and encompassing East Bay. Extension of the west jetty in the 1960's prevented the bypassing of sand to downdrift shores. In the meantime, lowering of the water levels resulted in less erosion of the bluffs to the east, such that between 1974 and 1983 the river mouth became wide open and the East Bay was connected to the lake. Since 1983 the inner East Bay area began to fill with sand (likely because of higher lake levels in the mid to late 1980's which caused more bluff

erosion), separating the bay from the lake and a wide river mouth was developed, as seen with the 1992 and 1993 shoreline positions. Since 1993, with the decline in water levels and the resumed sand bypassing, the wide river mouth area filled with sediment and a straight shoreline was created by 1999. Once the shoreline had been rendered relatively straight, the river mouth began to migrate towards the west at a rate of approximately 120 m/year between 1999 and 2004 and 60 m/year between 2004 and 2006. It is expected that the migration rate will slow with time, as the river approaches its full possible extension to the west.

Across the west end of the West Bay sediment has been accreting lakeward to create the Town Beach. Around the southwest corner of West Bay the shoreline has been accreting in both lakeward and westward directions. This process has recently shifted the mouth of Carpenter Creek toward the west. This depositional zone is likely a result of the longshore transport of sand along the south shores of the bay. The irregular outline of this shore is likely a result of temporally and spatially discrete pulses of sand arriving at the shore.

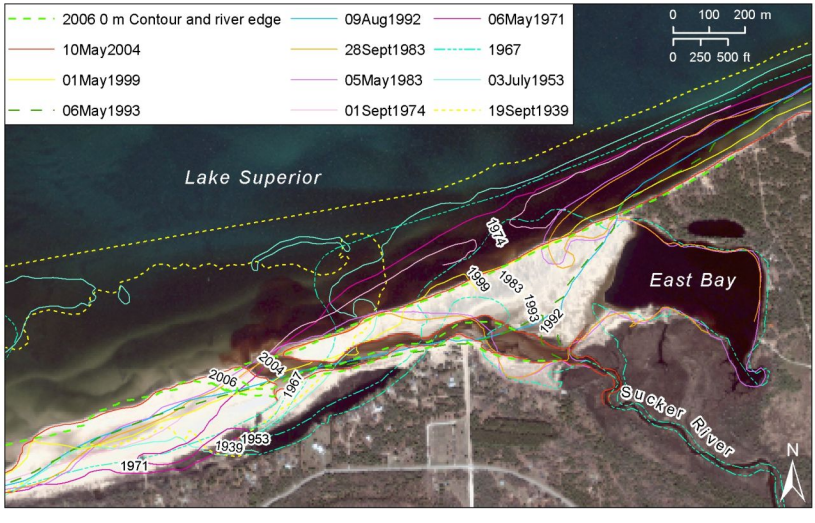

Fig. 4. Shoreline response at Lonesome Beach between 1939 and 2006

Bathymetry Comparison

A comprehensive hydrographic survey of the area was conducted in May 2006. This survey was compared to a number of previous surveys. Figure 5 shows the change in bottom elevation between 1967 and 2006. The 1967 contours were digitized from the 1967 USGS DRG map. It is observed that the old pile dike beach sediment has moved and deposited towards the south and west. Volume calculations within the comparison area (shown by the dashed line) indicate 1,900,000 m^3 of accretion of sediment in the old

harbor basin. This corresponds to an infilling rate of 48,000 m^3/year over the past 39-year period. A dash line dividing the comparison area into two sections on both sides of the proposed 55 degree breakwater is also shown in Figure 5. Accumulation rates to the east and west of this line are 21,000 and 27,000 m^3/year respectively. The bypassing shoal and some accumulation on the east side of the east jetty are also observed

.

Figure 6 shows the surface comparison results between 2003 and 2006 surveys. In this figure the survey data points are also shown as an indication of accuracy. The movement of sand along the bypassing shoal as a series of sand pulses is well captured in this figure. Total accumulation volume in the dash line comparison area is 354,000 m^3 over the 3 years. Accumulation rates to the east and west of the proposed breakwater line are 19,000 and 89,000 m^3/year, respectively. Comparison of the 2006 survey with a limited survey of the inner harbor basin conducted in 2002 by the Corps shows an accumulation rate of 48,000 m^3/year over the past 4 years in the inner harbor basin west of the proposed breakwater line. In either case, it is clear that the sediment infilling volume into the West Bay has increased significantly in recent years. This may be attributed to complete infilling of the eastern half of the harbor basin, disappearance of remnants of Gull/Lost Island, which has made the inner West Bay more exposed to the action of waves (in particular N and NE waves), and resumption of full sand bypassing around the harbor jetties to the downdrift east shores, making more sand available for transport. With the recent rates of accumulation, the whole West Bay will likely be filled in with sediment in less than 100 years and probably as soon as 50 to 60 years from now.

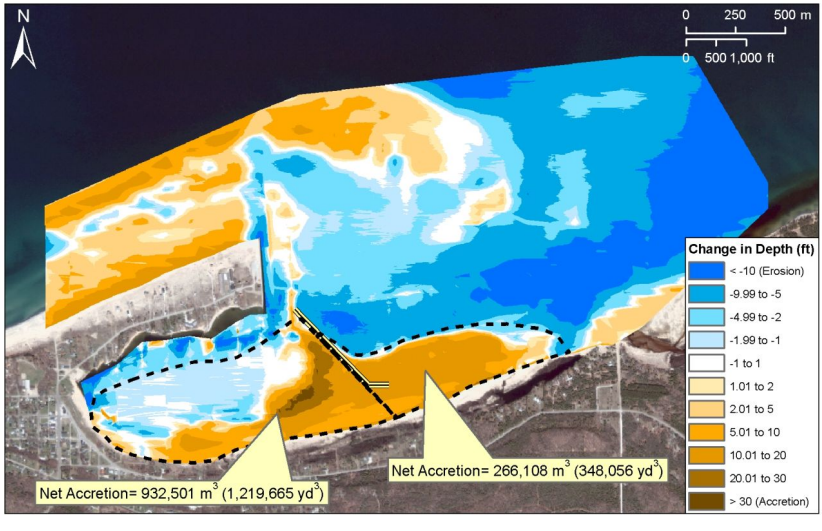

Fig. 5. Bathymetry comparison and volume calculations (1967-2006)

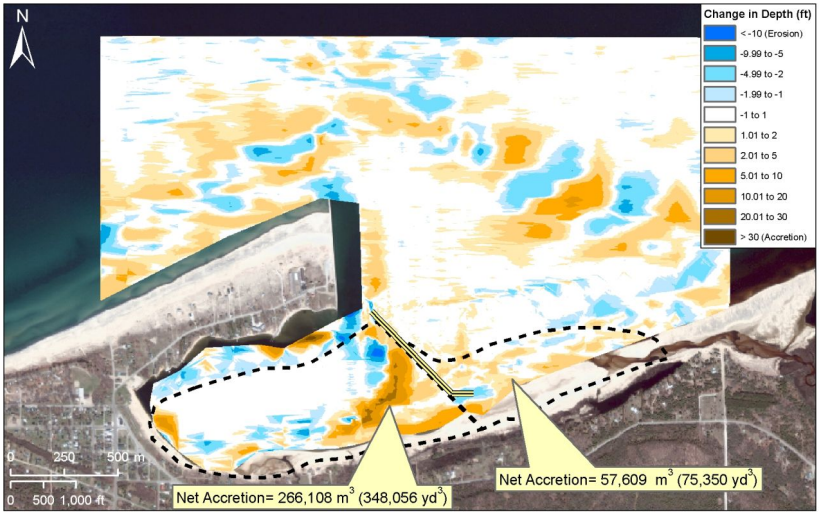

Fig. 6. Bathymetry comparison and volume calculations (2003-2006)

NUMERICAL MODELING

Offshore Waves

An 18-year (1984 to 2002) hindcast offshore wave climate at Grand Marais was generated in the using a 1D parametric model. The offshore wave rose is shown in Figure 7. The wave climate at Grand Marais is multidirectional with waves arriving from east to north and to west. N, NW and W waves, however, are predominant (53% of the time). The lake is calm (no waves) for 31% of the time. Wave heights greater than 3 m occur 2.1% of the time and have periods of 8 to 12 s. They mostly but not always come from the N to W quadrant. Wave height is less than 1 m and 2 m for 72% and 92% of the time (including calm periods), respectively. Ice conditions happen in January to March but are not considered in the present analysis because of uncertainties in climate change in upcoming years.

HYDROSED Modeling

Numerical modeling using *HYDROSED* was undertaken to transform offshore waves and calculate waves and their corresponding nearshore currents and sediment transport that occur in the harbor area. *HYDROSED* is a 2DH hydrodynamic and sediment transport state of the art model for coastal areas. It consists of a spectral wave transformation model (where the wave field is calculated by the spectral energy conservation equation of Karlsson 1969, with the breaking dissipation term of Isobe, 1987), a hydrodynamic model (Nishimura, 1988) to describe wave generated nearshore currents and circulations (driven by radiation stresses predicted with the spectral wave transformation model) and a sediment transport model presented by Dibajnia et al (2001). The sediment transport

model considers the influence of non-linear orbital velocities and undertow and is based on the sheet flow transport formula of Dibajnia and Watanabe (1992), which was extended by Dibajnia (1995) to consider suspended transport over ripples as well as the bedload transport. Dibajnia et al (2001) also conducted a sensitivity test of their model and showed that the model response under various actual nearshore wave environments is satisfactory. For a given wave condition, *HYDROSED* provides a full spatial description of nearshore currents in and around the harbor.

The nearshore wave transformation mesh had 477×675 grids (cross-shore × alongshore) with a constant grid spacing of 40 m in both directions. The depth at the offshore boundary of the calculation domain was approximately 150 m. The calculation domain for the harbor area, which used the 2006 bathymetry at a 0.2 m water level, featured a 662×692 mesh (cross-shore × alongshore) with grid size of 5 m. The depth at the offshore boundary of the inner calculation domain was approximately 16 m.

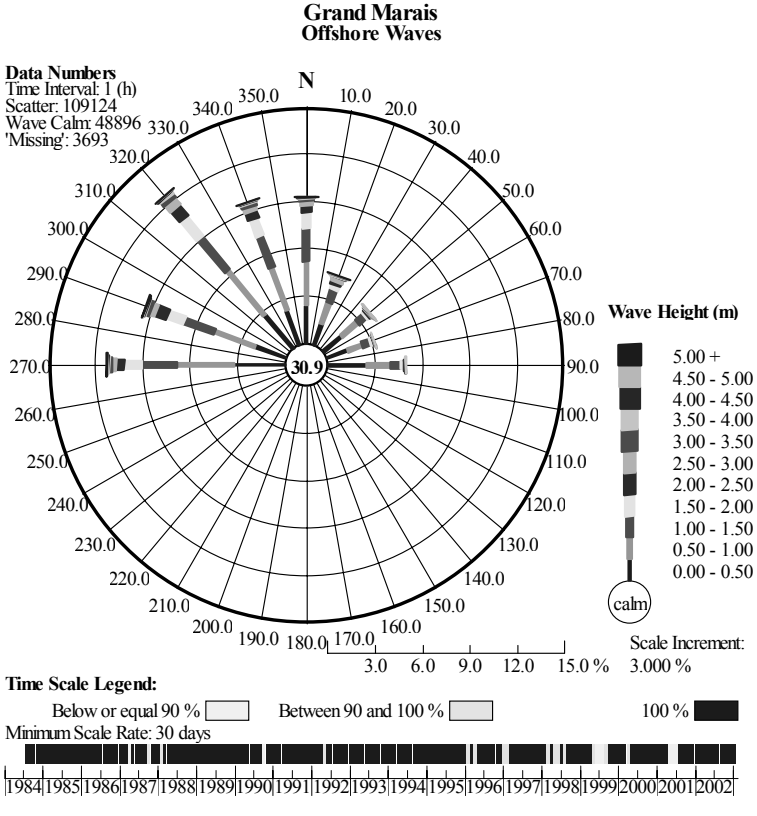

Fig. 7. Grand Marais Offshore Wave Rose

Existing Conditions

The model was run for 143 wave conditions with the existing bathymetry and harbor conditions. The selected wave conditions were representative of the predominant and extreme events of the 18-year hindcast dataset. Figure 8 shows sample results for nearshore currents under 3 m, 8 s waves from the NW direction. (a typical large wave condition at this site). The longshore current from this wave condition flows along the Superior Beach, bypasses the jetties and continues over the bypassing shoal towards the Sucker River mouth where it divides into separate eastward and westward components. A clockwise circulation is also created around the east jetty causing a northward outgoing current through the navigation channel. Although this current is not a very strong current, it is sufficient to counteract the movement of sediment by nonlinear wave orbital motions into the navigation channel. Under large NE waves, the westward longshore current partly bypasses the jetties, but mostly flows into the West Bay south shores as well as the harbor basin and again northward into the navigation channel. Therefore, under most large wave conditions there is a northward outgoing current through the navigation channel, which is likely helping to keep the channel clean and free of sediments.

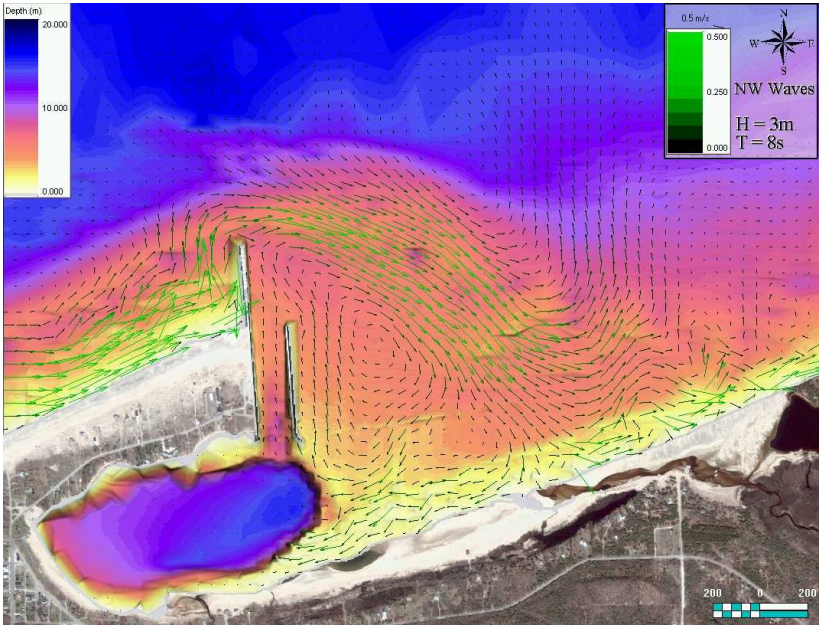

Fig. 8. Nearshore currents under 3 m, 8 s NW waves (existing conditions)

Model results for 143 representative wave conditions were tabulated as lookup tables for a simple numerical interpolation program that stepped through the 18-year time series of

hourly wave data to determine the long-term average sediment transport rate across several cross- sections in the calculation domain. The results are summarized in Figure 9. In summary, *HYDROSED* predicts a net eastward transport of 50,000 m^3/year that fully bypasses the jetties and reaches the downdrift shorelines. The bypassed sediment reaches the downdrift shores through the bypassing shoal (30,000 m^3/year) and over the shallow shelf between the bypassing shoal and the east jetty (20,000 m^3/year). The predicted eastward and westward components of transport are 70,000 and 20,000 m^3/year, respectively. The 20,000 m^3/year westward transport at Lonesome Point is also trapped in the study area. As a result, 70,000 m^3/year is available for accumulation in the harbor basin and on its south shores. The predicted transport rate into the West Bay area is 50,000 m^3/year and is in fair agreement with the estimated volumes through bathymetry comparisons. The remaining 20,000 m^3/year is accumulated in the South Beach area. Note that values in Figure 9 are long-term average figures and maybe different in individual years depending on wave conditions in each year.

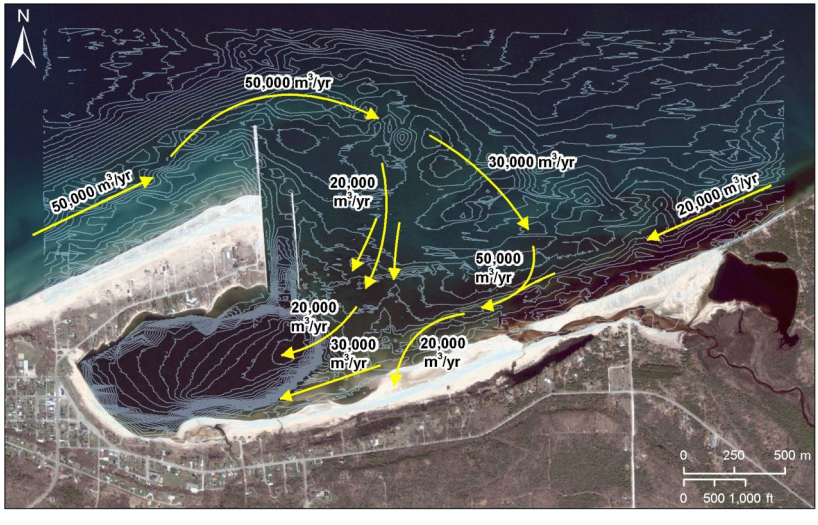

Fig. 9. Sediment budget predicted by *HYDROSED* for the existing conditions

55 degree Breakwater

Figure 10 shows the nearshore current results for 3 m, 8 s waves from the NW direction for the proposed 55 deg breakwater. The westward longshore current, west of the Sucker River mouth, is effectively blocked by the 55 degree breakwater. The clockwise circulation near the east jetty does not go through the navigation channel. Large NE waves and the resulting westward longshore current are partly blocked by the breakwater and partly diverted northward towards the entrance channel where it joins a small circulation entering into the navigation channel. Long-term analysis of *HYDROSED* results predicts accumulation rate against the breakwater of about 60,000 to 70,000 m^3.

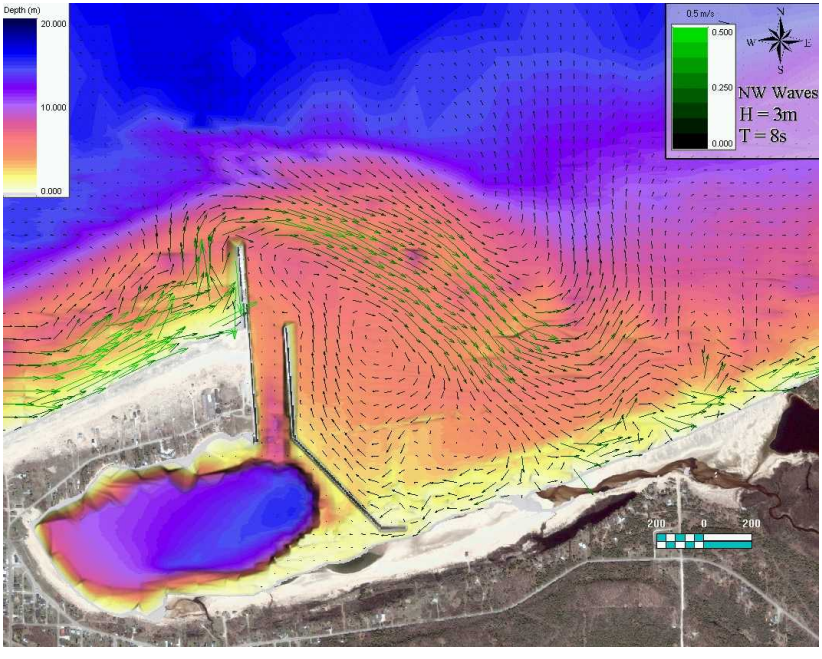

Fig. 10. Nearshore currents under 3 m, 8 s NW waves (55 degree breakwater)

CONCLUSIONS

Based on the numerical modeling results and the geomorphic analysis presented in the above sections, it is concluded that Figure 11 provides a reasonable sediment budget for the Grand Marais area. Based on our geomorphic assessment and numerical analysis, therefore, a net eastward transport of 40,000 to 60,000 m^3/year exists that fully bypasses the jetties and reaches the downdrift shorelines. There is also about 20,000 to 40,000 m^3/year supply from bluff erosion east of the Lonesome Point to the harbor area. As a result, 60,000 to 100,000 m^3/yr is available for accumulation in the harbor basin and on its south shores.

Projections of the future shorelines for the proposed alternative and the No Project condition were completed. An average accumulation rate of 80,000 m^3/yr was used in the calculations. Predictions of future shoreline conditions were made for 5, 10, 20 and 30 years out from the present. It is noted that these predictions are approximate and that the potential error of the prediction becomes larger as the duration of the prediction increases. The future water levels and frequency/intensity of storm events (both waves and river floods) have a significant influence on the Sucker River mouth location. Dramatic river switches (back to the east) are more likely to occur under high lake level and river flood conditions under all scenarios. After each switch, however, the river

mouth will start to migrate to the west once the water levels are back to normal or low levels.

Figures 11 and 12 show the predicted shorelines for the No Project condition and the 55 degree breakwater, respectively. With the No Project condition the historic trend of lakeward and westward advancement of the shoreline are projected to continue. Land-connected accumulation rates (for the beaches and basin) were 60,000 m^3/year and the remaining 20,000 m^3/year was considered to fill the deeper basin. Actual rates may be higher or lower than predictions, depending on the number and frequency of storm events that occur in the future. The West Bay basin will also continue to infill under the No Project condition.

With the 55 degree breakwater alternative (Figure 12) the main area of accumulation is offshore and to the east of the new breakwater structure. The volume of accumulation is greater than that of the No Project scenario because the basin is no longer infilled once the breakwater is constructed and this sediment is instead trapped next to the breakwater. With No Project and the 55 degree breakwater scenarios the bluff erosion to the east will continue resulting in erosion of the Lonesome Beach on the north side of the Sucker River. The 55 degree breakwater presents little or no restriction to the westward extent of migration compared to the No Project condition.



Fig. 11. Predicted future shorelines for the No Action scenario



Fig. 12. Predicted future shorelines for the proposed 55 degree breakwater

ACKNOWLEDGEMENTS

The authors would like to thank the USACE, Detroit District, for supporting this study.

REFERENCES

Dibajnia, M. (1995). "Sheet flow transport formula extended and applied to horizontal plane problems", *Coastal Engineering in Japan*, 38(2), 179-194.

Dibajnia, M., Moriya, T. and Watanabe, A. (2001). "A representative wave model for estimation of nearshore local transport rate", Coastal *Engineering Journal*, 43(1), 1-38.

Dibajnia, M. and Watanabe, A. (1992). "Sheet flow under nonlinear waves and currents", *Proceedings of 23rd International Conference on Coastal Engineering*, Venice, ASCE, 2015-2028.

Isobe, M. (1987). "A parabolic equation model for transformation of irregular waves due to refraction, diffraction and breaking", *Coastal Engineering in Japan*, 30(1), 33-47.

Karlsson, T., 1969. "Refraction of continuous ocean wave spectra", *Journal of Waterways and Harbors Division,* Proceedings of ASCE, 95(WW4), 437-448.

Nishimura, H., (1988). "Computation of nearshore currents", In: Horikawa, K. (Editor), Nearshore Dynamics and Coastal Processes, University of Tokyo Press, Tokyo, 271-291.

SUCCESSFUL BEACH MODELLING, MONITORING AND MANAGEMENT FOR A LARGE LNG FACILITY

Jonathan A. Kemp[1], Tom C. Coates[1], Richard Head[2], Jenny S. Harcourt[1]

1. HR Wallingford Ltd, Howbery Park, Wallingford, OX10 8BA, UK jak@hrwallingford.co.uk, jsh@hrwallingford.co.uk, ttc@hrwallingford.co.uk,
2. ELNG, Building No 2, Port Said Road, Cairo, Egypt richard.head@egyptianlng.com

Abstract: A temporary construction harbour was built for the Egyptian Liquified Natural Gas (ELNG) facility in Abu Qir Bay on Egypt's Mediterranean Sea coast, west of the Rosetta Nile. A shoreline impact assessment was undertaken during the planning process which involved modelling the existing beach processes as well as shoreline development during construction, operation, decommissioning and recovery. Based on this assessment and modelling, a schedule of shoreline management and monitoring was proposed to ensure that the temporary harbour did not have a negative impact on the shoreline over its three year life. ELNG followed the proposed programme under scrutiny from the Egyptian Shoreline Protection Agency (SPA) and successfully restored the beach to its pre-construction state. This paper discusses the ELNG project, beach modelling, monitoring and the management programme as a case study, and assesses the beach modelling against the unique field data set

INTRODUCTION

The Egyptian LNG facility, located within Abu Qir Bay on the Mediterranean Sea coast (Figure 1), receives natural gas from wells offshore of the Nile Delta (West Delta Deep) and exports liquefied natural gas (LNG. The liquefaction plant and the associated marine facilities for tanker export were built between 2002 and 2005. A construction dock was required for the off-loading of plant from shallow draft barges directly to the site. Given the exposed nature of the site, the dock was protected within a small dredged harbour formed of rock breakwaters at the shoreline, with a dredged navigation channel connecting to deeper water. Tanker facilities for LNG export were built further offshore to minimise the need for maintaining a dredged channel across the shallow nearshore zone and LNG was piped to the tankers using a 3km long trestle (Figure 1).

As it was recognised that the harbour could have a significant impact on coastal processes, it was planned to be a temporary structure. The impact was to be monitored and managed

throughout its life, with the intention of reinstating the shoreline to its natural form following removal. This approach was intended to satisfy the regulating authorities, but also ensured that the LNG facilities would not be at risk from erosion or flooding as a result of the disruption to beach evolution processes. A management plan based on desk studies and numerical modelling was agreed and then implemented and scrutinized by the Egyptian Shoreline Protection Agency (SPA) over the period from construction in the spring of 2003 to removal of the harbour in the autumn of 2005.

The intensive management period resulted in an extensive beach data set from the pre-existing natural beach through construction, operation, removal and reinstatement. These data provided an opportunity to assess model predictions against measured shoreline changes, and the success of the proposed management plan.

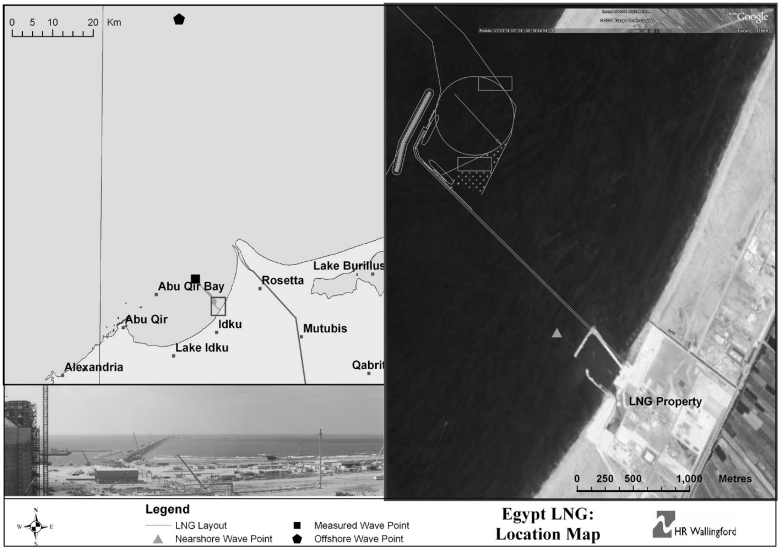

Fig. 1. Location Map

SITE DESCRIPTION

Abu Qir Bay is less than 20m deep and about 33km wide from the partially sheltered area in the lee of the reefs and islands off Ras Abu Qir in the west, to the rapidly eroding delta of the Rosetta Nile in the northeast. The shallow waters of Idku Lake lie just behind a barrier beach in the southern part of the Bay. The shore is exposed to dominant north-westerly waves, driving a strong easterly longshore drift along most of the Nile Delta coast (Fanos *et al*., 1995 and Frihy *et al*., 1991) but with a local south-westerly drift direction along the shore of Abu Qir Bay to the north of the ELNG plant location. The Bay has a small tidal range (typically ~0.2m), and the main driving forces for currents and sediment transport are wind and waves. Fresh water flows into the Bay via the Rosetta Nile and Idku Lake, although both sources are now low volume and considered to have little impact on coastal processes in relation to winds and waves.

Understanding of the coast and seabed evolution is based on information derived from historic maps and charts, satellite images, published research papers, unpublished reports, project specific field surveys and numerical modelling of sediment transport. In summary, the seabed and beaches are formed of fine sand and silt, subject to continuing change due to the dramatic reduction in sediment supply from the Rosetta Nile following construction of the Aswan dams, combined with the moderately high energy wave conditions typical of the Egyptian north coast. The net longshore shoreline drift is from northeast to southwest in the area of the ELNG plant, but is subject to short term reversals and a high level of annual variability. There is evidence, from sediment sampling, of offshore transport of silt and some fine sand to deeper water across the mouth of the Bay. At decadal timescales the shoreline is considered to be stable or slowly accreting in the area of the LNG facility, with a reasonable balance between sediment transport alongshore and losses offshore.

Previous beach and nearshore surveys carried out by CoRI (Coastal Research Institute, Egypt) over the 12 years prior to construction of the facility indicated that the natural shoreline and nearshore seabed levels were subject to substantial short term variability in response to seasonal conditions, up to ± 40m relative to a mean position, Fanos (2001).

It was anticipated that sand would accumulate to the north of the harbour, and that there would be areas of erosion to the south. An updrift accretion could potentially cause problems of infilling in the harbour and downdrift erosion could result in unacceptable loss of land to the LNG property or further along the coast. The nearshore bed was also expected to change both seasonally and over longer time periods, with some transport around the seaward face of the breakwaters, possibly causing infill of the dredged navigation channel.

SHORELINE IMPACT MODELLING

Potential impacts of the construction harbour on the shoreline were assessed using a suite of numerical models. Offshore wave conditions were defined and then transformed to create a time series of nearshore conditions as input to longshore drift predictions for the open coast and in the presence of the harbour breakwaters.

The wave climate offshore from the ELNG facility was evaluated by a combination of numerical modelling methods, with the offshore wave climate established using “Eurowaves”, which are model data based on the ECMWF (European Centre for Medium Range Weather Forecasts) hindcast model. At the time of this study seven years of sequential Eurowaves data (1992 – 1999) were available for the model point 30.5°E 32°N (Figure 1). The offshore wave predictions were calibrated against wave measurements made over a six-month period (November 2001 to April 2002) at the seaward end of the proposed approach channel (Figure 1).

Nearshore wave conditions over the seven year period were then modelled at a number of locations along the ELNG site on the 6m contour below Chart Datum (CD – approximately LAT at Alexandria). The time series of six-hourly predicted values of wave height, period and direction at a point just offshore from the northern harbour breakwater was used to model the likely changes to the shoreline.

The simplest measure of sand transport along a beach is the “potential mean annual transport rate”, denoted here as Q_{mean}. This single statistic allows an initial assessment of the scale and

pattern of any beach erosion / accretion following installation of coastal structures. It must be emphasised that Q_{mean} is:

- Subject to considerable uncertainty, because of the difficulties involved in calculation (i.e. it is extremely sensitive to the precise wave conditions and the beach orientation at any given point along the frontage;
- Averaged over a number of years and may be subject to substantial annual variability; and
- Dependent on the availability of suitable sediment to feed the drift.

The nearshore time series waves were transformed up to the breaking point of each condition. The values of wave height, period and direction at breaking were then used to derive the instantaneous longshore transport rate for sand for each six hour period using the CERC formula modified by Ozasa and Brampton (1980). The cumulative transport rates at the end of each month and year were defined. Finally, all the results were averaged over the seven years to produce the predicted mean annual nett transport rate, Q_{mean}. The best estimate prediction of Q_{mean} was approximately 480,000m^3/ year (south-westerly), as presented in Table 1, with a standard deviation of 196,000m^3/year. These figures give an indication of the potential variability in annual longshore drift, albeit from a small sample.

Table 1 provides a breakdown of the contributions to the drift rate produced by various categories of nearshore wave. Waves arriving from 310°N - 010°N produce a northeast to southwest drift (positive values), while waves arriving from 260°N - 300°N produce a southwest to northeast drift (negative values). The dominating effect of the waves between 1.5m to 2.5mH_s can be appreciated by considering the entries in the "Total" column, which show that these wave heights generate over 60% of the nett "positive" drift. The effect of the largest waves on drift direction is also important, indicating that very stormy periods are likely to be associated with drift reversals.

Table 1. Annual drift and % Wave height

Resultant wave height (m)	Direction sector (°N)									Total	% Wave Height
	275 - 285	285 - 295	295 - 305	305 - 315	315 - 325	325 - 335	335 - 345	345 - 355	355 - 005		
0.0 - 0.5	-263	-172	-23	1,193	1,259	978	1,946	2,324	511	7,751	15.91
0.6 - 1.0	-525	-5,131	-967	37,743	23,645	13,295	14,655	7,371	2,900	92,986	32.42
1.1 - 1.5	-426	-20,283	-7,036	57,570	18,058	15,893	22,844	12,007	615	99,244	22.23
1.6 -2.0	..	-28,789	-22,089	100,526	43,162	11,170	24,483	4,604	..	133,065	14.67
2.1 - 2.5	..	-29,176	-23,819	147,537	45,452	8,860	11,708	..	..	160,563	8.25
2.6 - 3.0	..	-26,248	-11,793	80,032	16,891	2,992	..	..	..	61,874	3.49
3.1 - 3.5	..	-19,550	-15,885	36,165	8,273	..	..	..	..	9,003	1.28
3.6 - 4.0	..	-7,883	-10,623	11,549	6,784	..	..	..	..	-173	0.55
4.0 +	..	-75,668	-86,721	71,009	7,612	..	..	..	..	-83,768	1.22
Total	-1,225	-212,901	-178,955	543,324	171,136	53,188	75,637	26,306	4,036	480,547	100

Table 1 also shows that about 60% of the mean annual drift rate is produced by waves with heights in excess of 1.5m. Such waves occur for less than 30% of the time (see Table 1), and hence it can be appreciated that a "calm" year, with fewer than average storms, will be likely to produce a very different drift rate to a "stormy" year with more storms.

Figure 2 shows the calculated variations in the nett longshore transport rate from month to month over the seven-year period. This indicates that transport is relatively constant in direction and rate during the summer months, at approximately 50,000m^3/month towards the southwest, but during the winter months the drifts can be much stronger, in one month alone the drift rate is equal to a years mean drift and in some cases there may be a reverse in drift direction. This had implications for the harbour entrance, since there was a danger that infill could occur by sand travelling from southeast to northwest.

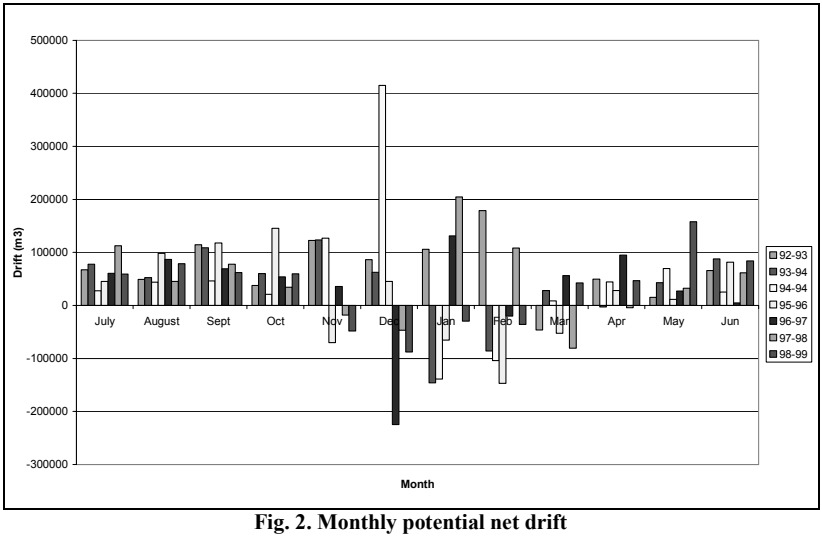

Fig. 2. Monthly potential net drift

The figure for Q_{mean} of 480,000m^3/ year at the north end of the harbour was considered to be a conservative prediction (i.e. overestimating) and the actual rate may be less due to the nearshore wave predictions not accounting for dissipation effects during storms from the shallow silty seabed. Furthermore the drift calculation is sensitive to the assumed beach orientation and sensitivity tests indicated that a change to the beach orientation of 1° gives a corresponding value of Q_{mean} altered by approximately 240,000m^3/ year. Therefore as the shoreline curves continuously, Q_{mean} will decrease significantly along the site towards the south, potentially even reversing immediately south of the LNG frontage. The sensitivity of drift predictions to small changes in wave direction is also similar. Since it is hardly possible to measure, let alone predict, nearshore wave directions to accuracies better than ±5°, then the uncertainty of the computed Q_{mean} value can be appreciated.

BEACH PLAN SHAPE EVOLUTION

Introduction

The changes in the plan shape of the beach around the temporary harbour were examined through the use of the HR Wallingford BEACHPLAN 1-line beach model, (HR Wallingford 2004 and Ozasa & Brampton 1980). This model uses the same wave conditions gathered at the LNG site as used in the drift calculations, in the form of a time series (from July 1992 to

June 1999). Ideally, when predicting shoreline evolution the model is calibrated against historical shoreline positions and detailed up to date beach and nearshore profiles are used to assess the active beach. A lack of suitable data for this study required the need for a conservative approach to predicting drift rates so that the potential for shoreline changes and subsequent mitigation measures would not be underestimated. Similarly, to be on the conservative side, no attempt was made at simulating the bypassing of sand around the seaward end of the harbour and although no nearshore survey data was available at this time it was assumed that the cross-shore extent of significant transported extended to at least the 5mCD contour. These and other model parameters were all chosen on a basis of experience and using a conservative approach in order to provide suitable guidance for the pattern and scale of beach changes and the subsequent mitigation requirements i.e. recycling.

The BEACHPLAN model was run for a number of different scenarios to provide initial assessment of the potential beach response to the proposed construction harbour. The model runs presented within this paper consider the following:

- Beach response to the harbour over 3 years, assuming no management measures.
- Beach recovery over 3 years following removal of the harbour.

Modelling runs: Natural response to the harbour

The model was first used to examine the potential changes in the shoreline following the construction of the harbour breakwaters. The model was run for three years to simulate the beach changes likely to develop over the life span of the harbour. Figure 3 shows the predicted beach plan-shape six months after the completion of the harbour. Substantial accretion of up to 150m is predicted, after 3 years, on the east side of the causeway, and a maximum of up to 100m of landward movement of the coastline to the west of the western breakwater. This figure also presents the predicted changes after 1, 2 and 3 years. The beach position after 1 year is very similar to the beach position after 6 months and it could be interpreted that the beach has not moved a great deal in this time period. However on examination of the results in more detail, on a monthly basis for example, it was predicted that the beach varies a great deal and as a result of storm activity, the drift rate is higher and more variable, often with periods of a reversal, as shown in Figure 2. The variations in the wave climate therefore resulted in a predicted beach position after 12 months similar to the one seen after 6 months. The longshore extent of predicted accretion and erosion was about 3km either side of the harbour. This is considered to be a qualitatively realistic though conservative scenario.

The model was not set up to indicate the potential volume of sand that may by-pass the breakwaters, which would largely be expected to be deposited within the dredged navigation channel leading to the dock, and would therefore result in more accretion on the updrift side. The results indicate that under conditions of “average annual” littoral drift substantial accretion was expected east of the temporary harbour with high rates of coastal erosion to the west.

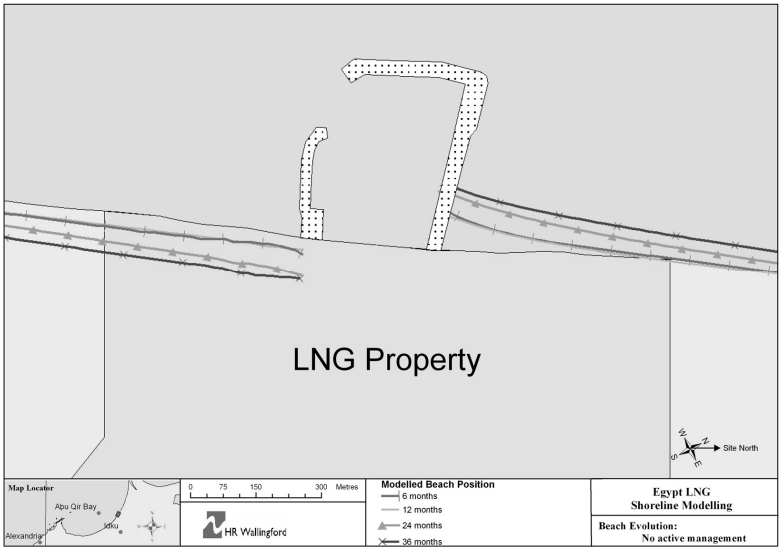

Fig. 3. Modelling of beach plan shape evolution

Modelling runs: Beach recovery

The model was also used to examine the changes in the shoreline after removal of the harbour. The initial situation was taken as the final shoreline position after three years with the harbour in place. The model demonstrated an initial rapid beach response followed by a gradual reorientation of the beach towards its original alignment over time. It is predicted that in less than three years from removal the beach would recover to its pre-construction state.

BEACH MANAGEMENT

A beach management plan was prepared for ELNG to minimise any impacts of the temporary harbour on the natural environment, as required by the Shoreline Protection Agency. The main aims and objectives of the management plan were to:

- Keep both the accumulation of beach material on the north-east side of the harbour and erosion south-west of the harbour to within agreed limits representing the envelope of beach variation under natural conditions;
- Minimise the rate of siltation of dredged areas in the harbour or its approach channel; and
- Return the shoreline to its pre-construction equilibrium state following removal of the harbour.

An envelope of acceptable shoreline movement was defined, based on the recorded movement of the shoreline over the previous decade, Fanos (2001) and the beach plan-shape modelling. The acceptable limits recognised that the beach would re-orient itself to a new position following the installation of the harbour and was considered not to be a problem as

the shoreline would rapidly return to its pre-construction position. Provided that the shoreline stayed within this envelope, no immediate management action was required. A further envelope of tolerable short-term erosion and accretion was defined allowing the contractor some leniency while undertaking bypassing operations. Variation outside this envelope was considered contractually unacceptable.

In order to maintain the beach within the agreed limits regular bypassing was proposed to move sand from areas of accumulation to areas of erosion. It was also proposed that any clean sand dredged from the navigation channel or the dock area would be deposited onshore for beach management purposes. A sand bypassing scheme using trucks was recommended as more efficient and flexible than any schemes involving pumps or dredging plant. It was anticipated that bypassing of up to 40,000m³ of sand might be required each month, but that this rate would vary in response to seasonal and storm conditions. The actual volumes of beach material moved are presented in Table 2.

A flexible management system was recommended because the beach and drift modelling highlighted that actual beach changes can occur very quickly (Figure 2) and are subject to the vagaries of the wave climate. It was not possible to determine the exact location of sand pick up and set down positions for sand bypassing and it was recommended that this would be determined by means of regular shoreline and nearshore monitoring.

A beach and nearshore survey programme was instigated to monitor the changes as a result of the temporary construction harbour and to facilitate in the management of the shoreline adjacent to the harbour.

The programme involved an assessment of the pre-construction shoreline and nearshore bathymetry, with frequent monitoring throughout the life of the facility. The survey programme comprised six-monthly bathymetric surveys out to about the 6mCD contour, two-monthly beach profile surveys accompanied by photographs and fortnightly waterline surveys. Furthermore volumes of any dredging and sand bypassing required to maintain the shoreline position were logged.

As shoreline data were recorded at frequent and regular intervals throughout the life of the harbour, an efficient data management and analysis system was set up. ArcMap GIS was used to store and analysis the data as it allowed efficient data management, a rapid analysis of shoreline changes and a cost effective method for monitoring contractor performance and compliance with SPA's requirements.

Table 2. Management Activities

Date	Activity	Volume Removed	Volume Added	comments
Feb-03	Construction of the temporary harbour begins			
Apr-03	Capital dredging begins	120,000m	10,700m	109,300 stored onsite
May-03	Temporary harbour complete			
Jun-03	Removal of sand from north beach	400m		Used to fill voids in breakwater
Aug-03	Maintenance dredging	38,200m	38,200m	
Nov-03	Sand Bypassing	22,000m	20,000m	
Jun-04	Maintenance dredging	15,200m	15,200m	
Apr to Oct-04	Sand Bypassing	44,750m	42,750m	
Jun-05	Removal of temporary harbour	Redistribution of sand		

ANALYSIS OF SURVEY DATA

Nearshore Surveys

The beach and nearshore surveys collected every six months, eight in total, illustrate clearly the response of the shoreline to the presence of the temporary construction harbour. Although these surveys only represent the situation on individual days they also show the patterns of accretion and erosion.

The February 2003 survey (Figure 4) was completed prior to any construction work. The contours are largely parallel, with a distinct nearshore channel/bar system typical of a "winter" beach condition. By the April 2003 survey (Figure 5) the harbour was part built, and was beginning to have an impact on the nearshore processes. The nearshore bar is still clearly present to the north of the breakwater, but to the south there is a channel, indicating a loss of about 2m elevation. There is also a deep scour hole (5m deeper than the surrounding seabed) near the end of the breakwater, which was thought to be caused by waves reflecting off the structure and possibly by longshore currents being turned offshore.

Over the summer of 2003 the bathymetry changed in a way that is often observed on sandy shorelines and by the October 2003 survey, the nearshore channel/bar system had flattened off, leaving a more even slope down from the beach typical of a "summer" profile i.e. the bars had migrated onshore. This indicated a continued loss of total sediment volume, despite the dumping of some 49,000m^3 of dredged sand onto the beach during the late summer 2003. There was also an accretion of sand to the north of the harbour, extending out to the contractual limit agreed with the SPA. As the harbour arm was extended for the completion of the harbour (Table 2), the scour hole migrated further offshore to form a stable but extensive feature off the northwest corner, Whitehouse (2005). This scour hole caused an instability of the trestle structure that runs alongside the temporary harbour and as a consequence a section of the northern arm of the harbour breakwater was realigned to a parallel orientation approximately 50m to the south, as shown in Figure 6.

By April 2004 the nearshore profile had again adopted a "summer" shape with a reduced nearshore bar, but there was still a clear build up to the north of the dock and a much steeper

profile to the south. The south beach was also affected by the presence of a 300m long rock revetment built along the backshore, although the survey plot does not show this. The effect of the revetment was to limit the landward migration of the waterline, but it did not slow the total loss of material from the beach and nearshore and downdrift erosion occurred beyond the site of the LNG. The rock revetment was removed during the summer of 2004.

Despite the management effort between April and October 2004 (Table 2), the October 2004 survey (Figure 6) clearly showed a continued build up of material to the north of the harbour. There was also a build up of sand around the outer edge of the breakwater indicating that natural bypassing processes were occurring, with likely infilling of the dredged channel. It is also evident that the south beach had a much steeper profile and there were no signs of the bar and channel system that existed pre-harbour construction, as shown in Figure 5. The April 2005 survey showed a similar pattern of sand movement with a continued build up of material to the north of the harbour.

During the period February 2005 to July 2005 the removal of the construction harbour took place. The final survey was undertaken in July 2005 and is presented in Figure 7. This Figure clearly shows that the shoreline had largely returned to its natural position except for the small residual promontory between profiles 10 and 11, and the remaining cut-back south of the ELNG site at profiles 21 – 23. The offshore contours still exhibit the effects of the harbour, with a substantial build up remaining in the area north of the harbour. The nearshore loss to the south, and particularly the loss of the nearshore bar feature, is a cause for concern, as the beach may no longer be able to respond to severe wave conditions in a natural and dynamic way.

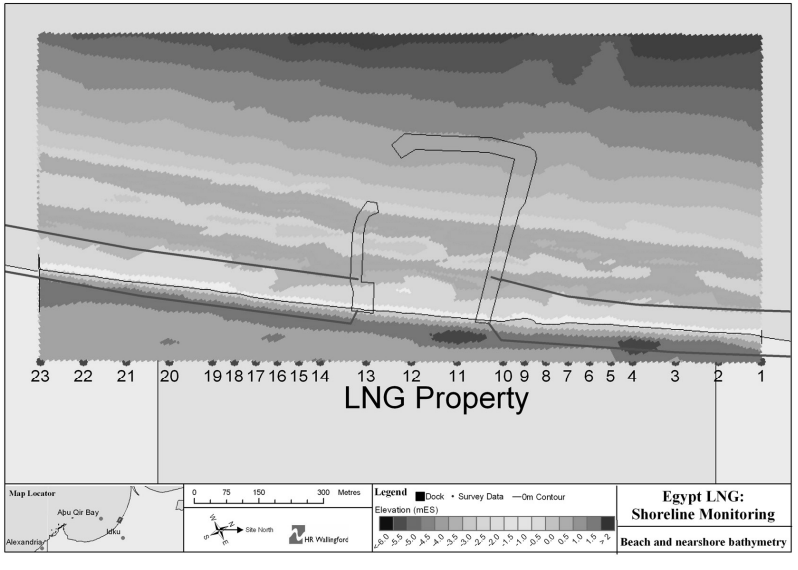

Fig. 4. Pre-construction beach/bathymetric contours: February 2003

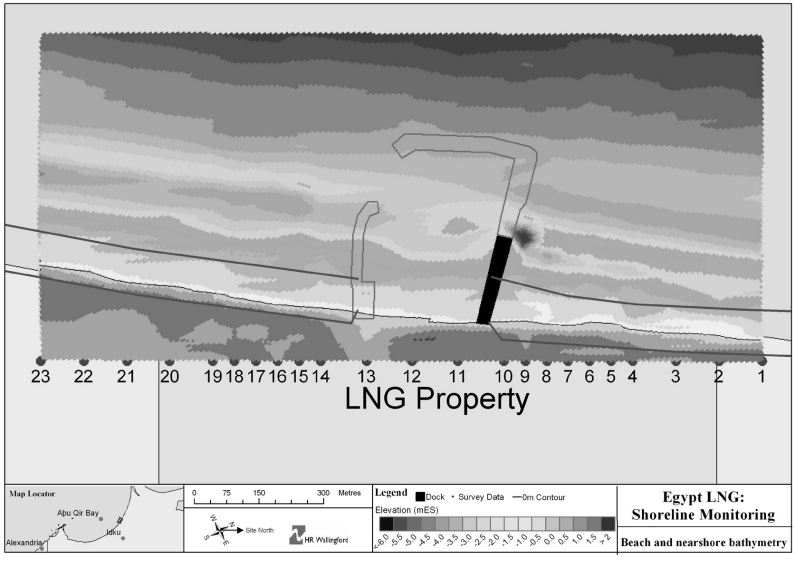

Fig. 5. Beach and bathymetric contours: April 2003

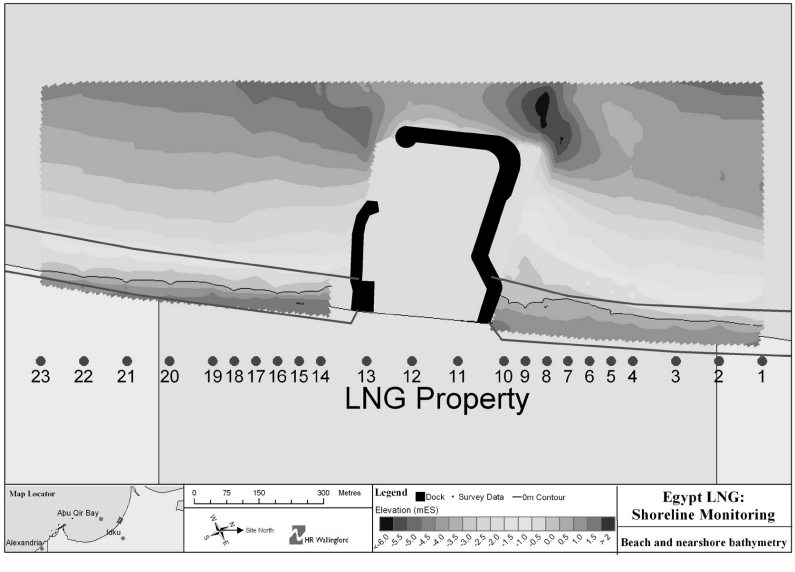

Fig. 6. Beach and bathymetric contours: October 2004 (Note new dock layout)

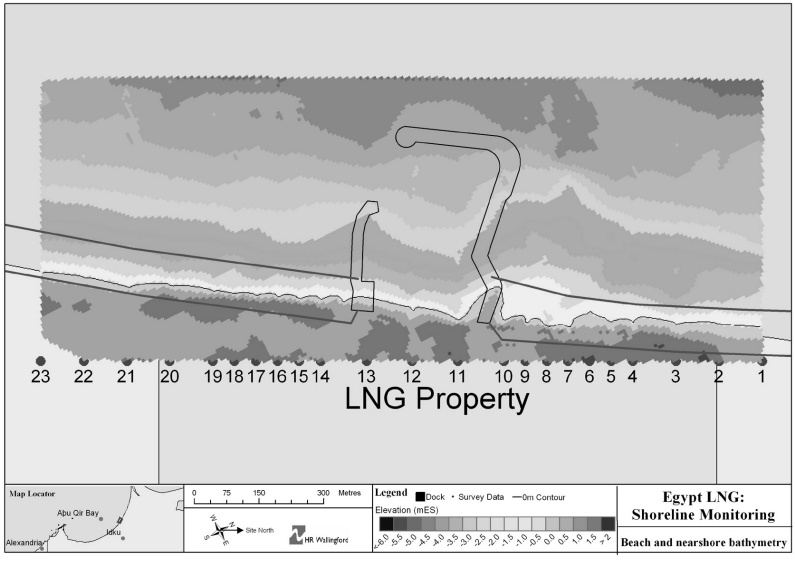

Fig. 7. Beach and bathymetric contours: July 2005 (note dock now removed)

Shoreline Position

The intended fortnightly waterline position surveys were actually completed at intervals from weeks to months. Measurements of the distance from a fixed baseline to the waterline were taken at intervals along the ELNG frontage to assess short term variability. The method used was simple and rapid and therefore allowed the contractor to respond to shoreline changes before the more detailed surveys and therefore keep the shoreline within the agreed limits of variation.

The peak rate of change in shoreline position was calculated and shows that the shoreline was accreting by 2.5m/wk at the north beach and was eroding by 1.3m/wk at the south beach during the first few weeks following construction and highlights the rapid response needed to effectively manage the shoreline.

MODEL PERFORMANCE

Prediction of accurate drift rates by numerical models is notoriously difficult, especially on open coastlines where there is little accurate historical data or even obstructions to the drift to provide evidence of the direction and intensity of the sediment transport rate. The monitoring programme at the ELNG has provided a unique dataset of measured beach evolution over the whole project (including removal of structures), therefore allowing an assessment of the performance of the numerical modelling undertaken as part of the initial shoreline impact predictions.

The use of GIS to store and plot both the modelled shoreline positions and the subsequent measured shoreline positions has allowed a direct comparison to be made between the two data sets, as shown in Figure 8. This figure clearly demonstrates that the modelled shoreline

position after 6 and 12 months closely match the corresponding measured shoreline position (August 2003 and February 2004) to the north of the harbour. The maximum amount of accretion against the north harbour arm after 6 months was predicted by the modelling to be 78m and when this is compared with the 83m accretion measured by the August 2003 survey, it is clear the model was accurately predicting the shoreline evolution. The predicted figure also compares well against the shoreline position measurements over the same time period. Looking further ahead in time, 24 and 36 months, the predicted shorelines do not match the measured. This is understandable as the shoreline was required to be maintained within agreed limits of movement and beach bypassing was undertaken in a responsive manner beginning in November 2003. Volume calculations of the survey data, although of a crude nature also tie in to the average longshore drift along the modelled stretch of coastline.

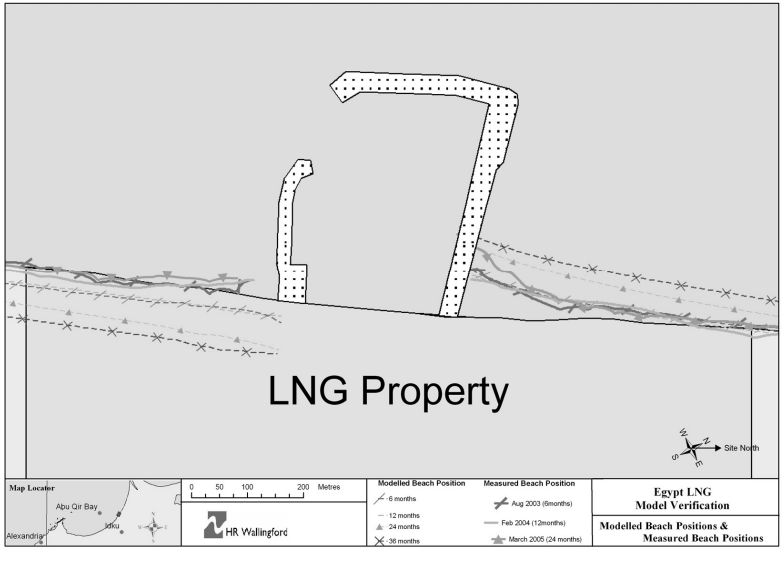

Fig. 8. Comparison of predicted beach positions and monitored beach positions

On the beach south of the harbour the surveyed positions do not match the shoreline position predicted by the modelling. However, the weekly shoreline position measurements tie in with the rate of erosion predicted at this location and as a result of the rapid erosion beach management (Table 2) was required before the August 2003 survey. Furthermore a rock revetment was placed along the shoreline to restrict any further landward movement of the shoreline south of the harbour. Therefore the surveyed shoreline position will not match the predicted shoreline position.

The beach plan shape model predicted that the beach would return to its pre-harbour position within three years after removal. Following removal of the harbour the waterline was artificially restored to its pre-existing state and it has subsequently not been possible to verify the recovery element of the modelling.

CONCLUSIONS

A comprehensive desk study of coastal processes was undertaken to assess the impact of the temporary construction harbour for the ELNG facility, before the BEACHPLAN model was used to predict future beach evolution. This model is applied as a first-stage tool in understanding coastline behaviour and the impact of engineering works upon it.

Drift rates are notoriously difficult to accurately predict and are sensitive to small changes in beach orientation (or wave direction). Caution must therefore be exercised when calculating them and sensitivity test should be carried out. In this study a shift in beach orientation of only 1° led to a 50% change in drift rates. This is clearly important when modelling along a curved shoreline such as the one in this study and led us to make a conservative estimate of the drift rates for the purpose of providing guidance to the required beach management.

Following the analysis of the survey data a comparison between measured and predicted beach position revealed that the modelling turned out to be reasonably accurate, despite the lack of any suitable calibration data. In situations where there is a lack of good data for calibration a comprehensive desk study and the undertaking of sensitivity tests gain increasing importance and any modelling should be done with a suitable amount of caution and conservatism.

As a result of the identification of the scour hole its subsequent impact on the trestle, it was recognised that that it is important to carry out a separate study to assess these impacts using a 2-D wave/current sediment transport model.

REFERENCES

Fanos AM, Khafagy, AA and Dean, RG (1995). "Protective works on the Nile Delta coast*," J. of Coastal Research*. V11-2, pp516-528.

Fanos AM (2001). "Coastal and sedimentation processes along the Abu Qir Bay." Report prepared for HR Wallingford.

Frihy OE, Nasr, MH and El-Raey, M (1991). "Temporal bottom and shoreline changes of the inner continental shelf off the Nile Delta, Egypt*," J. Coastal Research*, 7,2,465-475.

HR Wallingford (2004). "BEACHPLAN model description IT509."

Ozasa H and Brampton A H. (1980) "Mathematical Modelling of Beaches Backed by Seawalls," *Coastal Engineering.*

Whitehouse R (2006). "Scour at Coastal Structures," *Proceedings of International Conference on Scour and Erosion.*

THE DESIGN OF STABLE AND AESTHETIC BEACH FILLS: LEARNING FROM NATURE

Paul D. Komar

College of Oceanic & Atmospheric Sciences
Oregon State University, Corvallis, OR 97331
pkomar@coas.oregonstate.edu

ABSTRACT: Beach fills come in two forms, the most common being the nourishment of a beach with sand to improve its recreational use and to enhance its capacity to buffer backshore properties from wave attack. The other form is a cobble berm (dynamic revetment), similarly used to protect shorefront properties, involving the construction of a cobble beach ridge. Both tend to be acceptable as shore-protection strategies due to their having natural forms found on coasts, acceptable where seawalls and conventional stone revetments are unacceptable. The design of beach fills should include considerations of the characteristics of their natural counterparts, so they have the visual aesthetics of natural beaches and respond to ocean processes during storms in much the same manner, increasing the probability that the fill will be stable in forming a permanent beach and in providing the desired level of protection for backshore properties.

INTRODUCTION

The term "beach fill" is broadly used to include the practice of restoring an eroded beach by the importation of sediment, or the development of a recreational beach where one had not previously existed. This of course is the common practice of beach nourishment, with sand generally being the material employed. Another form for a beach fill, one less common, is the use of gravel and cobbles to construct a beach ridge that provides protection to backshore properties. It has been observed by coastal geologists and engineers that natural cobble beaches can impart significant degrees of shore protection, and there has been a few examples where their artificial counterparts were constructed as beach fills to protect coastal developments; those fills are alternately termed "cobble berms' or "dynamic revetments". Beach fills

therefore come in a variety of forms, but the underlying objective in their construction is to restore a beach or to provide a natural form of shore protection. Having this natural form, their installation tends to be more readily acceptable within the framework of coastal management, including within jurisdictions where the use of hard structures is outright forbidden, or locally within parks or similar environments where soft solutions are preferred over the use of conventional seawalls and revetments.

It is apparent that the design of beach fills should include considerations of the characteristics of their natural counterparts, so these artificial fills have the visual aesthetics of natural beaches rather than it being apparent that they had been designed by an engineer. Conformity with the natural forms found in Nature will likely also increase the probability that the fill will be stable in forming a more permanent beach and in providing the desired level of protection for backshore properties. This assumes a level of "intelligence" on the part of Nature, with her having formed beaches composed of sand, gravel and cobbles that represent levels of stability necessary for them to remain along the shore. Viewed another way, the beaches we find along the coast represent examples of "survival of the fittest", implying that they have naturally evolved in their morphologies to maximize their stabilities.

The implication is that we can learn from Nature in our design of beach fills, in effect to "Design with Nature". This was the title of a book published in 1969, written by the Scotsman Ian McHarg, a town planner and landscape architect. With advances in the science of ecology during the latter half of the 20th century, efforts were made to determine what constitutes a balanced and sustainable environment, making possible man's prosperity while minimizing our adverse impacts on the environment — McHarg's book is a reflection of that idealism. It is telling that the first environment he considered is the coastal zone, with his primary focus having been on barrier islands and their fragility. As outlined above, I tend to put a somewhat different spin on the concept of designing with Nature, that we can learn from it in our search for improved ways to develop the coast and to protect those developments from the forces of Nature that seem bent on our destruction. The objective of this paper is to explore that concept in the application and design of beach fills, for both beach nourishment projects and cobble berms, drawing on the designs of Nature to serve as a guide. But it will be seen that on occasion Nature make mistakes, resulting in unstable beaches, but her mistakes can also serve as guides in our development of more stable beach fills.

BEACH MORPHODYNAMICS — THE KEY FOR STABLE BEACH FILLS

Whenever coastal scientists and engineers undertake investigations of beaches, they make observations and collect data that potentially are of value in the design of artificial beach fills. Specifically, in those designs we need to adopt a profile for the fill that takes into account the morphologies of natural beach profiles and how they are effective in dissipating the energy of storm waves, thereby surviving the storm. Specifically, we need to know how the slope of the beach depends on the grain sizes of its sediments and the wave conditions, and perhaps even how the wave swash sorts

the ranges of particle sizes and shapes into regular patterns across the profile, this being a particularly distinctive feature of gravel and cobble beaches. High on the scale of relevance to beach-fill design is an understanding of how natural beaches respond to the forces of extreme waves and elevated tides during major storms, their response in general being to move some of their sediment offshore to yield a profile that is more effective in dissipating the energy of the storm waves. From our research on beaches over the decades, we have acquired a reasonable understanding of how Nature acts to maximize the stabilities of its beaches, to be drawn upon in the design of beach fills.

This stability is an inherent component in the classifications of beaches, particularly the morphodynamics classification of Wright and Short (1983), and that of Jennings and Shulmeister (2002) that considers the full range of beach types depending on their proportions of sand versus a coarse-grained component, gravel and cobbles. The well-known classification of Wright and Short includes beach categories that range from Dissipative to Intermediate to Reflective, defined on the basis of their contrasting profiles and accompanying differences in wave breaking and surf-zone processes. A Dissipative Beach is one having a low average slope and a wide surf zone, whereas a Reflective Beach at the other extreme has a steep beach face and a relatively narrow swash zone that experiences the direct forces of the runup and backwash of the breaking waves. The distinction between these extremes in the classification is fundamental in that on the low slope of a Dissipative Beach, the waves break well offshore and progressively loose their energy while they travel as bores across the wide surf zone. Whenever the heights of the waves increase during a storm, they simply break further offshore, with a minimal increase in the incident-wave energy at the shore (although there is an increase in the long-period infragravity motions). The morphology of a Dissipative Beach therefore effectively acts to dissipate the energy of the waves, a successful design by Nature. In contrast, on the steep Reflective Beach the incident waves break close to shore with little prior loss of energy. However, some of that energy is reflected from the steep beach face, generating waves that return seaward; hence the term "reflective". The Intermediate Beach categories incorporate a series of morphological types that are more three dimensional, and cannot satisfactorily be represented as simple two-dimensional profiles. The morphology may include the presence of complex patterns of nearshore currents, including rip currents that locally erode embayments into the beach, each becoming the site of localized “hot-spot” erosion that represents a hazard to shorefront properties.

The ramification of the morphodynamics classification of Wright and Short (1983) to the design of beach fills, where stability is of prime importance, is that it is preferable to have a Dissipative Beach. Reflective beaches can also be reasonably stable in that a significant portion of the incident wave energy is reflected, and in the case of steep beaches composed of gravel and cobbles, much of the remaining incident wave energy is expended as it washes up the beach face, with some of its water percolating into the permeable gravel. Therefore, within the scope of the morphodynamics classification the Intermediate categories tend to be the least stable and experience the

greatest morphological change, with the highest prospects of there being property erosion. The ramification for beach-fill design is clear — Intermediate beaches are to be avoided.

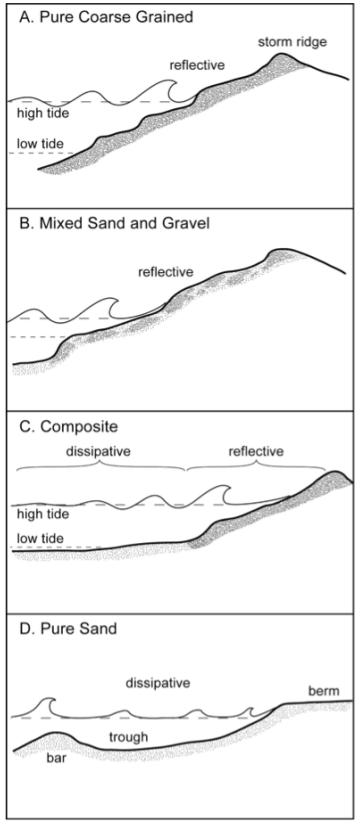

Fig. 1. The classification of beaches depending on the proportions of sand versus gravel and cobbles. [*after* Jennings and Shulmeister (2002)]

Also relevant to the design of beach fills, specifically of beach berms or dynamic revetments consisting of gravel and cobbles, is the classification of Jennings and Shulmeister (2002), Figure 1, that places beaches into four categories depending on their relative proportions of sand versus the coarse-grained component, and how Nature has sorted those fractions across the profile. The vast majority of coastal research has focused on the two extremes, coarse-grained beaches containing minimal quantities of sand, and sand beaches where the quantity of gravel is sufficiently small it does not affect the morphology and dynamics of the beach. Of interest are the mixed sand-and-gravel beaches and composite beaches, Figure 1, differing in how

Nature has dealt with the range of sediments available to form the beach; in the former there is an intimate mixing of the two size fractions in the beach face (Kirk 1980), whereas in composite beaches the sand and coarse-grained fractions are largely separated across the profile, the upper foreshore or backshore ridge being composed of gravel and cobbles while the lower foreshore is sand, there generally being a distinct boundary between them. Again, this classification has ramifications to the design of stable beach fills to be used for shore protection. The presence of the sand within the mixed sand-and-gravel beach acts to reduce the deposit's permeability and capacity to dissipate the energy of the wave swash, while the composite beach is ideal in having combined a Dissipative sandy foreshore and Reflective cobble backshore, the two most stable forms in the morphodynamics classification. We therefore recognize in these classifications where Nature has been most successful in the development of stable ocean beaches, and it behooves us to follow her directions in the design of artificial beach fills.

COARSE-GRAINED BEACH FILLS FOR SHORE PROTECTION

Coastal geologists and engineers involved in the study of natural gravel or cobble beaches have come to recognize that given sufficient volumes of coarse sediment to construct a beach ridge, Nature can provide her own solution for the protection of backshore properties. I came to my "eureka moment" on the Oregon coast after having seen several examples, Figure 2, only to later read the publications of others to find that my observations had not been unique.



Fig. 2. A cobble beach on the Oregon coast, providing natural protection to a sea cliff. [*photo courtesy of* Jonathan Allan]

It is unclear when or where such observations were followed by the construction for the first time of an artificial coarse-grained beach specifically for shore protection. There are early papers on the nourishment of gravel beaches, adding similar material to an already existing gravel beach (e.g., Muir Wood 1970). However, that practice differs from what has come to be known in the engineering literature as the construction of a "dynamic revetment", or is alternatively referred to as a “cobble berm”, a preferable name in coastal management in having diluted the implication of it being a type of revetment. On the other hand, the term dynamic revetment provides a contrast with a conventional “stable” revetment that consists of large quarry stones, where stone movement can lead to the failure of the structure. A further extension of the concept is that of rubble-mound breakwaters, and artificial islands that have been constructed to serve as oil-drilling platforms. The earliest published paper I have found that might be considered to involve the design and construction of an artificial gravel beach in the form of a cobble berm is that of van Hijm (1974), the application having been along the bank of the entrance to Rotterdam Harbor in the Netherlands, but needed to dissipate wave energy rather than to serve as shore protection. Whatever the origin of the concept, the basic strategy has evolved into one of building a gravel or cobble beach that can adjust and deform in response to storm wave action, being dynamic in expecting stone movement rather than static as in revetments of large quarry stones. By being dynamic, the cobble berm is effective because the mound of gravel and cobbles is able to disrupt and dissipate the wave energy, partly through its absorption of the runup by the permeability of the deposit, and it can alter its overall morphology just as a natural cobble beach does at the time of a storm.

The initial research into dynamic structures was undertaken at the Delft Hydraulics Laboratory, having been directed toward the design of the wave-dissipating structure to be built in Rotterdam Harbor, but relevant also for the design of rubble breakwaters for harbors, or artificial islands. Accordingly, those experiments were undertaken in a laboratory wave channel with deep water in front of the structure. Ahrens (1990) extended the research through additional laboratory investigations, but with shallow water fronting the rubble mound. Even then the laboratory studies differed from the typical situation where one wants to construct a cobble berm/dynamic revetment for the protection of shorefront properties, with it commonly being placed at the back of an active, sand beach.

A preferred approach upon which to base the design of cobble berms for use in shore protection is to investigate their natural occurrences, morphologies, and responses to extreme storms. There is a wealth of relevant information in the published literature to be drawn upon. To cite a few examples: the origin and distinctive characteristics of gravel and cobble beaches (e.g., Carter and Orford 1984); the movement of the particles depending on their shapes and sizes (e.g., Carr 1974; Nicholls and Wright 1991); the resulting patterns of particle shapes across the beach profile (e.g., Bluck 1967; Orford 1975; Williams and Caldwell 1988); the rates of gravel abrasion (e.g., Matthews 1983; Dornbusch et al. 2002); and the unique morphodynamics of mixed sand-and-gravel beaches (Kirk 1980).

Particularly informative are the field studies of cobble beaches that specifically had the objective of collecting data to be used in the design of cobble berms. Everts et al. (2002) investigated natural cobble beaches on the coast of southern California, with the objective to design a cobble berm for shore protection in Ventura. We have undertaken similar investigations of cobble beaches on the Oregon coast, to compare their dynamics with a cobble berm that was constructed in Cape Lookout State Park in response to major problems with erosion and flooding (Allan and Komar 2002, 2004). Its design was based primarily on surveys of nearby cobble beaches to determine their natural slopes, and the elevations reached by the combined tides and wave-swash runup that had occurred during an extreme storm in March 1999, the storm that in particular had impacted the park. The design of the cobble berm therefore focused on potential extreme water levels in order to prevent its overtopping during major storms, and the volumes of coarse sediments needed to provide those elevations; in this respect, the design represents something of a hybrid between that of a riprap revetment where elevations are important, and a conventional beach nourishment project where sediment volumes are most important. This cobble berm has been monitored since its completion in 2000 by a program of seasonal surveys, tracing the mobility and net transport of the cobbles with PIT-tags, and a documentation of the changing grain sizes and sorting patterns (Allan and Komar 2004; Allan et al. 2006); similar investigations are underway on natural cobble beaches along the Oregon coast, in order to provide comparisons with the process-responses and evolution of the constructed cobble berm. To date, the cobble berm, backed by a re-constructed sand dune, have been successful in providing protection for the park, and have remained fairly intact under the forces of major storms, including extreme events when both the cobble berm and artificial dune were overtopped.

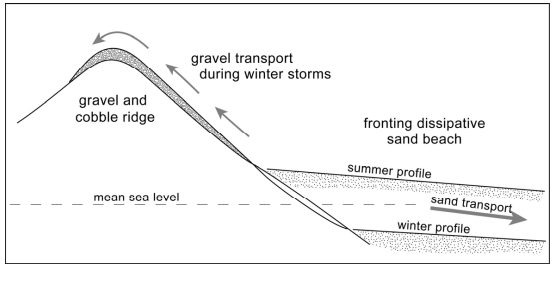

Fig. 3. The contrasting patterns of sediment movement on the cobble ridge and fronting sand beach of a composite beach during storms.

The investigations by Everts et al. (2002) of cobble beaches on the coast of southern California, and ours on the Oregon coast (Allan and Komar 2002, 2004), compliment one another in their observations and conclusions. Both involved composite beaches in the classification of Jennings and Schulmeister (2002), consisting of Dissipative sand beaches fronting Reflective cobble beaches; on the California coast the cobbles

have tended to accumulate in ridge deposits, whereas on the Oregon coast they primarily form sloping beaches in front of sea cliffs or high sand dunes. Of particular interest, documented in both studies, are the contrasting responses of the sand and coarse-grained deposits during storms, depicted in Figure 3, or as part of the overall seasonal shifts in profiles from summer to winter. As expected, during a storm the sand beaches erode due to the offshore transport of the sand from what had been the dry summer berm, into offshore bars, this being the typical seasonal cycle for sand beaches along the West Coast. With the lowered elevations of the fronting sand beaches in the fall to early winter, the waves are only then able to reach and impact the cobble deposits. During a storm the increased intensities and elevations of the runup move cobbles landward, while the backwash weakened by percolation produces less offshore movement. The general result is accretion and a steepened profile of the cobble beach, Figure 3, and an increase in its maximum elevations, particularly if the storm waves result in overwash of the cobble ridge. Everts et al. (2002) found that the most substantial episodes of cobble-ridge accretion occurred during the 1982-83 El Niño and during the most extreme storm of the study period in January 1988, events when the sand beaches experienced their greatest degrees of erosion. A similar response has been found for the cobble berm constructed at Cape Lookout State Park, with storms steepening the slope of the berm due to the accumulation of cobbles at the base of the dunes, enhancing their protection from the forces of the storm waves, even during overwash events.

During the summer months with the return of sand to the fronting beach, the cobble deposits are partly to entirely covered. While this sand cover improves the recreational use of the beach during the summer, it potentially has a detrimental effect on the stability of the cobble beach with the return of the fall storms, since the sand fills the voids within the deposit and thereby increases the intensities of both the swash runup and backwash. Usually that sand is removed by the first storms of the fall, but Everts et al. (2002) reported on a site where in 1995 more than a million cubic meters of sand was placed atop and in front of the cobble beach; this led to its erosion during the next winter, even though the storm waves were relatively modest. Also of importance to the stability of the cobble deposits are their patterns of net longshore transport in the winter, during the few months when the waves are able to impact them. Everts et al. (2002) found on the California coast that while the net longshore transport of the sand on the fronting beach is to the south, there is not a net longshore transport of the cobbles, this enhancing their stability and effectiveness in protecting backshore properties. In contrast, on the Oregon coast there is not a net longshore transport of the sand (being confined within "pocket-beach" littoral cells with bounding headlands), but the cobble-tagging experiments of Allan et al. (2006) have documented a significant northward transport due to the dominant approach of the winter storm waves from the southwest. In such a case where the longshore transport results in a net loss of material from a constructed cobble berm, it requires periodic maintenance of the structure by the addition of gravel and cobbles.

Our experience with the construction of this cobble berm on the Oregon coast has illustrated the advantages of this shore-protection strategy (Allan and Komar 2004),

discussed more generally by Ahrens (1990). In keeping with its dynamic nature, the stone sizes are significantly smaller than required for armor in a traditional static revetment. Accordingly, its construction can use the small-size debris from a quarry that is often considered to be waste, although at times the demand is for pre-rounded cobbles, for aesthetic reasons, requiring that the source be a gravel-bed stream or another beach where there is an excess of material so some extraction is possible (this having been the source for the Oregon cobble berm). In reality the requirement that the introduced cobbles be rounded may be unnecessary, as investigations of the rates of gravel abrasion have shown that it can occur quite rapidly, rounding the sharp edges of the particles within a couple of years (Matthews 1983; Dornbusch, et al. 2002). In addition, the placement of the gravel and cobbles in the berm during its construction is straight forward, only requiring its grading into what is assessed to be the approximate equilibrium slope of a natural cobble beach having those particle sizes; in contrast, the construction of a conventional riprap revetment ideally involves the individual placement of the stones to insure their stability. The consequence is that the construction of a cobble berm will be much less expensive than a conventional structure, a riprap revetment or a seawall; in the case of the cobble berm and artificial dune at Cape Lookout State Park, the total cost was about $125,000, whereas the estimated cost for a riprap revetment for that site was $500,000. In addition to these practical advantages derived from constructing a cobble berm for shore protection, its natural and aesthetic form makes it ideal for a park setting, our impression being that few if any people visiting Cape Lookout State Park recognize the cobble berm and artificial dune for what they are, shore-protection structures.

The initial incentive for including the artificial dune backing the cobble berm, to protect the park, was to downsize the berm so that smaller volumes of cobbles were required. As a result, the cobble berm alone would have been insufficient in providing protection to the park, the monitoring program having shown that during even modest storms and high tides, the cobble berm is overtopped (Allan and Komar 2004). The dune was therefore needed to provide back-up protection, to reduce overwash occurrences and flooding of the park's campground. In order to enhance its stability, the dune was constructed with a core of geotextile bags, each filled with sand, covered with loose sand planted with native dune grass. Although the dune does contain this artificial structural component, this combination of a sand dune backing a cobble berm still conforms with the "Design with Nature" philosophy, since one can see this combination at many locations along the West Coast, including within Cape Lookout State Park. As found naturally, this combination has been particularly effective in protecting the park, with the cobble berm primarily having the role of reducing the wave-swash impacts on the dune, while the presence of the dune has reduced the occurrences of overwash and flooding into the park grounds, and has largely prevented the waves from hurling cobbles ballistic-fashion into the campground. A similar hybrid solution could be employed in the protection of sea cliffs that are experiencing erosion, in that case constructing a dynamic cobble berm that fronts a structure of large stones meant to be fixed in position at the base of the cliff; with a sufficient level of wave dissipation by the cobble berm, this backup structure could in effect be a downsized riprap revetment, but constructed to have the

appearance of its being a continuation of the cobble beach, again just as one finds naturally along the coast.

BEACH NOURISHMENT — THE STABILITY OF BEACH FILLS OF SAND

The practice of beach nourishment involves the importation of large quantities of sediment, generally sand, to widen a beach that has experienced erosion, the objective being to restore its recreational uses and to improve the capacity of the beach to buffer shorefront properties from wave attack. In more extreme examples (e.g., the Mediterranean coast of Spain), the undertaking might involve the placement of sand to form a recreational beach where one had not previously existed. Both represent examples of beach fills, akin to the construction of cobble berms but differing in the approaches of their designs as well as sediment sizes. Beach nourishment in particular focuses on the selection of the sand so it provides a reasonable match with the sand already present on the beach, in terms of both its composition and grain sizes, this being a clear instance of "Design with Nature". Another important aspect in the nourishment design is a decision as to how the imported sand will be placed on the beach: should it be spread evenly across the profile, including the surf zone and offshore bars?; should the sand be added only to the visible beach?; should some of the sand be used in the construction of a dune at the back of the beach? Guidance can be derived from Nature as to what to do, or what not to do.

Nature is far less fussy than we are, it working with the sediments available and then molding those sediments into beach forms that are compatible with the forces of the ocean's waves and currents. Here our guidance mainly comes from how Nature designs its beaches in terms of the sediment particle sizes it selects to form the beach, how it sorts those particles according to their sizes and densities, and the morphologic forms acquired by the beach as a whole that yields a degree of stability. For example, on the Oregon coast Nature has a wide spectrum of sediment sizes to work with, from silt and sand contributed by its rivers, to gravel and cobbles eroded from basaltic headlands. Massive landslides are a frequent contributor, containing the full range of particle sizes. It is amazing how rapidly the waves and currents can deal with even the largest inputs of sediment, removing the unwanted silt and fine sand to the offshore, and concentrating the coarser sand into a beach that is effective in dissipating the energy of the waves. If present in the original range of particle sizes supplied to the shore, the gravel and cobbles are selectively transported onshore by the waves to form a cobble ridge at the back of the sandy beach, forming a composite beach (Fig. 1) that maximizes the stability of the shore by having incorporated both Dissipative and Reflective elements in the profile.

One lesson to learn from Nature is that she can take care of herself. If the sand imported for a beach nourishment project contains silt, so be it — so does the sediment supplied by rivers. We tend to underestimate the resilience of Nature, her ability to separate out the grain sizes that best suit her purposes for that coastal site, "flushing" the unwanted silt to deep water with minimal lasting consequences. The same can be said for the placement of the imported sediment on the beach in the nourishment project. No matter where the sand is placed, Nature will go to work on

its rearrangement, just as she does when the delivery is from a river or landslide. It can be argued that the placement should approach as closely as possible the expected natural equilibrium profile — with less sediment redistribution being required, the argument is that less sand will be lost from the nourishment site due to its offshore and longshore transport. This practice, however, would require that the imported sediment be spread evenly across the profile, including through the surf zone and offshore bars, not easily accomplished and increasing the cost of the project. It can equally be argued that the imported sand be placed on the visible portion of the beach, its berm and possibly with some used to construct a foredune. Analyses have shown that this placement temporarily maximizes the protection of backshore properties from the forces of storms, the storm surge and waves, at least until those processes succeed in redistributing the sand into an equilibrium profile by moving a portion of it into the surf zone (Hansen and Byrnes 1991).

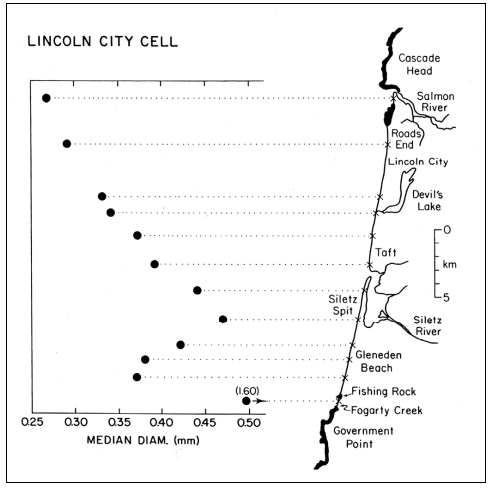

Fig. 4. The longshore variation in beach sediment median grain sizes within an Oregon littoral cell, due to the introduction of coarse sediment by sea-cliff erosion south of Siletz Spit. [*after* Shih and Komar (1994)]

We should not mistakenly accept that Nature always gets it right. Her experiments with forming beaches have not always been successful in terms of maximizing their stability, but we can learn from her mistakes. Again, an example is found on the Oregon coast (Shih and Komar 1994), where Nature is in the process of undertaking her own beach nourishment project, but one that has turned out badly by having rendered the beach more unstable. The shore of interest is the central stretch of beach within the Lincoln City Littoral Cell, Figure 4, a "pocket beach" cell trapped between rocky headlands, where there is a seasonally reversing longshore sediment transport but with the net transport in the long term being effectively zero. Initially this beach would have been composed of a medium-grained sand (0.25 mm), typical of the

Oregon coast; with that grain size it would have been a Dissipative beach in the morphodynamics classification of Wright and Short (1983), and therefore would have been relatively stable. The beach nourishment experiment undertaken by Nature is interpreted to have begun about 300 hundred years ago, precisely on 26 January 1700 when a magnitude-9 subduction earthquake caused this stretch of coast to abruptly drop down by 1 to 2 meters, resulting in the inception of the sea-cliff erosion that continues today. The cliff immediately south of Siletz Spit and along the shore of Gleneden Beach is composed of Pleistocene coarse sand and granules, with some small-diameter gravel. Nature's beach nourishment project was therefore forced to use this coarser sediment, and its introduction at that site has resulted in the longshore variation in beach sediment median grain sizes graphed in Figure 4, produced by the spreading (diffusion) of the introduced sand. The beach at the nourishment site now has a median diameter of 0.47 mm, whereas at the far north end of the Cell's shoreline (Roads End) the median diameter is still 0.25 mm. Nature's experiment with beach nourishment here on the Oregon coast would appear to conform with our general practice of selecting a somewhat coarser sediment for the material to be added to the beach, the expectation being that it would reduce offshore losses and enhance the stability of the beach. Nature's experiment on the Oregon coast has had just the opposite response; the addition of the coarser sediment increased the beach slopes in the Gleneden Beach and Siletz Spit areas, so they were converted from stable Dissipative beaches into highly dynamic Intermediate beaches. As a result, this stretch of shore now has one of the highest rates of erosion along the Oregon coast; in contrast, the beach at the far north end of the Cell, where the sand still has a 0.25mm diameter, has remained Dissipative and relatively stable under identical wave conditions. With the local enhanced sea-cliff erosion at Gleneden Beach, still more coarse-grained sediment is being added to the beach, continuing Nature's experiment, and unfortunately in doing so is further exacerbating the erosion problems.

In terms of the coasts of the United States, the above example has the primary relevance to the West Coast where the combination of relatively fine-grained beaches and swell waves of low steepness result in the beaches being Dissipative. If one is to undertake a beach nourishment project, caution is required not to add sediment that is of sufficient coarseness it converts the beach into an Intermediate category in the classification of Wright and Short (1983), as this will likely insure that there are increased problems with erosion. On the other hand, on the East Coast the beaches are generally already Intermediate, with that at the Field Research Facility of the U.S. Army Corps of Engineers, in Duck, North Carolina being a well-studied example [see Lippmann and Holman (1990) in the context of placing its morphodynamics into the classification of Wright and Short (1983)]. In this case, in principle it would be good from a stability standpoint to add sufficient quantities of coarse-grained sediment to push the beach into the Reflective category, but this would likely be objected to on the basis of its recreational uses. However, my impression is that the beach at the Field Research Facility provides a natural example where the stability might be improved by the addition of relatively small quantities of gravel. At that site the natural presence of the gravel has resulted in its concentration at the base of the beach face, forming something of a step along the seaward edge of the swash zone. As a

result, although the offshore bars have experienced the dramatic cycles one expects of Intermediate beaches under the changing wave conditions, the beach face and width of the sand berm have been more stable than found on other East Coast Intermediate beaches where a gravel component is not found. Nature may be telling us something in this example, holding a key to the improved stability of those beaches.

SUMMARY AND DISCUSSION

The theme of this paper has been that we can learn from Nature in the development of new strategies directed toward increasing the stability of our coasts, approaches that are aesthetic in having adopted natural forms while providing sufficient protection to shorefront properties. We have examined a range of beach fills, from cobble berms (dynamic revetments) that involve the construction of an artificial beach composed of imported gravel and cobbles, to the common practice of beach nourishment with sand. Research completed over the years on their natural counterparts found along coasts can serve as the basis for the designs of these beach fills, with recent investigations having focused specifically on gathering data from the natural beaches on coasts where cobble berms are to be constructed.

It is apparent that these natural strategies will seldom provide the same degree of shore protection as a massive riprap revetment or seawall that has been properly designed by an engineer. Therefore, their use will likely be primarily in natural settings such as parks where those conventional structures are undesirable, or in jurisdictions where they are outright forbidden. In order to enhance their abilities to provide sufficient protection, it may be necessary to employ combinations of forms, hybrids, just as commonly found in Nature. For example, we have seen that composite beaches (Fig. 1) can yield the greatest degree of stability, where a sand beach fronts a cobble berm, each contributing to the dissipation of the storm-wave energy. Similarly, the constructed cobble berm might be backed by a down-scaled static revetment of large stones, blended to give more of a continuum as found naturally along rocky coasts. Otherwise, as constructed at Cape Lookout State Park on the Oregon coast, the cobble berm could be backed by an artificial sand dune reinforced with a core of sand-filled geotextile bags to enhance its stability. We need to be more imaginative in our approaches directed toward shore protection, as in those combinations, so the resulting structure maintains a natural appearance while at the same time offers a significant measure of stability.

With this approach to restoration and protection being rather unconventional, its undertaking might best be accomplished as a team effort, including a coastal engineer and a geologist who is familiar with the details of the natural beach forms; and where the placement of the beach fill is within a park, a landscape architect could also make a contribution.

REFERENCES

Ahrens, J.P. (1990) “Dynamic revetments,” *Proc. 22nd Int. Conf. on Coastal Engr.,* ASCE, 1837-1850.

Allan, J. C., and Komar, P. D. (2002) "A dynamic revetment and artificial dune for shore protection," *Solving Coastal Conundrums, Proc. 28th Int. Conf. on Coastal Engr.*, ASCE, 2044-2056.

Allan, J. C., and Komar, P. D. (2004) "Environmentally compatible cobble berm and artificial dune for shore protection," *Shore & Beach*, 72(1), 9-18.

Allan, J.C., Hart, R., and Tranquile, J. V. (2006) "The use of Passive Integrated Transponder (PIT) tags to trace cobble transport in a mixed sand-and-gravel beach on the high-energy Oregon coast, USA," *Marine Geology*, 232, 63-86.

Bluck, B.J. (1967) "Sedimentation of beach gravels: Examples from South Wales," *Journal of Sedimentary Petrology*, v. 37, p. 128-156.

Carr, A.P. (1974) "Differential movement of coarse sediment particles," *Proc. 14th Int. Conf. on Coastal Engr.*, ASCE, 851-870

Carter, R.W.G., and Orford, J.D. (1984) "Coarse clastic barrier beaches: A discussion of the distinctive dynamic and morphosedimentary characteristics," *Marine Geology*, 60, 377-389.

Dornbusch, U., Williams, R.B.G., Moses, C., and Robinson, D.A. (2002) "Life expectancy of shingle beaches: measuring in situ abrasion," *Journal of Coastal Research*, Special Issue 36, 249-255.

Everts, C.H., Eldon, C.D., and Moore, J. (2002) "Performance of cobble berms in Southern California," *Shore & Beach*, 70(4), 5-14.

Hansen, M., and M. R. Byrnes (1991) "Development of optimum beach fill design cross-section," *Coastal Sediments '91*, ASCE, 2067-2080

Jennings, R., and Shulmeister, J. (2002) "A field based classification scheme for gravel beaches," *Marine Geology*, 186, 211-228.

Kirk, R.M. (1980) "Mixed sand and gravel beaches: Morphology, processes and sediments," *Progress in Physical Geography*, 4, 189-210.

Lippmann, T. C., and Holman, R. A. (1990) "The spatial and temporal variability of sand bar morphology," *Journal of Geophysical Research*, 95(C7), 11,575-11,590.

Matthews, E. R. (1983) "Measurements of beach pebble attrition in Palisser Bay, southern North Island, New Zealand," *Sedimentology*, 30, 787-799.

Muir Wood, A.M. (1970) "Characteristics of shingle beaches: the solution to some practical problems," *Proc. 12th Int. Conf. Coastal Eng.*, ASCE, 1059-1075.

Nicholls, R.J., and Wright, P. (1991) "Longshore transport of pebbles: experimental estimates of K," *Coastal Sediments '91*, ASCE, 920-933.

Orford, J.D. (1975) "Discrimination of particle zonation on a pebble beach," *Sedimentology*, 22, 441-463.

Shih, S.-M., and Komar, P. D. (1994) "Sediments, beach morphology and sea cliff erosion within an Oregon coast littoral cell," *Journal of Coastal Research*, 10, 144-157.

Van Hijm (1974) Equilibrium profiles of coarse material under wave attack: *Proc. 14th Int. Conf. Coastal Engr.,* ASCE, 939-957.

Williams, A. T., and N. Caldwell (1988) "Particle size and shape in pebble-beach sedimentation," *Marine Geology*, 82, 199-215.

Wright, L. D., and Short, A. D. (1983) Morphodynamics of beaches and surf zones in Australia: In *Handbook of Coastal Processes and Erosion*, edited by P. D. Komar, pp. 35-64, CRC Press, Boca Raton, Florida.

VARIATION IN THE ORGANISATION OF GRAVEL-DOMINATED COASTAL SYSTEMS: EVIDENCE FROM NOVA SCOTIA AND SOUTHERN ENGLAND

Julian D. Orford[1], Simon C. Jennings[2*]

1. School of Geography, Archaeology and Palaeoecology, Queen's University, Belfast, BT7 1NN, UK j.orford@qub.ac.uk
2. Inst. of Culture, Tourism and Development, London Metropolitan University, London, N7 8DB UK (*Deceased)

Abstract: Over the last two decades, a model of coastal gravel barrier evolution dependent on paraglacial reworking of limited, point-sourced glacigenic deposition has been proposed based on the Holocene evolution of the Nova Scotia Atlantic shoreline. Essential controls in this sequence were dependent on relative sea-level rise rate, sediment supply, basement structure and wave climate. Key in this sequence was the move from drift-aligned to swash-aligned barriers as a one-way process, with an emphasis that such swash alignment induced relative stability of barrier in the face of wave climate variability. Contemporary evidence from Nova Scotia following an extreme event and inferred environmental reconstruction of the gravel dominated barriers of southern England, suggest that swash-alignment is not as stable as hitherto identified, and that reversals from swash to drift-alignment and quick breakdown by extreme storm need to be considered as part of the potential sequence of gravel barrier evolution.

INTRODUCTION

The mesoscale dynamics and organization of gravel dominated coasts including source, transport and sink elements has been developed in a series of papers (Orford et al. 1991; 1996; 2002) dealing with the Eastern Shore of Nova Scotia (NS) (Fig.1A). These developments have been noted particularly in the context of; fast relative sea-level rise (RSLR: c.4mm a^{-1}); finite paraglacial sediment source supply in the form of drumlins; and discordant lithified basement plan-geometries (estuaries and headlands); all contributing to coastal barrier evolution over time scales of c 2-3ka. A key element in

this barrier evolution sequence was the move from sediment-rich, drift-aligned (DA) barriers to sediment-deficit swash-alignment (SA) barriers, with an emphasis that once SA was achieved there was a domain shift in spatial barrier activity as longshore transport transformed into cross-barrier transport through barrier rollover processes. Orford et al. (1991) identified the basic sequence of such barrier morphological change based on the limited glacigenic sediment sources characteristic of the NS coastline. The swash domain was thought to occupy a longer time phase compared with the drift domain, eventually transforming into a breakdown phase. The conditional basis for this transformation has remained uncertain, given that the SA barrier was thought to be well tuned to storm events: even to catastrophic events (Orford et al. 2003). Hurricane activity on the Eastern Shore (Sept 2003) provided the forcing to address the extreme event issue and possible barrier breakdown. This NS barrier sequence has yet to be tested elsewhere, so this paper also addresses how in comparison the gravel-dominated shoreline of southern England (Fig.1B) evolved in the mid- to late-Holocene. The use of similar concepts of sediment cell development and associated morpho-sedimentary assemblages are considered in the light of both limited RSL change and sediment supply, but where spatial freedom of barrier morphology is radically restricted by lithified basement morphology that is strongly cliff-controlled, unlike the low-lying NS coastline.

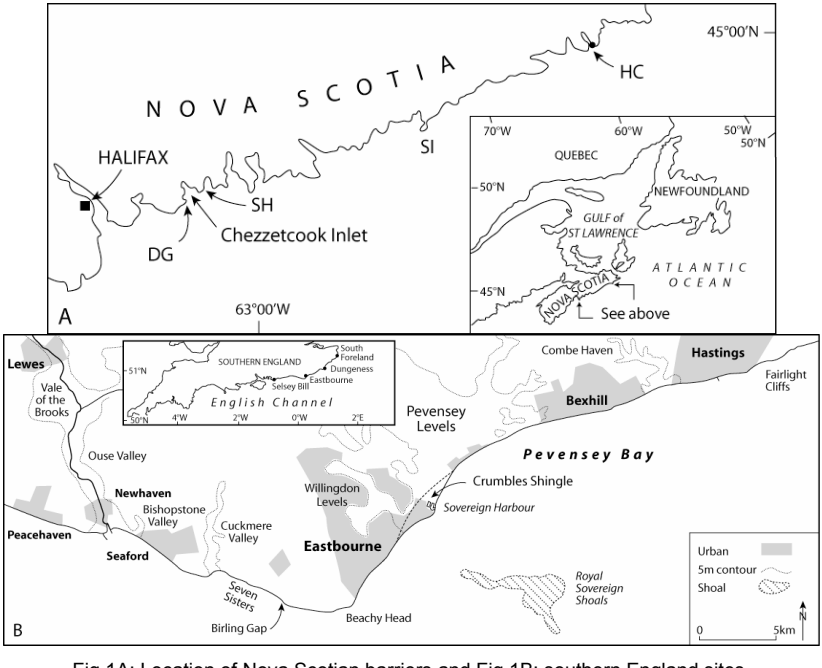

Fig.1A: Location of Nova Scotian barriers and Fig.1B: southern England sites.

METHODS

The analysis of Nova Scotian barriers (pre-2000AD) was based on comparison of serial air photography (over 50 years), and field survey of barriers and nearshore morphology. Recent extreme event forcing of morphology post-2000AD, along the NS coast has been examined from two sources: aerial photography taken pre- and post Hurricane Juan (28.9.03) (courtesy of N.S. Dept Natural Resources) and satellite images post-2003 (via Google Earth™). The H. Juan imagery is only available for the hurricane track path that crossed the NS coast east of Halifax, and offers GIS vector overlays of shoreline change post hurricane passage (DNR 2003). This allows direct shoreline examination of two key SA barrier sites from previous analyses: Story Head and Grand Desert (both at the mouth of Chezzetcook Inlet). These hurricane change outlines have been superimposed on existing barrier retreat data over the period of c 1933 to 1987 (Orford et al. 1996 2002) and allow examination of both barrier morphology and barrier retreat. This source of post-hurricane analysis is not available for positions at the eastern end of NS, however examination of two further key SA sites in this eastern zone (Sober Island and Haulover Cove) using Google Earth imagery (albeit at small scale) allows definition of major domain changes in both barriers since 2000AD.

The reconstructions of southern English barriers are based on an analytical deduction process by which published lower-estuary stratigraphies (Table 1) are translated into phases of environmental control on estuary deposition through the presence or absence of cross-estuary mouth barriers sufficient to allow organic deposition, or marine sands/silts respectively, to dominate the estuary fill.

Table 1. Sources of information used for stratigraphic data and palaeoenvironmental reconstruction of southern England barriers.

Site/former estuary	Publications
Ouse Valley	Burrin & Scaife (1984); Jones (1971); Thorley (1981); Waller & Hamilton (2000)
Bishopstone Valley	Jennings & Smyth (unpublished)
Willingdon Levels (Eastbourne)	Jennings & Smyth (1987, 1990, 1991); Jennings et al. (2003)
Pevensey Levels	Moffat (1986)
Combe Haven (Hastings)	Jennings & Smyth 1987; Smyth & Jennings (1988, 1990)

RECENT BARRIER ACTIVITY IN NOVA SCOTIA

Nova Scotian Model

In Nova Scotia the speed and totality of the exhumation of point sediment sources (drumlins) under fast RSLR (c.4mm a-1) has generally led to single mesoscale cycles of variable longshore sediment transport dominated by early rising limbs of sediment surplus, and later falling limbs of sediment deficit, both of which define the cycle. These two domains of sediment supply have led to temporal overlapping of dual semi-synchronous phases of sediment aggradation through DA and then subsequent sediment cannibalisation leading to SA. The clarity of these morpho-sedimentary phases and the cessation of longshore sediment supply from the source area means that the

cannibalisation phases appear to be dominant in contemporary shorelines, such that resultant morphologies are dominated by a single crested SA ridge that is being forced towards breakdown phases under fast RSLR.

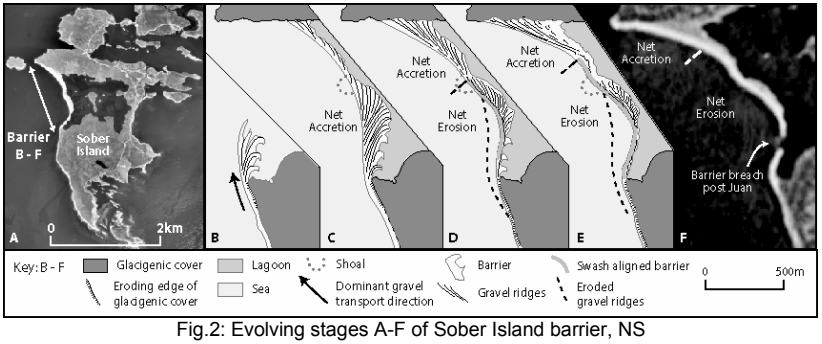

Fig.2: Evolving stages A-F of Sober Island barrier, NS

Figure 2 shows the likely spatial sequence of barrier development at Sober Island (75km east of Halifax) as an example of this barrier evolution. Figure 2A shows SI in the late 1980s with longshore sequences of SA and DA beach ridges. A period of a prior DA spit growth (Fig.2B) under high sediment transport rate relative to sink shoreline length, has changed into proto SA as the barrier sink distance expands relative to diminishing sediment volume from the drumlin source (Fig.2C-E). Cannibalisation of the old drift barrier, as witnessed by the expanding SA section, is supplying sufficient sediment to maintain a down-drift DA section, though this process is controlled by the extent to which the SA barrier can remain coherent as it is forced further backwards by rollover, and extends northwards as longshore cannibalization continues. The natural rock basement to the north of the barrier acted as a groyne and prevented loss of gravels further down-drift away from the barrier system. This lack of onward down-drift transport appeared to be the control on rate of longshore swash-alignment encroachment. In 2000AD this barrier appeared to be transport-deflected from complete swash-alignment, as shown by other previously mixed alignment systems (e.g. Haulover Cove: Fig.3A).

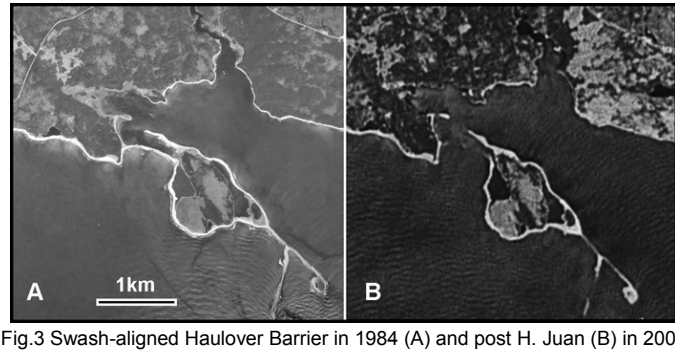

Fig.3 Swash-aligned Haulover Barrier in 1984 (A) and post H. Juan (B) in 2003

Swash-alignment was thought to be the stable long-term barrier configuration, especially when RSL rise was not fast (<2mma^{-1}). Barrier stability has to be considered in terms of the barrier volume being stretched over an increasing barrier extension distance, as it retreats through both RSL rise, and by rollover. However, in areas of fast RSL (and with an eye on future management problems of accelerated RSL) stability of swash-alignment is somewhat of a moot point. If swash alignment leads to stability, then the length of shoreline with swash-alignment features should be high relative to existing barrier length, though this would diminish as RSLR increases. Jennings et al. (1998) suggest that with RSLR of >8mma^{-1}, barrier coherence is radically threatened and breakdown likely. In NS there is a scarcity of SA, (<10% of the Atlantic NS coastline), which while being greater than DA, is significantly less than what would be expected given the potential of basement structure and sediment sources. However given that the rate at which barriers could move into the breakdown phase is unknown, the long-term stability of SA remains unknown.

Extreme events have been identified as a significant forcing in gravel barrier retreat (e.g. Orford et al. 2002), however evidence for catastrophic breakdown has been limited. Post Hurricane Juan (Sept.2003) an assessment of what a severe extreme event can do to swash alignment can be made. Hurricane Juan was, a Category 2 event that made landfall west of Halifax NS (28.09.03), and is regarded by Dept of Natural Resources (NS) as NS's worst 20th century coastal storm (DNR 2003). Juan generated southerly waves with H_s of 9m off Halifax harbour and H_{max} of 19-20m at hurricane landfall, while moving onshore associated with a 1.5m surge at Halifax harbour (Bowyer 2003).

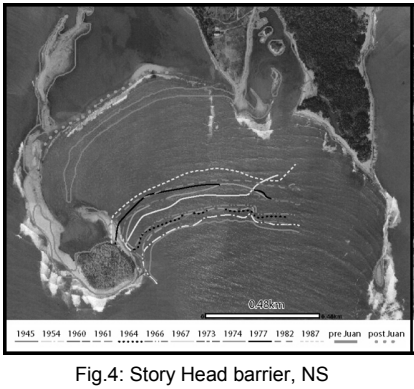

Fig.4: Story Head barrier, NS

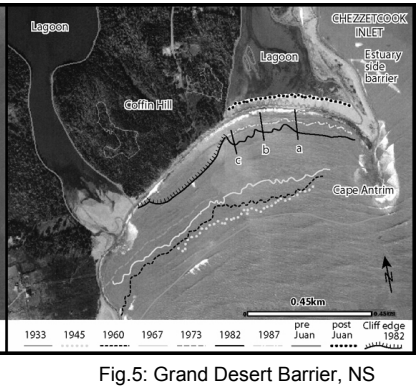

Fig.5: Grand Desert Barrier, NS

Story Head is a SA barrier (25km east of Halifax, Fig.4) facing south at the eastern side of Chezzetcook Inlet entrance. It had a well-documented rapid barrier retreat history between 1930-90 (Orford et al. 1996), but post-Juan is now broken down into wave washed shoals. Story Head was a low barrier (crest height at <4m NAD (1928)) and height appears to be a major factor in breakdown, given that Grand Desert barrier (western side of Chezzetcook, Fig.5) at 8-9m NAD (1928) crest height, also facing directly into the wave path was forced to retreat, but retained its overall SA structure.

The severity of the storm reduced towards the east, but was sufficient, as Fig.2F indicates, for Sober Island's SA section to be breached, with the northerly hard rock groyne now overlapped by reworked barrier sediments under southerly wave activity, identifying a new sediment pathway by which the sediment volume of the barrier can be reduced. Haulover Cove (120km east of Halifax: Fig.3B) exhibits a total reduction of the SA barrier to a sub-tidal elevation. SA barriers in both cases were evidently insufficient (in terms of barrier height and width) to resist the wave climate extremes and in the case of Haulover, to rebuild the barrier in the manner identified by Orford et al. (2003), i.e. the sediment volume was insufficient to recreate a stable profile.

MID- TO LATE-HOLOCENE BARRIER CHANGES IN SOUTHERN ENGLAND

This issue of overall spatial organization of gravel-dominated barriers and the balance of DA to SA has to be reconsidered when the context of sediment supply and RSL change rates are restricted. The south coast of England represents a near-iconic gravel dominated (≈ shingle) coastline with world-known classic depositional structures in Chesil Beach and Dungeness Foreland. In particular the gravel systems of Sussex (central southern England: between Brighton - Beach Head – Hastings – Dungeness: Fig1B)), which may have linked to the major Dungeness Foreland gravel accumulation, have had limited consideration in terms of source and transport corridors. The contemporary coast is one that is gravel starved (and sand starved; Anthony 2002), yet is managed through a process of beach replenishment and profile maintenance into a posture of barrier coherence implying SA around hard points of Tertiary cliffs and 20th century built-infrastructure.

This coastline presents a difficult task in establishing barrier reorganization given the scarcity of sediment record under the managed volumes. To obtain a perspective on how past barriers have evolved, stratigraphical analysis of freshwater and salt water organic phases as well as minerogenic deposition have been considered in six estuaries operating along this coast (Table 1: Fig.1B). Because there is no evidence for any RSL fall along this coast during the last 5ka, it is likely that the consolidation of barrier beaches principally controlled these regressive organic deposition/episodes. Barrier consolidation is likely to reflect periods of greater sediment input and throughput, and therefore, by implication, a period of stronger longshore transport, with cell elongation and greater spacing between cell boundaries. Under these conditions, the inlets to the six estuaries narrowed or closed, depending on the volume of river discharge. Conversely, periods when estuarine or marine silty clays and fine sands were deposited represent transgressive episodes resulting principally from inlet widening as a consequence of reduced longshore sediment transport. Such episodes would have been associated with cell breakdown and reduced cell boundary spacing, the boundaries located principally around the inlets. On this basis four time-slices in the last 5ka have been identified in which varying storminess and access to sediment have been specified to account for barrier structure. The full establishment of the total drift cell was probably only achieved briefly during some of the stormiest conditions of the Little Ice Age (16th - 17th centuries AD), a perturbation which has dominated coastal cell development and management lasting to the present day.

The early Holocene legacy

The reconstruction of cell development, discussed below, begins around 5,000 Cal yrs BP. This is because prior to this period, RSL was below –5 m O.D. and the configuration of the coastline was controlled more than it is today by the shape of the buried channel systems emanating from these former estuaries and coalescing with the palaeovalley system eroded into the bed of the English Channel (Antoine et al. 2003). Potentially, this more indented coastline of the early Holocene would have had a very different sediment transport system to that of the mid- to late-Holocene, with greater control exerted by headlands. Under this scenario, as RSL rose sufficiently to drown these headlands, the potential for the development of more extensive transport corridors increased. However, the abundant sediment available in the early Holocene, inherited from Pleistocene periglacial processes, probably facilitated an active drift system with sediment able to by-pass headlands. Therefore, early-Holocene barrier inception and consolidation was likely, together with the segregation of sand and gravel into discrete depositional zones within the English Channel (Anthony 2002).

The drowning of this landscape had two major consequences on the subsequent macroscale development of cell formation. First, it transferred shoreline processes to areas of flatter relief associated with former interfluves and to shore platforms whose formation may have been initiated under previous high RSL episodes. Second, it trapped and drowned extensive gravel deposits in the palaeovalleys of the English Channel (Bellamy 1995; Antoine et al. 2003), effectively removing a substantial body of sediment from contributing to the later-Holocene sediment transport system. Consequently, the coastline entered a phase of gravel sediment starvation, relying on very limited supplies from near-shore deposits, which were/are in sufficiently shallow water to be activated and moved onshore by (storm) waves, on the re-working of isolated raised beach deposits to the west (e.g. at Selsey Bill and Brighton) and on 'freshly' weathered flint from chalk cliffs, the latter providing only low volumes of material.

Cell development episodes

Four episodes of cell development from 5,000 Cal yrs BP have been identified, based principally upon the nature of estuary infill, as discussed above.

Episode 1: 5,000 Cal yrs BP (Fig. 6). At this time the estuaries to the west of Beachy Head (BH on Figs.6-9) were accumulating organic, regressive sediments, associated with freshwater fen (Thorley 1981; Jones 1971). However, estuaries generally to the east of Beachy Head were open to the sea (Jennings & Smyth 1987 & 1990). The Royal Sovereign Shoals, immediately to the east of Beachy Head would have been above MHW, effectively forming an extension to Beachy Head. The shoals today are exposed at LWST, and it is likely that they formed a significant landmass during the early- to mid-Holocene. Therefore, sediment was being transported in sufficient quantities to restrict tidal access in the western estuaries, and it is likely that a transport corridor existed east to the Royal Sovereign Shoals. Because eastern estuaries were open to the sea, this transport corridor must have had a boundary on the Royal Sovereign Shoals

(Fig. 4), with sand and gravel accumulating in the down-drift segment of the cell.

The form of the coastline to the east of Beachy Head was very different to that of today.

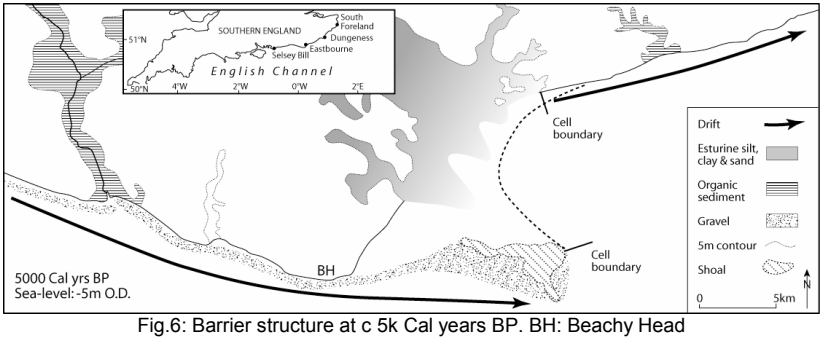

Fig.6: Barrier structure at c 5k Cal years BP. BH: Beachy Head

A broad estuary fronting Willingdon and Pevensey Levels (northeast of Beachy Head) probably extended southeast towards the Royal Sovereign Shoals. Evidence for this, is the existence of mid-Holocene estuarine sediments that reach the present coast at Willingdon Levels, and therefore are likely to have extended beyond this point.

Episode 2: 4,000 cal yrs BP (Fig.7). By 4000 years, western estuaries had opened while eastern ones had closed. The regression establishing largely freshwater conditions in these estuaries identifies a period of approximately 700 years when all the eastern estuaries of East Sussex may have been closed, and a single drift cell established: similar conditions to that from the inception of the current cell (in the 12th century – see Episode 4) to its modern breakdown.

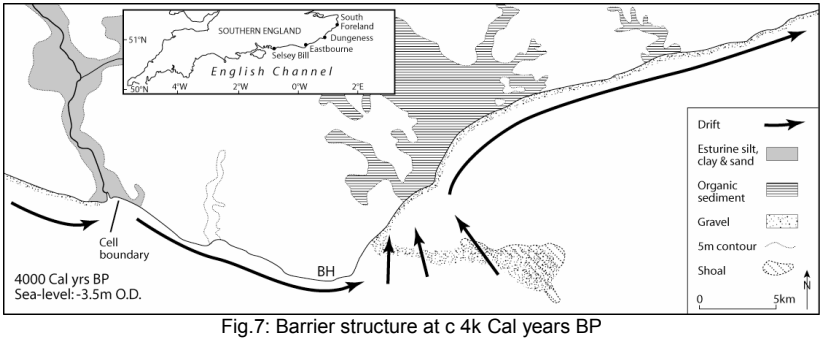

Fig.7: Barrier structure at c 4k Cal years BP

The opening of the western valleys indicates the establishment of a cell boundary at their entrance, and was likely to have triggered the formation of an ebb-tidal delta, imparting a positive feedback to the establishment of a cell boundary. As a consequence, sediment in the down-drift section of the former cell, now cut off from up-drift supplies, would have

been cannibalised and the associated gravel barrier would have broken down. This is depicted on Fig.5 by arrows showing sediment moving from the Royal Sovereign Shoals onto the adjacent section of coast at Willingdon and Pevensey Levels. Such a breakdown of the down-drift section of a former cell would have injected sediment in sufficient quantity to close off the former estuary mouth and create a stronger sediment transport corridor from Willingdon Levels eastwards, ultimately feeding Dungeness, the store at the down-drift end of the cell. Long & Innes (1993) provide evidence for gravel accumulation at Dungeness at around this time. These changes to cell positions and size, and the re-distribution of gravel from stores to adjacent sections of shoreline occurred approximately at the start of a period of increasingly wetter (and stormier?) conditions (Blackford 2000).

Episode 3: 2,500 Cal yrs BP (Fig.8). This period of the mid- to late-Holocene was characterised by a very slow rate of RSL rise, and therefore resulted in very limited sediment input from freshly weathered gravel. Also, most of the offshore, 'inherited' gravel sediment had been transferred onshore, although there may have been a remnant on the Royal Sovereign Shoals. As a consequence of this diminished sediment supply, the two cells present in the previous episode broke down into a number of smaller units, their boundaries located at estuaries. This fragmented and diminished drift system caused all the estuaries to be open. The continuation of this episode of fragmented cell development to the present day was prevented by a major perturbation that re-activated the sediment transport system. This re-activation resulted in major geomorphological changes, in particular the re-establishment of barrier beaches (as drift-dominated) and a switch from open to closed estuaries, resulting from the establishment of a single coastal cell defining an active and extensive transport corridor. This perturbation was driven by a climatic change to the increasingly stormier and colder conditions of the Little Ice Age, which had set in by the mid-13th century and ended by the mid-19th century (Higgitt 2001).

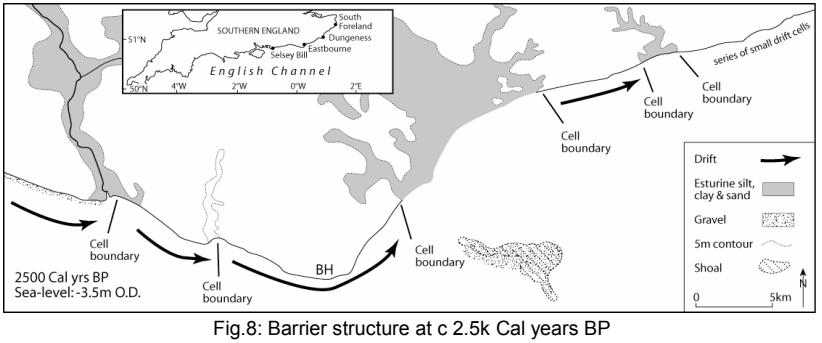

Fig.8: Barrier structure at c 2.5k Cal years BP

Episode 4: 12th to 17th centuries (Fig. 9). Evidence for the inception of the present cell system, dating to around the 12th century, is reclamation on Pevensey Levels (Salzman 1910; Dulley 1966) and on the marshes adjacent to the Rye barriers (Eddison 1998), which appears to correspond to a period of increased sediment supplies, at least locally.

For example, near Pevensey a tide mill was becoming inoperative by the second half of the 12th century, due to reduced tidal flow (Salzman 1910). Salt working on Pevensey Levels ceased in the mid-13th century (Dulley 1966) due to the cessation of regular tidal inundation, and gravel drifting across inlets is in evidence at Hastings by the 14th century (Ward 1920). This build-up and transport of gravel was probably the consequence of the initial stages in the formation of a major gravel assemblage known as the Crumbles Shingle (Fig.9).

The development of the Crumbles Shingle begins with the prior extensive estuarine conditions (Episode 3) at the mouth of the former Willingdon and Pevensey estuaries, inferring a possible ebb delta origin (Jennings & Smyth 1987). This substantial sand body subsequently formed a foundation for gravel accumulation, a pattern that is similar to the development of Dungeness (Basa et al. 1997; Long et al. 2006). The trigger for a change from a sand-dominated to a gravel-dominated system at the Crumbles means a re-activation of gravel supplies feeding onto the dissipative shoals. Jennings & Smyth (1990 &1991) have argued that the source of this gravel was more likely from offshore than longshore, as gravel deposits originating from alongshore were limited in extent, and the size of the former Crumbles was substantially bigger (Waghenaer's chart of 1588 and John Norden's map of 1595 indicate a 2km shoreline seaward of the present day) than local cliff-sourced longshore sediments could supply.

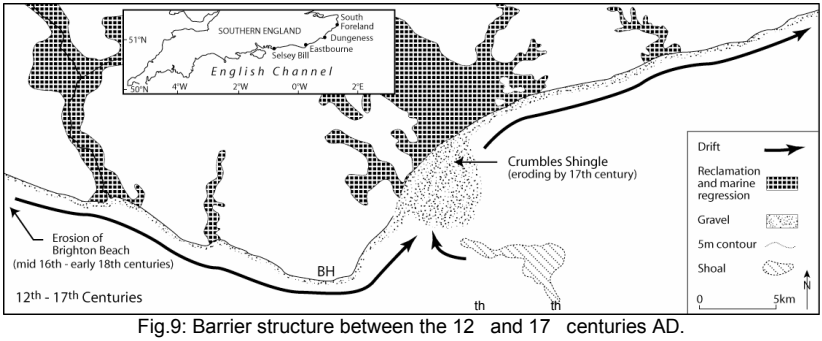

Fig.9: Barrier structure between the 12th and 17th centuries AD.

The proximity of the shoreline of the original Crumbles Shingle to the Royal Sovereign Shoal infers a sediment transfer from those shoals onshore and onto the sand body that lay between the Royal Sovereign Shoals and the entrance to Willingdon and Pevensey inlets. Under the initial prevailing dissipative conditions, gravel would have accumulated on the sand body until it had formed a structure large enough to establish reflective morphodynamic conditions (Jennings & Smyth 1990). Once that had occurred, longshore drift would have been initiated due to changes in the breaker characteristics as reflective conditions replaced dissipative ones.

This reconstruction of the origin of the Crumbles Shingle assumes a residual body of gravel on the Royal Sovereign Shoals following Episode 3, and its re-activation shoreward under the increased storminess of the Little Ice Age. Precisely dating the

origin of the Crumbles Shingle is problematic as it occurred at a time that pre-dates detailed documentary and map evidence, but a date of around the 12th century is commensurate with the documentary evidence summarised above. Intriguingly the re-entry and reworking of Crumble gravels into the eastern drift system did not appear to alleviate the sediment deficit position of the East Sussex barrier (e.g. SA) linking via the Rye barrier to the Dungeness Foreland. The period from the 12th to the 15th centuries witnessed numerous marine floods that regularly threatened reclamation attempts (Dulley 1966; Brandon 1972) and gave rise to substantial coastal re-alignment, especially in Rye Bay (adjacent to eastern limit of Fig. 1B). The possible 'breakdown' of the Rye Bay Barrier corresponds to a sequence of storms between 1250 to1291AD (Eddison 1998) leading to a pattern of continuous or episodic retreat of the barrier, rather than breakdown *per se*, a continuation of a process that started as the barrier rolled-over during Episode 3, as a consequence of diminished sediment supplies. Edison (1998) estimates the rollback as c. 2 km in approximately 300 years. This gives an approximate (minimum) retreat rate of 7 m a^{-1}. This realignment isolated Dungeness from up-drift supplies of gravel.

The early development of the Crumbles could be described as a localised redistribution of near-shore supplies. By the 16th to 17th centuries sufficient volumes of gravel were being transported along the coastline to the east of Beachy Head to prevent regular flooding, for example, at Pevensey (Salzman 1910; Dulley 1966). This period also saw major progradation of gravel ridges to the south of Rye, (Eddison 1998) which failed to connect with Dungeness due to the major indented realignment of the transport corridor by the rapid retreat of the original Rye barrier (cf. Long et al. 2006). This increase in the volume and spatial extent of longshore drift was largely due to erosion of the Crumbles Shingle, with the gravel being transported eastwards into Rye Bay.

Therefore, by the 16th century the re-distribution of gravel from the Crumbles was largely responsible for the establishment of an extensive cell and marked a significant change to the morphodynamics of the East Sussex coast. The consolidation of gravel beaches and barriers signaled the emergence of predominantly reflective conditions, which was a pre-requisite for the formation of an extensive cell. This cell, to the east of Beachy Head, functioned principally to re-distribute gravel from the Crumbles to the Rye Bay barrier. This episode of cell development ended 'naturally' soon after the 17th century. Cell fragmentation, resulting from decreasing volumes of sediment redistributed from the Crumbles would have been inevitable. However, the interplay between coastal management and cell fragmentation has modified cell development over the last two hundred years. The construction of groynes since the mid-19th century, and more recently gravel recharge on the Crumbles Shingle area has slowed erosion there. However, this has caused acceleration in the fragmentation of the down-drift part of the cell, with severe erosion occurring from Pevensey Bay eastwards. This coastline is now only stabilized through constant management by gravel recharging.

DISCUSSION

In Nova Scotia, of the four SA barriers monitored, H. Juan forced a breach in one, broke down two and forced major retreat in the fourth – all occurring in a storm whose wave excitation was of a 110 year return period. In a 2-3ka organizational span of drumlin-sourced barriers in NS, this return periodicity drives a high statistical likelihood that SA barriers will be moved into a breakdown phase and associated shoal features. The low percentage of SA along the NS coastline is interpreted as showing that the breakdown transition may occur more often than hitherto identified. If this is the case, then SA barriers should not be considered as sustainable features, with obvious implications for future management of such barriers. This perspective has to be constrained by three other factors: (1) the RSLR rate which sets the tempo of barrier change, (2) the spatial density of hinge positions on the basement relief upon which SA is fixed relative to sediment availability for barrier linkage; and (3) the consistency of longshore sediment supply. The last point is critical, as it is noticeable in NS that those SA barriers that are less prone to storm damage, are those with a major sand component that appears via a distinct foreshore apron and nearshore dissipative bottom that attenuate severe wave attack. In effect, the greater the domination by the gravel component of barrier volume, the more reflective the beach face is, and the longer and deeper the plan-view arc of the barrier (and concomitant loss of barrier height with increasing barrier length), then the more likely rapid rollover and final breakdown by storms will occur.

Southern England barriers show overall barrier behavior fitting into a punctuated self-organization of gravel barrier coasts (Forbes et al. 1995) that is characteristic of NS. In southern England over a time resolution approximately similar to the NS cycle, there have been periods of quiescence, characterised here by fragmented cells and open estuaries, that were interrupted by shorter episodes of rapid reorganization, marked by gravel barrier genesis and breakdown, and the establishment of active longshore sediment transport corridor and inlet closure. The major contrast has been in the variation of the basement zone in which these periods of reorganization have been able to take place. NS has a wider horizontal freedom whereas southern England has a constrained corridor. The narrowness of the coastal zone has seen barrier reorganization overlying barriers in a similar spatial position (building limited palimpsest) during the last 4-5ka, hence suggesting a different model of spatial organization than that identified for Nova Scotia. It is still one controlled by sediment supply and position of sources, but one where such sources are spatially constrained and barriers constantly cannibalised at smaller length and diminishing time scales as the overall volume of gravel availability declines. The four-time slices identify a changing gravel barrier organization with the development of DA that closes estuaries, and then reopens as the barriers segment into SA units. There is a revitalization of barriers that relates to a redistribution of gravel sinks into new phases of DA, though the overall reduction of such gravel sinks leads to a progressive thinning and segmentation of barriers. The survival of these depleted barriers as SA features has now more to do with post mid-19th century coastal defence policy than anything else. Without this defensive element these barriers would have now moved into a breakdown phase.

CONCLUSION

Swash-aligned barriers are not now thought to be long-term semi-equilibrium features, as they are prone to breakdown with extreme storms likely to be the agent of such breakdown. The breakdown process is controlled by the virtual cessation of longshore sediment transport, sufficient for swash alignment to develop as a precursor to breakdown. Where revitalization of transport rates is available, then SA barriers can be restructured as DA, as seen in southern England. The major difference between Nova Scotia and southern England barrier development is in the effective spatial width of the coastal pathway in which barriers were built. Where RSLR is low and basement morphology exerts spatial constraints on the barrier building, then forcing changes are more likely to allow revitalization of existing barriers, so that sequences of DA to SA to DA barriers can occur. Coastal defences (as in southern England) can deflect barrier breakdown and by masking breakdown trends may account for contributing towards the supposed resilience of swash-aligned barriers.

ACKNOWLEDGEMENTS

JDO appreciates the assistance of Christine Smyth in accessing material from the estate of Simon Jennings. The graphics support of Maura Pringle (QUB) is also gratefully acknowledged, as is the material provided by DNR (Nova Scotia).

REFERENCES

Anthony, E.J. (2002). Long-term marine bedload segregation, and sandy versus gravely Holocene shorelines in the eastern English Channel. *Marine Geology* 187, 221-234.

Antoine, P., Coutard, J-P, Gibbard, P. Hallegouet, B., Lautridou, J-P & Ozouf, J-C. (2003). The Pleistocene rivers of the English Channel region. *Journal of Quaternary Science* 18, 227-243.

Basa, T., Greensmith, J.T. & Vita-Finzi, C. (1997). The sub-surface Holocene Middle Sands of Dungeness. *Proc. Geologists' Assoc.* 108, 105-112.

Bellamy, A.G. (1995). Extension of the British landmass: evidence from shelf sediment bodies in the English Channel. In: Preece, R.C. (ed.) Island Britain: a Quaternary Perspective Special Publication 96. Geological Society Publishing House, Bath, 47-62. ISBN 1-897799-32-2

Blackford, J. (2000). Palaeoclimatic records from peat bogs. *Trends in Ecology & Evolution* 15, 193-198.

Bowyer, C. (2003) Hurricane Juan summary http://www.atl.ec.gc.ca/weather/hurricane/juan/summary_e.html

Brandon, P.F. (1972). Agriculture and the effects of floods and weather at Barnhorne, Sussex, during the late Middle Ages. *Sussex Archaeological Collections,* 109, 69-93.

Burrin, P.J. & Scaife, R.G. (1984). Aspects of Holocene valley sedimentation and floodplain development in southern England. *Proc.Geologists' Assoc.*,95, 81-96.

DNR(2003) Hurricane Juan preliminary assessment, Nova Scotia Dept. Natural Resources, http://gis2.gov.ns.ca/website/juan/viewer.htm

Dulley, A.J.F. (1966). The Level and Port of Pevensey in the Middle Ages. *Sussex Archaeological Collections,* 104, 26-45.

Eddison, J. (1998). Catastrophic changes: a multidisciplinary study of the evolution of the barrier beaches of Rye Bay. In: In: Eddison, J., Gardiner, M. & Long, A.J. (eds.) *Romney Marsh: Environmental Change and Human Occupation in a Coastal Lowland.* Oxford University Committee for Archaeology Monograph No. 46 the Alden Press, Oxford 65-87.

Forbes, D.L., Orford, J.D., Carter, R.W.G., Shaw, J. & Jennings, S.C. (1995). Morphodynamic evolution, self-organization and instability of coarse-clastic barriers on paraglacial coasts. *Marine Geology*, 126, 63-85.

Grove, J.M. (1988). *The Little Ice Age*. Methuen, London.

Higgitt, D.L. (2001). A brief time of history. In: Higgitt, D.L. & Lee, E.M. (eds.) *Geomorphological Processes and Landscape change: Britain in the Last 1000 Years*, Blackwell, Oxford, 1-26. ISBN 0-631-22273-1

Jennings, S. & Smyth, C. (1987). Coastal sedimentation in East Sussex during the Holocene. *Progress in Oceanography*, 18, 205-241.

Jennings, S. & Smyth, C. (1990). Holocene evolution of the gravel coastline of East Sussex. *Proc. Geologists' Assoc*., 101, 213-224.

Jennings, S. & Smyth, C. (1991). Holocene evolution of the gravel coastline of East Sussex: reply to correspondence. *Proc. Geologists' Assoc*., 102, 306-308.

Jennings, S., Greatorex, C., Smyth, C. & Spurr, G. (2003). The environmental archaeology of the Late Bronze Age occupation platform at Shinewater, near Eastbourne, U.K. In: Howard, A.J., Macklin, M.G. and Passmore, D.G. (eds.) *Alluvial Archaeology in Europe*. Balkema, Rotterdam, 93-110. ISBN 90 5809 561 4

Jennings, S., Orford, J.D., Canti, M., Devoy, R.J.N. & Straker, V. (1998). The role of relative sea-level rise and changing sediment supply on Holocene gravel barrier development: the example of Porlock, Somerset, U.K. *The Holocene*, 8, 165-181.

Jones, D.K.C. (1971). The Vale of the Brooks. In: Williams, R.B.G. (ed.) Guide to Sussex Excursions. *Trans. Institute of British Geographers*, 43-46.

Long, A.J. & Innes, J.B. (1993). Holocene sea-level changes and coastal sedimentation in Romney Marsh, southeast England, UK. *Proc. Geologists' Assoc*., 104, 223-237.

Long, A.J., Waller, M.P. and Plater, A.J. (2006). Coastal resilience and late-Holocene tidal inlet history: The evolution of Dungeness foreland and the Romney Marsh depositional complex (U.K.). *Geomorphology*, 82, 309-330.

Moffat, B. (1986). The environment of Battle Abbey estates (East Sussex) in medieval times; a re-evaluation using analysis of pollen and sediments. *Landscape History*, 77-93.

Orford, J.D., Carter, R.W.G. and Jennings, S.C. (1991). Coarse clastic barrier environments: evolution and implications for Quaternary sea-level interpretation. *Quaternary International*, 9, 87-104.

Orford, J.D., Carter, R.W.G. and Jennings, S.C. (1996). Control domains and morphological phases in gravel-dominated coastal barriers. *Journal of Coastal Research*, 12, 589-605.

Orford J.D., Forbes D.L. & Jennings S.C. (2002). Organisational controls, typologies and time scales of paraglacial gravel-dominated coastal systems. *Geomorphology*, 48, 51-85.

Orford, J.D., Jennings, S.C. and Pethick, J. (2003). Extreme storm effect on gravel-

dominated barriers. Coastal Sediments'03. In Davis, R.A. (ed). *Proceedings of the International Conference on Coastal Sediments 2003.* CD-ROM published by World Scientific Publishing Corp. and East Meets West Productions, Corpus Christi, Texas, USA. ISBN 981-238-422-7, 12pp.

Salzman, L.F.(1910). The inning of Pevensey Level. *Sussex Archaeological Collections,* 53, 32-60.

Thorley, A. (1981). Pollen analytical evidence relating to the vegetation history of the Chalk. *J.Biogeography,* 8, 93-106.

Waller, M. P. and Hamilton, S. 2000. Vegetation history of the English chalklands: a mid-Holocene pollen sequence from the Caburn, East Sussex. *J.Quat. Sci*.15, 253-272.

Ward, E.M. 1920. The evolution of the Hastings coastline. *Geographical Journal* 56, 107-123.

PROFILE DYNAMICS AND PARTICLE TRACER MOBILITY OF A COBBLE BERM CONSTRUCTED ON THE OREGON COAST

Jonathan C. Allan and Roger Hart

Oregon Department of Geology and Mineral Industries, Coastal Field Office,
P.O. Box 1033, Newport, OR 97365, USA. jonathan.allan@dogami.state.or.us.

Abstract: In response to the erosion of Cape Lookout State Park on the Oregon coast, a cobble berm (dynamic revetment) was constructed for shore protection, designed to be similar to a natural cobble beach. For added protection it is backed by an artificial dune reinforced with a core of sand-filled geotextile bags. We have monitored these structures since 2001, including periodic surveys and measurements of cobble mobility through particle tagging. The surveys have demonstrated profile responses to storms that are the same as found for natural cobble beaches, while the particle tagging has documented a high degree of cobble mobility, including a significant net longshore transport. To date the structures have survived five winters, including several major storms that have resulted in periodic overtopping, providing the desired level of protection to the park. However, due to the loss of cobbles from the cobble berm, its long-term stability is uncertain.

INTRODUCTION

Gravel beaches, consisting of pebbles to large cobbles, have long been recognized as an effective form of natural coastal protection, exhibiting a remarkable degree of stability in the face of sustained wave attack while also minimizing the potential for overtopping and inundation (Nicholls and Webber 1988; Sherman 1991; Bradbury and Powell 1992). This is because gravels exhibit a greater propensity for onshore movement compared with sand-size particles, partially due to their high threshold of motion and because of the asymmetry of shoaling waves and swash velocities on the beach face. As a result, the gravels accumulate landward of the swash zone where they form a high, steep sloping gravel beach that is able to disrupt and dissipate the incident-wave energy, adjusting its morphology to the prevailing waves. Thus,

artificially constructed gravel beaches have been suggested as a viable approach for protection from coastal erosion (van Hijum 1974; Ahrens 1990). However, few studies have demonstrated the effectiveness of such structures on high energy shores.

During the past decade, significant erosion has occurred along the Pacific Northwest coast of Oregon produced by an unprecedented number of severe storms and as a result of the occurrence of major El Niños. This erosion has been especially chronic at Cape Lookout State Park (CLSP), Figure 1, located at the south end of Netarts Spit on the northern Oregon coast (Komar 1998).

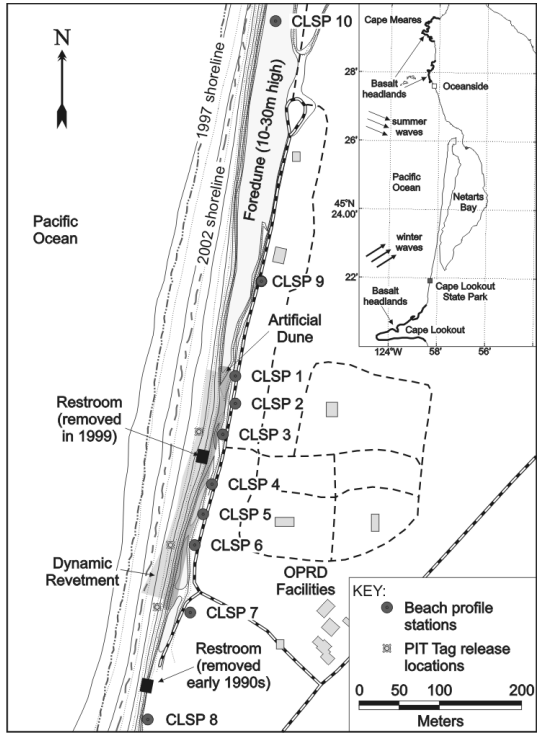

Fig. 1 Location map of Cape Lookout State Park showing the beach monitoring sites and the gravel tracer release points.

Netarts Spit has a history of alternating phases of erosion, followed by subsequent beach and dune rebuilding. For example, Stembridge (1975) observed that the spit was breached at multiple locations as a result of a period of intense storm activity during the winter of 1939. However, the breaches soon filled and the spit remained stable up until the early 1980s. Erosion returned to Netarts Spit as a result of the 1982-83 El Niño (Komar 1986), which produced a combination of high ocean water levels coupled with large waves. The arrival of the storm waves from the southwest resulted in "hotspot" erosion at the south end of the spit, with the sand having been

removed to offshore bars and to the north as the result of longshore transport. The erosion eventually destroyed a wooden bulkhead constructed in the 1960s seaward of the campground by the Oregon State Parks and Recreation Department (OPRD). While the beach did rebuild during the late 1980s, the amount of aggradation was generally small. Erosion returned during the late 1990s, first as "hotspot" erosion associated with the major 1997-98 El Niño (Komar 1998; Revell et al. 2002), followed by the extreme 1998-99 winter characterized by four 100-year storms (having been estimated in 1997 to be a 10-m significant wave height). The largest storm generated 14.1 m significant wave heights that effectively destroyed the remaining foredune fronting the park's campground, flooding the park and damaging its facilities. The cumulative erosion of these two winters resulted in the dune toe receding landward by on average 18 m, while the estimated volume of sand lost from the foredune along Netarts Spit was about 1.2 million m^3.

It was clear that CLSP could expect additional damage during subsequent winters, unless some form of shore protection was installed. However, instead of constructing a conventional riprap revetment commonly used along the Oregon coast, the decision was made by the OPRD to construct a cobble berm (dynamic revetment), in effect a gravel beach backed by an artificial dune reinforced with sand-filled geotextile bags (Figures 2 and 3)(Allan and Komar 2002; Komar et al. 2003; Allan and Komar 2004). The construction of the cobble berm/dynamic revetment at CLSP has presented a unique opportunity to investigate the stability and effectiveness of a prototype structure in a high-energy environment, and to compare the dynamics of such structures with natural cobble beaches. The objective of this paper is to examine two components of gravel beach stability, the profile responses during storms and the use of Passive Integrated Technology (PIT) tag tracers to measure the mobility of the gravels.

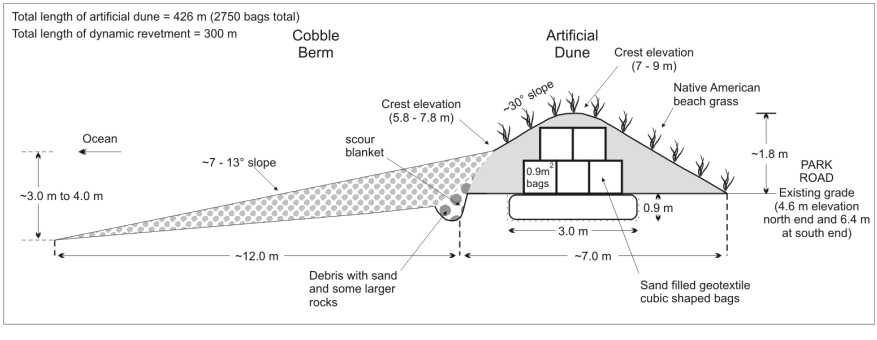

Fig. 2 Conceptual design elements of the gravel beach and artificial dune constructed at Cape Lookout State Park.

STUDY SITE

Cape Lookout State Park is located at the southern end of the Netarts littoral cell, a 15 km sandy shore bounded by two prominent headlands; Cape Meares marks the northern boundary while Cape Lookout is at the south, extending some 3.2 km out

into the Pacific Ocean. The park itself is located approximately 2 km north of Cape Lookout. The beaches within this cell are composed of fine sand and are characterized by low slopes (~2.3º), making them fully dissipative in the morphodynamics classification of Wright and Short (1983). Along the southern 4 km of the spit, a narrow (10 to 15 m wide) gravel beach backs the otherwise sandy beach, with the crest of the gravel beach ranging in elevations from 6 to 7 m relative to the North American Vertical Datum 1988 (NAVD88); NAVD88 is approximately 0.1 m above Mean Lower Low Water (MLLW) at CLSP. Mean grain-sizes along the gravel beach range from –5.5Ø to –7.2Ø (45 to 147 mm), very coarse gravel to large cobbles, the deposit is moderately well sorted and there is little evidence of either cross-shore or longshore sorting of the gravels along the beach. The gravels are entirely basalt in origin and have a mean hardness of 47.3 N/mm^2 (Newtons/mm^2) (standard deviation of 3.7 N/mm^2). With this beach consisting of a steeply-sloping upper foreshore or backshore ridge composed of gravel, fronted by a lower foreshore of sand (Figure 3A), with a distinct boundary between them, it can be classified as a "composite beach" using the classification system of Jennings and Shulmeister (2002).

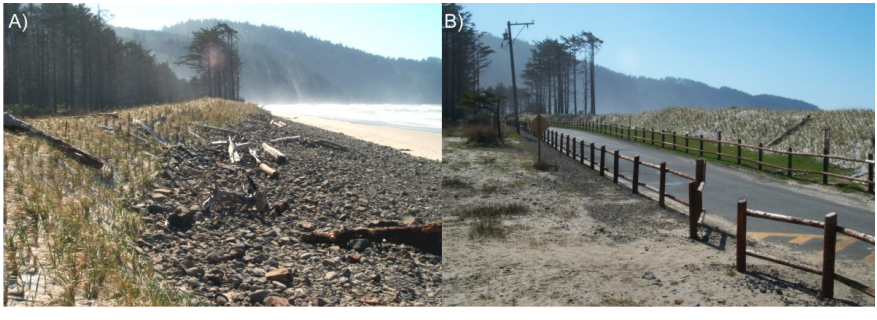

Fig. 3 A) The completed cobble berm (dynamic revetment) and artificial dune in March 2001. B) Landward view of the artificial dune.

COBBLE BERM DESIGN AND CONSTRUCTION

The basic concept of a cobble berm (dynamic revetment) is the construction of a gravel beach that can adjust and deform its morphology in response to the prevailing waves (Figure 3), being dynamic in permitting particle movement as opposed to being static as in a conventional revetment where large riprap stones are used. As a result, the construction of such structures is simpler compared with conventional riprap revetments since the particles used (gravel) are smaller, and their placement of the gravel does not require special care (Ahrens 1990). The major design elements can therefore be reduced to a few critical aspects: the size and type of gravel, the slope of the gravel face, the volume of material, and the determination of an appropriate crest elevation. Of these, the identification of a suitable gravel source is probably the most problematic, with distant sources possibly precluding the construction of dynamic revetments due to the high costs involved to transport the material to a site (Allan et al. 2005).

Since there are a number of gravel beaches present along the Oregon coast that offer protection to shorefront properties, the decision was made to base the design elements on the morphology of natural cobble beaches found along Netarts Spit and elsewhere (Komar et al. 1999). Surveys of the natural gravel beaches yielded slopes on the order of 11º to 14º (between 1-in-5 and 1-in-4), and this was recommended for the constructed dynamic revetment. The required elevations were based on an application of the wave runup model developed by Ruggiero et al. (2001), which considers the combined effect of the measured tides plus the calculated swash runup level achieved during storms. Analyses of potential extreme events yielded swash runup levels of 7 to 8 m, which when added to a Spring tide yielded total water elevations ranging from about 9 to 10.5 m NAVD88. Surveys of the gravel beach to the north of CLSP supported these estimates since their crest elevations were found to range from 7 to 8.5 m. Accordingly, it seemed reasonable to construct the dynamic revetment to attain a crest elevation of 8 to 9 m to prevent overtopping during extreme storms. However, because the volume of gravel required to construct the cobble berm to such specifications was found to be substantial, the decision was made by the OPRD to develop an artificial dune landward of a smaller scale cobble berm (Figure 2 and 3). Thus the artificial dune would form the backbone of the overall structure, providing both mass as well as the necessary height needed to minimize wave over-topping. Figure 2 depicts the overall design elements of the artificial dune, which was completed in April 2000. The dune was subsequently covered with a jute/coconut fiber cloth and planted with Native American grasses (Figure 3).

Construction of the cobble berm at CLSP was initiated early in the 2000 winter. Gravel were extracted from the natural cobble beach in the north along Netarts Spit (~3000 m^3) and from the south end (~2300 m^3) of the cell in areas where it was believed that more than sufficient volumes were present to protect the dunes and where no park infrastructure is present. The cobbles were carried to the construction site on a front loader, and placed evenly across the pre-existing profile. The volume added along the length of the constructed dynamic revetment varied depending on the antecedent beach morphology. The top of the added cobble overlaid a scour blanket placed beneath the artificial dune (Figure 2). No attempt was made to provide toe protection for the placed cobbles; the natural deposit of cobbles extends below the sand beach, providing the only toe support. The total cost of the structures was $125,000, and was able to be kept to a minimum since the construction phase was carried out with the aide of work-released labor from the State penitentiary.

METHODS

In order to understand the dynamics and effectiveness of the cobble berm, we initiated a research program to quantify its responses to storms through a monitoring program that has included repeated surveys and analyses of its response to storms, measurements of evolving grain-size statistics, and observations of particle movement by tagging experiments. At the same time, similar data are being collected on nearby gravel beaches for comparisons.

Monitoring of the cobble berm and artificial dune was initiated in July 2001, six months after the structures were completed. Our initial monitoring efforts focused on seven transects (CLSP 1 through 7 in Figure 1), but was eventually expanded to 10; seven of the profiles, spaced approximately 35 m apart, cross the cobble berm, while 3 profiles are located on natural cobble beaches to the north and south of the structures. Surveying was initially undertaken using a conventional Total Station theodolite. Since December 2004, measurements of the beach morphology have been accomplished with a Trimble 5700/5800 Real Time Kinematic-Differential Global Positioning System (RTK-DGPS), using procedures outlined in Ruggiero et al. (2005). The surveying has typically been concentrated in the winter to capture the effects of storms, with fewer surveys occurring in the summer.

Assessment of cobble transport was undertaken using a variety of approaches. Initial experiments focused on using painted particles to document their mobility. However, due to the extreme wave and current regime at CLSP, this approach was soon abandoned as our recovery rates were low, likely due to the particles having been buried. We also experimented with magnetized tracers but discovered that the cobbles at CLSP are strongly magnetic, which meant that this approach also had to be abandoned. Our attention then turned to using Radio Frequency Identification technology (RFID) to detect Passive Integrated Transponder (PIT) tags inserted in the cobbles (Allan et al. 2006). This approach has been used extensively for tagging fish and most recently has been experimented with in a sediment transport study undertaken in a gravel bed river (Lamarre et al. 2005).

The RFID system consists of three main components, the transponder "PIT" tags that are inserted into the cobbles, a palmtop computer and RFID reader unit, and an antenna; we developed RFID systems based around a 0.3 m and a larger 1.0 m diameter antenna. A complete description of our approach is described in Allan et al. (2006). Our experiments used 32 mm long PIT tags that have a detection range of up to 1.0 m. The tags are glass-encapsulated with each tag factory programmed with a unique identification number, and have an estimated potential lifespan of 50 years. A range of cobble sizes were collected from the cobble berm and a tag inserted into each and cemented in place; the particles ranged in size from -6.0Ø (64 mm) to -7.5 Ø (181 mm), with a dominant size mode centered at -6.5Ø (90.5 mm). Each of the cobbles was weighed and analyzed to determine its general characteristics, including orthogonal measurements of the particle's long (*L*), intermediate (*I*) and short (*S*) axes using a digital caliper, and measurements of its mass and hardness. A total of 200 particles were initially released at four locations on 15 March 2004; two injection points were established respectively at CLSP 6 and 3 (Figure 1). An additional 200 particles were released on 31 January 2005 at CLSP 7 bringing the total number of tracers presently being tracked to 400.

Relocating the tracer particles is technically simple, albeit time consuming. An operator simply drags the antenna and RFID reader unit across the gravel and sand beach, walking track lines. The discovery of a PIT tag tracer is identified by an audible noise from a siren attached to the RFID unit, followed by the particle's

identification number appearing on the palmtop screen. Having identified the location of the tracer, its' position is then observed using the Trimble 5700/5800 RTK-DGPS system. Relocation of the tracers has been accomplished on several occasions over the past two and half years, with the most recent complete survey having been carried out in May 2006. Over time, a number of the tracers have been removed from the beach in order to assess whether the cobbles have undergone measurable abrasion according to their weight reduction. On 14 December 2006, forty-five of these cobble tracers were re-released onto the cobble berm near the sand/cobble junction at CLSP 6 just prior to a major storm in order to assess their response to a significant wave event. At the same time 150 gravel particles were released (the particles ranged in size from -4.3Ø (20 mm) to -6.5Ø (91 mm), with a mean size of -5.9Ø (59.9 mm)), tagged by having painted them, in order to document the mobility of these smaller particles compared with the cobbles.

RESULTS

The CLSP cobble berm has a mean elevation of 6.4 m, and is steepest in the south (~8º) compared with the north (5º). The elevations of both the berm and the artificial dune vary along the shore, Figure 4, with the highest elevations (8.9 m) located near CLSP 5 at the south end, decreasing to the north and south; with the exception of a beach access path (Figure 4), the dune crest reaches its lowest point (6.7 m) adjacent to CLSP 2. Figure 4 also documents that the cobble berm aggraded in the north during the years 2002 to 2005, having raised the berm crest by on average 0.5 m. This response was accompanied by an overall steepening of the berm's slope. In contrast, the elevation of the cobble berm decreased by almost 1.0 m south of the CLSP 6 profile site. As will be shown below, this change is due to the movement of gravels from the south, and their redistribution to the north. Between profiles CLSP 6 and CLSP 4, the cobble berm has remained essentially unchanged.

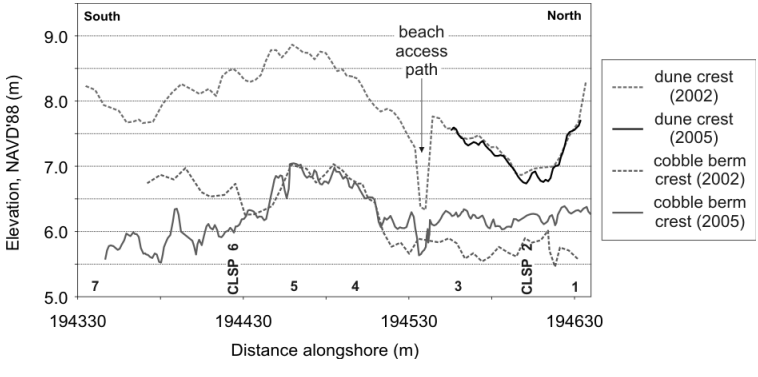

Fig. 4 Changes in the alongshore variability in the elevations of the cobble beach and artificial dune at CLSP

Figure 5 presents a summary of the measured profile changes at CLSP 2 located at the north end of the structures (Figure 1). The figure identifies the profile elevation on the right axis, while the left axis depicts the difference between the minimum and

maximum envelope of change. The latter provides a measure of the range of variability across the sand beach and cobble berm (graphed as the red dashed line in Figure 5) and is derived from almost 30 surveys of the beach. An average profile is also shown (black line), while results from the most recent survey (24 December 2006) of the beach are plotted in blue.

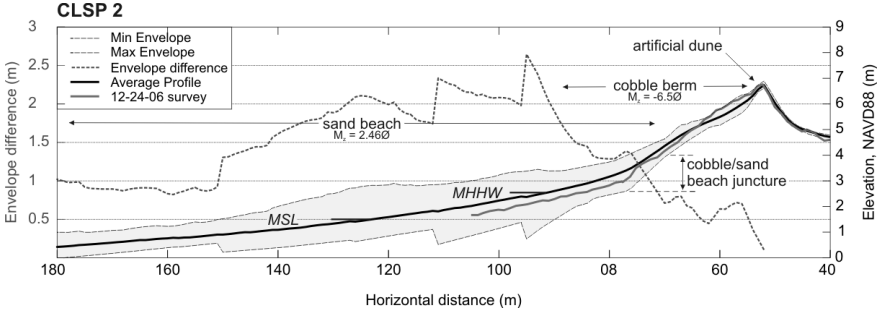

Fig. 5 Beach profile responses at profile CLSP 2, including the average beach profile and envelope of variability. Note: MSL denotes Mean Sea Level and MHHW indicates Mean Higher High Water.

The most noticeable feature of Figure 5 is the greater variability shown for the elevation of the sandy portion of the beach, and the degree to which it covers the cobble berm. Typically, the sand beach aggrades against the cobble berm over the summer months, which causes the junction between the sand beach and gravel foreshore to be positioned further landward and at higher elevations, compared with the winter when the sandy beach is eroded and its profile morphology is lowered. As a result, the lower cobble face typically experiences negligible gravel transport for several months, until the sand beach has lowered sufficiently in the following winter, allowing waves to once again mobilize the cobbles. The largest vertical excursion seen in Figure 5 occurred in January 2004, when a rip embayment formed in front of the cobble berm and lowered the sand beach elevation by 2.5 m. These changes clearly contrast with the magnitude of change observed across the cobble berm, having experienced a maximum vertical excursion of no more than 0.5 m, while the standard deviation of vertical change is ±0.1 m. This small level of response highlights the resilience of the cobble berm to storms.

Figure 6A documents the major cross-shore profile changes found in the surveys of the cobble berm at CLSP 2, while Figure 6B depicts the response of the berm at five select contour elevations (6.5, 6, 5.5, 5, and 4.5 m) during the five years of surveys, contrasting the trends in the upper portion of the berm's profile compared with its lower half. The results indicate that the central to lower part of the cobble berm initially eroded, with some of the gravel having been transported up the berm to produce the progradation of the 5.5 m contour during the 2001/03 winter. However, the response shown between July 2001 and 17 November 2002 for changes at the 4.5 and 5.0 m elevations, Figure 6A, probably incorporates some component of the sand beach also having been eroded; the sand beach at the time was in its most aggraded

state while subsequent summer surveys have been characterized by smaller sand volumes. By 27 January 2003, the cobble berm had prograded approximately 6 m seaward in response to the arrival of a slug of gravel at the site, transported en mass in the longshore direction along the cobble beach. Some gravel was also transported up the cobble berm face, raising the berm crest elevation slightly (Figure 6).

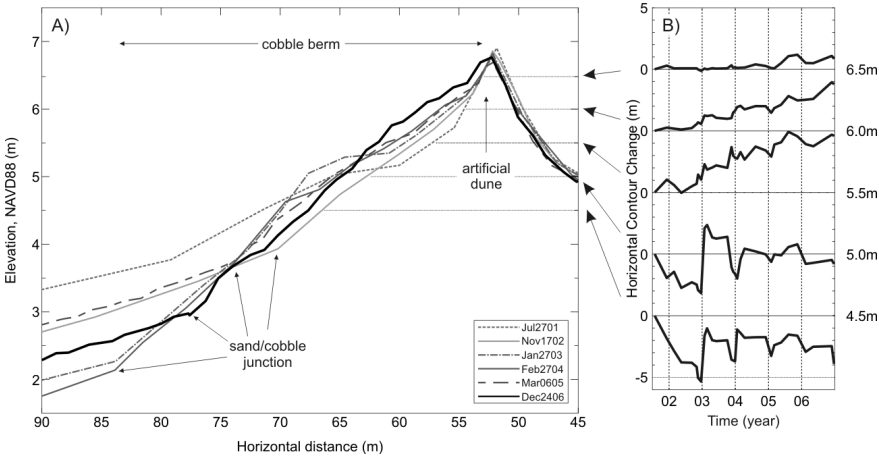

Fig. 6 A) Major morphological changes derived from the beach surveying. B) Long-term response of the cobble berm as defined by the response of the berm face at five select contour elevations.

Aside from an early phase of erosion during the 2003/04 winter, the cobble berm continued to gain material, resulting in further aggradation at its crest. The most recent survey (24 December 2006) reveals that this process has continued, with the berm having raised its crest elevation to such an extent that cobbles are now periodically carried over the artificial dune during major storms (Figure 7). This last aggradation phase occurred primarily as a result of a major storm on 21 December 2006, which generated an 8.2 m significant wave height (H_s) and a peak spectral wave period (T_p) of 16 seconds. The calculated total water level (wave runup plus tide) for this event using the Ruggiero et al. (2001) wave runup model was 6.9 m NAVD88, which produced minor overtopping of the artificial dune in the north (Figure 7). The patterns shown in Figure 6B reveal that the most significant morphological changes on the cobble berm occur during the winter, while the summer months are characterized by little to no change, this of course being expected since the waves are only able to impact the berm during the winter months. While the upper portion of the cobble berm has clearly gained material over time, the lower section of the berm continues to experience alternating phases of erosion and accretion, as particles are transported to the site and then subsequently removed. These patterns are consistent with observations by Everts et al. (2002) of natural cobble beaches on the southern California coast, whereby aggradataion and profile steepening occur during winter storms, as the cobbles and gravel are carried up the beach face.

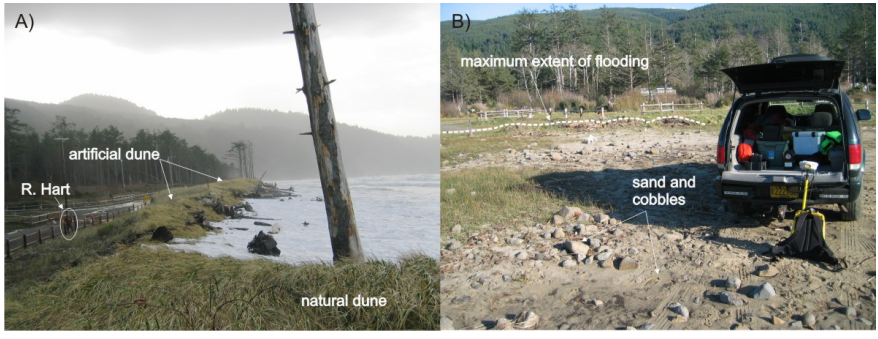

Fig. 7 A) wave overtopping on 21 December 2006. B) A major storm on 3-4 February 2006 overtopped the entire structure. This event transported a significant amount of gravel over the artificial dune and into the park.

To understand the patterns of cobble transport responsible for the profile changes, we have undertaken a series of experiments to track the movement of individual cobbles by inserting PIT tags into 400 cobbles as described in the METHODS section (Allan et al. 2006). Recovery rates have been very good, 90% one month after their release, while our most recent survey in May 2006, 27 months after the particles were released, yielded a recovery rate of ~33%. This most recent survey includes the results of particles injected at the CLSP 7 profile site on 31 January 2005 (Figure 8A). Much of the decrease in particle recovery over time can be attributed to the offshore transport of the cobbles down the berm's face, to its lower reaches that are exposed during the winter. With the return of summer, the sand beach aggrades across the lower cobble berm, burying those tracer cobbles to depths where they cannot be detected (recall that the PIT tags used have a maximum detection depth of about 1.0 m, while the sand beach envelope of change may reach as much as 2.5 m). Our survey undertaken in May 2006, following the re-exposure of the lower cobble berm during the 2005/06 winter, confirmed the presence of those cobble tracers, and also discovered a number of cobble tracers that had not been seen since they were first injected onto the cobble berm two years earlier. Nevertheless, Figure 8A reveals that several tracers have been transported significant distances (up to 334 m) along the cobble berm during a relatively short period of time (essentially 16 months). As a result, it is also possible that we may not be covering a sufficiently large area when scanning for the tracers, with part of the reduction in recovery rates being accounted for by extreme longshore transport distances.

As shown in Figure 8A, the cobble tracers on average document a net northwards transport along the shore, consistent with the morphological response of the cobble berm, with the surveys having indicated that its south end has experienced a net loss of gravel. The updated results presented here confirm our earlier observations of northward cobble transport, discussed in greater detail by Allan et al. (2006). Unexpected, the cobble tracers released at CLSP 7 appear to be moving at a faster rate along the beach, indicated both by their greater dispersion and distance of transport compared with the tracers released earlier in March 2004. This is despite

the fact that these latter cobbles are comparable in size to those earlier tracers. Allan et al. (2006) observed that the predominant northward transport of the gravels was due to the prevalence of waves from the west to southwesterly directions, which results in their breaking obliquely to the shore forming strong northward-directed longshore currents. In contrast, summer wave conditions are characterized by lower wave energy levels (from west to northwest directions), and with the eventual return of a fronting sand beach, the cobbles are not transported back to the south. These findings contrast with observations by Everts et al. (2002), who found no evidence for a net longshore transport of the cobbles on the coast of southern California.

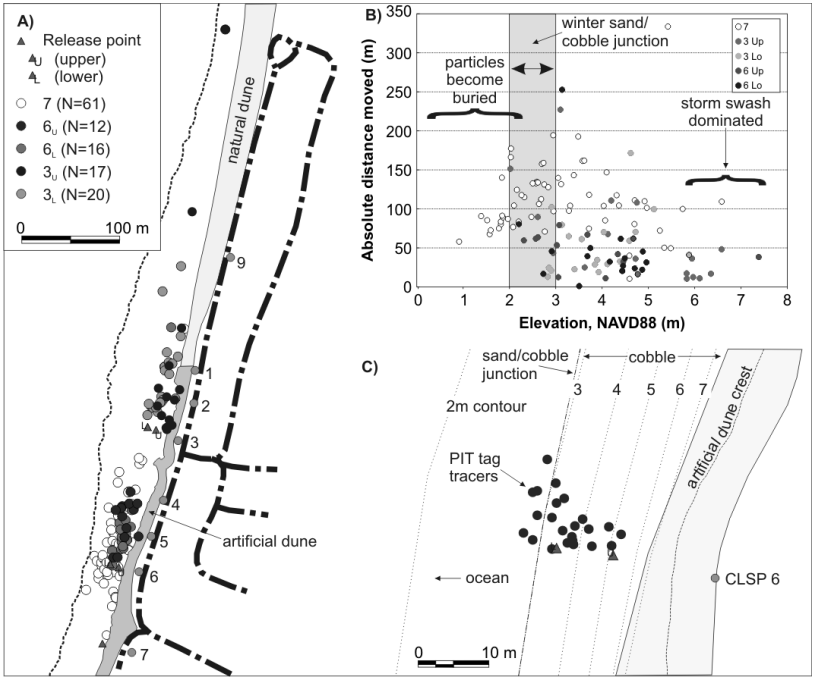

Fig. 8 A) Particle tracking results as of May 2006. B) Relationship between gravel tracer movement (absolute values) versus the elevations of the tracers on the cobble berm. C) Particle dispersion in response to a single storm on 21 December 2006.

Of interest, the bulk of the cobble tracers (61% of those recovered) tended to be located close to the sand/gravel beach junction, approximately between the 2 to 4 m contour elevations (Figure 8B). The cobble tracers also locally exhibit a strong cross-shore transport, characterized by both upslope and downslope movements, with a few being carried out onto the sand beach. As a result, those particles that are transported down the cobble berm face, below the 2.5 m contour elevation, may experienced negligible transport for extended periods of time, as the sand aggrades against the cobble berm during the summer. Future movement of these tracers will therefore be dependent on sufficient lowering of the sand beach elevation. Similarly, those particles that are transported up the cobble berm (e.g. above the 6 m contour) may

also exhibit slow to negligible transport rates, since at those high elevations their movement depends on occurrences of rare major storms that occur at high tides (Figure 8B). Within the mid-range of elevations are those particles that are moving quickly along the shore, since this is the region dominated by a higher incidence of swash runup excursions.

Comparisons between the particle size, as determined by the intermediate (*I*) and short (*S*) axis of the cobbles, revealed some evidence of preferential sorting with distance along the shore. Initial observations by Allan et al. (2006) indicated that the larger particles were tending to outrun the smaller particles. However, our updated results suggest that this process is beginning to reverse, with the smaller particles (~60-80 mm size range) tending to outrun the larger cobbles (i.e. *I*-axis greater than 80 mm). Nevertheless, the plots were characterized by considerable scatter, indicating that all grain-sizes were capable of moving both short and long distances. Our monitoring of the gravel tracers has also revealed evidence of particle abrasion over time that is correlated with the net distance moved by tracers (Allan et al. 2006).

Finally, Figure 8C shows the response of the cobble tracers during a storm on 21 December 2006. A total of 45 cobble tracers were released prior to the event at the sand/gravel junction on profile CLSP 6. In addition, these cobble tracers were supplemented with 150 painted gravel-size particles, 75 released at each of two positions across the profile on 12 December 2006; the injection points were the same as those used during our initial release in March 2004 (Figure 8A). These gravel particles had a mean grain-size of -5.9Ø (59.9 mm), significantly smaller than the cobble tracers, the objective of this experiment having been to document their different mobility during the storm. Figure 8B shows the dispersion of the tracers based on their relocation immediately following the storm. The results indicate that the cobble tracers were dispersed in the cross-shore direction, with several of the particles having been transported up the cobble berm, while the majority of the cobbles were transported in a northward direction. This response is consistent with our observation of the other PIT tag tracers as depicted in Figure 8A and 8B. The painted gravels were exposed to two separate events, with the first event occurring on 15 December 2006. Those gravels injected near the sand/cobble junction disappeared entirely, while the gravels released higher up on the berm were dispersed mainly in the cross-shore direction, but remained congregated around their injection point. Following the second storm on 21 December, we were unable to relocate any of the painted gravels, highlighting the limitation of tagging particles by painting them. However, the experiment did provide evidence for the extreme mobility of the gravel under the vigorous swash of those storm waves, a significantly greater mobility and transport than experienced by the cobbles. Efforts to understand these patterns and the response of the gravels to swash activity during individual storms is ongoing.

CONCLUSION AND DISCUSSION

Since its construction in 2000, the cobble berm and artificial dune constructed at CLSP have performed well, having survived several major storms, when both structures were overtopped. To date, damage to the structures has been generally

minor, suggesting that they can be a viable alternative to conventional engineered solutions.

Our beach monitoring efforts have revealed that the cobble berm has over time tended to aggrade along its northern end, while its southern half has remained essentially unchanged; in contrast the berm south of the CLSP 6 profile site has progressively eroded over time. Results from the beach surveying also demonstrate the resilience of the cobble berm, which has been characterized by a maximum vertical excursion of no more than 0.5 m, while the standard deviation of vertical change has been only ±0.1 m. This reinforces the perception that gravel beaches are an effective buffer in the face of sustained wave attack. Assessments of particle transport using RFID technology and PIT tags inserted in 400 cobbles has revealed a predominant net northward transport of the cobbles over time, with the particles tending to congregate near the sand/cobble beach junction due to its greater susceptibility to wave swash activity. The tracer experiments also revealed significant cross-shore movement, with the particles tending to move in both upslope and downslope directions during major storms. Of concern, the existence of a predominant net northward migration of the cobbles documented by the tracer experiments will in time degrade the reliability of the structure due to the net loss of gravel and cobbles, leading to the need for periodic 'top-ups' to maintain the structure's integrity.

ACKNOWLEDGEMENTS

This work was conducted under the National Shoreline Erosion Control Development and Demonstration Program (Section 227) authorized by the Water Resources and Development Act of 1996 (Public Law 104-303, 110 Stat. 3658), under contract number W912HA-04-C-0028. We are grateful for the assistance provided by Dr. Don Ward and Mr. Bill Curtis from the Engineer Research Development Center (ERDC) of the U.S. Army Corps of Engineers. We are especially grateful to Dr. Paul Komar who provided comments on the manuscript, and Dr. Alan and Wendy Niem for their assistance with sample preparation.

REFERENCES

Ahrens, J. P. (1990). "Dynamic revetments," *Proceedings 22nd Conference on Coastal Engineering*, ASCE, 1837-1850.

Allan, J. C., Hart, R. and Geitgey, R. (2005). "Dynamic revetments for coastal erosion stabilization: A feasibility analysis for application on the Oregon Coast," Special Paper-37, Oregon Department of Geology and Mineral Industries, Portland, Oregon.

Allan, J. C., Hart, R. and Tranquilli, V. (2006). "The use of Passive Integrated Transponder tags (PIT-tags) to trace cobble transport in a mixed sand-and-gravel beach on the high-energy Oregon coast, USA," *Marine Geology*, 232(1-2): 63-86.

Allan, J. C. and Komar, P. D. (2002). "A dynamic revetment and artificial dune for shore protection," *Proceedings of the 28th Conference on Coastal Engineering*, ASCE, 2044-2056.

Allan, J. C. and Komar, P. D. (2004). "Environmentally compatible cobble berm and artificial dune for shore protection," *Shore & Beach*, 72(1): 9-18.

Bradbury, A. P. and Powell, K. A. (1992). "The short term response of shingle spits to storm wave action," *Coastal Engineering*, 16: 2695-2707.

Everts, C. H., Eldon, C. D. and Moore, J. (2002). "Performance of cobble berms in Southern California," *Shore & Beach*, 70(4): 5-14.

Jennings, R. and Shulmeister, J. (2002). "A field based classification scheme for gravel beaches," *Marine Geology*, 186: 211-228.

Komar, P. D. (1986). "The 1982-83 El Nino and erosion on the coast of Oregon," *Shore and Beach*, 54(2): 3-12.

Komar, P. D. (1998). "The 1997-98 El Niño and erosion on the Oregon coast," *Shore & Beach*, 66(3): 33-41.

Komar, P. D., Allan, J. C. and Winz, R. (2003). "Cobble beaches - The "design with nature " approach for shore protection," *Coastal Sediments' 03, 5th International Symposium on Coastal Engineering and Science of Coastal Sediment Processes*,

Komar, P. D., Revell, D. and Good, J. (1999). "Erosion and protection of Cape Lookout State Park, Oregon," Oregon State Parks and Recreation Department, Salem.

Lamarre, H., MacVicar, B. and Roy, A. G. (2005). "Using passive integrated transponder (Pit) tags to investigate sediment transport in gravel-bed rivers," *Journal of Sedimentary Research*, 75(4).

Nicholls, R. and Webber, N. (1988). "Characteristics of shingle beaches with reference to Christchurch Bay, S. England," *Proceedings of the 21st Conference on Coastal Engineering*, ASCE,

Revell, D., Komar, P. D. and Sallenger, A. H. (2002). "An application of LIDAR to analyses of El Niño erosion in the Netarts littoral cell, Oregon," *Journal of Coastal Research*, 18(4): 792-801.

Ruggiero, P., Komar, P. D., McDougal, W. G., Marra, J. J. and Beach, R. A. (2001). "Wave runup, extreme water levels and the erosion of properties backing beaches," *Journal of Coastal Research*, 17(2): 407-419.

Ruggiero, P., Kaminsky, G. M., Gelfenbaum, G. and Voight, B. (2005). "Seasonal to interannual morphodynamics along a high-energy dissipative littoral cell," *Journal of Coastal Research*, 21(3): 553-578.

Sherman, D. J. (1991). "Gravel beaches," *National Geographic Research & Exploration*, 7(4): 442-452.

Stembridge, J. E. (1975). "Shoreline changes ad Physiographic Hazards on the Oregon Coast," Ph.D Dissertation Thesis, University of Oregon, Eugene, 202 pp.

van Hijum, E. (1974). "Equilibrium profiles of coarse material under wave attack," *Proceedings 14th Conference on Coastal Engineering*, ASCE, 939-957.

Wright, L. D. and Short, A. D. (1983). "Morphodynamics of beaches and surf zones in Australia," In: Komar, P. D. (Editor), Handbook of coastal processes and erosion. CRC Press, Boca Raton, FL, pp. 35-64.

MIXED SEDIMENT BEACH PROCESSES: KACHEMAK BAY, ALASKA

Peter Ruggiero[1], Peter N. Adams[2], Jonathan A. Warrick[3]

1. Department of Geosciences, Oregon State University, 104 Wilkinson Hall, Corvallis, OR, 97331, USA. ruggierp@science.oregonstate.edu
2. Department of Geological Sciences, University of Florida, 241 Williamson Hall, P.O. Box 112120 Gainesville, FL, 32611, USA. adamsp@ufl.edu
3. Coastal and Marine Geology Program, USGS Pacific Science Center, 400 Natural Bridges Drive, Santa Cruz, CA 95060, USA. jwarrick@usgs.gov

Abstract: Mixed sediment beaches are morphologically distinct from and more complex than either sand or gravel only beaches. Three digital imaging techniques are employed to quantify surficial grain size and bedload sediment transport rates along the mixed sediment beaches of Kachemak Bay, Alaska. Applying digital imaging procedures originally developed for quickly and efficiently quantifying grain sizes of sand to coarse sediment classes gives promising results. Hundreds of grain size estimates lead to a quantitative characterization of the region's sediment at a significant reduction in cost and time as compared to traditional techniques. Both the sand and coarse fractions on this megatidal beach mobilize into self-organized bedforms that migrate alongshore with a seasonality reflecting the temporal pattern of the alongshore component of wave power. In contrast, the gravel bedforms also migrate in the cross-shore without significant seasonality suggesting that swash asymmetry is sufficient to mobilize the gravel even during low energy summer conditions.

INTRODUCTION

The majority of our knowledge of nearshore sediment transport and associated beach morphodynamics is derived from studies of beaches dominated by a single sediment type. Typically that sediment type is sand, and numerous studies have documented the rates of sediment transport along well-sorted, sand-rich beaches resulting in correlations (and models) relating sediment transport to forcing by waves and currents. To a lesser extent, gravel (shingle) beaches have also been the focus of numerous coastal studies but predictions of coarse-grained transport are often unreliable (Osborne, 2005). The

dynamics of mixed-grain size beaches, however, have received relatively little attention in the scientific literature (Mason and Coates, 2001) in spite of the fact that heterogeneous sedimentary environments comprise approximately 80% of the worlds' non-rocky coastal regions (Holland et al., 2004). Mixed sediment beaches occur on shores where glaciation has provided significant sources of sands and gravels and are recognized as being morphologically distinct from and more complex than either sand only or gravel only beaches (Kirk, 1980). Two recent studies of mixed-sediment beaches, Osborne (2005) and Allan et al. (2006), reveal interesting relationships between transport rates and coarse-grained material size and shape. Unfortunately, a detailed understanding of the processes governing mixed-sediment transport remains elusive.



Fig. 1. Study location. Kachemak Bay is located on the Eastern shore of Cook Inlet in south central Alaska. The star marks the location of the Argus cameras used in this study.

The tectonically active, megatidal (spring tide range greater than 8m), and sea dominated beaches of Kachemak Bay, AK (Figure 1) exhibit a wide range of interesting characteristics and provide an ideal natural laboratory for investigating mixed sediment beach processes. The surficial sediments range from fine sand to large boulders and this broad range of sediment size is reflected in intriguing morphodynamics in which self-organized bedforms composed of fine-to-medium sand migrate as coherent packages over a coarse substrate which is also dynamic (Figure 2). Understanding sediment transport patterns and rates along the north shore of Kachemak Bay is particularly

important as net southeasterly transport is primarily responsible for maintaining the Homer Spit (Figure 1), the economic engine of the region, at engineering/planning time scales.

Our goals in this paper are to first characterize the mixed sediment environment of the north shore of Kachemak Bay, AK, then quantify the rates and modes of sediment transport. We achieve these goals through the application of three novel digital imaging techniques. Due to the general lack of detailed understanding of mixed-sediment systems as discussed above, our approach here is to build, and report on, a high quality data set which will be used to develop sediment transport and morphological evolution models for these systems in future efforts.



Fig. 2. Proto-typical mixed sediment beach along the north shore of Kachemak Bay, AK. Note the discrete sand bedform in the far field migrating over the coarse substrate and the mobile gravel berm (near field).

METHODOLOGY

Understanding the range of natural variability of mixed sediment beaches is essential to the management of these complex systems. Historically, quantitative characterization of surficial grain size variability has been difficult because standard techniques are inadequate due to the sampling and processing efforts required and because of the volumes of material that must be handled to capture the full range of variability. Quantifying sediment transport patterns at event-seasonal-interannual scales on these beaches also poses complex sampling problems. Here we apply three digital imaging techniques (beachball camera, cobble-cam, and an Argus Beach Monitoring System) to overcome these sampling issues in investigating the mixed sediment dynamics along the north shore of Kachemak Bay, AK.

Beachball Camera

Recently, Rubin et al., (2006) developed digital imaging methodologies for quickly sampling surficial bed sediments in a variety of field environments. Images of surficial sediment, either sub-aqueous (flying eyeball) or sub-aerial (beachball), sand are taken by simply pressing a watertight camera system into the bed. Grain-size analysis from the digital images requires a calibration process in which sediments from the field area are sieved at quarter-phi size intervals and digitally photographed. An autocorrelation algorithm (Rubin, 2004) between pixels in the digital images has been developed to compute the average grain size of sediment on the bed and the grain size distribution of bed sediment. This emerging technique is extremely rapid and has the potential to revolutionize our ability to quantify grain size information in heretofore inaccessible regions.

The 'beachball' camera is simply a grain-imaging digital still camera fitted with macro lenses and housed in a watertight plastic case. In summer 2004 we collected approximately 150 images using this system on the north shore of Kachemak Bay, AK. Images were collected at low tide and only on the self-organized sand bedforms that exist in the region. Figure 3a shows the spatial distribution of many of the beachball images (red asterisks) overlaid on a gridded topographic surface derived from GPS measurements of the beachface during the same sampling period that the images were taken.

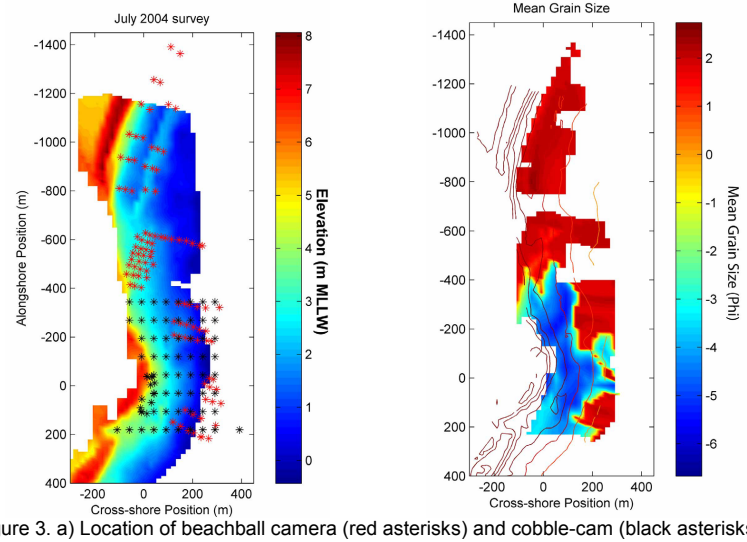

Figure 3. a) Location of beachball camera (red asterisks) and cobble-cam (black asterisks) images overlaid on 2004 gridded topographic surface. b) Gridded surface of surficial sediment grain size.

Cobble-Cam

We are extending the methodology developed by Rubin et al. (2006) to also estimate the size distribution of the coarse component of the region's sediments (Harney et al., in press, Warrick et al., in prep.). The 'Cobble-Cam' consists of a digital still camera mounted on a downward looking, vertically-telescoping tripod designed for capturing a population of coarse grained material. A bubble level on the tripod enables horizontal positioning while an adjustable, rotating extension arm allows for the camera to be mounted looking downward at the sediment surface without capturing the legs of the tripod in the field of view. Typically, the camera is mounted approximately 1.5 m above the bed and images are triggered using a remote control to minimize camera movement. Two images at each location are taken and a scale bar in one of the image's field of view enables the development of a conversion factor defined as the number of pixels in the image equal to 1 mm ground distance. In a summer 2004 pilot effort we collected cobble-cam images at a handful of locations while in summer 2005 we collected approximately 70 images approximating a 50x50 m rectilinear grid as shown in Figure 3a (black asterisks).

For each digital photograph, a regular spaced (200-pixel) grid was overlain producing a 9-by-12 matrix for the photograph using the commercially-available Abode Photoshop computer application. The longest exposed length of each rock underlying each grid intersection was then measured in pixels using a line-drawing tool. If there was no distinguishable rock under the grid point, the rock directly up and to the left was measured. Notes were made if the rock was partly buried (<50% of rock perimeter buried), mostly buried (>50% of perimeter buried), and/or off of the photograph. A second length measurement was then made for each rock along the "short" axis, which was defined to be the longest visible distance perpendicular to the "long" axis measurement. Rocks that were too small to be measured with the resolution of the photograph (typically 3-4 pixel length, ~1.2-mm long) were defined to be "sand" and given an arbitrary grain-size equal to the mean of the beachball samples. These length measurements in pixels were then converted to actual distances using the conversion factor for each photograph.

Argus

In February 2003 we installed an Argus Beach Monitoring System (Lippmann and Holman, 1989; Holman et al., 1991; Holman et al., 1993) along the north shore of Kachemak Bay, AK to observe and quantitatively document the mixed sediment dynamics of the region (Adams et al., in press). The system consists of 8 digital cameras spanning a field of view of approximately 220º. Within this field of view, a geometry solution is computed allowing for the conversion from oblique merged panoramic views (Figure 4) to merged planform views, thereby defining true geographic coordinates to each pixel in the merged planform image. Typically snapshots and time averaged exposures (approximately 3 minutes) for each camera are taken each hour. However, since summer 2005 we sample each camera every 15 minutes during spring tides. Utilizing low tide images in which bedforms are exposed and a tidal contouring algorithm (Plant and Holman, 1997, Aarninkhof et al., 2003) we quantify the rates and

directions of sediment transport exhibited by the sand and cobble fractions of the bi-modal sediment distribution, respectively.

RESULTS

Intertidal beach sediments along the north shore of Kachemak Bay are composed of a poorly sorted coarse component (glacial till), consisting of fist-sized cobbles (5-10 cm) to Volkswagen-sized boulders (1-3 m), and a fine component, fine-to-medium, well-sorted sand. The average mean grain size of the sand bedforms estimated from the approximately 150 digital sand samples collected is 0.29 mm (medium sand), ranging from 0.15 mm (fine sand) to 0.83 mm (coarse sand). In general, the sand fraction is well sorted; however, there is a trend of coarsening toward the trailing edge of individual sand bedforms with finer sands at the leading edge (Figure 3b).



Fig. 4. Merged panoramic images from the Homer, AK ABMS site; top panel: June 2004; bottom panel: June 2005.

For two of the 70 cobble-cam samples approximately 15-20 rocks were labeled in the field and then removed following photographing to allow for physical measurements of the rock dimensions. For both samples, the size estimate of the major (long) axis derived from the photo method (pixel counting) compared extremely well with the physical measurements of the major axis of the rock. The correlation coefficient between the two techniques exceeded 0.97 (Figure 5a) indicating the point counting method is sufficiently accurate to quantify the mean grain size of each cobble-cam image. The mean grain size derived from all of the cobble-cam images was 44 mm (coarse gravel) while the estimated means ranged from 10 mm to 105 mm.

Calibration curves, similar to those developed for Rubin's (2004) autocorrelation algorithm for sand grains, were constructed by Warrick et al., (in prep.) from coarse

samples extracted from a similar mixed sediment beach at the mouth of the Elwha River in Port Angeles, WA. Surprisingly, the Kachemak Bay images, when processed with the autocorrelation algorithm using the Elwha calibration curves, showed remarkable agreement between point count size estimates and computer derived size estimates (Figure 5b). This result suggests that estimates of coarse grain sizes may be computed with significant reduction of cost and time as compared to traditional techniques.

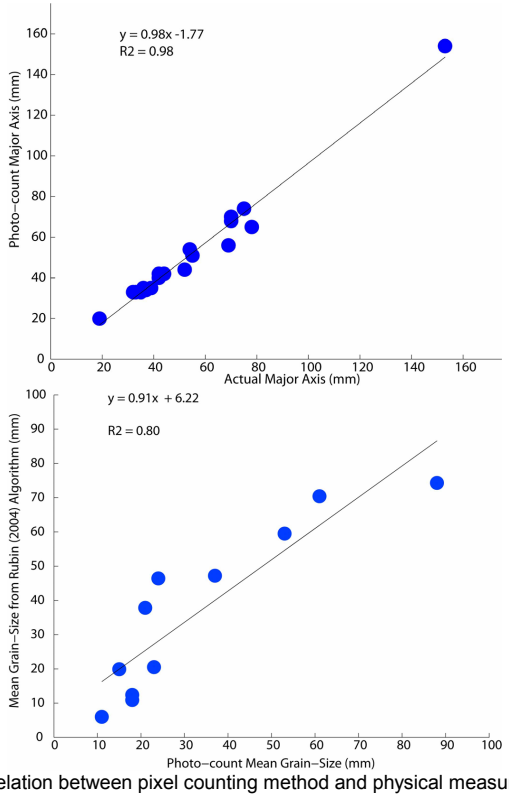

Fig. 5. top) Correlation between pixel counting method and physical measurements of grain size for a single cobble-cam image. bottom) Relationship between mean grain sizes estimated from the Rubin (2004) algorithm and pixel counting size estimates.

The beachball and cobble-cam results give us reasonably accurate estimates of mean grain size at over 220 locations within the field of view of the Homer Argus cameras. From these data we develop a gridded surface of the surficial grain size in the study area (Figure 3b). While in this example we combine data collected over a two year period to construct a composite surficial sediment surface, our goal here is to demonstrate that these relatively simple techniques can be applied to accurately and efficiently characterize the range of variability in heterogeneous environments.

Alongshore migration rates of intertidal sand bedforms, 1-2 m amplitude and ~200m wave length (Figure 2), over the coarse gravel substrate have been documented to be approximately 250 m/yr (Adams et al., in press). Strong seasonality in alongshore migration rates is evident with the majority of sand body movement, up to weekly-averaged rates of movement exceeding 6 m/day, occurring during large wave events. The seasonal signal of the alongshore bedform migration rate (proxy for bedload transport) is well correlated with seasonal variability in the alongshore component of wave power suggesting that the sand component of this mixed sediment system behaves much as most sand beaches with strong net longshore sediment transport rates.

The cobble substrate, over which the organized sand fraction is transported, is dynamic as well. Field observations (Figure 2), Argus video measurements (Figure 4), and ground surveys (Figure 6) have documented the growth and migration of a large gravel bedform over a life cycle of more than two years.

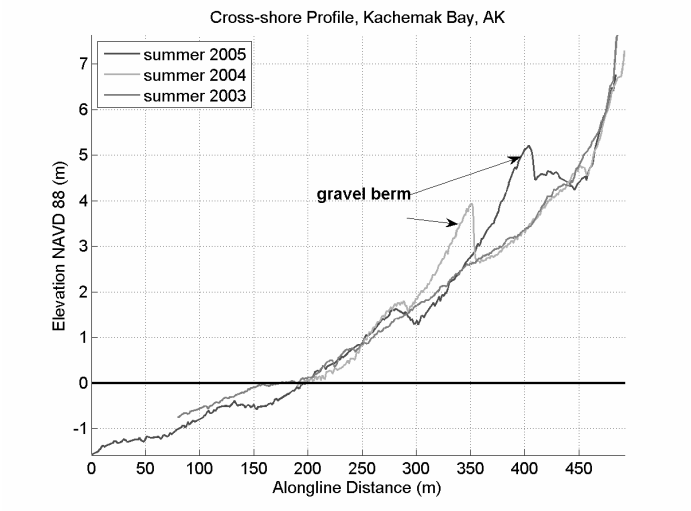

Fig. 6. Profile view of development and onshore migration of gravel berm. Data collected by walking cross-shore transects with RTK-GPS.

The cobble bedform was initially formed during late fall early winter 2003/2004 (note that the feature does not exist in summer 2003 in the cross-shore profile shown in Figure 6) by a now abandoned tidal slough outlet (flows typically exceed 1 m/s) immediately to the west of the Argus cameras. Human intervention may have played a role in the formation of the gravel feature in that the outlet of the slough was forced to the west in late 2003 as it had been steadily migrating toward the east and was beginning to threaten private property with erosion. The coarse material associated with the remnant stream

bed was then impacted by only marine processes rather than the balance between marine and fluvial processes that previously existed. While it is difficult to resolve the detailed processes associated with the formation of the feature with the Argus cameras (poor weather caused unusable images), the feature soon became large enough to accurately track using the cameras. By spring 2004 (Figure 4) the bedform had organized into a mobile gravel berm with a landward slipface approximately 1.5 m high and a cross-shore length of about 50 m. During the following year this feature increased in volume and migrated approximately 50 m in the cross-shore and over 100m in the alongshore direction while the berm crest gained over 1.0 m in vertical elevation (Figure 6).

By mapping the location of the gravel bedform in subsequent merged rectified Argus images we quantify the pattern and rate of migration of this feature much in the same manner as Adams et al., (in press) quantified the sand body migration rates at the same site. Figure 7 illustrates the gravel bedform's footprint at three distinct times in its life cycle. From the initial development of the feature until late spring 2005 the primary direction of transport was in the alongshore (with some cross-shore movement). From summer 2005 until the feature's eventual collapse, the bedform primarily moved onshore. The gravel feature also elongated during its life cycle from extending approximately 100 m in early 2004 to over 300 m in late 2005.

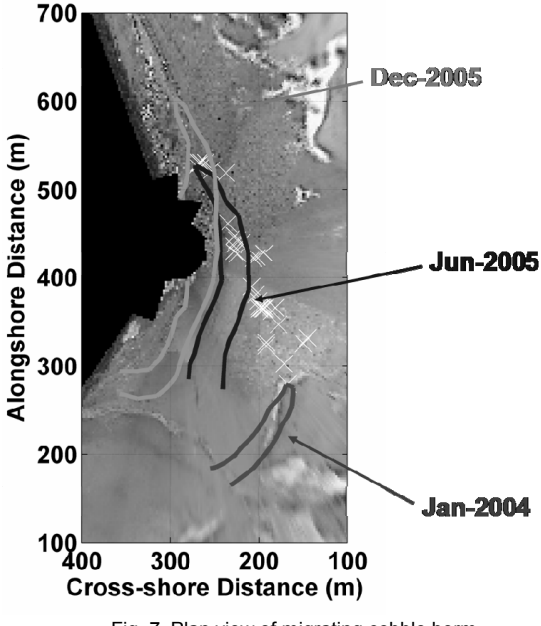

Fig. 7. Plan view of migrating cobble berm.

The white asterisks in Figure 7 represent the position of the easternmost tip (toward the top of the page) of the gravel bedform at approximately bi-weekly intervals, every spring tide from early 2004 until late 2006. This data is used to estimate the migration rate of the gravel berm as illustrated in Figure 8. Similar to the transport pattern of the sand bodies (Adams et al., in press), the cobble berm migration rate experiences a significant seasonality to its movement. In early 2004, when storm waves were still frequent, the gravel berm migrated at a rate of approximately 0.7 m/day (primarily in the alongshore direction). During the relatively calm spring and summer months of 2004 the gravel berm halted only to resume its movement when waves increased in late fall/winter. During the first year of its existence the gravel berm migrated approximately 150 m resulting in an annual average migration rate of 0.4 m/day.

The megatidal nature of Kachemak Bay is ideally suited for quantifying beach changes using tidal contouring methods (Plant et al., 1997, Aarninkhof et al., 2003). Knowing the time of each merged rectified time averaged exposure and the corresponding tidal elevation (taken from the NOAA tide gage located at Seldovia, AK on the south shore of Kachemak Bay approximately 25km south-southwest of Homer) we construct monthly cross-shore beach profiles at three alongshore locations (Figure 9). Unfortunately, because ponding occurs on the landward side of the gravel berm as the tide recedes, we are not able to resolve the slip face of the gravel berm and the beach face immediately landward of the bedform (Figure 9b).

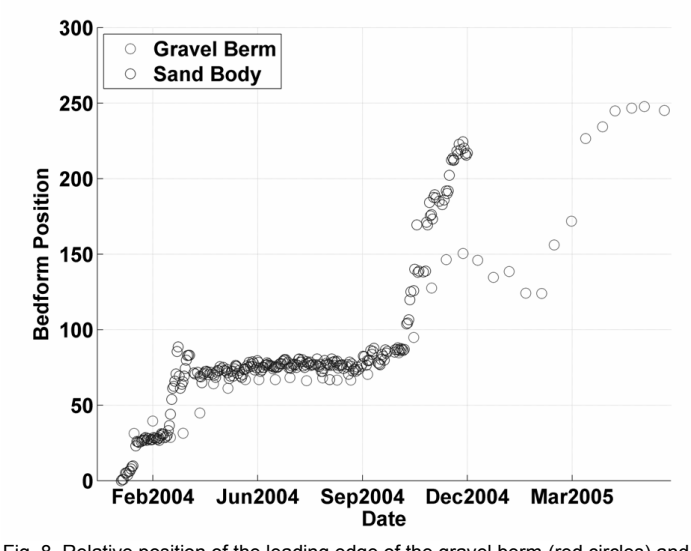

Fig. 8. Relative position of the leading edge of the gravel berm (red circles) and the approximate center of mass of a single sand body (blue circles).

In order to accurately resolve the cross-shore migration of the gravel berm we extract the cross-shore position of the 4.5 m (MLLW) contour at monthly intervals (Figure 10). At all times when the gravel feature is present at a particular alongshore location, the 4.5 m contour is on the seaward sloping face of the bedform. Therefore, tracking this contour serves as a reasonable proxy for the cross-shore migration of the gravel berm. Figure 10 illustrates that the migrating gravel berm reaches the transect located at alongshore position 400 m (Figure 9) in November 2004, as evidence by over 75 m of offshore migration of the contour. From February 2005 until December 2005 the 4.5 m contour migrates steadily onshore with an average rate of 0.1 m/day.

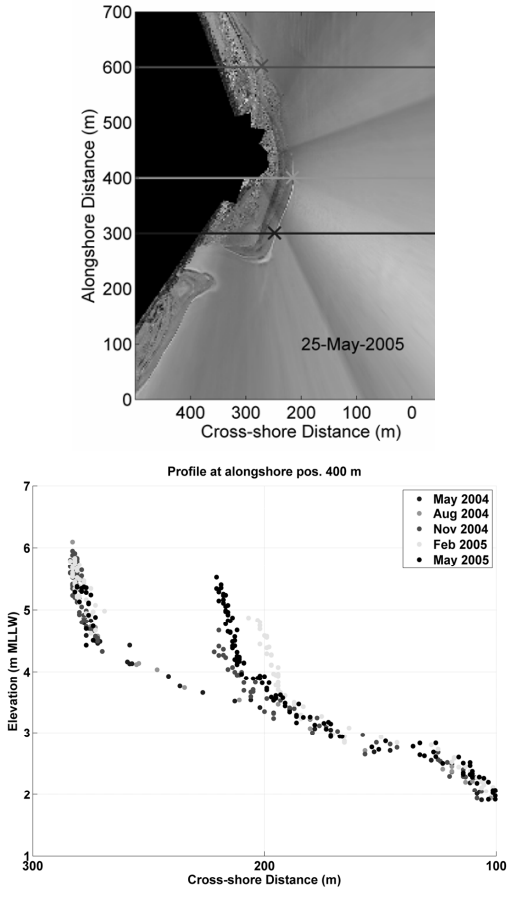

Fig. 9. top) Plan view demonstrating tidal contouring methodology. bottom) Quarterly cross-shore profiles extracted from tidal contouring method at alongshore position of 400 m.

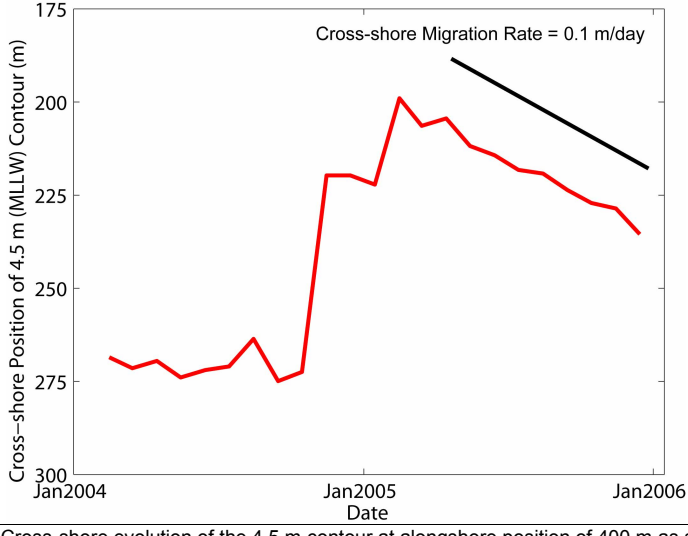

Fig. 10. Cross-shore evolution of the 4.5 m contour at alongshore position of 400 m as shown in Figure 9 (top).

CONCLUSIONS

New digital imaging techniques now available for quantifying grain size allow for quick, inexpensive, and relatively accurate characterization of mixed sedimentary environments. We have initiated the extension of a technique initially developed for sand (Rubin et al., 2006) to produce sufficiently accurate estimates of coarse sediment (gravel and cobble) sizes in order to resolve the cross-shore and alongshore gradients of surficial sediments in a highly heterogeneous sedimentary environment.

Along the sea-dominated, megatidal, mixed sediment environment of Kachemak Bay, AK, both the sand and gravel fractions are highly mobile with the dominant mode of sediment transport being the migration of self-organized bedforms. Employing merged rectified Argus images we estimate the annual migration rate of the sand bedforms to be approximately 0.75 m/day (Figure 8, blue circles) while the gravel bedform migrates at 0.4 m/day. Surprisingly however, the bedforms of different size components migrate in the alongshore with a similar seasonality which is well correlated with the seasonality in the alongshore component of wave power. This result suggests that simple models, similar to the "CERC formula" (Komar and Inman, 1970; U.S. Army Corps of Engineers, 2002), for alongshore bedload transport of the coarse fraction may be developed, at least for this system.

Intriguingly, the cross-shore migration rate of the gravel berm is relatively constant during most of 2005 (February to December) without exhibiting seasonality. This perhaps suggests that the asymmetric swash motions on the seaward flank of the gravel

bedform are always sufficient to mobilize the coarse sediment, even during the relatively calm summer conditions. Presumably the permeability of the gravel bedform produces a net onshore shear stress over the swash backwash cycle leading to net onshore transport. Future experiments performed using Argus images and Argus time stacks will specifically test this hypothesis by determining whether or not swash velocities are sufficient to mobilize the gravel bedform throughout the year.

ACKNOWLEDGEMENTS

The U.S. Geological Survey supported this work through the 'Geological Characterization and Sedimentary Processes of Nearshore Habitats in Kachemak Bay, Alaska' project. Logistical support was provided by the Kachemak Bay Research Reserve. We thank Guy Gelfenbaum, Jodi Harney, and Jodi Eshleman for stimulating scientific discussions and excellent field support. Special thanks go to Dr. Paul Eneboe who continues to allow us to maintain our Argus cameras on his lovely property. Finally, we would like to thank Carl Schoch for his continued vision and strong support of sediment dynamics studies in Kachemak Bay.

REFERENCES

Aarninkhof, S.G.J., Turner, I.L., Dronkers, T.D.T., Caljouw, M., and Nipius, L., 2003. A video-based technique for mapping intertidal beach bathymetry, Coastal Engineering, 49, 275-289.

Adams, P.N., Ruggiero, P., Schoch, G.C., and Gelfenbaum, G., in press. Intertidal sand body migration along a megatidal coast, Kachemak Bay, Alaska, J. of Geo. Res. – Earth Surface.

Allan, J.C., Hart, R., and Tranquili, J.V., 2006. The use of Passive Integrated Transponder (PIT) tags to trace cobble transport in a mixed sand-and-gravel beach on the high-energy Oregon coast, USA, Marine Geology, 232, 63-86.

Harney, J. N., Ruggiero, P., Lam, A., Gelfenbaum, G., in press. Grain-size analysis of a dynamic, mixed-sediment shoreline: Kachemak Bay, Alaska. US Geological Survey Open File Report 2006, 12 p.

Holland, K.T., and Kaihatu, J.M., 2004. The influence of sediment heterogeneity on coastal hydrodynamics. Eos Trans. AGU 84(52), Ocean Sci. Meet. Suppl., Abstract OS41L-03.

Holman, R.A., Lippmann, T.C., Oneill, P.V., and Hathaway, K., 1991. Video Estimation of Subaerial Beach Profiles, Marine Geology, 97, 225-231.

Holman, R.A., Sallenger, A.H.J., Lippman, T.C., and Haines, J.W., 1993. The application of video image processing to the study of nearshore processes, Oceanography, 6, 78-85.

Kirk, R.M., 1980. Mixed sand and gravel beaches: morphology, processes and sediments. Progress in Physical Geography 4, 189-210.

Komar, P. D. and Inman, D. L., 1970. Longshore sand transport on beaches. Journal of Geophysical Research, 75: 5514-5527.

Lippmann, T.C., Holman, and R.A., 1989. Quantification of Sand-Bar Morphology - a Video Technique Based on Wave Dissipation, Journal of Geophysical Research-Oceans, 94, 995-1011.

Mason, T. and Coates, T.T., 2001. Sediment Transport Processes on Mixed Beaches: A Review for Shoreline Management." Journal of Coastal Research 17(3): 645-657.

Osborne, P.D., 2005. Transport of gravel and cobble on a mixed-sediment inner bank shoreline of a large inlet, Grays Harbor, Washington, Marine Geology, 224, 145-156.

Plant, N. G. and Holman, R. A., 1997. Intertidal beach profile estimation using video images, Marine Geology, 140, 1-24.

Rubin, D.M., 2004. A simple autocorrelation algorithm for measuring sediment grain size in digital images. Journal of Sedimentary Research, 74(1):160-165.

Rubin, D.M., Chezar, H., Harney, J.N., Topping, D.J., Melis, T.S., and Sherwood, C.S., 2006. Underwater Microscope for Measuring Spatial and Temporal Changes in Bed-Sediment Grain Size, U.S. Geological Survey Open-File Report 2006-1360, Version 1.0 http://pubs.usgs.gov/of/2006/1360/.

U.S. Army Corps of Engineers, 2002. Coastal Engineering Manual. Coastal and Hydraulics Laboratory EM 1110-2-1100, http://chl.erdc.usace.army.mil/CHL.aspx?p=s&a=Publications;8.

Warrick, J.A., Todd, E., Rubin, D.M., Harney, J.N., Ruggiero P., in prep. Cobble cam photographs of mixed sediment beaches for grain-size calibration. U.S. Geological Survey Open-File Report.

MIXED SAND AND GRAVEL BEACH DESIGN AND CONSTRUCTION FOR HABITAT RESTORATION

David Simpson[1], Michael Wray[2], Jon Houghton[3], John Klekotka[4]

1. Coast & Harbor Engineering, Inc., 110 Main Street, Suite 103, Edmonds, WA 98020 USA. dave@coastharboreng.com.
2. Berger/ABAM Engineers Inc., 33301 Ninth Avenue South, Suite 300, Federal Way, WA 98003, USA. wray@ABAM.com.
3. Pentec Environmental, 120 Third Ave South, Ste 110, Edmonds, WA 98020-8411, USA. jon@pentecenv.com.
4. Port of Everett, PO Box 538, Everett, WA 98206, USA. johnk@portofeverett.com.

Abstract: A mixed sand and gravel beach 1,100 feet (335 m) in length was designed and constructed during 2005-2006 in Puget Sound as beach restoration, and is being monitored for changes in sediment distribution and profile shape. The beach is to function as improved habitat specifically for salmon, provide public access to the shoreline, and to control erosion of backshore fill. The beach was designed to mimic to the extent feasible the beach face slopes, elevations, and materials of a natural Puget Sound shoreline. Design beach dimensions and morphology were patterned after those of beaches documented at other Puget Sound locations. Forebeach material size gradation was designed from published relationships and judgment based on measured gradations at beaches having similar wave exposure and habitat as targeted for the project site. Construction monitoring assured the intent of the design was implemented. Post-construction monitoring has shown that the constructed beach is performing as designed.

INTRODUCTION

A beach in central Puget Sound, Washington, USA was rehabilitated for a distance of 1,100 feet (335 m) as part of a pier construction project owned by the Port of Everett. Figure 1 is a location map of the project area. The reach of shoreline containing the project had been degraded by industrial activities of several different owners for over a century. Figure 2 shows the pre-project beach and rock bulkhead. Objectives of the restoration are to (1) create a beach that will function as improved habitat specifically

for salmon, (2) provide public access to the shoreline, and (3) control erosion of backshore fill by maintaining morphology and material types of natural, functioning Puget Sound beaches. Beach construction and monitoring are elements of a Conservation Measures and Monitoring Plan (CMMP) developed during environmental permitting of the overall pier project. The beach restoration is not required mitigation, but a rather proactive measure undertaken by the Port of Everett to enhance the environmental and physical functions of the beach.

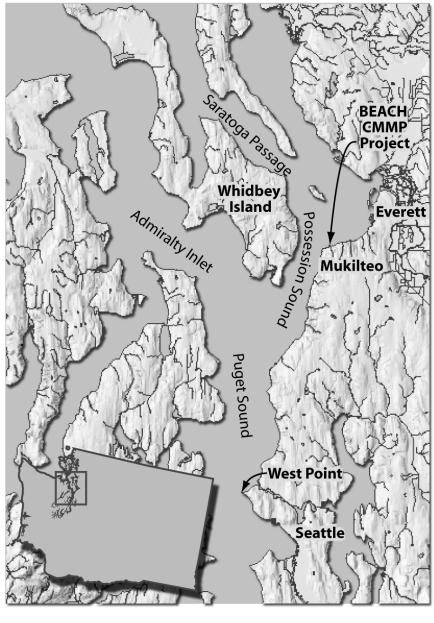

Fig. 1. Location map of constructed beach



Fig. 2. Pre-project shoreline at pier project site

Typical Puget Sound shorelines are backed by bluffs composed of glacial outwash deposits. Bluff erosion is a mechanism for delivering sediments to the shore. The site is exposed to moderate or low wave energy and an 11-ft diurnal tide range. When the sediment budget is balanced the resulting beach surface has a slope and distribution of sediments that form habitat for food sources of endangered fish species. Topography channels winds in central Puget Sound in predominantly northerly, and secondarily in southerly directions. The project area has a generally north-facing shoreline, and is exposed to a fetch having an effective length of 7.5 nautical mi (13.9 km). Deepwater significant wave heights reach 3 to 4 ft in strong winter storms. Predominant longshore transport direction is from west to east as interpreted from shore forms and erosion patterns.

BEACH DESIGN

Beach design accounted for the physical processes that would modify the constructed beach during placement and during the project life. Prototype beaches and their physical environment provided the basis of design that would maintain morphology and beach composition that create desired habitat. Typical self-formed morphology of northern Puget Sound beaches consists of a low-gradient low tide terrace composed of silt and sand, and a steeper high tide beach composed of coarse sand and gravel, and in some cases cobbles (Keuler 1988).

Criteria

Habitat performance criteria were established in consultation with the project biologist and regulatory agencies at the start of the design process and were balanced with engineering criteria of physical functionality, ability to provide shore protection, longevity, constructability, and economics. Sediment predominantly in the size range of medium sand to pea gravel is required in the beach surface material to serve as habitat in the upper elevation zone for forage fish spawning (WDFW Undated a, b). Evidence of Pacific sand lance usage, although sparse, was found in the pre-existing beach, despite the beach's degraded state. For the rehabilitation to be judged successful, the completed beach will be required to develop improved biological functions, compared to the area covered.

Project design must therefore mimic the morphodynamics of a self-formed beach composed of a mixture of sediment sizes. The beach form must be stable in a design storm even though the beach contains fine sediments. The concept developed for the beach cross section is a core and berm composed of coarse material in the size range that is found at the berm crest on natural beaches. The forebeach is constructed with a sand and gravel mixture known as "habitat mix," because the distribution of material sizes has a significant component in the range of coarse sand to fine gravel. The back beach is composed of sand with a zone of soil to support riparian vegetation.

Design Process

Mixed sand and gravel beaches differ from shingle beaches in that the high percentage of sand in mixed beaches reduce swash infiltration in the beach face. The resulting uprush and downrush velocities are more symmetrical in the zone of higher sand content, creating a flatter slope than is found where only gravel is present. Quick and Dyksterhuis (1994) noted in their study of a limited range of wave heights and mixed beach compositions that a mixture having a sand percentage greater than a certain amount behaved nearly as sand. That sand percentage varied with the energy of the incident waves. A design objective was to specify a beach face slope and sediment gradation that function as habitat and remain in dynamic equilibrium with the wave environment after natural sorting of sediment. The design process consisted of the following tasks.

- Document existing site conditions
- Analyze wave and water level statistics
- Test applicability of design formulas
- Specify target grain size for forebeach
- Apply formulas to calculate combinations of median grain size, size gradation, and beach face slope for selected wave conditions
- Determine berm crest elevation and berm width
- Complete final engineering design, plans, specifications, and cost estimates

Pre-project beach surface sediment sizes were documented with an initial field reconnaissance. Tide level statistics are listed in feet above mean lower low water (MLLW) in Table 1 below. Mean higher high water (MHHW) is 11.02 ft above MLLW at the site. Wave statistics applicable to the site were developed with wave hindcasts using wind data from the northern quadrants recorded at the West Point lighthouse (see Figure 1).

Table 1. Extreme Value Statistics for Tides, Winds, and Waves for Beach CMMP Project Site

Return Period, year	Tide Level, feet	Wind Speed, mi/hr	Hmo Wave Height, feet	Spectral Peak Period, sec
5	13.50	36.3	3.61	3.87
10	13.71	38.4	3.86	3.99
20	13.90	40.4	4.11	4.10
50	14.11	42.7	4.40	4.22

Note: Tide elevations of Glendale, Whidbey Island, in feet above MLLW. Wind speeds developed from west and north winds measured (2-min average) at West Point, WA 1984-2002.
Hmo is zero-moment wave height.

A relationship developed by Powell (1993) among median particle size (d_{50}), beach grading (ratio of d_{84} and d_{16} sizes), incident wave height and period, and beach face slope was applied in the design of the forebeach because it incorporates a measure of the size distribution of sediments as well as the median grain size. The maximum grading of beach sediments which Powell included in his laboratory studies was 8.3, with median size of 6.7 mm, which does not describe the "habitat mix" size distribution, however. Figure 3 shows gradations of habitat material from a natural Puget Sound beach, a commercially produced habitat mix, and calculated median diameter and d_{84} and d_{16} sizes corresponding to a 7:1 slope using the Powell formula. Prediction of equilibrium states between sediment size distribution and foreshore slope is less certain for habitat mix because the sand content is typically higher than in beaches that Powell studied. Formulas for equilibrium beach slopes of Powell (1993), van der Meer and Pilarczyk (1986), and for on- or off-shore transport of Ahrens and Hands (2000), and those listed in Larson and Kraus (1989) were applied to the 5-year wave height and period and observed beach face slope. Formulas based on a single grain size generally indicated that most of the material termed the natural Puget Sound beach in Figure 3 would remain in place or be moved onshore by the design waves. The formula incorporating gradation indicated the equilibrium slope was flatter than that measured at Puget Sound beaches.

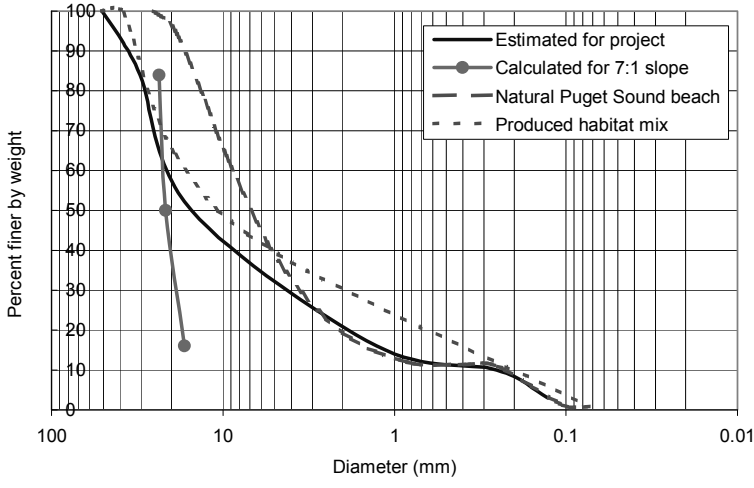

Fig. 3. Shore structures and beach in project reach

Wave heights and periods corresponding to the 5-year exceedance probability were input with a 7H:1V slope to formulas referenced above to predict combinations of median particle size and grading for designing the foreshore material. Gradations were developed through the formulas as a starting point, then modified in consideration of gradations measured at natural beaches, and to account for gradations of commercially available material that could be used to construct the project. The design gradation of the project habitat mix is shown in Figure 4. Size characteristics of the gravel core of the designed beach cross section were determined using a 4H:1V slope and wave of the 20-year exceedance frequency (Figure 4). The design gradation for the project habitat mix is also shown in Figure 3 to compare with gradations of other habitat material. The design slope of the foreshore is 7H:1V, but the slope calculated as being in equilibrium with the design habitat mix is 12H:1V according to the Powell formula. Designing the habitat mix gradation relied more on observed gradations than on formulas in their current state. This difference is cause for concern because the project would not be considered successful if the foreshore flattened to the predicted 12H:1V slope. Post-construction monitoring will focus on the performance of this material and the foreshore slope.

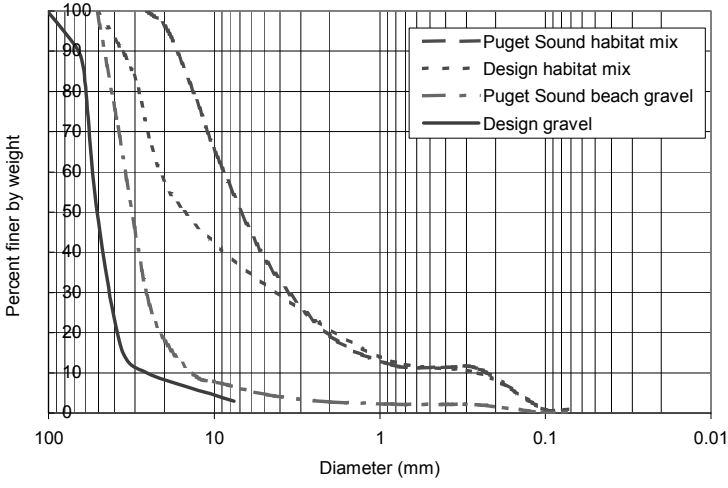

Fig. 4. Observed and calculated gravel and habitat mix gradations

The model RBREAK2 (Kobayashi and Poff 1994) simulated wave runup and overtopping of the berm designed to various heights. Model output assisted in determining the berm elevation and dimensions that would minimize wave overwash on the back beach and maximize stranding of large woody debris on the berm crest. The optimum berm elevation was 13 ft MLLW and back beach width was 30 ft.

Transitions of the designed berm to unimproved shorelines at both the east and west ends of the project were based on the interpreted net eastward longshore sediment transport pattern. The eastern transition to the unimproved beach included a beach sill composed of cobbles. The sill is a permanent feature to retain beach material that would otherwise be transported alongshore to the east. The estimated average replenishment rate of habitat mix is based on a projected loss rate of initially placed material. The loss rate was calculated with the shoreline diffusivity parameter, as defined in Coastal Engineering Manual (2002) Part III Chapter 2, using pre- and post-project beach face slopes, which influence the location and height of waves at breaking. The ratio of diffusivity parameters is the basis of the estimated 10 percent loss rate after construction. The renourishment cycle was assumed to be once per 5 years.

Design Plan, Section, and Specifications

Figure 5 shows the design plan of the beach rehabilitation. The plan accommodated construction of a beach face on which habitat would develop and meet other project objectives and criteria, with the minimum quantity of imported material. The greatest increase in beach elevation from pre-project to design surface is 6 ft, at the location of the berm crest at the eastern end of the project. The widest footprint of the designed beach is 115 ft. Four beach sections include designs for conveying storm water

through the constructed beach from existing culverts located at the back beach, two by culvert extensions and two by means of a porous cobble portion designed into the section. Access paths descended from the upland to merge with the berm crest at two locations. The path was supported with structural fill, which was protected at its base above the beach with rock revetment, vegetation, and anchored logs.

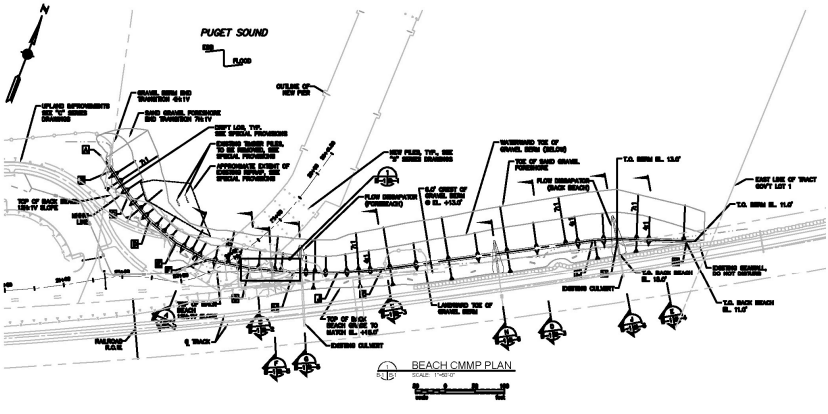

Fig. 5. Plan of beach rehabilitation

Size gradations specified for habitat mix are shown in Figure 6. Beach material quantities were specified by tons and costs were estimated on an in-place basis. Quantities were determined by computing with CADD the volumes of the separate materials between the surface constructed with the pre-project beach surface and the design beach surface. Volume was converted to weight with the factor 1.7 tons per cubic yard. The specified tolerance of the completed beach surface was plus or minus 4 inches of the design surface. Beach construction was to proceed in reaches 300 ft in length, which were to be accepted by the Engineer before the Contractor could finish the next reach in sequence. After the Engineer accepted a reach the Contractor was to minimize construction impact to that section, but was also no longer responsible for repairing damage of the section caused by natural processes.

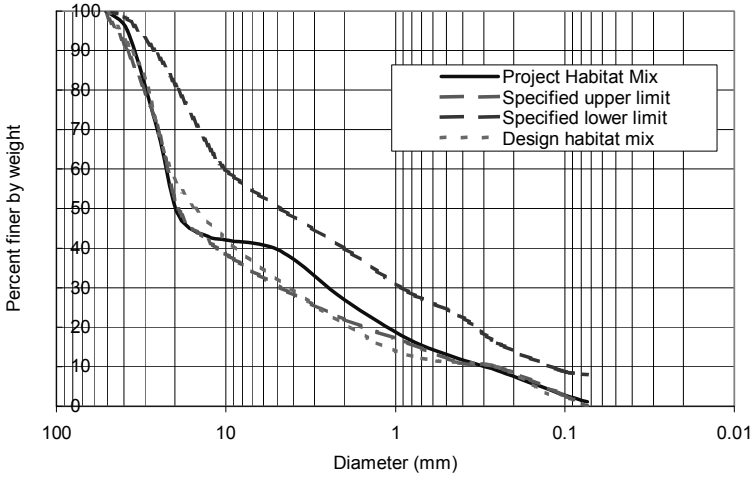

Fig. 6. Gradations of specified and supplied habitat mix for constructed foreshore

CONSTRUCTION

All beach materials were transported over surface streets to the site with dump trucks and stockpiled. Gradation curves of materials proposed for constructing the beach were evaluated for conformance to the construction documents and were visually assessed before the material was placed in the project. Beach rehabilitation construction began in September 2005. A single 22-cu-yd capacity off-road truck transported beach material from the stockpile to where it was placed. A small dozer bladed and compacted the material to lines and grades. The rate of material placement by this operation was 220 tons per hour on the eastern extent of the project, farthest from the stockpiles.

Locations requiring cobbles were constructed first. Gravelly core material was then placed and used as a haul road to advance the placement toward the eastern end of the project. With this sequence, operation was unimpeded by high tide levels. After the core section at the eastern terminus was constructed, back beach sand placement alternated with habitat mix placement, as tide height permitted. The Engineer verified that the finish surfaces of the beach components were within specified tolerance, using the construction surveys. The Contractor constructed 750 feet of beach by November 3, 2005, and delayed further beach construction until tide levels during daylight were more favorable, starting in January 23, 2006. Beach construction was completed with transition to the pre-existing armored fill at the western end of the project by the end of January 2006.

The placed quantities of materials were within 8 percent of the design volumes, except for the habitat mix, which had a significant over-run. The overrun could have been caused by loss of some of the fines in the habitat mix into the porous structure of

the gravelly core as well as washed into Puget Sound during initial tidal inundation. The 2005 cost of the constructed beach was $585 per lineal foot, not counting landscaping and irrigation for new vegetation on the back beach.

PERFORMANCE ASSESSMENT

Monitoring program

A monitoring program to evaluate beach performance against success criteria was developed during the permitting process and was finalized with an agreement among the Port of Everett and resource agencies before environmental permits were granted. Monitoring results will be reviewed to determine the need for beach renourishment, document the constructed beach response to waves and tides, and assess the accuracy of predictive relationships that were the basis of design.

The monitoring program specified establishment of a minimum of six transects in the project area for surveying beach cross sections after construction is complete and in the late summer after 1, 2, 3, and 5 years following construction, and within one month following a significant storm from the north. Monitoring will be extended to years 7, 10, and 20 unless it has been shown that a significant storm from the north produces no long-term changes in the beach profile or substrate. With every monitoring, sediment is sampled at four locations on each transect and analyzed for size distribution. Photo points are to be established and reoccupied for photographing and comparing beach appearance through time. Figure 7 shows locations of monitoring transects A through F.

Beach rehabilitation success is measured with biological and physical factors. The physical measures of successful rehabilitation listed in the CMMP (Pentec 2004) are the following:

- Beach profiles will not change by more than +/- 1.5 foot by Year 5
- Substrate composition along the upper beach will be suitable for forage fish spawning over a minimum of 50 percent of the beach length enhanced
- No adverse impacts to eelgrass in the adjacent lower beach areas will result from material lost from the rehabilitated beach

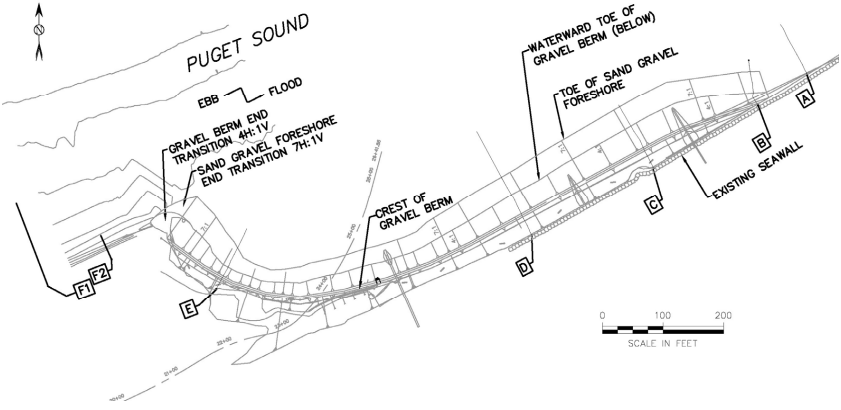

Fig. 7. Location of monitoring transects

Beach Cross Section

By November 2006, the constructed beach had not been impacted by design waves. Wind speeds from the north that produced a hindcast significant wave height of 2.6 ft incident on the rehabilitated beach occurred only in February and April 2006. Figure 8 shows monitoring transect D (see Figure 7) surveyed on May 26, 2006 and November 16, 2006 as an example of beach response to the wave climate since the time of construction. The beach face above mean tide level had remained at a slope of 7H:1V in both May and November. The slope below mean tide level to the intersection with the pre-project profile was 7.5H:1V in May. The berm crest elevation increased to 14 ft above MLLW from the constructed elevation of 13 ft. Some material has been lost from the western end of the project, where the shoreline angle with respect to incident waves is most oblique. Thus far the design intent of providing the specified beach face slope has been met. The transition section at the eastern end of the project (Transect B) has undergone the greatest change, exhibiting retreat and lowering as the plan form attained a smoother transition to the unimproved beach. Sediment volume adjustment of the constructed beach is being monitored as surveys are repeated at the monitoring transects.

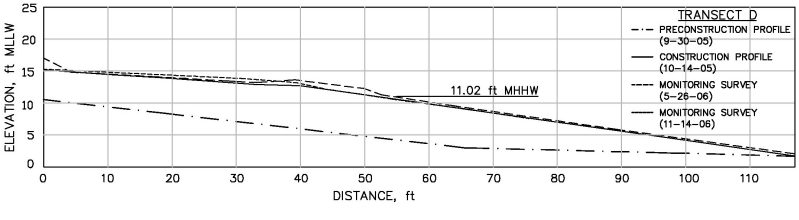

Fig. 8. Profiles of monitoring transect D, May and November 2006

Sediment Analysis

Sediment samples were taken from the beach surface and below the surface along the monitoring transects on May 26 and November 16, 2006 at the times the cross sections were surveyed. Samples are identified by survey shot numbers in Figures 9 and 10. Sediment size distributions of surface samples taken on the beach face at about elevation 9 ft on Transects C and D on the two monitoring dates are plotted in Figure 9. The gradation of the placed material is shown in the figure for comparison. Modification of the gradation by natural sorting is evident for some samples, but other sample pairs show remarkable similarity from May to November. At some locations the surface material became coarser from May to November and at other locations the sediment became finer (Figure 9). Figure 10 compares the gradation of the beach surface material and the material below the surface layer at the same location and time. The surface layer thickness was one to two diameters of the larger particles in the layer. Size statistics of the surface samples and the subsurface samples are plotted separately in Figure 11 as median size versus ratio of d_{84} and d_{16} sizes. For comparison, statistics of the beach sediments used to develop the empirical equation of Powell (1993) are also shown along with gradations of other Puget Sound beach samples are also plotted for comparison. The figures show that the habitat mix placed in the project and sorted by the wave climate, as well as other natural Puget Sound beaches, have larger ratios of d_{84} and d_{16} sizes than do sediments used in developing the formula.

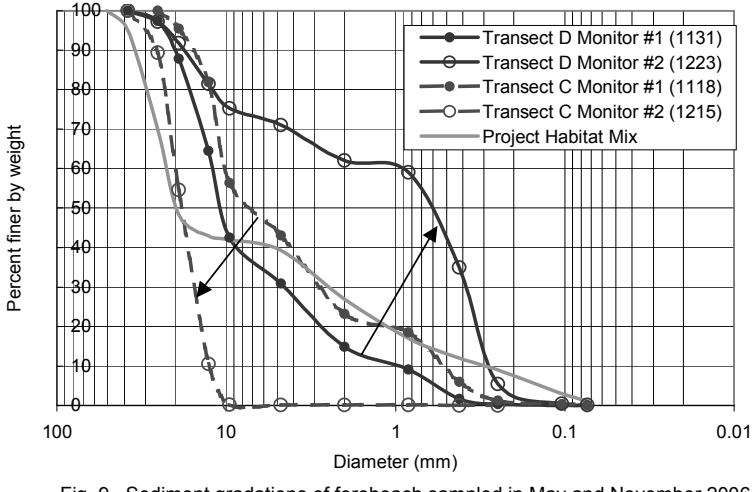

Fig. 9. Sediment gradations of forebeach sampled in May and November 2006

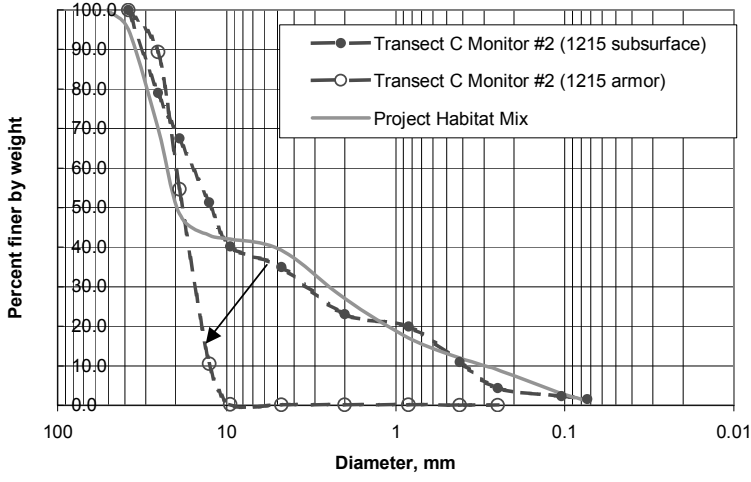

Fig. 10. Sediment gradations of forebeach surface and subsurface, November 2006

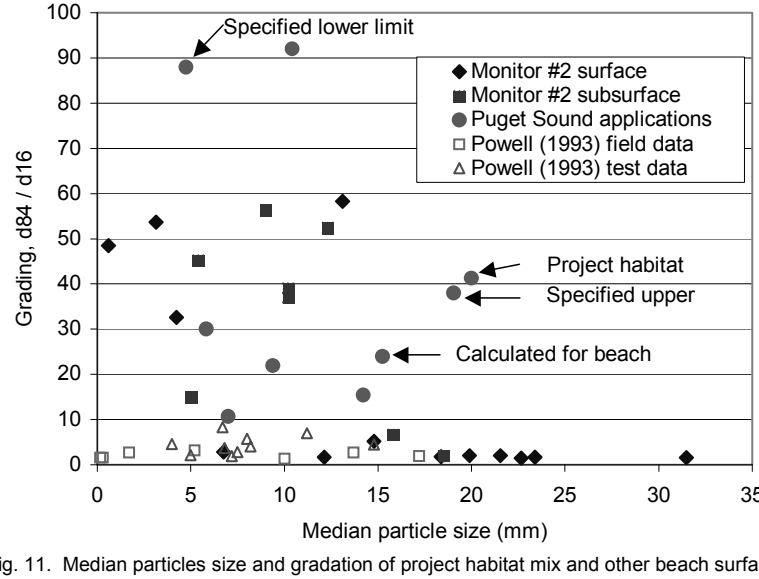

Fig. 11. Median particles size and gradation of project habitat mix and other beach surfaces

Beach Appearance

Photographs of the beach taken in 2004 before construction and November 2006 (after construction) show that the beach features desired to be created have been maintained over the first year since placement. Comparison of Figures 12a and 12b illustrate the distinct beach berm and woody debris that accumulated on the beach crest after construction.



Fig. 12. Beach appearance before and after beach construction, view toward east

SUMMARY DISCUSSION

A beach composed of sand and gravel was constructed at a Port of Everett property with three objectives: habitat restoration, shore protection, and public access. Size gradations of material comprising the forebeach and the gravelly core and berm were designed using knowledge of sediment gradation of naturally formed Puget Sound beaches, and with the aid of empirical formulas that accounted for both sediment median size and ratio of d_{84} and d_{16} sizes. Empirical formulas appear to have limitations in design of Puget Sound habitat beaches because these beaches have a greater sand percentage than those from which the formulas were developed. The beach has been in place for parts of two winter seasons. Habitat features of beach slope, surface material size distribution and beach dimensions that were the design goal have been maintained. The project shows the viability of constructing mixed sand and gravel beaches in particular Puget Sound locations when design procedures are followed.

ACKNOWLEDGEMENTS

The authors gratefully acknowledge the support of the Port of Everett in constructing and monitoring the beach at its Rail/Barge Transfer Facility, and the permission by the Port of Everett to publish this information.

REFERENCES

Ahrens, John and Hands, Edward (2000). "A Simple Perspective on Cross-Shore Sediment Movement," *Shore & Beach,* Vol. 68, No. 4, pp.3 – 14.

Keuler, Ralph (1988). "Map Showing Coastal Erosion, Sediment Supply, and Longshore Transport in the Port Townsend 30-Minute Quadrangle," *Folio of the Port Townsend Quadrangle*, Miscellaneous Investigation Series, Map I-1198-E. U.S. Geological Survey, Arlington, VA.

Kobayashi, Nobuhisa and Poff, Michael (1994). "Numerical Model RBREAK2 for Random Waves on Impermeable Coastal Structures and Beaches," *Research Report No. CACR-94-12*, *Center for Applied Coastal Research*, University of Delaware, Newark, DE.

Larson, Magnus and Kraus, Nicholas C. (1989). "SBEACH: Numerical Model for Simulating Storm-Induced Beach Change," *Report 1: Empirical Foundation and Model Development*, Technical Report 89-9, US Army Engineer Waterways Experiment Station, Vicksburg, MS.

Pentec Environmental (2004). "Conservation Measures and Monitoring Plan, Port of Everett Rail/Barge Transfer Facility Everett, Washington," *Revised Draft Appendix F*, Prepared for Berger/ABAM Engineers, Inc and the Port of Everett.

Powell, K. A. (1993). "Dissimilar Sediments: Model Tests of Replenished Beaches Using Widely Graded Sediments," *Report SR 350*, HR Wallingford.

Quick, Michael C., and Dyksterhuis, Patricia (1994). "Cross-shore Transport for Beaches of Mixed Sand and Gravel," *Proceedings, International Symposium: Waves-Physical and Numerical Modelling*, Canadian Society of Civil Engineers, pp. 1443-1452.

van der Meer, J. W. and Pilarczyk, K. W. (1986). "Dynamic Stability of Rock Slopes and Gravel Beaches," *Proceedings International Conference on Coastal Engineering*, American Society of Civil Engineers, N.Y., pp. 1713-1726.

Washington Department of Fish and Wildlife (WDFW). Undated a. Washington State Surf Smelt Fact Sheet. Olympia, WA

Washington Department of Fish and Wildlife (WDFW). Undated b. Washington State Sand Lance Fact Sheet. Olympia, WA

INFLUENCE OF CHANGING MANAGEMENT REGIMES ON THE MORPHODYNAMIC RESPONSE, OF A MIXED GRAVEL AND SAND BARRIER BEACH

Andrew P. Bradbury[1], and Julian D. Orford[2]

1. Channel Coastal Observatory, National Oceanography Centre, Southampton, SO14 3ZH, UK
   Andy.Bradbury@noc.soton.ac.uk
2. School of Geography, Archaeology and Palaoecology, Queen's University, Belfast, Northern Ireland, BT8 8AT UK `
   j.orford@qub.ac.uk,

Abstract: The morphodynamic response of a mixed gravel and sand barrier is considered, by reference to storm conditions of varying magnitude, and under differing management regimes. Observations focus on evolution of the barrier at the temporal scale of the storm event, but the response during these episodic events is placed in context with potential impacts on longer term decadal scale geomorphological evolution. Decadal scale evolutionary trends indicate that the total volume of the barrier is declining and that the frequency of overwashing events and rate of rollback of the barrier is likely to increase. Changing profile and sediment sorting responses are evident during the interim phase, immediately following changes in management practice. Modifications to management practice present new issues that may include the possibility of fragmentation on the barrier.

INTRODUCTION

The mixed gravel and sand barrier between Blakeney and Salthouse, lies on the North Norfolk coast of the UK (Figure 1); it is an integral part of a complex coastal geomorphic system that also provides the first line of defence against tidal flooding to the villages of Cley and Salthouse, during extreme surges.

The 11km long barrier forms part of a macro tidal environment, with a mean spring tidal range of 4.4m. The distal terminus is very active, extending through a sandy ebb delta

system. Historical records indicate that that the barrier has migrated at a rate of circa $1ma^{-1}$ since the 16th century. Episodic storm surge events have historically resulted in extensive overwashing and flooding (Orford et al, 2003).

The back barrier area has historically been subject to considerable intervention. Some natural development of intertidal saltmarsh system occurs towards the distal end of the barrier, but extensive reclamation of the proximal end of the back barrier during the 20th century, to form coastal grazing marsh with an extensive drainage system, has substantially reduced the intertidal area (Orford et al 2003). This reclamation has reduced the potential for flood inundation via the estuary, but has also modified the geometry of the back barrier area over which the barrier rolls back. This compounds the complexity of future possible evolution of the barrier, by modifying the accommodation space and by increasing the surface emergent cross-section area; this effectively reduces the potential rate of roll back. . The grazing marshes and freshwater habitats defined and protected by Blakeney barrier are of the highest habitat value particularly for ornithology and are protected by a range of national and international designations.

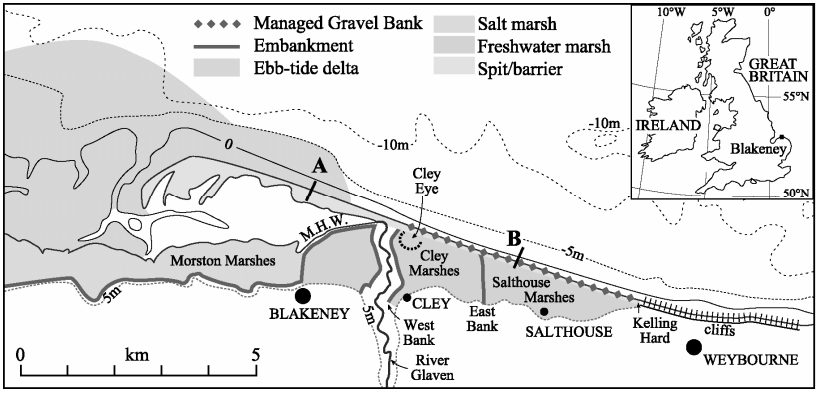

Figure 1. Location and Structure of Blakeney-Salthouse Gravel Barrier (source Orford et al 2003).

The western section of the barrier has remained unmanaged for the last 50 years and has been allowed to evolve naturally. By contrast, the proximal eastern section of the barrier was managed at least since the 1950s until 2005, with mechanical plant used to profile the beach following storm events. This management practice has been considered to be unsustainable, both financially and also environmentally, especially with regard to the EU Habitats Directives. The UK government requirement on returning 95% of designated sites to a satisfactory level by 2010AD means that the barrier management regime has recently been altered to one of virtual non-activity in physically managing the barrier, so as to enable "natural' evolution of the barrier and allow back-barrier area to revert back to a more natural form. Following some fifty years of management this approach presents some complex issues and there is some uncertainty regarding the

likely future patterns of evolution, whilst the barrier adjusts to the new regime.

This investigation seeks to examine the early stages of transition from a managed barrier, to a more naturally evolving system. The implications of earlier management practice on long term evolution are examined. Morphodynamic responses and evolutionary patterns are examined, with respect to defined hydrodynamic conditions, prior to and following changes in management practice. Hypotheses are examined to examine predictions for future changes. For the purposes of comparison the beach is divided into two segments reflecting the unmanaged and managed beach sections (Figure 1).

FIELD OBSERVATIONS

Field observations span the period 1992-2006 and include some 30 independent surveys of beach profiles spaced at approximately 1km intervals (Figure 1). These are supplemented with more detailed recent surveys derived from LIDAR (0.25m resolution), covering the whole of the barrier and back barrier area. Post storm beach profile survey data also provides evidence of beach evolution, during events that have followed the changes in management policy. A series of orthorectified aerial surveys, spanning epochs from 1946-2004, provide the basis for determination of plan shape changes. Hydrodynamic data are provided by tide gauge (Cromer 1km west of the site) and wave measurements, and hindcast offshore wave data, transformed to nearshore locations.

MANAGEMENT PRACTICE

Prior to 2005 two distinct management practices were evident on the barrier (Figure 1). The beach exhibits differing performance and evolutionary characteristics on each section. Active management of the barrier ceased during 2004, since when the barrier has been allowed to modify naturally.

Unmanaged beach

The morphodynamic evolution of the unmanaged beach section is consistent with the classical processes normally associated with gravel barriers (Orford et al, 1995). The classical dynamic equilibrium shingle beach profile (Powell, 1990) develops whilst conditions are sufficiently benign that wave run-up cannot exceed the crest; this provides a distinct berm, breaker-step and toe at the seaward limit. The dynamic equilibrium profile can be predicted reliably for given combinations of wave, water level and sediment size under such conditions. Clearly defined ephemeral berms form beneath the crest, in response to the dynamics of the wave and water level conditions. As the combination of wave period and water level conditions become more severe however, wave-run up may exceed the crest and at this point the predictive profile model fails to function, as it is not designed to deal with a cross-section of finite area (Bradbury, 2000).

Overtopping may occur as conditions become more severe. The swash limit is initially small as a result of the high beach permeability and most water percolates harmlessly through the permeable structure. Modification of the crest may occur with build up of

sediment arising under such conditions (Orford et al. 1991). Evolution of the crest is confined to those conditions where sufficient wave energy reaches the crest to cause sediment movement. Saturation of the beach occurs under the most severe conditions and this may result in larger scale movements of sediment resulting in overwashing, which can reduce crest height (Carter and Orford, 1993, Carter et al 1993).

Beach sorting processes result in general coarsening of grain-size, and increasing permeability of the beach sediment towards the crest. The crest is generally characterized by coarse open-work shingle, whilst the sandy component washes through towards the base and toe of the beach. Layering and intermixing of sand layers with coarser gravels is sometimes evident, but these layers are usually ephemeral, arising from rapid changes in deposition in overwashing events, within the more severe storm events. Long term processes gently wash the finer fraction from the surface layers maintaining a permeable structure over much of the beach.

Maintained beach

Regular maintenance of the shingle ridge has been carried out for at least 50 years, to the east of Cley Eye (Figure 1). The beach cross-section has been maintained with an artificially high crest elevation and over-steep upper beach crest ridge. The crest elevation has typically been maintained at between 8-9mODN, some 2-3m higher than the typical crest of the natural beach. This has been achieved by bulldozing beach material landwards with mechanical plant, to reform the crest ridge following storm activity. This practice of cross-shore recycling has several impacts. Cross-shore movement of beach material results in a modified profile shape, which is much steeper than would form naturally. Additionally, the mechanical profiling process results in movement of the finer fraction of material from the lower beach to the beach crest, mixing of coarse and fine sediments, and compaction by the mechanical plant to form a cohesive matrix; this is able to stand close to a vertical angle, until undermined and reworked by wave activity. Permeability of the beach and any infiltration by water is reduced, thereby generating greater overland flow on the beach face under backwash. No additional beach recharge material has been added to the system – though some longshore sediment transfers are likely.

Following mechanical profiling of the beach, changes to the modified profile are rapid under wave action, as the beach seeks to reproduce a more natural dynamic equilibrium profile. The cohesive matrix of the upper beach is maintained until the whole of the upper beach has been reworked. As maintenance of the crest ridge has continued for more than 50 years, the reworking process has not been permitted to complete this cycle. A reflective upper beach face is formed therefore, which accelerates the return of beach material to the lower foreshore and modification of the profile towards a dynamic equilibrium shape. Although the lower beach is reworked, this does not generally occur above an elevation of about 4mODN. A hard impermeable core has resulted within the unworked section of the barrier crest. On rare occasions wave activity is able to reach the crest in severe events, but the beach crest performs with similar characteristics to an impermeable vertical seawall under these conditions, resulting in overtopping of the

crest and waves plunging vertically onto the lee face of the beach and forming deep runnels. The sediment characteristics of the beach are defined by a heavily mixed foreshore and an oversteep crest ridge of matrix dominated fine materials, with occasional clasts.

Geometric characteristics of managed and unmanaged sections

The geometric characteristics of the managed and unmanaged sections of the beach provide some marked contrasts. Whilst the natural crest elevation of the unmanaged beach lies at between 5-6.5mODN (MHWS=2.45mODN), the managed beach sections are typically within the elevation range 8-9mODN. The beach cross-sectional area above MHWS is however typically approximately 60% larger on the unmanaged beach section than the managed section. This is significant in context with the predictive approach to the threshold of barrier overwashing (Bradbury et al, 2005), which suggests that the surface emergent cross-section area at the storm peak provides the most significant geometric control. Threshold conditions leading to overwashing might reasonably be expected to be somewhat less severe on the managed section therefore. Although the beach cross-section area varies between the managed and unmanaged sections, the wave climate conditions are very similar along much of the barrier length. Differing beach responses are likely to be a function of beach geometry and sediment structure therefore.

DECADAL SCALE EVOLUTION

The unmanaged western 5km of the barrier exhibits classical gravel barrier evolution characteristics (Orford et al 1991), with high permeability, regular overtopping, overwashing and landward transgression during extreme events. Decadal scale evolution of the back barrier fringe, determined from aerial surveys, suggests an annual average rate rate of 0.9m a^{-1} for the period 1946-2004 (Box, 2005). Profile analysis demonstrates the episodic nature of crest and back barrier evolution. For instance, a single event (19 February 1996) is responsible for transgression of the back barrier fringe by approximately 25m, and reduction of the crest elevation by 1m. Regular crest evolution and overwashing is clearly evident within a 15 year evolutionary sequence of profile data (Figure 2). Washover fans that do not reach the back barrier margin can extend as far as 40m from the beach crest. Changes in crest elevation are typically small (<1m) even under the most extreme events. Numerous events have resulted in deposition of veneer deposits 0.1-0.2m thick under overtopping conditions. The crest has been within a building phase for most of the period.

By contrast, the pattern of evolution on the managed beach is somewhat unclear. A lower rate of barrier migration (0.6m a^{-1}) is suggested by aerial survey data; this rate has been controlled however, largely by the mechanical reprofiling process that has resulted in artificial holding of the crest line and limited evolution of the back barrier margin. As the barrier inertia is somewhat lower on the managed section of beach a more rapid rate of transgression might reasonably be expected under naturally evolving conditions.

Profile analysis indicates net losses in the upper beach volume (above MHWS) over the period 1992 to 2004 of approximately 300,000m^3 spread equally between the managed and unmanaged sections of the barrier (Halcrow, 2006). This represents a total proportional loss of 13%, from the original total volume of 2.3million m^3 above this elevation. The downward trend appears to be reasonably linear. The implications of these losses and the ongoing trend of a gradually reducing effective cross-section area, combine with factors such as relative sea level rise, and increasing intensity of wave climate; these variables increase the vulnerability of the barrier to overwashing processes and future rates of change of evolution. As losses continue, the frequency of overwashing events is expected to increase. Whilst the freeboard of the managed section of the beach is consistently higher than the unmanaged beach, the cross-section area is generally significantly smaller. Cross section areas above MHWS on the managed barrier vary from about 160-250m^2, whilst those on the managed barrier vary between 100-220m^2. The cross-section area of the unmanaged beach is on average 60% higher than the managed beach, which suggests that a more volatile response might be expected on the managed beach section. It is clear that without supply of additional beach material from new sources the beach volume will continue to decline and the frequency of overwashing will increase.

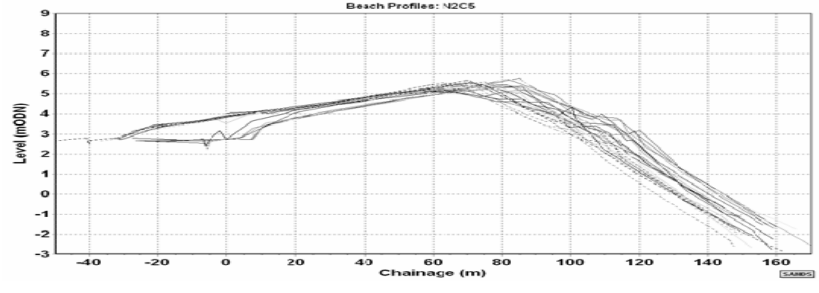

Figure 2 Evolution of the unmanaged barrier from 1992-2005

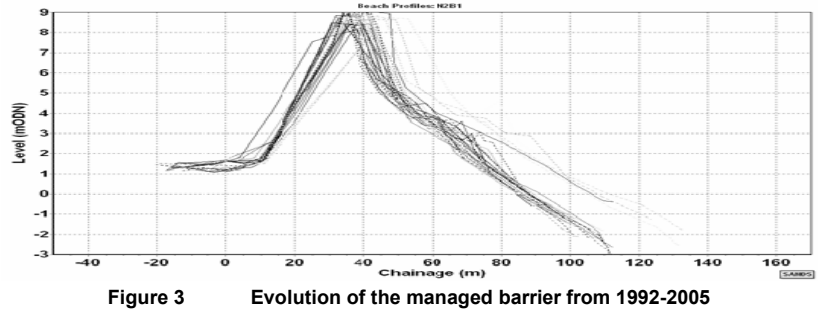

Figure 3 Evolution of the managed barrier from 1992-2005

A variable longshore wave energy gradient is evident but this is inconsistent along the length of the barrier. Although sediment transport calculations (Halcrow, 2006) suggest differential rates that might possibly induce the formation of tears and fragmentation in the barrier, the transport rates are consistently low, with the exception of the distal end of the spit. Given the potential limitations of the modeling exercise the differentials identified could be within the expected scatter of results. There is no evidence of tears forming within the beach at this stage, although two sections do show signs of preferential thinning.

WAVE CLIMATE

The Met-Office UK waters regional wave model provides the source time series data (1986-2006) for generation of an offshore wave climate. The lengthy time series is extrapolated using a Weibull probability distribution to provide an estimate of extreme conditions (Table 1). The regional wave climate is dominated by the most severe wave conditions occurring from the north-northeast sector (300-60°). Historically, all recorded events that have resulted in overwashing of the barrier have arisen from waves generated from this direction sector.

Numerical modeling of shallow water wave transformations provide nearshore conditions at a series of points, above the 10mCD depth contour (see Figure 1); this provides wave conditions in an effective water depth of 10-15m, across the tidal range, in conditions close to the seaward limited of wave driven sediment movement or depth of closure. Provision of the nearshore wave climate across this range of water depths provides the most appropriate conditions for input to investigations of models of barrier profile development, including estimation of the overwashing threshold conditions (Bradbury, 2000).

Table 1. Offshore and Nearshore 3-hourly Extreme Wave Conditions for All Directions.

Return period (years)	Extreme offshore wave height H_s (m)	Extreme nearshore wave heights H_s (m)
0.1	4.51	2.71
0.2	4.83	2.91
0.5	5.23	3.17
1	5.52	3.36
2	5.79	3.54
5	6.14	3.77
10	6.40	3.95
20	6.65	4.11
50	6.97	4.33
100	7.20	4.49
200	7.43	4.64

Key storm events have been hindcast and transformed to the nearshore locations (Table 2). The three events described have all resulted in overwashing at some location on the barrier. Individual storm events are placed in a probabilistic return period context relative to the regional wave climate. Extreme water levels are shown in similar context, based upon earlier investigations (Halcrow, 2006). Sensitivity testing of the longshore

gradient and variability of the wave climate for these extreme conditions indicates very small changes in conditions along the length of the barrier, with the exception of the distal recurves where the wave intensity is reduced and the angle of wave attack much more oblique. Significantly, the nearshore conditions result in virtually normally incident wave conditions at the barrier site for each event.

Table 2. Nearshore Storm Characteristics of Events Resulting in Barrier Overwashing

Event peak	Hs (m)	Tz (s)	Tp (s)	Dirn O	Wave Return period (yrs)	Water level (mODN)	Surge Residual (m)
21/02/1993 06:00	3.5	7.2	8.4	2.1	2	3.45	2.3
19/02/1996 06:00	3.1	6.6	7.9	17.5	0.5	2.96	1.5
08/04/2005 18:00	2.6	6.5	7.8	2.8	0.1	3.00	0.5

Storm profiles

The storm profiles of major events provide a valuable insight into the hydrodynamic conditions impacting on the barrier. Both major events shown (Figures 4 and 5) have resulted in major overwashing and flooding.

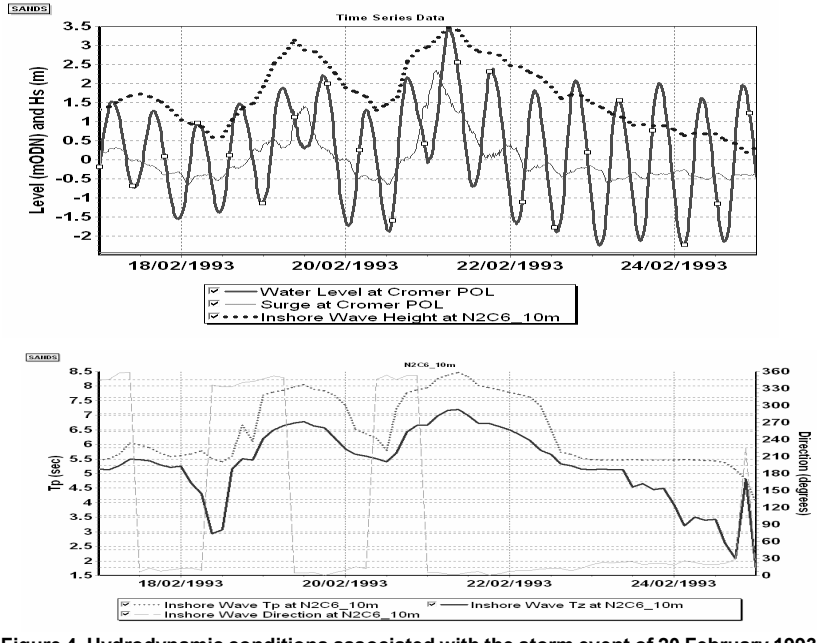

Figure 4. Hydrodynamic conditions associated with the storm event of 20 February 1993

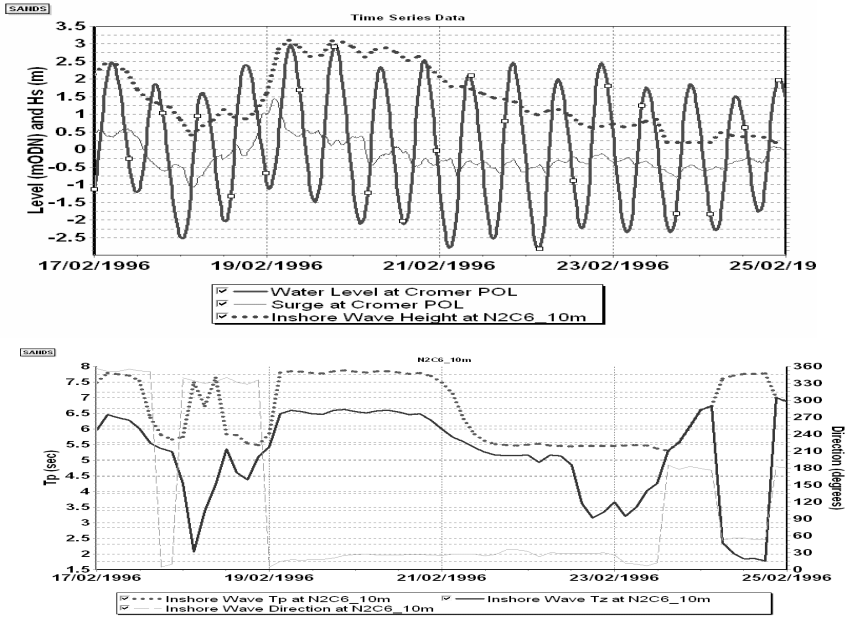

Figure 5. Hydrodynamic conditions associated with the storm event of 19 February 1996

The characteristic conditions for both events show some similarities, with major storm surges (>1m) being associated with both events. Although the storm event of 20 February 1993 provides the most severe combination of significant wave height and extreme water level conditions, profile analysis demonstrates that more extensive evolution of the barrier is evident during the event of 19 February 1996. This may reflect maintenance of the storm intensity over a period of several tidal cycles around the 19 February 1996 event (Figure 5), during which period the resistance of the barrier would have been significantly reduced following initial overwashing. Storm duration is considered to be a significant factor in the rate of evolution, if the overwashing threshold has been exceeded and insufficient material is available to enable a dynamic equilibrium profile to form within the beach cross-section.

POST MANAGEMENT REGIME EVOLUTION

Since the change of management policy in 2004, wave conditions have generally been relatively benign, by comparison with the major flooding events (Figures 4 and 5). A storm event of moderate intensity on 8 April 2005 (Figure 6) provides an opportunity to examine the early stage impacts of modification of the management policy on the beach response. The storm peak is coincident with the high spring tide, which is also supplemented by a small storm surge.

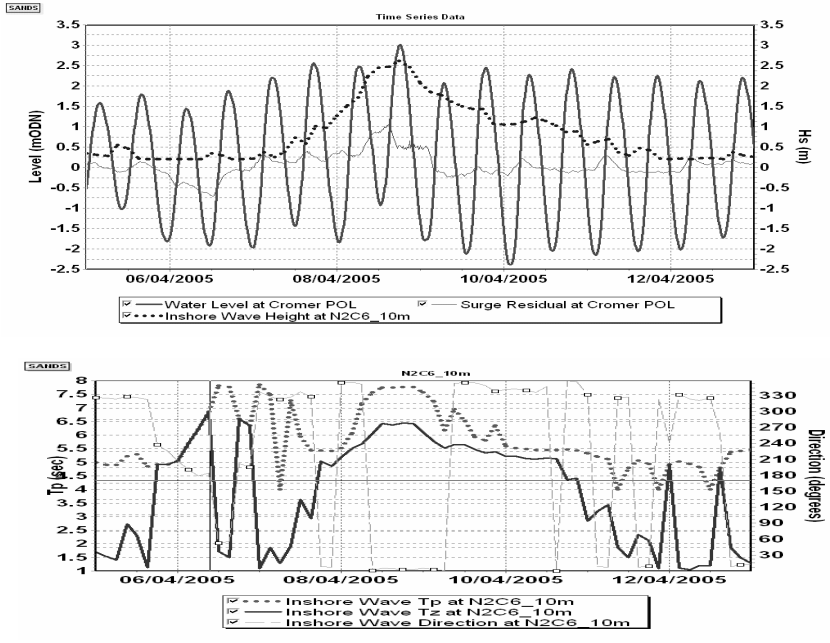

Figure 6. Hydrodynamic conditions associated with the storm event of 8 April 2005

Sample profiles are presented, representing the beach response at various locations (Figure 7). Contrasting responses are evident according to pre-storm cross-section area and previous management practice. The beach performance on the unmanaged beach section is very similar to responses observed previously (Figure 7a). Conditions are very close to the overwashing threshold, with evidence of a thin veneer of washover deposits extending beyond the crest ridge, but with maintenance of the crest elevation.

The storm has resulted in reworking of the over-steep crest ridge over most of the length of the previously managed barrier. Observations made during and following the storm demonstrate clearly that the overwashing threshold was exceeded (Figure 8) at several isolated locations; this was confined to those areas of the beach where the pre-storm beach cross-section area above MHWS was below 110m^2. The extent of washover fans is limited to approximately 10-12m length to landwards (Figure 7b). The relatively small changes in the profile response, and maintenance of a sharp crest ridge suggest that conditions were close to the overwashing threshold. Profile analysis demonstrates that gradual thinning of the oversteep beach crest has occurred since maintenance has ceased. This is particularly pertinent on sections of the beach with low cross-section area.

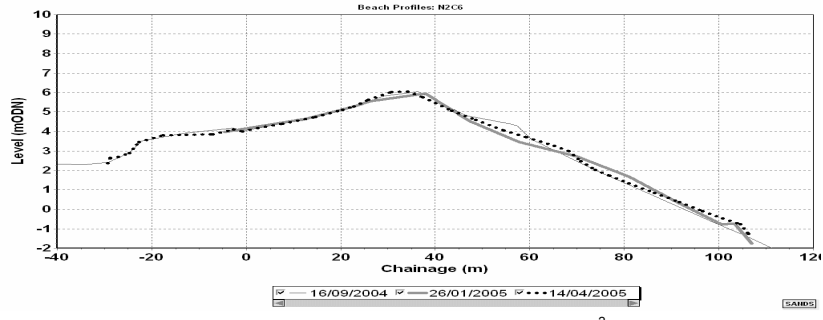

7a. Unmanaged beach section (CSA = 155m^2)

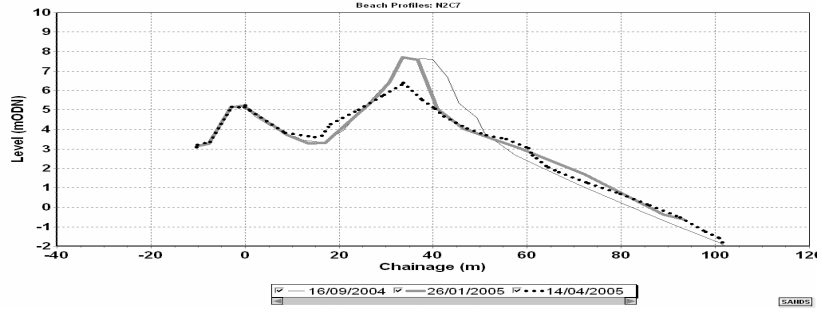

7b. Previously managed beach section with small cross-section area (CSA=110m^2).

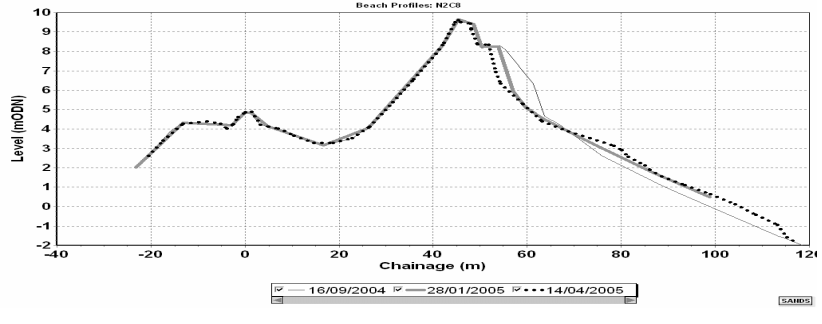

7c. Previously managed beach section with high freeboard (CSA= 220m^2).

Cross-sectional areas are all above MHWS (2.45mODN

Figure 7 Post storm profile response to storm event of 8 April 2005

Elsewhere on the beach there is evidence of erosion of the crest ridge and typically reduction of the crest width, but the upper crest ridge has maintained its steep upper profile (Figure 7c). Initial erosion of the crest ridge has resulted from waves that have been unable to reach the beach crest. Undermining of the steep beach face has resulted in cut back of the crest ridge and drawdown by reflected waves. The remaining upper beach crest remains matrix dominated and highly impermeable. The beach zone below an elevation of about 4mODN is showing signs of better sorting however. A steep leeward slope has been maintained, although there is evidence of plunging overtopping waves causing runnels in this area.



Figure 8. Stages in overwashing during the storm event of April 8 2005
(Images courtesy Bernard Bishop)

DISCUSSION

There is evidence that some parts of the barrier are already adapting and following a more natural evolutionary form, following changes to the management regime; this is more clearly evident where the crest elevation is low or the barrier cross-section is relatively small. There is clear evidence that the profile form is changing as better beach sorting, arising from re-working, results in increased localized permeability. The barrier crest remains matrix dominated at those locations where reworking has not yet occurred. A broader more well sorted foreshore is evident in the zone from mean tide level to about 2m above MHW, which is showing clear signs of increased permeability and sorting with clast domination.

Several stages are evident in the transition process. Firstly, the whole of the previously engineered cohesive barrier crest must be subject to wave activity and all sediment reworked before the barrier can evolve in a natural manner. On the basis of changes observed in profile trends since 2004, it seems likely that a further period of 3-5 years will elapse before this transitional process is complete. In the event of a major storm event, such as the February 1993 or 1996 events, this period could be substantially shortened.

Overwashing may occur at many locations prior to the completion of the re-working process. The elevation of the beach is so high at some locations that wave run-up is unable to reach the beach crest. Overwashing will arise as a result of undermining and

thinning of the crest at such locations. The cross-section area above MHWS exhibits high spatial variability, which lies in the range 100-250m^2. Regular (annual) overwashing can be expected where the cross-section is less than about 160m^2, based on historical trends on the unmanaged section. More frequent overwashing might reasonably be expected where the cross-section is smaller. Once the crest ridge has been reworked and overwashing processes become more regular, the rate of rollback is likely to increase. The long term loss of sediment from the system is likely to accelerate the overwash process, provided that this trend is maintained. Without further supply of material to the system, the barrier is expected to decline in volume further. Losses might reasonably be expected to occur at the historical rate observed between 1992-2004 (23,000m^3 a^{-1}), at least until such time as the barrier becomes more precisely swash aligned, when more volume might be maintained.

The impacts of back barrier controls will become much more significant on long term evolution. Features such as the glacial eye deposits could have a major impact on interruption of the rollback process. These will provide local restrictions on the rate of roll back at some locations, acting as headland structures. Fragmentation of the barrier is possible at these hard points, as tears may develop arising from differential resistance of the barrier. The potential breakdown of the barrier into smaller barriers
is linked also with uncertain issues related to sediment supply, and differential sediment transport rates along the length of the barrier. The major question arising is - will the barrier continue to form as a coherent single entity? Breakdown will depend upon many factors including tear propagation. The position of the 'eyes' is likely to hold up the ridge and push tear development as perturbations in a consistent spatial rate of barrier retreat - hence the possibility of smaller barrier segments

The elevation of the reclaimed land behind the previously managed beach will slow the rate of recession, providing greater effective cross section. Reworking of fine reclaimed material is likely to become a significant process that will modify the geometry and response of the lower beach zone. Similarly, migration over a back barrier of varying topography will present compaction issues, given the organic basis of the back barrier facies.

.

The historical management practice has enabled more mature development of features such as saline lagoons which are naturally ephemeral features and has also preserved shingle vegetation which might normally be destroyed. It is expected that
with greater overwash the saline lagoons (as a priority designation in the EU) may be better maintained. However the increased flood routing that has occurred in the back barrier (new sluice gates for storm discharge) might mitigate against that.

CONCLUSION

The mixed gravel and sand barrier between Cley and Salthouse is in a transition phase as it reverts from a heavily managed barrier to more natural structure. Changes in beach response have become evident within one year of the change in management practice. Transition phases will be followed by periods during which rate of overwashing and

rollback is expected to increase. Subsequently, the back barrier geometry will become a more dominant control on evolution. Ongoing monitoring of the transition from a managed barrier to more natural evolution will provide further evidence of changes in morphology and response.

ACKNOWLEDGEMENTS

We wish to thank the Environment Agency for provision of data used in the preparation of this paper.

REFERENCES

Box S.J., (2005) Coastal Evolution Studies of Cley Barrier Norfolk Unpublished MSc. Thesis, University of Southampton.

Bradbury, A.P., Cope S.N. and Prouty D.B. (2005) Predicting the response of shingle barrier beaches under extreme wave and water level conditions in southern England. *Proc. Coastal Dynamics 05* ASCE

Bradbury, A.P. (2000) Predicting Breaching of Shingle Barrier Beaches-Recent Advances to Aid Beach Management. *Proc. 35th. Annual MAFF Conference of River and Coastal Engineers*.05.3.1-05.3.13

Carter, R.W.G., and Orford, J.D., (1993). The morphodynamics of coarse clastic beaches and barriers: a short- and long-term perspective. *J. Coastal Research,* 15, 158-179.

Carter, R.W.G., Forbes, D.L., Orford, J.D., Jennings, S.C., Shaw, J., and Taylor, R.B., (1993). Long-term morphodynamic evolution of beaches and barriers: examples from paraglacial coasts, *Proc.. Large scale coastal behaviour 93*, U.S Geological Survey Report 93-381, 238

Halcrow Group (2006) Cley to Salthouse Shingle Ridge Management Coastal Process Analysis. Report to the Enivironment Agency.

Orford, J.D., Jennings, S.C. and Pethick, J. (2003) Extreme storm effect on gravel-dominated barriers. Coastal Sediments'03. In Davis, R.A. (ed). 2003. *Proceedings of the International Conference on Coastal Sediments 2003*. CD-ROM published by World Scientific Publishing Corp. and East Meets West Productions, Corpus Christi, Texas, USA. ISBN 981-238-422-7, 12pp

Orford, J.D., Carter, R.W.G., and Forbes, D.L., (1991). Shingle barrier migration and sea level rise; some observations from Story Head, Nova Scotia, Canada. *J. Coastal Research*, Vol. 7; 477-488.

Orford, J.D., Carter, R.W.G., McKenna.,J., and Jenkins, S.C., (1995). The relationship between the rate of mesoscale sea-level rise and the rate of retreat of swash aligned shingle - dominated barriers, *Mar.Geol.*Vol. 124 177-186.

Powell, K.A., (1990). Predicting short-term profile response for shingle beaches. Hydraulics Research Report SR219.

THE INFLUENCE OF GROUNDWATER ON PROFILE EVOLUTION OF FINE AND COARSE SAND BEACHES

Diane P. Horn[1], Tom E. Baldock[2], Ling Li[2,3]

1. School of Geography, Birkbeck College, University of London, Malet Street, London WC1E 7HX, UK. d.horn@bbk.ac.uk.
2. School of Engineering, University of Queensland, Brisbane, Queensland, 4072, Australia. t.baldock@uq.edu.au.
3. Centre for Eco-Environmental Modelling. Hohai University, Nanjing 210098, People's Republic of China. l.li@uq.edu.au.

Abstract: This paper reports on laboratory experiments carried out on fine and coarse sand beaches under raised and lowered back beach groundwater levels. Onshore sediment transport was enhanced when the groundwater level was lowered under both accretionary and erosive conditions, whereas higher groundwater level promoted offshore sediment transport. Under swell conditions, the coarse beach showed accretion at all groundwater levels. In contrast, on the fine sand beach, lowering the groundwater level was able to induce accretion on a previously erosive profile. The groundwater level had less effect on beach profile evolution under storm conditions, suggesting that artificially lowering groundwater levels would not help much in the control of storm erosion, but could promote post-storm accretion on permeable beaches. Agreement between measured and modelled head levels was better on the coarse beach than on the fine beach, and better in the swash zone and within the beach than in the surf zone.

INTRODUCTION

The relative importance of infiltration and exfiltration for sediment transport and beach profile evolution in the swash zone has not yet been resolved. Many researchers have suggested that infiltration losses in the swash provide a mechanism by which beach accretion occurs above the still water level (e.g. Bagnold 1940; Duncan 1964; Nelson and Miller 1974; Packwood 1983; Turner and Nielsen 1997; Masselink and Li 2001). Because the uprush and backwash are relatively shallow, a small change in water volume

due to infiltration losses could influence uprush/backwash flow asymmetry and therefore the energy available for sediment transport (Nelson and Miller 1974). The potential for infiltration or exfiltration has been linked to beach watertable elevation, with a low watertable favouring infiltration and onshore sediment transport and a high watertable favouring exfiltration and offshore sediment transport (Grant 1946, 1948). A practical application of this concept is the use of beach dewatering systems, where the watertable is artificially lowered within the beach by a system of drains and pumps. However, attempts to modify beach morphology by controlling groundwater levels or through beach drainage have had mixed success and the effectiveness of the dewatering concept in maintaining beach stability and controlling coastal retreat is yet to be convincingly demonstrated at the prototype scale (Turner and Leatherman 1997). In addition, the conditions under which infiltration is a significant process have not yet been definitively determined. Numerical studies have suggested that the effects of infiltration/exfiltration on sediment transport are greater in the uprush than in the backwash (Packwood 1983; Turner and Masselink 1998; Masselink and Li 2001). However, the inferences drawn from this modelling about infiltration effects in the swash has not yet been verified. A number of studies also indicate that infiltration in the swash zone may only be important for profile evolution on coarse-grained beaches (Bagnold 1940; Quick 1991; Packwood 1983). The beachface gradient has been shown to increase with the amount of swash infiltration (Quick 1991; Masselink and Li 2001), and infiltration loss in the swash is often given as the reason why gravel beaches are steeper than sand beaches. This has led to the suggestion that hydraulic conductivity is an important factor in the different response of fine and coarse-grained beaches, and therefore that beach groundwater dynamics play an important role in beach profile evolution.

EXPERIMENTAL SETUP

The experiments reported here were carried out in a section of the Coastal Wave Basin in the Department of Civil Engineering, University of Queensland, Australia. The section used in the experiments was 27.3 m long, 1.4 m wide and 0.8 m deep, with a working depth of 0.5 m (Figure 1). The experimental setup was designed to simulate a coastal barrier dividing the ocean from a relatively constant back beach water level, conditions approximating a closed off lagoon system or beach aquifer. Under this scenario, the backshore water level was fixed at an elevation that was either higher than, lower than, or the same as the still water level (SWL), comparable to varying the groundwater level according to the tidal stage. Thus at high tide the groundwater level at the beach boundary may be raised above that inland, whereas at low tide it may be lower, with wave runup subsequently further influencing the groundwater levels in the beach. Varying the back beach groundwater level influenced a much larger region of the upper beach than if a point or line drain were used. The water level in the basin was kept constant using a small inflow near the wave generator and a weir behind the beach. The back of the beach was supported by a wire mesh located 0.2 m from the back wall of the flume, which prevented the loss of sediment while allowing water flow in and out of the permeable beach. The water level behind the beach was controlled by an adjustable pipe which was connected through the back wall.

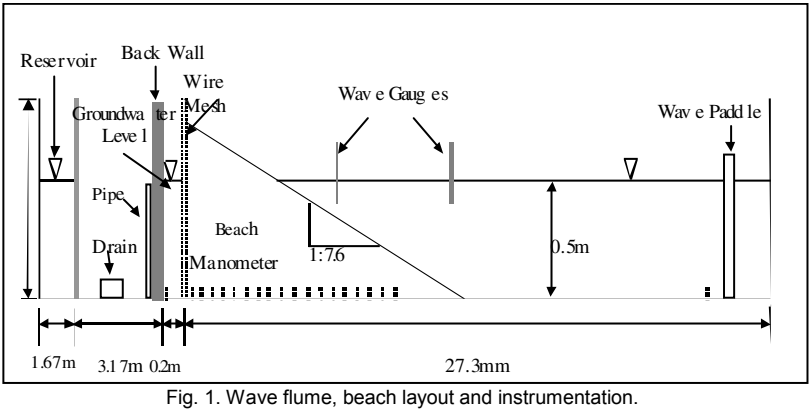

Fig. 1. Wave flume, beach layout and instrumentation.

At the start of each experimental run, the watertable behind the beach was set at a chosen level (nominally 0 to ± 0.075m) relative to the offshore level and the piezometric head levels recorded. A series of regular waves were then generated by the wavemaker and wave parameters were measured with two surface-piercing wave gauges. A set of 20 damped manometer tappings on the bed of the flume provided time-averaged mean piezometric head levels in the cross-shore direction from offshore of the breakpoint to the back of the beach. According to Dupuit-Forchheimer theory, the piezometric heads can be assumed to give the watertable elevation as long there is no significant vertical flow (Kirkham 1967). The water level in the manometer tubes responded quickly to uprush and backwash, and eventually reached steady state conditions.

Table 1. Experimental runs for each grain size

Run	H (m)	f (Hz)	Ω (H_b/w_sT)	Profile Type
1-3	0.05	0.4	0.15	swell
4-6	0.1	0.4	0.31	swell
7-9	0.15	0.4	0.46	swell
10-12	0.05	0.6	0.23	swell
13-15	0.1	0.6	0.46	swell
16-18	0.12	0.6	0.7	swell/storm
19-21	0.15	0.6	0.56	storm
22-24	0.05	1	0.39	storm
25-27	0.1	1	0.77	storm
28-30	0.15	1	1.16	storm

Two sets of experiments were carried out, one with coarse sand (d_{50}=0.84 mm) and one with fine sand (d_{50}=0.197 mm). In all experiments, the initial beach profile was planar, with a slope of approximately 1:7.6, with the beach gradient starting from the weir mesh and extending 5.4 m from the back wall. The beach was regraded between runs so that each run started with the same initial profile. The relative back beach water levels and wave heights were set to simulate the typical tidal range and wave heights on a micro-mesotidal beach. For each sediment size, experiments were run with regular waves at three wave frequencies (0.4, 0.6 and 1 Hz), three wave heights (0.05 m, 0.1 m and 0.15 m), and three groundwater levels in the beach (0.05 m above SWL, 0.05 m below SWL and equal to SWL), in order to simulate high tide, low tide and mid-tide conditions (Table 1). Note that three runs were carried out at each wave setting in order to vary the groundwater levels for these waves. All tests were run for an hour. Manometer readings were taken at the start of the experiment and at 10, 20, 35 and 55 minutes into each run. The beach profile was measured along the centre line of the beach at the start of the experiment and at 15, 30 and 60 minutes into each run.

BEACH PROFILE EVOLUTION

Figure 2 shows the initial planar beach profile and the measured beach profiles for the fine and coarse sand beaches after 60 minutes for swell conditions for the case where the back beach groundwater elevation was the same as the SWL (run 7 on Table 1). Under these conditions, onshore transport and accretion above the SWL were observed on the coarse sand beach, with a berm developing on the upper beachface. In contrast, the fine sand beach showed offshore transport, with the upper beachface eroding and a bar developing in the same offshore position where the coarse sand beach showed erosion (approximately 2-3 metres from the back wall).

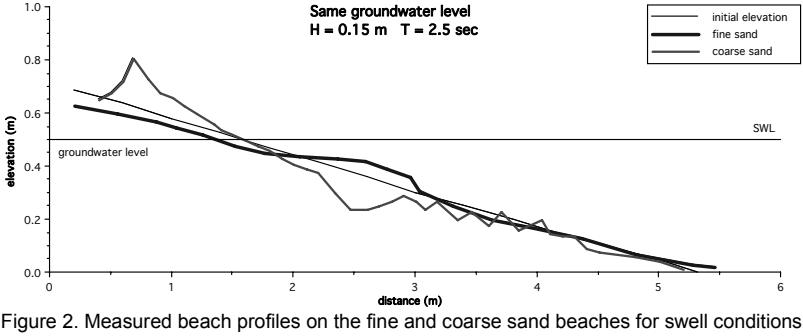

Figure 2. Measured beach profiles on the fine and coarse sand beaches for swell conditions (T=2.5 sec, H=0.15m), with the inland groundwater level the same as the SWL

Figure 3 shows the initial profile and the profiles after 60 minutes for the fine and coarse sand beaches for swell conditions when the back beach groundwater elevation was lower than the SWL (run 8). In contrast to the situation when the groundwater level in the beach was the same as the SWL (run 7, shown in Figure 2), both beaches showed onshore transport and accretion above the SWL with a lowered back beach groundwater

level. However, only a small amount of accretion was observed on the fine sand beach, whereas a large berm developed on the coarse sand beach. One bar developed below the SWL on the fine sand beach. As in the previous case, the coarse sand beach showed erosion below the SWL, with a series of small bars developing further offshore.

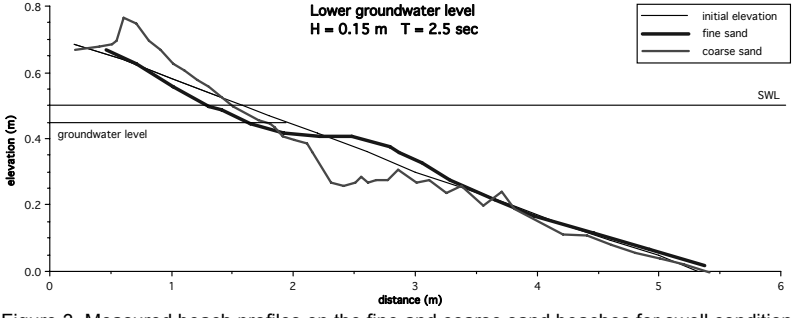

Figure 3. Measured beach profiles on the fine and coarse sand beaches for swell conditions (T=2.5 sec, H=0.15m), with the inland groundwater level lower than the SWL

Figure 4 shows the initial profile and the profiles after 60 minutes for the fine and coarse sand beaches for swell conditions when the back beach groundwater elevation was higher than the SWL (run 9). The results show the same pattern as run 7, with onshore transport on the coarse beach and offshore transport on the fine beach. However, with raised inland groundwater levels, much less accretion occurred on the coarse beach, whereas the amount of erosion on the fine beach was similar to that in run 7. This suggests that the reduced infiltration due to the raised groundwater level affected sediment transport on the coarse beach, but had little effect on transport on the fine beach, where the profile was virtually identical to that in run 7.

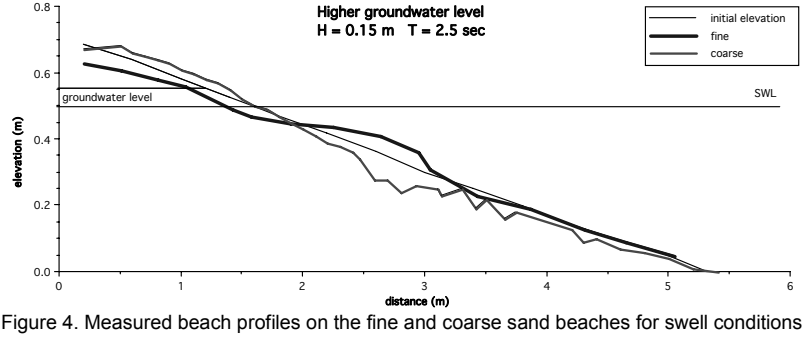

Figure 4. Measured beach profiles on the fine and coarse sand beaches for swell conditions (T=2.5 sec, H=0.15m), with the inland groundwater level higher than the SWL

Figure 5 shows the initial profile and the profiles after 60 minutes for the fine and coarse sand beaches for storm conditions when the back beach groundwater elevation was the

same as the SWL (run 25). Under storm conditions, as expected, offshore transport occurred on both the fine sand and the coarse sand beach. However, the coarse sand beach appeared to show more erosion above the SWL and bar development below the SWL than the fine sand beach. In contrast, the fine sand beach showed relatively little change from the initial profile. Field experiments have also shown that the amount of profile change on coarse beaches is often greater than on fine beaches (e.g. Van Wellen et al. 2000; Kulkarni et al. 2004; Horn and Li 2006).

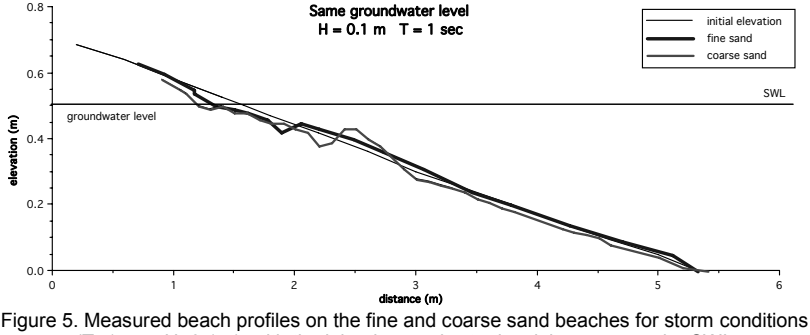

Figure 5. Measured beach profiles on the fine and coarse sand beaches for storm conditions (T=1 sec, H=0.1m), with the inland groundwater level the same as the SWL

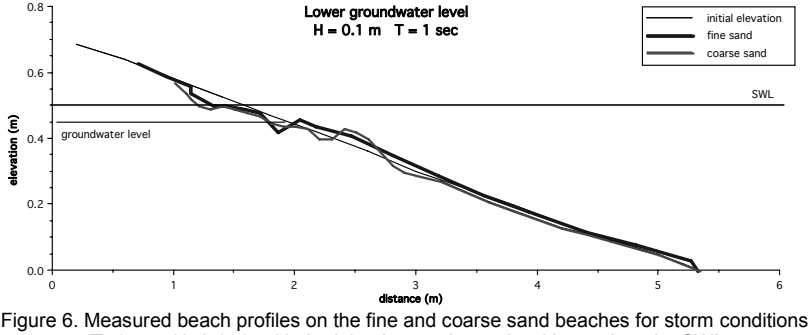

Figure 6. Measured beach profiles on the fine and coarse sand beaches for storm conditions (T=1 sec, H=0.1m), with the inland groundwater level lower than the SWL

Figure 6 shows the initial profile and the profiles after 60 minutes for the fine and coarse sand beaches for storm conditions when the back beach groundwater elevation was lower than the SWL (run 26). Again, more erosion was observed above the SWL on the coarse beach than on the fine beach. The upper beachface on the coarse beach under the lowered groundwater level was considerably steeper than in run 25, whereas the profile on the fine beach was very similar to the profile in run 25.

Figure 7 shows the initial profile and the profiles after 60 minutes for the fine and coarse sand beaches for storm conditions when the back beach groundwater elevation was

higher than the SWL (run 27). Again, the profile on the fine beach was very similar to that in runs 25 and 26, although there was slightly more erosion above the SWL and the bar developed a bit further offshore. The erosion on the coarse beach occurred at a lower elevation above SWL, but the pattern was otherwise comparable to runs 25 and 26.

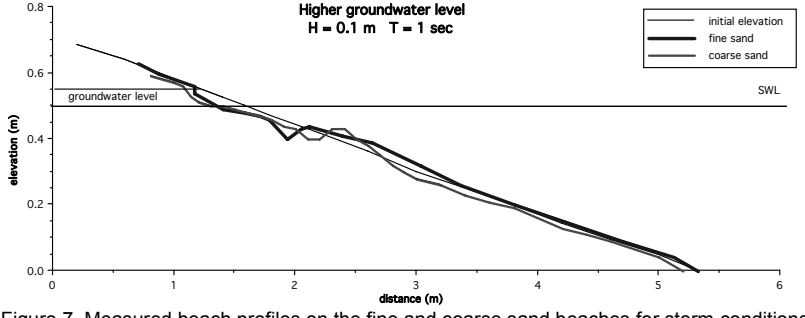

Figure 7. Measured beach profiles on the fine and coarse sand beaches for storm conditions (T=1 sec, H=0.1m), with the inland groundwater level higher than the SWL

In terms of flow through the beach, the coarse sand beach is comparable to a gravel beach at full scale. The laboratory experiments indicated that infiltration played a significant role in beach profile development on the coarse beach, with onshore transport and berm development under all inland groundwater levels, particularly when the inland groundwater level was lowered. In contrast, accretion above the SWL on the fine sand beach only occurred when the inland groundwater level was lowered, suggesting that only under these conditions was infiltration significant. Although saturation levels in the beach were not measured during these experiments, the implication is that the sand above the watertable on the coarse sand beach was always unsaturated, whereas on the fine sand beach the sand was only unsaturated when the groundwater level in the beach was lowered. Lowering the groundwater level on the coarse beach under swell conditions increased the amount of accretion and raising the groundwater level decreased the amount of accretion, but accretion occurred at all groundwater levels on the coarse beach.

Only a few of the results appear to support the conceptual model of Grant (1946, 1948), who suggested that a dry beach (which he interpreted as one with a low watertable) is associated with net onshore transport and beach accretion and a wet beach (which he interpreted as one with a high watertable) is associated with net offshore transport and beach erosion. In the case shown here (runs 7 to 9), and in a few other cases, a lowered groundwater level on the fine sand beach resulted in a small amount of accretion on the upper beach, with erosion occurring everywhere on the beachface under the same wave conditions for the other two groundwater levels. The results of these experiments therefore do not confirm previous suggestions that infiltration only plays a significant role in profile evolution on coarse-grained beaches and does not affect fine-grained beaches. In fact, these experiments suggest that altering the groundwater level is only

able to induce accretion on an eroding profile on a fine sand beach.

Although beach groundwater did influence profile evolution in almost all of the runs, the changes in groundwater elevation in these experiments were usually not sufficient to change an erosive profile to an accretive profile or *vice-versa*. In general, however, onshore sediment transport was enhanced when the groundwater level was lowered under both accretionary and erosive conditions, whereas the back beach groundwater level had less effect on beach profile evolution under storm conditions. This suggests that artificially lowering groundwater levels would not help much in the control of storm erosion, but could promote post-storm accretion on permeable beaches.

MODELLING

The laboratory measurements were compared to simulations using the BeachWin model (Li et al. 2002), a numerical model that simulates interacting wave motion, beach groundwater flow and sediment transport in the swash zone and part of the surf zone. The BeachWin model has been used to investigate the effect of infiltration on swash zone hydrodynamics and sediment transport on sand and gravel beaches. Simulations carried out by Masselink and Li (2001) showed that on a relatively impermeable beach (fine sand, hydraulic conductivity 0.01 cms^{-1}), beach profile development was characterised by offshore sediment transport resulting in steepening of the beachface and the formation of a bar/step feature below the still water level. On a permeable beach (gravel, hydraulic conductivity 1.6 cms^{-1}), the beach profile showed onshore transport and development of a bar/step feature at the beginning of the simulation, followed by onshore transport and berm development. Li et al. (2002) showed the results of simulations with both high and low watertables. With a low watertable, significant infiltration occurred in the swash zone, with a smaller amount of exfiltration on the lower profile; whereas with a high watertable, no infiltration occurred during runup. Their profile simulations showed that with a lower watertable, swash infiltration enhanced onshore sediment transport, leading to the formation of a steeper beach and a large berm. However, none of these simulations were validated against field or laboratory data. While analytical and numerical models for beach groundwater have been verified against data at tidal frequencies, the only known validation at wave frequencies are those of Horn et al. (2003), Ang et al. (2004) and Horn and Li (2006).

In the present study, BeachWin was set up identically to the experimental arrangement and using the measured hydraulic conductivity of the beach sediment (0.001 ms^{-1} for the coarse sand and 0.0001 ms^{-1} for the fine sand). Two sets of model runs were carried out for each experimental run, one in fixed beach mode, i.e. without profile evolution over time, and one where the profile was allowed to change during the model run. Only the comparisons of the measured and predicted piezometric heads from the model runs in fixed beach mode are shown here. The mobile bed modelling, including comparisons of measured and simulated beach profile evolution, will be shown in a later paper (Baldock et al. forthcoming). Model-data comparisons are shown only for the first 10 minutes of each run, as despite the often significant profile changes described above, the groundwater levels generally exhibited steady state conditions after that. At this time the

groundwater level had reached equilibrium with the waves and beach morphology, but the changes in morphology from the initial plane state were small. Subsequent tests suggested that later changes in morphology lead to only minor changes in overall piezometric head levels. Differences between model predictions for small changes in morphology are also minor. Hence, taking the beach boundary as the initial plane state has little effect on the model predictions and model-data comparisons (Ang et al. 2004).

Figure 8 shows the measured and modelled groundwater levels on the coarse sand beach after 10 minutes for swell conditions when the back beach groundwater elevation was the same as the SWL (run 7). The initial beach profile and the profile after 60 minutes are also shown on Figure 8. The model overpredicts the head levels in the surf zone and underpredicts landward of the SWL. Agreement between measured and simulated head levels is reasonably good in the swash zone and within the beach, suggesting that the model's representation of the internal flow within the beach is correct. A similar pattern can be observed for the lowered back beach groundwater level (Figure 9, run 8); however, the agreement between the measured and simulated head levels is not as good when the inland groundwater level is lowered (Figure 9) or raised (Figure 10, run 9).

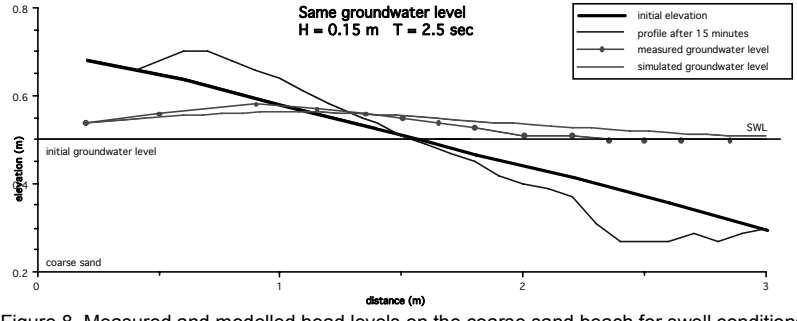

Figure 8. Measured and modelled head levels on the coarse sand beach for swell conditions (T=2.5 sec, H=0.15m), with the inland groundwater level the same as the SWL

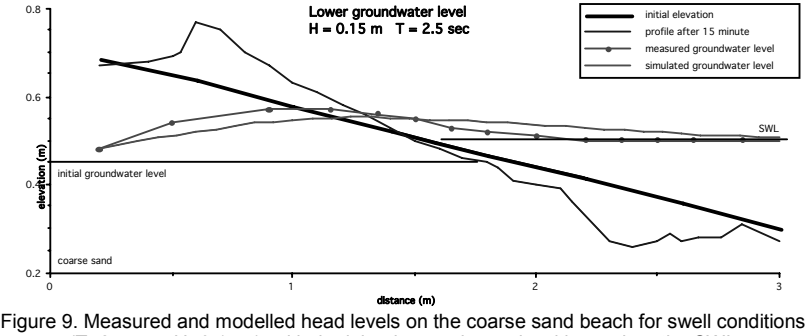

Figure 9. Measured and modelled head levels on the coarse sand beach for swell conditions (T=2.5 sec, H=0.15m), with the inland groundwater level lower than the SWL

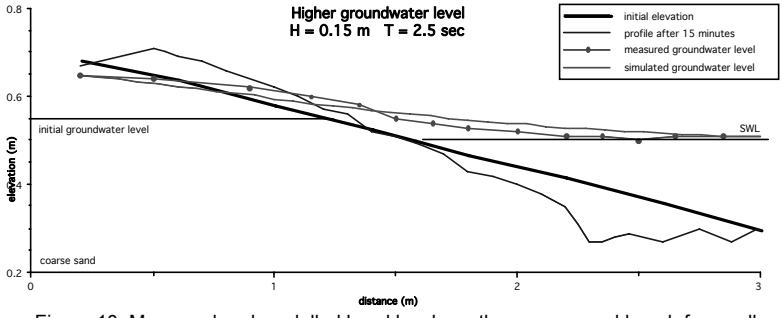

Figure 10. Measured and modelled head levels on the coarse sand beach for swell conditions (T=2.5 sec, H=0.15m), with the inland groundwater level higher than the SWL

Figure 11 shows the measured and modelled groundwater levels on the fine sand beach after 10 minutes for swell conditions when the back beach groundwater elevation was the same as the SWL (run 7). In this case, the model overpredicts the head levels both offshore and onshore of the shoreline, and agreement between measured and modelled head levels is less good than in the coarse sand beach. This pattern is also observed when the inland groundwater level is lowered (Figure 12, run 8) and raised (Figure 13, run 9).

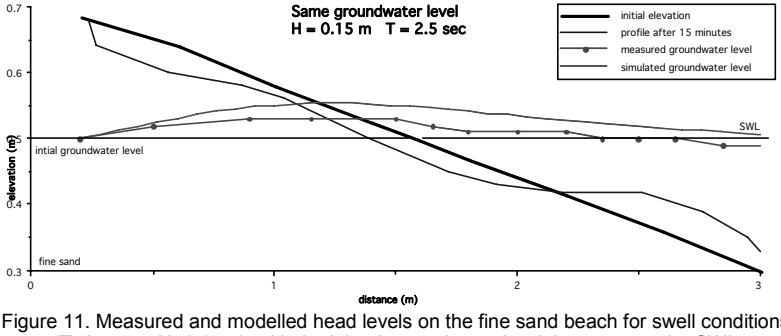

Figure 11. Measured and modelled head levels on the fine sand beach for swell conditions (T=2.5 sec, H=0.15m), with the inland groundwater level the same as the SWL

Similar results were observed under erosive conditions. Figure 14 shows the measured and modelled groundwater levels on the coarse sand beach after 10 minutes for storm conditions when the back beach groundwater elevation was the same as the SWL (run 25). Figure 15 shows the measured and modelled groundwater levels on the comparable run on the fine sand beach after 10 minutes for storm conditions when the back beach groundwater elevation was the same as the SWL (run 25). On the coarse beach, simulated head levels were overestimated offshore and underestimated landward of the SWL. On the fine sand beach, simulated head levels were always higher than measured.

These patterns were similar for the other runs (26 and 27), which are not shown here, and also very similar to the predictions under swell conditions.

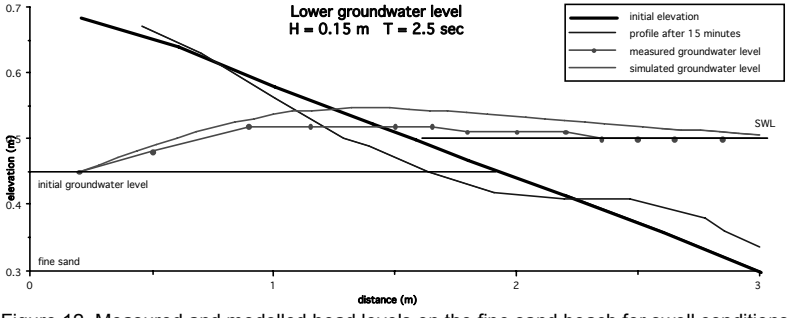

Figure 12. Measured and modelled head levels on the fine sand beach for swell conditions (T=2.5 sec, H=0.15m), with the inland groundwater level lower than the SWL

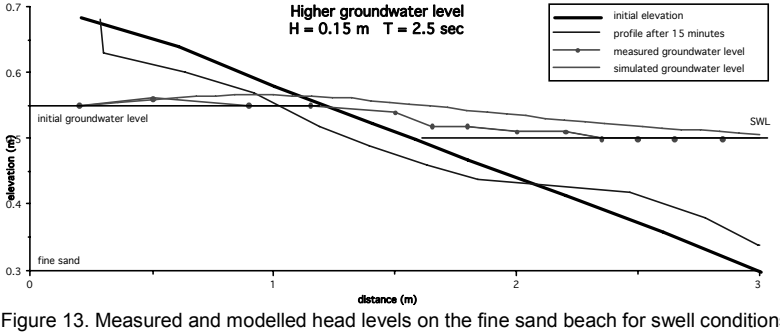

Figure 13. Measured and modelled head levels on the fine sand beach for swell conditions (T=2.5 sec, H=0.15m), with the inland groundwater level higher than the SWL

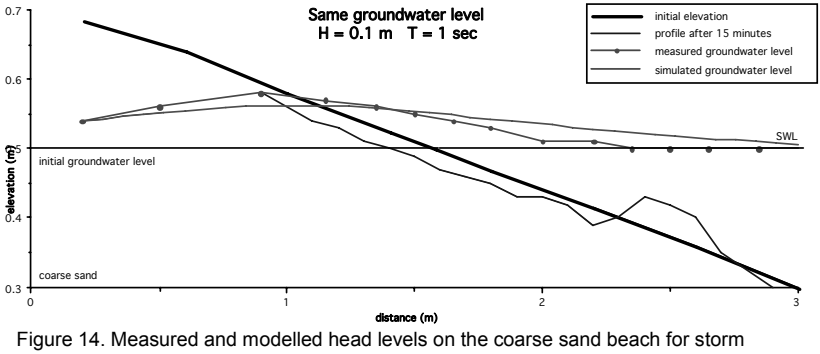

Figure 14. Measured and modelled head levels on the coarse sand beach for storm conditions (T=1 sec, H=0.1m), with the inland groundwater level the same as the SWL

The two main boundary conditions influencing the beach groundwater head levels are the back beach water level and the surf zone setup due to waves, which interact through the flow within the beach. For longer wave periods the back beach water level appears to have little effect on the head offshore of the initial shoreline, indicated by near constant setup in the surf zone, irrespective of the back beach water level (Ang et al. 2004). For a shorter wave period and smaller wave height (f=1Hz, H=0.1m) the measured data show that the back beach ground water level can influence the setup in the inner surf and swash zones, with smaller setup observed for a lower overall beach groundwater (Ang et al. 2004). These observations are consistent with the influence of swash-swash interactions on nearshore setup, which becomes proportionally larger for shorter period waves (Baldock and Holmes 1999).

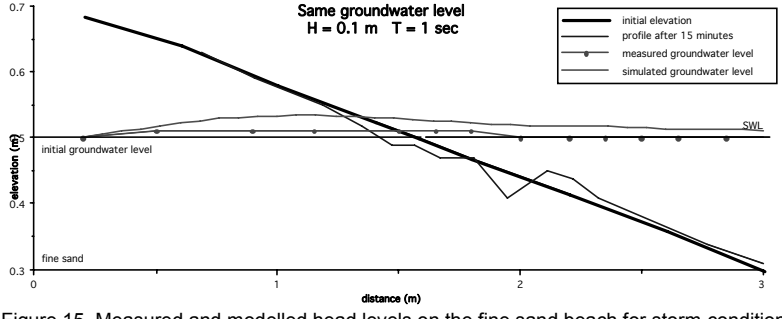

Figure 15. Measured and modelled head levels on the fine sand beach for storm conditions (T=1 sec, H=0.1m), with the inland groundwater level the same as the SWL

Profile evolution had little effect on measured or modelled head levels, which were primarily governed by the back beach head level and the wave runup limit (Ang et al. 2004). Overall, model predictions are better for the coarse beach than for the fine beach, because measured head levels were higher on the coarse beach due to greater infiltration. The model tends to underestimate groundwater levels for longer period waves and overestimate groundwater levels for shorter period waves. Model predictions are better in the swash and within the beach than offshore. The reason for this appears to be a significant overestimation of the wave setup in the inner surf zone, which may be related to the energy dissipation routine within the model (Ang et al. 2004). Thus the main discrepancies between measured and simulated head levels appear to be a result of inaccurate prediction of the nearshore hydrodynamics rather than poor representation of the internal flow in the beach. Since the main aim of these experiments was to improve understanding of the effect of beach groundwater on beach profile evolution, the poor prediction of surf zone head levels is not a significant problem; however, it does suggest that in future the wave component of the model will require modification.

CONCLUSIONS

1. Accretion above the SWL occurred at all groundwater levels on the coarse beach suggesting that infiltration played a significant role in beach profile development.

Onshore transport and berm development occurred under all inland groundwater levels, and particularly when the inland groundwater level was lowered.

2. Accretion above the SWL on the fine sand beach only occurred when the inland groundwater level was lowered. This suggests that altering the groundwater level is only able to induce accretion on an eroding profile on a fine sand beach, in contrast to previous suggestions that infiltration only plays a significant role in profile evolution on coarse-grained beaches and does not affect fine-grained beaches.

3. Although beach groundwater did influence profile evolution in almost all of the runs, the changes in groundwater elevation in these experiments were usually not sufficient to change an erosive profile to an accretive profile or *vice-versa*.

4. Onshore sediment transport was enhanced when the groundwater level was lowered under both accretionary and erosive conditions, whereas the back beach groundwater level had less effect on beach profile evolution under storm conditions. This suggests that artificially lowering groundwater levels would not help much in the control of storm erosion, but could promote post-storm accretion on permeable beaches.

5. The data provide the first controlled experimental verification of a numerical model which simulates wave and beach groundwater interaction in the coastal zone with forcing at wave frequencies. Profile evolution had little effect on measured or modelled head levels, which were primarily governed by the back beach head level and the wave runup limit. Agreement between measured and simulated head levels is better for the coarse beach due to greater infiltration. The main discrepancies between measured and simulated head levels appear to be a result of inaccurate prediction of the nearshore hydrodynamics rather than poor representation of the internal flow in the beach.

ACKNOWLEDGEMENTS

This research was funded by the Australian Research Council (International Linkage Award, grant number LX0454743), and the UK Environment Agency and Defra (UK Department for Environment, Food and Rural Affairs) Joint R&D Programme, Project FD1923. The laboratory measurements were carried out by Lea Sian Ang, Christine Sum, Raphaelle Bourgouin and Guillaume Samson.

REFERENCES

Ang, L.S., Sum, C, H.-Y., Baldock, T.E., Li, L. and Nielsen, P. (2004). "Measurement and modelling of controlled beach groundwater levels under wave action," *Proceedings of 15th Australasian Fluid Mechanics Conference*, CD-ROM.

Bagnold, R.A. (1940). "Beach formation by waves: some model-experiments in a wave tank," *Journal of the Institution of Civil Engineers*, Paper No. 5237, 27-53.

Baldock, T.E. and Holmes, P. (1999). "Simulation and prediction of swash oscillations on a steep beach," *Coastal Engineering* 36, 219-242.

Baldock, T.E., Horn, D.P. and Li, L. forthcoming. "Laboratory investigation of beach profile evolution with controlled beach groundwater elevation," *Continental Shelf*

Research (proceedings of International Coastal Symposium, Gold Coast, Australia, April 2007).

Duncan, J.R. (1964). "The effects of water table and tidal cycle on swash-backwash sediment distribution and beach profile development," *Marine Geology* 2, 186-197.

Grant, U.S. (1946). "Effects of groundwater table on beach erosion," *Geological Society American Bulletin* 57, 1952. (abstract)

Grant, U.S. (1948). "Influence of the water table on beach aggradation and degradation," *Journal of Marine Research* 7, 655-660.

Horn, D.P., Li, L. and Holmes, P. (2003). "Measurement and modelling of gravel beach groundwater response to wave run-up," *Proceedings Coastal Sediments '03*, CD-ROM published by East Meets West Production, Corpus Christi, Texas ISBN 981-238-422-7, 11p.

Horn, D.P. and Li, L. (2006). "Measurement and modelling of gravel beach groundwater response to wave run-up: effects on beach profile changes," *Journal of Coastal Research* 22(5), 1241-1249.

Kirkham, D. (1967). "Explanation of paradoxes in Dupuit-Forchheimer seepage theory," *Proceedings of the Soil Science Society of America* 10, 58-68.

Kulkarni, C.D., Levoy, F., Monfort, O. and Miles, J. (2004). "Morphological variations of a mixed sediment beachface (Teignmouth, UK)," *Continental Shelf Research* 24, 1203-1218.

Li, L., Barry, D.A., Pattiaratchi, C.B. and Masselink, G. (2002). "BeachWin: modelling groundwater effects on swash sediment transport and beach profile changes," *Environmental Modelling and Software* 17, 313-320.

Masselink, G. and Li, L. (2001). "The role of swash infiltration in determining the beachface gradient: a numerical study," *Marine Geology* 176, 139-156.

Nelson, C.L. and Miller, R.L. (1974). "The interaction of fluid and sediment on the foreshore," University of Chicago, Department of Geophysical Sciences, Fluid Dynamics and Sediment Transport Laboratory Technical Report No. 15, 175 p.

Packwood, A.R. (1983). "The influence of beach porosity on wave uprush and backwash," *Coastal Engineering* 7, 29-40.

Quick, M.C. (1991). "Onshore-offshore sediment transport on beaches," *Coastal Engineering* 15, 313-332.

Turner, I.L. and Leatherman, S.P. (1997). "Beach dewatering as a 'soft' engineering solution to coastal erosion: a history and critical review," *Journal of Coastal Research* 13(4), 1050-1063.

Turner, I.L. and Masselink, G. (1998). "Swash infiltration-exfiltration and sediment transport," *Journal of Geophysical Research* 103(C13), 30,813-30,824.

Turner, I.L. and Nielsen, P. (1997). Rapid watertable fluctuations within the beachface: implications for swash zone sediment mobility?," *Coastal Engineering* 32, 45-59.

Van Wellen, E., Chadwick, A.J. and Mason, T. (2000). "A review and assessment of longshore sediment transport equations for coarse-grained beaches," *Coastal Engineering* 40(3), 243-275.

EFFECTS OF PERMEABILITY ON THE PERFORMANCE OF MIXED SAND-GRAVEL BEACHES

Kaiming She[1], Louise Trim[2], Diane Horn[3], Paul Canning[4]

1. School of Environment, University of Brighton, Lewes Road, Brighton BN2 4GJ, UK, k.m.she@bton.ac.uk.
2. Black & Veatch, Grosvenor House, 69 London Road, Redhill, Surrey RH1 1LQ, UK, triml@bv.com
3. School of Geography, Birkbeck College, University of London, London, WC1E 7HX, UK, D.Horn@bbk.ac.uk
4. Rivers and Coastal, Atkins Water, 280 Aztec West, Bristol, BS32 4SY, UK, Paul.Canning@atkinsglobal.com

Abstract: This paper examines the performance of a mixed sand-gravel beach in comparison with that of a pure gravel beach through a series of controlled laboratory experiments. The gravel beach was modelled using anthracite of a uniform (single) grain size while the mixed sand-gravel beach modelled by means of graded anthracite of the same median sediment size (D_{50}). The two model beaches were tested under identical wave conditions and beach profile changes were recorded. Significant differences were observed in the performance of the two beaches. The reduced permeability of the mixed sand-gravel beach seems to have the effect of reducing the onshore transport but increasing the offshore transport.

INTRODUCTION

Mixed sand and gravel beaches are particularly common in the UK, where over one third of the beaches in England and Wales, and almost all of the beaches on the heavily populated south coast, are composed of combinations of sand and gravel (Fuller and Randall 1988). Beaches with an important component of gravel are estimated to occur along approximately 19,000 km of the British coast, with pure gravel beaches estimated to occur along almost 3500 km (Randall et al. 2001). Mixed beaches in the UK range from predominantly sand, with small proportions of visible gravel along the upper beach, through sand platforms with a distinct sandy gravel

upper beach ridge, to predominantly gravel (or cobble) barrier beaches extending to low water mark or beyond. However, even the best known gravel ridge beaches often have a mixed zone at their toe, which may be more apparent on a seasonal basis, or are known to have high proportions of sand below their surface layer. A recent report on mixed beaches in the UK concluded that it is perhaps more sensible to consider all 'shingle' ridge and mixed beaches as elements of a continuous spectrum in which the sediment type should not be defined by a single size parameter (Defra 2003). Many of these mixed beaches constitute an important defence against erosion and flooding, forming barrier beaches in front of low-lying marshes, toe protection along eroding cliffs, and wide prograding areas where local conditions promote deposition, which help to protect substantial urban areas and high value agricultural, recreational and environmental assets (MAFF 1999, Defra 2003). Many of these coarse-grained beaches are subject to long term erosion with a concurrent risk of flooding of adjacent low-lying land (Coates et al. 2001).

Although interest in mixed sand and gravel beaches has increased in recent years, processes on mixed beaches are less well understood than on sand beaches or gravel beaches. While a mixed but dominantly gravel beach may be expected to behave to a large degree like a pure gravel beach, it is now also recognised that, due to the presence of sand, a mixed sand-gravel beach tends to have a significantly reduced permeability compared to a pure gravel beach (Mason 1997), which may greatly alter the performance of the beach. The objective of this study is to look at how the reduced permeability of a mixed sand-gravel beach affects its behaviour compared to a pure gravel beach, when subjected to the same wave conditions.

EXPERIMENTAL SETUP

The experiments were carried out in a wave flume of 10m in length, 0.45m in width and 0.5m in depth. The model material was graded anthracites with a density of 1400 kg/m^3. Both model beaches had the same dimensions and these are shown in Figure 1.

The sediment characteristics of the two beaches are shown in Figure 2. Assuming a model scale of 1:30, the corresponding prototype sediment sizes can be estimated in terms of the threshold of motion criterion or onshore-offshore criterion. The median size of the prototype beaches is of an order of 15mm, thus the model beach of a uniform (single) grain represents a pure gravel beach free from the influence of sand. The mixed beach model represents a prototype sand-gravel beach containing approximately 10% sand. The prototype water depth at the toe is 4.8 m.

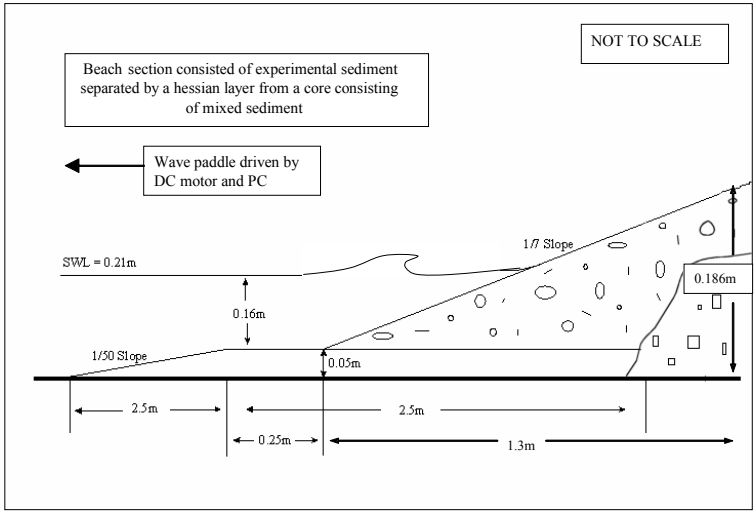

Fig. 1. Schematic of beach model set-up.

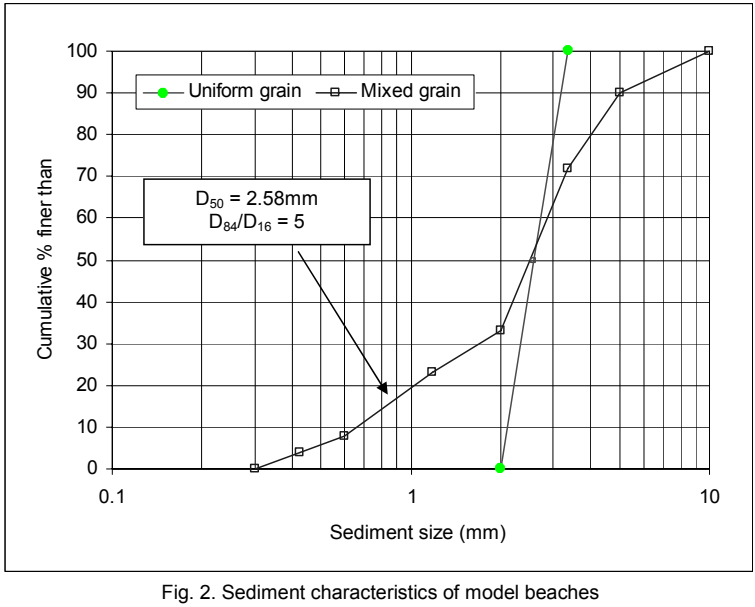

Fig. 2. Sediment characteristics of model beaches

TEST CONDITIONS

Waves were produced by a PC operated DC piston-type wave generator supplied by HR Wallingford. The test conditions included both monochromatic and random waves of a range of wave height and period, as given in Table 1. The random waves were generated based on the Jonswap Spectrum. Both model beaches were subjected to the each wave condition for a duration of 30 minutes, which is approximately 3 hours under prototype conditions.

Table 1. Experimental wave conditions

EXPERIMENTAL CONDITIONS			
Model Frequency	Model Wave Height	1 in 30 Scale	
		Prototype Frequency	Prototype Wave Height
Monochromatic Wave Conditions			
0.53Hz	0.02m (A), 0.04m (B)	0.10Hz	0.6m, 1.2m
1.05Hz	0.02m (C), 0.04m (D), 0.06m (E)	0.19Hz	0.6m, 1.2m, 1.8m
1.58Hz	0.02m (F), 0.04m (G), 0.06m (H)	0.29Hz	0.6m, 1.2m, 1.8m
Random Wave Conditions			
0.53Hz	0.052m (I), 0.084m (J)	0.10Hz	1.6m, 2.5m
1.05Hz	0.033m (K), 0.053m (L), 0.069m (M)	0.19Hz	1.0m, 1.6m, 2.1m
1.58Hz	0.025m (N), 0.04m (O), 0.052m (P)	0.29Hz	0.8m, 1.2m, 1.6m

With an initial slope of 1:7, the beach profiles were manually measured at 10 minute intervals. This was done by marking the profiles with coloured markers onto the glass sidewalls of the tank during the test. At the end of each test, the marked profiles were measured and recorded. Each profile consisted of an elevation measurement for each 50mm chainage to an accuracy of 1mm. Differences were present between the profile readings on the two sidewalls. Complete symmetry in the evolution of a 2D beach model can never be attained, partly due to the imperfections in the initial beach slope and partly due to the variations of sediment sizes across the beach. At a result, the average readings of the two walls are used for the final analysis.

RESULTS

In general, the beach underwent rapid changes within the first few minutes and a pseudo-steady state was attained after 10 minutes, as demonstrated in Figures 3 and 4. Both summer and storm profiles were observed under both monochromatic and random wave conditions. The general trend of profile evolution was similar for both model beaches but there were significant differences in the quantity of sediment movement. The first difference is that, where the onshore transport took place, the mixed beach experienced less movement of material. This can be clearly seen from Figures 5, 6 and 7 under monochromatic wave conditions, and Figures 8, 9 and 10 under random wave conditions. In the case of offshore transport, the profiles of the mixed beach showed greater losses of material from the beach head. This may be seen from Figures 11, 12 and 13 under monochromatic wave conditions, and Figures 14, 15 and 16 under random wave conditions.

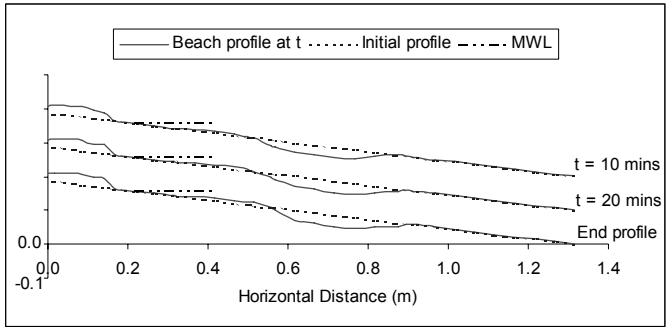

Fig. 3. Profiles recorded under monochromatic wave conditions (f = 0.53Hz, H_s = 0.04m - condition B) with a mixed grain anthracite model

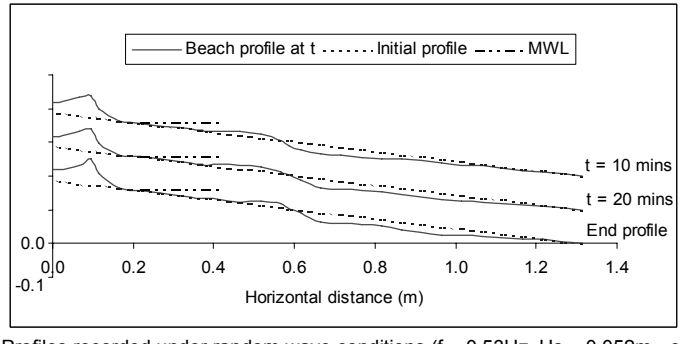

Fig. 4. Profiles recorded under random wave conditions (f = 0.53Hz, Hs = 0.052m - condition I) with a mixed grain anthracite model

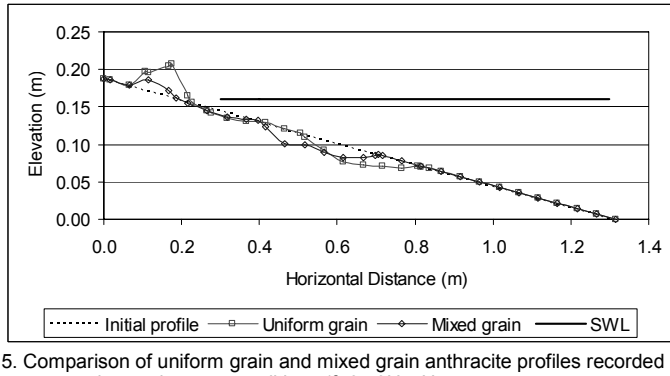

Fig. 5. Comparison of uniform grain and mixed grain anthracite profiles recorded under monochromatic wave conditions (f=0.53Hz, H_s = 0.02m – condition A)

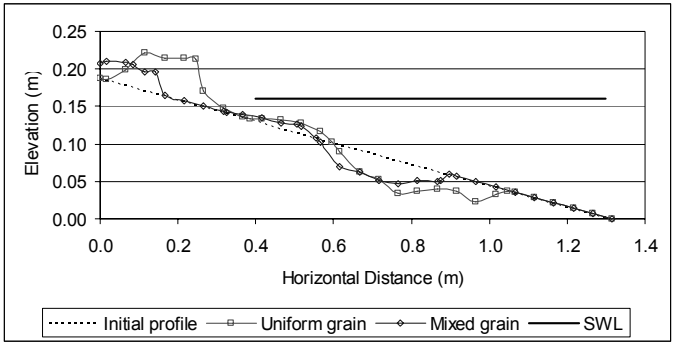

Fig. 6. Comparison of uniform grain and mixed grain anthracite profiles recorded under monochromatic wave conditions (f=0.53Hz, H_s = 0.04m – condition B)

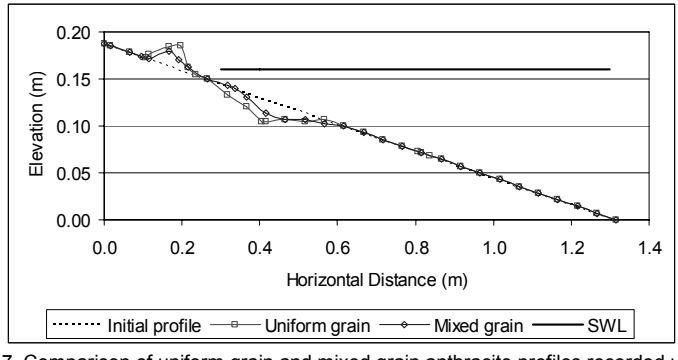

Fig. 7. Comparison of uniform grain and mixed grain anthracite profiles recorded under monochromatic wave conditions (f=1.05Hz, H_s = 0.02m – condition C)

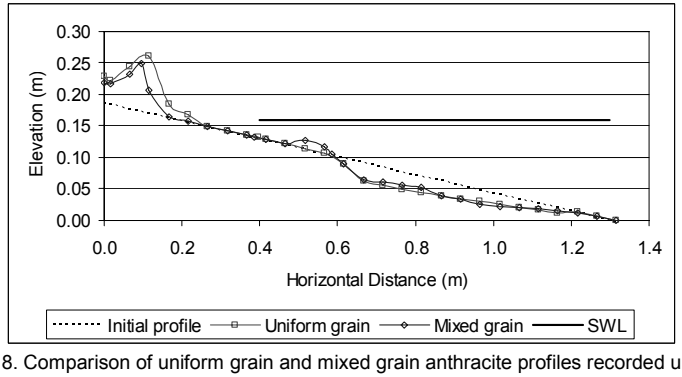

Fig. 8. Comparison of uniform grain and mixed grain anthracite profiles recorded under random wave conditions (f=0.53Hz, H_s = 0.052m – condition I)

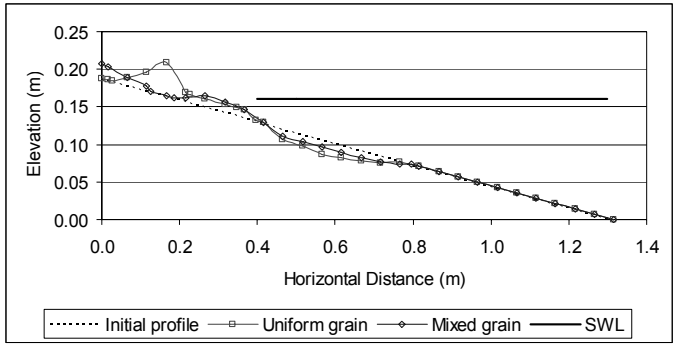

Fig. 9. Comparison of uniform grain and mixed grain anthracite profiles recorded under random wave conditions (f=1.05Hz, H_s = 0.033m – condition K)

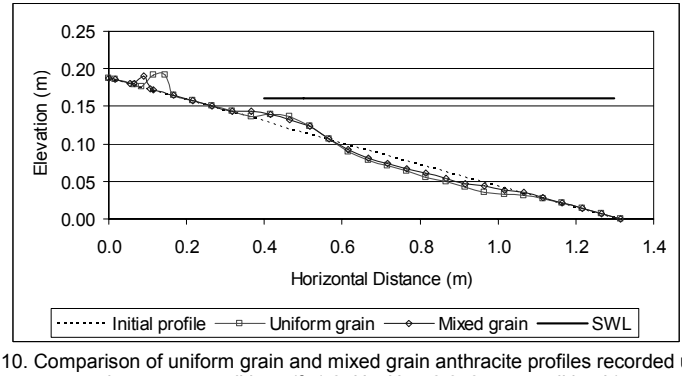

Fig. 10. Comparison of uniform grain and mixed grain anthracite profiles recorded under random wave conditions (f=1.05Hz, H_s = 0.053m – condition L)

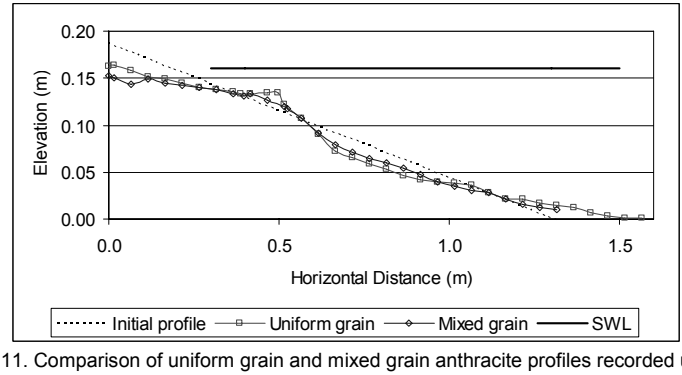

Fig. 11. Comparison of uniform grain and mixed grain anthracite profiles recorded under monochromatic wave conditions (f=1.05Hz, H_s = 0.06m – condition E)

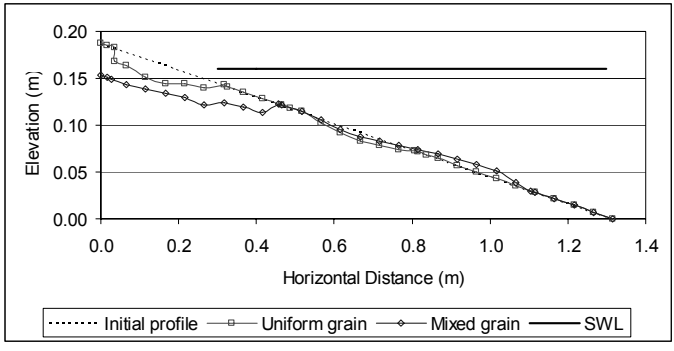

Fig. 12. Comparison of uniform grain and mixed grain anthracite profiles recorded under monochromatic wave conditions (f=1.58Hz, H_s = 0.04m – condition G)

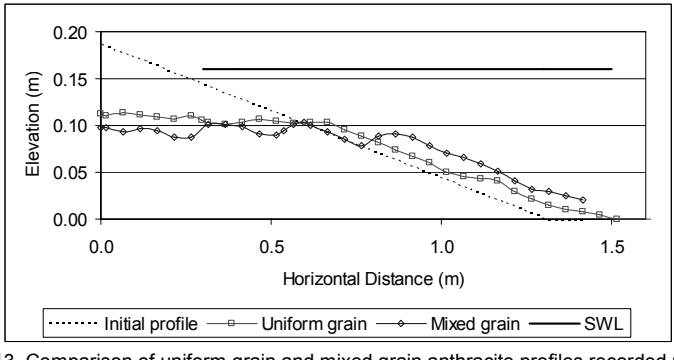

Fig. 13. Comparison of uniform grain and mixed grain anthracite profiles recorded under monochromatic wave conditions (f=1.58Hz, H_s = 0.06m – condition H)

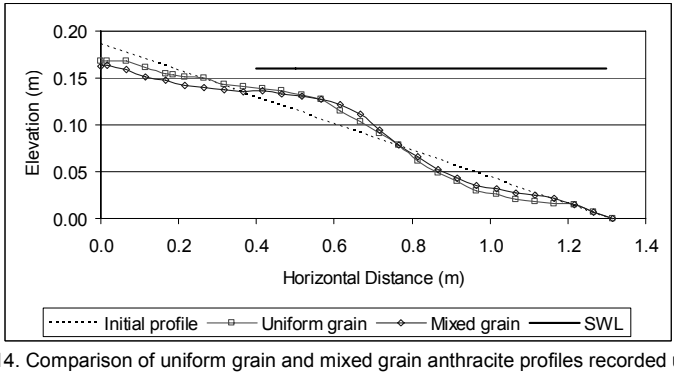

Fig. 14. Comparison of uniform grain and mixed grain anthracite profiles recorded under random wave conditions (f=0.53Hz, H_s = 0.084m – condition J)

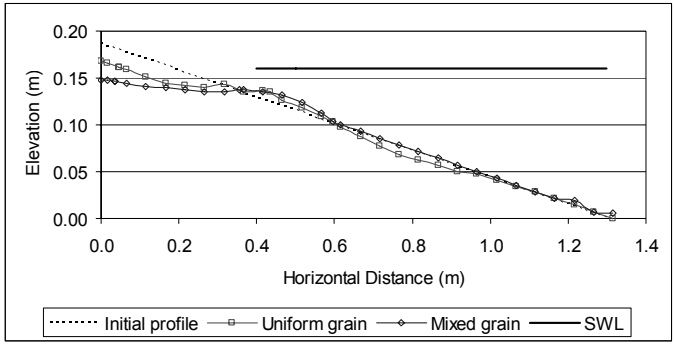

Fig. 15. Comparison of uniform grain and mixed grain anthracite profiles recorded under random wave conditions (f=1.58Hz, H_s = 0.052m – condition P)

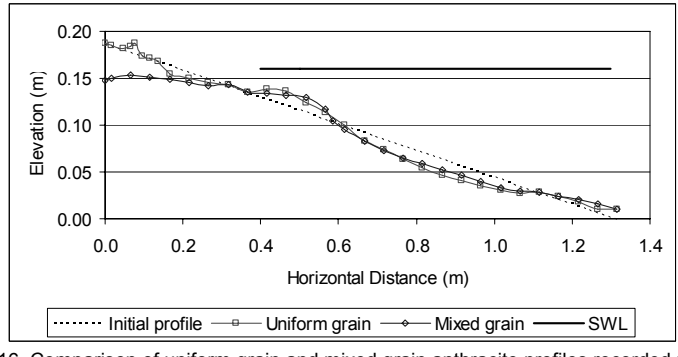

Fig. 16. Comparison of uniform grain and mixed grain anthracite profiles recorded under random wave conditions (f=1.05Hz, H_s = 0.069m – condition M)

DISCUSSIONS

The differences observed between the two beaches may be explained with reference to the permeability of the beaches. Note that the uniform grain beach model represents a pure gravel beach while the mixed beach model represents a mixed sand-gravel beach. The two beaches have the same D_{50}. A critical difference between the two beaches is in their permeability. The study of Mason (1997) showed that the sediment mix as a result of adding a small percentage of sand into gravel tends to have significantly reduced permeability compared to that of gravel without any sand. She et al (2006) further demonstrated that the percentage reduction in the sediment permeability is inversely proportional to the sand percentage. Assuming 10% of sand in the mixed beach model, its permeability is estimated to be 30% smaller than that of the uniform grain beach model, which will have a fundamental impact on the behavior of the beach.

Due to their difference in the permeability, the percolation flow in the uniform grain (gravel) beach is much greater than that in the mixed beach. In the cases where the wave energy and period are such that the onshore transport takes place, the wave breaking brings the sediment particles into temporary suspension and at the same time creates an uprush that takes the sediment up the beach surface. The subsequent backwash brings some of the sediment back down. The net sediment deposition is the difference between the sediment taken up during the uprush and that taken down by the back wash. The gravel beach allows much greater percolation flow into the beach, thus reducing the uprush but more significantly the backwash. As a result, greater onshore transport takes place on a gravel beach than on a mixed beach even though the wave conditions are identical.

In storm conditions, the backwash carries sufficient energy to moves more sediment than that by the uprush, due in part to the slope advantage of the backwash and in part to a more saturated upper beach above the mean water level. In comparison, a mixed beach is more saturated due to smaller percolation flow within the beach, which may be identified in terms of an increased ground water level in the upper beach. This means an increased backwash on the mixed beach compared to a gravel beach. The result is that, under the same wave conditions, a mixed beach loses more material than a gravel beach.

CONCLUSIONS

The performance of a mixed beach was investigated by testing two laboratory models under controlled wave conditions. The presence of sand in a mixed beach was shown to lead to reduced permeability, which in turn affects the sediment transport processes on the beach. The results from the study indicated that a mixed sand-gravel beach will tend to lose more beach material than a pure gravel beach when subjected to storm wave attacks while less material may be recovered under swell wave conditions

The second implication is that the hydraulic conductivity of the sediment bed is of great significance in influencing the sediment transport processes on the beach. Reducing the sand fraction seems to hold the key to improved hydraulic conductivity and thus the beach performance but the question is how to improve the beach recharge techniques to achieve this.

ACKNOWLEDGEMENTS

This work was part of a research project funded by the Department of Environment, Food and Rural Affairs (Contract F1923).

REFERENCES

Coates, T.T., Brampton, A.H. and Powell, K.A. (2001). “Shingle beach recharge in the context of coastal defence: principles and problems”. In Packham, J.R., Randall, R.E., Barnes, R.S.K., Neal, A. (eds.) Ecology and geomorphology of

coastal shingle. Westbury Academic and Scientific. Otley, Yorkshire, 394-403.
Defra (Department of Environment, Food and Rural Affairs), (2003). "Development of predictive tools and design guidance for mixed beaches, stage 2". Final project report FD1901.
Fuller, R.M. and Randall, R.E., (1988). "The Orford Shingles, Suffolk, UK – classic conflicts in coastline management". Biological Conservation 46(2), 95-114.
MAFF (Ministry of Agriculture, Fisheries and Food), (1999). "Development of predictive tools and design guidance for mixed beaches". Final project report FD1304.
Mason, T., (1997). "Hydrodynamics and sediment transport on composite (mixed sand/shingle) and sand beaches". Unpublished PhD thesis, University of Southampton.
Randall, R.E., Barnes, R.S.K., Neal, A. (eds.) (2001). "Ecology and geomorphology of coastal shingle". Westbury Academic and Scientific. Otley, Yorkshire, 23-55.
She K., Horn D. and Canning P. 2006, "Cliffing of mixed sand-gravel beaches – causes and possible solutions". 41st Defra Flood & Coastal Management Conference, York, July 2006, 9.9.1-9.9.5.

Cross-shore and longshore transport of tracer pebbles on a macrotidal mixed sediment beach, Somme Estuary, France.

J. Curoy , U. Dornbusch, C.A. Moses, D.A. Robinson, R.B.G. Williams

University of Sussex, Postgraduate Pigeonholes, Department of Geography, SOCCUL, BN1 9QJ Falmer, UK. Email: jc77@sussex.ac.uk

Abstract

Data on the transport of material on mixed sand and shingle beaches using newly designed synthetic pebbles has been collected on a macrotidal beach at Cayeux-sur-Mer in northern France. Deployment occurred on three separate days at three locations: on the upper, the middle and the lower part of the beach, down to depths of ~ 30 cm. The recovery rates varied from 26% after one tide to 95% at the end of the experiments. The pattern of pebble behaviour after one tide on the lower, middle and upper parts of the beach seemed to be consistent. Pebbles injected on the lower and middle beach showed a clear longshore displacement whereas pebbles injected at the top of the beach were mostly displaced cross-shore (seaward). The distance pebbles travelled varied with the location in which they were placed, with pebbles from the upper beach tending to travel further than pebbles placed in the middle and lower parts of the beach. Wave conditions and water level also influenced pebble movement.

Introduction

Shingle and mixed sand-shingle beaches are present in many parts of the world, especially in mid to high latitudes, and act as a valuable natural coastal defence. They have attracted growing scientific interest over the past 30 years, and many studies have been made of their morphology and erosional dynamics. Particular attention has been paid to investigating longshore and cross-shore sediment transport.

In order to study pebble behaviour *in situ* and to quantify longshore transport on shingle and mixed beaches, many tracer techniques can be used: fluorescent paint (e.g. Jolliffe 1961), aluminium pebbles (e.g. Van Wellen *et al.* 1998), electronic pebbles (Workman *et al.* 1994), non-indigenous pebbles (e.g. Hattori and Suzuki 1978), radioactivity (e.g. Kidson 1959). Tracers are non-invasive and can be used successfully in high-energy conditions, even if the input parameters for the calculation of transport rates remain uncertain and require further evaluation (Van Wellen *et al.* 2000). Many previous research studies have used tracers trying to appreciate of how pebbles behave.

Despite all these efforts to monitor shingle movement, tracer studies are still not completely reliable. Bodge and Kraus (1991; in Van Wellen 1999) concluded that estimates of total longshore transport volumes derived from tracers can be in error by a factor of 4 due to limitations in sampling methodology (or the recovery rate, when dealing with individually identifiable tracers).

Cross-shore and longshore sediment transport changes the morphology of beaches and the positions of shorelines (e.g. Pedrozo Acun□a 2005). Due to the coarse grain size, steep seaward slopes are usually sustained on shingle (e.g., Longuet-Higgins and Parkin 1962), inducing a high reflective potential and also a high degree of stability under wave attack. Mixed sand and shingle beaches are generally characterised by lower slopes and a larger foreshore, allowing the incident waves to progress further inshore. Breaking is rapid and a parallel breaker line often forms directly in contact with the beach without the creation of a surf zone. All the wave energy is therefore transferred to an incident swash motion. This leads to the conclusion that most of the transport occurring on gravel and mixed sand-shingle beaches is linked to swash processes (e.g. Austin and Masselink 2006). The precise mode of transport on gravel and/or mixed beaches remains contentious. Austin's (2006) observations led him to claim that transport occurs as bed load (in accordance with Horn and Mason 1994) and as sheet flow through the swash motion, with some quasi-suspended load at the point of bore collapse, as confirmed by Pedrozo's (2005) research. However, in laboratory experiments on a scale model beach Coastes (1994) observed more suspended load than anticipated, which shows how little is actually known about the processes responsible for sediment transport. Van Hijum & Pilarczyk (1982) used hydraulic laboratory experiments to try to identify the effects of various factors on pebble behaviour, and concluded that the transport of material takes place essentially as a single moving layer, and not as the independent responses of individual sediment fractions, because the larger pebbles impede the movement of the smaller ones (e.g. Carter 1988). They also concluded that flatter pebbles are carried further than round ones. These results contradict those of Allan *et al.* (2006) who found no relationship between particle shape and distance moved in the field.

A further complication is that pebble transport rates are dependent on their location on the beach, which influences the time that they spend under the influence of the swash. Van Hijum & Pilarczyk (1982) showed that differences in the distances covered in a

given time are a reason for the sorting often observed across beaches and for possible differences in the amounts of longshore transport. They also proved through their laboratory experiments that when the angle between the wave crest line and the beach increases, the transverse component of the motion becomes smaller and the longitudinal component larger. All this has important implications for the study of how pebbles behave on actual beaches.

This paper presents tracer pebble measurements obtained on a mixed sand and shingle beach in the north of France at Cayeux-sur-Mer. The measurements were made under varying wave conditions over a complete neap-spring tide cycle from October 28 to November 11, 2005. The tracers were of a new type made of epoxy resin with copper cores to allow recovery by both visual searches and metal detection. A differential GPS was used to determine locations. Deployments were normally made at three locations: on the upper, middle and lower part of the beach, at the surface and down to depths of up to 20 cm or occasionally 40 cm. It was hoped to obtain a picture of the overall movement of the pebbles on the beach, and to provide data for the long-term management of beaches of similar type, as well as to create an opportunity to calibrate and create predictive longshore transport formulae.

Field site and method

The beach at Cayeux-sur-Mer experiences strong longshore transport in an overall northerly direction. It is part of a 40-50 million m^3 mixed sand and shingle spit that extends from chalk cliffs at its southern end 16 km northwards to the mouth of the River Somme. This spit has developed during the last 2500 years. Between 1500 and 1900 it grew 6 km northwards without any major human intervention. However, cliff retreat to the south is no longer supplying shingle in sufficient volume to sustain the growth of the spit. To combat shingle loss and possible flooding of the land behind, groynes have been built northwards from Ault to just south of Cayeux-sur-Mer where at present the beach is still wide enough to prevent any flooding. Each year, 70 000 to 80 000 m^3 of sand and shingle are removed from the northern end of the spit and dumped on the beach at Cayeux (just downdrift of the northernmost groyne) in the form of a ridge 450 m long. This recycling is intended to balance the natural drift.

At Cayeux-sur-Mer (figure 1) the beach is aligned N20-30º and the tidal range is 6.6 to 11.2 m. The beach material has bi-modal distribution with a peak in the gravel size range (10 to 20 mm) that is sometimes mixed with sand, and a peak in the cobble size range (40 to 50 mm; Dolique 1998). The beach volume is composed about 20% of sand. This study site was north of the most northerly groyne and was selected because of its simple morphology and bathymetry, absence of groynes, and abundance of flint shingle, thus conforming to the recommendations of Van Wellen (1997).

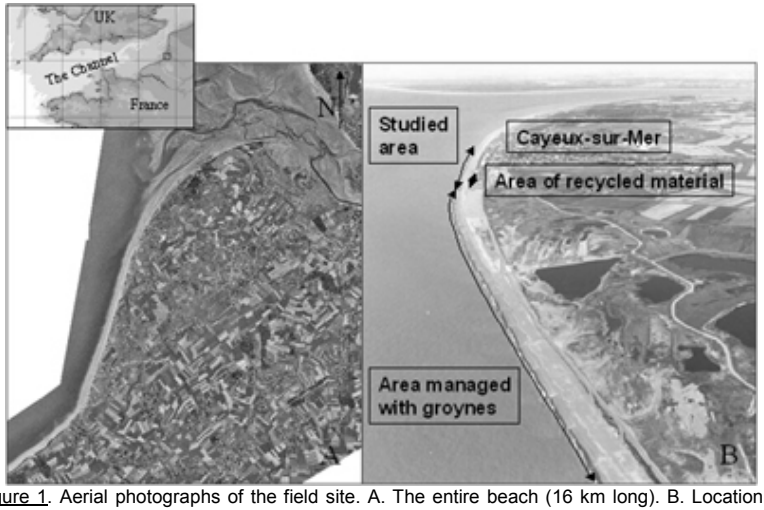

Figure 1. Aerial photographs of the field site. A. The entire beach (16 km long). B. Location of the field site.

The resin tracer pebbles were 6-7 cm long (a-axis) and 4-5 cm wide (b and c-axis), and individually numbered. Their copper cores allowed them to be re-found using a metal detector even when buried to depths of up to 30 cm. Having the same density as natural flint pebbles of the same size, they could be expected to provide realistic data.
The tracer pebbles were deployed on a cross-shore transect at elevations of +0.34 m, +2.10m and +3.86m above mean low water level. On the first day of the experiment the upper deployment was located 8 m along the transect from the most recent berm and 16 m from the artificial seawall. The lowest deployment was made 8 m landward from the base of the shingle. The middle deployment was midway (15 m) between the top and lowest deployments. Deployments took place on the 31st October, the 7th and 8th of November. The study period ended on the 11th of November.

The experiment was designed to investigate variations in transport rates in relation to the cross-shore profile. The top of the beach mainly experiences a dynamic of swash/backwash, and is only reached at high tide. By contrast, the bottom of the beach over a tidal cycle is subjected to a strong but short swash/backwash phase when the tide rises; then a long period under breaking waves; and finally another short period of swash/backwash when the tide falls. Tracer recovery took place during every other low tide following deployment at the preceding low tide. Each pebble was searched for by the metal detector. Buried tracers had to be excavated to identify them. Metal detection took place by walking along tracks at least 70m long downdrift from the injection area.

Location and depth were recorded with a Topcon RTK-DGPS. A total of 510 pebbles were deployed on the beach over the study period. The hydrodynamic conditions were recorded with an S4 directional wave recorder located directly on the sandy lower foreshore.

Results

The inshore tidal signal, is a typical intertidal, semi-diurnal and macrotidal signal. During the study period the water level changed from neap to spring and back to neap tide (Figure 2). The wave climate was representative of the year wave height climate with significant wave heights (Hs) ranging from 0.4 m to 2.7 m, punctuated by two storm events on the 1st and 4th of November 2005. The incident waves were from the west, with an angle of incidence to the beach of between 7 and 60° and an average of between 15 and 40°. Almost half (49.7%) of the significant wave heights (Hs) were less than 1 m, 96.4% less than 2 m, and only 3.6% exceeded 2 m. The wave period varied between 4 and 9 s and two distinct wave periods were clearly be identified. Firstly, a group of waves that were the most representative with a period of between 4 and 6 s and secondly, a group with a period of between 6 and 9 s. During the tidal cycle, current velocities were the strongest at mid-tide and weakest at high tide. Current direction was mainly northward in accordance with the waves and the expected longshore drift direction.

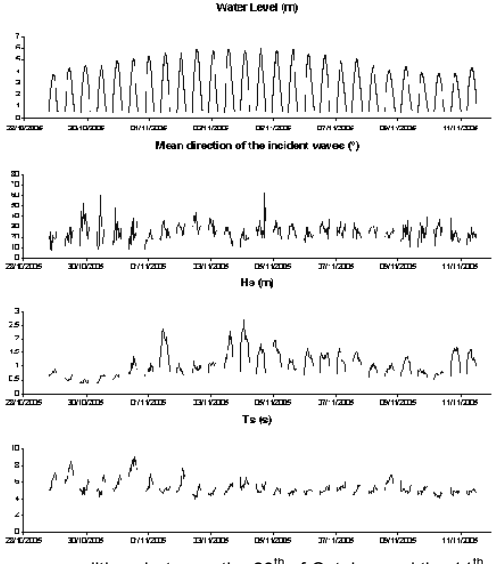

Figure 2. Inshore wave conditions between the 28th of October and the 11th of November 2005.

Date of deployment	Location of the injection	Recovery rates (Total of pebble recovered)		
		After 1 tide	After 3 tides	At the end of the experiments
31/10/05	Upper beach	47% (37)	59% (47)	86% (68)
	Middle beach	39% (31)	65% (52)	95% (76)
	Lower beach	26% (13)	58% (29)	88% (44)
07/11/05	Upper beach	44% (22)	56% (28)	60% (30)
	Middle beach	64% (32)	84% (42)	92% (46)
	Lower beach	42% (21)	76% (38)	88% (44)
08/11/05	Upper beach	78% (39)	84% (42)	88% (44)
	Middle beach	70% (35)	78% (39)	82% (41)
	Lower beach	48% (24)	62% (31)	68% (34)

Table 1: Recovery rates for tracer deployments on the 31st of October, the 7th of November and the 8th of November 2005. The figures in brackets are the cumulative number of tracer pebbles recovered at the time indicated.

Recovery rates for three deployment days, at the three locations (upper, middle and lower beach) and over different time periods (after one tide, three tides and finally at the end of the observation period) are shown in Table 1. Recovery rates varied from 26% to almost 95%, depending on the location and date of deployment. Recovery rates increased with time. Despite the lower recovery rates recorded after one tide, after 3 tides they reached, or were very close to expected recovery rates for a "passive" tracers i.e. ≥ 60% (Allan *et al.* 2006). By the end of the experiment, the recovery rates were mostly above 80%, which is higher than that described from other studies.

After one tide, the lowest recovery rates were recorded on the lower beach and the highest recovery rates on the upper beach, except on the 7th of November. At the end of the experiments, recovery rates from the tracers injected at the middle of the beach were the highest (almost > 90% recovery). Such high recovery rates confirm firstly that the technique used in this experiment allows successful relocation of tracer pebbles even during stormy or relatively agitated conditions, and secondly that the results are reliable enough to track pebble movement patterns and beach topographic changes under different wave and tide conditions.

The locations of tracer pebbles recovered after one tide and at the end of the experiment have been mapped for each of the deployment dates (31th October, 7th and 8th of November; Figures 3, 4 and 5). On each survey, the tracers were scattered to the north of their injection point in accordance with the expected drift direction under south westerly waves. During the period of the experiment no tracers were found to have moved in an updrift direction. The movement pattern shown by tracers between the 31st of October 2005 and the 11 of November 2005 is representative of the entire experiment (Figure 3). After one tide the longest-travelled tracer pebble was recovered 30.9 m from its injection point. At the end of the experiment, 21 tides after deployment, the longest-travelled tracer pebble was 311.4 m from its injection point. After one tide the shortest-travelled

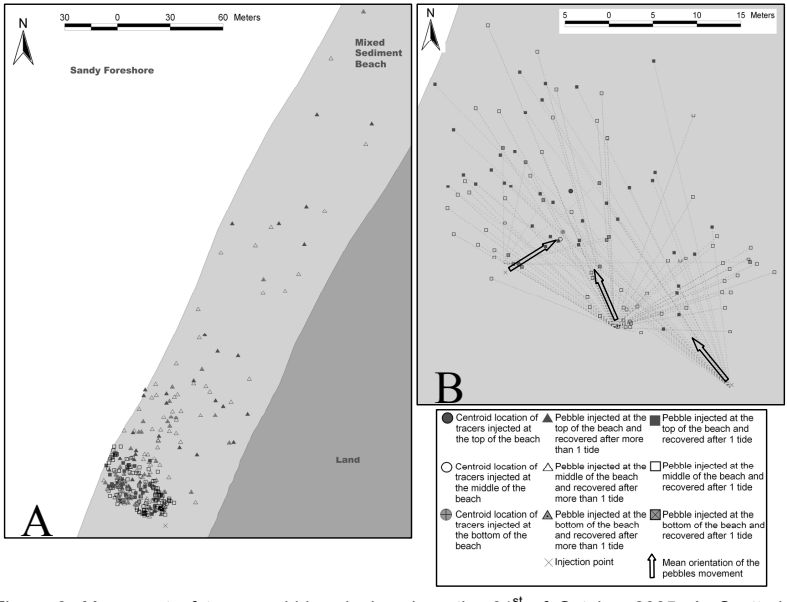

Figure 3. Movement of tracer pebbles deployed on the 31st of October 2005. A. Scattering observed over the whole survey period. B. Scattering observed after one tide.

tracer pebbles was only 0.3 m from its injection point whilst after 21 tides the shortest-travelled pebble was only 2.8 m from its injection point. Over this single tide, the wave approach angle ranged from 8 to 38° and averaged 22.7°; the significant wave height ranged from 0.77 to 1.36 m, averaging 1.1 m; the mean wave period ranged from 6.8 to 9.1 s and averaged 7.9 s (Figure 2). The centroid location obtained from the cloud of pebbles recovered for each deployment location, showed that the mean distance travelled after one tide by the tracers deployed at the top of the beach was 28.77 m. Tracers deployed in the middle and lower beach travelled only 11.55 m and 7.66 m respectively. This initial observation indicates that pebbles located at higher elevations on the beach have the potential to travel further than those at lower elevations. However, this observation does not take into account the bearing of the centroid trajectory from its deployment point. The angle of the trajectory has been calculated for each deployment using the beach angle ($N23^{o}$) as the direction of longshore movement from the original injection points. All tracer movements up the beach, in a landward direction, recorded a positive value whilst those that moved down the beach, in a seaward direction, recorded a negative value. The results indicated that tracers injected in the upper beach had a trajectory angle of -84.2°. Those injected into the middle beach recorded a trajectory

angle of -53°. Tracer pebbles that were injected into the lower beach unexpectedly recorded a trajectory angle of +38°.

In summary, pebbles injected at the top of the beach tended to travel across the beach in a seaward direction and also longer distances than the other tracers. Those injected in the middle of the beach also recorded a cross-shore scattering in a seaward direction but it was less than those injected into the upper beach. Pebbles injected into the middle of the beach typically travelled less than half the distances recorded by those deployed on the upper beach. Finally, the pebbles deployed on the lower beach travelled the shortest distances but showed a tendency to scatter up the beach in a landward direction.

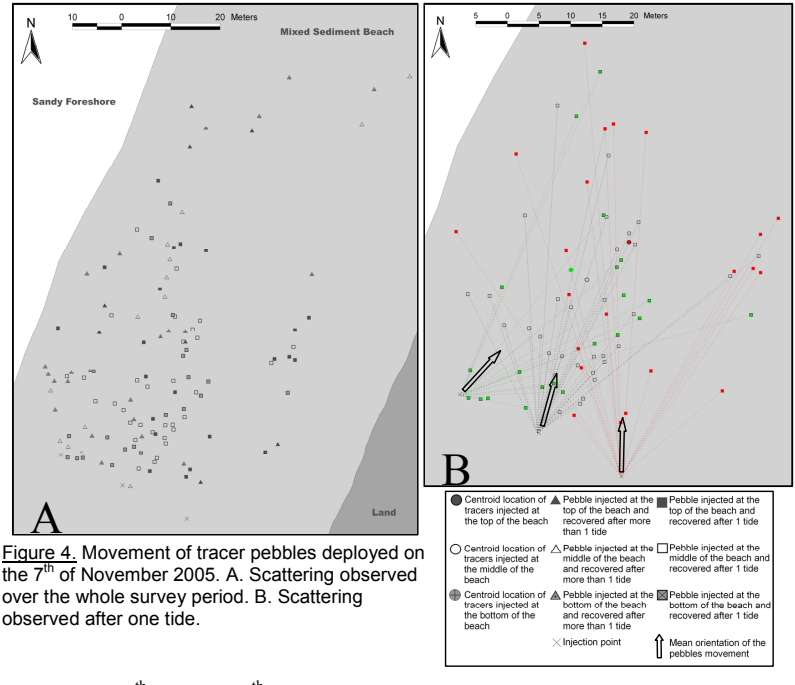

Figure 4. Movement of tracer pebbles deployed on the 7th of November 2005. A. Scattering observed over the whole survey period. B. Scattering observed after one tide.

Between the 7th and the 11th of November 2005 (Figure 4) the furthest-travelled pebble recovered was 101.6 m away from its injection point on the 11th of November 2005 (7 tides after deployment). After one tide, tracers were scattered distances of between 1.34 and 68.88 m from their injection points. The location and orientation of centroids after one tide on the upper, middle and lower beach were, respectively: 33.42 m with an angle

of –21.3°, 21.5 m with an angle of –1.6° and 21.6 m with an angle of +31.3°. Here again, the pattern observed previously is displayed.
In addition, the mean angle of scatter of tracers deployed on the upper beach on the 31st of October was significantly greater than that recorded on the 7th of November. On that particular tide, the angle of wave approach was between 20.1 and 30.4° (average 27.6°); the wave height ranged from 0.74 to 1.14 m (average 0.95 m) and the mean wave period varied between 4.6 and 5.9 s (average 5.1 s; see Figure 2).

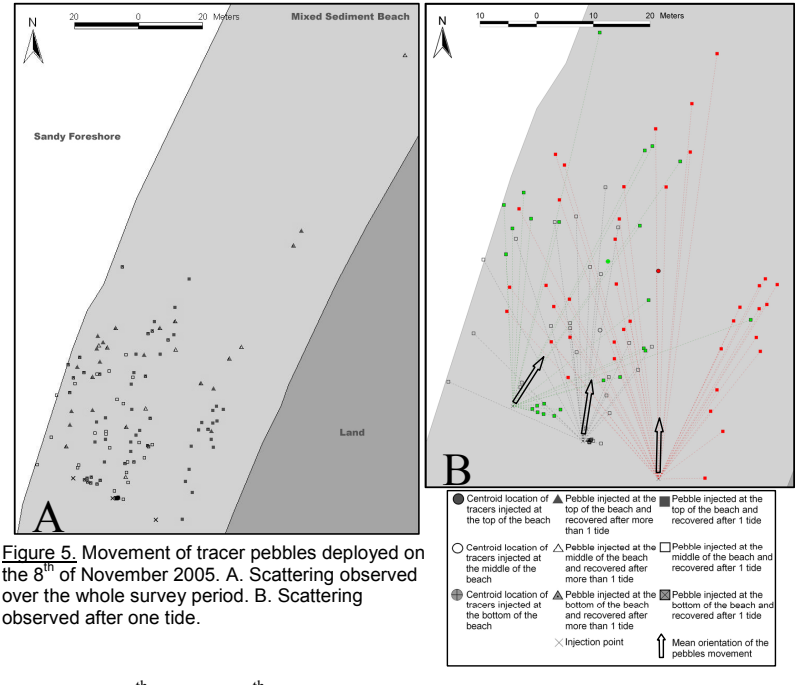

Figure 5. Movement of tracer pebbles deployed on the 8th of November 2005. A. Scattering observed over the whole survey period. B. Scattering observed after one tide.

Between the 8th and the 11th of November 2005 (9 tides in total), the furthest-travelled tracer pebble after one tide was 75.5 m from its injection point and after seven tides 101.6 m (Figure 5). The centroid locations, from the upper to lower beach, of each tracer scattering after one tide show respectively: a mean distance travelled of 34.7 m with a mean angle of –25.5°, a mean distance travelled of 14 m with a mean angle of –27.2° and a mean distance travelled of 24.11 m with an angle of +9.6°. The results displayed the same tendencies as the two previous cases in both the distance travelled and the orientation of the tracer movements. However, the tracers injected into the middle of the beach travelled a significantly shorter distance than was expected from the first two

examples. On that date, the wave approach was between 14.4 and 30.4° (average 22.4°), the wave height ranged between 0.62 to 1.36 m (average 1.09 m) and the mean wave period between 4.8 and 5.7 s (average 5.01 s; see Figure 2).

The results of the experiment have revealed patterns of tracer pebble movement that are dependent on location of the injection point. Tracers deployed on the upper beach travelled the furthest distances. These pebbles were also subject to the most significant cross-shore movement in a seaward direction in comparison to those deployed in the middle and lower beach. Tracers deployed in the middle and lower beach travelled similar distances but moved in different directions. Pebbles deployed in the middle of the beach showed a tendency to migrate seaward, but the main component of their movement was alongshore rather than across-shore. In contrast, pebbles deployed on the lower beach displayed a tendency to migrate landwards, although the main component of movement was again in the longshore direction.
In addition, tracers deployed at different times during the experiment travelled different distances. Those deployed on the 31st of October travelled, on average, a shorter distance than those injected on the 7th and the 8th of November 2005. They also recorded a stronger cross-shore movement component than those deployed on the two later dates.

Discussion

One possible explanation for the low recovery rate of pebbles injected into the lower part of the beach was movement of pebbles from the beach onto the adjacent sandy foreshore. However, no pebbles were ever detected during regular surveys of a two metre wide track along the sandy platform directly in front of the beach toe. This suggests that pebble exchanges between the foreshore and mixed sand and pebble beach are rare even during relatively agitated periods and cannot be the cause of the low recovery rates.

Nevertheless, the shingle beach toe is an area of important topographic change induced by the change of slope and the combined effect of wave breakage and swash during each tidal cycle. As a result, the most likely explanation for the low recovery rates of pebbles placed on the lower beach is their burial within the indigenous beach material to depths below the detection limits of the metal detector.

Burial of the tracers to depths below the detection limit is probably the explanation also for the “abnormally” low recovery rate for those injected into the top of the beach on the 7th of November. On this occasion burial most probably resulted the change in water level between the spring and neap tides of the tidal cycle. At the time the tracers were injected, wave and tide conditions were transporting the coarser beach material up-beach to create a berm which probably trapped and buried many of the tracers below detection depths.

Despite the low recovery rates after just one tide, the recovery rates achieved by the end of the experiment are sufficient to give a high level of confidence regarding the pattern of transport they display (Table 1). It is apparent that those injected in the upper beach demonstrate a clear tendency to move seawards across-shore and move further than those injected in the mid and lower beach (Figures 3, 4 and 5). It is well known that on a steep coarse grained beach, the width of the swash zone may be significantly greater than that of the surf zone. It has been shown in models and experiments (e.g. Van Wellen 1999; Pedrozo Acun□a 2005), that most of the morphological changes on a steep beach profile occur in the swash zone. The difference in distance travelled is a function of the greater time swash is active and is the reason why pebbles from the upper beach move furthest. Regarding the strong seaward cross-shore tendency, Van Hijum and Pilarczyk (1982) showed the distance covered is a function of time spent in the swash. However, this does not explain why the tracers injected at the lower beach migrate landward while pebbles from the top of the beach migrate seaward.

Nielsen (1997) identified ground water dynamics in the swash zone as one of the processes that might be important for predicting net sediment transport in this area. Ground water flows are a determining factor of variations in the morphology of beaches with a high permeability (Elfrink and Baldock 2002). These flows are even more significant when the tidal range is larger, which creates high hydraulic gradients between the water table and the water level (Turner 1995). The three sites where tracers were injected were in completely different ground water environments. The injection site on the upper beach was above the water table throughout the tidal cycle. The site where the tracers were injected in the middle of the beach was also above the water table at low tide but when the tide rises is quickly saturated by water. At the bottom of the beach considerable quantities of water drained out of the sediment even at low tide.

Observation of the tracers as the tide rose over the lower site, showed that they were immediately mobilised and quickly disappear, apparently due to seaward migration. This may result from swash flows interacting with the groundwater flow. The consequence of downward directed pressure gradients increases the effective weight of the sediment, stabilises the bed and decreases the potential of sediment to be transported during the uprush. In contrast, during backwash the upward directed pressure gradient increases sediment transport reducing the effect of the weight of sediment. The net effect of this process is movement towards the offshore direction (Hughes *et al.* 1997; Nielsen 1997). However, the majority of the tracers from the lower beach eventually move up the beach. This may be explained by the fact that after a short period of time, with the rising tide, the water level and the water table are at an equal height and this impedes the ground water flow, resulting in the uprush becoming dominant and beach material being moved up the beach. This uprush only affects a thin surface layer of sediment. As the water level continues to rise, the steepness of the beach face causes the waves to break directly onto the beach. As a result a lot of energy is delivered to the beach face in a very short period of time which results in entrainment, mixing and movement of a greater

depth of material. During this period the tracers at the surface of the sediment are likely to become well mixed with the beach sediment and buried at depth, where the backwash during the falling tide cannot remobilise them. The net result is for the pebbles to migrate landward. This is in addition to the main tendency for them to move down-drift, alongshore.

The middle of the beach is above the water table level and as a result all the wave energy released in the uprush will transport the surface sediment landward. At the same time infiltration into the beach face will strongly reduce the energy of the backwash. This tendency changes when the water table and the water level reach the same elevation. At that point, the sediment will be saturated by water, and seaward currents will be strong enough to remobilise the beach material during the high tide (at least that of a comparable size to the tracers used). In addition, the backwash during the falling tide drags surface material down across the beach. During the three days of deployment of the tracers, wave breakage at high tide occurred between the shingle beach toe and just below the point where the middle tracers were injected. Under the breaking waves, some tracers were buried deep enough not to be removed by the decreasing tide and the associated swash.

It has been identified that on the 7th and the 8th of November the centroid of tracer movement was at a smaller angle than that of the 31st of October, whilst the mean distance travelled was greater than on the 31st (Figures 3,4 and 5). On the 7th and the 8th of November berm accretion occurred, and this coincided with the changeover of tidal level from a spring tide to a neap tide. As a consequence, coarse material on the upper beach was pushed landward to build up the berm. In contrast, on the 31st of October, this berm suffered erosion as a consequence of the tidal range going toward a spring tide and the coarse upper beach material was spread out across the beach as described previously. It is mainly pebbles from the upper beach area that contribute to the berm construction. The distance travelled by the tracers is mainly due to the energy delivered by the wave onto the shore face. Looking at the wave conditions and the water level (Figure 2), there was little difference in Hs, water level and wave direction during the periods displayed. However, there was a significant difference in the significant wave period (Ts). It is well known that the longer the wave period, the greater the longshore wave energy. This probably explains why the distances travelled are greater on the 7th and the 8th of November than on the 31st of October.

Conclusion

Observations of hydrodynamic conditions inshore, morphological changes and sediment motion from one low tide to the following have been made on a mixed sand and shingle beach at Cayeux-sur-Mer, France. The results highlight constant patterns of movement for a specific grain size over time and for specific wave conditions. Good recovery rates allow a high level of confidence in the results. The new findings provide a better insight to particle behaviour on mixed sand and shingle beaches, drawing on existing

knowledge of hydrodynamic conditions, swash flows, groundwater flow, beach slope and grain size.

Material from the upper part of the beach tends to migrates seaward and further down-drift than the other parts of the beach. It is suggested that this is linked to a continuous swash action from the high tide to the low tide. Pebbles from the lower beach tend to migrate up the beach, although alongshore transportation is dominant. It is suggested that these movements are explained by the combined effect of the groundwater flow, the swash flows and the action of breaking waves. Pebbles from the middle of the beach display a preference to move down the beach which may also be explained by the interaction between the groundwater flow, swash flows and the action of the breaking waves. Alongshore drift is again significantly greater than cross-shore movement.

The experiments show that pebble material on a mixed sediment beach is extremely sensitive to position on the beach profile and to changes in the water level and wave conditions associated with tidal conditions. Formulae and models for longshore drift fail to take this differential transport on such beaches into account and this could be one of the main reasons for their inaccuracy. Future work will seek to first validate the hypothesis of pebble movement suggested in this paper by more field measurements and then include it into an improved model or a formula for better predicting longshore drift on mixed sand and pebble beaches.

Acknowledgments
Fieldwork was part-funded by INTERREG III (Beaches At Risk).

References

Allan, J. C., Hart, R., Tranquili, J.V. (2006). "The use of Passive Integrated Transponder (PIT) tags to trace cobble transport in a mixed sand-and-gravel beach on the high-energy Oregon coast, USA." *Marine Geology* 232: 63-86.

Austin, M. J., Masselink, G. (2006). "Observations of morphological change and sediment transport on a steep gravel beach." Marine Geology 229: 59-77.

Bodge, K. R., Kraus, N.C. (1991). "Critical examination of longshore transport rate magnitude." *Coastal Sediment '91 Conference, American Society of Civil Engineers*: 139-155.

Carter, R. W. G. (1988). "Coastal Environments: an Introduction to the Physical, Ecological and Cultural Systems of Coastlines." *Academic press., London*: 617 pp.

Coates, T. T. (1994). "Effectiveness of control structures on shingle beaches: physical model studies." *HR Wallingford Report* SR 387.

Dolique, F. (1998). "Dynamique morphosédimentaire et aménagements induits du Littoral Picard au sud de la Baie de Somme." *PhD thesis, Université du Littoral*: 388 pp.

Elfrink, B. andBaldock, T. (2002). "Hydrodynamics and sediment transport in the swash zone: a review and perspectives." *Coast. Eng.* 45(149–167).

Hattori, M., Suzuki, T. "Field experiment on beach gravel transport." *Proceedings of the 16th International Conference on Coastal Engineering, American Society of Civil Engineers*: 1688–1704.

Horn, D. P., Mason, T.E. (1994). "Swash zone sediment transport modes." *Marine Geology* 120(3-4): 309-325.

Hughes, M. G., Masselink ,G., Brander, R.W. (1997). "Flow velocity and sediment transport in the swash zone of a steep beach." *Marine Geology* 138: 91-103.

Jolliffe, I. P. (1961). "The use of tracers to study beach movements; and the measurement of littoral drift by a fluorescent technique." *Revue de Geomorphologie dynamique* XII(2): 81-98.

Kidson, C., Carr (1956). "The movement of the shingle over the seabed close inshore." Geogr. J. CXXV.

Longuet-Higgins, M. S., Parkin, D.W. (1962). "Sea waves and beach cusps." *Geogr. J.* 128: 194–201.

Pedrozo Acun□a, A. (2005). "Concerning Swash On steep Beaches." *PhD thesis, University of Plymouth*: 214 pp.

Nielsen, P. (1997). "Coastal groundwater dynamics." *E.B. Thorton (Editior), Coastal Dynamics '97. ASCE, Plymouth, UK*: 546-555.

Turner, I. L. (1995). "Simulating the influence of groundwater seepage sediment on sediment transpoted by the sweep of the swash zone across macrotidal beaches." *Marine Geology* 125(1-2): 153-174.

Van Hijum, E., Pilarczyk, K.W. (1982). "Equilibrium profile and longshore transport of coarse material under regular and irregular wave attack." *Waterloopkundig laboratorium delft hydraulics laboratory* 274.

Van Wellen, E., Chadwick, A. J., Bird, P. A. D., Bray, M., Lee, M.,Morfett, J. (1997). "Coastal sediment transport on shingle beaches." *Proceedings of Coastal Sediments '97, American Society of Civil Engineers*: 38-47.

Van Wellen, E., Chadwick, A. J., Lee, M., Baily, B., Morfett, J. (1998). "Evaluation of Longshore Sediment Transport Models on Coarse Grained Beaches Using Field Data: A Preliminary Investigation." *Proceedings of the 26th International Conference on Coastal Engineering, American Society of Civil Engineers* 3: 2640-2653.

Van Wellen, E.. (1999). Modelling of swash zone sediment transport on coarse grained beaches. *PhD thesis, University of Plymouth*, 279 p.

Van Wellen, E., Chadwick, A. J., Mason, T. (2000). "A review and assessment of longshore sediment transport equations for coarse-grained beaches." *Coastal Engineering* 40: 243-275.

Voulgaris, G., Workman, M., Collins, M.B. (1999). "Measurement Techniques of Shingle Transport in the Nearshore Zone." *Journal of Coastal Research* 15(4): 1030-1039.

Workman, M., Smith, J., Boyce, P., Collins, M.B. and Coates, T.T. (1994). "Development of the electronic pebble system." *HR Wallingford Report* SR405.

WHY ARE SHINGLE BEACHES REPLACING SANDY BEACHES?
(coastal zone of NW Portugal)

Helena Granja[1], Eduardo Loureiro[2]

1. University of Minho, Earth Sciences Center, Campus de Gualtar, 4710-057 Braga, Portugal.
   hgranja@dct.uminho.pt
2. University of Minho, Earth Sciences Center, Campus de Gualtar, 4710-057 Braga, Portugal.
   eduardo.marinha@clix.pt

Abstract: The progressive thinning of sandy beaches in NW Portugal has exposed: large areas of rocky outcrops in the low tide and sub-tidal zones; older marine deposits in the sub-tidal zone; and older beach deposits in the foreshore. All these environments were previously covered by sands.

As a result, sandy beaches have progressively been replaced by shingle beaches. This phenomenon migrates from north to south along the coast. Morphological change generally pass through a state where sand and gravel coexists in a beach cusp morphology (the beach horns being made of pebbles) until the sand disappears and only pebbles, cobbles and boulders remain.

The main purpose of this study is to understand shingle behaviour under different wave climate conditions and the mechanisms that led the shingle beaches to be more stable than the sandy beaches they replaced.

INTRODUCTION

Gravel beaches did not dominate the coastal landscape of Northwest Portugal some years ago (Fig. 1). On the contrary this coastal zone was dominated by extensive sandy beaches with dune systems, from the Little Ice Age (LIA), at the backshore (Fig. 2a).

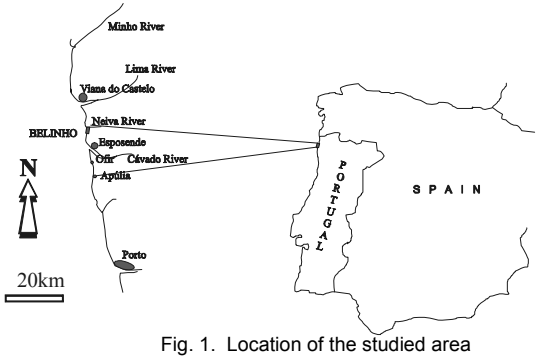

Fig. 1. Location of the studied area

However, on the most northern sector of the coast (between the Minho and Lima rivers; Batista, 1992), small pocket gravel beaches, between rocky headlands, have dominated the coastal landscape for more than a century. These small and narrow beaches did not show large yearly or seasonal morphological changes (except during overwashing; Alves, 1996), though, in time, they have been slowly migrating inland (e.g. Gelfa Beach). The gravels of these beaches cover medieval salt pans, like in Areosa (Almeida, 1979). They are swash-aligned barriers.

But since 2000, gravel beaches (Fig. 2c) that have become a progressive and dominant feature of the coastal landscape in the coastal zone between the Lima and Cávado rivers, are a new phenomena, involving mechanisms acting very fast in time. Unfortunately, the understanding worldwide of the behaviour of gravel beaches is still very rudimentary compared to that of sandy beaches as worldwide (Sherman, 1991).



Fig. 2. Belinho Beach (Esposende). a. sandy beach (June1994); b. sandy and gravel beach (June1998); c. gravel beach (June 2003)

One particular character of these new gravel beaches is that they are progressively, and irreversibly, replacing the former sandy beaches, though maintaining the dune systems on their backshore (Fig. 2). The new coastal landscape is composed by exposed rocky abrasion platforms, steep gravel beaches (with cobbles and pebbles, and, sometimes, small sand aprons), and dunes (composed of fine sand), inherited from the previous sandy beach morphology.

This paper, through the description of the development and facies change of a wave dominated, high energy beach (Belinho Beach), tries to give an explanation about probable mechanisms that changed it from a dissipative state (sands) to a reflective state (pebbles, cobbles and boulders), which has become the new permanent equilibrium.

GEOMORPHOLOGICAL BACKGROUND OF THE STUDY SITE

The sector of the NW coastal zone of Portugal where gravel beaches have been replacing sandy beaches is characterized by a narrow coastal zone, extending from the sea till a dead cliff, and composed of two rocky platforms (Fig. 3), the lower one extending underwater, which have been exposed over the last years.

The dead cliff and the associated higher platform are carved from Hercynian granite, with several fault systems. This granitic intrusion has metamorphosed the Palaeozoic rocks (Teixeira *et al*., 1969) that compose the lower platform, which is part of a NW-SE oriented complex syncline. The Ordovician quartzitic beds are present in both flanks, interbedded with Ordovician schists and a conglomerate with elongated quartz pebbles (due to post-Devonian tectonic deformation) on the western flank. At Belinho Beach, the rocky platform is made of the schists.

The surface of the lower platform is slightly irregular, with some depressed areas due to some probable faults. In these depressions, a thin Holocene formation is present (Granja, 1999; Ribeiro, 2003). The base of these depressions consists of a layer of marine pebbles, probably reworked from fluvial deposits and marine gravel ridges of Pleistocene age, which are present on the higher areas of the same platform (Soares de Carvalho *et al*., 2006).

Due to the strong erosion of this coastal zone over the last years (since 1995-1996), different sedimentary deposits are now exposed. Holocene deposits, including lagoon, beach deposits, and gravel ridges, have been exposed in some sectors of the beaches, due to accelerated dune cliff retreat. At the same time, sand has been lost from the beaches, and large areas of the low abrasion platform on the intertidal zone have been exposed.

On the inner shelf, till –20m depth, some preliminary data from SCUBA campaigns have already shown (Granja and Ferreira, 2006): a marine sea level stand at –15m depth, revealed by the presence of a N30ºW notch; channels with the same orientation, between rocky outcrops with 18m height walls; many pebbles and

boulders; and clasts exclusively composed of organic detritus (shell hash). Sand is very fine and silty, and only confined to a narrow band along the coast.

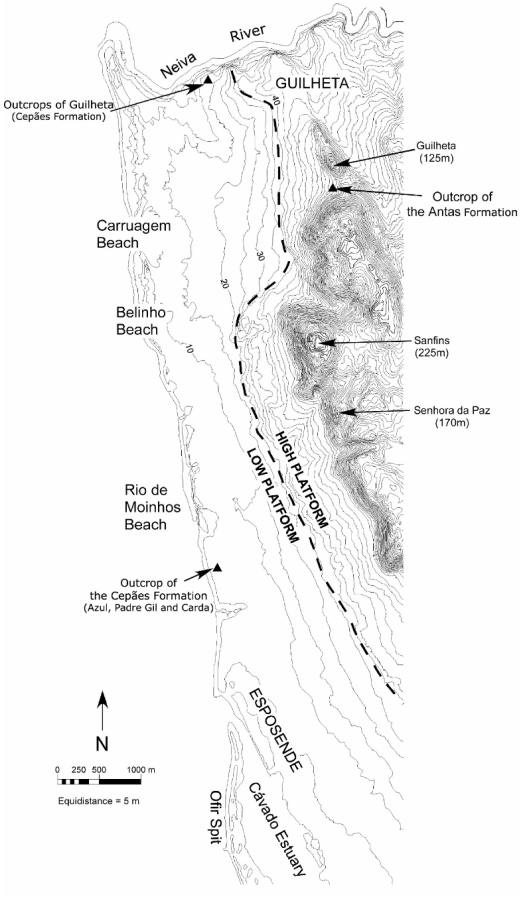

Fig. 3. Main landscape features of the coastal zone between the Neiva and Cávado rivers. Crowded contour lines indicate the position of fault scarps (dead cliff) (after Soares de Carvalho *et al*, 2006)

THE EVOLUTION FROM A SANDY TO A GRAVEL BEACH STATE

Belinho Beach is one of the beaches where the replacement of sand by gravel was the most spectacular. For this reason it was chosen as case-study.

For more than two decades, erosion has been a constant along the NW coastal zone of Portugal (Teixeira, 1980; Granja, 1990; Veloso Gomes, 1993; Oliveira, 1997;

Oliveira *et al*., 1982, Carvalho *et al*., 1986, Dias, 1990, Mota-Oliveira, 1990, Ângelo, 1991. Ferreira and Dias, 1991; Bettencourt and Ângelo, 1992, Carvalho and Granja, 1992, in Magalhães, 1999; Veloso Gomes *et al*., 2002). Inland beach migration, thinning of beaches and cliff retreat are the geoindicators of that phenomenon (Carvalho *et al*., 2002).

However, only from 1996 onwards, beaches began definitively to loose sand, which has been replaced by much coarser sediments – like pebbles, cobbles and boulders. This process was initiated in Castelo do Neiva (north of the Neiva River) by the end of the 1980's, when sandy beaches began to show beach cusps with horns composed of pebbles (intermediate state, with sand and gravel). These beaches evolved progressively towards a gravel state, extending southwards along the coast. Today, gravel beaches extend till Redonda Beach, at the town of Esposende (Fig. 1).

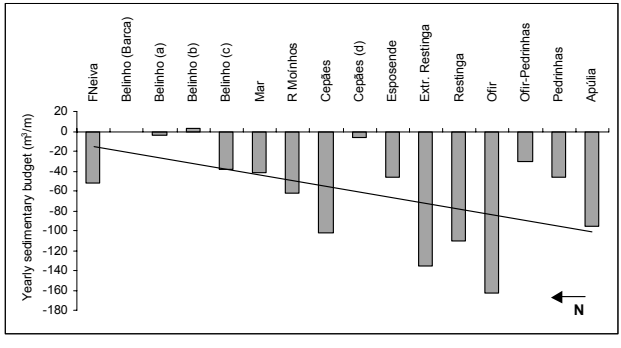

Fig. 4. Sedimentary budget along the beaches, between the Neiva River and Apúlia (2001-2004)

The coast of NW Portugal is of mixed energy, wave and tide-dominated, according to the classification of Davis and Hayes (1984). Tides are mesotidal, semi-diurnal, with maximum amplitude of 3.9m and a minimum of 0.2m. The wave climate is characterized by a mean H_s and T_s of 2m and 9s, respectively; the main direction is from NW (79% of frequencies). The net sedimentary drift is from North to South, though at some points this is inverted due to the presence of outcrops or shoaling bars (as around the ebb tidal delta of the Cávado mouth) that refract and diffract the dominant NW incoming waves. The presence of some engineering structures (groynes and revetments) also contributes to some interference patterns on the general circulation, promoting up-drift wedge beaches against groynes, thinning of beaches in front and excavation on both sides of the revetments.

According to Short (1999) spatial changes in beach type are driven by changes in both wave climate and sediment characteristics. However, the available wave data is scarce and not continuous. The number of recorded data of the Hydrographic Institute (IH) at the Leixões wave-buoy, although significant, shows a series of breaks in the sequences. The common situation of sample collection produces 240

monthly data (8 per day). But, between 1981 and 1985, the data from storms are very rare, probably due to technical problems (Coelho, 2005).

With these limitations, and due to the impossibility to use data from pressure transducers (PTs), it is extremely difficult to find any explanation based on wave climate changes. However, even taking into consideration the scarcity of data, there are some slight changes concerning the breaker heights and the steepness of incoming waves, that can help to explain some changes in beach behaviour (Fig. 5).

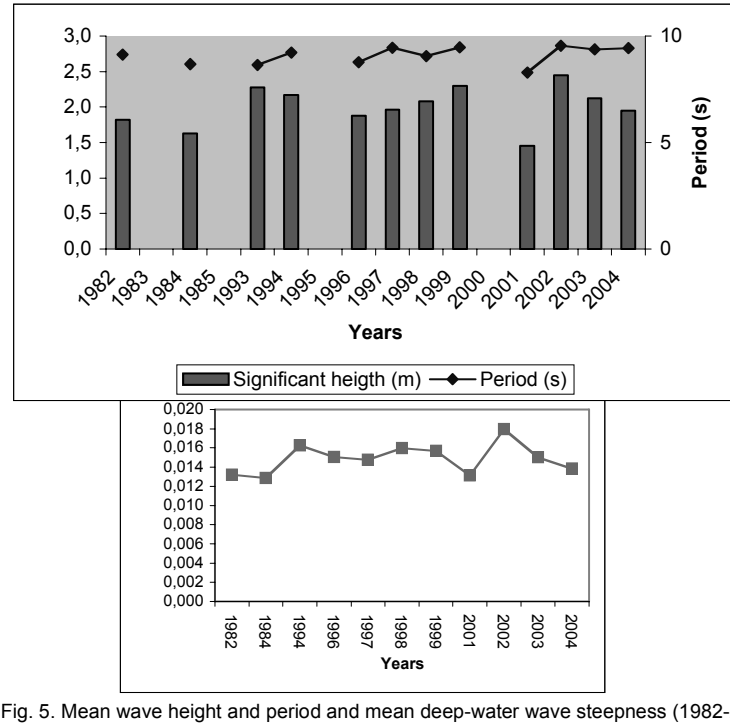

Fig. 5. Mean wave height and period and mean deep-water wave steepness (1982-2004)

Beach facies

The coastal segment between Belinho and Mar is 3000m long. Till 1995, Belinho was a sandy, 100m wide dissipative beach, with a slope of 0.07, well-developed 30-40m wide berm dipping landward, and a smooth beach face (Fig. 2a and Fig.6).

After1995, the beach evolved progressively into an intermediate state one, as did also facies and grain size of sediments (Fig. 2b and Fig.6). The emergence of rocky outcrops of the platform contributed to a change of wave refraction and the formation of large-scale rip circulation. This mechanism, associated to the ridge-and-runnel systems, produced variations in the wave breaker heights parallel to the shore and on the direction of approach. The morphology stimulated deposition at the lee side of the bars, the growth of megacusp horns, and the scouring in the bays due to higher diverging waves. As the morphology helps to reinforce and attenuate the dynamics, the morphodynamic coupling is maintained with continued low waves (Short, 1999). Bars will move shoreward while the megacusps horns will grow seaward, producing scarping in the rip embayment. Progressive shoreward moving will create a low tide terrace.

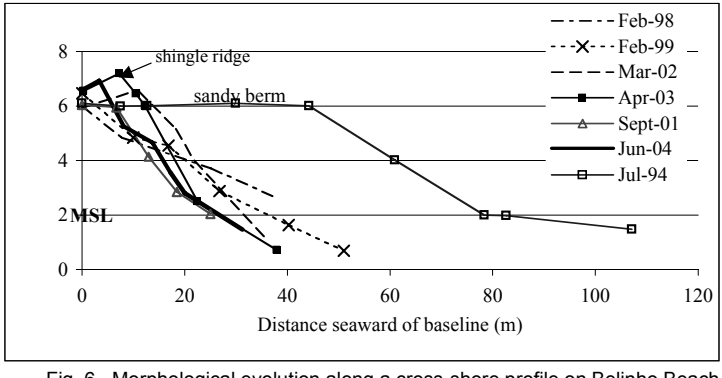

Fig. 6. Morphological evolution along a cross-shore profile on Belinho Beach

Today, and since 2000, the gravel beach is fully reflective (Fig. 3c and Fig.9). It shows a 10-20m wide berm, oriented N10ºE-N40ºW, and backed by a dune cliff, where four active overwashing areas cut through it. The steep beach face shows several series of beach cusps with different wavelength (Fig. 7a). In the intertidal zone there are extensive rocky outcrops of the lower platform.



Fig.7. a. Series of beach cusps in Belinho Beach (June 2006, fair weather conditions); b. smooth profile after storm (November 2006)

The sedimentary cover of the beach is composed of gravel, pebbles, cobbles and boulders of different lithology (quartzite, the most abundant, schist, conglomerate, quartz and granite) and shape (discs, rods, spheres, and blades). The dominant size lies within the 45-64mm range (Loureiro and Granja, 2001). Sometimes, some sandy aprons are present on the lower beach face during fair weather conditions.

Shingle shape zonation on the beach is a function of wave energy conditions. The wave climate and the existence of rocky outcrops in the intertidal and subtidal zones have an important role in the distribution and selection of pebbles on the beach, contributing to the existence of different morphosedimentary behaviours.

Over the year, the shingle beach of Belinho may exhibit a range of facies responses to the wide spectrum of wave energy it receives. Different shape particles react differently to wave conditions, permitting the subdivision of the beach into different morphodynamic zones (Loureiro and Granja, 2001).

Beach Dynamics

On reflective beaches, seaward of the breaker point, shoaling waves induce onshore sediment transport as well as a preferential shoreward movement of coarse sediments, that will accumulate in the swash zone. The waves breaking at the base of the beach face expend all the remaining energy in the swash zone. Much of the energy goes into the wave uprush which builds a steep beach face aided by coarser sediments (Short, 1999).

Cusps are a product of sub-harmonic edge-waves, meaning that the waves have a period twice that of the incoming wave (Wright *et al*., 1979, in Short, 1999). The edge wave period and the beach slope determine the edge wave-length, which in turn determines the cusp spacing, which on swell coasts can range from 20 to 40m (Short, 1999), like here, in Belinho (Fig. 10).

The distribution of particle size across a beach profile shows a decrease from the ridge crest to the bay of the beach cusps. The accumulation of large discs and spheres in the berm of the beach occurs during storm periods. Small spheres are also projected by the waves and lodged among the bigger particles.

During storms, the beach profile is smoothed with the destruction of the cusp morphology and pebble imbrication, while the build-up of the berm crest turns the profile steeper (Fig. 7b).

METHODS

Foreshore morphology

The topographic surveys consisted of cross-shore profiles along the beaches using a Leica theodolite (all surveys are referred to ZH level, the national hydrographic level, 2m below mean sea-level and to Hayford/Gauss Datum). Each profile was surveyed between the low tide line and the top of the dunes on which crests fixed reference points were established. Sediment budgets and beach slopes were thus calculated. The

sedimentary volumes were calculated along 17 profiles covering about 1000m of beach extension in 1994, 1998, 1999, 2002, 2003, and 2004.

The shoreline retreat was based on the sample mean standard deviation and the maximum shoreline landward movement (Byrnes and Hiland, 1994; Anders *et al.* 1990 *in* Gorman *et al*., 1998). The volume calculation was obtained with the program Surfer, version 8.0, using the Trapezoidal, the Simpson and the 3/8 of the Simpson methods, with a relative error lower than 0.05%.

The morphological vulnerability index (Larson and Kraus, 1995), a resilience measure of the beach face to adverse marine agitation conditions, was determined.

Wave measurements

In the absence of pressure transducers, IH data were used to calculate wave parameters. Wave characteristics were obtained by statistical averaging of significant wave heights and periods. These analyses were based on wave data from 1982 till 2004. Breaker height was estimated in the surf zone according to Komar and Gaughan (1972) and the deep-water wave steepness (H_s/L_0) was calculated.

The surf scaling parameter $\varepsilon=(2\pi^2 H_b)/(gT^2 \tan^2\beta)$, the surf similarity parameter $\Sigma=\tan\beta/(H_b/L_0)^{0..5}$ and the Dean's number $\Omega= H_b/(WsT)$ were calculated. The beach was classified according to its morphodynamic state and the type of wave breaker (Short, 1999).

Sediment sampling

The morphometric indexes (R.I and F.I) and the shape of the pebbles were determined along the beach transects during a field campaign in 1998, when the beach was already in a reflective state, but with only a series of beach cusps (Fig. 2 b). 1405 quartzitic pebbles and cobbles were sampled on the ridge crest and on horns and bays of beach cusps, using a square metre sampling net (Loureiro and Granja, 2001).

RESULTS

Sediment characteristics

Considering the total of the beach, discs were the most abundant shapes (43%), followed by spheres (29%), rods (19%) and blades (11%). The percentage of discs shows an increasing trend with size, while rods and blades show a decreasing trend. Spheres are abundant in all size classes. There is an increase of the roundness index with the decrease of particle size, while the flatness index shows a slight increase with increasing sizes.

A seawards decrease of size particles was observed across shore. This particle size differentiation can be due to an asymmetric swash flow, the size gradient depending on the pulsation of a distinct groundwater surface flow operating in conjunction with backwash (Orford *et al*., 2002). The larger sizes at the berm crest are due to storm conditions, when onshore transport is dominant at the top of the beach.

Discs represent the most frequent shape on the ridge, horns and bays of cusps (80%, 81% and 77%, respectively), being predominant in the highest size ranges (40-50 to 60-70mm). Rods (76% in the ridge; 59% in the cusp horns; 42% in the cusp bays) are represented most in the lower size ranges, decreasing in the higher ranges. Spheres and blades are regularly distributed over all size ranges. In the cusp bays there are all the shapes in the lowest ranges (<20mm) and their absence in the range size 60-70mm, while in the ridge and cusp horns only the shapes <20mm are absent (Fig. 8).

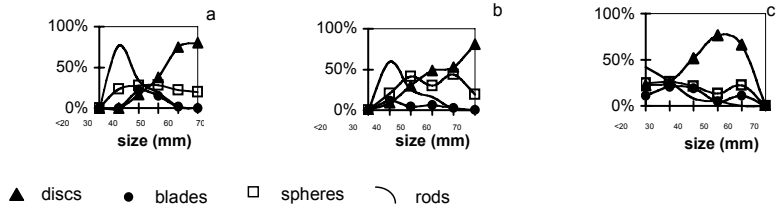

Fig. 8. Pebble shape percentages: a. ridge crest; b. horn of beach cusps; c. bay of beach cusps (after Loureiro and Granja, 2001)

It is interesting to note that on Belinho Beach, size ranges for cusp horns and bays are higher than those of other beaches cited by authors like Sherman *et al.* (1993). For example, in bays, discs are mostly in the 40-60mm size range, a higher range than the ones presented by those authors.

In the beach cusps, the mean value of the R.I. (585±100) in the bay is higher than that of the horns (519±190). In the ridge crest the R.I. is 514±104. Along the beach, R.I decreases from north to south. The presence of larger outcrop areas on the southern sector of the beach would reduce the pebble mobility, explaining perhaps the decrease of R.I.

Wave climate

Between 1982 and 2004 the mean wave characteristics concerning height and period were calculated (Table 1) from the IH records as was the deep water wave steepness (Fig. 5).

The yearly mean of the wave height was 2.0m and 9.1s for the period, though with important seasonal variations. During winter (2.6m) and fall (2.5m) the mean height values exceeded by about 1m those of summer and spring. The differences between the maximum and the minimum of the means was about 1.6m. The maximum height was observed in October 2003 (9.2m) and in February 2002 (7.4m).

Observing the mean wave heights for each year of this period of time (Fig. 5), there is a slight decrease between 1993 and 1994 and a more accentuated one between 1999 and 2001. From 2002 till 2004 there is also a decrease. The highest values of

the period were observed during fall (10.1s) and winter (11.0s), while the lowest was registered in summer (7.9s).

Between 1981 and 2004, the strongest situations of marine agitation occurred during the year 2002, with waves H_s>3m during 106 days and T_s>12s during 88 days of the year.

Deep water wave steepness shows an irregular behaviour (Fig. 8). The highest values prevailed during part of 1993 (0.018), 1999 and 2002 (0.016), while the lowest values (0.013) were related to small waves during the years 1982, 1984 and 2001. Although irregular, a small decreasing trend was observed between 1994 and 1996, 1999 and 2001, 2002 and 2004. In 1994, the beach was still dissipative, the change to an intermediate state having occurred by 1996 with a great loss of sand. Looking at Fig. 6, those periods correspond to steeper beach face profiles. The steeper beach face and higher ridge crests correspond to April 2003, when the wave steepness and wave height diminished.

Table 1. Wave Climate Statistics, 1981-2004, Esposende

Time Period	Mean Height, m	Mean Yearly Max Height, m	Maximum Height, m	Mean Period, s
Winter (Jan-Mar)	2.6	4.2	7.4	11.0
Spring (Apr-Jun)	1.7	3.7	6.3	8.6
Summer (Jul-Sep)	1.3	2.6	3.7	7.9
Fall (Oct-Dec)	2.5	4.1	9.2	10.1
Yearly Mean	2.0	3.7	2.5	9.1

Beach morphology

Today, Belinho Beach is characterised by Ω values between 0.15 and 0.10, which means that this coastal segment is reflective with plunging breakers, the beach face presenting a high steep slope during all the year.

The dominant morphology of the beach, today, is a 7 to 12m wide shingle ridge (boulders, cobbles, and pebbles) parallel to the foredune, a steep beach face where the pebbles show imbrication, series of pebble beach cusps with different wavelength (7 to 18 m), and small areas of coarse sand between the lower beach face and the rocky outcrops (sand aprons). During storm conditions, pebbles and cobbles overwash the foredune.

With breaking wave heights Hb<0.5m, in some sectors of the beach, pebbles accumulate between the lower beach face and the rocky outcrops, where they are covered by sand transported from seawards during summer.

The retreat of the sandy cliffs between 1994 and 1997 was between 20 and 40m, but from 1998 till 2004, the mean retreat has decreased to 5m due to the presence of the

shingle ridge in front of it. Only in the overwashing areas the retreat had a maximum of 30m.

Between 1998 and 2004, the base of the beach face was subjected to a yearly mean lowering of about 0.7m, and the width of the berm decreased by about 2m. The mean retreat of the sandy cliffs in this sector was about 4±2.5m, with a maximum retreat of 8m in the overwashing areas (Fig. 6).

Table 2. Morphodynamic Parameters (mean values concerning 2001-2004)

Belinho Beach	Slope (tanβ)	Foreshore width (m)	Grain size (mm)	Ω	Σ	ξ
Yearly	0.15	25	≥50			
winter				0.15	0.91	1.8
summer				0.10	0.93	1.7

Concerning the vulnerability index, before 2001 the behaviour of the beach was weak (0.36 to 0.62), but after then, when shingle definitively replaced sand, the beach changed to a robust behaviour (0.02 to 0.26).

DISCUSSION

This is a good example of a beach segment with a fast and extreme evolution trend. The change from a sandy state to a gravel state was reached in just a few years. This is not situation of stripping of beach sands during winter storms and the exposure of a cobble/boulder lag deposit, a temporary change of sediment and beach type, as documented by Shepard (1963) or Short (1984). Here it is a permanent state. The fundamental question here is why a sandy, dissipative beach turned into a very coarse, reflective gravel beach. The evolution from a dissipative state to a reflective state is exactly the opposite of all those beaches that evolve into a dissipative state at some stage, although most never reach the fully dissipative state according to Short (1999).

On Belinho Beach, the present reflective state should be analogous to the one responsible for the emplacement of the fossil gravel beach ridges situated under the LIA dunes. Orford *et al.* (2003) have presented a similar case in NE Ireland and discussed the mechanisms responsible for the decoupling of gravel and sand into different modal-sized components in Holocene coastal sedimentary environments, or how two distinctive coastal domains with radically different morphodynamic beach contexts could alternate to generate superimposed units of widely contrasting particle size.

One of the explanations for that superimposition suggested by Orford *et al.* (2003) points to different energetic conditions, the gravel source being preferentially deposited under high-energy conditions, followed by the fine sediment when the gravel supply is exhausted. But if so, why are there no observable significant wave climate changes, over the last 20 years, when the replacement from sand to gravel state took place?

Another mechanism discussed by the same authors is that gravel ridges were emplaced under a reflective morphodynamic regime that would deplete the sediment source. The superimposition of the dune cover would follow it, with sand moving into the beach to replace or possibly bury (the case of Belinho) the gravel component residing on the beach face (the ante-LIA ridge). According to them, such a switch in sediment source may also have resulted from a joint occurrence of energy and sediment source changes. In the case of Belinho Beach, it would mean that, during LIA, the sand availability was large and the winds strong enough to mobilize it (which is confirmed by historical texts, see Felgueiras, 1998), under a regime of high-energy wind-blown sand.

The dunes superimposed on gravel beach ridges is thought to be the result of an alternating sediment decoupling (modulated by falling sea level) rather than a sequential sediment sourcing, according to Orford *et al.* (2003).

The presence of outcrops in the lower foreshore contributes to sediment accretion on the beach, making the seaward cross-shore and alongshore sediment transport more difficult (pebbles have smaller R.I.), which leads to an increase of the berm height and of the beach face slope. The ridge protects the foredune cliffs against a direct attack of the waves, and also stimulates the infiltration of water from the swash, decreasing the backwash over the beach face. This contributes to a strong reduction of sediment movement offshore.

Like in other cases (e.g. Portmore Beach, Sherman *et al*, 1993), Belinho Beach is a beach subject to a wide range of energy conditions and constantly reworked, though maintaining a sedimentary equilibrium (Fig. 4).

Although the beach slope is 0.13 (>0.10), the deep-water wave steepness is in the range of 0.016-0.013, higher than what was proposed (<0.01) by Bauer and Greenwood (1988) (cited by Sherman *et al*., 1993) for the occurrence of reflective conditions under all wave regimes. Plunging breakers are the dominant wave breaker type, and during high tide, in the zones where the beach is steep enough ($\tan\beta$=0.15 to 2.0), the waves are of the collapsing breaker type.

The volumetric changes (Fig. 4) since the beach became fully reflective are small and the erosive processes affect the beaches only during storms, when partial foredune overwashing occurs. The small difference between the maximal and minimal sediment volumes in this sector indicates that the beaches keep some morphodynamic stability. Consequently, the beach shows a robust behaviour, resulting in some stability following a new morphodynamic equilibrium.

CONCLUSIONS

Between 1981and 2004, the beach characteristics of Belinho Beach (Esposende coast) show a trend to: 1) increase in grain size; 2) change in sediment composition (quartz sands to quartzite pebbles and cobbles); 3) increase in rocky-outcrop areas in

the intertidal zone; 4) increase in negative sedimentary budget and cliff retreat; 5) gradual shift from dissipative to reflective morphotypes.

Between 2001 and 2004, the cliff retreat and the sediment budget were different along the coastal zone of Esposende, although mainly erosive (Fig. 6). The negative sediment budget recorded today on the beaches can possibly be the result of a lack of significant sediment sources available, sand starvation on the shoreface which is now beginning to be confirmed by diving campaigns, and sea-level rise (Granja, 1999). Sand starvation and increasing water-depths resulting from sea-level rise, leads to a decreasing sediment transport shoreward. Also, the predominance of the plunging breaker type promotes a strong backwash, which contributes to an important cross-shore transport seawards, increasing the erosion of the beach.

However, today on Belinho Beach and on the other gravel beaches, the erosional processes are less accentuated than on the still sandy beaches of the Esposende coastal zone.

Sediment transport is conditioned by local factors such as: 1) the strong wave refraction over a bigger or smaller intertidal area of rocky outcrops, reducing the alongshore component of the energy flux; 2) a different orientation of the beaches in relation to the approaching waves; 3) local bathymetric characteristics; 4) the existence of different circulation cells; 5) the availability and grain size of the sediments; 6) the Cávado river mouth; 7) the presence of groynes and breakwaters.

However, what has led and still leads to a general loss of sand on these beaches and to the change from a dissipative to a reflective state? Wave climate change? From the 20 years wave data available from IH there is no evidence of significant changes. Sand starvation? Undoubtedly yes, especially if the inner shelf cover is also considered. But, if so, where is the sand going? The sand trapped against the groynes and breakwaters southwards and into the estuary of the Cávado River is not enough to justify the losses from adjoining beaches.

At times of maximal sand deficit, the morphodynamic regime of the beach face switches to one of inner-beach reflectivity, which is a response to gravel ridge development at high-water positions, which in turn will be fixed during dissipative conditions, after a new influx of fine-grained sediment. These cycles of sediment renewal would be related to variations in the rate of sea level drop and reworking of near-shore sediment (Orford *et al.*, 2003). On Belinho Beach, if one of the gravel sources could be in the beach ridges under the LIA dunes, another is certainly on the inner shelf itself, which is being reworked under present sea level rising and higher frequencies of storms.

In the case of coastal risks today, the northern segment (Belinho) of the Esposende coast is less vulnerable to storm surge flooding and infrastructural damage due to an undeveloped shore, predominance of large outcrop areas in the intertidal zone, a shingle ridge parallel to the foredune, and a well-developed dune system. The

southern sector, with intermediate and dissipative beaches (Esposende and Ofir spit), is prone to higher risks due to a flat beach face and intensively developed backshores without protective dunes.

ACKNOWLEDGEMENTS

We greatly appreciate the cooperation of Dr. Carlos Coelho from the University of Aveiro, concerning wave data information and we are very grateful to Dr. Th. de Groot for the revision of the English text. We acknowledge the Área de Paisagem Protegida do Litoral de Esposende and the Câmara Municipal de Esposende, that have sponsored this work. All wave data used is from the Hydrographic Institute (IH).

REFERENCES

Almeida, C. A. B. (1979). Salinas medievais entre Cávado e Neiva. *Brácara Augusta XXXIII,* (75-76), 391-407.

Alves, A. M. C. 1996. Causas e processos da dinâmica sedimentar na evolução actual do litoral do Alto Minho. *PhD thesis,* Universidade do Minho, Braga, 442 p.

Batista, J. L. M. (1992). As indústrias líticas pré-históricas do litoral minhoto (Portugal) no seu contexto cronoestratigráfico e paleoambiental. *PhD thesis,* Universidade do Minho, Braga.

Bluck, B. J. (1967). Sedimention of beachs gravels: examples from South Wales *Journal of Sedimentary Petrology,* 37: 128-156.

Carter, R. W. G., and Orford, J. D. (1993). The morphodynamics of coarse clastic beaches and barriers: a short-and long-term perspective. *Journal of Coastal Research,* Special Issue No. 15: 158-179.

Carvalho, G. S., Granja, H. M., Gomes, P., Loureiro, E., Henriques, R., Ribeiro, I., Costa, A. L., and Ribeiro, P. (2002). New data and new ideas concerning recent geomorphological changes in the NW coastal zone of Portugal. In: Eurocoast Assotiation (ed), *LITTORAL 2002 6th International Symposium proceedings - The Changing Coast,* Porto, Vol 2, 339-410.

Coelho, C. (2005). Riscos de exposição de frentes urbanas para diferentes intervenções de defesa costeira. *PhD thesis,* Universidade de Aveiro, 404 p.

Felgueiras, J. (1998). A Pilotagem e os Pilotos Mores da barra de Esposende. Subsídios para a História Marítima de Esposende. Separata do *Boletim Cultural de Esposende* Nº 19, 15-30.

Gorman, L., Morango, A., and Larson, R. (1998). Monitoring the coastal environment; Part IV: Mapping, shoreline changes, and bathymetric analysis. *Journal of Coastal Research*, 14(1), 61-92.

Granja, H. M. (1999). Evidence for Late Pleistocene and Holocene sea-level neotectonic and climate in coastal zone Northwest Portugal. *Geologie en Mijnbouw,* vol. 77: 3-4.

Granja, H., and Ferreira, V. (2006). Geomorfologia da plataforma continental interna ao largo de Esposende (um caso de estudo – nota preliminar). *3º Congresso Nacional de Geomorfologia*, Funchal, Madeira.

Komar, P. D., and Gaughan, M. K. (1972). Airy wave theory and breaker height prediction. In: *Proceedings of the 13th International Conference on Coastal*

Engineering ASCE, 405-418.
Loureiro, E., and Granja, H. M. (2001). Short-term morphodynamics of a shingle beach (Esposende, Northwest Portugal). In: Packham, Randall, Barnes and Neal (eds.), *Ecology and Geomorphology of Coastal Shingle,* 148-159.
Larson, M., and Kraus, N. C. (1989). Prediction of cross-shore sediment transport at different spatial and temporal scale. *Marine Geology*, 126:11-127
Magalhães, F. (1999). *Os sedimentos da Plataforma Continental Portuguesa: contrastes espaciais, perspectiva temporal, potencialidades económicas*. PhD thesis, Universidade de Lisboa, 289 p.
Oliveira, I. B. M. (1997). Proteger ou não proteger ou sobre a viabilidade de diferentes opções face à erosão da costa oeste portuguesa. *Colectânea de Ideias sobre a Zona Costeira de Portugal.* Associação Eurocoast-Portugal, Porto, 205-228.
Orford, J. D., Forbes D. L., Jennings S. C. (2002). Organisational controls, typologies and time scales of paraglacial gravel-dominated coastal systems. *Geomorphology*, 48: 51-85
Orford, J. D., Murdy J. M., Wintle A. G. (2003). Prograded Holocene beach ridges superimposed dunes in north-east Ireland: mechanisms and timescales of fine and coarse beach sediment decoupling and deposition. *Marine Geology*, 194: 47-64
Ribeiro, I. M. C. (2003). Deformação neotectónica pós-plistocénica na zona costeira entre os rios Minho e Ave. *PhD thesis,* Universidade do Minho, Braga, 357 p.
Shepard, F. P. (1963). *Submarine Geology*. 2nd Edition, Harper and Row, New York, 577 p.
Sherman D. J. (1991). Gravel Beaches. *National Geographic Research & Exploration*, 7 (4): 442-452.
Sherman D. J., Orford J. D., Carter R. W. G. (1993). Development of cusp-related, gravel size and shape facies at Malin Head, Ireland. *Sedimentology*, 40:1139-1152
Short, A. (1984). Beach and nearshore facies, southeast Australia. *Marine Geology*, 60:261-282
Short, A. (1999). *Handbook of beach and shoreface morphodynamics*. Jonh Wiley & Sons, Ltda., 379 p.
Soares de Carvalho, G., Granja, H. M., Loureiro, E., and Henriques, R. (2006). Late Pleistocene and Holocene environmental changes in the coastal zone of Northwestern Portugal. *Journal of Quaternary Science,* vol 21, 8: 859-877.
Teixeira, C., Medeiros, A. C., Alves, C. A. M., and Moreira, M. M. (1969). Carta geológica de Portugal na escala 1/50 000. Notícia explicativa da folha 5C – Barcelos. Lisboa, Serviços Geológicos de Portugal, 49 p.
Veloso-Gomes, F., Taveira-Pinto, F., Barbosa, J. P., Neves, L., and Coelho, C. (2002). High risk situation in the NW Portuguese coast: Douro river-cape Mondego, *Proceedings LITTORAL 2002*, 6th International Symposium, organised by Eurocoast-Portugal, 22-26 September 2002, Porto, II:411-421.
Wright, L. D., and Short, A. D. (1985). Morphodynamics of beaches and surf zones in Australia. In: Komar P. (ed.) Handbook of coastal processes and erosion CRC Press, Inc. Florida, 35-64.

FIELD MEASUREMENTS OF SHORE CONDITIONS TO ASSESS BULKHEAD EFFECTS IN THURSTON COUNTY, SOUTH PUGET SOUND

Susan P. Tonkin[1], Tim Abbe[2], José Carrasquero[2] and Steve Morrison[3]

1. Moffatt & Nichol, 710 Second Ave South #720, Seattle, WA 98104, USA. stonkin@moffattnichol.com.
2. Herrera Environmental Consultants, 2200 Sixth Avenue #110, Seattle, WA 98121, USA. tabbe@herrerainc.com and jcarrasquero@herrerainc.com.
3. Thurston Regional Planning Council, 2424 Heritage Court SW #A, Olympia, WA 98502, USA. morriss@co.thurston.wa.us.

Abstract: This study investigated the effects of bulkheads and other armoring on beach conditions in Thurston County, Washington. Beach characteristics were measured at paired beach sites – neighboring and otherwise similar sites with and without bulkheads or other armoring. The study focused on beach characteristics relevant to spawning habitat for pacific sand lance and surf smelt, known as forage fish because of their importance to salmon. Armored locations, particularly in reaches of the shoreline where armoring was common, were found to have narrower beaches, with the greatest loss of beach typically at the higher elevations. Beach slope and sediment size were not significantly affected by the armoring. In a separate GIS-based investigation, it was determined that smaller, typically unnamed creeks contribute insignificant amounts of sediment in this area compared to the potential sediment supply from larger rivers or (most likely the largest contribution) from landslides and other mass wasting.

INTRODUCTION

Thurston County is located at the southern tip of Puget Sound, WA (see Figure 1). The county has 120 miles of marine shoreline along four north-trending inlets: Totten, Eld, Budd, and Henderson. The shoreline is macrotidal, with generally coarse and narrow beaches backed by coastal bluffs, predominantly composed of quaternary glacial

outwash. Approximately 36% of the shoreline is armored, largely with vertical bulkheads.

The study described here was performed to evaluate the effect of shoreline armoring, particularly bulkheads, on spawning habitat for forage fish (pacific sand lance and surf smelt) – specifically, the availability of sand and gravel beach at elevations between Mean Tide Level (MTL) and Mean Higher High Water (MHHW). Secondary aims of the study were to understand sediment sources in the area, and general geographical trends within the inlet. A more detailed description of the study background, aims, activities, and results is given in Herrera Environmental Consultants (2005).

METHODS

An intensive field program during the summer of 2003 measured beach characteristics at paired beach sites – neighboring and otherwise similar sites with and without bulkheads. The purpose of the field survey was to document and categorize the various geomorphic beach characteristics present, to identify the effect of bulkheads on sediment and beach characteristics, and to aid in identification of sediment sources and sinks. The field survey was supplemented by a GIS study of existing aerial photographs and digital elevation data that identified mass wasting sites (landslides) feeding the littoral system.

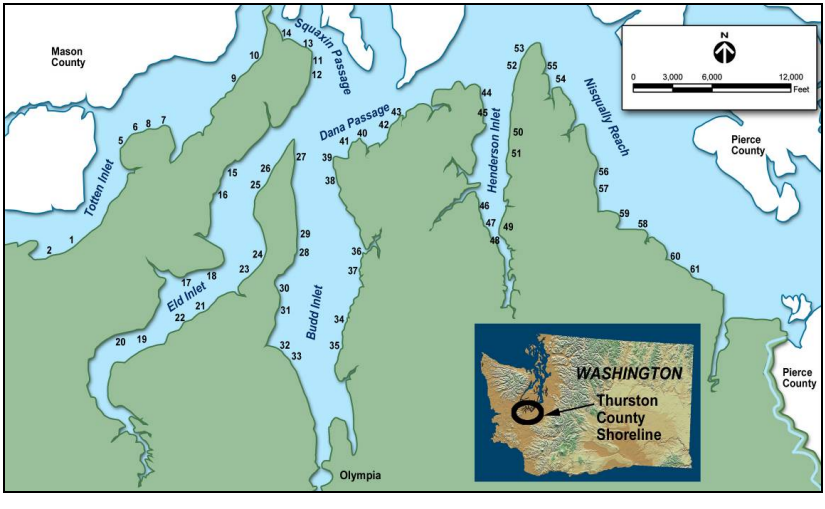

Fig. 1. Vicinity map including the location of beach sites

The majority of the field work was performed between August 25 and August 28, 2003. The marine shoreline of Thurston County was analyzed using 29 pairs of beach sites; the individual sites are shown in Figure 1. Each pair of beach sites consisted of one armored and one unarmored location. Three additional sites, not shown in Figure 1, were used to investigate the characteristics of small creeks. As is typical of the marine shoreline of

Thurston County, the beach at each site was backed by armoring or a bluff face. The majority of the armoring consisted of concrete bulkheads, although a few sites with riprap revetment and/or anchored logs were selected.

The following criteria were used in selecting each pair of sites, in order that they be as well matched as possible:

- Located in the same drift cell, as mapped by Schwartz and Hatfield (1982);
- Similar aspect;
- Similar geology;
- Similar slope and bluff relief upland of the sites;
- No recent landslide activity nearby;
- At least 250 feet and preferably about 500 feet between the two sites;
- No significant features protruding into the water between the two sites.

In some locations, bulkheads were originally constructed encroaching on the beach. These were typically indicated by return walls, of the same construction as the main bulkhead, used to retain upland fill. Such locations were not selected as beach sites.

The full beach profile was measured at each of the 58 sites. The beach profiles were measured at relatively low tide (no higher than MTL and much lower when possible). The beach profiles were measured from the lowest elevation available by wading to the armoring or bluff face. The most common and secondary sediment types (boulder, cobble, gravel, sand, fines, or other – generally shell hash) were determined visually and recorded at each point along the profile. The presence or absence of the following characteristics was noted:

- Hardpan, either exposed or a few inches below the beach surface;
- Coarser sediments on the beach surface (surface armoring, indicating erosion);
- Barnacles (indicating relatively low wave energy);
- Woody debris, either driftwood or locally sourced through mass wasting.

As a separate effort, six mass-wasting sites were surveyed in September 2003 to field-verify the landslide identification from the GIS analysis, described below.

All sampling locations were georeferenced using a Trimble® GeoExplorer3 handheld global positioning system (GPS) unit (resolution 6 to 16 feet).

FIELD PROGRAM RESULTS: BEACH CHARACTERISTICS

Figure 2 illustrates a typical beach in Thurston County, while Figures 3 and 4 are typical of the beach profiles measured. The photographs were taken, and both profiles were measured, in Henderson Inlet. Figure 3 is typical of those cases where the unarmored and armored beach profiles were very similar, while Figure 4 is typical of those cases where the armored beach is narrower than the unarmored beach.



Fig. 2. Typical Thurston County Beach (photographs in Henderson Inlet, unarmored site 49)

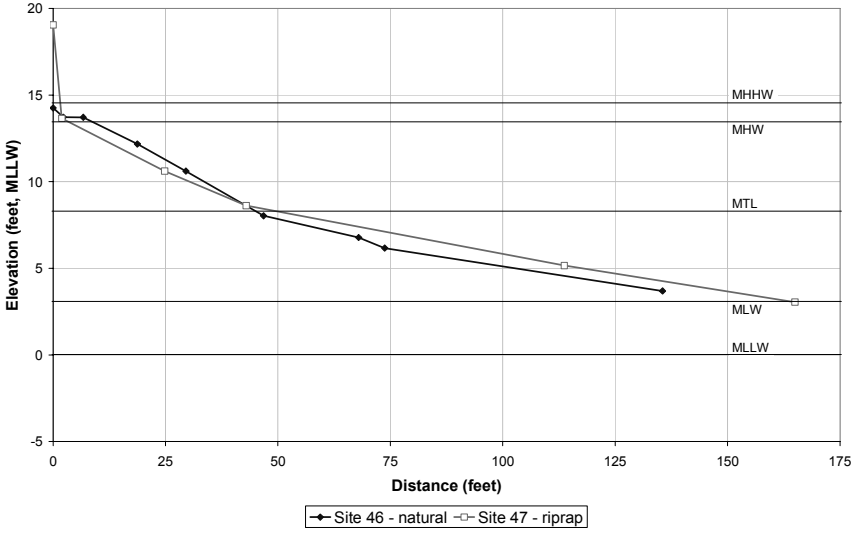

Fig. 3. Paired beach profiles where the armored and armored beach are similar (Henderson Inlet, sites 46 and 47)

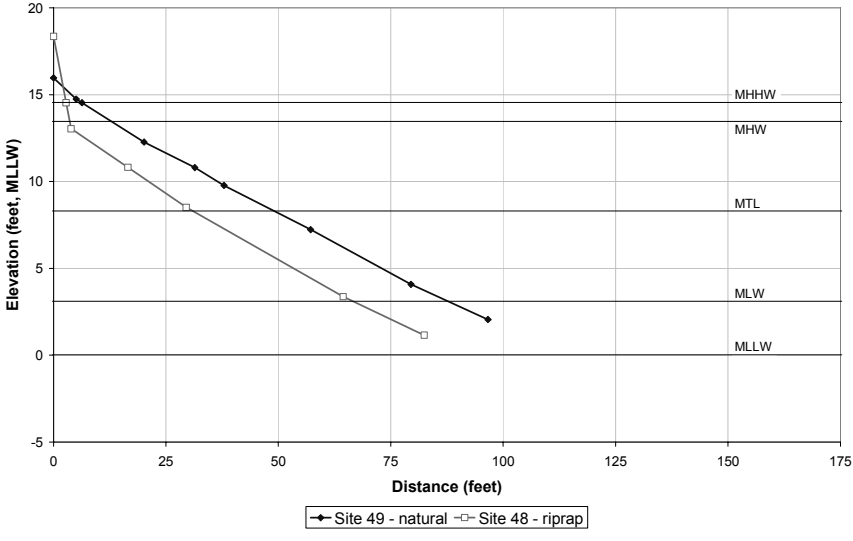

Fig. 4. Paired beach profiles where the armored beach is lower than the unarmored beach (Henderson Inlet, sites 48 and 49)

The average beach slope (between MHHW and the lowest limit measured), the width of the upper beach (from MHHW to MTL), and the width of the upper beach suitable for forage fish spawning (that part of the upper beach where the substrate was sand or gravel) were calculated for each profile, and the results compared for armored and unarmored sites.

Table 1 shows the results of this analysis. It indicates that armored shorelines differ significantly from unarmored shorelines in that the bulkheads effectively encroach on the upper beach – leading to a lower beach crest elevation and a generally narrower beach. (The beach crest is defined here as the point where the beach meets the bulkhead, other armoring, or bluff face). However, the beach slope, sediment characteristics, and the apparent wave energy on the beach (indicated by the presence of barnacles as well as by sediment characteristics) are not affected by local armoring. Woody debris is more likely to be present in unarmored areas, although this is likely to result from beach grooming by landowners rather than being a direct effect of the armoring. A slight but not statistically significant difference between the beach sediment grain size for armored and unarmored beaches was observed (Figure 5).

Table 1. Beach Characteristics Compared for Armored and Unarmored Beaches

Attribute	Median Difference *	Probability difference occurred by chance	Statistically Significant?
Upper Beach Width, feet (m)	-8.5 (-2.6)	p < 2.5%	Yes
Beach Width Suitable for Spawning, feet (m)	-9.4 (-2.9)	p < 2.5%	Yes
Slope, %	0.2%	p > 25%	No
Elevation of Beach Crest, feet (m)	-1.8 (-0.5)	p < 2.5%	Yes
Hardpan Exposure, yes/no	N/A	p > 25%	No
Beach Surface Coarsening, yes/no	N/A	5% < p < 10%	No
Presence of Barnacles, yes/no	N/A	p > 25%	No
Presence of Woody Debris, yes/no	N/A	p < 2.5%	Yes

* Median values of (armored-unarmored) measurements, for numerical measures

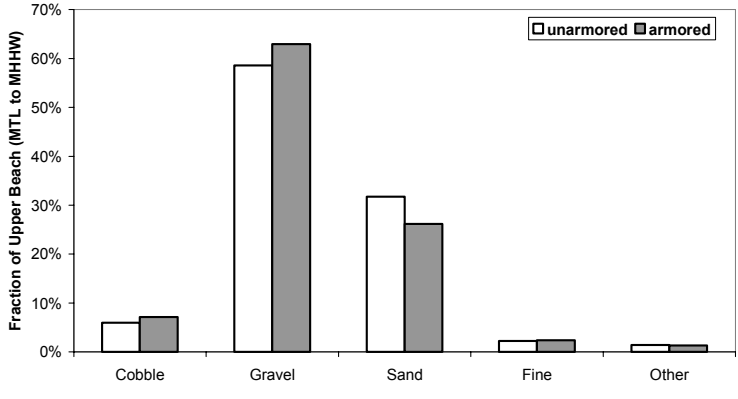

Fig. 5. Sediment size characteristics

At ten out of 23 armored sites where the armoring consisted of bulkheads, the bulkhead footing was exposed (e.g., Figure 6). This suggests that the decrease in beach width has resulted from erosion (with the upper beach fixed by the bulkhead rather than retreating along with the beach), and not simply to encroachment at bulkhead construction.

The relative decrease in crest elevation when comparing armored to unarmored beaches was found to be greater in those parts of the shoreline where armoring is common – defined here as those locations where more than 50% of the shoreline within 600 feet is armored. Beaches adjacent to isolated bulkheads are little affected by the armoring. The fact that the beach crest elevation is affected more by armoring in areas where armoring is common could be a cumulative effect due to long-term impoundment of bluff

sediments behind bulkheads. Alternatively, it could simply be the case that property owners are more likely to construct armoring along erosional stretches of beaches.



Fig. 6. Exposed bulkhead footing, Totten Inlet. August 25, 2003.

As a separate observation, the beach sediments generally coarsened from south to north, reflecting an increase in wave energy to the north.

Observed differences between armored and unarmored sites within each individual inlet, while not statistically significant (due to the smaller sample size), were consistent with the results described above.

GIS RESULTS: SEDIMENT SOURCES

A major aim of the GIS study was to identify the most significant sediment sources for the marine coastline of Thurston County. The three general sediment sources considered were: mass wasting (including landslides and bluff erosion); larger rivers; and smaller (typically unnamed) creeks.

The marine shoreline of Thurston County is typical of Puget Sound, with beaches set against steep, forested hillslopes composed of relatively unstable glacial sediments. Feeder bluffs are hillslopes that contribute sediment to the shoreline either through chronic surficial erosion or through periodic landsliding. The GIS study estimated only the sediment quantity delivered to the littoral zone through landsliding. As such, the results given here do not include sediment supply from chronic surficial erosion and represent a lower limit on the sediment supply from mass wasting.

Vegetation and topographic relief were used in the GIS analysis to identify and measure the area of each landslide. The approximate age of each landslide was estimated based on vegetation characteristics at the site; see, for example, Figure 7. A subset of the landslides was spot checked in the field. The landslides were further compared to those shown on available Washington Department of Natural Resources (WDNR) geologic maps as landslide deposits (WDNR 2003a-e, 2004a). WDNR only recorded landslides in

areas where the landslide obscures the underlying geology and consequently did not map many smaller landslides that were mapped in this study.



Fig. 7. Example of landslide in Eld Inlet. Riparian vegetation indicates slide is approximately 10 years old.

The annual volume of sediment supplied from mass wasting was estimated using this GIS analysis of landslide areas and ages together with field observations of recent landslides that suggested that the landslide depth was typically 3-5 feet (1-1.5 m). It was assumed that 30 percent of the sediment supplied to the beach by landslides was sand or gravel, and was therefore able to contribute significantly to the littoral sediment supply. The potential coarse sediment supply delivered by landslides – a lower limit of the total supply from mass wasting – is summarized in Table 2 for each inlet and reach.

Table 2. Estimated lower limit on the potential sediment supply due to mass wasting

	Totten Inlet *	Squaxin Passage	Eld Inlet	Budd Inlet	Dana Passage	Henderson Inlet
Potential supply, cubic yards (cy)/year (m^3/year)	1,300 (1,000)	50 (40)	3,200 (2,500)	1,700 (1,300)	400 (300)	2,500 (2,000)

* Thurston County shoreline only.

The potential sediment supply from larger rivers was evaluated based on dredging records from Capitol Lake, reported by Thurston Regional Planning Council (2002). Capitol Lake, which is located in Olympia at the southern tip of Budd Inlet, is formed by impoundment of the Deschutes River, so that the sedimentation rate in the lake is equal to the volume rate of sediment transport by the river. At present, this sediment is not available to the littoral system. For the other rivers, an estimate of sediment transport was

based on the relative watershed areas of the different rivers. The fraction of coarse sediment (sand sized or larger) was also based on dredging records from Capitol Lake.

Table 3 gives the estimated potential sediment supply from large rivers for the different inlets and reaches. It is possible that a large fraction of the coarse sediment is immediately transported offshore and is not delivered to the littoral system – meaning that the volumes given here provide an upper limit on the sediment supply from larger rivers to the littoral system. The quantities shown in Table 3 are of a similar magnitude to the quantities in Table 2, indicating that the sediment supply from large rivers is similar to or less than the sediment supply due to mass wasting.

Table 3. Estimated potential sediment supply from large rivers for each inlet and reach in Thurston County

Inlet / Reach	Potential Supply	Notes
Totten Inlet, cy/year (m^3/yr)	1,900 (1,500)	Half the total input to Totten Inlet; the western shore is in Mason County.
Squaxin Passage, cy/year (m^3/year)	0 (0)	No significant rivers.
Eld Inlet, cy/year (m^3/yr)	2,300 (1,800)	
Budd Inlet, cy/year (m^3/yr)	2,600 (2,100)	In addition to this quantity, the potential supply from the Deschutes River (currently impounded) is 9,500 cy/year.
Dana Passage, cy/year (m^3/yr)	0 (0)	No significant rivers.
Henderson Inlet, cy/year (m^3/yr)	2,900 (2,300)	

Small, typically unnamed creeks individually transport small quantities of sediment. However, there are many such creeks. Additionally, a small creek that flows over the top of a beach, rather than cutting through it, could deposit all of its sediment on the beach. This is in contrast to some larger rivers which can deposit much of their sediment so far offshore to that the material is unable to return to the littoral system. For these reasons, it is important to assess whether the small creeks, in aggregate, provide a significant sediment supply to the littoral system.

An analysis of the watershed areas of larger rivers (included in Table 3) and other areas, assumed to be drained by smaller and unnamed creeks, showed that minor creeks have a much smaller watershed area, even in aggregate, than the larger rivers. Furthermore, recent work by Haugerud (2003) indicates that forest vegetation effectively "froze" the topographic expression of the Puget Sound Lowlands shortly after the continental ice sheet receded 10,000 years ago. This suggests that historically, all but the larger rivers were relatively minor sediment sources.

This watershed analysis suggests that the sediment input from small creeks is insignificant compared to the input from larger rivers. The sediment input from small creeks is also insignificant compared to that from mass wasting. Individual small creeks could be important for small drift cells but, in the aggregate, their effect on the littoral sediment budget appears minor. Consequently, a program of culvert removal for smaller creeks would not be effective in increasing the sediment supply to the littoral zone. There may, of course, be other good reasons (such as fish passage) for culvert removal in smaller creeks.

CONCLUSION

The study found the following statistically significant differences between unarmored and armored shorelines within Thurston County:

- Armored shorelines have a reduced beach area, with a beach crest elevation that is lower compared to unarmored shorelines;
- As a consequence, the armored shorelines have less spawning area suitable for forage fish;
- Less woody debris is found on the armored shorelines.

The loss of upper beach area is more pronounced as the percentage of shoreline protection increases. This may be a cumulative effect (e.g., due to impoundment of feeder bluff sediment behind armoring), or it may simply result from a greater tendency for landowners to armor their property in highly erosional areas.

The study found no statistically significant differences in the following areas:

- Beach slope;
- Beach substrate (i.e., grain size);
- General indicators of wave energy including hardpan exposure, beach surface coarsening, and the presence or absence of barnacles.

These results are entirely consistent with the concept of passive erosion: the armoring fixes the upper limit of the beach in generally erosional areas, causing the beach to narrow relative to unarmored areas. The results do not specifically support the concept that the effective wave energy is increased by reflection from bulkheads.

The analysis of sediment sources shows that both mass wasting and the larger rivers have the potential to supply significant quantities of sediment to the littoral zone. The sediment from larger rivers may be delivered directly offshore, bypassing the narrow littoral zone, indicating that the landslides are likely more significant than larger rivers as an effective sediment source. Small, typically unnamed creeks do not and have not historically provided a significant source of sediment.

REFERENCES

Haugerud, R. (2003) Geomorphic Map Units and Landscape Evolution in the Puget Lowland. U.S. Geological Survey. University of Washington, Department of Earth & Space Sciences. Available online at: <http://gsa.confex.com/gsa/2003AM/finalprogram/abstract_67526.htm>.

Herrera Environmental Consultants (2005). Marine Shoreline Sediment Survey and Assessment: Thurston County, Washington. Prepared for Thurston Regional Planning Council by Herrera Environemntal Consultants, Moffatt & Nichol, and Aspect Consulting.

Schwartz, M. L. and Hatfield, D. M. (1982). Thurston County, Washington, Net Shore-Drift. Compiled by Washington Department of Ecology into Schwartz, M.L., et al. 1991. Net Shore-Drift in Washington State: Volume 2, South Puget Sound Region. Shorelands and Environmental Assistance Program, Washington Department of Ecology, Olympia, WA.

Thurston Regional Planning Council (2002). Capitol Lake Adaptive Management Plan.

WDNR (2003a). Geologic map of the Lacey 7.5-minute Quadrangle, Thurston County, WA: Washington Division of Geology and Earth Resources Open File Report 2003-9. Prepared by Logan, R.L., T.J. Walsh, H.W. Schasse, and M. Polenz.

WDNR (2003b). Geologic map of the McNeil Island 7.5-minute Quadrangle, Pierce and Thurston Counties, WA: Washington Division of Geology and Earth Resources Open File Report 2003-22. Prepared by Walsh, T.J., R.L. Logan, and M. Polenz.

WDNR (2003c). Geologic map of the Nisqually 7.5-minute Quadrangle, Thurston and Pierce, Counties, WA: Washington Division of Geology and Earth Resources Open File Report 2003-10. Prepared by Walsh, T.J., R.L. Logan, M. Polenz, and H.W. Schasse.

WDNR (2003d). Geologic map of the Squaxin Island 7.5-minute Quadrangle, Mason and Thurston Counties, WA. Washington Division of Geology and Earth Resources Open File Report 2003-23. Prepared by Logan, R.L., M. Polenz, T.J. Walsh, and H.W. Schasse.

WDNR (2003e). Geologic map of the Tumwater 7.5-minute Quadrangle, Thurston County, WA: Washington Division of Geology and Earth Resources Open File Report 2003-25. Prepared by Walsh, T.J., R.L. Logan, H.W. Schasse, and M. Polenz.

WDNR (2004). Geologic map of the Summit Lake 7.5-minute Quadrangle, Thurston and Mason Counties, WA: Washington Division of Geology and Earth Resources Open File Report 2004-10. Prepared by Logan, R.L. and T.J. Walsh.

CORAL-GRAVEL STORM RIDGES: EXAMPLES FROM THE TROPICAL PACIFIC AND CARIBBEAN

Bruce M.Richmond[1] and Robert A. Morton[2]

1. U.S. Geological Survey, Pacific Science Center, 400 Natural Bridges Drive, Santa Cruz, CA 95060, brichmond@usgs.gov.
2. U.S. Geological Survey, 600 Fourth St. S., St. Petersburg, FL, USA rmorton@usgs.gov

Abstract: Extreme storms in reef environments have long been recognized as a mechanism for depositing ridges of reef-derived coarse clastic sediment. This study revisits the storm ridges formed by Tropical Cyclone Bebe (1972) on Funafuti, Tuvalu and Tropical Cyclone Ofa (1990) on Upolu, Western Samoa in the South Pacific, and Hurricane Lenny (1999) on Bonaire, Netherlands Antilles in the Caribbean. Ridge characteristics produced by these storms include: heights of 1-4 m, widths of 8-50 m, and lengths up to 18 km. The ridges tend to be higher and steeper on their landward margins than on their seaward margins and are composed mostly of re-worked coral rubble derived from reef front settings with smaller amounts of fresh broken coral (5-30%). Characteristics of these modern gravel storm ridges can be used to help identify ancient storm deposits and to differentiate between other coarse-grained deposits such as those created by tsunamis.

INTRODUCTION

Extreme storms in coral reef environments are capable of constructing large ridges of reef-derived coarse sediment that can ultimately lead to island growth (Maragos et al., 1973). As early as 1904, David and Sweet (1904) recognized the importance of storms as an island-building mechanism and described older "hurricane banks" as an important component of atoll islet development from Funafuti, Tuvalu (Figure 1). McKee (1959) and Blumenstock (1961) were some of the first to examine storm impacts and sedimentation resulting from an extreme storm in a reef setting (Jaluit Atoll, Marshall Islands). Their observations included geomorphology and sedimentology descriptions of storm deposits such as reef flat gravel ridges

(ramparts), shore ridges, and gravel sheets.

This paper examines the characteristics of storm ridges created by Tropical Cyclone Bebe (1972) on Funafuti, Tuvalu, South Pacific, Tropical Cyclone Ofa (1990) on Upolu, Western Samoa, South Pacific, and Hurricane Lenny (1999) on Bonaire, Netherlands Antilles, Caribbean Sea. This study is not intended to be a synthesis of all storm-ridge deposits, but rather a description of particular sites where significant coral-gravel ridges were created by known events, and where the sizes, morphologies, textures, and positions with respect to sea level and the shoreline could be established.

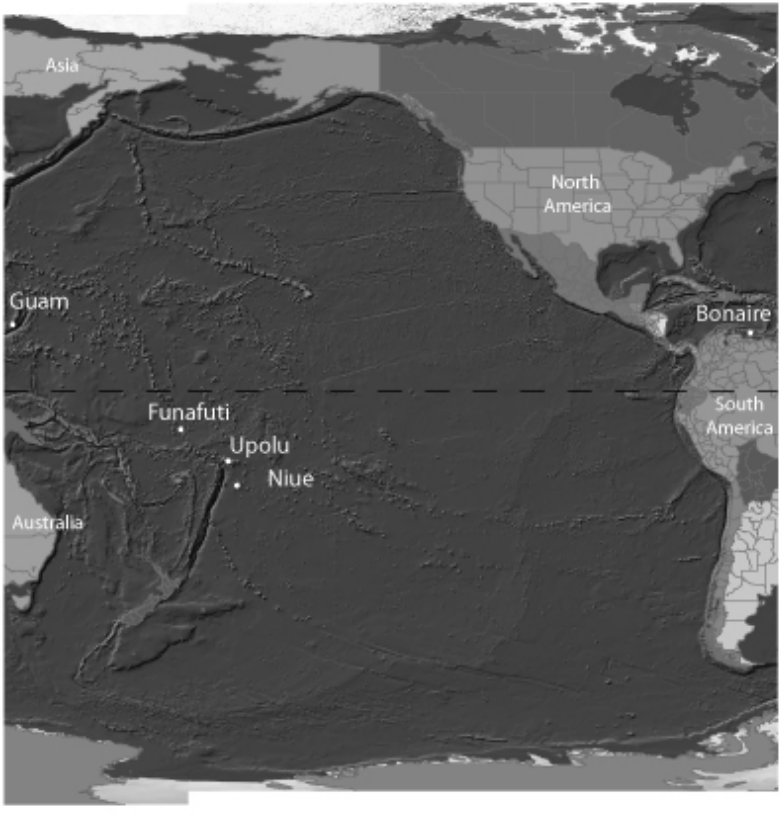

Figure 1. Locations of coral-rubble storm ridges studied.

CORAL-GRAVEL STORM RIDGE FORMATION

Brief Descriptions of the Studied Islands and Storms

The island of Funafuti is an atoll with near continuous islet development along its eastern (windward) margin and scattered islets along the western (leeward) and northern margins. A narrow reef rim surrounding a central lagoon is dissected by several deep passages that allow water exchange between the lagoon and open ocean. Tropical Cyclone Bebe was a category 3 storm (Saffir-Simpson scale) and one of only three severe storms to strike Funafuti in the last 140 years (Maragos et al. 1973). The slow-moving storm approached from the east with the eye passing directly over the atoll (note: cyclonic storms in the southern hemisphere rotate in a clockwise direction with most of the damage occurring in the left front quadrant). Much of the eastern side of the island was inundated by a wave (storm surge?) that exceeded 3 m (Baines et al. 1974).

Upolu is a high volcanic island bordered by both fringing and barrier reefs. The north shore of Upolu is characterized by a narrow coastal plain fronted by fringing reef that is reduced in width or absent opposite the major stream valleys (Richmond 1992a). Tropical Cyclone Ofa occurred in early February 1990 and was the strongest storm to strike Western Samoa in over 160 years (Elmqvist et al. 1994). The category 4 storm had winds in excess of 210 km/hr and passed within 160 km west of Upolu. Deepwater wave heights exceeded 7 m and were superimposed on a storm surge of 1.6 m (Rearic 1990). The strong winds and high waves caused extensive damage to buildings, roads, and natural habitats along the north coast of Upolu.

Bonaire is an uplifted and tilted high limestone island with a volcanic core and is surrounded by a narrow fringing reef system. Fringing reef and reef flats are best developed along the western shores. Much of the windward (east) coast is characterized by low coastal cliffs fronted by a steep nearshore zone. The cliffs are underlain by last interglacial reef deposits and vary in elevation from near present sea-level in the south, 5-8 m along the east and northeast coast, 3-9 m along the west and northwest coast, and 15 m along the north coast (Scheffers 2005). Hurricane Lenny was a category 3-4 storm that moved in an unusual easterly direction passing about 200 km north of Bonaire in November, 1999 (National Oceanic and Atmospheric Administration 1999). Lenny was the strongest storm to impact Bonaire in nearly 100 years and produced waves 6-8 m high along the Bonaire coast causing significant impacts along the western shores.

Although the islands studied represent three distinct types (atoll, high volcanic, and uplifted limestone), they have many similar characteristics including: impacts by infrequent major storms, prolific coral reef growth, well-developed reef flats, and nearshore reef areas capable of storing reef debris for subsequent mobilization and re-deposition by major storms.

Storm Ridge Characteristics

Studies by Maragos et al. (1973) and Baines et al. (1974) documented the impacts of Tropical Cyclone Bebe on the atoll of Funafuti. Bebe created a coral-gravel ridge in

excess of 18 km long and up to 4 m high along the southeast reef platform. The Bebe ridge averaged about 37 m in width and 30 m from the seaward edge of the reef. The base of the ridge on the reef flat was intertidal and the crest was above normal tide levels. The initial seaward face was concave in profile while the landward face formed a steep escarpment or avalanche face and the entire ridge was separated from the islet shorelines by a moat (Figure 2). The deposit was composed of cobble to boulder size coral rubble consisting of approximately 5% "fresh" coral and the remaining 95% previously rounded and re-worked coral clasts that had been stored in reef front environments. Internally the deposit was poorly sorted with some evidence of crude stratification. In addition to the storm ridge, "rubble tracts" or sheets of coral rubble, were deposited in some areas of the reef flats and islets. Landward of the Bebe ridge there is one or more older and higher storm ridges that form the backbone of windward Funafuti (David and Sweet 1904; Dickinson 1999; Richmond 1992b).



Figure 2. From right to left, the steep landward margin of the Bebe ridge, moat, and eroded beach from Funafuti. Photograph by Jim Maragos, December 1972.

Rearic (1990) examined the "cyclone banks" created by Tropical Cyclone Ofa along the north coast of Upolu a few months after their formation. In general, the ridge formed discontinuous segments (longest about 2 km long) presumably related to source material availability and offshore bathymetric conditions. The ridges were deposited on the intertidal reef flat approximately 10-20 m from the seaward reef edge and contain occasional low sections that are flooded during high tide resulting in the appearance of separate ridge segments. The ridge averaged 2-3 m in height with a maximum width of about 50 m. The landward avalanche face was steeper (~ 40 ^{o}) than the seaward face (~ 20°) (Figure 3). The internal ridge structure was generally

disorganized, clast supported, and with little or no sand present in the upper meter. There are no older ridge deposits landward of the Ofa ridges; however, rubble sheets on the reef flats may represent older re-worked cyclone deposits.



Figure 3. The seaward face of the Ofa ridge about two years after original deposition. Landward migration and reworking of the ridge has resulted in a sheet of coarse rubble on the seaward (to the right) reef flat (backpack for scale).

Scheffers (2005) described the characteristics of Hurricane Lenny deposits on the island of Bonaire. Lenny formed discontinuous coral gravel ridges along more than 18 km of west-facing Bonaire shoreline. The Lenny ridges were typically 1 m high, with a maximum of ~ 4 m, and they were relatively narrow at 8-10 m wide. There was no broad intertidal reef flat on Bonaire, therefore ridge deposition occurred just seaward of the existing shoreline. A coral-rubble spit was deposited partially across an embayment in northwest Bonaire where the maximum Lenny ridge elevation of 4 m was recorded (Figure 4). The Lenny deposits were composed of coral rubble with about 20-30% of the clasts being "fresh" coral fragments. The deposits were clast supported with minor initial sand component. As with the Bebe and Ofa ridges, the landward slope of the ridge was stepper than the seaward face. In many places the Lenny deposits lie seaward of older and higher gravel ridges.



Figure 4. Coral-rubble ridge constructed by Hurricane Lenny on the northwestern coast of Bonaire. This spit-like feature was reworked by Hurricane Ivan in 2004.

DISCUSSION

Storm Ridge Characteristics

There are several features common to the Bebe, Ofa, and Lenny storm ridges (Table 1), these include: a) A relatively even, gently curved seaward edge that is roughly reef/shore parallel; b) A sinuous landward edge with debris tongues and embayments; c) Ridge heights ranged from 1-4 m above the reef flat surface and varied from ~8-50 m wide; d) In cross section the ridges have steep faces on both their seaward and landward margins with the highest part of the ridge usually near the seaward edge and the steepest face occurring along the landward edge; e) The ridges are formed mostly of gravel-sized coral rubble derived from the adjacent reef. Most of the rubble is composed of previously eroded and rounded coral fragments that were stored in reef depositional sites and subsequently reworked and deposited by the storms. A smaller percentage of material (5-30 %) was derived from living coral that was broken during the storms; f) The gravel clasts of the seaward margin tend to be imbricated seaward, whereas the internal structure of the ridges are more disorganized but may contain some crude sub-horizontal bedding; g) Megaclasts of meter-sized reef material were moved by the storms but form a relatively minor component of the overall deposits; h) The ridges are subject to subsequent reworking by waves and tides and landward migration has resulted in a reduction of ridge size, and in the case of Bebe (Baines and McLean, 1976) and Lenny (Scheffers and Scheffers, 2006) deposits they have

merged with the pre-storm shorelines.

Table 1. Summary of Storm Ridge Characteristics

Ridge Characteristics	T.C. Bebe Funafuti, Tuvalu	T.C. Ofa Upolu, Western Samoa	H. Lenny Bonaire, N.A.
Height (m)	3.5 (ave) 4 (max)	2-3	1 (4 max)
Width (m)	37 (ave) 21-50 (range)	50+ (max)	10 (max)
Length (km)	19 (continuous)	2+	Discontinuous (4 km max)
Composition	Coral Rubble (~5% "fresh") (cobble-boulder size) (minor sand)	Coral Rubble (minor sand)	Coral Rubble (20-30% "fresh") (cobble-boulder size) (minor sand)
Maximum clast size	7x3x3 m	Boulder ?	12 t (Curaçao)
Distance from reef edge (m)	30 (ave)	10-20	Beach Ridges
Slopes(degrees) **L = landward** **S = seaward**	"steep escarpment" L 20-30 S (concave)	40 L 20 S	Steep L Gentler S
Older Ridge(s) Present	1+	None	1+
Internal Structure	Poorly-sorted	Clast supported. Disorganized	Clast supported.

The formation of coral-gravel storm ridges has been noted from a number of tropical settings but they are not produced on a regular basis during extreme storm events and the reasons for this paradox remain unclear. Funafuti, Upolu, and Bonaire are subject to seasonal high waves and storms but are outside of the main cyclonic storm pathways; hence, extreme storms are a relatively rare event for these islands. Islands that are impacted by storms annually, but only infrequently subjected to extreme storms, may produce and rework reef debris, storing it on the reef where it is available for storm ridge building during extreme events (Scoffin, 1993). It is possible that islands regularly impacted by hurricane force storms are less likely to accumulate reef debris in shallow submarine environments for later storm redeposition as ridges. For example, the island of Guam in the western Pacific is regularly struck by typhoons. Studies in the aftermath of Typhoon Russ (1990) on a coral rubble islet on the barrier reef rim of southern Guam, documented coral-gravel sheet deposition over island surfaces rather than ridge deposition on the reef flat (Jaffe and Richmond, 1992). Most of the island washover sediment was derived from the pre-storm beach with very little sediment originating from the living reef and shallow marine environment.

Older Storm Ridges

Although the processes of gravel ridge formation are poorly understood, there are several conditions that are necessary to develop a ridge structure and morphology. These include: elevated water levels associated with the storm passage, extreme waves, an abundant supply of coarse sediment, a suitable depositional substrate, and ample time (hours) for clast excavation, transport, and construction by the high frequency waves. Flooding before and concurrent with deposition of the ridge is necessary for construction of the steep avalanche face that characterizes the landward margin of a ridge. Rearic (1990) thought that the ridge structure may be analogous to a bedform (break-point bar?) formed predominantly by bedload transport under elevated water levels and extreme waves. On both Funafuti and Bonaire there are older, higher, and more massive ridge deposits than those formed either by Bebe or Lenny. For example, Figure 5 is a photograph of an older coral-gravel ridge from the southwest coast of Bonaire showing a wide range of sediment sizes (sand through gravel), crude bedding and distinct sand layers, and seaward imbrication of some of the larger clasts. The ridge stands nearly 5 m above the adjacent toe of the beach, is steep on both landward and seaward margins, and has ridge and swale topography landward of the crest (Figure 6). Although Bebe and Lenny are major storms of the last century there are geologic records of deposition by greater storm on both Bonaire and Funafuti.



Figure 5. Photograph of an older coral-gravel ridge on the southwest coast of Bonaire. The ocean is to the right. The red ticks on the scale are 10 cm apart.



Figure 6. Small-scale (meters) ridge and swale topography on landward side of coral-rubble ridge shown in Figure 5.

Along the east coast of Bonaire, there are spectacular coral-gravel ridges that dwarf the storm deposits described here (Morton et al. 2006; Scheffers, 2005). Compared to the deposits described in this paper, the windward ridges of Bonaire are larger, contain bigger clasts, and occur both near sea level and on elevated Pleistocene-reef wave-cut platforms 5 or more meters above present sea level. These ridge deposits contain many of the storm ridge characteristics described here, but on a larger scale. Their origin however has been ascribed to the work of a few extreme tsunami waves rather than multiple extreme storm wave events (Scheffers, 2004, 2005). Some of the criteria used by Scheffers (2004, 2005) to identify the windward ridges as tsunami depositional features include the presence of megaclasts (> 2 t), bimodal sediment distribution (i.e. sand and gravel mixture), deposition up to 400 m inland from the shore, and deposition on elevated reef platforms.

The characteristics of the coral-gravel storm ridges described in this paper and studies in the aftermath of the 2004 Indian Ocean Tsunami provide important criteria for distinguishing extreme storm-wave deposits from those produced by a tsunami. For example, the Indian Ocean tsunami of 2004 impacted thousands of kilometers of coastline bordered by coral reefs, yet no comparable ridge-like deposits have been described. Rather, tsunami generated deposits of coarse debris include coral boulder

fields of individual clasts and relatively thin sheets (< 1 m) of beach and reef sediment (Richmond et al. 2006). There is also some question regarding the relative ability of storms versus tsunami to transport megaclasts above sea level (Morton et al. 2006). Recent studies by Hall et al. (2006) have demonstrated that storms can quarry and transport megaclasts up to 50 m above sea level and form coarse-clast ridges. Another modern example is for Cyclone Heta, which in 2004 deposited 4-ton reef blocks 20 m above sea level on the cliff coast of the high limestone island of Niue (Russell Howorth, SOPAC, Suva, Fiji, pers. comm.).

Not all extreme storms in reef environments create ridge deposits and it is not clear why some storms create ridges and others do not. It does not appear to be storm power related, but rather a complex relationship involving sediment availability, storm characteristics including duration, and physical setting. What are the mechanisms that lead to ridge versus sheet deposition? What is the role coastal orientation relative to the storm track and how important is cross-shore versus longshore sediment transport processes in ridge formation? Does storm frequency and magnitude dictate whether or not a ridge forms? These are questions that remain unanswered.

CONCLUSIONS

Coral-gravel storm ridges are important depositional features in low-latitude coastal environments subject to intense cyclonic storms. The three depositional ridges studied here occur on diverse island types, but with similar physical settings including:

- Areas of relatively high reef productivity (i.e. abundant sediment source).
- Nearshore areas suitable for the storage of reef debris.
- Infrequent large storms that allow the accumulation of reef debris between events.
- Suitable coastal environments for storm deposits to accumulate (reef flats).

General characteristics of the three storm ridges include: ridge heights ranging from 1-4 m above the reef flat surface and varying from ~8 to 50 m wide; in cross section the ridges have steep faces on both their seaward and landward margins with the highest part of the ridge usually near the seaward edge and the steepest face occurring along the landward edge; the ridges are formed mostly of cobble-boulder sized coral rubble derived from the adjacent reef and most of the rubble is composed of previously eroded and rounded coral fragments; the gravel clasts of the seaward margin tend to be imbricated seaward, whereas the internal structure of the ridges are more disorganized but may contain some crude seaward-dipping beds; and, megaclasts of meter-sized reef material were moved by the storms but form a relatively minor component of the overall deposits.

ACKNOWLEDGEMENTS

We are grateful to Anja and Sander Scheffers and Dieter Kelletat for sharing their knowledge of the Bonaire deposits and for many interesting and provocative discussions regarding extreme waves and their deposits. Bruce Jaffe and Guy

Gelfenbaum provided hours of discussion both in and outside of the field and we thank them for many fruitful discussions. We greatly appreciate Jim Maragos for providing photographs of the initial Bebe deposits. Theresa Fregoso assisted with the figure preparation. This is dedicated to the memory of Doug Rearic.

REFERENCES

Baines, G.B.K., Beveridge, P.J., and Maragos, J.E., (1974). Storms and island building at Funafuti Atoll, Ellice Islands. *Proceedings 2nd International Coral Reef Symposium* 2,485-496.

Baines, G.B.K. and McLean, R.F. (1976). Sequential studies of hurricane deposit evolution at Funafuti Atoll. *Marine Geology* 21, M1-M8.

Blumenstock, D.I. (editor; 1961). A report on typhoon effects upon jaluit Atoll. *Atoll Research Bulletin* 75, 1-105.

David, T.W.E. and Sweet, G., (1904). The Geology of Funafuti, *in:* "The Atoll of Funafuti: Borings into a coral reef and the results," The Royal Society, London, p. 61-124.

Dickinson, W.R. (1999). Holocene sea-level record on Funafuti and potential impact of global warming on central pacific atolls. *Quaternary Research* 51, 124-132.

Elmqvist,T., Rainey, W.E., Pierson, E.D., and Cox, P.A. (1994). Effects of Tropical Cyclones Ofa and Val on the structure of a Samoan lowland rain forest. *Biotropica* 26(4), 384-391.

Hall, A.M., Hansom, J.D., Williams, D.M., and Jarvis, J. (2006). Distribution, geomorphology and lithofacies of cliff-top storm deposits: examples from the high-energy coasts of Scotland and Ireland. *Marine Geology* 232, 131-155.

Jaffe, B.E. and Richmond, B.M. (1992). Overwash variability on the shoreline of Guam during Typhoon Russ. *Proceedings 7th International Coral Reef Symposium* 1, 257-264.

Maragos, J.E., Baines, G.B.K., and Beveridge, P.J., (1973). Tropical cyclone creates a new land formation on Funafuti Atoll. *Science* 181, 1161-1164.

McKee, E.D., (1959). Storm sediments on a Pacific atoll. *Journal of Sedimentary Petrology*, 29: 354-364.

Morton, R.A., Richmond, B.M., Jaffe, B.E., and Gelfenbaum, G, (2006). Reconnaissance investigation of Caribbean extreme wave deposits – preliminary observations, interpretations, and research directions. U.S. Geological Survey Open-File Report 2006-1293 (available on-line at: http://pubs.usgs.gov/of/2006/1293/).

National Oceanic and Atmospheric Administration, 1999, Preliminary Storm Report on Hurricane Lenny, Nov. 16-19 1999 (http://www.srh.noaa.gov/sju/lenny.html)

Rearic, D.M. (1990). Survey of Cyclone Ofa damage to the northern coast of Upolu, Western Samoa. SOPAC Technical Report 104. SOPAC Technical Secretariat, Suva, Fiji.

Richmond, B.M., (1992a), Coastal geology of Upolu, Western Samoa, In: Keating, B.H. and Bolton, B.R., (eds.): *Geology and Offshore Mineral Resources of the Central Pacific Basin*, Circum-Pacific Council Monograph V. 14, pp. 101-125.

Richmond, B.M. (1992b). Development of atoll islets in the central Pacific. *Proceedings 7th International Coral Reef Symposium* 2, 1185-1194.

Richmond, B.M., Jaffe, B.E., Gelfenbaum, G., and Morton, R.A. (2006). Geologic impacts of the 2004 Indian Ocean Tsunami on Indonesia, Sri Lanka, and the Maldives. *Zeitschrift für Geomorphologie* Supplement Volume 146, 235-251.

Scheffers, A., 2004. Tsunami imprints on the Leeward Netherlands Antilles (Aruba, Curaçao, Bonaire) and their relation to other coastal problems. *Quaternary International* 120, 163-172.

Scheffers, A., 2005. Coastal response to extreme wave events – Hurricanes and tsunami on Bonaire. *Essener Geographische Arbeiten* Band 37, 96 pp.

Scheffers, A. and Scheffers, S. (2006). Documentation of the impact of Hurricane Ivan on the coastline of Bonaire (Netherlands Antilles). *Journal of Coastal Research* 22(6), 1437-1450.

Scoffin, T.P. (1993). The geological effects of hurricanes on coral reefs and the interpretation of storm deposits. *Coral Reefs* 12, 203-221.

FIELD OBSERVATIONS OF STEP DYNAMICS ON A MACROTIDAL GRAVEL BEACH

Daniel Buscombe[1], Martin J. Austin[2], Gerhard Masselink[3]

1. School of Geography, University of Plymouth, Drake Circus, Plymouth PL4 8AA. daniel.buscombe@plymouth.ac.uk
2. School of Earth, Ocean and Environmental Sciences, University of Plymouth, Drake Circus, Plymouth PL4 8AA. martin.austin@plymouth.ac.uk
3. School of Geography, University of Plymouth, Drake Circus, Plymouth PL4 8AA. gerd.masselink@plymouth.ac.uk

Abstract: A data set consisting of detailed measurements of the hydrodynamics, morphological and sedimentological change, and sediment transport, has been collected from the region of the beach step on a macrotidal gravel beach. The step is an accretionary feature which evolves with a different relaxation time to that of the berm. Initiation of the step requires relative tidal stationarity and is thought to be triggered by increasingly reflective conditions. Despite its location, the step has remarkably stable sedimentology, differentiated from the swash zone using sedimentary moments. Co-spectral analysis indicates that sediment transport in the region of the step is related to sub-incident wave frequencies. A reconstructed ensemble sediment transport event confirmed that sediment transport at the base of the step occurs as a negatively skewed wave, perhaps sensitive to wave groups. The transition matrix of the nearshore gravel bed motion data closely resembled that of a 'memoryless' queuing process.

INTRODUCTION

The step is a common feature on reflective coarse-grained sand and gravel beaches (Bauer and Allen, 1995). The presence of the step imposes a steep hydrodynamic gradient across the nearshore which controls wave breaking. In fact, the beach step has been considered analogous to a breakpoint bar common to sand beaches (Buscombe and

Masselink, 2006), which would imply it was a region of on/offshore sediment convergence. As well as controlling wave breaking, the importance of the step lies in the fact that it is a beach protective feature, providing a locally steepening the active beachface, thus maintaining reflectivity during storms (Hughes and Cowell, 1987). It is able to do this because it is remarkably responsive to the semi-diurnal tidal cycle (Strahler, 1966; Miller and Ziegler, 1958), even on macrotidal beaches. The lack of previous studies into beach step dynamics belittles its importance, and belies the fact that it is an interesting case study for coarse-grain beach morpho-sedimentary-dynamics. We sought to redress this fact by carrying out a series of detailed field experiments, taking a holistic approach to the step with context to its evolving hinterland, and measuring hydrodynamic forcing, morphological and sedimentological change, and sediment transport.

FIELD EXPERIMENT AND METHODS

A field experiment was carried out on 27th September 2005 at Slapton, a 4 km-long macrotidal gravel barrier beach in Devon, UK. According to the Jennings and Shulmeister (2002) classification scheme, Slapton is a 'pure' gravel beach morphotype. During the measurement period the intertidal gradient was tan β=0.23 (Fig. 1), with a median sediment size of ~6mm. For a more detailed description of the field site refer to Austin and Masselink (2006a). The aim was to collect high-resolution concurrent and co-located morphological, sedimentological and hydrodynamic data from the step region as it evolved over a 6 hour period around high tide (+/- 3 hrs). The experiment was one of a three similar experiments within a wider morpho-sedimentary monitoring campaign of Slapton, 16-30th September 2005 on a spring-spring tidal cycle. The 27th September data set was the most comprehensive, and coincided with a period of major berm building just after neap tide (Fig. 1). Until this time the beach had been morphologically relatively inactive (Fig. 1). This is the first time measurements of each hydro-, morpho-, and morpho-sedimentary-dynamics have been made in the field across the step on a gravel beach.

Two instrument rigs were deployed aligned cross-shore. The first maintained a pressure transducer (PT) and a bi-directional electromagnetic current meter (ECM) measuring water depth and cross-shore and alongshore velocity respectively, logging at 16Hz 3cm above the bed around mid-step position. The second was located at the base of the step and measured velocity at 0.1, 0.25 and 0.4 m above the bed with a vertical array of Acoustic Döppler Velocimeters (ADVs), logging at 32Hz, and an ECM logging at 16Hz. An underwater colour digital video camera was also located here to observe the bed, logging at 25Hz. Swash excursion was measured using an electrical resistance wire maintained at 2cm above the bed, logging at 16Hz. Morphological measurements were made every 5 minutes across the foreshore and nearshore beyond the base of the step using Sallenger and Richmond's (1984) rapid profile technique. In addition, manual sediment samples taken at regular 5 minute intervals on the foreshore, to be dried and sieved at 1/4Φ. An additional video camera recorded the entire experiment from an oblique position just beyond the berm crest.

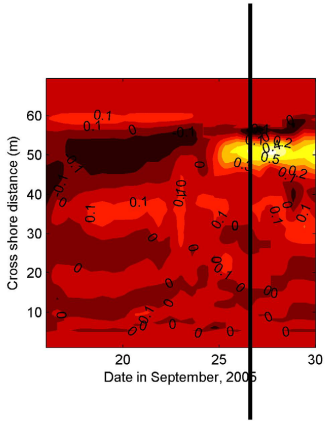

Fig (1) The antecedent morphological conditions prior to the experiment on the 27th (solid line) showing profile change (cm) relative to initial.

The size of gravel clasts and nature of gravel sediment transport precludes the use of optical and acoustic backscatter sensors to quantify sediment flux in the nearshore, which occurs almost exclusively as bedload and sheetflow. Instead, the underwater video was used as a measurement tool to quantify the magnitude of sediment transport (e.g. Williams, 1990; Stive et al. 2005). The video was decompiled into individual frames, converted to greyscale, and filtered for various sources to noise using powerful relaxed median (e.g. Hamza et al., 1999) and complex-valued log Gabor wavelet (Kovesi, 1999) filters. A two-dimensional correlation was applied between each consecutive frame, the reciprocal of which proved useful as a dimensionless 'bed motion coefficient', Ω sensitive to changes in bed 'texture' or gross (non-directional) bed mobility.

$$1/\Omega = \frac{\sum_m \sum_n \alpha\beta}{\sqrt{\left[\sum_m \sum_n (\alpha)^2\right] - \left[\sum_m \sum_n (\beta)^2\right]}} \quad (1)$$

where m and n denote dimensions of image ι, $\alpha = {}_{mn}(t) - \acute{\iota}_{mn}(t)$ and $\beta = {}_{mn}(t+1) - \acute{\iota}_{mn}(t+1)$ where the over-dash denotes mean and t denotes time. High values of Ω indicate poorer correlation, therefore most change, and most sediment transport.

RESULTS

Hydrodynamics

Figure 2 summarises the hydrodynamic forcing derived from the pressure record. Water depth varied by c. 0.75m on a slightly asymmetrical neap tide, wave height was maintained between 0.5 and 0.6m, and spectral wave period increased from c. 5 to 10s. The trend in wave skewness (Elgar and Guza, 1985) was one of increasingly negative skew, and the spectral wave field displayed two prominent peaks at 5 and 12 seconds, the relative prominence of the latter increasing with time. Directional deviations away from shore-normal were uncommon and unsustained.

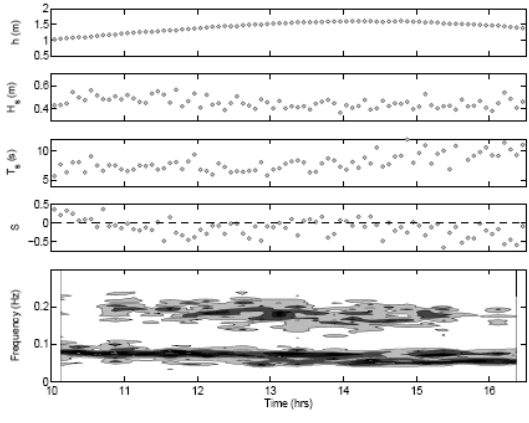

Fig (2). Hydrodynamic summary. Left panel (from top to bottom): water depth (m), significant wave height (m), significant wave period (s), wave skewness, and normalised spectral density (Hz m^2).

Morphodynamics

The pressure record was used to derived the surf scaling ε (Guza and Inman, 1975) and surf similarity ξ (Battjes, 1974) morphodynamic parameters for each 5 minute interval, using the 'active' intertidal slope, defined as the region of beachface between the 2% and 80% runup exceedance limits, measured with the resistance wire. The tidal translation rate (TTR) was calculated as the change in the 2% runup exceedance over consecutive 5 minute periods. The variation in these measures over the survey period may be seen in Fig. 3, where the period 10.45 – 11.30 has been highlighted since it was at this time that wave breaking regime moved from one of plunging/surging to fully surging. In the absence of significant change in wave steepness at this time, this change would have come about because the rising tide was advecting up an increasingly steep concave beach profile, making conditions more reflective. The surf scaling and similarity parameters are generally agreed to be taxonomic for sand beach morphodynamic state, but in the relative scarcity of a gravel beach studies it was thought prudent to substantiate and

validate the use surf similarity parameter to predict wave breaking on gravel beaches through independent means. Breakers were thus classified 'wave-by-wave' visually using the subaerial video record, and it was found that the agreement between visual observations and ξ was excellent. The wave breaker regime derived using visual observations from the video record is shown in the right panel of Fig. 3 (left), which shows the change in wave breaker type over the period 10.10 – 11.40, showing a marked transition between plunging and surging breaker types just before 11.00.

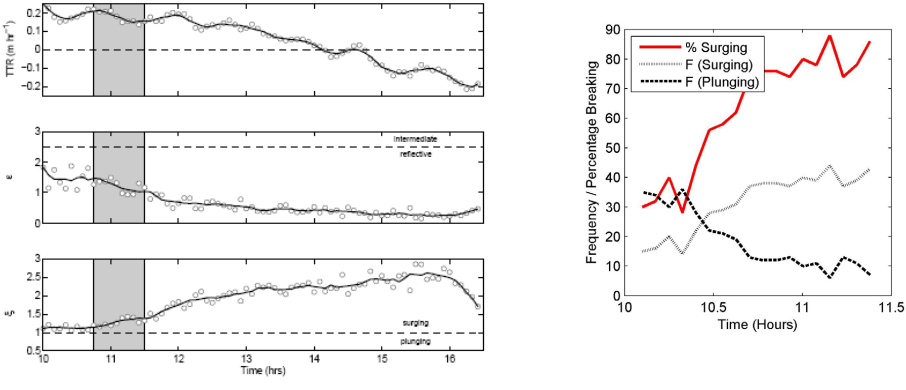

Fig (3). Left, from top to bottom: tidal translation rate (m hr^{-1}), surf scaling, and surf similarity. Grey patches on the right panels indicate the period 10.45 - 11.30 a.m. The solid black lines are a 5 point (25 minute) moving average. Right: changing wave breaker conditions based on video observations when step-berm morphologies begin to take hold.

A morphodynamic 'trigger' mechanism seems to control step initiation. Here, any causative relationships dictate that timing is crucial, i.e. whether the step begins to build before or after the change in wave breaking. If the step forms before the change in breaker type from plunging to surging, then that would be the necessary increase in slope to affect ξ, yet if the wave breaker transition precedes step formation then it is more likely that tidal excursion over a concave slope is key. The development of the step does not begin until after 11 a.m, by which time the change in hydrodynamic forcing has occurred.

Morphological change relative to initial was computed for every 5 minute survey of the beachface and nearshore, and the results are shown in the left panel of Fig. 4 (figures are in centimetres, therefore lighter shading represents relative accretion). The berm (at c. 53-50m) and step (at c. 58-56m) are clearly accretionary features, distinct from 'erosive' regions in the mid-swash (c. 56-53m) and nearshore (> 58m). Over the measurement period there is a net increase of 1.4 m^2 over each unit metre of beachface (contributed to predominantly by the berm). Incidentally, berm formation coincides almost exactly with the changing breaker regime, and we have no reason to suppose that berm formation did

not occur according to onshore swash asymmetry overtopping mechanisms of Hine (1979); Austin and Masselink (2006); and Weir et al. (2006), since gross morphological change is consistent with these earlier findings. The step and berm are effectively independent features forced by discordant timescales: the relaxation time of the berm is linked with spring-neap tidal cycle (Fig 1), whereas the relaxation time of step is linked with semi-diurnal tidal cycle, and relative tidal stationarity (Fig. 4), and with the mid-foreshore remaining a morphological 'pivot point'. With this latter point in mind, there is little evidence to support the notion that the step forms due to an onshore/offshore convergence of sedimentation (e.g. Miller and Ziegler, 1958).

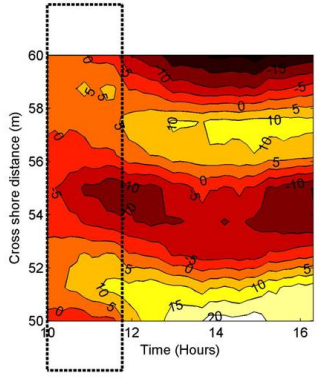

Fig (4) Morphological change, in cm, relative to initial (left panel) across the nearshore (seawards up the page) – light areas indicate accretion, dark depletion

Sediment Dynamics

The reported persistence of predominantly coarse sediments at the beach step (Miller and Ziegler, 1958; Bauer and Allen, 1995) dictates that the spatial and temporal characteristics of sediment size may have an important morphodynamic role, especially on gravel beaches (Sherman et al., 1993; Buscombe and Masselink, 2006) where the range of sediment size is so large. Spatial patterns of morpho-sedimentary variation are mixed over the entire foreshore (Fig. 5, both panels). Coarsening is associated with the development of step and berm features, but also with the depletion of material in the nearshore. Fining is associated with the upper foreshore, co-incident with removal of material, and step crest which is coincident with the deposition of material (Fig. 5, both panels). In a gross sense, each hydro-kinematic region thus has a distinct 'morpho-sedimentary domain', so it is possible to trace the gross trend of berm and step building-coarsening through time, and it may be seen that the mid-foreshore is a sedimentological as well as morphological pivot point. By contrast, the time-averaged grain size distribution remains relatively unchanged (i.e. no temporal trend).

Figure 6 reveals that step sediments are characteristically coarser skewed, more poorly sorted, and more platykurtic, than the sediments of the foreshore and berm. Despite the

location of the step, it has remarkably stable sedimentology, and it is thus possible to distinguish the step from the foreshore using sedimentary moments.

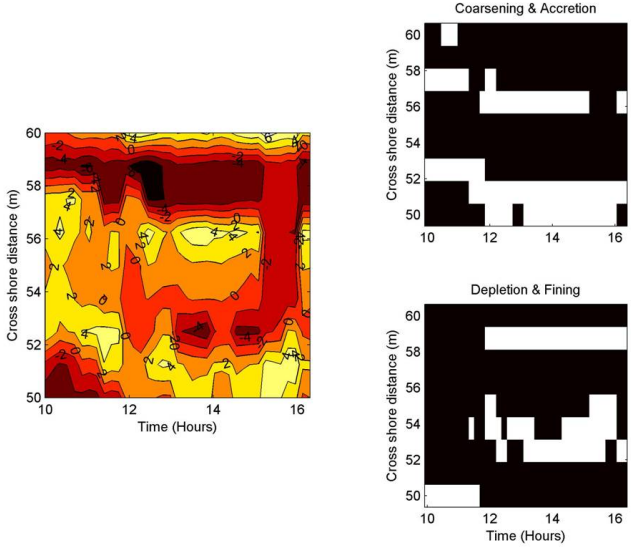

Fig (5) Sedimentological change (left panel), in mm, relative to mean size profile (lighter shading indicates coarsening); regions of morpho-sedimentary co-variation (right panels) – coexistence of relative sediment accretion and coarsening (top), and relative sediment depletion and fining (bottom).

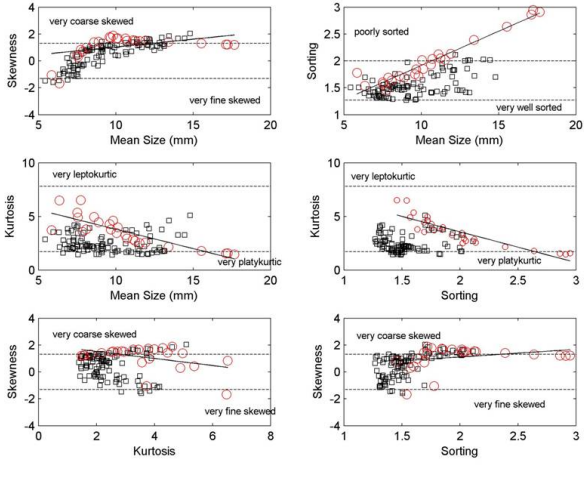

Fig (6) Bivariate scatterplots of geometric moments for swash/berm (black squares) and step (red circles) sediments. Solid lines show linear least squares fits through the step data;

dashed lines show dependent variable classification boundaries (Folk and Ward, 1957).

Sediment Transport

The limited amount of work which has quantified transport of gravel-sized sediment in coastal environments has been shown transport to be a highly irregular function of instantaneous fluid forcing and mechanistic properties of the bed. Heathershaw and Thorne (1985) demonstrated that the majority of gravel sediment transport under tidal currents occurs as short duration, turbulent and particular events, un-related to time-averaged flow parameters. Further work by Thorne (1986b), Williams (1990), Hardisty (1991) and others (generally in deeper water) demonstrated the role particle inertia and the various mechanical properties of the bed may have to play on the (therefore highly nonlinear) response of natural gravel sediments to nearshore flow velocity. What is clear from this work is that gravel sediment transport is dependent on both deterministic (e.g. oscillatory and mean flow velocities), and probabilistic phenomena (e.g. bed configurations, sediment properties, turbulence), but little work has been carried out to quantify sediment transport in the nearshore because of the measurement difficulties associated with such work. Recent researchers have emphasised the role of fluid accelerations (and associated horizontal pressure gradients) on coarse particle transport (e.g., Drake and Calantoni, 2001; Hoefel and Elgar, 2003; Stive et al., 2005).

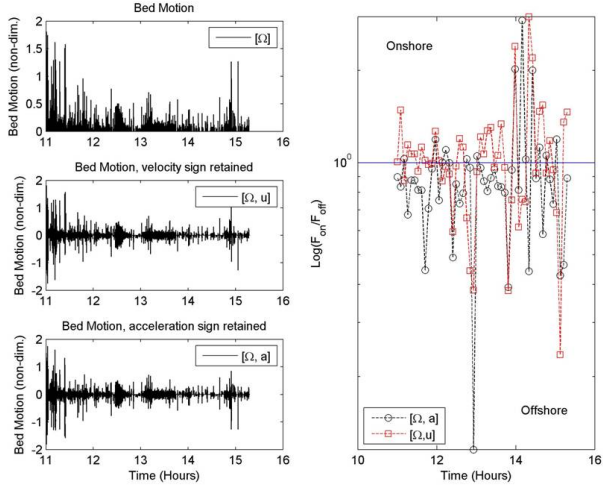

Fig (7). Magnitude-response diagram for Ω. The original time series of Ω is depicted in the upper left panel; the middle left panel shows Ω magnitude with the instantaneous directional component of velocity retained; and the lower left panel shows Ω magnitude with the instantaneous directional component of velocity acceleration retained. The right panel shows normalised bed motion magnitude (see text) for acceleration (black circles) and velocity (red squares).

The bed motion data was re-sampled to 4Hz to correspond with the velocity sample frequency. Upon visual inspection there was systematic bed motion response to neither velocity direction nor magnitude; acceleration direction nor magnitude. Indeed, bed motion induced by similar velocity or acceleration events was often very different in duration and magnitude. Assuming instantaneous sediment transport response to nearshore fluid motions, the sign of Ω was scaled according to the instantaneous directional component of velocity and acceleration (i.e. positive onshore, negative offshore), to yield +/-Ω_u and +/-Ω_a respectively, and the following calculations were performed for each 5 minute segment of data:

$$\delta_a = \log\left(\frac{\sum|\Omega_a|}{\sum|-\Omega_a|}\right); \quad \delta_u = \log\left(\frac{\sum|\Omega_u|}{\sum|-\Omega_u|}\right) \tag{2}$$

providing a ratio of time-averaged onshore:offshore dimensionless sediment flux, assuming instantaneous response to fluid forcing. Fig. 7 (right) shows these ratios over time, showing that in general values lie close to unity, however in general in can be seen that sediment flux which occurs when flows are accelerating offshore is greater than sediment flux which occurs when flows are accelerating onshore. Conversely, sediment flux is greater when velocity is directed onshore.

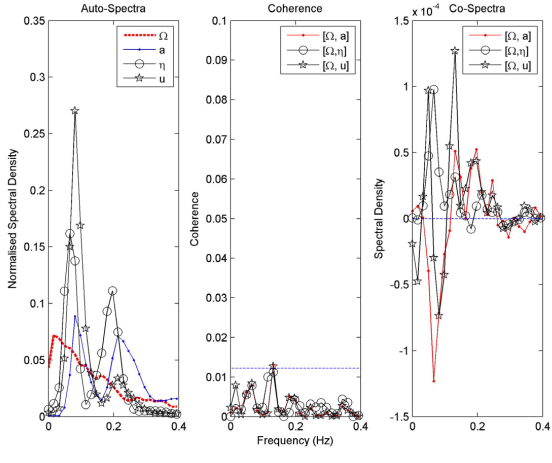

Fig (8) Spectral analysis of *u*, *a*, η and Ω. Left panel: autospectra of Ω (non-dim. Hz^{-1}) shown as red dashed line; η (m^2 Hz^{-1}) as open circles; *u* (ms^{-1} Hz^{-1}) as open stars; and *a* (ms^2 Hz^{-1}) as blue dots (note that the auto-spectra have been normalised by their total variance, e.g. m^2 $Hz^{-1}/\Sigma m^2$ Hz^{-1} for η). Middle panel: cross-spectral coherence (the dashed line is the 95% confidence interval) for [Ω, *a*], [Ω,*u*], and [Ω, η] denoted as red dots, open circles and stars respectively. Right panel: co-spectra for [Ω, *a*], [Ω,*u*], and [Ω, η] denoted as red dots, open circles and stars respectively

Figure 8 shows the spectral characteristics of the bed motion (Ω, Eq. 1) surface elevation (η), cross-shore current velocity (u) and cross-shore current acceleration (a). Auto-spectra for Ω showed peaks at low frequencies (0.03-0.05Hz), compared to the corresponding spectra of u and a which showed peaks at 0.08 and 0.2 Hz. These spectral peaks indicate a wave field composed of 12 and 5 second period waves, travelling in groups with a period of approximately 33 seconds. Cross correlation between the velocity envelope and a lowpass-filtered Ω (not shown – refer to Austin and Buscombe, *submitted*) shown a highly significant positive correlation at ~5 second lag. This could suggest that sediments respond strongest to sub-incident wave frequencies, which could mean that individual waves stir/destabilise sediments, and the largest wave(s) in a group carry out most of the transportation. Equally, it could indicate that the importance of the magnitude of the velocity event which transports most sediment is diminished, if the *sequence* of individual waves which are large enough to stir the bed is long enough. In which case, stress 'histories' are more important in the movement of clasts than instantaneous bed stresses (Paphitis and Collins, 2005).

Co-spectral analysis between Ω and u (e.g., Huntley and Hanes, 1987) showed very poor coherence and significance over the frequencies of interest (Fig. 8). Low coherence between velocity and transport suggests transport is highly intermittent, highly variable at swell frequencies, and clearly a highly non-linear function of flow velocity.

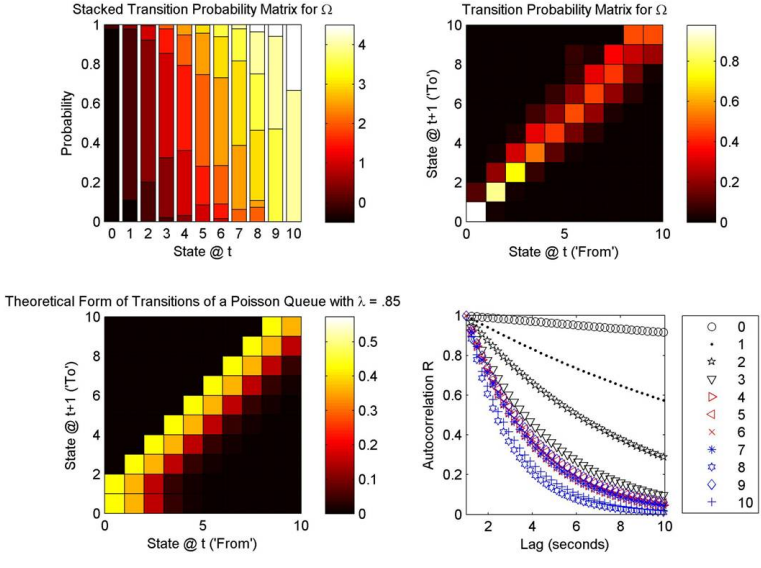

Fig (10) Sediment transport as a Markov chain: transition probability matrix for Ω_{rr} (top

panels); autocorrelation functions, R, for Ω_{rr} states (bottom panels)

In order to glean further information about the nature of bed motion, the data was analysed further using a probabilistic model in order to reconstruct an ensemble or 'typical' transport event. Dimensionless raw Ω was linearly rescaled to span the interval 0-10, and rounded to the nearest integer in order to obtain a discrete record Ω_{rr} which maintained similar resolution. A transition probability matrix (TPM) of the Ω_{rr} data was constructed (Fig. 10), and using Markov Chain theory (e.g., Kemeny and Snell, 1976), analysed for its general distributional form and persistence characteristics.

With reference to the TPM for Ω in Fig. 10, the absence of transitional extremes validates the sample frequency at which the data was collected. The transition matrix shows that sediment transport 'events' are in general negatively skewed. For example, the transition probabilities are not symmetrical about the inertial left-right diagonal, and the probability for an event of *increased* magnitude to follow an event of *given* magnitude is larger than the vice-versa (i.e. incline tendencies). Specifically, values of average magnitude have a larger transitional spread; therefore the skew in the wave will not be drawn by the mode (event peak) or tails but by the falling limb. In order to reconstruct the ensemble event the remaining information required is the persistence characteristics of every magnitude. The rank autocorrelation function of a Markov chain is given by (Basawa, 1972):

$$R = \frac{\sum_{i,j} ij\Theta_{ij} - \left(\sum_{i,j} i\Theta_{ij}\right)^2}{\sum i^2\Theta_{ij} - \left(\sum_{i,j} i\Theta_{ij}\right)^2} \tag{3}$$

where $\Xi_{ij} = \pi^T P^T$ such that $\Sigma_{ij}\Xi_{ij} = 1$, and where T, i,j, P, and π denote matrix transpose, row, column, transition matrix, and steady state probability vector, respectively. The steady state vector is found by solving the set of equations:

$$\pi = P\pi \tag{4}$$

subject to $\Sigma\pi = 1$. The autocorrelation functions for each magnitude are shown in Figure 10 (bottom right panel), showing an almost linear decrease in persistence with increasing magnitude. What this means in a physical sense is that a typical sediment transport event resembles a negatively skewed wave which is composed of a series of steps of increasing shorter length. This general form complies with visual inspection of the data, and could be interpreted as the first waves in a group 'clearing' the bed of a certain proportion of movable grains, until a threshold is reached where the conditions have been primed for the greatest amount of transport, after which the bed is relatively immobile. This implies a great deal of initial resistance to movement imposed by the micro-mechanical configurations of the bed (temporal and spatial distributions of grain size, 'hiding' factors, relative flow protrusion, etc).

The transition matrix for Ω (Fig. 10) resembled the theoretical form of a 'memoryless' Poisson queuing process, given by;

$$P_n(t) = e^{-\lambda t}\frac{(\lambda t)^n}{n!} \tag{5}$$

which expresses the probability of an event n in time t given by average number of occurrences per unit time, λ such that there would be λt events on average in t, implying inter-arrival times are exponentially distributed by $e^{-\lambda t}$, and the average number of events is the same for each unit interval of t, which is the 'memoryless' property (e.g. Kleinrock, 1975). For example, the TPM associated with a Poisson queue controlled by arrival rate λ=0.85 is depicted in Fig. 10 (bottom left). This draws strong parallels with similar work carried out on gravel sediment transport in fluvial settings (e.g. Einstein, 1937; Hassan et al., 1991).

CONCLUSION

The gravel beach step is an accretionary feature strongly linked to tidal stage, evolving with a different relaxation time to that of the berm. Initiation of step morphology requires tidal stationarity and is perhaps triggered by a change wave breaker type from plunging to surging. The beachface at short timescales is effectively a closed sedimentary unit although the step and beachface may be differentiated using sedimentary moments. Different morphological features such as the step have typical spatial sedimentary responses. Nearshore sediment transport is related to sub-incident frequencies (wave groups) but is not a linear function of either velocity magnitude or direction. Therefore, a better description of sediment transport requires instantaneous sediment size information, which has to be remotely sensed. It is possible to reconstruct an ensemble sediment transport event using the transitional properties of the data The transition matrix for bed motion resembled the theoretical form of a 'memoryless' Poisson queuing process.

ACKNOWLEDGEMENTS

Thanks to field assistants Tamsin Watt, Ben Allured, Jon Tinker, and George Graham. This work was funded by a faculty scholarship awarded to DB, and a post-graduate research grant awarded to MJA by the British Geomorphological Research Group. Thanks to Jon Tinker for improving the efficiency of the Markov chain computations.

REFERENCES

Austin, M.J., and Masselink, G. (2006a). "Observations of morphological change and sediment transport on a steep gravel beach," *Marine Geology* 229, 59-77.

Austin, M.J., and Buscombe, D. (submitted). "Morphological change and sediment

dynamics of the beach step on a macrotidal gravel beach," *Marine Geology.*
Bauer, B.O., and Allen, J. (1995). "Beach steps: an evolutionary perspective," *Marine Geology* 123, 143-166.
Battjes, J.A. (1974). "Surf similarity," *Proceedings 14th International Conference on Coastal Engineering* pp. 466-480, ASCE.
Buscombe, D., and Masselink, G. (2006). "Concepts in gravel beach dynamics," *Earth Science Reviews* 79, 33-52.
Drake, T.G., and Calantoni, J. (2001). "Discrete particle model for sheet flow sediment transport in the nearshore," *Journal of Geophysical Research* 106, 19859-19868.
Einstein, H.A., (1937). "*Bedload transport as a probability problem*," PhD Dissertation, Eidenoess. tech. Hochsch., Zurich, Switz. (English translation by W.W. Sayre, in "*Sedimentation"*, edited by H.W. Shen, Appendix C, H.W. Shen, Fort Collins, Colo., 1972).
Elgar, S., and Guza, R.T. (1985). "Observations of bispectra of shoaling surface gravity waves," *Journal of Fluid Mechanics* 161, 425-448.
Folk, R.L., and Ward, W.C. (1957). "Brazos River bar (Texas): a study in the significance of grain size parameters," *Journal of Sedimentary Research* 27, 3-26.
Guza, R.T., and Inman, D.L. (1975). "Edge waves and beach cusps," *Journal of Geophysical Research-Oceans* 80, 2997-3012.
Hamza, A.B., Luque-Escamilla, P.L., Aroza, J.M., and Roldan, R.R. (1999). "Removing noise and preserving details with relaxed median filters," *Journal of Mathematical Imaging and Vision* 11, 161-177.
Hassan, M.A., Church, M., and Schick, A.P. (1991). "Distance of movement of coarse particles in gravel bed streams," *Water Resources Research* 27, 503-511.
Heathershaw, A.D., and Thorne, P.D. (1985). "Sea bed noises reveal role of turbulent bursting phenomena in sediment transport by tidal currents," *Nature* 31, 339-342.
Hine, A.C. (1979). "Mechanisms for berm development and resulting beach growth along a barrier spit complex," *Sedimentology* 26, 333-351.
Hoefel, F., and Elgar, S. (2003). "Wave-induced sediment transport and sand bar migration," *Science* 299, 1885-1887.
Hughes, M., and Cowell, P. (1987). "Adjustment of reflective beaches to waves," *Journal of Coastal Research* 3, 153-167.
Huntley, D.A., and Hanes, D.M. (1987). "Direct measurement of suspended sediment transport," *Coastal Sediments '87*, pp. 723-737, ASCE.
Jennings, R., and Shulmeister, J. (2002). "A field based classification scheme for gravel beaches," *Marine Geology* 186, 211-228.
Kemeny, J.G, and Snell, J.L. (1976). "*Finite Markov Chains*, *2nd edition.*" Springer-Verlag, New York.
Kleinrock, L. (1975). *"Queueing Systems Volume 1: Theory."* Wiley Interscience, New York.
Kovesi, P. (1999). "Phase preserving de-noising of images," *The Australian Pattern Recognition Society Conference, DICTA'99*, pp. 47-67.
Miller, R.L., and Ziegler, J.M. (1958). "A model relating dynamics and sediment pattern in equilibrium in the region of shoaling waves, breaker zone, and foreshore," *Journal of Geology* 66, 417-441.

Paphitis, D., and Collins, M.B. (2005). "Sand grain threshold, in relation to bed 'stress history': an experimental study," *Sedimentology* 52, 827-838.
Sallenger, A.H., and Richmond, B.M. (1984). "High frequency sediment level oscillations in the swash zone," *Marine Geology* 60, 155-164.
Sherman, D.J., Orford, J.D., and Carter, R.W.G. (1993). "Development of cusp-related, gravel size and shape facies at Malin Head, Ireland," *Sedimentology* 40, 1139-1152.
Stive, M.J.F., Reniers, A.J.H.M., Terrile, E., and Verhagen, H.J. (2005). "Coarse particles' threshold of motion under shoaling waves," *Coastal Dynamics '05*, ASCE.
Strahler, A.N. (1966). "Tidal cycle of changes in an equilibrium beach Sandy Hook, New Jersey," *Journal of Geology* 74, 247-267.
Thorne, P.D. (1986b). "An intercomparison between visual and acoustic detection of seabed gravel movement," *Marine Geology* 72, 11-31.
Weir, F., Hughes, M., and Baldock, T.E. (2006). "Beachface and berm morphodynamics fronting a coastal lagoon," *Geomorphology* 82, 331-346.
Williams, J.J. (1990). "Video observations of marine gravel transport," *Geo-Marine Letters* 10, 1432-1157.

LARGE-SCALE SCOUR OF THE SEA FLOOR AND THE EFFECT OF NATURAL ARMOURING PROCESSES, LAND RECLAMATION MAASVLAKTE 2, PORT OF ROTTERDAM

Sander Boer[1], Edwin Elias[2], Stefan Aarninkhof[3], Dano Roelvink[4], Tiedo Vellinga[5]

1. Infram, PO Box 16, 8316 ZG Marknesse, The Netherlands, Tel. +31 (527) 241120, sander.boer@infram.nl
2. US Geological Survey, 345 Middlefield Road, m.s. 999, Menlo Park, CA 94025, USA, Tel. (650) 329-5475, eelias@usgs.gov (formerly Delft Hydraulics)
3. Royal Boskalis Westminster nv, P.O. Box 43, 3350 AA Papendrecht, The Netherlands, Tel. +31 (78) 6969415, s.g.aarninkhof@boskalis.nl (formerly Delft Hydraulics)
4. UNESCO-IHE and WL | Delft Hydraulics, P.O. Box 3015, 2601 DA Delft, The Netherlands, Tel. +31 (15) 2151715, d.roelvink@unesco-ihe.org
5. Delft University of Technology and Port of Rotterdam, P.O. Box 6622, 3002 AP Rotterdam, The Netherlands, Tel +31 (15) 2521309, t.vellinga@portofrotterdam.com

Abstract: Morphological model computations based on uniform (non-graded) sediment revealed an unrealistically strong scour of the sea floor in the immediate vicinity to the west of Maasvlakte 2. By means of a state-of-the-art graded sediment transport model the effect of natural armouring and sorting of bed material on the scour process has been examined. Sensitivity computations confirm that the development of the scour hole is strongly reduced due to the incorporation of armouring processes, suggesting an approximately 30% decrease in terms of erosion area below the -20m depth contour.

INTRODUCTION

Rotterdam is creating a prime new European location for port activities and industries which will be reclaimed from the sea, linking directly to the current port and industrial zone. The total land reclamation known as Maasvlakte 2 will consist of 1,000 hectares of commercial sites for deep sea container handling, chemical industry and distribution (figure 1).

The most obvious spot for the new port is situated in an area known as Natura 2000 site Voordelta, a Special Area of Conservation (SAC) (figure 2). Safeguarding the natural values of the Voordelta was one of the leading principles on which the design of Maasvlakte 2 is based.

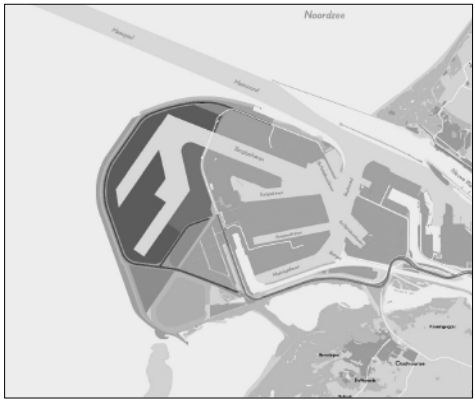

Figure 1. Design of Maasvlakte 2

The effects of the construction, presence and use of Maasvlakte 2 have been determined by means of an Environmental Impact Assessment (EIA) and an Appropriate Assessment (AP) of the effects on SAC. The Maasvlakte 2 project includes compensation projects for the natural values which will or may be lost. Compensation will be found in the realization of a 25.000 ha marine reserve and 35 ha new dunes. In this way the foundation is laid for the construction of a functional and optimal accessible port area, while impact on the natural features and the environment is limited and compensated to the greatest possible extent.

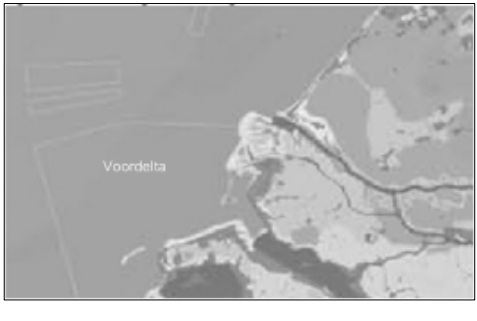

Figure 2. Natura 2000 site Voordelta

Within the framework of the Maasvlakte 2 project extensive studies have been executed to determine the impact of Maasvlakte 2 on the existing current pattern and the transport of sand and silt, and the resulting morphological changes.

In this paper specific attention is given on the issue of large scale scour of the surrounding sea floor, which is important from various perspectives, viz.:

- environmental effects: erosion of the sea floor below NAP -20m needs to be compensated in view of loss of habitat and loss of potential feeding area, for protected birds that tend to feed not deeper than -20m.
- maintenance need of the sandy sea defence of Maasvlakte 2: extent and location of the scour hole may cause additional erosion of the beach and dunes.
- dredging requirements: sand originating from the scour hole may cause additional accretion of the existing access channel to the port of Rotterdam (Maasgeul).

SCOUR DEVELOPMENT PRESENT SITUATION

The present port entrance dates from the period 1968-1976 (figure 3). Regular bathymetrical surveys have been carried out during construction and after completion of the works. Surveys were executed both in the immediate vicinity of the works in progress (Zuiderdam and Noorderdam) and in a larger sea area to the west of the Maasvlakte.

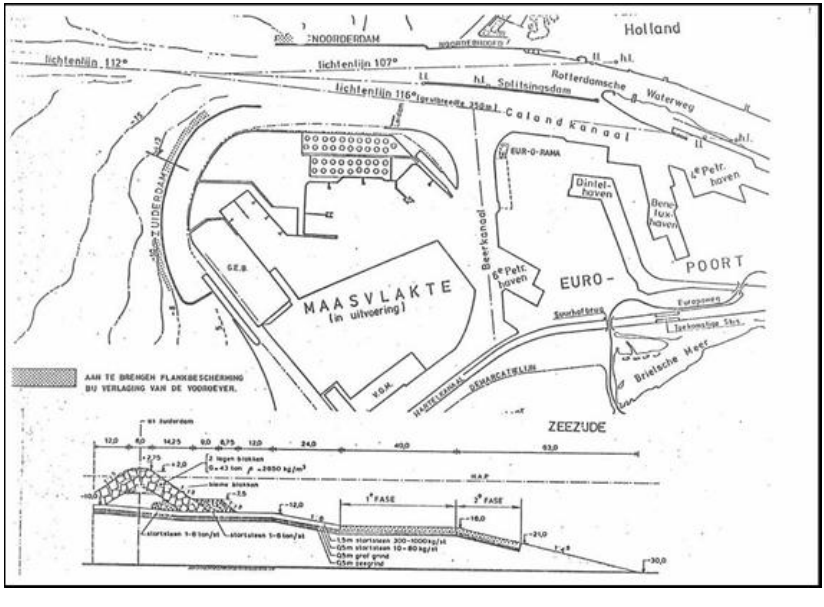

Figure 3. Original situation

During construction local erosion was observed along the Zuiderdam moving along with the temporary head of the structure. At two locations the erosion remained present during a longer period: along the southern bend of the Zuiderdam, at the transition from the rock protection to the sandy beach, and 2 km northward of it, approximately along the middle part of the Zuiderdam (figure 3).

During construction only limited erosion was observed at larger scale: erosion rates between 1970 and 1976 were approximately 0.1 to 0.2m per year in the immediate vicinity to the west of the Maasvlakte. Locally, also areas with some accretion were found: accretion rates were less than 0.1m per year.

After completion of the port entrance erosion in the sea area to the west of the Maasvlakte has continued. However, successive bathymetrical surveys indicate that the erosion process gradually has slowed down over the years. Presently, the scour hole has reached more or less an equilibrium state (figure 4). The scour hole exists nearly along the whole outer contour of the Zuiderdam covering an area of approximately 160 hectares. The maximum bottom depth is approximately NAP -18m. This implies that since 1970 a maximum erosion of approximately 6 m has occurred (based on the initial depth of NAP -12m).

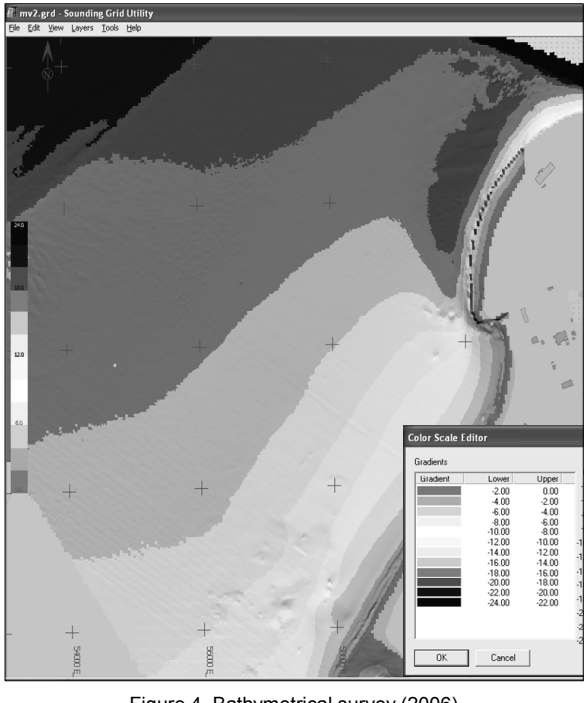

Figure 4. Bathymetrical survey (2006)

The design of Maasvlakte 2 shows much agreement with the presently existing situation. Computations for the situation of Maasvlakte 2 indicate that the main flow characteristics in the future situation will undergo only little changes as compared to the present situation. Therefore, it is reasonable to expect that the development of scour in the future situation with Maasvlakte 2 will show much resemblance to that of the present situation.

Table 1. Morphodynamic modules DELFT3D system

DELFT2D-MOR: this process based module which is a subset of DELFT3D system is designed to simulate sediment transports and morphological developments in coastal, river and estuarine areas (Roelvink and Van Banning, 1994). The 'standard' morphodynamic method involves a coupled simulation of waves, currents, transport and bottom changes. A morphological process is built up from morphological time steps, which consist of a simulation of wave-current interaction over a tidal cycle, followed by a number of intermediate steps where transport is computed and averaged over a tidal cycle, and the bottom is updated. The transport and bottom computations are repeated a number of times using "continuity correction" (= constant discharge trough cells), until bottom changes are so large that a full hydrodynamics computation is required. The method requires full transport computations through tidal cycle, which can be time-consuming especially when suspended-load transport induced by waves and currents in shallow areas is to be accounted for.
DELFT2D-RAM: this hybrid module which is also a subset of DELFT3D system can be applied for Rapid Assessment of Morphology (Roelvink et al., 2001). The RAM module can be characterized as a 'quick-and-dirty' bottom updating scheme (based on the "continuity correction') in combination with repeated detailed computations of hydrodynamics and sediment transport using DELFT2D-MOR.
DELFT3D-ONLINE: this module which is the latest refinement of Delft3D system can operate in 2DH and in 3D mode. The module is characterized by online coupling between hydrodynamic and transport/bottom modules which enables simultaneous computation of flows and transports and simultaneous feedback to bottom changes. Therefore, hydrodynamic flow calculations are always carried out using the correct bathymetry. Only the wave model is executed separately. Acceleration of the morphological developments is achieved by up-scaling the bottom developments during each time step by means of a so-called morphological scaling factor. In this project the Delft3D-ONLINE module was used in 2DH mode. The Maasvlakte 2 computations have been carried using a recently developed calculation scheme in which the simulation is split into a number of parallel processes, which all represent different conditions; at a given frequency all processes provide bottom changes to the merging process, which returns a weighted average bottom change to all processes which then continue the simulation (Roelvink, 2006).

MORPHODYNAMIC COMPUTATIONS

The morphological impact of Maasvlakte 2, including the issue of large scale scour of the surrounding sea floor, has been determined on the basis of morphodynamic computations. Thereby use has been made of the integrated modelling system Delft3D developed by WL|Delft Hydraulics, including the modules Delft2D-RAM, Delft2D-MOR and Delft3D-ONLINE (Table 1). For the various investigations, which were carried out in the course of time, always modules with latest functionalities and improved usability have been used.

In this paper only results from the most recent studies which were carried out in 2005 and 2006 for the current lay-out of Maasvlakte 2 will be presented (figure 1).

Study 2005 (Roelvink and Aarninkhof, 2005)

The set-up and execution of this study elaborated as much as possible on earlier investigations in order to enable the comparison of the results (e.g. wave- and current conditions, bed material characteristics, roughness size). However, the most important shortcomings of the previously used Delft2D-RAM/MOR module were overcome by:

- the use of the wave propagation model SWAN and the DELFT3D-ONLINE approach which was required for a realistic reproduction of bottom changes in the shallow areas of the Voordelta site.
- the incorporation of wave effects which was considered to be important for the development of the scour hole and the maintenance of the sandy beach and dunes.

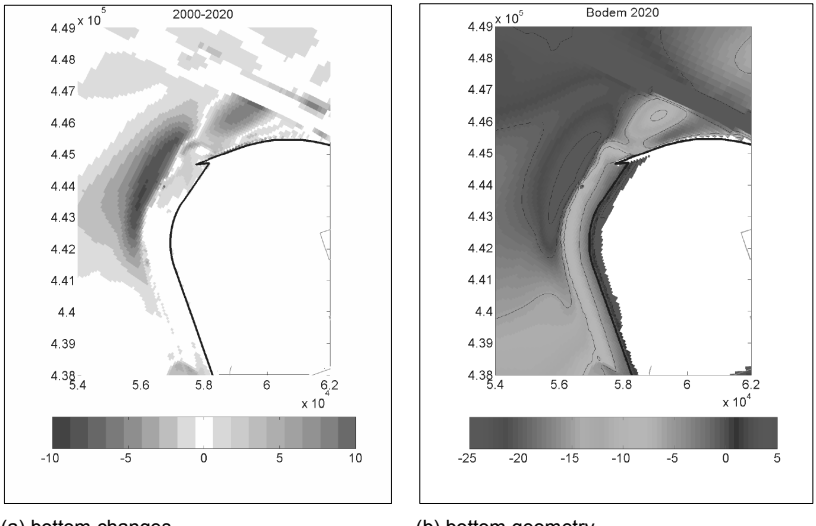

(a) bottom changes (b) bottom geometry

Figure 5. Computation DELFT3D-Online (2005)

In figure 5 a typical example of the morphological development is given after 20 years. Both (a) the erosion- sedimentation pattern and (b) the final bottom geometry are shown. It appears that a scour hole will develop almost along the entire north-westerly coastline of Maasvlakte 2. A depth of NAP-25m is exceeded in a rather large area. Sand originating from the scour hole is mainly deposited in the access channel but also in the area to the north of Maasvlakte 2 accretion can be observed.

The location of the scour hole agrees very well with the area with maximum tidal current velocities during flood phase (figure 6).

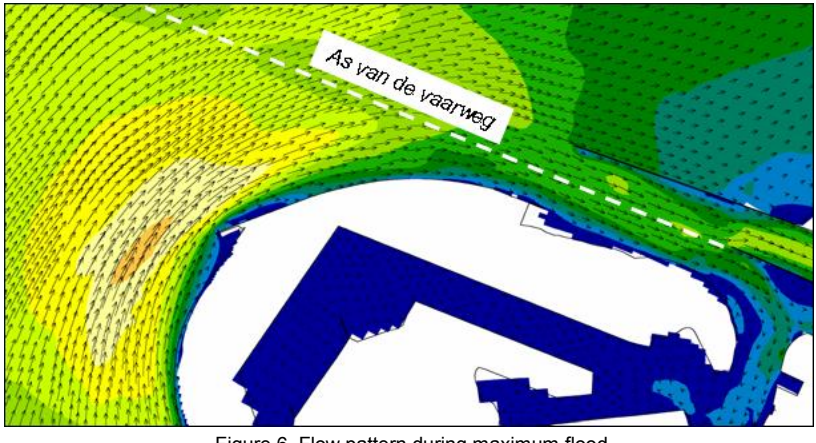

Figure 6. Flow pattern during maximum flood

In Figure 7 the time development of the scouring is shown in terms of (a) the area subjected to erosion with a depth larger than 1 m, (b) the area which is eroded below NAP-20m and (c) the maximum erosion depth. The applied model and the associated input parameters result after 20 years in a scour hole with a size of 1420 hectare. The area below NAP -20m is about 760 ha and the maximum depth is about NAP-27m.

From these figures it can be seen that the process of scour continues after 20 years and that equilibrium is not yet reached. A similar calculation for the existing situation (autonomous situation) also showed a persistent scour for the next 20 years. These unrealistically strong developments do not correspond with the experience from the existing Maasvlakte. The observed scour is much smaller than the calculated scour. The calculated size and depth of the scour hole for the situation of Maasvlakte 2 are therefore considered as rather conservative estimates.

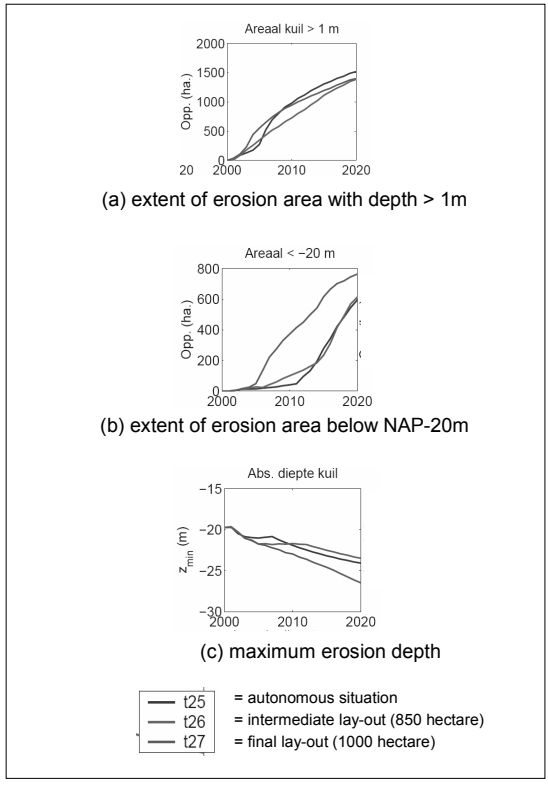

Figure 7. Computation DELFT3D-Online (2005)

Study 2006 (Elias et al., 2006)

Further analysis revealed that the overestimation could be related to the schematization of the sea floor by means of uniform non-graded sediment with a mean particle size of 160 micron.

From literature it is known that sorting of graded bed material and natural armouring of the surface bottom layer may result in a strong reduction of the scouring process. Also a heterogeneous composition of the sub-sea floor may have a strong impact. Until recently experience with the modelling of graded material was mainly restricted to river applications; for coastal areas such applications were still rare. However, with the latest version of DELFT3D this process can be simulated in a schematized way by distinguishing several sediment fractions and bottom layers.

Within the framework of the Maasvlakte 2 project the graded sediment model has been applied to carry out sensitivity computations. The computations are of a comparative nature not aiming at providing an accurate prediction of the location and extent of the scour hole. The latter can only be achieved by extensive calibration and verification of the model and the incorporation of the effect of both wave-induced and current-induced sediment transports.

1. Case IJmuiden

Because only little experience with the model existed, a concise investigation of the scour hole near the harbour moles of IJmuiden has been conducted firstly. The underlying reasoning is that this scour hole is well measured and documented. Also some studies with DELFT3D for this area have been carried out in the past (Roelvink et al., 1994; Lesser et al., 2004).

From these computations the correct functioning of the model was demonstrated. The sorting process of bed material in the scour hole by erosion of finer fractions and lagging behind coarser fractions could be reproduced in a satisfactory manner (figure 8). Also a lot of experience was obtained about the best way of schematisation, viz.: number of layers, layer thickness and fractional partition of bed material.

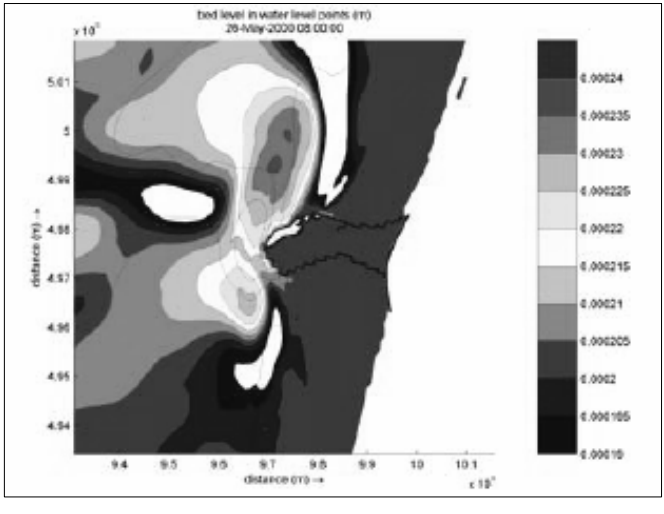

Figure 8. IJmuiden, spatial distribution of mean grain size (after 20 years)

2. Case Maasvlakte 2

Subsequently, computations have been performed for the situation of Maasvlakte 2 using the graded sediment model. The set-up of the model was, wherever possible, chosen in accordance with the previous study of 2005.

Computations were carried out for uniform and graded bed material. For the computations with uniform sediment a number of mean particle sizes have been distinguished, viz: 160 and 200 micron (overall values entire area) and 160/285 micron (with a distinction between the characteristics of seabed and cross-shore profile of Maasvlakte 2). The characteristics of the graded material have been derived from grading curves determined from soil drilling samples collected in the area during a survey in 2005 (figure 9).

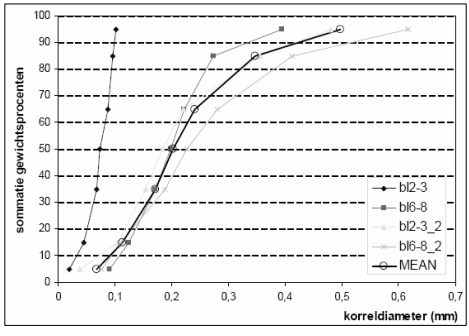

Figure 9. Grading curves from soil drilling samples collected in the area

The bed material is schematized using the average grading curve represented by 5 sediment fractions (Table 2).

Table 2. Sediment fractions

Fraction	D50 (micron)	relative distribution (%)
1	91	20
2	171	30
3	242	30
4	347	10
5	487	10

It appears that the average D50 of the bed material is 200 micron. This is considerably larger than the value of 160 micron which was used in all previous computations of Maasvlakte 2 (as a representative mean value of the whole study area). Further on it is seen that this difference in particle size will already have some impact on the development of the scour hole.

In the original computations several schematizations for the sub-sea floor were tested. The results presented in this paper only refer to the schematization with 15 bottom layers each layer having a thickness of 1 m.

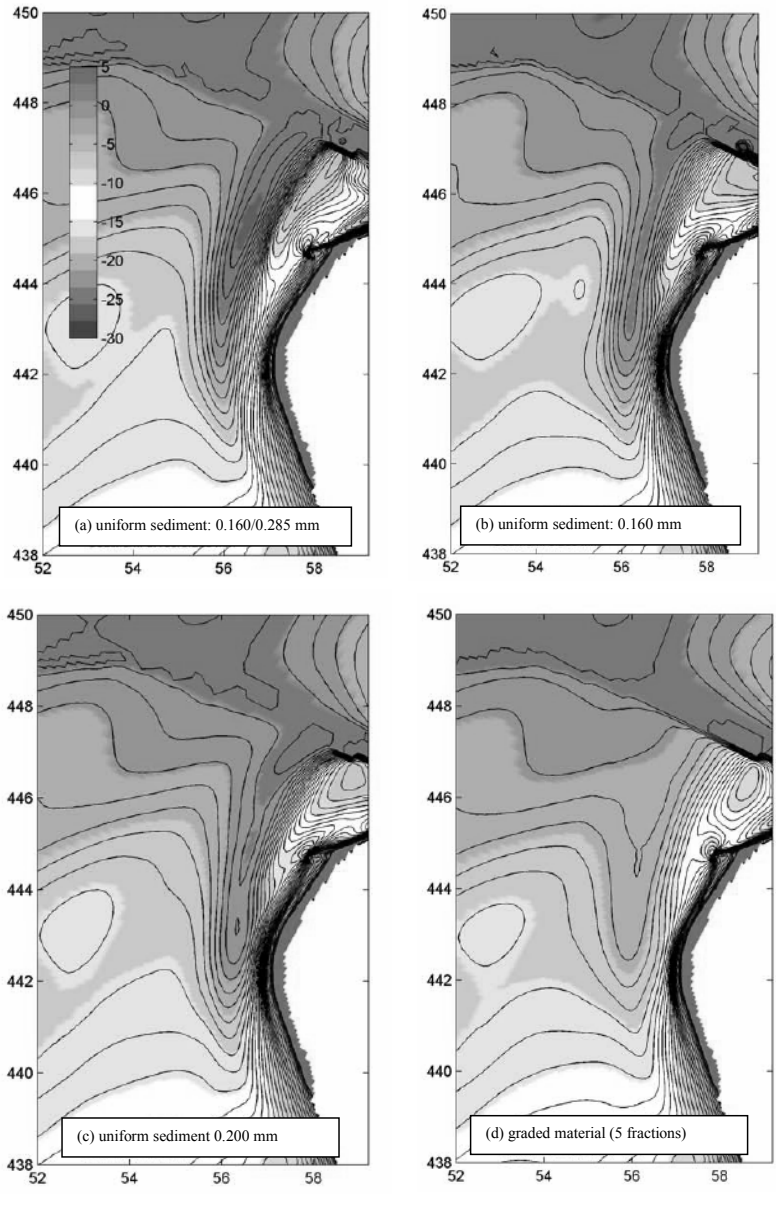

Figure 10. Example DELFT3D-Online (2006)

In figure 10 the calculated bottom geometry after 20 years is shown for the various simulations with uniform and graded bed material. From this figure the difference between graded and uniform material can be seen very clearly. With graded material the maximum erosion depth and the extent of the erosion area are strongly reduced. The results of the cases with uniform material are very similar to the results of previous studies. Some differences in extent and depth of the scouring hole can be observed, depending on the particle size. However, the general shape of the scouring hole remains the same in these cases.

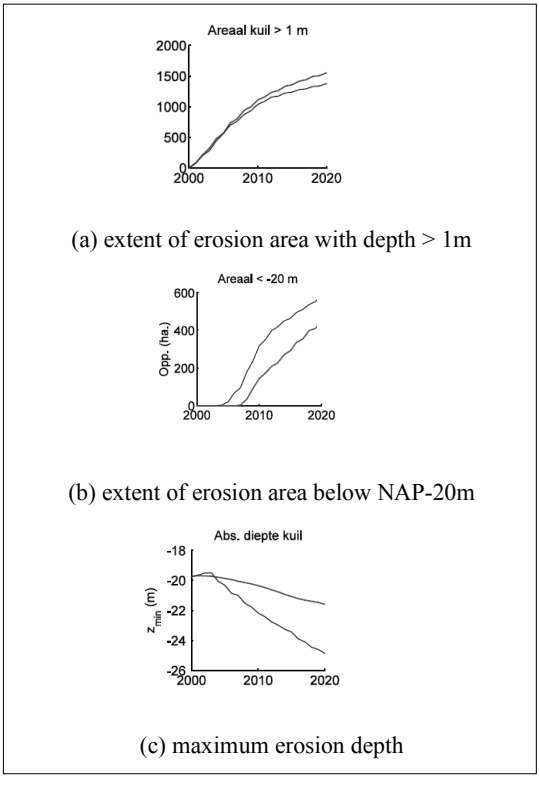

Figure 11. Example DELFT3D-Online (2006)
(bottom material: red - uniform; blue -graded)

In figure 11 a comparison is made between the computational results with graded bed material and uniform bed material (with a D50 of 200 micron). The differences between these two cases are both related to the maximum scour depth and the extent of the erosion area. With uniform bed material a maximum depth of more than 10m below the

original bottom level is reached after 20 years (NAP -26.5m). With graded material this is reduced to 4m (NAP-20.5m). With the effect of graded material incorporated the development of the scour hole is strongly reduced; an approximately 30% reduction in terms of the area below the NAP-20m depth contour is suggested.

CONCLUSION

Morphological predictions on the basis of uniform (non-graded) sediment revealed an unrealistically strong development of a scour hole in the area directly west of Maasvlakte 2. Additional calculations with a state-of-the-art graded sediment transport model have shown that armouring effects and sorting of the bed material do indeed reduce the depth and extent of the scour hole. By means of sensitivity calculations the impact of armouring on the scour development has been examined. The calculations confirm that the incorporation of armouring processes have a strong impact on the development of the scour hole, suggesting an approximately 30% decrease in terms of the area below the NAP-20m depth contour.

In summary, the use of an innovative, graded sediment transport model has shown the potential for improved prediction of the morphological evolution of scour holes. These techniques enable the Port of Rotterdam to anticipate well on the expected scour hole development, the resulting access channel maintenance and additional compensation for the scour below NAP-20m in the planned marine reserve. Additionally the model can contribute importantly to future EIA's for large-scale coastal interventions.

ACKNOWLEDGEMENTS

We thank the Port of Rotterdam Authority giving this opportunity to publish and to present the results of the research in question at the Coastal Sediments '07.

REFERENCES

Elias, E., Aarninkhof, S.., Roelvink, J.A. (2006). Ontwikkeling Ontgrondingskuil bij Maasvlakte 2, Z4114.00, WL| Delft Hydraulics (in Dutch).

Lesser, G.R., Roelvink, J.A., van Kester, J.A.T.M., Stelling, G.S., (2004). Development and validation of a threedimensional model, Coastal Engineering 51, pp. 883915.

Roelvink, J.A. and Banning, G.K.F.M. van (1994). Design and development of Delft3D and application to coastal morphodynamics, Hydroinformatics 94, Verwey, Minns, Babovic & Maksimovic (eds), Balkema, Rotterdam, 1994, pp. 451-455.

Roelvink, D., Boutmy, A., Stam, J.M. (1998). A simple method to predict longterm morphological changes. Proceedings of the 26th International Conference on Coastal, Engineering, Copenhagen. ASCE, New York, pp. 3224–3237.

Roelvink, J.A., Jeuken, M.C.J.L., van Holland, G., Aarninkhof, S.G.J. and Stam, J.M.T. (2001). Long-term, process-based modelling of complex areas. Proceedings of Coastal Dynamics '01, Lund, Sweden, June 2001. New York, ASCE, 383–92.

Roelvink, J.A., Aarninkhof, S.G.J. (2005). Onderbouwend onderzoek MER Maasvlakte2. Onderdeel Morfologie. Z3959, WL/Delft Hydraulics (in Dutch).

Roelvink, J.A. (2006). Overview of coastal morphodynamic evolution techniques, Coastal Engineering, Volume 53, Issue 2-3, 1 February 2006, Pages 277-287
Waterloopkundig Laboratorium, Scouring near the Port of IJmuiden, WL-report H460, 1988 (in Dutch).

DUNE EROSION PREDICTION METHODS INCORPORATING EFFECTS OF WAVE PERIODS

Marcel R.A. van Gent[1], E. Martijn Coeveld[1], Hans de Vroeg[1], Jan van de Graaff[2]

1. Delft Hydraulics, Wave Dynamics & Structures Group, P.O. Box 177, 2600 MH Delft, The Netherlands, Marcel.vanGent@wldelft.nl, Martijn.Coeveld@wldelft.nl, Hans.deVroeg@wldelft.nl.
2. Delft University of Technology, Section of Hydraulic Engineering, P.O. Box 5048, 2600 GA Delft, The Netherlands, J.VanDeGraaff@TUDelft.nl.

Abstract: Recently, the influence of wave periods on dune erosion was studied in a series of large-scale physical model tests (Van Gent *et al.,* 2006). In these tests dune erosion was simulated under extreme storm conditions. The aim of the study presented in this paper was to develop dune erosion prediction methods that take effects of wave periods on dune erosion into account. An existing dune erosion prediction method was used as starting point for the development. The obtained prediction method will be used to evaluate the dunes along the Dutch coast, where longer wave periods occur than previously assumed.

INTRODUCTION

Dunes in The Netherlands act as primary sea defense for the lowlands behind them. Since this is a densely populated area, it is important to assess their safety against flooding. Therefore, the strength of the dunes needs to be predicted under the hydraulic loads in a normative storm surge. In The Netherlands the normative conditions refer to rather small chances of failure ($\approx 10^{-4}$ to 10^{-5} per year). The strength of the dunes can be determined by predicting the volume of dune erosion during an extreme storm. Failure of the dunes takes place when the rate of dune erosion is so large that flooding of the lowlands behind the dunes occurs. In The Netherlands dune erosion is predicted by using rather simple empirical relations (Vellinga, 1986). These predictions are mainly based on the cross-shore dune profile before a storm, the expected storm surge level, the wave height at deeper water, and characteristics of the sediment.

Recent insights led to the conclusion that wave periods during an extreme storm event along the Dutch coast could be longer than previously assumed. In order to achieve information on possible effects of longer wave periods, large-scale physical model tests were performed in the Delta flume of Delft Hydraulics (Van Gent *et al.,* 2006). These tests indicated that the eroded dune volume increases for longer wave periods (*e.g.* an increase in the wave period of 50% led to an increase in dune erosion volumes of 15% to 25%). However, the method to predict dune erosion that has been applied in The Netherlands does not account for the influence of the wave period. Therefore, the aim of this study is to extend the existing method taking the effects of the wave period into account using the data obtained from the tests.

APPROACH

The scope of this study allowed only for an extension of a yet existing method for predicting dune erosion instead of developing an entirely new method. Several concepts of incorporating effects of wave periods into the existing formulations were already developed based on existing data and insights before the recent data from large-scale model tests (Van Gent *et al.*, 2006) became available. These large-scale dune erosion tests were used to verify and to optimize the developed concepts. The dune erosion prediction method that was used as a starting point in this study is described hereafter. A summary of the most important results of the recent large-scale dune erosion tests is also presented in this section.

Current dune erosion prediction method

In the safety assessment which is presently applied for the Dutch dunes (based on the method described by Vellinga, 1986), use is made of a 2DV description of the dune erosion profile after a very severe storm event with a characteristic significant wave height and water level. With this description of the shape of the dune erosion profile, the location of the dune erosion profile can be obtained by horizontally moving the shape of the dune erosion profile over the initial profile until the total erosion volume is equal to the total accretion volume, see Figure 1. This provides a prediction of the dune erosion volume above storm surge level (*A* in Figure 1). If this volume exceeds the initial volume above storm surge level, flooding occurs. This prediction method will from hereon be referred to as the 'current method'.

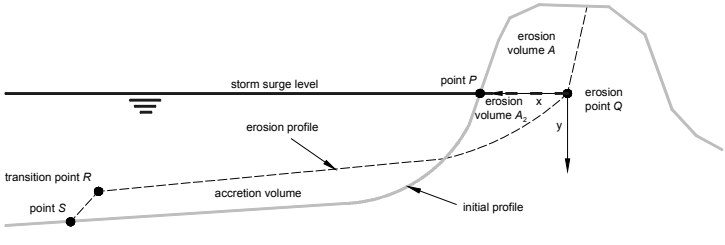

Fig. 1. Definition of characteristic erosion profile, erosion volumes and (erosion) points in a cross-shore profile.

The derived equation for the erosion profile (between point Q and R in Figure 1) is described by Vellinga (1986) and reads:

$$\frac{7.6}{H_{0s}} \cdot y = 0.4714 \left[\left(\frac{7.6}{H_{0s}} \right)^{1.28} \cdot \left(\frac{w}{0.0268} \right)^{0.56} \cdot x + 18 \right]^{0.5} - 2.0 \qquad (1)$$

where H_{0s} = significant wave height at a depth of Datum -20 m (m); w = fall velocity of a grain of sand with diameter $D = D_{50}$ (m/s); y = depth beneath storm surge level (m); and x = horizontal cross-shore distance from point Q (see Figure 1) positive in seaward direction. Point Q is defined at the maximum storm surge level and forms the origin $x = 0, y = 0$ in Equation 1. Equation 1 describes the erosion profile between point Q and transition point R, which is described by:

$$x_R = 250 \cdot \left(\frac{H_{0s}}{7.6} \right)^{1.28} \cdot \left(\frac{0.0268}{w} \right)^{0.56}$$
$$y_R = 5.717 \cdot \left(\frac{H_{0s}}{7.6} \right) \qquad (2)$$

The upward slope on the landward side ($x < 0$ and $y < 0$) is fixed at 1:1. The slope on the seaward edge between the erosion profile and the initial profile (between point R and S in Figure 1) is fixed at 1:12.5.

The equations above were derived on the basis of many experiments including series of large-scale tests for a basic situation with a wave height of $H_{0s} = 7.6$ m (prototype value) and sediment fall velocity of w = 0.0268 m/s. This basic situation can be clearly recognized as reference values in the equations. The equations were derived for waves with a peak wave period T_p = 12 s, corresponding to a wave steepness of $H_{0s} / L_0 = H_{0s} / 1.56 \cdot T_p^2 = 0.034$. Delft Hydraulics (1982a) states that the method is only valid for situations in which (1) the maximum storm surge level minus 1 m is exceeded for 5 to 6 hours, (2) the grain size diameter is 150 μm < D_{50} < 400 μm, and (3) the wave steepness is larger than $H_{0s}/L_0 = 0.02$. It is also noted that a post-storm beach profile as measured shortly after the storm will be a little lower than the predicted profile, because of a redistribution of sand after the peak of the storm.

Results of large-scale dune erosion tests

Large-scale dune erosion tests with different wave periods (Van Gent *et al.,* 2006) were carried out to provide the data necessary to verify the developed concepts. In the tests use was made of the same initial coastal profile (see Figure 2) based on a profile that is considered as characteristic for the Dutch coast. To translate this prototype profile to a model that fits in the flume, use was made of the set of scaling relations derived by Vellinga (1986) that was based on an extensive series of dune erosion tests on different scales and with different sediment diameters (see Section 3.3). In the present tests, geometrically distorted models needed to be applied to properly model the fall velocity

of the sediment with respect to the other relevant parameters. The dune erosion tests were carried out with a depth scale of $n_d = 6$. Sediment with a diameter of $D_{50} = 200$ µm was applied in the tests and a wave height of $H_{m0} = 1.5$ m. The tests used here were performed with a Pierson-Moskowitz spectrum with peak wave periods that varied from $T_p = 4.9$ s to $T_p = 6.12$ s to $T_p = 7.35$ s (model values), denoted with T01, T02 and T03 respectively. This corresponds to peak wave periods of $T_p = 12$ s, $T_p = 15$ s and $T_p = 18$ s in prototype. This means that there is an increase in wave periods (T_p, $T_{m-1,0}$ and T_m) with 50% between conditions T01 and T03. Note that T01 was performed with the same wave period as the condition on which the current method was based.

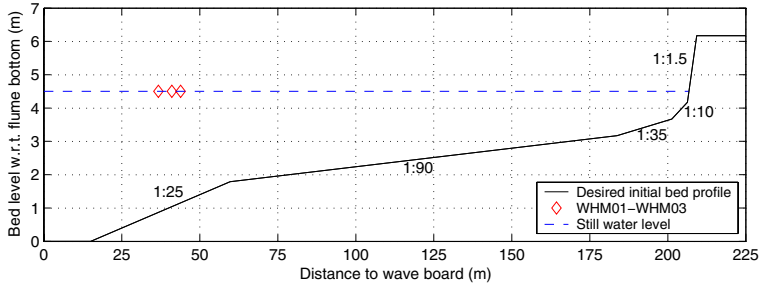

Fig. 2. Initial bed profile (WHM = wave height meter).

During the development of the current dune erosion prediction method (Section 2.1), a characteristic storm duration was defined at maximum storm surge level. This storm duration was 5 hours. At a depth scale of $n_d = 6$, a prototype storm duration of 5 hours corresponds to a test duration of 2.04 hours ($2.04 = 5 / \sqrt{n_d}$). The tests were carried out with a constant water level.

The tests included measurements of the bed profile, wave conditions, flow velocities and sediment concentrations. Furthermore, particle size distributions and fall velocities were determined for several sediment samples.

Figure 3 shows a comparison of the bed profile measurements after 6 hours (model scale) for Tests T01, T02 and T03. This figure shows that the retreat of the dune face (the relative steep part of the bed profile above the still water level) is largest in Test T03 (with the longest wave period) and smallest in Test T01 (with the shortest wave period). The differences in the shape of the bed profile for different wave periods are small, but the changes in dune foot location, slope of the beach profile and the shape of the deposit area for increasing wave periods are consistent. The dune foot is located at the intersection of the relatively steep dune face and the beach just in front of the dune face. It appears that the horizontal position of the dune foot moves more landward for the longest wave period, while the vertical position of the dune foot hardly varies. The slope of the bed profiles around and below the still water level is a bit gentler for the longest

wave period. The seaward edge of the deposit area is located farther seaward in Test T03 than in Test T01. Dune erosion volumes were obtained from the bed profile measurements. The volumes were based on the difference between the initial profile and the profile measured after a certain period of time. Tests T01 and T03 have each been repeated. Repetition of the tests led to differences of less than 2.5% in the total eroded volumes after 1, 2 and 6 hours. The differences after 0.1 and 0.3 hour were slightly larger. This indicates that the reproducibility of the results of the tests is good. Hereafter, for Tests T01 and T03 the average of the two test results with equal wave conditions has been used.

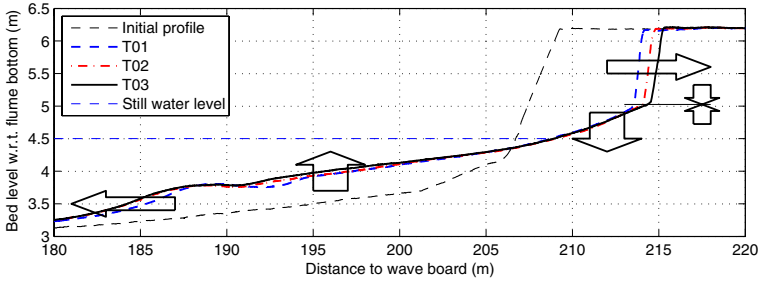

Fig. 3. Comparison of measured bed profiles after 6 hours (model scale) in Tests T01, T02 and T03 and indications of qualitative effects of wave period on erosion profile.

It was found that after 2.04 test duration (*i.e.* 5 hour storm duration in prototype) the dune erosion volume above the still water level increases with 24 % for an increase in wave period with 50% (Figure 4b). It should be noted that an equilibrium situation has not yet been established at that stage, see for example the development of the erosion volume above the still water level with time in Figure 4a.

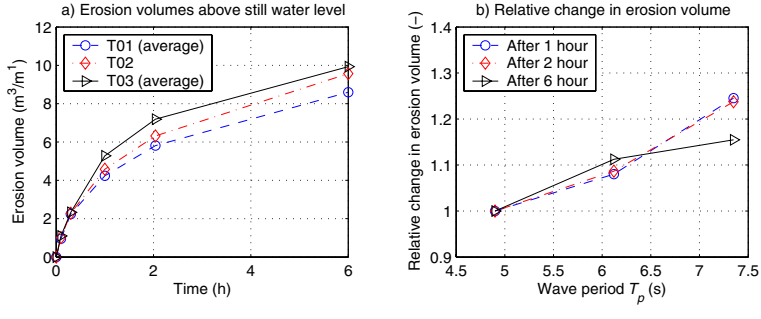

Fig. 4. Development of erosion volume above still water level (a) with time (left) and (b) depending on the wave period (right).

NEW DUNE EROSION PREDICTION METHODS

In this section new deterministic dune erosion prediction methods to take effects of the wave period into account will be discussed. These methods have the current method as a starting point. The methods were initially based on data that were already available prior to the execution of the described large-scale tests (Van Gent *et al.,* 2006). With the results of these large-scale tests, the methods were calibrated and evaluated. The methods are subdivided into two categories (1) period-dependent erosion volumes, and (2) period-dependent erosion profiles. In the first category, the shape of the erosion profile as described in Section 2.1 by Equations 1 and 2 remains unchanged and effects of the wave period on dune erosion are taken into account by means of a horizontal translation of the erosion profile based on an additional volume of dune erosion. This volume can be expressed as a function of the wave period (or wave steepness). Methods in this category are discussed in Section 3.1. In the second category, Equations 1 and 2 are extended in order to include effects of the wave period. Methods in this category are discussed in Section 3.2.

Category 1: Period-dependent erosion volumes

The first method, Method 1, is based on the assessment of a factor P_{extra} for the extra volume of dune erosion ($= P_{extra} \cdot A$) due to effects of an increased wave period compared to the condition for which the current method was derived. This method results in a dune erosion volume of $(1+P_{extra}) \cdot A$, in which A is the erosion volume above the water level calculated with the current prediction method, see Section 2.1.

This method can be considered as an extension of earlier methods described in Delft Hydraulics (2006) that were based on a limited number of small-scale tests reported in Delft Hydraulics (1982b). By also using small-scale tests by Coeveld *et al.* (2005) an improved fit could be made, resulting in the following relation between the wave steepness and the dune erosion volume:

$$\begin{cases} \dfrac{H_{0s}}{L_0} < 0.015 & P_{extra} = 0.31 \\ 0.015 \le \dfrac{H_{0s}}{L_0} \le 0.04 & P_{extra} = -16.5\left(\dfrac{H_{0s}}{L_0} - 0.034\right) \\ \dfrac{H_{0s}}{L_0} > 0.04 & P_{extra} = -0.10 \end{cases} \qquad (3)$$

This method was not adjusted based on the large-scale tests, although the large-scale tests showed less dependency on the wave period than Equation 3 (based on small-scale tests) would suggest. With Equation 3 an erosion volume is obtained, but not yet a dune erosion profile. In order to find also a shape of the dune erosion profile with this method it was chosen to deduce information on the erosion profile by letting the newly obtained dune erosion volume be the target volume in a series of iterative dune erosion

predictions with the current prediction method. In the iterative predictions the diameter of the sand is reduced until the target volume is obtained.

Category 2: Period-dependent erosion profiles

In this category two methods are considered, Method 2a and Method 2b. In Method 2a the dune erosion profile beneath storm surge level and the transition between the dune erosion profile and the initial profile are modified. A new equation was derived for the erosion profile using a methodology similar to the one applied in Delft Hydraulics (1982a). In Delft Hydraulics (1982a) the available profiles were all based on tests with a (prototype) peak wave period of about T_p = 12 s. Here, data from small-scale tests, including tests with other wave periods, were used for the derivation of Method 2a. Method 2a was not adjusted based on the results from the described large-scale tests. Also similar scaling relationships have been assumed here. This yielded a modified erosion profile beneath storm surge level, with gentler profile slopes for larger wave periods. Method 2a is described by Equation 4:

$$\frac{7.6}{H_{0s}} \cdot y = 0.4714 \cdot \left[\left(\frac{7.6}{H_{0s}} \right)^{1.28} \cdot \left(\frac{w}{0.0268} \right)^{0.56} \cdot x + \frac{\left(T_p + 6 \right)^2}{18} \right]^{0.5} - \left(\frac{T_p + 6}{9} \right) \qquad (4)$$

This equation gives the same result as Equation 1 for a peak wave period of T_p = 12 s, and the location of the dune foot does not shift (in other words: if $y = 0$ then $x = 0$). The slope between point R and S (see Figure 1) is equal to the slope in the current method (1:12.5). The transition point R is located at:

$$\begin{aligned} x_R &= 250 \cdot \left(\frac{H_{0s}}{7.6} \right)^{1.28} \cdot \left(\frac{0.0268}{w} \right)^{0.56} \\ y_R &= \left(\frac{H_{0s}}{7.6} \right) \cdot \left[0.4714 \cdot \left(250 + \frac{\left(T_p + 6 \right)^2}{18} \right)^{0.5} - \left(\frac{T_p + 6}{9} \right) \right] \end{aligned} \qquad (5)$$

This implies that the horizontal position of the transition point (x_R) relative to the dune foot is equal to the position in the current method. Since the erosion profile between the dune foot and the transition point changed (Equation 4 instead of Equation 1), the vertical position of the transition (y_R) is different.

Similar as for Method 2a, also for Method 2b the dune erosion profile beneath the storm surge level and the transition between the dune erosion profile and the initial profile are modified. The dune erosion profile is modified in a rather straightforward way, viz. by adding a term $(12 / T_p)^{\alpha}$ as indicated in Equation 6. In this way, the term for the wave period is included in a similar way as the wave height and the fall velocity (effect relative to reference value):

$$\frac{7.6}{H_{0s}} \cdot y = 0.4714 \cdot \left[\left(\frac{7.6}{H_{0s}} \right)^{1.28} \cdot \left(\frac{12}{T_p} \right)^{\alpha} \cdot \left(\frac{w}{0.0268} \right)^{0.56} \cdot x + 18 \right]^{0.5} - 2.0 \qquad (6)$$

The exponent α was initially determined with a fitting procedure on data from small-scale tests at $\alpha = 0.5$. The validation with the large-scale tests led to a small adjustment of this exponent to $\alpha = 0.45$. For wave periods longer than T_p=12 s, a smaller value for α leads to a smaller landward shift of the dune face and shows a steeper bed profile below the still water level. Equation 6 gives the same result as Equation 1 for a peak wave period of $T_p = 12$ s, and the location of the dune foot does not shift (in other words, if $y = 0$ then $x = 0$). The slope between point *R* and *S* (see Figure 1) is equal to the slope in the current method (1:12.5). The transition point *R* (see Figure 1) is located at:

$$\begin{aligned} x_R &= 250 \cdot \left(\frac{H_{0s}}{7.6} \right)^{1.28} \cdot \left(\frac{0.0268}{w} \right)^{0.56} \\ y_R &= \left(\frac{H_{0s}}{7.6} \right) \cdot \left[0.4714 \cdot \left(250 \cdot \left(\frac{12}{T_p} \right)^{\alpha} + 18 \right)^{0.5} - 2 \right] \end{aligned} \qquad (7)$$

Evaluation of prediction methods

The dune erosion prediction methods presented in Sections 3.1 and 3.2 were verified with the measurements of Tests T01, T02 and T03 (see Section 2.2). The validation was carried out by comparing the measured and predicted erosion profiles and erosion volumes above the still water level. For the comparison of the predicted and measured profiles reference is made to Figure 3, which summarizes the qualitative effects of the wave period on the shape of the erosion profile.

SCALE RELATIONS

Because the prediction methods should be applied for prototype conditions, all measured bed profiles are translated to a prototype situation for this purpose. Use is made of the set of scaling relations described by Vellinga (1986):

$$\begin{aligned} n_l &= n_l \cdot \left(\frac{n_d}{n_w^2} \right)^{0.28} \\ n_H &= n_d \\ n_T &= n_t = n_d^{0.5} \end{aligned} \qquad (8)$$

where n_l = scale factor for horizontal geometrical measures ($n_l = x_{proto} / x_{model}$); n_d = scale factor for vertical geometrical measures; n_w = scale factor for the fall velocity of the sediment; n_H = scale factor for the wave height; n_T = scale factor for the wave period;

and n_t = scale factor for the time. Vellinga (1986) concluded that the hydraulic and morphologic processes need to be scaled with the same time scale factor to appropriately simulate dune erosion on a smaller scale.

The fall velocity scale factor n_w in Equation 8 is obtained by dividing the prototype value of the fall velocity by the model value. For the prototype fall velocity a value of $w = 0.0268$ m/s is chosen, which was also used in earlier analyses and corresponds with the fall velocity of a grain diameter of $D_{50} = 225$ µm. To obtain a prototype profile the horizontal dimensions of the model are multiplied with the horizontal length scale factor n_l, and the vertical dimensions (*e.g.*, water depth and wave height) with the depth scale factor n_d. Prototype values for the wave period and the time at which profile measurements were carried out are obtained by multiplying the model values with the square root of the depth scale factor n_d. By multiplying the measured dune erosion volume (per linear meter) with $n_A = n_l \cdot n_d$ the prototype volume is obtained.

COMPARISON OF PREDICTION METHODS

A comparison between prediction methods is discussed here, primarily focused on the prediction of dune erosion volumes, not on the prediction of dune erosion profiles.

The current method, derived for a wave period of T_p=12 s, over-predicts the erosion volume above still water for this basic condition. This current method is used as starting point for the new methods. The new methods that take into account an extra amount of dune erosion for longer wave period will therefore also over-predict the measured dune erosion volumes, see left panel in Figure 5. Therefore, to obtain better insight into the relative performance of the methods, the erosion volumes have been normalized for T_p = 12 s, see right panel in Figure 5.

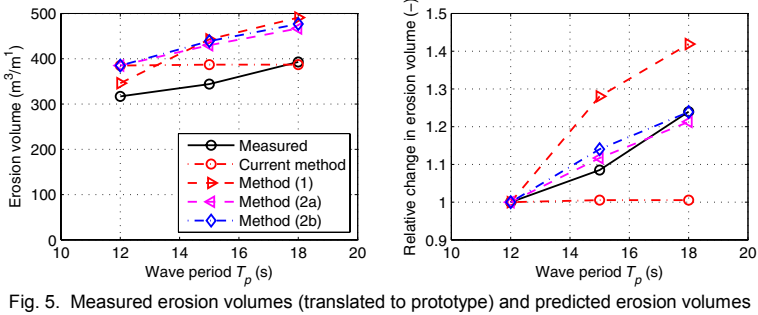

Fig. 5. Measured erosion volumes (translated to prototype) and predicted erosion volumes above still water level and change in erosion volume relative to volume in Test T01 (T_p = 12s)

For all three methods, the predicted erosion volume increases more between T_p = 12 s and T_p = 15 s, than between T_p = 15 s and T_p = 18 s, while for the measurements the opposite applies. Nevertheless, the predicted relative change in erosion volume between

T_p = 12 s and T_p = 18 s corresponds best to the measurements when using Method 2a or Method 2b.

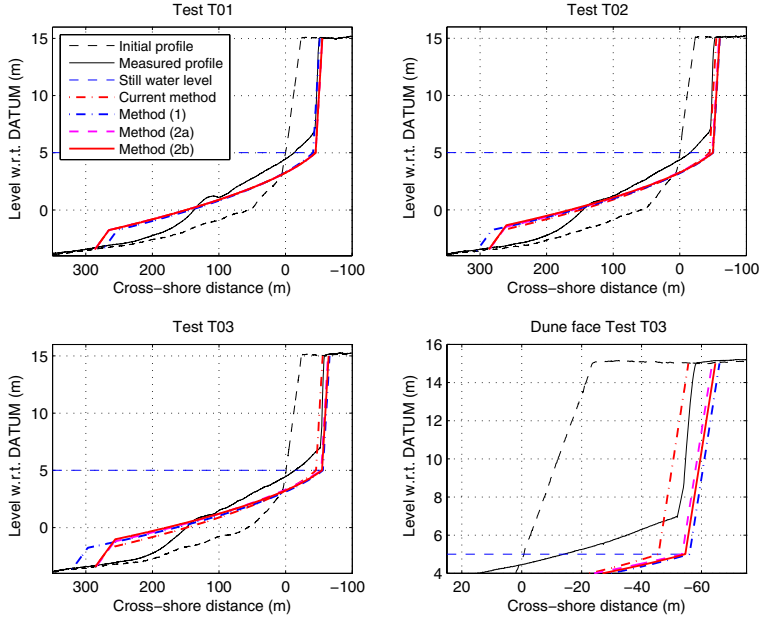

Fig. 6. Measured bed profiles (translated to prototype) and bed profiles predicted with Methods (1), (2a) and (2b) for Tests T01 (T_p = 12 s), T02 (T_p = 15 s) and T03 (T_p = 18 s).

The main goal of the prediction method is to predict the dune erosion volume. Nevertheless, attention is also paid to several aspects of the predicted bed profiles. Figure 6 shows measured and predicted bed profiles for Tests T01, T02 and T03 translated to a prototype situation. The bed profiles predicted with the current method (which is used as a starting point for the other methods) are equal in all tests, because the current method does not take the wave period into account. Furthermore, the following can be observed:

- With the current method the horizontal position of the dune face is predicted more landward than the measured position for Test T01. For Test T03 the opposite applies. By definition, the vertical position of the dune foot predicted with the current method is located at the still water level, while the measured location of the dune foot is well above the still water level. The horizontal position of the dune face

predicted with Methods 2a and 2b corresponds reasonably well with the measurements.

- The slope of the predicted profile directly seaward of the dune face is less steep than the measured profile. The correspondence of the bed profile below the still water level predicted with Methods 2a and 2b and the measurements is poor, which is also the case for the current method.
- The predicted deposit area extends significantly more seaward than the measured deposit area. Method 1 shows a larger influence of the wave period on the length of the deposit area, than the predictions of Methods 2a and 2b.

In general, the bed profile predictions do not correspond very well with the measurements irrespective of which prediction method is used. Because this is also the case for the current method, while the current method is used as a starting point for the new methods, no significant improvements can be expected with the new methods with respect to predicted bed profiles. The same is valid for the vertical position of the dune foot.

INFLUENCE OF WAVE SPECTRA ON DUNE EROSION

Based on dune erosion tests with double-peaked wave energy spectra Van Gent *et al.* (2006) concluded that the influence of wave spectra on dune erosion is more appropriately taken into account using the wave period $T_{m-1,0}$ than using the peak wave period T_p. The wave period $T_{m-1,0}$ can be incorporated in Equations 6 and 7 in the following way:

$$\frac{7.6}{H_{0s}} \cdot y = 0.4714 \cdot \left[\left(\frac{7.6}{H_{0s}} \right)^{1.28} \cdot \left(\frac{10.9}{T_{m-1,0}} \right)^{0.45} \cdot \left(\frac{w}{0.0268} \right)^{0.56} \cdot x + 18 \right]^{0.5} - 2.0 \qquad (9)$$

and

$$\begin{aligned} x_R &= 250 \cdot \left(\frac{H_{0s}}{7.6} \right)^{1.28} \cdot \left(\frac{0.0268}{w} \right)^{0.56} \\ y_R &= \left(\frac{H_{0s}}{7.6} \right) \cdot \left[0.4714 \cdot \left(250 \cdot \left(\frac{10.9}{T_{m-1,0}} \right)^{0.45} + 18 \right)^{0.5} - 2 \right] \end{aligned} \qquad (10)$$

The value 10.9 is based on the fact that the ratio $T_p/T_{m-1,0}$ comes close to a value of $T_p/T_{m-1,0} = 1.1$ for a standard single-peaked spectrum such as the Pierson-Moskowitz spectrum applied in the tests on which Equations 1-7 are based. Figure 7 shows the measured erosion volumes and the volumes predicted with Method 2b based on Equations 9 and 10.

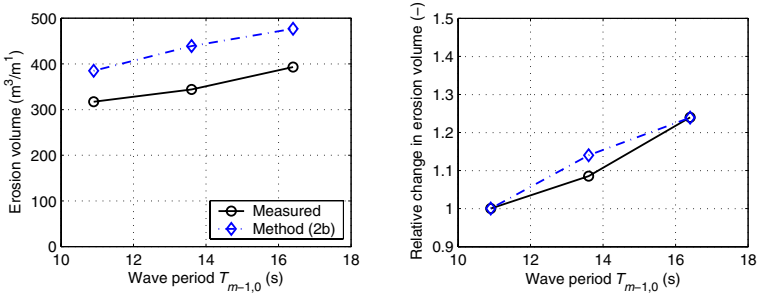

Fig. 7. Measured erosion volumes (prototype) and volumes predicted with Method 2b (Equations 9 and 10) and change in erosion volume relative to Test T01 ($T_{m-1,0}$ = 10.9 s).

DISCUSSION

Application of selected dune erosion method

Method 2b is selected to replace the current dune erosion prediction method in the safety assessment procedure for the Dutch dunes in the coming years, because of its simplicity.

Figure 8 shows the sensitivity of Method 2b to the input parameters H_s and $T_{m-1,0}$. A higher wave height leads to a longer deposition area, a more landward located dune face and a larger dune erosion volume. A longer wave period leads to gentler slopes of the bed profile below the still water level, a more landward located dune face and a larger dune erosion volume.

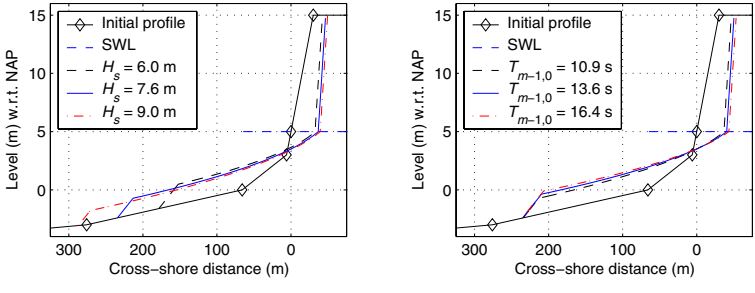

Fig. 8. Sensitivity of Method 2b to input parameters.

An example application of Method 2b is presented in Figure 9. The figure compares the current and the new dune erosion prediction method for a cross-section of an arbitrary Dutch dune for an extreme event. It shows that Method 2b predicts more dune erosion than the current method for the hydraulic conditions indicated in the figure. Obviously, the current method would have predicted the same bed profile for other wave periods.

The increase in erosion volume above the still water level between T_p = 12 s and T_p = 18 s is about 23 %, which agrees well with the observed increase in erosion volume in the physical model tests. It should be noted that the effects of the wave period on dune erosion depend on the initial bed profiles or hydraulic condition if they deviate significantly from the situation in the tests. Different initial profiles may lead to a significantly larger or a significantly smaller dependency on the wave period.

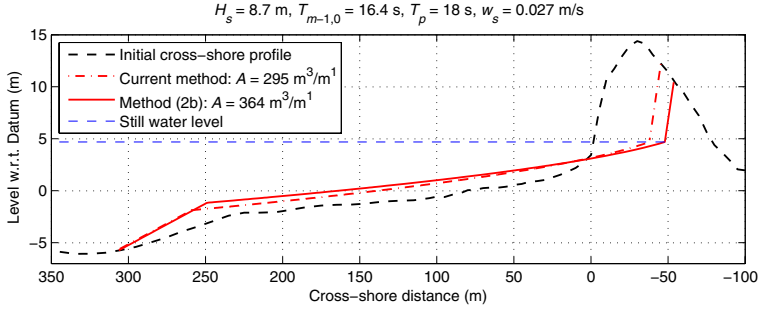

Fig. 9. Example application of current and new dune erosion prediction method for a cross-section of a dune (dashed line = initial bed profile, solid line = predicted erosion profile).

Method 2b has the same range of validity as the current method (see Section 2.1), except that for the wave steepness this method is considered valid for a wider range. Because of the limited amount of data for smaller wave periods, it is recommended to use Method 2b only for conditions with a deep water wave steepness of $0.02 < s_{m-1,0} < 0.063$ (or for standard single-peaked wave energy spectra of $0.017 < s_p < 0.04$).

Future developments

The method described above provides an indication of dune erosion volumes under extreme storm conditions. Because it is an empirical method, its validity is quite limited. For instance, the development and duration of a storm are strongly schematized, and the influence of the initial cross-shore profile cannot always be correctly reproduced. It is desirable to have methods available that do also account for these effects. Therefore, it is useful to develop a dune erosion prediction method that simulates dune erosion processes rather than an empirical representation of these processes. The large-scale tests will be analyzed to gain more insight into the physical processes underlying dune erosion.

CONCLUSIONS

The aim of the study was to develop a dune erosion prediction method that takes effects of the wave period on dune erosion into account. The dune erosion prediction method by Vellinga (1986) was used as a starting point for the new prediction method. Several prediction methods were developed on the basis of existing data and verified with the bed profiles and erosion volumes measured in recent large-scale dune erosion tests.

Based on the comparisons of predictions and measurements of dune erosion, it can be concluded that the relative increase in dune erosion volume for increasing wave periods observed in the tests corresponds well with the predictions of the newly developed methods. The new method can be used to predict dune erosion volumes, including effects of wave period. However, the shape of the bed profile below the still water level is not very well predicted. This is also the case for the current prediction method by Vellinga (1986). The new and current methods are therewith not very suitable to predict the bed profile below the still water level.

ACKNOWLEDGEMENTS

This research was carried out in an assignment of the National Institute for Coastal and Marine Management of the Dutch Ministry of Transport and Public Works. Dr. M. Boers of this institute is acknowledged for his contribution to this research.

REFERENCES

Coeveld, E.M., den Heijer, C., Van de Graaff, J., De Vroeg, J.H., and Steetzel, H.J. (2005). "The effect of the wave period on dune erosion", *ASCE, Proc. of 5th Int. Conf. on Coastal Dynamics 2005*, Barcelona, Spain.

Delft Hydraulics (1982a). "Computational model for the estimation of dune erosion during storm surge", (Rekenmodel voor de verwachting van duinafslag tijdens stormvloed.) Delft Hydraulics report M1263 part IV (in Dutch).

Delft Hydraulics (1982b). "Systematic investigation of parameters relevant for dune erosion", (Systematisch onderzoek naar kenmerkende factoren voor duinafslag.) Delft Hydraulics report M1819 part 1 (in Dutch).

Delft Hydraulics (2006). "Dune erosion, Deterministic dune erosion prediction methods", Delft Hydraulics Report H4357, January 2006, Delft.

Van Gent, M.R.A., Coeveld, E.M., Walstra, D.J.R, Van de Graaff, J., Steetzel, H.J. and Boers, M. (2006). "Dune erosion tests to study the influence of wave periods", *Proc. of 30th ICCE*, San Diego, USA.

Vellinga, P. (1986). "Beach and dune erosion during storm", Ph.D. thesis, Delft University of Technology; see also Delft Hydraulics Communication 372 and Report M1263-IV.

REEVALUATION OF EQUILIBRIUM BEACH PROFILE SCALE PARAMETER

Zhanxian Wang[1], Robert G. Dean[2]

1. Applied Research Associates, Inc. 8540 Colonnade Center Drive, Suite 307, Raleigh, NC 27615, USA. zwang@ara.com.
2. Department of Civil and Coastal Engineering, University of Florida, 365 Weil Hall, P.O. Box 116590, Gainesville, FL 32611-6590, USA. dean@coastal.ufl.edu.

Abstract: A modification of the equilibrium beach profile scale parameter is proposed to account for wave effects. The modification is expressed in terms of a multiplication factor applied to the profile scale parameter and considered to be a function of the fall velocity parameter. The recommended modification is based on large-scale wave flume tests. The differences between summer and winter profiles in nature can be explained qualitatively by the proposed model and the application of the model to predict seasonal shoreline changes is promising.

INTRODUCTION

The concept of an equilibrium beach profile (EBP) is one of the coastal engineer's most valuable tools in providing a framework to consider disequilibrium and thus cross-shore sediment transport (Kriebel and Dean 1985; Larson and Kraus 1989; Zheng and Dean 1997). Also many useful and powerful conceptual and design relationships are based on profiles of equilibrium (Dean 1991).

The commonly accepted EBP shape from Bruun (1954) and Dean (1977) is

$$h = Ay^{2/3} \tag{1}$$

in which h is the water depth at a seaward distance, y, and A is the profile scale parameter with dimensions of length$^{1/3}$. Dean (1977) found that this relationship is consistent with uniform wave energy dissipation per unit volume, D_*, within the breaking

zone. From linear shallow water wave theory, it can be shown that D_* and A are related by

$$A = \left[\frac{24 D_*}{5 \rho g^{3/2} \kappa^2} \right]^{2/3} \tag{2}$$

where ρ is the water mass density, g is gravity, and κ is a constant relating wave height to water depth within the surf zone.

Moore (1982) collected and analyzed a number of published beach profiles and developed a relationship between A and D_{50} (the grain size median diameter). Later, Dean (1987) transformed the A vs. D_{50} relationship to the A vs. w (the fall velocity) relationship. Table 1 presents the recommended A values (in $m^{1/3}$) vs. the median sand size in 0.01-mm increments over the range of sand sizes from 0.1 mm to 1.09 mm (Dean et al. 2001). A limitation in the relationships between A and D_{50} (or w) is that wave conditions are not included. Thus, as questioned by Pilkey et al. (1993), this representation cannot explain one phenomenon that occurs in natural beaches: the profiles are of milder slope in the winter under high wave energy, compared to the summer conditions associated with milder and less steep waves. In the present study, a modification function is developed to account for wave effects on EBP shapes.

Table 1. Recommended Profile Scale Parameter Values ($m^{1/3}$)

D_{50} (mm)	0.00	0.01	0.02	0.03	0.04	0.05	0.06	0.07	0.08	0.09
0.1	0.063	0.067	0.071	0.076	0.080	0.084	0.087	0.090	0.094	0.097
0.2	0.100	0.103	0.106	0.109	0.112	0.115	0.117	0.119	0.121	0.123
0.3	0.125	0.127	0.129	0.131	0.133	0.135	0.137	0.139	0.141	0.143
0.4	0.145	0.147	0.148	0.150	0.151	0.153	0.155	0.156	0.158	0.159
0.5	0.161	0.162	0.163	0.165	0.166	0.167	0.168	0.169	0.171	0.172
0.6	0.173	0.174	0.175	0.177	0.178	0.179	0.180	0.181	0.183	0.184
0.7	0.185	0.186	0.187	0.188	0.189	0.190	0.190	0.191	0.192	0.193
0.8	0.194	0.195	0.196	0.196	0.197	0.198	0.199	0.200	0.200	0.201
0.9	0.202	0.203	0.204	0.204	0.205	0.206	0.207	0.208	0.208	0.209
1.0	0.210	0.211	0.212	0.212	0.213	0.214	0.215	0.216	0.216	0.217

MODIFICATION OF EBP PROFILE SCALE PARAMETER

The fall velocity parameter (Dean 1973) includes information of both sediment size and wave conditions and has been used in many coastal problems. The hypothesis tested here is that a relationship exists between the profile scale parameter A and the fall velocity parameter H_b/wT as

$$A = f(D_{50}) \cdot F(\frac{H_b}{wT}) \tag{3}$$

in which the first term is determined from Table 1, and the second term is a modification term which is a function of the fall velocity parameter. To investigate this modification function, the large-scale wave flume experimental data from LWT (Kraus and Larson 1988) are analyzed. LWT used monochromatic waves and all commenced with an initial profile slope of 1:15. Most of the final profiles in this experiment had almost achieved equilibrium.

The analysis procedure is as follows: first using the wave transformation model of Dally et al. (1985) or from measurements, determine the breakpoints and the corresponding breaking wave heights in the final measured profiles; then, applying the least-squares method from the shoreline positions out to the breakpoint positions, determine the best-fit A values by assuming that the final profiles are in equilibrium. Figure 1 shows one example from Case 300 in the LWT experiments. For final profiles having multiple bars and a wide trough landward of the primary bar, such as LWT Cases 500 (Figure 2), they are fit to the breakpoint near the inner bars.

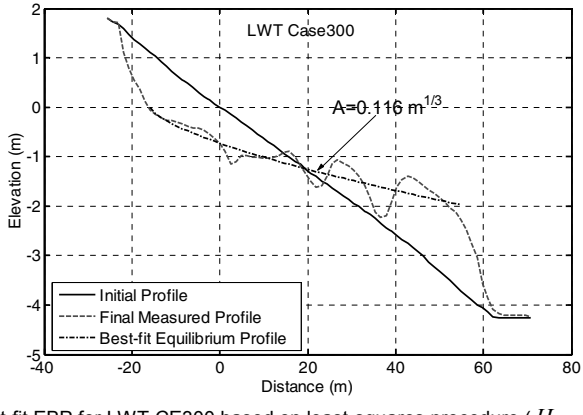

Fig.1. Best-fit EBP for LWT CE300 based on least-squares procedure (H_b = 1.88 m, T = 11.33 s, D_{50} = 0.22 mm). The A value based on Table 1 is 0.106m$^{1/3}$.

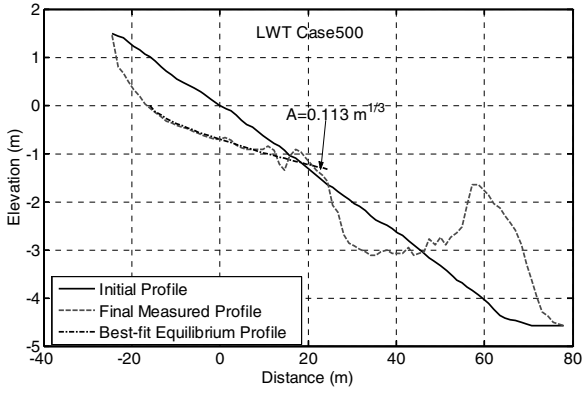

Fig.2. Best-fit EBP for LWT CE500 based on least-squares procedure (H_b = 1.88 m, T = 11.33 s, D_{50} = 0.22 mm). The A value based on Table 1 is 0.106m$^{1/3}$.

A plot of the ratio of the best-fit A values (A_{fit}) to the recommended values from Table 1 (A_{rec}) vs. the fall velocity parameter is presented in Figure 3. A reasonable fit to the data is

$$F(\frac{H_b}{wT}) = 0.868 + 1.406\left(\frac{H_b}{wT}\right)^{-1} \tag{4}$$

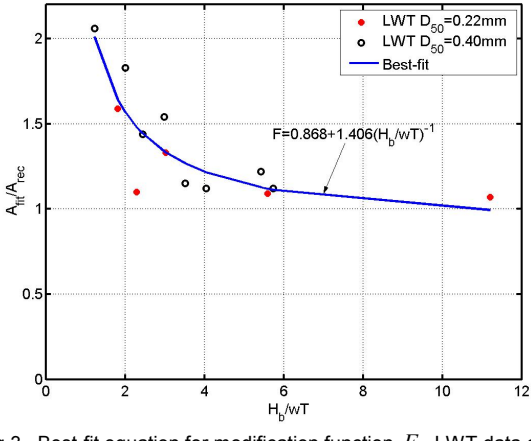

Fig.3. Best-fit equation for modification function F , LWT data only.

APPLICATION TO SEASONAL SHORELINE CHANGES

Of special interest, seasonal profile changes can be explained qualitatively on the basis of Eq.4: from winter to summer, the A value becomes larger with the fall velocity parameter decreasing, thus the profile becomes steeper in summer and the shoreline advances seaward relative to winter conditions.

Figure 4 shows an idealized scheme for the calculation of seasonal shoreline changes from summer to winter based on equilibrium beach profile concepts. This process is assumed to be reversible, which may not be exact when considering profile changes from winter to summer following the depth of closure concept. Considering volume conservation in Figure 4, the shoreline change, Δy , can be determined approximately as

$$\frac{\Delta y}{W_*} = -\frac{\frac{3}{5}\left(\frac{A_s}{A_w} - 1\right)}{\left(\frac{B}{h_*} + \frac{A_s}{A_w}\right)} \tag{5}$$

where A_s and A_w are the respective EBP profile scale parameters for summer and winter profiles determined from Eq.3, h_* is the depth of closure, B is the berm height, and $W_* = (h_* / A_w)^{3/2}$ is the active beach width.

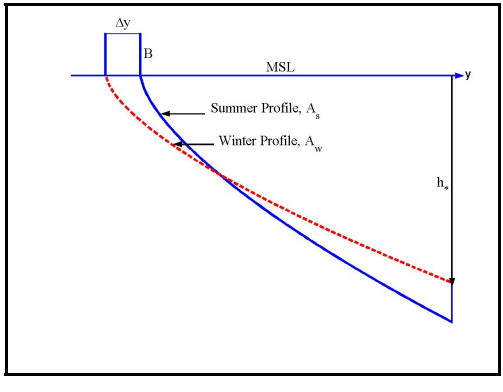

Fig.4. Scheme for calculating seasonal shoreline changes

For example: for Florida beaches, with a representative sediment size of 0.2 mm (Charles et al. 1994) which corresponds to a fall velocity of 0.03 m/s, the observed averaged seasonal shoreline change is in the range of 10 to 20 m (Dewall 1977). From Table 1, the recommended A value is 0.1 $m^{1/3}$. Taking the averaged wave conditions from the Wave Information Studies hindcast data (http://frf.usace.army.mil/wis/) on Florida beaches as: H_b = 0.6 m, T = 8 s in summer, and H_b = 1.0 m, T = 6 s during winter, the

modified A values are 0.143 $m^{1/3}$ and 0.112 $m^{1/3}$ for summer and winter profiles, respectively. Thus, the calculated potential seasonal shoreline change from Eq.5 is about 20 m ($h_* = 4$ m, and $h_* / B = 2.0$ based on the authors' experience), which is close to the observed value.

SUMMARY

The modification function proposed provides a basis to account for the effects of wave and sediment characteristics on equilibrium beach profiles through the fall velocity parameter. Based on investigation of the measured profiles from the large-scale wave flume experiments, an inverse relationship between the profile scale parameter and the fall velocity parameter was obtained. An example for seasonal shoreline changes on Florida beaches has demonstrated that the modified profile scale parameter model can be applied to predict reasonable seasonal shoreline changes; however, additional testing with more field data is needed to further verify and refine the model.

ACKNOWLEDGEMENTS

This study was sponsored by the Bureau of Beaches and Coastal Systems, Department of Environmental Protection, State of Florida, as part of the first author's doctoral research. The laboratory experimental data were kindly provided by Nicholas C. Kraus from the U.S. Army Corps of Engineers.

REFERENCES

Bruun, P. (1954). "Coast erosion and the development of beach profiles." Technical Memorandum No.44, Beach Erosion Board.

Charles, L., Malakar, S. B., and Dean, R. G. (1994). "Sediment data for Florida's east coast." UFL/COEL-94/014, Coastal and Oceanographic Engineering Department, University of Florida, Gainesville, FL 32611.

Dally, W. R., Dean, R. G., and Dalrymple, R. A. (1985). "Wave height variation across beaches of arbitrary profile." *Journal of Geophysical Research,* Vol.90 (C6), 11917-11927.

Dean, R. G. (1973). "Heuristic models of sand transport in the surf zone." *Proceeding of Conference on Engineering Dynamics in the surf zone,* Sydney, Australia.

Dean, R. G. (1977). "Equilibrium beach profiles: U. S. Atlantic and Gulf Coast." Ocean Engineering Report No.12, Department of Civil Engineering, University of Delaware, Newark, Delaware.

Dean, R. G. (1987). "Coastal sediment processes: Toward engineering solutions." *Proceedings of the Specialty Conference on Coastal Sediments'87,* ASCE, 1-24.

Dean, R. G. (1991). "Equilibrium beach profiles: Characteristics and applications." *Journal of Coastal Research,* Vol.7(1), 53-84.

Dean, R. G., Walton, T. L., and Kriebel, D. L. (2001). "Cross-shore sediment transport." *In Coastal Engineering Manual,* U. S. Army Coastal and Hydraulics Laboratory.

Dewall, A. E. (1977). "Littoral environment observations and beach changes along the Southeast Florida coast." Technical Paper 77-10, U.S. Army Corps of Engineers, Coastal Engineering Research Center.

Kraus, N. C., and Larson, M. (1988). "Beach profile change measured in the tank for large waves, 1956-1957 and 1962." Technical Report CERC-88-6, Coastal Engineering Research Center, U.S. Army Engineer Waterways Experiment Station, Vicksburg, MS.

Kriebel, D. L., and Dean, R. G. (1985). "Numerical simulation of time-dependent beach and dune erosion." *Coastal Engineering,* Vol.9, 221-245.

Larson, M., and Kraus, N. C. (1989). "SBEACH: Numerical model for simulating storm-induced beach change. Report 1: Empirical foundation and model development." Technical Report CERC-89-9, Coastal Engineering Research Center, U. S. Army Engineer Waterways Experiment Station, Vicksburg, MS.

Moore, B. D. (1982). "Beach profile evolution in response to changes in water level and wave height." Masters Thesis, Department of Civil Engineering, University of Delaware.

Pilkey, O. H., Young, R. S., Riggs, S. R., Smith, A. W. S., Wu, H., and Pilkey, W. D. (1993). "The concept of shoreface profile of equilibrium: A critical review." *Journal of Coastal Research,* Vol.9 (1), 255-278.

Zheng, J., and Dean, R. G. (1997). "Numerical models and intercomparisons of beach profile evolution." *Coastal Engineering,* Vol.30, 169-201.

SHOREFACE RESPONSE TO SEDIMENT DEFICIT

G.M. Kaminsky[1], M.A. Ferland[2], P.J. Cowell[3], H.R. Moritz[4], and P. Ruggiero[5]

1. Washington Department of Ecology, Coastal Monitoring & Analysis Program, P.O. Box 47600, Olympia, WA, 98504-7600, USA, gkam461@ecy.wa.gov
2. Central Washington University, Department of Geological Sciences, Lind Hall, Ellensburg, WA, 98926-7418, USA, ferlandm@cwu.edu
3. University of Sydney Institute of Marine Science, School of Geosciences, NSW 2006, Australia, cowell@mail.usyd.edu.au
4. U.S. Army Corps of Engineers, Portland District, P.O. Box 2946, Portland, Oregon, 97208, USA, hans.r.moritz@usace.army.mil
5. Oregon State University, Department of Geosciences, 104 Wilkinson Hall, Corvallis, OR, 97331-5506, USA, ruggierp@science.oregonstate.edu

Abstract: This paper evaluates shoreface change in response to a decrease in sediment supply over three timescales – Holocene (millennia), historical (century), and contemporary (interannual). The reduction of sediment supply is due to northern migration of the Columbia River ebb-tidal delta over the past few thousand years and construction of jetties during 1885–1917. Data analyzed include shoreface vibracores, historical regional bathymetry since 1868, and upper shoreface and beach profiles since 1997. At late Holocene to historical time scales the lower shoreface eroded while the upper shoreface and barrier accreted. At recent interannal time scale, the primary dune prograded. This behaviour resulted in a net rotation (i.e., steepening) of the shoreface and implies onshore sediment supply from the lower shoreface to the barrier. The study area is along northern Clatsop Plains, Oregon, USA.

INTRODUCTION

Shoreface rotation (i.e., progradation of the upper shoreface and deepening of the lower shoreface) has been observed on the Pacific Northwest coast, USA, both as a natural mean trend at millennial scale and as a response to engineering intervention at historical scale. This behaviour suggests that the inherited lower shoreface previously had a higher sediment supply and evolved toward a deeper equilibrium under both

natural and modified conditions. The lower shoreface erosion provided a sand supply for strandplain progradation under both sets of conditions, but at different rates.

The data are from the northern ~10 km reach of Clatsop Plains, Oregon, USA (Figure 1), where dramatic erosion of the lower shoreface ensued after construction of the south jetty (1885–1917) at the Mouth of the Columbia River (MCR). Jetty construction effectively eliminated sediment supply to the Clatsop shoreface (from shore to ~60 m water depth). Analysis of regional historical bathymetry since 1868 reveals an alongshore gradient of lower shoreface deepening, with the greatest magnitude of change close to the jetty. The erosion has substantially contributed to jetty deterioration, the need for several jetty rehabilitations, and more recently an evaluation of dredged-material management strategies for nourishing the shoreface.

This paper extends previous work (e.g., Kaminsky *et al.* 2001; Gelfenbaum *et al.* 2001; Moritz *et al.* 2003) that focused on the post-jetty multi-decadal evolution of the ebb-tidal shoals and adjacent coasts of the Columbia River mouth. The present work provides a detailed quantitative analysis of both pre-historic and historical evolution of the northern Clatsop sub-cell in order to better estimate future conditions and to inform management strategies for addressing the impacts of the sediment deficit. The study site and the available data are unique because they provide the opportunity to evaluate shoreface response to reduced sediment supply over millennial to inter-annual timescales. At millennial scale, the Columbia River entrance migrated northward across the present northern Clatsop shoreface. The river mouth also narrowed in width, implying that the ebb-tidal delta of a few thousand years ago also extended farther to the south than in historical time. Although the river mouth narrowed as the Clatsop Plains and sub-aerial Clatsop Spit prograded northward and seaward, the offshore area of the northern Clatsop Plains remained a broad ebb-tidal delta complex of shallow shoals and migrating channels affected by fluctuations in river discharge. Prior to jetty installation, the river mouth was approximately 9.6 km in width. Upon construction of both jetties, the width of the river mouth was reduced by two-thirds to approximately 3.2 km.

METHODS

This study presents results from 10 vibracores recently collected on the Clatsop shoreface (Kaminsky and Ferland 2003, 2005), which are interpreted in combination with previously-interpreted seismic reflection data (Twichell and Cross 2001). Radiocarbon (^{14}C) Accelerator Mass Spectrometry (AMS) dating and sediment grain size analysis of vibracore samples are also performed. In addition, this study analyzes historical shoreface change from four eras of extensive regional bathymetric data (1868, 1926, 1958 and 2000). Interpretations are informed by decadal-interval MCR condition surveys including exploration surveys beginning in 1841, several decades prior to jetty construction. Finally, a time series of upper-shoreface bathymetric surveys (< -12 m MLLW) from 1999 to 2006 and beach profiles from 1997 to 2005 are analyzed to compare contemporary shoreface and beach changes to recent decadal-scale trends.

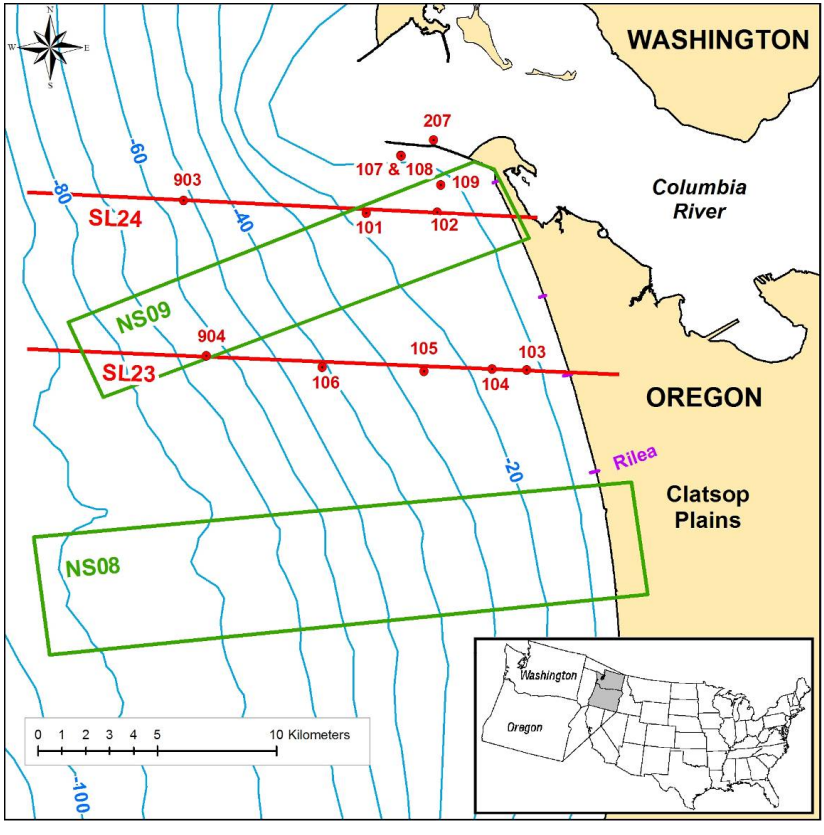

Fig.1. Clatsop Plains shoreface on the northern Oregon coast, including vibracore sites, shoreface profiles, and alongshore-averaged areas referenced in the text. Depth contours are in m relative to the North American Vertical Datum of 1988 (NAVD 88)[1].

ANALYSIS

Holocene Time Scale

In prehistoric time, the Columbia River valley was located south of the present location of the mouth. Figure 2 shows the lowstand surface (>14,000 years ago) interpreted from seismic reflection data (Twichell and Cross 2001) and reveals the shape and position of the ancient Columbia River valley that runs between the north and south transects of the Clatsop shelf cores.

[1] NAVD 88 m at the MCR = 0.16 m above Mean Lower Low Water (MLLW)

As sea level rose by some 110 m over 14,000 years, the Columbia River valley filled with sediment as the environment transitioned from fluvial to estuarine. Twichell and Cross (2001) indicate that as recently as 3,000 years ago, Clatsop Plains was narrow and did not extend as far north as it does now. Rather, the river mouth was even wider than it has been in recent historical time prior to jetty construction. This implies that the ebb-tidal delta of a few thousand years ago also extended farther to the south than in historical time. Evidence in the vibracores indicates long-term erosion of the inner shelf, which is consistent with a narrowing and substantial reduction in the size of the ebb delta from its previous, more southerly extent. As the environment transitioned from ebb delta to shoreface, the sediment of the delta was redistributed, resulting in a lowering of the seabed, as the historical and vibracore data indicate.

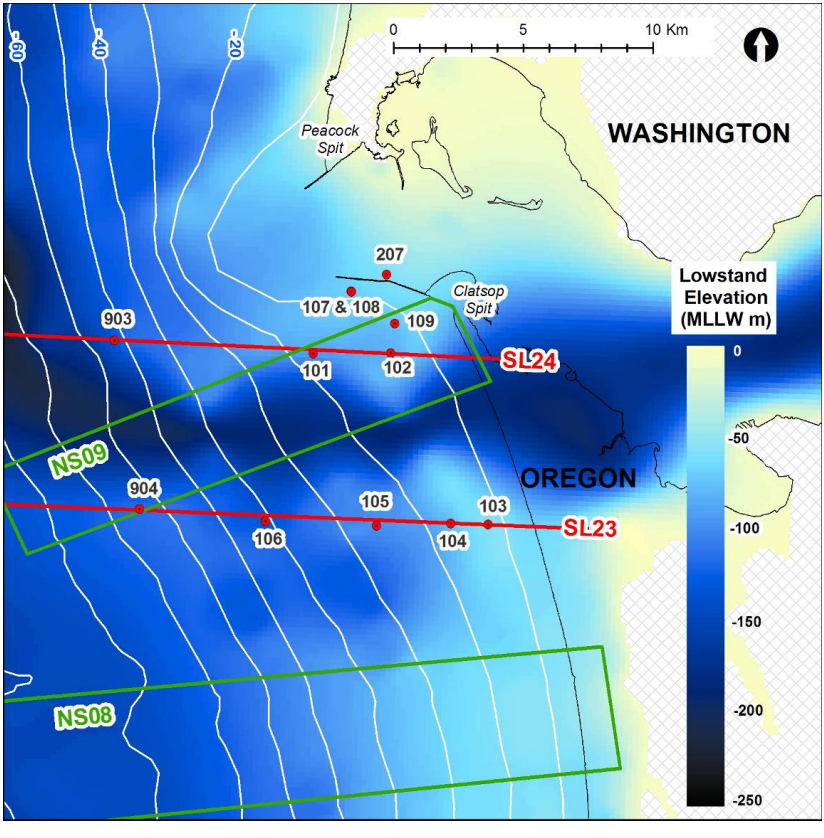

Fig. 2. Lowstand surface (>14,000 years ago) interpreted from seismic reflection data (Twichell and Cross 2001). For reference purposes, the figure includes the 1999 shoreline, the jetties, and the modern bathymetric depth contours in 10-m intervals.

Most of the vibracores collected on the Clatsop shoreface in 2002 and 2003 have laminated mud and sand units (cores 101, 102, 105, 106, 108, 109). In order for these units to be preserved in shallow water on this high-energy shoreface, they would have to be buried soon after deposition. The lack of bioturbation in these units supports this hypothesis of rapid burial. It is possible that the laminated mud and sand units were deposited at the margin of the once-wide and dynamic entrance with at least two major channels (north and south) separated by a large sand bank/shoal, and large, shore-connected shoals extending from the south and north (Clatsop Spit and Peacock Spit, respectively). Rapid burial would be possible, indeed likely, as ebb-delta shoals shifted and deposited sand. Erosional events were likely, and may be evidenced in the cores as sharp, angular contacts within the laminated unit that cut bedding at a low angle.

Samples from laminated units on the Clatsop shoreface have been analyzed by AMS, and the results indicate that these units are 'relict' (i.e., were not deposited in the last 1000 years). The calibrated ages of the organics within the laminated mud are youngest closest to the inlet (2000–2500 Before Present (BP)[2]; cores 108, 109) and are progressively older with distance from the inlet (> 4000 BP; cores 105, 106). In fact, within the present inlet, laminated mud and sand units in core 207 are younger than 339 BP, providing a modern analog to the relict deposits found on the shoreface. In contrast, the old dates near the surface of the shoreface cores indicate that relatively little sediment has accumulated on the Clatsop shoreface since the dated material was deposited, and/or that sediment has been eroded.

Additional evidence for long-term erosion on the Clatsop shoreface is provided by radiocarbon dates of carbonate material from two cores. In each core, the dates are not in stratigraphic order, because an older date occurs above a younger date. In core 104 (-17.3 m) a bivalve fragment collected at 112–116 cm depth interval returned a calibrated age of 2391 BP, whereas another bivalve fragment at 184–189 cm had a >Modern age. This result suggests that the seabed has been actively reworked to nearly 2 m along this shallow shoreface. Relatively old dates out of stratigraphic order were also found at lower depths in this core. A bivalve fragment at 322 cm returned a calibrated age of 4744 BP, while a shell fragment at 464–472 cm had a calibrated age of 3836 BP. Together, the dates in this core suggest recent sedimentation at the toe of the progradational (upper shoreface) sediment wedge over relatively older reworked sediment. In core 106 (-40.5 m) a bivalve fragment collected at 76–77 cm returned a calibrated age of 5649 BP, whereas another bivalve fragment at 184–185 cm returned a younger calibrated age of 4962 BP. This result is more likely when there is a slow rate of sediment accumulation, and sediment is eroded and redeposited locally. In addition, both of these relatively near-surface samples are old (another indicator of an erosional setting).

[2]0 calibrated ^{14}C years BP = Anno Domini (AD) 1950 (Gregorian calendar years)

The only exception to the trend of long-term erosion on the Clatsop shelf occurs in the shallow nearshore zone, adjacent to the central Clatsop Plains. In core 103, located in 10.8 m water depth, a sand dollar fragment at 133 cm returned a calibrated age of 558 BP, another sand dollar fragment at 237 cm had a calibrated age of 588 BP, and another sand dollar fragment at 549 cm returned a calibrated age of 1800 BP. These dates indicate sediment accumulation on the upper shoreface at rates on the order of 30 cm/100 years. This nearshore accumulation is not surprising given the history of long-term progradation of Clatsop Plains (Kaminsky *et al.* 1999; Peterson *et al.* 1999).

The radiocarbon ages and inferred accumulation rates derived from the vibracores are consistent with the historical bathymetric changes observed on the Clatsop shoreface. Relatively old radiocarbon dates occur at shallow depths within cores 101, 102, 105 and 106, and indicate very low sediment accumulation rates in the same areas where high rates of historical seabed erosion have been measured. Similarly, within core 103 young dates moderately deep within the core and indicate relatively high accumulation rates on the upper shoreface where historical seabed accumulation has been measured. In core 104, recent accumulation over old and out-of-sequence dates is consistent with the trends shown over historical time scales (next section). The old (and shallow) radiocarbon ages found on the Clatsop lower shoreface stand in sharp contrast to the much younger (and deeper) radiocarbon ages found on the Long Beach lower shoreface north of the MCR (Kaminsky and Ferland, 2005). The pattern of older radiocarbon ages and relict mud deposits in the southern-most and offshore Clatsop shoreface cores, and progressively younger dates associated with these deposits in the onshore and northerly direction, is consistent with the northward migration of Clatsop Spit over the past few thousand years and the subsequent movement of the ebb delta (Twichell and Cross 2001).

Historical Time Scale

Regional bathymetric changes for three historical periods are shown in Figures 3–5. These figures were developed from merged regional bathymetric surfaces developed by Buijsman *et al.* (2003) and include the locations of the vibracores. These figures illustrate the regional decadal- to century-scale morphological changes primarily attributed to the construction of the Columbia River jetties.

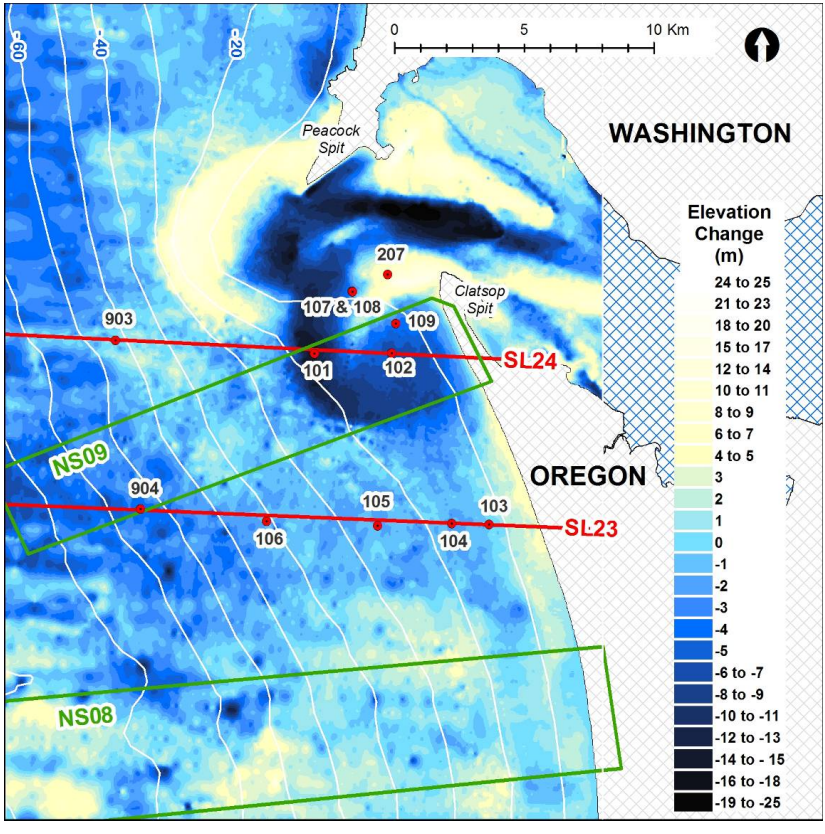

Fig. 3. 1868–1935 bathymetric change from Buijsman *et al.* (2003) shown with the vibracore sites. Data compiled from 1877 to 1926 for shelf; 1868 to 1926 for delta; and 1868 to 1935 for entrance and estuary. Bathymetric contours derived from data from 1998–2003 in meters relative to NAVD 88.

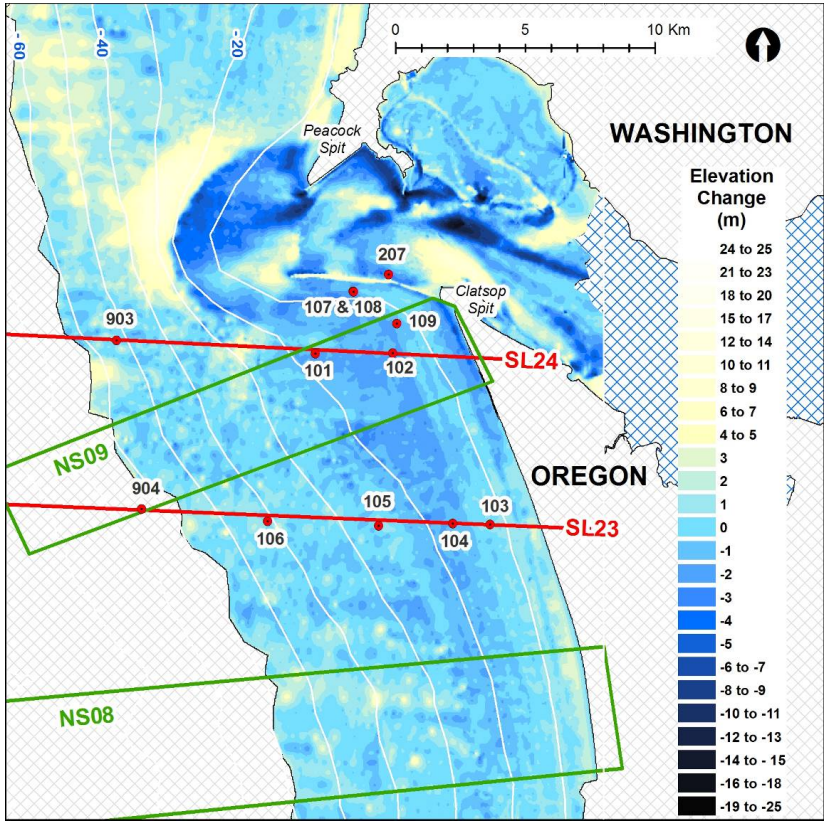

Fig. 4. 1926–1958 bathymetric change from Buijsman *et al.* (2003) shown with the vibracore sites. Data compiled from 1926 to 1958 for shelf, delta, and estuary; 1935 to 1958 for entrance. Bathymetric contours derived from data from 1998–2003 in meters relative to NAVD 88.

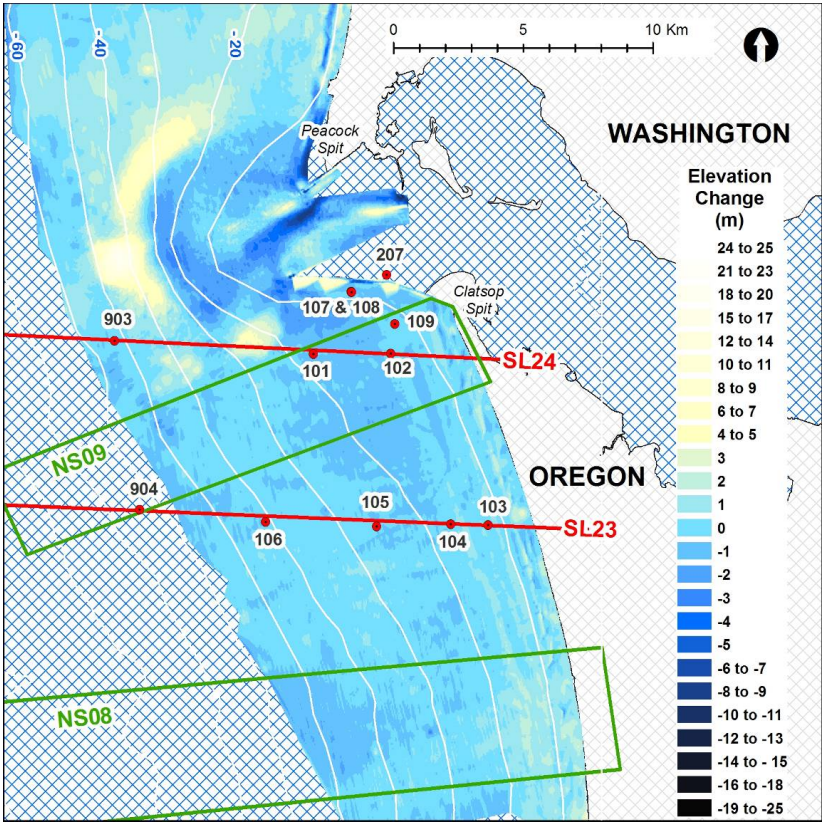

Fig. 5. 1958–2000 bathymetric change from Buijsman *et al.* (2003) shown with the vibracore sites. Bathymetric contours derived from data from 1998–2003 in meters relative to NAVD 88.

The historical erosion of the Clatsop shoreface has been most severe in the vicinity of core 101, often near the crest of the ebb-delta in the pre-jetty surveys. From 1868 to 1883 there was 3.7 m of vertical erosion at this site, and from 1883 to 2000 there was an additional 11.7 m of erosion at this site. Shoreface lowering at the site of core 102 from 1883–2000 was similar, at 9.7 m (Figure 6). Both cores 101 and 102 contain laminated mud units in the shallow subsurface. In core 101, the relict mud unit is less than 10 cm below the seabed, and only 85 cm below the seabed in core 102. Figure 6 shows the shoreface profile change from 1868 to 2000 at these core sites. The profile change shows the rapid initial adjustment from an ebb-shoal environment to a shoreface environment. The apparent shoal feature near km 3 in Figure 6 in the more recent profiles is Ocean Dredge Material Disposal Site A, where more than 18.25 million m^3 of dredged material was placed during 1956–1994.

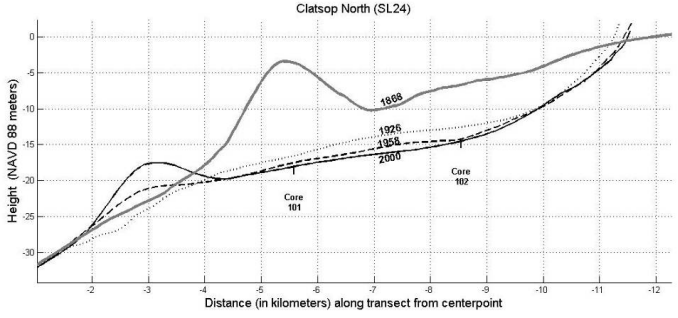

Fig. 6. Historical shoreface profiles and vibracore sites at the SL24 transect.

Figure 7 shows the historical shoreface profile change at the Clatsop south seismic line (SL23), where the progradation of the upper shoreface and the extensive lowering of the mid- to lower shoreface has occurred. Core 103 is located near the toe of the upper shoreface progradation. Profile analyses of the SL23 transect reveals that the toe of the upper shoreface progradation migrates from -10.5 m in 1868 to -17.5 m in 2000.

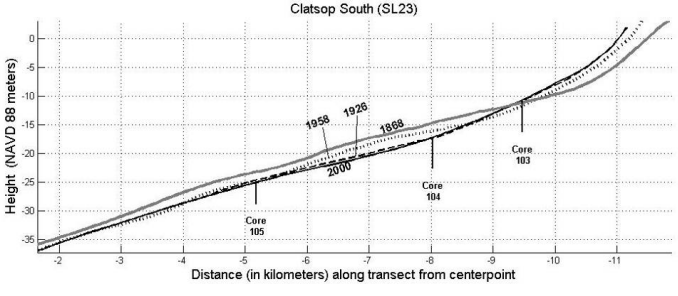

Fig. 7. Historical shoreface profiles and vibracore locations at the SL23 transect.

The major observation of change in the NS09 (along-shore averaged) profile is that of significant lowering of the profile to about 25 m water depth, as shown in Figure 8. During 1868–1926, the NS09 profile rapidly lowered, much more so than during any other period. Between water depths of -1.2 m and -24.9 m, the average rate of shoreface lowering was -9.6 cm/yr. The erosion peak occurred at an interval-average depth of -12.6 m at a rate of -17.8 cm/yr. During 1926–1958, the shoreface lowered between -0.8 m and -26.0 m at an average rate of -3.3 cm/yr, a substantial slowing from the previous period. The erosion peak during this period occurred at an interval-average depth of -14.0 m at a rate of -5.3 cm/yr. During 1958–2000, the shoreface continued to lower, but at a lower rate and with a greater extent offshore. The shoreface between -8.7 m and -26.2 m lowered by an average rate of -1.5 cm/yr, less

than half the rate of the previous period. The erosion peak occurred at an interval average depth of -16.3 m and had a rate of -2.3 cm/yr. Between -26.2 m and the end of the profile at -55.7 m, the profile lowered at an average rate of -0.7 cm/yr. Over the three intervals spanning 1868–2000, the average rates of lowering were -9.6 cm/yr, -3.3 cm/yr, and -1.5 cm/yr, while the peak rates of lowering were -17.8 cm/yr, -5.3 cm/yr, and -2.3 cm/yr.

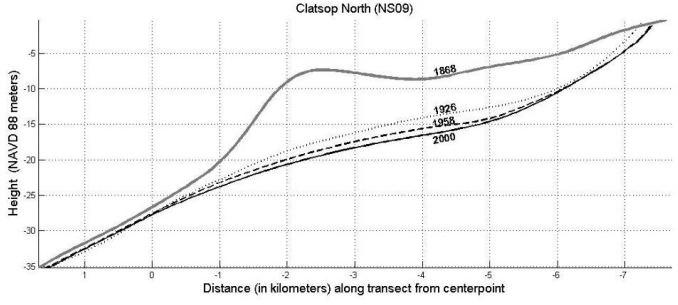

Fig.8. Historical shoreface profile change at the NS09 alongshore-averaged transect from 1868 to 2000.

Farther south, at the NS08 alongshore-averaged transect, the historical profiles suggest slight profile translation over the entire period from 1868 to 2000 (Figure 9). However, during the interval from 1958–2000, the lower shoreface slightly eroded with a minor increase in magnitude with distance offshore from the toe of the progradational sand wedge. This trend is consistent with a time lag in reduction of sediment supply since jetty construction, and follows the shoreline change trend presented in Kaminsky *et al.* 1999. We surmise that the rapid deflation of the profile in the northern sector provided a pulse of onshore and southerly migrating supply of sand to induce historical shoreface translation on the central Clatsop shoreface.

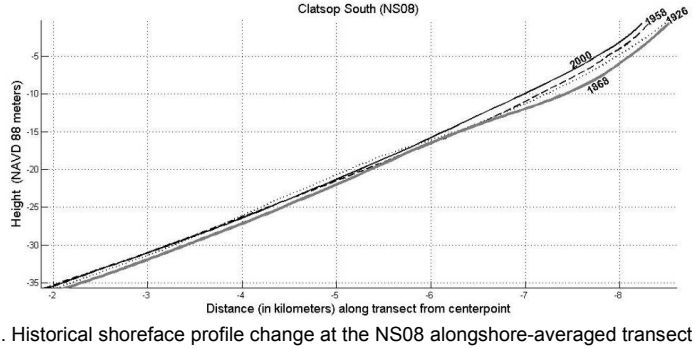

Fig. 9. Historical shoreface profile change at the NS08 alongshore-averaged transect from 1868 to 2000.

Interannual Time Scale

Since 1997 upper shoreface profile data have been collected from (typically) ~12-m water depth to landward of the primary dune (Ruggiero *et al.* 2005). Individual nearshore bathymetric profiles (Figure 10) along Clatsop Plains reveal that interannual morphodynamic variability within the upper shoreface is large, masking trends at these time scales. As demonstrated by Ruggiero *et al.* (2003), the variability is large in the nearshore zone and lower beachface but decreases landward and upward on the beach profile. In this case, we observe evidence of a net residual trend of onshore sediment supply from the lower shoreface that is resolvable at interannual time scales on the dune face (Figure 11). The time series of topographic beach profiles at Rilea (profile location indicated in Figure 1) reveals a consistent trend of dune face progradation at an average rate of ~2.5 m/yr during 1997–2006.

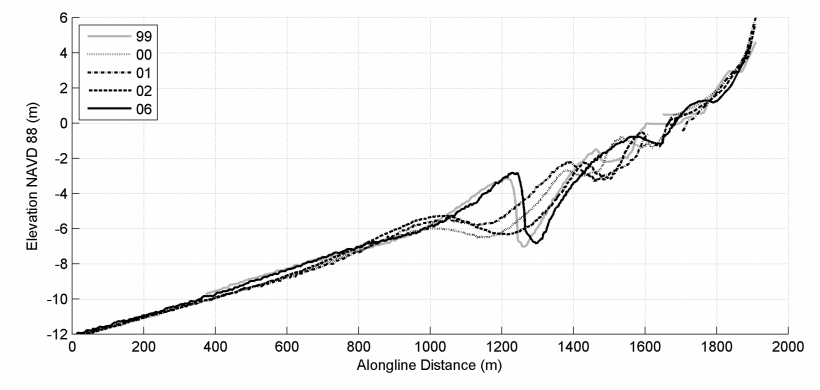

Fig. 10. Upper shoreface profile change at Rilea from 1999 to 2006.

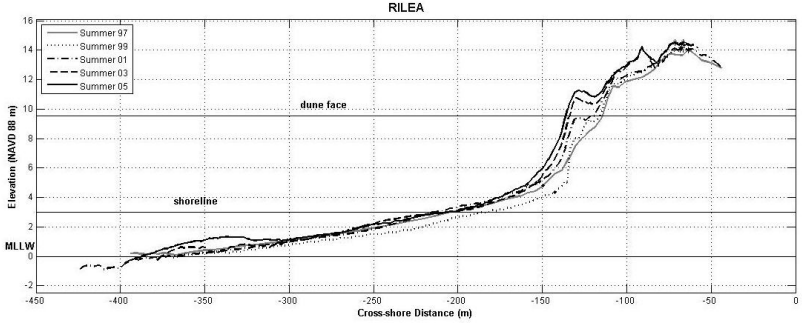

Fig.11. Beach profile change at Rilea showing the prograding dune face from 1997 to 2005.

CONCLUSION

Evidence of long-term erosion of the Clatsop lower shoreface comes from several sources. First, the vibracores contain relict laminated mud and sand units that occur near the top of many cores, 'old' radiocarbon ages, winnowed or lag deposits, and inferred rip-up clasts and mud clasts. Radiocarbon dates on carbonate that are out of stratigraphic order are indicative of re-working in a low sedimentation or erosional setting. Near-surface sediment samples across this shoreface are found to be significantly coarser than samples from the adjacent Long Beach shoreface north of the MCR. Next, the time series of historical bathymetric data from 1883 to 2000 shows a consistent erosion pattern that reveals as much as 10 m of shoreface deepening within a few km of the south jetty. Recent upper shoreface surveys suggest a gradient in morphology change, with highest erosion rates observed closest to the jetty (across the entire profile) and accretion only on the upper shoreface shallower than approximately -8 m MLLW several kilometers to the south, which is consistent with the longer term, regional data. Together, there is abundant evidence that the lower Clatsop shoreface has significantly eroded over contemporary, historical and late Holocene timescales. These results provide a sound basis for predicting future shoreface changes and informing management strategies to reduce the impacts of shoreface erosion due to a sediment deficit.

ACKNOWLEDGEMENTS

The authors are grateful for the funding provided by the University of Sydney Institute of Marine Science, the U.S. Geological Survey – Coastal and Marine Geology Program, the U.S. Army Corps of Engineers – Portland District, the Washington Department of Ecology, and the Northwest Association of Networked Ocean Observing Systems (NANOOS). We thank Bobbi Conard for supporting the processing of the vibracores at the Oregon State University Core Facility. Many individuals contributed to the collection of vibracores, beach topography and nearshore bathymetry. Dinah McCandless provided a wealth of GIS support and assistance with figures. We thank Candice Holcombe for help with formatting and preparation of this manuscript.

REFERENCES

Buijsman, M.C., Sherwood, C.R., Gibbs, A.E., Gelfenbaum, G., Kaminsky, G.M., Ruggiero, P., and Franklin, J. (2003). "Regional sediment budget of the Columbia River littoral cell, USA: Analysis of bathymetric- and topographic-volume change," U.S. Geological Survey Open File Report 02-281, 140 p.

Gelfenbaum, G., Sherwood, C.R., Peterson, C.D., Kaminsky, G.M., Buijsman, M.C., Twichell, D., Ruggiero, P., Gibbs, A., and Reed, C. (1999). "The Columbia River littoral cell: A sediment budget overview," *Proceedings of Coastal Sediments '99*, ASCE, 1660–1675.

Kaminsky, G.M., Buijsman, M., Gelfenbaum, G., Ruggiero, P., Jol, H.M., Gibbs, A.E., and Peterson, C.D. (1999). "Synthesizing geological observations and processes-response data for modeling coastal change at management scale," *Proceedings of Coastal Sediments '99*, ASCE, 1708–1723.

Kaminsky, G.M., Buijsman, M.C., and Ruggiero, P. (2001). "Predicting shoreline change at decadal scale in the Pacific Northwest, USA," *Proceedings of the 27th International Conference on Coastal Engineering*, ASCE, 3, 2400-2413.

Kaminsky, G.M., and Ferland, M.A. (2003). "Assessing the connections between the inner shelf and the evolution of Pacific northwest barriers through vibracoring," *Proceedings of Coastal Sediments '03*, CD-ROM Published by East Meets West Productions, Corpus Christi, TX ISBN-981-238-422-7, 12 p.

Kaminsky, G.M., and Ferland, M.A. (2005). "Vibracores at the Mouth of the Columbia River, Final Report," Washington Department of Ecology publication No. 05-06-020, 103 p.

Moritz, H.R., Moritz, H.P., Hays, J.R., and Sumerell, H.R. (2003). "100-years of shoal evolution at the Mouth of the Columbia River: Impacts on channel, structures, and shorelines," *Proceedings of Coastal Sediments '03*, CD-ROM Published by East Meets West Productions, Corpus Christi, TX ISBN-981-238-422-7, 14 p.

Peterson, C.D., Gelfenbaum, G., Jol, H.M., Phipps, J.B., Reckendorf, F., Twichell, D.C., Vanderburg, S. and Woxell, L. (1999). "Great earthquakes, abundant sand, and high wave energy in the Columbia Cell, USA," *Proceedings of Coastal Sediments '99*, 2, 1676–1691.

Ruggiero, P., Kaminsky, G.M., and Gelfenbaum, G. (2003). "Linking proxy-based and datum-based shorelines on a high-energy coastline: implications for shoreline change analyses," *Journal of Coastal Research*, SI 38, 57-82.

Ruggiero, P., Kaminsky, G.M., Gelfenbaum, G., and Voigt, B. (2005). "Seasonal to interannual morphodynamic variability along a high-energy dissipative littoral cell," *Journal of Coastal Research*, (21) 3, 553-578.

Twichell, D.C. and Cross, V.A. (2001). "Holocene evolution of the Southern Washington and Northern Oregon shelf and coast: Geologic discussion and GIS data release," U.S. Geological Survey Open-File Report 01-076, 28 p. (with CD).

THE CHALLENGES OF RESTORING LOUISIANA BARRIER ISLANDS: FROM DESIGN THROUGH CONSTRUCTION

Gordon G. Thomson, P.E.[1], Greg M. Grandy[2], and Rachel Sweeney[3]

1. Coastal Planning & Engineering, Inc. 2481 NW Boca Raton Blvd, Boca Raton, FL 33431, USA. gthomson@coastalplanning.net.
2. Coastal Engineering Division, Louisiana Department of Natural Resources 617 North 3rd St, 10th Floor, P.O. Box 44027, Baton Rouge, LA 70804-4027, USA. gregoryg@dnr.state.la.us.
3. NOAA, National Marine Fisheries Services, c/o Louisiana State University, South Stadium Drive, Military Science Building, Room 266, Baton Rouge, LA 70803-7535, USA. rachel.sweeney@noaa.gov.

Abstract: Louisiana's barrier islands provide not only habitat but protection for interior marshes. The loss of these islands would expose interior marshes to increased wave heights, flooding, and loss of wetland habitat. The restoration of Louisiana barrier islands poses a combination of challenges, starting with quantifying project goals, developing a project design based on meeting those goals, through to construction of the project. This paper outlines design and construction details unique to Louisiana barrier islands using East Grand Terre and the Chaland Headland Restoration CWPPRA projects as case studies.

INTRODUCTION

East Grand Terre and the Chaland Headland are part of a chain of barrier islands that separate the Gulf of Mexico from Barataria Bay. The islands are located approximately 80 km due south of New Orleans and provide a first line of defense against waves and storm surge during storm events. Figure 1 provides a location map of the two project areas.

The island restoration projects are being constructed under the Coastal Wetlands Planning, Protection and Restoration Act (CWPPRA) with the Louisiana Department of Natural Resources as the local sponsor and the National Oceanographic and Atmospheric Administration's (NOAA) National Marine Fisheries Service as the federal sponsor.

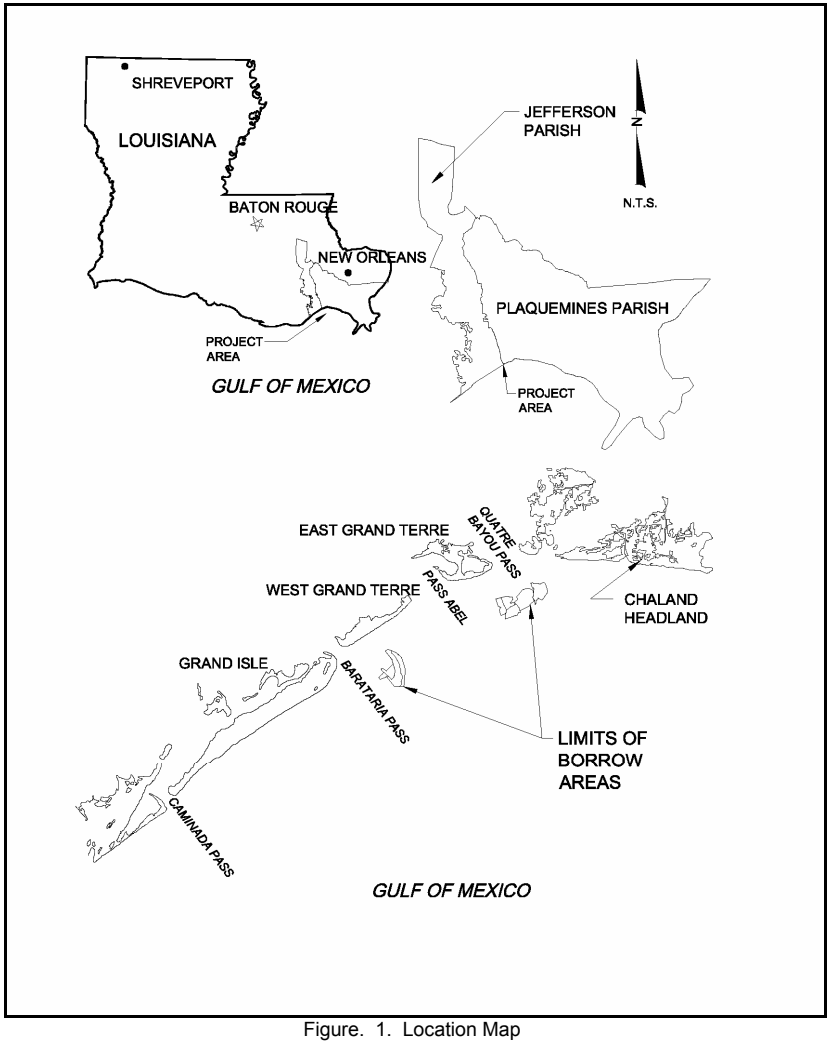

Figure. 1. Location Map

Some of the design challenges encountered with restoring Louisiana's barrier islands include: 1) Estimating the performance of a beach nourishment project that is composed primarily of sand, when the historic shoreline recession rates reflect the recession of islands that can contain upwards of 60% clay/silt material; 2) A relative sea-level rise rate (RSLR) that is amongst the highest in the world; 3) CWPPRA projects require a one-time construction event and a 20-year project life.

DYNAMIC MORPHOSEDIMENTARY PRINCIPLE

Mann and Thomson (2003) showed that at Holly Beach, Louisiana, the cross-shore profile changed from a sandy bottom to a silty bottom at approximately -1.7 m, MHW (-4 feet, NAVD). This change in the characteristic bottom sediment coincided with a break in the slope of the cross-shore profile. Above this elevation, the profile was a concave upward curve of the approximate form $y=ax^{2/3}$. Below this elevation, the profile was relatively flat with a slope of 1 Vertical (V):400 Horizontal (H). They suggested that this break in slope be used as the bottom of the active profile height for sand.

Campbell *et al*. (2006, in press) developed this concept further with a dynamic morphosedimentary model (DMSM) that explains the high shoreline recession rates observed along Louisiana barrier islands. The DMSM proposes that the beach is composed of a thin veneer of sand that overwashes the island during large storms. This exposes the marsh sediment that comprises the bulk of the barrier island. As the island erodes, silts and sand are released. The silts are transported offshore while the sand is concentrated along the beach face due to natural sorting by wave action. This reforms the sand veneer but in a more landward location. However, the high percentage of silt in the body of the island results in large shoreline recession until the sand veneer reforms. Overwash of the barrier islands also deposits sediment in the back marshes, which helps to counteract elevation loss due to relative sea level rise.

The construction of a wide sandy beach along the front of barrier islands should result in lower shoreline recession rates because the erosive marsh will not be exposed following storm events. However, overwash of the island is still important to maintain the back marsh elevation. While the constructed elevation of the beach can be minimized to allow overtopping during low frequency storm events, the additional width of the beach can reduce this effect. Therefore, nourishment of the back marshes is an integral component of the project.

PROJECT GOALS

Louisiana barrier islands constructed under coastal restoration authorities are evaluated differently from beach nourishment projects constructed elsewhere in the nation. The majority of current shoreline restoration projects in Louisiana are not evaluated using a typical cost-benefit analysis (USACE, 1999) that assesses infrastructure protection and recreational use. The CWPPRA program recognizes that these islands provide important habitat for flora and fauna, and protection against storm surge and wave action. Project performance of the restoration of barrier islands under CWPPRA is typically evaluated using a Wetland Value Assessment (WVA) (Environmental Work Group, 2002). The Barrier Island Community Model is used to determine the WVA and assess the performance of barrier island projects in providing fish and wildlife benefits.

The Barrier Island Community Model includes variables such as the percent of subaerial area that is classified as subtidal, intertidal, supratidal, or dune habitat, the percent of each subaerial area that is vegetated, percent vegetative cover by woody species, marsh

edge interspersion, and beach/surf zone features (Environmental Working Group, 2002). The definitions of these various habitat classes are shown in Table 1.

Table 1. Habitat Description (after Williams and Sweeney, 2005)

Habitat	Description
Dune	≥ +1.02m MHW (+5 feet, NAVD[1]) The portions of the dune platform anticipated to be above the specified elevation.
Supratidal	≥ +0.21m, MHW (+2 feet, NAVD) to < 1.02m, MHW (+5 feet, NAVD) Beach berms and portions of the fore and back slope of the dune within the elevation range. Also includes primary retention/ containment dikes for the period anticipated to remain in the elevation range. Generally includes major portion of the marsh platform until the time dewatering and consolidation reduce the elevation to intertidal.
Gulf Intertidal	≥ -0.5m, MHW (0 feet, NAVD) to < +0.1m, MHW (+2.0 feet, NAVD) Gulf side beach slope / shallow open water.
Bay Intertidal	≥ -0.50m, MHW (0 feet, NAVD) to < +0.1m, MHW (+2.0 feet, NAVD) Bayside elevations including vegetated wetlands, flats, and bayside open water areas.
Subtidal	≥ -0.96m, MHW (-1.5 feet, NAVD) to < -0.5m, MHW (0 feet, NAVD) or 300m (1,000 feet) bayward of the 0.0m contour Shallow Open water bayside area only.

1. NAVD – North American Vertical Datum

The application of the Barrier Island Community Model poses a challenge from an engineering design perspective, as the design must optimize different habitat area classifications along with the cost. The variables within the model are estimated for each year over the project life to develop expected benefits, which allows various alternatives to be compared.

Interestingly, the Wetland Value Assessment method does not address island integrity, which was omitted from the model to ensure that project evaluation is consistent with the CWPPRA authority (Environmental Work Group, 2002). It was considered that island integrity was an important factor in project design but that erosion of the barrier island would be reflected in a loss of habitat acreage and thus not needed to characterize habitat quality. However, an additional project goal for the East Grand Terre and Chaland Headland Projects is that the island would not be breached within the 20-year project life and that the minimum dune elevation would not be less than 0.7m, MHW following any storm event.

BEACH FILL DESIGN

The project design steps for East Grand Terre (Coastal Planning & Engineering, Inc, 2005) are outlined here. East Grand Terre was chosen because it involves a more

complex shoreline development than the Chaland Headland and provides some additional insight into the geomorphic changes that occur along Louisiana barrier islands.

East and West Grand Terre used to be one continuous island until a significant breach occurred in the center of the island in 1926, creating Pass Abel (Figure 2). The creation of Pass Abel has influenced shoreline retreat of the adjacent shorelines. After the creation of Pass Abel, the west end of East Grand Terre eroded until Bay Melville was open to the Gulf of Mexico. Since 1988, a spit has been extending in a west-northwesterly direction, enclosing Bay Melville once again. Shoreline recession calculations of the eastern side of the island were therefore used to analyze volume losses. The growth of the western spit enabled the development of a move complete sediment budget.

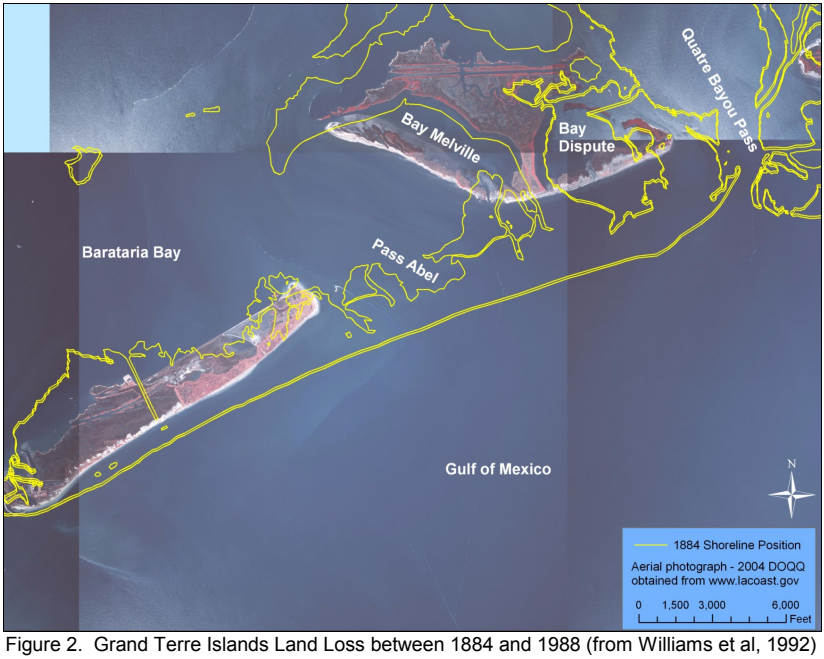

Figure 2. Grand Terre Islands Land Loss between 1884 and 1988 (from Williams et al, 1992)

The shoreline along the eastern side of East Grand Terre retreated at a rate of 8.0 m/year (26 feet/year) between 1884 and 1988 (CPE, 2005). The shoreline recession rate has increased in the last few years and has averaged 11.4 m/year (38 feet/year) since 1996. The island has narrowed significantly and small breaches have occurred in several areas along the island.

Typically shoreline recession rates can be correlated to volumetric erosion. However, while shoreline location data is available back to 1884, profile data along East Grand

Terre was only available from surveys conducted in November 2000 and August 2002. A comparison of volumetric changes and shoreline changes did not provide a strong correlation, possibly due to the short record. Therefore, volumetric change was developed along the island by multiplying the shoreline change by the active profile height and distance between profiles (CPE, 2005).

The top of the active profile was determined for each profile line from the August 2002 survey. Thus, there was a varying active profile height along the length of the island. The bottom of the active profile height was taken as the change in slope of the profile. The change in slope was observed to be approximately -1.5 m MHW (-5 feet, NAVD) at East Grand Terre.

Once the volumetric changes along the island had been established, a sediment budget was developed to distinguish between alongshore and cross-shore losses of silt and sand, as well as shoreline recession due to relative sea-level rise and overwash. By accounting for the various components, a longshore sand transport curve could be developed to assist in the prediction of sediment transport following construction.

The first element in developing the sediment budget was to estimate the sand percentage along East Grand Terre. The reformation of the western end as a spit like feature suggested that this end of the island should have a higher sand content than the western end. Vibracores collected along the dune crest and within the back bay showed that the west end of the island was composed primarily of sand (90%) while the east end of the island contained only 40% sand. It was assumed that the silt fraction would be transported offshore while the sand was transported in a longshore direction or overwashed into the back bay.

The second element was to determine the volumetric "loss" due to RSLR. Shoreline recession due to RSLR does not result in a net volume change in the cross-shore profile but simply a redistribution of the sediment across the profile. However, the volume change calculated from shoreline recession must be reduced to account for relative sea level rise prior to calculating the volume change used to develop the sand littoral transport rate. It was estimated using the Bruun rule (1962) that relative sea level rise results in a shoreline recession of 1.4 m/year (4.6 feet/year). The break in slope was used as the bottom of the active profile for application of the Bruun Rule.

The third element within the sediment budget was overtopping. The average crest elevation along East Grand Terre is low, approximately 0.6 m, MHW (3.4 feet, NAVD). As a result, sediment is transported over the top of the island by waves during storm events. This is the primary mechanism of island rollover. The landward movement of sediment conserves some sediment within the system despite the landward shift of the shoreline. The volume change, calculated from shoreline change, must be reduced to account for the conservation of sediment within the system. An estimate of overwash along the islands was estimated using the November 2000 and August 2002 profile data.

An overwash estimate of 4.8 m^3/m/year was developed by comparing the November 2000 and August 2002 surveys.

The sand conservation equation allows the littoral transport for adjacent reaches to be estimated using Equation 1.

$$LT_{out} = \Delta V_{measured} * \% \, sand + LT_{in} - V_{overwash} - V_{RSLR} \quad (1)$$

where LT_{out} = Littoral transport out of the reach; LT_{in} = Littoral transport into the reach (LT_{out} from updrift cell); $\Delta V_{measured}$ = Volume change calculated based on shoreline change; % sand = Factor applied to volume change to account for silt in island composition; $V_{overwash}$ = Volume of overwash = 4.8 m^3/m/year x reach length; V_{RSLR} = Volume associated with shoreline retreat due to relative sea level rise;

Typically a nodal point (a point of zero net sediment transport) is chosen as the starting point for the solution of Equation 1. It is easier to locate an area with zero net sediment transport than the transport rate elsewhere along the island (such as at the end) because the nodal point can usually be identified by the location with the highest shoreline recession rate. This was close to the eastern end. Aerial photograph interpretation, wave modeling, and analysis of the coastal processes along the island also suggested that there was sediment transport towards both ends of the island and that the nodal point was located close to the eastern end of the island. Solution of equation 1 along the length of the East Grand Terre provided the longshore sand transport rate shown in Figure 3.

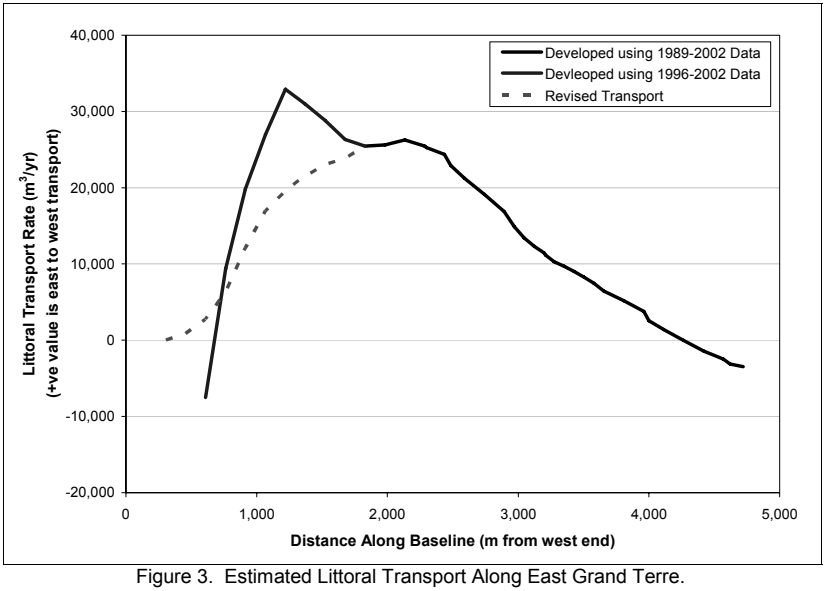

Figure 3. Estimated Littoral Transport Along East Grand Terre.

Figure 3 shows that two data sets had to be used to develop the longshore sand transport rate. This was due to limited available data along the west end. The general trend of sediment transport increasing from the east end towards the center of the island and then decreasing along the western spit agrees with features observed on the island. First, the spit feature at the eastern tip of the island is very small, which suggests that sediment transport is relatively low at this point. Second, the island has a distinct change in orientation where the western spit formation started and the sediment transport rate starts to decrease just around this bend. Third, the growth of the western spit would indicate a decreasing longshore transport rate. Lastly, the sediment transport at the western tip of the island must be small because a small tidal channel connecting Bay Melville to Pass Abel remains open. The tidal currents in this channel are weak because the tidal range in the project area is only 0.3m and Bay Melville is only 1.5 km^2. Therefore, a large sediment transport rate would be expected to overwhelm the tidal currents and close the pass.

A beach nourishment cross-section has two components: the design section, which is the fill volume required at TY20 to meet the project goals, and advanced nourishment, which is the sacrificial portion of the fill that will erode over the 20-year project life. This two-section design is in accordance with the National Research Council (1995) recommendations. The advanced nourishment volume can be estimated using the sediment budget. The design section was determined by cross-shore modeling using SBEACH (Larson *et al*. 1990).

Cross-shore modeling was used to determine the minimum design dune width necessary to meet the project goals. The cross-section has a 1V:30H landward slope, which is similar to the landward sides of the existing dunes. A 1V:45H seaward construction slope was adopted based on the post-construction profile slope attained during the Holly Beach Sand Management Project, Louisiana (CPE, 2003) using similar fill material. The constructed dune elevation was set to +1.3 m, MHW (+6 feet, NAVD), based on cross-shore modeling. The +1.3 m, MHW dune elevation is above the 20-year return period surge elevation (+1.2 m, MHW) estimated for target year 20 (includes relative sea level rise over the life of the project).

The USACE (2001) estimated that island breaching occurs when the overtopping rate exceeds 0.05 m^3/s (1.7 cfs), and this standard was used to evaluate the likelihood of breaching. The modeling suggested that the maximum overtopping rate will be 0.02 m^3/s (0.6 cfs) so breaching is not anticipated during a 20-year storm event.

The cross-shore modeling showed that the design cross-section to achieve the project goals is a 27.4m (90-foot) dune crest. The design cross-section is shown in Figure 4. This corresponds to an average fill density of 160 m^3/m (64 cy/ft) or a total of 708,750 m^3 (927,000 cubic yards) of beach fill over the 4.42 km (14,500 feet) project length.

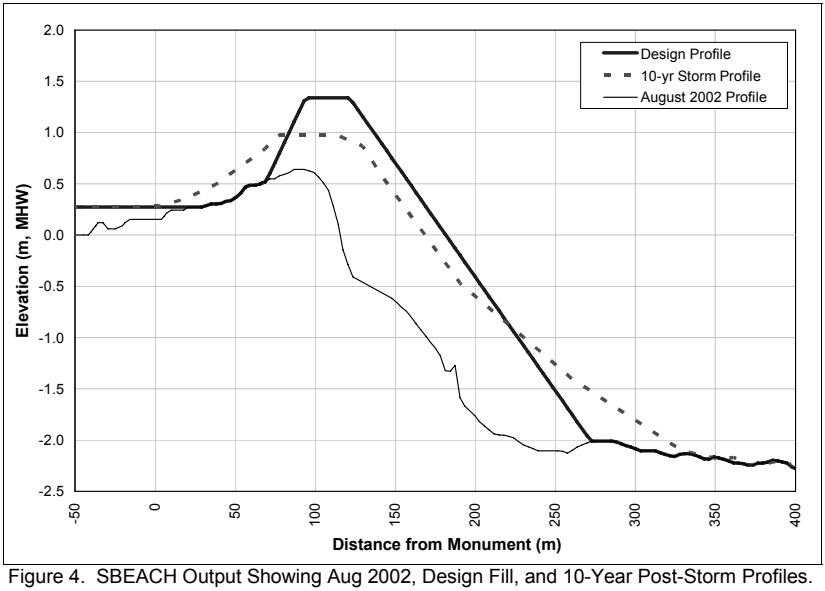

Figure 4. SBEACH Output Showing Aug 2002, Design Fill, and 10-Year Post-Storm Profiles.

The Generalized Model for Simulating Shoreline Change (GENESIS) (Hanson and Kraus, 1989) was used to optimize the fill placement. Since GENESIS assumes a fixed active profile height and does not account for mixed sediment, GENESIS was calibrated using the sediment transport rate developed through the littoral budget. The total volume of beach fill proposed at East Grand Terre is 1,163,000 m^3 (1,521,000 cubic yards).

While the design fill is placed uniformly along the project length to ensure that the design section is in place throughout the length of the project life, the advance nourishment is placed non-uniformly to account for the varying longshore transport. Since the eastern end of the island has a higher longshore transport rate, while the western side has been accretional, more than 80% of the advanced fill was placed on the eastern side of the island.

MARSH FILL DESIGN

The average elevation of the existing marsh platform was determined to be -0.2 m, MHW (+1.1 feet, NAVD) based on measurements taken along three survey lines. Ideally, to maximize intertidal functions, the marsh platform should have an elevation between mean high water and mean low water over the majority of the project life. Eustatic sea level rise will result in the mean high and mean low water levels rising an estimated 0.061 m (0.200 feet) over the 20-year project life (NRC, 1987). The marsh platform will drop in elevation as a function of three processes: geologic subsidence of the region; consolidation of the marsh fill material; and consolidation of the underlying soils due to the weight of the marsh fill.

The geologic subsidence is independent of the project and will occur under the without project condition as well as the with project condition. It is considered to be constant at 0.009 m/year (0.0292 feet/year) (NRC, 1987) over the 20-year project life. The extent of marsh fill consolidation will be a function of the classification properties of the borrow material (sand, silt, clay & organic content), the thickness of the lift and the placement techniques (i.e., dredge pipe discharge velocity and flow, containment and cell capacity). The soil underlying the marsh fill will consolidate due to the addition of an overburden (the constructed marsh). Settlement of the underlying soils is a function of the consolidation properties of the underlying soils, the area of the applied load and the amount of fill above the water table (surcharge load). Marsh settlement curves (Figure 5) were developed to help determine a target elevation for marsh construction that would maximize the time that the marsh elevation was intertidal during the 20-year project life.

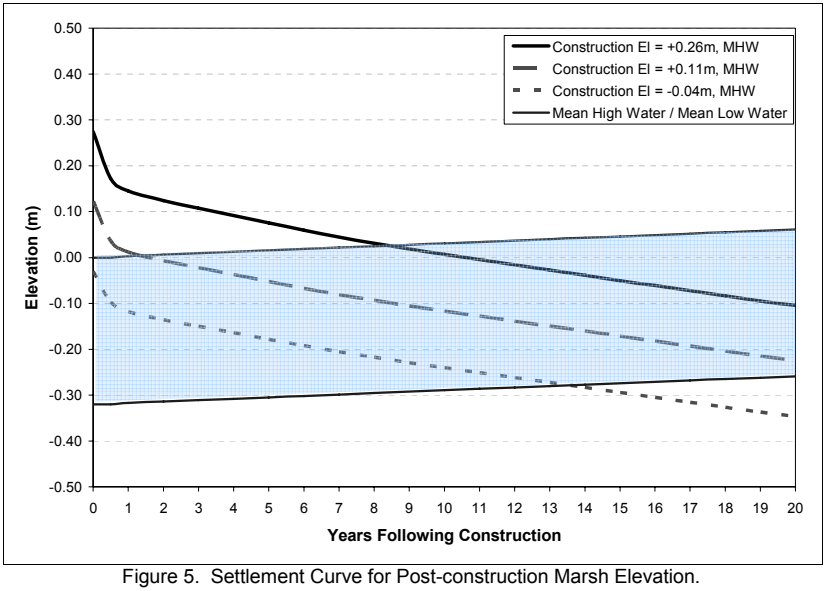

Figure 5. Settlement Curve for Post-construction Marsh Elevation.

The total volume of marsh fill proposed for the East Grand Terre Project is 1,390,000m^3 (1,817,000 cubic yards).

Chaland Headland Construction

The Chaland Headland Project bid package included the placement of 1,370,000m^3 (1,792,200 cubic yards) of beach fill, 726,500 m^3 (950,200 cubic yards) of marsh fill, along with other ancillary items. Bids were opened for the Chaland Headland Restoration (BA-38-2) CWPPRA Project on 19 July, 2005, just 41 days prior to landfall of Hurricane Katrina. It was envisioned that there would be changes to the project area between the development of the bid documents and the start of construction of the

project. Therefore, the project specifications allowed for changes to the project layout following the pre-construction survey. This proved useful as the eye of Katrina passed only 15km (9 miles) to the east of Chaland Headland forming a second breach and causing additional beach fill loss.

Shoaling of the contractor's access route (Robinson Canal) during the passage of Hurricane Katrina was not anticipated, necessitating additional permitting, oil infrastructure investigations, and oyster lease coordination. Hurricane Katrina also destroyed the closest monument requiring that this be reset prior to the start of the pre-construction survey.

Chaland Headland is similar to many Louisiana barrier islands in that there is significant oil infrastructure in and around the island. Photo 1 shows a pre-construction aerial of the project site. The dashed red line highlights the location of the "W" Canal, which was dredged to allow access to oil infrastructure. As can be observed in Photo 1, the "W" Canal has resulted in several breaches forming in the island, as the shoreline receded. The breaches then exacerbated the shoreline retreat.



Photo 1. Pre-Construction Aerial of the Chaland Headland with A Trace of the "W" Canal.

A field study was performed to determine the tidal currents flowing through the western breach and whether the pumping rate of a 30" cutterhead dredge would be sufficient to close this breach without having to resort to a structural solution. Several oil pipelines traverse the project area and it was preferred to avoid a structural closure solution. The analysis suggested that pumping rate of sand would be sufficient to close the breach. This was confirmed during construction as the contractor (Weeks Marine, Inc.) closed the breach with no difficulty.

Locating/ identifying sand resources in Louisiana has, and will continue to pose a challenge, to barrier island restoration. A borrow area (Quatre Bayou) was identified by Coastal Planning & Engineering, Inc approximately 5 km (3 miles) southwest of the project site. The Quatre Bayou borrow area was located in water depths of -4.0 m to -5.8 m, MHW (-12 to -18 feet, NAVD). The sand portion of the borrow area varied in thickness from 1 to 2.5m (3 to 8 feet) thick but was covered by a silt overburden that was between 0.5m and 3m (1 to 9 feet) thick. A portion of the overburden was used to construct the marsh, while the sand layer was used as beach fill material. The beach fill material was fine sand (0.11 mm) and had a silt content that ranged from 4% up to 40% percent. Similarly, the silt layer contained varying percentages of sand (5% to 50%).

The varying content of the different types of fill provides both a unique opportunity and challenge at the same time. It is useful to have a sandy marsh from both an ecological and engineering perspective. A sandy marsh will limit the amount of settlement that the marsh will experience and provide additional resistance to wave attack if it were to become exposed. A varying sand content in the borrow area also results in varying fill type through the marsh, which can add to habitat diversity. However, a varying sand content in the marsh fill material makes it challenging to achieve a specific elevation range. During the bidding process, dredge contractors indicated their concern for the tolerance of ±0.1 m (±0.3 feet) required in the specifications. This tolerance was required because the project performance relies on achieving the target marsh elevation. The contractor was capable of meeting the target elevations along the project though some sections of the marsh were sand and higher while other sections contained less sand and were slightly lower in elevation. Post-construction marsh surveys were conducted 30 days following the placement of fill in a given section to allow time for dewatering and initial settlement.

The Chaland Headland specifications required that the beach fill contain less than 15% silt and that the beach be constructed without confinement. The majority of the beach fill along the project length fulfilled the silt requirement. However, the beach fill at the far eastern end contained a higher volume of silt even though the vibracores and seismic records suggested that the section of the borrow area being dredged to supply the sand was the cleanest in the entire borrow area. The volume of overburden exceeded the volume required for marsh creation so the overburden was sidecast back in to the borrow area. It is hypothesized that the previously sidecast marsh fill material was flowing into the area being dredged, increasing the silt content. The depth of cut in this area was also the deepest in the entire borrow area creating a steep slope for the silty material to flow down.

The contractor experienced higher levels of sediment loss out of the template than originally anticipated (Johnson, 2006). It appears that there is a threshold silt level at which the silt acts to suspend the sand fraction and results in the sand being deposited further away from the discharge pipe. At Holly Beach, the silt content was less than 15%, the mean grain size was 0.13 mm, and the fill flowed approximately 100 m to 200 m (300 to 600 feet) from the discharge. At the Chaland Headland the average silt content was 15% to 30% with a grain size of 0.11 mm but the contractor used dikes up to 400 m (1,200 feet) long. The specifications allowed the contractor to request a change in the construction slope during the project. The construction slope was changed to 1V:30H above -0.2 m, MHW (1.0 feet, NAVD) and 1V:90H below -0.2 m, MHW. The Contractor reduced their losses when using this slope.

Overall, the Chaland Headland project was very successful with over 1,906,000m^3 (2,493,000 cubic yards) of beach fill placed. Approximately 706,000m^3 (924,000 cubic yards) of marsh fill placed. Photo 2 shows a photograph of the project area.



Photo 2. Aerial Photograph Mid-way during Construction.

Considerations for Future Louisiana Barrier Island Restoration Projects

Future projects may experience difficulty in finding sand deposits with low silt contents. Therefore, future projects may have to use borrow areas that have a high silt content. The dynamic morphosedimentary model (Campbell *et al*. 2006) will allow for prediction of barrier island performance with higher silt contents. Another option that is currently being investigated is the use of sand from the Mississippi River (Finkl *et al*. 2006).

The size of the marsh should be developed following delineation of the borrow area. Many of the borrow areas in Louisiana have an overburden that needs to be removed to access the sand deposit. Cost optimizations can be achieved by basing the size of the marsh on the volume of overburden to be removed. The marginal cost of pumping the overburden to a containment cell may be worth the additional benefits accrued under the project performance assessment method rather than sidecasting the material.

Monitoring of these projects and applying lessons from the projects, such as the Chaland Headland Project, are an important element of the design and construction process.

CONCLUSION

The Louisiana barrier islands provide an important first line of defense from waves and storm surges. Several challenges arise when designing and implementing restoration projects for these islands. The challenge of predicting shoreline performance can be overcome with the use of sediment budgets, which can differentiate between sand and silt movement and assess losses due to relative sea level rise. Marsh elevations can be designed and constructed to maximize project benefits. Construction specifications can be flexible to accommodate changes immediately prior to or during construction. Lastly, project monitoring and adaptive management must be implemented to meet the challenges of the design and construction of Louisiana's barrier islands.

ACKNOWLEDGEMENTS

The authors would like to acknowledge the support of the Louisiana Department of Natural Resources and NOAA National Marine Fisheries Service for their support of these projects.

REFERENCES

Bruun, Per, 1962. "Sea-Level Rise as a Cause of Erosion," Published Monthly of the Florida Engineering and Industrial Experiment Station, Vol XVI, No. 5, pp. 2-15.

Campbell, T., Thomson, G. and Benedet, L., 2006. "Design of the Restoration of Shell Island with Application of a Dynamic Morphosedimentary Model," *Proceedings of the 30th International Conference on Coastal Engineering*, ASCE, 13 p.

Coastal Planning & Engineering, 2003. *"Holly Beach Louisiana sand Management Project Completion Report,"* Coastal Planning & Engineering, Inc., Boca Raton, FL.

Coastal Planning & Engineering, Inc., 2005. "*East and West Grand Terre Island Restoration Project (BA-30): 95% Design Report*," Coastal Planning & Engineering, Inc., Boca Raton, FL.

Environmental Work Group, 2002. "*Coastal Wetlands Planning, Protection and Restoration Act: Wetland Value Assessment Methodology, Barrier Island Community Model*," U.S. Fish and Wildlife Service, Lafayette, LA, 21p.

Finkl, C.W., Andrews, J.L., Benedet, L., and Campbell, T. 2005. "*Geotechnical Investigation for Exploration of Sand Resources in the Lower Mississippi River and South Pass, and Exploration for Sand via Vibracoring in South Pelto Blocks 12 & 13*," Boca Raton, Florida: Coastal Planning & Engineering, Inc. 40p.

Hanson, H., and Kraus, N. C. (1989). "GENESIS: Generalized model for simulating shoreline change, Report 1: Technical reference," Tech. Rep. CERC-89-19, U.S. Army Engineer Waterways Experiment Station, Coastal Engineering. Research Center, Vicksburg, MS.

Johnson, G., 2006. Personal Communication with Gordon Thomson.

Larson, M., Kraus, N., and Byrnes, M.R., 2000. "*SBEACH: Numerical Model for Simulating Storm-Induced Beach Change; Report 2, Numerical Formulation and Model Tests*," U.S. Army Engineer Waterways Experiment Station, USACE, Washington, D.C.

Mann, D.W., and Thomson, G.G., 2003. "Beach Nourishment at the Holly Beach, Louisiana Breakwater Field," *Proceedings Coastal Sediments '03*, CD-ROM Published by East Meets West Productions, Corpus Christi, TX ISBN-981-238-422-7

National Research Council, 1987. "*Responding to Changes in Sea Level, Engineering Implications*," National Research Council, Washington.

U.S. Army Corps of Engineers, 1999. "*Engineering and Design for Civil Works Projects,"* ER 1110-2-1150, U.S. Army Corps of Engineers, Washington, D.C.

Williams, J.S., Penland, S., and Sallenger, A.H., 1992. "Atlas of Shoreline Changes in Louisiana from 1853 to 1995," U.S. Geological Survey, Denver.

Williams, P. and Sweeney, R., 2005. "Data Requirements to Support Environmental Benefit of Barrier Island And Headland Assessment with Community Models," National Oceanographic and Atmospheric Administration, National Marine Fisheries Service, Baton Rouge, LA, 8 p.

FIELD OBSERVATIONS OF WAVE-CURRENT-SEDIMENTS DYNAMICS, ATCHAFALAYA SHELF, LOUISIANA, USA

Sergio Jaramillo[1], Alex Sheremet[1], Mead Allison[2]

1. Civil and Coastal Engineering, 365 Weil Hall, University of Florida, Gainesville , FL 32611, USA. sjaram1@ufl.edu, alex@coastal.ufl.edu.
2. Earth and Environmental Sciences, Dinwiddie Hall, Tulane University, New Orleans, LA 70118, U.S.A. malliso@tulane.edu.

Abstract: Two instrumented platforms were deployed for over two months on the shallow (<8 m depth) Atchafalaya shelf in Spring 2006. The instruments monitored wave, sediment and current evolution throughout the entire water column. High-resolution measurements of near-bottom velocity and suspended sediment concentration show clearly the formation and erosion of fluid mud layers in response to wave and current forcing.

INTRODUCTION

The processes governing the interaction between surface waves and sediment bed on muddy coasts are poorly understood. Two classes of possible dissipation mechanisms have been proposed: friction-type direct bottom interaction, characterized by a direct transfer of energy from the wave-field to the soft muddy bottom, and indirect processes, where the energy transfer is mediated by additional mechanisms, typically related to the formation of near-bed high density suspensions. The former has been modeled using various approximations of mud rheology (percolation, Carter et al., 1973; poro-elastic beds, Yamamoto et al., 1978; Yamamoto and Takahashi, 1985; visco-elastic beds, Jiang and Mehta, 1995; Jiang and Mehta, 1996; visco-plastic beds, Mei and Liu, 1987; viscous Newtonian fluid mud, Dalrymple and Liu, 1978; and others). The latter, much less studied, might involve surface-lutocline wave interactions (Jamali et al. 2003a; Jamali et al. 2003b), and development of instabilities of the Kelvin-Helmholtz/Holmboe type (Mehta and Srinivas, 1993; Traykovski et al., 2000).

Laboratory and field experiments (Chou et al., 1993; Foda et al., 1993; Sterling and Strohbeck, 1975) suggest that realistic models of wave propagation over muddy sea beds have to address the issue of mud-state variability. The character of the muddy sea bed (and its wave-dissipation efficiency) changes in response to the sea state. Smooth and hard consolidated muds are no more dissipative than sandy bottoms (e.g. Lee, 1995). However, wave action can liquefy bottom sediment (Chou et al., 1993; Foda et al., 1993) producing fluid or soft, unconsolidated muds with non-Newtonian behavior and significantly higher wave dissipation efficiency (e.g. Gade, 1957). Catastrophic mud liquefaction events have also been recorded, leading to massive submarine landslides (Sterling and Strohbeck, 1975).

Modeling and laboratory research efforts suggest a number of possible mechanisms for wave-mud interaction. The range of applicability of each of these mechanisms is largely unknown, mainly due to the scarcity of coherent field observations of wave, currents and cohesive sediment dynamics. Here, we present a field experiment effort to assess the importance of wave-sediment coupling through high-resolution measurements of wave-current-sediment motion in the first 1 mab (meter above the bottom).

INSTRUMENTATION AND FIELD SITES

The instruments were deployed on the Atchafalaya shelf in spring 2006. Figure 1 shows a map of the Atchafalaya shelf with the approximate sediment distribution and the location of the instruments. The large amount of sediment discharged in the area by the Atchafalaya River is typically carried to the West by the nearshore currents associated with the prevailing winds and the Gulf of Mexico loop current. The instruments were deployed for approximately 2-week periods, interrupted by a short break for maintenance and data downloading. Two deployment configurations are shown in Figure 1. The experiment was timed to coincide with the part of the year characterized by the energetic waves and high river discharge.

An example of instrument cluster mounted on a deployment tripod is shown in Figure 2. The instruments include a high-resolution, downward-looking Sontek PC-ADP (pulse-coherent acoustic Doppler profiler) and an upward-looking RDI ADCP (acoustic Doppler current profiler). The PC-ADP provided high-resolution information of water and sediment motions in the first 50 cmab by sampling pressure and three-dimensional current velocity at 2 Hz, in 17 bins 3-cm high, continuously for the entire duration of a deployment (approximately 14 days). The ADCP measured current and directional wave motions in the upper water column in 30-cm bins. In addition to the directional wave information provided by the ADCP, waves were measured continuously a 2 Hz using a redundant array of pressure sensors (one independently logged and one on each of the profilers).

Near-bed sediment dynamics was monitored using OBS (optical backscatterance sensors). A pencil-beam 600-kHz ABS (acoustic backscatter sensor) was used to

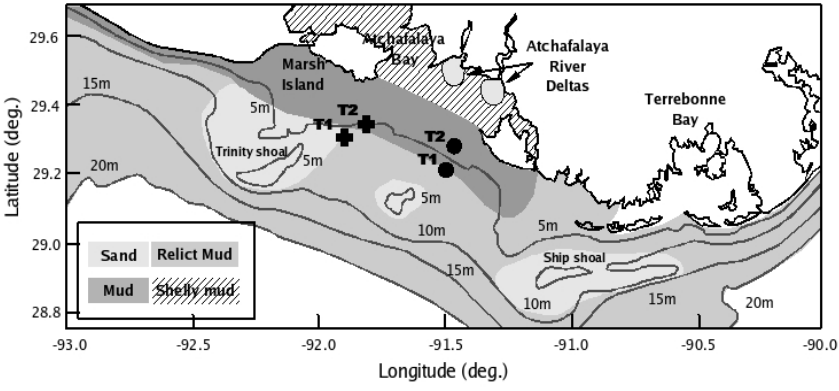

Fig. 1. Facies map of the surficial sediments of the Atchafalaya inner shelf, Louisiana, USA (Neill and Allison, 2005). Relict sediment units sometimes are mantled by thin (less than 20-cm thick), ephemeral modern mud. The locations of the two tripods (T1 and T2) are marked with circles / crosses.

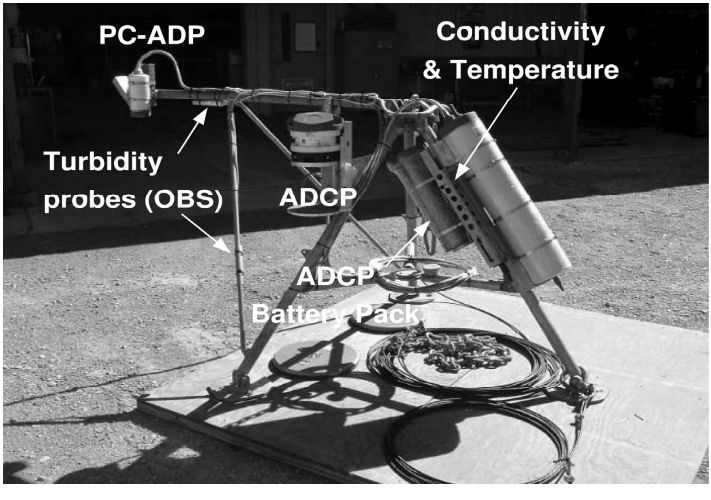

Fig. 2. An image of one of the instrument clusters (tripod T1, see Figure 1 for deployment configuration) before deployment, showing the type and mounting of the instruments. The height of tripod is approximately 1.2 m.

monitor the position of the bottom and strata formation. At this frequency the ABS signal can penetrate the lutocline and provide clear image of the evolution of fluid-mud layers. Later in the experiment, a Sequoia Scientific LISST (system for in-situ measurement of particle size and distribution) was also deployed. Additional details about the experiment can be found in Jaramillo et al. (2007).

OBSERVATIONS

The instruments were deployed in several configurations along the 5-m isobath on the shelf fronting Atchafalaya Bay (Figure 1). During the approximately 2 months of deployment, February through March 2006, a number of cold fronts swept through the area, accompanied by increased wave and current activity. Here we compare sediments response to two energetic storms that occurred March 8-13 and March 19-21 2006.

Figure 3 shows a summary of PC-ADP observations (T1 cluster, circles in Figure 2) of wave-current-sediment evolution during the storm of March 8-13 2006. At that time the tripods were distributed in the cross-shore configuration (circles in Figure 1). The storm was fairly energetic, with waves reaching over 2m significant height at the peak of intensity. The behavior of the spectral band with frequencies larger than 0.2 Hz (short waves, sea) and the band with frequencies below 0.2 Hz (long waves, swell) is typical of a frontal passage on the Atchafalaya shelf. Figure 3a shows the evolution of swell and sea wave height. Short waves are generated locally and show a fast response to intensifying surface winds. They spin up quickly to about 0.75-m height and stay at that level for the entire duration of the storm. The swell band develops more slowly and becomes significant only within a narrow 2-day time window (March 09-11). At the peak of activity the total wave height exceeded 2 m. The nearshore velocity profile is well correlated to the wave activity, reaching a peak of about 40 cm/s at about 50 cmab (Figure 3b) at the peak of activity.

Current profile observations (Figure 3b-c) also reveal indirectly details of sediment behavior. The two lines in Figure 3c mark the position of two surfaces: the continuous one represents the surface which reflects strongest the PC-ADP acoustic signal, which also coincides in some cases to an elevation characterized by very strong shear (e.g. March 11, in Figure 3c). The dashed line marks the position where the horizontal velocity becomes zero. The latter represents the hydrodynamic bottom, the deepest level where current and wave motion can penetrate. For the sake of argument we will define this level as the “solid bottom”. The solid bottom position coincides with the strongest reflector during the calm periods. There are though two events during which these two lines separate. These are fluid-mud events of about 15 cm thickness, lasting for about half a day to a day. Significant values of horizontal velocities recorded with the layer (that is below the strongly reflecting surface) suggest that both events are mobile fluid-mud layers, in one instance (March 11) moving against the average direction of the upper column layers.

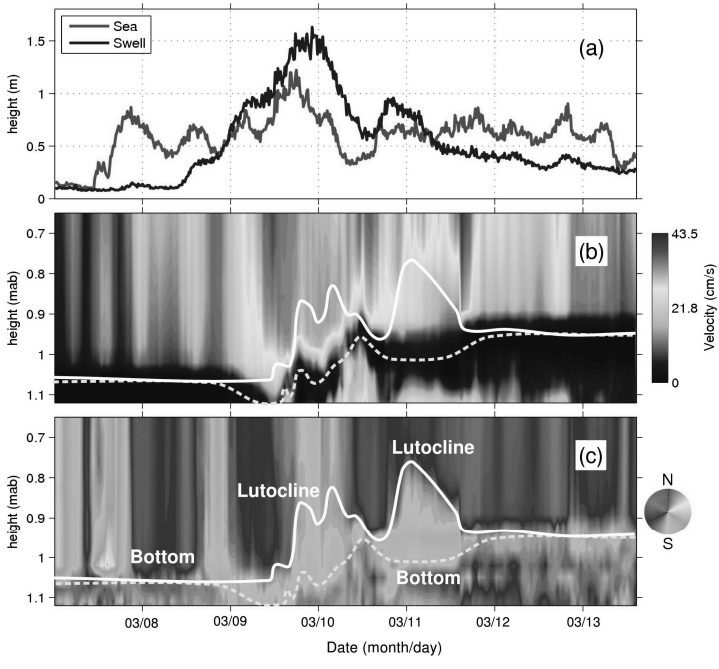

Fig. 3. PC-ADP observations of fluid mud formation during the storm of March 8-13 2006. Deployment configuration is shown in Figure 1 (circles). a) Wave heights (blue/dark line -- swell, frequency < 0.2 Hz; red/light line -- seas, frequency > 0.2 Hz). b) Velocity profile, magnitude. c) Velocity profile, direction. The continuous line marks the position of strongest-reflection surface (bottom and lutocline). Dashed line marks the position of zero horizontal velocity (hydrodynamic bottom).

The sequence and timing of the fluid-mud events with respect to wave and current activity suggests that the first event was due mainly to bed-liquefaction (note the dip in the position of the hydrodynamic bottom at the beginning of the storm) whereas the second event was probably a combination of resuspension-advection event. It is interesting to note here that T2 observations (not shown) do not indicate significant fluid-mud layer formation.

Figure 4 shows a summary of PC-ADP observations (T2 cluster, crosses in Figure 1) during the second storm March 19-21 2006. The ocean was calm throughout the first three days shown, but in the 4th day stronger winds associated with a fast approaching front produced relatively large high-frequency seas (Figure 4a) and strong northward currents (Figure 4b, direction not shown). Swell energy began to increase March 20, indicating that the peak of the storm occurred sometime on March 20-21. At the peak

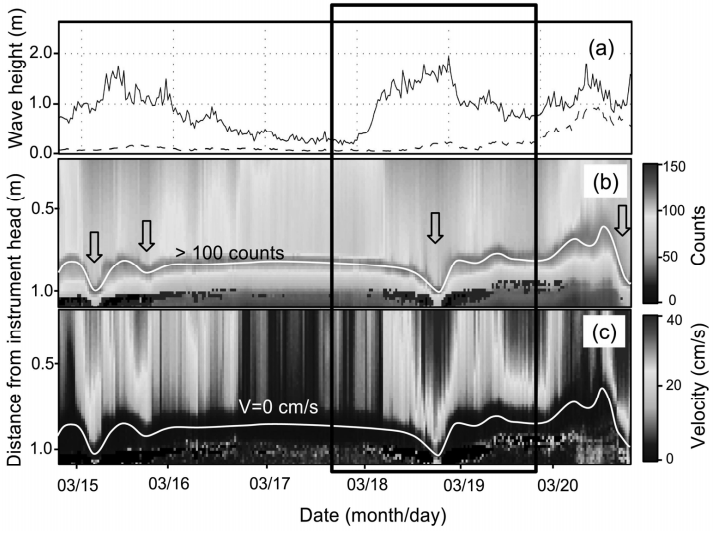

Fig. 4. PC-ADP observations of fluid mud formation and erosion (arrows) in response to currents. Deployment configuration is shown in Figure 1 (crosses). a) Wave heights (continuous line – swell, frequency < 0.2 Hz; dashed line -- seas, frequency > 0.2 Hz) b) Intensity of instrument return signal; white line contours the highest-return surface. c) Horizontal current velocity; the position of zero velocity (hydrodynamic bottom) is indicated by a white line. Details of the lutocline evolution within the time interval marked by the black rectangle are shown in Figure 5.

of wave activity the total significant height was just under 2 m, with mean near-bottom currents of approximately 40 cm/s. Sediment response as recorded (indirectly, as before) by the downward looking PC-ADP is shown in Figure 4c.

Figure 4b shows the strength of the PC-ADP acoustic signal return. Higher intensities (large "count" number) indicate strong reflection. The position of the maximum return strength is marked by a white line. In contrast to the March 8-13 observations, fluid-mud layers cannot be identified here based on periods of disagreement between the position of the hydrodynamic bottom (white line in Figure 4b) and the strongest reflecting surface (white line in Figure 4c), as they are virtually identical. It the reflecting surface is a lutocline, this observation suggests that these fluid mud layers are high density and stationary (in contrast to the first example). That this is indeed the case as supported by coherent, lower-frequency ABS measurements which can penetrate deeper into the layers. A 2-day detail of ABS observations (corresponding to the enclosed rectangle in Figure 4) is shown in Figure 5. The location of the "solid" bottom is relatively constant at approximately 1.1 m from the instrument head. The high-density suspensions during this event have typical suspended sediment

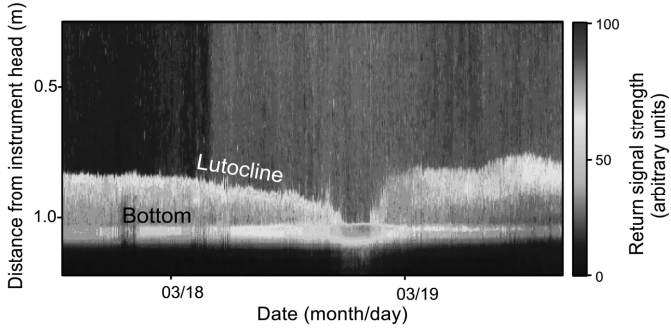

Fig. 5. Detail of ABS observations of near-bottom sediment showing the evolution of the lutocline during a current pulse (see Figure 4, time interval enclosed by rectangle). The PC-ADP signal is absorbed within the thick fluid mud layer and only the lutocline remains visible (Figure 4b). The 600-kHz ABS signal penetrates the lutocline and reveals the bottom location. The thickness of the fluid-mud layer is clearly visible.

concentrations in the range of 5-10 kg/m^3 and thickness of 15-20 cm. In this example, the maximum thickness is approximately 30 cm.

The pronounced difference between the dynamics of fluid muds in the two cases discussed is remarkable, given that the forcing conditions (waves and currents) are quite similar in magnitude. The fluid-mud layer events also differ significantly in duration.

Due to a dominant westward circulation on the shelf, the observation site (crosses in Figure 1) receives a large percentage of the sediment discharged inside the bay by the Atchafalaya River. During periods of calm (weak currents and waves) sediment settling contributes to the formation of fluid-mud (Allison et al. 2000; Sheremet and Stone 2003; Sheremet et al. 2005). While these processes likely play an important role in the formation and time span of the fluid mud events seen in Figure 4, their origin is not entirely apparent since they were present when the tripods were deployed at this site. However, Figure 4-5 illustrates their typical behavior in response to the near-bottom circulation. Increased turbulence at the lutocline level associated with high near-bed mean current velocities (arrows in Figure 2a) result in increased sediment resuspension and an erosion of the lutocline. Observed maximum velocities coincide with a minimum of fluid-mud thickness. In fact, the exception of the second event (evening of March 15th) all high velocity events shown in Figure 2 completely erode the fluid-mud layer. When the current weakens, the layer reforms likely through sediment settling. These processes can be recognized to affect also fluid muds at the first site (Figure 3, corresponding to circles in Figure 1). The last fluid mud event in Figure 3 (March 11) ends abruptly, being swept away by a strong current pulse which occurred about noon on March 11 (Figure 3b).

CONCLUSION

The experiment produced a significant amount of information. At the time of the writing of this account, the datasets resulting from this experiment are still being processed. Large segments of data have yet to undergo quality control procedures, while others have yet to be explored. We have not yet attempted any modeling of the processes observed. From the data analyzed so far, however, an interesting picture emerges of the interaction between hydrodynamic and cohesive sediments sediment processes.

Field and laboratory observations of wave-current-sediment interaction in muddy environments suggest that sediments respond to changes in the sea state on temporal and spatial scales similar to those characteristic of wave-current evolution. This hypothesis, however, have not been thoroughly verified in the field.

In an effort to fill in this gap, we deployed clusters of instruments to monitor water and sediment motions in the entire water column, with increased resolution in the first meter above the bottom, on Atchafalaya Shelf, an area dominated by cohesive sediments. The small subset of the data collected shown here illustrates the rapid response of fluid muds to variations in near-bed mean currents (shown here for the first time in field observations and a high resolution).

We identified at least two different types of fluid-mud dynamics, one associated with mobile, the other with stationary layers. These regimes seem to be associated with similar hydrodynamic forcing, but they appear to have different origins and generating mechanisms. In both cases, near-bottom currents appear to be the triggering factor in erosion processes.

Phenomena discussed here are only a small subset of the many processes that characterize the strong coupling between sediment and water-column hydrodynamics. Other aspects, which will be discussed elsewhere, include changes of consolidated mud state due to energetic wave-fields, triggers for gravity flow of the fluid muds, and the feedback these changes have on wave propagation processes.

ACKNOWLEDGEMENTS

The work presented here was supported by the Office of Naval Research and the Naval Research Laboratory at Stennis Space Center. We are indebted to Dr. T.K. Holland for valuable discussions, encouragement and instrumentation. Field data was collected with expert support by the Field Support Group in the Coastal Studies Institute, Louisiana State University, lead by Captain Steve Dartez.

REFERENCES

Allison, M.A., G.C. Kineke, E.S. Gordon, and M.A. Goni, Development and reworking of a seasonal flood deposit on the inner continental shelf off the Atchafalaya River, *Continental Shelf Res.* 20, p. 2267-2294, 2000.

Carter T.G., P.-L.F. Liu, and C.C. Mei, Mass-transport by Waves and Offshore Sand Bedforms, *J. Waterways Harbors and Coastal Eng. Division-ASCE 99 (NWW2*), p. 165-184, 1973.

Chou, H.-T., M.A. Foda, and J.R. Hunt, Rheological response of cohesive sediments to oscillatory forcing, In: *Nearshore and Estuarine Cohesive Sediment transport, Coastal Estuarine Sci., 42,* A.J. Mehta ed., p. 126-148, AGU, Washington DC, 1993.

Dalrymple, R.A. and P.L.-F Liu, Waves over soft muds: a two-layer fluid model, *J. Phys. Oceanogr. 8,* p. 1121-1131, 1978.

Foda, A.M., J.R. Hunt, and H.-T. Chou, A nonlinear model for the fluidization of marine mud by waves, *J. Geophys. Res. 98,* p. 7039-7047, 1993.

Gade, H.G., Effects of a non-rigid impermeable bottom on plane surface waves in shallow water, Ph. D. Thesis, Texas A&M University, 35 pp, 1957.

Jamali, M., B. Seymour, and G. Lawrence, Asymptotic analysis of a surface-interfacial wave interaction, *Phys. Fluids 15*, p. 47-55, 2003a.

Jamali, M., G. Lawrence, and B. Seymour, A note on the resonant interaction between a surface wave and two interfacial waves, *J. Fluid Mech. 491*, p. 1-9, 2003b.

Jaramillo, S., A. Sheremet, and M. Allison, Wave propagation over a muddy shelf: A field experiment, *Proceedings of the 30th International Conference on Coastal Engineering*, San Diego, CA, USA, 2007 (in print).

Jiang F. and A.J. Mehta, Mudbanks of the Southwest Coast of India IV: Mud viscoelastic properties, *J. Coastal Res. 11,* p. 918-926, 1995.

Jiang F. and A.J. Mehta, Mudbanks of the Southwest Coast of India V: Wave attenuation, *J. Coastal Res. 12*, p. 890-897, 1996.

Lee, S.C., Response of mudshore profiles to waves. PhD thesis, University of Florida, Gainesville, 1995.

Mei, C.C. and P.L-F. Liu, A Bingham-plastic model for a muddy seabed under long waves, *J. Geophys. Res. 92*, p. 14,581-14,594, 1987.

Mehta, A. and R. Srinivas, Observations of entrainment of fluid mud by shear flow, In: *Nearshore and Estuarine Cohesive Sediment Transport*, A. J. Mehta ed. American Geophysical Union, Washington, DC, p. 224-246, 1993.

Neill, C.F. and M.A. Allison, Subaqueous deltaic formation on the Atchafalaya Shelf, Louisiana, *Marine Geology 214*, p. 411-430, 2005.

Sheremet, A. and G.W. Stone, Observations of nearshore wave dissipation over muddy sea beds, *J. Geophys. Res. 108*, DOI 10.1029/2003JC001885, 2003.

Sheremet A., A.J. Mehta, B. Liu, and G.W. Stone, Wave-sediment interaction on a muddy inner shelf during Hurricane Claudette, *Est. Coastal Shelf Sci. 63*, p. 225-233, 2005.

Sterling, G.H., and G.E. Strohbeck, Failure of South Pass 70 Platform B in Hurricane Camille, *J. Pet. Tech. 27*, p. 263-268, 1975.

Traykovski, P., Geyer W.R., Irish J.D., Lynch, J.F., The role of wave-induced fluid mud flows for cross-shelf transport on the Eel river continental shelf. *Continental Shelf Res., 20*, p. 2113-2140, 2000.

Yamamoto, T., H.L. Koning, H. Sellmeijer, and E. van Hijum, On the response of a poro-elastic bed to water waves, *J. Fluid Mech. 87*, p. 193-206, 1978.

Yamamoto, T. and S. Takahashi, Wave damping by soil motion, *J. Waterway, Port, Coastal, and Ocean Eng. 3*, p. 62-77, 1985.

INVESTIGATION OF MORPHOSEDIMENTARY PROCESSES ON A SCHEMATIC LOUISIANA BARRIER ISLAND USING PROCESS-BASED NUMERICAL MODELING

Campbell, T.[1] de Sonneville, B[2]., Benedet, L.[3] Walstra, D.J.R.[4], and Finkl, C.W.[5]

1. Coastal Planning & Engineering 2481 NW Boca Raton Blvd, Boca Raton, FL, 33431, USA, and Delft University of Technology, 2600 GA Delft, The Netherlands. tcampbel@coastalplanning.net
2. Delft University of Technology, and WL | Delft Hydraulics, P.O. Box 177, 2600 MH, Delft, The Netherlands Ben.deSonneville@wldelft.nl
3. Coastal Planning & Engineering 2481 NW Boca Raton Blvd, Boca Raton, FL, 33431, USA, and Delft University of Technology, 2600 GA Delft, The Netherlands. lbenedet@coastalplanning.net
4. Delft University of Technology, and WL | Delft Hydraulics, P.O. Box 177, 2600 MH, Delft, The Netherlands. DirkJan.Walstra@wldelft.nl
5. Coastal Planning & Engineering 2481 NW Boca Raton Blvd, Boca Raton, FL, 33431, USA. cfinkl@coastalplanning.net

Abstract: Although basic causes of barrier island retreat and area loss of Louisiana Barrier Islands are known, there has been limited success in unraveling and quantifying how these processes interact to generate observed barrier island behavior. Processes that make up a conceptual-analytical dynamic morphosedimentary model (DMSM) are evaluated here using a process-based numerical model. The model is specifically used to investigate the morphodynamic behavior of non-cohesive (sand) and cohesive (fines) sediments under different hydrodynamic conditions (mild waves, cold fronts and tropical storms). The primary modeling focus is on the seaward limits of sand deposition during high wave energy conditions and the selective deposition of different grain sizes (sand, clay and silt, and mixed sediments) during low wave energy conditions.

INTRODUCTION

Louisiana barrier islands are naturally dynamic features that change in shape (length, width, height, and planform), geographic position, and orientation in response to waves,

relative sea-level rise (RSLR), sediment supply, winds and currents. Although basic causes of barrier island retreat and area loss are known, there has been limited success in unraveling and quantifying how these processes interact to generate the observed barrier island behavior.

Processes that make up a conceptual-analytical dynamic morphosedimentary model (DMSM), developed originally by Campbell (2005), are evaluated here using a process-based numerical model. The DMSM simplifies barrier island retreat, volumetric losses and recovery from the barrier islands into four basic stages. These four-stages include: Stage 1, the initial (relatively stable) state of barrier beaches, which is generically described in terms of a thin sand cap that sits on top of mixed (sand, silt and clay) deltaic sediments that also underlie relatively wide backbarrier marshes. Stage 2, when the sand cap is eroded (removal of protective beach), cohesive deltaic sediments are uncovered on the upper shoreface and marshes are exposed to the direct attack of Gulf waves. These sediments are easily eroded and transported offshore causing large shoreline retreat. Stage 3, loss of the protective beach and sandy cover on the upper shoreface which promotes erosion of deltaic sediments and marsh sediments. Sandy sediments are also released to the system, as the shoreline retreats. Stage 4, sandy sediments reworked in Stage 3 eventually deposit as a sand cap on top of the deltaic sediments and form a protective beach in front of residual marsh that is now much reduced in area, setting the stage for another morphosedimentary cycle of erosion (Figure 1).

The DMSM is based on some assumptions that include a limiting depth of sand transport that is shallower than for most open coast sandy environments and is linked to a 'break of slope' in the nearshore profile. This 'break of slope' is a noticeable transition between steeper, sandy profiles and flatter, muddy profiles and is commonly observed offshore Louisiana's barrier islands. The DMSM also assumes that the largest part of barrier island retreat is caused by erosion of fine sediments in post-storm periods, after the sandy beach is eroded away (by overwash and longshore transport processes) and the mixed sediment core of the island (silts and clays) are exposed to Gulf waves. It assumes that, while the sandy sediments remain above the break of slope, the fine grained sediments are deposited offshore of the break of slope. Many of the assumptions of the DMSM are supported by the existing literature as shown in table 1, while other assumptions have not been properly investigated in the field. The DMSM is commonly used to calculate volumetric requirements for barrier island restoration projects in Louisiana, as described by Campbell *et al.* (2006).

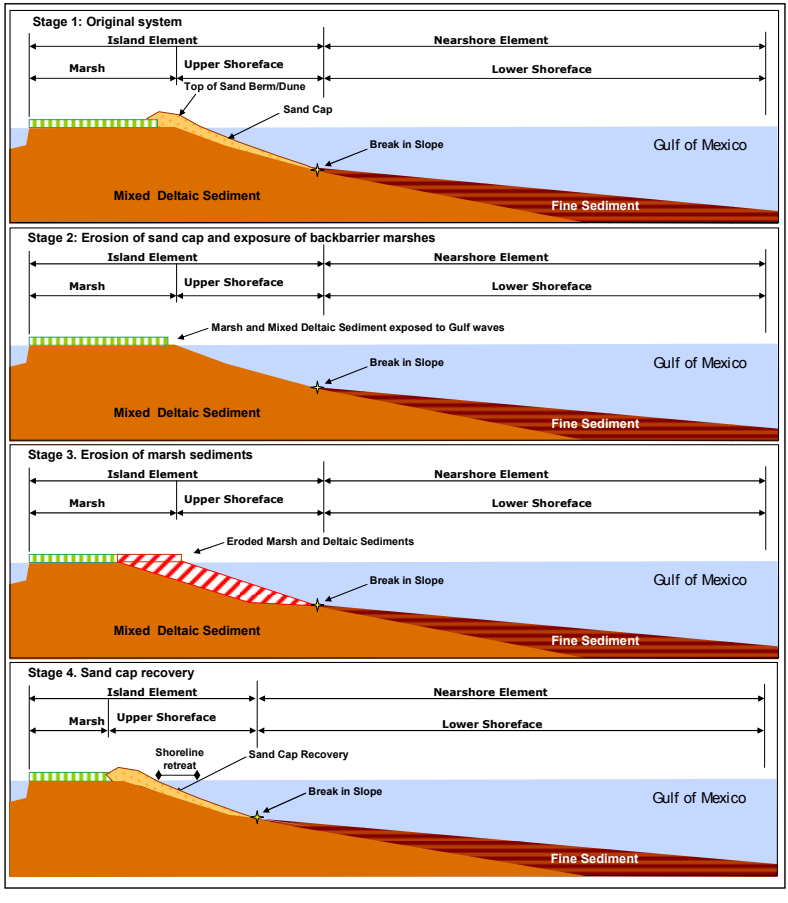

Figure 01: Four stage conceptual model that diagrammatically shows erosion, shoreline retreat, and recovery processes for Louisiana's barrier islands (after Campbell, 2005).

In this investigation a process-based numerical model (Delft3D), is used to investigate the morphodynamic behavior of non-cohesive (sand) and cohesive (fines) sediments under different hydrodynamic conditions (mild waves, cold fronts and tropical storms). The primary focus is on the seaward limits of sand deposition during high wave energy conditions and the selective deposition of different grain sizes (sand, clay and silt, and mixed sediments) during low wave energy conditions. The model setup is described in the following paragraphs.

Table 01: DMSM processes that are reported in literature and field research

Processes	Sample references
The general presence of a typical barrier island profile with a sandy shoreface shaped as a Dean equilibrium profile intersecting with a flatter profile at a 'break in slope'.	Williams *et al.* (1992) CPE (2000, 2003)
The sandy layer on the beach is overwashed or transported off- or alongshore during major storms, exposing highly erodable marshes.	Boyd *et al.* (1985)
Exposure of fine sediments to wave action on the Gulf side may accelerate the shoreline retreat.	Donnelly *et al.* (2004) and Everts (1985)
Barrier islands become narrower instead of rolling over, because the backbarrier marshes do not migrate landward at the same rate that the barrier islands erode.	Williams *et al.*(1992)
Transgressive barriers migrate landward while adapting to the rising sealevel by washover processes.	Roy *et al.* (1995)

NUMERICAL MODEL SETUP

To investigate the physical processes causing barrier island retreat, a simplified representative bathymetry is used. For this, the bathymetry of Shell Island is deduced from the Atlas of Sea-Floor Changes (SFC) (List *et al.*, 1994), slightly simplified, and implemented on a computational grid. For the model boundary conditions, two representative high wave energy conditions are distinguished to determine the limits of sand transport and a low wave energy condition to describe selective deposition of different grain sizes.

The model cases have constant water levels that depend on representative storm surge levels. Tides and winds are disregarded because focus is given to wave-driven processes. The cases were run in a cross-shore (two-dimensional-vertical – 2DV) model to investigate cross-shore morphodynamic processes contributing to barrier shoreline retreat. The same wave cases were also run in an area (two-dimensional-horizontal – 2DH) model to investigate alongshore processes contributing to barrier shoreline retreat, however due to space limitations we concentrate in the 2DV results.

2DV Model

The 2DV model has a cross-shore length of 10 km. For the barrier island bathymetry, representative cross-shore dimensions of Shell Island are selected. Because this former barrier island had a typical Louisiana barrier island profile with a break in slope around -2 m and an island height of 1.5 m. The depth profile (Figure 2) is obtained from of the Atlas of Sea-floor Changes (List *et al.*, 1994). From the break in slope (-1.7 m) to the top of the island (+1,5m) (*b*) a Dean Equilibrium profile for sandy beaches is applied with the concave shape of $h(y) = Ax^{2/3}$ (Dean, 1991). Backbarrier dimensions obtained from Campbell (2005) include elevation of +1,0 m with a width of approximately 250 m.

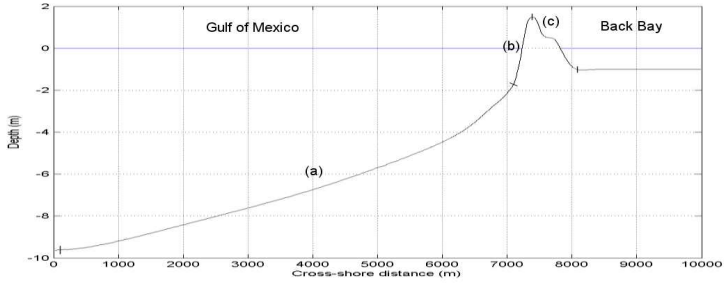

Figure 2. Cross shore profile use din the 2DV model.

Boundary Conditions

The wave climate and associated barrier island erosion in Louisiana is largely dependant on the occurrence of two typical events: 1) cold fronts and 2) tropical storms. The remaining days of the year are characterized by a relatively mild wave climate. Therefore, the modeling is divided into three cases: (1) cold front conditions, (2) tropical storm conditions and (3) average wave condition. Simulated waves approach the coast at normal angles.

To obtain representative wave heights, periods and duration, an analysis of existing wave data (USACE WIS station 132) was performed. For representative cold-front conditions, an active cold front year is chosen (1993). In this year, 24 cold fronts occurred (if a cold front is defined as an occasion where the wave height > 1m). Five major cold fronts (producing waves from 90-315°) were selected to determine the average wave height, period and duration of a typical cold front event. The resulting wave condition is shown in the Table 2. For representative tropical storm conditions, waves during Hurricane Lili (2002) were used. Wave information was provided by CPE (2003). Average wave height, angle and period calculated for the the Barataria shoreline, based on wave statistics from 1976 to 1995 calculated by CPE (2003) were used for the average wave case (Table 2).

Tides and relative sea-level rise were not considered in our short-term simulations. Therefore, filling of tidal basins is not considered and a constant water level boundary is prescribed at the seaward and back bay boundary. The height of the water level boundary depends on the storm surge during the three events (see Table 2).

For the first case (cold front conditions), a level of 0.4 m is selected (barrier island non-submerged), because water levels during cold fronts are relatively low (Pepper and Stone, 2002). During Hurricane Lili (2002), a storm surge of 2.0 m was observed (Alfegame and Cañizares, 2005). A storm surge level of 2 m used in the second case implies that the island is submerged during this event.

Table 2: Wave cases simulated.

	H_0	T_m	*Storm Surge*	*Duration*
Representative cold front conditions	2.0 m	6.1 s	0.4 m	60 hrs
Representative tropical storm conditions	3.0 m	10.0 s	2.0 m	24 hrs
Average wave conditions	0.8 m	5.0 s	0.0 m	1 week

Main Model Parameters

The overall regional Mississippi Delta sediment stratigraphy is fine-grained. Grain sizes range from fine sand to clays or silts. Although the distribution of the sediments is quite complex, numerous studies by the state and federal survey are available which link sediment characteristics to the depositional environments. Sand-rich environments include distributary channels, inner-shelf shoals, recurved spits and tidal inlets (Kulp *et al.*, 2005). Clay and silt-rich environments are predominantly found offshore and in the shallow backbarrier environments. According to measurements by CPE (2003) for the Barataria shoreline, a representative grain size is approximately 150. This value will be used in the model simulations for the sand fraction.

In the Delft3D-version used in this study, no distinction is made between clay and silts. All grain sizes smaller than 63 are assumed to be 'mud' and to behave as cohesive sediments. The morphodynamic behavior of these cohesive sediments is determined by the mud transport parameters, following the approach of Parteniades (1965). In this computation, erosion of mud (E) occurs once the critical bed shear stress for mud erosion (= 0.7 N/m2 in this study) is exceeded by the acting maximum bed shear stress ( ). A user specified erosion parameter (M = 2 Kg/m2/s) determines the speed of erosion. The amount of deposition (D) is controlled by the concentration in the near bottom computational layer and the fall velocity (= 0.0005 m/s) of the mud particles. All mud transport occurs by means of suspended load, as cohesive sediment transport usually does not occur in the form of bed load.

The value for of $\tau_{cr,d}$ is calculated with a relationship between critical shear stress and bulk density (ρ_b), that was derived during laboratory experiments performed on artificial mixed sediment beds (*e.g.* Mitchener and Torfs, 1996). The other mud transport parameters are left on their default value (cited above), because no calibration data specific to mud erosion is available. A sensitivity analysis was conducted to evaluate the effect of these parameters on model results. Sand transport calibration factors SusW and BedW are initially set at a commonly used value of 0.2 based on previous modeling experience (*e.g.* Walstra *et al.*, 2005).

A simulation timestep of 12s was used, for the 2DV model this resulted in a maximum courant number $\sigma = 9.8$, stable in Delft3D implicit scheme. Other model parameter settings include the horizontal and vertical eddy viscosity and diffusivity. Delft3D-FLOW with the roller extension computes the viscosity each time step and is therefore

self-regulating. The horizontal eddy viscosity and diffusivity are set at an initial value of 0.1 m²/s. For the 2DV cases, the vertical exchange of momentum and mass in is computed using the vertical eddy viscosity and diffusivity calculated with the k-ε turbulence model (WL Delft hydraulics, 2003).

Other model parameters not mentioned here are left on their default value. For the model spin up time, 240 min. is chosen, based on the fact that virtually all water level and velocity profile oscillations dampen after four hrs. The hydrodynamic simulation time is 20 hrs. For the morphodynamic development a morphological scale factor was defined for each wave case separately.

RESULTS AND DISCUSSION

Sand transport and profile change during storms

During cold front conditions, the magnitude of the velocity varies considerably in the nearshore zone (Figure 3). The highest flow velocities are observed from x = 7100 m to the shoreline, in the shoreward part of the breaker zone. The magnitude of the flow velocity has a maximum value of 0.18 m/s near the bed. In the top layers of the nearshore breaker zone (x = 7000 m to x = 7200 m), another slight increase in flow magnitude is observed. The flow circulates in the nearshore breaker zone, caused by wave-induced mass flux driving an onshore current in the top water layers, with a returning offshore current in the bottom layers. The return current is stronger than the shoreward current causing net erosion of the upper part of the profile (Figure 4).

During tropical storm conditions, higher wave-induced flow velocities are observed from x = 7200 m to x = 7400 m, above the island because the island is overtopped by a storm surge of 2 m prescribed in the model (Figure 3). The magnitude of the currents is larger in the top layers (1.8 m/s), decreasing slightly towards the bed. Lower flow velocities at the bed can be attributed to bed friction. Once the flow passes the island, it reduces gradually to a value of around 0.25 m/s. All flow is directed onshore in this case. There are no offshore directed or circulating currents. This is consistent with literature (*e.g.* Pirello, 1992) that also suggests a lack of return current when the storm surge level exceeds the island level during storm conditions. The localized water level set-down due to the increase in flow velocity above the island (Bernoulli's law) is clearly visible in Figure 3. Behind the island the flow slows down and the water level rises again.

During tropical storm conditions, both bed load and suspended load transport are directed onshore. This occurs because transport follows the water flowing over the island (See Figure 3). Secondly the suspended load reaches a high peak of $7.5 \cdot 10^{-3}\,m^3/ms$ on top of the barrier island, about 175 times the value of the offshore suspended sediment transport in the first few cases. This is caused by the high flow velocities and concentrations on top of the island. It also shows that, in this case, bed load is almost negligible compared to the suspended load transport. The suspended load transport starts far offshore near x = 4000 m with a relatively low value of $2 \cdot 10^{-3}\,m^3/ms$ and rapidly increases at approximately x = 7200 m, where the steeper slope area begins.

During the cold front the bed load is generally positive, indicating that it is onshore directed, following the wave direction. This transport is mainly caused by wave asymmetry and wave streaming, which in this case is larger than the offshore transports current related transports (explanation: prevails over the bed load transport, asymmetry and streaming acts on both suspended and bed-load! as it just a hydrodynimcal forcing). Highest values of bed load transport (up to $1.2 \cdot 10^{-5}$ m^3/ms) are observed in the breaker zone. The suspended load, on the other hand, is offshore directed following the net direction of the flow. The magnitude and volume of the suspended load is significantly larger than the magnitude of bed load. The highest peak value reaches ($4.2 \cdot 10^{-5}$ m^3/ms) occurs in the nearshore area where maximum sediment concentrations and flow velocities are observed.

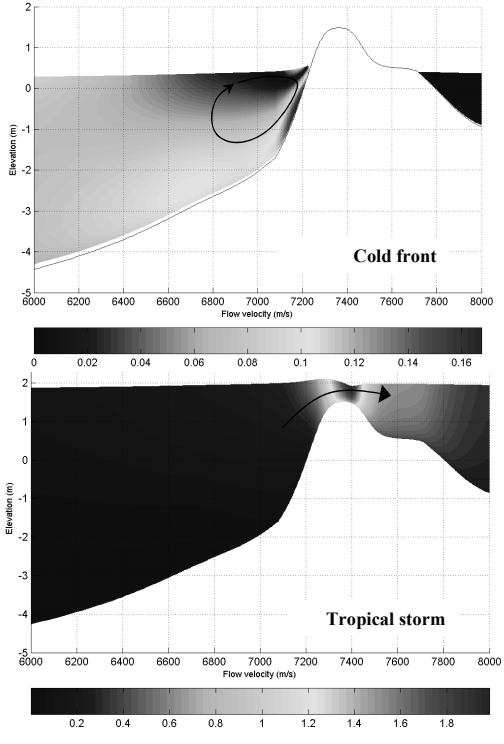

Figure 3: Predicted 2DV wave-induced flow velocities for the cold front (top plot) and the tropical storm case (bottom plot). For wave case parameters see table 1.

The offshore directed suspended load transport causes erosion in the upper part of the profile and deposition in the lower part of the profile. The morphological development

shows resemblance to a 'classic storm erosion profile', as described in Stive and Battjes (1984).

Two observations mark the area where sand deposition takes place. The main deposition takes place between x = 6900 and x = 7130 m near the break in slope (Figure 4). A very thin sand sheet is also deposited on the inner shelf from a distance of x = 5500 m (Figure 4). About 50% of the offshore sand transport is deposited between of 1 m and 2 m water depth, the remaining 50% are deposited between -2 m and -4.9 m water depth. The outer limit of sand transport is located at about 1500 m offshore from the shoreline. The main reason why sand transport takes place at a large offshore distance is the low shelf gradient that causes waves to break and dissipate energy far offshore thus causing seabed remobilization.

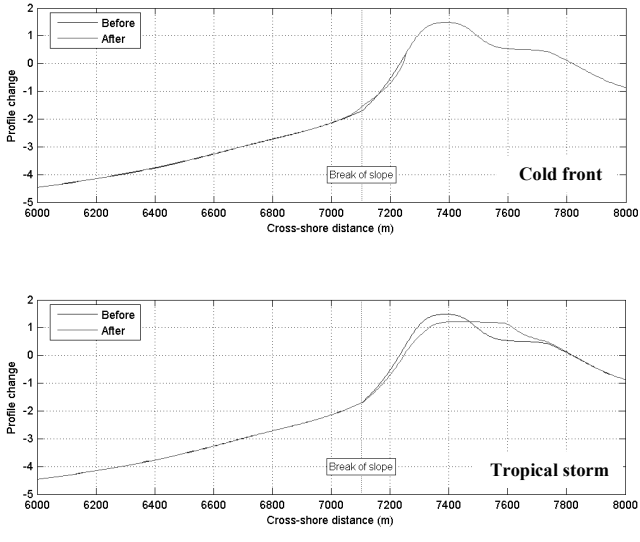

Figure 4: Profile change for a sandy barrier island during cold fronts (top plot) and tropical storm (bottom plot) conditions.

Within the context of the DMSM that considers the break in slope at around – 2 m as the seaward limit of sand transport, it is concluded that, according to profile modeling results, most of the sand is deposited at or near the break of slope, although sand can be transported beyond this limit during cold fronts. It remains unclear how much of this sand is transported onshore during the post-storm period since this is a difficult

phenomenon to evaluate by modeling. Experience with Louisiana beach profiling and sediment sampling, however, tends to indicate that most of the sandy sediments are confined to relatively shallow areas of the profile suggesting significant post-storm recovery. Phenomena of wave dissipation by fluid muds (*i.e.* Sheremet and Stone, 2003) were also not included in the model. For example, if wave energy were reduced by 50%, current velocities would be greatly reduced and the limit of offshore sand transport would be shifted landward to shallower water.

Movement of sand and mud during average wave conditions

During average wave conditions higher flow velocities are observed in the shoreward part of the breaker zone. The flow velocity is 0.14 m/s near the bed, decreasing in offshore and upward directions. In the top layers of the breaker zone a slight increase in flow magnitude is observed. The largest difference with the cold front case is the width of the surfzone and resulting offshore extent of higher bottom flow velocities. The surfzone in this average wave case is narrower resulting in currents confined to a zone much closer than in the cold front case. The circulating flow pattern of shore-directed current in the model upper layers and offshore-directed currents in the bottom layers is, however, similar to that of the cold front (Figure 3).

Suspended transport magnitudes and directions are shown in Figure 5, top plot. Negative values indicated offshore directed transport and positive values indicate onshore transport. Highest values of bed load transport (up to $0.8 \cdot 10^{-5}$ m^3/ms) are observed in the breaker zone. All bed load transport is directed onshore in the direction of the wave propagation. Sand suspended load is negative (offshore), because the net offshore directed currents at the surf zone transport the suspended sand particles offshore. The magnitude of the suspended load is significantly larger than the magnitude of bed load, reaching a peak of $3 \cdot 10^{-5}$ m^3/ms in the breaker zone. All suspended sand load deposits at the seaward boundary of the breaker zone (Figure 5). Mud transport is directed to the offshore at the breaker zone (x = 6700 m to x = 7100 m in Figure 5) with peak values reaching $2.7 \cdot 10^{-6}$ m^3/ms. Offshore of the breaker zone, onshore mud transport is observed, reaching to an offshore distance of x = 4000 m with a maximum magnitude of $6 \cdot 10^{-6}$ m^3/ms (Figure 5). Onshore transport seems illogical, with a mean offshore directed flow at the surf zone. However, the mud transport outside of the surf zone is dependent on other processes, like wave streaming, a process that occurs near the bed in the direction of wave propagation causing locally observed onshore transport.

Erosion and sedimentation of sand and mud fractions can also be visualized in Figure 5. Mud erosion takes place on a larger cross-shore length than in the sand erosion. On the other hand, erosion and sedimentation of the sand portion is confined to the surf zone and reaches higher magnitudes. The main observation concerning the mud deposition is that it occurs on a significantly longer length scale. It starts slightly (20 m) more offshore and is stretched out in offshore direction almost twice as far as the sand deposition to an offshore distance of about 6600 m. The deposition of mud occurs mostly offshore of the break in slope and the deposition of sand occurs landward of the break in slope in water depths shallower than –2 m (Figure 5) under average wave conditions.

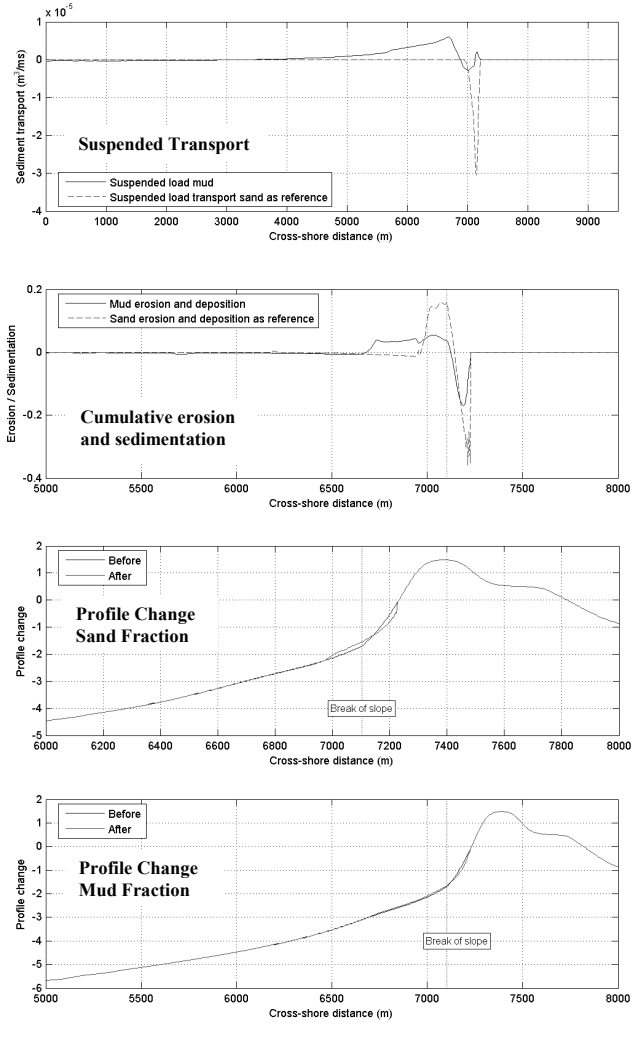

Figure 5: Suspended sediment transport, cumulative erosion and sedimentation and profile change during average wave conditions.

Simulations with sand and mud mixtures

The previous discussion compared the behavior of a sandy versus a muddy barrier island under average wave conditions. Delft3D-FLOW also allows for a computation with

multiple sediment fractions in the same model. Current model limitation is, however, that no interaction between the sand and mud particles is considered. The sediment types are assumed to erode and deposit independently. A new feature in Delft3D-FLOW is using a 'transport layer'. When this feature is enabled, Delft3D computes the volumetric changes of specified sediment types (*e.g.* 'sand' and 'mud') in a user specified top layer ('transport layer'). The relative volumetric percentage change ('fraction change') is computed for each time step. This enables observations of selective erosion and deposition of different sediment types.

Model simulations are performed with mixed sediment of the types 'sand' and 'mud'. Initial volume fractions are equally distributed (50%-50%). Because the sand and mud are assumed to behave morphologically independently and their behavior was discussed previously, we will only describe the sediment fraction change with time in this section. The volume fraction change of mud in the top sediment layer for 7 days of morphological development under average wave conditions is shown in Figure 6. Initially the volume fraction of mud is 50% (light green). The mud fraction changes significantly between x = 6700 m and x = 7200 m where the erosion and deposition was observed. In the rest of the model area the mud fraction remains 50%.

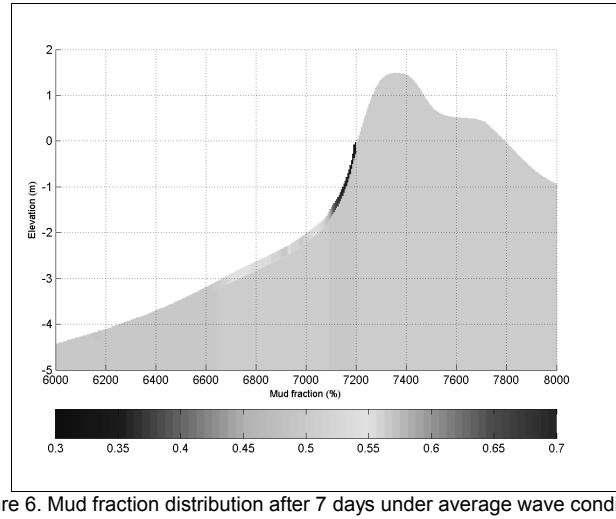

Figure 6. Mud fraction distribution after 7 days under average wave conditions.

The model results of this case show that, under average wave conditions the selective deposition of mud is located further offshore than that of sand. This selective deposition pattern can cause spatial variations of sediment grain sizes, creating zones in which certain sediment types dominate. Domination of certain sediment grain sizes could subsequently control profile characteristics (*e.g.* gradients), providing an explanation for the presence of a break in slope in Louisiana. An interesting detail is that, in these model

results, the fraction transition zone (the zone where the mud dominated volume fraction turns into sand dominated) lies close to the often observed break in slope in Louisiana (± 2 m), where sediments transition from sand to mud according to previous sediment sampling (*i.e.* CPE 2003).

CONCLUSIONS

The numerical modeling conducted here provides valuable insights into the processes behind the conceptual-analytical Dynamic Morphosedimentary Model (Campbell 2005). This study provides, for the first time, a possible process-based explanation for the prominent break in slope commonly observed in beach profiles obtained along the Louisiana Coast.

Sand transport is mainly directed offshore in cases where the island is not overtopped. When the island is submerged (strong tropical storms and hurricanes) there is no significant offshore sand transport and sand is transported onshore by overwash processes. Under low wave energy conditions, mud is transported offshore and deposition occurs offshore of the break of slope, while sand deposition is mostly confined to the surf-zone. Simulations of the behavior of mixtures of sandy and muddy sediments in the model predicted a transition between the sand-mud depositional zones around the break of slope, similar to what is observed in the field.

The selective transport and deposition of mud and sandy sediments can be explained by considering the mechanisms behind the sediment transport of the two sediment types. Outside of the surf zone, offshore directed suspended mud particles deposit. Simultaneously, onshore bed load transport of sand causes erosion in this zone. These processes combined increase the mud content in this area. In the inner surf-zone to the beach the onshore bed load of sand dominates, this process combined with mud erosion in suspended mode, causes the mud content to decrease significantly in the surf zone. Model results are, however, sensitive to variation of the mud transport parameters. Varying these parameters mainly affects how far offshore the muddy sediments move but do not result in mud deposition above the break of slope, in turbulent surf-zone waters.

REFERENCES

Alfageme, S., and Cañizares, R., 2005. Process-based modeling of a restored barrier island: Whiskey Island, Louisiana, USA. *Proceedings of Coastal Dynamics 2005,* Barcelona, Spain.

Boyd, R., Suter, J. and Penland, S., 1985. Relation of sequence stratigraphy to modern sedimentary environments. *Geology*, 17: 926-929.

Campbell, T., 2005. Development of Morphosedimentary Model for Design of Coastal Restoration Projects along the Louisiana Coast. *Journal of Coastal Research*, 44, 234-244.

Campbell, T., Thomson, G. and Benedet, L., 2006. Design of the Restoration of Shell Island with Application of a Dynamic Morphosedimentary Model. *Proceedings of the 30th International Conference on Coastal Engineering*, San Diego, California, 13 p.

Coastal Planning and Engineering, 2000. Holly Beach Breakwater Enhancement and Sand Management Plan. Boca Raton, Florida: Coastal Planning & Engineering, unpublished report, 101p.

Coastal Planning and Engineering, 2003. Chadland headland and Pelican Island barrier Shoreline restoration 30% Design Review. Boca Raton, Florida: Coastal Planning and Engineering, unpublished report, 81p.

Dean, R. G., 1991. Equilibrium Beach Profiles: Characteristics and Applications. *Journal of Coastal Research* 7(1), 53-84.

Donnelly, C.; Hung, N.M., Larson, M., and Hanson, H., 2004. One-line modeling of complex beach conditions: an application to coastal erosion at Hai Hau beach in the Red River Delta, Vietnam. *Proceedings of the 29th International Conference on Coastal Engineering.* Lisbon, Portugal, paper no. 429.

Everts, C.H., 1985. Sea-level rise effects on shoreline position. *Journal of Waterway, Port, Coastal and Ocean Engineering,* 111(6), 985-1000.

Kulp, M.; Penland, S.; Williams, S.J.; Jenkins, C.; Flocks, J., and Kindinger, J., 2005. Geological framework, evolution, and sediment resources for restoration of the Louisiana coast. *Journal of Coastal Research,* SI(44), pp. 56-71.

List, J.H.; Jaffe, B.E.; Sallenger, A.H.; McBride, R.A., and Penland, S. 1994. Atlas of sea-floor changes from 1878 to 1989. US Geological Survey in Cooperation with Louisiana Geological Survey. Miscellaneous Investigations Series I-2150-B.

Mitchener, M., Torfs, H., 1996. Erosion of mud/sand mixtures. *Journal of Coastal Engineering,* 29, pp. 1-25.

Partheniades, E., 1965. Erosion and Deposition of Cohesive Soils. *Journal of the Hydraulic Division,* ASCE, vol 91. No HY1.

Pepper, D.A. and Stone, G.W., 2002. Atmospheric forcing of fine sand transport on a low-energy inner shelf: south central Louisiana, USA. *GeoMarine Letters,* 22, 33-41.

Pirrello, M.A., 1992. The role of wave and current forcing in the process of barrier island overwash. MSc Thesis, Coastal and Oceanographic Engineering Department, University of Florida, Gainesville, FL, 117 p.

Roy, P.S.; Cowell, P.J., Ferland, M.A., and Thom, B.G., 1995. Wave dominated coasts. Reprinted from*: Coastal Evolution: Late Quaternary shoreline morphodynamics*. Ed. Carter, R.W.G. and Woodroffe, C.D. Cambridge University Press.

Sheremet, A, and Stone, G.W., 2003. Observations of nearshore wave dissipation over muddy sea beds. *Journal of Geophysical Research* 108., C11, DOI:10.1029/ 2003JC001885, 11 pp.

Stive, M.J.F., and Battjes, J.A., 1984. A model for offshore sediment transport. *Proceedings of 19th Conference for Coastal Engineering,* ASCE, 1420-1436.

Walstra, D.J.R., P. Ruggiero, G. Lesser, and G. Gelfenbaum, 2005. Modeling Nearshore Morphological Evolution at Seasonal Scale. *Proceedings of Coastal Dynamics 2005,* Barcelona, Spain

Williams, S.J.; Penland, S, and Sallenger, A.H., 1992. Atlas of Shoreline Changes in Louisiana from 1952 to 1995. US Geological Survey in Cooperation with Louisiana Geological Survey. Miscellaneous Investigations Series I-2150-A.

WL | Delft Hydraulics, 2003a. DELFT3D-FLOW, user manual. Version 3.10, Delft, The Netherlands.

RESTORATION-QUALITY SAND FROM SHIP SHOAL, LOUISIANA: GEOTECHNICAL INVESTIGATION FOR SAND ON A DROWNED BARRIER ISLAND

Syed M. Khalil[1], Charles W. Finkl[2], Jeff Andrews[3] Christopher P. Knotts[4]

1. Louisiana Department of Natural Resources, Coastal Engineering Division, 617 N 3rd Street, 10th Floor, P.O. Box 44027, Baton Rouge, LA 70804-4027; Syed.Khalil@la.gov
2. Coastal Planning & Engineering, Inc., 2481 NW Boca Raton Boulevard, Boca Raton, FL 33431, USA.; cfinkl@coastalplanning.net
3. Coastal Planning & Engineering, Inc., 2481 NW Boca Raton Boulevard, Boca Raton, FL 33431, USA.; jandrews@coastalplanning.net
4. Louisiana Department of Natural Resources, Coastal Engineering Division, 617 N 3rd Street, 10th Floor, P.O. Box 44027, Baton Rouge, LA 70804-4027; Chris.Knotts@la.gov

Abstract: In an effort to more accurately evaluate sand volumes that are potentially available for coastal restoration, high-resolution geophysical data were collected followed by detailed geotechnical investigations in two study areas in Ship Shoal Complex. Interpretation of vibracores helped to identify about 13.2 x 10^6 m^3 of clean sand (<5 % silt: D_{50} ~0.20 mm) in portions of Ship Shoal Blocks 88 & 89. Geotechnical exploration of South Pelto Blocks 12 & 13 also identified mostly clean sand (D_{50} grain size 0.15 to 0.2 mm) with less than 5% silt in upper stratigraphic units 4 to 6 m thick. Combined volumes of three closely spaced potential borrows amounted to approximately 21.6 x 10^6 m^3. Comparison of sediments on emergent barrier islands with those on the drowned barrier known as Ship Shoal indicates a high level of compatibility for restorative work on Isle Dernieres and Lafourche delta coastal segments.

INTRODUCTION

The degradation of mainland Gulf shorelines and deltafront barrier islands jeopardizes the vitality of strategic economic and biological resources (including aquatic habitat) as well as the protection of coastal residents from surge flooding. Unless significant efforts are made to restore barrier islands and coastal wetlands, Louisiana will lose productive and protective islands (beaches, dunes) and marshes (Penland *et al.* 2005; Campbell *et al.* 2005, Hester *et al.* 2005, Laska *et al.* 2005). The primary objective of mitigation is to attempt to stabilize the landward retreat and the disintegration of the barrier islands by adding sediment to the system and translating the barriers into various types of modified morpho-sedimentary environments (Khalil *et al* 2006). To promote large-scale restoration (*e.g*. beach nourishment, dune development, marsh creation) of the Louisiana coast, appropriate sand resources must be identified and quantified as these restoration efforts primarily depend on the emplacement of sand and suitable sediment to build up barrier and deltaic systems (Khalil *et al* 2006). Large accumulations of offshore sand provide a valuable resource for the supply of volume-needs required for building the first line of defense in shore protection. These integrated beach-dune-marsh environments, which themselves comprise a fragile coastal system, can protect the immediate Louisiana hinterland by absorbing wave impacts and diminishing the effects of surge flooding.

Restoration of Louisiana's barrier islands requires large volumes of sand (for beaches and dunes) and mixed sediments (for marshes). Such large volumes can only be obtained from offshore sources and consequently, marine sand searches originally focused on reconnaissance surveys in efforts to ascertain general trends in sediment distribution on the seabed. Preliminary or reconnaissance efforts (Suter *et al.* 1991; Kindinger *et al.* 2001) discovered potential sand sources in a range of depositional systems that include spit platforms, delta sheet sands, ebb-tidal deltas, distributary mouth bars, and distributary-channel fills, and inner shelf shoals. Although these types of deposits occur on the continental shelf, a single large deposit is attractive for island restoration because it is cohesive, not dispersed, and not covered by muddy overburden. According to the MMS (2004), estimates of total sand volumes comprising Ship Shoal are on the order of 1.2×10^9 m^3. The drowned barrier sediments range from very fine- to medium-grained sand that in volume are comprised of 112×10^6 m^3 in the shoal crest, 430×10^6 m^3 in the shoal front, and 640×10^6 m^3 within the shoal base. Kulp *et al.* (2001) estimate that there is an additional 123×10^6 m^3 of sand in distributary channel fill deposits under the shoal. As promising as these volumes estimates are, based on reconnaissance data, more detailed studies of the Ship Shoal sands indicate a scope that is limited by subsea infrastructures placed by the oil and gas industries, environmental concerns over dredging, and variability of deposits in the shoal. Nevertheless, these sediments are required for restorative purposes, as indicated below, however constrained by competing needs and restrictive human activities.

Detailed high resolution geophysical surveys were undertaken in 2003 by the Environmental Protection Agency and Louisiana Department of Natural Resources to address archaeological and hazard concerns in South Pelto Blocks 12 &13(CEI, 2003a)and Ship Shoal Blocks 88 & 89 (CEI, 2003b). Such surveys are also pre-requisite

for MMS to grant leases for future dredging in these areas. In both these study areas about 26 square kilometers of the area was covered by high resolution geophysical surveys (bathymetric, seismic, sonar, and magnetic) along approximately 660 line kilometers of track lines almost all trending east-west with a spacing of 50 m and a few north-south with 900 m spacing (CEI, 2003 a & b). Odom Echo Trac DF 3200 bathymetric system, EdgeTech 500 kHz side scan sonar, Edgetech Geostar SB 512i subbottom profiler, and Geometrics 880 cesium magnetometer were used for the geophysical surveys with C-Nav globally corrected GPS for positioning in both these areas (CEI, 2003a & b). CEI (2003a) identified twelve sonar targets and eleven magnetic clusters in the South Pelto Blocks 12 &13. This paper reports offshore geotechnical investigations in the South Pelto Blocks 12 &13. The results of this geotechnical investigation summarize the deposit in terms of its submarine geomorphology, sedimentology, and stratigraphy. Sediments in the study area appear to be suitable for barrier island restoration. Although good quality sediments occur in the Ship Shoal environment, the occurrence of cultural resources and petroleum industry infrastructure impede development of sand resources. The problem of locating sand resources for barrier island restoration is thus not simply a matter of marine exploration but also being cognizant of hazards to dredging and awareness of potential hazards posed by borrows to existing structures. Complex patterns of pipeline corridors and other infrastructures restrict exploration for sand resources and reduce potential volumes that can be dredged. Eight pipelines transit the study area and seven occur adjacent to it (CEI 2003a). Six production platforms and two wells (CEI 2003a) also exist just outside the bounds of the study area. These pipelines and structures are protected by 150 m buffer zones within which no dredging can occur.

STUDY AREA LOCATION AND GEOLOGICAL FRAMEWORK

Most of the seafloor beneath the study area consists of a large, submarine sand body that is locally known as Ship Shoal, the largest shoal off Louisiana. The potential of Ship Shoal as a source of sand for restoring parts of Louisiana's rapidly eroding coastline has been summarized by various researchers including Krawiec (1966); Suter *et al*. (1985); Penland *et al*. (1985, 1986); Williams *et al*. (1989); Kulp *et al*. (2001); Stone (2001); Finkl *et al.* (2005). A 40- to 45-m thick wedge of deltaic sediments, deposited by the Mississippi River during the Holocene, underlies the Ship Shoal region. Although processes of Mississippi River Delta formation have been intensively studied (*e.g*. Coleman and Gagliano 1996; Frazier 1967; Saucier 1994), they are briefly summarized here as they relate to the formation of the Ship Shoal environs. The shoal crest, with surface sand thickness >1 m occupying an area of about 560 km^2, forms an ancient barrier shoreline that has been modified by processes related to transgression and submergence of the Maringouin delta complex (Krawiec, 1966; Frazier, 1967; MMS, 2004).

A result of deltaic abandonment and marine transgression, Ship Shoal (Figure 1) is the largest and easternmost of a series of sand shoals on the inner continental shelf of Louisiana (Kulp *et al*. 2001). The elongated shoal, lying parallel to the coast approximately 12 to 19 km off Terrebonne Parish, measures approximately 50 km long in an east-west direction. The central portion of the shoal ranges 5 to 12 km in width, but its distal margins narrow to points.

South Pelto is located on the eastern segment of Ship Shoal, about 14 to 20 km offshore

the eastern part of the Isle Dernieres barrier chain (Figure 1). The area encompasses portions of five MMS lease blocks (12, 13, 14, 18, and 19) (MMS, 2004). In order to better appreciate the deposit geometry of South Pelto, sedimentary geology, and geomorphology, it is necessary to understand the stratigraphic implications of river diversion (avulsion and branching) and delta switching in major deltaic depositional environments. These processes contribute to the formation of transgressive sand bodies, such as Ship Shoal, and evolution of modern barrier islands such as those lying landward of the Shoal (*e.g.* Isles Dernieres and Timbalier).

Ship Shoal was formed about 7,000 years ago (early Holocene) in association with the abandonment and reworking of distal sediments from the Maringouin Delta Complex. The Isles Dernieres, located landward of Ship Shoal, are associated with the winnowing and reworking of sediments from the abandonment and submergence of the Caillou Bay headland (abandoned about 600 to 800 years ago) of the Lafourche delta complex (Penland *et al.,* 1988).

Deltas are dynamic depositional systems that exhibit a wide range of depositional features. The Mississippi deltaic plain is characterized by major river diversions that promote large-scale delta lobes. These delta complexes occur on millennial scales. Bay fills are built and abandoned in centennial time frames, whereas the smallest sub-deltas exist only for two centuries, on average (Coleman and Gagliano, 1964).

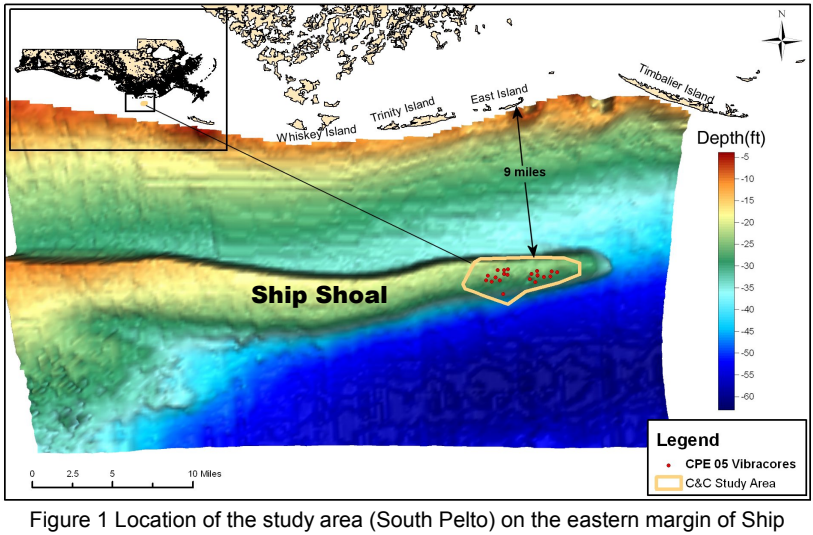

Figure 1 Location of the study area (South Pelto) on the eastern margin of Ship Shoal, in relation to the Isles Dernieres (Whiskey, Trinity, and East Islands) and regional bathymetry of Ship Shoal

Scruton (1960) employed the term *delta cycle* in reference to alternating phases in deltaic sedimentation. Each delta cycle is initiated by (1) sedimentation and rapid growth (a

constructional-progradational phase) that is followed by (2) systematic loss of flow efficiency, (3) sediment dispersal and abandonment of the delta by the sediment delivery system (delta switching), and concludes with (4) a destructional phase in the form of delta deterioration. The coastal plain of Louisiana exhibits all stages of the delta cycle, from the newly constructed Atchafalaya-Wax Lake bayhead deltas to abandoned destructive deltas (*e.g*, Lafourche) (Roberts, 1997). At the present time (Holocene epoch), eighteen delta lobes coalesce within six major delta complexes to make up the Holocene deltaic plain of Louisiana (Coleman *et al*., 1998; Kulp *et al*., 2005). The entire deltaic plain is transgressive, with the exception of the Birdfoot (Balize complex) and the Atchafalaya River delta complex. The most recent abandoned lobes are the Laforche and Plaquemines lobes of the modern Balize-Birdfoot delta.

Older lobes of the Mississippi delta began to accumulate sediment about 7,000 YBP (years before present), when the rate of sea-level rise decelerated and MSL (mean sea level) approached present levels (Fisk *et al*., 1954; Roberts, 1997). River avulsion (rapid channel switching) and diversion, which often result in delta switching, are responsible for the present complex and diverse geomorphology and stratigraphy of the Mississippi deltaic plain. Study of the sedimentary record suggests that delta building occurred at different locations about every 1000 to 2000 years (Roberts, 1997; Coleman *et al*., 1998. The Mississippi River has thus built a broad and complex coastal plain by these basic processes. Throughout the current deltaic plain, late Pleistocene mud-rich and stiff clay deposits underlie Quaternary depositional deltaic sequences. Typically, the Pleistocene facies is denser than overlying Quaternary sediments (compaction occurs mostly in Quaternary sediments). During late (destructive) stages of a delta cycle, abandoned delta complexes subside due to compaction (dewatering of clastic sediments and oxidation of organic-rich materials). As coastal processes rework the seaward margin, the delta lobe enters a transgressive-destructive phase where erosional headlands, flanking barriers, barrier island arcs and erosional headlands develop, as described by Penland *et al.* (1988). A mechanism for the genesis and evolution of transgressive depositional systems in the Louisiana deltaic plain is suggested by Penland *et al.* (1988) in a three-stage geomorphic model. This evolution begins when marine processes transform the abandoned delta complex into a Stage 1 erosional headland with flanking barriers. At this stage, sediment is supplied to flanking barrier development by shoreface erosion. Relative sea-level rise, land loss, and shoreface erosion leads to submergence of back barrier lands and the separation of the Stage 1 barrier from the mainland shoreline, forming the Stage 2 barrier island arc. When relative sea-level rise and overwash processes overcome the ability of the barrier island arc to maintain its subaerial integrity, submergence initiates the formation of inner shelf shoals under Stage 3. Following submergence, the drowned barrier islands continue to be re-worked by marine/coastal processes to form a marine sand body in the inner shelf. This is the last stage in the evolution of transgressive depositional systems. These evolutionary processes were collectively subsumed under the heading of "transgressive submergence" by Penland *et al*. (1988). According to Penland *et al.* (1988), Ship Shoal is an inner shelf shoal that represents Stage 3 of the model.

The controlling variables that differentiate transgressive submergence (Penland *et al.,* 1988) from other models of shoreline sand formation such as shoreface retreat (Fisher, 1961; Swift, 1975) and in-place drowning (Sanders and Kumar, 1975) are: (1) high rates of relative sea-level rise, (2) low gradients of continental shelves with limited local sand sources, and (3) a storm-dominated environment. Formation of barrier islands and shoals by mainland detachment processes and regression generally results in a coarsening upwards stratigraphic sequence (sediment grain size increases upwards from the bottom of the deposit toward the top) that is commonly found in barrier islands arc sequences and inner shelf shoals. Reworked inner shelf shoals exhibit a stratigraphic sequence that grades rapidly from silt and sand in the base, to shoal front sand capped by shoal crest sand and shell on the surface (Penland *et al.*, 1988). The sedimentology and stratigraphy of Ship Shoal is further discussed as follows.

SHIP SHOAL SEDIMENTOLOGY AND STRATIGRAPHY

The Ship Shoal system was characterized by Penland *et al*. (1988) and Suter *et al*. (1991) as a sandy submerged barrier island that is about 50 km long by 8 km wide in the central area to about 5 and 10 km on eastern and western margins, respectively. Local relief varies from about 7 m on the western margin to about 5 m elsewhere. Water depths range from 3 m on the west to 5 m on the eastern margin (Kulp *et al*., 2005). According to Penland *et al*. (1988), Ship Shoal has migrated to its present position under conditions of sea-level rise, shoreface erosion, and submergence. Landward asymmetry and stratigraphic position of the shoal indicates that it is a transgressive sand body that is migrating landward.

Penland *et al*. (1988) described seven (7) lithofacies on Ship Shoal that were based on texture, sedimentary structures, faunal assemblages, and stratigraphic position. However the upper three facies that are most relevant to sand resources and include the (1) shoal crest, (2) lower shoal or shoal front, and (3) shoal base. The shoal crest, the facies to explore over the short term, is located in the upper 5 m of the deposit and is comprised by very well sorted quartz sand (99% sand) that ranges from 0.13 mm to 0.16 mm in size. Sediments are very well sorted and coarser on the crest, associated with a general coarsening upward trend in a high-energy active zone where sediments are winnowed and sorted by waves and currents. The shoal front, subsequently overridden by the migrating crest, is slightly thinner (1.2 to 3.4 m thick) and contains finer-grained sand (0.12 to 0.15 mm) compared to the crest. The base of the shoal, underlying the shoal front, contains poorly sorted finer-grained sand that are interbedded with layers of silt and clay. Penland *et al.* (1988) estimates that the shoal crest unit alone contains more than 7.6×10^6 m^3 of sandy sediment. Although there may be large sediment volumes in Ship Shoal, the presence of oil infrastructure and obstructions (pipelines, flow lines, rigs, abandoned pipes, wrecks) may preclude exploration of in many areas.

The available evidence indicates that the majority of the 45 m of Holocene sediments underlying the study area is associated with the Maringouin Delta Complex and has been deposited over the last 7,500. These thick Holocene deposits rest on weathered, Pleistocene Prairie terrace deposits that represent floodplain, deltaic and open shelf sediments deposited between about 120,000 and

20,000 years BP (Frazier, 1974; Saucier, 1994). During low sea-level stands, large expanses of these Pleistocene surfaces were subaerially exposed and streams extended an extensive network of channels across them. Several relict channels trending northwest to southeast are incised into this deeply buried Pleistocene surface near the study area. These relict channels terminate at the head of Mississippi Canyon and represent channels of an ancestral Mississippi River course (Moore *et al*., 1978). About 18,000 to 20,000 years BP (Last Glacial Maximum in Wisconsinan time), shorelines stood approximately 90 m lower than present and approximated the edge of the outer continental shelf. Since that time, sea level has gradually risen and Pleistocene surfaces were drowned and buried by Holocene marine and deltaic sediments.

Analyses of sediments from Ship Shoal and the Isles Deniers indicates compatibility of grain sizes and sorting viz. 2.64-3.72 phi (0.165-0.076 mm) and 2.73-3.94 phi (0.149-0.063 mm) for Isle Dernieres sediment and Ship Shoal, respectively (based on Krawiec, 1966, and reported in MMS, 2004). Both areas contain fine to very fine sand that is very well to well sorted, making the deposits compatible and the Ship Shoal sand ideal for beach nourishment.

GEOPHYSICAL AND GEOTECHNICAL FIELD AND LAB METHODS

Cost effective exploration for offshore sand in deltaic environment needs a systematic approach (Khalil 2004, Finkl and Khalil 2005a). Most of the tasks associated with the phase-wise approach for sand search (Khalil 2004) was undertaken during 2003 when a detailed geophysical survey was conducted is Ship Shoal Blocks 88 & 89 (CEI 2003b) and South Pelto Blocks 12 &13 (CEI 2003a) as stated earlier. Based on the interpretation of bathymetric, seismic, sonar, and magnetic data, geotechnical investigation was undertaken by collecting vibracores (Finkl and Khalil 2005b).

Geophysical/geotechnical equipment and techniques used during this investigation included (Finkl *et.al* 2005):

- Differential Global Positioning System (DGPS) – Trimble GPS and Coast Guard Navigation Beacon (Provides accurate positioning of the survey vessel).
- Navigation/Survey Integration System – Hypack Inc.'s "HYPACK® MAX" (Integrates DGPS data with data collected during the survey).
- Vibracore Acquisition
- Sediment-Size Analysis

The technical methods, analytical tools, and equipment used in this geotechnical investigation for evaluation of sand deposits in the study area are described below.

Navigation System

The navigation and positioning system used during the survey was a Trimble DGPS Global Positioning System (GPS) that was interfaced to Hypack Inc.'s HYPACK® MAX. A Pro Beacon receiver provided differential GPS correction from the U.S. Coast Guard Navigational Beacon located at English Turn, Louisiana. The DGPS initially receives the civilian signal from the global positioning system (GPS) NAVSTAR satellites. The locator automatically acquires and simultaneously tracks the NAVSTAR satellites, while

receiving precisely measured code phase and Doppler phase shifts, which enables the receiver to compute the position and velocity of the vessel. The receiver then determines the time, latitude, longitude, height, and velocity ten times per second. The GPS accuracy, with differential correction used in this study, provides for a position accuracy of one (1) to four (4) feet, which is within the accuracy needed for geotechnical investigations for sediment sources. The U.S. Army Corps of Engineers (USACE) test of the U.S. Coast Guard beacons found an accuracy of at least five (5) feet approximately 94% of the time.

Survey Integration via Hypack Inc.'s HYPACK® MAX

The navigation system was interfaced with an onboard computer, and the data integrated in real time using Hypack Inc.'s HYPACK® MAX. HYPACK® MAX is a state-of-the-art navigation and hydrographic surveying system. Online screen graphic displays include the pre-plotted survey lines, the updated boat track across the survey area, adjustable left/right indicator, as well as other positioning information such as boat speed, quality of fix, and line bearing. All data are recorded on the computer's hard disk and transferred to a USB memory stick each day during the survey to back-up raw survey data. After post-processing, the navigation data (locational) stored in the HYPACK® MAX system was then exported to a *.dxf* file and imported into ArcGIS 8 in order to create a GIS shapefile for analysis and report preparation.

Vibracore Acquisition

A 271B Alpine Pneumatic Vibracore, configured to collect undisturbed sediment cores 20 feet in length, was used for this project. This self-contained, freestanding pneumatic vibracore unit contains the following components: an air-driven vibratory hammer assembly, an aluminum H-beam which acts as the vertical beam upright on the seafloor, a steel coring pipe (with a plastic core liner), and a drilling bit with a cutting edge. An air hose array provided compressed air from the compressor on deck to drive the vibracore. If penetration refusal occurred at less than 80% of expected penetration, the sampled portion was removed from the pipe, a new liner inserted, and a jet pump hose was attached just below the vibracore head. After lowering the rig to the bottom and jetting to one (1) to two (2) feet above the refusal depth, the jet was turned off and the vibrator turned on in order to collect the remaining core. The vibracore unit was deployed by a crane from the "liftboat" M/V *Stingray*.

Sediment-Size (Mechanical) Analysis

Sieve analyses were conducted for samples obtained by vibracoring in accordance with American Society for Testing and Materials Standard Materials Designation D422-63 for particle size analysis of soils (ASTM, 1987). This method covered the quantitative determination of the distribution of sand size particles. Results of the particle-size analyses were entered into gINT® software, which computes the mean and median grain size, sorting, and silt/clay percentages for each sample using the moment method described by Folk (1974).

RESULTS

Twenty (20) vibracores were obtained in the South Pelto study area. The core locations were selected on the basis of results from preliminary geophysical investigations conducted by CEI (2003a). Vibracore locations were overlaid on a three-dimensional (3D) bathymetric image (using NOAA-NOS historic bathymetric data mostly from 1979) to show the relationship between vibracore locations and morphology whereas the latest bathymetric data (CEI 2003a) collected was used to plan the vibracore acquisition. In the study area occurring on the eastern tip of Ship Shoal (Figure 1), water depths decrease from east (mostly between 6 to 9 m isobaths) to west (9 m isobath on the crest) as this inner-shelf ridge increases in width. Shoreward-facing (north) slopes are steeper than the seaward (south) side slopes. Vibracores were located on the eastern shoal crest and concentrated in two main areas (Figure 1). Vibracore #20 obtained off the south margin of the main shoal contained mostly clay and probably represented lagoonal sediments from the Marogouin delta that underlies the shoal base. Other vibracores on the shoal crest recovered mostly sand in surface layers and mixed fine sediments (sand, silt, and clay) in basal layers.

Potential borrow sites, targeted by results of prior work, were reported to be free from dredging obstructions. Figure 2 shows the location of the design borrow sites, buffers (no-dredge zones as defined by cultural resource surveys), vibracore locations (Finkl *et al*. 2005), location of fence diagrams, and MMS lease block boundaries. Potential borrow areas are labeled A, B and C (Figure 2).

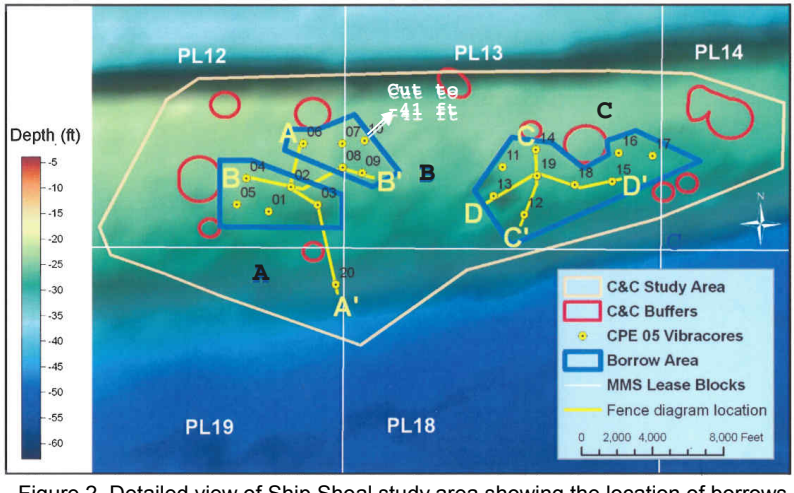

Figure 2. Detailed view of Ship Shoal study area showing the location of borrows.

Potential borrow area A contains five vibracores (Cores # 01, 02, 03, 04 and 05). Sand thickness varies from 3.6 to 4.8 m with greater thickness occurring in the vibracore closest to the center (#04). Figure 3 a fence diagram drawn perpendicular to the shoal

crest shows how the sand deposit thickens to the offshore as the shoal relief decreases and the underlying mud layer outcrops in the shoal seaward (south) side. Upper portions of vibracores generally contained clean sand (mean grain size ranges from 0.15 to 0.22 mm) whereas bottom layers contained clay and silty sand (mean grain size ranges from 0.12 to 0.15 mm). Figure 4, a schematic fence diagram drawn parallel to the shoal's crest illustrates how the sand thickness is constant along the shoal crest (W-E) in contrast to a rapid thinning offshore (N-S).

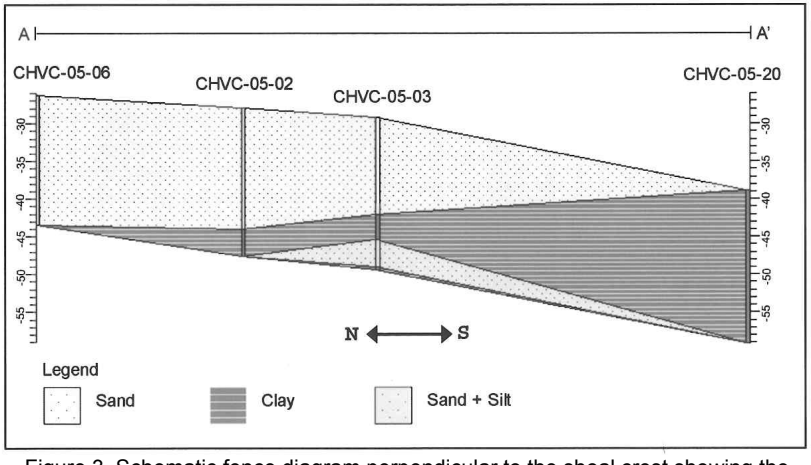

Figure 3. Schematic fence diagram perpendicular to the shoal crest showing the decrease of sand thickness towards the offshore (vibracore 20).

Five (5) vibracores were obtained in potential Borrow Area B (cores # 06, 07, 08, 09 and 10). Sand thickness ranged from 4.6 to 6 m with the greatest thickness occurring in vibracore 07. The fence diagram in Figure 3 illustrates that vibracore 06 contained clean sand from the core top down to the core base, the same pattern is observed in cores 08 and 09 illustrated in Figure 4. Thus, all vibracores along this area contained sand from the shoal crest and displayed a slight coarsening upward trend. Grain sizes range from finer grain sizes (0.15 to 0.18 mm) in the base of the core to slightly coarser sand sizes (0.19 to 0.51 mm, but mostly around 0.2 mm) near the top. Shell fragments and whole shells in the top 0.6 m of vibracore #10 accounted for coarser grains (0.51 mm).

Nine (9) vibracores were obtained within potential Borrow Area C. Sand thickness ranged from 3.9 to 5.7 m but mostly occurred in the 5 m range (see Figures 5 and 6). Silt decreased and mean grain size increased from the core base to the top. Sediments in the upper 3 m were generally cleaner and contained coarser-grained sand than basal layers. Vibracore #12, the seaward most core, contained the thinnest sand layer that at 4 m transitioned to clay (Figure 5). Clayey sediments occurred in basal layers of seven (7) out of the nine (9) vibracores from this area. Most clay layers occurred 5 m below the shoal surface.

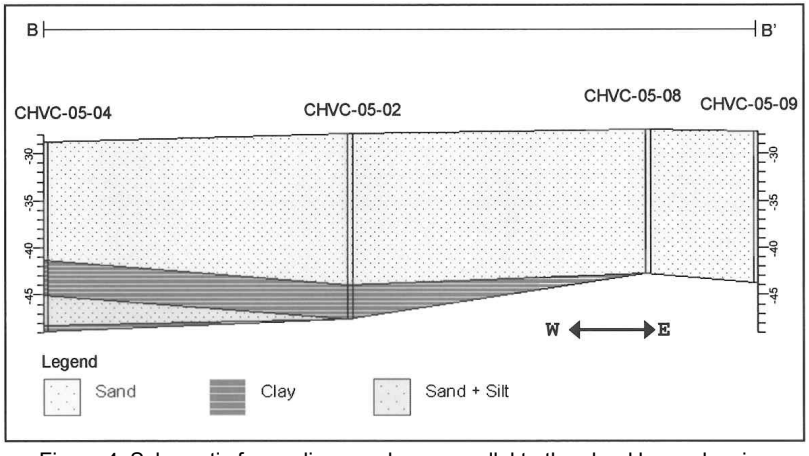

Figure 4. Schematic fence diagram drawn parallel to the shoal base showing relatively homogeneous sand thickness throughout the shoal base unit.

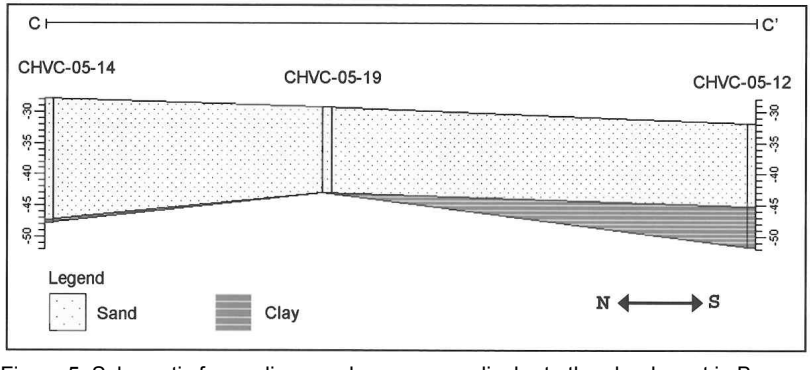

Figure 5. Schematic fence diagram drawn perpendicular to the shoal crest in Borrow Area C. The cleaner upper sand layers thin seaward (to the south).

Based on the interpretation of seismic data compared with historical cores, CEI (2003a) prepared a sand isopach map for the project area. The isopach indicated that sand thickness in the study area varies from 5.7 m on the shoal's crest to 0.3 m on the seaward (south) side of the shoal. Sand thickness decreases abruptly towards the south compared to a more gradual decrease observed to the north. Sand thickness in the Borrow Area C is slightly thinner than borrow areas A and B and ranges from 3.5 to 5.4 m.

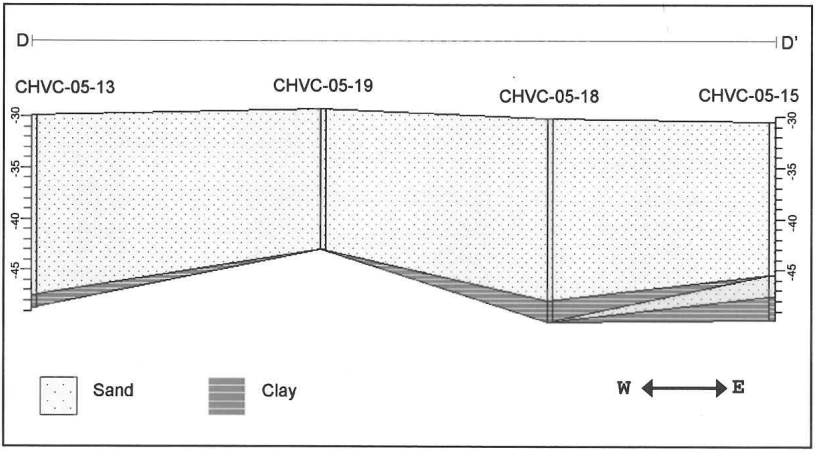

Figure 6. Schematic fence diagram drawn parallel to the shoal crest in Borrow Area C. Clean sandy sediments are associated with upper units (shoal crest and front).

Borrow area cuts were calculated using the isopach data provided by CEI (2003a) compared with vibracore results (thickness of clean sand and textural properties). Sand volume estimated in Borrow Area A is about 6.95 x 10^6 m^3, in Borrow Area B about 4.9 10^6 m^3, and in Borrow Area C about 9.75 10^6 m^3 with a total of about 21.6 x 10^6 m^3 of sand available from all these three borrow sites.

CONCLUSIONS

Sand resources along the southern Louisiana coast are relatively scarce given the large volumes of sand required for restoration of the rapidly degrading barrier systems. During this investigation, twenty vibracores were obtained from Ship Shoal, a well-known sand source offshore of the Isles Dernieres.

The study area along the eastern end of Ship Shoal, commonly known as South Pelto mainly contained very clean sand (less than 5% silt in the upper shoal units) that ranged in thickness from 4 to 6 m and generally ranged in grain size from 0.15 to 0.2 mm. About 21.6 x 10^6 m^3 of clean sand is estimated to occur in three borrow areas. Buffers around oil and gas infrastructures and other magnetic anomalies occurring in and around the study area were avoided during borrow area design to ensure quality of borrow sediments and safety of dredging operations. The sand deposits identified along South Pelto in this study have great potential to support large-scale coastal restoration of Lafourche Coastal segments. Sand from this borrow area is proposed to be used for restoration of Caminada Headland restoration project which is about 48 km. Transporting sand to this distance will be expensive. However in absence of any suitable deposit with adequate quantity of sand in the vicinity of the project area, this might be the only option left.

REFERENCES

Campbell, T., Benedet, L., and Finkl, C.W. (2005). "Regional Strategies for Coastal Restoration in Louisiana." In: Finkl, C.W. and Khalil, S.M., (eds.), Savings America's Wetland: Strategies for Restoration of Louisiana's Coastal Wetlands and Barrier Islands. *Journal of Coastal Research*, Special Issue No. 44, pp. 245-268.

Coastal Environment Incorporated (CEI, 2003a). *"New Cut Dune/Marsh Restoration Project Using Ship Shoal Sediment Coastal Terrebonne Parish, Louisiana: High Resolution Geophysical and Archaeological Survey of the South Pelto Area Block 13 Vicinity of Ship Shoal,"* C&C Technologies, Lafayette, LA, 43p.

Coastal Environment Incorporated (CEI, 2003b).*"Whiskey Island West Flank Restoration Project Using Ship Shoal Sediment Coastal Terrebonne Parish, Louisiana: High Resolution Geophysical and Archaeological Survey of the Portions of Blocks 87, 88, 89,94 & 95 Ship Shoal Area,"* C&C Technologies, Lafayette, LA, 43p.

Coleman, J.M. and Gagliano, S.M. (1964). "Cyclic sedimentation in the Mississippi River delta plain," *Transactions Gulf Coast Association of Geological Societies* 14, 67-80.

Coleman, J.M.; Roberts, H.H., and Stone, G.W. (1998). "Mississippi River Delta: an Overview. *Journal of Coastal Research*, Vol. 14, No. 3, pp. 698-716.

Fisher, A.G. (1961). Stratigraphic record of transgressing seas in light of sedimentation on Atlantic coast of New Jersey. *Am. Assoc. Petroleum Geologists*, v. 45, p. 1656-1667.

Finkl, C.W. and Khalil, S.M. (2005a). Offshore exploration for sand sources: General guidelines and procedural strategies along deltaic coasts. *In*: Finkl, C.W. and Khalil, S.M., (eds.), Savings America's Wetland: Strategies for Restoration of Louisiana's Coastal Wetlands and Barrier Islands. *Journal of Coastal Research*, Special Issue No. 44, pp. 203-233.

Finkl, C.W. and Khalil, S.M. (2005b). Vibracore. In: Schwartz, M.L., (ed.), *The Encyclopedia of Coastal Science*. Kluwer Academic, Dordrecht, The Netherlands, 1272-1284 pp.

Finkl, C.W.; Andrews, J.L.; Benedet, L., and Campbell, T. (2005). *Geotechnical Investigation for Exploration of Sand Resources in the Lower Mississippi River and South Pass, and Exploration for Sand via Vibracoring in South Pelto Blocks 12 &13*. Boca Raton, Florida: Coastal Planning & Engineering, Inc. 40p. (Report Prepared for the Louisiana Department of Natural Resources, Baton Rouge, LA).

Hester, M.W., Spalding, E.A., Franze, C.D. (2005). "Biological Resources of the Louisiana Coast: Part 1. An overview of coastal plant communities of the Louisiana Gulf Shoreline" In: Finkl, C.W. and Khalil, S.M., (eds.), Savings America's Wetland: Strategies for Restoration of Louisiana's Coastal Wetlands and Barrier Islands. *Journal of Coastal Research*, Special Issue No. 44, pp. 134-145.

Khalil, S.M. (2004). General Guidelines: Exploration for Offshore Sand Sources., Version-IV. Pdf. *Coastal Engineering Division. OCRM, Louisiana Department of Natural Resources,* Baton Rouge, LA.

Khalil, S.M., Knotts, C. P., and Tate, B. (2006). "Restoration of Louisiana Barrier

Islands: Engineering approaches to hazard mitigation by modulating coastal environments," *Proceedings ICCE 2006*, Published by World Scientific (in press)

Kindinger, J.; Flocks, J.; Kulp, M.; Penland, S., and Britsch, L.D., (2001). "Sand Resources, Regional Geology, and Coastal Processes for the Restoration of the Barataria Barrier Shoreline," Report to U.S. Army Corps of Engineers, New Orleans District, September 2001. *US Geological Survey Open File Report 01-384*.

Kulp, M., Penland, S., and Ramsey, K. (2001). "Ship Shoal, Sand Resource Synthesis Report" Coastal Research Laboratory, Department of Geology and Geophysics, University of New Orleans, New Orleans, LA July 2001.

Kulp, M., Penland, S., Williams, S.J., Jenkins, C., Flocks, J., and Kindinger, J. (2005). "Geological Framework and Sediment Resources for Restoration of the Louisiana Coastal Zone. In: Finkl, C.W. and Khalil, S.M., (eds.), Savings America's Wetland: Strategies for Restoration of Louisiana's Coastal Wetlands and Barrier Islands," *Journal of Coastal Research*, Special Issue No. 44, pp 56-71.

Laska, S., Woodell, G., Hagelman, R., Grambling, R., Farris, M.T. (2005). "At Risk: The Human, Community and Infrastructures Resources of Coastal Louisiana," In: Finkl, C.W. and Khalil, S.M., (eds.), Savings America's Wetland: Strategies for Restoration of Louisiana's Coastal Wetlands and Barrier Islands. *Journal of Coastal Research*, Special Issue No. 44, pp 90-111.

MMS (Minerals Management Service) (2004). "*Environmental Assessment: Issuance of Non-Competetive Leases for the Use of Outer Continental Shelf Sand Resources from Ship Shoal, Offshore Central Louisiana for Coastal and Barrier Island Nourishment and Hurricane Levee Construction,"* U.S. Department of Interior, Washington, DC, 114p.

Penland, S., Connor, P.F., Jr., Beall, A., Fearnley, S. and Williams, S.J. (2005). "Changes in Louisiana's Shoreline: 1855-2002. In: Finkl, C.W. and Khalil, S.M., (eds.), Savings America's Wetland: Strategies for Restoration of Louisiana's Coastal Wetlands and Barrier Islands," *Journal of Coastal Research*, Special Issue No. 44, 7-39.

Penland, S., Boyd, R., and Suter, J. R., (1988). "Transgressive depositional systems of the Mississippi River delta plain," *Journal of Sedimentary Petrology*, 58 (6), 932-949.

Roberts, H.H. (1997). "Dynamic changes of the Holocene Mississippi River delta plain: The delta cycle," *Journal of Coastal Research*, 13(3) 605-627.

Scruton, P. C. (1960). "Delta building and the deltaic sequence," In F. P. Shepard, (ed), Recent sediments, northwest Gulf of Mexico. *American Association of Petroleum Geologists*, Tulsa, OK. 82 - 102

Sanders, J.E. and Kumar, N. (1975). "Evidence of shoreface retreat and in-place drowning during Holocene submergence of barriers, shelf off of Fire Island, New York," *Geol. Soc. America Bull.*, v. 86, p. 65-76.

Suter, J. R., Penland, S., and Ramsey, K. E. (1991). "Nearshore Sand Resources of the Mississippi River Delta Plain: Marsh Island to Sandy Point". Coastal Geology Technical Report No. 8. Louisiana Geological Survey, Baton Rouge, LA, U.S.

Swift, D.J.P. (1975). "Barrier island genesis: Evidence from the central Atlantic shelf, eastern USA: *Sedimentary Geology*, v 14, p. 1-43.

Mississippi River Sand for Barrier Island Restoration in Louisiana: Geophysical & Geotechnical Investigations for Sand Mining

Jeffrey L. Andrews[1], Syed M. Khalil[2], Charles W. Finkl[1], and Lindino Benedet[1]

1. Coastal Planning & Engineering, Inc., 2481 NW Boca Raton Boulevard, Boca Raton, FL 33431, USA. cfinkl@coastalplanning.net; jandrews@coastalplanning.net; lbenedet@coastalplanning.net
2. Louisiana Department of Natural Resources, Coastal Engineering Division, 617 N 3rd Street, 10th Floor, P.O. Box 44027, Baton Rouge, LA 70804-4027; Syed.Khalil@la.gov

ABSTRACT Coastal land loss in the Mississippi River delta region contributes to loss of valuable habitat and coastal flooding hazards. Restoration of these ecosystems is a primary activity that requires large volumes of sand to rebuild beach-dune systems and restore wetland habitats. Sand sources have traditionally been sought offshore in the marine environment but there are problems associated with setbacks from oil and gas infrastructure, presence of muddy overburden, and limited reserves of beach-quality sediments. The potential of sand sources in channel and point bar deposits becomes an attractive alternative for barrier island restoration, especially because fluvial sediments are renewable. Results of preliminary geophysical and geotechnical investigations in the lower Mississippi River (south of New Orleans) along a 32-km stretch of the river indicate the presence of at least 23 million m^3 of usable sand.

INTRODUCTION

Land loss in Louisiana leads the nation in degradation of coastal wetlands and destruction of terrestrial, aquatic, and benthic habitats in and around the barrier island systems that are associated with the Mississippi Delta Plain viz. the Isle Denieres Barrier shoreline, Bayou Lafourche Barrier shoreline, Plaquemines shoreline, and Chandeleur Island shoreline. Numerous natural processes are responsible for coastal erosion and land loss in the deltaic environment of Mississippi River, one of the world's largest fluvial systems. Various experts estimate that about 30 percent of the land loss in coastal Louisiana is due to natural causes, the remaining 70 percent being attributable to both direct and indirect negative anthropogenic

effects on the environment (*e.g*. Boesch *et al*., 1994; Williams, Stone and Burruss, 1997). Some of the main causes include land subsidence, sea-level rise, decrease in sediment supply to coastal marshlands due to the levee system, fluid withdrawal from underlying strata by the petroleum (oil and gas) industry, dredging of access channels through wetlands, *etc*.(*e.g.* Penland and Ramsey, 1990; Roberts and Coleman, 1996).

Disappearing at a rate on the order of 65 to 90 km^2 per year, Louisiana looses nearly 9060 hectares coastal wetlands per year. Over the last century, as a result of human activities and natural coastal processes, the State of Louisiana lost valuable coastal wetlands on the order of 2430 to 3650 km^2. If nothing is done to mitigate coastal land loss in Louisiana, another 1760 km^2 could be lost over the next 50 years (LDNR, 2005). Although currently 30% of the total coastal marsh in the conterminous United States occurs in Louisiana, this state accounts for 90% of the coastal marsh loss.

In order to promote large-scale restoration of the Louisiana coast, appropriate sand resources must be identified and quantified (*e.g*. Suter, Penland and Ramsey, 1991; Kindinger *et al*., 2001; Finkl and Khalil, 2005a). Sand resources will supply materials needed for building the first line-of defense of this fragile coastal system, its beaches and dunes. This geotechnical and geophysical study of riverine deposits along the Lower Mississippi River (LMR) was conducted to ascertain the potential of using fluvial sediments for barrier island restoration along the Louisiana coast, northern Gulf of Mexico. Deposit sedimentology, stratigraphy, and relationship to previous work and geomorphic framework are presented here in reflection of prior work by Finkl *et al*. (2005, 2006).

Study Area in the Lower Mississippi River

Sand resources are investigated along the Lower Mississippi River (LMR) reach from Mile Marker [MM] 35 to MM 15 (Figure 1). This area was selected because of its proximity to Gulf of Mexico barrier islands via Adams Bay, Bastian Bay, and associated marshlands. Along the channelized section of the LMR, straight reaches of the river are about 800 m wide but may exceed 2400 m on bends with large point bars. Although river depths average about 20-25 m, they often approach 30 m in the thalweg. Geotechnical and geophysical investigations along the river target active and relict point-bar deposits as well as migrating sand waves on the riverbed. The sedimentary geology and geomorphology of the area is related to river diversions (avulsion) and delta switching, as occur in major deltaic depositional events throughout the region's geologic history.

Geological Framework

The LMR traverses the delta plain and cuts into deltaic deposits that are older than the present river position. Deltas are dynamic depositional systems that exhibit a wide range of sedimentary features. The Mississippi deltaic plain is characterized by major river diversions that promote the development of large-scale delta lobes (*e.g.* Kolb and Lopik, 1966; Roberts, 1997). These delta complexes occur on a millennial time scale. Bay fills are built and abandoned on a centennial time scale, whereas smaller sub-deltas exist for two centuries on average (Coleman and Gagliano, 1964).

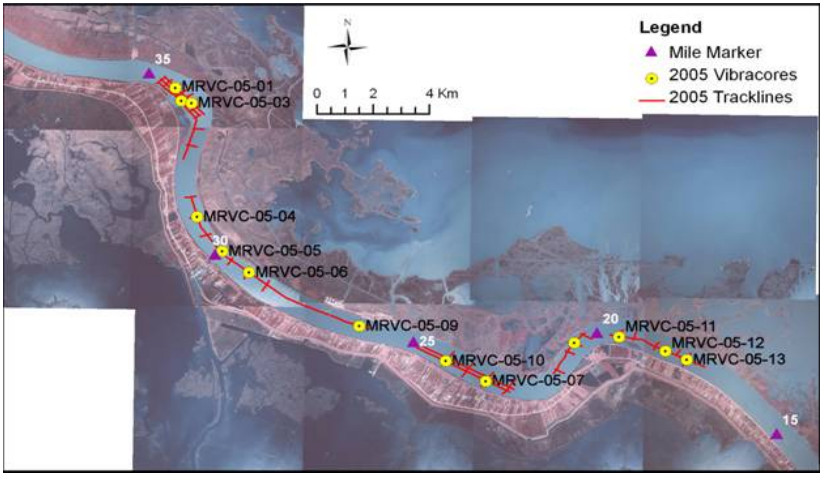

Fig. 1. Photomosaic showing the location of vibracores and geophysical tracklines in the Lower Mississippi River between Nairn (top left) and Ft. Jackson (bottom right).

Of particular interest to this study is the geological setting where the LMR cuts into the delta (alluvial) plain. The river valley is entrenched in the alluvial plain but itself contains bedload (traction materials) sands that continue to accumulate on relict point bars (since channelization and training of the river were initiated in the 1930s) and as channel margin, sheet (with rippled bedforms), and shoal deposits. Mixed sediments similar to those on the inner continental shelf and deltaic plain (Stanley *et al*., 1996) underlie the modern (Holocene) river channel. Because the channel is entrenched, classic morphological patterns associated with graded streams (*e.g*. oxbows, meanders, meander scars, Yazoo meaner loops) are not present in the LMR. Critical to rationalization of sediment patterns and strategies for sand searches in this fluvial-deltaic environment depends on comprehension of different stages of fluvial geomorphological development.

SAND RESOURCES IN THE LOWER MISSISSIPPI RIVER

One of the most studied, engineered and heavily trained rivers in the world (*e.g*. Kessel, 2003), the Mississippi River features flood control structures, levees, floodways, floodwater retention structures, and reservoirs. Today the LMR is the product of natural influences modified by engineered channel improvements constructed under the aegis of Mississippi River tributaries projects (Biedenharn *et al.,* 2000).

Studies relevant to riverine (fluvial) sand searches in the LMR include several noteworthy reports viz. Biedenharn *et al*. (2000), Dunbar *et al.* (1994), Fisk (1944, 1947, 1952 and 1961), Keown *et al.* (1977, 1981, 1986), Kessel (2003), Kolb and Van Lopik (1966), Kolb (1962), Mossa (1996), Nordin and Queen (1992), Saucier (1996), Smith (1996), among others. Based on nearly one hundred borings, Stanley *et al.* (1996) prepared a generalized stratigraphic description of the LMR deltaic plan. Results of their investigations showed a top-to-bottom sequence for the alluvial plain that comprehends Holocene progradational facies of deltaic sediments that overlie Pleistocene sandy sediments.

Holocene deltaic sediments (Deltaic Progradational Facies) range in thickness down river from 18 m in the vicinity of New Orleans to about 75 m at Head of Passes. Thickness of the deltaic sediments from MM 35 to MM 22 is about 30 m to 45 m (Stanley *et al.*, 1996). The texture (percent sand, silt, and clay) of the deltaic sediments varies from muddy (silty-clays) to sandy deposits that occur in paleo-meander point bars, crevasses, and low-relief natural levees. Deltaic sediments in the LMR (*i.e*. MM 34 to MM 22) are likely to contain sedimentary deposits similar in composition to those found on the inner shelf offshore Plaquemines Parish but accentuated by greater variation due to paleo-riverine deposits that are mixed within the Holocene deltaic sedimentary package. The Pleistocene sandy sediments in the Mississippi delta plain, defined by Stanley *et al.* (1996) as a late-Pleistocene to early Holocene Transgressive Facies (LPEHT), underlie the Holocene deltaic sediments. The Pleistocene sandy layer, about 4.5 to 7 m thick in the New Orleans area, decreases southward to about 2.4 to 5 m at Head of Passes and occurs beneath the Holocene sedimentary package.

Formation of new point bars is prohibited, because river-stabilizing structures prohibit lateral migration of meander belts in the modern Mississippi River (Smith, 1996). This observation is important because point bars are good sources of sand deposits in fluvial systems. Noting that the Mississippi River is a highly trained channel, Smith and Winkley (1996) report that the river now responds to channel-forming flows by building 'mid-channel bars,' also referred to as 'sand waves' (Allison, 2004; LeClair, 2004), instead of migrating and producing natural meander cutoffs. LeClair (2004) reports that macro sand waves are scaled by channel width and planform. Symmetric dunes at Red Eye Crossing in the LMR (MM 223 to MM 225, near Baton Rouge), for example, have lengths of about 120 m and heights of 3 m with superimposed asymmetric dunes about 11-m long and 1-m high. The mean flow depth was 27 m and velocity was about 1.8 m s^{-1} (LeClair, 2004). Similar small dunes migrate on the point bar but the main channel features larger dunes 69-m long by 2.6-m high with celerity up to 2 m h^{-1}. Study of probability-distribution curves for bedload in the main channel suggests steady sediment supply and transport rate (LeClair and Blom, 2005), parameters that are particularly important to evaluation of fluvial sand resources. Significantly, navigation maintenance of the LMR involves dredging of "problem reaches" where there is bed elevation (sedimentary aggradation) and chronic formation of mid-channel bars (sand waves, ripples).

From the point of view of sand searches, location of these problem reaches may fortuitously point to a renewable sand resource. Examination of sediment deposition rates and grain sizes in the LMR further indicates that bedload varies from fine sand to gravel depending on local geometry and hydraulic conditions (Smith and Winkley, 1996).

The LMR exhibits greater variability of thalweg elevation (due to the presence of mid-channel bars and sand waves) than many up- and downstream segments. Kessel (2003) suggests that variation of thalweg is a hydrodynamic response to decreased sediment input from upriver sources. Thalweg data presented by Kessel (2003) indicates that bed aggradation in this reach of the LMR may have resulted from larger bed loads in recent times. He thus concludes that because the river is no longer allowed to meander, sediment storage capacity of the channel is greatly reduced. Fisk (1944) long ago described downstream grain-size variation in terms of riverbanks that become progressively composed of finer deposits, a channel cross-sectional area that becomes narrower and straighter, and sandbars that become more infrequent.

Grain-size of bedload decreases downstream from sand-dominated deposits near the Atchafalaya diversion (Old Control Structure) to silt-dominated at Head of Passes (Mossa, 1996). Grain size decreases from 0.21 to 0.10 mm from MM 200 to MM 100 and from 0.17 to 0.05 mm between MM 100 and MM 0 (Keown *et al.*, 1981, 1986) and fluctuates from 0.19 to 0.28 mm between MM 28 and MM 30 (Allison and Nittrouer, 2004).

Temporal trends in composition of bed materials, initially reported by Robins (1977) and updated by Nordin and Queen (1992), were evaluated and again updated by Biedenharn *et al.* (2000) who report a general decrease in the D_{50} size since 1932. The Nordin and Queen (1992) study reported, however, that there has not been significant change in the character of the bedload since the pre-cutoff period (late 1920's to the present).

Allison and Nittrouer's (2004) seismic surveys of the LMR (from MM 86 at English Turn downstream to MM 0 at Head of Passes) mapped the active sand sheet that is formed by bedload sediment transport. The active sand layer (traction bedload deposits) is present throughout most of the study area in deeper parts of the river and ranges in thickness from 2 to 3 m. Point bars are now relatively inactive but may represent a significant source of sandy sediments (*e.g*. Smith, 1996; Kessel, 2003) due to the presence of river control structures (*e.g*. levees) in the LMR.

Nordin and Queen (1992), studying particle size distribution of bed sediments along the thalweg of the Mississippi River from Cairo (Illinois) to Head of Passes (Louisiana), acquired data from field sampling in 1989 using a WES drag sampler (a 10-cm inside diameter steel pipe 1.2-m long closed at one end and flared to about 20 cm diameter at the other end). The thalweg sediment samples obtained by Nordin and Queen (1992) in the project area (MM 35 to MM 15) range from 0.13 to 0.35 mm; sediment sorting is similar to inner shelf and beach environments (between 1 and 2 phi, or moderately sorted) except for a sample at MM 30.4 that contained very poorly sorted sediments (high variability attributed to a higher than normal percentage of fines). The thalweg data from Nordin and Queen (1992) also indicated that the relative percent of coarse sand (2 to 4.7 mm) and gravel sediments is reduced when compared to a sampling survey conducted in 1932. From MM 100 to MM 0, thalweg sediment composition is dominated by fine sand (0.15 to 0.25 mm) - percent silt is generally less than 10%, percent clay is generally less than 5% and percent gravel and coarse sand is generally less than 2%. The Nordin and Queen (1992) data indicate that favorable grain sizes (*i.e*. suitable for beach restoration) occur in reaches of the LMR. This information is, however, only a proxy of channel sand in the LMR because bank sediments differ from thalweg sediments.

McClelland (1988) indicates that previous USACE boring data for the Nairn Point Bar describe sand thicknesses of 21 m. The point bar deposit has two major sedimentary units: (1) a featureless (flat) mud bottom from the riverbank to about 8 m water depth and (2) a sand bottom with surface sand waves from 8 m to their survey depth limit (Figure 2). Sand composition is homogenous with a slight coarsening downward (fining upward) trend. The Nairn Point Bar, shown as a seismic image in Figure 2, is described as "a massive point bar at least 70 feet [21 m] thick" (McClelland, 1988). These reports indicate, based on 36 samples obtained from 16 vibracores in the Nairn Point Bar, an average (composite) grain size of 0.17 mm with 0.92 phi sorting.

Results of a recent study of river geomorphology (potamological interpretation of fluvial forms, bathymetry, sedimentary deposits, and hydrology) indicate that large volumes of sand may be available in the lower section of the river. Three primary potential sand targets were

identified between MM 35 and MM 22 (CPE, 2004). One target was located 3 to 6 km upriver from Empire between MM 32 and MM 34, near the City of Nairn and another near Empire between MM 31 and MM 25. The third target was located near Fort Jackson between MM 24 and MM 22. A smaller secondary potential target was identified between MM 20 and MM 18 at the Fort Jackson river bend.

Of these three deposits, greater sediment thickness was anticipated in a river meander where the presence of relict (vertically stacked) sand bars occurred. Surface samples obtained along a gentle river bend on the eastern side of the river had a mean grain size of 0.19 mm to 0.28 mm. Sand waves were about 2 m thick, but underlying sands may increase the total thickness of sand deposits. An additional target was identified along a riverbank about 10 km downriver from Empire and 3 km upriver from the Fort Jackson river meander. The 3-km long target is limited upriver and downriver by riverbank revetments. The secondary sand targets, *e.g.* those mapped along the Fort Jackson meander, may be morphologically and compositionally similar to the primary targets because they are located in a similar hydro-geomorphological setting (river meander-point bar).

GEOPHYSICAL, GEOTECHNICAL AND LAB PROCEDURES

The geophysical survey of the study area between MM 35 to MM 15 involved geographical positioning, bathymetric survey, magnetic survey, seismic sub-bottom profiling, and side-scan sonar survey of the riverbed. These geophysical methods were deployed to accurately determine water depth (bathymetry), types of fluvial bedforms (presence of planar beds, sand waves, megaripples), and the nature and thickness of sedimentary deposits between banks of the river (slipoff slopes, point bars, and thalweg). The purpose of the magnetometer survey was to ascertain the presence of shipwrecks and other artifacts of archaeological significance in addition to debris that could be harmful to dredging machinery. The geotechnical surveys involved vibracoring and grain-size determinations from subsamples of sedimentary layers in the cores.

Presurvey Planning

The first phase of a sand search involves literature searches and design of the exploration program. Experience (*e.g.* Finkl, Khalil and Andrews, 2002; Finkl *et al.*, 2005a,b) has shown that this phase is crucial to evaluation and re-interpretation of prior knowledge, to the development of conceptual models of sedimentary environments, and to guide the planning of future survey options. Thus, the purpose of literature (data) review is to familiarize survey planners with local environmental conditions and to flag any special conditions that require avoidance or focused attention. Unfamiliarity with peculiarities of local environments or geomorphological features holds potential for obtaining less than desirable results. Tasks proposed for this riverine sand search were adjusted to local conditions according to procedural strategies suggested by sand search guidelines (*e.g.* Finkl; Andrews and Benedet, 2002; Finkl and Khalil, 2003; Khalil, 2003; Finkl, Khalil and Andrews, 2005).

Navigation and Survey

A Trimble DGPS Global Positioning System (GPS), interfaced to HYPACK® MAX (A Pro Beacon receiver) was used for navigation and positioning. Differential GPS correction was provided by the U.S. Coast Guard Navigational Beacon located at English Turn, Louisiana. Navigational, magnetometer, and depth sounder systems were integrated in real time using HYPACK® MAX, a state-of-the-art navigation and hydrographic surveying system. After post-processing, the navigation data (locational) stored in the HYPACK® MAX system

was then exported to a *.dxf* file and imported into ArcGIS 8 in order to create a GIS shapefile for analysis and report preparation.

Bathymetric Survey

A single frequency portable hydrographic echo sounder (Hydrotrac, Odom Hydrographic Systems) was used for the bathymetric survey. The Hydrotrac operates at frequencies of 24, 33, 40, 200, 210, or 340 kHz and is a digital, survey-grade sounder. Prior to use, the sounder was calibrated and checked periodically throughout the survey. Speed of sound through water and other selected parameters were adjusted to accurately reflect physical water conditions in the survey area.

Magnetometer Survey

A Geometrics G-882 Digital Cesium Marine Magnetometer was used in a cursory investigation of magnetic anomalies within the potential borrow areas. The purpose of the magnetometer surveys was to establish the presence, and subsequent exclusion zones around, any petroleum pipelines within the potential borrow areas. The HYPACK® MAX software recorded magnetic anomalies directly from the Geometrics magnetometer.

Sidescan Sonar Survey

A sidescan sonar system (EdgeTech 4200 FS) was used to interpret morphological features on the unconsolidated sediment. The full-spectrum chirp technology delivered wide-band, high-energy pulses coupled with high resolution and superb signal to noise ratio echo data. The sidescan was towed at an optimum position and depth to ensure isolation from sources of interference and for optimum record quality. The resulting digital data was merged with positioning data (DGPS via HYPACK® MAX), video displayed, and recorded to disk for post processing and/or replay. The position of the sensor relative to the DGPS antenna was documented to ensure proper positioning of the data. Range scales were set at 150 m, providing over 100% coverage for the South Pass study area. Dual frequency provided a differential aid to interpretation.

Data was processed by Isis Sonar software in a geographical framework for target interpretation and delineation. The geo-encoded sonar imagery data were stored as *.xtf* files and then converted to *DDS_VIF* raster imagery files. Raster images were then imported into Triton Elics DelphMap software to be further processed, merged, and exported in the form of geo-referenced sidescan mosaics (*geo-tiff* files).

X-STAR Chirp 512i Sub-bottom Profile Survey

The EdgeTech SB512i system was used because it shows a distinct reflector at boundaries between sand deposits and finer-grained accumulations (*i.e.* submerged channel plugs, back levee fills, delta plain deposits). This wideband FM sub-bottom profiler collected digital normal incidence reflection data over many frequency ranges and generated cross-sectional images of the sea(river)bed to a depth of 15 m in this survey. Transmission of an FM pulse that is linearly swept over a full spectrum frequency range (called a “chirp pulse”) produces a tapered waveform spectrum that results in images that have virtually constant resolution with depth. Post-processing of the seismic data was accomplished with SonarWebPro®, a software program that can produce georeferenced HTMLs that can be incorporated into a GIS database.

Geological Investigation

Field investigations are required to ascertain correspondence between actual conditions in the study area compared to those described in the literature. In addition, specialized information is required to prove out potential borrow areas that were selected on the basis of literature reviews and inspection of proprietary reports. Because vibracores provide the kind of detailed information that is required (collection of undisturbed sediment samples), vibracore surveys are often conducted in tandem with geophysical investigations. Geophysical surveys and geotechnical work is thus able to definitively establish deposit geometry, and the quality and quantity of sand. Vibracores were thus deployed in this sand search investigation to determine the nature of sedimentary deposits in the river and to help calibrate the seismic reflection profiles obtained by the CHIRP 512i sub-bottom profiler, as described procedurally by LDNR (2003) and Finkl and Khalil (2005) for conditions in Louisiana.

Vibracore Survey Sediment cores 6 m in length were collected by a 271B Alpine Pneumatic Vibracore. This self-contained, freestanding pneumatic vibracore unit contains an air-driven vibratory hammer assembly, an aluminum H-beam which acts as the vertical beam upright on the riverbed, a steel coring pipe (with a plastic core liner), and a drilling bit with a cutting edge. An air hose array provided compressed air from the compressor on deck to drive the vibracore. Complete description of vibracore survey procedures may be accessed in Finkl and Khalil (2005b).

Sediment-Size (Mechanical Sieving) Analysis Sieve analyses were conducted for samples obtained by vibracoring in accordance with American Society for Testing and Materials Standard Materials Designation D422-63 for particle size analysis of soils (ASTM, 1987). This method covered the quantitative determination of the distribution of sand size particles. Mechanical sieving was accomplished using calibrated sieves, with a gradation of half phi intervals with the addition of sieves that represent key ASTM sediment classification boundaries. Grain-size frequency distribution curves were prepared for each vibracore and a composite compiled for each vibracore.

The basic procedures for sediment analysis via mechanical sieving involve weighing approximately 75-100g of representative material to the dish. Large clasts or other materials that are not characteristic of the sub-sampled horizon, or layer as a whole, were removed and noted in the comments field (composition and size) of the lab report sheet. The wet Munsell color should be obtained from the vibracore log. The sample was dried fro 12 hr at 110˚ C.

The dried sample was then weighed on a tarred electric scale and the weight recorded. The sample was totally immersed in deflocculent (approximately 80 g of sodium hexametaphosphate [Calgon] in 1 liter of water) and soaked for 3 hr. The sample was then placed on a #230 sieve and gently washed until the water draining from the bottom of the sieve ran clear. The washed sample was then returned to the dish and dried. When dry, the sample was reweighed. Bulk shell content and bulk carbonate content are estimated at this point (if appropriate).

The standard sieve stack was set up and the sample poured onto the top of the sieve nest. The sieve stack was hand shaken for 30-60 sec. After the weight of the sample dish was recorded, contents of the top (3/4) sieve were returned to the dish. Percent shell (if any) was recorded, as was the weight of the dish and the sample. The weight retained on each sieve was recorded in this manner through the #14 sieve. The remaining sieves were placed in a mechanical sieve shaker for 20-30 min. The weight retained and percent shell for the remaining sieves and pan were recorded. Weight retained was entered into a sieve analysis program (gINT® software),

which computes the mean and median grain size, sorting, and silt/clay percentages for each sample using the moment method (Folk, 1974).

RESULTS OF FLUVIAL SAND SEARCH INVESTIGATIONS

Geophysical and geotechnical investigation of selected reaches in the LMR permitted the identification of significant sand resources in point bar deposits on river bends and in bed load materials in the active channel. The active sediment transport layers and underlying relict deposits in the LMR collectively constitute good quality sand deposits that are suitable for restoration of barrier islands.

Sand Resources in the LMR (MM 35 – MM 15)

Thirteen vibracores and 23 line-miles of geophysical survey were obtained from the LMR between MM 35 and MM 15. Most of the cores contained relatively clean sand from top to bottom with exception of the cores obtained near riverbanks. Three cores were obtained in the Nairn Point Bar, downriver from MM 35. Vibracores MRVC-05-01 and MRVC-05-03 were obtained in 13 m and 18 m water depth and contained mostly siliciclastic sand with few fines (less than 3% fines) and a slight coarsening upward trend with sand grain size increasing from 0.14 mm at the base of the core to 0.22 mm in the top of the core (MRVC-05-01) and from 0.22 mm in the base to 0.24 mm in the top (MRVC-05-03). Recovered sand thickness was 5.2 m in MRVC-05-01 and 5.3 m in MRVC-05-03. Vibracore MRVC-05-02, obtained in shallower water (6.6 m deep), contained sand intercalated with clay and silt layers in the upper 4.2 m (mixed sediment layer) below which there is clean sand about 1.5 m thick.

Vibracores MRVC-05-07 and MRVC-05-10 were obtained on a wide bank downriver from MM 25 in -13 m and -17 m of water, respectively. Both vibracores recovered about 4.5 m of clean siliciclastic sand (less than 5% silt) with grain size slightly coarsening upward (from 0.13 mm to 0.20 mm in the base of the cores to 0.24 mm to 0.26 mm at the top).

Vibracores MRVC-05-11, MRVC-05-12 and MRVC-05-13 were obtained on the western side of the river downriver from MM 20, in an area commonly known as the Fort Jackson Point Bar. Vibracore MRVC-05-11, obtained in the narrower northern segment of the deposit in -16 m of water, contained 6 m of intercalated layers of sand and clay (mixed sediments). These mixed sediments are characterized by darker reflectors in the seismic imagery compared to lighter reflectors that characterize sand. Vibracore MRVC-05-12, located in the mid-section of the deposit in -12 m of water, contained clean sand in the upper 2.4 m and sand with two clay layers (2.5 to 3.4 m and 3.8 to 4.3 m). Vibracore MRVC-05-13, located in the wider southern segment of the deposit in -12 m of water contained mostly clean sand with basal clay lamina. Sand in this core showed a slight coarsening upward trend (0.13 mm at the base to 0.15 mm at the top) with less than 5% silt content overall. The lack of well-defined reflectors and uniform light tones in the seismic trace suggests the presence of sand below the depth of vibracore MRVC-05-13. Sand thickness in Fort Jackson Point Bar ranges to at least 15 m thick. Relative relief of these sand waves seldom exceeds 1 m and is thus subdued compared to surface bedforms previously described.

Sediments grade downriver from mixtures of silt and clay mixed with sand (vibracore MRVC-05-11) to predominantly sandy sediments (cores MRVC-05-12 and MRVC-05-13). Deposit width (distance between 10 m and the 21 m contours) increases downriver and the sub-bottom profile of the southern segment of the deposit shows light tones in the seismic trace and relatively homogenous seismic reflectors that are characteristic of riverine sand.

Sidescan sonar investigations were conducted in an effort to map the occurrence of potential dredging obstructions and bottom topography. Georeferenced sidescan mosaics, overlain on top of aerial photographs show surface sand waves that are generally orientated transverse to riverbanks. Well-developed sand waves, parallel to the direction of flow and transverse to riverbanks, occur near vibracores MRVC-05-01, 02 and 03 and near vibracores MRVC-05-04, -05, -06 and -09. As a general spatial trend, the sonar imagery tends to become darker (more reflectivity) near riverbanks and lighter (less reflectivity) towards the thalweg. This pattern is most prominent along the Nairn Point Bar and in the river bend between cores MRVC-05-04 and MRVC-05-05. Lighter toned sonar imagery is not infallibly associated with sandy sediments. The area where vibracore MRVC-05-10 was acquired, for example, is darker toned but composed of clean sandy sediments. Reflection patterns from sidescan imagery should not be used to assess surface (river bottom) sediment texture without further image processing, filtering and calibration (which is beyond the present scope of work).

Potential sand volumes were calculated from data contained in vibracores and seismic reflection profiles. Sand thickness was extrapolated beyond vibracore recovery length when seismic records indicated continuity (and extension) of the sand deposits. The total volume estimated from seven potential borrow sites is 23 x 10^6 m^3 of clean sand. These volumes were based on sediment thickness, as determined from vibracore and seismic data. Deposit volumes are summarized in Table 1. Deposits are named from north to south as MR (Mississippi River) potential borrows A, B, C, D, E, F and G in relation to mile markers.

Table 1. Estimated sand volumes in potential borrows in the Lower Mississippi River.

Borrow Area	Approximate Location	Volume (m^3)[1]
MR A	Nairn Point Bar, 0.8 km downriver from MM 35	2,164,000
MR B	Across river from Empire intersection, 2.4 km upriver to 3.2 km downriver from MM 30	11,422,000
MR C	1.6 km upriver from MM 25	1,010,000
MR D	About 150 m upriver from MM 25	187,000
MR E	Upriver Ft. Jackson Point Bar about 1.6 km downriver from MM 25	4,877,000
MR F	Ft. Jackson Point Bar 0.8 km upriver from MM 20	722, 000
MR G	Ft. Jackson Point Bar 2.4 km south of MM 20	2,737,000
Total		**23,119,000**

1. Based on Finkl *et al*. (2006).

CONCLUSIONS

Sand resources along the southern Louisiana coast, particularly along the Plaquemines coast, are relatively scarce. Alternative sand sources for the restoration of the Plaquemines coast were investigated in this study along the Lower Mississippi River (LMR).

Thirteen vibracores and 37 line-km of geophysical data (seismic reflection profiles, bathymetry, vibracore, and magnetometer surveys) were obtained along the LMR between MM 35 and MM 15. Thick sand deposits (15-20 m thick) comprised by clean (generally less than 5% silt) fine to medium sands (0.12 to 0.4 mm, but mostly around 0.2 mm) were found in most of the investigated sites. These deposits are composed of modern sands associated

with fluvial bedload transport in the upper 1 to 2 m (as sand waves) and relict riverine sands below these surface bedforms. The sand deposits identified in this study of the LMR have great potential to support large-scale coastal restoration of the Plaquemines coast. Total volumes estimated in seven deposits are on the order of 23 x 10^6 m^3. Bedload deposits in the Mississippi River may provide an important renewable resource for restoration of Louisiana's barrier islands. Feasibility studies are being conducted to determine the best mode of delivery of sand from the Mississippi River to the barrier islands, whether pumping through long pipelines, by barge, or combinations involving booster pumps or sediment staging areas.

REFERENCES

Allison, M. and Nittrouer, C.A. (2004). *Personal email communication.* Tulane University, New Orleans.

ASTM (1987). "Standard method for particle-size analysis of soils, designation D422-63," *In*: *1987 Annual Book of ASTM Standards, Volume 04.08 Soil and Rock; Building Stones; Geotextiles*. American Society for Testing Materials, Philadelphia:.

Biedenharn, D.S.; Thorne, C.R., and Watson, C.C. (2000). "Recent morphological evolution of the Lower Mississippi River," *Geomorphology* 34, 227-249.

Boesch, D.F.; Josselyn, M.N.; Mehta, A.J.; Morris, J.T.; Nuttle, W.K.; Simenstad, C.A., and Swift, D.J.P. (1994). "Scientific Assessment of Coastal Wetland Loss, Restoration and Management in Louisiana," *Journal of Coastal Research* Special Issue No. 20, 103p.

Coleman, J.M. and Gagliano, S.M. (1964). "Cyclic sedimentation in the Mississippi River delta plain," *Transactions Gulf Coast Association of Geological Societies* 14, 67-80.

Dunbar, J.B.; Blaes, M.R.; Dueitt, S.E.; May, J.R., and Stroud, K.W. (1994). "*Geological Investigation of the Mississippi River Deltaic Plain,"* U.S. Army Corps of Engineers, Waterways Experiment Station, Technical Report GL-84-15, 71p, Vicksburg, Mississippi: (Map scale 1:62,500).

Finkl, C.W.; Andrews, J., and Benedet, L. (2002). "Shelf sand searches for beach nourishment along Florida Gulf and Atlantic coasts based on geological, geomorphological, and geotechnical principles and practices," *Coastal Sediments 2003* (Clearwater, Florida), CD-ROM.

Finkl, C.W. and Khalil, S.M. (2005a). "Offshore exploration for sand sources: General guidelines and procedural strategies along deltaic coasts," *In*: Finkl, C.W. and Khalil, S.M., (eds.), Savings America's Wetland: Strategies for Restoration of Louisiana's Coastal Wetlands and Barrier Islands. *Journal of Coastal Research* Special Issue No. 44, pp. 203-233.

Finkl, C.W. and Khalil, S.M. (2005b). "Vibracore," *In*: Schwartz, M.L., (ed.), *The Encyclopedia of Coastal Science*. Kluwer Academic, Dordrecht, The Netherlands, pp. 1272-1284.

Finkl, C.W.; Khalil, S.M., and Andrews, J. (2005). "Sand search models in deltaic environments: Geological frameworks, geophysics and geotechnical exploration for marine sand resources," *Proceedings Hornefǿrður International Coastal Symposium* (Höfn, Iceland, June), CD-ROM.

Finkl, C.W.; Andrews, J.L.; Benedet, L., and Campbell, T. (2005). "Geotechnical Investigation for Exploration of Sand Resources in the Lower Mississippi River and South Pass, and Exploration for Sand via Vibracoring in South Pelto Blocks 12 & 13," Coastal Planning & Engineering, Inc., Boca Raton, Florida, 40p. (Prepared for the Louisiana Department of Natural Resources, Baton Rouge, Louisiana, by Coastal Planning & Engineering of Louisiana).

Finkl, C.W.; Khalil, S.M.; Andrews, J.; Keehn, S., and Benedet, L. (2006). "Fluvial sand sources for barrier island restoration in Louisiana: Geotechnical investigations in the Mississippi River," *Journal of Coastal Research* 22(4), 773-787.

Fisk, H.N. (1944). "Geological Investigations of the Alluvial Valley of the Lower Mississippi River," U.S. Army Corps of Engineers, Mississippi River Commission, Vicksburg, Mississippi, 78p.

Fisk, H.N. (1947). "Fine-grained Alluvial Deposits and Their Effects on Mississippi River Activity," US Corps of Engineers, Mississippi River Commission, Vicksburg, Mississippi, Vol. 1, 82p., Vol. 2, 74 plates.

Fisk, H.N. (1952). "Geologic Investigations of the Atchafalaya Basin and the Problems of Mississippi River Diversion," U.S. Army Corps of Engineers, Mississippi River Commission, Vicksburg, Mississippi, 145p.

Fisk, H.N. (1961). Bar-finger sands of the Mississippi River delta. *In*: Peterson, J.A. and Osmond, J.C. (eds.), *Geometry of Sandstone Bodies*. Tulsa, Oklahoma: American Association of Petroleum Geologists, pp. 22-52.

Keown, M.P.; Dardeau, E.A., Jr., and Kennedy, J.G. (1977). "Inventory of Sediment sample Stations in the Mississippi Basin," U.S. Army Corps of Engineers, Waterways Experiment Station, Tech. Rep. M-77-1, Vicksburg, Mississippi.

Keown, M.P.; Dardeau, E.A., Jr., and Causey, E.M. (1981). "Characterization of the Suspended Sediment Regime and Bed-Material Gradation of the Mississippi River Basin," U.S. Army Corps of Engineers, Lower Mississippi Valley Division, Potamology Program (P-1), Vicksburg, Mississippi, 2 volumes.

Keown, M.P.; Dardeau, E.A., Jr., and Causey, E.M. (1986). "Historic trends in the sediment flow regime of the Mississippi River," *Water Resources Research* 22, 1555-1564.

Kessel, R.H. (2003). "Human modifications to the sediment regime of the lower Mississippi River flood plain," *Geomorphology* 56, 325-334.

Khalil, S.M. (2004). "General Guidelines – Exploration for Offshore Sand Searches," Baton Rouge: Louisiana Department of Natural Resources, Coastal Engineering Division, Coastal Protection Systems Design Guidelines, 200p and Version III in pdf.

Kindinger, J.; Flocks, J.; Kulp, M.; Penland, S., and Britsch, L.D. (2001). "Sand Resources, Regional Geology, and Coastal Processes for the Restoration of the Barataria Barrier Shoreline," Report to U.S. Army Corps of Engineers, New Orleans District, September 2001. *US Geological Survey Open File Report 01-384*.

Kolb, C.R. and Van Lopik, J.R. (1966). "Depositional environments of the Mississippi River deltaic plain, southeastern Louisiana," *In*: Shirley, M.L. and Ragsdale, J.A., (eds.), *Deltas*. Houston Geological Society, Houston, Texas, pp. 17-62.

LDNR (Louisiana Department of Natural Resources) (2003). "General Guidelines – Exploration for Offshore Sand Searches," Department of Natural Resources, Coastal Engineering Division, Coastal Protection Systems Design Guidelines, Baton Rouge, Louisiana, 200p.

LDNR (2005). "Factoids about Louisiana's coastal wetlands," LaCoast Website at: http://www.lacoast.gov/education/factoid%20old.htm.

LeClair, S.F. (2004). "Multi-scale dunes of the Mississippi River: The analysis of time variability of probability distributions of bed elevation as a step toward the understanding of bedload sediment transport," *Geological Society of America Abstracts with Programs*, 36(5), p.461. [Session No. 198, Paper No. 198-8]

LeClair, S.F. and Blom, A. (2005). "A qualitative analysis of the distribution of bed elevation and the characteristics of associated deposits for subaqueous dunes," *In*: Blum, M.D.; Marriott, S.B., and LeClair, S.F., (eds.), *Fluvial Sedimentology VII*, Special Publication (International Association of Sedimentologists), 35, 121-134.

McClelland [McClelland Engineers] (1988). "Geotechnical Engineering, Restoration of Shell Island, Plaquemines Parish, Louisiana. Task II-3, Sand Borrow Source Evaluation – Sixty Mile Point, Volume 2," Unpublished report by McClelland Engineers, Harahan, Louisiana, 8p.

Mossa, J. (1996). "Sediment Dynamics in the Lowermost Mississippi River," *Engineering Geology* 45, 457-479.

Nordin, C.F. and Queen, B.S. (1992). "Particle Size Distributions of Bed Sediments along the Thalweg of the Mississippi River, Cairo, III to Head of Passes, September, 1989," U.S. Army Corps of Engineers, Waterways Experiment Station, Potamology Program, (P-1) Report 10, Vicksburg, Mississippi, 15p.

Penland, S. and Ramsey, K. (1990). Relative sea level rise in Louisiana and the Gulf of Mexico: 1908-1988. *Journal of Coastal Research*, 6(2), 323-342.

Roberts, H.H. (1997). "Dynamic changes of the Holocene Mississippi River delta plain: The delta cycle," *Journal of Coastal Research* 13(3) 605-627.

Roberts, H.H. and Coleman, J.M. (1996). "Holocene evolution of the deltaic plain: a perspective – from Fisk to present," *Engineering Geology* 45, 113-138.

Robbins, L.G. (1977). *"Suspended and Bed Material Studies on the Lower Mississippi River,"* Potamology Investigation Report 300-1, US Army Corps of Engineers, Vicksburg District, Vicksburg, Mississippi.

Saucier, R., T. (1996). "A contemporary appraisal of some key Fiskian concepts with emphasis on Holocene meander belt formation and morphology," *Engineering Geology* 45, 67-86.

Smith, L.M. (1996). "Fluvial geomorphic features of the Lower Mississippi alluvial valley," *Engineering Geology* 45, 139-165.

Smith, L.M. and Winkley, B.R. (1996). "The response of the Lower Mississippi River to river engineering," *Engineering Geology* 45, 433-455.

Stanley, D.J.; Warne, A.G., and Dunbar, J.B. (1996). "Eastern Mississippi delta: late Wisconsin unconformity, overlying transgressive facies, sea level and subsidence," *Engineering Geology* 45, 359-381.

Suter, J.R., Penland, S., and Ramsey, K.E. (1991). "Nearshore Sand Resources of the Mississippi River Delta Plain: Marsh Island to Sandy Point," Louisiana Geological Survey, Coastal Geology Technical Report No. 8, Baton Rouge.

Williams, S.J.; Stone, G.W., and Burruss, A.E. (1997). "A perspective on the Louisiana wetland loss and coastal erosion problem," *Journal of Coastal Research* 13(3), 593-595.

RE-ENGINEERING THE MISSISSIPPI RIVER AS A SEDIMENT DELIVERY SYSTEM

Harley S. Winer[1]

1. U.S. Army Corps of Engineers, New Orleans District, P. O. Box 60267, New Orleans, LA 70160-0267, USA. Harley.S.Winer@mvn02.usace.army.mil.

Abstract: Engineering works on the Mississippi River constrain the River in its present course and prevent flood waters from overflowing the river banks. Thus, very little of the river's sediment load goes into the wetlands, with the major fraction transported off the edge of the continental shelf into deep water. A realistic approach is presented that reconfigures the arrangement of structures at the Old River Complex so that a predominance of the sediment load would go down the Atchafalaya River where it would be deposited in the shallow waters of Atchafalaya Bay, thus creating a large expanse of marsh lands that would help to compensate for the loss of wetlands in the rest of southern Louisiana. The purpose of this paper is to advocate for a comprehensive analysis, in the form of a feasibility study, of the benefits and drawbacks of redirecting the sediment load at Old River.

INTRODUCTION

The average annual sediment load of the lower Mississippi River (below Old River Control Complex) is estimated to be 131 million tons. Because the natural delta building processes have been drastically altered, a very large portion of this sediment goes off the edge of the continental shelf and is deposited in the deep waters of the Gulf of Mexico. The deltaic processes that built the landmass of southern Louisiana have been altered by the river engineering that has provided flood protection to the local residents and navigation benefits to the region and the nation. At present only a small portion of the sediment load is directed into marsh building through the beneficial use of dredged materials program and engineered sediment diversions. To counter the steady loss of the Louisiana coastal wetlands, it is imperative that a method be found to fully utilize the Mississippi River sediment load by directing its totality into wetland creation. It is

unrealistic to think in terms of removing existing levees so as to allow the river to naturally flood its banks and deposit sediment in the adjacent wetlands. Annual flooding is not an option for the citizens of the developed areas along the Mississippi River corridor. A more realistic approach is presented that reconfigures the plumbing at the Old River Control complex so that the predominance of the sediment load would go down the Atchafalaya River where it would end up being deposited in the shallow waters of Atchafalaya Bay, thus creating a large expanse of marsh lands that would help to compensate for the loss of wetlands in the rest of southern Louisiana.

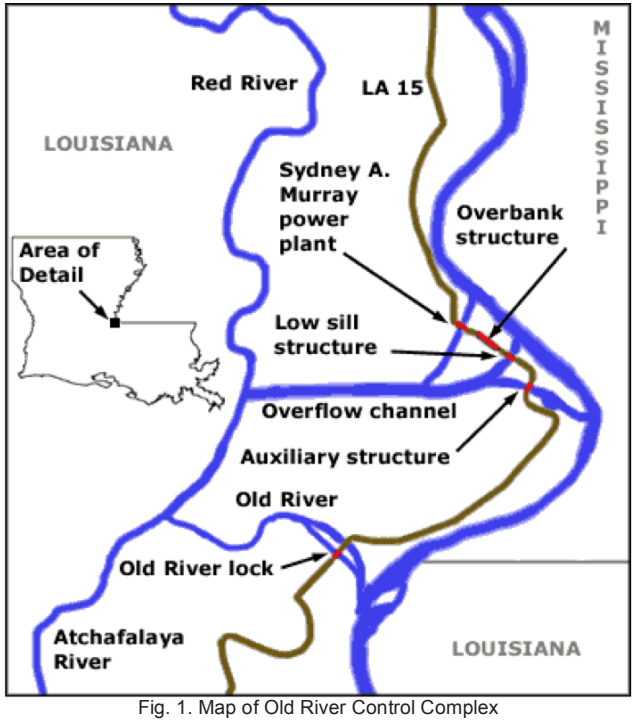

Fig. 1. Map of Old River Control Complex

The distribution of flow at the Old River Control Complex has been fixed by legislation. Seventy percent of the latitude flow (Latitude flow refers to the combined flow from the Mississippi and Red Rivers crossing the latitude of the Old River Control Complex) is to go down the Mississippi River and thirty per cent of the latitude flow is to go down the Atchafalaya. This was the distribution of flow at the time of the enabling legislation more than half a century ago. Although the enabling legislation provided for the same distribution of sediment, more than the allotted seventy per cent goes down the Mississippi River. The Old River Auxiliary Structure, which was built after the 1973 flood weakened the Old River Control Structure, was specifically designed so that the inflow channel would capture a sediment rich flow, and thus help to correct the sediment

distribution problem. However, shortly after the Auxiliary Structure was put in service, a hydroelectric power plant, with a sediment lean inflow channel was installed to take advantage of the head differential between the Mississippi and the Old River Outflow Channel. (See Figure 1 for a map of the existing structures at Old River.) Because of the operation of the hydroelectric plant, the legislated sediment distribution has not been met in recent years. Despite the fact that the Atchafalaya sediment load has been less than legislated, there is sufficient sediment so that there is delta formation at the mouth of the Atchafalaya and the Wax Lake Outlet. This is one of the few places in Louisiana where land is actually accreting. Figure 2 shows recent delta growth at the mouth of Wax Lake Outlet. If the sediment load in the Atchafalaya River were to be significantly increased, the rate of delta growth at Wax Lake Outlet and the mouth of the Atchafalaya River would be significantly increased.



Fig. 2. Delta Growth at Wax Lake Outlet and Atchafalaya river mouth.

Since the flow and sediment distribution at Old River is mandated by existing legislation, any change in the operation of Old River would require new legislation. The purpose of this paper is to advocate for a comprehensive analysis, in the form of a feasibility study, of the benefits and drawbacks of redirecting the sediment load at Old River. The arguments in favor of such a study are many fold. First and primary is the impact of coastal land loss in southern Louisiana and the potential impact upon the entire Gulf of Mexico ecosystem. Most of the commercial Gulf fisheries are dependant in one way or another upon fringing coastal wetlands. The Louisiana coastal wetlands are the largest

extent of these coastal wetlands fringing the Gulf of Mexico. It is imperative that new coastal wetlands be created to replace the on going loss in the rest of Louisiana. It is not feasible, either monetarily or technically, to pump all of the sediment out of the lower Mississippi. Only by directing the flow into shallow water and allowing for natural deposition, is it feasible to utilize the sediment load for land building. The advantage of using the Atchafalaya as opposed to a major river division into the Barataria or Breton estuaries is that deep draft navigation would not be impacted. Redirecting the sediment load to the Atchafalaya River would have another benefit of reducing the maintenance dredging in the lower Mississippi River. This would be a quantitative monetary benefit.

The technical problems of maintaining navigation, flood control and freshwater supplies to the lower Mississippi River corridor are easily solved, as are also the issues of how to reconfigure the control structures at Old River to accomplish the proposed flow regimes. These are presented in the paper. The major problems are not technical but political. This paper also discusses the political and social implications of changing the flow and sediment distribution at Old River.

HISTORY

The Mississippi River is a heavily engineered river. The proposed scheme in this paper merely suggests re-engineering the system to resolve problems created by the engineering.

In 1831, under the direction of Henry Shreve, a cut was made across a narrow neck of the River that eliminated Turnbull's bend. This cut reduced the river mileage by seven miles. It also removed the mouth of the Red River from the river, eliminating the problem of shoaling at the mouth of the Red. The part of the river formerly known as Turnbull's Bend that was eliminated from the main stem of the Mississippi River came to be known as the old river channel, hence the name Old River. The north portion of the old river eventually silted in. However, it can still be identified in aerial photos of the area. The south portion of the old river carried flows into or out of the Mississippi depending upon the relative magnitudes of flows in the Red and the Mississippi. The Old River channel would sometimes flow east to west into the Atchafalaya and at other times flow west to east into the Mississippi.

In 1839 the state removed a massive 30 mile long log jam in the Atchafalaya. The removal of this impediment to flow allowed greater flow to go down the Atchafalaya. This greater flow eroded a larger channel which in turn allowed ever increasing flow down the Atchafalaya. This was a gradual process. Eventually the flow in the Old River channel was almost entirely from east to west.

By the 1930s this increasing proportion of flow going down the Atchafalaya began to worry scientists and engineers involved with the management of the river. In 1941 the Mississippi River Commission engaged Harold N. Fisk, a geologist at Louisiana State University, and a team of geographers and geologists to investigate delta-lobe switching by the Mississippi. The report of this team (Fisk, 1944) contributed greatly to the

understanding of the physical mechanisms involved in river channel switching. The Fisk report stated that the Atchafalaya was in the process of capturing the flow of the Mississippi. Furthermore the report made the prediction that by 1972 if nothing was done to alter the situation, the channel switching would be irreversible since the predominance of the flow would be down the Atchafalaya.

Since this channel switching was seen as a potential disaster for flood control and navigation, the response was to prevent the river from switching course. Within a very short period of time a Chief of Engineers report with a recommendation was submitted to Congress, funds were appropriated, and the Old River Control Structure was designed and built. This structure, comprised of eleven gates each 44 feet wide, enabled the regulation of the flow distribution as mandated. It became operational in 1955. In 1973 there was a record flood on the Mississippi River. Scour caused the collapse of a wing wall and emergency measures were necessary to save the structure. Inspections after the flood receded revealed scour holes and support piles dangling in the water underneath the structure. Repairs were made to strengthen the structure but the need for structural redundancy was clearly evident to the river managers. The Old River Auxiliary Control Structure was thus authorized, designed and built. It became operational in 1987. In addition to structural redundancy, the auxiliary structure offered the important feature of the ability to pass more sediment to the Atchafalaya. This is because the intake channel of the original structure was located on the outside of a river bend in a sediment lean location, whereas the new structure had its intake channel located on the inside of a river bend, i.e. in a sediment rich location. Generally, the suspended sediment concentration is greater on the inside of a bend then on the outside of a bend. (If it were otherwise river meanders would be self correcting). This ability to pass more sediment was of importance because the congressional authorization mandated not only the distribution of flow but the distribution of sediment.

In 1985, construction began on the Sidney A. Murray, Jr. Hydroelectric Plant. It is situated just north of the Low Sill Structure (another name of the first structure) and has its intake from the Mississippi at a sediment lean location on the outside of a bend. This facility, sponsored and owned by the town of Vidalia, Louisiana produces power from the head difference between the Mississippi River and the outfall channel flowing to the Atchafalaya. The plant began full-scale operation in 1990. Since the power plant takes a large portion of the flow going from the Mississippi to the Atchafalaya and because it is a sediment lean flow, the sediment going to the Atchafalaya is often less than the 30 percent mandated. None-the-less, even with reduced sediment going down the Atchafalaya, there is delta growth at the two outlets of the Atchafalaya as shown in Figure 2.

The present policy of preventing the Mississippi River from changing course has maintained flood control, navigation and freshwater supply to the lower Mississippi but has had disastrous unintended consequences not anticipated by the designers of the Old River Control complex. Because the mouth of the Mississippi River in Southwest Pass has been extended to the edge of the continental shelf, the sediment load of the

Mississippi River is deposited in deep water off the edge of the continental shelf. By contrast the continental shelf at the mouth of the Atchafalaya River is quite wide as is shown in Figure 3. Because the continental shelf is wide at the mouth of the Atchafalaya, sediment carried by the Atchafalaya is deposited in shallow water and builds land as is seen in Figure 2.

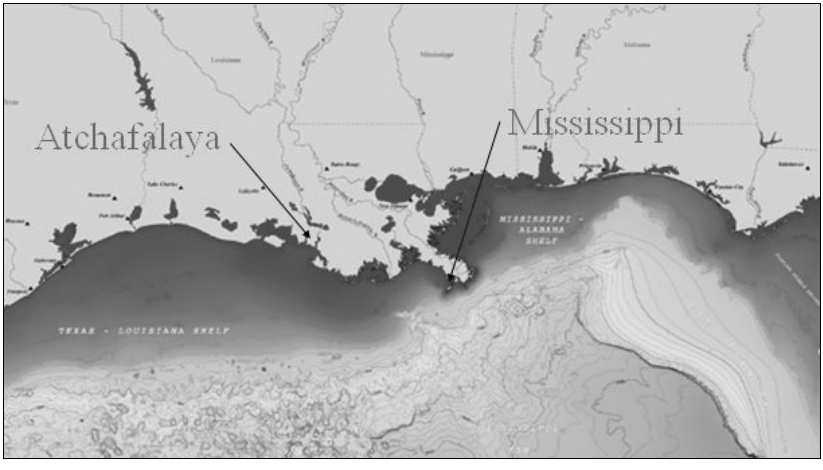

Fig. 3. Bathymetry of the Northern Gulf of Mexico. Dark (red in color version) shading is shallow water.

FLOW DISTRIBUTION

In a previous paper (Winer 2006) the author argued for a new paradigm in managing the flows of the lower Mississippi River. The proposed paradigm was "How do we provide for navigation, flood control and water supply along the lower Mississippi River corridor while allowing the River to change its course?" The suggested flow distribution was that for normal flows (i.e. neither flood flows or low flows) only the minimum flow necessary to keep the saltwater wedge out would go down the lower Mississippi and all of the rest of the flow along with the predominance of the sediment would go down the Atchafalaya. The minimum flow necessary to arrest the saltwater wedge was determined following the work of Soileau et. al. (1989). During flood flows the lower Mississippi would be utilized the same as it presently is along with flood control structures such as the Bonnet Carre Spillway. During low flows the scarcity of flow would be distributed the same as it is presently, as 70 percent of the latitude flow to the Mississippi and 30 percent to the Atchafalaya.

CONSTRUCTION SEQUENCING

The River could be allowed to change its course in a controlled manner through the construction of additional structures and the re-alignment of outfall canals from the existing structures. The sequencing proposed herein is meant as an initial stab at a feasible method of accomplishing the objective of allowing the River to change course to

the Atchafalaya channel. Only a detailed feasibility study can address all aspects of the river channel change and come up with the right and proper method.

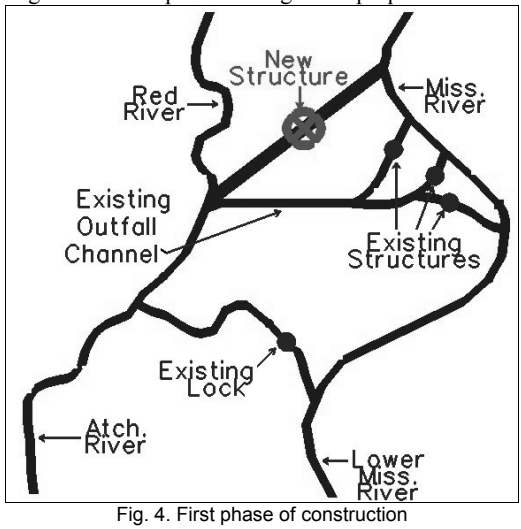

Fig. 4. First phase of construction

First, a new structure could be constructed in the dry and then have connecting channels dug to it. The new structure should be sufficiently large so as to be capable of passing the maximum flow determined. This structure could be located north of the existing complex of structures where the construction would not interfere with operation of the existing structures. This structure would also have a very low still for passing sediment. Upon completion of the new structure and the connecting channels as shown in Figure 4, this structure would be used for passing water to the Atchafalaya while the remaining phases of construction are taking place. There could be a time lag between the first phase and subsequent phases of construction, using this first structure to progressively increase flows in the Atchafalaya channel. Only a detailed study could estimate this time to allow the Atchafalaya channel to grow to accommodate increased flows.

The second phase of construction would be to realign the outfall channel so that the existing structures could be used to divert water into the lower Mississippi River. This would involve dredging a new channel and blocking the present outfall channel. By directing the outfall from the three existing structures to the lower Mississippi River and building a lock and dam across the lower Mississippi River just above the discharge of the outfall canal (see figure 5) the existing structures could then be used to divert flow into the lower Mississippi River. The lock and dam would need to be constructed at the same time as the realignment of the outfall canal (but not completed prior to the completion of the realignment of the outfall channel.) This would best be done swiftly so as to minimize the time that the hydro-electric plant is inoperable due to the channel realignment and/or insufficient heads. The lock and dam would need to be designed so

as to pass the projected flood flow in concert with the existing structures that would now be diverting water to the lower Mississippi River.

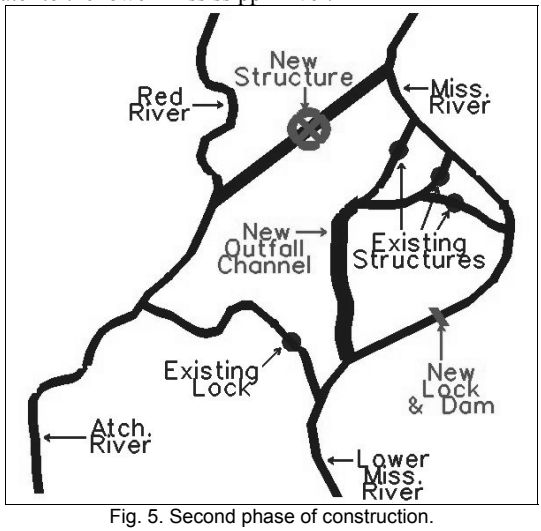

Fig. 5. Second phase of construction.

CHALLENGES AND OPPORTUNITIES

Reconfiguring the Old River Control Complex and increasing the flow distribution to the Atchafalaya will require extensive study and planning. The list presented here is only the beginning. A detailed study would inevitably add numerous issues to the list. First, the design and configuration of the structures at Old River needs to be optimized. A possible re-configuration has been presented but it requires considerable refinement. Second, a plan of gradually increased flows in the Atchafalaya would be necessary to increase the flow capacity of the Atchafalaya by allowing the river to carve a bigger channel. This would eventually necessitate the relocation of pipelines and bridges (both rail and highway) that cross the Atchafalaya. Levees and flood protection may also need to be relocated and raised.

Additional conveyance through the Teche ridge would also be necessary. The existing channels through the Teche Ridge (Wax Lake Outlet and the lower Atchafalaya River) would have to be enlarged or possibly an additional outlet would need to be created. At present the existing two outlets require a very high head to pass design flood flows.

Another issue is the possible change in stages along the Red River due to back water effects from increased stages in the Atchafalaya. This could impact agriculture along the river banks inside the levee system.

OPPOSITION

Opposition could come from those who would prefer to see marsh created near the metropolitan area of New Orleans in the hopes that it would provide protection from

hurricane storm surge. First, it is not certain that marsh creation is a viable hurricane protection method. Hurricane surge can travel great distances inland over low coastal lands. Second, even if it were a viable hurricane protection, there is no viable method to capture the entire sediment load of the lower Mississippi River and create marsh. Directing the flow along with the sediment load into shallow water is the only viable method of creating marsh lands with the river's sediment load. A major diversion of the River in the lower reach where there is deep draft navigation would require deep draft locks which would be a detriment to the shipping industry.

Opposition could also come from the citizenry and industries of the Morgan City area. Sending increased flows down the Atchafalaya and building a larger delta would radically affect Morgan City and the surrounding area. First, either an enlargement of the existing flow paths through the Teche ridge or an additional flow path would be required. This would involve the acquisition of real estate with all of the complication involved in dealing with private property ownership issues. Second, as the deltas grow, the length of the channel would also grow so that any particular location would be progressively further from the sea. This would result in a long term gradual increase in stages along the lower Atchafalaya channel. The businesses that use the riverfront of Morgan City would be impacted and in time the flood protection for Morgan City may need to be raised as the delta grows.

CONCLUSION

This proposal represents radical change. Change generally brings opposition. Radical change could well result in intense opposition. Political opposition, however, should not impede the discussion of this proposed alternative or the process to initiate a detailed feasibility study. There are indeed numerous impacts associated with this proposal. However, there are impacts to the present system of preventing the river from shifting course. The process of a feasibility study is to identify and address impacts either by removing, minimizing, or mitigating.

Holding the River in its present position means that a resource of millions of tons per year of sediment is lost off the edge of the continental shelf. Capturing all of that sediment through dredging is not feasible. Only large river diversions can capture and deliver all of the sediment. River diversions below Baton Rouge would require deep draft locks that would have huge costs both for construction and in terms of transit times.

The importance of the coastal wetlands to the entire eco-system of the Gulf of Mexico is well established. The proposed change of course of the river and its sediment load at Old River would insure that there will be emergent marsh in the future to replace the presently eroding marsh.

DISCLAIMER

The views expressed in this paper are solely those of the author and do not in any way reflect the position or policy of the Department of the Army, the Corps of Engineers, the United States government or any other agency of the U.S. government.

REFERENCES

Fisk, H.N. (1944). "*Geologic Investigations of the Alluvial Valley of the Lower Mississippi River,*" U. S. Army Corps of Engineers, Mississippi River Commission, Vicksburg, MS.

Soileau, C.W., Garrett, B.J., Thibodeax, B.J. (1989). "Drought Induced Saltwater Intrusion on the Mississippi River," *Proceedings of Coastal Zone '89 Conference*, ASCE.

Winer, H.S. (2006). "A New Paradigm for Managing the Lower Mississippi River," *Proceedings 30th International Coastal Engineering Conference*, ASCE, in press.

SEDIMENT FLUX AND FATE IN THE MISSISSIPPI RIVER DIVERSION AT WEST BAY: OBSERVATION STUDY

T. Mitchell Andrus[1], Samuel J. Bentley[2]

1. Coastal Engineering Consultants, Inc., 5745 Essen Lane, Suite 200, Baton Rouge, LA 70810, USA. mandrus@ceci-la.com
2. Memorial University of Newfoundland, St. John's, NL A1C 5S7, P.O. Box 4200, CANADA. sjb@esd.mun.ca

Abstract: Land-building sediment diversions, such as the Mississippi River Diversion at West Bay, are being used as important building blocks in the conservation and restoration of Mississippi Delta wetlands. We have studied sediment deposition and retention in the West Bay diversion outfall area through analyses of sediment cores, bathymetry, and hydrodynamics. Cores and x-ray samples were collected at twenty stations in March 2004, August 2004, November 2005, and April 2006. Cores were sub-sampled in 2 cm increments and analyzed for grain size distributions and ^{7}Be activities which can be linked to recent sediment deposition. Bathymetric surveys were conducted in November 2005 and April 2006 and will be used to compare significant elevation changes to bay bottom contours. Data analysis for the study focuses on the ^{7}Be results in comparison with hydrodynamic forcing functions such as river and diversion flows and major storm activity.

INTRODUCTION

In the modern Mississippi Delta, subdeltas represent important and dynamic components of the landscape and sediment delivery system. In a general sense, we understand the processes that influence the growth and decay of subdeltas. However, our knowledge is insufficient to allow prediction of sediment deposition and

retention within subdeltas, and so we cannot reliably model the processes and resultant dynamic geomorphology. This inadequacy is problematic, because subdeltas, like the one being built at West Bay, are being used as important building blocks in the conservation and restoration of Mississippi Delta lands and wetlands. The overall goal of this study is to elucidate our understanding of sediment dispersal and retention within subdeltas, thus enhancing assessment, planning, and predictive capabilities for the West Bay Diversion and for future land-building projects of comparable design.

Background

The West Bay Subdelta Complex is located in the Mississippi River Delta in Plaquemines Parish, Louisiana. It is one of the six subdelta complexes defined by Coleman and Gagliano (1964) comprising the most recent framework of the modern Birdfoot Delta as shown in Figure 1.

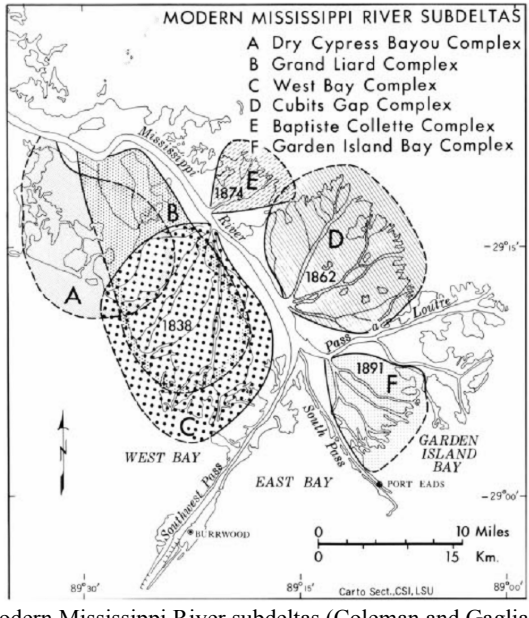

Fig. 1. Modern Mississippi River subdeltas (Coleman and Gagliano, 1964)

Historical dating through map studies has shown that the West Bay subdelta originated around 1838 as a break in the natural Mississippi River levee during flood stage creating an intricate land-building crevasse splay. The location of this break, which is still hydraulically open, is just below the present day town of Venice, LA and is know as "The Jump". Figure 2 shows a progression of subdelta growth and initial stage of deterioration over a timescale from 1845 to 1958.

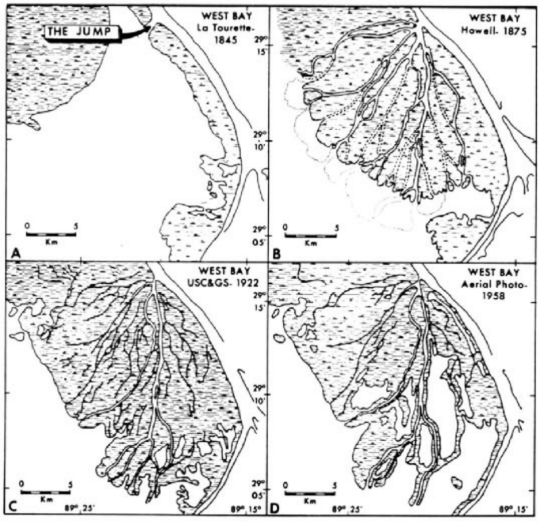

Fig. 2. West Bay subdelta evolution (Coleman, 2006)

This original subdelta growth work performed by Louisiana State University's Coastal Studies Institute (LSU CSI) (Fig. 2) can be extended further into time by comparing these past map studies with recent imagery. Figure 3 illustrates false-color IR imagery from 1998 of the West Bay/Head of Passes region, compared to a 1953 topographic map of the same area, at the same scale. Extensive regions mapped as marsh in 1953 are now open water. Our study area is outlined in black, west of the river.

1998 1953

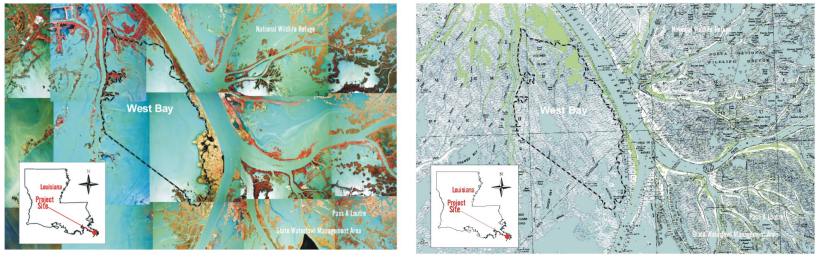

Fig. 3. Project area marsh loss comparison

The extensive mapping study by LSU CSI is summarized in the subdelta life cycle curve shown in Figure 4. The curve is a typical for a subdelta life cycle, which generally lasts from 100 to 150 years from inception to abandonment. In the mid 1900's, the West Bay subdelta entered the natural deterioration phase of its life cycle which was possibly accelerated by river channelization, canal dredging, and decreased sediment loads in the Mississippi River. As hydraulic efficiency of the subdelta decreased, the valuable inputs of fresh water, nutrients, and sediment declined and the marsh succumbed to erosion and subsidence.

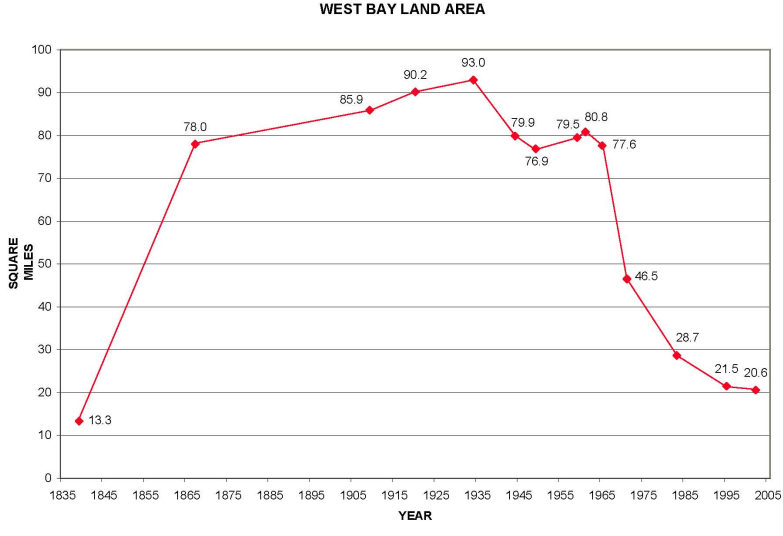

Fig. 4. West Bay Subdelta Complex life cycle curve (Coleman, 2006)

Restoration Efforts

The West Bay Sediment Diversion was one of the first projects approved by the Coastal Wetlands Planning Protection and Restoration Act (CWPPRA) on its first priority list in 1990 and was sponsored by the Louisiana Department of Natural Resources (LDNR) and the U.S. Army Corps of Engineers (USACE). The main goal set forth in the CWPPRA project monitoring plan was to create, nourish, and maintain 9,831 acres of emergent marsh within the project area over the 20 year project life by enhancing the natural process of delta growth and through the beneficial placement of material dredged during construction and maintenance. The project consists of a conveyance channel from the river into West Bay located at river mile 4.7 above Head of Passes along the right descending bank (LDNR, 2003). The initial and present capacity of the diversion is 20,000 ft^3/s (~570 m^3/s) with plans to increase its capacity to 50,000 ft^3/s (~1400 m^3/s) after sufficient monitoring.

Planning and engineering for the project began in 1990. Because of navigation concerns and land rights negotiations, the project was not constructed until late 2003. In November of 2003 dredging of the diversion channel was completed and sediment laden Mississippi River water once again flowed into West Bay.

Study Objectives

In bays, such as West Bay, that are actively receiving river sediment, the exact balance between sediment retention in the bays (i.e., sediment that builds land and wetlands) and sediment bypassing to the shelf is not known. However, the West Bay Sediment Diversion represents an excellent opportunity to study this phenomenon, and a complete quantitative understanding of such processes is essential to predicting the success of such enterprises (and to predicting impacts on downdrift coastal environments). Although the work presented herein represents only a small step toward an ability to understand and predict subdelta evolution, we suggest that these steps provide important insights applicable to future efforts to manage river sediment and build wetlands, particularly in settings where project design needs to be optimized for maximum sediment retention.

This study is intended to increase our understanding of sediment delivery by the diversion, sediment retention within the bay and, ultimately, the success of the diversion toward building deltaic wetlands. Our specific objectives are to: (1) describe sediment deposition patterns within the study area using proven sediment-radiochemical techniques dating techniques and (2) link these patterns to hydrodynamic forcing functions such as river and diversion flows and major storm events.

METHODS

^{7}Be Dating

Radioisotopes, such as Berillyum-7 (^{7}Be, ½-life 53.3 days) can be used to reconstruct the recent sedimentation history of the coastal seabed, particularly in river-influenced settings. In this study, ^{7}Be is used to track sediment flux from the diversion and determine short-term sediment accumulation rates. ^{7}Be is a naturally occurring radioisotope with a half-life of 53.3 days that is formed in the atmosphere by reactions between cosmic rays and nitrogen and oxygen. In fluvial-marine depositional systems, ^{7}Be geochronology is a powerful tool to document and estimate sediment flux and deposition over seasonal timescales (Sommerfield et al., 1999; Allison et al., 2000; Rotondo and Bentley, 2003). In fluvial marine systems where the catchment basin is larger than the region receiving sediment, (such as the Mississippi Delta), the cosmogenic, particle-reactive radioisotope ^{7}Be can be used as a tracer of sediments recently derived from the fluvial source. Sediments that contain significant ^{7}Be must have been deposited within several half-lives of ^{7}Be, or <200 days, based on its 53-day half life.

Sediment Sampling

Most of West Bay seabed is subtidal and > 1 m deep, so cores were collected from shallow-draft vessels using pushcores. Coring was coordinated with the hydrographic

surveys along established CWPPRA bathymetric survey lines at seventeen stations as shown in Figure 5. Sample locations were evenly distributed throughout the study area including areas near the diversion, open water deeper areas in the middle of the bay, shallower areas around the periphery of the bay, and semi-enclosed areas with less efficient hydraulic connections to the bay and diversion flows.

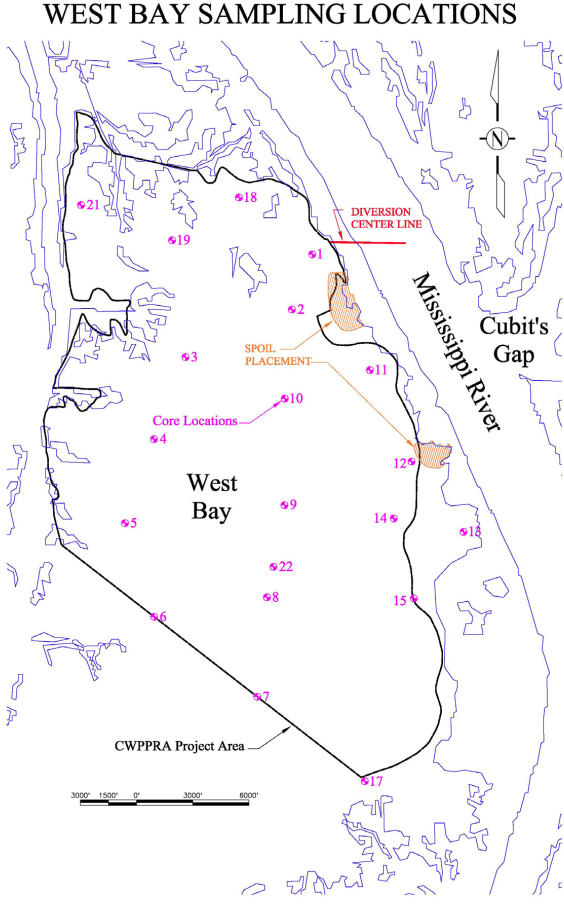

Fig. 5. West Bay Sampling Plan

Samples were collected in four separate events from 2004 to 2006, intended to capture conditions just before and after annual high water. The first sampling event was conducted on March 18-19 (2004) and the second sampling event was conducted on August 23-24 (2004). LDNR provided an airboat and two field personnel at no

cost for these efforts. Subsequently, funding was allocated through a grant from the Coastal Restoration and Enhancement through Science and Technology program (CREST) allowing for more robust data collection efforts. Funding for the CREST program is administered by the Louisiana Universities Marine Consortium (LUMCON) using funds provided by the National Ocean Service of the National Oceanic and Atmospheric Administration (NOAA). In the process of securing this funding, no sampling was conducted in the spring of 2005. The next two field collection events were undertaken by LSU CSI researchers and field support staff. Sampling was conducted from a shallow-draft bay boat that could access most sampling locations, with the exception of a semi-enclosed area which could only be reached by airboat. The third sampling event was conducted on November 3 (2005). It is important to note that this was approximately two months after Hurricane Katrina, which devastated lower Plaquemines Parish making lodging and other logistics very limited. The fourth sampling event was conducted on April 12-14 (2006).

Cores were collected using 10-cm-diameter PVC core barrels. Because this study focuses primarily on short-term accumulation rates produced by recent fluvial processes, core barrels were cut in short lengths of approximately 1 m long. The CSI field staff constructed an efficient self-sealing coring device designed to allow core extraction with minimal effort. The suction head was constructed out of an aluminum billet with a shoulder cut as a bearing surface for core insertion. The barrel was sealed to the suction head with hose clamps and tape. Venting of captured air and water was accomplished with eight (8), 1.75 cm vents that seal with a spring loaded, rubber-faced aluminum plate. Spring tension was adjustable to account for different viscosities of material being vented. When core extraction was initiated, a suction was created to the interior of the core barrel, facilitating removal of the core with minimal material loss. Capping is done once the core was recovered.

X-ray samples were acquired using three-sided Plexiglas trays employing a sliding panel as the fourth side. The tray was initially pushed into the bay floor then the fourth panel was slid into place guided by grooves in the side panels, thereby shearing the sample from the adjacent sediments and enclosing within the tray. The sample was then pulled from the bay floor and capped and sealed for storage and travel. In locations deeper than 1 m this was accomplished using SCUBA gear.

Sediment Analyses

X-radiographic subsamples were imaged soon after collection using a Thales Flashscan digital panel X-ray detector with 14 bit, 127 μm pixel resolution. Images were then stored as 16-bit TIFF files for subsequent study. Activities of ^{7}Be were determined by gamma spectroscopy of dried sediment (477.7 KeV peak for ^{7}Be). The sediment was weighed before and after drying for water content to be used in porosity calculations. A known mass of ground sediment was then placed in a 6 cm petri dish and sealed. The sealed samples were analyzed on a Canberra gamma detector.

RESULTS

The maximum depth of ^{7}Be occurrence is a useful indicator of short-term (months) sediment deposition and mixing because of its relatively short half life (53.3 days). Profiles of ^{7}Be activity in the seabed were determined for each core sampling station in west bay for the four sampling events. Beryllium activity at the time of field sampling (A) measured in decays per minute per gram of sediment (dpm/g) was calculated using the equation:

$$A = A_o e^{-\lambda t} \quad (1)$$

where A_o is the activity at the time of detection, $\lambda = 0.013\ d^{-1}$ is the decay constant for ^{7}Be, and t is the time elapsed between sample collection and detection. Figure 6 shows ^{7}Be activity profiles for station WB01, which is closest to the diversion outfall, and WB05, approximately 3.5 miles southwest of the diversion outfall.

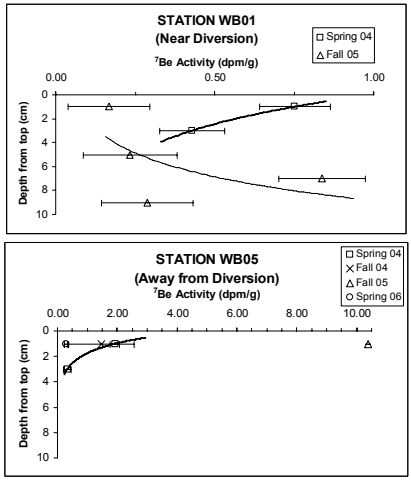

Fig. 6. Graphs of ^{7}Be Activity (dpm/g)

The WB01 results for the Spring 2004 sampling event show a typical logarithmic decrease from 0 to 4 cm depth in the core. The Fall 2005 WB01 results show an increase in activity with depth, suggesting strong physical reworking. Fall 2004 and Spring 2006 sampling events resulted in no detected ^{7}Be, possibly due to sediment erosion, considering the close proximity to turbulent diversion flows. ^{7}Be was detected near the surface of the cores at station WB05 for all sampling events with an exceptionally high amount of activity for the Fall 2005 sample. It is suspected that this is due to a large sedimentary event layer produced by Hurricane Katrina.

The X-radiographic images shown in Figure 7 taken at station WB05 also show evidence of this significant event layer. The Spring and Fall 2004 images show thin layers of fine sediment deposition. The top 4 cm of the these images are also more transparent indicating more recently deposited, less compacted sediments. This compares well with the ^{7}Be activity profiles from Figure 6 which indicate a ^{7}Be penetration of about 4 cm in this core (i.e., the top 4 cm of sediment are recently deposited). The Fall 2005 image shows a much thicker layer of relatively dense sediment above thin layers of lower density sediment identified in previous sampling events. The thickness and higher density of this layer may indicate coarser-grained sediment deposited by Hurricane Katrina. This layer also contains the highest ^{7}Be activity found during any sampling event. Thin layers of finer sediment become more evident above this layer in the Spring 2006 image and the ^{7}Be activity drops back down to below 0.5 dpm/g.

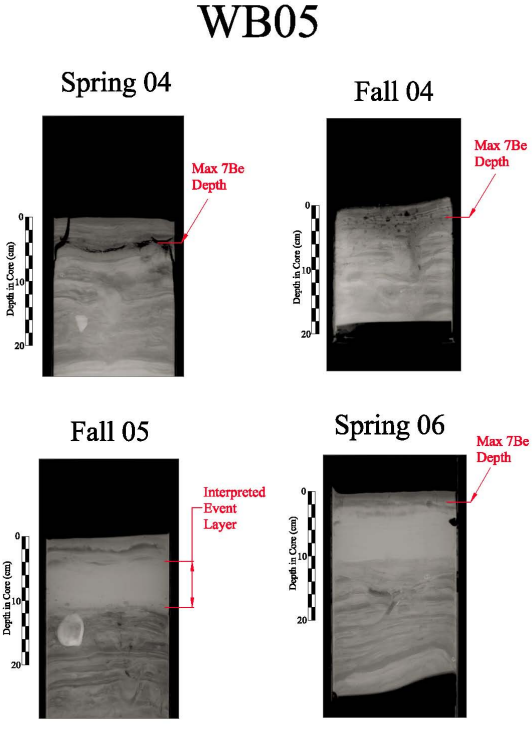

Fig. 7. X-ray images of sedimentary layers for station WB05. Bright zones indicate relatively high density (coarser grain size or lower water content), whereas darker shades indicate lower density, due to finer grain size and/or higher water content.

^{7}Be activity can also be reported on a volumetric basis, calculated as the product of the ^{7}Be activity the solids volume fraction (1-porosity), and the average density of the sediment (2.65 g/cm^{3}). Figure 8 shows ^{7}Be activity profiles for stations WB01 and WB05 after this conversion.

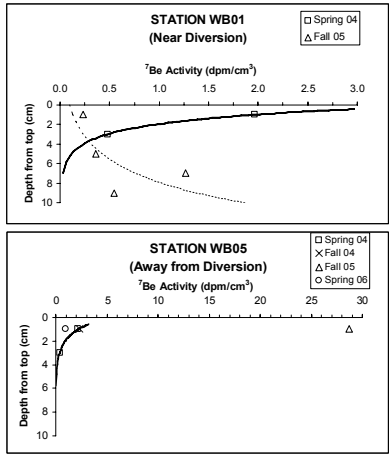

Fig. 8. Graph of ^{7}Be Activity (dpm/cm^{3})

Total inventories were then calculated by integrating volumetric ^{7}Be activity with respect to total core depth for each sampling event. A summary of ^{7}Be inventories for stations WB01 and WB05 are shown in Figure 9.

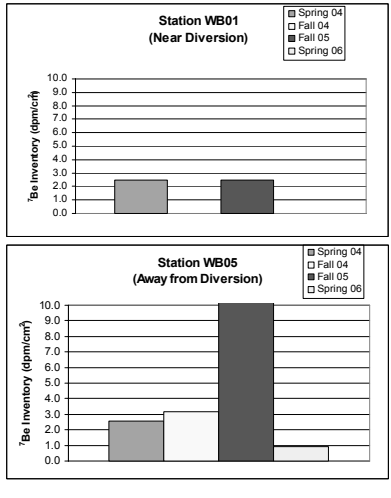

Fig. 9. Summary of ^{7}Be Inventory (dpm/cm^{2})

Figure 10 shows maps of ^{7}Be inventories for each station from all four sampling events. The highest inventories are interpreted to represent the most rapid sediment deposition. The magnitudes and distribution patterns appear to be related to the river hydrograph and corresponding diversion flows summarized in Figure 10 as well as hurricane related deposition and mixing. The Spring 2004 samples were taken after a river hydrograph peak of approximately 550,000 cubic feet per second (cfs). Results for this sampling event suggest fresh sediment deposition along the western margin of the bay, and show the highest ^{7}Be inventories of our study, with the exception of the Fall 2005 samples which were taken approximately two months after Hurricane Katrina. The Fall 2004 and Spring 2006 samples were collected after river hydrograph lows of less than 200,000 cfs. These observations suggest that deposition at relatively low river levels can occur in the middle of the bay, where water depths are on the order of 1-2 m.

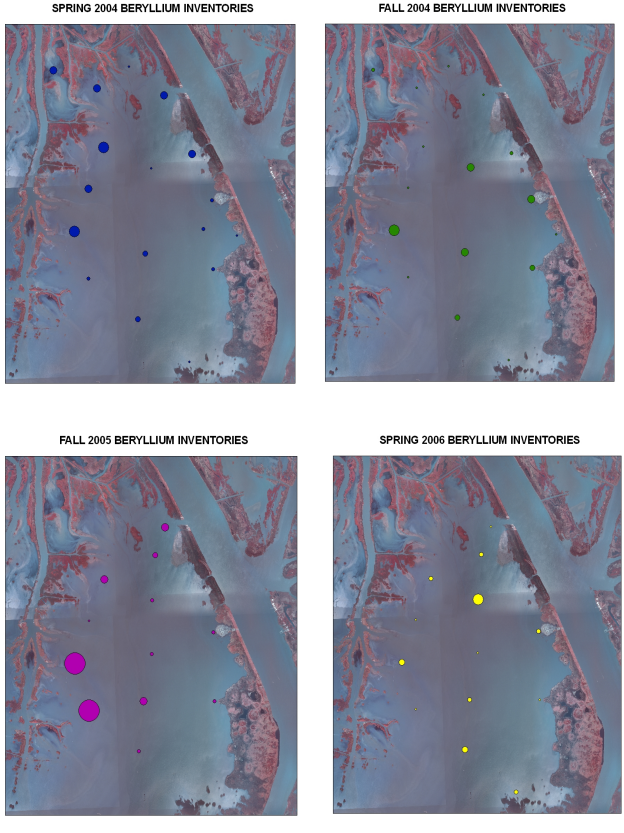

Fig. 10. Spatial distribution of ^{7}Be Inventories.

Figure 11 illustrates the river and diversion flow hydrographs (in cfs) along with total ^{7}Be inventories in dpm/cm^{2} for each sampling event. Total inventories were calculated by summing inventories from core sampling stations which were replicated for each sampling event. No flow data were collected from August to December of 2005 due to Hurricane Katrina. However, the highest total ^{7}Be inventory was calculated during this time period, indicating a large amount of sediment re-suspension, deposition, and physical mixing. The total inventories from the Spring 2004, Fall 2004, and Spring 2006 appear to track river flows and to a lesser extent, diversion flows. For example, the Spring 2004 samples resulted in more than twice the ^{7}Be inventory than that of the Spring 2006 samples which were taken during higher diversion flows but a lower river stage. This suggests that river flows, and therefore suspended sediment, are entering the study area through other avenues than only the diversion. River flows were measured at Venice near "the Jump" where a portion of the flow is diverted to Grand Pass which borders the study area on the western margin.

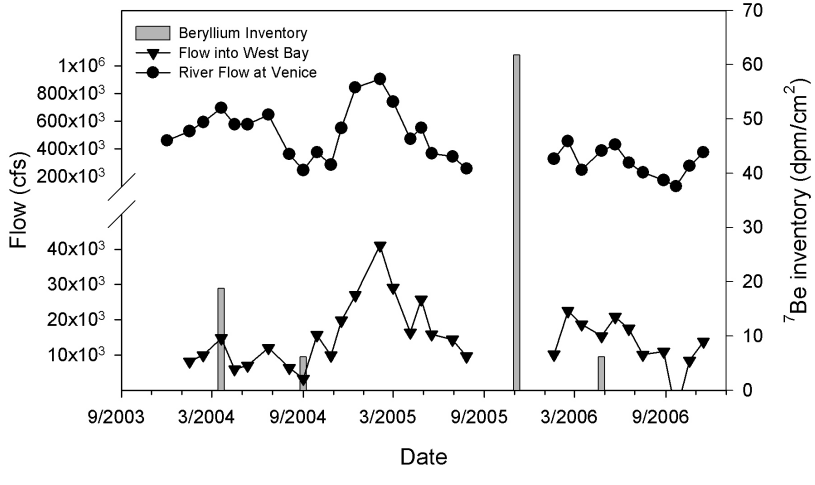

Fig. 11. West Bay Flow and Total ^{7}Be Inventory Analysis (USACE, 2006)

DISCUSSION

The strategy of the initial study plan was to track two (2) normal cycles of the Mississippi River hydrograph by timing sampling events with rising and falling limbs of river flow. The 2004 river hydrograph (Fig. 10) displayed a predictable pattern, however during 2005 irregular flow patterns were encountered. The Spring 2005 flow peak was significantly higher than those of the 2004 and 2006 spring

seasons. No sampling was conducted in Spring 2005, due to cost considerations. Following this peak, Hurricanes Katrina and Rita struck the Louisiana coast in late summer, devastating lower Plaquemines Parish. Flow records were not recorded for the following six months however the study team did manage to conduct a coring trip in November 2005. The results from these samples produced ^{7}Be inventories of much greater proportions than those of the other three coring trips (Fig. 10). From this data and evidence of substantial deposition layer seen in a number of the x-ray images taken during in the Fall 2005 and Spring 2006 (Fig. 7), it is evident the extreme energy of the hurricanes transported copious amounts of sediment with coarser grain size than the sediment being delivered by the diversion or other sources.

The 2006 river hydrograph returned to a more typical pattern resembling that of 2004, however with lower flow magnitudes. This is reflected in the Spring 2006 ^{7}Be inventory which is approximately one third of that found in Spring 2004 despite a higher diversion flow in 2006. This difference certainly warrants additional investigation into other factors which could be affecting the results. These factors could include river sediment loads, sediment loads being captured by the diversion, affects of wind and waves, and associated sediment re-suspension and transport within the bay.

As part of the study, additional data were collected but have not yet been analyzed. These data include continuous records of velocities and turbidity at the diversion cut and at two sites within the bay, as well as continuous wave measurements at the bay sites, bathymetric elevation surveys of both the diversion cut and bay bottom, and grain size analysis of the sediment cores.

Long term records of river flow and sediment loads are also available for additional analysis and insight. They will be used along with the diversion flow records to estimate net sediment influx into the bay and compared against sediment accumulation rates calculated at sampling locations from ^{7}Be activities and penetration depths. Through this analysis sediment retention rates within the project area will be estimated. Comparing ^{7}Be activities at West Bay to activities found at other sites in coastal Louisiana that have no riverine influence may also help decipher river and diversion induced sediment deposition from other background sources.

CONCLUSIONS

Analysis of ^{7}Be activities and inventories, x-ray images of sediment profiles, and diversion hydrographs all show strong indication that the West Bay Sediment Diversion is delivering sediment from the Mississippi River into West Bay. Data collected during the study period also shows strong evidence that sediment deposition in West Bay can also be attributed to major storm events and river flows entering the study area from locations other than the diversion. Upcoming analysis of sediment grain size, flow, suspended sediment concentrations, wind and wave

influences, bathymetry evolution, and previous studies will allow for further understanding of diversion function and performance.

ACKNOWLEDGEMENTS

We appreciate all of the cooperation and support provided by the CWPPRA partnering project sponsors LDNR and USACE. We also appreciate all funding and support from NOAA's CREST grant program and LSU CSI and look forward to continued collaboration with these personnel for a successful study.

REFERENCES

Allison, M.A., G.C. Kineke, E.S. Gordon, and M.A. Goni. (2000). "Development and reworking of a seasonal flood deposit on the inner continental shelf off the Atchafalaya River," Continental Shelf Research 20, 2267-2294.

Coleman, J.M., Boyd Professor, Louisiana State University, Coastal Studies Institute. (2006). Personal communication with Mitch Andrus and approval to use unpublished data on November 27, 2006.

Coleman, J.M. and Gagliano, S.M. (1964). "Cyclic sedimentation in the Mississippi River delta plain," Transactions Gulf Coast Association of Geological Societies 45, 67-80.

Louisiana Department of Natural Resources. (2003). "Monitoring Plan, Project No. MR-03, West Bay Sediment Diversion," Date: August 21, 2003, 11 p.

Rotondo, K.A., and Bentley, S.J., 2003, Deposition and resuspension of fluid muds on the western Louisiana inner continental shelf. Gulf Coast Association of Geological Societies Transactions 53: 722-731.

Sommerfield, C.K., Nittrouer, C.A., and Alexander, C.R.. (1999). "^{7}Be as a tracer of flood sedimentation on the northern California margin," Continental Shelf Research 19, 335-361.

U.S. Army Corps of Engineers. (2006). Personal communication between Mitch Andrus and Greg Miller, USACE Project Manager, and approval to use unpublished flow data from the Mississippi River and West Bay Diversion on November 30, 2006.

INITIAL MORPHOLOGIC AND STRATIGRAPHIC DELTA EVOLUTION RELATED TO BUOYANT RIVER PLUMES

Joep E.A. Storms[1], Marcel J.F. Stive[2], Dano (J.) A. Roelvink[2,3,4], Dirk Jan Walstra[2,4]

1. Delft University of Technology, Faculty of Civil Engineering and Geosciences, Section Geo-engineering, PO Box 5048, 2600 GA, Delft, Netherlands. j.e.a.storms@tudelft.nl
2. Delft University of Technology, Faculty of Civil engineering and Geosciences, Section Hydraulic Engineering, PO Box 5048, 2600 GA, Delft, Netherlands. m.j.f.stive@tudelft.nl
3. UNESCO-IHE, P.O. Box 3015, 2601 DA Delft, The Netherlands. d.roelvink@unesco-ihe.org
4. WL|Delft Hydraulics, P.O. Box 177, 2600 MH Delft, The Netherlands. walstra@wldelft.nl

Abstract: This paper presents the results of a numerical model study on initial delta formation in basins of different water depths. A process-based model (Delft3D-Online) is used to calculate fluid flow and sediment transport patterns at a newly formed river effluent. In absence of wave and tidal forcing, the river effluent is fully river dominated. The model results are interpreted in terms of morphology and stratigraphy. For the shallow basin case, the delta develops as a complex pattern of channels and shoals analogous to Wax delta. The simulated delta development in the deep basin is markedly different and resembles a classic prograding bird foot delta morphology. Typical clay-rich prodelta deposits underlie sandy bar and channel deposits. The top of the sedimentary sequence consists of a clay-rich delta plain deposit. The potential of the process-based model to simulate typical delta morphologies and a realistic stratigraphy provides many new opportunities to bridge typical engineering and geological research approaches.

INTRODUCTION

Numerical modeling in sedimentary geology has significantly attributed to the understanding of depositional systems and their preserved deposits since the 1970's. The

first models were based on simplified behavior of geometric rules and reproduced large scales (10-100 km) stratigraphic sequences that formed over long periods (10^4 to 10^6 years). To better understand the small-scale variability in sedimentary deposits, models generally became more refined and elaborate. As the level of understanding of depositional systems increased so did the degree of detail in the models. Behavior rules were partially replaced by process-rules leading to models that were constantly at the limit of the computational possibilities of the time. At present, improved processor speed and intelligent up scaling algorithms of sediment transport have led to a new cross-over situation where process-driven morphodynamic models developed by hydraulic engineers can be usefully applied to scales relevant to sedimentary geologists who study detailed sedimentology and stratigraphy. In this paper we apply the process-based model Delft3D-Online to simulate the initial stages of delta formation and view the results with 'geologic eyes'. As such, morphodynamic modeling of initial delta formation opens the opportunity to interpret modeling results in terms of combined morphologic and stratigraphic development. Hence, it provides a bridge to merge knowledge of long term (geological/ sedimentological) and short-term (hydraulic engineering) process understanding. Both fields of expertise have historically focused on deltas as an important research area, but due to the difference in approach relatively little new understanding has been gained by combining expertise. Studies such as these can therefore test the assumptions made in the engineering world for their validity in earth sciences.

This paper shows results of such an approach to a 'newly-formed' river effluent. To reduce the complexity in flow patterns at the effluent we will focus on a river-dominated effluent by assuming no waves and tides to be present. Furthermore, at this stage of our research we try to avoid too much complexity at the same time. Hence, complex flow patterns by salinity mixing effects and the associated flocculation of clay particles have been disregarded by restricting our simulations to homopycnal conditions, c.f. low sediment concentrations at the river effluent and a fresh water basin.

Validating a process-model is extremely difficult due to the vast amounts of processes that can be adjusted in the model. In addition, data time series relevant to delta development at a timescale between years and centuries are absent. Time series measurements are generally too short to determine the overall net sediment transport directions and rates at longer time scales. The sedimentary record provides only data of the preserved sediments and therefore is not a complete data record. Yet this scale is crucial to the understanding of initial delta formation, as well as to the further development of deltas. It is for this reason that numerical modeling can provide and test new hypotheses that relate stratigraphy to their formative processes and boundary conditions (Figure 1).

Numerical modeling of deltaic sedimentary systems can be used to test sedimentological concepts and dogmas thirty years after L.D. Wright's (1977) benchmark paper on deltaic depositional patterns at river effluents. We now can actually simulate river mouth processes and sedimentation during the initial stage of delta formation. According to

Wright (1977), the complexity of river mouth processes, in the absence of disturbance by tide and wave action, can be categorized into three effluent types that are dominated by either outflow inertia, turbulent bed friction and outflow buoyancy. Numerical morphodynamic modeling may enable us to test (1) the applicability of Wright's original ideas on *dominant effluent forcings*, (2) study the relation between variable effluent forcings *and intrinsic delta behavior*, c.f. mouth bar formation, channel bifurcation, channel abandonment, and (3) relate the *continuous range* in effluent forcings to morphological development of initial deltas.

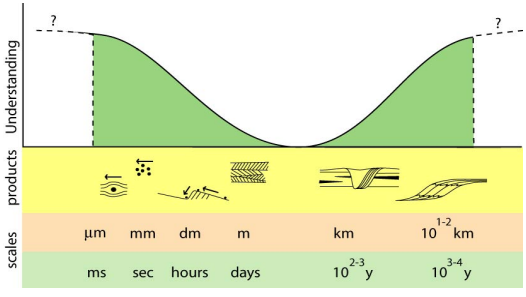

Fig.1. Schematic diagram showing our lack of understanding at the boundary between in situ measurements and stratigraphic data.

MORPHODYNAMIC MODEL

Delft3D-flow solves the unsteady shallow-water equations, that consist of the continuity equation, the horizontal momentum equations, the transport equation under the shallow water and Boussinesq assumptions (Elias 2006). Vertical accelerations are assumed minor compared to gravitational acceleration (shallow water assumption) reducing the vertical momentum equation to the hydrostatic pressure relation. By specifying boundary conditions for bed (quadratic friction law using a Chézy coefficient of 50 m½/s), free surface (no wind stress) and lateral boundaries (fixed water levels on the open-sea boundaries and total discharge at the river inflow with free-slip wall roughness conditions) the equations can be solved on a staggered grid using an Alternating Direction Implicit method (Stelling 1984; Leendertse 1987). Wave effects can be incorporated in the flow simulation by running the 3rd generation SWAN wave processor, but since we are primarily interested in the effluent forcings we have eliminated the effects of waves and tides.

The Delft3D Online Morphology add-on supplements the Delft3D-flow model results with sediment transport computations (Lesser et al. 2004). In this study the default Van Rijn (1993) transport formulation is used for non-cohesive sediment. The suspended load transport is calculated by solving the three-dimensional diffusion-advection equation. There, the sediment eddy diffusivities are a function of the fluid eddy diffusivities as

calculated by Delft3D-flow using horizontal large eddy simulation and grain settling velocity. The total sediment transport is obtained from the sum of the bed load and suspended load transports. Bed load transports represent the particle movements in the wave boundary layer due to currents and waves. Suspended load transports are the transports above the bed layer. Before bed-level updating, sediment transport rates are corrected for bed-slope effects. Overview of the implementation of the Van Rijn transport formulations (Van Rijn 1993) in Delft3D Online Morphology are presented by Walstra and Van Rijn (2003) nad Lesser et al. (2004).

Several methods exist to manage the communication between flow pattern and bathymetric change. Here, a method named 'Online' is used which updates flow, sediment transport and bathymetry all at the same small time steps (Roelvink 2006). The updating of the bottom takes very little computation time, however, this method does not take into consideration the difference in time scales between the flow and morphology. Therefore a simple device can be used, called the 'morphological factor' (Lesser et al. 2004). This factor increases the depth change rates by a constant factor n, so that after a simulation of one day we have in fact modeled the morphological changes over n days assuming that the hydrodynamic changes are small compared to the bed changes within that period. In a typical Delft3D-flow simulation we would apply a time step of 1 minute; with a high morphological factor of $n = 60$ this implies that we update the bathymetry every (morphological) hour. An advantage of this 'Online' method is, that short-term processes are coupled at flow time-step level, which makes it easy to include various interactions between flow, sediment and morphology, and which also removes the need to store large amounts of data between processes (Roelvink 2006).

Delft3D-flow can simulate water flow in three dimensions using a specified number of layers in the water column. However, these computations are extremely demanding. In this paper we exclude the effects of currents induced by tide, waves and density differences between the both fresh water masses (homopycnal). Experiments indicated that the results for 2DH simulations were comparable to the 3D simulations with 5 layers. Therefore all simulations shown in this paper are based on a 2DH approach.

SIMULATION EXPERIMENTS

Two simulations are shown in this paper which have a similar setup except for the receiving basin depth; one basin is shallow while the other basin is deep. Both basin and river effluent are generically modeled, i.e. they are not based on specific real-world river effluents, but both effluents are river dominated in the absence of waves and tides.

The imposed liquid discharge is 1000 m^3/s. The distributary channel and effluent initially are 2.5 m deep and about 200 m wide. The cross-sectional area of the initial channel design is intentionally undersized relative to the imposed liquid discharge. Therefore the initial flow velocity was reasonably high (1.4 m/s) but it is quickly reduced to about 1.1 m/s by the increase of the cross-sectional channel area due to erosion of the substrate (consisting of 50% sand and 50% clay). Sediment is introduced at the inflow point as a boundary condition. Total sediment load at the inflow point is 0.14 kg/m^3, of which half

is non-cohesive sand (125 μm) and the other half is cohesive clay. Local sediment load may be higher due to bed erosion. The maximum erosion depth in the initial channel is limited to 5m, which results in a maximum channel depth of 7.5 m. Total liquid discharge does not change in time. The morphological factor *n* is set to 50. Grid cells size is 50 x 50 m and the total model domain is 10 x 10 km. The time step is set to 60 seconds.

SIMULATED MORPHOLOGY

Figure 2 shows the morphological development of the incipient delta formation in a shallow basin (SIM A) and a deep basin (SIM B). The morphological development for both deltas is notably different. For SIM A, the initial sandy lunate bar is rapidly build up to a water depth of less than ½ m. The decreasing water depth at the lunate bar crest results in a dynamic equilibrium between the sand deposition and flow velocity. In other words, sand is bypassed over the lunate bar, which causes the lunate bar to grow basin ward rather than vertically. In addition to the lunate bar, a small middle ground bar (also named mouth bar) develops in front of the river effluent, which gradually separates the flow along the axis of the river. This preferential flow pattern leads to an inhomogeneous flow pattern across the lunate bar and gradually channels as well as shoals start to develop. In time, the initial channel and shoal pattern matures forming many small channels and a large number of elongated shoals. All shoals, including the middle ground bar, grow both basin wards and towards the river effluent. The area of the emerged delta plain continues to increase with time.

SIM B shows a different morphological development. Here the lunate bar is less extensive while the middle ground bar grows rapidly leading inevitably to flow separation. Instead of forming many shallow channels, two distinct channels form, which resembles a classic bifurcation pattern. It does however take quite a while before the middle ground bar actually emerges. Following the bifurcation, the right channel becomes dominant and discharges the most water. As a result it also becomes the deepest channel with the highest flow velocity. This high flow velocity causes a breach of the subaqeous levee, which leads to the formation of a new channel. Rapidly the old branch is abandoned and filled in. Meanwhile, the middle ground bar has emerged and the original left branch of the first bifurcation is slowly abandoned as well. The only remaining main channel now transports all the discharge and sediment and progrades rapidly in a basin ward direction thereby forming a new lunate bar and middle ground bar. This middle ground bar is at an angle relative to the bathymetric contour lines of the substrate and therefore develops asymmetrically. This leads to a clear preference of the left channel over the right channel, which therefore becomes the main channel. A new breach occurs at the right hand side levee about 1 km landwards from the most recent bifurcation. This breach develops into a crevasse splay and possibly develop into the new shortcut for the main channel, which thereby decreases its overall distance to the basin.

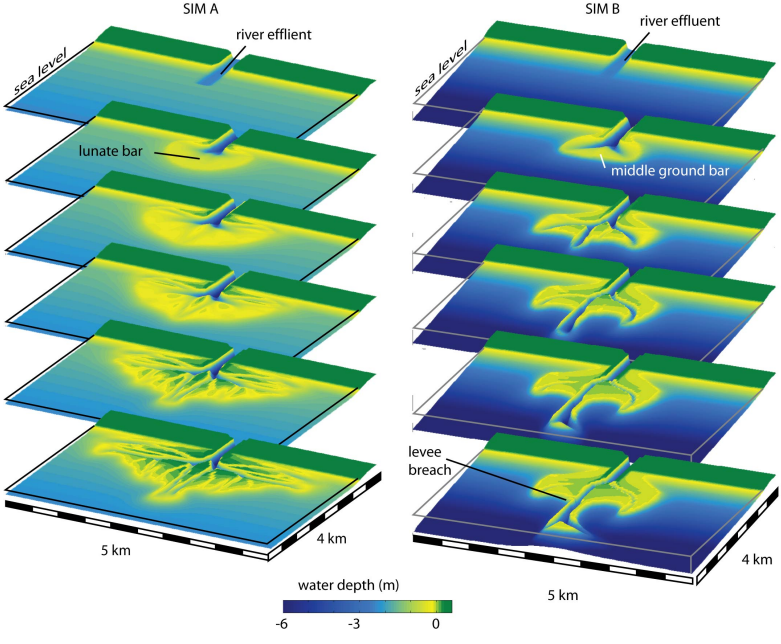

Fig. 2. Simulated delta evolution for SIM A (left) and SIM B (right). The only difference between the two simulations is the depth of the receiving basin.

STRATIGRAPHY

The simulated bimodal sediments distribution can be traced both in top view (Figure 3) as well as in cross section. Figure 4 shows cross sections of the initial lunate and ground middle bar formation just prior to emergence above sea level. The sand body consisting of both the lunate and middle ground bar for SIM A is longer than for SIM B. Yet, it also much thinner (< 1 m) due to the low basin depth (low accommodation space). The contact between clay and sand in both cases is sharp but non-erosive. The clay, which are prodelta deposits according to the classification of standard sedimentological textbooks, have a non-horizontal contact to the overlying sand deposits. This non-horizontal facies contact is not associated to any change in allochtonous forcings (c.f. sea level) but is caused by both the decreasing sand supply per unit area as the lunate bar becomes larger as well as by the high clay deposition rate at the basin ward edge of the lunate bar due to the rapidly decreasing flow velocity by flow expansion. Both sand bodies of SIM A and B show a fining upwards sequence in sediment grain size as would be expected and which is also commonly observed in the field.

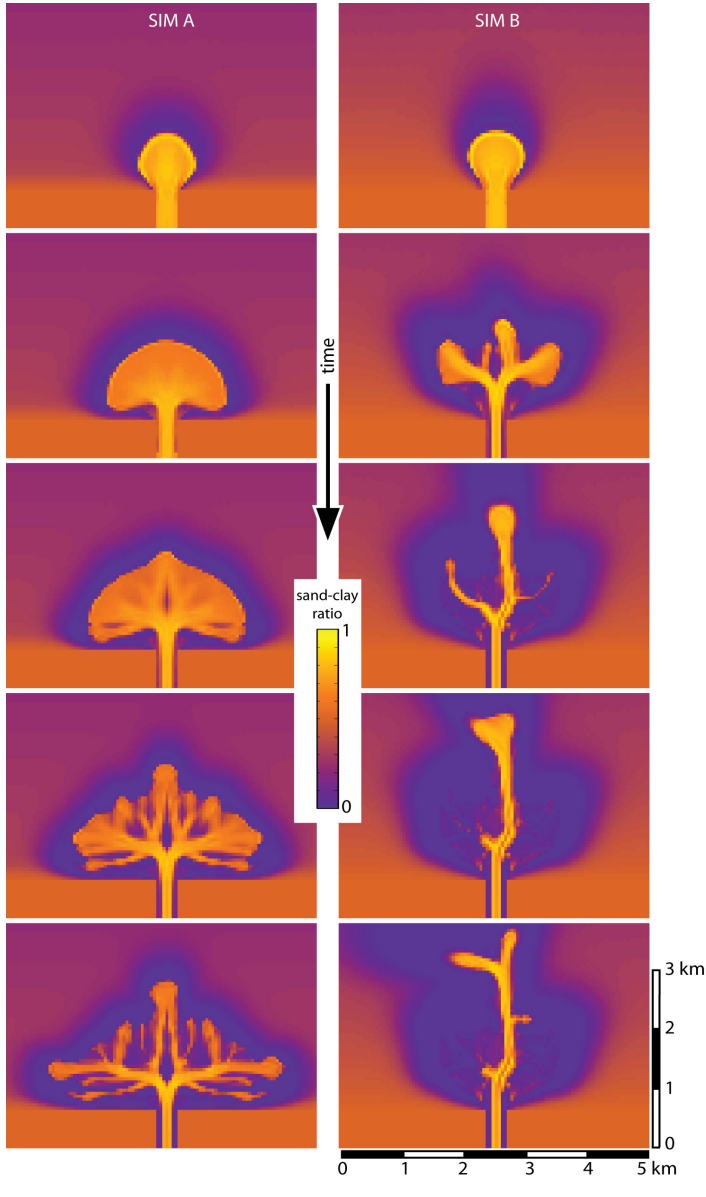

Fig. 3. Time sequence of the top view of the simulated sand-clay ratio in the upper 10 cm of the sediment bed (active layer) for SIM A (left) and SIM B (right).

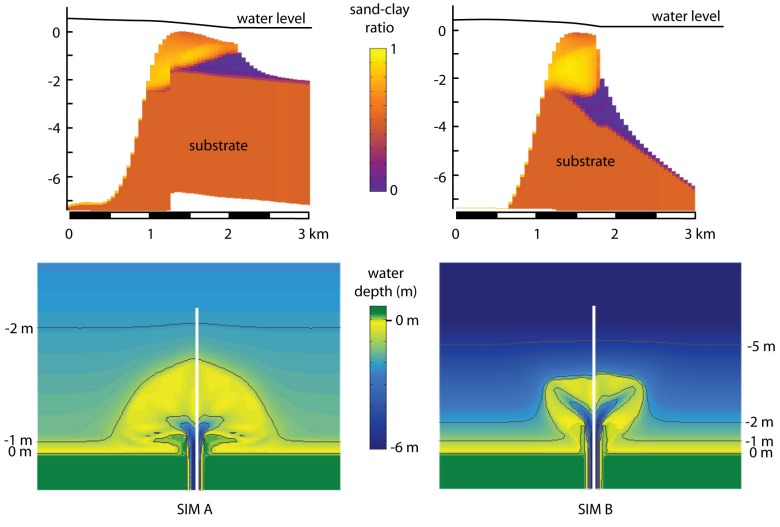

Fig. 4. Cross section (top) and top view (bottom) of the simulated initial bar development at the river effluent. SIM A (left) shows a lunate bar with a weakly developed middle ground bar. SIM B shows a weakly developed lunate bar with a distinct middle ground bar.

As the delta simulation progresses, the simulated stratigraphic record becomes increasingly complex due to the local and temporal formation of the channels and shoals. For SIM A, these channels are generally shallow and unable to erode deep into the initial stage deposits (Figure 5). Deposition through the dense channel network results in a sheet-like sand body that does allow for identification of individual channel sands. Closer to the main channels, large sections of the initial deposits have been eroded and reworked. Due to the fewer numbers of channels, SIM B shows a less complex stratigraphic record than SIM A (Figure 6). As the channels are located further apart, the interdistributary bays allow for clay deposition. Therefore, the sand bodies associated with individual channels can be recognized as the bounded by clay deposits that originate from the interdistributary areas.

In addition to the consistent sharp lower contact between the clay and sand, there is a generally more gradual upper contact between the sandy channel and bar deposits and the overlying clayey delta plain deposits (e.g. Olariu and Bhattacharya, 2006). Sand is generally best 'sorted' (c.f. the highest sand-clay ratio) in the lower portions of the sand deposits and become more mixed in the upper parts of the sand deposits. The timelines in Figure 4 and 5 show that although the sediments are generally near-horizontal deposits, the formation actually takes place as basin ward dipping clinoforms. Especially the clay deposits show the clinoforms in the timelines, which are capped by the sand deposits. This agrees well with field observations and geophysical field data of many other deltas.

The main channels that formed in SIM A have a negative channel bottom gradient. The large number of channels leads to a stepwise decrease in discharge per channel in basin ward direction. This low discharge affects the channel cross sectional area. As a result, inertia actually forces the water to flow uphill. Eventually, the large number of channels and the high flow resistance resulting from the large number of inefficient small channels, combined with the inverse gradient will lead to the dominance of one or a few main channels in time while the small channels will become abandoned. SIM B shows fewer channels than SIM A. Therefore, the decrease in discharge for the channels relative to the inflow is less obvious, making the decrease in channel size relatively small in basin ward direction.

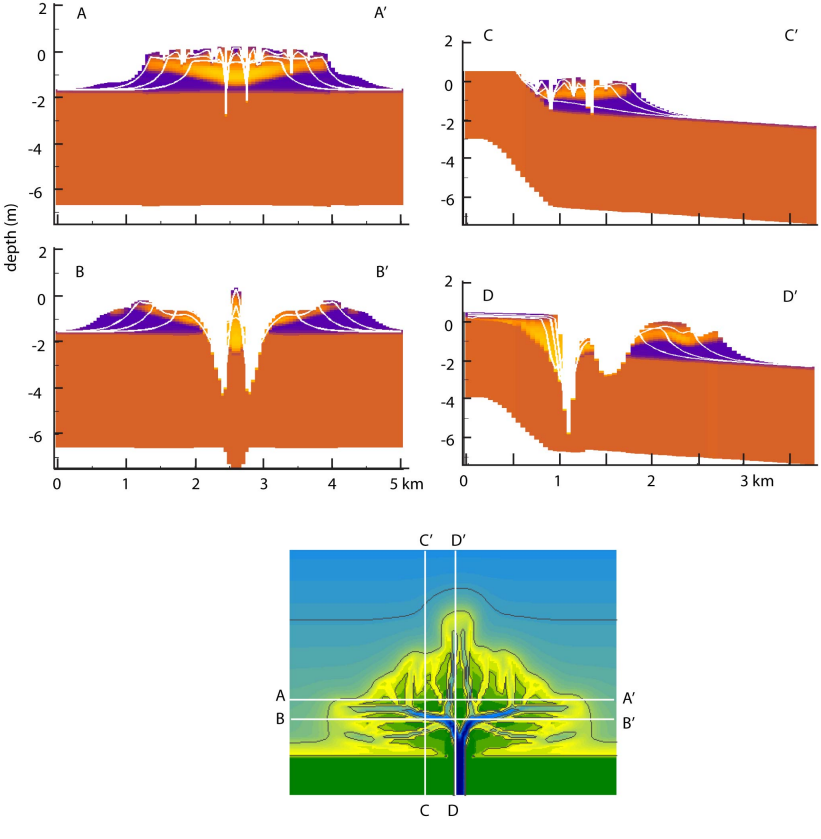

Fig. 5. Lithologic cross sections of the simulated delta deposits in the shallow basin (SIM A). The white lines are time-equivalent lines. The locations of the cross sections are indicated in the lower figure. The color bar for A, B, C and D is shown in Figure 3. The color bar of the lower figure is shown in Figure 2.

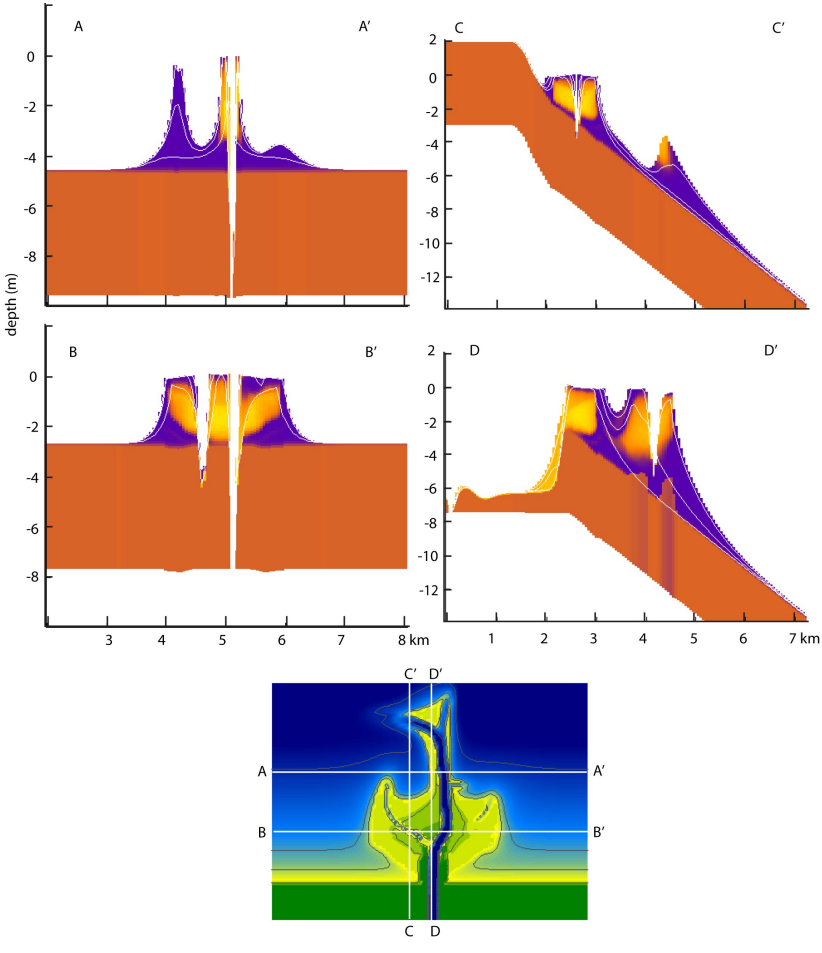

Fig. 6. Lithologic cross sections of the simulated delta deposits in the deep basin (SIM B). The white lines are time-equivalent lines. The locations of the cross sections are indicated in the lower figure. The color bar for A, B, C and D is shown in Figure 3. The color bar of the lower figure is shown in Figure 2.

DISCUSSION

A quick reality check of the simulated morphology and stratigraphy suggests that the simulations bear an interesting resemblance with both shallow basin and deep basin deltas from the real world. Although the simulations cannot be compared with any real world delta directly, the simulated morphology, stratigraphy and evolution have

similarities with bayhead deltas such as those in Atchafalaya bay. Wax delta has to some extent a comparable configuration of longitudinal shoals and channels as SIM A. However the angle at the initial bifurcation point in the model (nearly 90°) is much higher than for Wax delta. Those angles become more realistic for the downstream channel bifurcations. The lithologic cross section based on core data through Atchafalaya delta (Van Heerden and Roberts, 1988) and Wax delta (Majersky et al., 1997) shows similar lithologic boundaries as the simulated cross sections from SIM A.

One of the main difference between Wax delta and Atchafalaya delta is the width of the river effluent. To understand the effects of the width of the effluent on delta development in a shallow basin, additional simulations were ran that were comparable in setup to SIM A, but with different effluent widths. The results shows a change in morphology of the delta compared to SIM A. For SIM C and SIM D, a large number of small channels and shoals evolve, but for SIM C the flow of the main channel remains along the axis of the river effluent (Figure 7). Here, the width of the main channel prevents the development of the middle ground bar. As a result, no bifurcation occurs in the main channel downstream of the effluent. Shoals emerge predominantly along the main channel. This leads to an elongated delta morphology with shoals aligned along the channel levees. SIM D (Figure 7) has an intermediate channel width when compared to SIM A and SIM D. In contrast to SIM C, a middle ground bar develops that causes the main channel to bifurcate, similar to SIM A. However, the bifurcation angle of SIM C is much smaller than for SIM A compares well to that of Wax delta. The overall delta channel and shoal pattern has a radial pattern rather than an elongated pattern (c.f. SIM C).

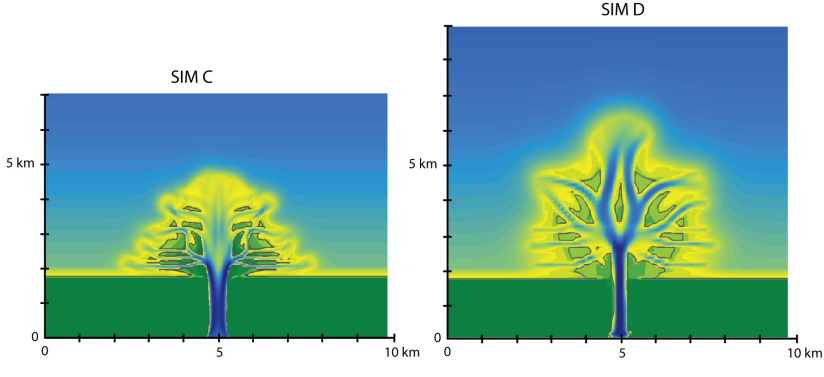

Fig. 7. Simulations of initial delta formation in a shallow basin with a wide (SIM C) initial channel and an intermediate initial channel width (SIM D). The thin black line indicates the coastline. The color bar is shown in Figure 2.

In the simulations, no floods are needed to for land to emerge, for a levee to be breached or for a middle ground bar to develop. This model behavior differs from the observations of Van Heerden and Roberts (1988) who concluded that floods are the dominating control on the initial stage of growth of the Atchafalaya delta. Also Wax delta emerged only after the big river flood of 1973 (Majersky et al., 1997). In our model case, the increase in hydraulic head over time raises the water level up to 0.5 m, which is sufficient to form land above sea level. However, a variable discharge regime with floods most likely will increase the rate at which these processes occur.

The deep-water delta (SIM B) has fewer channels and shoals and is much more elongated. It has more characteristics in common with the present-day Mississippi delta bird foot. There is one main channel that forms subaqeous levees, which are superimposed on prodelta clays in relatively deep water. These subaqeous levees prevent the channel mouth from forming a lunate bar as the flow velocity in the constrained channel remains high. Nevertheless, an elongated middle ground bar emerges which causes an inevitable bifurcation (Figure 4 and 6). As the channel progrades basin wards, the hydraulic head increases due to increase of friction leading to a local breach of a levee. This breach then opens the opportunity for the river to shorten its route thereby increasing its hydraulic gradient and a delta lobe switch has occurred.

Although the simulation results have a morphology and a stratigraphy that show a number of agreements with real-world deltas, care must be taken in its interpretation and application. Process models have many variables that must be set prior to modeling. Little experience exists in using process-based models for generic model applications such as this one and therefore the values of the model variables are not always evident. Yet they do affect the morphodynamic evolution of the delta. A rigorous sensitivity analysis should therefore be undertaken to understand the model behavior as well as the simulated delta behavior. The effect of the grid cell size, time step and morphological factor also need to be addressed for optimized time efficiency. Although the simulations shown in this paper only use two grain-size fractions, in theory it is desirable to use several, but these simulations are computationally very demanding. Also, the interplay between the grain-size classes (hiding effects and armouring for example) are not included in the model.

CONCLUSIONS

The simulations presented in this paper suggest that the smallest physically realizable scale of fluid flow and sediment transport computations can be used explain meso- and macro-scale behavior of fluvial dominated river deltas. The main mechanisms that play a role in delta evolution have been observed in the simulations (lunate and middle ground bar development, channel bifurcations, channel abandonment, channel infill, shoal formation, grain size separation). The model has no special modules for e.g. channel abandonment, it only follows rules of fluid dynamics and sediment transport. The constantly updated bathymetry leads to feedback mechanisms that results is recognizable

morphodynamic responses. As such, the numerical model approach can be very powerful in identifying which morphodynamic behavior will occur under which set of conditions.

REFERENCES

Elias, E.P.L. (2006). "Morphodynamics of Texel inlet," Ph.D. Dissertation Delft University of Technology. IOS Press. 262 p.

Leendertse, J.J. (1987). "A three-dimensional alternating direction implicit model with iterative Fouth order dissipative non-linear advection terms," Report WD-3333-NETH, Rijkswaterstaat.

Lesser, G.R., Roelvink, J.A., Van Kesteren, J.A.T.M. and Stelling, G.S. (2004). "Development and validation of a three-dimensional model," *Coastal Engineering* 51, 883-915.

Majersky, S., Roberts, H.H., Cunningham, R., Kemp, G.P., John, C.J. (1997). "Facies development in the Wax Outlet delta: present and future trends," Basin Research Institute Bulletin 7, 50-66.

Olariu, C. and Bhattacharya, J.P. (2006). "Terminal distributary channels and delta front architecture of river-dominated delta systems," *Journal of Sedimentary Research* 76, 212-233.

Roelvink, J.A. (2006). "Coastal morphodynamic evolution techniques". *Coastal Engineering* 53, 277-287.

Stelling, G.S. (1984). "On the construction of computational methods for shallow water flow problems," Rijkswaterstaat communication series No. 35, The Hague.

Van Heerden, I.L., and Roberts, H.H. (1988). "Facies development of Atchafalaya delta, Louisiana: a modern bayhead delta," *The American Associationof Petroleum Geologists Bulletin* 72(4), 439-453.

Van Rijn, L.C. (1993). "Transport of fine sands by currents and waves," *Journal of Waterway, Port, Coastal and Ocean Engineering* 119(2), 123-143.

Walstra, D.J., and Van Rijn, L.C. (2003). "Modeling of sand transport in Delft3D," Report Z3624. WL.Delft Hydraulics, Delft.

Wright, D.L. (1977). "Sediment transport and deposition at river mouths: a synthesis," *Geological Society of America Bulletin* 88, 857-868.

PHYSICAL AND NUMERICAL MODELING OF RIVER AND SEDIMENT DIVERSIONS IN THE LOWER MISSISSIPPI RIVER DELTA

Clinton S. Willson[1], Nathan Dill[2], William Barlett[2], Samantha Danchuk[2], Ryan Waldron[2]

1. Associate Professor (and corresponding author), 3513D CEBA, Department of Civil and Environmental Engineering, Louisiana State University, Baton Rouge, LA 70803; cwillson@lsu.edu
2. Graduate Research Assistants, Department of Civil and Environmental Engineering, Louisiana State University, Baton Rouge, LA 70803; ndill1@lsu.edu, samatfsu17@aol.com, wbarle1@gmail.com, rwaldr4@lsu.edu

Abstract: Over the past several thousand years the Mississippi River has formed one of the world's largest deltas. However, over the last 100 years or so this system has been deprived of most of the sediments vital for its regeneration and maintenance due to organized human interventions (e.g., levees). As a result, the natural channel shifting necessary for replenishment of the delta with fresh sediment is severely impeded. River and sediment diversions are being proposed as way to re-create the historical delivery of river water and sediments into the delta region. Two complementary tools useful for studying diversions are physical models and numerical modeling. First, we present some details and result from a distorted scale, movable bed physical model designed to provide insight into potential river and sediment diversions. We then present some approaches being taken to develop numerical models aimed at providing insight that cannot be obtained using the physical model.

INTRODUCTION

The current Mississippi River delta has been formed over the past 7,000 years (Coleman, 1988). Over the past 200 years, the delta has been deprived of most of the sediments vital for its regeneration, due to organized human interventions such as construction of the levee system for flood protection and navigation improvements. These levees impede the natural channel shift and bank overflow necessary for replenishment of sediment into the delta area. Also, the construction of many storage dams and reservoirs on rivers in the watersheds of the upper tributaries has greatly reduced the sediment load of the Mississippi River. The lost sediment totals between 150-200 million tons annually, which is almost half of the estimated load from the period of 1850 to 1963 (CREST,

2006). The reduction in sediment load in combination with the inability of the sediment to reach the deteriorating coastal wetlands is a major factor in the land loss. Over the past 50 years, coastal Louisiana has lost approximately 34 square miles of coastal wetlands on average per year (Mossa, 1995).

Coastal wetlands are very important to Louisiana's culture and economy (particularly, the petrochemical and fisheries industries) causing state authorities to recognize the necessity to reverse or, at very least, slow down the land loss processes. While impossible to save and/or restore all of the lost wetlands, reversing some of the more dramatic land loss may be possible by attempting to reinstate some of the natural flow patterns that allow the river to interact with the swamps (CREST, 2006).

One proposed method of reestablishing these flow and sediment patterns is use of river diversions (Mossa, 1995). While river diversions specifically designed to transport sediment into coastal wetlands systems are only beginning to be designed and tested, the combination of freshwater siphons and crevasses for delta splay creation have already been used successfully, suggesting that river diversions have the potential to restore wetlands (Miller 2004). A properly designed river and sediment diversion would provide a conduit into the coastal wetlands instead of into the Gulf of Mexico and off of the continental shelf. There is currently one river flow and sediment diversion operating in the lower Mississippi River delta-the West Bay Diversion. It is a sediment diversion built to directly connect the Mississippi River to the West Bay estuary in an attempt to reform a historic sub-delta and associated vegetated wetlands and aquatic habitats. If the diversion is successful, there is a possibility that it could be enlarged (Miller 2004).

Large river and sediment diversions are very complicated systems involving many design components and large amounts of data uncertainty. This makes the study and conceptual design of diversions very complicated. Options to study the potential success of diversions include field tests, numerical modeling, and physical modeling. Field tests are a very common practice used in science and engineering to develop an understanding of a process. If a similar process can be monitored in one place over a period of time, the data analysis might provide some insight into what might occur at a different, but similar location. Field studies, and the accompanying data collection effort, are also very important in the development and use of numerical and physical models. Another hydraulic system design tool is the numerical model. Advantages of numerical modeling include: typically inexpensive compared to field studies; it is easy to change system parameters; the ability to simulate realistic and/or ideal conditions; and the exploration of unnatural events. Among the drawbacks of computational modeling are discretization error (intrinsic to all), input data error, initial and boundary condition error, and modeling error. Physical modeling is often also used for the design of hydraulic systems. One of the major advantages of physical modeling is the ability to replicate complex flow situations which cannot be modeled numerically. One of the signficant limitations of physical modeling is due to scale effects. Scale effects are the "incomplete satisfaction of a full set of similitude criteria associated with a particular situation" and typically "increase in severity as the ratio of prototype to model size increases or the number of

physical properties to be replicated simultaneously increases" (Ettema et al. 2000).Oftentimes, physical and numerical models are used in a combination that accesses the strengths of each type of model.

The objective of this paper is to present complementary approaches for investigating the potential for using large-scale river flow and sediment diversions in the lower Mississippi River delta. First, an overview is presented of a distorted scale movable bed physical model which is capable of providing qualitative and semi-quantitative data on potential diversion scenarios. Next, our initial work directed at the development of numerical modeling of these diversions into coastal wetland systems is described. Finally, we provide some representative results from the SSPM experiments and demonstrate the complementary nature of the numerical modeling work.

SMALL-SCALE PHYSICAL MODEL

In 2002, the Louisiana Department of Natural Resources (LADNR), Office of the Coastal Restoration and Management, initiated and funded a project to use a small scale physical hydraulic model (SSPM) to explore the potential for using large-scale river diversions (150,000 – 500,000 cfs each) in their lower Mississippi River coastal restoration effort (DNR 2003**;** BCG et al., 2004). These large diversions are necessary to capture the spring flows; i.e, the flows which carry a large fraction of the total annual sediment load. The SSPM is currently housed in the Vincent A. Forte Coastal and River Hydraulics Laboratory (VAFCRHL) on the LSU campus.

The SSPM of the lower Mississippi river delta (Figure 1) is a distorted scale movable bed physical model with 1:12,000 horizontal and 1:500 vertical scales. Special care must be taken with distorted models to ensure that the important physics impacting the processes in the prototype are being properly replicated in the model. The important processes are determined from analysis of the problem being studied and the project objectives and then similitude theory is used to derive the appropriate non-dimensional parameters.

The SSPM originally covered 77 river miles (River Mile (RM) 59 to RM -18 (end of Southwest Pass)) and an area of about 3,526 square miles. The bathymetry and topography of the SSPM study region was collected by C&C Technologies of Lafayette, LA from various government and public sources. Each river cross-section is 600 m to the mean axis of the Mississippi River. Additional cross sections at 1200 m apart were used for Southwest Pass. In 2005, the SSPM was extended to replicate the river cross-sections up to RM 77.5 plus an additional seven miles upriver using the RM 77.5 cross-section. This extension was built to create a greater distance from the headbox to the Myrtle Grove region ensuring fully developed flow and sediment transport in the model. As constructed, the model has the capability to model three large (600K cfs) diversions, 12 small (100K -200K cfs) diversions, a slack-water navigation channel w/ two lock gates, the West Bay Sediment Diversion (50K cfs), and the Bohemia Spillway / Pointe a la Hache Relief Outlet (up to 250K cfs natural overflow to the east).

The model was designed and built according to the Froude similarity law. For free surface flow, gravitational effects dominate and hydraulic similitude can be established by equating the ratio of gravitational forces to that of inertial forces (i.e., Froude similarity). While the hydraulics are scaled based upon Froude number similarity, sufficient turbulent flow in the model produces the minimum Reynolds number required for transporting sediment particles in suspension. The size and density of the sediment material is scaled such that the material will move in the same manner for both the prototype and the model; i.e., the incipient motion and resuspension of the sediment occur in the same manner for both. Shields law was satisfied in order to properly scale incipient sediment particle entrainment. The SSPM model sediment has a density of 1050 kg/m^3 which represents coarse and fine sands. For large scale water diversion from the Mississippi River, sand transport and its deposition patterns are modeled directly by model sediment material simulating sands of particle size between 62 and 300 μm which comprise about 20% to 25% of the total sediment load transported by the Mississippi River. The deposition area of the remaining 75% to 80% of the sediment load, consisting of silts (particle size between 62 and 4μ) and clays (particles less than 4μ), are estimated using time-lapse photographs of dye patterns taken at regular intervals.

The hydraulic timescale, determined through the Froude similarity criteria is 1:537 or one year of prototype time equals a little over 16 hours of model time. The sediment time scale is based on the ratio of the times in the prototype and model to build the same feature out of sediment or to fill a certain volume with sediment. The SSPM sediment time scale was based on a similar physical modeling study performed by Sogreah for the Seine River Estuary (Sogreah, 2003). The resultant sediment time scale is 1:17,857 or one year of prototype time equals roughly 30 minutes of model time.

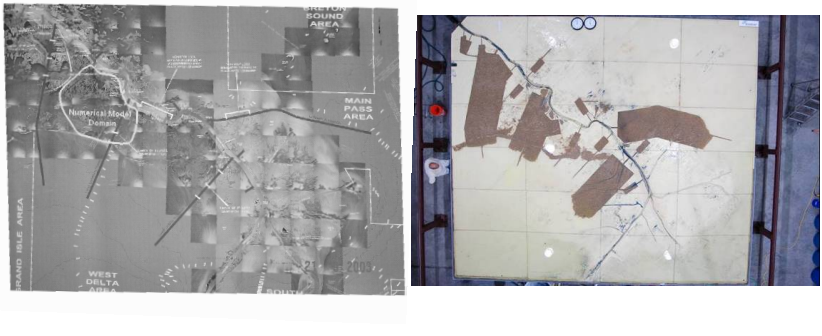

Figure 1: (left) map of the lower Mississippi River Delta; (right) overhead photo of the SSPM. Note that SSPM covers the same area as the map

A detailed discussion of the historical discharge and sediment loading conditions in the lower Mississippi River included in the model can be found in Sogreah (2003) and BCG (2004). In short, historical flowrates measured at Tarbert Landing gage from 1972-1997 were used to create an annual hydrograph. Sediment concentrations measured on a monthly basis at Belle Chase were used as the starting point for the sediment input into the model. The HEC-6 sediment transport model was used to calculate the sediment input at the upstream end of the model. Mississippi River stage data was collected from eight stations between Pointe a la Hache and Port Eads to use in the model calibration and verification.

Typical scenarios tested using the SSPM are for 50- or 100-years (i.e., 25 to 50 hours of model time). Two-year flow and sediment hydrographs are used in the experimental program. Projected subsidence and sea level rise of approximately one foot every 25 years is simulated in the model by raising sea level. The amount of sediment that flows out of Head of Passes and off the model is collected, weighed, and recorded as sediment lost to the Gulf of Mexico (GoM). If necessary, the model river is dredged in between cycles in order to maintain 48 ft navigation depth. The amount of sediment dredged is weighed and recorded. Gage readings at the 14 stationary gages within the model are recorded periodically and stage hydrographs at selected gages are measured every ten years. High-resolution overhead photos are taken every 4-6 years to document the temporal sediment deposition patterns. At various points in the experiments, fluorescent dye is injected into the model and time-lapsed photgography used to examine the flow patterns. After each scenario was finished, spatial characteristics of the deposited sediment are determined by collecting, weighing, and sieving the material based upon its spatial location.

To date, over six scenarios have been run along with a couple of replicates. The scenarios differ in the combination of "large" and "small" diversions that were used. Here, results from four tests will be presented: (1) the "Base Case" scenario where the model was run for 100 years without any diversions; (2) the "Large Diversion" scenario where one large (500,000 cfs) and two smaller (~250,000 cfs each) were open for 100 years; (3) the "Multiple Diversion" scenario where seven smaller (~200,000) channels were opened over a 28 year period with a total simulation time of 100 years; and (4) the "Eastern Slack-water Navigation" scenario where a new navigation route, controlled by a sail-through lock chamber, was opened on the east bank and two small diversion were opened on the west bank to reduce the head on the lock and divert some sediment into the wetlands.

NUMERICAL MODELING

Numerical hydrodynamic models of a hypothetical Mississippi River Diversion near Empire, LA were constructed to support the SSPM modeling effort by providing greater detail of the circulation patterns that might arise within the marsh due to the inflow from a diversion. The SSPM can provide a semi-quantitative estimate of how much sediment a particular diversion might capture over relatively long time scales while numerical

models with their greater spatial resolution can aid in understanding where the diverted water and sediment will eventually end up within the marsh. The location just above Empire, shown in Figure 1, was chosen because SSPM observations showed a relatively large amount of sediment captured by a diversion here.

Two popular hydrodynamic codes, RMA2 and ADCIRC, were chosen for the numerical models. Both are 2D finite element models that compute time dependent water surface elevation (WSE) and depth averaged current velocities within the model domain, and are supported by interfaces within the Surface Water Modeling System (SMS) software developed at the Environmental Modeling Research Laboratory at Brigham Young University in cooperation with the US Army Corp of Engineers.

RMA2 solves the depth-integrated Reynolds-averaged form of the Navier-Stokes equations for conservation of fluid mass and momentum (Donnell et al., 2005). The equations are solved by the finite element method using the Galerkin method of weighted residuals. Bottom friction can be specified using Manning n or Chezy's C, and may be calculated automatically. Eddy viscosity may be specified directly; or it may be calculated automatically varying with depth using the Peclet number, or varying with depth and velocity gradient using the Smagorinsky method. Elements may be 1D elements with trapezoidal cross-section or 2D triangles or quadrilaterals or various special elements used to represent control structures; elements must be quadratic and may have parabolic shaped sides. Wetting and drying can be simulated by a method of elemental elimination, or RMA2's marsh porosity option which allows for some flow through elements even when the WSE is below the nodal elevations of the element. This option is useful for simulating flow through wetlands where it is nearly impossible to resolve the micro-topography of sub grid scale streams and channels.

ADCIRC can be run in either a 3D or 2D depth-integrated mode. WSE is calculated by solving the continuity equation in its Generalized Wave Continuity Equation (GWCE) form (Luettich and Westerink, 2004). This formulation requires specification of a factor, TAU0, which weights the relative contributions of the primitive continuity equation and wave equation portions of the GWCE. After WSE's are found from the GWCE, velocities are computed by solving the Reynolds-averaged depth-integrated (for 2D mode) momentum equations. Bottom friction is specified with a drag coefficient which may be spatially variable or may be calculated during a simulation based on the computed depth. Eddy viscosity is specified directly and may vary spatially. Elements are linear triangles with only corner nodes. Wetting and drying can be simulated by elemental elimination.

Direct comparison of RMA2 and ADCIRC models would best be accomplished using meshes representing exactly the same geometry. For this reason the linear triangular mesh for ADCIRC was made first with the intention of simply adding mid-side nodes to make the RMA2 mesh. The mesh generation and GIS tools provided by SMS's map module were used for mesh generation for both models. First, a number of Digital Orthophoto Quarter Quadrangles (DOQQ's) covering the study area were downloaded

from www.atlas.lsu.edu in the form of MRsid files. These 2004 vintage aerial photographs were viewed in SMS and then used as a foundation on which to build the meshes. SMS allows the user to draw a feature map over the photos by clicking out a series of arcs with the mouse. The arcs are made up of a series of vertices linked together by straight lines. Arcs can be combined to form polygons which can be individually assigned a number of different properties including the type of mesh generation algorithm to be used inside that polygon. Once a feature map has been drawn, SMS is able to generate a mesh which preserves all feature vertices as nodes while also filling in the polygons with mesh.

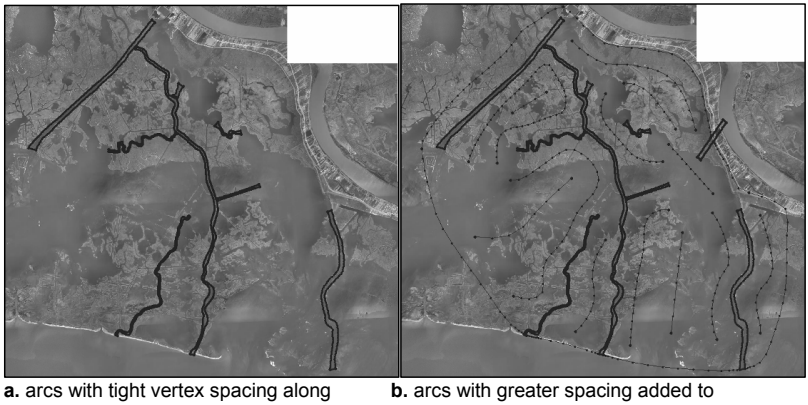

a. arcs with tight vertex spacing along channels

b. arcs with greater spacing added to stretch mesh in flatter areas.

Figure 2. Feature map drawn over DOQQs for generation of ADCIRC mesh.

Unstructured meshes have the advantage of providing higher spatial resolution in areas where it is needed and lower resolution in topographically uninteresting areas as element size can change gradually from one element to the next. For this reason arcs were drawn around some of the larger channels evident in the photographs with a minimum vertex spacing of 100 ft (Figure 2a). Once the channels were outlined in this way more arcs were drawn in the flatter areas with a maximum vertex spacing of over 3000 ft (Figure 2b). SMS's paving algorithm was then used to generate a 2D mesh which resolves the channels while increasing element size into the flatter areas with the overall goal of keeping the number of required elements as low as possible. At this point mesh quality was checked to conform with individual model geometric requirements.

Elevation data for the meshes came from two different sources. LIDAR data for land elevations were acquired from www.atlas.lsu.edu in the form of edited XYZ ASCII files. These data came from measurements made in 2002 and are also projected to the UTM zone 15 coordinate system with horizontal units of meters and vertical units of survey feet. Digital sounding data available from the National Ocean Service Hydrographic database at www.ngdc.noaa.gov were used for bathymetry. The bathymetry data were

also obtained as ASCII xyz files, but with geographic coordinates. All data sets refer to the same horizontal North American Datum 1983(NAD 83), while the LIDAR data refer to the North American Vertical Datum 1988(NAVD 88), and the Bathymetry are referenced to Mean Low Water(MLW). In order to combine the elevation data sets it is necessary to relate the geodetic datum NAVD 88 to tidal datum MLW for the area. The difference between these two data depends on the local tidal range and therefore differs at different Bench Mark locations. In this case NAVD 88 is approximately 0.5 feet lower than MLW. All data sets were converted to units of feet, translated to NAVD 88 if necessary, edited for consistency, and combined. Then the elevations of the mesh nodes were linearly interpolated from the elevation data. Once again the mesh quality was checked and the mesh was edited to smooth contours and remove steep gradients. Finally an 8500 ft long diversion channel was added to the mesh extending 1500 ft into the river.

After the mesh was geometrically complete, a discharge boundary was assigned along a string of nodes at the head of the diversion channel and WSE boundaries were assigned along areas of open water using SMS's ADCIRC interface. Figure 3 shows the resulting ADCIRC mesh containing 12,328 nodes and 24,457 elements, with color contours of the mesh elevation.

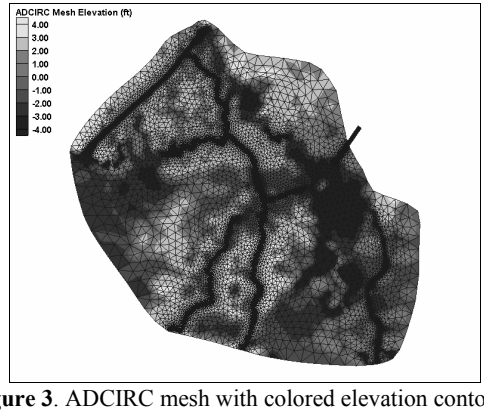

Figure 3. ADCIRC mesh with colored elevation contours.

Initially a RMA2 mesh was created by simply adding mid-side nodes to the finalized ADCIRC mesh. However this resulted in a mesh with 49,131 nodes on which simulations ran slower than real time on a 2.2 GHz Pentium 4 with 1.5 GB of RAM, making it unfeasible to use both ADCIRC and RMA2 meshes with exactly the same geometry. It was therefore necessary to create a RMA2 mesh with fewer elements which could be run with reasonable efficiency. This modification was done by going back to the feature map stage of mesh construction and increasing the vertex spacing on the feature arcs; the map used had a minimum vertex spacing of about 175 ft and maximum of over 4400 ft.

A mesh was generated from this map in the same way the ADCIRC mesh was generated. However quadrilateral elements were generated in addition to triangular elements to further reduce the number of nodes in the resulting mesh. This mesh was edited to maintain the same geometrical requirements as the ADCIRC mesh with the additional requirement that no quadrilateral element had an angle greater than 110 degrees. The nodal elevations for the RMA2 mesh were interpolated from the nodes of the ADCIRC mesh. Also nodal elevations greater than 4 ft were set to a maximum elevation of 4 ft. This was necessary because RMA2 is a "start wet" model requiring that the initial WSE for a model run be greater than the highest elevation in the mesh. In simulations where drying of elements is expected, as in this case, it in necessary to do an initial draw-down simulation to bring the WSE down from the highest nodal elevation to a more realistic elevation. Once the WSE is brought down to a realistic level, further simulations can be hotstarted from the end of the draw-down simulation. The final RMA2 mesh containing 16,070 nodes and 7173 elements (5617 triangles, 1556 quadrilaterals) is shown in Figure 4 with the colored elevation contours

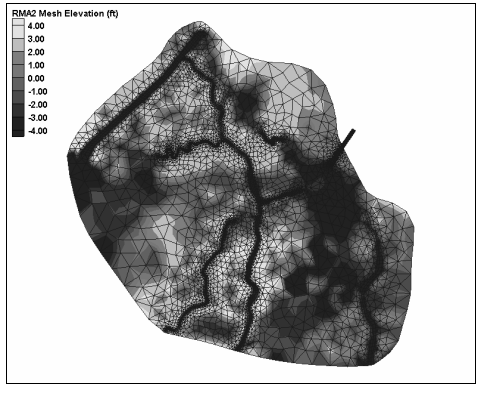

Figure 4. RMA2 mesh with colored elevation contours

Although it was possible to achieve the exact same diversion channel geometry (with rectangular elements), the necessary coarsening of the mesh for creating efficient RMA2 model resulted in the inability to represent all of the channels in the mesh with three elements across as was the case in the ADCIRC mesh.

RESULTS

SSPM Results

The SSPM has been used to simulate a number of potential lower Mississippi River flow and sediment diversion scenarios. One of the major issues in the lower river is the amount of material that must be dredged to maintain navigation. As can be seen from Table 1, the quantity of sediment dredged in the "Large Diversion" scenarios was almost an order-of-magnitude less than the "Base Case" and significantly less than the other

scenarios. The large reduction in the dredging costs could help offset the costs of building and maintaining these diversion structures. While the quantity of sediment dredged in the "Multiple Diversion" scenario seems large, it should be pointed out that a significant amount of the dredging, nearly 33%, occurred in the local vicinity of the diversions. Because the sediment deposition occurs farther upstream than in the "Base Case" scenario and close to the diversions, it could be more feasible to transport this dredged sediment into the wetlands. Additional results including high-resolution photographs depicting sediment distributions, results from dye tests, and other data can be found in BCG (2004).

Table 1: Representative Results from Several SSPM Scenarios. (quantities in parentheses are the percent of injected sediment)

Experiment	Duration [years]	Sediment Injected [Mtons]	Sediment Lost to GoM [Mtons]	Sediment Dredged [Mtons]	Sediment Deposited [Mtons]
Base Case	100	2000	106.9 (5.3%)	1344.1 (67.2%)	549 (27.5%)
Large Diversion	100	2000	400 (20.0%)	192 (9.6%)	1408 (70.4%)
Large Diversion (replicate)	50	1000	93.4 (9.3%)	63.0 (6.3%)	843.6 (84.4%)
Multiple Diversion	100	2000	74.4 (3.7%)	1115.7 (55.8%)	809.9 (40.5%)
Hang A Left	50	1000	64.0 (6.4%)	430.1 (43.0%)	505.9 (50.6%)

Numerical Simulations

A number of simulations were run with varying discharge into the diversion channel to see how the WSE at the head of the diversion channel would be affected at different flows, and conversely how much discharge could be expected for a given river stage and gulf sea level. Simulations for both models were run with steady inflow boundary conditions at the diversion channel and constant 1 ft WSE (very close to MSL in the NAVD88 datum) at the Gulf boundaries. These simulations were run until the velocity field and WSE gradient across the domain remained steady and are made to represent potential steady-state conditions for the hypothetical diversion. For both models the bottom friction parameters were set so that the bottom friction would be calculated as a function of the depth. Although RMA2 and ADCIRC used different formulations for varying bottom friction with depth, the parameters in each model were set so that this behavior would be nearly the same for both models. Similar values of spatially constant eddy viscosity were used for both models, 40 lb-s/ft^2 for RMA2 and 20 ft^2/s for ADCIRC. Wetting and drying in ADCIRC was accomplished using elemental elimination, while the marsh porosity option was used with RMA2.

The results for the stage in the diversion channel produced by 7 different values for inflow discharge between 50,000 cfs and 200,000 cfs is shown in Figure 5.

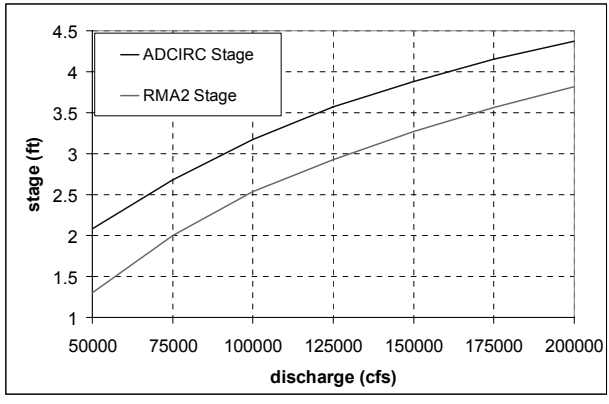

Figure 5. Rating curves for diversion channel for both RMA2 and ADCIRC models.

Overall the ADCIRC model results show a higher WSE in the diversion channel when compared to RMA2. This difference is like due to how wetting and drying is handled within the two models. ADCIRC's elemental elimination limits the flow to only the wet elements thus providing a greater restriction as water flows through the marsh land. RMA2's marsh porosity on the other hand allows for fraction of flow through the dry elements and does not channelize the flow through the marsh as much as ADCIRC.

Two additional simulations were run using a constant discharge of 150,000 cfs over a flat mesh with the elevation set 0.2 ft below the WSE boundary. These simulations were designed to more closely resemble the flat marsh area on the SSPM. After the currents were computed, a particle tracking model was run using the resulting steady-state velocity field to draw streamlines. The particles were initially placed across the diversion channel at points of equal fractional discharge so that the resulting space between any two streamlines represents approximately 0.5% of the total discharge. The particle tracking model was also run for the 150,000 cfs diversion cases where the topography was considered. The comparisons of the streamlines in Figure 6 illustrates the benefit of using numerical models for examining more detailed flow patterns within marsh area that cannot be modeled with the SSPM.

Future simulations which consider time varying river and gulf stage levels could be run using the above curve to assign a time varying inflow discharge based on records of Mississippi River stage for the area.

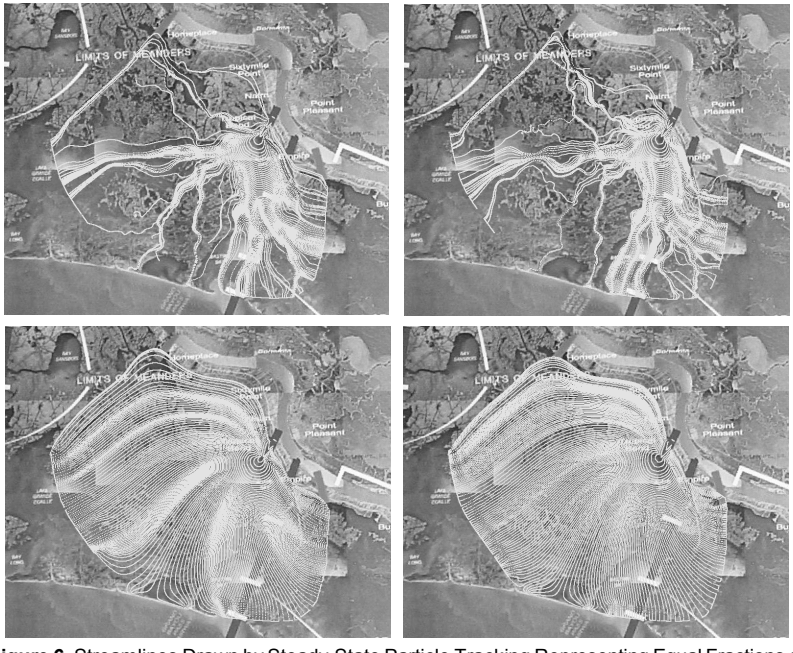

Figure 6. Streamlines Drawn by Steady-State Particle Tracking Representing Equal Fractions of Total Inflow, Steady 150,000 cfs diversion. Upper Left: RMA2 with topography; Upper Right: ADCIRC with topography; Lower Left: RMA2 with flat mesh; Upper Right: ADCIRC with flat mesh.

CONCLUSIONS

There are two main advantages of using the SSPM to study the potential for using large-scale diversions for reintroduction of flow and sediment into coastal wetland systems. The first is that visualization of sedimentation processes along the Mississippi River, through the selected diversion channels and into the wetlands enhances the general understanding of the project impacts on various relevant aspects of concern to the public and State and Federal Agencies. The second advantage is due to the model sedimentation time scale. Since the model is able to reproduce one year's evolution in 30 minutes, it can reproduce relatively long-term sedimentation processes within a few hours of testing time (e.g., 100 years of sedimentation processes in 50 hours of testing). Thus, the model helps to assess and compare the performance of project concepts, possibilities for their improvement, and makes site selection decision-making easier and decisive.

While the SSPM can be used to qualitatively, and semi-quantitatively, examine sediment deposition as a result of large-scale diversions, limitations due to the geometric scaling and distortion limit the insight and conclusions that can be reached. This is why we have begun to use numerical modeling to complement the physical modeling. While the numerical modeling is limited to smaller spatial domains and much shorter study times,

the results provide much needed insight into the role of topography on the flow, and ultimately deposition, patterns of the diverted water and on the potential for depositing finer sediment into the coastal wetlands.

ACKNOWLEDGEMENTS

The SSPM was funded by the Louisiana Department of Natural Resources (LA DNR). The LSU Vincent A. Forte Coastal and River Hydraulics Laboratory (VAFCRHL) was built with funding from the LSU College of Engineering. The physical modeling research is being funded by LA DNR with additional support from the Coastal Restoration and Enhancement through Science and Technology (CREST) program. The numerical modeling work is also supported by LA DNR and the Louisiana Board of Regents NSF EPSCOR Pfund Program.

REFERENCES

Brown, Cunningham, and Gannuch (BCG) Engineering Consultants, (2004) "Report of the Feasibility of Small Scale Physical Model of the Lower Mississippi River Delta for the Testing Water and Sediment Diversion Projects." State of Louisiana Department of Natural Resources DNR. Contract No. 2503-03-04. Dec. 2004.

Coleman, J.M. (1988). Dynamic changes and processes in the Mississippi River Delta. *Geological Society of America Bulletin*. 100, 999-1015.

CREST, (2006). On Reintroducing Riverine Processes in the Mississippi Delta Region, http://www.gulfcrest.org/docs/Diversions%20meeting%20report.doc, 20pp.

Donnell, B.P., Letter, J.V., McAnally, W. H., and others, (2005) "Users Guide for RMA2 Version 4.5," [http://chl.wes.army.mil/software/tabs/docs.htp].

Ettema, R., Arnd, R., Roberts, P., Wahl, T., (2000) "Hydraulic Modeling: Concepts and Practice", ASCE Publications, Reston, Va.

Sogreah, (2003). "Small-Scale Physical Model of the Mississippi Delta", Report No. 345044 submitted to Louisiana Department of Natural Resources, 47 pp.

Luettich, R., and Westerink, J. (2004). "Formulation and Numerical Implementation of the 2D/3D ADCIRC Finite Element Model." Available at http://www.adcirc.org/adcirc_theory_2004_12_08.pdf

Maynord, S. (2006). " Evaluation of the Micromodel: An Extremely Small-Scale Movable Bed Model." *Journal of Hydraulic Engineering* 132:4(343).

Miller, G. (2004). "Mississippi River – West Bay Sediment Diversion." *Critical Transitions in Water and Environmental Resources Management – proceedings from the 2004 World Water and Environmental Resources Congress: June 27 – July 1, 2004, Salt Lake City, UT*, ASCE, Reston, Va.

Mossa, J. (1996). :Sediment dynamics of the lowermost Mississippi River." *Engineering Geology* 45, 457-479.

A GEOMORPHIC PROCESS-RESPONSE MODEL FOR CHENIER-PLAIN EVOLUTION IN SOUTHWESTERN LOUISIANA, USA

Randolph A. McBride[1], Matthew J. Taylor[2], and Mark R. Byrnes[3]

1. Geology and Earth Science Program, Department of Environmental Science and Policy, George Mason University, Fairfax, VA 22030, USA. rmcbride@gmu.edu.
2. Department of Geography, University of Denver, Denver, CO 80208, USA. mtaylor7@du.edu.
3. Applied Coastal Research and Engineering, Inc., 766 Falmouth Road, Suite A-1, Mashpee, MA 02649, USA. mbyrnes@appliedcoastal.com.

Abstract: Coastal morphodynamics are evaluated to develop a more-advanced geomorphic model for chenier-plain evolution in southwestern Louisiana. Most ridges on the chenier plain represent open-Gulf paleoshorelines. Past movement trends of individual shorelines allow ridges to be further classified as transgressive, regressive, or laterally accreted. As such, a geomorphic hierarchy of landforms is refined relative to dominant coastal process. To understand long-term evolution of the chenier plain, modern tidal-inlet processes operating at Sabine Pass, Calcasieu Pass, and the Mermentau River mouth are examined relative to the inlet-stability ratio; historical shoreline-change data are used to document trends in shoreline behavior; and air-photo interpretation and topographic profiles are used to address form/process relationships of primary landforms. These datasets and others indicate that the geologic evolution of the chenier plain is more complicated than just channel avulsions of the Mississippi River and downstream delta switching. A six-stage geomorphic process-response model is presented that synthesizes chenier-plain evolution primarily as a function of: 1) the balance between sediment supply and energy dissipation, 2) local sediment reworking and lateral transport, and 3) tidal-entrance dynamics.

INTRODUCTION

The chenier plain of southwestern Louisiana, located west and downdrift of the Mississippi River deltaic plain, extends from Southwest Pass at Vermilion Bay westward almost 200 km to the Sabine River at the Texas/Louisiana border (Fig. 1).

To the west, the chenier plain merges with the barrier-island system of the Texas Gulf Coast. The chenier plain is a late-Holocene, marginal-deltaic environment, up to 30 km wide and is primarily a mud-dominated environment capped by marsh and interspersed with thin sand- and shell-rich ridges known as cheniers.

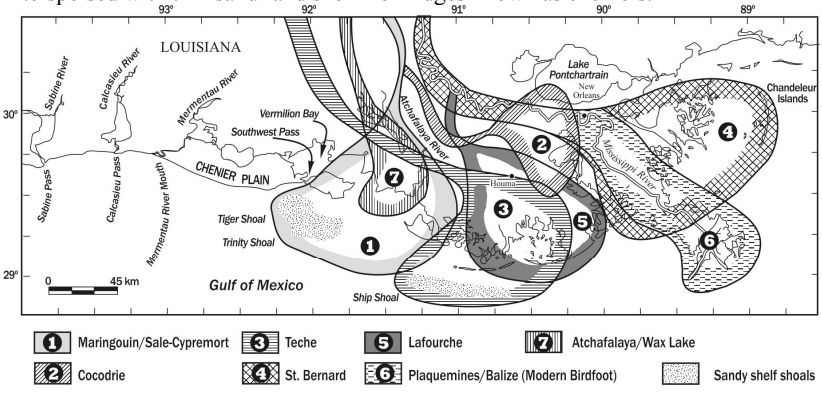

Fig. 1. Study area showing the delta plain of southeastern Louisiana and the chenier plain of southwestern Louisiana. The Mississippi River delta plain is composed of Holocene delta complexes that are illustrated chronologically from oldest (Maringouin/Sale-Cypremort) to youngest (Atchafalaya/Wax Lake) [modified from Frazier (1967), Coleman (1988), and Roberts (1997)].

Although many studies had discussed the geologic and geomorphic development of the chenier plain (Russell and Howe 1935; Howe et al. 1935; Fisk 1948; Gould and McFarlan 1959; Byrne et al. 1959), Hoyt (1969) presented the first detailed depositional model for chenier genesis and mudflat progradation (Fig. 2). According to Hoyt's (1969) model, chenier-plain development reflects changes in Mississippi River flow direction that are caused by channel avulsion, which results in downstream delta switching along the coast (Fig. 1). Channel avulsions of the Mississippi River occur approximately every 1000 to 1500 years (Coleman 1988; Roberts 1997). As the distributary mouth progrades into the Gulf of Mexico, the river course slowly lengthens and progressively becomes hydraulically unstable. To achieve hydraulic efficiency, the Mississippi River seeks a shorter, steeper course to the ocean (i.e., base level) and avulses on a semi-regular interval, resulting in delta switching (Fig. 3).

Hoyt's model is based solely on the delta-switching process. Hoyt correlates mudflat progradation with periods of Mississippi River discharge to the west (Figs. 2 and 3). When the river becomes hydraulically unstable and avulses eastward, fine-grained sediment supply to the chenier plain is reduced significantly, enabling wave reworking and erosion of mudflats, resulting in a transgressive ridge. Mudflat advance recurs when the Mississippi River avulses westward, completing chenier genesis (Fig. 2). Hoyt's hypothesis that the changing position of the Mississippi River is important to overall chenier-plain development is valid, but because it incorporates

only regressive mudflats and transgressive cheniers—omitting ridges created by other means—his model oversimplifies chenier-plain evolution in southwestern Louisiana (McBride et al., in press).

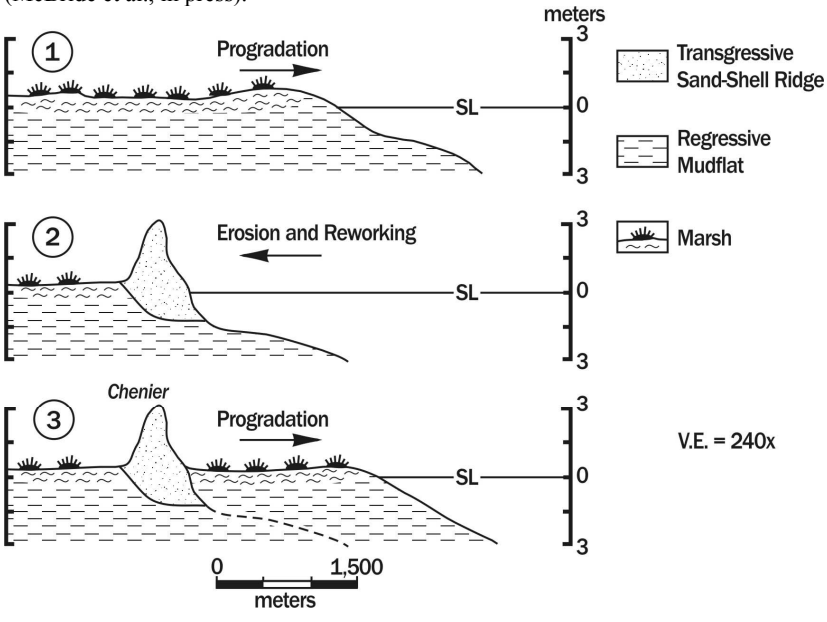

Fig. 2. Depositional model illustrating chenier-plain development through mudflat progradation (1), wave erosion and reworking to create a transgressive ridge (2), followed by mudflat progradation, which completes chenier genesis (3) [modified from Hoyt (1969)]. SL = sea level.

Thus, the purpose of this paper is to provide a more comprehensive understanding and explanation of chenier-plain evolution by examining the geomorphic development of the Louisiana chenier plain relative to regional and local coastal processes.

REGIONAL SETTING

Coastal Louisiana, which consists entirely of Holocene sediments deposited directly or indirectly by the Mississippi River, is divided into two primary geomorphic zones: the deltaic plain of southeastern Louisiana and the chenier plain of southwestern Louisiana (Figure 1) (see Fisk 1944; Gould and McFarlan 1959; Roberts 1997). Distinct ridges, most of which are former open-Gulf shorelines, are interspersed in the mud-dominated chenier plain. Ridges typically are oriented shore-parallel to subparallel, are 10 to 90 km long and < 1 to 5 m thick, and are < 1 km wide. Ridge relief ranges from 0 to 4 m above mean sea level (MSL). The shoreline is classified as a low-energy, microtidal (0.6 to 0.8 m), storm-dominated coast that experiences episodic sediment supply from the Mississippi River (Wells and Roberts 1981;

Byrnes et al. 1995). Net longshore sediment transport is to the west, in response to wind and waves that are predominantly from the southeast (Beall 1968; Becker 1972; USACE 1974; Crout and Hamiter 1981; NOAA 1985b; Hubbertz and Brooks 1989).

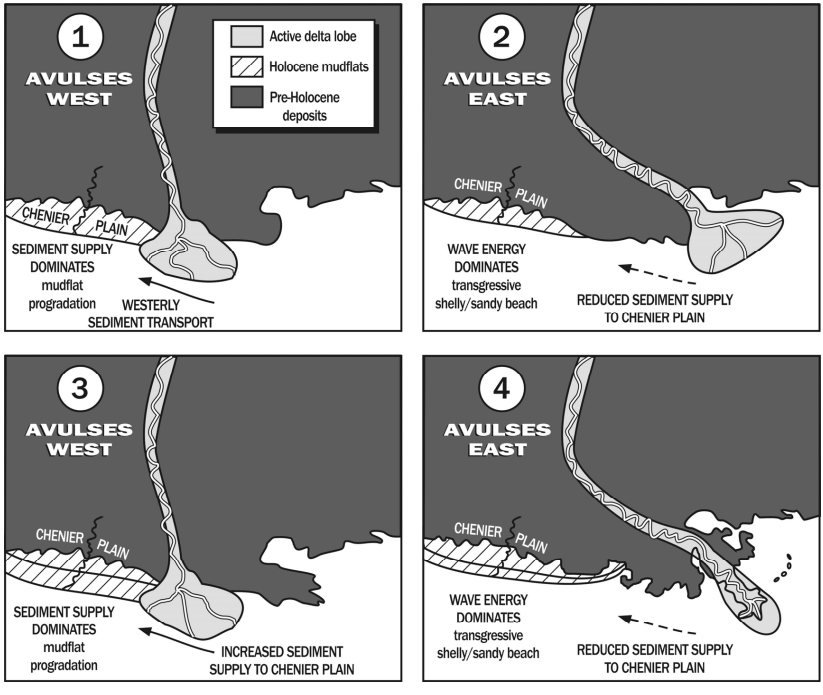

Fig. 3. Geologic model illustrating chenier-plain evolution in response to channel avulsions of the Mississippi River and the resultant downstream delta-switching process along the coast (from McBride et al., in press).

DATASETS AND METHODS

Investigation of the Louisiana chenier plain and construction of the geomorphic process-response model are based on the following data and methods: 28 topographic profiles, 104 sediment samples, and air-photo interpretation and geomorphic base-map construction (Taylor et al. 1995; Taylor 1996; Taylor et al. 1996; McBride et al., in press), historical shoreline-change data from 1883 to 1994 (Byrnes et al. 1995; McBride and Byrnes 1995), ground penetrating radar (GPS) reflection profiles (Zenero et al. 1995), and paleoecological analysis of molluscan assemblages (Anderson et al. 1998).

LANDFORM DEFINITIONS AND GEOMORPHIC HIERARCHY

In this paper we use the term "ridge" simply as a morphologic term for a narrow, linear or curvilinear topographic high (< 4.25 m elevation) that consists of sand and

shelly material accumulated by waves and other physical coastal processes. Under this definition, most ridges in the chenier plain represent relict shorelines. On the basis of past movement trends of individual shorelines, ridges can be further classified as transgressive, regressive, or laterally accreted. As McBride et al. (in press) discussed, transgressive, regressive, and laterally accreted ridges are topographic features that were created through landward, seaward, and lateral movement of the shoreline, respectively. A transgressive ridge that is surrounded by littoral mud deposits also is known as a chenier, a regressive ridge is known as a beach ridge, and a laterally accreted ridge is known as a spit or a recurved spit.

Furthermore, geomorphic zones that contain two or more regressive, transgressive, or laterally accreted ridges are termed *complexes*. A beach-ridge complex contains two or more parallel to subparallel, regressive ridges, and is net progradational, without extensive fine-grained interridge deposits. A chenier complex contains two or more parallel to subparallel, transgressive ridges that are separated by regressive, littoral mudflats (muddy units) and is net progradational. A spit complex contains two or more laterally accreted ridges that primarily have prograded laterally along the downdrift ends of ridges.

On the basis of these definitions, McBride et al. (in press) refined a geomorphic hierarchy of landforms relative to dominant process for the Louisiana chenier plain (Table 1). They defined a chenier plain as a first-order feature (5000 km^2) and as a marginal-deltaic environment because of its genetic link to the Mississippi River. The chenier plain is composed of three smaller, second-order features (30 to 300 km^2): chenier complex, beach-ridge complex, and spit complex. Individual ridges of each complex type are further separated into third-order features: chenier, beach ridge, and spit.

COASTAL MORPHODYNAMICS AND CHENIER-PLAIN EVOLUTION

Understanding the long-term evolution of a coastal depositional system requires recognizing the primary process-response mechanisms and trends along the modern coast. Present-day coastal processes operating along the outer shoreline of the chenier plain are central to providing a new perspective in the development of a more-advanced geomorphic model for chenier-plain evolution, and are synthesized below.

Tidal-Entrance Dynamics and Ridge Occurrence

Tidal prism (Ω) and the quantity of littoral sediment transport (M_{total}) are the primary factors that control inlet stability (Bruun et al. 1978). Greater discharge and/or tidal prism increase the potential for river and estuarine systems to (1) interrupt longshore sediment transport, (2) maintain and naturally stabilize tidal entrances, and (3) promote updrift deposition (Bruun 1967; Todd 1968). In classifying inlet stability, Bruun (1967) calculated an inlet-stability ratio (Ω/M_{total}) number for tidal entrances worldwide.

Table 1. Geomorphic Hierarchy and Landform Classification for the Southwestern Louisiana Chenier Plain [modified from McBride et al. (in press)]

Geomorphic Feature	Formation Process and Shoreline Movement	Order	Dimensions	References
Chenier plain	Net progradational	1	5000 km^2	Russell and Howe 1935; Howe et al. 1935; Fisk 1948; Price 1955; Gould and McFarlan 1959; Hoyt 1969; Otvos and Price 1979; Kaczorowski 1980; Kaczorowski and Gernant, 1980; Penland and Suter 1989; Taylor 1996; Taylor et al. 1996; McBride et al. in press
Chenier complex	Net progradational	2	30 to 300 km^2	Kaczorowski and Gernant, 1980; Taylor et al. 1996
Beach-ridge complex	Net progradational	2	30 to 300 km^2	Stapor 1975; Kaczorowski and Gernant, 1980; Gerdes 1982, 1985; Taylor et al. 1996
Spit complex	Lateral accretion (stationary shoreline) or net progradational	2	30 to 300 km^2	Kidson 1963; Kumar and Sanders 1974; Hine 1979; Kaczorowski and Gernant, 1980; Taylor et al. 1996
Chenier	Transgressive	3	30 to 500 m wide and up to 90 km long	Hoyt 1969; Kaczorowski 1980; Zenero et al. 1995
Beach ridge	Regressive	3	30 to 500 m wide and up to 30 km long	Stapor 1975; Kaczorowski 1980; Gerdes 1982, 1985
Spit	Lateral accretion	3	30 to 500 m wide and up to 10 km long	Evans 1942; Kidson 1963; Kumar and Sanders 1974; Kaczorowski 1980

According to Bruun et al. (1978), Ω/M_{total} is > 150 for stable inlets, between 100 and 150 for moderately stable inlets, and < 100 for unstable inlets. Unstable and moderately stable inlets will migrate laterally and are classified as wave-dominated, whereas stable inlets are much more stationary and are classified as tide-dominated (see Nummedal et al. 1977; Davis and Hayes 1984; and McBride 1999).

Table 2 summarizes river, estuary, and inlet characteristics along the chenier plain and reports the Ω/M_{total} for each tidal entrance. Tidal prism of chenier-plain estuaries increases from 0.94×10^7 to 4.10×10^7 m^3, while longshore sediment transport is about the same along the entire modern chenier-plain shoreline, at 0.62×10^5 to 1.0×10^5 m^3/yr (Bruun 1967; USACE 1971).

Table 2. Quantified Physical Processes along the Southwestern Louisiana Chenier Plain—Maximum River Discharge (Q_{max}), Suspended Sediment Discharge (SSQ), Mean Significant Wave Height (H_s), Wave Approach, Tidal Range, Tidal Prism (Ω), Quantity of Littoral Sediment Transport (M_{total}), and Inlet Stability (Ω/M_{total})[a] (from Taylor 1996)

River, Estuary, or Inlet System	Q_{max}[b] (m^3/s)	SSQ[c] (kg/yr × 10^9)	H_s[d] (m)	Wave Approach (°)	Tidal Range[e] (m)	Ω[e] ($m^3 \times 10^7$)	M_{total}[a,f] ($m^3/yr \times 10^5$)	Ω/M_{total}
Trinity (Texas)	207	0.50	1.1	135.0	0.61	21.00	NA	NA
Sabine (Louisiana)	234	0.29	1.0	157.5	0.76	4.10	0.62 to 1.0	661 to 410
Calcasieu (Louisiana)	73	0.15	1.0	157.5	0.61	3.90	0.62 to 1.0	629 to 390
Mermentau (Louisiana)	32	0.19	1.0	157.5	0.76	0.94	0.62 to 1.0	151 to 94
Atchafalaya (Louisiana)	4900	55.00	1.1	135.0	0.58	67.00	50	NA
Mississippi (Louisiana)	14,000	145.00	1.2	112.5	0.37	NA	NA	NA

[a] Bruun et al. (1978), [b] USGS (1995), [c] Mossa et al. (1993), [d] Hubbertz and Brooks (1989), [e] NOAA (1985a), [f] USACE (1971)

As McBride et al. (in press) discussed, Sabine Pass, which has good inlet stability (Ω/M_{total} = 410), has effectively interrupted longshore sediment transport, causing long-term shoreline advance immediately west and east of the inlet (Table 2). Calcasieu Pass has not always been as stable as its present channel. To the west, relict deflected channels of the Calcasieu River, e.g., Hamilton Lake and spits curving into this channel, indicate past periods of inlet instability that allowed longshore sediment transport to dominate fluvial and tidal processes. The presence of a regressive ridge complex adjacent to the present Calcasieu Pass denotes increased stability. Although present discharge of the Calcasieu River is much less than that of the Sabine River (73 vs. 234 m^3/s), tidal prism is of a similar volume and accounts for good inlet stability (Ω/M_{total} = 390) (Table 2).

Historically, the Mermentau River has been characterized as relatively unstable (Ω/M_{total} = 94). Although longshore sediment transport was not sufficient to fill the river mouth naturally, it was adequate to dominate fluvial discharge (32 m^3/s) and tidal exchange (9.4×10^6 m^3), forcing westward migration of the entrance and lateral shoreline accretion (Table 2). Thus, before human modification and stabilization efforts, the Mermentau River entrance would be classified as wave-dominated, Sabine Pass as tide-dominated, and Calcasieu Pass as tide-dominated to occasionally mixed, as discussed by McBride et al. (in press).

Geomorphic Process-Response Model of Chenier-Plain Evolution

Concentration of sand- and shell-rich deposits within the mud-dominated chenier-plain system and the overall response of ridges involve lateral variations in processes and landforms that are not explained fully by simple delta switching as it was

discussed by Russell and Howe (1935), Fisk (1948), Gould and McFarlan (1959), Hoyt (1969), and Penland and Suter (1989). As such, McBride et al. (in press) presented a more-advanced six-stage geomorphic process-response model that explains chenier-plain evolution primarily as a function of (1) the balance between sediment supply (Q_s) and energy dissipation (E), (2) local sediment reworking and lateral transport, and (3) tidal-entrance dynamics (Fig. 4).

The model begins by emphasizing the landward-most ridge trend that represents the Holocene highstand open-Gulf shoreline (Fig. 4, Stage 1). Before chenier-plain development, the open-Gulf shoreline transgressed across an exposed shelf from ~16 to ~4 kyr in response to the last post-glacial rise in eustatic sea level (see Anderson et al. 2004). Some type of transgressive barrier-beach/barrier-island system characterized the open-Gulf shoreline. As this transgressive barrier shoreline (i.e., transgressive ridge) experienced the apex of the Holocene highstand in sea level and/or an increase in sediment supply, and thus ceased its landward migration, the landward-most ridge trend (i.e., Little Chenier/Little Pecan Island paleoshoreline) was created. In Stage 1, vertically-aggraded mud deposits that were deposited landward of the highstand open-Gulf shoreline (landward-most ridge trend) represent estuarine and marsh environments, as Fisk (1948) and Penland and Suter (1989) described, but not progradational littoral mudflats, as Gould and McFarlan (1959) postulated. Past exposure to incident wave processes would cause the contact between the Pleistocene Prairie Complex and Holocene marshes to be curvilinear, not crenulated. Thus, the crenulated contact represents the Holocene bay shoreline (i.e., the leading edge of the Holocene transgression), not a Holocene open-Gulf shoreline. The difference between vertically-aggraded mud deposits laid down behind an open-Gulf shoreline and progradational littoral mudflats deposited in front of an open-Gulf shoreline is subtle, but critical.

Subsequently, the Mississippi River avulsed to a westerly position along the deltaic plain (Fig. 3), and westward-advected, fine-grained sediment was deposited in front of the landward-most ridge trend, resulting in littoral mudflat advance where $Q_s > E$ (i.e., regional processes dominate), as shown in Figure 4, Stage 1. The entire shoreline prograded extensively in response to increased sediment supply and net-westerly littoral drift. When the Mississippi River channel diverted to the east, fine-grained sediment delivery to the chenier plain was reduced, enabling wave energy to dominate ($Q_s < E$) and transgression to occur along major sections of the shoreline, thus concentrating coarser-grained material into ridges (Figs. 3 and 4, Stage 2). Suppose that two inlets also existed, an eastern one that is wave-dominated and unstable ($\Omega/M_{total} < 150$) and a western one that is tide-dominated and stable ($\Omega/M_{total} > 150$). As the shoreline eroded in some localities, creating sand- and/or shell-rich cheniers, most of the eroded sediment was transported downdrift and trapped through lateral accretion (recurved spits) at the wave-dominated inlet and through net shoreline advance (beach ridges) farther west, where inlet processes dominated longshore sediment transport at the tide-dominated inlet. A local reversal in longshore sediment transport occurred west of the tide-dominated inlet, probably in response to wave refraction around an ebb-tidal delta. As such, beach ridges were created on

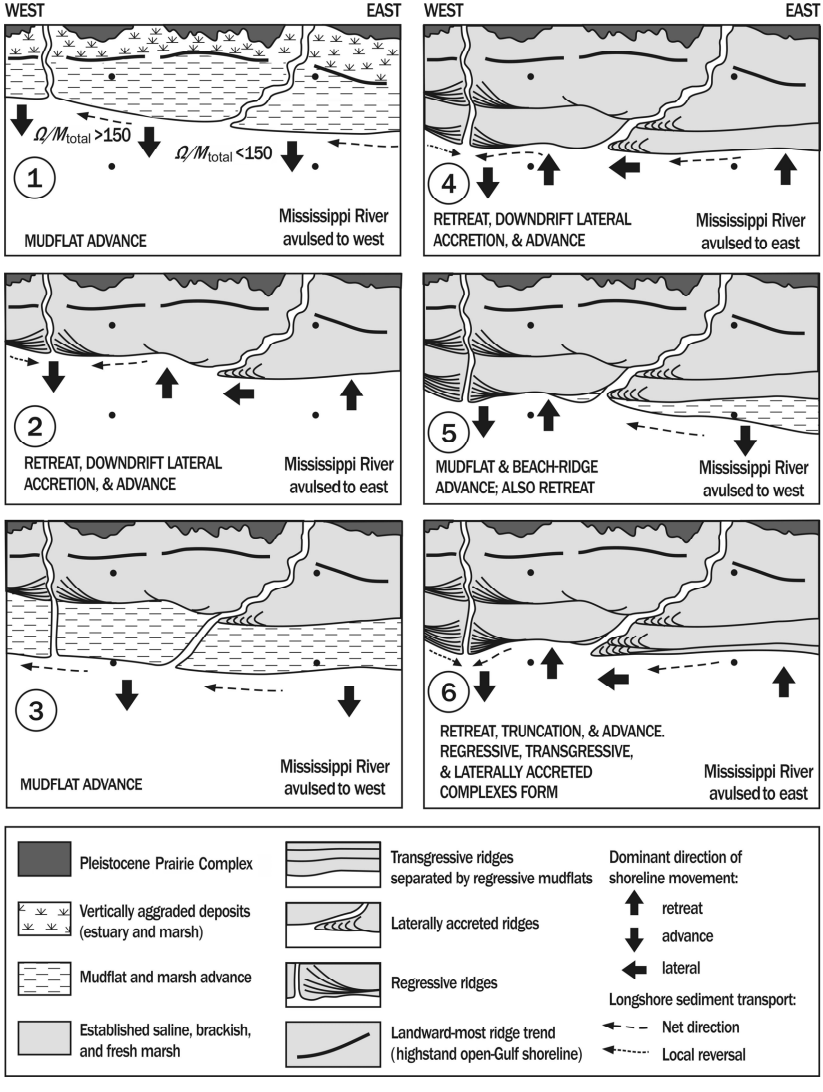

Fig. 4. Six-stage geomorphic process-response model illustrating evolution of the Louisiana chenier plain, where the geneses of three distinct ridge types (transgressive, regressive, and laterally accreted) typically occur contemporaneously along the same shoreline trend at different locations [from McBride et al. (in press)]. The four dots in each stage represent the same position through time.

either side of the tide-dominated inlet. Thus, the geneses of three distinct ridge types occurred contemporaneously along the same shoreline, but at different locations. The different locations represent local variations in shoreline behavior along the coast during periods of decreased sediment supply (i.e., local processes dominate). Moreover, coastwise zones of fresh, brackish, and saline marshes became established across the entire chenier plain in Stage 2, thus masking former environmental demarcations found in Stage 1. During Stage 3, the Mississippi River channel avulsed to the west again ($Q_s > E$), and littoral mudflats advanced seaward of the different ridge types that were formed during Stage 2 (Fig. 4).

When the Mississippi River switched back to the east (Fig. 4, Stage 4), fine-grained sediment supply was diminished, and transgressive, regressive, and laterally accreted ridges again formed contemporaneously while local processes dominated and shaped the coastal landscape, as indicated by historical shoreline-change trends (Byrnes et al. 1995). The unstable, wave-dominated inlet migrated farther west as the ridges accreted laterally with sediment from updrift erosion and ridge truncation (Fig. 4, Stage 4). The area around the stable, tide-dominated inlet advanced farther seaward.

During Stage 5, the Mississippi River occupied a more westerly position, and mudflat growth seaward of the ridges was renewed; however, fine-grained deposition did not extend along the entire chenier-plain shoreline, as it does today; rather, active mudflat advance occurred only along the eastern chenier plain (i.e., the Freshwater Bayou area). This permitted further erosion, reworking, and redistribution of ridge sediment to the west, with continued seaward advance of the shorelines adjacent to the stable inlet, as indicated by historical shoreline-change movements (Byrnes et al. 1995). During Stage 6, fine-grained sediment supply to the chenier plain was reduced again when the Mississippi River switched to the east (Fig. 4, Stage 6). Local transgression was more extensive, which allowed the active shoreline to truncate a greater number of older ridge deposits, thus releasing more trapped sediment into the littoral transport system for lateral accretion to the spit complex updrift of the unstable inlet. The regressive ridge complexes updrift of the stable inlet continued to advance seaward using sediment supplied from updrift erosion.

SUMMARY AND CONCLUSIONS

1. The Louisiana chenier plain contains not only transgressive ridges (traditional cheniers), but also regressive ridges (beach ridges) and laterally accreted ridges (spits or recurved spits). Thus, a geomorphic hierarchy of primary landforms relative to dominant coastal process is presented. "Chenier plain" is defined as a first-order feature and contains three smaller, second-order features: chenier complex, beach-ridge complex, and spit complex. Individual ridges of each complex type are further classified as third-order features: chenier, beach ridge, and spit.

2. Although the Mississippi River plays a primary role in chenier-plain development, chenier-plain evolution and ridge genesis cannot be attributed solely to channel avulsion and attendant delta switching along the southeastern Louisiana coast. Other primary depositional and erosional processes include local erosion, reworking, and

downdrift transport of sediment and the stability and sediment-trapping capability of tidal entrances. The location and level of inlet stability determine the genesis and distribution of beach ridges and recurved spits and their associated complexes. Regressive beach-ridge complexes develop at stable inlets ($\Omega/M_{total} > 150$), whereas laterally accreted spit complexes form at unstable inlets ($\Omega/M_{total} < 150$).

3. The more-advanced, six-stage geomorphic process-response model presented here synthesizes chenier-plain evolution primarily as a function of (a) the balance between sediment supply and energy dissipation in response to channel avulsions of the Mississippi River, (b) local sediment reworking and lateral transport, and (c) tidal-entrance dynamics. The geneses of three distinct ridge types (transgressive, regressive, and laterally accreted) typically occur contemporaneously along the same shoreline at different locations.

ACKNOWLEDGEMENTS

Research was funded by the U.S. Geological Survey Coastal and Marine Geology Program (cooperative agreement 14-08-0001-A0917, Byrnes and McBride co-principal investigators); the Office of Naval Research (Grants N00014-99-1-0817 and N00014-00-1-0247, McBride principal investigator); the Office of the Provost at George Mason University (Faculty Summer Research Grant to McBride); and the Louisiana Department of Natural Resources, Coastal Restoration Division. The R.J. Russell Foundation (Department of Geography and Anthropology, Louisiana State University) also funded a portion of the fieldwork for Taylor's masters thesis. Our thanks to Lisa Duvic, Feng Li, Mary Lee Eggart, Clifford P. Duplechin, and Callan Bentley for technical and cartographic assistance, and to Amanda and Victor Van Beuren of Van Beuren Publication Services and Claudia Holland for their editorial services. Mr. Guthrie Perry and employees at Rockefeller Refuge provided invaluable assistance, helicopter support, and accommodation. We also thank The Nature Conservancy for giving us permission to conduct research on Little Pecan Island. Our gratitude extends particularly to the many residents of the chenier plain for allowing us on their private property and for providing important local insight.

REFERENCES

Anderson, L.C., McBride, R.A., Taylor, M.J., and Byrnes, M.R. (1998). "Late Holocene record of community replacement preserved in time-averaged molluscan assemblages, Louisiana chenier plain," *Palaios*, 13, 488–499.

Anderson, J.B., Rodriguez, A., Abdulah, K.C., Fillon, R.H., Banfield, L.A., McKeown, H.A., and Wellner, J.S. (2004). "Late Quaternary stratigraphic evolution of the northern Gulf of Mexico margin: A synthesis," In: J.B. Anderson and R.H. Fillon (Editors), *Late Quaternary Stratigraphic Evolution of the Northern Gulf of Mexico Margin,* Special Publication No. 79, SEPM (Society of Sedimentary Geology), Tulsa, OK, 1–23.

Beall, A.O. (1968). "Sedimentary processes operative along the western Louisiana shoreline," *Journal of Sedimentary Petrology,* 38, 869–877.

Becker, R.E. (1972). "Wave Energy Studies Along the Louisiana Coast," Technical Report 12, Coastal Resources Unit, Center for Wetland Resources, Louisiana State University, Baton Rouge, LA, 22 p.

Bruun, P. (1967). "Tidal inlets on alluvial shores," In: A.A. Costonares and F.B. Phelger (Editors), *Lagunas Costeras, Un Simposio,* Universidad Nacional Autonoma de Mexico, Mexico City, 349–366.

Bruun, P., Mehta, A.J., and Johnson, I.G. (1978). *Stability of Tidal Inlets, Theory and Engineering,* Elsevier, Amsterdam, 506 p.

Byrne, J.V., LeRoy, D.O., and Riley, C.M. (1959). "The chenier plain and its stratigraphy, southwestern Louisiana," *Gulf Coast Association of Geological Societies Transactions,* 9, 237–259.

Byrnes, M.R., McBride, R.A., Tao, Q., and Duvic, L. (1995). "Historical shoreline dynamics along the chenier plain of southwestern Louisiana," *Gulf Coast Association of Geological Societies Transactions,* 45, 114–122.

Coleman, J.M. (1988). "Dynamic changes and processes in the Mississippi River delta," *Geological Society of America Bulletin,* 100, 999–1015.

Crout, R.L., and Hamiter, R.D. (1981). "Response of bottom waters on the west Louisiana shelf to transient wind events and resulting sediment transport," *Gulf Coast Association of Geological Societies Transactions,* 31, 273–278.

Davis, R.A., and Hayes, M.O. (1984). "What is a wave-dominated coast?," *Marine Geology,* 60, 313–329.

Evans, O.F. (1942). The origin of spits, bars, and related structures," *Journal of Geology,* 50, 846–865.

Fisk, H.N. (1944). "Geological Investigation of the Alluvial Valley of the Lower Mississippi River," Mississippi River Commission, U.S. Army Corps of Engineers, Vicksburg, MS, 82 p.

Fisk, H.N. (1948). "Geological Investigation of the Lower Mermentau River Basin and Adjacent Areas in Coastal Louisiana," Mississippi River Commission, U.S. Army Corps of Engineers, Vicksburg, MS, 40 p. and 26 plates.

Frazier, D.E. (1967). "Recent deltaic deposits of the Mississippi River: Their development and chronology," *Gulf Coast Association of Geological Societies Transactions,* 17, 287–311.

Gerdes, R.G. (1982). "Stratigraphy and history of development of the Caminada-Moreau beach ridge plain, southeast Louisiana," M.S. Thesis, Department of Geology, *Louisiana State University*, Baton Rouge, LA, 123 p.

Gerdes, R.G. (1985). "The Caminada-Moreau beach ridge plain," In: P.S. Penland and R. Boyd (Editors), *Transgressive Depositional Environments of the Mississippi River Delta Plain: A Guide to the Barrier Islands, Beaches, and Shoals in Louisiana.* Guidebook Series No. 3, Louisiana Geological Survey, Baton Rouge, LA, 127–140.

Gould, H.R., and McFarlan, E. (1959). "Geologic history of the chenier plain, southwestern Louisiana," *Gulf Coast Association of Geological Societies Transactions,* 9, 261–270.

Hine, A.C. (1979). "Mechanisms of berm development and resulting beach growth along a barrier spit complex," *Sedimentology,* 26, 333–351.

Howe, H.V., Russell, R.J., McGuirt, J.H., Craft, B.C., and Stephenson, M.B. (1935). "Reports on the Geology of Cameron & Vermilion Parishes," Louisiana Geological Survey Geol. Bulletin 6, Dept. of Conservation, New Orleans, 242 p.

Hoyt, J.H. (1969). "Chenier versus barrier, genetic and stratigraphic distinction," *American Association of Petroleum Geologists Bulletin,* 53, 299–306.

Hubbertz, J.M., and Brooks, R.M. (1989). Gulf of Mexico Hindcast Wave Information," Tech. Rep. WIS 18, U.S. Army Corps of Engineers Waterways Experiment Station, Coastal Engineering Research Center, Vicksburg, MS.

Kaczorowski, R.T. (1980). "The Louisiana chenier system–Some preliminary reinterpretations and refinements," *Gulf Coast Association of Geological Societies Transactions,* 30, 427–430.

Kaczorowski, R.T., and Gernant, R.E. (1980). "Stratigraphy and coastal processes of the Louisiana chenier plain and Louisiana chenier plain microfossil associations," In: *The Sedimentary Environments of the Louisiana Coastal Plain, A Field Trip Guidebook, Field Trip #4.* Gulf Coast Association of Geological Societies, Earth Enterprises, Inc., Austin, TX, 1–72.

Kidson, C. (1963). "The growth of sand and shingle spits across estuaries," *Zeitschrift fur Geomorphologie,* N.F.B, d. 7 (1-2), 177–201.

Kumar, N., and Sanders, J.E. (1974). "Inlet sequence: A vertical succession of sedimentary structures and textures created by the lateral migration of tidal inlets," *Sedimentology,* 21, 491–532.

McBride, R.A. (1999). "Spatial and temporal distribution of historical and active tidal inlets: Delmarva Peninsula and New Jersey, USA," In: N.C. Kraus and W.G. McDougal (Editors), *Coastal Sediments '99,* American Society of Civil Engineers, Reston, VA, 1505–1521.

McBride, R.A., and Byrnes, M.R. (1995). "A megascale systems approach for shoreline change analysis and coastal management along the northern Gulf of Mexico," *Gulf Coast Association of Geological Societies, Transactions*, 45, 405–414.

McBride, R.A., Taylor, M.J., and Byrnes, M.R. (in press). "Coastal morphodynamics and chenier-plain evolution in southwestern Louisiana, USA: A geomorphic model," *Geomorphology,* 28 p.

Mossa, J., Hudson, P., Wilder, M., and Lower, J. (1993). "Suspended sediment supply from large rivers entering the northern Gulf of Mexico," Technical report submitted in fulfillment of Contract No. DACA39-M-4918, U.S. Army Corps of Engineers Waterways Experiment Station, Coastal Engineering Research Center, Vicksburg, MS, 42 p. and 3 appendices.

NOAA (1985a). "National Estuarine Inventory Data Atlas," National Oceanic and Atmospheric Administration, Department of Commerce, Washington, DC, 87 p.

NOAA (1985b). "Gulf of Mexico Coastal and Ocean Zones Strategic Assessment: Data Atlas," National Oceanic and Atmospheric Administration, Department of Commerce, Washington, DC, 161 p.

Nummedal, D., Oertel, G.F., Hubbard, D.K., and Hine, A.C. (1977). "Tidal inlet variability: Cape Hatteras to Cape Canaveral," *Coastal Sediments '77,* American Society of Civil Engineers, New York, NY, 543–562.

Otvos, E.G., and Price, W.A. (1979). "Problems of chenier genesis and terminology—an overview," *Marine Geology,* 31, 251–263.

Penland, P.S., and Suter, J.R. (1989). "The geomorphology of the Mississippi River chenier plain," *Marine Geology,* 90, 231–258.

Price, W.A. (1955). "Environment and formation of the chenier plain," *Quaternaria,* 2, 75–86.

Roberts, H.H. (1997). "Dynamic changes of the Holocene Mississippi River delta plain: The delta cycle," *Journal of Coastal Research,* 13(3), 605–627.

Russell, R.J., and Howe, H.V. (1935). "Cheniers of southwestern Louisiana," *Geographical Review,* 25, 449–461.

Stapor, F.W. (1975). "Holocene beach-ridge plain development, northwest Florida," *Zeitschrift fur Geomorphologie,* Suppl.-bd., 22, 116–141.

Taylor, M.J. (1996). "Geomorphology and sedimentology of southwestern Louisiana cheniers," M.S. Thesis, Department of Geography and Anthropology, *Louisiana State University*, Baton Rouge, 133 p.

Taylor, M.J., Byrnes, M.R., and McBride, R.A. (1995). "Sediment texture and composition changes along the southwest Louisiana coast: Implications for sediment supply," *Gulf Coast Association of Geological Societies Transactions,* 45, 557–564.

Taylor, M.J., Byrnes, M.R., and McBride, R.A. (1996). "Form/process relationships and geomorphic evolution of the southwestern Louisiana chenier plain," *Gulf Coast Association of Geological Societies Transactions,* 46, 413–422.

Todd, T.W. (1968). "Dynamic diversion: Influence of longshore current-tidal flow interaction on chenier and barrier island plains," *Journal of Sedimentary Petrology,* 38, 734–746.

USACE (1971). "Survey of Holly Beach and vicinity, Louisiana," Serial No. 92, U.S. Army Corps of Engineers, Vicksburg, MS.

USACE (1974). "Mermentau River—Gulf of Mexico Navigation Channel," Draft Environmental Statement, U.S. Army Corps of Engineers, Vicksburg, MS.

USGS (1995). "Water Resources Data, Louisiana, Water Year 1995," Water-data report LA-95-1. *U.S. Geological Survey*, Reston, VA.

Wells, J.T., and Roberts, H.H. (1981). "Fluid mud dynamics and shoreline stabilization: Louisiana chenier plain," *Proceedings,* 17th International Coastal Engineering Conference, *American Society of Civil Engineers* 1382–1401.

Zenero, R.R., Seng, D.L., Byrnes, M.R., and McBride, R.A. (1995). "Geophysical techniques for evaluating the internal structure of cheniers, southwestern Louisiana," *Gulf Coast Association of Geological Societies Transactions,* 45, 611–620.

SEDIMENT ANALYSIS FOR HABITAT RESTORATION: ADAPTATION OF OPEN-COAST BEACH NOURISHMENT PRINCIPLES

Daniel J. Heilman[1], Joel T. Darnell[2], M. Cameron Perry[3]

1. HDR | Shiner Moseley and Associates, Inc., 555 N. Carancahua, Suite 1650, Corpus Christi, TX 78478, USA. daniel.heilman@hdrinc.com.
2. HDR | Shiner Moseley and Associates, Inc., 3100 South Gessner, Suite 540, Houston, TX 77063, USA. joel.darnell@hdrinc.com.
3. HDR | Shiner Moseley and Associates, Inc., 555 N. Carancahua, Suite 1650, Corpus Christi, TX 78478, USA. cameron.perry@hdrinc.com.

Abstract: Conceptually, the goals and engineering design associated with beach nourishment are very similar to those required for habitat restoration, with the primary component of both being placement of fill material. Similar analyses are required for characterization of historic geologic and environmental conditions, assessment of sediment compatibility, development of design and construction templates, application of coastal structures, and other design elements. With some modification, many of the design methodologies developed for beach nourishment can be adapted to the less-established field of wetlands restoration.

INTRODUCTION

Along the Gulf coast of the United States, estuarine environments such as intertidal wetlands and bird rookery islands have experienced significant losses over the past century. These losses have been caused by a variety of ongoing mechanisms that include accelerated subsidence, wave induced erosion, eustatic sea level rise, reduction of sediment supply, and direct anthropogenic impacts from urbanization and industry. Although traditionally valued primarily for ecological benefits, the storm-protection role of wetlands has gained attention over the past decade, especially following the active 2004 and 2005 hurricane seasons along the U.S. Gulf coast. This increased attention has led to a larger number of projects constructed along the Texas and Louisiana Gulf coasts. Site conditions coupled with rigorous success criteria for these projects pose significant challenges to designers, particularly in the shallow water and soft sediments encountered in bays and estuaries.

A key component of most restoration projects is placement of sediment as fill material. Similar to traditional open-coast beach nourishment projects, placing fill for habitat restoration requires borrow source identification, analysis of sediment compatibility, and prediction of fill performance and longevity. Although extensive guidance is available for locating and assessing sediments for beach nourishment (for example, Dean 2002), relatively little exists for habitat restoration (USACE 2000). Design items not traditionally considered for beach nourishment but typically required for habitat restoration include analysis of sediment nutrient content and sediment consolidation and settlement.

The purpose of this study is to review the components of sediment analysis required for open-coast beach nourishment and explore their application to estuarine habitat creation projects. Similarities and differences are drawn in terms of project goals, analysis and design methodology, and construction considerations. Recommendations are provided regarding design methodology for estuarine habitat creation.

DISCUSSION

Within the context of this study, "estuarine habitat creation" focuses on creation of new and/or replacement of historic wetlands and is simply referred to herein as "wetlands restoration." Unlike beach nourishment, which primarily replaces sand in eroding locations, wetlands restoration often replaces habitat at locations where wetlands may not have existed in the recent past. Typically, the overall goals of wetlands restoration are to (1) replace or create new area, (2) protect new or existing area, and/or (3) provide synergistic benefits to adjacent areas. These goals are also typical of beach nourishment, and the fundamental method of achieving these goals is placement of sediment as fill material[1]. The following discussion provides comparisons between beach nourishment and wetlands restoration in terms of these goals and associated engineering considerations.

Project Goals and Benefits

Table 1 presents a comparison of project goals between beach nourishment and wetlands restoration. Beach nourishment often includes breakwaters or other protective structures for sand retention and provides synergistic benefits through recreation, tourism, and storm-damage reduction to landward infrastructure. Similarly, wetlands restoration often includes breakwaters or other protective structures to minimize fringe recession and provides synergistic benefits through attenuation of storm surge, recreation, and ecotourism.

[1] An exception is the excavation of uplands to create wetlands, not discussed here.

Table 1. Comparison of Project Goals

	Examples	
Goal	**Beach Nourishment**	**Wetlands Restoration**
Replace or Create New Area	Create beach (sand dunes, wide berm, sand bars, feeder berm, etc.)	Create marsh complex (ponds, channels, vegetated area, mud and/or sand flats, etc.)
Protect New or Existing Area	Protect beach with breakwaters, groins, or nearshore berm.	Protect wetlands with breakwaters or reef.
Provide Synergistic Benefits to Adjacent Areas	▪ Storm protection to upland infrastructure ▪ Economic benefits (tourism, property values) ▪ Recreation ▪ Sand source for downdrift beaches	▪ Storm surge attenuation ▪ Economic benefits (ecotourism, fishing) ▪ Recreation (fishing, hunting) ▪ Compliment/expansion to overall ecosystem

Historical Site Conditions

Gathering and reviewing historical aerial photography, bathymetric and topographic data, oceanographic and meteorologic information, and other environmental data is a common step for assessment of physical conditions and geomorphic processes in coastal areas. Specific items of interest for beach nourishment design include analysis of historic shoreline and beach volume change for prediction of project longevity or long-term performance. In addition, analysis of sediment characteristics can provide an indication of historic sources and sinks for development of a sediment budget.

For wetlands restoration design, historic shoreline (or marsh edge) change is also important, although the interaction and relative contribution of wave-induced erosion, subsidence, sea level rise, interior fragmentation, and marsh accretion adds a significant degree of complexity to prediction of future change and project longevity. Analysis of sediment characteristics can provide an indication of the age of a marsh and help explain its origin (such as relic washover deposits, river deltas, tidal shoals, etc.).

A parameter that is unique to wetlands restoration design is the historical percent and geometry of open water (i.e., ponds and channels) within a marsh complex. The total percent open water may increase over time as a marsh progresses through its various stages of growth and development, fragmentation, and decay. Selecting an appropriate historical baseline condition for percent open water can be subjective and largely depends on habitat preference (such as aquatic versus avian). For example, at the Swan Lake restoration marsh in Galveston Bay, Texas approximately 35% open water was targeted to provide both intertidal and aquatic habitat (Figure 1). However, at a restoration marsh under construction by Cheniere Energy in western Louisiana near Sabine Pass, minimal open water was included at the request of the regulatory community.



Fig. 1. Construction of Swan Lake Restoration Marsh (photo courtesy of RLB Contracting, Inc., Port Lavaca, Texas)

Environmental Conditions

Analysis of waves, currents, tides, and storm surge is required for quantification of sediment transport and geomorphology of a beach fill project. These environmental conditions are also important for wetlands design, although primarily for erosion prevention and water circulation instead of geomorphology.

Sediment Compatibility

Borrow material investigations and analysis of sediment compatibility are key components of both beach nourishment and wetlands restoration. While the typical focus for beach nourishment is to locate an ample source of poorly graded (i.e., "clean") sand that resists consolidation and remains loose after placement, sediment for wetlands restoration is usually composed of cohesive material (silt or clay) that contains or attracts organic matter for plant nutrients. Assessing compatibility of beach sediments may include testing for grain size, sorting index, fines content, color, and toxicity. Although the criteria for wetlands sediments are generally less stringent, assessment of compatibility is still critical and may include testing for fines content, toxicity, and organic content. A comparison of required testing for sediment compatibility is summarized in Table 2.

Table 2. Comparison of Testing for Sediment Compatibility

Parameter	Beach Nourishment	Wetlands Restoration
Grain Size	Sieve Analysis ▪ ASTM C 136 ▪ ASTM C 117	Sieve/Hydrometer Analysis ▪ ASTM D 422
Sorting Index	Folk & Ward (1957)	Not Required
Fines Content	Sieve Analysis ▪ ASTM C 117	Sieve Analysis ▪ ASTM C 117
Toxic Content	EPA Methods 9071A, 8440, 3051, 9020B, 8260	EPA Methods 9071A, 8440, 3051, 9020B, 8260
Organic and Chemical Nutrient Content	Not Required	Various Agricultural (Soil Analysis) Testing

As documented by Finkl et al. (2006), detailed methods have been developed for locating and quantifying sand sources that meet project-specific compatibility criteria for beach nourishment. Techniques including review of geologic conditions, subbottom (seismic) profiling, jet probing, and soil borings can also be applied to borrow source investigations for wetlands restoration. Note that jet probing may have limited application where soils contain higher silt and clay content and/or turbid water limits visibility.

Unanticipated shoreline changes from wave refraction, shoaling, and/or reflection at offshore borrow pits have been documented for beach nourishment projects (Finkl 2004) and should be considered for marsh restoration. In addition to adverse shoreline change, borrow pits may cause unacceptable environmental impacts such as alteration or destruction of habitat, or anoxic conditions resulting in fish kills.

Underlying Soil Considerations

Although not typically required for placement of fill material on a sandy beach, underlying soil considerations often dictate the design approach for wetlands restoration projects. The soft soils typical of a marsh can cause fill material to be susceptible to instantaneous settlement (associated with lateral displacement of underlying soils during placement) and subsequent short- and long-term settlement associated with consolidation of underlying soils. In addition, the ability of excavated marsh soils to be mechanically sidecast and "stacked" to construct terraces or small containment levees is often critical. Determination of soil strength parameters and moisture content are therefore key elements of wetlands restoration design.

These design elements should also be considered for beach nourishment at sites where a thin veneer of sand overlies relic marsh sediments such as within the chenier plain extending along western Louisiana and eastern Texas. Without consideration of settlement, a beach fill project at such a location may require a much greater volume of sand than planned or settle to an unacceptable elevation subsequent to construction.

Fill Geometry

Extensive guidance is available for analysis and optimization of length, cross section, transition areas, and other geometry of beach fill projects. For example, equilibrium profile theory (Moore 1982) can be applied for relatively accurate prediction of the average slope of a nourished beach profile. And various numerical models such as GENESIS (Hanson and Kraus 1989) and SBEACH (Larson 1988) are available for prediction of long-term and storm-induced fill performance based on longshore and cross-shore sediment transport. These tools allow development of a design template and its associated construction template. The construction template provides the initial placement geometry and is largely based on constructability considerations. The design template is the desired target geometry of the project after prolonged exposure to waves.

The concept of design and construction templates also applies to wetlands restoration. For development of the design template, an existing reference marsh is typically selected to provide target planting bed elevations, geometry of ponds and channels, and total percent open water. As already mentioned, selection of an appropriate reference marsh for baseline conditions can be fairly subjective and is dependent upon the desired type of habitat. Other design tools include circulation modeling to assess water quality and channel stability and wave analysis to assess potential for marsh fringe erosion. Marsh fringe (or edge) is the area of a marsh immediately adjacent to open water (ponds and tidal channels) and has been recognized as a highly utilized habitat for a variety of significant fishery species (Rozas et al. 2005).

For wetlands restoration, once the design template has been developed, the construction template is determined based on sediment characteristics (of both the fill and insitu soil) and fill placement method. For hydraulic placement associated with pipeline dredging, sandier fill material can be considered for unconfined placement and the adaptation of equilibrium profile theory can be considered, depending on water depth and exposure to waves. However, silt and soft clay will generally require containment with small levees or existing adjacent marsh edge. If placed mechanically, containment is generally not required and much "steeper" side slopes can be achieved as may be desired to reduce fill volume and accommodate small ponds and channels. Mechanical placement allows greater control for constructing complex pond and channel geometry; in contrast, hydraulic placement generally requires more idealized open-water shapes. Figure 2 provides an example of hydraulic placement of dredged material to create "marsh mounds" at Delehide Cove in Galveston Bay, Texas. Note that the "ponds" and "channels" are the areas between the mounds that provide the desired open water.



Fig. 2. Delehide Cove Restoration Marsh (photo courtesy of Texas Parks and Wildlife)

Regardless of the type of fill material and placement method, higher planting bed elevations are usually specified for the construction template than the design template to accommodate settlement. Determining total settlement should consider both sediment characteristics and placement method. Although numerical methods such as the PSDDF model (Stark et al. 2005) can be applied, most were developed for traditional dredged material placement where relatively thick layers of fill are placed in confined disposal cells. Because fill material for wetlands restoration is typically only two to three feet (0.6 to 0.9 meters) thick and is often unconfined, prediction of total settlement often relies as much on experience and judgement as numerical techniques.

Protection with Structures

A common method of improving longevity of beach fill projects is construction of breakwaters, groins, reefs, and combinations thereof as sand retention and wave reduction structures. The extensive knowledge that has accumulated through application of such structures to beach nourishment can be applied for design of similar structures to protect restored (and existing) wetlands. Limiting factors in selection of structural protection in wetlands are soft soils with minimal bearing capacity, shallow water and limited construction access, and the need to maintain tidal exchange. Also, similar to application of structures on beaches, downdrift impacts associated with interruption of longshore sediment transport can be a concern. Additional impacts to adjacent wetlands or private property can occur due to wave reflection.

An example of a lesson learned from beach nourishment projects that is relevant for wetlands restoration is the return flow of water from wave overtopping at low-crested breakwaters. This process was determined to be a significant problem at the Prefabricated Erosion Prevention (P.E.P.) Reef project constructed at the Town of Palm Beach, Florida (Martin and Smith 1997). Consideration of this process may be a

particular concern for breakwaters along marsh edge. Such breakwaters are often low crested to promote water exchange during high tides. Chronic current from return flow along the leeward side of the breakwater may scour the edge of the marsh.

CONCLUSION

As coastal engineers continue to explore and establish successful techniques and develop guidelines for analysis, design, and construction of wetlands restoration, they will rely on experience gained from the more-practiced field of beach nourishment. Key principles of beach nourishment that can be applied to wetlands restoration include the following:

- Similar to helping determine historic flow pathways for a beach, analysis of historic sediment characteristics can provide an indication of the age of a marsh and help explain its origin and evolution (such as relic washover deposits, river deltas, tidal shoals, etc.).

- Assessing compatibility of beach sediments may include testing for grain size, sorting index, fines content, color, and toxicity. Although the criteria for wetlands sediments are generally less stringent, assessment of compatibility is still critical and may include testing for fines content, toxicity, organic content, and consolidation.

- Detailed methods have been developed for locating and quantifying sand sources that meet project-specific compatibility criteria for beach nourishment. Techniques including review of geologic conditions, subbottom (seismic) profiling, jet probing, and soil borings can also be applied to borrow source investigations for wetlands restoration.

- The concept of "design" and "construction" templates employed for beach nourishment design also applied to wetlands restoration and is directly related to sediment characteristics and fill placement method.

- Similar to beach nourishment, structures applied with wetlands restoration can cause downdrift erosion and other adverse impacts to adjacent areas. Limiting factors in selection of structural protection in wetlands are soft soils with minimal bearing capacity, shallow water and limited construction access, and the need to maintain tidal exchange.

ACKNOWLEDGEMENTS

The authors acknowledge and appreciate the sponsors for the various projects cited in this paper, including the Texas General Land Office, Texas Parks and Wildlife, U.S. Fish and Wildlife Service, Cheniere Energy, City of Texas City, National Oceanic and Atmospheric Administration, and the Texas Commission on Environmental Quality. The opinions expressed in this paper do not necessarily reflect those of the project sponsors.

REFERENCES

Dean, R.G. (2002). "*Beach Nourishment Theory and Practice*," Advanced Series in Ocean Engineering – Volume 18, World Scientific Publishing Co., 399 p.

Finkl, C.W., Khalil, S.M., Andrews, J., Keehn, S., and Benedet, L. (2006). "Fluvial Sand Sources for Barrier Island Restoration in Louisiana: Geotechnical Investigations in the Mississippi River," *Journal of Coastal Research*, 22(4):773-787.

Finkl, C.W. (Editor) (2004). "*Journal of Coastal Research*," Thematic Section on Impacts of Sand Mining, 20(1):1-154.

Folk, R.L., and Ward, W.C. (1957). "Brazos River Bar: A Study in the Significance of Grain Size Parameters," *Journal of Sedimentary Petrology*, 27:3-26.

Hanson, H., and Kraus, N. C. (1989). "GENESIS: Generalized model for simulating shoreline change, Report 1: Technical reference," Tech. Rep. CERC-89-19, U.S. Army Engineer Waterways Experiment Station, Coastal Engineering. Research Center, Vicksburg, MS.

Larson, M. (1988). "Quantification of Beach Profile Change," *Report No. 1008*, Department of Water Resources and Engineering, University of Lund, Sweden.

Moore, B.D. (1982). "Beach Profile Evolution in Response to Changes in Water Level and Wave Height," unpublished M.S. Thesis, University of Delaware, Newark, Delaware.

Martin, T.R., and Smith, J.B. (1997). "Analysis of the Performance of the Prefabricate Erosion Prevention (P.E.P.) Reef System, Toen of Palm Beach, Florida," CETN-II-36, U.S. Army Waterways Experiment Station, Engineer Research and Development Center, Vicksburg, MS, 8 p.

Rozas, L.P., Caldwell, P., and Minello, T.J. (2005). "The Fishery Value of Salt Marsh Restoration Projects," *Journal of Coastal Research*, Special Issue No. 40:37-50.

Stark, T.D., Choi, H., and Schroeder, P.R. (2005). "Settlement of Dredged and Contaminated Material Placement Areas I: Theory and Use of Primary Consolidation, Secondary Compression, and Desiccation of Dredged Fill," *Journal of Waterway, Port, Coastal, and Ocean Engineering*, 131(2): 43-51.

U.S. Army Corps of Engineers (2000). "Wetlands Engineering Handbook," ERDC/EL TR-WRP-RE-21, U.S. Army Waterways Experiment Station, Engineer Research and Development Center, Vicksburg, MS, misc. paginated.

SUBSURFACE EXPLORATION AND CONTAINMENT DIKE DESIGN CRITERIA FOR COASTAL LOUISIANA MARSH RESTORATION

Russ Joffrion[1], Michael Poff [2], Mitch Andrus[3]

1. Louisiana Department of Natural Resources, 617 North 3rd Street, 10th Floor, Baton Rouge, LA 70803, USA. russj@dnr.state.la.us.
2. Coastal Engineering Consultants, Inc., 3106 S. Horseshoe Drive, Naples, FL 34104, USA. mpoff@cecifl.com.
3. Coastal Engineering Consultants, Inc., 5745 Essen Lane, Suite 200, Baton Rouge, LA 70810, USA. mandrus@cecifl.com.

Abstract: Louisiana has embarked on the nation's most ambitious program to restore and protect their ecosystems, wetlands, and wildlife; provide storm protection; and support oil and gas development. Storm erosion has breached the majority of the barrier islands resulting in the development of fragmentary islands and new inlet openings. Environmentally sensitive marsh habitats have declined due to man's impact from oil and gas mining and Mother Nature's effects. One key strategy within the program is marsh restoration to stabilize the integrity of the barrier shorelines. Success criteria mandates that by Year 3 the marsh platform elevations are within the intertidal zone, defined from Mean High Water to Mean Low Water, and remain within this zone through Year 20. Critical steps in the platform design process include subsurface data collection, back-barrier sediment analyses, containment dike design, and prediction of the target platform elevation to achieve the success criteria.

INTRODUCTION

The strategies set forth in Louisiana's Coast 2050 program constitute the nation's most ambitious ecosystem restoration plan to provide storm and flood protection; enhance fisheries production; create, restore and enhance wetlands; protect wildlife resources; and support the activities of oil and gas development, navigation, and ecotourism. Hurricanes, overwash events and increased tidal prism have caused breaches along the majority of the barrier island shorelines resulting in the development of fragmentary islands and new inlet openings. Environmentally sensitive wetland and marsh habitats have declined due to man's impact from oil and gas mining, as well as Mother Nature's effects of sea level rise and storm erosion.

One of the key strategies within the program is restoration of marsh platforms to help stabilize the integrity of the barrier shorelines. The goals of the marsh restoration projects include the following:

- 20-Year project design life
- Create new back-barrier marsh at Year 1 with unrestricted tidal exchange
- Construct marsh platforms such that by Year 3 the platform elevations are within the intertidal zone, defined from Mean High Water (MHW) to Mean Low Water (MLW), and remain within this zone through Year 20
- Close breachments that have occurred due to storm and hurricane damage and prevent breaching during the design life
- Vegetate newly created marsh areas according to these criteria: approximately 25% of the marsh platform shall be 80% or greater vegetated after the first completed growing season after construction, and 100% of the marsh platform shall be vegetated after three complete growing seasons
- Construct tidal creeks and ponds to allow hydraulic exchange and circulation within newly created marshes.

Critical steps in the marsh platform design process include subsurface data collection, back-barrier sediment analyses, containment dike design, and prediction of the target marsh platform elevation to achieve the intertidal zone criteria.

PROCEDURES FOR SUBSURFACE INVESTIGATIONS

Examination of case studies and past projects has led to the establishment of subsurface investigation procedures to guide designers in developing geotechnical data acquisition programs for marsh creation projects. These procedures were developed using the Boussinesq Case for determining vertical soil stresses under embankment loadings and typical containment dike designs. The purpose of the investigations is to determine geotechnical engineering design soil parameters for geotechnical analyses. The locations of the borings shall coincide with the containment dike alignment as well as within the proposed marsh fill area. The boring data acquisition program shall be set according to the following guidelines (Table 1); however, they may vary due to site elevations, cultural constraints, and site specific knowledge of the designer (LDNR, 2005).

Table 1. Guidelines for Soil Boring Collection

Design Component	Location	Depth *	Spacing
Marsh Creation Fill Area	Open Areas per Designer	25' – 40' & (1 – 60')	1 per 50 - 100 acres (3 minimum per site)
Containment Dike	@ C.L.	30' – 60'	1 per 500' to 800'

* Depth is referenced from the mud line
C. L. denotes Centerline

Field data measurements shall include the following information specific to the borings:
- Horizontal position in state plane or latitude/longitude coordinates
- Elevation of existing grade (e.g. bay bottom) referenced to the project datum (e.g. North American Vertical Datum, 1988)
- Depth of penetration (i.e. length of boring)

Field sampling procedures recommended for back-barrier testing in cohesive and semi-cohesive soils follow ASTM D1587 and for non-cohesive soils, ASTM D1586. An appropriate sized drill rig shall be mobilized to the site and using accurate Global Positioning Equipment, the locations and elevations of each sample shall be established. The drill rig shall advance the boring to the desired depth using a three-inch diameter Shelby tube sampler (cohesive) or a split spoon sampler (non-cohesive). The sample and tube shall be extracted from the borehole and detached from the drill rig. Minimum intervals of five feet are recommended. The tubes shall be sealed in the field to protect the samples during transport as well as minimize moisture loss. Further, they are logged on chain of custody forms for transportation to the testing facility.

To ascertain the penetration resistance of the in situ sediments, standard penetration tests may be performed. A split spoon sampler shall be driven into the undisturbed sediment at the bottom of the boring with an appropriately weighted hammer having an appropriately measured stroke. The number of blows required to drive the sampler through two, 6-inch increments is recorded and serves as the measure of penetration resistance (STE, 2004).

BACK-BARRIER SEDIMENT ANALYSES

The following sediment parameters are recommended for testing to provide the necessary geotechnical engineering design criteria. Samples representative of the various sediment strata shall be classified using the Unified Soil Classification System (ASTM 2487). Classification tests shall include Atterberg Limits (ASTM D4318) for cohesive soils and sieve analyses and hydrometer tests (ASTM D422) for non-cohesive soils. Strength tests shall include the miniature vane (ASTM D4648), unconfined compression (ASTM D2166) and triaxial compression (ASTM D2850). Consolidation tests (ASTM 2435) shall be performed. Further, moisture content, organic content, and unit weights shall be determined.

CONTAINMENT DIKE DESIGN

In order to facilitate the placement of hydraulically dredged material, an earthen containment dike system should be designed capable of resisting lateral pressures and environmental effects. Utilizing the results of the back-barrier sediment testing, three geotechnical analyses should be performed to provide design criteria for the containment dike. First, due to the weight of the material, the primary consolidation settlement of the underlying soils is estimated using one-dimensional consolidation theory. Second, the self-weight consolidaton "shrinkage" of the uncompacted dike material is estimated based on soil density, moisture content, and past experience. Third, a global slope stability analysis is performed using the proposed containment dike configuration. This is done by assuming a failure surface and using both the circular arc "normal method of slices" and sliding block methodologies to evaluate the global stability of the dike. The side slopes of the dikes have two types of forces acting on them, driving forces and resisting forces, which depend on the geometry of the site. The driving forces include the soil weight and seepage forces, which can initiate sliding. The resisting forces include the soil shear strength, which opposes soil movement. The ratio of the sum of the resisting and sum of the driving forces is called the global slope stability factor of safety.

Parameters in these analyses include water depth and the initial freeboard of the dike. The freeboard equals the distance from the water surface elevation to the top of the containment dike. The total consolidation increases with increasing freeboard primarily due to the additional weight of dike material.

TARGET MARSH PLATFORM ELEVATIONS

Louisiana's Coastal Wetlands Planning, Protection, and Restoration Act (CWPPRA) designates marsh restoration projects as environmentally benefits based projects, which are funded according to the level of benefits produced versus fiscal constraints. To achieve the highest level of environmental benefits, the marsh platform shall be designed to lie within the intertidal zone, Mean Higher High Water (MHHW) to MLLW, for the significant majority of the design life. A similar analysis employed for the dike design is utilized wherein the total settlement rate, accounting for settlement due to the weight of the marsh fill over the underlying back-barrier sediments and self-weight consolidation within the fill, is predicted.

CASE STUDY

Project Setting

The Bay Joe Wise Headland is located approximately 50 miles southeast of New Orleans, Louisiana, in the Plaquemine's Parish, Coast 2050 Region 2, Barataria Basin (Figure 1). The reach proposed for restoration extends from Pass Chaland in the west to Grand Bayou Pass in the east. The barrier island fronts the Gulf of Mexico and protects the shallow interior bay, Bay Joe Wise, and adjacent wetlands and marsh (Figure 2).

Based upon historical profile characteristics and site observations, the beach and dune along the Headland are low-lying with average berm elevation of +3 to +4 feet NAVD88 and berm slope ranging from approximately 1:20 to 1:30. The dry beach width varies from 0 (non-existent) to approximately 50 feet.



Figure 1: Location Map

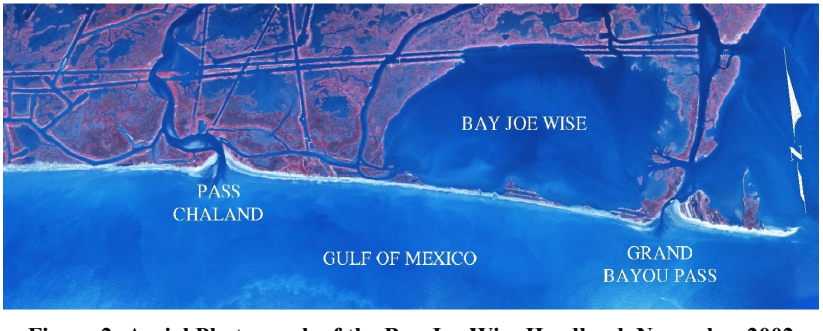

Figure 2: Aerial Photograph of the Bay Joe Wise Headland, November 2002

The offshore slope varies from approximately 1:80 to 1:130. Both Pass Chaland and Grand Bayou Pass are shallow inlets with fairly sizable ebb shoals and relatively small flood shoals. Bay Joe Wise is a shallow interior bay with average water depths of 3 to 4 feet.

The Headland has experienced significant erosion, such that, it has receded to critical width and has breached during recent storm and hurricane activity, e.g. Hurricanes Lili and Isidore in 2002, and Hurricane Katrina in 2005, whose eye passed directly over the Headland. Numerous breaches are open and water exchange is evident from bay to gulf. The marsh, wetlands, beach and dune habitats within the Project reach have undergone significant loss not only due to these extreme events and other natural processes such as sea level rise, and subsidence, but also man-influenced activities including oil and gas exploration and related canal dredging.

The Project area is one of, if not the, most rapidly disappearing areas in Louisiana, experiencing a loss rate of over 73 acres per year since 1988 (Coastal Research Laboratory (CRL), 2000). A photographic analysis was conducted to determine the acreage of land versus water, land acreage change, and breakdown of land mass into distinct habitats. In 2000, the land versus water acreage was estimated to be approximately 1,039 acres and 3,503 acres respectively. The habitat inventory estimated 769 acres of marsh, 41 acres of uplands, 200 acres of shrubs, 7 acres of inter-tidal, and 22 acres of beach. By applying the loss rate of 73 acres per year, the short–term year of disappearance was predicted to be 2014 (CRL, 2000).

Project Proposal

To address the significant land loss and natural resource habitats within this area and restore the structural integrity of the barrier island, the National Marine Fisheries Service (NMFS) and the Coastal Restoration Division of the Louisiana Department of Natural Resources (LDNR) have proposed an ecosystem restoration plan which is being funded and authorized in accordance with the provisions of the Coastal Wetlands Planning, Protection, and Restoration Act (CWPPRA) under 16 U.S.C.A., Sections 3951-3956. The Project is entitled *Pass Chaland to Grand Bayou Pass Barrier Shoreline Restoration Project* (BA-35, CWPPRA Priority Project List 11).

The Project construction proposes to construct a marsh platform approximately 1,000 feet wide contiguous with the northern side of the Gulf shoreline of Bay Joe Wise. It is estimated that approximately 2.67 million cubic yards of dredged material consisting of clays, silts and sands will be required to construct the marsh platform. Further, the construction template includes a beach and dune component to address the severity of erosion along the gulf-front shoreline and multiple breachments that have occurred due to recent storm and hurricane damage. It is estimated that approximately 1.55 million cubic yards of dredged material consisting primarily of sand will be required to construct the beach and dune component. A plan view of the proposed fill template and typical cross section are presented in Figures 3 and 4, respectively.

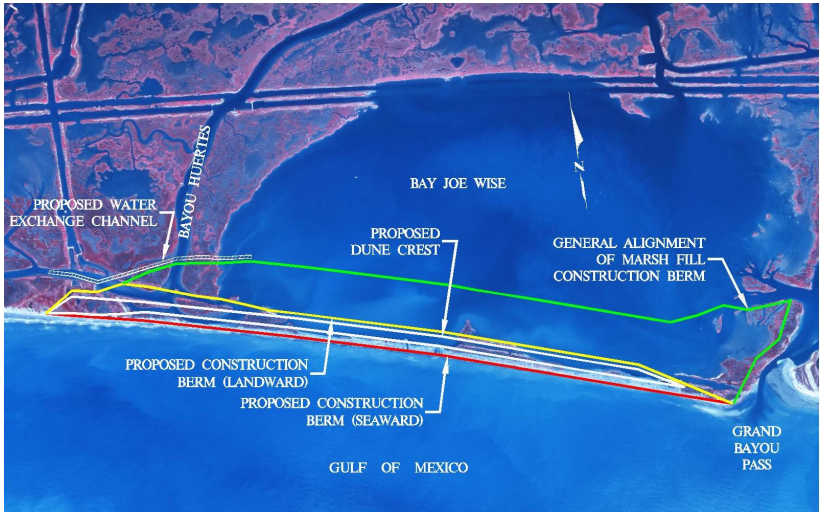

Figure 3: Plan View of Proposed Construction

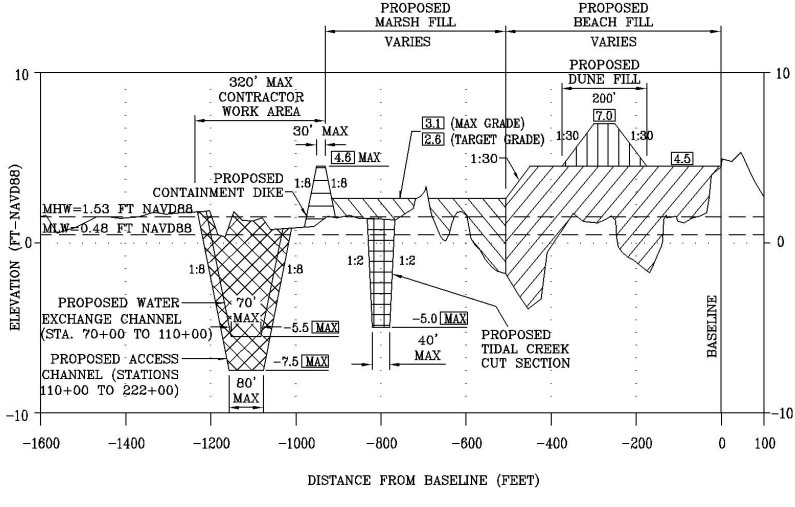

Figure 4: Cross Section View of Proposed Construction

Dike Design Parameters

Tidal Parameters

The mean lower low water (MLLW) elevation and the mean higher high water (MHHW) elevation in the Project area are 0.4 feet NAVD and 1.6 feet NAVD respectively. In order to ensure adequate stability of the dike, MHHW was used as the reference datum to determine the water depth in the fill templates, and MLLW elevation was used as the reference datum to calculate the height of the dike above the water surface, that is, the freeboard of the dike relative to the water surface.

Safety Factors

Soil Testing Engineers, Inc. (STE) (2004) determined that for the Project's geologic setting, sediment parameters and design objectives, a dike side slope of 1(V):8(H) would be needed to maintain a stable dike. Table 2 provides an excerpt from a table of the safety factors presented in STE (2004). Values of 1.3 or higher are considered safe (USACE, 1987). Figure 5 displays a graph of the stability factor data along with regression lines, regression line equations, and R^2 values of the regression. These regression results were used to interpolate the safety factor for varying freeboard heights at water depths of 4 feet and 6 feet, which are typical depths anticipated to be encountered for dike construction, assuming a crest width of 20 feet.

Table 2. Slope Stability Analysis

Initial Freeboard (ft)	Water Depth (ft)	Safety Factor for a Side Slope of 1(V):8(H)
1	4	2.6
2		2
3		1.6
4		1.4
1	6	2.3
2		1.9
3		1.6
4		1.4

Total Effective Settlement

Decreases in the fill and dike elevations are due to the total effective settlement. The total effective settlement accounts for settlement due to the weight of the fill or dike, self-weight consolidation within the fill or dike, geologic subsidence, and sea level rise. The settlement due to the weight of the fill or dike and self-weight consolidation within the fill or dike were calculated by STE (2004) based on the sediment conditions sampled and analyzed in Bay Joe Wise. Both the geologic subsidence and sea level rise occur at an approximate rate of 0.025 feet per year (SJB Group and CEC, 2005).

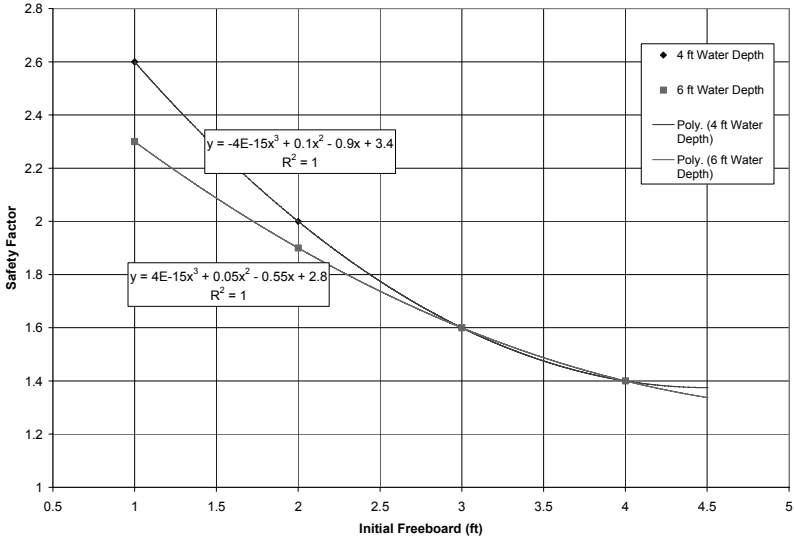

Figure 5. Slope Stability Analysis

Figure 6 depicts the relationships between initial freeboard and the estimated total effective settlement extrapolated from calculations by STE (2004) for varying time periods at the typical bay depth of 4 feet. These relationships were used to calculate the total effective settlement for varying freeboard heights and water depths and served as design criteria for determining the optimal primary dike and marsh fill elevations.

Fairly rapid settlement caused by the weight of the dike or fill and self-weight consolidation occurs over the first two years following construction. Following the initial two years, a steadier settling takes place which is dominated by the fairly constant geologic subsidence and sea level rise. Thus, the dike design life was set at two years.

Bay Joe Wise Wave Analysis

Due to the expanse of the bay, and additional analysis was conducted considering that the primary dike to contain the marsh fill will be exposed to waves from Bay Joe Wise. During the anticipated six month period that the fill is dewatering, the containment dikes must reasonably protect the fill from potentially damaging waves. An analysis of the potential wave propagation across the bay under various scenarios was performed using CEDAS-ACES Version 2.01G (Leenknecht et al., 1992). This analysis was conducted at two points on the proposed dike corresponding to the extreme eastern and western ends of the dike that will potentially be exposed to waves from the bay at points maximizing the potential fetch length.

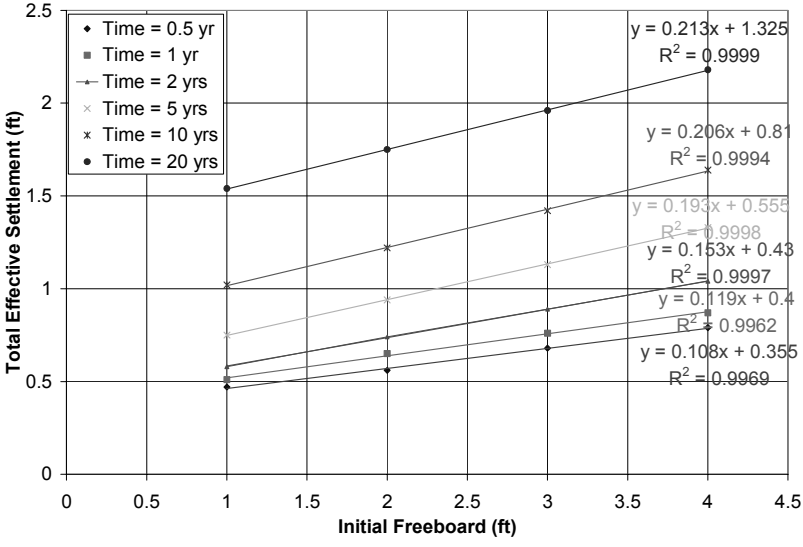

Figure 6. Total Effective Settlement vs. Initial Freeboard in 4 Feet of Water

Design wind and stage data available for the Project area (SJB Group and CEC, 2005) were used as input to the CEDAS-ACES model. Table 3 displays results of the predictive scenarios ran with CEDAS-ACES for the annual, 2-year, 3-year, 4-year, and 5-year storm scenarios.

To further evaluate the overtopping potential, an additional analysis of the wave run-up was performed in CEDAS-ACES. Given the information generated by CEDAS-ACES and the side slopes of the proposed dikes of 1(V):8(H), the maximum wave run-up was calculated to be 1.6 feet for the 2 year storm. The 2 year storm stage of 1.6 feet NAVD plus the wave run-up of 1.6 feet gives a total elevation of 3.2 feet NAVD for the design criteria.

Table 3. Predicted Wave Heights

Storm	Wave Height East (ft)	Wave Height West (ft)	Stage & Wave East (ft NAVD)	Stage & Wave West (ft NAVD)
Annual	1.1	1.1	2.7	2.7
2-Year	1.1	1.1	2.7	2.7
3-Year	1.5	0.7	4.2	3.4
4-Year	1.8	0.3	5.2	3.7
5-Year	1.9	0.1	5.9	4.1

Primary Dike

The primary dike for the marsh platform will be sited along the northern boundary of the marsh fill template. The general native soil elevation along this boundary is -3 feet NAVD or shallower. In order to maintain a conservative estimate of material that may be needed to construct this dike, the design toe elevation of -3 feet NAVD shall be used.

Using the total effective settlement relationships with freeboard and water depth, a trial and error analysis was performed to determine the design dike elevation, 4.5 feet NAVD, which meets and exceeds the 2-year design criteria. Figure 7 depicts the results of the analysis. The initial freeboard of the dike equals 4.1 feet, which has a safety factor of approximately 1.4. The figure shows the total effective settlement for six different water depths. These six scenarios range from the dike constructed on dry ground, that is, 0 feet of water, to the dike constructed in 10 feet of water. The total effective settlement increases for increasing water depth primarily due to the weight of the extra material required to reach the water surface. MHHW and MLLW are denoted on the figure for evaluation of the scenarios. In sections where the dike elevation is above MHHW, the surface of the dike will rarely become inundated with water.

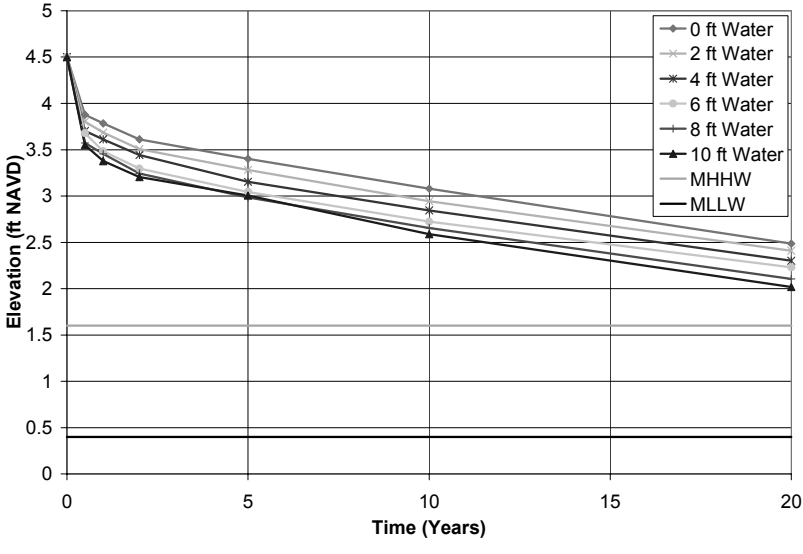

Figure 7. Settlement of Marsh Fill Containment Dike in Various Water Depths

Settlement calculations predicted the dike is likely to settle as much as 0.8 feet within the first six months immediately following dike construction. Examining the results of the Bay Joe Wise wave analysis, the proposed primary marsh dike elevation of 4.5 feet NAVD should be sufficient to protect the marsh fill from storms of a magnitude less than or equal to that of the average two-year storm events. Since the fill should be completely

dewatered within a six month time period, this should provide a reasonable amount of protection to the fill until it is settled in place.

Marsh Platform

A similar analysis was performed to determine the optimal design elevation of the marsh platform, 2.6 feet NAVD, for achieving the Project's design objective for marsh construction, that is, achieve an elevation such that the marsh fill elevation lies within this zone through the majority of the 20 years. Figure 8 presents the results of this analysis. Although the marsh fill elevation generally remains above MHHW until Year 5, it remains above MLLW for the 20-Year design life.

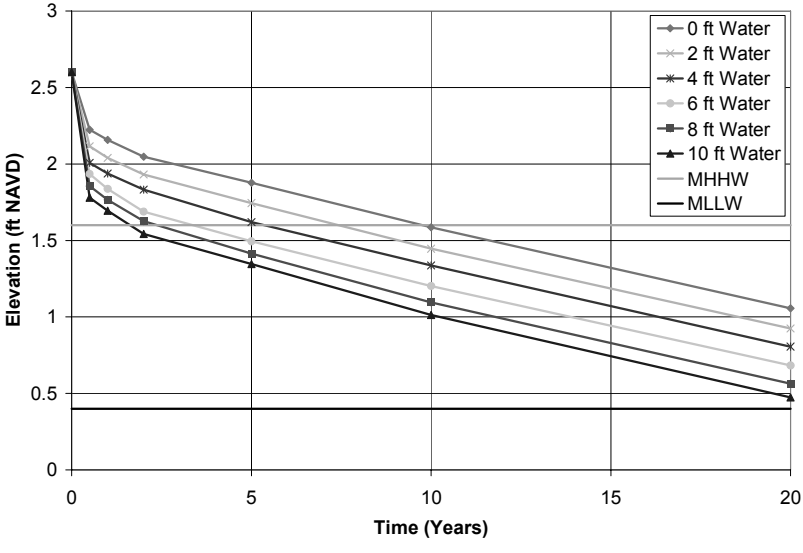

Figure 8. Settlement of Marsh Fill in Various Water Depths

Material Sources and Alternatives

The primary marsh containment dike will be approximately 16,000 linear feet long and require approximately 526,000 cubic yards. There are three (3) sources of material for dike construction. They are the inlet ebb shoals, interior channels, and Bay Joe Wise sediments. Field work was accomplished during Project design to sample the inlet ebb shoals and interior channels (SJB Group and CEC, 2005). Based on visual observations, the sediments are comprised primarily of fine sand with silts and clays and should be suitable for dike construction. STE (2004) determined the bay sediments are also suitable for dike construction.

CONCLUSION

Coastal Louisiana is disappearing at alarming rates resulting in the loss of pristine and unique estuarine systems, wildlife habitats, and recreational and commercial fishing; not to mention the decline in opportunities to mine oil and gas reserves and safely transport and distribute these valuable resources to the country. The state has embarked on its Coast 2050 program to hold the line and offset a significant amount of these impacts. The program includes dozens of marsh restoration projects to stabilize the integrity of the barrier shorelines. Key design steps in these projects include the siting, form and function of containment dikes to hold hydraulically placed fill within the marsh platform, and target elevations of the dikes and marsh platform to achieve environmental benefits based success criteria. The guidelines presented herein are recommended to the designer to enhance their understanding of the geotechnical data collection and sediment analyses required to properly design these key project components and achieve the success criteria. A case study is presented demonstrating the design of the marsh creation component of a Barrier Island Restoration project within the Barataria Basin wherein many of the guidelines were applied in the containment dike and marsh platform design. The project is slated for construction in 2007.

ACKNOWLEDGEMENTS

The authors thank the staff of LDNR's Coastal Engineering Division and National Marine Fisheries Service for their valuable input on marsh restoration design processes and blending of engineering principles with the biology and ecology of healthy marshes. Further, the authors thank the staffs of Coastal Engineering Consultants and consulting partner, SJB Group of Baton Rogue, Louisiana, for their support and contributions to this paper and to the Coast 2050 restoration program.

REFERENCES

Coastal Research Laboratory, University of New Orleans. (2000). "Barataria Barrier Island Restoration: Shoreline Change Analysis." Final Report submitted to Tetra Tech EM Inc., Baton Rouge, Louisiana. Contract No. 00RM-S0003.

Leenknecht, D.A., Szuwalski, A., Sherlock, A.R. (1992). *Automated Coastal Engineering System User's Guide Version 1.06*. Vicksburg, MS: Coastal Engineering Research Center, Department of the Army.

Louisiana Department of Natural Resources. (2005). "Coastal Protection Systems Design Guidelines."

SJB Group, Inc. and Coastal Engineering Consultants, Inc. (2005). "Final Design Report for the Pass Chaland to Grand Bayou Pass Barrier Shoreline Restoration Project (BA-35)." Louisiana Department of Natural Resources.

Soil Testing Engineers, Inc. (2004). "Report of Geotechnical Investigation, Pass Chaland to Grand Bayou Pass, Barrier Shoreline Restoration Project BA-35, Bay Joe Wise Area, Plaquemines Parish, Louisiana." Louisiana Department of Natural Resources, Coastal Resources Division and SJB Group, Inc.

U. S. Army Corps of Engineers. (1987). "Engineering and Design for Civil Works Projects." EM 1110-2-5027. Washington, D.C.

ICE RAFT FORMATION, DISPERSION AND SEDIMENTATION ON NEW ENGLAND SALT MARSHES

Brittina A. Argow[1], Zoe J. Hughes[2], and Duncan M. FitzGerald[2]

1. Wellesley College, Department of Geosciences, 106 Central St, Wellesley, MA 02481, USA. bargow@wellesley.edu
2. Boston University, Department of Earth Sciences, 675 Commonwealth Ave, Boston, MA 02215, USA. zoeh@bu.edu; dunc@bu.edu

Abstract: Ice-rafting of sediment is a major winter process in New England coastal marshes, increasing in intensity northwards. A survey of ice rafts conducted across three back-barrier salt marshes characterizes and quantifies sediment loads. The mean concentration of sediment in ice rafts increases to the north: 10.4g/L at Nauset, MA; 20.3g/L at Essex, MA, and 26.2g/L at Wells, ME. Inorganic sediment dominates 70% of ice rafts sampled. Ice raft dispersion across the marsh surface, while highly stochastic, is influenced by tidal amplitude, channel network density, meteorological conditions, and marsh surface elevation. A numerical model of ice-rafted sediment deposition on New England salt marshes is derived. Mechanisms of ice raft sediment incorporation and dispersion, conceptual models of ice raft formation, and estimates of the relative magnitude of vectors are presented, with implications for the vertical accretion of northern marshes in a regime of rising sea level.

INTRODUCTION

Winter processes such as ice-rafting are an important sedimentation vector to northern high marsh environments. Ice rafts are a secondary sedimentation process, redistributing sediment within the back-barrier system. The transfer of inorganic sediment from tidal creek bottoms, tidal flats, and pannes to the marsh surface plays a critical role in the geomorphic evolution of the marsh, and may be a key factor in the survival of northern marshes in a regime of accelerated sea-level rise.

Background

Differences between northern and southern marshes may result from processes directly or indirectly attributable to climate (Chmura et al., 1997; Pennings and

Bertness, 1999; Morris et al., 2002). Shorter summers and a lower angle of incident sunlight reduce the growing season, and most marshes experience complete winter die-off of above-ground vegetation north of Cape Cod. Progressively longer winters increase the magnitude of cold-weather processes northward along the New England coast (Fig. 1). Despite the current global warming trend, winter processes may remain significant on northern marshes. Climate trends from the past 55 years at Portland, ME, show an increase in monthly mean minimum temperatures for all months (mean = +3.16°C) except January, which has become colder on average (-0.88°C)(data from NCDC, NOAA). Shorter winters that are nevertheless more severe are another unexpected effect of global warming that may impact sedimentation and bioproductivity on the marsh surface.

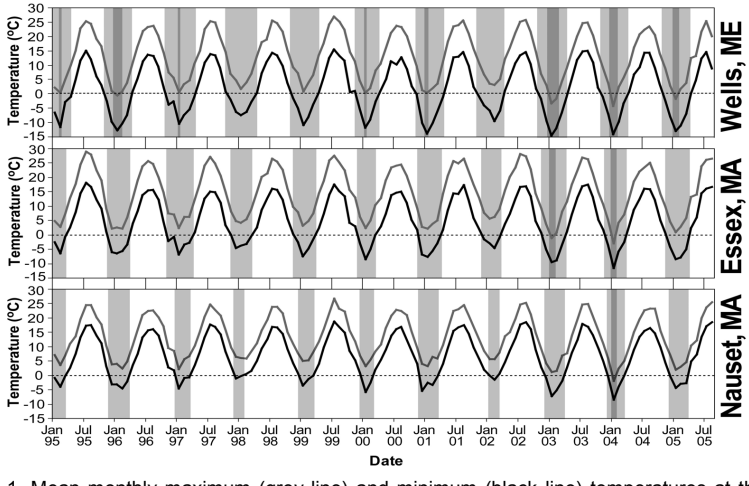

Fig. 1. Mean monthly maximum (grey line) and minimum (black line) temperatures at three New England field sites. Grey bars denote periods when mean daily minimum temperatures for the month were ≤ 0°C; darker grey bars indicate monthly mean maxima were ≤ 0°C. Data from NCDC (National Climatic Data Center), NOAA (National Oceanic and Atmospheric Administration).

Recently more attention has been focused on the role that winter ice plays in northern salt marshes (e.g. Ewanchuk and Bertness, 2003; Chmura and Hung, 2004; van Proosdij et al., 2006). Ice rafts deliver a large amount of sediment to the marsh surface in late winter or spring at break-up (Gordon and Desplanque, 1983; Wood et al., 1989; Dionne, 1988, 1989, 2000; Chmura et al., 1997; Ollerhead et al., 1999; Pejrup and Andersen, 2000; Chmura et al., 2001; Staats et al., 2001; Davidson-Arnott et al., 2002; van Proosdij et al., 2006). Ice-rafted sediment was found to significantly influence both the sediment budget and the morphology of intertidal and supratidal salt marshes in studies attempting to quantify this process (Dionne, 1989; Ollerhead et al., 1999; Pejrup and Andersen, 2000; Argow, 2006). Several of the mechanisms by which this sediment is incorporated into ice rafts in New England back-barriers differ from those described in the literature of open coasts. These processes may be specific

to these sub-environments of northern back-barriers: platform-type marshes dominated by high marsh, tidal flats in sheltered, enclosed embayments, tidal creek bottoms and creek banks, and tidal pools or pannes.

In intertidal environments, sediment may be frozen in a layer 10 to 15 cm thick onto the base of ice cover on mudflats or marshes, and later lifted and transported by ice (Gordon and Desplanque, 1983; Dionne, 1988, 1989, 1993; Chmura et al., 2001a). Blocks of ice may be stacked, partially melted, and re-frozen to create layered ice-rafts, observed on several marshes (Gordon and Desplanque, 1983, Dionne, 1988, 1989; Wood et al., 1989; Ollerhead et al., 1999; Pejrup and Anderson 2000; van Proosdij et al., 2006; Argow, 2006). At higher latitudes thick ice buildup on the surface of the marsh is capable of ripping up sections of marsh surface peat during break-up (Gordon and Desplanque, 1983; Dionne 1988; 1989), or planing off peat blocks from the leading edge of a fringing marsh (Pejrup and Anderson, 2000; vanProosdij et al, 2006), contributing to the erosion of the marsh and creating pannes on the marsh surface. In New England, the geomorphic effects of ice reported in the literature include ice-rafting as a mechanism of salt marsh colonization or expansion (Redfield. 1972; Richard, 1978). Ice-shearing of vegetation has also been observed (Redfield, 1972; Hardwick-Witman, 1985; Hardwick-Witman, 1986; Roberts and Robertson, 1986; Bertness, 1999; Ewanchuk and Bertness, 2003).

This paper presents observations of freezing and sediment entrainment processes on three New England marshes and provides conceptual models for ice raft formation and characterization. The thickness of ice deposits formed in situ on the surface of the marsh is discussed relative to elevation and geomorphic features. Data from surveys of representative ice-rafts stranded on three salt marshes in February, 2005 serve to characterize the nature of ice rafts and ice-rafted sediment in this region. The data and these models have implications for larger-scale processes on the marsh surface, such as the development of salt pannes, the evolution of tidal creeks, salt marsh expansion and colonization, and near-term coastal evolution in response to climate change.

Study Areas

Three representative back-barrier salt marshes were selected at different latitudes in New England to explore the variation in intensity of winter processes based on climatic differences. Webhannet River marsh (hereafter referred to as "Wells marsh"), located at 43°18'N in Wells, Maine, is a 7-km^2 back-barrier salt marsh formed behind a stabilized, highly-developed barrier island (Fig. 2). Essex River and Castle Neck River marsh ("Essex marsh") represents the southerly extent of the large barrier complex developed along the shore of the Merrimack River Embayment, and is located at 42°40'N on the north-facing coast of Massachusetts west of Cape Ann. The total area of the back-barrier is approximately 4645 acres (18.8 km^2). Nauset marsh, located between Eastham and Orleans, Massachusetts on the Atlantic shore of Cape Cod at 41°50'N, is a back-barrier marsh and lagoon system covering 2335 acres (9.45 km^2).

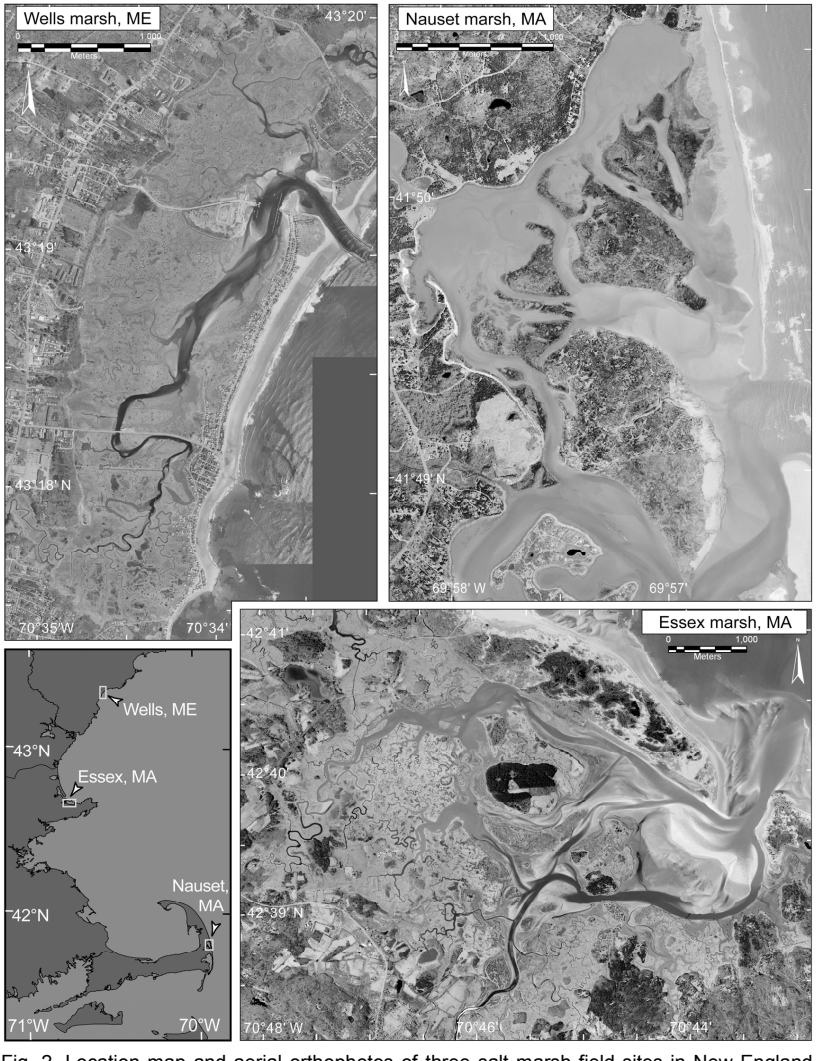

Fig. 2. Location map and aerial orthophotos of three salt marsh field sites in New England. Photo scales are per photo. (Apr 2001 photos from: Maine, Massachusetts State GIS).

All three marshes experience semi-diurnal tides and are lower mesotidal (Wells =2.7m, Essex =2.8m, Nauset =1.9m). The salt marshes are dominated by high marsh species (*Spartina patens, Distichlis spp, Juncus spp,* short form *S. alterniflora*)(Nixon and Oviatt, 1973; Nixon, 1982) and are deeply incised by tidal creeks. These supratidal expanses are completely flooded only ~3-6 days per tidal cycle (based on comparison of NOAA NOS data and modal surface elevation). Flood tidal waters

carry a modest suspended sediment load to the marsh surface in New England, generally an order of magnitude less than that reaching most southern wetlands (3.4—17.2 mg/L in the Webhannet River estuary, Wells, ME)(Ward, 2004). This mineral sediment influx, together with the accumulation of organic material due to the bioproductivity of *Spartina spp*., is an essential mechanism for vertical accretion of salt marshes, and helps to determine whether they will keep pace with rising sea level or be inundated (Reed, 1995; Callaway et al., 1996).

Climate variation between the sites is reflected in several quantifiable parameters. Over the last decade, the severity and duration of the winter season increases consistently to the north among the study locations (Fig. 1). During winter 2004-05 (Dec-Mar), Wells marsh experienced 53 days when the maximum air temperature did not exceed freezing, and 163 days when minimum temperatures were at or below 0º C. Mean air temperature was -4.1º C, comparable to the 20 year average (NCDC, NOAA; Wells NERR). In comparison, Essex marsh experienced 29 days when temperature maxima were ≤ 0º C, 138 days of minima ≤ 0º C. Mean winter temperatures = -1.38 ºC (2004-05, NCDC, NOAA). Near Nauset marsh, the southernmost site, records of minimum air temperatures indicate 87 days ≤ 0º C, maxima ≤ 0º C on 23 days. Nauset marsh experienced a mean temperature of 0.8º C over the winter of 2005-05 (data from NCDC, NOAA). Total snowfall received was 90.2cm at Wells marsh, 100.3cm at Essex marsh, and 14.5cm at Nauset marsh. These data give some indication of the different climate regimes of the three study sites and the expected magnitude of winter processes at each.

METHODS

Shore-fast ice (formed on and frozen to marsh surface) thickness was measured in early February, 2005, following a ten-day cold spell. A hand auger was used to take replicate (n=3x5) measurements at ~50 m intervals along upland-normal transects at each study site. Elevation was derived from LIDAR and TOTAL station data. 100 representative ice rafts were observed and sub-sampled along upland-normal transects at each study site after break-up in early March, 2005. Ice and incorporated sediment were weighed and sediment characterized by dominant sediment type based on grain size and composition. The average bulk density of aggregate samples was determined. Numerical relationships between physical and spatial parameters were determined using MSExcel and Matlab.

RESULTS

Ice thickness

Greatest thickness of shore-fast ice on the high marsh surface is observed at elevations closely corresponding to mean high water (MHW), and ice deposit elevations range from 1.25—1.46m above MSL (NAVD 88). Analysis of LIDAR elevation data for the Webhannet River estuary reveals that modal elevations for the back-barrier region as a whole are between 1.3—1.4 m above MSL, near the elevation of MHW (Fig. 3).

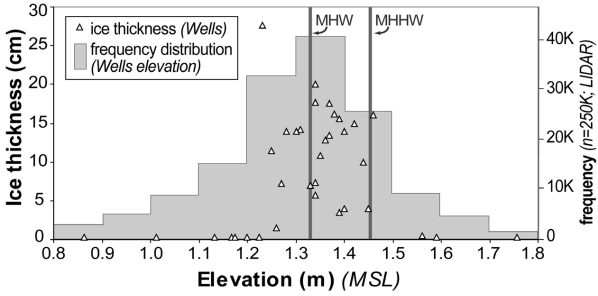

Fig. 3. Relationship between shore-fast ice thicknesses (Feb 2005) and marsh surface elevation at Wells marsh, ME. Histogram shows relative proportion of marsh surface area per elevation in the intertidal zone (LIDAR data, NOAA). All non-zero sample sites are located on high marsh (defined by plant species).

Ice-raft survey

Over 90% of the ice-rafts sampled on three New England marshes exhibited layering when the ice textures were closely examined. Most rafts showed regelation textures within layers. In this survey, relatively few (17%) had measurable sediment layers (>0.5 cm thick) frozen between ice layers, but nearly all (97%) had visible sediment adhered to the base. Mean thickness of ice rafts observed at the study sites varied; Wells and Essex were comparable, while Nauset ice rafts were thinner (22.5, 25.4, and 11.7 cm, respectively; Table 1). Similarly, mean thickness of the individual layers observed in ice rafts at Wells and Essex marshes was comparable (8.3 and 7.8 cm, respectively; mean 3 layers per raft), while Nauset rafts had fewer and thinner layers (4.7 cm, 2 layers per raft). The thickness of the ice rafts was positively correlated to the number of visible layers at all sites (r^2=0.72). At all sites, most rafts exhibit 2-3 layers (Table 1).

Table 1. Descriptive statistics of ice rafts surveyed on three New England marshes.

	Wells, ME (n=35)	Essex, MA (n=35)	Nauset, MA (n=30)	NE ave. (n=100)
sediment (g) per ice (L):				
mean:	26.2	20.3	10.4	19.9
mode:	0-1	1-2	5-6	0-8
range:	0.2-160.9	0.1-190.1	2.7-29.8	0.1-190.1
total raft thickness (cm):				
mean:	22.5	25.4	11.7	19
mode:	15	15	4	15
range:	6.0-45.0	8.0-70.0	2.0-32.0	2.0-70.0
thickness per layer:				
mean:	8.3	7.8	4.7	6.7
mode:	5	7.5	5	5
range:	3.0-15.0	2.0-18.0	2.0-8.0	2.0-18.0
number of layers:				
mean:	3	3.6	2.4	2.9
mode:	3	3	2	3
range:	1-8	1-9	1-6	1-9

Sediment concentration in ice rafts varies within (0.1-190.1 g/L_{ice}) and between sites, generally increasing northward (10.4-26.2 g/L_{ice}; Table 1). The modal 50% of ice rafts had relatively low concentrations of sediment relative to the carrying capacity of

sea ice (Fig. 4a). The top 10% of ice rafts having the highest sediment concentration define a trend roughly equivalent to the wet bulk density of fine sand (1.35 g/cm^3), although the sediment incorporated into those rafts was not exclusively sand (Fig. 4b).

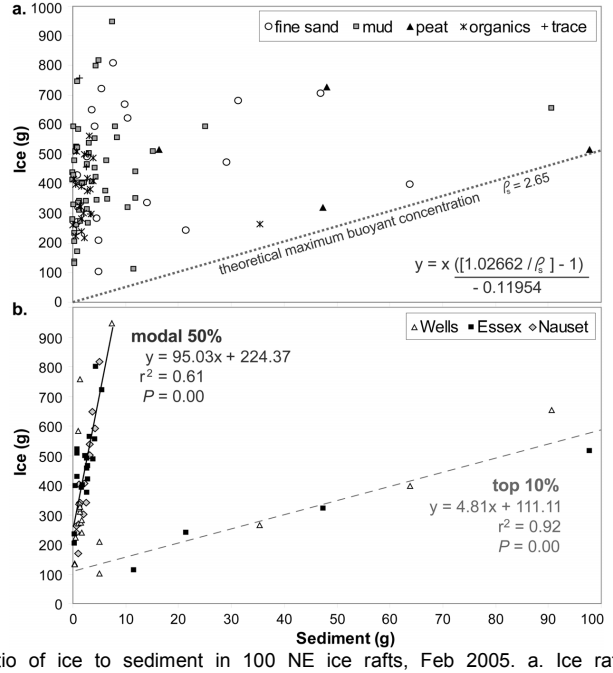

Fig. 4. Ratio of ice to sediment in 100 NE ice rafts, Feb 2005. a. Ice raft sediment concentration, classified by sediment type. Grey dotted line represents theoretical maximum sediment concentration in neutrally buoyant ice rafts, based on seawater at 3ºC and 33.5 ppt salinity (ρ_{sw}=1.03g/cm^3), density of sea ice (ρ_i=0.91 g/cm^3), and maximum density of incorporated sediment (quartz; ρ_s=2.65 g/cm^3). b. Solid line represents regression through points within the modal sediment/ice concentration (1-8 g/L; 50% of total points); dashed line represents regression through the top 10% of rafts based on sediment concentration.

Sediment incorporated into each ice raft was removed and characterized. Fifty-four percent of ice rafts sampled were silt-dominated (mud; Fig. 5a)(BD_{wet}=1.1 g/cm^3). Fine sand concentration decreased southwards (Fig. 5a,b)(BD_{wet}=1.35 g/cm^3). Peat, characterized by a cohesive, well-developed root mat and low wet bulk density (BD_{wet}=0.8-1.2 g/cm^3) was least commonly sampled in ice rafts at all sites (Fig. 5a), but made up the greatest total concentration of sediment at Essex marsh (Fig. 5b). No clear relationship between sediment type and concentration in ice rafts could be determined (Fig.4a,5b). However, patterns emerge when ice-rafted sediment concentration and type are compared to spatial parameters on the marsh surface. Sediment concentration decreases logarithmically with increasing distance from the nearest creek for all sites (y = -8.5 ln(x) + 41.6, r^2=0.68 (Nauset marsh); Fig. 6).

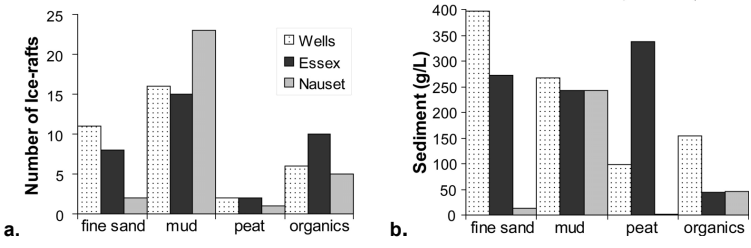

Fig. 5. Number of ice rafts and concentration in those ice rafts classified by sediment type. a. Predominant sediment type in ice rafts surveyed. b. Sediment concentration by type.

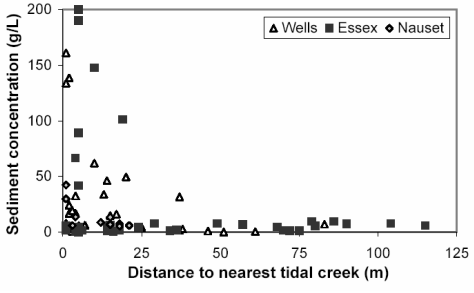

Fig. 6. Inverse relationship between distance to the nearest tidal creek on the marsh surface and the amount of sediment incorporated in surveyed ice rafts at three study sites.

DISCUSSION

Ice thickness measurements

Nauset marsh had the thinnest measurable ice deposits and the least total surface area covered by ice, as would be expected at the most southerly study site. Thicker shore-fast ice deposits were observed at Essex marsh and Wells marsh, correlating to the amount of snowfall at each site. Shore-fast ice deposits were thickest in the mid-to-fore marsh, near the leading edge of the geomorphically-defined high marsh platform, at elevations close to MHW (Fig. 3). This finding agrees with observations from northern climates (Nova Scotia; van Proosdij et al., 2006). At lower elevations, frequent tidal inundation prevents build-up and regelation of snow; at higher elevations, wind may remove drier snow.

During our on-going study of New England marshes, no fresh scars that seemed attributable to ice-plucking of peat from an unbroken marsh surface have been observed, as has been reported farther north (Dionne 1988, 1989; Gordon and Desplanque, 1983). Shore-fast ice on salt marshes in the Bay of Fundy (45 º49'N) has been reported at thicknesses up to 1.5 m (Ollerhead et al., 1999); resultant ice rafts are certainly capable of tearing up and transporting even large tufts of peat at break-up (Dionne, 1976, 1984, 1988). It may be that shore-fast ice on New England marshes rarely if ever reaches the thicknesses required to generate enough buoyancy to rupture an undisturbed, healthy *Spartina* root mat. However, numerous instances of ice-plucking from the edges of creeks and pannes and in otherwise disturbed areas have been observed at temperate latitudes; this process of peat incorporation into ice-rafts

is addressed in the conceptual models of ice raft formation and sediment incorporation which follow.

Ice raft survey

Ice raft thickness and layering is believed to be primarily a function of seasonal conditions, and varies from year to year. During the 2005 study, most ice rafts contained 2-3 layers (Table 1). The consistent pattern of layering of the ice rafts at all sites suggests a mechanism of formation governed by repetitive, cyclical processes, such as tidal processes, precipitation patterns, or daily temperature fluctuations. The number of layers may indicate the approximate duration of the ice-raft forming process relative to these cycles. The quantity of sediment incorporated into ice rafts is highly variable (Fig. 4); however, ice-raft sediment concentration increases as both the number of layers and total thickness of the raft increase (Table 1), suggesting that the incorporation of sediment into ice rafts also may be related to ice-raft layering, and be governed by the same cyclical processes, such as tidal fluctuations.

Most ice rafts surveyed were carrying relatively low concentrations of sediment (Fig. 4). Comparing the mass of sediment incorporated in ice rafts to the mass of the ice reveals that the majority of ice rafts contain more than 100 times the mass of ice relative to sediment (Fig. 4a). Therefore, the sediment concentrations of most sampled ice rafts fall well below the theoretical maximum concentration based on physical parameters, indicating that few rafts are at the carrying capacity for sediment. In fact, due to its low bulk density (as low as 0.80 g/cm^3 when saturated with seawater), peat can be ice-rafted even when dramatically out-weighing the ice component of the raft, a phenomenon often observed in the field (Fig. 7).



Fig. 7. Ice raft stranded on high marsh 1.5m from the creek bank in the mid-back marsh, Wells marsh, late Feb 2004. The ice raft contains a thick basal layer of low marsh peat, a layer of organics (ice-sheared *S. patens*), a thick, muddy fine sand layer (upper), and several trace layers (arrows). Lens cap for scale (circled).

Numerical Model of Ice Raft Sediment Concentration

Given the relative densities of ice, sediment, and cold seawater (3ºC, 33.5 ppt), surveyed ice rafts easily carry observed sediment loads (Fig. 4). Interestingly, the top 10% of ice rafts based on sediment concentration form a statistically significant trend ($r^2 = 0.92$, $P = 0.00$; Fig. 4b). These results may be taken to suggest the maximum amount of sediment that can realistically be incorporated into ice rafts transported

onto New England marshes. This "maximum carrying potential" is described by the relationship:

$$M_i = 4.8\ M_s + C, \quad (1)$$

where M_i is the mass of ice in the ice raft, M_s is the mass of frozen sediment, and C is a constant most likely dependent upon climate. This trend is quite similar to the limit of maximum theoretical sediment concentration described earlier (Fig. 4a).

If we consider the modal 50% of rafts based on sediment concentration (1-8 g/L), we derive a more conservative estimate for the quantity of sediment carried to the marsh surface by ice-rafting. A trend through this subset of the data yields a relationship wherein:

$$M_i = 95\ M_s + C \quad (2)$$

(r^2=0.61, C is a constant equal to 224 for New England)(Fig. 4b). This relationship may be useful in providing very rough estimates of the amount of sediment that is being transported to the marsh surface over a winter season by ice rafting, based on aerial and ground surveys of stranded ice rafts, which observe volume. Based on the volume of ice rafts deposited on a New England marsh:

$$M_s = 0.01\ V_i - C \quad (3)$$

where C = 2.36 for northern New England.

Classification and Origin of Ice-rafted Sediment

Despite the fact that the majority of all ice rafts sampled were carrying predominantly mud (Fig. 5a), nearly equal total masses of ice-rafted mud and fine sand were measured (Fig. 5b), due to the higher bulk density of sand and the observed tendency of sand layers in sampled ice rafts to be thicker, whereas mud laminations were often quite fine (Fig. 7). A sand-rich sediment layer implies that these ice rafts incorporated sediment in a sandy creek bottom or tidal flat (Fig. 8). Such sand-bottomed creeks and sheltered intertidal flats are present at all three study sites.



Fig. 8. A nearly-melted ice raft deposits a 5 cm thick layer of sandy sediment on the high marsh surface at Essex marsh, mid-Feb, 2004. The muddy fine grey sand texturally and compositionally matches sediment in the bed of a nearby tidal creek.

When peat was observed in ice rafts at all sites, the dense root mat tended to create an unusually thick sediment layer relative to the thickness of the ice raft (Fig. 7), accounting for the high mass of peat recovered from relatively few ice rafts. Peat can be frozen into ice rafts most readily at locations where the root mat has already been disturbed, such as slumping creek banks or the edges of salt pannes or pools. These environments are common in New England marshes.

Most ice rafts at all three sites carried sediment dominated by mud, suggesting that they formed in environments with muddy substrate. Two types of mud-dominated sediment were observed in ice rafts: a sandy mud with few organics and occasional

shells, and an organic-rich mud bearing rare *S. alterniflora* rhizomes and often characterized by a blackened anaerobic zone. The sandy mud is similar in grain size and composition to sediment found in the channels of the distal or upper reaches of tidal creeks at all sites. Organic-rich mud is characteristic of sediment found in low marsh ramps at the leading edge of the marsh and in slumped or gently sloping areas along major creek banks, both environments present at all sites.

Most ice rafts bearing "organics" (15% of total) included dense mats of sediment-laden algal matter, commonly found in pannes, ponds, and disturbed areas on the high marsh (Fig. 9). Rafts from frozen pannes are common; solid ice excavated from a panne on Essex marsh in January, 2005 revealed algal mats adfrozen to the ice layer. Sediment removed from pannes via ice-rafting is observed at all sites (Fig. 9). Some rafts contain sheared vegetation (5%) from stranding on the marsh surface (Fig. 7).

The four types of sediment incorporated in ice rafts suggest four potential sources from within the back-barrier environment: tidal flats, creek beds, creek banks, and salt pannes. Sediments from each of these sub-environments of the marsh are incorporated into ice rafts via different processes, described in conceptual diagrams of ice-raft formation.

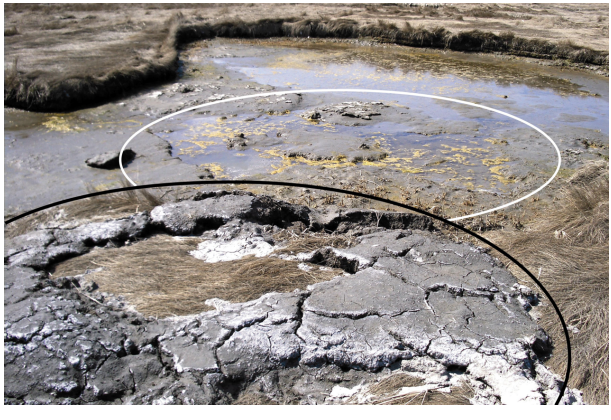

Fig. 9. Muddy algal-rich sediment lifted from the bottom of a nearby panne by ice rafting and deposited on the high marsh on Essex marsh, Apr 2005 (black circle). The upper surface of the muddy deposit is covered by algal mat and gastropods. Visible in the panne in the background is a scar closely matching the contours of the ice-rafted sediment deposit (white circle).

Ice Raft Dispersion

The concentration of sediment in surveyed ice rafts decreases sharply with increasing distance from the nearest creek (Fig. 6), suggesting that ice rafts laden with greater volumes of sediment may not travel as far from their probable source as may clean drift ice. Sandy ice rafts stranded closest to tidal creeks. Muddy ice rafts, formed primarily in mid-to-back marsh creeks and drained pannes, stranded at elevations of 1.2-1.4m above MSL (NAVD'88). This is a narrow range compared to sandy rafts, which were stranded at elevations between 0.9-2.0m, and rafts carrying dominantly organics, which stranded at 0.7-1.6m. Peat and algal rafts were found closer to salt pannes and ponds, as were many rafts bearing mud containing sparse S. *alterniflora* rhizomes.

Conceptual models

Conceptual models are based on data and observations over the period 2002-06 and describe processes of ice raft formation in distinct environments on the marsh surface: shallow tidal flat, creek bottom, creek bank and salt panne.

Tidal Flat Model: In northern marshes, the leading edge of the high marsh is often cliffed, abutting tidal flats. In winter, surface seawater freezes in sheltered embayments with limited wave activity, forming a layer of drift ice. As tide ebbs, sea ice strands on the tidal flat. A layer of sediment freezes to the bottom of the ice blocks. Ice is re-floated on next flood tide, and then strands and fractures repeatedly during successive tides until spring flood occurs. Note that peat calving at the leading edge of the marsh may also become frozen to ice rafts. During a spring tide event, the ice will raft onto the marsh surface. With the ebb tide, many ice rafts are stranded on the surface of the marsh, where in spring they melt and deposit characteristic sediment (Fig. 8). Ice rafts originally formed from drift ice may also become trapped in creeks, repeating the cycle of sediment adfreezing and layering until finally being rafted onto the marsh surface, into the embayment, or melting. Rafts may float out the inlet to open water.

Creek Bed and Bank Models: In summer, sub-surface flow drains peat to creeks (Fig.10a; arrows). In winter, sub-surface seepage builds up a layer of ice on creek banks and beds (Fig.10b,c) in a period of ~two weeks of freezing temperatures (drift ice requires shorter periods but colder temperatures to form). Limited daily melting contributes to thicker ice deposits on banks by increasing sub-surface flow (Fig.10c). Ice fractures due to micro-slumping or creep of the underlying peat and hydraulic pressure of tidal waters. Water continuously seeps from the peat, freezes onto the banks and bed, and, during flood tide, may break free as a sediment-laden ice raft (Fig.10b,d). During neap tides, ice may strand on the channel bottom and freeze to an additional layer of ice and sediment (Fig. 7). During spring tides, ice may raft onto the surface of the marsh with flood tides (Fig.10d), sometimes traveling great distances from the nearest creek (up to 500 m observed) before stranding. Ice in these rafts does not exhibit regelation textures, and sediment may range from mud to gravel, depending on the location and configuration of the creek channel.

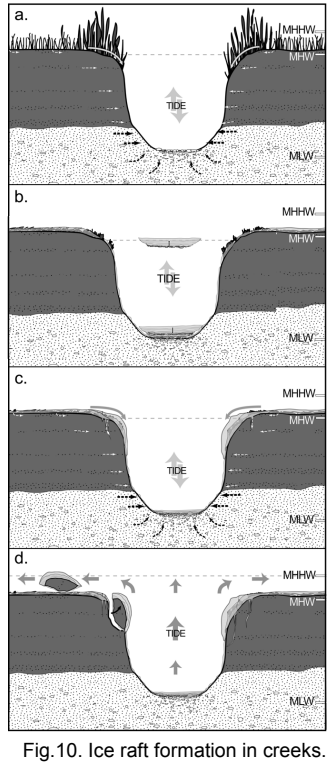

Fig.10. Ice raft formation in creeks.

Ice raft formation is an effective, possibly dominant, mechanism of tidal creek enlargement on northern New England salt marshes. This

process transfers sediment from creek banks and beds to the marsh surface, expanding tidal creeks and increasing vertical relief. Due to flood dominance of tidal creek channels (Leonard et al., 1995; Blanton et al., 2002; Davidson-Arnott et al., 2002), tidal sediment moves headward and replaces ice-removed sediment. Peat lost from creek banks, however, is not replaced in the same fashion; creek widening results. If sea level remains constant or rises very gradually, channel infilling may lead to shallowing as tidal currents slow, allowing colonization of intertidal creek-edge ramps by *S. alterniflora*, eventually narrowing the creek. In a time of rapidly rising sea level, however, enlarged channels will facilitate conduction of increased tidal flow through the marsh, and creek widening will continue.

Panne Model: The high marsh surface of New England marshes is marked by the presence of numerous small ponds and shallow, waterlogged depressions, herein collectively referred to as salt pannes (Erwin et al. 2004)(Fig.11a). During cold winters, these pannes freeze over; shallow pannes may freeze to depth (Fig.11b,c). This process forms ice rafts when ice and incorporated sediments are fractured and buoyed from the panne by flood tides (Fig.11d). Rafts may be identified by the particular sediment carried: a basal layer of sediment-laden algal mat and smaller clumps or ribbons of high-marsh peat torn from the edge of the panne. The formation of ice rafts effectively deepens and widens existing pannes on the marsh surface (Fig.11e). In disturbed areas, this mechanism of ice raft formation may also be responsible for panne initiation.

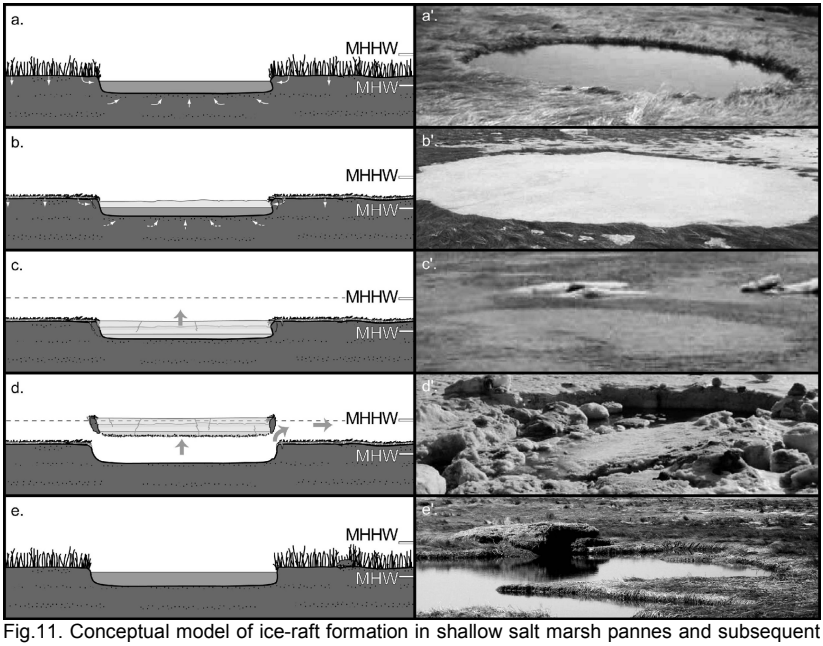

Fig.11. Conceptual model of ice-raft formation in shallow salt marsh pannes and subsequent panne enlargement. Letter primes are representative photos (2003-2005).

Relative magnitude of the four processes of intra-marsh ice-raft formation

Each of these mechanisms of ice raft formation is active in New England marshes, but their relative importance in the sediment budget varies. By considering the percentage of diagnostic sediment types contained in surveyed ice rafts (Fig. 5a,b), a rough measure of the magnitude of these processes at each study site can be obtained.

At Wells marsh, ~50% of ice-rafted sediment was fine sand, suggesting ice raft formation in large creek bottoms and tidal sand flats. Rare peat rafts suggest that ice was not as effective at removing peat from channel sides over the 2005 winter season, relative to previous observations. Sixteen percent of rafts bore organics, and most likely formed on the marsh surface and in pannes. Nearly 30% of the sediment carried in ice rafts was dominated by mud, most likely adhered to ice rafts in the upper reaches of tidal creeks, farther from the main source of sand (Wells inlet).

Essex marsh, where 30% of ice-rafted sediment was peat, has man-made ditches in the study area wherein peat from the sides is actively slumping and available to ice rafts. Over half of ice-rafted sediment appears to come from tidal channels or tidal flats, and little evidence of algal mats from salt pannes was observed in this study; however, due to ditching, relatively few pannes mark this section of the marsh.

Nauset marsh ice rafts bore little sediment, and were dominantly silty or muddy. Nauset tidal channels are generally sand-bottomed, suggesting that most ice-rafts formed in the muddier shallow reaches of the marsh distal to the inlet. Panne ice raft formation was represented. Few sandy rafts were sampled, due to the short ice season and relatively open hydraulics of the system, inhibiting channel ice-raft development.

CONCLUSIONS

Ice rafting of sediment is a secondary process of sedimentation in the back-barrier; rafts move sediment from tidal flats, creeks and pannes to the surface of the marsh, aiding vertical accretion. The volume of ice rafted onto the high marsh surface can be used to estimate the total quantity of ice-rafted sediment deposited on the marsh. Despite global warming, ice processes remain relevant as winters become shorter but more severe.

While research worldwide has led to significant advances in our understanding of salt marsh processes and our ability to numerically model these complex systems, there remains some disconnect between our general understanding of marsh processes and their application to coastal systems in northern latitudes. Differences in morphology and climate are responsible for variations in the physical, chemical and biological processes of the salt marsh at a variety of time scales, from a single tidal cycle to historical or Holocene records (e.g. physical processes: Davidson-Arnott et al., 2002; Argow and Fitzgerald, 2006; van Proosdij et al., 2006; biological processes: Bertness and Ewanchuk, 2002; Morris et al., 2002; Chmura and Hung, 2004). These differences can result in significant deviation from what is considered the “norm” in wetlands processes, and should be accounted for in models seeking to predict coastal response to sea-level rise in northern temperate latitudes, including New England.

REFERENCES

Argow, B.A., 2006. Winter processes on New England salt marshes. Dissertation, Boston University, Boston, MA. 379 pp.

Argow, B.A. and FitzGerald, D.M., 2006. Winter processes on northern salt marshes: Evaluating the impact of in-situ peat compaction due to ice loading, Wells, ME. Estuarine, Coastal and Shelf Science, 69(3-4): 360-369.

Bertness, M.D., 1999. The ecology of Atlantic shorelines. Sinauer Associates, Sunderland, Massachusetts, 465 pp.

Bertness, M.D. and Ewanchuk, P.J., 2002. Latitudinal and climate-driven variation in the strength and nature of biological interactions in New England salt marshes. Oecologia, 132(3): 392-401.

Blanton, J.O., Lin, G.Q. and Elston, S.A., 2002. Tidal current asymmetry in shallow estuaries and tidal creeks. Continental Shelf Research, 22(11-13): 1731-1743.

Callaway, J.C., Nyman, J.A. and DeLaune, R.D., 1996. Sediment accretion in coastal wetlands; a review and a simulation model of processes. Current Topics in Wetland Biogeochemistry, 2: 2-23.

Chmura, G.L., Chase, P. and Bercovitch, J., 1997. Climatic controls of the middle marsh zone in the Bay of Fundy. Estuaries, 20(4): 689-699.

Chmura, G.L., Coffey, A. and Crago, R., 2001a. Variation in surface sediment deposition on salt marshes in the Bay of Fundy. Journal of Coastal Research, 17(1): 221-7.

Chmura, G.L., Helmer, L.L., Beecher, C.B. and Sunderland, E.M., 2001b. Historical rates of salt marsh accretion on the outer Bay of Fundy. Canadian Journal of Earth Sciences, 38(7): 1081-1092.

Chmura, G.L. and Hung, G.A., 2004. Controls on salt marsh accretion: a test in salt marshes of eastern Canada. Estuaries 27(1): pp. 70-81;.

Davidson-Arnott, R.G.D., van Proosdij, D., Ollerhead, J. and Schostak, L., 2002. Hydrodynamics and sedimentation in salt marshes: examples from a macrotidal marsh, Bay of Fundy. Geomorphology, 48(1-3): 209-231.

Desplanque, C. and Bray, D.I., 1985. Winter ice regime on the tidal estuaries of the northeastern portion of the Bay of Fundy, New Brunswick. Canadian Journal of Engineering, 13: 130-139.

Dethleff, D., 2005. Entrainment and export of Laptev Sea ice sediments, Siberian Arctic. Journal of Geophysical Research, 110: 17.

Dionne, J.C., 1988a. Characteristic features of modern tidal flats in cold regions. In: P.L. de Boer, A. van Gelder and S.D. Nio (Editors), Tide-influenced sedimentary environments and facies. Sedimentology and petroleum geology. D. Reidel Publishing Company, Utrecht, Netherlands, pp. 301-332.

Dionne, J.C., 1988b. An estimate of shore ice debris content, upper St. Lawrence Estuary, Quebec, Program with Abstracts - Geological Association of Canada; Mineralogical Association of Canada; Canadian Geophysical Union, Joint Annual Meeting, St. John's, NF, Canada, pp. A33.

Dionne, J.C., 1989a. An Estimate of Shore Ice Action in a Spartina Tidal Marsh, St Lawrence Estuary, Quebec, Canada. Journal of Coastal Research, 5(2): 281-293.

Dionne, J.C., 1989b. The role of ice and frost in tidal marsh development; a review with particular reference to Quebec, Canada. In: E.F. Bird and D. Kelletat (Editors), Zonality of coastal geomorphology and ecology; Proceedings of the Sylt symposium. Verlag Ferdinand Schoemingh, Paderborn, Germany, pp. 171-210.

Dionne, J.C., 1993. Sediment load of shore ice and ice rafting potential, upper St. Lawrence Estuary, Quebec, Canada. Journal of Coastal Research, 9(3): 628-646.

Dionne, J.C., 2000. Recent erosion of the high marsh at Sainte-Anne-Anne-de-Beaupre, Quebec. Geographie Physique Et Quaternaire, 54(1): 69-89.

Dionne, J.C., 2002. Sediment content of the ice-cover in muddy tidal areas of the turbidity zone of the St. Lawrence Estuary and the problem of the sediment budget. In: T. Healy, W. Ying and J.-A. Healy (Editors), Muddy coasts of the world; processes, deposits and function. Proceedings in Marine Science, v.4, pp. 463-478.

Erwin, R.M., Sanders, G.M. and Prosser, D.J., 2004. Changes in lagoonal marsh morphology at selected Northeastern Atlantic coast sites of significance to migratory waterbirds. Wetlands, 24(4): 891-903.

Ewanchuk, P.J. and Bertness, M.D., 2003. Recovery of a northern New England salt marsh plant community from winter icing. Oecologia, 136(4): 616-626.

FitzGerald, D.M., Buynevich, I.V. and Argow, B.A., 2006. Model of tidal inlet and barrier island dynamics in a regime of accelerated sea-level rise. Journal of Coastal Research(SI 39): 789-795.

Gordon, D.C. and Desplanque, C., 1983. Dynamics and environmental effects of ice in the Cumberland basin of the Bay of Fundy. Canadian Journal of Fisheries and Aquatic Sciences, 40(9): 1331-1342.

Hardwick-Witman, M.N., 1985. Biological consequences of ice rafting in a New England salt marsh community. Journal of Experimental Marine Biology and Ecology, 87(3): 283-298.

Hardwick-Witman, M.N., 1986. Aerial survey of a salt marsh: Ice rafting to the lower intertidal zone. Estuarine, Coastal and Shelf Science, 22(3): 379-383.

Leonard, L.A., Hine, A.C., Luther, M.E., Stumpf, R.P. and Wright, E.E., 1995. Sediment Transport Processes in a West-Central Florida Open Marine Marsh Tidal Creek - the Role of Tides and Extra-Tropical Storms. Estuarine Coastal and Shelf Science, 41(2): 225-248.

Morris, J.T., Sundareshwar, P.V., Nietch, C.T., Kjerfve, B. and Cahoon, D.R., 2002. Responses of coastal wetlands to rising sea level. Ecology, 83(10): 2869-2877.

Nixon, S.W., 1982. The ecology of New England high salt marshes: A community profile. FWS/OBS-81/55, U.S. Fish and Wildlife Service, Office of Biological Services, Washington, D.C.

Nixon, S.W. and Oviatt, C.A., 1973. Ecology of a New England Salt Marsh. Ecological Monographs, 43(4): 463-498.

Ollerhead, J., van Proosdij, D. and Davidson-Arnott, R.G.D., 1999. Ice as a mechanism for contributing sediments to the surface of a macro-tidal saltmarsh, Bay of Fundy, Canadian Coastal Conference 1999, pp. 345-358.

Pejrup, M. and Andersen, T.J., 2000. The influence of ice on sediment transport, deposition and reworking in a temperate mudflat area, the Danish Wadden Sea. Continental Shelf Research, 20(12-13): 1621-1634.

Pennings, S.C. and Bertness, M.D., 1999. Using latitudinal variation to examine effects of climate on coastal salt marsh pattern and process. Proceedings of the OECD Workshop on Global Change and Wetlands. Journal of Biogeochemisty, 3: 100-111.

Redfield, A.C., 1972. Development of a New England salt marsh. Ecological Monographs, 42: 201-237.

Reed, D.J., 1995. The response of coastal marshes to sea-level rise; survival or submergence. Earth Surface Processes and Landforms, 20(1): 39-48.

Richard, G.A., 1978. Seasonal and environmental variations in sediment accretion in a Long Island salt marsh. Estuaries, 1(1): 29-35.

Roberts, B.A. and Robertson, A., 1986. Salt marshes of Atlantic Canada: Their ecology and distribution. Canadian Journal of Botany-Revue Canadienne De Botanique, 64(2): 455-467.

Staats, N., de Deckere, E., Kornman, B., van der Lee, W., Termaat, R., Terwindt, J. and de Winder, B., 2001. Observations on suspended particulate matter (SPM) and microalgae in the Dallard Estuary, The Netherlands: Importance of late winter ice cover of the intertidal flats. Estuarine, Coastal and Shelf Science, 53: 297-306.

van Proosdij, D., Ollerhead, J. and Davidson-Arnott, R.G.D., 2006. Seasonal and annual variations in the volumetric sediment balance of a macro-tidal salt marsh. Marine Geology, 225(1-4): 103-127.

Ward, L.G., 2004. Variations in Physical Properties and Water Quality in the Webhannet River Estuary (Wells National Estuarine Research Reserve, Maine). Journal of Coastal Research(SI 45): p. 39-58.

Wood, M.E., Kelley, J.T. and Belknap, D.F., 1989. Patterns of Sediment Accumulation in the Tidal Marshes of Maine. Estuaries, 12(4): 237-246.

EFFECTS OF LARGE SCALE MORPHOLOGICAL CHANGES TO A BACK-BAY SYSTEM

Lee L. Weishar[1], Theodore Keon[2], Donald K. Stauble[3]

1. Woods Hole Group, 81 Technology Park Drive, East Falmouth, MA 02536, USA. lweishar@whgrp.com.
2. Town of Chatham, 549 Main Street, Chatham, MA 02633. tkeon@chatham-gov.ma
3. U.S. Army Engineer Research and Development Center, Coastal and Hydraulics Laboratory, 3909 Halls Ferry Road, Vicksburg, MS 39180-6199, USA. Donald.K.Stauble@erdc.usace.army.mil.

Abstract: The Nauset barrier spit breached during a strong Northeast storm in January 1987, creating a new tidal inlet. Nauset Beach has historically undergone an approximate 135 year cycle of spit elongation followed by breaching and new inlet formation. The creation of the tidal inlet resulted in dramatic changes to the hydrodynamic processes within the Pleasant Bay estuarine system including an increase in tidal range, tidal currents, formation of ebb and flood tidal deltas, and an increase in wave energy transmitted into the previously quiescent back-bay region. A notable change was a loss of fringing salt marsh within the estuary. In the 10 year period after the breach there was a 14% decrease in fringe marsh followed by a 5% and 12% increase during the next 11 years. Since 1998, the Town has removed approximately 482,000 yd^3 of dredged material that has been used to maintain unarmored important Town beaches along the interior shoreline.

INTRODUCTION

Tidal inlets play an important role in the dynamics of the coastal ecosystems because they provide conduits for nutrients and fauna both into and out of the lagoon or estuary they serve. The efficiency of the conduit often dictates the relative health of the estuarine ecosystem. If the tidal inlet efficiently flushes the estuary there most likely is an adequate flow of oxygen and nutrients into the estuary resulting in healthy populations of Submerged Aquatic Vegetation, fish, shellfish, and other wetland resources that are important to the socio-economic viability and health of the estuarine ecosystem.

Additionally, the tidal inlet often provides an important navigation access to ports and harbors for commercial and recreational vessels. Historically, many of the inlets within the United States provided vital links for commerce carriers and fisherman to access trade routes and fishing grounds that lay off the nearshore areas of the coast.

Tidal inlets are often unstable if the longshore littoral transport exceeds that natural flushing capability of the tidal inlet. If this condition occurs and the tidal inlet is commercially important it is often artificially maintained by structures, by dredging, or a combination of both. Many estuaries within the United States are served by a single tidal inlet. However, when a second inlet forms in a single inlet system, the system normally becomes unstable and one of the inlets will close because the dominant inlet successfully captures tidal flows and reduces the tidal volume and velocities within the tidal channel served by the secondary inlet. This instability may go on for years however, eventually, one of the inlets gains dominance and the secondary inlet closes. When a new inlet opens or an old inlet closes there may be significant changes within the back-bay system. These changes may include impacts to navigation, shoreline orientation (both within the back-bay area and on the open coast), and expose previously sheltered areas of the back-bay shoreline to significant amounts of wave energy. These changes can have significant social, environmental, and economic impacts to the back-bay estuarine region.

This was the case when a new tidal inlet formed during a northeaster in Chatham, MA on January 2, 1987 (Figure 1). This storm was not a storm of record nor was it particularly damaging along much of the coast of New England. However, the storm breached the Nauset Barrier Beach forming a new tidal inlet. The formation of this inlet had been predicted by scientists however, the breach caught most people and state agencies by surprise and therefore, they were unprepared for the changes that occurred after the inlet formed. While the consequences of New Inlet have been far ranging and profound, this paper will concentrate on the effect of New Inlet on the fringe marsh resources within the back-bay area and the problems associated with maintaining navigation channels within this dynamic and ever changing system.

SETTING

The study area for this project is within the Pleasant Bay Estuary in Chatham, Massachusetts, located on Cape Cod (Figure 2). Nauset barrier beach forms a continuous strip of barrier beach free of any coastal engineering structures or other impediments to sediment transport. This uninterrupted section of beach extends approximately 17 km from Nauset Inlet to New Inlet. Prior to the formation of New Inlet the barrier beach extended an additional 8 km to the south (Figure 1). This southern 8 km of the barrier beach was cut off after the formation of New Inlet and transformed that section of the barrier beach into a barrier island. Nauset barrier beach provides protection to Chatham Harbor, Bassing Harbor, Crows Pond, Ryder's Cove, Pleasant and Little Pleasant Bays. Additionally, within the estuary there are many rivers, creeks and islands that provide a wide diversity of habitats. The entire estuary comprises approximately 2,833 ha of open water habitat (Pleasant Bay Management Alliance, 1998).



Fig. 1. Chatham Harbor showing the pre- and post breach conditions and New Inlet



Fig. 2. Study location, Chatham, Massachusetts on Cape Cod

There are an additional 467 ha of salt marsh within the estuary. However, approximately 142 ha of 467 ha of salt marsh is composed of fringing salt marsh while the rest resides in larger tracts and is not characterized as fringing salt marsh. Nauset Barrier Beach

protects the estuary from the waves and storm surge associated with the Atlantic Storms that frequent Cape Cod during the fall, winter, and spring seasons. During the January 2, 1987 northeast storm the Nauset Barrier Beach was initially breached by an overwash that flowed water only at high tide. The overwash area was approximately 1 meter wide and could be stepped across however; the overwash rapidly grew in size over the next several months until today it now measures approximately 1.3 km in width. The geologic history of the Nauset Barrier beach was studied by Giese (1988). He predicted that the barrier beach would be breached and would break-up and reform a number of times prior to migrating to the south. Weishar *et al*. (1989) and Weishar and Fields (1993 and 1994) used Giese's model to make predictions on how the back-bay shoreline would respond to the rapidly changing inlet morphology.

The formation of New Inlet and subsequent morphological changes associated with the inlet resulted in many changes within the back-bay system. The tide range increased approximately 0.5 m within the first year after the inlet formed (Wilhelm 1989). The tide range within the estuary increased because after New Inlet formed, approximately 8 km of narrow sinuous tidal channel that connected the estuary to the Atlantic Ocean was eliminated thus; reducing tidal friction and the length the tide had to travel to reach Pleasant Bay. However, the formation of New Inlet also allowed more wave energy to travel directly into the estuary from the Atlantic Ocean. Previously these areas had been sheltered by the barrier beach and as a result, large lengths of the shoreline previously protected were now subject to direct wave attack during severe storms. As New Inlet grew in size and dominance, it eventually captured all of the tidal flow from the old Chatham tidal inlet. As New Inlet increased in size, new tidal channels formed along with large flood- and ebb-tidal shoals (Stauble 2001). The change in wave energy and increase in tide range created many changes within the estuary however, this paper is going to address only the changes induced by New Inlet on the loss of fringing salt marsh, navigation, and shoreline erosion mitigation. The fringe marsh and dredge management areas are shown in Figure 3.

CHANGES IN SALT MARSH RESOURCE

Prior to the formation of New Inlet, much of the Pleasant Bay Estuary had a fringing marsh that varied in width from a ½ m to 10 to 12 m. The fringing marsh is primarily composed of *Spartina alterniflora* that grows in the region between the Mean- and High-Tide lines and is positioned between the open water of the estuary and the glacial bluffs and coastal banks that frequent the shoreline within the estuary. The fringing marsh is an important resource within the estuary because it provides habitat diversity, sequesters nutrients, provides refugia for small fish and crustaceans, and provides food in the form of detritus for primary producers.

Prior to the formation of New Inlet the coastal bluffs and banks that are composed of glacial till and outwash were largely unarmored, well vegetated and stable. A typical transect would begin at the top of the coastal bank and progress seaward and cross a well vegetated stable bank slope to the toe of the bank.



Fig. 3. Location diagram showing the Pleasant Bay estuary, the fringe marsh study area, and the dredge management area including New Inlet

The transect would continue seaward from the toe of the bank across a narrow sand beach and then across a narrow strip of fringe marsh into the intertidal region.

The formation of New Inlet along with the increase in tidal range had a profound effect on the stability of the coastal banks and the viability of the fringing marsh. In some areas, the fringing salt marsh was eroded directly by the increase wave energy that traveled through the New Inlet however; these areas were confined to the region near the opening of New Inlet.

In most of the estuary, the increase in tidal range allowed locally wind generated waves to reach further landward. The combined action of increased tide range and storm surge allowed the locally generated wind waves to reach higher on the beach and in most cases reach the toe of the coastal bank. As a result, many of the fringing salt marshes were subjected to more frequent wave attack from larger waves and were inundated for longer periods of time. While increasing the tide range and inundation time will not kill the salt marsh, it will weaken the *Spartina* species until it can readjust to the new dynamic

regime. The increased tidal range permitted waves to reach the base of the previously stable coastal banks and bluffs during even moderate storms. As a result, the previously stable coastal banks began to erode which inundated the fringing marsh with sediment. The combination of the weakened plants, longer tidal inundation, and covering with relatively large amounts of sediment resulted in a loss of fringing salt marsh within the estuary. The change in the salt marsh resource associated with the formation of New Inlet had been observed but not previously been quantified. In order to quantify the observed change in the fringing salt marsh resource a sub-section of the Pleasant Bay estuary was chosen for study. The study area was located within the lower portion of the estuary and was composed of Bassing Harbor, Ryder's Cove, and Crows Pond (Figure 4). The study area has an open water area of approximately 146 ha and approximately 9 ha of fringing salt marsh. This area was chosen because it is a confined series of embayments that offered a well delineated study area, the wetland resources are dominated by fringe marsh, and it is characteristic of the rest of the Pleasant Bay estuary. A series of vertical aerial photographs were obtained that included coverage beginning before the formation of New Inlet and spanning the 21 year period between the 1984 and 2005 vertical aerial photographs (Table 1).



Fig. 4. Fringe marsh study area and location of sub-embayments

Table 1. Date and scale of vertical aerial photographs used in this study

Date	Data Source	Scale	Comments
1984	Col-East	1:6,000	
1994	MAGIS web site	1:48,000	
2000	Town of Chatham (East Coast Mapping)	1:6,000	
2003	MAGIS web site	1:2,500	Not used; photos acquired at or near high tide
2005	Town of Chatham (James W. Sewall Co.)	1:12,000	

The 2005 and 1994 aerial photographs were obtained from MAGIS and were georectified. The 1984 and the 2000 aerial photographs were scanned, imported into ArcMap, and georectified. We researched other sources of aerial photography to obtain additional coverage however, these were the only time series available. Once all photographs were georectified, Arc Map was used to create polygons of fringe marsh. The results of the analysis are shown in Figure 5. There was a relatively extensive fringing marsh within the study area prior to the formation of New Inlet. After New Inlet formed, the dynamics within the estuary changed and as a result the fringe marsh area declined from 90,207 m^2 to 77,435 m^2.

While the decline in fringe marsh between 1984 and 1994 is dramatic it may have been more extensive because the only set of vertical aerial photographs for the Pleasant Bay estuary available after the formation of New Inlet were acquired in 1994, 10 years after the formation of New Inlet. The decline may have been more extensive immediately after the hydrodynamics changed within the estuary and the fringe marsh may have already been recovering by 1994. Even taking this short-coming into account the trend in the data is clear. After the breach there was a decline in the aerial coverage of fringe marsh. We hypothesize that the fringe marsh decline stopped and began recovering because the eroding coastal banks had either been armored or had reached a new dynamic stability by 1994 thus, eliminating the episodic covering of the fringing salt marsh with sediments eroded from the banks. Additionally, the increase in tidal range provided additional area for the fringing salt marsh to expand into because the tide range between Mean- and High-Tide lines increased vertically by approximately 0.75 ft. This increase in vertical range provided additional area for the *Spartina alterniflora* to expand into where there was either beach or other relatively flat areas to colonize.

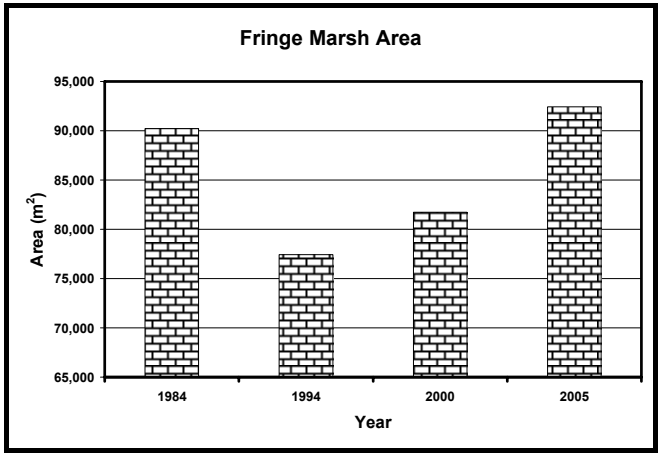

Fig. 5. Results of the fringe marsh analysis showing the decrease in fringe marsh area after the formation of New Inlet and subsequent growth of fringe marsh within the study area

NAVIGATION

The formation of New Inlet relocated the primary opening through Nauset Barrier beach approximately 8 km to the north. The opening of New Inlet also created a new shorter navigation channel and new ebb- and flood-shoals. As the system adjusted to the new hydrodymics, the flood shoal grew rapidly, rapidly changed position, and increased in volume (Stauble 2001). This situation presented challenges for the Town to manage dredging for navigation, mooring, and constructive use of dredged material.

Navigation within Chatham Harbor is critical because Chatham has one of the largest commercial fishing industries in New England and Chatham's municipal Fish Pier, which is its primary fish offloading facility, is located just over a mile north of New Inlet. Chatham's close proximity to some of the prime northeast fishing grounds provides the opportunity to travel to and from the fishing areas in a single day. Chatham's fishing fleet is comprised of about 60 to 70 smaller "day-boats" typically in the 9 to 15 m class with drafts between 1 and 2.4 meters. Additionally, the US Coast Guard, Station Chatham, also maintains vessels at the Fish Pier because it provides the most direct route to the Atlantic Ocean for search and rescue operations. The ability for fishing boats to make single day fishing trips results in higher prices for their fishing catch. Therefore, maintaining the navigation channel to Aunt Lydia's Cove is of vital importance for the commercial fishing fleet and the US Coast Guard utilizing the Fish Pier.

Soon after the break in Nauset Beach, the traditional navigation channels were overwhelmed with sediment from two sources. Sand already within the harbor system was now becoming more mobile due to the increase in tidal velocities and wave energy. In addition, significant volumes of new sand were being swept into the harbor from the outer littoral system creating new shoals which migrated as a unit into the harbor (Fitzgerald and Montello 1993, Liu *et al*. 1993, Stauble 2001). This resulted in drastic changes in the form and location of the traditional channels and limited the ability of the fishing vessels to traverse the shoals to enter and exit the harbor.

In the late 1980's, US Army Corps of Engineers (USACE) initiated studies to investigate the impacts of the break on the surrounding shorelines and navigation channels, and examined the potential for federal interest for corrective strategies. Ultimately, the USACE developed a small draft (-2.5m MLW by 30.5m) federal navigation project (Section 107) for Aunt Lydia's Cove to maintain fishing fleet access to the Fish Pier. The object of the dredging project was to provide navigation access into Chatham Harbor and to the Fish Pier through the rapidly changing flood shoal morphology (Figures 1 and 6; Stauble 2001, Fitzgerald and Montello, 1993). Access over the outer bar (ebb-tidal) delta, while still difficult at certain tidal conditions, was not included in the authorized project.

The location of the 1995 initial federal dredging maintained the channel entrance at its historic position. The initial dredging of the federal project was completed in 1995 with approximately 120,000 cubic yards (yd^3) of material removed by a hydraulic cutterhead

dredge from the old entrance channel as well as the more sheltered mooring basin located to the west of Tern Island (Figure 6).

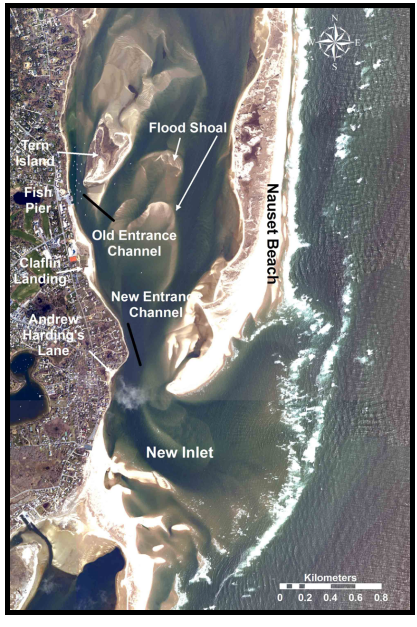

Fig. 6. Location of dredged channels, Fish Pier and beach nourishment areas

The dredged material was clean fine sand and disposal was upland on the adjacent Tern Island which had been historically used as a disposal site for smaller dredging projects. Dredging of the channel was difficult because the channel was infilling with freshly supplied sand even while the dredging was underway. Ultimately this channel completely shoaled and was closed to navigation within approximately 6 months. The USACE did not return for maintenance dredging until June of 2000 when the special purpose hopper dredge "Currituck" instead of a hydraulic dredge was used to dredge the navigation channel through the flood shoal. The Currituck has subsequently been providing annual spring maintenance since 2000 removing from 30,000 yd^3 to over 95,000 yd^3 of sand from the navigation channel on a typical annual cycle.

Prior to the return of the USACE dredge Currituck in the Spring of 2000, the morphology and history of the flood shoal was re-evaluated to develop dredging strategies to improve the longevity of the navigation channel. In addition, given the ongoing erosion of many of the vulnerable surrounding shorelines, a dedicated effort was made to re-utilize the dredged sand for beneficial re-nourishment. The goal was to develop a comprehensive Channel/Sand Management Plan that enabled flexible dredging and disposal strategies that would be more responsive to highly dynamic shoal

morphology and changing hydrodynamic conditions. The Channel/Sand Management Plan acknowledged the highly mobile nature of the flood shoal, and identified a "zone of potential dredging" in lieu of a fixed channel footprint. This approach did not restrict the dredging to set channel coordinates and instead allowed the dredging to be more mobile and follow actual or potential natural channel positions. This plan proved to be a more effective strategy from the perspective of both channel longevity and cost effectiveness.

The first significant dredging following the USACE initial project completion in 1995 was conducted in March 1998 utilizing the Barnstable County 14-inch hydraulic cutterhead pipeline dredge "Codfish". This was the first time that the navigation channel was substantially relocated to take advantage of the change in flood shoal morphology (Figure 6). Specifically, the channel was relocated to take advantage of developing marginal ebb dominated channels along the western edge of the flood shoal adjacent to the mainland shoreline. These ebb dominated channels were dredged to enhance flow through the dredged cut to encourage natural tidal action to assist in reducing sand from depositing into the channel. This strategy has been successfully implemented for the past several years for both the local and federal dredging efforts.

As the flood shoal complex continued to evolve, increasing quantities of sand were transported northward into the Fish Pier access channel and the mooring basin. This condition threatened to deny commercial and private fishing boats access to both the Fish Pier and the mooring basin. Twice yearly dredging was often required to keep the channels open sufficiently for the fishing fleet due to the rapid infilling of the channel and mooring basin (Table 2).

Table 2. History of dredged material quantities and location of disposal by year

AUNT LYDIA'S COVE DREDGING SUMMARY					
Date		Dredge Type	Dredge Location	Total QTY	Disposal Location
1995		ACE: Cutterhead	Mooring Basin	120,000	Tern Island
1998	Mar	Mechanical	Entrance	1,000	Tern Island
	May	County-Cod Fish	Entrance	9,300	Direct Pumpout to Claflin (5K); truck haul to asst'd Landings (4K)
	May	County-Cod Fish	Mooring Basin	1,500	Town Landing
	Oct	County-Cod Fish	Entrance	9,000	Direct Pumpout to Andrew Hardings
1999	May	County-Cod Fish	Entrance	9,800	Direct Pumpout to Andrew Hardings
	Oct	County-Cod Fish	Entrance	6,000	Direct Pumpout to Andrew Hardings
2000	May	County-Cod Fish	Mooring Basin	9,800	Direct Pumpout to Claflin (1.8K) ; truck haul to asst'd landings (8K)
	May	ACE-Currituck	Entrance	30,000	Sub-acqueous: Outside bar
	Oct	County-Cod Fish	Mooring Basin	8,400	Direct Pumpout to Claflin
2001	June	ACE-Currituck	Entrance	60,000	Sub-aqueous: Outside bar & Inside bar near shore
2002	Mar	County-Cod Fish	Mooring Basin	8,300	Direct Pumpout to Claflin (2K); truck haul to asst'd landings (6.3K)
	June	ACE-Currituck	Entrance	60,000	Sub-aqueous: Outside bar & Inside bar nearshore
2003	June	ACE-Currituck	Entrance	60,000	Sub-aqueous: Inside bar near shore
2004	June	ACE-Currituck	Entrance	50,000	Sub-aqueous: Inside bar nearshore
	Oct.	County-Cod Fish	Entrance	10,200	Direct Pumpout to Andrew Hardings
2005	June	ACE-Currituck	Entrance	97,000	Sub-aqueous: Inside bar nearshore
	Oct.	County-Cod Fish	Entrance	2,100	Direct Pumpout to Claflin
			Mooring Basin	8,000	Direct Pumpout to Andrew Hardings
2006	May	ACE-Currituck	Entrance	42,400	Sub-aqueous: Inside bar nearshore
			TOTAL QTY	**602,800**	**cubic yards**

Total to Tern Island: 121,000 cys
Total to Andrew Hardings: 43,000 cys
Total to Claflin: 19,300 cys
Total to Town Landings: 19,800 cys
Total to Sub-aqueous: 369,400 cys

Notes: ACE - Army Corps of Engineers

The Town quickly realized that the appropriate dredging strategy would be to use the Currituck for removal of larger volumes of sand from the primary entrance channel while utilizing the Cod Fish for supplemental dredging in the entrance channel when necessary and to maintain the relatively small mooring basin where the larger Currituck was unable to maneuver. It should be stressed that the volume of material that was removed by either the Currituck or the Cod Fish was more often a reflection of the funding available at the time of each project than the true need or actual volume that should have been removed. The Town had limited funds to apply to these projects and significant efforts were devoted to maximize the effectiveness of the dredging to conserve these resources. In addition, the USACE, Currituck had a limited window of time to work on-site, and their goal was to remove the maximum amount of sand from the most severely shoaled channel sections in the allotted time period rather than maintaining the overall project dimensions.

Given the highly dynamic nature of the flood shoal and sediment movement, the Town's dredging strategy has been to identify the most critical areas for dredging to provide for the greatest navigation channel longevity. As the flood tidal shoal continued to evolve, the shoal and channel morphology was frequently reviewed to incorporate a more creative approach that included a form of advanced maintenance dredging that incorporated the following:

- Shifting the orientation of the channel and dredged cut to facilitate natural tidal flushing.
- Dredging of deposition basins adjacent to the channel to trap sand prior to entering the channel.
- Over-depth dredging to provide greater capacity of the channel for shoaling.
- Over-dredging along the leading edge of the flood shoal adjacent to channel in anticipation of rapid infilling.

While these strategies have proven reasonably effective at maintaining navigation access to the Fish Pier, the highly dynamic nature of the flood shoal and the entire inlet and flood/ebb shoal complexes have created a littoral environment which continues to pose considerable challenges for maintaining navigation through the inlet into the Fish Pier and mooring basin.

DISPOSAL/NOURISHMENT STRATEGIES

The Town's dredging requirements provided the opportunity to constructively use the dredged sand from the navigation projects to mitigate shoreline erosion associated with New Inlet. The Town established an internal policy to re-utilize the dredged sand as beach and shoreline nourishment whenever possible. Chatham is fortunate that the dredged material from Chatham Harbor is very clean medium to fine grained beach quality sand and therefore, can easily be reused for beneficial purposes. The Town has actively renourished shorelines eroded after New Inlet formed through a variety of means including the direct pumpout of material via the pipeline dredge, truck-hauled placement of both dewatered dredged material and mined upland sand, as well as by sub-aqueous

placement of material in the nearshore (approximately -1.8 to -6.1m MLW) by the USACE split-hulled hopper dredge, the Currituck.

Dredging with the hydraulic cutterhead Codfish, has provided the opportunity to directly pump-out the dredged sand onto beaches for beneficial nourishment. There are two Town-owned beaches and/or landings within the effective direct pumpout range (approximately 1.6 or less 5 km with a booster pump) of the Codfish. These beaches Andrew Harding's Lane and Claflin Landing are Town owned landings and have not been armored. Both of these sites have undergone considerable erosion, recession and loss of public access due to the proximity to New Inlet. Therefore, both Andrews Harding and Claflin Landings were designated as priority locations for beneficial beach nourishment and dune building projects. Utilizing these two public landings provided cost effective dredge material disposal sites and helped mitigate the on-going shoreline erosion.

Since 1998 over 19,000 yd^3 of sand has been placed at Claflin Landing while Andrew Harding's Lane has received approximately 43,000 yd^3. Almost 20,000 yd^3 of additional sand was pumped to Claflin Landing but this excess material was dewatered on-site in diked containment areas and hauled by dump trucks to several other Town owned beaches and landings. Erosion at Claflin Landing has begun to stabilize over the past few years partly as a result of the continued southerly migration of the southern tip of Nauset Beach. The migration of the barrier beach has reduced the exposure of this shoreline to wave energy, thereby reducing the loss of material from the shorefront.

Andrew Harding's Lane is located closer to the inlet and it is a small "pocket beach" located between two substantial sections of stone revetments built post-inlet formation. Andrew Harding's Lane, however, continues to undergo considerable erosive losses because it is located closer to New Inlet and is directly exposed to waves traveling through the inlet from the Atlantic Ocean. The initial beach and dune nourishment projects (1999 & 2000) were able to mitigate the erosion at this location and as a result a substantial dune had begun to develop after installing sand fencing on the back-beach. However, in 2003 and 2004 the beach began to erode at a much higher rate and the shoreline receded almost to its original 1999 pre-nourishment position. The increase in erosion is attributed to increased tidal current scour due to changes in the orientation of the primary ebb and flood channels.

As changes in the configuration of the outer ebb bar system progressed, the main tidal channel became more directed onto the shore. This change in morphology caused incoming flood currents to become focused onto the nourished beach at Andrew Harding's Lane resulting in rapid loss of sediment once the sand was suspended due to wave action. Additional beach and dune nourishment projects have partially mitigated the increased erosion and have prevented complete breaching of the dune system. This heightened erosion has moderated somewhat during 2006 because the primary tidal channel once again has shifted position into a more shore parallel orientation and the associated tidal currents are not as focused onto the shoreline.

Despite the reduced erosive losses during 2006, the Town is continuing to investigate alternatives to mitigate the erosion at Andrew Harding's Lane because this is a popular small recreational beach. The opportunistic beach nourishment during ongoing dredging may not be sufficient to maintain the shoreline given the uncertainty of the frequency or scale of future nourishment dredging projects. Therefore, various structural shore protection alternatives are being considered to supplement the ongoing sand nourishment. These structures include groins, offshore breakwaters, perched beach systems, training dikes and other similar shoreline erosion mitigation measures. Based on a preliminary analysis, the use of groin-like training dikes placed at either end of the beach appear to be the most promising option. Their function would be similar to training dikes in a fluvial system, which are constructed to deflect river currents away from river banks to prevent scour. At Andrew Harding's Lane these structures would be placed to deflect tidal currents as well as provide some sheltering from waves in the lee of the structure to reduce the loss of sand. Whether the Town will ultimately choose to pursue installation of these features will be dependent upon the changing morphology and on the associated severity and rate of future erosion.

CONCLUSIONS

The formation of New Inlet produced long ranging changes within the Pleasant Bay estuary. The shorelines along Pleasant Bay have experienced a re-adjustment following the break due to the increase in tidal range which resulted in heightened erosion. These conditions initially resulted in an influx of sediment into the system as the estuarine shorelines receded and readjusted to the new hydraulic regime during the first few years after formation of New Inlet. The sediment input has decreased as these shorelines began to form a new equilibrium profile.

Several of the most dramatic changes included an initial reduction and subsequent recovery of the fringing salt marsh, transmission of wave energy onto previously sheltered shorelines, and the growth of a large flood shoal. These changes have placed the estuary in a state of flux that continues to change 19 years after the formation of New Inlet. The increase in tidal range resulted in a loss of fringing marsh within the estuary. This loss was the result of increase tide range and storm surge that allowed waves to reach higher onto the back-beach and ultimately to the destabilization of coastal banks. The initial loss of fringing salt marsh stopped approximately 10 years after New Inlet formed. The aerial coverage of fringing salt marsh has been recovering over the past 14 years and has now exceeded pre-breech conditions. We hypothesize that the increase occurred because of the additional suitable growing area associated with the increase in tide range that occurred after the formation of New Inlet.

The formation of New Inlet 8 km north of the old inlet changed the hydrodynamic conditions within Chatham Harbor. The changing conditions led the Town to develop a flexible Channel/Sand Management Plan that is a living document. The Plan continually re-assesses the shoal morphology and the location of the navigation channel. The flexibility of the Plan allows the Town to use limited resources to maximize the dredging efforts to maintain navigation to the Town Fish Pier and the mooring basin.

The beneficial reuse of dredged material has proved effective at nourishing a number of public and private shorelines throughout Chatham. The Town has also provided supplemental nourishment utilizing sand from upland sources. This sand serves as a suitable additional source of material to provide for nourishment when the sand from dredging projects is not available. Recently, the erosion at Andrew Harding's beach has begun to abate because a change in the ebb shoal morphology has changed the orientation of the inlet channel. While the Town is encouraged by this change, it is developing plans for a more permanent solution if the channel should once again change position and the erosion increases at this location.

ACKNOWLEDGEMENTS

Some funding and data support was provided by the USACE New England District and Town of Chatham. Permission to publish has been granted by the Chief of Engineers.

REFERENCES

FitzGerald, D. & Montello, T. (1993). Backbarrier and inlet sediment response to the breaching of Nauset Spit and formation of New Inlet, Cape Cod, Massachusetts," In: "*Formation and Evolution of Multiple Tidal Inlets*", eds. D. Aubrey and G. Giese, pp. 158-185. American Geophysical Union, Washington, DC, 237p.

Giese G. (1988). Cyclical behavior of the tidal inlet at Nauset Beach, Chatham, Massachusetts. In: "*Hydrodynamics and Sediment Dynamics of Tidal Inlets*", eds. D. Aubrey and L. Weishar, pp. 269-283. Springer-Verlog, New York, 454p.

Liu J., Stauble, D., G. Geise, & Aubrey, D. (1993). Morphodynamic evolution of a newly formed tidal inlet. In: "*Formation and Evolution of Multiple Tidal Inlets*", eds. D. Aubrey and G. Giese, AGU, Washington, DC, 237p.

Pleasant Bay Resource Management Alliance. (1998). The Pleasant Bay resource management plan (Draft), Harwich, MA, The Pleasant Bay Resource Management Alliance.

Stauble D. (2001) Impacts of navigation channel maintenance on the coastal processes of Chatham, Massachusetts, Tech. Rep. ERDC/CHLTR-01-26, Coastal and Hydraulics Laboratory, Vicksburg, MS.

Weishar L., Stauble, D., & Gingerich, K. (1989). A study of the effects of the new breach at Chatham, Massachusetts, "A reconnaissance report to New England Division", Vicksburg, MS, U.S. Army Engineer Waterways Experiment Station, Vicksburg, MS.

Weishar L. & Fields, L. (1993). Phase I: Final environmental impact report shore protection structures Aunt Lydia's Cove to Beach and Tennis Club, Chatham, MA, Prepared for the Town of Chatham, MA, Aubrey Consulting, Inc. Falmouth, MA.

Weishar L. & Fields, L. (1994). Phase II: Final environmental impact report Tennis Club to Morris Island, Chatham, MA, Prepared for the Town of Chatham, MA, Aubrey Consulting, Inc, Falmouth, MA.

Wilhelm R. (1989). Report on the Pleasant Bay water quality study Cape Cod, Massachusetts, The Friends of Pleasant Bay Inc., Harwich, MA.

This page intentionally left blank

Subject Index

Page number refers to the first page of paper

Aggregates, 2394
Alabama, 1047, 2002
Alaska, 463
Australia, 1033, 1417

Backwashing, 1947
Barrier beaches, 492
Barrier islands, 647, 671, 685, 699, 976, 1153, 1179, 1722, 1988, 2002, 2011, 2254
Barriers, 434, 814, 935, 1731, 1910, 2084
Bars, 2111, 2124
Bathymetry, 1877, 2191
Bays, 341, 463, 814, 856, 1311, 2137, 2151
Beach erosion, 1142, 1311, 1601
Beach nourishment, 776, 2279, 2358, 2418, 2501, 2515
Beaches, 300, 314, 378, 406, 420, 463, 477, 506, 520, 531, 545, 584, 626, 935, 1019, 1227, 1269, 1455, 1696, 1708, 1740, 1787, 1851, 1865, 1947, 1661, 2111, 2241, 2265, 2402, 2460
Bed load, 56
Belgium, 1431
Berms, 449
Brazil, 1455
Breaking waves, 42, 2124
Breakwaters, 2402, 2460
Bulkheads, 561

California, 1696, 1740, 1851, 2501
Canada, 351
Caribbean, 572
Case reports, 1391
Channels, 1431, 1571, 1678, 2164, 2213, 2345, 2358, 2372
Chesapeake Bay, 2306
Cliffs, 1696
Climatic changes, 963, 1214
Closed form solutions, 15
Coastal engineering, 434, 1241, 1405
Coastal environment, 179, 207, 449, 828, 842, 1117, 1129, 1283, 1475, 1647, 1669, 1813, 1827, 1900, 1910, 1924, 2084, 2151, 2321
Coastal morphology, 1, 137, 272, 364, 492, 671, 736, 814, 828, 842, 986, 1019, 1033, 1165, 1200, 1297, 1354, 1363, 1417, 1455, 1529, 1571, 1582, 1589, 1635, 1938, 2011, 2025, 2137, 2199, 2345
Coastal structures, 2432
Colorado River, 1502
Currents, 42
Cyclones, 935

Damage, 1008
Deep water, 1, 341
Deltas, 207, 736, 749, 828, 882
Design, 420, 785, 1988
Dikes, 392, 785, 1008
Dredge spoil, 2358
Dredging, 2372, 2382, 2394
Dunes, 612, 897, 951, 1033, 1089, 1241, 1283, 1813, 1961, 1975
Dynamics, 584

Empirical equations, 1431
Environmental issues, 1827
Equilibrium, 897, 2241
Erosion, 96, 612, 1722, 1799, 1813, 1961, 2037, 2074, 2265, 2321
Esthetics, 420
Estimation, 1008, 2372, 2382
Estuaries, 531, 1200, 1609, 1623, 1669, 2487
Evaluation, 626

Failures, 392, 1008
Field investigations, 661
Fills, 2402, 2418

Florida, 151, 378, 1047, 1297, 1326, 1377, 1582, 1589, 1877, 2199, 2265
Flumes, 124
Forecasting, 1813
Forests, 1117
France, 531

Geology, 2151, 2473, 2487
Geometry, 1787, 2002, 2177
Geomorphology, 165, 762, 2097, 2292, 2306
Grain size, 259, 314, 1255, 1623, 2229, 2241, 2446
Gravel, 477, 492, 520, 572, 584, 2473
Gravity waves, 1, 235
Great Lakes, 392
Ground water, 506
Gulf of Mexico, 935, 1515

Harbors, 1431, 2292
Hawaii, 1227
Hazards, 1799
Heterogeneity, 921
History, 364, 867
Hurricanes, 151, 882, 888, 911, 976, 986, 996, 1047, 1466, 2306
Hydrodynamics, 221, 1297, 1489, 1557, 1582, 1787, 1924
Hydrographs, 1827
Hydrologic models, 1669

Ice formation, 798
Imaging techniques, 1886
Indonesia, 1019
Infiltration, 506
Inlets, waterways, 1165, 1297, 1326, 1354, 1363, 1377, 1391, 1475, 1489, 1502, 1515, 1529, 1543, 1557, 1589, 1468, 2199, 2331
Integrals, 286
Islands, 1340, 1708, 1722, 1865

Japan, 1269, 1354, 1900, 2460

Laboratory tests, 68, 235, 248
Lagoons, 1708
Land reclamation, 598
Latin America, 2345
Littoral currents, 1405
Littoral drift, 165, 179
Louisiana, 647, 661, 671, 685, 699, 762, 785, 888, 911, 921, 1165, 1179, 2254

Mapping, 2487
Marshes, 785, 1571
Maryland, 1340
Massachusetts, 814, 856, 1142
Mathematical models, 1075
Measurement, 221, 561, 1609, 1678, 1947
Mexico, 996, 2279
Michigan, 392, 2292
Mississippi, 1466
Mississippi River, 699, 712, 722, 749, 882, 2177
Models, 300, 406, 897
Monitoring, 406
Morphology, 235, 1391, 1557, 1900, 2199
Mud, 1660, 1669, 1690

Navigation, 1431, 1502, 1678, 1768, 2345, 2372
Nearshore, 1, 56, 584, 951, 1886
Netherlands, 1129, 1363
New England, 798
New York, 1722, 2331
New Zealand, 1441, 1910
North Carolina, 327, 963, 1153, 1543, 1837, 2229
North Sea, 2124
Numerical analysis, 1089
Numerical models, 341, 671, 736, 749

Oregon, 449, 1754, 2137
Outwash, 2049, 2074, 2084

Parameters, 124, 626
Permeability, 520
Plumes, 736, 2382
Porous media, 2321
Portugal, 545, 1557
Predictions, 314, 612, 1103
Probability, 272
Progressive waves, 2191

Radar, 1900
Reefs, 572, 1647

Remedial action, 1601
Restoration, 647, 685, 699, 776, 785
River basins, 1647
River beds, 2177
Rivers, 842

Salts, 798
Sand, 42, 68, 96, 193, 248, 259, 314, 477, 492, 506, 520, 545, 584, 685, 699, 1255, 1269, 1340, 1405, 1609, 1708, 2164, 2191, 2254, 2432, 2446, 2460, 2473, 2501
Sandbars, 28
Scour, 598, 1609, 1851, 2213
Sea floor, 598, 1635, 1660, 2487
Sea level, 1153, 1179, 1193, 1200, 1214
Sediment, 15, 28, 207, 300, 463, 531, 633, 661, 671, 712, 722, 736, 749, 776, 867, 951, 1047, 1075, 1103, 1283, 1326, 1635, 1647, 1768, 1877, 1988, 2229, 2292, 2382, 2473, 2515
Sediment transport, 42, 56, 68, 82, 96, 110, 124, 137, 151, 179, 193, 221, 286, 351, 911, 996, 1117, 1241, 1405, 1441, 1669, 1678, 1754, 1924, 1938, 2037, 2049, 2446, 2460
Sedimentation, 798, 1377
Seismic effects, 856
Shear stress, 193, 1947
Sheet flow, 286
Ship motion, 110
Ships, 685, 2213
Shoaling, 921, 1311
Shoreline changes, 327, 364, 378, 392, 888, 1129, 1142, 1214, 1227, 1417, 1601, 1740, 1754, 1799, 1837, 2306
Shores, 561, 633
Simulation, 259, 2097
Simulation models, 1623
Skewness, 137
Slopes, 137, 165
South Carolina, 1787, 2151
Spatial distribution, 2037
Spits, coastal, 351
Sri Lanka, 842, 1061
Statistics, 1799, 2177
Stones, 531
Storm surges, 996, 1466
Storms, 951, 963, 1813, 1886, 2061
Stratification, 1635
Structural design, 2432
Subsurface environment, 82
Subsurface investigations, 785
Surf zone, 82, 151, 1455, 1865
Surface waters, 1690
Suspended sediments, 221, 248
Switzerland, 2321

Texas, 1475, 1502, 1515, 1529
Tides, 1129, 1179, 1354, 1417, 1543, 1589, 1731, 1768, 2164
Time dependence, 193, 867, 1690
Topography, 867, 1623, 1837, 1865, 1938, 2061, 2097
Tracers, 449
Transport rate, 179
Tropical regions, 1731, 2061
Tsunamis, 842, 1008, 1019, 1033, 1061, 1075, 1089, 1103, 1117
Turbulence, 15

United Kingdom, 434, 1200

Vegetation, 1571
Velocity, 15, 28, 2382
Virginia, 364, 2402

Washington, 561, 1311, 1754
Water circulation, 327
Water levels, 963
Wave groups, 110
Wave runup, 272, 1075, 1089, 1924, 1938, 1947, 1961, 1975
Wave tanks, 259
Waves, 661, 1660, 1690, 1731
Wetlands, 722, 1179, 1193
Wind, 1255

This page intentionally left blank

Author Index

Page number refers to the first page of paper

Aagaard, Troels, 951, 2124
Aarninkhof, Stefan G. J., 598, 1975
Abbe, Tim, 561
Adams, Mark B., 1142
Adams, Peter N., 463
Alfageme, Santiago R., 2345, 2432, 2025
Allan, Jonathan C., 449, 2137
Allison, Mead A., 661, 882
Alonso, Ignacio, 1283
Alsina, J. M., 272
Amaro, Venerando E., 1731
Anderson, Carl M., 1529
Andrews, Brian D., 2487
Andrews, Jeffrey L., 685, 699, 2515
Andrus, T. Mitchell, 722, 785
Argow, Brittina A., 798
Arsenault, Matthew A., 2473
Asano, Go, 1623
Ashton, Andrew D., 327, 341, 351, 1214
Austin, Martin J., 584

Baba, Yasuyuki, 1938
Baig, Stephen, 1466
Baldock, Tom E., 272, 286, 506, 1947
Baldwin, Wayne E., 2151, 2487
Barcak, Ronnie G., 1502
Barlett, William, 749
Barnard, Patrick L., 2501
Barnes, Matthew P., 272, 1947
Barnhardt, Walter A., 856, 2151
Barthélemy, Eric, 235
Bass, Gregory P., 1340
Batten, Brian K., 1515
Beck, Tanya M., 1377, 1582
Bell, Paul S., 1886
Bell, Robert G., 1441
Bender, Christopher, 151
Benedet, Lindino, 671, 699, 2515
Benoit, Jeff, 1601
Bentley, Samuel J., 722, 1441
Bergeron, Emile, 2487
Bliss, James D., 2473
Boer, Sander, 598
Bokuniewicz, Henry, 1722
Bolinger, Daniel L., 2254
Bradbury, Andrew P., 492
Brehin, Florian G. A., 1297, 2199
Briére, C., 137
Brocchini, M., 1635
Brown, J. M., 1609
Buonaiuto, Frank, 1722
Buschman, Frans, 1647
Buscombe, Daniel, 584
Butman, Bradford, 2487
Byrnes, Mark R., 762, 1754

Calliari, Lauro J., 1455
Calvete, D., 2111
Camenen, Benoît, 15, 56, 1938
Campbell, T., 671
Cañizares, Rafael, 2025, 2345
Canning, Paul, 520
Carrasco, Ana R., 2084
Carrasquero, José, 561
Carter, Joshua, 1489
Clarke, Linden B., 1975
Cleary, William J., 1543
Cleveringa, Jelmer, 1129
Coates, Tom C., 406
Coeveld, E. Matrijn, 612, 1975
Conley, D. C., 1635
Connell, Kenneth J., 2011
Cowell, P. J., 633
Cox, Andrew, 1466
Crowley, Tom, 1214
Curoy, J., 531

Dalon, Matthew M., 2137
Dan, Sebastian, 207
Danchuk, Samantha, 749
Danforth, William W., 2487
Darnell, Joel T., 776

Dartez, Dane, 911
Dartnell, Peter, 1851
Das, Himangshu, 1466
Davies, A. G., 1609
Davis, Richard A., 1582
de Alegria Arzaburu, Amaia Ruiz, 996, 1865, 2279
de Sonneville, B., 671
de Vroeg, Hans, 612
Dean, Robert G., 626
Dekker, Frank, 1117
Dellapenna, Timothy M., 882
Denny, Jane F., 2151, 2487
Dias, Alveirinho, 1557
Dias, João A., 2049, 2084
Dibajnia, Mohammad, 392, 2097, 2292
Diesing, Markus, 2394
Dill, Nathan, 749
Dohmen-Janssen, C. Marjolein, 1019
Donnelly, Chantal, 2061
Dornbusch, U., 531
Dougherty, Amy J., 1910
Driscoll, Neal, 2151
Durham, William McKinney, 82

Edge, Billy L., 2074
Edwards, Brian D., 1851
Elias, Edwin P. L., 598, 1363
Elkan, Peter, 2402
Elko, Nicole A., 378
Espinal, Juan C., 996, 2279
Esteves, Luciana S., 221, 1886

Falchetti, S., 1635
Falqués, A., 2111
Farris, Amy S., 1837
Fauver, Laura A., 897
Ferland, M. A., 633
Ferreira, Óscar, 1557, 2049, 2084
Finkl, Charles W., 671, 685, 699, 2515
FitzGerald, Duncan M., 798, 856, 1165, 1179, 2164
Fitzpatrick, Kathy, 1326
Fletcher, Charles H., 1227, 1799
Foster, David S., 2487
Foye, Peter, 2265
Frazer, L. Neil, 1799
Friedrichs, Carl T., 2382

Fujii, Hiroyuki, 1008
Fukuhama, Masaya, 259, 1008, 1623
Furuike, Kou, 314

Galal, El Sayed, 1900
Galofre, Jordi, 2241
Garcia, Marcelo H., 2191
Garnier, R., 2111
Gayes, Paul T., 1787, 2151
Gelfenbaum, Guy R., 1103, 1117, 1768
Genz, Ayesha S., 1799
Georgiou, I., 2177
Georgiou, Ioannis, 1179
Gibeaut, James C., 1193
Giese, Graham S., 1142
Giosan, Liviu, 828
Goff, James R., 1033, 1061
Goff, John A., 2473
Goñi, Miguel A., 882
Gonzalez, Mauricio, 300
Grandy, Greg M., 647
Granja, Helena, 545
Grasmeijer, Bart, 1
Grasso, Florent, 235
Griffee, Sarah F., 1754
Griggs, Gary B., 1740, 2501
Grosskopf, William G., 1340
Grüne, Joachim, 248
Guannel, Gregory, 28
Guard, P., 286
Guedes, Rafael M. C., 1455
Guidroz, Walter S., 911
Guillén, J., 2111
Gunawardena, Yohama, 1865
Gunn, James R., 2306

Haghshenas, S. Abbas, 1690
Hall, Kevin, 1660, 2213
Haller, Merrick, 28, 2137
Hamilton, Stuart, 986
Hansen, Mark, 2002
Hanson, Hans, 15
Hapke, Cheryl J., 1696
Harcourt, Jenny S., 406
Hardaway, C. Scott, Jr., 2306
Harikai, Souichi, 1269
Hart, Roger, 449
Hashimoto, Koji, 1354

Hatchett, Lyle, 1466
Hayashi, Kentaro, 1354
Head, Richard, 406
Headland, John R., 2432
Healy, Terry R., 165, 2358
Heilman, Daniel J., 776, 1502
Hein, Christopher J., 856
Higgins, Stephen, 2265
Higman, Bretwood, 1103
Hoekstra, Piet, 1647
Hoitink, Ton, 1647
Holland, K. Todd, 1455
Holman, Rob A., 1975
Honma, Akihiro, 1354
Hopf, Frank, 1241
Horn, Diane P., 520, 506
Horwitz, Mark H., 1047
Hotta, Shintaro, 1255, 1269
Houghton, Jon, 477
Houser, Chris, 986
Howes, Nick, 1179
Hsu, Tian-Jian, 1669
Hughes, Michael G., 1417
Hughes, Zoe J., 798, 1179
Hulscher, Suzanne J. M. H., 1019, 1813

Ilic, Suzana, 1865
Inukai, Takushi, 1623
Irwin, Barry J., 2487
Ishii, Toshimasa, 96
Ishikawa, Toshinori, 259, 314, 2460
Ishino, Kazuo, 842
Izzo, Dominic, 2254

Jaffe, Bruce, 1103, 1117
Jaffe, David A., 867
Jaramillo, Sergio, 661
Jenkins, Chris J., 2473
Jennings, Simon C., 434
Jiménez, José, 1283
Joffrion, Russ, 785
Jose, Felix, 921, 935

Kaminsky, George M., 633, 1768
Kana, Timothy W., 2229
Kato, Fuminori, 1008
Kemp, Jonathan A., 406
Keon, Theodore, 814
Khalil, Syed M., 685, 699
Kheiashy, K., 2177
Khondker, Masood, 2025
Kirby, James T., 28
Kirwan, Matthew L., 1571
Klekotka, John, 477
Knaapen, Michiel A. F., 1200
Knotts, Christopher P., 685
Kobashi, Daijiro, 921
Kolberg, Mark O., 1708
Komar, Paul D., 420
Kos'yan, Ruben, 248
Kotulak, Peter, 2432
Kozuka, Masayuki, 96
Kraus, Nicholas C., 193, 1377, 1475, 1502, 1515, 1529, 1961, 2011, 2331
Krecic, Michael, 151
Kremkau, Kevin, 1326
Kroon, Aart, 951, 2124
Krynock, Laural, 2402
Kubota, Susum, 1255, 1269
Kumada, Takayuki, 314, 2446
Kuriyama, Yoshiaki, 179, 2037

Landry, Blake J., 2191
Larson, Magnus, 56, 1924, 2011
Li, Ling, 506
Lillycrop, W. Jeff, 888, 1827
Limber, Patrick W., 1837
Lin, Lihwa, 1502, 1515
Lisniowski, M. A., 221
List, Jeffrey H., 221, 327, 1837
Littlewood, Ryan, 341, 351
Liu, Baozhu, 935
Long, Bernard F., 124
Lorente, Paloma, 1283
Loureiro, Eduardo, 545
Lovelock, Catherine, 1441
Lynett, Patrick, 1103

Maathuis, Ben H. P., 1019
MacDonald, Neil J., 110, 2213
Macon, Christopher L., 1827
Madsen, Ole Secher, 82, 96
Mahoney, Tucker, 2345
Mai, Stephan, 2321
Makowski, Christopher, 2265
Mann, Douglass W., 1405

Manoonvoravong, P., 272
Mark, David J., 1311
Masselink, Gerhard, 584
Matias, Ana, 2049, 2084
Matsumoto, Hideo, 1678
Matsumoto, Ryosuke, 1900
Matsura, Seizo, 1354
McBride, Randolph A., 364, 762
McCorquodale, J., 2177
McKillip, Doris J., 1768
Medellin, Gabriela, 2241
Medina, Raúl, 300, 2241
Meilianda, Ella, 1019
Merrifield, Mark A., 1227
Meselhe, E., 2177
Meyer-Arendt, Klaus, 986
Michallet, Hervé, 235
Mimura, Nobuo, 96
Miner, Michael D., 1165, 1179
Momose, Kazuo, 96
Montreuil, Stéphane, 124
Moore, Andrew, 1103
Morán, Diana K., 996, 2279
Morang, Andrew, 1311
Morgan, Michael J., 2331
Moritz, Hans R., 633, 1754, 1768
Morris, Brad, 2049
Morrison, Steve, 561
Morton, Robert A., 572, 1061, 2151, 2487
Moses, C. A., 531
Mouraenko, Oleg, 2372
Mulder, Jan P. M., 1813, 1019
Murray, A. Brad, 341, 351, 1214, 1571
Mustain, Neomi, 2501

Nairn, Robert B., 392, 1708, 2097, 2292
Nakagawa, Hajime, 842
Nakagawa, Yasuyuki, 1678
Nakamura, Nagatomo, 1255
Nawarathna, Bandara, 842
Neto, Francisco Santos, 1731
Nichol, Scott L., 1061, 1910
Nicholls, Robert J., 1200
Nichols, David R., 2487
Niedoroda, Alan W., 1466
Nielsen, P., 286

Özkan-Haller, H. Tuba, 28

O'Brien, Thomas F., 2487
O'Donoghue, Tom, 42
Odroniec, Kristen, 151
Ojeda, E., 2111
Oltman-Shay, Joan, 1768
Oravetz, Jonathan, 986
Orford, Julian D., 434, 492
Osborne, Philip D., 110
Oumeraci, Hocine, 248
Oveisy, Ali, 1660
Overton, Margery, 2074

Pacheco, André, 1557
Palmsten, Meg L., 1975
Park, Young Hyun, 2074
Parkinson, Shaun, 110
Pawlak, Geno, 1227
Penland, Shea, 1179
Pereira, Pedro S., 1455
Perotto, H. L. S., 221
Perry, M. Cameron, 776
Phillips, Eleyne L., 1851
Placido Jr., Jose S., 1731
Podymov, Igor, 248
Poff, Michael, 785
Pope, Joan, 963

Quartel, Susanne, 951

Ramsey, John, 1326
Ranasinghe, Roshan Suminda, 68
Ranasinghe, Roshanka, 1417
Reid, Dave, 1696
Reniers, Ad J. H. M., 1975
Requejo, Soledad, 300
Revell, David L., 1740
Reynolds, B. M., 1787
Ribas, F., 2111
Ribberink, Jan S., 1, 42
Richardson, Trent M., 364
Richmond, Bruce M., 572
Risk, Michael J., 1708
Roberts, Susan, 1601
Roberts, Tiffany M., 1961
Robertson, William, V., 1877
Robinson, D. A., 531
Roblin, Rachel R., 392
Rodríguez-Herrerías, Manuel, 1283

Roelvink, Dano (J.) A., 598, 736
Rosario-Llantin, Jo-Ann, 2199
Rosati, Julie Dean, 1988
Rosenberg, Lee, 2402
Rossington, Kate, 1200
Ruessink, Gerben, 1
Ruffman, Alan, 1075
Ruggiero, Peter, 463, 633, 1768
Ruthven, Trey, 1326

Sánchez, José C., 2279
Sabatier, François, 207
Saifee, Shabbar, 1466
Sakagami, Takeharu, 96
Sakamoto, Hikari, 179
Sallenger, Asbury H., 179, 888, 897, 976, 2061
Salles, Paulo, 996, 2279
San-nami, Toshiro, 314
Santo, Renato E., 1455
Sasaki, Takayuki, 1354
Sasakura, Shinya, 1900
Sato, Shinji, 68, 1089
Sayah, Selim M., 2321
Schmeltz, Edward J., 2254
Schmidt-Koppenhagen, Reinold, 248
Schupp, Courtney A., 1340
Schwab, William C., 2151, 2487
Seabergh, William C., 1391
Seaver, Kathryn, 1722
Selegean, James P., 392, 2292
Serizawa, Masumi, 259, 314, 2446, 2460
She, Kaiming, 520
Shepsis, Vladimir, 1489
Sheremet, Alex, 661, 882
Sherman, Douglas J., 1241
Shibayama, Tomoya, 1690
Shimozono, Takenori, 1089
Short, Andrew D., 1417
Simpson, David, 477
Slott, Jordan, 1214
Smith, David E., 1075
Smith, Eric, 2432
Smith, Ernest R., 193, 1502
Smith, Jane M., 1311
Smith, S. Jarrell, 2382
Soltanpour, Mohsen, 1690
Son, Minwoo, 1669
Son, P. Kim, 272
Soulsby, Richard L., 1075
Spiers, Kyle C., 2358
Stauble, Donald K., 814, 2418
Stive, Marcel J. F., 207, 736, 1363, 1589, 1975
Stockdon, Hilary F., 976
Stolper, David, 1153
Stone, Gregory W., 911, 921, 935, 1988
Storlazzi, Curt D., 1227, 1851
Storms, Joep E. A., 736
Suzuki, Takayuki, 2037
Swales, Andrew, 1441
Sweeney, Rachel, 647

Tajima, Yoshimitsu, 96, 1089
Takagi, Toshimitsu, 1008, 1623
Takeuchi, Maiko, 2037
Takewaka, Satoshi, 1900
Talmon, A. M., 137
Tanaka, Hitoshi, 842
Tarya, Ayi, 1647
Taylor, David, 2213
Taylor, Matthew J., 762
Teakle, I., 286
Thieler, E. Robert, 2487
Thomas, Robert C., 1502
Thompson, David M., 897, 976
Thomson, Gordon G., 647, 2265
Tidwell, David K., 1377
Tomoda, Naoki, 2037
Tonkin, Susan P., 561
Trim, Louise, 520
Tsuru, Masahito, 96
Tung, Tran Thanh, 1589
Twichell, David C., 2487

Uda, Takaaki, 259, 314, 2446, 2460
Uijttewaal, Wim S. J., 1975

Valdemoro, Herminia I., 1283
Valentine, Page C., 2487
Valvo, Lisa, 1214
van de Graaff, Jan, 612, 1589
van den Bergh, Gert, 1647
van der Burgh, L. M., 1813
van der Spek, Ad J. F., 1129
van der Werf, Jebbe J., 1, 42

van Gent, Marcel R. A., 612
van Heteren, Sytze, 1129
van Koningsveld, M., 1813
van Ormondt, M., 137
van Rijn, Leo V., 1, 137
van Thiel de Vries, Jaap S. M., 1975
Vanderbeke, Nicole, 2402
Vatvani, Deepak, 1117
Vellinga, Tiedo, 598
Verwaest, Toon, 1431
Vidal, César, 2241
Vila-Concejo, Ana, 1417, 1557, 2049
Vincent, Chris E., 248
Vital, Helenice, 1731
Vitousek, Sean, 1227

Waldron, Ryan, 749
Walstra, Dirk Jan R., 137, 207, 671, 736, 1589
Wamsley, Ty V., 1924
Wang, Ping, 378, 1047, 1377, 1582, 1961
Wang, Zhanxian, 626
Warren, Jeffrey D., 1837
Warrick, Jonathan A., 463
Weaver, Robert, 1466
Weber, Kathryn M., 1837
Weishar, Lee L., 814
Welsh, John M., 1543
White, James, 2402
Whitman, Dean, 1877
Whitmeyer, Shelley J., 2164
Wijnberg, K. M., 1813
Williams, Deidre D., 1529
Williams, Jon J., 221, 1886
Williams, R. B. G., 531
Williams, S. Jeffress, 1153, 2473
Willson, Clinton S., 749
Winer, Harley S., 712
Wise, Larry A., 2372
Worley, Charles W., 2487
Wozencraft, Jennifer M., 1827
Wray, Michael, 477
Wren, P. A., 1787
Wright, C. Wayne, 888

Yamaguchi, Satomi, 2037
Yano, Shinichiro, 842

Zarillo, Gary A., 1297, 2199
Zhang, Keqi, 1877



Coastal Sediments '07

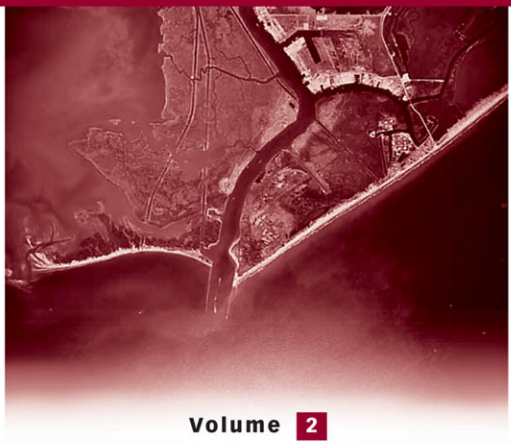

Volume 2

ASCE

Edited by
Nicholas C. Kraus
Julie Dean Rosati

Coasts, Oceans, Ports, and Rivers Institute
An Institute of The American Society of Civil Engineers

COASTAL SEDIMENTS '07

VOLUME TWO

PROCEEDINGS OF THE SIXTH INTERNATIONAL SYMPOSIUM ON COASTAL ENGINEERING AND SCIENCE OF COASTAL SEDIMENT PROCESSES

May 13–17, 2007
New Orleans, Louisiana

SPONSORED BY
Coasts, Oceans, Ports, and Rivers Institute (COPRI)
of the American Society of Civil Engineers

IN COOPERATION WITH
American Shore and Beach Preservation Association
Dept. of Oceanography and Coastal Science, Louisiana State University
Geological Society of America
International Association of Geomorphologists
International Union of Geological Sciences
U.S. Army Corps of Engineers, Coastal Inlets Research Program
U.S. Geological Survey, Coastal and Marine Geology Program

EDITED BY
Nicholas C. Kraus
Julie Dean Rosati

ASCE

Published by the American Society of Civil Engineers

Library of Congress Cataloging-in Publication Data

International Symposium on Coastal Engineering and Science of Coastal Sediment Processes (6th : 2007 : New Orleans, La.)
Coastal sediments '07 : proceedings of the sixth International Symposium on Coastal Engineering and Science of Coastal Sediment Processes, May 13–17, 2007, New Orleans, Louisiana / sponsored by Coasts, Oceans, Ports, and Rivers Institute (COPRI) of the American Society of Civil Engineers in cooperation with American Shore and Beach Preservation Association ... [et al.] ; edited by Nicholas C. Kraus, Julie Dean Rosati.
p. cm.
Includes bibliographical references and index.
ISBN-13: 978-0-7844-0926-8
ISBN-10: 0-7844-0926-9
1. Coast changes--Congresses. 2. Coastal sediments--Congresses. I. Kraus, Nicholas C. II. Rosati, Julie Dean. III. Coasts, Oceans, Ports and Rivers Institute (American Society of Civil Engineers) IV. Title.

GB450.2.I58 2007
627'.58--dc22 2007009073

American Society of Civil Engineers
1801 Alexander Bell Drive
Reston, Virginia, 20191-4400

www.pubs.asce.org

Any statements expressed in these materials are those of the individual authors and do not necessarily represent the views of ASCE, which takes no responsibility for any statement made herein. No reference made in this publication to any specific method, product, process, or service constitutes or implies an endorsement, recommendation, or warranty thereof by ASCE. The materials are for general information only and do not represent a standard of ASCE, nor are they intended as a reference in purchase specifications, contracts, regulations, statutes, or any other legal document. ASCE makes no representation or warranty of any kind, whether express or implied, concerning the accuracy, completeness, suitability, or utility of any information, apparatus, product, or process discussed in this publication, and assumes no liability therefore. This information should not be used without first securing competent advice with respect to its suitability for any general or specific application. Anyone utilizing this information assumes all liability arising from such use, including but not limited to infringement of any patent or patents.

ASCE and American Society of Civil Engineers—Registered in U.S. Patent and Trademark Office.

Photocopies and reprints.
You can obtain instant permission to photocopy ASCE publications by using ASCE's online permission service (www.pubs.asce.org/authors/RightslinkWelcomePage.html). Requests for 100 copies or more should be submitted to the Reprints Department, Publications Division, ASCE, (address above); email: permissions@asce.org. A reprint order form can be found at www.pubs.asce.org/authors/reprints.html.

Photo Credit.
Top: East Island, Isle Dernieres, Louisiana, October 20, 1990. Bottom: Belle Pass and Port of Fouchon, Louisiana, November 3, 1989. *Images Courtesy USGS*

Copyright © 2007 by the American Society of Civil Engineers. All Rights Reserved.
ISBN 13: 978-0-7844-0926-8
ISBN 10: 0-7844-0926-9
Manufactured in the United States of America.

Foreword

The COASTAL SEDIMENTS '07 conference was organized as a technical specialty conference devoted to the physical aspects of sediment processes and morphology change in the coastal and inlet environment. Following previous conferences in the Coastal Sediments series that were held in 1977, 1987, 1991, 1999, and 2003, COASTAL SEDIMENTS'07 celebrated 30 years of the Coastal Sediments series and promoted exchange of information and views among specialists in the fields of coastal engineering, geology, oceanography, and related disciplines. The theme of COASTAL SEDIMENTS '07 was "Coastal Engineering and Science in Cascading Spatial and Temporal Scales," which established the trend of thinking and approach of the conference, as well as determined in part the composition of the papers that were presented. This theme was chosen to stimulate research devoted to the various scales of processes and their interactions at which coastal engineers and scientists must work in developing knowledge and capabilities to assist society in managing the coast under present and future conditions. Emphasis was on papers that recognize and relate to coastal morphology change of long-term consequence.

The COASTAL SEDIMENTS '07 conference returned to the site of the 1987 conference, New Orleans, Louisiana, because of the extraordinary morphologic change along the coasts of Louisiana, Mississippi, and Texas, caused by Hurricanes Katrina and Rita that struck in August and September, respectively, of 2005. In addition to the recent hurricanes, this coast is experiencing long-term natural and anthropogenic change including rapid and differential subsidence, severe reduction in renewable sediment supply, deltaic adjustment of fine-grained material, and oil and gas exploration and extraction. The theme is intended to generate papers and discussion of coastal sediment processes from the micro-scale to the regional scale at which integrated coastal design and management must be accomplished. Participants were given an overview of recent hurricane damage within the context of the long-term morphologic change in Louisiana in the Keynote Address delivered by Mr. James R. (Randy) Hanchey, Deputy Secretary of the Louisiana Department of Natural Resources.

Professor Leo van Rijn of Delft Hydraulics and the University of Utrecht, The Netherlands, accepted the 2007 Coastal Award at the Conference Awards Luncheon on May 16th. Starting in 2001, the Coastal Award has been presented every 2 years alternately at the Coastal Dynamics conference and the Coastal Sediments conference through coordination between the organizing committees of these two technical specialty conferences. The Organizing Committee of Coastal Sediments '07 joins conference participants and the extended research community in celebrating Professor van Rijn's research contributions that have greatly influenced engineers and geologists working in the areas of coastal sediment transport and morphology change.

These *Proceedings* volumes are the permanent record of the conference, containing the latest thinking and progress of the world's leading scientists and

engineers in the areas of coastal sediment transport and morphology change. The contents are a valuable source of information on coastal sediment and morphology processes ranging from basic research to case studies and lessons learned. The papers contained herein provide the most recent results and ideas in a wide range of approaches and viewpoints not assembled elsewhere in both quality and breadth. The *Proceedings* were produced in hard copy in two volumes in black and white and also provided to conference participants as a CD ROM with searchable index of PDF files in color. All papers are available to the public in PDF format via the ASCE Research Library at www.ascelibrary.org.

Three-hundred fifty abstracts were submitted to the Conference Steering Committee. On average, each abstract received five reviews, and 225 submissions were invited for development into full papers and presentation over 3 days of technical sessions. The 197 papers appearing in these Proceedings originated from approximately 24 countries, demonstrating the international scope of COASTAL SEDIMENTS '07. Each paper included in these *Proceedings* received positive peer review. Each paper is eligible for discussion in the *Journal of Waterway, Port, Coastal and Ocean Engineering* and can be nominated for ASCE awards.

The Steering Committee of COASTAL SEDIMENTS '07 gratefully acknowledges the assistance of many individuals, both known and anonymous, in the 2 years of preparations by an all-volunteer committee. Numerous individuals assisted the Steering Committee in review of abstracts and final papers. The efforts of the following persons are acknowledged: Matthew Arsenault, U.S. Geological Survey (USGS); Mark Byrnes, Applied Coastal Research and Engineering, Inc.; Duncan FitzGerald, Boston University; Guy Gelfenbaum, USGS; Cheryl Hapke, USGS; John Headland, Moffatt & Nichol; Todd Holland, Naval Research Laboratory; Peter Howd, USGS; Bruce Jaffe, USGS; Magnus Larson, University of Lund; Jeffrey List, USGS; Randy Parkinson, Coastal and Environmental Geological Consulting; Robert Morton, USGS; James O'Connell, Woods Hole Oceanographic Institution; Lisa Robbins, USGS; Vladimir Shepsis, Coast and Harbor Engineering; Donald Stauble, U.S. Army Corps of Engineers; Marcel Stive, Delft Hydraulics; Hilary Stockdon; USGS; and Curt Storlazzi, USGS.

We also thank the session moderators for agreeing to lend their time and experience to run the conference smoothly and productively. We are indebted to the tour leaders and their organizations for arranging and conducting memorable and stimulating technical trips. The "Geology of the Louisiana Coastal Zone: Implications for Coastal Management and Restoration" tour was led by Mark Kulp, University of New Orleans (UNO); Mike Miner, UNO; Duncan FitzGerald, Boston University; and Ioannis Giorgiou, UNO. The "Wax Lake-Atchafalaya Delta Complex Sedimentation, Stratigraphy" tour was led by Harry Roberts, Louisiana State University. Finally, we thank Lucy King of ASCE for assisting and often leading in conference logistics; Donna Dickert of ASCE for accurately producing the Proceedings; and Lesa Rair and Chris Hanson of COPRI for assisting with conference arrangements, including exhibitors and sponsors.

We also would like to thank our exhibitors and sponsors for Coastal Sediments 2007 for their support:

Sponsors

Applied Coastal and Research Engineering Inc.
Coastal Engineering Consultants, Inc.
Coast & Harbor Engineering
Great Lakes Dredge & Dock Co.
NortekUSA
Olsen Associates, Inc.
Weeks Marine, Inc.

Exhibitors

American Vibracore Services, Inc.
COPRI
Frontier Surveying Co.
Louisiana Dept. of Natural Resources
Moffatt & Nichol
N.S. Nettles & Associates, Inc.
NortekUSA
SonTek/YSI
Taylor Engineering, Inc.
Teledyne RD Instruments
Tensar Earth Technologies, Inc.
U.S. Army Corps of Engineers, Coastal Inlets Research Program
U.S. Army Corps of Engineers, Navigations Systems Research Program
U.S. Army Corps of Engineers, Regional Sediment Management Program
U.S. Geologic Survey, Coastal and Marine Geology Program
University of New Orleans
URS Corporation
Weeks Marine, Inc.

To everyone who participated, we thank you for contributing to this remarkable conference that is precious to all of us.

Conference Steering Committee

Nicholas C. Kraus
Conference Co-Chair
U.S. Army Engineer
Research and Development Center

Hans Hanson
University of Lund, Sweden

Julie Dean Rosati
U.S. Army Engineer
Research and Development Center

S. Jeffress Williams
U.S. Geological Survey,
Coastal and Marine Geology Program

William G. McDougal
Conference Co-Chair
University of Florida

Luke Le Bas
Coastal Engineering Division,
Louisiana Department of
Natural Resources

Ping Wang
University of South Florida

Harley S. Winer
U.S. Army Corps of Engineers,
New Orleans District

Contents

Volume One

Sediment Transport Fundamentals I

Wave-Related Transport and Nearshore Morphology 1
Leo van Rijn, Gerben Ruessink, Bart Grasmeijer, Jebbe van der Werf, and Jan Ribberink

Closed Form Solution for Threshold Velocity for Initiation of Sediment Motion under Waves 15
Hans Hanson and Benoît Camenen

Influence of Velocity Moments on Sand Bar Movement During CROSSTEX 28
Gregory Guannel, H. Tuba Özkan-Haller, Merrick C. Haller, and James T. Kirby

Development of a New Practical Model for Sand Transport Induced by Non-Breaking Waves and Currents 42
Jebbe J. van der Werf, Jan S. Ribberink, and Tom O'Donoghue

A Total Load Formula for the Nearshore 56
Benoît Camenen and Magnus Larson

Sediment Transport Fundamentals II

Longshore Sand Transport Rate Measurements Using Small-Scale Physical Models 68
Roshan Suminda Ranasinghe and Shinji Sato

Pressure-Induced Subsurface Sediment Transport in the Surf Zone 82
Ole Secher Madsen and William McKinney Durham

Tracking Sediment Particles under Wave-Current Coexisting Field 96
Yoshimitsu Tajima, Masayuki Kozuka, Masahito Tsuru, Toshimasa Ishii, Takeharu Sakagami, Kazuo Momose, Nobuo Mimura, and Ole S. Madsen

Sediment Transport in Response to Wave Groups Generated by High-Speed Vessels 110
Philip D. Osborne, Neil J. MacDonald, and Shaun Parkinson

Sediment Transport Fundamentals III

Flume Experiments under Cat-Scan to Measure Internal Sedimentological Parameter During Sediment Transport 124
Stéphane Montreuil and Bernard F. Long

The Effects of Bed Slope and Wave Skewness on Sediment Transport and Morphology 137
D. J. R. Walstra, L. C. van Rijn, M. van Ormondt, C. Briére, and A. M. Talmon

Sediment Transport off Northeast Florida Outside the Surf Zone during Hurricanes 151
Michael Krecic, Christopher Bender, and Kristen Odroniec

Longshore Transport

Geomorphic and Sedimentologic Evidence for Net Littoral Drift—A Review 165
Terry Healy

Cross-Shore Variation of Predominant Longshore Sediment Transport Rate 179
Yoshiaki Kuriyama and Hikari Sakamoto

Longshore Sand Transport Calculated by Time-Dependent Shear Stress 193
Ernest R. Smith and Nicholas C. Kraus

Sediment Budget of the Danube Delta Coastal Zone 207
Sebastian Dan, Marcel Stive, Dirk Jan Walstra, and François Sabatier

Field Measurements and Modeling of Longshore Sediment Transport 221
J. J. Williams, L. S. Esteves, M. A. Lisniowski, and H. L. S. Perotto

Sediment Transport Fundamentals IV

Infragravity Waves in Mobile-Bed Laboratory Experiments 235
Florent Grasso, Hervé Michallet, and Eric Barthélemy

Large-Scale Laboratory Modeling of Suspended Sand Concentration Fluctuations under Irregular Waves 248
Joachim Grüne, Ruben Kos'yan, Hocine Oumeraci, Igor Podymov, Reinold Schmidt-Koppenhagen, and Chris E. Vincent

Change in Longitudinal Profile Using Sand of Mixed Grain Size in Large Wave Tank and its Numerical Simulation 259
Massaya Fukuhama, Takaaki Uda, Masumi Serizawa, and Toshinori Ishikawa

Probabilistic-Deterministic Modelling of Swash Zone Morphology 272
T. E. Baldock, P. Kim Son, P. Manoonvoravong, M. P. Barnes, and J. M. Alsina

Modelling Sheet Flow Sediment Transport Using Convolution Integrals 286
P. Guard, I. Teakle, P. Nielsen, and T. Baldock

Shoreline Change Modeling

A Middle-Term Evolution Model for Beaches 300
Soledad Requejo, Raul Medina, and Mauricio Gonzalez

Model for Predicting Beach Changes on Coast with Sand of Mixed Grain Size Based on Bagnold's Concept 314
Masumi Serizawa, Takaaki Uda, Toshiro San-nami, Kou Furuike, Toshinori Ishikawa, and Takayuki Kumada

A Circulation Modeling Approach for Evaluating the Conditions for Shoreline Instabilities 327
Jeffrey H. List and Andrew D. Ashton

An Alternative Explanation for the Shape of 'Log-Spiral' Bays 341
Ryan Littlewood, A. Brad Murray, and Andrew D. Ashton

The Response of Spit Shapes to Wave-Angle Climates 351
Andrew D. Ashton, A. Brad Murray, and Ryan Littlewood

Observed Shoreline Change

Historical Shoreline Changes and Morphodynamics of Parramore Island, Virginia (1852-2006) 364
Trent M. Richardson and Randolph A. McBride

Temporal and Spatial Scales of Profile and Planform Adjustment on a Nourished Beach 378
Nicole A. Elko and Ping Wang

Shoreline Response to Dike Failure at Grand Marais Harbor, Lake Superior, Michigan 392
Rachel R. Roblin, Mohammad Dibajnia, Robert B. Nairn, and James P. Selegean

Successful Beach Modelling, Monitoring and Management for a Large LNG Facility 406
Jonathan A. Kemp, Tom C. Coates, Richard Head, and Jenny S. Harcourt

Gravel Coasts I

The Design of Stable and Aesthetic Beach Fills: Learning from Nature 420
Paul D. Komar

Variation in the Organization of Gravel-Dominated Coastal Systems: Evidence from Nova Scotia and Southern England 434
Julian D. Orford and Simon C. Jennings

Profile Dynamics and Particle Tracer Mobility of a Cobble Berm Constructed on the Oregon Coast 449
Jonathan C. Allan and Roger Hart

Mixed Sediment Beach Processes: Kachemak Bay, Alaska 463
Peter Ruggiero, Peter N. Adams, and Jonathan A. Warrick

Mixed Sand and Gravel Beach Design and Construction for Habitat Restoration 477
David Simpson, Michael Wray, John Houghton, and John Klekotka

Gravel Coasts II

Influence of Changing Management Regimes on the Morphodynamic Response of a Mixed Gravel and Sand Barrier Beach 492
Andrew P. Bradbury and Julian D. Orford

The Influence of Groundwater on Profile Evolution of Fine and Coarse Sand Beaches 506
Diane P. Horn, Tom E. Baldock, and Ling Li

Effects of Permeability on the Performance of Mixed Sand-Gravel Beaches 520
Kaiming She, Louise Trim, Diane Horn, and Paul Canning

Cross-shore and Longshore Transport of Tracer Pebbles on a Macrotidal Mixed Sediment Beach, Somme Estuary, France 531
J. Curoy, U. Dornbusch, C. A. Moses, D. A. Robinson, and R. B. G. Williams

Why Are Shingle Beaches Replacing Sandy Beaches? (Coastal Zone of NW Portugal) 545
Helena Granja and Eduardo Loureiro

Gravel Coasts III

Field Measurements of Shore Conditions to Assess Bulkhead Effects in Thurston County, South Puget Sound 561
Susan P. Tonkin, Tim Abbe, José Carrasquero, and Steve Morrison

Coral-Gravel Storm Ridges: Examples from the Tropical Pacific and Caribbean 572
Bruce M. Richmond and Robert A. Morton

Field Observations of Step Dynamics on a Macrotidal Gravel Beach 584
Daniel Buscombe, Martin J. Austin, and Gerhard Masselink

Large-Scale Scour of the Sea Floor and the Effect of Natural Armouring Processes, Land Reclamation Maasvlakte 2, Port of Rotterdam 598
Sander Boer, Edwin Elias, Stefan Aarninkhof, Dano Roelvink, and Tiedo Vellinga

Dunes and Profiles

Dune Erosion Prediction Methods Incorporating Effects of Wave Periods 612
Marcel R. A. van Gent, E. Martijn Coeveld, Hans de Vroeg, and Jan van de Graaff

Reevaluation of Equilibrium Beach Profile Scale Parameter 626
Zhanxian Wang and Robert G. Dean

Shoreface Response to Sediment Deficit 633
G. M. Kaminsky, M. A. Ferland, P. J. Cowell, H. R. Mortiz, and P. Ruggiero

Louisiana Coast

The Challenges of Restoring Louisiana Barrier Islands: From Design through Construction 647
Gordon G. Thomson, Greg M. Grandy, and Rachel Sweeney

Field Observations of Wave-Current-Sediments Dynamics, Atchafalaya Shelf, Louisiana, USA 661
Sergio Jaramillo, Alex Sheremet, and Mead Allison

Investigation of Morphosedimentary Processes on a Schematic Louisiana Barrier Island Using Process-Based Numerical Modeling 671
T. Campbell, B. de Sonneville, L. Benedet, D. J. W. Walstra, and C. W. Finkl

Restoration-Quality Sand from Ship Shoal, Louisiana: Geotechnical Investigation for Sand on a Drowned Barrier Island 685
Syed M. Khalil, Charles W. Finkl, Jeff Andrews, and Christopher P. Knotts

Mississippi River Sand for Barrier Island Restoration in Louisiana: Geophysical and Geotechnical Investigations for Sand Mining 699
Jeffrey L. Andrews, Syed M. Khalil, Charles W. Finkl, and Lindino Benedet

Mississippi River Delta

Re-Engineering the Mississippi River as a Sediment Delivery System 712
Harley S. Winer

Sediment Flux and Fate in the Mississippi River Diversion at West Bay: Observation Study 722
T. Mitchell Andrus and Samuel J. Bentley

Initial Morphologic and Stratigraphic Delta Evolution Related to Buoyant River Plumes 736
Joep E. A. Storms, Marcel J. F. Stive, Dano (J.) A. Roelvink, and Dirk Jan Walstra

Physical and Numerical Modeling of River and Sediment Diversions in the Lower Mississippi River Delta 749
Clinton S. Willson, Nathan Dill, William Barlett, Samantha Danchuk, and Ryan Waldron

A Geomorphic Process-Response Model for Chenier-Plain Evolution in Southwestern Louisiana, USA 762
Randolph A. McBride, Matthew J. Taylor, and Mark R. Byrnes

Marshes and Wetlands

Sediment Analysis for Habitat Restoration: Adaptation of Open-Coast Beach Nourishment Principles 776
Daniel J. Heilman, Joel T. Darnell, and M. Cameron Perry

Subsurface Exploration and Containment Dike Design Criteria for Coastal Louisiana Marsh Restoration 785
Russ Joffrion, Michael Poff, and Mitch Andrus

Ice Raft Formation, Dispersion and Sedimentation on New England Salt Marshes 798
Brittina A. Argow, Zoe J. Hughes, and Duncan M. FitzGerald

Effects of Large Scale Morphological Changes to a Back-Bay System 814
Lee L. Weishar, Theodore Keon, and Donald K. Stauble

Volume Two

Deltas and River Mouths

Morphodynamic Feedbacks on Deltaic Coasts: Lessons from the Wave-Dominated Danube Delta 828
Liviu Giosan

Coastal and River Mouth Morphology Change in Sri Lanka Due to 2004 Indian Ocean Tsunami 842
Hitoshi Tanaka, Kazuo Ishino, Bandara Nawarathna, Hajime Nakagawa, and Shinichiro Yano

Holocene Evolution of the Merrimack Embayment, Northern Massachusetts, Interpreted from Shallow Seismic Stratigraphy **856**
Christopher J. Hein, Duncan M. FitzGerald, and Walter A. Barnhardt

The Use of Historic Topography for the Characterization of Time-Dependent Geomorphic Change and Sediment Delivery **867**
David A. Jaffe

Impact of Hurricanes Katrina and Lili on the Inner Shelf of the Mississippi-Atchafalaya Delta **882**
Mead A. Allison, Timothy M. Dellapenna, Miguel A. Goñi, and Alex Sheremet

Storms I

Coastal-Change Impacts during Hurricane Katrina: An Overview **888**
Asbury Sallenger, C. Wayne Wright, and Jeff Lillycrop

Modeling Dune Response Using Measured and Equilibrium Bathymetric Profiles **897**
Laura A. Fauver, David M. Thompson, and Asbury H. Sallenger

Sediment Transport along the Southwestern Louisiana Shoreline: Impact from Hurricane Rita, 2005 ..... **911**
Walter S. Guidroz, Gregory W. Stone, and Dane Dartez

Heterogeneity and Dynamics on a Shoal during Spring-Winter Storm Season, South-Central Louisana, USA **921**
Daijiro Kobashi, Felix Jose, and Gregory W. Stone

Winter Storm and Tropical Cyclone Impacts on the Short-Term Evolution of Beaches and Barriers along the Northeastern Gulf of Mexico **935**
Gregory W. Stone, Baozhu Liu, and Felix Jose

Storms II

Impact of a Major Storm on Sediment Exchanges between the Dunes, Beach, and Nearshore **951**
Aart Kroon, Susanne Quartel, and Troels Aagaard

Storm Patterns and Climatic Trends Based on Water Level Fluctuations: Duck, North Carolina, USA **963**
Joan Pope

Hindcasting Potential Hurricane Impacts on Rapidly Changing Barrier Islands **976**
Hilary F. Stockdon, David M. Thompson, and Asbury H. Sallenger, Jr.

EOF Analysis of Morphological Response to Hurricane Ivan **986**
Chris Houser, Stuart Hamilton, Klaus Meyer-Arendt, and Jonathan Oravetz

Storm Surge and Sediment Process Owing to Hurricane Isidore in Terminos Lagoon, Campeche **996**
Juan C. Espinal, Paulo Salles. A de A, and Diana K. Moran

Tsunami I

Tsunami Damage Estimation in Consideration of Beach Transformation and Dike Failure 1008
Fuminori Kato, Masaya Fukuhama, Hiroyuki Fujii, and Toshimitsu Takagi

Beach Morphology at Banda Aceh, Indonesia in Response to the Tsunami on 26 December 2004 1019
Ella Meilianda, C. Marjolein Dohmen-Janssen, Ben H. P. Maathuis, Suzanne J. M. H. Hulscher, and Jan P.M. Mulder

Dune Morphology as an Indicator of Paleotsunamis 1033
James R. Goff

Sedimentological Characteristics of Regional-Scale Washover Deposits Caused by Hurricane Ivan 1047
Mark H. Horwitz and Ping Wang

Tsunami II

Impacts of the 2004 Indian Ocean Tsunami on the Southwest Coasts of Sri Lanka 1061
Robert A. Morton, James R. Goff, and Scott L. Nichol

Reconstructing Tsunami Run-Up from Sedimentary Characteristics—A Simple Mathematical Model 1075
Richard L. Soulsby, David E. Smith, and Alan Ruffman

Numerical Study of Tsunami Run-Up over Erodible Sand Dunes 1089
Takenori Shimozono, Shinji Sato, and Yoshimitsu Tajima

Predicted Sedimentary Record of Reflected Bores 1103
Bretwood Higman, Guy Gelfenbaum, Patrick Lynett, Andrew Moore, and Bruce Jaffe

Tsunami Inundation and Sediment Transport in Vicinity of Coastal Mangrove Forest 1117
Guy Gelfenbaum, Deepak Vatvani, Bruce Jaffe, and Frank Dekker

Sea Level Rise I

From Transgression to Regression: Coastal Evolution near The Hague, The Netherlands, around 5000 Years BP 1129
Ad J. F. van der Spek, Jelmer Cleveringa, and Sytze van Heteren

Changing Orientation of Ocean-Facing Bluffs on a Transgressive Coast, Cape Cod, Massachusetts 1142
Graham S. Giese and Mark B. Adams

Modeling Barrier Island Response to Sea-Level Rise in the Outer Banks, North Carolina 1153
Laura J. Moore, Jeffrey H. List, S. Jeffress Williams, and David Stolper

1880 to 2005 Morphological Evolution of a Transgressive Tidal Inlet, Little Pass Timbalier, Louisiana 1165
Michael D. Miner, Duncan M. FitzGerald, and Mark A. Kulp

Sea Level Rise II

Impacts of Rising Sea Level to Backbarrier Wetlands, Tidal Inlets, and Barrier Islands: Barataria Coast, Louisiana 1179
Duncan FitzGerald, Mark Kulp, Zoe Hughes, Ioannis Georgiou, Michael Miner, Shea Penland, and Nick Howes

Modeling Future Coastal Wetland Transition Induced by Relative Sea-Level Rise 1193
James C. Gibeaut

Morphological Interactions within UK Estuaries: A Preliminary Analysis of Critical Rates of Sea-Level Rise 1200
Kate Rossington, Robert J. Nicholls, and Michiel A. F. Knaapen

Variable Shoreline Responses to Sea-Level Rise and Climate Change 1214
A. Brad Murray, Lisa Valvo, Jordan Slott, Andrew Ashton, and Tom Crowley

Model Scenarios of Shoreline Change at Kaanapali Beach, Maui, Hawaii: Seasonal and Extreme Events 1227
Sean Vitousek, Charles H. Fletcher, Mark A. Merrifield, Geno Pawlak, and Curt D. Storlazzi

Wind-Blown Sand

Aeolian Processes, Coastal Dunes, and the *Coastal Engineering Manual*, Part III, Chapter 4—"Wind-Blown Sediment Transport" 1241
Frank Hopf and Douglas J. Sherman

Distribution of Horizontal Distance Traveled by Saltating Sand Grains in Air 1255
Shintaro Hotta, Susumu Kubota, and Nagatomo Nakamura

Beach Stabilization Works Against Wind Blown Sand on Beaches: Experiences from Japan 1269
Susumu Kubota, Souichi Harikai, and Shintaro Hotta

Coastal Dunefield Evolution in Conditions of Limited Sediment Availability: Natural and Anthropogenic Controls on the Corralejo Dunes 1283
Herminia I. Valdemoro, José A. Jiménez, Ignacio Alonso, Paloma Lorente, and Manuel Rodriguez-Herrerias

Coastal Inlets I

Hydrodynamic and Morphologic Modeling at Sebastian Inlet, FL 1297
Gary A. Zarillo and Florian G. A. Brehin

Erosion and Channel Migration at the Shoalwater Bay Reservation, Willapa Bay, Washington 1311
Andrew Morang, David J. Mark, and Jane M. Smith

Sediment Management Plan Development for the St. Lucie Inlet, Martin County, Florida 1326
John Ramsey, Trey Ruthven, Kevin Kremkau, and Kathy Fitzpatrick

Sand Bypassing Restores Natural Processes to Assateague Island, Maryland 1340
Courtney A. Schupp, Gregory P. Bass, and William G. Grosskopf

Morphological Responses to Jetty Construction at Tidal Inlet: Lake Saroma, Japan 1354
Kentaro Hayashi, Koji Hashimoto, Takayuki Sasaki, Akihiro Honma, and Seizo Matsura

Coastal Inlets II

Morphodynamics of Texel Inlet, The Netherlands 1363
Edwin P. L. Elias and Marcel J. F. Stive

Sedimentation Patterns in a Stabilized Migratory Inlet, Blind Pass, Florida 1377
Ping Wang, David K. Tidwell, Tanya M. Beck, and Nicholas C. Kraus

Approaches to Understanding Multiple-Inlet Stability 1391
William C. Seabergh

Engineering Guidelines for the Siting of Sand Bypassing Discharges 1405
Douglass W. Mann

Shoreline Implications of Flood-Tide Delta Morphodynamics. The Case of Port Stephens (SE Australia) 1417
Ana Vila-Concejo, Andrew D. Short, Michael G. Hughes, and Roshanka Ranasinghe

Mud Coasts I

Using Simple Semi-Empirical Models for Integrated Assessment of Scenarios for a Navigation Channel. The Case of the Port of Ostend, Belgium 1431
Toon Verwaest

Sediment Processes and Mangrove-Habitat Expansion on a Rapidly-Prograding Muddy Coast, New Zealand 1441
Andrew Swales, Samuel J. Bentley, Catherine Lovelock, and Robert G. Bell

The Influence of Mud on the Inner Shelf, Shoreface, Beach, and Surf Zone Morphodynamics—Cassino, Southern Brazil 1455
Lauro J. Calliari, K. Todd Holland, Pedro S. Pereira, Rafael M. C. Guedes, and Renato E. Santo

The Hurricane Katrina Storm Surge in Mississippi 1466
Alan W. Niedoroda, Lyle Hatchett, Himangshu Das, Andrew Cox, Robert Weaver, Stephen Baig, and Shabbar Saifee

Texas Inlets

Coastal Inlets of Texas, USA 1475
Nicholas C. Kraus

Cedar Bayou—Inlet Dynamics and Engineering 1489
Vladimir Shepsis and Joshua Carter

Navigation Improvements, Mouth of the Colorado River, Texas 1502
Ronnie G. Barcak, Nicholas C. Kraus, Lihwa Lin, Ernest R. Smith, Daniel J. Heilman, and Robert C. Thomas

Long-Term Inlet Stability of a Multiple Inlet System, Pass Cavallo, Texas **1515**
Brian K. Batten, Nicholas C. Kraus, and Lihwa Lin

Morphologic Response to a New Inlet, Packery Channel, Corpus Christi, Texas **1529**
Deidre D. Williams, Nicholas C. Kraus, and Carl M. Anderson

Coastal Inlets III

Evolution of a Relocated Tidal Inlet: Mason Inlet, NC **1543**
John M. Welsh and William J. Cleary

Present Hydrodynamics of Ancão Inlet, 10 Years after its Relocation **1557**
André Pacheco, Ana Vila-Concejo, Oscar Ferreira, and Alveirinho Dias

The Influence of Tidal Prism and Vegetation on Tidal Channel Morphology: Implications for Marsh Stability **1571**
Matthew L. Kirwan and A. Brad Murray

Natural and Anthropogenic Influences on the Morphodynamics of Big Sarasota Pass, Florida **1582**
Richard A. Davis, Ping Wang, and Tanya Beck

Morphological Behavior of Seasonal Closure of Tidal Inlets **1589**
Tran Thanh Tung, Marcel J. F. Stive, Jan van de Graaff, and Dirk-Jan R. Walstra

Estuaries

The National Academies Report on Mitigating Shore Erosion along Sheltered Coasts **1601**
Jeff Benoit and Susan Roberts

Field Measurement and Modeling of Scour Pit Dynamics in a Sandy Estuary **1609**
A. G. Davies and J. M. Brown

Projection of Topographic Change of an Estuary Terrace by Horizontal 2-D Simulation Model, Considering Grain Size **1623**
Toshimitsu Takagi, Go Asano, Takushi Inukai, and Masaya Fukuhama

Examining the Contribution of Sediment Stratification to the Evolution of Seabed Morphology **1635**
S. Falchetti, D. C. Conley, and M. Brocchini

From River Basin to Barrier Reef: Pathways of Coastal Sediments **1647**
Piet Hoekstra, Ton Hoitink, Frans Buschman, Ayi Tarya, and Gert van den Bergh

Mud Coasts II

Wave Evolution on Fluid Mud Bottom **1660**
Kevin Hall and Ali Oveisy

A Fine Sediment Transport Modeling Framework and its Application to Fluid Mud Processes **1669**
Tian-Jian Hsu and Minwoo Son

Field Measurement of Fine Sediment Transport Process around Navigation Channel 1678
Yasuyuki Nakagawa and Hideo Matsumoto

Time Dependent Mud Fluidization and Irregular Wave Transformation on Muddy Profiles 1690
Mohsen Soltanpour, S. Abbas Haghshenas, and Tomoya Shibayama

Volume Three

Regional Processes I

Regional Beach/Cliff System Dynamics along the California Coast 1696
Cheryl J. Hapke and Dave Reid

Factors Influencing the Long-Term Stability of the Carbonate Sand Beaches of Mauritius 1708
Michael J. Risk, Robert B. Nairn, and Mark O. Kolberg

Evolution of Erosion Hot Spots on a Barrier Island: Fire Island, New York 1722
Kathryn Seaver, Frank Buonaiuto, and Henry Bokuniewicz

Tropical Mixed Wave/Tide Dominated Barrier-Spit System: A Case Study from NE Brazil 1731
Helenice Vital, Francisco Santos Neto, Jose S. Placido Junior, and Venerando E. Amaro

Regional Shoreline and Beach Changes in the Santa Barbara Sandshed 1740
David L. Revell and Gary B. Griggs

Regional Processes II

Engineering Activities Influencing Historical Sediment Transport Pathways at the Columbia River Mouth, WA/OR 1754
Mark R. Byrnes, Sarah F. Griffee, and Hans R. Moritz

Implementing Regional Sediment Management to Sustain Navigation at an Energetic Tidal Inlet 1768
Hans R. Moritz, Guy R. Gelfenbaum, George M. Kaminsky, Peter Ruggiero, Joan Oltman-Shay, and Doris J. McKillip

Decadal Evolution of Shoreface Geometry in South Carolina, USA 1787
B. M. Reynolds, P. A. Wren, and P. T. Gayes

Improving Statistical Validity in Calculating Erosion Hazards from Historical Shorelines 1799
Ayesha S. Genz, L. Neil Frazer, and Charles H. Fletcher

Linking Coastal Evolution and Super Storm Dune Erosion Forecasts 1813
L. M. van der Burgh, K. M. Wijnberg, S. J. M. H. Hulscher, J. P. M. Mulder, and M. van Koningsveld

LIDAR and ARGUS

***CHARTS*-Enabled Data Fusion for Coastal Zone Characterization** 1827
Jennifer M. Wozencraft, Christopher L. Macon, and W. Jeff Lillycrop

Using Topographic LIDAR Data to Delineate the North Carolina Shoreline 1837
Patrick W. Limber, Jeffrey H. List, Jeffrey D. Warren, Amy S. Farris, and Kathryn M. Weber

Exploring Rippled Scour Depressions Offshore Huntington Beach, CA 1851
Eleyne L. Phillips, Curt D. Storlazzi, Peter Dartnell, and Brian D. Edwards

A Study of Intertidal Bar Dynamics Using the Argus Video System 1865
Amaia Ruiz de Alegria Arzaburu, Suzana Ilic, and Yohama Gunawardena

Depth of Closure Derived from Airborne Laser Bathymetry 1877
William Robertson V, Keqi Zhang, and Dean Whitman

Remote Sensing

Assessing Nearshore Bar Movements during Storms Using Time-Averaged X-Band Radar Images 1886
Luciana S. Esteves, Jon J. Williams, and Paul S. Bell

Longshore Migration of Coastal Features Observed with X-Band Radar 1900
Satoshi Takewaka, El Sayed Galal, Ryosuke Matsumoto, and Shinya Sasakura

Detailed 3-D Models of New Zealand Barrier Stratigraphy Provide Insight into Coastal Evolution in Various Spatial and Temporal Settings 1910
Amy J. Dougherty and Scott L. Nichol

Swash Zone

A Formula for Longshore Sediment Transport in the Swash 1924
Magnus Larson, Ty V. Wamsley

Importance of the Swash Longshore Sediment Transport in Morphodynamic Models 1938
Yasuyuki Baba and Benoît Camenen

Direct Bed Shear Stress Measurements in Bore-Driven Swash and Swash Interactions 1947
Matthew P. Barnes and Tom E. Baldock

Limits of Beach and Dune Erosion in Response to Wave Runup Elucidated from SUPERTANK 1961
Tiffany M. Roberts, Ping Wang, and Nicholas C. Kraus

Interaction of Dune Face and Swash Zone 1975
Jaap S. M. van Thiel de Vries, Linden B. Clarke, Stefan G. J. Aarninkhof, E. Matrijn Coeveld, Rob A. Holman, Meg L. Palmsten, Ad J. H. M. Reniers, Marcel J. F. Stive, and Wim S. J. Uijttewaal

Barrier Island Breaching

Critical Width of Barrier Islands and Implications for Engineering Design 1988
Julie Dean Rosati and Gregory W. Stone

Barrier Island Vulnerability to Breaching: A Case Study on Dauphin Island, Alabama 2002
Mark Hansen and Asbury H. Sallenger

Morphologic Modeling of Multiple Barrier Island Breaches for Regional Application 2011
Kenneth J. Connell, Magnus Larson, and Nicholas C. Kraus

Breach Stability and Growth Analysis Using a Morphological Model 2025
Santiago R. Alfageme, Masood Khondker, and Rafael Canizares

Spatial Distribution of Cross-Shore Sediment Transport Rate for Berm Formation and Erosion 2037
Takayuki Suzuki, Maiko Takeuchi, Naoki Tomoda, Satomi Yamaguchi, and Yoshiaki Kuriyama

Overwash and Washover

Sediment Transport Patterns During Overwash 2049
Ana Matias, Ana Vila-Concejo, Óscar Ferreira, Brad Morris, and João A. Dias

Characterization and Modeling of Washover Fans 2061
Chantal Donnelly and Asbury H. Sallenger

Experimental Study of Overwash 2074
Billy L. Edge, Young Hyun Park, and Margery Overton

Backbarrier Evolution and Complete Overwash Occurrence 2084
Ana R. Carrasco, Óscar Ferreira, Ana Matias, and João A. Dias

Sand Bars, Beach Cusps

Geomorphic Features Shaped by Crossing Waves 2097
Robert B. Nairn and Mohammad Dibajnia

Observation and Modeling of Crescentic Bars in Barcelona Embayed Beaches 2111
F. Ribas, R. Garnier, E. Ojeda, A. Falqués, J. Guillén, and D. Calvete

Mesoscale Behaviour of Longshore Bars—Net Onshore or Net Offshore Migration 2124
Troels Aagaard and Aart Kroon

Morphological Characteristics of Rip Current Embayments on the Oregon Coast 2137
Matthew M. Dalon, Merrick Haller, and Jonathan Allan

Geologic Framework of the Long Bay Inner Shelf: Implications for Coastal Evolution in South Carolina 2151
Walter Barnhardt, Jane Denny, Wayne Baldwin, William Schwab, Robert Morton, Paul Gayes, and Neal Driscoll

Sand Waves and Channels

A Relic Sand Wave Field in a Tidal Channel 2164
Shelley J. Whitmeyer and Duncan FitzGerald

Geometric and Statistical Characteristics of Bed Forms in the Lower Mississippi River 2177
K. Kheiashy, J. McCorquodale, I. Georgiou, and E. Meselhe

Bathymetric Evolution of a Sandy Bed under Transient Progressive Waves **2191**
Blake J. Landry and Marcelo H. García

Analysis of Sebastian Inlet, FL, Morphologic Changes Using Complex Empirical Orthogonal Functions (CEOF) **2199**
Florian G. A. Brehin, Jo-Ann Rosario-Llantin, and Gary A. Zarillo

Investigating Ship Induced Scour in a Confined Shipping Channel **2213**
David Taylor, Kevin Hall, and Neil MacDonald

Beach Nourishment

Evolution of Grain-Size Distribution on Bogue Banks: Implications for Selection of Borrow Material **2229**
Timothy W. Kana

New Findings in Equilibrium Grain Size Distribution **2242**
Jordi Galofre, Raúl Medina, Gabriela Medellin, and César Vidal

Determination of Overfill Factor for Offshore Sand in Barrier Island Restoration on the Louisiana Coast **2254**
Daniel L. Bolinger, Dominic Izzo, and Edward J. Schmeltz

Broward County Beach Demonstration Project: From Beers to Beaches **2265**
Christopher Makowski, Gordon Thomson, Peter Foye, and Stephen Higgins

Beach Nourishment Evolution in the Cancún Beach, Quintana Roo, México **2279**
Diana K. Morán, Paulo Salles, A de A, José C. Sánchez, and Juan C. Espinal

Case Studies

Geomorphic Response and Elements of Sediment Budget at St. Joseph Harbor, Southeast Lake Michigan **2292**
Mohammad Dibajnia, Robert B. Nairn, and James P. Selegean

Chesapeake Bay: Headland Control Systems Performance Including Hurricane Isabel **2306**
C. Scott Hardaway, Jr. and James R. Gunn

Coastal Protection against Wind-Wave Induced Erosion Using Soft and Porous Structures: A Case Study at Lake Biel, Switzerland **2321**
Selim M. Sayah and Stephan Mai

Physical Processes Study of Goldsmith Inlet, New York **2331**
Michael J. Morgan and Nicholas C. Kraus

Dredging

Design of Navigation Channel Deepening Works Using a Morphological Model in Barranquilla, Columbia **2345**
Rafael Cañizares, Santiago Alfageme, and Tucker Mahoney

Beach Renourishment through Spoil Disposal Downdrift of a Dredged Entrance Channel **2358**
Kyle C. Spiers and Terry R. Healy

Desktop Methodology for Estimating Maintenance Dredging Requirements for Widened and Deepened Navigation Channels 2372
Larry A. Wise and Oleg Mouraenko

A Mass-Balance, Control-Volume Approach for Estimating Vertical Sediment Flux and Settling Velocity within Dredge Plumes 2382
S. Jarrell Smith and Carl T. Friedrichs

What Does "Physical Regeneration" of Marine Aggregate Dredging Sites Mean? 2394
Markus Diesing

Beach Nourishment and Structures

Performance of Beach Fill and Nearshore Breakwaters at East Ocean View Beach, Norfolk, VA 2402
Peter Elkan, Laural Krynock, Nicole Vanderbeke, James White, and Lee Rosenberg

Assessing Fill Compatibility through Project Performance Evaluation 2418
Donald K. Stauble

Coastal Structure Design for Shore Protection and Sand Retention: Practical Aspects 2432
John R. Headland, Santiago Alfageme, Eric Smith, and Peter Kotulak

Quantitative Evaluation of Controlling Effect of Headland on Longshore Sand Transport Using Model for Predicting Changes in Contour Lines and Grain Size 2446
Takayuki Kumada, Takaaki Uda, and Masumi Serizawa

Evaluation of Controlling Effect of Sand Transport by Detached Breakwaters Built on Dynamically Stable Beach 2460
Takaaki Uda, Masumi Serizawa, and Toshinori Ishikawa

Seafloor Mapping

Geologic Characterization of Offshore of Shelf Areas Using usSEABED for GIS Mapping, Modeling Processes and Assessing Marine Sand and Gravel Resources 2473
S. Jeffress Williams, James D. Bliss, Matthew A. Arsenault, Chris J. Jenkins, and John A. Goff

USGS Advances in Integrated, High-Resolution Sea-Floor Mapping: Inner Continental Shelf to Estuaries 2487
Jane F. Denny, William C. Schwab, David C. Twichell, Thomas F. O'Brien, William W. Danforth, David S. Foster, Emile Bergeron, Charles W. Worley, Barry J. Irwin, Bradford Butman, Page C. Valentine, Wayne E. Baldwin, Robert A. Morton, E. Robert Thieler, David R. Nichols, and Brian D. Andrews

A Rapid Compatibility Analysis of Potential Offshore Sand Sources for Beaches of the Santa Barbara Littoral Cell 2501
Neomi Mustain, Gary Griggs, and Patrick L. Barnard

Presence of Beach-Compatible Sediments in Offshore Borrows: New Challenges and Trade Offs in Developing Codifications **2515**
Charles W. Finkl, Jeffrey L. Andrews, and Lindino Benedet

Indexes

Subject Index **I-1**

Author Index **I-5**

VOLUME TWO

This page intentionally left blank

MORPHODYNAMIC FEEDBACKS ON DELTAIC COASTS: LESSONS FROM THE WAVE-DOMINATED DANUBE DELTA

Liviu Giosan[1]

1. Woods Hole Oceanographic Institution, MS#22, Department of Geology and Geophysics, 360 Woods Hole Road, Woods Hole, MA 02543, USA. lgiosan@whoi.edu.

Abstract: In natural conditions, the dynamics of the Danube delta coast has been largely determined by the interaction between fluvial deposition and a strong southward wave-induced longshore transport near the mouths of the river. River-mouth morphodynamics is highly nonlinear, involving multiple feedbacks on the longshore sediment transport. These include a *groin effect* of the river plume and subaqueous delta, a *shoaling effect* of the downdrift offset subaqueous delta, and a *barrier steering effect* of the downdrift barrier islands or spits. As a result, a net sequestration of sediments occurs near the river mouth that aids and speeds up delta lobe development. Downdrift of the mouth, barriers may form after extreme river floods, but also due to increased shoreline instability under high angle waves. Although river mouth processes are complex, the resulting morphology of wave-dominated delta lobes exhibits a tendency to self-organize.

INTRODUCTION

Deltas are home to a disproportionate fraction of the world's population. Moreover, a few remaining less developed deltas have some of the highest biodiversity on the planet. However, deltas are fragile geomorphic features, which can change dramatically with modest modifications in boundary conditions. Their complex morphology is the result of a dynamic equilibrium between fluvial discharge, marine energy conditions, accommodation, and the overall geological framework. Low relief makes deltas susceptible to floods, storms and sea level change, vulnerabilities exacerbated by sediment deficits following extensive river damming. Understanding the influence of

waves on deltaic coasts, in particular, is critical as deltas are increasingly becoming wave-dominated under these large fluvial sediment deficits (e.g., Ericson et al. 2006). In spite of the importance of deltas, a quantitative understanding of deltaic deposition is limited due to their intrinsic complexity (see e.g., Overeem et al. 2005).

Morphodynamics of deltaic coasts and shelves has been a less explored aspect in the evolution of deltas, although the morphodynamic paradigm has been widely used in coastal studies (e.g., Carter and Woodroffe 1994; Cowell et al. 2004). Feedbacks between the evolving morphology of a delta forced by the continuous sediment output from the river and modified by basinal hydrodynamics remain inadequately known, as are the interactions between contemporaneous lobes within a delta (e.g., Komar 1973; Wright 1985; Cowell et al. 2004) or the influence exerted by a delta on the dynamics of adjacent non-deltaic coasts and vice-versa (e.g., Penland and Suter 1989; Corregiari et al. 2005). While there has been much recent progress in understanding suspended sediment deposition from river plumes (e.g., Syvitski and Bahr 2001; Geyer et al. 2004), the dynamics of coarse sediments at river mouths (Wright 1977) has received little attention recently, in large part due to the inability of conventional techniques to provide direct reliable measurements.

Existing morphodynamic models (e.g., Komar 1973; Cowell et al. 2003) identify the *rotation of the shoreline* as the principal phenomenon associated with delta development. Shoreline rotation is responsible for changes in longshore drift along deltaic coasts. Several other hydrodynamic-morphodynamic feedback loops related to bedload sedimentation at river/distributary mouths by have been identified by Giosan et al. (2005) and are explored herein for the particular case of the Danube delta. Furthermore, numerical modeling (Ashton and Murray 2005; Ashton and Giosan 2006) suggested that shoreline instability is more to be expected on the downdrift coast of wave-dominated lobe than updrift of the feeding river mouth. A conceptual model for wave-dominated deltas proposed by Bhattacharya and Giosan (2003) is modified in here to account for this latest understanding of delta coast morphodynamics.

BACKGROUND

Danube River

The Danube river is the second largest European river after the Volga in terms of catchment area (817,000 km2) and length (2870 km) as well as water and sediment discharge. The average annual discharge reported between 1840 and 1995 is ~6240 m3/s, with the highest measured annual discharge of ~9250 m3/s in 1970 (Bondar and Blendea 2000). The peak discharge during the year occurs in late spring (Vörösmarty et al. 1998), following snowmelt and there is a factor of 2 variability between the spring (high) and the fall (low) discharge (Reschke et al. 2002).

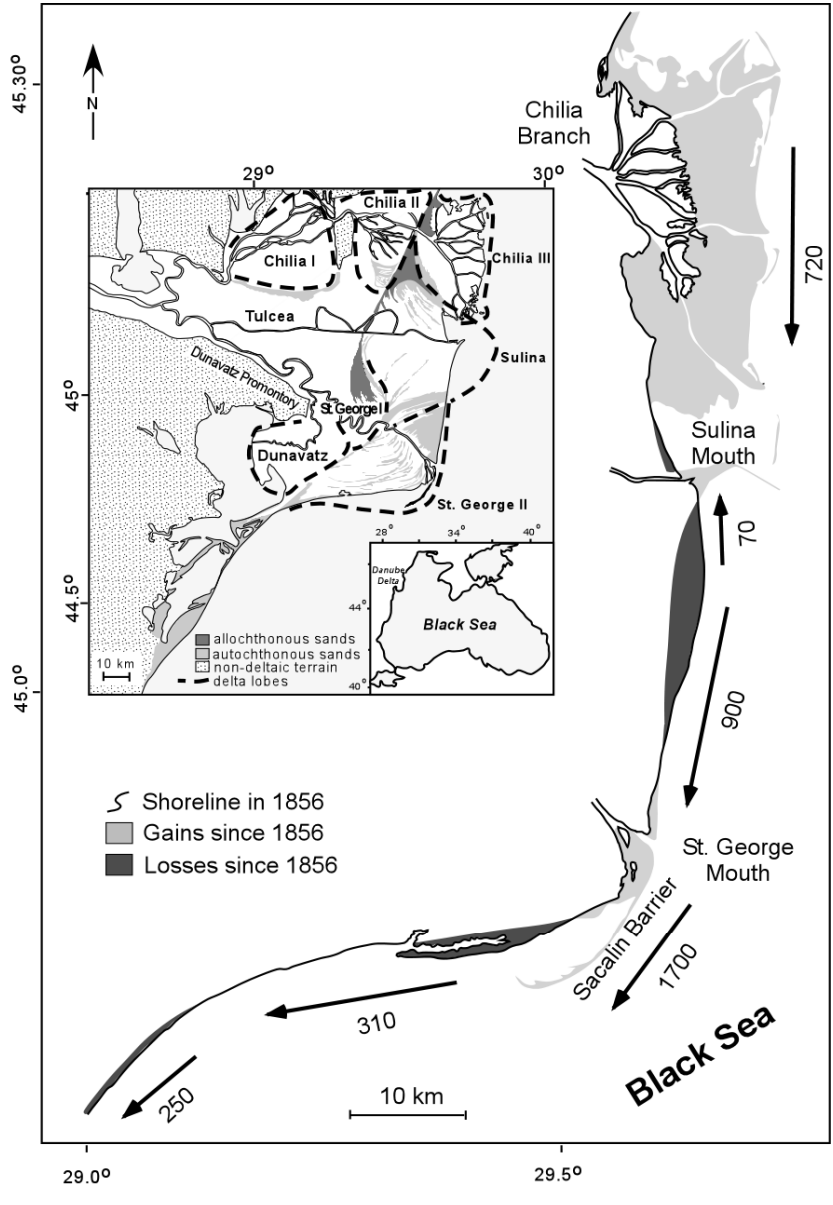

Fig. 1. Danube delta coast: shoreline changes from 1856 to 2003/05 (after Giosan et al. submitted). Cartography: S. Constantinescu. Inset: Danube delta morphology and sand facies distribution (after Giosan et al. 2006)

Extensive damming, especially in the lower basin, has reduced the suspended sediment discharge at the apex of the delta from ~67×10^6 t/year between 1921 and 1960 to ~25-35×10^6 t/year at present. The bed-load sediment discharge at the Danube mouths has been estimated to range between ~4.6 and ~5.3×10^6 t/year (Bondar et al. 1992).

In the delta, Danube splits into three main distributaries (Fig.1): the Chilia (Kilia), the Sulina and the St. George (Sf. Gheorghe). Since 1856 when the first estimates of the flow were made by the European Danube Commission, discharge through main navigation route, the Sulina arm, has steadily increased (from 7% to 19%), while St. George and Chilia have compensatorily decreased their flow (from 30% to 23% and from 63% to 57% respectively) as a consequence of sustained maintenance and improvement projects for navigation on Sulina and intensive channelization in the delta. After similar human interventions on the St. George arm in 1980's, the discharge of this distributary started to increase. Reported values for suspended and bed-load sediment discharge on the three distributaries are 55% and 57-65% for Chilia, 21% and 19-25% for Sulina, and 23% and 19%-21 for St. George, respectively (Bondar and Harabagiu 1992).

Black Sea

Danube flows and builds its delta into the Black Sea, a semi-enclosed basin connected to the World Ocean via the Sea of Marmara and the Mediterranean. Black Sea is a microtidal basin with a semi-diurnal tide with a range between 7 and 12 cm. Long term relative sea-level rise has been minimal at the Danube delta (Giosan et al. 2006), although a recent acceleration to 2.7 mm/year has been observed (Cazenave et al. 2002). The average wind speed along the Danube coast is between 5 and 6.5 m/s (Bulgakov et al. 1992). Winds from the north-east quadrant are dominant. Based on visual observations offshore Constantza, the wave regime is higly skewed (82%) arriving dominantly from the left hand side relative to the regional direction of the coast (i.e., north-east quadrant); for the 1972-1981 measurement period, the annual average significant wave height was 0.8 m, with an annual standard deviation of 1 m, and a mean period of 5 seconds (Giosan et al. 1999).

Danube Delta

Two distinct delta plain regions have been classically recognized (Antipa 1915) based on distinct morphologies defined by the distribution of channels, flood basins and lakes, and sand ridge geometries. The "fluvial delta", composed of the Tulcea, Chilia I and II, and Dunavatz lobes (Fig. 1; Giosan et al. 2006), developed in the former Danube Bay, which was probably sheltered by a barrier (Spratt 1860). The "marine delta" developed largely outside the Danube Bay and exhibits a clear wave-influenced morphology (Fig. 1). After reaching the barrier coast, Danube distributaries built four laterally offset lobes. Open-coast delta lobes are wave-dominated (Fig. 1), with the exception of the Chilia III, the youngest lobe, which shows primarily a fluvial-dominated morphology. The wave-dominated lobes exhibit an asymmetric morphology (Bhattacharya and Giosan 2003). Amalgamated beach ridges formed extensive beach ridge plains updrift (north) of (paleo)distributary mouths and are capped in places by dune fields with heights up to ~12 m (Fig. 1). Non-amalgamated beach ridges organize in barrier beach plains located

downdrift (south) of (paleo)distributary mouths. They resemble chenniers, with a succession of elongate sandy ridges separated by mud-filled marshy/lacustrine elongate depressions (Fig. 1). Beach ridges have been recognized to represent former shorelines of the delta (Bratescu 1922); their groupings in sets that are laterally juxtaposed allows the identification of the lobe development sequence for the "marine delta" (Fig. 1). Early interpretations of beach ridge juxtaposition patterns established a relative chronology for the open-coast lobes (de Martonne 1931; Zenkovich 1956). The St. George I was the first lobe built at the open-coast, followed by Sulina; subsequently, the St. George arm was reactivated developing a second lobe St. George II (Fig. 1). Chilia III is the youngest lobe built at the open coast. Based on AMS radiocarbon and optical dating, Giosan et al. (2006) have established that the "marine" part of the delta has started to develop no earlier than 5500 years BP.

Giosan et al. (1999) analyzed the longshore sediment transport pattern along the Romanian sector of the deltaic and associated lagoonal coast (Fig. 1) and found that the magnitude of the sediment drift was extremely high, with average values of ~900,000 m^3/year along sectors of the coast that are not sheltered from the eastern-northeastern dominant waves. Since 1856, when the European Danube Commission first surveyed the Danube delta coast in detail, the Chilia lobe experienced massive progradation (Fig. 1), although it has become increasingly wave dominated since 1940s (Giosan et al. 2005). The St. George lobe, with a new barrier (Sacalin) development, appears to be in a relative equilibrium, while the Sulina lobe has been reworked by waves.

MORPHODYNAMIC FEEDBACKS

Morphodynamics addresses the coupled adjustments between hydrodynamic processes, sediment transport, sedimentation, and morphology, and has become an established paradigm for studying coastal evolution (e.g., Carter and Woodroofe 1994; Wright 1985). Compared to other clastic coasts, the morphodynamics of deltas is complicated by the continuous or episodic delivery of freshwater and sediment to the coast by one or several rivers through one or multiple mouths. The solid load discharged by the river comprises of both suspended fine sediment within the river plume and coarse bed-load. Sedimentation of the coarse-grade sediments appears to be a dominant factor in river mouths evolution (Wright 1995) and further, in determining the facies architecture of wave-dominated deltas (Bhattacharya and Giosan 2003).

At the coast, delta forms a discrete subaqueous protuberance; in most cases, the protuberance is also expressed at the shoreline, which progrades relative to the adjacent coasts. From a hydrodynamical perspective, this deltaic "bulge" can be viewed as a morphological perturbation to the regional circulation system. Morphodynamic adjustments between the deltaic morphology and the fluvial and basinal hydrodynamics are most intense at the river mouths. Morphodynamics of wave-dominated deltaic distributary mouths is highly non-linear, involving multiple feedbacks between subaerial deltaic progradation, deposition on the subaqueous delta, current and wave hydrodynamics as well as wave-current interactions (Fig. 2; Giosan et al. 2005). These

feedbacks are particularly well expressed at the St. George mouth/deltaic lobe coast of the Danube delta.

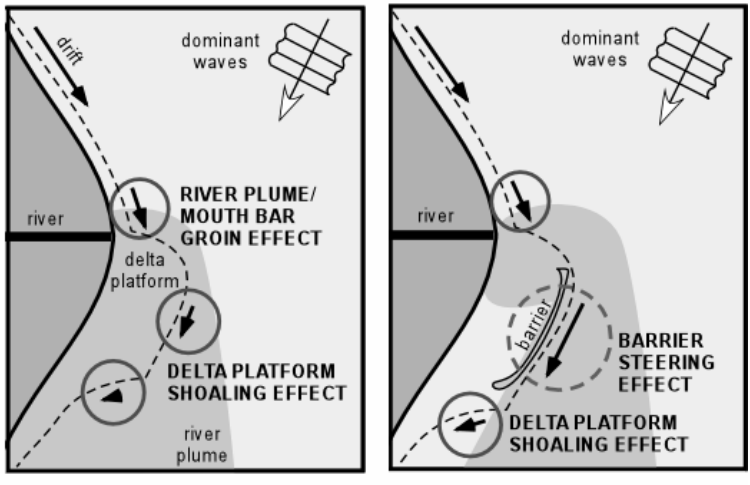

Fig. 2. Effects leading to sediment trapping on the subaqueous delta for a wave-dominated asymmetric deltaic coast with and without barrier. Convergence/divergence of the sediment drift is indicated by shortening/lengthening of arrows and continuous/dashed line circles, respectively.

Groin Effect

The morphology of the mouth shows that the submarine lobe built by the St. George branch is completely offset to the south of the mouth (Fig. 3; Constantinescu et al. submitted) in the direction of the longshore drift and the preferred orientation of the distributary's plume (Fig. 1; Bondar 1964). The coast updrift of the mouth is separated from the mouth by a subaqueous levee, it is multibarred, and evolves much like a beach on a sand-rich non-deltaic coast (Giosan et al., submitted; Vespremeanu-Stroe, A., Constatinescu, S., Ovejanu, I., Filip, F., Giosan, L., in prep., Impact of Danube high discharge events on the morphology and sedimentation at the mouth of St. George arm). Sands updrift of the St. George mouth are texturally more mature than the sands downcoast (Giosan 1993) suggesting again that fluvial material from St. George distributary does not contribute significantly to the updrift wing of the delta lobe, but instead has been built by sediment eroded from the Sulina lobe.

To explain the development of the subaqueous levee and the composition of the updrift coast, Giosan (1998) invoked the interaction between the river plume and the surface waves (Fig. 2). The convergence of the longshore sediment transport updrift of the river mouth due to this interaction has been termed as the hydraulic groin effect of the plume (Todd 1968; Komar 1973). This effect occurs regardless of the presence of suspended sediment in the plume. However, the increase in plume's density by addition of suspended sediment leads to an increase in the density contrast between the plume and the coastal waters, resulting in a more rapid breaking of the waves when they encounter the plume (e.g., Rodriguez et al. 2000). Furthermore, the subaqueous delta *per se* developed offshore the river mouth (including the subaqueous levee) also acts like an obstacle to the sediment drift (Fig. 2), much like an ebb shoal restricts bypassing of sediment downcoast (Bruun and Gerritsen 1959; Kraus 2000).

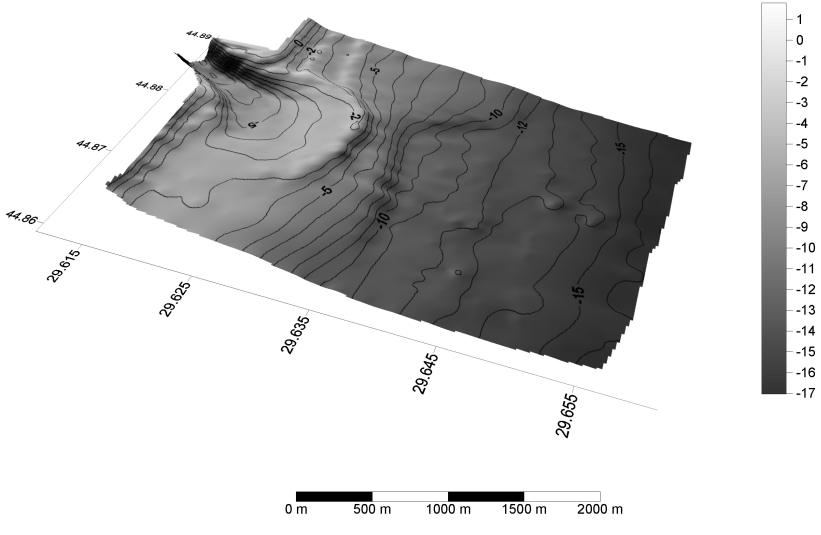

Fig. 3. DEM of the St. George mouth (after Constatinescu et al., submitted). Depth scale (in m) is on the left. Coordinates are in degrees latitude-longitude. Cartography by S. Constantinescu.

Where the longshore drift reaching the mouth is significant, a positive feedback loop develops between the progradation of the updrift coast caused by this combined groin effect of the river plume and subaqueous delta (Fig. 2), leading to a mouth that is progressively more sheltered from waves, which in turn, results in an increase in sedimentation on the subaqueous delta platform and less sand bypassing around the mouth. Sediment trapping within the delta is one of the net results of this feedback mechanism.

Shoaling Effect

On the updrift side of the mouth, the longshore drift obstructed by the river plume builds a deltaic beach ridge plain mostly of sediments brought in from updrift. Development of a subaqueous delta strongly offset to the opposite downdrift side of the mouth is accomplished with sediments brought in by the river. The asymmetry of this subaqueous delta relative to the river mouth activates another positive feedback between morphology and wave hydrodynamics (Fig. 3; Fig. 4a). The vast, shallow delta platform offset to the south of the river mouth shelters the mainland deltaic coast as waves dissipate almost completely over it. Although at a larger scale, this phenomenon is similar to the reversal of the wave-driven sediment transport on the downdrift side of ebb-shoals at inlets, due to the sheltering provided by the shoal itself (e.g., FitzGerald 1984).

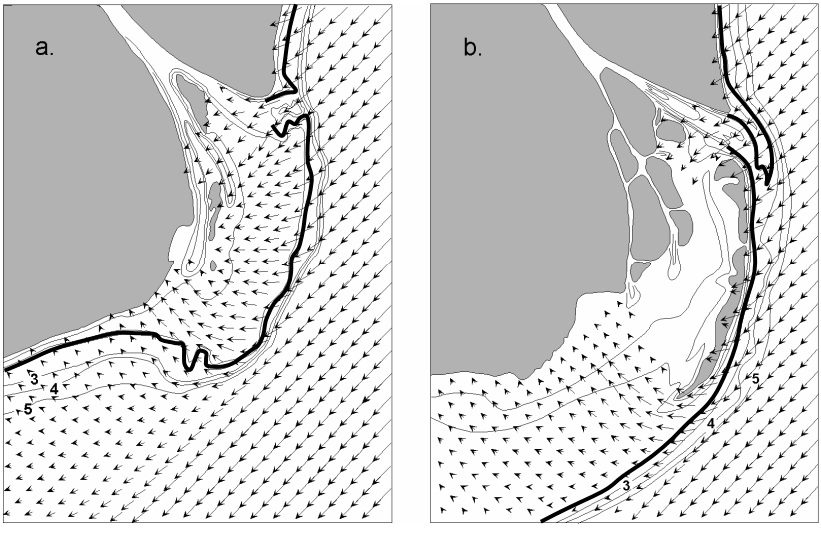

Fig. 4. Wave transformation of a typical wave field (NE from 30 m depth, with a 1 m height represent by initial arrow length and 4.5 s period; after Giosan et al. 2005) on bathymetries of St. George mouth: (a) 1856 and (b) 1935. Extent of subaqueous delta platform is shown by the 2 m depth contour (thick line). STWAVE (Smith et al. 2001) runs by F. Buonaiuto.

The convergence of the drift along the subaqueous delta is seen in modeling exercises (Fig. 4a) as waves refract and shoal less updrift of the mouth, where no the subaqueous delta is present, than downdrift of the mouth, where a massive submarine delta exists. This dynamic interaction between the morphology, with an ever expanding subaqueous delta driven by river sediment discharge, and the wave hydrodynamics acts as another positive feedback (Fig. 2), leading to larger entrapment of sands within the delta. The downdrift offset of the subaqueous delta promotes a stronger, more rapid dissipation of waves over it, than updrift of the mouth where no subaqueous delta is present; this results in more quiescent conditions favoring expansion of the subaqueous delta.

Barrier Steering Effect

Similar to other deltas (e.g., Rodriguez et al., 2000), the barrier at St. George mouth was probably built by waves reworking sediments delivered by the extreme river floods (at the end of 19th century; Bratescu 1922). By 1935, Sacalin barrier doubled in length (Fig. 4b) while rolling-over to the mainland under the influence of overwash and breaching processes (Giosan 1998). The submarine lobe appears to have continued to prograde into the dip direction until mid-19th century (Giosan et al., submitted), albeit slowly, but its slope became flatter as the delta platform retreated with the barrier island toward mainland. However, after Sacalin's emergence, the submarine lobe elongated to southwest (Fig. 4b) at a dramatic rate of over 200 m/year, compared to less than 100 m/year previously.

Wave transformations performed using the STWave model (Fig. 4b) for the case when a barrier is present show that the nearshore is steep along the barrier and incoming waves reach the coast of the island incompletely shoaled and refracted, inducing an intense longshore drift that is steered (guided) and redirected to the south by the barrier island shore (Giosan et al. 1999). This phenomenon, which we term barrier steering (or channeling) of the longshore drift, is another feedback loop developed between morphology and wave hydrodynamics (Fig. 2), contributing to the dramatic southward extension of the submarine lobe after Sacalin's emergence (Giosan et al. 2005). Development of a shallow subaqueous delta platform downdrift of the mouth allows deposition of mouth bars to be displaced offshore to the edge of the platform during floods, exposing them to a more intense wave activity. Waves elongate these bars into barrier islands fronting the delta platform via the longshore drift. As the emergent barrier becomes the new shoreline for the downdrift half of the delta, it activates this new feedback loop between the wave hydrodynamics and the delta morphology. Waves can no longer dissipate over the shallow delta platform; they reach the barrier shore incompletely refracted resulting in a steering of the longshore drift (i.e., intensification of the drift guided along the shore of the barrier); this in turn leads to a more rapid development of the subaqueous delta in the alongshore direction. This mechanism is also a positive feedback loop because as the subaqueous delta is built alongshore it advances gradually into deeper waters and, thus, immobilizes sand there rather than bypassing it to the downcoast. The barrier also keeps most of the river plume offshore of it and steers it downcoast. This steering forces sedimentation from the suspended load to aid development of the subaqueous delta at its downcoast tip into gradually deepening waters.

Shoreline Rotation and Instability

Morphodynamic models (e.g., Komar 1973; Cowell et al. 2003) identify the rotation of the delta shoreline as a phenomenon responsible for changes in the longshore drift along a wave-dominated deltaic coast. Assuming that the offshore wave regime is not significantly skewed to one side of the regional orientation of the coast, as a delta protrusion advances, the wave angle of attack increases along both sides of the mouth driving a larger drift away from the mouth. Changes in the drift magnitude can be

thought as a feedback loop between subaerial morphology of the delta and waves, which ultimately limits the growth of the deltaic protrusion.

For numerical modeling purposes, rotation is generally conceptualized as a two-dimensional problem by assuming that the nearshore profile is invariable for the entire deltaic coast. Even with such a drastic simplification, recent one-line modeling showed that, for the same sediment supply and wave energy, deltas prograde faster and attain a more pronounced aspect ratio when the proportion of high-angle waves is increased, for wave regimes that remain symmetrical relative to the regional orientation of the coast (Ashton and Murray 2005). In cases where the offshore wave direction is skewed toward one side of the coast, the shoreline instability on the downdrift delta wing is enhanced leading to the development of overwashing spits (Fig.5; Ashton and Murray 2005; Ashton and Giosan 2006). This seems to be the case for the St. George shoreline in 1856 (Fig. 1), when a spit was present on the downdrift wing of the lobe.



Fig. 5. Simulation result for deltas with a one-line model (Ashton et al. 2001; Murray and Ashton 2004;) with asymmetrical wave distribution (more waves from the left; after Ashton and Murray, 2005).

CONCLUSIONS

Based on a survey of the morphology of several deltas and/or deltaic lobes, Bhattacharya and Giosan (2003) introduced a conceptual model for wave influenced deltas that classifies them into symmetric, asymmetric and deflected types. We modify this model to account for the role played by the subaqueous delta in establishing the morphodynamic feedbacks discussed above (Fig. 5). In cases where the longshore drift is relatively strong at the river mouth asymmetry index >200; Bhattacharya and Giosan, 2003), it can interact with fluvial delivery of sediment leading to an asymmetry in the morphology and facies distribution of the delta (see above for St. George's case). Furthermore, the

shoreline instability on the downdrift delta wing could lead to the development of overwashing spits (Ashton and Murray 2005; Ashton and Giosan 2006). In the extreme case where the longshore drift is dominant over a relatively low or episodic fluvial discharge, a deflected delta develops (Fig. 6). In this case, the mouth of the river runs subparallel to the coast most of the time during the delta evolution with the river being separated from the sea by a sandy spit-levee (Wright 1985). Subaqueous deposition in this case is not localized and never reaches a volume large enough to have an effect on sediment trapping. The delta progrades as a series of randomly distributed, quasi-parallel sand spits and channel fills.

At river mouths where the net longshore sediment transport is small (asymmetry index <200; Bhattacharya and Giosan, 2003), wave-influenced deltas are symmetric in morphology and facies (Fig. 1). In this case, where the river discharges a significant suspended load besides sandy bed load, a subaqueous delta advances periodically in front of the mouth (Van Maren 2005) with beach ridges or barriers developing subsequent on both sides of the mouth. The mechanism to generate these barriers is still unclear: Van Maren (2005) believes that onshore sediment transport by wave asymmetry is responsible, while we would argue based on Giosan (1998) that river floods are probably the main mechanism for barrier nucleation and longshore transport is the mechanism responsible for their further development. However, in these cases of symmetrical deltas, both the groin effect and the barrier steering effect would apply acting on both sides of the mouth.

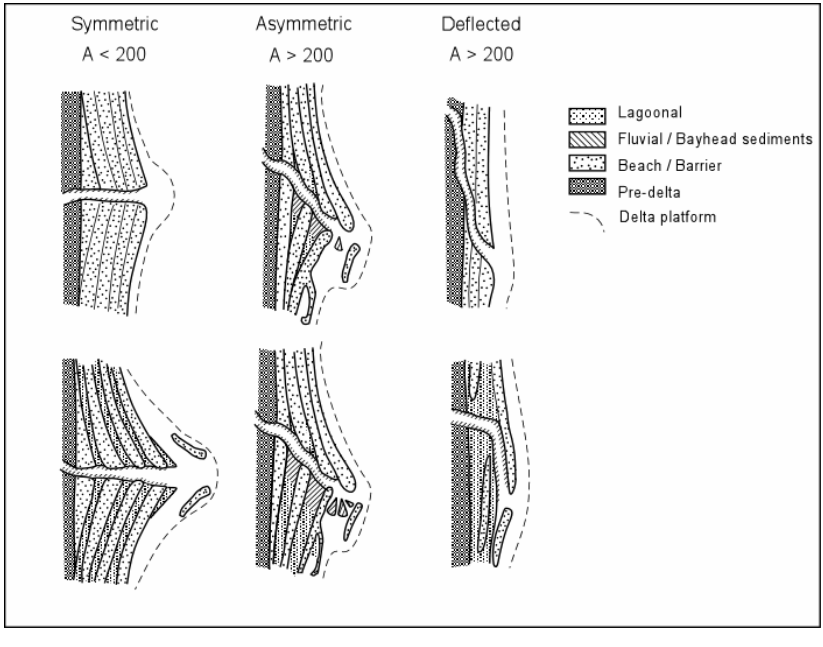

Fig. 6. Process diagram for wave influenced deltas (modified from Bhattacharya and Giosan, 2003). The upper row includes deltas preserving a lower proportion of fluvial mud compared to the cases in lower row that are more typical for rivers with high suspended load.

Asymmetric development of delta lobes has been documented around the world by Bhattacharya and Giosan (2003). In the case of the Danube delta, besides the St. George lobe, asymmetry with development of downdrift barrier occurs also on the previously fluvially-dominated Chilia lobe coast at several secondary mouths (Fig. 1), indicating a tendency to for river mouth to self-organize at various scales. The asymmetry in facies is also displayed by older marine lobes of the Danube delta (Fig. 1: Giosan et al. 2005) indicating a strong and sustained southward-directed longshore drift and suggesting that the wave-driven morphodynamics of the deltaic coast has always played a fundamental role on the entire development of the external delta plain. In conclusion, morphodynamic feedback mechanisms linked to the existence of a subaqueous delta appear to be essential in determining the morphology and facies of wave-dominated deltas and they should be considered in modeling exercises.

ACKNOWLEDGEMENTS

I thank Janok Bhattacharya, Andrew Ashton, and my Romanian colleagues S. Constantinescu, F. Filip, I. Ovejanu, and A. Vespremeanu-Stroe for good scientific discussions and help in the field and lab.

REFERENCES

Antipa, G. (1915). "Wissenschaftliche und wirtschaftliche Probleme des Donaudeltas," *Anuarul Institutului de Geologie al Romaniei*, 7, 88 p.

Ashton, A.D., and Murray, A.B. (2005). "Delta simulations using a one-line model coupled with overwash;" *Proceedings Coastal Dynamics '05*, Barcelona, Spain, 1-13.

Ashton, A. D., and Giosan, L. (2006). "Emergent shoreline behaviors reflected in the depositional history of wave-dominated deltas: Examples from Danube delta," American Geophysical Union Fall Meeting, *EOS Transactions* 87(52), NG53A-02.

Ashton, A., Murray, A. B., and Arnoult, O. (2001). "Formation of coastline features by large-scale instabilities induced by high-angle waves," *Nature*, 414, 296-300.

Bhattacharya J.P., and Giosan L. (2003). "Wave-influenced deltas: geomorphologic implications for facies reconstruction," *Sedimentology*, 50, 187-210.

Bondar, C. (1964). "Date asupra distributiei spatiale a salinitatii in jurul gurilor Dunarii," *Studii de Hidraulica*, 11, 229-245.

Bondar, C. and Blendea, V. (2000). "Water and sediment transport by the Danube into the Black Sea during 1840-1995," Intergovernmental Oceanographic Commission, *Workshop Report No.145*, IOC/UNESCO, Paris, 58-63.

Bondar, C. and Harabagiu, E. (1992). "Regimul depunerilor de aluviuni la gura canalului Sulina," *Studii de Hidraulica*, 33, 131-141.

Bondar, C., State, I., Cernea, D., Harabagiu, E. (1992). "Scurgerea de apa si aluviuni a Dunarii la gurile bratelor Dunarii in anii 1858-1988," *Studii de Hidraulica*, 33, 57-71.

Bratescu, C. (1922). "Delta Dunãrii. Geneza si evolutia sa morfologicã si cronologicã," *Buletinul Societatii Regale Romane de Geografie*, 41, 3-39.

Bruun, P., and Gerritsen, F. (1959). "Natural by-passing of sand at coastal inlets," *Journal of Waterways and Harbors Division*, ASCE, WW4, 75-107.

Bulgakov, N.P., Golubev, Y.N., Kuftarkov, A.Y. (1992). "Energy active zones of the Black Sea," *Doklady Rossiyskoy Akademii Nauk*, 326, 177-180.

Carter, R.W.G., Woodroffe, C.D., (eds.) (1984), "*Coastal evolution: late Quaternary shoreline morphodynamics*," Cambridge University Press, 539 p.

Cazenave A., Bonnefond, P., Mercier, F., Dominh, K., Toumazou, V. (2002). "Sea level variations in the Mediterranean Sea and Black Sea from satellite altimetry and tide gauges," *Global and Planetary Change*, 34, 59-86.

Constatinescu, S., Vespremeanu-Stroe, A., Ovejanu, I., Filip, F., Giosan, L. (2008). "Morphodynamics of the Danube delta coast [2]: Natural and far-field anthropogenic effects on the evolution of St. George mouth," *Journal Coastal Research*, submitted.

Corregiari et al., (2005). "Depositional patterns in the late-Holocene Po delta system," In: Giosan, L., Bhattacharya, J.P. (Eds.), *River Deltas: Concepts, Models and Examples*, *SEPM Special Publication 83*, 365–393.

Cowell, P.J., Stive, M.J.F., Niedoroda, A.W., de Vriend, H.J., Swift, D.J.P., Kaminsky, G.-M., Capobianco, M. (2004). "The Coastal-Tract (Part 1): A conceptual approach to aggregated modeling of low-order coastal change," *Journal of Coastal Research*, 19, 812–827.

van Maren, D.S. (2005). "Barrier formation on an actively prograding delta system: The Red River Delta, Vietnam," *Marine Geology*, 224, 123-143.

de Martonne E. (1931). "*Europe Centrale*," Volume II: Paris, Editeur Armand Colin, 786-787.

Ericson, J.P., Vorosmarty, C.J., Dingman, S.L., Ward, L.G. and Meybeck, M. (2006). "Effective sea-level rise and deltas: Causes of change and human dimension implications," *Global and Planetary Change*, 50, 63-82.

FitzGerald, D.M. (1984). "Interactions between the ebb-tidal delta and landward shoreline; Price Inlet, South Carolina," *Journal of Sedimentary Petrology*, 54, 1303-1318.

Geyer, W.R, Hill, P.S., Kineke, G.C. (2004). "The transport, transformation and dispersal of sediment by buoyant coastal flows," *Continental Shelf Research*, 24, 927-949.

Giosan, L. (1993) "*Studiul evolutiei dinamice a sedimentelor in zona litorala din fata deltei Dunarii*," unpubl. Diploma thesis, Bucharest University, 75 p.

Giosan, L. (1998). "Long term sediment dynamics on Danube delta coast, 1998," in Dronkers, J. and M.B.A.M. Scheffers (eds.), *Physics of estuaries and coastal seas: proceedings of the 8th International Biennial Conference on Physics of Estuaries and Coastal Seas*, the Hague, Netherlands, 9-12 September 1996; A.A. Balkema, 365-376.

Giosan, L., Bokuniewicz, H., Panin, N., Postolache, I. (1999) "Longshore sediment transport pattern along the Romanian Danube delta coast," *Journal of Coastal Research*, 15, 859-871.

Giosan, L., Constantinescu, S., Vespremeanu-Stroe, A., Filip, F., Ovejanu, I. (2008) "Morphodynamics of the Danube delta coast [1]: Natural and anthropogenic influences on subaqueous delta evolution," *Journal Coastal Research*, submitted.

Giosan, L., Donnelly, J.P., Vespremeanu, E.I., and Buonaiuto, F.S. (2005) "River delta morphodynamics: Examples from the Danube delta," in Giosan, L. and Bhattacharya, J.P., eds., *River deltas - Concepts, models, and examples, SEPM Special Publication*, 83, 87-132.

Komar, P.D. (1973). "Computer models of delta growth due to sediment input from rivers and longshore transport," *Geological Society of America Bulletin*, 84, 2217-2226.

Kraus, N. C. (2000). "Reservoir model of ebb-tidal shoal evolution and sand bypassing," *Journal of Waterway, Port, Coastal, and Ocean Engineering*, 126, 305-313.

Murray, A.B., and Ashton, A.D. (2004). "Extending a 1-line modeling approach to explore emergent coastline behaviors," *Proceedings of the 29th International Conference on Coastal Engineering*, 2035-2047.

Overeem, I., Syvitski, J.P.M., and Hutton, E.W.H. (2005). "Three-dimensional numerical modeling of deltas," In: Giosan, L., Bhattacharya, J.P. (Eds.), *River Deltas: Concepts, Models and Examples*, *SEPM Special Publication 83*, 13–30.

Penland, S. and Suter, J.R. (1989). "The geomorphology of the Mississippi River chenier plain," *Marine Geology*, 90, 231-240.

Reschke, S., V. Ittekkot and N. Panin (2002). "The nature of organic matter in the Danube River particles and north-western Black Sea sediments," *Estuarine, Coastal and Shelf Science*, 54, 563-574.

Rodriguez, A.B., Hamilton, M.D., and Anderson, J.B. (2000). "Facies and evolution of the modern Brazos Delta, Texas; wave versus flood influence," *Journal of Sedimentary Research*, 70, 283-295.

Syvitski, J.P.M. and Bahr, D.B. (2001). "Numerical models of marine sediment transport and deposition," *Computers & Geosciences*, 27, 617-618.

Todd, T.W. (1968). "Dynamic diversion: influence of longshore current-tidal flow interaction on chenier and barrier island plains." *J. Sed. Petrol.*, 38, 734-746.

Vörösmarty, C.J., Fekete, B., and Tucker, B.A. (1998). River Discharge Database, The Institute for the Study of Earth, Oceans, and Space, University of New Hampshire, *http://www.rivdis.sr.unh.edu/*

Wright, L.D. (1977). "Sediment transport and deposition at river mouths: a synthesis," *Geological Society of America Bulletin*, 88, 857-868.

Wright, L.D. (1985). River Deltas. in: A.R. Davis (ed.), *Coastal Sedimentary Environments*, Springer-Verlag, 1-76.

Zenkovich, V.P. (1956) Zagadka Dunaiskoi Delty, *Priroda*, 45, 86-90.

COASTAL AND RIVER MOUTH MORPHOLOGY CHANGE IN SRI LANKA DUE TO THE 2004 INDIAN OCEAN TSUNAMI

Hitoshi Tanaka[1], Kazuo Ishino[2], Bandara Nawarathna[3], Hajime Nakagawa[4] and Shinichiro Yano[5]

1. Department of Civil Engineering, Tohoku University, 6-6-06 Aoba, Sendai 980-8579, Japan. tanaka@tsunami2.civil.tohoku.ac.jp
2. Taisei Corporation, 344-1 Nasecho Totsuka-ku Yokohama-shi, Kanagawa 245-0051, Japan. kazuo.ishino@sakura.taisei.co.jp
3. Taisei Corporation, 344-1 Nasecho Totsuka-ku Yokohama-shi, Kanagawa 245-0051, Japan. nwrbnd00@pub.taisei.co.jp
4. Kyoto University, Gokasho Uji-shi, Kyoto 611-0011, Japan. nakagawa@uh31.dpri.kyoto-u.ac.jp
5. Kyushu University, 6-10-1 Hakozaki Higashiku Fukuoka-shi, Fukuoka 812-8581, Japan. yano@civil.kyushu-u.ac.jp

Abstract: Field observation on coastal and river mouth morphology change in Sri Lanka induced by 2004 Indian Ocean Tsunami has been carried in May 2005 by a survey team delegated by the Committee on Hydroscience and Hydraulic Engineering, Japan Society of Civil Engineers (JSCE). The survey area covers southeastern, southern and southwestern parts of Sri Lanka. It is found that dependent on the tsunami waver height and vegetation condition covering the sand surface, various level of erosion has occurred along the coast.

INTRODUCTION

Sri Lanka received extensive damage due to the Indian Ocean Tsunami caused by the earthquake that occurred off the coast of Sumatra in December 2004. In order to investigate this tsunami and related damages from the costal and hydraulic viewpoints, the Committee on Hydroscience and Hydraulic Engineering, Japan Society of Civil Engineers (JSCE) delegated its members whose majors are coastal engineering, river engineering, hydraulic engineering and hydrology (The Committee on Hydroscience and Hydraulic Engineering JSCE 2005). The present paper mostly

deal with coastal and river mouth morphology change in Sri Lamka, whereas other river-related topics, such as tsunami propagation into a river and bridge damages, have been reported elsewhere (Tanaka et al. 2007).

Several field investigations have already been carried out on tsunami run-up around the Sri Lankan coastal areas (Liu et al. 2005; Shibayama et al. 2005; Koibuchi 2005; Choi et al. 2005; Tomita et al. 2006). According to these results, it was over 10m along the east coast facing Sumatra, the source area of the earthquake. Although it gradually decrease from the southeast coast to the southwest areas, heavy human and physical damages were caused there, because there is a concentration of relatively large urban and resorts in these areas. For this reason, the rivers and the areas shown in Figure 1 were chosen as the subject of the field investigation by the JSCE survey team. Among them, the sites framed with rectangle will be dealt with herein, whereas survey results at the rest will be shown elsewhere (Tanaka et al. 2007).

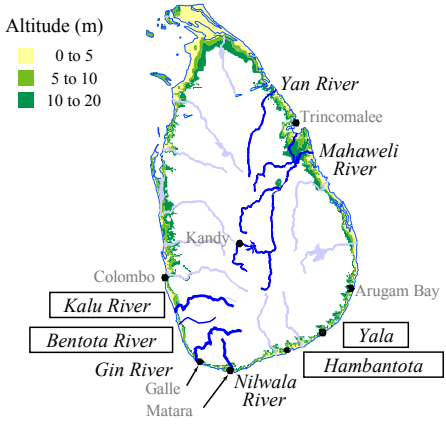

Fig.1. Study areas of JSCE survey team

SAND SPIT EROSION BY OVERTOPPING AT KALU RIVER MOUTH

The Kalu River is located in the central part of Sri Lanka, with the river basin area of 2,690m^2 with a length of approximately 100km. The Kalu River basin can be divided into the upstream valley region (Ratnapura District) and the downstream low-lying region (Kalutara District) (Komatsu et al. 2005). The difference in altitude between the mountainous land of the headwaters and the mouth of the river is approximately 2,250m, but since the altitude abruptly drops from 2,250m to 14m in the first 36km from the riverhead, much of the river channel has a steepness of only approximately 1/5,000. Along the sandy coast in Sri Lanka, elongated sand spit can commonly seen at river entrances due to predominant longshore sediment movement (The Committee on Hydroscience and Hydraulic Engineering JSCE 2004). The Kalu River is one of typical examples of Sri Lankan river with 3km long sand spit as seen in Figure 2.

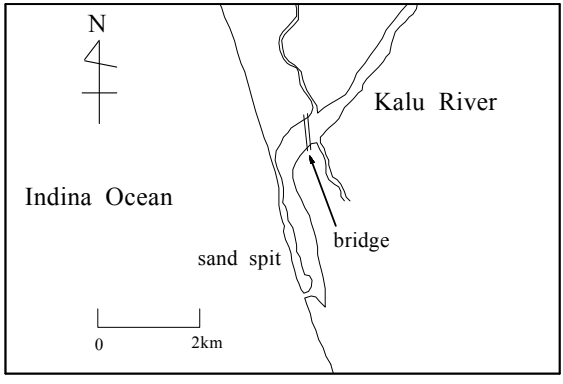

Fig. 2. Mouth of the Kalu River

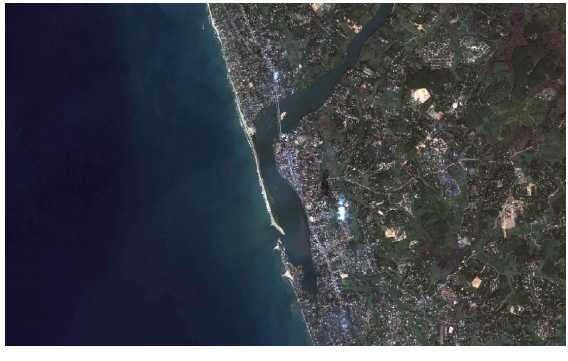

Photo 1. Satellite image at Kalu River before tsunami
(Hitachi Software Engineering Co., Ltd. 2006)

Photo 1 and Photo 2 respectively show satellite images before and during the Indian Ocean Tsunami around the sand spit at the Kalu River, located on southeast coast of Sri Lanka. Photo 2 indicates the instant of tsunami backwash, when the waterline in the upper part of the image advanced seaward by 340m. It is also seen that at the river entrance, strong seaward current from the river formed a flow pattern of turbulent jet spreading in the sea area. Although the breaching of the sand spit did not occur on the sand spit in Photo 2, the field survey revealed that there was slight erosion on the sand spit as seen in Photo 3 and Photo 4. Since the spit surface is covered with the dense vegetation, tsunami wave energy was dissipated during overtopping. It is noted tat sediment deposit in Photo 4 is similar to overwash caused by wind-generated waves (e.g., Ritchie and Penland 1990).

The tsunami height in coastal area in Kalutara, which is located near the river mouth, was 3.5m above MSL (Koibuchi et al. 2005). On the other hand, the field investigation showed that the height of the sand spit was 2.6m. From this result, it is estimate that the maximum of overflow depth was about 0.9m during the tsunami. In addition, it is reported by Tanaka et al. (2007) that the tsunami propagated further upstream along the Kalu River up to 20km from the river mouth, and that there is possibility of soliton fission occurrence in the river according to witness of workers along the river, although field data recorded by a water level gauge could not be obtained.



Photo 2. Satellite image at Kalu River during tsunami
(Hitachi Software Engineering Co., Ltd. 2006)



Photo 3. Erosion of sand spit by tsunami overtopping



Photo 4. Sediment intrusion due to wave overtopping on Kalu River sand spit

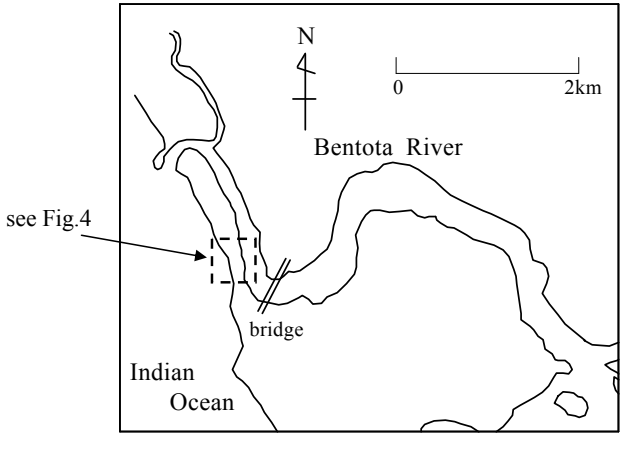

Fig. 3. Map of Bentota River mouth

SAND SPIT BREACHING AT BENTOTA RIVER MOUTH

Bentota is one of the most attractive beach resort area in Sri Lanka, located about 65km south of Colombo on the southwest coast. Similar to the Kalu River, predominant longshore sediment movement has formed a narrow spit of land almost 2km long as illustrated in Figure 3, which is the main beach area and resort hotel center for the Bentota area.

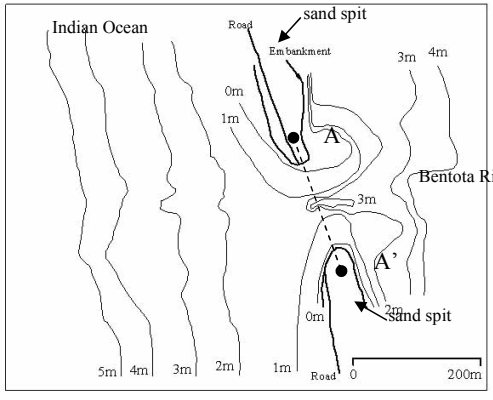

Fig. 4. Breached sand spit at the Bentota River mouth

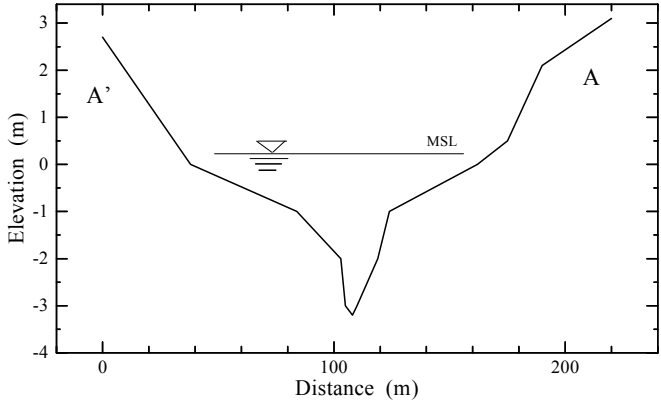

Fig. 5. Cross-section of breached sand spit (A-A' section)

On the contrary to the Kalu River, a sand spit at the Bontota River mouth was breached completely. Since several resort hotels are located near the tip of the sand spit beyond the eroded section, it was highly required to recover the access road going to the hotels. Thus, in order to make a plan for recovery work, detailed bathymetric survey has been performed immediately after the tsunami in January 2005, as shown in Figures 4 and 5. It is seen that very severe erosion occurred up to 4m deep below MSL and 200m wide, although there might have sediment intrusion into the breached section due to wind-generated waves before bathymetry surveying in January.



Photo 5. Recovery of breached sand spit by sand fill

When the present surveying was carried out in May 2005, the breached section has already been artificially filled with sand as shown in Photo 5.

SAND DUNE EROSION DUE TO OVERTOPPING IN HAMBANTOTA

Hambantota is a town in southern coastal area of Sri Lanka (Figure 6). It is also the capital of the district Hambantota in the Southern Province of Sri Lanka. Severe erosion of sand dune was observed at three places in the coastal area of Hambantota depicted in Figure 6. The tsunami height in this area was about 10m (Koibuchi 2005), whereas the sand dune is about 8m high. Thus, it is estimated that the overtopping water depth that caused severe erosion was about 2m above the dune crest.

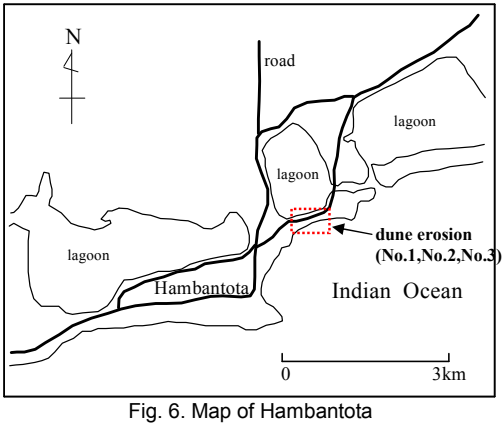

Fig. 6. Map of Hambantota



Photo 6. Dune erosion by tsunami overtopping (No.1)



Photo 7. Dune erosion by tsunami overtopping (No.2)

Each site of severe erosion will hereafter be referred to as No.1, No.2 or No.3 from the westernmost one. Photo 6 shows No.1 erosion taken from the lagoon side behind the dune. According to an interview to local people, although a scouring hole was created behind the dune at No.1 by strong overflowing water, it has already been filled up with debris caused by the tsunami disaster before the present field survey. Most severe erosion can be seen at No.2 site shown in Photo 7; a scouring hole filled with water still exists behind the dune as seen in Photo 8, with a partial landfill with debris after tsunami. Meanwhile, Photo 9 shows No.3 erosion, which is quite similar to No.2, but no scouring hole was formed.



Photo 8. Dune erosion by tsunami overtopping (No.2)



Photo 9. Dune erosion by tsunami overtopping (No.3)

EROSION IN YALA

Investigation for the damages in Yala National Park was carried out mainly around the beach where 50 people including 8 Japanese were killed (Figure 7). The height of the tsunami in this coastal area was 7-7.5m, judging from the withered leaves in the trees. Some trees were ruptured at around the height of 2m, and sand surface near the lodge and the trees was eroded up to the depth around 0.6m (Photo 10 and Photo 11).

Photo 12 and Photo 13 show the damages of the road, which also acts as an embankment for a small reservoir behind the lodge. The tsunami ruptured the embankment as can be seen in Photo 12. In the ruptured area in Photo 12, there was a channel on the beach that had not existed before the occurrence of the tsunami. The water in the channel was stagnant at the time of the field investigation, and its mouth facing the sea was already closed due to sediment deposit by waves.

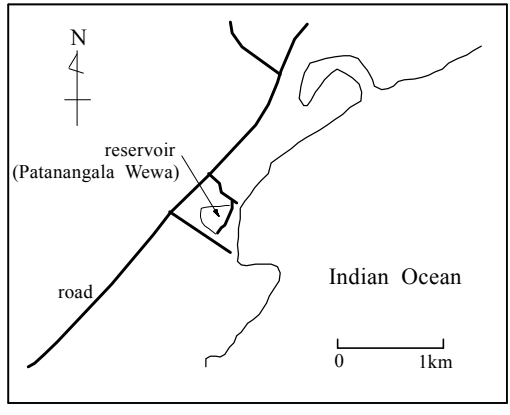

Fig. 7. Map of Patanangala in Yala area



Photo 10. Beach erosion by tsunami in Yala



Photo 11. Beach erosion around a tree



Photo 12. Breaching of reservoir embankment



Photo 13. Severe erosion of seaward surface of embankment

It is noted that shoreward surface of the embankment was more severely eroded than landward surface as illustrated in Photo 13. The mechanism of such a different erosion patter on the both surface may be as follows:

(1) Figure 8(a) illustrates on-offshore cross-section from the sea to the reservoir before the tsunami occurrence.
(2) During the run-up of tsunami waves, water level rise occurred too quickly to allow erosion on the both surface of the embankment. (Figure 8(b))
(3) After reaching the highest water level, the water stored in the reservoir drained gradually, while the water level in the sea had descended more quickly. The large difference of water level inside and outside of the reservoir caused strong overflowing current, resulting in severe erosion on the seaward surface of the embankment as seen in Photo 13 (Figure 8(c)).

(4) After breaching of the embankment due to overflow, a channel connecting the reservoir and the sea was created by the strong seaward current (Figure 8(d)).

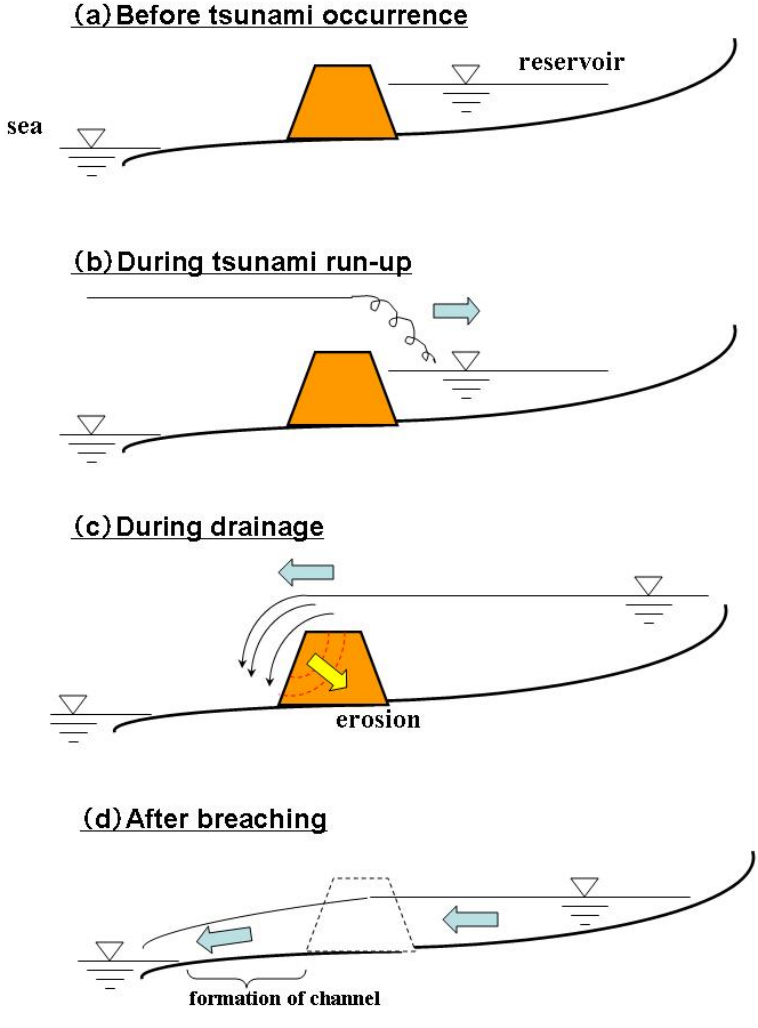

Fig. 8. Mechanism of erosion on seaward slope surface of embankment

CONCLUSION

This study highlights erosion of sandy coast and sand spit at a river mouth in Sri Lanka due to the 2004 Indian Ocean Tsunami, based on a field investigation by JSCE survey team.

At the Kalu River mouth, slight erosion was induced on the sand spit by tsunami overtopping, while at the Bentota River mouth, the spit was breached by strong current by tsunami. Such a different response in river mouth morphology change may depend on the tsunami height, the geological formation around the river mouth and on the characteristic features of the river. Furthermore, dune erosion in Hambantota coast and embankment erosion in Yala are surveyed. In particular, a role of return flow is discussed in connection with slope erosion of embankment in Yala.

ACKNOWLEDGEMENTS

The authors would like to express their grateful thanks to Foundation of River and Watershed Environment Management for their financial support to the present field investigation. The authors' appreciation should be extended to Lanka Hydraulics Institute (LHI) for their kind offer of the bathymetric data, Japan International Cooperation Agency (JICA) and various other organizations and institutions for their kind assistance in conducting the field investigation.

REFERENCES

Choi, B. H., Siripong, A., Sundar, V., Wijetunge, J. J. and Disposaptono, S. (2005). "Post runup survey of the December 26, 2004 Earthquake Tsunami of the Indian Ocean", *Proceedings of the Special Asia Tsunami Session at APAC (Asian and Pacific Coasts) 2005*, 1-20.

Hitachi Software Engineering Co., Ltd. (2006). http://hitachisoft.jp/News/News295.html.

Koibuchi, Y., Honda, T., Welhena, T., Ranashinghe, S. and Sato, S. (2005). "Localized tsunami disaster surveyed on southwest coast of Sri Lanka due to Indian Tsunami", *Proceedings of Japanese Conference on Coastal Engineering*, 52, 1411-1415. (in Japanese)

Komatsu, T., Tanaka, H., Toda, K., Shimizu, Y., Fujita, M., Ishino, K., Kazama, S., Ushiyama, M., Katsuhama, Y., Herath, S. and Nawarathna, B. (2005). "Field investigation of the flood disaster in south-west area of Sri Lanka occurred in May 2003", *Journal Hydroscience and Hydraulic Engineering*, 23(2), 43-53.

Liu, P. L. F., Lynett, P., Fernando, H., Jaffe, B.E., Fritz, H., Higman, B., Morton, R., Goff, J. and Synolakis, C. (2005). "Observations by the international tsunami survey team in Sri Lanka", *Science*, 308(5728), 1595.

Ritchie, W. and Penland, S. (1990). "Aelion Sand Bodies of South Louisiana Coast", in *Coastal Dunes -Form and Process-*, (edited by Nordstrom, K.F., Tsuty, N. and Carter, B.), John Wiley & Sons, 105-127.

Shibayama, T., Okayasu, A., Wijayaratna, N., Sasaki, J., Suzuki, T., Jayarantne, R.

(2005). "The December 26, 2004 Sumatra Earthquake Tsunami, Tsunami Field Survey around Southern Part of Sri Lanka", http://www.cvg.ynu.ac.jp/G2/srilanka_survey_ynu_e.html.

Tanaka, H., Nawarathana, B., Ishino, K., Nakagawa, H., Yano, S., Yasuda, H., Watanabe, Y. and Hasegawa, K. (2007). "Field investigation of disasters in Sri Lankan rivers caused by the 2004 Indian Ocean Tsunami". (submitted)

The Committee on Hydroscience and Hydraulic Engineering JSCE (2004). "*2003 Sri Lanka Flood Damage Investigation Report*", 76p. (in Japanese)

The Committee on Hydroscience and Hydraulic Engineering JSCE (2005). "*Sri Lanka Damage Investigation Report for the 2004 Indian Ocean Tsunami*", 132p. (in Japanese)

Tomita, T., Imamura, F., Arikawa, T., Yasuda, T. and Kawata, Y. (2006). "Damage caused by the 2004 Indian Ocean tsunami on the southwestern coast on Sri Lanka", *Coastal Engineering Journal*, 48(2), 99-116.

HOLOCENE EVOLUTION OF THE MERRIMACK EMBAYMENT, NORTHERN MASSACHUSETTS, INTERPERTED FROM SHALLOW SEISMIC STRATIGRAPHY

Christopher J. Hein[1], Duncan M. FitzGerald[2], Walter A. Barnhardt[3]

1. Department of Earth Sciences, Boston University, 675 Commonwealth Ave., Boston, MA 02215, USA.
   hein@bu.edu
2. Department of Earth Sciences, Boston University, 675 Commonwealth Ave., Boston, MA 02215, USA.
   dunc@bu.edu
3. United States Geological Survey, Woods Hole Science Center, 384 Woods Hole Road, Quissett Campus, Woods Hole, MA 02543-1598, USA.
   wbarnhardt@usgs.gov

Abstract: Recent multi-beam, backscatter, and bottom sediment data demonstrate that a large sand sheet was formed in the inner shelf by the reworking of the Merrimack River lowstand delta and braid plain (12 kya) during the Holocene transgression. Seismic data reveal the presence of widespread channel cut-and-fill structures landward of the delta suggesting that much of the sand sheet consists of braided stream deposits. These features map into several sets of cut-and-fill structures, indicating the avulsion of the primary river channels, which creates the lobes of the paleo-delta. Truncations of these cut-and-fill structures suggest that the braid plain deposits were probably reworked during the Holocene transgression and may have contributed sand to developing barriers that presently border the Merrimack Embayment.

INTRODUCTION

Global warming is causing increased melting of ice caps and mountain glaciers and the expansion of surface ocean waters, which is accelerating sea-level rise (SLR). The 2001 IPCC Report predicted SLR by 2100 to be between 48 and 88 cm (Church 2001). Concurrently, riverine supply of sediment to the coastal zone in northern latitudes has diminished due to dam construction and natural depletion of glacial sediment sources. The lack of new sand sources has led to pervasive beach erosion and shoreline retreat not only in New England, but throughout the US and the world. Thus, the potential sand reservoirs of the inner continental shelf and the mechanisms of sand exchange between beaches and barriers and the offshore are vital topics of research for the coastal community (Pilkey and Field 1972). Presently, the pathways, volumes, and net direction of sand exchange between the nearshore zone and offshore (the inner shelf) are not known (Morton et al. 1994). However, if shoreface sand is being lost to the inner shelf sand sheet, as suggested by several recent studies (e.g. Gayes et al. 1997; Swift and Thorne 1991), then the coastal zone and the populations and infrastructure it supports ($3 trillion along the US East and Gulf Coasts alone (USGS 2006)) may be under serious threat from accelerated SLR.

To investigate the reworking of nearshore sediments in a regime of accelerated SLR, it is crucial to understand the processes that govern the origin and distribution of sand bodies on continental shelves. To understand the source and behavior of these sediments, it is important to understand both their sedimentologic history and the present processes driving sediment transport. This paper presents a preliminary analysis and interpretation of nearly 4,000 km of shallow seismic data from the nearshore region of the Merrimack Embayment in the western Gulf of Maine and provides a sedimentologic framework for developing an evolutionary model of the 34 km-long barrier system within the embayment.

Physical Setting

The Merrimack Embayment in the Gulf of Maine is a mixed-energy, tide-dominated coast, extending from Cape Ann in northern Massachusetts north to Great Boar's Head in New Hampshire (Figure 1). It is the longest barrier island chain in Massachusetts (approximately 34 km long) with a backbarrier system consisting primarily of marsh and tidal creeks that often open to small bays near the inlet openings (Smith and FitzGerald 1994). The barrier islands are pinned to bedrock or glacial promontories with the tidal inlets are situated in drowned river valleys (FitzGerald et al. 2002). The Merrimack River heads in the White Mountains of New Hampshire with a catchment of approximately 13,000 km^2. The river drains regions dominated by granitic plutons, the weathering of which produced extensive sandy glacial deposits. Sediments discharged from the mouth of the Merrimack are subsequently reworked in a southeasterly alongshore direction as a result of strong northeasterly storm waves associated with Northeasters (FitzGerald et al. 2002).

Stone et al. (2004) used a variety of data to construct a sea-level curve that incorporates a rheological model for the region (Koteff et al. 1993). Following the Wisconsin sea

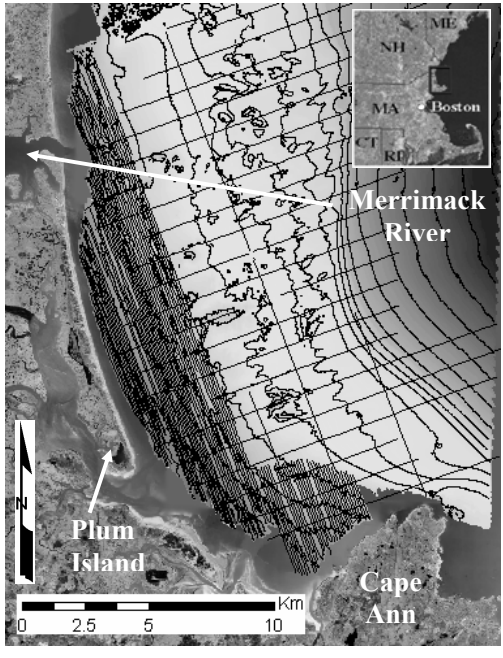

Fig. 1. Study area in northern Massachusetts. Offshore study area shown in grayscale bathymetry with black isobath lines (contour interval = 5m). Parallel track lines (black) run shore parallel with shore normal tie lines.

level highstand (+33m) at ca.17,000 cal yr. BP, this region experienced rapid isostatic rebound resulting in a -45 m lowstand at 12 kya. During this time, the Merrimack River deposited a large delta that is currently located approximately 6 to 7 km offshore and trends parallel to the present coast (Oldale et al. 1983; Edwards 1988). The paleo-delta is 20 km long, 4 to 7 km wide, up to 20 m in thickness and contains about 1.3 billion m^3 of sediment (Oldale et al. 1983, 1993). Earlier seismic records showed that eastwardly-dipping delta foresets were truncated during the early Holocene transgression of this region (Oldale et al. 1983). Much of the surface of the delta exhibits a ravinement surface that is inferred to be a time transgressive unconformity formed during the Holocene marine transgression and subsequently overlain by beach or bar deposits (Oldale et al. 1983). Edwards (1988) described these sandy deposits as a discontinuous, planar, palimpsest shelf surficial sand sheet of varying thickness and in disequilibrium with present-day processes. Edwards (1988) also reported "linear ridges" that he hypothesized formed during the transgression or as post-transgressive features; i.e. either degraded barriers that formed as sea level rose and sediments were reworked in an onshore direction or active shoreface-connected ridges that form in the present day in response to peak flow conditions during northeasters.

Several papers have since reexamined the formation and evolution of the barrier system in relation to the offshore paleo-delta (Oldale et al. 1993; FitzGerald et al. 1994). However, these efforts have relied on the interpretation of limited (2 km spacing) seismic data and only 4 vibracores that provided little information on the detailed morphology and nature of the sub-bottom stratigraphy. Recent multi-beam, shallow

seismic, and bottom sediment data provide new evidence for the partial reworking of the paleo-delta deposits that continues to the present time.

METHODS

During February - March 2004, September 2005, and September 2006 the sea floor of the Merrimack Embayment (323 km^2 area) from the nearshore zone to about 17 km offshore was mapped using single beam, multibeam, and side scan sonar. Additionally, 3,857 km of shallow seismic track lines were taken in the study area using an Edgetech SB-512 CHIRP sub-bottom profiler. Shallow seismic track lines were primarily oriented shore parallel and were taken within the first 1-2 km of the present shoreline (depths of less than 30 m) with 100 m spacing between lines (Figure 1). Several sets of shore normal lines with approximately 750 m spacing were also taken.

Analysis of backscatter data was used to select the position of more than 100 bottom videos and sediment samples, collected simultaneously with the seismic data. Videos and grain size data were used to ground truth the backscatter image, allowing identification of features such as the sand sheet and areas in the vicinity of bedrock outcrops. Shallow seismic data were georeferenced and analyzed using ESRI's ArcGIS Desktop software package. Cut-and-fill features in the shallow seismic profiles were traced across profiles and mapped throughout the study region.

RESULTS

Shallow Seismic Surveys

The locations of shallow seismic profiles analyzed in this section are given in Figure 2. Shallow seismic data from the paleo-delta region exhibit pervasive shallow, seaward dipping reflectors that become tangential with the sediment bottom in an offshore direction. In most cases, the surface of the clinoforms are truncated and overlain by thin flat-lying deposits. Track lines normal to the coast show a consistent pattern of seaward dipping clinoforms and a pronounced ravinement surface, confirming previous observations that the upper portions of the delta were eroded during the Holocene transgression (Figure 3). However, it is still not known how much of the upper delta was removed during the reworking process.

Shore parallel profiles reveal the existence of channel cut-and-fill structures in the region onshore of the paleo-delta. These features trend in an E-W direction and are commonly several meters in thickness, varying in width from about 25 to several hundred meters. Several large sets of cut-and-fill features range from 500 to 600 m wide and 10 to 15 m deep. Shore normal seismic lines confirm the nearly shore normal orientation of these features. In some locations, the orientation and geometry of these features closely resembles that of underlying bedrock surfaces (Figure 4). Several of the cut-and-fill features exhibit structures interpreted as the result of river terracing; i.e. sets of parallel horizontal reflectors on either side of a deeper incised channel (Figure 5). Within any given region, the spatial distribution of cut-and-fill features varies from a highly organized network to a random distribution. However, several examples exist of a single structure retaining an identical geometry across numerous parallel profiles representing hundreds of meters in a shore normal direction (Figure 6).

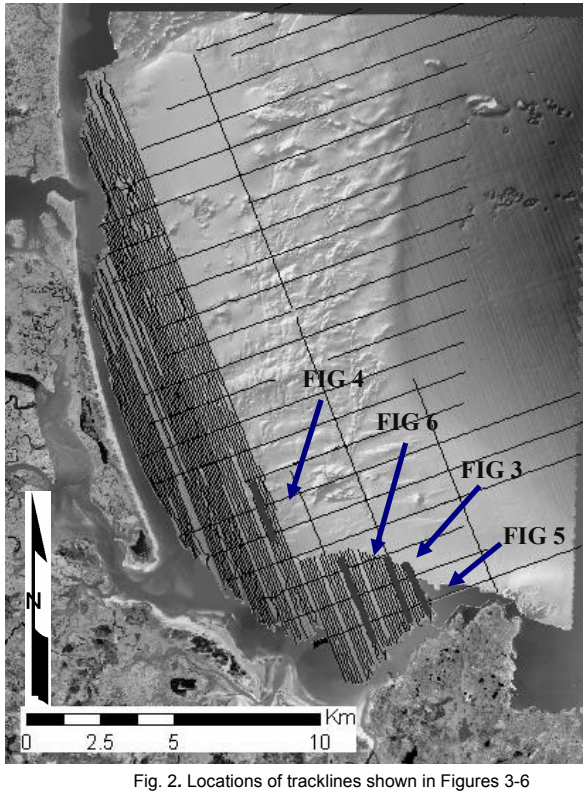

Fig. 2. Locations of tracklines shown in Figures 3-6

A continuous, near-horizontal reflector, interpreted to be an erosive ravinement surface, overlies the cut-and-fill features. This layer is in turn overlain by several (3-8) meters of sediment, interpreted to be Holocene deposits (Figure 3). Generally, the thickness of this Holocene layer decreases in a shoreward direction, resulting in a shallowing of the ravinement surface in the profiles. In the nearshore profiles the channel cut-and-fill features loose their distinct character and are not ubiquitous. In the most nearshore profiles, the cut-and-fill features breach the subsurface and appear to be within a zone of active reworking. These changes in the character of the sub bottom likely reflect reworking during the Holocene.

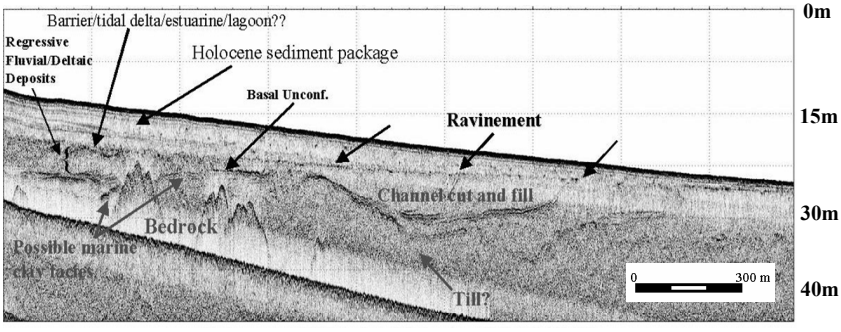

Fig. 3. Sample shallow seismic line indicating general features seen in both shore normal and shore parallel transects (Seismic shot L101f1).

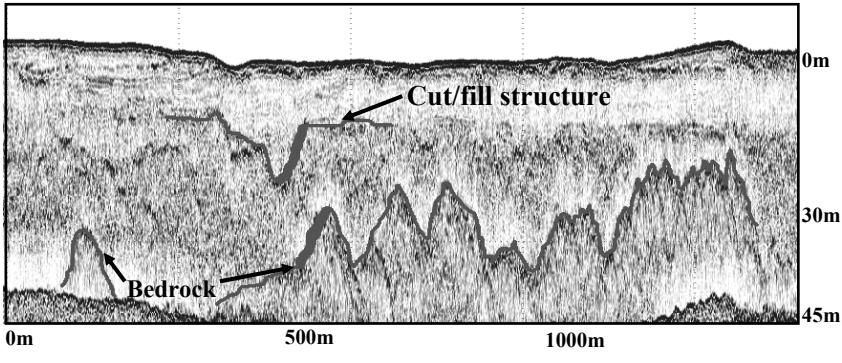

Fig. 4. Sample shallow seismic line indicating a channel cut-and-fill structure overlying bedrock. The bolded lines highlight the close correlation between the geometry of the bedrock and the side of the channel (Seismic shot L5f2).

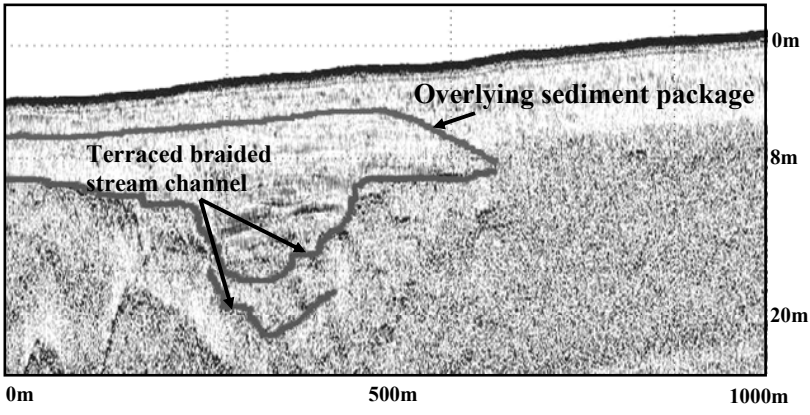

Fig. 5. Evidence of terracing in channel cut-and-fill structures (Seismic shot L106f1).

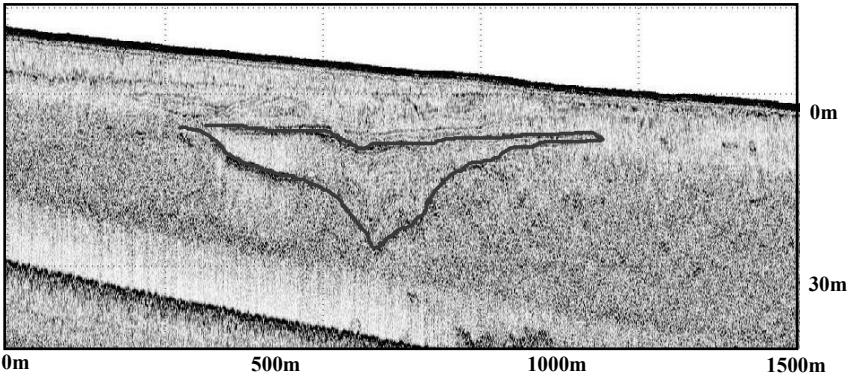

Fig. 6. Example of typical channel cut-and-fill feature mapped near Cape Ann. The form exhibited in this feature is easily traced across several parallel track lines (Seismic shot L97f5).

Channel cut-and-fill structures identified in sub bottom profiles were mapped onto a surficial bathymetric map of the Merrimack Embayment (Figure 7). Three sets of shore normal channel cut-and-fill structures are identified. The southern set continues towards the Parker River Inlet at the southern end of Plum Island (Set A, Figure 7). A central set tracks towards the northern end of a remnant drumlin at the southern end of Plum Island (Set B, Figure 7). The northern-most set trends toward the center of Plum Island near a

low marshy region (Set C, Figure 7). Additionally, at the very southern end of the Merrimack Embayment there is some evidence of a forth set of cut-and-fill features that trend towards the present-day Ipswich River Inlet.

ANALYSIS AND DISCUSSION

Braided Stream Deposits

Seismic profiles of the region of the Merrimack Embayment inshore of the paleo-delta reveal an irregular basement overlain by channel cut-and-fills, flat lying reflectors, and acoustically transparent regions. Bedrock outcrops extending through the sediment surface increase in extent to the north. Our records and those collected by Oldale et al. (1983) suggest that glacial and bedrock topography strongly controlled the course of the river system while it was delivering sediment to the lowstand delta. Presently, bedrock outcrops continue to stabilize much of the lower river and estuary region.

The earlier studies of the Merrimack Embayment (Oldale et al. 1983; Edwards 1988; Oldale et al. 1993) did not report the pervasive channel cut-and-fill features characterizing the region landward of the delta. However, the channel cut-and-fill structures observed in our seismic profiles suggest that the delivery system conveying sediment to the delta consisted of a braided stream complex. Moreover, the size and morphology of the paleo-delta suggest that the delta was deposited in a series of lobes indicating significant river migration and/or avulsion (Figure 7). Present-day topographic evidence supports this conclusion. A ridge landward of the backbarrier marsh west of Plum Island may have controlled drainage landward edge of potential drainage (Figure 7).

Edwards (1988) postulated that distributary drainage through the paleo-Merrimack occurred at or near the present-day mouth of the Merrimack River. Sediment would have been deposited along northern end of paleodelta and then reworked to the south to form the southern lobe. However, evidence from this study indicates that paleo-drainage of the Merrimack River was indeed to the south through various avulsion channels. Few cut-and-fill features are seen near the present-day mouth of Merrimack River; however thick (>20 m) layering of sediment overlying bedrock indicates a large input of sediment from the present-day Merrimack River.

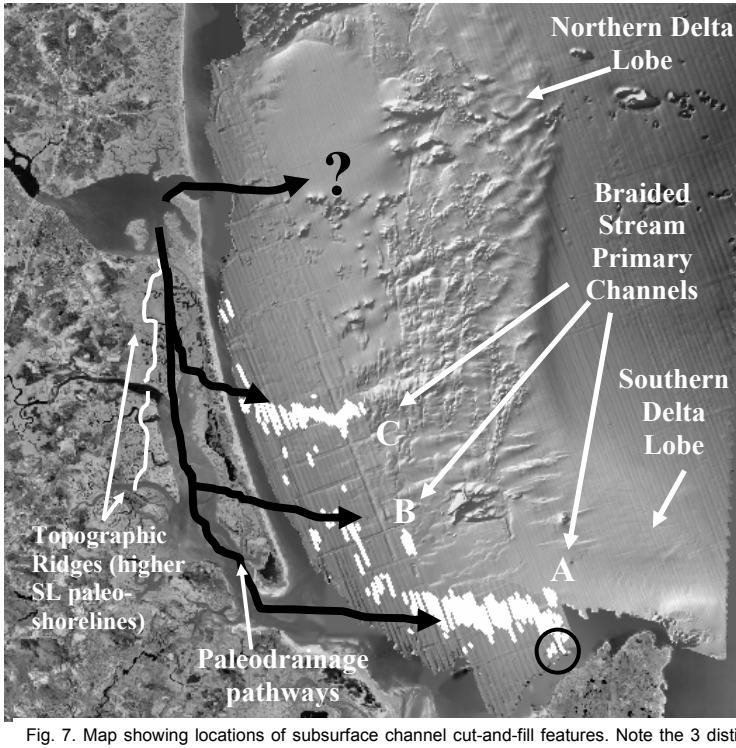

Fig. 7. Map showing locations of subsurface channel cut-and-fill features. Note the 3 distinct sets of features denoting possible locations of braided streams, labeled A-C. The possible forth set of features is circled just north of Cape Ann. Edwards (1988) identified a braided stream complex directly offshore of the present-day mouth of the Merrimack River, however, no channel cut-and-fill features were mapped in that location from data in this study.

Formation of the Merrimack Embayment Barriers and Subaqueous Sand Sheet

Surficial sediments in the Merrimack Embayment have been substantially reworked during the Holocene, as indicated by the existence of a broad sand sheet (18km x 7km) extending from approximately 2 km north of Cape Ann to 4 km north of the mouth of the Merrimack River and from the nearshore (-10 m) to the paleo-delta front (-45 m). This sand sheet consists of silty sand in the outer reaches near the delta and coarse-grained sand further inshore. An expansive (32 km^2), featureless coarse-grained sand deposit is centered off the Merrimack River. Fine-grained sand overlies this deposit in many locations, although it is not continuous, and forms asymmetrical bedforms (Hein et al. 2007).

Notably in shoreward regions, channel cut-and-fill features are truncated suggesting that the braided stream deposits themselves were reworked during the Holocene marine transgression. Shallow seismic profiles show a basal unconformity located immediately below a set of regressive fluvial / deltaic deposits. Capping these deposits is a pronounced ravinement surface, which extends from the delta to the nearshore of the Merrimack Embayment, indicating extensive reworking of the fluvial-deltaic lithosome during the Holocene transgression.

Granularmetric analyses indicate that the delta sediments are bimodal containing poorly sorted silt and fine sand components, which is characteristic of fluvio-deltaic sediments (Giosan and Bhattacharya 2005). Cores through the paleo-delta generally show intercalated silty clays and fine to medium silty sands. The upper 20 to 30 cm of the cores consists of medium sand with coarse pebbles and shell fragments (Edwards 1988). The cores that extend between 3 and 8m confirm that the delta is composed largely of fine-grained sediments, unlike the sediments that comprise the sand sheet.

The sediments composing the broad Merrimack Embayment sand sheet are likely sourced from the braided stream deposits that were reworked during the Holocene transgression and not from the delta itself. Furthermore, though FitzGerald et al. (1994) postulate that the reworking of paleo-delta sediments contributed to the formation of Plum Island and the other barriers in the Merrimack Embayment, it is likely that these coarser braided stream deposits were the true offshore source for any barrier sediments. The sand sheet and barriers were likely generated during the Holocene transgression when shoreface processes reworked both delta and braided stream deposits. Additional sand may have been derived from the Merrimack River (FitzGerald 1994).

CONCLUSIONS

1. New shallow seismic data indicate a widespread system of channel cut-and-fill structures inshore of the Merrimack paleo-delta having a depth of 5-10 m and an apparent width of 25 – 300 m.

2. The channel geometry and spatial extent of the cut-and-fill features are consistent with those of braided streams. Several distinct sets of channel cut-and-fill features represent avulsion of the primary distributary channel of the paleo-Merrimack River.

3. This braid plain system was responsible for delivering a large volume of sediment (1.3 billion cubic meters) to a multi-lobate lowstand delta during late Pleistocene (12 kya, at -45 m, Oldale et al. 1983).

4. Sediment comprising this braid plain was reworked during the Holocene transgression and likely contributed sediment to the present day barrier system in the Merrimack Embayment.

ACKNOWLEDGEMENTS

This study was funded by the Minerals Management Service of the US Department of the Interior and Massachusetts Coastal Zone Management. The authors would like to extend our appreciation to Bror Jonsson of Boston University and Brian Andrews, Seth Ackerman, and the rest of the team at the USGS Science Center for Coastal and Marine Geology in Woods Hole, MA for their assistance in the collection and processing of the raw data. Additional thanks to the crews of the R/V Connecticut (Groton, CT) and the F/V Venture (Gloucester, MA).

LITERATURE CITED

Edwards, Gerald B. (1988). Late Quaternary geology of northeastern Massachusetts and Merrimack Embayment, Western Gulf of Maine. Boston, MA: Boston University, Master's thesis, 213p.

FitzGerald, D.M., Rosen, P.S., and van Heteren, S. (1994). New England Barriers, *In*: DAVIS, R.A. (ed.), *Geology of Holocene Barrier Island Systems*, Berlin, Germany: Springer-Verlag, pp. 305-394.

FitzGerald, D.M., Buynevich, I.V., Davis, R.A., AND Fenster, M.S. (2002). New England tidal inlets with special reference to riverine-associated inlet systems, *Geomorphology*, 48(1), 179-208.

Hein, C.J., FitzGerald, D.M., and Barnhardt, W. (2007). Holocene reworking of a sand sheet in the Merrimack Embayment, Western Gulf of Maine. Journal of Coastal Research, SI 50 (Proceedings of the 9th International Coastal Symposium), Gold Coast, Australia, ISBN.

Koteff, C., Robinson, G.R., Goldsmith, R., and Thompson, W.B. (1993). Delayed postglacial uplift and synglacial sea levels in coastal central New England, Quaternary Research, 40(1), 46-54.

Oldale, R.N., Wommack, L.E., and Whitney, A.B. (1983). Evidence for a postglacial low relative sea-level stand in the drowned delta of the Merrimack River, western Gulf of Maine, *Quaternary Research*, 19(3), 325-336.

Oldale, R.N., Colman, S.M., and Jones, G.A. (1993). Radiocarbon ages from two submerged strandline features in the western Gulf of Maine and a sea-level curve for the northeastern Massachusetts coastal region, *Quaternary Research*, 40(1), 38-45.

Smith, J.B., and FitzGerald, D.M. (1994). Sediment transport patterns at the Essex River Inlet ebb tidal delta, Massachusetts, U.S.A., *Journal of Coastal Research*, 10, 752-774.

Stone, B.D., Stone, J.R., and McWeeney, L.J. (2004). Where the glacier met the sea: Late Quaternary geology of the northeast coast of Massachusetts from Cape Ann to Salisbury, *In*: Handson, L. (ed.), Proceedings of the *New England Intercollegiate Geological Conference*, Salem, Massachusetts, B-3, pp. 25.

THE USE OF HISTORIC TOPOGRAPHY FOR THE CHARACTERIZATION OF TIME-DEPENDENT GEOMORPHIC CHANGE AND SEDIMENT DELIVERY

David A. Jaffe[1]

1. Pacific Advanced Civil Engineering, Inc. (PACE), 17520 Newhope St., Ste. 200, Fountain Valley, California, USA.
djaffe@p-a-c-e.com

Abstract The Santa Clara River, draining one of the largest watersheds in Southern California (1,634 sq-mi [4,232 sq-km]), is a major source of coastal sediments. Future development on the watershed has the potential to alter sediment delivery and cause erosion both along the coast and within the River. Unfortunately, long-term, historic sediment transport data is unavailable for Santa Clara River. Because of the paucity of the available data, an alternative means of determining a baseline geomorphic and sediment delivery condition is needed.

Time dependent geomorphic change was calculated based on topographic data dating from 1906 to 2005. At least one cross-section was chosen for each hydraulically distinct subreach of the study area. A sectional analysis based on elevation change of the bed (area computation of the section) was conducted to determine time dependent geomorphic change. Analysis finds that sections show geomorphic change between 1947 and 2005 ranging from -8.0 to 3.1 feet (-2.44 to 0.95 m).

INTRODUCTION

The following technical investigation provides a detailed and focused evaluation of the long-term stability of the Santa Clara River for the reach between Interstate 5 and the Los Angeles-Ventura County Line (7.0 miles [11.3 km])(Figure 1). The Santa Clara River fluvial system extends from Acton, California in the east to the Pacific Ocean, the River's natural terminus, in the west. The River is a major source of coastal sediments along Southern California beaches. Both historical and future development along the River within the study reach has the potential to modify the fluvial response of the watershed through changes in the runoff and reduction in the sediment supply from the developed areas. Until approximately the 1960's, development in the watershed upstream of the study reach was primarily agricultural, however, more recent development has been

suburban housing and commercial uses. Future modifications to the river system and uplands have the potential to modify the fluvial operation of the floodplain and cause changes to the stream mechanics. These changes to fluvial mechanics have the potential to impact the delivery of sediment to the coast. The intent of this analysis is to evaluate changes in the floodplain fluvial operation over the long-term, and estimate the extent to which these changes have been a function of riverine and uplands development.

Modifications to the river system are measured as bed adjustment in feet. Positive adjustment indicates bed aggradation while negative adjustment indicates bed degradation. Of the several types of adjustment, only long-term adjustment is considered in this study. Long-term adjustment consists of fluvial processes that occur over many rainy seasons and contribute fluctuation of bed elevation of a river or creek.

The primary objective of this study is to develop the technical engineering analysis to assess river bed impacts from potential modifications of fluvial operation from long-term watershed development west of Interstate 5.

PREVIOUS STUDIES

Three sediment transport studies have been conducted within the study reach between Interstate 5 and the Los Angeles/Ventura County line in the last 25 years. The first study conducted by Sikand Engineering was submitted in June 2000, and revised November 2004. The primary focus of the study was the long-term degradation of the river bed. Grain size distribution plots indicate poorly graded sand with gravel and a D_{50} of approximately 1 mm in the vicinity of the Castaic Creek confluence. The study found that for seven subreaches in the present condition, the bed is in steady state, but that the proposed conditions are expected to cause minimal degradation (an average of one foot [0.3 m]) in some subreaches and minimal aggradation (an average of three feet [0.9 m]) in some subreaches. The study also analyzed the historical record of gage data at the county line from 1953 to 1993. By comparison, USGS data (*Sediment Discharge in The Santa Clara River Basin, Ventura and Los Angeles Counties, California*) notes in Table 3 that in 1971 at 1470 cfs (41.6 cms), 99% of the transport was silt at the county line. It is important to note that the results of this study were not accepted by Los Angeles County Department of Public Works (LADPW), and the comments on the last review of the study in 2004 were not addressed.

The second study produced by Simons, Li, and Associates (SLA) and submitted November 1990, sought to provide information for flood and fluvial process management in the Santa Clara River from Soledad Canyon to Castaic Creek. The study included multiple tasks including data collection, quantitative analysis and mathematical modeling, and other assignments. For the portion of the River downstream of Interstate 5, the bed was found to be adjusting between -0.1 to +1.0 feet (-0.03 to 0.31 m). The study notes that the River appears to be in “pseudo-equilibrium” and “shows no trend toward either aggradation or degradation and significant lateral migration of the channel is not apparent.” The SLA report was reviewed in detail by LADPW and response to comments made, however, the report was not revised to obtain final LADPW approval.

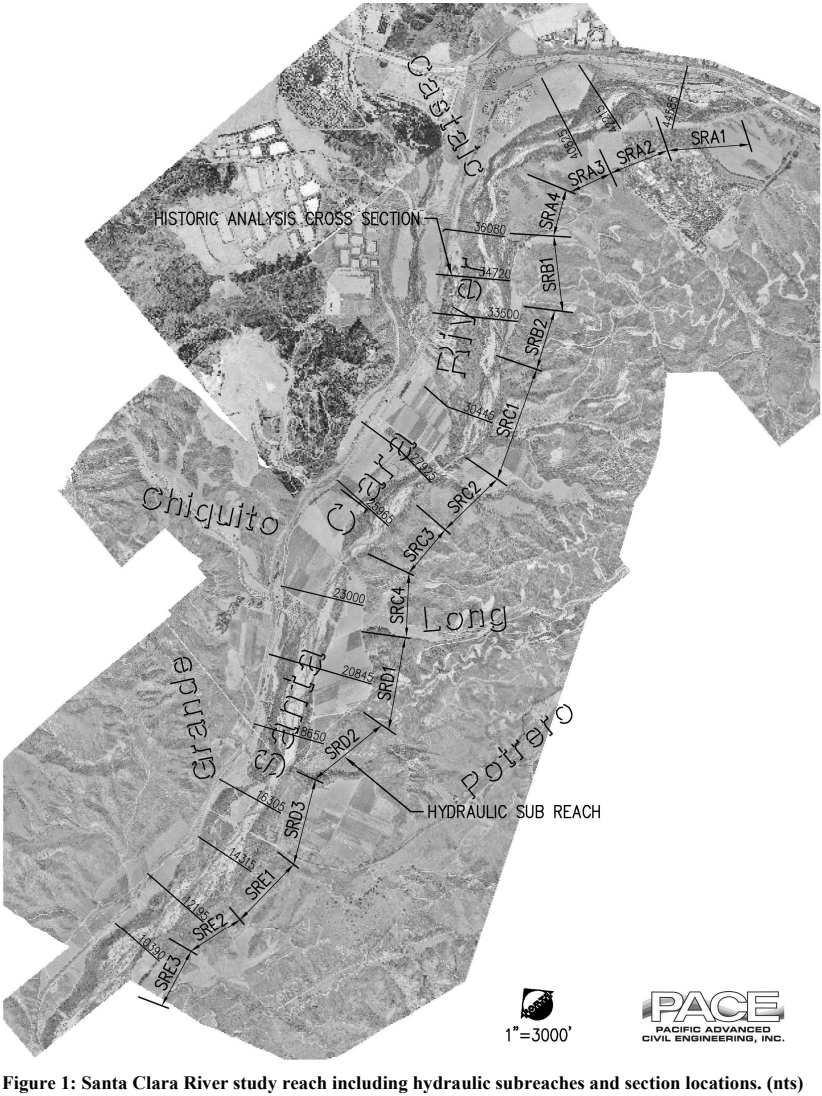

Figure 1: Santa Clara River study reach including hydraulic subreaches and section locations. (nts)

The final study was conducted by the United States Geological Survey and completed in August 1979. The study sought to determine the sediment discharge in the Santa Clara

River Basin in Los Angeles and Ventura Counties using sediment trap (1968-1975) and historical discharge data (1928-1975). Sediment data was collected for the period 1967 to 1975 at the Los Angeles/Ventura County line. During the short-term period (1968-1975), total sediment discharge was 63.5 million tons (5.76×10^{10} kg), 59.5 million tons (5.43×10^{10} kg) of which was carried in suspension. Coarse sediment accounted for 28% of the total sediment discharge (17.7 million tons [1.61×10^{10} kg]). Transport of the majority of sediment occurred during only a few days of flood flow each year (55% of the total sediment within 2 days and 92% within 53 days). Sediment deposited in reservoirs resulted in a 6% reduction of sediment to the River basin during the historical period (1928-1975) and 12% during the period most affected by dams (1953-1975). Castaic Creek interception of sediment reduced the amount of sediment in the River by another 2% from 1928-1975 and 4% from 1953-1975. It is not clear how these reductions are directly related the completion of the Castaic Creek Dam because it was not completed until 1971.

SEDIMENT CHARACTERIZATION AND ANALYSIS

To characterize the sediment of the river bed and by extension the possible bed load of sediment during discharge events, a sediment grain size analysis was conducted. The goal of the analysis is to gain a statistical representation of the size distribution of soil components of the river bed.

Sediment collection for the Santa Clara River along the study reach was conducted by Allen Seward Engineering Geology, Inc. Eighteen samples were collected along the river with a five samples taken at the tributaries. The relevant sampling locations are compiled in Table 1. All sampling was conducted using grab samples of the upper foot of the active or recently active portion of the bed. At least three samples at different locations within a sampling station were taken at each River sampling location.

For this study, no fine material is included in analysis because fine material is generally transported as wash load, which is not of concern here. Distribution data has been averaged on a station by station basis. Averaging is accomplished by taking the mean of the three samples from a given station. Averaging provides a single representative sediment grain size distribution for a given station that can be used for analysis. Plots of the mean grain size distribution for each sampling station are presented in Figure 2.

A review of the raw gradation curves indicates that most samples are comprised of poorly graded sands with gravels and silts. The D_{50} values for all samples ranged from 0.25 to 4.67 mm with an average of 0.80 mm. The averaged D_{50} values range from 0.50 to 1.00 mm. Additionally, previous SLA study noted above also found similar sandy characteristics, however, the average grain size was found to be approximately D_{50}=1.30 mm, somewhat more coarse that the current sampling. An armoring layer was not observed in field measurements, Seward field studies or SLA boring logs.

Table 1: Santa Clara River Location and Average D_{50} of Sediment Samples

Reach	Station	Sample Number	Reach Average D_{50} (mm)[1]
A & B	37135	CB1	0.5
	37135	CB2	
	36515	CB3	
C	28500	HR1	1.0
	28500	HR2	
	28500	HR3	
	24115	LC1	
	24115	LC2	
	24115	LC3	
D	22195	AC1	1.0
	22195	AC2	
	22195	AC3	
D & E	15335	MC1	1.0
	15335	MC2	
	15335	MC3	

1: Reach average is the average of all samples I the reach.

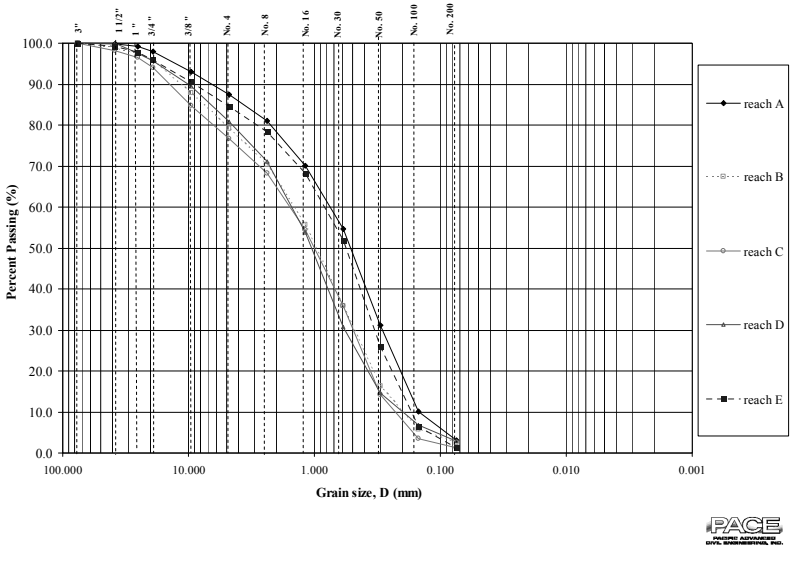

Figure 2: Santa Clara River Grain Size Gradation Curves

LONG-TERM ADJUSTMENT

Long-term adjustment was calculated based on historical records in the form of topographic data. First, topographic data dating from 1906, 1930, 1947, 1963, 1999, 2004 and 2005, was obtained and digitized. This was accomplished by determining a common coordinate system and creating contour lines within the study area. Topographic data was available in several formats including digital elevation maps (1999, 2004, 2005), topographic surveys (1963) and quad maps (1906, 1930, 1947). Digital elevation maps were only adjusted for horizontal location. Cross-sections were next cut at the locations of select numerical model sections for each historical topography (Figure 1). At least one cross-section was chosen for each hydraulically distinct subreach based on engineering interest. The sections chosen are section 10390, section 12195, section 14315, section 16305, section 18650, section 20845, section 23000, section 25965, section 27925, section 30445, section 33500, section 34720, section 36080, section 40825, section 42215, and section 44585. Section 36080 is actually in SRB1 not SRA4, although it was chosen since it is directly upstream of a tributary and near the proposed Commerce Center Drive Bridge. Areas of the 1947, 1963, 1999, 2004 and 2005 sections are calculated and these areas are used to calculate the average change in bed elevation over time. The 1930 topography is not used to calculate average change in bed because of the impacts of the failure of the St. Francis Dam in 1928. The 1906 topography is excluded from this study because it of insufficient resolution. To calculate the area of a given cross-section the lowest historical point on the section is determined and the area of each vertical foot (0.31 m) of the section in one-foot (0.31 m) intervals is calculated, as shown in Figure 3a-c, for each topography. (Space restrictions prevent the publication of all 16 sections so the upstream, middle and downstream sections are presented and discussed below for brevity.) The area of a section is the sum of the one-foot area intervals, also shown in Figure 3a-c. All areas for a given section have a common toe and top from which the area is calculated. The relative average change in depth for a given section and topography is calculated as the area divided by the top width, where the top width is taken as the width of the upper most one-foot (0.31 m) area. The top width in this sense is not a hydraulic characteristic but a physical one, which along with the sectional area determines the maximum capacity of the section. Moreover, the calculated depth is a relative physical value based on the section area and represents an average physical characteristic of the section as a whole.

Several events within the available historical record (1930 to present) have had an impact on the River bed and fluvial mechanics. These events include failure of the upstream St. Francis Dam, construction of bridges spanning the River, agricultural infill along the River banks, and periodic burning of surrounding vegetation during forest fires. These different historical events can be placed into two categories: the St. Francis Dam failure in 1928, and those both prior to and following Dam failure. The most significant historical event in the formation of the present bed condition was the aforementioned failure of the Dam. The consequence of this event is tied to the River's recovery from the erosion caused by the extremely high flow of floodwater (1.7×10^6 cfs [4.8×10^4 cms] at the dam-break). Within the project reach, the failure of the Dam appears to have resulted in the severe scouring of the bed in some locations. Placement of bridges does not appear

to have had a measurable impact on long-term bed characteristics, except for very local characteristics. The Interstate 5 Bridge has not been outflanked by bed migration since its construction. Moreover, despite narrowing of the bed locally, bridge placement does not appear to have led to general bed degradation on the River as a whole. Periodic fires have burned the flora of the watershed historically, and as recently as the summer of 2006. Fires are important to changes of the River bed because these fires deplete vegetation stalks and root systems that hold soil in upland areas, thereby leading to increased erosion on slopes and increased sediment delivery to creeks and rivers. Agricultural fills are also important to the historic River fluvial mechanics because the fills limit the extent to which the River may migrate, and in turn cause vertical erosion of the creek bed. LADPW has noted that lateral erosion of agricultural fill has occurred periodically although no data is presently available to date to gage the extent or depth of this erosion. Certainly, the volume of agricultural fill laterally eroded is not sufficient to prevent vertical bed erosion.

Table 2a shows the long-term historical cross-sections area from 1947 to 2005. The table lists the area for each historical section in a given subreach. The table also lists the difference between historical sections (e.g. 1947 section 23000 area – 2005 section 23000 area). Table 2b shows the historical cross-section average depth and average depth change by section and year. As noted above, the average depth is the area of a given section by year divided by the section geometric top width for that year. The difference between historical areas is also shown. It is important to note that the vertical elevation for each section is the same.

Section 42215 (SRA2) appears to have greatly down cut and widened since 1947, degrading an average 8.1 feet (2.47m) along the section. Some of the observed long-term change may be related to the presence of the theme park and water treatment facility on the bank at this location. In recent years (1999-2005), the creek appears to have become relatively stable: area has increased from 17946 to 17101 over the period (Figure 3a). The River is relatively wide at this location although a bend is present. Development has occurred on both banks with agricultural development on the north bank and the Magic Mountain theme park on the south bank. Historical development may have led to the observed degradation, although at present the bed appears to be stable or degrading only slightly. The impacts of woody vegetation in this section may have played a role in the recent degradation. Finally, the 2004-2005 winter was very wet and high flows were present on the River. During the heavy storms of December 2004 and January 2005, approximately 4.4 acres (17,806.2 m^2) of the south bank was lost to the Santa Clara River. Some of the single-season degradation may possibly be attributed to this event. The features located at station 775 and 1325 in the 1999 topography are expected to be related the aerial surveying methodology.

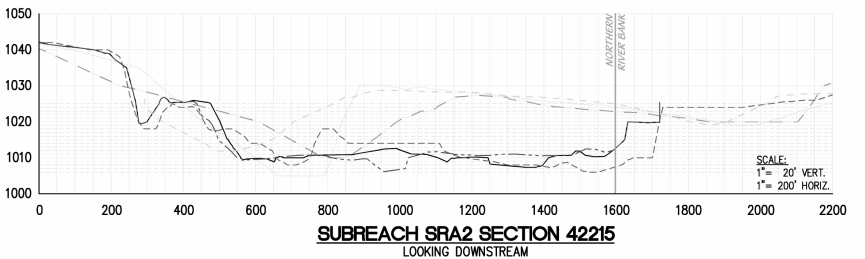

CROSS SECTIONAL AREAS AT STA 42215 (sf)					
ELEV	1947	1963	1999	2004	2005
1007.0	0.0	0.0	58.7	31.4	0.0
1008.0	0.0	0.0	112.6	79.5	95.4
1009.0	0.0	0.0	370.2	95.4	148.4
1010.0	0.0	0.0	502.0	183.9	223.1
1011.0	0.0	80.5	641.6	412.8	588.7
1012.0	7.2	114.1	679.1	920.5	898.3
1013.0	86.6	146.5	709.3	1055.3	1028.1
1014.0	136.6	178.9	736.3	1093.5	1073.1
1015.0	181.3	211.3	1041.4	1115.8	1090.6
1016.0	222.4	243.5	1067.9	1129.1	1104.3
1017.0	254.2	274.7	1099.1	1134.2	1110.1
1018.0	286.0	305.7	1143.3	1140.1	1115.7
1019.0	317.8	336.6	1284.1	1146.4	1121.9
1020.0	395.8	367.6	1309.9	1159.8	1133.8
1021.0	509.5	692.9	1326.8	1263.7	1245.8
1022.0	601.5	843.7	1341.2	1301.3	1260.7
1023.0	700.1	1008.7	1357.4	1315.9	1275.2
1024.0	802.4	1236.4	1380.0	1329.3	1289.6
1025.0	1107.8	1398.5	1697.5	1342.9	1304.2
Area	5609.2	7439.6	17858.4	17250.9	17107.1

LEGEND:
2005 TERRAIN
2004 TERRAIN
1999 TERRAIN
1963 TERRAIN
1947 TERRAIN
1930 TERRAIN

PACE
PACIFIC ADVANCED CIVIL ENGINEERING, INC.

Figure 3a: Subreach SRA2 Historical Sections.

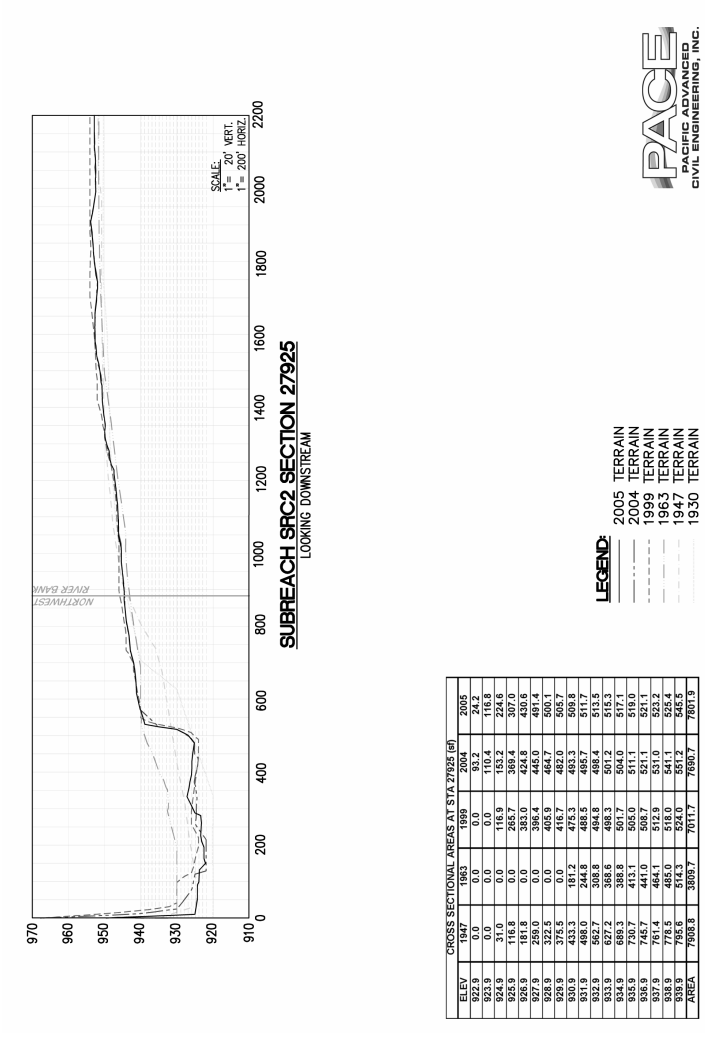

CROSS SECTIONAL AREAS AT STA 27925 (sf)

ELEV	1947	1963	1999	2004	2005
922.9	0.0	0.0	0.0	93.2	24.2
923.9	0.0	0.0	0.0	110.4	116.8
924.9	31.0	0.0	116.9	153.2	224.6
925.9	116.8	0.0	265.7	369.4	307.0
926.9	181.8	0.0	383.0	424.8	430.6
927.9	259.0	0.0	396.4	445.0	491.4
928.9	322.5	0.0	405.9	464.7	500.1
929.9	375.5	0.0	416.7	482.0	505.7
930.9	433.3	181.2	475.3	493.3	509.8
931.9	498.0	244.8	488.5	495.7	511.7
932.9	562.7	308.8	494.8	498.4	513.5
933.9	627.2	368.6	498.3	501.2	515.3
934.9	689.3	388.8	501.7	504.0	517.1
935.9	730.7	413.1	505.0	511.1	519.0
936.9	745.7	441.0	508.7	521.1	521.1
937.9	761.4	464.1	512.9	531.0	523.2
938.9	778.5	485.0	518.0	541.1	525.4
939.9	795.6	514.3	524.0	551.2	545.5
AREA	7908.8	3809.7	7011.7	7690.7	7801.9

Figure 3b: Subreach SRC2 Historical Sections.

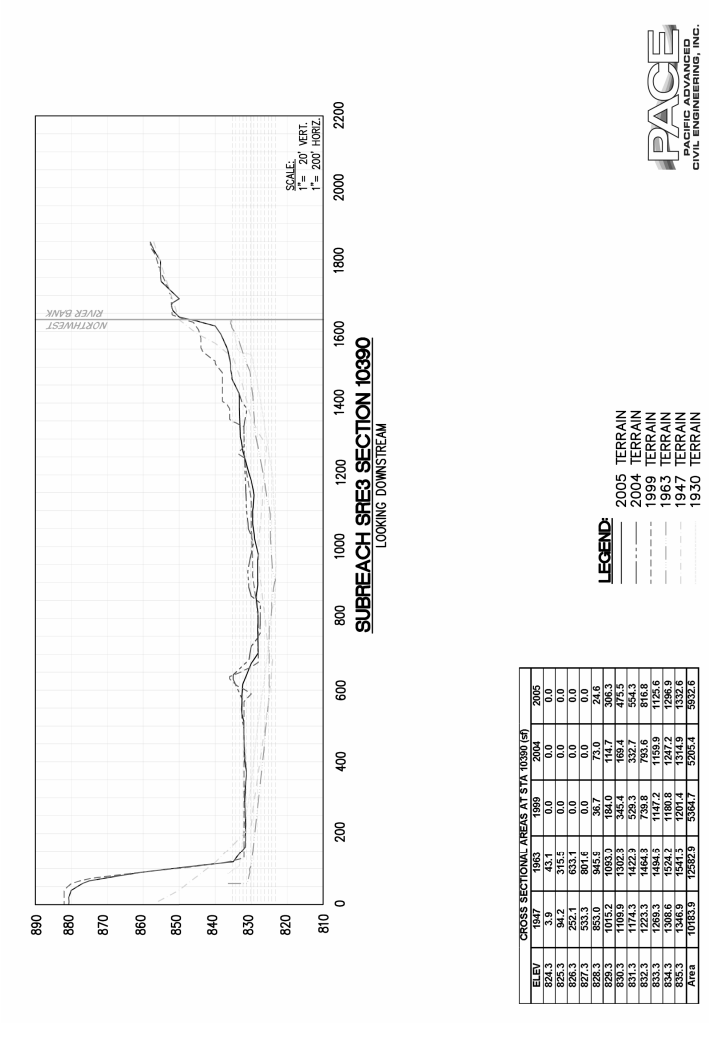

CROSS SECTIONAL AREAS AT STA 10390 (sf)

ELEV	1947	1963	1999	2004	2005
824.3	3.9	43.1	0.0	0.0	0.0
825.3	94.2	315.5	0.0	0.0	0.0
826.3	252.1	633.1	0.0	0.0	0.0
827.3	533.3	801.6	0.0	0.0	0.0
828.3	853.0	945.5	36.7	73.0	24.6
829.3	1015.2	1093.0	184.0	114.7	306.3
830.3	1109.9	1302.3	345.4	169.4	475.5
831.3	1174.3	1422.9	529.3	332.7	554.3
832.3	1223.3	1464.8	739.8	793.6	816.8
833.3	1269.3	1494.3	1147.2	1159.9	1125.6
834.3	1308.6	1524.2	1180.8	1247.2	1296.9
835.3	1346.9	1541.5	1201.4	1314.9	1332.6
Area	10183.9	12582.9	5364.7	5205.4	5932.6

Figure 3c: Subreach SRE3 Historical Sections.

Table 2a: Santa Clara River Long-term Historical Cross-Section Area & Area Change 1947-2005

Subreach	Station	Area by Year (sf)			Δ Area by Year (sf)			
		1947	2004	2005	47-05	Change	04-05	Change
SRA1	44585 [1,3]	9209	12312	14990	-5781	DEGRADE	-2678	DEGRADE
SRA2	42215	5609	17251	17107	-11498	DEGRADE	144	AGGRADE
SRA3	40825	4761	7403	10210	-5449	DEGRADE	-2807	DEGRADE
SRA4	36080 [2]	12270	21059	21208	-8938	DEGRADE	-149	DEGRADE
SRB1	34720	14344	16868	19520	-5176	DEGRADE	-2652	DEGRADE
SRB2	33500	9132	14857	16523	-7391	DEGRADE	-1666	DEGRADE
SRC1	30445	9172	13898	13351	-4179	DEGRADE	547	AGGRADE
SRC2	27925	7909	7691	7802	107	AGGRADE	-111	DEGRADE
SRC3	25965	7734	9757	9519	-1785	DEGRADE	238	AGGRADE
SRC4	23000	18321	14968	13563	4758	AGGRADE	1405	AGGRADE
SRD1	20845	20069	14737	16091	3978	AGGRADE	-1354	DEGRADE
SRD2	18650	9589	10838	12011	-2422	DEGRADE	-1173	DEGRADE
SRD3	16305	11158	9704	11772	-614	DEGRADE	-2068	DEGRADE
SRE1	14315	8670	12499	13590	-4920	DEGRADE	-1091	DEGRADE
SRE2	12195	6839	6657	8034	-1195	DEGRADE	-1377	DEGRADE
SRE3	10390	10184	5205	5933	4251	AGGRADE	-728	DEGRADE

1 - Long-term change analyzed using 1963 data instead of 1947 data because 1947 data is unavailable at this section

2 - STA 36080 was chosen to represent sra4 because the downstream confluence is of particular engineering interest to that subreach

3- STA 44585 1947 area uses 1963 data since 1947 data is not available.

Table 2b: Santa Clara River Historical Cross-Section Average Depth & Average Depth Change Aggradation/Degradation Change 1947-2005

Subreach	Station	Average Depth by Year = Area/Top Width (ft)			Δ Average Depth by Year (ft)			
		1947	2004	2005	47-05	Change	04-05	Change
SRA1	44585 1,3	16.0	18.4	17.8	-2.8	DEGRADE	0.6	AGGRADE
SRA2	42215	5.1	12.8	13.1	-8.0	DEGRADE	-0.3	DEGRADE
SRA3	40825	4.5	7.4	9.7	-5.2	DEGRADE	-2.3	DEGRADE
SRA4	36080 2	11.6	14.2	14.3	-2.7	DEGRADE	-0.1	DEGRADE
SRB1	34720	9.9	11.4	13.1	-3.2	DEGRADE	-1.7	DEGRADE
SRB2	33500	6.4	8.8	9.8	-3.4	DEGRADE	-1.0	DEGRADE
SRC1	30445	7.3	8.9	8.6	-1.3	DEGRADE	0.3	AGGRADE
SRC2	27925	9.9	14.0	14.3	-4.4	DEGRADE	-0.3	DEGRADE
SRC3	25965	5.7	7.6	7.4	-1.7	DEGRADE	0.2	AGGRADE
SRC4	23000	8.5	7.3	6.6	1.9	AGGRADE	0.7	AGGRADE
SRD1	20845	7.8	5.9	6.4	1.4	AGGRADE	-0.5	DEGRADE
SRD2	18650	5.6	5.6	6.2	-0.6	DEGRADE	-0.6	DEGRADE
SRD3	16305	5.6	5.1	6.3	-0.7	DEGRADE	-1.2	DEGRADE
SRE1	14315	6.1	6.5	7.1	-1.0	DEGRADE	-0.6	DEGRADE
SRE2	12195	5.3	5.1	6.2	-0.9	DEGRADE	-1.1	DEGRADE
SRE3	10390	7.6	4.0	4.5	3.1	AGGRADE	-0.5	DEGRADE

1 - Long-term change analyzed using 1963 data instead of 1947 data because 1947 data is unavailable at this section

2 - STA 36080 was chosen to represent sra4 because the downstream confluence is of particular engineering interest to that subreach

3- STA 44585 1947 area uses 1963 data since 1947 data is not available.

At section 27925 (SRC2), the upstream degradational trends diminish and historic topographic data begin to indicate a bed that is fluctuating about a mean (Figure 3b). Section 27925 is quite narrow and adjacent to historic agricultural practice. The channel

at this section is confined between steep bluffs on the left bank and tree-lined agricultural embankments on the right. Data in Table 2b indicate that the section has degraded 4.4 feet (1.34 m) over the period of record and 0.3 feet (0.09 m) during 2005 season. A relatively low-radius bend in the River is also present here.

Section 10390 (SRE3) illustrates 3.1 feet (0.95 m) of aggradation from 1947 to 2005 and 0.5 feet (0.15 m) of degradation between 2004 and 2005 (Table 2a). In this subreach, the River is relatively very wide and braided. Little woody vegetation is observed on the banks and steep bluffs dominate both banks, although a small farm plot sets the bluff on the right bank back. Figure 3c indicates that the bed is recovering from scouring related to the 1928 dam break. The observed feature in the 1999 and 2004 topographies at station 625 appears to be the south bank of the thalweg.

Based on the above analysis and Table 2, sections above approximately 25965 appear to be degrading, while sections below appear to be stable or fluctuating around a mean elevation. This may be the result of historic development within the overbank areas or owing to the presence of the generally narrower, winding channel bed in the upstream portion of the study reach. The lower portion of the study reach is relatively flat, broad and straight.

With historical topography from successive years, estimates of single-season change can be developed. The 2004-2005 rain season was wet on Santa Clara River with strong rain events occurring on already saturated soils both in December 2004 and January 2005. These events produced very high discharges on the River (≈ 50-year return period discharge). Topography from before and after these events provides a tool to estimate the impacts of a single large-discharge event, in general, and single season cumulative impacts. The 2004 and 2005 beds are described in Table 2a-b and Figure 3a-c. The table and figures illustrate that the bed elevations show alternating degradation and aggradation. Degradation ranges from 0.1 to 2.3 feet (0.03 to 0.70 m), on average, with most degrading sections changing less than one foot (0.31 m), on average. Aggrading sections change from 0.2 to 0.7 feet (0.06 to 0.21 m), on average. More sections degrade than aggrade. The pattern of aggradation and degradation over the single season does not appear to be a function of proximity to a river confluence.

CONCLUSION

This technical study provides an evaluation of the long-term stability of Santa Clara River between Interstate 5 and an area generally west of the Los Angeles/Ventura County line. Future development along the River within the study area has the potential to modify the fluvial mechanics of the River. This sectional-area-based analysis evaluates changes to the river bed and in the floodplain fluvial operation over the long-term despite a paucity of available historical data.

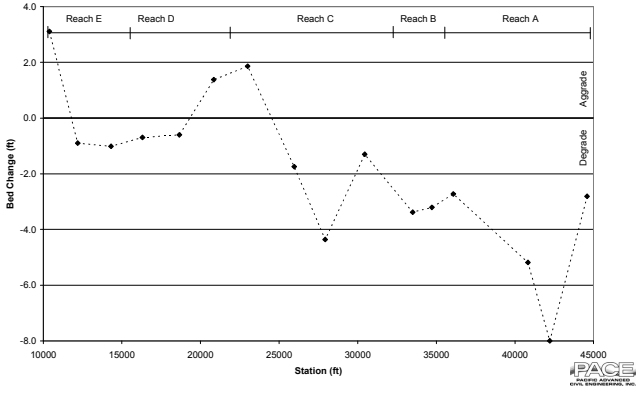

Figure 4: Santa Clara River Historic Long-term Bed Elevation Change

Three sediment transport studies were previously conducted within the study reach in the last 25 years. The first study conducted by Sikand Engineering (June 2000, and revised November 2004) was to provide a sediment transport analysis for the Santa Clara River and to determine the possible effects of future development on river bed stability. The second study, produced by SLA (November 1990), sought to provide information for flood and fluvial process management in the Santa Clara River. The final study was conducted by USGS, whereby the study collected sediment data from 1967 to 1975 at three sites in the Santa Clara River basin including the Los Angeles-Ventura County line. The study estimated long-term sediment discharge by applying the sediment and water discharge relationship observed from 1967 to 1975.

Long-term adjustment was calculated based on historical records in the form of topographic data. Topographic data dating from 1906, 1930, 1947, 1963, 1999, 2004 and 2005, was digitized. Cross-sections were cut at the locations of select modeling sections for each historical topography. At least one cross-section was chosen for each hydraulically distinct subreach. Areas of the 1947, 1963, 1999, 2004 and 2005 sections are calculated and the areas of the 1947, 2004 and 2005 bed are used to calculate the average change in bed elevation over time. The 1930 topography is not used to calculate average change in bed because the trends in bed change that occurred during this year occurred immediately following the failure of the St. Francis Dam upstream of the project site, while the 1906 data is of insufficient resolution for inclusion. Several events within the available historical record (1930 to present) have had an impact on the River bed and fluvial mechanics. These events include failure of the upstream dam, construction of bridges spanning the River, agricultural infill along the River banks, and periodic burning of surrounding vegetation during forest fires. The most significant historical event in the formation of the present bed condition was the failure of the Dam. Within the project reach, the failure of the Dam appears to have resulted in the abrupt scour of the bed.

The sectional analysis finds that some historical sections (SRD2, SRD3, SRE1, SRE2) show little change between 1947 and 2005 suggesting an approximate equilibrium state for these subreaches. Between 1947 and 2005, 0.5, 0.7, 1.0, and 0.8 feet (0.15, 0.21, 0.31, and 0.24 m), respectively, of cumulative degradation appears to have occurred on these sections. A combination of limited development on the banks and local topographic features are possible causes for the limited degradation. It should be noted that the degradation observed on these reaches is similar to that predicted by the Sikand (2000) study, but the opposite of that predicted by the SLA (1990) study where aggradation of approximately 1 foot (0.31 m) was expected. Upstream sections SRA1 to SRC3 (SRC2: Figure 3b) show continuous degradation over the period of record from 1947 to the present. Degradation ranged from -1.3 feet (0.40 m) at section SRC1 to -8.0 feet (2.44 m) at Section SRA2 (Figure 3c). This degradation appears to be caused by a combination of local topography, development of the banks, and local scour related to bridge placement. Three sections, SRC4, SRD1 and SRE3 (Figure 3c) aggraded cumulatively between 1947 and 2005 by 1.9, 1.4, and 3.1 feet (0.58, 0.43, and 0.95 m) on average, respectively. While it is unclear why the observed aggradation occurred, it is presently believed to be the result of bed recovery from the 1928 St. Francis Dam failure combined with affects of local topography. By way of comparison with previous studies the SLA (1990) study predicted aggradation of approximately 1 foot (0.31 m) while Sikand (2000) predicted degradation, as noted above.

Degradation seems to be more prevalent on the upper half of the study reach while mild fluctuations about a mean are more apparent on the lower half. This appears to result from the relatively steep, narrow, winding upper portion of the study reach versus the relatively flat, wide, braided channel in the lower portion of the study reach of the River. Agricultural activities occurred, primarily in downstream sections but in upstream sections as well, so some of the observed channelization may have resulted from these activities. Non-agricultural development is more prevalent on the banks of upper portion of the study reach and this development may contribute to the observed degradational trends, also.

In general, the data presented here suggests that erosion has increased on the study reach over the period of historical record. Data suggest that the observed erosion has resulted from impacts to the floodplain by development. It is not clear from this study, however, if the increased scour is localized or if the increased scour will impact sediment delivery at the coast. Certainly the implication here is that continued development of the banks will reduce the sediment from uplands, increasing bed scour, and reducing delivery to the coasts unless future development sediment inflows are managed carefully.

ACKNOWLEDGEMENTS
The author would like to thank Allen Seward Engineering Geology for assistance with sediment sampling data and historical topographies; and Los Angeles County Department of Public Works for assistance with previous studies.

REFERENCES

Sikand Engineering (2000). In the *Newhall Ranch Santa Clara River HEC-RAS Study,* June.

Simons, Li & Associates (1990). Fluvial Study of Santa Clara River and the Tributaries, November.

US Geological Survey (USGS) (1979). Sediment Discharge in the Santa Clara River Basin, Ventura and Los Angeles Counties, California. Water Resource Investigations 79-78, August.

IMPACT OF HURRICANES KATRINA AND LILI ON THE INNER SHELF OF THE MISSISSIPPI-ATCHAFALAYA DELTA

Mead A. Allison[1], Timothy M. Dellapenna[2], Miguel A. Goñi[3], Alex Sheremet[4]

1. Earth and Environmental Sciences, Dinwiddie Hall, Tulane University, New Orleans, LA 70118, U.S.A. malliso@tulane.edu.
2. Marine Sciences, Texas A & M University at Galveston, Galveston, TX 77553; dellapet@tamug.edu
3. Dept. of Oceanography, Oregon State University, Corvallis, OR 97331; mgoni@coas.oregonstate.edu
4. Civil and Coastal Engineering, 365 Weil Hall, University of Florida, Gainesville , FL 32611, USA. alex@coastal.ufl.edu.

Abstract: Box cores collected on the Louisiana continental shelf immediately following Hurricanes Lili (2002) and Katrina (2005) allow comparison of sediment event layer formation on the actively accreting Mississippi delta adjacent to Southwest Pass (Katrina) and the Atchafalaya delta (Lili). Post-Katrina box core sites in water depths of <40 m show evidence of an erosional surface at the sediment-water interface, indicating the water depth that critical erosion stresses are found in these large storms. Erosional deflations from Katrina and Lili ranged from 2-15 cm, controlled by water depth (shallower caused greater incision) and degree of consolidation of the pre-existing seabed sediments. In water depths of >25 m, post-Katrina cores display event layer deposition 1-25 cm thick above the incision surface: post-Lili cores from the Atchafalaya show similar thicknesses dependent on proximity to the storm path, but also extending into shallower water (shallowest station sampled was 4 m).

INTRODUCTION

Tropical cyclones, because of the enormous wave orbital velocities and strong mean flows they create in the benthic boundary layer, may have a disproportionate impact on the transport, deposition and burial of sediments on continental shelves where they are active. Study of the shelf seabed response to tropical cyclones, whether erosional, depositional, or a combination of the two, is complicated by the wide range of sediment types and shelf geometries that are present in areas prone to these storms, as

well as the individual nature of storm tracks, pressures and wind fields. River-dominated continental shelves are generally the only shelf type where modern fine-grained sediment deposition is taking place on the inner to mid shelf region (Nittrouer and Wright, 1994; McKee et al., 2004) most impacted by storm-induced waves and surges. As such, large reservoirs of soft sediments are available for mobilization in these areas, which may have significant implications for controlling the geometry and location of the shelf sediment depocenter. Previous investigations of tropical cyclone seabed response have involved the examination of a shelf area immediately following the event in an area recently studied for another purpose. This before-and-after approach aids in minimizing a complicating issue—definitively identifying the sediment deposit or erosional surface associated with the storm.

On October 3, 2002 the southwestern coast of Louisiana was struck by Hurricane Lili, a tropical cyclone that took a northwesterly route across the Gulf of Mexico and reached Category 4 status with maximum winds of 232 km/h (125 knots) and a minimum pressure of 940mb at 0000 GMT on October 3rd, before weakening to Category 2 status at landfall 13 hours later (Fig. 1). Beginning 4 days after landfall, a

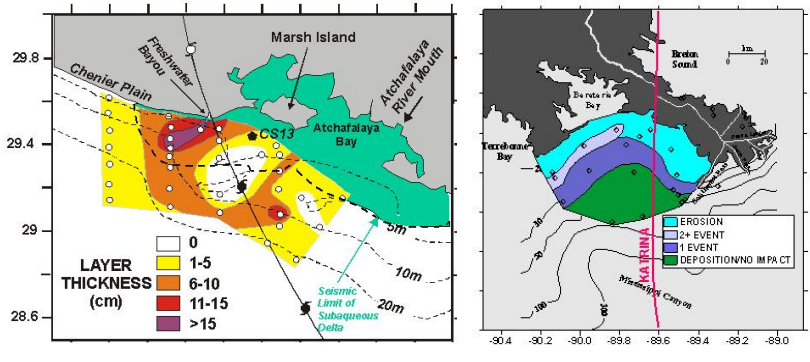

Figure 1. Thickness map of the Lili event layer on the Atchafalaya Shelf (left). Path of the center of the eye is shown. Box core locations are also shown as white circles and the LSU Coastal Studies Institute monitoring platform #3 is plotted. The seismic limit of the Atchafalaya subaqueous delta is from Neill and Allison (2005). The extent of the post-Katrina event layer and box core locations, shown in the panel at right, are relative to the storm path. Areas are divided into 1) a region where shelf incision and no event layer were found (Erosion), 2) a region where shelf incision was followed by deposition of an event layer (1 Event), 3) a region similar to the 1 Event zone but where stacked earlier (Ivan) and/or later (Rita) event layers were also preserved (2+ Event), and 4) a deeper region where no shelf incision was observed and event layers were documented or no impact was observed (Deposition/No Impact).

seabed box coring cruise was conducted on the inner shelf in the area of storm passage. This area, which includes the Atchafalaya subaqueous delta and adjacent inner shelf offshore of the West Louisiana Chenier Plain, has been the subject of recent sediment transport and accumulation studies (Allison et al., 2000; Draut et al., 2004; Neill and Allison, 2005; Kineke et al., 2006). The core data collected on this

cruise on the R/V *Longhorn*, combined with meteorological, sea surface and water column current data over the period of the storm from a nearby observational platform (Fig. 1) operated by Louisiana State University's Wave-Current-Surge Information System for Coastal Louisiana (WAVCIS) provided a unique opportunity to examine fluid and flow characteristics of the storms and the seabed response over a heterogeneous shelf inner shelf of modern muds and relict (sandy) deltaic shoals. The sedimentology and organic geochemistry of the Lili storm deposits have been reported previously in Allison et al. (2005) and Goñi et al. (2006).

The landfall of Hurricane Katrina along the southeastern Louisiana coast on August 29, 2005 provided an opportunity to conduct another early response study of this deltaic coast to a tropical cyclone: in this case immediately west of the main Mississippi shelf. Hurricane Katrina made landfall in Louisiana as a transitional Category 3-4 storm, after having reached Category 5 status on 28 October. A coring and seismic cruise on the R/V *Longhorn* was carried out over this area of the Barataria Bight (Fig. 1) on 1-6 October. This area has been analyzed recently for sediment accumulation and surficial seabed mobility (Corbett et al., 2004; Corbett et al., 2006), allowing a comparison with recent, but pre-storm, seabed character. These studies have shown that modern mud accumulation is focused further offshore along this section of the coast relative to the Atchafalaya shelf. The primary objective of the present paper is to outline the erosional and depositional response of the Mississippi deltaic shelf (15-70 m water depth) to Hurricane Katrina, and to compare these seabed response results with the earlier Lili dataset, which was collected, processed and analyzed utilizing the same methods.

OBSERVATIONS

The 18 box cores collected on the Katrina cruise were subsampled with tray cores and x-rayed for stratigraphy with a portable x-ray machine at 15 mA//70 keV. X-radiographs show that the sample sites can be divided into four categories based on A) the presence or absence of an irregular, basal erosional surface that marks the transition from pre-storm (below) and Katrina event layer (above) deposits (Fig. 2), and B) the presence or absence of a fining-upward event layer attributable to the storm. As in the Lili studies, this event layer was attributed to Katrina based on the relatively homogenous (when corrected for grain size variations) activity of the particle-reactive, short-period radiotracer ^{7}Be (half life = 53 days), which tends to be high in activity on river-derived particulates, and, secondarily, on the fining upward stratigraphy. The event layer and erosional basal surface was interpreted in the Lili deposit (see Allison et al., 2005) as being a result of seabed erosional deflation during the period of maximum wave heights and onshore, surge-induced currents, followed by gradual reduction in water column energies with passage of the eye onshore. This waning phase would be marked by re-deposition of particles suspended by the storm and runoff of additional particles from the land surface, associated with the surge backflow. Gradual reduction of energies would result in fining upward stratigraphy, with a sharply coarser basal layer above the erosional surface (Fig. 2). In several Katrina cores, this coarse basal layer reached 5-7 cm thick and was marked by x-

bedding in the sands—indicative of bedload transport of sandy lags from the erosion of the underlying seafloor.

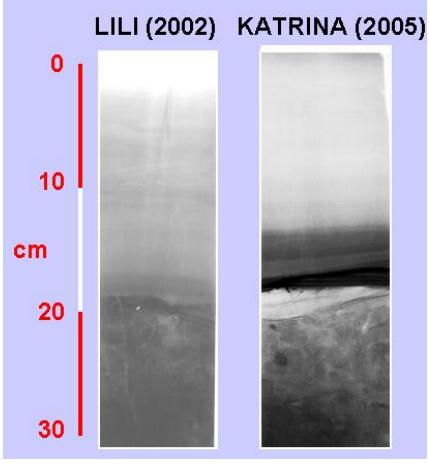

Figure 2. X-radiograph positive images (dark=coarser) of box core subcores showing characteristic examples of the event layer stratigraphic record left by Hurricanes Lili and Katrina. In both cases, a basal incised surface of pre-storm deposits is bound at about 19 cm depth in the cores. Above this surface is a basal deposit of coarser material: in the case of the Lili deposit, this is a thin (2 cm) sandy silt, while the Katrina deposit is a laminated sand 5 cm thick. The difference is ascribed to the limited sand available for reintroduction by seafloor incision in the Atchafalaya subaqueous delta versus the sandier deltaic deposits on the inner-mid Mississippi deltaic shelf. Above this basal layer is a massive to laminated, low consolidation, silty clay deposited in the waning phase of the storms in both cases.

The zonations shown in Figure 1 for the Katrina event strongly correlate with water depth. In water depths of less than about 25 m, box cores showed no event layer preservation and an erosional sediment surface. These cores were uniformly composed of relatively highly consolidated and burrowed muds. At three of these sites, were were able to compare box core X-radiographs from the post-Katrina cruise with those collected at the same locations in May 2005 by a NOAA-funded, Texas A&M University hypoxia study (Steve DiMarco, lead PI). Using subbottom layers, we were able to measure seafloor deflations of 2, 3, and 8 cm, presumably due to the storm, with the deepest erosion at a site closer to Southwest Pass and underlain by more recent Balize lobe sediments, rather than older, more consolidated Lafourche lobe sediments at the sites further west. Seaward of 25 m to about 40 m water depth, the basal erosional surface was covered by a fining-upward event layer of similar morphology to the Lili event layer (Fig. 2). At two of the three sites shown as "2+ Events" in Fig. 1, the surface of the Katrina deposit was incised by a later, erosional surface-event layer packet we attribute to the impact of Hurricane Ivan which made landfall at the Texas-LA border the week prior to our cruise and caused large waves as far eastward as our study sites. Potentially, this event also contributed to the seabed deflation thicknesses mentioned above. At all three "2+ Event" sites, the Katrina deposit was underlain by another erosional surface-event layer packet that is probably associated with Hurricane Ivan in 2004. It is uncertain why this multiple deposit is observed in this zone at water depths (20-25 m) that in adjacent regions (Fig. 1) show no event layer preservation, but may be related to water and sediment emitted from the exits from adjacent Barataria Bay. Seaward of about 40 m water depth, no incision surface was observed, suggesting that combined wave-current

shear stresses were below critical erosion stress at these water depths during the storm. In several of these sites, an event layer was still observable in X-radiographs as a change in fabric (grain size), supported by the presence of ^{7}Be activity. No event layer was recognizable in some of these deeper sites, which may indicate that fabric changes were too subtle with underlying sediments, or that no storm deposition took place, and only normal, ^{7}Be penetrations of a few centimeters were present due to bioturbation. A more widespread mapping of these deeper sites was carried out further west of the present study area by a second, NSF-funded and simultaneous cruise on the R/V *Hatteras* (Goñi and Corbett, PI's). This study (Walsh et al., 2006) recognized a Katrina event layer as far west as the Atchafalaya shelf, where it overlapped with a more substantial Rita event layer, and as deep as the floor of Mississippi Canyon.

CONCLUSIONS

Several conclusions about the impact of tropical cyclones on river-dominated continental margins can be drawn from an examination of the event layers formed by Hurricane Katrina and from comparison with the earlier Lili dataset. They are:

1) Katrina generated seafloor incision in the Barataria Bight to water depths of about 40 m. The removal of surficial sediments down to a relict fluvio-deltiac material up to several thousand years old at inner sites suggests that tropical cyclones are a primary mechanism for keeping most of the inner shelf (<20 m) swept from modern sediments, despite the large flux of Mississippi-derived particulates moving alongshore in the westward-flowing coastal current. Further, this deflation by successive storms over decades, likely is a major additional factor generating retreat of inactive Mississippi deltaic lobe headlands. While winter cold-fronts also likely contribute to this on the innermost shelf and shoreface (<10 m), significant wave heights (<2 m) during these events are generally too small to generate resuspension at greater depths.

2. The deposition of an event layer on shallow (5-20 m) areas of the Atchafalaya shelf after Hurricane Lili, where only erosion is observed in the Katrina event at these water depths, suggests a wave-seafloor feedback, where the presence of extensive soft muds on the Atchafalaya subaqueous delta dissipates sufficient wave energy that deposition can take place in the waning phase of the storm. This is evidence of the important role that soft muds play protection of adjacent shorelines from wave attack during tropical cyclones. Significant deposition of an event layer in deeper water from Katrina than was observed during Lili is likely a function of the offshore-oriented vector of particle transport in the waning phase. The lower gradient Atchafalaya shelf requires particles to traverse greater distances prior to settling relative to the Barataria Bight to reach equivalent water depths.

3. Interannual preservation of tropical cyclone event layers on river-dominated continental margins, such as could be utilized for studies of paleo-hurricane frequency and intensity are likely to be limited to 1) areas of active subaqueous lobe

deposition, 2) water depths sufficient to avoid total incision by subsequent winter and tropical storms, and 3) areas that are sufficiently shallow that a basal erosional surface is formed, which aids in identification of the storm event layer.

ACKNOWLEDGEMENTS

The Katrina work presented here was supported by the Office of Naval Research, Coastal Geosciences Program. Financial support for the Lili work was provided to M.A. Goñi by the National Science Foundation (OCE-0223119)

REFERENCES

Allison, M.A., A. Sheremet, M.A. Goñi, G.W. Stone (2005). "Storm layer deposition on the Mississippi-Atchafalaya subaqueous delta generated by Hurricane Lili in 2002", *Continental Shelf Research* 25, 2213-2232.

Allison, M.A., G.C. Kineke, E.S. Gordon, and M.A. Goñi (2000). "Development and reworking of an annual flood deposit on the inner continental shelf off the Atchafalaya River", *Continental Shelf Research* 20, 2267–2294.

Corbett, D.R., B.A. McKee, and M.A. Allison (2006). "Nature of decadal-scale sediment accumulation in the Mississippi River deltaic region", *Continental Shelf Research* 26, 2125-2140.

Corbett, D.R., B.A. McKee, and D. Duncan (2004). "An evaluation of mobile mud dynamics in the Mississippi River deltaic region", *Marine Geology* 209, 91-112.

Goñi, M.A., E.S. Gordon, N.M. Monacci, R. Clinton, R. Gisewhite, M.A. Allison, and G.C. Kineke (2006). "The effect of Hurricane Lili on the distribution of organic matter along the inner Louisiana shelf (Gulf of Mexico, USA)", *Continental Shelf Research* 26, 2260-2280.

Kineke, G.C., E.E. Higgins, K. Hart, and D. Velasco (2006). "Fine-sediment transport associated with cold-front passages on the shallow shelf, Gulf of Mexico", *Continental Shelf Research* 26, 2073-2091.

McKee, B.A., R.C. Aller, M.A. Allison, T.S. Bianchi, and G.C. (2004). "Transport and transformation of dissolved and particulate materials on continental margins influenced by major rivers: benthic boundary layer and seabed processes", *Continental Shelf Research* 24, 899–926.

Neill, C.F. and M.A. Allison (2005). "Subaqueous deltaic formation on the Atchafalaya shelf, Louisiana", *Marine Geology* 214, 411–430.

Nittrouer, C.A and L.D. Wright, L.D. (1994). "Transport of particles across continental shelves", Reviews of Geophysics 32, 85–113.

Walsh, J.P., D.R. Corbett, D. Mallinson, M. Goni, M. Dial, C. Loewy, K. Marciniak, K. Ryan, C. Smith, C., A. Stevens, B. Sumners, and T. Tesi (2006). "Mississippi delta mudflow activity and 2005 Gulf hurricanes", *EOS, Transactions of the American Geophysical Union* 87, 477-478.

COASTAL-CHANGE IMPACTS DURING HURRICANE KATRINA: AN OVERVIEW

Asbury Sallenger[1], C. Wayne Wright[2], Jeff Lillycrop[3],

1. U. S. Geological Survey, 600 4th St. South, St. Petersburg, FL 33701, USA. asallenger@usgs.gov
2. National Aeronautics and Space Administration, Wallops Flight Facility, Wallops Island, VA 23337, USA. charles.w.wright@nasa.gov
3. U.S. Army Engineer District-Mobile, Joint Airborne Lidar Bathymetry Technical Center of Expertise, 109 St. Joseph Street, Mobile, AL 36602. Jeff.Lillycrop@sam.usace.army.mil

Abstract: As part of an ongoing cooperative effort between USGS, NASA and USACE, the barrier islands within the right-front quadrant of Hurricane Katrina were surveyed with airborne lidar both before and after landfall. Dauphin Island, AL was located the farthest from landfall and wave runup intermittently overtopped its central and western sections. The Gulf-side of the island experienced severe erosion, leaving the first row of houses in the sea, while the bayside accreted. In contrast, the Chandeleur Islands, LA did not experience this classic 'rollover'. Rather, the island chain was completely stripped of sand, transforming a 40-km-long sandy island chain into a discontinuous series of muddy marsh islets. Models indicate that storm surge likely submerged the entire Chandeleur Island chain, at least during the latter part of the storm. The net result was destructive coastal change for the Chandeleur Islands, while Dauphin Island tended to maintain its form through landward migration.

INTRODUCTION

On August 29, 2005, Hurricane Katrina made landfall on the Mississippi delta as a Saffir-Simpson Category 3 storm. Earlier, it had reached Category 5 intensity in the central Gulf of Mexico but fortunately weakened as it approached land. Regardless, Hurricane Katrina—with winds at landfall estimated at 110 kts—was the most costly and one of the five most deadly hurricanes in United States history (Knabb et al., 2005).

The U.S. Geological Survey (USGS), National Aeronautics and Space Administration (NASA) and U.S. Army Corps of Engineers (USACE) are working together to quantify the changes forced by Katrina along the coast of the northern Gulf of Mexico, focusing on the chain of barrier islands from Louisiana to Alabama within the hurricane's right-front quadrant (Fig. 1). Our primary tool is airborne lidar that over the past decade has revolutionized the quantification of coastal change by surveying hundreds of kilometers of coast in hours with high spatial data densities. For example, USGS, NASA, and USACE were able to survey, before and after landfall, the impact zones of all four hurricanes that came ashore in or near Florida in 2004 (Sallenger et al., 2006). For more information about the USGS, NASA, and USACE extreme storms research effort, including preliminary results from other 2005 hurricanes (e.g. Rita), see: http://coastal.er.usgs.gov/hurricanes/

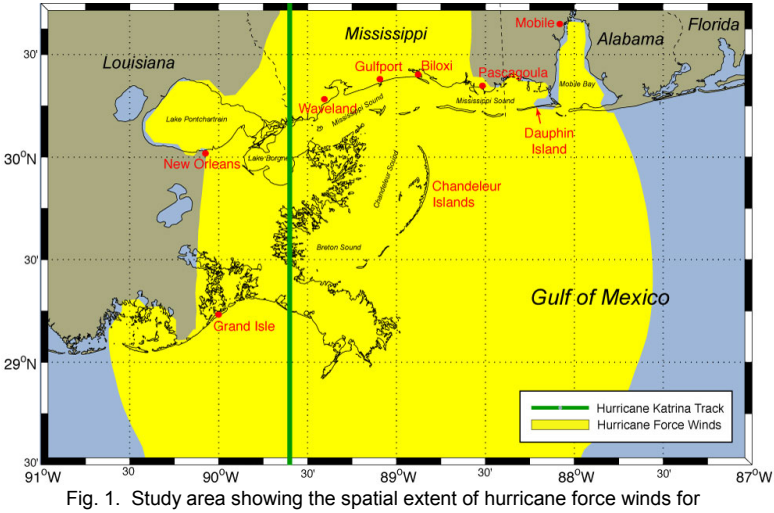

Fig. 1. Study area showing the spatial extent of hurricane force winds for Hurricane Katrina. Wind fields were calculated by NOAA's Hurricane Research Division, Miami, Florida.

METHODS

Two different lidar systems were used to survey the study area before and after landfall of Hurricane Katrina: U.S. Navy and USACE CHARTS (Compact Hydrographic Airborne Rapid Total Survey) and NASA EAARL (Experimental Advanced Airborne Research Lidar; Wright and Brock, 2002). In addition, the USGS acquired pre- and post-storm oblique aerial photography and video to assist in interpreting the lidar data.

Lidar—once an acronym for "light detection and ranging" and now an accepted word, like radar—typically acquires estimates of ground elevation with spatial densities of about one shot every square meter within a swath width of several hundred meters. Multiple surveys of a 70-km long reach of coast on the same day have shown vertical

accuracies of elevation estimates of about 15 cm RMS for another NASA lidar: Airborne Topographic Mapper (Sallenger et al, 2003). Both CHARTS and EAARL should have comparable accuracies for topography. They are also designed to obtain bathymetry, although the post-Katrina survey, collected several days after landfall, encountered water too turbid to allow sufficient laser penetration for accurate measurements of depth.

OBSERVATIONS

In this paper, we compare and contrast hurricane-induced coastal changes on developed Dauphin Island, Alabama, near the outer extent of hurricane force winds, to changes on undeveloped Chandeleur Islands, Louisiana, located relatively close to landfall (Fig. 1). Further, to help put the extreme changes during Katrina into perspective, we compare them to changes from other recent hurricanes, such as Ivan in 2004 and Lili in 2002, for which we have acquired comparable lidar surveys.

Dauphin Island, Alabama

In May 2004, lidar topography of a central section of Dauphin Island showed a narrow barrier island with four rows of houses and a central road, the road appearing in the topography as a depression below the surrounding sand (Fig. 2A). Category-3 Hurricane Ivan came ashore east of this area on September 16, 2004. Even though on the weak side of the storm, Dauphin Island experienced overwash sufficient to fill the depression containing the road (Fig. 2B). An elevation difference map shows this accretion (in shades of green), as well as erosion on the Gulf-side of the island (in shades of red; Fig. 3A). The houses were not removed from the topographic data; hence in the difference map, lost houses appear as red (erosional) rectangles. Within this central section, ~17 houses were lost as a result of Hurricane Ivan.

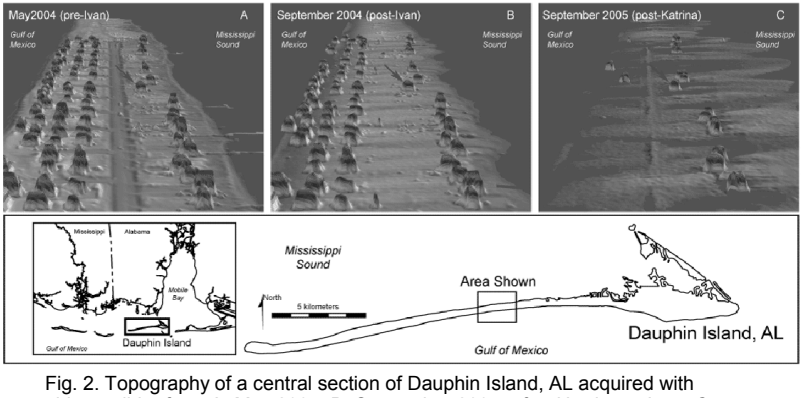

Fig. 2. Topography of a central section of Dauphin Island, AL acquired with airborne lidar from A. May 2004. B. September 2004, after Hurricane Ivan. C. September 2005, after Hurricane Katrina. The hotter colors are higher elevations. The highest elevations here are the roofs of houses. In each map, the red arrow points to the same house.

The post-Katrina topography shows a more extensive coastal-change response (Fig. 2C), as the island width was completely overwashed from Gulf to bay (Fig. 3B). The pattern is the same as for Ivan, with erosion on the Gulf-side of the island and accretion farther landward, but the scale of change was far greater during Katrina. On the Gulf-side of the island, sand was eroded from under the first row of houses leaving their pilings stranded in the water. Overwash extended into the back bay where sand was deposited building the island landward. In the classic sense for a barrier island, it 'rolled over' or migrated, like a large bedform. Over 100 houses were destroyed in the section shown (Fig. 3B) and most of their remains were likely swept with the sand into the back bay.

Chandeleur Islands, Louisiana

Hurricane Lili came ashore west of the Chandeleur Islands in 2002 and forced a similar overwash regime as observed on Dauphin Island, where waves transported sand from the Gulf-side of the island to its central part (Fig. 4). Note that the island eroded on its Gulf-side, but remained intact as a barrier island. Lili was a relatively weak storm, Category 1, generating a maximum storm surge along the Chandeleurs of only 0.6 m, according to NOAA SLOSH model simulations.

In contrast, Hurricane Katrina, with an average storm surge along the Chandeleurs of 3.2 m, forced a very different response than overwash. The sand was completely removed from the subaerial island (Fig. 5), including dunes that in places reached ~6 m high before the storm. Discontinuous marsh islets were left in the storm's wake (Fig. 6), with maximum elevations of approximately 2 to 3 m. Post-Katrina surveys were collected several days after landfall and, by that time, what remained of the Chandeleur Islands no longer satisfied the definition of sandy barrier islands.

Discussion

Along the Chandeleurs, at some point during Katrina, the storm surge (3.2 m) was likely greater than the post storm elevation of the remnant muddy islets (2-3 m), creating the inundation regime of Sallenger (2000). Under these conditions, the islands were continuously underwater (as opposed to being intermittently overtopped by waves during overwash.) It was a submerged shoal and the currents that removed the sand would have been driven by gradients in sea level across the island. Such gradients would have varied in direction and strength as the counterclockwise circulation of the storm moved past the island.

A major research question is where the removed sand was transported during the storm: landward of the island into the back bay? or offshore of the island into the Gulf? We hope to address this question through modeling the currents across the island and working with USGS and University of New Orleans colleagues who are conducting coring and sampling studies on and offshore of the Chandeleurs after Katrina.

CONCLUSIONS

The processes causing coastal change to barrier islands at varying distances from Katrina's landfall were different. Near the outer limits of hurricane force winds, surge

and wave runup were high enough that waves intermittently overtopped the island, forcing it to rollover. Closer to landfall, storm surge was sufficient to submerge the island and all sand was removed from its surface. Under this inundation regime, the system changed destructively, diminishing in size, compared to normal overwash regime, when the island would have maintained its overall dimensions.

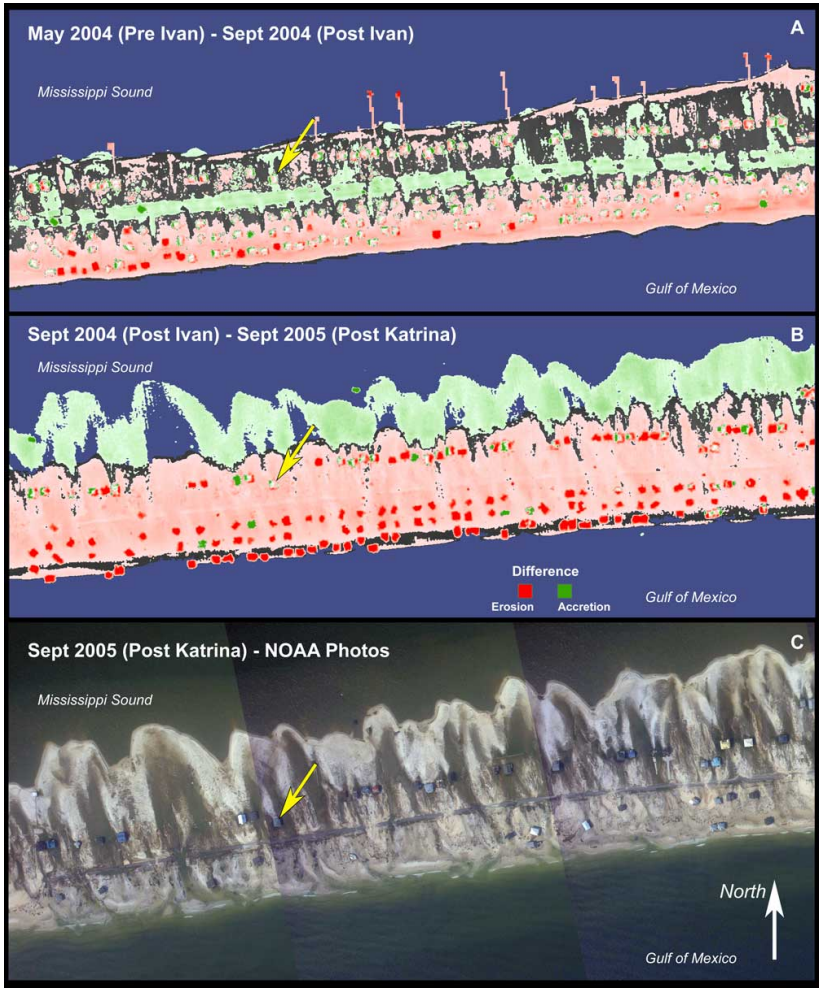

Fig. 3. Maps of elevation change derived from differencing elevations shown in Fig. 2. A. September 2004 elevations minus May 2004 elevations. B.

September 2005 elevations minus September 2004 elevations. C. Vertical photograph of the same area acquired by NOAA after Hurricane Katrina.

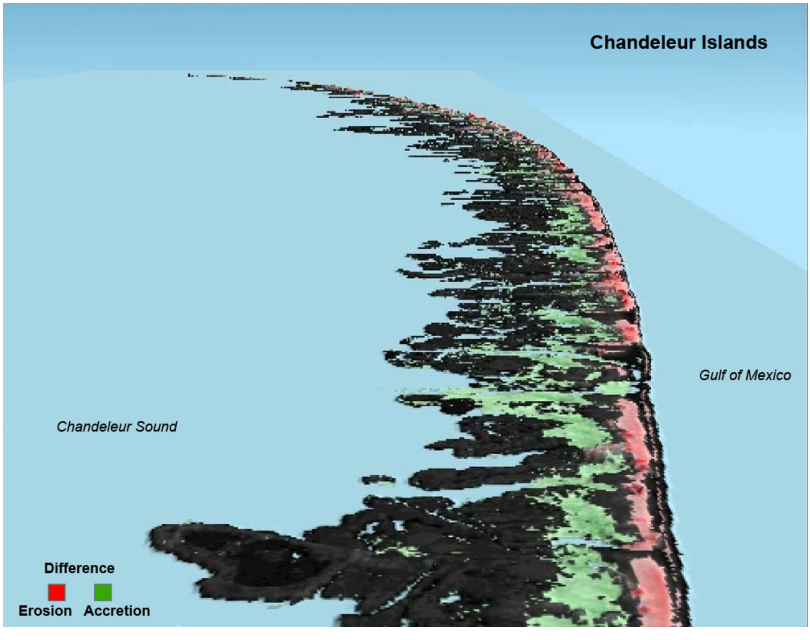

Fig. 4. Three-dimensional view of the northern Chandeleur Islands showing the impact of Hurricane Lili in 2002. Colors indicate vertical change on the island derived from comparisons of before- and after-Lili lidar topography. This vertical change is draped on pre-storm island topography shown in gray scale.



Fig. 5. Before and after Katrina oblique aerial photographs taken from an altitude of ~170 m above the northern Chandeleur Islands. Aircraft is over Gulf of Mexico looking towards the west across the island. Location of the aircraft when photos were acquired is shown in Fig. 6. A. pre-storm photo taken on July 17, 2001. B. post-storm photo taken on August 31, 2005.

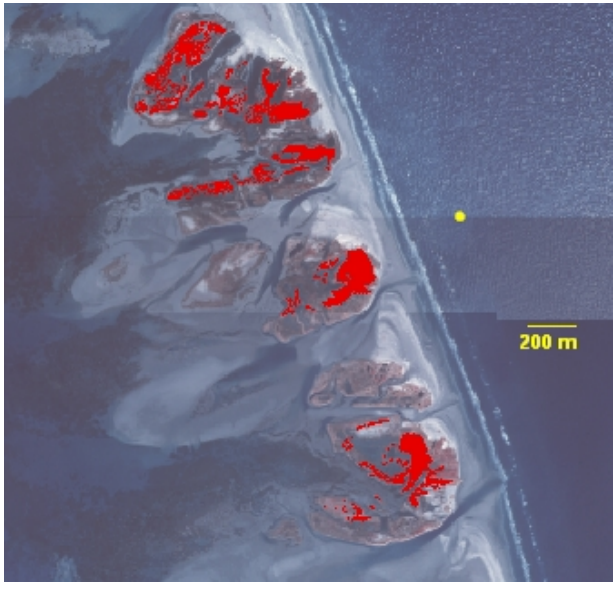

Fig. 6. Pre-storm vertical aerial photographs from the location of the photo pair in Fig. 5. Position of the aircraft from which the photo pairs were taken is shown as a yellow circle. Superimposed on the vertical photo, is what remained of the Chandeleur Islands as of the post-storm lidar survey. The mean high water contour was determined from lidar data and filled with red. The area not shown in red was water in the days after Hurricane Katrina.

ACKNOWLEDGEMENTS

Many people contributed to the acquisition and analysis of the Hurricane Katrina data sets. We thank the other members of the USGS Extreme Storms Research Team (Karen Morgan, Peter Howd, Kristy Guy, Hilary Stockdon, David Thompson, Billy Reynolds, Mark Hansen, Peter Howd Dennis Krohn), the NASA EAARL acquisition and analysis team, and the USACE CHARTS acquisition and analysis team.

REFERENCES

Knabb, R., Rhome, J., and Brown, D., (2005). Tropical Cyclone Report, Hurricane Katrina, 23-30 August 2005, NOAA, National Hurricane Center, 43 p. (Available online at http://www.nhc.noaa.gov/pdf/TCR-AL122005_Katrina.pdf)

Sallenger, A.H., (2000). "Storm impact scale for barrier islands," *J. Coastal Research*, 16 (3): 890-895.

Sallenger, A.H., Krabill, W., Swift, R., Brock, J., List, J., Hansen, M., Holman, R.A., Manizade, S., Sontag, J., Meredith, A., Morgan, K., Yunkel, J.K., Frederick, E., and Stockdon, H. (2003). "Evaluation of airborne scanning lidar for coastal change application," J*ournal of Coastal Research,* v. 19, no. 1, p. 125-133.

Sallenger, A., Stockdon, H., Fauver, L., Hansen, M., Thompson, D., Wright, C.W. and Lillycrop, J., (2006). "Hurricane 2004: an Overview of the Characteristics and Coastal Change." *Estuaries and Coasts*, 29(6A): 880-888.

Wright, C.W., and Brock, J. (2002). "EAARL: A lidar for mapping shallow coral reefs and other coastal environments, " *in* Seventh International Conference on Remote Sensing for Marine and Coastal Environments, Miami, Fla., 20-22 May 2002, Proceedings: Ann Arbor, Mich., Veridian International Conferences, CD-ROM.

MODELING DUNE RESPONSE USING MEASURED AND EQUILIBRIUM BATHYMETRIC PROFILES

Laura A. Fauver[1], David M. Thompson[1], Asbury H. Sallenger[1]

1. U.S. Geological Survey, Florida Integrated Science Center, 600 Fourth Street South, St. Petersburg, FL 33701, USA. lfauver@usgs.gov.

Abstract: Coastal engineers typically use numerical models such as SBEACH to predict coastal change due to extreme storms. SBEACH model inputs include pre-storm profiles, wave heights and periods, and water levels. This study focuses on the sensitivity of SBEACH to the details of pre-storm bathymetry. The SBEACH model is tested with two initial conditions for bathymetry, including (1) measured bathymetry from lidar, and (2) calculated equilibrium profiles. Results show that longshore variability in the predicted erosion signal is greater over measured bathymetric profiles, due to longshore variations in initial surf zone bathymetry. Additionally, patterns in predicted erosion can be partially explained by the configuration of the inner surf zone from the shoreline to the trough, with surf zone slope accounting for 67% of the variability in predicted erosion volumes.

INTRODUCTION

Long-term coastal erosion along the east and gulf coasts of the United States is exacerbated by short-lived, high-intensity extreme storm events. The hurricane seasons of 2004 and 2005 produced eight major hurricanes (Category 3 or higher) that made landfall on U.S. coastlines, causing extensive shoreline retreat, dune erosion, and coastal overwash events (Sallenger et al., 2006). Coastal engineers and planners typically use numerical beach erosion models such as SBEACH to predict coastal change due to extreme storms. SBEACH is a two-dimensional, cross-shore model that takes into account the pre-storm beach profile, as well as wave heights and periods, water levels, and wind speeds.

This study focuses on the sensitivity of SBEACH to the details of pre-storm bathymetry. Recent SBEACH studies have utilized light detection and ranging (lidar) data for the

pre-storm topography, while an equilibrium shape was used to represent the profile seaward of the shoreline (Fauver, 2005). Advances in lidar technology now allow the measurement of nearshore bathymetry with lidar sensors developed by the Naval Oceanographic Office (NAVO) and the U.S. Army Corps of Engineers (USACE) (Wozencraft and Lillycrop, 2003). In this study, the SBEACH model is tested with two initial conditions for pre-storm bathymetry, including (1) measured bathymetry from lidar, which is referred to as "Case A", and (2) calculated equilibrium profiles, which is referred to as "Case B."

The SBEACH model takes into account the shape of the pre-storm beach and offshore profile, as well as the hydrodynamic conditions of the storm. At each time step, wave height and water level profiles are calculated between the offshore boundary and the shoreline, and are utilized to calculate sediment transport rates across the profile (Larson and Kraus, 1989; Larson et al., 1989). Calculations of wave height in the surf zone are sensitive to water depth, and therefore pre-storm bathymetry can play an important role in model accuracy (Kraus and Wise, 1993). Traditionally used as a proxy for real bathymetry, equilibrium profiles decrease monotonically with depth, whereas many beaches along U.S. coastlines are known to display bar configurations. Nearshore bars cause waves to break seaward of the shoreline, dissipating energy offshore and lessening the impact of the storm. Additionally, observed surf zone profiles can display significantly different slopes than modeled equilibrium profiles, which affects the distance from the shoreline at which the wave breaks and the rate of energy dissipation across the nearshore zone.

BACKGROUND

Study Area

The study site is a 1.2 km stretch of shoreline within the city of Destin, FL on the Gulf of Mexico coastline (Figure 1). The selected area is an undeveloped stretch of coast within Henderson State Park, which consists of recreational public beaches and several inland parking lots. The park is characterized by continuous, linear sand dunes with a mean peak elevation of 5.0 m (σ = 0.4 m). On September 16, 2004, Hurricane Ivan made landfall in Gulf Shores, AL as a Category 3 hurricane. Hurricane force winds extended 140 km to the east of landfall, with the study area falling within the outer edge of these limits. The NOAA Hurricane Research Division's (HRD) H*Wind grids provide a maximum surface wind speed estimate of 65.8 kts directly offshore of the study site.

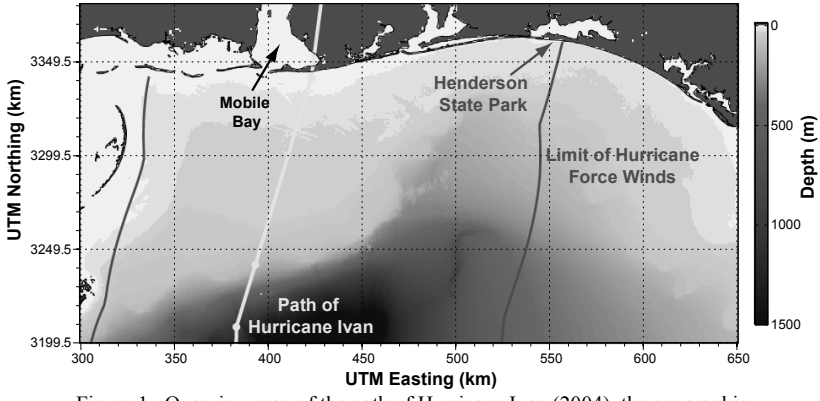

Figure 1. Overview map of the path of Hurricane Ivan (2004), the geographic extent of hurricane force winds, and the location of Henderson State Park.

Lidar measurements show that offshore of Henderson State Park, a non-rhythmic, three-dimensional sandbar was positioned approximately 150 m from the shoreline (Figure 2). Within the western portion of the study area, the bar is attached to the shoreline over a distance of approximately 120 m in the longshore direction. Along this section of shoreline, the surf zone slope is shallower than the surrounding area, and a bar and trough configuration is not detectable in cross-sectional profiles. Within the study area, the mean bar height and width are 1.1 m and 87.6 m respectively (σ = 0.5 m and 23.1 m). The mean water depth at the bar crest is 2.6 m below mean sea level.

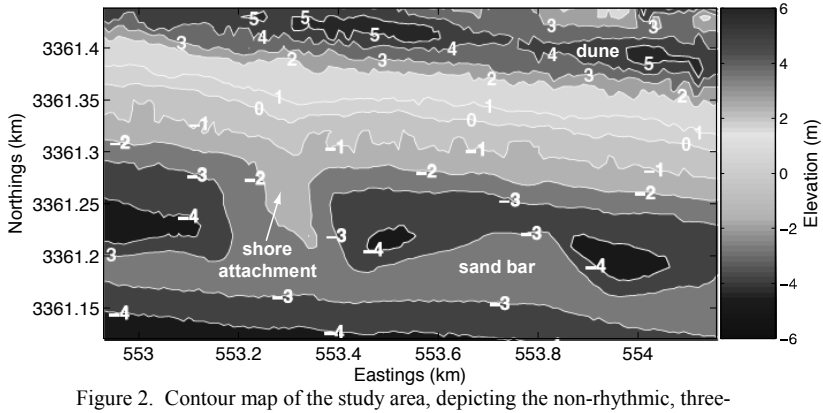

Figure 2. Contour map of the study area, depicting the non-rhythmic, three-dimensional bar configuration.

Model Description

SBEACH is a macroscale beach erosion model, invoking sediment transport over length scales of meters, and time scales of hours (Larson and Kraus, 1989; Larson et al., 1989).

At each time step, input values of offshore wave height and period are used to calculate the cross-shore wave height profile. A two-dimensional form of the conservation of energy flux equation is used to compute wave heights from the offshore boundary to the shoreline:

$$\frac{d}{dx}(F\cos\theta) = \frac{k}{d}(F - F_s) \tag{1}$$

where F is wave energy flux, F_s is the energy flux of a stable wave, θ is the local wave angle, k is the wave decay coefficient, and d is total water depth including surge and setup. Additionally, the location of the break point is determined by an empirical equation for the value of γ, the ratio of wave height to water depth at which the wave breaks.

The wave height calculations obtained from Equation 1 are used to compute sediment transport rates, which are applied to the conservation of mass equation in order to calculate profile change. Within the surf zone, sediment transport rates are calculated with the empirical formula:

$$Q_s = K\left[D - D_{eq} + \frac{\varepsilon}{K}\frac{dh}{dx}\right] \tag{2}$$

where Q_s is the sediment transport rate, D is wave energy dissipation, D_{eq} is the energy density required to maintain the instantaneous profile form, K is the transport rate coefficient, ε is an empirical coefficient, and dh/dx is the local bed slope. Model calibrations were performed to determine best-fit values for the coefficients in Equation 2, including $K = 1.0\text{x}10^{-6}$ m^4/N, and $\varepsilon = 0.0045$ m^2/s. The wave energy dissipation term D is proportional to the wave height squared, and therefore the sediment transport rate is directly affected by the surf zone bathymetry.

METHODS

Measured and Equilibrium Profiles

Lidar surveys were flown along the Florida panhandle coast in May 2004, four months before Hurricane Ivan made landfall in Alabama. Topographic data were collected with the Compact Hydrographic Airborne Rapid Total Survey (CHARTS) system, and bathymetric data were measured with the Scanning Hydrographic Operational Airborne Lidar Survey (SHOALS) sensor. Surveys were flown in a cooperative research agreement USACE, NASA, and the USGS. Cross-shore profiles were extracted from the lidar data set every 20 m along the beach, and used as the initial profile conditions for SBEACH model runs of Hurricane Ivan. A total of 61 profiles along 1.2 km of beach were used to evaluate the SBEACH model.

Two sets of initial bathymetric profiles are used to evaluate the sensitivity of SBEACH to the configuration of the surf zone. The first set of profiles consists of topographic data from CHARTS lidar, as well as the measured bathymetric lidar data. These profiles

display a bar and trough configuration along most of the study site. A notable exception occurs within the western portion of the study area where the bar is welded to the shoreline, creating a more planar nearshore profile. Profiles taken from bathymetric lidar and the corresponding SBEACH results will be referred to "Case A."

The second test case consists of equilibrium profiles calculated using a standard $h=Ax^{2/3}$ offshore profile as described by Dean (1977). Topographic data from lidar was appended with the calculated equilibrium profile seaward of the shoreline. The shape of the profile is dependent on median grain size, which is measured to be 0.33 mm at mean high water (Taylor Engineering Inc., 2003). For the remainder of this paper, these equilibrium profiles and corresponding SBEACH results will be referred to as "Case B."

Along a majority of the study site, the Case A profiles exhibit a wide bar and a steeper surf zone slope than Case B profiles (Figure 3a, Figure 4). The slope of the inner surf zone, measured from the shoreline to the deepest section of the trough, ranges from 0.017 to 0.045 for Case A. In contrast, profile slope is uniform about a mean of 0.025 for Case B equilibrium profiles. A shallower slope and smaller bar volumes are observed on Case A profiles that are located where the longshore bar attaches to the shoreline and fills in the deep trough (Figure 3b, Figure 4). Due to this attachment, the volume of the bar also decreases in this same location.

The two working hypotheses for these test cases are that (1) the bar-type configuration of the Case A profiles will produce statistically significant differences in SBEACH model results when compared with results from Case B profiles, and (2) the longshore variations in Case A bathymetry will lead to longshore variability in the modeled erosion signal. In contrast, the homogeneity of the Case B bathymetry is expected to contribute to a relatively uniform longshore erosion signal.

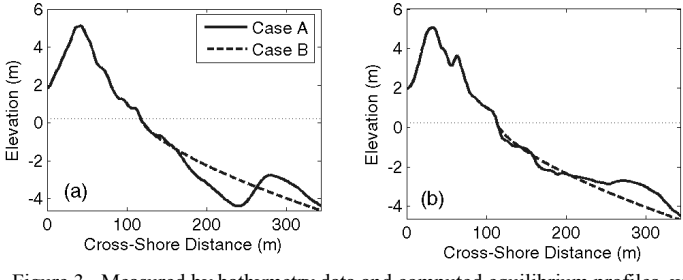

Figure 3. Measured by bathymetry data and computed equilibrium profiles, where (a) depicts a profile displaying a large offshore bar, and (b) is an example of a profile where the longshore bar has attached to the shoreline.

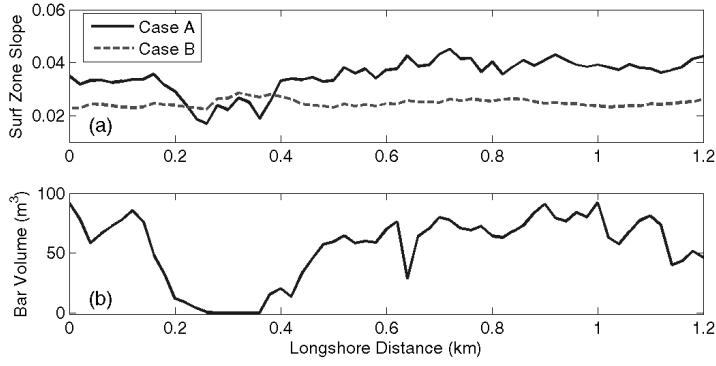

Figure 4. Alongshore variation of (a) surf zone slope as calculated from the shoreline to the deepest point of the trough, and (b) bar volume. A noticeable decrease in surf zone slope corresponds to the location where bar volume is at a minimum.

Wave Height and Water Level

The SBEACH model was initialized with time series of wave height, wave period, water level and wind speed. No wave buoys or tide gauges were located near the study area, and therefore waves and water levels for Hurricane Ivan were modeled with Delft3D (Thompson et al., 2006). A time series of nearshore water levels was extracted from the Delft3D model results 2 km offshore of the study site, in order to avoid boundary affects associated with land. These water levels were used as input values for the SBEACH model runs (Figure 5). Wave heights for SBEACH model runs were extracted offshore of the study site at a depth of 20 m, which is intermediate water depth for the given storm conditions (Figure 5).

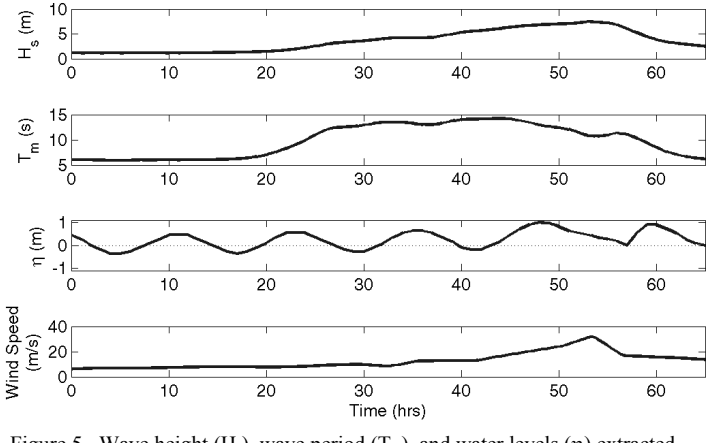

Figure 5. Wave height (H_s), wave period (T_m), and water levels (η) extracted from Delft3D model runs, and wind speeds extracted from HRD H*Wind grids.

RESULTS

SBEACH model runs were completed for each of the two sets of pre-storm profiles described in the previous section, including measured bathymetric profiles (Case A) and equilibrium profiles (Case B). Results can be divided into two groups, those for barred profiles and those for non-barred profiles. SBEACH model results for a barred profile are plotted in Figure 6, with the area of profile change enlarged in the right panel. The SBEACH model predicts greater profile change over the Case A (bar) profile, as opposed to the Case B (equilibrium) profile. This result is consistent throughout the study area for profiles with a bar-type configuration. SBEACH model results are plotted for a non-barred profile in Figure 7. For non-barred profiles, SBEACH model results converge for Case A and Case B.

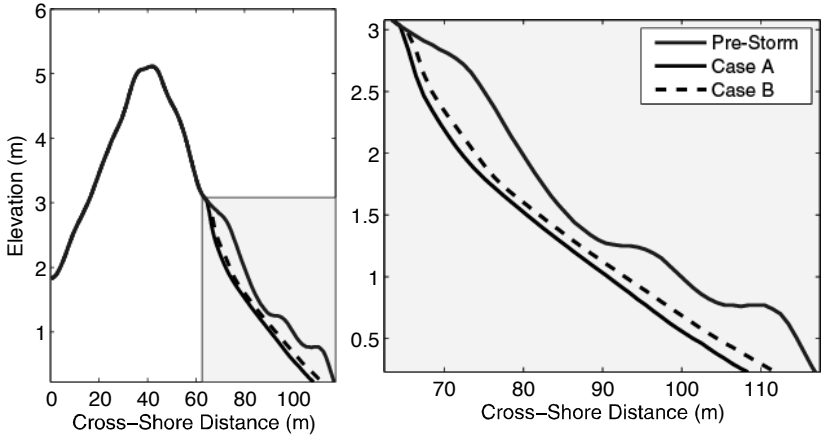

Figure 6. Comparison of SBEACH model results for the two test cases. The pre-storm profiles are the same as shown in Figure 3a, which has a distinct offshore bar and is typical of a majority of the study site.

Two calculations were used to quantify differences in model results. The first calculation is the root-mean-square (RMS) vertical difference between the two predicted profiles, measured between the shoreline and the dune crest:

$$RMS = \left[\frac{1}{N} \sum_{i=1}^{N} (z_{i,A} - z_{i,B})^2 \right]^{1/2} \tag{3}$$

where z_A is the elevation of the Case A predicted profile, and z_B is the elevation of the Case B predicted profile. For all profiles tested, the mean RMS value is 0.13 m, with a standard deviation of 0.04 m (Table 1). This result is considerably less than originally expected, given the large differences in initial bathymetric configuration. However, when the results are separated into barred and non-barred profiles, the

mean values of RMS are 0.14 m and 0.06 m respectively. These mean RMS elevation differences are statistically different at the 95% confidence level.

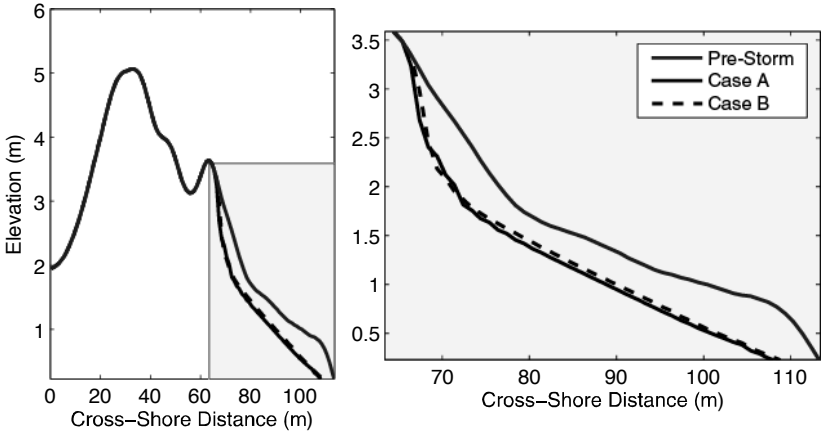

Figure 7. Comparison of SBEACH model results for the two test cases. The pre-storm profiles are the same as shown in Figure 3b, which has a shallow slope and planar nearshore profile, corresponding to the shoreline attachment of the offshore bar.

The second calculation is of the gross volume difference (GVD) between the two predicted profiles, measured from the shoreline to the dune crest:

$$GVD = \sum_{i=1}^{N} \left| z_{i,A} - z_{i,B} \right| dx \tag{4}$$

where *dx* is the horizontal distance between elevation points (set at 0.1 m). The mean value of GVD for all of the profiles is 6.0 m^3/m, with a standard deviation of 2.1 m^3/m. For barred and non-barred profiles, the means are 6.4 m^3/m and 2.7 m^3/m respectively. These means are also significantly different at the 95% confidence level. Calculations of RMS and GVD confirm that model results for Cases A and B converge over the non-barred profiles where initial bathymetry is similar, and diverge over barred profiles where bathymetric differences are more pronounced.

Table 1. Mean statistics describing differences in model results for Cases A and B.

Profiles	Mean RMS (m)	Std RMS (m)	Mean GVD (m^3/m)	Std GVD (m^3/m)
All profiles (N=61)	0.13	0.04	6.0	2.1
Barred (N=54)	0.14	0.03	6.4	1.6
Non-barred (N=7)	0.06	0.03	2.7	2.5

In order to address the question of longshore variability in the erosion signal, a quantitative measurement of erosion is established. Gross volume change (GVC), a proxy for total erosion volume, was calculated between the shoreline and the dune crest:

$$GVC = \sum_{i=1}^{N} \left| \hat{z}_i - z_{i,pre} \right| dx \tag{5}$$

where $\hat{z}$ is the elevation of the predicted profile, and z_{pre} is the elevation of the pre-storm profile. In the longshore direction, an interesting pattern emerges in the predicted erosional signal (Figure 8). For Case A results, a significant drop in GVC is displayed within the western half of the study area, in the location corresponding to the shoreline bar attachment. In this area, no bar is present and surf zone slopes are shallow due to the filling in of the trough. Beyond this area where the bar-type configuration persists, the predicted GVC signal is relatively consistent. For Case B results, the erosion signal is uniform along the entire study area. These results conform to the original hypothesis, which stated that greater longshore variability in erosion was expected for Case A results, due to longshore variations in initial surf zone bathymetry.

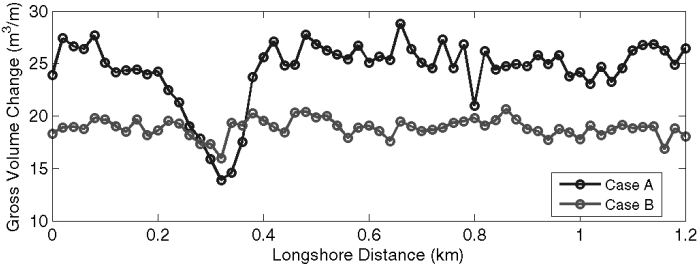

Figure 8. Longshore patterns in predicted GVC are shown for the two test cases.

DISCUSSION

The SBEACH model results show that more erosion was predicted on Case A profiles displaying a bar-type configuration, as opposed to Case B profiles with an equilibrium profile form. This result seems contrary to conventional wisdom, which says that for barred beaches, waves will break over the bar and dissipate energy, therefore producing less erosion on the subaerial profile. For Case B, energy should dissipate gradually over the equilibrium profile in the surf zone, allowing greater wave heights closer to shore and hence greater erosion of the subaerial beach. The results from this study do not fall in line with this hypothesis, and therefore modeled wave height profiles are inspected for further insight. Modeled wave heights are extracted from SBEACH at the time of maximum offshore waves (Figure 5). The cross-shore wave height profile is plotted with the corresponding beach profiles modeled by SBEACH in order to examine patterns of breaking over nearshore bathymetry. Results are shown for both a barred profile (Figure 9) and a non-barred profile (Figure 10).

Over the barred-profile, waves break slightly over the bar and then reform over the trough. Alternatively, dissipation of energy is gradual and decreases monotonically moving towards the shoreline over the corresponding equilibrium profile. Landward of the trough, the Case A and Case B wave height profiles diverge due to differences in surf zone slope. The steeper slopes associated with Case A profiles allow waves to break closer to the shoreline, producing greater erosion on the subaerial beach. In contrast, over a non-barred profile, the Case A and Case B wave height profiles are not significantly different from one another (Figure 10).

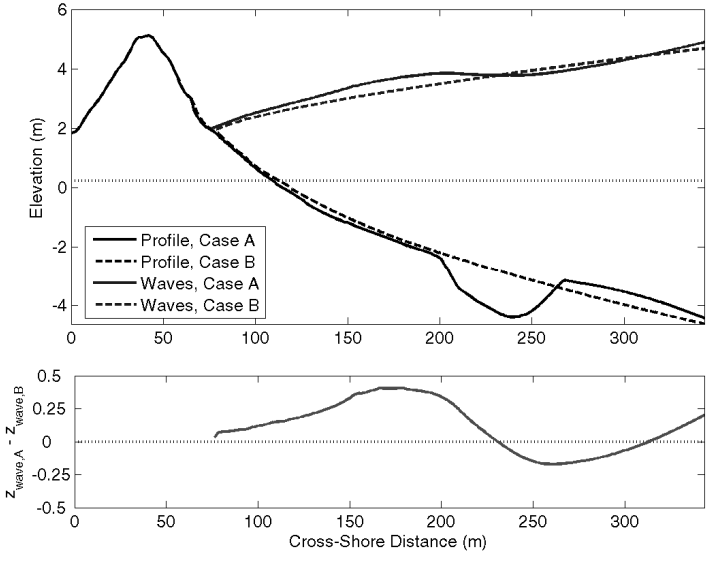

Figure 9. SBEACH predictions of wave height and profile shape at the time of maximum wave height (53 hrs) for a barred profile. Near the shoreline, wave heights are greatest over the measured bathymetry, which exhibits a bar and a deep trough. Nearshore wave heights are smaller over the equilibrium profile, due to the shallower surf zone slope.

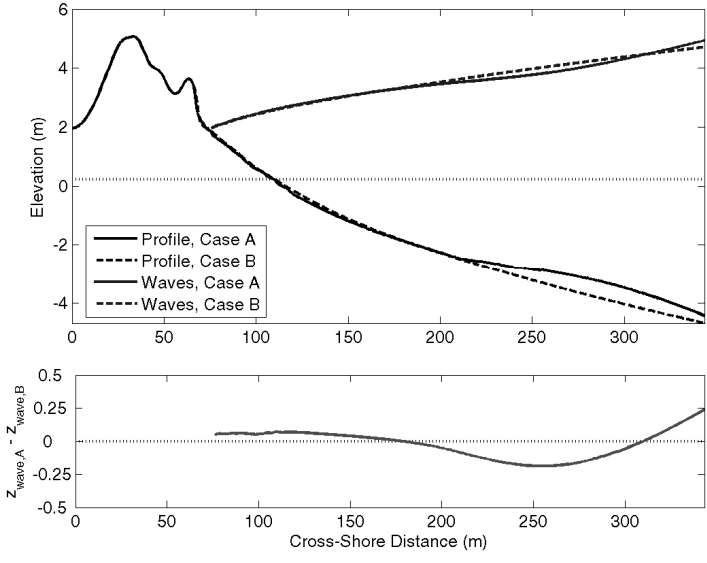

Figure 10. SBEACH predictions of wave height and profile shape at the time of maximum wave height (53 hrs) for a non-barred profile. Near the shoreline, wave heights are comparable for both test cases, due to the similarity in surf zone configuration.

Predictions of GVC were compared to surf zone slope and bar volume, in order to determine potential relationships between bathymetry and model predictions of erosion. Plots of GVC and slope show a linear relationship with an r^2 value of 0.67, which is significant at the 95% confidence level (Figure 11a). Results are clustered into two groups, with ample spread observed within each group. The first group contains those profiles with low slopes, including all of the Case B equilibrium profiles, and those Case A profiles with a non-barred configuration. These profiles display lower predicted GVC values than the second grouping. The second cluster of profiles are Case A profiles with a bar-type configuration and higher slopes and correspondingly higher GVC values.

Alternatively, the relationship between bar volume and predicted GVC (plotted for Case A only) shows no significant trend (Figure 11b). This result suggests that the bar did not play a significant role in the erosion of the subaerial profile. This finding is explained by the modeled wave height profiles which show minimal breaking over the bar and immediate reformation over the deep trough (Figure 9).

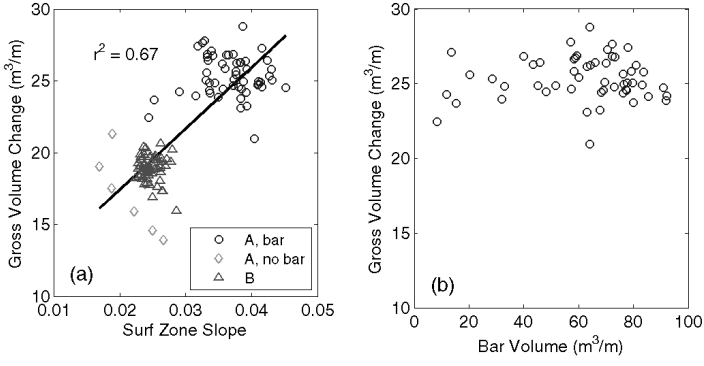

Figure 11. (a) GVC as a function of pre-storm surf zone slope for both test cases. The calculated r^2 value of 0.67 is significant at the 95% confidence level. (b) GVC as a function of bar volume, showing that in this specific case, bar volume is not a significant variable in affecting erosion of the subaerial profile.

CONCLUSIONS

Model results for Cases A (measured bathymetry) and B (equilibrium profiles) converge over non-barred profiles where initial bathymetry is similar, and diverge over barred profiles where bathymetric differences are more pronounced. The mean volume difference between the two predicted profiles was 6.0 m^3/m, which is smaller than expected based on differences in initial surf zone bathymetry. When this calculation is separated into barred and non-barred profiles, the respective means of 6.4 m^3/m and 2.7 m^3/m are significantly different at the 95% confidence level. Additionally, longshore variability in model predictions is observed for Case A profiles. The surf zone configuration changes sharply over a 120 m wide attachment of the bar to the shoreline, which occurs within the western half of the study area. The predicted erosional volumes drop sharply in this region, to as little as half of the predicted erosion on surrounding profiles (Figure 8). In contrast, predicted erosion is uniform throughout the study area for Case B model results. Patterns in predicted erosion can be partially explained by the configuration of the inner surf zone from the shoreline to the trough, with surf zone slope accounting for 67% of the variability in predicted erosion volumes (Figure 11a).

The predicted erosional volume on the subaerial profile was consistently greater for Case A results than for Case B results. This observation is contrary to the original hypothesis, which suggested that waves would break over the bar and dissipate substantial energy seaward of the beach, therefore producing less erosion on the subaerial profile. While the bar was expected to play a significant role in erosional trends, no relationship emerged in a comparison of bar volume and gross volume change (Figure 11b). Inspection of modeled wave heights over barred profiles shows that waves break minimally over the bar, and immediately reform landward of the bar over the deep trough (Figure 9). Over the equilibrium profile, wave heights decrease gradually over the monotonic profile form. Modeled wave height profiles for Cases A and B diverge

significantly landward of the trough. The divergence is caused by differences in surf zone slope, which allows larger waves to shoal closer to the shoreline over Case A profiles. Accordingly, the specific configuration of the profile, including the height and depth of the bar, the depth of the trough, and the surf zone slope will all play important roles in determining the magnitude of erosion predicted by SBEACH.

ACKNOWLEDGEMENTS

Many thanks are due to Peter Howd (USGS), Hilary Stockdon (USGS), and Chantal Donnelly (University of Lund) for lending their expertise in statistics and dune modeling. Karen Morgan, Kristy Guy, and Charlene Sullivan of the USGS were all instrumental in processing lidar data and profiles used in this study. Lidar surveys were performed in cooperation with Jeff Lillycrop of the U.S. Army Corps of Engineers and the Naval Oceanographic Office. This work is funded under the USGS Hurricane and Extreme Storm Impact Studies project, which is part of the USGS National Assessment of Coastal Change Hazards.

REFERENCES

Dean, R.G. (1977). Equilibrium beach profiles: U.S. Atlantic and Gulf coasts. *Ocean Engineering Technical Report No. 12*, University of Delaware, Department of Civil Engineering, Newark, DE.

Fauver, L. (2005). Toward predicting barrier island vulnerability: Simple models for dune erosion. *M.S. Thesis*, College of Marine Science, University of South Florida, St. Petersburg, FL.

Kraus, N.C., and Wise, R.A. (1993). Simulation of January 4, 1992 storm erosion at Ocean City, Maryland. *Shore and Beach*, 61(1), 34-41.

Larson, M., and Kraus, N.C., (1989). SBEACH: Numerical model for simulating storm-induced beach change; Report 1: Empirical foundation and model development. *Technical Report CERC-89-9*, U.S. Army Engineer Waterways Experiment Station, Coastal Engineering Research Center, Vicksburg, MS.

Larson, M., Kraus, N.C., and Byrnes, M.R. (1989). SBEACH: Numerical model for simulating storm-induced beach change; Report 2: Numerical formulation and model tests. *Technical Report CERC-89-9*, U.S. Army Engineer Waterways Experiment Station, Coastal Engineering Research Center, Vicksburg, MS.

Sallenger, A.H., Stockdon, H.F., Fauver, L., Hansen, M., Thompson, D., Wright, C.W., and Lillycrop J. (2006). "Hurricanes 2004: An overview of their characteristics and coastal change." *Estuaries and Coasts* 29(6A), 880-888.

Taylor Engineering, Inc. (2003). Beach management feasibility study: Walton County and Destin, Florida. *Report C2000-032/033*, Jacksonville, FL.

Thompson, D.M., Howd, P.A., and Sallenger A.H. (2006). Nearshore wave climate variability during Hurricane Ivan. *2006 Ocean Sciences Meeting*, Honlulu, HI.

Wozencraft, J.M., and Lillycrop, W.J. (2003). Airborne coastal mapping, past, present, and future. *Journal of Coastal Research,* Special Issue(38), 207-215.

SEDIMENT TRANSPORT ALONG THE SOUTHWESTERN LOUISIANA SHORELINE: IMPACT FROM HURRICANE RITA, 2005

Walter S. Guidroz[1], Gregory W. Stone[2], Dane Dartez[3]

1. BP North America Inc., 501 Westlake Park Blvd., Houston, TX 77079, USA. walter.guidroz@bp.com.
2. Louisiana State University, Coastal Studies Institute and Department of Oceanography and Coastal Sciences, 316 Howe-Russell, Baton Rouge, LA 70803, USA. gagreg@lsu.edu.
3. Louisiana State University, Hurricane Center, Baton Rouge, LA 70803, USA. ddarte2@lsu.edu.

Abstract: The landfall of Hurricane Rita in 2005 significantly altered physical and morphological characteristics along the southwestern Louisiana coastline and interior marshes. An excessive storm surge event linked to Rita resulted in widespread, storm-induced overwash deposits in Cameron and Vermilion Parishes, Louisiana. These deposits superseded prior deposits and were aligned parallel to predominant flow patterns associated with the storm's counter-clockwise circulation. These responses became more pronounced farther west and culminating at eyewall impact. Excessive salinity levels resulting from salt-water intrusion severely impacted local vegetation several kilometers inland and over the longer term may exacerbate the loss of vegetation that retards coastal erosion and attenuates waves and storm surge during high-energy events. Massive water levels introduced onshore by surge remained locally ponded several weeks after the hurricane; however, morphological patterns along the coastline had begun facilitating the return flow of water and sediment to the Gulf of Mexico.

INTRODUCTION

A significant coastal sediment transport and storm surge event occurred along the southwestern Louisiana shoreline concurrent with the landfall of Hurricane Rita on September 24, 2005. This hurricane, which made landfall as a Category Three storm near the Texas/Louisiana border, significantly altered coastal sediment transport patterns through (1) the effects of a strong storm surge, and (2) the post-storm return flow to the

Gulf of Mexico of elevated water levels within inland bays and marshes. Additionally, coastal morphology was influenced by post-storm beach recovery as indicated by bar welding to the lower shoreface only several weeks after the passage of Hurricane Rita.

Research by the Coastal Studies Institute of Louisiana State University revealed sand overwash deposits and evidence of excessive storm surge and salt-water intrusion along the southwest Louisiana coast. These responses became more pronounced farther west and closer to eyewall impact near the Texas/Louisiana border. Excessive salinity levels resulting from salt-water intrusion severely impacted local vegetation both along the coast and several kilometers inland. These impacts may locally exacerbate existing problems linked to coastal erosion through the loss of vegetation that retards coastal erosion and attenuates waves and storm surge during high-energy events.

Storm surge associated with the passage of Hurricane Rita infiltrated tens of kilometers inland. Ponded surge water remained trapped even several weeks after Hurricane Rita struck the southwestern Louisiana coast. However, distinct return flow patterns of water and sediment were observed along the southwestern Louisiana coastline, which indicate active processes by which excessive water volume returns to the open Gulf.

STORM HISTORY AND SEA STATE

Hurricane Rita began as a tropical depression just east of the Turks and Caicos Islands on September 17, 2005 and intensified steadily over the next several days as it moved westward through the Florida Straits. The eye of Hurricane Rita passed approximately 50 miles (80 km) south of Key West, Florida on September 20 and thus missed the U.S. mainland as it approached southern Florida as a Category 2 hurricane on the Saffir-Simpson scale. However, upon entering the Gulf of Mexico, Rita intensified rapidly and attained Category 5 status and a peak sustained wind strength of 175 mph (78 m/second) within only 24 hours. The barometric pressure recorded during this phase of the storm reached 897 millibars, the third-lowest ever recorded for a tropical system in the Atlantic Basin at that time. This pressure reading simultaneously displaced to fifth-lowest the 902 millibar minimum pressure measurement from Hurricane Katrina recorded only one month earlier (National Hurricane Center, 2005; Knabb et al., 2006). However, both of these measurements were subsequently displaced one level lower in October 2005 by Hurricane Wilma, which yielded the lowest barometric pressure ever recorded to date in the Atlantic Basin, at 882 millibars (Pasch, et al., 2006).

Wind and wave conditions during Hurricane Rita were measured by a series of buoys maintained by the National Data Buoy Center. While still at sea in the Gulf of Mexico, the eye of Rita passed approximately 2 miles (3 km) southeast of Buoy 42001, the data buoy closest to the path of the storm (Figure 1). A barometric pressure of 926 millibars was recorded at 6:00 PM (2300 Z) on September 23, about 8.5 hours prior to landfall. The maximum significant wave height measurement was 38 feet (11.6 m), sustained winds were measured at 100 mph (45 m/second), and maximum gusts were measured at nearly 136 mph (61 m/second) approximately 7 hours prior to landfall. As Rita neared the coast, C-MAN station SRST2, located near Sabine Pass on the upper Texas coast

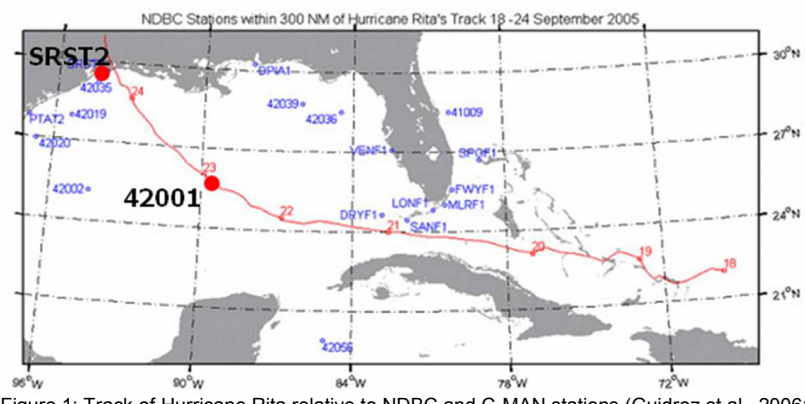

Figure 1: Track of Hurricane Rita relative to NDBC and C-MAN stations (Guidroz et al., 2006; reprinted by permission of the GCAGS whose permission is required for further use)

(Figure 1), recorded a barometric pressure of 951 millibars at 1:00 AM on September 24 (approximately one hour prior to landfall).

Hurricane Rita weakened as it approached the north-central coast of the Gulf of Mexico on September 23, eventually becoming a Category 3 hurricane as it made landfall. The hurricane moved ashore between Sabine Pass and Johnson's Bayou, Louisiana early on September 24 with sustained winds of 120 mph (54 m/second). Concurrent with its onshore arrival and wind field, Rita initiated a substantial storm surge east of its center that reached a maximum of 18-20 feet (5-6 m). Rita then weakened rapidly as it continued northward through east Texas and western Louisiana, eventually turning northeastward and merging with an advancing cold front on September 26, 2005.

OBSERVATION METHODS

A helicopter overflight was taken to observe post-hurricane coastal conditions along practically the entire south-central and southwestern Louisiana coastlines and interior marshlands (Figure 2). The coastal flight path began near the Atchafalaya and Wax Lake Delta, extended westward toward Marsh Island and Vermilion Bay, and concluded at Sabine Pass in Cameron Parish, Louisiana. An interior marshland flight pass was then made that extended eastward from Sabine Pass and continued through Cameron, Calcasieu and Vermilion Parishes. Digital photos were taken throughout the trip as were a constant stream of video data that provided a continuous record of the entire trip. Photos were calibrated to a GPS to ensure accurate positioning of each picture so that sedimentologic and morphologic changes detected in potential follow-up trips could be accurately calibrated to those from this original flight.

RESULTS

Several unique phenomena were observed during the overflight. Massive overwash deposits were observed on the backside of many beaches along the coast. These became



Figure 2: Helicopter overflight route, southwestern Louisiana, October 16, 2005 (satellite image available at http://www.geology.com/satellite/louisiana-satellite-image.shtml)

more pronounced farther west and culminated near where the eye moved ashore at Johnson's Bayou. In addition, excessive storm surge and salt-water intrusion also became more evident farther west as indicated by the loss of vegetation in inland marshes as well as the catastrophic infrastructure and property loss in locations such as Holly Beach and Cameron. Scour effects and sediment re-distribution patterns were also noted, particularly in association with several series of rock jetties located just offshore from the southwestern Louisiana coast. Despite the destructive nature of the phenomena observed, the initial phases of post-storm recovery were also detected, primarily through bar welding to the lower shoreface as sediment was being reworked from offshore by post-storm waves.

Storm Surge and Return Flow Observations

Overwash deposits were observed in western Vermilion Parish and continued westward through most of Cameron Parish. These overwash deposits were typically located approximately 30-50 feet (9-15 m) behind the immediate coastline and were approximately 40 feet (12 m) wide (Figure 3). In many cases, ripple beds were detected on top of overwash deposits, indicating significant wave-induced currents. In other cases, overwash deposits were seen as distinct lobes in tandem with distributary patterns that appeared to consist of relatively finer-grained, muddier material (Figure 4).

However, overwash was not detected continuously along the coast. This fact may stem from either the lack of an initial, sand-sized offshore sediment supply or from localized variations in coastline morphology. In some cases, distinct incision events were detected across a broad mud apron along the immediate shoreline and seemed to indicate evidence of return flow of water and sediment to the Gulf of Mexico (Figure 5). These dendritic-shaped patterns continued from the shoreline southward to a hinge point just offshore where they appeared to bifurcate and form subaqueous channels directed offshore. Although significant onshore sediment movement occurred during Hurricane Rita, this evidence indicates that steady, post-storm sediment and water movement had been taking place in the offshore direction.



Figure 3: Overwash deposits, eastern Cameron Parish, Louisiana (inset shows rippled overwash deposits and return flow features)

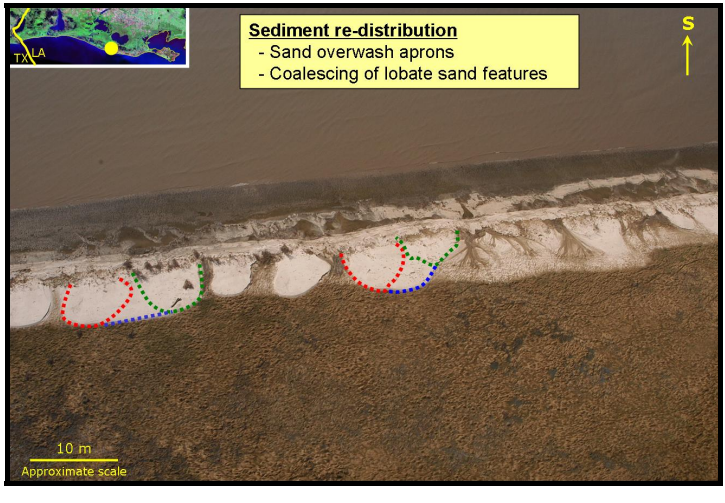

Figure 4: Lobate sand overwash deposits, Vermilion Parish, Louisiana (Guidroz, et al. 2006; reprinted by permission of the GCAGS whose permission is required for further use)

Hurricane Rita generated a significant storm surge event that resulted in substantial salt water intrusion, much of which occurred as far as 25 miles (40 km) inland. Evidence for this intrusion was noted by several different means. First, severe vegetation loss was noted during the October 2005 overflight, primarily through marsh grass that had been

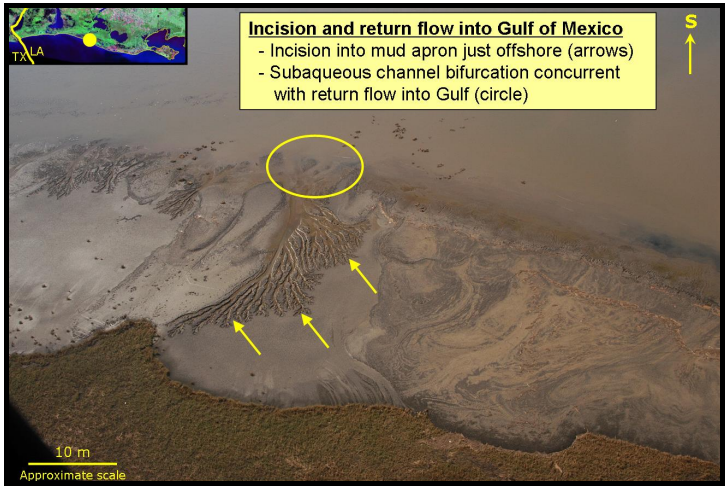

Figure 5: Drainage and return flow channelization, Cameron Parish, Louisiana (Guidroz, et al. 2006; reprinted by permission of the GCAGS whose permission is required for further use)

killed off through saline seawater intolerance. Second, numerous debris fields were observed, particularly near Cameron and Holly Beach, Louisiana and all were aligned in a southeast-northwest direction, indicating how surge had transported both beach and man-made material parallel with the hurricane's predominant counter-clockwise flow. Third, ponded water, remaining from the surge event three weeks earlier and trapped from re-entering the Gulf by localized topographic relief, was also clearly evident along the coast (Figure 6). Fourth, a series of high-water observations was undertaken by staff from the LSU Hurricane Center to visually observe storm surge water level heights based on markings from debris and water levels carried inland by storm surge.

Storm Surge Water Levels

Field observations of high water marks along the coast and inland for several kilometers were obtained by the LSU Hurricane Center (LSUHC; Figure 7) and the Federal Emergency Management Agency (FEMA; Figure 8; URS Group, Inc., 2006). Both data sets are in generally good agreement. Maximum water levels associated with Rita were observed at 14-15 feet (4-4.5 m) at Cameron and slightly farther to the east (all elevations were measured relative to NAVD88). Inland along the margins of Calcasieu Lake, storm surge was significantly attenuated, and high water marks ranged between 3-10 feet (1-3 m). To the east as far as Vermillion Bay, storm surge water levels remained significant and high water marks of up to 12 feet (3.7 m) were measured.

High-water surge observations noted in the field were compared to publicly available numerical models (SLOSH and AdCirc; FEMA, 2005, Figure 9). The datasets generally agree on the relative intensity of storm surge along the immediate southwestern Louisiana coast although the FEMA model consistently under-predicted surge levels at

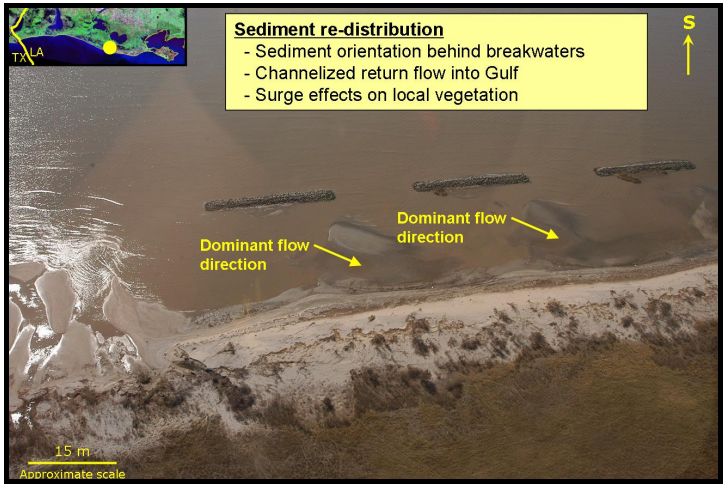

Figure 6: Channelized return flow features, Vermilion Parish, Louisiana (Guidroz, et al. 2006; reprinted by permission of the GCAGS whose permission is required for further use)

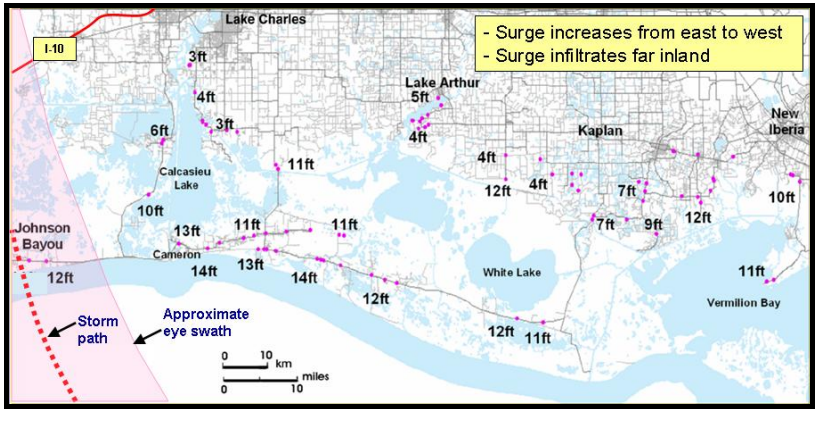

Figure 7: LSUHC high-water mark field observations, southwestern Louisiana (Guidroz, et al. 2006; reprinted by permission of the GCAGS whose permission is required for further use)

the coast. Inland, however, the model results diverged greatly. The FEMA model, which was run in hindcast mode, vastly over-predicted surge levels inland. The latter may be a direct function of the inability of these models to account for differences in bottom friction between water and marsh.

West of the eyewall impact along the upper Texas coast, storm surge levels were much lower compared to areas east of eyewall impact in southwestern Louisiana. The counter-

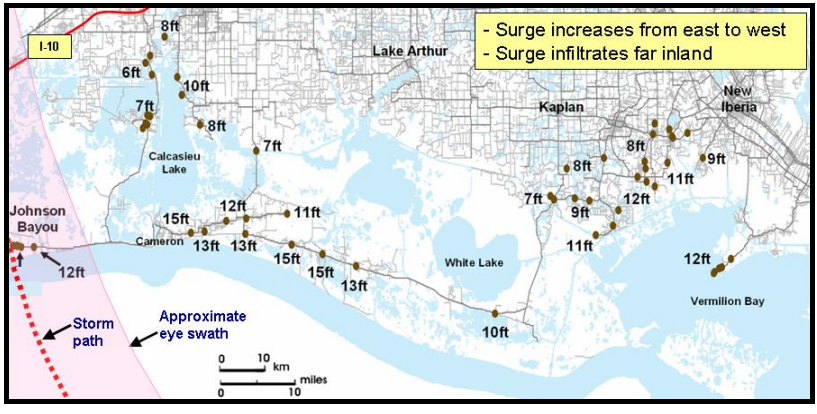

Figure 8: FEMA high water mark field observations, Hurricane Rita, southwestern Louisiana (URS Group, Inc., 2006)

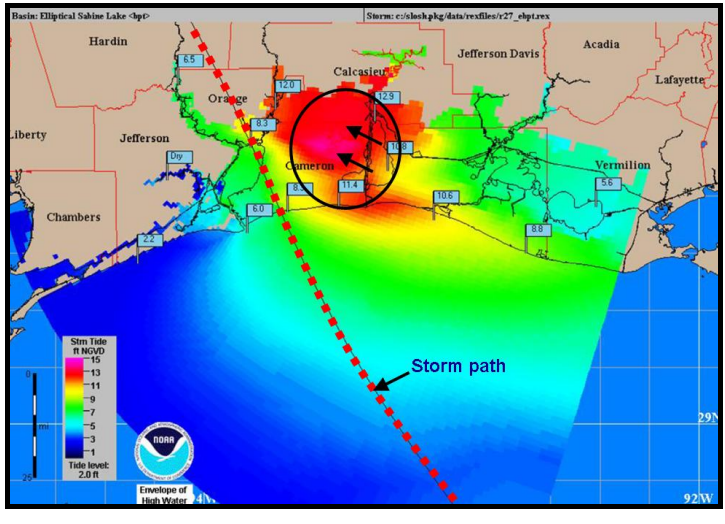

Figure 9: SLOSH model, Hurricane Rita (URS Group, Inc., 2006; available at http://www.fema.gov/pdf/hazard/flood/recoverydata/rita)

clockwise circulation associated with Rita resulted in a primary wind field along the upper Texas coast from the north and northeast. This flow direction suppressed any excessive surge events and therefore minimized morphologic effects west of the point of eyewall impact. Preliminary observations along the upper Texas coast have confirmed these findings (King, personal communication, 2006).

LONG TERM CONSEQUENCES

Since 1901, at least 55 tropical storms and hurricanes have made landfall within Louisiana, implying a long-term average of one storm about every-other year (Stone et al., 1997). However, storm frequency along the central and southwestern Louisiana coasts is nearly twice that of eastern Louisiana with a peak in activity usually occurring

in the month of September. The relatively high frequency of storms along this section of the Gulf coast therefore exerts a cumulative effect on and can significantly alter coastal geomorphology from year-to-year. Previous sand overwash deposits have been noted along the southwestern Louisiana coastline (Williams, 2006) as driven by excessive storm surge events. However, post-storm adjustments to these effects also play a critical role. As an example, post-storm recovery has been previously documented along several Louisiana barrier islands after Hurricanes Juan (1985), Danny (1985) and Gilbert (1988; Stone et al., 1999; Guidroz et al., 2006). Although post-storm recovery depends upon the degree of damage and the availability of sediment within the coastal system, more investigation is needed to further quantify the full effects. This overflight was only the initial investigation into documenting destruction and recovery effects; follow-up observations are required to adequately address the pace and efficiency of future beach recovery.

CONCLUSION

The observations noted in the aftermath of Hurricane Rita demonstrate several distinct phenomena prevalent within the coastal environment after severe storms. Storm surge, combined with post-storm water and sediment return flow back to the open Gulf, can greatly influence sediment patterns along and adjacent to nearshore and inland coastal areas. The observations made during the study will serve as the basis for future investigations to document longer-term effects on local sediment distribution patterns as a result of Hurricane Rita. However, these effects may be interrupted, and possibly delayed, by future tropical cyclones that impact the north-central and northwestern Gulf of Mexico coasts.

ACKNOWLEDGEMENTS

The authors would like to thank BP America, Inc. for underwriting costs associated with this overflight. We also thank the Coastal Studies Institute of Louisiana State University for their support in arranging overflight logistics. Xiongping Zhang and Felix Jose of the Coastal Studies Institute acquired digital photo images and video data during the flight that were used in assembling this paper.

REFERENCES

Guidroz, W.S., G.W. Stone and D. Dartez (2006). "Hurricane Rita, 2005: Assessment of a storm-induced geological event along the southwestern Louisiana coast and adjacent interior marsh," *Gulf Coast Association of Geological Societies Transactions* 56, 229-239.

King, D.B. (2006). Personal communication, Engineer Research and Development

Center, United States Army Corps of Engineers, Vicksburg, MS.
Knabb, R.D., D.P. Brown and J.R. Rhome (2006). "Tropical Cyclone Report, Hurricane Rita, 18-26 September 2005," National Hurricane Center, Miami, FL, 33 p.
National Hurricane Center (2005). "Monthly Tropical Weather Summary, September 2005," Miami, FL, 3 p.
Pasch, R.J., E.S. Blake, H.D. Cobb III and D.P. Roberts (2006). "Tropical cyclone report: Hurricane Wilma, 15-25 October 2005," National Hurricane Center, Miami, FL, 25 p.
Stone, G.W., J.M. Grymes III, J.R. Dingler and D.A. Pepper (1997). "Overview and significance of hurricanes on the Louisiana coast, U.S.A.," *Journal of Coastal Research* 13(3), 656-669.
Stone, G.W., P. Wang, D.A. Pepper, J.M Grymes III, H.H. Roberts, X. Zhang, S.A. Hsu and O.K. Huh (1999). "Studying the importance of hurricanes to the northern Gulf of Mexico coast," *Eos, Transactions, American Geophysical Union* 80, 301-305.
URS Group, Inc.(2006). "Hurricane Rita Rapid Response: Louisiana Coastal & Riverine High Water Mark Collection," Federal Emergency Management Agency, Hazard Mitigation Technical Assistance Program, Contract No. EMW-2000-CO-0247, Task Orders 445 & 450, Gaithersburg, MD, 42 p.
Williams, H.F. (2006). "Hurricane Rita storm surge deposits in southwest Louisiana: preliminary fieldwork results," *Gulf Coast Association of Geological Societies Transactions* 56, 881 (abstract only).

HETEROGENEITY AND DYNAMICS ON A SHOAL DURING SPRING -WINTER STORM SEASON, SOUTH-CENTRAL LOUISIANA, USA

Daijiro Kobashi[1], Felix Jose[2], Gregory W. Stone[3]

1. Coastal Studies Institute, Department of Oceanography and Coastal Sciences, Louisiana State University, 218A Howe-Russell Geoscience Complex, Baton Rouge, LA 70803, USA. dkobas1@lsu.edu
2. Coastal Studies Institute, Louisiana State University, 216 Howe-Russell Geoscience Complex, Baton Rouge, LA 70803, USA. felixjose@lsu.edu
3. Coastal Studies Institute, Department of Oceanography and Coastal Sciences, Louisiana State University, 316, Howe-Russell Geoscience Complex, Baton Rouge, LA 70803, USA. gagreg@lsu.edu

Abstract: Ship Shoal, a shore-parallel elongate sand shoal and a remnant of a late Holocene active delta has a unique heterogeneous sedimentary feature strongly affected by winter storms and fluvial sediment input from the Atchafalaya River. The interaction between fluvially derived sediment and subsequent deposition on the shoal has not been quantified; implications for hydrodynamic modeling are profound given that the shoal surface vacillates between sand and fluid mud. Thus, attenuation effects on waves and currents vary greatly. The results of a field survey undertaken during spring flood and winter storm periods showed that during fair weather, river-borne sediments transported to the shoal, forms a distinct fluid mud layer. Bottom sediments were re-suspended and transported by storm-induced waves and prevailing northerly/southerly

trends of currents over the shoal during the period. Data presented here suggest that the high sediment transport during the storms and the ephemeral deposition of fine-grained sediments could form transient sediment distribution on the shoal without leaving any modern sedimentary records, as reported by recent core surveys.

INTRODUCTION

Much of the Louisiana continental shelf is characterized by fine-grained sediment due to fluvial inputs from the Mississippi and Atchafalaya rivers, their distributaries, and frequent hurricane and winter storms. Submerged transgressive sand shoals off Louisiana, which are remnants of past active deltas, form thick sandy sequences on the inner shelf (Penland et al., 1986).

Physical processes along the Louisiana coast are strongly affected by high energy events such as hurricanes and quasi-periodic winter storms. The muddy coast along western Louisiana also causes unique physical process responses (e.g. Sheremet and Stone 2003; Sheremet et al., 2005; Stone et al., 2006) as well as biological processes (e.g. Stone et al. 2006). Recent articles demonstrate the effects of the Mississippi and Atchafalaya River plumes on the Louisiana continental shelf, based on hydrological and geological surveys and satellite image analysis (e.g. Allison et al., 2000; Walker and Hammock, 2000; Bentley, 2002).

It is now well documented in the scientific literature that coastal Louisiana has experienced substantial wetland loss and beach/barrier island erosion due to high rates of subsidence, storms, shortage of sediment supply from adjacent fluvial systems and human intervention such as dam and levee construction. Federal and state governments are exploring potential sand sources offshore to restore eroding barrier islands and beaches (Drucker et al., 2004). Offshore sand resources have been considered one of the highest priorities for sand resources for coastal restoration given proximity to the target areas and for sand quality (Drucker, B., pers. com.). Ship Shoal, which is a remnant of the paleo-Maringouin delta, located 20 km offshore Isles Dernieres, is a high priority target sand resource to aid in the restoration of the Isles Dernieres Barrier Chain (Drucker et al., 2004). Numerous studies of the area have been undertaken particularly in terms of geological and physical processes (Penland et al., 1986; Pepper, 2000; Stone et al., 2006). Studies of the physical processes include wave-climate, bottom boundary layer, and sediment transport processes based on field surveys and spectral wave model studies (Pepper 2000; Stone et al. 2004). These studies concluded that waves substantially transform as they

propagate over the shoal by comparing the result of pre- and post-sand mining scenarios (Stone et al., 2004). Although they provide detailed mechanisms of hydrodynamics and non-cohesive sediment transport at the shoal, recent surveys suggest that the area has a complex sedimentary environment, which has not previously been researched. To fully understand the mechanism of wave-bottom sediment interactions and sediment transport processes, field surveys and numerical modeling studies were conducted and a synopsis of the data are presented here. The overall purpose of this paper is to describe wave and current dynamics affecting the bottom boundary layer, and sediment transport over the shoal during a field survey conducted in Spring 2006.

DATA AQUISTION

During spring flood and the winter storm season, an array of oceanographic instrumentation was deployed at three locations along the northern and southern

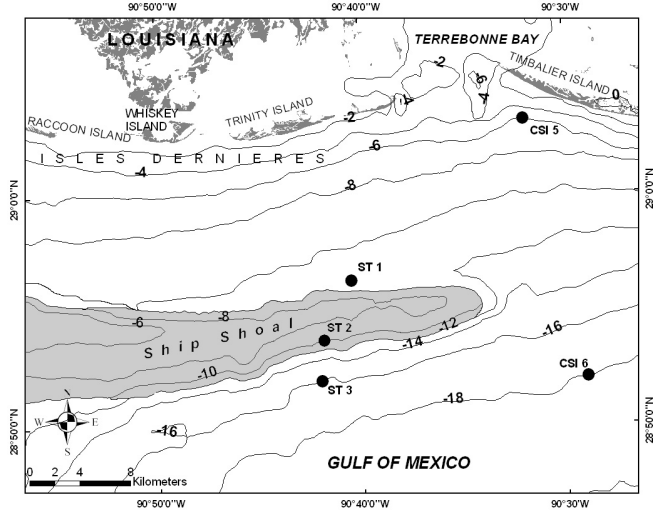

Figure 1 Map of 2006 survey stations, ST1, ST2 and ST3

edges of the shoal and the crest of the shoal, to collect wave, current and suspended sediment concentration data (Figure 1). The instruments at the middle station (ST2) consisted of a 1.5 MHz SonTek^{R} pulse-coherent Doppler profiler, a Druck^{R} pressure sensor, and two D&A^{R} optical backscatter sensors. A 5.0 MHz SonTek^{R} Acoustic Doppler Velocimeter and a ParoScientific^{R} pressure sensor were deployed at both

edges of the shoal (ST1, ST3). Two D&A^R optical backscatter sensors were also deployed at the north station (ST1). Each instrument system was tethered to nearby oil platforms for a robust deployment.

DATA ANALYSIS

Significant wave height, peak wave period, and dominant wave direction were calculated from pressure and current data based on the spectral method by Earle (1995) (see also Stone et al. 2006). Directional wave spectra were calculated by the PUV method using DIWASP, a Matlab package (DIWASP, 2001).

Suspended sediment concentration (hereafter referred to as SSC) was estimated from the data collected using optical backscatter sensors (hereafter referred to as OBS) after calibration using water and sediment samples taken from the stations by ponar grab. The calibration studies were conducted at the CSI field support facility. Bottom sediment samples were incrementally added to distilled water in a black bucket and stirred using a hand-held electric agitator. OBS sensors were immersed in the bucket and measurements were taken for 2 minutes. Water samples were taken after the OBS measurements and were filtered; the SSC were estimated from the weight of the dried sediments and the water volume (Stone et al., 2006).

SSC was also estimated from the ADV and the PCADP single frequency acoustic backscatter intensity with appropriate calibration. The acoustic backscatter intensity is a by-product of the PCADP and the ADV, and is proportional to the SSC estimated from the OBS. This method includes inevitable noise because the backscattering is affected by various parameters such as sediment type, size and composition. All are difficult to quantify by single frequency backscatter sensors and there remain limitations associated with optical and acoustic instruments (Hamilton et al., 1998). In spite of these limitations, estimating the relative sediment concentration profile based on the acoustic backscatter intensity is a cost-effective method which enables us to monitor the SSC trend over time. A more detailed method of estimating the SSC from the OBS and the PCADP/ADV is presented in Stone et al. (2006). The SSC at ST3 was estimated from the relationship between the OBS and the ADV backscatter intensity at ST1.

Wave orbital velocity, shear velocity, shear stress, and apparent bottom roughness were calculated to examine boundary layer dynamics. For the calculation of shear velocity and shear stress, four methods were used: (i) linear wave theory, (ii) log-linear method, (iii) Reynolds stress method, and (iv) quadratic stress law method (Sternberg, 1972; Komar, 1976; Pepper, 2000). Critical shear stress for non-cohesive

sediments was calculated by the Shields parameter combined with the modified Yalin parameter (Pepper, 2000). The critical shear stress for cohesive sediments is difficult to specify and needs further laboratory experiment to determine parameters which are site-specific (Mehta et al., 1989). Mean critical shear stress for erosion and deposition is suggested to be 0.15 N/m^2 and 0.1 N/m^2, respectively, based on a wide variety of studies in the U.S. and was used in this study (DHI, pers. com.).

RESULTS AND DISCUSSIONS

Meteorological and hydrological characteristics

Tropical cyclones (i.e. hurricanes and tropical storms) and extra-tropical storms (i.e. winter storms) are the two important meteorological events that affect the Louisiana coast. Particularly, frequent passage of winter storms between October and April causes cumulative effects on waves, hydrodynamics and sediment transport along the Louisiana coast because of their frequency, compared to less frequent landfall of tropical cyclones (Pepper, 2000; Stone et al., 2004; Kobashi et al., 2005). Generally, as cold fronts approach the coast, strong southerly winds can generate significant wave height on the shelf from 3-5 m, barometric pressure shows a marked decrease and thus characterizes the pre-frontal phase. After the front passes, air temperature abruptly decreases and wind direction changes from the southern to northern quadrants representing the post-frontal phase. The above described trend is evident in the time series of wind data obtained from a nearby meteorological station, WAVCIS CSI-6 (90° 29' W, 28° 52' N) (Figure 2 left). The dominant wind direction is 173 degrees (i.e. wind from SSE), which is a common characteristic during the fair weather conditions and a force to generate longshore current, generally directed westward, off south-central Louisiana (Figure 2 right).

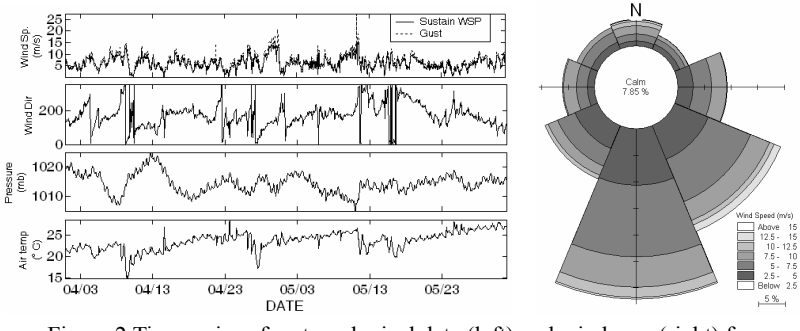

Figure 2 Time series of meteorological data (left) and wind rose (right) from WAVCIS CSI-6

Significant amounts of fluvial sediment discharged from both the Mississippi and Atchafalaya rivers, and distributaries, are also highly significant in introducing sediment to the shelf thereby playing an important role on hydrological processes that affect physical and biological processes on the Louisiana inner continental shelf. In the study area, maximum river discharges of 310,000 cubic feet per second (cfs) were recorded at Simmesport located upstream on the Atchafalaya River on March 30th, 2006 and 250,000 cfs on May 8th, 2006, resulting in significant influxes of muddy sediments along the western/south-central Louisiana coast (Stone et al., 2006).

Bottom sediment characteristics

Bottom sediments collected during a biological cruise conducted for the entire shoal that included ponar grabs along the eastern flank of the shoal before and after bottom boundary layer equipment deployment (Figure 3, shaded triangles), show a unique shoal sedimentary environment. Bottom sediment grain size distribution for the entire shoal, surveyed in late May, 2006, shows that the grain size is finer along the western part of the shoal than its eastern flank; we attribute this to the influence of fluvially derived material from the Atchafalaya River (Figure 3, left).

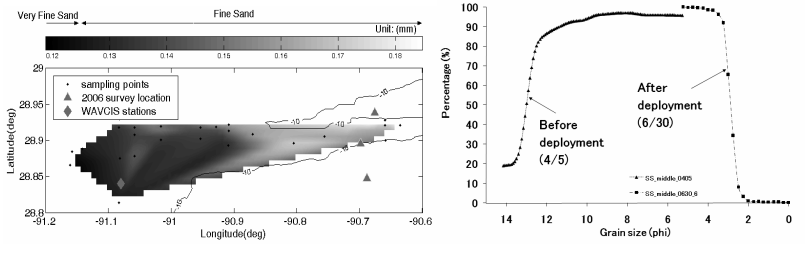

Figure 3 Mean grain diameter for the entire shoal (samples taken May 25th, 2006) (left) and grain size distribution taken before and after the deployment (right)

Bottom sediment taken from the eastern portion of the shoal shows a dramatic change in sediment grain size before and after the deployment (Figure 3, right). Sediment sampled before the deployment was mainly clay with a median grain diameter of 2 microns, probably originating from the Atchafalaya River; sediment sampled after the deployment was fine sand with a median grain diameter of 143 microns, suggesting the effect of sediment reworking due to storm-induced waves. This unique behavior of the bottom sediments was not found during previous field surveys undertaken along the western flank of Ship Shoal in January, 1998 (Pepper, 2000). The fine

grained sediments from the Atchafalaya River are usually transported west due to a longshore coastal current (Wells and Kemp, 1981). However, during winter storms, strong southerly wind-induced currents with sufficient sediment supply can transport this fine grained sediment to the south/southeast, occasionally reaching Ship Shoal (Kobashi et al., submitted). Such a sediment dispersal pattern was confirmed by satellite imagery obtained during our deployment and also reported by Walker and Hammock (2000).

Wave characteristics

During the cold frontal passages, pre-and post-frontal phases have a significant effect on the wave field along the northern Gulf. Lower frequency waves dominate the spectrum during pre-frontal conditions. As winds veer to the north, higher frequency waves occur in the bays/estuaries and wave energy levels drop significantly on the shoreface (Figure 4d,e). Waves can become higher after the storms because of relatively strong southerly wind induced by a high pressure system covering the area (e.g. April 10th, 2006) (e.g. Pepper, 2000; Kobashi et al., 2005).

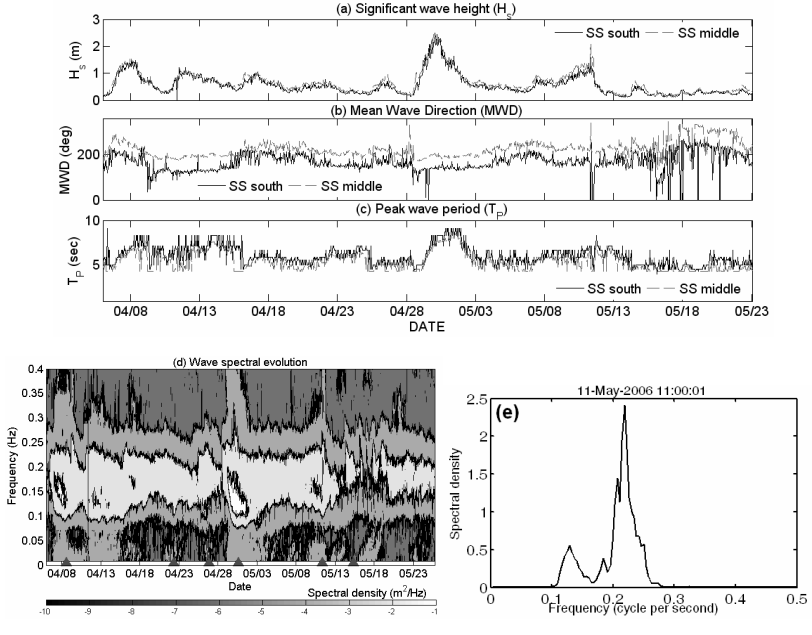

Figure 4 (a-c) Time series of wave parameters, (d) Wave spectral evolution, (e) spectral distribution during a post-front. Triangles show passage of cold fronts.

Current velocity and circulation patterns

Bottom currents are strongly affected by local bathymetry and associated turbulence as well as currents due to tides. Current direction near the bottom is different from that at the surface, suggesting current modulation due to local bathymetry, wave-induced turbulence, or wind-induced Ekman transport. Currents due to tides are generally small (i.e. less than 5 cm/s) and strong currents occur during winter storms. The strong northeast/southwest osciallation of current direction during winter storms is clearly apparent in Figure 5, and is associated with the rotating storm wind direction. During fair weather, currents are weak and highly variable when compared to storm conditions; however, surface currents were often westward (not in the figure) due to longshore currents driven by prevailing south-easterly waves. In addition to the longshore currents, tidally-induced currents when combined with higher energy waves during winter storms result in additional currents with a period of around 5 to 10 days, a mean frequency consistent with winter storms.

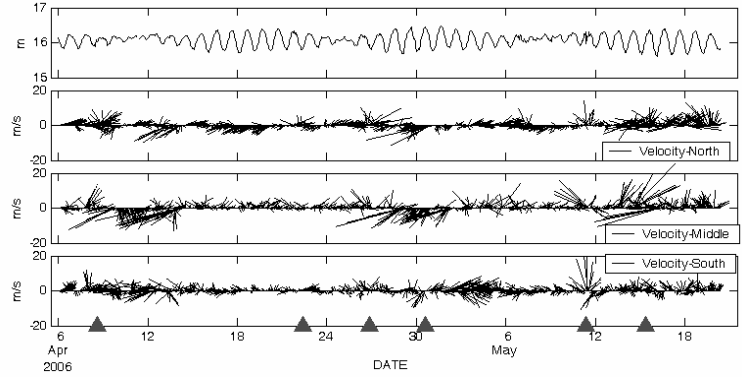

Figure 5 Stick vector of bottom current velocity at each station. Triangles indicate passage of storms

Suspended Sediment Concentration

Suspended sediment concentration is also strongly associated with winter storms. Figure 6 shows that high sediment concentrations occur during winter storms at all three stations, suggesting that strong storm-induced waves cause high bottom sediment re-suspension compared to that during fair weather. Particularly, during late April, high concentration of suspended sediments associated with a storm occurred. At ST1, SSC attained saturation level and lasted approximately 2 days. At ST2 and ST3, high SSC also occurred during the waning phase of the storm as well as during

the pre-frontal stage, suggesting the occurrence of substantial deposition of cohesive sediments (The latter is discussed in more detail below). High SSC during April 8th and May 10th shows the input of river-borne sediments from the Atchafalaya River, also confirmed by satellite images and altimeter data during this period (Kobashi et al., submitted).

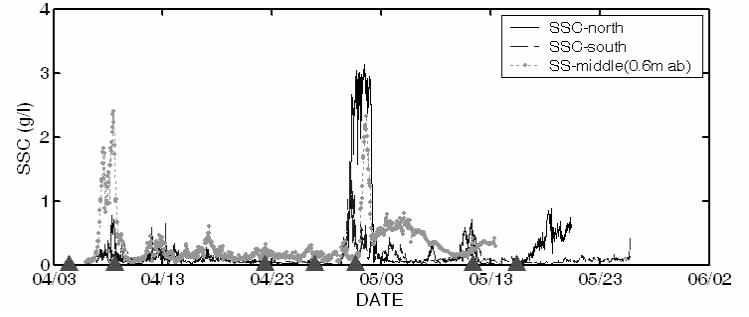

Figure 6 Time series of sediment concentration at each deployment station. Triangles indicate passage of storms.

Bottom boundary layer parameters and sediment flux

Shear velocity and shear stress are high during winter storms. Bottom orbital velocities associated with winter storms attained a maximum of 60 cm/s during a storm in late April (Figure 7). The periods of high orbital velocity, shear velocity, and shear stress match those of the high SSC shown in Figure 6.

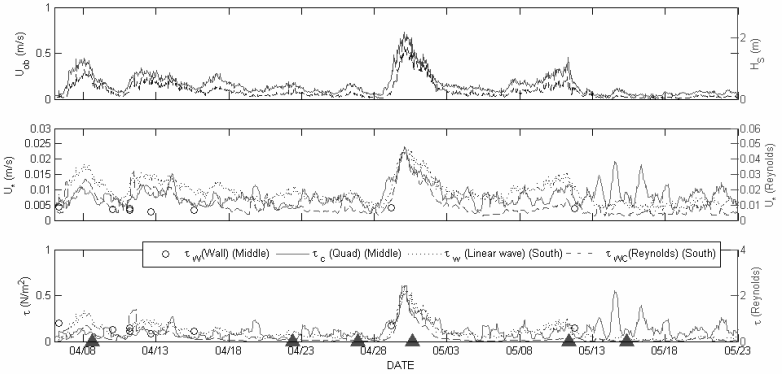

Figure 7 Time series of bottom boundary layer parameters: (a) wave orbital velocity (Uob), (b) shear velocity (U*), and (c) shear stress (τ) during the deployment at the middle station

The sediment flux, calculated by the product of horizontal velocity and sediment concentration, is shown in Figure 8. The direction of sediment transport is different among stations, and is significantly influenced by current direction. Northerly/southerly currents during winter storms drive the highest transport in the region, although current direction is dependent on other factors such as local bathymetry and tides. It is evident that in-situ observation of sediment flux is much higher than non-cohesive sediment transport derived numerically (not in the figure). It is also evident sediment flux occurs during fair weather, a finding that contradicts the results of previous work (e.g. Wright et al., 1997).

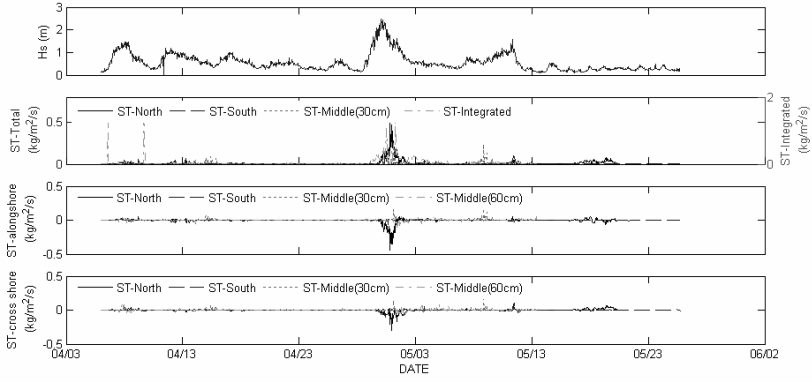

Figure 8 In-situ sediment transport measurements for each deployment station

Resuspension, mixing, and settling processes of fluid mud during a storm

Waves, currents, and sediment transport are intensified by winter storms, and the bottom sediment of the shoal uniquely varies during these events. Figure 9 shows the time series variation of bottom boundary layer parameters and SSC during a storm which passed the region in late April, 2006. Wave height reached approximately 2.5 m during the pre-frontal phase, consistent with a maximum wind speed of 18 m/s. When wave height reached approximately 1 m, the shear stress exceeds the threshold for sediment re-suspension (i.e. τ_{ce}), which is consistent with the increase of bottom SSC (Figure 9c). Bottom sediments are re-suspended strongly during the pre-frontal phase (Re-suspension period), causing highest sediment transport during the storm because of high horizontal velocity. Subsequently, the transport rates decrease due to decreased horizontal velocity and an increased vertical velocity causing vertical mixing during the storm passage (Mixing period). During the waning phase of the storm, substantial sediment deposition occurs in spite of the high sediment transport

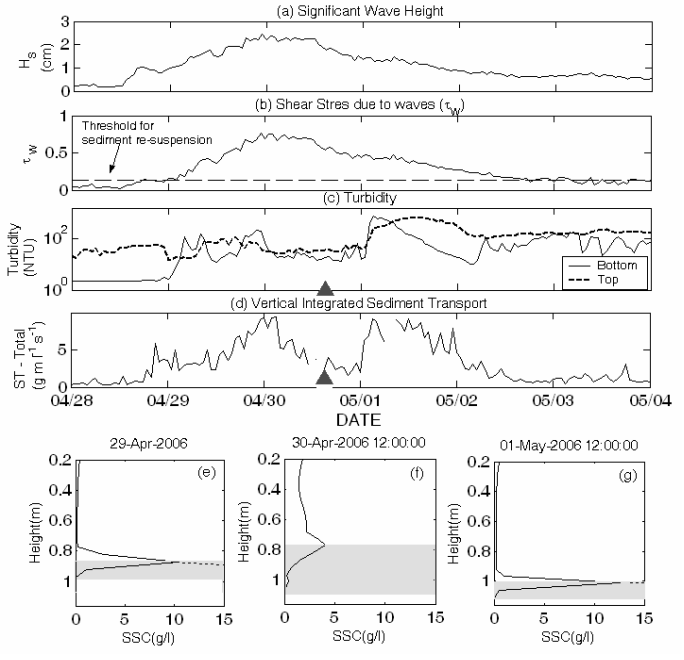

Figure 9 Time series of (a) significant wave height, (b) shear stress due to waves, (c) turbidity, (d) vertical integrated sediment transport, (e)-(g) sediment concentration profiles. Triangles indicate passage of a storm

rates (Settling period). The SSC profile in Figure 9 (e, f, g) demonstrates the above. Prior to storm passage, the peak sediment concentration was measured near the bottom, suggesting the existence of a fluid mud layer (SSC>10 g/l) delivered by hyperpycnal flows originated from the Atchafalaya River. The peak of the SSC strongly decreased below the lutocline since the acoustic signal was strongly attenuated below it (cf. Traykovski et al., 2000). The high frequency acoustic pulse cannot penetrate consolidating muddy bed or sandy bed below fluid mud. Based on this, the thickness of the layer was estimated to approximate between 10 and 15 cm (Figure 9e-g, shaded area). The high value of the SSC disappeared during the storm peak and the peak of the SSC shifted upward, suggesting the layer was vertically diffused due to high vertical velocity. During the waning phase of the storm, the fluid mud layer was re-established. However, the layer is highly unstable according to the SSC profile during the deployment (not in the figure). It is implied that this unstable

layer, which can easily be re-suspended, could not be settled long enough to become consolidated, because of the frequency of the winter storms. Allison et al. (2000) demonstrated that sediment cores taken on the southwest of Ship Shoal had no modern sedimentary records, implying these muddy sediments on the sandy relict sediments cannot become consolidated hard mud bed without leaving any modern sediment records as reported by the recent core surveys at the southwest of the shoal.

There are few data available to prove this hypothesis. It is still unclear as to the fate of this transient mud sediment covering the sandy bottom. Surveys will be undertaken to examine bottom sediments using box cores and underwater cameras to better understand mud distribution during various seasons. Also, the ongoing modeling studies of waves, currents and cohesive sediment transport should provide a more comprehensive analysis of the shoal and its unique processes, which are important to the physical and biological processes of the study area, and for future sand dredging activities.

CONCLUSIONS

To examine wave-climate and wave-bottom interactions over a heterogeneous shoal, field surveys were conducted and the following results were obtained. (I) Bottom sediments on the shoal vary substantially depending on fluvial sediment inputs and winter storms; (II) The north-south trend in current direction during storms suggests a dominant sediment transport direction during the deployment; (III) Rates of transport for cohesive sediment is much higher than those numerically derived non-cohesive sediment transport during the deployment; (IV) A fluid mud layer is formed during fair weather on the shoal and is re-suspended, mixed and re-deposited during storms, implying fine-grained sediment are ephemeral resulting in no sedimentary records on the deposited sediments previously reported by Allison et al. (2000).

ACKNOWLEDGEMENTS

This study is funded by the U.S. Minerals Management Service, Department of Interior and Louisiana Department of Natural Resources. The authors would like to thank CSI field support crews for assisting in the field survey. Yuliang Chen assisted with cartography.

REFERENCES

Allison, M.A., Kineke, G.C., Gordon, E.S., Goni, M.A. (2000). Development and reworking of a seasonal flood deposit on the inner continental shelf off the

Atchafalaya River. *Continental Shelf Research* 20 (16), 2267-2294.

Bentley, S.J. (2002). Dispersal of fine sediments from river to shelf: process and product, *Transaction*, Gulf Coast Association of Geological Societies, v.52, 1055-1067.

DIWASP (2001). DIWASP, a directional wave spectra toolbox for MATLAB®: User Manual. Research Report WP-1601-DJ (V1.1), Centre for Water Research, University of Western Australia.

Drucker, B.S., Waskes, W., and Byrnes, M.R. (2004). The U.S. Mineral Management Service Outer Continental Shelf Sand and Gravel Program: Environmental studies to assess the potential effects of offshore dredging operations in federal waters, *Journal of Coastal Research*, 20 (1), 1-5.

Earle, M.D. (1996). Nondirectional and Directional Wave Data Analysis Procedures, NDBC Technical Document 96-01, National Data Buoy Center, NOAA, 37pp.

Hamilton, L.J., Shi, A., and Zhang S.Y., (1998). Acoustic backscatter measurement of estuarine suspended cohesive sediment concentration profiles, *Journal of Coastal Research*, 14(4), 1213-1224.

Kobashi, D., Jose, F., and Stone, G.W. (2005). Hydrodynamics and sedimentary responses within bottom boundary layer: Sabine Bank, western Louisiana, *Transaction*, Gulf Coast Association of Geological Societies, v.55, 392-399.

Kobashi, D., Jose, F., and Stone, G.W. (2006). Impacts of river discharges and winter storms on a heterogeneous sand shoal off south-central Louisiana, U.S.A., *Journal of Coastal Research*, SI 50, *Submitted.*

Komar, P.D. (1976). The transport of cohesive sediments on continental shelves, In: Stanley and Swift, eds, Marine Sediment Transport and Environmental Management, 107-125.

Mehta, A.J., Hayter, E.J., Parker, W. R., Krone, R.B., and Teeter A.M. (1989). Cohesive Sediment Transport I: Process Description, Journal of Hydraulic Engineering Vol. 115, No.8, 1076-1093

Penland, S., Suter, J.R., and Moslow, T. F. (1986). Inner-shelf shoal sedimentary facies and sequences: Ship Shoal, Northern Gulf of Mexico, SEPM Core Workshop No.9, Modern and Ancient Shelf Clastics, 73-123.

Pepper, D.A. (2000). Hydrodynamics, bottom boundary layer processes, and sediment transport on the south-central Louisiana shelf: The influence of extra tropical storms and bathymetric modification. Unpublished *dissertation*, Louisiana State University, Baton Rouge, 159p.

Sheremet, A, and Stone, G. W., (2003). Observations of nearshore wave dissipation

over muddy sea bed, *J. Geophys. Res.*, 108(C11), 2257, doi: 10.1029/2003JC001885, 2003.

Sheremet, A., Mehta, A.J., Liu, B., Stone, G.W. (2005). Wave–sediment interaction on a muddy inner shelf during Hurricane Claudette. *Estuarine, Coastal and Shelf Science*, v.63, 225–233.

Stone, G.W., Pepper, D.A., Xu, J. and Zhang, X. (2004). Ship Shoal as a Prospective Borrow site for barrier island restoration, Coastal south-central Louisiana, USA: Numerical wave modeling and field measurements of hydrodynamics and sediment transport. *Journal of Coastal Research*, 20(1), 70-89.

Stone, G.W., Condrey, R., Fleeger, J. (2006). Environmental investigation of long-term use of Ship Shoal sand resources. Year 2 annual report, MMS/LDNR, 59p.

Sternberg, R.W. (1972). Predicting initial motion and bedload transport of sediment particles in the shallow marine environment. In: Swift, Duane, and Pilkey (eds.), Shelf sediment transport: Process and Pattern. Stroudsburg, PA: Dowden, Hutchinson, and Ross, Inc., 61-82.

Traykovski, P., Geyer, W.R., Irish, J.D., and Lynch, J.F. (2000). The role of wave-induced density-driven fluid mud flows for cross-shelf transport on the Eel River continental shelf. *Continental Shelf Research*, Vol. 20. 2113-2140.

Walker, N.D. and Hammack, A. B. (2000). Impacts of winter storms on circulation and sediment transport: Atchafalaya-Vermilion Bay Region, Louisiana, U.S.A., *Journal of Coastal Research*, 16(4), 996-1010.

Wells, J.T. and Kemp, P. (1981). Atchafalaya mud stream and recent mudflat progradation: Louisiana Chenier plain. *Transaction*, Gulf Coast Association of Geological Society, v.31, 409-416.

Wright, L.D., Sherwood, C.R. and Sternberg, R.W. (1997). Field measurements of fair-weather bottom boundary layer processes and sediment suspension on the Louisiana inner continental shelf, *Marine Geology*, 140, 329-345.

WINTER STORM AND TROPICAL CYCLONE IMPACTS ON THE SHORT-TERM EVOLUTION OF BEACHES AND BARRIERS ALONG THE NORTH-EASTERN GULF OF MEXICO

Gregory W. Stone[1], Baozhu Liu[2], and Felix Jose[3]

1. Coastal Studies Institute, Department of Oceanography and Coastal Sciences, Louisiana State University, 218A Howe-Russell Geoscience Complex, Baton Rouge, LA 70803, USA. gagreg@lsu.edu
2. Coastal Studies Institute, Louisiana State University, 218A Howe-Russell Geoscience Complex, Baton Rouge, LA 70803, USA. bliu2@lsu.edu
3. Coastal Studies Institute, Louisiana State University, 218A Howe-Russell Geoscience Complex, Baton Rouge, LA 70803, USA. felixjose@lsu.edu

Abstract: Here we present data indicating the complexity and highly variable response of barrier islands and beaches to the impacts of tropical cyclones and winter storms along the northern Gulf of Mexico. Data indicate that (1) barrier islands can conserve mass during catastrophic hurricanes; (2) less severe hurricanes and tropical storms can promote rapid dune aggradation and contribute sediment to the entire barrier system; (3) cold fronts play a critical role in the post-storm adjustment of the barrier by deflating the subaerial portion of the overwash terrace and eroding its marginal lobe along the bayside beach through locally generated, high frequency, steep waves; and (4) barrier systems along the northern Gulf do not necessarily enter an immediate post-storm recovery phase, although nested in sediment-rich nearshore environments. The fluid mud environment off west Louisiana coast plays a significant role in damping wave energy associated with tropical cyclones. However, no significant surge attenuation appears apparent. It is anticipated that these findings will have important implications for the longer-term evolution of coastal systems in the northern Gulf of Mexico.

INTRODUCTION

Recent data suggest that the North-central Gulf of Mexico coast has undergone an increase in the number of tropical cyclone landfalls over the past decade. Louisiana State University and the USGS have monitored the Florida panhandle and Alabama coast since the mid 1990's using airborne LIDAR and field surveys. The resultant data sets provide a unique time series capturing morphological change and post-storm adjustment due to three powerful events (Opal, 1995, Ivan, 2004 and Katrina, 2005), weaker hurricanes and numerous tropical storms. It is the objective of this paper to identify, quantify and elucidate storm responses and post-storm adjustment along a heterogeneous and geologically complex coastal region. The concept of "barrier mass conservation" is further examined. Study sites along the Florida panhandle (A on Fig. 1), Mississippi, (B) and south-central Louisiana (C, D and E) are used to investigate the effects of geological variability on storm response. The significance of locally generated, high frequency waves in estuaries/bays during winter storms is also investigated and interpreted within the context of short-term coastal evolution.

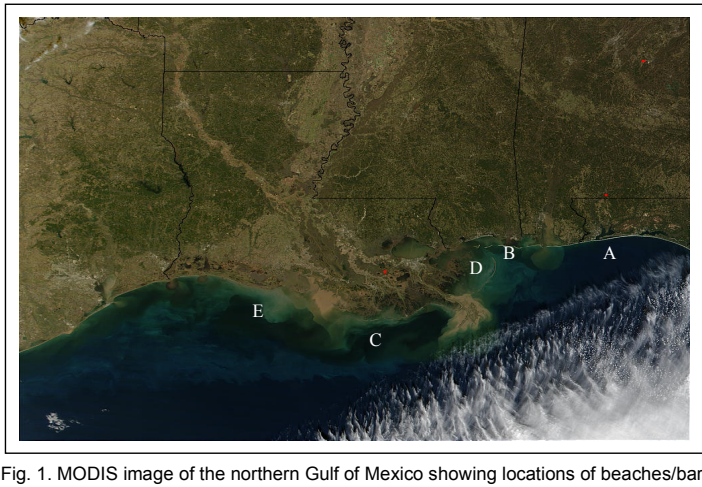

Fig. 1. MODIS image of the northern Gulf of Mexico showing locations of beaches/barriers monitored during the study program discussed in text.

GEOLOGICAL VARIABILITY

In an otherwise tectonically stable region of the northeastern Gulf of Mexico, the coast appears to be storm dominated and undergoing a reduction in sediment volume in the sub-aerial barrier unit, a phenomenon that appears attributable to storm dominance (barrier islands off Mississippi coast are the typical example, location B on Figure 1).

Along the Louisiana coast, barrier islands are routinely breached and/or stripped of their coarser (fine sand) fraction of sediment that overlays an organic, silty-muddy, cohesive core (location C on Figure 1). While the sand veneer is typically infused into the finer-grained bay sediments, the organic and fine-grained core material is exposed due to turbulence associated with storm waves. This response was noted after Hurricane Andrew (1992) (Stone and Finkl, 1995), Tropical Storm Isidore (2002) and Hurricane Lili (2002) (Stone et al., 2003; Allison et al., 2005). Larger chains that constitute those barriers west of the modern delta were not significantly impacted by either Hurricane Katrina or Rita (2005) (Stone et al., 2005; Guidroz et al., 2006; 2007). Similar to during Hurricane Ivan (2004), the Chaundeleur Islands (location D on Figure 1) were severely breached during Hurricane Katrina (2005).

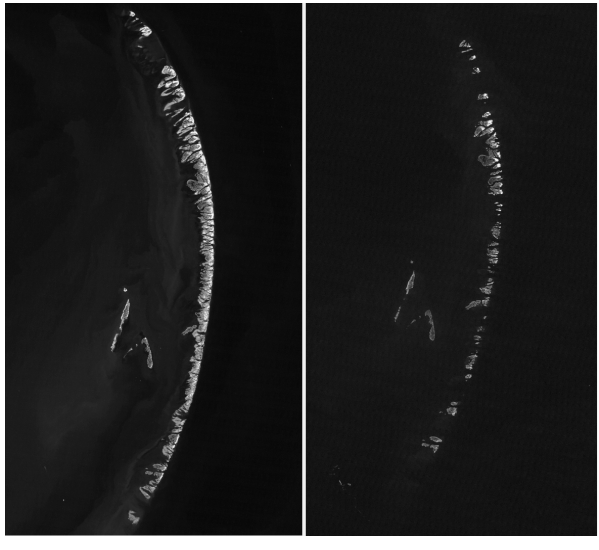

Fig. 2. Chandeleur Islands, Louisiana, before hurricane Katrina, on 13 October 2004 (left) and after, 16 September 2005. Images courtesy of USGS.

West of the Atchafalaya delta (location E on Figure 1) a predictable response occurred along the Chenier plain and the coast farther west during Hurricanes Lili (2002) and Rita (2005). Fine sand was eroded from the upper shoreface and beach and deposited on the adjacent marsh surface as a well defined veneer which widened considerably to between 100-150 m west towards the point of landfall near the Louisiana-Texas border. Guidroz et al., (2006; 2007) reported extensive damage to the coastal marsh vegetation, even up to 25 km inland, due to super elevated storm surge associated with Hurricane Rita. Overwash deposits and evidence of excessive

salt water intrusion were observed for the Cameron and Vermilion Parishes, (Figure 3) southwestern Louisiana. However, the aerial observation study also reported initial post-storm beach recovery, within a matter of two weeks from the day of landfall. Significant contrasts in post-storm adjustment are evident over decadal time-scales on contrasting the sediment rich Florida-Alabama coast and the barriers of South-central Louisiana. Longer-term monitoring along the Florida coast implies post-storm adjustment can take up to 10 years for recovery of approximately 75% of the sediment budget after major events (e.g., Hurricanes Frederic, 1979 and Opal, 1995) (Stone et al., 1999). Although post-storm adjustment of the Louisiana coast is



Fig. 3. Holly Beach, Louisiana, before Hurricane Rita, on 16 June 2001 (upper) and after, 28 September 2005. Images courtesy of USGS, Coastal Hazard Team.

considerably slower, infusions of sand from updrift and offshore sources are apparent. Nevertheless, the multi-decadal increasing trend in storminess is causing a distinct down-turn in the sediment budget.

FIELD DATA

As a case study, topographic and bathymetric surveys have been conducted for a 6 km stretch along the western half of Santa Rosa Island (location A, Figure 1) over a 10 year period. Altogether 30 surveys were conducted since February 1996 and pre and post storm island morphology associated with all major storm events were monitored during this decade long field study program. The details of the transects and the methodology adopted are given in Stone et al., (2004). The morphological evolution of the island in terms of change in volume of sediments is presented in Figure 4. For uniformity, shoreline location was defined as NGVD zero. To study the different responses of the various sub-environments, the cross-island profile was divided into four sections as follows: Gulf beach (foredune to -1.5 m NGVD), dune (foredune to bay beach dune), bay beach (dune to Mean Low Water), and bayside platform (MLW- -1.5 m NGVD).

STORM IMPACTS ON MORPHOLOGY

Stone et al., (2004) described in detail the post-storm morphological adjustment of the island after Hurricane Opal (1995). The study revealed that approximately 90% of the sediment eroded from the foredune-beach-nearshore environment was deposited as expansive overwash deposits on the interior and bayside flanks of the barrier. The barrier increased by an average of approximately 40 m in width along the bay side suggesting that the system conserved mass during Hurricane Opal. As a consequence of this mass conservation response, the Gulf side shoreline of the island retreated an almost equal distance. During the ensuing 2 years this newly deposited wedge of material along the adjacent bay was significantly reworked by northerly waves during the post-frontal phase of cold fronts which resulted in a significant shoreline recession (Stone et al., 2004). The response of north facing beaches/nearshore to these high-frequency steep waves generating in the bay during winter time are discussed in more detail later in this paper.

The time series volume change data for the study area over the period February 1996 – August 2005 is given in Figure 4 and Table 1. These data include the signatures of 7 storms and 10 cold front seasons, which contained over 300 winter storms. Even though the impact of Tropical Storm Josephine resulted in a net loss of sediments from the system, the barrier immediately regained sediment during the period November 1996 and July 1997. Due to the sustained southerly winds during Hurricane Danny a significant amount of sediment migrated from the nearshore and was re-desposited on the berm and overwash platform. The increased vegetation density during the summer also helped the re-deposition of sediment. Prior to

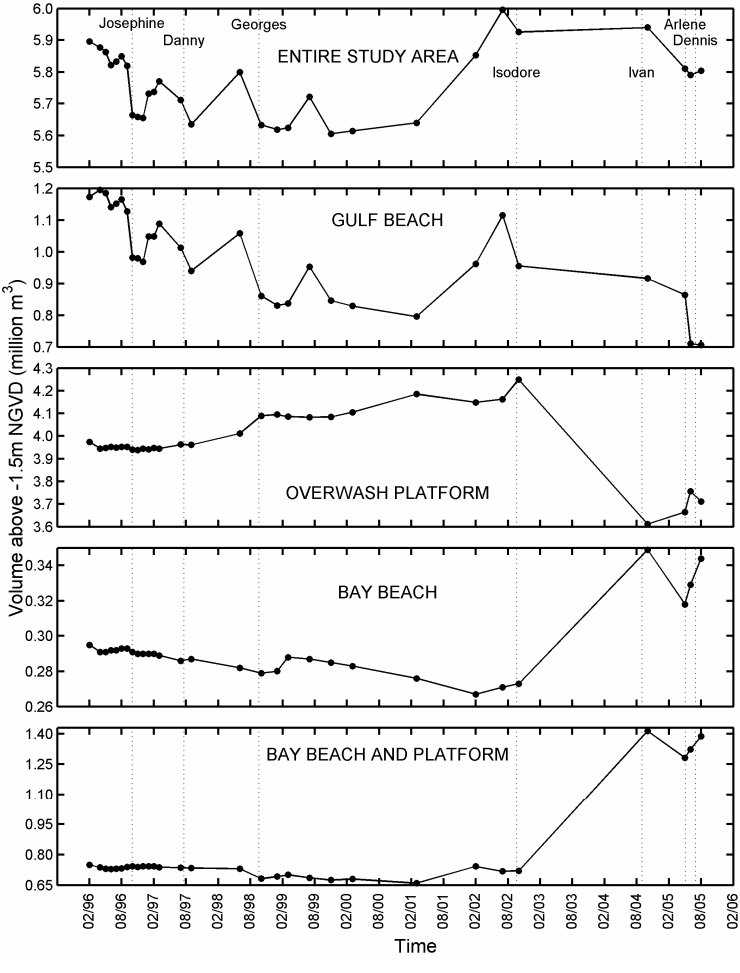

Fig. 4. Volume change for each of the barrier sub-environments from 2/96-8/05 at the Santa Rosa Island site, west Florida.

landfall of Hurricane Georges, the barrier went through a phase of sustained accretion, particularly along the gulf beach. The impact of this storm resulted in the migration of considerable volumes of sediment, eroded from the berm, across the

Table 1. Sediment Volumes of the Entire Study Area and each Sub Environment: (calculated by BMAP to -1.5 m NGVD)

Survey	Entire Area (10^6 m^3)	Gulf Beach (10^6 m^3)	Dune (10^6 m^3)	Bay Beach (10^6 m^3)	Bay Beach & Bayside Platform (10^6 m^3)
Feb-96	5.896	1.173	3.974	0.295	0.749
Apr-96	5.877	1.195	3.945	0.291	0.737
May-96	5.863	1.185	3.947	0.291	0.731
Jun-96	5.822	1.141	3.952	0.292	0.729
Jul-96	5.833	1.152	3.95	0.292	0.731
Aug-96	5.85	1.165	3.952	0.293	0.733
Sep-96	5.819	1.127	3.952	0.293	0.74
Tropical Storm Josephine					
Oct-96	5.664	0.982	3.94	0.291	0.742
Nov-96	5.658	0.98	3.938	0.29	0.74
Dec-96	5.655	0.968	3.945	0.29	0.742
Jan-96	5.732	1.048	3.941	0.29	0.743
Feb-97	5.737	1.048	3.947	0.29	0.742
mar-97	5.771	1.088	3.945	0.289	0.738
Hurricane Danny					
Jul-97	5.712	1.013	3.963	0.286	0.736
Sep-97	5.635	0.94	3.961	0.287	0.734
Jun-98	5.8	1.058	4.011	0.282	0.731
Tropical Depression Georges					
Oct-98	5.633	0.861	4.09	0.279	0.682
Jan-99	5.618	0.831	4.095	0.28	0.692
Mar-99	5.624	0.837	4.086	0.288	0.701
Jul-99	5.722	0.953	4.083	0.287	0.686
Nov-99	5.605	0.846	4.084	0.285	0.675
Mar-00	5.614	0.829	4.105	0.283	0.68
Mar-01	5.64	0.796	4.185	0.276	0.659
Feb-02	5.853	0.962	4.149	0.267	0.742
Jul-02	5.996	1.115	4.163	0.271	0.718
Tropical Storm Isidore					
Oct-02	5.926	0.955	4.25	0.273	0.721
Hurricane Ivan					
Oct-04	5.94	0.916	3.611	0.349	1.413
May-05	5.811	0.864	3.665	0.318	1.282
Tropical Storm Arlene					
Jul-05	5.79	0.711	3.756	0.329	1.323
Hurricane Dennis					
Aug-05	5.804	0.706	3.711	0.344	1.387

island to form a series of overwash terraces. This resulted in a considerable reduction in the volume of sediments in the gulf beach environment. This downward trend in gulf beach volume was reversed after May 2001, six years after landfall of Hurricane Opal. However, Tropical Storm Isidore (September 2002) again reversed that trend

and subsequently, the gulf beach has been undergoing a sustained erosional phase which was exacerbated by the land fall of Hurricane Ivan (2004), Tropical Storm Arlene (2005) and Hurricane Dennis (2005). As per our latest survey in August 2005, the sediment volume along the gulf beach was at its lowest level during the entire span of the study period.

The overwash platform, however, has been following a different trend over this decade of monitoring. Beginning May, 1997, two years after landfall of Opal, the overwash platform had been showing a steady increase in volume, mainly at the expense of episodic migration of sediments from the nearshore and beach, driven by sustained southerly waves and storm surge associated with the occasional hurricanes and tropical storms. However, a conspicuous downturn in volume occurred with the landfall of Hurricane Ivan in September 2004. For the track and other meteorological details of the Hurricane Ivan, see Stone et al., (2005). Persistent southerly waves and storm surge associated with landfall of Hurricane Ivan, a category 3 hurricane, resulted in substantial transport of sediment from the dune and overwash platform to the bay beach/nearshore. In addition, the island breached across the study area at a few locations and channels occurred in the backshore area. However, contrary to the gulf side environment, the overwash platform had been gradually gaining in sediment volume since Fall 2004 and underwent erosion during Hurricane Dennis (July 2005).

As discussed in Stone et al., (2004), the bay beach is susceptible to frequent cold front generated winter storms and the morphodynamics of this environment are variable. During our survey period, the bay beach sediment volume increased since 2002. Apparent increases in the volume of sediment were observed immediately after landfall of Hurricane Ivan. Sediments reworked from the gulf shore and overwash platforms were redistributed and deposited on the bay beach and the adjacent platform during this event. However, these sediment deposits were reworked by the northerly waves associated with winter cold fronts and a net reduction in volume was observed until the land fall of Tropical Storm Arlene (2005). The trend had been reversed and the net sediment volume in this environment was increasing until our last survey.

DISCUSSION

Influence of Storms on Morphodynamics

Data indicate the importance of overwash events in supplying sediments to the bayside beaches along Santa Rosa Island, and the importance of cold fronts in rapidly eroding the overwash deposits and causing a significant amount of deflation on the subaerial portion of the barrier. These data have added significantly to our

understanding of the longer-term morphological maintenance of barrier islands in the Gulf and the importance of extratropical and winter storms (see Figure 5). Few studies have been conducted on the post-storm adjustment phase of barrier islands. Moreover, those that have been conducted (cf. Sexton and Hayes, 1991; Dingler and Reiss, 1995) are limited to annual topographic surveys, which significantly reduce the resolution of morphological recovery of the barrier system. Profiles are typically conducted during the same month in successive post-storm years, restricting conclusions to the net amount of sediment deposited on the barrier during the post-storm phase (Dingler and Reiss, 1995).

Given that >90% of sand comprising largely the subaerial barrier mass at the Florida study site could be accounted for after two severe hurricanes, the implications are highly significant for (a) the source of material during post-storm recovery, and (b) the prevailing concepts that sediment eroded from, in particular, the upper shoreface during storms, is transported offshore to the continental shelf and lost from the barrier system. These issues have not been adequately addressed in the barrier island literature. In addition, these preliminary data have potentially significant bearing on the application of existing models to the upper shoreface-foreshore (see Swift 1976; Swift et al., 1985).

Barrier islands along the northern Gulf of Mexico are oriented generally east-west from southern Louisiana to the Florida panhandle (Fig. 1). North-facing beaches on the bay side of these barrier islands are particularly susceptible to wave attack during northerly winds, which generally accompany the passage of cold fronts. Significant erosion has been observed in areas where the adjacent fetch in the sound or bay is relatively long (Stone and Morgan, 1993; Chaney and Stone, 1996; Armbruster et al., 1995; Armbruster, 1997).

During winter seasons, three distinct end-member type cold fronts impact the northern Gulf of Mexico (Lewis and Hsu, 1992; Pepper, 2000; Pepper and Stone, 2004): 1) the mid-latitude cyclone; 2) the Arctic surge; and 3) the Gulf cyclone. The extratropical weather systems produce local variations in wind direction, intensity, and duration, and thereby significantly affect wave and sediment transport processes along the back-barrier beach. Fronts cross the northern Gulf approximately 30 times each year and with the exception of tropical storms and hurricanes, are the only known natural mechanism to generate relatively high waves in these bay/sound environments. A common regional weather phenomenon accompanying the passage of cold fronts is the strong post-frontal northerly wind. Due to the sheltering effect of the island, southerly winds are not capable of generating high waves along the back-barrier beach. Influences of the Gulf swell are minimal except in the vicinity of the

tips of the islands and inlets. Strong northerly winds, therefore, constitute the primary driving force for modifying the bayside barrier beach system.

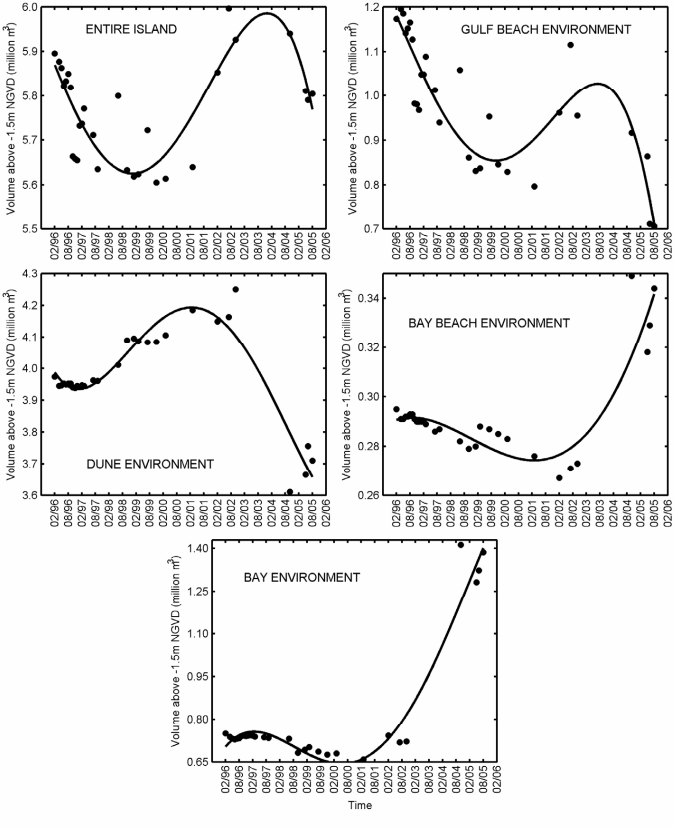

Fig. 5. Time series of volumetric change along the northern Gulf for 3 sub-environments and the entire barrier system 1996-2006 with an applied fourth order polynomial curve to identify apparent trends.

The general morphological characteristics of these back-barrier beaches are fundamentally different from the features developed by storm overwash processes (Schwartz, 1981; Otvos, 1982), which are critical to the origin and supply of sediment to these systems (Stone, 1998). These differences indicate the existence of

a general mechanism/s governing the dynamics and morphological maintenance of the back-barrier beach.

Post-Frontal Forcing

It is reasonable to assume that due to the sheltering effect of barrier islands along the northern Gulf (Stone and McBride, 1998), nearshore sediment transport along the back barrier beach is not significant during southerly winds. Where the northerly wind has a long fetch and is capable of generating relatively high waves, water-level setup occurs. Our work to date indicates that the strong northerly wind is the primary energy supply to the back-barrier beach in terms of significant sediment transport and morphological change. We acknowledge the longer-term role of relative sea level rise in these areas but take the position that the critical forcing mechanism/s for mobilizing and transporting sediment are a primary function of wave-current and wind forcing. The area is microtidal and thus, tidal currents play a lesser role in sediment resuspension in shallow water.

The frontal event has distinct meteorological and sea state signatures associated with its pre- and post-frontal phases. In Figure 6 we present a time series of wind speed (A), wind direction (B) and significant wave height (C) for a frontal passage in December 2002. The data were obtained from a WAVCIS (www.wavcis.lsu.edu) metocean station located at the 6 m isobath in Mississippi Sound, north of West Ship Island. Winds blow from the south prior to arrival of the front at the site and reach a maximum speed of approximately 7 m/s. Southerly wind speeds decrease as wind direction veers clockwise to the north over a matter of a few hours (B). Wind speeds rapidly increase across the Sound and peak at approximately 13.5 m/s. During the pre-frontal phase, wave heights are low in the Sound, <0.2 m (C), due to the sheltering effect of West Ship Island. Wave response to wind forcing is rapid and heights of 0.6 m are attained. Spectral evolution of the wave field is presented in Figure 7 and illustrates that energy is concentrated in the higher frequency bands due to wind veering to the north. Northerly winds persist for several days and maintain high wave energy levels along the north-facing beach resulting in erosion. As wind speed decreases wave energy levels show a concomitant decrease and winds veer clockwise to the east during this phase, resulting in extremely low wave energy conditions in the Sound. These data support the contention that winter cold fronts play the key role in north-facing beach erosion over short-term time scales. The prevalence of fronts over the northern Gulf explains the continued loss of sediment from the bay beach as presented earlier. What is less clear, however, is the actual pathway of sand transport during these events. Our data indicate that sediment is being removed from the foreshore during post-frontal events. The transport and ultimate fate of the material eroded is not yet understood. Our preliminary data indicate a sequence of events during the post-frontal northerly winds. The existence

of the commonly observed erosional scarp extending along the high water mark, and the flat extensive platform indicates to us, a significant contribution of sediment transported from the upper shoreface, offshore. The mechanisms driving this apparent offshore sediment transport are poorly understood.

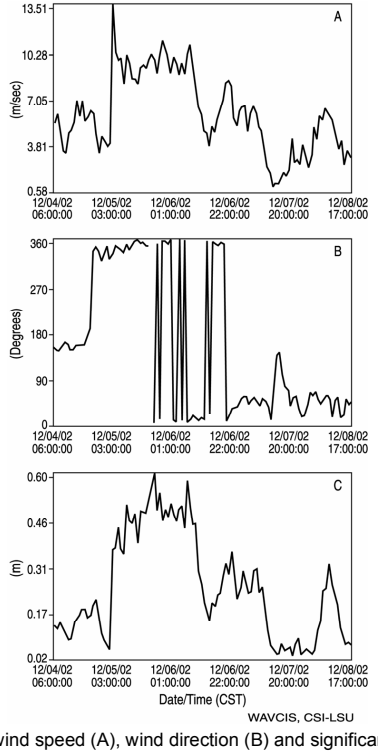

Fig. 6. Time series of wind speed (A), wind direction (B) and significant wave height (C) during a frontal event obtained from a WAVCIS metocean array in Mississippi Sound. (Modified from Stone et al., 2004).

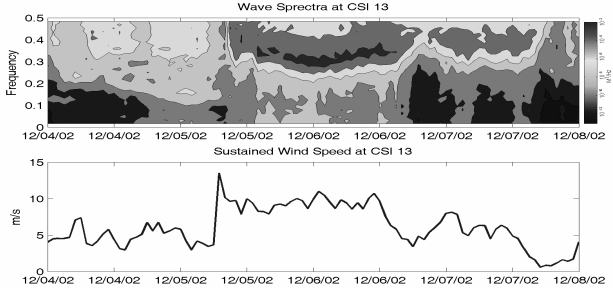

Fig. 7. Spectral evolution of waves from WAVCIS in Mississippi Sound (Modified from Stone et al., 2004).

Implications for Short-term Barrier Evolution

The data presented suggest that weaker hurricanes, such as Danny and Georges, can rework considerable amounts of sediment to the berm and relict overwash terrace. Bay beach accretion through overwash or aeolian deposition is short lived however, and frontal passage during the ensuing winter typically results in net loss to the system. This sequence of events implies that the barrier crosses a threshold initiated by a catastrophic storm, e.g. Ivan, and over the shorter-term, barrier degradation results due to net sediment loss from the system in its entirety. Storms such as Lili and Rita resulted in little beach erosion due to wave attenuation across the muddy inner shelf along western Louisiana.

CONCLUSIONS

Several important conclusions have been reached based on the data presented here: (1) where the inner shelf is comprised of cohesive sediments (fine silts and clays), typical of western Louisiana, pronounced wave damping and attenuation results in minor beach erosion. A clearly defined erosional-depositional couplet is a typical response during storms where fine sand eroded from the beach is overwashed across the interior marsh and an eroded marsh surface is exposed in the foreshore. What is not known, however, is the role of these cohesive sediments in surge attenuation. This is an important question that should be addressed by numerical modelers using data from carefully designed experiments involving in situ observations; (2) low-lying barrier islands, vulnerable to overwash, can conserve mass during catastrophic hurricanes (e.g., Hurricanes Opal and Ivan); (3) less severe hurricanes can promote rapid dune/berm aggradation and contribute sediment to the entire barrier system; (4) cold fronts play a critical role in the post-storm adjustment of the barriers by deflating the subaerial portion of the overwash terrace and eroding its marginal lobe

along the bayside beach; (5) considering seasonal time scales, post-storm recovery along the Gulf-facing beach/nearshore is not immediate and did not occur at some of the study sites until approximately 6 years after several events; and (6) bay facing beaches showed a continued decline in volume throughout the entire study period, a phenomenon we attribute to locally generated high frequency waves due to the passage of cold fronts along the northern Gulf of Mexico. There remains a need for field experiments to determine the source(s) and mechanisms responsible for sedimentation in these environments over various time and spatial scales and the development of models that elucidate the morphosedimentary dynamics of other mid-latitude, micro tidal barriers.

ACKNOWLEDGEMENTS

This work was funded by the National Science Foundation under awards AGS 9625709 and EAR9903984.

REFERENCES

Allison, M.A., Sheremet, A., Goni, M.A., Stone, G.W., 2005. Storm layer deposition on the Mississippi-Atchafalaya subaqueous delta generated by Hurricane Lili in 2002. *Continental Shelf Research* 25, 2213–2232.

Armbruster, C.K., Stone, G.W. and Xu, J.P., 1995. Episodic atmospheric forcing and bayside foreshore erosion: Santa Rosa Island, Florida. *Trans. Gulf Coast Assoc. Geol. Soc.*, v. XLV, 31-37.

Armbruster, C.K., 1997. Morphologic responses of a low-energy, micro-tidal beach to winter cold front passages: North shore Santa Rosa Island, Florida. *MS thesis*, Department of Geography and Anthropology, Louisiana State University, Baton Rouge, 166 pp.

Chaney, P.L. and Stone, G.W., 1996. Sound side shoreline erosion and implications for winter cold front forcing: West Ship Island, Mississippi, *Shore and Beach*, 64, 27-33.

Dingler, J.R. and Reiss, T.E., 1995. Beach erosion on Trinity Island, Louisiana caused by Hurricane Andrew. *In,* Stone, G.W. and Finkl, C.W. (eds.), 1995. Impacts of Hurricane Andrew on the coastal zones of Florida and Louisiana; August 22-26, 1992. *Journal Coastal Research* SI 21, 254-264.

Guidroz, W.S., Stone, G.W. and Dartez, D., 2006. Hurricane Rita, 2006: Assessment of a storm-induced geological event along the southwestern Louisiana coast and adjacent interior marsh. *Transactions, Gulf Coast Association of Geological Societies*, v.56, 229-239.

Guidroz, W.S., Poole, K.R., Stone, G.W., Dartez, D. and Pond, L.G., 2007. Contrasting sediment transport along the southwestern Louisiana and upper

Texas shorelines: Impacts from Hurricane Rita, 2005. *Shore & Beach*, in press.

Lewis, J.K. and Hsu, S.A., 1992. Mesoscale air-sea interactions related to tropical and extratropical storms in the Gulf of Mexico, *Journal of Geophysical Research*, 97, 2215-2228.

Otvos, E., 1982. Santa Rosa Island, Florida Panhandle, Origins of a Composite Barrier Island. *Southeastern Geology*, 23(1), 15-23.

Pepper, D.A., 2000. Hydrodynamic, bottom boundary layer processes and sediment transport on the south-central Louisiana inner shelf: the influence of extratropical storms and bathymetric modification. *Ph.D. dissertation*, Coastal Studies Institute and Department of Oceanography and Coastal Sciences, Louisiana State University, Baton Rouge, 159 p.

Pepper, D.A. and Stone, G.W., 2004. Hydrodynamics and sedimentary responses to two contrasting winter storms on the low-energy inner shelf of the Northern Gulf of Mexico, USA. *Marine Geology,* 210, 43-62.

Schwartz, R.K., 1981. Nature and genesis of some storm washover deposits. In S.P. Leatherman, (ed)., Overwash Processes, Hutchinson Ross Publishing Company, Stroudsburg, Pennsylvania, 229-260.

Sexton, W.J. and Hayes, M.O., 1991. The geologic impact of Hurricane Hugo and post-storm shoreline recovery along the undeveloped beaches of South Carolina, Dewees Island to the Sanatee Delta. *Journal of Coastal Research*, Special SI 8, 275-290.

Stone, G. W. and Morgan, J. P., 1993. Implications for a constant rate of relative sea-level rise during the last millennium along the Northern Gulf of Mexico: Santa Rosa Island, Florida. *Shore and Beach,* 61(4), 24-28.

Stone, G.W. and Finkl, C.W. (eds), 1995. Impacts of Hurricane Andrew on the Coastal Zones of Florida and Louisiana: 22-26 August, 1992. Journal of Coastal Research, SI 21, 364 pp

Stone, G.W., 1998. Hurricane impact and recovery on coastal island geomorphology: Hurricane Opal, October 1995, *NSF Report*, 9625709, 68 p.

Stone, G.W. and McBride, R.A., 1998. Louisiana barrier islands and their importance in wetland protection: Forecasting shoreline change and subsequent response of wave climate. *Journal of Coastal Research,* 14(3), 900-915.

Stone, G.W., Wang, P., Pepper, D.A., Grymes, J.M., Roberts, H.H., Zhang, X.P., Hsu, S.A. and Huh, O.K., 1999. Researchers Begin to Unravel the Significance of Hurricanes on the Northern Gulf of Mexico Coast. *EOS, Transactions of the American Geophysical Union,* 80(27), 301-305.

Stone, G.W., Sheremet, A., Zhang, X., He, Q., Liu, B. and Strong, B., 2003. Landfall of two tropical systems seven days apart along south-central Louisiana, USA. *Proceeding* , Coastal Sediments '03, 333-347

Stone, G.W., Liu, B., Pepper, D and Wang, P., 2004. The importance of extratropical and tropical cyclones on the short-term evolution of barrier islands along the northern Gulf of Mexico. *Marine Geology*, (210), 63-78.

Stone, G.W., Walker, N.D., Hsu, S.A., Babin, A., Liu, B., Keim, B.D., Teague, W., Mitchell, D. and Leben, R. 2005. Hurricane Ivan's Impact along the northern Gulf of Mexico. EOS, *Transactions of American geophysical Union*, 86(48), 497-508.

Swift, D.J.P., 1976. Coastal Sedimentation. *In*: Stanley, D.J. and Swift, D.J.P. (eds.) Marine Sediment Transport and Environmental Management. John Wiley and Son Inc., New York, 602 pp.

Swift, D.J.P., Niedoroda, A.W., Vincent, C.W. and Hopkins, T.S., 1985. Barrier island evolution, Middle Atlantic Shelf, U.S.A., Part I: Shoreface Dynamics. *Marine Geology,* 23, 69-85.

IMPACT OF A MAJOR STORM ON SEDIMENT EXCHANGES BETWEEN THE DUNES, BEACH AND NEARSHORE

Aart Kroon[1], Susanne Quartel[2] and Troels Aagaard[3]

1. Department of Geography, University of Copenhagen, Oster Voldgade 10, DK-1350 Copenhagen K., Denmark. ak@geogr.ku.dk
2. IMAU, Department of Physical Geography, Utrecht University, Heidelberglaan 2, 3584 CS Utrecht, Netherlands. s.quartel@geo.uu.nl
3. Department of Geography, University of Copenhagen, Oster Voldgade 10, DK-1350 Copenhagen K., Denmark. taa@geogr.ku.dk

Abstract: The morphologic and volumetric changes of the dune foot, beach and inner nearshore zone over a major storm are studied on Egmond beach. The shoreline configuration of this beach showed an alongshore variation of embayments and horns, with an alongshore spacing between 400 and 700 m and a cross-shore amplitude of about 25 m. The response of the dune foot and intertidal beach was closely coupled to this alongshore variation, with major changes in the embayments (more reflective conditions) and small changes at the horns (more dissipative conditions). Overall, the upper beach and dune foot were eroding and flattened and the lower intertidal beach was accreting. The inner nearshore slope showed a steepening and a landward movement of e.g., the -3 m depth contour. The mechanisms that caused the changes are discussed and coupled to observed water levels in the nearshore. These water levels altered and shifted the location of the transformed waves (asymmetric waves, breaking waves, bores and swash) in a cross-shore direction over the profiles

INTRODUCTION

The beach is the transition zone for sediment exchange between the dunes and the nearshore. Under accretive conditions with low- to moderate wave energy conditions in the nearshore, these beaches tend to grow in height and width due to successive onshore migration of intertidal bars, which may merge to the upper beach (see for a recent overview Masselink et al., 2006). During onshore winds, part of this accumulated

sediment will be further transported to the dunes by wind. However, under erosive conditions with a high influx of wave energy and a dissipative nearshore, the dunes often erode by incoming waves and much of the sediment on the upper and intertidal beach is transported to the inner nearshore zone. This intense wave action near the dune foot is caused by an increase of the mean water levels over the beach due to extra surge levels by the passage of a depression track (area of low air pressure), wave set-up and wave run-up. The offshore sediment transport of beach sediments is enhanced by undertow (bed return flows).

We studied the impact of an extreme storm on a sandy beach located at Egmond, the Netherlands. The paper will show results of the morphologic and volumetric changes of the beach and nearshore during an extreme storm event. The analysis is based on daily bathymetric surveys of the beach (DGPS) and 2 bathymetric surveys of the nearshore (WESP) over a 16 days period. Special emphasis is paid to the alongshore variations that might be caused by the variations in the initial observed alongshore morphology with alternation of beach horns and embayments. The alternations had a length scale between 400 and 700m. The mechanisms that caused the changes are discussed and coupled to observed water levels in the nearshore. These water levels altered and shifted the location of the transformed waves (asymmetric waves, breaking waves, bores and swash) in a cross-shore direction over the profiles, and might be responsible for the observed patterns.

FIELD SITE: EGMOND, THE NETHERLANDS

The field site at Egmond, the Netherlands is located at the central part of the Dutch coast (Figure 1). This is a mixed energy coast, influenced by waves and tides. The coastline is exposed to waves coming from S-SW to N directions. The mean annual offshore wave height is 1.3 m with wave periods of about 5 s. The mean semi-diurnal tidal range is 1.65 m and increases towards 2.1 m during spring tides. The tidal curve is asymmetric with a 4-h flood period and an 8-h ebb period. The tidal current direction is towards the N during flood and towards the S during ebb.

The area has two nearshore bars and an intertidal bar on the beach. These nearshore bars have their crest typically around -3 m (outer) and -2 to -2.5 m (inner) below mean sea level. The bar crests experience a net offshore migration, with generation in the inner nearshore and decay in the outer nearshore (e.g., Ruessink and Kroon, 1994; Wijnberg and Terwindt, 1995). The slope between the -1 m and -8 m depth contours is between 1:35 and 1:60. The outer bar is slightly crescentic in alongshore direction to relatively straight. The inner bar crest has a crescentic shape during low- to moderate wave conditions and straightens during storms . Weak rip channels can develop in the inner sub-tidal bar with a variable alongshore spacing of 200 to 500 m. The intertidal beach is between 50 and 100 m wide and often shows cell topography with intertidal bars, feeder channels and drainage rips. The intertidal bar often shows a landward migration and is flattened during storms (e.g., Masselink et al., 2006). The slope of the intertidal beach varies between 1:10 and 1:50.

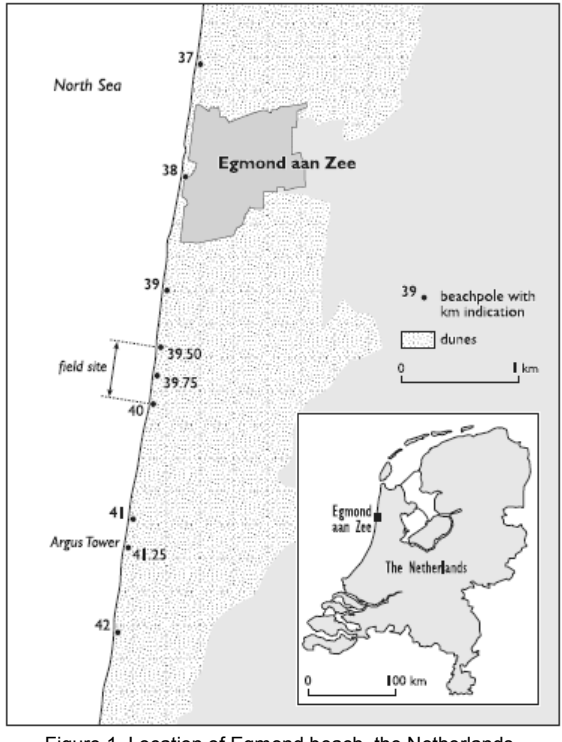

Figure 1. Location of Egmond beach, the Netherlands.

Figures 2 and 3 show the alongshore alternation of more dissipative bar horns (shoreline salients) and more reflective embayments. The typical alongshore length scale is about 400 to 700 m. The mean grain size of the intertidal beach sediments ranges between 250 and 300 μm and shows an offshore fining trend to 200 μm in the outer nearshore.



Figure 2. Argus video-image of Egmond beach with the alternation of horns and embayments on 21 October 2002 (Low-tide image with small waves breaking on the inner nearshore bar; Alongshore coordinate of camera position is 41.25 km; View to the N, decreasing alongshore coordinates)

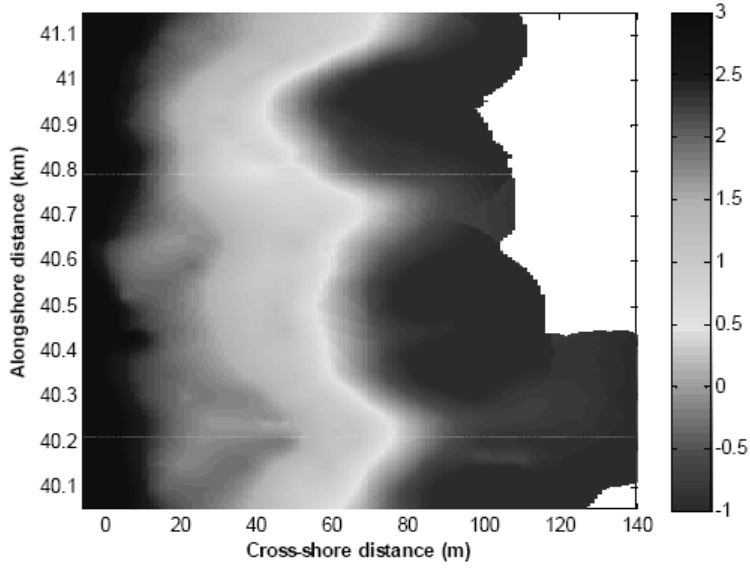

Figure 3. Beach survey with a DGPS of 21 October 2002 (see Figure 2)

CHARACTERISTICS OF THE MAJOR STORM EVENT

The studied storm event occurred on Sunday 27th of October 2002 (Figure 4). The event was registered as the fourth storm of the last 100 years along the Dutch coast (communication Royal Netherlands Meteorological Institute, KNMI). The maximum wind speed at the coastal station of IJmuiden, some 15 km S of Egmond beach, showed mean velocities over 25 m.s^{-1} and came in from the SW to W directions during the peak (270 degrees; shore normal). The wave height (*Hm0*) at about 8 km offshore reached maximum values over 6 m. The peak of the storm coincides with low-tide in the afternoon. The maximum surge level in the outer nearshore zone, computed as the difference between the measured water level and the predicted tidal level, was almost 2 m. The combination of SW to W wind and wave directions (relatively small fetch over the North Sea), and the peak at low tide caused relatively low values of the measured water levels above mean sea level. The duration of measured and predicted water levels over the storm event and over the period between two nearshore bathymetric surveys are presented in Figure 5 (left and right panel, respectively). Maximum water levels during the storm were about 2.3 m above mean sea level (≈ 0 m Dutch Ordnance Level).

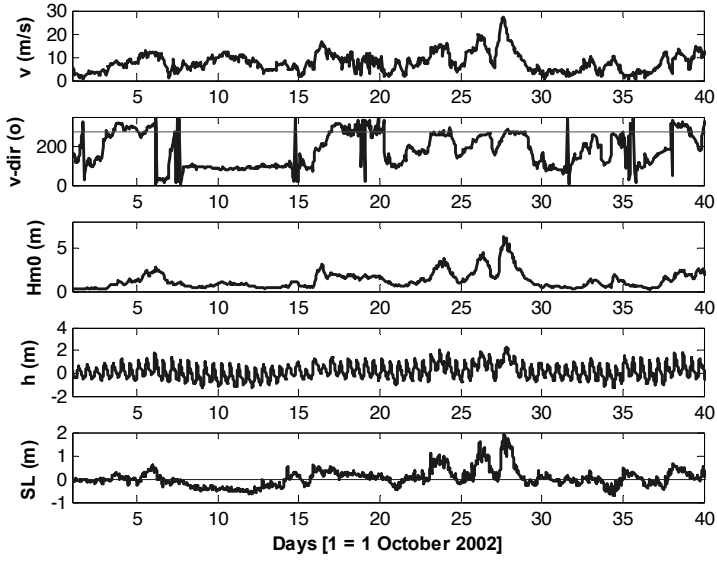

Figure 4. Wind velocity, wind direction, offshore wave heights, measured nearshore water levels, and observed surge levels (from top to bottom panel) in front of Egmond beach.

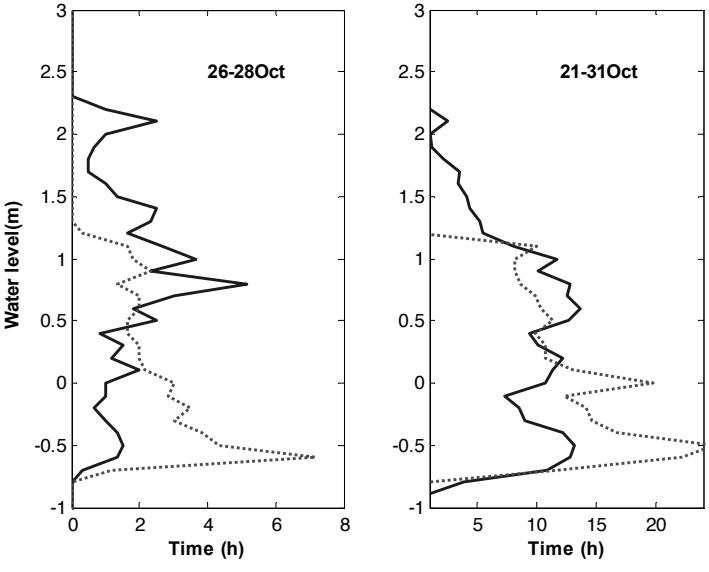

Figure 5. Water levels on the beach during the storm period (left panel) and the period between two WESP measurements (right panel). Solid line is measured water level in the nearshore; dotted line is predicted tidal water level.

MORPHOLOGIC RESPONSE OF THE BEACH AND NEARSHORE

Two bathymetric surveys of the dune, beach and nearshore area were used to describe the morphologic response of the storm event. These surveys were made on October 21st and 31st 2002 with the WESP, an amphibious vehicle with a height of 11 m. Most cross-shore profiles were measured from +3 m MSL, just above the dune foot, towards the -5m depth contour during the first survey and the -3 m depth contour at about 230 m from the dune foot during the last survey. The latter survey could not be extended further offshore, due to loose sediments in the trough landward of the outer nearshore bar. The alongshore spacing of the cross-shore profiles was about 50 m. and the total alongshore coastal stretch was 3.5 km from beach pole 39.00 km in the N towards beach pole 42.50 in the S. All profiles were made equidistant (cross-shore spacing of 0.1 m) and smoothed with a moving average method (window size of 10, which means 1 m average) in order to remove measurement spikes and small scale bed forms. The results are focused on the stretch between 39.10 km and 40.75 km where alongshore embayments and horns were observed (see Figures 2 & 3 and Aagaard et al., 2005).

The changes of the contour lines at the dune foot (+2.5 m), near the high water mark (+1.0 m) and halfway the intertidal beach at mean sea level (+0 m) are presented in Figure 6 (left panel). The dune foot showed an alternation of seaward and landward changes with a weak rhythmic pattern along the shore. The upper beach near the high

tide mark also showed an alongshore alternation, but the overall pattern was landward migration. However, the +0 m contour line showed an opposed trend with a majority of changes pointing in a seaward direction. This meant that there was an overall flattening of the upper beach that induced deposition halfway the intertidal beach. The changes of the contour lines in the inner nearshore (-2.0 m and -3.0 m) are presented in Figure 6 (right panel). Despite the large variation in the alongshore direction, the overall pattern was a slight seaward movement of the -2 m contour line and a landward movement of the -3 m contour line. This caused a steeper slope of this area during the storm.

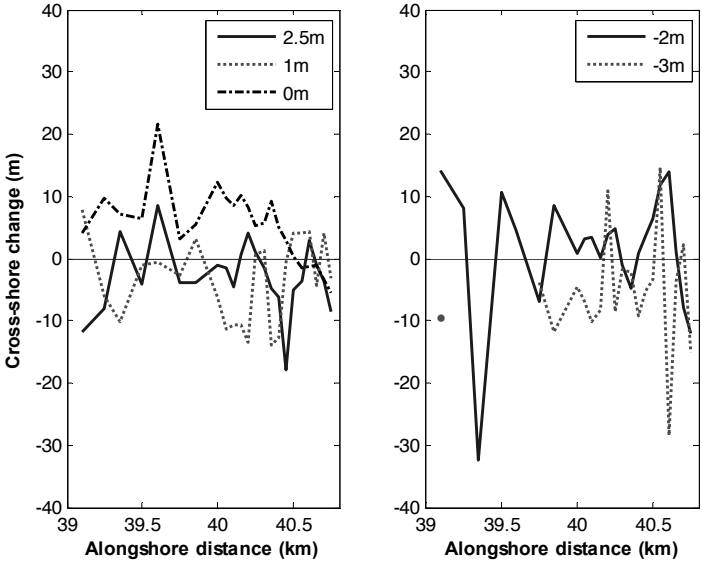

Figure 6. Alongshore variation of changes in contour lines between 21 and 31 October 2002. Left panel shows dune foot and intertidal beach contours, right panel shows inner nearshore contours.

The slopes of the upper part of the cross-shore profiles, between the dune foot (+2.5 m) and halfway the intertidal beach (+0 m), and of the lower part between +0 m and the -2 m depth contour in the inner nearshore is presented in Figure 7 (left panel). The slopes of the upper part were much steeper and showed a large alongshore variation with 2 flatter areas at 39.35 km and 40.25 km at the position of horns. Most of these slopes decreased over the storm event and the upper part of the cross-shore profile thus flattened. The slopes of the lower part were smaller, hardly showed any alongshore variation and steepened in most cases. The alongshore variation of the slopes for both the upper beach and lower beach and nearshore decreased during the storm event. However, alongshore variation in slopes of the upper beach was still significant.

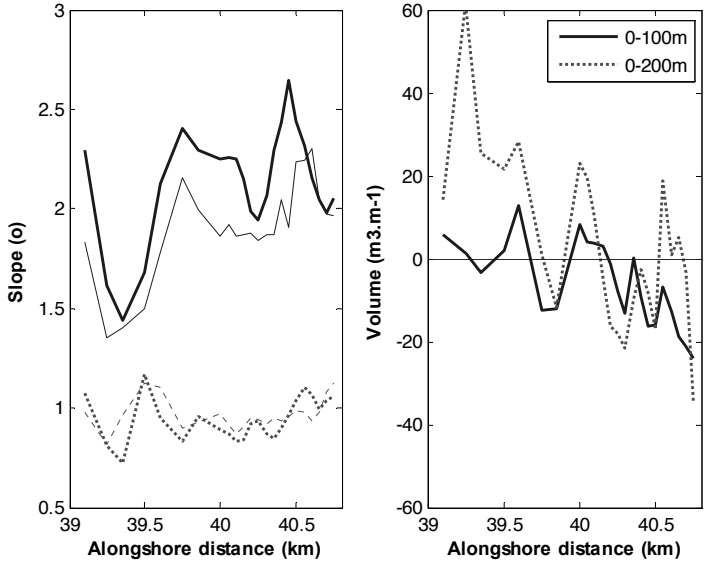

Figure 7. Alongshore variation of the slopes (left panel; thick line is 21 Oct, thin line is 31 Oct; solid line is between 2.5 and 0m contour lines, dotted line is between 0 and -2m contour lines) and volumetric changes (right panel; solid line is beach and dotted line is beach and nearshore) between 21 and 31 October 2002.

The volumetric changes on the upper beach were computed between the cross-shore position at x = 0 m (initial dune foot at +2.5 m) and the cross-shore position at x=100 m. The total changes in this cross-shore area are presented in Figure 7 (right panel). The volumetric changes showed a clear alongshore variation with a rhythmic pattern between accretion and erosion. Besides, the northern part (lower numbers of the alongshore distance) was more accretive than the southern part. The volumetric changes between x = 0 m (initial dune foot at +2.5 m) and the cross-shore position at x=200 m (inner nearshore) is also presented in Figure 7 (right panel). The alongshore variation of an alternation between erosive and accretive profiles was similar and in the order of 400 to 600 m. However, the absolute values of these volumetric changes were larger.

Daily bathymetric surveys of the dune foot, and the upper- and intertidal beach were measured with a DGPS system. The cross-shore profiles were about 100 to 150 m long and the alongshore spacing was 50 m. The alongshore coastal stretch measured 1100m, between alongshore beach positions 40.05 km and 41.15 km. The measured data were interpolated and computed to a regular grid with a spacing of 1 m. An example of intertidal beach bathymetry is presented in Figure 3. The alongshore alternation of steeper embayments and flatter horns was clearly visible. This pattern remained very prominent until the beginning of the storm. Bed level changes of the detailed surveys

around the storm, between 28th and 25th October 2002, are presented in Figure 8. The patterns were similar to those observed in WESP surveys over the 10 days period. The dune foot was heavily eroded and showed an alongshore variation that corresponded with the location of the horn-embayment structure (see Figure 3). The highest dune foot erosion rates were observed at the location of the embayments. Most of these eroded sediments and those of the upper beach were deposited on the lower intertidal beach. This induced an overall flattening of the whole area and a destruction of the intertidal barred features. However, visual observations of aeolian sediment transport during the peak of the storm from the upper beach and dune foot into the dune area were made, pointing at an extra loss of sediment over the landward boundary of the cross-shore profiles. Bed level changes of the detailed surveys after the storm, between 31st and 28th October 2002, are presented in Figure 9. Immediately after the storm, the intertidal morphology changed again towards a barred situation. This is also presented in the cross-shore profile evolution in Figure 10. The upper part of the beach and the dune foot were now landward located of the active profile, due to the reduced wave energy and surges levels (see Figure 4). The intertidal bar was generated in the upper intertidal area, between +0.5 and +1 m, and the seaward flank of this bar steepened. The profile adjustments of the storm were largest in the embayments. The initial profile here was steeper, while the initial profile of the horn profiles were already very flat and dissipative.

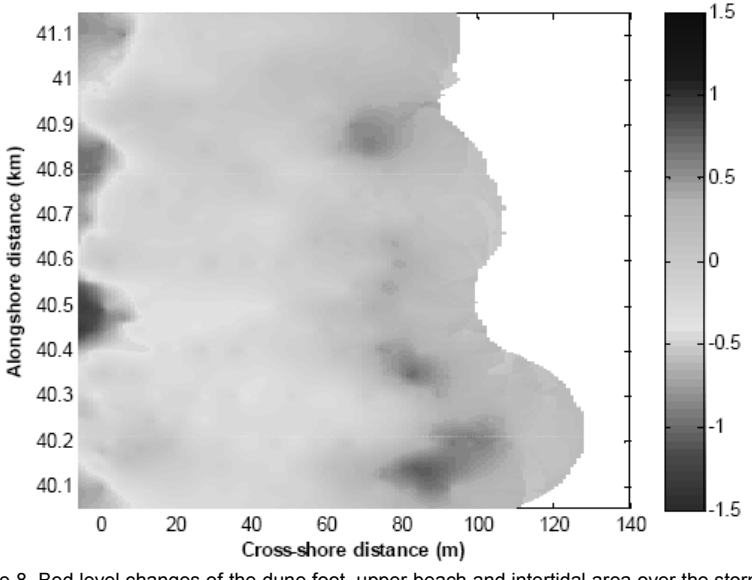

Figure 8. Bed level changes of the dune foot, upper beach and intertidal area over the storm. Changes are in m between 25th and 28th October 2002, positive values = accretion.

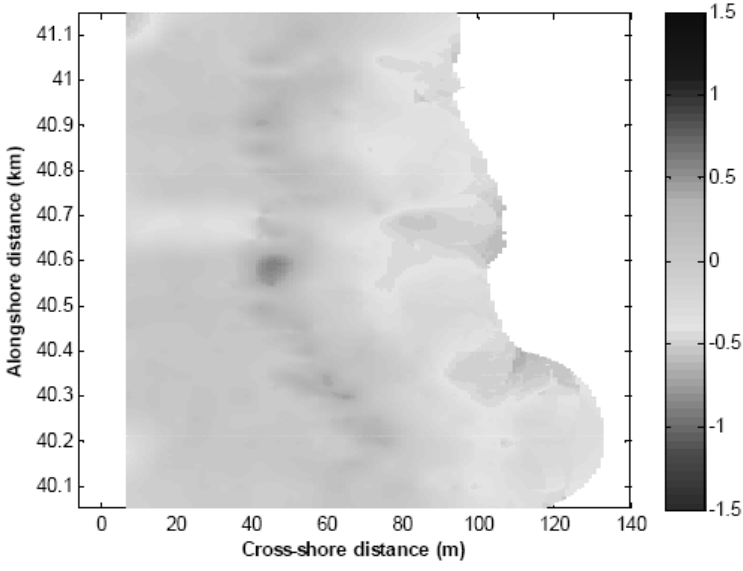

Figure 9. Bed level changes of the dune foot, upper beach and intertidal area after the storm. Changes in m are between 28th and 31st October 2002, positive values = accretion.

DISCUSSION AND CONCLUSIONS

The cross-shore response of the dune, beach and nearshore morphology along an embayment and horn differed. Quite often, the beaches on the horns were less steep (more dissipative) and showed hardly any morphologic changes during storms (Figure 10), where the beaches along the embayment showed erosion of the upper part and accretion on the lower intertidal beach and in the inner nearshore trough (see also Aagaard et al, 2005).

The causes of the different profile response were probably due to these initial cross-shore profile configurations. The wave transformation over the flat sloping beach at the horn was more dissipative. The water levels on the upper and intertidal beach were not extreme and the dune foot was especially eroded behind the embayments (Figure 8). The slope of the upper and intertidal beach hardly adjusted at the horn location and the overall lowering was probably caused by a slightly larger component of the undertow driven offshore mean sediment flux during high tide over the onshore directed sediment flux due to propagating bores and swash over very shallow water (with relative wave heights in the order of 1, see Masselink et al., 2006; Aagaard et al., 2005).

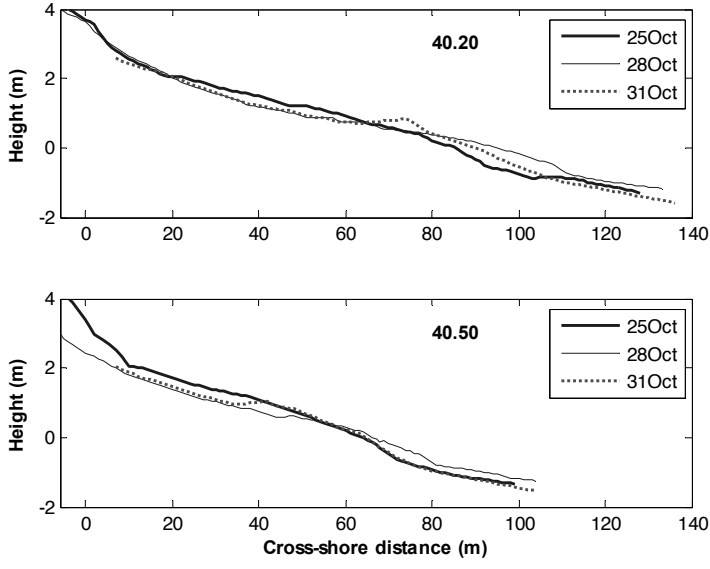

Figure 10. Profile adjustments at the location of a horn (upper panel; alongshore location 40.20km, see Figure 3) and at the location of an embayment (lower panel; alongshore location 40.50km).

The pattern of upper beach erosion and lower intertidal beach accretion during the storm (Figure 8) and generation of an intertidal bar at the upper intertidal beach after the storm (Figure 9) showed that a lot of the eroded sand stayed in the area (see also Figure 6 left panel) and was transported onshore after the storm. The mechanism responsible for this intertidal bar generation at the upper intertidal beach were initiated by the dissipation of incident wave energy over shallow water with a major role for surf zone bores. The tidal water levels altered and shifted the location of the transformed waves (from deep to shallow: asymmetric waves, breaking waves, bores and swash) in a cross-shore direction over the profiles. The actual location of this intertidal bar was probably determined by the duration of the swash and surf zone bore processes at the distinct position of the cross-shore profile (Masselink et al., 2006).

The alongshore variability of horns and embayments survived the storm event, despite the different morphologic and volumetric behavior at its units. The horns stayed almost at the same positions. However, the whole pattern was less pronounced in a cross-shore direction. The coupling between the alongshore variations with a length scale of 400 to 700 m in these crescentic patterns of the shoreline configuration to the alongshore configuration of the crescentic nearshore bar at about 400 m offshore could only be made for a restrictive area S of the Argus tower (see Figure 1; no data presented). The

bar was alongshore straightened during the storm, as generally described in Van Enckevort and Ruessink (2003), but the alignment still remained crescentic. The data set was unfortunately too small to correlate the alongshore alignments of the outer nearshore bar with the shoreline configuration.

ACKNOWLEDGEMENTS

This research was funded by the European Union through the CoastView-project (contract number EVK3-CT-2001-0054). We gratefully acknowledge the help with the bathymetric surveys by Rijkswaterstaat, directorate North-Holland and the help with the ARGUS video system by Rob Holman and his Coastal Imaging Laboratory at Oregon State University.

REFERENCES

Aagaard, T., Kroon, A., Andersen, S., Møller Sørensen, R., Quartel, S. and Vinther, N., 2005. Intertidal beach change during storm conditions; Egmond, The Netherlands. *Marine Geology* 218, 65-80.

Masselink, G., Kroon, A. and Davidson-Arnott, R.G.D., 2006. Morphodynamics of intertidal bars in wave-dominated coastal settings – A review. *Geomorphology* 73, 33-49.

Ruessink, G. and Kroon, A., 1994. The behaviour of a multiple bar system in the nearshore zone of Terschelling, the Netherlands: 1965-1993. *Marine Geology* 121, 187-197.

Van Enckevort, I.M.J. and Ruessink, B.G., 2003. Video observations of nearshore bar behaviour. Part 2: alongshore non-uniform variability. *Continental Shelf Research* 23, 513-532.

Wijnberg, K.M. and Terwindt, J.H.J., 1995. Extracting decadal morphological behaviour from high-resolution, long-term bathymetric surveys along the Holland coast using eigenfunction analysis. *Marine Geology* 126, 301-330.

STORM PATTERNS AND CLIMATIC TRENDS BASED ON WATER LEVEL FLUCTUATIONS: DUCK, NORTH CAROLINA, USA

Joan Pope[1]

1. U.S. Army Engineer Research and Development Center, Ft. Belvoir, Alexandria, VA, 22315, USA. Joan.Pope@hq02.usace.army.mil

Abstract: A twenty-year (1978-1998) record of open-coast atmospherically-induced water level fluctuations at the US Army Engineer Field Research Facility (FRF) at Duck, NC has been analyzed and correlated to the occurrence of both cyclonic and frontal storms. The time-series and statistical clustering of water level excursions from the predicted tide have been analyzed. The analytical technique and findings presented here reveal significant information on the characteristics of individual storm surge hydrographs and on both short and long-term climatic trends. A classification model for characterizing storm hydrographs is presented along with selected statistical summaries of water level and storm trends. The techniques presented here provide a simple method for assessing climatic variability and storm cycle trends using frequently available continuous tide records. A Storm Intensity Index parameter, bases solely on water level deviations is presented. This study suggests an approach to link shoreline evolution to metrological patterns.

INTRODUCTION

The U.S. Army Engineer Field Research Facility (FRF) at Duck, North Carolina has one of the most comprehensive, long-term process-response coastal data sets in the world (including local meteorology, water levels, waves, and beach profiles) (Savage and Birkemeier, 1987; Birkemeier, Savage, and Leffler, 1988). As such it offers the opportunity to consider decadal correlation patterns between water level events and beach evolution trends. It is also a site that is exposed to a variety of both tropical and extratropical storms. The classic concept of a storm surge is of a single well-defined peak rise in the water level (lasting several hours). However, an analysis of the

atmospherically-induced water level fluctuations in the FRF record reveal a variety of hydrographs including; sustained rise in the water surface lasting days to a week or more, periods of water depression (i.e., a "draw-down"), or vacillations in the surface demonstrating sequences of rises and draw-downs of the water surface in response to the shifting wind patterns of an extratropical storm and/or the passage of multiple lows.

The tide record from the FRF was used to extract atmospherically-induced deviations from the predicted tide (called "storm surge" throughout this paper). Selected events were compared to the regional meteorological record and correlated to either the occurrence of frontal passages, extratropical lows, or tropical storms; both near and far field. Time-series correlations between the FRF water level record and local weather conditions were used to understand local verses regional influences and the sensitivity of the event to wind directionality. Individual events were extracted from the record and parameterized. Each water level event has been characterized (duration, magnitude, range, etc) and classified. Through this process statistical summaries were developed that were used to identify climatologically-driven patterns of seasonal, annual, and decadal event clustering.

Coastal process analyses rarely consider the role of water level fluctuations as a suite of individual events or as cumulative trends in inducing cyclic geomorphic changes to the beach and nearshore. This work provides a foundation for linking annual and long-term meteorological trends to spatial and temporal patterns of water level fluctuations and the role of storm surges in promoting conditions of beach instability. Thus it is but one step in the process of assessing the cumulative effect of storm clustering in driving longer-period beach dynamics and coastal morphodynamic trends. It is further proposed that storm surge data, easily extracted from the tidal record, has value in assessing climate variability and trends. This analysis could assist coastal scientists in understanding the temporal influence of atmospherically-driven water levels in controlling beach evolution.

THEORY

Both tropical and mid-latitude cyclonic storms can affect the mid-Atlantic coast (Dolan and Davis, 1992; Davis, Dolan, and Demme, 1993). Tropical cyclones form between the equator and the Tropics of Cancer (Northern Hemisphere) and Capricorn (Southern Hemisphere) over warm ocean waters. The most intense tropical cyclones (wind speeds in excess of 120 km/hr) develop a distinctive 3-dimensional wind field and a central eye and are called either hurricanes in the Atlantic and eastern Pacific or typhoons in the western Pacific and Indian Ocean. Mid-latitude cyclones usually develop along the front of a high latitude (cold) air mass that is displaced into lower and warmer latitudes (specifically, between the polar circles and the tropics). Instability along the front associated with strong horizontal temperature gradients between the warm and cold air masses promotes the development of a perturbation, which becomes a wave, then a low pressure cell, and finally a fully developed cyclonic storm. Other commonly used names for mid-latitude storms are "non-tropical" or "extratropical" storms. Along the Atlantic seaboard of the United States they are commonly called "Nor-easters." These two major

populations of cyclones have different climatology, genesis, dynamics, structures and impacts to the coast (Perry and Walker, 1977; Bowden, 1983; Pugh, 1987).

The first distinction for the two classes of Earth's large-scale atmospheric cyclones; tropical and non-tropical, is the latitude of their genesis. In general, tropical cyclones originate in the tropics (between 23.5^0 N and S), while non-tropical, mid-latitude storms originate outside the tropics (between the 23.5 and 66.7^0 parallels). There are a number of other distinctive aspects between the two storm populations. Table 1 is a simplified summary that compares several major characteristics as well as the implications to the coast. Hurricanes are self-contained and self-maintaining cyclones that move (relatively) independent of synoptic scale air masses, while extratropical storms are usually generated and move along fronts between cold and warm air masses. The primary energy source for hurricanes is the latent heat released during the formation of heavy rains in convection cells, while the primary energy of extratropical storms is derived from the thermal contrast between two air masses. Hurricanes are well-organized storms with very steep pressure gradients and tight, circular isobars, near the eye.

Although, typically smaller then an extratropical storm, hurricanes are more intense (lower central pressures, steeper pressure gradients, and higher wind speeds). The typical hurricane has a diameter of about 650km, (less than half the size of a mid-latitude storm), will have maximum sustained surface winds in excess of 33 m/sec (74mph), and sea level central pressures of 950mb or less. Hurricanes are an intense warm-core low that occur during the warm summer and early fall. Extratropical storms have a cold core and, although they can occur year round, their frequency and intensity peaks during the winter and near-winter months (for the hemisphere of interest). Extratropical storms tend to move eastward within the mid-latitude westerlies. Hurricanes tend to move westward within the tropical trade-winds until they cross the 23rd parallel and into the mid-latitudes where zonal winds steer the hurricane toward the east. A typical hurricane season will spawn in the order of ten storms, while a hemispherical winter weather pattern may generate hundreds of extratropical lows. Thus, the typical extratropical cyclone is a less intense, longer lasting; but more frequent event that can affect a large area and redistribute a lot of sand along a beach.

Both tropical and extratropical storms can induce long wave fluctuations in the sea surface that impact the shore as a surge. These atmospherically-induced water level fluctuations extend the cross-shore impact zone of the wave field beyond that of the astronomical tide, causing instability (i.e., disequilibrium) to the beach profile. Most dramatic changes to the coast happen during storms in response to how the surge hydrograph distributes the wave field across the shore. The role of a single, major storm surge in causing large quantities of sand transport, coastal retreat, dune breaching, channel shoaling, and changes to the nearshore slope and profile are well established throughout the literature. However, extratropical storms generating lesser maximum surge events (particularly when of long duration or clustered) can accumulate a significant total quantity of elevated water levels and may have a greater affect on the beach profile.

Table 1. A Generalized Comparison of Tropical vs. Extratropical Storms

CHARACTERISTICS	TROPICAL	EXTRATROPICAL
Location of Cyclogenesis	Tropics, over Warm Ocean Waters	Mid-latitudes, over Land or Water
Size	Smaller (10-100's of Km)	Larger (100-1000's of Km)
Pressure Gradient	Extreme and Steep	More Subdued
Sustained Winds	Higher (<74mph)	Lower
Frequency of Impact to an Area	Decadal or Greater	Yearly or less
Structure	Well-organized (Defined Core), Self-contained	Disorganized, Affiliated with a Cold Front
Forward Speed	Faster	Slower
Period of Impact to an Area	Hours	Days
Classic Impact Locations	US East and Gulf Coasts, Caribbean, Pacific Ocean Islands, Australia, Indian Ocean	US East & Pacific Coasts, East Coast Canada, Great Lakes, North Europe, Mediterranean, etc.
Storm Surge	Steep, High, Short-lived Peak (i.e., Hours), Moves with Storm	Broad, Flatter, Lasting Days, May Move with or Propagate Away from Storm Center
When Occur	Summer-Early fall	Late Fall, Winter, early Spring
Primary Beach Impact Damages	Inundation – Flooding Inlet formation, Overtopping of dunes Transport of sand toward back beach	Retreat of the shoreline, significant loss of sand from beach berm, Sand transported offshore

Redundant weather patterns can trigger multiple lows impacting the same area resulting in week to month or longer sequences of water levels deviations from the predicted. For example, the record analyzed during this study record included as many as 5 or 6 water level events in a single month, with 75% or more of the days in that month experiencing greater then predicted water level ranges. The result is a long period of sustained high water and greater beach dynamism. An Intensity Index parameter for measuring the total cumulative water-level effect of an event or over a period has been developed for this study.

Storm-induced water-level fluctuations are more complex in both their manifestation and in their impacts than that suggested by the generally accepted use of a single water elevation parameter (usually the “maximum surge”). There is a direct relationship between the storm meteorology (particularly location, size, duration, and wind and pressure fields) and the characteristics of the water level fluctuation.

METHODOLOGY AND ANALYSIS

The methodology used in conducting this study required the following steps:

1) Acquire and process water level data including the filtering of the data to one hour increments and calculating the residual water level by subtracting the predicted tide from the measured water level.
2) Analyzing the database to identify and extract periods of excursion from the predicted water levels that complied with the criteria used in this study. Each became a sequentially numbered storm event.
3) Examination of individual storm events to characterize particular classes of surge hydrographs. A subset of the storms was compared to the meteorological conditions of the time to interpret the relationship between the meteorological event and the surge hydrograph.
4) Parameterize each storm event as to maximum or minimum peak, duration, and the area of the hydrograph (total meter hours).
5) Conduct a comparative trend analysis to examine seasonal and yearly trends.

Water Level Data

The National Ocean Service (NOS) of the National Oceanic and Atmospheric Administration (NOAA) maintains hundreds of water-level monitoring ("Tide Stations") throughout the United States (Harris, 1981). Some of the oldest, continuously operating, tidal stations in the nation, are located along the mid-Atlantic through New England coast (i.e., Boston Harbor, MA initiated in 1921; Sandy Hook, NJ in 1910; Atlantic City, NJ in 1911; and Sewells Point, Hampton Roads, VA in 1927). However, many stations have been established, abandoned, and then re-established at other location with extensive data gaps. Also of concern is that the majority of these stations are in protected waters within harbors or bays where a storm surge would be locally modified by the geometry of the bay and the orientation of the bay/harbor-mouth. The selection of a tide station for a study of storm-induced water level fluctuations should be based upon an analysis of the station's data history, exposure to storm surges, and availability of meteorological data.

The 20-year tide record at the FRF at Duck, NC was selected for the analysis presented here. The FRF is a unique source for continuous, synoptic data (representing each data class of coastal interest including beach changes) since 1981. In addition to this extraordinary and well-maintained database, the FRF has the additional advantage of being subject to both tropical and extratropical events. The tide station at the FRF is located at the end of a 560m long reinforced concrete pier at the approximate 7-m depth contour. Water level data collection started in August 1978. However, during the first couple of years (1978-1979) the gage experienced some technical difficulties and there are windows of invalid data and a tendency to fail during storms. Although water level data collection continues at this site, only data through December 1998 is included in this analysis. Water level is recorded at 6-minute intervals however; the data was filtered to 1-hour increments for the purposes of this analysis.

Selection of Storms

A suite of 351 extratropical and hurricane storms which have impacted the mid-Atlantic at Duck, North Carolina between 1978 and 1998 have been extracted from the water level record based upon elevation and duration of the residual surge (measured water level – predicted water level) according to the following criteria.

A Positive storm surge must have a:

1) Maximum residual water level greater then 0.299 m lasting at least 12 hours, or
2) Maximum residual water level greater then 0.599m lasting at least 8 hours, or
3) Maximum residual water level greater then 0.899m lasting at least 6 hours.

A Negative storm surge must have a:

1) Minimum residual water level less then -0.299 lasting at least 12 hours, or
2) Minimum residual water level less then -0.599 lasting at least 8 hours.

Levels complying with these criteria need not be continuous, but shouldn't drop below +0.25m or above -0.25m for more then a few hours. The plus or minus 0.299m as well as the 12 hour discriminating criteria for identifying a storm were developed after a complete review of the water level record and though comparison with both the meteorological and wave record. Any water level deviation from the predicted that fell between 0.299 and –0.299 is considered as insignificant in causing a change in the excursion of the wave climate across the profile. The 12-hour criteria encompasses one tidal cycle. The higher peaked, shorter criteria tend to capture the near field and direct hit tropical storms.

A total of 351 individual storm events were identified and selected for analysis during the period 1978-1998. The predicted astronomical tide was extracted from the actual water level hydrograph producing the storm hydrograph. Several statistics were extracted for each event including the maximum and minimum surge elevations and duration of the greater then 0.299m deviation from the predicted tide. In addition, a parameter was specifically developed for this analysis that is the total area of the hydrograph in units of meter-hours. This parameter provides a single metric of the storm's duration and intensity.

Storm Characterization and Analysis

Of the 351 storm surges examined only Hurricane Gloria, (1985) and Hurricane Bob (1991) were close to matching the idealized hydrograph shape of a steeply rising and falling hydrograph with a strong single peak. These were the only two direct hit hurricanes in the database. An example of the complexities associated with surge hydrographs are those that oscillated between positive and negative surge peaks over a water level range of 1.5 meters. A number of hydrographs displayed multiple surge peaks; either two or three significant peaks several days apart or even a frequent cyclic peaking pattern with a 12-hour periodicity (often found to be in phase with the falling astronomical tide).

There is a first order relationship between the resultant surge and whether or not the generating storm was a tropical or extratropical event. There is also a linkage between

the characteristics of the surge and whether or not the storm was a local meteorological event or a remote event. Storm surges that do not mirror changes in the local atmospheric pressure or wind field are those that are spawned and maintained by remote, and probably regional scale storms. Figure 1 was developed based upon a review and characterization of the 351 surge hydrographs analyzed through this study. Figure 1 dramatically illustrates a range of curve geometries including flat (little peakedness), several well-defined peaks, and negative peaks (drawdowns). These are each related to the meteorological event associated with that hydrographic signature. There is a significant range in surge duration (i.e., from 1 to 10 days) and variability as the storm meteorology evolves and changes location relative to the surge measurement site.

STORM TYPE	CLASSIC EXAMPLE STORM	GENERALIZED SURGE STATISTICS			CONCEPTUAL SURGE HYDROGRAPH SHAPE
		Trend	Max peak	Dur	
Direct-hit Hurricane	Hurricane Gloria Sep 26-28 1985	+	<1.0m	6-12hr	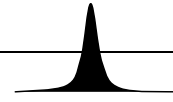
Passing Hurricane	Hurricane Edouard Aug 29 –Sep 3 1996	++	<0.3	1-2 days	
Near-field, Minor Extratropical	VERY FREQUENT EVENT	+	<0.3m	1-2 days	
Local Low Extratropical	FREQUENT Oct 23-26 1982	-+-	0.3-0.6m & >-0.3m	1-2 days	
Regional Extratropical	Mar 6-14 1989	+++	<0.6m	3-4 days	
Sequential Local Extratropicals	Dec 8-18 1989	-+-+-	0.3-0.6m & >-0.3m	5-8 days	
Sequential Regional Extratropicals	Oct 28- Nov 12 1991 Halloween Storm	+++0+++	<0.6	2-3 weeks	
Anti-cyclone (High) or Inland Low	Mar 13-18 1993 Storm of the Century	---	-0.3 to >-0.6	2 –3 days	

Figure 1. Classes and characteristics of storm hydrographs extracted from FRF record

Statistical Analysis

Parameters were developed per storm and per month. Figure 2 illustrated the summary statistics per storm, while Figure 3 is presented for per month. In all cases the parameters refer to the atmospheric surge elevation as the residual once the predicted tide has been removed from the measured water level. Maximum and Minimum values are the highest and lowest surges that occurred that during that month or per storm. Duration is the total number of hours that the storm surge elevation exceeded either plus or minus 0.299 m. An Intensity Index parameter is presented as meter-hours (m-hr). This parameter represents the area of the surge hydrograph during which the water rose or fell greater then 0.299 from the predicted tide. This parameter is the best single indicator of both the "intensity" of a storm and the "storminess" of the month.

Figure 2 compares water level parameters per storm. Figure 2a illustrates that most storms last less then 50 hours and produce less then a 0.6m rise in the water level. The longest duration storms are major regional extratropicals that can produce surges between 0.6 and 0.9m and last over 150 hours (6-8 days). These are significant beach erosion events. Most of the higher surge events are associated with hurricanes that move through the region fairly quickly. This comparison of duration to maximum surge height is not necessarily a good indicator of significant storms as it doesn't capture the duration of the highest water levels. Figure 2b and 2c is better at discriminating the more significant coastal events than Figure 2a.

For example, the highest Intensity Index (m-hr) event on record was Storm #335, which occurred February 3-10, 1998. This storm produced a maximum surge of 0.91 m, with a duration of 163 hours and an Intensity Index of 53.4 m-hr. There are storms that lasted longer and storms that produced higher surges. But this single storm dominates as the most intense on record as can be seen in Figure 2c. The second most intense on record is Storm #190 which occurred October 28- November 2, 1991. This storm lasted 120 hours, produced a peak surge of 1.01 m, and an Intensity Index of 38.14 m-hr. It was immediately followed by Storm #191, which occurred November 8-12, 1991, lasting 97 hours, producing a maximum surge of 0.933m, and intensity of 16.67 m-hr. There are few events that trigger a draw-down of the water level and these tend to be of short duration. The single most significant draw down event was Storm #225, which occurred March 13-16, 1993 associated with an extratropical low that traveled west of the FRF along the eastern seaboard (Kocin, et al., 1994). This actually caused a 0.56m draw down of the water level.

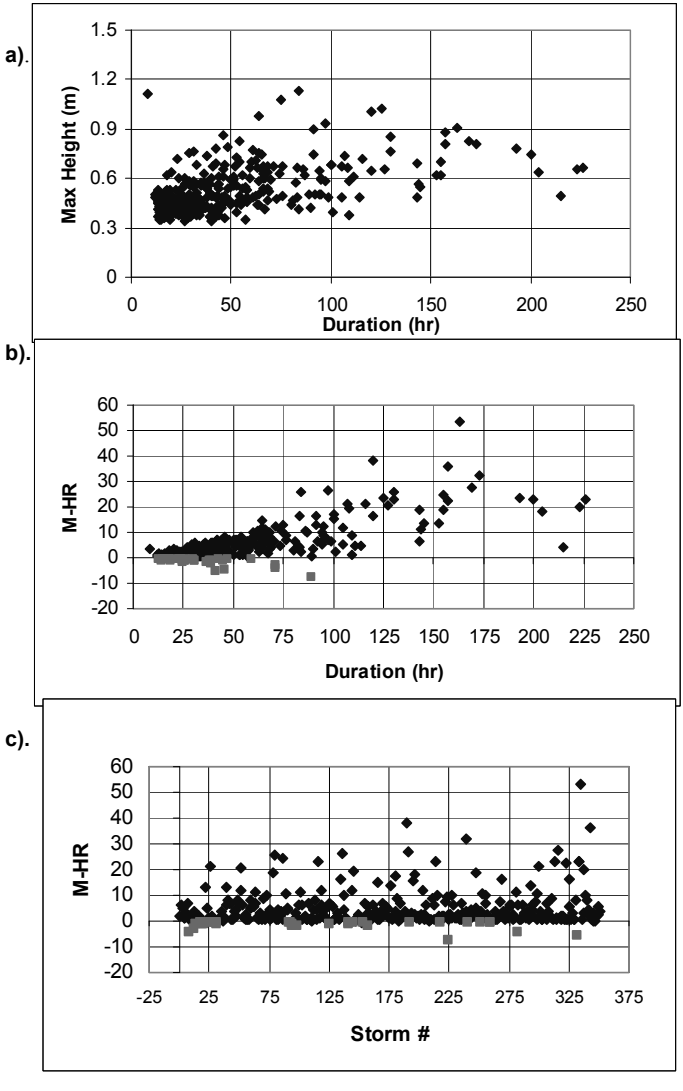

Fig. 2. Comparison of water level parameters for all 351 storms extracted from the FRF data set 1978-1998. Diamonds document each storm that had a positive surge while squares document each storm with a negative surge. Graph a) correlates maximum surge to duration. Graph b) compares the area under the curve (meter-hours) to duration. Graph c) demonstrates the trend of storm hydrograph area over time. Each storm is numbered sequentially with Storm #1 on Jan 1, 1980 and Storm #351 on Dec 30, 1998.

Figure 3 demonstrates the seasonality of these storm events. Figure 3a shows that surges of greater then 0.6 m or draw downs of the water surface greater then 0.3 m can occur during any month. However, Figure 3b, which compares the total number of hours of surge per month, and Figure 3c, which uses the m-hr intensity index parameter clearly indicates a tendency for the stormiest months to be from October through April. February tends to be the stormiest with 216.4 m-hr of surge, followed by October with 200.9 m-hr of surge. The highest recorded surge, 1.129 m, is actually associated with an extratropical storm, April 11-15, 1988. The next highest is 1.112 m with Hurricane Gloria, September 29, 1985. The least stormy month is July with only a single storm during the 20-year period, resulting in 147 hours of surge and an index of 6.2 m-hr.

Total storm intensity index (m-hr) per year is demonstrated in Figure 4. This figure suggests both a cyclical trend to the occurrence of stormy years and a tendency of increasing storminess over the 20-year record for this site. The years with the most storms are 1983, 1997, and 1998, with nineteen storms each. When considering the storm intensity index, 1991 is added to the list of the stormiest years. A storm intensity index of 212.6 m-hr was computed for 1998, 157.8 m-hr for 1991, 152.6 m-hr for 1997, and 131.0 m-hr for 1983. The quietest years on record are 1980-1982, 1986, and 1990; each year with a storm intensity index of less then 50 m-hr.

Discussion

The analysis presented here demonstrates the dynamism of meteorological patterns as they influence coastal processes. It also advances a relatively simple technique for documenting meteorological trends, critical in the evolution of the coast. As the position and intensity of the jet streams and the ocean temperature change, different air masses dominate a region influencing the genesis and evolution of storms. Meteorological conditions that tend to generate either tropical or extratropical storms are likely to spawn sequential storms resulting in a temporal clustering of higher energy events impacting a particular region. The greatest impact of this analysis may be in illustrating how, through the readily extractable parameter of water level excursions, the storm history for a region can be assembled.

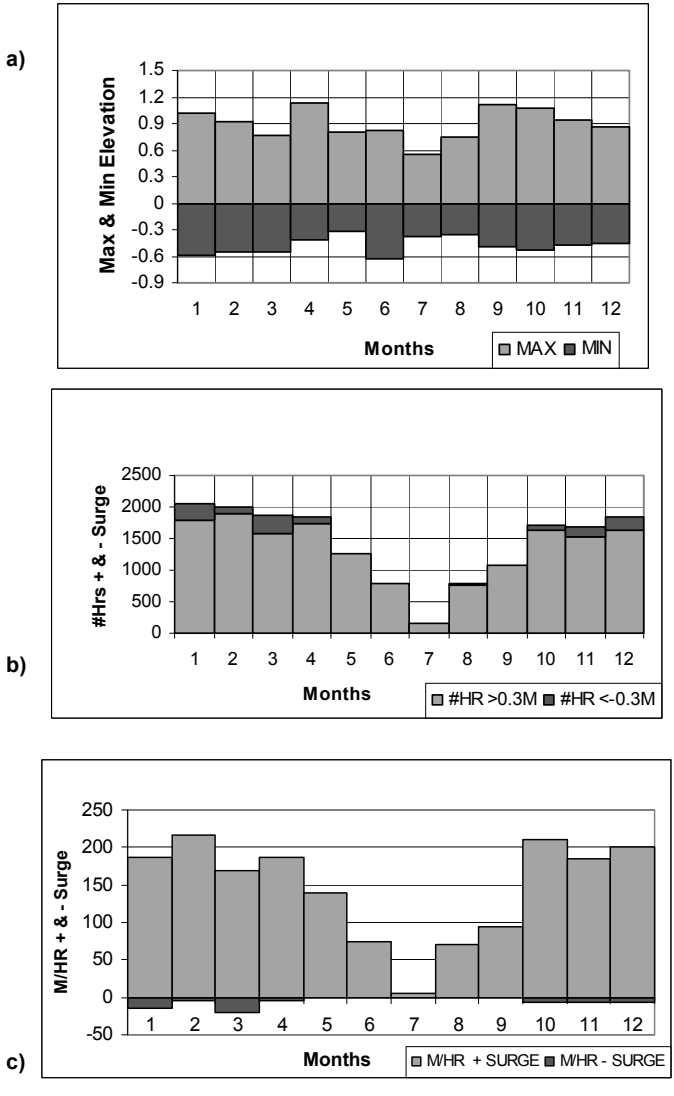

Fig. 3. Monthly statistics based upon all 351 storms extracted from the FRF data set 1978-1998. Graph a) documents the single occurrence maximum and minimum (negative or draw down) peaks experienced during that month over the 20 year record. Graph b) documents duration, cumulating the total hours during that month of storm surge influences over the 20 year record. Graph c) illustrates the total cumulative meter-hours of surge impact per month.

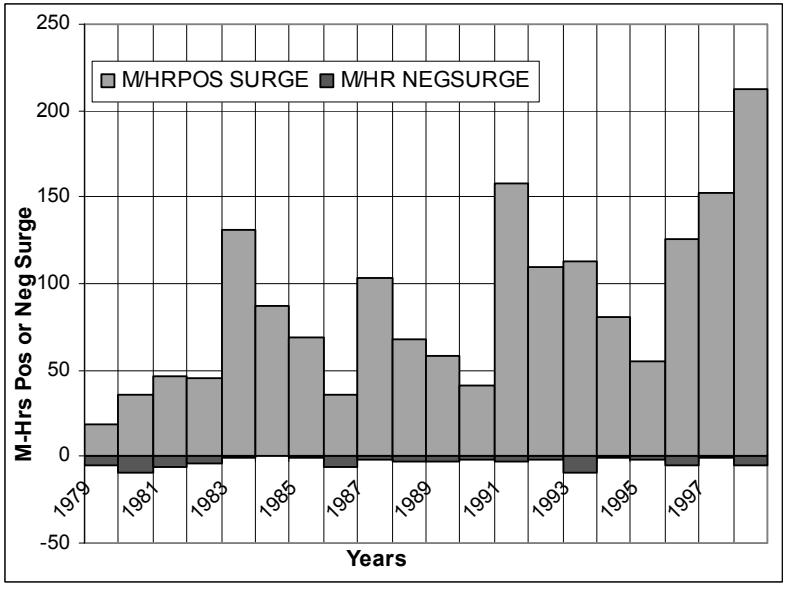

Figure 4. Storm Intensity Index (meter-hours) per year over the 20-year water level record for the FRF.

CONCLUSION

Storm surges number amongst the deadliest and most destructive of all natural disasters. They kill, flood the land, damage the coastal infrastructure, create and destroy inlets, erode beaches, and disrupt ecological systems. Yet their study has generally been limited to the high profile, direct-hit hurricanes which quickly overwhelm coastal communities. The work presented here provides a foundation for consideration of the full storm surge record including lower surge, but longer duration, and clustering of more minor events. Very little analytical work has been conducted on the range of characteristics, evolution, and impacts using prototype surge data. The study proposes an analytical approach and also a mechanism to correlate storm induced water level fluctuations as a means for better understanding trends in coastal evolution.

=

ACKNOWLEDGEMENTS

The direction and assistance of Drs. Robert Dolan and Patricia Wiberg, University of Virginia and Dr. Nicholas Kraus, U.S. Army Engineer Research and Development Center in framing this research and the constant prodding by many colleagues as well as my husband, Richard, is acknowledged. Cliff Baron and William Birkemeier at the U.S. Army Engineer Field Research Facility assisted greatly in the acquisition and initial processing of the FRF tide data. Amy Wibowo contributed significantly in the data processing and storm identification phases.

REFERENCES

Birkemeier, W. A., Savage, R. J., and Leffler, M. W. (1988). *A Collection of Storm Erosion Field Data.* Miscellaneous Paper CERC-88-9. US Army Engineers, Waterways Experiment Station. Vicksburg, MS., 285 p.

Bowden, K. F. (1983). *Physical Oceanography of Coastal Waters*. Ellis Horwood, Ltd. Chichester, England. 302 p.

Davis, R.E., Dolan, R. and Demme, G. (1993). "Synoptic Climatology of Atlantic Coast North-easters." *International Journal of Climatology*. Vol. 13, 171-189.

Dolan, R. and Davis, R.E. (1992) "An Intensity Scale for Atlantic Coast Northeast Storms." *Journal of Coastal Research*. Vol. 8, No. 4, 840-853.

Harris, D. L. (1981). *Tides and tidal datums in the United States.* U.S. Army Engineers, Coastal Engineering Research Center, Washington D.C. 382 p.

Kocin, P.J., Schumacher, P.N., Morales, R.F., and Uccellini, L.W. (1994) "Overview of the 12-14 March 1993 Superstorm." *Bulletin of the American Meteorological Society.* Vol. 76, No. 2, 165-182.

Perry, A. H. and Walker, J. M. (1977). *The Ocean-atmosphere System*. Lowe & Brydone Printers, Norfolk, U. K., 160 p.

Pugh, D. T. (1987). *Tides, Surges, and Mean Sea-Level*. John Wiley & Sons. New York, N.Y., 472 p.

Savage, R. J. and Birkemeier, W A. (1987). "Storm Erosion Data from the United States Atlantic Coast." *Proceedings Coastal Sediments '87*, ASCE, 1445-1459.

HINDCASTING POTENTIAL HURRICANE IMPACTS ON RAPIDLY CHANGING BARRIER ISLANDS

Hilary F. Stockdon, David M. Thompson, and Asbury H. Sallenger, Jr.

U.S. Geological Survey, Center for Coastal and Watershed Studies, 600 4th St. South, St. Petersburg, FL 33701, USA; hstockdon@usgs.gov

Abstract: Hindcasts of the coastal impact of Hurricane Ivan on Santa Rosa Island, Florida, using a storm-impact scaling model that compares hurricane-induced water levels to local dune morphology, were found to have an accuracy of 68% in predicting the occurrence of one of four impact regimes: swash, collision, overwash, and inundation. Errors were overwhelming under-predictions of the regime where the observed response was more extreme than had been expected. This is related to the evolution of the profile during the storm. Mean pre-storm dune elevations decreased by 1.9 m over the 75-km long island as most of the dunes were completely eroded during the storm. Dramatic morphologic change during a hurricane makes barrier islands more vulnerable to overwash and inundation than will be predicted based on pre-storm dune parameters. Incorporation of the timing of rising water levels relative to storm-induced profile evolution is required to improve model accuracy.

INTRODUCTION

In recent years, several large hurricanes have made landfall in the United States resulting in extensive damage to coastal communities and dramatic change to natural coastal systems including beaches, barrier islands, and wetlands. When Hurricane Ivan made landfall in Gulf Shores, Alabama, on September 16, 2004 much of the coastline of Alabama and the Florida panhandle experienced significant coastal change (Sallenger et al. 2006). In Orange Beach, Alabama, a 5-story condominium collapsed after the dune supporting its foundation was completely eroded by large waves. Just west of landfall in Pine Beach, Alabama, parts of the island were flooded during the storm, and a 1.8-m deep channel was scoured across its entire width. On

Santa Rosa Island, Florida, located over 55 km east of where Ivan came ashore, sand dunes were completely eroded and much of the 73-km stretch of island was overwashed. In order to mitigate the impact of these intense storms on existing and future Gulf and Southeast Atlantic barrier island communities, predictions of the coastal response to an approaching storm are essential.

One method for determining the likely mode of coastal change on barrier islands during a hurricane is to make use of a storm-impact scaling model that compares the elevations of local beach morphology and extreme water levels expected during a storm (Sallenger 2000). Based on these elevations, four storm impact regimes are defined, and within each the processes and magnitudes of coastal change are unique (Stockdon et al. in press). When extreme water levels (R_{high}), defined as the sum of storm surge, astronomical tide, and the 2% exceedence level for runup, are confined to the beach face, the system is within the *swash* regime and the magnitudes of coastal change are minimal. When R_{high} reaches the elevation of the base of the dune (D_{low}) the beach enters the *collision* regime, which is characterized by dune erosion. If R_{high} exceeds the crest of the dune (D_{high}) the beach will *overwash*, and sand will be transported landward, resulting in increased shoreline erosion and beach volume loss (Stockdon et al. in press). The most extreme regime, *inundation*, occurs when the storm-induced still water level (R_{low}), defined as the sum of wave setup and storm surge, exceeds the elevation of D_{high}. At this point, the island is continually submerged, and cross-island flows dominate the physical processes responsible for morphologic change.

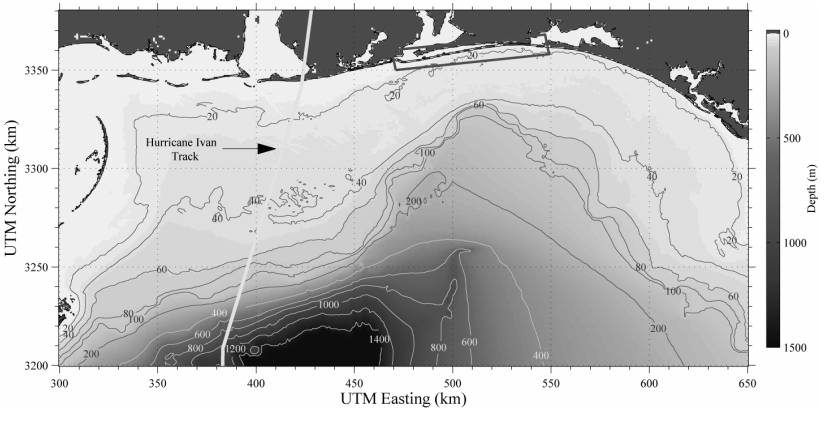

Fig. 1. Bathymetry grid (1-km x 1-km) for modeling wave and surge conditions during Hurricane Ivan along the northern Gulf of Mexico from eastern Louisiana to western Florida. The box shows the location of Santa Rosa Island, FL.

The predictive accuracy of this model is tested by hindcasting the spatially-variable coastal response of Santa Rosa Island, Florida, to the landfall of Hurricane Ivan on September 16, 2004 (Fig. 1). Santa Rosa Island is a 73-km long barrier that encompasses the communities of Pensacola Beach, Navarre Beach, and Okaloosa Island, as well as a portion of Gulf Islands National Seashore. Most of the island was subjected to hurricane-force winds (> 119 m/s) during the storm and, therefore, experienced striking morphologic change in response to large waves. The magnitudes of storm-induced shoreline change varied substantially along the length of the island: shoreline retreat of over 40 m was observed in some locations while change in adjacent areas was near zero.

METHODS

Hindcasts

Hindcasts of the coastal response to Hurricane Ivan were made every 20 m along the island by comparing measurements of pre-storm dune morphology to modeled water-level elevations. Storm surge and the nearshore wave climate were simulated using the Delft3D model (Delft 2003). The model domain consisted of a 2-km x 2-km grid with a nested 1-km x 1-km grid located closer to the study area (Fig. 1). The model was run for 66 hours beginning ~53 hrs before the storm made landfall. Observed winds and atmospheric pressure input were obtained from NOAA's Hurricane Research Division. Tides were simulated by inputting tidal constituents extracted from the TPXO6.2 global tide model (Egbert and Erofeeva 2002) at four points along the boundary of the Delft3D model domain. Wave heights and periods were verified in deep water using measurements collected at NOAA's National Buoy Data Center (Thompson et al. 2006).

The offshore wave height at each time step was extracted from the 20-m depth contour and, in conjunction with lidar-based measures of pre-storm beach slope, converted to the 2% exceedence elevation for wave runup, R_2, using the empirical formulation of Stockdon et al. (2006). Storm surge and astronomical tides, η, were extracted along the shoreline position, as defined by the mean-high-water (MHW) tidal datum. Hurricane-induced total water levels, R_{high}, were calculated every 20 m along the island as the sum of R_2 and η. Still-water levels, R_{low}, during the course of the storm were calculated as the sum of η and wave setup, also modeled empirically using offshore wave conditions and local beach slope (Stockdon et al. 2006).

The pre-storm elevations of the dune base, D_{low}, and crest, D_{high}, were extracted every 20-m along the island from a May 2004 lidar survey conducted by the US Army Corps of Engineers using the Naval Oceanographic Office CHARTS instrument. When a dune was not present, the height of the berm was taken as D_{high}. The elevations of D_{high} varied considerably along the island: mean, μ, D_{high} was 3.27 m while the standard deviation, σ, was 1.17m (Fig. 2).

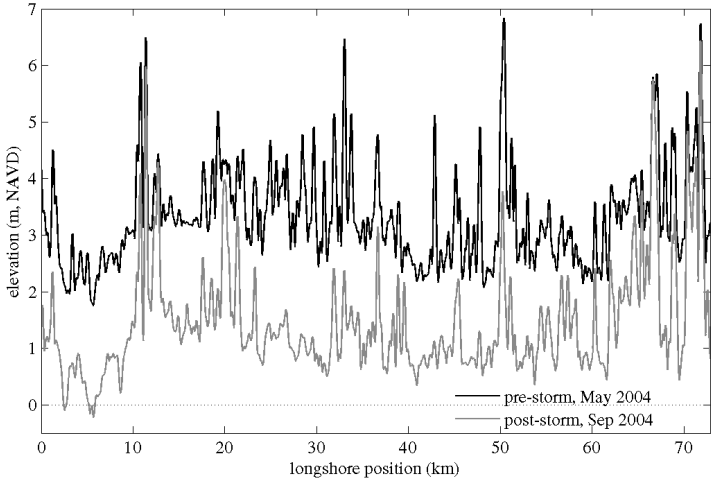

Fig. 2. Elevation of the dune crest, D_{high}, before (May 2004) Hurricane Ivan and of the same cross-shore position following the storm (Sep 2004). Mean elevation decreased by 1.9 m to 1.4 m.

To hindcast the impact regime expected during Hurricane Ivan, modeled water levels were compared to elevations of pre-storm dune morphology. When $R_{high}>D_{low}$, the beach was expected to fall in the collision regime and experience dune erosion; when $R_{high}>D_{high}$, the beach was expected to overwash (Fig. 3a); and when $R_{low}>D_{high}$, the beach was expected to inundate or breach (Fig. 3b). Examining the threshold quantities (R-D) at each time step of the progression of the storm reveals the time when thresholds were exceeded, as well as the magnitude and duration of exceedence (Fig. 3a). The spatial variability of the expected regime (Fig. 3a) is overwhelmingly due to an associated variability in beach morphology, which is included in the model both directly, through the elevation of dune parameters, and indirectly, through the beach-slope-dependent estimates of wave runup.

Observations

Hurricane-induced coastal change and the observed impact regime were quantified by comparing the May 2004 morphology to that measured three days after landfall, on September 19, 2004, using the NASA EAARL lidar. The observed impact regime was designated every 20-m along the beach by comparing cross-shore profiles of island topography. Locations showing dune erosion exceeding a 2.5 m^3/m threshold were classified to be within the collision regime. Areas with a decrease in dune elevation exceeding 1 m were identified as locations of overwash. Because overwash deposits extended into the bay behind the island where volumes of transported sediment could not be measured, objective measures of this regime were subjectively verified using lidar difference grids and post-storm aerial photography. Finally,

cross-shore profiles with peak post-storm elevations less than MHW (0.23 m NAVD) were likely submerged during the storm and, therefore, classified as falling within the inundation regime. Over 89% of the island was observed to have overwashed during the storm. Inundation was limited to a narrow area on the low, western end of the island and limited areas between longshore locations, y, = 38 - 41 km.

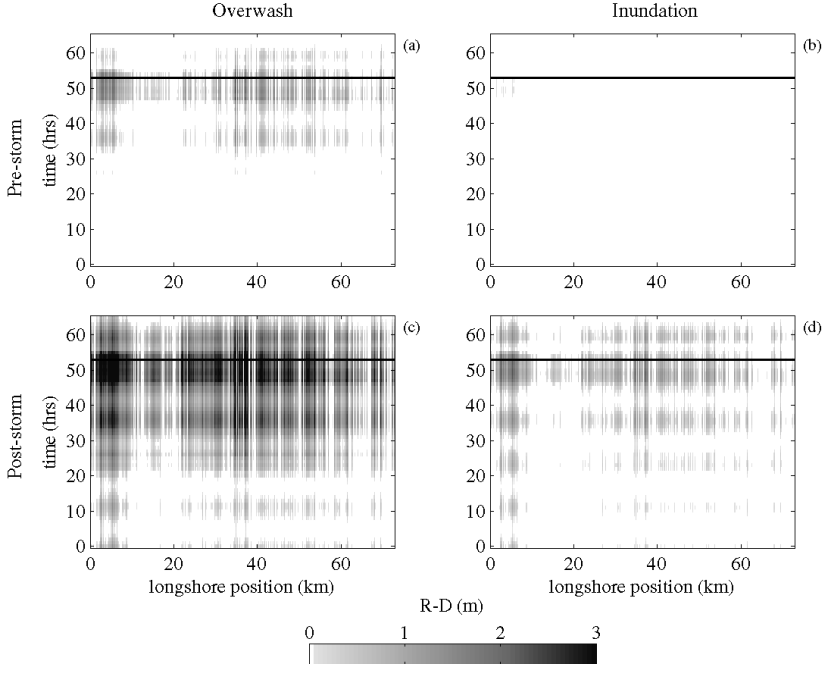

Fig. 3. Space-time plots of the predictive quantity for determination of the overwash (R_{high} – D_{high}, left column) and inundation (R_{low} – D_{high}, right column) regimes at all locations along Santa Rosa Island, Florida, for all time steps of the wave and surge modeling (66 hours), based on pre-storm (top row) and post-storm (bottom row) morphology. The black horizontal line marks the time of Hurricane Ivan's landfall. White areas indicate where R - D <= 0, meaning an area was not likely to be in that particular regime.

RESULTS

To evaluate the predictive accuracy of the model, the observed regime was compared to the hindcast regime at the time the maximum R_{high} was observed, which for most locations was the time of landfall. Mean modeled R_{high} along Santa Rosa Island was 3.55 m and the standard deviation was 0.37 m (Fig. 4). Elevated water levels in the central portion of the island result from higher runup in an area with steeper beach

slopes. Storm surge, which remained relatively constant (μ = 0.98 m, σ = 0.14 m) along the island, represents only 27.7% of the total water-level signal, with wave runup (swash and setup) contributing the remaining 72.3% (Fig. 4).

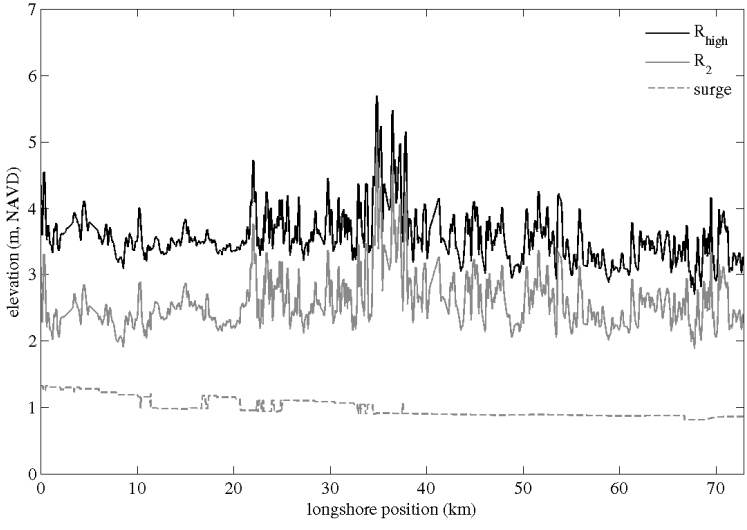

Fig. 4. Elevations of wave runup (R_2), storm surge, and total hurricane-induced water level (R_{high}) along Santa Rosa Island, Florida, as modeled during the peak of Hurricane Ivan.

The majority of the 73-km stretch of island (69.9%) was predicted to overwash while 28.2% of the island was predicted to experience dune erosion and only 1.9% was expected to inundate (Fig 3b). Comparisons to observations show an overall accuracy of predicting one in four regimes to be 68%. However, accuracy for a particular regime varied considerably. A confusion matrix that explicitly shows the number of correct predictions, *Nc*, total observations, N_o, and total predictions, N_p, for each regime can be used to examine regime-specific accuracies (Table 1). Positive predictive power, *P*, calculated as (N_c/N_p * 100), defines the probability that a particular regime will occur if predicted by the scaling model. Model sensitivity, *s*, is defined as (N_c/N_o * 100) and represents the probability that a particular regime was classified correctly. High sensitivity for the collision and overwash regimes (s = 77.2% and 72.4%, respectively) indicate the model's ability to identify locations most susceptible to dune erosion and overwash. Positive predictive power of 90.3% within the overwash regime shows that there is a high probability that an area predicted to overwash will, in fact, do so.

Table 3. Confusion matrix for regime-specific accuracy of Sallenger's scaling model (2000)

		Observed					
		Swash	**Collision**	**Overwash**	**Inundation**	N_p	P (%)
Predicted	**Swash**	0	0	0	0	0	n/a
	Collision	30	142	792	0	964	14.73
	Overwash	167	42	2158	24	2391	90.26
	Inundation	10	0	31	25	66	37.88
	N_o	207	184	2981	49	N = 3421	
	s (%)	0	77.17	72.39	51.02		

DISCUSSION

The majority of the hindcast errors were associated with the under-prediction of the response, such as the prediction of collision (dune erosion) in locations that experienced overwash. These errors may arise because a time-dependent process (profile evolution during a storm) is being examined using a non-time-dependent model. During a high tide 17 hours before the storm made landfall, water levels at the shoreline exceeded the elevation of the dune crest along 35.7% of the island. Five hours before landfall, R_{high} exceeded D_{high} at over 67% of the longshore locations, a total length of ~49 km. The dunes along these sections of the island (consistently between y = 2 - 7 km and intermittent locations between y = 35 - 60 km) were likely being overtopped for a full tidal cycle before the hurricane made landfall.

At a location near the middle of the island, y = 35 km, the time series of R_{high} modeled throughout the storm's approach show extreme water levels exceeding the crest of the dune for ~30 hrs (Fig. 5). While the total hurricane-induced water level remained high for many hours, this area was not predicted to inundate because the pre-storm D_{high} was higher than R_{low}. However, the profile changed dramatically over the course of the storm as the sand dune was completely eroded, making this location more vulnerable to extreme coastal change as the storm continued (Fig. 6). At y = 35 km, the maximum elevation was reduced by 1.1 m to 2.1 m, resulting in a post-storm dune elevation that was lower than the peak R_{low} (Figs. 5 and 6). Therefore, it is likely that this location was inundated at some time during the storm.

Likewise, many locations that were not vulnerable to overwash based on the pre-storm morphology showed substantial dune erosion as a result of the storm. The mean elevation at the cross-shore position of D_{high} decreased by 1.9 m (σ = 1.0 m), creating areas that were more vulnerable to overwash (Fig. 2). The increased vulnerability can be visualized by examining the predictive quantity for overwash (R_{high}-D_{high}) using the post-storm morphology rather than the pre-storm (Fig. 3c). While this parameter

cannot be used as a hindcast, it provides a qualitative look at the likely impact regime experienced during the storm, particularly at the time of landfall when the beach had already evolved in response to more than 20 hours of elevated water levels. When the post-storm morphology is considered, 92% of the island was shown to have conditions that were favorable for overwash, in closer agreement to the 89% that was observed to have overwashed. In some locations, such as the western 7 km of beach, peak water-level elevations exceeded the post-storm dune/berm elevations by 3 m.

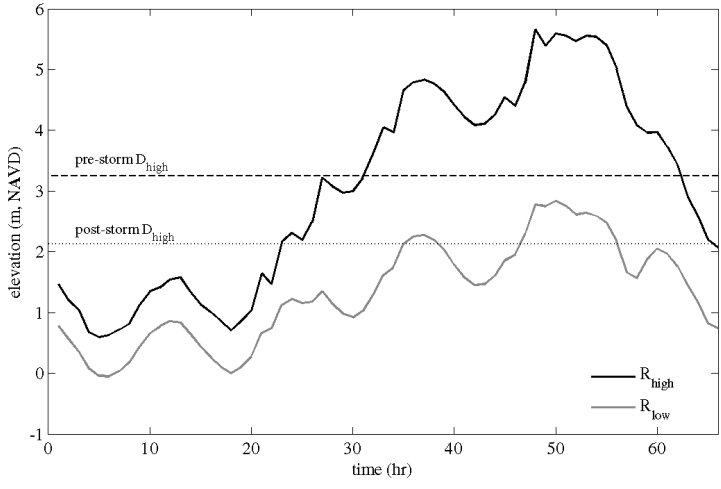

Fig. 5. Time series of modeled R_{high} and R_{low} during Hurricane Ivan at a single location (y = 35 km) along Santa Rosa Island. Horizontal lines indicate the elevations of the dune crest, D_{high}, before (3.25 m) and after (2.13 m) the storm.

The long duration of increased water levels contributed to significant profile evolution; however, the period of time that water levels exceeded threshold conditions did not directly correlate to the magnitudes of shoreline or beach volume change and, therefore could not explain the spatial variability of the observed coastal change. This is likely because, as a result of the storm, 43% of the island had conditions favorable for inundation (Fig. 3d). In the inundation regime, portions of the island are underwater and cross-shore flows will dominate the processes of sediment transport. During these extreme conditions, wave-driven processes such as swash and setup are not expected to scale with transport or the resulting coastal change.

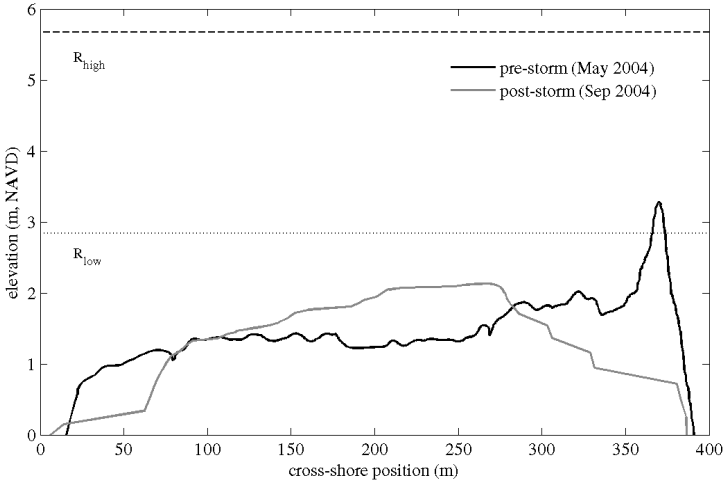

Fig. 6. Cross-shore profiles measured before (May 2004) and after (Sep 2004) the landfall of Hurricane Ivan. Cross-shore distance increases offshore with the Gulf of Mexico located to the right. Horizontal lines show the maximum value of R_{high} (5.67 m) and R_{low} (2.83 m) reached at this location during the storm.

In order to more accurately predict the type of coastal change expected during a hurricane, models will need to include information about the duration of elevated water levels and the magnitude of the difference between R_{high} and D_{high}. Of particular importance is the timing of water level increases relative to that of changes in beach morphology.

CONCLUSION

A storm-impact scaling model was used to hindcast the potential coastal impact of Hurricane Ivan on Santa Rosa Island, Florida. Comparisons to lidar-based measurements of coastal change and classification of regime indicate that the model has an overall accuracy of 68% in predicting one in four regimes. Based on measures of model sensitivity and positive predictive power, performance was best within the overwash regime where 72% (s) of overwashed locations were correctly predicted to do so, and there was a 90% (P) probability that an area predicted to overwash would respond as such. Most of the errors were an under-prediction of the impact regime. This is likely due to the evolution of the profile during the course of the storm. Seventeen hours before the storm made landfall, hurricane-induced total water levels exceeded the elevation of the dune or berm crest along 35.7% of the island. During the next high tide, five hours before water levels peaked, as much as 67% of the coastline was expected to be overwashed by waves and surge. Comparison of pre-storm morphology to that measured three days after the storm made landfall reveal large changes to the profile shape as storm waves eroded most of the sand dunes

along the beach. The mean elevation at the cross-shore position of pre-storm D_{high} was reduced by 1.9 m to 1.4 m, making this area more vulnerable to extreme coastal change as the storm slowly moved onshore. The predictive quantity (*R-D*) calculated using a post-storm measure of D_{high} shows that, because of significant erosion during the course of the storm, portions of the island likely entered a more extreme regime than expected based on the pre-storm morphology. In order to more accurately predict the mode of coastal change during a hurricane, models will need to include information about the duration and timing of increases in total water levels relative to profile evolution during the storm.

ACKNOWLEDGEMENTS

The lidar data were collected through a joint program between USGS, NASA, and USACE. We would like to thank C. Sullivan, J. Wozencraft, P. Howd, K. Morgan, and L. Fauver for technical assistance with data processing. This work was funded by the USGS Coastal and Marine Program's National Assessment Project.

REFERENCES

Delft Hydraulics. (2003). "Delft3D-FLOW: Simulation of multi-dimensional hydrodynamic flows and transport phenomena, including sediments." *User Manual*, WL | Delft Hydraulics, Delft, The Netherlands.

Egbert, G. D., and Erofeeva, S. Y. (2002). "Efficient inverse modeling of barotropic ocean tides." *J. Atmos. Oceanic Technol.*, 19(2), 183-204.

Sallenger, A. H. (2000). "Storm impact scale for barrier islands." *Journal of Coastal Research*, 16(3), 890-895.

Sallenger, A. H., Stockdon, H. F., Fauver, L. A., Hansen, M., Thompson, D. T., Wright, C. W., and Lillycrop, J. (2006). "Hurricanes 2004: An overview of their characteristics and coastal change." *Estuaries and Coasts*, 29(6A), 880-888.

Stockdon, H. F., Holman, R. A., Howd, P. A., and Sallenger, A. H. (2006). "Empirical parameterization of setup, swash, and runup." *Coastal Engineering*, 53(7), 573-588.

Stockdon, H. F., Sallenger, A. H., Holman, R. A., and Howd, P. A. (in press). "A simple model for the large-scale, spatially-variable coastal response to hurricanes." *Marine Geology*.

Thompson, D. M., Howd, P. A., and Sallenger, A. H. (2006). "Nearshore wave climate variability during Hurricane Ivan." *Eos Trans. AGU*, 87(36), Ocean Sci. Meet. Suppl., Abstract OS35E-05.

EOF ANALYSIS OF MORPHOLOGICAL RESPONSE TO HURRICANE IVAN

Chris Houser[1], Stuart Hamilton, Klaus Meyer-Arendt, Jonathan Oravetz

1. Department of Environmental Studies, University of West Florida, 11000 University Parkway, Pensacola, Florida, 32514. chouser@uwf.edu shamilton@uwf.edu kjma@uwf.edu jro8@students.uwf.edu

Abstract: Hurricane Ivan, a Category-3 hurricane, came ashore near Gulf Shores, Alabama, on September 16, 2004. Santa Rosa Island, Florida, was within the Northeast quadrant of the storm and subject to surge heights in excess of 3 m. As a result the area suffered significant sediment loss (>200 m^3 m^{-1}) and widespread overwash and breaching. Morphological changes were quantified by comparing LIDAR images collected before and after landfall. In general, the morphological changes exhibited an alongshore variation at a range of scales (<1 km), consistent with the variation in foredune height prior to the storm. Using multivariate statistics it is found that this variation not only depends on the height of the foredune (relative to the surge elevation) but also on the alongshore extent of the dune and the presence and relative location of the secondary dunes. This alongshore variation will affect the recovery of the dunes, reinforcing the observed patterns.

INTRODUCTION

Hurricanes and tropical storms produce elevated water levels and large waves, capable of eroding the beachface and causing overwash and barrier breaching. In general, the impact of a storm on a barrier island depends on the elevation of the storm surge relative to the vertical geometry of the coast, which in turn depends on the extent and height of foredune development (Thieler and Young, 1991; Sallenger, 2000).

Alongshore variations in dune morphology can force alongshore patterns in overwash and breaching during storms (Morton and Sallenger, 2003). While dunes along Cape Hatteras are relatively continuous, variations in dune height (in excess of 8 m) have

been noted at scales of kilometers to tens of kilometers (Elko *et al.*, 2002). Wetzell (2003) showed that the alongshore variation in storm impact was consistent with the variation in dune height and the Storm Impact Scale of Sallenger (2000). In areas where there is frequent and extensive overwash the dune field tends to develop as a mosaic of alongshore patches that vary in age and composition (Stallins and Parker, 2003). While the dunes will obstruct overwash penetration, surge water may be forced into the intervening areas of low elevation, which can become washover conduits (Morton, 2002). It is reasonable to expect that the concentrated flows within these conduits could impact adjacent foredunes through lateral erosion, which could increase overwash penetration where dune height is variable.

In recent years, Santa Rosa has been impacted by Hurricane Ivan (2004), Tropical Storm Arlene (2005), Hurricane Dennis (2005) and Hurricane Katrina (2005). During Hurricane Ivan, the dunes on Santa Rosa Island were again reduced in height through direct wave erosion and overwashing. It is hypothesized that the morphological response to Hurricane Ivan was conditioned by the alongshore variation in the height of the dunes that had recovered following Hurricane Opal (1995). The purpose of this study is to examine how the alongshore variation in dune height and extent affected the morphological response of Santa Rosa Island to Hurricane Ivan and the redistribution of dune and beachface sediment between the nearshore and overwash deposits.

STUDY SITE

Santa Rosa Island is a narrow sandy Holocene barrier island extending over 80 km in length, from East Pass near Destin in the east to Pensacola Pass in the west (Figure 1). The second-longest barrier island on the U.S. Gulf Coast, Santa Rosa Island is separated from the Pleistocene mainland coast by Santa Rosa Sound, a continuous lagoon 3 km wide in the west and tapering to less than 400 m in the east (Kwon, 1969). Although some scholars ascribe the origin of the island to erosion of a central Pleistocene "core" and longshore redistribution of sediments (Otvos, 1982), others (Stone, 1991; Stone *et al*., 1992; Stone & Stapor, 1996) attribute longshore sediments derived by bluff erosion east of Destin as contributing most to the island's formation. The island reached its present form by 3000 bp, and it has been characterized by overall transgression since then. On the basis of dated peat and tree stumps, Stone and Morgan (1993) estimated a landward shift of "one island width" over the past 800 years (cited in Otvos, 1997). This translates to a long-term shore retreat rate of about 2 ft/yr at the site of present-day Pensacola Beach.

Santa Rosa Island is microtidal, with an average tidal range of 0.43 m (Armbruster, 1997). In addition to strong wave action on the Gulf side, especially during tropical storms and hurricanes, the island experiences back-barrier shoreline erosion due to wind-driven waves generated by winter polar outbreaks. As a result, the roll-over effect commonly associated with transgressive island systems is largely absent, except following intense hurricanes that generate extensive overwash activity.

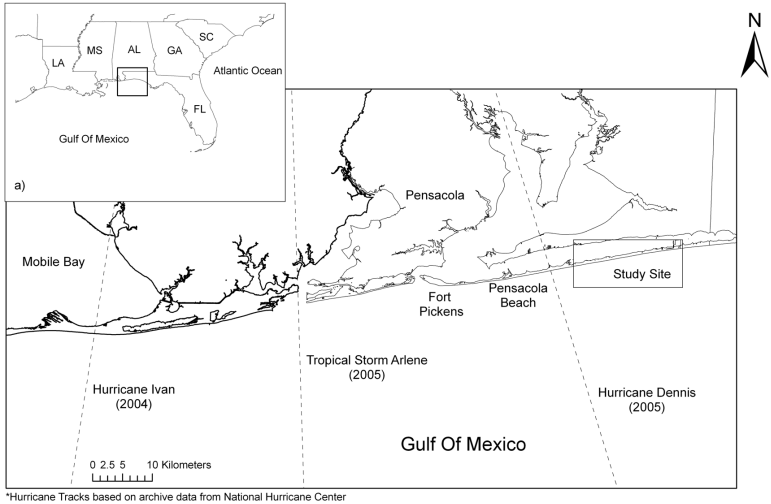

*Hurricane Tracks based on archive data from National Hurricane Center

Fig. 1. Map of study site showing location relative to the tracks of Hurricanes Ivan and Dennis and Tropical Storm Arlene.

Historically, Santa Rosa Island has been been struck by relatively few hurricanes, especially throughout most of the 20th century. In spite of hurricanes in 1906, 1916,and 1926 (when Santa Rosa Island was unpopulated), the island's shoreline position remained relatively stable from 1920 to 1993 (Foster *et al.*, 1999; Stapor, 1975).

Short-term shoreline changes have, on the other hand, been rather dramatic since 1995 because of the passage of several hurricanes and tropical storms, e.g. Erin (1995), Opal (1995), Georges (1998), and various tropical storms. Such changes have been well documented (e.g. Leadon *et al*., 1998; Leadon *et al.*, 1999; Liebens, 2000, and unpublished analyses by Olsen & Associates).

METHODOLOGY

Changes to the barrier morphology were quantified by comparing LIDAR images collected immediately before and after landfall using cross-shore transects spaced 50 m alongshore. The cross-shore geometry of the island was examined using empirical orthogonal function (EOF) analysis to identify to reduce the topographic data into common forms. EOF analysis is similar to principal component analysis, except that the variability structure is examined through space rather through time. The relationship between the primary modes of the pre- and post-storm topographic data was examined through canonical correlation analysis (CCA). This test is used to

investigate whether or not there are patterns that occur simultaneously in two different data sets and to describe the nature of those patterns.

RESULTS

A comparison of the pre- and post-storm alongshore variation in foredune elevation is provided in Figure 2. The foredune height exhibited considerable variability alongshore and was in some cases discontinuous with an average elevation above-sea-level of ~4.3 m prior to the storm. Through spectral analysis, it is found that the variation in dune height is periodic, with statistically significant spectral peaks at 9, 14, 31 and 76 transects. The average elevation within the foredune area was reduced to 2.3 m, with remnant dunes remaining only where relatively large continuous dunes had been present. The post-storm elevation data also exhibits an alongshore periodic variation at 31 and 76 transects and relatively muted variations at 9 and 14 transects.

The average pre- and post-storm cross-island profiles are presented in Figure 3. The net change in sediment volume ranged from an erosion of 238 to 43 m^3 per unit width of beach. The largest net losses of sediment (>150 m^3 per unit width of beach) were coincident with the location of breaches, which were observed where the dune crest elevation (based on a 9-point moving average) is at a minimum and close to the surge elevation (Figure 2). The crest of the dune at these locations would have been overtopped early in the storm and would have focused overwash that would eventually precipitate a breach. The breaches were reactivated during Hurricane Katrina (2005) and are activated during frontal storms that coincide with high tide.

The amount of sediment removed per unit width of beach exceeded 45% at the breach sites and ~20% on average. The loss of sediment is considerably larger than the volumetric changes presented by Stone *et al.*, (2004) for Hurricane Opal, although sediment volumes in that study were considered to a depth of 1.5 m on both the Gulf and Sound side of the island. Except for the breach areas, the amount of sediment lost from the profile does not exhibit a clear relationship with the pre-storm elevation of the foredune. This suggests that the height of the foredune is not the only control on the redistribution of sediment between overwash and erosion offshore.

Empirical Orthogonal Function (EOF) Analysis

In both the pre- and post-storm data, the first 5 modes were found to be statistically significant (ρ<0.05), with the percent of the total variance explained being 65 and 75% respectively. The primary eigenmode (E1) for the pre-storm morphology explains 21% of the variance and shows a secondary dune (positive factor weightings) ~170 m landward of the average primary dune (Figure 4a). Secondary dunes are also indicated by positive factor weightings for E3 and E5, at 67 and 117 m landward of the primary dune respectively. The second eigenmode (E2) explains 14% of the variance and exhibits negative factor weightings in the vicinity of the beachface and positive factor weightings on the landward slope of the primary dune.

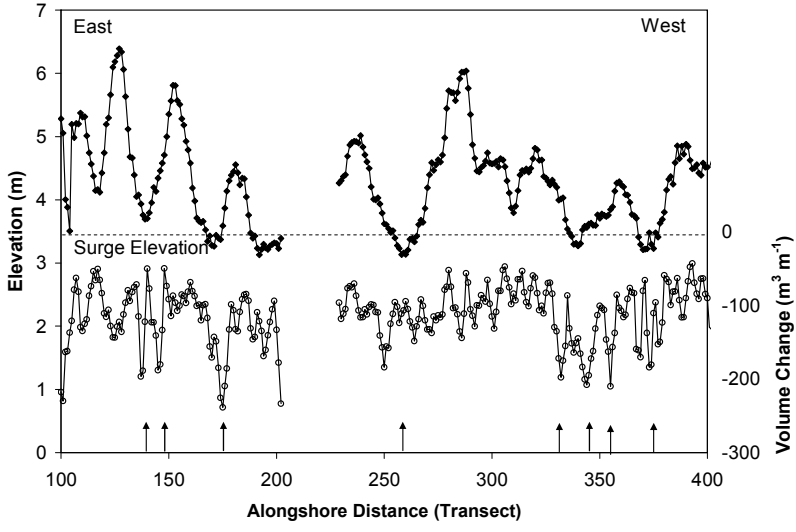

Fig. 2. Alongshore variation in dune height modelled using a 9-point moving average and the volume change between the pre- and post-storm profiles. Also shown with the arrows are the locations where breaches were observed.

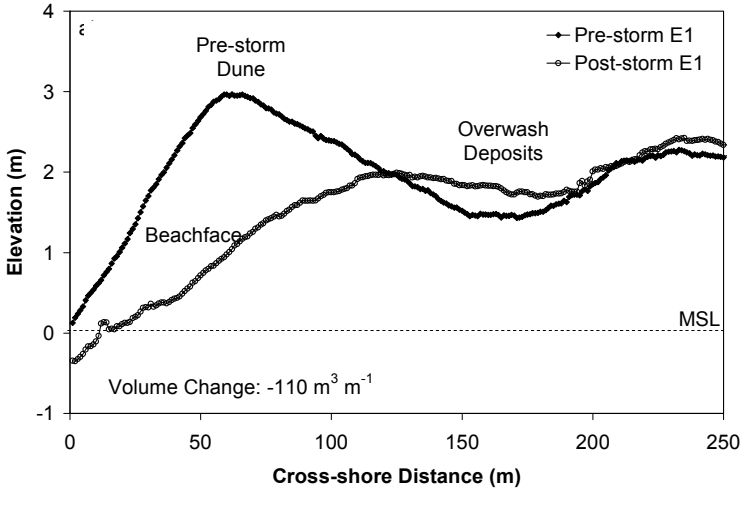

Fig. 3. Pre- and post-storm average cross-island profiles with major morphological features identified.

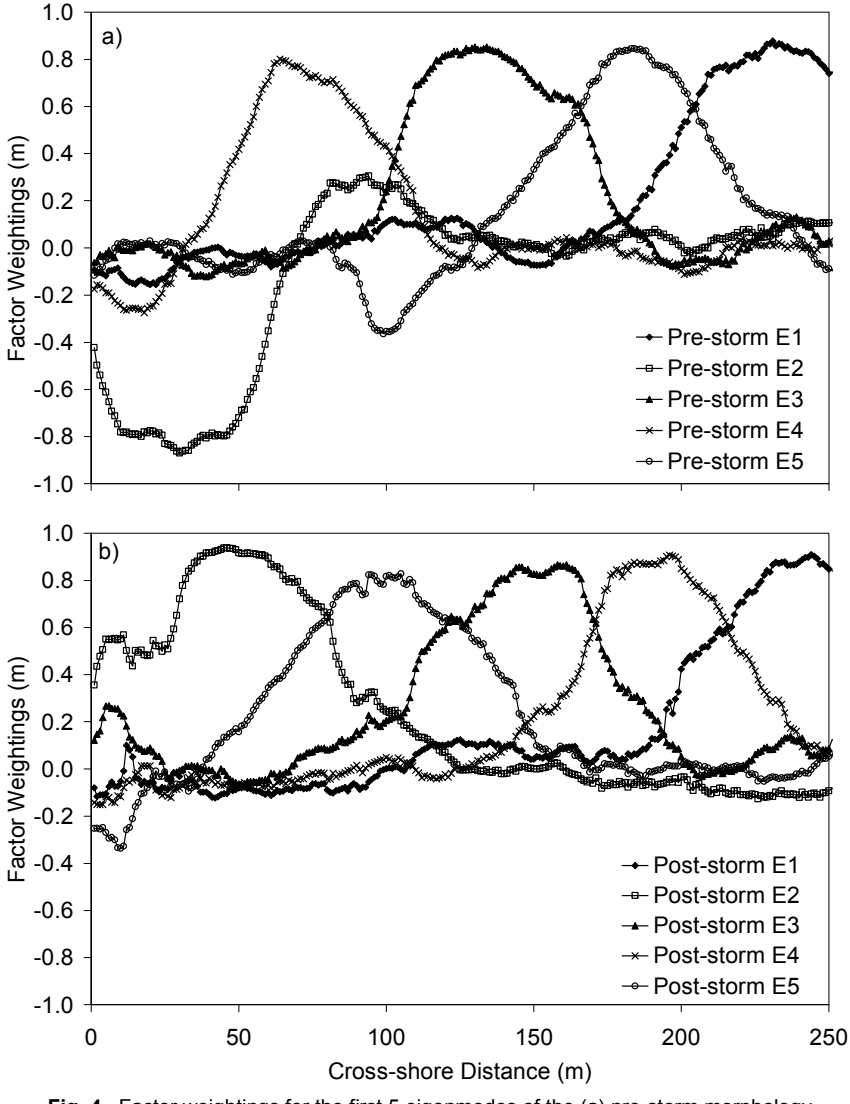

Fig. 4. Factor weightings for the first 5 eigenmodes of the (a) pre-storm morphology and (b) the post-storm morphology.

This profile is characterized by a single foredune that is ~20 m landward of the average foredune position and a relatively extensive foreshore and backshore. The fourth eigenmode (E4) has positive factor weightings at the crest of the foredune and is characteristic of a foredune that is ~0.80 m larger than the average dune (Figure 3).

In the post-storm morphology, 26% of the total variance is explained by E1and 25% of the variance is explained by E2. The primary eigenmode (E1) for the post-storm morphology exhibits positive factor weightings in the backbarrier similar in position and amplitude to the primary eigenmode for the pre-storm morphology (Figure 4b). Remnant secondary dunes are also apparent, to varying degrees, in the profiles for E3 and E4. The location and amplitude of these dunes is consistent with E3 and E5 for the pre-storm morphology. The second eigenmode exhibits positive factor weightings and accretion in the vicinity of the beachface, characteristic of either less beachface erosion or accretion relative to the average post-storm profile (Figure 3).

Canonical Correlation Analysis

As observed in the EOF analysis, there are similarities in the factor weightings of the pre- and post-storm morphology. Canonical correlation analysis between the factor scores for the pre- and post-storm morphology yields a correlation of 0.73 (ρ<0.05). Results of the analysis are presented in Table 1. The negative correlation (-0.79) between the pre-storm E2 and post-storm E2 is a reflection of how overwash penetration is inversely related to dune height and that significant overwash penetration and even breaching are observed in areas of low dune height (areas with a negative pre-storm E2). The positive correlation between pre-storm E4 and post-storm E5 is a reflection of increased beachface erosion and sediment loss to the offshore with increasing dune height. Overwash penetration is relatively small and in some cases absent where there is a strong positive pre-storm E4 (large dunes). The additional correlation between pre-storm E4 and post-storm E2 suggests that large dunes adjacent to smaller dunes (or areas where dune are absent) can be eroded through lateral erosion.

Table 1. Canonical correlation coefficients (*r*) between the pre- and post-storm profiles, with the largest coefficients (strongest relationships) highlighted.

		Post-storm Profiles				
		E1	**E2**	**E3**	**E4**	**E5**
Pre-Storm Profiles	**E1**	0.66	-0.06	0.16	0.18	0.14
	E2	0.13	-0.79	-0.07	0.10	0.02
	E3	0.08	-0.06	0.63	0.24	-0.05
	E4	-0.03	0.21	0.23	0.07	0.72
	E5	0.20	0.03	0.04	0.52	-0.24

DISCUSSION

It has been well demonstrated in previous studies that the response of a barrier island to an extreme storm depends not only the local magnitude of the storm but also the pre-storm morphology (e.g. Sallenger, 2000; Morton, 2002). The models developed in these studies provide reasonable estimates of storm impact (see Wetzell, 2003), but

the models only provide a first approximation based largely on foredune height and there is a need for verification in the prototype. In the present study, LIDAR data is used to examine how the response of Santa Rosa Island to Hurricane Ivan was directed by the pre-storm geometry. Results suggest that (to the first order) the morphological response partly varies with the height of the foredune relative to the elevation of the storm surge, which supports the storm impact model of Sallenger (2000).

The pre-storm height of the foredune exhibited considerable variation alongshore and the variation in the morphological response and profile volume exhibited a similar variation. Prior to the storm, the alongshore variation in the foredune height exhibited periodic variations at 76, 31, 14 and 9 transects. The larger-scale variations remained strong following the storm while the smaller-scale variations were significantly weaker following the storm. If the impact of this storm depended only on the relative elevations of the dune and storm surge, then these small-scale variations would have been maintained and potentially reinforced with larger and sustained impacts where there were small dunes. It is reasonable to expect that the absence of these small-scale variations following the storm is a result of lateral dune erosion and that the scale of variation that is removed (or weakened) by the storm depends on the magnitude and duration of the storm. As noted in a number of studies, surge water can be forced into areas with low dune heights (Morton, 2002) and the fast flowing water within these conduits is capable of eroding the dunes laterally.

The morphological response and redistribution of dune sediment was also found to depend on the cross-island geometry. Where there were no secondary dunes overwash and sediment erosion offshore were primarily dependent on the height of the foredune (Sallenger, 2000), which was the general case in the eastern section of the study site (transects 115 through 181). Numerous secondary dunes were observed in the western section of the study site (transects 229 to 400) with a periodicity of 38 transects. Where the primary and secondary dunes were closely spaced overwash was restricted and sediment erosion offshore was increased. This situation was analogous to having a large wide foredune (Thieler and Young, 1991). As the separation between the primary and secondary dune increased, overwash penetration was not restricted and the amount of sediment eroded offshore was reduced.

While the island appears to be uniformly covered an overwash terrace the results of this study have shown there to be considerable alongshore variability in the morphological response and redistribution of dune sediment. This variation will ultimately affect the recovery of the dune system, such that there will be alongshore variation in the height and extent of the next foredune. If the frequency of extreme storms increases the alongshore variation will be reinforced and the dunes will develop a mosaic of alongshore patches that have a cross-island orientation (Stallins and Parker, 2003). The secondary dunes on Santa Rosa Island are remnant features that not only survived Hurricane Ivan but had also survived Hurricane Opal in 1995. The alongshore periodicity of these features (~30 transects) is consistent with the

alongshore periodicity in the height of the foredune, suggesting that the alongshore response of the island is directed by a persistent variation in the island geometry that is a reflection of the storm frequency (Stallins and Parker, 2003).

CONCLUSIONS

While it has been well demonstrated in previous studies that the response of a barrier island to an extreme storm depends on the pre-storm morphology, these models only provide a first approximation based on foredune height. Results from the present study suggest that the morphological response not only depends on the foredune height but also on the presence and relative location of secondary dunes and breaks in the crest. Where there were no secondary dunes, overwash and sediment erosion offshore were primarily dependent on the height of the foredune. Where the primary and secondary dunes were closely spaced, overwash was restricted and sediment erosion offshore increased, analogous to having a large wide foredune. As the separation between the primary and secondary dune increases, overwash is not restricted and the amount of sediment eroded offshore is reduced. The alongshore variation in morphological response will ultimately control the recovery of the dune system, such that the alongshore variation in dune height and extent may redevelop and direct the response to the next extreme storm.

ACKNOWLEDGEMENTS

This study was supported by a grant from the National Park Service (P5320060026). LIDAR data was provided to the Park Service by the USGS Center for Coastal & Watershed Studies and the survey transects were prepared by the UWF Geodata Center.

REFERENCES:

Armbruster, C.K., 1997, Morphologic responses of a low-energy, micro-tidal beach to winter cold front passages: North shore Santa Rosa Island, Florida. M.Sc. Thesis, Louisiana State University, Baton Rouge, LA.

Elko, N.A., Sallenger, A.H., Guy, K., & Morgan, K.L.M., (2002). Barrier island elevations relevant to potential storm impacts; 2, South Atlantic: U.S. Geological Survey, Open-File Report 2002-288, 1 folded sheet.

Foster, E.R., Spurgeon, D.L., & Cheng, J., 1999, *Shoreline Change Rate Estimates: Escambia and Santa Rosa Counties*. Report No. BCS-99-03. Tallahassee: Florida Department of Environmental Protection, Office of Beaches and Coastal Systems.

Kwon, H.J., 1969, *Barrier islands of the northern Gulf of Mexico coast: Sediment source and development*. Coastal Studies Series 25. Baton Rouge: Louisiana State University Press.

Leadon, M.E., Clark, R.R., & Nguyen, N.T., 1999, *Hurricane Earl and Hurricane Georges: Beach and dune erosion and structural damage assessment and post-storm recovery plan for Panhandle coast of Florida*. Report No. BCS-

99-01. Tallahassee: Florida Department of Environmental Protection, Office of Beaches and Coastal Systems.

Leadon, M.E., Nguyen, N.T., & Clark, R.R., 1998, *Hurricane Opal: Beach and dune erosion and structural damage along the Panhandle coast of Florida*. Report No. BCS-98-01. Tallahassee: Florida Department of Environmental Protection, Office of Beaches and Coastal Systems.

Liebens, J., 2000, A simple method to evaluate the impact of tropical cyclones on the coast: Hurricane Georges and the Gulf Coast, *Shore and Beach* 68 (1): 17-24.

Morton R.A., (2002). Factors controlling storm impacts on coastal barriers and beaches - a preliminary basis for near real-time forecasting. *Journal of Coastal Research* 18(3): 486- 501.

Morton, R.A., and Sallenger, A.H., 2003. Morphological impacts of extreme storms on sandy beaches and barriers. *Journal of Coastal Research*, 19, 560-573.

Morton, R. A., and Paine, J. G., (1985). Beach and vegetation-line changes at Galveston Island, Texas; Erosion, deposition, and recovery from Hurricane Alicia: The University of Texas at Austin, *Bureau of Economic Geology Geological Circula*r 85-5, 39 p.Otvos, E.G., 1982, Santa Rosa Island, Florida panhandle: Origins of a composite barrier island, *Southeastern Geology* 23 (1): 15-24.

Otvos, E.G., 1997, *Northeastern Gulf Coastal Plain revisited: Neogene and Quaternary units and events—old and new concepts.* Guidebook, Louisiana to Northwest Florida Field Trip, Oct. 17-18, 1997. New Orleans: New Orleans Geological Society.

Sallenger, A. H., 2000. Storm impact scale for barrier islands. *Journal of Coastal Research*, 16, 890-895.

Stallins, J.A., and Parker, A.J., 2003. The influence of complex systems interactions on barrier island dune vegetation pattern and process. *Annals of the Association of American Geographers*, 93, 13-29.

Stapor, F.W., Jr., 1975, Shoreline changes between Phillips Inlet and Pensacola Inlet, northwest Florida coast, *Transactions, Gulf Coast Association of Geological Societies* 25: 373-378.

Stone, G.W., 1991. Differential sediment supply and cellular nature of longshore sediment transport along coastal Northwest Florida and Southeast Alabama since the late Holocene. Ph.D. Dissertation, University of Maryland, College Park, MD.

Stone, G.W. & Morgan, J.P., 1993, Implications for a constant rate of relative sea-level rise, etc., *Shore and Beach* 61 (Oct.): 24-27.

Stone, G.W. & Stapor, F.W., Jr., 1996. A nearshore sediment transport model for the northeast Gulf of Mexico coast, USA, Journal of Coastal Research 12: 786-792

Stone, G.W., Stapor, F.W., Jr., May, J.P., & Morgan, J.P., 1992, Multiple sediment sources and a cellular, non-integrated, longshore drift system: Northwest Florida and southeast Alabama coast, USA, *Marine Geology*105: 141-154.

Thieler, E. R., & Young, R. S., (1991). Quantitative evaluation of coastal geomorphological changes in South Carolina after Hurricane Hugo, *Journal of Coastal Research* (Special Issue) 8, 187–200.

STORM SURGE AND SEDIMENT PROCESS OWING TO HURRICANE ISIDORE IN TERMINOS LAGOON, CAMPECHE

Juan C. Espinal[1], Paulo Salles. A de A[2], Diana K. Morán[3]

1. Universidad Nacional Autónoma de México, Instituto de Ingeniería, Ciudad Universitaria, Coyoacán, México D. F., 04510, México. jespinalg@iingen.unam.mx
2. Universidad Nacional Autónoma de México, Instituto de Ingeniería, Ciudad Universitaria, Coyoacán, México D. F., 04510, México. psallesa@iingen.unam.mx.
3. Universidad Nacional Autónoma de México, Instituto de Ingeniería, Ciudad Universitaria, Coyoacán, México D. F., 04510, México. dmorang@iingen.unam..mx.

Abstract: The hydrodynamic response of Terminos Lagoon to the passage of Hurricane Isidore is presented. The field data analysis shows the changes of the hydrodynamic currents in the Carmen and Puerto Real inlets, as well as the water level elevation in the marine front and the interior of the Terminos Lagoon, due to the storm surge from the ocean, and the large fresh water discharges from land to the lagoon. Finally a brief interpretation of the system behavior is made, showing that in spite the large distance between the lagoon system and the hurricane trajectory (250 km), important effects in the hydrodynamics and sediment transport rates were reported. The identification of the hydrodynamic and sediment transport response to extreme events can help to better understand the physics of such systems, and can be applied to water quality and mass transport studies in semi-enclosed coastal bodies.

INTRODUCTION

Inlet hydrodynamics in coastal lagoons are complex. They result from the interaction between the fluid motion and the bottom floor, which often has a complicated spatial distribution (channels, bars, deltas, platforms…). The fluid motion is in turn generated both by currents (tidal-induced, wind-driven, wave-generated, river flow...) and by waves, which propagated at frequencies ranging from a few seconds to several hours or more.

The tide, propagating from deep to shallow water, suffers a distortion process (energy transfer to higher frequency components, energy loss energy due to friction), which

increases when the tide enters and propagates in a semi-closed body as can be a coastal lagoon. This distortion produces an imbalance between the flood and ebb tidal prisms, favoring the generation of residual currents. The variation of these residual currents over time is responsible for the net circulation through the inlet and for the net transport of silts and sand.

The hurricane Isidore to affect the variation in the hydrodynamic circulation, in all Terminos Lagoon. In order to analyze the effects of waves and storm surge on inlet dynamics, a series of projects have been conducted, including field measurements (waves, currents, suspended sediment), mathematical and numerical modeling. This study consists of numerical simulations of hydrodynamics response of the lagoon system and the changes of hydrodynamic system in Puerto Real inlet, flow (ebb).

STUDY AREA

The Terminos Laggon coastal system is located in the coastal plains of the State of Campeche. It communicates with the Gulf of Mexico through two natural inlets, Carmen and Puerto Real inlets, east and west of the Carmen barrier island, respectively, and Sabancuy Inlet, a small artificial inlet, 43 km northeast from Puerto Real Inlet. The system is composed by a main water body with 4.5 m average depth and a surface area of approximately 1,700 km^2, and a series of adjacent lagoons, some of which are the deltas of rivers entering the main lagoon (see Fig. 1), with a total surface area of 800 km^2. The flood area, up to the +1.0 m relative to the mean sea level, is 4,000 km^2 large.

The climate is tropical humid and is characterized by three stations, regulated by the rain intensity: little precipitation (March to May), heavy rains (June to October), and intermediate precipitations with strong northerly winds or Nortes (November to February). The average yearly precipitation is 1,805 mm (David et al., 1998), and the yearly evaporation has been estimated to be 1,512 mm, which give an average effective input, considered uniformly distributed over the entire system, of 23 $m^3.s^{-1}$. The predominant winds are moderate with north-northeast and east-southeast wind speeds lower than 5 $m.s^{-1}$, except during the Nortes season, in which frontal passages can have average sustained north-northwest wind speed in excess of 12.5 $m.s^{-1}$ (Mancilla et al., 1980).

Most of the fresh-water input to the system comes from three rivers (see Fig. 1): Palizada river with monthly-averaged discharges ranging from 115 to 510 $m^3.s^{-1}$ (288 $m^3.s^{-1}$ yearly average), Candelaria and Mamantel rivers, whose discharges occur in the Panlau lagoon, and range monthly from 23 to 197 $m^3.s^{-1}$ (72 $m^3.s^{-1}$ yearly average), and Chumpán river with discharges ranging from 0.3 to 50 $m^3.s^{-1}$ (18 $m^3.s^{-1}$ yearly average). The tide in the area is mixed-diurnal (Marina, 2001), with the diurnal components being the largest, as shown in Table 1. The average amplitude is 0.424 m, the high high water is 0.923 m and the low low water is –0.662 m, with respect to the mean water level (0.000 m). According to measurements of the water level fluctuations at the inlets and an intermediate point between the inlets (St. 12 in Fig. 1), the phase lag of the tide as it propagates inside the lagoon is important, as shown in Table 2. For instance, the high O_1

tide occurs 1.7 hours later at Carmen Inlet and 5.01 hours later at Station 12. It can be seen that the propagation of the tide is from northeast to southwest in that zone of the Gulf of Mexico. Furthermore, the propagation experiences selective dampening inside the lagoon, as a result of higher friction and energy transfer from one component to another.

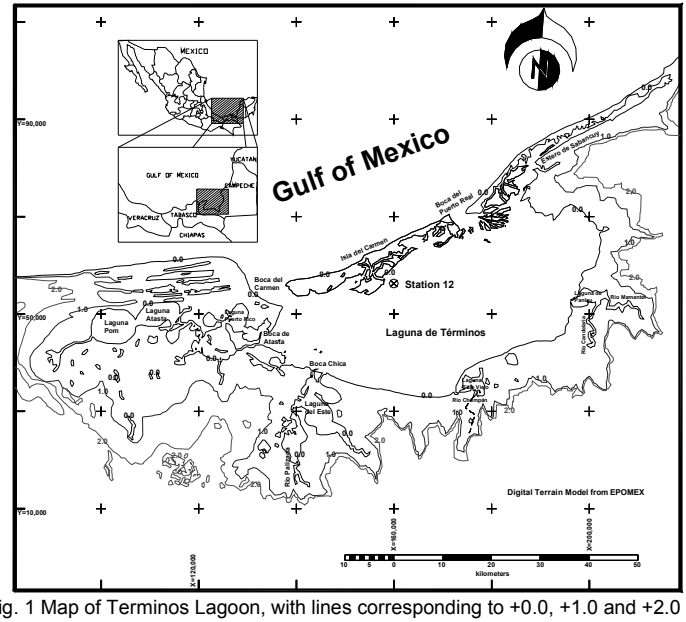

Fig. 1 Map of Terminos Lagoon, with lines corresponding to +0.0, +1.0 and +2.0 m.

Table 1 Main Harmonic Components

Component	M_2	S_2	N_2	K_1	O_1	P_1
H (m)	0.076	0.019	0.021	0.111	0.120	0.036
Phase (º)	78.58	73.63	67.35	315.17	318.93	321.44

Table 2 Phases of the Main Harmonic Components (in Degrees and Hours, minutes), relative to Puerto Real.

Component	M_2	S_2	N_2	K_1	O_1	P_1
Puerto Real	0	0	0	0	0	0
Carmen	-33 / 1:08	-8 / 0:16	-39 / 1:22	-36 / 2:24	-24 / 1:43	-27 / 2:01
St. 12	-134 / 4:38	-254 / 8:28	---	-67 / 4:27	-70 / 5:01	-41 / 3:04

Table 3 Dischargers in Terminos Lagoon during Hurricane Isidore effect.

	River			
Name	Palizada	Chumpan	Candelaria/mamantel	Las Coloradas
Discharge (m^3/s)	510	50	197	35

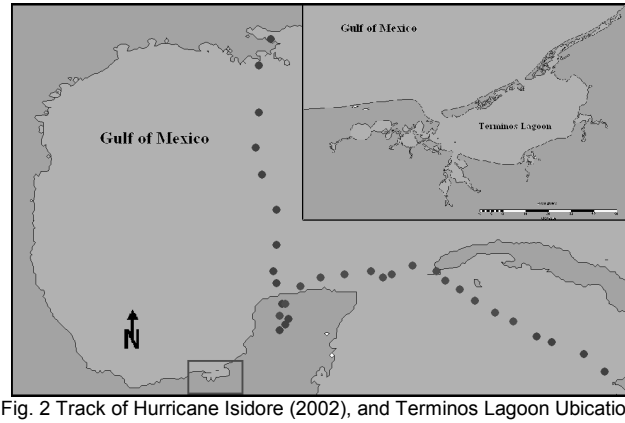

Fig. 2 Track of Hurricane Isidore (2002), and Terminos Lagoon Ubication

Location and Description of Oceanographic Equipments

In order to gather oceanographic data in the Terminos Lagoon, the Coastal and Ports Engineering Group (GICP) of the Engineering Institute of the UNAM and the Federal Electricity Commission (CFE) placed two oceanographic equipments to collect current and wave data, in the Puerto Real Inlet (GICP) and Carmen Inlet (CFE). Additionally, water level elevation data was collected with the Navy tide gage (SEMAR, 2001), located in the oriental margin of Carmen Inlet. During the campaign, hurricane Isidore stroke the coast of Yucatan (Fig. 2), which was recorded by the three instruments.

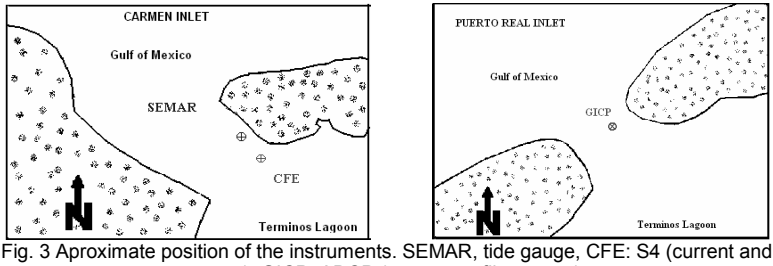

Fig. 3 Aproximate position of the instruments. SEMAR, tide gauge, CFE: S4 (current and waves), GICP: ADCP (current profile, waves).

NUMERICAL MODEL

Numerical simulations of the tidal dynamics in the system, using RMA-2V (Donnell et al., 1997), a vertically integrated finite-element model that solves the non-linear momentum and continuity equations, complemented with COPLA-2DH (COPLA-RD, 1998), a wave parabolic model for the wave propagation under the presence of currents, were performed in order to estimate the flow characteristics at the inlet. Finally, the bedload and suspended load sediment transport at different locations was computed by means of a combined wave-current bottom boundary layer flow model (e.g., USACE, 2001).

WAVE PROPAGATION

The wave propagation includes both inlets, with 1 and 3 m height waves whit 6 and 12 second period, respectively approaching from the North, which is the more common wave direction, according to the directional spectrum analysis of the data (Mantilla, 2004).

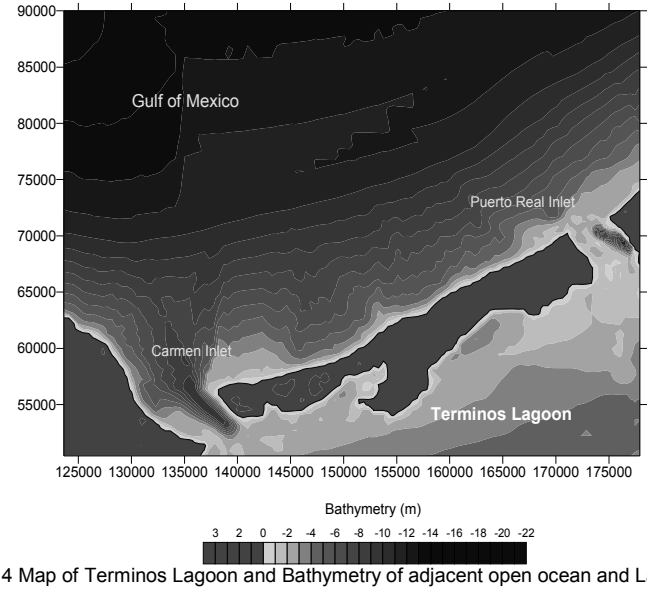

Fig. 4 Map of Terminos Lagoon and Bathymetry of adjacent open ocean and Lagoon.

In order to obtain the form of the wave and induced current characteristics at the Inlets, a model was used to propagate the waves, as shown in the following figures.

In the case of the 1m waves at Carmen Inlet (Fig. 5), the model results show that the induced currents, between 0.2 and 0.5 $m.s^{-1}$, are oceanward in the western boundary of the inlet and lagoon ward in the eastern section. In turn, the Puerto Real Inlet presents increasing induced currents after the waves pass the ebb delta and become more nonlinear (Fig. 6).

The effect of increasing the wave height in Carmen Inlet is that all the induced current becomes flood-oriented (Fig. 7). The increase of wave height and period in Puerto Real Inlet produces simply an increase in the induced current (Fig. 8).

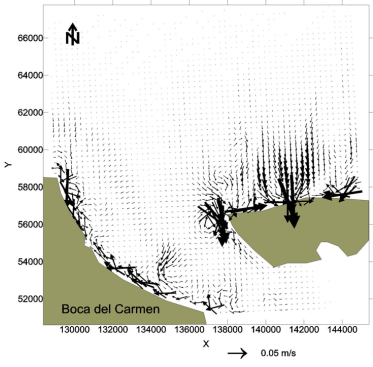

Fig. 5 Wave-induced current velocity vectors at Carmen Inlet with 1m waves (period=6s)

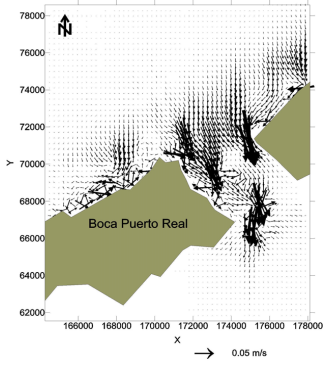

Fig. 6 Wave-induced current velocity vectors at Puerto Real Inlet with 1m waves (period=6s)

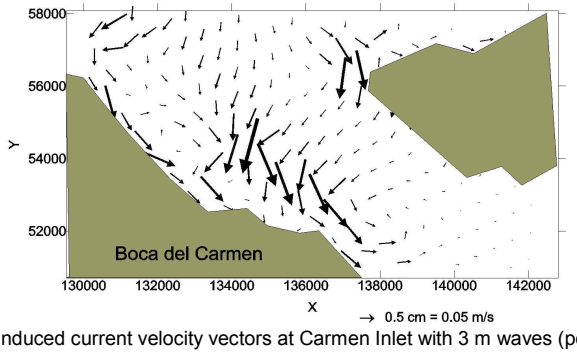

Fig. 7 Wave induced current velocity vectors at Carmen Inlet with 3 m waves (period = 12 s)

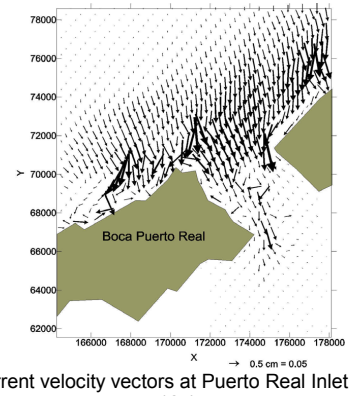

Fig. 8 Wave induced current velocity vectors at Puerto Real Inlet with 3 m waves (period = 12s).

LONG PERIOD CURRENTS

The modeled current velocities across the inlets were computed as the weighted average for the nodes of the cross-section, as shown in Fig. 9.

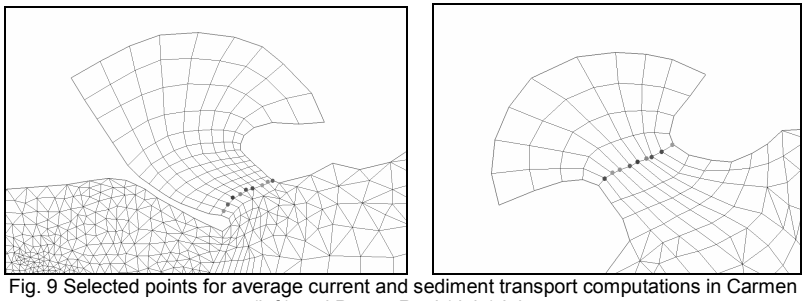

Fig. 9 Selected points for average current and sediment transport computations in Carmen (left) and Puerto Real (right) Inlets.

The hydrodynamic results include the effect of river discharges, and tide for a 20 day period encompassing the days during which Hurricane Isidore stroke the area. The tide gauge in Carmen and Puerto Real Inlets are shown in Fig. 10 and Fig. 11.

The hydrodynamic results to Carmen and Puerto Real Inlets was obtained by RMA2 Model implemented, next figures show the cross sectionally average flow velocity, in both cases flow negative is flood and positive ebb.

Although Fig. 10and 11 show stronger flood currents at both inlets, a closer analysis of the discharger (e.g., Espinal 2002) indicate that Carmen Inlet is a net exporter of water on normal conditions (before Isidore). While Puerto Real Inlet is a net import of water before on normal conditions.

Indeed, these same figures show that Carmen Inlet presented stronger and longer ebb flows during a small fraction of the first part of the Hurricane surge (22/09) but in fact remained directed to the lagoon (flood) during most of the Hurricane passage (Fig. 10). Inversely, the flow through Puerto Real Inlet was ebb oriented most of the duration of the Hurricane surge (Fig. 11). In other words, there was a reversal of the flows, Carmen became net importer of water, and Puerto Real net exporter.

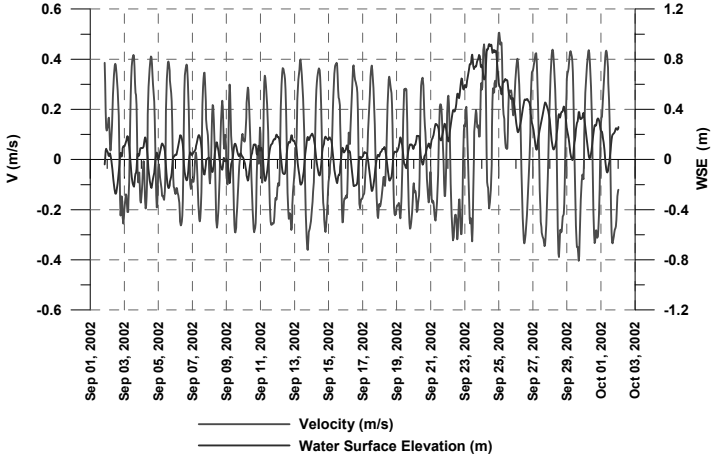

Fig. 10 Water surface elevation and cross-sectionally averaged flow velocity in Carmen Inlet (negative is flood).

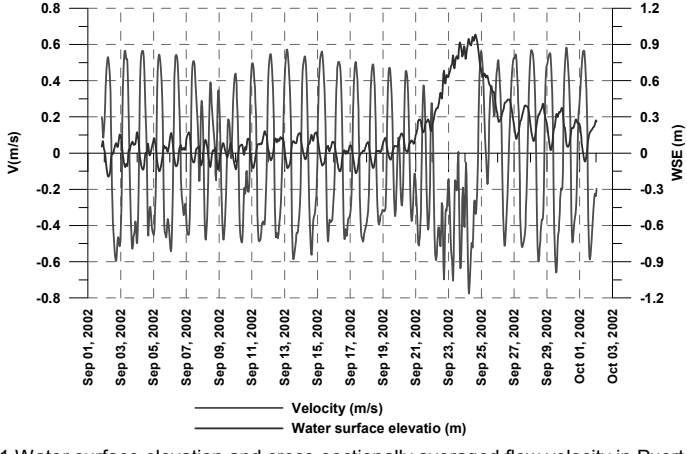

Fig. 11 Water surface elevation and cross-sectionally averaged flow velocity in Puerto Real Inlet (negative is flood)

Fig. 12 shows the current profile data at the Puerto Real site, during the passage of Hurricane Isidore. These data confirm the water export at Puerto real, found also in the model results presented above.

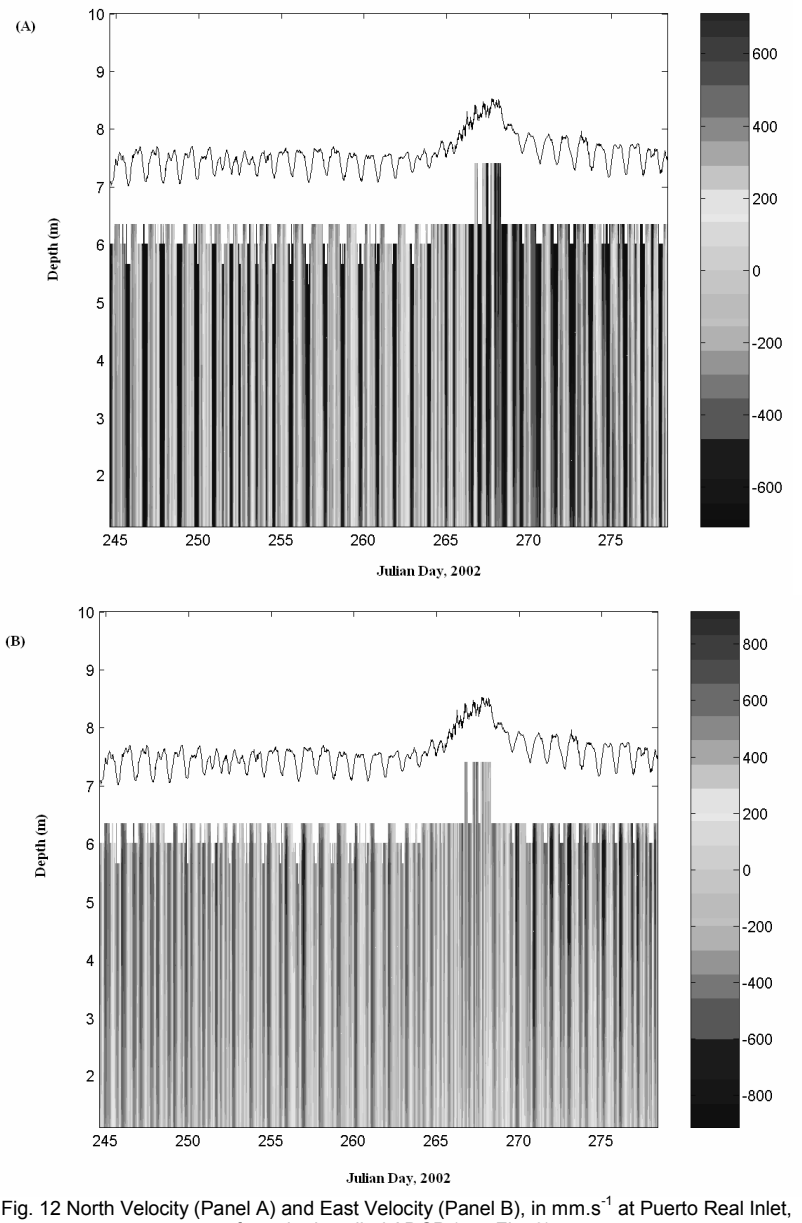

Fig. 12 North Velocity (Panel A) and East Velocity (Panel B), in mm.s^{-1} at Puerto Real Inlet, from the installed ADCP (see Fig. 3).

SEDIMENT TRANSPORT ACROSS THE INLETS

The transport of non-cohesive material is calculated by means of a combined wave-current bottom boundary layer flow model computed whit two conditions of wave and long period currents to normal and storm surge conditions (Hurricane Isidore) and rivers discharge.

The modeled effect of the Isidore Hurricane on the sediment transport rates at Carmen Inlet can be observed in Fig. 13 and at Puerto Real Inlet in Fig. 14.

The peaks are generally more uniform in all cross section, both inlets increased sediment transport rates, associated whit stronger velocity gradients presented during hurricane Isidore.

What can be seen from these figures is that the sediment transport rate (in $m^3.s^{-1}.m^{-1}$) during the passage of Hurricne Isidore decreased at Carmen Inlet and Increased at Puerto Real Inlet. In other words, and according to the hydrodynamics shown previously, Carmen imported small amounts of sand during Isidore, and Puerto Real exported large amounts of sand during that same period.

Although a thorough analysis of the effects of waves on sediment transport can be done analytically, this example simply shows the importance of considering waves when studying the morphological evolution of coastal features as inlets. In Terminos Lagoon, especially in the flood dominant Puerto Real Inlet, the wave effects on sediment transport are considerable. The large sediment transport capacity obtained when considering waves in this inlet is consistent with the observed morphologic evolution.

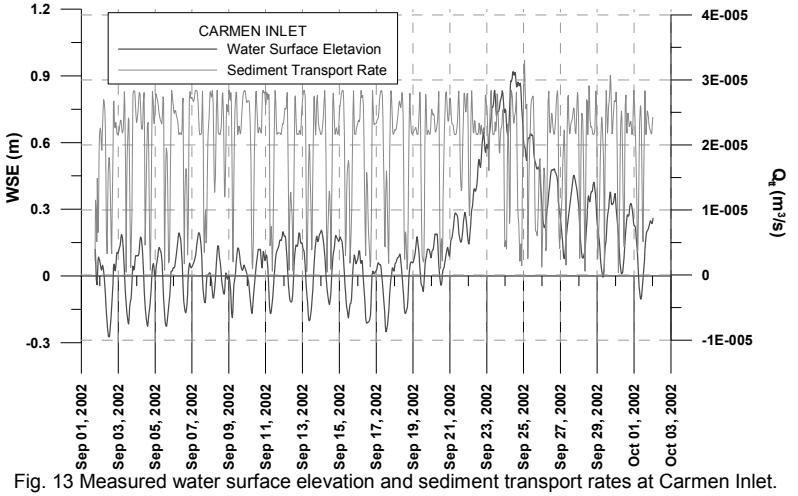

Fig. 13 Measured water surface elevation and sediment transport rates at Carmen Inlet.

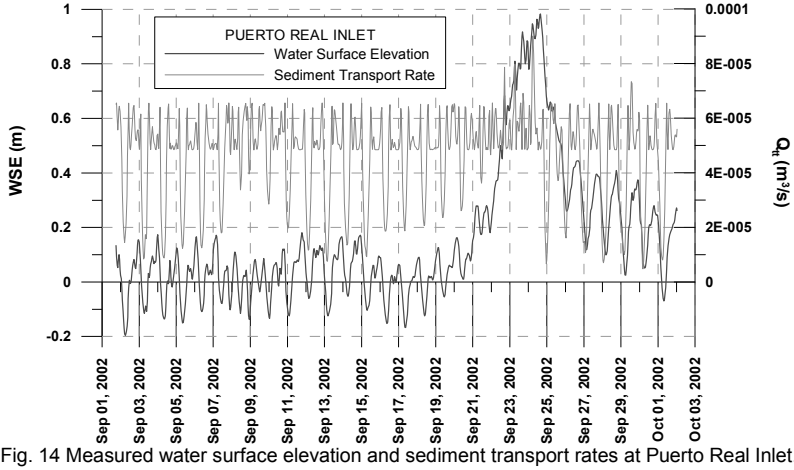

Fig. 14 Measured water surface elevation and sediment transport rates at Puerto Real Inlet.

CONCLUSION

The following conclusions can be made:

Terminos Lagoon is protected in a natural way by the configuration of the Gulf of Mexico and the Orientation of the Lagoon System.

Given the measured and modeled currents for the period of the passage of Hurricane Isidore, the water surface elevation increase that occurred at both inlets may have not been caused only by a storm surge, but also by large volumes of freshwater discharged by the rivers and surface runoff.

The storm surge can increase the rates of sediment transport, but for the case of Carmen Inlet it seems that the sediment transport decreased.

The combination of field data with modeling can be a useful tool to understand hydrodynamic and morphodynamic responses in coastal environments affected by large storm events.

ACKNOWLEDGETMENTS

The author of this paper would like to acknowledge the assistance of "Zona Naval 5 de la Secretaria de Marina, Armada de Mexico" and "Departamento de Oceanografía de la CFE." This work was partially supported by Instituto de Ingeniería, UNAM.

REFERENCES

COPLA-RD (1998). Modelo integral de propagación de oleaje y corrientes en playa., Manual de Usuario, versión 1.0. Universidad de Cantabria.

David, L. T. and B. Kjerfve (1998). "Tides and Currents in a Two-Inlet Coastal Lagoon: Laguna de Términos, México." Continental Shelf Research 18(10): 1057-1079.

Donnell, B. P., J. I. Finnie, J. V. Letter, W. H. McAnally, L. C. Roig and W. A. Thomas (1997). User's Guide to RMA2 WES Version 4.3. US Army Corps of Engineers - Waterways Experiment Station Hydraulics Laboratory.

Espinal G. J. C., 2002. "Caracterización del Transporte de Sedimentos en las Bocas del Carmen y Puerto Real en Laguna de Términos, Campeche". Tesis de Maestría, Posgrado Ingeniería UNAM. pp 100.

Mancilla, M. and M. Vargas (1980). "Los primeros estudios sobre la circulación y el flujo neto de agua a través de la laguna de Términos, Campeche, México." An. Instituto de Ciencias del Mar y Limología, UNAM 7(2): 1-12.

Mantilla T., Megumi, 2004. "Mediciones y análisis de datos para el estudio de los efectos del oleaje en la estabilidad de bocas estuarinas", Masters thesis Universidad Nacional Autónoma de México- Facultad de Ingeniería. March 2004

Marina, S. d. (2001). Tablas de Mareas, Golfo de México y Mar Caribe. Dirección general de Oceanografía Naval.

USACE (2001). Coastal Engineering Manual. Washington D.C.

TSUNAMI DAMAGE ESTIMATION IN CONSIDERATION OF BEACH TRANSFORMATION AND DIKE FAILURE

Fuminori Kato[1], Masaya Fukuhama[2], Hiroyuki Fujii[3], Toshimitsu Takagi[4]

1. National Institute for Land and Infrastructure Management, Asahi 1, Tsukuba 305-0804, Japan. katou-f92fr@nilim.go.jp
2. National Institute for Land and Infrastructure Management, Asahi 1, Tsukuba 305-0804, Japan. fukuhama-m92fc@nilim.go.jp
3. INA Corporation, Sekiguchi 1-44-10, Bunkyo-ku 112-8668, Tokyo, Japan. hr-fujii@ina-eng.co.jp
4. INA Corporation, Sekiguchi 1-44-10, Bunkyo-ku 112-8668, Tokyo, Japan. t-takagi@ina-eng.co.jp

Abstract: Quantitative estimation methods for tsunami damage to houses and humans are proposed in consideration of beach transformation and dike failure. Case studies were conducted for Kochi Coast, Japan, where dike subsidence caused by earthquake motions, topographical change by tsunami, and dike failure by toe scouring is expected. Damage to houses and humans on land increases with dike subsidence and dike failure, and public awareness of evacuation had a significant influence on the extent of human damage. The methods used in this study quantitatively evaluated the mitigation of tsunami damage achieved by making coastal dikes earthquake- and tsunami-resistant, and raising the level of evacuation awareness.

INTRODUCTION

Coastal areas in Japan are at risk of tsunami disasters although concrete-armored dikes are distributed along the long shoreline. The central and prefectural governments have conducted tsunami damage estimations assuming non-failure of coastal dikes during earthquake and tsunamis. However, even concrete-armored dikes could fail by strong earthquake motions or large tsunamis, resulting in tremendous damage to coastal zones. Dike subsidence caused by earthquake motions and dike failure by scouring should be taken into account in tsunami damage estimation in order to determine the most effective measures for tsunami damage mitigation. Moreover, topographical change caused by tsunamis should also be considered because tsunami runup transforms river-mouth bars that act as breakwaters and erodes sandy beaches that form the foundation of coastal dikes.

We propose a method for estimating tsunami damage to humans and houses taking into consideration beach transformation and dike failure, as shown in Figure 1.

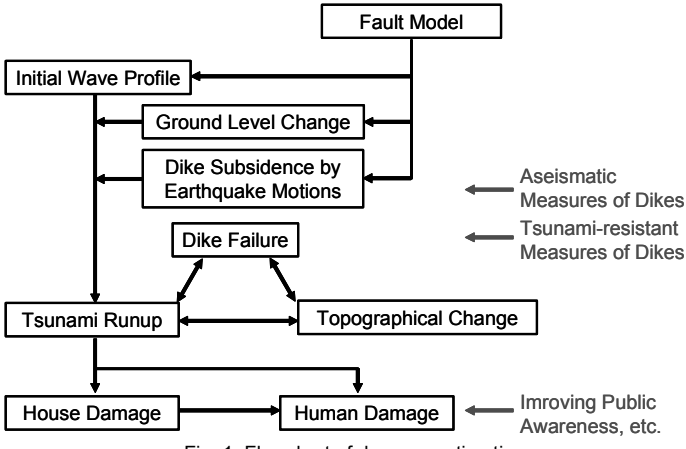

Fig. 1. Flowchart of damage estimation

TSUNAMI SIMULATION

Calculation Method

Case studies were conducted for Kochi Coast, Kochi Prefecture, Japan, where huge tsunamis generated by large-scale earthquakes are expected in the near future. Tsunamis were simulated using a fault model in which the Tonankai and Nankai Earthquakes occur at the same time as shown in Figure 2. Table 1 shows conditions for the case studies, which were taken into account in the tsunami simulations based on nonlinear long-wave equations. Grid size of calculation was refined from 2700 m to 11 m. Initial tide level was set at the mean monthly-highest level (0.945 m above the mean sea level in Tokyo Bay). Gates and sluices were assumed to be closed in the simulations.

Dike subsidence caused by earthquake motions was calculated using dynamic FEM analysis for the case in which the Tonankai and Nankai Earthquake occur at the same time (magnitude 8.6). In this analysis, the effects of concrete covering coastal dike were ignored for the Nino District (east of the Niyodo River) because the seaward slope of the dike is not covered with much sand. On the other hand, for the Nii District where considerable sand covers the seaward slope, the effects were taken into account. Therefore, dike subsidence was estimated at 3.44 m for Nino and 0.09 m for Nii. Besides this, the ground level was expected to fall by about 2 m on the Kochi Coast because of the earthquake. The post-earthquake crest height of the coastal dike was estimated to be T.P. +4.39 m (4.39 m above the mean sea level in Tokyo Bay) for Nino and T.P. +8.02 m for Nii.

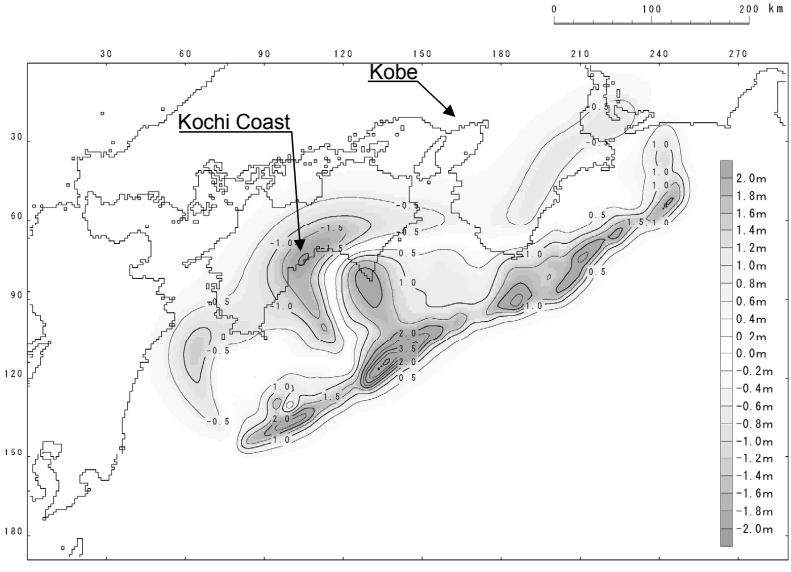

Fig. 2. Change in ground level (source: Central Disaster Prevention Council)

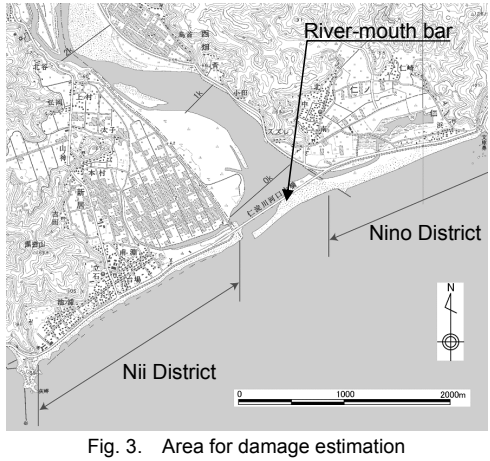

Fig. 3. Area for damage estimation

Table 1. Conditions for case studies

Case	Dike subsidence	Topographical change	Dike failure
A1	No	No	No
A2	Yes	No	No
B3	Yes	Yes	No
B4	Yes	Yes	Yes

As shown in Figure 4, tsunami simulation considering dike failure was conducted after that without dike failure in order to estimate the timing of failure. According to Takahashi et al. (1993), topographical change caused by tsunami was calculated using Brown's equations with bottom friction force based on Manning's formula, and the continuity equation proposed by Watanabe et al. (1984).

$$Q_s = \frac{u_*^5}{(\sigma/\rho - 1)^2 g^2} \frac{10}{d} \tag{1}$$

$$u_* = \sqrt{\tau/\rho} \tag{2}$$

$$\tau = \rho g n^2 (u^2 + v^2) / D^{1/3} \tag{3}$$

where Q_s = sediment transport rate; u_* = friction velocity; σ = sand density; ρ = water density; g = gravity acceleration; d = grain size; τ = sheer stress; n = Manning's roughness; u and v = horizontal velocity; and D = total water depth. Thickness of sand layer was set at 0 for grids corresponding to coastal dike because the dike is covered with concrete. Median grain size and pore ratio in the model were set at 2 mm and 0.4, respectively. Total scour depth was calculated by adding time series of scour depth to topographical change caused by tsunami, because scouring due to overflow is a dominant cause of topographical change near coastal dikes. Scour depth was calculated using the equation proposed by Noguchi et al. (1997) and the overflowing rate at the coastal dike. We assumed that the crest height of the coastal dike lowered to initial ground level near the coastal dike when ground level near the coastal dike fell to the residual water level in the coastal dike (T.P. +0.54 m).

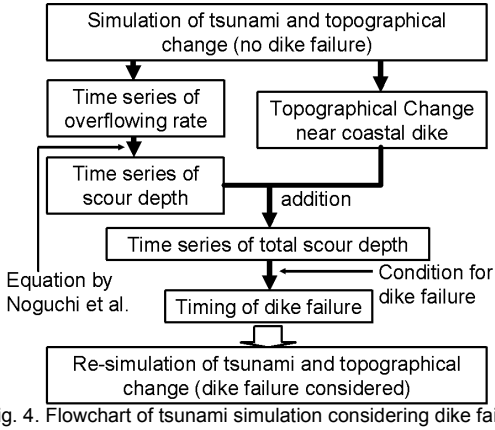

Fig. 4. Flowchart of tsunami simulation considering dike failure

Results of Calculations

Figure 5 shows the calculation results for water level and velocity in front of the coastal dike at Nino District for Case B3. The water level reached a peak (6.53 m) about 30 minutes after the earthquake, and fluctuated after the peak. Overflowing

occurred only near the peak water level, resulting in strong landward flow. The results indicate that only the first wave overtopped in Nino District. As for Case B4, the dike failed 33 minutes after the earthquake. The dike failure lowered the maximum water level by increasing the overflowing rate as shown in Figure 6, and increased the velocity after the second wave. On the other hand, overflowing did not occur in Nii District because dike subsidence was very small.

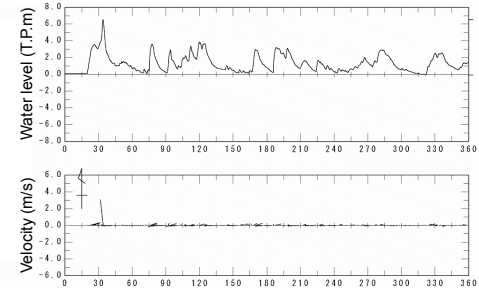

Fig. 5. Water level and velocity in front of coastal dike at Nino District (Case B3)

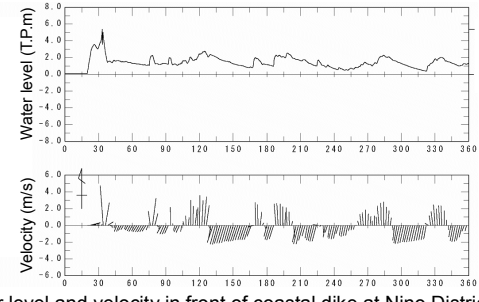

Fig. 6. Water level and velocity in front of coastal dike at Nino District (Case B4)

Figure 7 shows the maximum water level in each case. In Case A1, the maximum water level reached 7 -8 m in Nino and Nii, about 6 m seaward of the river-mouth bar, and less than 5 m in the Niyodo River because of the river-mouth bar. In Case A2 when dike subsidence was taken into account, the maximum water level in front of the coastal dike at Nino was about 1 m lower than that in Case A1. In Case B3 when topographical change and dike subsidence were considered, the maximum water level lowered by about 1 m on the river-mouth bar, but rose slightly in the river. In Case B4 in which even dike failure was assumed, the water level rose on the land in Nino, and inundation area expanded slightly.

Figure 8 shows the maximum water depth in each case. In Case A1, the maximum water depth was more than 6 m in front of the coastal dike in Nii and Nino, and more than 4 m on the river-mouth bar. In Case A2 in which dike subsidence was taken

into account, the maximum water depth exceeded 2 m in low areas of the hinterland. In Case B3 in which topographical change was also considered, the water depth was larger on the river-mouth bar than that in Case A2. In Case B4 in which dike failure was also considered, the maximum water depth on the land increased more.

Figure 9 shows the maximum velocity in each case. In Case A1, the velocity exceeded 5 m/s at the upstream side of the river-mouth bar during tsunami runup, and at the cutoff of the river-mouth bar during tsunami drawdown. In Case A2, the velocity on the land reached a peak of more than 5 m/s during tsunami runup. As shown in Cases B3 and B4, consideration of topographical change and dike failure increased the velocity on the land.

Figure 10 shows the extent of topographical change in Cases B3 and B4. A tendency to erode near the coastal dike and to accumulate in low areas of the hinterland was shown. Tsunami runup moved the river-mouth bar upstream, and tsunami drawdown caused accumulation off the cutoff of the river-mouth bar and off the point of dike failure. At the tip of the river-mouth bar, the ground level lowered by 2 m or more.

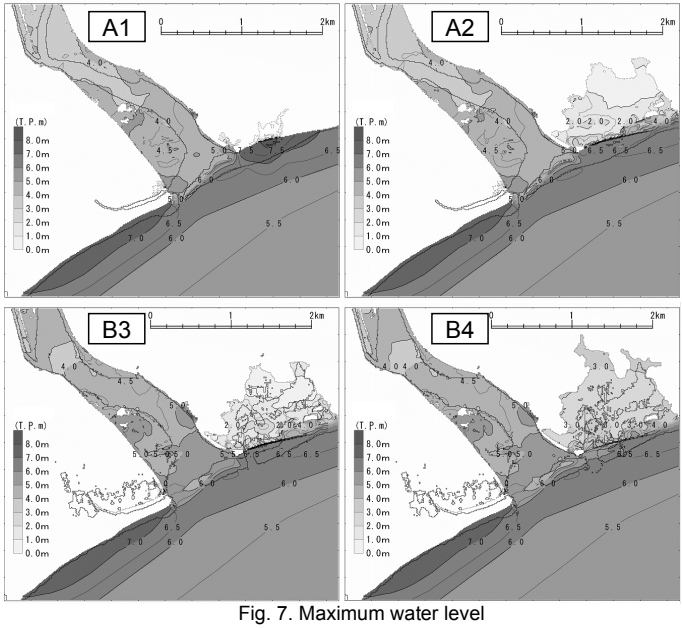

Fig. 7. Maximum water level

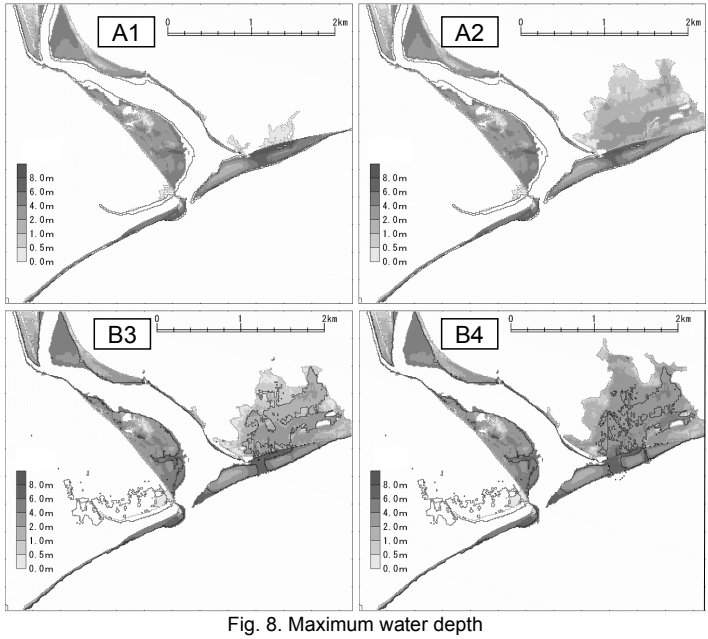

Fig. 8. Maximum water depth

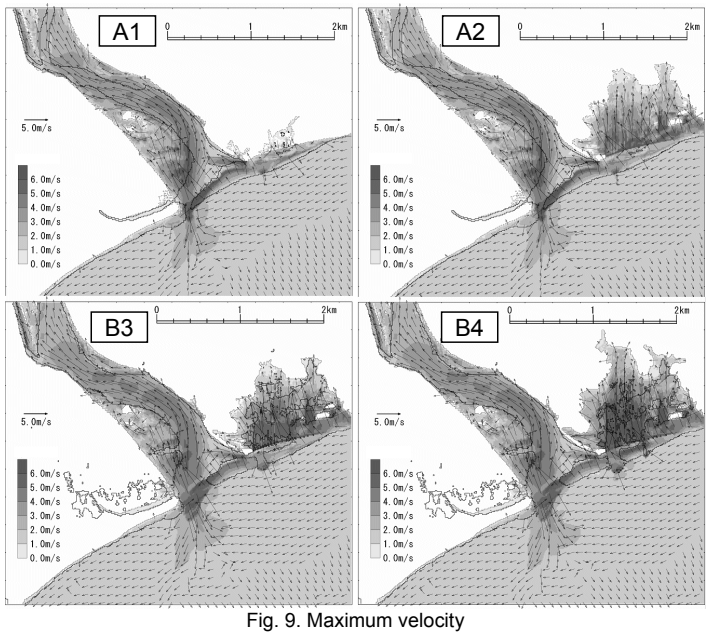

Fig. 9. Maximum velocity

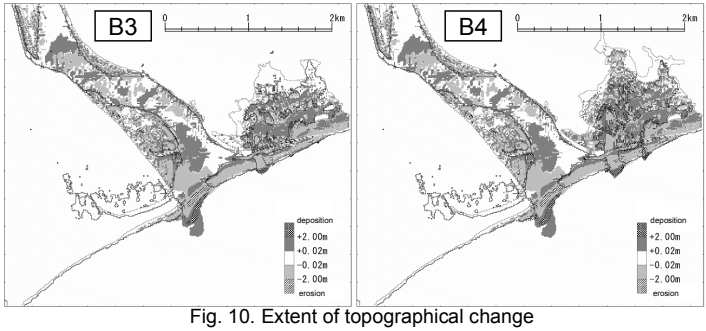

Fig. 10. Extent of topographical change

DAMAGE ESTIMATION

Estimation Method

Major damage functions for houses and human were selected from past tsunami damage estimations conducted by prefectures and the Central Disaster Prevention Council of Japan. House damage was estimated using Kanagawa Prefecture's damage functions (wooden houses, heavily destroyed: water depth > 4 m, partially destroyed: water depth > 2 m) and those of the Special Investigation Committee on the Tonankai and Nankai Earthquakes in the Central Disaster Prevention Council (as well as many prefectures) as shown in Table 2. Human damage was estimated using house damage or the maximum water depth with three functions shown in Table 3. In the method used by Kanagawa Prefectures, etc., the death toll and the number of injured people was estimated based on damages caused by the Tonankai Earthquake (1944) and Nihonkai-Chubu Earthquake (1983), respectively. Casualty estimation in the method used by Shizuoka Prefecture, etc., and the death rate in the method used by the Central Disaster Prevention Council were based on damage caused by the Hokkaido-Nanseioki Earthquake (1993). In the Central Disaster Prevention Council's method, four cases were set considering the difference between general and "tsunami" earthquakes in human behavior, and public awareness of evacuation. "Tsunami" earthquakes correspond to earthquakes which generate rather large tsunamis for small earthquake motions. The ratio of persons who did not complete evacuation varied with tsunami arrival time, which was set at a value for 33 minutes after the earthquake (average time of dike failure in the simulation).

Table 2. Criteria for evaluating house damage

Damage	Water depth	
	Wooden houses	Non-wooden houses
Heavily damaged	$H \geq 2.0$ m	-
Partially damaged	$1.0 \text{ m} \leq H < 2.0$ m	-
Slightly damaged	$0.5 \text{ m} \leq H < 1.0$ m	$H \geq 2.0$ m
Inundation below floor level	$H < 0.5$ m	$H < 0.5$ m

Table 3. Criteria for evaluating human damage

Method	Death toll	Number of people injured
Kanagawa Prefecture, etc.	$0.072(N_t+0.5N_c)^{1.018}$ N_t: Number of houses heavily damaged N_c: Number of houses partially damaged	Heavily injured: $0.00001074(N_t+0.5N_c)^{1.961}$ Slightly injured: $0.00004510(N_t+0.5N_c)^{1.961}$
Shizuoka Prefecture, etc.	$0.0424\exp(0.1763r_h)$ X (Population) r_h: $(N_t+0.5N_c)$/(Number of houses)	Heavily injured: $0.0340r_h$ X (Population) Slightly injured: $0.0822r_h$ X (Population)
Central Disaster Prevention Council (CDPC)	People evacuate: (Population affected) X (Ratio of persons who do not complete evacuation) X r_d People not evacuate: (Population affected) X r_d r_d =0.0282exp(0.2328 X (Water depth))	

Results of Estimation

Figure 11 shows the estimated number of damaged houses. The maximum water depth was less than 4 m for all cases, so that the number of houses partially damaged estimated using Kanagawa Prefecture's method was equal to the number of houses heavily damaged using the Central Disaster Prevention Council's method. In the results obtained with the Central Disaster Prevention Council's method, the number of houses heavily or partially damaged was 39 for Case A2 (dike subsidence considered) and 148 for Case B4 (dike subsidence, topographical change and dike failure considered), while only one house was inundated in Case A1. Dike subsidence and dike failure increased the water depth and flooded area on land, which greatly influenced the extent of house damage.

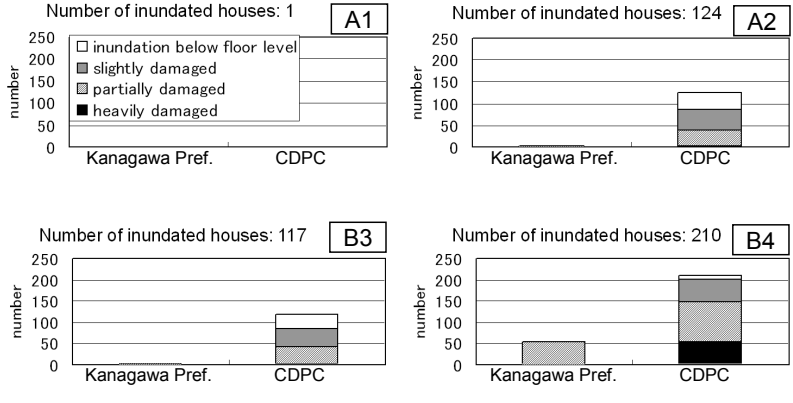

Fig. 11. Estimated house damage

Figure 12 shows the human damage estimated using the methods shown in Table 3. In the results obtained with Kanagawa Prefecture's method, the death toll was almost 0. In the results obtained using Shizuoka Prefecture's method, casualties increased with the number of houses damaged, reaching 90 for Case B4. In the results obtained using the Central Disaster Prevention Council's method, the death toll was very small when public awareness of evacuation was high, because the ratio of persons who evacuated was high and that of persons who did not complete evacuation was low. On the other hand, when public awareness of evacuation was low, the death toll for tsunami earthquakes was about two times that for general earthquakes, because the ratio of persons who did not complete evacuation was high. This indicates that improved public awareness of evacuation has a mitigating effect on the extent of human damage.

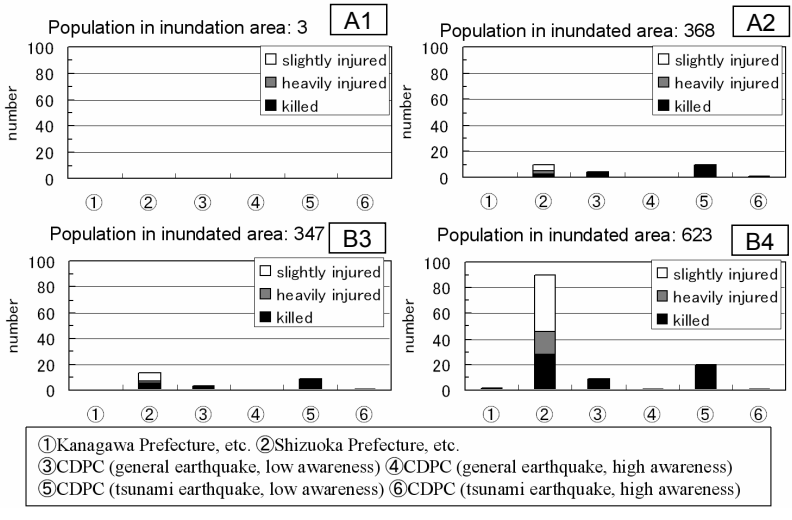

Fig. 12. Estimated human damage

CONCLUSIONS

As described above, the extent of damage to houses and humans on land was increased by dike subsidence and dike failure, and public awareness of evacuation had a significant influence on human damage. The methods used in this study quantitatively evaluated the mitigation of tsunami damage to humans and houses achieved by making coastal dikes earthquake- and tsunami-resistant, and raising the level of evacuation awareness.

ACKNOWLEDGEMENTS

We thank Kochi Office, Shikoku Regional Bureau, Ministry of Land, Infrastructure and Transport, for survey on earthquake-resistance of coastal dikes.

REFERENCES

Noguchi, K., Sato S., and Tanaka, S. (1997), "Large-scale experiments on tsunami overtopping and bed scour around coastal revetment", *Proceedings of Coastal Engineering, JSCE*, Vol. 44, 296-300 (in Japanese).

Shuto, N. (1988), "Tsunami disasters and problems on their countermeasures", *Proceedings of the 35th Japanese Conference on Coastal Engineering*, 237-241 (in Japanese).

Takahashi, T., Imamura, F., and Shuto, N. (1993), "Numerical simulation of topography change due to tsunamis", *Proceedings of the IUGG/IOC International Tsunami Symposium*, 243-255.

Watanabe, A., Maruyama, Y., Shimizu, T., and Sakakiyama, T., (1984), "Numerical model on 3-D beach transformation with structure construction", *Proceedings of the 31st Japanese Conference on Coastal Engineering*, 406-410 (in Japanese).

BEACH MORPHOLOGY AT BANDA ACEH, INDONESIA IN RESPONSE TO THE TSUNAMI ON 26 DECEMBER 2004

Ella Meilianda[1], C. Marjolein Dohmen-Janssen[2], Ben H.P. Maathuis[3], Suzanne J.M.H. Hulscher[4], Jan P.M. Mulder[5]

1. Water Engineering & Management (WEM), University of Twente, PO Box 217, 7500 AE Enschede, The Netherlands / / Syiah Kuala University, Banda Aceh, Indonesia, email: e.meilianda@utwente.nl
2. Water Engineering & Management (WEM), University of Twente, PO Box 217, 7500 AE Enschede, The Netherlands, email: c.m.dohmen-janssen@utwente.nl
3. Water Resources, International Institute for Geo-Information Science and Earth Observation (ITC), PO Box 6, 7500 AA Enschede, The Netherlands, email: maathuis@itc.nl
4. Water Engineering & Management (WEM), University of Twente, PO Box 217, 7500 AE Enschede, The Netherlands, email: s.j.m.h.hulscher@utwente.nl
5. Water Engineering & Management (WEM), University of Twente, PO Box 217, 7500 AE Enschede, The Netherlands, email: j.p.m.mulder@utwente.nl;

Abstract: A study of morphological response and development of beaches which were affected by the earthquake and the tsunami on 26th December 2004 has been conducted at two selected coastal sections of Banda Aceh, Indonesia. A simplified principle adopted from one-line shoreline theory in a geospatial analysis utilizing identified shoreline features across the foreshore zone is applied. The analysis yields a rough estimation of the shoreline and sediment volume changes since the tsunami. After the severe impact as revealed by a significant chaotic shoreline retreat, the morphological development in the following 6 months has shown that about 15% of the total sediment loss due to the tsunami on the northwest coast has further been eroded, while 60% of that on the west coast has been compensated by accretion. This leads to a conclusion that different coastal characteristics show different responses to, and developments after the tsunami.

INTRODUCTION

On 26th December 2004 at 7:58 hr. local time (i.e. North Sumatra Time = GMT + 7 hours), South-East Asia was hit by an earthquake with a magnitude of at least 9.0 (Stein and Okal, 2005), which generated tsunami waves. Being only 150 km away from the epicentre, the earthquake and the resulting tsunami destroyed almost everything in the coastal region of Banda Aceh and lead to a dramatic change of the coastal morphology.

Another big earthquake (8.7) subsequently occurred on 28th March 2005 at 23:09 hr local time (Anonymous, 2006) which epicenter was near Simeulue Island, ca. 300 km south of Banda Aceh. The earthquake caused severe land subsidence in the area around Banda Aceh, i.e. about 2 m at the west coast and about 0.3 – 0.6 m at the northwest coast (e.g. Gibbons and Gelfenbaum 2005). The tsunami caused extensive inland inundation, severe coastal erosion and large tsunami deposits inland (Jaffe et al. 2006).

The objective of the present study is to quantify the coastal morphological changes in response to the earthquake and the following tsunami waves and to determine how the morphology has developed since then. The importance of the present study is twofold: one, to quantify the magnitude of the changes and development in time; and two, to understand how the coast responses to this impact. In the present study, these phenomena are presented through an alongshore shoreline variability analysis and a volume change of the beach profiles over a relatively short term period (< 1 year).

This paper starts with a general description of the coastal zone of Banda Aceh followed by a more detailed assessment of the two selected areas. A qualitative description of the morphological changes due to the tsunami and the development since then is also included. Subsequently, the methods applied and their relevance to the objectives of the study is discussed. This is followed by descriptions of data analysis, shoreline features identification and the net volume change concept. The results of the applied methods are subsequently discussed and the paper ends with some general conclusions derived from the study.

STUDY AREA

To understand in more detail of the morphological changes in response to such a huge scale of disaster, we observe two small spatial scale coastal sections (~ 1 to 4 km) on the study area. Each coastal section has a different morphological characteristic. Here, we have to choose the part of the coast which has the best data quality. Our choice falls on the Ulee Lheue (reads: *Oo le le*) beach which is located on the northwest coast and Lampuuk beach (reads: *Lampoo ook*) which is located on the west coast of Banda Aceh. The lengths of the coastal sections are ca. 1 and 4 km, respectively. A map showing the overall study areas is presented in Fig. 1.

Ulee Lheue Beach, Northwest coast

Before the tsunami, almost the entire Ulee Lheue beach was protected by seawalls (Fig. 1b). They were constructed to protect the backshore from flooding during spring tides

and from severe wave attack. Moreover, the northwest coast had also subjected to significant erosion in the past few years before the tsunami. A short stretch of the beach remained open for recreational purposes near the Ferry port. The average elevation of the backshore was about 1.5 to 2.0 m above lowest low water level. This narrow coast separated a coast-parallel lagoon system from the sea.

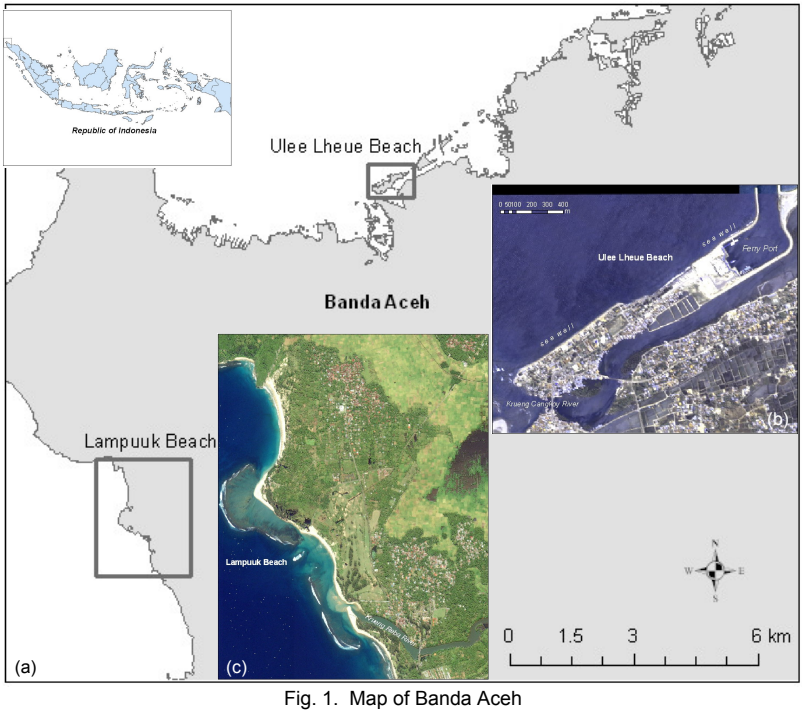

Fig. 1. Map of Banda Aceh

Since the tsunami, this low-lying northwest coast suffers from permanent inundation due to the breaching of its narrow sandy beach. It connected the lagoon and wetland area behind the beach with the sea. The breached beach was transformed into small barrier islands (Fig. 1a). The length of these barrier island formations ranges between 0.2 and 1.7 km. Recently, the active long shore transport seems to be inter-connecting the islands by the formation of the sand spits.

Based on a coastal survey on the northwest coast of Banda Aceh conducted in 2003 (Meilianda, et al. 2006), the wave climate was pre-dominantly coming from northwest (54%) during the northwest monsoon (June – October) and from northeast (40%) during the southeast monsoon (January - May). The significant wave height was 1.00 m with a peak period of 2.4 seconds. The tidal range of the coastal area of Banda Aceh is around 1.73 m high. The sediment transport was pre-dominantly in the west-to-east direction.

Lampuuk Beach, West coast

The west coast is a type of white sandy coast. The coastal plain is generally a higher ground above the mean sea level with beach slope between 1:30 and 1:100. It is bounded with coast-parallel ridges and some small promontories. The west coast has a persistent long shore sediment transport from south to north direction. The significant wave height is about 2.5 m with a period of 5 seconds. We assume the tidal range in this area to be similar to that at the northwest coast of Banda Aceh.

The impact of the earthquake and the tsunami is revealed by the trim line of the stripped-off vegetation along the feet of hills and headlands/promontories caused by tsunami waves attack. The shore-parallel dune system along the northern part of the west coast was also cut-back, some were flattened, and inlet mouths were eroded (widened). Recently, significant accretion is taking place along the west coast. This evident from the development of the dunes or elevated beaches which at some places overtopped the coastal roads. Closure of the inlet mouths occurs along the west coast. This effect is caused by the accreting beach development in front of them.

Lampuuk beach is located between a small headland on the north and Krueng Reba River mouth on the south of the west coast (Fig. 1c). An off-shore coral reef system exists in the middle of this 3.3 km coastal stretch. Sand bars were also found along the pre-tsunami's west coast. In our study, we extend the coverage length to another half kilometers to the south of the river mouth in order to observe the development in the vicinity of the inlet.

METHODS

An overall indicator for coastal problems is often concentrated to shoreline positions and trends, being used either by the scientists, coastal engineers or coastal managers. In many geospatial studies, it is common to represent coastal morphological development by rate of changes of comparative single or multiple shoreline positions (White and El Asmar, 1999; Solomon, 2005; Trebossen et al. 2005). These approaches may give an impression of changes in terms of horizontal position changes due to erosion-accretion processes. Alternatively, a quasi-three dimensional approach can be applied, for instance by comparing before and after coastal profiles using cut/fill methods (Zhang, et al., 2005) or a volumetric method (Morton et al., 1995).

Tides fluctuate on the foreshore between Mean Low Water Level (MLWL) and Mean High Water Level (MHWL). In the present study, we focus our observation on the foreshore zone. In this zone, the position of the waterline fluctuates continuously. We call the indicator of these different water level positions as 'shoreline features'. The measure to detect coastal morphological changes due to an extraordinary impact like a tsunami and the development since then is the net of erosion or accretion between the initial and later state of the morphology after the tsunami.

Data Analysis

Monitoring a morphological development in the geospatial studies requires information of the horizontal and vertical positions of a coastal feature (e.g. shorelines, coastal roads,

etc.) relative to the coordinate system to be used. From this information we can quantify, for instance, the distance and elevation of a feature. The data sources representing this information are, however, scarce in the present study. This is particularly the case for elevation data, such as topographic and bathymetric contours. Consequently, there is a gap of information needed for studying the morphological development in this particular area. To fill in this gap, we use any information contained in the available data sources, which in this case consists of four types: i) ortho-rectified aerial imagery; ii) satellite imagery; iii) tidal chart; and iv) coastal topographic contour. The details of the data sets are given in Table 1. All data uses Lowest Low Water Level (LLWL) as the datum (± 0.00 m).

Table 1. Image Acquisition and the Corresponding Tidal Elevation

Image data	Notation	Date	Local time	Tidal elevation*	Tidal stage
IKONOS sat. imagery	T_0 (west)	13 Jan 2003	11:12:39	0.7	MLWL
IKONOS sat. imagery	T_0 (northwest)	23 Jun 2004	10:54:29	0.5	MLWL
IKONOS sat. imagery	T_1	29 Dec 2004	10:55:41	1.2	1 hour to MHWL
Aerial Photograph	T_2	06 Jun 2005	ca. 08:30:00	1.5	MHWL
Coastal topographic	T_2	06 Jun 2005	ca. 08:30:00	1.5	MHWL

* Tidal chart source is from Hydro-Oceanographic Service of Indonesian Navy.

An ortho-rectified aerial imagery of Banda Aceh was obtained from an airborne survey conducted by the Norwegian Agency for Development Cooperation (NORAD) on behalf of the Survey and Mapping Agency of Indonesia (Bakosurtanal). The data has already been through a high standard image rectification process. This imagery is used as our base-map to register and to geo-reference other imageries and topographic data.

The topographic contour of Banda Aceh city was derived from this imagery and verified with ground control point surveys conducted by Japan International Corporation Agency (JICA). The contour line interval is 0.5 m which enables the careful study of the new developments along the coast.

High resolution IKONOS satellite images were provided by the International Institute for Geo-information Science and Earth Observations (ITC) in Enschede, The Netherlands. The multi-spectral IKONOS satellite imagery consists of 3 bands; i.e. red, green and blue. The images have been resampled to 2.5 m spatial resolution. These high resolution satellite images were enhanced to improve the appearance of the discernible features. Here, a minimum-maximum type of stretching for the three image bands was used. As the result, the water- and saturation lines were becoming more discernible.

Shoreline Feature Identification

To get an idea of which elevation each shoreline indicators represents, the first attempt is to overlay the image (with the identified shoreline features) with the coastal contour map.

The next step is to determine the instantaneous tidal stage of the image using a tide chart.

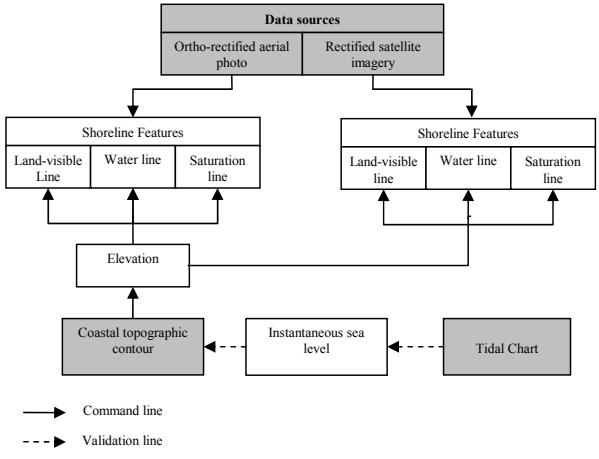

Fig. 2. Scheme of data source usage for shoreline feature identification and its validation

Boak and Turner (2005) stated that a shoreline feature is used as a proxy to represent the 'true' shoreline position. The proxies consist of three types: a feature that is visibly discernible in coastal imagery, the intersection of a tidal datum with the coastal profile, or a shoreline feature that is not necessarily visible to the human eyes but is based on the application of image-processing techniques. The choice for either one of these techniques in a shoreline analysis study very much depends on the data source and the chosen shoreline definition. Shoreline features in the present study are determined visually using the available data. Figure 2 shows the process of shoreline features identification in this study.

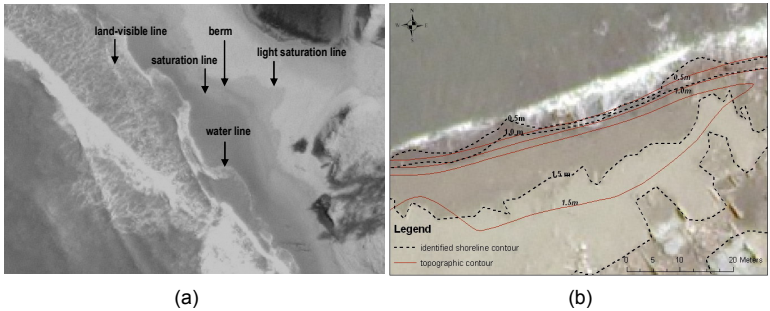

(a) (b)

Fig. 3. (a) Shoreline features. (b) Identified shoreline features based on the contour map and discernible features, validated by the tidal chart.

Figure 3 shows that to extract shoreline features from different kinds of image sources one has to treat each of them uniquely, either because of the image characteristics and

acquisition, or because of the tidal stage at the moment.

Here, the aerial photograph was used as the basis to identify the shoreline features. The high quality of the image (which was resampled to 0.3 m spatial resolution) enables the identification of the instantaneous shoreline dynamics. There are at least four different shoreline indicator features, which are as following (see also Fig. 2 and 3a):

- *Light saturation line*; the border line of maximum run up of the area which has smaller groundwater content and is not affected by the run-ups.
- *Saturation line*; the border of the area which is saturated by the groundwater (a similar feature was termed 'groundwater exit point' by Boak and Turner, 2005). The tone of sand color of this area is dark grey or dark brown, depending on the type of beach material.
- *Water line*; the border line of the instantaneous water body, which appears in green or blue color tone.
- *Land-visible line*; the border line of the water body where the submerged land just below the water is still visible.

By overlaying the contour map on top of the image, one can observe which contour elevations from the coastal contour map coincides with the interpreted shoreline features in the foreshore zone of the image. These were subsequently validated using the corresponding tidal stage. The tidal chart indicated for the time of image acquisition (see Table 1) was at MHWL which elevation was charted at +1.5 m from the datum.

The contours of the topographic map are generated from interpolation of several ground control points across the coastal area. We identify the elevation of the shoreline features by the proximity to the contour patterns. The line of these features shows that the alongshore variability which may, for example, be due to the formation of beach cusps. The contour of +1.5 m falls into the area of groundwater saturation which appears as a dark color of sandy beach. This feature is clearly discernible, especially along the accreting beach with a gentle slope. The saturation with groundwater is probably the result of a high intensity of water fluctuations due to wave run-ups. Therefore, we take the +1.5 m contour as representative for mean high water level (MHWL). This is confirmed by the tidal chart which showed that it was high tide (MHWL) with a water level of +1.5 m at the photograph's acquisition time.

Based on the contour map, the (instantaneous) water line is approximately following the contour elevation of +1.0 m. To identify this particular line is quite tricky because of either it is the 'true' instantaneous waterline (still water level) or the waterline in motion (e.g. run-ups and breaking waves). The color tone of this area (i.e. green or blue color tone for the 'true' waterline) in this case becomes an important control in order to avoid the confusion.

It turns out that due to the high tide the position of the +0.5 m contour falls into the watered area, although the color tone of land is still visible just below the water (mixture color of green-blue and brown). We observed that this feature is continuously connected

alongshore, sometimes in combination with the on-shore wave breaks. The light saturation line is not taken into account because this feature belongs to the instantaneous wave run-ups.

At this stage, from the four shoreline features, there are only three features left which we were able to validate using the other data sources (tide charts and contour map). These are: i) the saturation line (i.e. elevation +1.5 m); ii) the water line (i.e. elevation +1.0 m); and iii) the land-visible line (i.e elevation +0.5 m). These validated features is subsequently used as the reference to identify the shoreline features for the other images in order to complement the contour line information which is not available for the whole area studied.

The minimum boundary was set to the elevation ± 0.00 m. Since we study the foreshore zone, we assume that the elevation ± 0.00 m can be obtained by extending the slope of the foreshore, that is from the identified shoreline features (elevation of +0.5, +1.0 and +1.5 m). From here, the shoreline position as well as the steepness of the foreshore slope change in time can be observed.

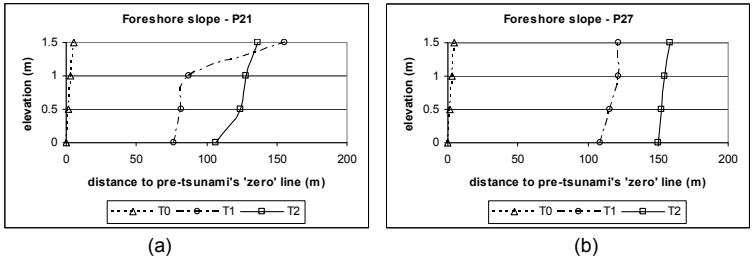

(a) (b)

Fig. 4. Examples of foreshore slope of early and 6 months after the tsunami at Ulee Lheue Beach. (a) Profile P21 (b) Profile P27. (See also Fig. 6a)

Figure 4 shows the foreshore slope change which also correlated to shoreline positions of two examples of the beach profiles. Here, we used the elevation zero line of the pre-tsunami as our reference. Shoreline positions of the pre-, early after- and 6-months after tsunami with respect to the pre-tsunami's elevation zero are denoted by T_0, T_1 and T_2, respectively (see also the data acquisitions correspond to the notations in Table 1 on page 5).

Concept of Net Volume Change

The shoreline feature identification has revealed the visual observation of the impact and the development since the tsunami. The subsequent attempt is to measure the magnitude of those changes. We adopt the principle of the one-line shoreline theory. The principle assumes that the coastal profile advances or retreats in response to shoreline accretion/erosion, while conserving its shape (Fig. 5). This means that the active part of the coastal profile identified by the height (H) is kept constant and the horizontal variable ΔY detects the changes of shoreline position. The magnitude (volume) of sediment loss ($Q_1<Q_2$) or gain ($Q_1>Q_2$) is subsequently obtained by multiplying the trapezoidal profile

with the distance (ΔX) between two profiles alongshore.

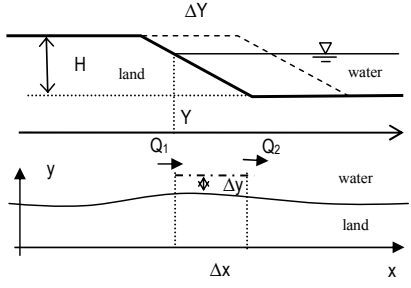

Fig. 5. Principle of one-line shoreline model.

We calculate the volume changes for two pairs of foreshore profiles by using the cut/fill operation in the spatial analyst tool in the Arc View software, which are: (1) the difference in sediment volume between the situation early after the tsunami and the pre-tsunami situation (T_1-T_0); (2) the difference in sediment volume between the situation 6 months after the tsunami and the pre-tsunami situation (T_2-T_0). Subsequently, we subtract volume (2) with volume (1) resulting in a loss or gain of sediment volume in the months after the tsunami.

ANALYSIS ON MORPHOLOGICAL RESPONSE AND DEVELOPMENT OF THE BEACH AFTER THE TSUNAMI

In this chapter we discuss the results from the applied methods to analyze the beach morphological changes and development in response to the earthquake and tsunami. The nature of the study gives a rise to some uncertainties. Uncertainties arise particularly from the fact that a simplified concept is used (i.e. one-line shoreline theory), and from a limitation of the presently available data, which is only valid for the foreshore zone.

Ulee Lheue Beach, Northwest coast

The morphological development of Ulee Lheue beach shows the erosion along with the re-distribution of sediment alongshore. The shoreline was retreating on average as far as 73 m from the pre-tsunami's shoreline. During the following 6 months the shoreline continued to retreat, resulting in an average distance from the pre-tsunami's shoreline of as large as 84 m.

We observe that a considerable portion of the beach sediment was eroded due to the tsunami. It may be brought outside the system, dumped over the coastal area during the tsunami, or transported off-shore within the active coastal zone. Profiles P1 to P6 in Fig. 6c show a small amount of volume change (erosion) between the pre-tsunami and both post-tsunami periods. This may be because the profiles are located in a semi-protected area in Krueng Cangkoy River mouth (see Fig. 1b). Profiles P14 and P19 reveal significant erosion in the development period after the tsunami (Fig. 6b), while in between the two profiles, the sediment seems to be re-distributed alongshore, as revealed

by the accretion on the profiles P11, P13, P17 and P18. Another interesting phenomenon is that the breached lands started to re-connected by sand accumulation between profiles P24 and P27. A graphic in Fig. 6c depicts these phenomena by the trend of alongshore erosion and re-distribution of sediments since the tsunami (comparison of the chaotic line due to the tsunami and the smoothed line of the development since then; see also Fig. 6b).

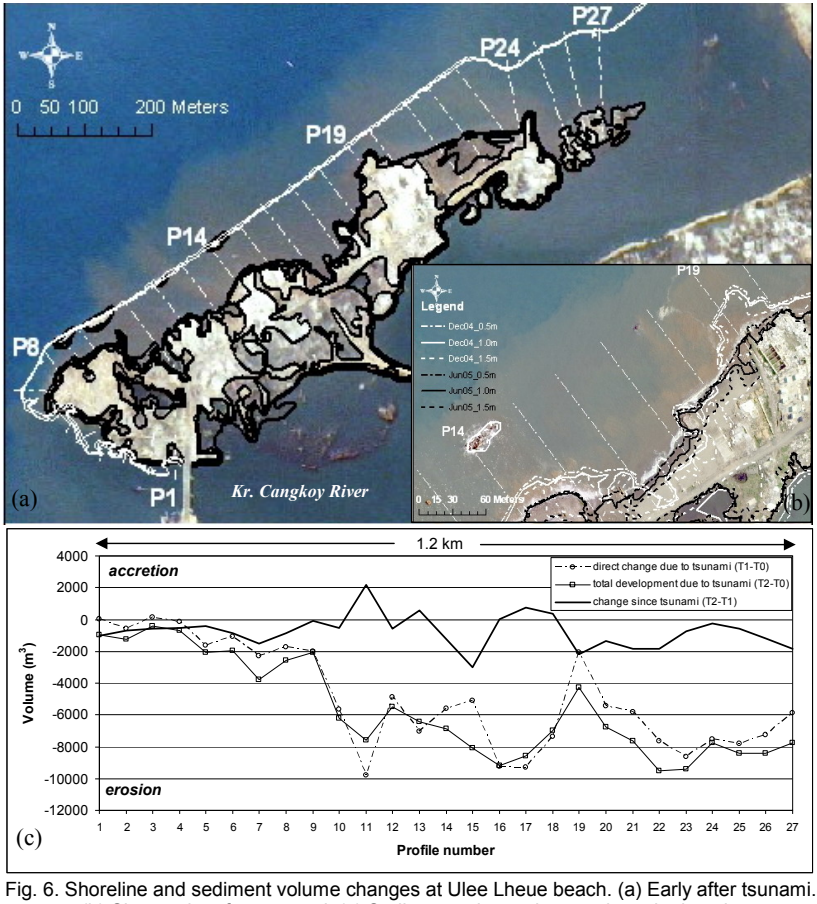

Fig. 6. Shoreline and sediment volume changes at Ulee Lheue beach. (a) Early after tsunami. (b) Six months after tsunami. (c) Sediment volume change along the beach.

The longshore transport seems to be pre-dominant on this particular coast which was indicated by the sediment re-distribution alongshore. There is no clear tendency of which direction the distribution is pre-dominant. Perhaps it is due to the fact that there are two opposite directions of the prevailing seasonal wave directions corresponding to the

monsoonal climate which influence the coast, as mentioned earlier in this paper.

The total amount of sediment loss in the initial response to the tsunami (T_1-T_0) and after six months (T_2-T_0) is 1.31x10^5 m^3 and 1.5x10^5 m^3, respectively. This implies that the development of the coastal section within 6 months after the tsunami was a further erosion, equals to 15% (1.9x10^4 m^3) of the sediment loss due to the tsunami.

Lampuuk Beach, West Coast

The morphological response of the west coast represented by Lampuuk beach reveals a similar effect of the chaotic shorelines (the black lines in Fig. 7a). Impact to the inlets is more obvious on this coastal section.

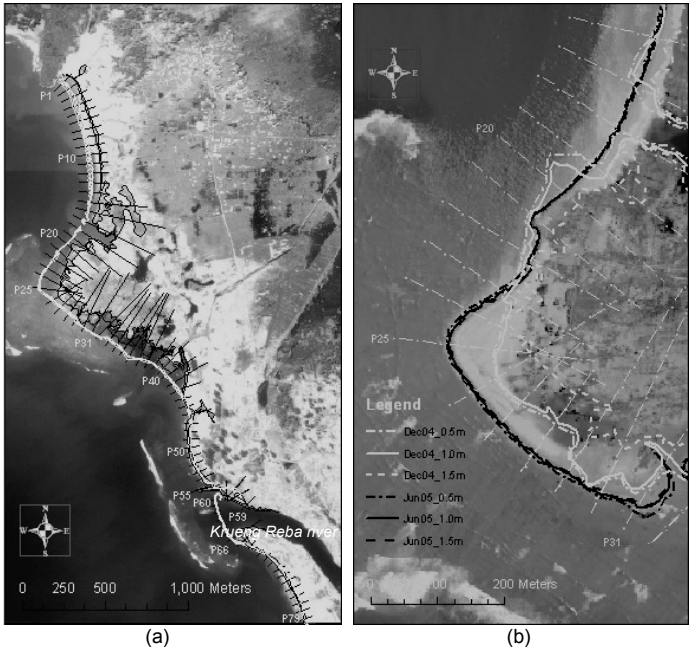

(a) (b)

Fig. 7.Shoreline changes at Lampuuk beach. (a) Early after tsunami. (b) Six months after tsunami.

The shoreline was retreating as far as 77 m early after the tsunami. In the following six months the shoreline was advancing on average 40 m with respect to the pre-tsunami's shoreline. Furthermore, Fig. 7 shows a significant difference of the morphological changes and development between profile P1-P44 and P45-P79. Figure 8 shows the trend of accretion during the 6 months of development after the tsunami (see also Fig. 7). This phenomenon is considerably different from what has occurred on the northwest coastal section (Ulee Lheue Beach).

Coastal section P1-P44 was heavily eroded due to the tsunami, while the adjacent part, i.e. P45-P79 was less eroded. We understood that coastal section P1-P44 was a non-protected sandy beach with a gentle slope, while the adjacent coastal section on the south was a beach with dune formation of ca. 10 m high above the ground, coastal protections such as beach revetment and training jetties were constructed in the vicinity of Krueng Reba river mouth (P51-P60). As the matter of fact, during our field visit in May 2005, we observed that the sea conifer trees behind the section P51 to P55 survived from the tsunami, and the beach revetment in front of them was still intact.

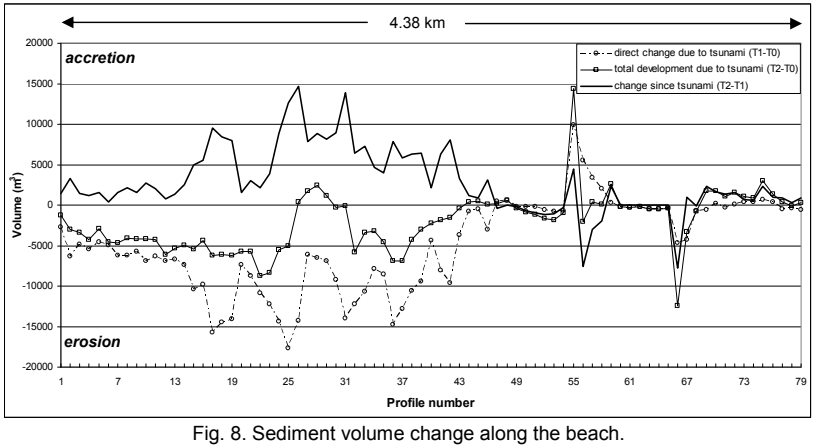

Fig. 8. Sediment volume change along the beach.

These different coastal settings may be the reason of different responses to the tsunami observed between coastal sections P1-P44 and P45-P79. Development of the morphology in the following 6 months shows the beach was accreting.

The small inlets at the profile P17 and P 18 used to be an inland depression behind the sandy beach in the pre-tsunami time. Due to the tsunami, the beach strip in front of this coastal feature was breached to form a small inlet. The beach on the vicinity was also flattened, as revealed by the elevation of the contour line in Fig. (7b). Morphological development during the following 6 months shows a tendency of considerable accretion, as can be seen from the positions of the contour lines (see the comparative white and black contour lines in Fig. 7b). Another interesting phenomenon is also observed on the beach promontory between profiles P20 and P40. The tip of the promontory was oriented northward during the development period.

Local discrepancy of the volume change appears in the graphic in Fig. 8 between profiles P55 to P66. This can be explained by the fact that at profile P55 there was training jetty which had not yet been constructed in our pre-tsunami's data (13 January 2003). Meanwhile, the profile P60 to P65 belong to the pre-tsunami's sand spit in front of Krueng Reba River mouth. Profile P66 shows the shifting of sand spit during the

morphological development after the tsunami.

The pre-tsunami's Krueng Reba river mouth was narrow with seasonal openings. Due to the tsunami, the instable part of the sand spit (profile P60 to P66) was breached and the river mouth was widening. Evidence of accretion that was taking place along the beach can also be observed on the Krueng Reba river mouth. The shift formation at the southern sand spit in recent development was oriented towards the river course. It suggests that besides the pre-dominant long shore sediment transport (south-north direction), the cross shore transport may also contribute to the beach/dune development; perhaps during the extreme wave condition where the spit was pushed inland and no significant discharge flowing in the river course. Furthermore, as mentioned in the earlier chapter, the dune formation was beginning to form again along the beach.

The overall impression of the development of the beach morphology after the tsunami not only occurred in the longshore direction but also in the cross shore direction. This process leads towards new beach equilibrium. The total amount of sediment loss in the initial response of the tsunami and in its development is 3.8×10^5 m^3 and 1.6×10^5 m^3, respectively. The volume of net change reveals that 2.2×10^5 m^3 or about 60% of sediment budget has been gained back into the beach stretch within 6 months.

CONCLUSION

We quantified the morphological response and development of beaches that were affected by the earthquake and the tsunami on 26th December 2004. It covers a small spatial scale (~ 1 to 4 km) of two different beach settings on the northwest and west coast of Banda Aceh city. Quantification of time-dependent shoreline features within the foreshore zone using a simplified principle adopted from one-line shoreline theory is applied. Three data sets of consecutive dates before, early after and several months after the event were used. After the severe impact as revealed by a significant chaotic shoreline retreat, the morphological development within the following 6 months has shown further erosion (about 15% of the sediment loss due to the tsunami) on the northwest coast. Meanwhile, 60% of the sediment loss on the west coast due to the tsunami has been compensated by accretion in the months after the tsunami. This leads to a conclusion that different coastal characteristics show different responses to and different developments after the tsunami. The nature of the study gives rise to some uncertainties. Uncertainties arise particularly from the fact that a simplified concept is used (i.e. one-line shoreline theory), and from a limitation of the presently available data, which is only valid for the foreshore zone. This uncertainty has hampered our effort to incorporate land subsidence quantifications, which we are looking forward to in our future study.

ACKNOWLEDGEMENTS

We address our acknowledgement to Bakosurtanal for providing the ortho-rectified aerial imagery, the coastal topographic map, and other supporting information under NORAD grant, distributed by SIM-centre, BRR, Banda Aceh. We also address our thanks to the Water Resource department of ITC, the Netherlands, for providing facility on image

processing and the satellite imagery data, and for providing the supervision (by Dr. Ben H.P. Maathuis; who is also the co-author in this paper). This study is made possible by the fund of Asian Development Bank (ADB) through the TPSDP Project of the Higher Education Department of Republic of Indonesia, and the University of Twente, the Netherlands.

REFERENCES

Anonymous (2006). Earthquake news and highlight archives, Earthquake Hazards Program, USGS, http://earthquake.usgs.gov/eqcenter/eqinthenews/index.php

Boak, E.H. and Turner, I.L. (2005). Shoreline Definition and Detection: A Review. *Journal of Coastal Research*, Vol. 21(4), pp.688-703

Gibbons, H. and Gelfenbaum, G. (2005). Astonishing wave heights among the findings of an international tsunami survey team on Sumatra. *Sound Waves March 2005 (monthly newsletter),* http://soundwaves.usgs.gov/2005/03/

Jaffe, B.E., J.C. Borrero, G.S. Prasetya, R. Peters, B. McAdoo, G. Gelfenbaum, R. Morton, P. Ruggiero, B. Higman, L. Dengler, R. Hidayat, E. Kingsley, W. Kongko, Lukijanto, A. Moore, V. Titov and E. Yuliantom. (2006). Northwest Sumatra and Offshore Islands Field Survey after the December 2004 Indian Ocean Tsunami. *Earthquake Spectra*, 22, S3, pp. S105–S135

McGlashan, D.J., Duck, R.W., Reid, C.T. (2005). Defining the foreshore: coastal geomorphology and British laws. *Estuarine Coastal and Shelf Science*, Vol. 62, pp. 183-192

Meilianda, E., Dohmen-Janssen, C. M., Hulscher, S. J. M. H., and Mulder, J.P. (2006). Inventory of physical characteristics of Banda Aceh coast (prior to the tsunami of 26th December 2004). Civil Engineering & Management research Report 2006W-002/WEM-002, University of Twente, The Netherlands.

Morton, R.A., Gibeaut, J.C., Paine, J.G. (1995). Meso-scale transfer of sand during and after storms: implications for prediction of shoreline movement, *Marine Geology*, Vol. 126, pp. 161-179

Solomon, S.M., (2005). Spatial and temporal variability of shoreline change in the Beaufort-Mackenzie region, northwest territories, Canada, *Geo-Mar Lett*, Vol. 25, pp. 127-137

Stein, S. and E.A. Okal. 2005. Speed and size of the Sumatra earthquake. *Nature,* Vol. 434, pp.581-582

Trebossen, H., Deffontaines, B., Classeau, N., Kouame, J., Rudant, J., (2005). Monitoring coastal evolution and associated littoral hazards of French Guiana shoreline with radar images, *C.R. Geoscience*, Vol. 337, pp. 1140-1153

White, K., El Asmar, H.M., (1999). Monitoring changing position of coastlines using Thematic Mapper imagery, an example from the Nile Delta, *Geomorphology*, Vol. 29, pp. 93-105

Zhang, K., Whitman, D., Leatherman, S. and Robertson, W. (2005). Quantification of beach changes caused by hurricane Floyd along Florida's coast using Airborne laser surveys, *Journal of Coastal Research,* Vol. 21(1), pp. 123-134

DUNE MORPHOLOGY AS AN INDICATOR OF PALEOTSUNAMIS

James R. Goff[1]

1. National Institute of Water & Atmospheric Research, PO Box 8602, Christchurch, NEW ZEALAND. j.goff@niwa.co.nz.

Abstract: Analysis of modern and past tsunamigenic features from within New Zealand and around the world have identified a suite of tsunami-related geomorphological features in dune systems including; Pedestals - remnant sections of dune ridge separated by scoured areas; Hummocky topography/Sand sheets - formed landward from pedestals (hummocky topography is the old, weathered equivalent of sand sheets); Parabolic dune fields - remobilised sand sheets landward of pedestals; Low Profile Sequences - post-tsunami feature indicative of changes to coastal sediment budget.

The type of features formed by a tsunami, and the ability to detect and interpret tsunami geomorphology by LIDAR (and also in the field) hinges on the interactions between five key criteria; the availability and type of sediment (e.g. sand/gravel); embayment type; a prograding or eroding coast; small or large accumulation space; and whether there is a wet or dry landward environment.

INTRODUCTION

New Zealand sits astride the boundary between the Pacific and Australian Plates (Figure 1). To the north in the Tonga-Kermadec-Hikurangi trench, the Pacific Plate is subducting from the east at a rate of 40 mm/yr. To the south in the Puysegur trench, the Australian Plate is being subducted from the west with a convergence rate of 35 mm/yr. In the centre of New Zealand, the plates are locked. This unique tectonic setting provides a wide range of potential tsunamigenic sources (Walters et al. 2006).

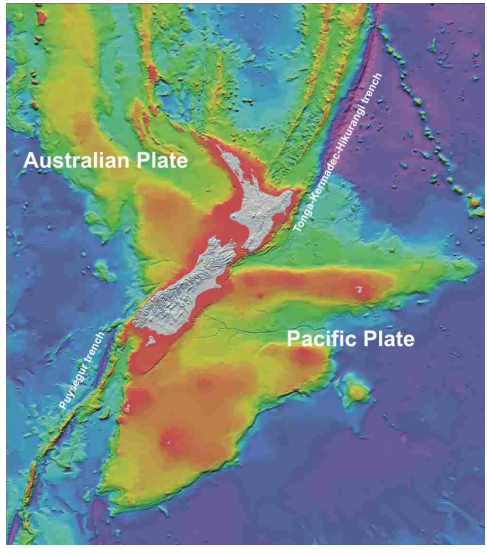

Fig. 1. New Zealand – showing key tectonic associations

An historical tsunami database for New Zealand records over 40 tsunamis (Berryman 2005). Additionally, a recently developed prehistoric tsunami database contains records from over 200 sites with details of more than 30 Holocene palaeotsunamis (Goff 2006). These geological signatures of tsunamis provide clues to a hazard that is poorly understood from historical records alone. Indeed, in northeast Japan, western North America, Norway, and Scotland, tsunami deposits serve as warnings of unusually large tsunamis (Nanayama et al. 2000; Atwater et al. 2005a; Bondevik et al. 2005). Tsunami deposits also afford estimates of tsunami recurrence (Pinegina et al. 2003; Cisternas et al. 2005; Kelsey et al. 2005), and can yield constraints on tsunami flow depth and velocity (Jaffe and Gelfenbaum 2002; Atwater et al. 2005b).

Researchers have also studied *tsunami-scour fans*. These form where a tsunami cuts a breach, or cleans out an existing one, through a beach ridge. Using material scoured from the breach, the tsunami builds a fan as it emerges from the breach. These combined features of erosion and deposition (scour and fan) were noted on opposite sides of the Pacific Ocean as by-products of the tsunami associated with the giant Chilean earthquake of May 22, 1960 (Kitamura et al. 1961; Bourgeois and Reinhart 1989; Atwater et al. 1999). Still other examples of tsunami scours have been reported from Kamchatka (MacInnes et al. 2005).

Similar features have been noted in New Zealand (Goff et al. in press). Unlike those reported by researchers in Chile, Japan, and the US, the New Zealand features are part of a geomorphological association purported to have been created by palaeotsunamis.

These include Hummocky Topography situated landward of coastal dune systems (Figure 2) and Pedestal features often associated with either hummocky topography or overwash deposits (Figure 3).

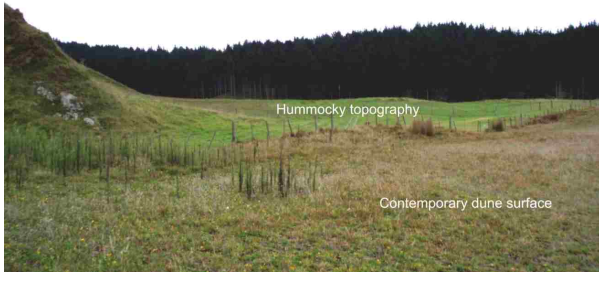

Fig. 2. Whangaruru North – hummocky topography inland of contemporary dune system (Photo: J. Goff).



Fig. 3. Great Barrier Island – resistant pedestal surrounded by palaeotsunami deposit (pebbles) – hummocky topography visible in distance (Photo: Scott Nichol, University of Auckland).

If such features can be identified centuries later by remote sensing, they can potentially be used to study the tsunami hazard on coastlines which have little or no historic record. With its high spatial density of data points (typically ~ 1-2 m) and accurate ground elevation fixes (typically to within a standard error of 0.15 m), LIDAR delivers topographic information that theoretically should be adequate to identify hummocky topography, pedestals, and scour-fan features if they have been preserved within the landscape.

FEATURES OF TSUNAMI GEOMORPHOLOGY

The 2004 Indian Ocean tsunami provided clear evidence that a large tsunami is required to leave a marked geomorphological signal in the landscape. The topographic extent of this signal is generally governed by antecedent sand supply (Figures 4 and 5).



Fig. 4. Sri Lanka: Top – large scale pedestals on sand-rich coast; Bottom – small scale foredune pedestals on sand-poor coast (arrows indicate pedestals). Smaller features are produced on coastlines with a reduced sand supply (Photos: J. Goff).



Fig. 5. Sri Lanka: Top – thick sand sheet landward of large scale pedestal formation shown in Figure 4 for sand-rich coast; Bottom – thin sand sheet landward of small scale foredune pedestals shown in Figure 4 for sand-poor coast (Photos: J. Goff).

The preservation of geomorphological features is affected by subsequent sand supply. Assuming similar post-tsunami conditions, in sand-rich areas there would be rapid rebuilding of coastal dunes and loss of pedestal topography, only the largest pedestals remain exposed. There are several variables, however:

1. Post-tsunami sand supply may be severely reduced if the tsunami entrains all available offshore sand (above and often considerably below storm wave base) and transports it inland. Subject to subaerial processes, this probably removes it from the coastal sediment transport cycle for some considerable time. Evidence of sand removed from the system would be preserved inland.

2. Post-tsunami sand supply may be severely reduced if the tsunami transports large quantities of sand from the shore and nearshore seaward beyond the normal storm wave base. This effectively removes it from the coastal sediment transport cycle. There would be no terrestrial evidence of the sand removed from the system.

3. Post-tsunami sand supply may increase markedly if the tsunami was generated by a large, local earthquake that led to large quantities of new sand being routed into the coastal zone from rivers (a delayed pulse can also occur in arid areas where years may pass between the earthquake and the next major rain event).

4. Other factors unrelated to tsunamis may affect sand supply conditions, such as extreme climatic events or anthropogenic land clearance.

Event magnitude and spatial extent are also important controls on tsunami generated morphology ("large" events are assumed to be in the region of 10m runup or greater). We believe that inundation by region-wide events would cause multiple breaching of dune systems as opposed, for example, to the isolated tsunami-scour fans. In other words, they would create multiple tsunami-scour fan assemblages during one inundation. The assemblages would include remnant dune ridges, or *pedestals*, between each breach, and the individual overwash fans would coalesce to form *sand sheets* that may or may not be mobile depending upon aeolian and dune swale conditions. This overall concept is not new. Minoura and Nakaya (1991) modelled the effects of tsunamis on a sandy barrier coastline and described the results in morphological terms.

Tsunamis in shallow water have the potential to carry large amounts of sediment. Tsunami overwash of dune ridges can reduce their height, create multiple breaches, transport eroded sediment into dune slacks (reworked aeolian dune sand and offshore sediments), and deposit a sand sheet across the landward topography – wet or dry. Dunes can also be remobilised by the passage of a tsunami (Bryant, 2001). If the sediment volume carried is large then, according to Bryant (2001) "a raised back barrier may form from coalescing overwash fans or small lagoons may be completely infilled. If these surfaces are not covered by seawater or quickly vegetated, they may be subject to wind deflation, with the [*landward*] formation of parabolic dunes (if the prevailing wind is onshore). Alternatively, sub-aerial processes may weather the sand in situ, developing a

hummocky topography. Bryant (2001) makes the point that storms tend to only surge through gaps in dunes, sporadically depositing lobate fans that rarely coalesce or penetrate far inland. This is a key difference generally, but there is room for confusion in areas of low accumulation space (e.g. in a small pocket beach, there may be insufficient accumulation space for more than one lobate fan and two pedestals).

Conceptual models

A series of conceptual models were developed to consider the major variables discussed above – namely sand supply and accumulation space. Examples are shown below (Figures 6-9).

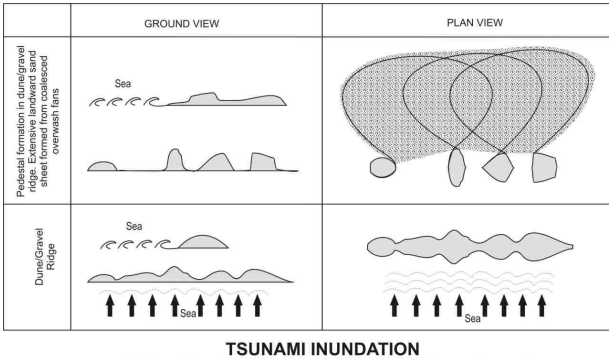

Fig. 6. Pedestal and overwash fan formation from tsunami inundation – light grey shading = in situ dune sand.

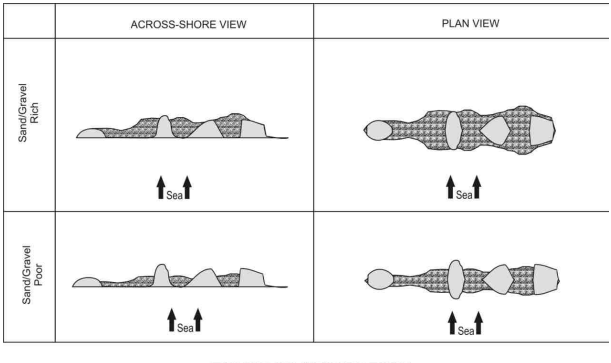

Fig. 7. Pedestal development over time in different sand supply conditions. Light grey shading = in situ dune sand, dark mottled shading = new sand supplied to the dune system following inundation.

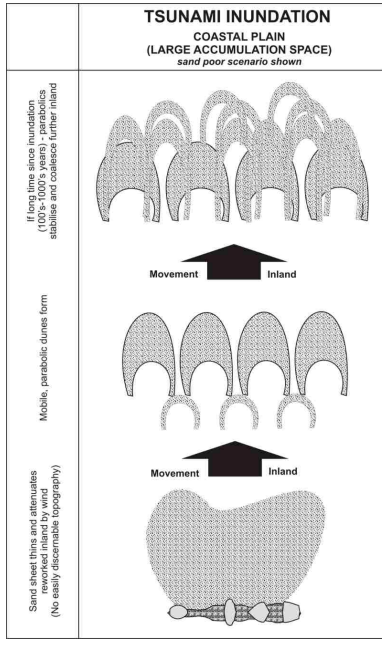

Fig. 8. Sand sheet–parabolic dune development (bottom to top of diagram) with large accumulation space AND dry ground conditions (in wet conditions the sand sheet is immobile and weathers). These are sand-poor conditions.

METHODS

For our analysis, LIDAR text files containing thinned ground strikes were read through a series of software packages to produce Triangulated Irregular Networks (TINs). Several edge detection techniques were then used to automatically identify possible features (refer to Goff et al, in press for full details of the methodology). Sites identified using these techniques were visited to geologically groundtruth the identified features.

STUDY AREA

We selected a series of sites along the coastline of the Otago region, New Zealand (Figure 1). A recent review of geological and archaeological information for the Otago coastline suggests that tsunami inundation has occurred since human occupation in the 13th century (Goff, 2006). If inundation did occur, it would seem likely that this was a rare event in the Holocene. The reasoning behind this assumption is that there are no obvious active local or regional earthquake sources thought to be significant enough to generate a large tsunami. Otago's coastal geomorphology may therefore prove useful for recognising tsunami inundation because only few (one?) large events have occurred

during the Holocene. If more that one large tsunami inundation has occurred, it is possible that they would have been infrequent enough to be recognisable as a separate suite of features.

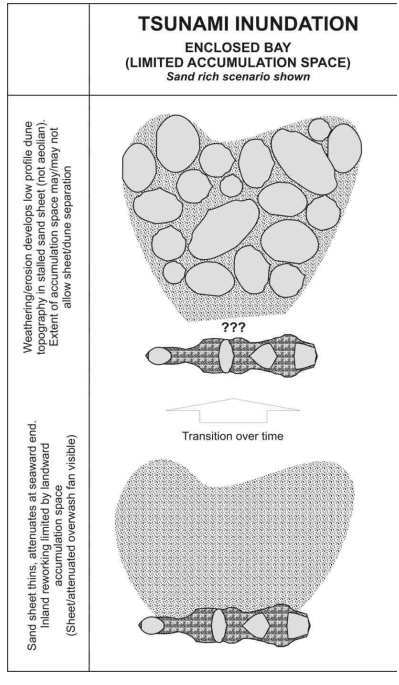

Fig. 9. Sand sheet–hummocky topography dune development with limited accumulation space AND wet/dry ground conditions. The upper section of the figure represents the formation of hummocky topography through time – the light grey shaded areas represent remnant small, low-profile dunes

RESULTS

We briefly discuss data from one site, Long Beach. Full details on this and other sites is available in Goff et al. (in press). The LIDAR image for Long Beach initially revealed a small embayment with two distinct sets of dunes. A fragmented landward set of higher elevation dunes, and an intact seaward group of lower elevation dunes, are separated by a wide, low-profile sequence of sand. The seaward dune system started to form around 1863 (Anderson, 1981). Our initial interpretation of the LIDAR image is shown in Figure 11. There is a section of well-defined hummocky topography landward of the higher elevation dunes. The fan of hummocky topography splays into a small wetland formed where a stream ponded behind the dunes. This pedestal-hummocky topography association is interpreted as tsunami geomorphology. Long Beach contains an important archaeological site that shows evidence of having been "washed by the sea" (Leach and

Hamel, 1981). During our groundtruthing survey (Figure 12), the evidence for "washing" by the sea was found to be a layer of pebbles and sand approximately 20 cm thick. In similar geomorphological associations elsewhere in the country, this type of sedimentary unit has been defined as a tsunami deposit (e.g. Nichol et al., 2004). Perhaps the important point to make here is that there is no other process capable of depositing such a sedimentary sequence - it is not diagnostic of a storm deposit (Goff et al., 2004).

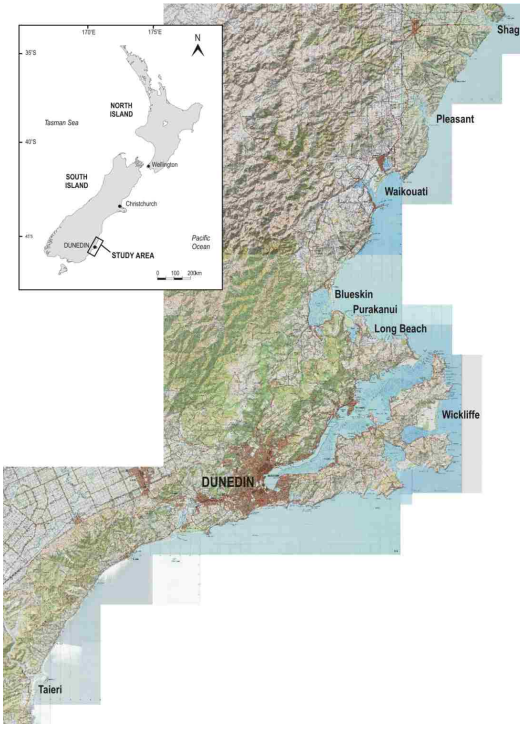

Fig. 10. Otago region coastal locations.

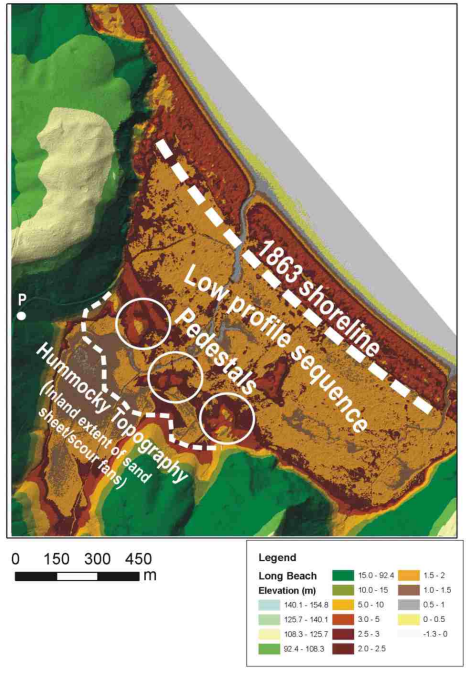

Fig. 11. Long Beach: Interpretation (P = Photo point for Figure 12)

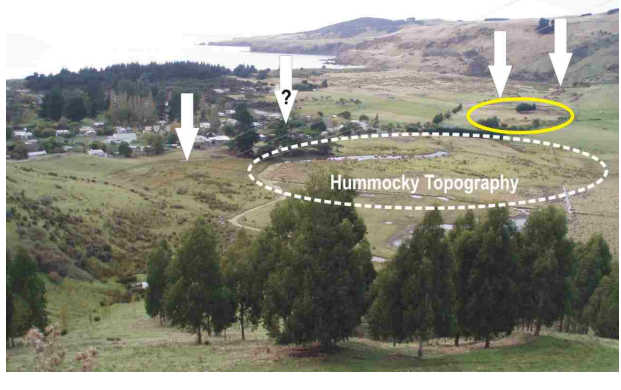

Fig. 12. Long Beach viewed from the NW. White arrows indicate remnant pedestals on the spit. The yellow ellipse is the archaeological site. The sand sheet/fan can be seen in the centre of the photo extending into the wetland (Photo: J. Goff).

DISCUSSION

Allowing that a coast has been subject to tsunami in the recent geological past, the ability to detect and interpret their geomorphic signature from LIDAR data, and also in the field, hinges on the interaction between five key criteria.

1. Availability and type of sediment (sand/gravel):
The spectrum of sediment availability ranges from sediment-rich to sediment-poor. In sediment-rich environments, tsunami geomorphology is more likely to be rapidly buried by incoming post-event material (10's of years). This is particularly pertinent for pedestals. In a sediment-poor system, geomorphology is more likely to be preserved for a much longer period (10^2-10^3 years).

2. Embayment type (n.b. – cliffed coasts were not a focus of this study):
Tsunami geomorphology in semi-enclosed embayments can be exposed to reworking by tidal and fluvial processes, whereas the latter are the main problem in small estuaries. Smaller pocket beach type embayments, such as Long Beach, which often have small streams and/or wetlands ponded behind coastal dunes, are more likely to preserve the features of tsunami geomorphology. This is because neither coastal nor fluvial processes are sufficiently energetic to rework tsunami-emplaced geomorphology.

3. Prograding/eroding coast:
An eroding coast is unlikely to preserve the complete geomorphological record of past tsunamis. Over time, the record will be lost. A prograding coast is more likely to preserve the geomorphology.

4. Small/large accumulation space:
A restricted landward accumulation space limits the development of tsunami geomorphology. On the other hand, there is less likelihood of post-tsunami remobilisation of the sand sheet (e.g. by wind, estuarine currents), thus hummocky topography is more likely to develop and be preserved (e.g. Long Beach). Differentiation of hummocky topography from conventional dune ridge formation will be complicated if multiple tsunami inundations add fresh sand volumes. Large accumulation spaces provide the potential for the development of tsunami geomorphology and the creation of remobilised sand dune phases as landward parabolic dune systems (e.g. Kapiti-Horowhenua coast – the conventional genesis of these dune systems is considered to be as a result of remobilisation caused by land clearance, although dune ages do not coincide – refer to Hawke and McConchie (2006) and Goff and McFadgen (2006) for opposing views). Where there is abundant space, sand sheets will most likely spread further and be thinner..

5. Wet/dry landward environment:
A wet landward environment (e.g. backshore swamp/pond) will stabilize inwashed sand . This is most likely to weather (in situ) over time to form low profile hummocky

topography. Since many dune systems are often associated with some form of ponded or blocked drainage system, low profile hummocky topography closely linked to a pedestal landscape would seem to be the most likely geomorphological association related to tsunami inundation. This is not always the case however, and dry landward environments could enable remobilisation of sand with the possible formation of a parabolic dune field or hummocky topography some distance landward of the original dune source.

CONCLUSIONS

LIDAR data analysis supplemented with brief ground surveys can identify the geomorphic signature of past large tsunamis. The type of geomorphological features and the chances of finding them depend largely upon the geomorphic setting. It is therefore important to know what to look for and where to look.

ACKNOWLEDGMENTS

This work was funded as part of NIWA's Capability Fund (Project CISA065) allocation from the Ministry of Research, Science & Technology. I am most grateful to Dr. Stephen Swabey of Otago Regional Council for permitting us to use coastal LIDAR imagery and their aerial photograph database for this project.

REFERENCES

Anderson, A.J. (1981). "A fourteenth-century fishing camp at Purakanui Inlet, Otago," *Journal of the Royal Society of New Zealand* 11, 201-221.

Atwater, B.F., Cisternas V.M., Bourgeois, J., Dudley, W.C., Hendley, J.W. II, and Stauffer, P.H. (1999). "Surviving a tsunami: lessons from Chile, Hawaii, and Japan," *U.S. Geological Survey Circular* 1187, 18p.

Atwater, B.F., Musumi-Rokkaku, S., Satake, K., Tsuji, Y., Ueda, K., and Yamaguchi, D.K. (2005a). "The orphan tsunami of 1700 – Japanese clues to a parent earthquake in North America," *U.S. Geological Survey Professional Paper* 1707, 133p.

Atwater, B.F., Bourgeois, J., Yeh, H., Abbott, D., Cisternas, M., Glawe, U., Higman, B., Horton, B.P., Peters, R., Rajendran, K., and Tuttle, M.P. (2005b). "Tsunami geology and its role in hazard mitigation," *Eos* 86, 400.

Bondevik, S., Løvholt, F., Harbitz, C., Mangerud, J., Dawson, A., and Svendsen, J. I. (2005). "The Storegga Slide tsunami – comparing field observations with numerical simulations," *Marine and Petroleum Geology* 22, 195–208.

Bourgeois, J., and Reinhart, M.A. (1989). "Onshore erosion and deposition by the 1960 tsunami at Rio Lingue estuary, south-central Chile [abstract]," *Eos* 70, Meeting Supplement, 1331.

Bryant, E. A. (2001). "*Tsunami: The underrated hazard*," Cambridge University Press, 320 p.

Cisternas, M., Atwater, B.F., Torrejón, F., Sawai, Y., Machuca, G., Lagos, M., Eipert, A., Youlton, C., Salgado, I., Kamataki, T., Shishikura, M., Rajendran, C.P., Malik, J.K., Rizal, Y., and Husni, M. (2005). "Predecessors to the giant 1960 Chile

earthquake," *Nature* 437, 404-407.

Goff, J.R. (2006). "*Draft palaeotsunami database*," National Institute of Water & Atmospheric Research unpublished report, New Zealand.

Goff, J.R., Hicks, D.M., and Hurren, H. (in press). "*Tsunami geomorphology in New Zealand*," National Institute of Water & Atmospheric Research Technical Report.

Goff, J.R., and McFadgen, B.G. (2006). "Shifting sands [abstract]," *Proceedings 12th Meeting of the Australian and New Zealand Geomorphology Group*, New Zealand. University of Auckland.

Goff, J.R., McFadgen, B.G., and Chagué-Goff, C. (2004). "Sedimentary differences between the 2002 Easter storm and the 15th century Okoropunga tsunami, southeastern North Island, New Zealand," *Marine Geology* 204, 235–250.

Hawke, R.M., and McConchie, J.A. (2006). "Dune phases in the Otaki-Te Horo area (New Zealand): a geomorphic history," *Earth Surface Processes and Landforms* 31, 633-645.

Jaffe, B.E., and Gelfenbaum, G. (2002). "Using tsunami deposits to improve assessment of tsunami risk," *Proceedings American Society of Civil Engineers, Solutions to Coastal Disasters '02, Conference*, 836–847.

Kelsey, H.M., Nelson, A.R., Hemphill-Haley, E., and Witter, R.C. (2005). "Tsunami history of an Oregon coastal lake reveals a 4600 yr record of great earthquakes on the Cascadia subduction zone," *Geological Society of America Bulletin* 117, 1009–1032.

Kitamura, N., Kotaka, T., and Kataoka J. (1961). "Ofunato-Shizugawa chiku [region between Ofunato and Shizugawa],. *In* Kon'no, E. (ed.) Geological observations of the Sanriku coastal region damaged by tsunami due to the Chile earthquake in 1960. *Contributions of the Institute of Geology and Paleontology of Tohoku University* 52, 28–40.

Leach, H.M., and Hamel, J. (1981). "Archaic and Classic Maori relationships at Long Beach, Otago: the artifacts and activity areas," *New* Zealand Journal of Archaeology 3, 109–141.

MacInnes, B.T., Bourgeois, J., Pinegina, T., Martin, M.E., and Kravchunovskaya, E. (2005). "Geomorphic effects of tsunamis in Asacha and Mutnaya Bays, Southern Kamchatka Peninsula, Russia [abstract]," *Eos 86(52),* Abstract T11A-0360.

Minoura, K., and Nakaya, S. (1991). "Traces of tsunami preserved in inter-tidal lacustrine and marsh deposits: some examples from northeast Japan," *Journal of Geology* 99, 265–287.

Nanayama, F., Shigeno, K., Satake, K., Shimokaka, K., Koitabashi, S., Miyasaka, S., and Ishii, M. (2000). "Sedimentary differences between the 1993 Hokkaido-nansei-oki tsunami and the 1959 Miyakojima typhoon at Taisei, southwestern Hokkaido, northern Japan," *Sedimentary Geology* 135, 255–264.

Nichol, S., Goff J.R., and Regnauld, H. (2004). "Sedimentary evidence for a regional tsunami on the NE coast of New Zealand," *Geomorphologie: Relief, Processus, Environnement* 1, 35–44.

Pinegina, T.K., Bourgeois, J., and Melekestsev, I.V. (2003). "A millennial-scale record of Holocene tsunamis on the Kronotskiy Bay coast, Kamchatka, Russia," *Quaternary Research* 59(1), 36–47.

Walters, R.A., Goff, J.R., and Wang, K. (2006). "Tsunamigenic sources in the Bay of Plenty, New Zealand," *Science of Tsunami Hazards* 24, 339–357.

SEDIMENTOLOGICAL CHARACTERISTICS OF REGIONAL-SCALE WASHOVER DEPOSITS CAUSED BY HURRICANE IVAN

Mark H. Horwitz[1], Ping Wang[1]

1. Department of Geology, University of South Florida, 4202 E. Fowler Ave., Tampa, FL 33620, USA. mhorwitz@mail.usf.edu; pwang@cas.usf.edu

Abstract: Washover deposits induced by Hurricane Ivan are examined along a 260-km stretch of northern Florida coast. Initial response to the overwash event is dominated by dramatic nearshore, beach, and dune erosion. Eroded sediment is in-turn redistributed landward across the barrier-island profile. Distinct sedimentological characteristics of the washover deposits are recognized in different barrier-island sub-environments. Deposits on the beach are bound by a basal erosional surface, and exhibit planar seaward-dipping stratification. Over the barrier interior, preservation of fresh, in-place vegetation below the washover indicates that limited erosion occurred prior to washover deposition landward of the foredune. Washover deposits over the interior platform are characterized by horizontal to sub-horizontal stratification. Increased accommodation space landward within flooded interior wetlands and the back-bay yields substantially thicker washover deposits characterized by steeply inclined sigmoid and tabular foreset stratification. Back-bay deposition locally accounts for 120 m of landward bayside-shoreline migration.

INTRODUCTION

Ivan, a strong category 3 hurricane, made landfall near the Florida-Alabama border on September 16, 2004 accompanied by extreme wind and wave energy. The storm induced regional-scale overwash extending as far as 260 km east of the storm's landfall position. Overwash occurs when water levels become elevated due to a combination of storm-surge and wave run-up, inducing cross shore flow landward beyond the beach-berm crest (Shepard, 1973). The process yields both erosional and depositional features, the latter referred to as washover deposits (Schwartz, 1975). Low lying barrier islands along the northern Florida coast are particularly vulnerable to overwash.

Notwithstanding the long-term gradual effects of deflation, the overwash process provides a primary mechanism for rapid and episodic redistribution of sediment landward across the barrier profile. Sedimentation can extend well into the back-bay resulting in landward barrier migration. Ivan induced regional-scale overwash produced a broad spectrum of impacts ranging from beach and dune erosion along the distal reaches of the storms wind-field, to inundation proximal to the storm center. The range of impact can be attributed to spatial and temporal variations in the magnitude of storm related forcing and antecedent morphologic and biologic conditions of the barriers and beaches. The broad range of overwash impact generated by Ivan provided a unique opportunity to study the sedimentological characteristics of regional scale washover deposits.

This study integrates trenching, coring, topographic profile survey, aerial photo, and ground penetrating radar (GPR) data in order to examine the sedimentological characteristics of washover deposits associated with Hurricane Ivan. The objectives of the study were: (1) to examine erosional and depositional characteristics of regional washover deposits, (2) to characterize their spatial distribution patterns in both the cross-shore and long-shore directions, and (3) relate the above to antecedent morphologic and biologic conditions of the barriers and beaches. These data should provide valuable insight into coastal response to intense storm events.

STUDY AREAS

The northwestern Florida coast, commonly referred to as the Florida Panhandle, is a low energy, wave dominated coast, punctuated by a discontinuous chain of barrier islands (Fig. 1). The region is considered micro-tidal with a range of less than 0.5 m (Morang, 1992). Significant wave heights average around 1.2 m during the winter months and 0.8 m during the summer. The 85-km long Santa Rosa Island is the westernmost Panhandle barrier. The island is oriented roughly east-west and has a maximum width of ~1- km. Further to the east, barrier-island orientations range from northwest to northeast, paralleling a broad Pleistocene headland. Owing to the additional sediment supplied by the headland, eastern Panhandle barrier-island widths can reach several km, with the wider portions of the islands being comprised of a sequence of beach ridges. Overall, relief on the barriers rarely exceeds 10 m.

Sediment along the Florida Panhandle coast is comprised of compositionally and texturally homogeneous quartz sand, 75% of which lies within the 0.2 to 0.4 mm grain-size fractions (Stone and Stapor, 1996). Shell-debris content is low, rarely exceeding 5%. Dark heavy minerals are common in the sediments and tend to concentrate in distinct laminae providing a basis for distinguishing bedforms and stratification.

This study examines seven sites located along a 260-km stretch of the Panhandle coastline, extending from Santa Rosa Island on the west to St. George Island on the east (Fig. 1). Santa Rosa Island hosts the four westernmost sites, which include from west to east, Fort Pickens Park (FP), Navarre Beach (NV), Eglin Air Force Base (EG) and Beasley Park (BP). The Inlet Beach (IB) site is located along a central Panhandle mainland stretch of beach, and the two eastern sites are located on St. Joseph Island (SJ)

and St. George Island (SG). The sites were chosen based on: (1) areas with limited anthropogenic modification, (2) proximity to the storm center, and (3) degree of morphologic and biologic diversity.

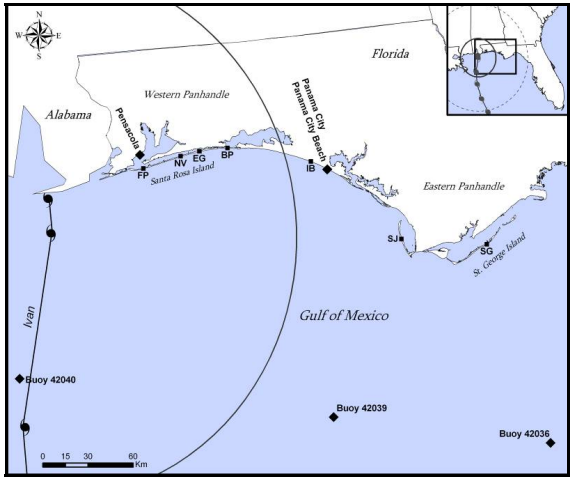

Fig. 1. Map showing track of Hurricane Ivan, wave and tide gauges (diamonds), and study sites (squares). The solid arc represents the extent of sustained hurricane force winds, and the dashed arc (in the insert) sustained tropical storm force winds at landfall.

The barrier-island study sites are characterized by a range of sub-environments (Fig. 2) which include, from bayside to Gulf: (1) mature woody vegetated dunes, (2) low-lying interior marsh and ephemeral wetlands, (3) broad flat interior platforms and hummocky dune fields (likely previous washover platform), and (4) a continuous to semi-continuous foredune ridge system populated with grassy vegetation, which merges seaward with the backbeach. The IB site, located along mainland beach is bound on the west by an artificially maintained narrow sinuous tidal inlet channel and on the east by residential development.

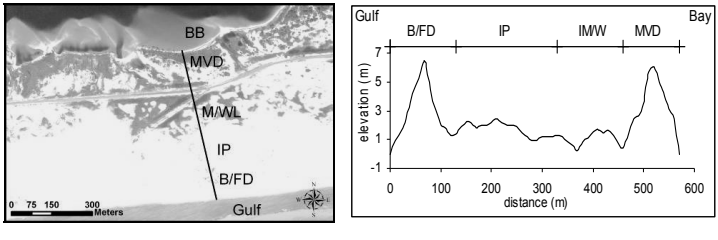

Fig. 2. Schematic showing typical northern Florida barrier island sub-environments. Sub-environments include; beach and foredune (B/FD), interior platform and hummocky dune-field (IP), interior marsh and wetlands (IM/W), mature vegetated dunes (MVD), and back-bay (BB).

Spatial variation of storm impact along the studied stretch of coastline was substantial. Employing the impact scale proposed by Sallenger (2000), inundation dominated the westernmost FP site. The NV site marks the transition from inundation to overwash, while overwash dominated the EG site. The BP site lies along the transition from overwash to collision regime, with scarping of higher dunes, erosion of lower dunes, and overwash penetrating inter-dune regions. East of the BP site, collision and swash regime dominated, with impact largely limited to beach erosion and dune scarping.

HURRICANE IVAN STORM CONDITIONS

On September 2, the ninth tropical depression of the 2004 hurricane season formed in the east Atlantic. Over the course of the next 24 hours, the storm intensified into Tropical Storm Ivan. Following a westerly course, Ivan further intensified into a Category 5 hurricane. On September 13, following passage through the Yucatan Channel, Ivan began a northwest track through the Gulf of Mexico, weakening slightly to Category 4, and eventually making landfall on September 16, as a strong Category 3 hurricane at Gulf Shores, Alabama, near the Florida-Alabama border (Fig. 1). The storm came onshore with extreme wind, wave, and surge.

Sustained tropical storm strength winds extended 475 km from the storm center, with sustained hurricane force winds extending 170 km (Fig 1). Significant and sustained surge was measured over a large area (Fig. 3). At the Pensacola tide gauge, the highest surge measured was 2.1 m above the Mean Low Low Water (MLLW), exceeding the gauge capacity. At Panama City Beach, the highest surge measured was 2.0 m above MLLW, nearly 4 times the typical tidal range. Surge levels exceeding 1.5 m (MLLW) persisted for over 10 hours (Fig. 3). Measured surge levels do not include contributions from wave setup and swash runup. Based on elevations of beach-profile changes, Wang et al. (2006) suggested that wave setup and swash runup account for ~50% of the total elevated water level during Ivan impact.

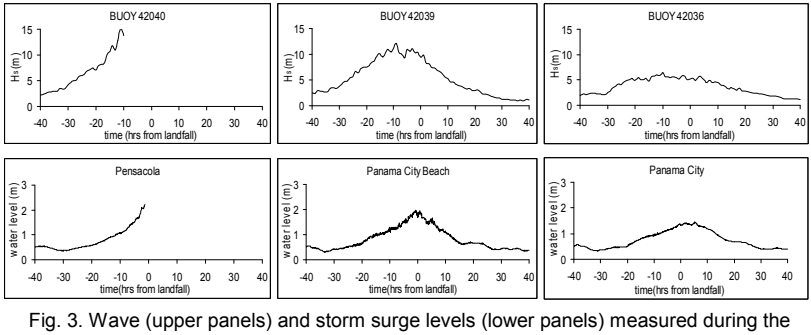

Fig. 3. Wave (upper panels) and storm surge levels (lower panels) measured during the passage of Ivan. Locations of the wave buoys and tide gauges are shown in Fig. 1. Water levels are relative to MLLW. Zero hour on time axis represents time of landfall.

Extremely high waves were measured offshore at the NDBC wave buoys. Shortly before landfall, 16-m waves were measured at the westernmost gauge 42040 (Fig. 3), which

apparently, was rendered inoperable. At gauge 42039, 220 km to the west, the highest wave measured was 12 m. Further east, at gauge 42036, the highest wave recorded was 6.4 m. Wang et al. (2005) measured wave heights higher than those reported by the NDBC buoys, with maximum wave height (H_{max}) reaching 28 m near Ivan's center. Overall, the highest waves at all three buoys were measured shortly before landfall.

METHODOLOGY

Coring, trenching, and GPR imaging were used to study the sedimentary characteristics of the Ivan washover deposits. Overall, 25 cores, 41 trenches, and approximately 30 line-km of GPR data were surveyed. Pre- and post-storm beach/dune and cross-island profiles were surveyed using an electronic total station and the data were referenced to NGVD 29 (National Geodetic Vertical Datum), which lies approximately 0.2 m below present sea level along the Panhandle region. At the BP, IB, SJ, and SG sites, profiles were surveyed 2 days prior, and 10 days following Ivan's landfall. Access limitations prevented pre-storm data collection west of the BP site. Core, trench and GPR data collection was initiated in October 2004, and continued during the 8 month post-storm period. During that period of time no appreciable storms impacted the studied region.

Sediment cores were obtained by driving a 7.6-cm diameter aluminum pipe into the subsurface with a sledge hammer. This procedure can penetrate up to 2 m below surface. Similar procedures of core description and sampling as used by Sedgwick and Davis (2003) were used here. Trenches of various shapes (e.g., T- or L-shape) and sizes (up to 6 m long and 1.5 m deep) were excavated in order to examine detailed sedimentological characteristics of the washover deposits. GPR transects were scanned adjacent to select trenches and core locations for ground truthing.

While traditional trenching and coring techniques provide valuable insight into detailed sedimentary characteristics, the methods are limited in spatial coverage. GPR, when employed in conjunction with coring and trenching can greatly expand spatial coverage, allowing for characterization of: (1) detailed internal sedimentary architecture, (2) transitional sedimentary features over a larger area, and (3) larger scale sedimentary features that may not be evident through single point data collection methods. GPR is a non-invasive geophysical technique which utilizes high-frequency electromagnetic (radar) waves to measure changes in the dielectric properties of earth materials. Abrupt changes in the dielectric properties of sediment layers (e.g., composition, texture, and porosity) result in some energy being reflected back to the ground surface, where it is recorded by a receiving antenna. The principals of GPR are discussed in detail by Daniels et al. (1988) and Davis and Annan (1989). Numerous studies describing the application of GPR in sedimentological studies are available in the literature (e.g., Jol et al., 1996; Bristow and Jol, 2003; Neal et al., 2003; Neal, 2004).

The GPR profile data were collected using a Sensors and Software Noggin SmartCart, equipped with a 250 MHz antenna and 100 V transmitter. Common mid-point (CMP) gathers were conducted at selected locations with a PulseEKKO 100 with a 200 MHz antenna and 400 V transmitter. The SmartCart data were collected in common offset

mode with the antenna separation fixed at 0.3 m, using a 0.05 m step size. Transect locations were established with a WAAS enabled GPS (Global Positioning System). The transects were surveyed for topographic control. The GPR data were processed using Sensors and Software EKKO Mapper software. All data were dewowed and scaled. Since imaging continuity of stratigraphic horizons and sedimentary structures were the primary goals of the GPR survey, an AGC (Automatic Gain Control) gain was applied employing max gain and pulse width settings of 400 and 1, respectively. This AGC gain settings tend to equalize signals by scaling in a manner inversely proportional to the signal strength. While some relative amplitude information is lost in this process (e.g., contrast between high and low amplitude reflections); lower amplitude reflections are enhanced, allowing better imaging of sedimentary structures. Common mid-point (CMP) gathers conducted at the NV, EG and BP sites yielded average signal travel velocities of 0.12 - 0.13 m ns^{-1} in the unsaturated sands, and 0.06 m ns^{-1} for the saturated sands below the water table. These velocities were used in the GPR interpretation, and depth scales were adjusted accordingly.

At the Santa Rosa Island sites, GPR penetration was on the order of 2 m. This relatively deep signal penetration can be attributed to the presence of a significant freshwater aquifer on the island as well as favorable sediment characteristics (medium quartz sands). Overall, data quality was good, and resolution was sufficient to image detailed sedimentary features observed in the cores and trenches. In contrast, at the central Panhandle IB site, shallow saline groundwater yielded rapid signal attenuation and nominal results. Owing to the limited cross shore extent of overwash along the eastern Panhandle, GPR surveys were not conducted at the SJ and SG sites.

Radar reflection profiles were interpreted following the techniques and terminology described by Neal (2004). The configuration and continuity of reflections provided the basis for establishing: (1) radar surfaces (radar boundaries), interpreted to represent depositional breaks, e.g., washover unit contacts, and (2) radar facies, interpreted to represent internal sedimentary structure. Interpreted profiles were correlated with sedimentary features observed in cores and trenches. This study focuses on the sedimentary characteristics of the Ivan washover deposits. Sedimentary units lying below the storm layer were not examined in detail.

RESULTS AND DISCUSSION

Pre and post-storm topographic surveys illustrate dramatic morphologic changes induced by Ivan extending over 260 km east of the storm center (Wang et al., 2006). The event yielded a broad spectrum of depositional as well as erosional features. These features are described within a spatial framework employing beach and barrier sub-environments as illustrated in Fig. 2.

Backbeach and Foredune Sub-environments

Representative pre- and post-storm profiles from the SG, IB and BP sites are shown in Fig. 4. Profile SG1 (Fig. 4a) illustrates typical backbeach and foredune response to the Ivan erosion and overwash event. Net erosion along the profile amounted to 20 $m^3 \cdot m^{-1}$,

with erosion reaching a maximum elevation of 2.7 m NGVD. A trench excavated along the backbeach revealed a 27 cm thick storm deposit here referred to as berm washover. The base of the washover is marked by antidunal bedforms punctuated by dark heavy mineral rich convex-up laminae (Fig. 5), and an abrupt transition from distinctly darker pre-storm bioturbated sediment to light colored quartz sand. The basal bedforms are overlain and truncated by horizontal to gently seaward dipping layers suggesting aggradation during the subsiding phase of the storm.

Further to the west, at the IB site, similar but more severe foredune and beach erosion were measured. Along the easternmost profile IB1 (Fig. 4b), net erosion amounted to 37 $m^3 \cdot m^{-1}$, with scarping of the foredune reaching a maximum elevation of 4.4 m NGVD (or roughly 4.2 m above MSL). A series of trenches excavated along the backbeach revealed a thickening seaward berm washover unit, 15 to 25 cm thick, characterized by horizontal to gently seaward dipping layers, overlying a sharp basal erosional surface (Fig. 4b), similar to the above SG site.

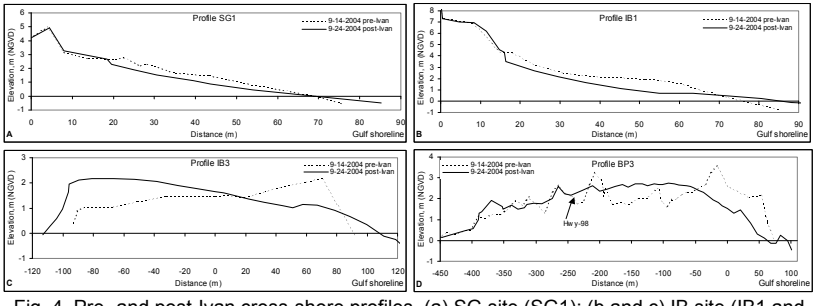

Fig. 4. Pre- and post-Ivan cross-shore profiles. (a) SG site (SG1); (b and c) IB site (IB1 and IB3); (d) BP site (BP3).

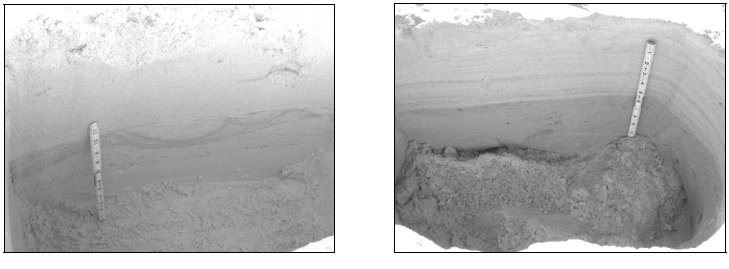

Fig. 5. Trenches excavated along profiles SG1 (left) and IB1 (right).

Located roughly 1-km to the west of IB1, profile IB3 (Fig. 4c) illustrates a significantly different pre-storm beach morphology. The site is characterized by a steep pre-storm shoreface and beach, which merges landward into broad flat platform (previous washover platform). Dunes are absent, and the beach and platform are bound on the west and north by a tidal inlet. Erosion along IB3 extended up the beach 75 m from MLW, yielding a net

loss of 40 $m^3 \cdot m^{-1}$ of sediment. Washover deposition further landward over the platform amounted to 75 $m^3 \cdot m^{-1}$, nearly twice the amount of sediment loss, suggesting longshore sediment transport may have contributed to the washover sediment supply. This is in contrast to the situation at BP site discussed in the next section.

Further to the west, along the eastern end of Santa Rosa Island, at the BP site, erosion dominates seaward of the foredune ridge. Along profile BP3 (Fig. 4d), the foredune ridge, with a pre-storm elevation of 3.6 m NGVD, was completely eroded, representing 76 $m^3 \cdot m^{-1}$ of sediment loss. Trenches excavated along the backbeach revealed a thickening landward berm washover deposit 20 to 33 cm thick, characterized by the horizontal to gently seaward dipping layers.

Fig. 6 shows a 270-m long shore-perpendicular GPR profile scanned at the BP site. The profile extends landward from the Gulf shoreface (left side), traversing the back-beach, foredune, interior platform, and interior marsh sub-environments. The profile contains: (1) a continuous undulating reflection lying between 0.5 and 1.6 m (labeled Iv) traceable across the entire profile, interpreted to represent the radar boundary separating the Ivan washover from pre-Ivan sediment; (2) semi-continuous horizontal and inclined, parallel to sub-parallel reflections overlying Iv representing internal structure within the Ivan washover deposit (Ivan radar facies); and (3) a continuous near horizontal reflection cutting across inclined reflections which represents the water table (labeled wt). Seaward inclined reflections imaged between 15 and 35 m correlate with layering observed within the berm washover. Between 70 and100 m, an eroded section of the foredune ridge was imaged. Reflective patterns suggest the Ivan washover thins substantially over the eroded dune and thickens rapidly landward. A general increase in accommodation space landward of the foredune would account for these patterns.

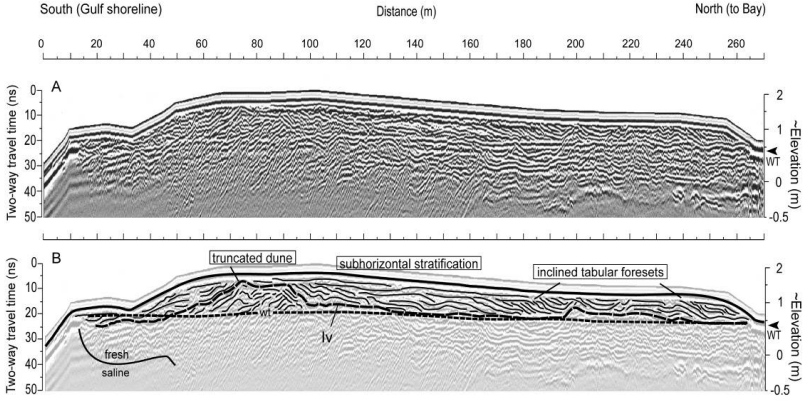

Fig. 6. Shore-normal GPR transect (upper) and interpreted profile (lower) at BP site.

Interior Platform and Hummocky Dune Field Sub-environment

In terms of aerial extent, the interior platform and associated hummocky dune field represent the largest portion of the barrier-island. This sub-environment is likely

washover from previous storms with recovering dunes. As shown in profile BP3 (Fig. 4d), erosion over the interior platform was largely focused to dunes lying above 2.5 m NGVD, with washover deposition dominating the lower elevations. Deposition along the profile amounted to 75 $m^3 \cdot m^{-1}$. This is roughly equal to the 76 $m^3 \cdot m^{-1}$ eroded from the beach and foredune along the profile, and suggests that while a significant volume of sediment redistribution occurs during an overwash event, overall barrier mass can be conserved. The average thickness of platform washover deposits based on 20 cores and trenches was 62 cm, with a maximum of 105 cm measured at the EG site. The washover is characterized by heavy mineral-rich horizontal to subhorizontal layers. The heavy minerals concentrate within the finer grain-size fractions (0.125 - 0.3 mm), and tend to form distinct laminae. Fresh, in-place and nearly upright grasses preserved along the base of the washover (Fig. 7) suggest erosion along the pre-storm surface was limited, and much less severe than the erosion on the backbeach and foredune areas.

GPR data over the interior platform (Fig. 6) show radar boundary Iv as a continuous horizontal to undulating reflection. The undulations appear to reflect hummocky dunes preserved along the pre-storm surface (Fig. 7). The Ivan radar facies is characterized by semi-continuous horizontal to slightly inclined landward reflections that downlap onto Iv. The reflective patterns illustrate a rapid thickening of the washover landward of the eroded foredune.

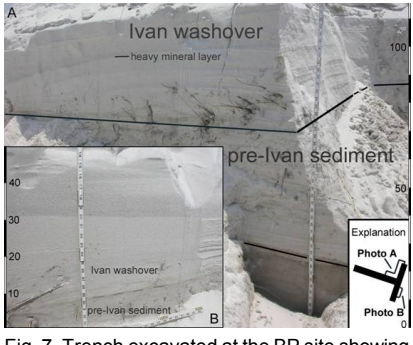

Fig. 7. Trench excavated at the BP site showing interior platform washover deposition occurring over a low-lying hummocky dune.

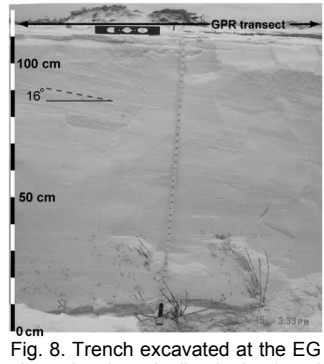

Fig. 8. Trench excavated at the EG site showing inclined landward tabular foreset stratification and marsh grasses along basal contact.

Interior Marsh and Ephemeral Wetlands Sub-environment

This sub-environment typically occupies low lying portions of the barrier islands, making it particularly susceptible to flooding during overwash. The pre-storm surface tends to be populated with marsh grasses, and in the case of ephemeral ponds, thin algal mats may develop along surface. The organic rich nature of the pre-storm sediment makes distinguishing the cleaner quartz sand washover deposits relatively straightforward.

Numerous existing studies (e.g. Schwartz 1975; 1982) have described the development of inclined tabular foreset bedding during washover deposition into lagoons and

washover ponds. Bedding features of this nature were apparent in both the trenches and GPR profiles examined in this study. At the EG site, a trench excavated along the margins of an active interior marsh (Fig. 8) exposed inclined landward tabular foreset bedding developed during progradational washover deposition into the flooded marsh. Fresh in-place marsh grasses extending up from the pre-storm surface indicate limited erosion occurred prior to washover deposition. Increased accommodation space within the low-lying wetlands yields an increasingly thicker washover relative to the seaward sub-environments, with washover thicknesses commonly approaching 1.20 m.

The GPR profile shown in Fig. 9 was scanned adjacent to the EG trench, and shows the Iv radar boundary extending across the profile at depths ranging from 0.8 to 1.2 m. The Ivan radar facies is characterized by semi-continuous inclined landward reflections that downlap onto Iv. Similar inclined reflective patterns were observed along the landward end of the BP GPR profile (Fig. 6), and correlate with washover deposition into a flooded interior marsh. The inclined reflections observed on the BP GPR profile however, are overlain by a series of semi-continuous horizontal to sub-horizontal reflections more consistent with platform type radar facies. The reflective patterns as well as trench data indicate that within the marsh-wetland sub-environment, inclined landward tabular foreset bedding translates upward into horizontal layering frequently. This transition of bedding features suggests a temporal variation in the mode of washover deposition. Initial deposition within the flooded wetlands occurs in a progradational manner as bedload sediment cascades down the terminal slope of the washover lobe. The in-filling of the accommodation space and the resulting increased elevations prompts a renewal of washover platform type aggradation yielding the overlying horizontal bedding. This aggradation should be dominated by sheet flow and suspended-load transport modes in shallowing water.

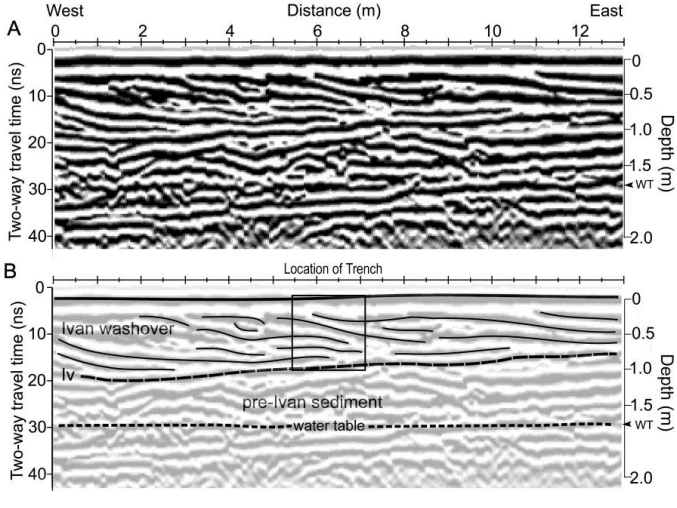

Fig. 9. GPR transect scanned adjacent to the trench (box outline) shown in Fig. 8.

Mature Vegetated Interior Dunes and Inter-dune Sub-environment

Along the western Panhandle, mature vegetated and less active interior dunes are commonly found landward of, or flanking the interior platform. The dunes rarely exceed 10 m in height, and frequently host woody plant species such as Scrub Live Oak and Myrtle, with vegetation commonly extending down to the inter-dune region. At the NV site, washover deposition occurred within the woody vegetated inter-dune region yielding a 45-cm thick deposit (Fig. 10a). The lower 15 cm of the washover is a massive layer containing abundant organic fragments and randomly disseminated dark heavy minerals, and is overlain by a series of thinner heavy mineral rich horizontal layers containing minor amounts of organic debris. A sharp boundary separates the washover from the organic rich pre-storm sediments. Numerous coarse woody roots and branches extend up from the pre-storm surface, suggesting that limited erosion occurred in the inter-dune region prior to washover deposition. The GPR transect scanned adjacent to the trench shown in Fig. 10 shows a continuous horizontal reflection at a depth of 0.5 m (labeled Iv) which correlates with the base of the of the Ivan washover unit. The Ivan radar facies is represented by a series of semi-continuous horizontal to sub-horizontal reflections. Numerous discrete hyperbolic reflections lying both above and below Iv represent coarse root and branch material.

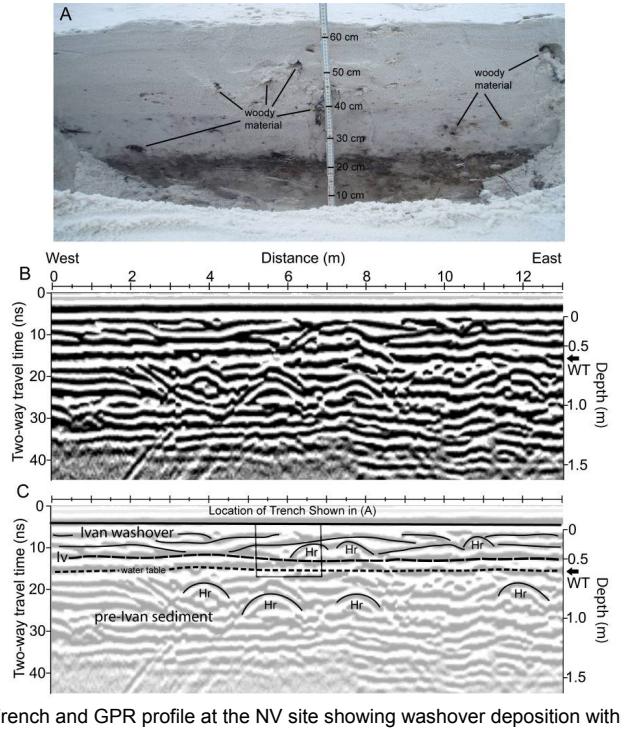

Fig. 10. Trench and GPR profile at the NV site showing washover deposition within vegetated inter-dune sub-environment.

Back Bay Sub-environment

The morphological characteristics of the bayside beach along the Panhandle coast include a narrow and steep shoreface and a shallow platform, typically less than 1.5 m deep extending up to several hundred meters into the bay (Stone et al., 2004). This platform, also referred to as low-tide terrace (Nordstrom, 1992), is common along estuary beaches worldwide. Ivan induced washover deposition into the back-barrier bay at the western FP, NV, and EG sites. Overwash into the back-bay took two forms. Along narrow sections of the barrier, where mature vegetated dunes are largely absent and the interior platform dominates the profile, inundation resulted in laterally continuous bayside washover deposition, in places amounting to 120 m of landward bayside shoreline migration. Along wider sections of the island, where mature dunes populate the bayside shoreline, deposition was largely confined to narrow shore normal runoff channels 50 to 80 m wide, yielding discrete washover tongues extending up to 100 m into the back-bay.

Landward progradation of the bayside shoreline is clearly evident when comparing the pre- and post-storm aerial photos of the FP site (Fig. 11c,d). A GPR profile scanned over the pre-storm bayside beach shoreface (Fig. 11a,b) shows an abrupt downwarping of Iv between 30 and 35 m which correlates with the pre-storm shoreface. Gulfward of the shoreface, the washover is characterized by semi-continuous subhorizontal reflections characteristic of washover platform radar facies. The platform facies merges landward (bayward) into steeply inclined sigmoid reflections lying tangential to Iv. Owing to the increased accommodation within the back-bay, washover thicknesses increase substantially, ranging from 1.5-2.0 m.

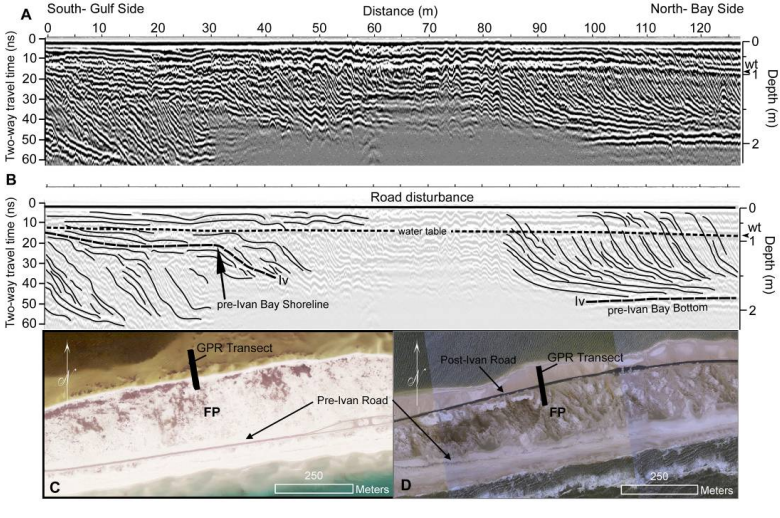

Fig. 11. GPR transect scanned at FP site, and pre- (C) and post-Ivan (D) aerial photos.

It is worth noting that along the Gulf side of the above GPR profile, below Iv, steeply inclined landward reflective patterns downlap onto a high amplitude landward dipping

reflector. The reflective patterns indicate an earlier phase of progradational deposition into the back-bay, suggesting that overwash constitutes a major process driving landward barrier island migration.

CONCLUDING SUMMARY

Regional overwash induced by Hurricane Ivan along the northern Florida coast yielded a range of spatially distinct erosional and depositional features. Nearshore beach and foredune response is initially dominated by erosion. Subsequent deposition over the beach, here referred to as berm washover, is characterized by basal high flow regime bedforms (e.g., antidune) or a sharp planar erosional surface overlain by horizontal to gently seaward dipping planar bedding. This berm washover deposits suggest aggradation occurred during the subsiding phase of the storm after the initial erosion. Owing to the limited accommodation space over eroded sections of the beach and foredune, the berm washover tends to be relatively thin.

Sediment eroded from the foredunes is in-turn transported landward and deposited across the entire barrier profile. Barrier response landward of the foredune is largely depositional; with limited erosion occurring in the low-lying areas as indicated by the widespread preservation of in-place vegetation below the washover deposits. Washover deposits over the interior platform and hummocky dune field are characterized by horizontal to subhorizontal inclined landward bedding. These bedding features correlate with horizontal and subhorizontal reflective patterns observed in the GPR data. Landward thickening of the interior platform washover can be attributed to a general landward increase in accommodation space.

Washover deposition within the flooded interior marsh and wetland sub-environment, coupled with increased accommodation space, yields thicker washover deposits. The washover is characterized by distinct inclined landward tabular foreset bedding that often translates upward into horizontal to subhorizontal inclined landward bedding. This transition of bedding features suggests a change in the mode of sediment transport and deposition. Initial deposition within the wetlands occurs in a progradational manner as bedload sediment cascades down the steep terminal slope of the washover lobe. The in-filling of the wetland depression and the resulting increased elevations prompts a renewal of washover platform type aggradation yielding the overlying horizontal bedding. This aggradation is believed to be dominated by sheet flow and suspended-load transport modes in shallowing water.

Proximal to Ivan's center, along narrow portions of Santa Rosa Island, inundation resulted in substantial washover deposition into the back-bay, in-places amounting to 210 $m^3 \cdot m^{-1}$ accumulation yielding up to 120 m of landward barrier migration. GPR reflective patterns indicate washover deposition within the back-bay is dominated by progradational sigmoid and inclined tabular foreset stratification. Owing to the significantly increased accommodation space, washover thicknesses within the back-bay commonly approach 2 m. Overall, the thickness of washover deposits is strongly controlled by the accommodation space.

ACKNOWLEDGEMENTS

This study is supported by the University of South Florida and the National Science Foundation's Geography and Regional Science Program.

REFERENCES

Bristow, C.S. and Jol, H.M. (Eds.) (2003) *Ground-penetrating Radar in Sediments*. Geological Society. London, Special publications, 211.

Daniels, D.J., Gunton, D.J. and Scott, H.F. (1988) Introduction to subsurface radar. *IEE Proceedings*, 135, 278-320.

Davis, J.L. and Annan A.P. (1989) Ground-penetrating radar for high-resolution mapping of soil and rock stratigraphy. *Geophysical Prospecting*, 37, 531-551.

Jol, H.M., Smith, D.G. and Meyers, R.A. (1996) Digital ground-penetrating radar (GPR): an improved and very effective geophysical tool for studying modern coastal barriers (examples fro the Atlantic, Gulf and Pacific coasts, U.S.A. *Journal of Coastal Research*, 12, 960-968.

Morang, A. (1992) Inlet migration and hydraulic processes at East Pass, Florida. *Journal of Coastal Research*, 18, 486-501.

Neal, A. (2004) Ground-penetrating radar and its use in sedimentology: principles, problems and progress. *Earth-Science reviews*, 66, 261-330.

Neal, A., Richards, J. and Pye, K. (2003) Sedimentology of coarse-clastic beach-ridge deposits, Essex, Southeast England. *Sedimentary Geology*, 162, 167-198.

Nordstrom, K.F. (1992) *Estuarine Beaches.* Elsevier Applied Science, 225 pp.

Sallenger, A.H. (2000) Storm impact scale for barrier islands. *Journal of Coastal Research*, 16, 890-895.

Schwartz, R.K. (1975) Nature and genesis of some storm washover deposits. *CERC Technical Memo 61*. U.S. Army Corps of Engineers, 69p.

Schwartz, R.K. (1982) Bedform and stratification characteristics of some modern small-scale washover sand bodies. *Sedimentology*, 29, 835-849.

Sedgwick, P.E. and Davis, R.A., Jr. (2003) Stratigraphy of washover deposits in Florida: implications for recognition in the stratigraphic record. *Marine Geology*, 200, 31-48.

Shepard, F. P. (1973) *Submarine Geology,* Harper & Row, New York, 517 pp.

Stone, G.W. and Stapor, F.W. (1996) A nearshore sediment transport model for the Northeast Gulf of Mexico Coast: *Journal of Coastal Research*, 12(3), 786-792.

Stone, G.W., Liu, B., Pepper, D.A. and Wang P. (2004) The importance of extratropical and tropical cyclones on the short-term evolution of barrier islands along the northern Gulf of Mexico, USA. *Marine Geology*, 210, 63-78.

Wang, D.W., Mitchell, D.A., Teague, W.J., Jarosz, E. and Hulbert, M.S. (2005) Extreme waves under Hurricane Ivan. *Science*, 309(5736), 896.

Wang, P., Kirby, J.H., Haber, J.D., Horwitz, M.H., Knorr, P.O., and Krock, J.R., 2006. Morphological and sedimentological impacts of Hurricane Ivan and immediate post-storm beach recovery along the northwestern Florida barrier-island coasts, *J. Coastal Res.*, 22(6), 1,382-1,402.

IMPACTS OF THE 2004 INDIAN OCEAN TSUNAMI ON THE SOUTHWEST COASTS OF SRI LANKA

Robert A. Morton [1], James R. Goff [2], Scott L. Nichol [3]

1. U.S. Geological Survey, 600 Fourth St. S., St. Petersburg, FL, USA rmorton@usgs.gov
2. National Institute of Water & Atmospheric Research Ltd., PO Box 8602, Christchurch, NZ j.goff@niwa.co.nz
3. University of Auckland, Bag 92019, Auckland, NZ s.nichol@auckland.ac.nz

Abstract: The 2004 Indian Ocean tsunami caused major landscape changes along the southwest coasts of Sri Lanka that were controlled by the flow, natural topography and bathymetry, and anthropogenic modifications of the terrain. Landscape changes included substantial beach erosion and scouring of return-flow channels near the beach, and deposition of sand sheets across the narrow coastal plain. In many areas tsunami deposits also included abundant building rubble due to the extensive destruction of homes and businesses in areas of dense development. Trim lines and flow directions confirmed that shoreline orientation and wave refraction from embayments and rock-anchored headlands locally focused the flow and amplified the inundation. Tsunami deposits were 1 to 36 cm thick but most were less than 25 cm thick. Deposit thickness depended partly on antecedent topography. The deposits were composed of coarse to medium sand organized into a few sets of plane parallel laminae that exhibited overall upward fining and landward thinning trends.

INTRODUCTION

A U.S. led multi-discipline multi-national survey team was dispatched to Sri Lanka two weeks after the 2004 Indian Ocean tsunami to conduct a rapid reconnaissance investigation of the impacts of this catastrophic event. The purposes of the survey were to obtain eyewitness accounts and to make observations and measurements regarding tsunami impacts that would likely be altered by the post-tsunami cleanup and reconstruction that began immediately (Liu et al., 2005, Goff et al., 2005). Nearly all of the post-tsunami field surveys conducted in Sri Lanka focused on the wave characteristics, water levels, and inundation distances (Wijetunge, 2006). In contrast, the U.S. led team also collected data to characterize the tsunami deposits. The types of tsunami data collected were water levels and wave run-up elevations (Fig. 1), flow

depths, inundation distance from the shore, and flow directions. Water level is the water elevation above a sea level datum, wave runup is the maximum elevation of water on the land, and flow depth is the water level minus the land elevation. Geological observations included geologic setting, nearshore topography, erosional and depositional changes, and tsunami deposit characteristics. This report summarizes the general morphological changes and sedimentological observations along the southwest coasts of the country between Colombo and Yala.

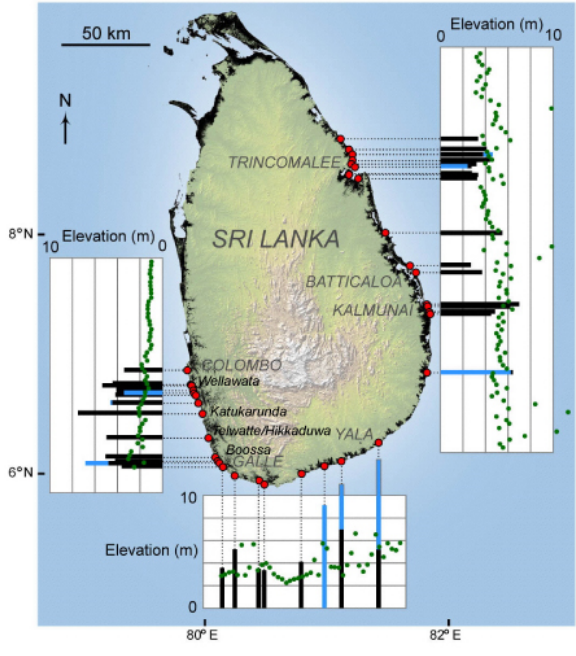

Fig. 1. Water levels in Sri Lanka associated with the 2004 tsunami. Measured tsunami runup (gray bars) and maximum wave heights (black bars). Gray-filled dots show the sites of elevation measurement. After Liu et al. (2005).

GEOLOGICAL SETTING

The island of Sri Lanka consists primarily of a Pre-Cambrian bedrock core that makes up the Central Highlands surrounded by lowlands and a fringing coastal plain composed of alluvial deposits (Swan, 1985). Long barriers with sandy beaches and interior lagoons occupy embayments between headlands that are bluff outcrops of resistant rock. Wave-cut platforms and other expressions of submerged outcrops extend offshore along much of the southwest coast (Swan, 1985). The lengths of sandy beach are greatest on the east and southeast coast but diminish to the west where cliff headlands are more common. These first-order morphological features controlled tsunami impacts such that the headlands blocked tsunami inundation and

prevented interior damage, whereas the embayments focused the waves and increased the limits of inundation and runup (Fig. 1).

The southeast coast of Sri Lanka near Yala is characterized by relatively wide zeta-curved sandy beaches and adjacent narrow coastal plains offset and separated by rock-anchored headlands and points. Small inlets that are connected to bays or lakes and associated upland drainages also bound coastal segments. Sand dunes are locally well developed on the southeastern beaches of Sri Lanka where sand supply is abundant and the climate is relatively dry. Sand dunes are largely absent on beaches of the southern and west coasts as a result of higher rainfall in the region. Beaches are composed predominantly of fine to coarse quartz sand with variable amounts of carbonate material consisting of shell and fragments of coral reef. Beach erosion was a serious problem for many Sri Lankan communities even before the tsunami. At some locations, shoreline stabilization structures such as gabions, riprap revetments, groins, and segmented breakwaters were heavily damaged or rendered ineffective by the tsunami.

2004 INDIAN OCEAN TSUNAMI

On December 26, 2004, rupture along a 1200 km segment of a megathrust fault west of northern Sumatra produced a magnitude 9.1 earthquake. The great subduction zone earthquake, which lasted for several minutes, deformed the seafloor an estimated 15 m (Lay et al., 2005) and generated a tsunami that propagated throughout the Indian Ocean, causing widespread destruction of coastal communities in 11 countries.

One of the countries hardest hit by the tsunami was Sri Lanka, owing to its location directly in the path of the highest waves and separated from the tsunami-generating source by only deep water. In Sri Lanka, where the tsunami arrived about 2 hrs after the earthquake, eyewitnesses reported that the first wave was a minor surge that flooded beaches but caused little damage to the infrastructure. The initial positive wave was followed by a large negative wave that caused the sea to withdraw several hundred meters, exposing the seafloor and coral reefs offshore. About 10 to 15 minutes later, the second positive wave struck causing most of the casualties and catastrophic impacts. North of Galle, a third wave was reported several hours after arrival of the first waves, indicating that the later wave followed a longer path, probably having been reflected off the Maldives or India (Liu et al., 2005).

TSUNAMI IMPACTS

In Sri Lanka, the low coastal areas with ocean-facing sand beaches provide easy access to the sea for commercial fishing and recreation. Consequently, they are densely developed and occupied by businesses and residences that are vulnerable to tsunami hazards. Most of the fatalities and structural damage from the 2004 tsunami occurred within a few hundred meters of the shore. Primary tsunami impacts at selected sites along the southwest coasts of Sri Lanka are summarized in Table 1. The following accounts, organized from northwest to southeast (Fig. 1), present the morphological impacts and deposit characteristics where the data are most complete. At all trench sites, tsunami deposits were sampled at 1 cm intervals.

Table 1. Summary of 2004 Tsunami Impacts on Southwest Coasts of Sri Lanka

Location	Primary Impacts	Max. Flow Depth m	Deposit Composition	Max. Thick. cm
Wellawatta*	Inundation, minor deposition	1.5	sand	7
Mt. Lavinia	Inundation, minor deposition	1.5	sand	
Moratuwa	Destruction and deposition	1.3	sd, boulders, bldg. rubble	
Katukurunda*	Inundation, deposition	3.5	sand and small boulders	36†
Paiyagala	Destruction, minor deposition	5.0	bldg. rubble and sand	
Ahungalla	Destruction, minor deposition	3.0	bldg. rubble and sand	
Telwatte*	Destruction, erosion, deposition	2.0	sd, boulders, bldg. rubble	20
Hikkaduwa*	Destruction, erosion, deposition	2.3	sand and bldg. rubble	23
Boossa*	Destruction, erosion, deposition	1.5	sand and bldg. rubble	5
Galle	Inundation, destruction	5.2	bldg. rubble	
Unawatuna	Inundation, destruction	1.5	bldg. rubble	
Weligama	Destruction, deposition	1.8	bldg. rubble and sand	
Matara	Destruction, deposition	2.3	bldg. rubble and sand	
Tangalla	Inundation, erosion	2.3	small boulders moved	
Hambantota	Destruction, deposition	5.5	sand and bldg. rubble	
Yala*	Destruction, erosion, deposition	4.6	sand and bldg rubble	22

* Tsunami deposits examined at these locations are described in the text.
† Thickness increased by artificial topography

Wellawata

South of Colombo, the densely developed communities of Wellawata and Mount Lavinia are characterized by straight and continuous sand beaches, which are approximately 30 m wide between the high water line (HWL) and the vegetation line. A narrow rock platform about 200 m offshore acts as a local breakwater for incoming waves. The coastal plain is an extension of the backbeach that gradually increases in elevation landward. Tsunami impacts along this coastal segment were primarily inundation, minor deposition, and slight damage to the infrastructure. Maximum flow depths were 1.5 m and inundation extended about 350 to 400 m inland from the beach where the waves generally were unrestricted by buildings. Sand was deposited as a washover sheet that extended about 30 m inland from the backbeach to the railroad embankment that runs parallel to the shore.

At Wellawata, eleven deposit thickness measurements were made along a cross-shore transect. The measurements showed that the tsunami washover sheet systematically increased and decreased in thickness landward from the HWL, ranging from 2 cm at 21 m, to 7 cm at 24 m, to 1 cm at 30 m, and pinch out at 31.7 m. The 7 cm deposit consisted of plane parallel laminations organized into two laminae sets, each about 3.5 cm thick (Fig. 2). The lower unit was composed of medium sand with abundant heavy mineral laminations and a slight upward fining of mean grain size. The upper unit also was composed of upward-fining medium sand that bracketed the same range of mean grain sizes as the lower unit, but did not contain the well defined segregation of heavy mineral laminations. Both of the laminae sets were moderately well sorted with sorting systematically improving upward. The tsunami deposits contrasted both

in color and texture with the older underlying deposits, which consisted of poorly sorted, very coarse orange sand and gravel (Fig. 2).

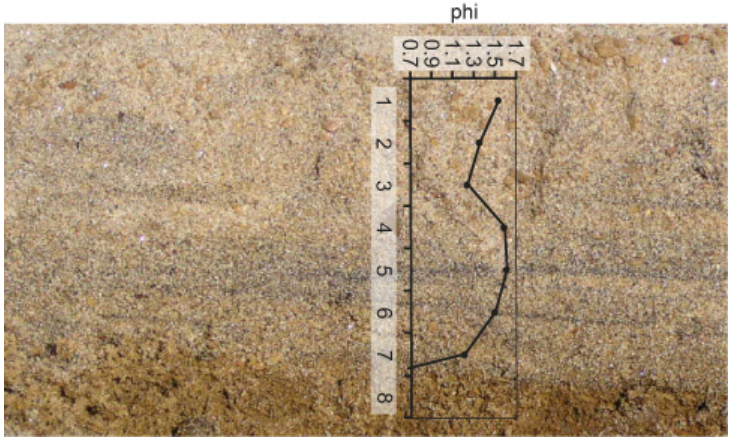

Fig. 2. Trench exposure at Wellawata located 24 m from the high water line.

Katukurunda

At Katukurunda, a broad lagoon separates a low narrow sand spit (150 m wide) from the mainland. The spit, which was approximately 1 m above sea level and developed with a three-story hotel complex and houses, was completely overwashed by the tsunami that generated a maximum flow depth of approximately 3.5 m. Beach width is highly variable owing to a field of offshore segmented breakwaters, each about 180 m long. The beach is about 140 m wide where it is attached to a breakwater as a tombolo and less than 25 m wide where the shore is unprotected between breakwaters. Post-tsunami observations were made at a site immediately landward of one of the breakwaters that was so severely damaged that rocks extracted from the structure were incorporated into the tsunami deposit.

On the low spit between the beach and hotel complex, rows of planted palm trees formed topographic highs, whereas the gaps between the trees formed topographic lows. The trees interfered with tsunami flow and scour increased around the tree bases. The tsunami washover sand deposits conformed to the landscaped topography and were thin around the tree root balls and relatively thick between them. A trench located 61 m from the HWL and between adjacent rows of trees showed that the tsunami deposit was 36 cm thick (Fig. 3).

The deposit was composed of medium to coarse sand that appeared to be homogeneous at the base and organized into plane parallel laminations toward the top. Vertical textural trends demonstrate that the tsunami deposit was organized into four units, each exhibiting upward-coarsening/upward-fining textural trends. Each component of each couplet was roughly equal in thickness and the couplets were

progressively thinner from bottom to top. The uppermost two couplets, each about 4 cm thick, consisted of clean sand laminae overlain by heavy mineral laminae. Within the deposit were two rip-up clasts about 3.5 cm in diameter composed of organic-rich sand derived from the underlying pre-tsunami soil, which was texturally finer than the tsunami deposit. Cobbles and small boulders (50 cm b axis) excavated from the offshore breakwater were scattered across the coastal plain close to the beach (Fig. 4). Concentration of the boulders at the surface indicated that they were probably part of the late-stage tsunami load that was mobilized and deposited after initial sand deposition.

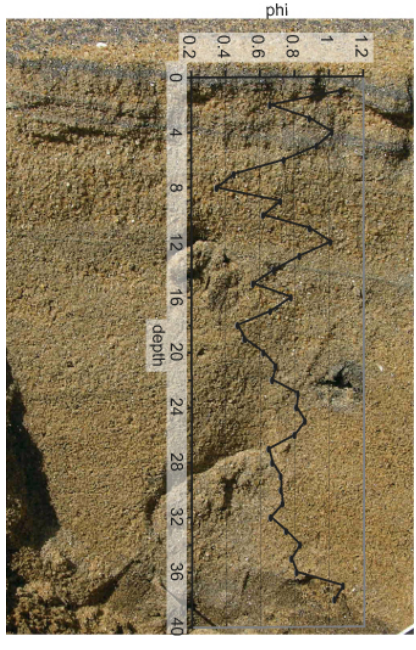

Fig. 3. Trench exposure at Katukurunda located 61 m from the high water line.

Telwatte

Low coastal plain elevations near Telwatte and an estuary mouth at North Hikkaduwa amplified tsunami inundation and led to near total destruction of buildings within 100 m of the sea. This coastal segment has a moderately wide beach (~70 m) and does not have a nearshore rock platform to protect the coastal infrastructure, such as the platform observed farther to the south at South Hikkaduwa. The sandy coastal plain near Telwatte is moderately wide, extending 0.5 to 1 km inland from the beach to a partly filled arcuate lagoon. The beach is relatively straight, long, and continuous, but it also is steep, narrow, and armored with riprap and short groins that protrude about 1 m above sea level. The coastal highway, which is located about 15 m from

the erosional backbeach scarp, and some houses were constructed on a low sand ridge that dominates the topography about 60 m inland from the beach. The ridge



Fig. 4. Small boulders on the Katukurunda beach emplaced by the 2004 tsunami.

influenced tsunami flow, the resulting morphological impacts, and the thicknesses of the tsunami deposits. Erosion and transport were the dominant processes across the ridge where flow depths were about 2 m. Deposits consisted of small coastal-structure boulders emplaced between the seaward edge of the ridge and the road, thin patches of sand, and accumulations of building rubble near and landward of the bare foundations that formerly supported buildings. The rapid tsunami flow and abrupt increase in water depth at the landward edge of the ridge produced a hydraulic jump that scoured pits roughly parallel to the ridge. Landward of the ridge and pits, tsunami deposits formed a sheet of sand and debris that extended inland more than 50 m.

Two trenches, each approximately 110 m from the HWL, exposed well sorted to moderately sorted medium to coarse sand 10 to 20 cm thick above an organic-rich soil. The soil zone was substantially coarser and more poorly sorted than the overlying tsunami deposits. The 10 cm tsunami deposit (Fig. 5) was organized into 3 laminae sets. The basal 4 cm were faintly laminated medium sand that exhibited upward-fining and upward-coarsening textural trends. A well-defined, possibly erosional surface of coarse sand and gravel formed the base of the second upward-fining laminae set, which was 2 cm thick. The third set was faintly laminated and upward fining to uniform in texture.

Where the Telwatte deposit was 20 cm thick it consisted of medium to coarse sand organized as plane parallel laminations into three laminae sets. Each laminae set was

about 6 cm thick. The basal laminae set, which was in erosional contact with the underlying dark brown

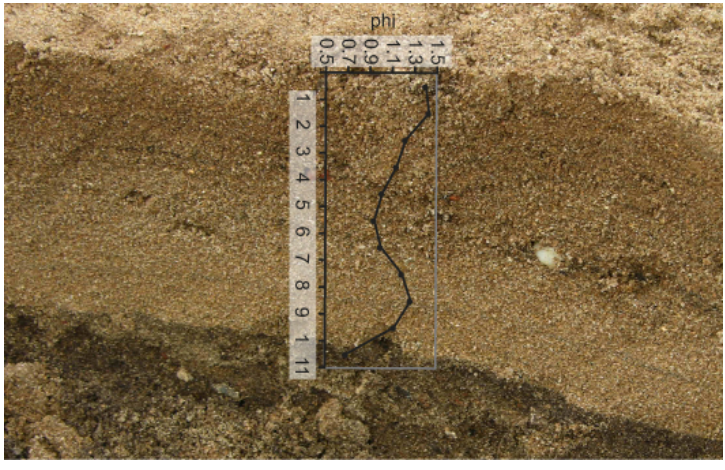

Fig. 5. Trench exposure at Telwatte located 110 m from the high water line.

organic-rich soil, was capped by a 0.5 cm unit marked by two faintly developed lamina enriched in heavy minerals. The intermediate and upper laminae sets were similar in grain size and composition; both contained pebble size clasts of masonry building material, but they were distinguishable by the slightly darker color of the upper unit.

South Hikkaduwa

The shore planform and beach dimensions at South Hikkaduwa are irregular owing to the presence of rock outcrops and a wave-cut shore platform at the toe of the sand beach. Although the beach typically is less than 10 m wide and embayed over distances of 150 to 200 m, it is densely developed with well-constructed commercial buildings including hotels and other businesses. The rock platform provided substantial protection from the tsunami and limited the impacts to beach erosion and deposition of a washover sheet and minor damage to buildings located between the beach and the coastal highway. Trapped debris and bark scars on trees indicated that flow depths across the backbeach and washover sheet were about 2.3 m, although there was evidence that the undulating rock platform influenced the runup, by focusing wave energy where there was a gap in the platform.

Tsunami deposits at Hikkaduwa exposed in a trench about 30 m from the HWL were 16 to 23 cm thick, and composed of well-sorted plane parallel laminated coarse sand with some shell fragments overlying a brown organic-rich sandy soil (Fig. 6). The tsunami deposit was organized into two laminae sets each about 8 cm thick and each exhibiting upward-fining textural trends. Upward-fining textures also characterized

the entire deposit. A slightly coarser lamina with some gravel separated the two laminae sets. Heavy minerals were disseminated throughout the deposit and were not concentrated into individual lamina as in other tsunami deposits.

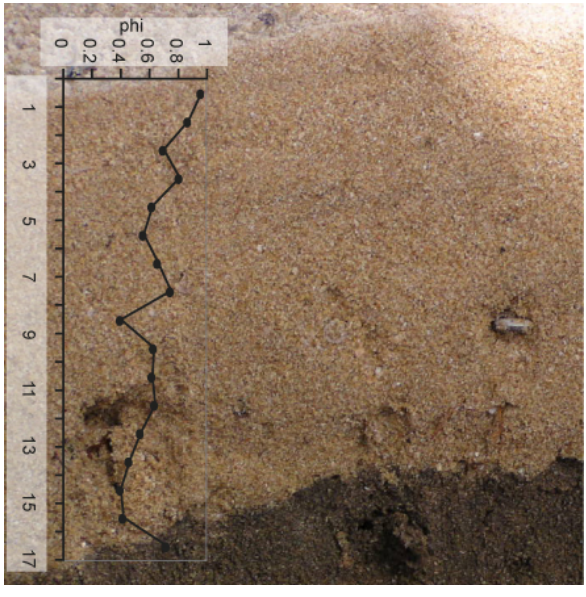

Fig. 6. Trench exposure at Hikkaduwa located 30 m from the high water line.

Boossa

Rock outcrops offshore and along the shore near Boossa create an irregular, slightly embayed shore platform that locally alters wave characteristics and produces variable beach dimensions. Locally increased wave heights and steepness were confirmed by the many surfers who favor the beach at Boossa for their sport. The steep narrow beach is about 10 m wide and only 10 to 100 m from the coastal highway. The tsunami eroded the beach, creating a scarp of densely matted tree roots and destroying houses that had been constructed near the coastal highway. Bent metal poles and broken concrete posts along the railroad tracks indicated both onshore and offshore flow directions. Maximum flow depths were about 1.5 m. Eyewitnesses reported that the first wave was low and moved rapidly, but the second wave, which came about 15 minutes later, was the most destructive.

Inundation by the tsunami produced a thin sand sheet and building rubble that covered the flat coastal plain near the shore at Boossa. Loading from pedestrian traffic had extensively modified the depositional surface and possibly the internal structure of the sand deposit. A trench located approximately 28 m from the HWL revealed 5 cm of homogeneous coarse sand overlying a dark organic-rich soil (Fig.

7). The sand was moderately well sorted and the minor vertical changes in mean grain size defined two slightly upward-coarsening units, each about 2 cm thick.

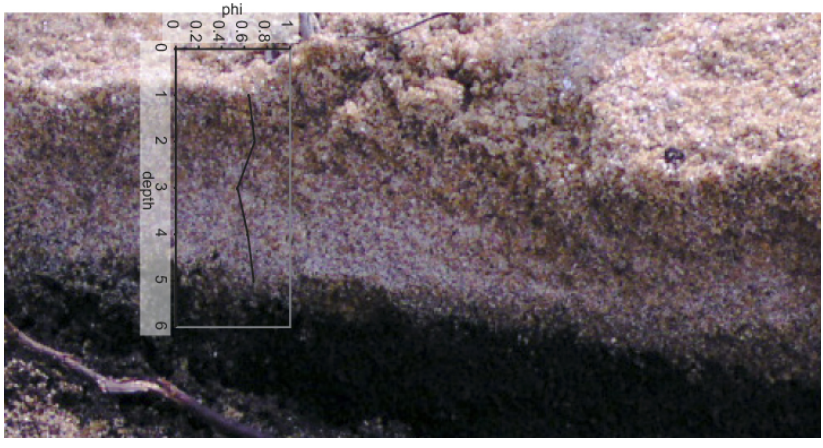

Fig. 7. Trench exposure at Boossa located 28 m from the high water line.

Yala

The shore of southeast Sri Lanka near Yala (Fig. 1) has a zeta-shape that is controlled by irregularly spaced rock promontories and embayments where minor local rivers cross the beach. As a result of this configuration, the shoreline is oriented slightly northeast, whereas embayed offsets face east. The coastal plain is about 2 km wide and relatively flat except for an ancestral dune ridge that is about 11.5 m high and 300 to 400 m inland from the modern beach and dune ridge. Grasses and shrubs stabilize the modern dune ridge, which is as much as 4 m high. Shore-parallel patterns on satellite images suggest long-term coastal plain progradation; however, field observations along the southern coast of Sri Lanka indicate a recent prolonged phase of beach erosion before the tsunami.

The unusual coastal setting, shoreline orientation, and refraction of the westward propagating tsunami wave produced a complex flow pattern at Yala that involved nearly simultaneous onshore (north) and alongshore (west) flow. West of the Yala study site, tsunami inundation extended more than 2 km inland where elevations were low along the estuary. The onshore and alongshore flows produced complex flow patterns that caused the destruction of two substantially built eco-tourism resort complexes. Destruction of one of the resorts (Fig. 8) was facilitated by intentional removal of the foredune ridge during resort development. Rubble derived from destruction of the buildings was incorporated into some of the more inland tsunami deposits. Open coast tsunami flow depths of 4.6 m were estimated at several sites from the heights of broken branches and debris trapped in trees, whereas a runup height of 12.5 m was measured from debris in shrubs on the ancestral dune ridge where flow depth was only about 1 m. Sand grains imbedded in surface pits of a

rough iron post near the beach indicated that the transported sand load in the water column extended at least 1.9 m above the pre-tsunami land surface.

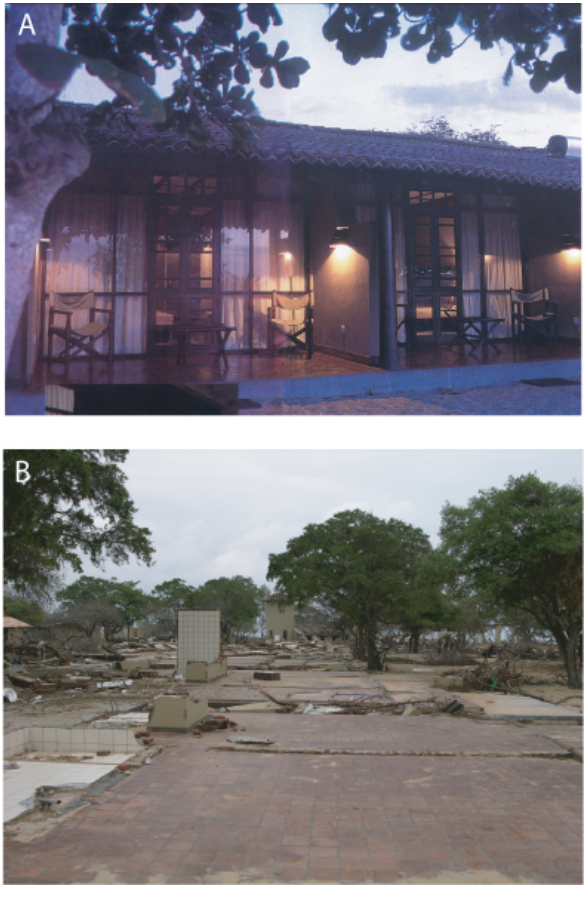

Fig. 8. Yala Safari Resort before and after the Indian Ocean tsunami.

The largest morphological changes observed at this site were erosion of the beach by onshore flow and scouring of incised channels near the beach by the return flow. Two weeks after the tsunami, a sand bar overwashed at high tide was rapidly migrating onshore to partly replace the sand lost during beach erosion and to fill the return flow channels (Fig. 9).

Tsunami erosion and inundation were exacerbated where the dunes had been removed intentionally and were minimized where the dunes were unmodified. Absence of the tsunami deposit in the lee of the dune ridge and bent grass and a small

boat resting on top (Fig. 9) demonstrated that the dune ridge was barely overtopped by the waves and it protected the area immediately landward from onshore flow.



Fig. 9. View at Yala of beach-recovery sand bar migrating onshore after the 2004 tsunami.

Three trenches, two sediment cores, and six supplementary depth measurements along a cross-shore transect at Yala were used to characterize the tsunami deposit. The overall landward-thinning deposit ranged in thickness from 19 cm near the beach, to 22 cm in the middle of the sand sheet, to 2.5 cm near the toe of the ancestral dune ridge. Re-construction of the pre-tsunami topography indicated that the thickest tsunami deposits were located in former topographic lows and the thinnest interior deposits were over former topographic highs including an unsealed road bed that was buried by the tsunami deposit.

The trench located 300 m from the HWL exposed 22 cm of plane parallel laminated well sorted to moderately well sorted sand. The sand was medium and coarse in texture and was found overlying an erosional basal contact and underlying truncated foreset stratification (Fig. 10). This deposit was visually subdivided into 3 units that were bounded by laminae of concentrated heavy minerals. The basal unit consisted of 12 cm of coarse-fine sand couplets composed of clean sand and heavy mineral laminations. The middle unit consisted of 5 cm of clean sand, whereas the upper 5-cm unit consisted of clean sand and heavy mineral couplets. The upper unit represented scour and fill deposits that decreased in thickness seaward. These late stage deposits probably were associated with a component of seaward-directed return flow. Sediment textures in the trench recorded four different vertical trends commencing with the basal 7-cm upward-coarsening trend overlain by 10 cm of relatively uniform

mean grain sizes. These trends were followed by 3-cm and 2-cm upward-fining trends that were separated by the finest textures in the tsunami deposit.

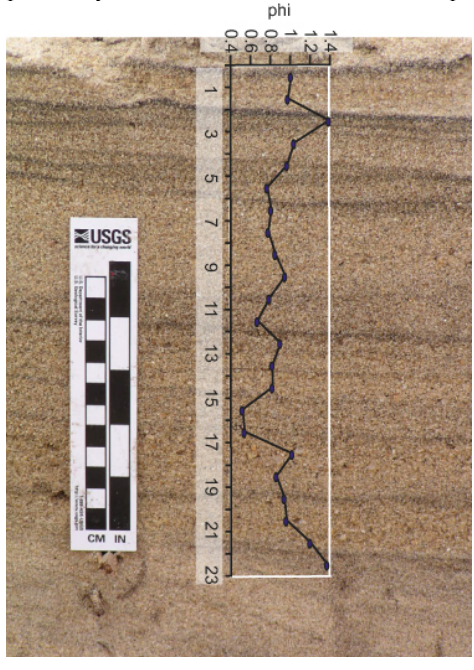

Fig. 10. Trench exposure at Yala located 300 m from the high water line.

DISCUSSION AND CONCLUSIONS

Field observations, trench measurements, sediment samples, and topographic profiles at sites spanning more than 250 km of the southwest coast of Sri Lanka provided a basis for interpreting the erosional and depositional phases of the tsunami event. The data show that sand deposits from the same tsunami event are highly variable in thickness, inland extent, geometry, and vertical textural trends. Deposits ranged in thickness from 1 to 36 cm but most were less than 25 cm thick. Local cross-shore variability in deposit thickness was partly related to antecedent topography with the deposits thinning over former topographic highs and thickening in topographic lows. The thickest deposit (36 cm at Katukurunda) was an artifact of a topographic low created by planted trees. The topographic dependence and upper limits on tsunami deposit thicknesses are consistent with those reported by Morton et al. (2007).

In Sri Lanka, the thin tsunami deposits tended to be homogeneous, whereas the thickest deposits exhibited better stratification, more laminae sets, greater textural variability, and more complex vertical textural trends. Visual subdivision of sandy tsunami deposits in the field only partly agrees with more detailed textural trends identified using mean grain size and sorting at 1 cm intervals. Vertical trends in mean

grain size included upward fining, upward coarsening, uniform, and highly variable. The most common vertical textural trend was upward fining. Cross-shore thickness measurements of the tsunami deposit at the two sites farthest apart where flow depths were the greatest (Yala) and least (Wellawatta) showed overall landward thinning. Comparison of the lowest laminae of the tsunami deposits and underlying soils indicated that the tsunami deposits are not texturally similar to the soils and therefore the soils are not the likely sources of the tsunami deposit sediments. Where present, the tsunami deposits have compositions and textures similar to the adjacent beaches and nearshore sediments from which they were derived. At several sites along the southern shore of Sri Lanka between Galle and Tangalla, there was very little sediment transported onshore. These sedimentological differences reflect the local influences that controlled the availability of sand and hydrodynamic characteristics of tsunami flooding.

At most tsunami impact sites in Sri Lanka, overland flow, sediment transport, and deposition were complicated so there is no simple direct correlation with the number of significant waves and the number of laminae sets or vertical textural trends in the deposits. Except for general spatial and textural trends such as landward thinning and upward fining, it does not appear that there are predictable geometric or textural patterns for these tsunami deposits.

ACKNOWLEDGEMENTS

We thank Ping Wang and Laura Fauver for reviewing the paper and improving its clarity. Betsy Boynton assisted with the illustrations.

REFERENCES

Goff, J., Liu, P., Higman, B., Morton, R., Jaffe, B., Fernando, H., Lynett, P., Fritz, H., and Synolakis, C. (2006). "The December 26, 2004 Indian Ocean tsunami in Sri Lanka" *Earthquake Spectra* 22 (S3), 155-172.

Lay, T., Kanamori, H., Ammon, C.J., Nettles, M., Ward, S.N., Aster, R.C., Beck, S.L., Bilek, S.L., Brudzinski, R., Butler, R., DeShon, H.R., Ekstorm, G., Satake. S., and Sipkin, S. (2005). "The great Sumatra-Andaman earthquake of 26 December 2004" *Science* 308 (5725) 1127-1133.

Liu, P. L.-F., Lynett, P., Fernando, H., Jaffe, B., Fritz, H., Higman, B., Morton, R., Goff, J., and Synolakis, C. (2005). "Observations by the international tsunami team in Sri Lanka" *Science* 308, 1595.

Morton, R. A., Gelfenbaum, G., and Jaffe, B. E. (2007). "Physical criteria for distinguishing sandy tsunami and storm deposits using modern examples", in Tappin, D.R., ed., Sedimentary features of tsunami deposits - their origin, recognition and discrimination *Sedimentary Geology Spec. Issue*

Swan, B. (1985). "Sri Lanka", in Bird, E. ed., *The Worlds Coastline* 749-759.

Wijetunge, J. J. (2006). "Tsunami on 26 December 2004: Spatial distribution of tsunami height and the extent of inundation in Sri Lanka" *Science of Tsunami Hazards* 24 (3) 225-239.

RECONSTRUCTING TSUNAMI RUN-UP FROM SEDIMENTARY CHARACTERISTICS – A SIMPLE MATHEMATICAL MODEL

Richard L. Soulsby[1], David E. Smith[2], Alan Ruffman[3]

1. HR Wallingford Ltd, Howbery Park, Wallingford, Oxfordshire OX10 8BA, UK (for correspondence) and Dept of Engineering Science, University of Oxford, UK. r.soulsby@hrwallingford.co.uk
2. School of Geography, Oxford University Centre for the Environment, South Parks Rd, Oxford OX1 3QY, UK. david.smith@ouce.ox.ac.uk.
3. Geomarine Associates Ltd, PO Box 41, Stn.M, Halifax, Nova Scotia B3J 2LJ, Canada. aruffman@dal.ca

Abstract: Tsunamis frequently leave a characteristic sediment deposit on the inundated land surface, which can be interpreted to deduce some of the features of the original tsunami wave. A simple trajectory-based theory of the tsunami hydrodynamics and sediment dynamics is presented here, yielding expressions for the landward variations in thickness and sediment composition of the deposit. Each grainsize contribution to the deposit thins linearly landwards, with the sediment run-up limit increasing with decreasing grainsize. The expressions can be fitted to observed sedimentary characteristics to deduce the run-up height and distance of the water. Example applications of the theory are given for the 1929 "Grand Banks" Tsunami, and the Holocene Storegga Slide Tsunami. Reconstruction of palaeo-tsunamis can help with assessments of present day risks from tsunamis.

INTRODUCTION

Evidence can be found at many locations around the world of thin layers of sand that are attributed to deposition by tsunamis. These have been observed after modern tsunamis, and can also be found in the recent geological record as evidence of tsunami inundation in the past. They typically run some 100s of metres inland of the (historic) shoreline and are up to some 10s of centimetres thick. Typically, they comprise a fine to medium sand with only small amounts of fine silt and clay, in a layer that thins from the shoreline landwards (e.g. Smith *et al.* 2004; Matsutomi *et al.*

2001; Dawson and Shi 2000; Moore 2001). Detailed grainsize analysis of vertically subdivided borehole samples generally reveals a pattern of landward fining, with upward fining in one or more sequences (Smith *et al.* 2004). Observations following modern tsunamis have shown that the height and landward extent of inundation by the water extend further than the limit of the sediment deposits (Tuttle et *al.* 2004) .

The aim of the present paper is to devise a simple mathematical model that contains the main physical (hydrodynamic and sediment dynamic) processes needed to predict the behaviour described above. The derived equations describing the characteristics of the sediment deposits are expressed in terms of the main descriptors of the coastal profile, the sediments and the tsunami hydrodynamics. Previous research workers have devised physics-based methods to re-construct the maximum inundation depths (Smith *et al.*, in press), maximum velocities (Jaffe and Gelfenbaum, in press), and characteristic velocities and depths together (Moore *et al.*, in press). The present approach extends these and other analyses (e.g. Matsutomi *et al.* 2001; Dawson and Shi 2000) by including a fuller description of the tsunami dynamics, while remaining mathematically tractable. A major motivation for this work is to facilitate re-construction of palaeo-tsunamis to assess the present-day risk of tsunamis at coastal sites, using the rationale outlined by Jaffe and Gelfenbaum (2002).

DERIVATION OF THEORY

Conceptual model

The scenario considered is sketched in Figure 1, which also shows the notation used. In order to keep the model mathematically tractable, a number of simplifying assumptions have been made. Everything is taken to be constant in the along-shore direction (1D assumption), and only the inundation flow onto and off the dry land is considered. The land surface is assumed to be plain and non-erodible, with a slope of 1:m. If R_z is the maximum run-up height of the water, then the maximum horizontal run-up distance is $R_w = mR_z$ from the still-water shoreline (SWL).

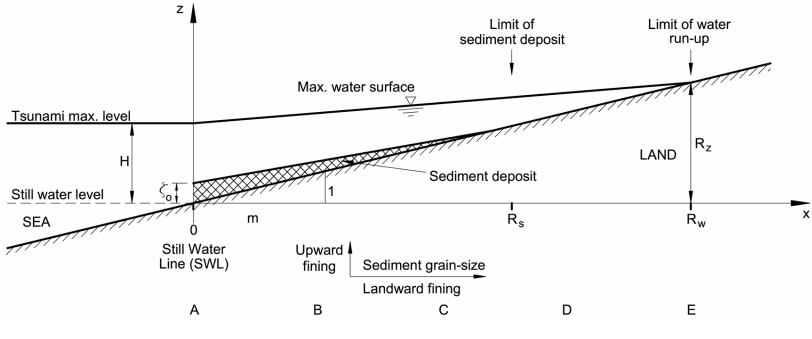

Fig. 1. Schematic of cross-section through land surface, with tsunami inundation and deposits. Snapshot at time $t = \gamma T$. ζ_o is deposit thickness at SWL.

Considering first the *hydrodynamics* of the tsunami wave, the maximum depth of inundation is assumed to decrease linearly with distance x from the SWL, from a depth H at $x = 0$ to zero at the maximum run-up point (Figure 1). The water depth $h(0,t)$ at the SWL (Point A in Figure 1) is assumed to increase with time linearly to H during the uprush ($0 < t < \gamma T$), then decrease linearly with time during the backwash ($\gamma T < t < T$), where T is the total time that the SWL is inundated (Figure 2a).

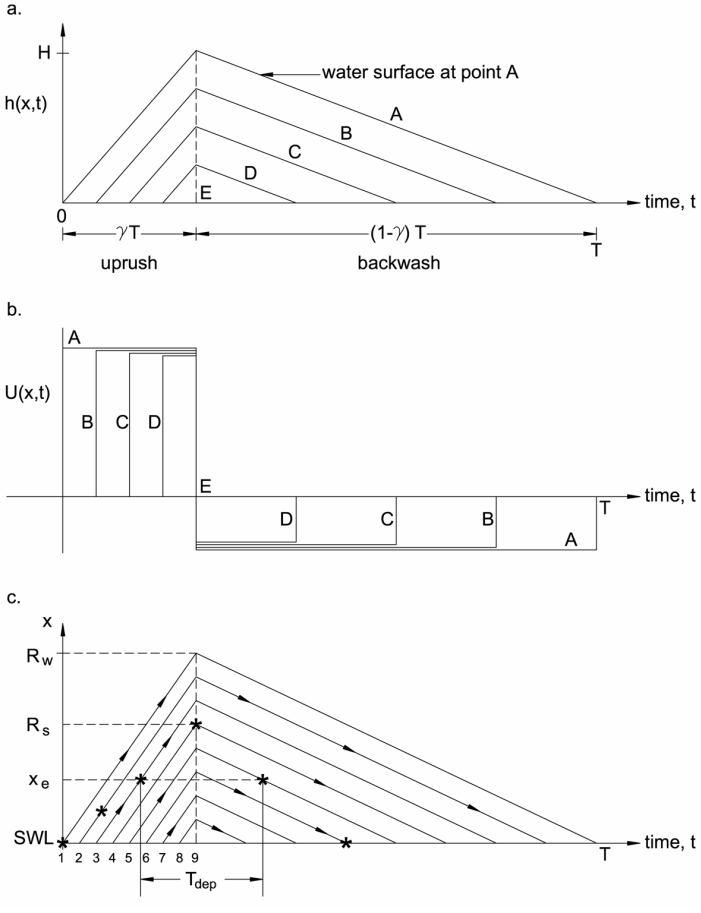

Fig. 2. Idealised tsunami characteristics for modelling purposes. (a) Depth variation with time at points A – E on Fig. 1. (b) Velocity variation with time at points A – E on Fig. 1. (c) Trajectories of water particles as distance (x) inland of SWL versus time for 9 different times of crossing the SWL. R_w and R_s are the horizontal run-up limits of water and sediment respectively, * marks points at which sediment deposition ceases for each trajectory, and T_{dep} is the duration over which sediment is deposited at example point x_e.

The time-variation of the water-level $h(x,t)$ at points between A and E also increases and decreases linearly with time, and the inundation durations decrease linearly with x from T at Point A to zero at Point E (Figure 2a). The time-lag between the time of maximum inundation at Point A and at the successive Points B to E is ignored, i.e. maximum water-level occurs everywhere at time $t = \gamma T$. Depth-averaged water velocities $U(x,t)$ are derived from the prescribed depths via the continuity equation (Figure 2b).

Next, considering the *sediment dynamics*, the wave is assumed to be heavily charged with suspended sediment eroded from the sea bed when it arrives at the SWL (Point A). The concentration (dry mass per unit volume) here is taken as constant (C_o) through the depth due to intense turbulent mixing, and constant in time over the uprush period $t = 0$ to γT during which sediment is advected onshore. Initially, the sediment is treated as having a single grain-size with settling velocity w_s. This is easily extended later to multiple grain-sizes. Judging from the observed thicknesses of deposits, the concentrations of suspended sediment must be very large (some 10s or 100s of kg/m^3), so that the downward settling flux $w_s C_o$ of sediment greatly outweighs the re-erosion flux. Accordingly, for the purpose of this simple model, the re-erosion flux is neglected. The settling is treated as if the sediment was in a moving settling column, i.e. the settling flux is given by a constant value of $w_s C_o$ until all the sediment in that water column has been deposited. This ignores the re-distribution of sediment vertically by turbulence. The thickness of the sediment deposit is assumed to be much thinner than the inundation depth, so that the changing bed elevation during the inundation does not significantly affect the hydrodynamics.

Mathematical model

A brief summary of the derivation of the model is presented here. The full mathematical derivation is available from the first author on request. Following Borthwick *et al.* (2005), the continuity equation is expressed in the form:

$$\frac{\partial h}{\partial t} + \frac{\partial q}{\partial x} = 0 \tag{1}$$

where the volumetric flux q of water (per unit shore-wise width) is given by: $q = Uh$ and q, U and h are all functions of x and t. From the prescribed form of depth time-series shown in Figure 2a, it can be seen that $\partial h/\partial t$ is a positive constant during the period $t = 0$ to γT, and a negative constant during the period $t = \gamma T$ to T. Solution of Eq. 1 during the uprush phase leads to a velocity that is constant in time and space (Figure 2b):

$$U_{up} = \frac{R_w}{\gamma T} \tag{2}$$

Likewise, during the backwash phase the velocity is also constant:

$$U_{back} = -\frac{R_w}{(1-\gamma)T} \tag{3}$$

Consider the nine trajectories of water particles shown in Figure 2c. Because of the assumptions made, the water depth remains constant along any trajectory. Thus

trajectory 1 is the locus of the wetting and drying line, has depth $h(x,t) = 0$, and reaches inland to the run-up limit R_w. Trajectory 3 starts at time $t = \gamma T/4$, has depth $h(x,t) = H/4$, and reaches inland to $x = (3/4)\,R_w$. Trajectories 5 and 7 have depths $H/2$ and $3H/4$, and reach inland distances $x = R_w/2$ and $R_w/4$ respectively. Trajectory 9 has a depth H, but because it starts (and finishes) at time $t = \gamma T$, it does not travel inland at all.

Applying the assumption that the sediment settles as it would in a settling column, the time taken for all the initially-suspended sediment to settle onto the bed, with settling velocity w_s, is h/w_s. Thus trajectories with greater depths will deposit sediment for longer times. Conversely, as seen above, these trajectories are also the ones with the shorter durations (from crossing the SWL on the uprush to re-crossing it on the backwash), and have the shorter penetrations inland. In Figure 2c, the point at which all the suspended sediment has been deposited is marked * on each trajectory. Trajectory 1 has zero depth, so all sediment is dropped immediately. Trajectories 2 and 3 have progressively greater depths, and complete the deposition at progressively later times and further distances inland. Trajectory 4 just completes its deposition at time $t = \gamma T$, when its distance inland is a maximum and it is about to return with the backwash. This distance, denoted R_s, is the maximum run-up distance for sediment deposition. Trajectories 5 and 6 are sufficiently deep that sediment is not only deposited during the uprush, but also through part of the backwash. Trajectory 6 just completes its deposition by the time it returns to the SWL. Trajectories 7 and 8 deposit sediment through their entire uprush and backwash journeys and carry some sediment back out to sea. Trajectory 9 does not carry sediment onto the land.

Now consider an arbitrary fixed point x_e on the land surface (see Figure 2c). No sediment arrives at point $x = x_e$ until trajectory 3 arrives. All the subsequent trajectories deposit sediment at $x = x_e$ until trajectory 5, which completes deposition on the backwash at $x = x_e$. Trajectory 6 deposits sediment briefly at $x = x_e$, but trajectories 7 and 8 do not even reach $x = x_e$. The time during which sediment is deposited T_{dep} extends from the time trajectory 3 reaches x_e on the uprush to the time trajectory 5 reaches x_e on the backwash. Moreover, with the settling column assumption, the rate of deposition during this time is constant $= w_s C_0$, so that the total mass of sediment deposited at point $x = x_e$ throughout the inundation is $w_s C_0 T_{dep}$. This applies to all points x_e between $x = 0$ and R_s, with T_{dep} decreasing landwards.

The run-up distance for sediment, R_s, can be related to the run-up distance for water, R_w (Figure 1), as follows. Suppose that trajectory i (which crosses the SWL at time $t = t_i$) is the one that just completes deposition at the time of velocity reversal, $t = \gamma T$ (marked as trajectory 4 on Figure 2c). Because depth at the SWL ($x = 0$) increases linearly with time during the uprush, the depth of this trajectory is:

$$h_i = \frac{t_i}{\gamma T} \cdot H \tag{4}$$

The time during which the trajectory is moving landwards is $(\gamma T - t_i)$, and this is equal to the time taken to deposit all the sediment, h_i/w_s. Thus:

$$\gamma T - t_i = \frac{h_j}{w_s} \tag{5}$$

Since the velocity on the uprush is given by Eq 2, the maximum distance R_s inland that sediment is deposited is (making use of Eqs. 2, 4 and 5):

$$\begin{aligned} R_s &= U_{up}\left(\gamma T - t_i\right) \\ &= R_w \cdot \frac{1}{w_s \gamma T / H + 1} \end{aligned} \tag{6}$$

For convenience, write $\alpha = \frac{w_s T}{H}$. Then the run-up of sediment R_s is related to the run-up of water R_w by the relationship

$$R_s = \frac{R_w}{1+\alpha\gamma} \tag{7}$$

Now calculate the thickness, ζ_o, of sediment deposited at the SWL ($x = 0$). Consulting Figure 2c, sediment starts to be deposited at $x = 0$ by trajectory 1, and finishes depositing at the end of trajectory 6. Denote this final depositing trajectory as trajectory j, which crosses the SWL on the uprush at time $t = t_j$, and reaches the SWL again on the backwash at time $t = t_k$. The trajectory has a depth h_j, and hence deposits all its sediment in a time h_j/w_s which is equal to the duration ($t_k - t_j$) of the trajectory. Thus:

$$t_k - t_j = \frac{h_j}{w_s} \tag{8}$$

The depth is given by (see Eq 4)

$$h_j = \frac{t_j}{\gamma T} \cdot H \tag{9}$$

and t_k is related to t_j by the respective velocities of uprush and backwash. The distance travelled inland is equal to U_{up} ($\gamma T - t_j$) on the uprush, and distance travelled back to the SWL is equal to $|U_{back}|$ ($t_k - \gamma T$) on the backwash. Equating these, and making use of Eqs 2, 3, 8 and 9 leads to:

$$\begin{aligned} t_k &= T - \frac{(1-\gamma)}{\gamma} \cdot \frac{\alpha\gamma T}{1+\alpha} \\ &= T \cdot \left[\frac{1+\alpha\gamma}{1+\alpha}\right] \end{aligned} \tag{10}$$

This gives the time $T_{dep,0} = t_k$ during which sediment is deposited at $x = 0$. Since sediment is deposited continuously at the rate $C_0 w_s$ through time $T_{dep,0}$, the mass deposited per unit area of bed at $x = 0$ is $C_0 w_s T_{dep,0}$. If the (dry) bulk density of the deposited sediment is ρ_B, where a typical value is $\rho_B = 1600\text{kg/m}^3$, the thickness deposited, ζ_o, is (using Eq. 10)

$$\zeta_o = \frac{C_0 w_s T}{\rho_B (1+\alpha)}(1+\alpha\gamma) \tag{11}$$

and, since $w_s T = \alpha H$,

$$\zeta_o = \frac{\alpha(1+\alpha\gamma)}{1+\alpha} \cdot \left(\frac{C_0}{\rho_B}\right) \cdot H \tag{12}$$

A full mathematical analysis following the same principles outlined above, and extended to all points inland, gives the distribution of the thickness $\zeta(x)$ deposited decreasing with distance x inland of the SWL according to the linear relationship:

$$\zeta(x) = \zeta_0\left(1 - \frac{x}{R_s}\right) \quad \text{for } x \le R_s, \text{ and 0 for } x > R_s \tag{13}$$

where ζ_o is given by Eq (12), R_s is given by Eq (7), and $\alpha = \frac{w_s T}{H}$.

Interpretation

The analysis given above enables the distribution of the thickness of sediment deposit, $\zeta(x)$, left by a single tsunami wave to be predicted for a wave of maximum height H at the SWL, with a period T from the time of first wetting to final drying at the SWL, in which the uprush occurs during a fraction γ of that period.

The deposit has a maximum thickness ζ_o occurring at the SWL, given by Eq 12. For a very fine-grained sediment (clay or fine silt), w_s is very small so α is very small and ζ_o tends to zero. Thus very fine sediments are hardly deposited at all, because they stay in suspension throughout the inundation. For coarser-grained sediment (coarse silt or sand), w_s is larger so α is larger, and the thickness ζ_o increases with grain-size (for a given concentration C_0). The thickness of the deposit is proportional to the concentration of suspended sediment just offshore of the SWL, and increases with the proportion γ of time occupied by the uprush. For very coarse-grained sediment, α is large and ζ_o tends to a value of $\alpha\gamma C_0 H/\rho_B = w_s(\gamma T)(C_0/\rho_B)$; in other words, all the suspended sediment is deposited during the uprush (γT) near the SWL.

The thickness of deposit tapers inland linearly with distance (x) from the SWL, as given by Eq 13, up to the sediment run-up distance R_s. Beyond this, no sediment is deposited, even though the water runs up further, to a distance R_w. R_s is smaller than R_w by a factor $(1+\alpha\gamma)$ as given by Eq 7. Thus, for a given γ, the larger that α is (coarse sediments), the shorter the sediment run-up. Very fine sediments will extend almost to the limit of water run-up, but gravel and coarse sand will be deposited closer to the SWL. For a given sediment size, the run-up distance R_s decreases as the proportion γ of time occupied by the uprush increases.

Mixed sediments

If interactions between different grain-sizes of a mixed sediment are ignored, Eqs 13, 7 and 12 can be applied separately to different grain-size fractions. Each fraction (subscript n) will have a characteristic settling velocity w_{sn} and characteristic value of α_n (for a tsunami of given H and T), and will have a concentration C_{on} just offshore of the SWL.

As an illustration, consider the case of a tsunami with a wave height of $H = 5$m, period $T = 10$ minutes, and uprush occupying 2.5 minutes ($\gamma = 0.25$), striking a coast that has a slope of 1:m = 1:30. The wave has entrained sediment characterised as follows into three grain-size fractions, each having a concentration of 20kg/m^3 (total concentration = 60kg/m^3). The fractions are, using subscripts $n = 1, 2, 3$:
Finest 1/3, represented by $d_{16} = 0.1$mm, with $w_{s1} = 0.006$m/s and $C_{01} = 20$kg/m^3
Middle 1/3, represented by $d_{50} = 0.2$mm, with $w_{s2} = 0.02$m/s and $C_{02} = 20$kg/m^3
Coarsest 1/3, represented by $d_{84} = 0.4$mm, with $w_{s3} = 0.053$m/s and $C_{03} = 20$kg/m^3

Suppose that the run-up height of the water is $R_z = 8$m, so that the run-up distance is $R_w = 8 \times 30 = 240$m. Using Eqs (12) and (7) for each fraction:

Fine sediment: $\alpha_1 = \dfrac{0.006 \times 10 \times 60}{5} = 0.72,\ \zeta_{01} = 0.031m,\ R_{s1} = 203m$

Medium sediment: $\alpha_2 = \dfrac{0.02 \times 10 \times 60}{5} = 2.4,\ \zeta_{02} = 0.071m,\ R_{s2} = 150m$

Coarse sediment: $\alpha_3 = \dfrac{0.053 \times 10 \times 60}{5} = 6.4,\ \zeta_{03} = 0.140m,\ R_{s3} = 93m$

When the three fractions are added together, it is seen that they form a landward-fining sequence. In addition, since the coarse fraction is deposited first, and the fine fraction last, at any point, they will form an upward fining sequence. The composition of each upward fining sequence could be calculated by an extension of the mathematical analysis that would give the time-sequence of deposition for each fraction at each point.

APPLICATION 1: THE 1929 "GRAND BANKS" TSUNAMI

On November 18th, 1929, a magnitude $M_s = 7.2$ earthquake on the Grand Banks south of Newfoundland triggered an offshore landslide that developed into a turbidity current moving down the Continental Slope and out onto the Abyssal Plain, cutting twelve trans-Atlantic telegraph cables. The resulting tsunami was observed from Newfoundland to the Caribbean, being felt most strongly on the south coast of the Burin Peninsula, southern Newfoundland. The tsunami run-up rose to 13m above the normal tide level in St. Lawrence, and to about 10m at Taylor's Bay, both south-facing bays. Widespread devastation took place on the Burin Peninsula and 28 persons lost their lives (Tuttle *et al.* 2004, Ruffman and Hann 2006).

The site from which the samples analysed in this paper were obtained is at Taylor's Bay, on the south side of the Burin Peninsula (Figure 3). At Taylor's Bay, a sand and gravel barrier circa 200m long encloses a small lagoon, landward of which an area of low-lying, largely peat-covered land, up to 20m above local datum, widens to nearly 1km behind the lagoon, then progressively narrows for circa 500m inland. The site is of particular interest for studying the effects of the tsunami because there are records of the arrival of the waves across the barrier and into the low-lying area and of the destruction caused, so that there is anecdotal evidence of the anatomy of the event (Tuttle *et al.* 2004). However, the particular value of the site lies in the extensive deposit of sand which was deposited by the tsunami and which is found a few cm

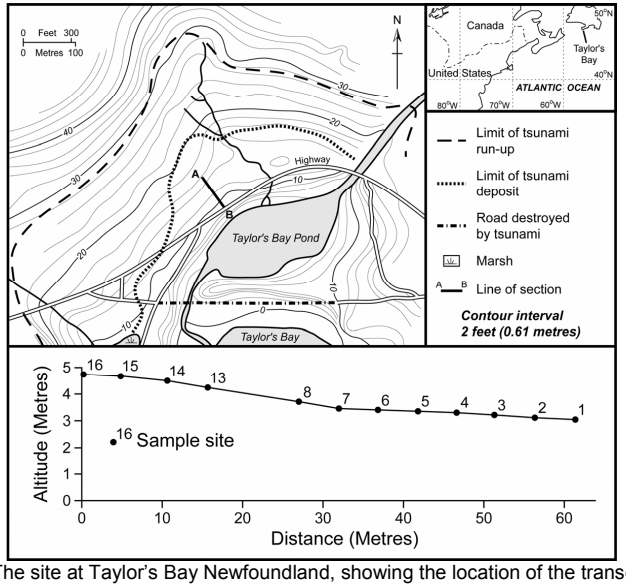

Fig. 3. The site at Taylor's Bay Newfoundland, showing the location of the transect from which samples were taken, together with the possible limits of tsunami run-up and deposit. Based partly on Tuttle *et al*.. 2004.

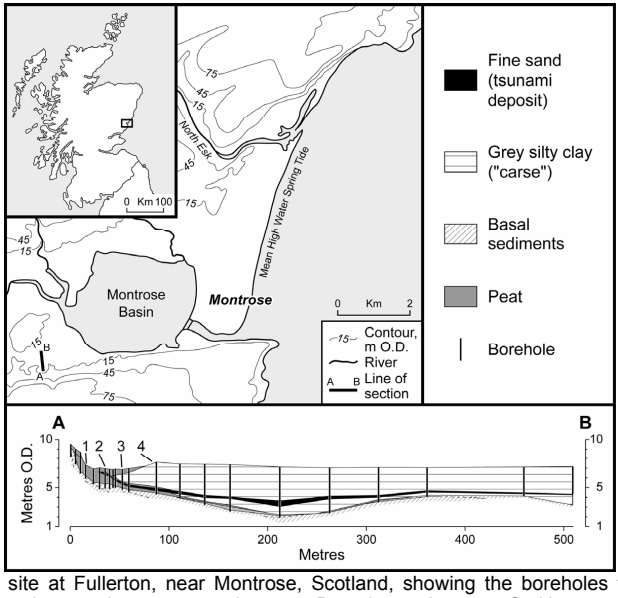

Fig. 4 The site at Fullerton, near Montrose, Scotland, showing the boreholes from which tsunami sand samples were taken. Based partly on Smith *et al*.. 2004.

beneath the surface of the peat. In recent work Moore *et al.* (in press) showed that the layer becomes thinner and fines landwards in general terms.

Monoliths from the peat containing the sand layer were taken at 5-10m intervals from the lagoon to the inland limit of the deposit (Figure 3). The location of each monolith was surveyed and its altitude levelled to local datum. On return to the laboratory, the sand layer at each monolith was sampled in contiguous 1cm slices and these samples analysed using a Malvern 2000 Mastersizer laser granulometer. Analyses involved pre-treatment using an acid digest to remove all organic matter, following the approach of Smith *et al.* (2004). The samples were obtained in August 1995 with the assistance of the Ottawa office of the Geological Survey of Canada and Erik Nielsen of Winnipeg, and analysed at Brighton University by Professor Callum Firth courtesy of Geomarine Associates Ltd.

Application of theory

The theoretical analysis can be applied to the twelve monolith samples taken along the shore-normal transect shown in Figure 3. The aim is to predict the water run-up distance from the observed sediment depositional characteristics. The SWL is taken as the shore of Taylor's Pond from extension of the line of section. The gradient of the land over this region increases landwards, with a mean gradient of about 1:22.

The Malvern granulometer gave results from each 1cm slice from each monolith as percentages of the total mass of sediment found in each of five grain-size fractions. The grain-size fractions with the largest masses of sediment were found to be those for 500-2000μm, 177-500μm, and 44-177μm, and these were chosen for the theoretical treatment. The percentages in all the slices for each monolith for a given grain-size fraction were summed, to give the percentage of sediment at that location attributable to that fraction. This was converted to give the contributions from each fraction to the thickness of deposit at that location. These are plotted for each of the three fractions and for the twelve locations in Figure 5a. Despite some scatter, due presumably to topographic features, it is seen that the thickness of each fractional deposit thins landwards. Linear trends have been fitted by least-squares regressions. From the trend-lines, the coarsest fraction (500-2000μm) has a thickness at the SWL of 3.4cm and a run-up distance of 115m. The corresponding figures for the medium fraction (177-500μm) are 4.1cm and 130m, and for the finest fraction (44-177μm) are 0.7cm and 166m. Thus, the run-up distances of the sediments (from the trend-lines) are greater for the finer sediments as predicted by the theory.

The settling velocities of the median diameters of each fraction (1000, 297, 88μm) are 0.114, 0.0368 and 0.00442 m/s for the coarse, medium and fine fractions respectively, using the formula of Soulsby (1997, Eq. 102) and assuming sea-water at 10°C and 35ppt with sediment density of 2650kg/m^3. Eq 7 can be applied to each fraction, yielding three equations in two unknowns, namely R_w and the quantity $B = \gamma T/H$ (with dimensions of inverse velocity), since the three values of R_s and w_s are known. A fitting procedure leads to an optimum value of B = 4.2s/m and R_w = 163m. The predicted run-up height is thus 163/22 = 7.4m above the local datum

(estimated tide level at the time of the tsunami). This compares with an observed run-up height from direct observations at the time of the tsunami of about 8.8m at this location (Tuttle *et al.* 2004) as seen in Figure 3.

APPLICATION 2: THE HOLOCENE STOREGGA SLIDE TSUNAMI

The Holocene Storegga Slide tsunami occurred around 8000 sidereal years BP. It is believed to have been generated by submarine sliding on the Continental Shelf and slope off South West Norway. The cause of the slide is unknown, but could have been due to crustal movement at the close of the last glaciation as Scandinavia became relieved of its ice burden (e.g. Smith *et al.* 2004).

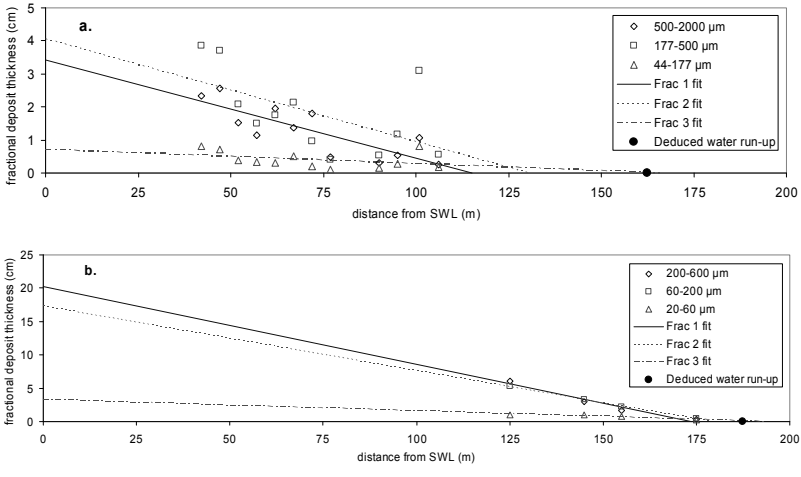

Fig. 5. Observed landwards variation of fractional deposit thickness, and fitted lines, for three grainsize fractions from (a) Taylor's Bay, Newfoundland, (b) Fullerton, Scotland.

The effect of the slide was to generate tsunami waves which inundated coastal areas as far apart as Iceland, the Faeroes, much of the Norwegian west coast, Scotland and northern England. At the time, sea surface levels lay up to 15m lower in the area (e.g. Mörner, 1980), but because of differential crustal depression following glaciation, relative sea levels across the coastlines involved were variable. The tsunami deposited in particular a distinctive layer of sand, normally less than 0.5m thick, across coastal peat, mudflat and saltmarsh. Subsequently, the layer was buried beneath later deposits of peat and coastal sediments. The layer is best preserved in former coastal inlets, usually gullies and small estuaries.

The sand layer at all sites was identified and sampled from shallow boreholes, using hand operated coring equipment. On return to the laboratory, contiguous 1cm samples were prepared for particle size analysis by removing all organic matter. Analysis was undertaken in a previous study by Shi (1995) using a Malvern 2600 laser granulometer as detailed by Smith *et al.* (2004).

The site used for this application is Fullerton (Figure 4), which lies at the western edge of the Montrose Basin, where a gully circa 1km long occurs in Late Glacial raised coastal terraces, to seaward of which raised Holocene estuarine sediments form an extensive surface. The tsunami sand layer can be traced along the gully and across its axis, and the sand has been analysed in four boreholes at the southern and of the transect. Two upward-fining sequences can be distinguished, but only the upper one is used in the present analysis as it is better defined. The site was described in Smith *et al.* (2004).

Application of theory

The theoretical analysis of the Fullerton section followed the same approach as for the Newfoundland example. Here, there were only four boreholes available. The origin of the *x*-coordinate (SWL) was taken at the lowest point on the section of the base of the sand layer, at about 210m on the section in Figure 4 where the elevation is 3.0mOD. The mean gradient of the land is about 1:30. The three grain-size fractions used in the analysis were 200-600μm, 60-200μm and 20-60μm. Roughly 10% of the sediments were finer than 20μm, but these were not used in the analysis. The thicknesses at the SWL, and the sediment run-up distances, taken from fitted lines (Figure 5b) for the coarse, medium and fine grain-size fractions were 20.3cm and 174m, 17.3cm and 179m, and 3.3cm and 194m respectively. The calculated settling velocities were 0.0447, 0.00682 and 0.000709m/s. The optimum values from the fitting procedure were B = 2.6s/m and R_w = 188m. The predicted run-up height is thus 188/30 = 6.3m above the assumed SWL, giving a total run-up height of 9.3mOD. In this case, there are no observations of water run-up, and the theory provides an estimate for an otherwise unknown quantity.

DISCUSSION

It is seen in both applications that the predicted run-up limit of the water is roughly equal to the projected limit of the finest sediment fraction. This is because the theory essentially equates the water run-up to the run-up of sediment with zero settling velocity, and the settling velocities of the finest sediments in both applications are very small. At Taylor's Bay, the observed water run-up height (about 8.8m) is rather larger than the predicted value (7.4m). This might be due to the simplifying assumption of no re-erosion of sediments in the theory, whereas in reality a thin layer of fine sediment deposited by the uprush could be eroded during the backwash.

Other departures of the idealised theory from the field situation include: (a) the actual topography is much more complex (gullies, ponds, ridges, vegetation) than the assumed smooth plane of constant slope, (b) laboratory experiments (O'Donoghue *et al.*, in press) show that the depth and velocity of a wave running up a sloping beach exhibit roughly parabolic and saw-tooth time-variations respectively, instead of the linear and constant time-variations respectively used in the simple theory, (c) the settling-column assumption for the sediments is an over-simplification. In practice, the sediment responds to a balance of erosion, deposition and diffusion processes.

In principle, a more sophisticated fitting technique between the theory and the data could be used. This could include the vertical grain-size variations, and might allow other tsunami characteristics such as wave height and period, water velocities, and suspended sediment concentrations to be deduced. However, the value of performing such a fitting would depend on how closely the idealisations of the theory conform to the geographical realities of individual sites.

The best way to overcome the deficiencies of the simple model would be to add sediment dynamics to a detailed numerical model of the tsunami hydrodynamics such as those of Borthwick *et al.* (2005) and O'Donoghue *et al.* (in press). This could model the two-dimensional flow patterns around complex topography, as well as the offshore sediment erosion, and the transport, deposition, re-erosion, convergence and divergence of sediment transport onshore. Optimisation of the input parameters such as height and period of the offshore wave could be performed to give a least-squares fit to the observed sediment thicknesses and grain-size compositions to achieve a full re-construction of depths, velocities and durations at all inundated points. More realistic tsunami inputs, such as multiple interacting waves, could also be modelled.

CONCLUSIONS

This analysis yields an equation for the maximum sediment run-up distance (R_s) in terms of the water run-up distance (R_w), and two additional parameters $\alpha = \frac{w_s T}{H}$, and γ = ratio (duration of uprush)/(duration of backwash) at the SWL. Here H is the height of the tsunami wave, and T the duration of inundation, at the SWL. A second equation gives the maximum deposit thickness (at the SWL) ζ_o in terms of α, γ, H, C_0 and the bulk density of the deposited sediment. The derived variation in thickness of the sediment deposit is found to decrease linearly with landward distance, from ζ_o at the SWL to zero at distance R_s. Applying the model with a range of grainsizes yields the following features, which agree with observations:

- The thickness of the deposit decreases uniformly with distance from the SWL
- The limit of the sediment deposit falls well short of the water run-up limit
- The landward extent of the sediment deposit increases with decreasing grain-size, so that the net result is a landward fining of the sediment
- Very coarse sediments are all deposited close to the SWL.
- Very fine sediments are almost entirely swept back out to sea
- Because of differential settling velocities, an upward fining sequence is formed
- Successive tsunami waves can give rise to multiple upward fining sequences

The theory has been applied to sediment samples from Newfoundland deposited by the 1929 "Grand Banks" tsunami, where the water run-up distance and height are known from observations at the time. Reasonably good agreement between predicted and observed run-up were found. The method has also been applied to sediment deposits in Scotland resulting from the Holocene Storegga Slide tsunami to deduce the water run-up distance and height, which in this case are not known. Thus

here the new method allows additional information to be deduced from the sediment deposits.

REFERENCES

Borthwick, A. G. L., Ford, M., Taylor, P. H., Weston, B. P. and Stansby, P.K. (2005). "Prediction of solitary wave run-up at an arbitrary plane beach," *Waves 2005, Conference Proc.*, *on CD-ROM, IAHR*, Paper No. 101, 9p.

Dawson, A. G. and Shi, S. (2000). "Tsunami deposits," *Pure and Applied Geophysics* 157, 875-897.

Jaffe, B. and Gelfenbaum, G. (2002). "Using tsunami deposits to improve assessment of tsunami risk," *Solutions to Coastal Disasters '02, Conference Proc., ASCE*, 836-847.

Jaffe, B. and Gelfenbaum, G. (in press). "A simple model for calculating tsunami flow speed from tsunami deposits," *Special Issue on Tsunami Deposits, Sedimentary Geology.*

Matsutomi, H., Shuto, N., Imamura, F. and Takahashi, T. (2001). "Field survey of the 1996 Irian Jaya Earthquake Tsunami in Biak Island," *Natural Hazards* 24, 199-212.

Moore, A. L. (2001). "Grain-size trends in a Holocene tsunami deposit from Cultus Bay, Puget Sound, Washington," *International Tsunami Society Proceedings*, Session 3(3-6), 503-510.

Moore, A., McAdoo, B. and Ruffman, A. (in press). "Landward fining from multiple sources in a sand sheet deposited by the 1929 Grand Banks tsunami, Newfoundland," *Special Issue on Tsunami Deposits, Sedimentary Geology*.

Mörner, N. A. (1980). "Late Quaternary sea-level changes in north-west Europe: a synthesis," *Geologiska Foreningens i Stockholm Forhandlingar* 100, 381-400.

O'Donoghue, T., Hondebrink, L. and Pokrajac, D. (in press). "Bore-driven swash on beaches: numerical modelling and large-scale laboratory experiments," *Proc. 30th International Conference on Coastal Engineering, World Scientific Publishing*.

Ruffman, A. and Hann, V. (2006). "The Newfoundland Tsunami of November 18, 1929: An Examination of the Twenty-eight Deaths of the "South Coast Disaster,"" *Newfoundland and Labrador Studies* 21(1), 97-148.

Shi, S. (1995). "Observational and theoretical aspects of Tsunami sedimentation," Unpublished PhD thesis, Coventry University.

Smith, D. E., Shi, S., Cullingford, R. A., Dawson, A. G., Dawson, S., Firth, C. R., Foster, I. D. L., Fretwell, P. T., Haggart, B. A., Holloway, L. K. and Long, D. (2004). "The Holocene Storegga Slide tsunami in the United Kingdom," *Quaternary Science Reviews* 23, 2291-2321.

Smith, D. E., Foster, I. D. L., Long, D. and Shi, S. (in press). "Reconstructing the pattern and depth of flow onshore in a palaeotsunami from associated deposits", *Special Issue on Tsunami Deposits, Sedimentary Geology*.

Soulsby, R. L. 1997. "*Dynamics of Marine Sands*", Thomas Telford, London, 249 p.

Tuttle, M. P., Ruffman, A., Anderson, T. and Jetter, H. (2004). "Distinguishing tsunami from storm surge deposits in eastern North America: the 1929 Grand Banks tsunami versus the 1991 Halloween storm," *Seismological Research Letters* 75(1), 117-131.

NUMERICAL STUDY OF TSUNAMI RUN-UP OVER ERODIBLE SAND DUNES

Takenori Shimozono[1], Shinji Sato[2], Yoshimitsu Tajima[3]

1. Department of Ocean Sciences, Tokyo University of Marine Science and Technology, 4-5-7 Konan, Minato-ku, Tokyo 108-8477, JAPAN. shimo@kaiyodai.ac.jp
2. Department of Civil Engineering, The University of Tokyo, 7-3-1 Hongo, Bunkyo-ku, Tokyo, 113-8654, JAPAN, sato@civil.t.u-tokyo.ac.jp.
3. Department of Civil Engineering, The University of Tokyo, 7-3-1 Hongo, Bunkyo-ku, Tokyo, 113-8654, JAPAN, yoshitaji@civil.t.u-tokyo.ac.jp.

Abstract: In numerical simulation of tsunami, the changing topography must be taken into account for some specific problems such as run-up over coastal dunes. In this paper, a numerical model for tsunami flooding over movable topography is presented. The model is based on the Boussinesq-type equation coupled with the sediment advection equation and existing empirical formulas for sediment transport. Laboratory experiment is conducted for the model verification on fixed bed, while its performance on movable bed is examined through comparison with available data. Finally, the dune erosion induced by tsunami is discussed on the basis of the model results.

INTRODUCTION

Coastal dunes are natural bedforms caused by wind and wave motions. They run parallel to the shoreline close to the beach and thus have an important role to protect land against potential ravages by storm waves or tsunami. A typical case was observed by authors in Hambantota, a city located in south coast of Sri Lanka, after the December 2004 Indian Ocean Tsunami. East part of the city has large-scale dunes along shoreline and hence suffered minor damages due to tsunami flooding. On the other hand, other part of the city without dunes or with small-scale dunes experienced serious damages. Since dunes undoubtedly reflect large part of flow energy, it is

essentially important to evaluate such protective effects against severe external forces such as tsunami.

Although numerous computational studies have been carried out on Tsunami flooding, only little studies focused especially on the tsunami hydraulics around dunes. The main difficulty in numerically solving the transient flow may be treatments of discontinuous phenomena such as breaking or hydraulic jump. In addition to the complexity of the flows, dry/wet boundary must be considered, which is usually troublesome. Conventionally empirical formulas are employed on an ad-hoc basis to overcome those difficulties. However such an approach may fail or degrade the accuracy due to arbitral choice of associated parameters.

In recent years, Shock Capturing Schemes have been widely used to solve hyperbolic problems. The schemes were first derived for scalar convection equation and then generalized for system equations by a technique known as approximate Riemann solver (Roe 1981). They are explicit schemes with conservative and shock capturing properties and higher order accuracy can be attained by giving the numerical dissipation required to maintain monotonicity of the solution. In the field of hydraulic engineering, the employment of the schemes to nonliner shallow water equation has become very popular especially in transient flow problems such as Dam break flow (Zoppu and Roberts 2002) or swash zone hydrodynamics (Brocchini 2001). In most cases the results show better agreements with experiments than those of conventional schemes.

Another important feature is that dunes are highly erodible under huge momentum of tsunami rushing from sea. If some part of dunes were washed out at initial stage of flooding, the ability of dune to reflect tsunami would become considerably small. The flow-induced sediment transport and the morphological change must be taken into account to accurately predict the flow rate over dunes. However, little is known about sediment transport induced tsunami partly because real-time field measurements are impossible. Moreover, only few data are available in physical experiments with limited spatial scales (Kobayashi and Lawrence 2004).

The objective of the present study is to develop a numerical model which can simulate tsunami flooding over erodible sand dunes and to investigate the ability to protect land from inundation via application of the model. The model is based on 1D Boussinesq-type equation coupled with sediment advection equation. Existing formulas for sediments exchange through bottom boundary are used for model closure. TVD-MacCormack Scheme(Vincent et al. 2001), which is classified as Shock Capturing Schemes, is employed with Roe's approximate Riemann solver to integrate the governing equations. The model performance on fixed bed is verified through comparison of the results with available data obtained in physical experiments carried out in the present study. For the case of movable bed, the model results are compared with data of Kobayashi(2004)

The paper starts with a description of numerical model. This is followed by a verification of the model. Finaly the protective effect of dune against Tsunami flooding is discussed on the basis of model results. The paper ends with some conclusions and brief remarks on future work.

MODEL DEVELOPEMENT

Nonlinear shallow water equation is used in many literatures for the simulation of tsunami on the assumption of hydrostatic pressure. Another equation widely used in coastal engineering is Boussinesq-type equation which accounts for dispersion effects due to non-hydrostatic pressure. Since dispersion term has an role of anti-steepeing, simulation based on NSWEs predicts wave breaking far offshore. In addition, the present target is flow around dune with steep slope so that vertical acceleration can not be negligible. For this reason, Boussinesq-type equations are employed in the present study.

Sediment transport is modeled on the basis of advection equation with bottom boundary condition specified by a balance of upward and downward sediment flux. Horizontal diffusion term is not explicitly introduced since the equation is integrated with Shock Capturing Scheme, in which numerical diffusion is automatically given to preserve monotonous distribution of sediments in horizontal direction. For the upward flux, which is entrainment of sediment from bed layer, total-load sediment is computed with a single formula.

Mass conservation equation of water and sediments must be fully coupled since time-scale of the bed level change is not smaller than that of water surface. Thus, at every time step, bed level change is considered in the calculation of the flow. Although the effects of horizontally varying concentration and momentum transfer due to sediment exchange are also significant in the simulation of highly concentrated flow(Cao et al. 2004), they are not taken into account here.

Governing Equations

Governing equations described above can be written as

$$\frac{\partial(h)}{\partial t}+\frac{\partial(uh)}{\partial x}=-\frac{\partial z}{\partial t} \tag{1}$$

$$\frac{\partial(hu)}{\partial t}+\frac{\partial}{\partial x}(hu^2+\frac{1}{2}gh^2)=-gh(\frac{\partial z}{\partial x}+s_f)+S_d \tag{2}$$

$$\frac{\partial(hc)}{\partial t}+\frac{\partial(huc)}{\partial x}=E-D \tag{3}$$

$$\frac{\partial z}{\partial t} = \frac{D - E}{1 - p} \tag{4}$$

where x = cross-shore coordinate positive in the seaward direction; h = total depth; u = depth averaged velocity; z = bed level; c = depth averaged sediment concentration; E = entrainment of sediment from bed layer; D =deposition flux of sediment; g = gravitational acceleration; s_f = friction slope; S_d = wave dispersion due to non-hydrostatic pressure; and p = prosity of bed material.

There are various formulations for the dispersion term S_d . In the present study, nonlinear dispersiton term derived for the large Ursell number is considered.

$$S_d = \frac{\partial}{\partial x}(\frac{h^3}{3}P_1 - \frac{h^2}{2}P_2) + \frac{\partial z}{\partial x}(\frac{h^3}{2}P_1 - hP_2) \tag{5}$$

where

$$P_1 = \frac{\partial^2 u}{\partial x \partial t} + u\frac{\partial^2 u}{\partial x^2} + (\frac{\partial u}{\partial x})^2 \tag{6}$$

$$P_1 = \frac{\partial z}{\partial t}\frac{\partial u}{\partial x} + \frac{\partial}{\partial t}(u\frac{\partial z}{\partial x}) + u\frac{\partial h}{\partial x}\frac{\partial u}{\partial x} + u^2\frac{\partial^2 h}{\partial x^2} \tag{7}$$

The dispersion term is identical to that of Peregrine(1967) if higher order terms of u are neglected from (6) and (7).

Model Closure

Empirical formulations of friction force and sediment exchange through bed are required for model closure. For the friction slope, conventional formulation is used,

$$s_f = \frac{n^2}{h^{4/3}}u\sqrt{u^2} \tag{8}$$

where n= the Manning roughness.

The entrainment of sediment from bed layer is calculated using total-load formula of Engelund and Hansen(1967),

$$E = 0.05\frac{u^2}{h}\left(\frac{\rho d}{(\rho_s - \rho)g}\right)^{1/2}\left(\frac{\tau_{be}}{(\rho_s - \rho)gd}\right)^{5/2} \tag{9}$$

where ρ = density of water; ρ = density of sediment; d= grain size and τ_{be} = effective bottom shear stress. To account for gravity effect due to bed slope, streamwise component of gravitational force is added to bottom shear stress by Wu(2004)'s method,

$$\tau_{be} = \tau_b + \lambda \tau_c \frac{\sin\theta}{\sin\beta} \tag{10}$$

where τ_b = bottom shear stress; τ_c = critical shear stress; θ = the bed angle with the horizontal; β = repose angle; λ = coefficient related with flow and sediment condition as well as bottom slope.

The deposition flux is evaluated with a general expression

$$D = w_s c_a = w_s \alpha c \tag{11}$$

where w_s = settling velocity of sediment; c_a =sediment concentration nearbed; α = the adaptation coefficient. For α, different values are used by many researchers. In the present study, α =2 is selected following Cao et al.(2004).

Numerical Scheme

Governing Equations are solved by a finite difference scheme with shock capturing property. TVD-McCormack (Vincent 2001) scheme is employed in the present study. The scheme is flux limited version of MacCormack scheme which has been widely used for hyperbolic equations. Non-physical oscillation associated with the classical MacCormack scheme is suppressed by correcting the flux to satisfy TVD (Harten 1983) condition. The reason for choosing this scheme is its superiority to keep the integration of source term in second order not like in other schemes. To describe the numerical scheme, governing equations are rewritten as follows

$$\frac{\partial Q}{\partial t} + \frac{\partial F}{\partial x} = S_1 + S_2 \tag{12}$$

$$Q = \begin{bmatrix} h \\ hu \\ hc \end{bmatrix} \tag{13}$$

$$F = \begin{bmatrix} hu \\ hu^2 + \frac{1}{2} g h^2 \\ huc \end{bmatrix} \tag{14}$$

$$S_1 = \begin{bmatrix} (D-E)/(1-p) \\ -gh(s_0 + s_f) \\ E - D \end{bmatrix} \tag{15}$$

$$S_2 = \begin{bmatrix} 0 \\ S_d \\ 0 \end{bmatrix} \tag{16}$$

The present numerical integration process can be divided into three steps.

Predictor Step

$$Q_i^p = Q_i^p - \frac{\Delta t}{\Delta x}(F_{i+1}^n - F_i^n) + \Delta t S_{1,i}^n \tag{17}$$

$$z_i^p = z_i^n + \Delta t \frac{D_i^n - E_i^n}{1-p} \tag{18}$$

Corrector Step

$$Q_i^c = Q_i^n - \frac{\Delta t}{\Delta x}(F_i^p - F_{i-1}^p) + \Delta t S_{1,i}^p \tag{19}$$

$$z_i^c = z_i^n + \Delta t \frac{D_i^p - E_i^p}{1-p} \tag{20}$$

TVD Step

$$Q_i^{n+1} = \frac{1}{2}(Q_i^p + Q_i^c) - \frac{\Delta t}{\Delta x}(F^T_{i+\frac{1}{2}} - F^T_{i-\frac{1}{2}}) + \Delta t S_{2,i}^n \tag{21}$$

$$z_i^{n+1} = \frac{1}{2}(z_i^p + z_i^c) \tag{22}$$

where F^T is correction flux. The predictor and the corrector steps are fully explicit, while TVD step should be implicit because the integration of the dispersion term ,which contains time derivatives of the variables, is included. If the bed level z and water depth h at new time step are approximated as solutions of the predictor and corrector step, (21) become tridiagonal about velocity u so that Thomas argorithm can be applied. If long propagation of wave is concerned, integration of the dispersion term should be improved.

The correction flux F^T is calculated by the conservative flux of the first order upwind scheme and second order lax-wendroff scheme as follows

$$F^T_{i+\frac{1}{2}} = (1-\Phi)(F^{UP}_{i+\frac{1}{2}} - F^{LW}_{i+\frac{1}{2}}) \tag{21}$$

where Φ is the flux limiter function which ensure the scheme is total variation diminishing (TVD). As solution become discontinuous, Φ approaches to zero so that numerical dissipation associated with the first order upwind scheme is introduced to eliminate spurious oscillation. F^T can be evaluated by using Roe's apporoximate

Riemann solver. The detailed description of how to calculate F^T is available in many literatures. (Vincent et al. 2001).

MODEL VERIFICATIONS ON FIXED BED

Laboratory experiments were performed in a wave flume with 30cm width, 80cm height and 30m length to obtain data for verification of the present model on fixed bed. As shown in Fig 1, the flume has a piston-type wavemaker at one end and constant slope of 1/30 at the other end. Water depth in flat bottom region is 20.0 cm. The toe of sloping beach is located 13m from wavemaker and sloping beach has length of 600cm to shoreline. The experiment conditions are shown in Table1. In case of U1, U2 and U3, solitary waves with different wave height are generated to observe wave run-up over uniform sloping beach. D1 and D2 are the cases in which dune-like structure having trapezoidal cross-section with different heights are installed at 50cm landward from the still water shoreline. In the present experiments, water surface elevations are measured by capacitance–type wave gauge every 10cm from the toe of the sloping beach up to maximum run-up point. Since number of wave gauge is limited, the measurement is conducted in several runs and the displacement of wave generator is recorded together for later synchronization of all data.

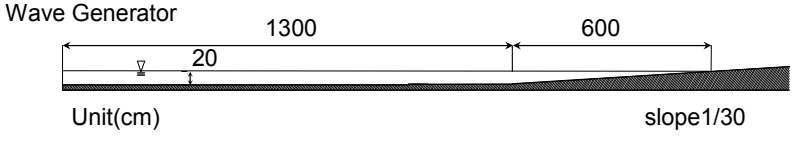

Fig. 1. Wave flume

Table 1. Experimental Conditions

Case	Wave Height, cm	Ratio of Wave Height to Water Depth	Bottom Topography
U1	5.0	0.25	Uniform Slope
U2	3.2	0.16	Uniform Slope
U3	1.8	0.09	Uniform Slope
D1	3.2	0.16	Dune(4cm height)
D2	3.2	0.16	Dune(6cm height)

Runup over Uniform Slope Beach(U1, U2 and U3)

The experimental and corresponding computational results of wave deformations over sloping beach for the case U1 , U2 and U3 are shown respectively with markers and lines at every 2.0 seconds in Figure 2. The line Z=0cm indicates still water level and the slope starts from X=300cm. In the computation, two different flux limiters

called Minmod and Superbee were employed for the flux correction. They are respectively the flux limiter giving the maximum and minimum numerical dissipation in the extent of TVD region (Sweby 1985). In order to make comparison easier, the offshore experimental data are given as the incident boundary condition of the simulations. The computational results reproduce the wave shoaling and breaking as well as formation of bore with excellent accuracy for all cases. The differences between two limiters become evident for the case of larger wave height. Superbee limiter preserves steeper wave profiles just before wave breaking, but underestimates the dissipation associated with the breaking.

Figure 3 shows wave run-up and backwash over sloping beach, which are subsequent profiles of Figure 4. In the figure, only results with Minmod limiter is shown for legibility since there is slight difference between two limiters. Bore formed after breaking collapses during run-up phase and thus the potential energy converted into kinematic energy. Therefore the flow velocity rapidly increases to rush water upward. After wave reaching its maximum run-up point, the backwash starts to form hydraulic jump around X=800cm. The computational results show good agreements with physical data except that waves are overestimated near the front during run-up for all cases. This may be because of the simple formulation of friction force as effects become dominant in small water depth.

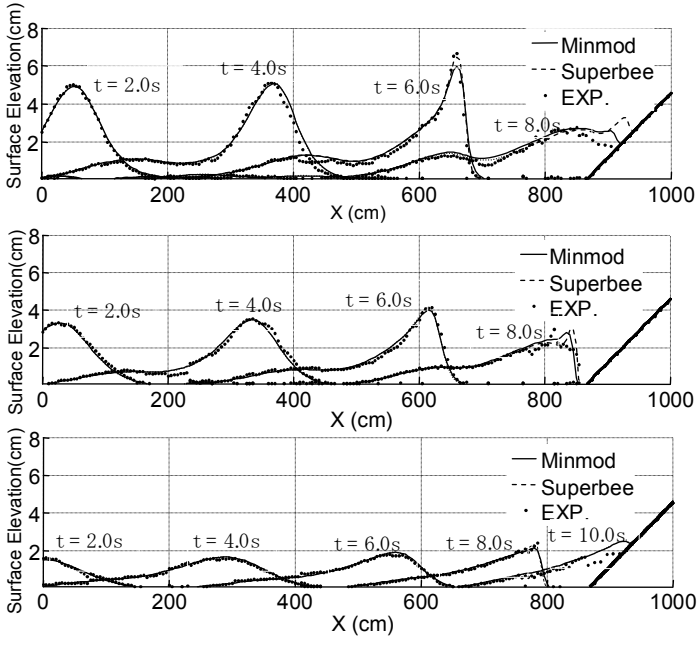

Fig. 2. Computed and experimental results of wave propagations over sloping beach

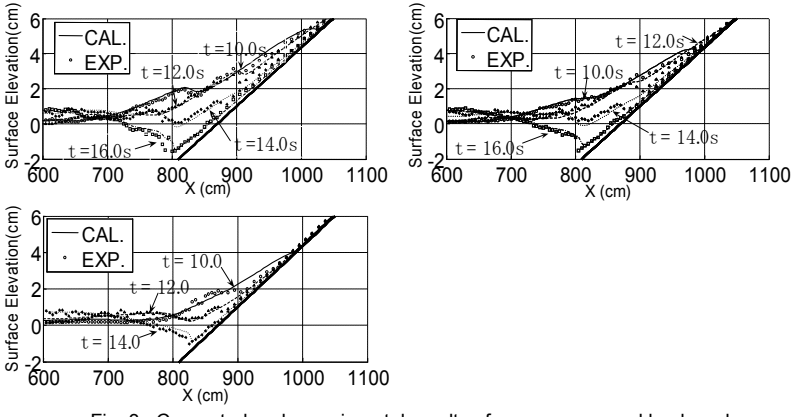

Fig. 3. Computed and experimental results of wave run-up and backwash

Runup over Dunes on sloping beach (D1 and D2)

Figure 4 shows the result for the case D1 and D2 with corresponding numerical results. Water surface profiles around dune-like structure at three different time stages are plotted. For the case D1, hydraulic jump is formed immediately after the wave front reaching the dunes while some amount of water overflows landward. In contrast, the wave is perfectly reflected by the dune-like structure if the height is larger in case of D2. Hence, it is confirmed that dune-like topography evidently has protective effect against tsunami if it is not erodible. From these figures, it is also confirmed that the present model reasonably predicts the run-up over dune-like topography.

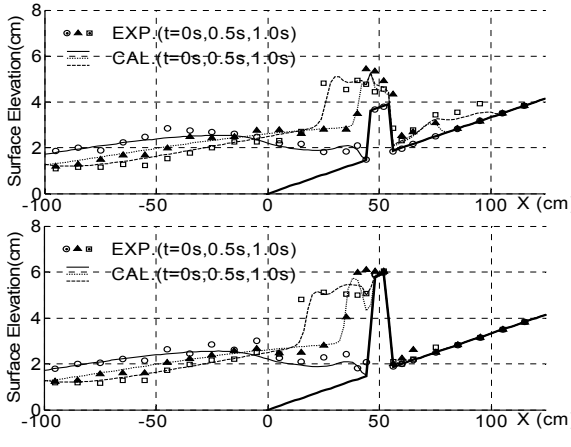

Fig. 4. Computed and experimental results of wave run-up over dune-like topography

MODEL APPLICATIONS ON MOVABLE BED

As described in former section, only few physical data is available for sediment transport due to tsunami. One of them is recently obtained by Kobayashi and Lawrence (2004). They conducted laboratory experiments in wave flume to investigate the beach profile change induced by breaking solitary wave. In order to examine the performance of the present model on movable bed, computations are carried out under the same conditions as adapted in the experiment. In the experiment, beach with initial slope of 1/12 was exposed to solitary wave with the wave height 0.216m. The grain size, measured settling velocity, porosity and the specific gravity of sand are 0.18mm, 2.0cm/s, 0.4 and 2.6 respectively.

Figure 5 displays the computed beach profile after 4 times exposition to the solitary wave. The experimental result shows the significant erosion at foreshore and the deposition seaward of still water shoreline as results of the wave plunging and subsequent strong downwash. The computed result well reproduces such a tendency and shows a good agreement in a quantitative sense.

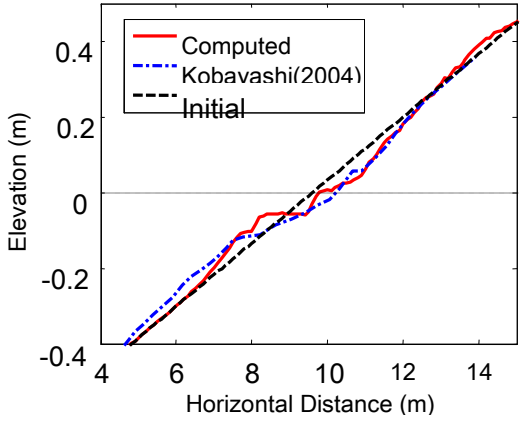

Fig. 5. Beach deformation induced by solitary wave

In order to investigate the beach deformation process in detail, the evolutions of water surface, bed level, velocity and the sediment concentration profiles during run-up and backwash are respectively displayed in Figure 6-8. Since a discussion with single wave is preferable, the incident wave height is increased to 0.35m to magnify the sediment transport. All figures start from the instance of furious breaking of the solitary wave approaching the shore. At this moment, the rapid transition from potential to kinematic energy produces a large velocity and thus the considerable amount of sediments are picked up from the bottom layer. The highly concentrated flow rushes up to the maximum run-up point losing its speed due to gravitational

effect and energy dissipation. Hence the entrainments become smaller than the deposition at certain height where sand is slightly accumulated as shown in the second figure. At the next moment, the flow changes its direction to initiate the backwash. During this stage, the flow velocity is accelerated by gravity so that the foreshore goes through the erosion again. Subsequently the suspended load settles down seaward of the still water shoreline.

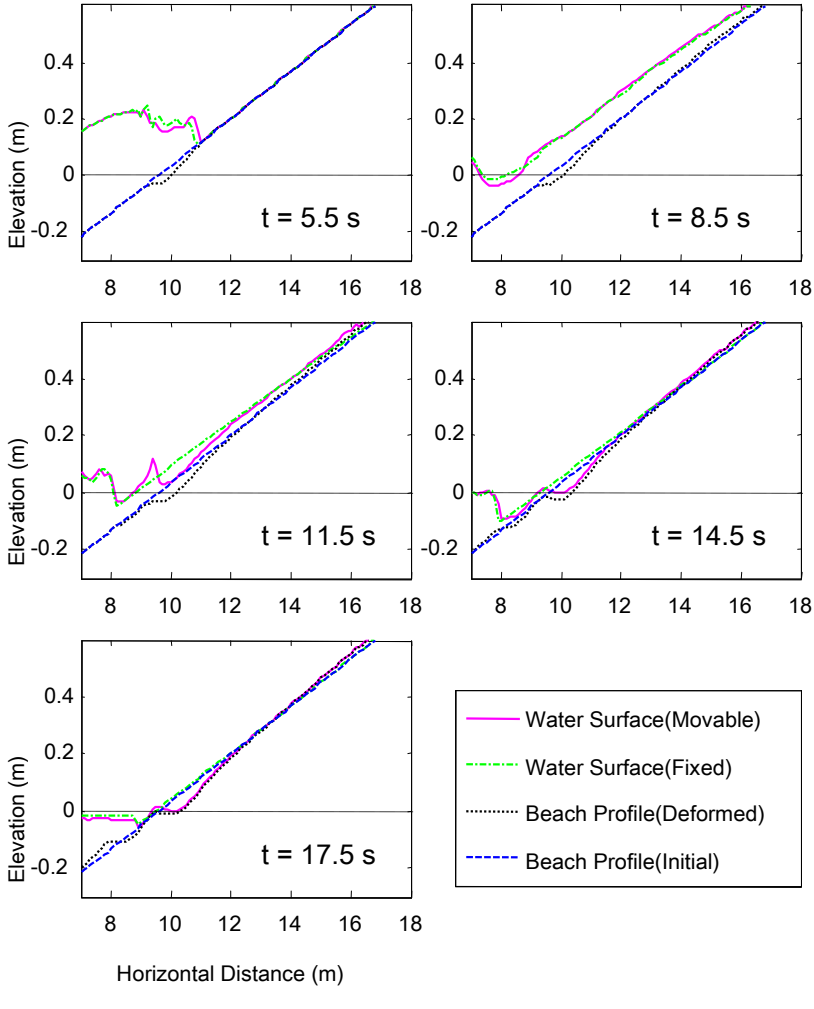

Fig. 6. Water surface and beach profile during run-up and backwash

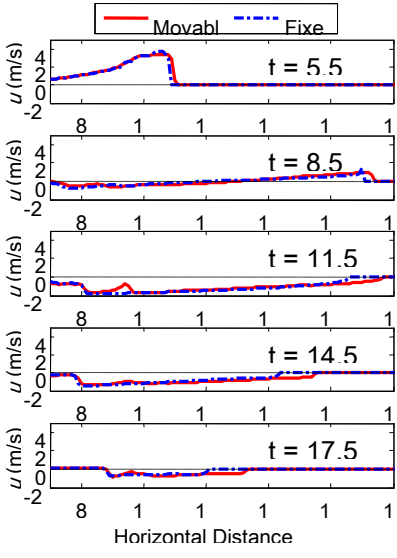

Fig. 7. Velocity profiles

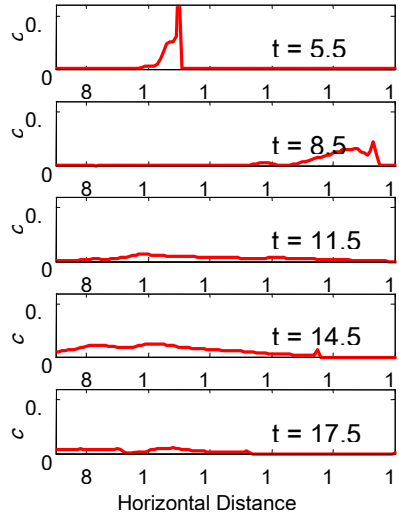

Fig. 8. Sediment concentration profile

TSUNAMI RUNUP OVER ERODIBLE SAND DUNE

Tsunami run-up over erodible dune is computed by the present model and the protective effects are discussed on the basis of the results. Dunes with different cross-section are introduced landward of shoreline on the beach with the same conditions as used in previous section. The shape of the dune is simply given with sech-squared profile. The region landward of the dunes is set as a flat bottom to avoid backwash from landside which makes the phenomena much more complicated.

A typical result from the computations is shown in Figure 9. The evolution of water surface and bed profiles around dune is plotted along with that from fixed-bed computations at 5 different times. Once waves overtop the dune, landside of the dune is severally eroded due to the flow descending along the downslope and the suspended sediments are later deposited on the flat bottom landward as shown in Figure 9. This is common to all the numerical tests especially with dunes having steep slope on landside. It is also confirmed by comparison of two results on fixed-bed and novable that the type of erosion does not significantly affect the overflowing rate. On a steep downslope, sand particle can move with smaller velocity due to gravitational effect. Once the landside of dune is eroded at lower part, its slope become steeper and such an effect become more significant. Consequently it results in large erosion. These results from the present computations are in accordance with

the observation of the real eroded dunes carried out by one of the authors in Sri Lanka. As shown in Figure 10, the landside of dunes, which experienced the overflow during 2004 Indian ocean tsunami, is violently scoured. The photograph on left hand side was taken from top of the dune, while one on right hand side shows landside of the dune.

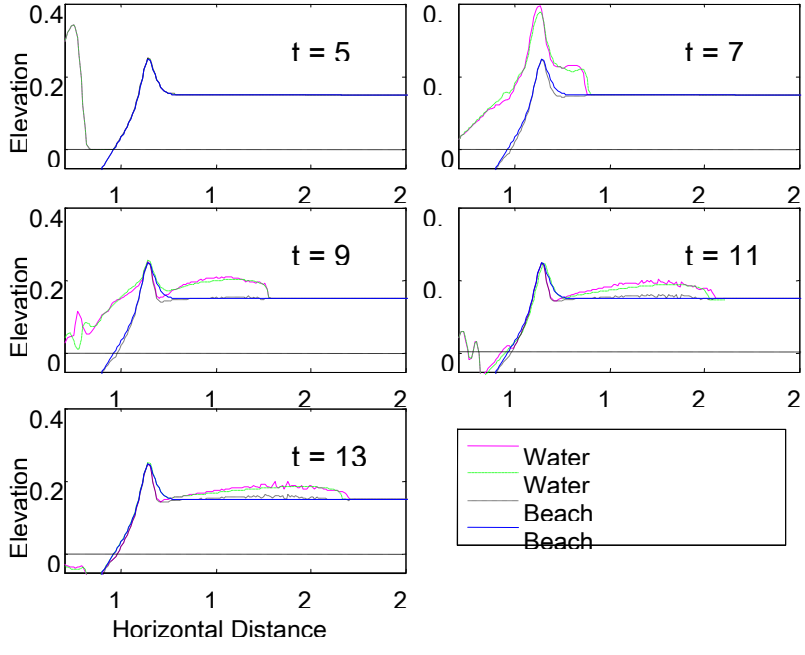

Fig. 9. Water surface and beach profile during run-up over dunes



Fig. 9. Eroded sand dune in Hambantota, Sli Lanka

CONCLUSION

A numerical model for simulation of tsunami flooding on movable bed is developed on the basis of Boussinesq-type equation coupled with sediment advection equation. The model has conservative and shock capturing property so that the flow containing discontinuities such as breaking or hydraulic jump can be handled without any special treatments. The model results are compared with available data both on fixed bed and movable bed. For the case of fixed bed, the model results show excellent agreements with the various experimental data relevant to solitary wave. Although verification is limited, the model outputs qualitatively reasonable results on movable bed problems such as tsunami run-up over dune. Since there are some empirical parameters to be determined, large-scale laboratory experiments must be conducted on movable bed for further improvement of the model.

REFERENCES

Brocchini, M., Bernetti, A. R., Mancinelli, A., and Albertini, G. (2001). "An efficient solver for nearshore flows based on the WAF method," *Coastal Engineering* 43, 105-129.

Cao, Z., Pender, G., Wallis, S. and Carling, P.A. (2004). "Computational dam-break hydraulics over erodible sediment bed," *Journal of hydraulic engineering* 130(7), 689-703

Engelund, F., and Hansen, E. (1967). "Comparison between similarity theory and regime formulae." Basic Research-Progress Report 13, Hydraulic Laboratory, Technical University of Denmark.

Harten, A. (1983). "High resolution schemes for hyperbolic conservation aws,",Journal of Computational Physics 49, 357–393.

Kobayashi, N. and Lawrence, A. R. (2004). "Cross-shore sediment transport under breaking solitary waves," Journal of Geophysical Research 109, C03047

Peregrine, D. H., (1967) "Long waves on a beach," *Journal of Fluid Mechanics* 27, 815–827

Roe P. L. (1981). "Approximate Riemann solvers, parameter vectors, and difference schemes" *Journal of Computational Physics* 43, 357–372

Sweby, P. K. (1985), "High resolution TVD schemes using flux limiters." *Lecture Note in Applied Mathematics* 22, 289–309.

Vincent, S., and Bonneton, P. (2001). "Numerical modeling of bore run-up on sloping beaches using a Maccormack TVD-Scheme," Journal of Hydraulic Research 39(1), 41-49.

Wu, W. (2004). "Depth-averaged 2-D numerical modeling of unsteady flow and nonuniform sediment transport in open channels." Journal of hydraulic engineering 130(10). 1013-1024

Zoppou, C. and Roberts, S. (2002) "Explicit Schemes for Dam-Break Simulations," *Journal of hydraulic engineering* 129. 11-34

PREDICTED SEDIMENTARY RECORD OF REFLECTED BORES

Bretwood Higman[1], Guy Gelfenbaum[2], Patrick Lynett[3], Andrew Moore[4], Bruce Jaffe[5]

1. Earth and Space Sciences, University of Washington, Johnson Hall 070, Box 351310, 4000 15th Ave. NE, Seattle, WA 98195-1310, USA. Hig314@U.Washington.edu.
2. USGS, 345 Middlefield Rd., MS999, Menlo Park, CA 94025, USA. GGelfenbaum@USGS.gov.
3. Coastal and Ocean Engineering Division, Department of Engineering Texas A&M University, College Station, TX 77843-3136, USA. PLynett@civil.tamu.edu.
4. Department of Geology, Kent State University, Kent, OH 44242, USA. AMoore5@Kent.edu.
5. USGS, 345 Middlefield Rd., MS999, Menlo Park, CA 94025, USA. BJaffe@USGS.gov.

Abstract

Where a steep slope blocks an inrushing tsunami, the tsunami commonly reverses direction as a reflected bore. A simple method for relating vertical and horizontal variation in sediment size to output from numerical models of depth-averaged tsunami flow yields predictions about the sedimentary record of reflected bores:

- Near the reflector, a abrupt slowing of the flow as the reflected bore passes is recorded by a normally graded layer that drapes preexisting topography
- At intermediate distances from the reflector, the deposit consists of a single normally graded bed deposited preferentially in depressions, possibly including a sharp fine-over-coarse contact. This contact records a brief period of erosion as the front of the reflected bore passes
- Far seaward of the reflector, grading in the deposit includes two distinct normally graded beds deposited preferentially in depressions separated by an erosional unconformity. The second normally graded bed records the reflected bore

INTRODUCTION

Geologists seeking paleo-tsunamis typically target beach plains and coastal marshes for study because they are good preservational environments. In the millennia since global sea levels stabilized in the middle Holocene, many beach-ridge and tidal-marsh plains have been building seaward. Some of these plains, which are vulnerable to attack by tsunamis, terminate at former sea cliffs or other steep slopes.

Depending on the width of a coastal plain and on the height and wavelength of a tsunami, strong flooding may or may not extend all the way to a steep inland limit. If fast-moving water does reach a steep slope at the end of the plain, it will likely form a reflected bore. The 2004 Indian Ocean tsunami reflected off beaches in Thailand (Fig. 1), and incoming tidal bores crossed exposed tidal flats to reflect off the shores of a macrotidal estuary in Alaska (Fig. 2b-d).

Nonlinear numerical tsunami run-up models predict the formation of reflected bores. In cases where a tsunami hits a steep slope at the landward limit of a horizontal plain, the reflected bore is one of the most prominent features in velocity time series—nearly as prominent as landward moving wave fronts (Fig. 2a).

As tsunamis flood beach plains, they usually carry marine sediment and leave it in a layer across the landscape. These tsunami deposits vary substantially in structure. Some deposits, such as the 1998 Papua New Guinea tsunami deposit (Gelfenbaum and Jaffe, 2003) and the 1992 Nicaragua tsunami deposit (Higman and Bourgeois, in press) have been characterized as quite simple—just one or two normally graded beds. However, even in these cases, variation in thickness, basal grain size, and rate of grading occurred through the deposit. For more complex deposits such as those from the 2004 Indian Ocean tsunami (Moore et al., 2006; Jaffe et al, 2006) and the 2001 Peru tsunami (Jaffe et al., 2003)) multiple layers are common, and grading within layers varies from normal to inverse. The number of layers in these deposits can vary both over hundreds of meters where the variation might be explained by large-scale evolution of the tsunami flow, and over a few meters where it more likely reflects local factors such as small variations in pre-existing topography.

In this paper, we explore grading predicted via simple flow sorting approximations (Fig. 3), to describe the expected grading for a simple reflected bore scenario (Fig. 4) and to interpret output from numerical tsunami inundation models (Figs. 5-6). By combining these approaches, we produce synthetic tsunami deposit structures.

Our ultimate objective, beyond this paper's scope, is to use the observed bedding of tsunami deposits to learn about paleo-tsunami flow conditions. For example, the spatial variation in grading in paleo-tsunami deposits may be used to determine whether the paleo-tsunami did impinge on a reflecting slope. Because the interaction of a reflected bore with the incoming wave is dependent on height and wavelength of the tsunami, it may be possible to interpret the characteristics of the paleo-tsunami from its deposits when the reflected bore was formed.

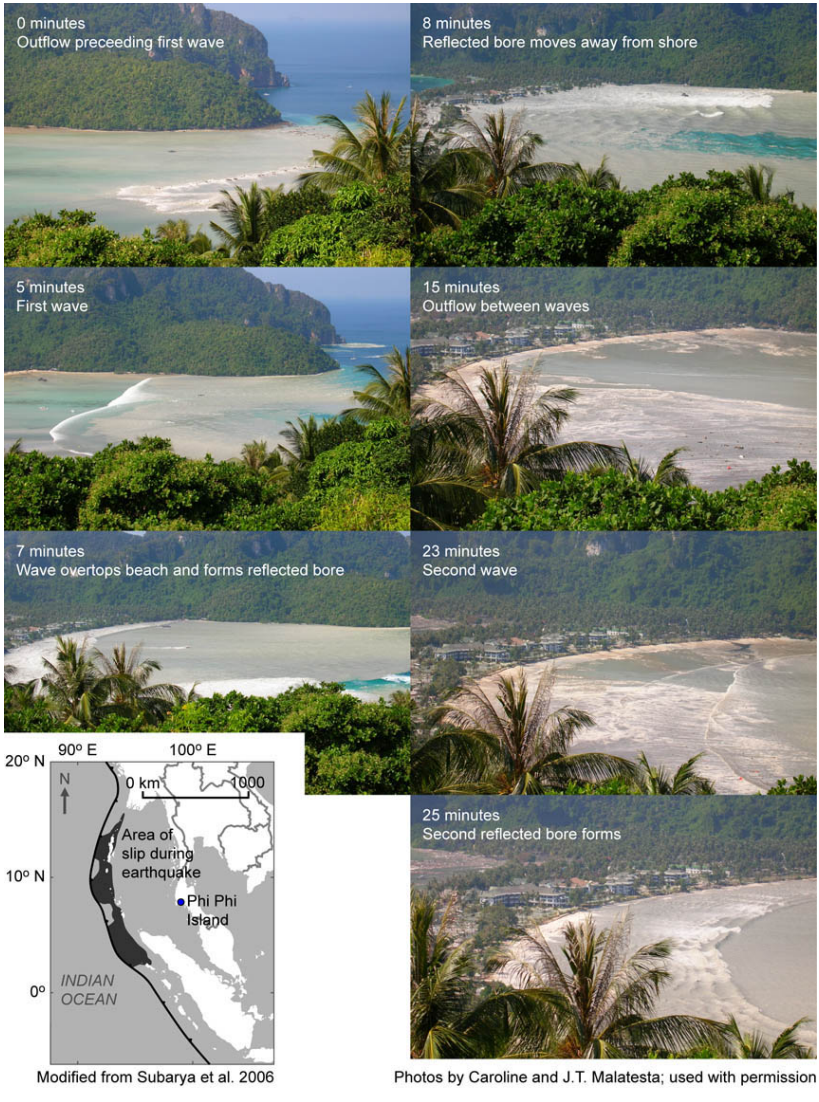

Modified from Subarya et al. 2006

Photos by Caroline and J.T. Malatesta; used with permission

Figure 1 Photos of the 2004 Indian Ocean tsunami attacking Phi Phi Island, Thailand. Reflected bores formed as both the first and second wave attacked the beach.

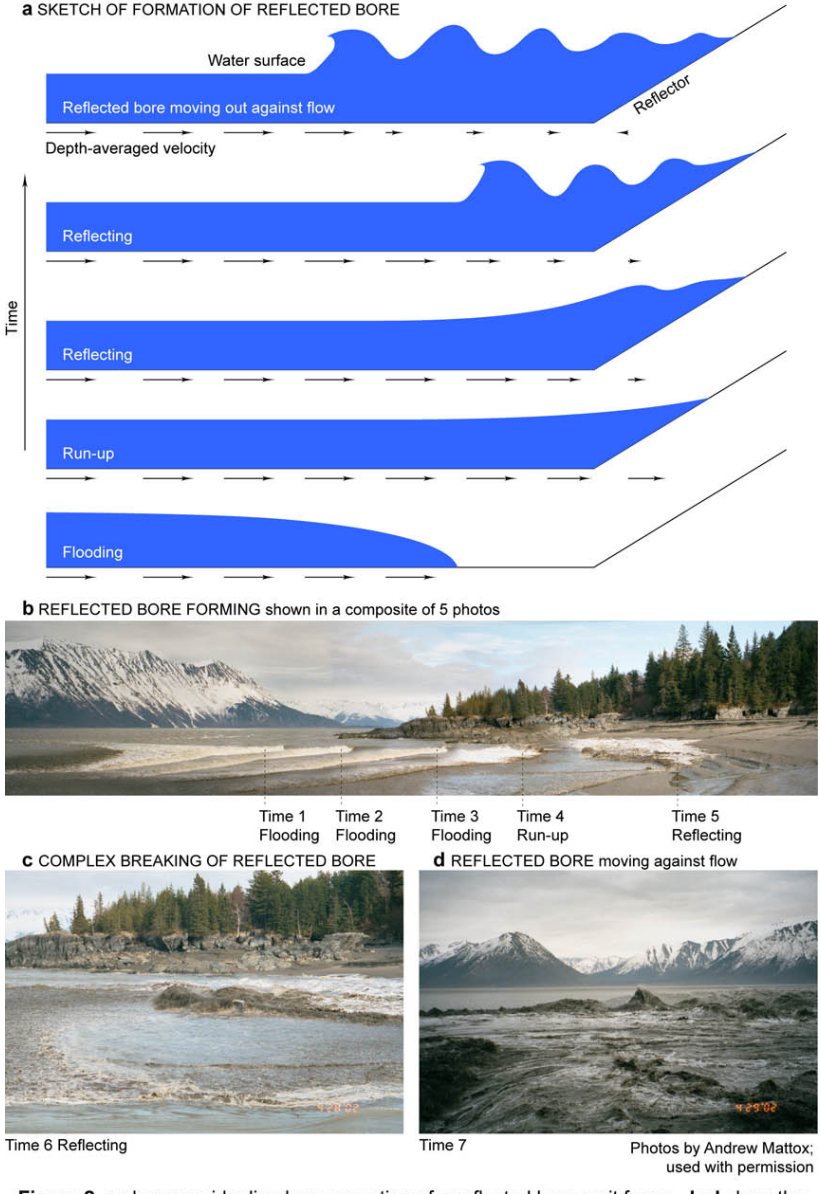

Figure 2 **a** shows an idealized cross-section of a reflected bore as it forms. **b-d** show the reflection of a tidal bore on Turnagain Arm, Alaska.

METHODS

In general, faster flows carry coarser sediment, and deposits form in areas of slowing flow. Thus coarse grains are observed in river beds in the mountains and fine sediments in flat areas, and deposition occurs in concave basins or where flows expand at delta fronts.

We apply this same conceptual model, here called the flow sorting approximations, to explain grading in tsunamis (Fig. 3)(originally applied to turbidites by Kneller, 1995). As the flow speed varies, the size and amount of sediment carried varies as well. When moving quickly, the flow will carry more and coarser sediment, and when it slows it will carry less and only the finest of available sediment. Deposition is assumed to be a function of whether the water passing over a point on the bed is slowing down or speeding up. This total time derivative of speed can be broken into a temporal and spatial term:

Total
Temporal Spatial

$$\frac{d|u|}{dt} = \frac{\delta|u|}{\delta t} + |u|\frac{\delta|u|}{\delta x}$$

where u is velocity, |u| is speed, t is time, and x is horizontal distance in the direction of the flow. Note that this latter definition is unusual in that the direction in which x increases changes each time the flow direction changes. The partial derivatives in space and time are defined at or across a single point (Eulerian perspective), while the total derivative is defined following an individual water particle (Lagrangian perspective). Although the *temporal* term—the change in speed at a given point—determines the change in grain-size distribution present in the flow, it is the sum of this term and the *spatial* term that determines whether deposition occurs. For example, where the flow brings progressively slower water past a point on the bed, it will usually be depositional. However, if the flow is speeding up through space to the point where the water experiences a *total* increase in speed then it will be erosional. Because we assume that the grain size of the sediment in the flow decreases along with flow speed, a normally graded deposit will be formed in this case. If the flow is speeding up, it will usually be erosional, but if there is some local variation in the bed such as a depression that leads to slowing through space, the water will experience a *total* decrease in speed and, because we assume that the grain size coarsens with increasing speed, an inversely graded sediment will be deposited.

The flow sorting approximations treats flow speed as the main variable controlling sediment sorting and deposition. A more thorough treatment would require tracking the variables more directly responsible for controlling sedimentation, such as bed shear stress and turbulent mixing in the water column. As a result of the simplifications the flow sorting approximations make, they do not resolve time-lags related to timescales of deposition and erosion.

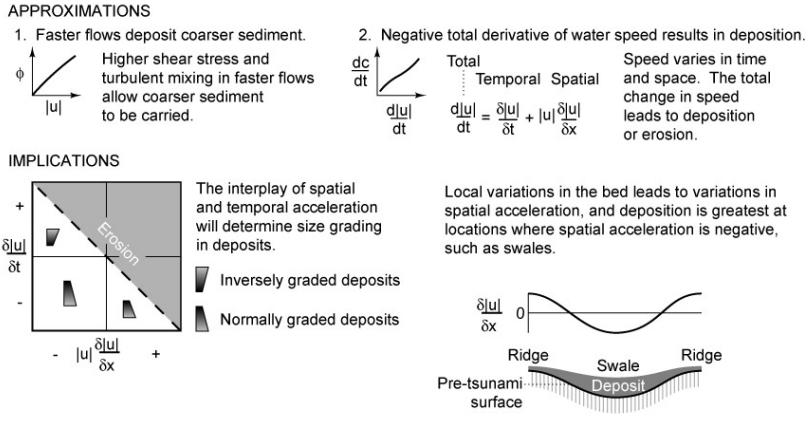

Figure 3 Flow sorting approximations

Here we present interpretation of output from two depth-integrated, nonlinear shallow -water wave models implemented for tsunami inundation: Coulwave (Lynett et al., 2002) and Delft3D (Stelling and van Kester, 1994). Though these models vary in the way they resolve moving limit of inundation and other important details, they both have been shown to accurately model most aspects of tsunami inundation. We are using them only to resolve general patterns of flow. In each case we run modeled waves across a horizontal plain with a slope at its landward limit.

In the next section, we present three realizations of bore reflection. The first is a qualitative sketch that describes some essential features of bore reflection using simplified (generally linear with discontinuities) time-series for speed and total change in speed (Fig. 4). The second presents numerical results from Coulwave for a single positive wave reflecting off a 2% slope (Fig. 5). The third presents numerical results from Delft3D for a wave train that reflects off a vertical wall (Fig. 6).

RESULTS

Reflected Bore

Figure 4 outlines the sequence of events as a tsunami crosses a beach plain and reflects off the distal slope. Figure 4a shows a simple profile of this sort, and 4b traces the paths of water particles across this beach plain. In 4b each water particle is averaged through depth, and separates constant volumes of water. Defined in this way, the water paths show the sudden change in direction that occurs with the passage of a reflected bore, generating a clear division between two distinct time-space domains. 4c shows a cartoon of the wave shape as the wave moves inland, and

4d shows the change in speed, velocity, and total derivative of speed through time. These variables can be combined using the flow sorting approximations to produce the time-grading diagrams in 4e.

This time-grading diagram emphasizes the evolution of the reflected bore's depositional pattern as it moves from the reflector. Near the reflector it starts fast and drops abruptly to very slow, dumping all the coarser sediment out of the water column. At intermediate distances from the reflector, the flow becomes abruptly more erosional, but it does not change in what grain size it is delivering to the deposit. Finally at locations far from the reflector the deposit records two distinct jumps in speed followed by gradual waning, each as a normally graded bed. The first bed records the inflow, the second records the outflow following the reflected bore. With some improvements in realism in 4f, the time-grading diagram can explain why the deposit varies depending on local topography. In lows, a more negative spatial derivative of speed leads to deposition even at times when the flow is erosional elsewhere. Finally 4g shows a deposit, both with and without annotation, that could be produced by this cartoon tsunami.

Figures 5-6 show a similar compilation of information for the Coulwave and Delft3D model runs. These are more realistic than the cartoon in figure 4, but are also likely to include complexities that are a function of the particular realization of fluid dynamics used in these models.

Deposit

Distal (near reflector) deposit: To form a reflected bore, a tsunami must be flowing quickly when it reaches the reflector. Given the flow sorting approximations, this fast flow will be carrying relatively coarse sediment. Because the tsunami slows continuously across the beach plain it will be depositing a continuously aggrading, normally graded sheet of this sediment. However, this deposit has only a moment to begin forming before the flow is abruptly stopped by the passage of the reflected bore. Relatively fine sediment rains out of this stilled water (Fig 4e, 5e, location A).

The flow sorting approximations fail to account for time lags in deposition from settling, dissipation of turbulence, and reversal of the boundary layer. As a result of these time lags, the abrupt drop in flow speed is recorded by a more gradual normal grading in the deposit. This normally graded deposit distinctly drapes topography, unlike deposits of more nearly steady flows that lap onto ridge crests. In the absence of larger incoming waves or strong reflector-parallel currents, it is likely that this drape will survive later reworking because later currents are expected to be weak. After the formation of this drape, gradually withdrawing water will leave a thin deposit that may be normally or inversely graded, possibly including discontinuous minor unconformities (Fig 4f, 5f, location A).

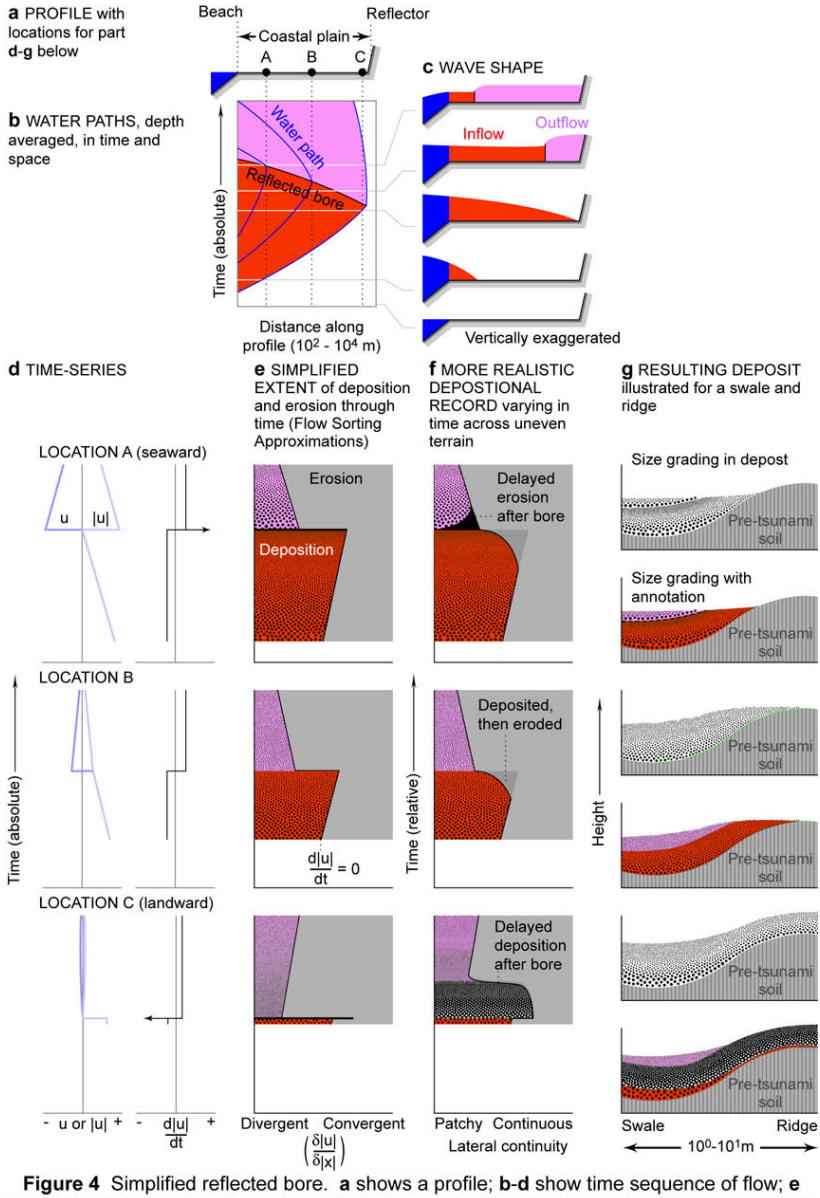

Figure 4 Simplified reflected bore. **a** shows a profile; **b-d** show time sequence of flow; **e** and **f** show the spatial extent of depositional record; and **g** shows the deposit implied by **f** on a local swale and ridge.

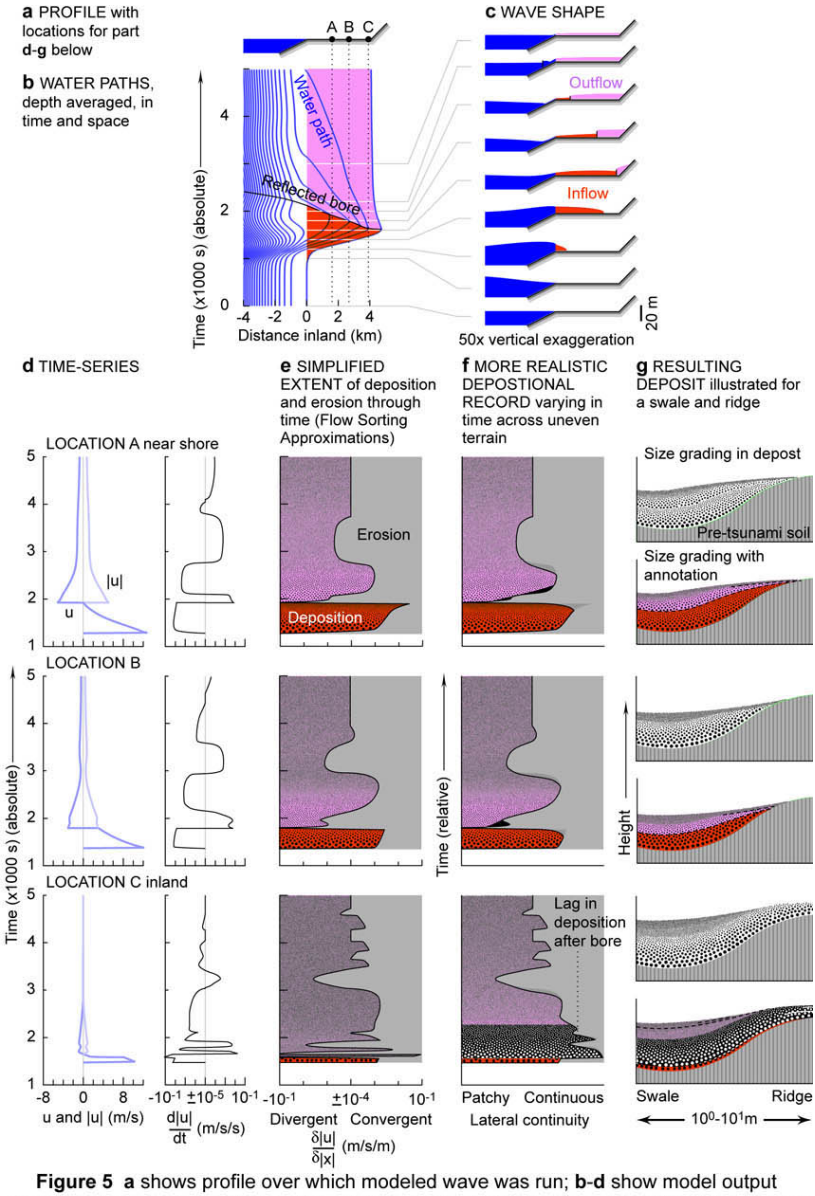

Figure 5 **a** shows profile over which modeled wave was run; **b**-**d** show model output (Coulwave); **e** and **f** show the spatial extent of depositional record; and **g** shows the deposit implied by **f** on a local swale and ridge.

Middle (between reflector and beach) deposit: The abrupt decrease in landward flow that distinguishes the distal deposit also occurs in more seaward locations. However, in these cases the magnitude of the change in flow is greater than the flow's speed, so the flow reverses and its speed (the scalar rate of motion relative to the bed) drops less than the flow velocity (the degree to which the flow is moving landward). There is some point where the abrupt decrease in landward velocity corresponds to no change in flow speed. Given our flow sorting approximations, there will be no abrupt change in grain size at this point, but there is likely to be a change in the total temporal derivative of speed that changes the spatial pattern of deposition on the bed. For example, a period of erosion can be recorded as an abrupt fine-over-coarse contact (figure 5e, location B). Allowing for time-lags in deposition and erosion scarcely alters this expected stratigraphic sequence (Fig 4f, 5f, location B).

Proximal (far from reflector) deposit: Where the arrival of the reflected bore occurs long after the passage of the leading tsunami front, there is time for the flow to slow down and possibly even stop or reverse before the reflected bore arrives. The slowing of the flow is recorded by a normally graded bed. When the reflected bore arrives the flow is again strong and slowly weakening, leaving a second normally graded bed (Fig. 4e, 5e, location C).

The reflected bore partially erodes the uppermost part of the first normally graded bed before deposition of a second normally graded bed. Because the flow needs time to entrain enough sediment to reach its transport capacity, the arrival of the reflected bore lags the beginning of deposition at this location (Fig. 4f, 5f, location C). The sediment in the reflected bore is limited to what can be eroded from the pre-existing tsunami deposit and pre-tsunami soil—provenance that may provide aid in distinguishing the reflected-bore deposit from that of a successive incoming wave or surge. Otherwise, a second normally graded bed may closely resemble the deposit of a second surge.

Most tsunamis includes multiple large waves. In these cases later waves may encounter water from earlier waves and form landward propagating bores. Also, multiple reflected bores will form. This multiplicity of flows is likely to produce the kinds of complexity shown in Fig. 6.

DISCUSSION

Many tsunami deposits have fairly simple structure, typically normally graded and thinning and fining landward (e.g. Gelfenbaum and Jaffe, 2003). These cases may be examples where the tsunami did not form a reflected bore. The most prominent expected record of a reflected bore is a relatively fine grained layer that thickens toward the reflector. However, detailed documentation of tsunami deposit structure, including lateral variability in layering, could provide evidence even of more subtle reflected bores, and allow one to untangle the signals of multiple bores and reflected bores crossing the beach plain. For example, in the 1992 Nicaragua deposit (Higman and Bourgeois, in press), a deposit in a lagoon with a steep slope at its landward limit includes a sharp contact where finer sediment overlies coarser

sediment, often associated with both heavy mineral laminae and concentrations of clay rip-ups (Fig 7). This feature may record the passage of a reflected bore.

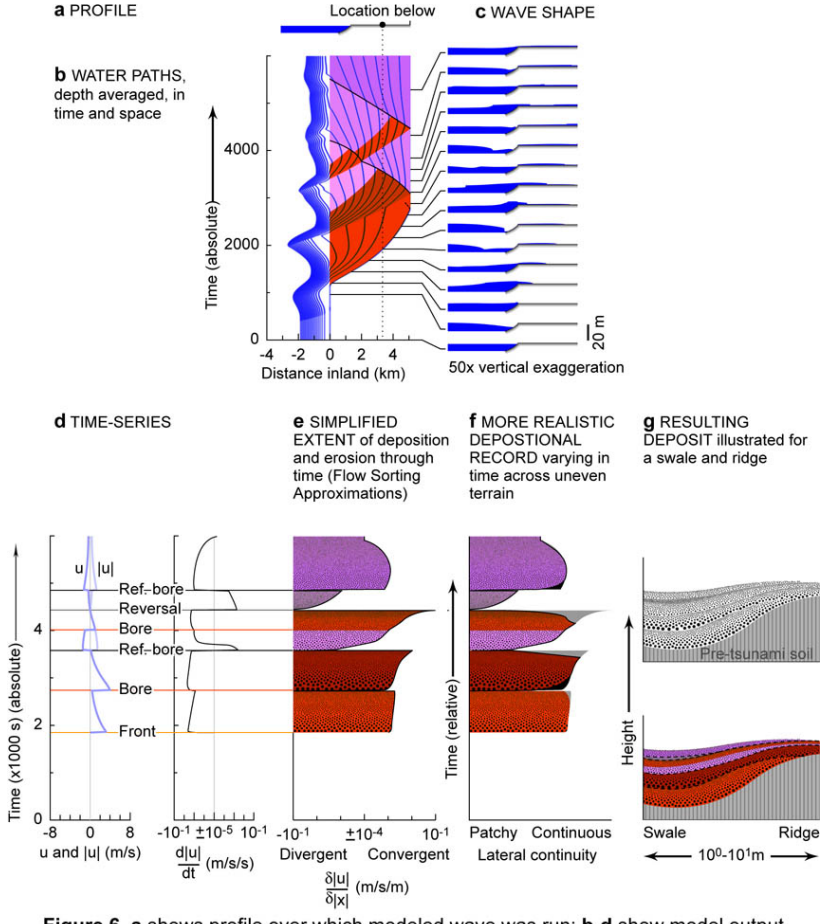

Figure 6 **a** shows profile over which modeled wave was run; **b**-**d** show model output (Delft3D); **e** and **f** show the spatial extent of depositional record; and **g** shows the deposit implied by **f** on a local swale and ridge.

The analysis presented here also provides a road-map for understanding other features of tsunami deposits. A number of non-linear shallow-water wave inundation models have been developed. These have been most widely used to estimate run-up values for tsunamis, but to achieve this they include dynamics that might be interpreted to better understand depositional patterns. Here we predict depositional signatures of reflected bores implied by numerical model output. We base our interpretation on a simple flow sorting approximation, along with some basic

sedimentary geology. This same procedure, preferably augmented by more sophisticated sedimentation models, could be used to predict deposition from other features in a tsunami, for example steep fronts propagating over dry ground or deposition in pot-hole lakes.

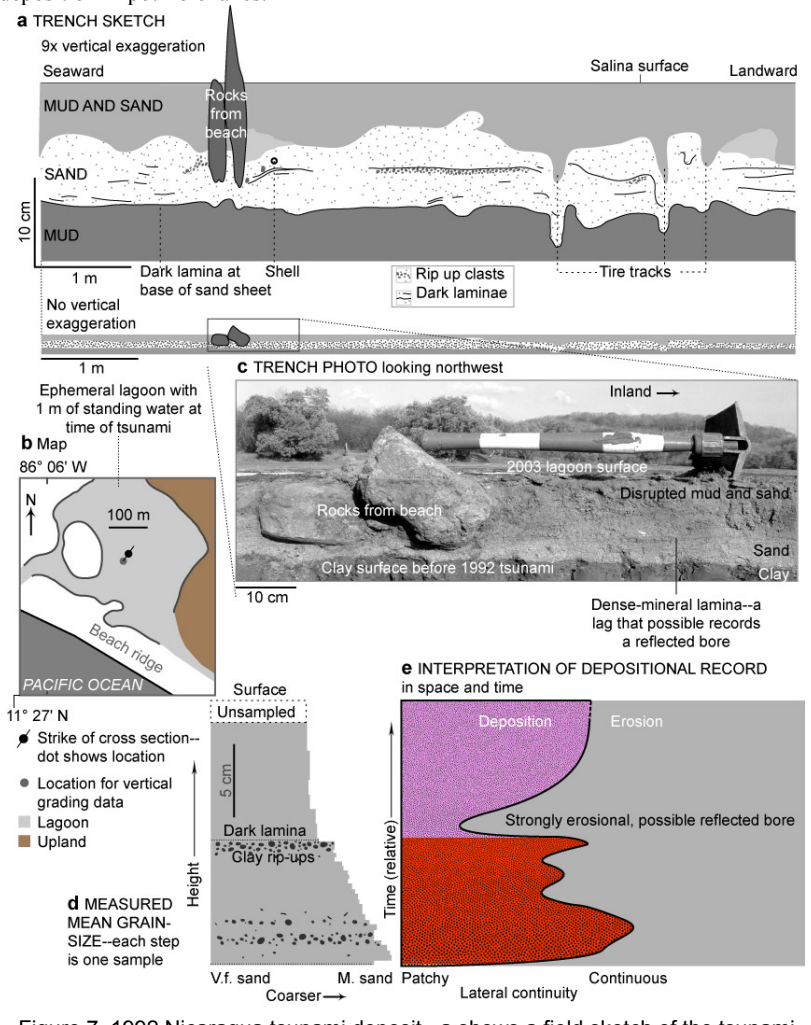

Figure 7 1992 Nicaragua tsunami deposit. **a** shows a field sketch of the tsunami deposit. **b** shows a map of the lagoon where the trench was dug. This lagoon rises steeply on its landward limit, making it a setting where a reflected bore is likely to form. **c** shows a photo of the trench. **d** shows measured vertical grading. **e** shows an interpretation of this deposit compiling measurement and sketch data in the style of figs. 4-6.

CONCLUSIONS

In a tsunami deposit that includes a record of a reflected bore, depositional patterns are likely to vary with location along a profile between the sea and the reflector: near the reflector, a thick normally graded drape; at intermediate distances from the reflector, a normally graded deposit possibly including a sharp contact; and far from the reflector, two normally graded beds.

These predicted features should be detectable in paleo-tsunami deposits, and we have seen similar features in modern deposits in settings where reflected bores are likely to form.

Beyond reflected bores, our methods could be applied to many features of tsunamis and their deposits. These qualitative tools for reading the paleo-tsunami record could greatly improve our understanding of tsunami hazard and of the events that generate tsunamis.

ACKNOWLEDGEMENTS

This manuscript was substantially improved by suggestions from Brian Atwater and Brian Collins. Also thanks to Caroline and J.T. Malatesta for permission to use their incredible photographs in figure 1, and to Andrew Mattox for his photos in figure 2 and for his unparalleled efforts as a field assistant.

REFERENCES

Gelfenbaum, G., & Jaffe, B.E. (2003). "Erosion and sedimentation from the 17 July 1998 Papua New Guinea tsunami," *Pure and Applied Geophysics* 160 (10-11), 1969-1999.

Higman, B., Bourgeois, J. (In press). "Deposits of the 1992 Nicaragua tsunami," *to be published in Tsunamiites—their features and implications. ed. Tsunemasa Shiki and published by Elsevier.*

Jaffe, B., Borrero, J., Prasetya, G., Peters, R., McAdoo, B., Gelfenbaum, G., Morton, R., Ruggiero, P., Higman, B., Dengler, L., Hidayat, R., Kingsley, E., Kongko, W., Lukijanto, Moore, A., Titov, V., Yulianto, E. (2006). "Northwest Sumatra and Offshore Islands Field Survey after the December 2004 Indian Ocean Tsunami," *Earthquake Spectra* 22, 105-135.

Jaffe, B., Gelfenbaum, G., Rubin, D., Peters, R., Anima, R., Swensson, M., Olcese, D. Bernales L., Gomez, J., and Riega, P. (2003). "Tsunami deposits: Identification and interpretation of tsunami deposits from the June 23, 2001 Perú tsunami," Proc. *Coastal Sediments '03*, 13p.

Kneller, B. (1995). "Beyond the turbidite paradigm; physical models for deposition of turbidites and their implications for reservoir prediction, in Characterization of deep marine clastic systems," *Geological Society Special Publications* 94, 31-49.

Lynett, P., Wu, T., Liu, P. (2002). "Modeling wave run-up with depth-integrated equations," *Coastal Engineering* 46, 89-107.

Moore, A., Nishimura, Y., Gelfenbaum, G., Kamataki, T., Triyono, R. (2006). "Sedimentary deposits of the 26 December 2004 tsunami on the northwest coast of Aceh, Indonesia," *Earth Planets Space* 58, 253-258.

Stelling, G.S., and van Kester, J.A.T.M. (1994). "On the approximation of horizontal gradients in sigma coordinates for bathymetry with steep bottom slopes," *International Journal for Numerical Methods in Fluids* 18, 915-955.

TSUNAMI INUNDATION AND SEDIMENT TRANSPORT IN VICINITY OF COASTAL MANGROVE FOREST

Guy Gelfenbaum[1], Deepak Vatvani[2], Bruce Jaffe[3], Frank Dekker[4]

1. U.S. Geological Survey, 345 Middlefield Rd., MS999, Menlo Park, CA 94025 USA. ggelfenbaum@usgs.gov.
2. Delft Hydraulics, P.O.Box 177, Delft, The Netherlands Deepak.Vatvani@wldelft.nl
3. U.S. Geological Survey, 400 Natural Bridges Drive, Santa Cruz, CA 95060, bjaffe@usgs.gov
4. Delft Hydraulics, P.O.Box 177, Delft, The Netherlands Frank.Dekker@wldelft.nl.

Abstract: Field measurements from Sumatra of tsunami wave height, erosion and deposition form a comprehensive data set that is tested against the Delft3D tsunami inundation and sediment transport model. Relative agreement between measured and modeled maximum water levels and sediment erosion and accumulation provides confidence that the model is reasonably characterizing the important processes of tsunami inundation. Adding a component to account for vegetation, the model is used to explore the effects of fringing mangrove forests on tsunami inundation and sedimentation. In model experiments, mangrove forests modify the water levels and flow speeds reached during tsunami inundation. Simulations with a mangrove forest result in sedimentation in the forest and not erosion, as occurs in the base case with no forest. This difference in sedimentation is important because the change in profile shape increases wave energy reflection off the beach and decreases wave energy penetration onto land.

INTRODUCTION

In recent years there has been a renewed interest in examining the beneficial effects of coastal defense structures in mitigating tsunami hazards. After the 2004 Indian Ocean tsunami, coastal managers, engineers and scientists have been asking if natural or man-made coastal structures could have helped reduce tsunami damage and casualties in

countries such as Sri Lanka, Indonesia, and Thailand. Whereas a tsunami warning system would have been beneficial for locations somewhat distant from the tsunami source, for locations so close to the source that a warning system would not have had enough time to be effective, education and coastal defense structures are viewed as important alternatives. For many years, the man-made coastal structures (seawalls and breakwaters) along the Japanese coast have played an important role in protecting the coast from tsunami hazards. Problems associated with man-made structures, such as high construction and maintenance costs, and modification of the natural environment are causing some managers to seek natural defense structures, such as coral reefs, sand dunes, or coastal forests (Figure 1) to complement their mitigation strategies.



Figure 1. Fringing mangrove forests, like this one near Simelue Island west of Sumatra, may reduce tsunami impact. The lower roots are exposed because of coastal co-seismic uplift.

Mangrove forests are known to provide coastal protection against normal wind waves and tidal currents, but the extent to which coastal forests reduce loss of life or protect coastal structures during tsunami inundation is less well known (United Nations Food and Agriculture Organization web site). Coastal forests can reduce tsunami impacts by 1) acting as a barrier against floating objects (e.g., boats, debris), 2) reducing tsunami impact such as inundation distance, wave height, or flow speed, 3) providing structures for people to climb or cling to during a tsunami, and 4) promoting development of dune

formation during fair-weather conditions (Harada and Imamura, 2005). Recent laboratory and numerical studies examine the reductions in tsunami energy associated with characteristics of coastal forests such as forest density, trunk diameter, tree height, and forest width (Harada and Imamura, 2005).

While the extent to which coastal forests act to reduce tsunami impacts are beginning to be elucidated, the associated sediment transport and morphological change around and within these forests have not been studied. For example, if a mangrove forest reduces tsunami flow speeds, what will the resulting sediment transport be in and beyond that zone? Will the reduced flow speed modify the sediment transport enough to cause different patterns of coastal erosion and sedimentation? This manuscript describes numerical simulations of tsunami inundation, sediment transport, and morphological change with and without fringing mangrove forests. The model presented here includes feedback between the flow, sediment transport, and morphological change, through regular bed updating. Prior to testing the effect of the fringing mangrove forest, the tsunami sediment transport model is validated with field data collected on the coast of Sumatra, Indonesia after the December 2004 Indian Ocean tsunami.

TSUNAMI INUNDATION AND SEDIMENT TRANSPORT MODEL

Model

The modeling approach employs the Delft3D-FLOW module to simulate the coastal flooding and the "online" sediment transport capabilities to calculate the erosion and deposition of sediment. Delft3D-FLOW has been shown to accurately simulate the propagation of the Indian Ocean tsunami away from the earthquake source (Vatvani et al., 2005). The hydrodynamics model solves the non-linear shallow water equations in 2D or 3D on a staggered grid with a finite difference scheme (Stelling and van Kester, 1994). A special solver is employed to handle rapid wetting and drying for use when simulating flooding and which has previously been validated for modeling dam-break waves and rapid inundation of dry areas (Stelling and Duinmeijer, 2003). Sediment transport is calculated by solving the conservation of mass equations within the flow module. This model has been tested against flume and analytical solutions and shown to be applicable under typical coastal sediment transport conditions (Lesser et al., 2004). Both bedload and suspended load transport are calculated using the transport formula of van Rijn (1993). Convergences and divergences of sediment transport are accounted for at each grid cell and result in deposition and erosion of sediment on the bed (Lesser et al, 2004). The model has been used successfully in a variety of coastal and estuarine settings to simulate sediment transport and morphological change for both event and long-term morphological evolution (Roelvink, 2006; Lesser et al., 2005; Gelfenbaum et al., 2003) but has only recently been tested under the conditions of tsunami inundation (Gelfenbaum, et al., 2006).

The model is used here to simulate the tsunami inundation at Kuala Meurisi, along the west Sumatra coast. A fine-scale rectangular grid extending from about 2 km offshore to 2 km landward of the shoreline, the extent over which accurate bathymetric and topographic data were obtained is used. Grid size varies from 10 m at the shoreline and

at the steep slope near the landward limit of inundation to 20 m in areas of slowly varying bottom elevation. A simulation time step of 0.3 s was necessary to minimize instabilities in the modeled water level. The earthquake rupture and sea-floor displacement are not simulated. Instead, a deep-water boundary condition along the outer boundary of the numerical domain was obtained from the Vatvani et al (2005) coarser-scale tsunami propagation model. The water-level time series from the Vatvani model is composed of numerous waves that leads with an initial trough that has an amplitude of -4 m in 18 m water depth at the offshore model boundary.

Field Data

As part of an International Tsunami Survey Team (ITST), field data of tsunami inundation and sediment deposits were collected in April 2005 along the west Sumatra coast. At several sites the ITST collected eyewitness accounts, topographic profiles, tsunami wave heights, inundation distances, tsunami deposit thickness, sediment samples for grain size analysis, and nearshore bathymetry (Jaffe et al., 2006). Topographic profiles were measured along shore-normal transects with a hand-held laser range finder and surveying rod with prism. Elevations were collected relative to water level at the time of the survey and later corrected to mean sea level. Tsunami wave heights were estimated by measuring the elevations of the highest freshly broken branches or of debris in trees left standing after inundation. Where possible, several water-level indicators were measured on nearby standing trees with the laser range finder and averaged. Small pits were dug along each transect to identify if the tsunami had eroded the surface or left a sedimentary deposit at that location. Where a tsunami deposit was found, its thickness was measured and sedimentary structures, vertical variation in grain size, and number of layers were noted. Samples of the tsunami deposit were collected for laboratory grain-size analysis. Nearshore bathymetric data were collected along cross-shore transects with a digital echo sounder to measure the water depth and GPS for horizontal position. The data were later tide-corrected to mean-sea level.

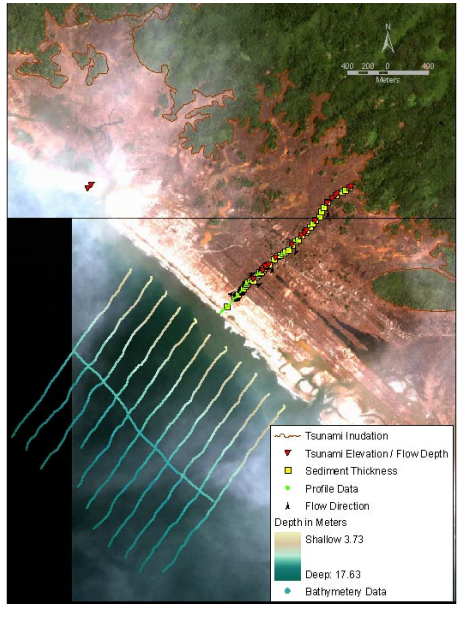

Figure 2. Satellite image of Kuala Meurisi with location of nearshore bathymetry, onland topography, water level, and sediment thickness measurements

At Kuala Meurisi, a site approximately 100 km south of Banda Aceh which will be used to test the model, a tsunami wave 15 m high inundated nearly 2 km across a coastal plain that was only 3-4 m above sea level. Eyewitnesses reported that the first wave arrived on land approximately 15-20 minutes after the earthquake, that the second and third wave arrived before the previous wave had completely receded, and that the third wave was the largest. The nearshore bathymetric data reveal a smooth shoreface profile to 18 m water depth, with a longshore bar at about 12 m depth and a concave shape up to 5 m. The bathymetric and topographic data were merged requiring interpolation between 5 depth m and the shoreline. Several trees remained standing across the coastal plain in the vicinity of this transect and reveal tsunami wave heights up to 15 m above mean sea level 1 km from the shoreline. The tsunami inundation extended 12 m up a hillside at a distance of 2 km from the shoreline.

The tsunami eroded the beach face and left a deposit that varied in thickness across the coastal plain from less than 1 cm to 34 cm. Comparison of satellite images from approximately 1 year before the tsunami and a few days after the tsunami suggest the shoreline moved approximately 75 m landward as a result of erosion during the tsunami and co-seismic subsidence, locally estimated to be 1-2 m. By the time of the ITST field survey, a new beach had formed along the shoreline with sand brought onshore (or perhaps alongshore) from fair-weather waves. During the field survey, moderate sized waves and average high tides combined to produce overwash of the dune and landward migration of the beach berm. Close to shore, the tsunami deposit includes one to three layers of sand above a dark brown soil. The sandy deposits are commonly normally graded and thin landward to muddy sand while a mud layer above the tsunami sand thickens. The deposit thickness consistently varies with local topography, thinning along ridges or local highs and thickening in the swales or low-lying areas. This pattern is characteristic of tsunami deposits and consistent with patterns observed in Papua New Guinea (Gelfenbaum and Jaffe, 2003) and in Sri Lanka (Goff et al., 2006) and other locations in Sumatra (Jaffe et al., 2006; Moore et al., 2005). The measurements at Kuala Meurisi of tsunami wave height, topography and bathymetry, and tsunami erosion and deposition form a comprehensive data set with which to test a tsunami inundation and sediment transport model (Figure 2).

Base Model Verification

Model simulations show several waves inundated the low-lying coastal plain of Kuala Meurisi, consistent with eye-witness accounts. Modeled maximum water levels at every cross-shore location fall within the scatter of field estimates of maximum wave height (Figure 3). Model and field data both give a runup of 12 m, the elevation of maximum landward inundation. Field estimates of maximum wave height in the center of the coastal plain may be somewhat higher than the model predicts, likely a result of uncertainties in the offshore boundary condition. Bottom roughness is set higher along the sub-aerial plain than for the part of the profile below mean sea level.

The sediment transport model predicts erosion of sediment along the beach. Accumulation of sediment occurs in an offshore bar and on land, across the coastal plain

(Figure 4). Sediment accumulation of up to 60 cm is predicted on land compared to measured deposit thickness of up to 34 cm. For this comparison, only one grain-size class (800 microns) is simulated yet sensitivity analyses show that deposit thickness is highly dependent on grain size. Both model simulations and field data show thicker deposits in local topographic lows or swales and thinner deposits (or erosion) on local topographic highs or ridges. The relative agreement between measured and modeled maximum water levels and sediment erosion and accumulation in the Kuala Meurisi case provides confidence that the model is reasonably characterizing the important fluid mechanics and sediment transport processes of tsunami inundation. By adding a component to account for vegetation, the model can be used to explore the effects of fringing mangrove forests on tsunami inundation and sedimentation.

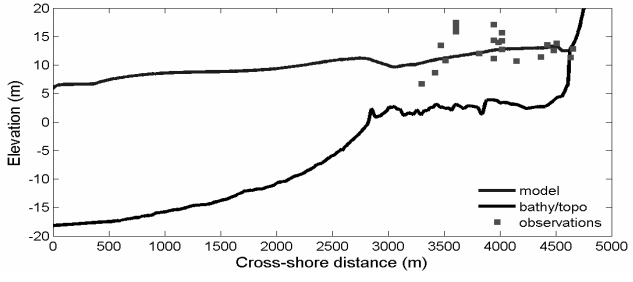

Figure 3. Cross-shore variation in maximum water level measured in the field (red squares) and modeled (blue line) after inundation of the tsunami.

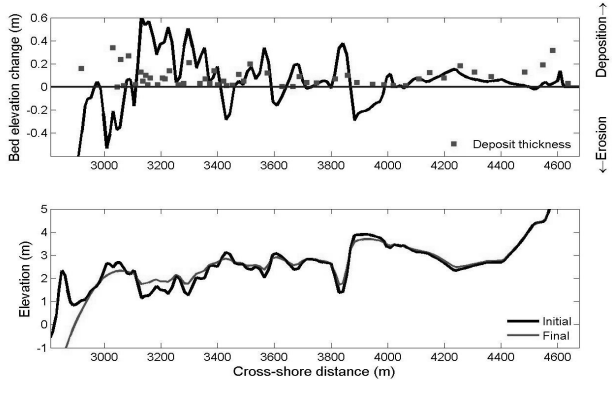

Figure 4. Model and data comparison of bed elevation change (erosion and deposition) along the beach and coastal plain at Kuala Meurisi. In top panel, red squares are measured tsunami deposit thickness and the black line is the model prediction. In lower panel, the thick black line is the initial topographic profile in the simulation and the thin red line is the final, predicted profile.

Mangrove Forest Parameterization

The influence of mangroves on the flow is included in the momentum equation by defining an extra force based on vegetation characteristics. Vegetation will lead to an extra resisting force acting on the flow. Following Baptist (2005) and Uittenboogaard (2003), the vegetation in Delft3D is modeled as a group of parallel, staggered or randomly arranged rigid vertical cylinders (stems) with homogeneous properties. The resistance force F per unit area can be expressed as:

$$F(z) = \tfrac{1}{2}\rho_0 \int_0^k C_D m(z) D(z) |u(z)| u(z) \qquad [N/m^3] \qquad (1)$$

Where:
ρ_0 = density of water
k = plant height
$C_D(z)$ = drag coefficient
$m(z)$ = cylinder density per unit area
$D(z)$ = cylinder diameter
$u(z)$ = time averaged, horizontal flow velocity

This parameterization is similar to the relation used by Mazda et al. (2005) and Wu et al. (2001). Vertical variations in the force generated by mangrove forests can be large due to the root-trunk-canopy structure of the tree. The flow velocity profile is assumed to be uniform inside the vegetation field. The continuity equation is corrected with the volume that is encompassed by the cross-sectional plant area.

In 3D simulations, all parameters in Eq. 1 are functions of the vertical coordinate z. In 2D simulations, the velocity u is uniform over the depth (depth averaged velocity), but C_D, m, D can still be a function of the vertical coordinate (i.e. the water level). When the water level rises above the vegetation height the influence of the vegetation (in the momentum and continuity equations) is reduced accordingly.

Table 1. Mangrove forest parameters for model experiments

Simulation	Mean Height, m	Stem diameter, m	Stem density, /m^2
Ma1	3	0.15	0.3
Ma2	3	0.15	0.6
Ma3	3	0.15	1.0

For the cases to be examined in this paper, the plant height and stem diameter are held constant and the stem density is varied from 0.3 to 1.0 stems/m^2 (Table 1). The width of the fringing mangrove forest in the numerical simulations is 175 m, with short transition zones on the seaward and landward edges of the forest (Figure 5). Although the actual

mangrove forest characteristics for the islands off Sumatra are slightly different, the parameters chosen for these numerical experiments allow examination of the influence of mangrove forests on coastal sediment transport during tsunami inundation. Model simulations include sandy sediment offshore and on the beach with a mean grain size of 400 microns and muddy sediment on land with a mean size of 50 microns. These sizes were chosen because they approximate the sediment sizes of the underlying soil and overlying tsunami deposit found near a mangrove forest (Figure 6).

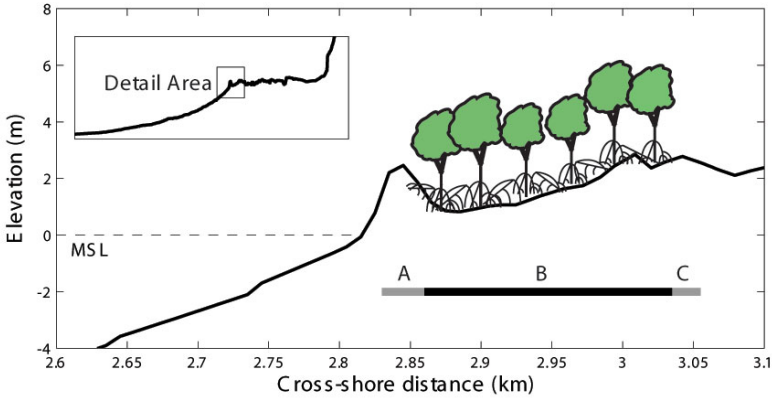

Figure 5. Location of the fringing mangrove forest along the coastal profile. Zones A and C are transition zones and zone B has stem densities of 0.3, 0.6, or 1 /m^2.



Figure 6. Photographs of sandy tsunami deposit overlying muddy organic rich soil in the vicinity of a mangrove forest.

MODEL RESULTS

A fringing mangrove forest can modify the maximum water level reached during tsunami inundation (Figure 7). Increasing the mangrove density decreases the maximum water

level across the coastal plain and the run-up. The maximum water level reached during the simulation, at a location approximately 200 m landward of the mangrove forest, is 80-91% of the maximum water level with no mangrove forest (the base case). Greater mangrove densities in the forest induce a greater reduction in water level.

Likewise, there is a reduction in maximum flow speed in the tsunami both within and landward of the mangrove forest. The flow reduction depends on several factors, and varies not only with mangrove density, but also from the first wave in the wave train to the last. The reduction in speed from the base case (no mangrove forest) varies from 49-91%. The greatest reduction in flow speed occurs for the third wave in the series (the largest in this simulation), in which the flow varies from 66-49% of the base case as the plant density increases.

The modified hydrodynamics have a significant impact on the sediment transport and resulting coastal morphological change (Figure 8). Both the onrushing wave and the seaward withdrawal result in erosion of the beach in the base case with no mangrove forest. Each of the simulations with a mangrove forest results in sedimentation in the zone of the forest and not erosion. This changes the amount of sedimentation further landward on the coastal plain, but more importantly, changes the profile shape, increasing wave energy reflection off the beach and decreasing wave energy penetration onto land. Deposition within the mangrove forest increases with increasing plant density, and deposition landward of the forest is less than in the base case with no forest.

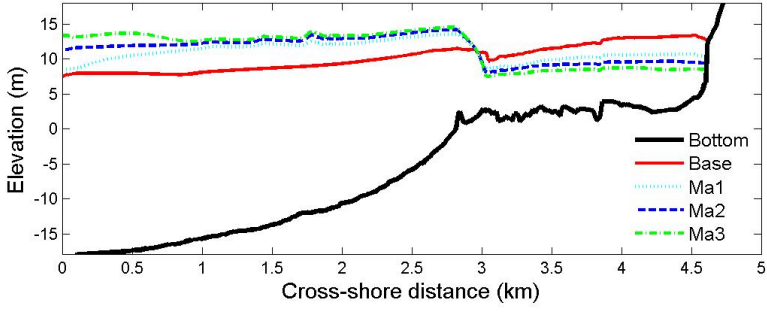

Figure 7. Cross-shore variation in predicted maximum water level for the base case and three cases with varying mangrove stem densities (see table 1 for explanation of cases).

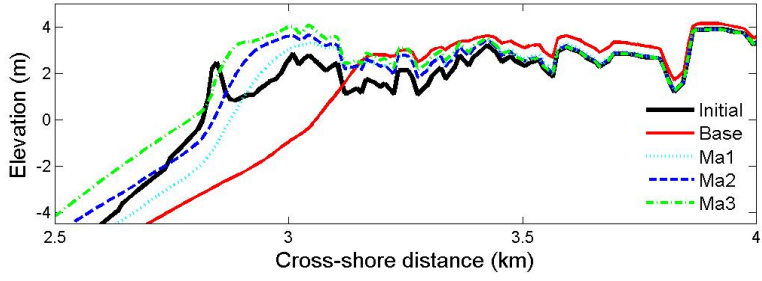

Figure 8. Cross-shore variation in predicted bed elevation for the base case and three cases of varying mangrove stem densities (see table 1 for explanation of cases).

CONCLUSION

Coastal communities at risk from tsunami inundation can benefit from a variety of man-made and natural defense structures. How helpful a particular coastal defense may be depends on many factors, and a validated process-based numerical model can be a very powerful tool in assessing the efficacy of various defense strategies. For "soft" defense structures such as sand dunes or fringing coastal forests, the feedback between the hydrodynamics, sediment transport, and morphological change can be critical. Laboratory experiments or models with fixed beds may not capture the important morphological changes that result from tsunami inundation, and that could have a significant impact on interpreting the usefulness of a particular structure. In the case of a fringing mangrove forest, the forest itself may modify the hydrodynamics and sediment transport enough to change the shape of the coast. In the example forest simulated here, the forest causes the beach to aggrade instead of erode, modifying the energy exchange as the tsunami impacts the coast.

ACKNOWLEDGEMENTS

Funding for this work came from the U.S. Geological Survey, Coastal and Marine Geology Program. We appreciate the efforts in the field of Andrew Moore, Robert Morton, Peter Ruggiero, Lori Dengler, Brentwood Higman, Widjo Kongko and Eko Yulianto. We also thank Andrew Stevens for assistance with the figures. Dirk-Jan Walstra and Edwin Elias contributed valuable conversations and Doug George and Andrew Stevens provided constructive comments to improve the manuscript.

REFERENCES

Baptist, M. (2005). Modelling floodplain biogeomorpholgy, Delft University Press, Delft, ISBN: 90-407-2582-9.

Dekker, F. (2006). Hydrodynamics and Morphodynamics in and around Mangrove

Forests, M.Sc Thesis, WL | Delft Hydraulics Report no. Z4158, Delft, The Netherlands.

Gelfenbaum, G., Lesser, G., Jaffe, J., Moore, A. (2006). Modeling Tsunami Erosion and Deposition, 100th Anniversary Earthquake Conference, Seismological Society of America Annual Conference, San Francisco, CA

Gelfenbaum, G., and Jaffe, B. (2003). Erosion and sedimentation from the 17 July 1998 Papua New Guinea tsunami. Pure and Applied Geophysics, v. 160, no. 10-11, p. 1969-1999

Gelfenbaum, G., Roelvink, J.A., Meijs, M., Buijsman, M., and Ruggiero, P. (2003). Process-based morphological modeling of Grays Harbor inlet at decadal time scales. Conference Proceedings Coastal Sediments '03, 15 pp.

Goff, J., Liu, P.L., Higman, B., Morton, R., Jaffe, B.E., Frenando, H., Lynett, P., Fritz, H., and Synolakis, C., (2006). The December 26th 2004 Indian Ocean Tsunami in Sri Lanka, Earthquake Spectra, v. 22, S3, p. S155-S172.

Harada, K., and F. Imamura (2005). "Effects of Coastal Forest on Tsunami Hazard Mitigation – A Preliminary Investigation" In Tsunamis: Case Studies and Recent Developments, ed. Kenji Satake, Springer, New York, Series VIII, Vol. 23.

Jaffe, B.E., Borrero, J.C., Prasetya, G.S., Dengler, L., Gelfenbaum, G., Hidayat, R., Higman, B., Kingsley, E. Lukiyanto, McAdoo, B., Moore, A., Morton, R., Peters, R., Ruggiero, P., Titov, V., Kongko, W. and Yulianto, E. (2006). The December 26, 2004 Indian Ocean Tsunami in Northwest Sumatra and Offshore Islands, Earthquake Spectra, v. 22, S3, S105-S136.

Lesser, G. R., Roelvink, J. A., van Kester, J. A. T. M., and Stelling, G. S. (2004). "Development and validation of a three-dimensional model" Coastal Engineering, 51, 883-915.

Mazda, Y., Kobashi, D., and Okada, S. (2005). Tidal-scale hydrodynamics within mangrove swamps, Wetlands Eco. Management, Volume 13, Number 6 .

Moore, A., Nishimura, Y., Gelfenbaum, G., Kamataki, T., and Triyono, R. (2005). Sedimentary deposits of the 26 December 2004 tsunami on the northwest coast of Aceh, Indonesia: Earth, Planets, and Space, v. 58, p. 253-258.

Roelvink, J. A. (2006). Coastal morphodynamic evolution techniques. Coastal Engineering, Vol. 53, Issues 2-3, pp 277-287.

Stelling, G. S., and S. P. A. Duinmeijer (2003). A staggered conservative scheme for every Froude number in rapidly varied shallow water flows. International Journal for Numerical Methods in Fluids, Vol. 43, No. 12, pp. 1329-1354

Stelling, G.S., and van Kester, J.A.T.M. (1994). On the approximation of horizontal gradients in sigma coordinates for bathymetry with steep bottom slopes. International Journal for Numerical Methods in Fluids 18, 915 – 955.

Uittenboogaard. R, (2003). Modelling turbulence in vegetated aquatic flows, International workshop on Riparian Forest Vegetated Channels: hydraulic, morphological and ecological aspects, 20-22 February 2003, Trento, Italy.

Van Rijn, L. C. (1993). "Transport of fine sands by currents and waves," Journal of Waterway, Port, Coastal and Ocean Engineering, 119(2), 123-143.

Vatvani D., Schrama E.J.O., Kernkamp H.W.J., Boon J.G. (2005). "Hindcast of Flooding caused by Tsunami in Aceh Sumatra." In *Proc. 5th Intl. on Ocean Wave*

Meas. and Analysis (WAVES 2005, Madrid, Spain, July 2005), ASCE Publ., paper 227.

Wu, R.A., Falconer, and J. Struve (2001). Mathematical modelling of tidal currents in mangrove forests, Environmental Modelling & Software, 16, pp 19-29.

www.fao.org/forestry/site/coastalprotection/en (2007). United Nations Food and Agriculture Organization web site

FROM TRANSGRESSION TO REGRESSION; COASTAL EVOLUTION NEAR THE HAGUE, THE NETHERLANDS, AROUND 5000 BP

Ad J.F. van der Spek[1], Jelmer Cleveringa[2], Sytze van Heteren[3]

1. TNO - *Geological Survey of the Netherlands*, P.O. Box 80015, 3508 TA Utrecht, The Netherlands *and* Delft University of Technology, Faculty of Civil Engineering and Geosciences, P.O. Box 5048, 2600 GA Delft, The Netherlands. ad.vanderspek@tno.nl.
2. Utrecht University, Faculty of Earth Sciences; *present address:* Alkyon Hydraulic Consultancy and Research, P.O. Box 248, 8300 AE Emmeloord, The Netherlands. cleveringa@alkyon.nl.
3. TNO - *Geological Survey of the Netherlands*, P.O. Box 80015, 3508 TA Utrecht, The Netherlands. sytze.vanheteren@tno.nl.

Abstract: The coast of the western part of The Netherlands changed from a transgressive, tide-dominated system, characterised by tidal inlets and tidal basins, into a prograding barrier coast, between 5500 BP and 3200 BP. Ypenburg, SW of The Hague, is situated on the seaward boundary of a transgressive tidal basin which evolved from a predominantly subtidal into a intertidal flat area. During this evolution the landward expansion of the basin stopped. The seaward side of the tidal flat area was reworked and built-up by waves; it formed a transgressive barrier. The limited thickness of the wave-dominated deposits and the lack of shells of open-marine molluscs indicate that this coast line was sheltered from open North Sea conditions. The infilling of the tidal basin and the associated decreasing tidal channel are the onset of coastal regression. The formation of a beach barrier further seaward was the start of coastal progradation.

INTRODUCTION

The Holocene coastal evolution of the western part of The Netherlands changed in nature from transgressive to regressive around 5000 BP (BP means years Before Present). Initially, this area was an open coast, with barriers, tidal inlets and tidal basins, that was shifting landward as a result of rapidly rising relative sea level and insufficient sediment supply. After a decline in the rate of relative sea-level rise (RSLR) after 6000

BP, the tidal basins were filled in with sediment and the tidal inlets gradually closed. The coastal system changed into a series of prograding beach barriers. Until recently, this major change in evolution had not been studied in detail.

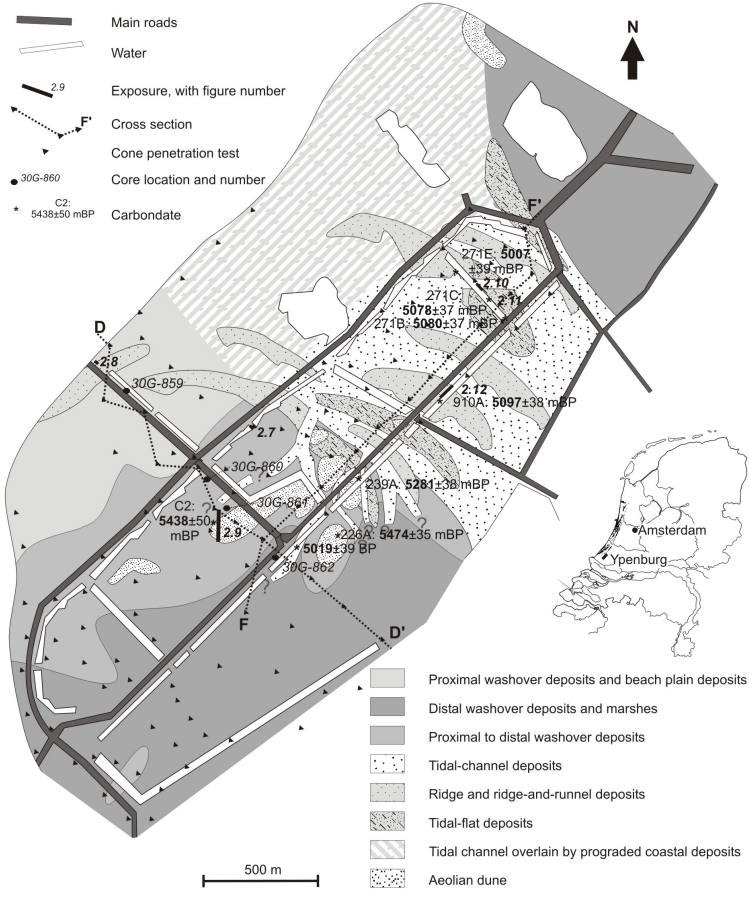

Fig. 1. Detailed map of the surface geology of the Ypenburg area. The top of the sand body in the western part is classified as 'proximal washover deposits'. The barrier series west of Ypenburg is indicated in the small-scale map of The Netherlands.

Ypenburg, a former military airfield, is situated on the boundary between the tidal back-barrier deposits of the transgressive coastal system and the beach-plain and beach-ridge deposits of the subsequent prograded coastal system (Fig. 1). In the subsurface of the Ypenburg area the remnants of the transition from the transgressive coastal system to the prograding coastal system are preserved. The expansion of the city of The Hague in recent years necessitated the transformation of Ypenburg into a suburb. The period of preparation for construction of this area allowed for a study of the deposits that were formed during this shift from transgressive to regressive coastal evolution. An extensive set of Cone Penetration Tests (CPT's) collected for foundation of constructions, temporary trenches, and other data provided an excellent opportunity to study the deposits in this area. Furthermore, Neolithic finds, including a well preserved burial site, triggered extensive archeological research, which provided additional subsurface data and facilitated geological research.

The morphology of transgressive coastal systems depends on the relative magnitude of waves and tides, and on the morphology of the substrate (see Boyd et al., 1992, for discussion and an overview). In general, the preservation potential of transgressive deposits from the seaward edge of the coastal system is very limited, because this part is constantly being eroded in the course of coastal retreat. Deposits from the landward part of the coastal system may escape erosion during transgression, and can be found in the shoreface and shelf sequence (Nummedal and Swift 1987). Prograded coastal sequences are abundant on many modern coasts. The preservation potential of prograded coastal deposits is high compared to that of transgressive coastal systems. A shift from transgression to progradation may results in the preservation of some transgressive deposits from the seaward side of a coastal system. In many cases the shift from transgression to progradation is associated with a shift from tide- to wave-dominated deposition (Davis and Clifton 1987), in most cases caused by the closure of the tidal inlets.

Aim of This Paper

The aim of this paper is to describe the change from a transgressive coastal system into a prograding barrier system on the basis of the analysis of the deposits at Ypenburg, and to summarize this transformation in a conceptual model. This paper will not present the detailed sedimentological analysis of the deposits, since this is partly done in an earlier publication (Cleveringa and Van der Spek 2000), which will be complemented by a paper in preparation.

Large-Scale Evolution of the Holland Coast

The Holland coast changed from an open, tide-dominated system, characterised by tidal inlets and tidal basins, into a prograding barrier coast dissected by the mouths of distributaries of the rivers Rhine and Meuse, between 5500 BP and 3200 BP. This evolution was triggered by the decrease in the rate of relative sea-level rise (RSLR) after 6000 BP to 0.3-0.4 m/century (Fig. 2), which tipped the balance between the creation of

sediment accommodation space by RSLR and sediment supply; the basins expanded less rapidly, allowing the sediment supply to infill the tidal basins (see Beets et al. 1992, and Beets and Van der Spek 2000, for more information). Sediment was supplied by the reworking of the North Sea bed, which included older coastal deposits and Early-Holocene deposits of the river Rhine. The major part of the sediment load of the river Rhine at that time was caught in the alluvial plain; no bed load reached the coastline (Beets and Van der Spek 2000).

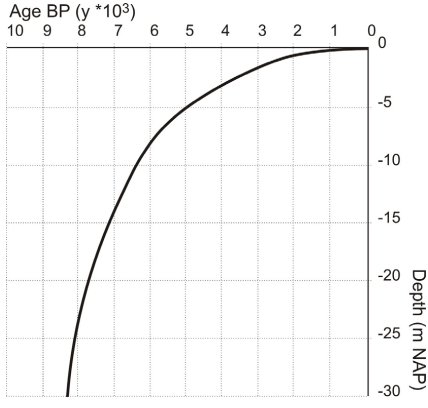

Fig. 2. Trend curve of Holocene relative sea-level rise in the western Netherlands.

When the relative sea level was rising rapidly, intertidal shoals were found bounding the tidal channels. Further away from the channels, where insufficient sediment was deposited, subtidal lagoons with predominant mud deposition existed. Going landward, these lagoons graded into freshwater swamps where peat was formed. With ongoing RSLR these basins expanded landward, leading to coastal erosion and consequent coastal retreat. The coastal retreat caused shoreface erosion which wiped out most of the traces of the former tidal basin deposits. Only the infill of deeply incised tidal inlets and channels escaped this erosion (Rieu et al. 2005).

Infilling with sediment of the tidal basins led to decreasing tidal prisms and, consequently, decreasing tidal inlet and channel dimensions. Finally, the inlets were closed. After closure of the tidal inlet, a stretch of coast started to prograde by formation of beach barriers. The latter were separated by beach plains. The beach barrier series near The Hague is over 8 km wide. This evolution was hitherto not known in detail. The data collected at Ypenburg allowed for a detailed analysis of the mechanism of inlet closure and the associated barrier formation.

Geological Setting of Ypenburg

The study area is located (south)east of The Hague, and borders the suburbs of Rijswijk and Voorburg. The area has been in use as a military airbase and until recently it was inaccessible for geological research. The airbase was closed in the 1990's and the area has been developed as a suburb of The Hague.

East of Ypenburg back-barrier sediments consist of sandy tidal-channel deposits with adjacent mud-flat deposits. The tidal channel system stretches eastward for about 12 km (Van der Valk 1996; De Gans et al. 1998). The back-barrier deposits form part of the transgressive coastal system.

West of Ypenburg the coastal stretch consists of a westward-thickening wedge of prograded coastal-barrier deposits (Van Straaten 1965; De Mulder et al. 1983; Roep et al. 1983; De Gans et al. 1998). The surface morphology of this area is dominated by a series of beach ridges and beach plains. Directly west of Ypenburg the oldest and most landward beach ridge is found, separated from the more westward ridges by a broad beach plain. The ridges are covered with low dunes, while the plains form lows which have subsequently been filled with peat. The most western part of the beach-ridge and beach-plain area is covered with high and relatively young dunes. The beach-ridge pattern can be traced 12 km to the northeast, up to the former mouth of the Old Rhine near Katwijk and Leiden. This branch of the Rhine was the main Rhine outlet from approximately 4300 BP until about 2900 - 2600 BP, when the Vecht became the active branch of the Rhine (Törnqvist 1993; Berendsen and Stouthamer 2001).

The deposits at Ypenburg can successfully be correlated with the succession found in a temporary exposure c. 3 km southwest of Ypenburg that has been described by Van der Valk (1996). This pit was deeper (down to 8 m - NAP) than any of the trenches in the Ypenburg area. The sandy coastal deposits in the construction pit are the equivalent of the sandy deposits in the western part of Ypenburg.

METHOD

Data on the subsurface of the Ypenburg area are derived from four undisturbed cores, numerous hand drillings, sections from trenches and pits, and a large number of cone penetration tests (CPT's). Cone penetration tests measure the resistance of the subsurface to vertical stress (cone resistance, indicated in Fig. 3) and torque stress. The ratio between vertical stress and torque stress gives a friction parameter. The combination of cone resistance and the friction parameter is a measure of the lithology (Amorosi and Marchi 1999, and references therein). Coarser sediment grain sizes cause higher resistance- and friction values. The inferred lithology from the CPT's can be verified with the lithology found in the continuously-core boreholes and sections from trenches. In this way CPT's can be used for stratigraphic correlations and sedimentological interpretations (Westerhoff et al. 1987; Beets et al. 1996; Amorosi and Marchi 1999). The top of the sedimentary sequence could be studied and sampled for radiocarbon dating in ditches and trenches dug for pipelines, cables, and dewatering

purposes. During preparation of the construction sites, extensive peat layers, including fossilized fully-grown oak trees, were removed, revealing the morphology of the original coastal landscape. This morphology included small-scale eolian dunes which showed abundant archeological traces and artefacts, reflecting intensive inhabitation.

Mollusc shells and tree leafs were collected from cores and trenches to determine the time of deposition with AMS radiocarbon (^{14}C) dating. Where possible, in-situ doublets of *Scrobicularia plana* were collected. Otherwise, doublets or undamaged single shells with remnants of the periostracum (the tissue covering the living shell) were taken. The doublets of *Scrobicularia* were found in living position within the sediment. All other shells were transported to their final resting-place, so their age is higher than the age of the site of deposition. However, the presence of periostracum on the selected shells indicates that transport and reworking can only have been limited. Therefore, radiocarbon ages will not deviate too much from the actual ages of deposits. The tree leafs were found within a clay layer among numerous other leaves and plant remains. The perfect condition of the leaves suggests that they have not been transported over a long distance and that their age is similar to the age of the sediment in which they were buried. A series of 38 shell samples and 1 tree leaf was dated. All ^{14}C ages on shells were corrected for the marine reservoir effect, which is 402 years for the North Sea. Ages are given in radiocarbon years BP (Before Present) throughout the text.

RESULTS

Geometry of Sediment Bodies

The CPT's facilitated the mapping of the extension and thickness of sand bodies in the area under study. In Fig. 3 two cross-sections are shown that were based on the CPT's. All CPT's show an abrupt increase in cone resistance around 15 – NAP. This jump indicates the top of the sandy Pleistocene deposits. All overlying deposits are of Holocene age. From East to West the following architecture is found. In the eastern part of cross-section D-D' (CPT's yp-65 and yp-PB8) continuous low friction values are found, indicating a sequence of about 10 m of muddy / clayey deposits with a very low sand content. In the western part of the cross-section a thick sand body is found from 12 m below NAP (NAP is the Dutch ordnance level called Nieuw Amsterdams Peil) upwards. This sand body can be traced to the east, in which direction it becomes thinner and less sandy. The CPT's yp-112 to 121 show interfingering of the thinning sand layers with the fine-grained deposits.

In the northern part of Ypenburg, another sandy sequence is found (cross-section F-F'; from yp-41 northwards). Within this sand body the CPT's yp-43 and yp-116 show highly variable resistances, indicative for alternations of sand and clay layers, reaching down to over 20 m. This pattern indicates the fill of a channel that has cut into the underlying Pleistocene sediments.

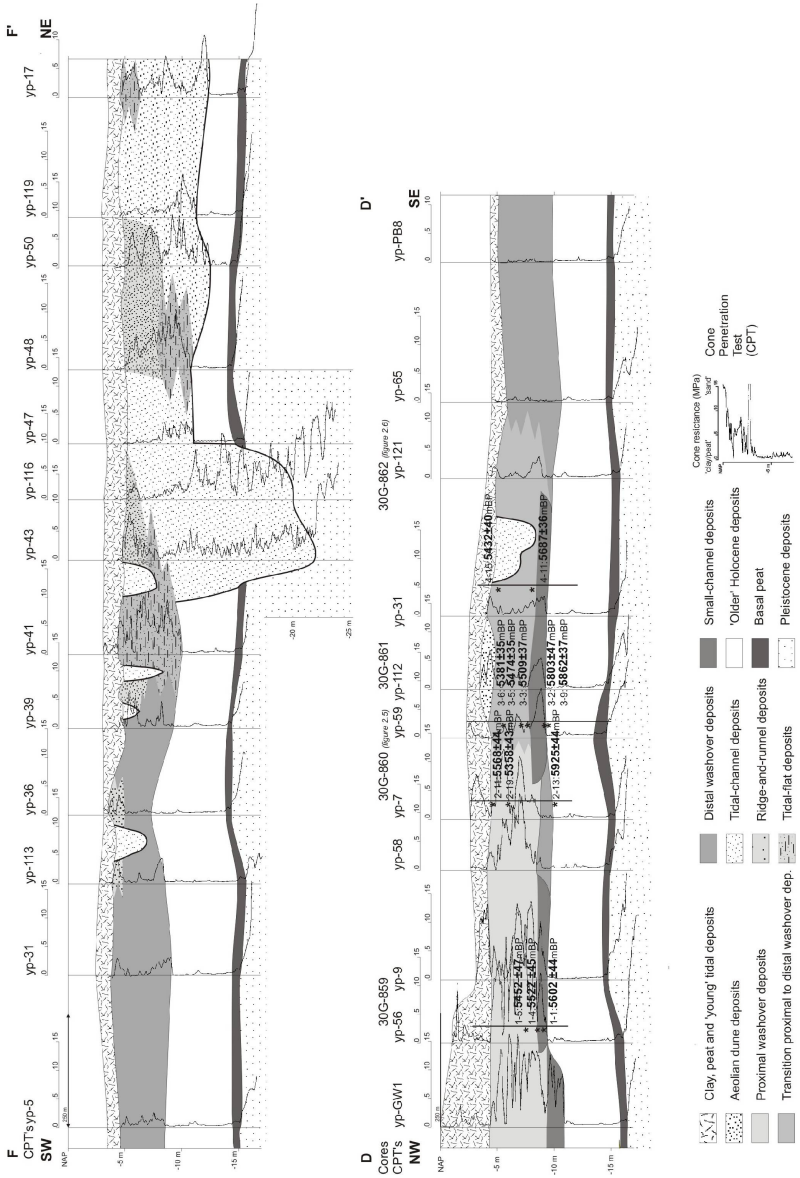

Fig. 3. Cross-sections normal (D-D') and parallel (F-F') to the paleo-shoreline at Ypenburg. The cross-sections are based on CPT's and four cores. See Fig. 1 for location.

Four continuously cored drilholes have been made along cross-section D-D' in order to sample all relevant deposits.

Sedimentary Sequence

This section describes the elementary characteristics of the deposits in the subsurface of Ypenburg, *viz.* lithology, major sedimentological elements, thickness and age (based on the ^{14}C ages), followed by the interpretation of the depositional environment. These descriptions are based on the drillings and field observations. Figure 4 shows an NW-SE cross-section based on the drillings.

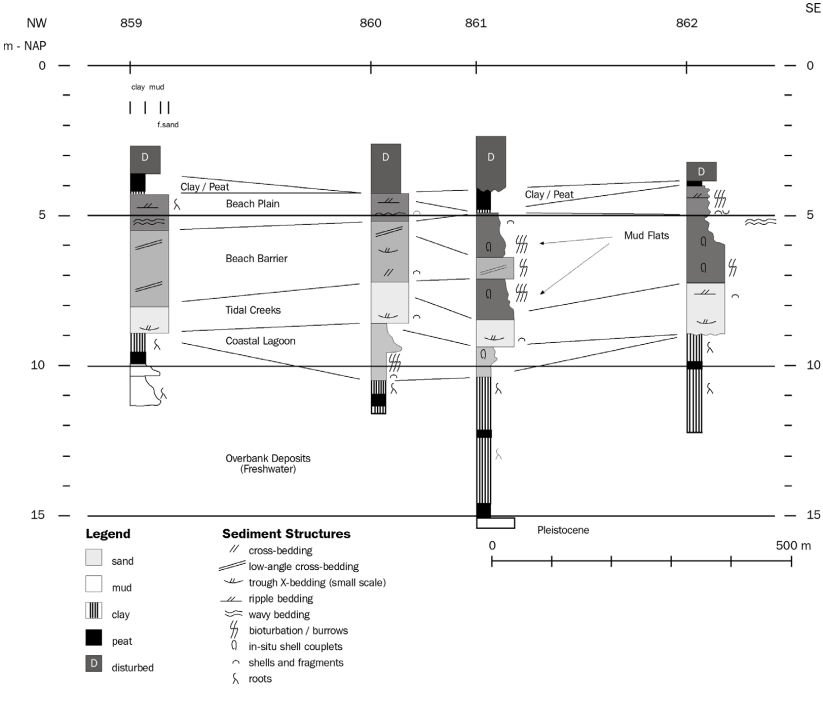

Fig. 4. Northwest-southeast cross-section of the sediment sequnce at Ypenburg, on the basis of 4 continuously-cored borings. See Fig. 1 for location.

The sediment sequence starts with a basal peat layer which is overlain by clay layers, intercalated with peat layers. Locally this sequence incorporates bodies of fine-grained sands. The clay usually contains plant remains. The unit is up to 5 m thick and deposited before c. 6000 BP. This sequence is interpreted as overbank deposits laid down on the alluvial plain of the river Rhine and in the most landward, freshwater parts of tidal basins.

Locally, see cores 860 and 861 in Fig. 4, the freshwater clays are overlain by mud which can be bioturbated, grading into sandy mud / muddy sand. Layers of small-scale sand lenses occur in the mud. The fauna is dominated by the mud snail *Hydrobia ulvae*. The deposit is 1 to 2 m thick and has an age of 5800 to 5900 BP. It is the deposit of a brackish, subtidal environment, possibly a coastal lagoon.

The freshwater clays and lagoonal muds are erosively overlain by a 1 to 1.5 m thick unit of cross-bedded, fine-grained sand with clay flasers and reworked shells of the Peppery Furrow Shell *Scrobicularia plana*. Shells of the Blue Mussel *Mytilus edulis*, the Baltic Tellin *Macoma balthica* and the Cockle *Cerastoderma edule* are found as well. These sands are dated at 5500 to 5700 BP. The were laid down by migrating tidal creeks or channels, possibly in a tidal-flat environment.

In the eastern part of Ypenburg these sandy channel deposits grade upwards into strongly bioturbated (sandy) muds with in-situ (layers of) shell couplets of *Scrobicularia plana*. These muds are 1.5 to 2 m thick and 5400 to 5600 radiocarbon years old. These are mudflat deposits.

The above mentioned sand body in the western part of Ypenburg consists of predominantly (low-angle) cross-bedded and laminated fine-grained sands, intercalated with layers of ripple bedding. Shells of predominantly *Macoma*, but also of *Cerastoderma* and *Mytilus* and, to the top of the sequence, *Spisula sp*. (the Trough Shell) occur on the foresets or dispersed within the sediment. This sandy unit is up to c. 3 m thick and was dated at 5450 to 5000 BP. The type of cross-bedding indicates the influence of swash and back-wash of breaking waves during deposition of the sand. The appearance of *Spisula* towards the top is an indication for an increasing (open) marine conditions (*Spisula* is found on the open North Sea shoreface in the present-day situation). Whether these sands were laid down on tidal flats along a tidal channel in which waves could penetrate from the North Sea or on a beach, can not be determined on the basis of cores. Equivalent deposits deposits from a pit about 3 km to the southwest were described by Van der Valk (1996) as beach deposits.

Both these sands and the mudflat deposits grade into alternations of cm-thick layers of sand and mud, (sub-)horizontally laminated, that can show intercalated layers and dispersed shells of *Macoma*- and *Scrobicularia*, some bioturbation and occurrence of rootlets. The sequence as about 1 m thick and is dated at 5100 to 5200 BP. Locally, these deposits are overlain by thicker sandy units with intercalated soils. The sand-mud alternations are interpreted as high-intertidal to supratidal beach-plain deposits, locally overlain by wash-over deposits and eolian dunes.

The second sand body in the northern part of Ypenburg has not been sampled by drilling. Observations on the top of this sequence in trenches show a lateral alternation of cross-bedded and bioturbated sandy deposits interpreted as tidal flats and ridge-and-runnel structures. The latter are erosively overlain by channel-like bodies of muddy sediments

that show concentric layering. These deposits are dated at 5000 - 5100 BP. The above described sequence is overlain by a clay layer that grades into peat.

INTERPRETATION AND DISCUSSION

The sedimentary sequence starts with a basal peat layer that was formed by deteriorating drainage, a consequence of the rising sea level. The overlying root-bearing clay with intercalated peat layers indicates continued drowning of the area. Since Ypenburg is situated at the northern boundary of the flood plain of the river Rhine, it is not clear whether these sediments were deposited in an alluvial or in a tidal-basin setting. The overlying lagoonal deposits that are overlain by tidal-flats indicate the approach of the North Sea. The tidal channel that cuts down into the Pleistocene subsurface in the northern part of Ypenburg is the major tidal channel in the area. It is known as the Rijswijk-Zoetermeer channel (Van der Valk, 1996). The tidal flats were bounding this channel. With transgression waves from the North Sea could gradually penetrate into the main tidal channel, influencing the sedimentation along the channel edges. The wave-built sand body in the western part of Ypenburg suggest the existence of a SW-NE running beach. However, the limited thickness of the sand body (the wave influenced interval is 2.5 m thick at the most), and the absence of shells of *Spisula*, the most common open marine mollusc species on the Dutch North Sea coast, suggest that this beach was not subjected to wave conditions normal at North Sea beaches (NB around 5500 BP wave conditions in the southern North Sea were only slightly less energetic as today (Stive 1987; Van der Molen and De Swart 2001). This suggest a sheltered position of this beach, protected from the bigger waves, possibly by a very shallow offshore morphology. The latter can either be caused by rapid coastal retreat or by sediment supply from the southwest, were older Holocene alluvial deposits were being reworked by marine processes (Van Heteren et al. 2003; in revision).

The deposition in the tidal basin eastward of the beach and tidal flats resulted in siltation and a decreasing tidal prism. The latter caused a decrease in dimensions of the tidal channel in the northern part of Ypenburg. The channel gradually became narrower and shallower, allowing the bounding tidal flats to expand. Continued sedimentation in the tidal flats, now protected by the beach in the west, resulted in vertical aggradation into a high-intertidal to supratidal environment. Close to the beach and the tidal channel this will have been a beach plain, further basinward this will haven been a salt marsh. The vertical aggradation, despite the ongoing rise in sea level, is caused by the positive sediment balance of the area. In the beach plain wash-over occurred during storm surges. During dry spells the wind could built small-scale dunes.

The architecture of the deposits shows a sandy to muddy tidal-flat area, bounding a tidal channel. On the seaward side, these tidal flats were reworked by waves, suggesting a position very close to a tidal inlet. The main tidal channel in the northern part of Ypenburg filled in and changed into a intertidal flat area. Although ridges and runnels have been found here, it is not clear whether sand transport by waves caused longshore transport and spit formation, contributing to the infilling of the channel. The limited

wave activity caused by the sheltered position (see above) makes significant spit formation unlikely.

During the final stage of evolution, from 5200 BP onwards, a large beach barrier formed about 2 km to the west of Ypenburg. This increased the sheltered position of Ypenburg and the area east of it, enhancing sedimentation. Only after the completion of the new barrier, the tidal inlet closed, leaving the tidal flats/beach plain as a relict feature. Subsequently, the tidal basin rapidly changed into a coastal peat bog.

The change from a transgressive to a prograding coastal system, despite a rate of RSLR that was 2-3 times higher than at present, was the result of an extensive supply of sediments from the southwest, were older Holocene alluvial deposits were being reworked by marine processes (Van Heteren et al. 2003; in revision).

CONCLUSION

Ypenburg is situated on the seaward boundary of a transgressive tidal basin which evolved from a predominantly subtidal into a intertidal flat area. During this evolution the landward expansion of the basin stopped. The formation of a wave-influenced sand body indicates the position of the coast line. The limited thickness of the wave-dominated deposits and the lack of shells of open-marine molluscs indicate that this coast line was sheltered from open North Sea conditions. This sand body can be considered a transgressive barrier. The infilling of the tidal basin and the associated decreasing tidal channel are the onset of coastal regression. The formation of a beach barrier further seaward is the start of coastal progradation which eventually resulted in a barrier sequence of over 8 km wide.

ACKNOWLEDGEMENTS

We would like to thank Hans Koot, the principal archeologist of the city of Rijswijk, who led the excavations at Ypenburg for facilitating and supporting the field work. Bastian van Dijck was a great help in the field, especially during the hand drilling campaign. Our understanding of the geology of Ypenburg and its surroundings improved significantly from discussions with Dirk Beets and Bert van der Valk.

REFERENCES

Amorosi, A., and Marchi, N. (1999). "High-resolution sequence stratigraphy from peizocone tests: an example from the Late Quaternary deposits of the southeastern Po Plain," *Sedimentary Geology* 128, 67-81.

Beets, D. J., and Van der Spek, A. J. F. (2000). "The Holocene evolution of the barrier and the back-barrier basins of Belgium and the Netherlands as a function of late Weichselian morphology, relative sea-level rise and sediment supply," *Geologie en Mijnbouw / Netherlands Journal of Geosciences* 79, 3-16.

Beets, D. J., Van der Valk, L., and Stive, M. J. F. (1992). "Holocene evolution of the coast of Holland," *Marine Geology* 103, 423-443.

Beets, D. J., Roep, T. B., and Westerhoff, W. E. (1996). "The Holocene Bergen Inlet:

closing history and related barrier progradation" In: D.J. Beets, M.M. Fischer and W. de Gans (eds.), *Coastal studies on the Holocene of the Netherlands, Mededelingen Rijks Geologische Dienst* 57, 97-131.

Berendsen, H. J. A., and Stouthamer, E. (2001). "*Palaeogeographic development of the Rhine-Meuse delta, The Netherlands,*" Koninklijke Van Gorcum, Assen, 268 p.

Boyd, R., Dalrymple, R. W. and Zaitlin, B. A. (1992). "Classification of clastic coastal depositional environments," *Sedimentary Geology* 80, 139-150.

Cleveringa, J., and Van der Spek, A.J.F. (2000). "Deposition and erosion during final transgression and initial progradation; Holocene coastal deposits at Ypenburg (Rijswijk, The Netherlands), in: J. Cleveringa, *Reconstruction and modelling of Holocene coastal evolution of the western Netherlands. Geologica Ultraiectina* 200, p. 25-55. Utrecht.

Davis, R. A., and Clifton, H. E. (1987). "Sea-level change and the preservation potential of wave-dominated and tide-dominated coastal sequences," In: D. Nummedal, O. H. Pilkey and J. D. Howard (eds.), *Sea-level fluctuation and coastal evolution, Society of Economic Paleontologists and Mineralogists Special Publication* 41, p. 167-178. Society of Economic Paleontologists and Mineralogists, Tulsa, OK.

De Gans, W., Kok, H., Zwaan, H., and Metten, R. M. (1998). "*Simplified Geological Map of The Hague and vicinity,*" Netherlands Institute of Applied Geoscience TNO - *National Geological Survey*, Haarlem (in Dutch).

De Mulder, E. J. F., Pruissers, A. P., and Zwaan, H. (1983). "Quaternary Geology of The Hague and vicinity,". In: E. F. J. de Mulder (ed.), *De Bodem van 's-Gravenhage, Mededelingen Rijks Geologische Dienst* 37-1, p. 12-43, Haarlem (in Dutch).

Nummedal, D., and Swift, D. J. P. (1987). "Transgressive stratigraphy at sequence-bounding unconformities: some principles derived from Holocene and Cretaceous examples." In: D. Nummedal, O. H. Pilkey and J. D. Howard (eds.), *Sea-level fluctuation and coastal evolution, Society of Economic Paleontologists and Mineralogists Special Publication* 41, p. 129-143. Society of Eeconomic Paleontologists and Mineralogists, Tulsa, OK.

Rieu, R., Van Heteren, S., Van der Spek, A. J. F., and De Boer, P. L. (2005). "Development and preservation of a mid-Holocene tidal channel network offshore the western Netherlands," *Journal of Sedimentary Research* 75 (3), 413-423.

Roep, T. B., Van de Plassche, O., Van der Valk, L., and Ruegg, G. H. (1983). "Sedimentology of the beach-barrier deposits below The Hague and Rijswijk." In: E. F. J. de Mulder (ed.), *De Bodem van 's-Gravenhage, Mededelingen Rijks Geologische Dienst* 37-1, p. 137-156, Haarlem (in Dutch).

Stive, M. J. F. (1987). "Main report Kustgenese: Large-scale evolution of the Dutch Coast," Report Rijkswaterstaat, Tidal Waters Division, The Hague, 83 p. (in Dutch).

Törnqvist, T. E. (1993). "*Fluvial sedimentary geology and chronology of the Holocene Rhine-Meuse delta, The Netherlands*," PhD Thesis, Utrecht University, Utrecht, 169 p.

Van der Molen, J., and De Swart, H. E., (2001). "Holocene wave conditions and wave-induced sand transport in the Southern North Sea," *Continental Shelf Research* 21, 1723-1749.

Van der Valk, L. (1996). "Geology and sedimentology of Late Atlantic sandy, wave

dominated deposits near The Hague (South-Holland, the Netherlands): a reconstruction of an early prograding coastal sequence." In: D.J. Beets, M.M. Fischer and W. de Gans (eds.), *Coastal studies on the Holocene of the Netherlands, Mededelingen Rijks Geologische Dienst* 57, 210-229.

Van Heteren, S., van der Spek, A. J. F., and De Groot, T. A. M., (2003). "Architecture of a preserved Holocene tidal complex offshore the Rhine-Meuse river mouth, The Netherlands," *Proceedings Coastal Sediments '03*, CD-ROM Published by East Meets West Productions, Corpus Christi, TX ISBN 981-238-422-7; 12 p.

Van Heteren, S., van der Spek, A. J. F., and De Groot, T. A. M., (in revision). "Architecture of a preserved Holocene estuarine complex offshore the Rhine-Meuse river mouth, The Netherlands," in revision for *Sedimentology*.

Van Straaten, L. M. J. U. (1965). "Coastal barrier deposits in South- and North-Holland, in particular in the areas around Scheveningen and IJmuiden," *Mededelingen van de Geologische Stichting, Nieuwe Serie* 17, 41-76.

Westerhoff, W. E., De Mulder, E. F. J. and De Gans, W. (1987). "Memoir Geological Map of The Netherlands, scale 1:50.000, Sheet Alkmaar West (19W) and Sheet Alkmaar East (19O)," Geological Survey of The Netherlands, Haarlem, 227 p (in Dutch with English summary).

CHANGING ORIENTATION OF OCEAN-FACING BLUFFS ON A TRANSGRESSIVE COAST, CAPE COD, MASSACHUSETTS

Graham S. Giese[1], Mark B. Adams[2]

1. Provincetown Center for Coastal Studies, 3 Holway Ave., Provincetown, MA 02657, USA. ggiese@coastalstudies.org .
2. Cape Cod National Seashore, US National Park Service, Wellfleet MA 02667, USA. Mark_adams@nps.gov .

Abstract: Erosion of the 24 km-long escarpment cut into the unconsolidated Pleistocene glacial deposits of outer Cape Cod, Massachusetts, by wave action during the Holocene transgression has supplied sediment for construction of spits and barrier beaches to its north and south. The major escarpment landforms produced by the erosion are steep coastal bluffs (upper c. 20 m), beaches, and a more gently sloping shoreface (to a depth of c. 10 m). Using differential GPS methods supplemented with LIDAR data we have re-surveyed the bluff portion of the escarpment along cross-shore transects originally surveyed in 1887-1889. Comparison of the surveys indicates that the bluffs erode at an overall century-scale rate of c. 0.8 m/yr, and that the erosion rate increases alongshore north-to-south by a factor of two. We suggest that the resulting change in coastal orientation results from relative sea level rise over the outer continental shelf and associated increase in wave energy from the southeast.

INTRODUCTION

Coastal bluff erosion is significant to environmental management largely due to two concerns: the threat it poses to coastal development, and the quantity and quality of sediment that it supplies to the littoral system. These concerns have motivated recent studies of bluff retreat on both ocean coasts of the United States as well as along the shores of the Great Lakes (Young and Ashford 2006; Kelley and Dickson 2000; Jibson and Odum 1994).

The focus of this study, the eroding east-facing bluffs of outer Cape Cod, Massachusetts, lie within the Cape Cod National Seashore (CCNS), and for that

reason their impact on coastal development is a relatively minor concern. They are critically important, however, as a sediment source. The bluffs together with the adjacent beach and shoreface (which extends to depths of more than 10 m) comprise a 24 km-long escarpment cut into unconsolidated Pleistocene glacial deposits by wave action during the Holocene transgression.

Erosion of the bluffs and shoreface is the sole source of sediment, not only for the beaches along the shoreline of the escarpment, but also for the spits and barrier beaches which make up the landforms north and south of the escarpment (Figure 1). Management of these depositional features and the bays, harbors and marshes associated with them is a matter of major concern for the CCNS and the region's municipalities.

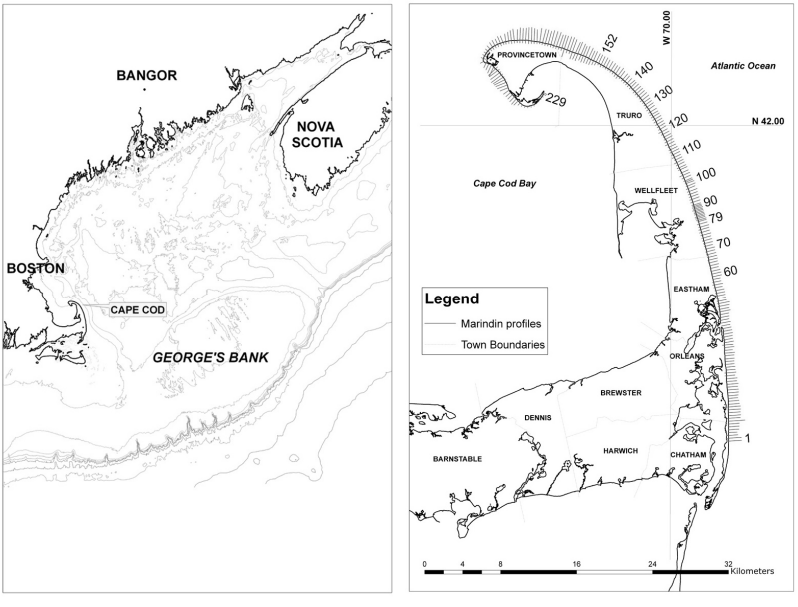

Fig.1. Cape Cod and the Gulf of Maine. The eroding bluffs surveyed in this study extend from "Marindin profile" MS56 to MS144.

While escarpment erosion appears to have been continuous throughout the transgression, construction of the depositional landforms does not, because the rates and direction of sediment transport have varied with sea level. For example, Provincetown Hook, north of the escarpment, is believed to have formed during the past approximately 6,000 years as the result of increased wave energy from the southeast due to increasing sea level over the outer continental shelf (Zeigler, et al. 1965).

Zeigler et al. (1964a, 1964b, 1965), using methods similar to (but technologically less advanced than) those described below, estimated the mean annual erosion rate of the bluffs to be approximately 0.8 m/yr over a seventy-year period. They also concluded that the bluff retreat rate remained constant alongshore for most of the escarpment. In general the reports suggested a steady state relationship between wave climate, escarpment erosion and sediment supply to landform systems to its north and south .

Pressing coastal management concerns together with restricted budgets for structural operations have motivated recent efforts to review and extend existing understanding of the physical underpinnings of sediment processes along this coast. Examples include studies of the region's beaches by O'Connell, Thieler and Schupp (2002) and of the lower shoreface and inner shelf by Poppe et al. (2006). The importance of re-examining the century-scale retreat of the bluff was recognized by Allen et al. (2001) who initiated the study which led to the present report.

METHODS

Henry L. Marindin (1889, 1891) surveyed 229 coastal profiles, normal to the shoreline of outer Cape Cod and reported latitude, longitude, azimuth and elevation for each line. For the present study, Marindin's profiles were resurveyed using Global Positioning System (GPS) receivers for navigation and measurement. To prepare the reported locations for use with GPS, Marindin's locations were converted from the original horizontal datum to the 1927 North American Datum (NAD27) by subtracting 0.6 seconds of latitude. This adjustment is based on available reference coordinates from local benchmarks (Curtis Crow, Massachusetts Division of Highways Geodesist, personal communication).

The results were then transformed to the current North American Datum of 1983 (NAD83) using ESRI ArcGIS software and loaded into Trimble differential GeoXT and Pathfinder ProXR GPS receivers for navigation. The GPS receiver's navigation mode reports distances from the origin station along the azimuth line. Distances from origin to current feature locations were recorded along each of profile (e.g., bluff crest, bluff toe, beach berm, swash zone). These distances were used to construct current profiles (without elevations) for comparison to the corresponding feature locations reported by Marindin.

Elevations were acquired for a few profiles using Trimble 5700 Real Time Kinematic GPS with a GPS base station for precise correction. Base station locations were corrected using the National Geodetic Survey's Online Positioning Service (OPUS). GPS locations were corrected using Trimble Geomatics Office software. Also, a complete set of elevations for all profiles was extracted from LIDAR data collected May 4, 2005, for the National Park Service (NPS) through a cooperative effort with NASA and the USGS Center for Coastal Studies in St Petersburg, Florida.

We report the century-scale bluff retreat in terms of change in location of the bluff

toe. The bluff toe was chosen as diagnostic of bluff retreat because it was specified in the 19th Century surveys, its position can be accurately determined in the field (the landward edge of marine deposits), and the negative feedback provided by bluff slumping produces a remarkably smooth alongshore lineation unequaled by other horizons.

RESULTS

The set of bluff toe locations as determined by our 2003-2004 survey is presented in Figure 2a. The data points with closer than usual spacing correspond to regions of special concern to the original surveyors (Marindin 1889). Larger gaps between data points occur at locations for which we encountered problems in the original data set. Two major sources of such problems were missing designations of the exact location of the bluff toe and obvious mistakes in the profile descriptive information (e.g., clearly erroneous latitude or longitude data).

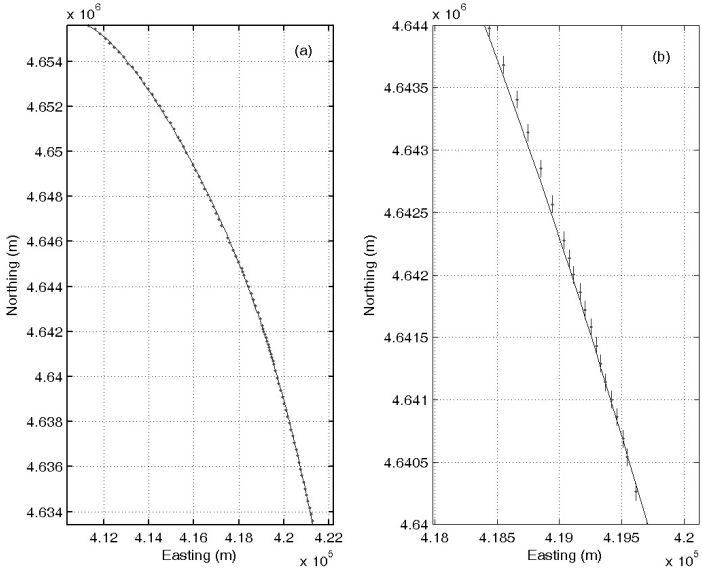

Fig.2. (a) Bluff toe locations from 2003-2004 surveys. (b) Enlargement of fitted polynomial with error bars described in text.

The general smoothness of the line of bluffs as defined by the bluff toe location is illustrated by the associated line, a fourth-order polynomial of "best fit" to the data. Deviations from the smooth curve are illustrated in Figure 2(b), which is an enlargement of one section of the first plot and includes error bars estimated to include at least 50% of the data points.

Century-scale change in location of the bluff toe was determined, as explained above, by the difference between the location of the feature along specific profiles in the 1887-1889 surveys and its location in the 2003-2004 surveys. The change was then expressed in terms of a long-term mean annual retreat rate by dividing the total change by the intervening time period. The results for specific profiles are represented in Figure 3, a scatter plot of data points plotted with respect to their alongshore distance north of the Marindin Station #1 (MS1).

Averaged over the entire length of the bluff section, 23.7 km, the mean value of the individual data points is 0.79 m/yr. However, Figure 3 indicates an overall northward decrease in bluff retreat over the time period between surveys. The oblique solid regression line represents the best approximation to the data using a linear relationship between the variables; the dashed and dotted lines are offset from the regression line by one and two standard deviation units respectively. The slope of the regression line indicates that the century-scale retreat rate decreases by approximately one-half along the section, from 1.03 m/yr to 0.53 m/yr, south to north.

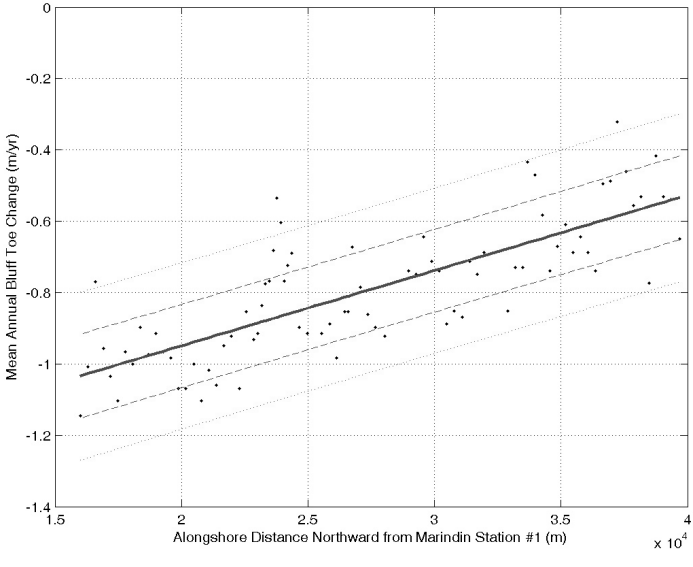

Fig.3. Scatter plot of century-scale bluff retreat rate showing linear regression line and that line extended by one and two standard deviation units.

To summarize, combining the results of our surveys during 2003-2004 with those of Henry Marindin's surveys during 1887-1889 to determine the century-scale change in the line of coastal buffs, we find that as measured at their toe they have retreated

overall at an average rate of 0.79 m/yr when expressed in terms of a long-term annual mean, and the rate of retreat varies linearly alongshore, decreasing by about one-half south-to-north over the 23.7 km section.

DISCUSSION

Coastal Orientation

While an average long-term retreat rate for the entire bluff section of approximately 0.8 m/yr is consistent with results of earlier studies (Uchupi et al. 1996), the previous results concluded that the retreat rate is constant alongshore for all but the northernmost part of the section (Zeigler et al. 1964b) in marked contrast to the present results. Nevertheless the finding of a northward decrease in bluff erosion does not come as a complete surprise. Geological reconstructions have indicated alongshore changes in coastal retreat during the Holocene (Uchupi et al. 1996), and studies of contemporary beach changes (O'Connell et al. 2002) show increasing erosion toward the south.

In addition, an alongshore change in bluff retreat rate as opposed to a constant rate may be more consistent with the overarching hypothesis of Zeigler et al. (1965): that relative sea level plays a dominant role in coastal processes along this shore by altering the depth of the extensive "Georges Bank" shoal on the outer continental shelf, thereby altering wave energy input from the southeast (North Atlantic basin). Applying this hypothesis, Zeigler et al. (1965) ascribed initiation of Provincetown Hook's development about 6,000 years ago to a reversal in direction of sediment transport, from southward to northward, resulting from submergence of George's Bank.

However, regional relative sea level has risen some 10 m since that time (Uchupi et al. 1996), presumably increasing wave energy from the southeast and thereby increasing the rate of net northward sediment flux. The expected coastal response with respect to orientation would be clockwise rotation (Giese 1964) which is consistent with the present results.

Net Sediment Flux

While such a change in the coastline orientation would provide negative feedback to counter the increased net northward sediment flux, a question arises as the relative rates of the two. The observed linear change in bluff retreat of about 0.5 m/yr over a distance of 23.7 km would produce a change in orientation of only about 1.2 degrees per 1,000 years. How would the resulting net flux decrease compare with the flux increase that would otherwise result from continuing relative sea level rise? The question has practical implications, especially in light of expected future increases in the rate of global sea level rise.

The answer requires information concerning wave climate and sediment flux not presently available as well as an analysis of the dynamics of their interaction. We

can, however, gain insight into the problem using recent LIDAR data and a simple kinematic analysis (Singh 2002).

Here we will consider the net alongshore sediment flux, that is, the net annual volume rate of alongshore transport, Qn, at a single location as the difference between the northward and southward annual fluxes at that point. Alongshore distance, y, will be positive toward the north. Were sediment volume to be conserved with no losses (sources or sinks) off- or on-shore, the alongshore gradient (i.e., divergence) of net flux, $\Delta Qn/\Delta y$, would equal the negative of the annual change in cross-shore area at that location, $\Delta A/\Delta t$.

For example, at a specific location a 1 cubic meter per year net flux increase per meter alongshore would result in a 1 square meter per year decrease in cross-sectional area, assuming sediment volume to be conserved. In our case, however, an estimated 18 % of the eroding glacial "source" material is lost offshore and does not contribute to depositional features (Zeigler et al. 1964a). Thus the relationship in this case can be expressed:

$$\Delta Qn/\Delta y = -0.82\,(\Delta A/\Delta t) \qquad (1)$$

where Qn = net alongshore sediment flux (m^3/yr); y = alongshore coordinate positive northward (m); A = cross-sectional area between successive "surveys" of individual profiles (m^2); t = time interval between successive "surveys" (yr).

To approximate $\Delta A/\Delta t$ at specific "Marindin lines" for the bluff portion of the sections, we plotted elevation vs. distance derived from the 2005 LIDAR data and compared the resulting profile with that provided by Marindin (1889). For the beach and shoreface sections, we simply translated the 1887-1889 profiles shoreward to match the profiles' bluff toe to the location of that feature as determined in our 2003-2004 surveys. Since all Marindin profiles reached at least a depth of 10 m, our submarine area calculations use a – 10m limit. Figure 4 provides an example of the method as applied to line MS100.

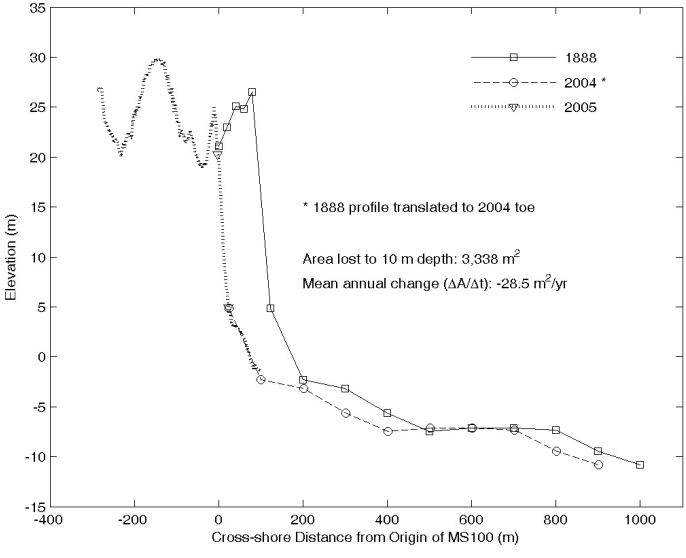

Fig.4. Comparison of cross-shore profiles at station MS100 as determined in 1888 and 2004-2005 (see text for details).

The value of $\Delta A/\Delta t$ for MS100 using this approximation is – 28.5 m^2/yr. Expressed in terms of the alongshore gradient of net flux using equation (1), this is equivalent to a $\Delta Qn/\Delta y$ value of 23.4 m^2/yr. This and the results of similar calculations carried out for several other representative lines are plotted in Figure 5. The large scatter of the values results primarily from the alongshore irregularity of bluff elevation. At MS152 (y = 42.3 x 10^3 m), the LIDAR and Marindin profiles coincide at the shoreline, marking this as the point of maximum net flux (i.e., $\Delta Qn/\Delta y = 0$).

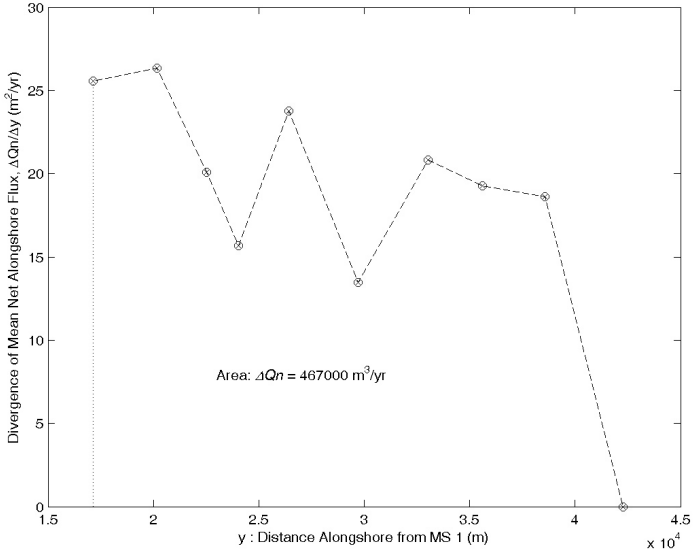

Fig.5. Scatter plot of alongshore divergence of rate of net alongshore sediment flux at selected bluff locations (see text).

Uchupi et al. (1996) estimate the total flux of sediment supplied to the Provincetown Hook as approximately 470,000 m^3/yr. Taking this as the value of the net flux, Qn, at MS152 ($y = 42.3 \times 10^3$ m) we can estimate the reduction of Qn, i.e., ΔQn, at another location southward along the bluff section through numerical intergration of $\Delta Qn/\Delta y$ over the interval of alongshore distance, Δy, between the other location and MS152.

Figure 5 illustrates that the result of this operation carried out between MS60 ($y = 17.2 \times 10^3$ m), which is near the southern limit of the eroding bluff section, and MS152 amounts to a net flux reduction of approximately 467,000 m3/yr. Despite the many approximations and assumptions employed, this suggests that at present, some 6,000 years after the submergence of Georges Bank, most if not all of the material eroded from the bluffs of outer Cape Cod is being transported northward to the Provincelands Hook. We plan to re-survey the bathymetric sections of Marindin's transects in the near future and, using these results, improve our sediment flux calculations for this section of the coast.

CONCLUSION

Results of recent surveys of the outer Cape Cod coast indicate that erosion of the section of exposed bluffs increases by a factor of two between the northern and southern ends of the section. We suggest that this increase and the resulting change in coastal orientation

are the result of continuing submergence of the Georges Bank shoal on the outer continental shelf southeast of Cape Cod. The change in orientation provides negative feedback to increased net northward sediment flux resulting from the shoal's submergence. However preliminary sediment transport calculations indicate that despite the changing orientation, most or all of the sediment supplied by bluff erosion is now transported northward.

ACKNOWLEDGEMENTS

We acknowledge the contributions of our colleague and friend, the late James (Jim) R. Allen, who initiated current resurveys of Henry Marindin's profiles and developed the initial coastal change protocol for the National Park Service's Inventory and Monitoring Program before his untimely passing.

Charles Labash of the University of Rhode Island Environmental Data Center transformed Marindin's coordinates to modern datums. Terri Smith, Dave Spang, Ben Bornstein, and Jim Gallagher provided valuable field assistance. The project has been generously supported from the beginning by the Provincetown Center for Coastal Studies, the Cape Cod National Seashore's Atlantic Research Center and the Town of Chatham. Additional community support was provided by the Cape Cod Five Cents Bank.

REFERENCES

Allen, James R., LaBash., C. T. and August, P. V., (2001). "Monitoring shoreline changes: a protocol for the long-term coastal ecosystem monitoring program at Cape Cod National Seashore," U.S. Geological Survey, Draft Report QX2001-13., 66p.

Giese, G. S. (1964). "*Coastal Orientations of Cape Cod Bay*," Masters Thesis, Graduate School of Oceanography, University of Rhode Island, 70 p.

Jibson, R. W., and Odum, J. K. (1994). "*Rates and Processes of Bluff Recession Along the Lake Michigan Shoreline in Illinois*," U.S. Geological Survey, Denver, CO.

Kelley, J. T., and Dickson, S. M. (2000). "Low-cost bluff-stability mapping in coastal Maine: Providing geological hazard information without alarming the public," *Environmental Geosciences* 7, 46-56.

Marindin, H. L. (1889). "Encroachment of the sea upon the coast of Cape Cod, Massachusetts, as shown by comparative studies, cross-sections of the shore of Cape Cod between Chatham and Highland Lighthouse," *Annual Report of the U.S. Coast and Geodetic Survey, 1889,* Appendix 13, 409-457.

Marindin, H. L. (1891). "On the changes in the shoreline and anchorage areas of Cape Cod (or Provincetown Harbor) as shown by a comparison of surveys made between Cape Cod and the Long Point Lighthouse," *Annual Report of the U.S. Coast and Geodetic Survey, 1891,* Appendix 9, 289-341.

O'Connell, J. F., Thieler, E. R., and Schupp, C. (2002). "New shoreline change data and analysis for the Massachusetts shore with emphasis on Cape Cod and the Islands: Mid-1800s to 1994*," Environment Cape Cod* 5(1), 1-14.

Poppe, L. J., Paskevich, V. F., Butman, B., Ackerman, S. D., Danforth, W. W., Foster, D. S., and Blackwood, D. S. (2006). "Geological interpretation of bathymetric and backscatter imagery of the sea floor off eastern Cape Cod," U.S. Geological Survey Open-File Report 2005-1048, DVD-ROM.

Singh, V. P. (2002). "Is hydrology kinematic?," *Hydrological Processes* 16, 667-716.

Uchupi, E., Giese, G. S., Aubrey, D. G., and Kim, D. J. (1996). "*The Late Quaternary Construction of Cape Cod, Massachusetts: A Reconsideration of the W. M. Davis Model,"* Geological Society of America, Special Paper 309, 69 p.

Young, A. P., and Ashford, S. A. (2006). "Application of airborne LIDAR for seacliff volumetric change and beach-sediment budget contributions," *J. Coastal Research* 22, 307-318.

Zeigler, J. M., Tuttle, S. D., Giese, G. S., and Tasha, H. J. (1964a). "Residence time of sand composing the beaches and bars of outer Cape Cod," *Proceedings 9th Conference on Coastal Engineering,* 403-416.

Zeigler, J. M., Tasha, H. J., and Giese, G. S. (1964b). "Erosion of the cliffs of outer Cape Cod: tables and graphs," Woods Hole Oceanographic Institution Tech. Rep. 64-21, 59 p.

Zeigler, J. M., Tuttle, S. D., Tasha, H. J., and Giese, G. S. (1965). "The age and development of the Provincetown Hook, outer Cape Cod, Massachusetts," *Limnology and Oceanography*, Redfield Volume R289-R311.

MODELING BARRIER ISLAND RESPONSE TO SEA-LEVEL RISE IN THE OUTER BANKS, NORTH CAROLINA

Laura J. Moore[1], Jeffrey H. List[2], S. Jeffress Williams[3] and David Stolper[4]

1. Department of Geology, Oberlin College, 52 West Lorain Street, Oberlin, OH 44074, laura.moore@oberlin.edu.
2. USGS Woods Hole Science Center, 384 Woods Hole Road, Woods Hole, MA 02543, jlist@usgs.gov.
3. USGS Woods Hole Science Center, 384 Woods Hole Road, Woods Hole, MA 02543, jwilliams@usgs.gov.
4. 2/68 Crown Road, Queesnscliff, Manly, NSW, 2095, Australia, davidstolper@yahoo.com

Abstract: An 8500-year Holocene simulation developed in GEOMBEST provides a possible scenario to explain the evolution of barrier coast between Rodanthe and Cape Hatteras, NC. Sensitivity analyses suggest that in the Outer Banks, the rate of sea-level rise is the most important factor in determining how barrier islands evolve. The Holocene simulation provides a basis for future simulations, which suggest that if sea level rises up to 0.88 m by AD 2100, as predicted by the highest estimates of the Intergovernmental Panel on Climate Change, the barrier in the study area may migrate on the order of 2.5 times more rapidly than at present. If sea level rises beyond IPCC predictions to reach 1.4-1.9 m above modern sea level by AD 2100, model results suggest that barrier islands in the Outer Banks may become vulnerable to threshold collapse, disintegrating during storm events, by the end of the next century. Consistent with sensitivity analyses, additional simulations indicate that anthropogenic activities, such as increasing the rate of sediment supply through beach nourishment, will only slightly affect barrier island migration rates and barrier island vulnerability to collapse.

INTRODUCTION

Barrier islands front a large percentage of the United States Atlantic and Gulf of Mexico Coasts. Because they are narrow and low-lying these landforms are extremely vulnerable to relative sea-level rise and storms. As sea level rises, a barrier island will respond either by migrating landward across underlying substrate to higher elevations or by disintegrating if there is no longer sufficient sand volume and relief above sea level to prevent inundation during storms. Disintegration of the Chandeleur Islands off of the

Louisiana coast during Hurricane Katrina may represent this type of threshold response whereby rapid rates of relative sea-level rise increase the vulnerability of migrating barriers allowing potentially irreversible destruction by storms to occur and ultimately leading to collapse of the barrier system. Several factors determine whether a barrier island will respond to sea-level rise by transgression or by submergence and collapse. These factors include the initial topography and morphology of the barrier, the geologic framework underlying the barrier, the availability and supply of sediment, the rate of sea-level rise, profile-response factors such as closure depth and anthropogenic modifications to the coast.

Recent predictions for the North Carolina Outer Banks, based on geologic interpretations, suggest sections of this barrier coast may collapse, becoming submerged within decades if sea level continues rising at current rates (Riggs and Ames, 2003). Our goal is to test the validity of this hypothesis by applying a morphological-behavior model, GEOMBEST, to 25-km of barrier coast expected to be among the first stretch of barrier to collapse in the Outer Banks. First, we simulate the Holocene evolution of the Outer Banks and perform sensitivity analyses to provide insight into which factors are most important in determining how the Outer Banks respond to sea-level rise. We then use the Holocene hindcast simulation as the basis for forward simulations to explore the potential response of the Outer Banks to future sea-level rise scenarios.

Study Area

The study area encompasses 25-km of barrier coast between Rodanthe and Cape Hatteras, NC (Figure 1), extending from the mainland to the shelf edge. The area is largely undeveloped including 17.5 km of National Seashore and the small towns of Avon and Salvo. The barrier island is narrow, ranging in width from 0.5 to 1.5 km and a discontinuous frontal dune provides only moderate relief across the study area. Longshore transport is to the south with a net volume of 5.9×10^5 m^3/yr lost between Oregon Inlet and Cape Hatteras (Inman and Dolan, 1989). Long-term shoreline change rates range from +2 to -4 m/yr (Morton et al., 2005).

METHODS

The Model

Because process-based models cannot yet address questions of large-scale coastal behavior, most predictions regarding future barrier island response to sea-level rise are based solely on geologic inference. Morphological-behavior models currently provide the only quantitative method for assessing how barrier islands evolve under changing conditions. These models are based on changes in sediment supply, sea-level rise and shoreface geometry (Cowell et al., 1995), but don't account for the physical processes of sediment transport. GEOMBEST (Geomorphic Model of Barrier, Estuarine and

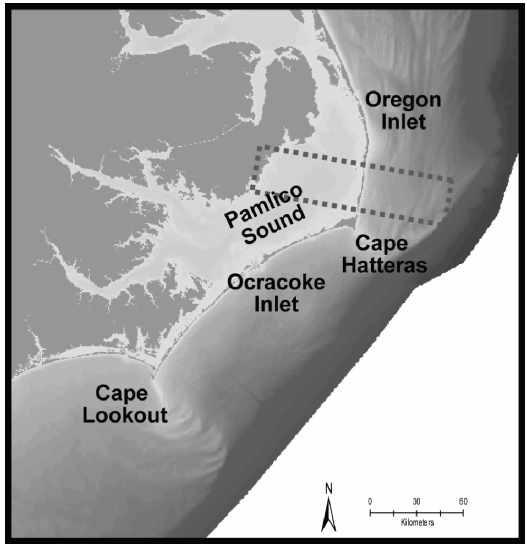

Figure 1. The study area is indicated by the rectangular box and encompasses 25-km of barrier coast between Rodanthe and Cape Hatteras, NC.

Shoreface Translations), as described by Stolper et al. (2005), is a profile-based, numerical morphological-behavior model that simulates the evolution of barrier island morphology and stratigraphy resulting from changes in sea level and sediment supply over time scales ranging from decades to millennia. The model incorporates information on the geologic framework and provides a quantitative means for testing the geometric feasibility of geologic hypotheses.

In an approach similar to that of Cowell et al. (1995), the model formulation in GEOMBEST is based on sediment conservation principles and behavior rules originating from "Bruun Rule" concepts, but with significant additional components allowing simulation of complex geological scenarios in which assumptions are relaxed, in an attempt to address concerns over the existence of equilibrium profiles (e.g., Pilkey and Cooper, 2004). The coastal tract in GEOMBEST extends from a user-defined distance offshore to the mainland and is divided into three functional realms including the shoreface, backbarrier and estuary (Figure 2). Each realm is treated separately in the model, but sediment is exchanged between them. GEOMBEST differs from other coastal evolution models by allowing specification of substrate characteristics along the coastal tract (i.e., erodibility and sand/mud ratio) and additional parameters allow for specification of open and changing sediment budgets. Morphological evolution is driven by disequilibrium between the coastal tract surface and a user-specified, equilibrium shoreface profile that maintains its vertical position

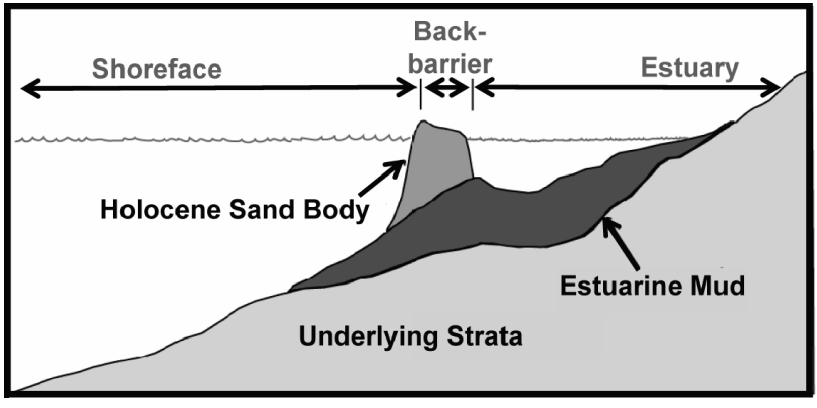

Figure 2. Cross-shore schematic showing three functional realms and stratigraphic units defined in GEOMBEST for a low-gradient barrier island coast. (After Stolper et al., 2005)

relative to sea level. Although the model drives toward equilibrium at each time step, it does not require equilibrium to be established. For example, the equilibrium profile will not be attained if the substrate is nonerodible or if sea-level rises too rapidly.

Input Parameters

The modern shelf morphology was obtained by averaging 18 alongshore transects spaced 1.5 km apart along the 25 km study area. To allow for substrate erosion, which is thought to have occurred in order to supply adequate amounts of sediment to the barrier system (McNinch et al., 1999) and which is supported by the presence of Pleistocene shells in the Holocene sand body (Wehmiller, 1999), an average of 5 m of vertical thickness was added to the modern shelf surface. Adding this layer of sediment provides an initial shelf surface across which an initial active sand body migrates landward throughout the Holocene simulation (Figure 3).

We begin the simulation with an active sand body that is approximately half the size of the Holocene active sand body currently located at the modern shoreline. Representative substrate characteristics and stratigraphy for the study area were determined for model input from cores, seismic sections and ground-penetrating radar data collected as part of a North Carolina Regional Study (Mallinson and Theiler, personal communication) (Figure 3).

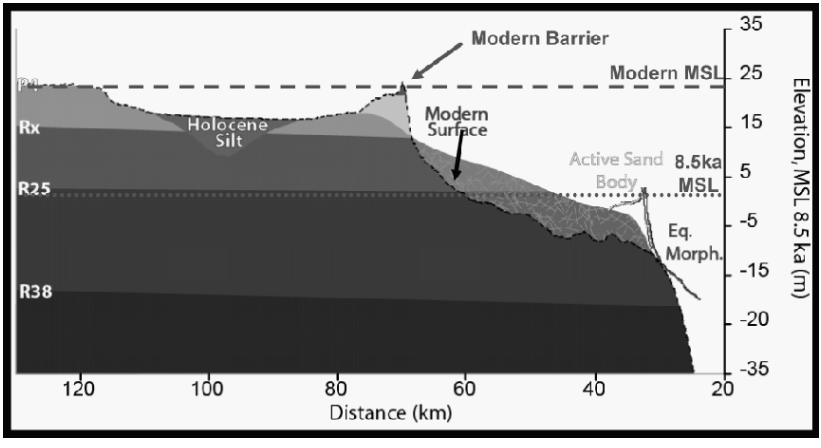

Figure 3. Stratigraphy (solid colors) and modern shelf surface (dashed black line) for the study area. 6 m of substrate is added to the modern surface (hatched area) and the active sand body (yellow) is moved offshore to create initial geometry for the Holocene simulation.

We begin the Holocene simulation 8.5 thousand years ago, when sea level was 22.5 m below modern sea level (MSL). Geometric contraints require the placement of the initial active sand body at both the shelf edge and at the farthest extent of the cape-associated shoals, which are believed to have been a major sink to the barrier island system throughout the Holocene (Pierce, 1969; Inman and Dolan, 1989; McNinch and Wells, 1999; McNinch and Luettich, 2000). Sea-level rise throughout the simulation follows the best available Holocene sea-level rise curve for North Carolina with rates of 0.5 m/100 yrs from 8.5 ka – 6.8 ka, 0.24 m/100 yrs from 6.8 – 4.2 ka and 0.15 m/100 yrs from 4.2 ka – 0 ka (Theiler et al., 2004). We assume a closure depth of 20 m based on shoreface and shelf morphology. This value agrees well with closure depths of 18.6 m and 21.6 m determined by Everts (1978) for Nags Head and Cape Hatteras, respectively. In order to bring the active sand body to its modern position while maintaining a modern sediment budget that matches closely the net loss of 5.9 x 10^9 m^3/yr reported by Inman and Dolan (1989) and to reproduce the modern shelf morphology, the sediment budget is varied throughout the simulation. The sediment budget is balanced from 8.5 ka – 6.8 ka, with 0 m^3/m/yr removed, negative from 6.8 – 4.2 ka, with 30 m^3/m/yr removed and negative from 4.2 ka – 0 ka, with 25 m^3/m/yr removed. Considered along the 25-km-long study area, the latter figure represents the removal of 625,000 m^3/yr, which comes close to the estimated net 590,000 m^3 transported to the south annually in the study area as estimated for recent decades (Inman and Dolan, 1989).

RESULTS AND DISCUSSION

Sensitivity Analyses

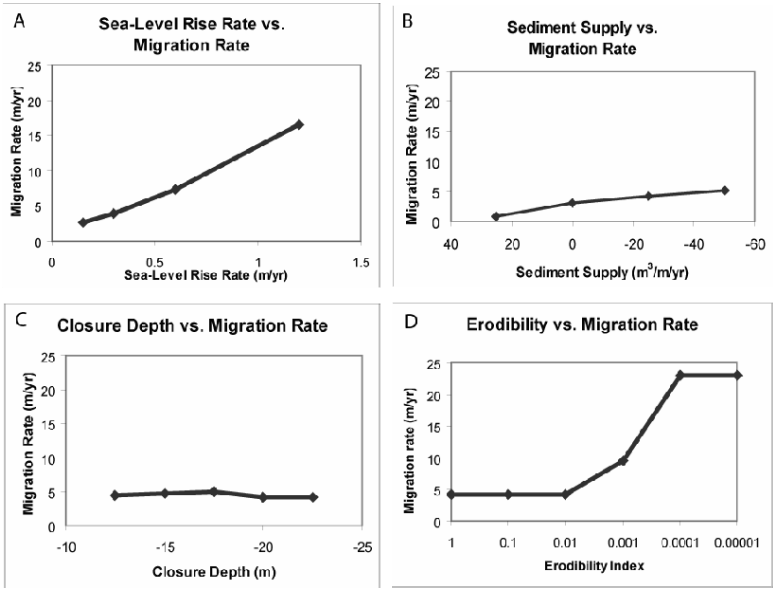

Figure 4. Results of sensitivity analyses demonstrating the effects on barrier island migration rate of changes in the rate of sea-level rise (A), rate of sediment supply (B), depth of closure (C) and substrate erodibility (D).

We explore the relative importance of sediment supply, sea-level rise rate, closure depth and substrate erodibility in determining barrier island response by varying one parameter at a time in the Holocene simulation. The relative importance of each factor is assessed by determining the degree to which changing the parameter produces a change in the rate of landward barrier island migration. Changing the sea-level rise rate by 100% from 0.3 m/100 yr to 0.6 m/100 yr produces increases migration rates 87% while decreasing the sediment budget in increments of 100% increases migration rates 40% as the sediment budget changes from balanced to -25m^3/m/yr (Figure 4). As closure depth changes from 12.5 m to 22.5 m by 2.5 m increments, migration rates change less than 6.5%. Migration rates are particularly insensitive to the erodibility of the substrate showing no change until the substrate is 1/1000 as erodible as a fully erodible unconsolidated sediment (Figure 4). Thus, given the range of sediment supply rates within the Outer Banks of North Carolina, sensitivity analyses indicate that barrier island migration rate is most sensitive to the rate of sea-level rise followed by the rate of sediment supply. Barrier island migration rate is less sensitive to closure depth and not sensitive to erodibility until the substrate is nearly nonerodible.

Holocene Simulation

The 8500-year hindcast simulation for the Outer Banks study area comes close to reproducing the morphology and stratigraphy of the modern barrier (Figures 5,6). For example, the edge of the modern shelf lies at a water depth of -11 m compared with -10 m reproduced by the simulation (Figure 6). A total of 4.5 x 10^9 m^3 of sediment is removed throughout the simulation. This sediment volume is of the same order of magnitude as the estimated volume (4.0 x 10^9 m^3) of the three cape-associated shoals (Diamond Shoal, Lookout Shoal and Frying Pan Shoal) as measured above the 12 m isobath (McNinch et al, 1999) suggesting that the volume removed throughout the simulation is reasonable. The Holocene simulation results in an average modern migration rate of -3.4 m/yr, which falls within the range of modern shoreline change rates for the study area of -4 to 2 m/yr (Morton et al., 2005), indicating that the simulation closely fits this additional observational constraint.

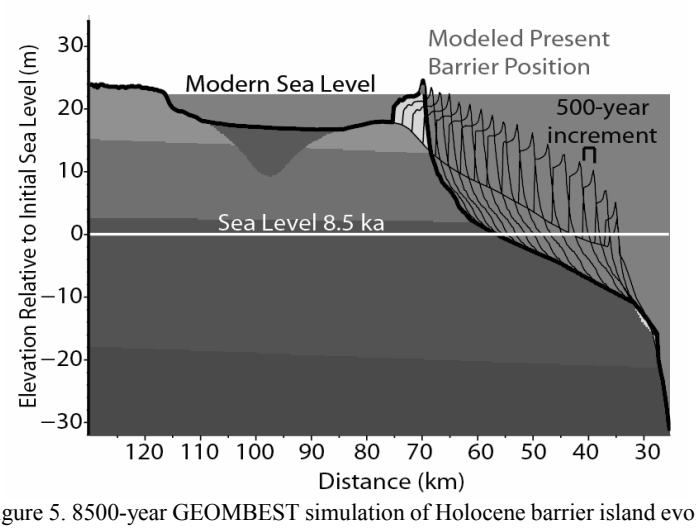

Figure 5. 8500-year GEOMBEST simulation of Holocene barrier island evolution for the study area. Pleistocene stratigraphy appears in brown. 500-year increments of time are shown as ghost traces and the final configuration of the shoreface is in bold.

Most critical to the reliability of forward simulations, for which the Holocene simulation serves as the basis, is comparison between the average modern surface (including the shelf, nearshore and active sand body), the initial surface used in the Holocene simulation, and the model-generated surface. This comparison indicates that the Holocene simulation reproduces closely the modern morphology and position of the Holocene sand body.

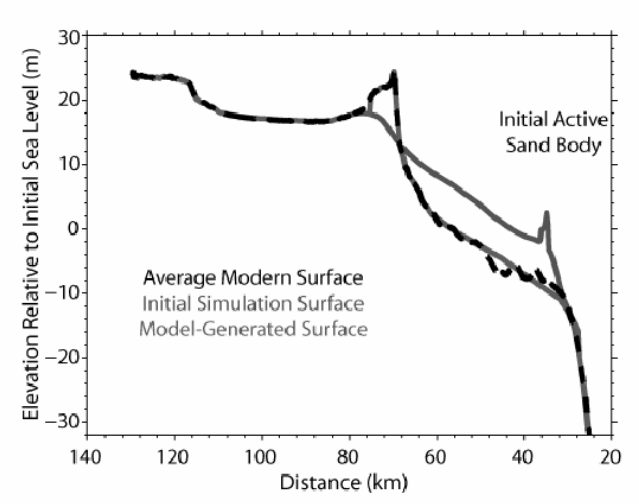

Figure 6. Comparison of the average modern surface (black dashed line), the initial surface used in the Holocene simulation (blue line), and the model-generated surface (red line).

Future Response to Sea-Level Rise

According to the Intergovernmental Panel on Climate Change (IPCC), sea level will likely rise between 0.09 and 0.88 m by AD 2100 (IPCC, 2001) unless there is a substantial reduction in greenhouse gas emissions. More recent studies suggest that IPCC estimates of sea-level rise may be too conservative and that conditions may be warm enough within the next century to cause melting of the Greenland Ice Sheet (GIS) and the West Antarctic Ice Sheet (WAIS), perhaps triggering many meters of sea-level rise (Gregory et al., 2004; Overpeck et al., 2006). If the GIS and the WAIS were to melt sufficiently, sea level could return to last interglaciation (LIG) levels of 4-6 m above present (Overpeck et al., 2006).

Forward simulations of potential barrier island response to several sea-level rise scenarios for AD 2100 start with the Holocene simulation described above and include an additional 100 years of barrier evolution with sea level rising linearly to specified elevation above modern MSL. A series of model runs based on the low- (0.09 m), mid- (0.48 m) and upper- (0.88 m) range of IPCC (2001) estimates for total sea-level rise by the year 2100, indicate future barrier migration rates of 2.3, 6.2 and 9.8 m/yr, respectively (Figure 7). The latter two results would represent an increase of up to nearly 2.5 times the fastest observed shoreline change rates in the study area, which range from 4 m of erosion to 2 m of accretion (Morton et al., 2005). Despite representing a significant increase, these rates are within the range of rates experienced by rapidly migrating barrier islands elsewhere today (Morton et al., 2004; Morton et al., 2005; Penland et al., 2005), suggesting that the barrier may remain intact even if the highest IPCC sea-level rise estimate is reached.

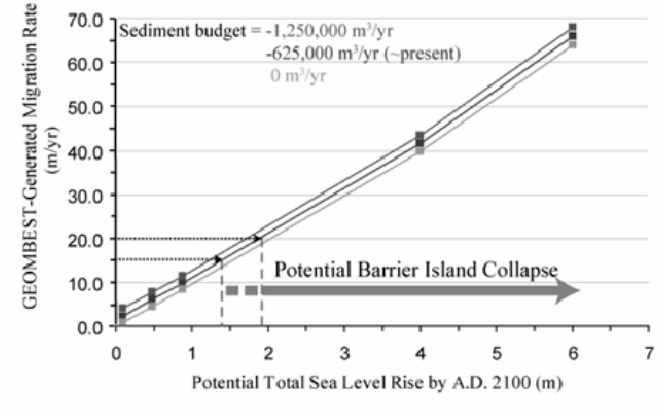

Figure 7. Model-generated barrier island migration rate as a function of total potential sea-level rise for scenarios in which the sediment budget remains similar to today, decreases by 100% and increases by 100%. The effect of an increase and decrease in sediment supply on the sea-level rise threshold is indicated by a vertical dashed green and blue line, respectively.

GEOMBEST simulations of barrier island response to 4 m and 6 m of sea-level rise by AD 2100 result in model-predicted barrier migration rates of 41 and 65 m/yr, respectively (Figure 7). These rates far exceed the highest average long-term barrier island erosion rates observed today along the Louisiana coast where the southern end of North Chandeleur Island eroded at average long-term rates of up to 18.6 m/yr (Morton et al., 2005) before disintegrating in response to Hurricane Katrina. This response to Katrina likely represents a threshold collapse whereby rapid rates of relative sea-level rise increase the vulnerability of migrating barriers allowing potentially irreversible destruction of the subaerial landform to occur during storms. In 1978, the Isle Dernieres off the coast of central Louisiana also entered into a period of rapid deterioration in response to a series of hurricanes (Williams et al., 1992) and recent measurements indicate these islands are eroding at average long-term rates of 5.2 to 17 m/yr (Penland et al., 2005). Relative sea level in Louisiana is rising 1.04 cm/yr (almost 10 times faster than the global average) (Penland and Ramsey, 1990) and sand supply is limited, making the barrier islands of Louisiana potentially viable analogs to islands that may experience similar conditions in the future. If barrier island observations in Louisiana can be applied to barriers in North Carolina, we can expect the Outer Banks to become vulnerable to threshold collapse when migration rates reach approximately 15-20 m/yr.

Model results for the five forward simulations suggest migration rates of 15 - 20 m/yr may occur if sea level rises approximately 1.4 - 1.9 m above modern MSL by AD 2100 (Figure 7). Additional simulations are consistent with the results of sensitivity analyses and suggest that changes in sediment supply plays a secondary role, modifying slightly the total sea-level rise at which barriers may become vulnerable to threshold collapse. For example, mitigating the negative sediment budget by 100% (e.g., nourishing the beaches with 625,000 m^3/year to create a balanced budget) decreases migration rates by 1.6 m/yr, which would offset barrier vulnerability to sea level rise by 0.2 m, while doubling sediment removal (from 625,000 m^3/year to 1, 050,000 m^3/year) increases migration rates by 1.6 m/yr, which would increase barrier vulnerability to sea-level rise by 0.2 m (Figure 7, green and red lines, respectively). Thus, regardless of the minor effects of possible anthropogenic modifications, our findings suggest barrier islands may become vulnerable to threshold collapse if the IPCC (2001) estimates are exceeded and sea level rises approximately 1.4 - 1.9 m above MSL by AD 2100.

CONCLUSIONS

Morphological-behavior models currently provide the only quantitative means by which to simulate barrier island evolution over long time scales. Using the morphological-behavior model GEOMBEST, we develop a Holocene simulation that closely reproduces the modern shelf and barrier morphology and provides a possible explanation for the evolution of the barrier coast between Rodanthe and Cape Hatteras, NC. Development of this simulation reveals that shoal morphology, shelf geometry and former sea levels are consistent with barrier island formation in the study area approximately 8500 years ago when sea level was 22.5 m below MSL. Sensitivity analyses suggest that in the Outer Banks, the rate of sea-level rise is the most important factor in determining barrier island migration rate and thus how barrier islands have evolved and will continue to evolve, in the future. Future simulations of barrier island response to sea-level rise, combined with modern observations, suggest that if sea-level rises ~0.9 m by 2100 AD, the Outer Banks may migrate up to 2.5 times more rapidly than at present, but will likely remain intact. However, additional results indicate that if sea-level rises beyond IPCC predictions by A.D. 2100, reaching 1.4-1.9 m above MSL, the Outer Banks may become vulnerable to "threshold collapse." Anthropogenic modifications to the sediment budget appear to only slightly mitigate increases in barrier island migration rate and vulnerability to collapse. This is consistent with the results of sensitivity analyses and may have significant implications for the future sustainability of coastal management practices.

ACKNOWLEDGEMENTS

This work was funded by U.S. Geological Survey and a sabbatical leave fellowship to Laura Moore from the Mellon-8 Consortium. The NSF-funded Oberlin College Beowulf cluster facility provided computer time.

REFERENCES

Cowell, P.J., Roy, P.S., and Jones, R.A., 1995, Simulation of large-scale coastal change using a morphologiacl-behaviour model: *Marine Geology*, v. 126, p. 45-61.

Everts, C.H., 1978, Geometry of profiles across inner continental shelves of the Atlantic and Gulf Coasts of the United States: Fort Belvoir, Virginia, U.S. Army Corps of Engineers, Coastal Engineering Research Center, p. 92.

Gregory, J.M., Huybrechts, P., and Raper, S.C.B., 2004, Threatened loss of Greenland Ice Sheet: *Nature*, v. 428, p. 616.

Inman, D.L., Elwany, M.H., and Jenkins, S.A., 1993, Shore rise and bar-berm on ocean beaches: Journal of Geophysical Research, v. 98, p. 181-199.

IPCC, 2001. *Climate Change 2001: The Scientific Basis. Contribution of Working Group I to the Third Assessment Report of the Intergovernmental Panel on Climate Change* [Houghton, J.T.,Y. Ding, D.J. Griggs, M. Noguer, P.J. vanderLinden, X. Dai, K.Maskell, and C.A. Johnson (eds.)]. Cambridge University Press, Cambridge, United Kingdom and New York, NY, USA, 881pp.

McNinch, J.E., and Wells, J.T., 1999, Sedimentary processes and depositional history of a cape-associated shoal, Cape Lookout, North Carolina: Marine Geology, v. 158, p. 233-252.

McNinch, J.E., Wells, J.T., and Snyder, S., 1999, The long-term contribution of pre-Holocene sands to transgressing barrier islands, *in* Kraus, N., ed., Proceedings of Coastal Sediments '99: Long Island, NY, American Society of Civil Engineers, p. 786-801.

McNinch, J.E., and LuettichJr, R.A., 2000, Physical processes around a cuspate foreland:: implications to the evolution and long-term maintenance of a cape-associated shoal: *Continental Shelf Research*, v. 20, p. 2367-2389.

Morton, R.A., Miller, T.L., and Moore, L.J., 2004, National Assessment of Shoreline Change:Part 1 Historical Shoreline Changes and Associated Coastal Land Loss Along the U.S. Gulf of Mexico, U.S. Geological Survey Open File Report 2004 -1043, p. 44.

Morton, R.A., and Miller, T.L., 2005, National Assessment of Shoreline Change: Part 2, Historical Shoreline Changes And Associated Coastal Land Loss Along The U.S. Southeast Atlantic Coast, USGS Open File Report 2005-1401, p. 14.

Overpeck, J.T., Otto-Bliesner, B.L., Miller, G.H., Muhs, D.R., Alley, R.B., and Kiehl, J.T., 2006, Paleoclimatic evidence for future ice-sheet instability and rapid sea-level rise: *Science*, v. 311, p. 1747-1750.

Penland, S., and Ramsey, K.E., 1990, Relative sea-level rise in Louisiana and the Gulf of Mexico: 1908 -1988: Journal of Coastal Research, v. 6, p. 323-342.

Penland, S., McBride, R.A., Williams, S.J., Boyd, R., and Suter, J.R., 1991, Effects of sea level rise on the Mississippi river delta plain, *in* Kraus, N., Gingerich, K., and Kriebel, D.L., eds., Coastal Sediments '91, Volume I: Seattle, WA, American Society of Civil Engineers, p. 319-334.

Pierce, 1969, Sediment budget along a barrier island chain: Sedimentary Geology, v. 3, p. 5-16.

Penland, S., Connor, P.F., Beall, A., Fearnley, S., and Williams, S.J., 2005, Changes in Louisisana's shoreline: Journal of Coastal Research, v. SI 44, p. 7 - 39.

Pilkey, O.P., and Cooper, A.G., 2004, Society and Sea Level Rise: *Science*, v. 303, p. 1781-1782.

Riggs, S.R., and Ames, D.V., 2003, Drowning the North Carolina coast: Sea-level rise and estuarine dynamics: Raliegh, NC, North Carolina Sea Grant, p. 152.

Stolper, D., List, J.H., and Thieler, E.R., 2005, Simulating the evolution of coastal morphology and stratigraphy with a new morphological-behavior model (GEOMBEST): *Marine Geology*, v. 218, p. 17-36.

Thieler, E.R., Colman, S.M., and Himmelstoss, E.A., 2004, Late Quaternary depositional events and their preservation on the U.S. Atlantic continental shelf; insights from a new compilation of radiocarbon age data *in* Belknap, D.F., Kelley, J.T., FitzGerald, D.M., and Buynevich, I.V., eds., IGCP Project 495, Quaternary Land-Ocean Interactions - Driving Mechanisms and Coastal Responses: University of Maine, Orono, p. 24.

Wehmiller, J.F., York, L.L., and Bart, M.L., 1995, Amino acid racemization geochronology of reworked Quaternary mollusks on US Atlantic coast beaches: implications for chronostratigraphy, taphonomy, and coastal sediment transport: *Marine Geology*, v. 124, p. 303-337.

Williams, S. J., Penland, S., Sallenger, A. H., Eds. 1992, *Atlas of Shoreline Changes Louisiana,* U.S. Geological Survey Open File Report 1-2150-A, Reston, Virginia.

1880 TO 2005 MORPHOLOGIC EVOLUTION OF A TRANSGRESSIVE TIDAL INLET, LITTLE PASS TIMBALIER, LOUISIANA

Michael D. Miner[1], Duncan M. FitzGerald[2], and Mark A. Kulp[3]

1. Pontchartrain Institute for Environmental Sciences, University of New Orleans, New Orleans, LA, 70148, USA. mminer@uno.edu
2. Department of Earth Sciences, Boston University, Boston, MA, 02215, USA. dunc@bu.edu
3. Department of Earth and Environmental Sciences, Pontchartrain Institute for Environmental Sciences, University of New Orleans, New Orleans, LA, 70148, USA, mkulp@uno.edu

Abstract: Rates of relative sea level rise in excess of 1 cm/yr are forcing rapid landward migration of barrier/tidal inlet systems along coastal Louisiana. Additionally, the conversion of interior wetlands to open water increases tidal prism, resulting in barrier degradation by means of increased inlet cross-sectional area and sediment sequestration in ebb tidal deltas. Historical bathymetric maps (dating to the 1880's) and up-to-date bathymetric data for Little Pass Timbalier provide a time series that shows the morphological evolution of this tidal inlet. The historical evolution includes: landward and lateral migration of its main channel (44 m/yr and 28 m/yr, respectively); changes in inlet throat geometry; and formation of a new stable ebb channel. The inlet throat cross-sectional area increased from 3,117 m^2 in 1880 to 17,510 m^2 in 2005. The ebb tidal delta is prograding seaward leaving a quasi-progradational sand body on the inner shelf as the barrier islands migrate landward.

INTRODUCTION

The Mississippi River delta plain (MRDP) is undergoing rapid relative sea-level rise (RSLR) at a rate of 0.94 cm/yr as indicated by a 57 year tide gauge record (1947-2004) from Grand Isle (Miner 2007). This high rate of RSLR coupled with the effects of tropical cyclones and passages of frontal systems results in a highly transgressive regime that has produced landward-migrating, overwash-dominated barrier systems. Moreover,

ongoing conversion of back barrier and interior wetlands to open water bays and lagoons increases tidal prisms, which in turn has enlarged the flow area of the associated tidal inlets (O'Brien 1931; 1969; FitzGerald et al. 2004). The continuing increasing bay size-tidal prism together with the landward migration of the barrier systems results in a dynamic environment within which new tidal inlets are formed and existing inlets are subject to changes in cross-sectional area (deepening and/or widening of throat) and position.

Most of the erosional and depositional changes along barrier island shorelines occur at the ends of the barrier. These changes are directly attributable to tidal inlet processes both in the inlet and along the adjacent barrier shoreline (FitzGerald 1984; FitzGerald et al. 1984). Along transgressive barrier islands, most of the landward movement of sediment occurs at tidal inlets (Armon 1979) therefore, an understanding of these tidal inlet processes is crucial to understanding transgressive barrier island evolution. In Louisiana, knowledge of inlet processes is imperative for formulating barrier stabilization projects, determining sediment budgets, and predicting future changes. Currently, large scale coastal restoration initiatives are being formulated that might require inlet management.

In comparison to many well-studied inlets, such as those along the Atlantic coast of North America, the tidal inlets of the MRDP are unique because of their location along a microtidal, transgressive coast that is dominantly fine-grained in textural character. The dominance of storm processes and overall fine-grained composition of the barriers and tidal shoals compared to the well studied inlet systems elsewhere in the world indicate that a different set of factors be considered when managing Louisiana tidal inlets.

The rapid evolution and transgressive nature of the MRDP provide an opportunity to correlate the historical morphological shoreline changes with the landward retreat, lateral migration, and avulsion of the tidal inlets. In this way, the evolution of the inlet can be traced using historical data and can be related to the actual channel morphology and depositional processes. This work will result in the development of process-response models that will be used to improve understanding of transgressive tidal inlet morphology and evolution, as well as an exploration tool for sand resource surveys and barrier/inlet system management approaches.

STUDY AREA

Little Pass Timbalier separates East Timbalier and Timbalier Islands and is the conduit for daily tidal exchange between Timbalier Bay and the Gulf of Mexico (Fig. 1). It is located approximately 90 km west of the active Balize delta complex of the Mississippi River and 100 km south-southwest of New Orleans, Louisiana. The Timbalier Islands are downdrift flanking deltaic barriers that are located west of the Caminada-Moreau erosional headland. This headland is a result of distributary progradation and delta lobe development of the Lafourche subdelta that began progradation 1,500 yrs BP (McFarlan 1961; Törnqvist et al. 1996). Approximately 300 yrs BP, the once active distributary

system waned and became reworked by marine processes to generate the erosional headland and flanking transgressive barriers (Morgan 1974; Penland et al. 1988).

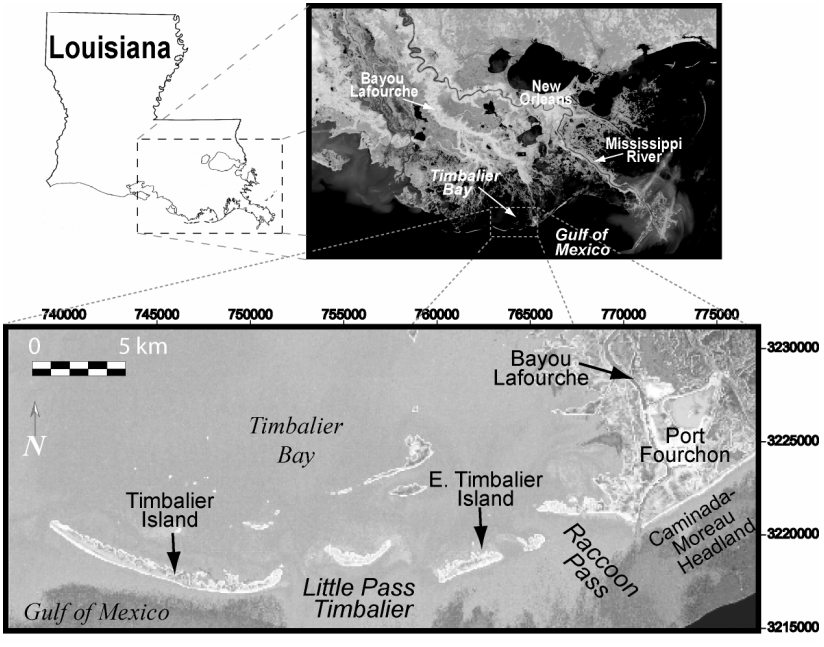

Figure 1. Little Pass Timbalier study area within the Mississippi River delta plain.

METHODOLOGY

Historical and recent bathymetric surveys are the primary datasets used in the analysis of Little Pass Timbalier. Historical surveys (dating from the 1880's –1980's) compiled by List et al. (1994) provide the framework for examining long-term trends. Details of data collection methods, processing techniques, and error assessment for the historical surveys can be found in List et al. (1994).

Recent (2005) bathymetric data of the study area were gathered using the University of New Orleans single-beam bathymetric rig mounted on the 21-foot *R/V Mudlump*. This bathymetric survey rig consists of an *Odom Hydrographics Hydrotrac* echosounder. Depth soundings are collected through a side-mounted *Odom Hydrographics* 200 kHz transducer with a beam width of 3°. The fathometer is equipped with a *Starlink Invicta* 210L differential global positioning system (DGPS) for navigation. Heave, pitch, and roll of the vessel are recorded using a *VT TSS Dynamic Motion Sensor Series-25* that is mounted vertically in-line with the DGPS antenna and the transducer. Thus, lateral offset errors between the DGPS antenna readings, transducer soundings, and vessel motion are cancelled minimizing vertical and horizontal errors in depth and navigation recordings.

The bathymetric, motion correction, and navigation data are recorded and integrated using *Coastal Oceanographics Hypack Max* hydrographic survey software.

The 2005 bathymetric data were processed using *Hypack Single Beam Editor* module and tide corrections were integrated using 6-minute interval data the NOAA tide gauge station (# 8762075) at Port Fourchon, LA. The water level elevation from the tide gauge was measured relative to mean lower low water (MLLW), a tidal datum based on the National Tidal Datum Epoch 1983 –2001.

After processing, the bathymetric data and historical datasets were used to make a series grids and ultimately digital elevation models (DEMs) for each date or time period (1880's, 1930's, 1980's, and 2005). The grids and DEMs were constructed using *Golden Software Sufer 8* contouring software. A kriging geostatistical algorithm was used to create the grid. Kriging is a distance weighting, moving average method that takes into account naturally occurring regional variables that are continuous from place to place (such as a linear bar or inlet channel), and assigns optimal weights based on the geographic arrangement of data point Z values taken from a variogram (Davis 1986; Krajewski and Gibbs 2003). Kriging was determined to be the most appropriate contouring method because it takes into account spatial characteristics of the local geomorphology and provides the best linear estimate that can be obtained from and irregular arrangement of data samples. Each DEM was then rectified and scaled relative to the other DEMs, allowing for the construction of a time series model that shows the morphological evolution of Little Pass Timbalier for the period from 1880 to 2005.

RESULTS

Inlet Morphology and Evolution

During the 1880's Little Pass Timbalier consisted of a relatively narrow, 1.5 km-wide tidal inlet with a single, 7 m-deep channel (Fig. 2) (List et al. 1994). The DEM for the 1880's indicates the presence of prominent flood and ebb tidal delta sediment bodies. The flood tidal delta was highly prominent during this early period and became less evident during subsequent stages. The flood delta morphology for the 1880's is comparable to those described by Hayes (1975) for Atlantic coast inlets and includes a flood ramp, flood channels, ebb shield, ebb spit, and spillover lobe (Fig 2). Noteworthy, is the fact that the ebb tidal delta is not as prominent at this stage as it is during subsequent stages. Ebb tidal volume for the 1880's was estimated to be 8×10^6 m^3, using the method proposed by Dean and Walton (1975). Inlet throat cross-sectional area was 3,177 m^2 in the 1880's.

Between 1880 and 1930 Little Pass Timbalier underwent a series of changes that led to breaching of the downdrift shoreline. According to U.S. Coast and Geodetic Survey maps, this process appears to have occurred prior to 1925 (U.S Coast and Geodetic Survey 1925) and possibly took place during a 1909 hurricane in which winds of 200 km/hr were recorded on the Louisiana coast and a tidal surge of 5 m was measured at Timbalier Island (Williams et al. 1992). The breaching of the adjacent shoreline resulted in an avulsion of the inlet and a displacement of the main channel 4.7 km updrift (west)

of the 1880 channel thalweg location. These changes contributed toward a widening of Little Pass Timbalier, from 1.5 km in 1880 to 8.6 km by 1930, increasing the throat cross-sectional area from 3,177 m^2 in the 1880's to 8,677 m^2. The wider inlet actually consisted of multiple channels separated by shoals, rather than a single, well-defined ebb channel (Fig. 2). The main ebb channel that formed at the site of the new breach was the deepest of the channels (7 m). Updrift, toward the east, the relict channel shoaled to 4 to 5 m and a third 4-m deep channel formed between the new breach channel and the relict channel. The ebb tidal delta of the former main channel eroded between the 1880's and 1930's (List et al. 1994), signaling a decrease in ebb current velocity in the former main channel. During that period waves reworked the ebb tidal delta sediment in a westward (downdrift) direction. The small portion of Timbalier Island that was located between the relict channel and the breach became a sand shoal, named Timbalier Shoal. Timbalier Shoal has remained ephemeral to date, becoming subaerially exposed during extended periods of calm weather and reworked to a subtidal shoal during tropical cyclone events. During the 1930's Little Pass Timbalier was characterized by a wide inlet with multiple channels separated by shoals. There were no prominent flood or ebb tidal delta deposits during this time period. Whereas the channel did migrate laterally during the period from 1880 to 1930 due to the avulsion and lateral spit migration, landward migration was approximately 1 km.

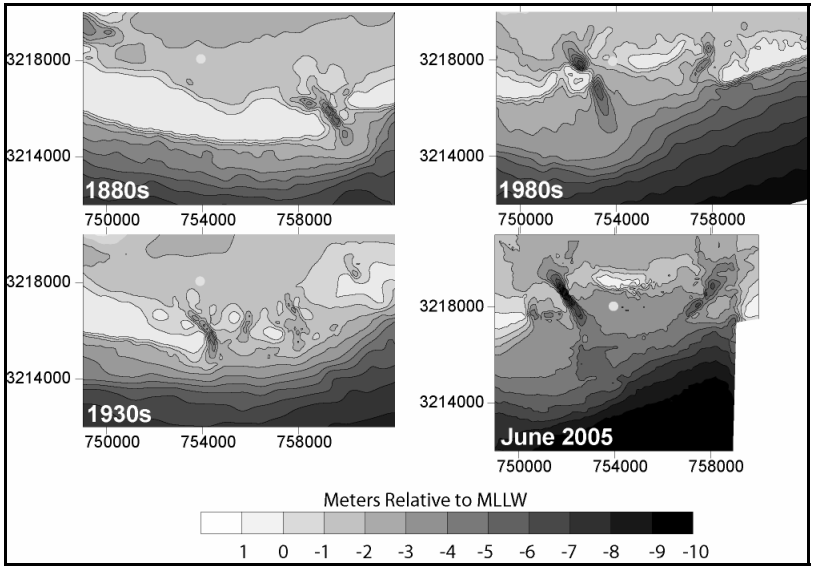

Figure 2. Morphological evolutionary model for Little Pass Timbalier. Note the yellow dot that remains geographically fixed for all time periods. Grid coordinates are in meters UTM zone 15. 1880's to 1980's bathymetric data from List et al. (1994).

Between the 1930's and the 1980's, the main channel migrated 1.9 km landward and 0.9 km laterally to the west. During the 1980's and subsequent timeframes, the inlet consisted of two ebb channels (the relict and new breach) separated by Timbalier Shoal (Fig. 4). Marginal flood tidal channels existed along the flanks East Timbalier and Timbalier islands, as well as along the flanks of Timbalier shoal. The inlet width at the throat was 7 km for the 1980's, a reduction of 1.6 km since the 1930's. However, cross-sectional area increased from 8,677 m^2 in the 1930's to 9,129 m^2 in the 1980's. During this period, Timbalier Shoal was subaerially exposed having an arcuate-shaped form built by an amalgamation of swash bars. During extensive periods of calm weather, swash bars migrate landward across the ebb tidal delta and eventually weld onto Timbalier Shoal. This phenomenon results in the vertical aggradation and subaerial exposure of Timbalier Shoal (Miner et al. 2005).

In the 1980's the two ebb channels of Little Pass Timbalier consist of differing morphologies. The deepest and westernmost channel was 7 to 8 m deep, whereas the eastern channel was 4 m deep (List et al. 1994). At the western channel site a large ebb tidal delta had become prominent since the 1930's due to increasing tidal prism (Fig. 2). The ebb tidal delta volume for the 1980's was estimated to contain 53 x 10^6 m^3 of sediment, an increase of 45 x 10^6 m^3 since the 1880's. The deepest point of the main channel did not exist at the throat during this time, but rather a large scour hole was present landward of the throat, having a depth of 8 to 9 m (List et al. 1994). According to the 1980's DEM, the easternmost channel of Little Pass Timbalier for the 1980's displayed no ebb or flood tidal delta features.

The morphology of Little Pass Timbalier reflected in the 2005 DEM is similar to that of the 1980's DEM exhibiting two ebb channels separated by Timbalier Shoal and marginal flood channels flanking the spits. However, the backbarrier scour hole disappeared and the deepest part of the main ebb channel is located at the inlet throat (Fig. 2). Dredging for the Louisiana Department of Natural Resources (LDNR) Project TE-40 Timbalier Island Dune/Marsh Restoration, resulted in the removal of approximately 3.5 x 10^6 m^3 of sediment from distal portions of the channel margin linear bar and central ebb tidal delta. This sediment was placed along the downdrift shoreline of Timbalier Island in 2004 (Shaw Coastal 2005). Of note is that between the 1980's and 2005 the ebb tidal delta ceased its progradation onto the inner shelf. The terminal lobe has since begun to retreat landward and the ebb tidal delta has broadened in a downdrift direction. Between the 1980's dataset (List et al. 1994) and the 2005 survey the inlet throat of the main channel migrated 2.1 km in a landward direction and 1.1 km alongshore to the west, and throat width widened from 8.1 km to 9.8 km. The main ebb channel increased in depth from 7 to 8 m deep in the 1980's to 9 to 10 m deep in 2005 and the secondary ebb channel deepened from 4 m to 6 m during that time. The throat cross-sectional area increased from 9,129 m^2 in the 1980's to 17,510 m^2 in 2005.

DISCUSSION

Morphologic Evolution

The morphological evolution of Little Pass Timbalier is complex and encompasses:

1) landward and lateral migration of its main channel (44 m/yr and 28 m/yr, respectively for the 1930 – 2005 time frame), 2) changes in inlet throat geometry, 3) formation of a new stable ebb channel through the combined processes of channel avulsion and breaching of the adjacent shoreline, and 4) increased ebb tidal delta sediment volume (Table 1; Figs. 2 and 3).

Table 1. Morphologic Evolution Summary

Time Period	Number of Ebb Channels	Throat Width, km	Throat Depth, m	Throat Cross-sectional Area, m^2	Ebb Delta Volume, m^3	Landward Migration, km	Lateral Migration, km
1880's	1	1.5	7	3,177	8×10^6	-	-
1930's	3	8.6	7	8,677	-	0.9	4.7*
1980's	2	8.1	9	9,129	53×10^6	1.9	0.9
2005	2	9.8	10	17,510	-	2.1	1.1

*Lateral migration due to island breach and ebb channel avulsion

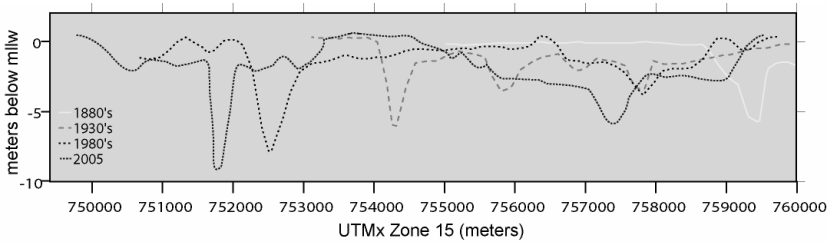

Figure 3. Shore-parallel bathymetric profiles across the Little Pass Timbalier tidal inlet throat for the years covered in this study. Profiles traverse the minimum inlet throat cross section for each period. 1880's, 1930's, and 1980's bathymetric data from List et al (1994).

Inlet channel migration and widening

Inlet throat migration is controlled by barrier landward migration in response to relative sea level rise, changes in tidal prism volume, the erodablity of the substrate (antecedent geology), longshore versus cross-shore transport processes, sediment supply, and frequency of storm impacts.

It has been established by previous tidal inlet studies along the Gulf of Mexico, Pacific, and Atlantic coasts of North America that inlet cross sectional area and bay tidal prism volume have a direct relationship (O'Brien 1939; 1969; Jarrett 1976), changes in the tidal prism volume will result in changes in inlet cross sectional area (O'Brien 1969; FitzGerald et al. 1984), and increasing tidal prism driven by wetland loss in Louisiana has resulted in increased tidal inlet cross sectional areas for the Louisiana coastal zone (FitzGerald et al. 2003; FitzGerald et al. 2004; Miner et al. 2005). At Little Pass Timbalier, increasing bay tidal prism volumes driven by backbarrier and interior land loss rates in the Timbalier/Terrebonne basin of 26.4 km^2/yr for a period from 1956 to

1990 (Barras et al. 1994) has forced this inlet widening process. Little Pass Timbalier has also increased in depth from 7 m in 1880 to 10 m in 2005 to accommodate the larger tidal prism volume (Fig. 3).

A breaching event sometime between 1880 and 1925 resulted in the formation of a second ebb channel down drift of the former inlet location. This second inlet channel has become the main ebb channel for Little Pass Timbalier and remains stable to date as part of a two-channel inlet system separated by an ephemeral shoal. Breaches and ephemeral inlets along the adjacent East Timbalier Island shoreline will eventually become stable tidal inlets in order to accommodate increasing tidal prism volume. The formation of additional tidal inlets along the Barataria shoreline in response to Barataria basin land loss has occurred during the past century as well (FitzGerald et al. 2004).

Ebb tidal delta expansion, precursory progradation, and retreat

Another consequence of the increasing tidal prism is the attendant increased volume of sediment sequestered in ebb tidal deltas (cf. Walton and Adams 1976). As the tidal prism of the Terrebonne/Timbalier basin increased between the 1880's and 1980's, the ebb tidal delta of Little Pass Timbalier enlarged by 45×10^6 m^3 and prograded onto the shelf as the barrier shoreline translated landward. This phenomenon of ebb tidal delta enlargement and seaward progradation in an overall transgressive regime has been noted by previous workers on the Louisiana coast (List et al. 1991; 1994; FitzGerald et al. 2003; FitzGerald et al. 2004). The volume increase in the ebb tidal delta occurs at the expense of the barrier islands, not only due to erosion of the tips of the barriers associated with inlet widening, but also because sand that builds the ebb tidal deltas would otherwise bypass the tidal inlet (FitzGerald et al. 2003).

During the period between 1980 and 2005 the ebb tidal delta began undergoing retreat after an initial stage of progradation (Fig. 4). This process is due to a progressive increase in the effective area of the ebb-tidal delta as it aggrades and progrades until its seaward extent is balanced by wave and shoreface erosional processes. Also, the continual landward and westward (lateral) migration of the inlet throat, where tidal current velocities are greatest, results in decreased ebb tidal current velocities along the updrift ebb tidal delta terminal lobe. The terminal lobe became starved of sediment and dominated by shoreface ravinement; forcing it to erode similarly to shoreface retreat, resulting in the transfer of sand to a downdrift lower shoreface depocenter. This proposed mechanism for ebb delta retreat and downdrift expansion after a period of seaward progradation is similar to that observed in flume experiments and stratigraphic investigations of a delta front conversion from the progradation stage to continuous retreat under constant relative sea-level rise and sediment supply as described by Muto and Steel (1992; 1997; 2001; 2002) and Muto (2001). The results are erosional processes dominating updrift portions of the ebb delta, and distribution of these sediments to downdrift flanking portions of the ebb delta, and along the adjacent downdrift shoreface.

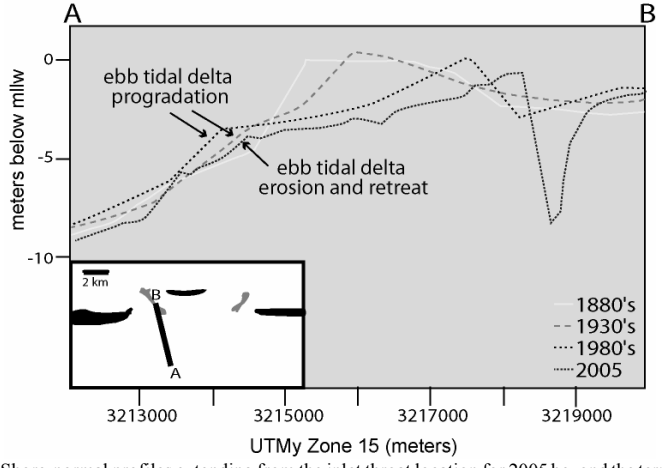

Figure 3. Shore-normal profiles extending from the inlet throat location for 2005 beyond the terminal lobe of the ebb tidal delta. 1880's to 1980's data from List et al. (1994).

Model Application

Transgressive Tidal Inlet Migration

The results of this study describe the morphological evolution of a transgressive tidal inlet that is dominated by increased throat cross-sectional area and landward channel migration. Because tidal inlet channels and inlet channel fill sequences have relatively high preservation potential during a transgression, the presence of inlet fills on the shelf have been used to document locations of relict barrier shorelines on the Atlantic shelf (e.g. Sheridan et al. 1974; Niedoroda et al. 1985). These interpretations are based on inlet fill models developed at modern inlets where lateral migration is the dominant control on inlet fill stratal geometry and sedimentary character. As shown here, the inlet migration pattern of a transgressive tidal inlet (shore perpendicular) is quite different than the laterally migrating inlet (shore parallel), and results in a distinctly different set of stratal architecture and facies successions (Miner 2007).

Shelf Sand Ridges

Lobate, shore oblique areas of accretion located offshore Timbalier Island have been identified by previous workers (List et al. 1994; Jaffe et al. 1997). However, the study conducted by Jaffe et al. (1997) did not identify a sediment source large enough to account for the accretion. A possible source for this sediment is the Little Pass Timbalier ebb tidal delta and suspended sediment transported out of the backbarrier through Little Pass Timbalier during ebbing tides. Sediment along distal portions of the ebb tidal delta is reworked by storm wave processes and deposited along the lower shoreface of Timbalier Island as shore oblique, lobate accumulations of sediment. Similar shore oblique, sediment transport trends and attendant bedforms along the middle and lower shoreface and shoreface-connected sand ridges have also been observed along the Atlantic coast (Ludwick 1978; Swift et al. 1978; Swift et al. 1985) and have been attributed to transgressive shoreface-shelf dispersal systems (Swift et al. 2003; Tillman

and Martinsen 1984), deposition as a lowstand shoreface during a forced regression (Posamentier et al. 1992), and sourced from abandoned ebb tidal deltas during a transgression (McBride and Moslow 1991; Snedden et al. 1994; 1999). The Atlantic examples are hydraulically maintained, and movement of the sediment within the ridges occurs during peak storm flow and downwelling (Wright et al. 1986; Swift et al. 1986; 2003).

Long-term landward migration of Timbalier Island combined with the enlargement and progradation of the Little Pass Timbalier ebb tidal delta resulted in the decoupling of the sediment transport pathway to the shoal from the upper shoreface and littoral systems. It has been proposed that, unlike the Atlantic lobes, the sediment transported downdrift along the lower shoreface of Timbalier Island is not lost to offshore sinks, but eventually becomes reintroduced to longshore processes downdrift at the Isles Dernieres (Jaffe et al. 1997). By the 1980's, the lateral accretion of lobes had been transported past the downdrift inlet Cat Island Pass and became a source of sediment that nourished the eastern Isles Dernieres barrier shoreline, where shoreline erosion rates are now about half of pre-bypassing rates (Jaffe et al. 1997).

During the period from the 1880's to 1980's, ebb tidal delta volume increased at Little Pass Timbalier from 8 x 10^6 m^3 to 53 x 10^6 m^3, resulting in its seaward progradation while at the same time the barrier and inlet channel system migrated landward. This morphological development is a response to increasing tidal prism. Since the 1980's, the ebb tidal delta of Little Pass Timbalier has shifted from seaward prograding to downdrift migrating. This shift results in shore-parallel downdrift growth of the ebb tidal delta and sediment transport and deposition along the downdrift lower shoreface of Timbalier Island.

A model for the formation and evolution of shoreface attached and detached sand ridges that develop from ebb tidal delta abandonment due to inlet migration or overstepping by transgression was proposed by McBride and Moslow (1991). One paradigm based on correlation between the location and orientation of existing sand ridges and the presence of relict or active tidal inlets along the modern shoreline, is that abandoned ebb tidal deltas act as an initial sand source for the generation of sand ridges (McBride and Moslow 1991). Radiocarbon age-dated vibracore and high resolution shallow seismic data collected on the New Jersey Atlantic shelf provide chronostratrigraphic evidence to support the correspondence between inlets and shelf sand ridges, however, the exact genetic process is still unknown (Snedden et al. 1994; 1999). The modern processes of transgressive tidal inlet morphodynamics at Little Pass Timbalier in which ebb tidal deltas expand and prograde seaward as the inlet channel and barrier migrate landward and their possible relationship to the formation of lobate accretionary zones along the downdrift lower shoreface along Timbalier Island have implications for the genesis of sand ridges and transgressive sand-sheets on the Holocene Atlantic (Swift et al. 2003) and northern Gulf of Mexico continental shelves (McBride et al. 2004), as well as sand sheets identified within the subsurface of the Holocene MRDP (Penland et al. 1988). A coast-wide bathymetric survey of Louisiana is currently in progress as a cooperative

study between the UNO Pontchartrain Institute for Environmental Sciences, U. S. Geological Survey, and Louisiana Department of Natural Resources. The results of this study will provide insight as to the recent depositional and erosional trends along the lower shoreface of Timbalier Island and evolution of the shore-oblique accretionary features.

CONCLUSIONS

Shoreface retreat along the barrier islands, driven by a relative rise rate of approximately 1 cm/yr, causes the Little Pass Timbalier tidal inlet system to migrate landward at a rate of 44 m/yr. Westward lateral migration of the main ebb channel is also occurring at a rate of 28 m/yr, resulting in a widening of the inlet. Widening is due in part to the fact East Timbalier Island can not accrete westward and is drowning in place due to its rip-rap lined shoreline.

The dominant control on the morphological evolution of Little Pass Timbalier since the 1880's has been increasing tidal prism driven by interior wetland loss. This has resulted in changes in inlet throat geometry (widening and deepening) and relocation of a new stable ebb channel to a site along the adjacent barrier that was breached during major storm. Increasing tidal prism has also resulted in increased volumes of sediment sequestered in the ebb tidal delta. In response to storm events and tidal prism changes, Little Pass Timbalier has evolved from an inlet having both an ebb and flood deltas in the 1880's to an inlet morphology having no prominent flood or ebb tidal delta but rather a system with multiple ebb channels separated by intra-inlet shoals by the 1930's. Most recently (1980's to 2005), the distribution of tidal channels and sand bodies reflects ebb dominance with a large ebb tidal delta and negligible flood tidal deltas.

The growth of the ebb tidal delta in a seaward direction ceased between the 1980's and 2005 and instead the ebb delta built in a downdrift direction. This downdrift dispersal of sediment explains genesis of a zone of accretion along the Timbalier Island lower shoreface, which appears to be attached to the Little Pass Timbalier ebb tidal delta. This genetic relationship between ebb tidal deltas and zones of lower shoreface accretion has implications as a possible analog for shelf sand ridge formation and transgressive sand sheet development.

REFERENCES

Armon, J. W., 1979, Landward Sediment Transfers in a Transgressive Barrier Island System, Canada, S.P. Leatherman, ed. Barrier Islands from the Gulf of St. Lawrence to the Gulf of Mexico: New York, New York, Academic Press, p. 65 – 80.

Barras, J. A., Bourgeois, P. E., and Handley, L. R., 1994, Land Loss in Coastal Louisiana 1956 –1990: National Biological Survey, National Wetlands Research Center, Open File Report 94-01, 10 p., 4 plates.

Davis, J. C., 1986, Statistics and Data Analysis in Geology, Second Edition: New York, John Wiley and Sons, 646 p.

Dean, R. G. and Walton, T. L., Jr., 1975, Sediment Transport Processes in the

Vicinity of Inlets with Special Reference to Sand Trapping: in L.E. Cronin, ed. Estuarine Research: New York, Academic Press, p. 129 –149.
FitzGerald, D. M., 1984, Interactions Between the Ebb-Tidal Delta and Landward Shoreline: Price Inlet, South Carolina: Journal of Sedimentary Petrology, v. 54, p. 1303 –1313.
FitzGerald, D. M., Penland, S., and Nummedal, D., 1984, Changes in Tidal Inlet Geometry Due to Backbarrier Filling: East Friesian Islands, West Germany: Shore and Beach, v. 52, no. 4, p. 2 –8.
FitzGerald, D. M., Kulp, M. A., and Penland, S., 2003, Tidal Prism Changes within Barataria Bay and its Effects on Sedimentation Patterns and Barrier Shoreline Stability: Gulf Coast Association of Geological Societies Transactions, v. 53, p. 243 –251.
FitzGerald, D. M., Kulp, M. A., Penland, S., Flocks, J., and Kindinger, J., 2004, Morphologic and Stratigraphic Evolution of Muddy Ebb-Tidal Deltas Along a Subsiding Coast: Barataria Bay, Mississippi River Delta: Sedimentology, v. 51, p. 1157 –1178.
Hayes, M. O., 1975, Morphology of Sand Accumulations in Estuaries, in L.E. Cronin, ed. Estuarine Research: New York, Academic Press, p. 3-22.
Jaffe, B. E., List, J. H., and Sallenger, A. H., Jr., 1997, Massive Sediment Bypassing on the Lower Shoreface of a Wide Tidal Inlet – Cat Island Pass, Louisiana: Marine Geology, v. 136, p. 131 –149.
Jarrett, J. T., 1976, Tidal Prism – Inlet Area Relationships: General Investigation of Tidal Inlets Report no. 3, U.S. Army Engineer Waterways Experiment Station, Vicksburg, MS, 32 p.
Krajewski, S. A. and Gibbs, B. L., 2003, Understanding Computer Contouring: Boulder, Gibbs and Associates, poster, 1 sheet.
List, J. H., Jaffe, B. E., and Sallenger, A. H., 1991, Large-scale Coastal Evolution of Louisiana's Barrier Islands: American Society of Civil Engineers, Proceedings Coastal Sediments 1991, p. 1532 –1546.
List, J. H., Jaffe, B. E., Sallenger, A. H., Jr.,Williams, S. J.,McBride, R. A., and Penland, S., 1994, Louisiana Barrier Island Erosion Study: Atlas of Seafloor Changes from 1878 to 1989: Reston, Virginia, U.S. Geological Survey and Louisiana State University, Miscellaneous Investigations Series I-2150-A, 81p.
Ludwick, J. C., 1978, Coastal Currents and an Associated Sand Stream off Virginia Beach, Virginia: Journal of Geophysical Research, v. 83, no. C5, p. 2365 –2372.
McBride, R. A. and Moslow, T. F., 1991, Origin, Evolution, and Distribution of Shoreface Sand Ridges, Atlantic Inner Shelf, U.S.A.: Marine Geology, v. 97, p. 57 – 85.
McBride, R. A., Moslow, T. F., Roberts, H. H., and Diecchio, R. J., 2004, Late Quaternary Geology of the Northeastern Gulf of Mexico Shelf; Sedimentology, Depositional History, and Ancient Analogs of a Major Shelf Sand Sheet of the Modern Transgressive Systems Tract, in Anderson, J. B. and Fillon, R. H. (eds.), Late Quaternary Stratigraphic Evolution of the Northern Gulf of Mexico Margin: Society for Sedimentary Geology SEPM, Special Publication, v. 79, p. 55 –83.
McFarlan, E., Jr., 1961, Radiocarbon Dating of Late Quaternary Deposits, South

Louisiana: Geological Society of America Bulletin, v. 72, p. 129 –158.
Miner, M. D., FitzGerald, D. M., and Kulp, M. A., 2005, Morphologic Evolution of a Transgressive Tidal Inlet, Little Pass Timbalier, Louisiana: Gulf Coast Association of Geological Societies Transactions, v. 55, p. 532 –542.
Miner, M. D., 2007, Long and Short-Term Morphologic Evolution and Stratigraphic Architecture of a Transgressive Tidal Inlet, Little Pass Timbalier, Louisiana: Ph.D. Dissertation, University of New Orleans, New Orleans, 156 p.
Morgan, J. P., 1974, Recent geological history of the Timbalier Bay area and adjacent continental shelf: Louisiana State University, Museum of Geoscience, Melanges, no. 9, 17 p.
Muto, T., 2001, Shoreline Autoretreat Substantiated in Flume Experiments: Journal of Sedimentary Research, v. 71, n. 2, p. 246 –254.
Muto, T. and Steel, R. J., 1992, Retreat of the Front of a Prograding Delta: Geology, v. 20, p. 967 –970.
Muto, T. and Steel, R. J., 1997, Principles of Regression and Transgression: The Nature of the Interplay between Accommodation and Sediment Supply: Journal of Sedimentary Research, v. 67, n. 6, p. 994 –1000.
Muto, T. and Steel, R. J., 2001, Autostepping During the Transgressive Growth of Deltas: Results from Flume Experiments: Geology, v. 29, p. 771 –774.
Muto, T. and Steel, R. J., 2002, Role of Autoretreat and A/S Changes in the Understanding of Deltaic Shoreline Trajectory: A Semi-quantitative Approach: Basin Research, v. 14, p. 303 –318.
Niedoroda, A. W., Swift, D. J. P., Figueiredo, A. G., Jr., and Freeland, G. L., 1985, Barrier Island Evolution, Middle Atlantic Shelf, U.S.A., Part II: Evidence from the Shelf Floor: Marine Geology, v. 63, p. 363 – 396.
O'Brien, M. P., 1931, Estuary Tidal Prisms Related to Entrance Areas: Journal of Civil Engineers, v. 1, no. 8, p. 738 –739.
O'Brien, M. P., 1969, Equilibrium Flow Areas of Inlets on Sandy Coasts: American Society of Civil Engineers, Journal of Waterways and Harbors, no. WW1, p. 43 – 52.
Penland, S., Boyd, R., and Suter, J. R., 1988, Transgressive Depositional Systems of the Mississippi Delta Plain: A Model for Barrier Shoreline and Shelf Sand Development: Journal of Sedimentary Petrology, v. 58, no. 6, p. 932 –949.
Penland, S. and Ramsey, K. E., 1990, Relative Sea-Level Rise in Louisiana and the Gulf of Mexico: 1908-1988: Journal of Coastal Research, v. 6, n. 2, p. 323 –342.
Posamentier, H. W., Allen, G. P., James, D. P., and Tesson, M., 1992, Forced Regressions in a Sequence Stratigraphic Framework: Concepts, Examples, and Exploration Significance: American Association of Petroleum Geologists Bulletin, v. 76, p. 1678 – 1709.
Shaw Coastal, Inc., 2005, Timbalier Island Dune/Marsh Restoration Project, CWPPRA/State Project no. TE-40, Project Completion Report, 8 p., 8 appendices with plates.
Sheridan, R. E., Dill, C. E., Jr., and Kraft, J. C., 1974, Holocene Sedimentary Environment of the Atlantic Inner Shelf off Delaware: Geological Society of America Bulletin, v. 85, p. 1319 – 1328.

Snedden, J. W., Kreisa, R. D., Tillman, R. W., Schweller, W. J., Culver, S. J., and Winn, R. D., Jr., 1994, Stratigraphy and Genesis of a Modern Shoreface-attached Sand Ridge, Peahala Ridge, New Jersey: Journal of Sedimentary Research, v. B64, p. 560 – 581.

Snedden, J. W., Kreisa, R. D., Tillman, R. W., Culver, S. J., and Schweller, W. J., 1999, An Expanded Model For Modern Shelf Sand Ridge Genesis and Evolution on the New Jersey Atlantic Shelf, in Bergman, K. M. and Snedden, J. W. (eds.), Isolated Shallow Marine Sand Bodies: Sequence Stratigraphic Analysis and Sedimentologic Interpretation, Society for Sedimentary Geologists SEPM, Special Publication, no. 64, p. 147 – 163.

Swift, D. J. P., Sears, P. C., Bohlke, B., and Hunt, R., 1978, Evolution of a Shoal Retreat Massif, North Carolina Shelf: Inferences from Areal Geology: Marine Geology, v. 27, p. 19 –42.

Swift, D. J. P., Niedoroda, A. W., Vincent, C. E., and Hopkins, T. S., 1985, Barrier Island Evolution, Middle Atlantic Shelf, USA, Part 1: Shoreface Dynamics: Marine Geology, v. 63, p. 331 –361.

Swift, D. J. P., Han, G., and Vincent, C. E., 1986, Fluid Processes and Sea-floor Response on a Modern Storm-Dominated Shelf: Middle Atlantic Shelf of North America, Part 1: the Storm Current Regime, in Knight, R. J. and McLean, J. P. (eds.), Shelf Sands and Sandstones: Canadian Society of Petroleum Geologists, Memoir no. 11, p. 99 –119.

Swift, D. J. P., Parsons, B. S., Foyle, A., and Oertel, G. F., 2003, Between Beds and Sequences: Stratigraphic Organization at Intermediate Scales in the Quaternary of the Virginia Coast, USA: Sedimentology, v. 50, p. 81 –111.

Tillman, R. W. and Martinsen, R. S., 1984, The Shannon Shelf Ridge Sandstone Complex, Salt Creek Anticline Area, Powder River Basin Wyoming, in Tillman, R. W. and Siemers, C. T. (eds.), Siliciclastic Shelf Sediments, Society for Sedimentary Geology SEPM, Special Publication, no. 34, p. 85 – 142.

Törnqvist, T. E., Tristram, R. K., Autin, W. J., van der Borg, Klaas, de Jong, A. F. M., Klerks, C. J. W., Snijders, E. M. A., Storms, J. E. A., van Dam, R. L., and Wiemann, M. C., 1996, A Revised Chronology for Mississippi River Subdeltas: Science, v. 273, p. 1693 – 1696.

United States Coast and Geodetic Survey, 1925, Mississippi River to Galveston: United States Coast and Geodetic Survey, Chart no. 1116, scale 1:458,596, 1 sheet.

Walton, T. L., and Adams, W. D., 1976, Capacity of Inlet Outer Bars to Store Sand: American Society of Civil Engineers, Proceedings Fifteenth Coastal Engineering Conference, Honolulu, Hawaii, 1919 –1937.

Williams, S. J., Penland, S., and Sallenger, A. H., Jr., 1992, Louisiana Barrier Island Erosion Study, Atlas of Shoreline Changes in Louisiana from 1853 to 1989: Reston, Virginia, U.S. Geological Survey and Louisiana State University, Miscellaneous Investigations Series I-2150-A, 103 p.

Wright, L. D., Boon, J. D., III, Green, M. O., and List, J. H., 1986, Response of the Mid Shoreface of the Southern Mid-Atlantic Bight to a 'Norteaster': Geo-Marine Letters, v. 6, p. 153 –160.

IMPACTS OF RISING SEA LEVEL TO BACKBARRIER WETLANDS, TIDAL INLETS, AND BARRIER ISLANDS: BARATARIA COAST, LOUISIANA

Duncan FitzGerald[1], Mark Kulp[2], Zoe Hughes[1], Ioannis Georgiou[2], Michael Miner[2], Shea Penland[2], and Nick Howes[1]

1. Department of Earth Sciences, Boston University, Boston, MA 02215, USA. dunc@bu.edu, zoeh@bu.edu, nchowes@gmail.com.
2. Department of Earth and Environmental Science, Pontchartrain Institute for Environmental Sciences, University of New Orleans, New Orleans, LA 70148, mkulp@uno.edu, igeorgiou@uno.edu, michaeldminer@gmail.com, spenland@uno.edu.

Abstract: The Barataria barrier system within the Mississippi River delta plain, is experiencing some of the highest relative sea-level rise (SLR) rates in the continental USA (0.94 cm/yr). This has led to substantial wetland loss in Barataria Bay (16.9 km^2/yr, from 1935-2000). This conversion of wetlands to intertidal and subtidal environments results from several linked processes including subsidence, marsh front erosion, and catastrophic scour during large magnitude hurricanes. Increasing open water within Barataria Bay has amplified tidal exchange with the ocean. Between 1880 and 2006, an increase of 400% took place in the combined cross-sectional areas of the major tidal inlets of Barataria Bay, associated with the enlarging tidal prism. This expansion of the inlets has been at the expense of the adjacent barrier islands, evident in the concomitant progradation of the ebb-tidal deltas. Since the 1880's the ebb delta at Barataria Pass built seaward more than 2.0 km, sediment cores show that sand constitutes the upper 1-2 m of the ebb delta. Movement of sand offshore, regional subsidence and increasing bay tidal prism produce segmentation of the barriers, forming new inlets such as Pass Abel. Acceleration in eustatic sea level rise will lead to further wetland loss and thus ultimately barrier disintegration. The Barataria barrier chain will be transformed into an island-only system similar to the Isle Dernieres and Timbaliers.

INTRODUCTION

Salt marshes cover extensive areas of estuarine and deltaic environments. They are one of the most productive ecosystems on Earth, and provide a variety of essential ecosystem services to humanity (Mitsch and Gosselink 1993; Sharitz and Pennings 2006). The marsh is maintained through delicate balances between: accretion and subsidence; erosion and vegetative stabilization; and tidal prism and drainage efficiency. Salt marshes today are threatened worldwide by a forecasted acceleration in the rate of sea-level rise (SLR) (Church et al. 2001) brought on by global warming. Recent studies indicate that the acceleration is already occurring (Church and White 2006; Donnelly 2006; Gehrels 1999; Nydick et al. 1995). The destruction of wetlands may provide a powerful positive feedback mechanism for increasing greenhouse gases and global warming by converting organic matter to carbon dioxide and methane.

The fragmentation and inundation of salt marshes due to SLR are intrinsically linked to changes in the configuration and stability of barrier island systems that separate them from the open ocean. A relative rise in sea level leads to an increase in the tidal prism of the bay, expansion of tidal inlets, sequestration of sand offshore in ebb-tidal deltas and erosion of barrier islands. These changes impact the overall hydrodynamics of the inlet-bay system leading to increased erosion of the back barrier and a positive feedback causing further deterioration of wetlands (FitzGerald et al. 2003, 2004). The region becomes more susceptible to both hurricanes and the intrusion of saltwater into freshwater wetlands. As the stability of a marsh is contingent upon elevation relative to mean sea level, the ecological fabric of the marshes is also threatened (Mitsch and Gosselink 1986; Gornitz 1995).

The objective of this paper is to report our results concerning the impacts of wetland loss along the central coast of Louisiana and discuss how increasing bay area and tidal exchange have affected the morphodynamics and sedimentation trends of tidal inlets and barrier islands. Barataria Bay was chosen for this study due to the extensive historical documentation that exists for this region including wetland loss (Britsch and Dunbar 1993; Barras et al. 1994, 2003) shoreline trends (Williams et al. 1992), bathymetric changes (List et al. 1994), and relative sea level data (Grand Isle; Penland and Ramsey 1990; Miner 2007). Previous discussions of the evolution of the Louisiana tidal inlets and barriers can be found in Levin (1993), List et al. (1997), and FitzGerald et al. (2004).

Rapid Sea Level Rise

The Barataria Basin is a natural laboratory in which to study the effects of accelerated SLR because it is experiencing one of the highest SLR rates in the country (0.92 cm/yr for 1947-2006 period; Miner 2007). This rapid rate of rise is attributed to many natural and anthropogenic causes including: 1. flexure of the lithosphere due to isostatic loading and growth; 2. fault motion within Cenozoic strata; 3. sediment compaction; 4. far-field isostatic adjustment (forebulge collapse) associated with retreat of the Laurentide Ice Sheet (Mitrovica and Milne 2002), 5. incidence of hurricane and storm surges; 6. reduced sediment supply due to leveeing and channelization of the Mississippi River; 7. withdrawal of fluids associated with oil and gas production (Morton et al. 2005); and

8. eustatic sea level rise. In a recent study using radiocarbon dated basal peat, Gonzalez and Tornqvist (2006) reported that widespread subsidence in the lower Mississippi delta appears to be unrelated to fault motion, but that glacio-isostasy may be a significant contributor. This is in addition to the process of locally significant sediment compaction, which is suggested to take place most rapidly above thick, recently deposited deltaic sediments (Penland and Ramsey 1990).

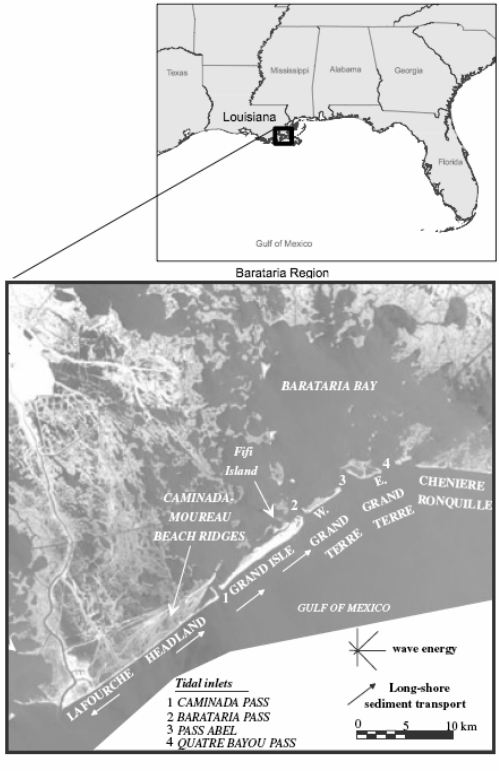

Fig. 1. Location of Barataria Bay and fronting barrier island complex. Tidal exchange between the bay and the Gulf of Mexico occurs through four tidal inlets. This basin has developed between the Lafourche headland to the west and the Plaquemine headland to the east.

Physical Setting

The Barataria barrier island complex is situated between the active Plaquemines delta lobe to the east and the Lafourche delta headland to the west (Fig. 1). The barrier chain that fronts Barataria Bay has formed from sediment shed from these two distributary

headlands, including the beach ridge/chenier systems of Caminada-Moureau beach ridges to the west and Chenier Ronquille to the east. Similar to much of the Gulf of Mexico, the Barataria coast is low-energy with a microtidal range of 0.4 m that increases to about 0.6 m during spring tides. Generally, breaking waves are small along the coast (< 0.4 m). However, during the passage of winter storms nearshore wave heights as high as 3.0 m can prevail for days (Stone and Muller 2003). Infrequent hurricanes (1 every 7 years; Muller and Stone 2001) cause the greatest impact on the shoreline resulting in widespread erosion, washovers, and tidal inlet formation (Boyd and Penland 1981; Stone et al. 2003).

DATA BASE

The areal extent and rate of wetland loss for Barataria Bay were derived from compilations produced by Britsch and Dunbar (1993) and Barras et al. (1994 , 2003). Land loss attributed to Hurricane Katrina was determined by Barras (2006). Documentation of historical changes in tidal inlet cross sectional area and longitudinal transects across the ebb-tidal delta were derived from an Atlas of Sea Floor Changes (List et al. 1994) and additional bathymetric data files (List, pers. comm.). Present-day tidal inlet bathymetry was determined from single beam surveys conducted in August 2006. During that field session, tidal current velocity distributions were recorded across the inlet throat using an Acoustic Doppler Current Profiler (ADCP). Additional current data were measured by Moffat-Nichols (LA DNR, pers. comm.). Approximately, 200 grab samples were collected throughout the inlets to determine the surficial facies characteristics of the inlet channels and ebb-tidal deltas.

RESULTS

Wetland Loss

During the past half-century rapid relative sea-level rise (0.94 cm/yr, Grand Isle tide gage: 1947-2006) and erosional processes within Barataria Bay have led to substantial wetland loss, converting more than 1,100 km^2 of wetlands to open water (16.9 km/yr) since 1935. Conversion of wetlands to intertidal and subtidal environments is a product of several linked processes including subsidence, marsh front erosion, and catastrophic scour during large magnitude hurricanes. Although a temporal plot of wetland loss and relative SLR in Barataria Bay shows similar directions in trend during the past 50 years, a comparison of their slopes indicates no close correspondence (Figure 2). Thus, other forcings must be operative. For example, Morton et al. (2003, 2005) have demonstrated convincingly that accelerated wetland loss in adjacent Terrebone Basin is related to rapid subsidence following peak volume fluid production from nearby oil and gas fields. A large number of oil and gas fields also exists in the Barataria Basin, which have likely contributed to subsidence in this region as well (Morton et al. 2006).

The formation of ponds and bays within wetland regions leads to marsh edge erosion by local wind generated wave attack. As open-water areas grow in size, a positive feedback exists whereby increasing fetch produces larger waves accelerating marsh edge retreat (Schwimmer 2001). In addition to the stratigraphy of the wetlands, which largely controls the resistance of the marsh to wave abrasion and undercutting, erosion rates are

related to fetch length and shore orientation with respect to storm and prevailing wind regimes.

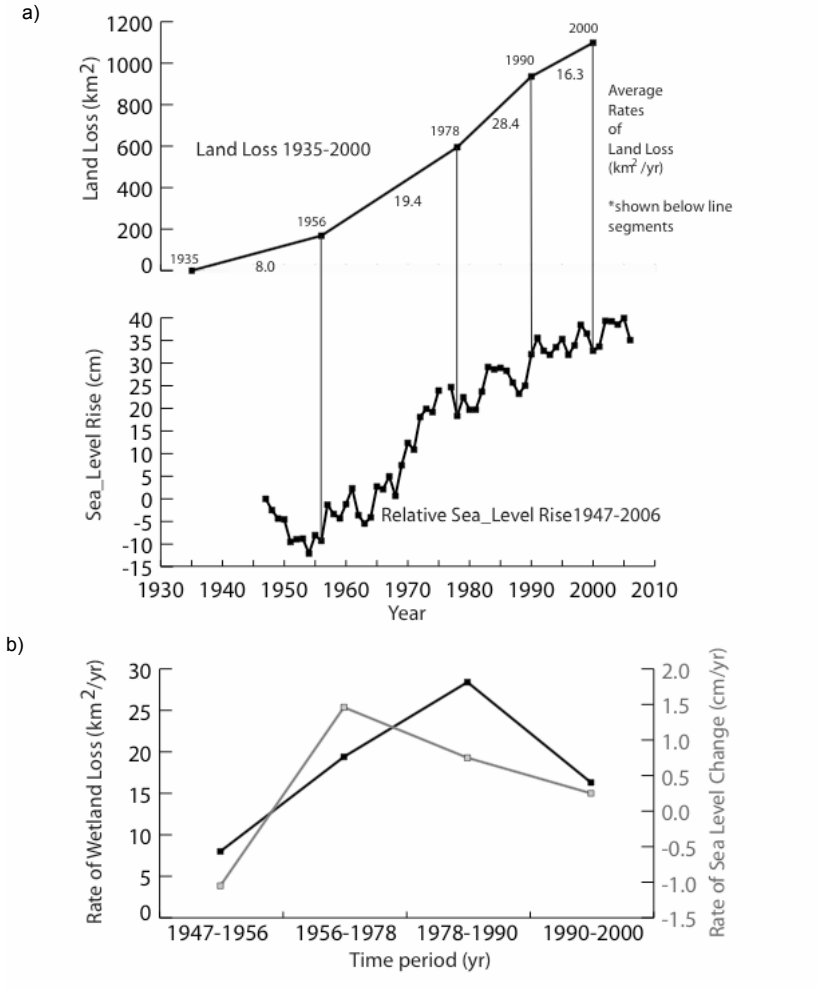

Fig. 2. Temporal plots of a). wetland loss and relative sea level since the mid-1900's and b). rate of wetland loss and sea level rise. Sea level curve from the Grand Isle gage (Miner 2006).

A recent study of marshes in Barataria Bay, Breton Sound, and the Balize Delta showed that wave erosion produces a 50 cm scarp at the marsh edge. This scarp transitions to a steep slope and then flattens with the bay bottom at a depth of 1.0 to 1.5 m (Wilson 2006). The retreating marsh produces a ravinement surface that is eventually covered by a shelly bay mud facies. It is interesting that nearshore transects surveyed off numerous marsh islands in Barataria Bay and Breton Sound show that the erosion processes produce a near same equilibrium profile (Wilson 2006).

In addition to the ongoing processes that are operative in converting wetland to open water, significant losses also occur during single large magnitude events such as 2006 Hurricanes of Rita and Katrina. Barras et al. (2006) showed that the Louisiana marshes lost a total 562 km^2 between 2004 and 2005, which can largely be attributed to Rita and Katrina that produced maximum storm surges of 5.5 and 8.0 m, respectively (IPET 2006; Hsu et al. 2006) and wave heights of 3 to 4 m. As seen in Figure 3, a direct connection exists between the path of the hurricanes and land loss. The greatest amount of wetland loss occurred in Mermentau and Breton Sound, which coincide with areas immediately east of where Rita and Katrina (respectively) made landfall accompanied by their strongest wind velocities.

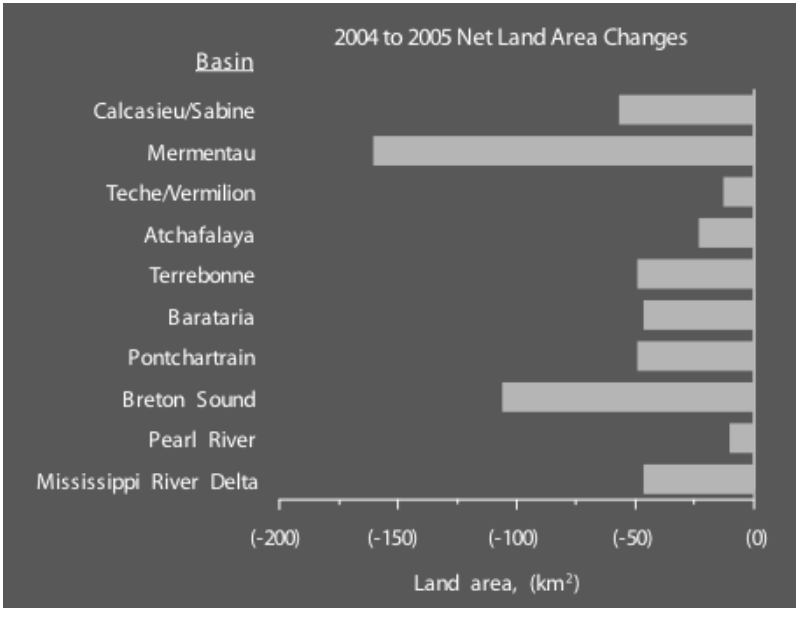

Fig. 3. Land loss resulting from the impact of Hurricanes Rita and Katrina. Note the significant increase in wetland loss immediately east of the hurricane landfalls.

A map of wetland loss in Barataria Bay resulting from the hurricanes of 2005, and primarily the impact of Hurricane Katrina, reveals that the majority of lost marshlands

occurred on the northward facing shorelines of the bays and ponds. This trend is especially apparent in large open water areas such as the shoreline along Little Lake, but is also observed in protected areas such as the terraced wetland regions east of Golden Meadow. There are exceptions, but this pervasive pattern would suggest that the return flow and the northerly winds following the passage of Katrina caused the most damage to the wetlands. Extensive loss of marshlands in the semi-protected region of Point a la Hache indicates a different erosional process. We suggest that return flow from the storm surge cascading over the western levee excavated the wetlands in this region.



Fig. 4. Map of wetland loss in Barataria Bay shown by red colored areas (from Barras 2006).

The pattern of wetland loss attributed to Hurricane Katrina appears to duplicate historical trends as seen in Figure 5. Although the map insets demonstrate that erosion occurs in all sectors between 1985 and 2000, the north and northeastward facing shorelines exhibit a more continuous and greater amount of erosion as compared with other shoreline orientations.

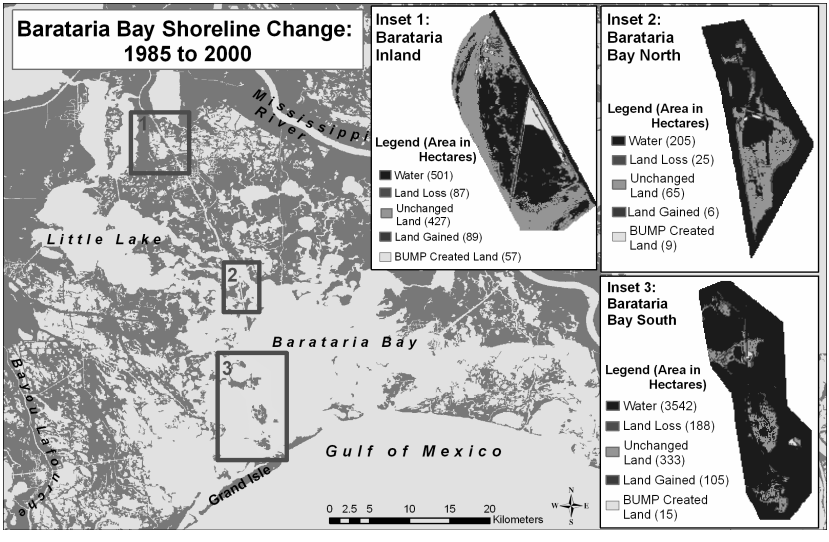

Fig. 5. Representative areas within the Barataria Basin illustrating patterns of marsh loss between 1985 and 2000.

Tidal Discharge And Tidal Prism

Long term conversion of wetlands to open water (> 125 years) has steadily increased tidal exchange between Barataria Bay and the Gulf of Mexico resulting in larger inlet tidal prism. Two direct consequences of the increasing tidal discharge are the enlarging tidal inlet geometry and growth of ebb-tidal delta shoals (List et al. 1997; FitzGerald et al. 2004). Recent data collected during the summer of 2006 allow an updating of hydraulic and morphologic trends previously established for the Barataria Bay barrier system for the period between 1880-1980.

Simultaneous synoptic ADCP surveys were conducted across the inlet throat of Caminada, Barataria Pass, Pass Abel, and Quatre Bayou Pass to obtain discharges through time and calculate tidal prisms for each pass. The surveys could not be conducted at night, hence the peak discharges of the flood tidal cycle were not measured. As a result, the ebb tidal volumes were used in the tidal prism versus cross sectional inlet area plots.

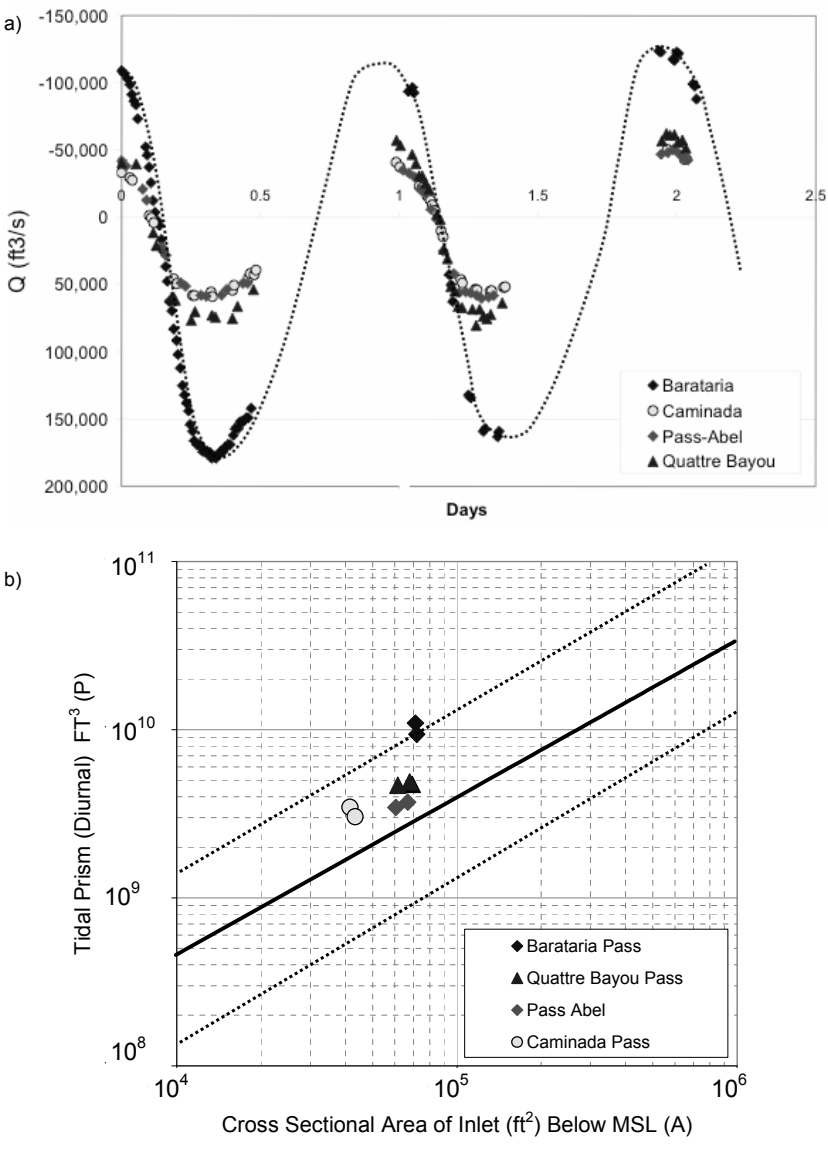

Fig. 6. ADCP data collected across the inlet throats were a) fitted to a sine curve and then used to determine tidal prisms for two ebb cycles for each inlet and then b) plotted against their corresponding maximum cross sectional area for that day. The graph also shows the Jarrett (1976) curve for unjettied Gulf Coast Inlets, as well as the 95% confidence limits.

The missing data to compute the calculation of ebb tidal prism volumes were filled by curve-fitting a distorted sine function. The function distortion lies in the slope of the rising and falling limbs of the tide and hence the discharge through the inlets. The distortion slopes of the sine function were obtained from data during this survey and data collected during the summer of 2006.

Cross sectional areas of the Barataria tidal inlets are plotted against their tidal prism (for two ebb cycles) and shown on Jarrett's (1976) regression curve for unjettied tidal inlets along the U.S Gulf Coast (Fig. 6). As seen in Figure 6, Caminada Pass, Pass Abel, and Quatre Bayou Pass plot well within the 95% confidence limits, but the Barataria Pass data points plot at the edge and outside of this field. As compared to the other Barataria inlets, and Gulf Coast inlets in general, Barataria Pass has a relatively small cross section given its tidal prism. One explanation for its relatively small size maybe related to the stratigraphy of the region, and perhaps the inlet channel is eroded into consolidated clays, which resist erosion.

Table 1. Inlet Cross Sectional Area (m^2)

Year	Abel	Barataria	Caminada	Quatre Bayou	Total X-sect area
1880	0	3996	809	133	4938
1930	395	7079	1353	2590	11417
1980	4193	8712	1532	3777	18214
2006	6669	7541	3372	6726	24308

Tidal Inlet Historic Morphologic Changes

Long-term wetland loss and increasing tidal prism have steadily enlarged the size of the tidal inlets. As seen in Table 1, Pass Abel and Quatre Bayou Pass have shown the greatest increase in area, and Caminada Pass the least, although it quadrupled in size. Interestingly, Barataria Pass doubled in size between 1880 and 1980, but subsequently shoaled by about 1,300 m^2 during the following 26 years. In Figure 7, the total inlet cross sectional areas is plotted for four time periods from 1880 to 2006. The regression analysis indicates a remarkable temporal correlation of increasing total inlet cross-sectional area, however this may be fortuitous. As most of the existing wetland area is now situated some distance from the tidal inlets (Fig. 4), the conversion of marsh area to open water will have an increasingly smaller effect of tidal prism due tidal wave attenuation and frictional factors within Barataria Bay.

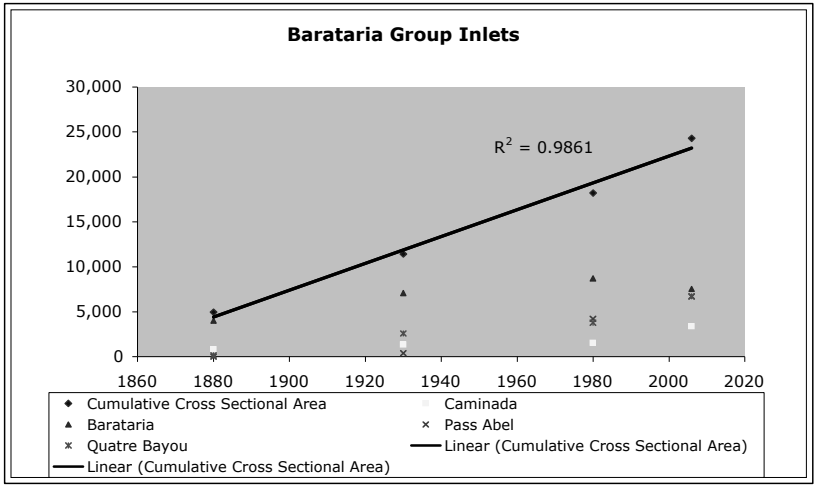

Fig. 7. Barataria tidal inlet cross-sections through time.

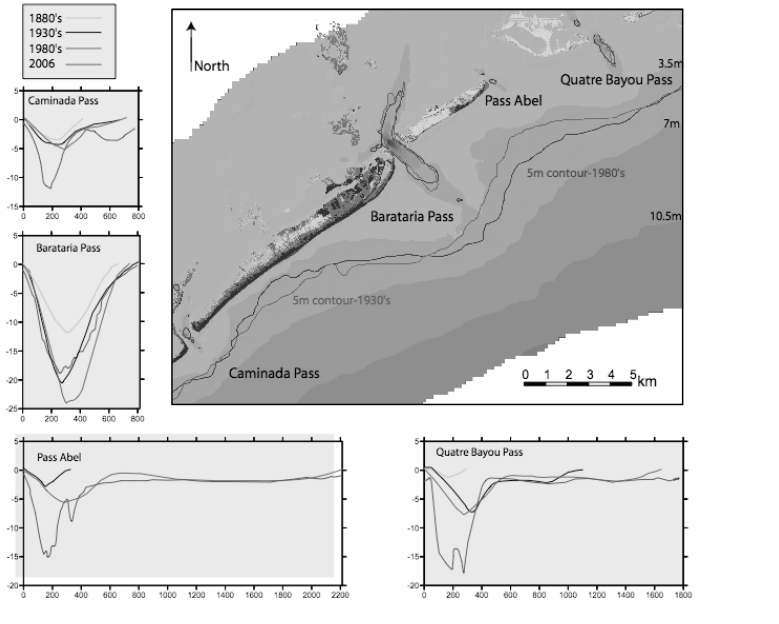

Fig. 8. Historical morphological changes in tidal inlet throat morphology between 1880 and 2006.

Historical changes in the throat geometry of the tidal inlets are illustrated in Figure 8. The most apparent trend at all the inlets is a deepening of the channel thalweg through time, with the exception of Barataria Pass that shoaled between 1980 and 2006. Although the total Barataria inlet cross-sectional areas increased since 1880, the decrease in size of Barataria Pass may be related to a capture of a portion of its former 1980 tidal prism by the adjacent inlets. Both nearby Pass Abel and more distant Quatre Bayou Pass substantially increased in size since 1980, deepening by more than 10 m. In addition, Caminada Pass doubled in size and deepened by 7 m to 12 m in depth.

CONCLUSION

Long-term conversion of wetland areas to open water in Barataria Bay is a product of the high rate of relative SLR and is attributed to both natural and anthropogenic causes. In addition to subsidence, land loss is due to marsh edge erosion and catastrophic scour during major hurricanes. Examination of wetland loss maps covering decadal time scales and after the impact of Katrina indicate that north and northeastward facing shorelines experience preferential erosion. Although the historic loss of wetland area corresponds with rising sea level, there is no direct correspondence in the rate of wetland loss and the rate of sea level rise. Expanding open water area has led to increased tidal exchange and enlarging tidal prisms. In response to this forcing, tidal inlets have grown in size and ebb-tidal deltas have prograded seaward. Total inlet cross sectional area has quadrupled in size since 1880. Although there is a very strong correlation between increasing total inlet throat section and time, the lack or marshlands close to the inlets and frictional attenuation of the tidal wave deep into the bay will reduce the historic rate of increasing tidal prism.

AKNOWLEDGEMENTS

The authors would like to thank Jeff Motti, Phil McCarty, Mike Brown and Dallon Weathers for their help in the field. This project was funded by NOAA's Pontchartrain Restoration Program.

REFERENCES

Barras, J. A., Bourgeois, P. E. and Handley, L. R. (1994). Land loss in coastal Louisiana 1956-90. National Biological Survey, National Wetlands Research Center Open File Report 94-01. 4 p.

Barras, John A. (2006). Land area change in coastal Louisiana after the 2005 hurricanes—a series of three maps: U.S. Geological Survey Open-File Report 06-1274.

Boyd, R., and Penland, S. (1981). Washover of deltaic barriers on the Louisiana coast. Gulf Coast Assoc. of Geol. Soc. v. 31, p. 243-248.

Britsch, L. D., and Dunbar, J.B. (1993). Land loss rates: Louisiana coastal plain: Journal of Coastal Research, v. 9, p. 324-338.

Church, J.A., Gregory, J.M., Huybrechts, P., Kuhn, M.,Lambeck, K., Nhuan, M.T., Qin, D., Woodworth, P. (2001). Changes in Sea Level. in, Douglas, B.C. and Ramirez, A, eds.., Climate Change 2001: The Scientific Basis. Cambridge Univ. Press, NY, p. 14, p. 670-679.

Dunbar, J.B., Britsch, L.D., and Kemp, E.B. (1992). Land loss rates: Louisiana coastal plain, Technical Report GL-90-2, USACE-WES, Vicksburg, MS, 121 p.

FitzGerald, D.M., Kulp, M., Penland, P., Flocks, J., and Kindinger, J. (2004). Morphologic and Stratigraphic Evolution of Ebb-Tidal Deltas along a Subsiding Coast: Barataria Bay, Mississippi River Delta, Sedimentology, v. 15, p. 1125-1148.

FitzGerald, D.M., Penland, S., and Kulp, M. (2003). Tidal prism changes within Barataria Bay and its effects on sedimentation patterns and barrier shoreline stability, The Gulf Coast Association of Geological Societies. v. 23, p. 213-225.

Hsu, S.A., Braud, D., and Blanchard, B. (2006). Rapid Estimation of Maximum Storm Surges Induced by Hurricanes Katrina and Rita in 2005, Coastal Studies Institute, Louisiana State University, http://www.nwas.org/ej/pdf/2006-EJ9, 10 p.

IPET (Interagency Performance Evaluation Task Force). (2006). Performance Evaluation of the New Orleans and Southeast Louisiana Hurricane Protection System. Draft Final Report of the Interagency Performance Evaluation Task Force. Vol. 1 - Executive Summary and Overview. 1 June 2006. Available online at https://ipet.wes.army.mil

Gornitz, V. (1991). Global coastal hazards from future sea level rise. Palaeogeography, Palaeoclimatology, Palaeoecology Global and Planetary Change Section., v. 89, p.379-398.

Jarrett, J.T. (1976). "Tidal prism-inlet area relationships," U.S. Army Corps of Engineers, GITI Report 3, 32pp.

Levin, D., 1993. Tidal inlet evolution in the Mississippi River delta plain. Jour. of Coastal Research, v. 9, p. 462-480.

List, J.H., Jaffe, B.E., Sallenger, A.H. Jr., Williams, S.J., McBride, R.A., and Penland, S. (1994). Louisiana barrier island erosion study: Atlas of seafloor changes from 1878 to 1989: Reston, Virginia, U.S. Geological Survey and Louisiana State University, Miscellaneous Investigations Series I-2150-A, 81 p.

List, J.F, Jaffe, B.E, Sallenger, A.H, Hansen, M.E. (1997). Bathymetric comparisons adjacent to the Louisiana barrier islands--processes of large-scale change: Journal of Coastal Research, v. 13, p. 670-678.

Mitrovica, J.X., Milne, G.A. (2002). On the origin of late Holocene sea-level highstands within equatorial ocean basins, Quaternary Science Reviews, 21(20-22), p.2179-2190.

Miner, M. D. (2007). Long and Short-Term Morphologic Evolution and Stratigraphic Architecture of a Transgressive Tidal Inlet, Little Pass Timbalier, Louisiana: Ph.D. Dissertation, University of New Orleans, New Orleans, Louisiana, 156 p.

Morton, R.A., Tiling, G., and Ferina, N.F. (2003). Causes of hotspot wetland loss in the Mississippi delta plain: Environmental Geosciences, v. 10. p. 71-80.

Morton, R.A., Bernier, J.C., Barras, J.A., and Ferina, N.F. (2005). Rapid Subsidence and Historical Wetland Loss in the Mississippi Delta Plain: Likely Causes and Future Implications, USGS Open-File Report 2005-1216, 115 p.

Morton, R.A., Bernier, J.C., and Barras, J.A. (2006). Evidence of regional subsidence and associated interior wetland loss induced by hydrocarbon production, Gulf Coast region, USA, Environmental Geology, v. 50, p. 261-274.

Muller, R.A., and Stone, G.W. (2001). A Climatology of tropical storm and hurricane

strikes to enhance vulnerability prediction for the southeast U.S. coast. Journal of Coastal Research, v. 17, p. 978-991.

Penland, S. and Ramsey, K.E. (1990). Relative sea-level rise in Louisiana and the Gulf of Mexico. Journal of Coastal Research, v. 2, p. 323-342.

Stone, G.W., and Muller, R.A. (2005). Meteorological effects on coasts, in: Encyclopedia of Coastal Science, Schwartz, M., ed., p. 345-347.

Schwimmer, R. (2001). Rates and processes of marsh shoreline erosion in Rohoboth Bay, Delaware. Journal of Coastal Research, v. 17, p. 672-683.

Williams, J., Penland, S., and Sallenger, A.H. Jr. (1992). Atlas of shoreline changes in Louisiana from 1853 to 1989: Reston, Virginia, U.S., Geological Survey and Louisiana State University, Miscellaneous Investigation Series I-2150-A, 103 p.

Wilson, C.A. (2006). An evaluation of erosional sediment dynamics in southeastern Louisiana coastal marshes: Barataria Bay, Breton Sound, and Balize Delta. Masters Thesis, Dept of Earth & Env Sci, Tulane University, New Orleans, LA, 142 p.

MODELING FUTURE COASTAL WETLAND TRANSITION INDUCED BY RELATIVE SEA-LEVEL RISE

James C. Gibeaut[1]

1. Bureau of Economic Geology, Jackson School of Geosciences, The University of Texas at Austin, University Station Box X, Austin, TX 78713, USA. jim.gibeaut@beg.utexas.edu.

Abstract: Using a 1-m lidar digital elevation model and detailed wetlands mapping, we developed an inundation model that projects future wetland distribution caused by sea-level rise. Vertical accretion, edge erosion, and land-subsidence components are also included in the model. Applying the model to a section of Galveston Island, Texas, and using the actual annual record of ocean level recorded by a nearby tide gauge shows the complicated interplay of decadal-scale water-level variation and topography in determining the future distribution of wetlands. Total wetland coverage declines by 22% in 30 years but recovers to a net loss of just 5% within 90 years. Uplands transitioning to high-marsh wetlands more than offset the effects of inundation, allowing high-marsh wetlands to increase in coverage by 132%. Low-marsh wetlands, however, decrease by 77% at the end of the 90-year model period.

INTRODUCTION

Distribution of barrier-island subenvironments is strongly related to elevation above or below mean sea level. The style of transition of estuarine habitats during rising sea level depends largely on the slope of the upland and sediment supply, Brinson et al. (1995). Fringing wetlands on the barrier islands of the upper Texas coast exist within a narrow elevation range, with shifts from barren tidal flat to marsh to upland vegetation occurring across areas with just a 50- to 60-cm rise in elevation, Gibeaut et al. (2003a). On the bay sides of barrier islands, this amount of topographic change occurs on a small scale and in complicated patterns across relict geomorphic features, such as storm-surge channels, washover and flood-tidal delta deposits, and beach ridges and swales.

For this research, a wetland map derived from manual interpretation of color infrared photography and extensive field checks, White et al. (2004), is combined with a high-resolution (1-m postings and .1- to .15-m vertical accuracy) lidar-derived digital elevation model (DEM), Smyth et al. (2003), to quantify topographic relationships of barrier-island wetland types. The combined data set forms the basis of an inundation model to determine the likely transition of wetlands during expected future sea-level rise. The model is applied to a section of Galveston Island, Texas USA, a sandy barrier island on the upper Texas coast.

MODEL

The DEM is classified using elevation intervals assigned to the following wetland types in order of increasing elevation: (1) low-flat; (2) low-marsh; (3) high-flat; and (4) high-marsh. Elevation is the primary factor in determining these environments, but not the only factor, thus causing some inconsistencies with the photography-mapped classifications. Noise in the elevation data and coarser-scale photographic mapping compared to the DEM also cause differences. Therefore, to arrive at an optimal and realistic classification, the lower boundary of the low flat is determined, and then the upper boundary of the high marsh, which is the wetland/upland boundary, is adjusted until the total area of wetland matches what was actually mapped on the photography. Elevation intervals for other wetland environments are then adjusted so that they have the same area as what was mapped.

In addition to changes caused by inundation, wetlands may erode along the bayward fringes as a result of waves and tidal currents. Therefore, rates of shoreline change computed by comparing historical shorelines from the 1930's, 1950's, 1980's, and 1995/2002 are incorporated into the wetland change model, Gibeaut et al. (2003b). Vertical sediment accretion occurs and partly offsets the inundating effects of relative sea-level rise. A sedimentation model that describes vertical accretion as a function of elevation is also contained in the wetland model. The sedimentation function is based on measured accretion rates in similar settings in the Gulf of Mexico that indicate slower rates at higher elevations, Callaway et al. (1997). The highest vertical accretion rate occurs at the elevation of the lower low-marsh boundary and is set equal to the long-term relative higher high water rise rate, as measured from 1908 through 2002 and adjusted for local land subsidence. Below the low-marsh boundary the rate is zero. Above the boundary, the function decreases the accretion rate according to the expected duration of tidal inundation. At the high marsh/upland boundary, the vertical accretion rate is zero and is zero above that level.

The record of mean annual levels of mean higher high water, as measured at the Pier 21 tide gage on the bayside of Galveston Island from 1908 through 2002, was used to calculate water-level input for the model. Because wetlands are not expected to respond to water-level fluctuations within a year's time, the running average of the previous 3 years of water level was used. The 3-year running average was differenced to provide the amount of water-level change for annual iterations of the model. The pier 21 tide gage measures relative sea-level change at its location, but relative sea-level change varies

along the barrier islands because of varying land subsidence rates. To account for this, various releveling surveys conducted along the main coastal highway from the 1950's to the 1970's were used to estimate subsidence rates relative to the pier 21 tide gage location. A differential subsidence grid was developed from these data using guidance from geologic studies showing the thickness of relatively compactable Holocene sediment beneath the islands.

MODEL RESULTS

The model test area is a 7.5-km-long, undeveloped part of the bay side of Galveston Island (Fig. 1). Relict storm-surge channels create a highly crenulated bay shoreline dominated in low-marsh environments by *Spartina alterniflora* (smooth cordgrass), with high-marsh environments characterized by *Borrichia frutescens* (sea oxeye), *Spartina patens* (saltmeadow cordgrass), and other plants. The diurnal tide range is 30 cm, but the elevation of the wetland/upland boundary is about 1 m above mean sea level. Episodic high wind tides cause a higher encroachment of estuarine wetlands than would be expected from the tide range. Rate of relative mean higher high water rise, as measured from 1908 through 2002, is 6.5 mm/yr; however, considerable interannual and decadal variation has occurred. Estimates of differential local subsidence, as described previously, indicates that long-term relative water-level rise varies from about 6.4 to 7.5 mm/yr in the study area.

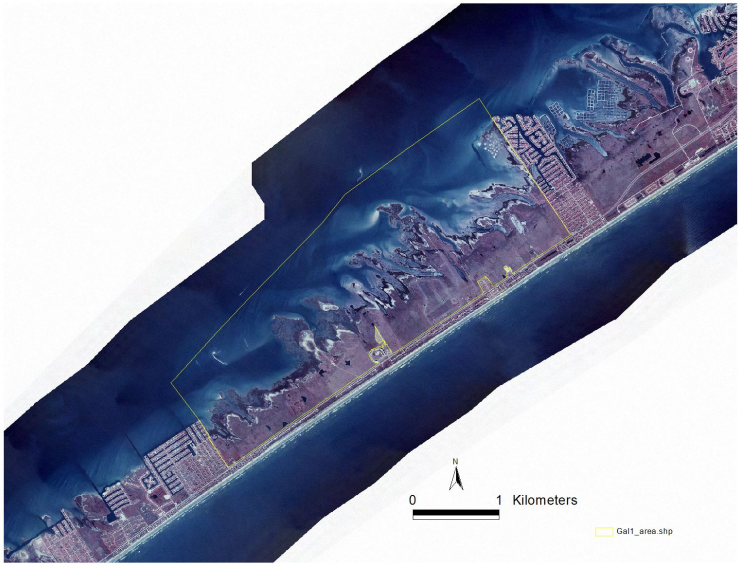

Fig. 1. Color infrared aerial photograph of model test area on Galveston Island, Texas. The Gulf of Mexico is toward the lower right and West Bay toward the upper left. The study area is outlined.

The wetlands model was run 90 years into the future. In 2002, 402 ha of wetland, which included low flat, low marsh, high flat, and high marsh, were mapped with 46% of it being low marsh and 32% high marsh (Fig. 2). After 30 years, the model projects an overall decline in wetland of 22%, but low marsh declines 58% and high marsh increases 47% (Fig. 3). High marsh continues to increase and low marsh decrease until 90 years when the model projects just 5% less total wetland than in 2002. By 90 years, however, low marsh has decreased by 77% and high marsh has increased by 132% (Fig. 4). Shoreline retreat caused the loss of about 30 ha (16%) of the low marsh but did not affect high marsh.

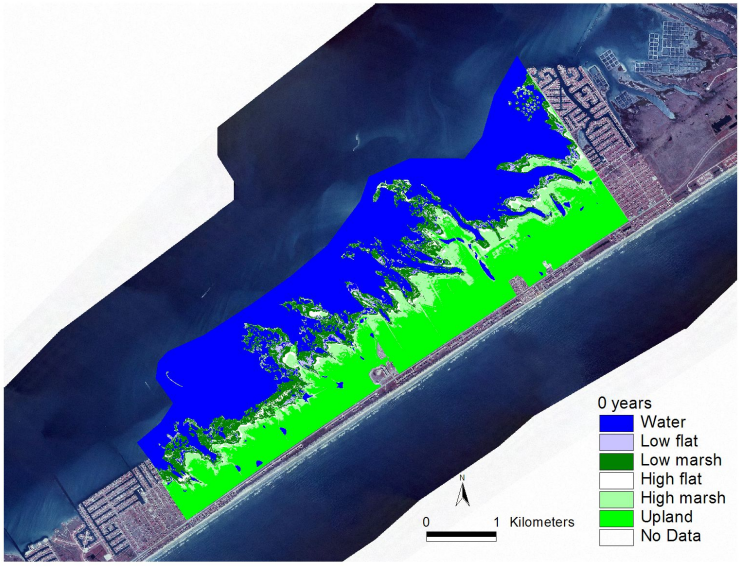

Fig. 2. Classification of wetlands according to elevation. Zero years is the beginning of the model run and represents wetland status in the year 2002.

DISCUSSION

The model shows marsh, particularly high marsh, migrating up the gently sloping back barrier in a complicated pattern dictated by the relict geomorphology but disappearing on the bayward side owing to inundation and shoreline retreat. Similar patterns and rates of change are observed when comparing 1956 and 2002 aerial photography. During that 48-year time period, there was about a 26% loss of marsh area. High- and low-marsh environments were not broken out on the 1956 photography, so comparing marsh types is not possible. However, observed marsh upland migration patterns and an overall similar decrease in marsh area indicate that assumptions in the model, particularly the vertical accretion function, shoreline retreat, and marsh-elevation relationships, are reasonable.

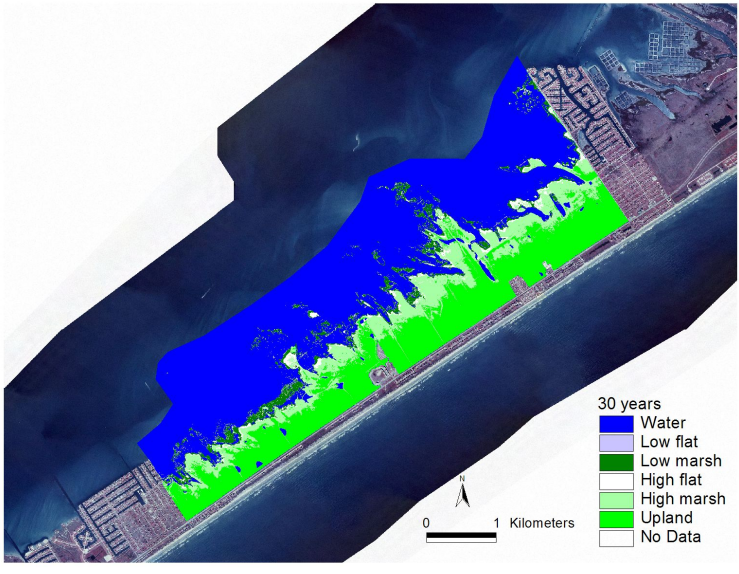

Fig. 3. Projected wetland distribution after a model run of 30 years.

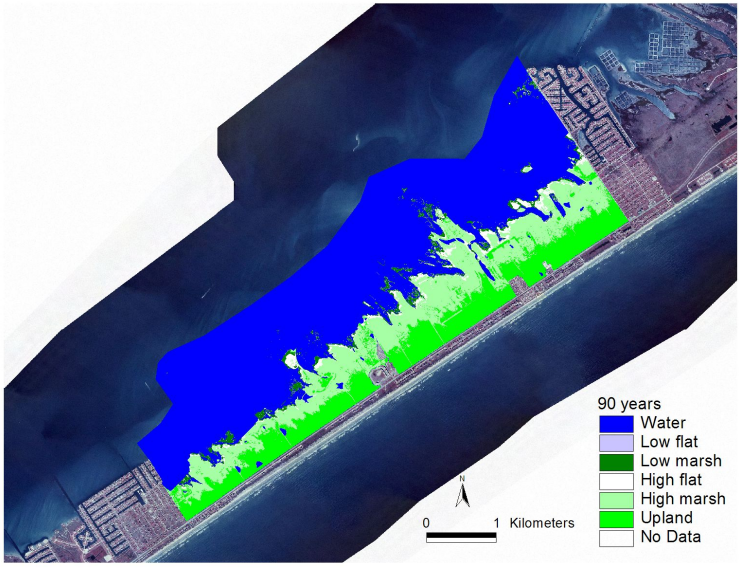

Fig. 4. Projected wetland distribution after a model run of 90 years.

The variability of wetland change over the projected 90-year period is a result of the complicated interplay of topography and decadal variation of mean higher high water level that is superimposed on a long-term rising trend. This variation causes ranges in water-level change rates input to the model to be several times the magnitude of the long-term trend for several years at a time. At the end of 90 years, upland migration allows for little net change in the combined area of the four wetland environments. However, the low marsh environment decreases dramatically. The low marsh is a crucial environment for fishery juveniles. The high rate of low-marsh decline is partly offset by upland migration in this undeveloped setting. Development is now occurring, however, and more is proposed in areas where the model projects an upland transition to wetlands. This development will also curtail the development of future high marsh. Furthermore, no increase in the rate of sea-level rise, as predicted in global warming studies, is included in the model.

We are currently refining and applying the model to other barrier islands where we have developed the necessary data sets. Model projections of wetland distributions could be used to establish buffer zones where development is restricted or to guide the acquisition of uplands for conserving future wetlands. The model will also allow experimentation to determine the relative importance of the various processes that determine the style of transition of barrier island environments during relative sea-level rise.

CONCLUSION

The wetlands inundation model shows the importance in considering annual to decadal variation in sea-level curves and detailed topography when projecting future wetland distributions, particularly in microtidal settings. Results from the 90-year model run presented here are based on a historical sea-level-change record without accounting for any increase in rate of sea-level rise due to climate change. Nonetheless, the important low marsh environment decreases drastically (77%). Some of this decrease is offset by upland migration of wetland, but future development of back barrier areas will eliminate the space needed for wetlands to migrate landward. Results from this study can be used to draw buffer zones for migrating wetlands.

ACKNOWLEDGEMENTS

This research was financed through grants from the U.S. Environmental Protection Agency through the Texas Commission on Environmental Quality.

REFERENCES

Brinson, M.M., Christian, R.R., and Blum, L.K., 1995, Multiple states in the sea-level induced transition from terrestrial forest to estuary: Estuaries, v. 18, p. 648-659.

Callaway, J.C., DeLaune, R.D., and Patrick, J., W. H. (1997). Sediment accretion rates from four coastal wetlands along the Gulf of Mexico: Journal of Coastal Research, v. 13, p. 181-191.

Gibeaut, J.C., White, W.A., Smyth, R.C., Andrews, J.R., Tremblay, T.A., Gutiérrez, R., Hepner, T.L., and Neuenschwander, A. (2003a). Topographic variation of barrier

island subenvironments and associated habitats, Coastal Sediments '03: Crossing disciplinary boundaries: Proceedings, Fifth International Symposium on Coastal Engineering and Science of Coastal Sediment Processes, Volume CD-ROM: Clearwater Beach, Florida, 10 p.

Gibeaut, J.C., Waldinger, R., Hepner, T., Tremblay, T.A., and White, W.A. (2003b). Changes in bay shoreline position, West Bay system, Texas: Austin, Texas, Bureau of Economic Geology, The University of Texas at Austin, p. 27.

Smyth, R.C., Gibeaut, J.C., Andrews, J., Hepner, T., and Gutiérrez, R. (2003). The Texas Shoreline Change Project: coastal mapping of West and East Bays in the Galveston Bay System using airborne lidar, final report prepared for the Texas General Land Office, under GLO Contract Number 02-520 C: Austin, Texas, Bureau of Economic Geology, The University of Texas at Austin, p. 41.

White, W.A., Tremblay, T.A., Waldinger, R.L., and Calnan, T.R. (2004). Status and Trends of Wetland and Aquatic habitats on Barrier Islands, Upper Texas Coast, Galveston and Christmas Bays: Austin, Bureau of Economic Geology, Jackson School of Geosciences, The University of Texas at Austin, p. 67.

MORPHOLOGICAL INTERACTIONS WITHIN UK ESTUARIES: A PRELIMINARY ANALYSIS OF CRITICAL RATES OF SEA-LEVEL RISE

Kate Rossington[1], Robert J. Nicholls[2], Michiel A.F. Knaapen[3]

1. School of Civil Engineering and the Environment, University of Southampton, Southampton, SO17 1BJ, UK. skr102@soton.ac.uk
2. School of Civil Engineering and the Environment, University of Southampton, Southampton, SO17 1BJ, UK. r.j.nicholls@soton.ac.uk
3. School of Civil Engineering and the Environment and School of Ocean and Earth Science, University of Southampton, National Oceanography Centre Southampton, European Way, Southampton, SO14 3ZH, UK mafk@noc.soton.ac.uk

Abstract: This paper uses historic bathymetry data for five UK estuaries to examine past morphological changes and to calibrate an equilibrium-based morphological behaviour model of estuarine evolution (ASMITA - Stive *et al*., 1998). After calibration, ASMITA is used to predict the maximum rate of sea-level rise (SLR_{crit}) which each estuary can experience without losing all intertidal areas. SLR_{crit} varies significantly between estuaries suggesting that some are quite vulnerable to sea-level rise (e.g., Southampton Water) and others are more resilient (e.g. the Ribble). Estuary area, sediment supply, sediment transport potential and human interference all appear to influence the sensitivity of an estuary to sea-level rise.

INTRODUCTION

Over 170 estuaries with a variety of physical characteristics, spatial extents and management issues dissect the coastline of the United Kingdom (Pontee and Cooper, 2005). Many have some form of nature protection designation and intertidal areas are particularly important for numerous species, especially migrating birds (Townend, 2002). Intertidal areas may also provide important natural coastal defences,

strengthening the flood protection of the low lying land surround estuaries, by dissipating wave energy (Möller, 2006).

Many estuaries have urbanised shorelines, with towns, cities and other developments around the estuary often being built on low-lying, flood prone land. In less developed areas, the land surrounding estuaries may be fertile farm land. Low-lying developed and agricultural areas are usually protected by embankments and sea walls. Estuaries are also used for recreational activities such as sailing, fishing and walking and are economically important as ports (with associated dredging), fishing grounds and for aggregate extraction (Townend, 2002).

The diverse uses and morphologies of estuaries can lead to complex and sometimes conflicting management demands. In order to manage estuaries effectively it is important to be able to predict how they are likely to change in the future, both due to natural and anthropogenic forcing.

Sea-level rise is predicted to accelerate over the 21st Century, with a global-mean rise of 9 to 88 cm, with the largest relative sea-level rise in the UK in the south (Hulme *et al*., 2002). Hulme *et al.* (2002) predict that by the 2080s the relative rate of sea-level rise around the UK could be between 0.3 and 12 mm/year with the highest rates of rise in the south west. This is likely to be a major driver of change within estuaries, possibly resulting in loss of intertidal areas, erosion of shorelines, and flooding of low lying areas around estuaries. Changes to shoreline management, such as increased use of managed realignment may also influence the morphological behaviour of estuaries (Townend and Pethick, 2002).

This paper has a main focus on the critical rate of sea-level rise when estuaries will lose their intertidal areas. It presents a) historic morphological changes for a sample of five UK estuaries covering a range of behavioural morphological types described in FutureCoast (Dyer, 2002), as shown in Table 1; and b) the use of ASMITA, which is an equilibrium-based morphological behaviour model of estuarine evolution (Stive *et al*., 1998). Previously, ASMITA has mainly been applied in lagoonal environments. This is the first time that it has been applied to and calibrated for estuaries with widely differing morphological characteristics and this research gives valuable insight into the behaviour of different estuaries under rising sea levels.

METHOD

Study Sites

Five estuaries were selected from around the United Kingdom (Fig. 1) to cover a range of morphological types, based on the behavioural characterisation of estuaries given in FutureCoast (Dyer, 2002): Ribble, Dart, Southampton Water, Langstone Harbour and Chichester Harbour. The main characteristics of each estuary are summarized in Table 1.



Fig. 1. Locations of the five study estuaries: 1) Ribble, 2) Dart, 3) Southampton Water, 4) Langstone Harbour and 5) Chichester Harbour. Reproduced from Ordnance Survey map data by permission of the Ordnance Survey © Crown copyright 2001.

Table 1. Summary of the major characteristics of the five study estuaries (Dyer, 2002).

	Estuary	Morphological Type	Area (ha)	Length (km)	Mean Tidal Range (m)	Mean river flow (cumec)	Tidal Asymmetry	Sediment	Human Influences
1	Ribble	Funnel shaped	11920	28.4	7.9	43.87	Flood dominant	Mainly sandy	Extensive reclamation, training walls & dredging
2	Dart	Ria without spits	863	19.8	4	11.07	Ebb dominant	Rocky	Training walls & some dredging in upper estuary
3	Southampton Water	Single spit enclosed estuary	3975	20.2	4	18.1	Ebb dominant	Muddy with some gravel	Extensive reclamation, capital & maintenance dredging
4	Langstone Harbour	Symmetrical tidal inlet	1925	7.7	4.2	0.36	Strongly ebb dominant	Mainly muddy	Reclamation & aggregate extraction from ebb-tidal delta
5	Chichester Harbour	Symmetrical tidal inlet	2946	8.1	4.2	0.71	Weakly ebb dominant	Muddy	Gravel extraction from ebb-tidal delta

Data on the historic morphologies of the Ribble and Dart estuaries, Langstone Harbour and Chichester Harbour were digitised from historic hydrographic charts obtained from the UK Hydrographic Office (UKHO). For Southampton Water, digital point elevation data were supplied by ABP Marine Environmental Research (ABPmer). The dates, types and sources of data used in this study are summarised in Table 2. Additional data and literature relating to the study sites has been reviewed for information such as amounts of dredging, dates of land reclamations and other significant human interventions.

Table 2. Summary of data used for each estuary.

Estuary	Data Type	Dates	Source
Ribble	Admiralty Charts	1904, 1951, 1977, 1990	UKHO
Dart	Admiralty Charts	1853, 1900, 1952, 1972, 1983, 1995	UKHO
Southampton Water	Point elevation data	1783, 1911, 1926, 1951, 1965, 1976, 1996	ABPmer
Langstone Harbour	Admiralty Charts	1955, 1961, 1968, 1974, 1997	UKHO
Chichester Harbour	Admiralty Charts	1955, 1961, 1968, 1974, 1997	UKHO

The data from the hydrographic charts were stored and manipulated using ArcView 9.0 Geographical Information System (GIS). All charts were georeferenced using known control points and transformed to British National Grid for comparison. Spot heights, depths, bathymetric contours and coastline were digitised from the hydrographic charts and converted to metres below ordnance datum (approximately mean sea level).

The point and contour data were interpolated to give a continuous bathymetry surface using ArcView's "Topography to Raster" interpolation method. This method was chosen because it is designed for catchment analysis and should create hydrologically realistic digital elevation models. It is the only interpolation technique available that can accept point elevation and contours as inputs. The area and volume of the tidal flats, channel and ebb-tidal delta (where present) were calculated using the Area/Volume tool in ArcView 9.0. The definitions of the tidal flats, channel and ebb-tidal delta are the same as those used in ASMITA (Fig. 2) and the area and volume data from the GIS analysis are used directly with the model.

Potential error in the volume and area data may come from numerous sources, including survey error, digitising and interpolation error. Survey error was estimated to be +/- 0.5 m for surveys conducted before 1968 and +/- 0.25 m for later surveys (van der Wal and Pye, 2004; Friend *et al*., 2006). Digitising and interpolation errors were calculated to be +/- 5 % of the element volume, in addition to the survey errors. A comprehensive

review of potential error when using historic charts and maps to investigate coastal change is given by Carr (1980).

ASMITA

ASMITA was first presented as a behaviour-based model "describing morphological interaction between a tidal lagoon or basin and its adjacent coastal environment" (Stive *et al*., 1998). The model consists of a schematisation of a tidal inlet system with the major morphological elements being viewed at an aggregated scale (Fig. 2). The major assumption of ASMITA is that, under constant hydrodynamic forcing, each element tends towards a morphological equilibrium which can be defined as a function of hydrodynamic forcing and basin properties (van Goor *et al*., 2003). Empirical relationships are used to define the equilibrium volume of each element (Stive *et al*, 1998).

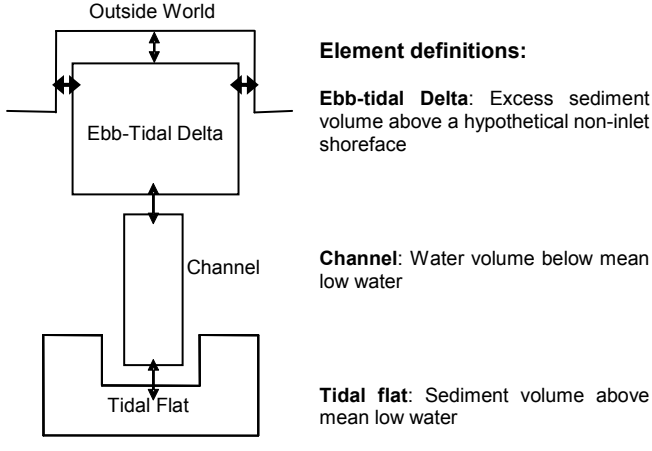

Fig. 2. ASMITA schematisation and element definitions (from van Goor *et al*., 2003).

The morphological elements in ASMITA, intertidal area, channels and ebb-tidal delta, interact through sediment exchange and this interaction plays an important role in the morphological evolution of the whole system, as well as that of the individual elements (van Goor *et al*., 2003). In cases where morphological elements are not present (e.g., ebb tidal delta), reduced element models can be applied. Long-term, residual sediment exchange is assumed to occur between adjacent model elements and it is assumed that development of the tidal inlet does not affect the availability of sediment in the outside world, represented by the global equilibrium concentration (van Goor *et al*., 2003). Volume changes within elements and sediment exchange between adjacent elements are described by equations 1, 2 and 3.

$$\delta_{fc} \cdot (c_f - c_c) = Ws_f \cdot A_f \cdot (c_{fe} - c_f) \quad (1)$$

$$\delta_{fc} \cdot (c_c - c_f) + \delta_{cd} \cdot (c_c - c_d) = Ws_c \cdot A_c \cdot (c_{ce} - c_c) \quad (2)$$

$$\delta_{do} \cdot (c_d - C_E) + \delta_{cd} \cdot (c_d - c_c) = Ws_d \cdot A_d \cdot (c_{de} - c_d) \quad (3)$$

Where δ_{fc}, δ_{cd} and δ_{do} are coefficients for horizontal exchange between the flat and channel, the channel and delta, and the delta and outside world; A_n is the area of element n; Ws_n is the vertical exchange coefficient for element n; c_n is the actual concentration and c_{ne} is the element's local equilibrium concentration, defined in equations 4, 5 and 6. Subscripts, f, c and d, refer to the tidal flat, channel and ebb-tidal delta elements, respectively.

$$c_{fe} = C_E \cdot (V_f / V_{fe})^r \quad (4)$$

$$c_{ce} = C_E \cdot (V_{ce} / V_c)^r \quad (5)$$

$$c_{de} = C_E \cdot (V_d / V_{de})^r \quad (6)$$

Where V_n is elements n's current volume; V_{ne} is elements n's equilibrium volume; C_E is the global equilibrium concentration and r is greater than 1 and is usually taken as 2 in compliance with a third power of sediment transport and a non-linear function of flow velocity (van Goor, 2001).

Model Application

In the current study, ASMITA was used to estimate the critical rate of sea-level rise (SLR_{crit}) for each estuary (van Goor *et al*., 2003). SLR_{crit} is the maximum rate of sea-level rise (SLR_{crit}) an estuary can keep pace with before it can no longer maintain equilibrium morphology and intertidal area is lost, with consequences for the habitat and natural flood defence functions of the estuary. SLR_{crit} is smallest in the tidal flat element, indicating the sensitivity of intertidal areas to sea-level rise. Below SLR_{crit}, intertidal flat volume progressively decreases and the channel volume increases (van Goor *et al*., 2003).

ASMITA was applied to each of the five study estuaries and calibrated to estimate a range of suitable sediment exchange coefficients (vertical exchange (Ws_n) and horizontal exchange (δ_{nm})) for each estuary. These coefficients were assumed to be the same for each element within the estuary. Southampton Water, the Ribble estuary and the Dart estuary do not have identifiable ebb-tidal delta elements and a two-element form of ASMITA comprising just the tidal flat and channel elements was used for these estuaries. The principles and base equations are the same for this two-element

ASMITA, but the channel interacts directly with the outside world. The three element model described above was used for Chichester and Langstone Harbours.

In order to calibrate ASMITA, first the value of C_E was estimated. The estimate was based on the relative availability of sediment at each site and does not represent a real or measurable concentration. The earliest area/volume data set was used to give the initial morphological conditions for each estuary. The ASMITA predictions from these initial conditions were compared with the volume data for later dates and the sediment transport coefficients (Ws_n and δ_{nm}) adjusted so that predictions fell within the error range of the data. Within this range, a least-squares approach was used to select the parameters giving the "best-fit" between the model predictions and the observed volumes.

Table 3. Total estuary area, intertidal area and % intertidal area of the earliest and latest data sets used for each estuary (numbers in brackets give error range).

Estuary	Date	Total Area (x 10^6 m^2)	Intertidal area (x 10^6 m^2)	% intertidal
Ribble	1990	127.9 (117.8 – 138.0)	98.8 (93.9 – 104.1)	77
	1904	131.6 (114.3 – 148.9)	106.8 (97.8 – 115.0)	81
Dart	1995	8.3 (7.0 – 9.6)	1.7 (1.0 – 2.3)	20
	1853	7.3 (6.0 – 8.5)	1.2 (0.6 – 1.9)	17
Southampton	1996	27.2 (25.6 – 27.4)	6.1 (4.6 – 7.6)	22
Water	1783	35.6 (35.2 – 38.3)	16.0 (12.7 – 19.8)	45
Langstone	1997	18.5 (18.1 – 18.8)	12.5 (11.9 – 13.8)	68
Harbour	1955	19.1 (18.8 – 19.4)	12.7 (11.0 – 14.3)	66
Chichester	1997	29.3 (29.0 – 29.6)	17.5 (15.6 – 19.5)	60
Harbour	1955	29.5 (29.2 – 29.7)	17.5 (15.3 – 19.7)	59

RESULTS

The data suggests differing morphological behaviour for each estuary. Southampton Water and the Ribble Estuary have been heavily modified over the last 100 – 200 years, with extensive reclamations and dredging; the influence of these disturbances can be seen in the sudden changes in element volumes, particularly in the flat element (Fig. 3 and Fig. 4). By contrast, the Dart Estuary and Chichester Harbour (Fig. 5) are relatively unaltered by human interference. Langstone Harbour has under gone reclamations in the past, and these may still be affecting the harbour's morphological evolution. Overall changes in estuary area and intertidal area are shown in Table 3.

Once calibrated, ASMITA predictions showed good agreement with observed data for all of the estuaries (Fig. 3, Fig. 4 & Fig. 5). In Southampton Water the volume of the tidal flats has decreased over the study period and the channel volume has increased over the same period. In the Ribble estuary, channel volume is approximately constant, but tidal flat volume has increased over the last century. In Chichester and Langstone Harbours and the Dart estuary, the channel and tidal flat volumes show only small

variations over the study periods, with ASMITA predicting the general behaviour well. The ebb-tidal deltas of Chichester and Langstone Harbours are more variable and have high error estimates. ASMITA represents the general behaviour of the ebb-tidal deltas but does not predict the detailed behaviour due to the nature of the model.

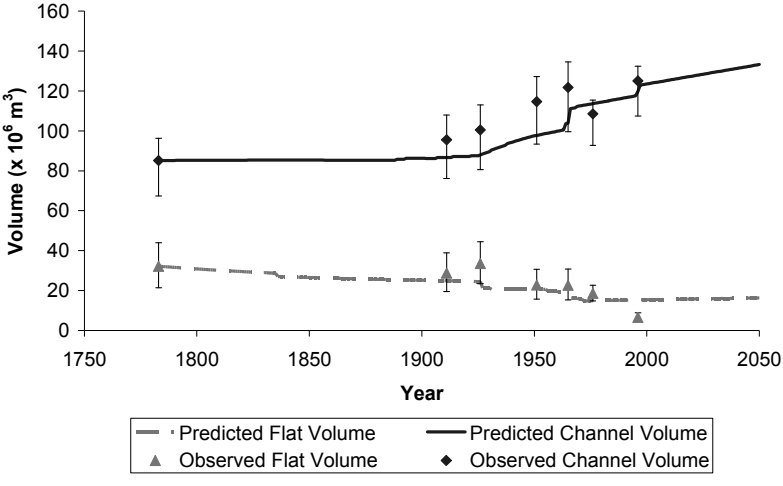

Fig. 3. Observed and predicted tidal flat and channel volumes in Southampton Water, assuming a historical rate of sea-level rise of 1mm/year.

The sediment transport coefficients producing the best fit to the data and the corresponding SLR_{crit} values are presented in Table 4. The Ribble is estimated to have a relatively high sediment availability, and hence $C_E = 0.0005$. The Dart has relatively low sediment availability ($C_E = 0.0001$) and Southampton Water, Chichester Harbour and Langstone Harbour have intermediate sediment availabilities ($C_E = 0.0002$).

Values of the vertical exchange coefficient (Ws_n) giving the best fit to the data varied between estuaries. Ws was smallest in Southampton Water ($Ws_n = 0.000001$). The other estuaries had vertical exchange rates approximately one order of magnitude larger than the Southampton Water value (Table 4) suggesting that sediment dynamics in Southampton Water differ considerably from nearby estuaries.

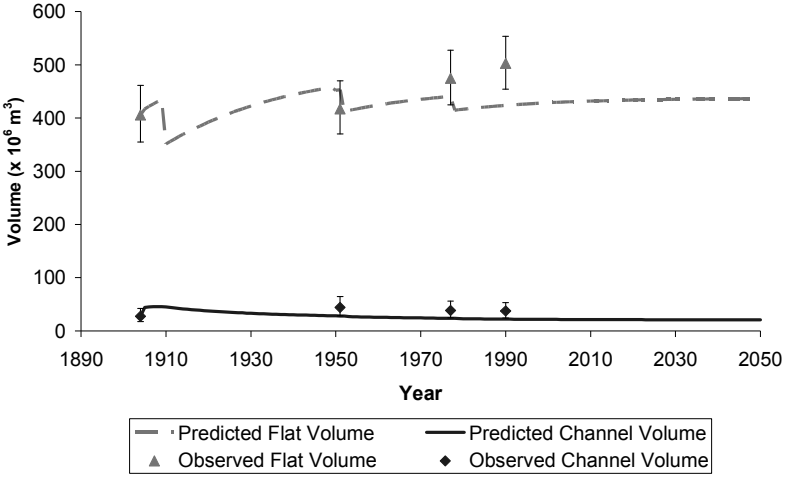

Fig. 4. Observed and predicted volumes for the tidal flats and channels in the Ribble Estuary.

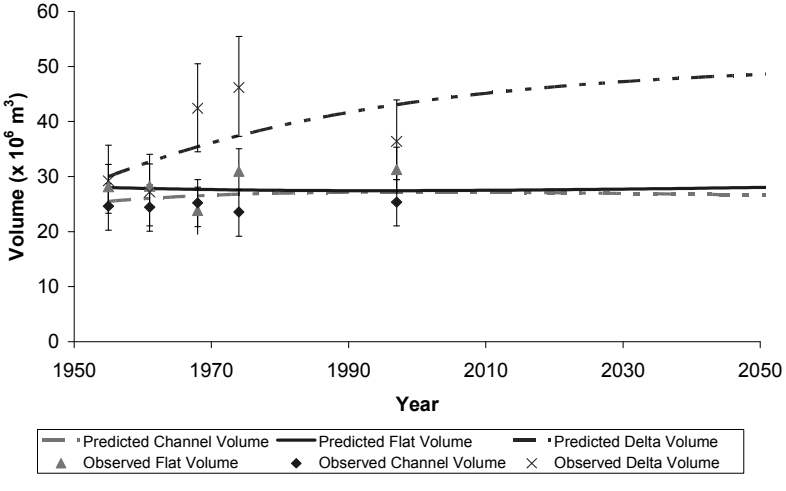

Fig. 5. Observed and predicted volumes for the tidal flats, channels and ebb-tidal delta in Chichester Harbour, assuming a historical rate of sea-level rise of 1mm/year.

Table 4. Values of CE, Ws_n and δ_{nm} giving the best fit for each estuary.

Estuary	C_E	Ws_n	δ_{nm}	SLR_{crit} (mm/year)
Ribble	0.0005	0.00003	1700	90.9
Dart	0.0001	0.00002	1500	56.7
Southampton Water	0.0002	0.000001	400	5.6
Langstone Harbour	0.0002	0.00001	200	17.9
Chichester Harbour	0.0002	0.00001	200	10.9

The value of the horizontal exchange coefficient (δ_{nm}) also varied between estuaries. The best fit value is given in Table 4; however a range of horizontal exchange coefficients gave a good fit for each estuary. In the Ribble, δ_{nm} varied between 1500 and 2500, giving a range of SLR_{crit} values of 82 to 122.5 mm/year. The Dart estuary also had a large range of δ_{nm} (400 to 3000). SLR_{crit} in the Dart appears relatively insensitive to the value of δ_{nm} within this range, with values of 40.3 to 59.7 mm/year.

For Southampton Water, δ_{nm} varied between 100 and 1500 and SLR_{crit} between 4.2 and 6.1 mm/year. In Langstone and Chichester Harbours the range of δ_{nm} and the SLR_{crit} values were similar: in Langstone Harbour, δ_{nm} ranged from 100 to 500 and SLR_{crit} was between 8.1 and 26.8 mm/year; in Chichester Harbour δ_{nm} was between 200 and 500, and SLR_{crit} between 10.9 and 21.7 mm/year. The range of predicted SLR_{crit} values for each estuary are summarised in Fig. 6.

DISCUSSION

The range of SLR_{crit} values varies considerably between the study estuaries, with Southampton Water having the smallest predicted SLR_{crit} and the Ribble estuary having the largest (Fig. 6). Langstone Harbour and Chichester Harbour, located next to each other on the south coast of England, were predicted to have very similar SLR_{crit} ranges. For comparison, van Goor *et al*. (2003) estimated the SLR_{crit} for Amelander zeegat and Eierlandse Gat to be 10.5 mm/year and 18 mm/year respectively. These are similar to the values for Langstone Harbour and Chichester Harbour, which are morphologically most similar to these inlets.

Predictions for the Ribble estuary suggest that sedimentation can keep pace with sea-level rise for rates of between 80 and 120 mm/year. Predicted rates of sea-level rise for the Ribble area in the 2080s are between 0.3 and 10.7 mm/year, suggesting that the intertidal areas of the Ribble estuary are unlikely to be threatened by sea-level rise in the next century. High values of Ws_n and δ_{nm} suggest the sediment transport potential is large. This is supported by the Ribble's large tidal range. The predicted SLR_{crit} values seem large and it is possible that they over estimate the capacity of the Ribble to adapt to sea-level change. The Ribble estuary, however, is flood dominant suggesting a net landward sediment transport into the estuary from the sea. It also has a plentiful supply of sediment from deposits on the floor of the south eastern Irish Sea (van der Wal *et al*., 2002).

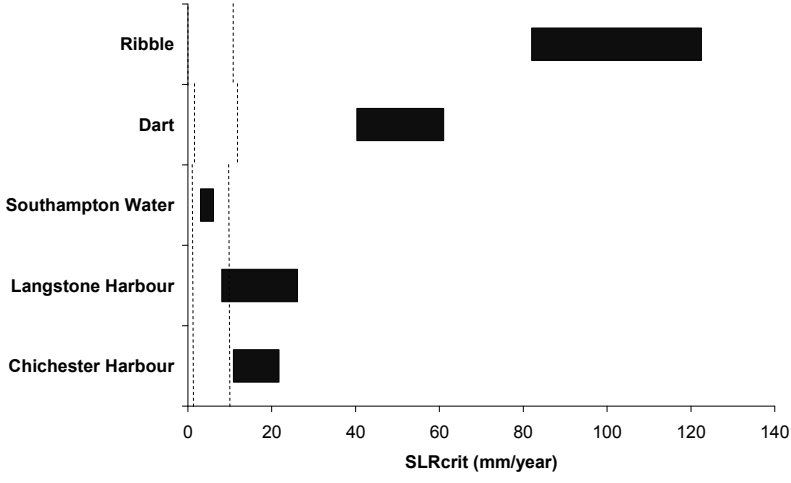

Fig. 6. Ranges of SLR_{crit} predicted for each estuary; the dashed lines represent the range of relative sea-level rise rates predicted for each region for the 2080s (Hulme et al, 2002).

The SLR_{crit} predictions for the Dart estuary suggest a high resilience to sea-level rise, with SLR_{crit} values of 40 to 60 mm/year. Again, this is much greater than the maximum predicted rate of 12 mm/year by 2080 (Hulme *et al*., 2002). These values seem high given the limited sediment supply to the Dart estuary from the coast, however, intertidal area is relatively small ($17x10^5$ m^2), and accounts for just 20 % of the estuarine area, so the volume of sediment needed to keep pace with sea-level rise is much smaller than in estuaries with large intertidal areas. A study of sediment dynamics in the upper Dart estuary suggests there has been recent sedimentation in line with what is observed in the current study (Dart Estuary Environmental Management, 2004).

SLR_{crit} for Southampton Water was predicted to be between 4.2 and 6.1 mm/year, falling within the predicted rates of sea-level rise for the 2080s (1 to 10 mm/year, Hulme *et al*., 2002). Major morphological changes and intertidal loss are likely in Southampton Water, if the model predictions are correct, and are consistent with current significant intertidal losses (Williams, 2006). The low threshold values for Southampton Water reflect the small value of Ws_n used for this estuary. Ws_n affects the rate of erosion and deposition in ASMITA. The low value for Southampton Water suggests that erosion and deposition rates may be extremely low. Bray *et al* (2004) suggest that sediment deposition in the channel is restricted by strong ebb-tidal currents and sediment transport in Southampton water is limited compared to other UK estuaries because it is sheltered from wave action by spits at the mouth and has a relatively small tidal range. Regular dredging in Southampton Water makes deposition in the channel effectively zero and it is possible that the calibrated value of Ws_n is artificially low because of this human influence. It is difficult to separate the effects of dredging and other man-made changes

from the natural behaviour of the estuary. It is also possible that the extensive reclamations and dredging in Southampton Water contribute to the sensitivity of the estuary to sea-level rise.

Langstone Harbour and Chichester Harbour had similar SLR_{crit} ranges, 8.1 – 26.8 mm/year and 10.9 to 21.7 mm/year respectively). In Langstone Harbour the range of SLR_{crit} values overlaps slightly with the maximum predicted sea-level rise for the 2080s. Best fit values of Ws_n and δ_{nm} were the same for the two harbours, but the best fit SLR_{crit} is predicted to be slightly higher in Langstone Harbour. This difference is explained by the differences in intertidal area between the harbours. As in the Dart estuary, the harbour with the smaller intertidal area (Langstone) requires less sediment for intertidal accretion to keep pace with sea-level rise.

There are a number of potential sources of uncertainty in the predictions. Use of the same parameter values for each model element means that all of the model elements have the same sediment transport potential. This is unlikely to be true in reality where current velocities and wave impacts are likely to vary with water depth. Using individual coefficients for each element increases the number of free parameters in the model and increases the uncertainty and complexity of the calibration. Further work is needed to improve this and to link the sediment transport parameters used in ASMITA to physical processes operating in estuaries. For example Ws_n, representing vertical sediment exchange in ASMITA, could be linked to wave climate and sediment type. In the current study these factors are not included; however, there is a trend for larger values of Ws_n in estuaries that are less sheltered from externally generated waves, such as the Ribble.

The estimation of C_E is also a source of uncertainty and needs further work to develop a reliable method of estimating C_E for the UK. It is possible that the value of C_E selected influences the sediment transport parameters to a greater extent than it affects the value of SLR_{crit}. The effect of varying C_E has so far only been investigated in the Ribble estuary. It was found that altering C_E causes the best fit values of the other parameters to shift, whilst the SLR_{crit} range remains approximately the same.

Improving estimates of C_E for UK estuaries is important because it represents sediment availability and affects the values of the sediment transport coefficients, which may influence estuarine management decisions. Cowell *et al*., (2003) found that sediment supply may be more important than sea-level rise rates in determining estuary evolution so improved estimation of C_E is potentially very important for accurately predicting future estuarine evolution. van Goor *et al*., (2003) used $C_E = S/Q$, where S is the bulk sediment transport along the barrier beaches and Q is the longshore wave generated discharge to estimate C_E for inlets in the Dutch Wadden Sea. It is outside of the scope of the current study to collect and analyse the data needed to estimate C_E by this method. It is also possible that the van Goor *et al*., (2003) method is not appropriate for UK estuaries where littoral drift and sediment bypassing at estuary mouths may be small.

Estimates of C_E based on suspended sediment concentration may be more suitable for UK estuaries, but cannot currently be directly related to C_E.

Planned future work includes the addition of extra study sites to better sample the range of UK estuaries, including Portsmouth Harbour and the Blackwater Estuary, investigating links between model parameters and physical processes and linking model predictions to holistic management approaches.

CONCLUSION

The ASMITA approach (Stive *et al*., 1998) has been successfully applied to a number of UK estuaries, indicating the generic value of this approach. The values of SLR_{crit} predicted for the five estuaries in the sample varied considerably. For some estuaries, such as Southampton Water, ASMITA predicts very low tolerance to sea-level rise, and SLR_{crit} could be reached within the next century with major morphological changes and intertidal loss and consequences for wildlife and flood defences. In contrast, ASMITA forecasts that other estuaries (especially the Ribble) are highly resilient to the full range of sea-level rise scenarios expected during the 21st Century.

Estuary area, sediment supply and sediment transport potential all influence the ability of an estuary to adapt to sea-level rise. Human interventions, including dredging, can also have important effects on the ability of estuaries to keep pace with increasing rates of sea-level rise, and this signal cannot always be separated from the natural behaviour, hindering interpretation of the model results.

The next stage of this work is to increase the number of sample estuaries to cover different morphological types and management issues and to examine the linkages between model parameters and physical processes operating in estuaries in more detail.

ACKNOWLEDGEMENTS

The authors would like to thank Marcel Stive & Tjerk Zitman from TU Delft for help and advice on applying and calibrating ASMITA; ABPmer for supplying bathymetry data for Southampton Water and UK Hydrographic Office for their assistance in finding historic data for other estuaries. Funding for this research was provided the Engineering and Physical Sciences Research Council.

REFERENCES

Bray, M. J., Carter, D. J., and Hooke, J. M. (2004). "Coastal Sediment Transport Study: Report to Coastal Groups," SCOPAC, available online at: http://www.scopac.org.uk/scopac sediment db/default.html.

Carr, A. (1980). "The significance of cartographic sources in determining coastal change," *Timescales in Geomorphology*, (R. A. Cullingford, D. A. Davidson, and J. Lewin, eds), John Wiley & Sons Ltd, 69-78.

Cowell, P. J., Stive, M. J. F., Niedoroda, A. W., Swift, D. J. P., de Vriend, H. J., Buijsman, M. C., Nicholls, R. J., Roy, P. S., Kaminsky, G. M., Cleveringa, J., Reed, C. W., and de Boer, P. L. (2003). "The coastal-tract (part 2): Applications of

aggregated modelling of lower-order coastal change," *Journal of Coastal Research* 19(4): 828-848.

Dart Estuary Environmental Management (2004). "Upper reaches of the River Dart Estuary: sustainable dredging for habitat protection," Dart Estuary Environmental Management.

Dyer, K. R. (2002). "*FutureCoast estuary assessment,"* Swindon, DEFRA.

Friend, P. L., Velegrakis, A.F., Weatherston, P. D. and Collims, M. B. (2006). "Sediment transport pathways in a dredged ria system, southwest England," *Estuarine, Coastal and Shelf Science* 67(3): 491 – 502.

Hulme, M., Jenkins, G. J., Lu, X., Turnpenny, J. R., Mitchell, T. D., Jones, R. G., Lowe, J., Murphy, J. M., Hassell, D., Boorman, P., McDonald, R., and Hill, S. (2002). "Climate Change Scenarios for the United Kingdom: The UKCIP02 Scientific Report," Tyndall Centre for Climate Change Research, School of Environmental Sciences, University of East Anglia, Norwich.

Möller, I. (2006). "Quantifying saltmarsh vegetation and its effect on wave height dissipation: Results from a UK East coast saltmarsh," *Estuarine, Coastal and Shelf Science*, 69, 331-351.

Pontee, N. I. and N. J. Cooper (2005). "Including Estuaries in Shoreline Management Plans*," Maritime Engineering* 158(MAI): 33-40.

Stive, M. J. F., Wang, Z. B., Capobianco, M., Ruol, P., and Buijsman, M. C. (1998). "Morphodynamics of a tidal lagoon and the adjacent coast," *Physics of Estuaries and Coastal Seas*, Rotterdam, Balkema.

Townend, I. (2002). "Identifying change in estuaries," *Littoral 2002, The Changing Coast*, Portugal.

Townend, I., and Pethick, J. (2002). "Estuarine flooding and managed retreat," *Philosophical Transactions of the Royal Society of London A*, 360, 1477-1495.

van der Wal, D. and Pye, K. (2004). "The use of historical bathymetry charts in a GIS to assess morphological change in estuaries," *The Geographical Journal* 169(1): 21-31.

van der Wal, D., Pye, K., and Neal, A. (2002). "Long-term morphological change in the Ribble Estuary, northwest England," *Marine Geology* 189: 249-266.

van Goor, M. A. (2001). "Influence of relative sea level rise on coastal inlets and tidal basins: Are the Dutch Wadden capable of following the rising sea level?, " MSc Thesis, Delft University of Technology, Delft.

van Goor, M. A., T. J. Zitman, Wang, Z. B., and Stive, M. J. F. (2003). "Impact of sea-level rise on the morphological equilibrium state of tidal inlets," *Marine Geology* 202: 211-227.

Williams, E. C. R. (2006). "The Change in level and distribution of saltmarsh and mudflats on Southampton Water," MSc Thesis, University of Southampton, Southampton.

VARIABLE SHORELINE RESPONSES TO SEA-LEVEL RISE AND CLIMATE CHANGE

A. Brad Murray[1], Lisa Valvo[1], Jordan Slott[1], Andrew Ashton[2], Tom Crowley[1]

1. Division of Earth and Ocean Sciences, Nicholas School of the Environment and Earth Sciences; Center for Nonlinear and Complex Systems, Duke University, Box 90230, Durham, NC 27708-0230, USA. abmurray@duke.edu, jordan.slott@duke.edu, lisa.valvo@duke.edu, tcrowley@duke.edu.
2. Woods Hole Oceanographic Institution, Clark 257, MS # 22 Woods Hole, MA, 02543, USA. aashton@whoi.edu.

Abstract: Researchers and coastal managers are addressing how climate change will affect shorelines (Gornitz 1991; Titus, Richard et al. 1991; Anderson, Rodriques et al. 2001; Field, Boesch et al. 2001; Brown, Few et al. 2004). Important questions include: How far will a sandy shoreline retreat as sea level rise accelerates (Cowell, Roy et al. 1995; Zhang, Douglas et al. 2004)? And, how far landward will the effects of possibly intensified storms reach (Zhang, Douglas et al. 2000)? These questions are most often investigated in a cross-shore profile framework, (Brunn 1962; Cowell, Roy et al. 1995) fostering the implicit assumption that coastline responses will be approximately uniform in the alongshore direction. However, we describe here experiments with a recently developed numerical model of coastline change involving shoreface geology and sediment-transport processes (Ashton, Murray et al. 2001; Valvo, Murray et al. 2006) which suggest that the responses to sea-level rise are likely to be alongshore-heterogeneous. The interactions between accelerating sea-level rise, alongshore sediment transport, and spatially variable underlying material will tend to cause spatially variable retreat rates. We compare these sea-level-rise effects to other climate-change related shoreline impacts suggested by recent modeling work. Slott et al. (2006) have suggested that as storm behaviors and wave climates change, shifts in complex large-scale coastline shapes will cause alongshore variation in shoreline-change rates that could be an order of magnitude greater than sea-level-rise-related shoreline changes.

INTRODUCTION

When addressing the effects of sea-level rise on sandy coastlines, researchers usually consider cross-shore transport processes (Bruun 1962; Cowell, Roy et al. 1995; Zhang, Douglas et al. 2004). Assuming that the cross-shore profile shape of the nearshore seabed (the 'shoreface') and sub-aerial barrier are maintained by wave action and remain constant over time, cross-shore transport will tend to cause landward retreat of the shoreline (Bruun 1962; Cowell, Roy et al. 1995). This cross-shore focus fosters the implicit assumption that sea-level rise will tend to produce alongshore-uniform shoreline retreat. However, considerations involving alongshore-transport processes, and how they interact with shoreface lithology (the 'geologic framework'), call this assumption into question.

Wherever shoreline erosion is sustained, the underlying geology will eventually emerge on the seabed, and will be transformed ('weathered') into mobile sediment. Where the underlying material weathers into grains that are coarse enough to remain in the high-energy nearshore environment (i.e. sand and gravel)—and erosion does not outpace the maximum weathering rate—the conversion into mobile sediment should not directly affect shoreline evolution. However, if some segment of the shoreline is underlain by a greater proportion of fine-grained material (e.g. muddy lagoon deposits) than are adjacent segments in the alongshore direction, these composition variation will affect shoreline change, as Valvo et al. (2006) have recently investigated with a numerical model. Using this model, we show in the third section how composition variations, coupled with alongshore transport, will tend to cause alongshore-heterogeneous shoreline change during a period of accelerating sea-level rise.

In the fourth section we discuss the effects of changes in the angular-distribution of wave influences, including stochastic variations in these 'wave climates' as well as variations associated with changing storm behaviors (e.g. increasing tropical-storm intensity) (Slott, Murray et al. 2006). These wave-climate shifts produce alongshore variations in shoreline change (including localized accretion as well as erosion) that will likely overwhelm sea-level-rise related shoreline changes—suggesting that simple shoreline retreat caused by sea-level rise may not be the most important aspect of shoreline response to climate change.

BACKGROUND AND METHODS

The magnitude of wave-driven alongshore flux can be related to deep-water wave height, and to the wave approach angle in deep water (before nearshore refraction), relative to the shoreline orientation (Fig. 1); the alongshore sediment flux reaches a maximum for relative wave-approach angles of approximately 45° (Ashton, Murray et al. 2001; Ashton and Murray 2006 a). On a sandy coastline, alongshore gradients in this sediment flux, Q_s, tend to cause changes in the shoreline position, η (Fig. 1):

$$\partial \eta / \partial t = -(1/D) \partial Q_s / \partial x, \qquad (1)$$

where D is the seabed depth to which erosion or accumulation extends. Large-scale (> kms) bends in a shoreline cause gradients in alongshore flux that alter the shoreline shape. When deep-water waves approach from nearly straight offshore, gradients in alongshore transport cause the large-scale shoreline shape to become smoother (Fig. 1). However, when waves approach from angles greater than approximately 45° ('high-angle' waves), plan view shoreline undulations grow (Ashton, Murray et al. 2001).

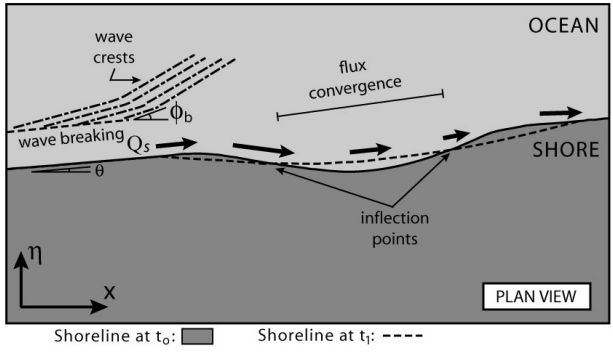

Fig. 1. Schematic illustration of gradients in the magnitude of alongshore sediment flux, caused by changes in shoreline orientation, and the consequent zones of erosion and accretion. The accretion (erosion) where the shoreline has seaward-concave (convex) curvature, shown here, occurs with low-angle waves. (From Valvo et al. 2006.)

Ashton et al. (2001) developed a numerical model to explore what shoreline behaviors might arise as undulations grow and interact with each other along an extended coastline. Using a 'one-line' model extended in a way that allows arbitrarily complex shoreline shapes to develop, they found that different shapes including cuspate capes and spits evolve under different wave distributions (characterized by the proportions of high- and low-angle waves, and by the degree of asymmetry—the proportion of wave influence from the left versus right, looking offshore) (Ashton, Murray et al. 2001). Valvo et al. (2006) incorporated geological-framework effects into this modeling framework, to investigate how they influence coastline evolution. Here we use these models to address shoreline responses to climate change—sea-level rise and changing wave climates (from changing storm behaviors). The model algorithms are described in detail elsewhere (Ashton, Murray et al. 2001; Murray and Ashton 2004; Ashton and Murray 2006 a; Valvo et al. 2006); here we recapitulate the main points.

A new deep-water wave angle is chosen daily from a probability distribution function representing a wave climate (e.g. Fig. 2). Breaking-wave height and angle relative to local shoreline orientations are calculated assuming refraction and shoaling over shore-parallel contours. Alongshore sediment fluxes, Q_s, are based on the commonly used CERC equation (Komar and Inman 1970; Komar 1998):

$$Q_s = KH_b^{5/2}\sin(\phi_b-\theta)\cos(\phi_b-\theta), \qquad (2)$$

where H_b and ϕ_b are breaking-wave height and crest angle, θ is local shoreline orientation (Fig. 1), and K is an empirical constant equal to 6.4 x 10^4 m^3d^{-1}. The model domain is discretized into cells, and shoreline changes are determined by a discretized form of (1).

Where protruding shoreline features block other coastline segments from the current deep-water wave-approach angle, no sediment transport occurs in the 'shadowed' segments.

To explore how these geologic influences interact with alongshore sediment transport processes, Valvo et al. (2006) imposed a landward retreat across the model domain, by removing sediment from each shoreline cell at a uniform rate. Here we interpret this shoreline retreat to be caused by sea-level rise. (The landward retreat rate can be roughly related to the rate of sea-level rise by multiplying the later by 100—a common but crude conversion that involves an assumed average slope to the shoreface profile of 1/100 (Brunn 1962; Dean and Maurmeyer 1983).

To represent the geologic framework, in each model cell the amount of mobile sediment and underlying, unweathered material are separately accounted for. The rate that the underlying material weathers, W, decreases with the thickness of mobile sediment covering it, Th. This basic relationship represents the assumption that as the amount of sediment on a shoreface decreases, the underlying material will be exposed more often to the complex set of physical, chemical and biological processes that transform it to loose sediment. We choose an exponential decrease, $W = ke^{-Th}$, as a simple parameterization roughly consistent with terrestrial bedrock weathering (Heimsath, Chappell et al. 2000; Anderson 2002), in lieu of empirical data on which to base such a relationship for the shoreface. k is a weathering coefficient equal to the assumed maximum rate for bare rock with no sediment cover—k = 20 m/yr in simulations presented here. The exact form of the weathering curve does not affect any of these results, because in these experiments the underlying material weathers at least as fast as alongshore and cross-shore transport processes uncover it.

The proportion of coarse (representing sand and gravel) and fine (representing silt and clay) grains composing the underlying material is defined in each cell at the beginning of a simulation. Then, as that material is weathered, the coarse fraction is transformed into mobile sediment, and the fine fraction disappears from the domain. This volume loss will tend to create an indentation in the shoreline corresponding to the alongshore extent of a fine-grained deposit (Fig. 2). Considering these geologic influences alone, the indentation should deepen landward as long as shoreline retreat—such as that caused by sea-level rise—continues.

However, in most locations alongshore transport will tend to fill in the indentation (Fig. 1). Most local wave climates are dominated by low-angle waves, even in areas such as the Carolina Capes where the regional wave climate is high-angle dominated (because of local shoreline rotation and wave-shadowing effects) (Ashton and Murray 2006 b). In

addressing geologic-framework effects, we therefore assume a local wave climate that tends to smooth the shoreline.

In experiments conducted by Valvo et al. (2006), as composition-related indentation deepens, the shoreline curvature and related alongshore-transport gradients increase; the rate of shoreline smoothing increases. Therefore, the model indentation's amplitude, or 'offset,' approaches a steady state (Fig. 2) in which alongshore transport redistributes sandy material into the indentation as fast as mud volume is lost there. Shoreline retreat rate thus becomes alongshore uniform (Fig. 2), with a rate reflecting the combined influences of sea-level rise and alongshore-averaged fine-sediment loss (Valvo, Murray et al. 2006) (Fig. 3a).

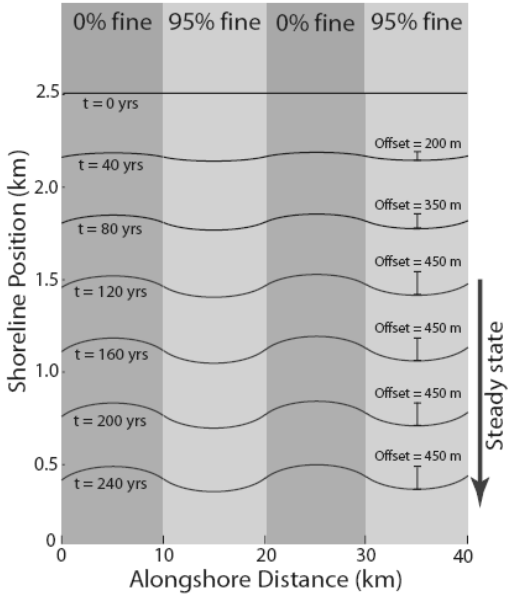

Fig. 2. Model results showing the plan-view evolution of a shoreline with two different lithologies alternating alongshore—one composed of material that weathers into 95% fine sediment (i.e. mud) that is not retained the nearshore system, and one that weathers into coarse sediment (i.e. sand or gravel). An indentation forms where fine-sediment is lost. However, alongshore transport redistributes into the indentation sediment liberated as the coarse lithology weathers. Steady-state indentations result, as shown by the offset values and highlighted by the red shoreline shapes (which are exaggerated in the cross-shore direction). (After Valvo et al. 2006.)

HETEROGENEOUS RESPONSE TO ACCELERATING SEA-LEVEL RISE

The steady-state offset in experiments such as that depicted in Fig. 2 depends on several factors, including the compositional contrast between adjacent shoreline segments, and the alongshore length of those segments (Fig. 3b). In the next section we will examine the consequence of the offset's dependence on wave climate; as the effective shoreline diffusivity (Ashton, List et al. 2003; Falques 2003; Ashton and Murray 2006 a; Ashton and Murray 2006 b) increases (a wave climate weighted more heavily toward low-angle waves), smaller curvatures are required for alongshore transport to redistribute sediment into the finer-grained shoreline segments as fast as fine material is lost there, so that indentations will exhibit smaller offset.

In this section we focus on the offset's dependence on the overall shoreline retreat rate, interpreted here to be driven by sea-level rise (Fig. 3b). As the overall retreat rate increases, the rate that fine sediment is lost in the fine-grained domains increases. Therefore, shoreline curvatures become higher and consequently indentation offset becomes greater before a steady-state evolves. If a steady-state shoreline configuration evolves under one rate of sea-level rise, and then the rate of sea-level rise and overall retreat increases, offsets will increase. Therefore, as the rates of sea-level-rise and coastal retreat accelerate in coming decades and centuries, the subtle indentations in present sandy shorelines (Riggs, Cleary et al. 1995; Honeycutt and Krantz 2003) will likely deepen; during this acceleration, shoreline retreat rates related to sea-level rise will not be alongshore uniform.

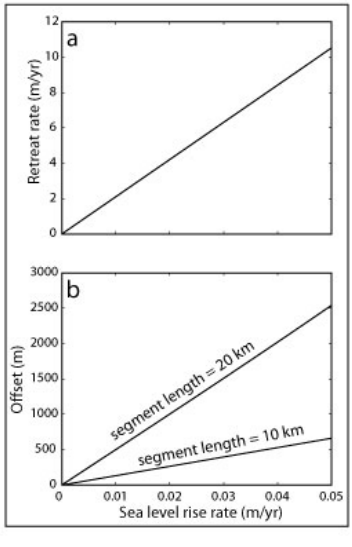

Fig. 3. Summaries of multiple model experiments like that depicted in Fig. 2, showing the variation of **a** retreat rate and **b** indentation offset, as functions of the rate of sea-level rise, for alternating fine and coarse shoreline segments with alongshore lengths of 10 km and 20 km.

The model experiments depicted in Fig. 3 predict that, if the sea-level-rise rate doubles on a time scale of a century (IPCC 2001), from 0.0025 m/yr to 0.05 m/yr, the offset will increase by approximately 300 m for 10-km long fine-grained segments, and by approximately 1200 m for 20-km segments. This amounts to a *difference* between the retreat rates in coarse and fine shoreline segments of approximately 3 m/yr for 10-km segments and 12 m/yr for 20-km segments, during the period of sea-level rise acceleration. Thus, these experiments suggest that the alongshore variation in erosion rate from growing indentations could be comparable to or greater than the alongshore-averaged retreat rate.

Because of poorly constrained model parameters, including shoreface compositions and alongshore length of compositional segments, the results in Fig. 3 should not be considered quantitatively reliable predictions. For example, a smaller alongshore-averaged fine-sediment content will produce slower overall retreat rates. However, this exploratory modeling exercise suggests that because the composition of underlying material commonly varies alongshore (Riggs, Cleary et al. 1995), the qualitative result of alongshore variability in shoreline loss should be widespread as sea-level rise increases.

DISCUSSION: WAVE-CLIMATE VARIATIONS

Two recent modeling studies suggest, however, that shoreline change caused by sea-level rise might be difficult to detect on many shorelines—they suggest that variations in wave climates, either stochastic or systematic, could cause alongshore variations in shoreline change that could swamp sea-level-rise related shoreline change.

Erosion Hot Spots

First, in the Valvo et al. (2006) experiments, indentation offset fluctuated significantly around the long-term, steady-state value. In the model, this behavior arises from stochastic variations in the short-term wave climate, as different mixes of wave-approach angles result from different sequences of daily random draws from the probability density function that represents the long-term wave climate. During periods in which the effective wave climate is less heavily weighted toward low-angle waves than is the long-term wave climate, the effective shoreline diffusivity is decreased. During these periods, offset increases, just as it decreases during periods in which the short-term wave climate more diffusive than the long-term average. Increasing offset corresponds to accentuated shoreline retreat in the finer-grained indentations, while decreasing offset corresponds to accentuated erosion in the coarser domains, which form subtle promontories. Surprisingly, in the Valvo et al. (2006) experiments, the periods in which either the subtle indentations or promontories acted as erosion hot spots lasted from years to decades.

This interaction between alongshore transport, the geologic framework, and shifting short-term wave climates could be responsible for decade-scale erosion hot spots on various coastlines. Recent observations on the northern Outer Banks, North Carolina,

USA, suggest that paleo-river channels (with abundant coarse sediment) outcrop on the shoreface offshore of the major decade-scale hot spots (Schupp, McNinch et al. 2006; Bill Birkemeier, pers. comm.). Examination of the shoreline shows these areas to be subtle promontories (unpublished observations). Ashton et al. (2003) showed that the major erosion and accretion patterns over a 20 year time span result from a smoothing of the coastline—in other words, to accentuated erosion of the promontories and even accretion in the indentations (Fig. 4). Is this erosion hot-spot behavior caused by a shift toward a more diffusive wave climate in recent decades? Further work is needed to investigate this potential explanation. However, Fig. 4 indicates that over decadal time scales, alongshore heterogeneities in shoreline change can overwhelm alongshore-averaged shoreline retreat from sea-level rise.

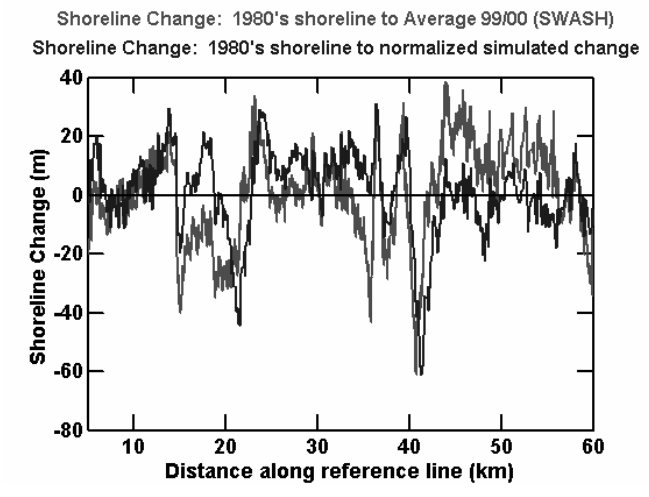

Fig. 4. Modeled and observed shoreline change along the northern Outer Banks of North Carolina, USA. The red line shows observed shoreline change over 20 years, and the blue line shows the results of a model experiment that used the observed coastline shape (1980) as an initial condition, and was forced with a wave climate based on WIS hindcasts in the region (USACE 2005). The magnitude of the model changes were normalized so that the maximum change in the model matched the maximum change in the observations. Because the regional wave climate is weighted toward low-angle waves, the model results represent smoothing of the initial coastline shape. (After Ashton et al. 2003.)

Changing Storm Behaviors

The warming of the atmosphere and oceans expected in coming centuries (IPCC 2001) will likely cause storm behaviors to change. Although how storm distributions will change cannot currently be predicted with confidence, extra-tropical and tropical cyclones may well change in frequency and severity (Emanuel 1987; Lambert 1995; Geng and Sugi 2003; Emanuel 2005; Webster, Holland et al. 2005). Shifts in storm behavior will alter the wave climates felt on coastlines, changing the relative amounts of

wave energy approaching from various directions. Model experiments indicate that sandy coastline shapes can depend sensitively on the angular distribution of approaching wave energy (Ashton, Murray et al. 2001; Ashton and Murray 2006 a), so that changing wave climates could cause significant shoreline change along some coastlines as large-scale shapes adjust.

Slott et al. (2006) recently explored how rapid changes in wave climate would affect a cuspate coastline shape (Fig. 5). The model coastline in Fig. 5b resembles the shape of the Carolina Capes, from Cape Hatteras, NC, to Cape Fear, SC, USA (Fig. 5a). To produce the coastline in Fig. 4b, Slott et al. forced the model with a wave climate based on 20 years of wave hindcast off of the Carolina coast (Wave Information Study station 509 (USACE 2005)). Mid-latitude winter storms off of the US East Coast produce waves that tend to approach from the northeast at high-angles relative to the trend of the Carolina coastline, and Atlantic tropical storms produce high-angle waves from the south. These two storm influences combine to produce a regional wave climate dominated by high-angle waves, as well as a moderate asymmetry (net transport would be to the southwest along a straight coastline with the overall trend of the Carolina Capes, Fig. 5a).

In the model, developing a cuspate pattern with the length scales shown in Fig. 5b requires millennia (starting from an unrealistic, approximately straight initial condition), and the rate of shoreline change slows with time (Ashton and Murray in press a). Fig. 5b shows the changes in the coastline over a further 200 years of evolution under a constant wave climate; the large-scale coastline shape changes relatively little on human timescales under these conditions, although continued southwestward translation of the capes does cause shoreline changes approaching a kilometer/century near the capes, consistent with historical observations (Pilkey, Neal et al. 1998).

Fig. 5c-e shows the results of model experiments that started with the same initial coastline as in Fig. 5b, but then involved 200 years of evolution under altered wave climates. Figure 5c shows how the simulated coastline changes under a wave climate that features a 10% greater proportion of high-angle waves, and a 10% lower asymmetry (an increase in waves from the right), compared to the wave climate that shaped the initial coastline. These changes along the Carolina Capes would correspond to an increase in the relative influence of tropical-storm waves. Figure 5d shows the effects of a 10% increase in the proportion of high-angle waves and a 10% higher asymmetry (increase in waves from the left). For the Carolina coast, this would correspond to an increase in the influence of extra-tropical winter storms. Figure 5e shows how the shoreline shape would change if the proportion of high angle waves decreases by 10%, which would occur along the Carolina Coast if the relative energy from tropical and extra-tropical storms decreased.

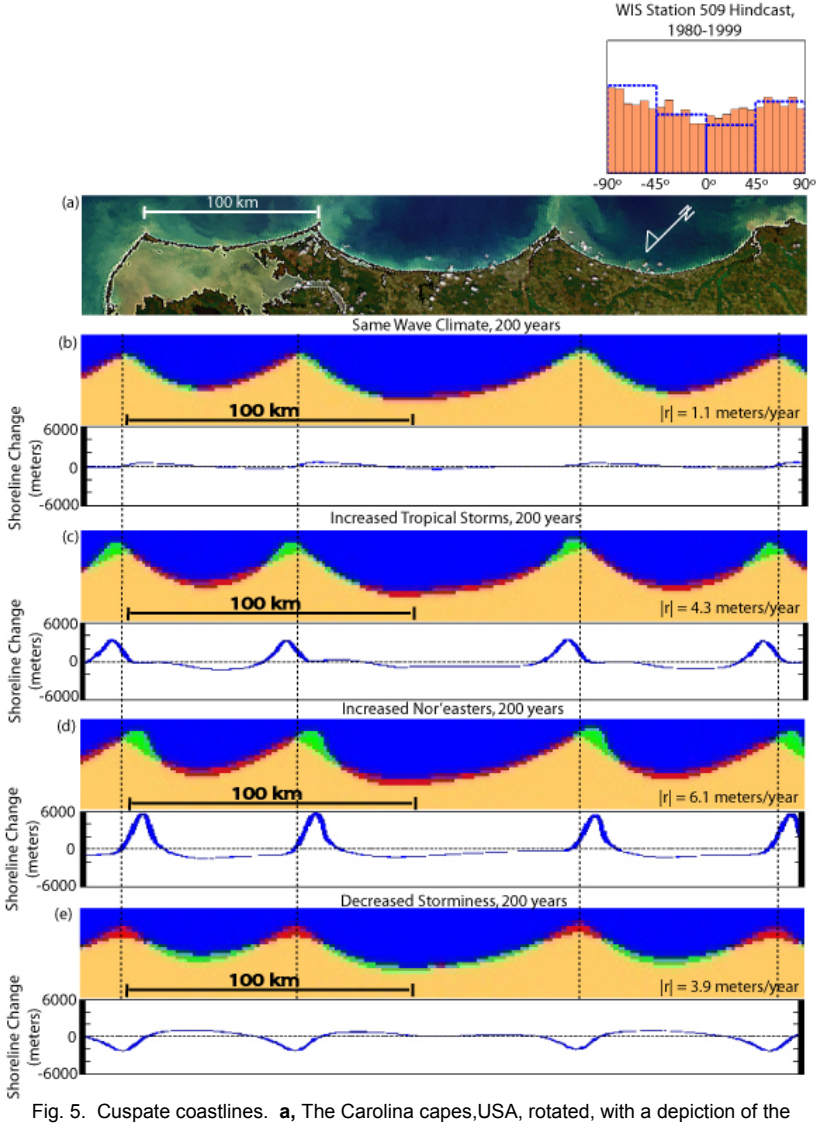

Fig. 5. Cuspate coastlines. **a,** The Carolina capes,USA, rotated, with a depiction of the regional wave climate. **b,** Model shoreline shape produced using a constant wave climate (blue bin outlines in the histogram), and the shoreline changes occurring over 200 years with this same wave climate; red indicates shoreline erosion, and green accretion. The alongshore average of the magnitude of shoreline-change rates is denoted by |r|. **c-e**, coastline changes over 200 years with altered wave climates. Satellite image courtesy of the SeaWiFS Project NASA/GSFC and ORBIMAGE. (From Slott et al. 2006.)

These experiments suggest that changing wave climates will tend to increase the alongshore-averaged shoreline-change rates considerably, relative to the case with a constant wave climate, and that maximum shoreline change rates could approach an order of magnitude higher than the maximum rates with the unchanged climate (Fig. 5). In addition, each changed-climate scenario in Fig. 5 exhibited markedly alongshore-heterogeneous shoreline change, featuring areas of accretion as well as erosion.

The model experiments, which involve several millennia with a constant wave climate followed by an abrupt shift, should not be taken too literally. Climate has shifted on various time scales in recent millennia, and global-warming induced climate change will not occur instantaneously. However, these experiments suggest that if wave climates have changed slowly enough for coastline shapes to maintain quasi-equilibrium, and then shift more rapidly, relatively rapid rearrangement of coastline shape should be expected on complex-shaped coastlines, including parts of the US Southeast and Gulf coastlines and the northwest Alaska coast. On such coastlines, the component of the shoreline change signal related to sea-level rise will be especially difficult to detect.

CONCLUSIONS

Alongshore variations in the composition of the underlying geology will tend to create alongshore variations in shoreline retreat rates during an acceleration in sea-level rise. The magnitude of these alongshore variations in retreat rates could be comparable to the overall retreat rate induced by sea-level rise (and loss of fine-grained material) (Fig. 3). However, shifting wave climates, interacting with the geologic framework, will tend to superimpose alongshore variations in shoreline change that could obscure the sea-level-rise effect. Decade-scale shoreline changes along a well studied coastline suggest that neither the alongshore-uniform nor the alongshore-varying components of sea-level-rise-related changes are currently the most important drivers of shoreline change (Fig. 4). Finally, on complex-shaped coastlines, climate change and associated wave-climate changes could cause rapid and alongshore-varying shoreline changes—shoreline change rates that locally exceed those expected from sea-level rise alone by an order of magnitude (Fig. 5).

If worst-case scenarios for rapid sea-level rise on the order of meters occur on human time scales, the effects on sandy coastlines will undoubted be severe. However, the model explorations described here suggest that coastline responses to sea-level rise are not likely to alongshore homogeneous, and may not be the most important component of climate-related shoreline change in many locations. These initial results suggest that researchers should consider alongshore as well as cross-shore processes when addressing coastline responses to sea-level rise and climate change, and that coastal management strategies should not be based on the assumption of approximately alongshore-uniform shoreline response to climate change.

ACKNOWLEDGEMENTS

The Duke University Center on Global Change and the National Science Foundation (DEB 05-07987) supported this work.

REFERENCES

Anderson, J., A. Rodriques, et al. (2001). "Researchers focus attention on coastal response to climate change." *EOS Trans.* 82, 513-520.

Anderson, R. S. (2002). "Modeling the tor-dotted crests, bedrock edges, and parabolic profiles of high alpine surfaces of the Wind River Range, Wyoming." *Geomorph.* 46, 35-58.

Ashton, A., J. List, et al. (2003). *Investigating Links Between Erosional Hot Spots and Alongshore Sediment Transport Using Field Measurements and Simulations*. Coastal Sediments '03, Clearwater, CDROM: World Scientific Publishing Corp, and East Meets West Productions, Corpus Christi, Texas, USA.

Ashton, A. and A. B. Murray (2006 a). "High-angle wave instability and emergent shoreline shapes: 1. Modeling of sand waves, flying spits, and capes." *J. Geophys. Res.* 111, F04011, doi:10.1029/2005JF000422.

Ashton, A. and A. B. Murray (2006 b). "High-angle wave instability and emergent shoreline shapes: 2. Wave climate analysis and comparisons to nature." *J. Geophys. Res.* 111, F04011, doi:10.1029/2005JF000423.

Ashton, A., A. B. Murray, et al. (2001). "Formation of coastline features by large-scale instabilities induced by high-angle waves." *Nature* 414, 296-300.

Brown, K., R. Few, et al. (2004). Responding to climate change: inclusive and integrated coastal analysis, Tyndall Centre project T2.42.

Bruun, P. (1962). "Coastal erosion and the development of beach profiles." *Proceedings of the ASCE, Journal of Waterways and Harbors Division* 88, 117-130.

Cowell, P. J., P. S. Roy, et al. (1995). "Simulation of large-scale coastal change using a morphological behavior model." *Marine Geology* 126, 45-61.

Dean, R. G. and E. M. Maurmeyer (1983). Models of beach profile response. *CRC Handbook of Coastal Processes and Erosion*. P. D. Komar and J. Moore. Boca Raton, CRC Press**,** 151-165.

Emanuel, K. A. (1987). "The dependence of hurricane intensity on climate." *Nature* 326, 483-485.

Emanuel, K. A. (2005). "Increasing destructiveness of tropical cyclones over the past 30 years." *Nature* 436, 686-688.

Engineers, U. A. C. o. (2005). http://frf.usace.army.mil/wis/.

Falques, A. (2003). "On the diffusivity in coastline dynamics." *Geophys. Res. Lett.* 30(21), 2119,doi:10.1029/2003GL017760.

Field, J. C., D. F. Boesch, et al. (2001). Potential consequences of climate variability and change on coastal areas and marine resources, US Climate Change Research Program**,** www.usgcrp.gov/usgcrp/nacc/coasts/default.htm.

Geng, Q. and M. Sugi (2003). "Possible change of extratropical cyclone activity due to enhanced greenhouse gases and sulfate aerosols - Study with a high

resolution GCM." *J. Clim.* 16, 2802-2805.
Gornitz, V. (1991). "Global coastal hazards from future sea-level rise." *Global and Planetary Change* 89(4), 379-398.
Heimsath, A. M., J. C. Chappell, et al. (2000). "Soil production on a retreating escarpment in southeastern Australia." *Geol.* 28(9), 787-790.
Honeycutt, M. C. and D. E. Krantz (2003). "Influence of the geologic framework on the spatial variability of long-term shoreline change, Cape Henlopen to Rehoboth Beach, Delaware." *Jour. Coastal Res.* special issue 38, 147-167.
IPCC (2001). Climate Change 2001: Impact, adaptation, and vulnerability. Contribution of working group II to the third assessment report of the Intergovernmental Panel on Climate Change., Cambridge University Press, Cambridge.
Komar, P. D. (1998). *Beach Processes and Sedimentation*. Upper Saddle River, New Jersey, Simon & Schuster.
Komar, P. D. and D. L. Inman (1970). "Longshore sand transport on beaches." *Jour. Geophys. Res.* 75, 5914-5927.
Lambert, S. J. (1995). "The effect of enhanced greeenhouse warming on winter cyclone frequencies and strengths." *J. Clim.* 8, 1447-1452.
Murray, A. B. and A. Ashton (2004). *Extending a 1-line modeling approach to explore emergent coastline behaviors*. Coastal Engineering 2004, Lisbon.
Pilkey, O. H., W. J. Neal, et al. (1998). *The North Carolina shore and its barrier islands*. Durham and London, Duke University Press.
Riggs, S. R., J. C. Cleary, et al. (1995). "Influence of inherited geologic framework on barrier shoreface morphology and dynamics." *Marine Geol.* 126, 213-234.
Schupp, C. A., J. E. McNinch, et al. (2006). "Nearshore shore-oblique bars, gravel outcrops, and their corelation to shoreline change." *Marine Geol.* 233, 63-97.
Slott, J. M., A. B. Murray, et al. (2006). "Coastline responses to changing storm patterns." *Geophys. Res. Lett.* 33, L18404, doi:10.1029/2006GL027445.
Titus, G. T., A. P. Richard, et al. (1991). "Greenhouse effect and sea level rise: The cost of holding back the sea." *Coastal Management* 19, 171-204.
Valvo, L., A. B. Murray, et al. (2006). "How Does Underlying Geology Affect Coastline Change? An Initial Modeling Investigation." *J. Geophys. Res.* 111, F02025, doi: 10.1029/2005JF00340.
Webster, P. J., G. J. Holland, et al. (2005). "Changes in tropical cyclone number, duration, and intensity in a warming environment." *Science* 309, 1844-1846.
Zhang, K. Q., B. C. Douglas, et al. (2000). "Twentieth-Century storm activity along the U.S. East Coast." *Jour. of Climate* 13(10), 1748-1761.
Zhang, K. Q., B. C. Douglas, et al. (2004). "Global warming and coastal erosion." *Climate Change* 64(1-2), 41-58.

MODEL SCENERIOS OF SHORELINE CHANGE AT KAANAPALI BEACH, MAUI, HAWAII: SEASONAL AND EXTREME EVENTS

Sean Vitousek[1], Charles H. Fletcher[1], Mark A. Merrifield[2], Geno Pawlak[3], Curt D. Storlazzi[4].

1: Department of Geology and Geophysics, 1680 East-West Rd. POST Room 721, Honolulu, Hawaii, 96822, USA. seanfkv@hawaii.edu and fletcher@soest.hawaii.edu.
2: Department of Oceanography, 1000 Pope Road, MSB 317, Honolulu, HI 96822,USA. markm@soest.hawaii.edu.
3: Department of Ocean Resource Engineering, 2540 Dole St., Holmes Hall 404, Honolulu, Hawaii 96822,USA. pawlak@hawaii.edu.
4. USGS Pacific Science Center 400 Natural Bridges Drive Santa Cruz, CA, 95060, USA. cstorlazzi@usgs.gov.

Abstract: Kaanapali beach is a well-defined littoral cell of carbonate sand extending 2 km south from Black Rock (a basalt headland) to Hanakao'o Point. The beach experiences dynamic seasonal shoreline change forced by longshore transport from two dominant swell regimes. In summer, south swells (H_s = 1-2 m T_p = 14-25 s) drive sand to the north, while in winter, north swells (H_s = 5-8 m T_p = 14-20 s) drive sand to the south where it accumulates on a submerged fossil reef. The Delft3D modeling system accurately predicts directly observed tidal currents and wave heights around West Maui, and is applied to simulate shoreline change. Morphologic simulations qualitatively resolve the observed seasonal behavior.

INTRODUCTION

Numerical modeling allows for simulations of coastal behavior provided that physical processes involved in sediment transport and morphologic development are well

resolved. Thus effort is needed to observe and, through modeling, reproduce wave and current fields with adequate spatial resolution.
The Delft3D modeling system accurately reproduces hydrodynamic behavior at a number of field sites (Elias et al. 2000; Klein et al. 2001; Luijendijk 2001; Walstra et al. 2001, 2003). Delft3D also reproduces observed sediment transport patterns in laboratory tests and morphologic simulations (Lesser 2000; Lesser et. al. 2004; Elias 2006) using the Van Rijn 1993 transport formulations. As an extension of these successes, it is hoped that adequate resolution of water levels, waves, and currents allow the model to reproduce sediment transport patterns in carbonate reef environments.

Kaanapali

Kaanapali Beach, located on the west coast of Maui, Hawaii, lies within a well-defined littoral cell extending 2 km south from Black Rock (a basalt headland) to Hanakao'o Point. Kaanapali Beach is at the center of the Maui Nui complex shown in Figure 1, which consists of the islands of Molokai, Lanai, Maui, and Kahoolawe. Shadowed by these islands, Kaanapali is exposed to direct swell from limited windows: north (350-10°), south (210-170°), west (280-260°), as well as refracted swell from the remaining directions.

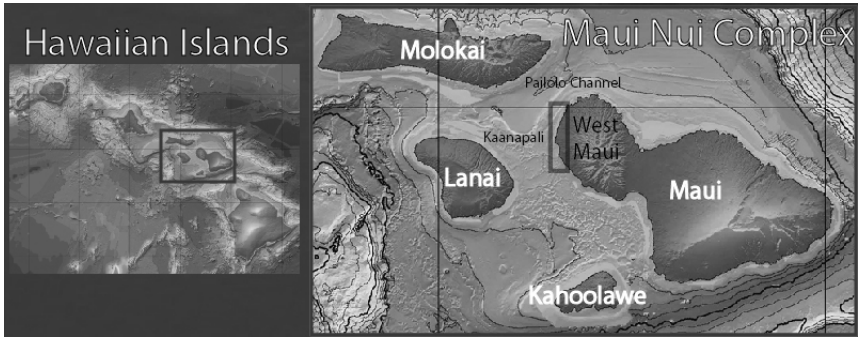

Figure 1 –Hawaiian Islands, Maui Nui, and Kaanapali.

Like the wave field, the Maui Nui current field is also spatially complex due to mean flows through the Pailolo Channel, which have been investigated in (Flament et al. 1996; Sun 1996; Storlazzi et al. 2006). Eversole (2003) characterized Kaanapali as an alongshore system that transports approximately 30,000 m^3 of sand to the north during summer months driven by south swell, which later returns to the south in winter months forced by north swell. This volume of sand can result in dramatic beach width changes of more than 50 m.

Erosion Event

In early July 2003, Kaanapali experienced a rapid-onset erosion event that undermined resort landscaping and infrastructure landward of Hanakao'o Point. This event was likely the result of unusually high sea levels resulting from a series of

mesoscale eddies that arrived over spring and summer months as seasonal sea level increased due to water column warming. Mesoscale eddies, investigated in Firing et al. (2004), can persist for weeks to months and produce sea levels 15-20 cm above normal.

The Kahului tide station on Maui reached its highest recorded hourly water levels during the mesoscale eddy sequence of 2003. While 15-20 cm may seem like a small sea-level signal, in micro-tidal areas such as Hawaii (tide range = 0.6-0.8 m), these eddies represent a significant percentage of the tide range, and a significant increase on sandy shorelines otherwise exposed to nearly constant water levels. It is unlikely that the sea-level signal produced by these events would be able, by themselves, to cause significant erosion. However, when these coincide with spring tides and swell, the conditions for significant erosion exist. Mesoscale eddies are an episodic phenomenon today that represent a future permanent condition in coming decades due to eustatic sea-level rise on the order of 3 mm/year.

South swell associated with the July eddy in 2003 reached a significant wave height of only 0.75 m at 10 m water depth (Tp = 15 s, breaking wave height = 1.3 m), which is considerably lower than the annually recurring deep-water significant wave height of 2 m (Tp = 17 sec, breaking wave height = 2 m). These factors emphasize the importance of sea level as a contributing factor to erosion, and seem to be a clear case of unprecedented water levels in combination with uneventful waves leading to unprecedented erosion.

Seasonal Change

Seasonal profile changes at Kaanapali beach are pronounced. Accretion periods can be idealized as two simple, different systems: accretion updrift of a headland (acting as a barrier to longshore transport, similar to a groin) and accretion on a flat fossil reef. Accretion updrift of a groin has been widely studied and is a common occurrence on coastlines in the US and abroad. The case of sand accretion on a perched beach is much less common, receiving only limited scientific attention.

Beach widening at Hanakao'o Point during winter months is an acute example of accretion on a perched beach, and poses one of the most interesting questions presented by the dynamic cycle of accretion and erosion at Kaanapali. Accretion at Hanakao'o is much more concentrated and dramatic than at Black Rock, even though the north end has an obvious accretion mechanism in place: the physical barrier of Black Rock. It is likely that the shallow, rough reef at Hanakao'o slows southward propagating alongshore currents generated by north swell leading to bed deposition. Hanakao'o also marks the point where swell regimes change from surging breakers in the northern portion of the beach at Black Rock where swash transport may play an important role in beach morphology to offshore dissipative breakers on the reef (characterizing the southern portion of the beach). Because of the difference in offshore depth and wave breaking characteristics, Hanakao'o likely marks the termination of swash zone transport. Improving an understanding of the various

processes governing beach dynamics is critical to defining the role of eddy-generated water-level changes in episodic erosion.

METHODS

Data

An array of instruments shown in Figure 2 (including CTD/OBS and ADCP's) was deployed at the 10 m depth contour along West Maui in 2003 as part of the USGS coral reef project to monitor physical processes affecting formation and lifespan of coral reef systems (Storlazzi et al., 2006). Another instrument (PUV) was deployed at Kaanapali in the summer of 2006 for further monitoring of waves and currents in shallow water.

Modeling

The Delft3D-FLOW module (v. 3.24.03 used here) solves the unsteady shallow-water equations with the hydrostatic and Boussinesq assumptions. In 2D mode the model solves two horizontal momentum equations (see Eq. 1-2), a continuity equation (Eq. 3) and a transport (advection-diffusion) equation (Eq. 4) shown below:

$$\frac{\partial u}{\partial t}+u\frac{\partial u}{\partial x}+v\frac{\partial u}{\partial y}+g\frac{\partial \eta}{\partial x}-fv+\frac{\tau_{bx}}{\rho_w(h+\eta)}-\frac{F_x}{\rho_w(h+\eta)}-\nu_e\left(\frac{\partial^2 u}{\partial x^2}+\frac{\partial^2 u}{\partial y^2}\right)=0 \quad (1)$$

$$\frac{\partial v}{\partial t}+u\frac{\partial v}{\partial x}+v\frac{\partial v}{\partial y}+g\frac{\partial \eta}{\partial y}-fu+\frac{\tau_{by}}{\rho_w(h+\eta)}-\frac{F_y}{\rho_w(h+\eta)}-\nu_e\left(\frac{\partial^2 v}{\partial x^2}+\frac{\partial^2 v}{\partial y^2}\right)=0 \quad (2)$$

$$\frac{\partial \eta}{\partial t}+u\frac{\partial[(h+\eta)u]}{\partial x}+v\frac{\partial[(h+\eta)v]}{\partial y}=0 \quad (3)$$

$$\frac{\partial[hc]}{\partial t}+\frac{\partial[huc]}{\partial x}+\frac{\partial[hvc]}{\partial y}=h\left[\frac{\partial}{\partial x}\left(D_H\frac{\partial c}{\partial x}\right)+\frac{\partial}{\partial y}\left(D_H\frac{\partial c}{\partial y}\right)\right] \quad (4)$$

where u and v = the horizontal velocities in the x and y directions respectively; t = time; g = gravity; η = free surface height; h = water depth; f = coriolis force; ρ_w = density of water; τ_b = bed friction; F = external forces due to wind and waves, ν_e = horizontal eddy viscosity; D_H = horizontal eddy diffusivity; and c = concentration of suspended sediment. The equations are solved on a staggered finite difference grid using the Alternating Direction Implicit (ADI) method after Stelling (1984).

Computational Grids

The computations of Delft3D are performed on orthogonal curvelinear grids shown in Figure 2. Modeling for this project involves two flow grids: a regional model covering the West Maui coast and a local Kaanapali model. These grids are linked either by domain decomposition (DD) or interpolation of boundary conditions from the regional grid to the local grid. The use of DD models is very elegant, although primarily used here to validate the flow field in the smaller models, and justify the use of the local grid by itself. The use of just a local grid for simulations offers an

improvement in computation time over domain decomposition models, especially if the single domain models return results similar to the DD models.

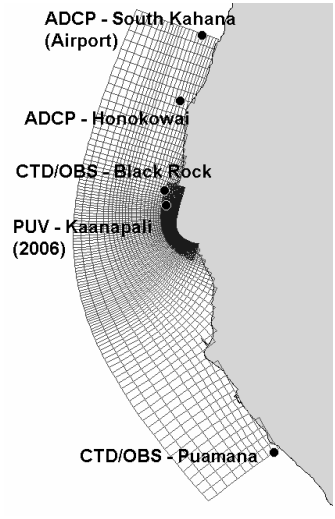

Figure 2 - Instrument locations and grid layout.

Boundary Conditions

West Maui experiences a propagating tide, where gradient phases and amplitudes of tidal constituents exist along the coast, and tidal velocities are directed shore parallel (Storlazzi et al., 2006). Boundary conditions ideal for modeling this particular tidal configuration have been expressed in Roelvink and Walstra (2004), using water-level boundaries at the open (offshore) boundary and water-level gradient (Neumann) boundary conditions at lateral boundaries to solve for alongshore tidal velocities.

The boundaries use a harmonic forcing type, which facilitates use of the harmonic tidal components in water-level boundaries and determining water-level gradients. Water-level gradient boundary conditions can be determined simply from the amplitudes and phases of the tidal constitutes at each lateral boundary using the equations given in Roelvink and Walstra (2004):

	Given tidal constituent	Gradient amplitude:	
Amplitude:	η_i	$\eta_i \left(\frac{\phi_i^{north} - \phi_i^{south}}{d_{ts}} \right)$	(5)
Phase:	ϕ_i	$\phi_i + \pi/2$	(6)

where η_i = amplitude of the tidal constituent (m); ϕ_i = phase of the tidal constituent ($\phi_i^{north}, \phi_i^{south}$ for north and south boundaries respectively (radians)) and d_{ts} = distance between the lateral boundaries (m). With these boundary conditions prescribed, the bed roughness is tuned to match the observed current magnitude. These boundary conditions have been shown to provide accurate simulations of tidal velocities in Roelvink and Walstra's modeling studies (2004) at Egmond (Netherlands). This study provides another example of the excellent performance of boundary conditions developed from this scheme (see Results).

The wave boundary conditions are determined from model hindcasts (WaveWatch III) because there are no recorded buoy observations that include wave direction. These hindcasts adequately resolve observed wave heights and periods at a number of buoy locations in Hawaii. In this study, hindcast values of significant wave height, peak period and direction are applied uniformly at the open boundaries of the largest SWAN model, and a series of nested grids resolve the wave field down to the nearshore scale (10m grid) at West Maui and Kaanapali Beach. The SWAN nesting scheme is shown on Figure 3.

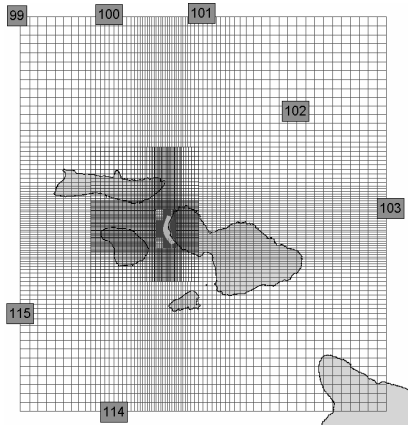

Figure 3 - SWAN nesting scheme. WaveWatch III hindcast locations are shown in boxes.

RESULTS

Model calibration has been carried out with the USGS data set. The model shows good comparison to the observed data set for tidal water levels, wave heights, and currents.

Good comparisons of tidal water levels are readily achieved with the use of a water-level boundary at the open boundary. The modeled and observed tidal components at the instrument location are shown in Table 1.

Table 1 - Observed vs. modeled tidal constituents at instrument locations

Airport

	Obs Amp [m]	Mod Amp [m]	Obs Phase [deg]	Mod Phase [deg]
M2	0.175	0.173	-124.1	-124.0
N2	0.029	0.029	157.9	157.7
S2	0.062	0.061	79.4	79.4
K1	0.182	0.181	79.4	79.2
P1	0.048	0.048	85.9	85.1
O1	0.105	0.105	-148.2	-148.5
K2	0.029	0.028	-107.5	-108.3

Honokowai

	Obs Amp [m]	Mod Amp [m]	Obs Phase [deg]	Mod Phase [deg]
M2	0.176	0.174	-122.6	-121.6
N2	0.029	0.029	159.1	160.3
S2	0.061	0.06	81.2	82.1
K1	0.18	0.18	79.0	78.6
P1	0.048	0.048	86.3	85.3
O1	0.105	0.104	-148.5	-148.9
K2	0.028	0.028	-107.1	-106.6

Black Rock

	Obs Amp [m]	Mod Amp [m]	Obs Phase [deg]	Mod Phase [deg]
M2	0.177	0.174	-119.3	-118.3
N2	0.029	0.029	161.1	163.6
S2	0.059	0.058	85.3	86.0
K1	0.178	0.177	78.9	77.7
P1	0.048	0.047	86.9	85.2
O1	0.104	0.102	-148.3	-149.3
K2	0.027	0.027	-106.3	-103.7

Puamana

	Obs Amp [m]	Mod Amp [m]	Obs Phase [deg]	Mod Phase [deg]
M2	0.179	0.177	-107.4	-106.8
N2	0.028	0.029	174.4	175.8
S2	0.052	0.052	100.0	100.6
K1	0.168	0.169	75.0	74.9
P1	0.045	0.045	84.4	85.0
O1	0.096	0.096	-150.8	-150.9
K2	0.025	0.025	-95.4	-93.4

Agreement between modeled and observed currents is more difficult to achieve because of unresolved current-generating sources including mean flows through the Pailolo channel, internal tides, and the influence of the mesoscale eddy. Nevertheless the model shows good comparison with the observed currents, especially for stations dominated by barotropic flow, shown in Figure 4 and Figure 5.

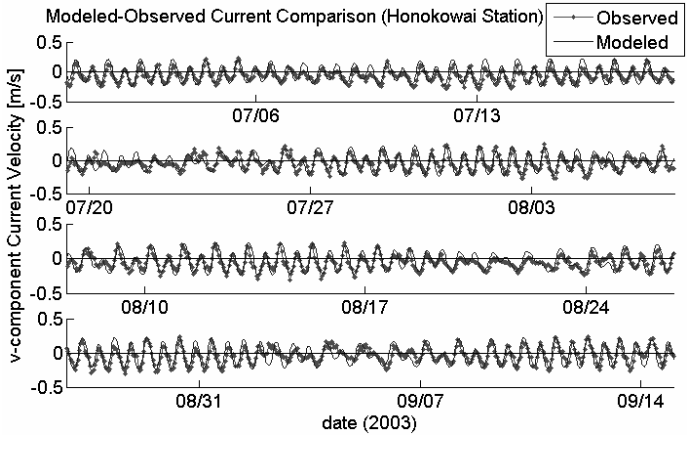

Figure 4 - Modeled vs. observed current comparison for Honokowai station.

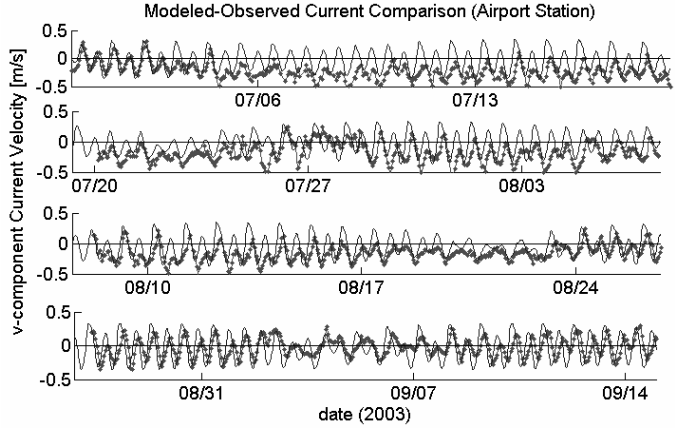

Figure 5 - Modeled vs. observed current comparison for the South Kahana (Airport) station.

Use of the SWAN model appears to resolve spatial variability around and inside of the Maui Nui complex. Modeled wave heights show good comparison with observations at instrument locations shown in Figure 6.

Tidal residuals from two dominant swell regimes are shown in Figure 7, which show significant longshore currents at Kaanapali.

Morphologic simulations under dominant north and south swell conditions are shown in Figure 8 with aerial photographs of the seasonal beach states when these swell regimes dominate.

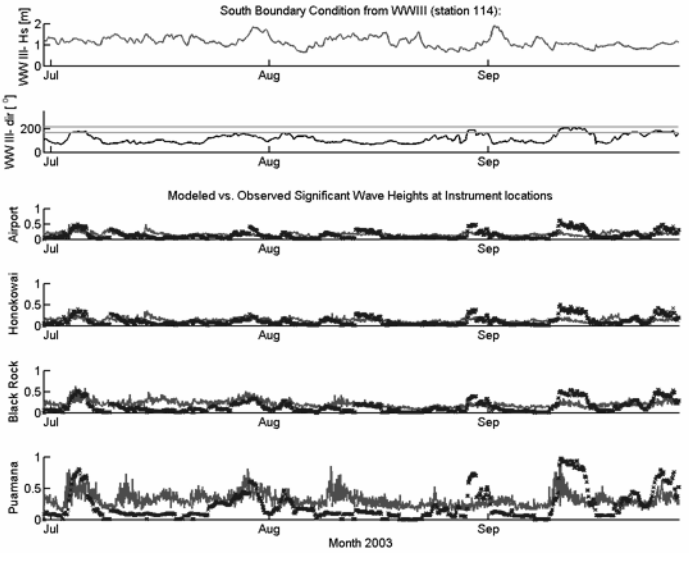

Figure 6 - WaveWatch III boundary conditions and comparisons of modeled (x) and observed (-) wave heights [m] at instrument locations. The lines on the second subplot represent the south swell window (170-210°).

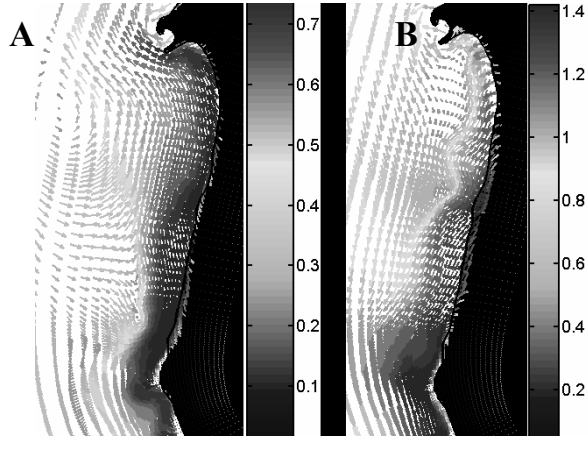

Figure 7 - Tidal residuals [m/s] for South (A) and North (B) swell at Kaanapali Beach

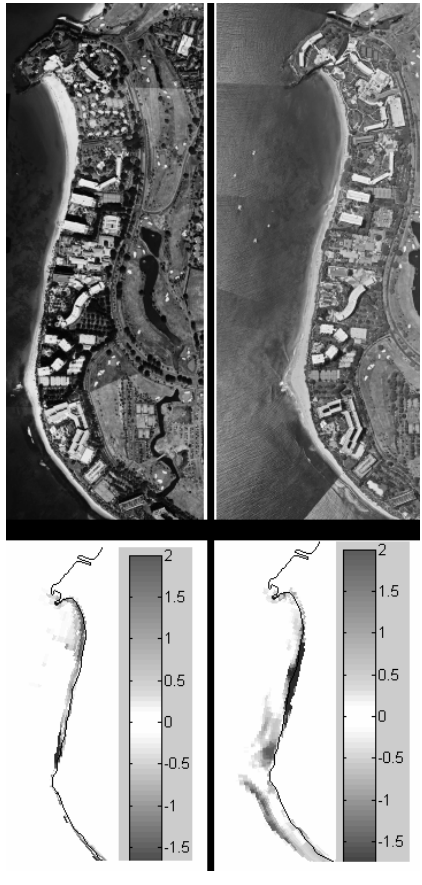

Figure 8 – Observed (above) and simulated (below) beach states (accretion - red; erosion - blue [m]) during summer (left) and winter (right) swell conditions.

DISCUSSION

Using Delft3D with water-level gradient boundary conditions prescribed in Roelvink and Walstra (2004) provide excellent resolution of current velocities in regions dominated by barotropic tidal flow. For regions influenced by mean flows and internal tides, more physical processes need to be accounted for to better resolve observed velocities. It appears the Honokowai station (Figure 4) is well resolved, while the South Kahana (Airport) station (Figure 5) is influenced by the presence of mean flows and internal tides. Despite the influence of unresolved processes, the models show good comparison with the observed flow velocities.

Mean flows observed at the South Kahana (Airport) Station appear to be related to wind direction, and may be related to island-trapped wave events (Merrifield 2002; Storlazzi 2006). Figure 9 shows the time series of wind speed and mean flow and their inter-relationship.

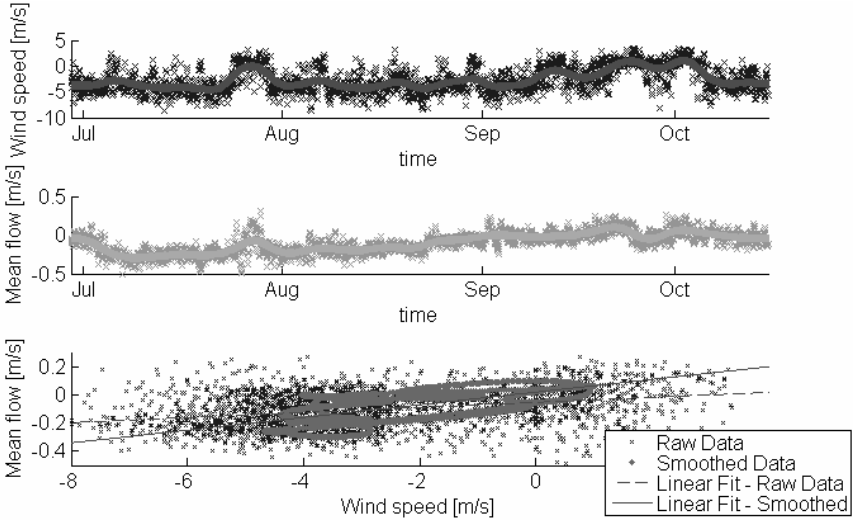

Figure 9 - Relationship between winds and mean flow through the Pailolo Channel.

Wind speed and mean flow seem to mirror each other. A notable event in the time series is the decrease in wind speed in late July which leads to a corresponding decrease in the mean flow through the channel. Although the model accounts for wind forcing, the mean flow is not resolved. If the mean flow is due to wind forcing, the inability to resolve the mean flow is probably due to the limited coverage of the model domain: inability to develop significant wind-generated currents, and/or the topographic influence of West Maui which may cause local acceleration of the wind field.

The mean flow observed at South Kahana seems unlikely, from the two observed time series, to extend past the Honokowai station and potentially affect currents and sand transport at Kaanapali Beach. The major influence in sand transport at Kaanapali seems to be the wave-generated currents that arise from obliquely incident waves from north and south swell breaking on the westward-facing shoreline.

While simulations of shoreline accretion and erosion forced by the dominant swell regimes show a qualitative morphologic behavior, the ultimate goal of modeling is to reproduce or predict transport volumes and resulting changes in the beach profile. Modeling beach profile changes often captures observed changes in mean state, but is

less successful at predicting significant erosion and accretion events. While the model seems to perform adequately for scenarios on timescales of a few days, variability of wave and current conditions on longer timescales make simulations on timescales of months to years more difficult to resolve. Comparisons of observed and modeled profile changes, in Figure 10, show that the model tends to overpredict accretion (indicated by the frequency of records in quadrant 2 and above the perfect fit line) and to miss large erosion and accretion events in the end members of the littoral cell (Black Rock and Hanakao'o). Bias towards accretion is likely due to the persistence of small wave states during the 3-month simulation, and inability to resolve swell events that lead to significant change. The effects of 2D vs. 3D modeling on accretion predictions should also be investigated.

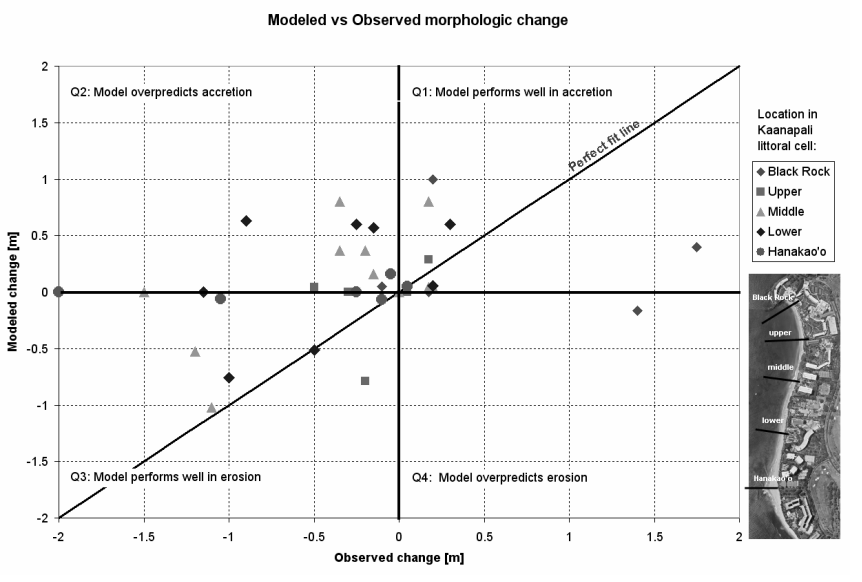

Figure 10 - Observed vs. modeled beach profile changes over 3 months at a number of locations at Kaanapali, Summer 2000.

Additionally, there appears to be no significant difference in modeling the summer 2003 erosion event with and without the presence of the small sea-level signal contributed by mesoscale eddies. This is likely the result of discretization by the model. There is an inherent problem simulating natural processes using discrete numerical simulations, especially when variability of a particular process, in this case sea level in its vertical and horizontal position, exists on a smaller scale than the discrete grid is capable of resolving. Another process we are not effectively resolving in the model is the action of swash transport producing morphologic changes in the beach face. The model does, however, have a scheme to replicate morphologic beach face changes by applying a relative amount of erosion or accretion in wet grid cells to

adjacent dry grid cells. While this scheme is a practical solution to an extremely complex problem, it does leave a potentially important processes unresolved.

We can, however, make interesting conclusions about sand transport from simulations of simple scenarios. Morphologic simulations of transport due to north swell with a uniform bed roughness demonstrate transport of a considerable amount of sand around Hanakao'o Point. Increasing the simulated roughness for the submerged fossil reef offshore from Hanakao'o Point causes the sand to accumulate in this location. This is consistent with field observations.

Inability of the model to resolve the signal of the mesoscale eddy should not cause us to dismiss its influence. Simple Bruunian models assign sea-level position paramount influence, although the presence of reef surfaces may change this simple dynamic. It appears that increased sea level on a normal shoreline profile (not perched) may exist in unstable equilibrium until wave energy initiates transfer to a new position. The duration of mesoscale eddies is sufficient to begin this transition as evidenced by the considerable erosion observed in summer 2003 at Kaanapali. The event also suggests that increased sea-level signals may cause accelerated seasonal response in alongshore systems.

CONCLUSIONS

Robust numerical models allow for realistic shoreline change simulations. Adequate observations are indispensable to ensure realistic performance. Poor modeling performance arises from inadequate tuning, unresolved processes, and spatial discretization of continuous natural processes. Use of water-level gradient boundary conditions given by observations of tidal components and the equations used in Roelvink and Walstra (2004) successfully model tidal velocities. Scenario-based modeling of seasonal shoreline change is qualitatively successful, whereas real-time, long-term simulations often to not capture significant changes in beach profile and shoreline position.

Mesoscale eddies and accretion on perched beaches atop rough reef substrates play a potentially significant role in beach morphology of Hawaiian shorelines, and merit continued investigation.

ACKNOWLEDGMENTS

The authors would like to thank Edwin Elias, Dolan Eversole, Chris Conger, Jeff List, Capt. Joe Reich, Lamber Hulsen, Dano Roelvink, Dirk-Jan Walstra, Everyone at Delft3D support: Johan Dijkzeul, Arjen Luijendijk, and Meo de Rover. This paper is funded by a grant/cooperative agreement from the National Oceanic and Atmospheric Administration, Project # R/EP-26, which is sponsored by the University of Hawaii Sea Grant College Program, SOEST, under Institutional Grant No. NA05OAR4171048 from NOAA Office of Sea Grant, Department of Commerce. The views expressed herein are those of the author(s) and do not necessarily reflect the views of NOAA or any of its subagencies. UNIHI-SEAGRANT-OP-07-06.

REFERENCES:

Elias, W.P.L. (2000). "Hydrodynamic validation of Delft2/3D with field measurements at Edmond," Proc. 27th ICCE, Sydney, Australia.

Elias, W.P.L. (2006). "Morphodynamics of Texel Inlet," Ph. D. thesis. Delft University of Technology, The Netherlands.

Eversole, D., Fletcher, C.H., (2003). "Longshore Sediment Transport Rates on a Reef-Fronted Beach: Field Data and Empirical Models Kaanapali Beach, Hawaii," Journal of Coastal Research: Vol. 19, No. 3, pp. 649–663.

Firing, Y. L., and Merrifield, M. A., (2004). "Extreme sea level events at Hawaii: Influence of mesoscale eddies," Geophys. Res. Lett. 31, L24306

Flament, P., Lumpkin, C., (1996). "Observations of currents through the Pailolo Channel: Implications for nutrient transport," In: Wiltse, W. (Ed.), Algal Blooms: Progress Report on Scientific Research, West Maui Watershed Management Project, pp. 57 –64.

Klein, M.D., Elias, E.P.L., Stive, M.J.F., Walstra, D.J.R., (2001). "Modelling inner surf zone hydrodynamics at Egmond, The Netherlands," In: Hanson, H., Larson, M. (Eds.), Proc. 4th Int. Conf. on Coastal Dynamics '01. ASCE, Reston, pp. 500–509.

Lesser, G.R., (2000). "Computation of Three-dimensional Suspended Sediment Transport within the DELFT3D-FLOW Module," Master's thesis. Delft University of Technology, The Netherlands.

Lesser, G.R., Roelvink, J.A., van Kester, J.A.T.M., Stelling G.S., (2004). "Development and validation of a three-dimensional morphological model," Coastal Engineering. v. 51. pp. 883–915.

Luijendijk, A.P., (2001). "Validation, calibration and evaluation of Delft3D-FLOW model with ferry measurements," Master's thesis. Delft University of Technology, The Netherlands.

Merrifield, M.A., Yang, L., Luther, D.S., (2002). "Numerical simulations of a storm generated island-trapped wave event at the Hawaiian Islands" Journal of Geophysical Research 107 (C10), 3169.

Roelvink, J.A., Wasltra, D.J., (2004). "Keeping in simple by using complex models," 6th International Conference on Hydroscience and Engineering, Advances in Hydro-Science and Engineering, Brisbane, Australia.

Stelling, G.S., (1984). "On the construction of computational methods of shallow water flow problems," Rijkswaterstaat communications, No. 35

Storlazzi, C.D., McManus, M.A., Logan, J.B. McLaughlin, B.E., (2006). "Cross-shore velocity shear, eddies and heterogeneity in water column properties over fringing coral reefs: West Maui, Hawaii," Continental Shelf Research 26 (2006) 401 –421

Sun, L.C., (1996). "The Maui algal bloom: the role of physics," In: Wiltse, W. (Ed.), Algal Blooms: Progress Report on Scientific Research. West Maui Watershed Management Project, pp. 54 –57.

Walstra, D.J.R., Roelvink, J.A., Groeneweg, J., (2000). "Calculation of wave-driven currents in a 3D mean flow model," Proc. 27th Int. Conf. on Coastal Engineering. ASCE, New York, pp. 1050– 1063.

Walstra, D.J.R., Van Rijn, L.C., Boers, M., Roelvink, J.A., (2003). "Offshore sand pits: verification and application of hydrodynamic and morphodynamic models," Proc. 5th Int. Conf. on Coastal Sediments '03. ASCE, Reston, Virginia

Aeolian Processes, Coastal Dunes, and the *Coastal Engineering Manual*

Part III, Chapter 4 - "Wind-Blown Sediment Transport"

Frank Hopf [(1)] and Douglas J. Sherman [(2)]

1) Department of Geography, Texas A&M University, College Station, Texas, 77843-3147 – Corresponding author fhpf@neo.tamu.edu

2) Department of Geography, Texas A&M University, College Station Texas, 77843-3147 sherman@geog.tamu.edu

ABSTRACT

Along many shorelines, the coastal foredune plays a key role in protecting against coastal flooding while providing a unique environment for specialized flora and fauna. Over the past 20 years, researchers with backgrounds in engineering, geography, geology, and geomorphology have expanded our understanding of the coastal aeolian processes that build and shape these landforms. In 2002, the U.S. Army Corps of Engineers (U.S.A.C.E.) replaced its *Shore Protection Manual (SPM*) with the *Coastal Engineering Manual* (*CEM*). The *CEM* is intended to provide "*in a single source the current state-of-the-art in coastal engineering to provide appropriate guidance for application of techniques and methods to the solution of most coastal engineering problems*" (*CEM* 2002, p. I-1.1), thus establishing it as the legal standard for coastal engineering practice in the U.S. Chapter 4 in Part III, "Wind-Blown Sediment Transport" is intended to provide engineers such guidance where wind blown sand is a part of the problem or the solution. This paper reviews Chapter III-4 and compares it to the published research to assess the degree to which this section communicates and codifies "state-of-the-art" understanding of coastal aeolian processes and landforms. Our review suggests that three specific areas require revisiting: (1) the "Transport Rate" section should be revised to direct the user to conservative transport rate estimation methods; (2) the coastal aeolian and dune process descriptions should be expanded to incorporate recent research findings, especially those that encourage and permit the engineer to incorporate more natural processes and landforms in solutions; and (3) an outdated and incorrect recommendation should be removed immediately.

INTRODUCTION

"Engineering is not applied science. Our limited understanding of nature is one constraint, but it is far from the only one, seldom the hardest one, and almost never the limiting constraint for coastal engineering design." (*CEM* 2006, p.V-3.18)

"Engineers, geographers, oceanographers, geologists and other scientists have made significant contributions to our present understanding of the coastal environment. As usual, however, interdisciplinary communication has not been good because each discipline is engrossed in specific problems. Nonetheless, if demands on the coastal system continue to increase, the cooperative efforts of all coastal workers are necessary to avert environmental disaster." (Ritter *et al*. 2002, p. 434)

In 2002, the U.S. Army Corps of Engineers (USACE) published the *Coastal Engineering Manual* (*CEM*) to provide coastal engineers "*the current state-of-the-art in coastal engineering to provide appropriate guidance for application of techniques and methods to the solution of most coastal engineering problems*." (*CEM*, 2002, p I-1.1) In the first section, the *CEM* identifies Ritter's '*engineers, geographers, oceanographers, geologists and other scientists'* as producing a 'coastal science' that it defines as a "*suite of interdisciplinary technologies applied to understanding processes, environments and characteristics of the coastal zone*." (*CEM*, 2002, p I-1.2) It continues: "*Coastal engineers use these understandings to develop physical adaptions to solve problems and enhance the human interface with the coast.*" (*CEM*, 2002, p I-1.2) This introduction admonishes users that proper design and implementation of solutions to coastal problems requires understanding of coastal processes. The *CEM* lays a heavy burden on coastal engineers to incorporate understanding of all processes working on the harbors, navigation channels, shore protection projects, flood control projects, and environmental preservation and restoration efforts that they design. The manual attempts to provide all of the necessary knowledge, an effort that helps explain why the *CEM,* at 2838 pages, is almost three times longer than the *Shore Protection Manual* (1984) it replaces. The U.S.A.C.E. developed the *CEM* to document both the state-of-the-art in coastal engineering designs and procedures and the scientific understanding of coastal processes and landforms.

If Ritter *et al*. (2002) are correct about the communication challenges between coastal engineers and coastal scientists, the question arises: Does the *CEM* reflect and communicate our best understanding of coastal processes? If it does not, what changes move us closer to this goal? This paper addresses these questions as they pertain to Chapter III-4 to assess whether it meets the "state of the art" standard. Through its identification with this standard, the U.S.A.C.E. has elevated the *CEM* to status of preemptive authority for the courts, in political debate and in public discussion. This importance dictates that geomorphologists and ecologists as well as coastal engineers provide critical review of the *CEM* to achieve and maintain this standard. The knowledge codified in the *CEM* finds it way into most designs and construction contracts for coastal work in the United State as the U.S.A.C.E retains project management and engineering responsibilities for the U.S. government. Moreover, U.S.A.C.E.'s translation of the *CEM* into many other languages, including Chinese and Catalonian, and the provision of free internet access only serve to increase its global impact.

This paper involves comparing the *CEM*'s Chapter 4 in Part III, "Wind-Blown Sediment Transport" (hereafter referred to as Chapter III-4) with the recent literature on aeolian processes and coastal dunes. To gauge Chapter III-4's degree of currency as of its publication on 30 April 2002, preference was given to articles published between 1990 and early 2001. To assess Chapter III-4's success, the question was posed: Does it provide the necessary guidance and information to maximize an engineer's chance to develop a sustainable, cost-effective, environmentally acceptable solution when assigned to develop a flood protection "sand dune" or to stop wind-blown coastal sand from encroaching on infrastructure or agricultural lands? For example, could the guidance of Chapter III-4 prevent the inundation of a city with sand from its beach nourishment project, such as occurred at Riells, Spain in 1988 and 1994? (Marques *et al*. 2001). If not, how could the guidance be improved?

ALTERNATIVE PERSPECTIVES

The typical technical code or design manual provides engineers two basic types of standards, (1) a prescriptive standard where the ways and means to attain an end result are fully defined; or (2) a performance-based standard where a specific description of the end result to be attained is defined and the engineers is required to determine how this is to be achieved (American Society of Civil Engineers 2006). Implicit in a prescriptive standard is the code writer's promise that if applied as prescribed, the solution will be conservative enough to not fail because of other (reasonable) factors that were not considered. Professors and textbooks inoculate neophyte engineers against failures by stressing the importance of conservative calculations and design. They emphasize early in the academic training the importance of applying generous safety factors or "factors of ignorance" that help reduce the number of "*sleepless nights wondering if those he has used are sufficient*" (McCormac 1967, p. 4). Similarly, performance-based standards presume the engineer has adequate scientific knowledge to apply to the problem. The C*EM* functions as a technical standard and more, with Part I through IV providing the "scientific foundation on which the engineering-based parts rely." (*CEM* 2002, p. I-4-3). The U.S.A.C.E. intended Chapter III-4 to provide state-of–the–art knowledge of aeolian processes and landforms at work in the coastal zone.

While our analysis to date cannot be considered complete, we feel that as currently constituted, Chapter III-4 does not provide the engineer with adequate, and in some cases correct, information to properly work with, specifically:

> 1) It prescribes (without the prescriptive language defined in American Society of Civil Engineers 2006) a method to calculate aeolian transports rates that is scientifically flawed and that does not produce conservative predictions.
> 2) The discussion of aeolian processes and coastal dunes is not adequate or current enough to meet the "state-of-the-art" standard. As published, Section III-4 provides weak foundation to develop successful performance-based solutions that will be effective and efficient.

3) While some of the text is only "weakly correct" or ignores established best practices, the chapter also includes text that perpetuates a relic recommendation to utilize an invasive plant species to stabilize sand dunes.

Predicting wind-blown sand transport rates

Chapter III-4 prescribes primitive methodologies for obtaining the data needed for predicting aeolian transport rates, prefaced by an out-of place description of "Wind Regimes in the US" (in Section III-4-2). Although generically interesting, this description offers little to assist an engineer facing a local challenge. Except in the rarest of cases, regional climate patterns and data will not produce the level of detail needed for successful estimates. A more appropriate start to Chapter III-4 would be a general introduction to the aeolian boundary layer and sampling methodologies.

Many of the protocols presented assume that the project engineer will not have the necessary resources to gather the appropriate data for transport rate estimates. For example, the discussion begins with a presentation of the "Law of the Wall:"

$$u_z = \frac{u_*}{\kappa} \ln\left(\frac{z}{z_0}\right) \quad (1)$$

where u_z is the wind speed at elevation z above ground, u_* is the shear velocity, z_0 is the roughness length, and κ is von Karman's constant (about 0.4), and d is the mean grain size. Estimation of u_* is the critical step for predicting transport rates as it is the fundamental parameter in most transport models. To determine u_*. estimates or measurements of u_z at height z are required. The standard practice is to use arrays of three to six anemometers to measure the wind speed profile at the location of interest, determine statistical best-fit line, and use the slope, m, and intercept, b, of that line to estimate: (Bauer *et al.* 1992)

$$u_* = m\kappa, \quad (2)$$

$$\text{and } z_0 = e^{-(b/m)} \quad (3)$$

Chapter III-4 describes processes for deriving estimates of roughness length and shear velocity using either one or two anemometers, rather than the preferred statistical analysis of wind profiles measured with three or more anemometers. Before continuing our review of this protocol, it is important to note that, given the normal cost of a three-cup anemometer between US$50 and $400, the recommendation to deploy only one or two anemometers will save the project engineer less than $1000 at a cost of inferior estimates for key transport parameters. Chapter III-4 suggests that roughness length can best be calculated by measuring wind speeds at two different elevations and then solving for z_0. If the relevant profile is perfectly log-linear, then this method will yield results identical to those obtained using the statistical protocol provided above. However, perfect log-linearity is rarely found in empirical wind data and even small departures from this state will lead to large degrees of uncertainty roughness length estimates. More importantly, however is the fact that if you have two (or more) anemometers and a log-linear profile, there is no need to estimate roughness length because estimates of u_* can be obtained directly from Equation 2. However, Chapter III-4 continues, somewhat contradictorily,

to argue that because velocity measurements at two elevations are rarely available, u_* could be determined from the relationship:

$$u_* = 0.044\, U_{2m} \quad (4)$$

where U_{2m} is the average hourly wind velocity measured two meters above the beach. Chapter III-4 also identifies that the constant for surface types other than a smooth beach varies from 0.037 for a tidal flat to 0.093 for the lee side of a dune, while admonishing that this relationship only holds for the grain size and sorting for which they were developed (although these values are not reported).

There are three flaws in this one-anemometer approach. First, there are several methods to estimate roughness lengths if the sand grain size is known or can be approximated (although such methods must, perforce, ignore complicating factors such as the presence of ripples, local topography, vegetation, etc.). For example, from the work of Nikuradse:

$$z_0 = d/30 \quad (5)$$

where d is the diameter of uniform grains. For non-uniform grain-size populations Namikas (2003), suggests the relationship:

$$z_0 = 2d/30 \quad (6)$$

where d is the mean grain diameter. This later relationship should be included because this condition is common to most beach surfaces and it could be used to estimate aeolian interactions with sand from potential beach or dune nourishment sources. Combining Equations 1 and 6 includes more information about a specific site:

$$u_z = \frac{u_*}{\kappa} \ln\left(\frac{15z}{d}\right) \quad (7)$$

The second flaw associated with the use of one (or two) anemometer(s) as described in Chapter III-4 concerns recommended measurement heights. For one anemometer, the recommended height is two meters, for two anemometers it is suggested that they be placed three, four, or more meters apart, vertically. At these elevations, however, there is a chance that the instruments would be above the internal boundary layer developing over a beach. The height, δ, of such a boundary layer increases with distance, X, down wind of a change in surface roughness or orientation – *e.g.*, the transition from wind flow over water to over sand Granger *et al.* (2005) suggest:

$$\delta = 0.18X^{0.62} \quad (8)$$

for relatively smooth conditions such as those over a sand surface. For a site 100 m from the water line, for example, this would put the top of the internal boundary layer at about 3 m. For a distance of 50 m, from the water line, berm crest, or dune crest, the estimate of δ decreases to about 2 m. Wind speeds should be measured conservatively below these elevations in order to best represent the conditions acting on the sand surface.

The third flaw arises from treating the roughness length as a constant. Since the work of Owen (1964), we have known that the presence of saltating grains produces an apparent roughness length, z_0' that is proportional to the shear velocity:

$$z_0' = \frac{Cu_*^2}{2g} \quad (9)$$

where C is a constant and g is gravity acceleration. A similar, but alternative formulation, is that of Raupach (1991):

$$z_0' = \left(\frac{Cu_*^2}{2g} \right)^{1-r} z_0^r \tag{10}$$

where r is the ratio of the threshold shear velocity to shear velocity. Either Equation 9 or 10 can be used with wind speed measured at one elevation to solve Equation 1 iteratively for shear velocity. Again, this approach includes much more environmental information than the approach presented in Chapter III-4. Any one of these three flaws could be enough to distort the critical estimates of shear velocity that would result from their use. Therefore, we conclude that these protocols do not represent best practice.

Section III-4-3 "Transport Rates" presents an incomplete review of transport rate equations that include only the models of Bagnold (1936), O'Brien and Rindlaub (1936), Zingg (1953), and Hsu (1971). At this point, instead of continuing to identify the many other formulas developed by researchers such as Kawamura (1951), Kadib (1964), Lettau and Lettau (1977), Horikawa *et al.* (1984), Sørensen (1991), and Spies et al. (1991), Chapter III-4, justified on the basis of Chapman's (1990) paper, jumps to the designation of **the one best** formula, that of Hsu (1971):

$$q = K \left(\frac{u_*}{\sqrt{gd}} \right)^3 \tag{11}$$

where q equals sand transport rate in gm/cm-s, u_* is shear velocity, d is mean sand grain diameter and K = dimensional aeolian sand transport coefficient, which in turn equals:

$$K = e^{-9.63+4.91d} \tag{12}$$

In selecting this formula as the prescribed transport estimation relationship, Chapter III-4 ignores the analyses of Svasek and Terwindt (1974), Sarre (1988), Bauer *et al*. (1990), Pye and Tsoar (1990), Sherman and Hotta (1990), Arens (1996) and Sherman *et al*. (1998). All of these studies tested the various models in various environments and collectively showed that none of the transport models provide consistent, accurate results. The recommendation to use the Hsu (1971) model even ignored Chapman's summary analysis (1990, p. 752) that of the models reviewed, including Hsu (1971), "*it is clear that there is no unequivocally 'best' method."*

There are many local factors that mitigate against the success of a general transport model that incorporates only wind speed (shear velocity) and grain size as independent variables. However, even without these complications, the different transport models produce a wide range of predicted transport rates. For a constant grain size and an identical range of shear velocities, Sherman *et al*. (2005) showed that the different models produce a set of predictions that vary by more than 700%. Pye and Tsoar (1990) had earlier identified this magnitude of variability. Researchers have not been able to narrow this variability in part because so many other factors (as listed by Arens (1996) and Sherman *et al.* (2005), for example) affect the rate. Beaches are also subject to significant temporal and spatial variations in wind speed over small time and space scales (Arens 1996; Gares *et al*. 1996) that complicates this problem further.

When the general transport models are corrected for moisture, the discrepancies between the predictions may increase depending on the moisture correction model used and the

moisture content for the sediments being evaluated. Many researchers have recognized that moisture content can be the third most important factor affecting transport rates (Sarre 1988; Gares 1988; Pye and Tsoar 1990; Sherman and Hotta 1990; Namikas and Sherman 1995; and Cornelius and Gabriels 2003).

Chapter III-4 contains four flaws in the treatment of sediment moisture content. First, it is presumed that moisture content is important only for days where precipitation exceeds evaporation. This is problematic for four reasons: 1) it requires reliance on data from weather stations that might be remote from the site under consideration; 2) it requires assessment on a daily basis, thereby ignoring the much shorter duration of many transport events; 3) it requires prediction of a daily evaporation total, a complicated process ignored in the chapter; and 4) perhaps most seriously, it presumes that precipitation is the only source of sediment moisture on a beach – this is clearly nonsense.

The second flaw is that only the Hotta *et al*. (1985) model is considered to represent the moisture influence on threshold shear velocity. There is no independent verification of the propriety of this designation (see review by Cornelius and Gabriels, 2003), and the predicted effects of moisture content vary widely depending on the model chosen (Namikas and Sherman, 1995). The third flaw is the assumption, based loosely on the field data of Svasek and Terwindt (1974) that the sand moisture content is either 2.5% or 0%, depending on the balance between precipitation and evaporation. Sand moisture is difficult to measure but readings vary from 1% to 25% with a recommended default value of 4% not recently flood by rain or tides (Sherman *et al.* 2005). Several researchers have developed correction factors for moisture, which Namikas and Sherman (1995) found could produce widely different results.

The fourth flaw associated with the moisture content analysis is that there is no way, according to the protocol spelled out in the chapter, to actually apply the results of a predicted effect because the Hsu (1971) equation does not include a term for threshold shear velocity. Indeed, examination of Tables III-4-4 and III-4-5, illustrating the use of moisture information for transport prediction, indicates that the moisture content effect either prevents transport entirely (nonsense) or has no effect at all (also nonsense).

At this point we can return to our premise that one duty of the engineer is to provide conservative estimates for project planning and design. Clearly, the protocols presented in Chapter III-4 cannot produce such estimates as only one outcome is possible for a particular data set. This ignores the large degree of variability that exists in transport (and related) models. It is more appropriate to provide a selection of approaches that would provide maximum and minimum likely transport rates. Following Sherman *et al*. (2005) we recommend that the engineer concerned about potentially damaging blowing sand (such as occurred on the nourished beach at Riells, Spain (Marques *et al*. 2001) use a model that yields an upper limiting calculation. Kawamura's (1951) model does this:

$$q = C\frac{\rho}{g}(u_* - u_{*_t})(u_* + u_{*_t})^2 \qquad (13)$$

where q is the transport rate, C is an empirical constant (typically 2.78), u_{*_t} is the threshold shear stress and ρ is the density of the sediment. This model could be used with a conservative moisture correction, such as that of Hotta *et al*. (1984):

$$u_{*_{tw}} = u_{*_t} + 7.5w \tag{14}$$

where $u_{*_{tw}}$ is the wet threshold shear velocity, which substitutes in equation 12 for u_{*_t}, combining equations 13 and 14:

$$q_{wet} = C\frac{\rho}{g}(u_* - u_{*_t} - 7.5w)(u_* + u_{*_t} + 7.5w)^2 \tag{15}$$

where q_{wet} is the moisture corrected transport rate.

One the other hand, for the engineer needing to estimate a potentially beneficial impact from blowing sand, (*e.g*. building a dune), a method that consistently gives low estimates should be considered, such as Zingg's (1953) modification of the Bagnold model:

$$q = C(\frac{d}{D})^{3/4}\frac{\rho}{g}u_*^3 \tag{16}$$

where q is the sediment transport rate, C is 0.83, and D is the reference grain size of 0.25mm. In this case, moisture correction should be applied and the method that identifies the largest reduction in rate, the Belly (1964) model, should be applied. It works by calculating the wet threshold shear velocity:

$$u_{*_{tw}} = u_{*_t}(1.8 + 0.6\log_{10} w) \tag{17}$$

Since the Zingg formula does not include a threshold shear velocity term, the moisture correction is made by increasing Bagnold's (1942) reference grain diameter D by solving for d in Equation 18 for the wet threshold velocity. D_{wet}, the moisture compensated equivalent reference grain diameter (Sherman *et al.* 2005) is determined by:

$$D_{wet} = \frac{u_{*_{tw}}^2}{A^2 g(\frac{\rho_s - \rho}{\rho})} = \frac{u_{*_t}^2(1.8 + 0.6 * \log_{10} w)^2}{A^2 g(\frac{\rho_s - \rho}{\rho})} \tag{19}$$

D_{wet} then substitutes for D in Equation 16 to obtain the conservative transport estimate:

$$q_{wet} = C(\frac{d}{D_{wet}})^{3/4}\frac{\rho}{g}u_*^3 \tag{20}$$

An example of the range of transport rates calculated by the two recommended methods, the Chapter III-4 method, and Bagnold's (1936) original model is shown in Figure 1.

The engineer can also compensate for other the factors that affect transport rate estimates for a given site, but it is important to establish the worst case estimates, whether they be low or high.

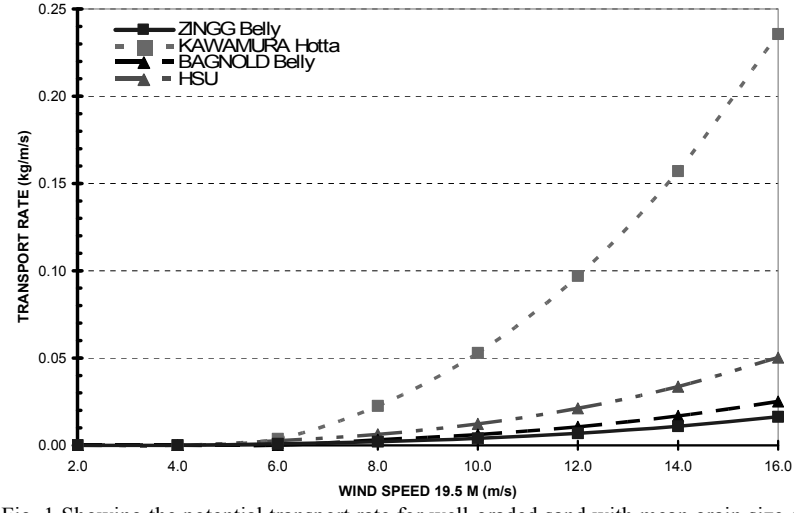

Fig. 1 Showing the potential transport rate for well-graded sand with mean grain size of 0.125mm with moisture content of 3.0% using various models mentioned in text for various measured wind speeds.

Scientific information about dunes and aeolian processes

Chapter III-4's relatively short section "Dunes and dune processes" begins with "*Sand dunes are important coastal features that are created, enlarged, and altered by wind–blown sand…. These dunes often result from the natural accumulation of wind blown sand originating on the beach face: however, they may also be man-made. Whether natural or man-made, they are subject to continued growth, alteration and movement due to natural wind transport processes. When present and if sufficiently large, foredunes can provide protection from coastal flooding, shoreline erosion, and wave damage. Dunes can also shelter the area landward from wind-blown sand*." (*CEM* 2002, p. III-4-47) Unfortunately, this promising introduction is not backed with sufficient information to help an engineer with the assignment of creating a protective dune with a given performance requirement (such as it shall provide a volume of 50 cubic meters/meter length above the 100-year flood level.) A short list of the critical scientific concepts that such an engineer should be aware of include:

1) A dune created by natural aeolian processes, in whole or in part, can be more effective in resisting storm waves and be more aesthetically pleasing than mechanically piled sand (Brunsden and Moore 1999, Psuty and Ofiara 2000, Nordstrom and Lotstein 1989)
2) Stabilization by native vegetation offers many advantages over fencing but there are situations where properly designed sand fencing will be required to create / maintain the dune. (Hotta *et al*. 1987; Nordstrom *et al*. 2000; Miller *et al*. 2001)

3) The foredune provides a niche microenvironment that should be preserved, or mimicked as much as possible. (Nordstrom and Allen 1978; McLachlan 1990)
4) Where they exist, foredunes are a critical element of the dynamic, linked offshore bar-beach-dune system where sediment budgets (natural and augmented) play a key role in the morphology of the elements. (Short and Hesp 1982; Sherman and Bauer 1993; van der Wal 2000; Garcia-Mora *et al.* 2001)
5) Dune blowouts are a natural part of the coastal sediment system and may not require immediate stabilization if the movement of sand is acceptable. (Hesp and Hyde 1996; Arens and Geelen 2006)

The bottom line is that Chapter III-4 does not provide the user with enough information to pursue engineered solutions that incorporate, reflect, or mimic natural aeolian processes and landforms. No other chapter of the *CEM* picks up the slack. Chapter VI is content to explain that "*Dune construction is the piling up of beach quality sand to form protective dune fields to replace those washed away during severe storms*" (VI-2.5). A levee or mechanically piled sand is the default "sand dune" solution. Chapter III-4 leaves the engineer with inadequate information to determine if there is sufficient sand, wind, and space to develop a more self-sustaining and environmentally acceptable dune solution. As noted by Brunsden and Moore, (1999) where the "*scientific knowledge of the coast is poor, the safest practice is to use an engineering solution, …often a 'heavy' solution…" CEM*'s Chapter III-3 acknowledges that "heavy" solutions (seawalls, groins, jetties, artificial reefs are breakwaters) are increasingly challenged, discouraged, and even outlawed because of fairness, cost, and environmental concerns. While a sand "levee" or dune with a sheetpile reinforced heart is not specifically listed as a "hard" solution, it shares issues with those structures on the list.

In one respect, this lack of guidance is disappointing because much relevant research is available. Nordstrom's (2000) book, published two years before the *CEM*, covered many of the same topics as Chapter III-4, but was directed to coastal managers. It refers to 699 research articles, books and papers, of which 613 were published after the *Shore Protection Manual* publication date of 1984, indicating substantial recent research interest in the subject. In contrast, Chapter III-4 cites a mere 36 research articles and books, only nine of which were published since 1984. Numbers alone do not guarantee quality but the disparity raises concerns about comparative currency and completeness. This is more concerning when one notes that Chapter III-4 is missing critical references to works such as Short and Hesp (1982), Bauer *et al.* (1990), Psuty (1990), Pye and Tsoar (1990), Arens (1996), Nordstrom *et al*. (2000), Nordstrom (2000), and van der Wal (2000), to name a few.

Correcting obvious problems

While it is simple error, Chapter III-4's recommendation to plant European beach grass *(Ammophila arenaria)* to stabilize West Coast dunes should be corrected By 2002, European beach grass had indeed stabilized many dunes on the Pacific Coast but it had done so in a manner that damaged the form of the coastal dunes while choking out all native species, causing state and Federal agencies to conduct very expensive and difficult

eradication efforts all along the coast north of San Francisco. (Wiedeman and Pickart, 1994) The recommendation also appears in with similar wording in *CEM* Chapter V-4 (p. 77).

CONCLUSIONS

The U.S.A.C.E. took on a difficult task in creating the *Coastal Engineering Manual*. It intends to provide both a breath of subject matter and the rigorous standard of being "state-of-the-art." This standard implies a close connection of the document to the research program of the larger community of coastal engineers and scientists. Although the *CEM* is not even five years old at this writing, most sections (with the exception of Chapter III-4) have already been revised at least once. While this paper reviews only particular aspects of Chapter III-4, it is clear that (1) the chapter should immediately be revised to prescribe conservative aeolian sediment transport rate estimates; (2) the aeolian process and dune description section needs to be revised to allow engineers the knowledge and tools to at least consider incorporating natural processes in designs and solutions, and (3) outdated references promoting use of invasive plants in designs should be purged from all sections of the *CEM*.

The long-term success of the *CEM* depends on the updating process. Given the scope and status, the review process could serve as a focal point for communication among Ritter's "*engineers, geographers, oceanographers and geologists*" to both share the findings of current research and to help set important areas where additional research needs to be conducted. While this paper identified shortcomings in Chapter III-4's explanations of coastal science's understanding aeolian process and landform science to engineers, as Nordstrom (2000) observed, coastal science is itself currently limited to offering knowledge of natural coastal processes because "*the state of knowledge of human-altered landforms is still primitive, in part, because so few geomorphological investigations have been conducted of these landforms.*" Clearly much work remains.

REFERENCES

American Society of Civil Engineers. (2006). "Standards Writing Manual of ASCE Standards Committees,"http://www.asce.org/files/pdf/instfound/standardswriting 06april.pdf, last accessed 1-8-2007.

Arens, S. M. (1996). "Rate of aeolian transport on a beach in a temperate humid climate," *Geomorphology* 17, 3-18.

Arens, S. M., and Geelen, L.H.W.T. (2006)."Dune landscape rejuvenation by intended destabilization in the Amsterdam water supply dunes," *Journal of Coastal Research* 22, 1094-1107.

Bagnold, R. A. (1942). The *Physics of Blown Sands and Desert Dunes,* New York: W. Morrow and Company, 265 p.

Bauer, B.O., and Davidson-Arnott, R. G. D. (2002). "A general framework for modeling sediment supply to coastal dunes including wind angle, beach geometry, and fetch effects," *Geomorphology* 49, 89-108.

Bauer, B.O., Sherman, D. J., and Wolcott, J.F. (1992)."Sources of uncertainty in shear stress and roughness length estimates derived from velocity profiles," *Professional Geographer* 44, 453-464.

Bauer, B.O., Sherman, D. J., Nordstrom, K. F., and Gares, P. A. (1990). "Aeolian transport and measurement across a beach and dune at Castroville, California," in: Nordstrom, K.F., Psuty, N.P., and Carter, R.W.G. (Eds.), *Coastal Dunes: Form and Process,* New York: Wiley Press, 39-55.

Belly, P.-Y. (1964). "Sand Movement by Wind," U.S. Army Corps of Engineers, Coastal Engineering Research Center Technical Memorandum 1, 24 p.

Brunsden, D., and Moore, R. (1999). Engineering geomorphology on the coast: Lessons from west Dorset," *Geomorphology* 31, 391-409.

Chapman, D. M. (1990). "Aeolian sand transport – an optimized model," *Earth Surface Processes and Landforms* 15, 751-760.

Coastal Engineering Manual. (2006). EM-1110-2-1100, U.S. Army Engineers Waterways Experiment Station, Washington, D. C.: U. S. Government Printing Office. 2838 p.

Cornelius, W.M., and Gabriels, D. (2003). "The effect of surface moisture on the entrainment of dune sand: an evaluation of selected models" *Sedimentology,* 50, 771-790.

Garcia-Mora, M.R., Gallego-Fernandez, J.B., Williams, A.T., and Garcia-Novo, F. (2001). "A coastal dune vulnerability classification – A case study of the SW Iberian Peninsula," *Journal of Coastal Research* 17, 802-811.

Gares, P.A. (1988). "Factors affecting aeolian sediment transport in beach and dune environments," *Journal of Coastal Research* S13, 121-126.

Gares, P.A., Davidson-Arnott, R.G.D., Bauer, B.O., Sherman, D.J., Carter R.W.G., Jackson, D.W.T., and Nordstrom, K.F. (1996). "Alongshore variations in aeolian sediment transport: Carrick Finn Strand, Ireland," *Journal of Coastal Research,* 12, 673-682.

Granger, R.J., Essery, R., and Pomeroy, J.W. (2005). "Boundary layer growth over snow and soil patches: Field observations," *Proceedings, 62nd Eastern Snow Conference*, 95-104.

Hesp, P.A., and Hyde, R. (1996). "Flow dynamics and geomorphology of a trough blowout," *Sedimentology* 43, 505-525.

Horikawa, K., Hotta, S., Kubota, S., and Katori, S. (1984). "Field measurement of blown sand transport rate by trench trap," *Coastal Engineering in Japan* 27, 214-232.

Hotta, S., Kubota, S., Katori, S., and Horikawa, K., (1984). "Blown sand on a wet sand surface," *Proceeding 19th Coastal Engineering Conference*, New York: American Society of Civil Engineers, 1263-1281.

Hotta, S., Kraus, N.C., and Horikawa, K. (1987). "Functioning of sand fences in controlling wind-blown sand," Co*astal Sediments 87*, New York: American Society of Civil Engineers, 772-787.

Hsu, S. (1971). "Wind stress criteria in eolian sand transport," *Journal of Geophysical Research* 76, 8684-8684.

Kadib, A.A. (1964). Addendum II: Sand transport by wind, studies with sand (c. 0.145 mm diameter)," *U.S. Army Corps of Engineers, Coastal Engineering Research Center Technical Memorandum 1:* II.1-II.10.

Kawamura, R. (1951). *Study of sand movement by wind," HEL-2-5*, Berkeley: University of California Hydraulics Engineering Laboratory, 1-38.

Lettau, K., and Lettau, H. (1977). "Experimental and micrometeorological field studies of dune migration," in Lettau, K., and Lettau, H. (eds.) *Exploring the World's Driest Climate,* Madison: University of Wisconsin Press, 110-147.

Marques, A.A., Psuty, N.P., and Rodriguez, R. (2001). "Neglected effects of eolian dynamics on artificial beach nourishment: The case of Riells, Spain," *Journal of Coastal Research* 17, 694-704.

McCormac, J. C., (1967). *Structural Steel Design*, Scranton, PA.: International Textbook Company, 542 p.

McLachlan, A., (1990). "The exchange of material between dune and beach systems," in: Nordstrom, K.F., Psuty, N.P., and Carter, R.W.G. (eds.), *Coastal Dunes: Form and Process*, New York: Wiley Press, 201-213.

Miller, D.L., Thetford, M., and Yager L. (2001). "Evaluation of soil fence and vegetation for dune building following overwash by Hurricane Opal on Santa Rosa, Island, Florida," *Journal of Coastal Research* 17, 936-948.

Namikas, S.L, (2003). "Field measurement and numerical modeling of aeolian mass flux distributions on a sandy beach," *Sedimentology* 50, 303-326.

Namikas, S.L. and Sherman, D. J. (1995). "A review of the effects of surface moisture content on aeolian sand transport," in Tchakerian, V.P. (ed.), *Desert Aeolian Processes*. New York: Chapman and Hall, 269-293.

Nordstrom, K.F. (1990). "The concept of intrinsic value and depositional coastal landforms," *Geographical Review,* 80, 68-81.

Nordstrom, K.F. (2000). *Beaches and Dunes of Developed Coasts*. Cambridge: Cambridge University Press, 336 p.

Nordstrom, K.F., and Allen, J.R. (1978). "Dynamic geomorphology as a basis for coastal land use planning," *Proceedings of Coastal Zone '78*, New York: American Society of Civil Engineers, 1371-1385.

Nordstrom, K.F., and Lotstein, E.L. (1989). "Perspectives on resource use of dynamic coastal dunes," *Geographical Review* 79, 1-12.

Nordstrom, K. F., Lampe, R., and Vandemark, L.M. (2000). "Reestablishing naturally functioning dunes on developed coasts," *Environmental Management* 25, 37-51.

O'Brien, M., and Rindlaub, B. (1936). "The transportation of sand by wind," *Civil Engineering* 6, 325-327.

Psuty, N.P. (1990). "Foredune mobility and stability, Fire Island, New York," in Nordstrom, K.F., Psuty, N.P., and Carter, R.W.G. (eds.), *Coastal Dunes: Form and Process*., New York: John Wiley and Sons, 159-200.

Psuty, N.P., (2005). "Coastal foredune development under a diurnal wind regime, Paracas, Peru," *Journal of Coastal Research* SI 42, 68-73.

Psuty, N.P., and Ofiara, D.D. (2002). *Coastal Hazard Management,* New Brunswick, New Jersey: Rutgers University Press, 429 p.

Pye K., and Tsoar, H. (1990). *Aeolian sand and sand dunes*, London: Unwin Hyman, 396 p.

Owen, P.R. (1964). "Saltation of uniform grains in air," *Journal of Fluid Mechanics* 20, 225-242.

Raupach, M.R. (1991). "Saltation layers, vegetation canopies and roughness lengths," *Acta Mechanica*, Supplement 1, 83-96.

Ritter, D.F., Kochel, R.C., and Miller, J.R. (2002). *Process Geomorphology*, Boston: McGraw-Hill, 560 p.

Sarre, R. (1988). "Evaluation of aeolian sand transport equations using intertidal zone measurements, Saunton Sands, England," Sedimentology 35, 671-679.

Sherman, D.J., and Bauer, B.O. (1993). "Dynamics of beach-dune systems," *Progress in Physical Geography* 17, 413-447.

Sherman, D.J., Jackson, D.W.T., Namikas, S. L., and Wang, S. (1998). "Wind-blown sand on beach: an evaluation of models," *Geomorphology* 22, 113-133.

Sherman, D.J., Jackson, N.L., Nordstrom, K.F., Hesp, P.A., and Arens, S.M. (2005). "Predicting maximum and minimum aeolian sand transport rates to provide a basis for assessing management actions for beaches and dunes," in Sanjaume, E., and Mateu, J.F., (eds.), *Geomorfologia Litoral I Quaternari*, Univerisitat de Valencia, 483-496.

Short, A.D., and Hesp, P.A. (1982). "Wave, beach, and dune interactions in southeastern Australia," *Marine Geology* 48, 259-284.

Sørensen, M. (1991). "An analytic model of wind-blown sand transport," *Acta Mechanica,* 1, 67-81 (Supplement)

Spies, P.-J., McEwan, I.K., and Butterfield, G.R. (2000). "One-dimensional transitional behaviour in saltation," *Earth Surface Processes and Landforms*, 25, 437-453.

Svasek, J. N., and Terwindt, J. H. J. (1974). "Measurements of sand transport by wind on a natural beach," *Sedimentology* 21, 311-322.

van der Wal, D. (2000). "Modeling aeolian sand transport and morphological development in two beach nourishment areas," *Earth Surface Processes and Landforms* 25, 77-92.

Walker, I.J. (2005). "Physical and logistical considerations of using ultra sonic anemometers in aeolian transport research," Geomorphology 68, 57-76.

Wiedemann, A.M., and Pickart, A. (1996.) "The *Ammophila* problem on the northwest coast of North America," *Landscape and Urban Planning* 34, 287-299.

Zingg, A. W., (1953). "Wind tunnel studies of the movement of sedimentary material Proceedings 5th Hydraulics Conference, Institute of Hydraulics, Iowa City, 111-135.

DISTRIBUTION OF HORIZONTAL DISTANCE TRAVELED BY SALTATING SAND GRAINS IN AIR

Shintaro Hotta[1], Susum Kubota[2], Nagatomo Nakamura[3]

1 Advanced Research Institute for Sciences and Humanities, Nihon University,
Kudan-kita 4-2-1, Chiyoda-ku, Tokyo, 102-0073, Japan
shotta @arish.nihon.ac.jp
2 Dept. of Civil Engineering, Nihon University,
Kanda-surugadai 1-8-14, Chiyoda-ku, Tokyo, 101-8308, Japan
kubota@civil.cst.nihon-u.ac.jp
3 Faculty of Economics, Sapporo Gakuin University,
Bunkyo-dai 11, Ebetu, Hokkaido, 069-8555, Japan
nagatomo@sug.ac.jp

Abstract: The distribution of the horizontal distance traveled by the sand grains in saltation, which is equal to the distribution of the falling sand grain rate in the region from the end of the sand bed and down wind, is quite similar to the vertical distribution of sand transport rate above the sand surface. This observation is explained by assuming that the height of the trajectories of transported sand grains in the air is different but the trajectories are similar in form. The wind tunnel experiment showed that the equation for the distribution of horizontal distance traveled by the grains converted from the vertical distribution of sand transport rate can be applied.

INTRODUCTION

An important problem for the coastal areas is how to stabilize sandy beaches against wind-blown sand. Wind-blown sand generated on beaches intrudes and disturbs activities in neighboring areas, which may be economically important for farming, industry, transportation, and recreation. In order to control wind-blown sand it is crucial to understand the detailed motion of the sand grains transported by the wind. There is a considerable amount of knowledge about wind-blown sand, but little of this focuses on the detailed motion of the grains. Blown sand grains exhibit characteristic types of motion, known as surface creep, saltation, and suspension.

The great bulk of grains (over 80% of total blown sand) moves by saltation. Only limited knowledge is available concerning saltation motion and no reliable quantitative information exists on the distance traveled by the saltating sand grains. Hotta and Horikawa (1991) reported that the distribution of the horizontal distance traveled by the sand grains in saltation, which is equal to the distribution of the falling sand grain rate in the region from the end of the sand bed downwind, is quite similar to the vertical distribution of sand transport rate above the sand surface that can be described with a theoretical formula derived by Kawamura (1951). This behavior is explained by assuming that the height of the trajectories of transported sand grains in the air is different but the trajectories are similar in form. However, the experiment by Hotta and Horikawa was limited to a sand grain size of 0.3 mm in median diameter and to shear velocities below about 100 cm/s. Thus, to re-examine these results and to establish a reliable predictive formula for the distribution of horizontal distance traveled by saltating sand grains for engineering purposes, a laboratory experiment was carried out using four different kind of grain sizes and a wide range of wind speeds employing a large wind-tunnel. The overall objective of this paper is to report on the experimental data and the associated results obtained through analysis of the collected data.

THEORETICAL BACKGROUND

The equation for the distribution of horizontal distance traveled by the grains converted from the vertical distribution of sand transport rate can be expressed as,

$$q(x) = G_0\left[\lambda\left\{2\sqrt{2}K_0(\zeta) - 2\sqrt{2}\beta\sqrt{\frac{l_0}{g}}\zeta K_1(\zeta)\right\} + \frac{1}{\sqrt{2}}\frac{a\beta\sqrt{0.75l_0}}{g}\zeta^2\{K_0(\zeta) + K_2(\zeta)\}\right] \quad (1)$$

$$\zeta = \sqrt{2x/l_0}, \qquad \lambda = \overline{u_1}/\sqrt{2gl_0}, \qquad \beta = 3\pi\mu d/m, \qquad \int_0^\infty lf(l)dl = l_0$$

where $q(x)$ is the falling sand grain rate at the distance x from the origin (the downwind end of the sand bed), g is the acceleration of gravity, $u(z)=a\sqrt{z}$ is the average horizontal component of transported sand grains when grains are set in motion from the sand surface, μ is the dynamic viscosity, d is the diameter of a sand grain, m is the mass of a sand grain, a is an experimental constant, G_0 is the mass of sand being entrained from a unit area of the sand surface per unit time, K_0, K_1, K_2 are the modified Bessel functions, and l_0 is the average horizontal distance traveled.

EXPERIMENTAL FACILITIES AND PROCEDURES

Facility

The experiment was carried out using a blow-off type wind tunnel with a test section that was 1.1 m high, 1.0 m wide, and 20 m long. A mobile sand bed was formed with a thickness of 10 cm from the upwind end of the tunnel to a distance of 16 m downwind. The mobile bed was retained by a timber board with a thickness of 9 mm and a height of 10 cm that was tapered upwind with a gradient of 45 degrees. Adjacent to the board on the downwind side, a horizontal distribution-type trap was

placed at the center of the tunnel in the transverse direction. Figure 1 shows the horizontal distribution-type trap used that has the same shape as the trap employed by Hotta and Horikawa (1991), but the width and arrangement in the horizontal of the segments were somewhat different.

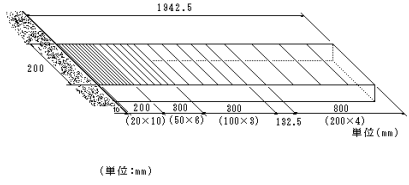

Fig. 1. Horizontal distribution-type trap

Four types of sand taken from a natural beach were used in the experiment. The sand was sieved to yield median diameters of around 0.15, 0.25, 0.48, and 0.68 mm. For convenience, hereafter we refer to the sands with median diameter of 0.15, 0.25, 0.48, and 0.68 mm as D15, D25, D48, and D68, respectively. Figure 2 shows the grain size cumulative curves for the four sand sizes studied.

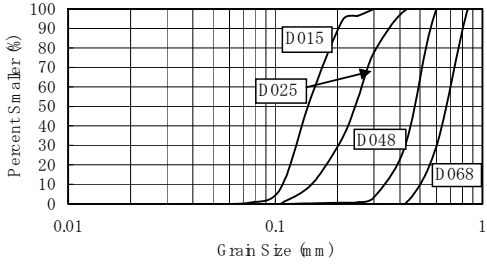

Fig. 2. Grain size cumulative curves.

The vertical distribution of wind speed was measured with a hot-film anemometer array consisting of fifteen anemometers at a location 13 m from the upstream end of the tunnel. The elevations of the measurement points were approximately 2.5, 5.0, 7.5, 10.0, 12.5, 15.0, 17.5, 20.0, 22.5, 25.0, 27.5, 30.0, 40.0, 50.0, and 60.0 cm above the sand surface.

Procedure

The sand was spread over the 15-m long test section in the tunnel and the sand surface was carefully flattened. After that wind was generated, where the time intervals for blowing the wind over the bed varied from two minutes to ten minutes, depending on the wind speed employed. After stopping the wind, the sand volume which passed the downstream end of the test section where the trap was placed was collected from the remaining portion of the wind tunnel (5 m long) and in the sand collection chamber located at the downstream end of the tunnel, and weighed. The sand trapped in the each segment of the vertical distribution-type trap was also

measured. After weighing the sand it was brought back and placed along the test section, the sand surface was flattened again, and additional sand was supplied as necessary. The same procedure was repeated for all experimental cases.

RESULTS AND DISCUSSION

Vertical Distribution of Wind on the Sand Surface

Figure 3 shows a semi-logarithmic plot of the vertical distribution of the wind speed on the sand surface. From Figure 3 it is clear that the distribution obeys the logarithmic law below an elevation of about 30 cm and that the wind speed is approximately constant in the upper region above 30 cm, although some scatter exists in the data. The wind speed may be described by:

$$u_z = 5.75u_* \log_{10}\frac{z}{z'} + u' \tag{2}$$

The vertical profiles of the wind speed measured on the four sand beds yielded the same basic results. It was difficult to detect any difference in the range of elevations where the logarithmic law is satisfied for four sands investigated. This observation implies that the thickness of the boundary layer developed near the surface is almost the same and the variation in sand surface roughness for the sands employed in the experiment did not have any significant influence on the formation of the boundary layer. The shear velocity was calculated from the vertical distribution of wind speed below an elevation of 30 cm. The focal point values (Bagnold, 1973) read form the Figure 3 are (330 cm/s, 0.28 cm) for D15, (320 cm/s, 0.24 cm) for D25, (510 cm/s, 0.75 cm) for D48, and (540 cm/s, 0.90 cm).

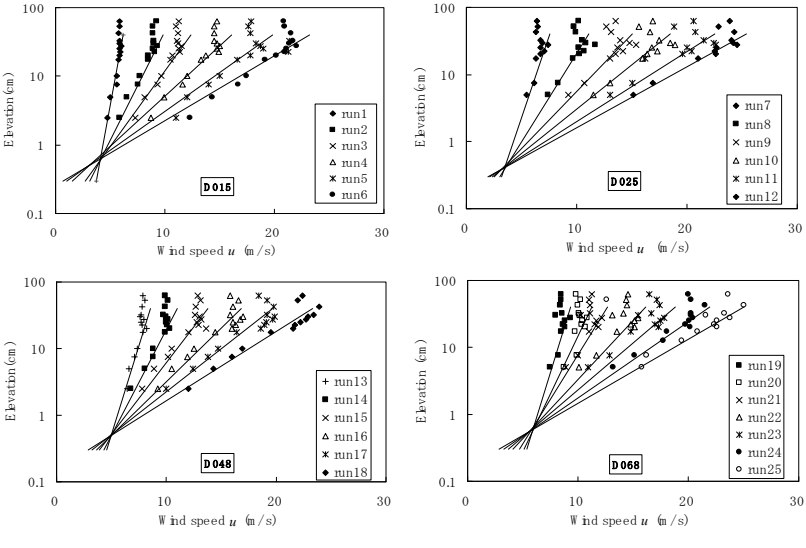

Fig. 3. Vertical distribution of wind speed

Total Sand Transport Rate

Here we define the total sand transport rate as the entire sand mass per unit time that passed the transverse section of the downstream end of the sand bed, where the horizontal distribution-type trap was placed. This quantity is often referred to as "the transport rate", but in this paper we use the word "transport rate" to denote the transport rate per unit height in the vertical direction in agreement with a related paper (Hotta et al., 2006). Therefore, to avoid misunderstanding, we use "the total sand transport rate" for the former quantity. Figure 4 shows a plot of the total transport rate versus the shear velocity on a semi-logarithmic paper. The curves displayed in Figure 4 are obtained by using the predictive formula for the total sand transport rate given by Kawamura (1951), taking the critical shear velocity to be 31.1 cm/s for a diameter of 0.48 mm. Kawamura's formula is,

$$q = K \frac{\rho_a}{g} \left(u_* + u_{*c}\right)^2 \left(u_* - u_{*c}\right) \tag{3}$$

where q is the total sand transport rate, g is the acceleration of gravity, u_{*c} is a threshold shear velocity, and K is an experimental coefficient.

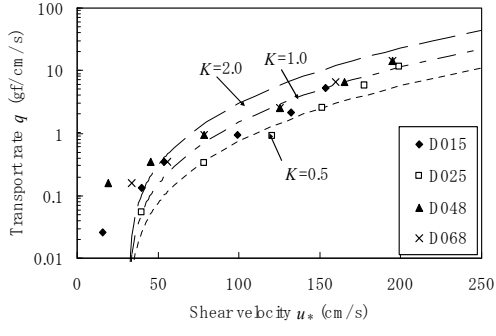

Fig. 4. Total sand transport rate

It is difficult to find a significant difference in the total transport rate between the four types of sand. The total transport rate for the four sands is almost the same and the scatter in the data is within the experimental error. This means that the difference in the median diameter is not significant enough to produce a difference in the transport rate (taking into account the experimental error) for the conditions investigated, although the median diameters determined by the sieving test were indeed quite different. The Kawamura formula can describe the total transport rate with an experimental coefficient of about 0.8. However, the value of 0.8 is somewhat smaller than that obtained in previous studies.

Trapping Efficiency of the Employed Horizontal Distribution-type Tap

Figure 5 shows the trap efficiency for the utilized distribution-type trap. Here the trap efficiency is defined by the ratio of the total amount of sand caught by the trap and one–fifth of the total amount of sand through the tunnel width (the width of the trap is 20 cm and the width of the tunnel is 100 cm). The trap efficiency becomes smaller with an increase in the shear velocity. Careful observation of the trapping conditions during the experiments suggested that this might be caused by the fact that an increase in wind speed leads to an increase in the amount of sand grains that rebound from the trap when the falling sand touched the trap. The trapping efficiency of the original trap used by Hotta and Horikawa (1991) was about 0.59 for a shear velocity between about 25 cm/s and 100 cm/s.

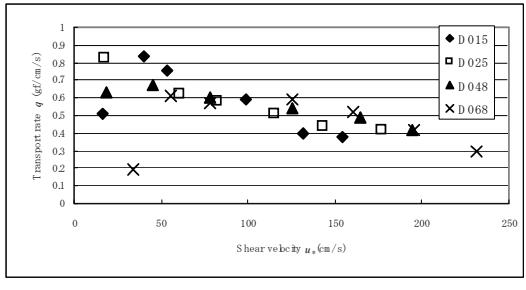

Fig. 5. Trapping efficiency of horizontal distribution-type trap.

Distribution of the Horizontal Distance Traveled by the Sand Grains

Figure 6 shows examples of the measured distribution of the horizontal distance traveled by the grains. Here *q(x)*, the falling sand grain rate at the distance *x,* is corrected by the trapping efficiency obtained. In Figure 6 curves are also drawn corresponding to Eq. 1, where suitable experimental coefficients or parameters were fitted by using trial and error. Figure 6 indicates that Eq. 1 describes the experimental data fairly well, although a discrepancy exists between the predicted curves and the data in the region close to the end of the sand bed and for locations where the dimensions of the segments changed. There is also a discrepancy between the curves and data in a region beyond 1 m downwind for sand sizes D15 and D25. Thus, it may be concluded that Eq. 1 converted from the expression of the vertical distribution of sand transport rate can be applied for the distribution of the horizontal distance traveled by the grains.

Figure 6 shows that a large amount of sand grains will fall within a distance of 20 cm downwind, if a sand bed does not exist. The falling rate becomes one order of magnitude smaller at a location of about 20 cm downwind from the end of the sand bed than that close to the end of the sand bed, and two orders of magnitude smaller at a location about 100 cm downwind.

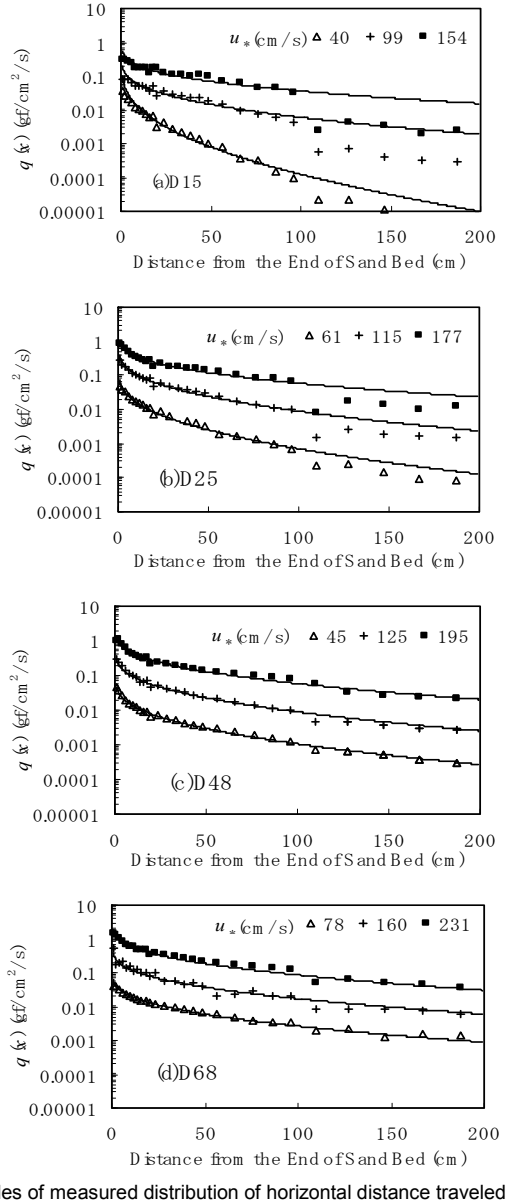

Fig. 6. Examples of measured distribution of horizontal distance traveled by sand grains

ESTIMATION OF EXPERIMENTAL COEFFICIENTS IN PREDICTIVE EQUATION

Estimation of Experimental Coefficient *a*.

In derivation of Eq. 1, the power law with a power of (1/2), $u(z)=a\sqrt{z}$ is assumed for the vertical distribution of wind speed in the moving sand layer near the surface. This assumption was made to facilitate theoretical development and not based on the theoretical background. However, Kawamura (1951) showed that the experimental results could be approximately described in the layer below a level of about 10 cm above the sand surface using a power law with the power of (1/2).

For the analysis in this experiment we used data points on wind speed obtained below 10 cm in elevation where moving sand were highly concentrated. Values of *a* determined under these conditions are plotted against the shear velocity in Figure 7. It is difficult to distinguish any differences in *a* for the studied grain sizes. Thus, it may be concluded that the value on the experimental coefficient *a* is independent of grain size in the present experiment. From Figure 7, the following experimental relationship may be developed:

$$a = 1.33\,u^* + 104.5 \qquad (4)$$

In this formula the dimension of *a* is $\sqrt{\text{cm}}$ /s and of u_* cm/s.

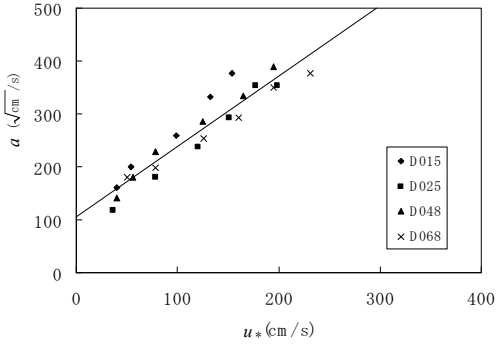

Fig. 7. Relationship between *a* and u_*

Estimation of Experimental Coefficient G_0

Figure 8 shows a plot of G0 versus u* in a log-log diagram. The straight line drawn through the data is the best fitted one by visual judgment. It is difficult to distinguish any differences in the value of G0 with respect to grain size. A general equation for the best-fit line is given by,

$$G_0 = 1.75\times10^{-7}\times u_*^{2.5} \qquad (5)$$

where the value of 1.75×10^{-7} is a dimensional constant with the unit gf/cm^5/s.

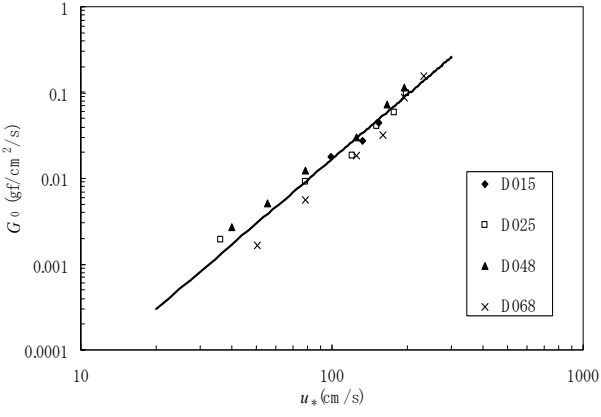

Fig. 8 Relationship between G_0 and u_*

Estimation of Experimental Coefficient l_0

Figure 9 shows the plot of l_0 versus u_* for the collected data. It is clear that l_0 and u_* display a linear relationship for all grain sizes and that the gradient of the straight lines becomes steeper with increase in grain size. Thus, the following general form can be assumed for the lines in Figure 9,

$$l_0 = B' u_* + C' \tag{6}$$

where B' and C 'are constants.

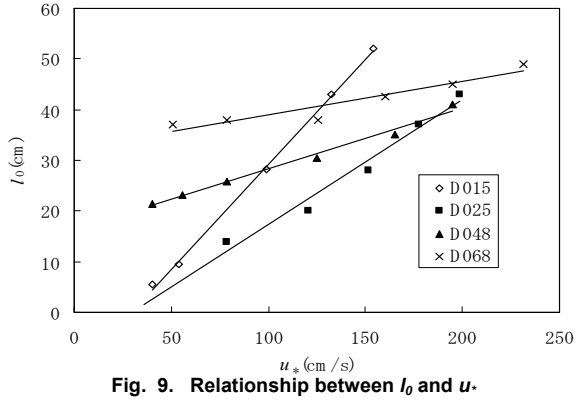

Fig. 9. Relationship between l_0 and u_*

The values of *B* 'and *C* 'can be derived from the straight lines in Figure 9 as the gradient and the intercept on the l_0 –axis, respectively,. Figure 10 shows a plot of *B'* versus the grain size *d*. The variables *B'* and *d* exhibit a linear relationship and from Figure 10 we can obtain the relationship:

$$B' = -6.2\,d + 0.45 \tag{7}$$

Figure 11 shows the plot of *C* versus *d* in a log-log diagram. The variables *C* and *d* display a linear relationship and the following equation may be derived:

$$C' = 873\,d + 26.8 \tag{8}$$

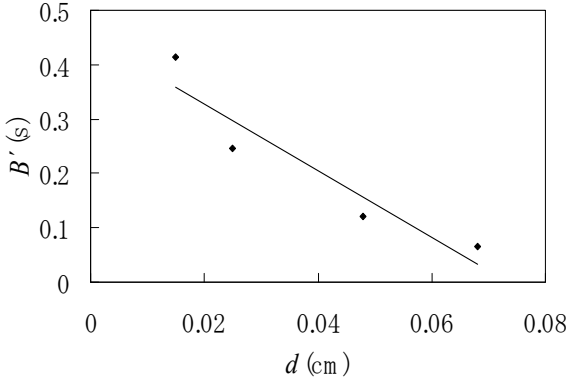

Fig. 10. Relationship between *B*' and *d*

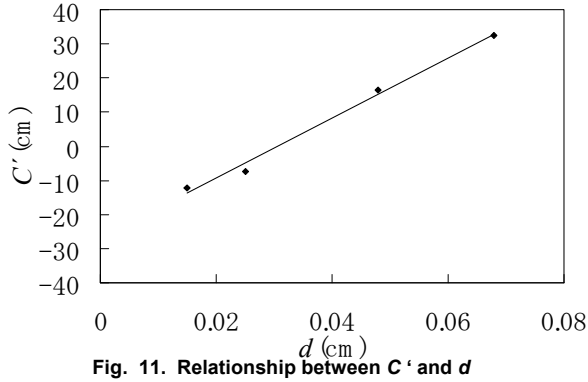

Fig. 11. Relationship between *C* ' and *d*

Substituting Eqs. 7 and 8 into Eq. 6 yields,

$$l_0 = (- 6.2\, d + 0.45\,)\, u_* + (873\, d + 26.8) \qquad (9)$$

where the dimensions of l_0, u_*, and d are (cm), (cm/s), and (cm), respectively.
Thus, the experimental coefficients and parameters a, G_0, and l_0 in Eq. 1 can be determined from Eqs. 4, 5, and 9, respectively.

EXAMINATION OF EQ. 1

In numerical calculations with Eq. 1, it was demonstrated that the second, third, and fourth terms are considerably smaller than the first term. In the following, a comparison is made of the four terms within the square brackets of Eq. 1.

The numbers in parentheses are the order of the parameters, coefficients, and variables that is under consideration ($0 < \zeta < 10.0$). Dividing the first and the second terms by $\lambda\, 2\sqrt{}2$, the order of the first term and the second term are:
$K_0(\zeta)$

Second term
$\lambda(0)^{-1} \cdot \beta(0) \cdot l_o(0)^{1/2} \cdot g\,(-3)^{1/2} \cdot \zeta\,(0) \cdot K_1(\zeta) = (-3) - ^{1/2} \cdot \zeta\,(-1 \text{ or } 0) \cdot K_1(\zeta)$

$= (-2) \text{ or } (-3) - ^{1/2} \cdot K_1(\zeta)$

The functions $K_0(\zeta)$ and $K_1(\zeta)$ are almost of the same order. Thus, the second term must be smaller than the first term by two orders, implying that the second term can be neglected.

For the third and fourth terms the order of the constants, coefficients and parameters yields:

$1 \cdot 2^{-1/2} \cdot 0.75\,(0)^{1/2} \cdot a\,(2) \cdot \beta(0) \cdot l_o(0)^{1/2} \cdot g(-3)^{1/2} = (0) \cdot \quad (-1)^{1/2}.$

The functions $K_0(\zeta)$ and $K_2(\zeta)$ increase to infinity when ζ approaches zero from the value of 1.0, and $K_0(\zeta)$ and $K_2(\zeta)$ approach zero when ζ becomes larger than 1.0 (see Figure 12). Therefore, we may estimate that $\zeta^2 \cdot K_0(\zeta)$ and $\zeta^2 \cdot K_2(\zeta)$ become small when ζ takes on small and large values compared to 1.0.

However, $\zeta^2 \cdot K_0(\zeta)$ and $\zeta^2 \cdot K_2(\zeta)$ take on significant values when ζ is around 1.0. The third and fourth terms are considerable smaller than the first term, but it is not possible to know how much smaller they are than the first term and whether the third term and fourth term can be neglected or not. Thus, numerical experiments were carried out using obtained values on coefficients and appropriate values on governing parameters.

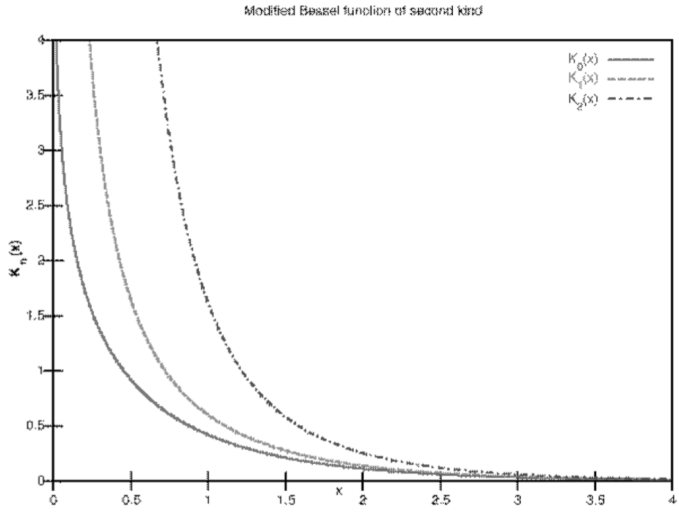

Fig. 12. Behavior of $K_0(\zeta)$, $K_1(\zeta)$, and $K_2(\zeta)$
(From wikipedia)

Figure 13 shows examples of the results of the calculations. The third and the fourth terms in $q(\zeta)$ contribute with around 3 or 4 % when ζ exceed 4.0 for cases when the third and the fourth terms attain large values (Fig. 13 (a)). However, the third and the fourth terms in $q(\zeta)$ contribute around 1 or 2 % when ζ exceed 4.0 for cases when the third and the fourth terms attain small values (Fig. 13 (b)). These results depend on the values of a, β, and l_o.

The region of ζ where the third and the fourth terms have large values is far from the region near the sand bed (ζ is small). Therefore we may typically neglect the third and the fourth terms in Eq. 1 and the simplified transport equation becomes:

$$q(x) = 2\sqrt{2}\lambda G_0 K_0(\xi) \tag{12}$$

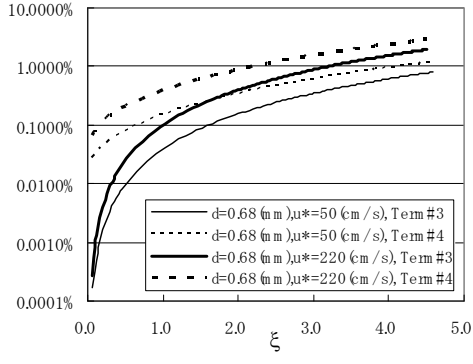

(a)

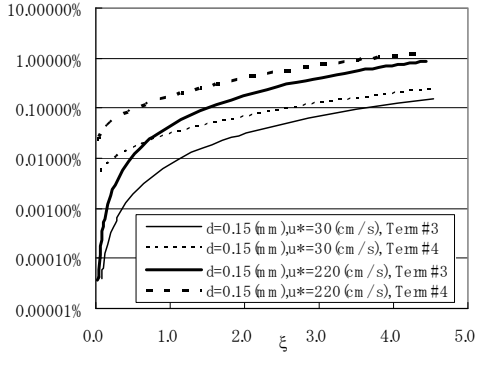

(b)

Fig. 13. Examples of calculated results for third and fourth terms in Eq. 1.

CONCLUDING REMARKS

Equation (1), which is converted from the equation for the vertical distribution of sand transport rate derived by Kawamura, described the experimental data fairly well and the experimental coefficients a, G_0, and l_0 in Eq. 1 were determined as empirical functions of the grain diameter d and the shear velocity u_*. Therefore, the distribution of the horizontal distance traveled by the sand grains can be predicted if the grain diameter d and the shear velocity u_* is known.

Equation 1 is converted from the equation originally expressing the vertical distribution of the sand transport rate, assuming that the height of the trajectories of transported sand grains in the air is different but the trajectories are similar in form. Thus, the experimental parameters and coefficients in Eq. 1, except quantities

(experimental parameters and coefficients) related to the vertical direction, must be the same as those of the vertical distribution of transport rate, if both experiments measuring the vertical distribution of transport rate and the falling rate of sand grains are correctly performed. In an experimental study for the vertical distribution of sand transport rate, Hotta et al. (2006) obtained an experimental relationship for a and G_0 according to:

$$a = 1.88u_* + 210.0 \tag{10}$$

$$G_0 = 2\times10^{-9} d^{-2} u_*^{2.5} \tag{11}$$

Equation (11) contains the grain diameter d as a variable but Eq. 5 does not contain the grain diameter. The authors can not explain this difference between the experiments on the vertical and horizontal distribution. Experiments were carried out for the same conditions, except for the traps employed that were of the vertical distribution-type or the horizontal distribution-type. Therefore, G_0 must be the similar if the experiments were correctly carried out at the same condition for both traps (vertical and horizontal), and if both traps collected sand with the same efficiency. Our assessment is that the discrepancy is related to a lower sand trapping efficiency for the upwind part (near sand bed end) of the horizontal trap.
However, we need further well-controlled experiments with a trap that has better efficiency to confirm this assessment.

ACKNOWLEDGMENTS

We are grateful for support provided by the Nihon University Multidisciplinary Research Grant for 2005 and 2006 for the Synthetic Study on Countermeasures for Watershed Development and Environmental Preservation in Waters.
We also would like to express our appreciation to Mr. Takashi Tamura, graduate student, for his support during the study period.

REFERENCES

Bagnold, R. M. (1973). "*The physics of blown sand and desert dunes*," Chapman & Hall Ltd, London, 265p.

Hotta, S., Kubota, S., Nakamura, N. and Hosaka, K. (2006). "Wind-tunnel study of vertical distribution of sand transport rate by sind," *Proceedings of 31th International Conference of Coastal Engineering,* ASCE, (in press)

Hotta, S. and Horikawa, K. (1991). "Vertical distribution of sand transport rate by wind," *Coastal Engineering in Japan*, 36(1), JSCE, 91-110.

Kawamura, R. (1951). "Study on Sand Movement by Wind," Rep. of the Inst. of Science and Technology, Univ. of Tokyo, 5(3/4), 95-112. (in Japanese). English translation available in: Research Tech. Rep. HEL-2-8, Hydraulic Eng. Lab. Univ. of Calf., Berkely,1964, 38pp.

BEACH STABILIZATION WORKS AGAINST WIND BLOWN SAND ON BEACHES: EXPERIENCES FROM JAPAN

Susumu Kubota[1], Souichi Harikai[2], and Shintaro Hotta[3]

1. Prof., Dept. of Civil Engineering, Nihon University,
   Kanda-surugadai 1-8-14, Chiyoda-ku, Tokyo, 101-8308, Japan
   kubota@civil.cst.nihon-u.ac.jp
2. President, Coastal Engineering Consultants Co., Ltd.
   Tukudo-hachiman 2-21, Shinjuku-ku, Tokyo, 162-0815, Japan
   harikai@coastal-con.com
3. Prof., Advanced Research Institute for Sciences and Humanities, Nihon University
   5-bancho 12-5, Chiyoda-ku, Tokyo, 102-8251, Japan
   shotta@arish.nihon-u.ac.jp

Abstract: At present, many beaches in Japan are experiencing severe erosion and prevention works to combat this erosion forces changes to the conventional works used to control wind blown sand in the past. Detailed field inspections were carried out of the wind blown sand controlling works and windbreaks at beaches in the central part of the main island of Japan. This study reports precious results obtained by the field inspections.

INTRODUCTION

Reducing damages from strong wind and controlling wind blown sand are important issues in beach stabilization and effective beach utilization. In Japan, a strong wind blows over the country from Northwest to West in the winter. During this season, the wind often causes damage to infrastructure and buildings, as well as to the natural environment (e.g., trees and plants), and significant transport of wind blown sand occurs on the beaches facing the Japan Sea. On some Pacific Ocean beaches wind blown sand is also generated by these winds, but on other Pacific beaches wind damage and wind blown sand occur in the different seasons. The beaches on the Japan Sea side are exposed to rain or snow in the winter, whereas the prevailing

climate on beaches located on the Pacific Ocean side is mostly fine during this period.
Thus, meteorological and topographical conditions are very different from one coast of Japan to the other.

To reduce wind damage and to control wind blown sand many types of prevention works have been employed in Japan. In order to develop effective and suitable systems of prevention works on beaches, the method of trial and error was applied in former times, implying that systems emerged that are specific for each beach. At present, different types of systems are found in different parts of the country depending on the local conditions at the beach, such as climatic, oceanographic, and geographical conditions as well as the economical importance of the region. The main objectives of this study is to introduce characteristic prevention works utilized in Japan, to point out problems faced, and to attempt to find fundamental principles for the successful usage of these prevention works as windbreaks and for controlling wind blown sand. The present paper constitutes a first preliminary report on the main findings.

STUDY AREA AND PROCEDURE

The field areas that were the focus in the present study were located on coastal stretches along the central part of the main island of Japan (Fig. 1). Detailed field inspections were carried out of the prevention works and wind breaks, documenting their design and general characteristics. The history of the works as well as the design procedures employed were also recorded as far as possible and photographic documentation were frequently employed. The effects on the beach morphology in terms of induced topographic change were determined using topographic maps.



Fig. 1. Study field site

RESULTS

The following results were obtained based on the field surveys and associated analysis.

Fundamental System of the Prevention Works

The fundamental system employed for the prevention works was a combination of vegetation works, sand fences (or wind breaks), foredune, and conservation forests from shore to inland, although variations in this system could be found where certain parts were not included. This system has functioned well with appropriate maintenance at non-eroding beaches. Photo 1 shows typical examples from wide beaches. The foredune in the Photo 1 (a) has been created by repeated emplacement of sand fences on a dune formed by buried old sand fences. In order to keep the foredune, fencing works are still continuously maintained. The beach grass in front of the dune grows naturally. Photo 1 (b) shows vegetation work with beach grass, windbreaks (sand fences) framed by thinned timber logs, and afforestation works by pine trees.



(a) A foredune with sand fences (Kashima Coast)

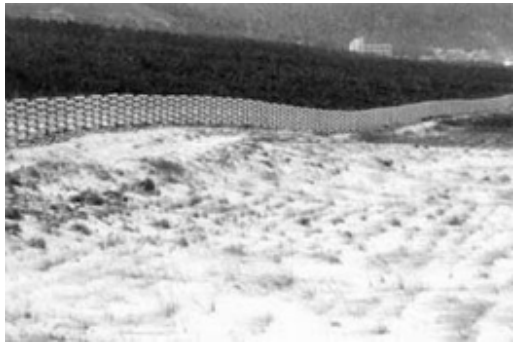

(b) A system of prevention works (Shounai Coast)

Photo 1. Examples of wind blown sand controlling works

At present, on many beaches, foredunes formed by fencing works have started to erode. Photo 2 shows examples of beaches where erosion has reached the foot of the foredune formed by using repeated emplacement of sand fences.

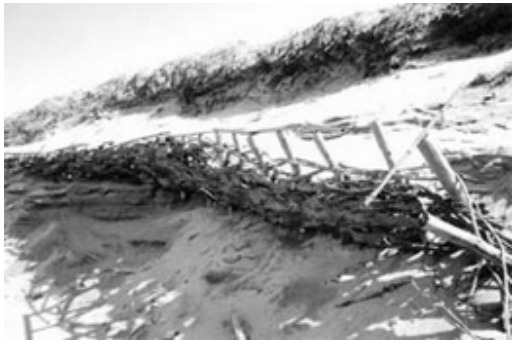

(a) A beach at Shounai Coast



(b) A beach at Ensyuunada Coast

Photo 2. Foredunes on eroding beaches

Countermeasures to combat beach erosion forces changes to the conventional works used to control wind blown sand in the past. However, there are no technical standards or guidelines how these beaches should be treated at present.

Photo 3 shows examples of eroding beaches where countermeasures have been completed. Photo 3 (a) shows a beach at Ishikawa Coast where detached breakwaters, a seawall, and an artificial embankment were constructed. The crown of the seawall is used as a bicycle road along the shore. This artificial embankment have multiple protective functions, that is, to trap wind blown sand, to stop wave splashing, to reduce the effects of storm surges and tsunamis, and to work as a windbreak for the area behind. Photo 3 (b) shows a beach at Ensyuunada Coast where a seawall and a sea dike located on the landward side as countermeasures against beach erosion have just been constructed. The countermeasures in Photo 3 (b) are chosen as an option to remedy the conditions shown in Photo 2 (b).



(a) A beach protected by multi-defense works (Ishikawa Coast)



(b) A foredune protected by structures (Ensyuunada Coast).

Photo 3. Examples of protected beaches

For the eroding beaches there is no clear indication regarding the kind of countermeasures needed, whether hard coastal structures, such as seawalls or revetments, or soft structures, such as artificial nourishment, would be most appropriate to employ.

However, when employing structures some additional considerations are needed. On protected beaches wind blown sand might be generated by the local disturbance of the wind field due to the coastal structures, as long as a sandy beach exists. In addition, structures often cause violent wave breaking with high and abundant splashing during stormy conditions. Thus, the possibility to induce damage from salt transport by wind in combination with wave splashing increases.

Site-Specific Design of the Prevention Works

Each beach almost always has a site-specific design of the prevention works. There are windbreaks, sand fences, and different kinds of artificial embankments and protection works for sloping surfaces.

Windbreaks

Photo 4 shows examples of windbreaks (fences) formed by thinned timber logs. The purpose of these windbreaks is different. The type in (a) has been widely used any place where windbreaks were needed. The type (b) has mainly been employed to protect shrubberies, whereas the type (c) was used to protect the front of afforestation works. The windbreak efficiency of these fence types varies greatly and the efficiency becomes lower in the order which they are shown in (a), (b), and (c).



(a) Timber windbreaks at Ishikawa Coast



(a) Timber windbreaks at Ensyuunada Coast



(b) Timber windbreaks at Niigata Coast



(c) Timber windbreaks at Syounai Coast

Photo 4. Windbreaks formed by thinned timber logs

Many other kinds of windbreaks (fences) are employed as well. Fences are ordinarily higher than 1.8 m (about 6 feet). The fence material most commonly employed is bamboo because many kinds of bamboo abundantly grow in Japan and it is economically beneficial to use. Fabric or metal fences are also commonly employed for protecting important facilities and obtaining fences with a long life. Photo 5 shows examples of bamboo and metal fences.



(a) Bamboo fence.

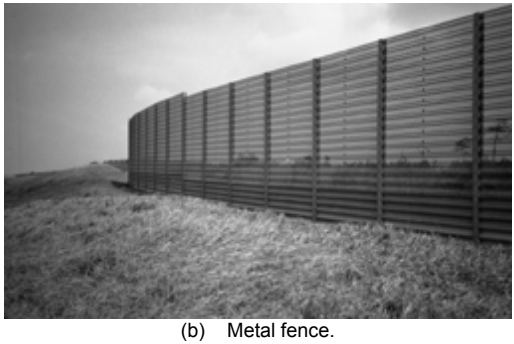

(b) Metal fence.

Photo 5. Bamboo and metal fences

Sand Fences

Many kinds of sand fences with regard to type and material are employed for trapping and keeping wind blown sand. Typical fence material used is fern, reed, brush, and bamboo, which all decompose with time. Thus, no long-life fabrics and metals are used. The height of ordinary sand fences is about 1 m (about 3 feet), and the slat-type sand fences that are commonly used in the United States has not yet been utilized in Japan. Photo 6 shows a typical bamboo sand fence. A summary of the

characteristics of windbreaks and sand fences may be found in the Proceedings of Coastal Sediments '87 and '91 (Hotta et al., 1987; Hotta et al., 1991).



Photo 6. Bamboo sand fences (Shounan Coast)

Artificial Embankments

Recently artificial embankments have been frequently employed instead of foredunes formed by fencing works, because construction of the embankment can be rapidly and economically done by using large earth-moving construction machines. Photo 7 (a) and (c) show artificial embankmenst positioned at the upper part of a beach that is relatively wide. The foreslope is vegetated with beach grass and it is not armored by any hard material. In Photo 7 (a) it is also possible to see examples of windbreaks (fences) formed by thinned timber logs from afforestation works on the crown. Other representative examples are displayed in Photo 3 (a) and photo 7 (d) where the embankment is located near the shoreline and its foreslope is armored by hard materials such as stones or precast concrete armor units. This type of embankment has multiple protective functions with respect to wind and wave action, as described before.

The cross-sectional shape of the embankment is typically designed as follows: a foreslope of 1:1 – 1:3, a backslope of 1:1 – 1:2, a crown width of 1–5 m, and a height of 3–10 m. The dimensions adopted have no engineering basis and are employed according to site experience.



(a) Cross sectional view of an embankment (Ishikawa Coast)

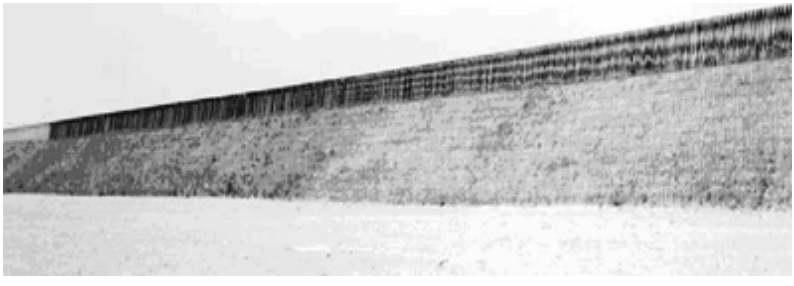

(b) Front view of the embankment (a)



(c) Another type of embankment



(d) Slope armored embankment and an access path to the shore

Photo 7. Artificial embankment as a substitute of a foredune

Oblique Foredunes

A specific foredune arrangement was found in the eastern part of the Ensyuunada Coast for controlling wind blown sand. This arrangement is based on the idea of "*making the wind turn aside*", as demonstrated in Fig. 2. In the figure, α is the azimuth of the shoreline. When the wind blows from the west, the wind blown sand generated on the beach surface sweeps into the sea if α is smaller than 90 degrees, and the blown sand is transported towards the inland if α is greater than 90 degrees.

The predominant direction of the wind on the Ensyuunada Coast is west in the winter and the azimuth of the shoreline on the eastern part of the Ensyuunada Coast is greater than 90 degrees and smaller than 135 degrees.

Considering conditions described in Fig. 2, formation of foredunes is attempted by using repeated placement of sand fences. Foredunes formed by this method function well. The blown sand from the west direction turns aside and sweeps into the sea. The height of formed foredunes is 5-10 m and the azimuth of the dune crest direction is from 120 degrees to 135 degrees.

Foredunes formed here represent oblique artificial foredunes.

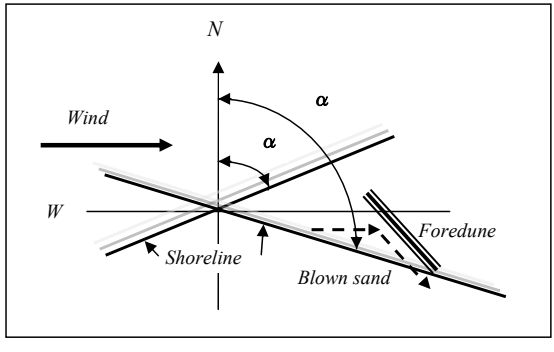

Fig. 2. Schematic illustration of an oblique artificial foredune

Concerning the oblique artificial foredunes, Takezawa et al. (2002) offered a simple model that gives the relationship between the slope gradient, wind incident angle and the crest direction of the embankment.

Design guidelines for artificial embankments

To develop technical standards for designing embankments, Hotta et al. (2000) carried out an experimental study using a wind tunnel which was 1.1 m high, 1.0 m wide, and 20 m long. Two series of embankments were included in the experiments. One series involved trapezoidal-type embankments where the foreslope changed

between 1:0, 1:0.5, 1:1, 1:2, 1:3, and 1:5 keeping the ratio of B/H = 1.0 (where B is the crown width and H is the height of the embankment) and where the backslope was kept at 1:1. The other series encompassed rectangular-type embankments with varying ratios of B/H = 0.05, 0.5, 1.0, and 2.0. Two main types of measurements were carried out, namely a tracer experiment to visualize the flow pattern and measurements of the wind speed field. The experiments produced the following results: In order to obtain a large area where the wind speed decreases on the windward side of the embankment, the foreslope of the embankment should be steeper than 1:1 and the ratio B/H should be smaller than 1.0. An area where the wind accelerated appeared behind the embankment at elevations from H to 5H. The area of acceleration considerably decreased when the foreslope became gentler than 1:1 and the ratio of B/H became larger than 1.0. The wind speed amplification at the upwind edge of the embankment crown was the largest when the foreslope of embankment was 1:1 and the width of the crown did not influence the wind speed amplification.

Considering general practice for construction in the field and the experimental results, Hotta et al. (2000) concluded that the appropriate dimensions are a foreslope of 1:3, a backslope of 1:2, and a crown width of 0 m. It is acceptable that both slopes, the foreslope and the backslope, are made steeper if needed, providing that surface protection of the slopes is carried out.

Problem of access to shore

It was found that the access to the beach is seriously interrupted when the foredunes, artificial embankments, and conservation forests are extended for a considerable distance alongshore. Then illegal access paths were made by residents for daily usage or by people who want to go beach for reasons such as surfing, swimming, fishing, and walking. Photo 8 shows example of the illegal access paths.



Photo 8. An example of illegal access path through artificial embankment

The alongshore distance between illegal access paths varied greatly depending on the local condition of the seashore and coastal area. The distance between these paths is more or less random and it ranges from about 300 – 400 m to more than 2 km. This means that access paths to the beach must be prepared in a suitable distance to avoid illegal paths. This is a difficult problem which concerns the management of the coastal area. At present there are no standards on the suitable distance between access paths.

To create and maintain access paths to the shore result in other problem. There is a possibility that tsunami or storm surge waves may intrude through the path openings, if parts of the embankments or foredunes are cut by access paths.

Concluding remarks

At present, many beaches in Japan are experiencing severe erosion and prevention works to combat this erosion forces changes to the conventional works used to control wind blown sand in the past. Some parts of the beaches protected by hard concrete structures have lost the sandy shore, but some parts of the beaches still have the limited narrow sandy beaches. On protected beaches the wind blown sand will be generated as long as a sandy beach exists. At present, no considerations of wind blown sand and increase in the possibility for salty wind damage are given when countermeasures for beach erosion are designed.

It was found that many artificial embankments have been constructed all over the investigated field sites. The high elevation of the constructed embankments is blocking the view towards the sea as well as disturbing the landscape. This problem is never discussed when embankments are designed.

In addition to the above, in order to develop new systems for protection the following matters must be studied in greater detail:

1) Which is a good selection of countermeasures and whether to employ hard coastal structures or soft structures, such as artificial nourishment, when erosion has reached the foot of the foredune?

2) Is the mechanism of wind blown sand generation on narrow beaches with structures the same as that on the wide flat beaches? Concerning this problem, Ugai et al. (2005, 2006) offered the interesting studies that the local disturbance of the wind field by structures (local currents or wakes, or cell currents around structures) mainly govern the wind blown sand phenomenon.

In conclusion it is possible to state that the trial and error to develop for controlling wind blown sand on erosive beaches begins.

ACKNOWLEDGMENTS

We are grateful for support provided by the Nihon University Multidisciplinary Research Grant for 2005 and 2006 for the Synthetic Study on Countermeasures for Watershed Development and Environmental Preservation in Waters.

REFERENCES

Hotta, S., Kraus, N. C., Horikawa, K. (1991). "Functioning of multi-row sand fences in forming foredunes," *Proceedings Coastal Sediments '91*, 261-.275.

Hotta, S., Kraus, N. C., Horikawa, K. (1987). "Function of sand fences in controlling wind blown sand," *Proceedings Coastal Sediments '87*, 772-787.

Hotta, S., Hatanaka, K., Tanaka, H., Koizumi, K., and Ohtsuka, K. (2000). "Determination of cross-sectional shape of artificial embankment by wind tunnel study," *Journal of the Japan Society of Erosion Control Engineering,* 53(2), 22-33. (in Japanese)

Takezawa, M., Zhang, T., Kubota, Z. and Hotta, S. (2002). "A brief examination of prevention works for sand and dust storm in the main land China and proposition of a new prevention work," *Proceedings of the 10th Symposium on Blobal Environments*, *JSCE,* 22, 475-480. (in Japanese)

Ugai, M., Tamura, T., Kubota, S. and Hotta, S. (2006). "Wind-tunnel study for suspended wind blown sand crossing over wind-breaks," *Annual Journal of Civil Engineering in the Ocean*, *JSCE,* 22, 475-480. (in Japanese)

Ugai, M., Hosaka, K., Kubota, S. and Hotta, S. (2005). "Suspended wind blown sand crossing over wind-breaks," *Annual Journal of Civil Engineering in the Ocean, JSCE*, 21, 415-420. (in Japanese)

COASTAL DUNEFIELD EVOLUTION IN CONDITIONS OF LIMITED SEDIMENT AVAILABILITY. NATURAL AND ANTHROPOGENIC CONTROLS ON THE CORRALEJO DUNES

Herminia I. Valdemoro[1], José A. Jiménez[1], Ignacio Alonso[2], Paloma Lorente[3], Manuel Rodríguez-Herrerías[3]

1. Laboratori d'Enginyeria Marítima, ETSECCPB, Universitat Politècnica de Catalunya, c/Jordi Girona 1-3, Campus Nord ed D1, 08034 Barcelona, Spain. herminia.valdemoro@upc.edu, jose.jimenez@upc.edu
2. Departament of Physics, Universidad de Las Palmas de Gran Canaria, Las Palmas, Spain. ialonso@dfis.ulpgc.es
3. Dirección General de Costas, Ministry of Environment, Plaza San Juan de la Cruz s/n, Madrid, Spain.

Abstract: This paper analyzes the main characteristics of the aeolian dynamics and dune evolution in the Corralejo coastal dunefield. This is an area with limited sediment supply and subjected to the action of a quasi-unidirectional wind regime. The governing conditions induce a long-term migration of the dune field in the direction of the wind with an expected long-term change in the landscape due to a change in the sediment supply to the dunefield through the upwind end due to natural and human-induced factors.

INTRODUCTION

The Corralejo dunefield is located in the NE coast of Fuerteventura (Canary Islands, Spain, Fig. 1). It has an extension of an approximated surface of 1,900 ha comprising the adjacent beaches and the dunefield itself, which is composed by transverse, barchan and barchanoid dunes. This sedimentary environment is one of the main resources of Fuerteventura island in terms of environmental quality –natural values contributing to its geodiversity and biodiversity- as well as in terms of landscape quality. This last one can be translated to economic values since the landscape is the most distinctive value of the Island for tourism, which is the main economic activity.

Due to its importance, the area is protected under the figure of Natural Park, which regulates the kind of activities to be permitted. In spite of this, the human influence is clearly observed through the presence of urbanized areas in its northern and western limits and by a road crossing the dunefield. These perturbations are products of the tourism development and, due to the dynamic conditions of the area they are behaving as threats to the physical conservation of the area.

The main aim of this paper is to analyze the dune dynamics in the area and to identify the potential effects of the cut in the sediment supply on the long-term behavior of the dunefield.

THE CORRALEJO DUNEFIELD

The study area is located in Corralejo, at the NE coast of Fuerteventura Island, Spain (Fig 1). Fuerteventura is located in front of the Saharian coast in the Atlantic Ocean and it is under the influence of the action of the Trade winds. The Corralejo dune field is located in the NE corner of the island. It occupies a rectangular surface with its larger axis oriented along the N-S direction along 8 km approximately and with an average width of 2 km (Fig. 1).

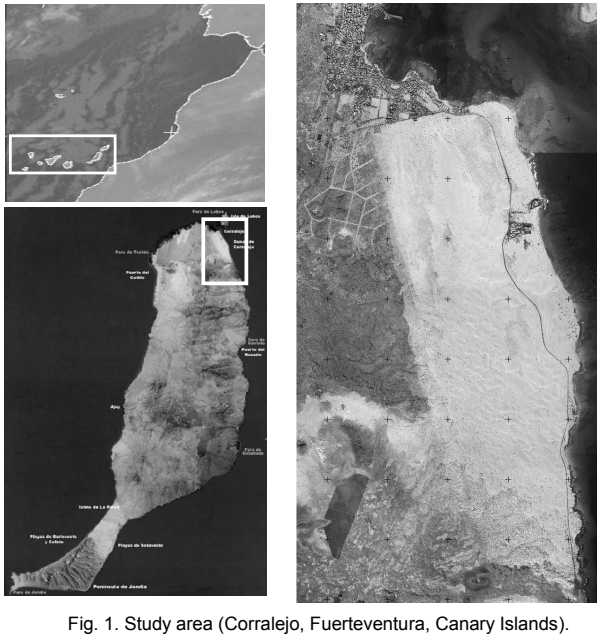

Fig. 1. Study area (Corralejo, Fuerteventura, Canary Islands).
Distance between crosses in the figure at the right is 1 km.

The climate in Fuerteventura is arid, without significant precipitation because, in contrast to the other Canary Islands, due to its very low altitude clouds brought by the action of the Trade winds are not stopped by the island relief. Fig. 2 shows the seasonal distribution of temperature and precipitation in the island.

The islands are subjected to the action of Trade winds which, in practical terms, it means that the area is affected by winds blowing from a quasi-constant direction, N-NNW (Fig. 2). These dominant directions are also the ones with the largest velocities. In general terms, the wind in the area can be characterized by a N wind with a mean velocity of 5.4 m/s with a standard deviation of the velocity of 2.4 m/s and where the 82.5 % of the year the wind velocity is lower than 8 m/s (Fig. 2).

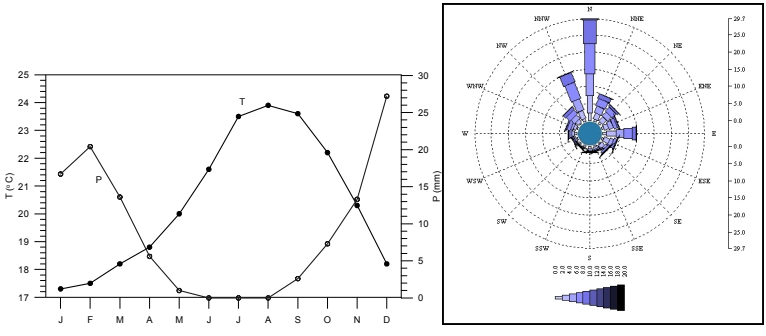

Fig 2. Left: Seasonal distribution of monthly averaged temperature and precipitation recorded in Fuerteventura airport (adapted from Gobierno de Canarias, 2002). Right: wind rose for records in Corralejo meteorological station.

According to Meco *et al.* (1997), sand forming dune fields in Fuerteventura are bioclastics and they come from marine deposits from Messinian containing warm water fauna from late Miocene and early Pliocene and large quantities of calcareous algae. These sands were exposed during the post-Messinian regression to wind action that reworked them forming the original dunes and, in some areas, they were covered by lava deposits from different volcanic eruptions. On these lava accumulations from 0.4 millions of years, new dune deposits were accumulated in a sedimentary activity that is associated to the middle Peistocene, between 0.181 ky and 350 ky ago. In the case of Corralejo dune field, the dunes are limited at the south by Montaña Roja and Apartaderos Malpais (lava flows).

These sand deposits were activated by wind action forming new generations of dunes until arriving to the actual mobile dunes. The alternation of active and inactive periods of aeolian transport was due to the alternation of dry and wet climatic periods. During the dry periods, the aeolian transport was important whereas during the wet ones the alteration of the basaltic substratum was favored (Damnati *et al.,* 1996).

These bioclastic sands are composed by a minimum of 85 % of carbonates (in some cases up to 95 %), with the high magnesium calcite with more than 18% of $MgCO_3$ being dominant (Coudé-Gaussen, 1991). Table 1 shows the mean values of textural parameters of sands in the area. They have been grouped into three main environments: mobile dunes, relict areas and beaches (Fig 3). As it can be seen, mean grain sizes are slightly coarser in beaches than in dune deposits (both active and relict). Thus, we shall find coarse sands of 0.6 mm in beaches whereas sediment mean size in dunes is about 0.4 mm. In the aeolian sub-environments (active dunes and relict areas) whereas the mean grain size is quite similar, they show a very significant difference in sediment sorting that is significantly larger for relict areas due to the presence of large shell fragments together fine sediments.

Table 1. Mean and standard deviation (between brackets) of textural parameters of sediment in each sedimentary environment of the dune field.

environment	mean (Φ)	mean (mm)	sorting	skewness	Kurtosis
mobile dunes	1.563	0.367	0.590	0.071	1.167
	(0.275)	(0.074)	(0.092)	(0.134)	(0.256)
relict areas	1.540	0.416	1.365	-0.264	1.971
	(0.707)	(0.236)	(0.556)	(0.199)	(0.863)
beaches	0.926	0.595	0.624	0.039	1.132
	(0.485)	(0.193)	(0.209)	(0.169)	(0.290)

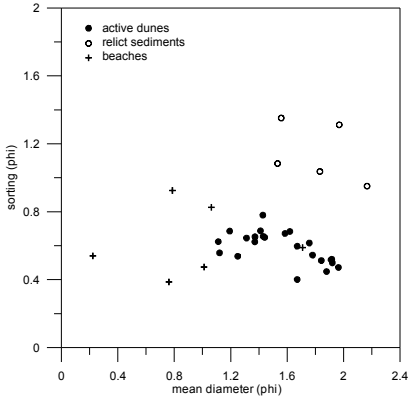

Fig. 3. Sediment characteristics in the sedimentary sub-environments of the dunefield.

These climatic conditions acting on the existing sand deposits have determined the actual evolutionary stage of the area. At present, the dune field can be described as a

sedimentary environment characterized by the presence of different sub-environments in terms of sediment and processes. Thus, the northern part and the westward border are formed by a land strip without dunes with a very narrow sand layer on the top of ancient sediments which area visible as outcrops in many locations. There is an important vegetal cover and it can be assumed that, at present, this area is not playing any significant role in the dynamics of the dune field (Fig. 4). Southward of this area, the thickness of the sand layer increases and, simultaneously, the vegetation decreases and, as a consequence, the sand mobility increases. This area is occupied in its central part by a sand body with a NNW-SSE orientation which is surrounded by stabilized areas. In this part there are no significant dunes and the outcrop of older sediments seems to indicate that active sand stocks are being progressively exhausted in some parts.



Fig. 4. Aspect of different areas of the dune field. Top: stabilized northern area. Middle: active sand without significant dunes in the Northern area. Bottom: example of dune types in the Central-Southern part of the dune field.

From this limit towards the Southern end, the field is covered by a layer of active sands forming dunes migrating in the southward direction. Dunes in the area are not homogeneous and, in fact, different dune trains and with different shapes can be

observed. Among them, barchans, barchanoids and transverse dunes dominate (Fig. 4), which are typical of environments subjected to the action of unidirectional winds (*e.g.* Lancaster, 1995). This area is limited in the southward end by the Malpais (lava flows) and in its eastern boundary by the sea. Within this area there are two artificial elements: (i) a road along the eastern boundary that it is easily crossed by mobile sands and, in consequence, its influence on the dune behavior is limited because it does affect sediment transport and, (ii) two hotels that affect the sediment dynamics in the adjacent area, specially the one located in the middle of the active zone.

Dune heights were determined from a topographic field campaign performed between September 2004 and March 2005 by Hidtma-Iberinsa for the Ministry of Environment. The averaged dune height (measured as the maximum height along the dune front) was about 8.4 m with maximum heights of about 29 m. The dune height distribution across the area was not uniform, with the Northern and Southern ends being the areas with the lowest height. This could be associated to the fact that the N area is behaving as a generation area whereas the S end is a way out area since the dune starts to move on to the lava flows area (malpais).

DUNEFIELD DYNAMICS

In order to characterize the present evolution of the dunefield, the first task was to estimate the changes in the surface occupied by the different dynamic sub-environments. This is shown in Table 2 for dunes, sand and stabilized areas to the East and to the West of the road crossing the area obtained from aerial photographs taken in 1987 and 2002.

The area of dynamic sands but without dunes located at the N area maintains its form with a slight surface increase. This increase is related to a redistribution of sediments under the action of winds which tend to enlarge the area along its southern end. Since there is no new sediment input in the area from the N, it is expected that the sediment thickness will progressively decrease, which is already visible in some parts (outcrops of older materials).

The area with mobile dunes (westwards of the FV-1 road) suffers during the monitored period a change that can be simply described as a southward displacement of the southern end (Fig. 5). This is easily explained by the continuous action of Trade winds on sediment deposits that transport them into the lava flows. In this southern end, the averaged displacement of the front is 80 m (with a maximum displacement of 240 m) which is equivalent to an averaged migration rate of the dune field into the lava flow of 5.3 m/y. This modification of the southern end means that the surface of the dunefield has increased about 42 ha during the 1987-2002 period (Jiménez et al., 2006). However, this increase cannot be understood as a gain of sedimentary material because it is due to a redistribution of the existing sediment volume.

This surface increase without new sediment inputs should imply that the averaged thickness of the sediment cover would decrease in time. Moreover, in the case of

stationary climatic conditions this behavior would tend to force the migration of the entire dunefield towards the south since the sediment transported in such direction from the Northern areas should not be replaced.

The evolution of the vegetated and stabilized areas within the dunefield does not present a systematic behavior. There is an apparent decrease in the stabilized surface probably due to the migration of dunes and burial of areas with isolated vegetation or outcrops in the inter-dune spaces (see Fig. 4) in such a way that changes are detected across the entire field.

Finally, in the area eastwards of the FV-1 road, the most significant change is an increase in the urbanized land due to the expansion of one of the existing hotels (already present in 1987). In addition of this, there was also an increase in the stabilized sands southwards (downwind) of the hotel area. The increase of the stabilized area from 1987 to 2002 was estimated in 3.5 ha.

Table 2. Surface (ha) of the main sedimentary environments of the Corralejo dunefield in years 1987 and 2002. FV-1 is the road along the Eastern coast.

Type	1987	2002
Westward of FV-1		
T1 –sands-	47.5	56.9
T2 –dunes-	636.7	679.1
T3 –stabilized-	97.3	78.8
Eastward of FV-1		
T1 & T2 –sands & dunes-	149.3	145.8
T3 – stabilized	9.8	13.2

Once the change in the sediment-dynamics sub-environments were estimated, the second step consisted in the evaluation of aeolian transport rates and dune migration rates within the mobile dune area. To estimate them, dune fronts were identified in the 1987 and 2002 photographs and the displacement in different sections of the front were measured (Fig. 5). The estimated dune migration rate was 5.8 m/y towards the South with a maximum value of 11.4 m/y (Table 3). It has to be stressed that this averaged value is nearly the same than the averaged rate of displacement of the southern end of the dunefield into the lava flows (5.3 m/y).

This mean value obtained for the period 1987-2002 is of the same order of magnitude than the reported by Hollerman (1982) for earlier stages and, this should be indicating that the actual conditions of sediment availability and mobility under the action of Trade winds have been steady during the last decades.

Finally, if dune migration is spatially analyzed, the lowest migration rates are observed in the N and S strips of the active area (Fig. 5), with the largest gradient in migration rates being located in the N end (difference in spatially averaged rates up to 2.5 m/y).

Table 3. Basic statistics of dune migration from 1987 to 2002. Analyzed dunes are showed in Fig 5.

Parameter	Displacement, m	Migration rate, m y^{-1}
Mean	87	5.8
Stand dev	30	2.0
Maximum	171	11.4
Minimum	29	1.9

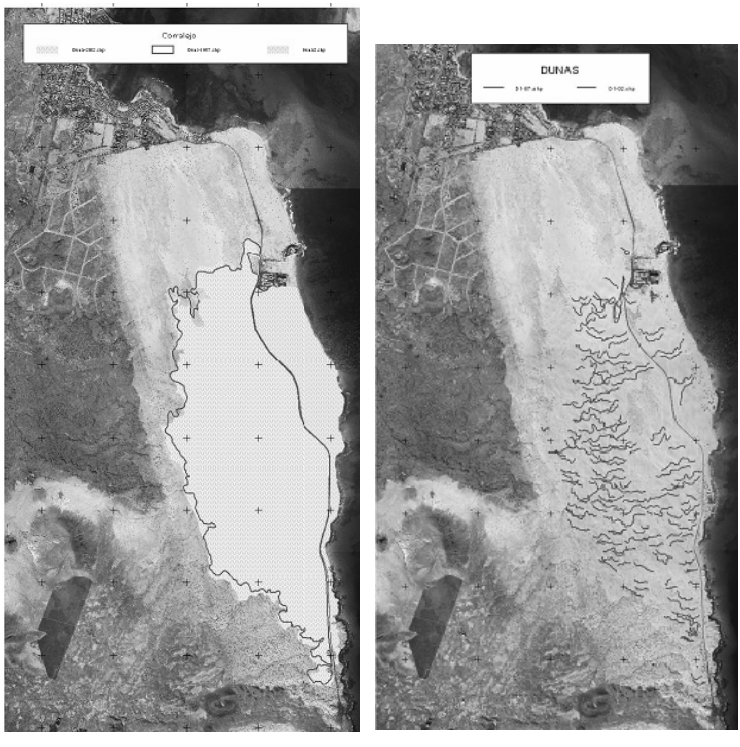

Fig. 5. *Left*: Evolution of the surface occupied by mobile dunes from 1987 (line) to 2002 (colored). *Right*: Dune migration from 1987 (green) to 2002 (red). Distance between crosses is 1 km (adapted from Jiménez et al., 2006).

Taking into account the measured migration rates and the averaged dimensions of dunes measured in 2005 we made an estimation of the aeolian transport in the area. To do this, we assume that actual dunes are migrating without experiencing any change in volume, i.e. they are in equilibrium, and as a consequence, sediment transport producing such

migration is simply the product of the migration rate by the dune height (see e.g. Illenberger and Rust, 1988). With this, net transport rates across the dunefield were estimated to have a mean value of 37 m^3/m/y with a standard deviation of 19 m^3/m/y. This transport rate should be acting in the direction normal to the dune fronts and, according to the distribution of the dunes in the W-E direction (Fig. 5), there will be significant changes in transport rates across the dune field.

Finally, these estimations from the observed dune behavior were compared to theoretical ones obtained by applying s-o-a formulations. Thus, the Bagnold (1941) model was applied to the conditions of the area. First, the probability of exceedence of mobility conditions in the dunefield was calculated by estimating the threshold velocity (impact velocity) associated to the different grain sizes across the area. Once this velocity was calculated, the probability of occurrence was obtained from the long-term wind velocity distribution. Table 4 shows the obtained values for the mean sediment sizes of the different environments. As it can be seen, and as it was expected, the larger mobility (probability of exceedence of transport conditions) is associated to sediments composing mobile dunes, followed by relict areas and finally the beaches. It has to be mentioned that these calculations were done for sediment of density 2710 kg/m^3, which was the value measured in laboratory for the carbonate sands of the area.

Table 4. Mean grain size dor the different sub-environments of the dunefield, impact threshold velocity and probability of exceedence.

environment	d50 (mm)	u_t (m/s)	P ($u \geq u_t$)
dunes	0.367	7.41	0.2132
stabilized-relict	0.416	7.81	0.1753
beach	0.595	9.09	0.0499

Due to the presence of coarse carbonate fragments (such as shells) in the sediment, the presence of sediment showing bimodal distributions was not infrequent. Under these conditions, the use of a mean grain size could be unrealistic and it would not be properly representing the selective action of wind on sediments (see *e.g.* van der Wal, 2000). To take into account this potential effect, computations were also performed by splitting each bimodal distribution –when present- into two sediment classes (Fig. 6). For each sediment type, the threshold velocity was calculated and the final probability was calculated as the weighted sum of the respective probabilities of exceedence. Final results do not differ too much from the ones showed in table 4, although in general, an increase in the mobility was obtained. It has to be stressed that threshold conditions for sediment composing stabilized areas only take into account the sediment size. However, the sediments show a high degree of compaction and, due to this, it is expected that the real mobility should be lower than the calculated one.

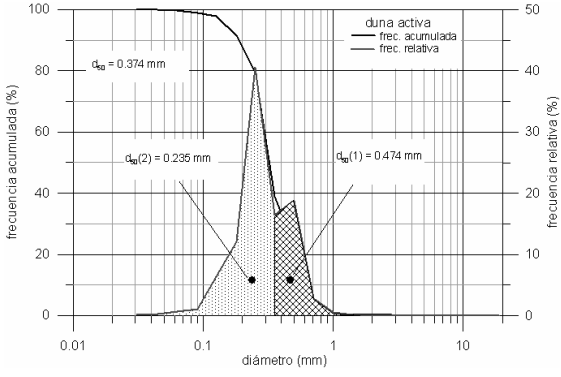

Fig. 6. Schematization of bimodal grain size distribution into two populations.

Once the minimum conditions for aeolian sediment transport were calculated, the following step was to estimate the potential transport rates. There exists a relative large number of transport models, all of them depending on some calibration coefficients in such a way that when applied to a given set of conditions they predict transport rates significantly different (see e.g. Sherman *et al.,* 1998). In this work we have estimated the potential transport rates in the area by using the Bagnold (1941) model that according to the comparative analysis done by Sherman *et al.* (1998) gives predictions in the intermediate range.

Although this model does not explicitly includes threshold conditions, it has been applied only for wind conditions exceeding the calculated threshold conditions for the given sediment environment (see e.g. Craig, 2000). Fig. 7 shows the aeolian sediment transport rose calculated for the area where it can be seen that the directional distribution of Trade winds induce a sediment transport with a resultant direction to the south as it was already observed in the dune migration analysis. This type of distribution is typical for areas with barchans and, transverse dunes in areas of good sediment availability (Lancaster, 1995).

The calculated averaged potential transport rate ranged from 3 m^3/m/y for the sediment composing the dunes to 5 m^3/m/y for the ones in beaches. This difference is only due to differences in sediment grain size and it does not include any possible variation in wind conditions across the dune field.

When comparing with transport rates obtained from dune migration, this rate is 3 times lower. This under-prediction of theoretical models against transport rates estimated from dune migration was also observed by Craig (2000) and Illenberger and Rust (1988), although other authors have found conditions in which they claim the Bagnold's model to over-predict real transport rates (*e.g.* Goldsmith *et al*., 1990).

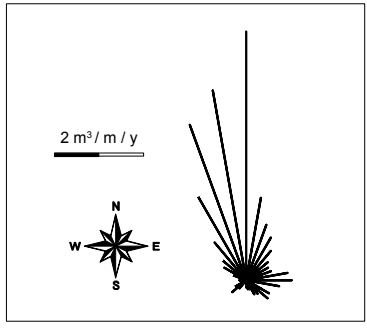

Fig. 7. Aeolian sediment transport wind rose for Corralejo.

CONDITIONS AFFECTING THE SEDIMENT SUPPLY

As it was shown in the previous section, the Corralejo dunefield is experiencing a southward migration with sand going out the former limits through the south towards the lava flows and through the SE towards the sea. Under these conditions, this means that unless new sediment will get into the system towards the N end, the dunefield will progressively migrate towards the S and, at the same time, part of the sediment will be removed and transported to the sea.

Due to this, it is important to know the actual situation of the potential sediment supplies to the system through the Northern limit. Nowadays, sediment sources in the area has nearly disappeared due to two main causes: **(i)** a very long term natural one, which is the progressive exhaustion of the sand sources in the coastal shelf, in such a way that at present it can be assumed that no sediment is susceptible to be transported towards the dune field. This can be detected in the distribution of sediment facies in the coastal shelf, where rocky outcrops are dominant along the shallower part of the area with sediment rich areas being unconnected to beaches (Fig. 8); **(ii)** a medium/long human-induced one –decadal scale-, due to the progressive urbanization of the Northern coast.

This last point is illustrated in Fig. 9 where the evolution of the urbanization in the northern border of the dune field is shown from 1941 to 2002. It can be clearly seen that whereas in 1941 only a small fishing village existed, nowadays (2002), the area is fully urbanized due to the growth of the original village and, specially, due to the construction of tourist resorts (tourism is the main economic activity of Canary Islands in general and this area in particular).

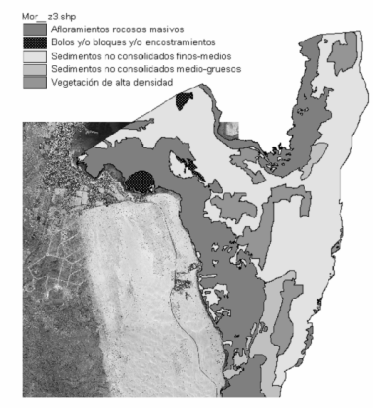

Fig 8. Sedimentary facies in the northern coast (brown: massive rock outcrops; black: cobbles and boulders; yellow: fine and medium sands; orange: medium-coarse sands; green: high density vegetal cover –Cymodocea-, adapted from Jiménez et al., 2006).

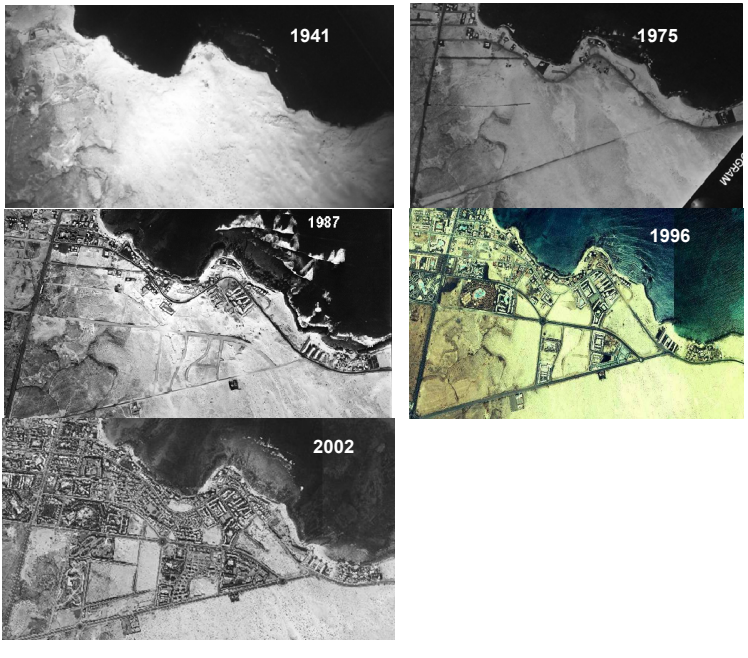

Fig 9. Evolution of the urbanization in the Northern coast of the Corralejo dunefield.

This urban growth acts on the sediment supply to the dune field by two ways: **(i)** as a barrier for the sediment that potentially could be incorporated to the aeolian dynamics of the area and; **(ii)** by eliminating a large volume of sand already existing in the area due to land occupation, preventing its mobilization and transport by wind. Thus, the loss of useful sand surface due to the urbanization of the northern coast has been estimated in 86.73 ha (measured in 2002).

These two effects have generated a gradient in the aeolian transport just southward of the urbanized area (the northern border of the dune field) during the last decades because the sediment transported towards the south is not been replaced by new sediment. This is behaving as the main boundary condition for the evolution of the dunefield and will determine in the long-term (assuming steady climatic conditions in about 6 centuries) a drastic change in the landscape. Thus, it is expected that dunes will progressively disappear from the Northern areas, decreasing the thickness of the sand cover and increasing the areas with vegetation (southwards displacement of the actual stabilized northernmost strip). The active dunes will move on to the lava flows across the actual southern end with also a progressive loss of sediment to the sea across the SE end.

CONCLUSIONS

In this paper, we have shown the main characteristics of the aeolian dynamics and resulting dune evolution in a coastal dunefield subjected to limited sediment supply and subjected to the action of a quasi-unidirectional wind regime. The dune field which is formed by carbonate sediment (bioclastic sands) is experiencing moderate dune migration rates and, in the upwind field limit is beginning to show the exhaustion of sediment. This results in a long-term migration of the dune field in the direction of the wind with an expected long-term change in the landscape due to a change in the boundary conditions at the upwind limit due to natural and human-induced factors. The migration of the overall dunefield at the downwind end which is formed by lava flows has been estimated to be of about 5.3 m/y, which is of the same order of magnitude of dune migration rates in the area (6.8 m/y). These rates together the dunefield dimensions seem to indicate that the change in landscape will occur in a very long-term scale (several centuries). However, although slow, this is continuous process provided climatic conditions remain stable.

ACKNOWLEDGEMENTS

This work was promoted and funded by the Dirección General de Costas (Spanish Ministry of Environment). The second author tanks to the Government of Catalonia by its support through a University Research Promotion Award for Young Researchers.

REFERENCES

Bagnold, R.A. (1941). "*The physics of blown sand and desert dunes,"* Methuen, London, 265 p.

Coudé-Gaussen, G. (1991). "La contribution des poussières aux limons sables et paléosols de Fuerteventura (Iles Canaries)." In: *Les poussières sahariennes*, Editions John Libbey Eurotext, 291-329.

Craig, M.S. 2000. "Aeolian sand transport at the Landsphere dunes, Northern California." *Earth Surface Processes and Landforms,* 25, 239-253.

Criado, C. (1987). "Evolución geomorfológica y dinámica actual del jable de Corralejo". *Revista de Geografía de Canarias*, 2, 29-52.

Damnati, B., Petit-Marie, N., Fontugne, M., Meco, J. and Williamson, D. (1996). "Quaternary paleoclimates in the Eastern Canary islands," *Quaternary International*, 31, 37-46.

Gobierno de Canarias. (2002). *"Plan rector de uso y gestión del parque Natural de Corralejo."* Consejería de Política Territorial y Medio Ambiente. Dirección General de Ordenación del Territorio.

Goldsmith, V., Rosen, P. and Gertner, Y. (1990). "Eolian transport measurements, winds, and comparison with theoretical transport in Israeli coastal dunes," In, Nordstrom, K.F., Psuty, N.P. and Carter, R.W.G. (Eds), *Coastal dunes: form and processes*, John Wiley, 79-101.

Hollermann, P. (1982). "*Studien zur aktuellen Morphodynamik und Geoökologie der Kanarinsel Teneriffe und Furteventura,"* Abhandl Akad, Wissensch, 406 p.

Illenberger, W.K. and Rust, I. (1988). "A sand budget for the Alexandria coastal dunefield, South Africa," *Sedimentology*, 35, 513-521.

Jiménez, J.A., Valdemoro, H.I. and Alonso, I. (2006). "*Estudio del estado actual de los sistemas dunares de Corralejo y Jandía (Fuerteventura). Identificación de problemas y propuestas de actuación,*" Dirección General de Costas, Ministerio de Medio ambiente.

Lancaster, N. (1995). "*Geomorphology of desert dunes,"* Physical Environment Series, Routledge, 290 p.

Meco, J., Petit-Maire, N., Fontugne, M., Shimmield, G. and Ramos, A.J. (1997). "The Quaternary deposits in Lanzarote and Fuerteventura (Eastern Canary Islands, Spain): An overview." In: Meco, J., Petit-Maire, N. (Eds.), *Climates of the Past, Proceedings CLIP Project*, 123-136.

Sherman, D.J., Jackson, D.W.T., Namikas, S.L. and Wang, J. (1998). "Wind-blown sand on beaches: an evaluation of models," *Geomorphology,* 22, 113-133.

van der Wal, D. 2000. "Grain-size-selective aeolian sand transport on a nourished beach," *Journal of Coastal Research*, 16, 896-908.

HYDRODYNAMIC AND MORPHOLOGIC MODELING AT SEBASTIAN INLET, FL

Gary A. Zarillo [1] and Florian G. A. Brehin[2]

1. Department of Marine and Environmental Systems 150 West University Blvd. Florida Institute of Technology Melbourne, FL 32901
zarillo@fit.edu
2. Department of Marine and Environmental Systems 150 West University Blvd. Florida Institute of Technology Melbourne, FL 32901
fbrehin@fit.edu

Abstract: Numerical model simulations of tidal inlet hydrodynamics, sand transport and topographic change were performed using the Coastal Modeling System (CMS) to investigate the morphological response to time varying forcing, sediment texture, and the influence of rock reef outcrops within the Sebastian Inlet system. The presence or absence of rock within the inlet throat and in the surf zone on the south side of the inlet resulted in distinctive differences in topographic changes to the ebb shoal over a year long simulation. Comparisons between three sand transport formulations over a shorter period (2 months) showed some variation among the formulations, but predicted net topographic changes were well within an order of magnitude. Comparisons between predicted and measured net topographic changes demonstrated agreement in terms of pattern. Agreement in absolute terms improved as the model spatial resolution was refined by decreasing cell sizes.

INTRODUCTION

Inlet/bay systems and their morphologic features exist in dynamic equilibrium, with sand fluxes between shoal sand reservoirs due to complex interactions with the surrounding forcing mechanisms. The accurate modeling of the morphologic evolution of tidal inlet shoals is an important management tool, since they control sediment budgets. Inlet hydrodynamics depend on physical forcing, inlet and bay geometry, bottom topography, and presence of stabilizing structures that influence

sedimentation and flow patterns. Controlling jetties have been constructed at most of the smaller tidal inlet systems of the U.S East and Gulf Coasts to prevent shoaling and safety of navigation channels and stabilize the inlet location. Stabilization may also influence inlet evolution by enhancing the formation of ebb shoal and flood shoal deposits. Net longshore sediment transport and wave forces reshape the ebb shoal through a mechanism in which sediment is bypassed around the inlet, forming a bypass bar and eventually an attachment bar which connects the ebb shoal to the downdrift beach. As the shoal system of a stabilized inlet evolves, variations within the wave climate can abruptly increase or decrease the volume of sediment on the ebb or flood shoals and cause temporary, but large variations in the volume of sand bypassing the inlet (Zarillo et al., 2003).

Regional sand management has become a national issue that requires data collection and monitoring of tidal inlets and surrounding beaches as well as better predictive tools for predicting morphology changes. Computationally efficient numerical models to reproduce and predict sedimentation patterns at inlets such as ebb-shoal growth, scour patterns around structures, cross shore transport between shoals have been developed under the Coastal Inlets Research Program (CIRP) at the Coastal and Hydraulics Laboratory of the U.S. Army Water Ways Experiment Station. Termed the Coastal Modeling System (CMS) the suite of models provides realistic simulations of inlet behavior. However, the remaining limitations of numerical modeling include the computation times, which increase with spatial resolution, limited morphologic constraints to prevent over prediction of topographic change, and the lack of extensive field data to calibrate model results. The model application presented in this paper summarizes the results based on the state of the CMS technology as of the middle of 2006.

OVERVIEW OF THE MODELING APPROACH

The CMS is based on the M2D model, which is a time-dependant, 2-D finite difference circulation and morphology model, which calculates water surface elevations, two components of the current and sediment transport on a rectilinear grid (Militello et al., 2004). Coupling of M2D with the Steady Spectral wave model STWAVE (Smith et al, 2001) was performed through the Surface Modeling System interface (SMS) using the steering process to include the radiation stresses and wave induced currents (Zundel, 2000).

The CMS includes three sediment transport modules: Watanabe formulation (Watanabe. 1987), the Lund-CIRP formulation, and Advection-Diffusion (AD) enhancement of the Lund Formulation ((Buttolph et. al, 2006). The sediment transport formulations are directly coupled to the M2D model along with a continuity-based calculation of morphologic change that considers sediment volume exchanges among computational cells (Buttolph et al., 2006). The Watanabe formulation for total load is a function of an empirical coefficient for wave irregularity, bed shear stress, critical shear stress of incipient motion, the water density, gravitational acceleration and total depth averaged current velocity. The Lund-CIRP formulation is more complex including the added the benefits of writing out bed load and total transport as separate values and calculating the wave energy

dissipation. In the AD formulation diffusivity terms in the horizontal dimensions are added are added to enhance sediment motion. Another important feature included in the model calculations is the representation of non-erodible cells (Hanson and Militello, 2005).that can be used to represent shore protection structures including breakwaters and jetties, as well as natural features.

MODEL APPLICATION AT SEBASTIAN INLET, FL

This paper presents several examples from an ongoing modeling effort at Sebastian Inlet, FL to investigate the sediment transport and morphological evolution. Numerical simulations of the coupled circulation/wave models (M2D/STWAVE) are discussed under the followings topics: 1. preliminary hydrodynamic runs and calibration, 2. hard bottom subroutine testing, 3. shorter term (2 months) model test cases run applying different sediment transport formulations. Computed topographic changes were analyzed and compared with measured data from bathymetric surveys.

Sebastian Inlet is located in the southern part of the Indian River Lagoon (IRL) on the east coast of Central Florida. Rock outcrops of coquina line the bottom of the inlet throat and form a rock reef area exposed in the surf zone on the southern side of the inlet. The inlet is also characterized by a small throat cross section area and a large bay (IRL), which promotes strong currents through the. The present Sebastian Inlet was artificially cut into the coquina of the Late Pleistocene Anastasia Formation in the late 1940's and stabilized by offset jetties from 1950's to 1970's. The present configuration of the inlet (Figure 1a &1b.) includes a 250 meter-long curved north jetty and a shorter straight south jetty of approximately 75 meters.

The main morphologic features include the ebb shoal and bypass bar, which is obliquely oriented to the southern beaches and connects to the attachment bar about 700 m south of the inlet entrance, a large flood shoal, and an excavated sand trap (Figures 1a &1b). The mean tidal range is approximately 1 meter. The east central Florida wave climate is moderate having a mean annual wave height of 0.6 meter (Zarillo *et al*., 2003). However the wave regime is subject to strong seasonal variations in energy and approach, punctuated by the higher wave energy from northeasters and tropical storms and hurricanes. Analysis of the 15 years of surveys of the inlet indicates that the inlet is in state of quasi-equilibrium in terms of shoal volumes, but the dynamic ebb shoal can gain or lose more than 100,000 m^3 of volume in a single year and controls the inlet sediment budget. The net sand budget of about 120,000 to 230,000 cubic m^3/yr is thought to be driven by a few extratropical storms creating southerly drift, whereas tropical systems from the south tend to drive longshore sediment transport toward the north (Zarillo et al., 2003). Figure 2 summarizes the wave climate in terms of the longshore component of wave power. The cumulative plot indicated that the net component is directed south but that reversals and strong variations in magnitude are common.

Model Setup

In the Sebastian Inlet region the model grid was setup on the inner continental shelf and shoreface from approximately 12 km north of the Inlet to 12 km south of the inlet (Figure 2). Data sets for model grid development and model boundaries include

topographic data, wave data from the Wave Information System (WIS) and from local monitoring programs, water level data, and sedimentologic data available from local sand source investigations, and beach condition surveys.

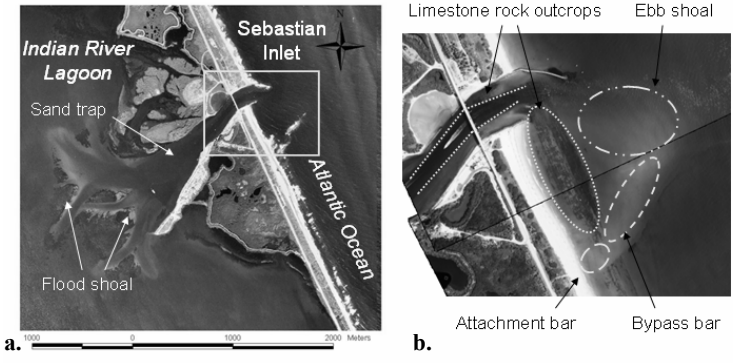

Figure 1. Study area. Note the waves breaking around the southern bypass bar. Hard bottom appears as dark bands on the aerial image.

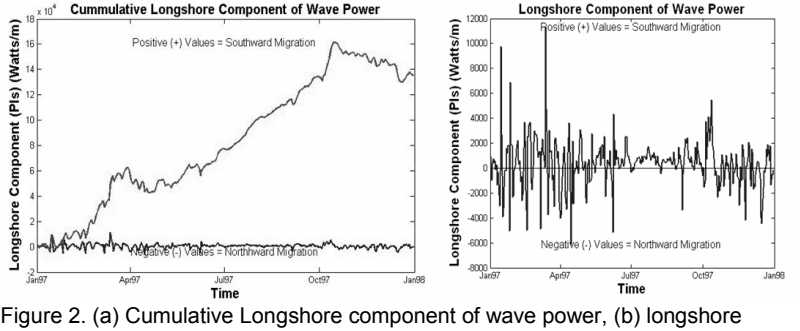

Figure 2. (a) Cumulative Longshore component of wave power, (b) longshore component of wave power.

Topographic data from the National Geodetic Data Center (NGDC) was combined with shoreface data from 1997. The simulation was forced by three measured water surface elevation (WSE) time series applied at the north lagoon, south lagoon, and ocean boundaries of the model grid. Wave inputs into STWAVE consisted of 365

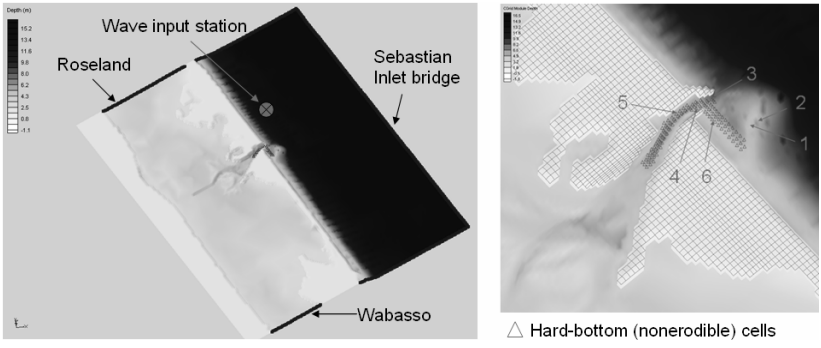

Figure 3. M2D grid and water surface elevation boundaries. The bottom topography contours are in meters.

directional spectra for coupling to M2D through a steering module that updated the wave field every 24 hours. Hind cast wave data from a nearby WIS station were propagated within a regional STWAVE grid to obtain the nearshore wave climate. The wave climate during the simulation time mainly consists of fair weather conditions with some storm events in summer and more frequent storms in fall and winter months. The largest wave heights were approximately 2 meters along with periods ranging from 4 to 15 s. The M2D grid cells corresponding to rock outcrops were selected and tagged as non-erodible (Figure 3). The depth of maximum erosion was set to 20 cm to account for occasional sand layers on the hard substrate. Observation cells were selected at different points of the model domain to extract time series of model outputs for analysis. For the longer term model runs (12 months) and testing the hard bottom routine, the circulation and wave model resolution was set to 50 meters. The two model cases used the Watanabe transport formula, sediment grain size set at 0.2 mm, the Watanabe sediment transport coefficient A set to 0.5, and total simulation time set to one year (8760 hours). For the three model cases comparing sand transport formulations and topographic changes between formulations the offshore cell sizes were set to 50 meters and refined to 25 meters in the inlet vicinity. Sediment grain size was set to 0.2 mm and simulation time was set to 1344 hrs (56 days).

Calibration and Preliminary Hydrodynamic Runs

A first step prior to sediment transport computations consisted of calibrating the hydrodynamic model. Predicted time series of water surface elevations were compared with measured elevations in terms of amplitude and phase. No measured current data were available for the model period. A comparison between computed and measured water surface elevations for Wabasso, FL tide station near the south boundary of the model is shown in Figure 4. Computed and measured elevations were found to match closely in terms of amplitude and phase. An example of computed current magnitude and direction during the ebb stage is displayed in Figure 5. Average computed velocities ranged from near zero behind the flood shoal to around 2 m/s between the two jetties confining the inlet throat. Stronger currents were found

in the inlet channel and throat. The model represents the ebb jet feature in between the jetties, where tidal currents peak and eddies forming on both sides and propagate offshore as current decreases around the ebb shoal. Current velocity was found to be strongly attenuated by the shoals.

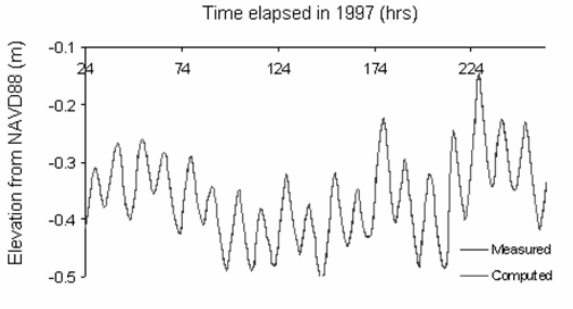

Figure 4. Model calibration: measured versus computed water surface elevations at Wabasso, FL.

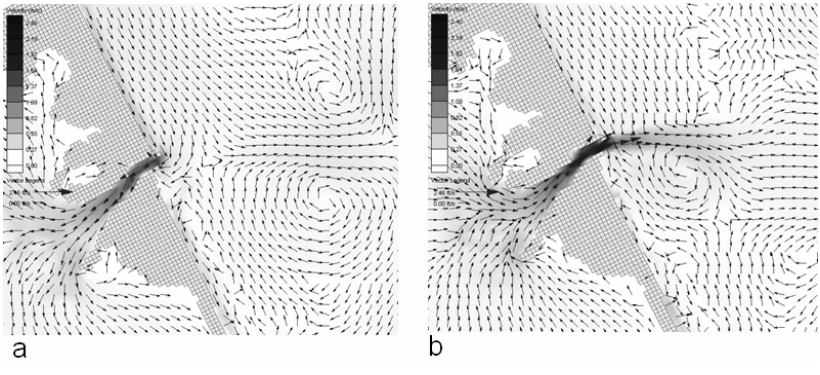

Figure 5. Current magnitude and directions extracted during a) flood stage and b) ebb stage.

During tests of the wave model wave height and direction were extracted for two cases: a northeaster and storm waves approaching from the south (Figure 6). Shoaling over the crest of the ebb shoal and along the bypass bar increased wave heights followed by a decrease and breaking at the shoreline. Strong wave refraction occurred around the ebb shoal/bypass bar area, especially when waves approached from the North East. Wave penetration into the inlet throat was predicted when waves were coming from the South East.

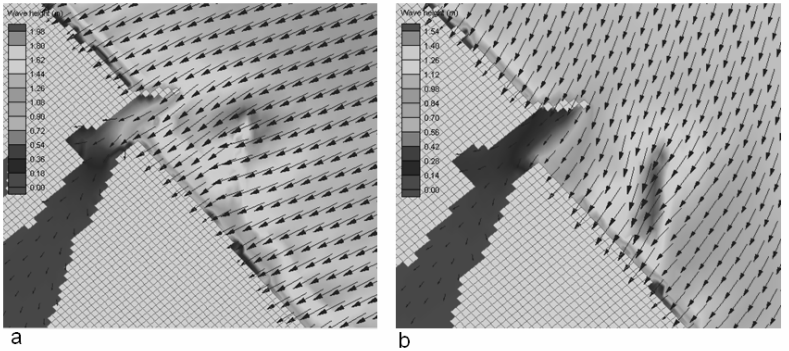

Figure 6. Predicted wave height and direction for a) swell approaching from the south typical of tropical systems b) Extratropical northeaster storm.

Long Term Runs

Model test cases were run with and without selected mode cells tagged as non-erodible to simulate the influence of rock outcrops on inlet dynamics. Computed net topographic change after a one year simulation under the Watanabe sand transport formulation is shown in Figure 7. Erosion areas corresponding to negative values are represented by blue colors and deposition areas (positive values) are represented by red colors. In the two model cases, channel bank erosion was observed, as well as scour at the seaward end of the offset jetties corresponding to areas of maximum current velocities during ebb and flood stages. Patches of erosion alternating with accretion were predicted on north and south shoreface areas, as well as over the flood shoal. For the south beaches and attachment bar, more complex patterns with patches of accretion and erosion alternating on the upper shore-face, probably due to interactions with rock reef.

Transient and permanent sand deposition is also predicted within the inlet throat section and ebb shoal complex and in both cases, a substantial net growth of the ebb shoal is predicted. When model cells were tagged as non-erodible through main inlet conveyance channel bank erosion increased as the inlet adjusted to a larger equilibrium cross-sectional area and the terminus of the ebb shoal extended farther from the inlet throat. Cross-shore transport on the bypass bar was observed for both runs, but deposition and erosion areas were reversed.

The hard bottom influence at specific cells corresponding to rock reef outcrops was investigated by extracting time series of topographic changes at high temporal resolution (Figure 8). Observation points 1, 2 and 3 were cells tagged as non-erodible with an initial layer of sand of 20 cm. At point 1, located on the reef in the outer surf-

zone of the south beaches, slight erosion of about 5 cm was predicted in the run, whereas net erosion to a depth of 0.5 meters was predicted in the run without non-erodible cells. At observation point 2 on the south side of the inlet throat episodic scour and deposition was predicted along with net erosion after about six months. The hard bottom run shows a less variable pattern of scour and deposition but with maximum erosion limited to 20 cm. Point 3 in a channel margin area west of the inlet throat experienced episodic scour and deposition without hard bottom and deposition when tagged as a hard bottom cell.

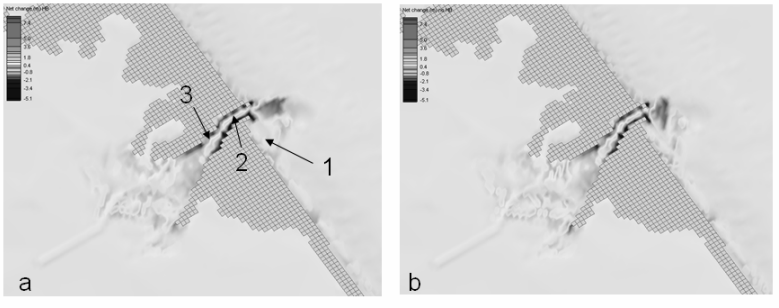

Figure 7. Computed Net topographic change after 1 year run under Watanabe formulation a) hard bottom and b) no hard bottom. Numbers correspond to observation cells for time series extraction.

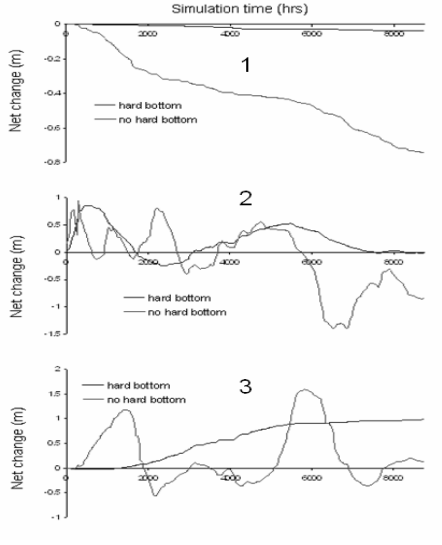

Figure 8. Extracted time series at observation stations for 1 year run (1997) under Watanabe formulation hard bottom versus no hard bottom.

Comparisons Between Sand Transport Formulations

Computed net topographic change after two months of simulation (1344 hours) is compared for the runs applying the Lund-CIRP formulation (Figure 9), Watanabe (Figure 10), and Advection Diffusion formulation (Figure 11). For all runs, the greatest erosion occurred along the margins of the inlet channel, whereas deposition is observed in the inlet channel. The Advection-Diffusion formulation showed more complex patterns, with less sand deposition in the channel, more deposition on the shoreface. All formulations agree in terms of sedimentation pattern including sand transport over the bypass bar with erosion on the outer part and deposition on the inner bar. However, the AD formula is the only one to reproduce natural bypassing and patches of sand accumulation on the attachment bar and shore-face between the south jetty and attachment bar. Under the Lund formulation, a small amount of sand was bypassed, but erosion was the dominant pattern between the beach and the first reef line. Over the flood shoal calculated net topographic changes very are small and mostly concentrated on the margin of the sand trap consistent with reality. Similar to the ocean side of the inlet patchy sand deposition is predicted by the AD calculations.

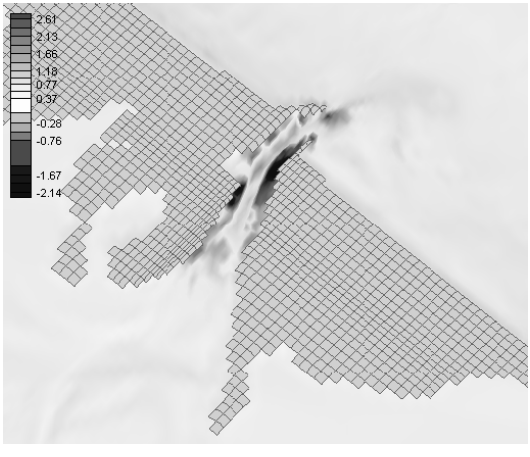

Figure 9. Computed net topographic change after 2 months of simulation under Lund-CIRP formulation.

Time series of bottom topography extracted at five observation cells shown in Figure 3 were used to compare the net predicted bottom change from each formulation. The sedimentation time series shown in Figure 12 agree well with visual observations of net change including erosion on the outer part of the bypass bar (point 2) and

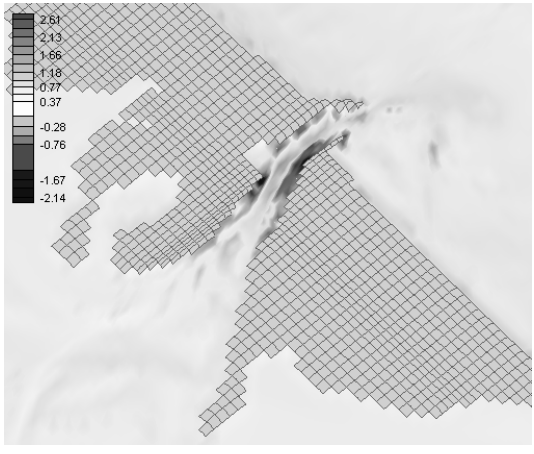

Figure 10. Computed net topographic change after 2 months of simulation under Watanabe formulation.

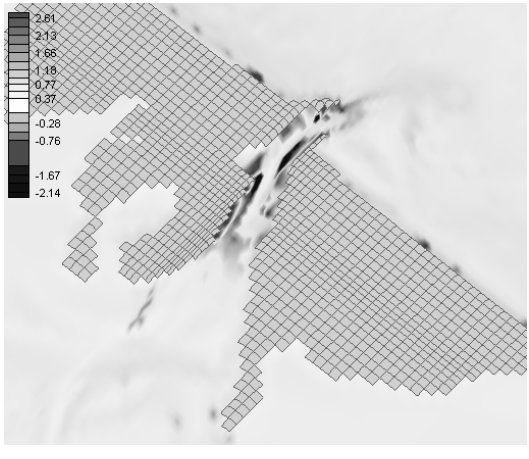

Figure 11. Computed net topographic change after 2 months of simulation under Advection-Diffusion formulation.

accretion on the inner part (point 1). For the three formulations, the overall trend is in accretion. Under Lund and AD formulas, the same trends of scour and deposition were observed, with the main difference in the magnitude of the net change. Computed net erosion at observation cell 2 was predicted by the three formulas. However, the magnitude of the net topographic change under the Watanabe formula was smaller compared to Lund and AD. Observation cell 3 is located off the east tip

of the North jetty. Here accretion was predicted by the three sediment transport formulas. Under the AD formula the predicted time series was more variable, whereas Lund and Watanabe formulas produced a more linear increase in net topographic change. Observation cell 4, 5, and 6 (Figure 2) were tagged as hardbottom cells. At cell 4 located off the tip of the south jetty, between the inlet channel and jetty structure the largest deposition was observed under the AD formula. Results diverge by the end of the run when scour was predicted by Lund. Model results at observation cell 5 on the North Channel margin of the inlet throat are similar for about half the simulation. However during the second half net deposition at this hardbottom cell under the AD formulation decreased while the other formulations continued to predicted a net increase. Model results at cell 6 is located on the rock reef outcrops located on the shoreface south of the inlet entrance indicated near zero net change under all three formulations. Only the AD results showed episodes of slight deposition and erosion.

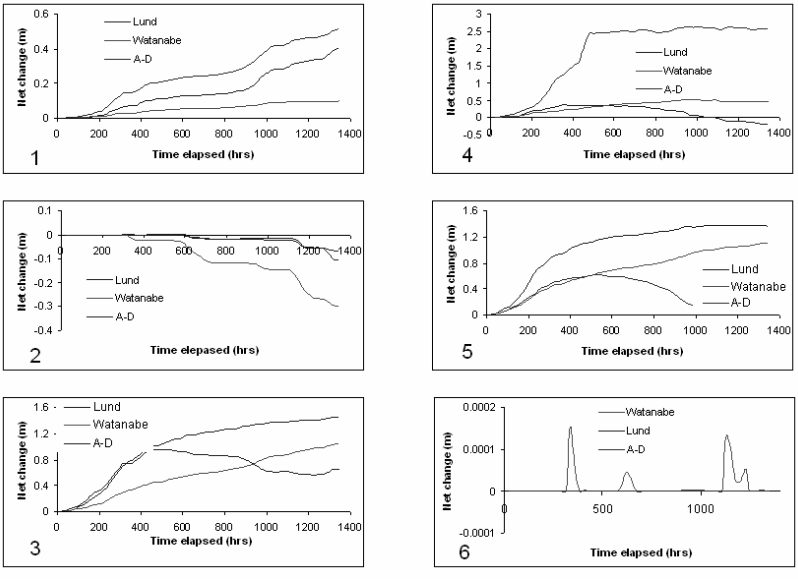

Figure 12. Time series of net bottom change extracted at each observation point.

SUMMARY AND DISCUSSION

Computed tidal currents were well within the range of magnitude determined by field measurements. The circulation model reproduced the expected ebb-jet during ebb stage, as well as the expanding turbulent wake. Through the longer term model runs wave driven currents were predicted on the upper-shoreface cells to the north and south of the inlet entrance, whereas tidal currents controlled sand transport within the inlet entrance. Predictions from the wave model reproduced complex wave refraction

and breaking over the ebb shoal and bypass that influence local sand transport directionality. During extratropical storms wave driven circulation patterns induced northward sand transport on the south side of the inlet between the south jetty and the attachment bar.

The largest computed net topographic changes were related to the hydrodynamic regime within the inlet/bay system. Channel bank erosion occurred, as well as scour at the seaward end of the offset jetties corresponding to areas of maximum current velocities during ebb and flood stages. Transient and permanent sand deposition was predicted within the inlet throat section and ebb shoal complex. The presence or absence of rock within the inlet throat and in the surfzone on the south side of the inlet resulted in distinctive differences in topographic changes to the ebb shoal over a year of real time simulation. When model cells were tagged as non-erodible through main inlet conveyance channel, bank erosion increased as the inlet adjusted to a larger equilibrium cross-sectional area. Episodic scour and deposition patterns across the shoreface were associated with storm conditions frequency and intensity and reversal in longshore transport.

Comparisons between sand transport equations showed some variation among the formulations but net topographic changes predicted from the formulations were well within an order of magnitude. However, the AD formula was the only one to reproduce bypassing and sand accumulation on the attachment bar. Under the Advection-Diffusion formulation, more complex sedimentation patterns were predicted. Less deposition occurred in the channel, which may be due to increased quantity of sediment in suspension in the channel.

Comparisons between predicted and measured topographic changes on an annual basis qualitatively agreed in terms of morphological evolution pattern. Agreement in absolute terms improved as the model spatial resolution was refined by decreasing cell sizes. Figure 13 is a comparison between predicted and modeled topographic changes at the entranced of Sebastian Inlet between March and September of 1997. The model predicted erosion and deposition patterns observed over the ebb shoal and bypass bar area and erosion along the south jetty. However, predicted deposition in a topographically low area off the end of the north jetty was not present in the survey data. Some of this difference could be due to inadequate representation of the north jetty and may require better resolution and further tuning of sand transport calculations. In addition, the sand transport module considered uniform grain sizes over the entire inlet. Material is usually coarser in areas of intense hydrodynamics, such as around the jetty fillets and on the ebb shoal. A more recent version of the M2D model now allows a variable grain size to be specified over the model grid.

CONCLUSIONS

Numerical simulations of coupled circulation, wave and sediment transport models were applied to Sebastian Inlet to calculate the morphology change and determine the influence of limestone rock outcrops on inlet dynamics. Evolution of morphology at Sebastian Inlet was found to be associated with the ebb-jet and wave-induced transport. General patterns of ebb shoal growth, sand bypassing, and scour of the

channel banks and around the jetties were reproduced by the CMS-M2D. The hard-bottom feature of the M2D model was effective in reducing the sediment transport in the channel and on the shoreface to the south of the inlet where natural rock reef outcrops occur. The inclusion of hardbottom cells though the main inlet channel induced erosion of the channel banks as the inlet adjusted to a larger equilibrium cross-sectional area. Adjustments to the ebb shoal topography in the model simulations was controlled by interactions between tidal and wave forces. Specifying non-erodible cells along model inlet channel produced deposition over the seaward portions of the ebb shoal most likely as a result of decreased sediment impoundment and increased regions of channel margin areas. Known patterns of topographic change on the shoreface were reproduced by the model cases, with erosion on the outer part and deposition on the inner part of the bypass bar. Predicted and measured topographic changes at Sebastian Inlet qualitatively agree. Further tuning and refinement of sand transport calculations are required to improve the match between model and real topography.

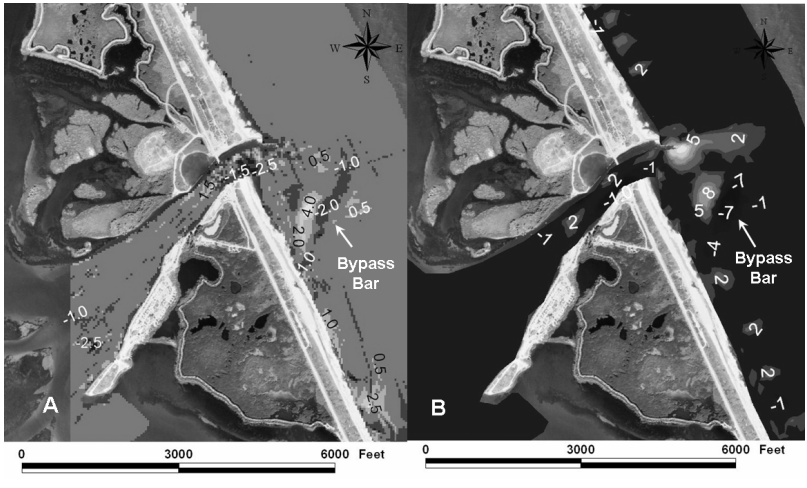

Figure 12. Comparison between predicted (A) modeled (B) topographic changes between March and September of 1997. Values of topographic change are in feet.

ACKNOWLEDGEMENTS

The U. S. Army Corps of Engineers (USACE) Coastal Inlets Research Program (CIRP) provided support for this research. The Sebastian Inlet Tax District kindly provided survey data and hind cast directional wave data. The St. Johns River Water Management District provided water level time series used to drive model

REFERENCES

Buttolph, A. M., Reed, C. W., Kraus, N. C., Ono, N., Larson, M., Camenen, B., Hanson, H., Wamsley, T., and Zundel, A. K. (2006). "Two-Dimensional Depth-Averaged Circulation Model CMS-M2D: Version 3.0, Report 2, Sediment Transport and Morphology Change," ERDC/CHL TR-06-09, U.S. Army Engineer Research and Development Center, Vicksburg, MS.

Dombrowski, M. R., 1993, "Inlet and Management Practices: Southeast Coast of Florida", Journal of Coastal Research Special Issue n. 18, pp. 29-57.

Hanson, H. and Militello, A., 2005, "Representation of non-erodible (hard) bottom in two-dimensional morphology change models", Coastal and Hydraulic Engineering Technical Note ERDC/CHL CHETN-IV-63, U.S. Army Engineer Research and Development Center, Vicksburg, MS.

Hoeke, R.K., 2001. Decadal time scale where morphodynamics determined from remotely sensed shoreline positions. *Master's Theses, Division of Marine and Environmental Systems, Florida Tech,* Melbourne, FL.Lin, L., Kraus, N. C., and Barcak, R. G., 2003. "Modeling Coastal Sediment Transport at the Mouth of the Colorado River, Texas", Estuarine and Coastal Modeling, 8th International Conference on Estuarine and Coastal Modeling Malcolm L. Spaulding - Editor, Nvember 3–5, 2003, Monterey, California, USA.

Militello, A., C.W. Reed, A.K. Zundel, and N.C. Kraus. 2004. Two-Dimensional Depth-Averaged Circulation Model M2D: Version 2.0, Report 1: Technical Documentation and User's Guide, ERDC/CHL TR-04-02, Vicksburg, MS: U.S. Army Engineer Waterways Experiment Station.

Smith, J. M., A.R. Sherlock, D.T. Resio. 2001. STWAVE: Steady-State Spectral Wave Model User's Manual for STWAVE, Version 3.0. TR-01-1 Vicksburg, MS: U.S. Army Engineer Waterways Experiment Station. Zarillo, G. A., Kraus, N. C., and Hoeke, R. K., 2003, "Morphologic Analysis of Sebastian Inlet, Florida: Enhancements to the Tidal Inlet Reservoir Model", Proceedings Coastal Sediments '03.

Zundel, A. K., 2000, "Surface water modeling system reference manual", Brigham Young University, Environmental Modeling Research Laboratory, Provo, UT.

EROSION AND CHANNEL MIGRATION AT THE SHOALWATER BAY RESERVATION, WILLAPA BAY, WASHINGTON

Andrew Morang, David J. Mark, and Jane M. Smith

U.S. Army Engineer Research and Development Center, Coastal and Hydraulics Laboratory, 3909 Halls Ferry Road, Vicksburg, MS 39180-6199, USA
Andrew.Morang@erdc.usace.army.mil
Jane.M.Smith@erdc.usace.army.mil
David.J.Mark@erdc.usace.army.mil

Abstract: Cape Shoalwater, at the north side of the mouth of Willapa Bay, Washington, has experienced some of the most severe erosion in the United States, exceeding 30 m per year during most of the 20th century. Morphological studies have documented that the rate of shore retreat near the Shoalwater Reservation has slowed to almost zero since the mid- to late-1980's. The reason is the presence of outcropping hard strata, a very dense, brown Pleistocene Terrace unit. This finding was unexpected because previous studies suggested that the shoreline would continue to retreat and that there were unlikely to be any practical engineering solutions to help stabilize the remnants of North Cove. Water diversion structures, such as dikes are impractical because they would need to be massive to have any effect in controlling the ebb- and flood-currents. Wave analysis verified that the waves causing local flooding in the reservation were generated in the fetch of the bay and that Pacific Ocean waves are effectively dampened as they pass over the Willapa ebb shoal.

INTRODUCTION

The Shoalwater Bay Indian Reservation is located on the northern side of Willapa Bay, on the Pacific coast of the state of Washington (Figure 1). Cape Shoalwater, at the north side of the mouth of the bay, has experienced some of the most severe erosion in the United States, exceeding 30 m per year during most of the 20th century (Komar 1998; Terich and Levenseller 1986) (Figure 2). The reservation, deeded in trust to the tribe by

President Andrew Johnson in 1866, formerly consisted of a land area and a protected bay where the tribe harvested shellfish. Because of the severe shore retreat, much of this bay has disappeared and the livelihoods of the tribe's members are threatened. In 2001, Congress directed Seattle District of the U.S. Army Corps of Engineers (NWS) to develop alternatives to arrest erosion and prevent storm and flood damage. NWS coordinated a study among the Coastal and Hydraulics Laboratory (CHL), Washington State Department of Ecology (WA DOE), and U.S. Geological Survey (USGS).

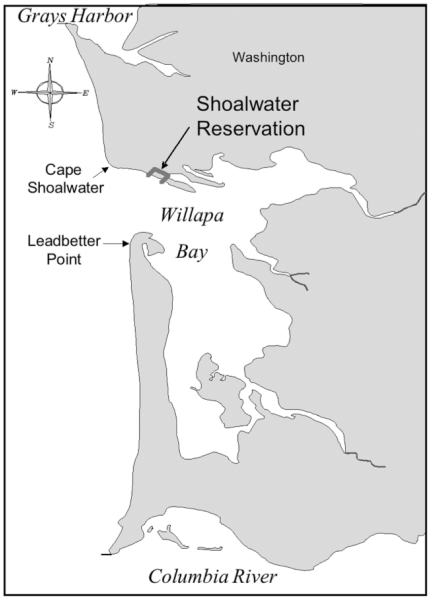

Figure 1. Study area, Willapa Bay, WA

In support of this study, from 2002 to 2004, a team of researchers from CHL conducted research on:

- Historical erosion, morphological changes and conditions, and potential future impacts
- Numerical model simulations of various hydraulic alternatives proposed by the USACE and the tribe
- Simulated flooding and storm overwash.

MORPHOLOGY AND HISTORICAL CHANGES

Bathymetric Data

The NWS has conducted hundreds of hydrographic surveys of portions of Willapa Bay in the last 150 years. Historical bathymetry data were imported into ESRI® ArcView™ v 3.2 software. Data were contoured and grids created with the Spatial Analyst module. Some of the data already existed in project files from the previous Willapa Bay project (Kraus 2000). Once the bathymetry was gridded, the thalwegs were visually traced (Figure 3).

The plot of all the thalwegs reveals some important details. In the east, the Willapa River has barely deviated from its channel over a century. South of the reservation bay, the Willapa River and the main bay channels join at a junction near cross-section line 7. The location of this junction has been surprisingly constant over time. Further west, the thalwegs showed a steady progression to the north, a rotation with the pivot point at the junction. Over 75 years, the thalweg changed from an east-west orientation to a southeast-northwest orientation. But, the rate of change decreased, and after 1996, the thalweg essentially stopped migrating.

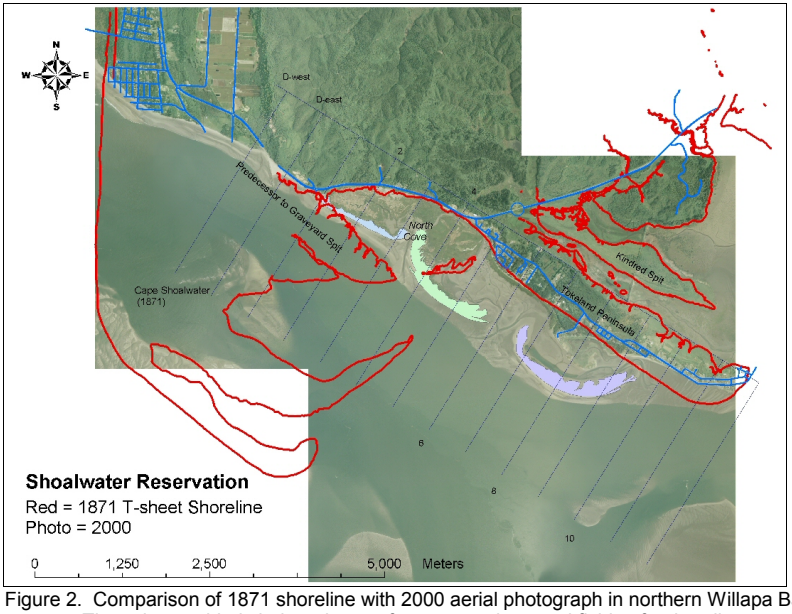

Figure 2. Comparison of 1871 shoreline with 2000 aerial photograph in northern Willapa Bay. The spits provided sheltered water for oyster culture and fishing for the tribe.

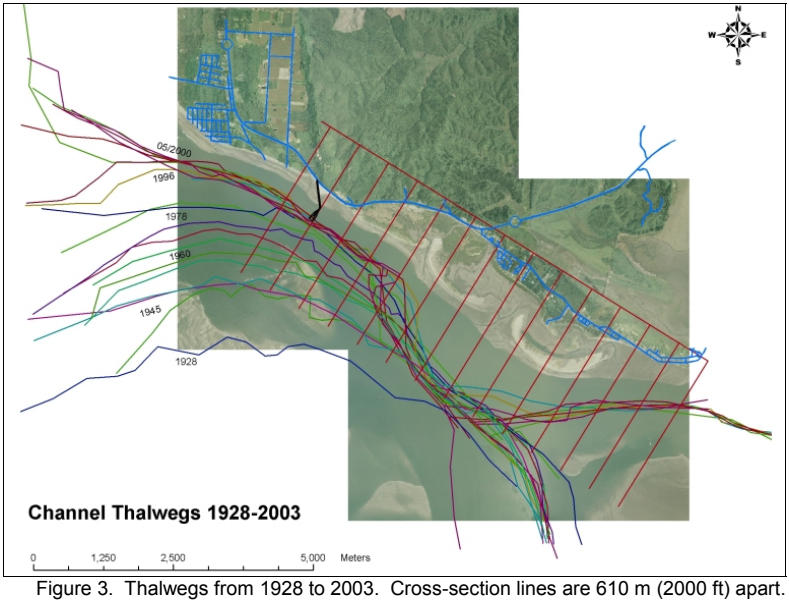

Figure 3. Thalwegs from 1928 to 2003. Cross-section lines are 610 m (2000 ft) apart. Background photo: Oct. 2000

Aerial photography and historical charts

Aerial photographs and U.S. Coast and geodetic Survey T-sheets were an invaluable source of information on changes at Graveyard Spit, the islands, the bay, and the nearby shorelines over the last 130 years. The 1942, 1945, and 1955 photographs came from the archives of the USACE's Beach Erosion Board (Morang 2003). NWS and the WA DOE provided more recent photographs as well as historical shorelines based on T-sheets. To convert the photographs into photomosaics, paper prints had to be scanned and processed in a multi step procedure, with CHL supplying many of the scanned files and WA DOE performing the mosaicing. CHL traced the shorelines and outlines of the spits and islands from the photomosaics by visually interpreting the wet-dry line. Figure 4 is a composite of the changes that have occurred to Graveyard spit and the sand islands.

To determine if the retreat rate has changed over the years, the position of the shoreline versus time were plotted. Plots for cross-section line 2 are shown as an example. Here, as at the other cross-section lines, the retreat of the shoreline and the thalweg paralleled each other (Figure 5). The cross-section curves show that the north flank of the channel was fixed for over a decade, while the south flank was irregular (Figure 6). The same phenomenon could be seen at other locations and was particularly noteworthy at cross-section line 4 (Figure 7).

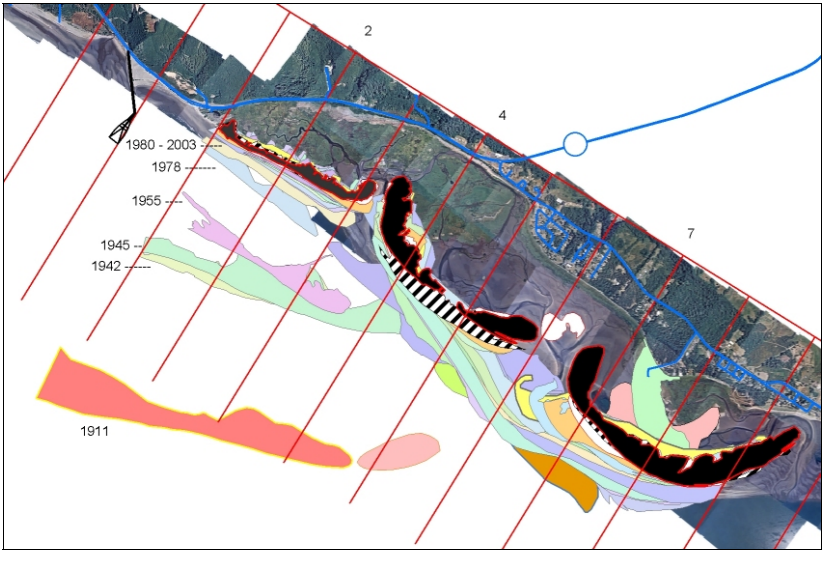

Figure 4. Plan view of Graveyard Spit and sand islands from 1911 to 2003. The spit moved much more rapidly during the first few decades of the 20th century. By 1980, the spit had stabilized in approximately the same position that it occupies today. Background photograph: July 2002. North is to the top

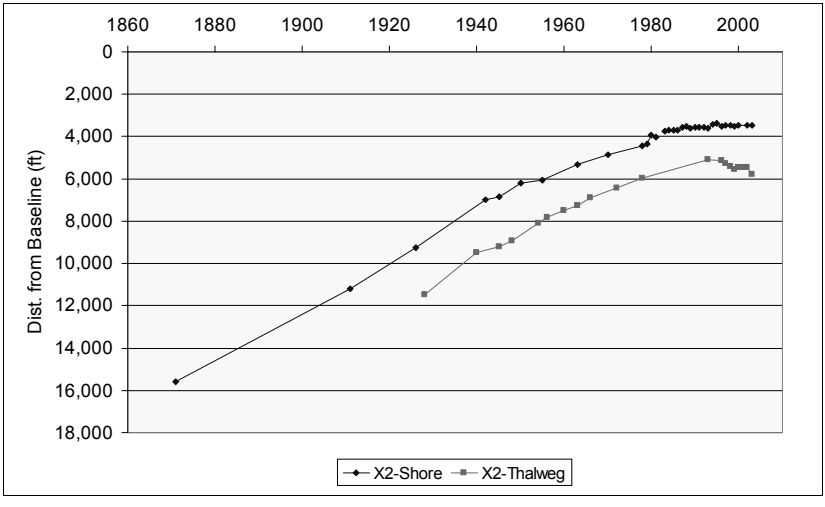

Figure 5. Cross-section line 2: shoreline and thalweg position. The shoreline stabilized in the early 1980's, while the thalweg moved away from shore (to the south) after 1996.

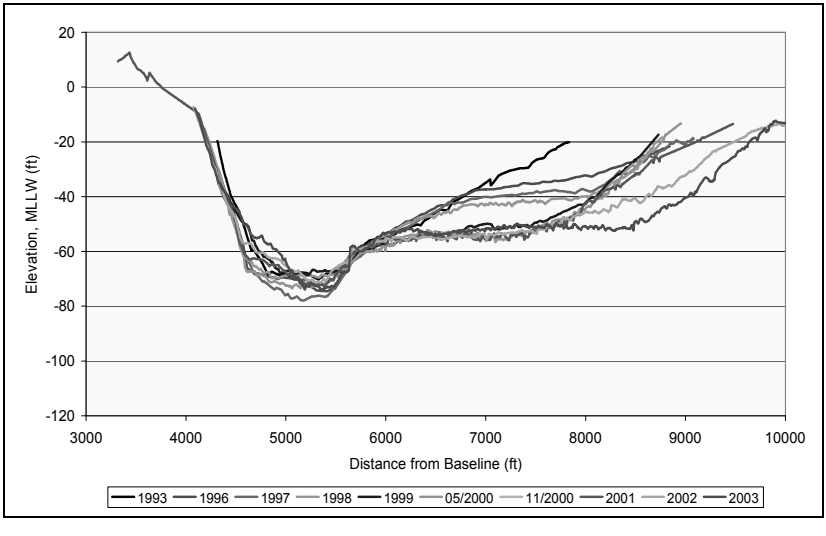

Figure 6. Cross-section line 2: channel sections. North is to the left. After 1993, the south flanks of the channel began to deepen, although the thalweg remained in approximately the same position. Note that the north flank remained fixed for a decade

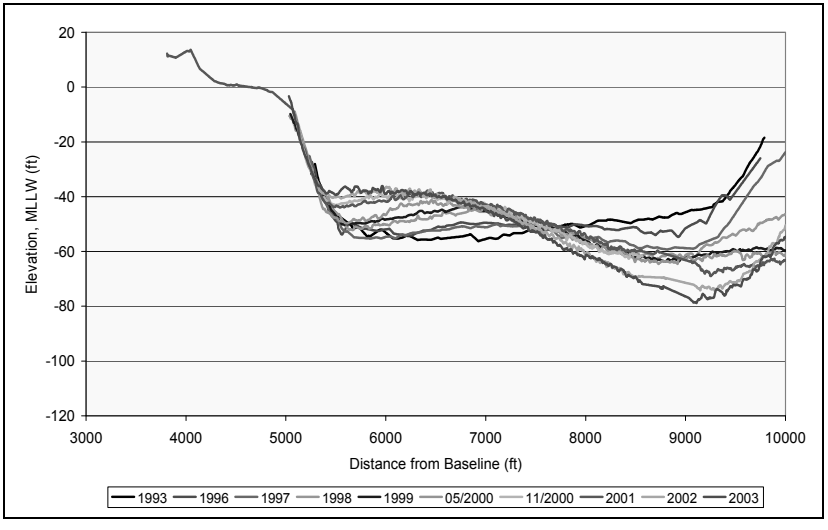

Figure 7. Cross-section line 4: channel sections. Since 1993, the north edge of the channel was fixed. Over time, the thalweg migrated south (to the right) as the area beyond 8,000 ft (2400 m) to the south deepened

Morphological findings

A number of trends emerged from the analyses which indicated that an engineering solution could be developed to protect the reservation from storm flooding and retard continued degradation of the remaining shellfish bay. As stated earlier, the thalweg stopped migrating northward after the mid-1990s. West of cross-line 2, the bottom became deeper as the thalwegs clustered along one path during the 1980s and 1990s. The channel was unable to continue moving northward, and as a result, the bottom became deeper as the flow was concentrated against the shore. From cross-lines 2 to 8, there is no evidence that the bottom is deepening near the spits or islands (i.e., the channel is not progressively moving north). This conclusion is verified by examining the cross-section curves.

Another finding was that the north sides of the channel had not migrated in over a decade and that the slope remained constant. This suggested that some form of harder strata was outcropping along the channel wall which was resistant to erosion. When the Washington State Department of transportation rerouted part of SR-105, they made a number of borings along the proposed highway route. At borings B-1-97, B-2-97, and B-3-97 (not shown in the above figures) they encountered a unit they identified as "very dense, brown Pleistocene Terrace" (Jackson, Allen, and Lowell 1997). We believe this unit extends under the Shoalwater bay and under the present spit and islands. Therefore, the remaining islands and spits are perched on a relatively stable base, although they are still vulnerable to overwash and loss of sand during flood events.

HYDRAULIC ALTERNATIVES

Members of the Shoalwater Bay Indian Tribe proposed investigating training structures, or dikes, as a possible remedy for controlling the extreme erosion along the North Cove shoreline. The purpose for these structures would be to deflect the high current away for the shore or to divert the flow in the North Channel such that it opens and maintains the Middle Channel to the open ocean. Seven locations for dikes were proposed, of which four were evaluated with the ADCIRC model, alternatives 1, 3, 4, and 6 (Figure 8). These four were selected because they are the closest to the tribal lands, thereby having the greatest potential to deflect the current away from the shore compared to the remaining alternatives.

The base or existing-condition grid was adapted for each alternative by adjusting the nodal positions and adding nodes so that each alternative is highly resolved in the grid. In all cases, the structure protrudes above the water surface and no water overtopping of the structure was permitted. Each alternative was tested under spring tide conditions, and no wind forcing was imposed in the simulation. Furthermore, the yearly mean river inflow was specified at the upstream boundary of the Willapa River. Peak spring ebb and flood currents were extracted from each simulation and analyzed as to their effectiveness.

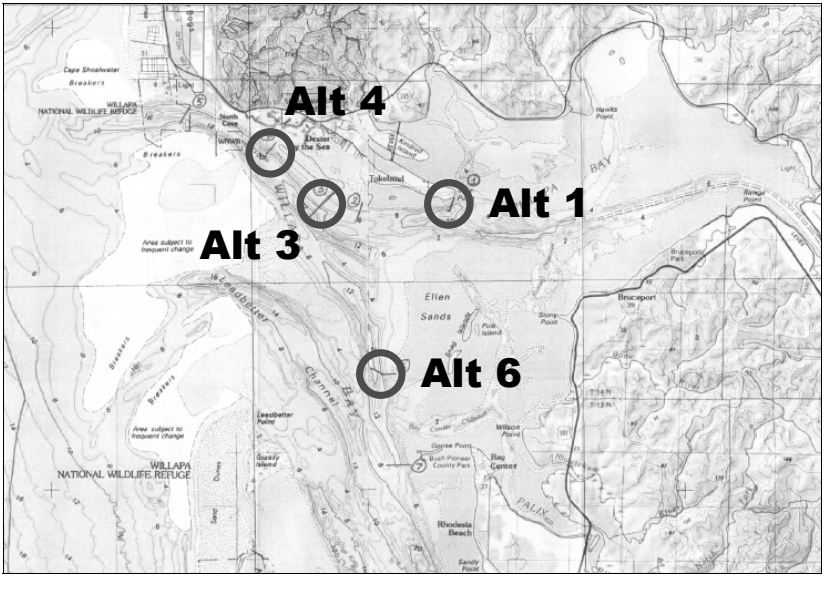

Figure 8. Proposed locations for training dikes

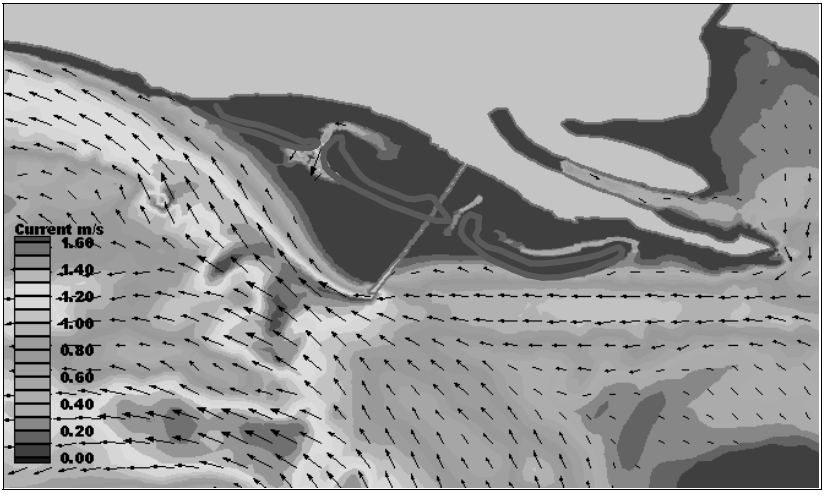

Figure 9. Peak spring ebb current with Alternative 3 in place

Alternative 3 extends directly across the North Cove and into the channel. The structure is 3,900 m long and extends 2,400 m into the channel. Peak spring ebb current in the vicinity of the North Cove for with-alternative condition is presented in Figure 9. The structure reduces the peak ebb current along the western extent of Empire Spit, and, to a lesser extent, at the eastern end of the spit. Current along the eastern end of the Spit is reduced during flood tide, whereas a small reduction in current is found to the west.

Two consequences of training structures is the creation of gyres, a circular or spiraling current, on the lee-side of the structure, and impediment of sediment transported along the shore. Although the gyres are weaker than the main current, the spiraling gyre will still suspend the sediment along the shore, and transport it into deeper water; with the structure preventing movement of sediment along the shore, the area being eroded by the gyre is not replenished, leading to a loss in land.

This investigation found that flow modifications caused by a training structure are localized, and if a structure is constructed, it must be in close proximity to the North Cove to have any impact on the current. Furthermore, the structure must be massive to divert or deflect the strong current away for the shoreline. For example, Alternative 3 measured 3,900 m in length, and extended into the channel to a depth of about 21 m. To have an appreciable impact on current, the remaining structures must block a significant portion of the channel in order to reduce the current speed along the shoreline. Each training structure reduces the conveyance of flow within the channel. As such, the current increases when it flows past the structure. As shown in the numerical experiments, the increase in current will induce the formation of a scour hole at the toe of

the structure. To prevent potential failure of the structure, regular maintenance will be required to prevent toe from sliding into the hole.

FLOODING AND STORM OVERWASH

The long-term erosion of the North Cove shoreline has been driven by the strong tidal currents that hug the shoreline, but waves also play a role in dune erosion during storms. The numerical model STWAVE (Smith et al. 2001) was used to transform waves into Willapa Bay for evaluation of alternatives. Smith and Ebersole (2000) measured and modeled waves in Willapa Bay and concluded:

- The incident wave climate at Willapa Bay is severe, with storm wave heights exceeding 7 m (as measured by the Grays Harbor Buoy, Station 03601).
- The shoals extending north from Leadbetter Point substantially attenuate incident waves. The tide level modulates waves within the bay, with more wave energy penetrating the bay at high water levels and less at low water levels.
- Field measurements validated the wave transformation model STWAVE for wave transformation and attenuation across the shoals and into the bay.
- The STWAVE model demonstrated that wave-current interaction is significant in the outer Willapa entrance channel where currents can exceed 2 m/sec, but is relatively insignificant in the interior channels.

Figure 10 shows incident offshore waves from the Grays Harbor Buoy and the nearshore Cape Shoalwater wave and water level measurements for the period 6-31 December 2002. Note the event with incident waves exceeding 5 m during 13-16 Dec (Julian days 347 through 350). These data illustrate that waves within Willapa Bay are strongly attenuated across the shoals and are modulated by the tide elevation. The relationship between water level and interior bay wave height is almost linear (see Figure 11; simulation results for 1-5 March 1999 storm). During storm events with elevated water levels, more wave energy penetrates into Willapa Bay. The elevated water levels allow waves to attack higher elevations on the dunes and shorelines.

The channel migration and shoreline retreat rates within Willapa Bay have slowed over recent years, but degradation of the barrier dunes protecting the Reservation shoreline indicate continued damage to the dunes and flooding of tribal land during storms with elevated water levels. To investigate protection from wave attack provided by the dunes, STWAVE was used to compare waves at the shoreline with and without the barrier dunes in place.

A grid of the dune and shoreline area was developed with a resolution of 30 m. This grid nested into the larger Willapa Bay grid and focuses on the North Cove area. Two versions of the grid were developed: one with the dunes as they exist based on 2002 bathymetry, and one with the barrier dune elevations above mean high water removed (Figure 12). The existing condition is referred to as the 'with-dune' case and the altered bathymetry as the 'without-dune' case. The offshore boundary conditions for the nested

grid runs are taken directly from the larger-scale STWAVE simulations, including local generation in southern Willapa Bay.

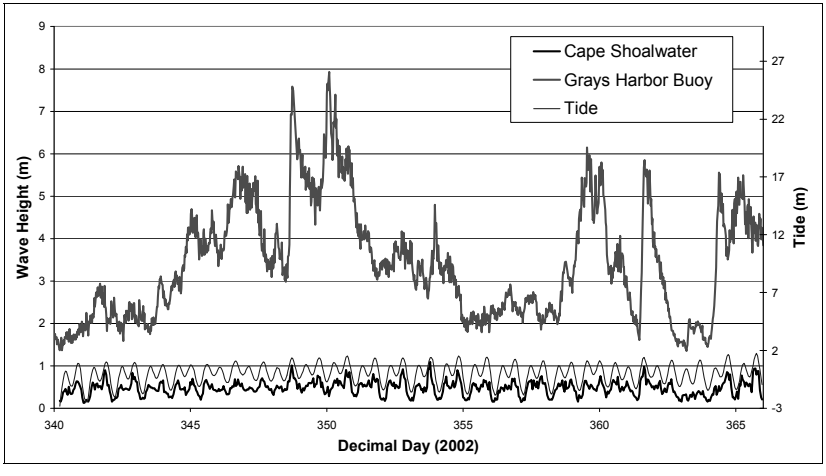

Figure 10. Measured waves and water levels (December 2002)

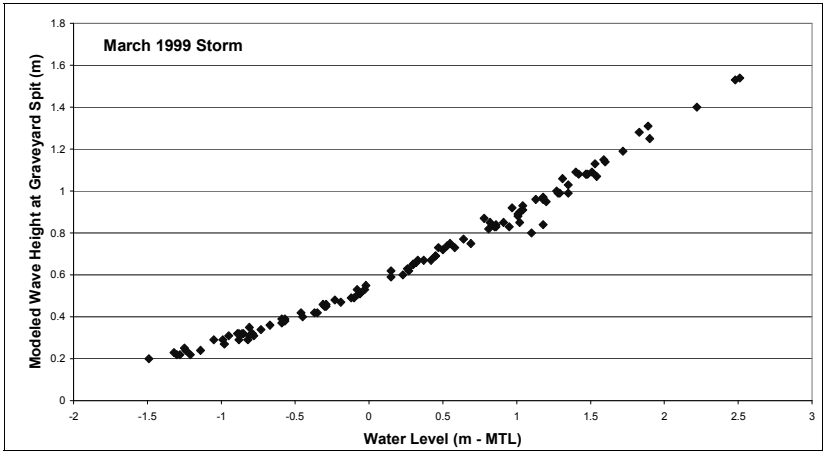

Figure 11. Relationship of modeled wave heights and water levels at Station 1 for March 1999 storm

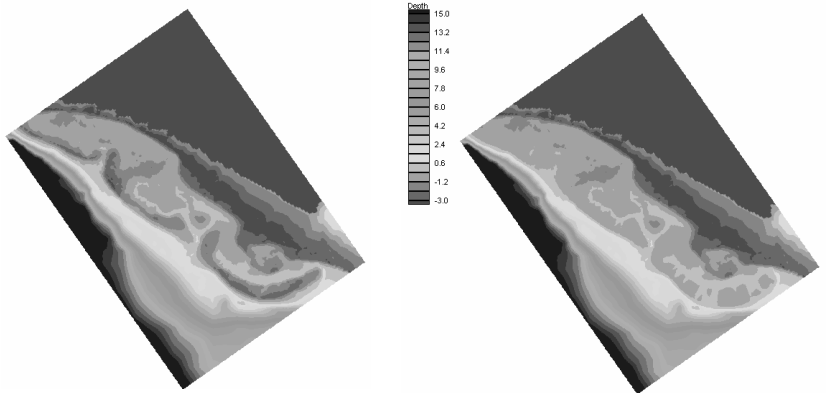

Figure 12. Bathymetry grids for nested grid simulations with and without dunes (with dunes on left and without dunes on right, depths in meters)

The March 1999 storm (the storm of record) was selected to simulate the with- and without-dune cases. The results are shown in a series of figures. Figures 13 and 14 show a snap shot of the wave heights for the with- and without-dune cases, respectively, for 3 March at 0900. The warmer colors (orange to green) indicate larger wave heights and the blues indicate lower heights. These plots are representative of the storm. The orange regions represent where waves shoal and break as they propagate up the slope to the dune. In the with-dune case (Figure 13), waves continue to break up to the crest of the dune. Wave energy also passes through some gaps in the dune line. In the without-dune case (Figure 14), waves exceeding 1 m in height pass over the lowered dunes and strike the shoreline. Eight station locations are indicated in Figures 13 and 14, with Sta 1 being the furthest to the northwest and Sta 8 to the southeast. Figure 15 shows the wave height for the 8 alongshore stations at the peak of the March 1999 storm (same hour as Figures 13 and 14) for the with- and without-dune simulations. The wave height is significantly reduced at the shoreline for the with-dune case for all stations except Sta 6, which is behind a gap in the dune line. Wave heights for these 8 stations are plotted in Figure 16 for the duration of the March 1999 storm. The filled symbols indicate simulations with the dunes and open symbols indicate without the dunes. Wave height is plotted as a function of water level (similar to Figure 11, which showed waves seaward of the dunes). The figure shows quantitatively, the protection provided by the dunes. With the dunes in place (existing condition), wave heights at the shoreline are generally less than 0.6 m, but without the dunes, wave heights are approximately twice as large. In summary, the existing dunes provide significant protection to the shoreline. Loss of the dunes would increase wave heights at the shoreline (increases storm damage) and increase overwash into North Cove.

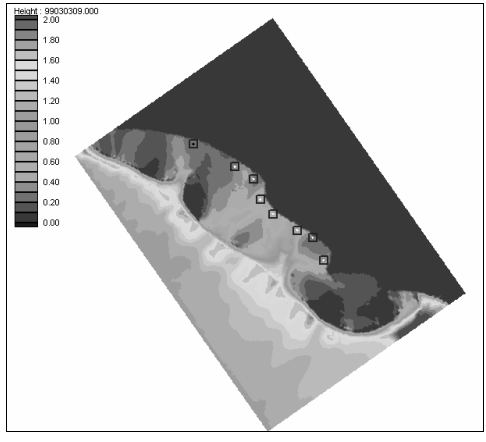

Figure 13. Contour plot of wave height with dunes for 3 March 1999 at 0900 (wave height in meters)

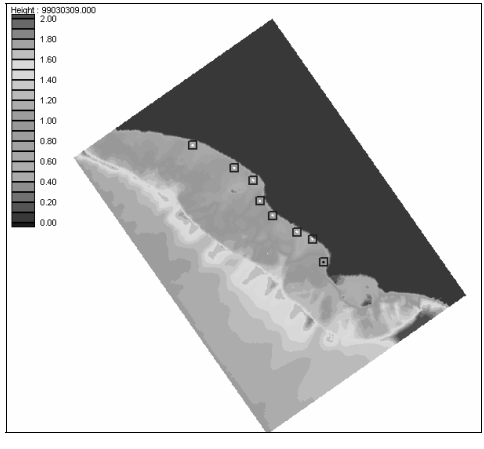

Figure 14. Contour plot of wave height without dunes for 3 March 1999 at 0900 (wave height in meters)

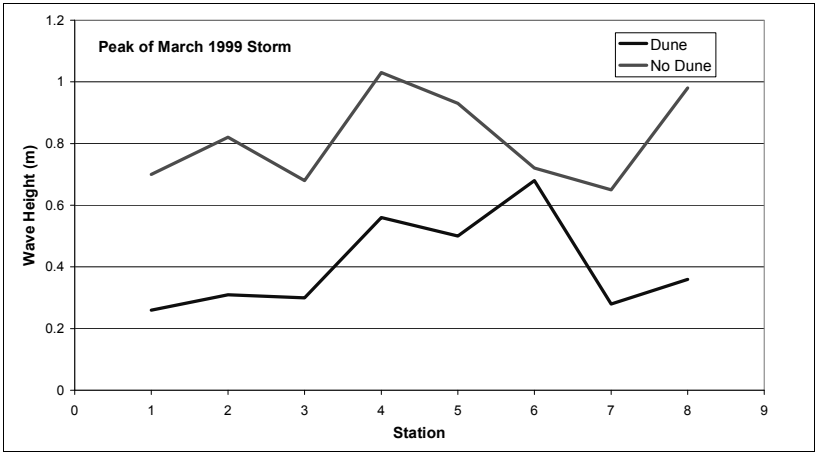

Figure 15. North Cove alongshore distribution of wave heights with (lower curve) and without dunes (upper curve), 3 March 1999 at 0900.

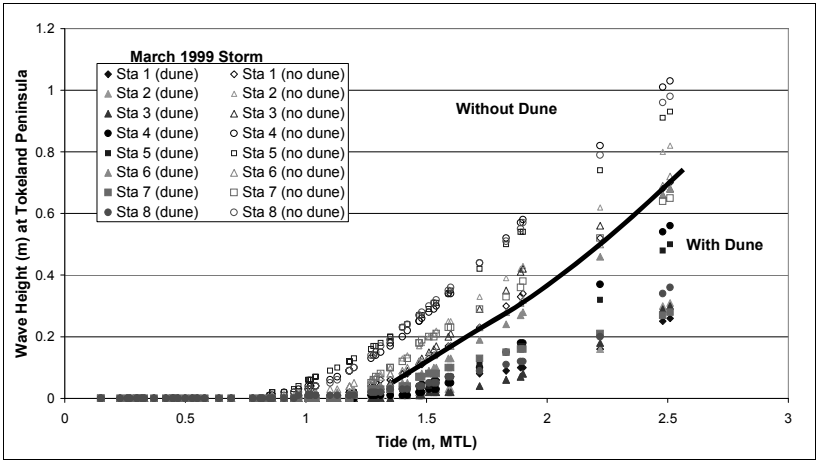

Figure 16. North Cove wave heights with and without dunes for March 1999.

Waves are attenuated across the shoals at the mouth of Willapa Bay, and water level over the shoals is the critical limiting parameter. Offshore-generated waves reaching North Cove are generally in the range of 0.3 to 1.0 m. During storms, water levels are elevated across the shoals and the larger wave heights occur. Also during storms, local winds from the south generate waves in southern Willapa Bay. The total wave heights (offshore plus local generation) at the project site are potentially in the range of 1.5 to 2.0 m. The wave heights simulated for the March 1999 storm peaked at 1.6 m along the

spit. Even as the overall shoreline erosion rate is reduced by reduction in the Willapa channel migration, waves will continue to act on the barrier spit during storm events (surge and southerly winds). This will result in continued flooding, overwash, and loss of dune elevation. Model results showed that the existing dunes provide significant protection to the shoreline, and further loss of dune elevation will exacerbate flooding and storm damage.

CONCLUSIONS

Although Cape Shoalwater was notorious during most of the 20th century for its rapid erosion, the north shoreline inshore (east) of the ebb shoal appears to have largely stopped migrating north. The analysis of historical bathymetry and aerial photographs demonstrates that retreat rates of the thalweg and the shoreline along north Willapa Bay were almost identical during the 20th century. We believe that the thalweg's movement has largely driven or been the forcing factor for the shoreline retreat. Since the mid-1980's, slope of the north bank of the main channel has been constant and has remained in a fixed position. The reason is that the channel encountered hard strata that are resistant to erosion, probably the very dense, brown Pleistocene terrace unit recovered in borings made by the Washington State Dep. of Transportation (Jackson, Allen, and Lowell 1997).

As the thalweg rotated to the north and northeast, the spits and islands that formerly protected the bay also moved north. After 1985, Graveyard Spit stabilized, but the islands to east continued to retreat due to loss of sand supply. Since the mid-1990s, the islands also semi-stabilized in position but become narrower and lower as a result of storm overwash.

The apparent end of gross shoreline retreat and the stabilization off the channel's north flank was an unexpected finding of this study. It meant that a relatively simple construction project could provide protection for the reservation without being washed away within a few months or years. The project will include dune restoration on islands using dredged material. The dunes will need 460,000 m^3 on 10-year maintenance interval. Along the Tokeland shoreline, a low rock flood berm will be extended to an elevation of +5.1 m MLLW. Construction of the flood berm is scheduled for mid-2007 to mid-2008, and dune restoration for 2009 to 2010. Work is dependent on continued Congressional funding, and there is no local cost-sharing at this project beyond provision of lands, easements and rights-of-way by the Shoalwater Bay Indian Tribe.

In Willapa Bay, flow diversion structures were eliminated from further consideration because they did not appear to be either cost effective or environmentally acceptable, or verifiable as to the beneficial effect in reducing the flood and coastal storm damage threat to the Reservation. Because of the volume of tidal flow from Willapa Bay, only massive dikes or jetties on the scale of Dutch control structures would have any hope of modifying the ebb or flood flow. The cost would be vastly greater than would ever be allocated for this setting, which is no longer used for deep-draft navigation.

ACKNOWLEDGEMENTS

We appreciate the cooperation of the Shoalwater Tribe and various collaborators in this rewarding study. We thank Steven Babcock, Eric Nelson, Larry Scudder, and Joyce Rolstad (NWS) and George Kaminsky and Dinah McCandless (WA DOE) for support and for providing valuable historical data from their agencies' archives. Yen-hsi Chu and Edward Hands (both now retired) and Gary Ray (ERDC Environmental Laboratory) participated in the CHL project team. Steven Babcock reviewed this paper. Permission was granted by Headquarters, U.S. Army Corps of Engineers to publish this information.

REFERENCES

Jackson, D., Allen, T.M., and Lowell, S. M. 1997. SR-105: Geological Study of the North Channel of Willapa Bay – Vicinity of north Cove, Washington. Geotechnical Report, Willapa Bay Channel Restoration Project, C.S. 2532, OL- 2431, Washington State Department of Transportation, Olympia, WA.

Komar, P.D. 1998. The Pacific Northwest Coast: Living with the Shores of Oregon and Washington. Duke University Press, Durham, NC.

Kraus, N.C. (Editor). 2000. Study of Navigation Channel Feasibility, Willapa Bay, Washington. Technical Report ERDC/CHL TR-00-6, Engineer Research and Development Center, Vicksburg, MS.

Morang, A. 2003. Photographic Archives of the Beach Erosion Board. *Shore and Beach,* Vol. 71, No. 4, pp. 17-21.

Smith, J. M., and Ebersole, B. A. 2000. Modeling and Analysis of Short Waves. Chapter 5 in Study of Navigation Channel Feasibility, Willapa Bay, Washington. Technical Report ERDC/CHL-00-6, N. C. Kraus (ed.), U.S. Army Engineer Research and Development Center, Vicksburg, MS, 23 p.

Smith, J.M., Sherlock, A.R. and Resio, D.T. 2001. STWAVE: Steady-state Spectral Wave Model; User's Manual for STWAVE V 3.0. Technical Report SR-01-1, US Army Engineer Research and Development Center, Vicksburg, MS.

Terich, T., and Levenseller, T. 1986. The Severe Erosion of Cape Shoalwater, Washington. *Journal of Coastal Research,* Vol. 2, No. 4, pp. 465-477.

SEDIMENT MANAGEMENT PLAN DEVELOPMENT FOR THE ST. LUCIE INLET, MARTIN COUNTY, FLORIDA

John Ramsey[1], Trey Ruthven[2], Kevin Kremkau[3], Kathy Fitzpatrick[4]

1. Applied Coastal Research and Engineering, Inc., 766 Falmouth Road, Suite A1, Mashpee, MA 02649, USA. jramsey@appliedcoastal.com.
2. Applied Coastal Research and Engineering, Inc., 766 Falmouth Road, Suite A1, Mashpee, MA 02649, USA. truthven@appliedcoastal.com.
3. Gahagan & Bryant Associates, Inc., 3802 West Bay to Bay Boulevard, Suite B22, Tampa, FL 33629, USA. kmkremkau@gba-inc.com.
4. Martin County, 2401 SE Monterey Road, Stuart, FL 34996, USA. kfitpat@martin.fl.us.

Abstract: A comprehensive approach was used to evaluate recent changes to the St Lucie Inlet system and was used as the basis for the evaluating future sand transfer and shoreline stabilization projects associated with the region. The analysis relied extensively upon hydraulic, bathymetric, and coastal monitoring conducted over multiple years and dredging cycles to evaluate impacts upon the hydraulics of the St. Lucie Inlet and Estuary. The monitoring data was used to assess the effects of the impoundment basin dredging on tidal prism/circulation patterns, navigation, and shoaling patterns/sediment transport pathways. Analysis of coastal processes through the development of numerical modeling tools in the vicinity of the inlet provided baseline information for management decisions.

INTRODUCTION

St. Lucie Inlet is located along the east coast of Florida in Martin County and links the Atlantic Ocean with the Indian River Lagoon. To the north side of the inlet lies Hutchinson Island, with the residential development of Sailfish Point being located adjacent to the inlet. Jupiter Island is located south of the inlet, where approximately the northern six miles of the island are undeveloped State and Federal property. The estuarine system landward of the Jupiter-Hutchinson Islands barrier complex consists of the Indian River to the north, St. Lucie River to the west, and Great Pocket to the south. The Intracoastal Waterway (ICWW) runs parallel to the barrier beach system along the

landward side. Regionally, the ICWW provides a direct connection between St. Lucie Inlet and nearby inlet/estuarine systems: Ft. Pierce Inlet to the north and Jupiter Inlet/Loxahatchee River to the south.

Similar to many tidal inlets along Florida's east coast, St. Lucie Inlet requires periodic maintenance dredging to ensure navigation safety. To address concerns related to inlet management, Applied Technology and Management, Inc. (ATM) was hired by the Florida Department of Environmental Protection and Martin County to assess inlet sand resource management, as well as safe navigation. The inlet management plan (ATM, 1995) provided the first comprehensive assessment of the relationship between the coastal engineering structures stabilizing the inlet and sediment management. In addition, the management plan recommended the following elements:

- Continued maintenance of the navigation channels, with dredge material placed on Jupiter Island beaches at least 14,000 feet south of the inlet
- Use of beach compatible material from interior shoals for nourishment programs within the Town of Jupiter Island
- Raising a 350 ft section of the north jetty, sand tightening a 250 ft portion at the west end of the north jetty to limit the weir section to 450 ft, and potentially expanding the impoundment basin
- Assess the feasibility of extending the south jetty by 400 ft

The St. Lucie Inlet Technical Advisory Committee (TAC) was initiated in 1996 to provide a link between the various stakeholders and the U.S. Army Corps of Engineers (USACE). The USACE is responsible for maintaining St. Lucie Inlet for navigation purposes. The local sponsor, Martin County, organized the TAC to ensure that various interests affected by inlet management practices were addressed through the USACE planning process. In addition, the TAC provided a mechanism for developing a 'locally preferred plan' that contained additional design elements that could not be funded as part of the Federal navigation project.

Since the development of the 1995 inlet management plan, a series of management strategies have been implemented to reduce maintenance dredging frequency and improve sediment bypassing at the inlet. In addition, the St. Lucie Inlet Design Memorandum (USACE, 2000) recommended a number of inlet improvements that have not been constructed at this time. The Design Memorandum was developed in close coordination with the TAC; therefore, primary concerns of the various stakeholders were reviewed as part of the USACE design process.

As originally proposed, the inlet management plan was designed to be a 'living document' that would require periodic updates. Since this plan was written, the USACE and Martin County have funded and constructed some of the elements described in the plan; however, new information developed by the Corps led to some changes from the Inlet Management Plan. Specifically, The USACE St. Lucie Inlet Design Memorandum addressed several of the elements described in the inlet management plan; however, the

planned placement location for bypassed sediment was altered to reduce potential maintenance costs. The locally preferred alternative includes beach placement of sand dredged from the impoundment basin at least 9,800 feet south of the south jetty along Jupiter Island.

Based on recommendations included in the St. Lucie Inlet Design Memorandum, the impoundment basin was enlarged in 2002-2003. Creation of the larger impoundment basin initially caused modifications to the sediment transport pathways, as tidal currents were influenced by the modified inlet cross-section. These alterations, combined with implementation of different sand management practices within the vicinity of the inlet, required an updated analysis of regional sediment transport processes.

ANALYSIS APPROACH

To update the analysis of the regional sediment transport and the management of sediment, a comprehensive inlet monitoring, numerical modeling, and analysis program was developed. Further data was required to supplement information developed during these previous efforts. Updated inlet surveys, beach profiles, aerial photography, tidal elevation information, and inlet tidal currents studies were performed to evaluate recent changes to sediment transport patterns resulting from the inlet improvements.

This comprehensive approach was used to evaluate recent changes to the inlet system, however it can be used as the basis for the evaluating future sand transfer and shoreline stabilization projects associated with St. Lucie Inlet. The program included components needed to characterize the immediate changes as well as facilitate future planning including:

- identification of shoreline and volumetric changes;
- refining the inlet sediment budget;
- identifying any hydraulic effects of flood shoal dredging and future inlet improvements;
- evaluating the benefits of sand transfer;
- providing advance planning for maintenance of navigation within the inlet by identification of channel depths and the sedimentation rate within the channel; and,
- providing a basis for design of future sand transfer and shoreline stabilization projects.

BATHYMETRIC CHANGE WITHIN ST. LUCIE INLET

Surveys of the inlet were conducted to provide the data necessary to identify shoaling and scouring within the inlet. In this manner, the surveys could be used for advanced planning for maintenance dredging and sand transfer and to update the sediment budget. Annual bank-to-bank hydrographic and topographic surveys were completed to accurately document the bathymetric change within the inlet prior to and following the impoundment basin construction, as well as throughout the subsequent years as the inlet adjusted to its new equilibrium state. Accurate observations of the actual bathymetric

change were necessary to properly parameterize the sediment transport model, to assist in determination of sediment transport pathways, and to evaluate maintenance dredging needs.

Bathymetric change within the inlet throat was computed for the time periods of June 2002 – March 2003 and March 2003 – June 2004. Three regions were selected based on observations of bathymetric change in the inlet, as well as the sediment transport modeling (Applied Coastal 2006). Specifically, the demarcation between Area I and Area II represents the separation between the sediment entering the inlet over/through the north jetty (Area I) and sediment derived from the beaches and or ebb shoal deposits to the south of the navigation channel (Area II). Area III represents the seaward portion of the flood shoal. The limits of the bathymetric change areas are shown in Figure 1.

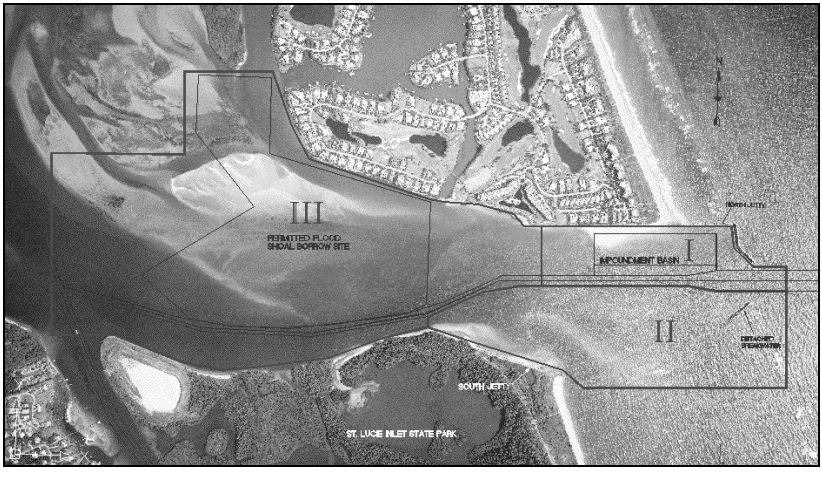

Figure 1. Bathymetric change areas.

A summary of the observed bathymetric change following the impoundment basin improvements is shown in Table 1. Significant accretion is observed for both Areas I and II, and much of this accretion is offset by erosion in Area III. During the latter half of 2003, the inlet was adjusting to its new equilibrium form, where the cross-section of the inlet throat increased significantly as a result of the navigation channel and impoundment basin dredging. Initially, larger flood and ebb tidal currents across the flood shoal caused sediment to migrate both east and west off the shoal. As a first approximation, 50% of the approximately 142,000 cubic yards could be expected to migrate to the east (into Areas I and II) and the remaining material migrated west and north toward the St. Lucie and Indian River Lagoon, respectively. Both the observed bathymetric change and the sediment modeling indicate that the dredged channel is self-scouring and likely prevents significant accumulation of material derived from the flood shoal. Conversely, the more efficient inlet has slightly lowered current velocities across the southern half of the inlet

throat, allowing settling of flood shoal derived material in this region. Figure 2 shows the significant region of accretion associated with Area II. If it is assumed that material eroded from Area III is split 25% to Area I and 75% to Area II, the sediment derived from other sources would be approximately 113,000 cubic yards and 52,000 cubic yards for Areas I and Areas II, respectively. This result indicates that shoaling from the south does not account for more than about 30% of the shoaling within St. Lucie Inlet.

Table 1. Analysis of Bathymetric Change within St. Lucie Inlet for the period March 2003 - June 2004.

Area I	**Volume (cy)**
Erosion	75,202
Accretion	205,622
Net Difference	130,420
Area II	**Volume (cy)**
Erosion	103,052
Accretion	208,597
Net Difference	105,545
Area III	**Volume (cy)**
Erosion	336,254
Accretion	169,126
Net Difference	-167,128
Corrections for Dredging	
Sailfish Point Maintenance (cy)	25,429
Adjusted Net Difference	-141,699
Total Erosion (cy)	514,508
Total Accretion (cy)	583,345
Total Net Change (cy)	68,837
Adjusted Net Change (cy)	**94,266**

COASTAL PROCESSES ANALYSIS

Analysis of coastal processes in the vicinity of the inlet provided baseline information for future management decisions. Specifically, sediment management within the inlet throat has been a chronic problem for navigation safety and has led to extensive shoreline retreat south of the inlet. The proposed improvements to the inlet are designed to reduce maintenance dredging frequency and to encourage placement of dredged material south (downdrift) of the inlet's "zone of influence". To support inlet management strategies, the following quantitative analysis techniques were performed:

- collection of tide and current information as necessary to alterations to inlet circulation resulting from inlet modifications;

- revise and update existing hydrodynamic and sediment transport models for the inlet (utilizing tide and current information previously collected, as well as updated information developed during this project); and,
- update the inlet sediment budget by utilizing bathymetry data, regional shoreline change information, and developing a wave and wave-induced sediment transport model for the coastal region surrounding St. Lucie Inlet.

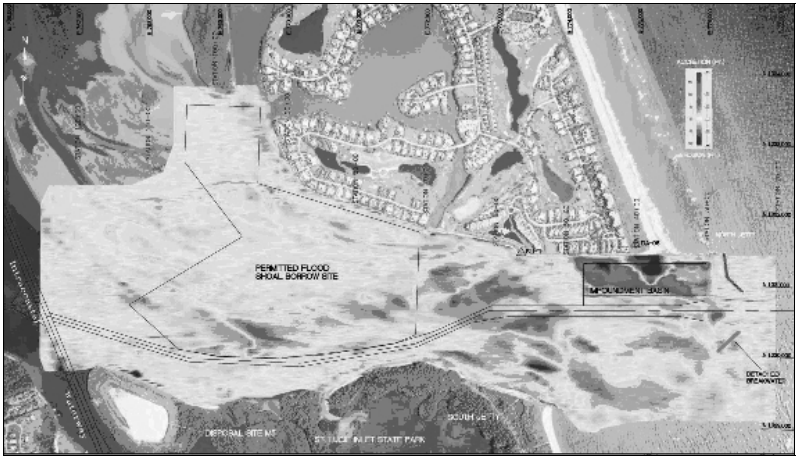

Figure 2. Observed bathymetric change between March 2003 and June 2004. Red areas define regions of accretion and blue areas define regions of erosion.

Modifications to the St. Lucie Inlet jetties and impoundment basin modified both tidal circulation patterns and sediment transport dynamics within the inlet throat. A two-dimensional hydrodynamic and sediment transport model was developed to evaluate the proposed inlet modifications and to provide a predictive tool for determining impacts of future flood shoal dredging events on tidal circulation and/or sediment transport. The sediment transport model was calibrated with available bathymetric change information.

To assess sediment movement within the inlet, it was critical that the volume of material entering the inlet from both Jupiter and Hutchinson Islands is accurately determined. Regional spectral refraction wave modeling and historic shoreline change data were incorporated into the updated calculation of the inlet sediment budget (Applied Coastal 2006). The numerical model results were utilized to alter or "fine-tune" assumptions from previous sediment budget estimates. The analysis was verified with recent bathymetric change information within the St. Lucie Inlet system.

ANALYSIS OF SEDIMENT MOVEMENT

One of the primary goals of the data collection and numerical modeling effort was to update the existing sediment budget for St. Lucie Inlet. The original Inlet Management Plan based the sediment budget on regional beach profile information, inlet dredging

records, and limited bathymetric change data. The present effort relies on much of the same types of information; however, bathymetric change analyses incorporated detailed surveys within the inlet throat and the seaward section of the flood shoal for 2000, 2002, and 2003. In addition, numerical modeling of coastal processes was utilized to determine, as well as verify, different components of the sediment budget.

The initial step in developing an inlet sediment budget is to define the various features comprising the inlet. By evaluating data and modeling/analysis results associated with each of these features, sediment transport pathways and quantities can be constrained within reasonable bounds. St. Lucie Inlet can be defined as a stabilized inlet; however, due to its relatively large size, the inlet exhibits features of an unstabilized inlet. For example, the existing jetty system does not confine the inlet to a narrow self-scouring channel. Instead, the confining cross-section (the smallest inlet cross-section, where tidally-induced velocities typically are highest) exists landward of the north and south jetties. Figure 3 illustrates the features used to define sediment transport pathways within the St. Lucie Inlet system. As shown, a large marginal ebb shoal exists to the south of the navigation channel, extending from approximately 2,000 feet west of the south jetty tip (inclusive of the shoal deposit along the south shore of the inlet immediately seaward of the flood shoal) and terminating seaward of the breakwater. Although the seaward extent of this feature likely is influenced by the existence of the breakwater, this region of sand accumulation is related to ebb shoal formation along the channel margins. For the purposes of this analysis, the flood shoal is defined as the region immediately landward of the most constricted inlet cross-section. Although part of the flood shoal, a region of sediment deposits north of the defined flood shoal in the Indian River lagoon is shown separately. Both the impoundment basin and the outer dredged navigation channel are combined, due primarily to their hydraulic connection and similar water depth.

From a longer-term perspective, sediment management practices have changed since 1993, where material dredged from the inlet is taken out of the local littoral system (either disposed of offshore or deposited in nearshore berms several miles downdrift of the inlet). Therefore, the updated sediment budget analyses does not consider the shoreline south of the inlet to be dominated by significant accretion associated with sand placement, rather the short-term shoreline change rate between 1999 and 2003 indicates a stable or moderately accreting shoreline to the north of where the attachment bar joins the shoreline (Applied Coastal 2006). The coastal management practices have been relatively consistent north of St. Lucie Inlet, the longer-term shoreline change is appropriate to assess beach volume change for the sediment budget analysis. The annual volumes of sediment retained by the beach south of the inlet was determined to be approximately 39,800 cubic yards and the by the beach north of the inlet (fronting Sailfish Point) was 6,200 cubic yards per year.

Numerical modeling of wave induced transport yielded updated gross and net longshore sediment transport rates, as well as ratios between the north and south directed transport which was useful for modifications to the previous assumptions utilized for the previous

sediment budgets (ATM 1995 and Bodge 1999). Results from the spectral wave modeling and longshore sediment transport analysis indicate a reduction in south-directed transport between Bathtub Reef and the north jetty. Protection from offshore waves is afforded by the natural reef system fronting Sailfish Point. South of St. Lucie Inlet, available sediment is controlled by the bypassing efficiency of the inlet; therefore, sediment transport potential only serves as a relative guide to realized longshore sediment transport rates. Since no sediment is available for southerly transport at the south jetty, only north-directed transport is realized at this location. Within the immediate region influenced by the inlet, sediment availability is controlled directly by (a) sediment traveling along the bypass bar and (b) sediment derived from the inlet via the marginal ebb shoal system. In addition, the local wave climate generates significant north-directed sediment transport into the inlet (around the south jetty).

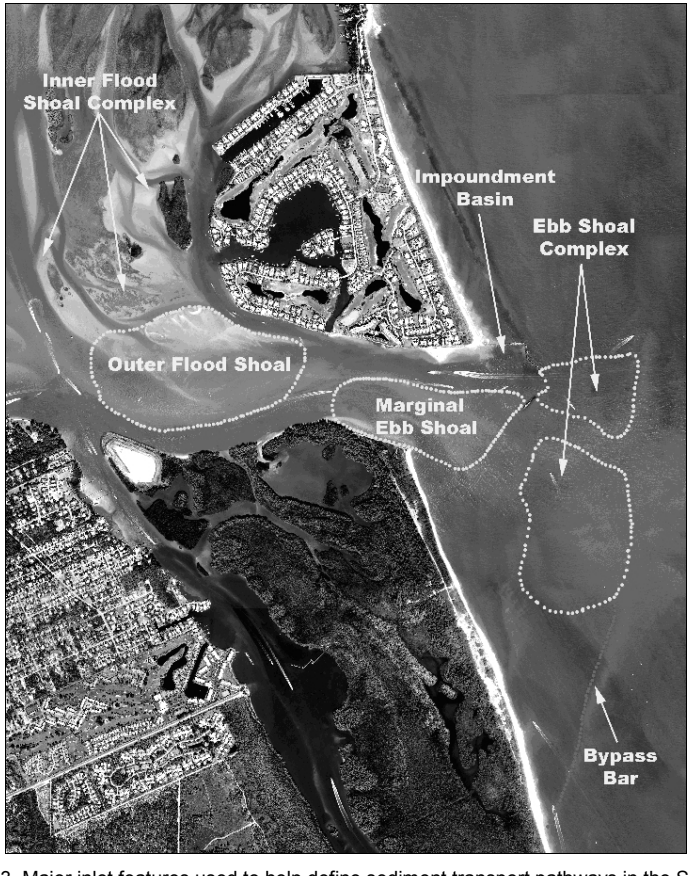

Figure 3. Major inlet features used to help define sediment transport pathways in the St. Lucie Inlet region.

The result of the wave-induced longshore sediment transport analysis is the net south-directed transport at the updrift boundary is approximately 260,000 ± 50,000 cubic yards per year. Modeling also indicated south-directed sediment transport at the north jetty weir section is approximately 150,000 ± 29,000 cubic yards per year (Applied Coastal Research 2006).

Since longshore sediment transport along the south side of St. Lucie Inlet is governed by sediment bypassed across the inlet, likely only the ratios of north and south directed sediment transport are applicable to the sediment budget analysis. At the downdrift boundary the modeled ratio of north-directed to south-directed transport is approximately 1:2. However, it should be noted, the area within the limits of the bypass bar (north of the shore attachment of the bypass bar) is sediment-rich relative to areas further south. This condition is a direct result of the tidal current-induced sediment transport discussed below. Therefore, north-directed transport within this region is more available in the littoral system and the 1:2 ratio of north-directed to south-directed transport likely overestimates the contribution the southerly littoral drift at the downdrift boundary of the sediment budget.

The sediment transport pathways within the St. Lucie Inlet system are strongly influenced by the various structural improvements made since 1929: the north jetty (including the weir section), the breakwater, the impoundment basin, and the south jetty. Based on a review of the inlet bathymetry data and the hydrodynamic modeling results, it is apparent that the controlling inlet cross-section (the smallest cross-section through the inlet throat) is not between the two jetties, but rather about 2,000 feet west of the inlet mouth, near the western limit of the south jetty. Based on the 2004 bathymetric survey, the cross-section between the south jetty tip and the north jetty was approximately 23,340 ft^2 and approximately 22,430 ft^2 at the narrowest section of the inlet. Although this represents only a 4% reduction in inlet cross-section between the two stations, it indicates that sediment accretion is more likely seaward of the restriction during the ebbing portion of the tidal cycle.

In addition to observed changes, the hydrodynamic and sediment transport modeling results provided further insight into sediment transport pathways. The tide elevation signal for the estuary exhibits generally flood-dominant behavior (Applied Coastal 2006), indicating that the estuary tends to be a sediment sink. A more detailed analysis of tidal currents within the main channel and across the marginal ebb shoal reveals overall sediment transport pathways through the throat of the inlet. A simple analogy for typical tidal inlets, similar to St. Lucie Inlet, is that they behave as a “drain” during the flooding portion of the tide cycle and a “jet” during the ebbing portion of the tide cycle. At St. Lucie Inlet, the relatively wide ocean entrance allows water to enter the inlet from a variety of directions including over/through the north jetty, between the breakwater and north jetty, and across the extensive ebb shoals. In general, there is no hydraulically preferred path for water to follow and water velocities across the entire entrance are fairly uniform (similar to a “drain”). After the estuary fills and the tide

begins to ebb, the least restrictive pathway back to the ocean is via the deep navigation channel. This deep channel acts as a "jet", where tidal flow preferentially is directed along this route as indicated by higher velocities in this portion of the inlet during the ebb cycle.

Quantitatively, an analysis of modeled tidal currents through the main navigation channel and across the marginal ebb shoal was used to determine likely sediment transport pathways. Tidal ebb currents through the navigation channel are significantly stronger than flood currents, indicating that the channel tends to export sediment in the direction of the ocean. However, the channel margins exhibit slightly flood-dominant behavior, where the flood velocities are greater than the ebb velocities. For St. Lucie Inlet, currents through the impoundment basin and across the marginal ebb shoal tend to drive sediment into the estuary. A constituent analysis of the tidal currents was used to determine the degree of flood or ebb dominance. Friedrichs and Aubrey (1988) describe this methodology in more detail. The analysis of modeled currents indicated that the navigation channel adjacent to the north jetty weir section is strongly ebb dominant and the marginal ebb shoal exhibits slight flood dominant behavior. Comparison of these results with tidal currents shows excellent agreement, where ebb velocities are higher than flood velocities in the navigation channel and ebb velocities are slightly lower than flood velocities across the ebb shoal. Based on this analysis, general sediment transport pathways were developed between the series of shoals within the inlet throat (shown in Figure 4). Sediment entering the inlet appears to be dominated by material entering the system across the north jetty weir section. Migration of this material along the Sailfish Point shoreline is responsible for annual maintenance dredging requirements for the navigation channels along the northern shoreline. A significant volume of this material also is deposited on the flood shoal, and likely is resuspended, where a portion is deposited within the marginal ebb shoal. In addition, the high ebb currents within the navigation channel transport material from the channel to the ebb shoal. The south-dominated wave-induced transport continually moves ebb shoal deposits to the south and flood dominant currents south of the breakwater drive a portion of this sediment onto the marginal ebb shoal. This analysis of tidal current asymmetries within the outer portion of the inlet indicates a bypassing mechanism across the weir section of the north jetty to the marginal ebb shoal in addition to the traditional bar bypassing driven by the net littoral drift. This significant mode of sediment transport within the inlet throat is unique for inlets along the east coast of Florida, due to the relatively wide entrance that allows formation of significant shoal areas within the inlet constriction.

SEDIMENT BUDGET

The quantitative and qualitative information above was used to develop a comprehensive sediment budget for St. Lucie Inlet. The sediment management practices for the inlet have been modified since assumptions were developed for the previous sediment budget calculations. Primarily, beach compatible sediment dredged from the impoundment basin and channel no longer are placed along the beach immediately south of the south jetty. Sediment basin improvements also altered the sediment transport pathways within the inlet throat. Dredging of the enlarged impoundment basin removed a

significant volume of bedrock along the northern side of the outer inlet navigation channel. This dredging increased tidal exchange along the general route of the navigation channel and caused a slight reduction in the outer flood shoal volume. Although the system continues to equilibrate to this modification in inlet bathymetry, the influence of the new sediment basin geometry represents a long-term shift in sediment transport pathways. The slight increase in tidal exchange and velocities over the existing shoal system likely will cause landward migration of the outer portion of the flood shoal, as well as enhanced accretion of the inner portions of the flood shoal and the marginal ebb shoal.



Figure 4. Generalized sediment transport pathways based upon numerical modeling of tidal currents, southerly-directed littoral drift north of the inlet, and northerly-directed littoral drift south of the inlet. Red arrows represent ebb-dominant transport and green arrows represent either flood-dominant transport or wave-induced sediment transport.

Numerical model results also were utilized to alter or "fine-tune" assumptions from previous sediment budget estimates. Wave modeling provided the driving force for wave-induced sediment transport estimates along the shorelines to the north and south of St. Lucie Inlet. Hydrodynamic and sediment transport modeling within the inlet was performed to quantitatively and qualitatively evaluate sediment transport pathways. By "calibrating" the sediment transport model with available bathymetric change information, as well as evaluating both short- and long-term bathymetric change, a more complete determination of shoaling and erosion rates within the inlet were developed. In addition to the numerical modeling efforts, the full range of bathymetry and shoreline position data sets were reviewed and analyzed for incorporation into the sediment

budget. Improved bathymetric surveys of the flood shoal, marginal ebb shoal, navigation channel, and impoundment basin serve as a baseline for future inlet management decisions.

Figure 5 summarizes the sediment budget analysis results from this study. Along the southern shoreline of Hutchinson Island, sediment transport potential decreases from approximately 260,000 cubic yards per year toward the south at Bathtub Reef to about 150,000 cubic yards per year. It was assumed that littoral drift in this region not accounted for by the reduction in south-directed transport or local beach volume change was bypassed to the ebb shoal system (approximately 129,000 cubic yards per year). Accretion on the ebb shoal east of the north jetty/breakwater system was assumed to be 12,000 cubic yards per year, based on the previous work in the original inlet management plan (ATM, 1995).

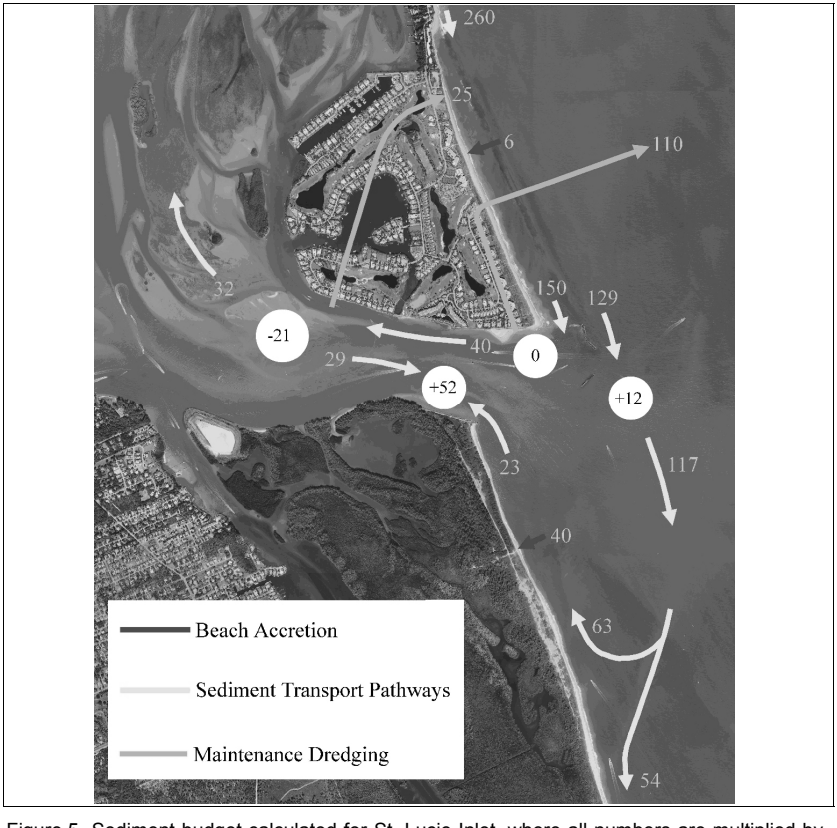

Figure 5. Sediment budget calculated for St. Lucie Inlet, where all numbers are multiplied by 1000 cubic yards per year. White circles represent areas of measure or assumed accretion/erosion.

The remaining 117,000 cubic yards per year was available to the littoral system south of the inlet, including the extensive marginal ebb shoal. As noted previously, the littoral system along the northern portion of Jupiter Island is not sediment-rich; therefore, it likely is inappropriate to use sediment transport potential calculations directly to determine the sediment budget in this region. A more appropriate technique is to utilize ratios of south- to north-directed transport as a guideline. At the shore attachment location of the bypass bar, south-directed sediment transport potential was computed to be 208,700 cubic yards per year. At the south jetty, north-directed transport was computed to be 81,500 cubic yards per year. The computed ratio of north-directed to south-directed transport for this case is 0.39. Since cross-shore transport from the marginal ebb-shoal influences the volume of bypassed material that reaches the beaches in this region, the aforementioned ratio likely is the most defensible. Based on beach accretion and requirements of balancing the sediment budget within the interior portion of the inlet, the south-directed transport at the shore attachment location of the bypass bar was determined to be 54,000 cubic yards per year and north-directed transport at the south jetty was determined to be 23,000 cubic yards per year. The ratio of north-directed to south-directed transport was 0.43, which is nearly identical to the ratio computed from sediment transport potential at these locations.

Within the inlet, the 150,000 cubic yards that enter the impoundment basin and outer navigation channel are distributed between maintenance dredging (recorded to be 110,000 cubic yards annually) and flood shoal accretion (40,000 cubic yards per year). The 110,000 cubic yards of material generated from maintenance dredging historically has been taken outside the region represented by the sediment budget; therefore, Figure 5 represents this “loss” to the system as an offshore directed arrow. The outer flood shoal is eroding at a relatively small rate of approximately 21,000 cubic yards per year, based on surveys between 1996 and 2002. The analysis of sediment transport pathways indicates that much of this eroded material migrates to the marginal ebb shoal region (29,000 cubic yards annually) and the remainder migrates to the inner flood shoal (32,000 cubic yards annually, from ATM, 1995). Only a portion of the recent significant accretion on the marginal ebb shoal can be attributed to the long-term sediment budget. The remainder of the accretion likely was caused directly from the impoundment basin improvements, as described above.

REFERENCES

Applied Coastal Research and Engineering, Inc., 2006. Physical Monitoring And Numerical Modeling Analysis To Support The St. Lucie Inlet Management Plan, Martin County, FL. Prepared for the Martin County Public Services Department and Florida Department of Environmental Protection.

Applied Technology and Management, Inc., 1995. St. Lucie Inlet Management Plan, Martin County, Florida. Prepared for the Department of Environmental Protection and Martin County Board of Commissioners.

Bodge, K.R., 1999. Inlet Impacts and Families of Solutions for Inlet Sediment Budgets. Proceedings, Coastal Sediments '99, ASCE, Reston, VA, pp. 703-718.

Friedrichs, C.T. and D.G. Aubrey (1988). "Non-linear Tidal Distortion in Shallow Well-mixed Estuaries: a Synthesis." Estuarine, Coastal and Shelf Science (27), pp 521-545.

USACE, 1968. Beach Erosion Control Study on Martin County Florida. Jacksonville District.

USACE, 2000. St. Lucie Inlet Design Memorandum and Final Environmental Assessment, St. Lucie Inlet, Martin County, Florida. Jacksonville District, South Atlantic Division.

SAND BYPASSING RESTORES NATURAL PROCESSES TO ASSATEAGUE ISLAND, MARYLAND

Courtney A. Schupp[1], Gregory P. Bass [2], William G. Grosskopf [3]

1. Assateague Island National Seashore, 7206 National Seashore Lane, Berlin, MD 21811, USA. Courtney_Schupp@nps.gov
2. US Army Engineer District, Baltimore, P.O. Box 1715, Baltimore, MD 21203-1715, USA. Gregory.P.Bass@nab02.usace.army.mil
3. Offshore Coastal Technologies, Inc., P.O. Box 1368, Chadds Ford, PA 19317, USA. wgrosskopf@offshorecoastal.com

Abstract: The North End Restoration Project uses a regional sediment management approach to address jetty-induced sediment deprivation and accelerated erosion on Assateague Island, Maryland. The biannual sand bypassing project dredges sand from the ebb and flood tidal deltas and places it in the nearshore area of the project site rather than on the upper shoreface, thereby replicating natural sediment transport processes and minimizing adverse impacts to subaerial habitats. Calm weather has prevailed since sand bypassing began, and accretion occurred at all depths within the placement area and at shallow depths to the north and south. Erosion occurred at lower depths and north of the ebb tidal delta attachment bar, which may block sand transport to the northernmost shoreface and where and where wave refraction over the ebb tidal delta and unique tidal circulation patterns contribute to upper shoreface erosion.

INTRODUCTION

Since its construction in 1935, a jetty system at Ocean City Inlet has caused unnatural sediment deprivation on northern Assateague Island, Maryland, thereby accelerating the natural erosion rate and causing associated habitat degradation. Assateague Island was later established as a National Seashore, and because the National Park Service (NPS) is required to reestablish natural functions and processes, NPS partnered with the U.S. Army Corps of Engineers (USACE) to address the ongoing and future effects of the jetties. The North End Restoration Project uses a regional sediment management approach to re-establish an historic, pre-inlet sediment transport to the northern 13.2 km of the island.

The method chosen to restore natural sediment transport processes at Assateague Island is known as sand bypassing, the hydraulic or mechanical movement of sand from an area of accretion to a downdrift area of erosion, across a barrier to natural sand transport such as large-scale jetty structures. Most sand bypassing projects around the world build permanent pumps to move sand across inlets and onto beaches (see Boswood and Murray, 2001 for an extensive list). A less common approach, and the one chosen for Assateague Island, is to use dredge boats to bypass sand to the nearshore or surf zone rather than onto the beach. This method has been successful at several locations including Tweed River, Australia, and Mount Maunganui, New Zealand, where placed sand remained in the nearshore and beach system at least one year later (Foster et al., 1994; Dyson et al., 2002).

The North End Restoration Project at Assateague Island will develop information concerning the effectiveness of restoring natural barrier island processes through the systematic nearshore placement of bypass sand and regular topographic and shoreline surveys over a 25-year period. For the purposes of this study, "surf zone" is defined as the area of breaking waves, and "nearshore" is defined as the subaqueous region extending offshore from the mean high water (MHW) line out to the depths at which waves begin to be significantly altered by the shoaling bathymetry, an area which encompasses the survey depth limit of -10 m (North American Vertical Datum, NAVD88). The biannual sand bypassing project, which began in January 2004, dredges sand from the ebb and flood tidal deltas and places it in the nearshore area of the project site rather than on the upper shoreface, thereby minimizing adverse impacts to subaerial habitats. An additional advantage of this method is a reduction in dredging needed to maintain the inlet navigation channel.

REGIONAL SETTING

Assateague Island is a barrier island that extends 58 km along the coast of Maryland and Virginia (Figure 1). Island width ranges from 300 m to 1200 m, and elevations are generally around 2 m (NAVD88), though dunes may rise up to 10 m high. Its northern end is bounded by Ocean City Inlet, which has an associated flood tidal delta and a large ebb tidal delta that extends both north and south of the inlet, curving to form a 300-meter wide attachment bar that currently meets the shoreline between 650-950 m south of the inlet (Figure 1). The growth of the ebb tidal delta since inlet formation, and its shoreline attachment by 1980, are well documented (Dean and Perlin, 1977; Leatherman, 1984; Underwood and Hiland, 1995; Rosati and Ebersole, 1996; Stauble, 1997; Kraus, 2000). This attachment bar is a significant bathymetric feature in the nearshore, rising 3.5 m above the surrounding seafloor, and steeper on its south flank (1:46 slope) than its north flank (1:180 slope).

The coast is classified as wave-dominated (average height of 1 m) and microtidal (0-2 m tide range) with spring tides fluctuating from -1 m to 3 m relative to mean low water (MLW) (Field 1979). Winter storms and high wave energy create a low, flat beach with sand stored in a nearshore sand bar; summer beach profiles are steeper. Depth of closure, defined as the depth beyond which sediment transport of engineering significance does

not occur (Hallermeier, 1981), is estimated to be -6.2 m NAVD88 (Stauble, 1994) and is typically found about 275 to 400 m from the high tide line. Net alongshore sediment transport is southward due to strong winter northeasters; in the summer, waves from the southeast drive sand transport less vigorously northward. As a result, the net annual alongshore transport is estimated to be between 115,000 and 214,000 m³/yr toward the south (Underwood and Hiland, 1995).

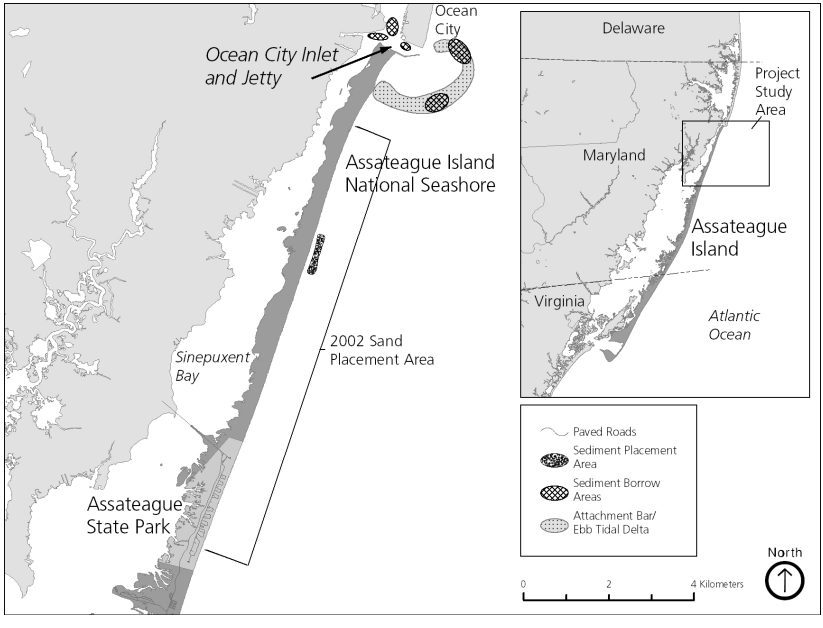

Figure 1. Location of project study area and major sediment features.

The majority of the island is managed as a National Seashore and has little infrastructure along its length, with the exception of the section 10-13.2 km south of the inlet. In that section, a state park constructed high dunes to protect extensive park infrastructure, and maintenance sometimes involves scraping the beach and importing clay to stabilize beach access over the dunes.

North of the state park, most of the northern 10 km of Assateague Island is a dynamic environment composed of a beach and low berm on the ocean side of the island, with a low elevation, sparsely vegetated back barrier flat and a narrow fringing salt marsh with overwash fans along an estuary. This dynamic area is prime habitat for state- and federally-listed endangered species and protects the mainland directly to the west from storm tides and waves.

The northern end of Assateague Island is classified by the U.S. Geological Survey as having 'very high vulnerability' because of its low elevation, frequent overwashing, and high rates of shoreline erosion (Pendleton et al., 2004). This vulnerability is thought to be caused primarily by an interruption in alongshore sediment transport by the jetties built around the Ocean City Inlet in 1935 (Rosati and Ebersole 1996). Along the northern 13.2 km of the island, the shoreline erosion rate more than doubled when the inlet was stabilized, from a pre-inlet rate (1850-1933) of -1.5 m/yr to a post-inlet rate (1942-1997) of -3.70 m/yr.

This increase in shoreline erosion is associated with a volume loss in the active profile (from the beach berm offshore to the depth of closure) that increased after the inlet was stabilized from an estimated 150,000 m^3/yr to 370,000 m^3/yr. Because detailed historical bathymetric data do not exist for this project site, this volumetric loss rate was approximated using a method established by Hanson and Kraus (1989) that integrates the active profile depth, the pre- and post-inlet shoreline change rates, and the assumption that shoreline change is represented as a horizontal and uniform translation of the profile. This assumption and the resulting volume calculations do not include the area north of the attachment bar, where the depth of closure and active berm are quite different from the shoreline directly southward.

North End Restoration Project

USACE predicted that without mitigation, the north end of the island would destabilize and eventually breach during storms in the near future (USACE, 1998). Should this occur, it would have both a significant impact on the values and purpose of Assateague Island National Seashore and serious implications for the adjacent mainland communities, including infrastructure vulnerability, loss of estuarine habitats, and increased maintenance needs for Ocean City Inlet.

To mitigate the loss of natural sand transport processes, local and national government agencies created a comprehensive two-phase restoration plan. The first, short-term phase of the restoration program intended to replace some of the sediment lost since inlet stabilization, estimated to be 9.7 million m^3 in the northernmost 12 km of the island by 1996 (USACE, 1998). During this phase, 1.4 million m^3 of sand was placed just seaward of the mean high water line in September 2002 in an area extending from 2 to 12.5 km south of the inlet (Figure 1).

The second, long-term (25-year) sand management phase is intended to restore sand transport to northern Assateague Island at a pre-inlet rate. The intent of the project is neither to create a fixed-width beach nor to stop erosion, but rather to reduce the erosion rate to the pre-inlet conditions by restoring the sediment transport pathway. Beginning in January 2004, and recurring every early spring and fall, a hopper dredge takes approximately 72,000 m^3 of sand from the ebb and flood tidal deltas (borrow sites delineated in Figure 1) and deposits it just seaward of the surf zone on Assateague Island approximately 2.5 to 5 km south of the inlet (Table 1). Unlike a typical beachfill project in which the material is pumped high on the beach, the bypassed borrow material is

deposited on the crest and just seaward of the nearshore bar, which has an approximate crest elevation of -1.45 m to -1.75 m NAVD88. The loaded hopper dredge, which drafts approximately 2.4 m, enters the placement area perpendicular to the shore until the bow makes contact with the bar. The hopper doors (approximately 30 m long and 7.6 m wide) are then slowly opened. As the material starts to exit the hopper and the load lightens, the vessel attempts to move shoreward to deposit the remaining material as close to shore as possible. The dredge deposits the majority of sand in depths of -1.5 to -5 m (NAVD88) and about 80-250 m from shore (Figure 1). Ideally, because the sediment is placed landward of the depth of closure, waves and alongshore transport processes then move this material onshore, shaping this sand into a natural configuration in the surf zone and on the beach.

Sand is not deposited along the northernmost 2.5 km of the island because USACE hydrodynamic models indicate that within that region, sediment has a localized net northward transport. The net northward transport is apparently caused by wave refraction and wave breaking on the ebb tidal delta and attachment bar (Buttolph et al., 2006).

Table 1. Sources and Volumes of Borrowed Sand Delivered to Assateague Island

Time Period	Borrowed from Inlet and Flood Tidal Delta (m^3)	Borrowed from Northern Ebb Tidal Delta (m^3)	Borrowed from Southern Ebb Tidal Delta (m^3)	Total delivered to Assateague Island (m^3)
Spring 2004 (1/30 – 4/1)	10964	45090	0	56054
Fall 2004 (10/1 – 11/26)	3280	0	66814	70094
Spring 2005 (3/29-4/28)	776	0	24332	25108
Fall 2005 (9/18-11/13)	12374	49386	0	53140*
Total	27394	94476	91146	204396

*8620 m^3 of the total borrowed volume was delivered to Ocean City.

Design studies performed prior to the short-term phase of the restoration project indicated that the native beach sediments in the active profile of the project area had a mean grain size of 0.25 mm and a standard deviation of 0.88 mm (moderately sorted sand), with finer sand seaward of the storm bar (USACE, 2001). Samples collected in 2004 and 2005 from the ebb and flood shoals indicate that the mean diameter of the sediments range from .17 mm to .65 mm, or fine to coarse sand and moderately well to well sorted.

Storm activity during the bypassing phase, from January 2004 through December 2005, was relatively minor, according to observations at the USACE wave and water level

gauge located about 3 km north of the inlet in about 9 meters of water. It is not uncommon for the gauge to record wave heights in excess of 3 meters several times a year, with a maximum wave height of 4.2 meters being recorded during the January 1992 northeaster. In contrast, between January 2004 and December 2005, wave heights exceeded 3 m during only one event. It should be noted, however, that the gauge was inoperable during the first half of 2005.

METHODS

To monitor the effects of the restoration project and the sand permanence, nearshore bathymetric profiles are surveyed annually and shoreline position is mapped quarterly, as described below.

Volume Change

Nearshore bathymetry profiles were surveyed just after the second round of dredging each fall. The profiles extended in an offshore direction from the beach berm out to about -10 m NAVD88. Surveys relied on a towed survey sled and an optical total station and were tied to monuments established along the island. The towed sled surveys have been performed on an irregular time interval since 1986, usually in response to engineering activities or storm events, and have been surveyed annually since 2003 as a part of the North End Restoration Project. The surveys analyzed for this paper were collected November 14-16, 2003, November 7-9, 2004, and November 11-13, 2005. Each survey followed mild frontal passages with minor waves, tides and sediment transport activity, so that the surveys could be performed during the offshore winds and calmer surf zone activity that follow the fronts.

Due to the distance between each of the nearshore profiles, true volume changes cannot be calculated, and were instead approximated using the following method. The change in cross-sectional area at each transect during each year was calculated for four different depth categories:

1. the beach, from 2 m to 0.36 m NAVD88 (MHW);
2. the shallow water, from 0.36 m (MHW) to -3 m NAVD88 (active profile zone);
3. deep water, from -3 m NAVD88 down to the closure depth as observed in graphs of the three surveys at each transect line; and
4. the total area from 2 m NAVD88 down to observed closure depth (varies for each transect).

The observed closure depth varied between transects and did not always extend to the generalized depth of closure for two reasons: not all transect surveys were collected out to the documented depth of closure; and for each transect line, the three surveyed profiles closed (joined at depth with no change in bathymetry on the three survey dates) within the survey area and at a unique depth.

Next, to approximate volume change over the two year period, the average area change of adjacent transects was multiplied by the distance between the two transects to get the approximate volume change between each pair of transects. These approximated

volumes were then summed for a total volume change estimate. This process was used for each depth category.

Shoreline Change

To calculate shoreline change rates, several sources of shoreline positions were used. The seven historic shoreline positions from 1850 to1980 came from various sources, including NOS T-sheets and aerial photographs. Recent high tide shoreline positions, collected from 1994 to the present, were surveyed quarterly at Assateague Island during near-average tidal ranges when the predicted high tides ran close to MHW. The high tide line, as evidenced by the wet/dry line or deposited wrack, was collected with a kinematic differential GPS receiver mounted on an ATV, and was post-processed.

The linear regression rates of shoreline change (LRR) were calculated using DSAS (Thieler et al., 2005), which cast shore-perpendicular transects at 50 m intervals between a user-defined baseline and each shoreline position. It then fit a least-squares regression line to all shoreline points for a particular transect and assigned the slope of the line as the change rate. Negative rates indicate erosion; positive rates indicate accretion. Although this method tends to underestimate the rate of change relative to other statistical methods, such as end point rate (Dolan et al., 1991), it offers the following benefits: all the data are used, regardless of changes in trend or accuracy; the method is purely computational and does not require any other analysis such as error measurements; and it is based on accepted statistical concepts (Thieler et al., 2005).

To examine the patterns in shoreline change related to the restoration project, several eras were selected. The long-term shoreline change rate was calculated for 1850-2005, and the shoreline change related to the long-term restoration phase was calculated from the positions surveyed between February 2004 and December 2005, which was a relatively calm weather period, with recorded wave heights exceeding 3 m (moderate intensity) during only one event. For comparison, shorelines from December 1994 through December 1997 were used to calculate the shoreline change rates for a pre-restoration period with similar weather. During that period, there was relatively little storm activity; wave heights at the gauge reached or just exceeded 3 m on only three occasions.

RESULTS

Nearshore Volume Change

As a whole, the study area experienced net accretion in the first year and erosion in the second year (when less sand was bypassed, Table 1), resulting in a net volume loss (Table 2). In the two-year period, net volume loss occurred at nearly all profile locations, with the exceptions of the attachment bar location, the sand placement location, and the state park (Figure 2A). After two years, the majority (63%) of volume increase lay in two places: within the placement area (96299 m^3) and on the attachment bar (32339 m^3).

Volume changes at each profile and in each depth category varied, with net accretion in the beach and shallow areas and net erosion in deeper areas (Table 2, Figure 2). Despite

the large volume of sand deposited in the nearshore of Assateague Island, and despite a relatively calm period of weather, there was a net volume loss in the active profile of Assateague Island. Most of this loss was at depth.

Table 2. Volume Changes by Depth Category 2003-2005

Depth Category (NAVD88)	2003-2004 (m^3)	2004-2005 (m^3)	2003-2005 (m^3)
Beach (2 to 0.36 m)	135718	-25415	110303
Shallow (0.36 to -3 m)	507596	-127531	380065
Deep (-3 m to deepest)	-628462	-370623	-999085
Total Profile	14852	-523569	-508717

The beach (2 m to 0.36 m NAVD88) accreted some sand the first year and then lost 30% of that volume the second year, resulting in an overall accretion along the 13.2 km study area (Table 2). The majority of this accretion was measured within two sites: the 2.5 km region centered on the sand placement site, and the point at which the attachment bar meets the beach (Figure 2B).

The shallow region (0.36 m to -3 m NAVD88) experienced net accretion over the two years (Table 2, Figure 2C). During the first year of the project, sand accreted at every transect location with one exception: north of the attachment bars (Table 2, Figure 2). During the second year, the shallow region experienced a 30% net loss of this accreted sand along much of the study area. As a result, over two years, the net change at this depth was erosional north of the attachment bar but accretional along most of the shoreline, particularly in and north of the placement area and in the northern section of the state park, where a large bar moved shoreward into shallower water.

At depth (below -3 m NAVD88), sand eroded at every transect location every year, with three exceptions: within the placement area, which gained sand both years; where the attachment bar meets the beach; and at one location within the state park, where a large bar migrated landward, moving into the 'shallow' depth category (Figure 2D). Most (60%) of the sand loss occurred in the first year (Table 2).

The volume of sand bypassed to Assateague during the first year of the project accounts for only 20% of the net volume of sand accreted in the beach and shallow areas that year. Over the two-year study period, the volume gained in the beach and shallow regions accounts for only 41% of the combined volume of bypassed sand and sand lost from the deep water (1.2 million m^3, Tables 1 and 2). The active profile area north of the attachment bar, represented by the northernmost two transects, accounts for a net volume loss of -129891 m^3, or 34% of the net volume loss along the whole study area (11% of the combined bypassed and lost volume).

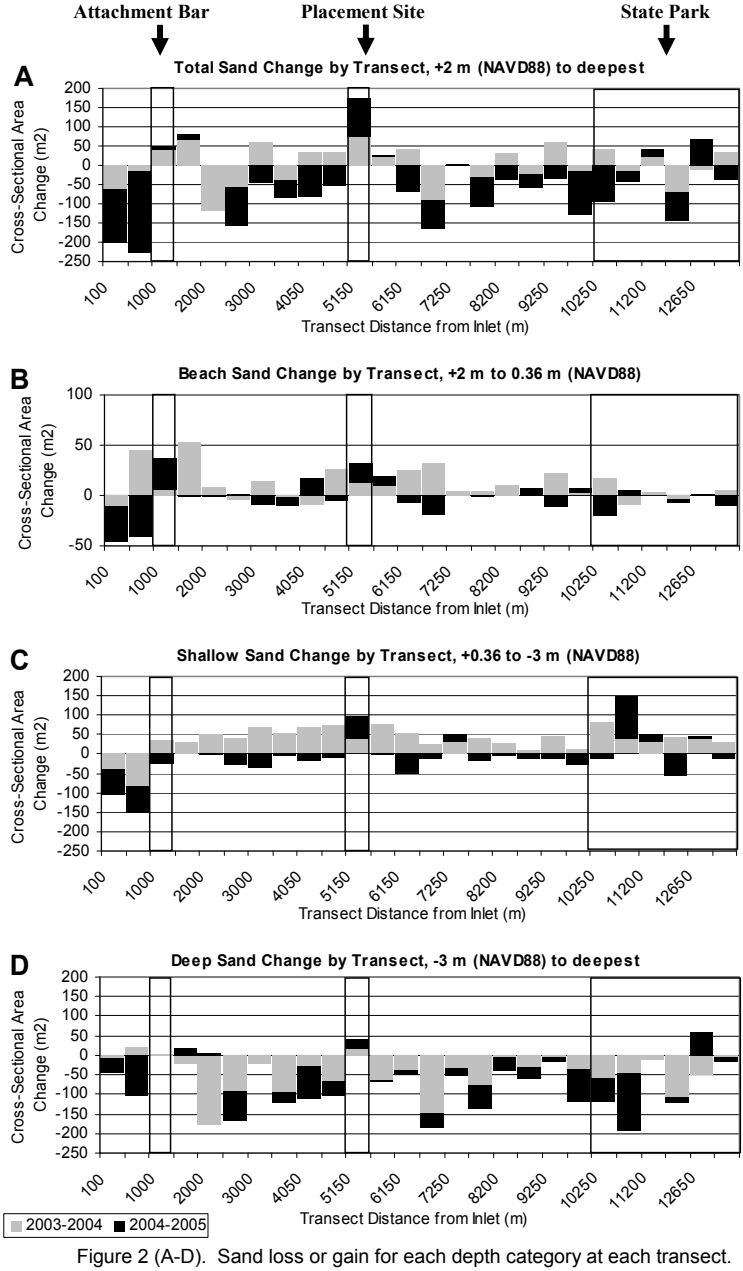

Figure 2 (A-D). Sand loss or gain for each depth category at each transect.

Shoreline Change Rates

The long-term (1850-2005) shoreline change rate in the 13.2 km study area averages -3.25 m/yr (erosion), with a slightly lower erosion rate in the area south of where the attachment bar developed (Table 3, Figure 3). Because the rate is calculated over a longer period of time with fewer shorelines, the standard deviation is lower than for the short-term rates (Table 3).

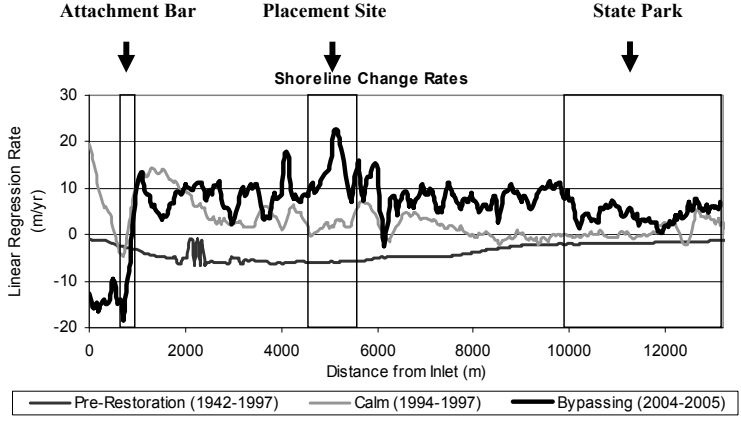

Figure 3. Linear regression rates of shoreline change before and during the long-term restoration project. Positive rates indicate accretion; negative rates indicate erosion.

Table 3. Linear Regression Rates of Shoreline Change by Era

Time Period	LRR (m/yr) in Study Area	Standard Deviation (m/yr)	LRR (m/yr) in Study Area, South of Attachment Bar	Standard Deviation (m/yr)
1850-2005	-3.25	1.96	-3.02	2.01
1994-1997 (calm weather, pre-restoration)	1.87	2.39	1.87	2.39
2004-2005 (calm weather, sand bypassing)	6.22	6.49	7.69	3.82

The tendency of the shoreline to accrete during calm years was evident during a calm-weather period (1994-1997) just before the restoration project began, when the shoreline in the northern 13.2 km study area was stable or accreting along its entire length, with the exception of the area north of the attachment bar, where the shoreline eroded (Figure 3). The two-year study period (February 2004 through December 2005) experienced a similar lack of major storms in addition to sand bypassing, and the accretion rate along the entire 13.2 km study area shoreline was even higher, although erosion quadrupled in

the area north of the attachment bar (Figure 3). In the state park, the shoreline also accreted during the recent period, but at a lower rate (Figure 3).

DISCUSSION

Correlation of Shoreline Change and Volume Change

The alongshore trend of shoreline accretion and erosion over the two-year period reflects the alongshore pattern of sand gain and loss in all depth categories. The volume loss seen north of the attachment bar is reflected in the high shoreline erosion rate there, and the high shoreline accretion rate at the northern end of the placement site is also reflected in the volumetric gain in all depth categories. Appropriately, the shoreline change rate is tied more closely to the alongshore volume changes on the beach than to the changes in other depth categories. The large sand gains in the beach and shallow regions were associated with a high accretion rate along most of the shoreline, particularly in the sand placement area, which had a large net volume increase (96,300 m^3).

Sand Sources and Sinks

Although the processes driving the volumetric changes along Assateague Island are difficult to ascertain based on two years of monitoring data, the likely sources of sand transport are known.

The long-term natural processes of barrier island retreat, which have driven Assateague Island toward the west, likely have continued. These processes include recession of the entire active profile and would account for the continued loss of material seaward of the -3 m contour. The sediment that is lost from the active profiles is being transported in possibly all four directions, along with the bypassed sand that was placed in the nearshore. The lost material probably did not move seaward of what is assumed to be the maximum depth of the active profile. Because the period 2003-2005 lacked major storms, it is assumed that the wave energy was not sufficient to move sand from the beach and shallow areas and into deeper waters; instead, waves would tend to deposit sand onto the beach and shallow areas, a process described by Hoefel and Elgar (2003).

Some of the sand from below the -3 m contour, along with the large amount of sand bypassed to the nearshore, would have been transported onshore by long period waves. This process accounts for the significant gains of sand above the -3 m contour and the associated shoreline accretion. Much (45%) of the sand remained within the nearshore placement area, a tendency documented in a similar project site at Mount Maunganui, New Zealand, where all of the placed sand remained in the placement area one year later (Foster et al., 1994). The retention difference may be attributed in part to the reduced wave energy and larger placement area at the New Zealand site.

Although topographic volume changes were not quantified for this study, it can be assumed that some of the sand carried into the shallow areas may have been carried farther onto the island as overwash fans, which have been measured on Assateague as accreting by 20 to 90 cm in one year (Kochel and Dolan, 1986). Sand may also have blown inland from the lower beach; Leatherman (1976) found that deposition by aeolian

sand transport could dominate even overwash processes, particularly in wide low areas such as the north end of Assateague Island. Likely, some of the bypassed sand was also transported southward from the placement area, along the island and out of the study area, as indicated by the effects in the shallow and beach areas diminishing with distance from the placement site, and by the absence of recognizable effects on the deeper areas (Figure 2). The muted accretion in the state park likely reflects the combination of increased sand supply from the north and the impacts of dune construction and maintenance; beach scraping can result in compaction, altered morphology (slope), and sediment transport (Conaway and Wells, 2005).

Northerly transport toward the inlet and into the ebb shoal complex due to tidal circulation occurs almost continuously and probably in large volumes. The assumption of northward transport is supported by the expectation of northward transport in the absence of storms, the shoreline accretion and volumetric gain on the attachment bar, and the trend of volume loss increasing with distance north of the placement site. The attachment bar appears to have blocked the northward transport of sand, as there was no sand accretion north of the attachment bar. The northward-moving sand likely welded to the bar both within the profile survey area and farther offshore as sand was shunted eastward around the curve and toward the inlet. Some natural accretion at the location where the attachment bar joins the shoreline is typical of tidal inlets (Fenster and Dolan, 1996), but the increased accretion can probably be attributed to the increased sand supply from the south.

The localized tidal circulation pattern contributes to the erosion of the island north of the ebb shoal attachment point. The expansion of the ebb tidal shoal and southward movement of the attachment bar has expanded the reach of erosive tidal currents north of the attachment bar, translating those profiles landward. This erosion was probably exacerbated by jetty tightening in 2002 and 2003, which in reducing jetty permeability also reduced sand transport to the areas adjacent to the jetty and shunts sand further offshore (Buttolph et al., 2006).

Future Work

The two-year period of data used in this paper helps to document sediment transport processes and the evolution of various features of the island. However, the period is far too short to examine long-term or weather-related trends, and is considered anomalously calm compared to typical conditions on Assateague Island. As more storminess occurs, other processes will become evident, such as overall beach erosion throughout the active profile, while other processes will become more pronounced, such as island overwash and both alongshore and cross-shore transport. Continued monitoring of bathymetry and shoreline position over the 25-year project period will shed great insight on the sand bypassing effects, including sand borrow and placement location, the feasibility of restoring natural sediment transport processes, and the effectiveness of restoring natural barrier island processes through nearshore sand placement. A fuller understanding of the project effects will be gained by statistically analyzing the correlation between changes in both shoreline position and sand volume; by including subaerial volumetric changes

driven by wind and overwash; and by comparing the performance of the bypassed sand project to that of the traditional beachfill project at neighboring Ocean City, MD.

CONCLUSION

The reduced erosion of the shoreface in the project site and the increase in shoreline accretion indicate that the sand bypassing project is effective in delivering beach-quality sand to the surf zone and shoreline of the project site. When assessing the effects of nearshore sand bypassing, volumetric changes must be assessed not only along the total depth profile but also within various process-related depths. In the two-year study period, which lacked major storms, the sand spread both north and south of the project area, and accreted only on the beach and at shallow depths. Much of the sand lost at depth is believed to have accreted to the ebb tidal delta and upper shoreface, with significant volume also being transported alongshore and out of the study area.

ACKNOWLEDGEMENTS

Thanks to Andrew Roach for the location figure.

REFERENCES

Boswood, P.K., and Murray, R.J. (2001). "World-wide sand bypassing systems: data report," State of Queensland Environmental Protection Agency Conservation technical report 15 (R20), Queensland, Australia.

Buttolph, A.M., Grosskopf, W.G., Bass, G.P. and Kraus, N.C. (2006). "Natural Sand Bypassing and Response of Ebb Shoal to Jetty Rehabilitation, Ocean City Inlet, Maryland, U.S.A," Proceedings 30th International Conference on Coastal Engineering, World Scientific Publishers, in press.

Conaway, C.A., and Wells, J.T. (2005). "Aeolian dynamics along scraped shorelines, Bogue Banks, North Carolina," *Journal of Coastal Research* 21(2), 242-254.

Dean, R.G., and Perlin, M. (1977). "Coastal engineering study of Ocean City Inlet, Maryland," *Proceedings Coastal Sediments '77*, ASCE, Reston, Virginia, 520-540.

Dolan, R., Fenster, M. S., and Holme, S. J. (1991). "Temporal analysis of shoreline recession and accretion," *Journal of Coastal Research* 7(3), 723-744.

Dyson A., Lawson, S., Victory, S., Boswood, P., Mahon, B., Trucchi, L., and Cummings, P. (2002). "Tweed River Entrance Sand Bypassing Project Post Commissioning Coastal Behaviour," Smith, Jane M. [ed.] *Coastal Engineering 2002: Proceedings of the 28th International Conference*.

Fenster, M., and Dolan, R. (1996). "Assessing the impact of tidal inlets on adjacent barrier island shorelines," *Journal of Coastal Research* 12(1), 294-310.

Field, M.E. (1979). "Sediments, Shallow Subbottom Structure, and Sand Resources of the Inner Continental Shelf, Central Delmarva Peninsula," CERC-TP-79-2, U.S. Army Engineer Waterways Experiment Station, Vicksburg, MS.

Foster, G.A., Healy, T.R., and De Lange, W.P. (1994). "Sediment budget and equilibrium beach profiles applied to renourishment of an ebb tidal delta adjacent beach, Mt. Maunganui, New Zealand," *Journal of Coastal Research* 10(3), 564-575.

Hallermeier, R. J. (1981). "A profile zonation for seasonal sand beaches from wave climate," *Coastal Engineering* (4), 253-277.

Hayes, M.O. (1979). "Barrier island morphology as a function of tidal and wave regime," Leatherman, S.P. [ed.] *Barrier Islands from the Gulf of St. Lawrence to the Gulf of Mexico*, Academic Press, New York.

Hanson, H., and Kraus, N. C. (1989). "GENESIS: Generalized Model for Simulating Shore Change, Report 1, Technical Reference," Technical Report CERC-89-19, U.S. Army Engineer Waterways Experiment Station, Vicksburg, MS.

Hoefel, F. and Elgar, S. (2003). "Wave-induced sediment transport and sandbar migration," *Science* 299, 1885-1887.

Kochel, R.C., and Dolan, R. (1986). "The role of overwash on a mid-Atlantic coast barrier island," *Journal of Geology* 94, 902-906.

Kraus, N.C. (2000). "Reservoir model of ebb-tidal shoal evolution and sand bypassing," *Journal of Waterway, Port, Coastal, and Ocean Engineering*, 305-313.

Leatherman, S.P. (1984). "Shoreline evolution of North Assateague Island, Maryland," *Shore and Beach* 52(3), 3-10.

Leatherman, S.P. (1976). "Barrier island sediment dynamics: overwash processes and eolian transport," *Proceedings of the 15th Conference on Coastal Engineering*, 1958-1973.

Pendleton, E.A., William, S.J., and Thieler, E.R. (2004). "Coastal vulnerability assessment of Assateague Island National Seashore (ASIS) to sea-level rise," U.S. Geological Survey Open-File Report 2004-1020.

Rosati, J.D., and Ebersole, B.A. (1996). "Littoral impact of Ocean City Inlet, Maryland, USA," Edge, Billy L. [ed.] *Coastal Engineering 1996: Proceedings of the 25th International Conference*. 3: 2779-2792.

Stauble, D.K. (1994). "A physical monitoring plan for northern Assateague Island, Maryland," U.S. Army Engineer Waterways Experiment Station, Coastal Engineering Research Center, Vicksburg, MS.

Stauble, D.K. (1997). "Appendix A: Ebb and flood shoal evolution," *Ocean City, Maryland, and Vicinity Water Resources Study, Draft Integrated Feasibility Report and Environmental Impact Statement*, U.S. Army Corps of Engineers, Baltimore District, Baltimore, Maryland.

Thieler, E.R., Himmelstoss, E.A., Zichichi, J.L., and Miller, T.L. (2005). "Digital Shoreline Analysis System (DSAS) version 3.0: An ArcGIS© extension for calculating shoreline change," U.S. Geological Survey Open-File Report 2005-1304. Available online at <http: http://woodshole.er.usgs.gov/project-pages/dsas/>.

Underwood, S.G., and Hiland, M.W. (1995). "Historical Development of Ocean City Inlet Ebb Shoal and Its Effect on Northern Assateague Island," U.S. Army Engineer Waterways Experiment Station, Coastal Engineering Research Center, Vicksburg, MS.

U.S. Army Corps of Engineers. (1998). "Ocean City, Maryland, and Vicinity Water Resources Study Final Inegrated Feasibility Report and Environmental Impact Statement, Appendix D, Restoration of Assateague Island," Baltimore, Maryland.

U.S. Army Corps of Engineers Baltimore District. (2001). "Assateague Island, Maryland Environmental Restoratoin Project, Design Report," prepared by Civil Works Branch, Engineering Division, Baltimore District, April.

MORPHOLOGICAL RESPONSES TO JETTY CONSTRUCTION AT TIDAL INLET; LAKE SAROMA, JAPAN

Kentaro Hayashi[1], Koji Hashimoto[2], Takayuki Sasaki[3],
Akihiro Honma[4], Seizo Matsura[5]

1. Alpha Hydraulic Engineering Consultants Co., Ltd., 9-14 Hassamu Nishi-ku, Sapporo, Hokkaido, 063-0829, JAPAN.
   k-hayashi@ahec.jp.
2. Alpha Hydraulic Engineering Consultants Co., Ltd., 9-14 Hassamu Nishi-ku, Sapporo, Hokkaido, 063-0829, JAPAN.
   hashimoto@ahec.jp.
3. Alpha Hydraulic Engineering Consultants Co., Ltd., 9-14 Hassamu Nishi-ku, Sapporo, Hokkaido, 063-0829, JAPAN.
   sasaki@ahec.jp.
4. Cold Region Port and Harbor Engineering Research Center, 8 Kita 7 Nishi 2 Kita-ku, Sapporo, Hokkaido, 060-0807, JAPAN.
   honma@kanchi.or.jp.
5. National Institute for Land and Infrastructure Management, 3-1-1 Nagase, Yokosuka, Kanagawa, 239-0826, JAPAN.
   matsura-s2ec@ysk.nilim.go.jp

Abstract: Empirical orthogonal function (EOF) analysis is applied to examine the morphological responses to jetty construction at the first entrance of Lake Saroma, Japan with a 14-year bathymetric survey data set. The result clearly shows that the erosion trend along the channel and the accretions of ebb shoal far offshore appear during and after the jetty construction. Moreover, the volume change around the entrance is investigated, and the result agrees with that from EOF analysis. The entrance was found to be stable in analyzing the relationship between the tidal prism and the cross-sectional area.

INTRODUCTION

There are a few tidal lakes in Japan. Among them, Lake Saroma is famous for the basin size. Lake Saroma has the 3rd largest basin (151.7 km^2) in Japan and is facing the Sea of Okhotsk, located in the northern region. The tidal range at this lake is 1.12

m. The tidal prism is 9.83×10^7 m^3 (Kondo et al. 1988). In the past, an entrance was located at the east end of the lake. The old entrance was opened artificially every spring, and it closed naturally due to the littoral drift during winter. At present, two inlets, which were artificially opened on the eastern side (so-called first entrance) and western side (so-called second entrance), connect the lake to the ocean (Fig. 1). The distance between two entrances is about 13k m. The first entrance was opened in April 1929 and has never closed. And the narrowest width is about 250 m. A jetty began to be constructed at the western side in 1990 and was completed in 1997. The total length of the jetty is 443m. In this study, the morphological characteristics at this entrance are examined. The second entrance was open in 1979and is 50 m wide, which is much smaller than the first entrance. In addition, the bed and sides are protected by concrete and has dual jetties (100 m length). Two large scour holes have subsequently appeared at both the ocean and lake sides; however, the inlet has been stable. Inside the lake, there are many aquacultural work facilities for scallops, oysters and so on, and also serves as a refuge from high waves during stormy weather. Therefore, these inlets are extremely important for fisheries.

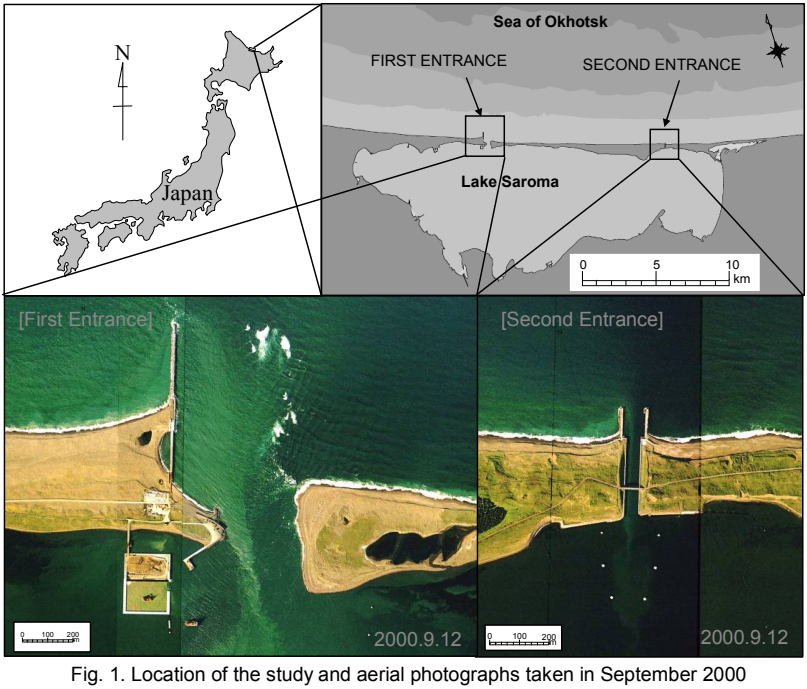

Fig. 1. Location of the study and aerial photographs taken in September 2000

There is one long-term wave observatory in the Sea of Okhotsk; Monbetsuminami. One of the most significant characteristics of this ocean is that the drift ice across the sea stays at the coast from the middle of January to the beginning of April. During

the term, the severe winter waves are prevented from attacking the coast. The observatory is located at about 28 km western from the inlet and the depth is 52.6 m. In this study, the observed result (2001.1.1 through 2004.12.31) is analyzed. From spring to summer, the wave climate is relatively clam and wave incidence toward shore from the east increases. From autumn to winter, the wave energy increases from NE and NNE.

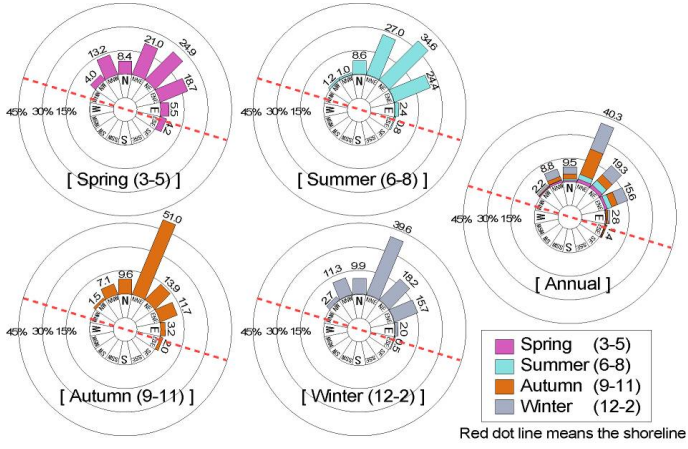

Fig. 2. Wave energy flux ratio for each direction observed at Monbetsuminami

There is no long-term current observatory along the coast. According to Fukushima et al. (1970), the maximum tidal current at the entrance was observed at more than 2.0m/s. A current observation was conducted from September to November in 1999. In this observation, an Acoustic Doppler Current Profiler (ADCP) was used to measure the current velocity at each vertical layer. Fig. 3 shows the measured points and the result at points 2.5 and 8.5m below the surface. The maximum ebb flow was 2.3m/s and the maximum flood flow was 1.7m/s.

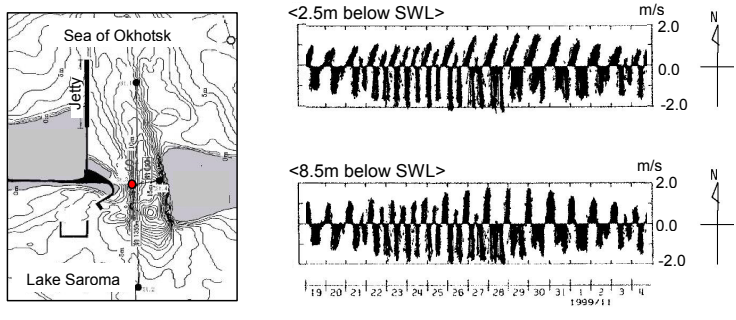

Fig. 3. Location and Result of Current Measurement in 1999

In terms of the longshore sediment transport, some researchers have studied it and made estimates. The predominant direction of longshore sediment transport is reported westward by Kikuchi et al. (1991). On the other hand, Uda et al. (2005) estimated that the longshore sediment transport eastward is dominant, which was investigated from comparison of aerial photographs, which was taken in 1947 and 2001. It is, therefore, difficult to determine the dominant direction and magnitude of longshore sediment transport on this coast.

Kikuchi et al. (1991) summarized the characteristic of grain size around the entrance and the coast. The median grain size at the entrance was very coarse and the maximum grain size was 15.5 mm. On the other hand, sediment around the entrance is comparatively fine. The average median grain size around the shorelines was less than 1.0 mm.

BATHEMETRIC ANALYSIS

Since its opening in 1929, many surveys were conducted at the western inlet. Fig. 4 describes the progress of the bathymetry, influenced by the jetty construction. Before jetty construction, Kikuchi et al. (1991) reported that the characteristic of the morphological changes at the inlet mouth, which is greatly influenced by the tide and wave, was for the channel thalweg to curve to the western offshore. The spit is growing from the east side due to the dominant longshore sediment transport and the tide breaks through the spit and then the channel thalweg made straight toward offshore. After the jetty construction, the channel thalweg has been kept straight toward offshore without curving westward, and the end of the terrace also has moved far offshore.

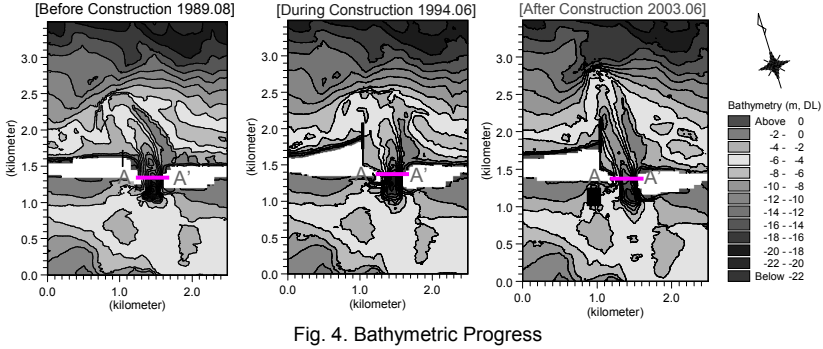

Fig. 4. Bathymetric Progress

When the cross-sectional profiles at A-A' (see Fig. 4) of the inlet-entrance are compared, during the construction of the jetty, the depth increased at the center of the entrance, and the west side has been gradually eroded. After construction was completed, the west side eroded continuously eroded and the depth at the center of the entrance became shallow, because the tidal thalweg have been shifted toward the

west jetty. On the other hand, the spit on the east side has been accumulated. However, the average cross-sectional area has not changed greatly, presumably controlled by the tidal prism of the lake (see Table 1).

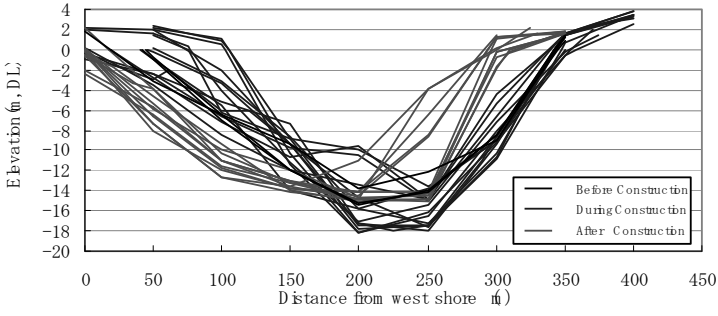

Fig. 5. Cross-sectional profiles at inlet mouth

Table 1. Cross-sectional area at inlet mouth

Time Period	Averaged Cross-sectional Area below DL, m^2
Before Construction (1989-1990)	2700
During Construction (1990-1997)	2720
After Construction (1997-2003)	2800

In consideration of the equilibrium cross-sectional are of this inlet, it is difficult to determine how much area is influenced by each inlet. In this study, the cross-sectional area is supposed to be the same as the sum of the narrowest profiles of both inlets. According to Fig. 6, the total area falls inside at the 95% confidence limits of the trend equation between cross-sectional channel area and the tidal prism (Jarrett 1976). Therefore, the inlet mouth has almost achieved equilibrium.

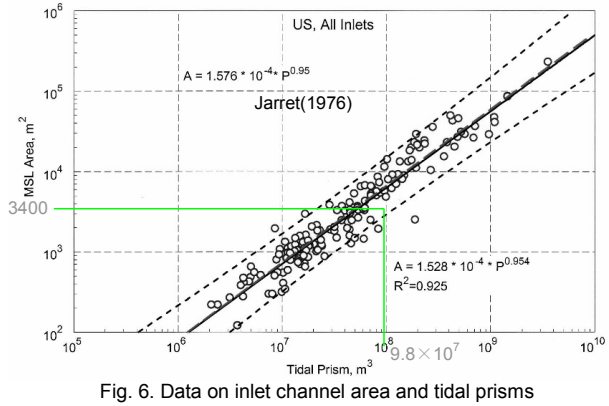

Fig. 6. Data on inlet channel area and tidal prisms

EOF ANALYSIS

Empirical orthogonal function (EOF) analysis, which is also referred to as principal component analysis (PCA), is one of the useful statistic methods to compress complicated variability of three-dimensional bathymetric data either in space and in time into the fewest possible number of modes. This method is widely applied for analyzing the morphologic characteristics (e.g. Katoh et al. 1980; Kuriyama 2002; Uchiyama et al. 2003). This method is basically different from the basic analysis, which includes Fourier analysis, and empirically determine the $e_n\ (x,y)$ and $C_n(t)$ based on the observed three-dimensional data. In this analysis, the observed data is expressed by

$$z(x,y,t) = \sum_n C_n(t) e_n(x,y) \tag{1}$$

where $z(x,y,t)$ = the observed data (m); x = offshore distance (m); y = the alongshore distance (m); $e_n\ (x,y)$ is the variable in space; $C_n(t)$ = the variable in time (m); and the subscript n is the n-th principal components.

In this study, 23 surveys during 14 years are analyzed to investigate the morphological characteristics, because the origin point in the old surveys is not more accurate than those surveyed in recent years. The surveyed area covers a 2.5km alongshore and a 3.5km on-offshore, from the offshore region at the 20m water depth (i.e. D.L.-20.0m) to the lake at about 5m water depth. Here, D.L. is the local datum level and is equivalent to the mean lower low water (MLLW) of the area.
In order to make the influences of jetty construction clear, the observed time period is divided into two intervals; Term A (1990~1997), focused on the construction of the jetty, and Term B (1997~2003), after the construction of the jetty is complete.

Table 2. Variances from EOF analysis

	Term A	Term B
Mode 1	35.3%	53.6%
Mode 2	23.6%	17.0%
Mode 3	10.4%	7.0%

Table 2 shows the variances for each mode. The total sums of the variances are 69.3% in Term A and 77.6 % in Term B. This shows that these three modes seem to mostly describe the morphological change in this area. The results of the first mode are displayed in Fig. 6. In Term A, the C_1 is decreasing constantly for first several years. This means the bathymetric change is constant. In other words, the channel thalweg at the entrance is eroded due to the changed direction of tidal flow straight toward offshore and the ebb shoal is accumulated offshore. After the several years, the constant C_1 means the channel keeps straight toward offshore. Also, the western shore is advanced offshore by the jetty construction. During Term B, the C_1 is decreasing constantly. Regarding to Fig. 7, the jetty construction trains the tidal flow along the jetty and push the sand offshore and right side.

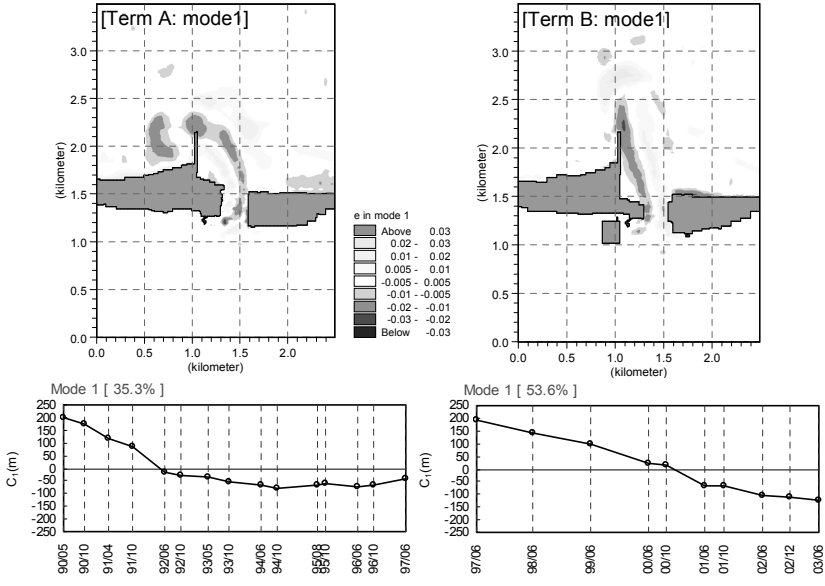

Fig. 7. Result of EOF analysis

VOLUMETRIC ANALYSIS

The surveyed area is divided into 5 sections (A through E) to understand the trend of volume change during and after the jetty construction. Fig. 8 shows the accumulated volume change for each area. The result is summarized by Fig. 9.

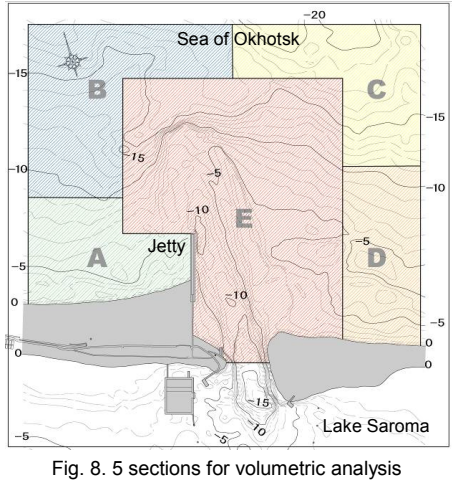

Fig. 8. 5 sections for volumetric analysis

As seen in Fig. 9, during the jetty construction, Section A has an accretion trend gradually and the other sections are almost constant, although they have both erosion and accretion trends. The volumetric change ratio in Section E, however, is greater than the other sections. These trends are clearly shown in the result of EOF analysis. After jetty construction, all sections have an accretionary trend for several years. Especially, Section E accumulates over 1 million m^3. This could be the influence of trapping longshore sediment transport. After several years, Section E starts to be eroded and the other sections seem to be almost stable.

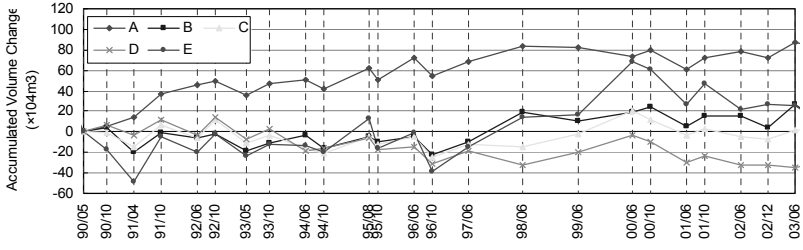

Fig. 9. Accumulated volume change for each section

CONCLUSION

The result of the EOF analysis is in agreement with observed the significant morphological characteristics at the western inlet, Lake Saroma, Japan. The constant erosion in the thalweg and the accretion in the offshore ebb shoal appear to be represented successfully. Also, when the cross-sectional volume is examined, this inlet was found to be stable. Since 2003, at the east side, new jetty construction was also started. In future work, we would like to apply a numerical approach to the morphological change at this site and continue to monitor the morphology influenced by the new jetty.

ACKNOWLEDGEMENTS

We would like to express appreciation to the cooperation and efforts of Abashiri Port and Harbor Office, Hokkaido Regional Development Bureau, Ministry of Land, Infrastructure and Transport, Japan for providing the great number of bathymetric survey data and aerial photographs. We appreciate a critical review of this paper given by Dr. Nicholas C. Kraus, of the U.S. Army Engineer Research and Development Center, Coastal and Hydraulics Laboratory, and Dr. Hideo Kondo, of Alpha Hydraulic Engineering Consultants Co., Ltd.

REFERENCES

Fukushima, H., Ozaki, A., Kashimamura, M., Yakuwa, I., and Takahashi, M. (1970). "Hydrodynamics at Lake Saroma," *Proceedings of 17th Japanese Conference on Coastal Engineering*, JSCE, 211-217p (in Japanese).

Jarrett, J. T. (1976). "Tidal Prism-Inlet Area Relationships," *GITI Report 3*, U.S. Army Engineer Waterways Experiment Station, Vicksburg, MS, USA.

Katoh, K., and Yoshimatsu, A. (1984). "A New Method of Three-Dimensional Empirical Eigenfunction Analysis for Contour Maps," *Report of the port and harbour research institute*, Ministry of Transport, JAPAN (in Japanese).

Kikuchi, K., Uda, T., Kawamori A., and Sasaki, T. (1991). "Morphological change at the entrance of Lake Saroma," *Proceedings of the Coastal Engineering Conference in Japan,Vol.38(1),* JSCE, 341-345p. (in Japanese)

Kondo, H., Nitta, N., and Toma, S. (1988). "Tidal Entrances in the okhotsk coast, JAPAN," *Proceedings of 9th IAHR Ice Symposium 1988 Sapporo*, 103-111p.

Kuriyama, Y. (2002). "Medium-term bar behavior and associated sediment transport at Hasaki, Japan," *J. Geophys. Res., Vol. 107, No. C9, 3132, doi:10.1029/ 2001JC000899*.

Uchiyama, Y., and Kuriyama, Y. (2003). "Complex Principal Component Analysis of Medium-term Nearshore Geomorphology at North Sendai Coast, Japan," *Proceedings of Coastal Structure '03*, ASCE.

Uda, T., San-nami, T., Hoshigami, Y., Serizawa, M., Kumada, T., and Sakai, K. (2005). "Beach erosion caused by obstruction of continuous longshore sand transport – an example of coastline between Monbetsu port and Lake Saroma in hokkaido," *Annual Journal of Civil Engineering in the Ocean Vol.21*, JSCE, 451-456 p.

MORPHODYNAMICS OF TEXEL INLET, THE NETHERLANDS

Edwin P.L. Elias[1,2], Marcel J.F. Stive[2]

1. WL | Delft Hydraulics, PO Box 177, 2600 MH Delft, The Netherlands. edwin.elias@wldelft.nl.
2. Faculty of Civil Engineering and Geosciences, Hydraulic and Offshore Engineering Division, Delft University of Technology, P.O. Box 5048, 2600 GA Delft, The Netherlands. m.j.f.stive@tudelft.nl.

Abstract: Different aspects of both the short- and long-term morphological evolution of Texel Inlet, and the underlying processes and mechanisms were studied, ranging from long-term descriptions of historic inlet evolution, 1550 A.D. to present, to detailed analyses of hydrodynamics and morphodynamics on the process scale using the latest state of the art process-based models. It is shown that the morphodynamic evolution of the inlet is governed by human intervention. At present a large sediment import (5-6 Mm^3/year) prevails as a result of a second-stage adaptation process to the effects of Closure of the Zuiderzee in 1932.

INTRODUCTION

Texel inlet, the largest inlet in the Dutch Wadden Sea, has undergone drastic changes in the morphology of its back-barrier basin, ebb-tidal delta and adjacent coastlines after the closure of the Zuiderzee (1926-1932). As a result large sand losses were observed along the adjacent coastlines and still until today the maintenance of this part of the coast is the most intensive of the entire Dutch coast. The processes controlling the sediment exchange between the North-Holland and Texel coasts, the ebb-tidal delta, tidal inlet and back-barrier basin are insufficiently understood despite intensive monitoring and analysis. This paper summarizes the results of a 4-year study aiming to acquire more understanding of this sediment exchange and of the inlet morphodynamics in general. The research covered a wide range of temporal and spatial scales ranging from long-term descriptions of historic inlet evolution, from 1550 A.D. to present, to detailed analyses of hydrodynamics and morphodynamics on a tidal and seasonal process-scale.

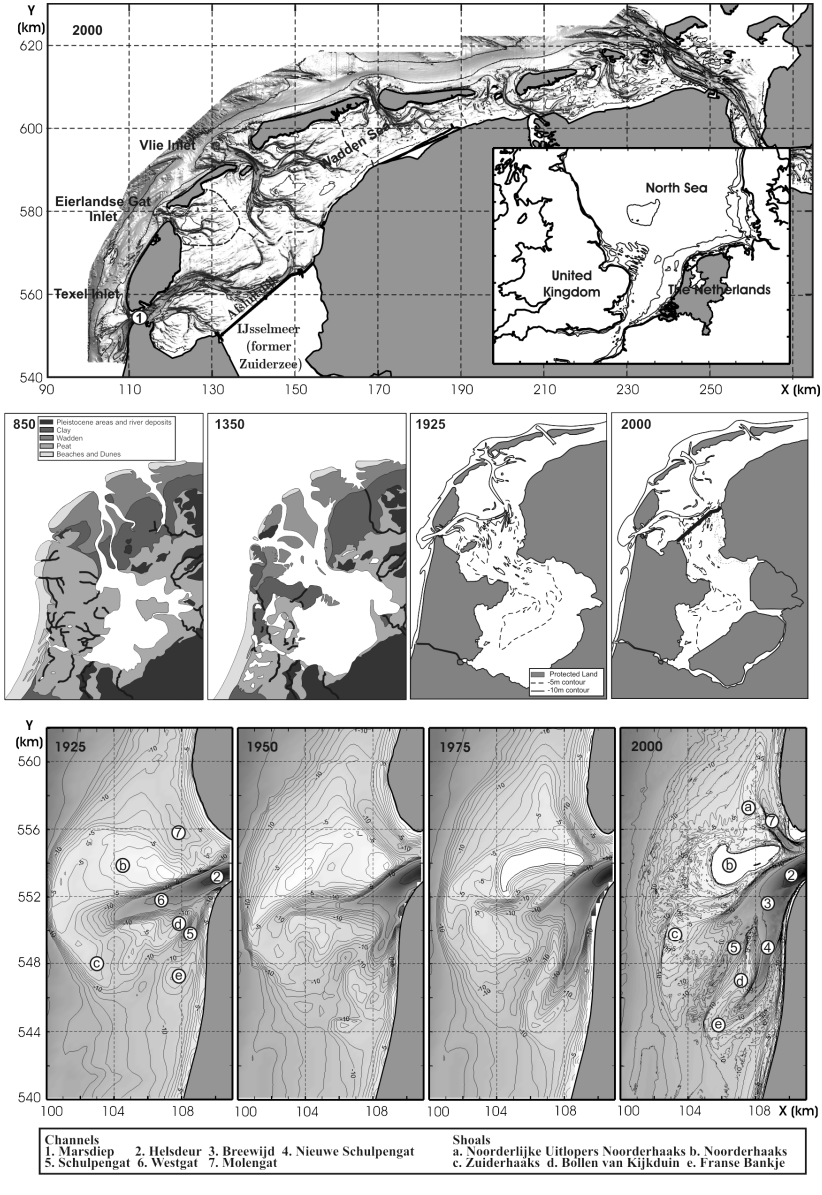

Figure 1: Location map of Texel Inlet in its present form (top panel), development of the inlet and basin through time 850 A.D - 2000 A.D. (middle panels), and evolution of the ebb-tidal delta in detail since closure of the Zuiderzee completed in 1932 (bottom panels).

STUDY AREA

Texel Inlet is the largest tidal inlet of the Dutch Wadden Sea, and is located in the north-western part of The Netherlands between Den Helder and the barrier island of Texel (Fig. 1 top panel). With bathymetric data of the inlet and ebb-tidal delta being available since the 16th century, the inlet is probably the longest regularly monitored inlet worldwide.

Tides and wind-generated waves are the dominant (natural) processes governing the morphological developments. Only a small supply of fresh water through the discharge sluices in the Afsluitdijk is present. Following the classification of Hayes (1979) the inlet qualifies as mixed-energy wave-dominated, even under spring tide conditions. However, the morphology of the inlet shows tide-dominated characteristics such as a large ebb-tidal delta. This is caused by the large tidal prism and the relatively low wave energy.

The inlet gorge is formed by Marsdiep that is about 2.5-km wide with a maximum depth of 53 m. The semi-diurnal tide with a mean tidal range of nearly 1.4 m in Marsdiep produces an average tidal prism through the inlet of $1x10^9$ m^3 with maximum tidal velocities ranging between 1.0 and 2.0 m/s. At present, the ebb-delta shoals protrude approximately 10 km seaward and stretch 25 km alongshore, determining the nearfield bathymetry of the adjacent North-Holland coast in the south and the Texel Island coast in the north (see Fig. 1 bottom panel 2000 for details).

Most of the bed sediment in the basin consists of fine sand with a median grain size around 200 μm. Grain size diameter decreases towards the mainland. Near the inlet sediment diameters over 450 μm are observed locally. On the ebb-tidal delta largest grain diameters (exceeding 450 μm) are observed in the inlet channel and proximal ebb-delta channels. Generally, in seaward direction the grain size decreases towards values between 150 and 200 μm on the shoals and 250 to 350 μm in the distal parts of the channels. The varying bed composition, presence of erosion resistant layers and coastal defence works must have played a role in the present stable state of the ebb-delta (Elias and van der Spek, 2006).

LONGTERM INLET EVOLUTION

To a varying degree of accuracy Texel Inlet's ebb-tidal delta bathymetry has been monitored over the last 400 years forming a globally unique morphodynamic dataset. This series of regular bathymetric observations allows the description of the inlets long-term morphodynamic evolution.

Texel Inlet is believed to have evolved from a small local drainage channel (Fig 1, 850 A.D.) that connected to the inland Zuiderzee around the 12th century A.D. after a series of severe storm events (Fig 1, middle panel 1350 A.D.). The size of the inlet increased with time as a result of subsidence of the surface level due to excavation and drainage of low-lying peat areas bordering the inlet's initial basin for agricultural use. With increasing basin volume the tidal prism through the inlet increased considerably causing the inlet channels to scour and increase in depth and width. Up to c. 1600 A.D. this

natural feedback mechanism of erosion and increasing tidal prisms governed the development of the inlet system. Ever since an increasing impact of major engineering works (e.g. construction of dykes, embankments, coastal protection works in the inlet gorge and recently the damming of the Zuiderzee completed in 1932 (Fig. 1925 and 2000) have governed the morphodynamic behavior and evolution of the system.

The well-monitored changes in ebb-tidal delta morphology, each characterized by specific orientations of the main channels and shoals, clearly show the impact of the inlet modifications and anthropogenic changes in the back-barrier basin (see Elias and van der Spek, 2006 for details). Prior to construction of extensive coastal defense works on the southern shore of the inlet in 1750 A.D. (predecessors of what is now known as Helderse Zeewering) the ebb-tidal delta showed a downdrift asymmetry, while the inlet gorge migrated southward. Periodic shoal breaching and downdrift channel relocation were the dominant mechanisms for sediment bypassing (major shoal bypassing). This period is most representative for the 'natural' behavior. After construction of the coastal defense works, a stable ebb-tidal delta with a westward stretching main ebb-channel developed over a period of c. 60 years. Sediment bypassing took place as minor shoal bypassing; the main channel remained in a westward position and smaller parts of the swash platform (periodically) migrated landward over the ebb-tidal delta to attach to the downdrift Texel coast. See Fig. 1, bottom panel, 1925 for a representative bathymetry for this situation.

The closure of the Zuiderzee (1925-1932) is the largest single intervention ever constructed in the Wadden Sea. Preceding the closure, the Texel and Vlie tidal basins covered the southwestern part of the Wadden Sea and the former Zuiderzee (Fig. 1, middle panel 1925). In total, the basin covered a surface area over 4000 km^2 with a basin length of 130 km. After the closure, the basin area reduced substantially to an area of roughly 712 km^2 (Fig. 1, middle panel 2000) and a length of about 30 km. The closure considerably altered the hydrodynamics and morphodynamics in the remaining active part of the basin (Elias *et al*., 2003 and Elias and Van der Spek 2006). The tidal characteristics changed from predominantly propagating to a more standing tidal wave resulting in an increase of the tidal range and tidal prism through Marsdiep by approximately 26%. With these large changes in hydrodynamics and particularly in basin geometry pronounced changes in the morphology of the inlet have taken place. The closure separated the back part of the basin (Zuiderzee) that contained a relative large portion of shoals. In the remaining active part of the basin the remaining shoals area was too small compared to the channel area, therefore, a morphologic adjustment of the basin was to be expected.

On the ebb-tidal delta a two-stage adaptation is observed. The initial (first-stage) response of the ebb-tidal delta lasted approximately 40 years. In this period the changed tidal characteristics of the basin and increased tidal prisms through the inlet forced an asymmetrical ebb-tidal delta development with updrift (southward) directed main channels (Fig. 1 bottom panels). Over 200 million m^3 of sand was eroded from the ebb-tidal delta and coastlines (due to scouring of channels) and deposited in the basin. The re-orientation of the main channels on the ebb-tidal delta since closure has had large

consequences for the coastal maintenance of the adjacent coasts. Both, the Texel and the North-Holland coastline are still subject to structural erosion and maintenance of these stretches of coast belongs to the most intensive of the entire Dutch coastal system (Mulder, 2000; Roelse, 2002).

The morphodynamic adjustment process is interesting as the observed behaviour of ebb-tidal delta and basin cannot be described by generally accepted empirical relations. For example, an increase in tidal prism through Marsdiep was observed despite the apparent reduction of basin area after closure. This increase is related to the changes in tidal wave characteristics from a propagating to a more standing wave character, and amplification of the tide due to reflection at the closure dam (Elias *et al.* 2003). A second interesting aspect is the decrease in ebb-delta volume. According to the empirical relation of Walton and Adams (1976) the volume of sand confined in the ebb-tidal delta (V_0) relates to the tidal prism magnitude (P) and an empirical constant ($V_O = cP^{1.23}$). With the 26% increase in tidal prism magnitude after closure an increase in ebb-delta volume was expected. In reality large sand losses were observed. One of the main reasons for these discrepancy between observed and based on empirical relations expected behaviour is the dominant effect of the human interventions. The well-monitored large-scale changes on the ebb-tidal delta, which were initiated by the construction of the coastal defence works and closure of the Zuiderzee, show that in-corporation of inlet modifications and back-barrier processes is vital for a correct description of the ebb-tidal delta dynamics and processes of Texel Inlet (Elias and van der Spek, 2006).

SEDIMENT BUDGET SINCE CLOSURE OF THE ZUIDERZEE

The sediment import into the Wadden-Sea was identified as one of the major sources of sand loss in the Dutch coastal sand balance (Stive and Eysink, 1989; Mulder, 2000). Partly, this sediment import is related to relative sea-level rise (Louters and Gerritsen, 1994), and partly import relates to the infilling of closed of channels after the damming of the Zuiderzee (Elias *et al.*, 2003; Elias, 2006). Previous studies agreed on the net sediment influx into the basin since the Zuiderzee damming, but estimates of the present import rates and predictions on future evolution varied between 0 - 3 Mm^3/year.

A major reason for this large variation in import rates is that these studies assumed that the individual inlets in the Wadden Sea can be defined as 'more or less' unconnected sub-systems separated by tidal divides. In principal basin and ebb-delta form a coherent morphological system and the volume change of ebb delta and basin are related; if the ebb-tidal delta erodes a corresponding rate of sedimentation in the basin is expected. Comparing the sediment volume change of Texel and Vlie basin and ebb-tidal delta in detail (upper plots of Fig. 2) we can observe a clear imbalance between ebb-tidal delta and basin changes on individual inlet level; the Texel ebb-tidal delta looses nearly 100 Mm^3 of sediments, while the basin volume remains near constant. A similar but opposite discrepancy is observed in the Vlie inlet system. An important conclusion from the individual sand balances is that we cannot describe the sediment budgets of the inlets separately.

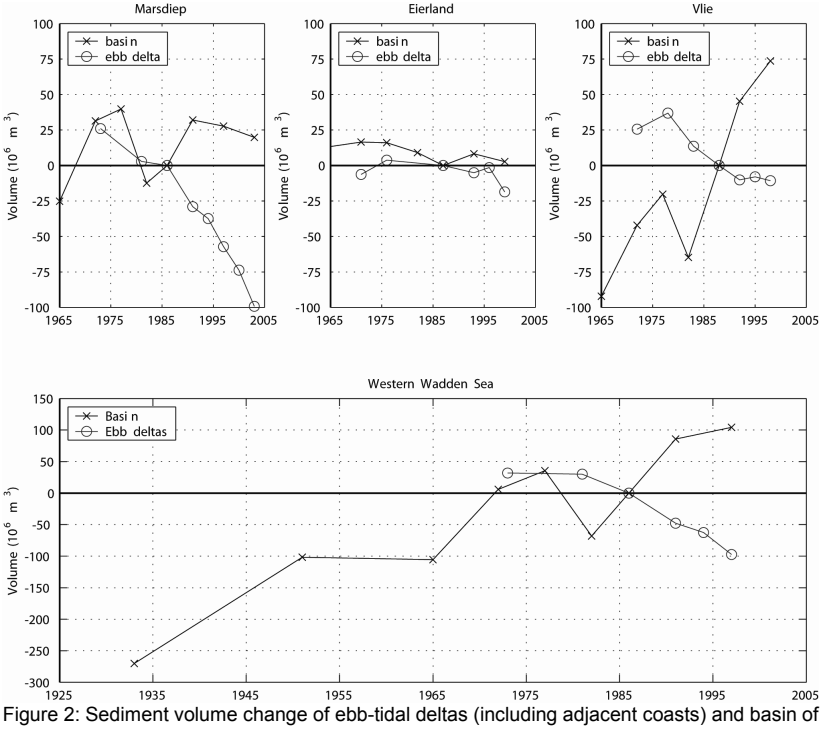

Figure 2: Sediment volume change of ebb-tidal deltas (including adjacent coasts) and basin of the western Wadden Sea. Upper plots: sediment budgets on inlet level over the period 1965 - 2003, lower plot: sediment budget for Texel, Vlie and Eierlandse Gat inlet combined (1927-1997). All plots relative to the 1986 volume.

The sediment budget of the entire western Wadden Sea (Texel, Vlie and Eierlandse Gat inlet combined) shows a near 400 Mm^3 of sediment deposition in the basin over the period 1927 – 1997 (Fig 2). The relative large fluctuations between 1950 and 1986 possibly relate to 18.5 year tidal modulations, or an indication of the measuring accuracy. The recent sediment import (1986 to present) ranges between 9 to 10 Mm^3/year of which most of the sediments, 5-6 Mm^3/year, are supplied by Texel inlet.

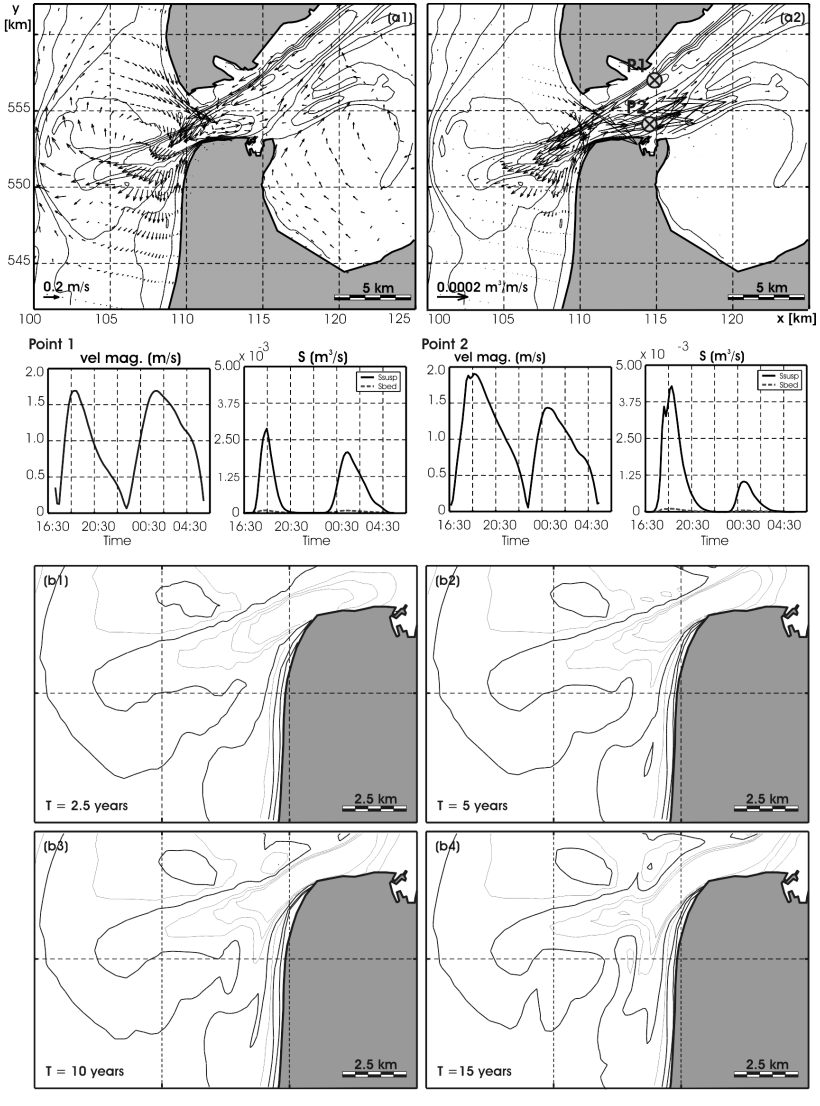

Figure 3 (a1 and a2): Delft3D Online morphology representation of residual flow and transport vector fields for the 1933 situation (directly after closure, before morphodynamic updating), (point 1 and 2) selected time-series for modeled flow and transport magnitude in point 1 and 2 during spring tide conditions, (b1 – b4) modeled development of a two-channel system on the ebb-tidal delta after 2.5, 5, 10 and 20 years of simulation (tidal forcing only).

INITIAL RESPONSE OF TEXEL INLET TO CLOSURE OF THE ZUIDER SEA

Elias and Van der Spek (2006) conclude that during the adaptation stage following the engineering works the large changes in the ebb-delta morphology cannot be described in terms of natural hydrodynamic processes such as the ratio of wave versus tidal energy alone. Moreover, these authors hypothesize that the morphodynamic ebb-tidal delta evolution after closure was triggered by the changed hydrodynamics in the basin. The altered tidal characteristics, the northward displacement of the basin centre, the closing of southward channels and the amplified tidal prism increased the discharges through Texelstroom. Texelstroom determines the ebb outflow into the inlet gorge that re-orientated resulting in a more southward-directed outflow onto the ebb-tidal delta. The expression back-barrier steering was introduced to describe this 'forcing' induced by the basin on the ebb-tidal delta.

Short-term hydrodynamic and morphodynamic process-based simulations (using Delft3D Online Morphology) were used to explore the importance of the main tidal asymmetries for the large sediment influx in the basin (not shown here), and the back-barrier steering mechanism (see Elias et al 2005 and Elias 2006 for details). Back-barrier steering is investigated by running the flow model for a 1-month period under tidal forcing using the buildin Van Rijn 1993 sediment transport solver (Lesser *et al.*, 2004). The tide-averaged flow and sediment transport patterns presented in Fig. 3 summarize the main model results. An interesting characteristic is the imbalance between the location of the largest residual flow and transports, and the position of the main channels (Fig. 3 a1 and a2). The main channel orientation is westward, whereas largest instantaneous and residual flow velocities and transports are directed southwestward towards Schulpengat. Major gradients in residual transport rates are observed at the locations where Molengat and Nieuwe-Schulpengat developed (erosion) and in Westgat (sedimentation). This inequality between flow and bathymetry, directly after closure before morphological updating, is interpreted as a manifestation of the back-barrier steering effect. With ongoing morphological adaptation of the bathymetry, filling in of Westgat and the scouring of Schulpengat and Molengat, the imbalance between transports and bathymetry and the residual transport rates decrease. The sediment influx is dominated by the large flood-dominant transports along the North-Holland coastline (point 2) that exceed the minor ebb transports along the Texel coastline (point 1). The suspended-load component dominates over the bed-load.

A model forced by tides only is capable of reproducing the major developments on the southern part of the ebb-delta (although time scales differ). Nieuwe Schulpengat enlarges and extends along the North-Holland coastline. Similarly to the observations first an ebb-chute develops along the coastline (Fig. 3 b3) that gradually increases in depth and length forming the main ebb channel. After 15 years of simulation (Fig. 3 b4) a two-channel system arises separated by a linear shoal (similar to the 1975 in the observations). The formation of the two-channel system is due to the segregation of ebb and flood flow. Ebb currents dominate the main channel and form a hydrodynamic obstacle for the flood currents. Flood currents are pushed seaward along the ebb-shield front. Already Van Veen (1950) showed the formation of separate ebb and flood channels separated by

shoals due to the evasive action of the ebb and flood flow. Although the scouring of the channels in the southern part of the ebb-delta is predicted, the landward migration and deformation of Noorderhaaks is not reproduced. This deficit indicates that Noorderhaaks developments are dominated by wave-driven processes that are not included in the present model.

SECOND-STAGE EFFECTS ON INLET MORPHODYNAMICS

With ongoing adaptation of the channels on the ebb-tidal delta a decrease in sediment import rates was expected. However no decrease can be observed by looking at the sediment budget (Fig. 2). The ongoing sediment re-deposition from the ebb-tidal delta into the basin is interpreted as a second-stage response to the effects of closure of the Zuiderzee. The majority of the Noorderhaaks deposits originate from the pre-closure ebb-tidal delta configuration wherein the main-ebb channel (Westgat) was westward orientated. Noorderhaaks was formed as an ebb shield balancing seaward supply of sediment by the ebb-tidal currents and landward wave-driven transports (Elias *et al.*, 2003). The closure of the Zuiderzee distorted this balance as the changed tidal characteristics of the basin forced an asymmetrical ebb-tidal delta development with updrift directed main channels (Fig. 1 bottom panels). This initial (first-stage) response lasted approximately 40 years, and the scouring of the large tidal channels eroded over 200 Mm^3 from the ebb-tidal delta. Due to the large tidal prism and corresponding large tidal transports involved, the channels regained an equilibrium state in a faster rate than the shoal areas (e.g. the abandoned ebb-shield Noorderhaaks). The present ebb-tidal delta development is dictated by the ongoing adjustment of these shoal areas.

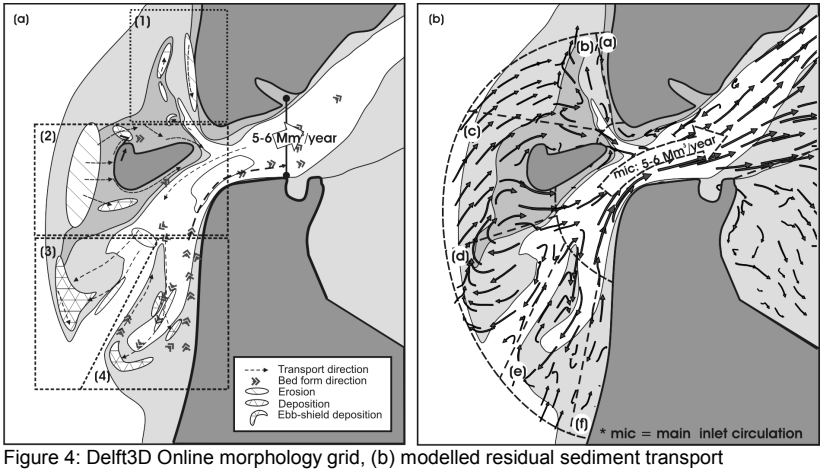

Figure 4: Delft3D Online morphology grid, (b) modelled residual sediment transport

Insight in the present-day behaviour of the Texel inlet system is obtained by focusing the analysis on recent measurements (1986-2003) that were obtained accurately, after stabilization of the channels on the ebb-tidal delta. A schematic depiction of the present-day flow and sediment transport patterns on the ebb-tidal delta based on the analysis of

recent measurements on flow, bedforms, sedimentary structures and sedimentation-erosion patterns is presented in Fig. 4a (based on Elias, 2006).

Despite a relative stability in the shape and form of the main channel and shoal areas on the ebb-tidal delta over the period 1986-2003 there are large morphological changes. Analysis of the sedimentation-erosion patterns shows that sediment redistribution, and local interaction between channels and shoals dictate the present morphological developments. In the north the landward migration of the Noorderlijke Uitlopers of Noorderhaaks and the corresponding displacement of Molengat induce severe erosion of the Texel coastline (Fig. 5, area 1). The central part of the ebb-tidal delta is dominated by landward displacement of sediments; erosion of the western margin of Noorderhaaks and deposition north and south of the supra-tidal part of Noorderhaaks (area 2). The channels Schulpengat and Nieuwe Schulpengat enlarge in depth. In the south we distinguish two areas, separated by Schulpengat, with dissimilar morphological behaviour; Zuiderhaaks (area 3) forms the spill-over lobe of the Nieuwe Lands Diep and Schulpengat channel showing a trend of sedimentation and southward growth. The Nieuwe Schulpengat area (4) is governed by the local interaction of the channel with the adjacent shoals. The Bollen van Kijkduin shoal migrates southward, inducing a small southward displacement and clock-wise rotation of Nieuwe Schulpengat and land-ward migration of the adjacent Franse Bankje shoal. Slip-face asymmetries of the dominant bedforms, derived from analysis of high-resolution multi-beam data, indicate that large flood dominant transports along the North-Holland coast into Marsdiep and towards Texelstroom prevail. The total sedimentation of the ebb-tidal delta is small compared to the erosion volume. As also the adjacent coastlines lose sediment a net sediment transport towards the basin must exist.

Delft3D Online morphology is used to identify the relevance of the governing processes and mechanisms, and to obtain insight in the physics behind the observed morphodynamic changes. The Delft3D Online Morphology model calculates morphologic changes simultaneously with the flow calculations (Fig. 5a shows the model grid). One of the major assets of this type of model is the capability to increase the spatial and temporal resolution of point-oriented field observations. Observations are used to force the model as realistically as possible (quasi real-time by measured time-series of wind, waves and tides) and the model results provide synoptic more or less realistic data of high spatial and temporal resolution over the entire inlet domain. Analysis of this data can provide valuable information on governing flow and sediment transport patterns in the instrumented and the uninstrumented areas. Additionally, such model approach allows for identification of the dominant processes systematically checking mechanisms by varying the forcing conditions. As a first step we modeled tidal transport patterns in order to understand the tidal rectification by interaction of the alongshore, northward, propagating open-sea tidal wave with the cross-shore inlet currents and compound ebb-delta bathymetry (Fig. 5c3). Interaction of tides with ebb-delta topography is known to result in compound flow patterns with local circulation patterns and complex morphodynamic behavior. Next we focused on the morphodynamic behavior by analysis of sediment transport patterns, month-averaged transport magnitudes and governing mechanisms. Here, we present example patterns on ebb-delta scale only.

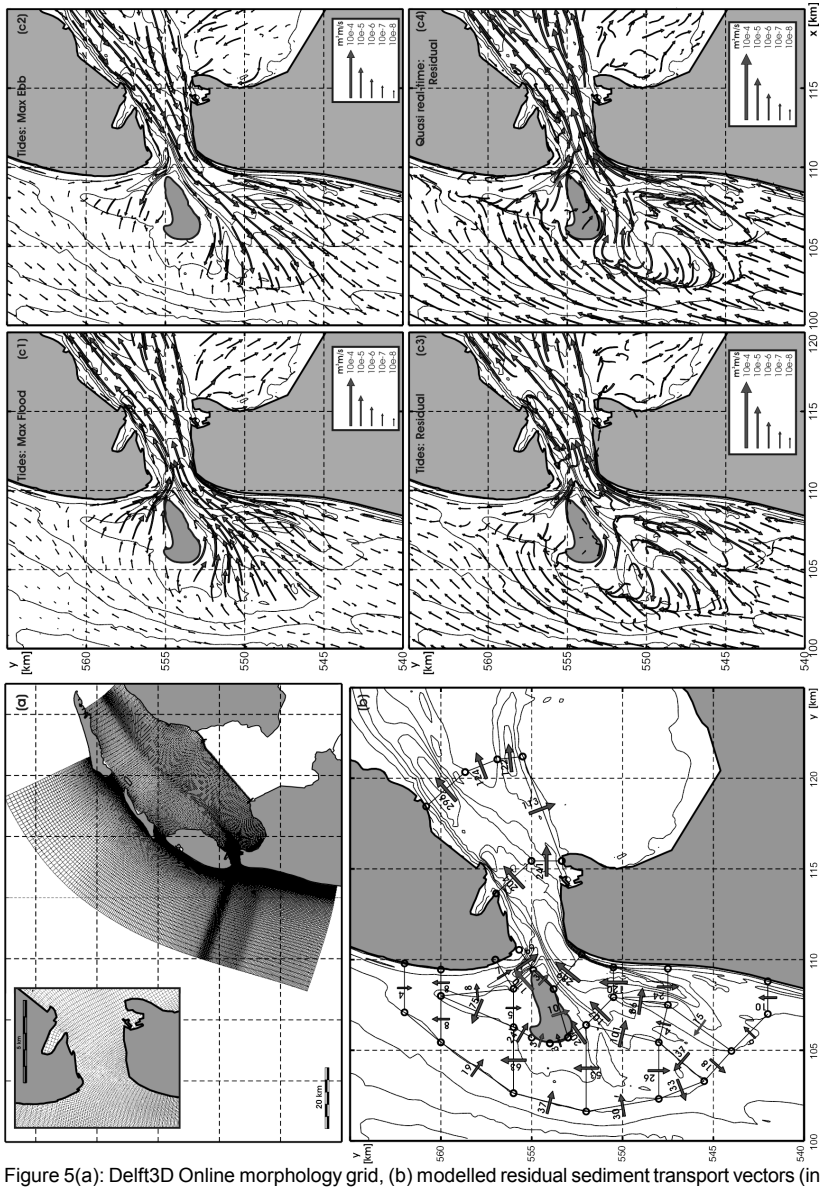

Figure 5(a): Delft3D Online morphology grid, (b) modelled residual sediment transport vectors (in 0.01 Mm3/year) over a 10-month period through a number of selected transects, sediment transport patterns for maximum flood and ebb (c1 and c2), tide-averaged sediment transport patterns for tidal and quasi real-time forcing (c3 and c4).

Figure 5 provides impressions of the modeled sediment transport patterns and transport magnitudes. Outside the ebb-delta domain (roughly bounded by the -15m depth contour) instantaneous and residual sediment transport rates are small compared to the large transports in the inlet channels. The qualitative correspondence in residual transport patterns between tidal and quasi real-time forcing in the southern part of the ebb-delta (Fig. 5c and 5d respectively) illustrates that the interaction of the inlet currents with the compound ebb-delta topography forms the principal mechanism for sediment transports. Due to the non-linearity between flow and transport the major contribution to the residual transport pattern occurs around maximum ebb and flood. During ebb the majority of the transports is flushed seaward onto the southern part of the ebb-delta (Fig. 5c2). Sediment transports through Nieuwe Schulpengat contribute to the accumulation of sand in the Bollen van Kijkduin and Franse Bankje shoals. Transports through Schulpengat and Nieuwe Westgat induce the outbuilding of Zuiderhaaks. Ebb-tidal transports on the western margin of the ebb-delta are minor due to the sheltering effect of Noorderhaaks. Flood transports enter the ebb-delta from the south increasing substantially towards the inlet gorge (Fig. 5c1) due to accelerated velocities. Near Helsdeur transports are further increased due to contraction of flow around the sharp curvature of Helderse Zeewering. As a result in the proximal part of the ebb-delta the flood flow and transports exceed the ebb resulting in a net import of sediment (Fig 5c3). Addition of non-tidal processes (mainly set-up in the inlet gorge) enhances the sediment import rates (Fig 5c4).

Despite relative small residual velocities (compared to the channels) the tidal transports on the western margin of Noorderhaaks show a distinct northward and landward direction. Waves augment these transports. The large shoal complex forms a wide 'surf-zone' area as the location of wave-breaking varies over this domain depending on wave-heigth; large waves lose their energy well ofshore on the ebb-delta front, while smaller waves can propagate relatively undisturbed to the major shoal areas. Similar to normal surfzone processes such as observed along the uninterrupted Holland coast loss of momentum and dissipation of wave energy due to wave-breaking become dominant contributors to the sediment transport The non-tidal mechanisms enhance the landward and northward transport of sediment on the Noorderlijke Uitlopers of Noorderhaaks. Most of the sediments supplied to the northern part of the ebb-delta are transported back into the main inlet circulation along the northern margins of the supra-tidal part of Noorderhaaks, through the Molengat channel, and into Marsdiep. As a result of this circuitous route only little sand actually bypasses the inlet onto the downdrift Texel coastline. Sediment bypassing mechanism at Texel inlet is probably more of an episodic phenomenon; sand accumulates in the downdrift Noorderlijke Uitlopers of the Noorderhaaks spit that eventually will breach and attach to the downdrift shoreline. Figure 4b summarizes the model results (Elias, 2006).

Analysis of monthly-averaged transport rates in Marsdiep indicates that sediment import into the basin is a more-or-less continuous process wherein both tidal and non-tidal contributions play an important role. The non-tidal part consists of near equal but opposite directed wind- and wave-driven contributions, and a larger input by set-up. Most of the sediments are supplied through the southern part of the ebb-delta. Tide and

wave-driven transports along the southern margin of the supra-tidal Noorderhaaks and setup driven contributions through Nieuwe Schulpengat form the major part. A minor part is supplied by the tide-driven sediment transports through Molengat.

CONCLUSIONS

The morphodynamics of Texel Inlet are studied over a wide range of temporal scales, ranging from long-term descriptions of historic inlet evolution, 1550 A.D. to present, to detailed analyses of hydrodynamics and morphodynamics on the tidal and seasonal process scale. A range of methodologies, varying from morphological interpretation of maps to understand long-term morphological developments and behaviour, to numerical process-based modelling and detailed analysis of field measurements to obtain fundamental knowledge of inlet processes was applied.

Over 400 years of regular bathymetric surveys of Texel Inlet and its ebb-tidal delta form a globally unique morphodynamic dataset. During the inlet's recorded history substantial changes in ebb-tidal delta evolution have occurred under the influence of the cumulative effects of human intervention. After construction of the coastal defence works in the inlet gorge (Helderse Zeewering) a stable ebb-tidal delta with a westward stretching main ebb-channel developed over a period of c. 60 years. Damming of the Zuiderzee, completed in 1932 A.D., separated the major part of the back-barrier basin and distorted this stable state; a two-stage adaptation of the ebb-tidal delta is observed. The initial (first-stage) response of the ebb-tidal delta lasted approximately 40 years. In this period the changed tidal characteristics of the basin and increased tidal prisms through the inlet forced an asymmetrical ebb-tidal delta development with updrift (southward) directed main channels. Over 200 million m^3 of sand was eroded from the ebb-tidal delta and coastlines (due to scouring of channels) and deposited in the basin. Tides are identified as the main process for these first-stage developments. Due to the large tidal prism and the corresponding large tidal transports involved, the channels regained equilibrium at a faster rate than the shoal areas (e.g. the abandoned ebb-shield Noorderhaaks).

The present-day ebb-tidal delta development is best described as a second-stage self-organizing process of sediment redistribution, sediment recirculation and sediment exchange to obtain a natural equilibrium state adapted to the changed configuration of the main-ebb channels. Sediment is eroded from the ebb-delta (including adjacent shorelines) and deposited in the basin. Largest erosion prevails on the western margin of Noorderhaaks were tides and waves are important for the landward displacement of sediments. Locally, sedimentation and erosion patterns are governed by channel-shoal interactions; the interaction of the channels Molengat and Noorderlijke Uitlopers of Noorderhaaks induces sediment loss of the Texel coastline, while the Nieuwe Schulpengat-Bollen van Kijkduin channel-shoal-system determines the development of the adjacent North-Holland coast. The presence of large flood-dominant channels along the coast induces a major sediment loss towards the basin. The sediment import in the basin through Marsdiep is estimated to range at 5 to 6 Mm^3/year. A number of aspects contribute to this large influx; (1) sediment deficit in the basin caused by the loss of intertidal shoal areas due to closure of the Zuiderzee and relative sea-level rise, (2)

availability of a vast amount of sediment in the abandoned ebb-delta front Noorderhaaks, and (3) transport capacity due to the large tidal prisms through the inlet.

The large ongoing sediment import into the basin shows that the effects of closure of the Zuiderzee are far from damped out, and it will take many decades before a new equilibrium will be reached.

REFERENCES

Elias, E. P. L., Stive, M. J. F., Bonekamp, J. G., and Cleveringa, J. (2003b). "Tidal inlet dynamics in response to human intervention" *Coastal Engineering Journal*, 45(4), 629-658.

Elias, E. P. L., Stive, M. J. F., and Roelvink, J. A. (2005). "Impact of back-barrier changes on ebb-tidal delta evolution" *Journal of Coastal Research*, 42(SI), 460-476.

Elias (2006). "*Morphodynamics of Texel Inlet*". Thesis, Delft University of Technology, Delft, 262 pp.

ELias, E. P. L., and Van Der Spek, A. J. F. (2006). "Long-term evolution of Texel Inlet and its ebb-tidal delta (the Netherlands)." *Marine Geology*, 225(1-4), 5-21.

Hayes, M. O. (1979). "Barrier Island morphology as a function of tidal and wave regime", Barrier Islands: From the Gulf of St Lawerence to the Gulf of Mexico, S. P. LEATHERMAN, ed., Academic Press, New York, 1-27.

Lesser, G. R., Roelvink, J. A., Van Kester, J. A. T. M., and Stelling, G. S. (2004). "Development and validation of a three-dimensional model", *Coastal Engineering*, 51, 883-915.

Louters, T., and Gerritsen, F. (1994). The Riddle of the Sands. A Tidal System's Answer to a Rising Sea Level., Report RIKZ-94.040. Rijkswaterstaat, The Hague.

Mulder, J. P. M. (2000). Zandverliezen in het Nederlandse kustsysteem. Advies voor dynamische handhaven in de 21e eeuw (in Dutch), Report RIKZ/2000.36. Rijkswaterstaat RIKZ, The Hague.

Roelse, P. (2002). Water en zand in balans. Evaluatie zandsuppleties na 1990; een morfologische beschouwing (in Dutch), Report RIKZ/2002.003. Rijkswaterstaat RIKZ, The Hague.

Stive, M. J. F., and Eysink, W. D. (1989). Voorspelling ontwikkeling kustlijn 1990-2090. fase3. Deelrapport 3.1: Dynamisch model van het Nederlandse Kustsysteem (in Dutch), Report H825. Waterloopkundig laboratorium, Delft.

Walton, T. L., and Adams, W. D. (1976). "Capacity of inlet outer bars to store Sand" *Proc. 15th International Conference on Coastal Engineering*, Honolulu, 303-325.

Van Veen, J. (1950). "Eb en vloedschaar systemen in de Nederlandse getijwateren" *Tijdschrift Koninklijk Nederlands Aardrijkskundig Genootschap*, 303-325.

Ridderinkhof, H., Van Haren, H., Eijgenraam, F., and Hillebrand, T. (2002). "Ferry observations on temperature, salinity and currents in the Marsdiep tidal inlet between the North Sea and Wadden Sea." Proc. 2nd int. conf. on EUROGOOS. Operational oceanography: implementation at the European and regional scales. Flemming, N.C. *et al.*, eds., Elsevier Oceanography Series, 66, pp: 139-148.

SEDIMENTATION PATTERNS IN A STABILIZED MIGRATORY INLET, BLIND PASS, FLORIDA

Ping Wang[1], David K. Tidwell[1], Tanya M. Beck[1], Nicholas C. Kraus[2]

1. Department of Geology, University of South Florida, 4202 E. Fowler Ave., Tampa, FL 33620, USA. pwang@cas.usf.edu
2. U.S. Army Engineer Research and Development Center, Coastal and Hydraulics Laboratory, 3909 Halls Ferry Road, Vicksburg, MS 39180-6199, USA. Nicholas.C.Kraus@erdc.usace.army.mil.

Abstract: The shoaling rate in Blind Pass entrance channel approximately equals the net southward longshore sediment transport rate. Most of the shoaling occurs along the northern side of the channel. Flow measurements and numerical modeling reveal that the ebb current is approximately twice as strong in the thalweg along the south side as compared to the rest of the channel. In contrast, the flood current is mainly uniform across the inlet and is stronger than the ebb flow over the northern portion. This flow-velocity distribution induced by a nearly 90-deg bend of the channel contributes to the shoaling pattern. Two years after the 2000 dredging, the shoal along the north side became shallow enough to induce wave breaking. Distinctive shoaling patterns influenced by seasonal wave climate were observed. Sediment deposition in the channel is closely related to the passages of cold fronts, which significantly increases the sediment supply by longshore transport.

INTRODUCTION

Tidal inlets are links between the coastal ocean and back-barrier bays, exchanging water, sediments, nutrients, and pollutants between them. Many inlets also serve as navigation channels. Because tidal inlets interrupt the continuity of shore processes, they often influence the sediment budgets and can cause beach erosion. Dean (1988) concluded that more than 80% of the erosion along the Florida coast can be directly linked to tidal inlets. Maintaining stable and deep navigation channels and also allowing for adequate sand bypassing provides a major challenge to coastal engineering. Understanding the processes that control shoaling at inlet channels is, therefore, an important challenge.

Blind Pass, a small stabilized migratory inlet, provides an excellent case for the study of inlet shoaling and interactions with adjacent beaches.

Blind Pass and the adjacent Johns Pass service a portion of Boca Ciega Bay along the west-central Florida coast (Fig. 1). The entire area, from the beach to the inlets to the back-bay, is heavily developed. The origin of Blind Pass is not clear. Before the opening of Johns Pass by a hurricane in 1848, Blind Pass was a major inlet along this stretch of the coast with large flood and ebb shoals. As Johns Pass captured a substantial portion of the tidal prism, Blind Pass became a wave-dominated inlet and started rapid southward migration. It was eventually stabilized with a series of hard structures. Following the stabilization, chronic shoaling of the channel and subsequent dredging occurred, along with a persistent erosion problem at the downdrift Upham Beach.

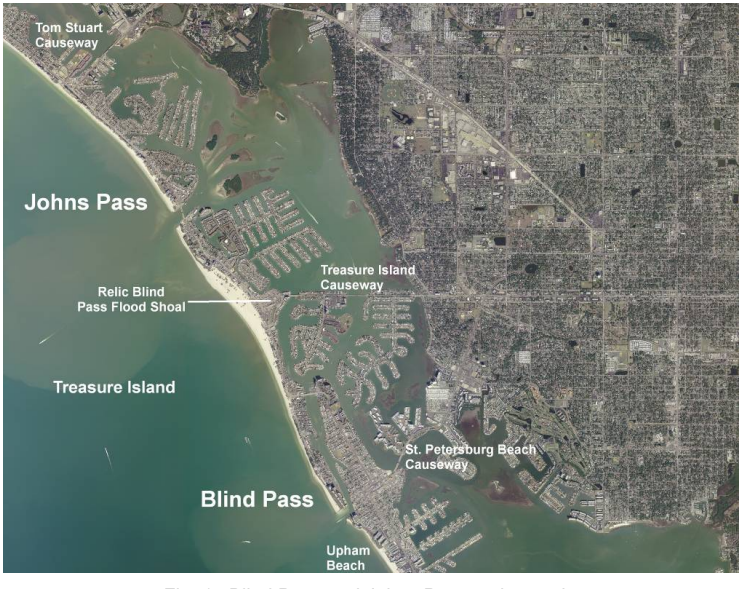

Fig. 1. Blind Pass and Johns Pass to the north.

This study quantifies the channel shoaling and associated processes following the last dredging in 2000. Time-series bathymetry surveys and flow measurements were conducted along with circulation modeling of the Blind Pass and Johns Pass system. The overall goals of this study are to understand the rate and processes of shoaling in the inlet channel and its interaction with adjacent beaches. Specific objectives include: 1) quantifying the shoaling and scouring pattern in the inlet channel, 2) investigating wave conditions and tidal flow velocities, particularly in relation to the inlet morphology change, and 3) determining the relationship between morphology change and the driving forces.

HISTORICAL EVOLUTION AND ENGINEERING AT BLIND PASS

Blind Pass is one of the most artificially modified inlets along the west-central Florida coast (Davis and Barnard 2000). Most of the engineering efforts are aimed at halting lateral inlet migration and reducing shoaling in the inlet entrance channel. The jetties have successfully stopped the longshore migration; however, channel shoaling has continued, and severe and persistent downdrift erosion was induced. The inlet needs to be dredged periodically and the sand used to nourish the adjacent beaches, especially Upham Beach, located directly to the south and downdrift.

Before 1848, Blind Pass was a fairly large inlet and was located directly gulfward of its flood shoal (Fig. 1). The opening of Johns Pass that year started a substantial trend of decreasing tidal prism at Blind Pass. As a result, the inlet began to migrate rapidly to the south so that, by 1926, the inlet had migrated more than 2 km. The year 1937 marks the beginning of direct stabilization with initial dredging and construction of the south jetty and seawall. Continued sediment shoaling in the inlet entrance channel led to extension of south jetty in 1951 and construction of the north jetty in 1962. Also, between 1940s and 1960s, extensive dredge-and-fill construction was conducted in Boca Ciega Bay (Fig. 1). The artificially created land, as well as construction of several causeways, resulted in significant reduction of back-bay area, and thus a further decrease in tidal prism. The south jetty was extended in 1975, and a weir with a 12-m gap was added in 1986. The weir was closed in 2004. The north jetty was extended in 1976 and 1983. These structures along with the significantly decreased tidal prism have made Blind Pass channel a trap of the southward longshore transport allowing little to no bypassing. In order to maintain the channel, the inlet was dredged in 1937, 1964, 1969, 1975, 1979, 1983, 1990, and 2000.

Artificial interferences on the morphodynamics of Blind Pass are illustrated well by time-series aerial photographs (Fig. 2). Blind Pass is characterized by a nearly 90-deg. turn before entering the Gulf of Mexico. We focus on the entrance channel at and gulfward of the turn. In 1926 (Fig. 2A), the inlet was still in pristine condition. A large ebb shoal and southward sand bypassing are apparent. By 1942 (Fig. 2B), the south side had been stabilized. The ebb delta and southward bypassing are still visible, but to a reduced degree. Beach erosion at Treasure Island to the north becomes obvious. By 1957 (Fig. 2C), the ebb shoal and southward bypassing are still visible. At the same time, erosion at the updrift Treasure Island had become severe. By 1969 (Fig. 2D), both sides of the inlet were stabilized. The ebb shoal and southward bypassing diminished substantially. Through a combination of jetty, groin field, and beach nourishment, erosion at the updrift Treasure Island was mitigated. However, severe erosion at downdrift Upham Beach to the south developed. Shoaling of the inlet channel and severe erosion downdrift are the main features of the 1984 photo (Fig. 2E), which was taken a year after the 1983 dredging. The ebb shoal and southward bypassing become indistinguishable. This trend continued and is shown in the 2000 photograph (Fig. 2F) just before the last dredging to date. The present study on shoaling in the channel was commenced after the 2000 dredging.

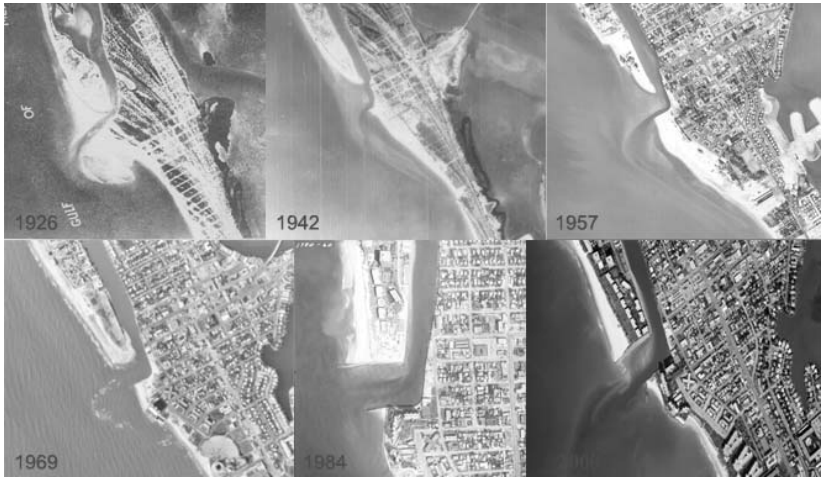

Fig. 2. Time-series aerial photos of Blind Pass.

METHODOLOGY

The present study examines sediment shoaling in the Blind Pass entrance channel via a series of field investigations, through which a numerical model of circulation was established. Time-series bathymetric surveys were conducted, as well as flow measurements. Bathymetric surveys were conducted roughly quarterly from August 2002 to June 2004. The surveys were conducted with a combination of precision echo sounder for depth and a synchronized Real-Time-Kinematic (RTK) Global Positioning System (GPS) for position. Water level variations were measured to cross-check the tidal influence on the floating platform survey. During the study, the northern side of the inlet became too shallow to survey by boat. Level-and-transit surveys using an electronic total station were conducted there monthly from February 2003 to February 2004. The monthly survey of 9 lines over the northern shoal, extending to roughly 1.5 m water depth, was designed to capture the infilling rate and pattern over this active shoaling area (Fig. 3). Surveys are referenced to NGVD29, which is roughly 0.15 m below mean sea level in this area.

Tidal flow patterns through the inlet were measured using an upward-looking acoustic Doppler current profiler (U-ADP) in combination with a side-looking ADP (S-ADP). Therefore, flow patterns both through the water column and across the channel were measured. The flow measurements were conducted at two locations with one near the mouth and one near the bend, each for approximately one month (Fig. 3). In addition, flow velocities were measured simultaneously using two U-ADP placed in the thalwegs near the entrances of Johns Pass and Blind Pass. These data are valuable for examining the interaction of the two inlets and for validating the circulation model.



Fig. 3. The north shoal profiles and locations and times of current meter deployments.

A two-dimensional finite-difference model of depth-averaged circulation, the Coastal Modeling System (CMS)-M2D (Buttolph et al. 2006), was set up to simulate tidal-driven flow patterns at both Johns Pass and Blind Pass. A grid consisting of 15x15 m elements and covering approximately the hydraulic circulation extent of the back-bay was generated based on a 2006 bathymetry survey conducted by this study. The model was driven by water-level measurements obtained in January 2001 at Johns Pass and verified with the flow data as described in the above paragraph. The CMS-M2D model has been applied extensively in tidal inlet modeling (e.g., Kraus and Militello 1999; Militello and Kraus 2003; Bounaiuto and Militello 2004). The CMS is a product of the U.S. Army Corps of Engineers' Coastal Inlets Research Program.

RESULTS AND DISCUSSION

Sediments along the west-central Florida coast are composed of fine quartz sand with various amounts of, typically larger, shell debris. At present, sediment in the Blind Pass channel varies greatly from the channel thalweg to the shoal area. The surface sediment in the channel thalweg is mostly shell lag with grain size ranging from several mm to several cm. The mean grain size of sediment along the slope of the main channel averages about 0.35 mm, with a considerable amount of shell debris. The mean grain size of sediment in the shoal area averages about 0.18 mm, predominantly fine quartz sand. Sediments in the shallow area close to the north jetty tend to be coarser, averaging 1.1 mm, with a large amount of shell debris. This variation in sediment grain size is controlled by selective sediment transport by currents and waves. Stronger currents in the channel thalweg produce the coarse lag; and breaking waves along the north jetty are responsible for the coarse sediment there.

Tidal Flow Patterns

The tide in the study area is mixed diurnal and semi-diurnal. Spring tides, with a range approaching 1 m, tend to be diurnal. A secondary cycle of typically less than 20 cm in range usually occurs on the rising phase of spring tide (Fig. 4). Neap tides ranging to about 0.5 m are mostly semi-diurnal. Therefore, although spring tide has greater overall range, the rate of water level change during the rising phase is not greater than the semi-diurnal neap tide; however, the rate of the falling phase is greater.

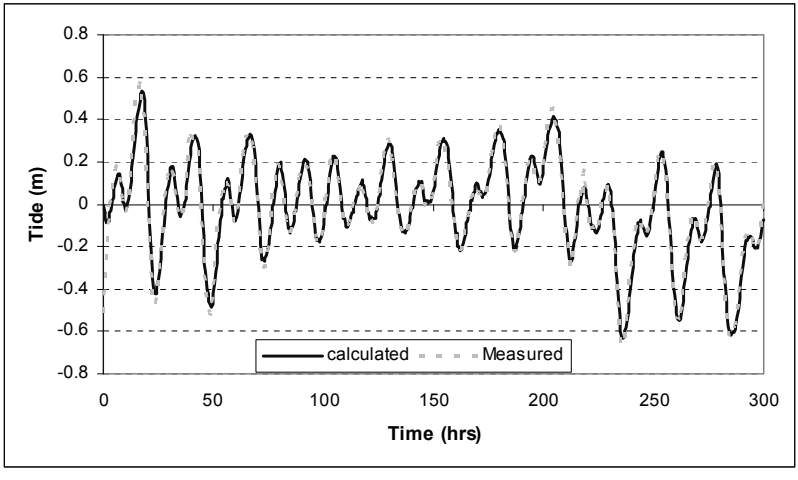

Fig. 4. Measured and calculated tidal water level at Blind Pass, January 12 to 25, 2001.

The measured flow velocity through Blind Pass exhibits the aforementioned tidal water-level characteristics (Fig. 5). The peak flood velocity is fairly uniform through time, with the weaker velocity appearing during the transition from the semi-diurnal neap to the diurnal spring tide. The peak ebb velocity shows large variation. The peak ebb velocity during spring tide is almost twice the magnitude of the peak flood velocity during neap tide in the channel thalweg. As discussed in the following, spatial variation patterns of flood and ebb currents across the channel also influence the peak magnitude.

Vertical velocity profiles are uniform throughout the water column from 1 m above the bed (Fig. 6). Vertical velocity profile measurements were conducted in the channel thalweg. A similar homogeneous trend was demonstrated by nearly all the measurements at the two different channel locations and during the different times (Fig. 3). In addition, overall flow velocity and trends through the channel thalweg, measured in January 2001 shortly after the dredging and in August-November 2002 after significant accumulation on the north shoal, are similar. The similarity indicates that the flow through the channel thalweg along the south side of Blind Pass is not significantly influenced by either the dredging or the shoaling that mainly occur along the north side.

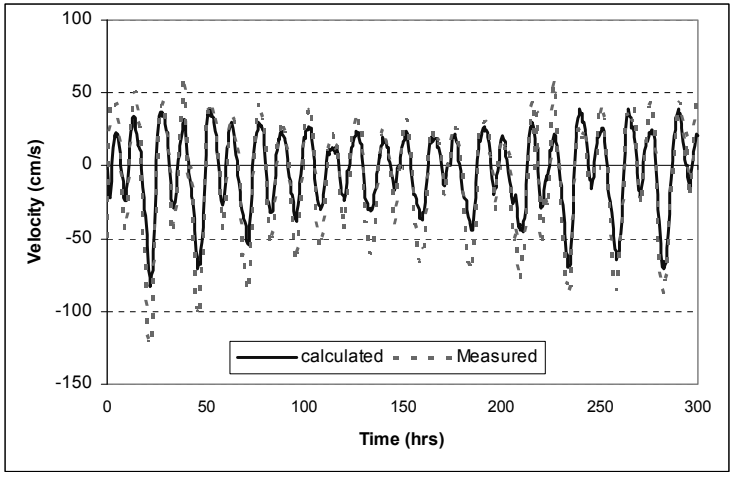

Fig. 5. Measured and calculated tidal flow velocity, January 12 to 25, 2001.

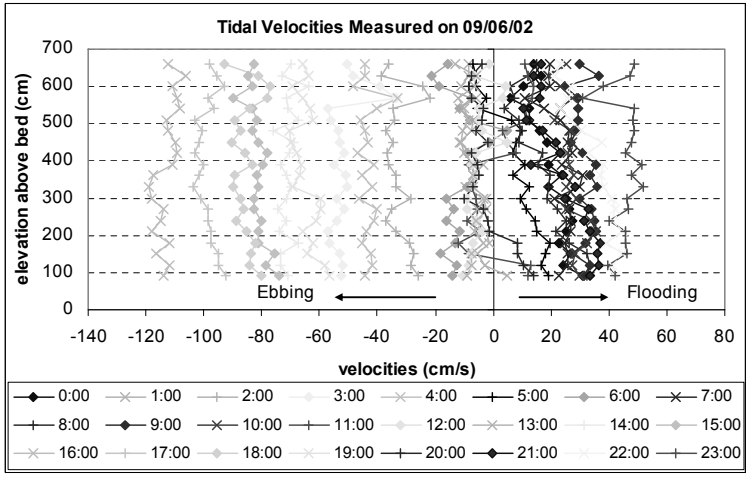

Fig. 6. Typical vertical profiles of current during spring tide.

In contrast to the homogeneous vertical velocity profiles, tidal flow velocity exhibits substantial horizontal spatial variation across Blind Pass channel. In addition, the cross-channel distribution pattern differs between ebb tide and flood tide (Fig. 7). During ebbing tide, flow velocity measured at the channel thalweg is 3 to 4 times greater than that measured over the north shoal. The peak ebb velocity through the channel thalweg approaches 1 m/s, the equilibrium velocity documented at many inlets (Bruun 1978). During flooding tide, flow velocity is primarily uniform across the channel, peaking at

about 0.5 m/s. This distribution of tidal flow velocity across the inlet channel can be attributed to the nearly 90-deg bend. The northern side of the inlet lies in the shadow zone of the ebb current as it turns around the corner. Such a sharp bend is common for migratory inlets, resulting from extension of the updrift barrier island and recession of the downdrift barrier. Therefore, the tidal flow distribution shown in Fig. 7 is likely not unique to the Blind Pass entrance channel.

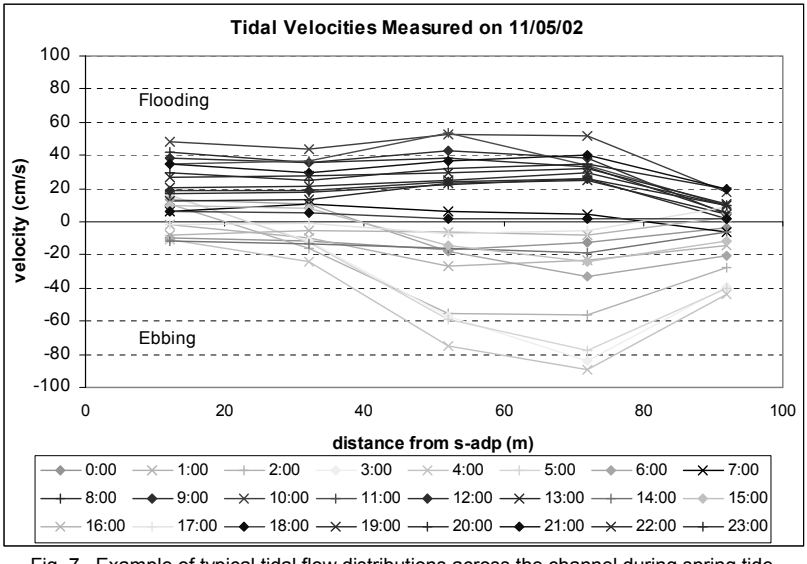

Fig. 7. Example of typical tidal flow distributions across the channel during spring tide.

Given the uniform vertical flow profile and substantial horizontal variation, a depth-averaged circulation model, such as the CMS-M2D, is a suitable and valuable tool to examine the Blind Pass hydrodynamics. The 2-week model run, spanning a spring and neap tide cycle, reproduced the measured water level well (Fig. 4). Measured velocity was also reproduced well, especially during flood (Fig. 5). The under-predicted peak ebb velocity may be related to the fact that a point measurement is compared to an averaged velocity over a 15x15 m grid. The substantial spatial (horizontal) variation of the ebb flow and the exact location of the flow meter may cause a slight inconsistency. Overall, results from the CMS-M2D represented the observations well over the 2-week period.

The predicted horizontal tidal flow patterns across the inlet channel also compare well with the measured pattern (Figs. 7 and 8). The ebb flow tends to hug the south side over the channel thalweg with a peak flow of approximately 1 m/s, whereas flow over the north shoal is much weaker (Fig. 8A). The flood flow tends to be uniform across the channel, peaking at about 0.5 m/s (Fig. 8B). This cross-channel flow pattern is closely related to the shoaling pattern, discussed in the next section.

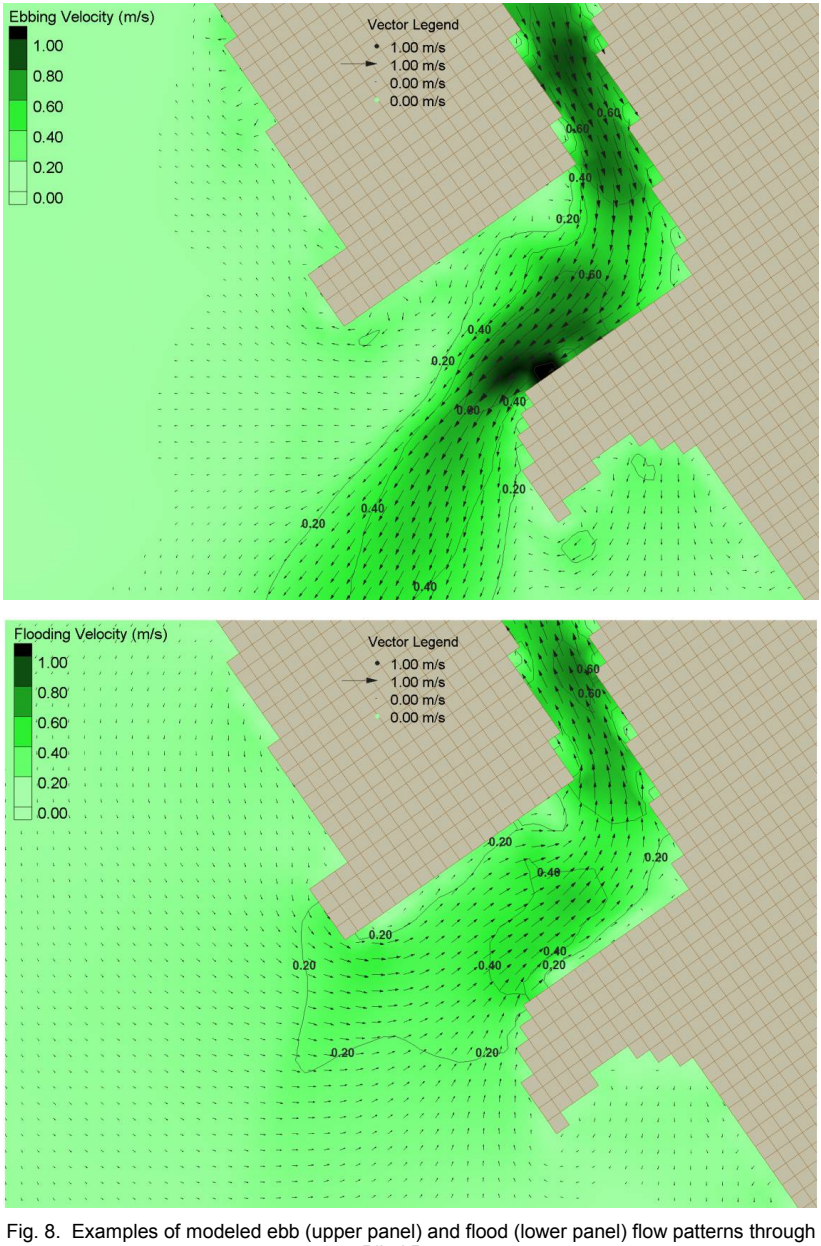

Fig. 8. Examples of modeled ebb (upper panel) and flood (lower panel) flow patterns through Blind Pass.

Shoaling in the Blind Pass Entrance Channel

Six bathymetric surveys were conducted by this study, in addition to one survey by the USACE, Jacksonville District, in July 2000 shortly after the last channel dredging. Significant shoaling is apparent in the time-series surveys (Fig. 9). Active shoaling occurred in three areas: along the north side, at the eastern corner, and along the south weir jetty. By far, most shoaling occurred along the north jetty. Comparing the July 2000 and August 2002 surveys, net sedimentation of 70,000 m^3 occurred during this 2-year period, or 35,000 m^3 per year. This rate roughly equals the net southward longshore sediment transport rate as obtained by Elko and Wang (2007) from measurements of erosion of the down-drift Upham Beach. This result indicates that Blind Pass has served as a total trap to southward longshore transport.

From August 2002 to August 2003, net sedimentation of 17,000 m^3 occurred, as the sum of 25,000 and 2,800 m^3 accumulation from August 2002 to December 2002 and from August 2002 to May 2003, respectively, and 11,000 m^3 of erosion from May 2003 to August 2003. From August 2003 to June 2004, net accumulation of 26,000 m^3 occurred. For both years, net accumulation occurred in the winter months and net erosion in the summer months. This seasonal trend is reflected more clearly in the monthly north-shoal survey, discussed in the following. The reduced amount of sedimentation during 2003 and 2004 is related to sediment backpassing around the corner of the inlet. A beach has developed on the back side of Treasure Island since 2003 and is growing (Fig. 10).

This shoaling pattern relates clearly to the southward net longshore sand transport and tidal flow distribution across the channel. Little shoaling occurs in the channel thalweg due to active flushing by the strong ebb flow. The north side is directly downdrift of the longshore sediment source. The weak ebb flow is not capable of flushing the sand deposited by the longshore transport, whereas the relatively strong flood flow tends to transport the sand deposited near the mouth further into the channel.

Sedimentation on the north shoal was monitored through monthly surveys of nine lines (Fig. 3). Four areas with different patterns of accumulation and erosion in the shoal can be distinguished as the: mouth area (lines 1 and 2), middle area 1 (lines 3 and 4), middle area 2 (lines 5 and 6), and the inner area (lines 7 through 9). From February to August, or the summer of 2003, a considerable amount of scour occurred in the mouth area (Fig. 11A). Little change was observed during the next two months. A tremendous amount of shoaling occurred in the mouth area between October and December of 2003, or at the beginning of the winter season. Scour was measured during the late winter between December 2003 and February 2004. Further into the inlet in middle area 1, little change occurred during the summer (Fig. 11B). A large amount of shoaling occurred at the beginning of winter, followed by further accumulation during late winter. Even further into the inlet at middle area 2, little change was observed during most of 2003 (Fig. 11C). A tremendous amount of shoaling occurred in the late winter. Near the bend of the inlet at line 9, southward progradation of the shoal occurred throughout the year (Fig. 11D). A large amount of shoaling was also observed during late winter.

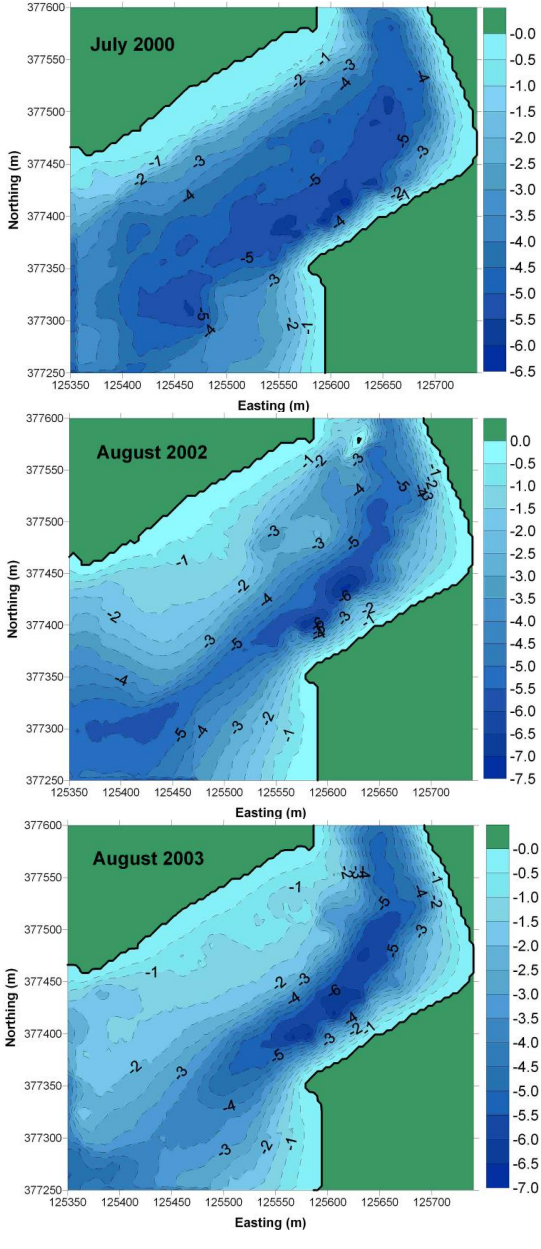

Fig. 9. Shoaling in Blind Pass entrance channel.



Fig. 10. Beach development along the back side of Treasure Island at Blind Pass, looking north.

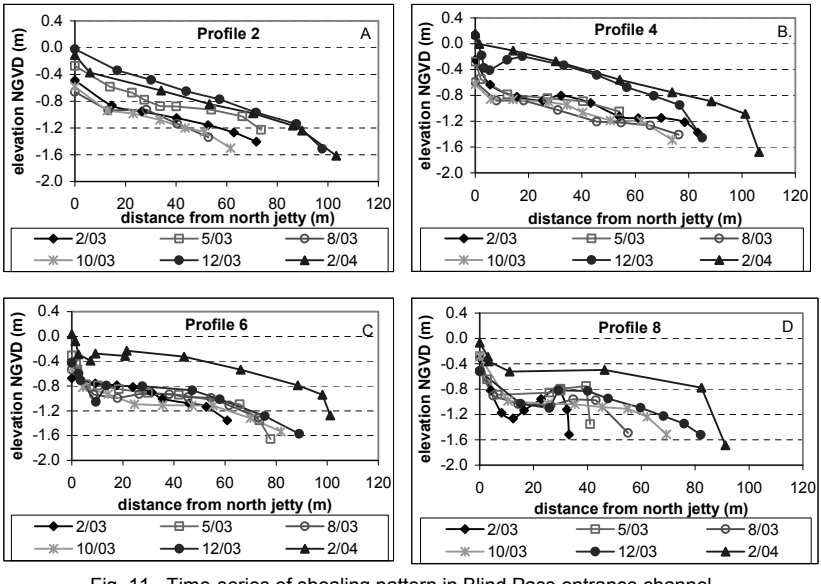

Fig. 11. Time-series of shoaling pattern in Blind Pass entrance channel.

Fig. 11 demonstrates both seasonal and event-driven shoaling and scouring at Blind Pass. During the summer when southwest wind dominates, and little sediment is trapped in the inlet because the sediment supply from the eroding Upham Beach to the south is limited. Furthermore, ebb flushing along the south side is active. As a matter of fact, scour was observed on the north shoal near the inlet entrance, indicating that the sand at the mouth area is being moved further into the inlet, and around the bend. Significant sediment shoaling occurred at the mouth area during the early winter starting in late October,

especially after the passages of the first several cold fronts. The northerly winds and waves are a major mechanism in driving southward longshore sand transport. The longshore moving sand can deposit readily into the space that was created during the summer season at the mouth area. This body of sand migrates further into the inlet during the winter. Therefore, shoaling in the Blind Pass entrance can be summarized as event-driven (particularly by cold fronts) supply of sediment, followed by redistribution during both low- and high-energy conditions.

The relatively strong flood current over the north shoal is a major mechanism transporting sand further into the inlet and around the bend to the back of Treasure Island. This has effectively limited development of an ebb shoal at Blind Pass. In addition to the flood current, wave breaking over the shallow north shoal and the resulting landward moving surf bore should also contribute significantly to landward sand transport, especially during high waves (Fig. 11). The development and significant growth of the beach on the back side of Treasure Island are results of the landward sand redistribution, in contrast to typical seaward sand transport by ebb flow and development of an ebb shoal.

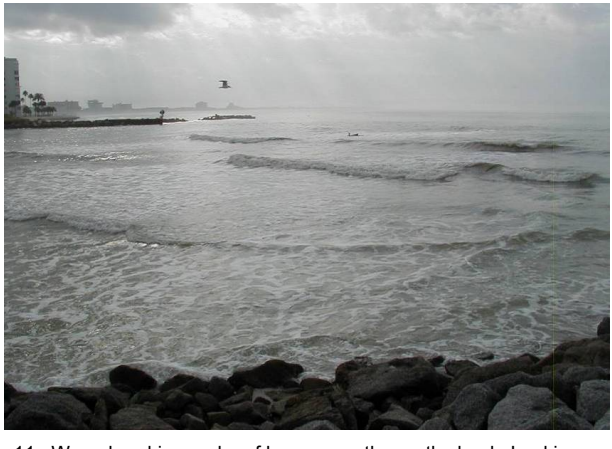

Fig. 11. Wave breaking and surf bores over the north shoal. Looking south.

CONCLUDING DISCUSSION

Blind Pass represents an example of a stabilized migratory inlet. Both in-situ flow measurements and numerical modeling revealed that ebb flow was approximately twice as strong in the channel thalweg along the downdrift side as compared with the rest of the channel. This strong ebb flow maintains the deep channel there. Flood flow, in contrast, was primarily uniform across the entrance and is stronger than the ebb flow over the northern portion of the inlet. This flow-velocity distribution across the inlet channel, which controls the shoaling patterns, relates to the nearly 90-deg. turn at its entrance to the Gulf of Mexico. The CMS-M2D model reproduced the measured tides and currents accurately.

Active sand accumulation occurs in the Blind Pass entrance channel, which is maintained by periodic dredging. The shoaling rate in Blind Pass channel approximately equals the net southward longshore transport rate. The inlet is presently serving as a total trap for southward longshore transport. Most of the active sediment shoaling occurs along the north side of the inlet, corresponding to 1) its proximity to the sand source, 2) weak ebb flushing, and 3) stronger flood current. Wave breaking over the shallow north shoal also contributes to the sand re-distribution further landward into the inlet.

Accumulation and erosion patterns at the Blind Pass entrance north shoal demonstrate distinct trends influenced by seasonal wave climate. High-energy waves, especially those driven by passages of cold fronts, play key roles in transporting littoral sand to the inlet channel. Active shoaling in the Blind Pass entrance channel occurs during the winter. This is followed by redistribution of the sand further into the inlet during the summer. The north side of Blind Pass and the growing beach behind Treasure Island are effectively functioning as an impoundment area for sand that is transported southwestward by the longshore current.

ACKNOWLEDGEMENTS

This study was supported by the Coastal Inlet Research Program (CIRP) at the U.S Army Engineer Research and Development Center, Vicksburg, MS.

REFERENCES

Bounaiuto, F., and Militello, A. (2004). Coupled circulation, wave, and sediment transport modeling for calculation of morphology change, Shinnecock Inlet, New York. *Proc. 8th Int. Estuarine and Coastal Modeling Conf.*, ASCE, 819-838.

Bruun, P. (1978). Stability of tidal inlets: Theory and engineering. *Developments in Geotechnical Engineering*, Vol. 23, Elsevier Scientific Publishing Co., NY, 510 p.

Buttolph, A.M., Reed, C.W., Kraus, N.C., Ono, N., Larson, M., Camenen, B., Hanson, H., Wamsley, T., Zundel, A.K. (2006). Two-dimensional depth-averaged circulation model CMS-M2D: Version 3.0, Report 2, sediment transport and morphology change, *ERDC/CHL TR-06-9*, U.S. Army Engineer Research and Development Center, Vicksburg, MS, 149 pp.

Davis, R.A., and Barnard, P.L. (2000). How anthropogenic factors in the back-barrier area influence tidal inlet stability: examples from the Gulf of Coast of Florida, USA. In K. Pye and J.R.L. Allen (eds.) *Coastal and Estuarine Environments: sedimentology, geomorphology, and geoarchaeology*. Geological Society, London, Special Publications, 1975, 293-303.

Dean, R.G. (1988). Sediment interaction at modified coastal inlets: Processes and policies. *Lecture Notes on Coastal and Estuarine Studies*, Vol. 29, 412-439.

Elko, N.A., and Wang P. (2007). Immediate profile and planform evolution of a beach nourishment project with hurricane influences. *Coastal Eng.*, 54(1), 49-66.

Kraus, N.C., and Militello, A. (1999). Hydraulic study of multiple inlet system: East Matagorda Bay, Texas. *J. Hydraulic Res.*, 125(3), 224-232.

Militello, A., and Kraus, N.C. (2003). Numerical simulation of sediment pathways at an idealized inlet and ebb shoal. *Proc. Coastal Sediments 03*, East Meets West Productions, CD ROM, 14 pp.

APPROACHES TO UNDERSTANDING MULTIPLE-INLET STABILITY

William C. Seabergh[1]

1. U.S. Army Engineer Research and Development Center, Coastal and Hydraulics Laboratory, 3909 Halls Ferry Road, Vicksburg, MS 39180-6199, USA.. William.C.Seabergh@erdc.usace.army.mil.

Abstract: The morphologic response of inlets that are part of a multiple inlet system, defined here as two or more coastal inlets connected to the same bay, is a complex problem. It has been thought that one inlet will eventually dominate, and that other inlets will close. Of course, in nature, there is a full range of situations and physical realities that complicate this situation. As more experience and historical information become available, various approaches can be tested. There may be multiple inlet systems serving a bay region that have naturally developed and coexisted for many years in some cases or there may be newly developed multiple inlet systems whose inlets immediately respond to each other, with the more efficient inlet creating a decline in the size of the other inlet, probably at a varying rate proportional to their efficiencies. An example of this type situation at two inlets on the Guatemalan coast is examined in this paper.

INTRODUCTION

This paper discusses recent understanding of multiple inlet stability and then examines a multiple inlet stability case study that may be considered common in engineering practice. A multiple inlet system is defined here as two or more inlets connecting one bay region to an ocean, sea or lake, i.e., a body of water much larger than the bay, and which typically is tidal and forces currents into and the out of the bay over a flood/ebb tidal cycle.

The inlet stability application concerns adding a flood relief inlet to an existing small navigable inlet system presently used extensively by local charter boats. An iterative process of examining Escoffier stability curves is applied to determine the response of both inlets while making reasonable assumptions for the system's representation. The

major question to be investigated is the relative stability of each inlet on the Escoffier stability curve.

BACKGROUND

Many inlet-bay systems with multiple inlets that connect with one bay respond, over time, in a manner where one inlet becomes predominant over the other inlet (or inlets, if more than two). This is the more commonly accepted concept about multiple inlet response, and is especially obvious when a large storm breaches a barrier at a location that is hydraulically "more efficient". For example, a new inlet cuts a channel through a barrier island that provides a shorter distance between bay and ocean. If this new, efficient inlet is not closed within a reasonable time, it can enlarge, capturing an increasing portion of the tidal prism admitted to the bay, reducing tidal prism of the original inlet. The original inlet may then have a tendency to decrease in size due to reduced velocity and channel shoaling. Also, the newly breached inlet would most likely not be associated with ebb or flood shoals, increasing its initial hydraulic efficiency and flow capturing capacity. If the new breach remains open, the original inlet may start to reduce in size. Also, existing constraints, such as preservation of bridges and roads may require closing the newly formed inlet before significant channel development occurs, requiring expensive changes to the existing infrastructure. Headland et.al. (1999) discuss impacts of breaches and multiple inlet systems.

Inlet Equilibrium Area

The equilibrium-area concept for a tidal inlet has been a useful approach to understand the adjustment of an entrance channel's minimum cross-sectional area to the basic hydraulic and sedimentation characteristics of the coastal inlet and bay it serves. Wave-generated and other currents along the coast move sand into the inlet channel, reducing its cross-sectional area. Inlet flow, produced by tidal, wind-generated, seiche-generated or river inflow currents, will tend to scour any excess deposition and that increases the channel cross section area above its equilibrium value. Using a a concept originated by LeConte (1905), O'Brien (1931, 1969) examined field data from tidal inlets through sandy barriers on the West coast of the United States. O'Brien determined a relationship between the minimum cross-sectional flow area of the entrance channel and the tidal prism (the volume of water flowing into the bay during the flood tidal cycle or conversely, the volume of water flowing out of the bay during the ebb portion of the tidal cycle). The form of this equation was:

$$A_c = CP^n \qquad (1)$$

With A_c the minimum inlet cross-sectional area in the equilibrium condition, C is an empirically determined coefficient (small regional differences may exist), P is the tidal prism (typically for spring tide), and n is an exponent usually slightly less than one unit, determined by best fit to data sets.

Escoffier (1940, 1977) combined the O'Brien relationship (Eq. 1) with an analytic model for the inlet hydraulics. He proposed a diagram for inlet stability analysis in which two curves are plotted (Figure 1). One curve, the "Equilibrium Velocity Curve" in Figure 1 is derived from a form of Equation 1 above. The second curve, the "Inlet Maximum

Velocity" curve, is created by solving an inlet hydraulics model for velocity for various values of inlet area. Figure 1 shows the graphical form of the solution for the Unstable and the Stable equilibrium points. These points will be discussed below. Seabergh and Kraus (1997) discuss the formulation of a PC program to create this plot. If an inlet has jetties, the equilibrium velocity curve would be defined by (in metric units)

$$A_c = 7.489 x 10^{-5} P^{0.86} \quad (2)$$

The necessary information to perform this analysis includes the tide range in the ocean, tidal period (12.42 hr in this study to represent a semi-diurnal tide), the surface area of the tidal basin, the channel length, channel width, a frictional coefficient for the channel, such as Manning's n, and estimates of entrance and exit loss coefficients.

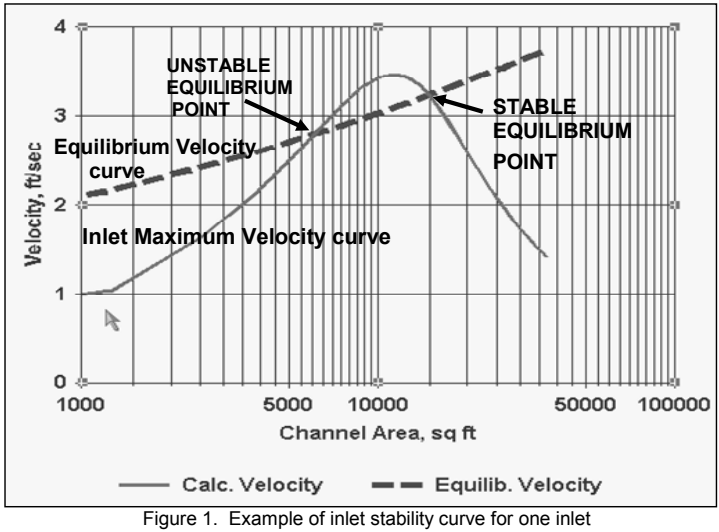

Figure 1. Example of inlet stability curve for one inlet

Referring to Figure 1, the solid line is the inlet's maximum velocity versus the inlet's cross-sectional flow area, A. A single curve represents changing inlet cross-section area conditions if ocean tide parameters and bay and inlet plan geometry remain fixed. As area approaches zero, velocity approaches zero because of increasing frictional forces, which are inversely proportional to channel area. As channel area increases, friction forces are reduced, but on the far right side of the curve, velocity decreases, as tidal prism has reached a maximum (bay fills to same level as ocean, if neglecting inertial term in flow equation), and any increase in channel area decreases velocity, as determined by the continuity equation. This curve can be constructed by calculating the maximum velocity V, resulting by varying channel area A. The maximum velocity V can be determined by an analytical or numerical model. The dashed-line curve is an empirical stability criterion curve such as O'Brien's discussed above (Eqns. 1 or 2). Therefore, as wave action supplies sand to the inlet channel and tends to reduce the cross-sectional area, the inlet flow will scour any depositions which reduce the channel cross section below its equilibrium value.

In Figure 1, the two curves may intersect at two locations, one location (a tangent), or not intersect. In the first case, the right-side intersection is a stable root in that any deviation in area returns movement along the stability curve to its starting point. If channel area increases (moves right on the curve from the stable equilibrium point), velocity will fall and more sediment can fill in the channel to bring it back to equilibrium. If area decreases, velocity will increase, scouring to the equilibrium point. The point of intersection on the left side is an unstable root, where if the area decreases, velocities decrease until the inlet closes. Moving to the right of this point, as velocity increases, area increases until the velocity starts falling and the stable root on the right is reached. If the stability curve is tangent to or below the stability criterion curve, the inlet will close. If the inlet area is to the right of the unstable equilibrium point, and a storm occurs provides a large sediment input to the inlet region, a possibility would exist that it could shift the area to the left of that point and the inlet will close.

Multiple-Inlet Stability

Initially van de Kreeke (1985) took the single inlet Escoffier analysis (1940, 1977) and extended it to multiple inlets. He maintained the simple hydrodynamic approach typically used in the original one-inlet Escoffier analysis. His procedure included the usual simplified assumptions that the bay water surface fluctuated uniformly as the tide entered and exited the bay through multiple inlets and the bay surface area was constant. With these assumptions, van de Kreeke (1990) concluded for multiple inlets connecting the same bay to ocean that for a two-inlet bay system analytical model, there exist no set of equilibrium flow areas, implying that ultimately one or both inlets close.

Van de Kreeke and Borsje (1994) found that if the stringent restraints for natural systems of a uniform bay rise with a constant value bay surface area, discussed above, are removed, and a semi-analytic approach is used with numerical computations, a set of unconditionally stable inlets is possible. Brouwer (2006) supplemented this approach, and found that a uniform water level in basin was too restrictive for shallow, long basins. He connected two bay basins at the topographic high by an interior channel and found three conditions, dependent on the channel's length and area. For small channels, inlets behaved nearly independently, and maintained two stable inlets. For a large connecting channel, one inlet would close, and for intermediate areas, there can be two unconditionally stable inlets in equilibrium.

As more historical information about multiple inlet systems has become available, it is known that some multiple inlet systems have remained as multiple inlets for a long duration compared to human lifetime. This is not to say that the inlets themselves have remained static. An example is the dual inlet system of Pass Cavallo and Matagorda Ship Channel on the Texas coast (Figure 2). Pass Cavallo was a naturally occurring inlet and the ship channel was dredged through the barrier island in the 1960s. Initially this change caused significant reduction in Pass Cavallo's size (Ward 1982) while scour occurred in the newly dredged Ship Channel. Recent analysis by Kraus et.al. (2006) indicated that the width of Pass Cavallo has remained stable since the mid-1990s or even

widened. Therefore this dual inlet system apparently has so far had a continual life of greater than 40 years.

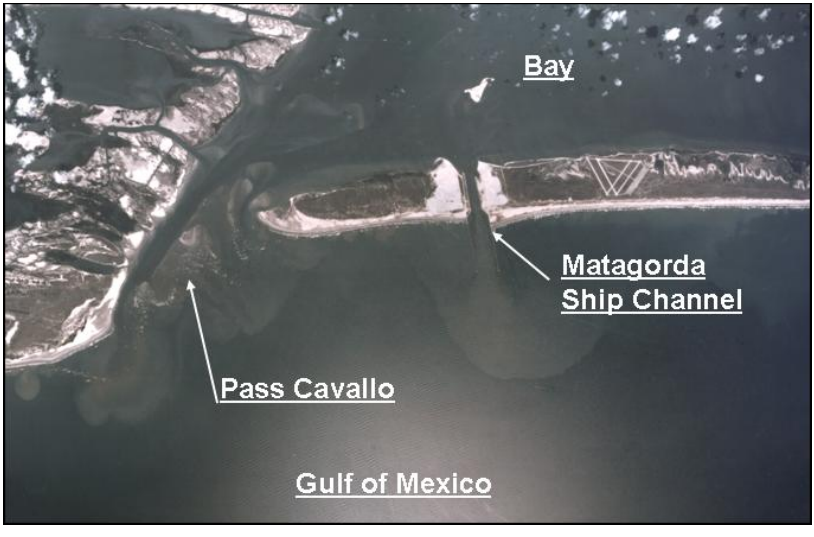

Figure 2. Pass Cavallo-Matagorda Ship Channel multiple inlet system, Texas

Freidrichs et. al. (1993) discussed a cyclical multiple inlet system instability at Chatham Harbor-Pleasant Bay tidal estuary, Cape Cod, Massachusetts. This inlet system has a 150-yr cycle, with a complex variation of inlet change, causing significant change in inlet hydraulics.

Other locations where dual-inlet systems have had one inlet close include Johns Pass (open)/Blind Pass (closed) on the Florida west coast and St Andrews Bay (open)/ East Pass (closed) on Florida's Panhandle, Gulf Coast. The Blind Pass portion of the first pair had reduced tidal prism due to anthropogenic infilling of the bay. For the second pair, East Pass shoaled relatively rapidly due to it's long channel.

In summary, for a bay with two inlets, if the bay is heavily segmented by wetlands, or man-made barriers to flow in the bay, such as causeways, than the bay serving one inlet may not be significantly affected by the other inlet. For this case, inlet interaction may be reduced, and the inlets will operate nearly independent of one another. As the connection in the bay is opened, there is more likely to be stable multiple inlet systems. As the connection between bay segments increases and the bay responds more uniformly to elevation change, one inlet will tend to dominate.

Of possible interest is information for the inlet pairs discussed earlier. Where one inlet closed in this group, the bay for each system was one that filled completely. This situation is also the response of an inlet that has reached equilibrium in Escoffier's

analysis for a single inlet. In contrast, the Pass Cavallo-Matagorda Ship Channel system bay response indicates about fifty percent filling. This is indicative of an inlet system where the inlet areas have a potential to increase in size until the bay fills completely. This might indicate that until the bay reaches a near bay-filling status, an equilibrium situation, one may have change from a stable (but not equilibrium area) two inlet system to a stable (with a true equilibrium area) one inlet system. This would require significant change to the bay planform and/or inlet cross-sectional areas, but could occur as a result of human intervention. It was noted in Seabergh (2003) that the time for a single inlet to evolve to an equilibrium condition can be considerable, if at all, unless there is some man-made change to reduce the energy loss in a system, e.g., entrance channel deepening or greater depth in the bay to reduce friction and create better connectivity between the two inlets. In other words, if the system can evolve to a "simpler" system, one where the bay fills completely and there is good connectivity between the multiple inlets, then one falls back to a single inlet evolution as the final configuration, as Van de Kreeke initially found.

SAN MARINO AND IZTAPA INLETS, GUATEMALA

Background

As part of a reconnaissance trip to the Guatemala coast, the San Marino Inlet and Iztapa Inlet system was examined to understand causes and remediation measures for channel shoaling at San Marino Inlet, an important channel for the local charter boat industry. San Marino and Iztapa Inlets both connect the Pacific Ocean with the same bay or lagoon region. Iztapa Inlet also serves as the closest exit to the sea for the Rio Maria Linda, a small river, but has been associated with flooding at the town of Iztapa. Figure 3 shows the two inlets. Historically there had been periods when only one inlet was open connecting the bay and ocean. Table 1 shows results of an examination of aerial photos. The inlets were consistently located in the region of today's inlets. This is of interest because some non-jettied inlets migrate along the shoreline and can be at very different locations along the coast over their history. Thus these inlets appear to be relatively stable with respect to their location along the shoreline in their pre-structured state, when they were open. The opening and closing of inlets can be associated with large waves, storms and riverine flood conditions. San Marino Inlet was permanently stabilized with two jetties in 1991, and Iztapa Inlet was stabilized in location with two jetties in 2003 (Figures 4 and 5). Apparently the structured inlets were appropriately sited due to their stable location.

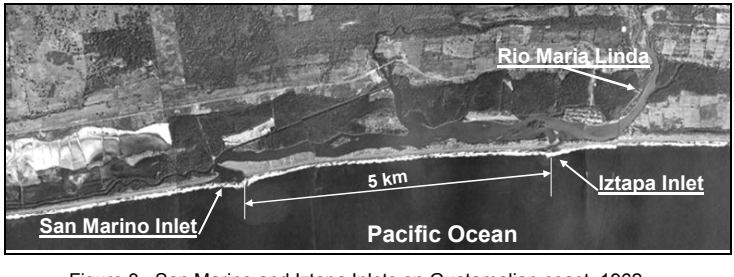

Figure 3. San Marino and Iztapa Inlets on Guatamalian coast, 1962



Figure 4. San Marino Inlet in 1991, just after construction.



Figure 5. Iztapa Inlet under construction in 2003.

However, as seen from Table 1, this dual-inlet system in its entirity does not consistently support two inlets. This instability can occur for a number of reasons. Iztapa Inlet, before being structured, most likely was a function of river inflow, as it is located near the exit of the Rio Maria Linda into the estuary. In the dry season, it would be likely to close, before it became a jettied inlet. The Iztapa Inlet jetties were constructed to relieve flooding of the town of Iztapa, located just adjacent to the river near the coast. Flooding conditions would lead to a breach at pre-jetty Iztapa Inlet once water levels had reached a high level in the lagoon. San Marino Inlet historically served a larger lagoon area than it does now, as the construction of Port Quetzal (in 1983) may have taken in some of the lagoon and blocked a region which previously drained into San Marino Inlet. The Port location would lie in the bottom left corner of Figure 3.

Table 1. Examination of Arial Photos

Date of Photo	Inlet at approximate San Marino location- Is it open ?	Inlet at approximate Iztapa location- Is it open ?
01/16/54	Yes-size not discernable*	Yes-size not discernable
01/23/62	Yes –width approx. 100 m	Yes-width approx. 50 m
02/06/67	Yes-width approx 50 m	No
03/11/80	No	Yes-width approx. 100 m
12/02/88	Not shown on photo	Yes-width approx. 80 m
02/01/91	Yes-stabilized inlet in place with width of 30 m	Yes- width approx. 30 m

*High altitude photos with low resolution, so inlet width estimates very rough

Inlet Cross-Sectional Stability and Tidal Prism

On 23 Jun 04, both San Marino and Iztapa Inlets were visited during a falling ocean tide. Consequently, the currents in the inlet channels were ebbing seaward. Using a tethered current meter, tidal currents were collected in each inlet at a time near peak ebb for that day. These measurements were useful in calibrating the numerical model for the stability analysis. The calibration procedure involved examination of photographs and maps to estimate the surface area of the bay. Because the bays are interconnected, a trial-and-error procedure was performed for each inlet, assuming different splits of the bay surface area until current measurements from the field matched the simple 1-D numerical model. Figures 6 and 7 show tidal elevations and currents for the calibrated models of each inlet. Table 2 shows the values used for model calibration. Also shown are estimated tidal prisms, or volumes of water that flow through the inlet during a flood or ebb tide for the calibration day of 23 June 04.

As noted from the tidal elevations, the bay tide ranges nearly equal the ocean tidal range. No measurements of bay tide range were available; however visual observation of bay tide range appeared to be in accordance with the calculations. If both inlets remain open, this should indicate good flushing of the bay system. Maximum velocities in the channel are in the range of 1.0 m/s, which is a value that indicates the inlet cross-section area is near an equilibrium value for tidal inlets (Bruun 1978). This indicates that both inlet systems appear to co-exist near inlet equilibrium states. This will now be examined by referencing the Escoffier stability plots for each inlet.

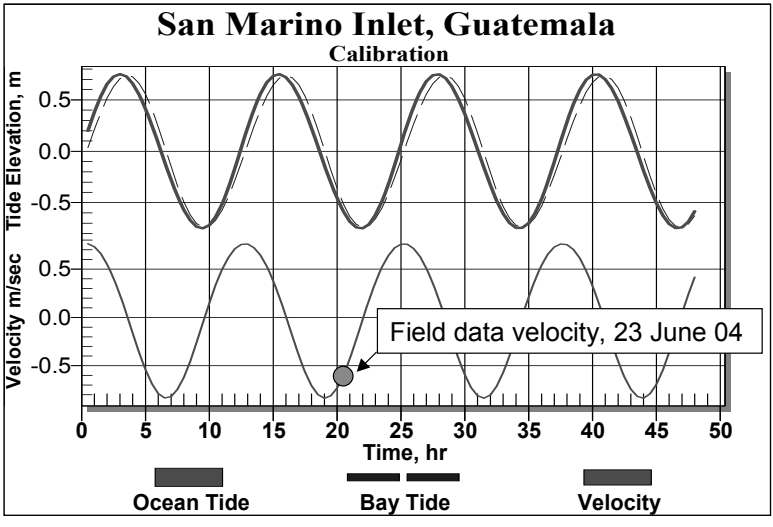

Figure 6. Calibration of San Marino Inlet hydrodynamics

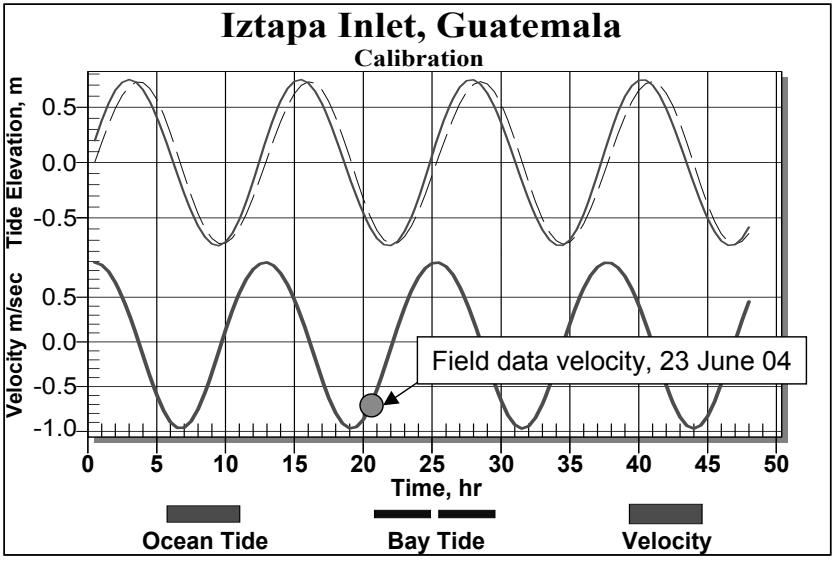

Figure 7. Calibration of Iztapa Inlet hydrodynamics

Table 2. Inlet Parameters and Tidal Prism

Parameter	San Marino Inlet	Iztapa Inlet
Bay surface area (sq meters)	500,000	2,200,000
Hydraulic radius (meters)	1.5	2.0
Channel length (meters)	400	500
Channel width (meters)	42	134
Calibration channel area (sq meters)	65	244
Entrance loss coefficient	1.0	1.0
Exit loss coefficient	0.5	0.5
Manning's n	0.030	0.030
Calibration ocean tide range (meters)	1.5	1.5
Calibration tidal prism (cubic meters)	735,000	3,234,000

Escoffier Analysis of Inlet Stability

The Escoffier plots for both inlets were determined based on the calibration of the hydrodynamics discussed above. Figure 8 shows the San Marino Inlet plot in the form discussed earlier.

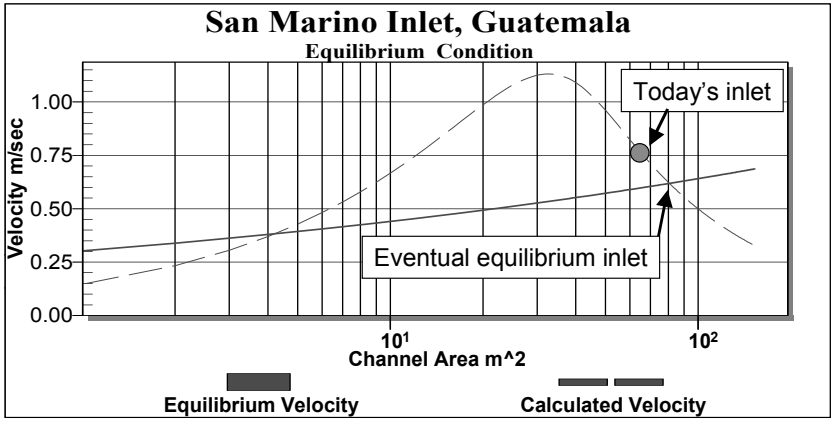

Figure 8. Escoffier plot showing today's inlet area with respect to eventual equilibrium area.

Figure 8 indicates that San Marino Inlet is close to its expected equilibrium value based on existing inlet hydrodynamics and the parameters given in Table 2. Some slight

changes could be expected if dredging were performed and the channel length shortened. At this time the channel into the bay follows a sinuous path. The inlet area is 65 sq m, moving toward an equilibrium value of 80 sq m. This would mean an average depth of about 1.9 m would be expected based on a tide range of 1.5 m. This depth is relative to mid-tide at the inlet and is less than would be expected if Iztapa Inlet was not opened.

Figure 9 shows the stability diagram if only San Marino Inlet was open to the bay and Iztapa Inlet was not present. Figure 9 indicates that the existing inlet area would have strong currents, near 2 m/s, probably similar to those that occurred historically in San Marino Inlet after the jetties were constructed in 1991, but before 2003, when Iztapa Inlet was opened and its jetties constructed. The jetties at San Marino Inlet are relatively short and probably never permitted the inlet to obtain its maximum equilibrium area of 334 sq meter (depth would then be 7.8 m), as sediment could come around the jetties and enter the channel fairly easily. Estimated equilibrium area would be 240 sq m (depth would be 5.6 m) if the prism relationship for an unprotected inlet were applied. This analysis is discussed to illustrate the change that can occur if a bay system is transformed from one primary inlet to a two-inlet system. Thus the creation of a permanent Iztapa Inlet has taken a part of the San Marino Inlet tidal prism and indicates a reduction in channel cross-section area and, therefore, a reduction in depth at San Marino Inlet. The next section examines the state of the Iztapa Inlet.

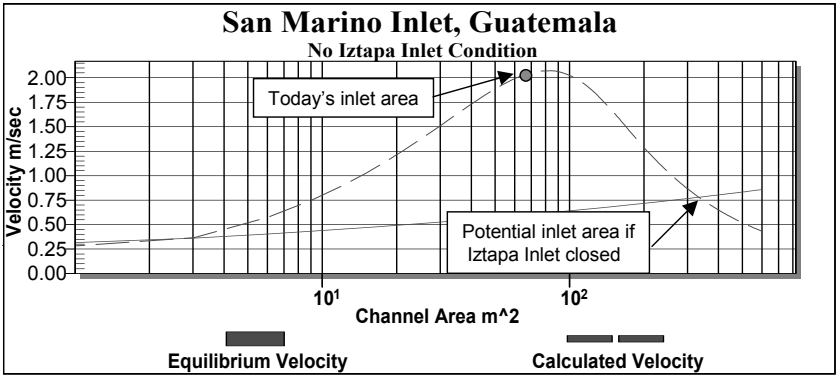

Figure 9. Escoffier plot showing what would occur at San Marino Inlet if Iztapa Inlet were not open (pre-2003)

Iztapa Inlet channel stability is shown in Figure 10. The existing area of 244 sq m is approaching the equilibrium area of 288 sq m. This indicates a potential average depth of 2.4 m. This depth is relative to mid-tide level at the inlet. Possible flooding from the Rio maria Linda could cause, temporally, an increased depth to occur in the channel between the jetties.

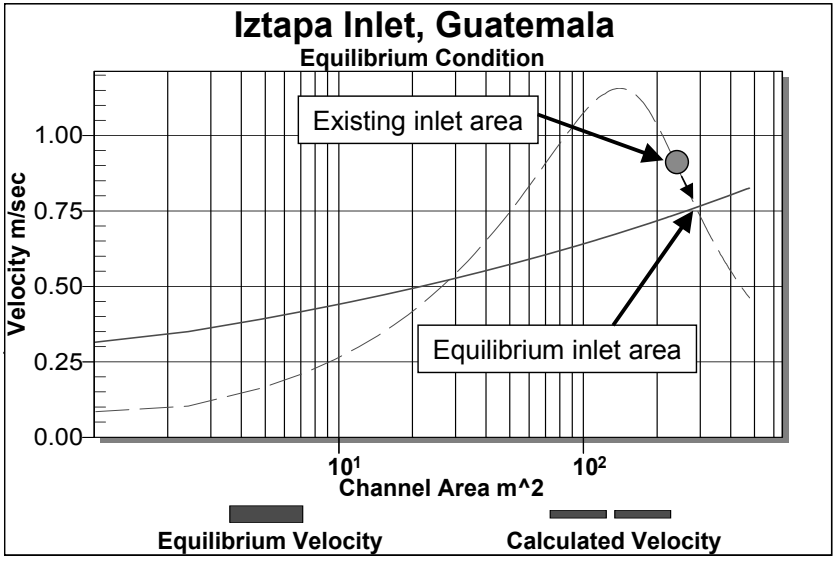

Figure 10. Escoffier plot showing today's inlet location with respect to channel area and eventual equilibrium area.

Historical Note and Summary of Inlet Stability

Important in the examination of inlet cross-sectional area stability are changes that occur in bay size. Anthropogenic changes in bay surface area and flow distribution can alter inlet stability. Most likely the bay size served by the San Marino Inlet was reduced by construction of the Port of Quetzal in the early 1980's. Inlet widths at the natural San Marino Inlet were noted to be as great as 100 m before port construction. Inlet area (and thus width) is proportional to the bay area drained by the inlet. Now, with the addition of a permanent Iztapa Inlet, there is a smaller bay surface area serving San Marino Inlet and, therefore, a smaller equilibrium cross-section area is expected, and thus less depth, for the given width between the jetties. This was seen in the previous analysis in comparing today's San Marino Inlet existing condition with the no Iztapa Inlet condition.

The original San Marino Inlet was stabilized with jetties in 1991. The spacing of the jetties constructed in 1991 at San Marino Inlet was 31 m and relatively narrow for the bay it served and, therefore, strong currents were reported funneling through the entrance channel. The positive aspect of this was that the strong currents would flush sediment from the channel and keep an easily maintained navigable depth. Negative impacts of this type of inlet would include potential navigation problems with respect to vessel control as the currents accelerate towards the inlet, and during ebb, or seaward flowing currents, the interaction of the outgoing current with the approaching waves from the sea can create increased wave height and breaking waves in the channel. Previous maximum currents were probably on the order of 2 m/s at San Marino Inlet, while today's

maximum currents are about 1 m/sec. The weaker currents result in a shallower channel depth and less forcing of the sediments to an ebb shoal seaward of the inlet entrance. Observation at the inlet indicated little evidence of a significant ebb shoal. The ebb shoal typically helps to function as a wave breaker and reduces wave energy entering the channel. Observation showed waves continually breaking at the entrance to the jetties. The depleted alongshore sediment supply due to blockage by Port Quetzal also contributes to a smaller ebb shoal.

Iztapa Inlet in its natural state (pre-2003) would be expected to be influenced by the flow of the Rio Maria Linda. It apparently opened due to floods and probably closed during the dry season when littoral currents on the coast created by waves moved sand into the inlet. Iztapa Inlet was constructed in 2003. This dual-jettied inlet has spacing between the jetties of 122 m. It is relatively shallow and continually had waves breaking at its entrance. It is near its equilibrium area and thus depth of 2.4 m, which is slightly greater than San Marino Inlet depths of 1.9 m. This is due to the greater tidal prism that the inlet serves. The tidal prism of San Marino Inlet was calculated to be 735,000 m^3 and Iztapa Inlet 's prism is 3,234,000 m^3s, about four times greater than San Marino's prism.

Careful observation of the San Marino-Iztapa system must be made to see if this system responds as two independent systems now that both inlets are stabilized with jetties, or to determine if there is still an interaction, since there is a direct channel connection between the inlets.

CONCLUSIONS

Recent work on a multiple inlet-one bay system by Van de Kreeke and others indicates there is a gradation in inlet interaction that can permit three possible outcomes. The multiple inlets can be relatively independent of each other and coexist. They can be interactive and maintain independent stability or if they are too closely interconnected, one will dominate and the other close, as shown in earlier theory.

Inlet channel cross-sectional area is proportional to the surface area of the bay it serves. If an inlet is added to a bay system, the surface area of the bay is apportioned between the two inlets and the original inlet will be reduced in size. In adding a stabilized Iztapa Inlet to the bay system, the San Marino Inlet responded by becoming shallower (since width between the jetties was constant).

The existing depths (2004) at San Marino and Iztapa Inlets are near an equilibrium value (based on limited field data for this analysis). The equilibrium depths at mean tide level are 1.9 m at San Marino Inlet and 2.4 m at Iztapa Inlet. The existing width between the jetties at San Marino Inlet should be appropriate for the present two inlet-system, with reduced maximum velocity for safer navigation.

ACKNOWLEDGEMENTS

Permission was granted by Headquarters, U.S. Army Corps of Engineers (USACE), to publish this information. Thanks go to Mr. Pete Robinson and Mr. Leo Cain of the

Mobile District, USACE, for their guidance and support in this study. Also thanks to Ms. Julie Rosati and Dr. Nicholas Kraus for reviewing this manuscript.

REFERENCES

Bruun, P. (1978). *Stability of Tidal Inlets*, (Developments in geotechnical engineering; v. 23), Elsevier Scientific Publishing Co., The Netherlands.

Brouwer, R.L. (2006). Equilibrium and stability of a double inlet system ,(M. SC. Thesis), Delft University of Technology

Escoffier, F.F. (1940). The stability of tidal inlets," *Shore and Beach* 8(4), 114-115.

Escoffier, F.F. (1977). Hydraulics and stability of tidal inlets," GITI Report 13, U.S.Army Engineer Waterways Experiment Station, Vicksburg, MS.

Friedrichs, C.T., Aubrey, D.G., Giese, G.S., and Speer, P.E. (1993). "Hydrodynamical modeling of a multiple-inlet estuary/barrier system, 95-112, *Formation and evolution of multiple inlets*, David G. Aubrey and Graham S. Giese (eds), (Coastal and Estuarine Studies; 44)

Headland, J.R., Rasmussen, C., Bocamazo, L., Smith, W.G., and Herrman, M. (1999). "Tidal inlet stability at Fire Island, Moriches and Shinnecock Inlets, Long Island, New York," *Proceedings Coastal Sediments '99*, ASCE, 2249-2264.

Kraus, N.C., Lin, L., Batten, B. K, and Brown, G L. (2006). "Matagorda Ship Channel, Texas: Jetty stability study," Technical Report ERDC.CHL-06-7, U.S. Army Engineer Research and Development Center, Coastal and Hydraulics Laboratory, Vicksburg, MS, 153 p.

LeConte, L. J. (1905). "Discussion of "Notes on the improvement of river and harbor outlets in the United Stated," Paper No. 1009 by D. A. Watts, *Transactions, American Society of Civil Engineers* LV, December, 306-308.

O'Brien, M. P. (1931). "Estuary tidal prisms related to entrance areas," *Civil Engineering* 1(8), May, 738-739.

O'Brien, M. P. (1969). "Equilibrium flow areas of inlets on sandy coasts," *Journal of Waterways and Harbors Division* 95(WW1), 43-52.

Seabergh, W.C., and Kraus, N.C., 1997. PC Program for Coastal Inlet Stability Analysis Using Escoffier Method, Coastal Engineering Technical Note, CETN IV-11.

Seabergh, W.C. (2003). "Long-term coastal inlet channel area stability," *Proceedings Coastal Sediments '03*, CD-ROM Published by East Meets West Productions, Corpus Christi, TX ISBN-981-238-422-7, 8 p.

Van de Kreeke, J. (1985). "Stability of tidal inlets - Pass Cavallo, Texas," Estuarine, *Coastal and Shelf Science 21*, 33-43.

Van de Kreeke, J. (1990a). "Can multiple tidal inlets be stable?," *Estuarine, Coastal and Shelf Science 30,* 261-273.

Van de Kreeke, J. (1990b). "Stability analysis of a two-inlet system," *Coastal Engineering* 14, 481-497.

Van de Kreeke, J., and Borsje, _ "Cross-Sectional Stability of Two-inlet bay Systems," at INTERNATIONAL SYMPOSIUM COASTAL HYDRO- AND MORPHODYNAMICS in honor of Prof. Jurjen Battjes, 14 May 2004, abstract

Ward, G.H. (1982). "Pass Cavallo, Texas: Case study of tidal-prism capture," *Journal of Waterway, Port, Coastal and Ocean Division 108(WW4),* 513-525.

ENGINEERING GUIDELINES FOR THE SITING OF SAND BYPASSING DISCHARGES

Douglas W. Mann, P.E.[1]

1. Coastal Planning & Engineering, Inc. 2481 N.W. Boca Raton Blvd, Boca Raton Florida 33431, USA dmann@coastalplanning.net

Abstract: This paper summarizes the limited existing guidelines for the establishment of sand bypassing discharges adjacent to tidal inlets. Two recent case studies are presented where discharge siting was analyzed via a review of the littoral transport. Based on these case studies, rational procedures for discharge siting are proposed for any inlet and bypassing system.

INTRODUCTION

The blocking of littoral sediment transport by tidal inlets has been a frequent cause for many coastal engineering projects. One method of maintaining the regional littoral transport and navigation within the inlet has been to mechanically transport the sand to the downdrift beach. Methods to accomplish this include dredging from within the channel or deposition basin, or by dredging sand from the updrift beach and nearshore, bypassing the channel, and discharging the sand on the downdrift beach. Bruun (1978, 1990) and the USACE (1991) provide some design guidance and documentation on the various types of pumping systems used in bypassing sand across tidal inlets or from navigational channels. The design guidance is focused on the pumping operation without much attention to siting discharge operations.

Due to the dearth of specific guidance for siting dedicated discharge pipelines, this paper reports on the results of two discharge pipe siting case studies (Coastal Planning & Engineering, Inc. (CPE), 2004, 2005). The studies identified that the recommended discharge siting should be based on site-specific coastal processes. From these studies, existing engineering guidelines are enhanced for application at any inlet bypassing operation.

LITERATURE REVIEW

While much has been written on the need to bypass sand, only a limited number of papers have focused on the disposal of the sand on the downdrift beach. Among them are the following papers, which provide supportive ideas to the specified subject matter.

Weggel (1981) provides an overview of basic design principles associated with weir jetties. As weir jetties are intricately linked to the bypassing of the littoral drift, one might suppose that discharge location siting may receive some consideration in the report. Nevertheless, Weggel (1981) only briefly summarizes downdrift discharge siting by indicating that it should be located far enough from the jetty to avoid the wave shadow of the jetties.

The USACE (1982) describes the discharge of the Oceanside Harbor sand bypassing system. The sand discharge would be up to 3100 m from the harbor and would include multiple discharge points to permit selective discharge of sand to the beach. No details of the design of the multiple discharge points were presented.

Bruno (1988) performed a feasibility study at Manasquan Inlet, New Jersey, using wave hindcasted transport rates. Bruno (1988) concluded that based on sediment transport properties near the inlet, bypassed sand should be placed at least 490 m north (downdrift) of the north jetty to re-enter the net northerly transport and avoid relatively long "residence time". Bruno stated that within 490 m, the bathymetry was affected by the inlet and would result in southerly net littoral drift.

Clausner (1988) summarizes the Nerang River (Queensland, Australia) sand bypassing system and its early performance. For that system, three discharges are located from 295 m, 440 m, and 520 m from the downdrift jetty. Clausner (1988) notes that during the initial operation, there was some concern that the discharge points were not located sufficiently downdrift of the inlet and that extending the discharge locations may be necessary.

Clausner et al. (1991) provide an overview of the design of the sand bypassing plant at Indian River Inlet, Delaware. They describe the beach disposal pipeline as extending up to 457 m on the downdrift shoreline and that the actual length of the pipeline is flexible. Rambo et al. (1991) state that during the first year of bypassing, the discharge location varied from 122 m to 183 m downdrift of the inlet to produce "an adequate distribution of sand along the beach."

USACE (1991) summarize sand bypassing system selection and briefly describe discharge siting for any bypassing operation. For unidirectional sand transport, a distance from the jetty of 305 m is proposed as a minimum and that the distance should be increased based on the length of the jetties and the size of the ebb shoal. The USACE recommends wave refraction studies to determine a location where inlet dominated processes cease.

If the sediment transport is bidirectional, the USACE (1991) recommends identifying the littoral forces on the downdrift shoreline and identifying any transport reversals. It is recommended that statistical wave data, wave refraction and diffraction diagrams and data on nearshore currents be incorporated. The use of coastal structures to reduce sediment transport (reversals) back to the inlet was also suggested. No specifics were presented on how to apply these prudent suggestions.

In two recent efforts, Bailard (2006) and Applied Technology & Management (2005) utilize the GENESIS shoreline model downdrift of Santa Barbara, California, and Lake Worth Inlet, Florida, respectively. The model was used to simulate the shoreline response downdrift of the harbors under varying sand placement scenarios.

One may conclude from the above literature, that for each inlet, the following guidelines apply to siting a sand discharge point:

a. There may an optimal location to bypass sand to.
b. Flexibility in the discharge location may be important.
c. The optimal location is not immediately against the downdrift jetty.

APPROACH

Given the guidelines above, the most prudent method of determining the optimal location for siting of a sand discharge is the development of a littoral budget for the downdrift shoreline. This should identify gradients in the littoral drift, and any reversals that are occurring. Only after the littoral budget is developed can siting of sand discharges be determined with engineering confidence. In this paper, littoral budget development is discussed and two case studies are presented to provide a range of applications of this approach. From the two case studies, enhanced engineering guidelines on the siting of sand bypassing discharges are presented.

LITTORAL BUDGET THEORETICAL CONSIDERATIONS

The conservation of sand in one dimension along a downdrift shoreline can be expressed as:

$$\frac{dQ}{dx} = \frac{-dV}{dt} + q(x,t) \qquad (1)$$

where Q is the alongshore sediment transport, V is the volume of sand within the beach, q is a source of sediment into the beach cell, and x and t are dimensions in space and time (Figure 1). The volume of sand within the beach, V, or the change in beach volume with time dV/dt, can be determined directly from beach surveys or estimated from shoreline comparisons using an assumption regarding the profile response to a shoreline change such as:

$$\frac{dV}{dt} = \left(b + d_c\right)\frac{dy}{dt} \tag{2}$$

where y(t) is the shoreline position, b is the elevation of the berm and d_c is the depth of closure for the beach profiles (Figure 1).

Solving Eq. 1 for the sediment transport requires some estimation of the sources of sediment. For this paper, the sources are limited to the natural bypassing of sand across an ebb shoal where the re-attachment of the ebb shoal bar is well defined, say at x =xs, or the mechanical bypassing of sand through a pipeline located at a specific location, xp.

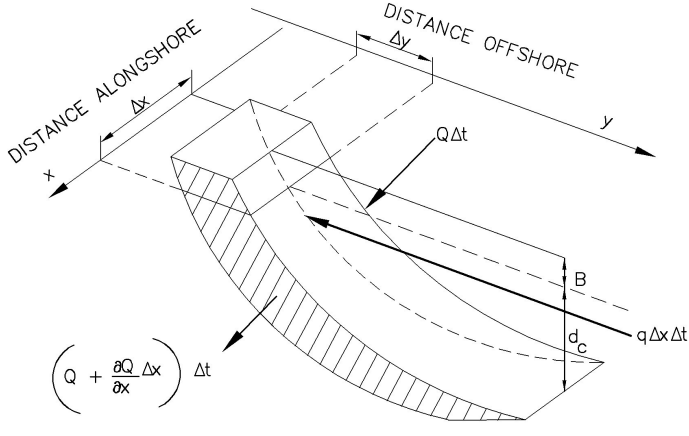

Figure 1. Definition Sketch of a Beach Cell.

Case Study 1: South Lake Worth Inlet, Florida

South Lake Worth Inlet (SLWI) is a manmade tidal inlet constructed in the 1920's to provide flushing of the south end of Lake Worth. While originally designed for flushing, the inlet is also used for small craft navigation. The inlet contains a rock bottom and has a fixed bridge over the inlet, which limit the size of vessels using the inlet. The curved north jetty is approximately 103 m longer than the south jetty and the downdrift beach is significantly offset to the west (Figure 2).

The inlet has an ebb shoal which bypasses a portion of the alongshore sediment transport to the downdrift beach. The ebb shoal bypassing bar attaches itself to the beach between approximately 670 m and 810 m south of the inlet (CPE, 2004). To

counteract the influence of the inlet on the remainder of the alongshore sediment transport, sand has been mechanically bypassed with fixed plants since 1937. Sand is currently discharged to the downdrift (south) beach through a single discharge located 207 m south of the south jetty (Figure 2).

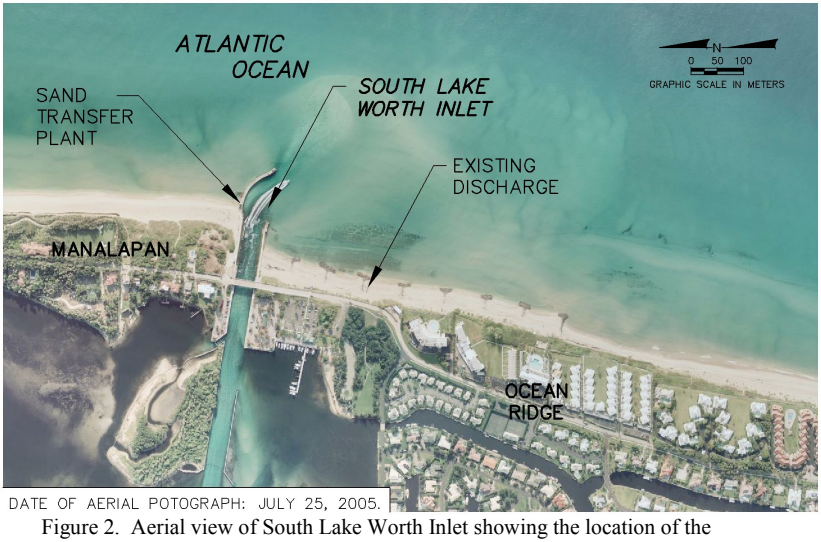

Figure 2. Aerial view of South Lake Worth Inlet showing the location of the bypassing plant, existing discharge and the south adjacent shoreline.

Palm Beach County owns the downdrift beach for the first 240 m. The next 990 m of upland property is privately owned. The first 2285 m of shoreline downdrift of the inlet is part of a Federally authorized shore protection project which includes 8 T-head groin structures and periodic nourishment with sand from offshore borrow areas (Olsen Associates, Inc., 1996).

Palm Beach County currently owns and operates the sand transfer plant at SLWI, which was last relocated in 1967. The current plant has reached the end of its useful life and is scheduled for replacement in 2007. As part of the design for a replacement plant, the County requested recommendations on the siting of the discharge pipe (CPE, 2004).

In this first case study, q (x,t) is expressed as two point sources of sand for the mechanical and natural bypassing. Due to limited data, Eq. 1 was solved on an average annual basis, so $q(x,t) = q(xp)$ for the mechanical bypassing, $q(x,t)= q(xs)$ for the bar bypassing, and $q(x,t)=0$ for all x other than xs, and xp. From Eq. 1, Q(x) was estimated and the littoral transport south of the south jetty is shown in Figure 3.

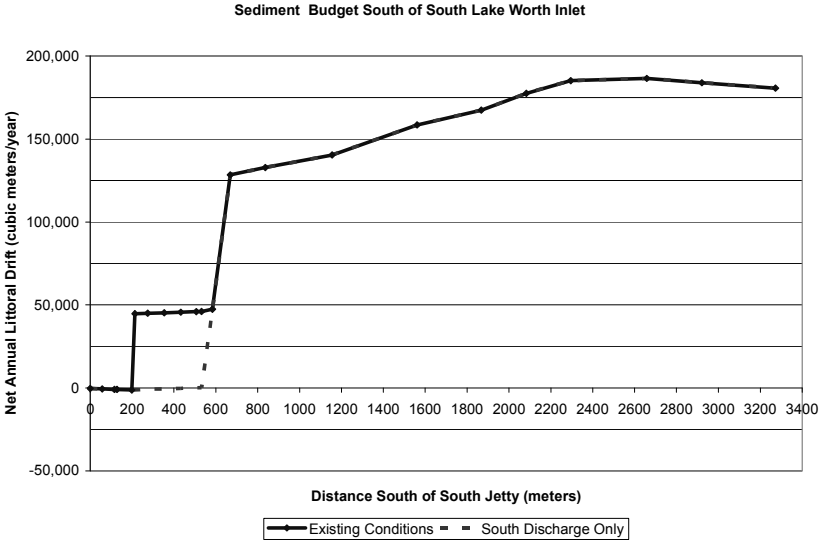

Figure 3. Existing and Proposed Sediment Transport South of South Lake Worth Inlet.

Immediately south of the inlet, the net annual littoral drift is low with an assumed loss back to the inlet of 380 m^3 per year. This value is consistent with the interior shoaling of the flood shoal area. The transport jumps abruptly at the existing discharge pipe (207 m) and at the point of the ebb shoal bar bypassing bar connection to the beach (670 m). South of the bar bypassing connection point, the littoral drift increases abruptly and approaches an asymptotic transport. Figure 3 shows that the wave induced littoral transport is just barely large enough to move the mechanically bypassed sand south along the beach. In fact, the T-head groin field appeared to be over performing. Discharging sand further south where the transport rate is higher appeared to be warranted.

CPE (2004) considered several alternative placements ranging from utilizing just the existing discharge at 207 m, to adding a second discharge at locations ranging from 584 m to as far south as 1130 m. Some of the suggestions were not solely based on technical justification and included upland owner input. A review of the pumping capacity of the proposed sand transfer motor, pump and pipeline system was performed (Four Jays Consulting, Inc., 2003). The review determined that the proposed system could pump a sand slurry to the last T-head groin (584 m) without risking sediment deposition within the discharge pipe.

The littoral drift curve (Figure 3) was adjusted assuming all mechanically bypassed sand was discharged through a second discharge located at the last groin in the T-head groin field (584 m). According to Figure 3, the bypassed sand will be discharged at a location of much greater wave induced sediment transport than at its current location; thus, the effectiveness of the bypassing should increase. From this analysis, support for extending a second discharge to the 584 m was recommended (CPE, 2004). While the use of q(x,t) as point sources is a useful tool, it results in abrupt changes in the wave driven littoral transport, which could be viewed as unrealistic.

The recommendation, for the addition of a second discharge at 584 m, was accepted by Palm Beach County (owner and operator of the plant). Nevertheless, the proposed location fronts private upland property, whose owners are disapproving the placement of the discharge in front of their property. The protection of private property rights is maintained under the State of Florida's beach preservation statute (Chapter 161, F.S.). For the time being, the proposed plant will continue to utilize the existing discharge at 207 m.

Case Study 2: Lake Worth Inlet, Florida

In contrast to the bar bypassing inlet at SLWI, the Lake Worth Inlet (LWI) is a deep draft navigation inlet with no ebb shoal and no natural bypassing of sand (Figure 4). The inlet was dredged in the early 20th century and was deemed a federal navigation project by 1925. The construction of twin jetties impacted the littoral drift significantly. As a result, a sand bypassing plant was constructed in 1958 to bypass a portion of the littoral transport to the downdrift beach. The remainder of the transport is allowed to shoal in the channel where it is dredged. The original discharge was within 25 m of the south jetty.

The plant operated more or less continuously until 1990 when the plant was damaged in a storm and when the steel discharge pipelines were found to be corroded. The plant set idle for several years until two new HDPE pipelines were directionally drilled under the inlet in 1996. Due to the limitations in directional drilling, the discharges were located approximately 64 m south of the south jetty. Since the resumption of bypassing in 1996, the beaches immediately downdrift of the inlet accreted significantly. This implies that only a portion of bypassed sand was being transported to the remainder of the Town of Palm Beach.

Aside from the publicly held lands that contain the south jetty, the upland property along the southern shoreline for several thousand m is privately owned. The Town does hold a beach access parcel at approximately 740 m south of the south jetty. This access parcel is used to deploy heavy equipment on the rare occasion that the existing discharges become landlocked.

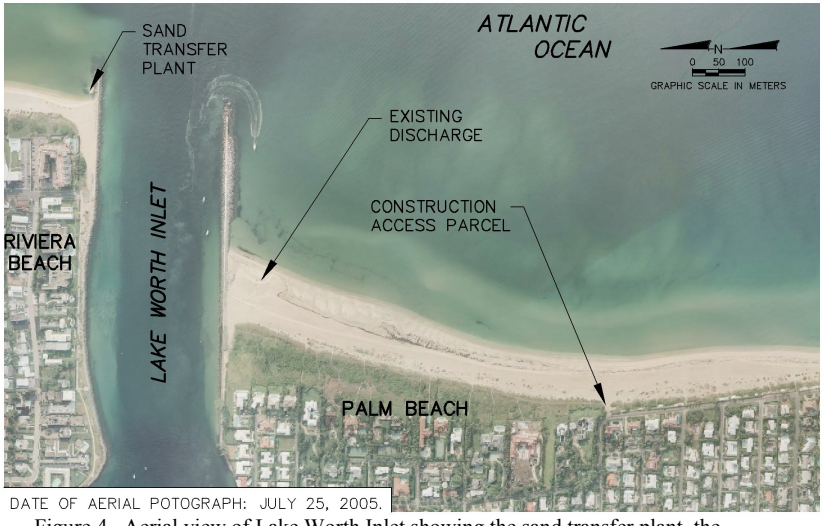

Figure 4. Aerial view of Lake Worth Inlet showing the sand transfer plant, the existing discharge and the south adjacent shoreline.

While the plant continues to operate, there is consensus that the existing sand transfer plant has reached the end of its life cycle and requires a major overhaul or replacement. Prior to initiating engineering of the pump and motors, the Town of Palm Beach requested an analysis of the optimum location of the discharge pipes and to determine if alternative locations would result in less beach accretion and more sand bypassing the immediate downdrift region.

In the second case study (CPE, 2005), the bypassing of sand in Eq. 1 is handled differently. Eqs. 1 and 2 are combined and q(x,t) is set to zero as there is no natural bypassing of sand at Lake Worth Inlet due to the maintained deep draft navigation channel.

The pipeline-bypassed sand is modeled after the diffused sand distribution described by Dean (2002). Dean (2002) states that for an initial narrow planform of sand along a straight beach, that the shoreline position with time, y_d (x,t) is:

$$y_d(x,t) = \frac{N}{\sqrt{4\pi G t}} e - \left(\frac{x^2}{4Gt}\right) \tag{3}$$

where N is the square footage of the initial planform, and G is the shoreline diffusivity (Dean, 2002). N was estimate for each bypassing event by dividing the bypassed volume by the active profile height ($b+d_c$). By doubling the value of N and

taking only half of the solution (positive x), the equation describes the shoreline response downdrift of an impervious jetty subject to a single bypassing event.

The initial diffusion of the narrow area was validated by comparing the resulting shoreline after one month of time for typical average wave conditions. At the end of one month the majority of the area had diffused away. This is consistent with observations of the actual discharge.

To determine the resulting net shoreline from M months of bypassing, the total bypassed induced shoreline change is then the summation of the shoreline responses for the corresponding remaining time intervals,

$$y_{dtotal}(x, M) = \sum_{i=1}^{M} \frac{N_i}{\sqrt{4Gt_i}} e - \left(\frac{x^2}{4Gt_i}\right) \tag{4}$$

where t_i = M-i + 1 in months:

The diffused shoreline response, y_{dtotal} , is then subtracted from the observed shoreline changes dy/dt, and Eqs. 1 and 2 are used to determine the wave induced sediment transport south of the jetty. The resulting net annual littoral drift curve is shown in Figure 5. In contrast to the abrupt changes in the SLWI case study, the littoral drift curve is a smooth transition from zero littoral drift at the inlet to a consensus value 1100 m downdrift of the south jetty.

Figure 5 clearly shows that the bypassing of an annual average of 131,000 m^3 per year to the existing discharge (64 m south of the south jetty) will result in deposition because the location has insufficient wave induced sediment transport to move such a large quantity of sand. Figure 5 also shows that by extending the discharge to approximately 740 m, that the littoral drift is approximately 85 percent of its maximum value and is greater than the volumetric rate of bypassing. The transport rate at 740 m is an order of magnitude greater than at the existing discharge. CPE (2005) recommended construction of a second discharge between 740 m and 1100 m south of the south jetty.

A review of the proposed bypassing pump and motors was undertaken assuming the existing HDPE pipes under the inlet were going to continue to be utilized (Four Jays Consulting, 2005). The proposed pump and motors were found to have the capability to pump a sand slurry to the existing discharge, but not to 740 m south of the jetty. A remotely operated booster pump on the south jetty was recommended if the discharge was to be lengthened.

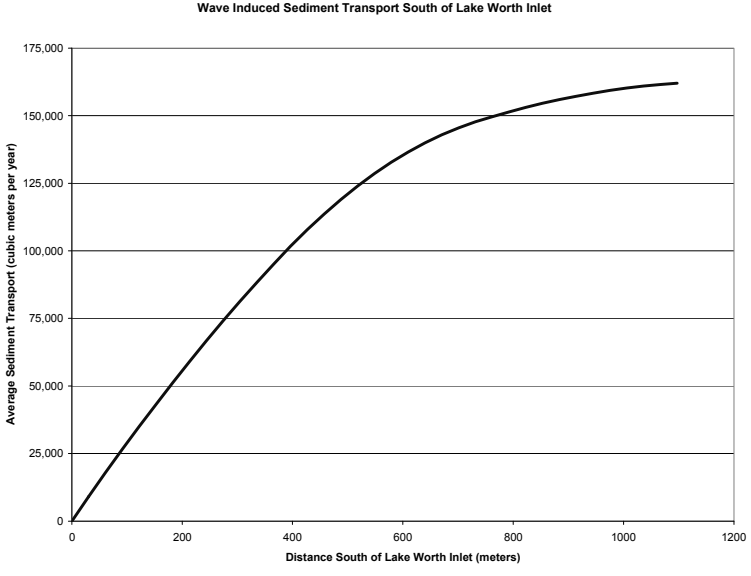

Figure 5. Average Sediment Transport South of Lake Worth Inlet.

The Town of Palm Beach accepted the recommendations and is pursuing the upland owner easements necessary to install a discharge pipe along the beach, and a booster pump at or near the south jetty.

CONCLUSIONS

Based on the previous two case studies and the findings of Bailard (2006), the following guidelines for the siting of sand discharges are offered:

a. Discharges should not be located immediately adjacent to the downdrift jetty. The littoral transport is either too small to transport sand away from the discharge or will transport sand back to the inlet. Neither achieves the objective of sand transport along the downdrift beach.

b. Dedicated sand bypassing systems should utilize two discharges at a minimum. This not only creates an engineering redundancy, but provides flexibility in discharging sand to the instantaneously optimal location as wave climates vary over a year.

1. The first discharge should be located close to the downdrift jetty (<100 m) to reinitialize the net sediment transport. If the inlet is not jettied, the distance should be increased such that reintroduction of sand back into the inlet is minimized. The volume of sand bypassed to this location should be limited to the wave induced sediment transport at this location.

2. The second discharge location should be at or downdrift of any bar bypassing feature, and at a distance from the downdrift jetty such that the wave induced sediment transport is greater than the annual bypassing rate. When the wave induced sediment transport is subject to significant annual fluctuations, additional flexibility in the second discharge location, may be warranted.

c. Discharges must be sited in cooperation with the design of the sand pumping system. Excessively long pumping distances may result in increased capital and operational costs by requiring increased horsepower, larger diameter pumps and pipelines, or thicker pipelines to account for the required increase in pressure in the pipe.

d. All locations should consider appropriate factors of safety (NRC, 1995) and include the effects of variable sediment budgets (Mann, 1999).

ACKNOWLEDGEMENTS

The author would like to thank the Town of Palm Beach and Palm Beach County for authorizing release of this data and for sponsoring the previous studies. The author also acknowledges the contributions of Christin Perkinson and Joseph Chaison, P.E. to the previous studies, and several CPE reviewers of this paper for their constructive comments.

REFERENCES

Applied Technology & Management, "Town of Palm Beach Lake Worth Inlet Sand Transfer Plant, Analysis of Longshore Transport and Discharge Alternatives," report to the Town of Palm Beach, January 2005.

Bailard, J., "Improving Sand Bypassing at Santa Barbara Harbor." Proc. of 30th International Conference on Coastal Engineering, San Diego, 2006.

Bruun, P., Stability of Tidal Inlets, Elsevier Scientific Publishing, 1978.

Bruun, P., "Beach Nourishment through Better Profiling and Backpassing" J. of Coastal Research, Vol. 6 (2), pp. 265-277, 1990.

Bruun, 1993. "An Update on Sand Bypassing Procedures and Prices," J. Coastal Research, SI No. 18, pp. 277-284, Fall 1993.

Clausner, J. "Jet Pump Sand Bypassing at the Nerang River Entrance, Queensland, Australia," Proceedings of the Beach Preservation Technology 88 Conference, Florida Shore and Beach Preservation Association, Tallahassee, Florida, pp.345,-356, 1988.

Clausner, J., Gebert, J., Rambo, A. and Watson, K., "Sand Bypassing at Indian River Inlet, Delaware," Coastal Sediments '91, American Society of Civil Engineers, pp.1177-1191.

Coastal Planning & Engineering, Inc., "South Lake Worth Inlet Management Program Update," report to Palm Beach County, Town of Manalapan, Town of Ocean Ridge, and the Florida Department of Environmental Protection, January 2004.

Coastal Planning & Engineering, Inc., "Lake Worth Inlet Sand Transfer Plant Discharge Location Evaluation," Report to the Town of Palm Beach, Florida, August 2005.

Dean, R. *Beach Nourishment: Theory and Application*, World Scientific Press, 2002.

Four Jays Consulting, Inc. "Proposed Sand Pumping Facility, Engineering Overview and Multiple Discharge Points," report to the South Lake Worth Inlet Technical Review Committee, November 2003.

Four Jays Consulting, Inc. "Lake Worth Inlet Sand Transfer Facility," report to the Town of Palm Beach, February 2005.

Mann, D. "The Importance of Inlet Littoral Budget Variability," Proceeding of Coastal Sediment '99, pp. 688-702, 1999.

National Research Council, *Beach Nourishment Protection*, National Academy Press, 1995.

Olsen Associates, Inc. and Palm Beach County Environmental Resources Management, "Palm Beach County Florida, From Martin County Line to Lake Worth Inlet and From South Lake Worth Inlet to Broward County Line, Shore Protection Project, General Design Memorandum Addendum for Ocean Ridge Segment with Final Supplement to the Environmental Impact Statement," August, 1996.

Rambo, A. Clausner, J. and Henry, R., "Sand Bypass Plant Indian River Inlet, Delaware," Proceedings of the 1991 National Conference on Beach Preservation Technology, Florida Shore & Beach Preservation Association, Tallahassee, Florida, 1991.

USACE, Los Angeles District, Oceanside Harbor, Oceanside, California, Report on a program for Installing, Monitoring, and Evaluating the Effectiveness of a Sand Bypassing System as a Means of Maintenance of the Harbor Channels, March 1982.

USACE, "Sand Bypassing System Selection," EM1110-2-1616, Washington D.C., January 1991.

Weggel, R. "Weir Sand-Bypassing Systems," Special Report No. 8, USACE Coastal Engineering Research Center, Fort Belvoir, VA, April 1981.

SHORELINE IMPLICATIONS OF FLOOD-TIDE DELTA MORPHODYNAMICS. THE CASE OF PORT STEPHENS (SE AUSTRALIA)

Ana Vila-Concejo[1], Andrew D. Short[2], Michael G. Hughes[3], Roshanka Ranasinghe[4]

1. Coastal Studies Unit. School of Geosciences, The University of Sydney, Sydney, NSW 2006, Australia. aconcejo@geosci.usyd.edu.au
2. Coastal Studies Unit. School of Geosciences, The University of Sydney, Sydney, NSW 2006, Australia. A.Short@geosci.usyd.edu.au
3. Coastal Studies Unit. School of Geosciences, The University of Sydney, Sydney, NSW 2006, Australia. michaelh@mail.usyd.edu.au
4. NSW Department of Natural Resources, GPO Box 39, Sydney, NSW 2001, Australia. E-mail: Rosh.Ranasinghe@dnr.nsw.gov.au

Abstract: Flood-tide deltas are dynamic features that are linked to the morphodynamics of the associated estuarine beaches and shorelines. Flood-tide delta morphodynamics remain largely unknown. Historic aerial photographs from Port Stephens, a ria-like estuary located in NSW (Australia), are analysed using Geographic Information System (GIS) techniques. Port Stephens is used as a case study to define flood-tide delta morphodynamics that will be applicable to similar systems elsewhere. The waterline is chosen to represent the evolution of the estuarine beaches because they are reflective in a microtidal environment. Boundary definition for the flood-tide delta needs further work since it is a submerged feature and the photographs have different quality and correspond to different tidal levels. It is suggested that image processing techniques may help to solve this problem in the future. More studies, both morphologic and hydrodynamic, are needed to establish the sediment paths and magnitudes within the Port Stephens flood-tide delta.

INTRODUCTION

Flood-tide deltas (or shoals) are caused by sediment accumulation at the landward end of inlets. They are often fan- or horseshoe-shaped with a broad ramp that slopes up to the surface in the landward area (Hayes, 1979; 1980; Davis, 1996). This ramp is a shoaling continuation of the inlet channel and delivers sediment to the tidal delta during flooding

tides. Flood-tide deltas are dynamic features that have not been the subject of many investigations; their formation processes are well understood but their morphodynamics remain largely unknown. Flood tide deltas can also be associated with adjacent estuarine beaches whose morphodynamics are linked to the delta. Consequently, the adequate management of these beaches requires in-depth knowledge of the short-, medium- and long-term morphodynamics of delta system.

The objectives of this paper are: (1) to present some of the existing knowledge of flood-tide delta morphodynamics in a micro-tidal estuary at short to medium temporal scales; (2) to identify future directions of research to establish flood-tide delta morphodynamics and their relationship with the associated shorelines; and, (3) to present some preliminary results in the decadal evolution of the flood-tide delta and associated shorelines of a flood-dominated estuary.

STUDY AREA

Port Stephens is located in New South Wales (NSW), SE Australia (Figure 1) 230 km north of Sydney. It is a ria-like drowned river valley estuary (Roy *et al*., 2001) and has an east-west orientation with a total length of 23 km and a surface area of 140 km^2. Two well differentiated basins can be distinguished inside it: the inner and the outer basins, also known as upper and lower ports. The estuary is shallow and that has prevented further development as a commercial/industrial harbour. At present it is the most popular tourist destination on the 1,000 km long NSW coastline.

Tides in the area are semidiurnal and microtidal with mean tidal ranges of 1.6 m and 1.3 m for spring and neap tides respectively (Short, 1985). According to Short and Trenaman (1992), the deepwater wave climate is moderate with mean significant wave heights (H_s) of 1.5 m and 8 s mean wave period (T). The same authors state that the central NSW coast receives few low-energy waves (<1 m, 10%) and a significant amount of high-energy waves (2-3 m, 21%; 3-5 m, 5%). Waves from the NE dominate during summer and E-SE waves are prevalent for the rest of the year; although SE storms may occur at any time of the year, they are more frequent between April and September (Short and Trenaman, 1992).

Rainfall data from the Australian Bureau of Meteorology (BOM, 2006) show that the average yearly rainfall between 1884 and 2004 is 1345 mm; minimum monthly rainfall occurs in October - November (75-80 mm) and increases to reach maximum rainfall in May - June (150-155 mm). Winds in the area are strongly influenced by a daily sea breeze pattern with onshore winds (>30 km/h) occurring in the afternoon from spring to autumn; W-SW winds with speeds over 30 km/h dominate the winter months (BOM, 2006).

Under the framework of Roy *et al*. (2001) classification for SE Australian estuaries, Port Stephens is classified as a tide-dominated estuary because tidal processes dominate the overall estuarine dynamics. Tidal attenuation inside the estuary is negligible because it has a wide mouth (1.24 km); however, it is located on a wave-dominated coast where

ocean waves do not allow ebb-tide delta deposition and propagate into the estuary affecting the flood-tide delta and the associated shorelines.

Port Stephens has a well developed flood-tide delta (Figure 1) that is occasionally affected by swell propagation into the estuary. Several authors (e.g., PWD, 1985; PWDS, 1999) have also emphasised the role of locally generated wind-waves in influencing the flood-tide delta and associated beaches. According to PWDS (1998) the spring tidal prism at the entrance is 168×10^6 m^3 for ebbing and 165×10^6 m^3 for flooding. The same authors provide values for maximum tidal currents at the entrance in excess of 1 m/s.

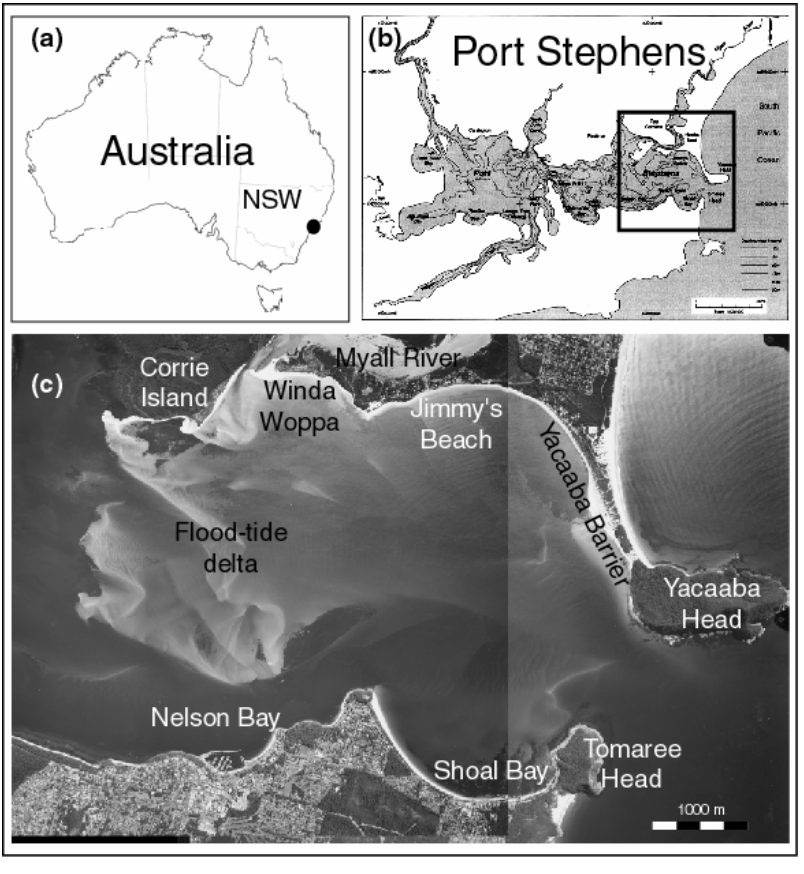

Figure 1. (a) Location of Port Stephens inside Australia; (b) Map after DPWS (1999) showing two well differentiated basins and the study area; (c) Aerial photo of the study area (April 2006) courtesy of the NSW Department of Natural Resources

METHODS

Present Work

The methodology includes an extensive search on Port Stephens to review existing knowledge on the study area. Historic data on Port Stephens include aerial photographs, maps and bathymetric charts of the area; data obtained from technical and scientific publications; and forcing mechanisms records (waves, tides, winds, rainfall). Data is then included in a Geographic Information System (GIS) that is set using ESRI ARC-GIS 9.1. The GIS allows the organisation of the data and the accurate measurement of the evolution of the morphologic features and shorelines. Four photographs from 1963, 1986, 1994 and 2006 have been georectified and used in this study.

Present measurements include: (a) location and evolution of the northern shorelines and Winda Woppa Spit; (b) location and evolution of the shoreline at Shoal Bay; and (c) definition and evolution of the flood tide delta. As a preliminary approach, shorelines are identified as the intersection between the water and the land. The waterline, or instantaneous-shoreline, cannot be always taken as representative of "normal" or "average" conditions (Smith and Zarillo, 1990) because short-term variations can be high. Short-term variability depends mostly on beach slope (tan β), tidal range and wave energy. Estuarine beaches in Port Stephens are reflective: beach measurements in Shoal Bay in October 2006 had an average tan β of 0.12 (i.e. 1 m variation in the water level would imply 8.3 m across-shore displacement of the shoreline). Simultaneously, it is not often that waves propagate into the estuary and they do not seem to be significant in the aerial photographs used for this study. Therefore, taking into consideration the amplitude of mean spring tides (0.8 m) and the average beach slope, the maximum error associated to taking the instantaneous shoreline would be $\pm$7 m across-shore.

Once the shorelines are identified the area of every morphologic feature is calculated using GIS; the evolution of the areas is made by comparing the areas obtained for consecutive years. It should be noted that data presented in this study refer to the extent of the morphologies instead of volumes of sediment.

Future Work

More aerial photographs (1951 to present) and historic maps will be included in the GIS to obtain a more complete evolution of the area over a longer period. More accurate measurements will be made with the possible application of image processing techniques as suggested by Aarninkhof *et al*. (2000), Hoeke *et al*. (2001), Aarninkhof (2003) and Boak and Turner (2005) to identify the shorelines in a more rigorous and accurate way.

Future work will also include the surveying of the flood-tide delta and the associated estuarine beaches in Port Stephens to obtain digital terrain maps (DTM). DTMs will then be included in the GIS and compared with the historic data. The topographic and bathymetric monitoring will be coupled with simultaneous hydrodynamic measurements using acoustic Döppler current profilers (ADCPs) and data from other sources such as wave, tidal and wind data. The combined analysis of the data will allow the

establishment of present and historic flood-tide delta morphodynamics and association with the morphodynamics of estuarine beaches.

PORT STEPHENS: EXISTING KNOWLEDGE

The shorelines on both sides of the estuary have experienced ongoing erosion that threatens public and private property resulting in several engineering interventions being undertaken to manage coastal erosion, namely at Jimmy's Beach, Shoal Bay and Nelson Bay (Figure 1). There has also been scientific interest on the presence of a large sandwave on the Yacaaba Barrier. Therefore, there have been several technical and scientific studies made at the area in order to propose management options and to monitor undertaken engineering interventions. These studies include several reports on Jimmy's Beach erosion (i.e., PWD, 1985; 1992); reports on Nelson Bay (PWD, 1979); a detailed study on the evolution of the sandwave at Yacaaba Barrier (Cholinski, 2004); and more general in-depth geomorphological studies such as Thom *et al*. (1992) and PWDS (1999).

Erosion at Jimmy's Beach and Winda Woppa

Jimmy's Beach and Winda Woppa are part of a sand spit that corresponds to the southern bank of the Myall River mouth (Figure 1). According to Thom *et al*. (1992) the spit was initiated about 1820 and reached its maximum length about 1910; a storm in 1927 caused the breaching of the spit some 1300 m from its end, creating a sand bank that migrated landwards to form a beach on Corrie Island. The same authors point to some westward extension of Winda Woppa occurring before 1992. Figure 2 shows that Winda Woppa spit has been one of the most dynamic features of the estuary; its dynamics seem to be related with the hydrodynamics of the lower Myall River. Thom *et al*. (1992) also stated that the flood-tide delta had undergone a net loss of sand since accurate charts became available (1851) thus facilitating spit breaching during the 1927 storm. The same authors proposed an alternative evolution where the sand spit breaching occurred due to the high energy conditions and extreme flooding that occurred during the 1927 storm, stating that it could be completely independent from the flood-tide delta evolution.

Jimmy's Beach and Winda Woppa have been undergoing erosion for over 40 years (PWD, 1985; 1992; PWDS, 1999). They are narrow reflective estuarine beaches that are backed by a sand scarp of some 2-4 m. The development of the area for residential uses started in the 1960s (Watson, 2000) and at present constitutes expensive beachfront real estate. Recession rates on the beach reach 1.1 m/yr with an average rate of removal of sediment of 8,000 m^3/yr (PWDS, 1999). As a consequence, there have been several studies of Jimmy's Beach and it has been nourished several times (PWD, 1985; 1992; PWDS, 1999). The first nourishment intervention was undertaken in March 1984 and by 1998 a total of 372,000 m^3 had been placed in the area (Watson, 2000)

Some of the studies (i.e., PWDS, 1999) have computed a net eastward direction for the sediment transport along the beach with the application of numerical models. They stated that the main forcing mechanism contributing to the net loss of sediment on

Jimmy's Beach was wind waves generated by westerly winds. They therefore identify the sandwave along Yacaaba Barrier (Figure 1 and 2) as a suitable source of sediment for future nourishment interventions.

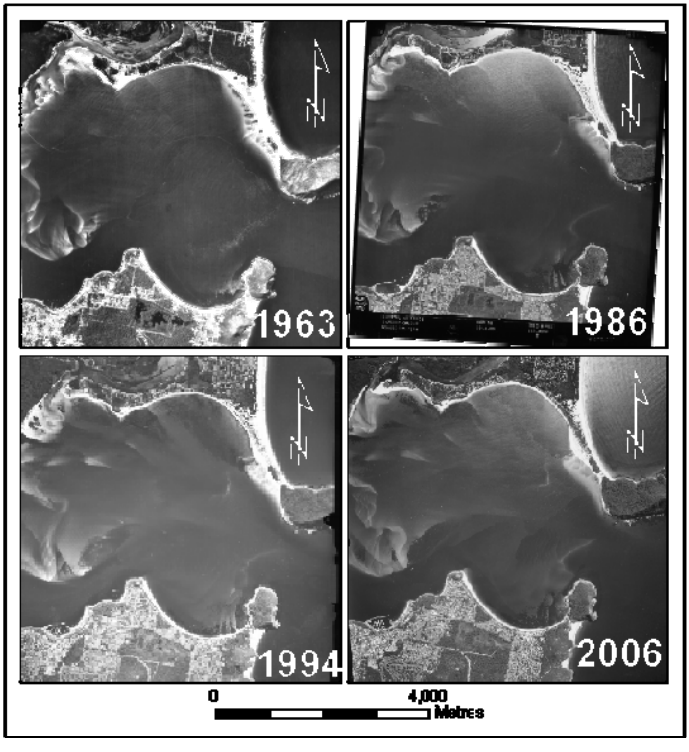

Figure 2. Georectified aerial photos of the study area.

Shoal Bay and Nelson Bay

Shoal Bay is located westward from Tomaree Head (Figure 1 and 2) on the southern shore of Port Stephens; it is an embayed estuarine beach that is aligned to the swash refraction patterns inside the estuary. Its more protected part, next to the headland, is narrow and with mean grain size about 0.25 mm. The most exposed section of the bay is wider with coarser sediments (mean grain size between 0.75 and 1.00 mm). Beach cusps are often present from the middle part of the bay to the westernmost end with typical wavelengths between 20 and 25 m. Westwards longshore transport appears to occur in this beach, evidenced by updrift sediment accumulation on the eastward side of a boat ramp located on the eastern end of the beach

Nelson Bay is the next westward embayment from Shoal Bay. It has been undergoing erosion processes since at least the 1940s, when a concrete slab and revetments were

placed on the beach for protection with limited success (PWD, 1979). A seawall was built in 1940 and it lasted only two years (PWD, 1979). According to the same authors the alignment of the shoreline underwent considerable variation between 1959 and 1977. They state that sediment transport along the beach is eastward directed as a consequence of locally generated wind waves, and attribute some of the erosion problems to the construction of a breakwater at the westernmost end of the beach. They also relate erosion problems to the nearby presence of the main ebb tidal channel (Figures 1 and 2).

Yacaaba Sand Wave Dynamics

Yacaaba Barrier is a sandy isthmus that separates the estuarine area of Port Stephens from Fens Embayment to the North (Figure 1). It is a typical low-energy reflective beach that is located eastwards from Winda Woppa and Jimmy's Beach. It is characterised by a sandwave that forms near the entrance and migrates landwards (Cholinski, 2004). Cholinski (2004) analysed sandwave evolution between 1951 and 2003. The same author identified several sandwaves in the area and concluded the following: (1) the first sandwave was observed in 1981; (2) the average migration rate was 70 m/yr to the west; (3) the sandwaves do not seem to migrate any further than the middle zone of the Yacaaba Barrier; (4) sandwaves increase their size by attaching submerged transverse bars; and, (5) the width of Yacaaba Barrier increased during the study period.

Flood-tide Delta Morphodynamics

The flood-tide delta at Port Stephens occupies most of the outer estuary and is related with the dynamics of Myall's river mouth and Winda Woppa spit (Thom *et al*., 1992) as well as with the adjacent estuarine beaches. It is a shallow delta (Figure 1 and 2) with depths that are mostly less than 5 m. Thom *et al*. (1992) described a net sand loss in the flood-tide delta since 1851 and speculated that Winda Woppa's breaching occurred due to the erosion of the flood-tide delta that caused the deepening of the area.

The morphodynamics of the flood-tide delta are controlled by tidal currents, swell waves that propagate into the estuary and locally generated wind waves. The relative importance of these mechanisms ultimately controls the evolution of the flood-tide delta. Tidal currents in the estuary are not well known. PWDS (1998) measured tidal currents and water levels during two consecutive days in September 1993; the measurements were restricted to the estuary entrance, the mouth of the Lower Myall River, the estuary constriction at Soldiers Point (which separates the outer estuary from the inner estuary, Figure 1) and Karuah River mouth in the north-west of the inner estuary. The estuary has maximum tidal flows occurring during the two hours following mid-tide and minimum tidal flows (slack water) occurring within one hour after high and low tide (PWDS, 1998). The same authors found that the tidal range is amplified along the estuary; they measured 1.13 m at the entrance and 1.31 m at the mouth of the Karuah River on the 29th September 1993.

PRELIMINARY RESULTS ON THE RECENT MORPHOLOGIC EVOLUTION

Figure 2 shows four georectified aerial photos of the study area. These photos are analysed using GIS technology.

Evolution of the Northern Shoreline and Winda Woppa Spit

The area comprising Yacaaba Barrier, Jimmy's Beach and Winda Woppa spit (Figure 3) underwent accumulation of $120x10^3$ m^2. The most significant changes were the accumulation due to Yacaaba's sandwave, mostly in 1994 and 2006; and at the westernmost point of Winda Woppa that showed westwards growth during the study period. The entire area showed no significant variations between 1963 and 1986 (Figure 4). An increase in $60x10^3$ m^2 occurred both for 1986-1994 and 1994-2006 (Figure 4). The westward growth of Winda Woppa Spit was high for 1963-1986, there was some retreat for 1986-1994 and was the greatest for 1994-2006 with approximately 275 m. Jimmy's Beach underwent approximately 50 m of shoreline retreat between 1963 and 2006; retreat between 1994 and 2006 has been between 10 and 20 m.

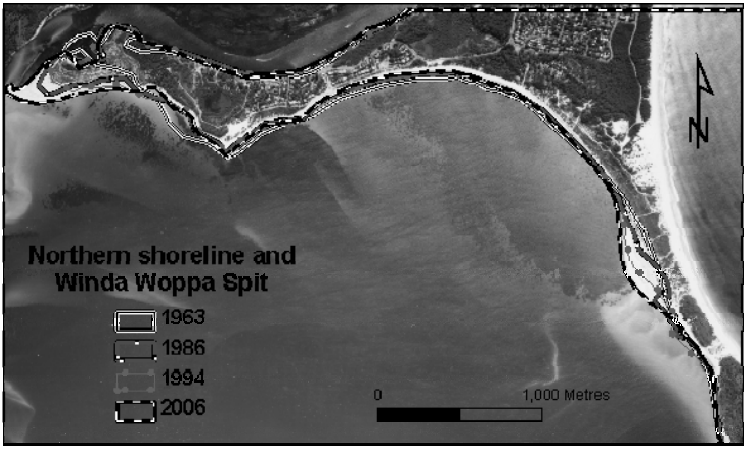

Figure 3.Evolution of northern shoreline/ Winda Woppa 1963-2006. The photo is from 2006.

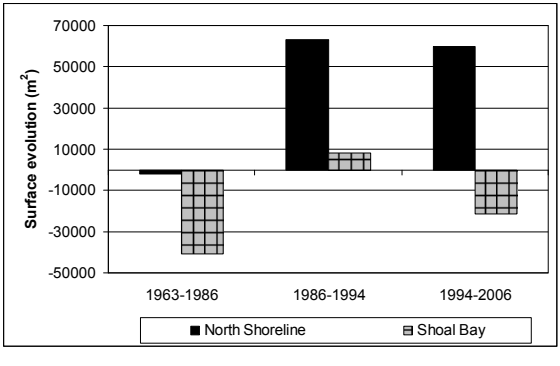

Figure 4.Surface evolution for the Northern Shoreline and Shoal Bay.

Evolution of Shoal Bay

Shoal Bay reduced its surface during most of the study period (Figures 4 and 5). Total erosion implied an area reduction of -55x10^3 m^2. The highest surface reduction occurred on the western part of the beach (Figure 5) with shoreline retreat approximately over 30 m. The largest erosion occurred for 1963-1986 with -40x10^3 m^2.

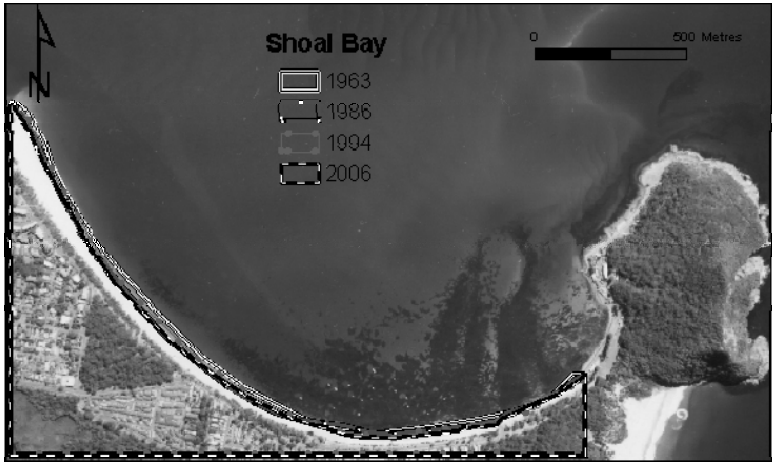

Figure 5.Evolution of the shoreline on Shoal Bay 1963-2006. The photo is from 2006.

Evolution of the Flood-Tide Delta

The definition of the morphological boundaries of the flood-tide delta is not clear and has yet to be defined. However, some approximation was made by enclosing the areas that showed the highest accumulation of sand and the qualitative results are in Figure 6. According to the data, there seems to have occurred a massive accumulation of sediment during the study period. However, it is important to note that the flood-tide delta is a submerged morphology and therefore its visibility highly depends on the tidal level and the quality of the aerial photos. Further work is required to correct the tidal levels, include other data that might help in the analyses and also, to develop a technique that allows the definition of the flood-tide level boundaries that does not require elevation data.

Figure 6 shows the preliminary attempt made to define the boundaries of the flood-tide delta. The western limit is given by the photograph from 1986, and the northern limit was selected to avoid the inclusion of Winda Woppa spit. The southern limit is easier to define because the ebb channel runs along the southern margin of the estuary. The main problem is the eastern limit because it is a continuum, from deeper flood channels next to the mouth, to shallower flood-delta on the westward side. The eastward limit is also heavily dependent on the tidal level.

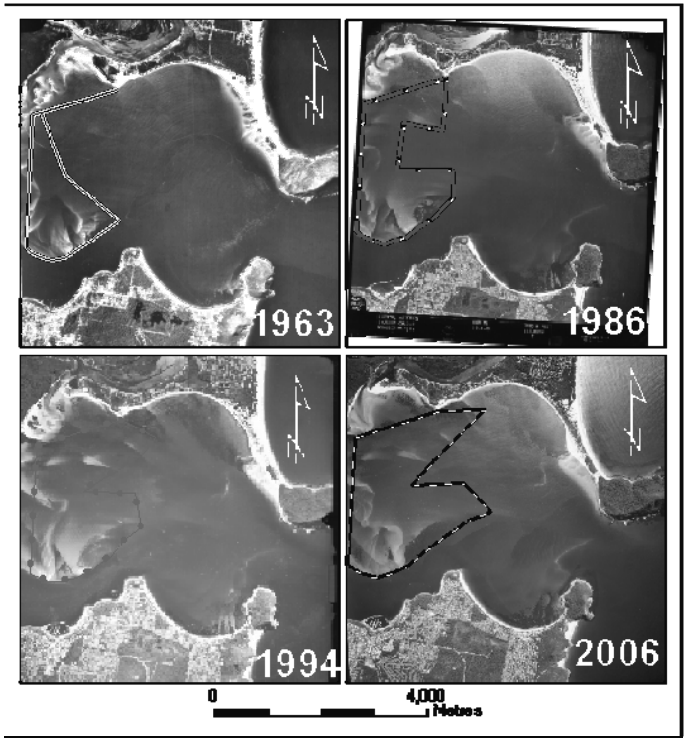

Figure 6. Preliminary attempt to delimit manually the flood-tide delta. Tidal levels are not the same in every photo and the resolution and photo quality also change.

DISCUSSION

Port Stephens is comparable with many ria-type estuaries in NSW and other parts of the world where fluvial processes have relatively less impact today on morphology and hydrology than during periods of low sea-level (Roy *et al*., 1980).

Data presented allows some preliminary analyses on the evolution of the flood-tide delta and associated shorelines in Port Stephens. The basic approach used in this study shows a general accumulative trend along the northern shoreline (Figure 3 and 4) that includes Yacaaba barrier, Jimmy's Beach and Winda Woppa spit (Figure 1). Therefore, when measuring area increase/decrease, the sediment accumulation due to Yacaaba's sandwave and to the westward growth of Winda Woppa spit seems to be of greater magnitude than the erosion occurring at Jimmy's Beach. Between 1984 and 1998 a total of $372x10^3$ m^3 of sand was placed on Jimmy's Beach (Watson, 2000); however, according to the shorelines measured in this work (Figure 3) and *in situ* observations (Figure 7) Jimmy's beach is still undergoing erosion. The westward growth of Winda

Woppa spit had already been described by Thom *et al.* (1992); data between 1994 and 2006 (Figure 3) show an intensification of the westward growth of the spit.

Results from numerical modelling have shown that the effect of wind generated local waves is the dominant control on Jimmy's Beach and therefore there is a net longshore transport from Jimmy's Beach towards Yacaaba Barrier (i.e., PWDS, 1999, Watson, 2000); PWDS (1999) therefore identify Yacaaba's sandwave as an ideal sediment source for future nourishment interventions on Jimmy's Beach. Results from Cholinski (2004) contradict the numerical models stating that the sandwave is rapidly migrating landwards (70 m/year). Further, and according to the same author, the first sandwave observation corresponds to 1981 and the sandwaves do not pass the central part of Yacaaba barrier. Further work is needed to correctly establish the sediment transport paths in this area. Data herein presented also show significant westward accretion of Winda Woppa spit; it is not clear which are the processes involved but spit dynamics seem to be linked not only to the estuary and flood-tide delta dynamics but also to the fluvial dynamics of the Myall River mouth. What appeared as a catastrophic breaching in 1927 might be a cyclic process involving sediment bypassing from the east to the west of the inlet that constitutes the mouth of the Myall River in what would be a typical sediment bypassing mechanism for geographically stable inlets (FitzGerald *et al.*, 2001). Further studies are needed to identify the sediment transport paths and magnitudes involved in the general evolution of the area.

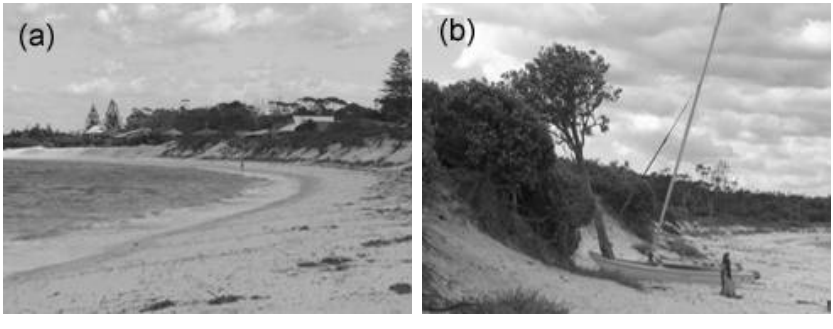

Figure 7. Jimmy's Beach location photos. (a) The beach is narrow with private property behind the scarp; (b) a tree and a tree stump are found in the beach due to strong erosion [Photos by Vila-Concejo, April 2006]

Shoal Bay underwent shoreline retreat during 1963-1986 and 1994-2006 mostly in the central and western part of the beach where shoreline retreat was over 30 m. The southern shoreline westward from Shoal Bay, Nelson Bay (Figure 1), was not analysed in this study but it has been undergoing erosion (PWD, 1979). A more detailed GIS analysis should be made in order to determine the shoreline evolution for the entire south shoreline. Several problems have been encountered when delimiting the flood-tide delta using aerial photos (Figure 6). As it is a submerged feature, the quality of the photograph

and the tidal levels are key factors that should be taken into account. It seems, however, that the flood-tide delta increased its area during the study period.

Roy *et al*. (1980) stated that Port Stephens and similar systems elsewhere are undergoing sand loss processes that are related to: (a) littoral drift; (b) aeolian transport into transgressive dunes; and (c) offshore transport of sand by seaward-flowing bottom currents. It is important to note that the mechanisms controlling sediment exchange through the entrance and outer estuary have not been investigated and therefore are a source of uncertainty for present conceptual models of behaviour that could be applied to Port Stephens and similar estuaries elsewhere.

Future work

The basic approach used in this study allowed the definition of general accretion and erosion/retreat areas. It is not clear however, if the use of the instantaneous shoreline (i.e. the waterline) is a good indicator of the system's variability; data presented in this paper seem to indicate that variations in the system are significantly larger than the associated ±7 m across-shore error. Additionally, Aarninkhof *et al*. (2000) and Aarninkhof (2003) extracted proxy shoreline features from digital coastal images that are not necessarily visible to the human eye. Hoeke *et al*. (2001) also proposed image processing techniques to define the shoreline using GIS. It seems likely that similar techniques will be useful to delimit submerged features taking into account a tidal level correction.

The morphologic evolution of Port Stephens should be coupled with the historic records of wave, tidal, wind and rainfall data to identify which are the processes governing the changes in the system. Present dynamics will be investigated by measuring the morphology and the forcing mechanisms. It is expected that establishing the present morphodynamics of Port Stephens flood-tide delta will help to understand its recent evolution and it will be applicable to other similar estuaries elsewhere.

CONCLUDING REMARKS

Flood-tide deltas are dynamic features that are often linked to estuarine beaches and shorelines. Flood-tide delta morphodynamics need to be established to understand the process-response of the system and to improve future management not only of the flood-tide delta but also of the associated beaches and shorelines.

The flood-tide delta in Port Stephens seems to have increased its extent since 1963. The north shoreline underwent general accumulation with sandwave accretion on the east and spit progradation on the west that has been intensified between 1994 and 2006. The central area of the north shoreline underwent erosion that was managed through sand nourishment but it is still undergoing erosion at present. Shoal Bay (on the southern margin of the estuary) has undergone erosion which, in some parts, has shown over 30 m of shoreline retreat. More studies, both morphologic and hydrodynamic, are needed to establish the sediment paths and magnitudes within the Port Stephens flood-tide delta.

A GIS is a useful tool to analyse the morphologic evolution of estuaries. Using the instantaneous shoreline (waterline) inside an estuary seems to represent shoreline evolution with enough accuracy. The definition of the flood-tide delta needs further development. It is suggested that image processing tools could be applied to determine the boundaries of the flood-tide delta. The extension of the flood-tide delta will have to be further corrected for the tidal levels.

ACKNOWLEDGEMENTS

This work is partially funded by the Australian Research Council (ARC) grant number: LP0668979; Ana Vila-Concejo is also funded by ARC. The authors would like to acknowledge the New South Wales (NSW) Department of Natural Resources (Australia) and the councils of Port Stephens and Great Lakes for financial support.

Dave Hanslow, Doug Lord, Christine Gray and Robert Clout from the Department of Natural Resources (NSW; Australia) kindly helped by providing aerial photos and access to technical reports. Allan Gordon and Des Mitchell from the Department of Commerce (NSW, Australia) provided essential help in finding bathymetries and charts of the study area. We would like to thank Michelle Frolich for her great contribution with the literature search. Also to the UNSW-GEOS3731 students that helped with the measurements on Shoal Bay.

REFERENCES

Aarninkhof, S.G.J., 2003. *Nearshore Bathymetry derived from Video Imagery*. PhD Thesis. Technische Universiteit Delft, 175 pp.

Aarninkhof, S.G.J.; Caljouw, M., and Stive, M.J.F., 2000. Videobased, quantitative assessment of intertidal beach variability. *Proceedings of the 27th International Conference on Coastal Engineering* (Sydney, Australia), 3291–3304.

Boak, E.H. and Turner, I.L., 2005. Shoreline definition and detection: a review. *Journal of Coastal Research*, 21/4, 688-703.

BOM 2006. Australian Bureau of Meteorology web site: http://www.bom.gov.au/cgi-bin/climate/cgi_bin_scripts/windrose_selector.cgi. October 2006.

Cholinski, M.P., 2004. *Sandwave Dynamics at Port Stephens, NSW*. School of Geosciences, University of Sydney, Australia. Honours Thesis. 150 pp.

Davis JR., R.A., 1996. Coasts. Prentice-Hall, New Jersey, 274 pp.

FitzGerald, D.M., Kraus, N.C. and Hands, E.B., 2001. *Natural mechanisms of sediment bypassing at tidal inlets*. ERDC/CHL CHETN-IV-30, U.S. Army Engineer Research and Development Center, Vicksburg, MS. (http://chl.wes.army.mil/library/publications/chetn)

Hayes, M.O., 1979. *Barrier island morphology as a function of tidal and wave regime.* In: Leatherman, S.P., (Ed.), Barrier Islands: From the Gulf of St. Lawrence to the Gulf of Mexico. Academic Press, New York, N.Y., 1-27.

Hayes, M.O., 1980. General morphology and sediment patterns in tidal inlets. *Sedimentary Geology*, 26, 139-156.

Hoeke, R. K., Zarillo, G. A., and Synder, M., 2001. *A GIS based tool for extracting shoreline positions from aerial imagery (BeachTools)*, Coastal and Hydraulics

Engineering Technical Note CHETN-IV-37, U.S. Army Engineer Research and Development Center, Vicksburg, MS.

PWD, 1979. *Nelson Bay Erosion Study*. Department of Public Works, NSW, Coastal Engineering Branch, Report No. PWD 79003, 64 pp.

PWD, 1985. *Jimmy's Beach Management Report*. Great Lakes Shire Council in conjuction with Public Works Department NSW, Report No. 85012, 18 pp.

PWD, 1992. *Jimmys Beach Summary of Great Lakes Shire Council Beach Surveys*. Department of Public Works, NSW, Coasts and Rivers Branch.

PWDS, 1998. *Port Stephens tidal data collection September 1993*. NSW Department of Public Works and Services, Manly Hydraulics Laboratory, Report No. MHL716.

PWDS, 1999. *Port Stephens/Myall Lakes Estuary Processes Study*. Manly Hydraulics Institute, Department of Public Works and Services, Report No 913.

Roy, P.S., Thom, B.G. and Wright, L.D., 1980. Holocene sequences on an embayed high-energy coast: an evolutionary model. *Sedimentary Geology*, 26, 1-19.

Roy, P.S., Williams, R.J., Jones, A.R., Yassini, I., Gibbs, P.J., Coates, B., West, R.J., Scanes, P.R., J.P. Hudson and Nichol, S., 2001. Structure and function of south-east Australian estuaries. *Estuarine, Coastal and Shelf Science*, 53, 351-384.

Short, A.D., 1985. Rip-current type, spacing and persistence, Narrabeen Beach, Australia. *Marine Geology*, 65, 47-71.

Short, A.D. and Trenaman, N.L., 1992. Wave climate of the Sydney region, an energetic and highly variable ocean wave regime. *Australian Journal of Marine and Freshwater Research*, 43, 765-791.

Smith, G.L. and Zarillo, G.A., 1990. Calculating long-term shoreline recession rates using aerial photographic and beach profiling techniques. *Journal of Coastal Research*, 6/1, 111–120.

Thom, B.G., Sheperd, M., Ly, C.K., Roy, P.S., Bowman, G.M., and Hesp, P.A., 1992. *Coastal Geomorphology and Qaternary Geology of the Port Stephens-Myall Lakes Area*. Department of Biogeography and Geomorphology, A.N.U. Monograph No. 6, 407 pp.

Watson, P., 2000. Jimmys Beach, Port Stephens, NSW. An expensive learning experience in coastal management. *Proceedings of International Conference Coastal Engineering*, 2000, Sydney, Australia, 3566-3579.

USING SIMPLE SEMI-EMPIRICAL MODELS FOR INTEGRATED ASSESSMENT OF SCENARIOS FOR A NAVIGATION CHANNEL. THE CASE OF THE PORT OF OSTEND, BELGIUM.

Toon Verwaest[1]

1. Flanders Hydraulics Research, Berchemlei 115, B-2140 Antwerp, Belgium, toon.verwaest@mow.vlaanderen.be

Abstract: Scenarios for a new navigation channel to the port of Ostend (Belgium) are to be assessed. Regarding coastal sediments dynamics, two aspects are of importance: first the maintenance dredging of the navigation channel itself (functional aspect), secondly the impact on the surrounding environment. The latter involves primarely the impact on the morphology of the sea bottom and the impact on the turbidity of the coastal waters. Available results of in situ-measurements, numerical modeling and laboratory experiments for the Belgian coastal zone were gathered, as well as general scientific literature. It could be concluded that the state of knowledge on coastal sediment dynamics in the Belgian coastal zone is to limited to be able to completely validate a process-based numerical model. A simple semi-empirical model was built, that is able to represent the essence of the impact on coastal sediment dynamics of a new navigation channel.

INTRODUCTION

The assessment of master plans of coastal ports comprises an assessment of the impact of scenarios regarding coastal sediment dynamics. A functional assessment as well as an environmental assessment are needed. Recent European legislation on environmental impact assessment (EIA) stipulates the use of a cascade approach in two steps : first an assessment of scenarios of masterplans (a strategic EIA) and secondly a more detailed assessment of scenarios of infrastructure works that implement a chosen master plan (a project EIA). This regulation –adding the concept of a strategic EIA- aims at considerations of environmental impact already to be taken into account in the earliest stages of design.

Thuss, for master plan studies a multidisciplinary approach has to be followed. Integration of the different disciplines is very important. Using simple semi-empirical models that can be easily understood by non-experts, but still are able to represent the essence of the impact on coastal sediment dynamics are very usefull in such a framework.

THE CASE OF IMPROVING THE NAVIGATION CHANNEL TO THE PORT OF OSTEND, BELGIUM

For the accessibility of larger ships to the port of Ostend an improved navigation channel is needed, amongst other infrastructure works (e.g. larger breakwaters). The port of Ostend is situated at the Belgian coastline in the southern part of the North Sea. Scenarios for an improved navigation channel have to be assessed, taking into account not only the accessibility for the largest ships but also other functional and environmental issues. Regarding impact on coastal sediments dynamics, two aspects are of importance: first the impact on maintenance dredging of the navigation channel itself (functional aspect), secondly the impact on the surrounding environment. The latter involves primarely the impact on the morphology of the sea bottom (erosion due to dredging nearby) and the impact on the turbidity of the coastal waters. To assess these impacts a.o. a semi-empirical model was elaborated taking into consideration all the available expertise on coastal sediment dynamics in the area that is relevant for the assessment of improved navigation channel scenarios.

STATE OF KNOWLEDGE ON COASTAL SEDIMENT DYNAMICS IN THE AREA

The sea bottom morphology is characterised by the presence of shore parallel sandbanks and swales. This is illustrated on Figure 1. On this figure the present navigation channel and the most probable future navigation channel are indicated.

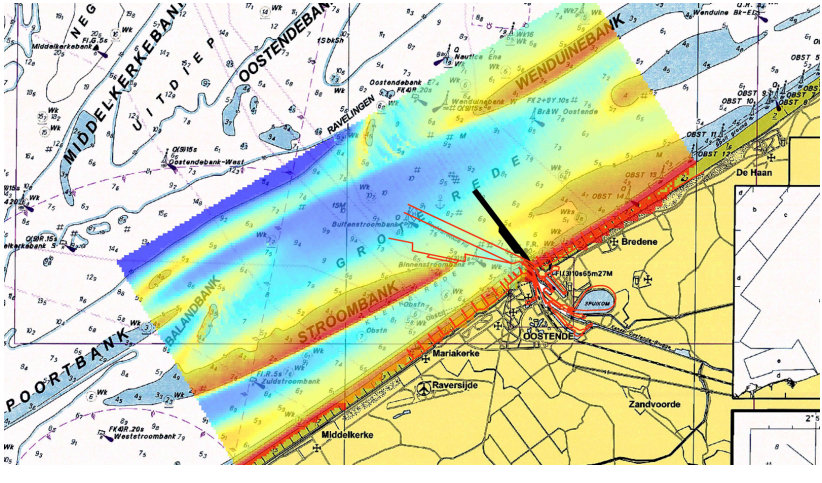

Fig. 1. Sea bottom in front of Ostende, with indication of the most probable future navigation channel (in black) and the present navigation channel (in red)

The sea bottom sediments in the area of the new navigation channel are a mixture of sand and mud particles. From in situ measurements –although limited in number- the relative mass percentages are determined as 50 % sand particles (> 63 μ) and 50 % mud particles (< 63 μ). This composition is based on measurements of surfacial sediment samples. Only a few analyses of drillings are available. Thin layers of soft mud are found in patches on the sea bottom, especially in the lower lying areas after calm weather and neap tides. Waves or spring tide currents remobilises this soft mud.

Prevailing residual tides, winds as well as waves all result on a yearly basis in a net transport from SW to NE. From operational hydrodynamic models, which have been calibrated and validated through many years of oceanographic research around the Belgian Continental Shelf, it follows that a water particle takes on average ca. 4 weeks to cross the Belgian coastal waters (65 km in length, from SW to NE).

The dynamics of mud particles and sand particles are very different. Their dynamics is treated separately, assuming no interaction of mud and sand. Process based models for mud transport as well as sand transport in the Belgian coastal zone are still work in progress. Several decades of research have not yet resulted in completely validated models, indicating the complexity of the coastal sediment dynamics.

Mud dynamics

Regarding mud dynamics the state of knowledge on the large scale is described in Fettweis et al (2005). The major natural transport of mud in the area is a yearly net transport of ca. 15 M TDS (Million Ton Dry Solids) mud per year through the Dover Strait and continuing along the coastline of Belgium (from SW to NE). Mud is advected with the residual water flow. The major antropogene mud transport is by maintenance dredging of the navigation channels and coastal ports in Belgian coastal waters. It amounts to ca. 10 M TDS mud per year. All dredged mud is also dumped in Belgian coastal waters. From several years of remote sensing observations (satelite SeaWIFFS, MODIS Aqua and MODIS images) as well as in situ profile measurements the concentration of mud in suspension is determined as ca. 50 mg/l on average for the more shallow coastal waters (from the coastline to ca. 25 km out the coastline). The resulting amount of mud in suspension is calculated as ca. 2 M TDS mud. The mud on the sea bottom which is readily available for transport, it is the patches of thin layers of mobile soft mud, is roughly estimated to be ca. 20 M TDS on average –although not enough measurements are available for a reliable estimate. The yearly erosion of consolidated mud (in areas where clayey soil outcrops) and the yearly sedimentation+consolidation of mud (in some sheltered areas) are of the magnitude of a few M TDS mud per year, and are more or less compensating each other.

Sand dynamics

Regarding sand dynamics the state of knowledge on the large scale is described in Van Lancker et al (2005). Large scale sand dynamics in the area is determined by a yearly net

alongshore transport in the direction of the prevailing currents and waves (from SW to NE). However, this net sand transport is the result of alternating gross sand transport intensities that are an order of magnitude (factor 10) larger. The momentous sand transport alternates mainly between SW to NE and NE to SW (parallel to the coastline), in accordance with the alternating current direction. The current climate and the wave climate are known accurately, but the resulting net sand transport cannot be determined accurately from this hydrometeo climate because there is no completely validated sediment transport formula available.

From historical nautical maps the morphological response to a navigation channel across the sandbanks can be observed. In the beginning of the 20th century for the first time a navigation channel across the shore-parallel sandbank "Oostendebank" was dredged. During the 20th century this navigation channel, called "Rechtstreekse Kil", has been deepened progressively as the draft of the ships in use became larger and larger. The morphological response caused by the creation, maintenance and deepening of this navigation channel appears to extend much further than the location of the dredging works itself. Relatively accurate historical nautical maps are available every ca. 5 years for this area for the period from the mid 20th century until present. From this time series the area where the influence of the navigation channel is dominant is determined. This influence area is ca. 10 km^2, for a navigation channel of less than 1 km^2. This influence area corresponds to the establishment of a morphological equilibrium slope of ca. 1/200. A clear correlation between the depth of the navigation channel and the sediment volume in the influence area is determined. This correlation is shown in Figure 3.

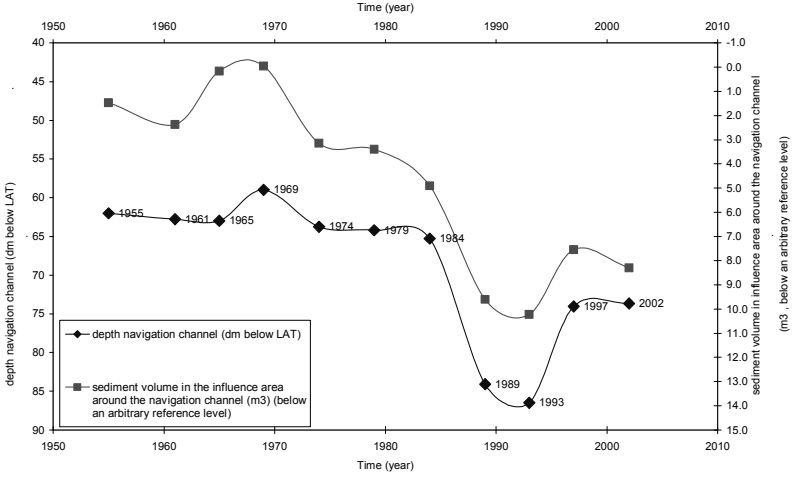

Fig. 3. Correlation between the depth of the navigation channel and the sediment volume in the influence area around the navigation channel

SEMI-EMPIRICAL MODELS FOR MUD AND SAND DYNAMICS

The state of knowledge is incorporated in these semi-empirical models.

Mud dynamics

A distinction is made between an equilibrium, steady state and a state of transition (between successive equilibrium states). The equilibrium state for mud is described in Figure 4.

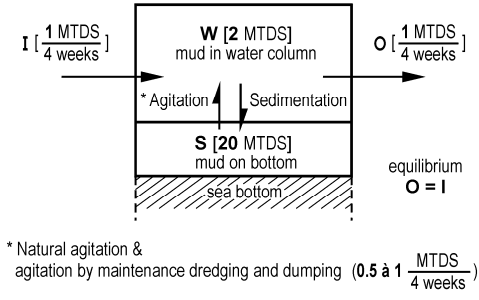

Fig. 4. Concept of equilibrium mud dynamics in the Belgian coastal waters

If one of the boundary conditions changes then the equilibrium state changes. For example, when due to the dredging of an improved navigation channel an additional, permanent source of mud sediment is created, after some time the amounts of mud in the water column, on the bottom and transported per time unit out of Belgian coastal waters will be increased correspondingly. Following a linear approximation the new equilibrium state is then described by the Figure 5.

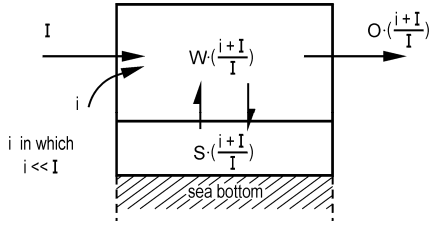

Fig. 5. Effect of an additional, permanent source of mud on the equilibrium steady state

where W = amount of mud in the water column (M TDS); S = amount of mud on the bottom (M TDS); I = transport of mud into Belgian coastal waters (M TDS / 4 weeks); O = transport of mud out of Belgian coastal waters (M TDS / 4 weeks); i = additional source of mud into Belgian coastal waters (M TDS / 4 weeks);

It is convenient to define r as the ratio of the additional source of mud relative to the major transport into Belgian coastal waters (Eq. 1).

$$r = \frac{i}{I} \qquad \text{with } r << 1 \tag{1}$$

The basic assumption is to consider a linear system with two system constants, α and γ (Eq. 2).

$$\alpha = \frac{W}{S} \qquad ; \qquad \gamma = \frac{W}{O} \tag{2}$$

The system constant α is describes the equilibrium between the processes of agitation, natural as well as antropogene, and the processes of sedimentation. The system constant γ is the average resident time in Belgian coastal waters of a mud particle that (by chance) never reaches the bottom.

From conservation of mass for mud and substution of Eq. 2 (Eq. 3) it follows that the transition from one equilibrium state to a new equilibrium state is then described by an exponential decay curve with a half time τ given by Eq. 4 (integration of Eq.3).

$$\frac{dW}{dt} + \frac{dS}{dt} = \frac{dW}{dt} + \frac{dW}{dt}\frac{1}{\alpha} = I + i - O = I + i - W\frac{1}{\gamma} \tag{3}$$

$$\tau = \gamma\left(1 + \frac{1}{\alpha}\right)\ln(2) \tag{4}$$

where τ = the time it takes to reach the mean state between two successive equilibrium states. The transition from the initial equilibrium state (with i=0) to a new equilibrium state (with i=i) is mathematically described by Eq. 5.

$$W(t) = W_1 + (W_2 - W_1)\left(1 - \exp\left(-\frac{t}{\tau}\right)\right) \tag{5}$$

where W_1 = amount of mud in the water column for the initial equilibrium state (M TDS); W_2 = amount of mud in the water column for the new equilibrium state (M TDS);

Sand dynamics

The semi-empirical model for sand states that the sedimentation of sand in a navigation channel is the sum of two processes. First there is sedimentation of a fraction of the sand which is transported along the Belgian coastline. Second there is sedimentation of the sand which is eroded in the "upstream" part of the influence area of the navigation channel. "Upstream" signifies SW from the navigation channel given the net sand transport from SW to NE. The sand which is eroded in the "downstream" part of the influence area is transported away from the navigation channel. This semi-empirical model is schematically described in Figure 6.

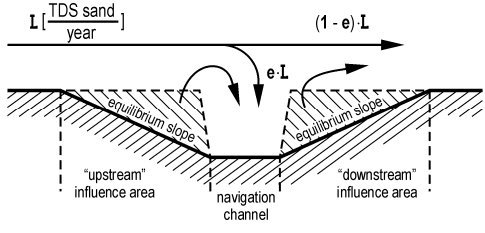

Fig. 6. Concept of sand dynamics in and around a navigation channel

where e = the trapping efficiency factor (-); L = the net sand transport along the Belgian coastline (M TDS / year).

The basic assumption is to consider no interaction between both processes for sedimentation of sand in the navigation channel (Eq. 6).

$$Q_{sum} = Q_1 + Q_2 \tag{5}$$

where Q_{sum} = the sedimentation rate of sand in the navigation channel (M TDS / year); Q_1 = the sedimentation rate of sand transported along the Belgian coastline (M TDS / year); Q_1 = the sedimentation rate of sand that is being eroded in the influence area around the navigation channel, which is caused by the dredging of the naivigation channel itself (M TDS / year).

The first contribution Q_1 is calculated as (Eq. 6)

$$Q_1 = eL \tag{6}$$

in which the trapping efficiency factor e is calculated using the engineering approach given in Van Rijn (2005) which is introduced in Van Rijn (1987).

The second contribution Q_2 is calculated as (Eq. 7)

$$Q_2 = E \tag{6}$$

in which E is the erosion rate of the upstream influence area (M TDS/year).

APPLICATION RESULTS

The described semi-empirical models are applied for different scenarios of improved navigation channels to the port of Ostend. For each scenario this results in a projection of the evolution of the necessary yearly maintenance dredging works –separately for sand and mud-, and in projections of the evolution of the increased turbidity and the extent of the erosion zone surrounding the navigation channel.

The results for one of the scenarios are given here after. Details can be found in Verwaest (2005). However, because the study is still ongoing no quantitative results are given in this paper.

The projection of the evolution of the maintenance dredging works is given in Figure 7. One can note that during the first ca. 3 years after the capital dredging works important quantities of sedimentation are to be expected, which are caused by the erosion in the influence area around the navigation channel where there is a gradual process of slopes flattening towards the equilibrium morphological slope.

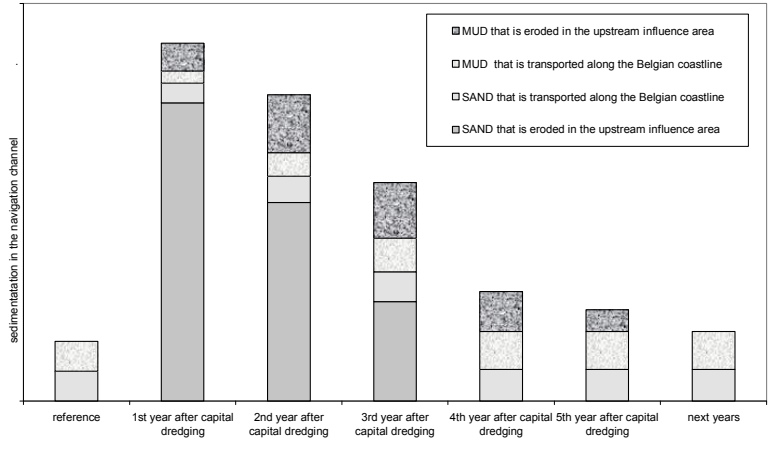

Fig. 7. Necessary maintenance dredging works after the capital dredging for a scenario of a new navigation channel to the port of Ostend.

Projections for increased turbidity in Belgian coastal waters are shown in Figure 8. A maximum increase after ca. 3 years and a half time τ equal to ca. 61 weeks can be seen.

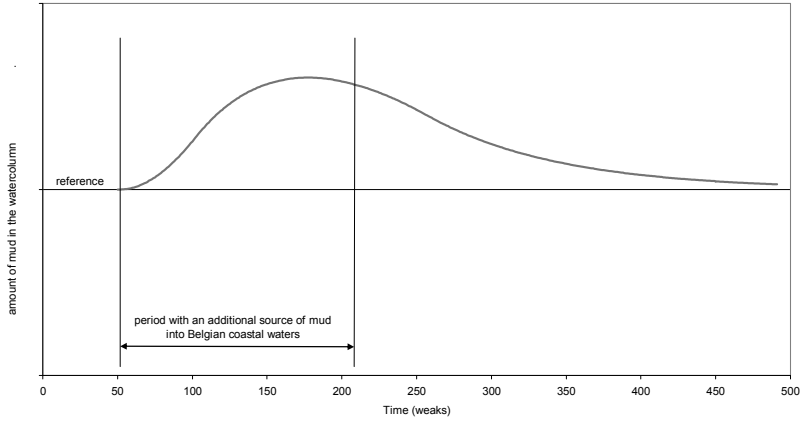

Fig. 8. Impact on turbidity in Belgian coastal waters of an additional source of mud of ca. 1,5 M TDS which is released during a period of 3 years (with a decreasing rate).

Projections of the extent of the erosion zone around the new navigation channel are made in a GIS. Using an average equilibrium slope of ca. 1/200 it is shown that an erosion zone of ca. 5 km^2 is affected, with the surface area of the navigation channel itself only ca. 0,5 km^2.

CONCLUSION

A simple semi-empirical model was built that is able to represent the essence of the impact on coastal sediment dynamics of a new navigation channel in the Belgian coastal zone. The model treats mud dynamics and sand dynamics separately. Using this model projections for maintenance dredging, erosion, and turbidity increase are successfully made for scenarios of a new navigation channel to the port of Ostend.

REFERENCES

Fettweis M., Francken F., Van den Eynde D., Houziaux J.-S., Vandenbergh N., Fontaine K., Deleu S., Van Lancker V., Van Rooij D, (2005). *"Mud origin, characterization and human activities (MOCHA): Characteristics of cohesive sediments on the Belgian Continental Shelf"*, Scientific Report Year 1, Belgian Science Policy, 70 p.

Van Lancker V., Deleu S., Bellec V., Du Four I., Verfaillie E., Fettweis M., Van den Eynde D., Francken F., Monballiu J., Guardino A., Portilla J., Lanckneus J., Moerkerke G. & Degraer S. (2005). *"Management, research and budgeting of aggregates in shelf seas related to end-users (Marebasse)*", Scientific Report Year 3.

Belgian Science Policy, 103 p.
Van Rijn L. (1987). *"Mathematical modeling of morphological processes in the case of suspended sediment transport"*, PhD thesis, Delft University of Technology, the Netherlands.
Van Rijn L. (2005). *"Principles of sedimentation and erosion engineering in rivers, estuaries and coastal seas"*, Aqua Publications.
Verwaest T. (2005). "Haven van Oostende – verbeterde haventoegang – impact op de baggerwerken", Tech. Rep. MOD 627/6, Flanders Hydraulics Research, Antwerpen, Belgium.

SEDIMENT PROCESSES AND MANGROVE-HABITAT EXPANSION ON A RAPIDLY-PROGRADING MUDDY COAST, NEW ZEALAND

Andrew Swales[1], Samuel J. Bentley[2], Catherine Lovelock[3], Robert G. Bell[1]

1. NIWA, National Institute of Water and Atmospheric Research, P.O. Box 11-115 Hamilton, New Zealand. a.swales@niwa.co.nz, r.bell@niwa.co.nz
2. Earth-Sciences Department, 6010 Alexander Murray Building, Memorial University of Newfoundland, St John's NL, Canada A1B 3X5. sjb@esd.mun.ca
3. Centre for Marine Studies, University of Queensland, St Lucia, Queensland, QLD 4072, Australia. C.lovelock@uq.edu.au

Abstract: Mangrove-habitat expansion has occurred rapidly over the last 50 years in the 800 km^2 Firth-of-Thames estuary (New Zealand). Mangrove forest now extends 1-km seaward of the 1952 shoreline. The geomorphic development of this muddy coast was reconstructed using dated cores (^{210}Pb, ^{137}Cs, ^{7}Be), historical-aerial photographs and field observations to explore the interaction between sediment processes and mangrove ecology. Catchment deforestation (1850s–1920s) delivered millions of m^3 of mud to the Firth, with the intertidal flats accreting at 20 mm yr^{-1} before mangrove colonization began (mid-1950s) and sedimentation rates increased to ≤ 100 mm yr^{-1}. ^{210}Pb data show that the mangrove forest is a major long-term sink for mud. Seedling recruitment on the mudflat is controlled by wave-driven erosion. Mangrove-habitat expansion has occurred episodically and likely coincides with calm weather. The fate of this mangrove ecosystem will depend on vertical accretion at a rate equal to or exceeding sea level rise.

INTRODUCTION

Enhanced sedimentation is occurring globally in estuaries due to increased catchment sediment yields associated with land-use changes (e.g., Thrush et al., 2004) particularly in the small and mountainous catchments that characterise the active-tectonic margins of the Pacific Rim (Milliman and Syvitski, 1992). Increased soil erosion has accelerated the infilling of estuaries, which have become progressively intertidal. In many temperate and tropical settings these intertidal flats have been colonized by mangroves (Neil, 1998; Ellis et al., 2004). Once established, mangroves influence estuarine sedimentary processes and long-term geomorphic evolution (Thom et al., 1975). Mangroves enhance mud accumulation by dampening currents and attenuating waves so that sediment accumulation rates (SAR) are highest within the fringes of mangrove forests, and decline with distance from the mangrove fringe (Furukawa et al., 1997). While mangroves may

stabilize sediments, provide fish nurseries and enhance water quality, mangrove-habitat expansion is not always desirable. In estuaries that previously had sandy substrates mangrove colonization and/or habitat expansion enhances long-term mud accumulation. This major change in substrate type from sand to mud, results in loss of biodiversity and changes in benthic community structure (Ellis et al., 2004).

In New Zealand (N.Z.), the grey mangrove (*Avicennia marina*), which is a frost-sensitive species, occurs in North Island estuaries above 38°S latitude and can colonize intertidal flats down to mean sea level (MSL), where seedlings are submerged for ≤ 6 hr per tide (Clarke and Myerscough, 1993). Mangrove-habitat expansion has occurred in many estuaries within their range in recent decades (Burns and Ogden 1985; Ellis et al., 2004) as has also occurred for introduced-invasive species such as the Cordgrass, *Spartina anglica*, (Swales et al., 2004). This process has been exacerbated by estuary infilling, forming extensive intertidal flats potentially suitable for colonization. This natural infilling process has accelerated over the last 150 years as sediment loads have increased due to catchment deforestation and SAR of < 0.5 mm yr^{-1} before deforestation have increased by an order of magnitude (Hume and McGlone, 1986, Swales et al., 2002). However, mangrove-habitat expansion observed over the last 50 years has occurred decades after catchment deforestation. Alternative explanations for this relatively recent expansion include climate change and increasing nutrient inputs associated with agricultural activities.

Mangrove-habitat expansion has been particularly rapid in the Firth of Thames, which is a 800 km^2 meso-tidal estuarine embayment on the east-coast of the North Island (37°S 175.4°E) 70-km south-east of Auckland (Fig. 1). Captain James Cook visited the Firth in 1769 and noted the presence of mangrove along the lower Waihou river (Brownell, 2004).

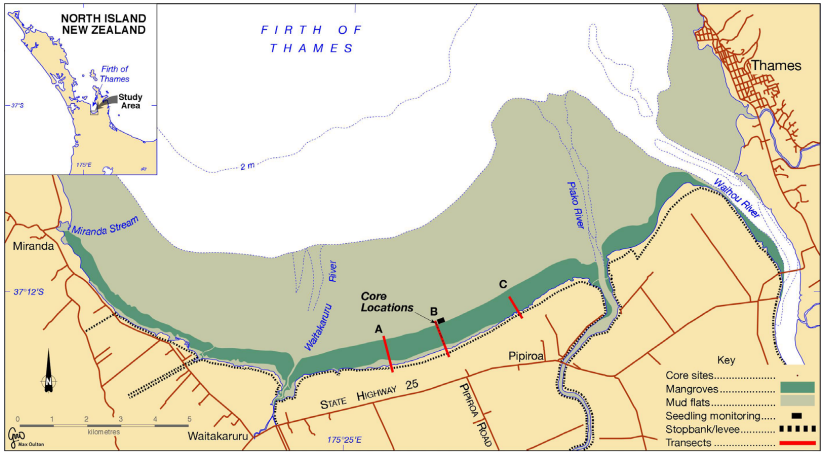

Fig. 1. Location of the study area, southern Firth of Thames, New Zealand.

Aerial photographs show that mangrove-habitat was restricted to delta deposits at river mouths as recently as the early 1950's. Today, mangrove habitat in the southern Firth extends 1-km seaward of the 1952 shoreline and covers 11 km^2 of former intertidal mudflat. The seabed elevation is now 0.1–0.2 m above mean high-water spring (MHWS) tide level so that the mangrove forest is only infrequently inundated.

This rapid mangrove-habitat expansion raises a number of questions that are relevant to the fate of mangrove systems and estuaries: what has triggered mangrove-habitat expansion decades after deforestation; how are mangroves altering estuaries; how does seedling recruitment occur on wave-exposed mudflats; and what is the long-term fate of these mangrove systems given the potential effects of climate change? In this paper we reconstruct the recent geomorphic development of this muddy coast and consider the interaction between sediment processes, geomorphology and mangrove ecology.

STUDY SITE

The Firth of Thames estuarine embayment occupies the Hauraki Depression, which is a structural graben (Healy, 2002) bounded to the east and west by the Coromandel and Hunua Ranges respectively. To the south are the low-lying Hauraki Plains, which are underlain by estuarine sediments (Woodroffe et al., 1983). The Firth receives runoff from a 3600 km^2 catchment and primarily from the Waihou (1966 km^2) and Piako (1476 km^2) Rivers, which deliver an estimated 150,000 t yr^{-1} and 35,000 t yr^{-1} of suspended sediment respectively. The Waihou River has delivered sediment to the Firth for the last 20,000 years. Shoreline-progradation rates have averaged 1.7 m yr^{-1} over the last 6,500 years (Brownell, 2004) and a chenier plain has formed in the last 3,600 years along the western shore of the Firth (Woodroffe et al., 1983).

History

Pre-human catchment landcover consisted of podocarp–hardwood forests on the steeplands while the Hauraki Plains were occupied by freshwater marshes and swamp forests of the podocarp Kahikatea. Maori arrived about 1,000 years ago and forest clearance was restricted to the rivers banks. European settlers arrived in the mid-1800s and large-scale deforestation began shortly after in the Coromandel ranges associated with logging and gold-mining activities (Brownell, 2004). These activities substantially increased sediment loads to the Firth. Hydrographic surveys conducted by the Public Works Department in 1882 and 1918 indicate that *c.* 6.9 x 10^6 m^3 of sediment was deposited within a 16 km^2 area of the lower Waihou River and its tidal delta (Fig. 1) and an estimated 36.7 x 10^6 m^3 was deposited in the 210 km^2 southern Firth. Development of the Hauraki Plains was delayed until drainage works began in 1905 with a stop-bank/levee constructed along the southern shore of the Firth and the tidal reaches of the rivers. By 1920 some 162 km^2 of swamp had been converted to pasture (Brownell, 2004). The 1932 storm flooded the entire Hauraki Plains and consequently the heights of stop-banks were increased. These engineering works constrained floodwaters to the river channels and are likely to have increased sediment delivery to the Firth.

Estuary characteristics

The Firth shoals from a maximum depth of 35 m at its inlet. Tides are semi-diurnal, with average spring- and neap-tidal ranges of 2.8-m and 2-m respectively. Tidal-current speeds are typically ≤ 0.2 m s^{-1} on the intertidal flats. Estuarine circulation and residual-tidal currents trap river-borne suspended sediments within the Firth (Healy, 2002). Northerly winds generate short-period ($T < 6$ s) waves typically < 1 m high (Woodroffe et al., 1983). The historical rate of sea level rise at Auckland (1904–1999) has averaged 1.3 mm yr^{-1}. The large tidal range, shallow bed slope (0.03°) and fine-sediment supply has built some 70 km^2 of intertidal-mudflats along the southern shore of the Firth (Fig. 1). Mudflat morphology is similar to that described for the muddy coast of Surinam, South America (Augustinus, 1980; Wells and Colman, 1981). The lower-intertidal flat is characterized by fluid mud, while a "mud bastion" morphology of isolated consolidated-mud mounds ≤ 20-cm high develops on the middle–upper intertidal flat above 0.7 m MSL. On the Surinam coast, these features have been interpreted as remnants of an eroded mudflat (Augustinus, 1980, Fig. 7). Above 0.8 m MSL, the mud bastions are replaced by a 300-m wide band of large-scale "mud forms" that resemble an irregular ridge-runnel system. These shore-normal, often bifurcating ridges, are ≤0.25 m high with wavelengths ≤2 m and sinuous crests up to 50 m long. These features are not drainage channels as the runnels are isolated from each other. This intertidal morphology is characteristic of a mesotidal, moderately wave-exposed, muddy coast, with large mud supply, high suspended sediment concentrations (SSC) and rapid sedimentation. In similar muddy-coast environments, near-bed SSC in the range 10^3–10^4 mg l^{-1} increase fluid density sufficiently to attenuate shoaling waves (Wells and Coleman, 1981; Mehta, 2002).

METHODS

Mangrove-habitat mapping, forest structure and pore-water salinity

Mangrove-habitat expansion was mapped from vertical aerial photographs of the southern Firth taken between 1952 and 2002. The digitized photographs were geo-referenced and analyzed using ARC-GIS software. Mangrove-forest structure was characterized at *c*. 20-m intervals across-shore using the point-center-quarter method (Cintrón and Schaffer-Novelli, 1984). Pore-water salinity at 30-cm depth was measured using the methods of McKee et al. (1988). A relationship between pore water salinity and forest height was tested using regression analysis.

Intertidal-flat elevation and tides

Intertidal-flat elevations were measured along three transects (A–C) at *c*. 2-km intervals alongshore and up to 1200-m seaward of the stop-bank/levee (Fig. 1) to determine the large-scale shore morphology and relate the sediment-cores to the mean sea level (MSL) datum. Elevations were measured to ±0.5 cm using a Geodimeter Model 464 total station. A sea-level record (1992– present) from Tararu (3 km north of Thames, Fig. 1) was analyzed to determine: (1) the duration of tidal inundation (2004–2006) of the mangrove forest; and (2) exceedance probability (%) for predicted high-tide levels (1900–1999 AD). The inundation time for specified vertical levels was determined for predicted tides (using tidal constituents for 2004-2006); and the measured (storm) tides.

Sediment cores

Replicate sediment cores 7.5-cm-diameter and ≤ 1.9-m long were collected from the mangrove forest along Transect B (February 2005) using a piston corer (Fig. 1, **LC sites** 3–11). A 0.7-m-long push core (site LC-12) was also 50-m seaward of the mangrove seaward edge of vegetation (SEV). Cores were also collected from the mudflats (**T sites,** Feb. 2006) up to 1-km seaward of the mangrove SEV using open-ended, three-sided Perspex trays (0.7 m deep, 2.5 x 19 cm). The trays were pushed into the sediment and then the fourth side inserted to minimize fabric distortion. Core names (e.g., T-50) indicate the seaward distance (m) of the site from the mangrove SEV. Core-compression was < 5% in all cases. The LC cores were logged and sub-sampled at intervals in 2-cm-thick slices for radioisotope, bulk density and particle-size analysis. Particle-size was determined using an Ankersmid CIS-100 "time-of-transition" (TOT) stream-scanning-laser particle sizer. Sediment samples were wet-sieved through a 2-mm sieve to remove vegetation fragments and shell hash and dispersed in an ultra-sonic bath for 10 minutes before and during analysis. Sediment fabric was determined from x-radiographs prior to sub-sampling. The cores were sectioned into 2-cm-thick longitudinal slabs and imaged using a Phillips Model Macrotank 205 X-ray generator with Kodak AA400 film (50 kV, 5 mA, 1.1 min) and digitized using a Nikon D1x digital SLR camera (ISO 125, TIFF). X-radiographs of the T-site cores were obtained using a Thales Flash-scan 35 digital X-ray panel detector, illuminated by a Kramex PX15HF portable X-ray generator (60 kV, 15mA, 3 s). After imaging, these cores were sub-sampled at 1–2 cm intervals for analysis of beryllium-7 (^{7}Be, half life, $t_{1/2}$ 53 days) by gamma spectrometry.

SAR were estimated from lead-210 (^{210}Pb, $t_{1/2}$ 22.3 yr) and caesium-137 (^{137}Cs, $t_{1/2}$ 30 yr). The cosmogenic radioisotope ^{7}Be is particle reactive and tends to be concentrated in aquatic systems, making it a useful sediment tracer in fluvial-marine systems at seasonal timescales. Radioisotope concentrations expressed in S.I. units of Becquerel (disintegration s^{-1}) per kilogram (Bq kg^{-1}) were determined by gamma-spectrometry. Dry samples (50–60 g) were counted for 23 hrs using a Canberra Model BE5030 hyper-pure germanium detector. The unsupported or excess ^{210}Pb concentration ($^{210}Pb_{ex}$) was determined from the ^{226}Ra ($t_{1/2}$ 1622 yr) assay after a 30-day ingrowth period for ^{222}Rn ($t_{1/2}$ 3.8 days) gas in samples embedded in epoxy resin. Gamma spectra of ^{226}Ra, ^{210}Pb and ^{137}Cs were analysed using Genie2000 software. ^{7}Be concentrations in the T-core sediments were also obtained by gamma spectrometry, with10-g dry samples sealed in petri dishes counted for 24 h. The $^{210}Pb_{ex}$ profiles in each core were used to determine: (1) time-averaged SAR from regression analysis of natural log-transformed data; (2) $^{210}Pb_{ex}$ inventory (A, Bq cm^{-2}) and; (3) mean annual supply rate (P, Bq cm^{-2} yr^{-1}) based on the ^{210}Pb decay co-efficient (k, 0.0311 yr^{-1}). These data were compared with the ^{210}Pb atmospheric flux (0.006 Bq cm^{-2} yr^{-1}) measured at Auckland. SAR were estimated from ^{137}Cs profiles based on the maximum depth of ^{137}Cs in each core and included corrections for sediment mixing indicated by ^{7}Be profiles. In NZ, ^{137}Cs deposition from the atmosphere was first detected in 1953 (Swales et al., 2002).

Propagule and seedling establishment and recruitment

The establishment and survival of recently-settled propagules and seedlings on the wave-exposed mudflat was monitored over a 180-day period from January 2006 in an area immediately east of Transect B (Fig. 1). Three replicate sites *c.* 100-m apart alongshore were monitored each with ten 0.16 m^2 quadrats located on the top of the mud forms at. 20 m, 70m and 120 m from the mangrove SEV. Propagule and seedlings numbers and their developmental stage (i.e., # of leaf pairs) were recorded and measurements repeated after 23, 44, 60 and 180 days. Data were pooled for each site by proximity grouping and cumulative survivorship was calculated as the proportion of propagules or seedlings remaining. Survivorship data were log transformed and analysed by repeated measures ANOVA where either site or proximity to the mangrove were fixed effects in the model.

RESULTS

Mangrove-habitat expansion

Historical-aerial photographs show that mangroves colonized the mudflat close to LC-3 between 1952 and 1963 and some 300-m seaward of the 1952 shoreline (Fig. 2a) and by 1963 had formed a 50-m wide stand. Subsequently, the mangrove forest spread seaward and, to a more limited extent, landward. By 1977 the mangrove SEV was located near LC-6 and by 1987 the SEV had extended to LC-8, some 726-m from the 1952 shoreline. By 2002 the mangrove-forest distribution was similar to that we surveyed in 2005.

Large-scale mudflat morphology and tides

The shore profile has a convex-upward shape (Fig. 2a) that is characteristic of stable or prograding muddy-coasts (Mehta, 2002).

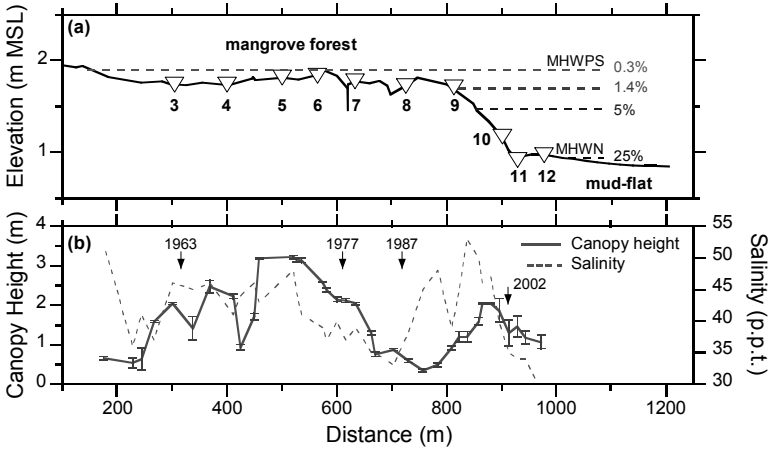

Fig. 2. Transect B: (a) bed elevation, tidal inundation (% of total time) and core locations (3–12); (b) average canopy height (std err = 0.01 – 0.03 m) and sediment pore-water salinity (parts per thousand). The positions of historical mangrove seaward fringes are also shown.

The profile is characterized by a uniformly flat surface within the mangrove forest, with elevations of 1.7–1.89 m above MSL and close to the MHWPS tide at 1.87m MSL, apart from a tidal creek (1.49-m MSL). The elevation maximum occurs near LC-6, which coincides with the tallest trees in the forest. This cross-shore sequence is repeated for the present mangrove SEV at 850–950 m. The prograding beach face (LC-9 to LC-11) slopes seaward at 0.37° and is ten-times steeper than the adjacent mudflat. Mean high water neap tide (MHWN, 0.98m MSL) coincides with the mangrove SEV, so that the present fringe on the beach face is only inundated during fortnightly spring tides (Fig. 2a). Predicted MHWS-tide elevation is 1.60 m above MSL. The length of tidal inundation rapidly decreases with increasing intertidal elevation and reduces from 25% on the mangrove SEV to < 1.4% for much of the mangrove-forest above 1.7 m MSL. The landward boundary of the mangrove forest is close to MHWPS, which is inundated ≤0.3% of the time. Comparison with predicted tides indicates that the measured meteorological or storm tides increase the length of time that the mangrove forest (above 1.7 m MSL) is flooded by *c*. 40%, which is equivalent to an additional 30 hrs per year. The largest storm tide during 2004–2006 (18 Sept. 2005) at 2.33 m MSL was 0.6 m higher than predicted.

Mangrove-forest structure

The mangrove-forest that has developed over the last 50 years displays a wide range of structure. Canopy height varies from < 0.5m to 3.5 m (Fig. 2b). Tree architecture also varies from open, spreading tree forms, which are indicative of trees that have grown in high-light environments without competition on colonizing edges, to trees with very straight trunks that have grown competing for available light. Variation in forest height did not significantly correlate with distance from the 1952 shoreline or porewater salinity. A repeating pattern of taller trees giving way to short, dwarf trees was evident along the cross-shore transect. For example, the current seaward fringe (850-1000 m seaward of the 1952 shoreline) gives way to a dwarf stand, with average canopy heights <0.5 m, between 650–800 m. Landward of these dwarf mangroves, are found the tallest trees (450–600 m), with an average-canopy height of 3 m, where a well developed and clearly older forest occurs. Lichen accumulation on the bark of trees in this tall forest is substantial. The tallest stand gives way to shorter forest again at 560 m, after which forest height increases before declining to be replaced by saltmarsh dominated by glasswort (*Sarcocornia quinqueflora*).

Sediment properties

Sediments deposited since the early-1950's on the mangrove flat (LC-3 to LC-9) are composed of homogenous muds, with median (D_{50}) and mean particle diameters ≤ 20 μm (Figs. 3a–c). Vertical profiles to 1.9-m depth show little variation except near the base of cores LC-8 and LC-9, which show abrupt increases in particle size at about 0.1–0.2 m above MSL. Sediment wet and dry bulk densities are between 1–2.4 g cm^{-3} and 0.4–0.8 g cm^{-3} respectively. Cores LC-10 and LC-11 collected on the mangrove fringe near the base of the actively prograding beach (0.9–1.2 m MSL) sample older deposits down to 0.8 m below MSL. The upper 0.8–1 m of these cores is also composed of homogenous fine-grained mud (D_{50} *c*.15 μm), below which an abrupt increase in particle size occurs (D_{50} > 40 μm) at 0.17 m above MSL (Figs. 3d–e).

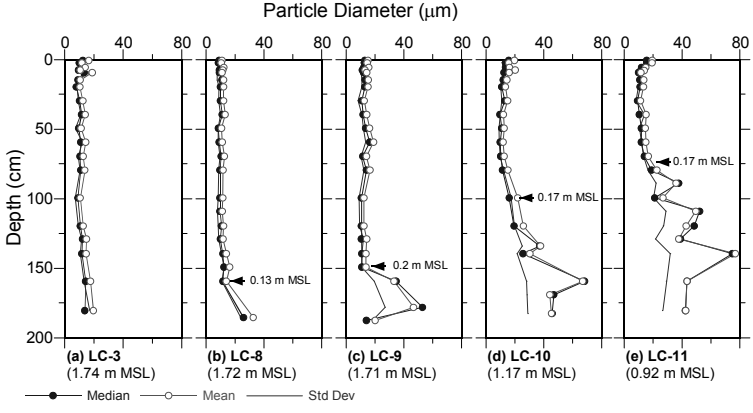

Fig. 3. Particle-size profiles for selected cores from the mangrove-forest (LC-3 to -9), seaward fringe (LC-10) and adjacent mudflat (LC-11). Surface elevation at sites is also shown.

Below this *c*. 1-m-thick mud layer, x-radiographs clearly show laminated clays, silts and fine sands overlaying abundant shell valves and hash of cockle (*Chione stuchburyi*) and estuarine trough shell (*Mactra ovata*), which is a suspension feeder characteristic of estuarine intertidal flats. The thickness of the laminations increase in scale with depth from mm to cm. X-radiographs of the T cores (Fig. 4), collected on the open mudflats, are characterized by two distinct zones of contrasting sedimentary fabric.

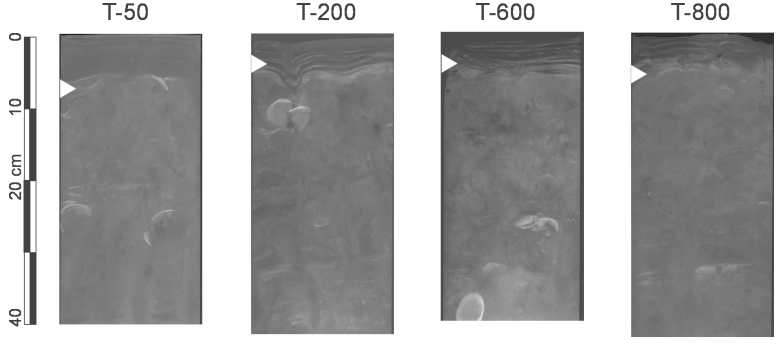

Fig. 4. X-radiograph negatives of the T-series cores from the mudflats. Bright shades indicated high-density or coarser sediment, and dark shades indicate low density or finer sediment. ^{7}Be penetration depth indicated by white triangles. Shell valves are of *M. ovata*.

A surficial layer, 3-7 cm thick, contains prominent laminations and cm-scale beds that display sharp basal contacts, and grade upward from coarser (light gray in X-radiographs) to finer (darker gray) sediments. These sediments have relatively high water content, as indicated by the dark shades in X-radiographs, and are mostly unbioturbated. Below this stratified surface layer, sediments display a range of biogenic

structures, including indistinct mottling and clearly defined burrows (mostly of polychaetes and *M. ovata*). These biogenic structures have overprinted mm-to-cm-scale stratification that is similar to the surface layer, but less clearly preserved, due to post-depositional bioturbation. Grain-size distributions in open-mudflat cores are slightly coarser than those observed in surface sediments of mangrove cores, with mean particle sizes of 25-43 μm, including 0-13% sand (concentrated in coarser beds evident in Fig. 4).

Radioisotope distributions

All profiles of ^{210}Pb in cores display prominent changes in gradients that indicate changes in SAR over time (Fig. 5). The lowermost section of all cores is characterized by a clearly defined region of relatively low SAR (8-25 mm yr^{-1}). The upper boundary of this region ranges from 1.5 to 1.7 m below the sediment surface close to the landward margin, to ~0.25 m below the sediment surface on the open mudflats at LC-12. Above this basal zone, in cores LC-3 to LC 12, SAR increase (to 33-108 mm yr^{-1}). These sub-vertical gradients extend to the sediment surface in cores LC6 to LC-11 (with a prominent discontinuity in LC-6). The surface of core LC-3 is characterized by a less vertical gradient and SAR of 8 mm yr^{-1} from 0.25 m below the sediment surface to the core top. In contrast, the two seaward-most cores (LC-11 and LC-12) have approximately vertical ^{210}Pb profiles in the upper ~0.25m of core, suggesting either: extremely high deposition rates, rapid vertical mixing, or a combination of the two.

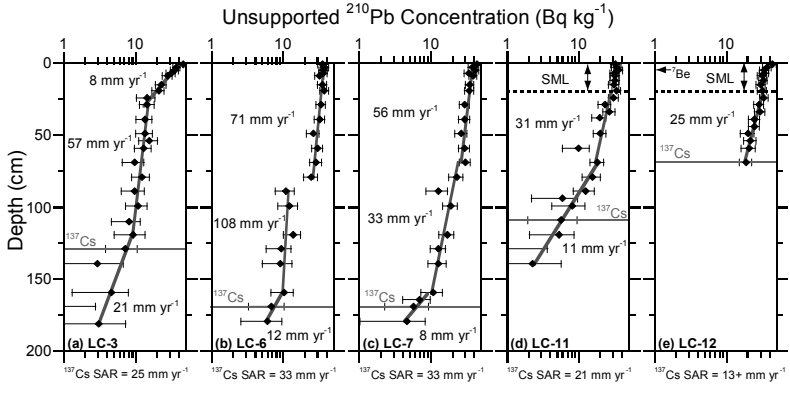

Fig. 5. ^{210}Pb$_{ex}$ concentration profiles and 95% conf. intervals and SAR for long-core sites (LC): mangrove forest (LC-3–LC-7); mangrove seaward fringe (LC-11); and mudflat (LC-12), Maximum ^{137}Cs depth and SAR also shown. SML = surface-mixed layer.

The presence of ^{137}Cs to 169-cm depth in LC-6 and LC-7 shows that these sediments have been deposited since the early 1950s and ^{137}Cs-derived SAR for the mangrove forest were 21–36 mm yr^{-1}. ^{7}Be occurs to 2-cm depth in cores LC-5 to LC-11 (mangrove forest) and to 4-cm depth in LC-12 (mudflat). Maximum SAR coincide with LC-8 and LC-9 located landward of the present-day mangrove fringe. The ^{210}Pb$_{ex}$ inventories (*A*) and mean annual supply rates (*P*) calculated for the long-cores display distinct spatial

patterns (Table 1). Inventories for cores LC-3 to LC-5 taken from the oldest (i.e., pre-1970s) mangrove forest gradually increase seaward.

Table 1. $^{210}Pb_{ex}$ inventories (A) and mean annual supply rates (P) and concentration factors (C) in the long cores.

Core	A (Bq cm^{-2})	P (Bq cm^{-2} yr^{-1})	C
LC-3	1.27	0.039	6.7
LC-4	1.40	0.044	7.4
LC-5	1.59	0.050	8.4
LC-6	3.75	0.117	19.8
LC-7	1.87	0.058	9.9
LC-8	1.73	0.054	9.1
LC-9	1.75	0.055	9.3
LC-10	1.21	0.038	6.4
LC-11	0.15	0.005	0.8

By comparison, A is similar for cores taken from mangrove forest established since the late-1970's (LC-7 to LC-9). At LC-6, A is more than double that measured at any other site. The concentration factor (C) indicates how P scales with the measured ^{210}Pb atmospheric flux (0.006 Bq cm^{-2} yr^{-1}). Table 1 shows that sediments in the mangrove forest are accumulating $^{210}Pb_{ex}$ at rates 6–20 times higher than expected if supplied by direct atmospheric deposition alone (i.e., $C = 1$).

Propagule and seedling establishment

Mangrove propagules settled on the mudflat in January 2006 over a 250-m wide band seaward of the present mangrove fringe. Propagule and seedling density at the first survey (28 January 2006) reached up to 187 m^{-2}, with a mean density of 36.4 ± 3.6 m^{-2} (± std error, n = 90). Propagule and seedling numbers declined rapidly and exponentially over time ($r^2 = 0.99$) so that < 10% of the initial propagules remained after 60 days and only one seedling remained after 180 days. Propagule attrition was not significantly influenced by site or distance from the mangrove fringe ($P > 0.05$). Despite the high-attrition rate of propagules, surviving seedlings were actively growing as shown by the proportion of seedlings that entered the 2–3 leaf pair stage after day 23 (Fig. 6).

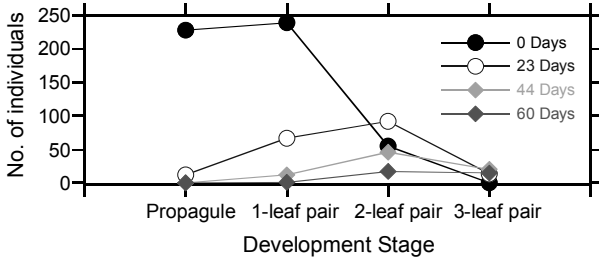

Fig. 6. Number of mangrove propagules and seedling in each development stage during the first 60 days of the monitoring.

DISCUSSION

The recent geomorphic evolution of the Firth is closely linked to historical increases in sediment loads following large-scale catchment deforestation and river-engineering works (1850s–1920s). The estimated 44 x 10^6 m^3 of mud was deposited in the southern Firth over a 36-year period to 1918 is equivalent to *c*. 280 years of present-day sediment loads. Cores record the physical effects of this mud influx on the Firth. Below the base of the 0.8–1.6-m thick homogenous mud layer at 0.2-m MSL are the original laminated silts and sands that are characteristic of energetic mixed-sediment intertidal-flats (Reineck and Singh, 1980). The abrupt transition to a pure-mud substrate indicates a fundamental change in the sediments and geomorphology of the Firth, which has initiated a sequence of large-scale environmental change. These changes include the rapid mangrove-habitat expansion that began in the 1950's, which continues today. Similar environmental changes have occurred in many N.Z. estuaries. However, the magnitude of these changes has been much larger in the Firth.

$^{210}Pb_{ex}$ profiles record the temporal and spatial sequence of initial mangrove colonization and mangrove-habitat expansion over the last 50 years. $^{210}Pb_{ex}$ profiles in cores from the oldest mangrove stand (LC-3 to LC-5) closest to the 1952 shoreline show a characteristic stair-step form (Fig. 5a), which are consistent with the known chronology of mangrove colonization and ^{137}Cs dating. Core LC-3 provides the longest record of sedimentation dating back to the 1920s (Fig. 5a) with SAR averaging 20 mm yr^{-1} that are similar to the present-day mudflat (25 mm yr^{-1}, Fig. 5e). These values are 5–10 times higher than SAR observed in other North-Island estuaries. Mangrove colonization resulted in a three-fold increase in SAR, with one metre of sediment deposited at LC-3 in little more than a decade. As the mangrove-forest expanded seawards so did the locus of maximum SAR. This process is recorded in cores from the oldest mangrove stand by an abrupt reduction in SAR to 8–11 mm yr^{-1} from the late 1960s onwards (Fig. 5a), as the sediment supply from open mudflats was cut off by forest expansion. Core LC-6 displays a discontinuity at 80–85-cm depth (Fig. 5b), with substantially lower $^{210}Pb_{ex}$ concentrations below this layer than above and SAR of 71–108 mm yr^{-1}. Cores LC-7 (Fig. 5c) to LC-9 also show that the mudflat was rapidly accumulating (21–33 mm yr^{-1}) even before mangroves colonised these sites (late 1970s–) and further increasing SAR (53–56 mm yr^{-1}). The present-day mangrove SEV established in last decade is also rapidly accumulating sediment (LC-11, Fig. 5d). X-radiographs and ^{7}Be profiles (≤ 7-cm) from the mudflat (Fig. 4) show that sediment resuspension and/or deposition introduces ^{7}Be into the seabed, rather than bioturbation. $^{210}Pb_{ex}$ inventories in the cores indicate that the mangrove-forest is a major long-term sink for fine sediments.

In many mangrove ecosystems canopy height reduces with distance from the seaward fringe. This reflects a reduction in tidal-water, nutrient and sediment inputs and an increase in salinity as evaporation exceeds tidal recharge (Smith, 1992). In the Firth, the complex variation in forest structure suggests multiple forest building events (Fig. 2b). This system provides an important case study of how mangrove forests develop through time, and a baseline to investigate how the function of mangrove ecosystems change as they undergo succession. Mortality of propagules and seedlings on the mudflat is primarily due to episodic wave-driven erosion of the substrate in which the seedlings are

rooted. In southern Australian, wind and wave conditions are also the most important factors influencing *A.marina* seedling mortality in estuaries (Clarke and Myerscough 1991). The early development of seedlings (Fig. 6) indicates that conditions are suitable for growth in the absence of physical disturbance. The repeating pattern of tall seaward-fringing forest and short/dwarf forest landward and observed high seedling mortality on the mudflats suggests that major phases of mangrove-habitat expansion have occurred infrequently and likely coincide with extended periods of unusually calm weather conditions that are required for successful seedling establishment

Mangrove colonization of the upper-intertidal flat at LC-3 occurred when the bed elevation was ≥ 0.5 m above MSL (Fig. 5a). This is well above the 0-m MSL lower-elevation limit (LEL) for grey mangrove (Clarke and Myerscough, 1993). The intertidal flat was rapidly accreting mud and by the 1950s eventually reached a critical elevation, with mangrove colonising the site during a period of calm weather. In nearby Tauranga Harbour, with its smaller wave fetch, the LEL for mangrove at wave-exposed sites is *c*. 0.3 m above MSL. Tidal range also influences the LEL for mangrove because wave-energy expended across the intertidal flats varies with water depth due to water-column attenuation and bed-friction effects for the short-period waves typical of New Zealand's fetch-limited shallow estuaries (Green et al., 1997; Swales et al., 2004). We normalised LEL for mangrove for both estuaries by the "king tide" amplitude to obtain a non-dimensional LEL of 0.3 for both estuaries. This approach could potentially be useful for predicting future mangrove colonization and habitat expansion in estuaries.

The fate of mangrove-forests primarily depends on the surface elevation increasing at a rate equal to or exceeding sea level rise (SLR). This has previously been assessed by comparing SAR derived from cores with SLR but is complicated by the effects of sediment auto-compaction (Cahoon et al., 1999). Furthermore, the frequency and duration of flooding by tides and freshwater runoff varies with elevation and controls sediment delivery, substrate oxidation and plant growth. Sedimentation-Erosion Tables (SET) have been used to apportion substrate elevation changes due to shallow subsidence and sedimentation. Cahoon et al. (1999) reported that: (1) surface-elevation gains lagged SAR at 50% of the 43 SET sites studied; and (2) surface-elevation change is a more suitable predictor of the future effects of SLR on mangrove/marsh stability. In the Firth, SAR of 8–100 mm yr^{-1} have substantially out paced SLR (1.3 mm yr^{-1}) so that the mangrove forest is now close to the upper limit of the tide and is very infrequently flooded. Surface elevations within the forest vary by < 20-cm despite large spatial variations in SAR. This suggests a complex feedback between the physical and biological processes controlling substrate elevation that has not yet been determined.

CONCLUSION

Rapid mangrove-habitat expansion in the Firth of Thames over the last 50 years is closely linked to historical increases in sediment loads due to catchment deforestation since the mid-1800s. The large quantities of mud deposited in the Firth over the next several decades buried the original laminated silt–sand substrate. Dated cores indicate that the upper-intertidal flats were rapidly accreting mud (20 mm yr^{-1}) for several decades. This initiated a sequence of large-scale environmental change that included

rapid mangrove colonization and habitat expansion since the 1950s. Mangrove-habitat expansion further increased SAR (≤ 100 mm yr^{-1}), rapidly building and elevating vegetated mudflats. The mangrove forest is a major long-term sink for fine sediments. Seedling recruitment is largely controlled by wave-driven erosion of the mudflat to ≤ 7-cm depth. Major periods of mangrove-forest expansion have been infrequent and have likely coincided with extended periods of calm weather. The lower-elevation limit for mangrove colonization at *c*. 0.5 m above MSL was higher than expected due to wave exposure. The mangrove forest is now near the upper limit of the tides and is infrequently flooded. Most sediment is deposited along the seaward fringe of the forest so that sedimentation decreases landward (50 to 8 mm yr^{-1}) due to reduced sediment supply and accommodation space. The long-term fate of this mangrove system depends on the surface elevation increasing at a rate equal to or exceeding SLR. This cannot be evaluated from sediment cores alone, due to the complications arising from shallow subsidence and the feedbacks between physical and biological processes.

ACKNOWLEDGEMENTS

Dr Terry Hume (NIWA) reviewed the paper and Mr Ron Ovenden (NIWA) undertook the elevation surveys and processed the sediment cores. Radioisotope analyses (LC cores) were conducted by the N.Z. National Radiation Laboratory. Dr Brian Sorrell (NIWA) participated in the ecological study. We thank Mr Rick Liefting (Environment Waikato) for supporting the initiation of this study. The study was funded by the NZ Foundation for Research Science and Technology (CO1X0307) and Environment Waikato. Funding to S. Bentley was provided through a NIWA visiting-scientist fellowship, and the US National Science Foundation (CAREER grant OCE-0093204).

REFERENCES

Augustinus, P.G.E.F. (1980). "Actual development of the chenier coast of Suriname (South America)," *Sedimentary Geology* 26, 91–113.

Burns, B.R. and Ogden, J. (1985). "The demography of the temperate mangrove (*Avicennia marinae* (Forsk.) Vierh.) at its southern limit in New Zealand," *Australian Journal of Ecology* 10, 125-133.

Brownell, B. (2004). "Muddy feet: Firth of Thames RAMSAR-site update 2004," Ecoquest Education Foundation, Pokeno, New Zealand, 198 p.

Cahoon, D., Day, J.W., Reed, D.J. (1999). "The influence of surface and shallow subsurface soil processes on wetland elevation: a synthesis," *Current topics in wetland biogeochemistry* 3, 72–88.

Cintrón, G. and Schaffer-Novelli, Y. (1984). "Methods for studying mangrove structures," p 91-113. *In*: S.C. Saenger, and J.G. Snedaker (*eds*.). The mangrove ecosystem: research methods. *UNESCO Monographs in Oceanographic Methodology 8*.

Clarke, P.J. and Myerscough, P.J. (1993). "The intertidal distribution of the grey mangrove (*Avicennia marina*) in southeastern Australia: The effects of physical conditions, interspecific competition, and predation on propagule establishment and survival," *Australian Journal of Ecology* 18, 307–315.

Ellis, J, Nicholls, P., Craggs, R., Hofstra, D. and Hewitt, J. (2004). "Effects of terrigenous sedimentation on mangrove physiology and associated macrobenthic

communities," *Marine Ecology Progress Series* 270, 71-82.
Mehta, A. J. (2002). "Mud-shore dynamics and controls," p 19–60. *In*: Healy, T., Yang, J.-A. Healy, (*eds*.) Muddy coasts of the world: processes, deposits and function.
Neil, D.T. (1998). "Moreton Bay and its catchment: seascape and landscape, development and degradation," *In* Tibbetts IR, Hall NJ, Dennison WC (*eds*.), Moreton Bay and Catchment, University of Queensland, p. 3–54.
Furukawa, K., Wolanski, E. and Mueller, H. (1997). "Currents and sediment transport in mangrove forests," *Estuarine, Coastal and Shelf Science* 44, 301–310.
Green, M.O., Black, K.P., and Amos, C. L. (1997). "Control of estuarine sediment dynamics by interactions between currents and waves at several scales," *Marine Geology* 144, 97–116.
Healy, T. (2002). "Muddy coasts of mid-latitude oceanic islands on an active plate margin – New Zealand," p 347–374. *In*: Healy, T., Yang, J.-A. Healy, (*eds*.) Muddy coasts of the world: processes, deposits and function.
Hume, T.M. and McGlone, M.S. (1986). "Sedimentation patterns and catchment use changes recorded in the sediments of a shallow tidal creek, Lucas Creek, Upper Waitemata Harbour, New Zealand," *N.Z. Journal of Marine and Freshwater Research*, 20, 677–687.
Milliman, J.D. and Syvitski, J.P.M. (1992). "Geomorphic/Tectonic control of sediment discharge to the ocean: The importance of small mountainous rivers," *Journal of Geology* 100, 525–544.
McKee, K. L., Mendelssohn, I.A. and Hester, M.W. (1988). "Re-examination of pore water sulfide concentrations and redox potentials near the aerial roots of *Rhizophora mangle* and *Avicennia germinans*," *American Journal of Botany* 75, 52–1359.
Reineck, H.E. and Singh, I.B. (1980). "Depositional Sedimentary Environments, second revised edition," Springer-Verlag, Berlin.
Smith, T. J., III. (1992). "Forest structure," *In* Robertson, A.I., and Alongi, D.M. (*eds*.), *Tropical Mangrove Ecosystems,* Coastal and Estuarine Studies, 41. American Geophysical Union. Washington DC. pp. 101-136.
Swales, A., Williamson, R.B., Van Dam, L.F. and Stroud, M.J. (2002). "Reconstruction of urban stormwater contamination of an estuary using catchment history and sediment profile dating," *Estuaries* 25(1), 43–56.
Swales, A., MacDonald, I.T. and Green, M.O. (2004). "Influence of wave and sediment dynamics on Cordgrass (*Spartina anglica*) growth and sediment accumulation on an exposed intertidal flat," *Estuaries* 27(2), 225–243.
Thom, B.G., Wright, L.D., Coleman, J.M. (1975). "Mangrove ecology and deltaic geomorphology: Cambridge–Ord River, Western Australia," *J. Ecology* 63, 203–232.
Thrush, S.F., Hewitt, J.E., Cummings, V.J., Ellis, J.I., Hatton, C., Lohrer, A., Norkko, A. (2004). "Muddy waters: elevating sediment input to coastal and estuarine habitats," *Frontiers in Ecology and Evolution* 2, 299-306.
Wells, J.T. and Coleman, J.M. (1981). "Physical processes and fine-grained sediment dynamics, coast of Surinam, South America," *Journal of Sedimentary Petrology* 51, 1053–1068.
Woodroffe, C.D., Curtis, R.J., McLean, R.F. (1983). "Development of a chenier plain, Firth of Thames, New Zealand," *Marine Geology* 53, 1–22.

THE INFLUENCE OF MUD ON THE INNER SHELF, SHOREFACE, BEACH AND SURF ZONE MORPHODYNAMICS – CASSINO, SOUTHERN BRAZIL

Lauro J. Calliari[1], K. Todd Holland[2], Pedro S. Pereira[1], Rafael M. C. Guedes[1], Renato E. Santo[1]

1. Fundação Universidade Federal do Rio Grande (FURG), Av. Itália, Km8, Campus Carreiros, Rio Grande, RS, Brazil. lcalliari@log.furg.br

2. Naval Research Laboratory, Code 7440.3, Stennis Space Center, MS 39525. tholland@nrlssc.navy.mil

Abstract: The inner shelf, shoreface and beach at Cassino, located in the southernmost sector of the Brazilian coastline, are characterized by marked differences in grain size and sediment composition compared to adjacent areas. This lateral heterogeneity in sediment properties controls the geomorphology of the inner continental shelf and shoreface, and influences the shoreline accretion rate and beach morphodynamic behavior along a 25 Km stretch of coast. Short-term effects are associated with episodic events of mud deposition on the beach during heavy storms that often result in strong gradients in hydrodynamic processes. These gradients in turn influence the morphodynamic behaviors on the sectors affected by the mud deposits and can create coastal hazards relating to beach usage. These findings are almost certainly applicable in other regions where significant sediment heterogeneity exists.

INTRODUCTION

The study of coastal regions with significant heterogeneity in sediment properties has been an important research topic within recent years (Holland et al. 2003). Textural maps indicate that heterogeneous bottom types composed of variable amounts of sand, silt, and clay cover some portions of the inner shelf and shoreface in front of Cassino beach, Brazil. Fine sediments provided by the Patos Lagoon are transported mainly toward the south and deposited offshore as fluid mud. Stormy conditions associated with periodic cold front passages, which occur frequently in the area, can rework and transport the fluid mud from the shoreface to the surf-zone and foreshore of Cassino

Beach causing lateral changes in the bottom sediment texture along the shoreface and surf-zone.

Such events have strong influence on the geomorphology of the inner continental shelf, surf-zone processes, beach morphodynamics, shoreline changes, and coastal hazards. The aim of this work is to describe and quantify the long and short-term effects of the mud deposits on the geomorphology of the shoreface and on related beach and surf zone morphodynamics within the different sedimentary regimes.

METHODS

Since 1984 long-term geologic superficial sampling, echosounding and side scan sonar has been used to define the location and type of sediments in the Cassino beach region (Calliari and Abreu, 1984). Approximately fifty piston and gravity cores have been collected within this region to define the historical boundary of the mud deposit (Calliari and Fachin, 1993, Calliari et al., 2001; 2005) and more than 150 beach sediment samples taken at 1 km spacing over a 25 Km interval have been analyzed by sieving (Figueiredo and Calliari, 2006; Calliari et al. 1996). Shoreline change along the same study region was determined using aerial photographs taken between 1947 and 2000 using the methodology based on the studies of Dolan *et al.* (1978, 1980) basically consisting of the superposition of a temporal series of aerial photographs under the same cartographic projection, on the definition of normal profiles taken at regular intervals and on the calculation of the differences between each shoreline over each profile.

Fifteen years of beach profile data combining automatic level and rod and total station surveys has also been obtained. After storms occurred on January 17 and March 10 of 1998 during a 14-month period, two sectors of the beach, one with mud deposits in the surfzone and shoreface and the other sector without, were systematically surveyed to monitor beach response. Additional high-resolution aerial photos using the ADAR system allow small mosaics to be constructed that indicate differences in surf zone morphology and hydrodynamics. In summary, these data represent a significant repository of observations concerning the influence of the fluid mud on coastal processes.

LONG TERM EFFECTS

The first long-term effect of the mud deposition identified adjacent to Cassino beach is on the geomorphology of the inner shelf and shoreface. Figure 1 shows the relief map of the upper 33 m of the continental shelf adjacent to Cassino beach, which includes the inner shelf and the shoreface. It is noticeable in this map the presence of three distinct morphologic regions: From the latitude of the lagoonal mouth down to 50 km to the south, the shoreface and inner shelf is extremely smooth and significant expressive topographic features are absent. This area is distinguished to the north and to the south by two irregular areas characterized by the presence of linear sand ridges with height differences up to 7 m between the crest and the trough.

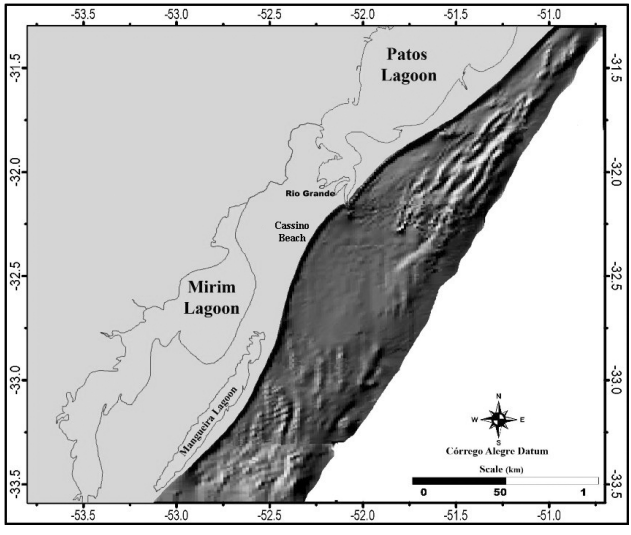

Fig. 1. Morphology of the inner continental shelf adjacent to Patos Lagoon inlet. Modified from Fachin, 1993.

The existence of this smooth area between two regions of irregular bathymetry suggests a different bottom type composed of mixtures of sand and mud. It is well known (Calliari and Fachin, 1993) that the influence of the muddy deposits of the "Patos Facies" (Martins et al. 1967) represented by silty clay, clayey silt, clayey sand and mixed bottoms types surpass the 20 m depth contour in this area. The presence of this homogenous bathymetric area between two irregular sand ridge fields (with all areas subjected to the same wave climate) can be explained in terms of different bottom sediment texture provided by the contribution of fine sediments (silt and clay) from the Patos Lagoon discharge into the ocean. During recent survey done on November of 2006, we were able to confirm the presence of continuous fluid mud and more consolidated mud deposits in the region offshore of the Patos Lagoon Inlet.

Another long term effect caused by the muddier shoreface in front of Cassino beach is the high rate of shoreline accretion on the order of 4.10 m/year found at 10 Km south of the inlet (figure 2). Studies of shoreline change adjacent to the four major inlets along the Rio Grande do Sul coastline (Lélis and Calliari, 2003) indicate that the Cassino beach displays highest accretion rates of all the studied sites. Historical records show that before the inlet stabilization and fixation by two jetties, alternated phases of shoreline accretion/erosion occurred in conjunction with the changeable morphology of

the ebb tide located at the lagoon mouth**.** After the end of the jetties construction, which begun in 1911 and ended in 1915, the shoreline started to accrete at higher rate. The shoreline accretion to the south of the inlet can be explained by the fact that the net littoral drift along the RS coastline is towards the northeast. However the higher rate of deposition coincides with the depocenter of the deposit mapped on basis of thickness of total mud content of the sediment cores (figure 3 from Calliari and Fachin, 1993) as well as the recent fluid mud thickness map (figure 4) of the shoreface obtained by coring and echobathymetric surveys in 2004 (Sperle et al. 2005). The stretch of beach adjacent to this area is also the place where mud deposits on the beach appear more frequently. These data strongly suggest that on a long-term basis there is an association between the shoreface mud deposits and the high shoreline accretion rate found in this area. The higher frequency of mud deposition at the beach and shoreface can substantially reduce the local wave energy and act like a sink for the sediments, which arrive there by littoral drift. Shoreline accretion and stabilization due to the presence of fluid mud on the shoreface has also been reported (Wells and Roberts 1980; Roberts et al 1989; Huh et al 1991) for sectors of the chenier plain coast of southwestern Louisiana.

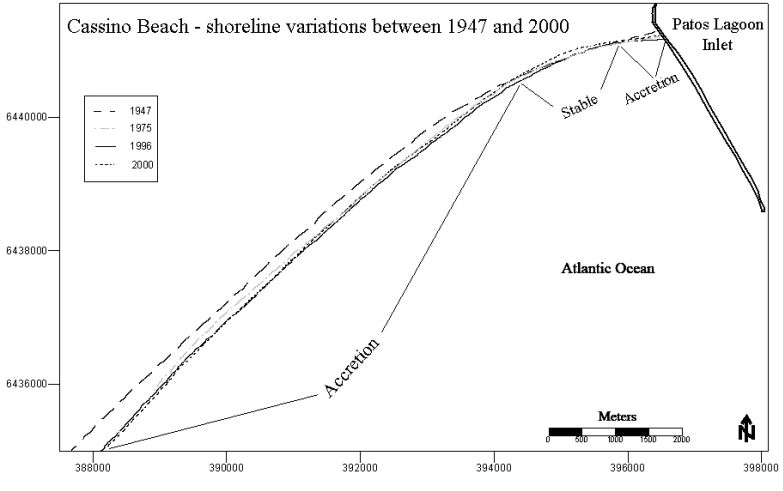

Fig. 2. Shoreline accretion between 1947 and 2000.

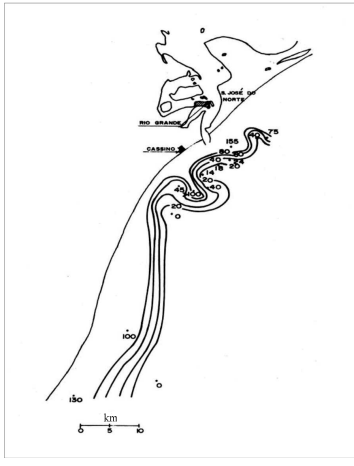

Fig. 3. Isopach map of total mud content (cm) displaying the depocenter of the mud deposit.

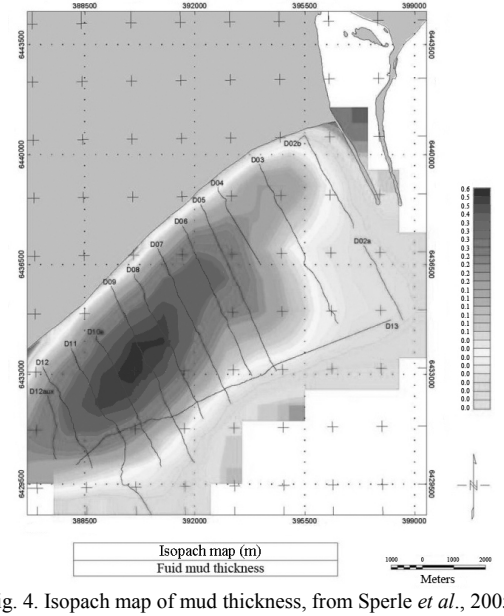

Fig. 4. Isopach map of mud thickness, from Sperle *et al*., 2005.

Alongshore changes in sediment texture also induce long term beach morphodynamic differentiation in the first 25 Km south of the Patos Lagoon inlet. Besides the silt and clay suspension load, Patos Lagoon contributes a substantial amount of very fine sand to the shoreface and adjacent beaches . Based on grain size distribution three main sectors were identified along this stretch of coast (Figueiredo and Calliari, 2006). The first sector called "West Jetty" which comprises the first 6 Km display the finest mean grain size of all RS coastline (2.9 phi units---very fine sand). The next sector the "Central" extends until Km 15 and the sand is slightly fine with a mean grain size of 2.7 phi. Between 15 Km and 25 Km the "Shipwreck" sector exhibit mean grain size of 2.3 phi units. Figure 5 displays the different sediment signatures between the central and shipwreck sectors as well as the long term different morphodynamic behavior between Querência beach located at the boundary of the first two sectors and the Shipwreck beach located at the end of the third sector. Querência beach displays higher beach width, a lower beach face slope and smaller changes in shoreline position and in the thickness of beach profile envelope when compared with the Shipwreck beach. One interpretation is that Querência is a typical dissipative beach and Shipwreck beach behaves more like an intermediate beach (Wright, 1984). Although these differences can be attributed to the fact that the presence of medium sand at Shipwreck beach contributes for its higher beach mobility, one cannot ignore the influence of muddy sediments found at shallower depths at Querência beach in terms of stabilizing the long-term morphodynamics.

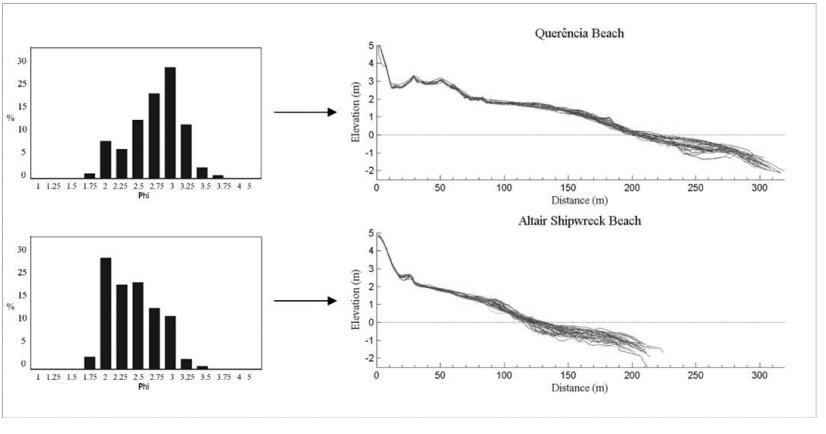

Fig. 5. Textural and morphodynamic long term differentiation between Querência and Shipwreck beach.

SHORT TERM EFFECTS

Short-term effects induced by mud deposition at the shoreface and surf-zone were detected during a mud deposition event which lasted for 14 months. Storms occurring on January 17 and March 10 of 1998 (Calliari et al. 2001**)** suspended and transported fluid mud deposits to the beach forming mud banks, which were exposed at the shoreline and in the surf-zone. The most obvious impact of these deposits over the depositional zone was the absence of surf-zone along vast stretches of beach (figure 6) that dramatically differed from adjacent areas with no shallow water mud deposits. Along these areas of the subaqueous deposits, rapid damping of wave energy could be visualized at distances of up to 6 Km offshore**.** Similar processes have been described by Wells and Coleman (1981) where waves transiting fluid mud bottoms along the coast of Surinam, South America were progressively attenuated nearshore without breaking**.** Similarly, Mathew et al. (1995) analyzed wave data from Kerala coast in India and found that wave height reduction as a result of wave propagation over fluid mud layers can reach 85%. According to these authors during the stage of mud banks formation along the southwest coast of India, the wave energy can be completely damped in a distance corresponding to a few wavelengths. All of these characteristics were obvious at Cassino suggesting that among other factors, the high viscosity of bottom sediments and the strong energy dissipation rate are the main causes of attenuation of the surface waves.



Fig. 6. Lateral variability in wave breaking associated with presence of mud.

A comparative study between two beach profile stations, monitored along Cassino beach, indicated that regions three kilometers apart displayed different behaviors in response to changes in the hydrodynamic conditions. Comparison of repeated beach profiles at the mud-free and muddy locations (Calliari et al. 2001) indicated that the mud-free site (Tourist Terminal) had much more variability compared to the more exposed, but muddier, beach (Rua Bahia) (figure 7). Such anomalous behavior, characterized by an inversion of the normal pattern of beach response, was due to the presence of nearshore and surf zone mud banks, which caused a wave attenuation effect.

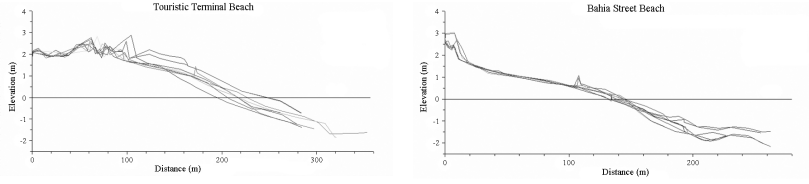

Fig. 7. Profiles showing more variability in the envelope of surveyed depths at the non-muddy site (left).

Micro-deltas, associated with the mouth of washouts that carried sand from the dune field to the beach appeared on the foreshore since the sand was not being remobilized by littoral drift due the complete absence of surf-zone during this period (figure 8). Additional morphodynamic effects relating to the mud deposits occurred with respect to beach protection as process similar to that described by Wells and Roberts (1980) along stretches of the Louisiana coast. During storms, due to the low set up in the area of mud deposits foredunes were protected from erosion. In this way the presence of the mud deposits certainly acted to stabilize the coast over short times and is consistent with the long-term observations previously described.

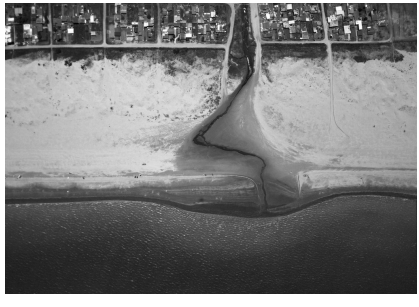

Fig. 8. Micro-delta features associated with the mouth of washouts.

COASTAL HAZARDS

On at least two occasions the presence of fluid mud in the surf-zone during episodes of high wave energy represented a potential hazard for surfers. Due to lateral gradients in wave energy along the surf-zone longshore currents transported surfers to areas where the surf zone was isolated from the beach by fluid mud which had thickness of 1.5 m or even more. Such situation caused surfers to get trapped in the surf zone under risk of life since they suffered hypothermia due to long exposure in autumn temperatures waters. There was some concern that they could be immobilized and buried by the fluid mud

deposits. Fortunately locals used cables and body boards to come across the surf-zone to rescue them.

The presence of mud between the beach face and backshore represents an additional risk for car traffic. The fact that Cassino beach is typically a highly dissipative wide and very fine sandy beach with a high degree of compaction (close-grained) encourages a steady flow of vehicles. Any mud deposited across the beach is rapidly covered by a thin layer of sand as soon as the sea level drops after the storms and acts as a trap for cars which get stuck in the mud sometimes reaching more than 0.3 m thick (figure 9). It becomes impossible to remove the cars without the use of heavy machines (caterpillar type). The accidents become more serious when cars in high velocity get suddenly stuck. Serious bodily injury resulted to tens of drivers during the duration of the mud deposit (14 months).



Fig. 9. Car trapped by mud deposits underneath a thin layer of sand.

CONCLUSIONS

The influence of offshore mud deposits on the otherwise fine sediment sandy beach in the Cassino area of Brazil is often extreme. With respect to regional morphodynamics, the flat shoreface and featureless inner continental shelf adjacent to the Patos Lagoon inlet results from the "Patos" facies composed predominantly by fine sediments from the lagoonal discharge. The high rate of shoreline accretion at 10 Km from the inlet is due to the association of the mud depocenter and the higher frequency of fluid mud deposition on the beach at this sector. The lagoonal source of very fine sand also induces beach morphodynamic differentiation in the proximities of the inlet as beaches located within 15 Km south of the inlet are ultra-dissipative. In contrast, south of this point, beaches are composed of mostly of fine and medium sand, display higher mobility and behave as intermediate.

Changes in sediment properties at the beach, surf zone and shoreface induce beach differentiation up to 25 Km south of the inlet. This lateral variability is identified by

three sectors with distinct morphodynamic behavior. In the first 6 Km (north sector), beach, surf-zone and shoreface are composed of very fine sands (the finest sand along the RS coastline). For the next 9 Km, which characterizes the central portion of Cassino, beach sediments are fine while the shoreface displays muddy sediments mostly composed of clayey silt, silty clay and silty sand. The lateral heterogeneity along the shoreface and surfzone of this beach also causes visible differences in beach morphodynamic behavior which is a response to the hydrodynamic conditions. Due the absence of mud in the shoreface, which can substantially reduce the wave energy, beaches in the first and third sector display more mobility and are subject to higher set-up when compared to the central sector of the region.

Similarly, sporadic mud deposition events during storms create short-term morphodynamic differentiation. Beach sectors under the influence of mud in the sub aerial beach, surf zone and part of the shoreface display low mobility and low hydrodynamics when compared with sectors without mud.
Mud deposition at the surf zone and beach can represent a non permanent potential coastal hazard for bathing, surfers and car traffic.

In short, many coastal sedimentary processes and properties are influenced by the presence of the offshore mud deposit. We expect that other regions with inlets having large sediment discharge rates may behave similarly.

ACKNOWLEDGEMENTS
This study is supported by the Office of Naval Research thru grant funding of the Fundação Universidade Federal do Rio Grande and thru base funding of the Naval Research Laboratory (PE #0601153N)

REFERENCES

Calliari, L.J. & Abreu, J.G., 1984. Litologia da plataforma continental interna adjacente a cidade de Rio Grande, RS, através da interpretação de sonar de varredura lateral e amostragem superficial. In: CONGRESSO BRASILEIRO DE GEOLOGIA, 33º *Anais...* Rio de Janeiro: SBG, vol. 2: 1553-1564.

Calliari, L.J. & Fachin, S. 1993. Lagoa dos Patos: Influência nos depósitos lamiticos costeiros. *Pesquisas* 20 (1) 57-69.

Calliari, L.J., Klein, A.H.F., Barros, F.C.R. 1996. Beach differentiation along the Rio Grande do Sul coastline (Southern Brazil). *Revista Chilena de Historia Natura*l, 69:485-493.

Calliari, L.J., Speranski, N.S., Torronteguy, M., Oliveira, M.B. 2001. The mud banks of Cassino beach, Southern Brazil: Characteristics, Process and Effects. *Journal of Coastal Research* (ICS) Proceedings 318- 325. New Zealand.

Calliari, L.J., Holland, T., Dias, M.S.,Vinzon, S., Thorton, E., Stanton, T. Experimento Cassino 2005: Uma síntese dos levantamentos efetuados na ante-praia e zona de arrebentação. Proceedings ABEQUA 2005 CD-ROM Published by META

Marketing & Eventos Ltda.Av. Nilo Peçanha, 50/1610 -20044-900, Rio de Janeiro.

Dolan, R., Hayden, B., Heywood, J. 1978. A new photogrammetric method for determining shoreline erosion. *Coastal Engineering*, 2: 21-39.

Dolan, R., Hayden, B., May, S. 1980. The Reliability of Shoreline Changes Measurements from Aerial Photographs. *Shore and Beach*, 48:22-29

Figueiredo, S.A., Calliari, L.J., 2006. Sedimentologia e suas implicações na morfodinâmica das praias adjacentes as desembocaduras da linha de costa do Rio Grande do Sul. Gravel (4) 73-87. Porto Alegre, RS.

Holland, K.T., Keen, T., and Kaihatu, J.M. 2003. Understanding coastal dynamics in heterogeneous sedimentary environments, Coastal Sediments '03, Clearwater Beach, FL.

Huh, O.K., Roberts, H.H., Rouse, L.J. and Rickman, D.A. (1991). Fine grain sediment transport and deposition in the Atchafalaya and chenier plain sedimentary system. Coastal Sediments ' 91 Proceedings Specialty Conference/ WR Div./ASCE Seatle, WA/June 25-27 p.817-830.

Lélis, R.J.F., Calliari, L.J., 2003. Variabilidade da linha de costa oceânica adjacente às principais desembocaduras do Rio Grande do Sul, Brasil. Abstracts of IX Congresso da Associação brasileira de Estudos do Quaternário-ABEQUA. Recife, PE, Brasil p. 133.

Martins, L.R., Urien, C. M. & Eichler, B. B., 1967. Distribuição dos sedimentos modernos da plataforma continental sul-brasileira e uruguaia. In: CONGRESSO BRASILEIRO DE GEOLOGIA. CBG, 21O. *Anais...* Curitiba, PR. Brasil : SBG, v. 2, p. 29-43.

Mathew, J., Baba, M., and Kurian, N.P., 1995. Mudbanks of the Southwest Coast of India. Wave Characteristics. *Journal of Coastal Research*, 11 (1), 168-178.

Roberts, H.H., Huh, O.K., Hsu, S.A., Rouse Jr., L.J. and Rickman, D.A. (1989). Winter storm impacts on the chenier plain coast of southwestern Louisiana. *Transactions of Gulf Coast Association of Geological Societies*. Vol. XXXIX p 515-522

Sperle, M., Vinzon, S., Calliari, L.J. , Rech, M., Fabri, J.B., Bispo, L., 2005. Aplicação de métodos geofísicos na avaliação da ocorrência de lamas fluidas na praia do Cassino, Rio Grande. II Proceedings Congresso Brasileiro de Oceanografia 09 a 12 de Outubro de 2005 - Vitória - ES – Brasil.

Wells, J.T., Roberts, H.H., 1980. Fluid mud dynamics and shoreline stabilization: Louisiana chenier plain. Proceedings of the Coastal Engineering Conference 17, 1382-1401.

Wells, J.T., and Coleman, J.M., (1981). Physical processes and fine-grained sediment dynamics, coast of Surinam, South America. *Jour. Sed. Petrology*, v.51, p. 1053-1063.

Wright, L.D. 1984. Morphodynamic variability of surf zone and beaches. A synthesis. Marine Geology 56 (1-4): 93-118.

THE HURRICANE KATRINA STORM SURGE IN MISSISSIPPI

Alan W. Niedoroda[1], Lyle Hatchett[2], Himangshu Das[3], Andrew Cox[4], Robert Weaver[5], Stephen Baig[6] and Shabbar Saifee[7]

1. URS Corporation, 1625 Summit Lake Drive, Suite 200, Tallahassee, FL 32317, USA. Alan_niedoroda@urscorp.com.
2. URS Corporation, 1625 Summit Lake Drive, Suite 200, Tallahassee, FL 32317, USA. Lyle_hatchett@urscorp.com.
3. URS Corporation, 1625 Summit Lake Drive, Suite 200, Tallahassee, FL 32317, USA. Himangshu_Das@urscorp.com.
4. Ocean Weather, Inc., 5 River Road, Cos Cobb, CT 80525-3152, USA. Andrewc@oceanweather.com.
5. Department of Civil & Coastal Engineering, Coastal & Oceanographic Engineering Program University of Florida, 548 Weil Hall, Gainesville, FL 32611 USA. rweaver@coastal.ufl.edu.
6. National Hurricane Center, 11691 SW 17th Street, Miami, FL 33165, USA. Stephen.r.baig@noaa.gov.
7. FEMA DFO, 500 C Street SW, Crystal City Room 906, Washington, DC 20472, USA. shabbar.saifee@dhs.gov.

Abstract: On August 29, 2005, Hurricane Katrina sent the largest-ever recorded storm surge into the central Gulf coast. The coastal surge penetrated more than 16 km (10 mi) inland in Jackson County to the east and Hancock County to the west. Wave destruction extended more that 1 km (0.6 mi) inland. Immediately after the storm, URS teams identified and surveyed 312 coastal high water marks (CHWM) in the three coastal counties. The USGS identified an additional 90 CHWM. These were checked, verified and surveyed to within 0.08 m (0.25 ft) vertical and 3.5 m (10 ft) horizontal. In this paper, the Hurricane Katrina storm surge is documented. By considering special features of both the oceanic and overland propagation of the surge it is possible the gain an understanding of why this storm surge was so much higher and spatially extensive than other previous major hurricane events along the coast.

INTRODUCTION

It is well accepted that coastal processes during storms strongly outweigh similar processes during normal weather. When Hurricane Katrina made landfall on the Mississippi coast near 7:30 a.m. (local) on August 29, 2005 it created one of the most devastating storm surges in U.S. history. Modern instruments, including satellites were able to develop a detailed data set on the meteorological properties of the hurricane. Additional insight into the storm surge development and behavior has been gained from post-event field studies and extensive simulations with numerical models. All of this permits us to develop a detailed description of the extreme coastal process that occurred. In this paper we concentrate on easternmost Louisiana and Mississippi because of the availability of our data and modeling.

HURRICANE HISTORY

Hurricane Katrina first made landfall on the southeast Florida coast north of Miami on August 25, 2005. It passed over the state and exited south of Naples early on August 26. It then continued on a westward track until the afternoon of the August 27 when it began a turn to the north. The storm made landfall on the lower Mississippi Delta and tracked across the lower delta in a northward direction. The eye passed between the eastern Louisiana shoreline and the Chandeleur Islands making landfall near the mouth of the Pearl River on the Mississippi/Louisiana border near 7:30 a.m. local time. Figure 1 shows a Doppler Radar Image of this storm just before it made landfall on the Mississippi coast.

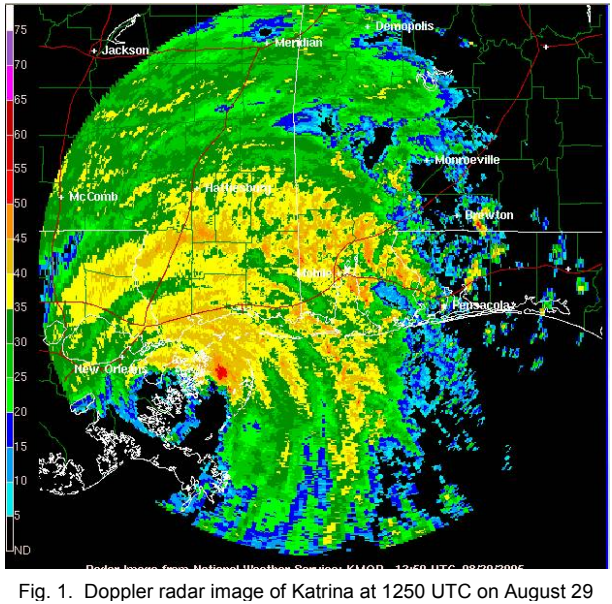

Fig. 1. Doppler radar image of Katrina at 1250 UTC on August 29

Much has been learned in recent years about the structure of hurricane wind fields and how these change in time. These changes are especially interesting to us as the storm centers come within about 150 km of the coast. As shown on Figure 2a, the Hurricane Katrina wind field was skewed to the east with the zone of maximum speed near the 2 o'clock position (i.e. NNE of the storm center) when the storm reached maximum intensity near 1100 hrs (local) on August 28. These winds diminished and the eastward asymmetry increased as the storm passed up the eastern Louisiana coast. Figure 2b shows that winds in excess of 70 meters per second (m/s) extended along the entire Mississippi coast at landfall. The radius to maximum winds at landfall have been variously estimated to be between 42 and 48 km.

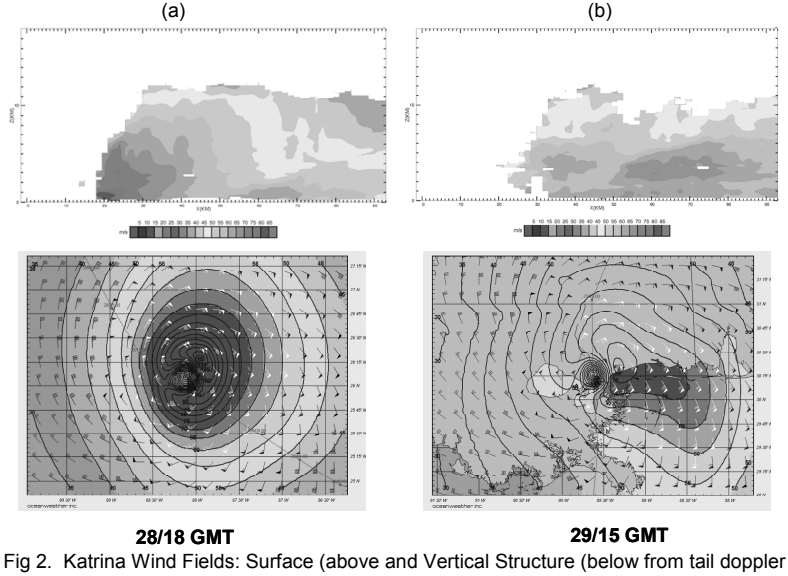

Fig 2. Katrina Wind Fields: Surface (above and Vertical Structure (below from tail doppler – source image from NHC) – (a) August 28, 1800 hrs UTC (b) Aug. 29, 1500 hrs

The details of these variations in the structure and intensity of the storm are very important to both the way that the storm surge developed and the ability of hydrodynamic models to accurately represent the details of the developing surge. For our study an exhaustive review of data sources was conducted to provide a comprehensive time-history of this storm. Hurricane hunter aircraft observations using GPS drops, Stepped Frequency Microwave Radiometer and Tail Radar were taken by NOAA several times a day. These data were combined with ocean data buoy measurements, land station meteorological observations, Doppler radar images, and satellite measurements. With this information the behavior of the OWI Tropical PBL Planetary Boundary Layer Model was adjusted to most closely match the best available interpretation of the wind field. This model was used to represent

conditions from the time that the storm entered the Gulf of Mexico to after landfall on the Mississippi coast.

SURVEY OF COASTAL HIGH WATER MARKS

When major storms make landfall the Federal Emergency Management Agency (FEMA) and other government agencies carry out surveys to describe the extent and maximum water levels over the areas that were flooded. The destruction of Hurricane Katrina was so great and widespread that this response was delayed for several days to avoid interfering with emergency crews. Coastal high water mark (CHWM) surveys were carried out by our crews working for FEMA and personnel from the U.S. Geological Survey (USGS).

CHWM surveys were carried out by personnel trained to identify evidence of the flood level and what each data point represents. A total of 402 points were located and surveyed in coastal Mississippi (312 URS/FEMA points and 90 USGS points). These points are deliberately divided between those reflecting the highest still water level, the highest level reached by the crests of waves propagating on the surge and the greatest wave run-up elevations on natural and constructed embankments.

Although still-water CHWMs are carefully selected from places where direct wave effects have been blocked (i.e. flood marks in interior rooms) it has been found that local spatial variability is unavoidable. In an extremely violent storm such as Katrina there must be large and rapid changes in the local wind and surge. In some rooms in damaged buildings we found evidence of turbulent conditions as waves crashed about and these can distort the watermarks, even in close adjoining closets. The amount and size of debris being piled up and tossed about is almost unimaginable. Locally this can temporarily dam up flow paths and amplify the maximum surges. Many other complicating factors can be envisioned.

With these difficulties in mind we have selected a total of 193 coastal high water marks as being the most reliable measurements of the maximum surge levels. Although, in actuality, as these measurements were first being reported by our field crew we were incredulous. The maximum CHWM elevations were 10.6 m (NAVD 88 datum) which were found near Pass Christian. Figure 3 shows some representative measurements along the shoreline and inland. This figure also has an outline of the inland extent of the surge as mapped by field parties.

We have conducted no mapping of the offshore barrier islands. The Coastal Services Group of the U.S. Geological Survey carried out Lidar elevation measurements a few days after the storm and showed that all of the islands were overtopped by the Katrina surge. They also report extensive erosion.

NUMERICAL MODELING

To better understand the extreme coastal conditions over the duration of the storm surge we have conducted a series of analyses with numerical models. The Ocean Weather PBL model, with the tailoring and adjustments noted above, provided a detailed and accurate time series of wind and atmospheric pressure fields that were

inputs to the other models. Waves were modeled with both WAM and SWAN. The (Parallel) ADvanced CIRCulation Model for Oceanic, Coastal and Estuarine Waters (ADCIRC) model was used to represent the hydrodynamics of the coastal surge.

Storm Waves

The wind and atmospheric pressure data provide by Ocean Weather were used as input to a Gulf-wide WAM model of ocean waves. These storm and wave conditions were then used as input to more detailed regional and local SWAN model grids covering the eastern Louisiana and entire Mississippi areas.

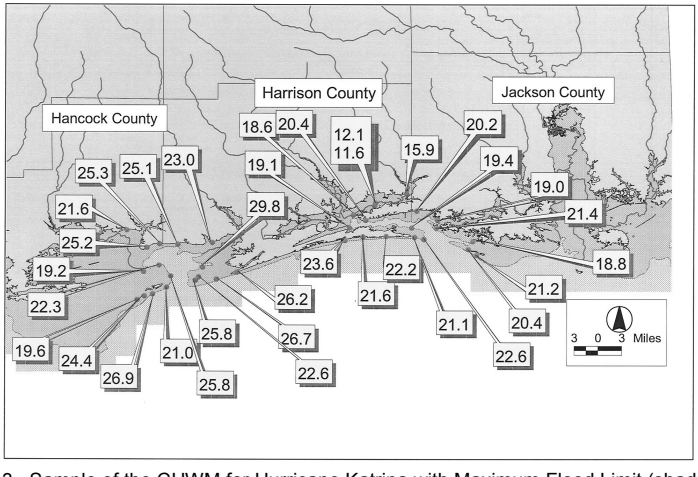

Fig. 3. Sample of the CHWM for Hurricane Katrina with Maximum Flood Limit (shaded)

The primary reason for the modeling of wave conditions during this event was to provide detailed representations of the breaking wave conditions so that the wave set-up component of the coastal surge could be determined.

Figures 4 and 5 show results from the regional SWAN model for August 29, 2005 conditions at 2130 hrs (local) on August 28 and 0730 hrs on August 29, respectfully. At 2130 hrs the barrier islands and shallow depths of both Chandelier Sound and the Mississippi Sound clearly protect the mainland coast. Within these sounds the wave periods are four seconds or less indicating that they are dominantly locally generated. The significant wave heights at this time are less than 2.5 m inshore of the barrier island. Figure 5, representing conditions at 0730 hrs on August 29 indicates this is where the coastal surge has overtopped the barrier islands. The corresponding extent of inland flooding also appears on this figure. Note that in spite of an increase in local water depths due to the developing storm surge on the order of 6 m., the wave periods indicate that the wave energy at the mainland coast is still largely dominated by wind-generated seas. The shoreface of the barrier islands absorbs the greatest share of the hurricane-generated waves from the open Gulf. Only a fraction of the open-Gulf

wave energy passes between the barrier islands. The shallow overtopping of the barrier islands allows them to maintain their important role in protecting the mainland shore.

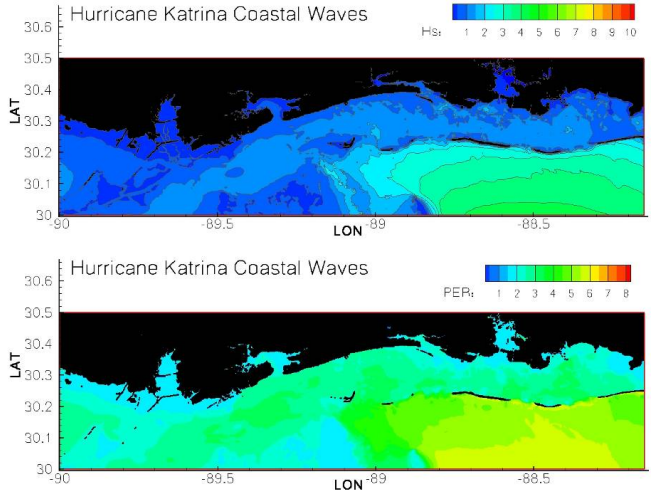

Fig. 4. Significant Wave Height (upper) and Period (lower) for 0430 hrs (UTC) Aug. 29.

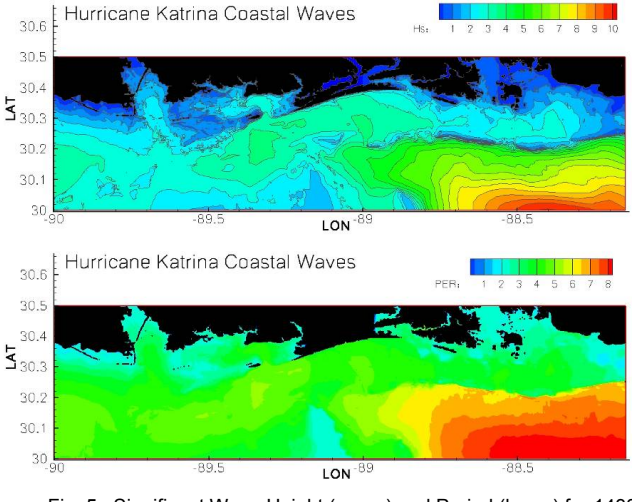

Fig. 5. Significant Wave Height (upper) and Period (lower) for 1430 hrs (UTC) Aug. 29.

This morphology of shallow sounds and low offshore barrier islands serves to restrict the maximum wave conditions and results in also restricting the contribution of wave set-up to the coastal storm surge at the mainland. Our calculations indicate that this component was generally less than 1 m.

Development of the Coastal Storm Surge

The time-history of the Hurricane Katrina coastal storm surge has been mapped out with the ADCIRC modeling. This model was calibrated using CHWM data from Hurricanes Camille, Betsy and Katina. Most of the work in these calibrations involved local adjustments in the way that topographic features were represented in the model grid. However, in the case of Camille and Betsy it was necessary to adjust the details of the wind fields in the OWI Tropical PBL Model. These adjustments were limited by the available data. That is the available data permitted a certain amount of judgment so long as measured behavior was not violated.

As Hurricane Katrina tracked northward on August 28 it strengthened alarmingly. A low barotropic wave propagated ahead of the storm and arrived at the Mississippi coast about a day ahead of landfall on the mainland. As the storm neared landfall on the Louisiana Delta coast just west of the river mouth, the coastal surge east of the river levees began to develop rapidly. The hydrodynamic model results clearly show a bulge of water about 5 m high that developed against the eastern levee system and was forced northward.

As this moved northward it became constrained by the levees protecting the areas around New Orleans. At this time the maximum winds were onshore with hurricane wind speeds extending over the entire coast of Mississippi and well into Alabama. Several factors combined to cause significant gradients in the height of the surge along the open Mississippi shore. The marked turn in coastline orientation from east-west in Mississippi to nearly north-south in eastern Louisiana certainly funneled and trapped the surge. The shallow depths and gentle bottom slopes of the Chandelier and Mississippi Sounds added to this effect. The surge attributable to these direct effects was certainly enhanced by the forced wave traveling up the eastern Louisiana levee systems.

Along the open coast the maximum surge elevations closely corresponded to the place where the strongest onshore winds occurred. The timing of the maximum wind and maximum surge closely correspond. Comparison of the maximum surge elevations shown on Figure 3 with the spatial distribution of the maximum onshore winds shown on Figure 2 is a good indicator of the role that the coastline geometry and offshore bathymetry played in amplifying the surge. The greatest surge developed in the Waveland-Pass Christian area. This surge remained high along the central Mississippi coast as far as Biloxi. Here the surge was held against the rapidly rising land level that parallels the shoreline. Further east, the winds were still strong, but the surge levels became lower.

The combined effects of gravity and wind stress also served to make the pattern of storm surge development irregular as it moved inland. Near the coast the pattern of

inland flooding is dominated by differences in the level of the surge along the entire coastline.

Comparison of how the surge propagated in eastern Louisiana compared to Mississippi show major differences due to local topographic relief. In the wide basins of the Pearl and Pascagoula Rivers the surge moves on a broad front up the drainage way in a manner similar to a progressive wave. However, much of the Mississippi coast has coastal streams in distinct valleys. The surge propagates up these and then spreads into adjacent low-lying areas. In the areas surrounding St. Louis Bay the sequence of wind stress had a strong controlling effect with considerably more flooding along the lowlands adjoining the Jourdan River which enters the bay from the west than in equivalent areas along the Wolf River which enters from the east. This effect was caused by the relative timing of the surge and the direction of the wind stress. The highest surges on the coast occurred around St. Louis Bay and were even higher in the bay itself. As the hurricane eye passed the strong west wind drove a pulse of water up Wolf River which enters the bay from the east. At this time the surge propagated against the wind up the Jordan River which enters the bay from the west. In the lowlands surrounding this river the maximum flood level was lower and its occurrence later than in the Wolf River because of this effect.

From the modeling results it is clear that the time of maximum storm surge levels and the times of maximum winds differed considerably in the different coastal areas. In St. Tammany Parish in eastern-most Louisiana places along the western side of the extensive wetland in the Pearl River floodplain had the storm surge maximum more than three hours later than the time of maximum winds. Inland flooding maximums for points several kilometers from the bays had a lag between one and three hours between maximum winds and maximum water levels. Many place in Harrison and Jackson Counties located between two and five kilometers inland had maximum surges lagging maximum winds by one half to one hour. Along the open coasts these time differences were small or absent.

CONCLUSIONS

This study clearly demonstrates how modern data collection programs combined with detailed numerical models can provide very detailed representations of the time history of a storm surge from a major hurricane and certainly points the way for developments in the near future where such analyses become feasible in a prognostic mode.

The study also shows the beneficial effect of barrier islands, even when they are severely overtopped. The whole mass of the barrier island platform, which extends across the shoreface to the inner shelf serves to cause the large waves to break, starting more than 10 km offshore. As a consequence wave conditions on the mainland coast are substantially less than what would be encountered on an unprotected shore.

The special role of the levees along the east bank of the Mississippi River and protecting the areas around New Orleans is noted. These appear to have served to enhance the surge along the western portion of the Mississippi coast.

The results also demonstrate that the inland propagation of a storm surge from a major storm such as Hurricane Katrina can be complex. The timing of maximum surge and maximum winds is not well correlated.

ACKNOWLEDGEMENTS
Much of the work that resulted in this paper was performed under Federal Emergency Management Agency (FEMA) contract HSFEHQ-06-D-0162. The authors express their appreciation for open source data and information provided by the National Oceanic and Atmospheric Administration.

COASTAL INLETS OF TEXAS, USA

Nicholas C. Kraus[1]

1. U.S. Army Engineer Research and Development Center, Coastal and Hydraulics Laboratory, 3909 Halls Ferry Road, Vicksburg, MS 39180-6199, USA. Nicholas.C.Kraus@erdc.usace.army.mil.

Abstract: Presently, 16 permanent inlets connect the inland coastal waterways and rivers to the Gulf of Mexico on the 560-km long coast of Texas. Processes controlling inlet stability in Texas are typically more complex than those acting on the Atlantic and Pacific Ocean coasts of the United States, where the astronomical tide dominates. The tide on the Texas coast is predominantly or fully diurnal and with small range; however, the large surface areas of most Texas bays produce large tidal prisms. Wind is strong throughout the year, either from the southeast in summer or as episodic northeasterly fronts in autumn and winter. Non-astronomical seasonal variations in water level are comparable to the tidal range of Texas bays. Creation of inlets on the Texas coast is ongoing for environmental, commercial, and recreational reasons, and this paper discusses the status and challenges posed to inlet creation, stability, and maintenance.

INTRODUCTION

The coast of Texas is approximately 540 km long and is fronted by sandy barrier islands or barrier spits (Fig. 1) with the exceptions of about 50 km each of mainland near Sabine Pass and Freeport. Texas inlets to the Gulf of Mexico originate as natural river mouths, relocated river mouths, natural entrances to bays, and artificial cuts through the barriers. There are eight federal channels: Sabine Pass, Galveston Pass, Freeport Ship Chanel, Mouth of Colorado River Navigation Channel, Matagorda Ship Channel, Aransas Pass, Mansfield Pass, and the Brazos-Santiago Pass. The Mouth of Colorado River and Mansfield Pass are shallow draft (at about 4-m depth), and the other six are deep draft at 13-m depth or greater. Permanent inlets of Texas are listed in Table 1, according to origin. Many inlets in Texas are named either as “passes” or as “cuts,” signifying the action of a hurricane or of human intervention in opening them. At the time of this writing, January 2007, 16 inlets along the Texas coast were open to the Gulf of Mexico.

Many inlets of Texas are described by U.S. Army Corps of Engineers ((USACE) 1992), and Morton (1977) studied morphologic response to seven federal Texas inlets with jetties (Mouth of Colorado River had not yet been opened).



Fig. 1. Location map for Texas coast with presently open and other inlets

The need for additional inlets along the Texas coast, in particular, for small inlets to allow exchange of water with the Gulf of Mexico and inland bays and lagoons, locally called "fish passes," was documented by Carothers and Innis (1960). In the mid 20th Century, two major inlets with jetties were constructed, Mansfield Pass (Hansen 1960; Kieslich 1977) and the Matagorda Ship Channel (Kraus et al. 2006). Some fish passes have been successful such as Rollover Pass opened to upper Galveston Bay opened in 1959 (Bales and Holley 1989) and Mitchells Cut opened to East Matagorda Bay in 1989 as a flood-relief channel (USACE 1992). Other inlets such as Yarbrough Pass to Baffin

Bay (Lockwood & Andrews 1952), most recently cut in 1952, and the Mustang Island Fish Pass opened in 1972 (Behrens 1979) have been unsuccessful by rapidly shoaling and closing. In contrast, Rollover Pass expanded greatly from its planned dimensions (because of a large phase difference between the Gulf and upper Galveston Bay) and had to be controlled be revetments and a channel weir. Other inlets located close to the Gulf have been considered for opening, including re-opening Parkers Cut to connect Matagorda Bay to the Colorado River Navigation Channel, and opening of a "Southwest Corner Cut" to connect East Matagorda Bay to the Colorado River Navigation Channel (Kraus and Militello 1999). Environmental and legal issues have reduced agency enthusiasm for opening fish passes, but inlet creation continues, as demonstrated by opening of Packery Channel in 2005 (Kraus and Heilman 1997; Williams et al. 2007) and interest in maintaining the long-lived ephemeral inlet Cedar Bayou Pass connecting the Gulf to Mesquite Bay (Simmons and Hoese 1959; Shepsis and Carter 2007). Concern has also been expressed by local interests in maintaining the San Bernard River Mouth (Lin et al. 2003).

Table 1. Coastal Inlets of Texas to Gulf of Mexico

Origin	Name	Comments
Inlets Open as of January 2007		
River Mouths	Sabine, Brazos, San Bernard, Colorado, Rio Grande	The modern Colorado River Mouth diverted into Matagorda Bay in 1992 Brazos River mouth relocated south of Freeport Ship Channel (original mouth) in 1929.
Natural Exchange Passes	Galveston, San Luis, Pass Cavallo, Cedar Bayou, Aransas, Brazos Santiago	Cedar Bayou is a long-lived ephemeral inlet to San Antonio Bay & Aransas Bay.
Artificial Inlets (Engineered Cuts)	Rollover Pass, Freeport Ship Channel, Mitchell's Cut, Matagorda Ship Channel, Packery Channel, Mansfield Pass	
Selected Ephemeral Inlets and Hurricane Passes		
Connecting to Gulf	Brown Cedar Cut & Greens Bayou; Corpus Christi Pass and Newport Pass	Likely will not open again because other inlets present
Proposed Passes to Rivers	SW Corner Cut to connect East Matagorda Bay and Colorado River Navigation Channel	Active discussion on opening this inlet
Attempted, but Failed Artificial Inlets		
Artificial Inlets	Mustang Island Fish Pass to Corpus Christi Bay; Yarbrough Pass to Baffin Bay	Both closed or became inefficient in short time.

Although Carothers and Innes (1960) provide design guidance for constructing fish passes along the Texas coast, it appears that an update based on more recent experiences and knowledge of Texas inlet processes would be beneficial to the coastal engineering and science communities. Creation of inlets can cause morphologic change on widely

varying space and time scales (Kraus 2006). It is the intent here to document recent observations and experiences with inlets along the Texas coast, updating the literature.

STABILITY OF TEXAS COASTAL INLETS

Many natural processes control the creation, stability, and navigability of coastal inlets. Main factors are:

1. Longshore sediment transport, including wind-blown transport.
2. Astronomical tide.
3. Wind tide.
4. Seasonal change in water level.
5. Regional precipitation and watershed characteristics.
6. River discharges for those inlets connected to rivers.
7. Sediment grain size and geological environment.
8. Human interventions, principally dredging, but also constriction of inlet width by jetties and reduction of longshore sediment transport reaching the inlet.
9. Hurricanes and tropical storms.
10. Relative sea-level rise.
11. Width to depth ratio of inlet channel with jetties, with smaller ratio providing a more hydraulically efficient channel (e.g., Kraus and Heilman 1997).

In this paper, the wind tide is examined, as its action is more regular and much more pronounced than along other coasts of the United States and dominates extreme water levels and currents at Texas coastal inlets. Relative sea-level rise (RSLR) on the Texas coast and varies from about 3 mm/year at the Port Isabel (Brownsville) tide gauge to greater than 10 mm/year at Freeport and Galveston. RSLR may increase bay and lagoon surface area, hence tidal prism, and promote inlet stability. On the other hand, protective jetties will become lower with respect to the water surface, allowing more littoral sediment to enter the entrance channels they protect. The sediment along the Texas coast is predominantly fine quartz sand with median grain size of 0.16-0.18 mm.

Because of the concave curvature of the Texas coast to the southeast, regional longshore sand transport is directed from north to south from Sabine Pass and from south to north from the Rio Grande to converge along central Padre Island (Carothers and Innis 1960; Watson 1971). Of course, there are local reversals, especially at inlets (e.g., Heilman and Edge 1996). Owing to the coastal curvature, widely varying magnitudes of net and gross longshore sand transport rates are expected. Volumes of sand dredged from inlet entrance channels indicate average rates of 100,000-300,000 m^3/year, but can reach 500,000 m^3/year.

Wind blowing from the Gulf of Mexico and surge by tropical storms elevate water at the shore, promoting longshore transport in the swash zone. Swash zone transport can cause spit growth into inlets without structures and sand back-passing (sand moving around landward side of a jetty) with spit growth for inlets with low jetties (Fig. 2). The longshore component of wind can also be strong, moving sand over portions of jetties located on the dry beach and contributing to shoal growth and channel infilling (Fig. 3).

Intrusion of channels by wind-blown sand can figure prominently in the closure of small inlets along the Texas coast (Kraus and Heilman 1997).

Hurricanes open many short-term and sometimes long-term ephemeral inlets in the Texas barrier islands (Hayes 1965). Examples of longer term ephemeral inlets are Cedar Bayou opening to Aransas Bay and San Antonio Bay through Mesquite Bay (Simmons and Hoese 1959; Shepsis and Carter 2007), and the presently closed Brown Cedar Cut at the eastern end of East Matagorda Bay (Mason and Sorenson 1971). Brown Cedar Cut will likely remain closed owing to artificial opening of nearby Mitchells Cut in 1989.

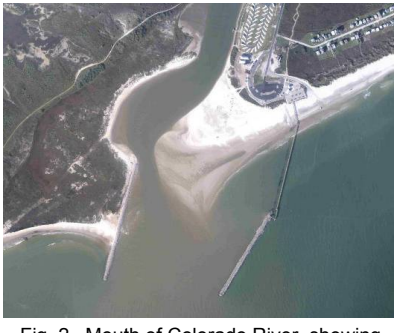

Fig. 2. Mouth of Colorado River, showing sand spit growing into channel from east (right) by transport landward of weir jetty, Jul 06

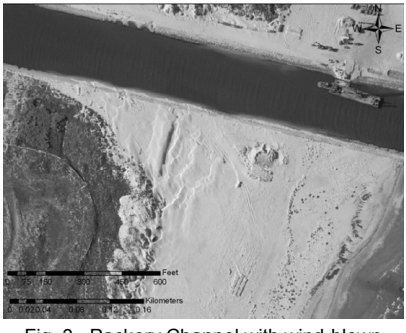

Fig. 3. Packery Channel with wind-blown sand covering the south (lower) jetty, Aug 06

Astronomical tide along the Texas coast is predominantly diurnal from Galveston to Sabine and fully diurnal from about Matagorda Bay to the Rio Grande. Gulf of Mexico tide range on this coast is on order of 0.6 m. Astronomical tide in the bays and lagoons is diurnal, and its range is considerably less than that of the open coast. Some large water bodies, such as Baffin Bay, are considered non-tidal by the National Ocean Service (tide range less than about 0.05 m), and others such as at Port Mansfield are marginally tidal.

In the bays and Texas along the coast, water level extremes and currents through inlets are controlled more by wind and seasonal variations than by astronomical tide. For example, Kraus and Militello (1999) report water level at two stations at the eastern (EMAT) and southwestern (SWEMAT) ends of the major axis of East Matagorda Bay from 7 Sep 1995 to 8 Feb1996 relative to Mean Lower Low Water (MLLW) (Fig. 4). The astronomical tide range in this bay is 0.1 m. The measurements show an almost 0.6-m tilt in water level over the 32 km between gauges during one strong northeast front with wind speed of 12 m/s, with a 0.2 to 0.3-m tilt being common during frontal passages. The bay is 37 km long, and typical depths are in the range of 0.6 to 1.2 m.

On the Texas coast, seasonal highs occur around May and October, and seasonal lows occur around August and December-January (Fig. 5). The seasonal range is about 0.2-0.3 m, which is comparable to or exceeds the tide range in many Texas bays and lagoons.

Figure 5 plots monthly water level for open coast tide gauges (Galveston, Bob Hall Pier at Corpus Christi; and bay gauges (Rawlings at Mouth of Colorado River; Lavaca, and Port Isabel in the lower Laguna Madre) for year 1999. Barge operators and others involved with inlet and coastal waterway navigation are aware of the seasonal highs and lows, and their possible benefit or impediment, respectively, to vessel transit.

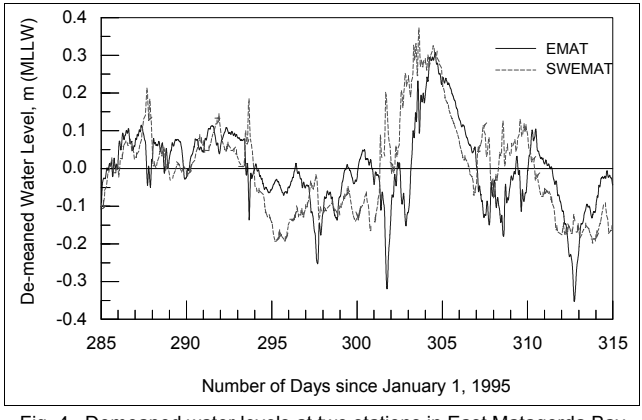

Fig. 4. Demeaned water levels at two stations in East Matagorda Bay

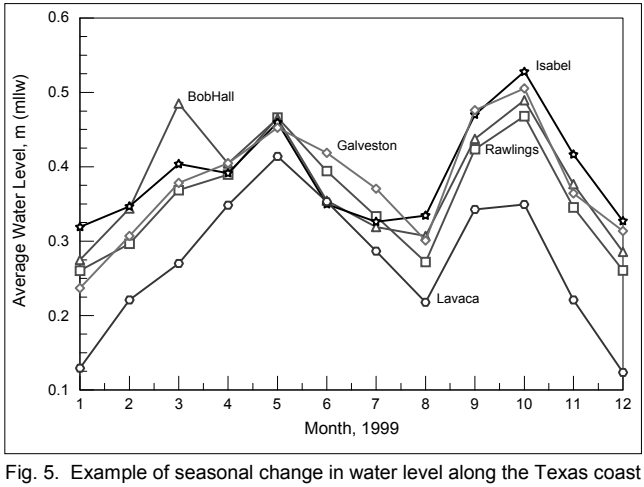

Fig. 5. Example of seasonal change in water level along the Texas coast

Strong wind from the north or northeast can overcome the astronomical tide in forcing water through Texas inlets, as shown in Fig. 6, based on measurements of the current, water level, and sustained wind from north at Packery Channel (Williams et al. 2007). Behrens (1979) explains how the strong wind from the southeast can enhance the flood current through inlets and strong wind from the north or northeast can enhance the ebb

current. For such reasons, Price (1952) noted that funnel-shaped inlets in the southwest corners of bays on the upper Texas coast or in the southeast corners of bays on the lower Texas coast tend to be the natural and stable inlets to the bays. Pass Cavallo in Matagorda Bay is such a southwest corner inlet, remaining open despite capture of much of the tidal prism by cutting of the Matagorda Ship Channel in 1966 (Kraus et al. 2006; Batten et al. 2007). Because wind tide and seasonal lows can dominate astronomical tide, the USACE Galveston District has defined a navigation datum called Mean Low Tide that is specific to location and lies below MLLW (Kraus et al. 1997). Seasonal lows in water level make marginally stable small inlets prone to closure.

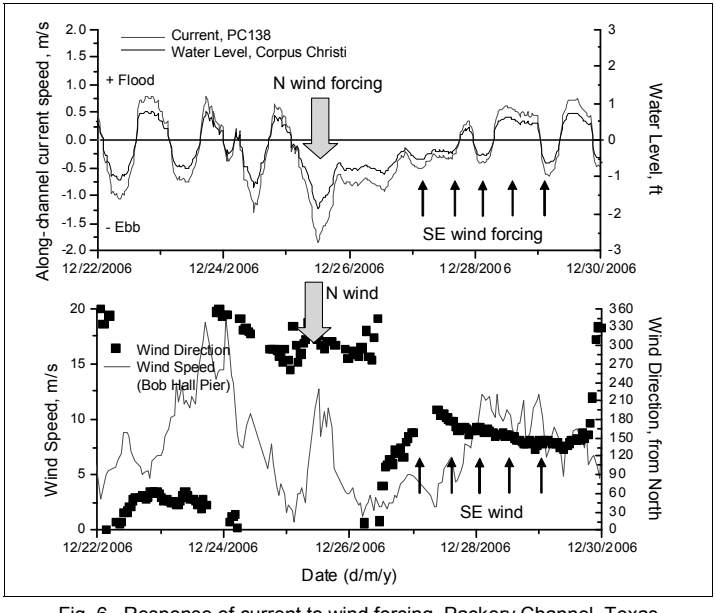

Fig. 6. Response of current to wind forcing, Packery Channel, Texas (from Williams et al. 2007)

TEXAS INLET STABILITY

Implications of Diurnal Tide

It is empirically known that a cross-sectionally stable inlet located on a sandy coast tends to have a mean-maximum velocity through it of approximately 1 m/s (Escoffier 1940; Bruun 1968). By "mean-maximum velocity" is meant the average of a regularly occurring maximum velocity, such as would occur on spring tide. If it is assumed that the discharge is solely related to the tidal prism and that there is a sinusoidal tide with one component, the maximum discharge D_m and tidal prism P can be related as:

$$P = \int_0^{T/2} D_m \sin\left(\frac{2\pi}{T} t\right) dt \tag{1}$$

where T is the tidal period, and t is time. The integration yields:

$$D_m = \frac{\pi}{T} P \tag{2}$$

Tidal prism is defined as the volume of water exchanged between an estuary or lagoon and the open sea during one tidal period (between high to low tide in the bay, giving an ebb-tidal prism, or between low to high tide in the bay, giving a flood-tidal prism). Therefore, the integration limit in Eq. 1 is taken to be $T/2$. Tidal prism can also be calculated as the product of the effective bay surface area served by the subject inlet times the tidal range, or from a computation of water discharge, as through a numerical model. By definition of a discharge, the mean-maximum velocity V_{mm} is:

$$V_{mm} = \frac{D_m}{A_C} \tag{3}$$

in which A_C is the minimum inlet channel cross-sectional area at mean sea level (msl).

Although refinements have been made in empirical predictive equations relating A_C and P, it is convenient for present discussion to consider the linear relation found by O'Brien (1969), based in part on analysis of inlets without jetties:

$$A_C = C\,P \tag{4}$$

where A_C is expressed in m^2, P is expressed in m^3, and $C = 6.6 \times 10^{-5}$ with units m^{-1}. The original units of this equation in feet were converted to metric units for the present work. Kraus (1998) derived a form of Eq. 4 by consideration of a balance of sand transport by the inlet channel-clearing current and the channel infilling by the longshore transport. This equation was also expressed directly in terms of water discharge through the inlet, in addition to tidal prism.

Substitution of Eq. 2 and Eq. 4 into Eq. 3 gives (O'Brien 1969):

$$V_{mm} = \frac{\pi}{CT} \tag{5}$$

For a semi-diurnal inlet, T = 12 hr, 25 min = 44,712 s. Then, Eq. 5 yields V_{mm} = 1.06 m/s, in agreement with empirical observations. For a tide that is primarily diurnal, the tidal period is 89,424 s, giving V_{mm} = 0.53 m/s. The conclusion is that an inlet in a diurnal tidal setting may require a smaller mean-maximum tidal velocity to maintain channel cross-sectional area stability as compared to inlets in a semi-diurnal setting, the more common type of inlet. The Texas coast is an ideal site to explore such a possibility, although the wind tide is expected to take as much a role as the astronomical tide in controlling stability of inlets on the Texas coast.

Implications of Wind Tide – Simple Model for Multiple Tidal Inlets

In this section, the consequence to the current of a wind tide is explored with a simple mathematical model of a bay with two inlets, and model parameters correspond to a bay similar to East Matagorda Bay. The model is a slight extension of a Keulegan bay

approach as discussed in Chapter 13 of Dean and Dalrymple (2002). Following their notation, we define:

$$F = K_{en} + K_{ex} + \frac{f\,L}{4R_H} \tag{6}$$

where K_{en} and K_{ex} = inlet entrance and exit loss coefficients (typically specified as 0.3 and 1.0, respectively), f = Darcy-Weisbach friction coefficient, L = effective length of inlet, and R_H = hydraulic radius of a rectangular cross-section inlet of depth h. Then, the equations of motion are, for two inlets serving the same bay:

$$\frac{dU_i}{dt} = -\frac{g}{L_i}\left(\eta_B - \eta_O \pm \delta\right) - \frac{F_i}{2\,L_i}\left|U_i\right|U_i \tag{7}$$

and

$$\frac{d\eta_B}{dt} = \frac{1}{A_B}\left(A_{C1}U_1 + A_{C2}U_2\right) + \frac{D}{A_B} \tag{8}$$

where U_i = velocity of inlet i = 1 or 2, t = time, g = acceleration of gravity (9.8 m/s^2), η_B = water-surface elevation of bay, η_O = water surface elevation of ocean (Gulf of Mexico in this paper), δ = tilt in water surface elevation across a bay as caused by wind, A_C = inlet cross-sectional area below mean sea level, A_B = surface area of bay, and D = discharge into the bay, as from a river. D was set to zero in this paper. The inlets are assumed to be located at the opposite ends of the bay, and the water level in the entire bay responds to each inlet. Other assumptions of a Keulegan bay apply.

The model formulation is similar to that of Seelig and Sorensen (1978), who included advective acceleration, omitted here, but did not include wind forcing. In a process-based model, the change in elevation by wind and associated current can be calculated by applying wind shear to the water surface, such as done for East Matagorda Bay by Kraus and Militello (1999) and described analytically by Kraus and Militello (2001), demonstrating that the tilt in water surface by wind blowing on a shallow bay is almost linear. The water surface responds rapidly to wind shear, and Kraus and Militello (1999) found it necessary to force the hydrodynamic model with 6-min averages of wind speed rather than 1-hr averages to obtain best agreement of the calculated water level and current with measurements. Here, the quantity δ describes the tilt directly and must be specified. A Matlab program was written to solve Eq. 7 and Eq. 8 in time-marching manner, and the results were checked against the Keulegan (1967) solution that neglects the acceleration term in Eq. 7 and water surface tilt.

The above simple model for a dual-inlet bay system was operated to explore the action of strong wind on a dual inlet. The example here pertains to a bay with surface area of $2\text{x}10^8$ m^2; primary inlet (denoted by subscript 1) of depth 3 m, width 300 m, and length 1,600 m; secondary inlet (denoted by subscript 2) on other side of bay of depth 1 m, width 50 m, and length 1,000 m; ocean forcing amplitude of 0.3 m (corresponding to a tidal range of 0.6 m) and sinusoidal diurnal tidal period of 89,424 s; and friction

coefficient $f = 0.06$. This arrangement roughly describes East Matagorda Bay, with the primary inlet being Mitchells Cut and the secondary inlet being the proposed SW Corner Cut as a narrow, shallow channel through marsh. The cross-sectional area of Inlet 1 is 18 times larger than that of Inlet 2, so the discharge is correspondingly larger.

The situation calculated with only tidal amplitude forcing is shown in Figs. 7 and 8. The figures are plotted for a time interval past the ramp of the solution and cover one diurnal tidal period starting with phase 0 for the Gulf water level forcing. Due to relatively strong friction in long and shallow inlets, the water level in the bay lags the Gulf of Mexico water level substantially and is greatly reduced in range. The current velocity is greater in Inlet 1, as expected, because of its greater depth. Although the tidal forcing is sinusoidal, the non-linear friction terms in Eq. 7 distorts the inlet current velocity. Positive directed current denotes flood, and negative denotes ebb.

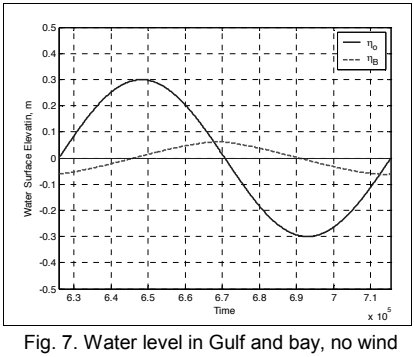

Fig. 7. Water level in Gulf and bay, no wind

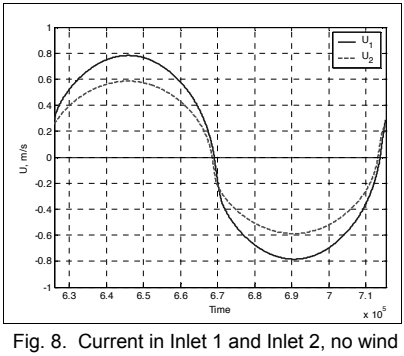

Fig. 8. Current in Inlet 1 and Inlet 2, no wind

The solution for a strong wind blowing such that the water surface is tilted upward 0.2 m toward Inlet 2 and downward 0.2 m at Inlet 1 is summarized in Figs. 9 and 10. In this situation, water can flow from the Gulf through the more efficient Inlet 1 of larger cross-sectional channel area, raising water level in the bay. The current through Inlet 2 increases greatly toward ebb, with the tidal flood current shown in Fig. 8 overcome by the wind tide to cause variable, but complete ebb flow through the tidal period (Fig. 10). The ebb current through the larger Inlet 1 is slightly reduced. The current through Inlet 2 is more distorted, with a longer duration during the latter portion of the tidal cycle.

The solution for a strong wind blowing such that the water surface is tilted upward 0.2 m toward Inlet 1 and downward 0.2 m at Inlet 2 is summarized in Figs. 11 and 12. In this situation, water can flow out of the bay and into the Gulf through the more efficient Inlet 1, lowering water level in the bay. The current through Inlet 2 increases greatly toward flood, with the tidal flood current shown in Fig. 8 overcome by the wind tide to cause variable, but complete flood flow through the tidal period (Fig. 12). The flood current through larger Inlet 1 is slightly reduced. The current through Inlet 2 is more distorted, with a longer duration during the initial portion of the tidal cycle.

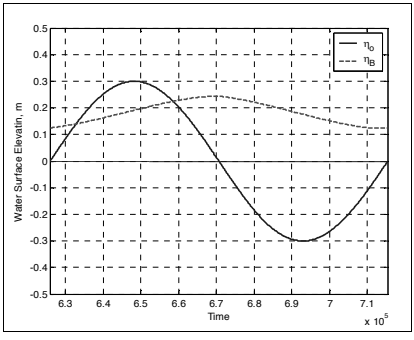

Fig. 9. Water level in Gulf and bay, water surface tilted upward toward Inlet 2

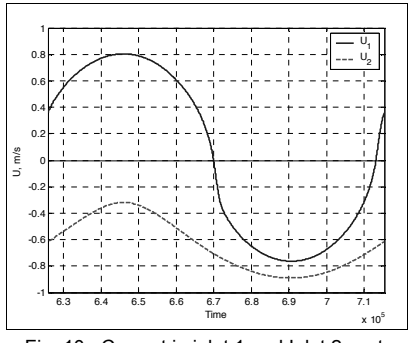

Fig. 10. Current in inlet 1 and Inlet 2, water surface tilted upward toward inlet 2

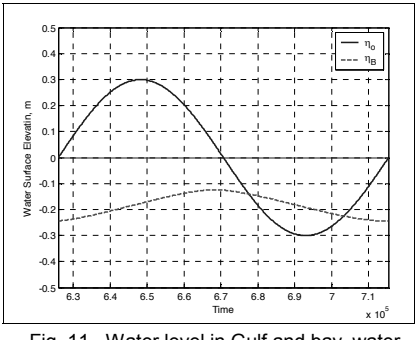

Fig. 11. Water level in Gulf and bay, water surface tilted upward toward Inlet 1

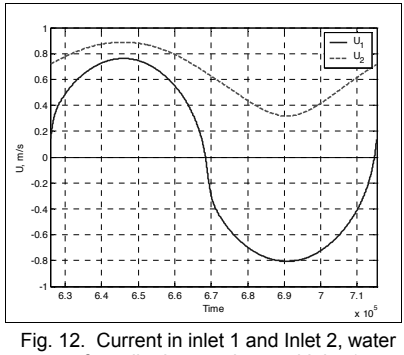

Fig. 12. Current in inlet 1 and Inlet 2, water surface tilted upward toward Inlet 1

CONCLUDING DISCUSSION

As is known to coastal engineers and scientists working along the Texas coast, as well as to ship pilots, barge operators, and fishing boat operators who transit its inlets and inland coastal waters, the water level in bays and current velocity through Texas coastal inlets are strongly influenced by wind and seasonal change in Gulf of Mexico water level. Both wind tide and seasonal change in water level can exceed astronomical tide range in Texas bays and lagoons. As a result, stability of Texas inlets is strongly controlled by wind. Because the wind tide can control the magnitude of the ebb (or flood) current, inlet area-tidal prism relations alone should be applied with caution. In a future paper, the author plans to introduce a formalism that accounts for wind tide in inlet stability analysis.

Intrusion of wind-blown sand into inlet channels is another and significant factor controlling stability of smaller inlets in Texas. The situation of the Colorado River Mouth (Fig. 2) demonstrates that longshore sand transport in the swash zone and wind-blown sand can greatly constrict an inlet channel.

Finally, the diurnal tide experienced on the Texas coast suggests that a smaller maximum current may be sufficient to maintain stability as compared to the more common semi-diurnal inlet. This potential behavior, together with wind tide, acts in favor of inlet stability on the Texas coast. At present, numerical modeling technology allows accurate representation of inlet hydrodynamics involving all water forcing, multiple inlets to the bays, rivers, and inter-bay connecting waterways, as has been demonstrated for the Texas coast (Brown et al. 2003). The challenge remaining is to reliably estimate sediment transport and morphology change at coastal inlets.

ACKNOWLEDGEMENTS

This paper was generated as an activity of the U.S. Army Corps of Engineers (USACE), Coastal Inlets Research Program. Support of inlet studies along the Texas coast over the years by the U.S. Army Engineer District, Galveston, is gratefully acknowledged. Discussions with Ms. Deidre Williams at TAMU-Corpus Christ are appreciated. Dr. Magnus Larson and Julie Dean Rosati provided helpful reviews of the first draft of this paper. Permission was granted by Headquarters, USACE, to publish this information.

REFERENCES

Bales, J.D., and Holley, E.R. (1989). "Sand transport in Texas tidal inlet," *J. Waterway, Port, Coastal, and Ocean Eng*. 115(4), 427-443.

Batten, B.K., Kraus, N.C., and Lin, L. (2007). "Long-term inlet stability of a multiple inlet system, Pass Cavallo, Texas," *Proc. Coastal Sediments '07*, ASCE, in press.

Behrens, E.W. (1979). "New Corpus Christi Pass, a Texas tidal inlet," *Shore & Beach* 47(4), 9-14.

Brown, M.E., Kraus, N.C., and Kieslich, J.M. (2003). "Regional circulation modeling of the Texas coast and inland coastal waters," *Proc. of 8th Estuarine and Coastal Modeling Conf.*, ASCE, 192-214.

Bruun, P. (1968). "*Tidal inlets and littoral drift*," Univ. Book Co., Oslo, Norway.

Carothers, H. P., and Innis, H. C. (1960). "Design of inlets for Texas coastal fisheries," *J. Waterways and Harbors Div.* 127(IV), 231-259.

Dean, R.G., and Dalrymple, R.A. (2002). "*Coastal Processes with Engineering Applications*," Cambridge U. Press, 475 p.

Escoffier, F.F. (1940). "The stability of tidal inlets," *Shore and Beach*, 8(4), 114-115.

Hansen, E.A. (1960). "Studies of channel through Padre Island, Texas," *J. Waterways and Harbors Div*. WW(3), 63-82.

Hayes, M.O. (1965). "Sedimentation on a semiarid, wave-dominated coast (South Texas) with emphasis on hurricane effects," Ph.D. Diss., U. of Texas at Austin, Austin, Texas, 351 p.

Heilman, D.J., and Edge, B.E. (1996). "Interaction of the Colorado River Project, Texas, with longshore sediment transport," *Proc. 25th Coastal Eng. Conf.,* ASCE, 3309-3322.

Keulegan, G.H. (1967). "Tidal flows in entrances: Water level fluctuations of basins in communication with seas," TB-14, Committee on Tidal Hydraulics, U.S. Army Engineer Waterways Experiment Station, Vicksburg, MS.

Kieslich, J.M. (1977). "A case history of Port Mansfield Channel, Texas," GITI Report 12, U.S. Army Coastal Engineering Research Center, Vicksburg, MS, 66 p.

Kraus, N.C. (1998). "Inlet cross-sectional area calculated by process-based model," *Proc. 26th Coastal Eng. Conf.*, ASCE, 3,265- 3,278.

Kraus, N.C. (2006). "Coastal inlet functional design: Anticipating morphologic response," *Proc. Coasta Dyanmics' 05*, CDROM, ASCE, 14 p.

Kraus, N.C., and Heilman, D.J. (1997). "Packery Channel feasibility study: Inlet functional design and sand management. Report 1 of a two-part series," TR TAMU-CC-CBI-96-06, Conrad Blucher Inst. for Surveying and Science, TAMU-Corpus Christi, Corpus Christi, TX.

Kraus, N.C., Lin, L., Batten, B.K., and Brown, G.L. (2006). "Matagorda Ship Channel, Texas: Jetty stability study," TR ERDC.CHL-06-7, U.S. Army Engineer Research and Development Center, Coastal and Hydraulics Laboratory, Vicksburg, MS, 153 p.

Kraus, N.C., and Militello, A. (1999). "Hydraulic study of multiple inlet system: East Matagorda Bay, Texas." *J. Hydraulic Res.* 125(3), 224-232.

Kraus, N.C., and Militello, A. (2001). "Analytical solution of one-dimensional bay forced by sea breeze," *Proc. Waves' 01 Conf.*, ASCE, 1,644-1,653.

Kraus, N.C., Thurlow, C.I., Heilman, D.J., Lindquist, A., and Earle, M.W. (1997). "Needs assessment for water level gauging along the Texas coast for the U.S. Army Corps of Engineers, Galveston District," TR CHL-97-29, U.S. Army Engineer Waterways Experiment Station, Vicksburg, MS.

Lin, L., Kraus, N.C., and Robinson, L.L. (2003). "Reduction of unanticipated Intracoastal Waterway current by relocating the San Bernard River Mouth, Texas," *Proc. Dredging '02,* ASCE, on CD ROM.

Lockwood & Andrews. (1952). "Proposed alterations and improvements, Yarbrough Fish Pass, Padre Island, Texas," Prepared for Game and Fish Commission, State of Texas, 37 p plus fold-out maps and drawings.

Mason, C.C., and Sorensen, R.M. (1971). "Properties and stability of a Texas barrier beach inlet," TAMU-SG-71-217, COE No. 146, Departments of Oceanography and Civil Engineering, TAMU, College Station, TX.

Morton, R. A. (1977). "Nearshore changes at jettied inlets, Texas coast," *Proc. Coastal Sediments 77*, ASCE, 267-286.

O'Brien, M.P. (1969). "Equilibrium flow areas of inlets on sandy coasts," *J. Waterways and Harbors Div*. 95(WW1),43-52.

Price, W.A. (1952). "Reduction of maintenance by proper orientation of ship channels through tidal inlets," *Proc. 2nd Coastal Eng. Conf.*, Council on Wave Research, 243-255.

Seelig, W.N., and Sorensen, R.M. (1978). "Numerical model investigation of slected tidal inlet-bay system characteristics," *Proc. 16th Coastal Eng. Conf*, ASCE, 1,302-1,319.

Shepsis, V., and Carter, J. (2007). " Cedar Bayou – Inlet dynamics and engineering," *Proc. Coastal Sediments '07*, ASCE Press, in press.

Simmons, E.G., and Hoese, H.D. (1959). "Studies on the hydrography and fish migrations of Cedar Bayou, a natural tidal inlet on the central Texas coast," *Publication Institute of Marine Sciences* 6, The Unversity of Texas, 56-80.

U.S. Army Corps of Engineers (USACE). (1992). "Inlets along the Texas coast," Planning Assistance to the States Program, Section 22, U.S. Army Engineer District, Galveston, Galveston, TX, 56 p.

Watson, R.L. (1971). "Origin of shell beaches, Padre Island, Texas," *J. Sed. Pet.*, 41 (4), 1,105-1,111.

Williams, D.D., Kraus, N.C., and Anderson, C.M. (2007). "Morphologic response to a new inlet, Packery Channel, Corpus Christi, Texas," *Proc. Coastal Sediments '07*, ASCE, in press.

CEDAR BAYOU – INLET DYNAMICS AND ENGINEERING

Vladimir Shepsis[1], Joshua Carter[2]

1. Coast & Harbor Engineering, Inc., 110 Main Street, Suite 103, Edmonds, WA 98020, USA. vladimir@coastharboreng.com
2. Coast & Harbor Engineering, Inc., 3410 Far West Blvd, Suite 210, Austin, TX 78704, USA. josh@coastharboreng.com

ABSTRACT

The paper presents results of a study conducted to identify the feasibility of restoring Cedar Bayou Inlet – a natural fish passage in the Texas Coastal Bend – to its historical, open conditions. The study included historical and new field data collection, empirical analysis, and numerical modeling as well as development and analysis of engineering alternatives. Through analysis and modeling, the connection between Cedar Bayou and Vinson Slough (an adjacent 22,000 acre wetland) was found to be a critical element in maintaining both inlets in an open condition. The primary element of the proposed engineering solution is the reconstruction of the historical connection between Vinson Slough and Cedar Bayou by opening the main channel through dredging. In addition, the dredged material is proposed be used beneficially to re-construction a submerged ebb shoal offshore of the mouth of the Cedar Bayou inlet, which promotes sediment bypassing of the inlet mouth and reduces channel sedimentation.

INTRODUCTION

Cedar Bayou is a natural inlet approximately 3 miles in length that provides a connection between the Gulf of Mexico and several bays in the Texas Coastal Bend Bay System, including Mesquite Bay, San Antonio Bay, Aransas Bay, and others. Figure 1 shows the Cedar Bayou vicinity based on a 1995 DOQQ aerial photo.

The Gulf of Mexico shoreline at the Cedar Bayou outlet is oriented from NE (45º) to SW (225º) and is composed of uniform, well sorted medium to fine sand, with a medium grain size diameter of 0.13 to 0.17mm. The bayward (northern) 2 miles of the Bayou are historically stable, with an average width of 590 ft and an average depth of 6.5 ft below Mean Sea Level (MSL). The seaward (southern) 1 mile of the

Bayou is much more dynamic. The widths and depths of this part of the Bayou vary at present from 570 ft to 30 ft wide, and from 8 ft to just inches deep.

Cedar Bayou, when open, provides a life cycle tidal route for biological resources of the Texas Coastal Bend bay system. During the last several decades, due to natural processes and various engineering activities, the flow through Cedar Bayou has diminished to a level that has affected the biological resources of the Texas Coastal Bend Bay system. A study has been initiated by the Texas General Land Office Coastal Erosion Planning and Response Act Program and Save Cedar Bayou, Inc. to determine the feasibility of restoring Cedar Bayou to its historical, open conditions. The study included historical and new field data collection, analysis and numerical modeling, and development and analysis of engineering alternatives for restoration of the Bayou.

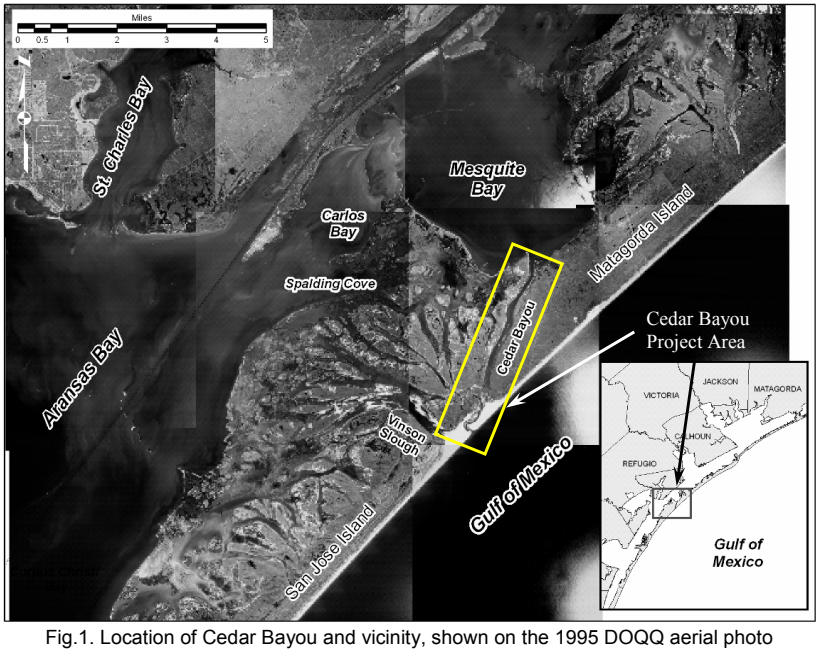

Fig.1. Location of Cedar Bayou and vicinity, shown on the 1995 DOQQ aerial photo

HISTORICAL INLET DYNAMICS

Limited literature exists that discusses the hydraulics of Cedar Bayou; references identified include Lockwood and Andrews (1953) and Simmons and Hoese (1959). This section discusses the inlet dynamics described in the existing literature and through analysis of available historical data.

Throughout the recorded history of Cedar Bayou from the mid 1800's to present time, Cedar Bayou's connection to the Gulf of Mexico has been described as "open" or

"closed". Historical maps as early as 1836 to 1927 show Cedar Bayou to be open, wide, and very shallow (Simmons and Hoese 1959). Figure 2 examines the time history of the opening and closing of Cedar Bayou based on available historical information, along with dredging events and major hurricanes that likely impacted the Bayou. Based on available maps, charts, and photos, Cedar Bayou has also maintained a connection to Vinson Slough, an adjacent 22,000 acre marsh system, and delivers Gulf water to an extensive marsh system and wetlands in Mesquite Bay.

Cedar Bayou has been dredged four times: 1939 (est. 200,000 cy), 1959 (est. 1 million cy), 1987 (est. 300,000 cy), and 1995 (est. 300,000 cy) with varying levels of success in regard to long-term stability of Cedar Bayou. During the most recent dredging in 1995, the dredged material from Cedar Bayou was placed across the mouth of Vinson Slough. The slough has been plugged and no direct connection between Vinson Slough and Cedar Bayou or Vinson Slough and the Gulf of Mexico have existed since.

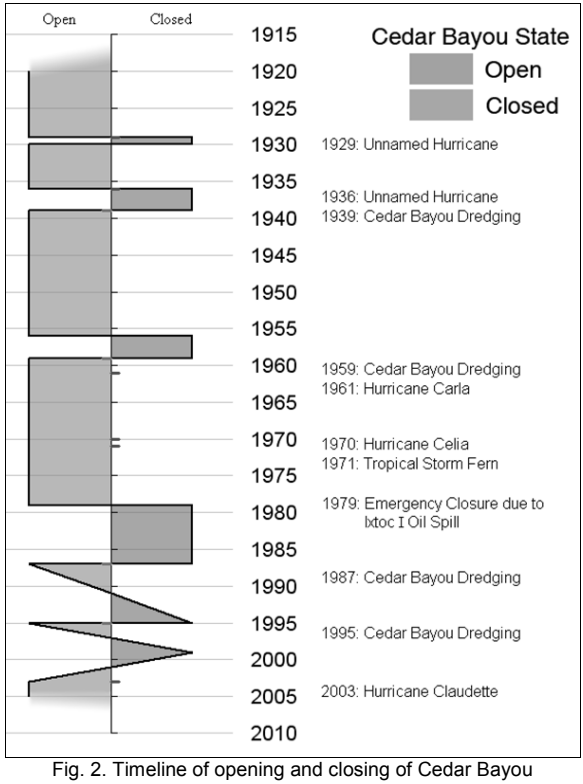

Fig. 2. Timeline of opening and closing of Cedar Bayou

The geomorphology of Cedar Bayou was investigated through a comparison of historical aerial photographs for the period from 1950 to 2003. Figure 3 is an example of the dataset of aerial photographs; it shows six aerial photos of the Cedar Bayou migration zone (the migration zone is the zone through which the Gulf mouth of Cedar Bayou has historically migrated) from 1953, 1973, 1984, 1987, 2001, and 2003. Analysis of photographs revealed that Cedar Bayou migrates from northeast to southwest, with the southwest boundary of migration at Vinson Slough. The Cedar Bayou – Vinson Slough connection typically occurs just upstream from flowing to the Gulf, although the point of connection migrates. Based on a review of aerial photographs, it appears that the Cedar Bayou – Vinson Slough hydraulic system is most stable when there is a substantial connection between the two channels. In addition, the inlet is maintained open for a longer period of time when Cedar Bayou and Vinson Slough are connected with a hydraulic connection with an area on the order of magnitude of the connection between Cedar Bayou and the Gulf of Mexico.

A potential explanation of this phenomenon relies on the hydraulic characteristics of the Cedar Bayou system. When connected to Cedar Bayou, Vinson Slough increases the total volume of flow through Cedar Bayou, which stimulates a higher flow gradient, and respectively, the flow velocities at the mouth of Cedar Bayou. It is likely that disconnecting Cedar Bayou from Vinson Slough (as occurred during the 1987 and 1995 dredging) has resulted in a reduction of the total volumetric flow at the mouth of Cedar Bayou. Consequently, flow velocities have diminished, and the ability of Cedar Bayou to maintain an open condition has decreased.

The ability of Vinson Slough to enhance the flow velocities in Cedar Bayou and increase self-maintaining capability was used as one of the major hypotheses of the project. Based on this hypothesis, the primary component of the engineering solution to restore Cedar Bay was developed to include reconnecting Cedar Bayou and Vinson Slough. Through testing with numerical modeling (as described below), the hypothesis still requires verification with field data because of the project's unique conditions. Therefore, the results of the engineering study and design include a recommendation for monitoring and adaptive management of the project after construction occurs.

The second hypothesis used for the study is that a construction of an ebb shoal offshore of the inlet mouth will promote sediment bypassing and reduce sedimentation in the Cedar Bayou inlet mouth. This hypothesis assisted with development of an engineering solution for disposal of the dredged material. This beneficial use solves the problem of sediment disposal and also adds benefit to the project's performance. The shoal will cause increased wave breaking on its seaward slope, and redirect longshore sediment transport along its seaward side. This would result in the bypassing of longshore sediment transport seaward of the mouth of Cedar Bayou, which would lead to a reduction of the sedimentation effect at Cedar Bayou and increase its longevity. Though not shown on historical hydrographic survey data, the existence of the ebb shoal in front of Cedar Bayou in the past (in the 1960s and 70s) was indicated by local residents and fishermen (Edwards 2006).

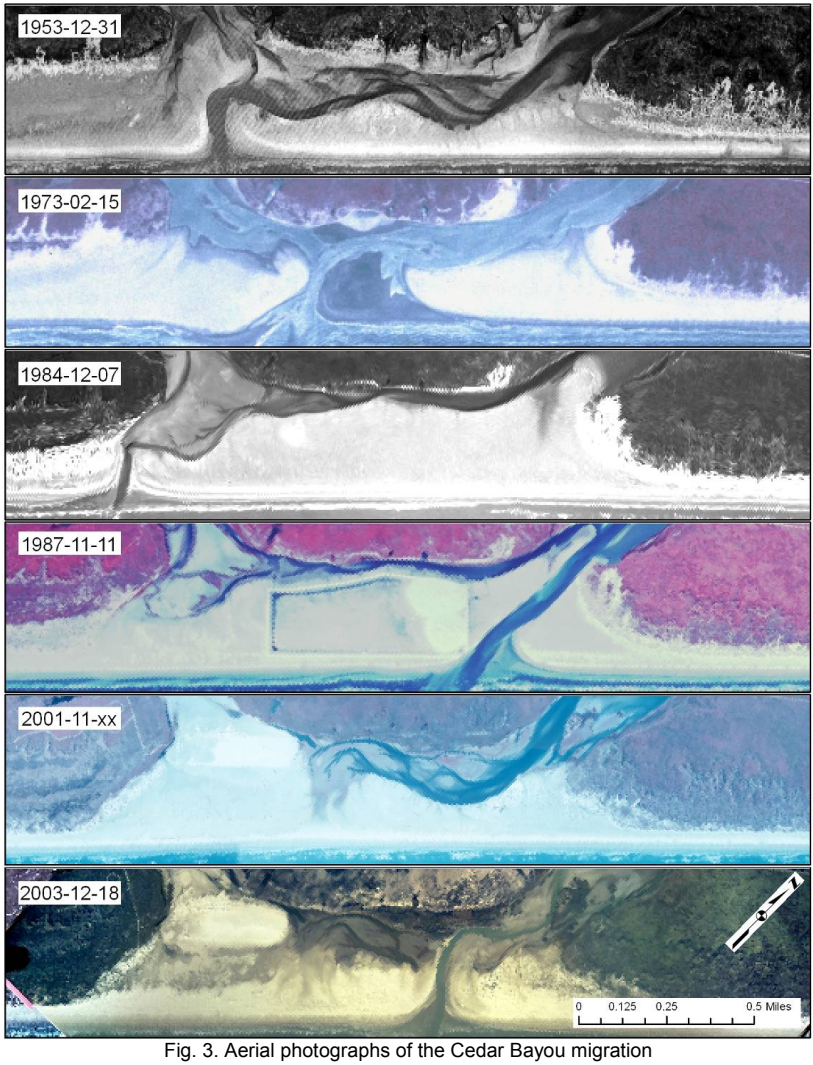

Fig. 3. Aerial photographs of the Cedar Bayou migration zone at the Gulf mouth of Cedar Bayou and Vinson Slough

ALTERNATIVES DEVELOPMENT AND ANALYSIS

The essential components of the Cedar Bayou Restoration Project solution were developed based on the two hypotheses described above. This included beneficial use of dredged material from Cedar Bayou and Vinson Slough for restoration of historical submerged ebb shoal. The restoration of the ebb shoal was proposed by creating a

source of sediment in the littoral zone in anticipation that this sediment will naturally form a submerged shoal in front of Cedar Bayou. The ebb shoal hypothesis was tested and supported through numerical modeling. Further, both of these hypotheses will be verified with field data during the post-construction monitoring program.

A set of various alternatives were developed to restore the Cedar Bayou hydraulic conditions and provide long-term opening of the inlet. These alternatives included various configurations of dredging channels between Cedar Bayou, Vinson Slough, and the Gulf of Mexico in conjunction with restoration of the submerged ebb shoal offshore of the mouth of Cedar Bayou. The most promising alternative, shown in Figure 4, was selected for detailed analysis and engineering. The alternative included dredging a straight Cedar Bayou connection to the Gulf, connection to Vinson Slough, and reconstruction of the submerged ebb shoal with dredged material. The alternative is plotted on the 2004 aerial photograph, and bathymetry is based on 2005 survey data.

Existing (pre-project conditions) are shown in Figure 5 using the same aerial photograph and bathymetric survey data. Note the large mound (red color) on the figure, which depicts the plug in Vinson Slough constructed from dredged material disposal during the 1995 dredging event.



Fig. 4. Layout of the mouth of Cedar Bayou for Alternative 1b, overlaid on the 2004 aerial photo

The evaluation of the proposed solution including testing the hypotheses and engineering design were based on two approaches: hydrodynamic numerical modeling and fitting to morphological analysis criterion. The numerical modeling was conducted to determine the flow discharge through the inlet for existing conditions and for the post-project conditions for various dredging cuts and ebb shoal dimensions. The numerical modeling was fit to the morphologic criterion in order to determine the stability of the inlet and ebb shoal for existing and post-project conditions.

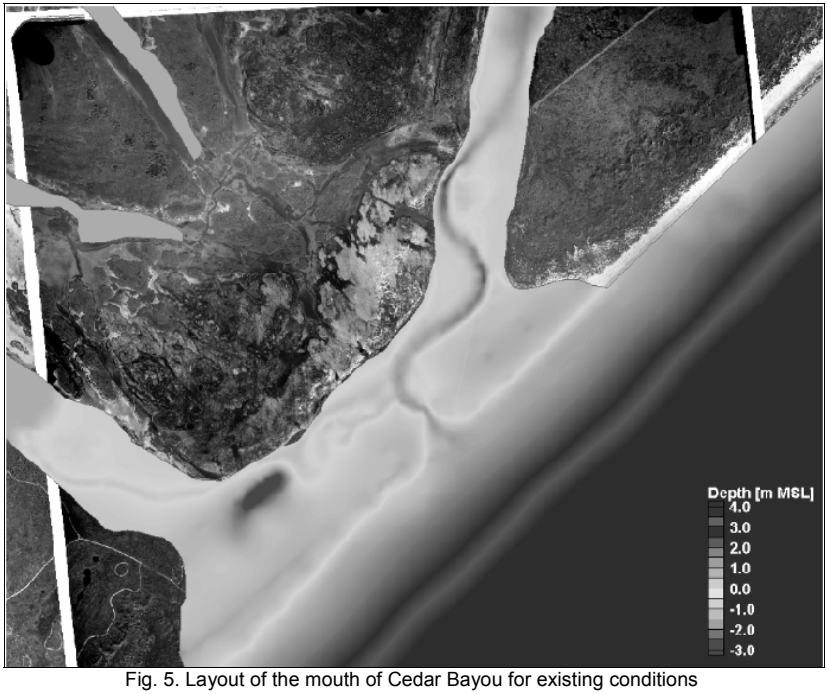

Fig. 5. Layout of the mouth of Cedar Bayou for existing conditions

The numerical modeling included tidal flow circulation and wave transformation modeling. Tidal flow circulation modeling was used to evaluate inlet channel dimensions and effectiveness. Wave modeling was performed to evaluate wave interaction with the inlet mouth. The input parameters were developed for the modeling, tidal range, wind, waves, and modeling grid, and are briefly discussed below.

The tidal range on the Bay side and Gulf side in the Cedar Bayou vicinity was determined by performing a harmonic analysis on the available long-term measuring stations, Bob Hall Pier and Rockport stations (TCOON 2006). The analysis results indicated that the average tidal range on both the Bay side and Gulf side of Cedar

Bayou is approximately 1.5ft. However, during extreme events this tidal range can be as much as 3-3.5ft.

The hindcast deepwater waves from Wave Information Study (WIS) were used for statistical analysis and to develop return periods of deepwater wave heights (WIS, 2006). An example of the extremal return period analysis is shown in Table 1.

Table 1. Extremal analysis of wave heights and corresponding periods for WIS Station 46

Return Period [years]	Significant Wave Height [ft]	Significant Wave Height [m]	Wave Period [sec]
2	14.0	4.3	11.2
5	16.3	5.0	12.3
10	17.5	5.3	13.0
20	18.9	5.8	13.7
50	20.6	6.3	14.6

Tidal flow modeling was performed using the two-dimensional Advanced Circulation Model ADCIRC (Luettich et al. 1992). ADCIRC simulates depth-averaged current velocities and water level fluctuations forced by tidal fluctuations at the boundaries of the modeling domain, and wind inputs over the entire modeling domain. The model domain was constructed extending 100 miles offshore (to the south), approximately 60 miles northeast, and 80 miles to the southwest (far from the project site to avoid boundary effects on the modeling results). The finite element mesh modeling domain is shown in Figure 6 for the entire domain (a) and in the project vicinity (b).

Tidal flow circulation modeling results were used to determine the change of the velocity and flow in Cedar Bayou. Figure 7 shows the velocity vectors at maximum ebb flow for both the existing and post-project (Alternative 1b) conditions. The maximum discharge velocities are increased from about 0.8 m/sec to more than 1.2 m/sec for post-project conditions.

Figure 8 shows the flow discharge across a cross-section in upper Cedar Bayou,near the discharge point from Cedar Bayou into Mesquite Bay. The figure shows the volumetric flow rate over 7 days of modeling with and without project conditions. Results indicate that construction of the project would increase flow by about a factor of 3, and greatly enhance the ebb flow rate through the pass. This increase in ebb flow is critical to the success of the project, as the ebb flow helps flush sediments out of the mouth and maintain a sufficient depth.

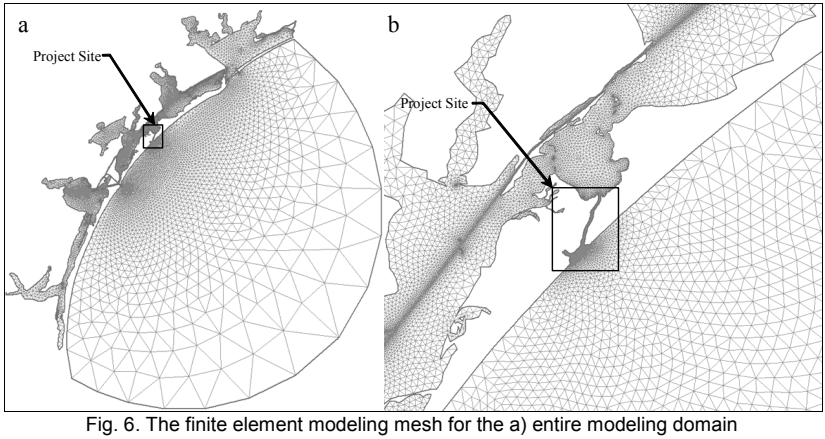

Fig. 6. The finite element modeling mesh for the a) entire modeling domain and b) near the project site

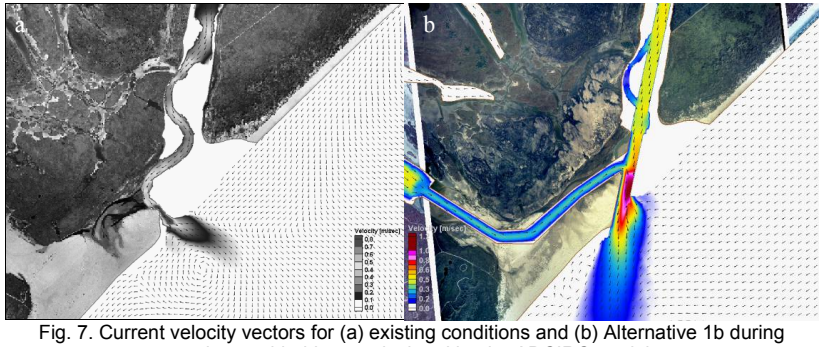

Fig. 7. Current velocity vectors for (a) existing conditions and (b) Alternative 1b during maximum ebb tide as calculated by the ADCIRC model.

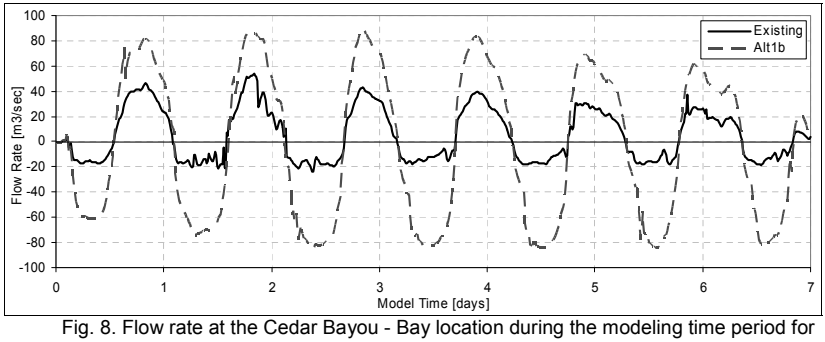

Fig. 8. Flow rate at the Cedar Bayou - Bay location during the modeling time period for the existing conditions and alternative 1b. Positive values are flood flow and negative values are ebb flow.

Wave transformation modeling was conducted to determine the effects from the ebb shoal on wave attenuation in the vicinity of the project. Wave transformation modeling was conducted using the two-dimensional model SWAN (Holthuijsen et al. 1993) and the two-dimensional model Bouss-2D (Nwogu 2001). The results of the wave modeling for a storm event with a 2-year return period showed that the wave heights at the shoreline were reduced 60% to 70% as a result of the ebb shoal construction. Details of the wave modeling analysis of the ebb shoal are available in Coast & Harbor Engineering (2007).

Fitting the project to morphologic criteria included determining inlet stability criterion and balancing the volume of the ebb shoal to the tidal flow rate through the new Cedar Bayou inlet. Final dimensions of the ebb shoal have not been determined at this time; for more details on the shoal dimensions, the reader is directed to Coast & Harbor Engineering (2007).

Fitting the inlet stability criterion was conducted using the Escoffier method. The Escoffier analysis relates tidal basin communication through an inlet to the maximum velocity possible through the inlet for a range of cross-sectional areas (Coastal Engineering Manual 2003). The Escoffier method was calibrated to the Cedar Bayou conditions using the ADCIRC circulation model. The Escoffier method was used to optimize the dimensions of the Cedar Bayou and Vinson Slough dredging cuts. The following is an example of Escoffier application methods to validate the channel dimensions.

An Escoffier curve is shown in Figure 9 for a Cedar Bayou channel dredged to a width of 80 m. The maximum velocity through the inlet was plotted with increasing depth for various inlet widths, along with the equilibrium velocity. The maximum velocity represents the velocity that is expected to occur through the channel for the given bay tidal prism and channel dimensions, while the equilibrium velocity is the velocity required to maintain a stable channel for a given channel area. The intersection of these two curves indicates the channel behavior as the channel dimensions (here, depth) vary. The first point where the maximum velocity and the equilibrium velocity intersect represents the critical unstable depth, and the second intersection represents the stable depth. These two points represent the lower and upper bounds of the depth for a given width of a channel. Based on the two methods - numerical modeling and the Escoffier analysis - the optimal dimensions of Cedar Bayou and Vinson Slough were determined to be:

- Cedar Bayou Channel: 100 m wide and 2.2 m (7 ft) deep
- Vinson Slough Channel: 100m wide and 2 m (6.5 ft) deep
- Mouth: 100 m wide and 2.2 m (7 ft) deep

To verify the hypothesis that the Vinson Slough (VS) connection to Cedar Bayou (CB) is critical for long-term stability of the channel, flow rates were extracted from the tidal circulation model at the inlet mouth, in CB upstream of the CB-VS connection, and in VS upstream of the CB-VS connection. Flow rates were calculated at these cross-sections for the case where CB only is connected to the Gulf

of Mexico, where VS only is connected to the Gulf of Mexico, and where CB and VS were connected together, then connected to the Gulf of Mexico. This allows for the evaluation of the addition of the VS flow to Cedar Bayou.

Results of this analysis are summarized in Figure 10, which shows the total flow rate during a seven day period averaged to the total daily flow rate for ebb and flood flows separately. Flow rates in VS are increased by a factor of 4 when CB is connected to VS. In upper Cedar Bayou, the addition of the connection with VS does not modify the flow rate substantially. However, at the inlet mouth, the addition of VS to CB increases the flow rate into and out of the mouth by nearly 70% - a substantial increase. Therefore, the hypothesis was proven to be correct based on numerical modeling. However, field verification is required to adequately prove or disprove the hypothesis. Therefore, a monitoring program has been built into the Construction phase to verify these results and allow for effective adaptive management.

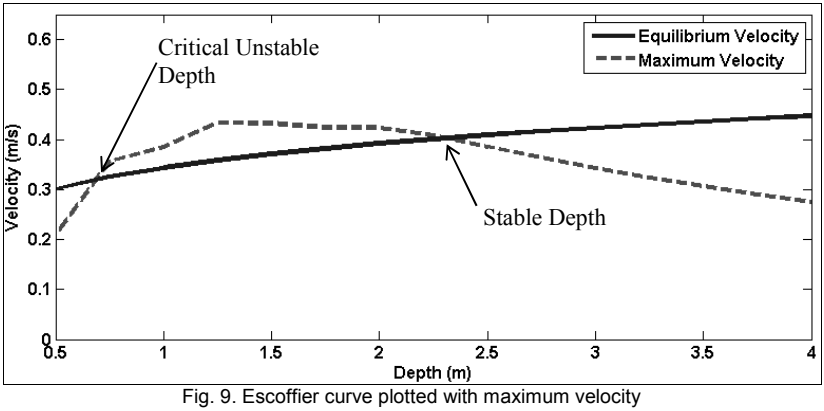

Fig. 9. Escoffier curve plotted with maximum velocity for a channel cross-section width of 80 meters

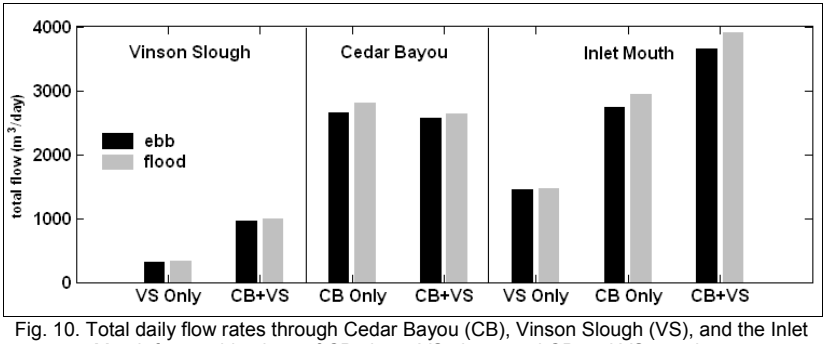

Fig. 10. Total daily flow rates through Cedar Bayou (CB), Vinson Slough (VS), and the Inlet Mouth for combinations of CB alone, VS along, and CB and VS together.

CONCLUSIONS AND RECOMMENDATIONS

Analysis of historical geomorphologic and hydrodynamic conditions at Cedar Bayou was the basis for developing two major hypotheses controlling Cedar Bayou inlet dynamics. These hypotheses are that the additional connection of Vinson Slough to Cedar Bayou is critical to the stability of Cedar Bayou, and that the restoration of an offshore ebb shoal allows for longshore sediment transport to bypass the inlet and therefore reduce the shoaling of the inlet itself. The hypotheses were tested and supported with numerical modeling.

An engineering solution for the restoration of Cedar Bayou was developed, and included deepening the existing Cedar Bayou Channel to the Gulf of Mexico, restoring the historical connection between Cedar Bayou and Vinson Slough, and beneficial use of the dredged material to construct a submerged offshore ebb shoal. Dimensions of the proposed solution were determined with numerical modeling, and were tested by through morphologic criteria including an inlet stability criterion and ebb shoal volume versus inlet flow volume.

The proposed solution was designed and is scheduled for construction in 2007-2008. A detailed monitoring program was recommended for the post-project conditions.

REFERENCES

Coast & Harbor Engineering, Inc. (2005). "Restoration of Cedar Bayou and Vinson Slough Phase 1 - Technical Feasibility: Hydraulic and Alternatives Analysis," prepared for Save Cedar Bayou, Inc., Fulton, TX.

Coast & Harbor Engineering, Inc. (2007; in production). "Restoration of Cedar Bayou and Vinson Slough Phase 2 – Optimization of Preferred Alternative," prepared for Save Cedar Bayou, Inc., Fulton, TX.

Edwards, L. (2006) Personal Communication. President, Save Cedar Bayou, Inc.

Holthuijsen, L.H., Booij, N. and Ris, R.C. (1993). "A spectral wave model for the coastal zone," *Proceedings 2nd International Symposium on Ocean Wave Measurement and Analysis*, New Orleans, LA, July 25-28, 1993, New York, pp. 630-641.

Lockwood & Andrews. (1953). Study of possible improvements, Cedar Bayou fish pass, St. Joseph-Matagorda Islands, Texas. UT Marine Science Library, Port Aransas, TX: SH 153 S793 1953.

Luettich, R.A., Jr., Westerink, J.J., and Scheffner, N.W. (1992). "ADCIRC: an advanced three-dimensional circulation model for shelves coasts and estuaries, report 1: theory and methodology of ADCIRC-2DDI and ADCIRC-3DL", Dredging Research Program Technical Report DRP-92-6, U.S. Army Engineers Waterways Experiment Station, Vicksburg, MS, 137p.

Nwogu, O.G. and Demirbilek, Z. (2001). "BOUSS-2D: A Boussinesq Wave Model for Coastal Regions and Harbors," Technical Report ERDC/CHL TR-01-25, U.S. Army Engineer Research and Development Center, Vicksburg, MS.

Simmons, E.G. and Hoese, H.D. (1959). Studies on the hydrography and fish migrations of Cedar Bayou, a natural tidal inlet on the central Texas Coast. Publ. Inst. Mar. Sci. Univ. Texas, 1959, pgs 56-80.

TCOON Texas Coastal and Oceanographic Observation Network. (2005). http://tcoon.cbi.tamucc.edu/TCOON/HomePage. Page last modified September 29, 2005 at 09:28 PM.

U.S. Army Corps of Engineers. (2003). Coastal Engineering Manual, Engineer Manual 1110-2-1100, U.S. Army Corps of Engineers, Washington, D.C. (in 6 volumes).

WIS. (2006). Wave Information Studies. http://frf.usace.army.mil/cgi-bin/wis/atl/atl_main.html

NAVIGATION IMPROVEMENTS, MOUTH OF THE COLORADO RIVER, TEXAS

Ronnie G. Barcak[1], Nicholas C. Kraus[2], Lihwa Lin[2], Ernest R. Smith[2], Daniel J. Heilman[3], Robert C. Thomas[3]

1. U.S. Army Corps of Engineers, Galveston District, 2000 Fort Point Road, Galveston, TX, 77550, USA. Ronnie.G.Barcak@swg02.usace.army.mil.
2. U.S. Army Engineer Research and Development Center, Coastal and Hydraulics Laboratory, 3909 Halls Ferry Road, Vicksburg, MS 39180-6199, USA. Nicholas.C.Kraus@erdc.usace.army.mil. Ernest.R.Smith@erdc.usace.army.mil. Lihwa.Lin@erdc.usace.army.mil.
3. HDR | Shiner Moseley and Associates, Inc., 555 N. Carancahua, Suite 1650, Corpus Christi, TX 78478, USA. daniel.heilman@hdrinc.com. robert.thomas@hdrinc.com.

Abstract: This paper describes an ongoing analysis of coastal and inlet processes at the mouth of the Colorado River Navigation Channel, Texas. A weir jetty system with impoundment basin down drift of the weir was constructed at the mouth of the Colorado River in 1985 to reduce the expected rate of dredging of the shallow-draft entrance navigation channel. The required rate of dredging has been about double the design estimate, however, due in part to diversion of the Colorado River away from its entrance to the Gulf of Mexico. A study is underway to better understand the processes involved, design a more efficient entrance, and provide the reduced dredging interval and volume originally desired, while placing the inlet processes within a regional sediment transport framework.

INTRODUCTION

The mouth of the Colorado River (MCR) is located on the Texas Gulf of Mexico coast approximately midway between Galveston and Corpus Christi (Fig. 1). It is a federally authorized shallow-draft navigation channel that experiences relatively weak water exchange between the Gulf of Mexico and East Matagorda Bay, connected through the 10.5-km (6.5 mile) long Colorado River Navigation Channel (CRNC) and the eastward section of the Gulf Intracoastal Waterway (GIWW). The flow system associated with the mouth of the Colorado River is separated from the Colorado River itself and (West)

Matagorda Bay through diversion of the river into the bay in 1992 as an environmental enhancement. Dual rubble mound jetties constructed in 1985 protect the entrance to the CRNC. The west jetty extends 333 m from the shoreline. The east jetty has a 333-m (1,090 ft) long weir section on its landward side with a sediment impoundment basin located westward of the weir. The entrance channel, 5 m deep by 65 m wide (17 ft by 200 ft), connects to the GIWW through a 4-m deep by 33-m wide (15 ft by 100 ft) channel.

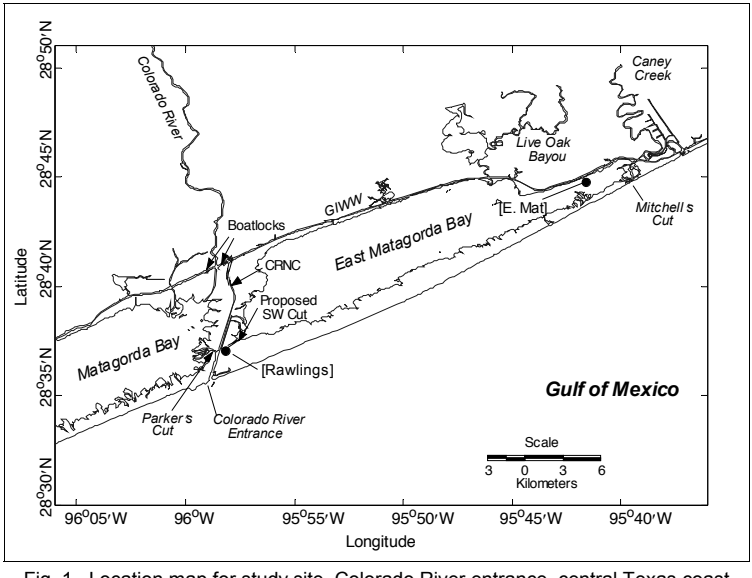

Fig. 1. Location map for study site, Colorado River entrance, central Texas coast

The coastal and inlet processes at the MCR, including circulation, waves, and longshore transport were numerically simulated by Lin et al. (2001). Local-scale modeling of sediment transport of the existing condition has recently been undertaken to analyze potential alternatives to the existing design for enhancing control of sedimentation of the navigation channel. This paper discusses the ongoing study at the MCR, the history, present study efforts, and what might be done in the future.

BACKGROUND

Before 1930, East Matagorda Bay and Matagorda Bay comprised a single Matagorda Bay. The bay was divided in 1935, when a large river delta was formed and moved across the bay after a logjam was freed in the river between 1925 and 1929 (US Army Corps of Engineers (USACE) 1992). The Colorado River began discharging into the Gulf of Mexico in 1935. Dual rubble mound jetties were constructed in 1985 to protect the entrance to the CRNC. Several designs to modify the entrance channel were considered, with the weir jetty and impoundment basin design being judged the most cost

effective for construction and subsequent dredging and bypassing of the sand dredged from the deposition basin and channel. At the time of design (in the 1960s), review (1970s), and construction (1980s), the Colorado River discharged to the Gulf of Mexico. The overall hydraulic system of the MCR is complex because of tide and wind forcing, connection of the CRNC to East Matagorda Bay, possibility of opening the SW Corner Cut to East Matagorda Bay (Kraus and Militello 1999), and possibility of opening the presently closed Parkers Cut to Matagorda Bay (Fig. 1).



Fig. 2. Entrance of Colorado River Navigation Channel, TX

As originally designed, the sediment impoundment basin was located between the weir section and the entrance channel (Fig. 2). The impoundment basin accommodated sand bypassing to the down-drift beaches by means of a pipeline dredge, with discharge in the surf zone on the west side of the MCR. The basin was designed to hold a 2-year supply of sediment estimated at 460,000 m^3 (600,000 cy) (USACE 1977). The jetties had to be placed at relatively large distance from each other to accommodate the deposition basin. The distance between the gulfward ends of the jetties is approximately 400 m (1,300 ft).

The Colorado River was rerouted in 1992 to discharge into Matagorda Bay through a diversion channel as part of an environmental enhancement project. A pair of locks was added to the GIWW at the junction of the Colorado River to mitigate the cross current at

the intersection of the river and GIWW. As a result, the Colorado River was diverted into Matagorda Bay, eliminating the river discharge as a means of scouring sediment from the entrance channel to the Gulf. The CRNC was thereby separated from the main river, but it is connected to the eastward section of the GIWW.

Initial dredging of the impoundment basin was completed in 1990. Since then, the basin has filled more rapidly than designed. The entrance mouth has experienced excessive sediment shoaling, and spits form on both the east and west sides of the landward ends of the jetties, encroaching on the navigation channel. Figure 3 plots volume of sediment dredged in the basin and CRNC from 1990 to 2002 and indicates that the total volume of dredging annually is about 425,000 m^3 (556,000 cy), approximately double the design estimate (in part due to contributions from the northern CRNC bottom and GIWW).

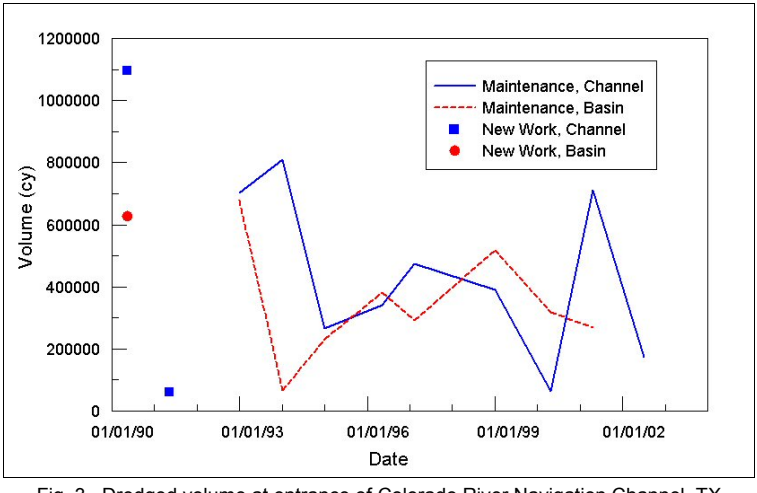

Fig. 3. Dredged volume at entrance of Colorado River Navigation Channel, TX

A 152-m (500 ft) long rock dike was constructed in September 2003 to function as a training structure for the deposition and reduce dredging requirements, as recommended by Kraus et al. (2003). Considered to be economically justified if it eliminated the need for one dredging cycle at annual frequency, it eliminated the need for almost two dredging cycles before being overwhelmed by wind-blow sand transport and swash-zone transport that occurred landward of the deposition basin during times of high water in the Gulf of Mexico. The sediment training structure was constructed shortly before the USACE was required to lower priority of maintaining shallow-draft channels, thereby greatly reducing dredging at the MCR. The beach accreted past the seaward end of the sediment training structure, and it is now almost buried (Fig. 4). Plans to raise the structure an additional 1.2 m (4 ft) to intercept wind-blown sand and swash-zone transport, as well as other incremental measures such as raising the weir jetty, have been considered (Kraus et al. 2003; Lin et al. 2003).



Fig. 4. Sediment training structure south, present west jetty in upper left corner, 6 Aug 06

COASTAL AND INLET PROCESSES EVALUATION

The tide on the central Texas coast is mixed, but mainly diurnal, having a period of approximately one tidal day (24.84 hr). The National Ocean Service (NOS) maintains a long-term tidal station at the Galveston Pleasure Pier, TX. The diurnal tide range calculated from the record for the 5-year period 1990-1994 was 0.65 m. Strong wind along the Texas coast can often dominate the water level in the river, and seasonal lows in water level in the Gulf of Mexico can be a concern for navigation (see Kraus 2007).

Nearshore wave data are available from gauges that were deployed at the 10-m depth contour 3.2 km offshore of the MCR, located 65 km south of the San Bernard River (King and Prickett 1998). The mean significant wave height was 0.6 m and the mean peak period was 5.9 sec over a 17-month period of data collected in 1991-1993. This dataset tends to under-represent the wave conditions during winter months. These waves can generate a strong nearshore current to transport the littoral sediment into the impoundment basin or along the shore in the swash zone to the entrance channel.

Samples taken in the entrance channel and impoundment basin between February 1994 and September 1995 indicate that sediments are primarily sand in the entrance channel, with some silt and clay in the basin. The sediment in the entrance channel has a median grain size of 0.12 mm and silt and clay fractions of 35 percent at some locations. The sediment in the impoundment basin has a mean grain size of 0.03 mm and contains 87 percent silt and clay fractions (Lin et al. 2003). Sediment samples taken in the CRNC show mean grain size of 0.04 mm and contained 60 to 80 percent silt and clay. The fine materials in the basin and CRNC, silt- and clay-sized particles, are consistent with the sediment found in the GIWW and from the river. The samples suggest that riverine sediments are reaching the MCR and likely settling into the impoundment basin.

Both the peak ebb and flood currents are weak, as indicate by data collected in January-February 2002 at Channel Maker 4 of the CRNC. The ebb-tidal current dominates the flow in the CRNC. The mean velocity was 0.013 m/sec (0.042 ft/sec) ebb dominant, and the average maximum current was 0.38 m/sec (1.25 ft/sec) at the throat of the entrance

channel, in a primarily tidal condition (weak wind). The mean velocity and the average maximum current become slightly greater, equal to 0.057 (0.19 ft/sec) and 0.40 m/sec (1.30 ft/sec), respectively, in a combined tide and strong wind condition. Because of weak tidal flow and the active littoral process in the nearshore, there is no appreciable ebb tidal shoal at the MCR.

Longshore Transport

The MCR General Design Memorandum (USACE 1977) estimated a net longshore transport rate of 229,000 m^3/year (300,000 cy/year) to the west and negligible transport to the east, based in part on observed impoundment at the Matagorda Ship Channel east jetty located to the 40 km (25 miles) southwest of the MCR. Heilman and Edge (1996) discussed sediment pathways and compiled estimates of longshore sediment transport on the Gulf of Mexico coast at the mouth of the Colorado River obtained from several sources and by different means of measurement or inference. They concluded that an average annual amount of 230,000 m^3 (301,000 cy/year) is necessary for sediment bypassing to the west beach at the entrance. King and Prickett (1998) estimated the net rate of transport at MCR to be 510,000 m^3/year (668,000 cy/year) to the west, with a gross rate of 670,000 m^3/year (877,000 cy/year), based on the SPM (1984) CERC equation and intermittent wave measurements at the 10-m contour at the site. These estimates (with K=0.35 for significant wave height) are greater than the average annual volume removal of 425,000 m^3, and so are questionable or can be considered an extreme upper limit.

Dredging volumes analyzed here for the 12-year interval 1990 to 2002 indicate the average annual volume removal was 425,000 m^3/year (556,000 cy/year). Of this amount, about 280,000 m^3/year (367,000 cy/year) is estimated to originate from longshore transport, in approximate agreement with the conclusion of Heilman and Edge (1996), and the remainder, 145,000 m^3/year (189,000 cy/year), is supplied by the river and GIWW as finer grained sediment. In the present study, transport rates were estimated with K=0.27 to achieve best agreement with the dredging data and shoreline position data interpreted by GIS analysis from rectified aerial photographs. These calculations gave a net transport rate of 212,000 m^3/year (278,000 cy/year) to the west was with a gross rate of 414,000 m^3/year (542,000 cy/year).

Regional Modeling

Tidal circulation, including influence of wind, at the MCR was examined with a finite-element circulation model ADCIRC (Lin et al. 2001). The model grid (Fig. 5) encompasses the MCR, East Matagorda Bay, Matagorda Bay, and surrounding GIWW based on the work of Kraus and Militello (1999). This grid was constructed as a regional model for the Texas regional coastal modeling study (Brown et al. 2003). The results of such modeling efforts have been used in the present study to force a local model of the circulation (current and water surface elevation) and sediment transport at the MCR, performed at high resolution.

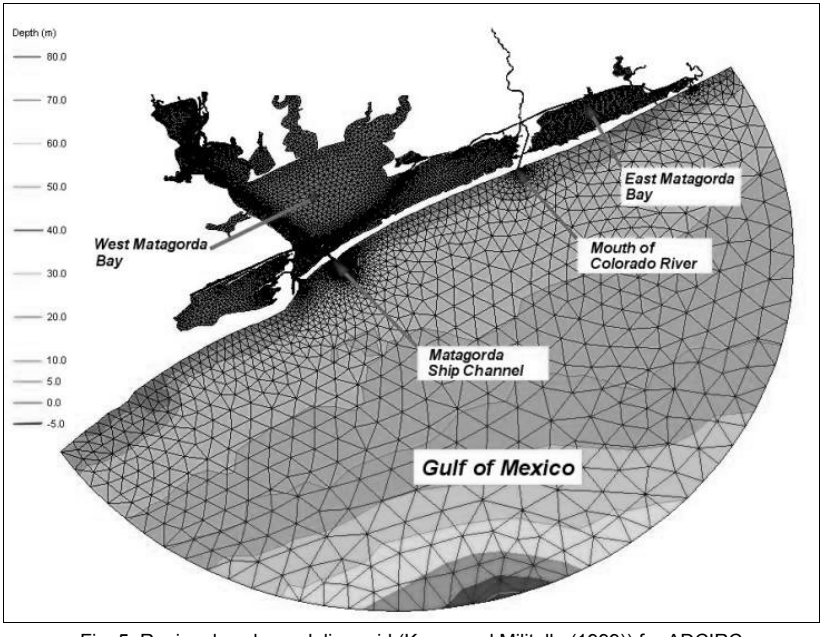

Fig. 5. Regional scale modeling grid (Kraus and Militello (1999)) for ADCIRC

Local-Scale Inlet Processes Modeling

For local-scale circulation modeling, M2D (Militello et al. 2004) was applied with wave forcing from WABED (Lin et al. 2006) to calculate tide, wind, river, and wave-forced currents and water level at the study site. Figure 6 shows the M2D and WABED grid coverage. The circulation and transport models are being run to evaluate the existing condition and construction of a new east jetty located approximately 153 m (500 ft) from the west jetty. Table 1 lists the alternatives being considered, as evaluated with this inlet-processes numerically modeling technology.

Table 1. Alternatives under Evaluation for Improvement of MCR

Alt	Description
-0-	Existing condition
1	150-ft channel with new jetty
2	200-ft channel with new jetty
3	150-ft channel with new jetty, open SW Cut
4	200-ft channel with new jetty, open SW Cut
5	150-ft channel with new jetty, open Parkers Cut
6	200-ft channel with new jetty, open Parkers Cut

This modeling technology and results are the culmination of several studies of the MCR as referenced in this paper. A new east jetty without weir that would be located approximately 153 m center to center from the existing west jetty will provide a much reduced channel width to depth ratio than the existing condition and, therefore, a more hydraulically efficient channel.

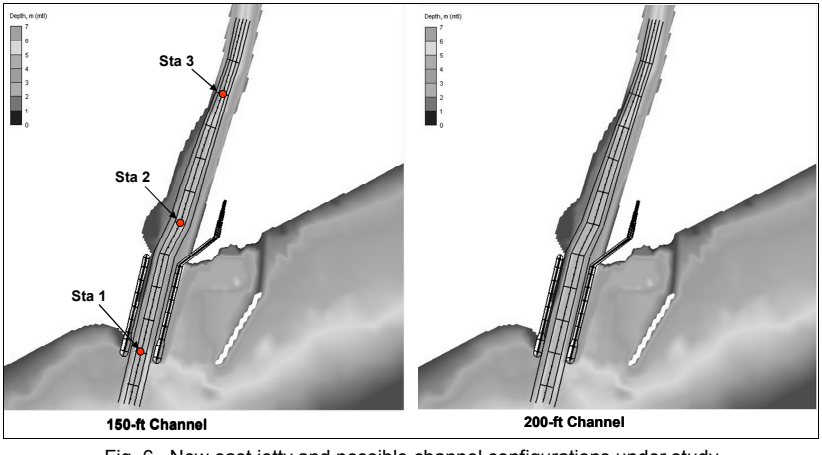

Fig. 6. New east jetty and possible channel configurations under study

Figures 7 and 8 show the calculated currents with the proposed new east jetty in place at maximum ebb (and including wind forcing and wave-induced current) for the situations without and with the presence of the SW Corner Cut. The current in the navigation channel can achieve almost double that measured and calculated for the existing condition, with the wind-dominated current in the SW Corner Cut (especially during winter) (Kraus and Militello 1999) increasing the ebb current hence scouring action at the entrance.

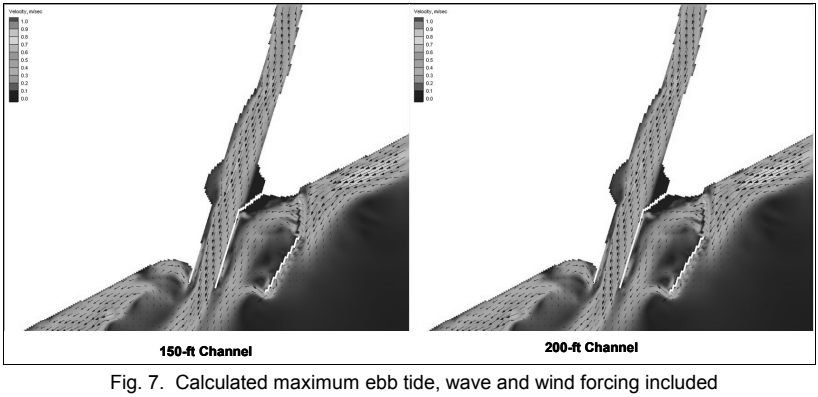

Fig. 7. Calculated maximum ebb tide, wave and wind forcing included

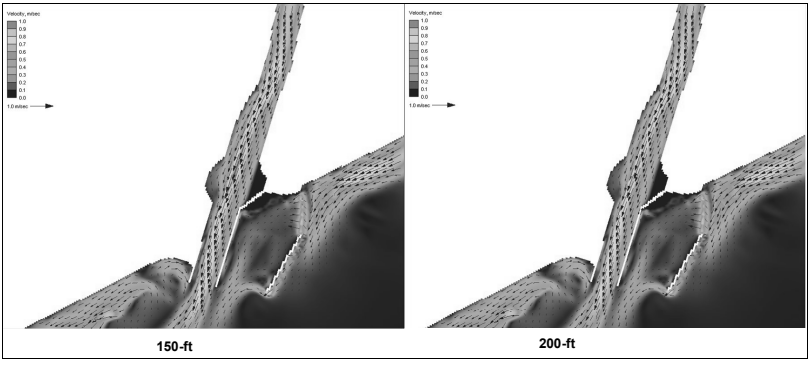

Fig. 8. Calculated maximum ebb tide, wave and wind forcing included, SW Corner Cut open

Shoreline Response to New East Jetty

The shoreline change rate was modeled to determine the existing condition and to predict the effect of proposed changes to the inlet. GENESIS (Hanson and Kraus 1989) was applied with WIS wave hindcast information (Tracy 2004), which gives hourly information on wave height, period, and direction. Based on model calibration using historical shoreline change and maintenance dredging records, a sediment transport factor of $K = 0.27$ in the CERC formula was determined. For the case without sand bypassing, the model predicts significant erosion on the western side of the jetties and accretion on the east side. Figures 9 and 10 plot the predicted shoreline change on the east and west sides of the jetties respectively after simulations from 5 to 20 years.

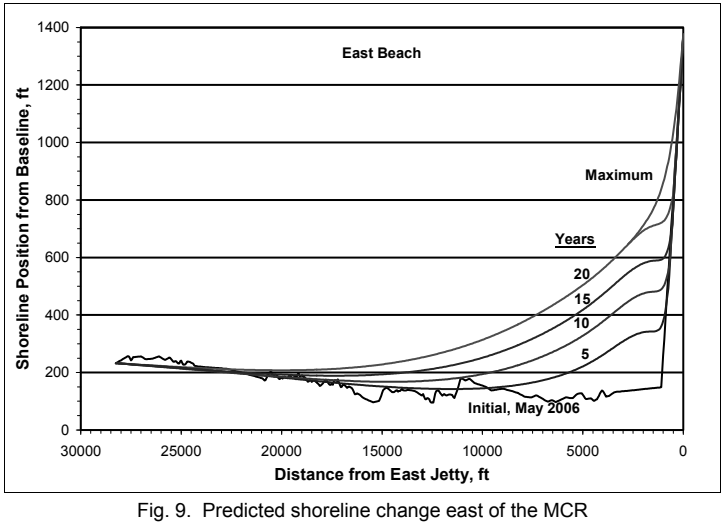

Fig. 9. Predicted shoreline change east of the MCR

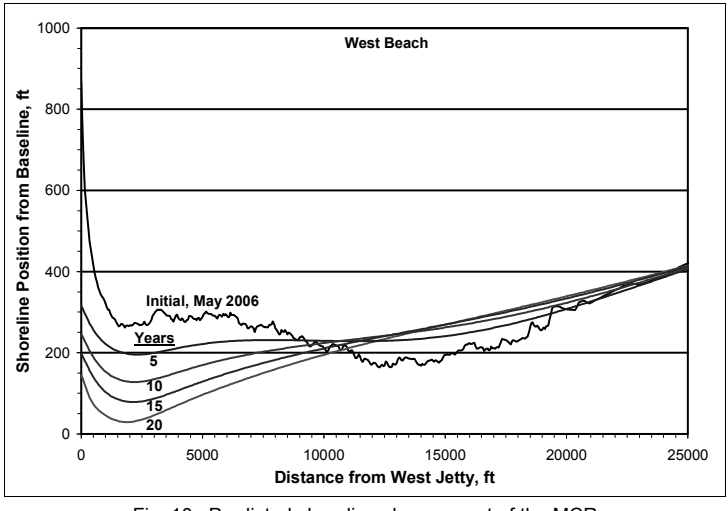

Fig. 10. Predicted shoreline change west of the MCR

Shoreline change also was also simulated including mechanical bypassing (dredging) of the up-drift accretion fillet at the east jetty. A volume of 306,000 m^3 (400,000 cy) was bypassed every 2 years and placed on the down-drift beach. Figure 11 indicates that bypassing is essential to maintain the beach to the west, continuing Galveston District practice, and not allowing a large fillet to form on the east, which would more readily allow littoral material to shoal in the entrance channel from the east beach.

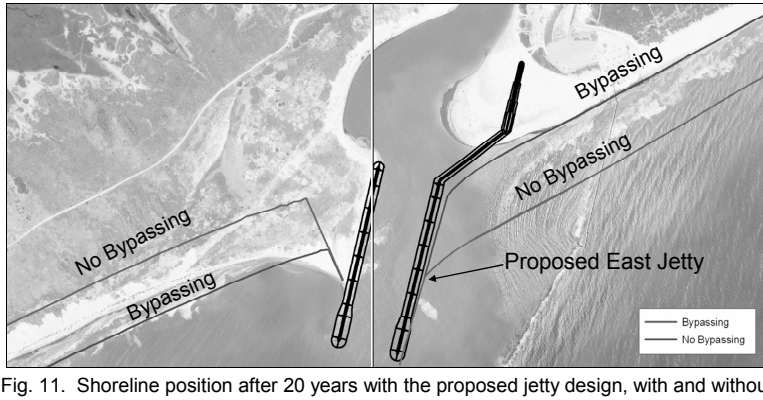

Fig. 11. Shoreline position after 20 years with the proposed jetty design, with and without sediment bypassing from up-drift to down-drift beaches (photograph May 2006)

Review of New East Jetty Concept

Inlet process modeling and shoreline change and sediment transport simulations indicate that the most feasible option for decreasing maintenance dredging requirements is construction of a new east jetty. The new east jetty would be similar to the existing west jetty. The primary difference in design is the proposed crest elevation of the landward section of the new jetty. Elevating the landward section of the jetty would reduce sediment infilling of the navigation channel due to wind-blown transport, swash zone transport, and washover during storms. Observation of the sediment training structure (Fig. 4) reveals the extent to which transport over the dry beach can occur.

The local-scale circulation and transport models are being applied to compare various designs for the new jetty and navigation channel. They indicate where and to what extent erosion and accretion are likely to occur. Shoreline change modeling indicates it essential that bypassing of sediment around the entrance be continued.

Lessons Learned at Other Jetties on the Texas Coast

Jetty design and construction technique can reduce initial construction cost of the proposed east jetty and reduce channel maintenance cost as well. There are nine jettied inlets on the Texas Gulf Coast, the earliest of which were constructed in the late 19th century. A review of these jetties by Sargent and Bottin (1989) provides insight on potential construction pitfalls to avoid in consideration of possible jetty modification or construction at the MCR. Most of the jetties were constructed with block-shaped granite cover stone. The shape of the cover stone increases hydraulic stability, but it makes placement difficult for side slopes steeper than about 3H:1V, especially in shallow water, therefore increasing construction cost for steep sides.

For land-based construction, jetty crest width should be at least 4.7 m (16 ft) to provide adequate room for maneuvering and operation of construction equipment. Although narrower cross sections are possible, they generally increase construction time and cost. Another consideration for land-based construction is the scour hole that tends to form as the jetty construction progresses offshore. The scour hole migrates with the end of the jetty as it is built seaward. Bedding stone is used to fill the scour hole, often resulting in rock overruns and increasing cost. A potential method to reduce such overruns is to use stone filled mattresses (Hughes 2006) instead of loose bedding stone. Finally, providing adequate elevation on the landward side of the jetty will reduce or eliminate bypassing of its landward side by wind-blown and swash zone sediment transport.

CONCLUDING DISCUSSION

A long-term plan for reducing maintenance dredging cost and increasing navigation channel reliability at the MCR is under development. The study entails examination of inlet processes and coastal processes, and modification of existing and construction of new structures. Numerical analysis has shown that a new east jetty without a weir and located closer to the original west jetty than the existing design should reduce the dredging interval by increasing channel hydraulic efficiency. A long-term bypassing plan

will ensure that the MCR navigation project will not cause erosion of the down-drift beach.

ACKNOWLEDGEMENTS

This study was supported by the U.S. Army Engineer District, Galveston. Permission was granted by Headquarters, U.S. Army Corps of Engineers, to publish this information.

REFERENCES

Brown, M.E., Kieslich, J.M., and Kraus, N.C. (2003). "Regional circulation modeling of the Texas Coast and inland coastal waters," *Proc. 8th International Conf. on Estuarine and Coastal Modeling*, ASCE, 192-214.

Hanson, H., and Kraus, N.C. (1989). "GENESIS: Generalized model for simulating shoreline change. Report 1: Technical reference," TR CERC-89-19, U.S. Army Engineer Waterways Experiment Station, Coastal Engineering Research Center, Vicksburg, MS.

Heilman, D.J., and Edge, B.L. (1996). "Interaction of the Colorado River Project, Texas, with longshore sediment transport," *Proc. 25th Coastal Eng. Conf.*, ASCE, 3,309-3,322.

Hughes, S.A. (2006). "Uses for marine mattresses in coastal engineering," CHETN – III-72, U.S. Army Engineer Research and Development Center, Vicksburg, MS.

King, D.B., and Prickett, T.L. (1998). "Mouth of the Colorado River, Texas, monitoring program," Monitoring Completed Navigation Projects Program. TR CHL-98-2, U.S. Army Corps of Engineers, Waterways Experiment Station, Vicksburg, MS.

Kraus, N.C. (2007). "Inlets along the Texas coast, USA," *Proc. Coastal Sediments '07*, ASCE, in press.

Kraus, N.C., Lin, L., and Barcak, R.G. (2004). "Alternatives to reduce channel shoaling, Mouth of Colorado River Navigation Channel, Texas," *Proc. Dredging 02*, ASCE, CD ROM, 13 pp.

Kraus, N. C., and Militello, A. (1999). "Hydraulic study of multiple inlet system: East Matagorda Bay, Texas," *J. Hydraul. Res*., 125(3), 224-232.

Lin, L., Kraus, N.C., and Barcak, R.G. (2001). "Predicting hydrodynamics of a proposed multiple-inlet system, Colorado River, Texas," *Proc. 7th International Conf. on Estuarine and Coastal Modeling*, ASCE, 837-851.

Lin, L., Kraus, N.C., and Barcak, R.G. (2003). "'Modeling coastal sediment transport at the Mouth of the Colorado River, Texas," *Proc. 8th International Estuarine and Coastal Modeling Conf*., ASCE, 988-1006.

Lin, L., Mase, H., Yamada, F., and Demirbilek, Z. (2006). "Wave-Action Balance Equation Diffraction (WABED) model, Part 1: Tests of wave diffraction and reflection at inlets," Coastal and Hydraulic Engineering Technical Note ERDC/CHL CHETN-III-73, U.S. Army Engineer Research and Development Center.

Militello, A., Reed, C. W., Zundel, A. K., and Kraus, N. C. (2004). "Two-dimensional depth-averaged circulation model M2D: Version 2.0, Report 1: Documentation and user's guide," ERDC/CHL TR-04-02, U.S. Army Engineer Research and Development Center, Vicksburg, MS.

Sargent, F., and Bottin, R. (1989). "Case histories of Corps breakwaters and jetty structures", REMR Report 9 Southwestern Division. January 1989, U.S. Army Corps of Engineers, Washington, D.C.

Shore Protection Manual (SPM) (1984). 4th ed., 2 Vol, U.S. Army Engineer Waterways Experiment Station, U.S. Govt. Printing Office, Washington, DC.

Tracy, B.A. (2004). "Wave Information Studies: Hindcast wave data for U.S. coasts," U.S. Army Engineer Research and Development Center, Vicksburg, MS. http://frf.usace.army.mil/cgi-bin/wis/atl/atl_main.html.

USACE (1977). "Mouth of Colorado River, Texas, Phase 1," General Design Memorandum (navigation features)," U.S. Army Engineer District, Galveston, TX.

USACE. (1992). "Inlets along the Texas Gulf Coast," Section 22 Report, Planning Assistance to the States Program, U.S. Army Engineer District, Galveston, TX.

LONG-TERM INLET STABILITY OF A MULTIPLE INLET SYSTEM, PASS CAVALLO, TEXAS

Brian K. Batten[1], Nicholas C. Kraus[2], Lihwa Lin[3]

1. Dewberry. 8401 Arlington Boulevard, Fairfax, VA 20231-4666, USA. bbatten@dewberry.com.
2. U.S. Army Engineer Research and Development Center, Coastal and Hydraulics Laboratory, 3909 Halls Ferry Road, Vicksburg, MS 39180-6199, USA. Nicholas.C.Kraus@erdc.usace.army.mil.
3. U.S. Army Engineer Research and Development Center, Coastal and Hydraulics Laboratory, 3909 Halls Ferry Road, Vicksburg, MS 39180-6199, USA. Lihwa.Lin @erdc.usace.army.mil.

Abstract: Matagorda Bay, Texas, is connected to the Gulf of Mexico by two inlets, Pass Cavallo and the Matagorda Ship Channel (MSC). Pass Cavallo is a natural inlet located at the southwest terminus of Matagorda Peninsula, and the MSC is an artificially cut, deep-draft federally maintained navigation channel approximately 7.2 km northeast. Pass Cavallo was historically stable until the 20th century, when the tidal prism was first reduced in 1935 by division of Matagorda Bay due to deltaic progradation of the Colorado River, and later in 1966 as a result of the construction of the Matagorda Ship Channel. In response to these reductions in tidal prism, the entrance width at Pass Cavallo reached historical minimums as Matagorda Peninsula and Matagorda Island prograded into the inlet. Long-term stability and potential of possible closure of Pass Cavallo are evaluated through theoretical and empirical relationships, and long-term analysis of morphologic change.

INTRODUCTION

Pass Cavallo, located on the south-central Texas coast (Figure 1), is the natural, permanent inlet between Matagorda Bay and the Gulf of Mexico. The inlet has existed for at least 2,600 years, being in approximately the same location for the past 200 years (Harwood 1973). The tidal prism through Pass Cavallo has been decreasing over the last century in response to natural processes and anthropogenic activities.

The first cause of this decrease was separation of the historic Matagorda Bay into East Matagorda Bay and the present Matagorda Bay, by growth of the Colorado River Delta across the bay from 1929 to 1935 (Wadsworth 1966; Bouma and Bryant 1969). This initial decrease in tidal prism resulted in shoaling (Harwood 1973) and difficulty in maintaining the commercial navigation channel through the inlet. These issues led to the construction of the Matagorda Ship Channel (MSC), the second and more dominant reason for decrease in the tidal prism at Pass Cavallo. The MSC entrance was cut through Matagorda Peninsula in 1963 approximately 5.5 km updrift of Pass Cavallo at that time. Construction of the jetties and dredging of the inner channel were completed in 1966 (U.S. Army Corps of Engineers (USACE1992)).

The deep-draft MSC enters the bay 7.2 km (as of December 2006) to the north of Pass Cavallo and is a more efficient tidal channel by joining with a deeper and more central portion of the bay. Due to this, the MSC has captured much of the tidal prism forming flowing through Pass Cavallo, resulting in a decrease in inlet width over the last half-century. Figure 2 shows the configuration of the inlet at the time of the opening of the MSC in 1965 and in December 2006.

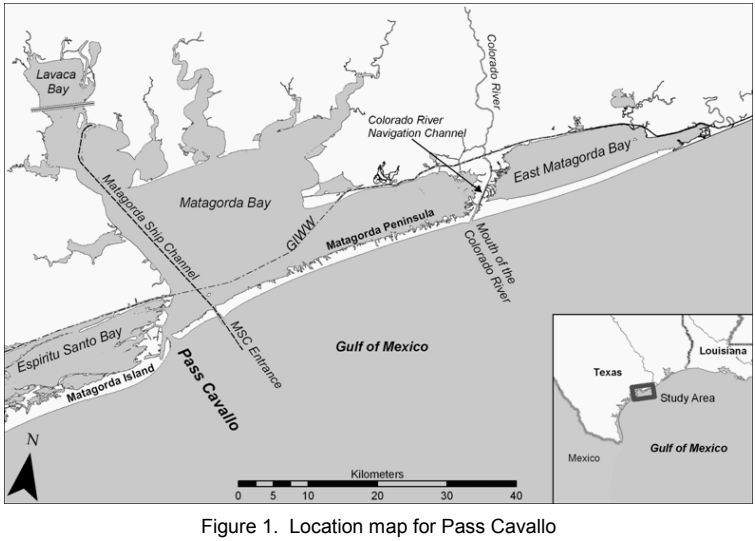

Figure 1. Location map for Pass Cavallo

Previous studies have not been unanimous about the long-term stability of Pass Cavallo. Ward (1982) concluded that the inlet was "shoal unstable," and van de Kreeke (1985) stated that Pass Cavallo would ultimately close because of the presence of the MSC entrance. Van de Kreeke (1990a, 1990b) concluded that multiple inlets to the same bay system cannot exist and that, eventually, at most one would remain. On the other hand, Price (1952) noted that northerly wind fronts, common along the Texas coast from October through May, force water into the southwest corners of Texas bays, promoting

existence and stability of channels in those corners (See Kraus 2007, this volume). Wind setup of water against the southwest shore of Matagorda Bay produces an ebb discharge (wind tide) that adds to that of the astronomical tide. Price (1952) also found that Texas bays from Matagorda Bay and to the south tend to have one inlet per bay, located in the southwest or southeast corners. Harwood (1973) concluded that Pass Cavallo would remain open based on geomorphic analysis and consideration of wind tides.

Therefore, there is uncertainty and concern that the existing MSC and possible enlargement of its entrance being considered might accelerate closure of Pass Cavallo. If Pass Cavallo were to close, the discharge at the MSC entrance would become greater, promoting scour and potentially compromising navigation reliability. The natural water exchange and path through Pass Cavallo for organisms and nutrients would also be lost.

This study proceeded by conducting four separate activities as (a) a tidal inlet morphologic analysis based on existing predictive equations, (b) survey of the entrance to Pass Cavallo, (c) numerical modeling of hydrodynamics, and (d) an analysis of inlet width and spit growth shoreline change.

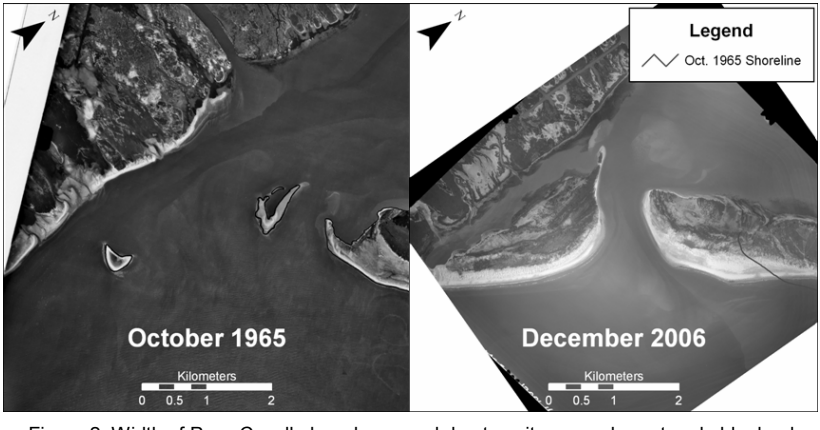

Figure 2. Width of Pass Cavallo has decreased due to spit encroachment and ebb shoal collapse since construction of the MSC.

ANALYSIS AND RESULTS

Empirical evaluation of inlet cross-sectional stability

It is empirically known that a stable inlet located on a sandy coast will have a mean-maximum velocity through it of approximately 1 m/sec (Escoffier 1940; Bruun 1968). By "mean-maximum velocity" is meant the average of a regularly occurring maximum velocity, such as would be generated during spring tide. The mean-maximum velocity V_{mm} can be obtained as:

$$V_{mm} = \frac{\pi}{CT} \quad (1)$$

where T is tidal period, and $C = 6.6 \times 10^{-5}$ is an empirical coefficient with units m^{-1}. For a semidiurnal inlet, T = 12 hr, 25 min = 44,712 sec. Then, Eq. 1 yields V_{mm} = 1.06 m/sec, in agreement with empirical observations for, at least, many semi-diurnal inlets. For a tide that is predominantly diurnal, the tidal period is 89,424 sec, giving V_{mm} = 0.53 m/sec (Kraus 2007). There are relatively few inlets worldwide in a diurnal tidal setting, making empirical validation of this result difficult.

The conclusion is that an inlet in a diurnal tidal setting may require a smaller mean-maximum tidal velocity to maintain channel cross-sectional area stability as compared to inlets in a semi-diurnal setting, the more common type of inlet. For Pass Cavallo, this smaller required value of V_{mm} by astronomical forcing may be an overestimate, because the contribution to the ebb discharge by wind setup in the bay was neglected. A smaller value of V_{mm} works in favor of the preservation of Pass Cavallo.

Tidal Prism

Harwood (1973) and Ward (1982) examined tidal prism at Pass Cavallo over the last century. Figure 3 plots data compiled from those two sources as well as a point for year 2004, in addition to data for a possible deepening and widening of the MSC, based on calculations with the ADCIRC model reported in Kraus et al. (2006). Harwood (1973) studied the Pass Cavallo flood shoal and computed the tidal prism through estimation of effective bay surface area, including a portion of Espiritu Santo Bay, multiplied by the estimated tidal range. Ward (1982) estimated tidal prisms based on measurements of the current and bathymetry in 1959 (prior to opening of the MSC) and in the 1970s. He found that, by the mid-1970s, the tidal prism at Pass Cavallo had decreased by half, similar to results of Harwood (1973).

In addition, Ward (1982) reports maximum values of the current ("during the race of tide") through Pass Cavallo to be on order of 1 m/sec in 1959 and of half that value in the 1970s. Ward (1982) notes that the tidal prisms for Pass Cavallo and the MSC in the 1970s were approximately the same, as can be seen in Figure 3. Our calculation for 2004, based on a calibrated two-dimensional model (Kraus et al. 2006), indicates that the present tidal prism at the MSC is approximately three times that at Pass Cavallo. The tidal prisms for Pass Cavallo and the MSC are large and comparable to the larger Pacific coast inlets, because the surface area of Texas bays is typically several times larger than the Pacific coast inlets, compensating for the relatively small tidal range as compared to the Pacific coast.

A bathymetric survey (Figure 4) was conducted by Frontier Surveying, Inc., Corpus Christi, TX, for the present study to determine the minimum cross-sectional area of Pass Cavallo. Depth across eight transects is shown in Figure 5. Maximum depth in the channel reaches 9 m MSL, and the cross-sectional area, calculated by integrating the curves to MSL, ranged from 3,470 m^2 along Transect 1 to a minimum of 2,060 m^2 along Transect 8. The latter transect was the limit of being able to navigate the survey boat abeam to incident waves in

the Gulf of Mexico that day. Transects 5-8 were interrupted to the south by a large shoal that approaches the channel from Matagorda Island.

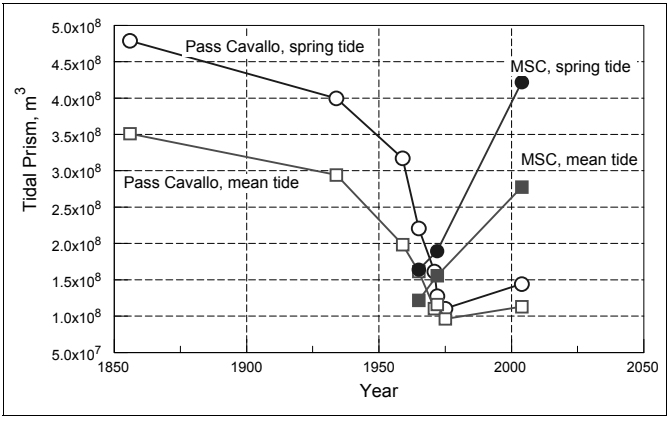

Figure 3. Estimated tidal prisms for Pass Cavallo and the MSC. Lines indicate trends and are not to be interpreted as representing intermediate values.

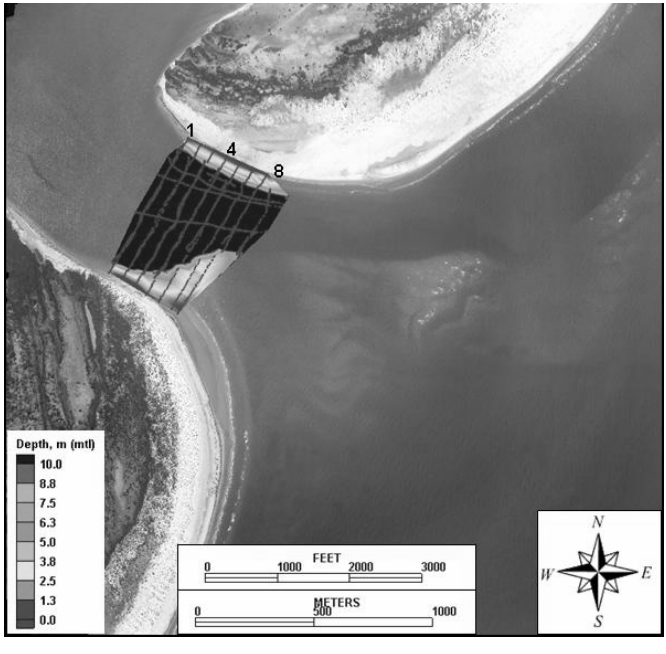

Figure 4. Pass Cavallo cross-sectional survey area of 23 May 2006, superimposed on photograph of 16 May 2006.

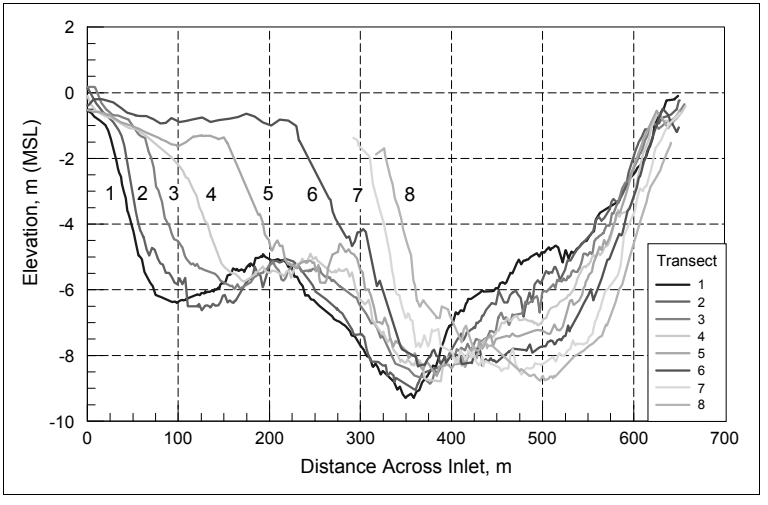

Figure 5. Surveys along eight transects in Pass Cavallo, 23 May 2006. Transect locations are numbered from 1 to 8, starting in Matagorda Bay and progressing seaward.

Accepted empirical relations are available that relate minimum inlet channel cross-sectional area below MSL for a stable inlet and tidal prism. Nishi et al. (2007) have shown that such considerations hold for tidal inlets world wide. Data compiled from six countries were consistent with the relation $A_C = 1.75\times10^{-04} P^{0.952}$ (A_C in m^2, P in m^3), which may be considered a global relation that can be applied if no data are available for a given inlet.

Jarrett (1976) analyzed 108 inlets (yielding 162 data points) along the Atlantic Ocean, Gulf of Mexico, and Pacific Ocean coasts of the United States. His objectives were to determine if inlets on the three coasts follow the same inlet cross-sectional area – tidal prism relation, and if inlet stabilization altered that relation. With relatively high correlation coefficients, all predictive relations were found to fit the form:

$$A_C = C P^n \tag{2}$$

in which C (similar to that in Eq. 1) and n are empirically determined. Jarrett (1976) found the exponent n to vary between 0.86 and 1.10 for inlets with no jetty or with a single jetty and between 0.85 and 0.95 for inlets with two jetties. .

For analysis of the stability of Pass Cavallo, the Jarrett (1976) relation describing unjettied and single inlets for the Gulf Coast, developed from 30 data points, was selected as most appropriate. This relation is $A_C = 6.992\times10^{-04} P^{0.86}$ (units of meters). With the 2004 value of tidal prism (1.44×10^8 m^3) from Figure 3, the result is A_C = 7,300 m^2. This predicted value of A_C is two to three times larger than those measured

from the recent channel cross-sections. This result indicates that Pass Cavallo is presently experiencing a surplus of sediment, and possible sources for this surplus are identified and discussed below.

Morphology change analysis

Aerial photographs were available for this study in both digital and 9' x 9' print format, sourced primarily from USACE archives. Print photographs were scanned on an UMAX 2100XL flatbed scanner at a resolution of 600 dpi and saved in tif format. Selected photographs were then rectified to 1995 1-m resolution digital orthophoto quarter quadrangles (DOQQ) available from the Texas Natural Resources Information System (TNRIS 1995). This photoset provided a high-accuracy (National Map Accuracy Standards, see Anders and Byrnes 1991), high-resolution (1 m pixel) base for rectification.

Few high-quality control points were available in the study area; therefore, control points were improvised from geomorphologic features and vegetation. Rectification quality was evaluated by the goodness-of-fit of the output image to the TNRIS DOQQs. Uncertainty of ground positions from the rectified imagery is estimated at 6-18 m. Images having apparent gross positioning errors were excluded from the study. Shorelines were digitized in the ArcGIS environment from the aerial base using standard techniques (Kraus et al. 2006). The study shoreline was identified as high-water line as defined by National Oceanographic and Atmospheric Administration (2000) and Leatherman (2003). Additional vector shorelines were retrieved from the National Ocean Service (NOS 2005), Texas Bureau of Economic Geology (BEG 2004), and the United States Geologic Survey (USGS) (Morton et al. 2004). In total, 28 shorelines were available from 28 unique dates between 1856 and 2006.

Spit growth was evaluated by establishing two baselines fronting the Gulf of Mexico shorelines of Matagorda Peninsula and Matagorda Island. For Matagorda Peninsula, the baseline originated at the west jetty of Matagorda Ship Channel. The origin of the Matagorda Island baseline was placed at the observed origin of the Matagorda Island spit. Spit growth along each baseline was measured in ArcView 3.2 using BeachTools (Hoeke et al. 2001). Analysis transects were generated along the baseline at 3-m intervals, and the distance of the last transect to intersect the spit shoreline was recorded.

The width of Pass Cavallo was measured from the limited shoreline data that extended into the channel from both sides of the inlet. Inlet width was evaluated in ArcMap from the westernmost extent of Matagorda Peninsula to the easternmost extent of Matagorda Island. Each measurement was recorded along a reference line aligned to the axial orientation of Matagorda Peninsula. This line was positioned at the narrowest section of Pass Cavallo, and then the distance across the inlet was recorded.

Inlet width and Spit Growth

Analysis of available shoreline data showed that the evolution of Pass Cavallo can be generalized into three eras of morphologic behavior (Figures 6 and 7): (1) relative

stability prior to 1963, (2) instability and rapid closure from 1963 to the mid-1980s, and (3) relative stability subsequent to 1990.

The initial decrease of tidal prism at Pass Cavallo due to subdivision of Matagorda Bay by the Colorado River caused significant shoaling within the inlet and a navigation concern (Harwood 1973; USACE 1992). Despite this, island morphology was stable, and minimal spit growth is observed during this time. Pass Cavallo maintained a width greater than 3 km between 1856 and 1965. Shoreline change during these years typically shows one or more (inter- or supra-tidal) islands in or around the entrance. The only emergent feature was a small island (called Pelican Island) between Matagorda Peninsula and Island, which first appeared in 1952. Hurricane Carla made landfall at Pass Cavallo in 1961 with an estimated maximum surge elevation of 3.7 m. Extreme conditions associated with this hurricane created 32 washovers along Matagorda Peninsula (Morton et al. 1976) and presumably forced sediment out of Pass Cavallo to create the maximum width of 3.5 km observed in 1965. Overall, Matagorda Peninsula receded approximately 90 m during Era I, while Matagorda Island remained unchanged.

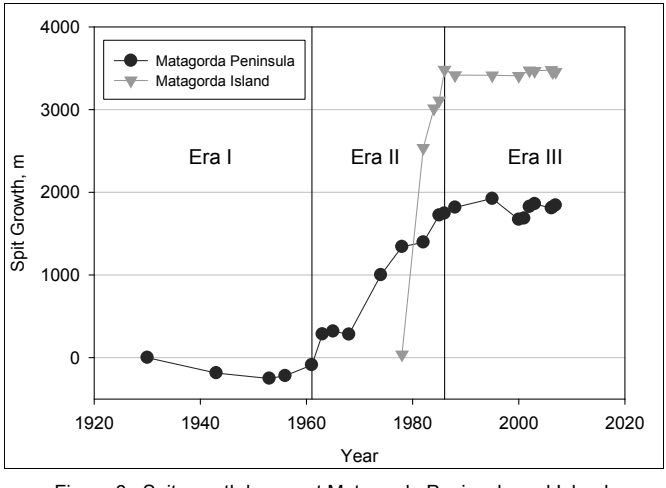

Figure 6. Spit growth by era at Matagorda Peninsula and Island.

The additional loss of tidal prism through Pass Cavallo due to the opening of the MSC (completed in 1966) resulted in significant morphologic change at the inlet, ushering in Era II. This timeframe is characterized by southwestward growth of Matagorda Peninsula that occurred in a rapid, step-wise fashion. Periods of rapid growth are followed by retarded growth and relative inactivity. Net progradation of Matagorda Peninsula between 1963 and 1988 was 1.53 km. In conjunction with this rapid growth on the east side of the inlet, a spit emerged from Matagorda Island in 1978 and rapidly prograded at a high rate to the north-northeast, recurving into Pass Cavallo by 1982. During this 4-year time span, the spit grew approximately 2.5 km. This high rate of

growth continued through 1986; when total spit length reached 3.49 km from the point of origin. Inlet width decreased by approximately 2.67 km, at a rate of 127 m/year over this 21-year period. Potential sources for this material are discussed in the following section.

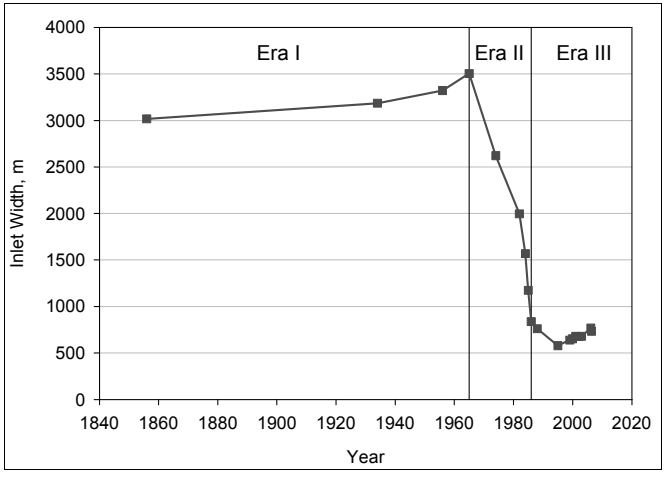

Figure 7. Width of Pass Cavallo, 1856 to 2006.

An apparent maturation of the system occurred in the mid-1980s, as Pass Cavallo achieved equilibrium with tidal forcing in the mid-1980s (Era III). Between 1986 and 2006, spit growth rates of Matagorda Peninsula and Matagorda Island decreased. Matagorda Peninsula prograded 95 m (~5 m/year), whereas the Matagorda Island spit receded west by 24 m (~ 1 m/year). Inlet width decreased by 160 m (9.5 m/year) over this time period.

In summary, Matagorda Peninsula prograded by 1.56 km from 1963 to 2003 and Matagorda Island prograded 3.45 km between 1974 and 2003. Overall, inlet width at Pass Cavallo decreased by 2.76 km. Shoreline change from 1965 through 2006 is shown in Figure 8. Note that although lateral growth of the spits decreased in the 1990s, the planforms began to extend seaward as more sediment was deposited within the inlet complex (1988-2006).

Sediment Sources

Tidal prism calculations indicated that Pass Cavallo was experiencing a surplus of sediment. Morphology change at the inlet subsequent to the opening of the MSC has confirmed that Pass Cavallo has been functioning as a sink within the local sediment budget. This section discusses potential sources for the large amount of material that has accumulated within the inlet complex over the last 40 years.

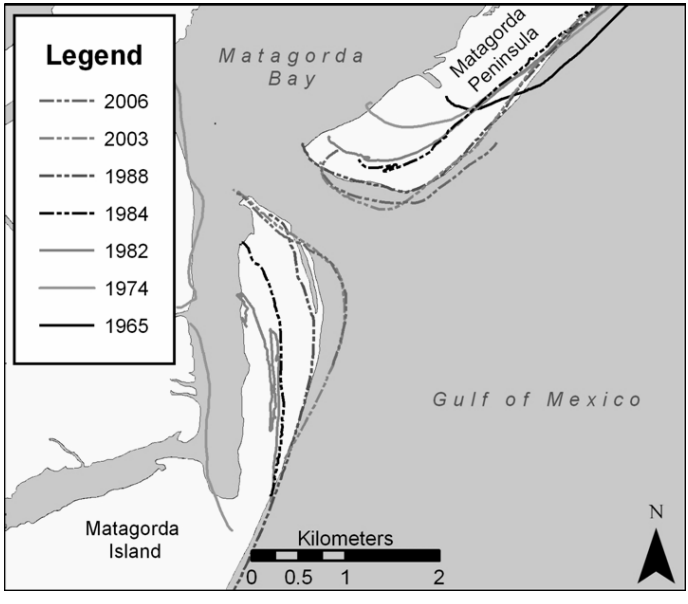

Figure 8. Shoreline time series showing spit progradation into Pass Cavallo.

Ebb-tidal shoals form as a balance between the transporting capacity of the ebb current at an inlet and the capacity of waves to transport material to and away from the inlet. Harwood (1973) studied the flood shoal at Pass Cavallo, which is an extensive sandy platform that protrudes into Espiritu Santo Bay. Flood shoals do not directly depend on wave action for their formation and consist of sediment entering the channel that is transported toward the bay by the flood current. Ebb shoals and flood shoals greatly differ in that, if the inlet reduces in size, migrates, or closes, the ebb shoal will be acted upon by waves and partially or completely disperse, whereas the flood shoal will remain intact. An entire ebb shoal or just a portion of it can become abandoned if an inlet is relocated, if jetties are constructed to confine the ebb current, or if the tidal prism, hence ebb current, decreases. Pope (1991) documents inlets on the southeast coast of the United States for which jetty construction restricted the width of the ebb jet and caused abandonment of lateral portions of the ebb shoal, which then migrated on shore. Kraus (2006) gives a more general discussion of ebb–shoal abandonment and cites other references to the literature. The abandoned portions of ebb shoals will migrate onshore, called "ebb-shoal collapse," if those portions are within the littoral zone.

Ebb shoal volume has been well correlated with tidal prism by Walton and Adams (1976), who concluded that ebb shoal volumes can be larger on coasts receiving less wave exposure, because there would be less transporting capacity to remove the sediment deposited by the ebb current. The following empirical formula was presented by Walton and Adams (1976) to compute the ebb shoal volume V_E for inlets in equilibrium on

mildly exposed (to waves) coasts. The Galveston Entrance, TX, and Aransas Pass, TX, were among the 16 inlets analyzed to obtain this correlation:

$$V_E = 8.458 \times 10^{-3} \; P^{1.23} \tag{3}$$

in which V_E and P are expressed in m^3, a conversion from units of cubic yards and ft^3, respectively, from the original formula.

For 1856, Harwood (1973) estimated the tidal prism of Pass Cavallo to be 4.79×10^8 m^3, and for year 2004, we estimate it at 1.84×10^8 m^3 (includes wind tide). By Eq. 3, these tidal prisms give V_E-values of about 400 million m^3 and 124 million m^3, respectively, assuming the ebb shoal achieved equilibrium volume for each of the tidal prisms. If these estimates are approximately correct, they indicate that since about 1966, when the MSC was cut, the excess volume (400 – 124 = 276 million m^3) has been abandoned by the gradually declining tidal prism at Pass Cavallo. Most of the abandoned sand-sized material in the ebb shoal will migrate down coast and on shore and be partially responsible for growth and volume increase of the spits to either side of the inlet.

The hypothesis for abandonment and collapse of a portion of the ebb shoal at Pass Cavallo is qualitatively supported by the analysis of Morton (1977), who noted that spit progradation and shoreline advance at Decros Point (western end of Matagorda Peninsula) did not appear compatible with recession of the shoreline downdrift of the MSC. Morton (1977) found excess material in the downdrift compartment, described the source as "problematic," and suggested bank and channel erosion as potential sources. These sources are considered by the authors to be inadequate to account for the observed long-term spit growth.

It is hypothesized here that sediment from offshore deposits are also contributing to growth at the end of Matagorda Peninsula and Matagorda Island. The likely source is partial abandonment and collapse of the ebb shoal at Pass Cavallo. This theory is supported by the limited bathymetric data available for the inlet (modern data are not available for comparison). Figure 9 shows a 1934 NOS hydrographic survey (NOS 1934) of Pass Cavallo, overlaid with the 1995 shoreline (BEG 2004). At the time of the survey, the inlet channel was located at the western side of the inlet, and a large ebb shoal is apparent offshore of the terminus of Matagorda Island. Shoreline recession along the eastern extent of Matagorda Island, in addition to the volume of material contained within this shoal, support the deposit as being the source of material for spit progradation into the inlet complex.

Most of the abandonment has occurred gradually over the 43 years since opening of the MSC. After the material in the abandoned shoal is depleted, a significant source of sand tending to close Pass Cavallo will be eliminated, and it is feasible that the inlet will grow (but not return to its historic maximum because of the reduction in tidal prism). The trend in Pass Cavallo for a new equilibrium or possible growth is consistent with the shoreline change analysis of inlet width.

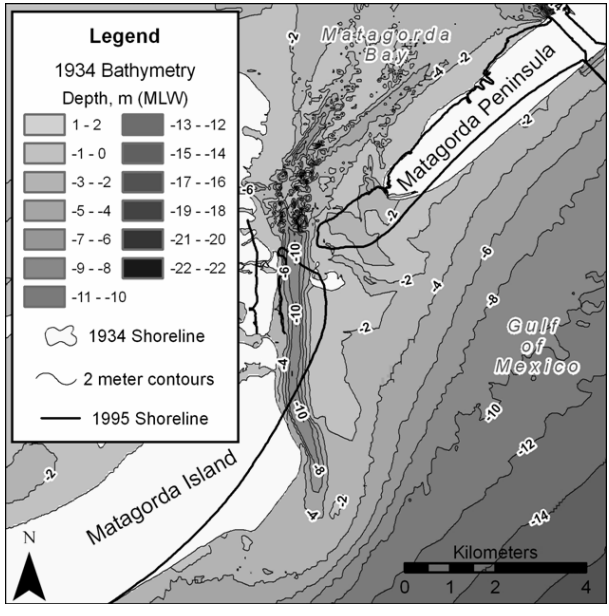

Figure 9. Pass Cavallo channel and ebb shoal in 1934.

Spit progradation on the west side of Pass Cavallo probably also occurs as part of the down-drift inlet offset process (Hayes et al. 1970). The predominant direction of littoral drift is from the northeast to the southwest along Matagorda Peninsula. There are reversals in transport during southerly winds and some storms. Under these conditions, a spit emerged from Matagorda Island and prograded 3.5 km northeast into the inlet. The southwest tip of Matagorda Island shoreline experienced recession (Paine and Morton 1989), and this eroded material could also contribute to support growth of the spit.

CONCLUDING DISCUSSION

Measurements and modeling indicate that the flow through Pass Cavallo is approaching a dynamic equilibrium. This natural inlet has withstood the ebb shoal collapse associated with reduced tidal prism and deposition within the inlet geomorphic complex. The evidence present herein demonstrates that it is not likely that Pass Cavallo will close in the near future. Simple theory indicates that tidal inlets on diurnal tide coasts require a weaker mean-maximum current for cross-sectional channel area stability (Kraus 2007), and the location of Pass Cavallo in the southwest corner of Matagorda Bay works to its favor in having an increased ebb flow due to wind prevalent from the north and northeast in the autumn and winter.

ACKNOWLEDGEMENTS

This research was supported by the Calhoun County Navigation District, through the U.S. Army Engineer District, Galveston, Texas. Permission was granted by Headquarters, U.S. Army Corps of Engineers, to publish this information.

REFERENCES

Anders, F.J., and Byrnes, M.R. (1991). "Accuracy of shoreline change rates as determined from maps and aerial photographs," *Shore & Beach* 59(1), 17-26.

Bouma, A.H., and Bryant, W.R. (1969). "Rapid delta growth in Matagorda Bay, Texas," *Coastal Lagoons, a Symposium*, Univesidad Nacional Autónoma de México, 171-189.

Bruun, P. (1968). "*Tidal inlets and littoral drift*," University Book Co., Oslo, Norway.

Bureau of Economic Geology (BEG). (2004). "Upper coast Gulf of Mexico vector shoreline data," Texas BEG, The U. of Texas at Austin, Austin, TX.

Escoffier, F.F. (1940). "The stability of tideal inlets," *Shore and Beach*, 8(4), 114-115.

Harwood, P.J.W. (1973). "Stability and geomorphology of Pass Cavallo and its flood delta since 1856, central Texas coast," M.A. thesis, The U. of Texas at Austin, Austin, TX, 185 p.

Hayes, M.O., Goldsmith V. and Hobbs, C.H. III (1970). "Offset coastal inlets," *Proceedings12th Coastal Engineering Conference*, ASCE, 1187-1200.

Hoeke, R. K., Zarillo, G. A., and Synder, M. (2001). "A GIS based tool for extracting shoreline positions from aerial imagery (BeachTools)," Coastal and Hydraulics Engineering Technical Note CHETN IV-37, U.S. Army Engineer Research and Development Center, Vicksburg, MS, 12 p.

Jarrett, J. T. (1976). "Tidal prism-inlet area relationships," GITI Report 3, U.S. Army Engineer Waterways Experiment Station, Vicksburg, MS.

Kraus, N. C. (2006). "Coastal inlet functional design: Anticipating morphologic response," *Proceedings Coastal Dyanmics '06*, CDROM, ASCE, 14 p.

Kraus, N. C. (2007). "Coastal Inlets, Texas, USA," *Proceedings Coasal Sediments '07*, ASCE, this volume.

Kraus, N.C., Lin, L., Batten, B.K., and Brown, G.L. (2006). "Matagorda Ship Channel, Texas: Jetty stability study," Technical Report ERDC.CHL-06-7, U.S. Army Engineer Research and Development Center, Coastal and Hydraulics Laboratory, Vicksburg, MS, 153 p.

Leatherman, S.P. (2003). "Shoreline change mapping and management along the U.S. east coast," *Journal of Coastal Research* Special Issue 38, 5-13.

Morton, R.A. (1977). "Nearshore changes at jettied inlets, Texas coast," *Proceedings Coastal Sediments '77*, ASCE, 267-286.

Morton R.A., Miller, T.L., and Moore, L.J. (2004). "National Assessment of Shoreline Change: Part 1, Historical Shoreline Changes and Associated Coastal Land Loss Along the U.S. Gulf of Mexico," USGS open file report 2004-1043, 44 p.

Morton, R.A., Pieper, M.J., and McGowen, J.H. (1976). "Shoreline changes on Matagorda Peninsula (Brown Cedar Cut to Pass Cavallo), an analysis of historical changes on the Texas Gulf shoreline," Geological Circular 76-6, Bureau of Economic Geology, The U. of Texas at Austin, Austin, TX, 37 p.

National Oceanographic and Atmospheric Administration (NOAA). (2000). "Tide and current glossary," U.S. Department of Commerce, NOAA, NOS, Center for Operational Oceanographic Products and Services, 29 p.

National Ocean Service (NOS). (2005). "Shoreline data rescue project of Matagorda Bay, Texas. Vector shorelines," National Ocean Service, National Oceanographic and Atmopheric Administration, Silver Spring, MD.

National Ocean Survey (NOS). (1934). "Lead-line survey of Gulf Coast of Texas at Pass Cavallo, NGDC number 03F11494, Survey H05864," U.S. Department of Commerce, NOAA, NOS, Silver Spring, MD.

Nishi, R., Kraus, N. C., and Kawamori, A. (2007). "Fundamenal study of inlet geomorphology: An approach for a global A-P relationship," *Proceedings Coastal Sediments '07*, ASCE, this volume.

Paine, J.G ., and Morton, R.A. (1989). "Shoreline and vegetation-line movement, Texas Gulf coast, 1974 to 1982," Texas Bureau of Economic Geology, Geological Circular 89-1, The University of Texas at Austin, Austin, TX, 50 p.

Pope, J. (1991). "Ebb delta and shoreline response to inlet stabilization, examples from the southeast Atlantic Coast," *Proceedings Coastal Zone '91*, ASCE, 643-654.

Price, W.A. (1952). "Reduction of maintenance by proper orientation of ship channels through tidal inlets," *Proceedings 2nd Coastal Engineering Conference*, Council on Wave Research, 243-255.

Texas Natural Resources Information System (TNRIS). (1995). Digital orthophotograph quarter quadrangles, 1 meter resolution, 20 February 1995, URL: http://www.tnris.state.tx.us/digitaldata/1mdoqs.htm.

U.S. Army Corps of Engineers (USACE). (1992). "Inlets along the Texas Gulf coast," Section 22 Report, Planning Assistance to States Program, U.S. Army Engineer District, Galveston, TX, 56 p.

Van de Kreeke, J. (1985). "Stability of tidal inlets - Pass Cavallo, Texas," *Estuarine, Coastal and Shelf Science* 21, 33-43.

Van de Kreeke, J. (1990a). "Can multiple tidal inlets be stable?," *Estuarine, Coastal and Shelf Science* 30, 261-273.

Van de Kreeke, J. (1990b). "Stability analysis of a two-inlet system," *Coastal Engineering* 14, 481-497.

Wadsworth, A.H. (1966). "Historical deltation of the Colorado River, Texas," in *Deltas in their Geological Framework*, M. L. Shirley, ed., Houston Geological Society, 99-105.

Walton, T.L., and Adams, W.D. (1976). "Capacity of inlet outer bars to store sand," *Proceedings 15th Coastal Engineering Conference*, ASCE, 1,919–1,937.

Ward, G.H. (1982). "Pass Cavallo, Texas: Case study of tidal-prism capture," *Journal of Waterway, Port, Coastal and Ocean Division* 108(WW4), 513-525.

MORPHOLOGIC RESPONSE TO A NEW INLET, PACKERY CHANNEL, CORPUS CHRISTI, TEXAS

Deidre D. Williams[1], Nicholas C. Kraus[2], Carl M. Anderson[3]

1. The Conrad Blucher Institute for Surveying and Science, Texas A&M University-Corpus Christi, 6300 Ocean Drive, Corpus Christi, Texas 78412. williams@lighthouse.tamucc.edu.
2. U.S. Army Engineer Research and Development Center, Coastal and Hydraulics Laboratory, 3909 Halls Ferry Road, Vicksburg, MS 39180-6199. Nicholas.C.Kraus@erdc.usace.army.mil.
3. U.S. Army Engineer District, Galveston, 2000 Fort Point Rd., Galveston, TX 77550. Carl.M.Anderson@swg02.usace.army.mil.

Abstract: In Jul 2005, Packery Channel was opened by Hurricane Emily during the second year of its construction. This inlet connects Corpus Christi Bay and Upper Laguna Madre to the Gulf of Mexico, and it is the first artificially cut inlet in Texas in 17 years. The inlet has remained open and navigable for shallow-draft recreational boats despite construction delays, and its parallel dual jetties were completed in Sep 2006. A physical process monitoring program was initiated prior to construction in 2003 to track the evolution of the channel, surrounding nearshore, and adjacent beaches. Maximum ebb current in the inlet often exceeds 1 m/s, and an ebb shoal has not yet formed. The shorelines adjacent to the jetties, as well as the seaward longshore bars, respond to seasonal changes in wind direction, hence direction of longshore sand transport. Shoreline change varies seasonally, but adjacent to the inlet the shoreline is nearly symmetrical.

INTRODUCTION

Environmental interests as well as the commercial and recreational fishing and boating communities in Texas have long been proponents for opening small inlets to connect its bays and lagoons to the Gulf of Mexico (Lockwood and Andrews 1952; Carothers and Innis 1960). Such inlets modulate salinity in the bays and lagoons, and provide a path for migration of juvenile marine organisms. In the early 1970s, such a “Fish Pass” was cut

across Mustang Island and into Corpus Christi Bay, but it gradually shoaled and closed (Behrens1979). The Texas experience with new small inlets is varied, with examples of inlets expanding and deepening too rapidly (Rollover Pass – Bales and Holley 1989), inlets closing too quickly (Yarbrough Cut – Lockwood and Andrews 1952), and yet other inlets being relatively stable (Mitchells Cut – U.S. Army Corps of Engineers (USACE) 1992). There is a general need for improved inlet design for the Texas coast (see Kraus, this issue, for related discussion). Newly created inlets will alter the surrounding coastal morphology at several space and time scales (Kraus 2006).

Historically, Corpus Christi Bay, Texas, was served by two natural inlets (Price 1952) or "passes" in local terminology, Aransas Pass (shared with Aransas Bay to the north) on the north side and Corpus Christi Pass on the south side, in the SSE corner (Fig. 1 and Fig. 2). Dredging of Aransas Pass started in 1912, and its re-direction into Corpus Christi Bay in 1924 caused Corpus Christi Pass to slowly shoal and become a flat ephemeral pass that was overwashed during more severe tropical storms and hurricanes (Price 1952). For many years, local interests have wanted to reopen the old Corpus Christi Pass through an existing dead-end channel called Packery Channel for water exchange. An additional navigational amenity is that access to the Gulf of Mexico from the Upper Laguna Madre and Corpus Christi Bay system would be about 3 miles (5 km) rather than the 23-mile (37 km) transit to Aransas Pass.

The North Padre Island (Packery Channel), Nueces County, Texas, Storm Damage Reduction and Environmental Restoration Project was authorized in the Water Resources Development Act 1999 as a Federal project with Nueces County, Texas, as the original local sponsor. The City of Corpus Christi assumed local sponsorship in 2000. Construction began in Oct 2003, and the inlet officially opened in Oct 2006. It is stabilized by two parallel jetties oriented 12 deg north of shore normal. The jetties are spaced 300 ft (91 m) apart extending 1,430 ft (427 m) into the Gulf of Mexico. The channel is to be maintained to a depth of 14 ft (4.3 m) MLLW. The original design study estimated that, after equilibrium, a dredging cycle of 1-3 years would be required (Kraus and Heilman 1997). Sand dredged from the channel as new work and maintenance material will be placed on adjacent beaches as a shore-protection element.

In Jul 2005, Packery Channel was opened by Hurricane Emily during construction of the jetties. The inlet connects Corpus Christi Bay and Laguna Madre to the Gulf of Mexico, the first new artificially created inlet in Texas in 17 years (Figs. 1 and 2), and now effectively defines the boundary between Padre Island and Mustang Island to the north. Inlet construction was in its second year when the storm surge eliminated the approximately 350-ft (107 m) wide sand plug that separated the channel from the Gulf and served as a land bridge for construction. The inlet has remained open since then.

This paper presents selected results of the 3 years of physical process monitoring of the channel, shoreline, nearshore bathymetry, and current. In addition to its general benefit for improving knowledge of coastal inlets, monitoring supports adaptive management of Packery Channel and adjacent beaches as a sediment-sharing system.

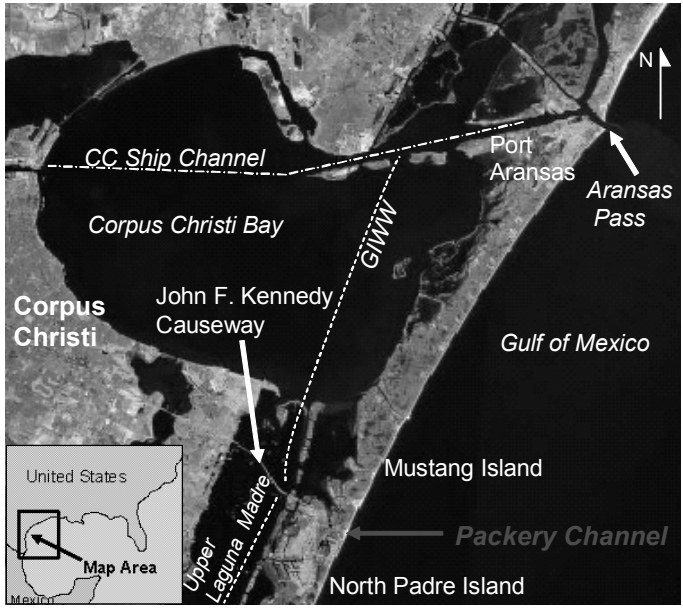

Fig. 1. Location map for region of Packery Channel, Texas.

MONITORING PROGRAM

In anticipation of construction, in Aug 2003 the USACE Galveston District initiated baseline and construction monitoring of morphology change at Packery Channel and the adjacent beaches through a contract with Texas A&M University-Corpus Christi (TAMU-CC). The functional design of Packery Channel identified probable responses in morphology (Kraus and Heilman 1997) and hydrodynamics (Brown and Militello 1997). The monitoring program includes surveys of the beach profile, ebb shoal, and channel; sediment sampling; measurement of channel current; aerial photography; shoreline and upper beach surveys; and development of a combined wave, circulation, and morphology change numerical model. Survey data are recorded relative to NAVD88, and depths are referenced to MSL (MSL = NAVD88 + 0.48 ft). The monitoring area encompasses 2.4 miles (3.8 km) of the Packery Channel inland waterway from the Gulf Intracoastal Waterway (GIWW) intersection to State Highway (SH) 361, the 1 mile (1.6 km) entrance channel west of SH361, and 8 miles (13.2 km) of adjacent beach from south of Bob Hall Pier on Padre Island to north of Mustang Island State Park.

Access to data, aerial photography, and real-time current measurements is available at the Texas Inlets Online website (http://goliath.cbi.tamucc.edu/TexasInletsOnline/). The physical processes monitoring program was described by Williams et al. (2005). An independent environmental monitoring program is also being conducted (HDR/Shiner Moseley 2006). Past monitoring was accomplished in part by coordination with construction milestones listed in Table 1.

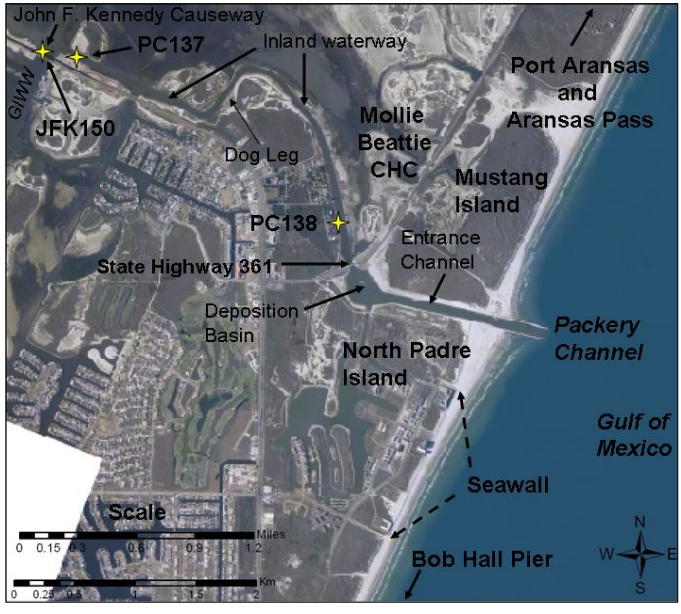

Fig. 2. Packery vicinity map, 16 Aug 2006 (Tobin Aerial Photography).

RESULTS

Water Level, Wind, and Channel Current

Packery Channel is located near two long-term tide gauges, a National Ocean Service (NOS) gauge in the Gulf of Mexico at Bob Hall Pier called "Corpus Christi," and the other on the bay side and along the original Packery Channel inland waterway (Fig. 2). Water level along the Texas coast is controlled by the astronomical tide, local wind, and seasonal change in Gulf water level. A seasonal or low-frequency fluctuation occurs with highs around May and October, and lows in August and December through January. The tide at the Corpus Christi gauge and Packery Channel is diurnal with diurnal range of 1.63 ft (0.50 m) and 0.38 ft (0.12 m) respectively.

The wind along the Texas Coast is strongly bimodal with persistent southeasterly wind from March or April to August or September. Northerly episodic winds accompany frontal passage from September or October to February or March. Southerly winds increase as fronts approach, with rapid reversal in direction as the systems move off the coast. With the opening of Packery Channel, the strong wind enhances water exchange between Corpus Christi Bay and the Gulf of Mexico. Persistent southeasterly and onshore directed easterly wind force water from the Gulf into the bay system, whereas northerly, particularly northwesterly wind, forces water toward the Gulf. Prior to opening of Packery Channel, northwesterly winds set up water in the SE corner of Corpus Christi Bay causing water to rise along the flats adjacent to SH361, now known

as the Mollie Beattie Coastal Habitat Community (CHC). With a pathway to the Gulf through Packery Channel, water exits this portion of the bay during frontal passages, greatly enhancing the ebb current flow in the inlet.

Table 1. Packery Channel Construction Timeline

Activity	Date	Comment
Construction begins	Oct 03	---
Dredge inner channel	Dec 03 - Apr 04	---
Land dredged to form channel; material placed on south beach	Apr – Jul 05	136,077 cy (104,038 m^3) bypassed
Channel opens (Hurricane Emily)	19 Jul 05	Removed sand plug
Narrow channel remains open	Jul - Dec 05	---
Channel dredged; material placed on beach south of inlet	Jan - Feb 06	679,089 cy (519,200 m^3) bypassed
S jetty completed to 1,430 ft (427 m)	Mar 06	---
N jetty completed to 1,430 ft (427 m)	Jun 06	Landward end incomplete
Scour hole at S Jetty filled with rock and concrete slabs	Aug 06	---
Landward end of N jetty completed	Sep 06	---
Official opening. Transfer to local sponsor in progress	Oct 06	---

Three current monitoring stations were deployed to measure the current in Packery Channel and in the GIWW near the Packery Channel intersection (Fig 2). The magnitude of the current is either enhanced or suppressed during periods of strong wind (Fig. 3). The primary Packery Channel current station, PC138, is located 0.25 mile (0.4 km) north of the SH361 Bridge (http://lighthouse.tamucc.edu/qc/138/). The current follows the phase of the tidal signal measured at the Corpus Christi gauge in the Gulf of Mexico. A second station, PC137, is located near the Packery water level station. The Packery stations were deployed during Sep 2005, each equipped with a side looking SonTek Argonaut mounted on existing structures at mid-depth. Data are collected remotely and posted in real time. The current speed at PC138 is an order of magnitude greater than at PC137. The difference in speed is related to distance from the inlet and change in channel orientation (dog leg). In the inland waterway of Packery Channel, the dog leg effectively separates the western section of the channel from the eastern channel. The entrance channel begins at the SH361 bridge and deposition basin.

Since deployment in Sep 2005, the average ebb and flood current speeds have been 0.44 and 0.38 m/s, respectively, and a maximum ebb current of 1.85 m/s and maximum flood current of 1.56 m/s have been measured during strong wind. Flood flow is enhanced by strong E-SE wind forcing water against the Gulf shoreline and into the bay/lagoon system through the channel (Fig. 4). Strong E-SE wind typically precedes frontal passage. Ebb flow is enhanced during frontal passage as water set-up along the northern

shore of the bay/lagoon system by E-SE wind is released, in part, through Packery Channel. Northerly winds can initiate abrupt reversal in current direction. Ebb flow will often continue for several days as the bay system returns to equilibrium level.

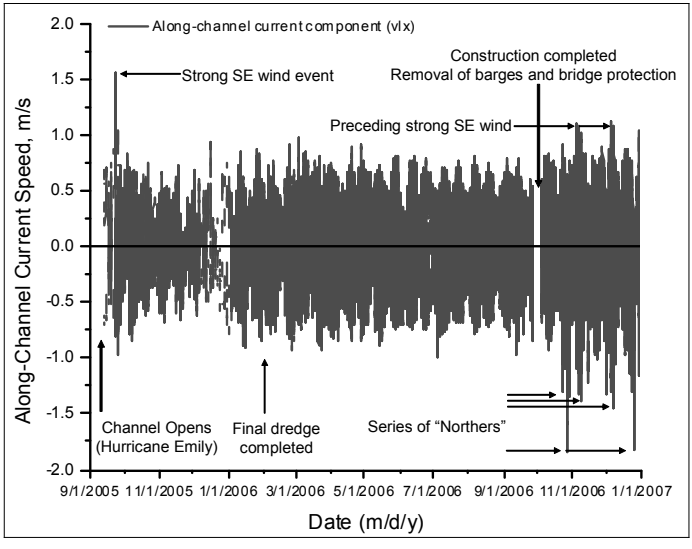

Fig. 3. Current record for PC138 showing key events.

The GIWW current meter (JFK150) is bottom mounted at a depth of 26 ft (8 m) in the center of the channel under the John F. Kennedy Causeway Bridge. Current in the GIWW is strongly influenced by the southeasterly wind that dominates the signal during the spring and summer (Fig 5). Although the signal follows the Gulf tide, flood flow pushing southward may be subdued or reversed during persistent SE wind. The current flows northward under solar diurnal SE forcing with reversals during frontal passage. The average current speed toward Corpus Christi Bay to the north is 0.23 m/s, and to the south it is 0.20 m/s. The maximum current speed toward the north recorded since Jun 2006 was 0.79 m/s and toward the south 0.78 m/s.

Sediment

Sediment in the study area is supplied by two sources. The bay and lagoon supply silt and shell hash introduced through erosion of flats and shoreline. North Padre and Mustang Island beaches supply fine sand. Finer grain size material with a component of shell hash is found in the inland waterway nearest to the GIWW where weaker currents allow deposition of sediment originating in the adjacent bay and lagoon. The deposition basin includes the influence sedimentation with fine material found around the periphery and deeper central sections. The entrance channel bottom is composed of fine sand with a median grain size of 0.15 mm. Sediment grain size increases moving toward the barrier islands where the median grain size of North Padre and Mustang Island sand is, on average, 0.16 mm.

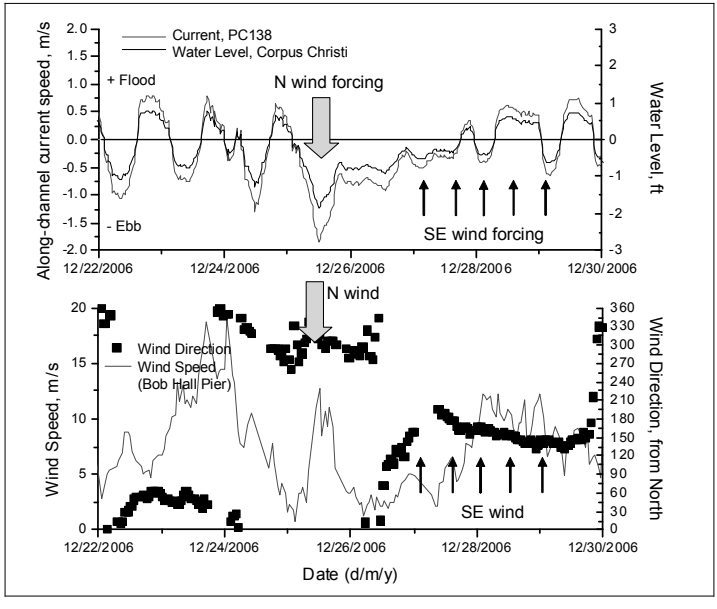

Fig. 4. Response of current to wind forcing at PC138.

Long-Term Shoreline Change and Longshore Sand Transport Rate

Along this coast, long-term shoreline change is recession of about 5 ft/yr (1.5 m/yr) (Morton and Pieper 1977). The design study for the project (Kraus and Heilman 1997) indicated that Packery Channel is located near a divergent nodal point in longshore sand transport. They estimated that the net direction of transport is to the south, with a gross rate of 150,000 to 250,000 cu yd/yr and net rate of 45,000 to 70,000 cu yd/yr.

Nearshore and Channel Morphology

In the early stages of jetty construction from Aug 2004 to Jul 2005, sand accreted between the short jetties. The sand plug that functioned as a land bridge for construction activities began to slowly advance seaward as did the adjacent shoreline to the north. Once the storm surge associated with Hurricane Emily removed this limiting feature, changes in morphology both within and adjacent to the inlet accelerated. In addition to Emily, Hurricanes Katrina and Rita increased flow in the new inlet during autumn of 2005. The narrow entrance channel remained open and navigable by small craft. In Jan 2006, with the channel still open, the entrance was dredged to facilitate barge operation associated with construction, as well as to replace sand eroded at the south end of the seawall during the active storm season. The incomplete north jetty limited the extent of dredging into the Gulf of Mexico.

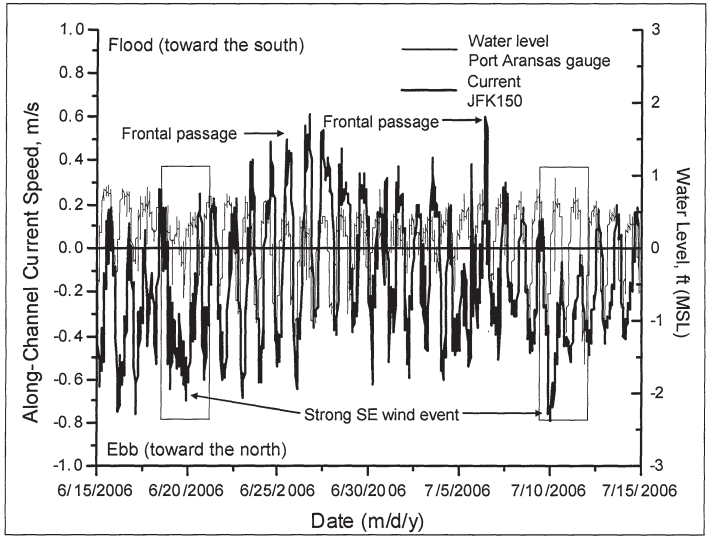

Fig. 5. Wind influence on GIWW current direction.

After the channel opened during Hurricane Emily, shoaling occurred at the existing mouth as observed on 29 Jul 2005 (Fig. 6). Depth in the channel where the sand plug had been was on the order of 2 to7.5 ft (0.6 to 2.3 m) with deepest areas in the center channel. The depth at the planned gulfward end of the jetties was 7 to 13 ft (2 to 4 m).

A survey was conducted on 6 Mar 2006 after completion of dredging in Feb 2006. The mouth of the channel had scoured, with shoaling evident adjacent to the jetties west of the mouth. Scour developed at the ends of the uncompleted north jetty and completed south jetty with depths of 20 to 22 ft (6 to 7 m) and 20 to 26 ft (6 to 8 m), respectively, where the pre-construction depths had been 10 to 13 ft (3 to 4 m) (Fig. 7). This broad region of scour extended beyond the jetties offshore of the mouth with depths of 17 to 20 ft (5 to 6 m). Seven months after Emily forced the channel open, no offshore bar or ebb shoal had formed.

The response of the channel to spring waves from the E-SE was captured in the 17 May 2006 survey (Fig. 8). A well-defined sand bar with crest at a depth of 7 ft (2 m) intersected the south jetty approximately 450 ft (137 m) from its seaward end. The south jetty was completed in Mar 2006, while construction of the northern jetty continued. No longshore bar adjacent to the north jetty appears in this survey. In the entrance channel, deposition occurred along the north jetty and erosion along the south jetty. A probable source for the sediment along the north jetty was a gap that existed between the channel revetment and the incomplete north jetty. This gap allowed transport of sand into the channel during storm surges prior to its closure in Aug 2006. Channel center depth varied from 9 to15 ft (3 to 5 m). Scour at the seaward ends of the north and south jetties decreased to 15 to 19 ft (4.5 to 5.8 m) and 18 to 20 ft (5.5 to 6 m), respectively.

Reduction in scour at the south jetty was related, in part, to placement of the final stone at the offshore extent. The two regions of jetty tip scour on the north and south merged and extended with depths of 15 to 20 ft (4.5 to 6 m) radiating offshore from the mouth and no ebb shoal was present.

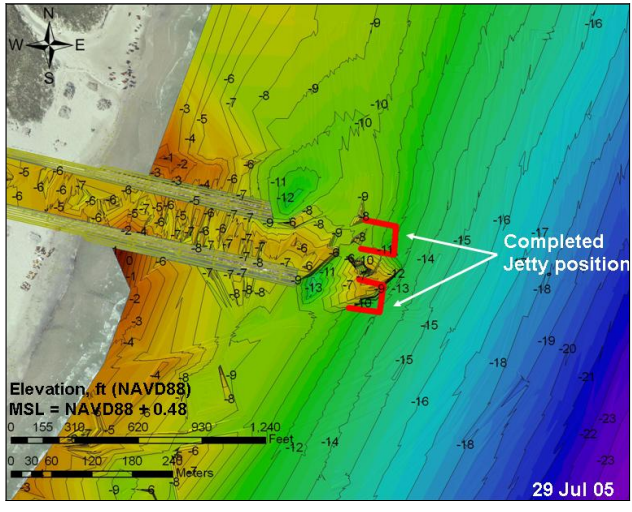

Fig. 6. Channel and nearshore morphology after Hurricane Emily (29 Jul 2005).

By Aug 2006, the offshore extents of both jetties were complete and onshore construction including the landward end of the north jetty was approaching completion. The south bar had become more defined under SE wind waves transporting sediment toward the north. This bar migrated 450 ft (137 m) offshore and was now in line with the end of the south jetty (Fig. 9). A possible jetty tip shoal developed to the north. In the channel, depth increased along the north jetty by 1 to 4 ft (0.3 to 1.2 m), while central channel depth remained variable with an average decrease of 1 to 2 ft (0.3 to 0.6 m). The offshore region of scour expanded, although a narrow, 40-ft (12-m) wide ridge developed between the jetty tip scour and offshore region of scour. Depth of the ridge was on the order of 16 ft (4.8 m). No ebb shoal or bypass bar was present.

The most recent (16 Dec 2006) survey was conducted after a transition period in weather patterns with numerous frontal systems moving off the coast. These abrupt, strong reversals in wind from SE to out of the NE-NW caused a reversal in sediment transport toward the south, changing the nearshore morphology adjacent to the inlet. In addition, prior to this time, the current had been astronomically dominated and only enhanced or subdued by SE wind forcing water from the Gulf into the bay-lagoon system. Two striking changes occurred as the nearshore responded to the reversal in the sediment transport system: 1) the south bar deflated and became less defined with a small shoal protruding offshore at northern end, and 2) a well defined bar developed north of the inlet (Fig. 10). Scour became more pronounced at the seaward end of the north jetty

where depths offshore of the mouth ranged from 14 to 25 ft (4 to 7.6 m) with the deeper region directly adjacent to the jetty. The narrow ridge identified 3.5 months prior widened to 190 ft (58 m), effectively separating the offshore scour from the jetty scour. The depth along the ridge decreased approximately 2 ft (0.6 m) to an average of 14 ft (4.3 m). No ebb shoal was present 1.5 years after the channel opened.

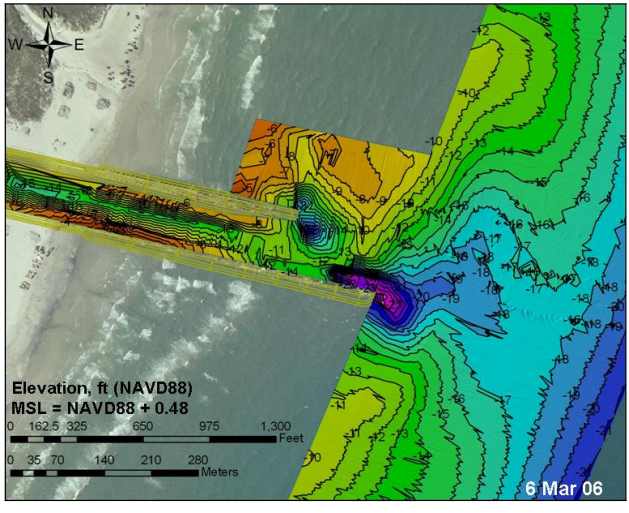

Fig. 7. Scour at channel mouth after final dredging (6 Mar 2006).

By 16 Dec 2006, the majority of the inner entrance channel had deepened, with transport of the scoured sediment toward the inlet mouth. Contours indicate forcing toward the Gulf (Fig. 10). No shoaling occurred at the channel mouth, with depths of 11 to 18 ft (3.4 to 5.5 m) across the entrance. The existence of this deep region at the mouth indicates that the source of the sand shoaling in the inner channel is from redistribution of existing channel sand. Scour along the jetties, particularly the northern jetty, is the likely source.

A strong ebb current exceeding 1.0 m/s with a maximum of 1.85 m/s was measured at PC138 from Oct 2006 through 16 Dec 2006. Over that period, ebb flow occurred more frequently and was sustained longer than flood flow due to strong forcing by N-NW wind during frontal passage. The persistent ebb flow is an effective forcing mechanism capable of redistributing channel sediment eastward toward the channel mouth and ultimately offshore into the Gulf of Mexico. The current in the entrance (between the jetties) will be stronger than that measured at PC138, because of the friction created by channel length and SH361 bridge piers between the entrance and PC138.

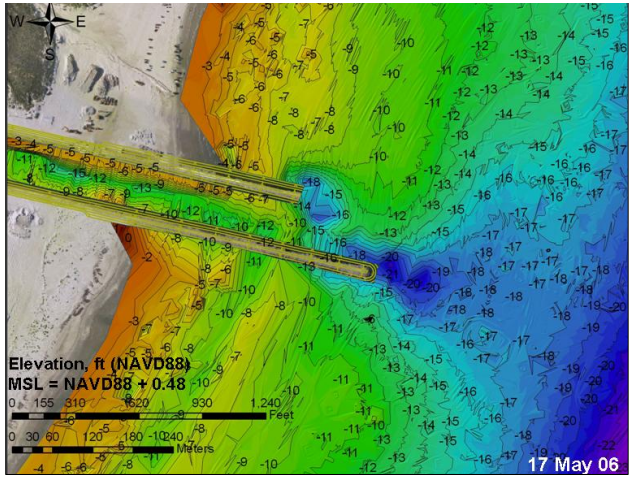

Fig. 8. Scour offshore of channel mouth (17 May 2006).

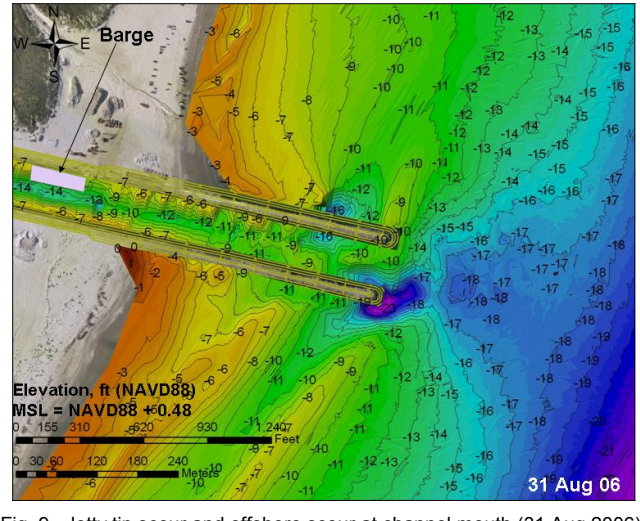

Fig. 9. Jetty tip scour and offshore scour at channel mouth (31 Aug 2006).

Shoreline Change and Beach Profile Response

Shoreline change beyond that attributable to seasonal and annual responses has so far been restricted to the region directly adjacent to the inlet and moderates within 1.5 miles (2.4 km) to the south and 1 mile (1.6 km) to the north. Surveys extended from south of Bob Hall Pier northward beyond Mustang Island State Park, a distance of 8.2 miles (13.2 km). The 1.5 to 2- ft (NAVD88) contour corresponds to the location of the berm crest and was selected for comparison to the Aug 2003 pre-construction baseline.

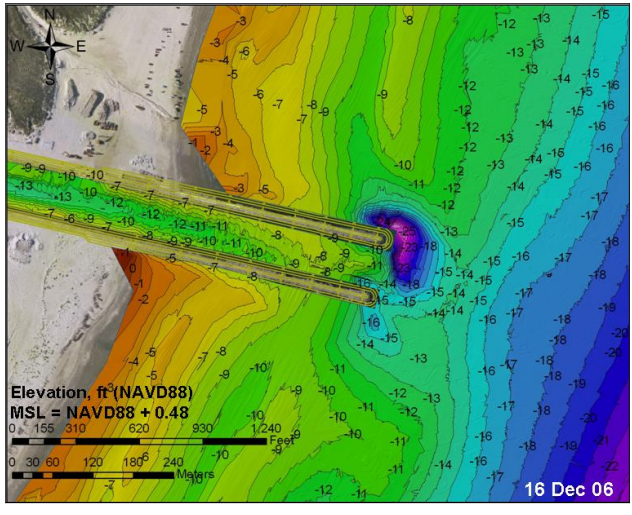

Fig. 10. Ridge between regions of scour offshore of channel mouth (16 Dec 2006).

The shoreline consistently advanced from the inlet to the south end of the seawall from Aug 2003 to Jul 2006. Near to the south jetty, the shoreline advanced a maximum of 400 ft (122 m). Advance in front of the seawall, ranging from a maximum of 200 ft (61 m) on the north end to a post-bypassing maximum of 155 ft (47 m) at the more variable south end, owes to mechanical bypassing (Fig. 11). After the active 2005 tropical storm season, the shoreline at the south end of the seawall receded some 100 ft (31 m), while the northern end remained stable. The shoreline maintained a net seaward position of on the order of 200 ft (61 m) nearest the north end of the seawall and a minimum of 80 ft (24 m) at the south end. Variability in shoreline position at the south end is likely related to distance from the sheltering by the jetties and may be exacerbated by the interaction of the terminus of the seawall and intersection of a paved access road that creates an unrestricted pathway for overwash during storm surge.

Shoreline change adjacent to the north jetty was more erratic, but moderated within 1 mile (1.6 km) of the inlet. During initial construction, shoreline advance near the north jetty was greater than that observed on the south side (Jul 2004 to Oct 2004). Shoreline recession to the 2003 baseline position from Oct 2004 to Jan 2006 was primarily due to sand lost around the incomplete landward end of the jetty during storm surge and may have been compounded by bypassing to the south around the incomplete seaward end of the northern jetty. Once the north jetty neared completion, the adjacent shoreline shifted to a maximum seaward position of 380 ft (116 m). As of Jul 2006, the northern shoreline advance was such that the north and south shoreline adjacent to the inlet were nearly symmetrical. The advance of the northern shoreline indicates at least intermittent transport to the south with impoundment at the jetty.

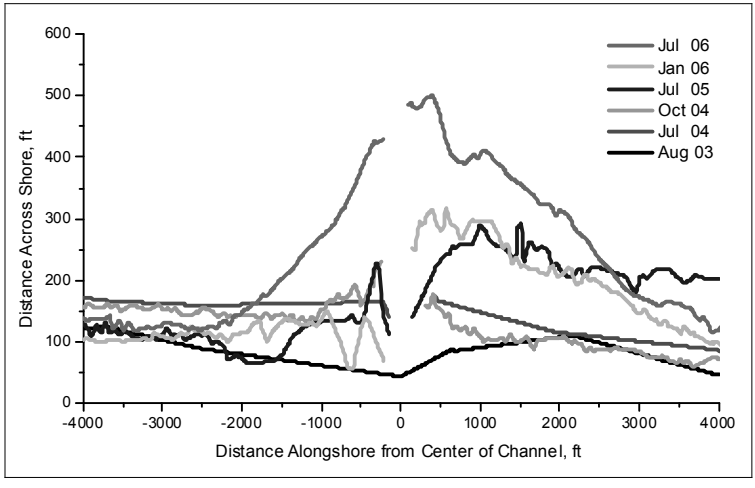

Fig. 11. Shoreline position change adjacent to the new inlet from Aug 2003 to Jul 2006.

CONCLUDING DISCUSSION

Over the 1.5 years since Packery Channel opened in Jul 2005, the channel has remained open primarily by scour induced by consistent, astronomically forced currents enhanced by seasonal wind tide. East-southeasterly directed frontal systems force flow and sediment toward the Gulf of Mexico. Current speed at PC138 is close to that, but as much as 0.35 m/s greater during wind events, than that predicted for the SH361 Bridge in the original design study of hydrodynamics by Brown and Millitello (1997). Therefore, it follows that current speeds on the order in excess of 1-1.35 m/s occur in the entrance channel. The greater observed speed is likely related to shallower channel water and higher than average wind speeds during the monitoring period. As a result of such strong sustained currents in the entrance channel, depth in the entrance channel has mainly increased with redistributed sand transported toward the channel mouth, forming a shoal to the west. The strong ebb flow not only forced the progradation of the shoal toward the Gulf, but, also, in combination with the longshore current, has induced scour at the mouth and contributed to the large region of scour offshore of the mouth. The speed of the ebb current has increased since the channel opened. No ebb shoal formation has been yet been detected.

Southerly directed longshore sediment transport dominates during the spring and summer induced by E-SE winds. The northerly directed transport during the spring and summer of 2006 induced migration of the seaward bars offshore to intersect with the south jetty tip. Autumn is typified by frontal passage and reversal in direction of longshore transport. The southerly directed transport caused rapid development of an offshore bar perpendicular to the north jetty during autumn 2006.

The southern shoreline adjacent to the inlet steadily advanced since 2003, but the northern shoreline position was erratic due to sediment loss around the incomplete north jetty. Once the jetties were completed, the northern shoreline advanced significantly and by Jul 2006 the shoreline was symmetrical with respect to the inlet. Northerly directed sediment transport is generally considered to occur during the summer, but the data indicates an intermittent southerly directed component. Development and dissipation of sand bars supports a strong seasonal bias in sediment transport in the nearshore. The rapid advance of the northern shoreline indicates that southerly directed sediment transport does occur during summer months and is related to the location of the channel at a divergent nodal area in the local longshore sediment transport system.

ACKNOWLEGEMENTS

This paper is a product of the USACE, Coastal Inlets Research Program. Permission was granted by Headquarters, USACE, to publish this information.

REFERENCES

Bales, J.D., and Holley, E.R. (1989). Sand transport in Texas tidal inlet. *J. Waterway, Port, Coastal, and Ocean Eng*., 115(4), 427-443.

Behrens, E.W. (1979). New Corpus Christi Pass, a Texas tidal inlet. *Shore & Beach* 47(4), 9-14.

Brown, C.A., and Militello, A. (1997). Packery Channel feasibility study: Bay circulation and water level, Report 2 of a two-part series. TR TAMU-CC-CBI-96-07, Conrad Blucher Inst. for Surveying and Science, Texas A&M Univ.-Corpus Christi, Corpus Christi, TX., 57 pp.

Carothers, H.P., and Innis, H.C. (1960). Design of inlets for Texas coastal fisheries. *J. Waterways and Harbors Division, Proc. of the ASCE,* 127(IV): 231-259.

Kraus, N.C. (2006). Coastal inlet functional design: Anticipating morphologic response. *Proc. Coastal Dynamics '05*, ASCE, CD ROM, 14 pp.

Kraus, N.C., and Heilman, D.J. (1997). Packery Channel feasibility study: Inlet functional design and sand management. Report 1 of a two-part series. TR TAMU-CC-CBI-96-06, Conrad Blucher Institute for Surveying and Science, Texas A&M Univ.-Corpus Christi, Corpus Christi, TX., 106 pp.

Lockwood and Andrews. (1952). Proposed alterations and improvements, Yarbrough Fish Pass, Padre Island, Texas. Prepared for Game and Fish Commission, State of Texas, Lockwood and Andrews, Houston, TX., 37 pp.

Morton, R.A., and Pieper M.J. (1977). Shoreline changes on Mustang Island and North Padre Island (Aransas Pass to Yarbrough Pass), An analysis of historical changes of the Texas Gulf Shoreline. BEG Geological Circ. 77-1, U. of Texas at Austin, Austin, Texas, 42 pp.

HDR/Shiner Moseley and Associates, Inc. (2006). Mollie Beattie Coastal Habitat Community. annual report: Baseline year 2-City Project 5122, prepared for the City of Corpus Christi, TX., 146 pp.

Price, W.A. (1952). Reduction of maintenance by proper orientation of ship channels through tidal inlets. *Proc. 2nd Coastal Engineering Conf*., Council on Wave Res., 243-255.

U.S. Army Corps of Engineers. (1992). Inlets along the Texas coast. Planning Assistance to the States Program, Section 22, U.S. Army Eng. District, Galveston, Galveston, TX, 56 pp.

Williams, D.D., Kraus, N.C.. and Anderson, C.M. (2005). Baseline and construction monitoring of Packery Channel, Corpus Christi, Texas. *Proc. Florida Shore and Beach Preservation Association,* http://www.fsbpa.com/publications.html, 16 pp.

EVOLUTION OF A RELOCATED TIDAL INLET: MASON INLET, NC

John M. Welsh[1] and William J. Cleary[2]

1. Gahagan & Bryant Associates, Inc., 295-A N. Green Meadows Drive, Wilmington, NC 28405-3933, USA. jmwelsh@gba-inc.com.
2. University of North Carolina-Wilmington, Center for Marine Science, 5600 Marvin K. Moss Lane, Wilmington, NC 28409, USA. clearyw@uncw.edu.

Abstract: Mason Inlet, situated between Figure Eight Island and Wrightsville Beach, N.C. was artificially relocated 850 m updrift of its former position at the southern terminus of a migrating barrier spit. Relocation that occurred in early 2002 was chosen from several management options due to the increased backbarrier infilling and southerly migration of the inlet that imminently threatened a resort complex and infrastructure on northern Wrightsville Beach. The relocated Mason Inlet provides an exemplary site to study the evolution and impacts of a recently relocated system from its inception while simultaneously assessing the relative success of the project. Jarrett's (1976) theoretical equation relating tidal prism (T_P) and cross-sectional area (A_C) appears to be a useful tool for estimation of the relocated Mason Inlet's T_P. However, ebb-tidal delta volume after 4.5 years remains well below the equilibrium volume predicted by Walton and Adams' (1976) model.

INTRODUCTION

Most of North Carolina's 19 inlets have been modified to some extent as a result of improved navigation via channel maintenance and removal of sand for beach nourishment. Hard stabilization techniques (engineering solution) by way of jetties or groins are traditionally used in the United States; however, North Carolina implemented a general statute, in 1984, that prohibits the use of hardened erosion-control structures along its coastline. As a result, soft protection techniques (e.g. dredging, beach nourishment, and sandbag installations) have become the mainstays of North Carolina's engineering solutions to these coastal hazard scenarios. Large-scale modification of inlets, associated with relocation or jetty emplacement, commonly alters the parameters (e.g. cross-sectional area, tidal prism, etc.) of an inlet and can result in substantial erosion of neighboring shorelines (Cleary *et al*., 1989;

Cleary and Marden, 1999). Concern over management issues (e.g. artificial inlet relocation) related to these modifications has increased due to severe impacts associated with these alterations and future modifications (e.g. dredging) slated for most of North Carolina's inlets.

Knowledge of how large-scale modification alters the physical parameters, current dominance, basin filling characteristics, as well as the impact on the offshore portion of specific inlet systems in southeastern North Carolina is generally lacking. A key element in evaluating the performance of an inlet where significant artificial changes have occurred is the application of the linear regression relationships derived by Jarrett (1976) and Walton and Adams (1976) for equilibrated inlets.

Mason Inlet, situated along the southeastern North Carolina coast, is characterized as a migratory system (Fig. 1). During the past 20 years the inlet has experienced considerable shoaling due to sand deposition in backbarrier feeder channels and a decrease in tidal prism (Cleary and FitzGerald, 2003). Since the early 1900's, the inlet has exhibited a net migration pattern to the southwest stretching along a 1.6-km corridor. Migration south caused erosion of the downdrift shoreline and eventually threatened to undermine a $22 million resort complex by 1997. Artificial relocation in March 2002 moved the inlet approximately 850 m northeast of its 2001 position and closed the former inlet. Over the past 4.5 years the new inlet has been adjusting to a larger tidal prism and retaining sand within an evolving ebb-tidal delta.

The intent of this paper is to provide a management framework from which the impacts of inlet relocation on tidal prism and inlet-related sand bodies can be better understood. The relocated Mason Inlet provides an ideal site to study the evolution and impacts of a recently relocated system from its inception by comparing the actual measured and derived values to predicted values obtained from regression equations associated with key inlet parameters.

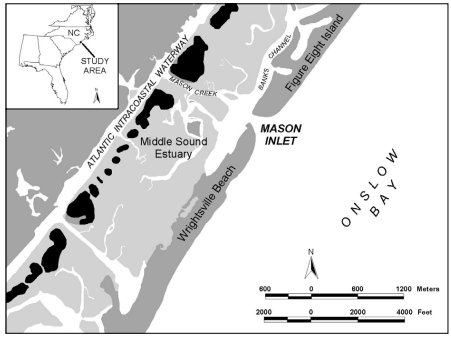

Figure 1. Location map of the study area. Dark features are dredge material islands.

PREVIOUS WORK

Inlet relocation, as a viable management option, has been made available to coastal managers under site-specific conditions. Relocation efforts have exclusively dealt with migrating inlets that have posed some degree of threat to the surrounding coastal zone (usually near field infrastructure) that borders an inlet.

Mason Inlet is not the first inlet along the North Carolina coast to be relocated. Tubbs Inlet, located 75 km to the southwest in adjacent Brunswick County, was relocated in January of 1970. After a period of adjustment the inlet began to migrate opposite its historic migration direction and the regional net littoral drift direction. Although Budde and Cleary (in press) have described morphologic changes in the inlet and their impact on the adjacent oceanfronts no published information exist that deals with the hydrodynamic evolution of the inlet.

Published studies documenting the effects of relocated tidal inlets along U.S. and foreign coastlines are uncommon. Studies of the 1983 relocation of Captain Sam's Inlet (mesotidal setting) near Charleston, South Carolina, include Kana and Mason's (1988) study that monitored the evolution and growth of the ebb-tidal delta, and the Kana *et al*. (1987) study that determined a sediment budget for the system. However, the inlet managed to migrate back to its approximate 1982 position twelve years after relocation (Kana and Mckee, 2003). Consequently, another artificial relocation of the inlet occurred in 1996. Both inlet relocation efforts are summarized in Kana and Mckee (2003). The study of Ancão Inlet's 1997 relocation, along the mesotidal, Ria Formosa barrier island system, in Portugal by Vila *et al*. (1999) determined that dramatic volumetric changes occurred during the first year of evolution, with the enlargement of the inlet and formation of well-developed flood and ebb deltas. Studies such as these are extremely important because they serve as case-studies for future inlet modifications elsewhere. Cleary and FitzGerald (2003) documented tidal prism changes intially induced by the relocation of Mason Inlet. Whereas, Erickson *et al*. (2003) also reviewed the relocation of Mason Inlet and the first year of observations of morphology and hydrodynamics in the system.

Certain fundamental parameters of an inlet system must be monitored as a new inlet system evolves to understand how relocation affects hydrodynamic and morphologic changes. Regression analyses of related morphologic and hydraulic characteristics of tidal inlets have been relatively successful in modeling inlet systems. These relationships between inlet parameters and processes have aided in the research of inlets worldwide (Kana *et al*., 1999). Jarrett (1976) refined Leconte's (1905) and O'Brien's (1931 and 1969) relationship between tidal prism and inlet cross-sectional area. Walton and Adams (1976) derived an empirical relationship between ebb-tidal delta volume and tidal prism.

STUDY AREA

Mason Inlet, situated in southwestern Onslow Bay along North Carolina's southeastern coastline, separates Figure Eight Island to the northeast from Wrightsville Beach to the southwest (Fig. 1). This region is characterized as a

microtidal and wave-dominated setting with mixed semi-diurnal tides (Hayes, 1994). The backbarrier region between the AIWW and Mason Inlet is the Middle Sound Estuary, which consists mostly of marsh incised by tidal creeks. Mason Creek and Banks Channel, two primary tidal channels within the estuary, provide the only navigable connection between the inlet and the AIWW.

Mean wave height and period in this region are 0.79 m and 7.9 seconds, respectively (Jarrett, 1977). The measured tidal range of this system has a mean range of 1.00 m, which increases to 1.20 m under spring tide conditions and decreases to 0.81 m under neap tide conditions. Mean sea level was determined to exist at an elevation of 0.20 m (National Geodetic Vertical Datum 1929 (NGVD 29)). The dominant direction of wave propagation is from the east-northeast and comprises 64% of the total wave energy that affects this area. Net longshore sediment transport is in the southerly direction and occurs at a rate of approximately 587,943 m^3/yr (USACE, 1982).

METHODS

This investigation utilized a relatively robust data set consisting of detailed photogrammetric, topo-bathymetric, hydrographic, and tidal survey information. All tidal and topo-bathymetric data were referenced horizontally to North Carolina State Plane 1983 and vertically to NGVD 29.

Flow Dynamics

A vessel-mounted RD Instruments® (RDI) Workhorse Monitor™ 1200 kHz Acoustic Doppler Current Profiler (ADCP) was used in collection of all flow data within the inlet throat. The ADCP was utilized during short-term deployments (e.g. 7–14 hr periods) for measuring flow velocities and direction, cross-sectional area, water levels, and calculating discharge and flow volume. The inlet throat was perceived as an extremely important location for data collection because a majority of inlet parameter relationships rely on throat measurements. Thus, ADCP surveys concentrated on determining variations in tidal prism and cross-sectional area at the inlet throat. These variations are important for characterizing the inlet's hydrographic nature. Typical surveys included traversing the throat profile a minimum of four times every half hour from the onset of the survey until completion of the tidal stage of concern.

An emphasis was placed on measuring the flood duration of the tide in order to determine tidal prism for a particular survey. Seven of eight surveys included data collection during a flood tide. That resulted in seven tidal prism values calculated from flow data collected by the ADCP between March 2002 and October 2003. No ADCP data were collected following October 2003.

Tidal prism (T_P), for the purposes of this study, is defined as the volume of water that enters an inlet on a spring flood tide (USACE, 2003). Cross-sectional area (A_C) is the channel section below mean tide level (MTL).

Ebb-Tidal Delta and Inlet Throat Analyses

Topo-bathymetric data collected by Gahagan & Bryant Associates, Inc. were used in measurements of throat parameters and sand volumetric analyses of the system. A total of eleven topo-bathymetric data sets spanning March 2002 to October 2006 allowed for the generation of digital terrain models (DTM).

Measurements of these DTM surfaces focused on two main regions. These included the newly evolving ebb-tidal delta and inlet throat for purposes of determining sand volume and A_C. A_C was measured below MSL (0.20 m NGVD) at the inlet throat.

Several studies describe a methodology for calculating the ebb-tidal delta volume by reference to idealized no-inlet bathymetry (Dean and Walton, 1975; Walton and Adams, 1976; Marino, 1986; Stauble, 1998). Hicks and Hume (1997) developed the residual method for analyses of ebb shoal shapes and volumes. In order to perform calculations on the ebb-tidal delta's volume, it was critical to define the boundary of the ebb shoal. Unfortunately, standardized techniques to determine these boundaries do not exist (Stauble, 1998). Volume of the evolving ebb shoal was determined using a variation of the method described by Dean and Walton (1975) for estimating quantities of sand stored in outer shoals of inlets on sandy coasts. Ultimately, the method used for this study followed closely after Stauble's (1998) Residual Method.

RESULTS

Inlet Throat and Tidal Prism

All pertinent ADCP flow data pertaining to the inlet throat are presented in Table 1. Discharge measurements collected during a flood tidal flow were manipulated for the purpose of calculating T_P during the course of the study. A large degree of variation

Mason Inlet Throat Parameters - ADCP Derived

Tides	Spring		Neap		Spring	Neap	Spring	Neap	Neap	Spring
Survey Date	3/28/2002		7/1/2002		7/25/2002	7/31/2002	6/27/2003	7/8/2003	9/5/2003	10/6/2003
Tidal Flow	Ebb	Flood	Flood	Ebb	Ebb	Flood	Flood	Flood	Flood	Flood
Duration (hr)	6.45	5.95	5.72	6.32	5.63	6.08	7.20	6.88	7.08	6.38
Max Velocity (m/s)	1.47	1.55	0.74	0.94	1.32	1.14	0.84	0.94	0.99	1.03
T_P (10^6 m^3)	6.41	7.34	2.66	2.1	2.68	4.03	4.76	4.15	6.25	4.71
Channel A_C (m^2)	298	384	191	105	212	227	310	276	396	286
*Tidal Range (m)	1.63	1.70	0.92	0.80	1.09	0.98	1.19	1.37	1.31	1.22

*Measured by water-level meter

Table 1. ADCP and tide range data for each of the eight throat surveys.

between these individual T_P values exists from one survey to the next. The first ADCP survey was conducted three weeks following inlet opening during a Spring tide with a flood range of 1.70 m. A relatively large T_P of 7.34 x 10^6 m^3 was calculated at that time. A 64% decrease in the T_P value occurred between the March 28, 2002 and July 1, 2002 surveys. Within the same month (July 1 to July 31, 2002) T_P increased by 52% to 4.03 x 10^6 m^3. The June 27, 2003 ADCP-derived T_P, an 18% increase from the previous survey almost a year earlier, was 4.76 x 10^6 m^3. Eleven days later the T_P decreased by 13%. A relatively large T_P volume of 6.25 x 10^6 m^3 was determined from the September 5, 2003 survey. A large Neap flood range of

1.31 m was measured for this survey and resulted in a 396 m^2 measured channel section. The final survey occurred on October 6, 2003 with calculations yielding a volume of 4.71 x 10^6 m^3. The mean calculated T_P value for the seven surveys was 4.84 x 10^6 m^3.

Correlation between T_P and flood tidal range was determined from acquired field data. As expected, a positive correlation (r = 0.87, significant at the 95% confidence level) was found to exist between these two inlet parameters. The correlation indicates that as tidal range rises or falls the T_P volume will respond in a like manner. Similarly, a positive correlation (r = 0.95, significant at the 99% confidence level) between ADCP-calculated T_P and ADCP-measured A_C was determined. This positive correlation indicates that larger A_C values result in greater T_P values or vice versa with diminished A_C values.

Ebb-Tidal Delta Development

Over the course of the past 4.5 years the ebb-tidal delta has experienced marked changes in morphology and volume. Between March and July 2002 the newly formed shoal had impounded 137,000 m^3 of material. A steady growth continued over the next 2.2 years and by October 2004 the shoal volume increased to 322,000 m^3. Between October 2004 and April 2005 a marked change occurred due to retention of an additional 96,000 m^3 yielding a total volume of 418,000 m^3. Continued growth occurred until October 2005 when the shoal reached its maximum volume of 440,421 m^3. Since October 2005 volumetric loss has characterized the ebb-tidal delta. In April 2006, shoal volume was 338,000 m^3 and by October 2006 the volume had decreased to 288,000 m^3.

Theoretical Relationships and Comparisons

The widely recognized relationship between T_P and inlet throat A_C was initially described by Leconte (1905) and later refined by O'Brien (1931, 1969) who elaborated upon the relationship's potential for estimating T_P. Jarrett (1976) furthered understanding of the relationship by grouping inlets into separate classes based on wave energy setting and on the presence or absence of jetties. Segregating the inlets allowed Jarrett to formulate unique linear regression equations for each class. Byrne *et al*. (1980) determined that relatively small tidal inlets situated within protected coastlines fail to apply to the predicted relationship of Jarrett (1976). Although Mason Inlet is not within a protected coastline, it is a relatively small inlet and consideration of that fact should be noted when utilizing this relationship. Utilizing the throat A_C and T_P derived values from data collected with the ADCP and topo-bathymetric surveys, it is possible to make comparisons between the new inlet channel and the predicted equilibrium cross-sections derived from these regression equations. For the purposes of this study, the frequently used regression equation derived by Jarrett (1976) for the Atlantic Coast was used in order to compare the values for the mean measured T_P and the calculated T_P (Equation 1):

$$A_C = 7.75 \times 10^{-6} T_P^{1.05} \quad (1)$$

where: A_C = throat cross-sectional area (ft^2) and T_P = tidal prism (ft^3). The cross-sectional area values used in Jarrett's equation represent the mean of the cross-sectional area values (A_C = 296 m^2) measured during each of the seven throat surveys conducted during flood tide conditions with the ADCP and the mean of the values (A_C = 291 m^2) measured across the six DTM surfaces. Based on Equation 1 and the A_C measured by the ADCP, the resulting calculated T_P was 4.53 x 10^6 m^3. The difference between this predicted T_P (4.53 x 10^6 m^3) and the mean ADCP-calculated T_P (4.84 x 10^6 m^3) was approximately 7%. The resulting predicted T_P, based on Equation 1 and the DTM-measured A_C, was 4.45 x 10^6 m^3; an 8% difference from the mean ADCP-calculated T_P (4.84 x 10^6 m^3). A t-test (t = 1.41) determined that the difference between the mean predicted values and the mean ADCP-calculated values were not significant (p-value = 0.21). The relatively small difference (7% and 8%) and statistical insignificance between these predicted T_P values and the mean ADCP-calculated T_P values suggest that Equation 1 was a comparable method and fairly useful tool for estimating T_P (Fig. 3).

Inserting A_C values derived from ADCP throat surveys into Equation 1, predicted T_P values were generated that ranged from 2.98 x 10^6 m^3 to 5.98 x 10^6 m^3. Extreme differences between these predicted T_P values and calculated T_P values ranged from <1% to 21%. It should be noted that the greatest difference of 21% occurred during the March 28, 2002 survey when the channel cross-section still maintained an artificial shape considered to be far from equilibrium. The next greatest difference was 13% and occurred in July 2002. Over time the difference between calculated and predicted values decreased as the channel section evolved. Individual ADCP-calculated T_P values were regressed against the corresponding predicted T_P values. A positive correlation was determined to exist (r = 0.97, significant with 99% confidence). This relationship was indicative of the comparativeness of these two different methodologies for estimating tidal prism. Both the ADCP and Equation 1 were useful for T_P estimation and appeared to compare more closely as the channel evolved over the study period.

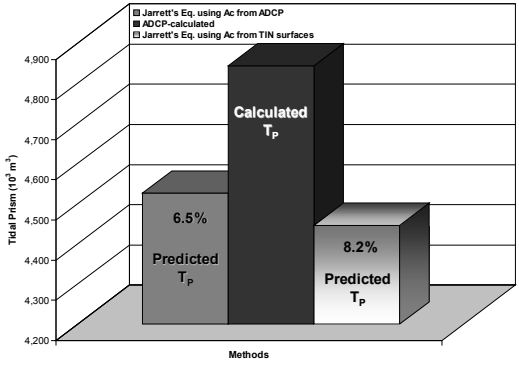

Figure 3. Bar graph illustrating differences in derived tidal prism values.

Based on the strong correlation found between ADCP-calculated and predicted T_P values over the first portion (March 2002 – October 2003) of the study period, Equation 1 was used as a tool to estimate T_P over the remainder of the study period (April 2004 – October 2006). No ADCP data existed for the inlet following October 2003. Utilizing the limited ADCP data acquired in the field, a mean T_P of 4.84 x 10^6 m^3 was calculated to exist between March 2002 and October 2003. Following this period, and based on six DTM-measured throat A_C values used with Equation 1, the inlet's T_P reduced over the second half of the study period to a mean value of 3.65 x 10^6 m^3. That mean value of 3.65 x 10^6 m^3 represents a reduction of T_P ranging 17 – 25% lower than values obtained during the first portion of the study.

A_C varied greatly over the entire length of the study. Initially, 1.6 years following relocation, changes in A_C varied considerably and averaged 46 m^2. However, over the latter portion of the study A_C changes diminished greatly and averaged 8 m^2.

Ebb-Tidal Delta Volume and Tidal Prism

Previous work by Walton and Adams (1976) described a strong correlation, by way of linear regression analyses, between the volume of sand stored in the ebb-tidal delta of an inlet and its T_P. According to their coastal energy classification scheme the inlets along the east coast of the U.S. (except in South Carolina), and Panhandle of Florida (Gulf Coast) fall within the moderately exposed coast range. T_P measurements used in their study were based on measurements from current data obtained at the throat of an inlet or by the "cubature method". The inlets analyzed in their study were considered equilibrated with respect to their surroundings. This study sought to compare ebb-tidal delta volumes derived from DTM surfaces to volumes ascertained from the empirical model of Walton and Adams' (1976). In order to accomplish this task, the mean ADCP-calculated T_P value was inserted in Walton and Adams' (1976) theoretical equation for moderately exposed coasts (Equation 2):

$$V_{ETD} = 10.5 \times 10^{-5} T_P^{1.23} \quad (2)$$

where: V_{ETD} = ebb-tidal delta volume (yd^3) and T_P = tidal prism (ft^3). The T_P value used in Equation 2 represents the mean of the T_P values (T_P = 4.43 x 10^6 m^3) calculated during each of the six ADCP throat surveys between July 2002 and October 2003. The March 2002 T_P value was not used in this analysis due to the artificial shape of the channel and the lack of an ebb shoal located offshore at that time. Using Equation 2 and the mean ADCP-calculated T_P, the resulting ebb shoal volume was predicted to be 963,000 m^3. The difference between this mean predicted V_{ETD} (963,000 m^3) and the final measured V_{ETD} (288,063 m^3) in October 2006 was approximately 70% (Fig. 4).

Ebb-Tidal Delta Volume and Cross-Sectional Area

As inlet throat A_C exhibits a direct correlation with T_P and is considered an easier inlet parameter to measure than T_P, Walton and Adams (1976) derived a correlation between volume of the ebb-tidal delta and A_C of the channel. In order to compare the

volume of material estimated in the ebb-tidal delta from DTM surfaces with the predictions of their empirical model, the mean DTM-measured A_C value was used in conjunction with Walton and Adams' (1976) theoretical equation for moderately exposed coasts (Equation 3):

$$V_{ETD} = 40.7\, A_C^{1.28} \quad (3)$$

where: V_{ETD} = ebb-tidal delta volume (yd^3) and A_C = cross-sectional area (ft^2). The A_C value used in Equation 3 represents the mean of the A_C values (A_C = 245 m^2) measured across the generated DTM surfaces between July 2002 and October 2006. The March 2002 A_C value was not used in this analysis due to the artificial shape of the channel and the lack of an ebb shoal located offshore at that time. Based on Equation 3 and the mean A_C measured across the DTM surfaces, the resulting predicted ebb shoal volume was 745,000 m^3. Comparisons of the individual measured V_{ETD} values with this predicted V_{ETD} (745,000 m^3) revealed that the initial July 2002 V_{ETD} (136,752 m^3) comprised only 18% of the predicted volume. By the end of the study, the shoal increased in size with an (October 2006) V_{ETD} measuring 288,063 m^3 and comprising only 39% of the predicted volume.

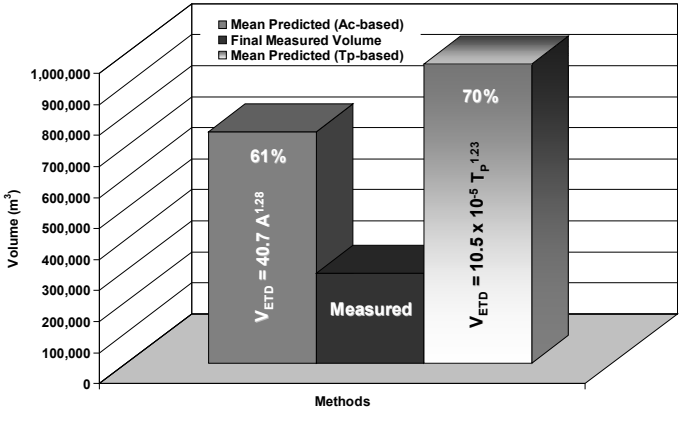

Figure 4. Bar graph illustrating differences in derived ebb-tidal delta values.

DISCUSSION

The regression equations of Jarrett (1976) and Walton and Adams (1976) have been used in this study to predict parameters for inlet conditions. Applicability of these equations to the newly developing system were assessed and provided a "measuring stick" of where the inlet and the parts that comprise it rank with regard to stability/equilibrium. These relationships provided insight into the performance of inlet.

Upon consideration of Jarrett's (1976) A_C and T_P relationship, a high correlation (r = 0.97) between predicted T_P, based on Equation 1 and A_C measured by the ADCP, and individual ADCP-observed T_P values shows a relationship indicative of the comparativeness of these two different methodologies for estimating tidal prism. The percentage differences (7% and 8%) between the ADCP-calculated T_P and Equation 1-derived T_P values are most likely related to extraneous factors such as wind and waves (Fig. 3). From a management perspective, the importance of using this tool is evident when considering that it approximates the potential T_P of the inlet. An adequate T_P is required to flush water through the inlet and reduce the tendency of inlet closure due to clogging of the backbarrier. The 2D hydrodynamic model used in the design phase of the relocation predicted that the relocated inlet would assume an equilibrium T_P of approximately 5.2 x 10^6 m^3 (Erickson *et al*., 2003). The current study revealed that this value has not been assumed. In fact, the latter half of the study indicated that T_P has apparently diminished from 4.84 x 10^6 m^3 to 3.65 x 10^6 m^3 (30% less than predicted by the 2D model). Infilling and shoaling of the backbarrier are believed responsible for T_P reduction and will impede the inlet from attaining the predicted T_P it was originally designed to sustain.

Another implication worthy of consideration is the issue of A_C equilibrium. Jarrett's (1976) empirical relationship was based on inlet A_C's equilibrated to their unique surrounding conditions. Obviously, this becomes an issue of concern for the current study. Unfortunately, there is no established definition for the determination of channel A_C equilibrium. Kana and Mason (1988) determined that the relocated Captain Sam's Inlet achieved channel A_C equilibrium within 250 days after opening with a measured equilibrium value within 5% of the area predicted by the empirical models of O'Brien (1969) and Jarrett (1976). Interestingly, the predicted values of A_C for Mason Inlet began closely approximating the measured A_C values (0.5% difference) 477 days after inlet opening and continued to remain at <8% difference for the remainder of the ADCP-portion of the study. Due to the high correlation (r = 0.97) between the individual ADCP-measured A_C values and the calculated A_C values, equilibration of the channel A_C was plausible. Considering Jarrett's (1976) equation was based on equilibrated A_C values supports this assumption. Based on findings by Kana and Mason (1988) for a relocated inlet with similar physical parameters and considering the high correlation (r = 0.97) between predicted and measured A_C's, it seems Mason Inlet assumed an equilibrated cross-section early in its post-relocation development. Unfortunately, with the lack of ADCP data after October 2003, continued monitoring of whether the actual measured throat section continued to remain close to predicted values proved impossible. Consequently, whether or not an equilibrated cross-section remained after October 2003 could not be determined.

Analyzing development of the ebb-tidal delta can further determine whether or not the inlet has achieved equilibrium within the period of study. Development of the ebb-tidal delta can be grouped into a period of initial accretion followed by volumetric loss. Although varying in its rate of accretion the shoal continually experienced growth volumetrically during the 3.5 years after relocation. Relatively

large-scale losses occurred over the final year of the study with the shoal losing 152,000 m^3. Initial gains were expected; however, losses in the ebb shoal were not projected to occur until after an equilibrated state had been assumed. Erickson *et al*. (2003) predicted that within five years, the ebb shoal would be at 90% equilibrium volume, and natural sand bypassing would be nearly established. Maintenance dredging of the inlet during February 2005, within the backbarrier region, is believed to have led to many of the changes on the ebb shoal. Removal of 140,000 m^3 of material from the flood shoal and inlet throat during the maintenance event first phase directly affected the A_C by deepening and widening the throat. Removing material from the sedimentation basin, situated landward of the throat, created a potential "sink" for sediment deposition. Material excavated from interior areas was used to nourish the oceanfront beach along the southern extent of Figure "8" Island. It is believed that the large gain measured in April 2005 on the ebb shoal was directly related to erosion and subsequent transport of fill material placed along the oceanfront in early 2005. The current trend of shoal volumetric loss is believed related to the latent effects of material removal from the backbarrier as a part of the maintenance event. Wave attack and most likely an increase in T_P has resulted in sand from the ebb shoal being relocated into the inlet's interior. Until the interior shoals adequately gain material the ebb shoal will likely continue to deflate. Induced changes (e.g. maintenance event) serve to disrupt the natural, established flow regime and limit the use of Walton and Adams' (1976) model (based on equilibrated systems) for this inlet.

Equations 2 and 3, used in the prediction of V_{ETD}, were based on data from equilibrated inlet systems. The ebb delta volume in October 2006 remained well below the predicted volume at 288,063 m^3 (between 30–39% of the predicted volume depending on the regression equation used). Even the largest measured ebb delta volume of 440,421 m^3 (October 2005) did not approximate the equilibrium volume predicted. Thus, Walton and Adams' equations did not adequately approximate the V_{ETD} for this inlet. When comparing the predicted V_{ETD} values (963,000 m^3 and 745,000 m^3) derived from Equations 2 and 3 with the actual delta size 4.5 years after opening, it is obvious that the inlet either had not reached equilibrium or did not necessarily conform to Walton and Adams' (1976) model (Fig. 4).

Inlet equilibration alone is not the only factor that possibly accounts for this large discrepancy between actual measured and predicted V_{ETD} values. Inlet size must also be considered since Walton and Adams' (1976) regression analysis included a majority of inlets considerably larger than Mason Inlet. Kana and Mason (1988) discussed this issue at length in their study of Captain Sam's Inlet's ebb-tidal delta evolution. The aforementioned study mentioned several additional factors besides equilibration that may be responsible for the observed difference in V_{ETD} values. One of these variables was that many of the inlets used in Walton and Adams' (1976) study were larger Florida and Texas microtidal inlets that were positioned along "mildly exposed" coasts and therefore were expected to exhibit little movement (Kana and Mason, 1988). Captain Sam's Inlet is quite similar to Mason Inlet in that it is a relocated, small-migrating inlet whose ebb-tidal delta only attained 35% of the

predicted volume 2.2 years after opening. The effectiveness of Walton and Adams' equation, for Mason Inlet, is brought into question due to its small size and poor comparison between measured and predicted V_{ETD} values. However, with regard to Mason Inlet, it is concluded that the size/volume of the ebb-tidal delta is most likely less than that predicted due to a decreased T_P and modifications within the inlet interior leading to a non-equilibrated system. Induced changes within the inlet interior are assumed to affect sediment storage capacity of the ebb shoal as evidenced by the maintenance event.

Based on the findings and time frame of this study, Mason Inlet may have failed to attain an equilibrated state with the surrounding forcing parameters. Several implications associated with the impacts of a non-equilibrated system should be considered, as the inlet will continue to adjust to its surroundings. As the ebb-tidal delta continues to adjust volumetrically and the lagoon infills with sediment the updrift shoreline of Figure "8" Island will likely continue to erode as sand will be transported to the ebb shoal and/or into the backbarrier channels. In addition to sand impounded on the ebb shoal, material is permanently lost from the littoral system when transported into the backbarrier (Cleary and FitzGerald, 2003). Cleary and FitzGerald (2003) concluded in their study of relocated Mason Inlet that the continued tendency of sediment transport into the backbarrier is indicated by flood dominance of the inlet (stronger flood than ebb tidal currents), residual flood flow, and deposition of material within the inlet interior after relocation. If left to its own devices lagoonal infilling will continue and T_P will be reduced over time perhaps leading to inlet closure.

Some degree of inlet equilibrium must be attained. The system continues to exhibit flood dominance and infills with sediment creating an unstable situation. As a result, the inlet's T_P is decreased. Stipulations of the relocation agreement require the inlet to remain within a 305-m corridor and allow dredging for this purpose. Dredging the inlet's feeder channels will aid in keeping the inlet channel in place by providing a larger T_P and flushing through the inlet throat. However, if that material is placed on the updrift shoreline of Figure "8" Island it will likely be transported back into the inlet or to the ebb shoal. Excessive dredging could adversely compromise Figure "8" Island enlarging T_P enough to cause the ebb-tidal delta to require more sand from the updrift shoreline. For this system, finding an equilibration state that works well for the entire system will be challenging.

CONCLUSIONS

Several broad based conclusions are drawn from the study of Mason Inlet over 4.5 years following the artificial relocation of the system in Marc 2002. T_P has been variable in this evolving system and is highly correlated to changes in A_C of the throat ($r = 0.95$) and fluctuations in tidal range ($r = 0.87$). Jarrett's (1976) theoretical equation relating T_P and A_C appears to be a useful tool for estimation of the T_P. From a management perspective, the empirical equation of Jarrett (1976) is important and can be useful in showing that the potential T_P is decreasing. Whether or not the inlet A_C equilibrated remains in question.

The volume of sand in the new ebb-tidal delta after 4.5 years remained well below (61–70% below) the equilibrium volume predicted by Walton and Adams' (1976) empirical relationship. This discrepancy may be related to the inlet's failure to attain equilibrium and/or its inability to conform to Walton and Adams' (1976) empirical relationship due to its relatively small size. Volumetric losses measured on the shoal are believed linked to the maintenance event. Induced changes to the system, that serve to disrupt any degree of equilibrium the T_P and ebb shoal may share, eliminate the usefulness of Walton and Adams' (1976) equations here.

ACKNOWLEDGEMENTS

This research would not have been possible without the aid of countless individuals at the UNCW's Center for Marine Science. A genuine debt of gratitude is extended to the students in the Coastal Geology Lab particularly Ben McGinnis, Chester Jackson, Adam Knierim, Kenny Willson, David Doughty, and Leighann Budde. Special thanks are also extended to Chris Gibson of Gahagan & Bryant Associates, Inc. for graciously providing detailed bathymetric data and aerial photographs.

REFERENCES

Budde, L.E. and Cleary, W.J., in press, Barrier progradaion related to inlet spacing and migration patterns , *Journal of Coastal Research,* Special Issue 39.

Byrne, R.J.; Gammisch, R.A., and Thomas, G.R., 1980. Tidal prism area relations for small tidal inlets. *Proceedings of the Seventeenth Coastal Engineering Conference,* ASCE, Sydney, Australia, pp. 2517–2533.

Cleary, W.J.; Hosier, P.E., and Gammil, S.P., 1989. Historic and dredging-induced shoreline changes, Bald Head Island, Cape Fear, NC. *Proceedings of Coastal Zone '89*, pp. 3017–3029.

Cleary, W.J. and Marden, T.P., 1999. Shifting Shorelines: A Pictorial Atlas of North Carolina Inlets. Raleigh, North Carolina: N.C. Sea Grant Publication No.99-X, 60p.

Cleary, W.J. and FitzGerald, D.M., 2003. Tidal inlet response to natural sedimentation processes and dreding-induced tidal prism changes: Mason Inlet, North Carolina. *Journal of Coastal Research,* 19(4), 1018-1025.

Dean, R.G. and Walton, T.L., JR., 1975. Sediment transport processes in the vicinity of inlets with special references to sand trapping. *In:* Cronin, L.E. (ed.), *Estuarine Research*, vol. 2, New York: Academic Press, pp. 129–150.

Erickson, K.M.; Kraus, N.C., and Carr, E.C., 2003. Circulation change and ebb shoal development following relocation of Mason Inlet, North Carolina. *Proceedings of Coastal Sediments '03,* (Clearwater Beach, Florida), CD-ROM.

Hayes, M.O., 1994. The Georgia Bight barrier system. *In*: Davis, Jr. R.A. (ed.), *Geology of Holocene Barrier Island Systems*, 7. New York: Springer-Verlag, pp. 233–304.

Hicks, D.M. and Hume, T.M., 1997. Determining sand volumes and bathymetric change of an ebb-tidal shoal. *Journal of Coastal Research*, 13(2), 407–416.

Jarrett, J.T., 1976. Tidal prism-inlet area relationships. Fort Belvoir, Virginia and Vicksburg, Mississippi: U.S. Army Corps of Engineers, Coastal Engineering Center and Waterways Experiment Station, *GITI Report #3*, 76p.

Kana, T.W.; Mason, J.E., and Williams, M.L., 1987. A sediment budget for a relocated tidal inlet. *Proceedings of Coastal Sediments '87,* American Society of Civil Engineers, New York, N.Y., pp. 2094–2109.

Kana, T.W. and Mason, J.E., 1988. Evolution of an ebb-tidal delta after an inlet relocation. *In*: Aubrey, D.G. and Weishar, L. (eds.), *Hydrodynamics and Sediment Dynamics of Tidal Inlets, Lecture Notes on Coastal and Estuarine Studies*, 29. New York: Springer-Verlag, pp. 382–411.

Kana, T.W.; Hayter, E.J., and Work, P.A., 1999. Mesoscale sediment transport at southeastern U.S. tidal inlets: conceptual model applicable to mixed energy settings. *Journal of Coastal Research,* 15(2), 303–313.

Kana, T.W. and Mckee, P.A., 2003. Relocation of Captain Sams Inlet – 20 years later. *Proceedings of Coastal Sediments '03,* (Clearwater Beach, Florida), CD-ROM.

Leconte, L.J., 1905. Discussion of "Notes on the Improvement of River and Harbor Outlets in the United States," Paper No. 1009 by D.A. Watts, Transactions, American Society of Civil Engineers, Vol. LV, Dec. 1905, pp. 306–308.

Marino, J.N., 1986. Inlet ebb shoal volumes related to coastal physical parameters. Gainesville, Florida: University of Florida, Gainesville, Coastal and Oceanographic Engineering Department, *UFL/COEL-86-017*, 116p.

O'Brien, M.P., 1931. Estuary tidal prisms related to entrance areas. *Civil Engineering*, 1(8), 738–739.

O'Brien, M.P., 1969. Equilibrium flow areas of inlets on sandy coasts. *Journal Waterways and Harbors Division*, New York: ASCE, 95, 43–52.

Stauble, R.K., 1998. Techniques for measuring and analyzing inlet ebb-shoal evolution. *Coastal Engineering Technical Note IV-13*, U.S. Army Corps of Engineers, Coastal Engineering Center & Waterways Experiment Station, Vicksburg, MS, 12p.

U.S. Army Corps of Engineers, 1982. Feasibility Report and Environmental Assessment of Shore and Hurricane Wave Protection, Wrightsville Beach, North Carolina. Wilmington, North Carolina: U.S. Army Corps of Engineers Publication.

U.S. Army Corps of Engineers, 2003. Engineering analysis at tidal inlets. *Proceedings of 4th Annual Tech-transfer Workshop '03,* Coastal Inlets Research Program, 26p. Available from World Wide Web <http://cirp.wes.army.mil/cirp/presentations/fsb03/Seabergh_EngAnalysis2003_H2.pdf>. PDF format.

Vila, A.; Alveirinho Dias J.M.; Ferreira, O., and Matias, A., 1999. Natural evolution of an artificial inlet. *Proceedings of Coastal Sediments '99*, American Society of Civil Engineers, New York, N.Y., pp. 1478–1488.

Walton, T.L., Jr. and Adams, W.D., 1976. Capacity of inlet outer bars to store sand. *Proceedings of the 15th Conference of Coastal Engineering* (New York, New York, ASCE), 2, pp. 1919–1937.

PRESENT HYDRODYNAMICS OF ANCÃO INLET, 10 YEARS AFTER ITS RELOCATION

André Pacheco[1], Ana Vila-Concejo[2], Óscar Ferreira[3], Alveirinho Dias[3]

1. CIACOMAR/CIMA, Universidade do Algarve, Avenida 16 de Junho s/n, 8700-311 Olhão, Portugal. ampacheco@ualg.pt
2. Coastal Studies Unit, School of Geosciences F09, University of Sydney, Sydney NSW 2006, Australia. aconcejo@geosci.usyd.edu.au
3. FCMA/CIMA, Universidade do Algarve, Campus de Gambelas, 8000 Faro, Portugal. oferreira@ualg.pt, jdias@ualg.pt

Abstract: Ancão Inlet (Southern Portugal) was relocated in 1997 and almost 10 years after its opening has the morphodynamic characteristics and migration pattern predicted by several authors. Its eastwards migration is mostly caused by high W-SW storm events, where the downdrift migration of the channel is accompanied by updrift spit growth and both deltas migrate asymmetrically. The inlet migration rates were computed between three new surveys and several inlet parameters measured, revealing the highest migration rates since inlet opening, an a relative stable inlet cross-section area, width and maximum depth at inlet throat through time. Inlet migration rate was compared with storm events and results showed a relation of this rate with the diminishing of E-SE storm events and an increase of magnitude of W-SW storms. Also, during an unusually powerful ex-tropical storm which affected the study area, an ephemeral inlet breached updrift from Ancão Inlet. The new inlet was competing for dominance of the tidal prism with Ancão Inlet, however it closed after three weeks, showing the hydraulic efficiency of Ancão Inlet nine years after its relocation.

INTRODUCTION

Tidal inlets are one of the most dynamic coastal features. The complex temporal and spatial interaction of waves, tides, and currents create and constantly modify the morphology and the sedimentary structure of tidal inlets. Despite being complex coastal systems and difficult to model, inlets are of extreme importance as navigation routes, as sediment suppliers to adjacent beaches, and as conduits that allow exchange of nutrients between backbarrier systems and the coastal zone (FitzGerald 1996).

Several engineering activities can be adopted in order to maintain an open inlet and avoid locational and/or geometrical instability and the subsequent coastal changes. Inlet relocation is a soft coastal management technique that, when applied to migrating inlets, involves the artificial opening of a new tidal inlet along the historic migration path of the inlet. This engineering technique was used to relocate Ancão Inlet (Ria Formosa barrier island system, Algarve, Southern Portugal).

In 1996 Ancão Inlet was in its limiting position (Vila-Concejo et al., 2004) showing severe infilling and meandering of the channel. Following a soft protection programme (Dias et al. 2003), the Portuguese Institute of Nature Conservation (ICN) decided to relocate the inlet 3,500 m to the west of its position in 1996. The new inlet was opened on 23rd July 1997. Since its opening, the new Ancão Inlet has been monitored and it was found to resemble the old inlet both in terms of its hydrodynamic characteristics and its morphology (Williams et al. 2003). According to Vila-Concejo et al. (2003; 2004), Ancão Inlet reached dynamic equilibrium one year after its opening (i.e. in July 1998) and has behaved like a natural inlet since that time.

Vila-Concejo et al. (2003) presented a four stage conceptual model for the natural evolution of artificially opened inlets (stage 1 is the artificially opened inlet; stage 2 corresponds to the developed inlet after reaching dynamic equilibrium; stage 3 represents the situation of a "natural" inlet after migration induced by normal longshore drift; and, stage PS "post-storm" represents the inlet morphological features after high-energy conditions). Williams et al. (2003) defined three morphological states based on three hydrodynamic regimes of Ancão Inlet which are synthesised in Table 1. H represents the wave conditions: H1 – non-storm conditions (prevailing fair-weather conditions), H2 – storm conditions for W-SW waves and H3 – storm conditions for E-SE waves.

Table 1. Three morphological states based on the three hydrodynamic regimes of Ancão Inlet (adapted from Williams et al., 2003)

Morphological state and frequency	Wave conditions
MOR 1 Ebb-tidally dominated period	$H1_A$: 90º<θ<180º, H_s <1 m, 4s <T_p <10 s
	$H1_L$: 180º<θ<270º, H_s <1 m, 4s <T_p <10 s
MOR 2 Post-storm wave-produced period	H2 245º<θ<275º, H_s > 3 m, 8s <T_p <18 s
	H3 120º<θ<140º, H_s > 3m, 6s <T_p <14 s
MOR 3 Transitional period	Establishment of $H1_A$ conditions

- H_s and T_p represent wave significant height and peak period, respectively
- $_A$ and $_L$ refer to mean Atlantic, W-SW and "Levante", E-SE, wave approach, respectively)

Morris et al. (2001) describes different morphological responses of Ancão Inlet and adjacent areas to the different hydrodynamic conditions, considering the status of the inlet as a tide- or wave dominated system, encompassing relationships between inlet morphology and the present and/or antecedent hydrodynamic conditions. The proposed model was supported by different numerical models and field evidence including the morphological conceptual model latter developed by Vila-Concejo et al. (2003). Using

video techniques, Morris et al. (2004) proposed a conceptual morphological model for inlet seasonal behaviour with three model stages (post-storm, transitional and extended calm morphological stage) that are closely related with the incident waves.

The present paper is focused on analysing the morphodynamics of Ancão Inlet 10 years after its relocation and comparing them with the estimates of several authors for its evolution (i.e. migration trend, morphological behaviour, response to oceanographic conditions). In order to achieve this objective, three new topo-bathymetric surveys were performed and several inlet parameters analysed (cross-sectional area, channel orientation, migration trend, and morphological features). Additionally, on the 11th October 2005 the remains of a tropical storm named Vince impacted the study area. It caused the breaching of Ancão Peninsula, near the location where Ancão Inlet was relocated in 1997 and a new inlet (Vince Inlet) was formed. Data presented in this study will show how Ancão Inlet responded to Vince Inlet.

STUDY AREA

Ancão Inlet is located in the Ria Formosa that is a multi-inlet barrier island system located in Southern Portugal (Figure 1). The system consists of five islands and two peninsulas separated by six tidal inlets: two relocated inlets (Ancão and Fuseta inlets), two artificially opened and stabilised inlets (Faro-Olhão and Tavira inlets) and two natural inlets (Armona and Lacém inlets). The backbarrier is characterised by large salt marshes, sand flats and a complex network of natural and partially dredged channels, covering 8.4×10^7 m^2 (Andrade 1990).

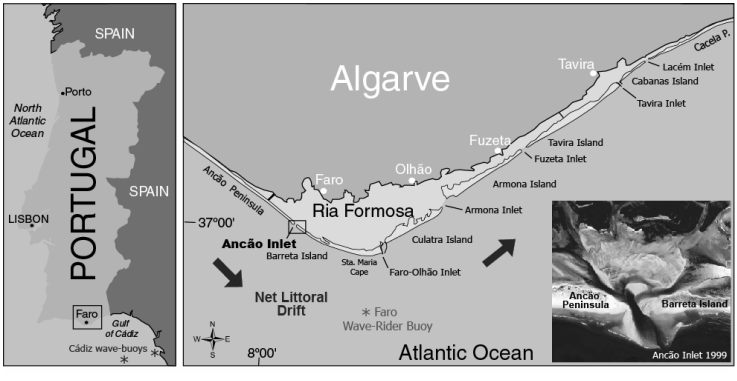

Fig. 1. Ria Formosa barrier island system (Algarve, Southern Portugal). In detail is a vertical aerial photo showing Ancão Inlet in 1999

Tides in the area are semi-diurnal, average ranges are 2.8 m for spring tides and 1.3 m during neap tides but maximum ranges of 3.5 m can be reached. Wave climate in the area is moderate to high (Ciavola et al. 1997). Predominant wave directions are from the W-SW, approximately 76%, while waves coming from the E-SE only account for 24%

of the observations (Costa et al. 2001). The dominant moderate sea state that prevails most of the time is sometimes disturbed by the occurrence of two types of storms: W-SW and E-SE storms. W-SW storms are associated with atmospheric low pressure centres in the south-eastern region of the North Atlantic Ocean, and occur mainly in winter, while E-SE storms occur when "Levante" (strong Mediterranean easterly wind) blows in the Gibraltar strait. "Levante" events may occur in all seasons and are of shorter duration (Pires 1998). The cuspate shape of the Ria Formosa system produces two areas differentiated in terms of exposure to wave action (Figure 1). The west flank is more energetic, being under the direct influence of dominant wave conditions (SW), while the east flank is only directly exposed to SE conditions.

Ancão Inlet is a small migrating inlet that has an average width of 300 m (Vila et al., 1999). The inlet undergoes a cyclic eastward migration (Weinholtz 1964; Esaguy 1986; Dias 1988; Pilkey et al. 1989). Vila-Concejo et al. (2002) analysed the historical development of Ancão Peninsula inlets from 1947 until 1996 and found that Ancão Inlet underwent two eastward migration cycles during this period. The eastward migration trends were very similar for both cycles, with the inlet showing an initial stage of readjustment (characterised by low migration rates), followed by a stage of high eastward migration rates, until reaching a limiting position; while migrating, Ancão Inlet maintains a stable cross-sectional area. This was distinguished as a high-energy migration pattern (HEMP) by Vila-Concejo et al. (2002; 2004).

METHODS

Inlet parameters

Since the relocation of Ancão Inlet a monitoring program has been carried out to study its evolution. Topo-bathymetric surveys were made from the opening (June 1997) until December 2002. The methodology and results of the monitoring program are presented by Vila-Concejo et al. (2003, 2004, 2006b) and included morphological, migration and channel evolution data (inlet width, depth and cross-sectional area).

Three new surveys were made at Ancão Inlet: June 2004, February 2005 and May 2006. These surveys included detailed topography of the adjacent barriers, ebb and flood shoals, as well as detailed bathymetry of the inlet and the adjacent channels (except February 2005 where detailed bathymetry was not possible for the entire area due to wave conditions). The topography was measured with a total station and a Real Time Kinematic DGPS (RTK-DGPS). Bathymetry was obtained by using an echo-sounder and the RTK-DGPS connected to a laptop, by using the HYPACK® 4.3a Gold software for data assimilation and navigation. The RTK-DGPS and echo-sounder were synchronised and measurements were taken at a frequency of 1 Hz. Using this system the recorded depth was immediately corrected for water level variations (i.e. tides and waves). Topographic and bathymetric data were then merged using SURFER® 8. A local metric co-ordinate system known as the Portuguese Melriça Grid (PMG) was used for the maps and the elevation is referenced to mean sea level (msl). Due to lack of bathymetric data, it was not possible to create a detailed topo-bathymetric map for the February 2005survey.

Key morphological parameters such as cross-sectional area (A_c), maximum depth (h_{max}), inlet width (I_w) and migration (M) were determined. This study followed the methodology proposed by Vila-Concejo et al. (2003) to allow comparison with previous studies.

Vila-Concejo et al. (2003) studied the inlet channel evolution in two different ways: (1) the inlet throat was defined for each map in order to analyse I_w, h_{max} and A_c below msl; and, (2) a longshore profile (profile 0 in Figure 2) was defined in order to analyse M by defining the changes of the location of the channel deepest point along the channel. All the gathered data, including those from by Vila-Concejo et al. (2003, 2004. 2006b) was stored and processed using GIS software (Arc View 8.3, ESRI software). The topo-bathymetric survey of 07/2001 was chosen as representative of the initial conditions to analyse the relation between inlet migration trend and the hydrodynamic conditions (measured between June 2001 and May 2006) for the present study.

Three periods were defined to compute M rate: June 2001-December 2002, January 2003-June 2004 and July 2004-May 2006. The last period was subdivided into two sub-periods (June 2004-February 2005 and March 2005-May 2006), in order to include the three new surveys performed and to study the particular effect of a W-SW Storm, the Vince storm. The M rate measurements, for each period and sub-periods, will be compared with the hydrodynamic conditions, in order to evaluate the impact of the most significant storm events.

Two RTK-DGPS topographic surveys were made to analyse the evolution of Vince Inlet that opened on 11/10/2005: these were undertaken on 26/10/05 and 04/11/05. The relative position of Vince Inlet and Ancão Inlet was measured using the maximum high water line (mhwl). The inlet width of both inlets was determined, as well as the distance between them. Additionally, several oblique photographs were obtained to analyse the morphologic evolution of Ancão Peninsula. Post-storm conditions were compared with those described by Morris (2001; 2004) and Vila-Concejo et al. (2003).

Hydrodynamic conditions

Tidal and wave data from the directional wave-rider buoy offshore of Sta. Maria Cape (location 36º54.3'N, 07º53.9'W at 93 m depth, Figure 1) provided by the Portuguese Hydrographic Institute (IH) were used for this study. The buoy records values of significant wave height (H_s), peak period (T_p) and wave direction (θ) for 20 min each 3 h, except during storm periods when data were recorded every half hour. Matias (2006) individualised the storms from June 2001 to June 2004 (defined as $H_s > 3$ m by Pessanha and Pires 1981). The data from Matias (2006) allowed identifying the major storm events for the two first periods of analysis (June 2001-December 2002, January 2003-July 2004), which will be compared with the measured M rates. The same author also characterised the wave climate by applying linear wave theory to estimate deep-water wave power (P). Due to the orientation of the southern coast of Portugal θ is always between 90º and 270º. P was then partitioned according to θ: W-SW ($\theta > 180$º) and E-SE, "Levante" ($\theta < 180$º).

Detailed wave data between July 2004 and May 2006, in order to characterise the storm events for the third period, were not available. However, it was possible to individualise storm events (from W-SW and E-SE) by analysing on-line IH graphs (http://www.hidrografico.pt). It should be noted that there were some gaps in the wave data records. Data from two Spanish wave buoys located offshore of Cádiz (Figure 1) were used to analyse storm occurrence during the IH gaps in the data: a wave-rider buoy (36º28.8'N, 6º57.6' W at 450 m depth) and a triaxys buoy (36º30.0' N, 6º20.0'W at 21 m depth). WAM (Wave Analysis Model) data provided by the Spanish Port Authority (http://www.puertos.es) which generates wave climate using a wind atmospheric/hydrostatic model, were also used. The WAM network node has a point located offshore of Ria Formosa system (approximate location 36º45.0'N, 08º00.00'W), thus allowing a double check of the storm data provided by the Cádiz wave-buoys. This methodology did not allowed to compute neither P value and storm duration.

RESULTS

Inlet parameters evolution

In June 2004 (Figure 2a) the inlet had a narrow updrift spit extending offshore and NW-SE oriented channel. In May 2006 (Figure 2b) the inlet's updrift margin was characterised by strong sediment accumulation. The channel is SSW-NNE oriented. In both maps the inlet presents all the features of a well developed inlet: well defined main and adjacent channel, ebb and flood-tidal shoals.

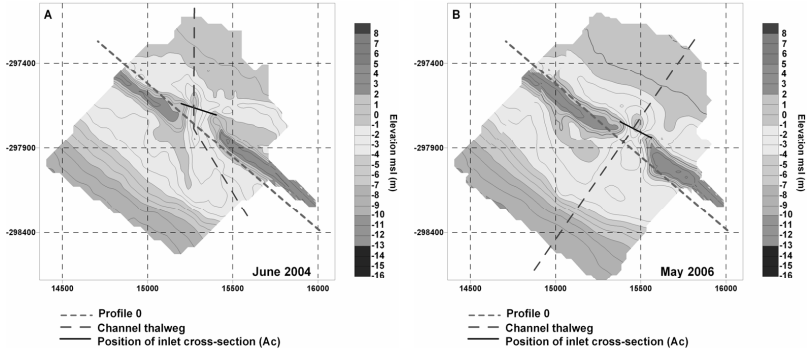

Fig. 2. Topo-bathymetric maps obtained for Ancão Inlet in June 2004 (a) and May 2006 (b). Metric co-ordinates refer to the Portuguese Melriça Grid. Elevation, in meters, is relative to msl.

Recent data show stable A_c values in accordance with previous data obtained by Vila-Concejo et al. (2003; 2004; 2006b, Figure 3). I_w also present small variations, with a minimum in April 2001, after which the inlet recovers to its normal width by May 2006. The survey performed in November 2001 presents the highest h_{max} and has been decreasing towards previous values since then. The A_c and h_{max} parameters, measured for the surveys performed in June 2004 and May 2006 (Figure 3), do not show

significant variations, although the occurrence of the ex-tropical storm Vince (11th October 2005). However, some increasing of I_w is observed.

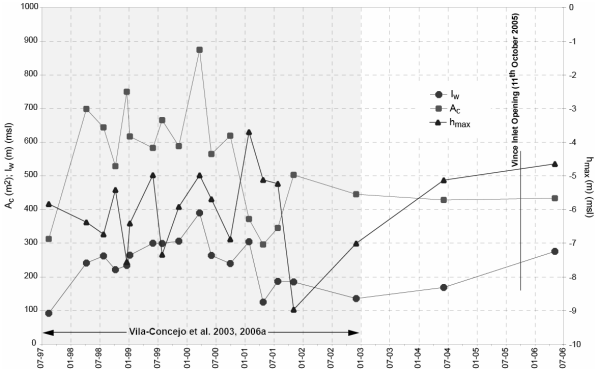

Fig. 3. Evolution of inlet cross-section (A_c), inlet width (I_w) and maximum depth at inlet throat (h_{max}) between August 1997 and May 2006

Inlet channel positions for the three recent surveys were plotted together with data from Vila-Concejo et al. (2003, 2004, 2006b) in relation to the Inlet Opening Position (IOP), and M rates obtained (Figure 4). The I_w, measured between the mhwl, was 50 m for Vince Inlet (shadow area, Figure 4) and 180 m for Ancão Inlet, showing that Ancão I_w did not significantly changed because of the storm (if compared with June 2004, Figure 3).

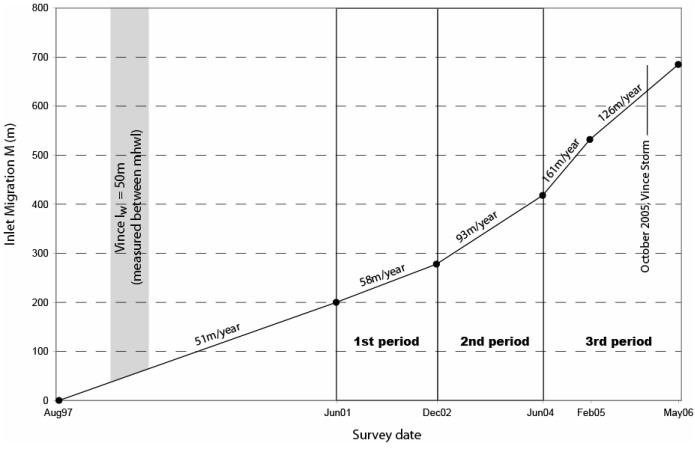

Fig. 4. Inlet migration from its opening position (IOP) until May 2006. The shadow area represents the relative Vince Inlet position and I_w in 26th October 2005

The inlet channel migrated approximately 685 m eastwards from its opening position (IOP) up until May 2006, which implies an 80 m/year migration rate. During the first period of this study (June 2001-December 2002), the inlet migrated ≅ 60 m/year, approximately the same rate measured between IOP and May 2001 (Figure 4). From January 2003 until June 2004 (2nd period), is observed an increase on M rate (≅ 95 m/year, Figure 4). The third period, divided into two sub-periods, present the highest M rate (≅ 140 m/year). The 3rd period M rate is higher between July 2004 and February 2005 (≅ 160 m/year, Figure 4), decreasing to ≅ 125 m/year between March 2005 and May 2006.

Hydrodynamic conditions

The number of storms from each sector (E-SE and W-SW) is shown in Table 2. Data for the two first periods (Jun01/Dec02 and Jan03/Jun04) were obtained from Matias (2006), and include total storm duration and P for all data. The most energetic storm from each sector is also in Table 2 taking into account maximum H_s and maximum storm duration. The H_s and storm duration can or cannot be coincident, i.e., a storm with higher H_s can have a lower duration and vice-versa. Storm data for the third period (Jul04/May06) were obtained from IH and Spanish port authority online graphs and the WAM model. Although it was possible to individualise storm events using maximum H_s, it was not possible to identify its duration and obtain P.

Table 2. Number of storm events from E-SE and W-SW for the three studied periods

Periods	E-SE Storms				W-SW Storms			
	Nº	Hours	Highest H_s (m)	Highest Duration (hh:mm)	Nº	Hours	Highest H_s (m)	Highest Duration (hh:mm)
Jun01/Dec02†	7	≅139	4.9 (17/12/01)	42:00 (19/10/02)	7	≅103	4.8 (17/12/02)	34:44 (17/12/02)
Jan03/Jun04†	3	≅30	5.7 (16/03/03)	25:43 (16/03/03)	11	≅103	4.2 (13/04/03)	39:45 (27/10/03)
Jul04/May06‡	8	*	4.0 (09/10/04)	* (09/10/04)	9	*	5.5 (11/10/05)	*

†adapted from Matias (2006)
‡obtained from IH and Spanish Port Authority online graphs and WAM model
*not possible to identify storm duration

During the first period (Jun01/Dec02), data obtained by Matias (2006) allowed the identification of seven storms from E-SE and seven from W-SW. The total duration was higher for storm events from E-SE than from W-SW. The maximum H_s recorded was 4.9 m for an E-SE storm event on 17th December 2001, however the maximum P was obtained for a W-SW event on the 17th December 2002 (≅150,000 $Jm^{-1}s^{-1}$, Matias 2006).

A small number of E-SE storms occurred during the second period (Jan03/Jun04), both in terms of events and duration (three storm events for a total duration of ≅30 hours). However, maximum H_s and P were recorded for an E-SE event occurring on 16th March 2003 (H_s=5.7 m and absolute P value >240,000 $Jm^{-1}s^{-1}$). The total duration of storm events from W-SW was the same as for the previous period (Table 2), although with higher number of storms. It should, however, be noticed that the maximum H_s of W-SW storm events was lower.

Data obtained using IH on-line graphs and the wave buoys of Cádiz allowed the identification of 17 storms between July 2004 and May 2006 (eight from E-SE and nine from W-SW). In general, W-SW had higher H_s and data allowed to individualise five storms with $H_s \geq 4$ m. The biggest storm, in terms of H_s, corresponds to ex-tropical storm Vince (11th October 2005). The storm, from W-SW, had an approximate duration of 16 hours and H_s of 5.5 m.

Plotted M rate values with maximum H_s for storms from E-SE and W-SW, allows to observe a M rate increase from the first to the second period, join with the decrease on number of E-SE and increase of W-SW storms (Figure5). The M rate increases significantly from the second to the third period, however in this case there is more equilibrium between events from both directions, although maximum H_s for the E-SE events are significantly lower. On the contrary, W-SW presents higher H_s and an extreme event, Vince storm (Figure 5).

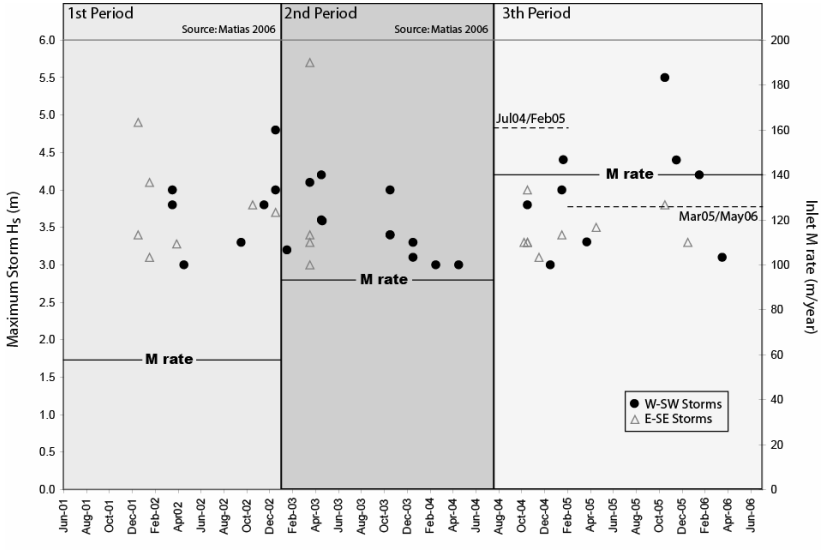

Fig. 5. Storm events between June 2001 and May 2006 plotted with M. The dashed lines marks the differences of M rate measured in the 3rd period.

DISCUSSION

The topo-bathymetric maps and the inlet parameters (Figure 2 and 3) show that despite the increase in M (Figure 4), the inlet has stable A_c, I_w and h_{max}. This is in agreement with Vila-Concejo et al. (2003, 2004, 2006b). The maintenance of a similar A_c represents that the overall inlet hydrodynamic behaviour was not affected by the migration, having a relatively stable tidal prism. Although the main channel presents different thalweg orientation (Figure 2), and some differences in I_w and h_{max} (Figure 3),

the inlet has a hydrodynamically efficient connection between the sea and the lagoon area, not being significantly affected by the wave-conditions and/or inlet migration.

Several storms occurred with different impact on M rates during the study period (June 2001 to May 2006). Morris et al. (2001) found that the combination of high tidal levels and storm events was a key factor for explaining the evolution of Ancão Inlet. The authors observed that a combination of large waves during spring high tide resulted in the most dramatic erosion of the vegetated areas on the downdrift margin. Once these areas erode, the inlet migrates rapidly. For the present paper more emphasis was given to the number of storms, storm duration and maximum H_s. It should be noted that a more detailed wave climate characterisation is needed in order to clearly individualise which storm events have impacted inlet behaviour, especially M.

During the 1st period (Jun01/Dec02) M rate was ≅60 m/year increasing to ≅95 m/year in the 2nd period (Jan03/Jun04). The duration of W-SW storms for both 1st and 2nd periods was about the same (≅103 hours); on the contrary, a decrease was observed in the number of E-SE storms (Figure 5). Since the fair-weather conditions were the same for both periods, the decrease of E-SE events could be related to the increase in M rates.

Within the 1st and 2nd periods, two extreme E-SE events occurred (17/12/2001 and 16/03/2003), with high values of P. The magnitude of these storms has a return period greater than 25 and 100 years, respectively (Pires 1998). Although it is recognised that E-SE events do not have an impact as severe as the W-SW storms at Ancão Inlet (Morris et al. 2001), historical data show that the inlet can widen significantly in a westerly direction (Vila et al., 1999; Williams et al. 2003). Vila-Concejo et al. (2003) recorded 80 m westward inlet migration between July 1997 and April 1998, with an I_w increase of ≅150 m. Thus, it seems plausible that even if westward migration did not occur, the extreme E-SE events can be responsible by episodes of reverse longshore drift (from east to west), attenuating the high eastward migration rates.

Assuming that fair-weather conditions for each period remain approximately the same, and considering that 80% of inlet migration occurs during storms (Williams et al. 2003), regulated by duration, magnitude and tidal level (Morris et al. 2001; Vila-Concejo et al. 2004), it seems likely that the high frequency and magnitude of E-SE events could have been responsible by the lower M rate found in the first period.

In the 3rd period (Jul04/May06) equilibrium in the number of occurrence between E-SE and W-SW events is observed (Table 2). The methodology used to individualise maximum H_s did not allow storm duration to be accurately obtained. It should be noted that the maximum H_s for E-SE storms was 4.0 m (Table 2). W-SW storms had higher magnitude and M was ≅140 m/year, showing a rapid eastward inlet migration that seems to be caused not only by ex-tropical storm Vince but also by the occurrence of four other storms with H_s ranging between 4-4.5 m (Figure 5). In fact, the highest M rate was recorded before the occurrence of the Vince storm (between Jul04/Feb05, M ≅160 m/year, Figure 4), raising the possibility of the occurrence of a W-SW storm

with higher duration and P, possibly during spring-tides (as suggested by Morris et al. 2001), which could have been responsible for the significant increase of the M rate. Thus, the Vince storm, although responsible for the opening of an ephemeral inlet updrift from Ancão Inlet, does not seem to be directly responsible for the high increase of the M rate found during the 3rd period. Possibly it effect could have been greater if the storm impacted the coast during spring-tides instead of the observed neap-tides (tidal amplitude of 1.2 m).

The Ancão Peninsula is a prograding feature owing to the net easterly sediment transport (Williams et al. 2003). Inlet migration is directly related to this fact. As occurs in other tidal inlet systems, the underlying, first order driving mechanism of the evolution of Ancão Inlet is related to storm events. A storm forces morphological changes so that the inlet moves from an essentially ebb-tide dominated condition to a wave-dominated condition (Morris et al. 2001, MOR1 under $H1_A$ Table 1). Following the passage of the storm, the inlet must then adjust its morphology back to a configuration determined by fair-weather conditions. The topo-bathymetric map of May 2006 (Figure 2) shows the inlet developing a fair-weather morphology, presenting the typical morphologies described by Williams et al. (2003) and Morris et al. (2004).

Morris et al. (2004) identified several post-storm morphodynamic features that can be also observed in Figure 6, an oblique photo taken after Vince storm: a down-drift orientation of the inlet channel, an inner sand spit developing in the backbarrier intertidal area of Barreta Island and a narrow across-shore ebb delta. After a series of winter storms, the inlet takes approximately three months to adjust back to its preferred fair weather condition configuration determined by fair-weather conditions (MOR 1, Table 1, Williams et al. 2003).

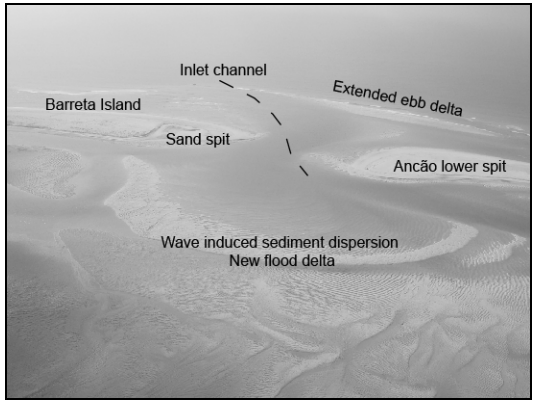

Fig. 6. Ancão Inlet at the end of November 2005, after the Vince storm, exhibiting the typical morphology of the post-storm morphodynamic conditions described by Morris et al. (2004).

Ancão Inlet exhibits a HEMP migration pattern (Vila-Concejo et al. 2002; 2006a). Figure 7 shows two aerial photographs of Ancão Inlet separated by eight years: Figure 7a shows Ancão Inlet one month after the relocation (08/1997) and Figure 7b one month after the Vince storm (11/2005). In the first the initial formation of the channel and a well developed dune field on Barreta Island can be observed. In the second the high eastward migration of Ancão Inlet and the development of a low-elevation spit on Ancão Peninsula can be observed. The dune field on Barreta Island has disappeared completely. The downdrift inlet area, due to its morphology, also has a high susceptibility to non-storm overwash events (Matias 2006). Vila-Concejo et al. (2006a) included the entire length of Ancão migration path inside the Inlet Hazard Area for the Ria Formosa.

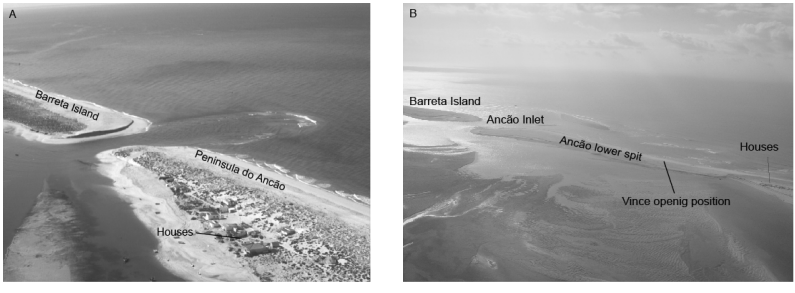

Fig. 7. Photos of Ancão Inlet at two times during its eastward migration cycle: A was taken one month after inlet opening (08/1997). B one month after the Vince storm (11/2005)

CONCLUSIONS

About 10 years after relocation, Ancão Inlet evolution and hydrodynamics were studied by using three new surveys. The obtained data was compared with previous data obtained by other authors. According to the morphological model proposed by Vila-Concejo et al. (2003), the Ancão Inlet is now in Stage 3, i.e., a "mature" migrating inlet, where the downdrift migration of the channel is accompanied by updrift spit growth and both deltas migrate asymmetrically. This stage is characterised by high eastward migration rates, as seems to be the case of the present inlet evolution without any significant changes in inlet parameters. During the study period an extreme event on 11th October 2005 was responsible for the opening of a small inlet in approximately the same place where the Ancão Inlet had been relocated in 1997. This ephemeral inlet remained open for three weeks before closing, showing the high hydraulic efficiency of Ancão Inlet. Migration rates obtained for Ancão Inlet with the three new surveys were the highest recorded since inlet opening. Although data presented within this study did not allow the direct relation of the inlet migration rate with the hydrodynamic data, some considerations can be made on the effect of storms in inlet behaviour: (1) a decrease on the number of E-SE storms seems to cause an increase of the inlet migration rates; and, (2) the Vince storm, although impacting on the M rate, did not seemed to be the major cause of the increase of this parameter, being probably related with a higher frequency of W-SW storms with $H_s > 4$ m.

ACKNOWLEDGEMENTS

This work is a contribution to the IDEM project – Inlet Dynamics Evolution and Management at the Ria Formosa, under contract POCI/MAR/56533/2004. Wave data from 2001 to 2004 was kindly provided by the Instituto Hidrográfico. The Ancão Inlet data corresponding to December 2002 was kindly supplied by the Instituto Portuário dos Transportes Marítimos de Portugal. The authors would like to thank Ana Matias for supplying the wave data treatment and also to Luis Pedro Almeida, Juan Severino Ibanhez and Piet Haerens, as well as to all CIACOMAR team, for helping during fieldwork. Thanks also to Brad Morris for his useful suggestions.

REFERENCES

Andrade, C. F. (1990). "O Ambiente Barreira da Ria Formosa, Algarve-Portugal". PhD Thesis, Universidade de Lisboa. 627 pp. (in Portuguese)

Ciavola, P., Taborda, R., Ferreira, Ó., Dias, J.A. (1997). "Field Measurements of Longshore Sand Transport and Control Processes on a Steep Meso-Tidal Beach in Portugal". *Journal of Coastal Research* 13 (4), 1119-1129.

Costa, M., Silva, R., Vitorino, J. (2001). "Contribuição para o estudo do clima de agitação marítima na costa Portuguesa". 2as Jornadas Portuguesas de Engenharia Costeira e Portuária in CD-ROM. (in Portuguese)

Dias, J.M.A. (1988). Aspectos geológicos do litoral algarvio. Geonovas (Lisboa), 10, 113-128. (in Portuguese)

Dias, J.A., Ferreira, Ó., Matias, A., Vila-Concejo, A., Sá-Pires, C. (2003). "Evaluation of soft protection techniques in barrier islands by monitoring programs: case studies of the Ria Formosa (Algarve-Portugal). *Journal of Coastal Research* SI 35, 117-131.

Esaguy A.C. Ria de Faro, Ilha do Ancão. Evolução 1950-1985. Direcção Geral de Portos Internal Report, 7p. (in Portuguese)

FitzGerald, D.M., Kraus, N.C., Hands, E.B. (2001). "Natural mechanisms of sediment bypassing at tidal inlets". ERDC/CHL CHETN-IV-30, U.S. Army Engineer Research and Development Center, Vicksburg, MS. 10pp.

FitzGerald, D.M. (1996). "Geomorphic Variability and Morphologic and Sedimentologic Controls on Tidal Inlets". *Journal of Coastal Research* SI 23, 47-71.

Matias (2006). "Overwash sedimentary dynamics in the Ria Formosa Barrier Islands". PhD Thesis, Universidade do Algarve. 253 pp. (in Portuguese)

Morris , B.D., Davidson, M.A., Huntley, D.A., (2001). "Measurements of the response of a coastal inlet using video monitoring techniques". *Marine Geology* 175, 251-272.

Morris , B.D., Davidson, M.A., Huntley, D.A., (2004). "Estimates of the seasonal morphological evolution of the Barra Nova Inlet using video techniques". *Continental Shelf Research* 24, 263-278.

Pessanha, L.E.V., Pires, H.O. (1981). Elementos sobre o Clima de Agitação Marítima na Costa Sul do Algarve. Internal Report, Instituto Nacional de Meteorologia e Geofísica. 66 pp. (in Portuguese)

Pilkey, O.H., Neal, W.J., Monteiro J.H., Dias, J.M.A. (1989). "Algarve Barrier Islands: a noncoastal-plain system in Portugal". *Journal of Coastal Research* 5(2), 239-261.

Pires, H.O., 1988. Project INDIA, *Preliminary Report on Wave Climate at Faro*. (unpublished). Instituto de Meteorologia – Instituto Superior Técnico, 37pp.

Vila, A., Dias, J.M.A., Ferreira, Ó., Matias, A. (1999). "Natural evolution of an artificial inlet". Proceedings Coastal Sediments'99 Conference (New York, U.S.A., ASCE), *1478-1488*.

Vila-Concejo, A., Matias, A., Ferreira, Ó., Duarte, C., Dias, J.M.A. (2002). "Recent Evolution of the Natural Inlets of a Barrier Island System in Southern Portugal". *Journal of Coastal Research* SI 36, 741-752.

Vila-Concejo, A., Ferreira, Ó., Matias, A., Dias, J.M.A. (2003). "The first two years of an inlet: sedimentary dynamics". *Continental Shelf Research* 23, 1425-1445.

Vila-Concejo, A., Ferreira, Ó., Morris, B., Matias, A., Dias, J.A. (2004). "Lessons from inlet relocation: examples from Southern Portugal". *Coastal Engineering* 51 (10), 967-990.

Vila-Concejo, A., Matias, A., Pacheco, A., Ferreira, Ó., Dias, J.M.A. (2006a). "Inlet hazard determination in the Ria Formosa barrier island system". *Continental Shelf Research* 26 (9), 1045-1060.

Vila-Concejo, A., Matias, A., Ferreira, Ó., Dias, J.M.A. (2006b). "Inlet sediment bypassing to a downdrift washover plain". *Journal of Coastal Research* SI 39, 401-405.

Weinholtz, M.B. (1964). "Contribuição para o Estudo da Evolução das Flechas de Areia na Costa Sotavento do Algarve". Separata do Boletim Trimestral de Informação da Direcção-Geral de Serviços Hidráulicos, 14. (in Portuguese)

Williams, J.J., O'Connor, B.A.O., Arens, S.M., Abadie, S., Bell, P., Balouin, Y., Van Boxel, J.H., do Carmo, A.J., Davidson, M., Ferreira, Ó., Heron, M., Howa, H., Hughes, Z., Kaczmarec, L.M., Kim, H., Morris, B., Nicholson, J., Pan, S., Salles, P., Silva, A., Smith, J., Soares, C., Vila-Concejo, A. (2003). "Tidal inlet function: field evidence and numerical simulation in the INDIA project. *Journal of Coastal Research* 19(1), 189-211.

THE INFLUENCE OF TIDAL PRISM AND VEGETATION ON TIDAL CHANNEL MORPHOLOGY: IMPLICATIONS FOR MARSH STABILITY

Matthew L. Kirwan[1], A. Brad Murray[2]

1. Nicholas School of the Environment and Earth Sciences, Duke University, Box 90229, Durham, NC 27708, USA. mlk13@duke.edu
2. Nicholas School of the Environment and Earth Sciences, Duke University, Box 90229, Durham, NC 27708, USA. abmurray@duke.edu

Abstract: A peculiar feature of tidal channel networks is that their geometry (e.g. channel length, width, density) scales better with watershed area than tidal prism. Platform elevation has little control on network morphology, suggesting that relative platform deepening following sea level acceleration or sediment supply reduction will not cause significant changes to the channel network, despite field observations to the contrary. We explain this paradox with a numerical model of platform and channel network evolution that incorporates feedbacks between vegetation and physical sediment transport processes. In the model, platform deepening stimulates vegetation growth, leading to more stable channel edges. In this situation, channels deepen rather than widen, leading to channel morphologies that do not reflect tidal prism. In an environment where sea level or sediment supply changes have significantly altered the platform elevation, vegetation disturbance will lead to rapid network expansion as channels return to a form determined by tidal prism.

INTRODUCTION

Networks of sinuous tidal creeks and channels typically dissect broad intertidal marshes. Channel networks carry water, sediment, and nutrients into and out of estuaries and on and off of vegetated marsh platforms (Rinaldo et al. 2004). Tidal creeks host many commercially and ecologically important fish and shell fish, and export organic material to estuarine and marine ecosystems (Turner 1977; Lynn et al. 1981; Costanza et al. 1989). In addition to ecological and economic interests, tidal networks often display beautiful morphologic patterns that are intellectually interesting. The evolution of

channel networks and the marsh platform that surround them are thoroughly coupled- the marsh elevation relative to sea level determines the volume of water flowing through the network, and the network distributes the sediment necessary for marsh accretion. Dense vegetation on the marsh platform and channel edges strongly influences the morphology of marsh systems by slowing water velocities, aiding platform accretion, and stabilizing creek banks (Fagherazzi et al. 2004).

Like terrestrial river channels, the shape and distribution of tidal creeks is largely controlled by the discharge of water passing through them. For example, tidal channel width and cross sectional area typically follow well established relationships with discharge (e.g. Rinaldo et al. 1999a). Tidal prism volume is defined as the volume of water passing through a single channel cross section during a tidal cycle. Drainage density, defined as the total channel length divided by the watershed area, increases as a function of tidal prism (Steel and Pye 1997; Marani et al. 2003; Novakowski et al. 2004). These types of relationships have contributed to the development of several morphologic models of channel network development and behavior (Allen 1997; Fagherazzi and Furbish 2001; D'Alpaos et al. 2007).

Recent analyses of remotely sensed channel networks have led to several insights regarding the processes that determine their morphology. One particularly interesting feature is that morphologic characteristics of tidal channels scale better with drainage area than tidal prism volume. For example, total network length increases linearly with drainage area at a rate consistent between several subbasins of the Venice Lagoon characterized by different elevations, vegetation, and tidal amplitude (Marani et al. 2003). On the other hand, network length increases linearly with tidal prism, but at a rate inconsistent among the different basins (Marani et al. 2003). Since tidal prism is determined by both the contributing watershed area, and the inundation height of water above the bed surface at all points within the watershed (e.g. Rinaldo et al. 1999a), Marani et al.'s (2003) measurements suggest that the relative elevation of the marsh platform is not an important influence on channel network morphology. Consistent with this interpretation, Hood (2007) analyzed the drainage density of 37 marsh islands, and found significant correlation with island area, but not island elevation. Moreover, Hood (2007) detected no significant relationship between island elevation and any channel metric, including channelized surface area, mainstem length, number of channels, or the outlet width of the largest channel.

Marani et al. (2003) and Rinaldo et al. (2004) hypothesize that the lack of influence of tidal prism volume on channel morphology reflects the ability for vegetation to "freeze" network morphology. Channel networks in marshes are thought to inherit much of their pattern from unvegetated mudflat or terrestrial sources (e.g. Friedrichs and Perry 2001). While mudflat channel networks are highly dynamic, channel networks bounded by a vegetated marsh surface tend to be highly stable. Indeed, channel migration is often nearly imperceptible in historical photographs (Marani et al. 2003 *and references therein*). However, we note that there have been several recent observations of channel expansion. Channel networks in New York (Hartig et al. 2002) and southeastern

England (Van der Wal and Pye 2004) have widened and lengthened dramatically, perhaps in response to local relative sea level acceleration.

The relationship between tidal prism volume and channel network morphology has significant implication for the response of channels to sea level and sediment supply change. Several numerical models predict that the elevation of the marsh platform, relative to sea level, will decrease in response to sea level acceleration or sediment supply reduction (Morris et al. 2002; Kirwan and Murray 2006; D'Alpaos et al. 2007). Platform deepening expands the tidal prism volume even as the drainage area remains constant (Kirwan and Murray 2006; Kirwan and Murray *submitted*). If changes in tidal prism volume cause changes in channel morphology, then channel networks should expand in response to sea level acceleration or sediment supply reduction. If, however, channel morphology does not respond to changes in tidal prism volume, then channel networks may be relatively stable to sea level and sediment supply change.

In this contribution, we present simple model experiments in which vegetation growth causes tidal channels to be unresponsive to tidal prism changes. In an environment undergoing relative sea level acceleration or sediment supply reduction, channel network morphologies will not reflect tidal prism volumes. In the model, this lack of response occurs because of stabilization of channel edges by vegetation that is more productive when the platform is deep in the tidal frame. Disturbance to vegetation, however, will tend to cause channels to return to a form determined by the tidal prism. In an environment where sea level or sediment supply changes have significantly altered the platform elevation, disturbance will lead to rapid expansion of the channel network and erosion of the marsh platform.

METHODS

To explore relationships between tidal prism volume and channel network morphology, we utilize a numerical model of tidal marsh evolution described in Kirwan and Murray (2006; *submitted*). The model simultaneously treats vegetation-influenced platform accretion and channel erosion processes, and is applicable over large spatial (km) and temporal (decades-millennia) scales. We have previously used the model to describe the response of platform morphology and accretion rates to changes in sea level rise rates.

Our basic approach is to model local elevation change calculated from erosion rates determined by simplified flow routing, and deposition rates determined as a function of water depth and the amount of vegetation growing in each cell. A model iteration begins with the marsh platform flooded to high tide level. We route water across the vegetated marsh platform and into the channel network according to a parametrically represented water surface. Flow directions on the platform are calculated according to the gradient of a constant curvature Poisson surface (Rinaldo et al. 1999b). In essence, the parametric water surface places watershed divides halfway between adjacent channels, and encourages platform flow perpendicular to the channel network. Within the channel network, flow is limited to cells with progressively decreasing along-channel distances to the outlet.

After all the water on the platform drains, local velocities are calculated by dividing the cumulative volume of water passing through each cell by cell width, depth at high tide, and a characteristic time period of high flow (see Kirwan and Murray *submitted* for details). We use $\tau_b = (\rho f_c v^2)/8$ to estimate bed shear stress (Dean and Dalrymple 1991). Erosion occurs when bed shear stress (τ_b) exceeds a critical value (τ_c=*0.4* N/m^2),

$$Erosion\ rate = m * \frac{\tau_b - \tau_c}{\tau_c} \quad (1)$$

where m is a constant equal to 0.0014 kg m^{-2} s^{-1} (Fagherazzi and Furbish 2001). Following Morris et al. (2002), the deposition rate in each cell is proportional to the vegetation biomass, B, and high tide water depth, d, of each cell. The deposition rate is additionally proportional to the concentration of suspended sediment, C_{ss}:

$$Deposition\ rate = (k_1 * C_{ss} + k_2 * B) * d \quad (2)$$

where k_1 (0.1848) and k_2 (0.000015) are proportionality constants adapted from Morris et al. (2002), and k_2 accounts for both the effect of sediment trapping by vegetation and the input of organic sediment.

We account for gravity driven processes such as creek bank slump by invoking a bed smoothing routine where sediment flux, $q_{s,g}$, is proportional to the slope, S, between neighboring cells:

$$q_{s,g} = (\alpha - \beta B) * S \quad (3)$$

The term $(\alpha - \beta B)$ is a topographic diffusivity that depends on the biomass, B, in the higher elevation neighbor, representing the stabilizing character of plant roots. We use α = 3.65 m^2 yr^{-1} and β = 0.0019 m^4 g^{-1} so that the slope driven transport is reduced by approximately two orders of magnitude for the maximum biomass densities, conservatively consistent with field experiments on terrestrial river banks (Murray and Paola 2003; Kirwan and Murray *submitted*).

In the model, we use biomass productivity as a proxy for total above ground biomass (Morris et al. 2002). We calculate biomass productivity as a function of high tide water depth:

$$Biomass\ productivity = aD + bD^2 + c \quad (4)$$

where a=28.2236, b=-0.0927661, and c=-272.847, which have been adapted from Morris et al. (2002) to fit a 4m tidal range using the methods of McKee and Patrick (1998).

This relationship yields highest productivity rates at some optimum water depth. In nature, salinity appears to limit growth at suboptimum depths and anoxia appears to limit growth at supraoptimal depths (Morris et al. 2002). When water depths are suboptimal, this relationship leads to relative stability of tidal marsh elevation relative to sea level (Morris et al. 2002). An increase in water depth would promote greater productivity, and more rapid deposition rates. However, water depths nearing or exceeding the optimal depth may promote instability of tidal marsh elevation (Morris et al. 2002). In this situation, a small increase in depth would cause a decline in vegetation productivity, and a reduction in deposition rates, causing further lowering of the marsh platform relative to high-tide level.

We calculate deposition and erosion per tidal cycle at the end of each model iteration and multiply by a time step to calculate bed elevation change. A model iteration, explicitly representing a single ebb tide, is multiplied by 120 to achieve a time step of 2 months, assuming 2 tidal cycles per day. Under a constant rate of sea level rise, an equilibrium platform and channel network morphology develops where the net rate of accretion (deposition minus erosion) everywhere equals the rate of sea level rise, and water depths remain constant through time (Kirwan and Murray 2006; Kirwan and Murray *submitted*).

In this contribution, we conduct several model experiments on a 9 km^2 marsh system, discretized into 25 m^2 cells. Each experiment begins with an equilibrium morphology created under a constant, 1 mm/yr rate of sea level rise. We subject the equilibrium morphology to an abrupt 10 mm/yr rate of sea level rise, and examine changes in tidal prism volume and the morphology of the channel network. We exclude vegetation from one experiment, and include it in the other. Model experiments end when a new equilibrium morphology has developed.

RESULTS

As reported elsewhere, an abrupt increase in the rate of sea level rise leads to marsh platform deepening and an increase in biomass productivity in the model (Kirwan and Murray, 2006 Kirwan and Murray *submitted*). This deepening continues until deposition rates, a function of biomass and water depth, increase to the new rate of sea level rise. At this point the marsh platform reaches equilibrium with the rate of sea level rise, and water depths, accretion rates, and biomass productivity remain temporally constant (Kirwan and Murray 2006). An increase in the rate of sea level rise from 1mm/yr to 10 mm/yr leads to about a 30cm depth increase when vegetation is present, and a 300cm depth change when vegetation is absent (Kirwan and Murray *submitted*). This platform deepening, together with channel expansion, converts a basin characterized by channels bounded by intertidal surfaces into a completely subtidal basin. Throughout the experiments, we define the channel network, even in a subtidal environment, as cells that are connected to the outlet by other channel cells and are at least 20mm lower in elevation than the highest platform cells.

In all model experiments, platform deepening leads to expansion of the tidal prism volume (Figure 1). Following a change in sea level rise rate from 1 mm/yr to 10 mm/yr, the prism in the unvegetated scenario approximately quadruples (Figure 1a). This causes water velocities in the channel network to increase and the channel beds to deepen. Slope driven transport, representing processes such as creek bank slump, actively widens channels as they deepen. We observe that the channelized portion of the marsh system slightly increases from about 50% to 55% in response to the 10 fold increase in sea level rise rate (Figure 1a). In this model experiment, channel widening dominates the total increase in channel area, although formation of new channels or the elongation of existing channels could also increase channelized area.

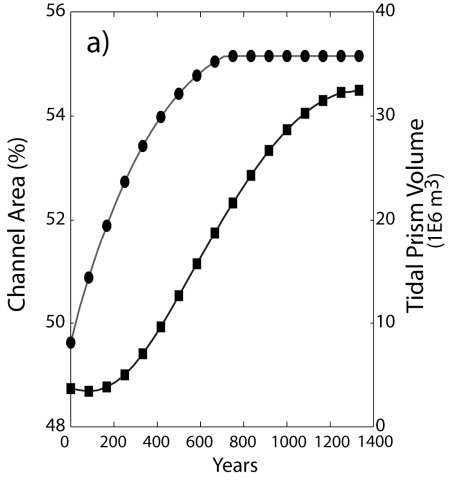

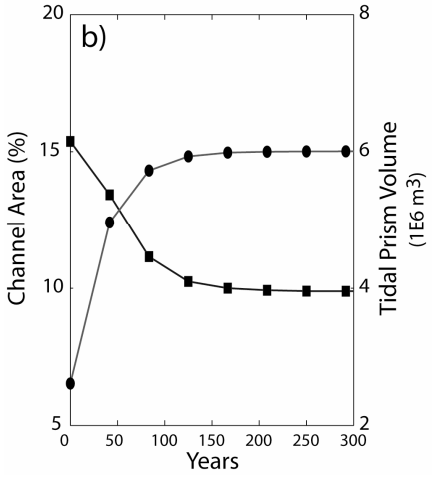

Fig. 1. Response of channel extent (squares, blue line) and tidal prism (circles, green line) to an abrupt increase in sea level rise rate. Vegetation is absent in a) and present in b). Platform deepening causes the tidal prism (green line) to increase in both scenarios, but stimulates biomass growth and resistance to creek bank slump in b). While an increase in tidal prism tends to enlarge channels (a), vegetation stabilization can exceed this effect (b).

Following a change in sea level rise rate from 1 mm/yr to 10 mm/yr, the prism volume in the fully vegetated scenario more than doubles in about 100 years (Figure 1b). While prism enlargement should tend to cause the channel network to erode and expand, we observe that the channelized portion of the marsh system decreases from about 15% to 10% over the same time interval (Figure 1b). We attribute this behavior to vegetation and its inhibition of channel widening processes. Increased platform depths cause increased biomass productivity and a decrease in gravity driven transport. Gravity driven transport processes determine channel width in our model, and in this experiment channels narrow in response to platform deepening.

Rather than eroding into the edges of a stable, vegetated platform, the modeled channel network accommodates the increased channel flow by eroding its bed and becoming deeper (Figure 2). In the vegetated scenario, the depth below high tide of channel cells increases about three-fold until a new equilibrium morphology develops. Therefore, the primary channel network response to sea level acceleration or sediment supply reduction is a decline in channel width-to-depth ratio.

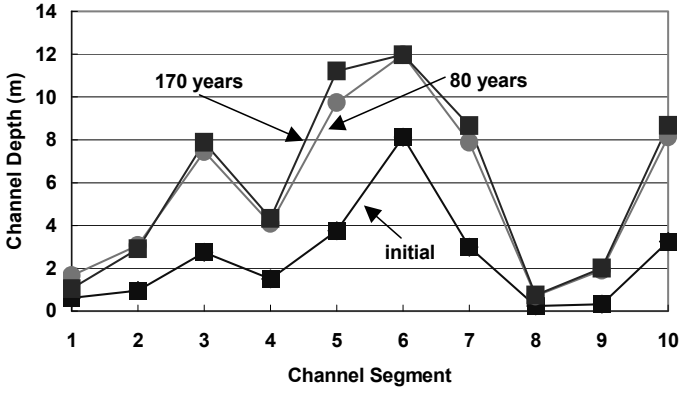

Fig. 2. Response of channel depth to an abrupt increase in sea level rise rate. Channel depths at representative points throughout the network measured as the difference between bed elevation and high tide.

DISCUSSION

Our model experiments suggest that tidal channels are responsive to tidal prism changes in the absence of vegetation, but unresponsive when vegetation is present. These experiments suggest that channel networks responding to increased rates of sea level rise, or decreased sediment supply, will have morphologic properties that do not reflect the current elevation of the marsh platform or tidal prism volume. The diversion of rivers flowing into Venice Lagoon, and the construction of dykes on the Skagit River Delta have resulted in decreased sediment delivery to marshes in these estuaries, and substantial lowering of marsh elevations relative to sea level (Marani et al. 2003; Hood 2007). A change in vegetation productivity in response to deepening could explain the disparities between tidal prism and drainage density in the Venice Lagoon (Marani et al. 2003) or the lack of correlation between platform elevation and any channel metric on the Skagit River Delta (Hood 2007). If true, these channel networks may be considered to be out of equilibrium with their present forcing conditions.

If enhanced vegetation growth leads to channels that are both narrower and deeper than their tidal prism would predict, then disturbance to vegetation may lead to significant morphologic change as channels adjust back to a form determined by prism volume. To address this possibility, we subjected the vegetated marsh surface at equilibrium with a 10 mm/yr rate of sea level rise to random vegetation disturbance. The disturbance consisted of removing all biomass in randomly selected platform cells (totaling 50% of all platform cells) and allowing it to grow back in disturbed cells after 10 years. As in previous simulations, the experiment ended when the platform and channel network morphology reached a new equilibrium.

Immediately following the initiation of disturbances, both the tidal prism and the channel network expanded (Figure 3). Unvegetated cells accreted more slowly than the

rate of sea level rise, leading to platform deepening and expansion of the tidal prism, even though the rate of sea level rise did not change. In this experiment, the tidal prism expanded only slightly, while the channelized area of the marsh system expanded from about 10% to about 60% in less than a hundred years. This suggests that channels expanded in response to increased gravity driven transport in disturbed cells, rather than in response to disturbance-generated tidal prism change. While additional model experiments should be conducted, a channel network out of equilibrium with platform morphology (i.e. network deeper and narrower than the platform elevation and tidal prism would determine) likely enlarges more than a channel network already at equilibrium with platform conditions. If true, disturbance to vegetation represents a process that can cause the channel network to regain a morphology that scales with platform elevation and tidal prism volume.

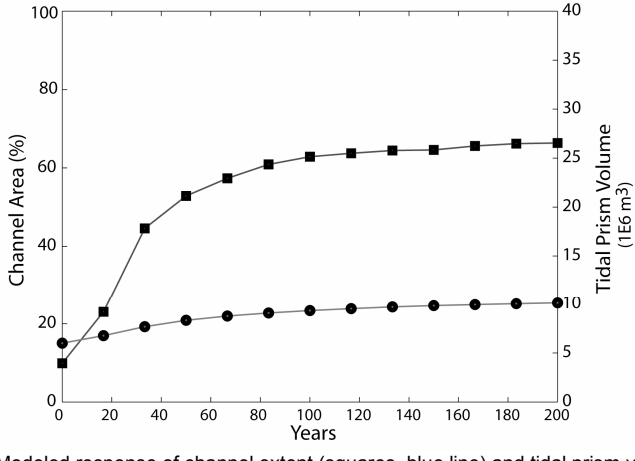

Fig. 3. Modeled response of channel extent (squares, blue line) and tidal prism volume (circles, green line), in a marsh at equilibrium with a 10 mm/yr rate of sea level rise, subjected to random vegetation disturbance (starting at time 0). While changes in the rate of sea level rise cause channel networks in fully vegetated marshes to abandon a plan view morphology determined by the tidal prism volume (e.g. figure 1), vegetation disturbance causes the network to return to a morphology determined by prism volume. In this case, vegetation disturbance leads to slight tidal prism enlargement, but large and rapid channel network expansion.

The disturbance experiment demonstrates that large and rapid changes in channel network morphology can occur after the marsh platform and channel network have stabilized in response to prior changes in sea level rise rates. This behavior is at least consistent with observed channel widening and elongation in New York (Hartig et al. 2002) and Southeastern England (Van der Wal and Pye 2004). In these regions, channels have expanded significantly over the last 50 years, despite accretion rates that mimic or exceed sea level rise rates.

Increased productivity of vegetation at greater water depths, and the ability of vegetation to resist channel widening processes, may have prevented network expansion in some marshes that have recently experienced increased sea level rise rates or decreased sediment delivery. If vegetation remains nearly intact, our model experiments suggest that drainage density will not reflect tidal prism volume. The resulting deep and narrow channels, however, may be particularly prone to vegetation disturbance. If disturbance to vegetation becomes more prevalent, our model experiments suggest that channels that have shown little response to sea level or sediment supply change in the past may widen dramatically in the future. Therefore, changes to channel depth may represent an initial stage of a channel network's response to accelerated sea level rise or sediment reduction. In this case, measurements of channel depth, or width-to-depth ratio, may forecast future change.

CONCLUSION

Our model experiments suggest that channel network morphologies will not reflect tidal prism volumes in an environment that has experienced accelerated sea level rise or sediment supply reduction. In these situations, vegetation productivity increases and channel edges become more stable as platform elevations become deeper in the tidal frame. In the continued presence of vegetation, channels respond to sea level acceleration or sediment supply reduction by deepening rather than widening. The resulting network geometry is metastable, prone to rapid change following vegetation disturbance. If relative platform elevations have changed significantly, vegetation disturbance can trigger widespread channel widening and elongation, as the network returns to a form determined by tidal prism.

ACKNOWLEDGEMENTS

The US National Science Foundation (EAR 1617209) supported the work financially.

REFERENCES

Allen, J. R. L. (1997). "Simulation models of salt-marsh morphodynamics: some implications for high-interval sediment couplets related to sea-level change," *Sedimentary Geology* 113, 211-223.

Costanza, R., Farber, S. C., and Maxwell, J. (1989). "Valuation and management of wetland ecosystems," *Ecological Economics* 1, 335-361.

D'Alpaos, A., Lanzoni, S., Marani, M., and Rinaldo, A. (2007). "Landscape evolution in tidal embayments: modeling the interplay of erosion, sedimentation, and vegetation dynamics," *In press, Journal of Geophysical Research*.

Dean, R. G., and Dalrymple, R. A. (1991). "*Water wave mechanics for engineers and scientists*," Advanced Series on Ocean Engineering, Volume 2: World Scientific Publishing Company, 353 p.

Fagherazzi, S., and Furbish, D. J. (2001). "On the shape and widening of salt marsh creeks," *Journal of Geophysical Research* 106, 991-1003.

Fagherazzi S., Marani, M., and Blum, L.K. (2004). "The ecogeomorphology of tidal Marshes," American Geophysical Union, p. 75-92.

Friedrichs, C. T., and Perry, J. E. (2001). "Tidal salt marsh morphodynamics: a synthesis," *Journal of Coastal Research* 27, 7-37.

Hartig, E. K., Gornitz, V., Kolker, A., Mushacke, F., and Fallon, D. (2002). "Anthropogenic and climate-change impacts on salt marshes of Jamaica Bay, New York City," *Wetlands* 22, 71-89.

Hood, W. G. (2007). "Scaling tidal channel geometry with marsh island area: a tool for habitat restoration, linked to channel formation process," *In press, Water Resources Research.*

Kirwan, M. L., and Murray, A. B. (2006). "Response of an ecomorphodynamic model of tidal marshes to varying sea level rise rates," *in* Parker, G. and Garcia, M. H. (eds.) *River, coastal, and estuarine morphodynamics: RCEM 2005, v.2,"* p. 629-634.

Kirwan, M. L., and Murray, A. B. "An integrated biologic and physical model of tidal marsh evolution," Submitted, Proceedings of the National Academy of Sciences.

Lynn, G. D., Conroy, P. D., and Prochaska, F. J. (1981). "Economic valuation of marsh areas for marine production processes (Florida)," *Journal of Environmental Economics and Management* 8, 175-186.

Marani, M., Belluco, E., D'Alpaos, A., Defina, A., Lanzoni, S., and Rinaldo, A. (2003). "On the drainage density of tidal networks," *Water resources research* 39(2), doi:10.1029/2001WR001051.

McKee, K. L., and Patrick, Jr., W. H. (1988). "The relationship of smooth cordgrass (Spartina alterniflora) to tidal datums: a review," *Estuaries* 11, 143-151.

Morris, J. T., Sundareshwar, P. V., Nietch, C. T., Kjerfve, B., and Cahoon, D. R. (2002). "Responses of coastal wetlands to rising sea level," *Ecology* 83, 2869-2877.

Novakowski, K. I., Torres, R., Gardener, L. R., and Voulgaris, G. (2004). "Geomorphic analysis of tidal creek networks," *Water Resources Research* 40, W05401, doi:10.1029/2003WR002722.

Rinaldo, A., Fagherazzi, S., Lanzoni, S., Marani, M., and Dietrich, W. E. (1999a). "Tidal networks 3. Landscape-forming discharges and studies in empirical geomorphic relationships," *Water Resources Research* 35, 3919-3929.

Rinaldo, A., Fagherazzi, S., Lanzoni, S., Marani, M., and Dietrich, W.E. (1999b). "Tidal networks 2. Watershed delineation and comparative network morphology," *Water Resources Research* 35, 3905-3917.

Rinaldo, A., Belluco, E., D'Alpaos, A., Feola, A., Lanzoni, S., and Marani, M. (2004). "Tidal networks: form and function," *In:* Fagherazzi S., Marani, M., and Blum, L. K. (eds.), *The ecogeomorphology of tidal marshes*. American Geophysical Union, p. 75-92.

Steel, T., and Pye, K. (1997). "The development of saltmarsh tidal creek networks: Evidence from the UK," *Paper presented at Canadian Coastal Conference,* Canadian Coastal Science and Engineering Association, Guelph, Ontario.

Turner, R. E. (1977). "Intertidal vegetation and commercial yields of penaeid shrimp," *Transactions of the American Fisheries Society* 106, 411-416.

Van der Wal, D., and Pye, K. (2004). "Patterns, rates, and possible causes of salt marsh erosion in the Greater Thames area (UK)," *Geomorphology* 61, 373-391.

NATURAL AND ANTHROPOGENIC INFLUENCES ON THE MORPHODYNAMICS OF BIG SARASOTA PASS, FLORIDA

Richard A. Davis[1], Ping Wang[2], Tanya Beck[3]

1. Coastal Research Laboratory, Department of Geology, University of South Florida, Tampa, FL 33620 rdavis@mail.cas.usf.edu
2. Coastal Research Laboratory, Department of Geology, University of South Florida, Tampa, FL 33620 pwang@cas.usf.edu
3. Coastal Research Laboratory, Department of Geology, University of South Florida, Tampa, FL 33620 tbeck1@cas.usf.edu

Abstract: Both natural and anthropogenic factors have played a role in producing the present morphodynamic conditions at Big Sarasota Pass. This inlet, of unknown origin and age, is located between Lido Key, a recently nourished barrier island, and Siesta Key, a classic drumstick barrier island. Stabilization of the south channel margin in the 1960s has resulted in an increase in the southerly shifting of the ebb-tidal delta which has produced a narrow and shallow outer channel. This has caused inlet bypassing of sediment to move beyond the updrift end of the island as is typical of natural offset inlets. The nourishment of Lido Key on the updrift side of the inlet has further exacerbated this condition with the result being erosion on the north end of Siesta Key and considerable accretion several hundred meters to the south.

INTRODUCTION

The west-central Gulf Coast of the Florida peninsula contains a wide range of barrier-inlet morphologies and is arguably the most complicated such system in the world (Davis 1987). This is the consequence of the low tidal range and wave climate coupled with a range of three orders of magnitude in tidal prism, the combination of which produces both stable and unstable inlets along with wave-dominated and mixed-energy barrier islands. The barrier inlet complex displays a generally north-to-south longshore transport of sediment except for a few local reversals (Davis, 1999).

The development of the barrier islands for residential and commercial purposes began after World War II (Fig. 1) with streets, infrastructure and residential construction

becoming widespread within a decade. At Lido Key significant anthropogenic impact began in the early 20th century when John Ringling filled a series of shoals and mangrove islands to make Lido Key and St. Armands Key just landward of it. This focused a geographically dispersed tidal prism into both New Pass on the north and Big Sarasota Pass on the south of Lido Key. Siesta Key, a classic drumstick barrier island, had its north or updrift end protruding well beyond Lido Key in the typical downdrift offset morphology of mixed-energy barrier/inlet systems (Fig. 1).

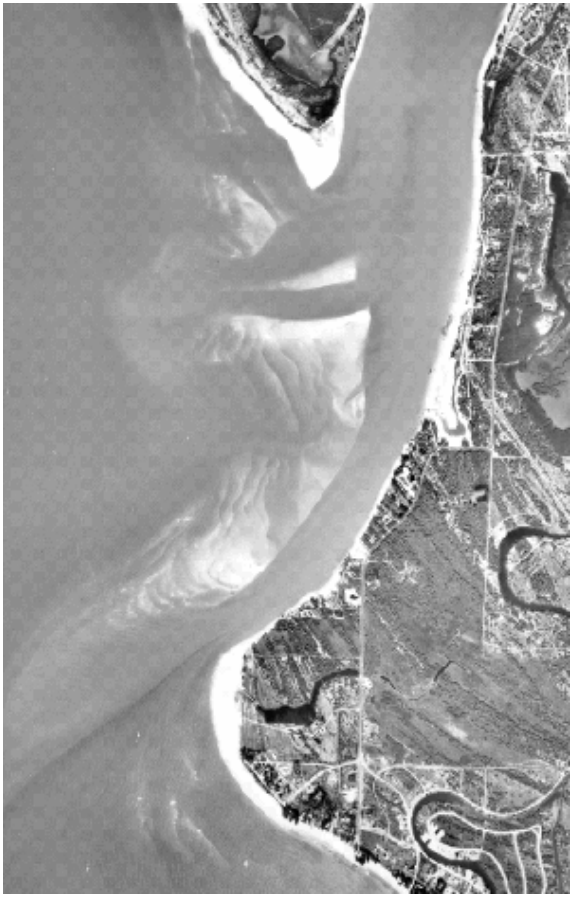

Fig. 1 – Aerial photograph of Siesta Key taken in 1948 showing the beginnings of development on the island overprinting the beach/dune ridges. Note also the flood channels cutting the ebb delta and the accretion at the north (right) end of Siesta Key.

The resulting inlet morphology was one of a strongly asymmetrical ebb-tidal delta (Fig. 1) and a southerly migrating tidal inlet (Big Sarasota Pass). The general process-response systems at such an inlet include the downdrift transport of sediment along the updrift barrier with significant sediment transported around the ebb-tidal delta thereby bypassing the tidal inlet with the remainder of the sediment carried across the ebb delta and into the main channel. Waves from the dominant northerly direction are refracted around the ebb delta causing a local reversal of longshore currents and resulting in a sediment sink at the end of the downdrift adjacent barrier island (Hayes 1974), in this case Siesta Key. This set of conditions produces prograding beach/dune ridges on the downdrift island as seen in Fig. 1.

HISTORICAL CHANGES

This discussion will consider both the natural and anthropogenic changes and consequences for Big Sarasota Pass and its associated barrier islands beginning with the first well-documented chart of 1883.

Predevelopment

The age and origin of Big Sarasota Pass are unknown although the age of adjacent Siesta Key has been documented at about 3000 BP by Stapor et al (1988). The prograding beach/dune ridges are at least 2000 years old implying that the inlet is at least that old. The first accurate chart is from 1883 and shows that Big Sarasota Pass is a maximum of 7 m deep with the shallowest part of the main channel being 2.3 m deep at the Gulfward end. The main channel deepened by the time of the 1953 survey to a maximum of 8 m deep and a minimum of 3.7 m. The first aerial photos available were from 1943 and show the pristine barriers on either side of the curved inlet. It is obvious from the early charts and this photo that the inlet channel is asymmetrical with the thalweg on the south or downdrift side. A plot of the inlet thalweg position shows a southerly migration over the period of record to that time (Fig. 2).

Development Stage

Road construction and other infrastructure installation began shortly after World War II. By the late 1950s there were many residences and commercial buildings present (Fig. 3). Landowners along the north end of Siesta Key along Big Sarasota Pass began to stabilize the shoreline using a combination of seawall, riprap, and groin field to prevent migration of the inlet channel into their property. This private and non-integrated effort did stop migration of the Big Sarasota Pass channel (Fig. 2) and the structures have remained in place to the present time.

Coupled with the stabilization of the south channel margin was the growth of the ebb-tidal delta at Big Sarasota Pass. Initially there were well-developed flood channels that crossed the large asymmetrical ebb-tidal delta (Fig. 1). These channels transported tidal prism and sediments into the main channel.

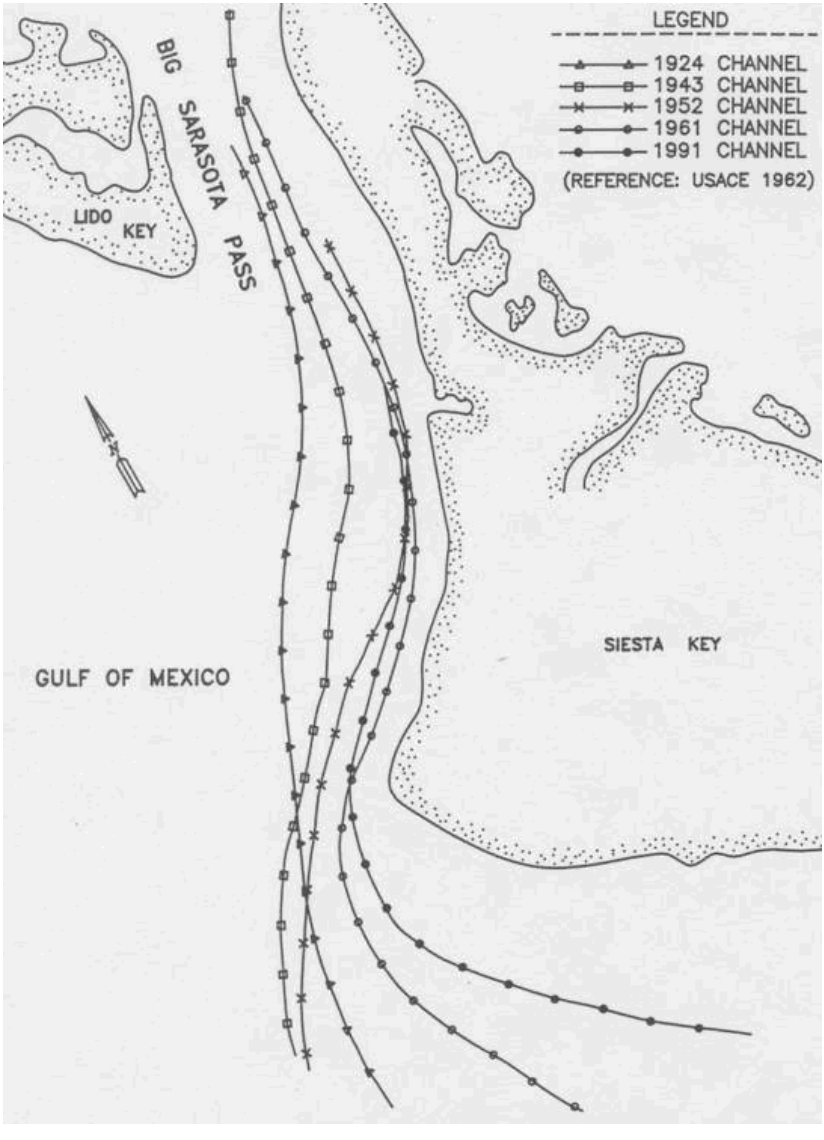

Figure 2 – Migration of the thalweg of Big Sarasota Pass through 1991.



Fig. 3 – Ebb-tidal delta at Big Sarasota Pass as it appeared in 1957 showing the asymmetrical nature of the ebb delta and the increase in development over the previous decade. Compare with Fig. 1.

As development of both Lido Key and Siesta Key proceeded there was need for nourishment on Lido which was not receiving substantial sediment from Longboat Key to the north. New Pass at the north end of Lido Key is tide-dominated with a pronounced channel margin linear bar to inhibit southward bypassing of sediment. As nourishment on Lido took place the ebb tidal delta at Big Sarasota Pass kept increasing in size due to the southward longshore sediment transport (Fig. 4). Bypassing of sediment at this inlet was facilitated by the pronounced offset of the adjacent barrier islands, the growth of the ebb delta and the shallow nature of the distal portion of the main channel. The most recent survey in 2006 showed a maximum depth of 9.3 m and a minimum at the channel mouth of 2.3 m.

As the ebb delta grew and the inlet channel tried to migrate south against Siesta Key, there was removal of sediment on the north end of that island without a means of replacing it. The result was substantial erosion causing residents to place riprap and various structures to protect their property (Fig. 5).

As this condition developed, the growth and extension of the ebb delta at Big Sarasota Pass, coupled with the very shallow distal portion of the channel has facilitated sediment bypassing. This bypassing is now focused several hundred meters from the north or updrift end of Siesta Key (Fig. 5) and has been for the past decade. This condition will continue in the future under the present conditions.



Fig. 4 - Oblique aerial photograph showing huge ebb-tidal delta and the asymmetric nature of Big Sarasota Pass as it appeared in 1994.

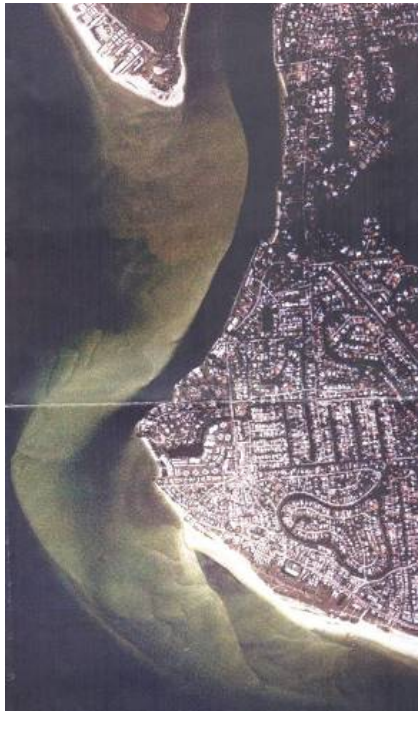

Fig. 5 - Vertical aerial photograph of Big Sarasota Pass in 2004 showing the absence of well-developed flood channels across the ebb delta, erosion on the north end of Siesta Key and considerable beach accretion where bypassed sand has migrated onto the shore area. Compare the north end of Siesta Key with the photos of 1948 and 1957; Figs. 1 and 3).

SUMMARY

Over the past century Big Sarasota Pass had experienced subtle but important modificants as the result of a combination of natural and human modified conditions. These can be listed chronologically to show their relative roles:

1 – Filling of mangrove islands and shoals to form Lido Key in the 1920s. This led to a more channelized tidal prism for both New Pass and Big Sarasota Pass.

2 – As a result of this channelization, Big Sarasota Pass carried an increased prism and migrated to the south (downdrift).

3 – Development of Siesta Key increased rapidly after World War II with residences being constructed along the south side of the Big Sarasota Pass channel. Non-integrated structures and rip-rap were placed along this channel in order to stop erosion. These efforts did halt channel migration.

4 – Because there were no structures on the updrift side of Big Sarasota Pass, the ebb-tidal delta was extended to the south thereby constricting the distal end of its channel. Sediment bypassing was being carried toward the south.

5 – Nourishment of Lido Key in the 1990s provided additional sediment that was transported to the south and caused the ebb delta at Big Sarasota Pass to grow and extend further to the south. This condition resulted in bypassed sediment being accreted to Siesta Key several hundred meters south of the north end and erosion to take place on the north end of the barrier.

REFERENCES

Davis, R. A. (1989). Morphodynamics of the west-central Florida barrier system: The delicate balance between wave- and tide-domination. *Proc.KNGMG Symp. Coastal Lowlands, Geology and Geotechnology*, Kluwer, 225-235.

Davis, R, A. (1999). Complicated littoral drift systems on the Gulf Coast of peninsular Florida. *Proc. Coastal Sediments '99,* ASCE, New York, 761-769.

Hayes, M. O. (1974). The importance of tidal deltas in erosional and depositional history of barrier islands. Geol. Soc. Am. Abstr. with Program 6, 785.

Stapor., F. W., Mathews, T.D., and Lindfors-Kearns, F.E. (1991). Barrier island progradation and Holocene sea-level history in southeast Florida. *Journal of Coastal Research*, 7, 815-838.

MORPHOLOGICAL BEHAVIOUR OF SEASONAL CLOSURE OF TIDAL INLETS

Tran Thanh Tung [1], Marcel J.F. Stive [2], Jan van de Graaff [3] Dirk-Jan R. Walstra [4]

1. Faculty of Civil Engineering and Geosciences, Delft University of Technology, P.O. Box 5048, 2600 GA, Delft, The Netherlands. T.TranThanh@tudelft.nl.
2. Faculty of Civil Engineering and Geosciences, Delft University of Technology, P.O. Box 5048, 2600 GA, Delft, The Netherlands. M.J.F.Stive@tudelft.nl.
3. Faculty of Civil Engineering and Geosciences, Delft University of Technology, P.O. Box 5048, 2600 GA, Delft, The Netherlands. J.vandeGraaff@tudelft.nl.
4. WL | Delft Hydraulics and Delft University of Technology, P.O. Box 177, 2600 MH Delft, The Netherlands. Dirkjan.Walstra@wldelft.nl.

Abstract: This paper documents the seasonal opening/closure features of tidal inlets and river mouths in a wave-dominated, micro-tidal environment along the central coast of Vietnam and discusses their formation, temporal morphological changes under typical conditions that are dominant in the dry and the wet season respectively. The interpretations are based on aerial photography, historical maps, satellite images and field observations. In addition a conceptual model of seasonal opening/closure features of tidal inlets in a wave dominated; micro-tidal environment under the influence of episodic river discharges is introduced and examined by numerical modeling.

INTRODUCTION

Seasonal closure and migration of tidal inlets and estuaries usually occur in micro-tidal, wave-dominated coastal environments where strong seasonal variations of river flow and wave climate are experienced. These inlets and estuaries close every year for a number of months due to the formation of a sand bar across the entrance or due to the growth of a sand-spit from updrift to downdrift. (Ranasinghe and Pattiaratchi, 2003). The phenomenon of seasonal closure of inlets or estuaries can be found at many coasts such as at the southern coasts of Australia, the southern coast of South Africa, the south-eastern coast of Brazil, and the south-western coasts of India and Sri Lanka.

The central coast of Vietnam has more than sixty inlets and river mouths connected to the South China Sea. They play a vital role in social-economic activities in the region. The closure of a tidal inlet or the shoaling of a river mouth cause significant negative impacts on the flood discharge capacity, coastal environment, ecological system, navigation and fishery sector, harming the socio-economical development in the region. Therefore, community interest in finding methods to keep these inlets permanently open has always been high. However, in order to find sustainable engineering solutions to keep these inlets perennially open, it is necessary to gain more insight into the morphodynamic processes governing seasonal opening/closure of those inlets and estuaries.

STUDY AREA

Situated on the south-west (SW) sector of the Gulf of Tonkin and the South China Sea, the central coast of Vietnam with a concave coastal plain (see Figure 1) stretches from 18°45' to 10°45' North latitude and from 105°06' to 109°28' East longitude. It consists of 12 provinces with a total area of 88,820 km^2 and population of 13.76 million.

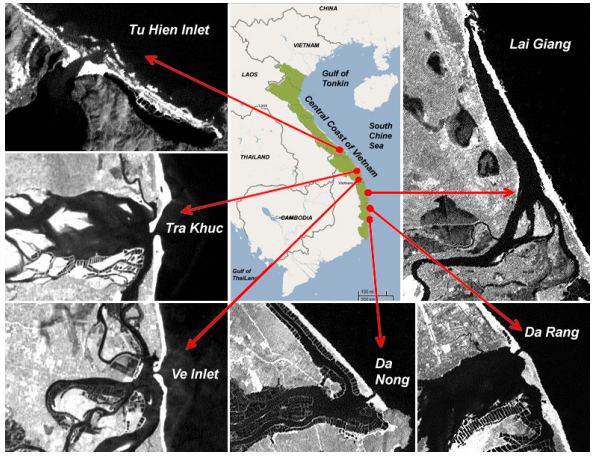

Fig. 1 Map of Central coast of Vietnam showing tidal inlets and estuaries

Vietnam is situated in a tropical region, where many atmospheric phenomena originating from the continent and the Equator Ocean meet. Consequently, climate in the region deeply suffers from the Asia monsoon regime, which originates from continental China in the period October till February and drives winds across the ocean from the north-east (NE). This is called the "winter monsoon" or "NE monsoon", with winds normally about 4 to 8 knots and with occasional strong winds up to 25 knots. In the period from May till August, when the continental high diminishes, the "summer monsoon" or "south-west monsoon" sets in and causes winds from the SW. Wind speeds are normally lower than in the winter months, up to 15 knots.

The long-stretching and narrow coastal plain in the central coast is frequently subjected to floods and storms. Every year, the central coast suffers directly from 3-5 storms and tropical depressions (50% of all SE Asian storms and tropical depressions hit Vietnam every year) causing heavy rain and subsequent flooding. The annual rainfall in the region ranges from 1500 mm to 4000 mm, mainly in the flood season (about 70% of the total yearly rainfall), between September and December. River flooding is a common annual phenomenon in the region as a result of this high rainfall intensity and uneven spatial rainfall distribution.

During extreme river floods the greatest effect is produced on tidal inlet and estuary morphology. The steep hinterland causes high peak discharges as well as high velocities as runoff is transported rapidly to the coast. Historical floodings have occurred 3 times in the past 70 years: 1953, 1983 and 1999. In November 1999, six provinces in the central coast experienced the heaviest rainfall due to effects of the tropical storm Eve. The entire hinterland was subjected to between 200 and 2000 mm of rainfall on a 6-day period. For example at Hue, the rainfall in a 12-hour period was approximately 770 mm. It caused severe flooding in the entire river basin with an estimated peak discharge of about 14,000 m^3/s. Such flooding events have a significant impact on an inlet configuration (closed inlets re-open and river channels widen, deepen and re-align).

Waves and sea level variations

Wave action is the dominant driving force in the morphological development of inlets/estuaries in the central coast of Vietnam. Along the coast waves, currents and sea level variations are defined mainly by the monsoon and storm regime. As a consequence, the wave regime in the central coast is NE dominated in wintertime and SW dominated in summertime. The offshore wave climates along the central coast have been determined from observations in Danang bay and off the Kyha Cape in the central coast from April 1997 to February 1998 and on the basis of a 36-year series of wave hindcast calculations from 1961 till 1997 (Nagai et al.,1998). The analysis showed that relative low waves are present from April till August; high waves may occur from September until February due to typhoons, tropical depressions and the NE monsoon. Waves from the NE are dominant resulting in a net southward littoral drift along the central coast.

Tides along the central coast of Vietnam are semi-diurnal with amplitudes varying from 0.5 m to 1.5 m. Spring tides seldomly exceed 2 m. The coast is therefore micro-tidal according to the classification of Davis (1964).

Coastal Morphology and Inlets Classification

The central coast is characterised by an abundance of small and medium size inlets/ estuaries formed at the mouth of rivers that discharge the rainfall of the steep hinterland. More than 60 rivers meet the South China Sea along 1500 km of coastline. Rivers usually are short and steep with gradients generally steeper than 1:100. The steep rivers with abundant natural but unevenly distributed flows during a year make the small and narrow coastal plains in the Central coast prone to flooding in the wet season, while the river is shallow and almost dry during the rest of the year. Specific topographical

features and the hydrological characteristics of the study area produce a particular highly seasonal variation of tidal inlet and river estuary configurations (from narrowing, shoaling or entirely closing during the dry season to widening and breaching in flood periods).

The coast is predominantly sandy as a result of high fluvial sediment input during flood periods, which nourish the mainland beaches and sandy barriers that form across estuary mouths and tidal inlets. Mainland beaches and barriers are typically steep and narrow and are dominated by cross-shore sediment transports. The sediment of the beaches and barriers is rather coarse. Based on morphological features, inlets and estuaries at the central coast can be classified into three major categories as follows:

1.Seasonal mixed tide-river-wave dominated inlets, connected to a lagoon or series of lagoons in the hinterland. The lagoons may receive water from a river, several rivers or might only receive natural surface run-off from the surrounding area. Tidal currents are the main driving forces maintaining an inlet open most of the time in a year. Meanwhile riverflood-generated currents are the driving force that widen and deepen the inlets in the wet season. Due to the fact that nearly all tidal inlets in the central coast of Vietnam are subject to a micro-tidal regime and wave dominated conditions, they are unstable and tend to narrow (or close) when tidal currents are much smaller than wave-induced currents.

2. Seasonal mixed river-wave dominated inlets are defined as those in which an inlet is maintained by river discharge and in which the tidal prism is too small to generate currents adequate to overcome wave-induced sediment transport in the nearshore that act to close the inlet. They are usually shallow in the dry season or closed for several years and re-open only during major river flood events. In the dry season, river discharges are usually too small or negligible in some cases. It causes estuary entrances to shoal easily and to close gradually due to longshore sediment transport or due to landward migration of offshore sand bars.

3. River-dominated estuaries with large river catchments are maintained by relatively higher river discharges during the whole year, thus the river entrances are kept open permanently. However, these estuaries often shoal, migrate or change their main channel due to the formation of sand-spits at the estuary entrance. These estuaries are not discussed here.

Hereafter, the formation, development and waning of the Tu Hien tidal inlet, which is representative for seasonal mixed tide-river-wave dominated inlets in central coast of Vietnam will be discussed based on historical maps, satellite images and field observations.

HISTORICAL EVOLUTION OF TU HIEN INLET

Located in the Thua Thien Hue Province, the Tu Hien inlet is one of two major inlets, which connect the Tam Giang - Cau Hai lagoon to the sea (see Fig.2A). The water body

of the Tam Giang - Cau Hai lagoon spreads over an area of 216 km^2 with a length of 68 km and an average wet volume of 300 million m^3.
The opening/closure cycle of the Tu Hien inlet starts with a breakthrough of the sand-spit across the closed inlet and forms a new inlet during an extreme river flood event. The inlet at this initial phase has its main channel in the orientation of NE-SW (see Fig.2B). Due to the dominant wave-induced currents in the SE direction the northern bank of the inlet is accreting and extending as a sand-spit in the SE direction. The inlet channel is then gradually lengthened and rotates to SE. When the sand-spit reaches the rocky headlands at the Vinh Phong Mountain, the inlet is then terminated and its morphological cycle is finished. The last entire morphological cycle of the Tu Hien inlet lasted for 9 years. In which the open period was 4 years (from 1990 till 1994) and the closed period was 5 years (from 1994 till 1999).

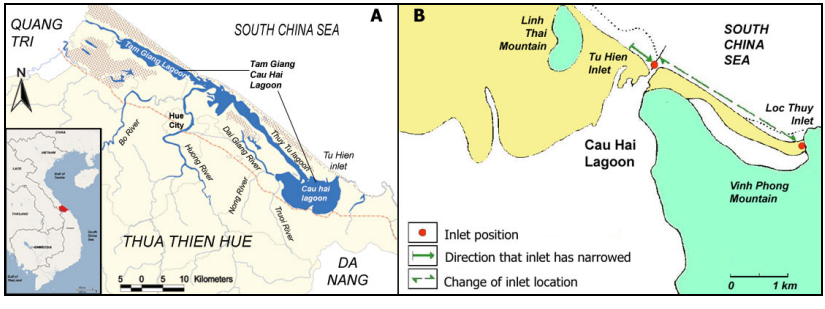

Fig. 2 Map of Hue and lagoon system (A)- Historical development of the Tu Hien inlet (B)

Figure 3 shows a series of the Landsat satellite images of the Tu Hien inlet from September 1999 till May 2005. In September 1999, just 2 months before the occurrence of the severe historical flooding in the region, a long sand-spit extending in SE direction blocked the Tu Hien inlet. A narrow inlet channel formed along the sand-spit connected to the sea through a small inlet namely the Loc Thuy. The inlet channel was flanked by the rocky headlands at the Vinh Phong Mountain and then turned to NE direction. During the historical flood in November 1999, flood-generated currents caused a breakthrough on the sand barrier at 5 places along 50 km of coastline and the Tu Hien inlet was re-opened. The re-opened inlet providing a short route for tidal exchange and flood discharge normally remains open while the less efficient inlets gradually close. Sediment accumulation on the southern bank of the new open inlet completely blocked the old channel formed along the sand-spit and isolated the old inlet from the lagoon. The historical development of an opening/closure cycle of the Tu Hien inlet is found similar to the model of inlet migration and spit breaching introduced by FitzGerald (1988).

In the classification of Hayes (1979), Tu Hien inlet is a micro-tidal inlet, in the wave-dominated region. Such a situation is characterised by long straight barriers, few inlets, well developed flood-tidal deltas and poorly developed ebb-tidal deltas. It means that the

offshore bars which are emergent at the inlet entrance during low tide and visible from the breaking wave patterns on the satellite image observed on March 2003, were not formed by ebb-tidal currents. They were formed as a consequence of river floods, when material which eroded from the flood-tidal delta and from the sand-spit during inlet widening, is pushed through the inlet and then deposited on the foreshore outside the inlet entrance. The satellite images also indicated that the ebb-shoals were elongated oblique to the shore over a distance of 200-300 m. Those were reworked further landward and finally incorporated into the sand-spit and into adjacent beaches in the form of a welded beach ridge. That is our explanation of how the sand-spits are forming on both sides of the inlet and why these are shaped like a triangle.

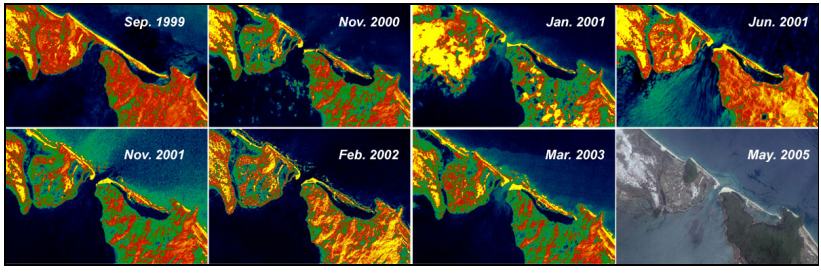

Fig. 3 The LandSat ETM+ satellite images of the Tu Hien inlet (Sep. 1999 till May 2005)

CONCEPTUAL MODEL OF SEASONAL OPENING/CLOSURE OF TIDAL INLETS

Based on the historical development of Tu Hien inlet, a general conceptual model of seasonal opening/closure for tidal inlets in the central coast Vietnam is proposed. The conceptual model is outlined below and in Fig.4. Three main stages are to be considered:

Formation stage

The opening/closure cycle of an inlet or estuary usually starts with a breach of the sand-spit across the inlet entrance during an extreme river flood event. Hence, the inlet formation stage is often occurring during the flood season (from August till December). The inlet or river mouth comprises of a narrow sandy channel with a sinuous course across the floodplain and changes its course along the barrier before the channel discharges to the sea (Fig. 4A and 4E). Long coastal barriers assume plan-form equilibrium with approaching waves.

During extreme flood events (Fig. 4B) floodplains are inundated and broad, while flood channels are produced by lateral scour of the floodplain. Large parts of the long barrier, opposite to the main flood channels are eroded. Also over-bank flow paths contribute to barrier erosion. Increasing flood discharge may breach the long barrier and formation of a new inlet or enlargement of the existing inlet. The breaching of the sand barrier or sand-spit across the inlet entrance removes the accumulated sediment from the estuaries and from the barrier. Sand from the barrier, together with additional sand from upstream of the river flood-plain is deposited as submerged sand bars offshore of the inlet

entrance. Those offshore sand bars are unstable in high wave energy environments and are not persistent for long time.

Development stage

The evolution of inlets/estuaries in this stage falls into two different categories, each discussed in the following two sections.

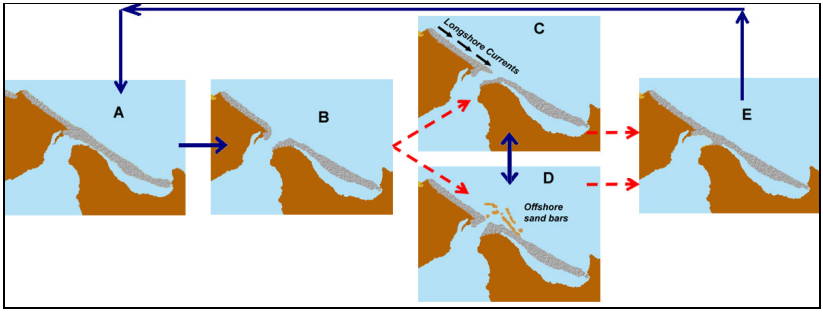

Fig.4 Conceptual model of opening/closure inlet/estuary

a. The development of sand-spits

The accumulation and expansion of sand-spits at an inlet entrance happened at many inlets/estuaries in the central coast such as Tu Hien inlet, Lai Giang inlet, and Da Nong inlet (see Fig.1). Those inlets are characterised by a long-narrow sand-spit forming parallel to the coast. The inlet entrance is usually located at the end of the sand-spit. The updrift bank of the inlet is accreting and extending as a sand-spit in the dominated littoral drift direction. The inlet channel is then gradually lengthened and changes its direction parallel to the coast. When the sand-spit reaches the rocky headlands or when it reaches its equilibrium condition the inlet is then gradually closed (Fig. 4C).

The accumulation and expansion of sand-spits at an inlet/estuary entrance is varying with time. Inlets/estuaries with large tidal prisms or strong river flood-generated currents will show slow expansion rates of sand-spits. Observations at the Tu Hien inlet indicated that the development of a sand-spit at the Tu Hien inlet was 4 years (from 1990 till 1994). Meanwhile, site investigations at the Lai Giang inlet in 2004 indicated that the sand-spit was fully developed in only 4 months, during the period of the NE monsoon.

b. The development of offshore sand bars in landward direction

After river floods decline the offshore sand bars are exposed to wave attack. The initially submerged sand bars rapidly become emergent and migrate landward into shallow water due to wave action. This causes shortening and widening of the bars, which gradually changes into an underdeveloped of a wave-dominated ebb-tidal delta (Oertel, 1975). Offshore sand bars become incorporated into the sand-spit by initially welding onto the beach, usually on the updrift side (Fig.4D). The subsequent landward migration under wave attack changes the bar into sand bodies elongated parallel to the coast (Cooper, 1990). Such mechanism was observed from series of satellite images and air-photos at Tu Hien inlet, Tra Khuc inlet, Ve inlet and Da Rang inlet.

Declining stage

The declining stage of a tidal inlet or estuary usually takes place when the inlet or estuary is much narrower and shallower compared to the initial situation at the formation stage. In the declining stage, wave energy continues to drive offshore sand bars landward onto the remaining breach. Overwash of the bar crest and transport of the forebeach sediment to the back-beach also contribute to this process (Cooper, 1990). Before final closure, the inlet may maintain a small bar similar to ebb-tidal deltas normally produced at small inlets and elongated in the downdrift direction, as in the longshore current-dominated model of Oertel (1975). The inlet may fully close at the beginning of the dry season, when river flows drop down significantly and inlets/estuaries suffer from severe NE monsoon events with high energetic wave conditions and a persistent wave direction for several days.

SIMULATION THE DEVELOPMENT OF AN IDEALIZED TIDAL INLET

An idealized inlet was developed and a process-based morphodynamic model, Delft-3D, was employed to examine flow, wave and sediment transport processes at the inlet area. The simulation purposes are to identify the morphological behaviour of an inlet under different tidal ranges and the variations of wave direction and to test two hypotheses on evolution of inlet closure.

Delft-3D, developed by WL| Delft Hydraulics, is a model system that consists of a number of modules for flow, waves, sediment transport and bottom changes, which are activated by a steering module. The hydrodynamic module is based on the depth-averaged shallow water equations, which are solved on a curvilinear staggered finite differences grid using an ADI scheme. The wave model in Delft-3D may employ the second-generation wave-model HISWA or the fully spectral third generation wave model SWAN (Holthuijsen et al., 1993). The transport model is based on the depth integrated advection diffusion equation for suspended-sediment transport and separately computes bed load transports (Lesser et al. 2004). All modules may operate on different computational grids, but the FLOW grid is used as the basis for data exchange between the modules.

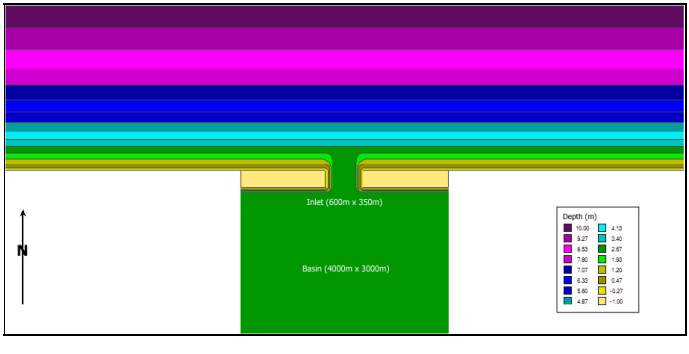

Fig.5 Grid and bathymetry of idealized inlet

Simulation setup and grid specifications

An idealized inlet and a computation grid (Fig.5) was setup for simulation in Delft-3D such that it has high resolution at the inlet entrance and in the surf-zone as the areas of interest and low resolution near the open boundaries which are of less interest. The cell size dimensions varied from 40 meters at the shoreline to 200 meters at the seaward boundary in cross-shore direction and from 60 meters at the inlet entrance to 200 meters at two lateral boundaries in longshore direction. The grid has a total of 110 grid cells in M-direction (in west-east direction) and 58 grid cells in N-direction (in north-south direction). The grid dimensions at sea are 13 km alongshore and 3 km in cross-shore direction. The seaward boundary is defined at the 10 meters depth contour line. The basin dimensions are 4 km by 3 km, with a uniform depth of 2 m. The inlet is located in the middle of the computation grid with dimensions of 700 meters by 400 meters.

Tide forcing for the FLOW model was represented as a harmonic wave having amplitudes varied from 0.1 m to 0.75 m and a period of 12.00 hr (semi-diurnal tide). The WAVE model is forced with offshore wave conditions which are defined at the seaward boundary. Wave height and period are representative of normal-wave conditions with a significant wave height of 1.5 m and a wave period of 7 seconds. The wave direction was varied from 315 degrees to 355 degrees relative to the North. A time step of 15 s was applied for FLOW simulations. The waves were updated every 20 minutes to accurately represent the changing flows due to tide and morphological development. Two sets of model simulation were run, one set which varied the tidal amplitudes (η) and other set which varied the wave directions (Table 1). In both cases, the same bathymetry and grid was used and the same representative tide and wave were employed. These simulations used the 2DH (online) mode of the Delft-3D model system and transport formulations by Van Rijn (1993). Both simulations were run for a period of 20 days. In dealing with the difference in time-scales between hydrodynamic and morphological developments, a morphological acceleration factor of 10 was used.

Table 1. Simulation scenarios with varying of tidal amplitudes and wave directions

RUN-ID	Tidal Amp. (cm)	Wave characteristics			RUN-ID	Tidal Amp. (cm)	Wave characteristics		
		Direction	H_s (m)	T (s)			Direction	H_s (m)	T (s)
W-315	25	**315**	1.5	7.0	**H-10**	**10**	325	1.5	7.0
W-335	25	**335**	1.5	7.0	**H-25**	**25**	325	1.5	7.0
W-345	25	**345**	1.5	7.0	**H-50**	**50**	325	1.5	7.0
W-355	25	**355**	1.5	7.0	**H-75**	**75**	325	1.5	7.0

Simulation results

Case 1- Variation of wave directions

Patterns of bed changes at the inlet entrance under varying wave directions are shown in Figure 6. All patterns of bed changes indicate the growing of a sand-spit from updrift to downdrift and development of ebb shoals at the inlet entrance. A flood delta is also observed inside the basin in all simulations. After 15 days, the inlet reduces 50% of its initial width for run W-355 and up to 75% for run W-315.

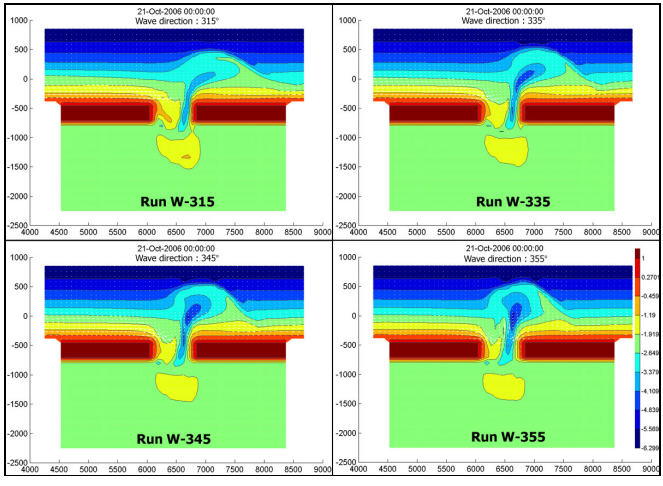

Fig.6 Inlet evolution with wave direction varied

The variations in wave direction causes different patterns of inlet channels and ebb-shoals in each simulation. In run W-345 and run W-355, when waves approach to the inlet at a small angle the inlet channels are formed in a drumstick shape and align perpendicular to the shoreline. In run W-315 and run W-335, the inlet channels section outside the inlet entrance seems to bend to downdrift because of the large wave angles. These channels tend to rotate perpendicular to the direction of the wave approach. The patterns of bed-changes in all four simulations show the seaward extension of the downdrift beach in a triangle shape. There might be a relationship between the enlargements of downdrift beach with the by-passing rate of ebb-shoals. The computed by-passing parameters (r) of 4 simulations, with a tidal prism (P) of 6M m^3, and the total littoral drift per year (M_{tot}) varied from 1.1×10^5 m^3 to 0.8×10^5 m^3 respectively, ranges from 54 to 75. According to Bruun and Gerritsen (1960), if the by-passing parameter ranges from 50 to 150, then the entrance bars are still pronounced and the by-passing at the inlet is a combination of bar-bypassing and flow-by-passing which is also observed from simulation results.

Case 2- Vaiation of tidal amplitudes

Patterns of bed changes at the inlet entrance with different tidal amplitudes are shown in Figure 7. The differences in tidal ranges cause distinct patterns of bed changes in four simulations. In the first simulation (H-10), the computed by-passing parameter (r) is 20. According to Bruun and Gerritsen (1960), the inlet is an unstable, non-permanent overflow channel. The inlet closed after 10 days and an equilibrium condition was reached after 15 days. In other simulations, the computed by-passing parameters are less than 150. It means that in those inlets ebb shoals at the inlet entrance are prominent and the by-passing type is a combination of both bar-by-passing and flow-by-passing. The patterns of bed changes in H-50 and H-75 simulations demonstrate the development of

ebb channels at the inlet entrance. The inlet channels are shifted to the right bank, deepen and extend further to the sea. Outside the inlet entrance, the inlet channel is exposed to the wave action thus it is bended to the downdrift beach. The by-passing mechanism through the ebb shoals is well illustrated in a series of patterns of bed changes which are observed in H-75 simulation (see Figure8).

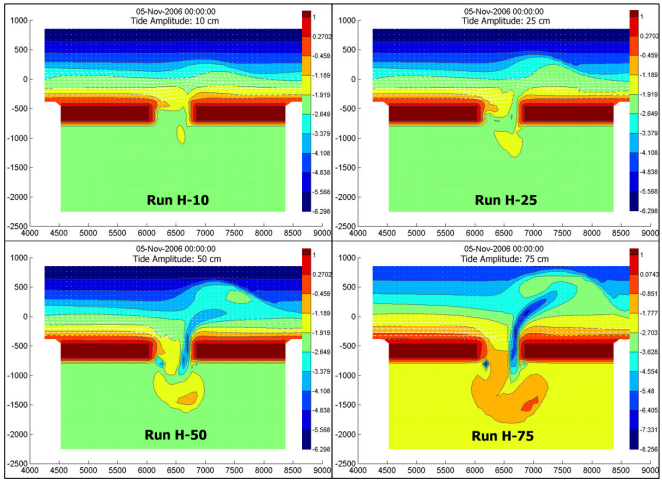

Fig.7 Inlet evolution with tidal amplitude varied

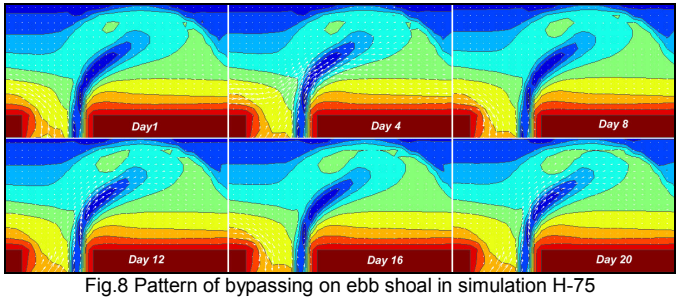

Fig.8 Pattern of bypassing on ebb shoal in simulation H-75

CONCLUSION

At most tidal inlets or estuaries, the existence and persistence of an entrance is dependent on the relative strength of inlet currents (tidal currents and river flood-generated currents) maintaining the entrance and wave-induced currents in the nearshore zone closing to entrance by depositing marine sediment. The balance between these processes determines the nature and the persistence of an inlet or a river mouth.

The morphological features of tidal inlets/estuaries at the central coast of Vietnam were investigated based on historical maps, satellite images and field observations. The historical development of an opening/closure cycle of the Tu Hien inlet was found

similar to the model of inlet migration and spit breaching introduced by FitzGerald (1988). Based on that, the formation, development and declination of an inlet is then generalised into a conceptual model for seasonal opening/closure. Two main mechanisms of inlet evolution were put forward in the conceptual model. The first mechanism is related to the narrowing of an inlet entrance due to the growing of a sand-spit. The second mechanism is controlled by nearshore wave-induced currents and landward movement of the offshore sand bars.

In order to identify the morphological behaviour of the seasonal closure of tidal inlets and to examine the hypotheses on inlet evolution, which were introduced in the conceptual model, a process-based morphological model was employed. The morphological model could successfully simulate the first hypothesis of inlet closure as well as the evolution of ebb-shoals due to the by-passing system. Further research on the second mechanism will be carried out in the future.

ACKNOWLEDGEMENTS

This research is supported by the Project Upgrading of the training capacity in coastal engineering in Hanoi Water Resources University, Phase 2; under the co-operation between Delft University of Technology, the Netherlands and Hanoi Water Resources University, Vietnam.

REFERENCES

Bruun, P. and Gerritsen, F., 1960. *Stability of Coastal inlets*, North Holland Publishing Co., Amsterdam, The Netherlands.

Copper, J.A.G., 1990. Ephemeral stream mouth bars at flood breach river mouths: comparison with tidal deltas at barrier inlets. *Mar. Geol*. 96, pp. 57-70.

Davies, J. L., 1964, A Morphogenic Approach to World Shorelines. *J. Geomorphology*. Vol. 8, pp 127-142.

FitzGerald, D. M. (1988). "Shoreline erosional-depositional processes associated with tidal inlets" *Hydrodynamics and sediment dynamics of tidal inlets*. D.G. Aubrey & L. Weishar, eds., Springer, Berlin, 186-225.

Hayes, M.O., 1979, Barrier Island Morphology as a Function of Tidal and Wave Regime. In: *Barrier Islands from the Gulf of St. Lawrence to the Gulf of Mexico,* S.P. Leatherman, ed., Academic Press, New York, pp 1-27.

Holthuijsen, L.H., Booij, N., Ris, R.C., 1993. A spectral wave model for the coastal zone, *Proceedings of the 2nd International Symposium on Ocean Wave Measurement and Analysis*, New Orleans, 630–641.

Lesser, G., Roelvink, J.A., van Kester, J.A.T.M. and Stelling, G.S., 2004. Development and validation of a three-dimensional morphological model, *Coastal Engineering*, 51, 883-915.

Nagai, K., Kono, S., and Quang, X.Q., 1998. Wave characteristics on the Central coast of Vietnam in the South China Sea. *Coastal Engineering J.*, Vol. 40, No. 4, pp.347-366.

Oertel, G.F., 1975. Ebb-tidal deltas of Georgia estuaries. In: L. E. Cronin (Editor), *Estuarine Research*, Vol. 2. Academic Press, New York, pp. 267-276.

Ranasinghe., R. and Pattiaratchi, C., 2003, The seasonal closure of tidal inlets: cause and effects. *Coastal Engineering J*., Vol. 45, No. 4: pp. 601-627.

Van Rijn, L.C., 1993. *Principles of Sediment Transport in Rivers estuaries and Coastal seas*. Aqua Publications, Amsterdam.

THE NATIONAL ACADEMIES REPORT ON *MITIGATING SHORE EROSION ALONG SHELTERED COASTS*

Jeff Benoit[1] and Susan Roberts[2]

1. SRA International, 3434 North Washington Boulevard, Arlington, VA 22201, USA. jeff_benoit@sra.com
2. Ocean Studies Board, The National Academies, 500 5th Street, NW, Washington, DC 20001, USA. sroberts@nas.edu

Abstract: Like ocean beaches, sheltered coastal areas experience land loss from erosion and sea level rise. In response, property owners often install structures that harden the shoreline as a way to prevent further erosion, but these structures cause changes in the coastal environment that alter landscapes, reduce public access and recreational opportunities, diminish natural habitats, and harm species that depend on these habitats for shelter and food. The National Research Council Committee on Mitigating Shore Erosion along Sheltered Coasts concluded that a regional management approach is needed to assess the costs, benefits, and cumulative impacts of structural approaches and to encourage erosion control alternatives that help retain the natural features of coastal shorelines.

INTRODUCTION

Throughout the coastal regions of the world there are a significant number of areas that are partially or fully protected from the high-energy regimes associated with open coastlines, such as ocean-facing beaches. These sheltered coastlines include environments such as estuaries, bays, lagoons, mud flats, and deltaic coasts and may be generally characterized as lower energy coastlines, but there is no quantitative formula that covers the diversity of conditions encountered on these more protected shorelines. Sheltered shorelines, though often contiguous with the open coast, border smaller, contained, bodies of water separated from the open ocean by islands, peninsulas, reefs, or other geomorphic features. Many of the processes that govern erosion and deposition on the open coast also apply to sheltered coasts, but generally the scale at which these processes function is significantly reduced within sheltered coastal areas. Also, unlike the typically long linear features associated with open coasts, sheltered coasts exhibit characteristics that are distinctively more compartmentalized with discrete areas of the coast encompassing a variety of

geomorphic and biological resources. Typical physical conditions associated with sheltered coasts include relatively low velocity tidal currents and mid-to-low energy wave climates associated with a limited fetch (distance from shore to shore). These conditions promote the formation of ecological complexes (i.e., mangroves, marshes, and mudflats) that often characterize habitats on sheltered coasts and are generally not found along open coasts.

Landowners frequently respond to the threat of erosion by armoring the shoreline with bulkheads, revetments, or other structures. Although the armoring of a few properties has little impact, the proliferation of structures along a shoreline can inadvertently change coastal environments and ecosystems. Managers and decision makers have been challenged to balance the trade-offs between protection of property and potential loss of landscapes, public access, recreational opportunities, natural habitats, and reduced populations of fish and other marine species that depend on these habitats.

At the request of the U.S. Environmental Protection Agency (EPA), the U.S. Army Corps of Engineers (USACE), and the Cooperative Institute for Coastal and Estuarine Environmental Technology, the National Research Council (NRC) conducted a study examining the impacts of shoreline management on sheltered coastal environments and evaluating strategies to minimize potential negative impacts to adjacent or nearby coastal resources. The report (NRC, 2007), released in October 2006, is summarized in this paper.

STUDY ORGANIZATION

The NRC committee met three times during the course of the study. The first meeting, held in Washington, DC, in June 2005, provided the committee with an opportunity to discuss the background and study expectations with the sponsors. In addition, the committee developed plans for a workshop that was subsequently held in Seattle, WA, in October 2005. The purpose of the workshop was to provide the committee with additional background information, largely focused on an analysis of options available to mitigate erosion of sheltered coasts. In planning this activity, the committee decided not to limit the discussion to marine or estuarine areas, but to include experts from the Great Lakes. The workshop explored the geomorphic settings of sheltered coasts as well as how various erosion measures affect those settings. The workshop brought together approximately 32 professionals with such diverse expertise as: state and federal regulatory matters, science, engineering, land use planning, and legal issues. The participants came from around the continental U.S. and provided expertise on the range of erosion problems in various coastal regions.

The committee's report identifies four broad categories of options to address erosion on sheltered coasts:

1) Land use regulation and management;
2) Vegetative stabilization;
3) Hardened structures (armoring the shoreline); and

4) Trapping or adding sediment.

These options are described in the context of the physical environment, ecosystem services and values, and the various regulatory, engineering, esthetic, and financial considerations that contribute to the decision-making process for mitigating erosion.

SHELTERED COASTS AND EROSION

Sheltered coasts are shorelines that face smaller bodies of water as compared to open ocean beaches. The water bodies are typically smaller, shallower, and have more varied shore morphologies, in part due to lower ambient wave energy. Lower energy conditions foster habitats and ecological communities, such as marshes and mud flats, typically not found on open coasts. Common shoreline profiles on sheltered coasts are illustrated in Figure 1. The unique characteristics of sheltered coasts affect the potential technological approaches and the consequences of actions taken to stem erosion and land loss from sea level rise.

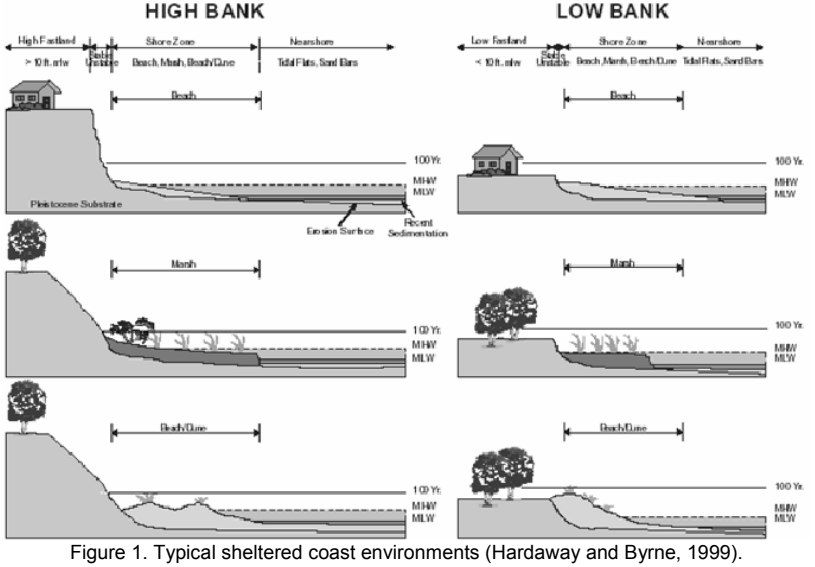

Figure 1. Typical sheltered coast environments (Hardaway and Byrne, 1999).

Erosion is caused by (1) winds; (2) waves, currents, and tides that transport shoreline sediments; and (3) weathering processes that destabilize landforms such as bluffs and cliffs. Although natural processes contribute to erosion, the rate may be accelerated by human activities such as construction of dams upstream of estuaries or installation of groins and seawalls that alter the magnitude and direction of sediment transport. Inundation can also increase because the ground sinks when sediments settle and compact or subsurface resources, such as groundwater and petroleum, are withdrawn. Other human activities that increase erosion include dredge and fill operations, wetland drainage, boat traffic, and channel dredging. Sea level rise will exacerbate

the loss of waterfront property and increase vulnerability to inundation hazards. It changes the location of the coast line, moving it landward and exposing new areas and landforms to erosion. Additionally, sea level rise is chronic and progressive, requiring a response that is correspondingly progressive (Figure 2).

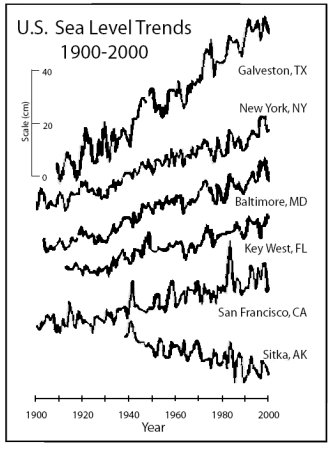

Figure 2. Relative sea–level trends in centimeters, for selected U.S. cities from 1900 to 2000. (Data from National Oceanic and Atmospheric Administration; graph available through the EPA [2000]).

CURRENT APPROACHES TO PROTECTING AGAINST EROSION

The pressure to develop and stabilize shorelines in sheltered coastal areas is increasing because coastal populations are growing. More people desire waterfront homes and coastal property values have risen. There are several types of strategies taken to stabilize shorelines. The most common response is a "hold the line" approach that hardens the shoreline with structures such as bulkheads and revetments. The following example illustrates the escalating rate of shore hardening and the consequent loss of natural coastal habitats.

Mobile Bay, Alabama

Mobile Bay is a shallow body of water (average depth about 3 meters) that empties into the Gulf of Mexico. The bay is approximately 51 kilometers long, 37 kilometers across at its widest point, and the overall length of the shoreline is approximately 160 kilometers. The bay area experiences extratropical storms and is subject to hurricanes from the Gulf of Mexico. With an average flow of 1,800 cubic meters per second, the Mobile Bay estuary has the fourth largest freshwater flow in the continental United States (Mobile Bay National Estuary Program, 2002). In 1997, a study was conducted that investigated the effects of bulkheads on the bay shoreline (Douglass and Pickel, 1999). The authors examined aerial photographs from 1955, 1974, 1985 to document the extent of

> bulkheads around the bay. Aerial video and site visits were used in 1997 to document the "present conditions." Results of the study reveal that the amount of armoring of the shoreline increased dramatically from 8 percent in 1955 to 30 percent in 1997. The study also documented that the rate of armoring from 1955 to 1997 corresponded to the rate of population growth in the area. This is a strong, but not surprising indication, that development trends increase the human impacts on sheltered coastlines. Of greater concern than the amount or rate of armoring was the associated loss of intertidal habitat, roughly estimated at 4 to 8 hectares (approx. 10 to 20 acres) corresponding to about 10 kilometers of intertidal beach shoreline.

There are alternatives to bulkheads, such as constructed marsh fringes, that are designed to preserve more natural shorelines while still reducing erosion (Figure 3). The selection of the type of response to prevent or offset land loss depends on understanding local causes of erosion or inundation. A shift away from the hold the line approach has been slow, in part because there is a greater familiarity with these methods than with alternative approaches such as constructing a marsh fringe or using vegetation to stabilize a bluff. Contractors are more likely to recommend structures such as bulkheads because they have experience with the technology and know the design specifications and expected performance. Landowners often assume that a hard, barrier-type structure will be required to prevent loss of property and protect buildings. In many regions, government regulations may unintentionally encourage shoreline armoring because it is simpler and faster to obtain the required permit(s). However, there are indirect costs associated with mitigation options that armor the shoreline. Many of these costs are borne by the public rather than the landowner. For example, installation of a groin to trap sand can affect neighboring beaches, while a bulkhead built on an eroding beach will eventually become the shore edge, replacing the beach that provided public access and scenic amenities. Construction on a marshy shoreline can lead to the loss of this highly diverse and productive plant and animal communities and their attendant ecosystem services—nursery areas for important fish stocks, removal of excess nutrients from land runoff, feeding areas for migratory birds, and sediment stabilization.

A NEW SHORELINE MANAGEMENT FRAMEWORK

Changing the current practice of armoring sheltered coasts will require a change in the shoreline management framework. Decision makers should appreciate the costs and benefits of the spectrum of potential solutions to shoreline erosion problems, including potential cumulative impacts on shoreline features, habitats, and other amenities. The management framework should encourage approaches that minimize habitat loss and enhance natural habitats in environments where such methods offer effective stabilization. Overcoming the obstacles associated with the current regulatory environment will require a number of societal and institutional changes in the following areas:

- **Improving Knowledge of Sheltered Shoreline Processes and Ecological Services**

Overall, less is known about physical process of sheltered coastal systems than of open coasts. In most areas, the scope and accessibility of information regarding the

causes of erosion at specific sites and the overall patterns of erosion, accretion, and inundation in the broader region (estuary, lagoon, littoral cell) is insufficient to



Figure 3. Planting vegetation offers an alternative for reducing erosion at some sites. Top photo shows a pre-project shoreline on Wye Island in Queen Anne's County, Maryland. Marsh grass was planted on sand fill and short, stone groins were placed. Middle photo is 3 months after installation. Bottom photo is six years after installation. Source: Hardaway and Byrne (1999).

support the development of an integrated plan for managing shore erosion. The report recommends that federal agencies (e.g., USACE, EPA, U.S. Geological Survey [USGS], and the National Oceanic and Atmospheric Administration [NOAA]), state agencies, and coastal counties and communities support targeted studies of sheltered coast dynamics to provide an informed basis for selecting erosion mitigation options that consider the characteristics of the broader coastal system rather than simply addressing immediate problems at individual sites.

- **Improving Awareness of the Choices Available for Erosion Mitigation**

Many decision-makers, particularly homeowners but also some state and federal regulators, are not sufficiently informed about the mitigation options available to them or the short and long term impacts of their choices. Decision makers need assessments of new techniques and materials designed to mitigate shore erosion. The report recommends that major federal agencies involved in permitting activities (EPA, USACE, and NOAA) initiate a national policy dialogue that can be used to develop guidelines for mitigating erosion on sheltered coasts. As part of this dialogue, the agencies should develop publications that contain objective information about erosion mitigation techniques, including descriptions of the conditions under which each option would be effective.

- **Considering Cumulative Consequences of Erosion Mitigation Approaches**

Cumulative impacts refer to the combined effects on legal, social, ecological, and physical systems. From a legal or regulatory standpoint, issuing permits may set a precedent, potentially facilitating the approval process for future requests for similarly situated structures. From an ecological standpoint, the cumulative impact of the loss of many small parcels will at some point alter the properties, composition, and values of the ecosystem. In addition, the economic, recreational, and esthetic properties of the shoreline will be altered, with potential loss of public use, access and scenic values. These cumulative effects are rarely assessed and hence are generally unknown, but an understanding of them is necessary to prevent an underestimation of the impacts of individual projects. The report recommends that cumulative effects be assessed in shoreline management plans, and that a precautionary approach be taken if there is insufficient information to determine cumulative effects.

- **Revising the Permitting System**

The current permitting system fosters a reactive response to the problem of erosion on sheltered coasts. Decision-making is usually parcel-by-parcel and based on relatively little environmental information. The path of least resistance drives choices through a rigid decision-making process, with inadequate attention to the cumulative effects of individual decisions. The decision-making process used for issuing permits for erosion mitigation structures should be revised for sheltered coasts and include consideration of potential cumulative impacts. This could be accomplished by a working group convened by state and federal agencies (EPA, USACE, and NOAA) to evaluate the criteria for sheltered coasts. The report recommends removing the often unintentional regulatory barriers for employing alternative erosion control approaches that have been proven to reduce erosion while preserving natural habitat.

- **Improving Shoreline Management Planning**

Creating a more proactive regional approach to shoreline management could address some of the unintended consequences of reactive permit decisions. The term "regional" is used in this report to reflect an area of shoreline that is defined by functional physical or ecological parameters such as littoral cells, or the scale of processes that affect sediment transport. Several examples of regional planning already exist for shorelines: the USACE Regional Sediment Management (RSM) program, EPA's National Estuary Program, and some special area management plans approved by state coastal management programs.

CONCLUSIONS

Until the government regulatory framework addresses the regional scale of the processes controlling sediment transport, stabilization of individual sites will often include structures that damage adjacent areas and create a domino effect of coastal armoring. The dimensions of the regulatory framework should match the scale of the processes that contribute to shore erosion. Currently there is no national mandate to document erosion processes on sheltered coasts or develop regional scale plans. No federal agency has been assigned to provide that scale of planning, although some states have become more proactive in shoreline management. Hence, implementation of a regional plan will require a new commitment for coordination among local, state, and federal programs, including a regional general permit. Overcoming the obstacles associated with the existing management framework will require a number of societal and institutional changes. The report recommends development of a new shoreline management framework to help decision makers evaluate the spectrum of available approaches to shoreline erosion problems in the context of the environmental setting. The new framework would include assessment of the physical and ecological properties of the shoreline and the potential cumulative impacts.

REFERENCES

Douglass, S.L. and B.H. Pickel. 1999. *"The Tide Doesn't Go Out Anymore"- The Effect of Bulkheads on Urban Bay Shorelines*. University of South Alabama, Civil Engineering and Marine Sciences Departments, Mobile. [Online] Available at: http://www.southalabama.edu/cesrp/Tide.htm [January 25, 2006].

EPA. 2000. *Sea Level Changes*. [Online] Available at: http://epa.gov/climatechange/science/recentslc.html [September 1, 2006].

Hardaway, C.S., Jr. and R.J. Byrne. 1999. *Shoreline Management in Chesapeake Bay.* Special Report in Applied Marine Science and Ocean Engineering, No. 356. College of William and Mary, Virginia Institute of Marine Science, Gloucester Point. 54 pp.

Mobile Bay National Estuary Program. 2002. *Comprehensive Conservation and Management Plan*. Mobile Bay National Estuary Program, Mobile, Alabama. [Online] Available at: http://www.mobilebaynep.com/Publications.htm [February 14, 2006].

NRC. 2007. *Mitigating Shore Erosion Along Sheltered Coasts*. National Academies Press. Washington, DC.

FIELD MEASUREMENT AND MODELLING OF SCOUR PIT DYNAMICS IN A SANDY ESTUARY

A.G. Davies[1], J.M. Brown[2]

1. School of Ocean Sciences, University of Wales (Bangor), Menai Bridge, Anglesey, LL59 5AB, U.K. a.g.davies@bangor.ac.uk.
2. School of Ocean Sciences, University of Wales (Bangor), Menai Bridge, Anglesey, LL59 5AB, U.K. osp05f@bangor.ac.uk.

Abstract: Field observations and model simulations are presented of the tidal flow over a scour hole at the mouth of the Dyfi Estuary, mid-Wales, U.K. This scour hole is maintained by locally high flow speeds resulting from convergence, and then divergence, of the flow over the hole. Fixed features of the local bathymetry may also have served to stabilise its location (over decades). Model simulations of steady flow over a variety of schematised pits of different elliptical shape on an otherwise flat bed are presented to show that shallow elongated pits can (almost) preserve the upstream flow speed at their centre point, making them potentially self-maintaining. Deeper pits reduce the flow speed and so will infill.

INTRODUCTION

A feature of many estuaries and channels is the occurrence of natural pits and scour holes. These fixed features often persist for decades in the erodible seabed sediment. The present paper highlights the dynamics one such scour hole in the mouth of the Dyfi Estuary in the middle of Cardigan Bay, mid-Wales, U.K. Here field observations were made as part of a model validation exercise aimed at demonstrating the ebb-dominant nature of the tidal flow in the Dyfi Estuary. This ebb dominance arises from the extensive areas of drying banks at low tide, together with the discrete channels, that characterise the interior of this predominantly sandy Estuary. The field observations are complemented by modelling work both of the tidal flow in the estuary, here with main emphasis on the area of the scour hole, and also of the flow above an idealized pit that is used to highlight the processes affecting scour-hole dynamics.

The behaviour of offshore sand pits was studied during the EU SandPit Project (2002-5) (Van Rijn et al., 2005). Here numerical models were intercompared in order to simulate both the infill rate and also the migration rate of pits and trenches, and comparisons were made with data from a variety of field and laboratory experiments involving combined waves and currents. Based on scenario model tests for a variety of offshore sand pits, coastal zone management issues were addressed relating to both the near- and far-field effects of these pits. For example, at the centre of the pits investigated it was found that both current velocities and sediment transport rates decreased quite markedly (by up to about 25% and 80%, respectively) compared with the situation without a pit. Work in SandPit was carried out at the University of Wales (Bangor) (UWB) using the Telemac Modelling System in which refinements were implemented relating to the bed roughness, the advection-diffusion scheme for suspended sediment and also the sand transport formulation (Davies and Villaret, 2003; Davies et al., 2005).

In the present study of the Dyfi Estuary the spring-neap tidal cycle has been modelled, and then combined with a schematized representation of the observed offshore annual wave climate. Even at high tide, waves are predicted, and also observed, to penetrate the estuary from offshore only to a limited extent; thus we focus here on the tidal flow over the scour hole at the estuary mouth without regard to waves. The main sections of the paper highlight the field observations made above the scour hole, the modelling of these flows using the Telemac System (Hervouet and Bates, 2000), and some consideration of the dynamics of pits aimed at addressing the question of whether natural scour holes can be self-maintaining and, if so, what shape of hole best serves this purpose.

FIELD STUDY IN THE DYFI ESTUARY

Validation data was obtained in a field campaign carried out in the Dyfi Estuary in January-February 2006 in order to confirm the model's hydrodynamic predictions at the estuary mouth, including the ebb dominance of the system. Figure 1 highlights the scour hole in the estuary mouth; the entire model domain is shown later in Figure 11.

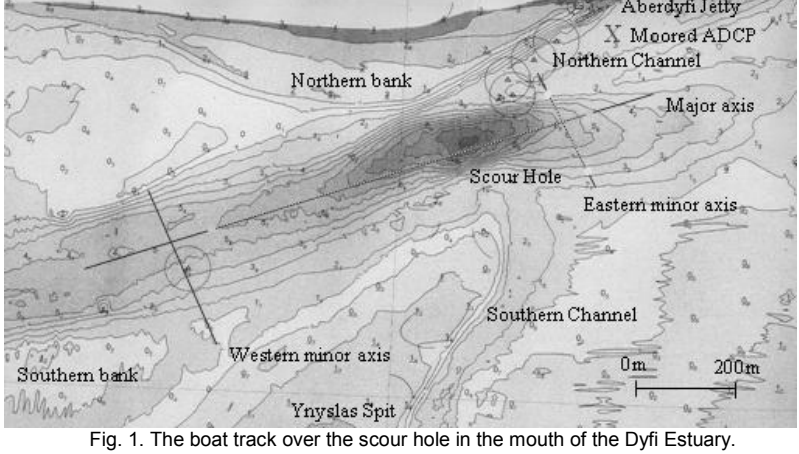

Fig. 1. The boat track over the scour hole in the mouth of the Dyfi Estuary.

The scour hole, which has been present as a fixed feature for decades, is approximately 800 m long, 150 m wide and 12 m deep, forming an asymmetrical elliptic shape. Data were obtained for both neap (24-25/01/06) and spring tides (31/01/01- 01/02/06), though here we highlight only the spring tide. Current data was obtained using a boat-mounted ADCP (the ADCP bin height was 0.25 m with a contaminated near-bed layer as shown). The boat tracked over the hole, following the double-cross shown in Figure 1, every 40 minutes during the tidal cycle. The flow was unstratified for the full spring tidal cycle and there was negligible wind and wave activity. The data presented here was collected along the major axis of the scour hole between the orange circles (Figure 3 and 7) and over the eastern minor axis between the yellow circles (Figures 4, 5, 8 and 9). The state of the tide corresponding to the data presented is indicated in Figure 2 by a red cross for peak flow on the flood tide and a blue cross for peak on the ebb. The water depth in Figure 2 was obtained by a bottom mounted ADCP moored in the main northern channel offshore from Aberdyfi jetty at the position indicated by the red cross in Figure 1.

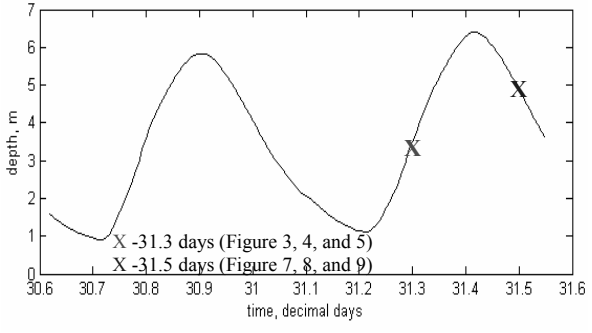

Fig. 2. The tidal curve off Aberdyfi jetty 31/01/06 -1/02/06 (spring tide).

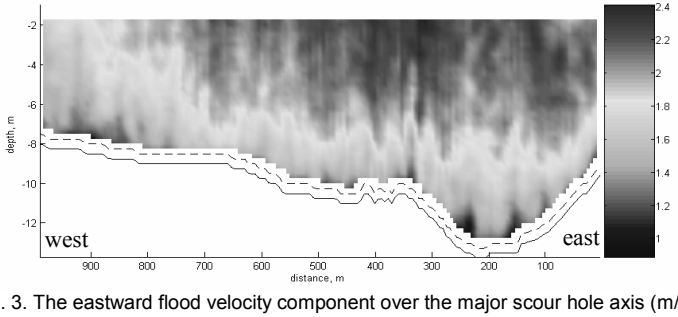

Fig. 3. The eastward flood velocity component over the major scour hole axis (m/s).

During peak flood flow the eastward (positive) velocity component over the hole was 2.4 m/s with maximum flow speeds occurring over the deepest parts of the hole. Figure 3 shows the flow along the main axis of the hole, while Figure 4 shows the flow through the eastern minor axis of the hole. The peak velocity occurred in a surface layer, just off

centre to the southern side of the hole. The change of sign of the northward velocity component (Figure 5) illustrates that the flow diverged as it left the hole on both sides of the eastern minor axis. The north-velocity component was weaker than the east-velocity component only reaching peak values of 0.5 m/s.

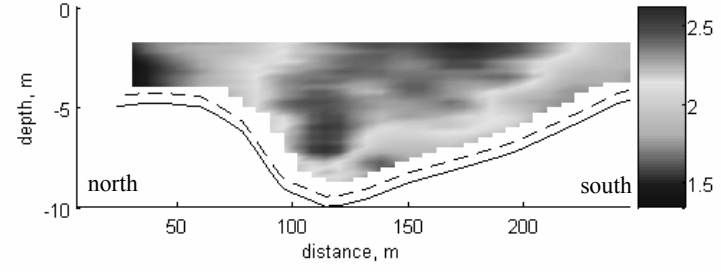

Fig. 4. The eastward flood velocity component over the eastern minor scour hole axis (m/s).

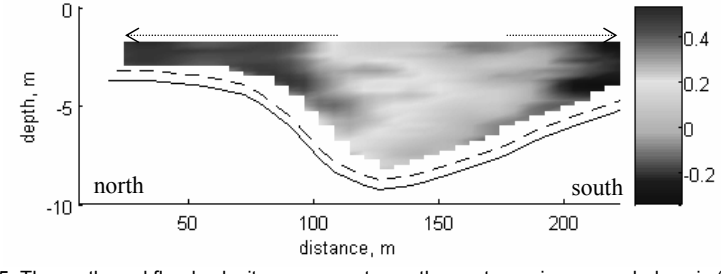

Fig. 5. The northward flood velocity component over the eastern minor scour hole axis (m/s).

It was found also that the flood tide along the north of the channel was deflected off the northern bank before entering the hole, directing the current in a more easterly direction (Figure 6). This also led to convergence over the deepest point of the hole, resulting in the large velocities seen in Figures 3 and 4.

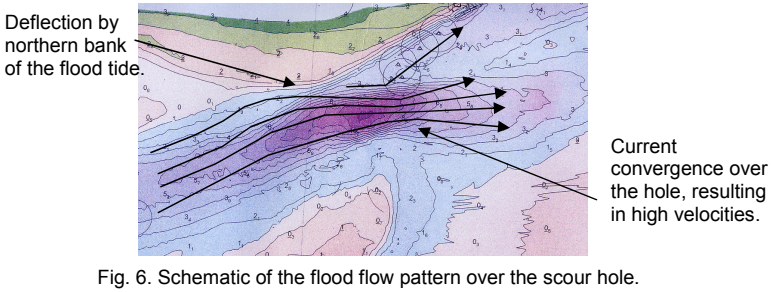

Fig. 6. Schematic of the flood flow pattern over the scour hole.

During peak ebb flow the eastward velocity component achieves maximum (negative) velocity of 2 m/s down stream of the hole (Figure 7). The flow was most pronounced

along the northern side of the hole (Figure 8) due to the main current stream entering the hole from the northern channel, which is ebb tide dominated. The northern channel passes Aberdyfi jetty (Figure 1) and is the main tidal channel in the estuary system. The change of sign of the northward velocity component (Figure 9) demonstrates that flow convergence occurred at the upstream end of the hole, the flow entering the hole over both sides of the eastern minor axis. This convergence may also be due to the northern and southern channels feeding the flow, a consequence of the falling water levels (Figure 2) restricting the flow to the estuary channels. Again the north-velocity component was weaker than the east-velocity component, achieving a peak magnitude of 0.7 m/s.

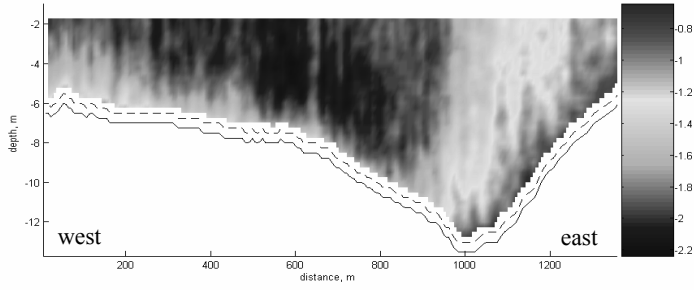

Fig. 7. The eastward ebb velocity component over the major scour hole axis (m/s).

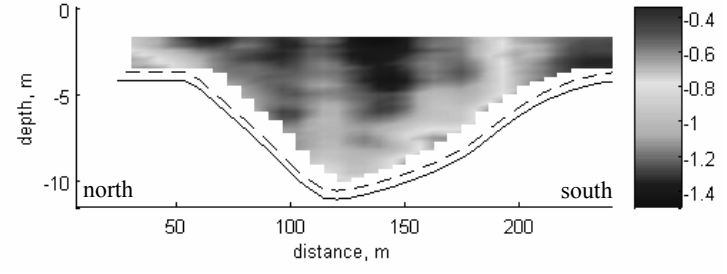

Fig. 8. The eastward ebb velocity component over the eastern minor scour hole axis (m/s).

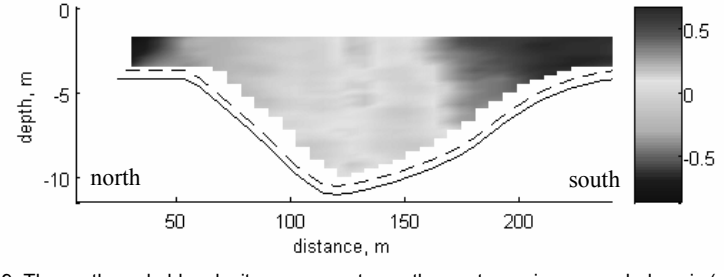

Fig. 9. The northward ebb velocity component over the eastern minor scour hole axis (m/s).

As the flow from the estuary channels met over the deep part of the hole (Figure 10) the flow increased and this process continued offshore giving rise to the peak velocity magnitude, seen to the west of the deepest point of the hole in Figure 7.

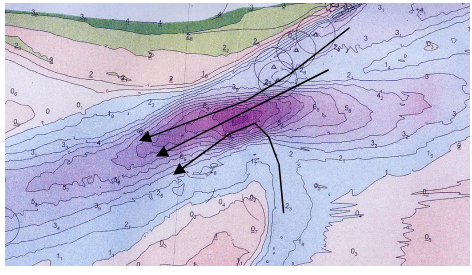

Fig. 10. Schematic of the ebb flow pattern over the scour hole.

In summary, the field data illustrate that over an elliptic hole, with the flow parallel to the major axis, converge/divergence occurs as the flow enters/leaves the pit. The question that then arises is whether this behaviour can cause an increase in velocity that is sufficient for the pit to be self-scouring. Van Rijn et al. (2005) noted the paucity of data of the kind presented here.

MODEL OF THE TIDAL FLOW IN THE DYFI ESTUARY

A complete description of the model of the Dyfi Estuary developed at UWB using the Telemac System is beyond the scope of this paper. Here we present only the details relevant to the present application. The model domain and bathymetry are shown in Figure 11. The offshore north-south boundary, where the water depth is typically 15 m, is 14 km long. The scour hole (marked with a blue cross) is located in the main channel seen entering the estuary. Within the sandy estuary itself large areas of drying banks dominate the bathymetry.

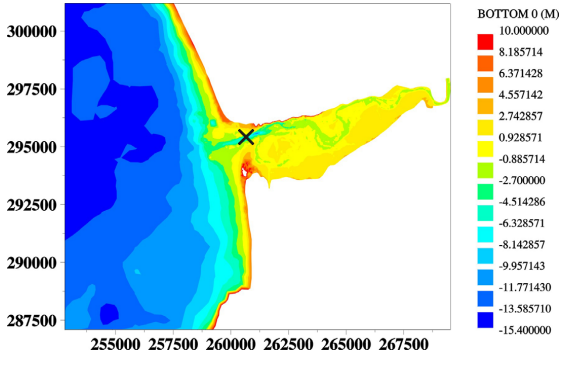

Fig. 11. Telemac model domain and bathymetry of the Dyfi Estuary

Telemac2D has been utilized with a mesh size of 500 m offshore reducing successively to 10 m over the area of the scour hole, thus allowing high resolution of the flow here. The tidal boundary conditions have been have been obtained from the operational POLCOMS model of the Irish Sea, but have here been simplified here by the retention of only the M2 and S2 constituents. A full spring-neap tidal cycle has been simulated with a model time step of 10 s. The field data have been used to undertake a limited amount of model tuning and the description of bottom friction has been matched with the known seabed type (sand with D_{50}= 0.24 mm). Following a spin-up period, the model cycle starts with the spring tide. In the offshore domain both the elevation and velocity fields are essentially symmetrical. This is not the case however in the estuary mouth, near to the region of the scour hole. Here Figure 12 shows that, while the tidal elevation is symmetrical, the velocity field is highly asymmetrical with a short (positive) flood flow into the estuary being followed by a much longer (negative) ebb flow out of the estuary. The reason for this ebb dominance, which has been confirmed by the field measurements, is attributable to the large areas of drying banks within the estuary.

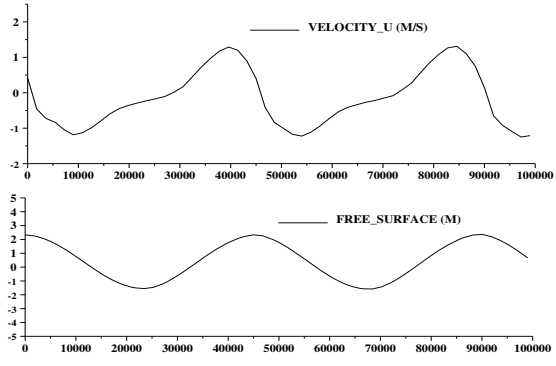

Fig. 12. East-west component of velocity (top), and free-surface elevation (bottom) in the mouth of the estuary.

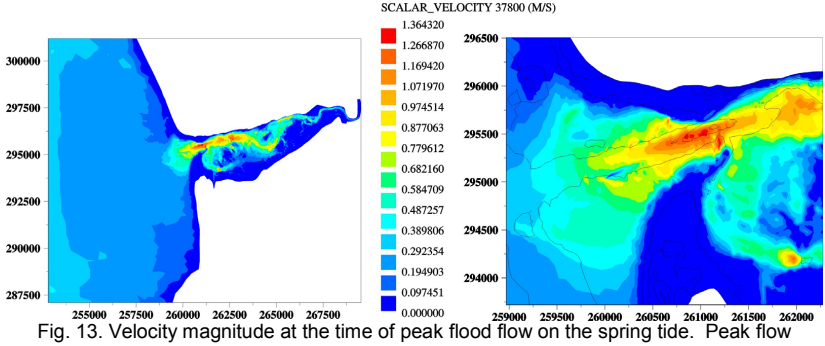

Fig. 13. Velocity magnitude at the time of peak flood flow on the spring tide. Peak flow speeds in the entire domain (left) occur over the scour hole (right, with bathymetry shown).

Figure 13 shows the velocity magnitude at about the time of peak flood flow into the estuary on the spring tide. Offshore the velocities are weak, but in the estuary mouth they are strong, attaining their largest values directly over the scour hole. On the ebb tide (Figure 14) the situation is analogous, though here the offshore directed velocities are maximum somewhat downstream of the point of maximum depth within the scour hole, consistent with the field results shown earlier in Figure 7.

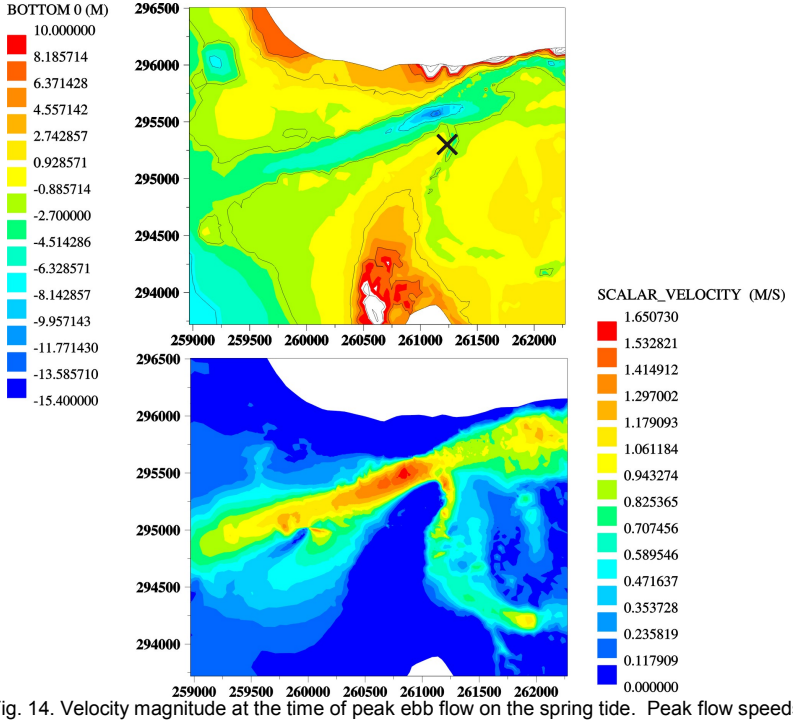

Fig. 14. Velocity magnitude at the time of peak ebb flow on the spring tide. Peak flow speeds again occur near the scour hole (bottom). The bathymetry of the pit is as shown (top).

Evidently both model and experiment show peak flows occurring in the vicinity of the scour hole. In the natural setting of the Dyfi Estuary, this velocity enhancement is caused partly by the funnelling effect of the sides of the estuary at its mouth and, possibly also, by topographic 'anchor points'. The area marked by the blue cross in Figure 14 is actually the site of ballast (rocky material) dumped by cargo vessels during the late 19th century. Although the underlying sediment is erodible, this ballast may have helped to stabilize the scour hole in its location nearby. What is clear is that the scour hole is a stable, persistent feature in the mouth of the Dyfi Estuary. What is less clear is whether its location and elongated geometry is simply forced by the nearby (fixed) topographic features, or whether its elongated shape results from a more fundamental interaction between the flow and the seabed topography.

A MODEL OF CHANNEL FLOW OVER A SCHEMATISED PIT

In order to address the question posed above, we consider next the results of Telemac2D simulations carried out for simple, steady, channel flows above idealized pits of elliptical plan area. The channel is 2000 m long and 1000 m wide, with an undisturbed depth h of 10 m. The nominal grid size is 50 m which reduces to 10 m in the region around the centre point of the channel where the pits are located. An upstream volume flux of $10^4 m^3/s$ imposed in all runs, and 'sliding' boundary conditions are imposed at the sides of the channel. At the downstream end the nominal depth of 10 m is imposed, and so here the (mean) velocity is 1 m/s exactly. To ensure convergence the duration of each run has been taken as 10^4 s with a model time step of 10 s (run time 12 min).

As the model spins up to convergence the surface elevation, which is 'free' at the upstream end of the channel, adjusts to its final value. For example, with a bed roughness of k_s = 0.05 m the perturbation (ζ) to the undisturbed depth h is $\zeta_{upstream}$= 0.058 m. It turns out that the surface slope along the channel is almost exactly uniform, corresponding in this case to -2.9×10^{-5}. Since the converged flow is horizontally non-uniform it is necessary to correct for this in obtaining the local bed shear stress τ_0, which may be obtained quite simply from the equation of motion as:

$$\tau_0 = \rho\left(g\left(h+\zeta\right)-U^2\right)\times\left\{-\,surface\;\;slope\right\}$$

where U is the local depth-averaged velocity along the channel, ρ is the water density, and g is the acceleration due to gravity. In the simple case of a flat bed the flow properties depend only upon one non-dimensional parameter, namely k_s/h. The behavior of the drag coefficient C_D defined in the usual way by $\tau_0 = \rho C_D U^2$ (and obtained in Telemac2D via the Chezy coefficient) is illustrated in Figure 15. This graph shows, for example, that doubling the depth decreases C_D by about 20%.

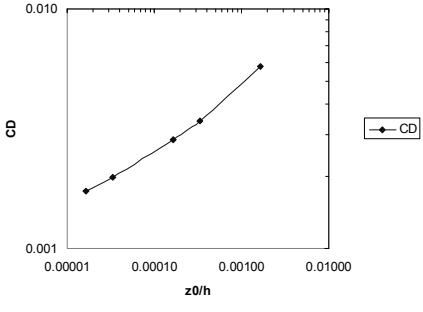

Fig. 15. Drag coefficient for steady flow in a channel (roughness length $z_0=k_s/30$)

Suppose next that we add a circular pit at the centre point of the domain, the pit being taken as an inverted cosine bell. If the depth of the pit below the undisturbed bed level is H and the radius of the pit (to the edge of the bell) is R, the properties of the flow now depend upon the three non-dimensional parameters: $\frac{k_s}{h}, \frac{H}{h}$ *and* $\frac{R}{h}$.

The effect of varying the two new parameters, while keeping k_s (and hence k_s/h) fixed (with k_s= 0.05 m) is shown in Figure 16. At the centre of the pit, the flux $U(h+H)$ increases significantly as H/h departs from its undisturbed value H/h= 0 indicating that fluid is being entrained into the pit from the surrounding area. However, the depth-averaged velocity U decreases as H/h increases, suggesting that such a pit shape is likely to promote infill. The results shown in Figure 16 for both the velocity and also the flux are strongly dependent upon H/h, but only very weakly dependent on R/h.

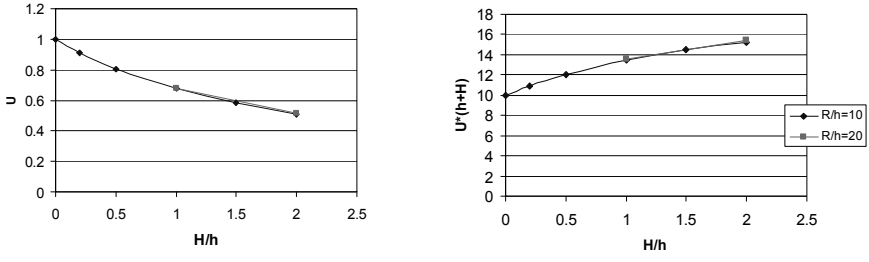

Fig. 16. Velocity (U m/s) (left) and flux ($U(h+H)$ m^3/s/m) (right) at the centre of the circular pit as H/h and R/h are varied with k_s/h fixed.

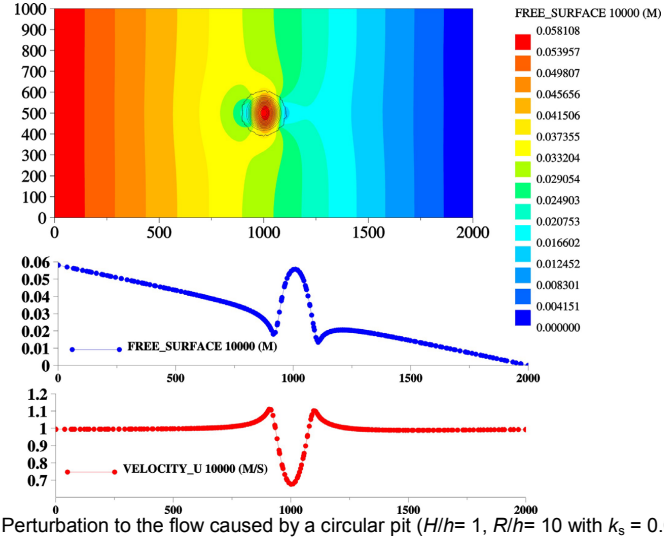

Fig. 17. Perturbation to the flow caused by a circular pit (H/h= 1, R/h= 10 with k_s = 0.05 m).

Some key results in a specific case are shown in Figure 17 in which the location of the pit is shown by the black contour lines. The colour map shows that the converged flow is down-slope from the left to the right of the domain, the surface slope being -2.9×10^{-5} as stated earlier. The pit perturbs the flow to a distance around it that scales on its radius R. The remaining graphs in Figure 17 show the free-surface and the streamwise

component of the depth-mean velocity, along the centre-line of the domain. On approaching the pit the flow accelerates causing the surface elevation to drop while, on entering the pit, the flow decelerates causing the surface elevation to rise. After passing the deepest point at the centre of the pit this pattern is reversed. Evidently the flow is sucked into the pit by the pressure field that is induced in the area surrounding it and Figure 16 shows that, as expected, increasing the depth of the pit reinforces this effect.

It may be inferred from the results above that a circular pit is likely to infill since U decreases as H/h increases. For a self-scouring pit we require the velocity to remain roughly constant (or ideally to increase) as H/h increases. The question that then arises is whether by changing the shape of the pit such an effect can be produced. In order to increase the domain of influence of the pit laterally (i.e. across the flow), it is necessary to increase the streamwise dimension of the pit. Next therefore we replace the circular pit (radius R) by an elliptical one (with streamwise semi-axis a, and transverse semi-axis b), doing this in such a way that the plan area of the pit remains unchanged (i.e. $\pi R^2 = \pi ab$ such that R is the 'effective' pit radius). The flow properties now depend upon four parameters: $\frac{k_s}{h}, \frac{H}{h}, \frac{R}{h}$ *and* $\frac{a}{R}$.

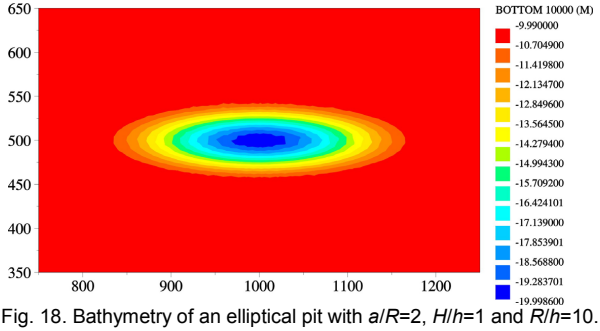

Fig. 18. Bathymetry of an elliptical pit with a/R=2, H/h=1 and R/h=10. Only the central area of the domain (500 × 250 m) is shown.

A typical elliptical pit, corresponding to a stretched cosine bell, is shown in Figure 18. The perturbation to the surface elevation caused by this pit can be seen in Figure 19 and the associated streamwise and transverse velocity components are shown in Figure 20. The effect of stretching the pit from a circle to an ellipse with its major axis in the streamwise direction is to suck more fluid into the pit from both of its now-longer sides. The results in Figure 20 show that the flow converges as it enters the pit and diverges as it leaves it, but the streamwise flow within the pit is now more intense than in the case of the equivalent circular pit. The depth mean velocity at the centre of the pit is 0.852 m/s, while at the upstream and downstream edges of the pit the velocity attains values of 1.068 and 1.083 m/s, respectively. The centre-point value may be compared with the much lower value for an equivalent circular pit of 0.676 m/s, and also with the undisturbed flat-bed value of 0.997 m/s, i.e. in the absence of a pit.

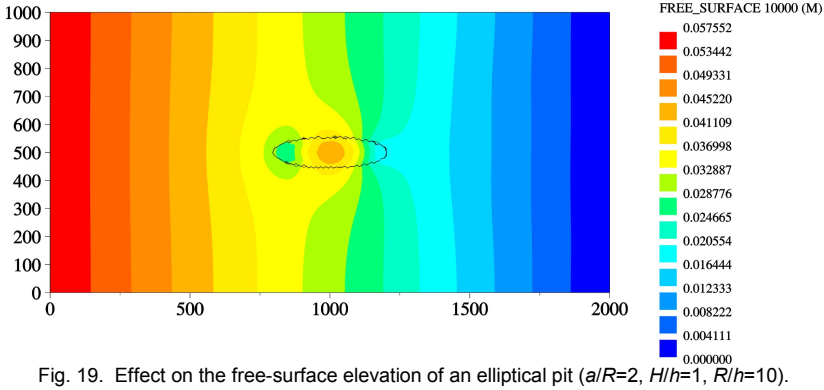

Fig. 19. Effect on the free-surface elevation of an elliptical pit (a/R=2, H/h=1, R/h=10). The perimeter of the pit is shown by the black line.

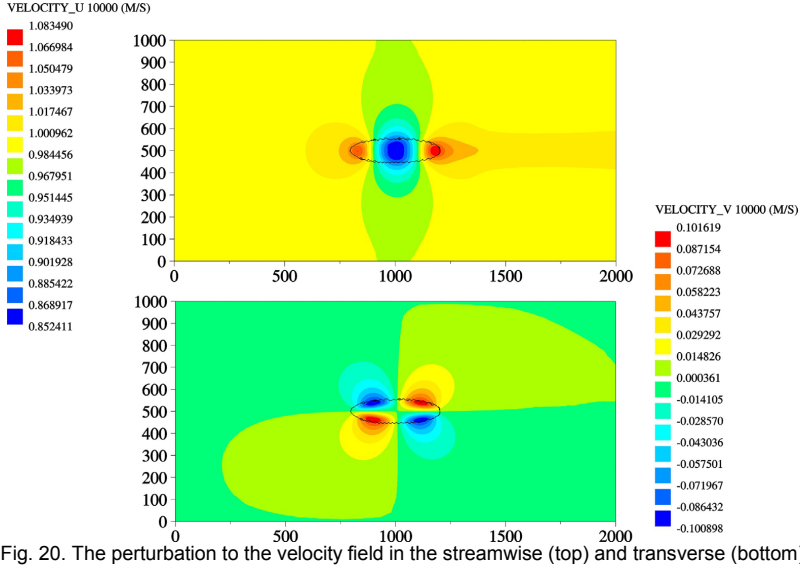

Fig. 20. The perturbation to the velocity field in the streamwise (top) and transverse (bottom) directions as a result of the pit shown in Figure 19 (a/R = 2, H/h = 1, R/h = 10).

The depth-mean velocity at the centre of a variety of elliptical pits is shown in Figure 21. With regard to the shape of the pit, the value a/R = 1 indicates a circular pit. In the limits $a/R \to 0$ and $a/R \to \infty$, the pit becomes, respectively, a trench and a longitudinal furrow. Shallow pits correspond to small values of H/h, while deep pits correspond to large values of H/h. Maximum longitudinal bed slopes only exceeded 10º in two of the cases considered, and were generally much smaller than this (< 5º). Thus flow separation within the pit would not be expected, and the use of a 2DH model is not unreasonable for an assessment of the dynamics.

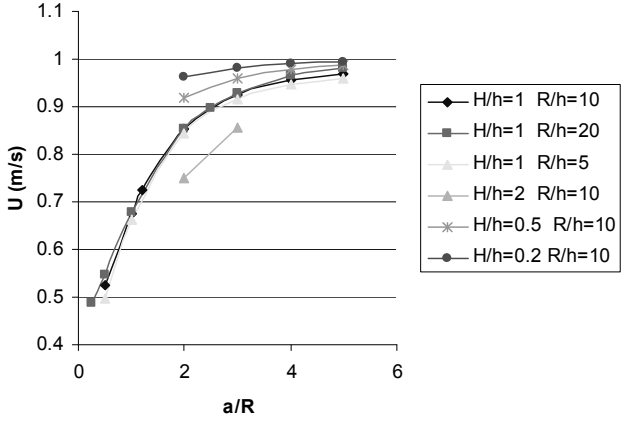

Fig. 21. Depth-mean velocity at the centre of elliptical pits defined by the parameters a/R, H/h and R/h, as indicated by the various symbols.

It is evident from Figure 21 that, if the major axis of the ellipse is across the flow in the transverse direction ($a/R < 1$), then the flow slows down considerably in the pit compared with its undisturbed value of 0.997 m/s (i.e. flat bed case with $k_s = 0.05$ m). However, if the major axis is in the longitudinal direction ($a/R > 1$), then the flow speed at the centre-point takes much larger values ($U > 0.9$ m/s for $a/R > 2$ for all but the deepest pits). The velocity at the centre of the longest shallow pit considered here ($a/R = 5$, $H/h = 0.2$, $R/h = 10$) is 0.993 m/s, virtually the same as the velocity in the undisturbed flow. The results in Figure 21 demonstrate the strong dependence of the maximum velocity upon a/R and H/h; the results are again very weakly dependent upon R/h, as found for circular pits.

DISCUSSION

The results in Figure 21 suggest that the flow at the centre of an elliptical pit may be unable to exceed the undisturbed value of 0.997 m/s. These results were obtained using a spatially constant value of the bed roughness k_s. If a spatially variable bed roughness is employed, the apparent constraint is relaxed. For example, taking $k_s = 0.05$m outside the pit and $k_s = 0.005$ m within it, the velocity at the centre-point increases to a value of 1.023 m/s which is somewhat larger than the undisturbed flat-bed value. However, whether or not this represents a physically relevant scenario when bed form dynamics are taken into account introduces factors other than those considered here.

Although it has been suggested that flow separation will not have occurred in any of the pits considered in Figure 21, three-dimensional helical flow effects are quite likely to play a role in the overall dynamics of sand pits. Such helical secondary flows (with their axes lying in the main flow direction) may be induced by the topography itself or by transverse variations in the bed roughness (McLean, 1981). For example, if the bottom of an elliptical pit is rougher than the seabed generally, then both the shape of the bed

and the roughness effect will complement one another to induce an up-slope secondary flow close to the bed that will help to stabilize the pit. In contrast, a relatively smooth pit interior will give rise to competing (positive 'topography' and negative 'roughness' driven) secondary helical flows that may have little net effect.

CONCLUSIONS

The field data from the Dyfi Estuary indicates velocity enhancement in the scour pit at the estuary mouth, and a tidal simulation of the Dyfi using Telemac2D has confirmed this velocity enhancement. In order to derive some generic results concerning scour hole dynamics, model tests have been carried out using schematized pits in steady flow. These tests have shown that :

- pits entrain additional fluid by perturbing the pressure field in the surrounding area.
- the depth-mean velocity decreases in circular pits, which are therefore likely to infill.
- for elliptical pits, the velocity at the pit centre depends strongly upon a/R and H/h, but only weakly on R/h and k_s/h (H = depth of the pit, h = undisturbed water depth, k_s = bed roughness, R = "effective" pit radius, a = semi-axis of ellipse in streamwise direction) .
- shallow, elliptical pits with major-axes in the streamwise direction may be self maintaining. However, if such a pit deepens, this process will not continue indefinitely.

In reality, apparently self scouring pits may rely on fixed bathymetric features (e.g. the presence of lateral channel banks or, in the Dyfi Estuary, dumped ballast in the estuary mouth). These issues require further study with regard to the sediment dynamics.

ACKNOWLEDGEMENTS

The authors thank the Aberdyfi Partnership for making funds available, through Martin Wright Associates, to support the field campaign reported here. Ben Powell of the School of Ocean Sciences, UWB, and Mark Roberts of Civil Engineering Solutions, Dolgellau, mid-Wales, are thanked for their valuable contributions to the field work.

REFERENCES

Davies A.G. and C. Villaret, 2003. "Sediment transport modelling for coastal morphodynamics," *Proceedings Coastal Sediments'03*, CD-ROM Published by East Meets West Productions, Corpus Christi, TX ISBN-981-238-422-7, 14pp.

Davies A.G., Berx B.E., Brown J.M. and Villaret C., 2005. "Morphological modelling of trenches and pits in wave-current flows." Pp. AS 1-14 in SANDPIT, Sand Transport and Morphology of Offshore Mining Pits, by L.C. Van Rijn, R.L. Soulsby, P. Hoekstra and A.G. Davies (Eds.), Aqua Publications, The Netherlands.

Hervouet J-M and Bates P., 2000. The Telemac Modelling System. *Hydrological Processes*, Vol. 14, (Special) Issue 13.

McLean S.R., 1981. The role of non-uniform roughness in the formation of sand ribbons. *Marine Geology*, 42, 1-4,49-74.

Van Rijn L.C., Soulsby R.L., Hoekstra P. and Davies A.G. (Eds.), 2005. *"SANDPIT, Sand Transport and Morphology of Offshore Mining Pits."* Aqua Publications, The Netherlands, 716pp.

PROJECTION OF TOPOGRAPHIC CHANGE OF AN ESTUARY TERRACE BY HORIZONTAL 2-D SIMULATION MODEL, CONSIDERING GRAIN SIZE

Toshimitsu Takagi[1], Go Asano[2], Takushi Inukai[3], Masaya Fukuhama[4]

1. INA Corporation, Sekiguchi 1-44-10, Bunkyo-ku 112-8668, Tokyo, Japan. t-takagi@ina-eng.co.jp
2. INA Corporation, Sekiguchi 1-44-10, Bunkyo-ku 112-8668, Tokyo, Japan. go-asano@ina-eng.co.jp
3. INA Corporation, Sekiguchi 1-44-10, Bunkyo-ku 112-8668, Tokyo, Japan. t-inukai@ina-eng.co.jp
4. National Institute for Land and Infrastructure Management, Asahi 1, Tsukuba 305-0804, Japan. fukuhama-m92fc@nilim.go.jp

Abstract: A numerical model for estimating the terrace topography changes caused by floods is introduced, by considering grain size of sediment discharged from a river. Applying this model to Fuji river-mouth, the sediment discharged during floods can be estimated with an aspect of quantity and quality. As the result, it was obvious that the major part of sediment discharged from Fuji river-mouth at floods is flushed out offshore in deeper than 20m depth, which can not contribute as the longshore sediment transport that nourish the neighborhood of the river-mouth.

INTRODUCTION

Fuji coast located at Suruga Bay in Japan (Fig.1) is formed by gravel and sand sediment supplied from Fuji River, which is 128km-long with 3,990km^2 basin (Fig.2). Since the sand-bar is developed from the east side of the river, the small river-mouth comparing with the river width is opened in the west side. In front of Fuji river-mouth the terrace topography is developed (Fig.3). The slope of river bed is very steep, so the river-flow discharge is a little in the usual condition. However during the rainy season, from June to July, and also in typhoon season, from August to October, the flow discharge increases rapidly in accordance with the precipitation. Much of the sediment movement along the river occurs during floods. During a flood,

a part of the sediment discharged from the river is deposited on the terrace; other is flushed out offshore, which can not contributed as longshore sediment transport that nourish the coastal area adjacent to the river-mouth. Since the offshore bottom slope is very steep, 1/3 (Fig.3), the sediment which transported to the deep area, deeper than 20m, will not come back to the shore again.

At Fuji coast, which located 10 km east from the mouth of Fuji River, has suffered from erosion since 1980. Cause of the erosion is decreasing volume of the longshore sediment due to obstruction of the sand flow by the breakwaters. The countermeasure, the sand and gravel fill, 105m^3 per year, has been carried out since 1996, and it has been shown the good results (Takagi et al., 2000). The material of sand and gravel fill is transported by tracks and ships from outside of the Fuji basin. However, it is difficult to obtain the large volume every year, because of the environmental damage in the borrow area and the cost for the transportation. Instead of bringing sediment from outside, discharged materials from Fuji River is reconsidered as useful for the nourishment material since it is a local in nature and the borrow area is closed to the site. A question was that how much amount of the sediment will remain on the terrace, without disappearing offshore.



Fig. 1. Location map

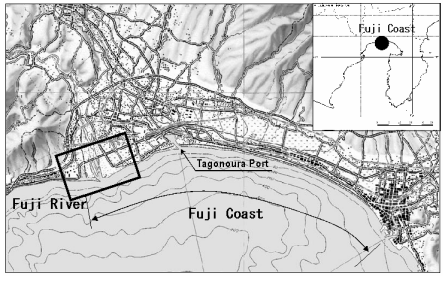

Fig. 2. Fuji River-mouth and Fuji Coast

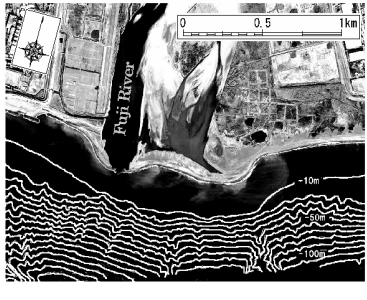

Fig. 3. Topography of Fuji River-mouth

In order to prevent losing the sediment to offshore bottom, a numerical model for estimating the terrace topography change caused by a flood is built. The numerical model is based on a horizontal 2-dimensional shallow water model, in which the sediment grain size is taken into account. The model is verified by depth-soundings and sediment surveys during several floods.

OBSERVATION FOR VERIFICATION

The observation for verification of a numerical model was carried out during several floods. From July to December 2004, 8 typhoons approached to Japan brought floods in Fuji River (Fig.4).

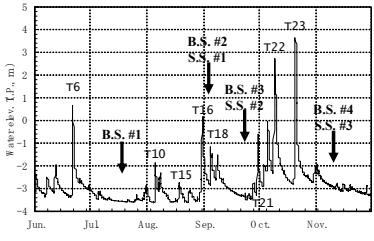

Fig. 4. Flood history and observation schedule

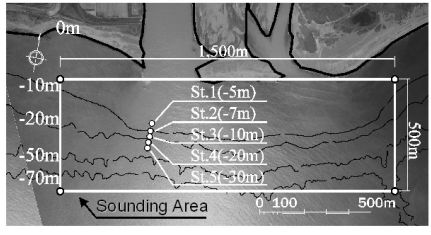

Fig. 5. Observation layout

In particular, Typhoon No.23 (T0423) caused a large flood. The peak discharge reached to 8,338m^3/sec., corresponding to a return period of 13 years in Fuji river. Bottom soundings (B.S.#1-#4) and sediment surveys (S.S.#1-#3) were carried out before and after floods respectively as shown in Fig.4 and 5.

The largest bottom change during the observation was found in the period from the 3rd to the 4th bottom soundings including floods caused by Typhoon No.22 and 23. The distribution of depth change, the comparison of cross section in the center of the river channel and the change volume of sediment in some blocks separated by depth and longshore distance are shown in Fig.6, 7 and Table 1 respectively. The largest depth change reached to about 15m deposition at about 30m depth offshore from almost center of the river channel. The sediment volume of deposition amounted to 366,000m^3 in the sounding area.

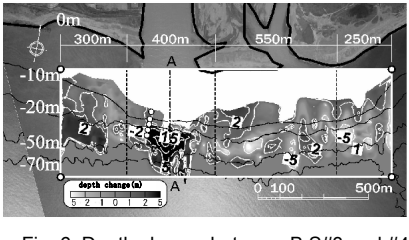

Fig. 6. Depth change between B.S#3 and #4

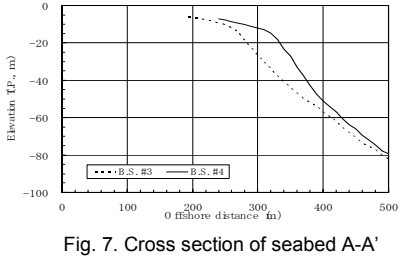

Fig. 7. Cross section of seabed A-A'

According to the depth change analysis, the critical water depth for sediment movement caused by waves was about 14-20m. If the sediment deposit below 20m depth did not come back to the shore by wave action, the amount of sediment about 240,000m^3 was assumed to be lost to offshore area.

Table 1. Change volume of sediment between B.S.#3 and #4

Contour depth	0-300 m	300-700m	700-1250m	1250-1500m	Total (10^3m^3)
≤T.P.-10m	1	13	34	15	100
T.P.-10 to T.P-20m	26	17	1	-7	
T.P.-20 to T.P-50m	63	158	-12	-29	236
≥T.P.-50m	5	66	-6	-9	
Total (10^3m^3)	95	254	17	-30	336

In the 3rd sediment survey after Typhoon No.23, the sediments at every station were mainly composed of gravel and sand on the surface of the bottom. But the sediment at St.3, 4 and 5 deeper than 10m depth included a little silt (Fig.8).

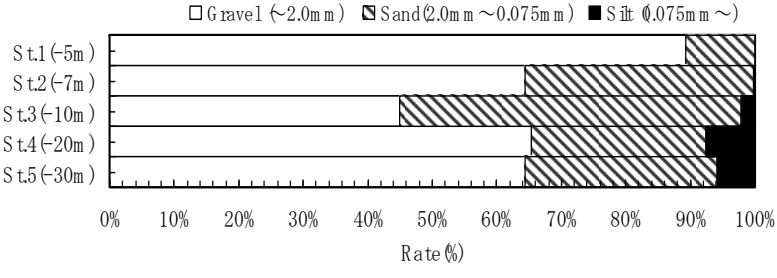

Fig. 8. Results of S.S. #3

NUMERICAL MODEL FOR TERRACE TOPOGRAPYH CHANGE

A numerical model is presented below; a horizontal 2-D model, treatment of bed load and suspended load, with consideration for sediment grain size. The governing equation for river and sea flow is the shallow water equations using depth-averaged velocity, neglecting the influence of mixture with salinity because the fresh water motion is dominant in the sea nearby the river-mouth during flood. The governing equation for bottom changes is yields from the conservation of sediment volume as follows:

$$\frac{\partial z_b}{\partial t} + \frac{1}{1-\lambda}\left\{\frac{\partial}{\partial x}\sum_l q_{bxl} + \frac{\partial}{\partial y}\sum_l q_{byl} + \sum_l (q_{sul} - w_{fl} c_{bl})\right\} = 0 \qquad (1)$$

where z_b is the bottom elevation, q_{bxl}, q_{byl} are components of bed load transport rates corresponding to grain size l, q_{sul} is the up-lift sediment transport rate from the bottom, w_{fl} is the settling velocity, c_{bl} is the suspended sediment concentration in the vicinity of the bottom, and λ is the sediment porosity. The bed load transport rate in each grain size is estimated by Ashida-Michiue Formula, as follows:

$$q_{bxl} = \sqrt{(\rho/\rho_s - 1) g d_l^3} \times 17 \times \alpha \times \tau_{*l}^{3/2} \left(1 - \frac{\tau_{*cl}}{\tau_{*l}}\right)\left(1 - \sqrt{\frac{\tau_{*cl}}{\tau_{*l}}}\right) P_l \frac{u}{\sqrt{u^2 + v^2}} \tag{2}$$

$$q_{byl} = \sqrt{(\rho/\rho_s - 1) g d_l^3} \times 17 \times \alpha \times \tau_{*l}^{3/2} \left(1 - \frac{\tau_{*cl}}{\tau_{*l}}\right)\left(1 - \sqrt{\frac{\tau_{*cl}}{\tau_{*l}}}\right) P_l \frac{v}{\sqrt{u^2 + v^2}} \tag{3}$$

in which:

$$\tau_{*l} = \frac{u_*^2}{\left(\sqrt{\rho/\rho_s - 1}\right) g d_1} \tag{4}$$

$$\tau_{*cl} = c_t \times \tau_{*cM} \tag{5}$$

$$c_t = \begin{Bmatrix} \dfrac{\log_{10} 19}{\log_{10}(19 d_1 / d_M)}, & (d_1/d_M \geq 0.4) \\ 0.85 \dfrac{d_M}{d_M} & (d_1/d_M < 0.4) \end{Bmatrix} \tag{6}$$

$$c_t = \begin{Bmatrix} 0.05, & R_* \geq 671.0 \\ 0.00849 \times R_*^{3/11}, & 671.0 > R_* \geq 162.7 \\ 0.034, & 162.7 > R_* \geq 54.2 \\ 0.195 \times R_*^{-7/16}, & 54.2 > R_* \geq 2.14 \\ 0.14, & R_* < 2.14 \end{Bmatrix} \tag{7}$$

$$R_* = \sqrt{(\rho/\rho_s - 1) g d_M^3} / v, \qquad d_M = \sum_l d_l P_l \tag{8}$$

where ρ is the water density, ρ_s is sand density, g is gravitational acceleration, d_l is the grain size, P_l is the percentage rate of the grain size, u_* is bottom friction velocity, $v = 1.14 \times 10^{-6}\,\mathrm{m^2/s}$, and α is the coefficient of sediment transport rate.

The suspended load is solved using the following equation:

$$\frac{\partial \overline{c_l}}{\partial t}+\frac{\partial(\overline{c_l}u)}{\partial x}+\frac{\partial(\overline{c_l}v)}{\partial y}=\left(q_{sul}-w_{fl}c_{bl}\right)/h \tag{9}$$

The up-lift sediment transport rate from the bottom is assumed as:

$$q_{sul}=\beta\times P_l\times \mathrm{K}\times\left(\alpha_*\frac{1}{\tau_{*l}}\frac{\rho}{\rho_s}u_*\Omega_l^*-w_{fl}\right) \tag{10}$$

$$\Omega_l^*=14\tau_{*l}^*-0.9 \tag{11}$$

The settling velocity is given by:

$$w_{fl}=\sqrt{\frac{2}{3}\left(\rho/\rho_s-1\right)gd_1+\frac{36\nu^2}{d_1^2}}-\frac{6\nu}{d_1} \tag{12}$$

The concentration of suspended load in the vicinity of the bed is expressed as follows:

$$c_{bl}=\frac{\phi_l\overline{c_l}}{1-\exp(-\phi_l)},\qquad \phi_l=\frac{6w_{fl}}{\kappa u_*} \tag{13}$$

where $\overline{c_l}$ is the concentration of depth-averaged suspended load, β is the coefficient of up-lift rate, K=0.008, α_*=0.14, κ=0.4. The up-wind boundary condition of concentration is given by:

$$\overline{c_l}=B\frac{q_{sul}}{w_{fl}\phi_l}\left[1-\exp(-\phi_l)\right] \tag{14}$$

in which B is an coefficient.

The equation of grain size change introduced the bottom change and exchange layer is:

$$\delta\frac{\partial P_l}{\partial t}+P_l^*\frac{\partial z_b}{\partial t}+\frac{1}{1-\lambda}\left\{\frac{\partial q_{bxl}}{\partial x}+\frac{\partial q_{byl}}{\partial y}+q_{sul}-w_{fl}c_{bl}\right\}=0 \tag{15}$$

$$P_l^*=\begin{Bmatrix}P_l & \left(\partial z_b/\partial t>0\right)\\ P_{l0} & \left(\partial z_b/\partial t<0\right)\end{Bmatrix} \tag{16}$$

where δ is the depth of exchange layer, and P_l is the rate of the grain size, P_{l0} is the rate of grain size in the origin bed. The governing equations are discritized by the Finite Element Method in space and by the selective lumping method (Kawahara et al., 1982) in time.

VERIFICATION OF NUMERICAL MODEL

The present model is verified by the observation data. The verification is carried out in the domain of the river channel and the sea as shown in Fig.9, which is discritized by triangular elements, as illustrated in Fig.10. The boundary conditions of the computation are set under the flow discharge, tidal elevation during the flood caused by Typhoon No.23 as shown in Fig.11. The initial rate of sediment grain size in the bottom is set as four kinds of grain sizes according to the field data as shown in Fig.12.

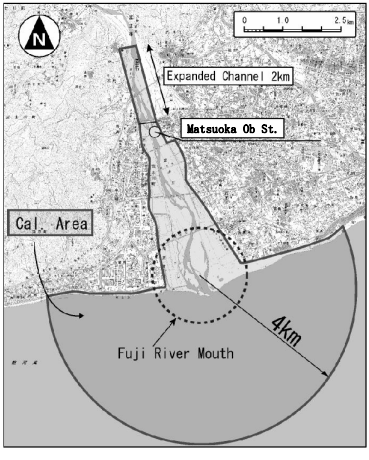

Fig. 9. Calculation area

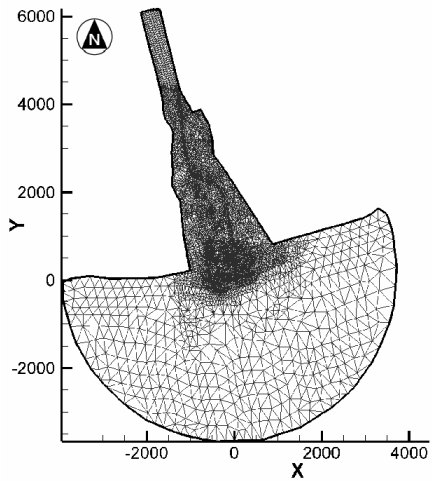

Fig. 10. Finite element mesh

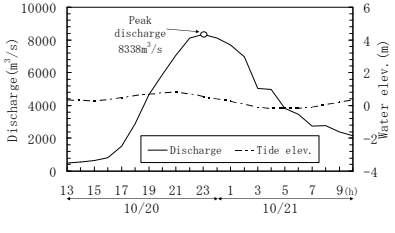

Fig. 11. Flow discharge and Tide level

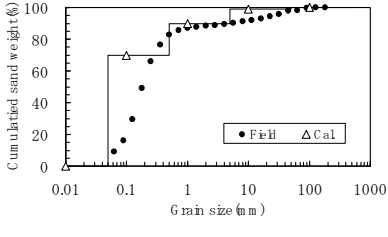

Fig. 12. Initial distribution of grain size

Fig.13, 14 and Table 2, 3, 4 show the horizontal distribution of depth change, the bottom topography in the cross-shore section, and the sediment volume after the flood, respectively.

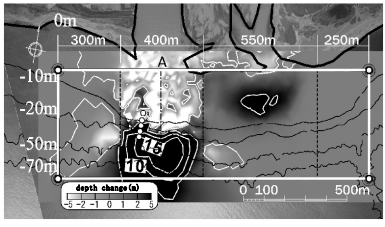

Fig. 13. Calculated depth changes

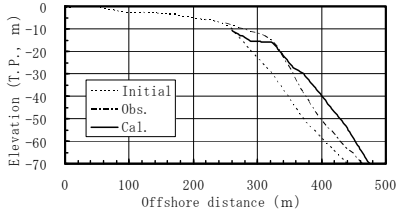

Fig. 14. Depth change in cross shore (A-A')

The sediment from the river deposits in deeper than 10m in front of the river channel is similar to observed data (Fig.5). In particular, the at most deposit area is located at about 30m depth, and it reaches to 15m depth change point, which is in almost agreed with the observed cross section. Moreover, the volume of deposition in the division from 0-700 m alongshore, 10-20m depth is about 45,000m^3, which is almost as same as the observed volume 51,000m^3 (Table 3). However, the sediment volume deeper than 20m depth in calculation exceeds 1,000,000m^3, which is about 3 times as compared to that of the observations. The grain size distribution at each station (St.1-5) is shown in Fig.15. In all stations, the grain size in calculation is rather finer than that of the observations. Also the grain size calculated in 4 hours after the peak discharge at St.1 and 2 relatively, are close to the observation data. Fig.16 shows the flow velocity and grain distribution of St.2 in three instances, one at peak discharge, the other at 4 hours after a peak discharge and at the final. At the time of a peak discharge, the water level is rising over the sand-bar, which was flushed offshore gradually, caused by the flood velocity is beyond 6.0m/sec., and the width of the river-mouth was expanded. At that time the distribution of sediment diameter in calculation is proximate to that of the survey. In 8 hours after a peak, the velocity is decreased, only the finer sediment is moving by then. As the result, the fine sediment is dominant at river-mouth. Above results are different from the sediment survey because of waves. In fact, the large waves which exceeded 5m in height attacked during the flood, the wave motion on the bottom caused fine sand to move toward offshore. Moreover, in this calculation, the sediment supplied from upstream on the boundary is determined by the velocity on the boundary, not considering the condition of the upstream region (Fig.17).

Table 2. Comparison of change volume (from T.P.-10m to T.P.-20m)

Contour depth	0-300 m	300-700m	700-1250m	Total
Observed (10^3m^3)	32	19	17	68
Calculated (10^3m^3)	0	45	10	55

Table 3. Comparison of change volume (from T.P.-20m to T.P.-50m)

Contour depth	0-300 m	300-700m	700-1250m	Total
Observed (10^3m^3)	72	230	32	334
Calculated (10^3m^3)	38	953	21	1012

Table 4. Calculated change volume in each grain size

Grain size	0.1mm	1mm	10mm	100mm	Total
Sediment vol.(10^3m^3)	781	16	08	1	806
Rate (%)	699	15	07	1	722

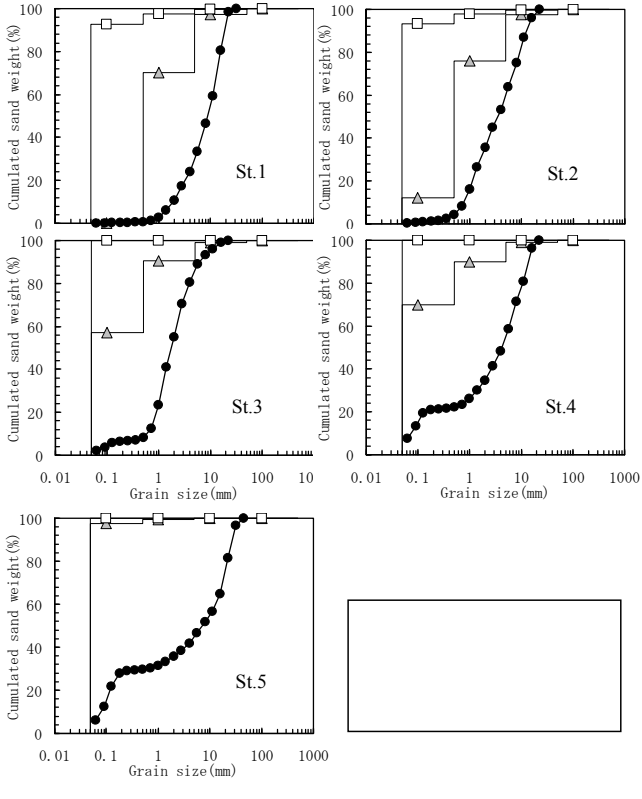

Fig. 15. Grain size distribution in calculation

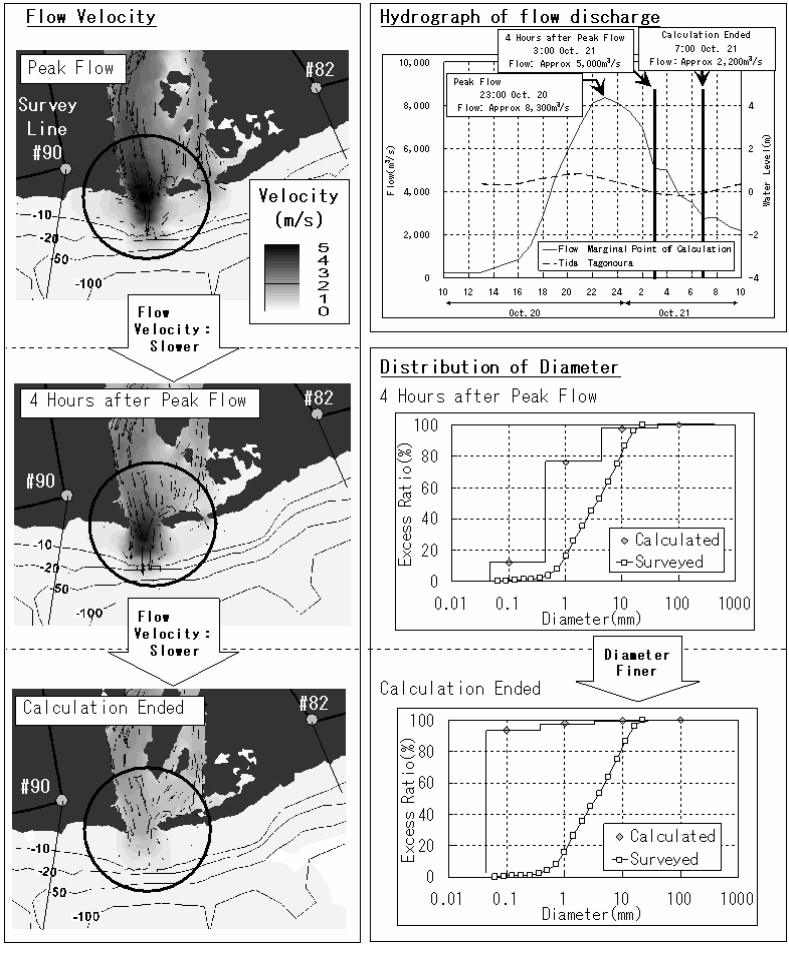

Fig. 16. Effect of flow velocity

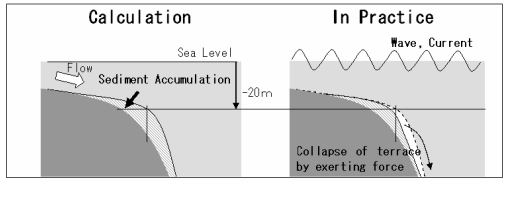

Fig. 17. Sediment accumulation in calculation and collapse of terrace in practice

ESTIMATION OF ANNUAL SEDIMENT DISCHARGE

It is very important to estimate the annual sediment discharge from Fuji River in order to understand the suitability of material as beach fill. The annual sediment discharge can be estimated as the expectation volume derived from the analysis using the results obtained by this return period model. Fig.18 shows the each volume of sediment remained on the terrace and lost to offshore be separated at 20m depth in the case of four kinds of floods. The total volume of discharged sediment increased together with amount of flow. However, the volume of sediment remained on the terrace does not correspond with the sediment volume lost into the offshore area. According the analysis using these results, the annual sediment volume which remained on the terrace is 240,000m^3 and the lost amount is 390,000m^3, approximately.

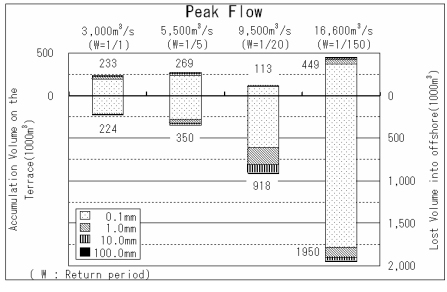

Fig. 18. Volume of sediment deposited on terrace and lost into offshore area at peak low

CONCLUSIONS

The numerical model for an estimation of a terrace topography change, considering sediment grain size, is presented. This model could be verified by the observation data obtained in Fuji river-mouth. In the case like the Fuji river-mouth, which faces the coast with the steep slope, it is obvious that almost 60% of the annual sediment discharged from the river is lost to offshore area. Therefore, the sediment contributed as the longshore sediment transport is well overestimated.

Furthermore, the volume of sediment remained on the terrace is not enough for the beach nourishment for Fuji coast. Since it is expected that the amount of sand discharge from Fuji River will not increase in near future, keeping the remained sediment at the beach is almost important. The present model can be a powerful tool to solve this problem.

ACKNOWLEDGMENT

This work was a part of the project of the countermeasure for erosion in Fuji coast, managed by Numazu Office, Ministry of Land, Infrastructure and Transport.

REFERENCES

Takagi, T., Sato, S., Yamamoto, K., Sakurai, W., Murano, U., Atsuzaka, Y., and Ding, Y. (2000). "Performance of gravel nourishment for erosion control at Fuji Coast", *Proceedings of International Conference on Coastal Engineering 2000*, ASCE, 3333-3344.

Kawahara, M., Hirano, H., Tsubota, K., and Inagaki, K. (1982). "Selective lumping finite element method for shallow water flow", International Journal for Numerical Methods in Fluids, 2(1), 89-112.

EXAMINING THE CONTRIBUTION OF SEDIMENT STRATIFICATION TO THE EVOLUTION OF SEABED MORPHOLOGY

S. Falchetti[1,2], D.C. Conley[1], M. Brocchini[3]

1. NATO Undersea Research Centre, Viale S. Bartolomeo 400, 19138 La Spezia, Italy. falchetti@nurc.nato.int; conley@nurc.nato.int.
2. D.I.Am., University of Genova, Via Montallegro 1, 16145 Genova, Italy. falchetti@diam.unige.it.
3. Università Politecnica delle Marche, Via Brecce Bianche 12, 60131 Ancona, Italy. m.brocchini@univpm.it.

Abstract: We investigate the near-bed sediment dynamics, that occurs in the oscillating boundary layer, observed during the SandyDuck '97 field experiment, through use of the k-ε turbulence module GOTM (1-D General Ocean Turbulence Model, *Burchard*, 1999). For most of the time, the value of the near-bed Richardson number of the high-energy events under examination exceeds the critical value of 0.25, suggesting suppression of turbulence by sediment-induced stratification. GOTM is used to simulate the onshore sandbar migration observed over a 5-day period during Duck'94 field experiment. Bar migration is predicted with a skill of 0.72 when including stratification effects. The accretion/erosion rates predicted using the same free parameters but neglecting stratification effects are approximately twice as large.

INTRODUCTION

Observations of near-bed sediment dynamics such as those collected by FOBS (Fiber Optical Backscatter Sensor) have highlighted the, at times dominant, role played by high-energy events, close to the bed where the sediment is mobilized and redeposited on time scales smaller than half a wave period (e.g. *Conley and Beach*, 2003). It has been proposed (e.g. *Conley*, 2005) that sediment stratification in this thin granular-fluid layer near the bed may have a strong role in such observed phenomena as the reversal of net cross-shore transport direction with height above the bed. It has been proposed that the stratification due to strong upwardly diminishing sediment concentration gradients can

enhance the role of near-bed dynamics by limiting the dispersion of sediment further into the water column. The result is a reduction in the contribution of the mean sediment transport from suspended sediments higher in the water column and an increase in the coherent transport that is biased to the high-velocity peaks under wave crests.

Turbulence damping by stratification is, typically, identified through the inspection of the gradient Richardson number (the non-dimensional ratio between the square of the buoyancy frequency and the square of the vertical gradient of the horizontal velocity which represents the ratio of flow-stabilizing-to-destabilizing forces):

$$Ri = N^2 \Big/ \left(\frac{du}{dz}\right)^2 = -g\frac{\partial\rho}{\partial z}\Big/\rho\left(\frac{du}{dz}\right)^2 = -gs\frac{dc}{dz}\Big/(1+cs)\left(\frac{du}{dz}\right)^2 \qquad (1)$$

where N = buoyancy frequency (1/s); u = velocity module (m/s); ρ = suspension density (kg/m^3); g = gravity acceleration (m/s^2); s = submerged specific gravity of the sediment (non-dimensional); c = sediment concentration (non-dimensional).

The effects of stratification are negligible until $Ri > 0.03$, and mixing is completely suppressed when $Ri >= 0.25$. While traditional applications of this parameter typically involve mean quantities on time scales of minutes or greater, we examine this parameter for very short periods of time (less than half a wave period) and observe that critical stratification is commonly achieved and that it has dramatic affects on the net sediment transport.

In this paper, we test the ability of the two-equations k-ε turbulence module GOTM (1-D General Ocean Turbulence Model, *Burchard*, 1999) to reproduce such stratification effects. Moreover we investigate the role that the above-mentioned increase in the coherent transport component close to the bed occurring during the analyzed events, can have as an additional cause for onshore sandbar migration.

The field data used for this aim belong to the Duck'94 field experiment (North Carolina), in which a 25-m onshore sandbar migration, observed over a 5-day period, has already been subject of study by many authors (*Thornton et al.,* [1996]; *Gallagher et al.,* [1998]; *Trowbridge and Young,* [1989]; *Hoefel and Elgar*, [2003]; *Henderson et al.,* [2004]; *Hsu et al.,* [2006]). Two different approaches to examine this issue can be found in the literature. The first assumes an energetics approach for the sediment transport model. Originally developed by *Bagnold* [1966], who relates the sediment transport rate for steady flows to the rate of work on the bed by the flowing fluid, it has been subsequently extended by *Bailard and Inman* [1981] to combined (oscillatory and steady) flows. The most recent significant modification to this model has been made by *Hoefel and Elgar* [2003], who showed that the addition of acceleration-skewness-dependent transport to the model of Bailard, leads to successful predictions of both the shoreward and the seaward bar migrations observed during the Duck94 experiment.

The other approach followed in literature, belongs to the wave-resolving eddy-diffusive model, the most recent version being proposed by *Henderson* [2004] and later by *Hsu et al.* [2006]. The common issue to their work is the inclusion of the nonlinear wave boundary layer processes in the determination of the shoreward sediment motion.

THE MATHEMATICAL/NUMERICAL METHOD

To gain insight in up-scaling realistic turbulence closure models under energetic sediment transport conditions, we have run numerical model simulations of sediment-stratified bottom boundary layers using the 1-D General Ocean Turbulence Model (GOTM). GOTM is an open source, two-equations (k-ε) turbulence closure model based on the hydrodynamic equations of motion and which makes use of the Boussinesq approximation (density only considered variable when multiplied with gravitational acceleration), the hydrostatic approximation and the eddy viscosity approximation. Since the time scale required to analyze the suspension events is shorter than one second, the model code used for this exercise has been slightly modified to account for sub-second processes.

A key parameter to model the flow velocity within a sheet flow is the bed roughness length, which depends on the viscosity of the water, the flow speed and the size of the physical roughness of the bed. Assuming hydrodynamically-rough flows, the bottom roughness reduces to:

$$z_0^b = 0.03 h_0^b + z_a \tag{2}$$

where z_0^b = bottom roughness (m); h_0^b = Nikuradse roughness (m); z_a = sediment transport component (m). The Nikuradse roughness is taken as 2.5 times the grain diameter; while for the sediment transport component, which arises from the momentum used by the flow to move the sand grains during intense sheet flows, standard GOTM implements the relation proposed by *Smith and McLean* [1977]:

$$z_a = \alpha_0 \left(u_{*b}^2 - u_{*c}^2\right) / \left[g\left(\rho_s - \rho_0\right) / \rho_0\right] \tag{3}$$

where α_0 = constant equal to 26.3; u_{*b} = actual bed shear stress (m/s); u_{*c} = critical bed shear stress (m/s); ρ_s = sediment density (kg/m^3); ρ_0 = water density (kg/m^3).

With the data at hand we found that the Smith and McLean's relationship over predicts the sediment transport component and that a better formula to quantify the total roughness length, comes from the relation proposed by *Nielsen* [1992]:

$$z_a = 5.67\left(\theta_{\omega s} - 0.05\right)^{0.5} d_{50} \tag{4}$$

where $\theta_{\omega s}$ = skin-friction Shields parameter (non-dimensional); d_{50} = representative sediment size (m). The increase of the roughness height over the corresponding values pertaining only to a clear fluid, due to the inter-granular and fluid-granular interactions in particle-laden flow over a mobile bed, is accounted for also by *Hsu et al.* [2006] to predict the onshore and offshore bar migration. They found that the best fit roughness height to the data available depends on the turbulence closure scheme; in particular for the k-ε closure scheme they suggest a modified Nikuradse roughness equal to 25 times the sediment diameter.

The conservation equation for suspended sediment mass, assuming a pure diffusion process (zero convective flux) reads:

$$\frac{\partial C}{\partial t}+\frac{\partial(\omega_s C)}{\partial z}=\frac{\partial}{\partial z}\left(\varepsilon_s \frac{\partial C}{\partial z}\right) \tag{6}$$

where C = sediment concentration (non-dimensional); ω_s = sediment fall velocity, a constant calculated from the grain diameter using the formula of *Soulsby* [1997] (m/s); ε_s sediment diffusivity (m^2/s). The equation is solved in two steps using a splitting technique by which the advective part is solved first:

$$\frac{\partial C}{\partial t}=-\frac{\partial F}{\partial z}; \qquad F=\omega_s C \tag{7}$$

The surface boundary condition is of zero mass flux F, while at the lowest interface the flux F is calculated with a one-sided first-order upstream discretization.
Instead for the diffusive part:

$$\frac{\partial C}{\partial t}=\frac{\partial}{\partial z}\left(\varepsilon_s \frac{\partial C}{\partial z}\right) \tag{8}$$

at the surface we impose a Dirichelet condition (zero flux), while at the lowest interface a Neumann condition is imposed:

$$C_{dw}=C_a\left[\frac{0.5z}{z_0^b}\frac{h-z_0^b}{h-0.5z}\right]^{-b}; b=\frac{\omega_s}{\kappa u_*^b} \tag{9}$$

where C_{dw} = sediment concentration at the lowest interface (non-dimensional); C_a = bottom reference concentration (non-dimensional); h = water depth (m); z = height of the lowest interface (m); b = Rouse number (non-dimensional); κ Von Karman constant.
A Lickian entrainment relation expresses the bottom reference concentration:

$$C_a=g_1\left[\left(u_*^b/u_*^c\right)^2-1\right] \tag{10}$$

where g_1 = non-dimensional parameter. If the value of z_0^b is computed by means of the α_0-dependent Smith and McLean formulation (3), g_1 is found to be equal to 1.56 E-03. On the contrary, if the formulation (4) proposed by Nielsen is used, a calibration of the sediment transport model is needed by determining g_1, through a least square fit of the available data.

As for the turbulent mixing of sediment ε_s has been parameterized using the reduced eddy diffusivity for passive tracers given by:

$$\varepsilon_s = \beta \frac{\nu_t}{\mathrm{Pr}_t}; \nu_t = C_\mu \frac{k^2}{\varepsilon} \tag{11}$$

where β = constant; ν_t = eddy viscosity (m^2/s); Pr_t = Prandtl number (non-dimensional); C_μ stability function (non-dimensional); k = turbulent kinetic energy (m^2/s^2); ε = dissipation rate (m^2/s^3). In the literature many different sets of stability functions can be found; they have the role to increase mixing in the case of unstable stratifications and decrease it for stable stratifications. We start with a simple choice of stability functions for the momentum equation, i.e. such that which, C_μ is a constant. Instead the stability function for tracers is related to the Richardson number through the Prandtl number as described in *Munk and Anderson* [1948]:

$$\mathrm{Pr} = \begin{cases} \mathrm{Pr}^0 \dfrac{(1+3.33Ri)^{3/2}}{(1+10Ri)^{1/2}}, \text{ for } Ri \geq 0, \\ \mathrm{Pr}^0 \qquad\qquad\qquad \text{for } Ri < 0 \end{cases} \tag{12}$$

where Pr^0 = constant Prandtl number for neutral stratification (non-dimensional); Ri = gradient Richardson number (non-dimensional). The buoyancy frequency used to compute the Richardson number takes into account the contribution due to the sediment concentration gradient. The reductive β parameter of equation (11) is used as a calibration parameter.

PREDICTING ONSHORE BAR MIGRATION

The numerical solution

We compare the onshore sandbar migration predictions given by the model with the erosive/accretive patterns observed during the Duck field experiment of 1994. The model is initialized with the 2-Hz time series of horizontal water velocity measured by near-bottom-mounted current meters extending from the shore to a location of about 4.5m depth. During the chosen period the current meter height above the bed remained of about 0.5m, i.e. sufficiently close to the bottom boundary layer. The seabed elevations used to initialize the model came from the measurements of the sonar altimeters deployed in conjunction with the majority of the current meters. The in-situ mean sediment grain sizes ranged from 0.30mm at the shoreline to 0.15mm at water depths of about 5m. For the numerical simulations we used a constant value of 0.2mm. The sensitivity to the cross-shore variations in grain diameter has been already tested by *Henderson et al.* [2004]. Indeed it is not clear the importance of neglecting the real distribution of sediment size, as for one of the offshore migration events they tested, the solution with constant sediment diameter (1-5 September) provided better results than that obtained with variable diameters, while for the other event (2-4 October) the contrary occurred. Moreover for the event characterized by an onshore sandbar migration, the model using a constant diameter provided a scarce prediction of the observed bathymetry, but not that bad to invalidate the assumption of constant sediment diameter.

The model described in the previous section was run repeatedly for each three-hour run

and for each current meter location. The transport rate signal of each instrument has been partitioned into wave, infragravity, mean and net contribution, the last one being the sum of the other three components. The wave and infragravity components are calculated from the raw co-spectrum of concentration and cross-shore velocity, choosing a cutoff frequency of 0.05Hz (*Conley,* 2003). The total, time-averaged and vertically-integrated transport values are estimated by simple integration of the flux values from the bed to the surface.

If it is assumed that the longshore sediment flux and the density of the sediment packing is constant, the mass conservation along the cross-shore direction yields (*Thornton et al.*, 1996):

$$\frac{dh}{dt} = \mu \frac{dQ_x}{dx} \tag{13}$$

where h = bed elevation (m); μ = packing factor (0.7); Q_x = cross-shore, time-averaged transport (m^2/s). The vertical morphological change appearing in equation (13) is estimated by fitting a continuous cross-shore profile of the sediment flux estimated at each current meter location (non-uniformly spaced in the cross-shore direction). The waves in the period tested were moderately energetic; with the significant wave height measured at 4 m depth slowly diminishing from a peak of 1.3 m to a minimum of 0.1 m mid-day on the 25th and then increasing briefly to a peak of 1.20 m (figure 1a). The mean wave period was approximately 7-8 s until mid-day on the 26th and then increased to a peak of 10 s towards the end of the period analyzed (figure 1a).

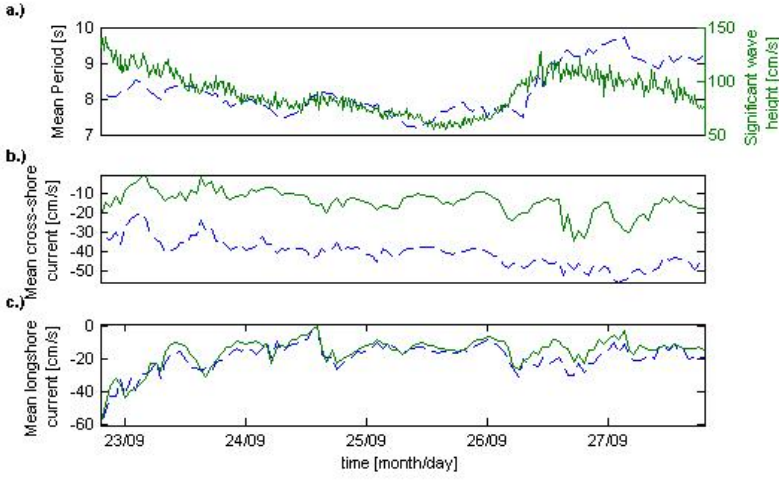

Figure 1 Plot of significant wave height (solid line) and mean period (dashed line) (a), mean cross-shore current near the bar crest (solid line) and trough (dashed line) (b), longshore current at the same locations (c).

Model results suggest that when mean-current-induced transport is small, wave-induced transport leads to the observed onshore bar migration (*Trowbridge and Young,* [1989]; *Hoefel and Elgar*, [2003]; *Henderson et al.,* [2004]; *Hsu et al.,* [2006]). Figure (1b) shows that, at last near the bar crest, the value of the cross-shore mean current for this period was generally low magnitude. As seen in figure (1c) the longshore current remained weak following the initial decrease from the post storm maximum at the beginning of the period.

To assess also the order of magnitude of the wave component to the sediment transport, figure (2) is used to show vertical profiles of one run-averaged (three hours) wave, infragravity, mean and net fluxes near the bar crest. The wave component, directed onshore, clearly exceeds the mean component directed offshore, causing a net sediment transport flux directed onshore. Note that the infragravity component does not affect significantly the net transport rate, its order of magnitude being 10 times lower than that of the wave component.

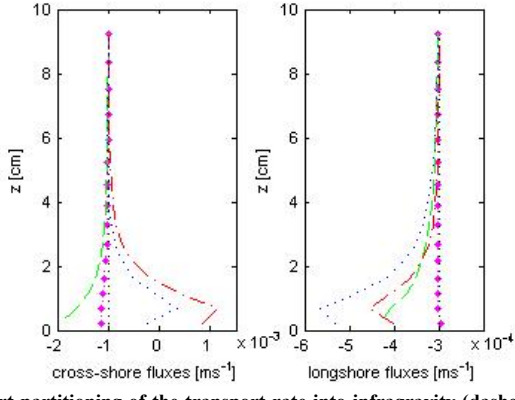

Figure 2 Transport partitioning of the transport rate into infragravity (dashed lines with solid circles), mean (dashed line), wave (dashed-dotted line) and net (dotted line) transport near the bar crest for the cross-shore flux (left panel) and long-shore flux (right panel) for a three-hour run.

Predicted beach profile

Observed and predicted beach profile evolutions are compared in Figure 3 and 4. To quantify the model skill at reproducing the observed morphological changes, we use the same approach proposed by *Gallagher et al.* [1998] and modified later by *Henderson et al.* [2004], who evaluates the model skill through the parameter:

$$S = 1 - \frac{\int_a^b (h_p - h_0)^2 \, dx}{\int_a^b (h_i - h_0)^2 \, dx} \qquad (14)$$

where S = model skill (non-dimensional); h_p= final predicted height (m) ; h_0 = final observed height (m); h_i = initial observed height (m); *a (b)* = most seaward(landward) location at which the current meter observations are available (m). If the model prediction was perfect, the model skill would be equal to 1. If the model prediction was more (less) accurate that the no-change assumption (S = 0), then the skill would be positive (negative).

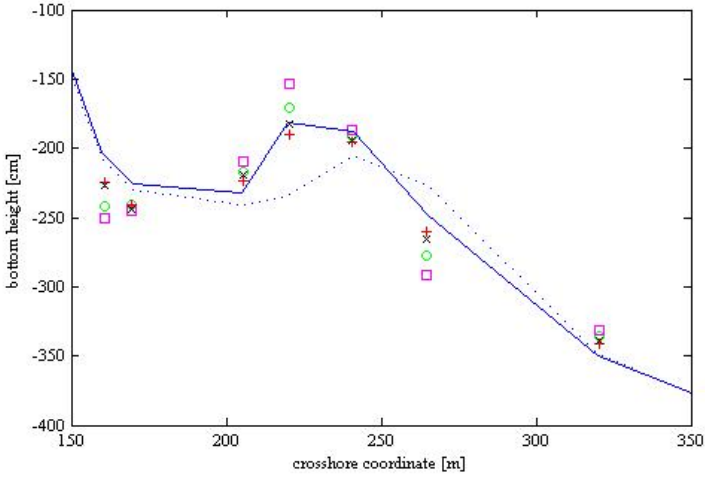

Figure 3 Onshore bar migration. Observations from 22 September 19:00 (dashed line) to 27 September 19:00 (solid line) are compared the numerical solution. Circles and squares represent the prediction with no stratification and , respectively, with g_1=1.80E-03, β=0.4 (S=0.17) and with g_1=2.30E-03, β=0.4 (S=-0.75). Pluses and crosses represent the prediction with stratification respectively for g_1=1.80E-03, β=0.4 (S=0.72) and g_1=2.30E-03, β=0.4 (S=0.58).

As seen in Figure (3), the model with sediment-induced stratification included (hereinafter, stratification included solution SIS), successfully predicts the shoreward bar migration (S=0.72) even if erosion onshore of 180 m is predicted against an observed slight accretion. Figure (3) also shows the sensitivity of the model to the reference concentration parameter: for the SIS, with β constant (0.4), and changing the value of g_1 from 1.80E-03 to 2.30E-03, the model skill decreases from 0.72 to 0.58. The effect of neglecting the sediment-induced stratification in the model predictions (hereinafter, no-stratification solution NSS), using the same calibration parameter, gives an accretion/erosion rate about twice that obtained with SIS. In particular the NSS becomes less accurate than the no-change assumption in the conditions characterized by a large concentration parameter (S = -0.75).

Figure (4) shows also the comparison of the predicted SIS profiles with different sets of the model calibration parameters. For g_1=1.80E-03 the highest skill (S = 0.72) is obtained, while changing the value of β from 0.4 to 1.0, leads to a prediction less

accurate that the no-change assumption (S = -1.29). The figure also reports the result obtained using the value of g_1 proposed by *Smith and McLean* [1977] and a sediment diffusivity equals to that used for the passive tracers. This latter case is characterized, again, by a negative skill, suggesting that the best choice for the model calibration parameter is β = 0.4 and g_1 = 1.80E-03 (giving S = 0.72).

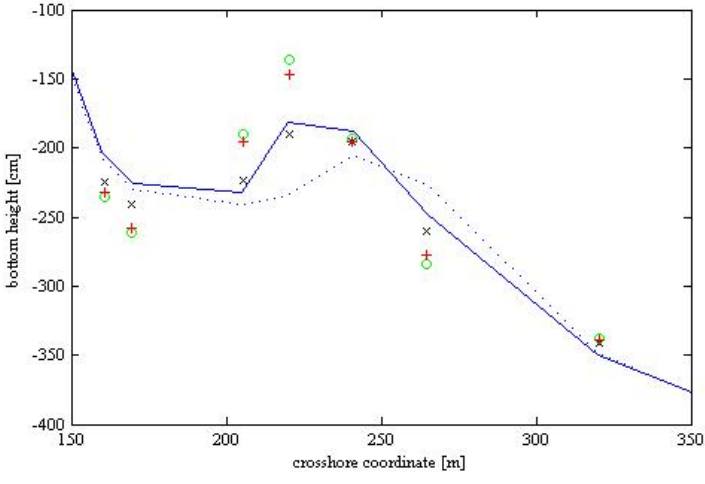

Figure 4 Onshore bar migration. Observations from 22 September 19:00 (dashed line) to 27 September 19:00 (solid line) are compared with the SIS. Circles represent the solution for (g_1, β) = (1.80E-03, 1.0), giving S = -1.29; crosses the solution for (g_1, β) = (1.80E-03, 0.4) giving, S = 0.72; pluses the solution for (g_1, β) = (1.56E-03, 1.0), giving S = -0.66.

Figure (5) shows the separate contributions to the sandbar migration caused by the various transport components. It is clear that the transport occurred around the bar-through location is almost entirely due to the wave component and that the mean and infragravity component have a reduced influence. Only seaward of the bar crest the mean and infragravity induced components of transport significantly affect the bed morphology, causing a large accretion. These model results are consistent with the previous studies (e.g.. *Thornton et al*. [1996]; *Gallagher et al*. [1998]; *Hsu et al*. [2006]) that suggest wave-induced component of transport being the cause of the observed net onshore sandbar migration.

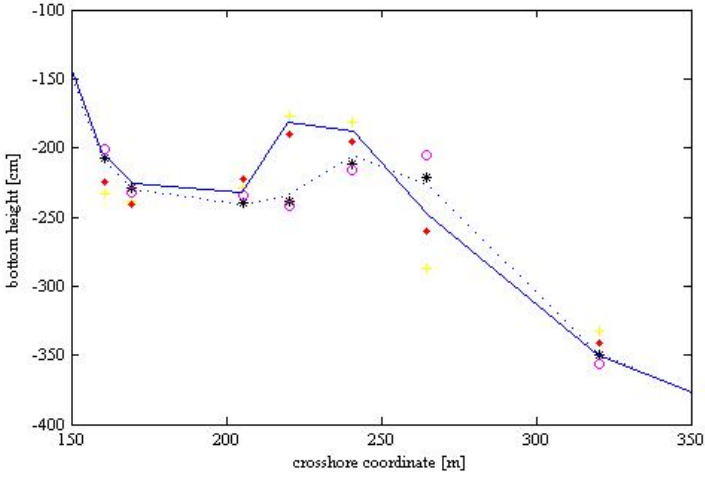

Figure 5 Onshore bar migration. Observations from 22 September 19:00 (dashed line) to 27 September 19:00 (solid line) are compared with the SIS obtained with (g_1, β) = (1.80E-03, 0.4) and the transport contributions highlighted as: infragravity-induced (stars), mean-induced (circles), wave-induced (pluses) and net-induced (dots).

DISCUSSION

The onshore bar migration is fairly well predicted with the calibrated SIS model ($\beta = 0.4$ and $g1$ = 1.80E-03), even if the accretion near the bar crest is slightly underestimated. This result and the small landward erosion predicted onshore of 180m instead of the observed accretion, are findings similar to those reached by *Hsu et al.* [2006] and *Henderson et al.* [2004]. The results obtained have highlighted and clarified the importance of the inclusion of the sediment-induced stratification in a model that reproduces the near-bed sediment dynamics (occurs in the oscillating bottom boundary layer). Neglecting sediment stratification would lead, with the same calibration parameters, to an approximate doubling in accretion/erosion rates. Hence, although in principle it could be attempted to reproduce the appropriate accretion/erosion rates through a specifically-calibrated NSS, we think this approach would obscure the overall physics of the phenomenon. The limited range of flow conditions tested (moderate wave forcing) suggests that extension of the above findings to a wider parameter space be made with care. In particular more tests are needed for strong wave conditions forcing offshore sandbar migration events.

We have attempted to compare our solutions to those provided by various wave-averaged and wave-resolving circulation models available in the literature. However, the different solution strategies and assumptions which are at the core of the various techniques makes such a comparison difficult and preclude a clear understanding of the fundamental phenomena influencing beach morphology evolution. For example, the model proposed by *Henderson et al.* [2004] differs from our SIS solver, because it

includes a second-order non-linear advective flux as well as a diffusive sediment flux in the suspended sediment mass conservation equation. Moreover the highest skill (S = 0.81) in reproducing the same sandbar migration event is achieved with a variable grain size in the cross-shore profile, against our constant value, and a greater value for the reference concentration parameter of 2.9E-03 with respect to the SIS model. However, the model, using the same parameters, fails to reproduce the offshore migration event of the 2-4 October; on the contrary a better results is obtained by means of a non-advective calibrated sediment transport model which makes use of a lower reference concentration parameter. The comparison with the model of *Hsu et al*. [2006], which uses a Meyer-Peter Mueller law for the dimensionless transport rate and a large roughness height (up to 25 times the grain size), to compensate for neglecting intergranular stresses and fluid-granular interactions is also difficult.

CONCLUSION

The onshore sandbar migration event, observed over a 5-day period during the Duck'94 field experiment, has been simulated through use of the k-ε turbulence module GOTM. On the basis of previous studies, which suggest the important role played by the sediment-induced stratification near the bed (*Conley,* [2005]), we investigated the main differences in predicting the observed beach profile change caused by the inclusion/neglection of sediment stratification effects.

The sediment transport model here in use, based on a Lickian entrainment relation for the bottom reference concentration and the relation proposed by *Nielsen* [1992] for the sediment transport roughness, predicts fairly well the onshore migration events under analysis. The result found when neglecting the stratification, show an almost-doubled accretion/erosion rates with respect to the solution which includes the near-bed sediment stratification. It seems possible, though physically undesirable, to obtain the same sediment transport rates and erosion/accretion patterns by means of a NSS obtained with specifically-calibrated model parameters.

ACKNOWLEDGEMENTS

We would like to express our gratitude to Dr. Steve Elgar for furnishing the Duck94 SPUVT data. We would also like to acknowledge the NATO Undersea Research Centre and the D.I.Am. of Genova University, for co-sponsoring the doctoral fellowship of the first author.

REFERENCES

Conley, D.C., and Beach, R.A. (2003). "Cross-shore sediment transport partitioning in the nearshore during a storm event", *J. Geophys. Res.-Oceans 108* (C3), 3065, doi:10.1029/2001JC001230.

Conley, D.C. (2005). "The role of sediment stratification in cross-shore sediment transport under waves", *Abstracts Coastal Dynamics 2005*, 226-227

Bagnold, R.A. (1966). "An approach to the sediment transport problem from general physics", *Prof. Paper 422-I U.S. Geol. Surv.*

Bailard, J.A., and Inman D.L. (1981). "An energetics bedload transport model for a

plane sloping beach: local transport", *J. Geophys. Res.-Oceans* 86, 2035-2043.
Burchard, H., Bolding, K., and Villarreal, M.R. (1999). "GOTM, a General Ocean Turbulence Model, Theory, Implementation and Test cases", European Commission, *Report EUR 18745*, 103 pp.
Gallagher, E.L., Elgar, S., and Guza, R.T. (1998). "Observation of sand bar evolution on a natural beach", *J. Geophys. Res.-Oceans* 103, 3203-3215.
Henderson, S.M., Allen, J.S., and Newberger, P.A. (2004). "Nearshore sandbar migration predicted by an eddy-diffusive boundary layer model", *J. Geophys. Res.-Oceans 109*, C06024.
Hoefel, F. and Elgar, S. (2003). "Wave-Induced Sediment Transport and Sandbar Migration", *Science 299*, 1885-1887.
Hsu, Tian-Jian, Elgar, S., and Guza, R.T. (2006). "Wave-induced sediment transport and onshore sandbar migration", *Coast. Engng 53*, 817-824
Munk, W. H., and Anderson E.R. (1948). "Notes on the theory of the thermocline", *J. Mar. Res. 3*, 276-295.
Nielsen, P. (1992). "Coastal bottom Boundary Layers and Sediment Transport". World Scientific Publishing, Singapore, *Advanced Series on Ocean Engineering, Vol. 4*, 1992.
Smith, J.D., and McLean, S.R. (1977). "Spatially averaged flow over a wavy surface", *J. Geophys. Res.-Oceans 82*, 1735-1746.
Soulsby, R. (1997). "Dynamics of marine sands", Thomas Telford, London.
Thornton, E.B., Humiston, R.T., and Birkemeir W. (1996). "Bartrough generation on a natural beach", *J. Geophys. Res.-Oceans 101*, 12097-12110.
Trowbridge, J., and Young, D. (1989). "Sand transport by unbroken waves under sheet flow conditions", *J. Geophys. Res.-Oceans 94*, 10971-10991.

FROM RIVER BASIN TO BARRIER REEF: PATHWAYS OF COASTAL SEDIMENTS

Piet Hoekstra[1], Ton Hoitink[1,2], Frans Buschman[1], Ayi Tarya[1] and Gert van den Bergh[3]

1. Department of Physical Geography, Institute for Marine and Atmospheric Research Utrecht (IMAU), Utrecht University, P.O. Box 80.115, 3508 TC Utrecht, the Netherlands.
   p.hoekstra@geo.uu.nl
2. Hydrology and Quantitative Water Management Group, Wageningen University, Department of Environmental Sciences, Wageningen University,
   6709 PA Wageningen, the Netherlands.
   ton.hoitink@wur.nl
3. Royal Netherlands Institute for Sea Research (NIOZ), P.O. Box 59, 1790 AB Den Burg, Texel, the Netherlands.
   gertb@nioz.nl

Abstract: The Berau delta and barrier reef system, East Kalimantan, Indonesia are subject of an integrated and multidisciplinary research programme that studies the transfer of water and sediment from upland river catchments towards estuaries and offshore located coral reef systems. Estuaries in the Berau delta have a certain trapping efficiency but a significant part of the suspended matter is still able to reach the marine environment. Seismic profiles, isotope analysis for deposition rates, estuarine and offshore measurements of salinity and turbidity patterns and ecological evidence, collected during a pilot study, provide clear evidence for this.

INTRODUCTION: ROLE OF TROPICAL RIVERS

Coastal sediment input by tropical rivers appears to be one of the main driving factors for changes in coastal morphology in tropical regions. Remarkably more than 70 % of the sediment load entering shelf seas and oceans is delivered by rivers in Southeast Asia and Oceania. For a variety of reasons such as the presence of a humid tropical climate,

high topographic relief, the degree of deforestation and the presence of erodible rocks and soils, in particular the Indonesian Archipelago is characterized by a huge input of sediment into the coastal zone (Hoekstra, 1989 and Milliman et al., 1999). The most recent estimates even suggest that 20-25 % of the global sediment transfer is delivered by tropical rivers in the East Indies (or Indonesian Archipelago; Latrubesse et al., 2005). Fluvial sediment entering the coastal zone will be subject to estuarine, deltaic and marine processes which eventually will determine the fate of the (suspended) sediment (Hoitink et al., 2003; van Maren and Hoekstra, 2005). The coarser fraction commonly directly contributes to estuarine deposition and delta growth but fine suspended matter will be dispersed across the shelf and occasionally may reach deeper oceanic waters. One of the larger islands of the Indonesian Archipelago is the island of Kalimantan and drainage basins on Kalimantan produce about 0.90×10^9 tons of sediment each year (Milliman et al, 1999) and are responsible for the development of some of the largest and most dynamic deltas in the Indo-Pacific region. Coastal progradation in, for example, the Mahakam delta, probably the largest delta in Indonesia, was about 60 km over the past 5000 years (Storms et al, 2005). In the present study we focus on a somewhat smaller system: the Berau river basin and delta, located along the Northeast coast of Kalimantan. The Berau river and delta (Fig. 1) is part of a larger coastal system that includes the delta with a number of estuarine branches (two northern and one southern branch), tidal channels and creeks and extensive mangrove swamps that are already partly converted into fishponds for aquaculture. In a seaward direction, the estuaries are connected with an extensive and relatively shallow lagoon / inner shelf, separated from more oceanic waters by a delta-front barrier reef (Tomascik et al., 1997) and the west part of the passage between the islands of Kalimantan and Sulawesi with some isolated oceanic reefs. Due to this specific coastal setting the Berau river is having a pronounced impact on the coastal zone in terms of water and sediment supply, the presence of nutrients and pollutants and the physical as well as ecological consequences that are associated with these factors such as fluctuations in salinity and turbidity (compare e.g Wolanski et al., 2004).

The purpose of the present paper is to give a general overview of the integrated Indonesian-Dutch research programme “From River Basin to Barrier Reef” that was launched in 2006 to study physical, ecological and socio-economic aspects of the Berau delta system. Leading theme is the transfer of water and sediment from upland river catchments towards estuaries and both shelf as well as oceanic reefs. The study focuses on the role of physical/biological coastal processes and human impact – in particular due to changing land-use patterns and large scale deforestation – on this system. In this paper we will address the fate of (estuarine) suspended sediment in relation to sediment input and dispersion into the coastal zone, based on a pilot study carried out in 2003. The paper starts with a short summary of the aims and objectives of the integrated programme. Next, the general characteristics of the Berau delta system are discussed and the first results from three of the six research programmes are presented. The paper ends with some first and preliminary conclusions based on the pilot campaign of 2003 and ongoing measurements that recently started in 2006.



Fig. 1. The Berau river basin and delta with two northern estuarine branches (light color in river due to suspended matter; coast both shallow and turbid water) and a tide-dominated southern branch

FROM RIVER BASIN TO BARRIER REEF

Physical and ecological conditions

The Berau river accounts for a substantial annual input of fresh water (delivering buoyancy) and sediment into the coastal zone, creating Regions Of Fresh water Influence (so-called ROFI; Simpson, 1997). This input of water and sediment and the development of a ROFI creates very specific environmental conditions that both provide opportunities as well as limitations for coastal (eco)systems. Sediment input directly contributes to estuarine dynamics and delta growth. Meanwhile, this water and sediment also determine the local and regional salinity, temperature, turbidity and suspended sediment load patterns and act as ecological stress factors for coastal ecosystems such as coral reefs. In particular, turbidity and siltation patterns associated to ROFI behaviour are key-controls of the zoning and morphology of coral reef systems. Likewise, these environmental stress factors will also be reflected by the growth pattern and characteristics of individual coral species and therefore provide high-resolution, proxy records to determine the local, regional or even global variability in climatic (and associated environmental) conditions in the recent past. The latter observation is very relevant since it provides a tool for understanding the natural dynamics of the system on an annual, decadal or even centennial time scale. Physical processes responsible for sediment delivery in the Berau system commonly operate on a range of temporal and spatial scales. Apart from the day-to-day tidal fluctuations (the ebb-flood but especially the spring-neap cycle), the river regime is subject to seasonal as well as annual fluctuations due to alternating wet and dry monsoons. In addition, inter-annual to decadal variability in river discharge, sediment load and marine conditions is determined by the El-Niño Southern Oscillation (ENSO cycle).

The socio-economic activities in the Berau river basin and coastal region are both affecting and affected by the natural dynamics of the system. However, these activities also have their own independent driving factors and momentum related to increasing population pressure, advancing processes of economic development and social change. In the near future, land, forest and reef degradation, man-induced changes in hydrological and fluvial regime, sedimentation and water pollution will result in a further degradation of the natural environment.

Integrated research programme

To study the complex interactions within such a coastal environment a research programme entitled "From River Basin to Barrier Reef" was recently launched. It is a joint Indonesian-Dutch initiative within the framework of the East Kalimantan Programme (2006-2010). The main objectives of this integrated and multidisciplinary study in the Berau delta are to:

- Analyse and define the interaction of physical, biological and socio-economic processes and developments in a river delta – barrier reef system that is at present characterized by a very large natural variability and still (partly) represents a pristine coastal environment;
- Asses the consequences of changing environmental conditions and increased human activities for the coastal and marine ecosystems;
- Use coral reef ecosystems as a bio-monitor for the state of the system.

The overall programme includes six different individual projects all dealing with specific aspects of the Berau system. The programme combines a range of disciplines, dominantly from natural sciences (physical geography, coastal oceanography, marine geology and coral ecology) but also including the human sciences (human geography). The programme includes the following projects: 1) Land degradation, estuarine dynamics and delta development in the Berau system; 2) Human Settlements in the coastal zone: effects of changing land-use patterns and deforestation; 3) Mixing and dispersion in marine waters surrounding coral reefs; 4) Coral condition, coral disease and algal/coral overgrowth in the Berau coral reef system; 5) High-resolution coral proxy analysis of the modern environment and reconstruction on a seasonal to centennial time scale; 6) Remote sensing of marine environment.

Sediment dynamics

Projects 1, 3 and 5 are all dealing with mainly the physical aspects of sediment delivery, dispersion and deposition and cover different aspects of the pathways and impact of coastal sediment. In the present paper we will concentrate further on these issues based on a pilot study carried out in East Kalimantan in July – August 2003 and on preliminary results obtained during recent and ongoing studies which started in September 2006 and will continue in 2007. The first project focuses on the effects of estuarine mixing processes – in relation to river discharges and tidal conditions – on the seaward transfer of water and sediment. The delivery of fluvial sediment itself depends on the hydrological sensitivity of the Berau drainage basin for seasonal and decadal scale climatic fluctuations in rainfall and the associated changes in soil erosion. The latter

process may be enhanced by man-induced changes in land-use patterns and deforestation. The third project aims to establish and understand the mixing and dispersal processes determinative to corals in the Berau barrier reef system. A link has to be established between processes acting on a regional scale such as tidal asymmetry up- and downwelling and the effect of buoyancy in a ROFI (Hoitink, 2004; Hoitink et al., 2003; Hoitink and Hoekstra, 2003; Wolanski, 2001) and the local process knowledge, on the scale of individual corals, of mixing and dispersion , for example in relation to the presence and characteristics of different types of hydrodynamic boundary layers (Shashar et al., 1996). Projects 1 and 3 both benefit from a combination of field measurements, modeling efforts and data obtained by remote sensing.

The coral proxy analysis (project five) determines the natural and anthropogenic induced environmental changes, based on a study of the temporal variability of conjugate proxies of banded massive *Porites* corals across a range of environmental settings in the Berau estuary – barrier reef system. Multi-proxy signals (e.g. high-resolution fluorescence measurements, isotope ratios) will be calibrated against in-situ time-series measurements of environmental parameters such as Sea Surface Temperature (SST), salinity and turbidity. The coral proxy analyis is based on handcores taken in the coral reef and laboratory analysis. During the pilot campaign in 2003 already seismic surveys were carried out and box cores were collected to establish the regional variability in grain size patterns of the clastic material in the area and the local deposition rates based on ^{210}Pb analysis.

COASTAL MORPHOLOGY AND SEDIMENTOLOGY

The seismic surveys, in combination with boxcores and bed samples demonstrate the presence of a lowstand and high-stand system tract (Fig. 2). The inner shelf between the present Berau delta and delta front barrier reef system is characterized by the delta platform and prodelta of the modern (Holocene) Berau delta, extending 25-30 km

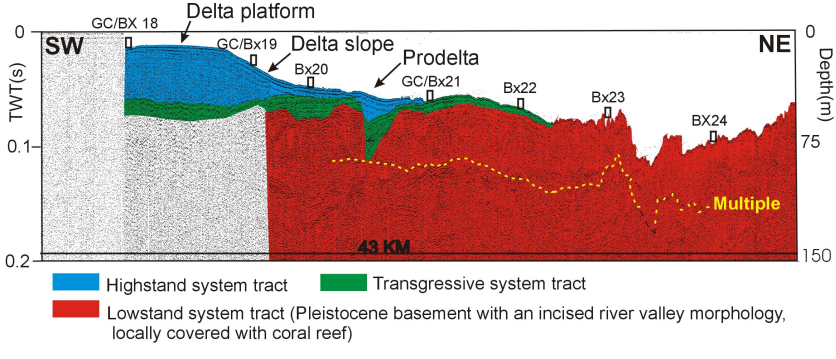

Fig. 2. Geological and morphological development of the Berau delta based on seismic surveys and samples taken from the sea bed.

offshore. The lowstand system tract represents the Pleistocene basement which shows a rather irregular and rugged topography due to the presence of incised river valleys. Locally, this Pleistocene surface is superimposed by transgressive and modern patch reef structures. The lagoon system reaches a maximum depth of about 75 m. Both system tracts are connected with each other by a transgressive system tract (Fig. 2).
Sediment properties vary with distance offshore. The delta platform and prodelta are characterized by very homogeneous, silty sediments; further seaward but still west of the barrier reef the bottom deposits exist of muddy sand alternating with reef structures. The zone between the delta front barrier reef and the oceanic reefs that are located on a

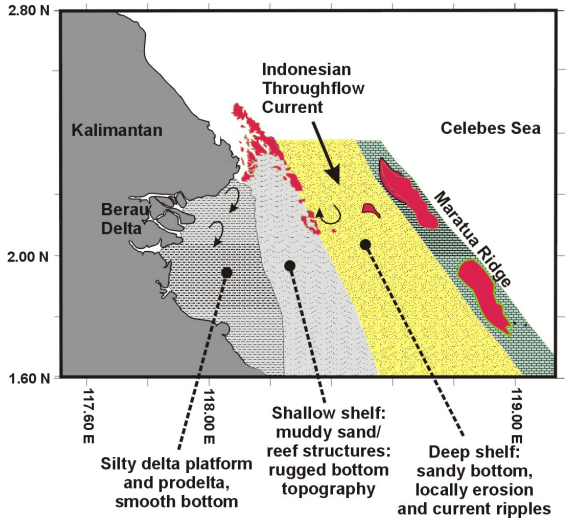

Fig. 3. Sediment properties in the prodelta and lagoonal/shelf environment; the dark red islands represent the coastal reefs, the delta front barrier reef and the oceanic reefs

topographic high, the Maratua Ridge, is characterized by sandy deposits showing the presence of contourites and sandwaves. The strong currents in this region are supposed to be the result of tidal flow in combination with the Indonesian Throughflow since the passage and Makassar Strait (in the south) partly form the link between Pacific and Indian Ocean.

ESTUARINE SEDIMENT DYNAMICS: TRAP OR CONDUIT ?

Hydrodynamic conditions

Rainfall in the river basin and lower catchment area probably varies between 2000 – 3000 mm per year with an average of about 2300 mm/year. The rainfall and associated discharge is not evenly distributed over the year and normally reaches peak values in the period December until March. Our present estimates of mean river discharge vary

between 1500 and 2000 m^3/s based on measurements in the Berau river channel upstream of the point where the river bifurcates in a number of estuarine branches. During the pilot campaign a fixed station was implemented and longitudinal surveys were carried out in both the northern and southern branch of the delta system (Note: this southern branch in the system seems to have a tidal origin instead of being an original part of the distributary network of the delta . Although it is presently connected with the main delta system, our hypothesis is that this connection may have been the result of both a landward extension by tidal erosion and avulsion processes).

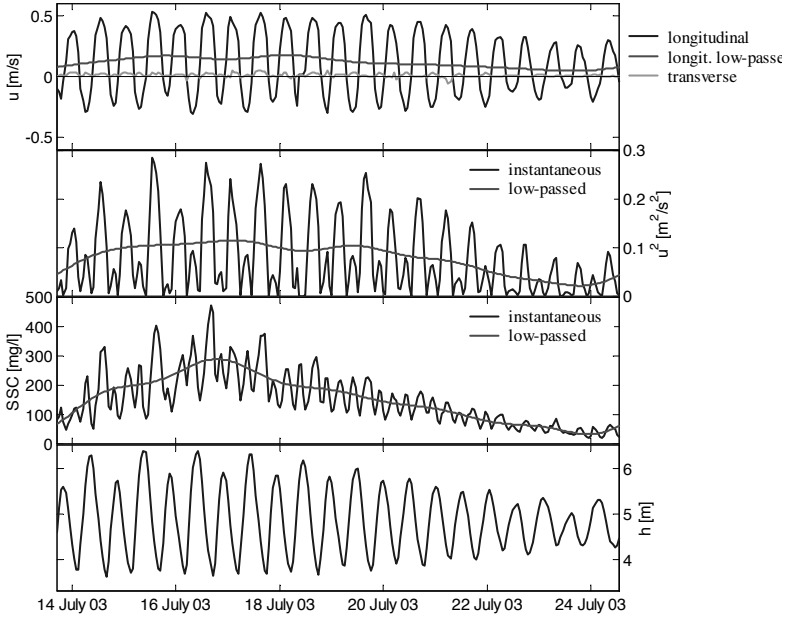

Fig. 4. Measurements in the main river channel of water levels, river flow including squared velocity values to represent shear stress and suspended sediment concentrations

The results of the permanent station upstream of the bifurcation are depicted in Fig 4 ; the station is located at a position approximately 40-45 km upstream of the northern river mouth. The offshore located delta front barrier reef is subject to a semidiurnal tide with tidal ranges varying from about 1.0 m during neap tide (when the tide is becoming diurnal) to about 2.6 m at spring tide (semidiurnal). The semidiurnal tide clearly propagates upstream in the main river channel and is still characterized by a significant tidal range showing a limited amount of damping. Consequently, bidirectional flow is observed with peak values occurring at low tide when river discharge and tidal flow enhance each other; maximum downstream velocities are about 0.5 m/s whereas

upstream flow reaches a magnitude of about 0.25 m/s. Recently measured values with a H(orizontal)-ADCP in a cross-section somewhat further upstream and mid-river show larger velocities in both an upstream and downstream direction. The low-pass filtered signal of the squared values of the velocities – more or less representing the shear velocities - partly correlates with the low-pass filtered trend in Suspended Sediment Concentrations (SSC) with local peak values of 450 mg/l (Fig. 4). Therefore, the trends in SSC are probably explained by a mixture of river discharge, local resuspension, advective transport and tidal mixing.

Longitudinal salinity patterns based on CTD surveys for both the northern and southern branch are illustrated in Fig. 5; the associated distribution in suspended matter is depicted in Fig. 6. Note: the bifurcation is located at km section 25 and the first part of

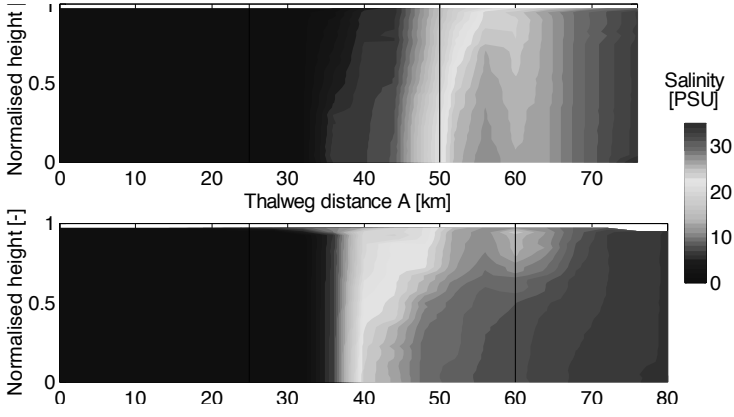

Fig. 5. Salinity patterns as a function of distance along the thalweg in the northern (top, A) and southern (bottom, B) branch; position in the vertical is normalized over depth

the profile (0-25 km) represents the main (single) river channel of the Berau river which is a common part for both branches. In the downstream part of the northern branch a salt wedge is absent and the location of the river mouth (km section 50) more or less coincides with a rapid increase in salinities. A river plume with less saline water masses (20-25 psu) is observed on top of more saline sea water. The buoyant river plume can be traced over an offshore distance of about 10-12 km and shows a kind of plunge point in the frontal zone. The southern branch though (river mouth at km section 60) shows the presence of a salt wedge upstream of the river mouth and the development of partly-stratified conditions in the lower part of the estuary. The fresh-salt interface is located about 20 km upstream of the river mouth.

Two major factors may be held responsible for the difference between both branches. First of all, the northern branch only has a limited depth of about 4 m and an extensive

system of mouth bars limits the landward intrusion of salt water masses. The southern branch though, with an average depth of about 10 m creates more favourable conditions for the tidal intrusion and the development of a salt wedge. Secondly, river discharge will probably vary over the two branches and it is presently assumed that a major amount of water and sediment is using the northern branch to reach the sea. A high river discharge will obviously reduce the amount of salt intrusion.

Estuarine Sediment distribution and offshore dispersion

Estuarine Turbidity Maxima (ETM's) can be observed in both branches. A relatively large turbidity maximum is located in the main river/estuarine channel, approximately at km section 12-14 (11-13 km upstream of the bifurcation) and a smaller one is observed in the southern branch, close to the bifurcation and somewhat landward of the salt wedge in the southern branch. The main ETM is located far upstream of the fresh -salt interface in the northern branch and shows values up to 400 mg/ltr. One may anticipate that the exact location of the ETM varies with the tide (ebb/flood – spring tide/neap tide). At ebb tide, for example, the ETM may be advected down the estuary and may show increasing concentrations due to erosion of sediment from the bed (compare Fig. 4). In this particular case the location of the ETM is located upstream from the fresh – salt interface which suggests that the presence of a null-zone and the existence of a gravitational circulation are less important for the development and location of this ETM. Normally, at the head of the salt wedge sediments settling from the upper seaward flowing layer and sediment carried in the landward flowing bottom layer accumulate – and depending on the actual settling velocity – create a zone of high turbidity, the ETM. Here, a more probable mechanism is local scour and resuspension of the river/estuarine bed in shallow water, in combination with tidal pumping (Dyer, 1997).

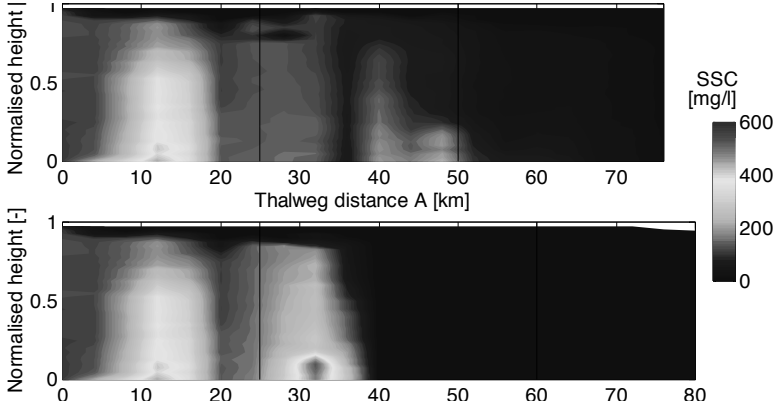

Fig. 6. Distribution of suspended in both the northern and southern branch showing the presence of a major turbidity maximum upstream of the main bifurcation in the delta

The development of (turbid) buoyant plumes, as observed in the field (and indicated in Fig. 7) clearly demonstrates that part of the suspended matter is able to reach the sea (lagoon/ inner shelf).Upstream in the delta, mid-channel bars and bedforms (megaripples and /or sandwaves) demonstrate that the effect of bedload transport cannot fully be ignored in the system. However, its effect rapidly reduces in a seaward direction and the coarsest fractions are building up mouth bars of substantial dimensions, in particular in front of the northern branch.
The offshore dispersion of suspended sediment is partly depicted in Fig. 7. Buoyant plumes are partly advected in a northward direction, as indicated by the low salinity, turbid water masses measured in the area between the mainland coast and the delta front barrier reef.

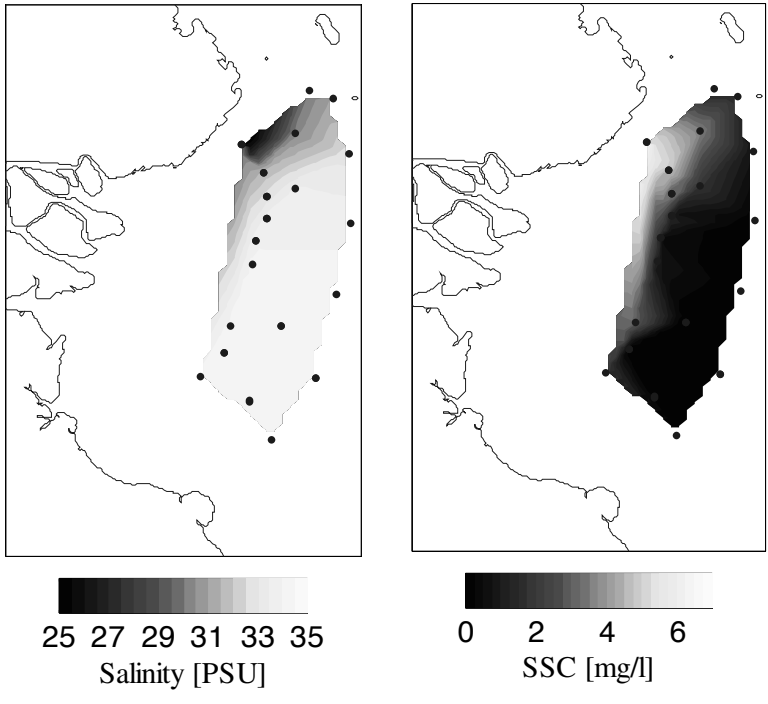

Fig. 7. Distribution of salinity and suspended sediment in the area between river delta and delta front barrier reef showing the offshore dispersion of (buoyant) water masses

DISCUSSION

The present results are based on a pilot study carried out in 2003 and provide more or less a snapshot of the system. The purpose of this pilot study and early reconnaissance

was to collect sufficient information for the definition and implementation of in-depth studies. These in-depth studies for the estuaries, lagoon and delta front barrier reef recently started and will continue in the coming years. Nevertheless, our preliminary results indicate that although the estuaries are able to trap part of the coarser sediment fractions, as visible by the existence of sand bars and mouth bars, a significant part of the suspended matter is still carried in a seaward direction due to the development of buoyant and turbid river plumes. Some of the finer sediment may also be retained in the estuaries, but most probably only on a temporary basis and contribute to the dynamics of the ETM. Main evidence for the seaward dispersion and, subsequently, deposition is the growth of the Holocene delta-platform and prodelta (Fig. 2). The silty and muddy sediments in this region, based on ^{210}Pb analysis of bed samples show deposition rates of about 0.2 – 3.1 cm/year due to the settling of suspended matter. Especially during high river floods the entire system is supposed to be flushed and may result in high deposition rates. As indicated in Fig. 7 part of the suspended matter is even further advected in a seaward direction due to buoyant plumes, tidal and residual currents. Especially the northern branch seems to be an important source for the input of less saline water and suspended matter. Occasionaly, resuspension of sediment may take place due to currents and waves. Wave effects in the northern part of the lagoon though are generally supposed to be limited due to the breakwater effect of the delta front barrier reef, the limited fetch of the lagoon and shallow depths.

Further evidence for the seaward and offshore dispersion of sediment is based on ecological data collected during the pilot campaign (pers. communication R.Bak, Royal NIOZ). There appears to be a clear zonation in coral reefs. Turbidity and suspended load are key-controlling factors in this respect. In the coastal zone, coastal reefs are facing a turbid and low light environment (zone 1). The delta front barrier reef (zone 2) belongs to an intermediate zone, whereas the oceanic reefs are subject to the most favourable conditions for coral growth. This zonation is based on a number of ecological parameters that show the following trends (from zone 1 to 3):

- Coral cover: dead coral cover is high in zone 1 but decreases offshore; likewise living coral cover increases and reaches a maximum in zone 3;
- Partial mortality: is decreasing from shore to open sea;
- Coral colony size: is increasing from shore to open sea;
- Spatial competition: overgrowth of corals is common offshore.

The three zones are also characterized by a difference in coral conditions as reflected by their coral metabolic functioning. The ecological data suggest that the coastal reefs are generally subject to relatively high turbidity levels whereas the delta front barrier reef probably occasionally is affected by higher turbidity levels. At least coral cores show low-density bands that are developed in the Porites skeleton and tend to correspond with luminescent bands, which are formed by the incorporation of land-derived humic acids during growth of the aragonitic skeleton. This suggests that low-density bands are formed during the rainy season, when river discharge and turbidity of the coastal waters increase and light intensity decreases. The offshore zone is characterized by low turbidity levels and very transparent water masses.

CONCLUSION

The Berau delta and its estuaries definitely have a certain trapping efficiency, as observed by the presence of sandy mid-channel bars and mouth bars. Some of the fine-grained suspended matter may be temporary retained within the estuaries and contribute to the development of an ETM. A significant part of the suspended matter, by means of buoyant river plumes and tidal and residual currents, is dispersed in a seaward direction and is able to reach the coral reefs along the coast and those reefs that are part of the delta front barrier reef.

Ongoing and in-depth studies have to reveal in more detail the physical, estuarine processes and mechanisms that operate in the Berau delta and are responsible for the development and dynamics of the ETM, the coastal-marine processes that generate a seaward transfer and dispersion of sediment and the way in which this sediment is finally able to reach the coral reefs.

ACKNOWLEDGEMENTS

The programme "From River Basin to Barrier Reef" is a joint Indonesian-Dutch research initiative sponsored by the Indonesian Institute of Sciences (LIPI) and the Netherlands Science Foundation (NWO), the Netherlands Foundation for the Advancement of Tropical Research (Wotro) and the Royal Netherlands Academy of Sciences and Arts (KNAW).

REFERENCES

Dyer, K.R. (1997). *Estuaries. A Physical Introduction*. John Wiley & Sons, Chichester, 195 p.

Hoekstra, P. (1989). Buoyant river plumes and mud deposition in a rapidly expanding tropical delta. *Netherlands Journal of Sea Research* 23, 517-527.

Hoitink, A.J.F. (2004). Tidally-induced clouds of suspended sediment connected to shallow-water coral reefs. *Marine Geology* 208, 13-31.

Hoitink, A.J.F. and Hoekstra, P. (2003). Hydrodynamic control of the supply of reworked terrigenous sediment to coral reefs in the Bay of Banten (NW Java, Indonesia). *Estuarine, coastal and shelf science* 58, 4, 743-755.

Hoitink, A.J.F., Hoekstra, P. and van Maren, D.S. (2003). Flow asymmetry associated with astronomical tides: implications for the residual transport of sediment. *Journal of Geophysical Research* 108 (C10), 3315, doi:10.1029/2002JC001539).

Latrubesse, E.M., Stevaux, J.C., Sinha, R. (2005). Tropical Rivers. *Geomorphology* 70, 87-206

Maren, D.S. van, and Hoekstra, P. (2005). Dispersal of suspended sediments in the turbid and highly stratified Red River plume. *Continental Shelf Research* 25, 503-519.

Milliman, J.D., Farnsworth, K.L., Albertin, C.S. (1999). Flux and fate of fluvial sediments leaving the large islands in the East Indies. *Journal of Sea Research* 41, 97-107.

Shashar, N., Kinane, S.,Jokiel, P.L., and Patterson, M.R. (1996). Hydromechanical boundary layers over a coral reef. *Journal of Experimental Marine Biology and*

Ecology 199 (1), 17-28.
Simpson, J.H. (1997). Physical Processes in the ROFI regime. *Journal of Marine Systems* 12, 3-15.
Storms, J.E.A., Hoogendoorn, R.M., Dam, R.A.C., Hoitink, A.J.F., Kroonenberg, S.B. (2005). Late Holocene evolution of the Mahakam delta, East Kalimantan, Indonesia. *Sedimentary Geology* 180, 149-166.
Tomascik, T., Mah, A.J., Nontji, A., and Moosa, M.K. (1997). The Ecology of the Indonesian Seas. Part Two. Periplus Editions, Oxford University Press, Oxford, UK, 727-788.
Wolanski, E., Richmond, R.H., and McCook, L. (2004). A model of the effects of land-based, human activities on the health of coral reefs in the Great Barrier Reef and in Fouha Bay, Guam, Micronesia. *Journal of Marine Systems* 46, 133-144.
Wolanski, E. (ed.). (2001). Oceanographic Processes of Coral Reefs: Physical and Biological Links in the Great Barrier Reef. CRC Press, Boca Raton, Florida, 356 pp.

WAVE EVOLUTION ON FLUID MUD BOTTOM

Kevin Hall[1] and Ali Oveisy[2]

1. Professor, Civil Eng. Dept., Queen's University, Kingston, ON. Canada, K7L 3N6, hallk@ce.queensu.ca
3. Graduate Student, Civil Eng. Dept., Queen's University, Kingston, ON. Canada, K7L 3N6, a_oveisy@ce.queensu.ca

Abstract: It is well known that surface water waves interact with the fluid mud on the sea bed. Wave-mud interaction results to high wave energy dissipation and mud mass transport. This kind of wave energy dissipation, which generally is much more significant than wave dissipation due to bottom friction, should be considered in simulation of wave evolution and transformation in muddy coastal environments. This paper presents a numerical model of wave evolution and dissipation on fluid mud . For this purpose, the spectral decay of wave due to mud is implemented in SWAN (a third generation numerical model for Simulating WAves Nearshore) using a multilayered wave-mud interaction model. In this numerical model it is assumed that mud layer has a visco-elasic-plastic behavior.

INTRODUCTION

Wave-mud interaction has been long the subject of the scientific research and some aspects of this interaction such as wave attenuation and mud mass transport have been well known. In coastal areas covered with soft mud bed, traveling waves generate inter-surface waves between the water layer and the fluid mud layer resulting to high wave attenuation due to of viscous damping of fluid mud layer. Wave energy dissipation due to wave-mud interaction should be considered in simulation of wave evolution and transformation in coastal muddy environments (Gade 1957; Tubman and Suhayda 1976; Sheremet et al. 2003; Oveisy and Soltanpour 2005 and 2006). In this paper the spectral decay of wave due to mud is calculated in a multilayered wave-mud interaction model which considers the mud layer as a visco-elastic-plastic material. The calculated wave attenuation coefficient is used in SWAN in order to simulate wave evolution and dissipation on fluid mud.

NUMERICAL MODEL

The simulation of wave evolution on fluid mud is carried out by introducing a two dimensional vertical wave-mud interaction model two SWAN. The multi-layered vertical model is used to calculate the wave attenuation rate on mud. The value of wave attenuation rate is then used in SWAN the same as the other dissipation factors to simulate wave dissipation on fluid mud bed.

Wave-Mud Interaction Model

Following Tsuruya et al. (1987), the fluid system is divided into N layers in which the water layer is represented by N=1.

Fig. 1 shows the sketch of the multi-layered model with the water layer on top.

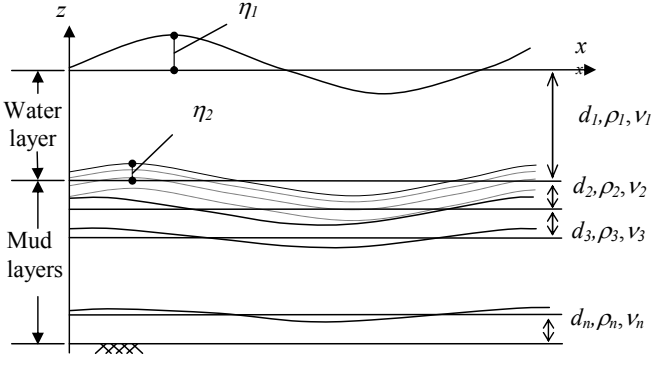

Fig. 1. Definition of multi-layered model

The linearized Navier-Stokes equations, neglecting the convective accelerations and the continuity equation for an incompressible fluid can be expressed as

$$\frac{\partial u_j}{\partial t} = -\frac{1}{\rho_j}\frac{\partial p_j}{\partial x} + \nu_{e,j}\left(\frac{\partial^2 u_j}{\partial x^2} + \frac{\partial^2 u_j}{\partial z^2}\right) \tag{1}$$

$$\frac{\partial w_j}{\partial t} = -\frac{1}{\rho_j}\frac{\partial p_j}{\partial z} + \nu_{e,j}\left(\frac{\partial^2 w_j}{\partial x^2} + \frac{\partial^2 w_j}{\partial z^2}\right) \tag{2}$$

$$\frac{\partial u_j}{\partial x} + \frac{\partial w_j}{\partial z} = 0 \tag{3}$$

where x and z are the horizontal and vertical coordinates, the subscripts j indicate the layers, and the parameters t, ρ, ν_e and p represent the time, density, kinematic viscosity of mud and dynamic pressure, respectively.

The separable, periodic solutions for $\hat{u}_j$, $\hat{w}_j$ and $\hat{p}_j$ are assumed as

$$\hat{u}_j(x,z;t) = u_j(z)\exp[i(kx-\sigma t)] \tag{4}$$

$$\hat{w}_j(x,z;t) = w_j(z)\exp[i(kx-\sigma t)] \tag{5}$$

$$\hat{p}_j(x,z;t) = p_j(z)\exp[i(kx-\sigma t)] \tag{6}$$

where k is the unknown complex wave number, namely

$$k = k_r + ik_i \tag{7}$$

Displacements of water surface and interfaces, η_j, are represented by:

$$\eta_j = a_j \exp[i(kx-\sigma t)] \tag{8}$$

where a_j is the amplitude of the displacement of the j_{th} layer and the water surface is expressed as η_1.Substituting the real and imaginary parts of wave number into Eq. (8), the expression of water surface and interfacial displacements can be obtained as

$$\eta_j = a_j \exp(-k_i x)\exp[i(k_r x-\sigma t)] \tag{9}$$

Therefore, the real part of the wave number, k_r, gives the wave length $L=2\pi/k_r$ and its imaginary part, k_i, presents the wave attenuation rate, assuming the exponential wave height decay. Substituting Eqs. (4) and (5) into the continuity Eq. (3) results to

$$u_j = \frac{iw_j'}{k} \tag{10}$$

where the prime represents the differential with respect to z. Introduction of Eq. (10) into Eq. (1) yields an expression for p_j

$$p_j = \frac{\rho_j \nu_{e,j}}{k^2}(w_j'''-w_j'\lambda_j^{\,2}) \tag{11}$$

where

$$\lambda_j^{\,2} = k^2 - i\sigma\nu_{e,j}^{-1} \tag{12}$$

Substituting p_j into the vertical momentum, Eq. (2), yields the forth order differential equation for w_j

$$w_j''''-(k^2+\lambda_j{}^2)w_j''+k^2\lambda_j{}^2 w_j=0 \tag{13}$$

The solutions can be obtained as

$$w_j(z)=A_j\sinh k(\sum_{n=1}^{j}d_n+z)+B_j\cosh k(\sum_{ne1}^{j}d_n+z)+$$

$$C_j\exp[\lambda_j(\sum_{n=1}^{j-1}d_n+z)]+D_j\exp[-\lambda_j(\sum_{ne1}^{j}d_n+z)] \tag{14}$$

where d_n is the thickness of n_{th} layer. The complex constants A_j, B_j, C_j, D_j, and the unknown variables k and a_j are determined from the boundary conditions.

5N boundary conditions are required for a viscous fluid model of N layers. The unknown constants and variables are determined from the boundary conditions at the water surface, the interfaces and the rigid bottom. The details can be found in Tsuruya et al. (1987).

Rheological Model of Mud

Proper rheological model of mud should be adopted in order to investigate wave-mud interaction. Mud in general can range from being a highly rigid and weakly viscous material to one that can be approximated as a purely viscous fluid, depending on the properties of the constituent sediment and the ambient fluid. Considering the complexity of rheological behavior, the visco-elastic-plastic model has been adopted in the present study to develop a predictive behavior model for wave-mud interaction (Shibayama and An 1993). The constitutive equations are expressed as:

$$\sigma_{ij}=2\mu_e\dot{e}_{ij} \tag{15}$$

$$\mu_e=\mu_1+\frac{iG}{\omega}\qquad \text{for}\quad (\frac{1}{2}\sigma_{ij}\sigma_{ij}\le\tau^2{}_y) \tag{16}$$

$$\mu_e=\mu_2+\frac{\tau_y}{\sqrt{4\,|\,\Pi_e\,|}}\ \text{for}\ (\frac{1}{2}\sigma_{ij}\sigma_{ij}>\tau^2{}_y) \tag{17}$$

where σ_{ij} is the deviator part of stress tensor, $\dot{e}_{ij}$ is the deviator part of strain rate tensor, G is the shear modulus of elasticity, μ_1 is the viscosity of mud in the viscoelastic state, μ_2 is the viscosity of mud in the viscoplastic state, τ_y is yield stress, ω is the angular frequency of wave and $4|\,\Pi_e\,|$ is expressed as

$$4\left|\Pi_e\right| = 2(\frac{\partial u}{\partial x})^2 + 2(\frac{\partial w}{\partial z})^2 + (\frac{\partial u}{\partial z} + \frac{\partial w}{\partial x})^2 \tag{18}$$

where u and w are velocity components in x and z direction, respectively. The rheological viscoelastic parameters of mud, i.e. shear modulus and viscosity, are calculated from the empirical equations offered by Shibayama and An (1993):

$$\mu_1 = 10^{(3.353-9.56\times10^{-3}W)} \times T \tag{19}$$

$$\log G = 3.761 - 1.05\times10^{-2}W + (0.147 - 3.38\times10^{-3}W)\times\log T - (0.522 - 1.23\times10^{-3}W) \tag{20}$$

where T is the wave period and W is the water content ratio of fluid mud (%). The viscoplastic parameters, μ_2 and τ_y were adopted from the laboratory experiments of Tsuruya et al. (1987):

$$\tau_y = 1.494\times10^6 W^{-2.452} \tag{21}$$

$$\mu_2 = 8.465\times10^3 W^{-1.344} \tag{22}$$

Equivalent Viscosity. In the viscoplastic state of the visco-elastic-plastic model, the objective $4|\Pi_e|$ of the representative viscosity, can be approximated by a viscoelastic field using an iterative method. The real parts of Eqs. (4) and (5) are written as

$$\hat{u}_j(z) = \left|u_j\right|\exp(-k_i x)\cos(k_r x - \sigma t + \alpha_j) \tag{23}$$

$$\hat{w}_j(z) = \left|w_j\right|\exp(-k_i x)\cos(k_r x - \sigma t + \beta_j) \tag{24}$$

where α_j and β_j are the arguments of u_j and w_j, respectively. Taking the partial derivatives of Eqs. (23) and (24) with respect to x and z

$$\frac{\partial \hat{u}_j}{\partial x} = -\left|k\right|\left|u_j\right|\exp(-k_i x)\sin(k_r x - \sigma t + \alpha_j + \theta_k) \tag{25}$$

$$\frac{\partial \hat{u}_j}{\partial z} = -\left|u'_j\right|\exp(-k_i x)\cos(k_r x - \sigma t + \alpha'_j) \tag{26}$$

$$\frac{\partial \hat{w}_j}{\partial x} = -|k||w_j|\exp(-k_i x)\sin(k_r x - \sigma t + \beta_j + \theta_k) \tag{27}$$

$$\frac{\partial \hat{w}_j}{\partial z} = -|w'_j|\exp(-k_i x)\cos(k_r x - \sigma t + \beta'_j) \tag{28}$$

where α'_j and β'_j and θ_k are the arguments of u'_j, w'_j and k, respectively. Substituting Eqs. (25) ~ (28) into Eq. (3) leads to

$$4|\Pi_e| = \frac{1}{2}\{|k|^2(2|u_j|^2 + |w_j|^2) + (|u_j'|^2 + 2|w_j'|^2)$$

$$- 2|u_j'||w_j||k|\sin(\beta_j + \theta_k - \alpha_j')\}\exp(-2k_i x) \tag{29}$$

Implementation in SWAN

The evolution of wave at SWAN is governed by wave action balance equation (Booij et al. 1999) expresed as,

$$\frac{dN}{dt} = \frac{\partial N}{\partial t} + \frac{\partial}{\partial x}(c_x N) + \frac{\partial}{\partial y}(c_y N) + \frac{\partial}{\partial \sigma}(c_\sigma N) + \frac{\partial}{\partial \theta}(c_\theta N) = \frac{S}{\sigma} \tag{30}$$

$N= E/\sigma$ is the action density (E is energy density), c_x and c_y are propagation velocities in x and y direction respectively, c_σ is propagation velocity in σ (relative frequency) space and c_θ is propagation velocity in θ (propagation direction) space. S includes all sources and sinks terms. A spectral sink term is needed to describe the wave-mud interaction (Zhang and Zhao 1999). Considering wave spectrum in space of σ, θ and exponential decay of wave height due to wave mud interaction,

$$E(\sigma_i, \theta_i) = \frac{1}{\Delta\sigma \cdot \Delta\theta} \cdot \frac{1}{2} a_{ix}{}^2 \tag{31}$$

$$a_{ix} = a_{i0} e^{-k_i (x - x_0)} \tag{32}$$

where a_{i0} is the amplitude of i-th wave component at point $x=x_0$, a_{ix} is the amplitude of i-th wave component at distant x from point x_0, and σ_i, θ_i are corresponding frequency and direction, the following equation can be derived for sink term in the right hand side of the action balance equation due to wave mud interaction.

$$S_{Mud} = 2k_i c N \tag{33}$$

where c is the propagation velocity and k_i is attenuation coefficient calculated in wave mud interaction model. Above mentioned dissipation term is implemented in SWAN to simulate wave-mud interaction.

MODEL PERFORMANCE AND DISCUSSION

Since wave attenuation of muddy banks in Louisiana coast has been well-known (Gade 1957; Tubman and Suhayda 1976) and significant measurement data are available, the model was used to simulate wave evolution along the Louisiana coast during a storm event which occurred from Jan 29 to Feb 01, 2001. In Fig. 2, CSI3 and CSI5 stations are parts of WAVCIS (Wave-Current Information System, wavcis.cis.lsu.edu), operated by Coastal Studies Institute of Louisiana State University. CSI3 is located in muddy part of the coast while CSI5 is on sandy bottom (Sheremet et al. 2003).

For this simulation wind data are extracted and interpolated on computational grid from ten metrological stations (Fig. 3) of NDBC (National Data Buoy Center), and spectral wave measurement in Buoy 42001 was used as offshore wave boundary condition.

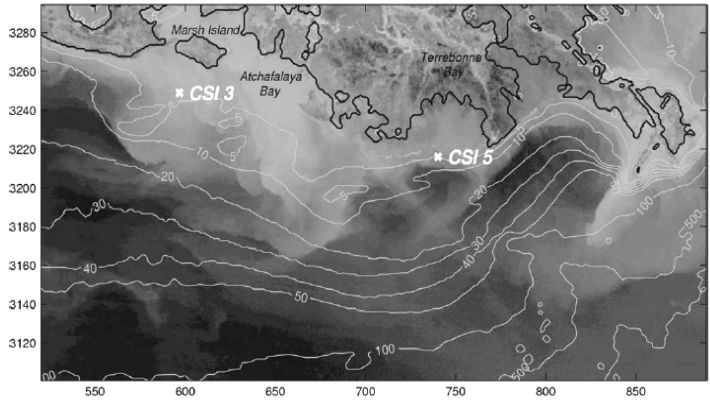

Fig. 2. Louisiana coast and shelf, Coordinates are in Kilometers and contours in meter (Terra-1 MODIS satellite image; Earth Scan Lab, LSU; Adopted from Sheremet et al., 2005)

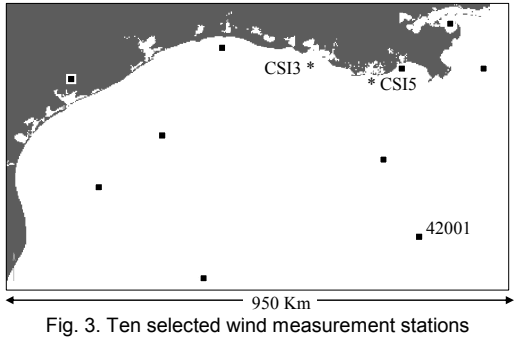

Fig. 3. Ten selected wind measurement stations

The simulation is conducted considering two scenarios. First, assuming no fluid mud layer. Second, 100 (cm) of high sediment concentration layer above the bed covering 8 (Km) around the CSI3. It was assumed that viscosity of the water-sediment mixture is two orders of magnitude greater than viscosity of water (Sheremet et al. 2005).

Fig. 4 shows spectral evolution during above mention storm at CSI3 and CSI5 for the two scenarios as well as measurement. Measurement obviously shows less spectral density in CSI3 than CSI5 (Fig.4-a). Fig. 4-b shows spectral evolution for the first scenario. With no mud dissipations, there is still less intensive spectral density in CSI3 comparing to CSI5. It can be due to the location of CSI3 which is surrounded by very shallow water (Fig. 2) resulting significant refraction and bottom dissipation.

The simulation results for second scenario shows significant wave attenuation. Higher attenuation is recognized for swells (waves with period greater than 5 seconds) since they have more interaction with bottom. The attenuation of short waves in measurement can be due to surface-interface wave interaction and three-wave interaction (Sheremet et al. 2005).

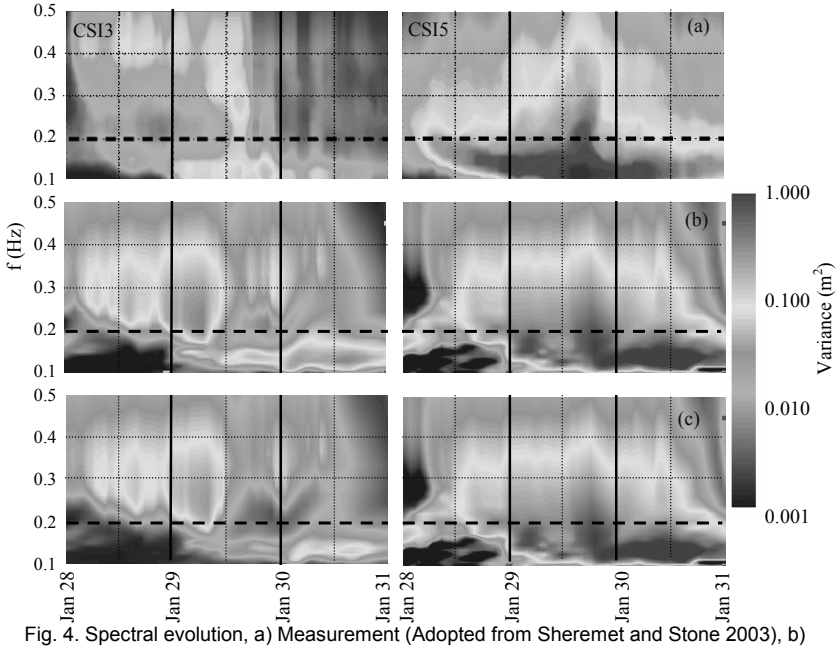

Fig. 4. Spectral evolution, a) Measurement (Adopted from Sheremet and Stone 2003), b) Simulated wave height no fluid mud, c) Simulated wave height with fluid mud

CONCLUSION

The wave attenuation on fluid mud was introduced as a part of dissipation terms in SWAN considering a multi-layer visco-elastic-plastic model. The model was used for simulation of a storm event from Jun 29 to Feb 01, 2001 in coast of Louisiana. The simulation result shows considerable wave height attenuation at CSI3 due to shoals around this point and wave-mud interaction.

REFERENCES

Booij, N., Ris R.C. and Holthuijsen L.H. (1999). "A third generation wave model for coastal regions: Part I: model description and validation," *Journal of Geophysical Research*, 104, p. 7649-7666.

Gade, H. G. (1957). "Effects of a non-rigid impermeable bottom on plane surfacewaves in shallow water," Ph.D. thesis, 35 pp., Texas A&M Univ., CollegeStation, Tex.._

Oveisy, A. and Soltanpour M. (2005). "Simulation of wave transformation on muddy coasts," CD *Proceeding 5th International Conference on Coastal Dynamics,* CD-ROM Published by ASCE.

Oveisy, A., Soltanpour M., Shibayama T. and Masuya Y. (2006), "Numerical and experimental study on wave propagation over mud," *30th International Conference on coastal Engineering* (Under publication)

Shibayama, T. and An, N. N. (1993). "A visco-elastic-plastic model for wave-mud interaction," *Coastal Engineering in Japan* 36, No. 1, p. 67-89.

Sheremet, A., Mehta A.J., Liuc B. and Stone G.W. (2005). **"**Wave–sediment interaction on a muddy inner shelf during Hurricane Claudette," *Estuarine, Coastal and Shelf Science* 63 p. 225–233.

Sheremet, A. and Stone G.W. (2003). "Wave dissipation due to heterogeneous sediment on the inner Louisiana shelf," *Proceedings of Coastal Sediments'03* p. 120-121.

Sheremet, A., Kaihatu J. M., Stone G.W., Zhang X. (2003). "Wave evolution in cohesive sedimentary environment: open problem," *GCAGS/GCSSEPM Transactions*, Volume 53, p. 765-771.

Tubman, M.W. and Suhayada J.N. (1976). "Wave action and bottom movements infine sediments_," *Proceedings of 15th International Conference on coastal Engineering.*

Tsuruya, H., Nakano, S. and Takahama, J. (1987). "Interaction between surface waves and a multi-layered mud bed," Rep. Port and Harbor Res. Inst., Ministry of Transport, Japan, 26, No. 5, p. 141-142.

Zhang Q. H., Zhao Z. D. (1999). "Wave-mud interaction: wave attenuation and mud mass transport," *Proceedings of Coastal Sediments'99*, Vol. 3, pp. 1867-1880

A FINE SEDIMENT TRANSPORT MODELING FRAMEWORK AND ITS APPLICATION TO FLUID MUD PROCESSES

Tian-Jian Hsu and Minwoo Son

University of Florida, Civil and Coastal Engineering, Gainesville, FL 32611, USA.

Abstract: A fine sediment transport modeling framework for estuary and coastal environments is developed based on simplified multiphase formulation. The model incorporates turbulence-sediment interactions in a two-equation turbulence closure and a rheology closure based on concentrated viscous suspension. The model has been demonstrated to capture the characteristics of tidal driven lutocline behavior observed at Amazon shelf and wave-supported gravity-driven mudflows observed at Po River prodelta (Hsu et al. 2007). However, these results are obtained by specifying an averaged floc diameter that is independent of flow condition. The floc density is then calculated by a prescribed fractal dimension. In this paper, we report a new but preliminary extension of this model with a more realistic formulation of floc dynamics for steady equilibrium condition. It is found that detailed floc dynamics is sensitive to the predicted suspended mud concentration and flow rate under a steady current.

INTRODUCTION

Understanding the fate of fine terrestrial sediments in the coastal ocean, including the initial sediment deposition from the river plume and the subsequent sediment resuspension, is of great importance for estuarine and coastal morphology. In this paper, a new modeling framework for fine sediment transport based on simplified multiphase formulation (Hsu et al. 2007) is introduced and we report new but preliminary model extensions toward a complete description of floc aggregation and break-up processes.

Fluid mud is highly concentrated suspended sediment from concentrations of about 10 g/l to a few hundred g/l above the consolidated bed (Ross & Mehta 1989). Since the last decade, multi-disciplinary approaches were adopted in several major field research programs, such as, AMASSEDS (e.g., Nittrouer et al. 1991), STRATAFORM (e.g.,

Nittrouer & Kravitz, 1996), EuroSTRATAFORM (e.g., Sherwood et al. 2004), and several others. Research findings resulted from these studies had advanced our understanding on fine sediment transport processes. However, they have also revealed some unexpected small-scale sediment transport processes that can not be captured with the conventional modeling approach. One of these interesting sediment transport problems is, for example, the wave-supported gravity driven mudflows (e.g., Wright et al., 2001; Kineke et al. 1996; Traykovski et al. 2000).

Accurate prediction of fine-sediment transport requires detailed water column models that resolve time-dependent flow velocity and sediment concentration (Winterwerp and van Kesteren, 2004). In general, the dynamics of sediment transport is a multiphase phenomenon. A multiphase approach provides rigorously derived balance equations that incorporate fluid-sediment interactions and granular rheology (Brennen 2005) and hence allows modeling transport continuously from concentrated aggregate network to dilute suspension. Existing water column models for mud suspension (e.g., Winterwerp 2001) incorporate the damping of flow turbulence due to sediment induced stratification, which is a crucial mechanism for the formation of fluid mud. However, the rheology of sediment is often neglected. In order to model the concentrated regime of mud consolidation and fluidization (e.g., Gibson et al. 1967) and other important applications, such as the dissipation of wave energy on muddy coasts (e.g., Dalrymple and Liu, 1978; Maa and Mehta 1987; Sheremet and Stone 2003), the rheology of mud shall be incorporated into the existing transport model.

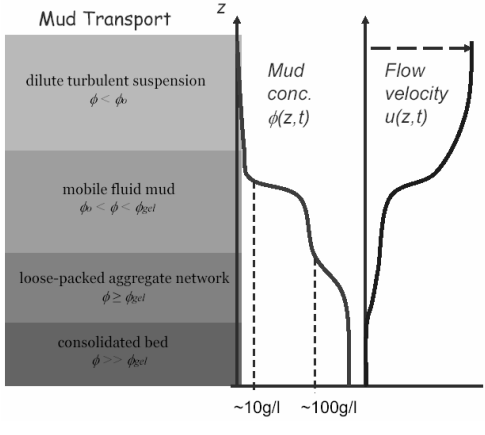

Fig. 1: Schematic description of mud transport according to Ross & Mehta (1988). The 1DV model presented in this paper calculates fluid mud transport above the concentrated aggregate network with $\phi<\phi_{gel}$.

Recently, Hsu et al. (2007) proposed a new fine sediment transport modeling framework based on simplified multiphase flow formulation. The 1DV water column model developed by Hsu et al. (2007) calculates the turbulent flow and mud floc concentration with given (constant) floc diameter and fractal dimension. Without incorporating detailed floc dynamics, they demonstrate that the model is able to capture the characteristics of tidal driven lutocline behavior observed at Amazon shelf (Kineke et al. 1996) and wave-supported gravity-driven mudflows observed at Po River prodelta (Traykovski et al. 2007). This is because the most important mechanism controlling the fluid mud dynamics appears to be the damping of carrier flow turbulence due to sediment (e.g., Trowbridge and Kineke 1994; Winterwerp 2001). However, in order to develop a complete fluid mud model, detailed floc dynamics must be incorporated. After a brief description on the model formulation, we focus on the new model implementation on the floc dynamics following Winterwerp (1998). Preliminary results with floc dynamics incorporated are presented.

MODEL FORMULATION

We consider sediment of diameter D, density s transported in a bottom boundary layer that is locally uniform in the cross-shore x and alongshore y directions. Assuming that fine sediment follows the ensemble-averaged carrier fluid velocities closely, the flow momentum equations for cross-shelf u and alongshelf v velocities are:

$$\frac{\partial u}{\partial t} = \frac{-1}{\rho^f(1-\phi)}\frac{\partial P}{\partial x} + \frac{-1}{\rho^f(1-\phi)}\left[\frac{\partial \tau_{xz}^f}{\partial z} + \frac{\partial \tau_{xz}^s}{\partial z}\right] + g_x\left[\frac{s\phi}{1-\phi}\right] \tag{1}$$

and

$$\frac{\partial v}{\partial t} = \frac{-1}{\rho^f(1-\phi)}\frac{\partial P}{\partial y} + \frac{-1}{\rho^f(1-\phi)}\left[\frac{\partial \tau_{yz}^f}{\partial z} + \frac{\partial \tau_{yz}^s}{\partial z}\right] + g_y\left[\frac{s\phi}{1-\phi}\right] \tag{2}$$

with ρ^f the fluid density, $s = \rho^m / \rho^f$ the sediment specific gravity and g_x, g_y the gravitational acceleration in the cross-shore and alongshore directions. For cohesive sediment, D is considered to be the floc diameter and the specific gravity of the floc is calculated by ρ^m, the floc density (see equation (5) in the next section). In the momentum equations (1) and (2) the flow momentum transport is caused by both fluid and sediment stresses τ_{xz}^f, τ_{xz}^s. The gravitational term contains sediment concentration and allows fluid flow to be driven by downslope gravitational force of the sediment. The cross-shore $\partial P/\partial x$ and alongshore $\partial P/\partial y$ pressure gradients are given as a prescribed flow forcing of the bottom boundary layer flow.

The sediment volume concentration ϕ is calculated by

$$\frac{\partial \phi}{\partial t} = -\frac{\partial}{\partial z}\left[\phi(1-\phi)T_P\left(1-s^{-1}\right)g_z - \frac{\nu_t}{\sigma_c}\frac{\partial \phi}{\partial z} + \frac{T_p}{\rho^s}\frac{\partial \tau^s_{zz}}{\partial z}\right] \tag{3}$$

The first two terms on the right-hand-side of (3) are the settling and turbulent suspension with T_p the particle response time calculated based on drag for sphere with correction for the effect of hindered settling using Richardson and Zaki (1954). The turbulent suspension is calculated here using an eddy viscosity. The third term on right-hand-side of (3) is the vertical gradient of sediment intergranular normal stress, which serves as an additional suspension mechanism for sediment. This is important in concentrated region of mud transport, including consolidation and fluidization of the mud bed (see figure 1, the region with ϕ near or greater than ϕ_{gel}).

Turbulence and rheology closures

In this study, the fluid turbulence and turbulent suspension are calculated by an eddy-viscosity with a two-equation k-ε closure. The effect of sediment on damping the carrier flow turbulence can be appropriately considered by deriving the balance equation of fluid turbulence kinetic energy (TKE) from the multiphase momentum equations (e.g., Hsu and Liu 2004). Detailed implementation on turbulence and its interaction with sediment are reported in Hsu et al (2007) and it not repeated here.

The present model also requires appropriate constitutive relations for mud rheology. Most prior studies on mud transport neglect rheology in the "mobile fluid mud" regime (see figure 1) but focus on sediment effective normal stress closure for mud consolidation (e.g., Gibson et al 1967). The rheology for sediment shear stress is often neglected in mud transport study, however, has long been considered important for studying hydrodynamic energy dissipation using a simple "layered" parameterizations for a high viscosity (e.g., Dalrymple and Liu 1978) or visco-elastic formulation (e.g., Maa and Mehta 1987). Because in the present model both the flow velocities and sediment concentration are calculated continuously across the water column, we adopt a set of rheology closures for both sediment shear and normal stresses that explicitly depends on concentration and shear rate based on concentrated viscous suspension theory (e.g., Zarraga et al. 2004). Detailed implementation of the rheology closure of the present model is referred to Hsu et al. (2007). For fluid mud process above the concentrated aggregate network, the mud concentration is much smaller than gelling concentration and the rheology is of less importance.

Sediment bottom boundary conditions

We use the continuous deposition concept here for the bottom boundary condition of cohesive sediments (e.g., Sanford and Halka 1993). The following simple parameterization for erosion (upward) flux is adopted:

$$E = m\left(\frac{\tau_b}{\tau_c} - 1\right) = mS \tag{4}$$

with m an empirical coefficient, τ_c the critical bottom stress. The bottom stress τ_b is calculated every time step through the flow velocity at the first-grid point above the bed based on logarithmic-law for rough bed. In reality, τ_c and m also depends on the amount of mud eroded and consolidation processes. Complete information requires in-situ sampling and characterization. Here, m and τ_c are considered to be constant for simplicity. Unless stated otherwise, τ_c is set to be 0.05 Pa in this paper and m is specified in the "Model Results" section.

Turbulence induced flocculation

When modeling fluid mud using the present model, the primary particle is not directly calculated. Instead, we prescribe aggregate (floc) diameter D and fractal dimension n_f (Winterwerp and van Kesteren, 2004). The density of the mud floc is given as

$$\rho^m = \rho^f + \left(\frac{D_0}{D}\right)^{3-n_f}\left(\rho^s - \rho^f\right) \tag{5}$$

with D_0 and ρ^s the diameter and density of the primary particle, taken to be $D_0 = 4\ \mu m$ and ρ^s=2650 kg/m^3. ρ^m is used to calculate the settling term in the balance equation (3) of concentration. The model calculates directly the mud floc volume concentration. The mass concentration c can be calculated from volume concentration ϕ as (Winterwerp 1998):

$$c = \phi\rho^s\left(\frac{D_0}{D}\right)^{3-n_f} \tag{6}$$

The floc dynamics is one of the most unique aspects of cohesive sediment. As summarized by Winterwerp (1998), the floc break-up and flocculation processes are in general controlled by several mechanisms but the dominant mechanism for coastal cohesive sediment is due to flow turbulence. Cohesive sediment particles, carried by turbulent eddies, can collide and form larger flocs. On the other hand, strong turbulent shear can also cause floc break-up. Based on such paradigm, Winterwerp (1998) propose a governing equation to describe the evolution of floc diameters:

$$\frac{dD}{dt} = K_A cGD^2 - K_B G^{3/2} D^2\left(D - D_0\right). \tag{7}$$

For simplicity, equation (7) is shown here for a special case with fractal dimension n_f=2, with K_A, K_B empirical coefficients and G the dissipation parameter calculated by turbulent dissipation rate ε and fluid viscosity ν:

The first term on the right-hand-side of equation (7) is a source term that represents the flocculation process. For higher concentration, it is more likely that flocculation occurs through collisions between floc particles carried by energetic turbulent eddies. The second term on the right-hand-side of (7) is a sink term that represents the floc break-up process due to shear generated by the turbulent eddies. According to (7), a simple relation for equilibrium floc size D_e is obtained for $dD/dt=0$:

$$D_e = D_0 + \frac{K_A c}{K_B \sqrt{G}} \tag{9}$$

Because the floc size is unlikely to be greater than the Kolmogorov length scale, an upper limited for D_e is also adopted here:

$$D_e = \min\left[D_0 + \frac{K_A c}{K_B \sqrt{G}}, \left(\frac{\nu^3}{\varepsilon}\right)^{1/4} \right] \tag{10}$$

In this paper, we present preliminary results of using (10) for equilibrium floc size. Given a prescribed fractal dimension $n_f=2$, the floc diameter and floc density are determined by equation (10) and (5), respectively. The dissipation parameter defined in (8) is calculated by model solution of turbulent dissipation rate ϵ through the k-ϵ closure.

MODEL RESULTS

A 1-DV water column numerical model is developed to calculate equations (1)-(3) for flow velocities and floc concentration with k-ϵ turbulence closure and appropriate rheology closure. The sediment flux boundary condition shown in equation (4) is utilized in this paper. Model results for tidal driven fluid mud and wave-supported gravity-driven mudflows without explicit consideration of floc dynamics are presented in Hsu et al. (2007) and are not repeated here. To demonstrate the new model capability for floc dynamics, equilibrium floc size formulation (10) is utilized.

Because the flocculation timescale can be very large (Winterwerp 1998), we exam fluid mud transport under a steady current. A constant pressure gradient is applied in the numerical model to drive the steady current (Hsu et al. 2007). The numerical model is initialized with zero flow velocities and mud concentration and marches in time until steady state solutions are obtained. Using suggested values of $K_A=14.6$ m^2/kg, K_B=14000 s$^{0.5}$/m^2 (Winterwerp 1998), model results for flow velocity, concentration, floc diameter and floc density are shown in Fig. 2 (solid curves). Because the current boundary layer extends to the entire water depth, considerable amount of sediment is suspended near the top of the water column. The floc size is smaller in the upper water column due to lower mud concentration. Near the bed the floc size reaches its maximum value about 500 μm.

Within the lower 20 cm above the bed, the floc size is limited by its maximum value, the Kolmogorov length scale (ϵ is usually very large near the bed). Due to small fractal dimension used (n_f=2) and large floc size calculated by the model, the resulting floc density (about 1020 to 1050 kg/m^3) is only slightly larger than the water density (1000 kg/m^3).

According to equation (10), the effects of flocculation due to higher concentration and floc break-up due to higher turbulence are controlled by the relative magnitudes between K_A and K_B. Therefore, model results (dashed curves in Fig. 2) are also shown for the same flow conditions but with K_A=1.46 m^2/kg (i.e., reduced by an order of magnitude). Due to reduced flocculation effect, the floc diameter becomes smaller (dashed curve in panel (c) is ranging from 150 μm near the bed to 50 μm far from the bed) when compared with results obtained by specifying larger K_A (solid curve). Consequently, the floc density becomes larger (dashed curve in panel (d)) according to equation (5). Notice that due to smaller floc diameter, the settling velocity is smaller (not shown) and more sediment is suspended under the same steady flow forcing (dashed curve in panel (b)). Visual inspection also suggests that the overall flow rate is larger for smaller flocs (dashed curve in (a)) because turbulence is damped more significantly due to more suspended sediments. This is the so-called the drag reduction due to the presence of sediment (Winterwerp 2001). Model results indicate that detailed floc dynamics has important effects on the overall suspended mud concentration and flow rate.

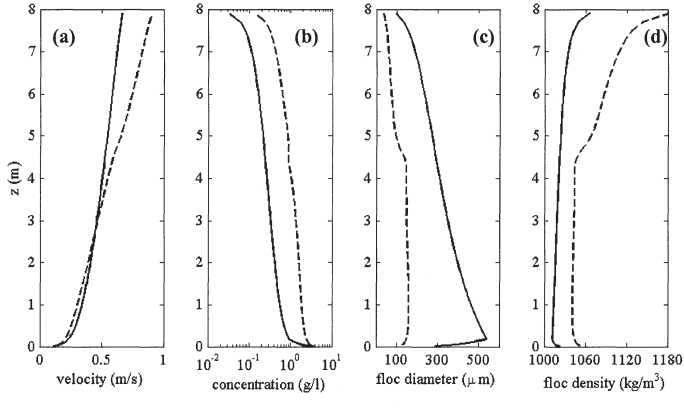

Fig. 2: Model results for (a) flow velocity, (b) mud concentration, (c) floc diameter and (d) floc density. Solid curves are model results with K_A=14.6 m^2/kg and dashed curves are model results with smaller K_A=1.46 m^2/kg. In both cases, the flow forcing used to drive the steady flow are identical. The *m* value in equation (4) for bottom erosion fluxes are specified in such way that both cases have the same magnitude of concentration at the bed.

both cases have the same magnitude of concentration at the bed.

CONCLUSION

Equilibrium floc diameter formulation of Winterwerp (1998) is incorporated in a fluid mud model to calculate steady boundary layer flow and mud suspension. The floc dynamics appears to be important to the overall mud suspension and resulting flow rate. More detailed non-equilibrium floc dynamic formulation shall be implemented in order to study fluid mud transport under tidal flow and waves.

ACKNOWLEDGEMENTS

Funding of this study is provided by U. S. Office of Naval Research (Coastal Geoscience) and South Florida Water Management District.

REFERENCES

Brennen, C. E., (2005) *Fundamentals of Multiphase Flow*, Cambridge University Press.

Dalrymple, R. A., and Liu, P. L.-F., (1978) Waves over soft mud beds: a two-layer fluid mud model. *Journal of Physical Oceanography*, 8, 1121-1131.

Gibson RE, Englund GL, Hussey MJL. (1967) The theory of one-dimensional consolidation of saturated clays. I. Finite non-linear consolidation of thin homogeneous layers. *Geotechnique*, 17(3), 261-273.

Hsu, T.-J. and Liu, P. L.-F., (2004), Toward modeling sand suspension under waves, *J. Geophys.Res.*, 109(C6), C06018.

Hsu, T.-J., P. A. Traykovski, G. C. Kineke, (2007) On modeling boundary layer and gravity-driven fluid mud transport, in press.

Kineke, G. C., Sternberg, R. W., Trowbridge, J. H., Geyer W. R., (1996), Fluid-mud processes on the Amazon continental shelf, *Cont. Shelf Res.*, 16, No. 5/6, 667-696.

Maa, P. -Y., and Mehta, A. J. (1989) Mud erosion by waves: a laboratory study, *Cont. Shelf Res.*, 7(11/12), 1269-1284.

Nittrouer, CA., DeMaster, D.J., Figueiredo, A.G. and Rine, J.M., 1991. AmasSeds: an interdisciplinary investigation of a complex coastal environment. *Oceanography*, 4, 37.

Nittrouer, C.A., and Kravitz, J.H., (1996). STRATAFORM: A Program to study the creation and interpretation of sedimentary strata on continental margins, *Oceanography*, 9(3), 146–152.

Richardson, J. F., and W. N. Zaki, (1954), Sedimentation and fluidization, part 1, *Trans. Inst. Chem.Eng.*, 32, 3553.

Ross, M. A., and Mehta A., (1989) On the mechanics of lutoclines and fluid mud, *J. Coast. Res.*, special issue 5, 51-61.

Sanford, L. P., and Halka, J. P., (1993), Assessing the paradigm of mutually exclusive erosion and deposition of mud, with examples from upper Chesapeake Bay, *Marine Geology*, 114, 37-57.

Sherwood C. R., J. W. Book, S. Carniel, L. Cavaleri, J. Chiggiato, H. Das, J. D. Doyle, C. K. Harris, A. W. Niedoroda, H. Perkins, P.-M. Poulain, J. Pullen, C. W. Reed, A. Russo, M. Sclavo, R. P. Signell, P. Traykovski and J. C. Warner, (2004), Sediment dynamics in the Adriatic Sea investigated with coupled models. *Oceanography*, 17(4), 58–69.

Sheremet, A., and G. W. Stone, (2003) Observations of nearshore wave dissipation over muddy sea beds, *J. Geophys. Res.*, 108(C11), 3357, doi:10.1029/2003JC001885.

Traykovski, P., Geyer W. R., Irish J. D., Lynch, J. F., (2000) The role of wave-induced fluid mud flows for cross-shelf transport on the Eel river continental shelf. *Cont. Shelf. Res.*, 20, 2113-2140.

Trowbridge, J. H., and Kineke, G. C., (1994), Structure and dynamics of fluid mud on the Amazon continental shelf. *J. Geophys. Res.*, 99(C1), 865-874.

Winterwerp, J. C., (1998) A simple model for turbulence induced flocculation of cohesive sediment, *J Hydraul. Res*., 36(3), 309-327.

Winterwerp, J. C., (2001) Stratification effects by cohesive and noncohesive sediment, *J. Geophys. Res.*, 106(C10), 22559-22574.

Winterwerp, J. C. and van Kesteren W. G. M., (2004) Introduction to the physics of cohesive sediment in the marine environments, Elsevier, Netherlands.

Wright, L. D., Friedrichs, C. T., Kim, S. C. and Scully, M. E., (2001), Effects of ambient currents and waves on gravity-driven sediment transport on continental shelves, *Marine Geology*, 175, 25–45.

Zarraga, I. E., Hill, D. A., Leighton, D. T., (2000), The characterization of the total stress of concentrated suspension of noncolloidal spheres in Newtonian fluids, *J. Rheology*, 44(2), 185-220.

FIELD MEASUREMENT OF FINE SEDIMENT TRANSPORT PROCESS AROUND NAVIGATION CHANNEL

Yasuyuki Nakagawa[1] and Hideo Matsumoto[2]

1. Port and Airport Research Institute, Coastal and Estuarine Environment Research Group, Nagase 3-1-1, Yokosuka, 239-0826, JAPAN. y_nakagawa@ipc.pari.go.jp
2. Chugoku Regional Development Bureau, Ministry of Land, Infrastr ucture and Transport, 2-10 Mikawa-cho, Naka-ku, Hiroshima 730-0029, JAPAN. matsumoto-h92y2@pa.cgr.mlit.go.jp

Abstract: The paper presents a set of observed sounding data which shows a tendency of siltation in the access channel for a port in a shallow muddy coast. The data shows the higher siltation rate at offshore part of the channel regardless of occurrence of disturbance by the wind waves. From the data monitored for 25 hours of current and suspended sediment distributions along the channel, apparent increase in the near bottom concentration of suspended sediment were observed around the offshore region of the channel. The high concentration event might be a potential source for the higher rate of siltation in the area. The sediment transport model has been developed for the study site and simulated the sediment transport process mainly dominated by the tidal current as a preliminary work for future study of the estimation of the channel siltation volume.

INTRODUCTION

The understanding of fine sediment transport processes has a significant importance in the economical and ecological aspects of coastal environment. The ability to predict the movement of fine sediments is necessary not only for estimation of a dredging cost to keep the safety ship navigations but also for management of contaminated sediment since that chemicals tend to absorb to fine sediment (e.g. National Research Council, 1997). Siltation in navigation channels and harbor basins at near shore coastal area is mainly caused by wave attacks and several studies have been worked on Japanese ports to minimize maintenance dredging volumes (e.g. Tsuruya et al., 1990). Many ship channels are still necessary to be extended and

dredged in the deeper off shore area for the requirements of economic growth and increase in vessel draft. In a macro- or meso- tidal coastal and estuarine environment, tidal current rather than short wind waves might be a principal external force of the sediment transport processes, resulting in channel siltations, in the relatively deeper region.

In the present study, for the purpose of understanding a shoaling mechanism of a navigation channel dredged through shallow muddy coast, fine sediment transport process especially by the effect of tidal currents are examined by analyses of field data measured in the Suoh-nada sea, Japan. A fine sediment transport model has been developed and the numerical results on the hydrodynamic features of tidal current and suspended sediment concentrations are validated by comparison with the field data as a preliminary work for future applications of siltation rate estimates.

FIELD OBSERVATIONS

Field measurements were carried out in the northern shore of Suoh-nada sea, which is shallow water system with the depth of less than 20 m (Figure 1). Tidal condition of the site could be classified as meso- tidal environment with the range of around 3 meters during spring tide period. A navigation channel with the depth of -12 m from the datum line (D.L.) has been maintained by dredging to the approximately 5 km offshore from the port of Ube through the shallow coastal area (Figure 2). Although further deepening of the channel is required for safety navigations of large draft ships, we should consider minimizing siltation and environmental impacts by the damping of dredged materials for the maintenance of the channel.

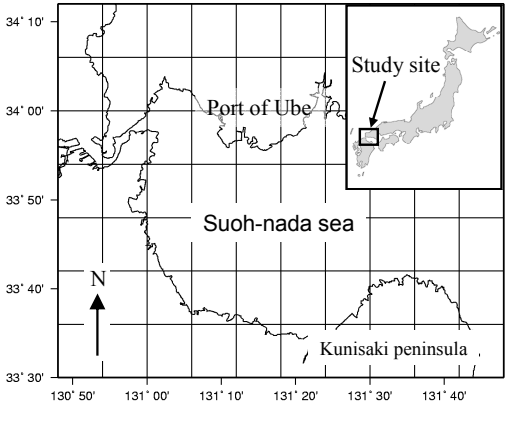

Fig. 1. Location of study site

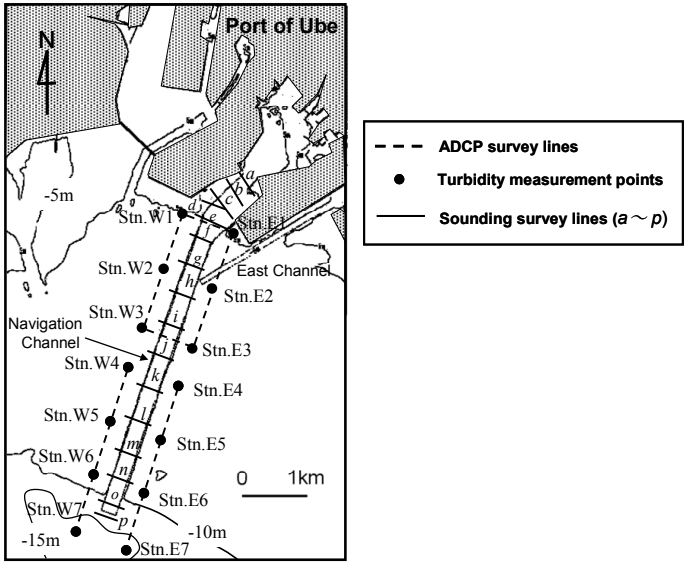

Fig. 2. Survey lines and turbidity measurement points

In order to grasp sediment properties of the study site and characteristics of the channel siltation, several measurements and data analyses were conducted. Bottom sediments were sampled in October, 2002 for the offshore stations (E4, W4, E6, W6 and W7) and in September, 2003 for the shallower stations (E1, W1, E2, W2, E3 and W3) and grain size analyses were carried out. Topography of the navigation channel has been monitored by the port office of the Japanese Ministry of Land, Infrastructure and Transport and some sounding data were used for the study to characterize the bathymetric change in the channel.

For the study of suspended sediment transport dynamics around the channel, current measurements were carried out with an ADCP (RD-Instruments, 1200kHz) towed by a boat running on the lines shown in the Figure 2. The offshore transects along the channel between the stations E4 - E7 and W4 - W7, were measured for 25 hours on October 22 and 23, 2002, and the other onshore transects between the stations E1, E3, W3 and W1 were on September 10 and 11, 2003, respectively. During the current measurement surveys, vertical profiles of suspended sediment concentrations (SSC) at the monitoring points on the ADCP lines were also measured by the operation of optical backscatter sensor (OBS) by another boat when the boat with ADCP run across an each point. OBS data was converted to SSC in mg/l by applying calibrations using sediment samples taken from the study site.

FIELD MEASUREMENTS RESULTS

Sediment properties and Siltation rates

Results of grain size analyses for bottom sediments sampled in the area are summarized in Figure 3. Coarse materials are dominant in the sediment of the shallower area near the port at the stations E1 and W1 and finer components, however, are major in the deeper region and the fraction of silt and clay is over 80 % in weight at the stations E6 and W7.

The channel with the depth of –12 m is maintained by dredging and Figure 4 shows bottom topographies inside and outside of the channel in the cross shore direction. The figure shows also the change in averaged depth during 3 months at each cross

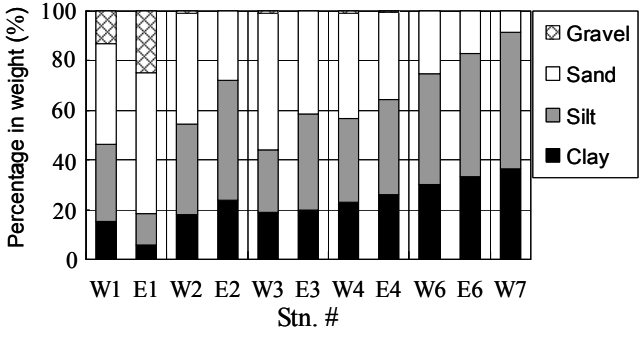

Fig. 3. Sediment characteristics in study area

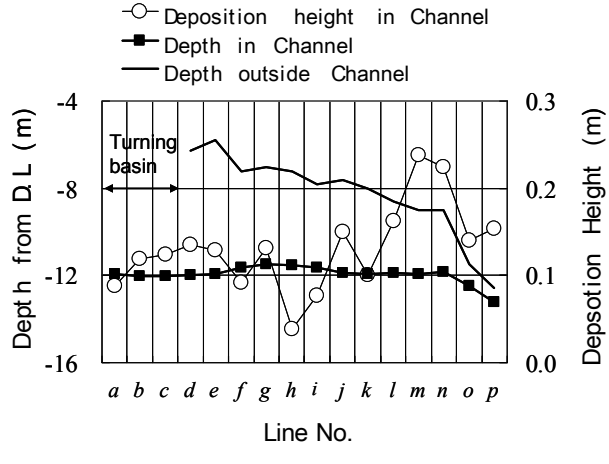

Fig. 4. Topographies inside and outside of channel and deposition height in channel between 3 months from September to December in 2005

section of the channel indicated as lines *a* through *p* in Figure 2. The difference in the averaged depth was analyzed with the sounding data measured in September and December, 2005. The highest deposition with the height of over 20 cm in the channel is observed at the lines *m* and *n* and these are located at the offshore tip of the artificially dredged waterway. Temporal change in the depositions during the monitoring period is shown in Figure 5 considering the data measured in October, 2005. There are high siltation event for all part of the channel during the first half period between September and October, 2005, where a heavy storm attacked the area with the averaged wind speed of over 20 m/s after the first sounding survey. On the other hand, the offshore area at lines *m* and *n* have still experienced higher siltation than other area even in the second half period without a sever storm condition,.

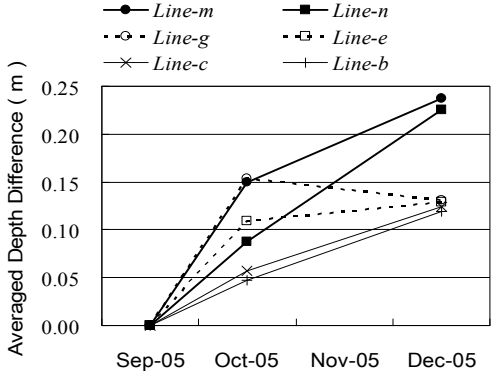

Fig. 5. Change in deposition height in channel during

Current and Suspended Sediment Distributions

Figure 6 (a) and (b) show current field patterns near the sea bed measured during flood and ebb currents of spring tide periods. The principal direction of the currents during both flood and ebb phase are across the navigation channel and it is to the north-west ward during the flood and to the south-east ward during the ebb tide. The current speed is approximately uniform in the offshore measurement line with the speed of over 30 cm/s and it slows down in the shallower region near the port.

In Figure 7, measured tide variation of suspended sediment concentrations (SSC) at 1m above the sea bed at the stations E4 and E6 compared with measured current speeds at the same level. The tide level in the figure is the measured data at the tide station in the port of Ube. The increases in SSC are observed during the ebb and flood periods with higher speed current. The tide variations of SSC at the offshore monitoring stations in the other side of the channel are also of the same pattern with the SSC increases during the ebb and flood tide phase. Vertical profiles of SSC during the high concentration events are shown in Figure 8 and the profiles in the

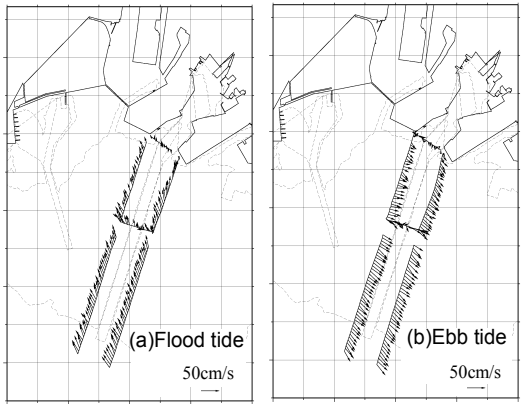

Fig. 6. Observed current vectors of flood and ebb tide current

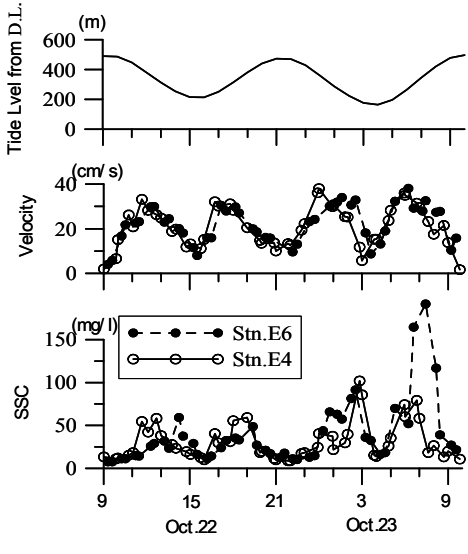

Fig. 7. Observed tide, current speed and suspended sediment concentrations measured at 100 cm above the bed

figure were obtained in the sequential ebb and flood current on October 23, 2002. Each profile clearly shows the rapid increase of SSC near the sea bed and it is considered that the high SSC might be due to resuspension of the sea bottom sediments in the area. The tide variation of SSC with higher concentration near the

bottom observed in the offshore area, however, was not be found in the near shore area, where tidal current becomes weak and coarse sand is dominant in the bottom sediment.

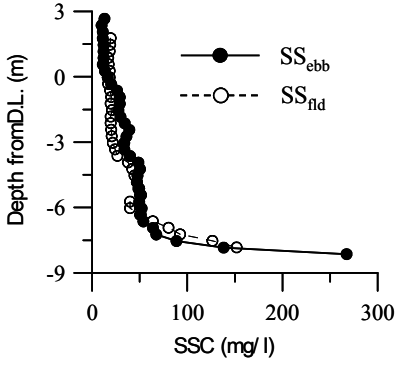

Fig. 8. Observed vertical distributions of suspended sediment concentration during ebb (●) and flood (○) tide

As mentioned above, considering that the high correlation between SSC and tidal current speed variations in the off shore area, resuspension process of the bottom sediments is one of the key factors for the observed increases in SSC. Since the tidal current flows across the navigation channel as shown in Figure 6, it is conceivable that a part of the resuspended fine sediments transported by the current might be deposited inside the channel and cause the higher siltation rate in the off shore area of the channel as shown in Figure 4 and 5.

NUMERICAL MODEL

Model Descriptions

In order to simulate the observed fine sediment transport process by the effect of tidal current in the area, a 3D numerical model was developed. The model consists of classical multilevel hydrodynamic model for flow field and advection-dispersion model for suspended sediment transport. Governing equations are solved with the finite difference scheme in a Cartesian grid system with z-grid in the vertical direction. Under the Boussinesq and hydrostatic approximations, the governing equations for the hydrodynamic model are the following continuity and momentum equations.

$$\left.\begin{aligned} w_{k-1/2} &= w_{k+1/2} - \frac{\partial M_k}{\partial x} - \frac{\partial N_k}{\partial y} \quad (k = 2,3,\cdots,K) \\ \frac{\partial \varsigma}{\partial t} &= w_{3/2} - \frac{\partial M_1}{\partial x} - \frac{\partial N_1}{\partial y} \end{aligned}\right\} \tag{1}$$

$$\frac{\partial M_k}{\partial t} = -\frac{\partial}{\partial x}\left(\frac{M_k^2}{H_k}\right) - \frac{\partial}{\partial y}\left(\frac{N_k M_k}{H_k}\right) - \left(wM\big|_{k-1/2} - wM\big|_{k+1/2}\right)/H_k + fN_k$$
$$- gH_k\left(\frac{\partial \zeta}{\partial x} + \frac{1}{\rho_k}\sum_{i=1}^{k}\left(H_i\frac{\partial \rho_i}{\partial x}\right) - \frac{1}{2}\frac{H_k}{\rho_k}\frac{\partial \rho_k}{\partial x}\right) + \left(\tau_{xz}\right)_{k-1/2} - \left(\tau_{xz}\right)_{k+1/2} + A_x\frac{\partial^2 M_k}{\partial x^2} + A_y\frac{\partial^2 M_k}{\partial y^2} \tag{2}$$

$$\frac{\partial N_k}{\partial t} = -\frac{\partial}{\partial x}\left(\frac{M_k N_k}{H_k}\right) - \frac{\partial}{\partial y}\left(\frac{N_k^2}{H_k}\right) - \left(wN\big|_{k-1/2} - wN\big|_{k+1/2}\right)/H_k - fM_k$$
$$- gH_k\left(\frac{\partial \varsigma}{\partial y} + \frac{1}{\rho_k}\sum_{i=1}^{k}\left(H_i\frac{\partial \rho_i}{\partial y}\right) - \frac{1}{2}\frac{H_k}{\rho_k}\frac{\partial \rho_k}{\partial y}\right) + \left(\tau_{yz}\right)_{k-1/2} - \left(\tau_{yz}\right)_{k+1/2} + A_x\frac{\partial^2 N_k}{\partial x^2} + A_y\frac{\partial^2 N_k}{\partial y^2} \tag{3}$$

where ζ is the water surface elevation, M_k and N_k are the horizontal flow rate in the x- and y-direction of the k-th layer respectively and $w_{k\text{-}1/2}$ is the vertical velocity between the k-th and (k-1)-th layers. In the momentum equations (Eq.(2) and (3)), g is the gravitational acceleration, ρ is the density of the sea water, A_x and A_y are the horizontal eddy viscosity coefficients and τ_{xz} and τ_{yz} are the x- and y-direction components of the shear stress between the layers.

The sediment transport model is expressed as,

$$\frac{\partial C_k H_k}{\partial t} + \frac{\partial M_k C_k}{\partial x} + \frac{\partial N_k C_k}{\partial y} + \left(\left(w - w_f\right)C\right)_{k-1/2} - \left(\left(w - w_f\right)C\right)_{k+1/2}$$
$$- \frac{\partial}{\partial x}\left(K_x H_k\frac{\partial C_k}{\partial x}\right) - \frac{\partial}{\partial y}\left(K_y H_k\frac{\partial C_k}{\partial y}\right) - \left(K_z\frac{\partial C}{\partial z}\right)_{k-1/2} + \left(K_z\frac{\partial C}{\partial z}\right)_{k+1/2} = 0 \tag{4}$$

where C_k represents suspended sediment concentration, w_f is the settling velocity of the suspended particles, and K_x, K_y and K_z are the eddy diffusion coefficients in the x-, y- and z-directions respectively. For the erosion rates of cohesive sediments, so called *Ariathurai-Partheniades'* type of equation is applied in the model as follows (e.g. van Leussen and Dronkers, 1988),

$$E = M\left(\frac{\tau_b}{\tau_e} - 1\right) \quad \text{for } \tau_b \geq \tau_e\,, \quad E = 0 \quad \text{for } \tau_b < \tau_e \tag{5}$$

$$D = w_f C_b \qquad \text{for all } \tau_b \tag{6}$$

where τ_b is the bottom shear stress, τ_e are the critical shear stress for erosion and

deposition and M is the erosion rate coefficient. In order to take the effect of the variability of the sediment quality on the erosion characteristic into account, the critical shear stress for erosion and the erosion rate coefficient depend on the mud content in the bottom sediments.

The parameters such as erosion rate constant and critical shear stress for the erosion flux estimation by Equation (5) are summarized, for examples, in Whitehouse et al. (2000). However the parameters depend on the sediment characteristics site by site and we obtained the parameters by using the relationship between observed bottom shear stress and total suspended load from the field data (Figure 9) in the present study. The erosion rates in the figure were estimated as the time difference of vertically integrated suspended load in the water column with observed SSC profiles. The bottom shear stress, on the other hand, was simply calculated by the quadratic law with observed current speed at 100cm above the sea bed. From the relationships between them for the stations from E4 through E7during the accelerating phase in the figure, erosion rate coefficient, M, is estimated as 0.019 mg/cm^2/min. and τ_{ec} as 0.021 Pa. The method is based on the assumptions of homogeneous of horizontal gradient of SSC and it could be applied reasonably well under such a condition that resuspension of the bottom sediment is dominant for the temporal change in SSC variation (e.g. Hill et al., 2003, Nakagawa et al. 2006).

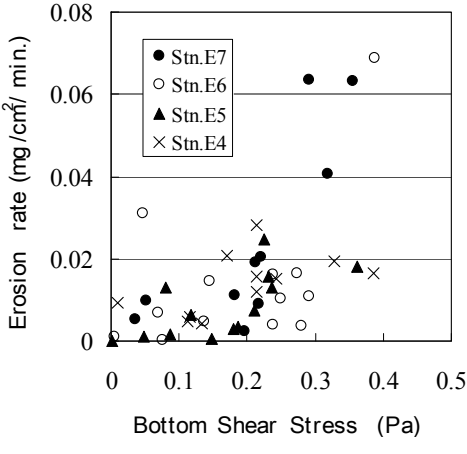

Fig. 9. Relationship between erosion rate and bottom shear stress

Numerical Results

Numerical results for the tide variations of water surface level, current velocities and SSC near the water surface at 100cm beneath and near the sea bottom at 100 cm above are shown in Figure 10 comparing with the field data of 25 hours under the spring tide condition. The model reasonably well reproduces the hydrodynamic

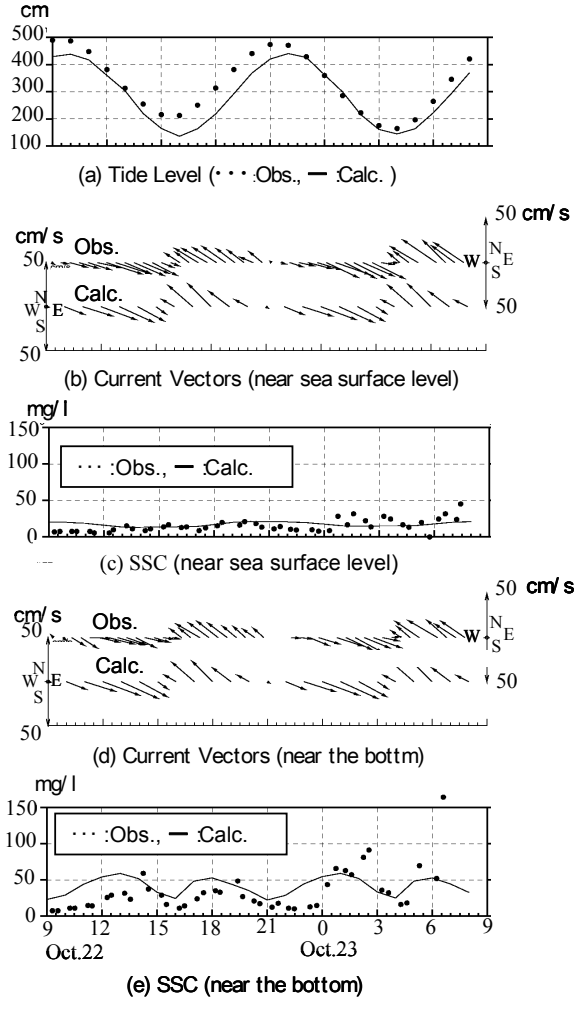

Fig. 10. Comparison between numerical results and observed data for tide, current velocities and SSC near surface and near bottom

features of the tidal currents and does simulate also well the temporal change in SSC especially near the bottom which has high correlation with the current speed variation. Furthermore, computed result of spatial distribution of SSC in the cross shore direction along the survey line is compared with observed data in Figure 11. The figure shows the snap shot at the high concentration event during the ebb tide current. Although the vertical resolution of the model does not so fine with at most 6 layers in

the area, the characteristics of the spatial distribution of SSC are reasonably reproduced by the model with the higher concentration in the offshore and the deeper

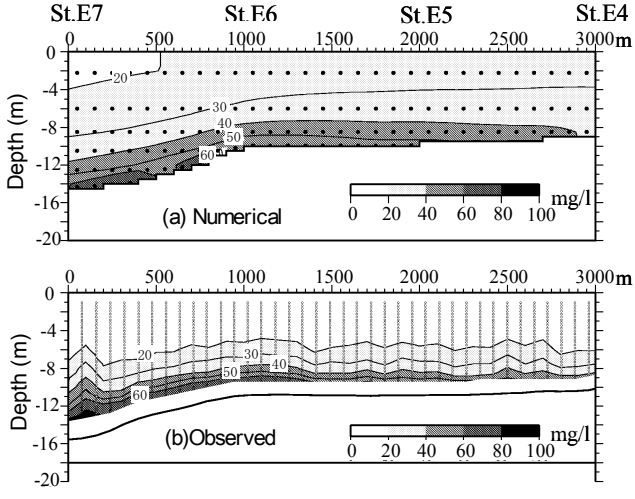

Fig. 11. Contours of numerical and observed data on suspended sediment concentration

area.

CONCLUSION

In this paper, we presented a set of observed sounding data which shows a tendency of siltation in the access channel for the port of Ube in a shallow muddy coast. According to the analyses of the data, the higher siltation rate was found at offshore part of the channel regardless of frequency of disturbance by storm events or wind waves. On the other hand, from the monitoring data of current and suspended sediment concentration, apparent increases in the near bottom concentration of suspended sediment were observed around the offshore region of the channel. The high concentration events are mainly due to the resuspension of the sediment around the channel by the tidal current and it might be a potential source for the higher rate of siltation in the area. The sediment transport model, furthermore, has been developed for the study area and the reasonable results were obtained for the fine sediment transport due to tidal currents. The model will be applied for the study to predict siltation rate in the channel. In a future work of siltation rate estimates in the channel, formation of fluid mud (e.g. Ross and Mehta, 1989) just above the sea bed by the settling of the observed suspended sediment should be also considered and modeled if necessary.

ACKNOWLEDGMENT

The authors would like to sincerely thank the Ube port office of the Ministry of Land, Infrastructure and Transport for their assistance of the field observation.

REFERENCES

Hill, D.C., Jones S.E. and Prandle, D. (2003). "Derivation of sediment resuspension rates from acoustic backscatter time-series in tidal waters," Continental Shelf Research, Vol.23, pp.19-40.

Nakagawa, Y. and Yoshida, H. (2006). "Field observation and modelling suspended fine sediment load in Ariake Bay, Japan," Proceedings for International Conference on Cohesive Sediments (INTERCOH) 2005, In press.

National Research Council, (1997). "Contaminated Sediments in Ports and Waterways," National Academy Press, 295p.

Ross, M. A. and Mehta , A. J. (1989). "On the mechanics of lutoclines and fluid mud," Journal of Coastal Research, Special issue, No.5, pp.51-62.

Tsuruya, H. Murakami, K. and Irie, I. (1990). "Mathematical modeling of mud transport in ports with a multi-layered model - Application to Kumamoto Port -," Technical Report of Port and Harbour Research Institute, Vol.29, No.1, 3-51.

van Leussen, W. and Dronkers, J. (1988). "Physical processes in estuaries:An introduction," in Dronkers, J. and van Leussen, W. (ed.), Physical processes in estuaries, Springer-Verlag, 560p.

Whitehouse, R. Soulsby, R., Roberts, W. and Mitchener, H. (2000). "Dynamics of estuarine muds," Thomas Telford Publishing, 210p.

TIME DEPENDENT MUD FLUIDIZATION AND IRREGULAR WAVE TRANSFORMATION ON MUDDY PROFILES

Mohsen Soltanpour[1], S. Abbas Haghshenas[2], Tomoya Shibayama[3]

1. Department of Civil Eng., K.N. Toosi University of Technology, No.1346, Vali-Asr St., P.C. 19697, Tehran, IRAN, soltanpour@kntu.ac.ir.
2. Department of Civil Eng., K.N. Toosi University of Technology, No.1346, Vali-Asr St., P.C. 19697, Tehran, IRAN, sahaghshenas@sina.kntu.ac.ir.
3. Department of Civil Eng., Yokohama National University, 79-5 Tokiwadai, Hodogaya-ku, Yokohama, JAPAN 240-8501. tomo@ynu.ac.jp.

Abstract: A numerical cross-shore model for wave-mud interaction is presented that can be used to predict time dependent variations of fluid mud thickness and irregular wave transformation along soft mud profiles. The rheological constitutive equations of visco-elastic (VE) material are adopted for the behavior of fluid mud layer under the wave action. Spectral calculation method is used for the simulation of irregular wave transformation. The application of the numerical model at a field site shows the capability of the model to predict the wave height transformation along muddy profiles.

INTRODUCTION

The upper part of muddy beds may be fluidized when high water surface waves travel on consolidated mud layers. The fluidized mud layer absorbs wave energy and, in turn, moves due to the wave action. The determination of the thickness of fluidized mud layer is essential for the simulations of wave height transformation and mud mass transport. Since Gade (1958), the interaction between water waves and muddy beds, particularly wave height attenuation and mud mass transport, has been studied in several ways. There have also been some efforts to formulate the fluidization of mud, based on the characteristics of the wave and undisturbed mud layer (Chou, 1989; Foda et al., 1993). Conducting a series of laboratory experiments, Mehta et al. (1995) presented an empirical equation for the time-dependent fluidization of mud layers. Recently, the effect of irregularity has also been included in few studies (e.g., Zhang and Zhao, 1999,

Soltanpour et al., 2004). Soltanpour et al. (2006) studied the fluidization of mud and wave transformation under irregular waves along real mud profiles. In spite of these researches, the effects of the time changes of the depth of fluidized mud layer along mud profiles have not been studied yet.

The present paper offers a numerical cross-shore wave-mud interaction model that can be used to determine the time-dependent thicknesses of the fluidized mud and the transformation of waves along muddy profiles during high wave conditions. The performance of the proposed model is examined by using laboratory experiments and field data.

FLUIDIZATION OF MUD LAYER

It is assumed that a water layer of a given thickness is sitting on top of a stratified two-layered mud bed, where the upper one is a generalized visco-elastic (VE) layer (Foda et al., 1993). The behavior of this fluidized mud layer is simulated, using a complex viscosity coefficient, which is a function of the imposed strain in some nonlinear manner. The lower stationary layer is assumed to be elastic. The thickness of the fluid mud layer is related to the resulting strains due to the imposed wave height. the experimental results of Mehta et al. (1995) are employed to include the time-dependent variations of mud fluidization

$$d(t) = M[1 - \exp(-0.021 t^{0.346})] \tag{1}$$

where t represents the total time under wave action, d is the time-dependent thickness of fluidized mud layer and M is the ultimate depth of fluid mud.

WAVE-FLUID MUD INTERACTION MODEL

After the fluidization, the fluid system above the stationary mud, i.e. the fluidized mud layer and water layer, is divided into N sub-layers, in which the water layer is represented by N=1 (Fig. 1). The vertical distribution of mud properties can be considered using different mud characteristics in the horizontal sub-layers of the fluid mud layer. The rheological equations of VE are used for fluid mud. The visco-elastic parameters are adopted from the laboratory experiments of Shibayama and An (1993). The governing equations are linearized Navier-Stokes equations and the continuity equations which are solved considering the boundary conditions. The mud mass transport in fluid mud as well as the wave attenuation rate, k_i, can be calculated by this wave-mud interaction model. The details can be found in the original work of Tsuruya et al. (1987).

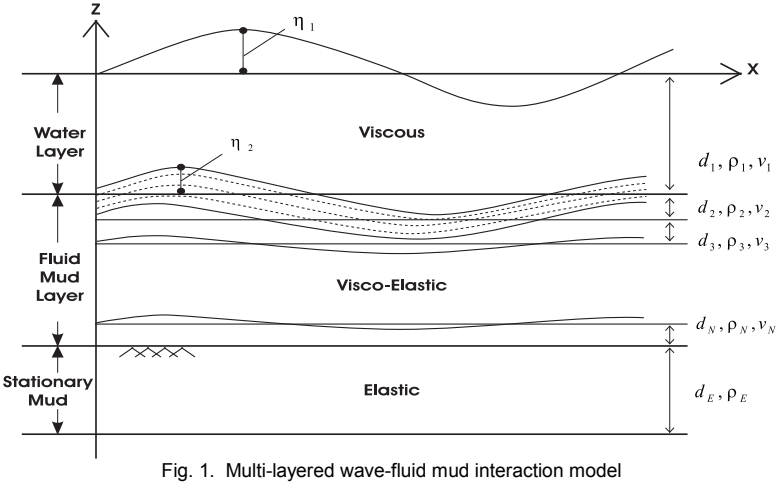

Fig. 1. Multi-layered wave-fluid mud interaction model

IRREGULAR WAVE TRANSFORMATION

Assuming the exponential decay of wave height over a horizontal mud bed, the energy dissipation rate of mud bottom is related to the wave attenuation rate, k_i (Soltanpour et al., 2003)

$$\varepsilon_{Dm} = -\frac{d}{dx}(C_g E) = 2C_g k_i E \tag{2}$$

where $E = \rho g H^2 / 8$ is the wave energy per unit surface area, ρ is the water density and C_g is the group velocity.

After the breaking line, energy dissipation rate reflects both dissipation effects of wave breaking and fluid mud.

$$\varepsilon_D = \varepsilon_{Dm} + \varepsilon_{Db} \tag{3}$$

where ε_D is total energy dissipation and ε_{Db} is the energy dissipation rate of wave breaking (Winyu and Shibayama, 1996).

Assuming that the irregular wave consists of an infinite number of component regular waves with different wave amplitudes and frequencies, the spectrum is divided into a number of wave components (Fig. 2). The irregular wave attenuation is simulated by superimposing the obtained regular component waves. The modeling wave spectra at $x = x_j$ is defined as

$$\hat{S}_j(\bar{f}_n) = \frac{1}{2} a_{jn}^2 \Delta f_n \tag{4}$$

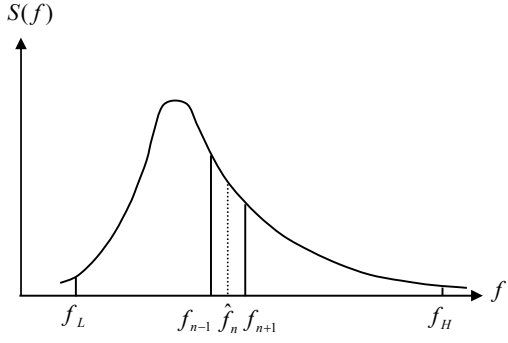

Fig. 2 Sketch used for definition of the amplitude and frequency of regular wave component

IRREGULAR WAVE-INDUCED MUD FLUIDIZATION

The fluidization model of Foda et al. (1993) is extended to irregular waves. Considering the periodic response of the imposed shear strain (Chou et al., 1993), the maximum shear strain of an irregular wave at the elastic mud line is calculated by superimposing of maximum shear strains of regular wave components, respectively

$$\gamma_{imp} = \sqrt{\sum_{n} \left(\gamma_{\max,n}{}^{2} \right)} \tag{5}$$

where $\gamma_{\max,n}$ is the maximum shear strain of each wave component at the elastic mud line. The thickness of the fluidized mud layer is determined by comparing the maximum shear strain, i.e. γ_{imp}, at the top of the elastic bed with the limiting or yield strain for the given mud material. A try and error procedure will result in the desired depth of fluidized mud layer under the overlaying irregular wave.

MODEL PERFORMANCE

Table 1 shows two cases of simulated and measured fluid mud thicknesses in a laboratory flume. As it is observed, the simulated ultimate depth of fluidized layer agrees with the observed data of Mehta et al. (1995). This supports the compatibility of different parts of the proposed fluidization model; i.e. time-dependent depth of fluid layer and ultimate depth of fluidization.

Table 1. Measured and Simulated Fluidized Mud Thickness (Data from Mehta et al., 1995)

Tests	Wave Period, s	Wave Height, cm	Water Depth, cm	*M* (cm) Measured	*M* (cm) Simulated
Case 1	1.00	4.00	19.0	18	20
Case 2	1.00	8.00	19.0	35	34

Fig. 3 shows an example of the measured and calculated wave spectra in monsoon conditions at a site offshore of the town of Alleppey in Kerala, India, where the measurements are at two stations with a distance of about 300 m (Mathew, 1992). A good agreement is observed between the measured and simulated wave spectra when the infinite time after wave action corresponding to the final fluidized depth, is reached. Two inshore wave spectra before final equilibrium state have also been presented. It is observed that considerable wave energy dissipation occurs at the initial stage of wave action, i.e. a few hours after the beginning of storm.

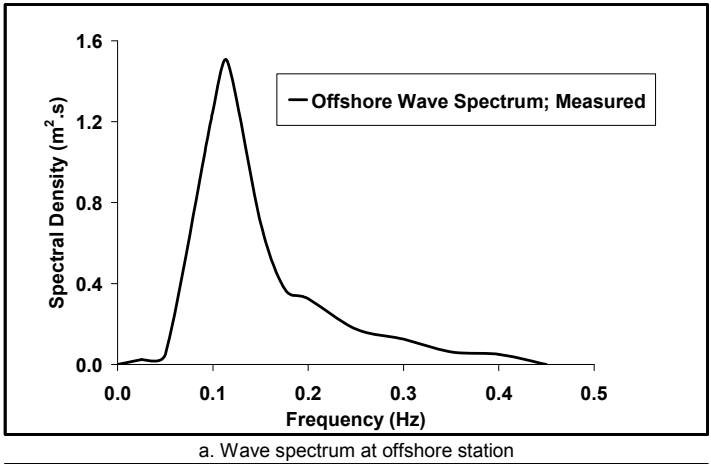

a. Wave spectrum at offshore station

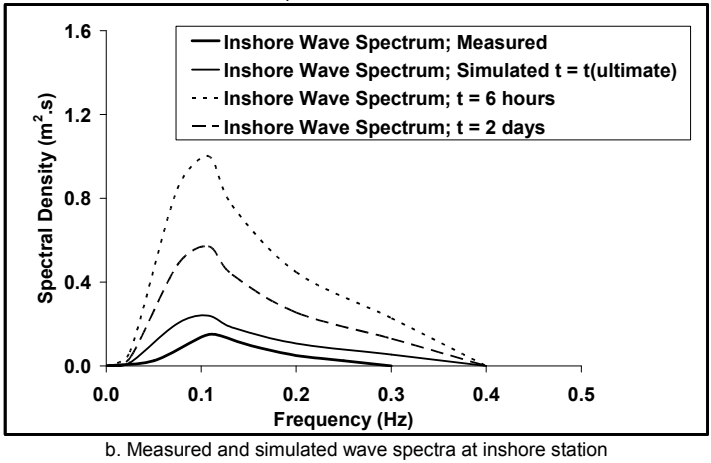

b. Measured and simulated wave spectra at inshore station

Fig. 3 Measured and simulated wave spectra at Alleppey in Kerala, India (Data from Mathew, 1992), (W=210%, G=5kPa, ρ_E=1300kg/m^3, ρ_{VE}=1250kg/m^3)

CONCLUSION

A dynamic fluidization model is introduced to predict the time-dependent depth of the fluidized mud under wave action. Irregular wave height transformation on muddy profiles is simulated and the results are compared with a field data. It is observed that the model is capable to predict wave heights along muddy beds. However, more wave measurements, particularly during high wave actions, are needed to validate model performance on muddy profiles.

REFERENCES

Chou, H. T. (1989). Rheological response of cohesive sediments to water waves, Ph.D. dissertation, University of California, Berkeley, 149 pp.

Chou, H. T., M. A. Foda, and J. R. Hunt (1993). Rheological response of cohesive sediments to oscillatory forcing, in Nearshore and Estuarine Cohesive Sediment Transport, Coastal Estuarine Sci. Ser., vol.42, edited by A. J. Mehta, chap. 8, AGU, Washington, D. C., pp. 126-148.

Foda, M. A., Hunt, J. R. and Chou, H. T. (1993). A nonlinear Model for the Fluidization of Marine Mud by Waves. American Geophysical Union, Journal of Geophysical Research, Vol. 58, No. C4, pp. 7039-7047.

Gade, H. G. (1958). Effects of a non-rigid, impermeable bottom on plane surface waves in shallow water, Jour. Marine Research, Vol. 16, No. 2, pp. 61-82.

Mathew, J. (1992). Wave-Mud Interaction in Mud banks, Ph.D. dissertation, Cochin University of Science and Technology, Cochin, Kerala, India.

Mehta, A. J., Wlliams, D. J. A., Wlliams, P. R. and Feng, J. (1995). Tracking dynamical changes in mud bed due to waves, Journal of Hydraulic Engineering, ASCE, Vol. 121, No. 6, June 1995, pp. 504-506.

Shibayama T., An, N. N. (1993). A visco-elastic-plastic model for wave-mud interaction, Coastal Engineering in Japan, Vol. 36, No. 1, pp. 67-89.

Soltanpour M., Shibayama T., Noma T. (2003). Cross-shore mud transport and beach deformation model, Coastal Engineering Journal, Vol. 45, N0. 3, pp. 363-387.

Soltanpour, M., Shibayama, T., Masuya, Y., Sabzevari, I. (2004). Wave attenuation and mud mass transport under irregular waves, Proc. 29th Coastal Eng. Conf., ASCE, pp. 1851-1860.

Soltanpour, M., Shibayama, T., Haghshenas S. A., (2006). Irregular Wave Transformation on Mud Profiles Including the Fluidization of Mud Layer, Proc. 30th Coastal Eng. Conf., ASCE, (under publication).

Tsuruya, H., Nakano, S., and Takahama, J. (1987). Interaction between surface waves and a multi-layered mud bed, Rep. No. 5, Port and Harbor Res. Inst., Ministry of Transport, Japan.

Winyu, R. and Shibayama, T. (1996). Cross-shore sediment transport and beach deformation model, Proc. 25th Coastal Eng. Conf., ASCE, pp. 3062-3075.

Zhang, Q. H., Zhao, Z. D. (1999). Wave-mud interaction: wave attenuation and mud mass transport, Coastal Sediments “99”, pp. 1867-1880.

This page intentionally left blank

Subject Index

Page number refers to the first page of paper

Aggregates, 2394
Alabama, 1047, 2002
Alaska, 463
Australia, 1033, 1417

Backwashing, 1947
Barrier beaches, 492
Barrier islands, 647, 671, 685, 699, 976, 1153, 1179, 1722, 1988, 2002, 2011, 2254
Barriers, 434, 814, 935, 1731, 1910, 2084
Bars, 2111, 2124
Bathymetry, 1877, 2191
Bays, 341, 463, 814, 856, 1311, 2137, 2151
Beach erosion, 1142, 1311, 1601
Beach nourishment, 776, 2279, 2358, 2418, 2501, 2515
Beaches, 300, 314, 378, 406, 420, 463, 477, 506, 520, 531, 545, 584, 626, 935, 1019, 1227, 1269, 1455, 1696, 1708, 1740, 1787, 1851, 1865, 1947, 1661, 2111, 2241, 2265, 2402, 2460
Bed load, 56
Belgium, 1431
Berms, 449
Brazil, 1455
Breaking waves, 42, 2124
Breakwaters, 2402, 2460
Bulkheads, 561

California, 1696, 1740, 1851, 2501
Canada, 351
Caribbean, 572
Case reports, 1391
Channels, 1431, 1571, 1678, 2164, 2213, 2345, 2358, 2372
Chesapeake Bay, 2306
Cliffs, 1696
Climatic changes, 963, 1214
Closed form solutions, 15
Coastal engineering, 434, 1241, 1405
Coastal environment, 179, 207, 449, 828, 842, 1117, 1129, 1283, 1475, 1647, 1669, 1813, 1827, 1900, 1910, 1924, 2084, 2151, 2321
Coastal morphology, 1, 137, 272, 364, 492, 671, 736, 814, 828, 842, 986, 1019, 1033, 1165, 1200, 1297, 1354, 1363, 1417, 1455, 1529, 1571, 1582, 1589, 1635, 1938, 2011, 2025, 2137, 2199, 2345
Coastal structures, 2432
Colorado River, 1502
Currents, 42
Cyclones, 935

Damage, 1008
Deep water, 1, 341
Deltas, 207, 736, 749, 828, 882
Design, 420, 785, 1988
Dikes, 392, 785, 1008
Dredge spoil, 2358
Dredging, 2372, 2382, 2394
Dunes, 612, 897, 951, 1033, 1089, 1241, 1283, 1813, 1961, 1975
Dynamics, 584

Empirical equations, 1431
Environmental issues, 1827
Equilibrium, 897, 2241
Erosion, 96, 612, 1722, 1799, 1813, 1961, 2037, 2074, 2265, 2321
Esthetics, 420
Estimation, 1008, 2372, 2382
Estuaries, 531, 1200, 1609, 1623, 1669, 2487
Evaluation, 626

Failures, 392, 1008
Field investigations, 661
Fills, 2402, 2418

Florida, 151, 378, 1047, 1297, 1326, 1377, 1582, 1589, 1877, 2199, 2265
Flumes, 124
Forecasting, 1813
Forests, 1117
France, 531

Geology, 2151, 2473, 2487
Geometry, 1787, 2002, 2177
Geomorphology, 165, 762, 2097, 2292, 2306
Grain size, 259, 314, 1255, 1623, 2229, 2241, 2446
Gravel, 477, 492, 520, 572, 584, 2473
Gravity waves, 1, 235
Great Lakes, 392
Ground water, 506
Gulf of Mexico, 935, 1515

Harbors, 1431, 2292
Hawaii, 1227
Hazards, 1799
Heterogeneity, 921
History, 364, 867
Hurricanes, 151, 882, 888, 911, 976, 986, 996, 1047, 1466, 2306
Hydrodynamics, 221, 1297, 1489, 1557, 1582, 1787, 1924
Hydrographs, 1827
Hydrologic models, 1669

Ice formation, 798
Imaging techniques, 1886
Indonesia, 1019
Infiltration, 506
Inlets, waterways, 1165, 1297, 1326, 1354, 1363, 1377, 1391, 1475, 1489, 1502, 1515, 1529, 1543, 1557, 1589, 1468, 2199, 2331
Integrals, 286
Islands, 1340, 1708, 1722, 1865

Japan, 1269, 1354, 1900, 2460

Laboratory tests, 68, 235, 248
Lagoons, 1708
Land reclamation, 598
Latin America, 2345
Littoral currents, 1405
Littoral drift, 165, 179
Louisiana, 647, 661, 671, 685, 699, 762, 785, 888, 911, 921, 1165, 1179, 2254

Mapping, 2487
Marshes, 785, 1571
Maryland, 1340
Massachusetts, 814, 856, 1142
Mathematical models, 1075
Measurement, 221, 561, 1609, 1678, 1947
Mexico, 996, 2279
Michigan, 392, 2292
Mississippi, 1466
Mississippi River, 699, 712, 722, 749, 882, 2177
Models, 300, 406, 897
Monitoring, 406
Morphology, 235, 1391, 1557, 1900, 2199
Mud, 1660, 1669, 1690

Navigation, 1431, 1502, 1678, 1768, 2345, 2372
Nearshore, 1, 56, 584, 951, 1886
Netherlands, 1129, 1363
New England, 798
New York, 1722, 2331
New Zealand, 1441, 1910
North Carolina, 327, 963, 1153, 1543, 1837, 2229
North Sea, 2124
Numerical analysis, 1089
Numerical models, 341, 671, 736, 749

Oregon, 449, 1754, 2137
Outwash, 2049, 2074, 2084

Parameters, 124, 626
Permeability, 520
Plumes, 736, 2382
Porous media, 2321
Portugal, 545, 1557
Predictions, 314, 612, 1103
Probability, 272
Progressive waves, 2191

Radar, 1900
Reefs, 572, 1647

Remedial action, 1601
Restoration, 647, 685, 699, 776, 785
River basins, 1647
River beds, 2177
Rivers, 842

Salts, 798
Sand, 42, 68, 96, 193, 248, 259, 314, 477, 492, 506, 520, 545, 584, 685, 699, 1255, 1269, 1340, 1405, 1609, 1708, 2164, 2191, 2254, 2432, 2446, 2460, 2473, 2501
Sandbars, 28
Scour, 598, 1609, 1851, 2213
Sea floor, 598, 1635, 1660, 2487
Sea level, 1153, 1179, 1193, 1200, 1214
Sediment, 15, 28, 207, 300, 463, 531, 633, 661, 671, 712, 722, 736, 749, 776, 867, 951, 1047, 1075, 1103, 1283, 1326, 1635, 1647, 1768, 1877, 1988, 2229, 2292, 2382, 2473, 2515
Sediment transport, 42, 56, 68, 82, 96, 110, 124, 137, 151, 179, 193, 221, 286, 351, 911, 996, 1117, 1241, 1405, 1441, 1669, 1678, 1754, 1924, 1938, 2037, 2049, 2446, 2460
Sedimentation, 798, 1377
Seismic effects, 856
Shear stress, 193, 1947
Sheet flow, 286
Ship motion, 110
Ships, 685, 2213
Shoaling, 921, 1311
Shoreline changes, 327, 364, 378, 392, 888, 1129, 1142, 1214, 1227, 1417, 1601, 1740, 1754, 1799, 1837, 2306
Shores, 561, 633
Simulation, 259, 2097
Simulation models, 1623
Skewness, 137
Slopes, 137, 165
South Carolina, 1787, 2151
Spatial distribution, 2037
Spits, coastal, 351
Sri Lanka, 842, 1061
Statistics, 1799, 2177
Stones, 531
Storm surges, 996, 1466
Storms, 951, 963, 1813, 1886, 2061
Stratification, 1635
Structural design, 2432
Subsurface environment, 82
Subsurface investigations, 785
Surf zone, 82, 151, 1455, 1865
Surface waters, 1690
Suspended sediments, 221, 248
Switzerland, 2321

Texas, 1475, 1502, 1515, 1529
Tides, 1129, 1179, 1354, 1417, 1543, 1589, 1731, 1768, 2164
Time dependence, 193, 867, 1690
Topography, 867, 1623, 1837, 1865, 1938, 2061, 2097
Tracers, 449
Transport rate, 179
Tropical regions, 1731, 2061
Tsunamis, 842, 1008, 1019, 1033, 1061, 1075, 1089, 1103, 1117
Turbulence, 15

United Kingdom, 434, 1200

Vegetation, 1571
Velocity, 15, 28, 2382
Virginia, 364, 2402

Washington, 561, 1311, 1754
Water circulation, 327
Water levels, 963
Wave groups, 110
Wave runup, 272, 1075, 1089, 1924, 1938, 1947, 1961, 1975
Wave tanks, 259
Waves, 661, 1660, 1690, 1731
Wetlands, 722, 1179, 1193
Wind, 1255

This page intentionally left blank

Author Index

Page number refers to the first page of paper

Aagaard, Troels, 951, 2124
Aarninkhof, Stefan G. J., 598, 1975
Abbe, Tim, 561
Adams, Mark B., 1142
Adams, Peter N., 463
Alfageme, Santiago R., 2345, 2432, 2025
Allan, Jonathan C., 449, 2137
Allison, Mead A., 661, 882
Alonso, Ignacio, 1283
Alsina, J. M., 272
Amaro, Venerando E., 1731
Anderson, Carl M., 1529
Andrews, Brian D., 2487
Andrews, Jeffrey L., 685, 699, 2515
Andrus, T. Mitchell, 722, 785
Argow, Brittina A., 798
Arsenault, Matthew A., 2473
Asano, Go, 1623
Ashton, Andrew D., 327, 341, 351, 1214
Austin, Martin J., 584

Baba, Yasuyuki, 1938
Baig, Stephen, 1466
Baldock, Tom E., 272, 286, 506, 1947
Baldwin, Wayne E., 2151, 2487
Barcak, Ronnie G., 1502
Barlett, William, 749
Barnard, Patrick L., 2501
Barnes, Matthew P., 272, 1947
Barnhardt, Walter A., 856, 2151
Barthélemy, Eric, 235
Bass, Gregory P., 1340
Batten, Brian K., 1515
Beck, Tanya M., 1377, 1582
Bell, Paul S., 1886
Bell, Robert G., 1441
Bender, Christopher, 151
Benedet, Lindino, 671, 699, 2515
Benoit, Jeff, 1601
Bentley, Samuel J., 722, 1441
Bergeron, Emile, 2487
Bliss, James D., 2473
Boer, Sander, 598
Bokuniewicz, Henry, 1722
Bolinger, Daniel L., 2254
Bradbury, Andrew P., 492
Brehin, Florian G. A., 1297, 2199
Briére, C., 137
Brocchini, M., 1635
Brown, J. M., 1609
Buonaiuto, Frank, 1722
Buschman, Frans, 1647
Buscombe, Daniel, 584
Butman, Bradford, 2487
Byrnes, Mark R., 762, 1754

Calliari, Lauro J., 1455
Calvete, D., 2111
Camenen, Benoît, 15, 56, 1938
Campbell, T., 671
Cañizares, Rafael, 2025, 2345
Canning, Paul, 520
Carrasco, Ana R., 2084
Carrasquero, José, 561
Carter, Joshua, 1489
Clarke, Linden B., 1975
Cleary, William J., 1543
Cleveringa, Jelmer, 1129
Coates, Tom C., 406
Coeveld, E. Matrijn, 612, 1975
Conley, D. C., 1635
Connell, Kenneth J., 2011
Cowell, P. J., 633
Cox, Andrew, 1466
Crowley, Tom, 1214
Curoy, J., 531

Dalon, Matthew M., 2137
Dan, Sebastian, 207
Danchuk, Samantha, 749
Danforth, William W., 2487
Darnell, Joel T., 776

Dartez, Dane, 911
Dartnell, Peter, 1851
Das, Himangshu, 1466
Davies, A. G., 1609
Davis, Richard A., 1582
de Alegria Arzaburu, Amaia Ruiz, 996, 1865, 2279
de Sonneville, B., 671
de Vroeg, Hans, 612
Dean, Robert G., 626
Dekker, Frank, 1117
Dellapenna, Timothy M., 882
Denny, Jane F., 2151, 2487
Dias, Alveirinho, 1557
Dias, João A., 2049, 2084
Dibajnia, Mohammad, 392, 2097, 2292
Diesing, Markus, 2394
Dill, Nathan, 749
Dohmen-Janssen, C. Marjolein, 1019
Donnelly, Chantal, 2061
Dornbusch, U., 531
Dougherty, Amy J., 1910
Driscoll, Neal, 2151
Durham, William McKinney, 82

Edge, Billy L., 2074
Edwards, Brian D., 1851
Elias, Edwin P. L., 598, 1363
Elkan, Peter, 2402
Elko, Nicole A., 378
Espinal, Juan C., 996, 2279
Esteves, Luciana S., 221, 1886

Falchetti, S., 1635
Falqués, A., 2111
Farris, Amy S., 1837
Fauver, Laura A., 897
Ferland, M. A., 633
Ferreira, Óscar, 1557, 2049, 2084
Finkl, Charles W., 671, 685, 699, 2515
FitzGerald, Duncan M., 798, 856, 1165, 1179, 2164
Fitzpatrick, Kathy, 1326
Fletcher, Charles H., 1227, 1799
Foster, David S., 2487
Foye, Peter, 2265
Frazer, L. Neil, 1799
Friedrichs, Carl T., 2382

Fujii, Hiroyuki, 1008
Fukuhama, Masaya, 259, 1008, 1623
Furuike, Kou, 314

Galal, El Sayed, 1900
Galofre, Jordi, 2241
Garcia, Marcelo H., 2191
Garnier, R., 2111
Gayes, Paul T., 1787, 2151
Gelfenbaum, Guy R., 1103, 1117, 1768
Genz, Ayesha S., 1799
Georgiou, I., 2177
Georgiou, Ioannis, 1179
Gibeaut, James C., 1193
Giese, Graham S., 1142
Giosan, Liviu, 828
Goff, James R., 1033, 1061
Goff, John A., 2473
Goñi, Miguel A., 882
Gonzalez, Mauricio, 300
Grandy, Greg M., 647
Granja, Helena, 545
Grasmeijer, Bart, 1
Grasso, Florent, 235
Griffee, Sarah F., 1754
Griggs, Gary B., 1740, 2501
Grosskopf, William G., 1340
Grüne, Joachim, 248
Guannel, Gregory, 28
Guard, P., 286
Guedes, Rafael M. C., 1455
Guidroz, Walter S., 911
Guillén, J., 2111
Gunawardena, Yohama, 1865
Gunn, James R., 2306

Haghshenas, S. Abbas, 1690
Hall, Kevin, 1660, 2213
Haller, Merrick, 28, 2137
Hamilton, Stuart, 986
Hansen, Mark, 2002
Hanson, Hans, 15
Hapke, Cheryl J., 1696
Harcourt, Jenny S., 406
Hardaway, C. Scott, Jr., 2306
Harikai, Souichi, 1269
Hart, Roger, 449
Hashimoto, Koji, 1354

Hatchett, Lyle, 1466
Hayashi, Kentaro, 1354
Head, Richard, 406
Headland, John R., 2432
Healy, Terry R., 165, 2358
Heilman, Daniel J., 776, 1502
Hein, Christopher J., 856
Higgins, Stephen, 2265
Higman, Bretwood, 1103
Hoekstra, Piet, 1647
Hoitink, Ton, 1647
Holland, K. Todd, 1455
Holman, Rob A., 1975
Honma, Akihiro, 1354
Hopf, Frank, 1241
Horn, Diane P., 520, 506
Horwitz, Mark H., 1047
Hotta, Shintaro, 1255, 1269
Houghton, Jon, 477
Houser, Chris, 986
Howes, Nick, 1179
Hsu, Tian-Jian, 1669
Hughes, Michael G., 1417
Hughes, Zoe J., 798, 1179
Hulscher, Suzanne J. M. H., 1019, 1813

Ilic, Suzana, 1865
Inukai, Takushi, 1623
Irwin, Barry J., 2487
Ishii, Toshimasa, 96
Ishikawa, Toshinori, 259, 314, 2460
Ishino, Kazuo, 842
Izzo, Dominic, 2254

Jaffe, Bruce, 1103, 1117
Jaffe, David A., 867
Jaramillo, Sergio, 661
Jenkins, Chris J., 2473
Jennings, Simon C., 434
Jiménez, José, 1283
Joffrion, Russ, 785
Jose, Felix, 921, 935

Kaminsky, George M., 633, 1768
Kana, Timothy W., 2229
Kato, Fuminori, 1008
Kemp, Jonathan A., 406
Keon, Theodore, 814
Khalil, Syed M., 685, 699
Kheiashy, K., 2177
Khondker, Masood, 2025
Kirby, James T., 28
Kirwan, Matthew L., 1571
Klekotka, John, 477
Knaapen, Michiel A. F., 1200
Knotts, Christopher P., 685
Kobashi, Daijiro, 921
Kolberg, Mark O., 1708
Komar, Paul D., 420
Kos'yan, Ruben, 248
Kotulak, Peter, 2432
Kozuka, Masayuki, 96
Kraus, Nicholas C., 193, 1377, 1475, 1502, 1515, 1529, 1961, 2011, 2331
Krecic, Michael, 151
Kremkau, Kevin, 1326
Kroon, Aart, 951, 2124
Krynock, Laural, 2402
Kubota, Susum, 1255, 1269
Kumada, Takayuki, 314, 2446
Kuriyama, Yoshiaki, 179, 2037

Landry, Blake J., 2191
Larson, Magnus, 56, 1924, 2011
Li, Ling, 506
Lillycrop, W. Jeff, 888, 1827
Limber, Patrick W., 1837
Lin, Lihwa, 1502, 1515
Lisniowski, M. A., 221
List, Jeffrey H., 221, 327, 1837
Littlewood, Ryan, 341, 351
Liu, Baozhu, 935
Long, Bernard F., 124
Lorente, Paloma, 1283
Loureiro, Eduardo, 545
Lovelock, Catherine, 1441
Lynett, Patrick, 1103

Maathuis, Ben H. P., 1019
MacDonald, Neil J., 110, 2213
Macon, Christopher L., 1827
Madsen, Ole Secher, 82, 96
Mahoney, Tucker, 2345
Mai, Stephan, 2321
Makowski, Christopher, 2265
Mann, Douglass W., 1405

Manoonvoravong, P., 272
Mark, David J., 1311
Masselink, Gerhard, 584
Matias, Ana, 2049, 2084
Matsumoto, Hideo, 1678
Matsumoto, Ryosuke, 1900
Matsura, Seizo, 1354
McBride, Randolph A., 364, 762
McCorquodale, J., 2177
McKillip, Doris J., 1768
Medellin, Gabriela, 2241
Medina, Raúl, 300, 2241
Meilianda, Ella, 1019
Merrifield, Mark A., 1227
Meselhe, E., 2177
Meyer-Arendt, Klaus, 986
Michallet, Hervé, 235
Mimura, Nobuo, 96
Miner, Michael D., 1165, 1179
Momose, Kazuo, 96
Montreuil, Stéphane, 124
Moore, Andrew, 1103
Morán, Diana K., 996, 2279
Morang, Andrew, 1311
Morgan, Michael J., 2331
Moritz, Hans R., 633, 1754, 1768
Morris, Brad, 2049
Morrison, Steve, 561
Morton, Robert A., 572, 1061, 2151, 2487
Moses, C. A., 531
Mouraenko, Oleg, 2372
Mulder, Jan P. M., 1813, 1019
Murray, A. Brad, 341, 351, 1214, 1571
Mustain, Neomi, 2501

Nairn, Robert B., 392, 1708, 2097, 2292
Nakagawa, Hajime, 842
Nakagawa, Yasuyuki, 1678
Nakamura, Nagatomo, 1255
Nawarathna, Bandara, 842
Neto, Francisco Santos, 1731
Nichol, Scott L., 1061, 1910
Nicholls, Robert J., 1200
Nichols, David R., 2487
Niedoroda, Alan W., 1466
Nielsen, P., 286

Özkan-Haller, H. Tuba, 28

O'Brien, Thomas F., 2487
O'Donoghue, Tom, 42
Odroniec, Kristen, 151
Ojeda, E., 2111
Oltman-Shay, Joan, 1768
Oravetz, Jonathan, 986
Orford, Julian D., 434, 492
Osborne, Philip D., 110
Oumeraci, Hocine, 248
Oveisy, Ali, 1660
Overton, Margery, 2074

Pacheco, André, 1557
Palmsten, Meg L., 1975
Park, Young Hyun, 2074
Parkinson, Shaun, 110
Pawlak, Geno, 1227
Penland, Shea, 1179
Pereira, Pedro S., 1455
Perotto, H. L. S., 221
Perry, M. Cameron, 776
Phillips, Eleyne L., 1851
Placido Jr., Jose S., 1731
Podymov, Igor, 248
Poff, Michael, 785
Pope, Joan, 963

Quartel, Susanne, 951

Ramsey, John, 1326
Ranasinghe, Roshan Suminda, 68
Ranasinghe, Roshanka, 1417
Reid, Dave, 1696
Reniers, Ad J. H. M., 1975
Requejo, Soledad, 300
Revell, David L., 1740
Reynolds, B. M., 1787
Ribas, F., 2111
Ribberink, Jan S., 1, 42
Richardson, Trent M., 364
Richmond, Bruce M., 572
Risk, Michael J., 1708
Roberts, Susan, 1601
Roberts, Tiffany M., 1961
Robertson, William, V., 1877
Robinson, D. A., 531
Roblin, Rachel R., 392
Rodríguez-Herrerías, Manuel, 1283

Roelvink, Dano (J.) A., 598, 736
Rosario-Llantin, Jo-Ann, 2199
Rosati, Julie Dean, 1988
Rosenberg, Lee, 2402
Rossington, Kate, 1200
Ruessink, Gerben, 1
Ruffman, Alan, 1075
Ruggiero, Peter, 463, 633, 1768
Ruthven, Trey, 1326

Sánchez, José C., 2279
Sabatier, François, 207
Saifee, Shabbar, 1466
Sakagami, Takeharu, 96
Sakamoto, Hikari, 179
Sallenger, Asbury H., 179, 888, 897, 976, 2061
Salles, Paulo, 996, 2279
San-nami, Toshiro, 314
Santo, Renato E., 1455
Sasaki, Takayuki, 1354
Sasakura, Shinya, 1900
Sato, Shinji, 68, 1089
Sayah, Selim M., 2321
Schmeltz, Edward J., 2254
Schmidt-Koppenhagen, Reinold, 248
Schupp, Courtney A., 1340
Schwab, William C., 2151, 2487
Seabergh, William C., 1391
Seaver, Kathryn, 1722
Selegean, James P., 392, 2292
Serizawa, Masumi, 259, 314, 2446, 2460
She, Kaiming, 520
Shepsis, Vladimir, 1489
Sheremet, Alex, 661, 882
Sherman, Douglas J., 1241
Shibayama, Tomoya, 1690
Shimozono, Takenori, 1089
Short, Andrew D., 1417
Simpson, David, 477
Slott, Jordan, 1214
Smith, David E., 1075
Smith, Eric, 2432
Smith, Ernest R., 193, 1502
Smith, Jane M., 1311
Smith, S. Jarrell, 2382
Soltanpour, Mohsen, 1690
Son, Minwoo, 1669
Son, P. Kim, 272
Soulsby, Richard L., 1075
Spiers, Kyle C., 2358
Stauble, Donald K., 814, 2418
Stive, Marcel J. F., 207, 736, 1363, 1589, 1975
Stockdon, Hilary F., 976
Stolper, David, 1153
Stone, Gregory W., 911, 921, 935, 1988
Storlazzi, Curt D., 1227, 1851
Storms, Joep E. A., 736
Suzuki, Takayuki, 2037
Swales, Andrew, 1441
Sweeney, Rachel, 647

Tajima, Yoshimitsu, 96, 1089
Takagi, Toshimitsu, 1008, 1623
Takeuchi, Maiko, 2037
Takewaka, Satoshi, 1900
Talmon, A. M., 137
Tanaka, Hitoshi, 842
Tarya, Ayi, 1647
Taylor, David, 2213
Taylor, Matthew J., 762
Teakle, I., 286
Thieler, E. Robert, 2487
Thomas, Robert C., 1502
Thompson, David M., 897, 976
Thomson, Gordon G., 647, 2265
Tidwell, David K., 1377
Tomoda, Naoki, 2037
Tonkin, Susan P., 561
Trim, Louise, 520
Tsuru, Masahito, 96
Tung, Tran Thanh, 1589
Twichell, David C., 2487

Uda, Takaaki, 259, 314, 2446, 2460
Uijttewaal, Wim S. J., 1975

Valdemoro, Herminia I., 1283
Valentine, Page C., 2487
Valvo, Lisa, 1214
van de Graaff, Jan, 612, 1589
van den Bergh, Gert, 1647
van der Burgh, L. M., 1813
van der Spek, Ad J. F., 1129
van der Werf, Jebbe J., 1, 42

van Gent, Marcel R. A., 612
van Heteren, Sytze, 1129
van Koningsveld, M., 1813
van Ormondt, M., 137
van Rijn, Leo V., 1, 137
van Thiel de Vries, Jaap S. M., 1975
Vanderbeke, Nicole, 2402
Vatvani, Deepak, 1117
Vellinga, Tiedo, 598
Verwaest, Toon, 1431
Vidal, César, 2241
Vila-Concejo, Ana, 1417, 1557, 2049
Vincent, Chris E., 248
Vital, Helenice, 1731
Vitousek, Sean, 1227

Waldron, Ryan, 749
Walstra, Dirk Jan R., 137, 207, 671, 736, 1589
Wamsley, Ty V., 1924
Wang, Ping, 378, 1047, 1377, 1582, 1961
Wang, Zhanxian, 626
Warren, Jeffrey D., 1837
Warrick, Jonathan A., 463
Weaver, Robert, 1466
Weber, Kathryn M., 1837
Weishar, Lee L., 814
Welsh, John M., 1543
White, James, 2402
Whitman, Dean, 1877
Whitmeyer, Shelley J., 2164
Wijnberg, K. M., 1813
Williams, Deidre D., 1529
Williams, Jon J., 221, 1886
Williams, R. B. G., 531
Williams, S. Jeffress, 1153, 2473
Willson, Clinton S., 749
Winer, Harley S., 712
Wise, Larry A., 2372
Worley, Charles W., 2487
Wozencraft, Jennifer M., 1827
Wray, Michael, 477
Wren, P. A., 1787
Wright, C. Wayne, 888

Yamaguchi, Satomi, 2037
Yano, Shinichiro, 842

Zarillo, Gary A., 1297, 2199
Zhang, Keqi, 1877



Coastal Sediments '07



Volume 3

Edited by
Nicholas C. Kraus
Julie Dean Rosati

ASCE

COASTAL SEDIMENTS '07

VOLUME THREE

PROCEEDINGS OF THE SIXTH INTERNATIONAL SYMPOSIUM ON COASTAL ENGINEERING AND SCIENCE OF COASTAL SEDIMENT PROCESSES

May 13–17, 2007
New Orleans, Louisiana

SPONSORED BY
Coasts, Oceans, Ports, and Rivers Institute (COPRI)
of the American Society of Civil Engineers

IN COOPERATION WITH
American Shore and Beach Preservation Association
Dept. of Oceanography and Coastal Science, Louisiana State University
Geological Society of America
International Association of Geomorphologists
International Union of Geological Sciences
U.S. Army Corps of Engineers, Coastal Inlets Research Program
U.S. Geological Survey, Coastal and Marine Geology Program

EDITED BY
Nicholas C. Kraus
Julie Dean Rosati

ASCE

Published by the American Society of Civil Engineers

Library of Congress Cataloging-in Publication Data

International Symposium on Coastal Engineering and Science of Coastal Sediment Processes (6th : 2007 : New Orleans, La.)
Coastal sediments '07 : proceedings of the sixth International Symposium on Coastal Engineering and Science of Coastal Sediment Processes, May 13–17, 2007, New Orleans, Louisiana / sponsored by Coasts, Oceans, Ports, and Rivers Institute (COPRI) of the American Society of Civil Engineers in cooperation with American Shore and Beach Preservation Association ... [et al.] ; edited by Nicholas C. Kraus, Julie Dean Rosati.
p. cm.
Includes bibliographical references and index.
ISBN-13: 978-0-7844-0926-8
ISBN-10: 0-7844-0926-9
1. Coast changes--Congresses. 2. Coastal sediments--Congresses. I. Kraus, Nicholas C. II. Rosati, Julie Dean. III. Coasts, Oceans, Ports and Rivers Institute (American Society of Civil Engineers) IV. Title.

GB450.2.I58 2007
627'.58--dc22 2007009073

American Society of Civil Engineers
1801 Alexander Bell Drive
Reston, Virginia, 20191-4400

www.pubs.asce.org

Any statements expressed in these materials are those of the individual authors and do not necessarily represent the views of ASCE, which takes no responsibility for any statement made herein. No reference made in this publication to any specific method, product, process, or service constitutes or implies an endorsement, recommendation, or warranty thereof by ASCE. The materials are for general information only and do not represent a standard of ASCE, nor are they intended as a reference in purchase specifications, contracts, regulations, statutes, or any other legal document. ASCE makes no representation or warranty of any kind, whether express or implied, concerning the accuracy, completeness, suitability, or utility of any information, apparatus, product, or process discussed in this publication, and assumes no liability therefore. This information should not be used without first securing competent advice with respect to its suitability for any general or specific application. Anyone utilizing this information assumes all liability arising from such use, including but not limited to infringement of any patent or patents.

ASCE and American Society of Civil Engineers—Registered in U.S. Patent and Trademark Office.

Photocopies and reprints.
You can obtain instant permission to photocopy ASCE publications by using ASCE's online permission service (www.pubs.asce.org/authors/RightslinkWelcomePage.html). Requests for 100 copies or more should be submitted to the Reprints Department, Publications Division, ASCE, (address above); email: permissions@asce.org. A reprint order form can be found at www.pubs.asce.org/authors/reprints.html.

Photo Credit.
Top: East Island, Isle Dernieres, Louisiana, October 20, 1990. Bottom: Belle Pass and Port of Fouchon, Louisiana, November 3, 1989. *Images Courtesy USGS*

Copyright © 2007 by the American Society of Civil Engineers. All Rights Reserved.
ISBN 13: 978-0-7844-0926-8
ISBN 10: 0-7844-0926-9
Manufactured in the United States of America.

Foreword

The COASTAL SEDIMENTS '07 conference was organized as a technical specialty conference devoted to the physical aspects of sediment processes and morphology change in the coastal and inlet environment. Following previous conferences in the Coastal Sediments series that were held in 1977, 1987, 1991, 1999, and 2003, COASTAL SEDIMENTS'07 celebrated 30 years of the Coastal Sediments series and promoted exchange of information and views among specialists in the fields of coastal engineering, geology, oceanography, and related disciplines. The theme of COASTAL SEDIMENTS '07 was "Coastal Engineering and Science in Cascading Spatial and Temporal Scales," which established the trend of thinking and approach of the conference, as well as determined in part the composition of the papers that were presented. This theme was chosen to stimulate research devoted to the various scales of processes and their interactions at which coastal engineers and scientists must work in developing knowledge and capabilities to assist society in managing the coast under present and future conditions. Emphasis was on papers that recognize and relate to coastal morphology change of long-term consequence.

The COASTAL SEDIMENTS '07 conference returned to the site of the 1987 conference, New Orleans, Louisiana, because of the extraordinary morphologic change along the coasts of Louisiana, Mississippi, and Texas, caused by Hurricanes Katrina and Rita that struck in August and September, respectively, of 2005. In addition to the recent hurricanes, this coast is experiencing long-term natural and anthropogenic change including rapid and differential subsidence, severe reduction in renewable sediment supply, deltaic adjustment of fine-grained material, and oil and gas exploration and extraction. The theme is intended to generate papers and discussion of coastal sediment processes from the micro-scale to the regional scale at which integrated coastal design and management must be accomplished. Participants were given an overview of recent hurricane damage within the context of the long-term morphologic change in Louisiana in the Keynote Address delivered by Mr. James R. (Randy) Hanchey, Deputy Secretary of the Louisiana Department of Natural Resources.

Professor Leo van Rijn of Delft Hydraulics and the University of Utrecht, The Netherlands, accepted the 2007 Coastal Award at the Conference Awards Luncheon on May 16th. Starting in 2001, the Coastal Award has been presented every 2 years alternately at the Coastal Dynamics conference and the Coastal Sediments conference through coordination between the organizing committees of these two technical specialty conferences. The Organizing Committee of Coastal Sediments '07 joins conference participants and the extended research community in celebrating Professor van Rijn's research contributions that have greatly influenced engineers and geologists working in the areas of coastal sediment transport and morphology change.

These *Proceedings* volumes are the permanent record of the conference, containing the latest thinking and progress of the world's leading scientists and

engineers in the areas of coastal sediment transport and morphology change. The contents are a valuable source of information on coastal sediment and morphology processes ranging from basic research to case studies and lessons learned. The papers contained herein provide the most recent results and ideas in a wide range of approaches and viewpoints not assembled elsewhere in both quality and breadth. The *Proceedings* were produced in hard copy in two volumes in black and white and also provided to conference participants as a CD ROM with searchable index of PDF files in color. All papers are available to the public in PDF format via the ASCE Research Library at www.ascelibrary.org.

Three-hundred fifty abstracts were submitted to the Conference Steering Committee. On average, each abstract received five reviews, and 225 submissions were invited for development into full papers and presentation over 3 days of technical sessions. The 197 papers appearing in these Proceedings originated from approximately 24 countries, demonstrating the international scope of COASTAL SEDIMENTS '07. Each paper included in these *Proceedings* received positive peer review. Each paper is eligible for discussion in the *Journal of Waterway, Port, Coastal and Ocean Engineering* and can be nominated for ASCE awards.

The Steering Committee of COASTAL SEDIMENTS '07 gratefully acknowledges the assistance of many individuals, both known and anonymous, in the 2 years of preparations by an all-volunteer committee. Numerous individuals assisted the Steering Committee in review of abstracts and final papers. The efforts of the following persons are acknowledged: Matthew Arsenault, U.S. Geological Survey (USGS); Mark Byrnes, Applied Coastal Research and Engineering, Inc.; Duncan FitzGerald, Boston University; Guy Gelfenbaum, USGS; Cheryl Hapke, USGS; John Headland, Moffatt & Nichol; Todd Holland, Naval Research Laboratory; Peter Howd, USGS; Bruce Jaffe, USGS; Magnus Larson, University of Lund; Jeffrey List, USGS; Randy Parkinson, Coastal and Environmental Geological Consulting; Robert Morton, USGS; James O'Connell, Woods Hole Oceanographic Institution; Lisa Robbins, USGS; Vladimir Shepsis, Coast and Harbor Engineering; Donald Stauble, U.S. Army Corps of Engineers; Marcel Stive, Delft Hydraulics; Hilary Stockdon; USGS; and Curt Storlazzi, USGS.

We also thank the session moderators for agreeing to lend their time and experience to run the conference smoothly and productively. We are indebted to the tour leaders and their organizations for arranging and conducting memorable and stimulating technical trips. The "Geology of the Louisiana Coastal Zone: Implications for Coastal Management and Restoration" tour was led by Mark Kulp, University of New Orleans (UNO); Mike Miner, UNO; Duncan FitzGerald, Boston University; and Ioannis Giorgiou, UNO. The "Wax Lake-Atchafalaya Delta Complex Sedimentation, Stratigraphy" tour was led by Harry Roberts, Louisiana State University. Finally, we thank Lucy King of ASCE for assisting and often leading in conference logistics; Donna Dickert of ASCE for accurately producing the Proceedings; and Lesa Rair and Chris Hanson of COPRI for assisting with conference arrangements, including exhibitors and sponsors.

We also would like to thank our exhibitors and sponsors for Coastal Sediments 2007 for their support:

Sponsors

Applied Coastal and Research Engineering Inc.
Coastal Engineering Consultants, Inc.
Coast & Harbor Engineering
Great Lakes Dredge & Dock Co.
NortekUSA
Olsen Associates, Inc.
Weeks Marine, Inc.

Exhibitors

American Vibracore Services, Inc.
COPRI
Frontier Surveying Co.
Louisiana Dept. of Natural Resources
Moffatt & Nichol
N.S. Nettles & Associates, Inc.
NortekUSA
SonTek/YSI
Taylor Engineering, Inc.
Teledyne RD Instruments
Tensar Earth Technologies, Inc.
U.S. Army Corps of Engineers, Coastal Inlets Research Program
U.S. Army Corps of Engineers, Navigations Systems Research Program
U.S. Army Corps of Engineers, Regional Sediment Management Program
U.S. Geologic Survey, Coastal and Marine Geology Program
University of New Orleans
URS Corporation
Weeks Marine, Inc.

To everyone who participated, we thank you for contributing to this remarkable conference that is precious to all of us.

Conference Steering Committee

Nicholas C. Kraus
Conference Co-Chair
U.S. Army Engineer
Research and Development Center

Hans Hanson
University of Lund, Sweden

Julie Dean Rosati
U.S. Army Engineer
Research and Development Center

S. Jeffress Williams
U.S. Geological Survey,
Coastal and Marine Geology Program

William G. McDougal
Conference Co-Chair
University of Florida

Luke Le Bas
Coastal Engineering Division,
Louisiana Department of
Natural Resources

Ping Wang
University of South Florida

Harley S. Winer
U.S. Army Corps of Engineers,
New Orleans District

Contents

Volume One

Sediment Transport Fundamentals I

Wave-Related Transport and Nearshore Morphology 1
Leo van Rijn, Gerben Ruessink, Bart Grasmeijer, Jebbe van der Werf, and Jan Ribberink

Closed Form Solution for Threshold Velocity for Initiation of Sediment Motion under Waves 15
Hans Hanson and Benoît Camenen

Influence of Velocity Moments on Sand Bar Movement During CROSSTEX 28
Gregory Guannel, H. Tuba Özkan-Haller, Merrick C. Haller, and James T. Kirby

Development of a New Practical Model for Sand Transport Induced by Non-Breaking Waves and Currents 42
Jebbe J. van der Werf, Jan S. Ribberink, and Tom O'Donoghue

A Total Load Formula for the Nearshore 56
Benoît Camenen and Magnus Larson

Sediment Transport Fundamentals II

Longshore Sand Transport Rate Measurements Using Small-Scale Physical Models 68
Roshan Suminda Ranasinghe and Shinji Sato

Pressure-Induced Subsurface Sediment Transport in the Surf Zone 82
Ole Secher Madsen and William McKinney Durham

Tracking Sediment Particles under Wave-Current Coexisting Field 96
Yoshimitsu Tajima, Masayuki Kozuka, Masahito Tsuru, Toshimasa Ishii, Takeharu Sakagami, Kazuo Momose, Nobuo Mimura, and Ole S. Madsen

Sediment Transport in Response to Wave Groups Generated by High-Speed Vessels 110
Philip D. Osborne, Neil J. MacDonald, and Shaun Parkinson

Sediment Transport Fundamentals III

Flume Experiments under Cat-Scan to Measure Internal Sedimentological Parameter During Sediment Transport 124
Stéphane Montreuil and Bernard F. Long

The Effects of Bed Slope and Wave Skewness on Sediment Transport and Morphology 137
D. J. R. Walstra, L. C. van Rijn, M. van Ormondt, C. Briére, and A. M. Talmon

Sediment Transport off Northeast Florida Outside the Surf Zone during Hurricanes 151
Michael Krecic, Christopher Bender, and Kristen Odroniec

Longshore Transport

Geomorphic and Sedimentologic Evidence for Net Littoral Drift—A Review 165
Terry Healy

Cross-Shore Variation of Predominant Longshore Sediment Transport Rate 179
Yoshiaki Kuriyama and Hikari Sakamoto

Longshore Sand Transport Calculated by Time-Dependent Shear Stress 193
Ernest R. Smith and Nicholas C. Kraus

Sediment Budget of the Danube Delta Coastal Zone 207
Sebastian Dan, Marcel Stive, Dirk Jan Walstra, and François Sabatier

Field Measurements and Modeling of Longshore Sediment Transport 221
J. J. Williams, L. S. Esteves, M. A. Lisniowski, and H. L. S. Perotto

Sediment Transport Fundamentals IV

Infragravity Waves in Mobile-Bed Laboratory Experiments 235
Florent Grasso, Hervé Michallet, and Eric Barthélemy

Large-Scale Laboratory Modeling of Suspended Sand Concentration Fluctuations under Irregular Waves 248
Joachim Grüne, Ruben Kos'yan, Hocine Oumeraci, Igor Podymov, Reinold Schmidt-Koppenhagen, and Chris E. Vincent

Change in Longitudinal Profile Using Sand of Mixed Grain Size in Large Wave Tank and its Numerical Simulation 259
Massaya Fukuhama, Takaaki Uda, Masumi Serizawa, and Toshinori Ishikawa

Probabilistic-Deterministic Modelling of Swash Zone Morphology 272
T. E. Baldock, P. Kim Son, P. Manoonvoravong, M. P. Barnes, and J. M. Alsina

Modelling Sheet Flow Sediment Transport Using Convolution Integrals 286
P. Guard, I. Teakle, P. Nielsen, and T. Baldock

Shoreline Change Modeling

A Middle-Term Evolution Model for Beaches 300
Soledad Requejo, Raul Medina, and Mauricio Gonzalez

Model for Predicting Beach Changes on Coast with Sand of Mixed Grain Size Based on Bagnold's Concept 314
Masumi Serizawa, Takaaki Uda, Toshiro San-nami, Kou Furuike, Toshinori Ishikawa, and Takayuki Kumada

A Circulation Modeling Approach for Evaluating the Conditions for Shoreline Instabilities 327
Jeffrey H. List and Andrew D. Ashton

An Alternative Explanation for the Shape of 'Log-Spiral' Bays 341
Ryan Littlewood, A. Brad Murray, and Andrew D. Ashton

The Response of Spit Shapes to Wave-Angle Climates 351
Andrew D. Ashton, A. Brad Murray, and Ryan Littlewood

Observed Shoreline Change

Historical Shoreline Changes and Morphodynamics of Parramore Island, Virginia (1852-2006) 364
Trent M. Richardson and Randolph A. McBride

Temporal and Spatial Scales of Profile and Planform Adjustment on a Nourished Beach 378
Nicole A. Elko and Ping Wang

Shoreline Response to Dike Failure at Grand Marais Harbor, Lake Superior, Michigan 392
Rachel R. Roblin, Mohammad Dibajnia, Robert B. Nairn, and James P. Selegean

Successful Beach Modelling, Monitoring and Management for a Large LNG Facility 406
Jonathan A. Kemp, Tom C. Coates, Richard Head, and Jenny S. Harcourt

Gravel Coasts I

The Design of Stable and Aesthetic Beach Fills: Learning from Nature 420
Paul D. Komar

Variation in the Organization of Gravel-Dominated Coastal Systems: Evidence from Nova Scotia and Southern England 434
Julian D. Orford and Simon C. Jennings

Profile Dynamics and Particle Tracer Mobility of a Cobble Berm Constructed on the Oregon Coast 449
Jonathan C. Allan and Roger Hart

Mixed Sediment Beach Processes: Kachemak Bay, Alaska 463
Peter Ruggiero, Peter N. Adams, and Jonathan A. Warrick

Mixed Sand and Gravel Beach Design and Construction for Habitat Restoration 477
David Simpson, Michael Wray, John Houghton, and John Klekotka

Gravel Coasts II

Influence of Changing Management Regimes on the Morphodynamic Response of a Mixed Gravel and Sand Barrier Beach 492
Andrew P. Bradbury and Julian D. Orford

The Influence of Groundwater on Profile Evolution of Fine and Coarse Sand Beaches 506
Diane P. Horn, Tom E. Baldock, and Ling Li

Effects of Permeability on the Performance of Mixed Sand-Gravel Beaches 520
Kaiming She, Louise Trim, Diane Horn, and Paul Canning

Cross-shore and Longshore Transport of Tracer Pebbles on a Macrotidal Mixed Sediment Beach, Somme Estuary, France 531
J. Curoy, U. Dornbusch, C. A. Moses, D. A. Robinson, and R. B. G. Williams

Why Are Shingle Beaches Replacing Sandy Beaches? (Coastal Zone of NW Portugal) 545
Helena Granja and Eduardo Loureiro

Gravel Coasts III

Field Measurements of Shore Conditions to Assess Bulkhead Effects in Thurston County, South Puget Sound 561
Susan P. Tonkin, Tim Abbe, José Carrasquero, and Steve Morrison

Coral-Gravel Storm Ridges: Examples from the Tropical Pacific and Caribbean 572
Bruce M. Richmond and Robert A. Morton

Field Observations of Step Dynamics on a Macrotidal Gravel Beach 584
Daniel Buscombe, Martin J. Austin, and Gerhard Masselink

Large-Scale Scour of the Sea Floor and the Effect of Natural Armouring Processes, Land Reclamation Maasvlakte 2, Port of Rotterdam 598
Sander Boer, Edwin Elias, Stefan Aarninkhof, Dano Roelvink, and Tiedo Vellinga

Dunes and Profiles

Dune Erosion Prediction Methods Incorporating Effects of Wave Periods 612
Marcel R. A. van Gent, E. Martijn Coeveld, Hans de Vroeg, and Jan van de Graaff

Reevaluation of Equilibrium Beach Profile Scale Parameter 626
Zhanxian Wang and Robert G. Dean

Shoreface Response to Sediment Deficit 633
G. M. Kaminsky, M. A. Ferland, P. J. Cowell, H. R. Mortiz, and P. Ruggiero

Louisiana Coast

The Challenges of Restoring Louisiana Barrier Islands: From Design through Construction 647
Gordon G. Thomson, Greg M. Grandy, and Rachel Sweeney

Field Observations of Wave-Current-Sediments Dynamics, Atchafalaya Shelf, Louisiana, USA 661
Sergio Jaramillo, Alex Sheremet, and Mead Allison

Investigation of Morphosedimentary Processes on a Schematic Louisiana Barrier Island Using Process-Based Numerical Modeling 671
T. Campbell, B. de Sonneville, L. Benedet, D. J. W. Walstra, and C. W. Finkl

Restoration-Quality Sand from Ship Shoal, Louisiana: Geotechnical Investigation for Sand on a Drowned Barrier Island 685
Syed M. Khalil, Charles W. Finkl, Jeff Andrews, and Christopher P. Knotts

Mississippi River Sand for Barrier Island Restoration in Louisiana: Geophysical and Geotechnical Investigations for Sand Mining 699
Jeffrey L. Andrews, Syed M. Khalil, Charles W. Finkl, and Lindino Benedet

Mississippi River Delta

Re-Engineering the Mississippi River as a Sediment Delivery System 712
Harley S. Winer

Sediment Flux and Fate in the Mississippi River Diversion at West Bay: Observation Study 722
T. Mitchell Andrus and Samuel J. Bentley

Initial Morphologic and Stratigraphic Delta Evolution Related to Buoyant River Plumes 736
Joep E. A. Storms, Marcel J. F. Stive, Dano (J.) A. Roelvink, and Dirk Jan Walstra

Physical and Numerical Modeling of River and Sediment Diversions in the Lower Mississippi River Delta 749
Clinton S. Willson, Nathan Dill, William Barlett, Samantha Danchuk, and Ryan Waldron

A Geomorphic Process-Response Model for Chenier-Plain Evolution in Southwestern Louisiana, USA 762
Randolph A. McBride, Matthew J. Taylor, and Mark R. Byrnes

Marshes and Wetlands

Sediment Analysis for Habitat Restoration: Adaptation of Open-Coast Beach Nourishment Principles 776
Daniel J. Heilman, Joel T. Darnell, and M. Cameron Perry

Subsurface Exploration and Containment Dike Design Criteria for Coastal Louisiana Marsh Restoration 785
Russ Joffrion, Michael Poff, and Mitch Andrus

Ice Raft Formation, Dispersion and Sedimentation on New England Salt Marshes 798
Brittina A. Argow, Zoe J. Hughes, and Duncan M. FitzGerald

Effects of Large Scale Morphological Changes to a Back-Bay System 814
Lee L. Weishar, Theodore Keon, and Donald K. Stauble

Volume Two

Deltas and River Mouths

Morphodynamic Feedbacks on Deltaic Coasts: Lessons from the Wave-Dominated Danube Delta 828
Liviu Giosan

Coastal and River Mouth Morphology Change in Sri Lanka Due to 2004 Indian Ocean Tsunami 842
Hitoshi Tanaka, Kazuo Ishino, Bandara Nawarathna, Hajime Nakagawa, and Shinichiro Yano

Holocene Evolution of the Merrimack Embayment, Northern Massachusetts, Interpreted from Shallow Seismic Stratigraphy **856**
Christopher J. Hein, Duncan M. FitzGerald, and Walter A. Barnhardt

The Use of Historic Topography for the Characterization of Time-Dependent Geomorphic Change and Sediment Delivery **867**
David A. Jaffe

Impact of Hurricanes Katrina and Lili on the Inner Shelf of the Mississippi-Atchafalaya Delta **882**
Mead A. Allison, Timothy M. Dellapenna, Miguel A. Goñi, and Alex Sheremet

Storms I

Coastal-Change Impacts during Hurricane Katrina: An Overview **888**
Asbury Sallenger, C. Wayne Wright, and Jeff Lillycrop

Modeling Dune Response Using Measured and Equilibrium Bathymetric Profiles **897**
Laura A. Fauver, David M. Thompson, and Asbury H. Sallenger

Sediment Transport along the Southwestern Louisiana Shoreline: Impact from Hurricane Rita, 2005 ..... **911**
Walter S. Guidroz, Gregory W. Stone, and Dane Dartez

Heterogeneity and Dynamics on a Shoal during Spring-Winter Storm Season, South-Central Louisana, USA **921**
Daijiro Kobashi, Felix Jose, and Gregory W. Stone

Winter Storm and Tropical Cyclone Impacts on the Short-Term Evolution of Beaches and Barriers along the Northeastern Gulf of Mexico **935**
Gregory W. Stone, Baozhu Liu, and Felix Jose

Storms II

Impact of a Major Storm on Sediment Exchanges between the Dunes, Beach, and Nearshore **951**
Aart Kroon, Susanne Quartel, and Troels Aagaard

Storm Patterns and Climatic Trends Based on Water Level Fluctuations: Duck, North Carolina, USA **963**
Joan Pope

Hindcasting Potential Hurricane Impacts on Rapidly Changing Barrier Islands **976**
Hilary F. Stockdon, David M. Thompson, and Asbury H. Sallenger, Jr.

EOF Analysis of Morphological Response to Hurricane Ivan **986**
Chris Houser, Stuart Hamilton, Klaus Meyer-Arendt, and Jonathan Oravetz

Storm Surge and Sediment Process Owing to Hurricane Isidore in Terminos Lagoon, Campeche **996**
Juan C. Espinal, Paulo Salles. A de A, and Diana K. Moran

Tsunami I

Tsunami Damage Estimation in Consideration of Beach Transformation and Dike Failure 1008
Fuminori Kato, Masaya Fukuhama, Hiroyuki Fujii, and Toshimitsu Takagi

Beach Morphology at Banda Aceh, Indonesia in Response to the Tsunami on 26 December 2004 1019
Ella Meilianda, C. Marjolein Dohmen-Janssen, Ben H. P. Maathuis, Suzanne J. M. H. Hulscher, and Jan P.M. Mulder

Dune Morphology as an Indicator of Paleotsunamis 1033
James R. Goff

Sedimentological Characteristics of Regional-Scale Washover Deposits Caused by Hurricane Ivan 1047
Mark H. Horwitz and Ping Wang

Tsunami II

Impacts of the 2004 Indian Ocean Tsunami on the Southwest Coasts of Sri Lanka 1061
Robert A. Morton, James R. Goff, and Scott L. Nichol

Reconstructing Tsunami Run-Up from Sedimentary Characteristics—A Simple Mathematical Model 1075
Richard L. Soulsby, David E. Smith, and Alan Ruffman

Numerical Study of Tsunami Run-Up over Erodible Sand Dunes 1089
Takenori Shimozono, Shinji Sato, and Yoshimitsu Tajima

Predicted Sedimentary Record of Reflected Bores 1103
Bretwood Higman, Guy Gelfenbaum, Patrick Lynett, Andrew Moore, and Bruce Jaffe

Tsunami Inundation and Sediment Transport in Vicinity of Coastal Mangrove Forest 1117
Guy Gelfenbaum, Deepak Vatvani, Bruce Jaffe, and Frank Dekker

Sea Level Rise I

From Transgression to Regression: Coastal Evolution near The Hague, The Netherlands, around 5000 Years BP 1129
Ad J. F. van der Spek, Jelmer Cleveringa, and Sytze van Heteren

Changing Orientation of Ocean-Facing Bluffs on a Transgressive Coast, Cape Cod, Massachusetts 1142
Graham S. Giese and Mark B. Adams

Modeling Barrier Island Response to Sea-Level Rise in the Outer Banks, North Carolina 1153
Laura J. Moore, Jeffrey H. List, S. Jeffress Williams, and David Stolper

1880 to 2005 Morphological Evolution of a Transgressive Tidal Inlet, Little Pass Timbalier, Louisiana 1165
Michael D. Miner, Duncan M. FitzGerald, and Mark A. Kulp

Sea Level Rise II

Impacts of Rising Sea Level to Backbarrier Wetlands, Tidal Inlets, and Barrier Islands: Barataria Coast, Louisiana 1179
Duncan FitzGerald, Mark Kulp, Zoe Hughes, Ioannis Georgiou, Michael Miner, Shea Penland, and Nick Howes

Modeling Future Coastal Wetland Transition Induced by Relative Sea-Level Rise 1193
James C. Gibeaut

Morphological Interactions within UK Estuaries: A Preliminary Analysis of Critical Rates of Sea-Level Rise 1200
Kate Rossington, Robert J. Nicholls, and Michiel A. F. Knaapen

Variable Shoreline Responses to Sea-Level Rise and Climate Change 1214
A. Brad Murray, Lisa Valvo, Jordan Slott, Andrew Ashton, and Tom Crowley

Model Scenarios of Shoreline Change at Kaanapali Beach, Maui, Hawaii: Seasonal and Extreme Events 1227
Sean Vitousek, Charles H. Fletcher, Mark A. Merrifield, Geno Pawlak, and Curt D. Storlazzi

Wind-Blown Sand

Aeolian Processes, Coastal Dunes, and the *Coastal Engineering Manual*, Part III, Chapter 4—"Wind-Blown Sediment Transport" 1241
Frank Hopf and Douglas J. Sherman

Distribution of Horizontal Distance Traveled by Saltating Sand Grains in Air 1255
Shintaro Hotta, Susumu Kubota, and Nagatomo Nakamura

Beach Stabilization Works Against Wind Blown Sand on Beaches: Experiences from Japan 1269
Susumu Kubota, Souichi Harikai, and Shintaro Hotta

Coastal Dunefield Evolution in Conditions of Limited Sediment Availability: Natural and Anthropogenic Controls on the Corralejo Dunes 1283
Herminia I. Valdemoro, José A. Jiménez, Ignacio Alonso, Paloma Lorente, and Manuel Rodriguez-Herrerias

Coastal Inlets I

Hydrodynamic and Morphologic Modeling at Sebastian Inlet, FL 1297
Gary A. Zarillo and Florian G. A. Brehin

Erosion and Channel Migration at the Shoalwater Bay Reservation, Willapa Bay, Washington 1311
Andrew Morang, David J. Mark, and Jane M. Smith

Sediment Management Plan Development for the St. Lucie Inlet, Martin County, Florida 1326
John Ramsey, Trey Ruthven, Kevin Kremkau, and Kathy Fitzpatrick

Sand Bypassing Restores Natural Processes to Assateague Island, Maryland 1340
Courtney A. Schupp, Gregory P. Bass, and William G. Grosskopf

Morphological Responses to Jetty Construction at Tidal Inlet: Lake Saroma, Japan 1354
Kentaro Hayashi, Koji Hashimoto, Takayuki Sasaki, Akihiro Honma, and Seizo Matsura

Coastal Inlets II

Morphodynamics of Texel Inlet, The Netherlands 1363
Edwin P. L. Elias and Marcel J. F. Stive

Sedimentation Patterns in a Stabilized Migratory Inlet, Blind Pass, Florida 1377
Ping Wang, David K. Tidwell, Tanya M. Beck, and Nicholas C. Kraus

Approaches to Understanding Multiple-Inlet Stability 1391
William C. Seabergh

Engineering Guidelines for the Siting of Sand Bypassing Discharges 1405
Douglass W. Mann

Shoreline Implications of Flood-Tide Delta Morphodynamics. The Case of Port Stephens (SE Australia) 1417
Ana Vila-Concejo, Andrew D. Short, Michael G. Hughes, and Roshanka Ranasinghe

Mud Coasts I

Using Simple Semi-Empirical Models for Integrated Assessment of Scenarios for a Navigation Channel. The Case of the Port of Ostend, Belgium 1431
Toon Verwaest

Sediment Processes and Mangrove-Habitat Expansion on a Rapidly-Prograding Muddy Coast, New Zealand 1441
Andrew Swales, Samuel J. Bentley, Catherine Lovelock, and Robert G. Bell

The Influence of Mud on the Inner Shelf, Shoreface, Beach, and Surf Zone Morphodynamics—Cassino, Southern Brazil 1455
Lauro J. Calliari, K. Todd Holland, Pedro S. Pereira, Rafael M. C. Guedes, and Renato E. Santo

The Hurricane Katrina Storm Surge in Mississippi 1466
Alan W. Niedoroda, Lyle Hatchett, Himangshu Das, Andrew Cox, Robert Weaver, Stephen Baig, and Shabbar Saifee

Texas Inlets

Coastal Inlets of Texas, USA 1475
Nicholas C. Kraus

Cedar Bayou—Inlet Dynamics and Engineering 1489
Vladimir Shepsis and Joshua Carter

Navigation Improvements, Mouth of the Colorado River, Texas 1502
Ronnie G. Barcak, Nicholas C. Kraus, Lihwa Lin, Ernest R. Smith, Daniel J. Heilman, and Robert C. Thomas

Long-Term Inlet Stability of a Multiple Inlet System, Pass Cavallo, Texas **1515**
Brian K. Batten, Nicholas C. Kraus, and Lihwa Lin

Morphologic Response to a New Inlet, Packery Channel, Corpus Christi, Texas **1529**
Deidre D. Williams, Nicholas C. Kraus, and Carl M. Anderson

Coastal Inlets III

Evolution of a Relocated Tidal Inlet: Mason Inlet, NC **1543**
John M. Welsh and William J. Cleary

Present Hydrodynamics of Ancão Inlet, 10 Years after its Relocation **1557**
André Pacheco, Ana Vila-Concejo, Oscar Ferreira, and Alveirinho Dias

The Influence of Tidal Prism and Vegetation on Tidal Channel Morphology: Implications for Marsh Stability **1571**
Matthew L. Kirwan and A. Brad Murray

Natural and Anthropogenic Influences on the Morphodynamics of Big Sarasota Pass, Florida **1582**
Richard A. Davis, Ping Wang, and Tanya Beck

Morphological Behavior of Seasonal Closure of Tidal Inlets **1589**
Tran Thanh Tung, Marcel J. F. Stive, Jan van de Graaff, and Dirk-Jan R. Walstra

Estuaries

The National Academies Report on Mitigating Shore Erosion along Sheltered Coasts **1601**
Jeff Benoit and Susan Roberts

Field Measurement and Modeling of Scour Pit Dynamics in a Sandy Estuary **1609**
A. G. Davies and J. M. Brown

Projection of Topographic Change of an Estuary Terrace by Horizontal 2-D Simulation Model, Considering Grain Size **1623**
Toshimitsu Takagi, Go Asano, Takushi Inukai, and Masaya Fukuhama

Examining the Contribution of Sediment Stratification to the Evolution of Seabed Morphology **1635**
S. Falchetti, D. C. Conley, and M. Brocchini

From River Basin to Barrier Reef: Pathways of Coastal Sediments **1647**
Piet Hoekstra, Ton Hoitink, Frans Buschman, Ayi Tarya, and Gert van den Bergh

Mud Coasts II

Wave Evolution on Fluid Mud Bottom **1660**
Kevin Hall and Ali Oveisy

A Fine Sediment Transport Modeling Framework and its Application to Fluid Mud Processes **1669**
Tian-Jian Hsu and Minwoo Son

Field Measurement of Fine Sediment Transport Process around Navigation Channel 1678
Yasuyuki Nakagawa and Hideo Matsumoto

Time Dependent Mud Fluidization and Irregular Wave Transformation on Muddy Profiles 1690
Mohsen Soltanpour, S. Abbas Haghshenas, and Tomoya Shibayama

Volume Three

Regional Processes I

Regional Beach/Cliff System Dynamics along the California Coast 1696
Cheryl J. Hapke and Dave Reid

Factors Influencing the Long-Term Stability of the Carbonate Sand Beaches of Mauritius 1708
Michael J. Risk, Robert B. Nairn, and Mark O. Kolberg

Evolution of Erosion Hot Spots on a Barrier Island: Fire Island, New York 1722
Kathryn Seaver, Frank Buonaiuto, and Henry Bokuniewicz

Tropical Mixed Wave/Tide Dominated Barrier-Spit System: A Case Study from NE Brazil 1731
Helenice Vital, Francisco Santos Neto, Jose S. Placido Junior, and Venerando E. Amaro

Regional Shoreline and Beach Changes in the Santa Barbara Sandshed 1740
David L. Revell and Gary B. Griggs

Regional Processes II

Engineering Activities Influencing Historical Sediment Transport Pathways at the Columbia River Mouth, WA/OR 1754
Mark R. Byrnes, Sarah F. Griffee, and Hans R. Moritz

Implementing Regional Sediment Management to Sustain Navigation at an Energetic Tidal Inlet 1768
Hans R. Moritz, Guy R. Gelfenbaum, George M. Kaminsky, Peter Ruggiero, Joan Oltman-Shay, and Doris J. McKillip

Decadal Evolution of Shoreface Geometry in South Carolina, USA 1787
B. M. Reynolds, P. A. Wren, and P. T. Gayes

Improving Statistical Validity in Calculating Erosion Hazards from Historical Shorelines 1799
Ayesha S. Genz, L. Neil Frazer, and Charles H. Fletcher

Linking Coastal Evolution and Super Storm Dune Erosion Forecasts 1813
L. M. van der Burgh, K. M. Wijnberg, S. J. M. H. Hulscher, J. P. M. Mulder, and M. van Koningsveld

LIDAR and ARGUS

***CHARTS*-Enabled Data Fusion for Coastal Zone Characterization** 1827
Jennifer M. Wozencraft, Christopher L. Macon, and W. Jeff Lillycrop

Using Topographic LIDAR Data to Delineate the North Carolina Shoreline 1837
Patrick W. Limber, Jeffrey H. List, Jeffrey D. Warren, Amy S. Farris, and Kathryn M. Weber

Exploring Rippled Scour Depressions Offshore Huntington Beach, CA 1851
Eleyne L. Phillips, Curt D. Storlazzi, Peter Dartnell, and Brian D. Edwards

A Study of Intertidal Bar Dynamics Using the Argus Video System 1865
Amaia Ruiz de Alegria Arzaburu, Suzana Ilic, and Yohama Gunawardena

Depth of Closure Derived from Airborne Laser Bathymetry 1877
William Robertson V, Keqi Zhang, and Dean Whitman

Remote Sensing

Assessing Nearshore Bar Movements during Storms Using Time-Averaged X-Band Radar Images 1886
Luciana S. Esteves, Jon J. Williams, and Paul S. Bell

Longshore Migration of Coastal Features Observed with X-Band Radar 1900
Satoshi Takewaka, El Sayed Galal, Ryosuke Matsumoto, and Shinya Sasakura

Detailed 3-D Models of New Zealand Barrier Stratigraphy Provide Insight into Coastal Evolution in Various Spatial and Temporal Settings 1910
Amy J. Dougherty and Scott L. Nichol

Swash Zone

A Formula for Longshore Sediment Transport in the Swash 1924
Magnus Larson, Ty V. Wamsley

Importance of the Swash Longshore Sediment Transport in Morphodynamic Models 1938
Yasuyuki Baba and Benoît Camenen

Direct Bed Shear Stress Measurements in Bore-Driven Swash and Swash Interactions 1947
Matthew P. Barnes and Tom E. Baldock

Limits of Beach and Dune Erosion in Response to Wave Runup Elucidated from SUPERTANK 1961
Tiffany M. Roberts, Ping Wang, and Nicholas C. Kraus

Interaction of Dune Face and Swash Zone 1975
Jaap S. M. van Thiel de Vries, Linden B. Clarke, Stefan G. J. Aarninkhof, E. Matrijn Coeveld, Rob A. Holman, Meg L. Palmsten, Ad J. H. M. Reniers, Marcel J. F. Stive, and Wim S. J. Uijttewaal

Barrier Island Breaching

Critical Width of Barrier Islands and Implications for Engineering Design 1988
Julie Dean Rosati and Gregory W. Stone

Barrier Island Vulnerability to Breaching: A Case Study on Dauphin Island, Alabama 2002
Mark Hansen and Asbury H. Sallenger

Morphologic Modeling of Multiple Barrier Island Breaches for Regional Application 2011
Kenneth J. Connell, Magnus Larson, and Nicholas C. Kraus

Breach Stability and Growth Analysis Using a Morphological Model 2025
Santiago R. Alfageme, Masood Khondker, and Rafael Canizares

Spatial Distribution of Cross-Shore Sediment Transport Rate for Berm Formation and Erosion 2037
Takayuki Suzuki, Maiko Takeuchi, Naoki Tomoda, Satomi Yamaguchi, and Yoshiaki Kuriyama

Overwash and Washover

Sediment Transport Patterns During Overwash 2049
Ana Matias, Ana Vila-Concejo, Óscar Ferreira, Brad Morris, and João A. Dias

Characterization and Modeling of Washover Fans 2061
Chantal Donnelly and Asbury H. Sallenger

Experimental Study of Overwash 2074
Billy L. Edge, Young Hyun Park, and Margery Overton

Backbarrier Evolution and Complete Overwash Occurrence 2084
Ana R. Carrasco, Óscar Ferreira, Ana Matias, and João A. Dias

Sand Bars, Beach Cusps

Geomorphic Features Shaped by Crossing Waves 2097
Robert B. Nairn and Mohammad Dibajnia

Observation and Modeling of Crescentic Bars in Barcelona Embayed Beaches 2111
F. Ribas, R. Garnier, E. Ojeda, A. Falqués, J. Guillén, and D. Calvete

Mesoscale Behaviour of Longshore Bars—Net Onshore or Net Offshore Migration 2124
Troels Aagaard and Aart Kroon

Morphological Characteristics of Rip Current Embayments on the Oregon Coast 2137
Matthew M. Dalon, Merrick Haller, and Jonathan Allan

Geologic Framework of the Long Bay Inner Shelf: Implications for Coastal Evolution in South Carolina 2151
Walter Barnhardt, Jane Denny, Wayne Baldwin, William Schwab, Robert Morton, Paul Gayes, and Neal Driscoll

Sand Waves and Channels

A Relic Sand Wave Field in a Tidal Channel 2164
Shelley J. Whitmeyer and Duncan FitzGerald

Geometric and Statistical Characteristics of Bed Forms in the Lower Mississippi River 2177
K. Kheiashy, J. McCorquodale, I. Georgiou, and E. Meselhe

Bathymetric Evolution of a Sandy Bed under Transient Progressive Waves **2191**
Blake J. Landry and Marcelo H. García

Analysis of Sebastian Inlet, FL, Morphologic Changes Using Complex Empirical Orthogonal Functions (CEOF) **2199**
Florian G. A. Brehin, Jo-Ann Rosario-Llantin, and Gary A. Zarillo

Investigating Ship Induced Scour in a Confined Shipping Channel **2213**
David Taylor, Kevin Hall, and Neil MacDonald

Beach Nourishment

Evolution of Grain-Size Distribution on Bogue Banks: Implications for Selection of Borrow Material **2229**
Timothy W. Kana

New Findings in Equilibrium Grain Size Distribution **2242**
Jordi Galofre, Raúl Medina, Gabriela Medellin, and César Vidal

Determination of Overfill Factor for Offshore Sand in Barrier Island Restoration on the Louisiana Coast **2254**
Daniel L. Bolinger, Dominic Izzo, and Edward J. Schmeltz

Broward County Beach Demonstration Project: From Beers to Beaches **2265**
Christopher Makowski, Gordon Thomson, Peter Foye, and Stephen Higgins

Beach Nourishment Evolution in the Cancún Beach, Quintana Roo, México **2279**
Diana K. Morán, Paulo Salles, A de A, José C. Sánchez, and Juan C. Espinal

Case Studies

Geomorphic Response and Elements of Sediment Budget at St. Joseph Harbor, Southeast Lake Michigan **2292**
Mohammad Dibajnia, Robert B. Nairn, and James P. Selegean

Chesapeake Bay: Headland Control Systems Performance Including Hurricane Isabel **2306**
C. Scott Hardaway, Jr. and James R. Gunn

Coastal Protection against Wind-Wave Induced Erosion Using Soft and Porous Structures: A Case Study at Lake Biel, Switzerland **2321**
Selim M. Sayah and Stephan Mai

Physical Processes Study of Goldsmith Inlet, New York **2331**
Michael J. Morgan and Nicholas C. Kraus

Dredging

Design of Navigation Channel Deepening Works Using a Morphological Model in Barranquilla, Columbia **2345**
Rafael Cañizares, Santiago Alfageme, and Tucker Mahoney

Beach Renourishment through Spoil Disposal Downdrift of a Dredged Entrance Channel **2358**
Kyle C. Spiers and Terry R. Healy

Desktop Methodology for Estimating Maintenance Dredging Requirements for Widened and Deepened Navigation Channels 2372
Larry A. Wise and Oleg Mouraenko

A Mass-Balance, Control-Volume Approach for Estimating Vertical Sediment Flux and Settling Velocity within Dredge Plumes 2382
S. Jarrell Smith and Carl T. Friedrichs

What Does "Physical Regeneration" of Marine Aggregate Dredging Sites Mean? 2394
Markus Diesing

Beach Nourishment and Structures

Performance of Beach Fill and Nearshore Breakwaters at East Ocean View Beach, Norfolk, VA 2402
Peter Elkan, Laural Krynock, Nicole Vanderbeke, James White, and Lee Rosenberg

Assessing Fill Compatibility through Project Performance Evaluation 2418
Donald K. Stauble

Coastal Structure Design for Shore Protection and Sand Retention: Practical Aspects 2432
John R. Headland, Santiago Alfageme, Eric Smith, and Peter Kotulak

Quantitative Evaluation of Controlling Effect of Headland on Longshore Sand Transport Using Model for Predicting Changes in Contour Lines and Grain Size 2446
Takayuki Kumada, Takaaki Uda, and Masumi Serizawa

Evaluation of Controlling Effect of Sand Transport by Detached Breakwaters Built on Dynamically Stable Beach 2460
Takaaki Uda, Masumi Serizawa, and Toshinori Ishikawa

Seafloor Mapping

Geologic Characterization of Offshore of Shelf Areas Using usSEABED for GIS Mapping, Modeling Processes and Assessing Marine Sand and Gravel Resources 2473
S. Jeffress Williams, James D. Bliss, Matthew A. Arsenault, Chris J. Jenkins, and John A. Goff

USGS Advances in Integrated, High-Resolution Sea-Floor Mapping: Inner Continental Shelf to Estuaries 2487
Jane F. Denny, William C. Schwab, David C. Twichell, Thomas F. O'Brien, William W. Danforth, David S. Foster, Emile Bergeron, Charles W. Worley, Barry J. Irwin, Bradford Butman, Page C. Valentine, Wayne E. Baldwin, Robert A. Morton, E. Robert Thieler, David R. Nichols, and Brian D. Andrews

A Rapid Compatibility Analysis of Potential Offshore Sand Sources for Beaches of the Santa Barbara Littoral Cell 2501
Neomi Mustain, Gary Griggs, and Patrick L. Barnard

Presence of Beach-Compatible Sediments in Offshore Borrows: New Challenges and Trade Offs in Developing Codifications **2515**
Charles W. Finkl, Jeffrey L. Andrews, and Lindino Benedet

Indexes

Subject Index **I-1**

Author Index **I-5**

VOLUME THREE

This page intentionally left blank

REGIONAL BEACH/CLIFF SYSTEM DYNAMICS ALONG THE CALIFORNIA COAST

Cheryl J. Hapke[1] and Dave Reid [2]

1. U.S. Geological Survey, Coastal Field Station, University of Rhode Island, 339 Woodward Hall, Kingston, RI 02881, USA. chapke@usgs.gov.
2. U.S. Geological Survey, Pacific Science Center, 400 Natural Bridges Dr., Santa Cruz, CA 95060, USA. dreid@usgs.gov.

Abstract: The coast of California is comprised of both sandy shorelines and cliffed coastline, and in many areas these features spatially coincide. In order to better understand the regional trends of change along the California coast, the U.S. Geological Survey is quantifying both sandy shoreline change and coastal cliff retreat for the state. The resulting database was used to examine the dynamics of the beach/cliff system. We found inconsistent evidence of a relationship between rates of cliff retreat and shoreline change on the spatial scale of 100-km cells. However, when the data are correlated within individual regions, a strong relationship exists between the geomorphology of the coast and the behavior of the beach/cliff system. Areas of high-relief coast show negative correlations, indicating that higher rates of cliff retreat correlate with lower rates of shoreline erosion. In contrast, low- to moderate-relief coasts show strong positive correlations.

INTRODUCTION

The coast of California is comprised of approximately 800 km of sandy shorelines. Additionally, 1300 km of coast are backed by cliffs and bluffs (California Department of Boating and Waterways and State Coastal Conservancy, 2002). In many areas, these geomorphic features coincide in that the sandy beaches are backed by low to moderate relief cliffs. Erosion of the beaches and retreat of the coastal cliffs are chronic hazards along the California coast, frequently resulting in property damage and land loss.

Several previous studies have included analyses of regional sandy shoreline change in California (U.S. Army Corps of Engineers 1971; Griggs and Savoy 1985; Griggs et al. 2005; Hapke et al. 2006), although most of these are compilations of existing data produced by different groups or agencies using a variety of techniques. The report by Hapke et al. (2006) is the first to systematically calculate and present rates for the entire state. Regional analyses of coastal cliff retreat are less available than shoreline change studies. The most comprehensive study to date is Hapke et al. (in press) where cliff retreat rates are calculated

for over 350 km of the California coast. Previous regional cliff retreat analyses are presented by Moore et al. (1999), where rates were determined for two California counties: Santa Cruz and San Diego.

Few previous studies have examined the spatial relationship between shoreline change rates and cliff retreat rates. Sallenger et al. (2005) documented the relationship between these systems during the 1997-98 El Niño along a single beach in Central California. Their analysis indicated that hotspots of cliff erosion correlated to areas of decreased beach width and beach elevation over time scales of individual storms or storm seasons. If this holds true over much longer temporal scales, it might be expected that areas undergoing high rates of sandy shoreline erosion in the long-term would correspond to areas with high rates of bluff retreat. Exceptions would include areas with wide beaches and cliffs that are undergoing only subaerial erosion (i.e. waves no longer reach the cliff base) and/or areas where the cliff is armored. This paper explores the relationship between coastal cliff retreat and shoreline change for California to determine if there are areas of chronic erosion in which both systems are behaving similarly (i.e. eroding at similar rates over the same temporal scale).

Coastal cliffs, as defined here, are steeply sloping geomorphic features, generally the seaward face of an elevated land surface, formed at the coast. Across the literature, "cliff" frequently refers to a slope formed in stronger more resistant rock units, whereas bluffs are slopes eroded in softer, unlithified material such as glacial till or ancient dunes. For the purposes of this paper the terms cliff and bluff are used interchangeably.

METHODS AND DATA

The U.S. Geological Survey has recently undertaken a nationwide assessment of historical shoreline change rates and trends for open-ocean coasts of the U.S. To date, analyses have been completed for the Gulf of Mexico (Morton et al. 2004), the Southeast U.S. (Morton and Miller, 2005) and the California coast (Hapke et al 2006). In addition, an analysis of coastal cliff retreat is currently underway for the California coast using a subset of the data sources used in the shoreline assessment. The primary data sources for the shorelines and cliff edges used in these studies are NOS T-sheets from the 1800s, 1930s and 1950s/70s for the historical shorelines, and lidar data (1998 or 2002) for the modern shoreline and cliff edge.

The historical shorelines are high water lines which are visual estimates of the high water line on the beach. The lidar shoreline, however, is a mean high water shoreline which is based on a local tidal datum. For this analysis, a proxy-datum adjustment was applied to the shoreline change rates (see Hapke et al. 2006, for details) to account for the bias in the data that occurs from using two different shoreline proxies. In order to statistically evaluate the relationship between cliff retreat and shoreline change, it was necessary to use the same data sources and generate rates over the same time period. As a result, shoreline change was generated as end point rates using only the 1930s and 1998/2001 shorelines rather than all four available shorelines because it was determined that the cliff edge was not a consistently valid feature on T-sheets from the other eras.

The cliff edge was digitized directly from the 1930s T-sheets after several pilot areas of

known low cliff retreat (e.g. granitic headlands) were evaluated to verify that the cliff and cliff edge as rendered on the T-sheets were valid features. The modern cliff edge was derived from the same lidar data used for the shoreline analysis. The data was gridded using a natural neighbors algorithm, at a 1 m cell size. A hillshade, which is a shaded surface based on the reflectance values and shading effects of surrounding surface features, was created from each grid. Hillshading is a useful tool for enhancing the visualization of a surface, and the resulting 3D rendering was used to interpret and hand-digitize the cliff edge using the visual break in slope. This visual rendering approach has advantages over slope or second-derivative methods of edge enhancement in that objects such as buildings or vegetation that are near the cliff edge are easier to identify and omit from the dataset. Oblique aerial photographs as well as historical maps were utilized during the digitization process to resolve ambiguities in the identification of the cliff edge.

The Digital Shoreline Analysis System (DSAS; Thieler et al., 2005) was used to calculate change along coast-perpendicular transects spaced at 20 m intervals. Although transects were generated along the entire coastline, only transects that intersected both the 1930s and 1998/2002 cliff edges and shorelines were used. There are large areas of data gaps for the cliff edges, as the edge was not used if it was an ambiguous feature on the historical maps, and there are many areas where the lidar data did not extend far enough inland to capture the cliff edge. In total, we were able to correlate the rates of change of the shoreline and cliff edge on 7,618 transects, covering a total of 152 km of the California coast. These data are assessed and presented for fifteen regions, as shown in Figure 1. Although data are distributed along the entire length of the coast, the number of transects per region varies dramatically (Table 1), as a function of both the geomorphology within each region and the data gaps described above. Central California consistently has the most data coverage. Northern and Southern California have more areas where sandy shorelines and coastal cliffs do not coincide.

RESULTS AND DISCUSSION

For the 152 km of coastline along which we calculated coincident shoreline change and cliff retreat, the average shoreline change rate (-0.1± 0.2 m/yr) is lower than the average cliff retreat rate (-0.3± 0.2 m/yr). In certain areas, the shoreline is prograding, and as such the net shoreline change contains averages of positive and negative values. The average shoreline *erosion* rate (the average of those transects with an erosional trend, 72% of the transects) is -0.3±0.2 m/yr, the same as the cliff retreat rate. This implies that based on a regional average, the beach and cliffs along the California coast are eroding at an equivalent rate.

It is important to note that the average change rates presented here will not be the same as those reported in Hapke et al. (2006) and Hapke et al. (in press), as different transects were generated for this analysis in order to increase the density of the data and to assure transects intersected both the 1930s and 1998/2002 shorelines and cliff edges. Additionally, there is a much more limited amount of data (covering a total of 152 km for the entire state) due to the requirement that there were coincident cliffs and shorelines for each transect.

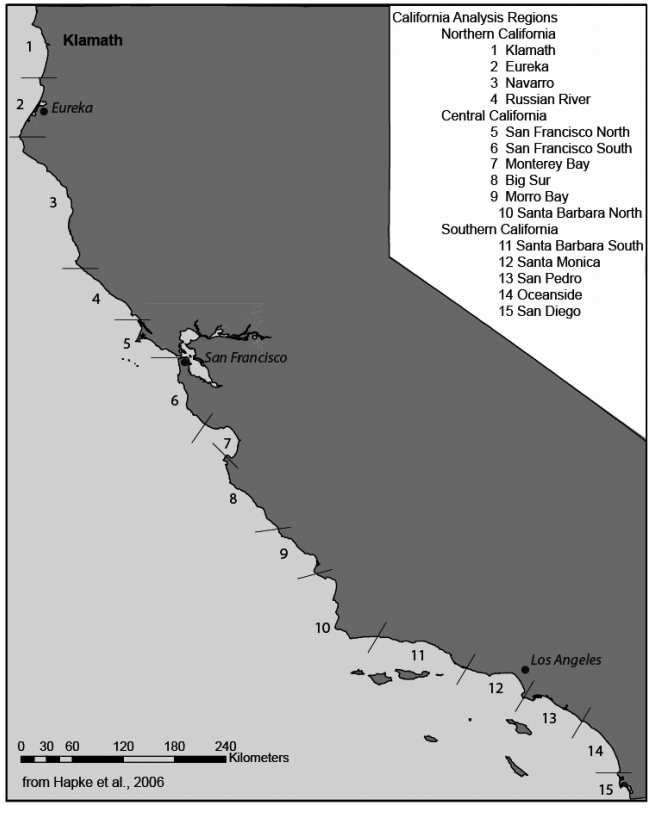

Figure 1. Location map of California showing the fifteen analysis regions.

Figure 2 shows the average rates of shoreline change and cliff retreat for each of the fifteen analysis regions. In general, the cliff retreat rates are highest in Central and Northern California, with the exception of the San Diego region in Southern California. Rates of shoreline change are highest in Central California. Besides some overlaps in these broad regional trends (i.e. high rates of both erosional shoreline change and high cliff retreat rates), there is no consistent evidence of a strong relationship between shoreline change rates and cliff retreat rates when values are averaged along the ~100-km analysis regions. In some regions where the average cliff retreat rates are high (>0.4 m/yr), such as the Eureka, Navarro San Diego regions, the average shoreline change is <0.1 m/yr. Central California exhibits the most consistent relationship between shoreline change and cliff retreat. It is likely that the lack of similar behavior between the beach and cliff in Southern California is related to the impact of human manipulations to the system (seawalls, groins, nourishments projects, etc.). In Northern California, the coastal system is dominated by high-relief, steep

slopes where large, deep-seated landslides are the dominant process of coastal retreat. Beaches tend to occur at river and stream mouths where valleys interrupt the coastal slope. Since the beach/cliff systems are rarely coincidental, it is not surprising that there is little apparent relation between the shoreline change and cliff retreat rates.

Table 1. Shoreline change and cliff retreat rate data for the 15 analysis regions

	Region	No. of transects	Length of coast (km)	Mean Shoreline Change Rate (m/yr)	Mean Cliff Retreat Rate (m/yr)
Northern California	Klamath	210	0.21	-0.3	-0.4
	Eureka	10	0.01	< 0.1	-0.5
	Navarro	350	0.35	0.1	-0.4
	Russian River	36	0.036	0.1	-0.1
Central California	San Francisco North	431	0.431	-0.4	-0.5
	San Francisco South	564	0.564	-0.3	-0.3
	Monterey Bay	547	0.547	-0.4	-0.6
	Big Sur	264	0.264	-0.1	-0.2
	Morro Bay	105	0.105	-0.3	-0.3
	Santa Barbara North	2273	2.273	-0.2	-0.2
Southern California	Santa Barbara South	15	0.015	-0.1	-0.2
	Santa Monica	829	0.829	< 0.1	-0.2
	San Pedro	219	0.219	-0.1	-0.1
	Oceanside	1712	1.712	0.1	-0.2
	San Diego	53	0.053	< 0.1	-0.6

One of the objectives of this analysis is to assess the relationship between the mechanisms of *retreat* of the coastline. Since the average rates of shoreline change contain both erosional and progradational data, they do not provide information only on shoreline retreat. To better understand the relationship between the trends of cliff retreat and shoreline retreat, we compared average rates of cliff retreat in areas were the shoreline is erosional to the cliff retreat rates in areas where the shoreline is accreting. The results of this are displayed in Figure 3, which demonstrates that cliff retreat rates are usually higher in the areas where the beach is eroding. Of the fifteen regions, 60% have higher cliff retreat rates where the beaches are undergoing long-term erosion. The average difference between the rates in these regions is -0.2 m/yr. Most of the regions where the cliff retreat rates are the same regardless of whether the beach is eroding or accreting are in Southern California, and again, this is likely related to the extensive manipulation of the beach and cliff systems in this part of the state. The Eureka region in Northern California is unusual in that it is the only region where the cliff retreat rate is higher where the shoreline is accreting. There are very little data available in this region (Table 1), and the specific location where the cliff and shoreline data coincide (10 transects) is the site of a large landslide complex just north of Cape Mendocino. The narrow beach is rapidly replenished by material from the landslide, thus resulting in high shoreline accretion rates where there are also high cliff retreat rates.

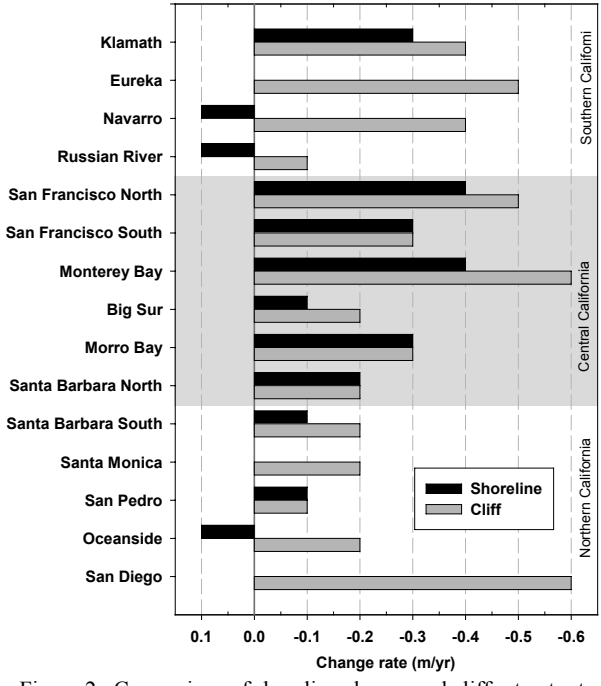

Figure 2. Comparison of shoreline change and cliff retreat rates for the fifteen regions analyzed in this study.

The previous discussion focused on assessing the average trends of the shoreline change and cliff retreat data on a large spatial scale (i.e. the state of California). In order to explore the relationship of the beach/dune system on a somewhat more localized scale, we generated plots of cliff retreat versus shoreline change for each of the fifteen analysis regions (Figures 4-6). The scatter plots show the relative distribution of the data and these data were correlated to assess the relationship between cliff retreat and shoreline change within each individual region.

Northern California

Figure 4 shows the cliff retreat versus shoreline change plots for the four regions in Northern California. Two of these regions (Eureka and Navarro) show a strong negative correlation between the data sets, which indicates that cliff retreat may be influencing rates of shoreline change. In areas of the coast where the characteristic geomorphology is steep, high-relief coastal slopes, large deep-seated landslides are the dominant process of coastal retreat. These landslides can contribute large volumes of material to the base of the slope, and this material may be stored on the subaerial beach, causing a seaward progradation of the shoreline.

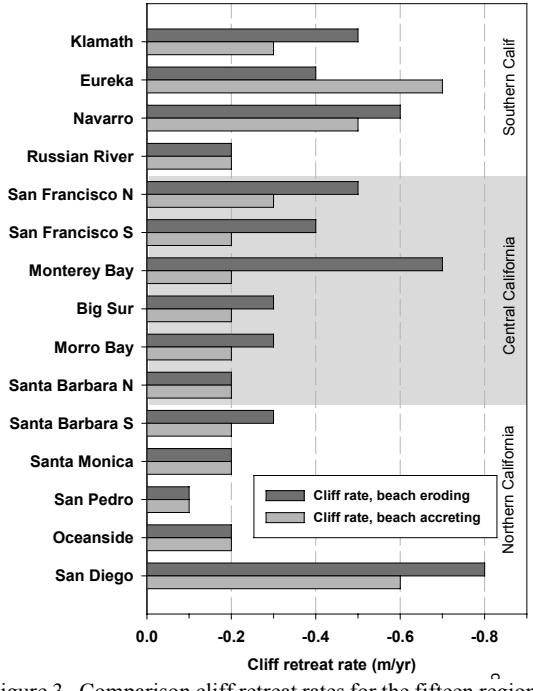

Figure 3. Comparison cliff retreat rates for the fifteen regions separated by whether the fronting beach is eroding or accreting.

Although the slopes of the regression lines in Figure 4, for the Eureka and Navarro regions, are not steep, there is evidence from the data that areas where cliff retreat is higher correlate to areas where the shoreline is prograding or retreating more slowly. The highest positive correlation and regression slope occur in the Klamath region (Figure 4). Although Northern California in general is dominated by high-relief coastal slopes, the areas for which we have Klamath data are all beaches backed by low cliffs or flat marine terraces. The processes resulting in retreat of these geomorphic settings tend to be lower volume, shallow failures of the cliff. Therefore, it is expected that the relationship between the beaches and cliffs will be different than in the large landslide-dominated regions.

Central California

All six of the analysis regions in Central California show some relationship between the beach and cliff system (Figure 5). In all regions except Big Sur, the correlation is positive, indicating larger cliff retreat rates in areas with larger shoreline retreat rates. As discussed above for the Klamath region, it appears that positive correlations occur in datasets from areas where the geomorphology is dominated by low- to moderate- relief cliffs that retreat via shallow failures of the cliff. This retreat mechanism results in a much lower

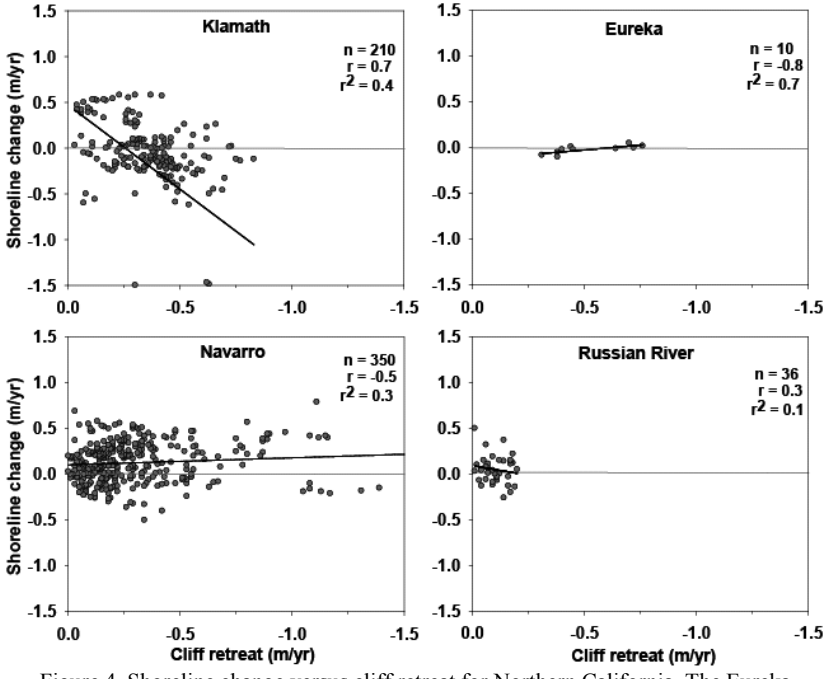

Figure 4. Shoreline change versus cliff retreat for Northern California. The Eureka and Navarro regions show a reverse trend between the rates Indicating lower shoreline retreat in areas of higher cliff retreat.

contribution of material to the beach system relative to that delivered by large, deep-seated landslides. It appears that in these low- to moderate-relief cliffed areas, the rates of shoreline retreat influence the retreat rates of the cliff. This observation is supported by the negative correlation in the Big Sur region (Figure 5) where the coastal geomorphology is much more dominated by large landslides, and the beach/cliff system behaves more similarly to that observed in Northern California. The Monterey Bay region has the strongest correlation in the state. In Figure 5, the dashed oval in the Monterey Bay region delineates data that is primarily from the southern part of the Bay where high rates of shoreline retreat and cliff erosion are well documented (Thornton et al., 2006). Based on our data, this area is the largest and most well-defined erosion "hotspot" in the state, at least over the temporal scale of the 70-years of this analysis.

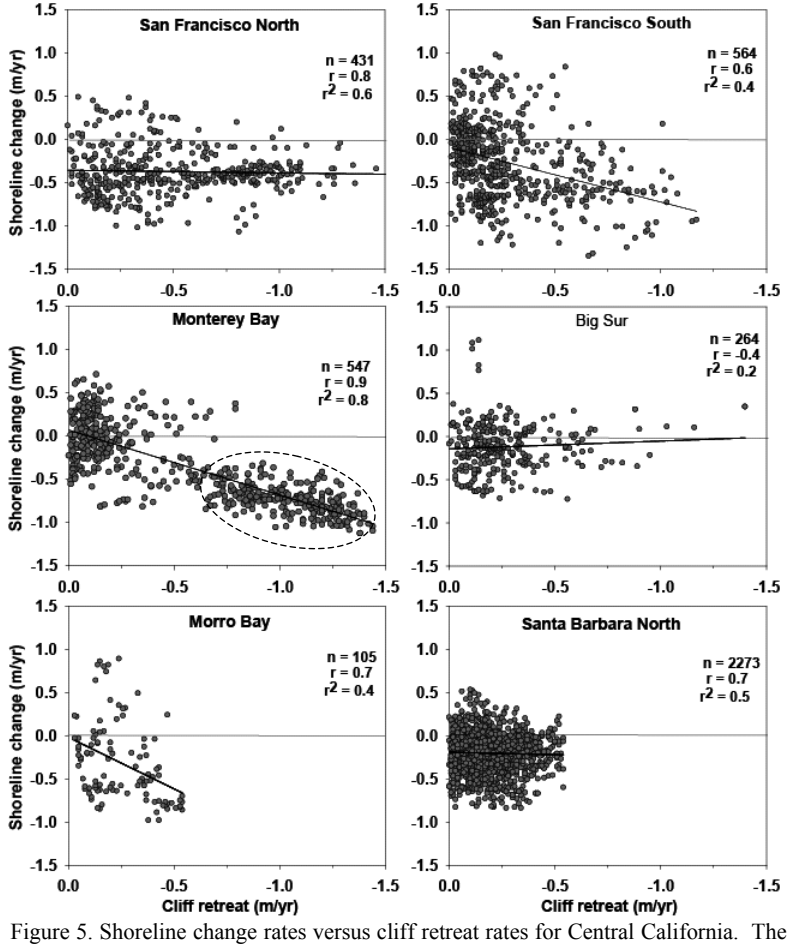

Figure 5. Shoreline change rates versus cliff retreat rates for Central California. The Monterey Bay region shows a strong correlation between high rates of shoreline and cliff erosion.

Southern California

Southern California, which is divided into five analysis regions for this study, has the most highly human-manipulated coastline in the state. As a result, the correlations between the shoreline change and cliff retreat datasets are poor (Figure 6). Most of the regions are lacking distinct trends in the data (i.e. Santa Barbara South, Santa Monica, San Pedro). The Oceanside and San Diego regions visually appear to have some positive trend in the data but

that correlation coefficients are relatively low (0.4). Santa Monica is the only region in the state to have a correlation coefficient of zero.

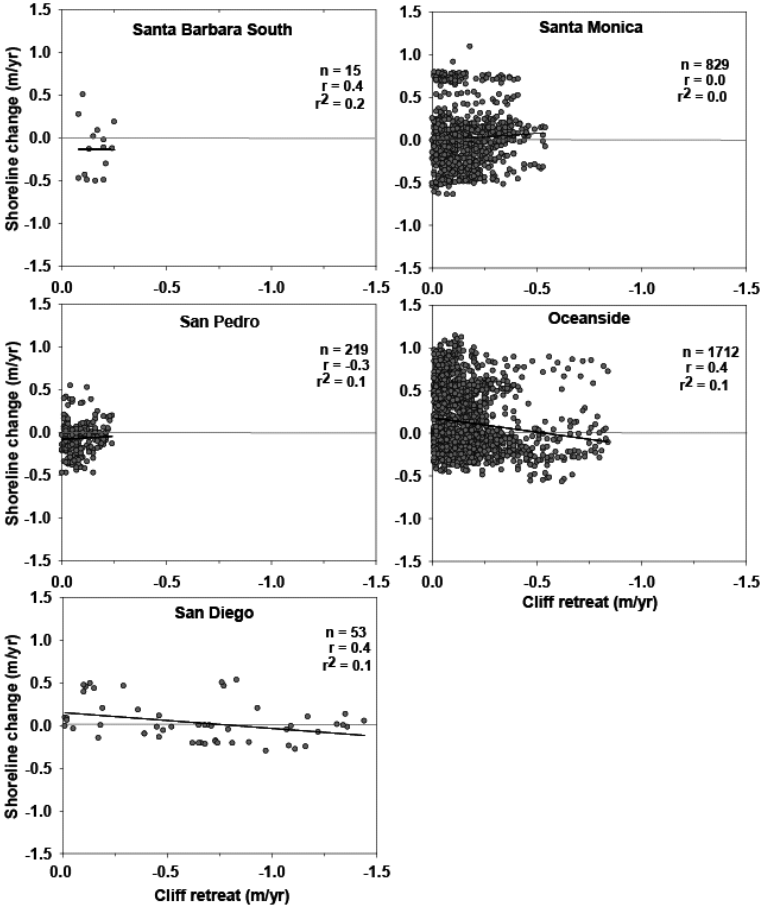

Figure 6. Shoreline change rates versus cliff retreat rates for Southern California. The regions all have low correlation values, and the Santa Monica region is the only one in the state to have a zero correlation.

CONCLUSIONS

Cliff edges and shorelines derived from 1930s historical maps and modern lidar data were used to produce a set of data whereby cliff retreat and shoreline change were calculated on the same transects and could therefore be statistically correlated to assess how the beach/cliff systems behave relative to one another. The final dataset covers 152 km of the California coast and samples the coastline along it entire length, albeit discontinuously.

Geomorphology and geology are strong controls on the relationship between the coastal retreat rates. In areas characterized by high-relief coasts, where the dominant coastal retreat process is movement on large, deep-seated landslides, the correlation between shoreline change and cliff retreat is negative. In these areas, transects showing higher cliff retreat rates correlate to areas of lower shoreline erosion or shoreline progradation. The mechanism of retreat, deep-seated landslides, results in the contribution of large volumes of material to the subaerial beach environment, thus slowing erosion or increasing accretion. Negative correlations were observed in the Eureka and Navarro regions in Northern California, and in the Big Sur Region in Central California.

In areas where the geomorphology is dominated by low- to moderate-relief cliffs, there tends to be a strong positive correlation between rates of shoreline change and cliff retreat such that areas of higher shoreline erosion are also areas of higher cliff retreat. In areas of more rapid shoreline erosion, waves will have more frequent opportunity to impact the cliff base. In addition the mechanisms of retreat of low- to moderate-relief cliffs (shallow landslides and slumps) do not contribute high volumes of material to the subaerial beach system. This positive correlation between cliff retreat and shoreline erosion was observed largely in Central California, with the exception of the Big Sur region. Additionally, the Monterey Bay has the highest positive correlation in the state, and the data indicate a chronic erosion hotspot in Southern Monterey Bay.

Human modified systems have the poorest correlation. This is demonstrated throughout Southern California where lack of correlation suggests that the beaches and cliffs behave independently in terms of rates of retreat.

ACKNOWLEDGEMENTS

We would like to thank Krystal Green (USGS), Mark Borrelli (URI) and Brian Spear (UCSC) for their assistance in generating many of the baseline data used in this study.

REFERENCES

California Department of Boating and Waterways and State Coastal Conservancy. (2002). "California Beach Restoration Study," Sacramento, California.

Griggs, G.B. and Savoy, L.E. (1985). "*Living With the California Coast,*" Duke University Press, 393 p.

Griggs G.B., Patsch, K., and Savoy, L. (2005). "*Living with the Changing California Coast,*" University of California Press, 540 p.

Hapke, C., Reid, D., Richmond, B., Ruggiero, P. and List, J. (2006). "National Assessment of Shoreline Change Part 3: Historical Shoreline Change and Associated Land Loss Along Sandy Shorelines of the California Coast," *U.S. Geological Survey Open-file Report 2006-1219*, 79 p.

Hapke, C., Reid, D., Green, K., and Borelli, M. (in press). "Historical Coastal Cliff Retreat Along the California Coast: An Addendum to the National Assessment of Shoreline Change Part 3: Historical Shoreline Change and Associated Land Loss Along Sandy Shorelines of the California Coast," *U.S. Geological Survey Open-file Report.*

Moore, L.J., Benumof, B.T., and Griggs, G.B. (1999). "Coastal Erosion Hazards in Santa Cruz and San Diego Counties, California," *Journal of Coastal Research Special Issue #28*, 121-139.

Morton, R.A., Miller, T.L. (2005). "National Assessment of shoreline Change: Part 2: Historical shoreline change and associated land loss along the U.S. South East Atlantic Coast," *U.S. Geological Survey Open-file Report 2005-1401*, 40 p.

Morton, R.A., Miller T.L, and Moore, L.J. (2004). "National Assessment of shoreline change: Part 1, Historical shoreline changes and associated coastal land loss along the U.S. Gulf of Mexico," *U.S. Geological Survey Open File Report 2004-1043*, 44 p.

Sallenger, A.H., Krabill W., Brock J., Swift R., Manizade S., Stockdon H. (2005). "Sea-cliff erosion as a function of beach changes and extreme wave runup during the 1997-1998 El Nino," *Marine Geology* 187(3), 279-297.

Thieler, E.R., Himmelstoss, E.A., Zichichi, J.L., and Miller, T.L. (2005). "Digital Shoreline Analysis System (DSAS) version 3.0; An ArcGIS© extension for calculating shoreline change," *U.S. Geological Survey Open-File Report 2005-1304.*

Thornton, E.B., Sallenger, A.H., Conforto Sesto, J., Egley, L. A. , McGee, T., and Parsons, A.R. (2006). "Sand Mining Impacts on Long-Term Dune Erosion in Southern Monterey Bay," *Marine Geology* 229(1-2), 45-58.

U.S. Army Corps of Engineers. (1971). "National Shoreline Study, California Regional Inventory," 106 p.

FACTORS INFLUENCING THE LONG-TERM STABILITY OF THE CARBONATE SAND BEACHES OF MAURITIUS

Michael J. Risk[1], Robert B. Nairn[2] and Mark O. Kolberg[3]

1. McMaster University, 1280 Main Street West, Hamilton, Ontario, CANADA L8S 4M1, riskmj@univmail.cis.mcmaster.ca
2. Baird & Associates, 627 Lyons Lane, Suite 200, Oakville, Ontario, CANADA L6J 5Z7, rnairn@baird.com
3. Baird & Associates, 627 Lyons Lane, Suite 200, Oakville, Ontario, CANADA L6J 5Z7, mkolberg@baird.com

Abstract: The long-term stability of the carbonate beaches of Mauritius is the result of the net balance of the supply of carbonate sand from the coral reef environment and the loss of sand to adjacent depositional beaches and through passes in the fringing coral reef to off-reef environments. Carbonate sand is supplied from the lagoon and the balance has been tipped in the favor of losses over supply due to a range of anthropogenic factors including: historic coral harvesting for lime kilns servicing the sugar cane refining industry; removal of coral for water ski lanes; coral health degradation through a decrease in water quality; over-fishing; and creation of navigational passes. This paper presents a technique for quantifying the supply of sand from the various lagoon facies using sediment constituent analysis and hyperspectral imagery. Numerical models are used to describe the sand loss. Non-structural management recommendations are designed to reverse the long-term beach erosion trend.

INTRODUCTION

The 320 km long coastline of the island of Mauritius, in the southwest Indian Ocean, is mostly surrounded by coral reef and associated lagoons. The economy is based to a large extent on tourism, with relatively stable sandy beaches being essential to the success of the tourism sector. Several cyclones pass by the east or west side of the island each year moving from north to south. Mauritius is also strongly influenced by swells generated in

the southern ocean due to forcing from the passage of extra-tropical cyclones. Wherever beaches exist, a near-continuous relict fringing reef system protects a wide shallow lagoon and the beaches along the shoreline from a high-energy wave environment. While beach erosion has been documented in the past, it is only over the last 10 to 15 years that the erosion has become apparently irreversible. This paper presents the results of an investigation of the factors influencing the net balance between the supply and loss of carbonate sand that results in either erosion or accretion at Flic en Flac beach on the west coast of Mauritius. This was one of several sites evaluated by Baird (2003) as part of an extensive study of coastal erosion in Mauritius for the Ministry of Environment.

EXISTING BEACH CONDITIONS

The Flic en Flac beach and coral reef-lagoon system is shown in Figure 1. Near the center of this system is one of the most heavily used public beaches on Mauritius. In 1995, in response to a growing erosion problem over the previous 10 years, a gabion wall and small gabion groynes were constructed to protect the southerly 450 m of public beach shoreline. By 2002, the gabion structures were in an advanced state of deterioration, particularly towards the south end of the wall (see Figure 2). Flanking erosion was also occurring at either end of the gabion wall.



Fig. 1. Oblique Aerial Photo of Flic en Flac Looking South Along the West Coast of Mauritius (November, 2002)

Based on a constituent analysis of the beach sand and reconnaissance of the 300 to 500 m wide lagoon, it was determined that sand along this shore is entirely derived from lagoon corals and the associated marine community (Baird 2003). The median grain size is temporally and spatially variable but on average has a D50 in the range of 0.3 to 0.5 mm. The beach sand quickly diminishes to a thin veneer of sand over Pleistocene reef rock in depths greater than a 1 m below MSL.



Fig. 2. Deterioration of the Gabion Wall and Groynes Protecting the Public Beach (November 2002)

This section of the Mauritius coast has suffered from a range of human impacts including: mining of beach and dune sand; removal of coral to feed a kiln to create lime used in processing sugar from the cane crops; construction of seawalls for hotel developments that encroached on the dynamic beach zone; removal of native coastal vegetation; over-fishing of the lagoon; and removal of coral for water ski lanes. Other sections of the Mauritius coast show initial signs of deterioration through algal growth related to excessive nutrient loading.

HISTORIC PROFILE AND SHORELINE CHANGE

The geomorphology of the beach and landform suggest that in the long-term this beach has been progradational, although accretion rates were likely slow (Baird, 2003). More recent shoreline changes were documented through GIS analysis of air photos from 1967 (prior to development of this section of Mauritius) and 1997. The results of this analysis for the south end of the Public Beach at Flic en Flac show that the vegetation line retreated 15 m during this period (see Figure 3).

Erosion along this shore typically occurs during cyclone events. The only available information on erosion in response to a cyclone were pre- and post-storm profiles completed for several locations on the island by McIntire and Walker (1964) before and after Cyclone Carol hit the island in February 1960 (see Figure 4). McIntire and Walker (1964) postulated that the berm marked by an "x' on the profile represents post-storm beach recovery and that the actual profile at the height of the storm may have featured much greater erosion. Based on the surveyed profiles, the beach crest retreated 4.6 m inland as a result of the cyclone and the eroded volume was approximately 10 m^3/m.

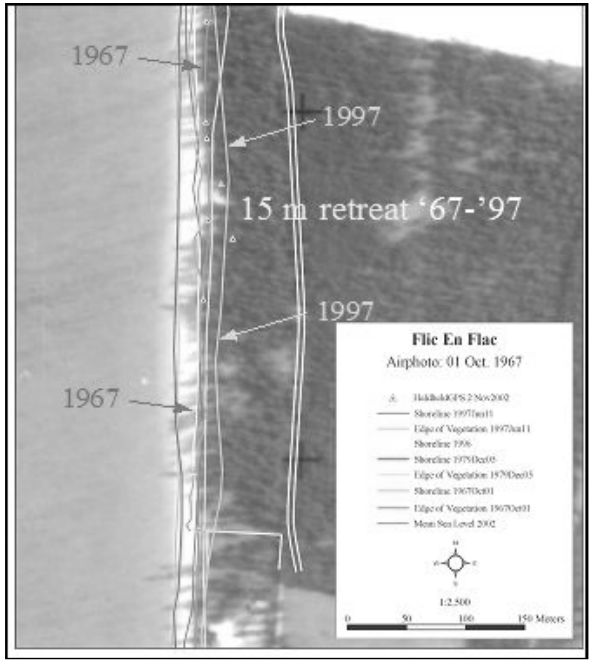

Fig. 3. Shoreline Change for the South End of Flic en Flac Public Beach

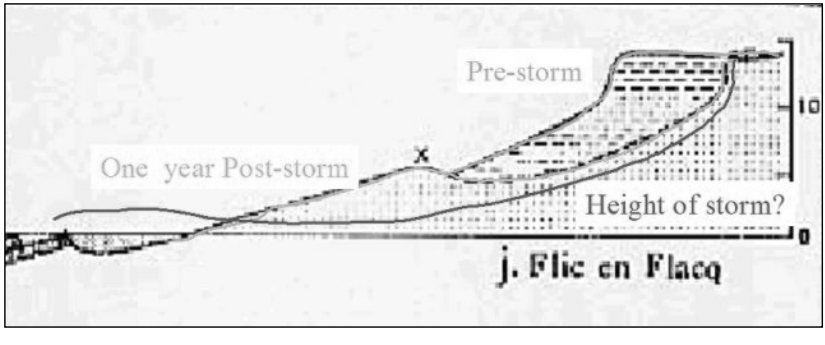

Fig. 4. Flic en Flac Profile Change Following Cyclone Carol
(interpreted from McIntire and Walker, 1964)

WAVE AND WATER LEVEL CLIMATE

The waves affecting Mauritius' coastal areas are generated through three different meteorological phenomena (Baird, 2003): 1) locally generated seas by the southeast trade winds (from which the Flic en Flac site on the west coast of the island is mostly sheltered); 2) swells generated by extra-tropical cyclones in the southern Indian Ocean; and 3) tropical cyclones that develop in the southwest Indian Ocean and typically approach Mauritius from east and north. Owing to the shallow reef protecting much of the island, beach erosion is primarily driven by surge and wave setup associated with tropical cyclones that allow wave energy to pass over the reef into the lagoon and towards the beaches. It is only the waves from tropical cyclones with associated storm surge that result in significant erosion of the island's beaches. A wave climate for all three sources of wave energy was modeled using a Baird-modified version of the well-known WAVAD model originally developed by Resio (1981) for the U.S. Army Corps of Engineers. A total of twenty-five different historical cyclones over the 1979 to 2002 time period were simulated. The model was validated against Waverider data for Cyclone Davina in 1999 with a peak measured H_s of 8.5 m (see Baird, 2003). Storm surges were also estimated for these historical cyclones. Figure 5 shows the cyclones that passed within 100 km of the island between 1979 and 2002. During this period, nine storms of tropical cyclone intensity passed within 100 km of Mauritius, or once every 2.5 years. These events feature peak significant wave heights in the range of 10 to 15 m with peak periods of 14 to 16 s. In addition to the detailed assessment for the period since 1979, a qualitative assessment of the frequency and intensity of cyclone attack dating back to 1848 was completed.

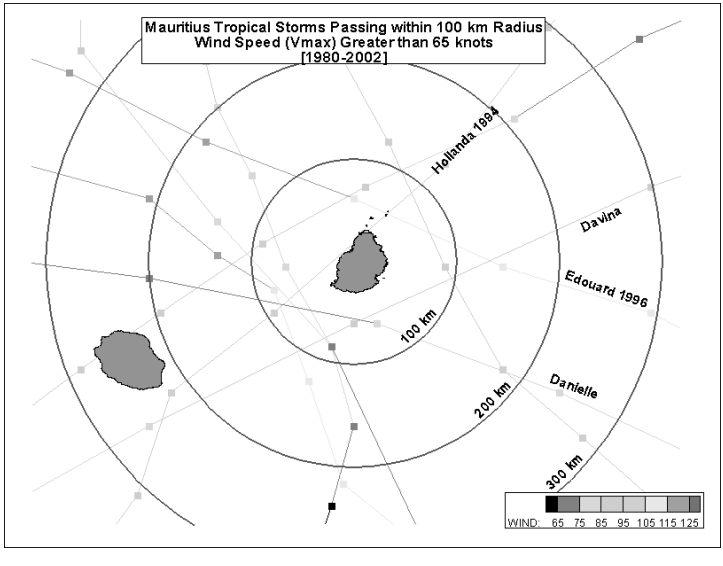

Fig. 5. Tracks for the Various Tropical Cyclones Simulated with WAVAD

As noted previously, the reefs surrounding Mauritius are wide and shallow-crested with the crest elevation being just slightly below low water level on this microtidal coast (typical tidal range of about 0.3 m to 0.5 m). The wave attenuation during average conditions and during cyclone storm surges was estimated with the COSMOS model (Nairn and Southgate, 1993). The ability of the model to predict wave attenuation across the reef was successfully tested against wave measurements made on either side of the reef (see Baird 2003). Figure 6 shows a sample of the COSMOS results for wave conditions with H_s=2 m and T=10 s and a surge of 0.3 m. The 90% reduction in incident wave height is representative of the degree of wave attenuation under most wave conditions.

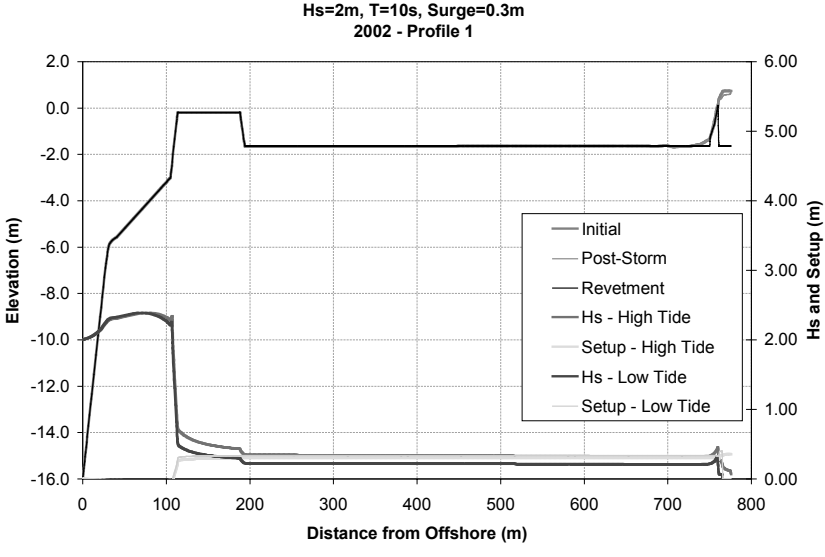

Fig. 6. Wave Height and Period Sensitivity Testing for Flic en Flac

SAND LOSS DUE TO CROSS-SHORE CHANGE AND LST GRADIENTS

During those cyclone events where storm surge and wave setup allows waves to pass over the protective reefs, the result is both cross-shore profile change (eroding the upper part of the steep 5:1 beach face) and longshore sand transport. The beach erosion at Flic en Flac was simulated for all the cyclones between 1979 and 2002 using the COSMOS model. The model was successfully validated against the estimated profile change immediately following Cyclone Carol (see Figure 7).

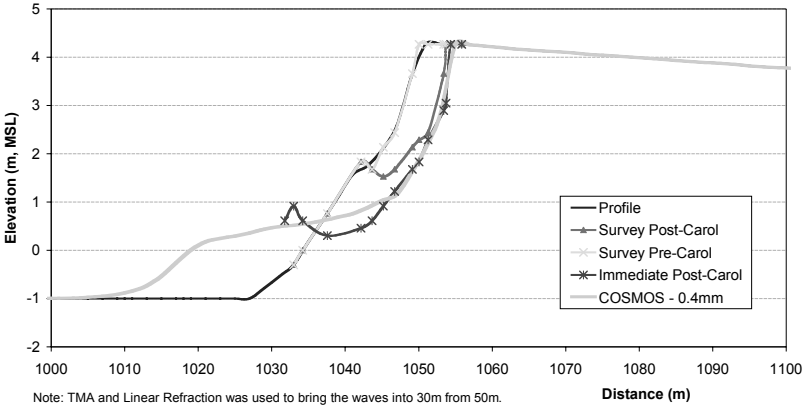

Fig. 7. Predicted vs. Measured Erosion for Cyclone Carol

Based on the COSMOS numerical model estimates, the rates of sand loss for all of the major cyclones during the period 1979 – 2002 were determined. Table 1 provides a summary of loss rates in terms of beach crest retreat and sand volume eroded.

Table 1. Lateral Crest Retreat and Eroded Volume for a Range of Cyclones

Return Period (years)	Greatest Retreat (m)	Erosion Volume (m^3/m)
5	7 – 10	12 – 17
10	8 – 11	13 – 19
25	8.5 – 12.5	16 – 23
50	9 – 13	17 – 24
100	11 - 14	20 - 27

For the Flic en Flac Beach sector, the gradients in longshore sand transport were also estimated with the COSMOS model. Sand is eroded from the middle section of the beach in the vicinity of the public park and transported to the north and/or south depending on the incident wave direction (see Figure 8). The sand that is eroded from the middle section of this sector is deposited in beaches to the north or south and also transported offshore through passes in the reef line and deposited in deepwater immediately offshore of the reef.

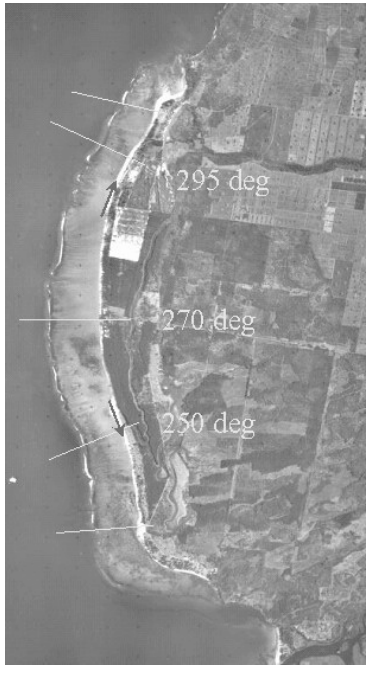

Fig. 8. Azimuths Along the Flic en Flac Shore and Direction of Longshore Sand Transport

QUANTIFYING THE CARBONATE SAND SUPPLY RATE

The coral reef habitat of the island of Mauritius was mapped with CASI (Compact Aerial Spectral Imagery) in 1996 for the Ministry of Fisheries. During the work by Baird, this data on coral reef facies was partially ground-truthed in specific areas of interest. The rate of supply of carbonate sand was estimated by integrating facies coverage by production rates estimated from previous work in the literature (e.g. Smith, 1973; Stearn et al. 1977; Hubbard et al., 1990). Using the CASI data and an estimated carbonate sand supply rate of 5 kg/m^2/year for the various reef areas, an estimate of the sand supply per meter of shoreline was made using GIS. This supply rate was successfully validated for the site on the east coast of Mauritius that featured long-term beach accumulation in a closed bay (see Baird, 2003).

Table 2 shows the range of carbonate sand supply rates along the shore reflecting the variability of coral patch reef coverage within the lagoon (with higher density of coral resulting in higher sand supply rates). The range in values for each reach represents the integrated uncertainty in production rates for different types of lagoon facies. The reaches are shown in Figure 9 and it is noted that the lowest supply rate corresponds to the reach

containing the public park shoreline at Flic en Flac. There is little or no patch reef in this zone, possibly owing to the historic harvest of coral in the mid-1900's to feed the lime kiln that is located at the north end of the park.

Table 2. Estimates of Sand Production Rates at Flic en Flac

Reach	Sand Production Rate (m3/m/yr)
A	0.43 – 0.84
B	0.43 – 0.65
C	0.57 – 1.00
D	0.52 – 0.77
E	0.95 – 1.34

SEDIMENT BUDGET

In order to evaluate the balance between sediment production and sediment loss, a sediment budget was completed for the period of shoreline change data from 1967 to 1995 (this latter date corresponding to the construction of the gabion wall at the Flic en Flac public beach). Only the sediment budget for the park area is presented here; the budget for the entire Flic en Flac reach is presented in Baird (2003). It may be recalled that the shoreline in the public park retreated 15 m during this period. This 15 m retreat over the 4 m beach height (from the beach toe to the beach crest) amounts to approximately 60 m^3/m of sand lost from the beach during the 28-year period.

Based on the simulation of historic cyclones, there were four 5-year events and one 10-year event during this period from 1979 to 1995, on the west coast of Mauritius. From 1967 to 1979 only two other events occurred (Gervaise in 1975 and Fleur in 1978). Taking the average values of 14.5 m^3/m and 16 m^3/m erosion loss during 5- and 10-year cyclone events respectively from Table 1, the total beach erosion for this period is estimated to be 74 m^3/m.

From Table 2, the estimated supply rate for Reach B for the 28-year period from 1967 to 1995 would be in the range of 12 to 18 m^3/m. Therefore, the predicted difference between erosion due to cyclones and supply from the reefs would be in the range of a 56 to 62 m^3/m net loss. This prediction compares well to the measured loss of 60 m^3/m for this period. However, it must be considered that the numerical model estimates of beach erosion did not consider any post-storm recovery.

IMPLICATIONS FOR LONG-TERM BEACH STABILITY AT FLIC EN FLAC

Net erosion in typical cyclones (i.e. with return periods of less than 1 in 10 years) is in the range of 5 to 10 m^3/m, once every 3 to 10 years giving a net loss rate in the range of 0.5 m^3/m/year (5 m^3/m every 10 years) to 3.33 m^3/m/year (10 m^3/m every 3 years). The low end is the long-term norm whereas the higher rate is more indicative of the last 25 years in Mauritius due to a greater than normal frequency of cyclones.

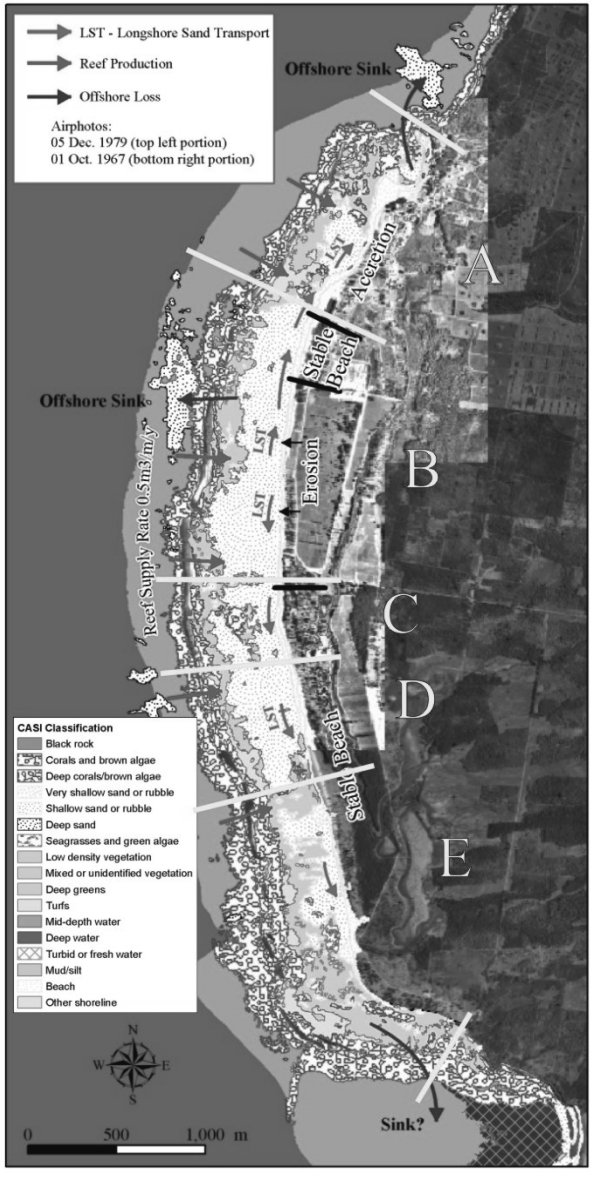

Fig. 9. Overview of Sediment Sinks and Sources at Flic en Flac

The GIS analysis of beach sand production from the reef-lagoon system found that the rates ranged from 0.4 to 1.3 m^3/m/year for the Flic en Flac lagoon depending on the extent and coverage of coral coverage in the lagoon. Therefore, in areas where coral is plentiful and healthy (i.e., high end of the range), the sand production rate will surpass the erosion rate under the normal frequency of cyclone attack and stable or accreting beaches will be the outcome. However, there is a fine balance between an accreting shore and an eroding shore in the long term. Once reef-lagoon sand production rates drop below about 0.5 m^3/m/year, even under normal cyclone frequency, long-term erosion will be sure to set in. While coastal zone managers have little control over the frequency of cyclones they can make a difference in preserving, protecting and even enhancing the reef-lagoon system and the resulting sand production rates.

MANAGEMENT ALTERNATIVES FOR BEACH PRESERVATION

At Flic en Flac, the local authorities initially believed the necessary solution was reconstruction of the gabion wall and groynes. However, the assessment of the root causes of erosion revealed that the solution at Flic en Flac was to redress the deficit in sand supply in order to re-establish the long-term stability of the beach. The recommended long-term solution consists of restoration of the lagoon coral in areas where production rates were determined to be less than 0.5 m^3/m/year. A hard substrate is to be placed above the hard, thinly covered bedrock floor of the lagoon in order to allow the coral spat to successfully recruit. It is anticipated that the coral restoration would sufficiently augment the natural supply within 5 to 10 years. The constant movement of a thin layer of sand supplied by the outer reef front across the bedrock lagoon floor explains why the patch coral has not naturally recovered since its removal to supply the lime kiln in the mid-1900's.

To address the short-term need to re-establish a healthy beach, it was proposed that the beach should be restored and widened through nourishment. Sand is typically sourced from licenced inland quarries. Another possible source of sand for the nourishment project is the large deposits of sand in approximately 10 m depth of water at the base of two passes in the reef at Flic en Flac. It was proposed that 12,000 to 24,000 m^3 of sand be placed along approximately 600 m of the public beach. This amounts to unit volumes of 20 to 40 m^3/m. Even if the frequency of cyclone attack were to continue at the current high rate, and providing that an even greater frequency or intensity of attack is not experienced, the nourishment quantity should last 10 to 20 years even without the benefit of the augmented supply through coral restoration.

It was recommended that the wider beach created with the beach nourishment should be planted with native vegetation layered from creepers to low shrubs to higher shrubs moving inshore promoting dune growth. This vegetation prevents the inshore loss of sand through wind and overwash during cyclone events. Once the beach nourishment, dune and vegetation are in place, it will be necessary to manage the beach by means of controlling pedestrian access by walkovers and limiting vehicle intrusions through designated parking areas. A final aspect of the proposed solution to the erosion problem

at Flic en Flac is the removal of a hotel seawall located immediately south of the public beach. It was shown in Baird (2003) that this seawall has also likely contributed to the erosion of the beach.

At other locations around Mauritius, the solutions also consisted of: implementing improvements to local water quality to preserve and restore coral reef health, implementation of development setbacks, controls on the construction of hard structures and strict guidelines on creation of artificial passes.

CONCLUSION

The beautiful carbonate sand beaches of Mauritius are generally well protected by coral reefs and are naturally stable or progradational. The onset of beach erosion at several locations on the island over the last 25 years has mostly resulted from a combination of the loss and removal of patch coral in the lagoons and a higher than average frequency of cyclone attack. There is a fine balance between supply of sand from the patch coral in the lagoons and loss of this sand to accretional zones and deposits offshore of passes. The reduction of supply from the lagoons was a direct result of several human factors including: coral mining to supply lime kilns in the 1950s; removal of coral for water ski lanes and navigation; degradation of water quality through elevated loadings of sediment and nutrients; and over-fishing. Preservation of the patch coral in the lagoon through management of these human activities and restoration of the coral where required are the fundamental long-term solutions to beach stability.

Based on this foundation of understanding the root causes of coastal erosion, an action plan was formulated with specific and general recommendations (Baird 2003). The recommendations represent a blueprint for integrated coastal zone management. A summary of these recommendations for each part of the reef-lagoon-beach system is depicted in Figure 10. Short-term and interim solutions consist of beach nourishment providing adequate sediment controls are implemented. Development setbacks must be implemented and enforced to prevent encroachment of structures in the coastal zone. Native coastal vegetation should be restored to reduce onshore losses of sand during cyclones. The preservation and restoration of the natural and integrated reef, lagoon, beach and coastal vegetation systems will help to avert the widespread onset of irreversible erosion.

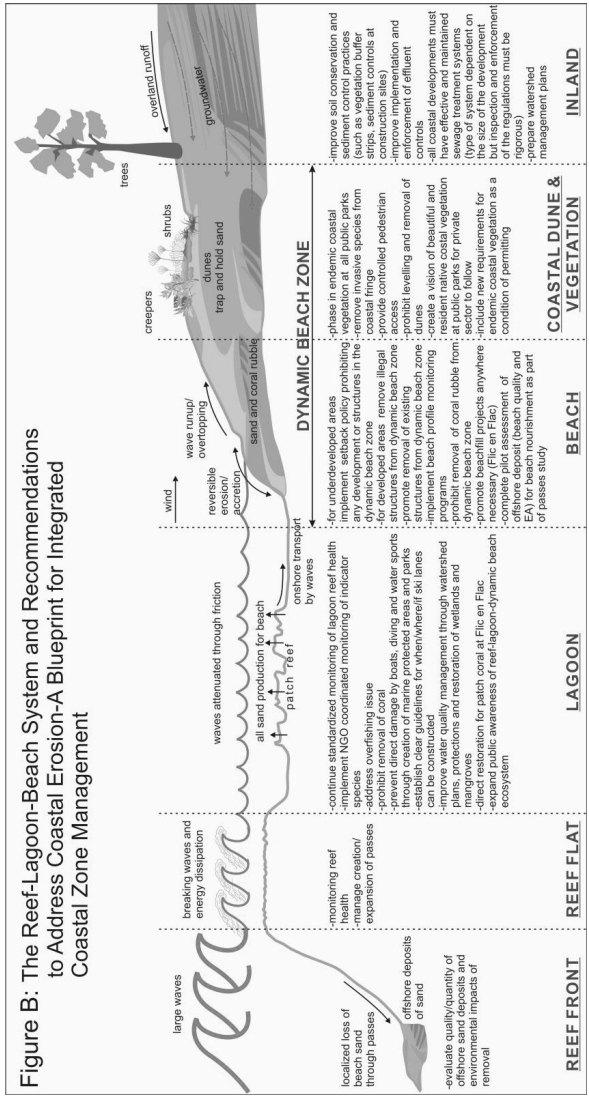

Fig. 10. Reef-Lagoon-Beach System and Recommendations to Address Coastal Erosion

ACKNOWLEDGEMENTS

The authors wish to thank Mr. S. Seebaluck, Permanent Secretary, Ministry of the Environment, Mr. Kallee, Chairman of the Coastal Erosion Study Steering Committee and all members of the Committee in Mauritius and Reef Watch Consultancy for the support provided to Baird during the course of the project.

REFERENCES

Baird (2003). "Study on Coastal Erosion in Mauritius, Final technical report for Ministry of Environment, Republic of Mauritius", August 2003.

Hubbard, D. K., Miller, A. I., and Scaturo, D. (1990). "Production and cycling of calcium carbonate in a shelf-edge reef system (St. Croix, US Virgin Islands): applications to the nature of reef systems in the fossil record," *J. Sedimentary Petrology* 60: 335-360.

McIntire, W.G., and Walker, H.J., (1964). "Tropical cyclones and coastal morphology in Mauritius," *Am. Ass. Am Geogr.* 54, 582-596.

Nairn, R.B. and Southgate, H.N. (1993). "Deterministic Profile Modelling of Nearshore Processes. Part II. Sediment Transport and Beach Profile Development,." *Coastal Engineering,* 19, 57-96.

Resio, D. (1981). "The Estimation of Wind-Wave Generation in a Discrete Spectral Model," *Journal of Physical Oceanography* Vol. 11, No. 4.

Smith, S. V. (1973). Carbon dioxide dynamics: a record of organic carbon production. , respiration and calcification in the Enewetak windward reef flat community," *Limnol. Oceanogr.* 18, 106-120.

Stearn, C. W., T. P. Scoffin and Martindale, W. (1977). "Calcium carbonate budget of a fringing reef on the west coast of Barbados. Pt. 1. Zonation and productivity," *Bull. Mar. Sci.* 27: 479-510.

EVOLUTION OF EROSION HOT SPOTS ON A BARRIER ISLAND: FIRE ISLAND, NEW YORK

Kathryn Seaver[1], Frank Buoniauto[2], Henry Bokuniewicz[3]

1. Department of Geology, Graham Building 101, East Carolina University, Greenville, NC 27858, USA.
   kathryn_seaver@yahoo.com
2. Hunter College, Department of Geography, New York, NY 10021, USA.
   Frank.buonaiuto@hunter.edu
3. Marine Science Research Center, Stony Brook University, Stony Brook, NY 11794-5000, USA.
   hbokuniewicz@notes.cc.sunysb.edu

Abstract: The distribution and evolution of local, shoreline features was examined by repeated mapping of the shoreline using a sub-meter GPS to map Fire Island from June to December. One region of erosion or "hot spot" was documented to migrate to the west, in the direction of the net longshore transport, at a rate of 2.1 m/day and then to the east at a rate of 4.2 m/day. Another shoreline feature followed the progression of a theoretical advection/diffusion model created earlier by other investigators to predict the migration of longshore sandwaves. This feature migrated to the west at 0.83 m/day. Similar features on the barrier island migrated to the west up to 51.5 m/day while others migrated to the east at rates up to 93.1 m/day. No trends in migration rate with the wavelength of the hot spot could be found. Rates tended to range between 1 and 100 m/day.

INTRODUCTION

Shoreline undulations are alternating landward and seaward displacements of the shoreline. Shoreline undulations manifest themselves in many different forms. Beach cusps, longshore sandwaves, and erosion hot spots are all classes of shoreline undulations. An erosion hot spot is defined for this paper as a specific section of the shoreline, of limited extent, which has become scoured of sand while nearby stretches of beach go relatively unscathed. The main goal of this study was to address whether or not erosion hot spots consistently appear in the same locations and whether or not

they migrate in the direction of net longshore transport. While mapping the ocean shoreline of a barrier island, Fire Island, we were able to study an erosional hot spot, a possible longshore sandwave and the wavelengths that compose undulating characteristics of the shoreline along the total length of Fire Island.

Study Area

Fire Island was chosen as the site for this research based on the previous works by Allen and Labash (1996), as described by Gravens (1999), and by Batten (2003). Fire Island is one of the south shore barrier beaches of Long Island, New York. It extends from Fire Island Inlet to Moriches Inlet and is approximately 50 km long and averages less than 0.5 km in width (National Park Service, 2006). Robert Moses State Park occupies its western extremity; to the east, Fire Island National Seashore encompasses most of its length and Smith Point County Park is found at its eastern terminus. Winds are primarily from the west but can vary from the southwest in summer to the northwest in winter. Waves generally approach from the south-southeast with an approximate wave height of 1 meter (Batten, 2003). Fire Island has a semi-diurnal tidal cycle (Batten, 2003). The direction of net longshore sand transport is from east to west (Gravens, 1999).

METHODS

The shoreline was mapped using an Ashtech Reliance Submeter GPS with an Ashtech BR2 Beacon Receiver and a Psion handheld controller. The technique used to map the shoreline was similar to that used by Allen and LaBash (1996), and described in Gravens (1999). The shoreline was defined as the boundary between the saturated and the unsaturated sand; this wet/dry contact is usually used in interpreting shoreline position from aerial photographs (Anders and Byrnes, 1991). Multiple surveys were conducted from June 2005 through December 2005. The surveys of individual features taken for this study were 4 hours or less in duration. Surveying the total length of Fire Island took about 4 to 5 hours to complete using four-wheeled vehicle, a Polaris Ranger.

Shoreline undulations were subjected to spectral analysis to look for dominant frequencies and changes of phase, which might indicate migration. The spectral analysis was conducted using MATLAB. The data was detrended using equal spacings of 1 meter. After the data was detrended it was run through a Fast Fourier Transform (FFT) in order to identify the dominant wavelengths. Individual wavelengths could then be processed using and inverse FFT (IFFT) in order to obtain information about changes in amplitude and shifts in phase.

RESULTS

Smith Point Hot Spot

On 12 June, 2005 a shoreline undulation or “hot spot” was first mapped approximately 5 km east of Smith Point County Park. Smith Point County Park was then surveyed seven more times during the five month interval of June through October and twice afterwards on 17 and 18 November and 1 December, 2005. The majority of the surveys were conducted during the falling tide in order to catch the

high tide shoreline as well as possible. The dune line remained stationary throughout the period. Several of the surveys were conducted specifically to see the results of a variety of passing storms. Between 12 June and 22 September, 2005 the hot spot became significantly less prominent in part because of shoreline recession to the east (Figure 1).

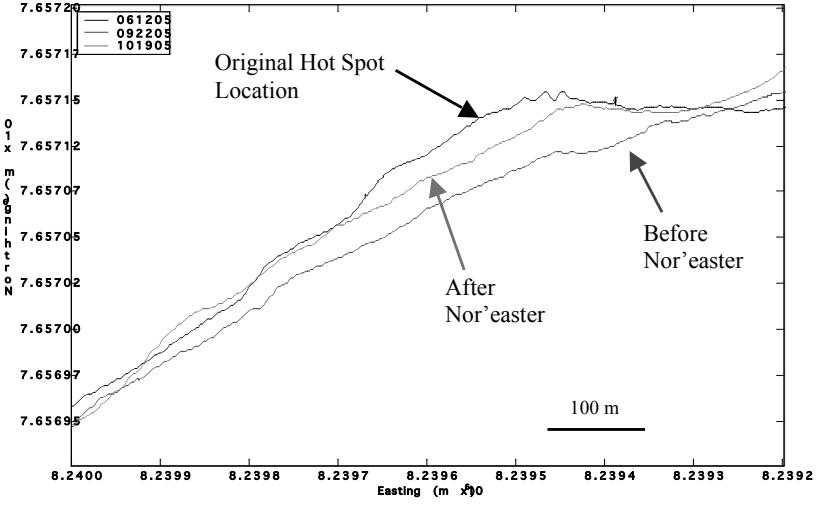

Figure 1. Condition of the Smith Point Hot Spot: original position, before and after a nor'easter in October, 2005.

In mid October, the area suffered the effects of a nor'easter that lasted for over a week. Wave heights were in excess of 5 meters and wave periods were over 14 seconds. The general direction of the storm waves were to the northwest, which would drive a westward longshore transport of sand. A survey was conducted on 19 October, 2005 after the storm had passed and the beach had experienced extensive damage. Significant change occurred between the 22 September, 2005 and 19 October, 2005. The erosional hot spot appeared to have persisted in the same location after the passage of the nor'easter (Figure 1).

To better visualize the changes in the dominant component of the Smith Point hot spot, its dominant periodicity was isolated by the IFFT as a sinusoid with a wavelength of 1000 m and an amplitude of 16.3 m (Figure 2). (In order to accurately compare the surveys the origin for each survey was chosen to be the easting value of 8239005 m.) Over time the hot spot had filled in or "healed" itself. There appeared to be no migration. This erosion hot spot healed in place reducing in amplitude at a maximum rate of about 0.1 m/day for a total reduction in amplitude to 6.5 m. By the end of the survey period (October 19, 2005), however, the amplitude had increased to

7.2 m and it seems to have migrated approximately 60 m to the west (Figure 2). This seemed to have been in response to the nor'easter of 7 October, 2005. Although the average westward migration over the 129 day period was about 0.5 m/day, almost all of the migration occurred in the last month when the westward migration rate was about 2.1 m/day over 27 days (Figure 2).

The two long surveys of Fire Island included the Smith Point hot spot and these were added to the other surveys of the Smith Point hot spot in order to see how the hot spot

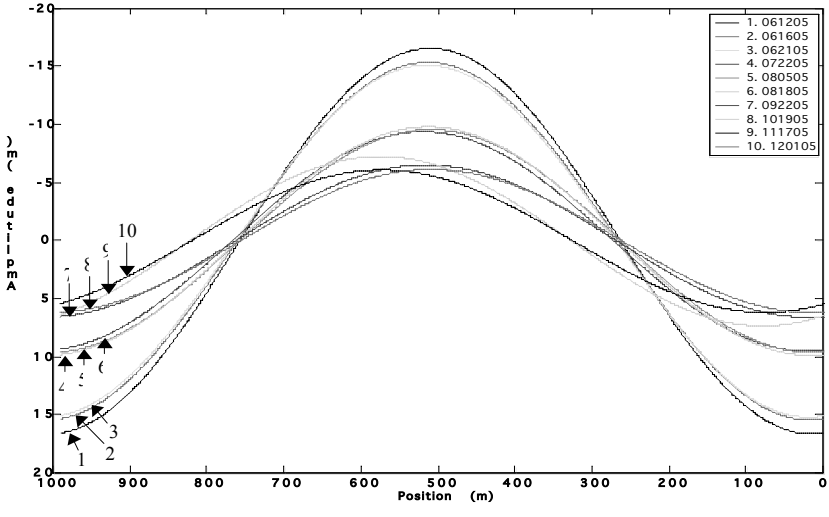

Figure 2. Principal component of Smith Point Hot Spot

had progressed after the nor'easter. The amplitude of the hot spot decreased with time to the approximate height as before the nor'easter (Figure 2). It can also be seen that the hot spot migrated back towards the east to almost its original location in between the two surveys at a rate of 4.2 m/day.

Kates Point

Another shoreline feature monitored at Smith Point was a seaward displacement of the shoreline equivalent to the sand packets or longshore sandwaves studied by Thevenot and Kraus (1995). The feature was found east of the Smith Point hot spot, and was referred to as Kates Point by local surfers. Over the period from 16 June to 19 October, 2005, Kates Point decreased in size and shifted westward in the direction of longshore transport (Figure 3). The erosional area west of Kates Point may have been caused by the point itself interrupting longshore transport and acting like a groin. Groin-like behavior of transient, natural features have been noted in other places (Jay Tanski, Sea Grant Cooperative Extension Service, 2006, personal

communication). Kates Point overall migrated to the west and simultaneously decreased in amplitude. The surveys of 17 and 18 November and 1 December showed that the erosional area has decreased in size at the same time that Kates Point has decreased in size. It appeared that sediment eroded from Kates Point was filling in the erosional area to the west. The position of each of these features has shifted to

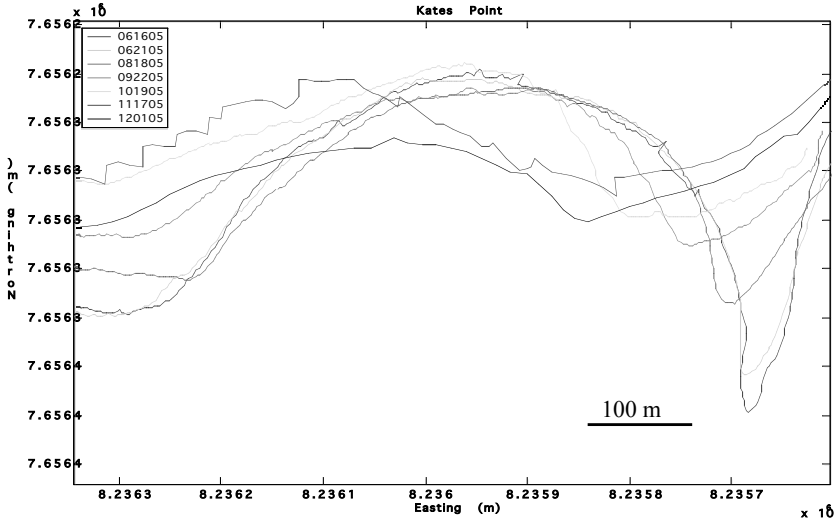

Figure 3. Surveys of Kates Point

the west. During this period the point migrated 110 m to the west at a rate of 0.88 m/day and simultaneously decreased in amplitude 80 m at a rate of 0.64 m/day (Figure 3).

Thevenot and Kraus (1995) had previously calculated a theoretical, advection-diffusion equation to model shoreline change and sand transport of longshore sand waves. Their model showed that the total sand wave body moved west and spread out with a substantial decrease in the amplitude. Although the scale of the model was much larger, the agreement in form suggests that Kates Point is, in fact, behaving according to the combination of longshore advection and diffusion processes.

Fire Island

On 17-18 November, 2005 and 1 December, 2005 surveys were conducted down the length of Fire Island over a four to five-hour period. The spectra generated for each survey were passed through a three-point running average to smooth the results. Dominant wavelengths of 1830 m and 1045 m were found by Gravens (1999) (labeled in red on Figures 4 and 5). From the survey on 17-18 November, 2005, dominant wavelengths appeared at 4779, 3186, 2811, 2276 and 1707 meters (Figure

4). From the survey on 1 December, 2005, dominant wavelengths appeared at 5973, 3186, 2515, 1911 and 1541 meters (Figure 5). The longer wavelengths emerged as the most important but we believe that was, in part, due to the large-scale trends that

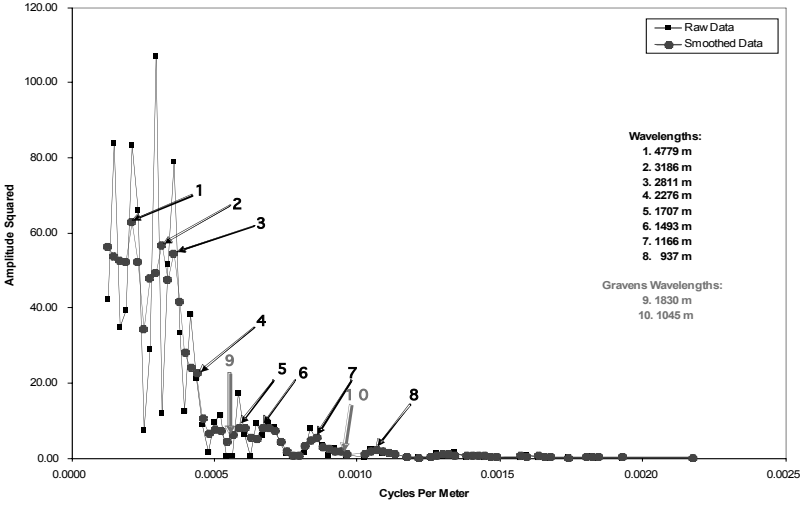

Figure 4. Fire Island Spectra of the survey on 17-18 November, 2005 smoothed with a three-point running average.

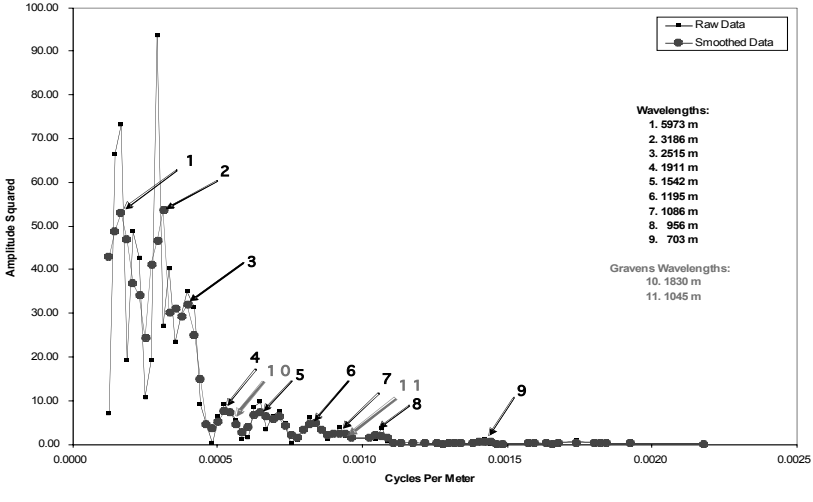

Figure 5. Fire Island Spectra of the survey of 1 December, 2005 smoothed with a three-point running average.

were not completely removed by the de-trending process. There may have been secondary peaks in the spectrum from November, 2005 at 1493 m, 1166 m and 937 m. Secondary peaks may also appear from December, 2005 at 1195 m, 1086 m, 956 m and, perhaps, even at 703 m. The component with a wavelength of 1086 m was close to that found by Gravens (1999) at 1045 m and approximately the size of the individual feature that was studied at Smith Point. The wavelength of 1911 m was also found by Gravens (1999) at 1830 m.

For any particular component, the change in phase between the November and December surveys was used to calculate the migration rate. Previous investigators had suggested that either larger wavelengths migrate faster or smaller wavelengths migrate faster, but these data cannot support either assertion. There does not seem to be a trend in migration rate. In addition, some wavelengths seemed to have migrated to the east in the same period that some migrated to the west. Waves during this period, as recorded at Buoy 44025 <www.ndbc.noaa.gov/station_history.php?station=44025>, would predominantly drive sand along shore from east to west but there were some reversals in the period. As Thevenot and Kraus (1995) remind us, local nearshore bathymetry can substantially influence the sand transport direction.

Some components for both the November and December surveys were of particular interest even though they were not dominant ones. The periodicity along the Fire Island shoreline with the largest wavelength was 24 km and appeared to move to the west at a rate of 44.1 m/day. The 15.9 km wavelength had the largest amplitude at 86.7 m. The 1291 m feature was the fastest migrating feature to the west at a rate of 51.5 m/day. The wavelength, 1493 m migrated the fastest to the east at a rate of 93.1 m/day. The wavelength, 2811 m had the greatest increase in amplitude, 0.27 m/day. It may be that components of different wavelengths respond differently to changing wave conditions but investigating such a phenomenon was beyond the scope of this work.

DISCUSSION

Migration rates of hot spots appear to be between 1 and 100 m/day. It seems, however, that there was no relationship between migration rates and wavelengths of erosional hot spots. In the specific case of the Smith Point Hot spot, the feature healed in place without migrating and migrated when storm activity caused it to grow. The sand packet referred to as Kates Point, on the other hand, migrated and dispersed according to advection-and-diffusion processes for longshore features. The undulations which are the superposition of a continuum of wavelengths had components which migrated at various rates and directions without an obvious pattern. They all were responding to the same water wave climate but that the net displacement over any particular period varied both in the direction and by the degree of the response.

Gravens (1999) suggested that shoreline undulations do not migrate from one end of Fire Island to the other but that migration within the range of the shoreline undulation is possible. Although it seems that shoreline features (e.g. Kates Point sandwave) do migrate in the direction of the long-term longshore transport over periods of weeks,

two considerations are noteworthy. First, individual components of the shoreline features may respond differently to the angle of wave attack. Particular wavelengths may preferentially migrate faster under waves arriving at different angles or slightly different direction. Second, depending on the speed of the longshore currents, it may be possible that some wavelengths migrate in the direction of longshore transport while others migrate in the opposite direction in a manner similar to the migration of antidunes in a river (Freedman and Sanders, 1978).

The presence and characteristics of shoreline undulations may have important implications for beach nourishment projects. Gravens (1999) suggested that nourishment projects be designed with a "shoreline undulation buffer" so that the average width of the beach is wide enough to accommodate the erosional hot spots that naturally develop. Dolan and Stewart (2006) further suggest that renourishment projects be designed to mimic the naturally occurring undulations in order to attempt to improve the rate at which ecological recovery takes place after the disturbance.

CONCLUSION

The behavior of shoreline undulations remains elusive. One feature studied in detail seemed to heal in place with little migration, but the other evidence is consistent with migration rates up to 100 m/day. Over long stretches of shoreline, the superposition of many different wavelengths of undulations obscures individual features and would make predictions difficult.

The sandwave, a positive feature referred to as Kates Point, evolved according to the modeled advection/diffusion process of Thevenot and Kraus (1995; Equation 1), migrating in the net longshore transport direction.

The data collected for this study was close to the results gathered by Gravens (1999). Gravens (1999) had shoreline undulations with amplitudes ranging from 20 to over 30 meters. The amplitude for the shoreline undulation at Smith Point Park was 16.3 m with a wavelength of 1 km. Gravens (1999) found dominant wavelengths of 3010 m, 1045 m, 2050 m, 2135 m, 1385 m, and 1310 m. We found dominant wavelengths of 3414 m, 6826 m, and 4779 m, similar in range to what Gravens (1999) found. Based on the power spectrum the dominant wavelengths for long beach distances were found to be 23893, 15928, 11964 m. Gravens (1999) had found similar wavelengths of 2135 m, 1830 m, 1065 m and 1045m as compared to the values found in our study at wavelengths of 2172 m, 1837 m, 1062 m and 1038 m.

This data does not support the contention that longer wavelengths migrate faster than smaller wavelengths or *visa versa*.

ACKNOWLEDGMENTS

We would like to thank the National Park Service at Fire Island National Seashore, especially Patricia Rafferty, for all their help during this project.

REFERENCES

Allen, J. and C. Lebash, 1996. Measuring shoreline change on Fire Island. *Maritimes*

39, 13 – 16.
Anders, F. J. and M. R. Byrnes, 1991. Accuracy of Shoreline Change Rates as Determined from Maps and Aerial Photographs. *Shore and Beach* 59: 17-26.
Batten, B., 2003. *Morphologic typologies and sediment budget for the ocean shoreline of Long Island, New York.* Ph.D. Thesis, State University of New York at Stony Brook. pp. 1 – 116.
Dolan, R. and D. Stewart, 2006. A Concept for Reducing Ecological Impacts of Beach Nourishment and Tidal Inlet Bypassing. *Shore and Beach* 74: 28 – 31.
Freedman, G.M. and J.E. Sanders, 1978. Principles of Sedimentology. John Wiley and Sons, NY: 792 pp.
Gravens, M. B. 1999. Periodic Shoreline Morphology, Fire Island, New York, *Proceedings of Coastal Sediments, '99*, American Society of Civil Engineers, NY, Vol. 2, pp 1613-1626.
National Park Service. http://www.nps.gov/fiis/NaturalResources.htm accessed 13 March. 2006.
Thevenot, M.M., and N.C. Kraus, 1995. Longshore sand waves at Southampton Beach, New York: observation and numerical simulation of their movement. *Marine Geology* 126, 249-269.

TROPICAL MIXED WAVE / TIDE DOMINATED BARRIER-SPIT SYSTEM: A CASE STUDY FROM NE BRAZIL

Helenice Vital[1], Francisco Santos Neto[2], José S. Plácido Junior[3], Venerando E. Amaro[4]

1. Pós-Graduação em Geodinâmica e Geofisica, Departamento de Geologia, Universidade Federal do Rio Grande do Norte, Laboratório de Geologia e Geofisica Marinha e Monitoramento Ambiental, Campus Universitário, P.O.Box 1596, Natal-RN, 59072-970, Brazil. helenice@geologia.ufrn.br.
2. Departamento de Geologia, University Federal do Rio Grande do Norte, Laboratório de Geologia e Geofisca Marinha e Monitoramento Ambiental, Campus Universitario, P.O.Box 1596, Natal-RN, 59072-970, Brazil. franciscosantoseto@yahoo.com.br.
3. Pós-Graduação em Geodinämica e Geofisica, Universidade Federal do Rio Grande do Norte, Laboratório de Geologia e Geofisica Marinha e Monitoramento Ambiental, Campus Universitário, P.O.Box 1596, Natal-RN, 59072-970, Brazil., USA. saraiva1000@hotmail.com.
4. Pós-Graduação em Geodinâmica e Geofisica, Departamento de Geologia, Universidade Federal do Rio Grande do Norte, Laboratório de Geoprocessamento, Campus Universitário, P.O.Box 1596, Natal-RN, 59072-970, Brazil. amaro@geologia.ufrn.br.

Abstract: This paper examines barrier-spit system morphodynamics on a tropical sandy coast, located on Diogo Lopes Village-RN, northeastern Brazil. The mechanisms of growth and elongation of the coastal spit and tidal inlets from Diogo Lopes are underway to reconstruct the historical evolution and dynamics. The general situation in this area is one of very energetic tidal conditions causing nearly continuous sediment mobility along the bottom close to the coast. The region experiences high-energy, coastal and shelf parallel currents driven by combined flows due to oceanic, tidal and wave processes. Natural inlet was cretaed by overwash processes during more energetic periods. Currents measured inside a new inlet show maximum speed of 85 cm/s during ebb phase, while nearhore it can reaches 100 cm/s. This data set is important to develop a detailed understanding of this kind of barrier-spit system evolution,

INTRODUCTION

The barrier literature has traditionally been dominated by one form of barrier, the barrier island (Hesp and Short 1999). Barrier islands, however, represent one end member in a spectrum of barrier types, with mixed wave/tide-dominated barrier islands and inlets in one direction (Davis 1994) and partially or completely joined to the mainland as a spit (Dingler and Clifton 1994), in the other direction. The Diogo Lopes barrier-spit system (Fig. 1) is a mixed wave/tide shoreline consisting of short barrier separated by inlets, which produce substantial ebb tidal deltas. This barrier-spit system experiences tidal processes but with no appreciable freshwater runoff. Others examples of this category are much of the Wadden Sea of The Netherlands and Germany.

Despite barrier islands have received a far greater proportion of attention from the scientific, engineering community, coastal managers and evironmentalists (e.g. Hayes 1974, 1994; Oretel 1985; Roy et al. 1994; Davis 1994), most of these studies were developed on the north hemisphere. Tropical coast barriers have been poorly studied in comparison to those on the high latitude

The aim of this paper is examine barrier-spit system morphodynamics on a tropical sandy coast. The mechanisms of growth and elongation of the coastal spit and tidal inlets from Diogo Lopes are underway to reconstruct the historical evolution and dynamics. This kind of data is important as contribution to the knowledge of the evolution, and the internal structures of tropical spits. Moreover, we hope these results can be used to comparisons with other barrier systems of the Brazilian coast and the world.

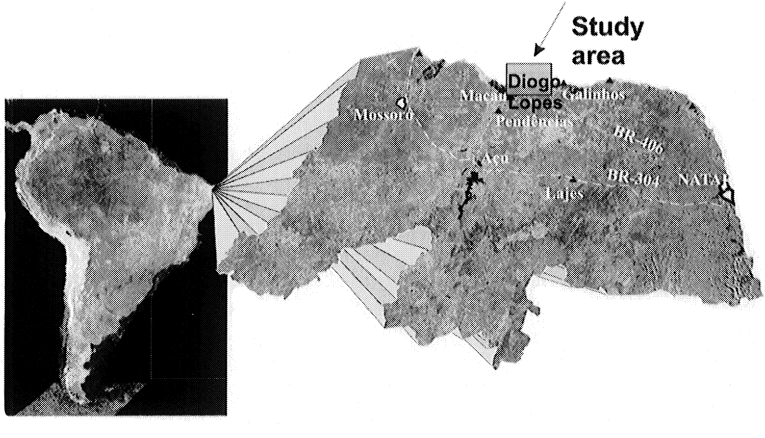

Fig. 1. Location of the study area.

COASTAL SETTING

Barrier island-spit systems on the Rio Grande do Norte cost can range from barrier spits (e.g. Galinhos), to barrier islands (e.g. Ponta do Tubarão, Amaro). Composed of sandy sediments, the barrier-spit systems are often capped by dunes. Evolution of these barrier systems has been cyclic (Xavier Neto et al. 2001; Lima et al. 2001, 2002; Silveira 2002; Souto 2002) indicating an ancient system of barrier islands developing into the current spits, and spits which were recently detached to form barrier islands. Studies of modern coastal environments and sediments in this area (Vital et al. 2003) show that barrier spits and barrier islands occur only on the EW North coast, and that they are confined between two important regional fault systems. But in the past barrier islands were abundant at least on the entire northern coast (Vital in press).

The Diogo Lopes area is located on northeastern Brazil (Fig.1), inserted on the Potiguar Basin. This basin has an economic regional importance because it is the most productive oil basin onshore in Brazil, and the second offshore. Nowadays, the study area is a State Sustainable Development Reserve.

The barrier-spit coast of northern Rio Grande do Norte State - NE Brazil (Fig. 1) is a mesotidal, mixed-energy coast according to the classification of Hayes (1975, 1979). Tides are semi-diurnal, with a maximum tidal height of 3.3 m and 2.5 m respectively during spring and neap tides. The overall wave energy is medium to low with maximum breaker heights of less than 80 cm (Silveira 2002, Chaves at al. 2006).

The Relative Tide Range - RTR (mean spring tide range - MSR / wave height - Hb) for this sector is $4 < RTR < 15$, and so in the mixed wave-tide group according to the classification of Masselink and Turner (1999, Vital in press). During periods of weak winds and waves with small heights the RTR is greater than 15 (predominantly 16-20); The maximum RTR registered was 27, and the beach was classified during this time as tide dominated. The presence of small ebb-tidal deltas along the barrier island-spit system, as well spits perpendicular to the coast indicate the strong tidal influence.

The longshore currents flow toward west-northwest (oblique to the coast) with a maximum of 97 $cm.s^{-1}$ during rising tides, and toward north (perpendicular to oblique to the coast) with a maximum of 50 $cm.s^{-1}$ during falling tides. They are by far the dominant contributor to the net sediment transport along the coast of Rio Grande do Norte. The sediment transport measured on this area is between 101 and 110 m^3/day (Chaves 2005; Vital et al. 2006).

The general situation in this area is one of very energetic tidal conditions causing nearly continuous sediment mobility along the bottom close to the coast. Sediment type in nearshore and barrier-spit system is consistent along the coast and is composed of fine to very fine quartz sand. The lagoon bottom sediments are composed mainly of silt, while tidal channels may have a higher shell content and, therefore, a coarser mean-grain size than the adjacent shorelines. No rivers provide new sediment to the coastal system. Since strong winds are present almost all the time, water masses are well mixed without

any characteristic stratification. Winds velocities measured direct on the coast reached a maximum of 9 m/s between August and October and a minimum of 4 m/s in April (Chaves et al. 2006). The months of worse coastal erosion in this area are related to the increasing wavy energy. This in turn, seems to be related to seasonal climatic variations, with the wave energy and tide currents speed increasing during months of minor precipitations (June to January).

The relative sea-level curves documented for the Northeastern Brazilian coast, for the last 7.000 years (Martin et al. 2003; Bezerra et al. 2003; Caldas et al. 2006; Stattegger et al. 2006) indicate that the sea level was some meters higher than the present, with a tendency to drop during the last 5.000 years.

METHODS

The methods used to attain these objectives included (a) Remote sensing Multitemporal remote-sensing images (aerial photographs and satellite images) and geographic information systems (GIS) were used for monitoring and interpretation ofshoreline change, nearshore bedforms and structural features. A range of digital image processing techniques were used and compared (e.g. Multitemporal Image Analysis, Water Index, Principal Components Analysis, Adaptative Filtering). The clear waters of the northeast Brazilian coast, produced by the dry climate and minimal organic turbidity, favor the visible imagery application. (b) Physical processes measurements: Hydrodynamic processes were measured with S4 and S4a sensor from InterOcean Systems (waves, tides, currents, temperature, conductivity, depth). The sensors were installed monthly for 24 hours during spring tides, one inside the inlet (S4) e the other (S4A) nearshore. Winds were measured with a portable meteorological station. (c) topographic and bathymetric survey: Hydroacoustic data were collected onboard small fishing boats with a Odom Hydrographyc System (echo sounder and side scan sonar) operating with a frequency of 200 kHz. The water depth was recorded both digitally and analogic while sonar data only analogic. Present topographic profiling were collected using a TOPCON HIPER LITE-RTK GPS system, and (d) Investigation of modern surficial facies were derived from vibracores and sediment samples collected using a Van Veen bottomgrab. Because the recovered cores were shorter than 3 m, informations from literature (Silva 1991) were incorporated.

RESULTS AND DISCUSSIONS

Barrier-spit System Morphodynamics

The Barrier on this area was completely joined to the mainland as a spit (Fig. 2A); around 1977 an inlet was created (inlet 1) and the barrier island was called Ponta do Tubarão (Fig. 2B). Since then this inlet is used as navigational access to the lagoon by the habitants from Barreiras and Diogo Lopes villages. The distance between this inlet and Diogo Lopes is quite large, creating public pressure for additional navigational access. Because the presence of a tidal inlet on a shoreline has the drawback that it traps a considerable amount of sand, creating significant potential for beach erosion on the adjacent beaches (Dean and Dalrymple 2002), professionals from the local University (UFRN) discouraged this action. However, in February 2006 a new inlet was created

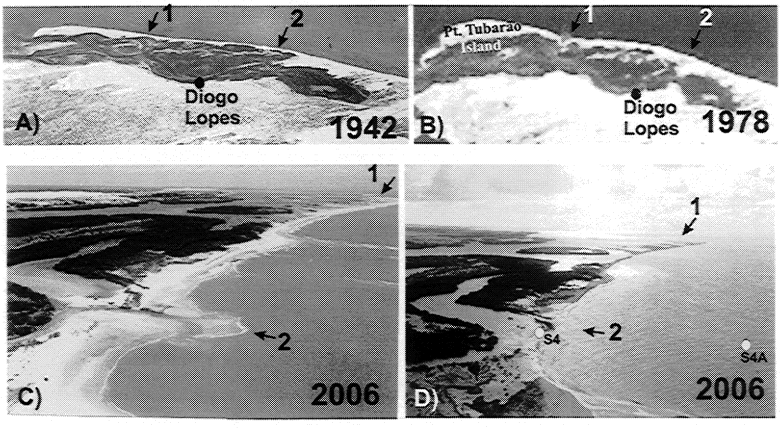

Fig. 2. View of the study area. A) Aerial picture from 1942; B) Landsat MSS image from 1978 (open of inlet 1); C) Low tide and D) High tide Aerial picture from 2006 (open of inlet 2).

(inlet 2, Fig. 2C,D). Waves measured nearshore have an average height of the 56 cm, with a maximum height of 123 cm. The calculated medium wave period for the area was 7.5 s. The broad shallow continental shelf bordering the RN coast causes deep-water swell in the area to decompose into these low, short-period waves. The short period waves tend to pass even this shallow shoreface with little modification in their direction. As a result, there is considerable refraction within the nearshore zone, which results in appreciable and persistent longshore currents. The primary direction of longshore current, from east to west, is controlled by the local shoreline orientation in combination with the direction of wave approach.

The bathymetric data show that the lagoon presents in general relatively shallow depths, between 1 and 3 meters, and maximum depth is 7 meters. Different bottom features were identified, such as small and big dunes (sensing of Ashley 1990), as well as flat bottom.

The new inlet (inlet 2 on Fig. 2) presented in February, one week after it was open, a shallow channel of 10 m width and 1 ,2 m initial depth during low tide. Two months later it shows 22 m width and 1,7 m depth. Six months after the inlet was open, the channel presents 25 m width and 1,6 m depth. At month eight it reaches the shallowest depth with o,6 m and since then becomes deeper until the depth of 1,4 m. However the width is continuously bigger. In month ten it reaches a width of 50 m. The Currents measured inside the channel (S4 sensor, for location see Fig.2D) shows speeds ranging from 85 cm/s during ebb phase to 10-30 cm/s during flood phase (Fig.3). Nearshore (S4A sensor, for location see Fig.2D) the currents reached until 100 cm/s.

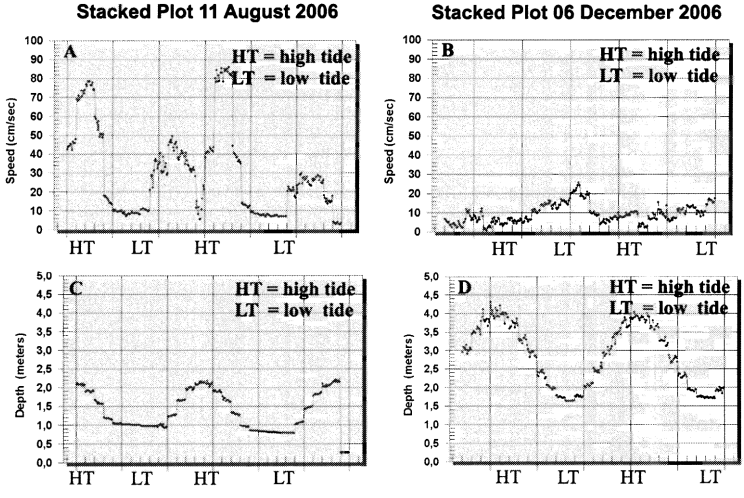

Fig. 3. S4 Stacked plots for August (A, C) and December (B, D) 2006 showing speed currents and depth in the inlet 2. For location of S4 see Fig. 2D.

Barrier-spit System Depositional facies

Diverse depositional facies associated with or immediately adjacent to the spit compose a complex depositional system. This system comprises the shore-parallel barrier island spit itself, the oceanic environment on its seaward side, the enclosed lagoon environment on its landward side, and the inlets that facilitate exchange of tidal.driven circulation. The bottom sediments collected in the channel, were classified in three main classes: terrigenous sandy mud, fine to very fine siliciclastic sands, and medium siliciclastic sands. The oceanic environment adjacent to the spit includes a shallow inner shelf with dune fields

The generalized Holocene stratigraphy of this area shows a transgressive sequence of restricted lagoon, lagoon and shoreface sediments followed by a regressive sequence of lagoon, tidal flats and fluvial sediments behind a barrier spit. The transgressive nature of this barrier-spit system is demonstrated by exposed mangrove muds and peats in the surf zone. Alluvial sediments of the Barreiras Group (Early Pleistocene and older) were reached at 9 meters depth in the landward most core, but the shoreface sediments are absent at this depth. A characteristic change in the environmental conditions towards more “open marine” environments is observed from bottom to top within this transgressive sequence. The basal, restricted lagoonal unit shows a very restricted microfauna, or the absence of microfossils. An intermediate lagoon unit shows a more open microfauna. Finally, the shoreface unit of the transgressive sequence presents a

normal marine microfauna. ^{14}C radiocarbon dating of shells from the base of the shoreface give an age of 6.060 ±80 yr BP and in the transgressive lagoon unit an age of 7.020 ± 100 yr BP (Silva 1991), suggesting an approximate age between 7 – 6 ka for the final stages of the Postglacial Marine Transgression.

The upper regressive sequence presents a greater variety of environments which characterize the prograding nature of this coastal plain. Lagoon, tidal flat and fluvial sediments are deposited behind a barrier spit, while tidal inlet, tidal flat and small secondary spit sediments are deposited seaward of the barrier spit. A restricted microfaunal assemblage is observed behind the barrier spit, while an open marine fauna is present in front of the spit. The environments observed seawards of the barrier spit represent the tidal inlet sub-facies of the ebb-tidal delta facies preserved in the subsurface as the ebb-tidal delta complexes are attached to the mainland promoting shoreline progradation. The contact between tidal inlet sediments and lagoon sediments is gradual, characterized by a change in the microfaunal association (Silva 1991).

Extensive ebb-tidal deltas in the inlets are the site of temporary important sand accumulations. These ebb-tidal delta deposits are composed of swash platform and tidal inlet sedimentary units. Swash platform units are lobate, concave-upwards sand deposits, laterally continuous over the entire ebb-tidal delta surface, usually having a thickness from 1 to 3 m.

Tidal inlet units are composed of sand/mud interbeds that occur in the bottom of the tidal inlets, as well as in the entire subsurface of the ebb-tidal deltas and in the subsurface of the coastal plain. Because of its greater thickness (3-10 m), and its deposition below wave base, the units are more likely to be preserved. The pattern of sand distribution in the littoral area is lobate, with elongate depocenters both parallel and perpendicular to the shoreline representing deposition in the barrier spits/ebb-tidal deltas and in the tidal inlets respectively. The resulting sand body geometry is both concave- or convex-upwards.

CONCLUSIONS

The Diogo Lopes coast has two active inlets, naturally occurring. The net drift is to the West-Northwest along this coast. Natural inlet formation was by breach of the narrow spit by overwash processes during more energetic periods.

The data base from this study suggest that littoral transport processes dominated these inlets with periods when the channel is deeper (maximum 1,7 m depth) and periods when the channel is shallower (minimum 0,6 m depth). If the hydrodynamic conditions persist, to maintain navigational interests, the inlet need to be stabilized over time.

Diverse depositional facies associated with or immediately adjacent to the spit compose a complex depositional system. This system comprises the shore-parallel barrier island spit itself, the oceanic environment on its seaward side, the enclosed lagoon environment on its landward side, and the inlets that facilitate exchange of tidal.driven circulation.

This data set is important to develop a detailed understanding of this tropical barrier-spit system evolution, to provide good architectural analogues for the nearby subsurface reservoir, and will enable the planners and ecologists to make the right decisions for a rational management of the coastal zone.

ACKNOWLEDGEMENTS

This work was funded by a CNPq grant for H. Vital (PQ process: 3508811999-5), and by funds from MAR-RN (FINEP/CTINFRA), PETRORISCO (REDE 05-FINEP/CNPQ/CTPETRO/ PETROBRAS), POTMAR (REDE 05-FINEP/CNPQ/ CTPETRO/PETROBRAS), UNIBRAL 021-04 (CAPES-DAAD). We would like to thank the Francisco Canindé, Jose Jr, Tiago, Marcel and the students participating in field and lab work.

REFERENCES

Ashley, G.M. (1990). "Classification of large-scale subaqueous bedforms: a new look at an old problem", *Journal of Sedimentary Petrology* 60, 160-172.

Bezerra, F.H.R., Barreto, A.M.F. and Suguio K (2003). "Holocene sea-level history on the Rio Grande do Norte State coast, Brazil". *Marine Geology* 196, 73-89.

Caldas, L.H.O., Stattegger, K. and Vital, H. (2006). "Holocene sea-level history: Evidence from coastal sediments of the northern Rio Grande do Norte coast, NE Brazil". *Marine Geology* 228, 39-53.

Chaves, M.S., Vital, H. and Silveira, I.M. (2006). " Beach morphodynamics of the Serra oil field, northeastern Brazil", Journal of Coastal Research Special Issue 39, 594-597.

Davis Jr., R.A. (ed) (1994). "*Geology of Holocene Barrier Island Systems*", Springer – Verlag, 464 p.

Dean, R.G., and Dalrymple, R. A. (2002). "*Coastal Processes*," Cambridge University Press, 475 p.

Dingler, J.R. and Clifton, H.E. (1994). "Barrier Systems of California, Oregon, and Washington". In: Davis Jr., R.A. (ed) *Geology of Holocene Barrier Island Systems*, Springer – Verlag, 464 p.

Hayes, M.O. (1974). "Morphology of sand accumulation in estuaries: an introduction to the symposium". In: L.E. Cronin (ed), *Estuarine Research*, Geology and engineering. Academic Press, 3-22.

Hayes, M.O. (1979). "Barrier island morphology as a function of tidal and wave regime". In: S.P. Leatherman (ed), *Barrier islands from the Gulf of St. Lawrence to the Gulf of Mexico*, Academic Press, 1-27.

Hesp, P.A. and Short, A.D. (1999). "Barrier morphodynamics". In: Short, A.D. (ed). *Handbook of Beach and Shoreface Morphodynamic*. John Wiley & Sons, 307-333.

Lima, Z.M.C., Alves, A.L., Amaro, V.E. and Vital, H. (2001). "Coastline Evolution of the Galinhos Spit (NE Brazil) Using Air Photography and Landsat TM Images", *Revista Pesquisas em Geociências*, 28, 497-507.

Lima, Z.M.C., Vital, H., Xavier Neto, P., Medeiros, W.E. and Andrade, P.R.O. (2002). "Sand spits from NE Brazil: high resolution Quaternary analogous for reservoir

model". Annual Meeting of American Association of Petroleum Geologist. Houston, EUA. Extended Abstracts CD-ROOM.

Martin, L., Dominguez, J.M.L. and Bittencourt, A.C.S.P. (2003). "Fluctuating Holocene sea-levels in eastern and southeastern Brazil: Evidence from multiple fossil and geometric indicators", *Journal of Coastal Research* 19, 101-124.

Masselink, G. and Turner, I.L. (1999). "The effect of tides on beach morphodynamics". In: Short, A.D. (ed.), *Handbook of Beach and Shoreface Morphodynamics*. John Wiley and Sons. 204-229.

Oretel, G.F. (1985). "The barrier island system". *Marine Geology* 63, 1-18.

Roy, P.S., Cowell, P.J., Ferland, M.A. and Thom, B.G. (1994). "Wave dominated coasts". In: Carter, R.W.G. and Woodroffe, C.D. (eds) *Coastal Evolution, Late Quaternary Shoreline Morphodynamics*. Cambridge University Press, 121-186.

Silva, C.G. (1991)."*Holocene Stratigraphy and Evolution of the Açu River Delta, Rio Grande do Norte State, Northeastern Brazil*". Ph.D. thesis, Duke University, Durham, 400 p.

Silveira, I.M. (2002). "*Monitoramento Geoambiental da região costeira do município de Guamaré-RN*". Master thesis, Universidade Federal do Rio Grande do Norte, Brazil, 112 p.

Souto, M.V.S. (2002). "*Análise multitemporal dos elementos geoambientais da dinâmica costeira da região da Ponta do Tubarão, Macau-RN, com base em produtos de sensoriamento remoto e GIS*". Relatório de Graduação, Universidade Federal do Rio Grande do Norte, Brazil, 67p.

Stattegger, K., Caldas, L.H.O., Vital, H. (2006). "Holocene coastal evolution of the Northern Rio Grande do Norte Coast, Brazil", *Journal of Coastal Research*, Special Issue 39, 150-155 .

Vital, H., Lima, Z.M.C., Silveira, I.M., Amaro, V.E. and Souto, M.V.S. (2003). "Barrier-Spit System From The Northern Rio Grande do Norte State Coast, NE Brazil: A Tectonic Control ?" Proceedings of The 3th Latin-American Congress on Sedimentology, 113-115.

Vital, H.; Chaves, M.S., Souto, M.V.S. and Amaro, V.E. (2006). "The Macau-Serra coastal erosion hotspot". Proceedings of The 4th Latin-American Congress on Sedimentology, Bariloche, CD-ROOM.

Vital, H. (in press). "The mesotidal barrier of Rio Grande do Norte" In: Dillemburg, S. and Hesp, P. (eds), *Geology of Brazilian Holocene Coastal Barriers*, Springer-Verlag.

Xavier Neto, P., Lima, Z.M.C., Andrade, P.R.O., Oliveira Jr., J.G., Medeiros, W.E. and Vital, H, (2001), "GPR images of the Galinhos Península, NE Brazil: the register of a geologic evolution from paleochannel to a sand spit ?" Porceedings of the I Symposium about GPR in sediments. Geological Society and UCL. London, CD ROOM.

REGIONAL SHORELINE AND BEACH CHANGES IN THE SANTA BARBARA SANDSHED

David L. Revell[1] and Gary B. Griggs[2]

1. Earth and Planetary Sciences, University of California, Santa Cruz, 1156 High Street Santa Cruz, CA 95064 USA. drevell@es.ucsc.edu
2. Institute of Marine Sciences, University of California, Santa Cruz, 1156 High Street Santa Cruz, CA 95064 USA. ggriggs@ucsc.edu

Abstract: Beach widths and shoreline change along Santa Barbara and Ventura Counties, California were evaluated using a 70-year record of rectified historic air photos. Beach widths have oscillated throughout the study period as opposed to narrowing as predicted by sediment supply reductions. Shoreline change rates evaluated using linear regression and end point rate analyses show differences between the wet/dry shoreline and back beach reference features. Most of these differences occurred along armored backed shorelines where the natural erosion of the back beach was halted while the wet dry shoreline continued to erode. Beach responses to single El Niño events form a predictable pattern of beach reorientation. Similar patterns of shoreline reorientation can be seen in the long-term shoreline change analyses providing evidence that El Niños may play an important role in long-term coastal evolution.

INTRODUCTION

Beaches are significant economic drivers of coastal communities and national economies, supporting commerce, recreation, and ecosystems (Heinz Center 2000, Griggs *et al.* 2005). Economists estimate that without California's beaches the state would lose about $5.5 billion annually and the U.S. economy would lose about $2.4 billion annually (King and Symes 2004). Beaches also provide hazard protection, it is estimated that over the next 60 years, 1 of 4 houses within 150m of the shoreline will be claimed by erosion (Heinz Center 2000). Erosion has threatened public facilities, infrastructure, and oceanfront property. The response has been an increase in shoreline armoring reducing habitat, recreation, and economic opportunities (Griggs *et al.* 2005).

The Santa Barbara Sandshed extends 245 km from the Santa Maria River in the north around Point Conception where the north-south trending shoreline takes an abrupt turn to a west-east trending shoreline orientation along the coast of southern Santa Barbara and Ventura Counties to the Point Mugu submarine canyon in the south (Figure 1).

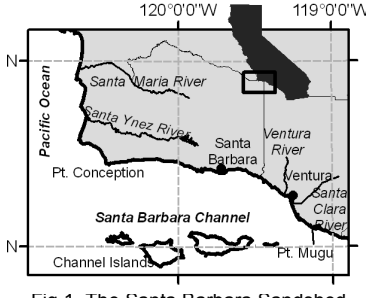

Fig.1. The Santa Barbara Sandshed

The Santa Barbara Sandshed (watershed + littoral cell), is a complex coastline with a variety of rocky outcrops, offshore reefs, and relatively narrow beaches. The beaches receive the majority of their sand inputs from four major rivers the Santa Maria, Santa Ynez, Ventura, and Santa Clara Rivers along with numerous small coastal drainages that pulse large sediment loads during episodic rain events (Inman & Jenkins 1999).

The presence of the Channel Islands to the south and Point Conception to the west create a narrow swell window that reduces and focuses much of the wave energy. The small swell window results in wave heights during 60% of the year of less than 1 meter. During the winter, longer period waves can achieve wave heights around 2.5 meters. Almost unidirectional wave conditions result in a longshore transport of sediment from west to east into the Santa Barbara Channel estimated to be around 1.7 km/yr (1 mi/yr) (Bailard and Jenkins 1982; Revell and Griggs 2006).

Major alterations to the Santa Barbara coastline began with the construction of the Santa Barbara Harbor in 1929 that provides the textbook example of down coast erosion causing by disrupting longshore transport (Wiegel 2002). The effects of dam impoundment and shore protection structures on sand delivery to the coast have been studied in the Santa Barbara cell and show an approximately 40% reduction in sand supplied to the sandshed by the major rivers (Willis and Griggs 2003, and Runyan and Griggs 2003). It was predicted that this reduction would correspond with a decline of sand volume dredged at the harbors. Using dredge records as a proxy for littoral drift, Runyan and Griggs found an average rate of sand at Santa Barbara Harbor since 1933 (~230,000 m3/year), and the Ventura Harbor since 1964 (~450,000 m3/yr) with no sign of reductions in dredge volumes (2002). One potential explanation for this lack of reduction in harbor dredge rates could be that the beaches were narrowing and supplying the sand found in the harbor dredge records.

This hypothesis was tested along the Isla Vista Coast, updrift of the Santa Barbara Harbor where it was found that beach widths had not narrowed but instead oscillated (Revell and Griggs 2006). The oscillations of beach width were found to relate to different phases of the Pacific Decadal Oscillation (PDO), a climate index of sea surface temperature with a periodicity of ~20 years (Mantua et al 1997). During positive PDO phases, El Niño-like patterns of increased precipitation and stream flow narrow beaches while during negative and calmer, drier PDO phases, beach widths widened (Revell and Griggs 2006). The driving mechanisms of beach changes were related to the change in wave directionality that during large El Niño events would more preferentially affect beaches that were normally sheltered in the Southern California Bight (Graham 2003).

The focus of this study has been to extend the beach width and shoreline change assessment to a 70km stretch of the Santa Barbara Sandshed extending from Ellwood Beach to Ventura Harbor in order to evaluate the response of beaches and shoreline to the sediment reduction, El Niños, and human alterations to the coastline.

METHODS

Historical aerial photographs provide one of the best data sources for long-term shoreline and beach change investigations. Many authors have utilized various shoreline reference features to examine changes to the beaches and shorelines (see Crowell and Leatherman 1999; Boak and Turner 2005 for a recent reviews). More recent acceptance of high accuracy lidar data enables a rapid assessment of long stretches of coast and provides additional information on beach volumes and regional shoreline changes caused by extreme storm events (Revell *et al* 2002; Sallenger *et al.* 2003).

The use of air photos for accurate shoreline change assessments requires an understanding of the potential sources of errors. Errors inherent in air photo interpretation can be broken down into 1) source error, 2) interpretation error, and 3) short-term natural variability errors (Morton and Speed 1998). Source error results from photo distortion, scale, and scanning errors (Moore 2000). Interpretation errors come from difficulty in locating shoreline reference features. Short-term variability errors arise from seasonal changes in beach profile and variations in water levels and wave run-up elevations that change the location of the shoreline reference features (Morton and Speed 1998, Ruggiero *et al.* 2003)

For this study, eighteen different sets of vertical air photos were obtained for the period from 1929 to 2003. Photographs selected for this study (at scale 1:24,000 or smaller) were taken during the calmer season (June to November) to reduce seasonal signals and ensure that beaches were near a maximum width. Due to the large study are and specific criteria, few photo sets were available with complete coverage of the study area.

To minimize errors, historic imagery was rectified using known coordinates of ground locations obtained through GPS surveys to reduce photo distortions (Moore 2000). For each image, two shoreline reference features were digitized - the wet/dry line identified

using tonal contrasts and the back beach or toe of the cliff or dune. The beach width is the distance between the wet/dry line and the back beach feature, generally the dry sand portion of the beach at the time of the photo.

Given the short-term variability of water levels, corrections to the wet/dry proxy- based shoreline reference features were based on the tide level portion of the total water level method discussed in Ruggiero *et al*. 2003. Tide level corrections adjusted the wet/dry shorelines to Mean Sea Level (MSL) (0.829m NAVD88) using the historic hourly water level data at Santa Barbara harbor available online from NOAA. These corrections translated the water level at the time of the historic photo onto an average summer beach slope calculated from historic profiles and from the 1997 lidar data for each shoreline segment. The beach slopes used in this tidal correction ranged from 0.045 (sand) to 0.11 (cobble). Due to the typical low energy waves found in the Santa Barbara Channel during the summer and fall, and the lack of hindcast wave data for most of the photography, a wave run-up adjustment was not included in the proxy based shoreline correction.

Error estimates for the identification and absolute spatial location of the shoreline reference features associated with shoreline change analysis are, +/- 9.7, and +/- 9.3 m for the early 1929 and 1938 photography respectively. More recent photography scanned at a higher resolution provides lower spatial errors on the order of +/- 7m. Unlike the shoreline change analysis that depends on different images, the errors in beach width measurements are spatially independent since both reference features can be seen in each of individual images. Therefore the beach width errors are +/- 5m and arise from reference feature identification and water level adjustments.

To better understand the changes caused during the 1997-98 El Niño event, NOAA, NASA, and USGS collected pre- and post- storm lidar surveys in October 1997 and April 1998 for most of this study area (Sallenger *et al.* 1999). Lidar data was obtained for Carpinteria and Isla Vista from the NOAA Coastal Service Center and processed to extract a MSL contour (0.829m NAVD88). The back beach reference feature was hand digitized using visual cues in cross-shore profiles, slope breaks, and hillshade layers. These two reference features were included in the BW change analyses, and the 1997 data set was included in the shoreline change analyses.

Shoreline change and beach widths for all imagery were measured along the same 50-meter transects using the USGS Digital Shoreline Analysis System (DSAS) (Thieler, *et al*. 2003). All shoreline change rates and error statistics discussed in this paper were calculated using DSAS version 3.2 (Thieler, *et al*. 2003). For this study, we focus on the shoreline change linear regression rates (LRR) and end point rates (EPR).

Beach widths were measured by individual years, by setting the back beach reference feature to one year after the date of the MSL shoreline so that the EPR calculation measured the beach width. Tide corrections were applied to the beach widths following DSAS measurement. Beach width measurements and the average beach slopes used in the tide level corrections were multiplied to calculate sand volumes above MSL by

transect (m3/m). These transect volumes were then multiplied by the 50m transect spacing and summed to provide a total volume for a chosen length of shoreline.

The intersection of the 50m transects and the individual MSL shorelines were used to calculate shoreline orientations. By drawing a straight line between adjacent transects at the intersection point between the MSL shoreline and the transect lines, an azimuth angle of this intersecting line was calculated in ArcGIS. From the azimuth angle, a shore normal, perpendicular angle was derived by adding 90 degrees to the azimuth angle. (Note: this azimuth angle is not to be confused with the azimuth angle derived by DSAS). Shoreline orientations were filtered to exclude all transects in front of shore protection structures and near creek and river mouths.

RESULTS

Beach Widths

The beach widths in the study area have varied widely throughout the 70-year time series (Figure 1). Two types of beaches can be identified - stable beaches and storage beaches. A stable beach maintains a wide minimum beach width and a storage beach is one that

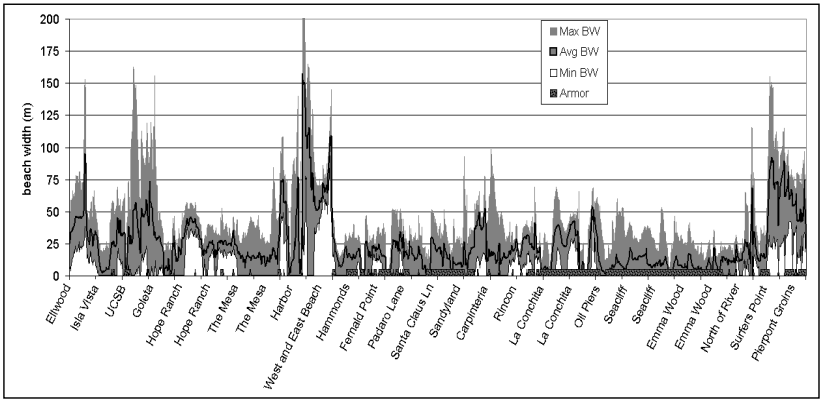

Fig. 2. Beach width variability along 70 km of southern Santa Barbara and Ventura Counties.

exhibits extreme natural variability but has zero minimum beach width. Stable beaches (e.g. Ellwood, Hope Ranch and Carpinteria) provide good locations to examine storm impacts, and provide good locations to observe pulses of sand moving along the coast. The best examples of a storage beach were UCSB and Goleta Beaches that reached their maximum widths (>150m) in the 1960s and 1970s (Revell and Griggs 2006).

This study area can be generally divided up into two locations based on the location relative to the Santa Barbara Harbor. The beaches to the west of the Harbor (toward Ellwood) face more southward and exhibit a wider range of beach widths. These beaches all had their minimum beach widths occur following either the 1982-83 or

1997-98 El Niño. The maximum beach widths for these beaches were reached mostly during the end of the last calm (negative) period of the PDO in the 1970s.

The beaches downdrift of the harbor (toward Carpinteria and Pierpont Groins) have smaller ranges of beach widths and are primarily armored shorelines (Figure 1). The minimum and maximum beach widths along this stretch do not fit any obvious pattern, although the analysis is limited by the lack of photo sets available prior to major transportation infrastructure projects completed in the early 1900s.

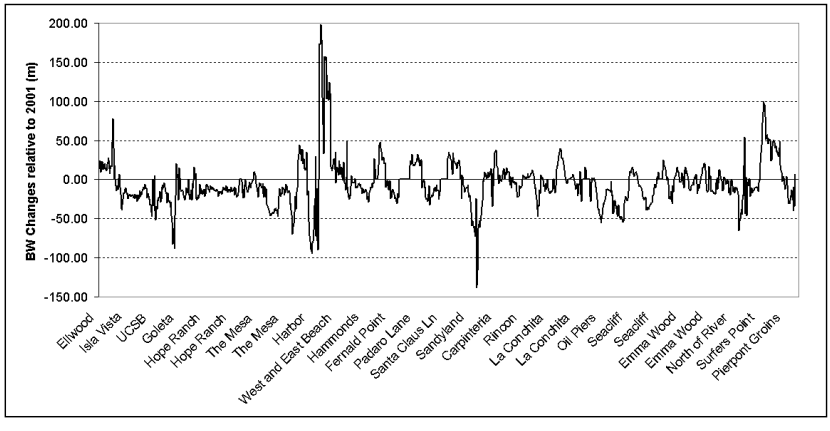

Fig.3. Long term beach width changes relative to the 2001 beach width. A negative beach width change indicates that the beach has narrowed, while a positive change indicates accretion.

One research objective was to examine the long-term changes in beach widths to ascertain whether the beaches may have narrowed supplying sand to the harbor dredge records to compensate for the reduction in sand supply. Figure 2 shows the long-term beach width changes relative to the 2001 beach widths. There does not appear to be a uniform narrowing of the beach widths across the study area.

The largest beach width changes in this study area are related to construction of the Santa Barbara Harbor. Other significant beach width accretions have occurred at the Pierpont groin field in Ventura, and Ellwood Beach. Ellwood Beach is uniquely situated facing west into the dominant wave direction, and is the only natural dune backed shoreline remaining in the study area. The greatest beach narrowing has occurred at both Carpinteria as a result of the Santa Barbara harbor construction and development of the former dunes, and at Goleta Beach as a result of the construction of the Santa Barbara airport and the loss of tidal prism at Goleta Slough (Revell and Griggs 2006). It is important to note that this end point beach width change analysis does not capture the oscillations in beach width that have been previously documented (Revell and Griggs 2006).

Shoreline Orientation

Due to the irregular shape of the coastline and the near uniform wave direction, wave exposure varies greatly depending on shoreline orientation. Periodicities observed in the long-term beach change width analysis (Figure 3) are related to changes in the shoreline orientations that partially control beach widths (Figure 4).

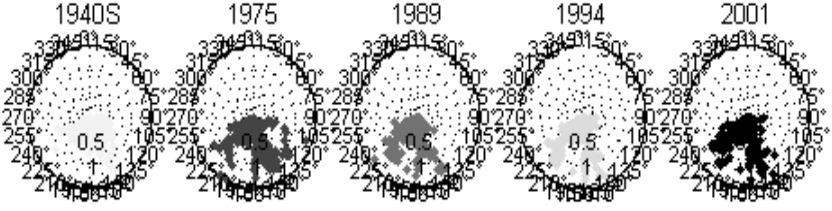

Fig. 4. Beach Widths plotted by Shoreline Orientation for separate years. Data points were extracted from the same shoreline transects and have comparable number of data points.

The shoreline orientation results indicate that most stable and widest beaches are those found facing SSW (255° to 210°, and SSE (165°-150°). The narrowest beaches are found facing close to south (210°-165°). The shoreline orientation analysis demonstrates the impacts of human alterations across the study area through time.

While air photo data from the pre-harbor construction era is sparse, it appears from historic oblique photos that most of the beaches were relatively narrow. By the 1940s (compilation data from 1943 and 1947), the beaches were relatively narrow with the widest being in the east (165°-150°) as a result of Santa Barbara Harbor construction and the trapping of sand to form the updrift Ledbetter Beach. The widest beaches in the west were found in the dunes of Ellwood Beach (255°-240°). By the 1975 data set, there were several human alterations creating wide beaches. The cluster located along 180 degrees is the beach continuously nourished by the sand bypassing at the Santa Barbara Harbor. In the late 1940s, the Pierpont groin field in Ventura oriented southwest (240°- 225°) filled in and has remained stable to present. 1975 was a wide sand year, and the SE facing UCSB storage beach (105°-120°) reached its widest width. By 1989, after the 1982-83 El Niño, the wide beach at UCSB was eroded (Revell and Griggs 2006). Throughout 1994 and 2001, beach widths continued to widen despite the large 1997-98 El Niño. By 2001, beach widths at Ellwood reached their maximum beach widths during the study period.

Shoreline Change

Shoreline change rates were calculated for both the wet/dry and the back beach shorelines at each transect along the entire study area (Figure 5) and summarized in Table 1. These broad rates do little to describe the spatial patterns and trends associated with the different shoreline segments (Figure 5). When averaged over the entire study area, the shoreline change rates calculated with both EPR and LRR are relatively low. The primary differences between the back beach and the wet/dry shorelines can be attributed primarily to the presence of shoreline armoring and engineered structures.

Table 1. Shoreline Change Rates

Shoreline Change (m/yr)	Average	Maximum	Minimum
EPR_Back Beach	0.01	3.10	-2.00
EPR_Wet/Dry	-0.02	2.89	-2.97
LRR_Back Beach	0.07	3.13	-1.59
LRR_Wet/Dry	-0.01	2.81	-2.37

Along an unarmored beach, beach widths would stay relatively stable over the long-term with the beach widths migrating landward or seaward depending on sea level, so one would expect the shoreline change rates for both reference features to be similar.

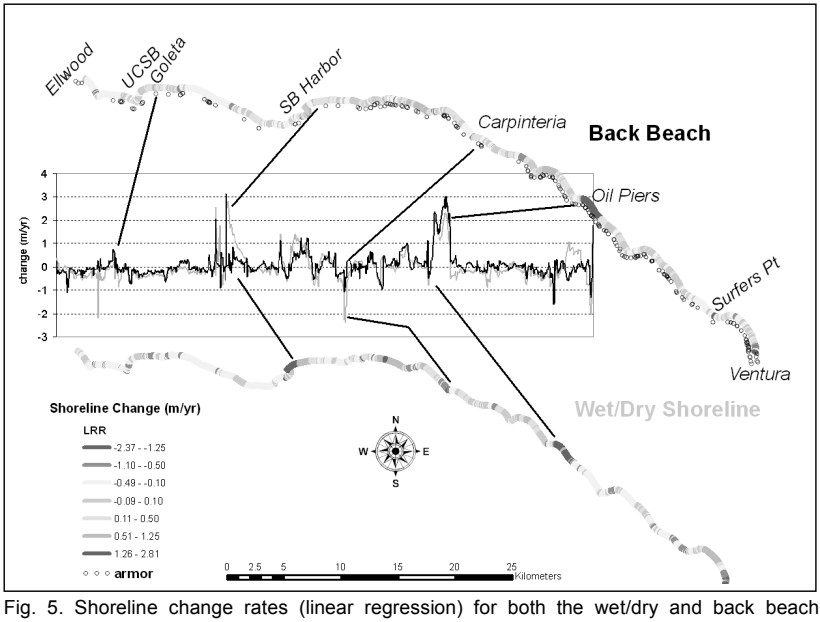

Fig. 5. Shoreline change rates (linear regression) for both the wet/dry and back beach shorelines.

Once the back beach is armored, then the back beach change would appear to accrete due to placement loss (determined by the footprint of the structure). As sea level continues to rise, and the wet/dry shoreline continues to retreat, passive erosion takes place.

Over the study area, the largest erosion rates detected using LRR occur at UCSB Beach, and at the inlet to Carpinteria Salt Marsh with both rates greater than –2 m/year (Figure 5). Maximum accretion rates are a direct result of engineered structures, the construction of the Santa Barbara Harbor and the construction of the oil processing facilities at Oil Piers resulted in 70 year shoreline change rates at ~3m/yr (figure 5). The regional analyses may facilitate regional sediment management, and a better understanding of

cumulative impacts however, most of the decisions directly affecting long-term beach widths and recreational and economic opportunities happen at a much smaller scale.

Case Study: Carpinteria Erosion

Breakwater construction and sand impoundment at the Santa Barbara Harbor led to a well documented erosion wave that migrated downcoast at ~1.7km/yr (~1mi/yr) (Weigel 2002). While the reporting of this erosion wave is not new, the application of the beach width methodology to study this erosion event provides new information on the response of the beach and shoreline (Figure 6).

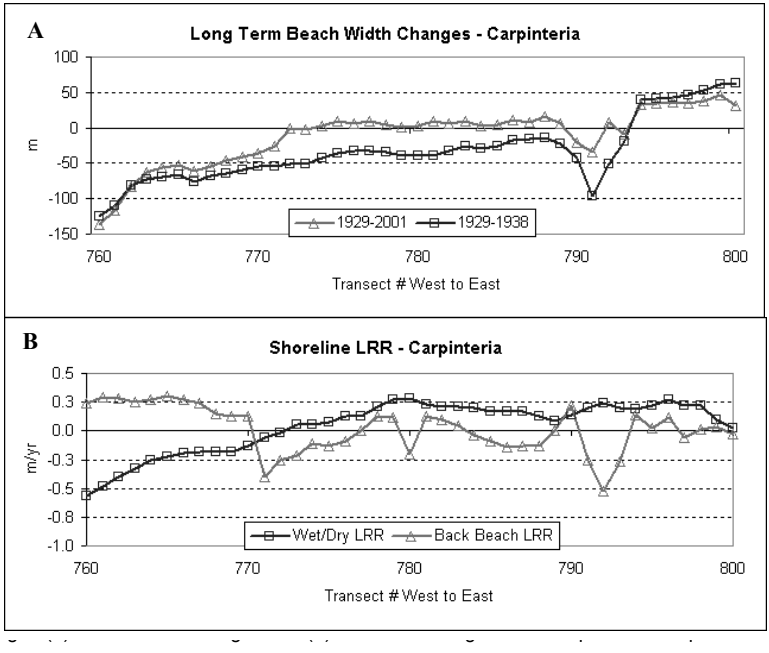

Figure 6 a shows the changes to the beach following the erosion wave determine by subtracting the differences in beach width between 1929-1938. While beach widths were largely eroded in the west (-150 m), there was also accretion of beach at the east end of the shoreline segment (~55m) (past the creek mouth located at transect 792) resulting in a change of the shoreline orientation. The beach has maintained this alignment for the following 63 years (1929-2001) although the center of the beach accreted some 50 meters over the longer time period.

In Figure 6b, the wet/dry shoreline change analyses shows a similar pattern of reorientation. However, the back beach shoreline change rate at the west end of the beach (transects 760-770) shows an accretion trend caused by the construction and encroachment of a revetment onto the beach. While the accretion "rate" of the back

beach is not valid after the structure is built, the reversal in shoreline change rate identifies the human alteration. The shoreline change immediately adjacent to the revetment along the city beach (transects 770-780) follows the overall pattern of reorientation depicted in the wet/dry shoreline change rates.

The beach width analysis was applied with the Lidar derived beach widths and air photos to examine impacts and recovery associated with the large El Niño events of 1982-83 and 1997-98 (Figure 7). By subtracting the Lidar beach widths of 1998 from

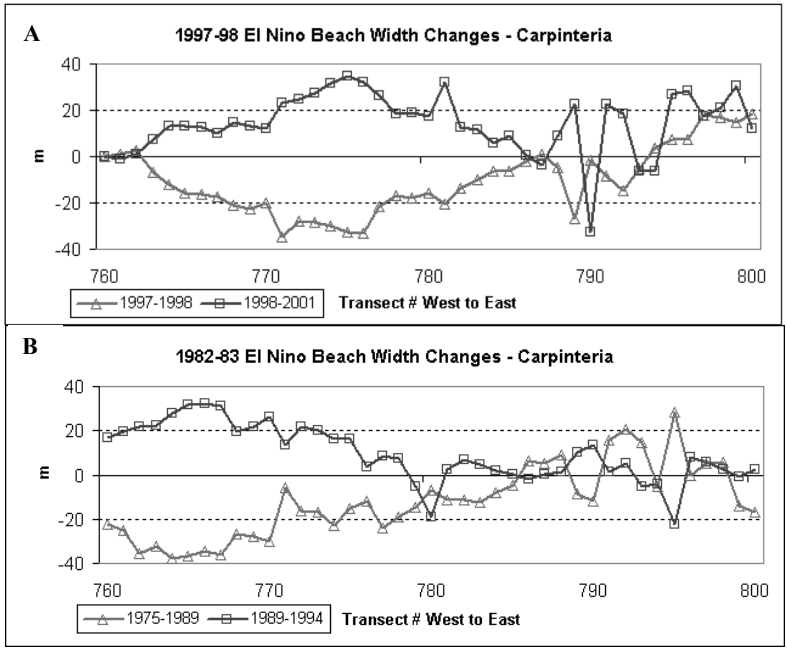

Fig. 7. Beach width changes and recovery following the 1997-98 (a) and 1982-83 (b) El Niños.

1997, the beach response revealed a similar pattern to the long-term beach width and wet/dry shoreline reorientation (Figure 7a). Erosion near the west end of the beach of ~40m was conversely related to east end accretion in beach width of ~20m. The recovery of the beach at the west end was complete by the time of the subsequent available air photo set in 2001 when the west end beach widths accreted nearly 40 meters. The net result by 2001 was that the beach had widened at the east end an additional ~20 meters from the 1998 survey.

The 1982-83 El Niño was the largest El Niño on record and had devastating impacts to UCSB beach (Revell and Griggs 2006). Due to the lack of available air photo sets, the closest available photo sets bracketing the event were taken in 1975 and 1989 (Figure 7b). The beach width changes were analyzed revealing the same pattern of

beach reorientation characterized by nearly 40m of erosion in the west end and ~20m of beach widening near the east end. By 1994, the next available photo set, this reorientation had recovered to the preexisting state in 1975. Note that the location of the maximum erosion shifted to the east roughly 500m between these two time periods (from Transect 767 to 777). Following the 1982-83 El Niño, the revetment was constructed to transect 761 resulting in a migration of the erosion hotspot downdrift.

DISCUSSION

Beach Widths

A 70 year record of beach widths changes were evaluated to determine if there was a long term narrowing of the beaches that could explain the discrepancy between a sediment supply reduction (Willis and Griggs 2003, Runyan and Griggs 2003) and a steady long-term average dredge volume recorded in the Santa Barbara harbor dredge records (Runyan and Griggs 2002). While he beach width analyses did not identify any systematic long term narrowing, the beach width envelopes identified locations of stable beaches, those with wide minimum beach widths and storage beaches, and those that exhibit extreme natural variability in widths and could potentially be a good site for beach nourishment.

The long-term beach width air analyses were complicated by the multiple dates and availability of sets of early air photos (ranging from 1929, 1938, 1943, and 1947). Further complicating the analyses were the beach changes associated with a variety of human alterations that pre-dated airplanes and air photos. Ideally, an air photo set taken during the late summer at lower tide prior to railroad construction (circa 1900), and a pre- harbor 1928 set would be compared to the existing photo sets to better examine this question of long term narrowing. The historic T-sheets provide some shoreline information, but the delineation of a back beach in the early maps is more of an artistic rendering rather than a substantive data set.

The use of shoreline orientation data provides additional information to understanding the response of beaches to wave exposure. The shore normal data aided in identifying stable beaches and storage beaches. Tot better assess the regional behavior and to calibrate the methodology, additional research is needed on less altered beaches. More research is also needed to understand long term changes to shoreline orientation, whether it is driven by a single catastrophic events such as an erosion waves or tsunami, or driven by repeated extreme events such as large El Niños or hurricanes.

Shoreline Change

Overall, the shoreline changes occurring throughout the study area are a balance of mild erosion and large-scale accretion caused by engineered structures. At a more localized scale, differences found between accretion of the back beach and erosion of the wet/dry shoreline can be used to identify locations of placement loss and passive erosion. Once a structure is constructed, and the placement loss occurs, then any rate of back beach shoreline changes largely becomes irrelative.

Storm Event response

The beach width response to the 1997-98 and 1982-83 El Niño match the long term pattern of reorientation observed at Carpinteria with erosion at the west end and accretion at the east end. This provides some evidence that extreme El Niños events may play an important role in creating or sustaining large scale, long-term coastal evolution. The data coverage bracketing the 1982-83 event was rather spread from the actual event, and may be recording a different erosion event. However if the pattern observed in 1989 is remnant from the 1982-83 event, the implication is that the 1982-83 event had a longer lasting impact on the coast than the 1997-98 event.

Beach width methodology

Beach width methodology when used in conjunction with shoreline change analyses provides additional information on the shape of the shape and response of the beach. When shoreline change rates along unarmored sections are similar between the wet/dry and back beach reference features indicating that beach widths remain relatively constant (among the oscillations) as the shoreline retreats. Along armored sections of coastline, however, we often see accretion of the back beach and the erosion of the wet dry line. The application of a beach width methodology can be used to detect both placement loss and passive erosion and assist coastal managers in quantifying and assessing cumulative impacts of shoreline armoring over a much broader spatial scale.

Human Alterations

Along the seventy kilometers of the study area, 60% (41.9km) of shoreline is armored with a variety of revetments and seawalls. Another ten kilometers (14.3%) has been altered by groins, breakwaters, or other littoral barriers. With the high rates of littoral transport, the cross-shore structures perform well at building up beach widths, while alongshore-oriented structures have resulted in placement loss, passive erosion, and had the net result of reducing beach widths. The construction of the revetment along Carpinteria following the 1982-83 event and the similar pattern of erosion in 1997-98 that was deflected down coast may provide some evidence that active erosion and flanking erosion is occurring at the end of the structure, but more research is needed.

CONCLUSION

The 70 year record of beach width changes in the Santa Barbara Sandshed did not reveal any long term beach narrowing that would be associated with a reduction in sand supply. Beach widths instead oscillated widely across the littoral cell. Updrift of the Santa Barbara harbor, beach widths are closely related to strong El Niños resulting in the narrowest widths measured following the events of 1982-83 and 1997-98. Down drift of the harbor, beach widths did not follow the similar El Niño pattern. The greatest narrowing of beach widths occurred at 1) Carpinteria caused by sand impoundment by the construction of the Santa Barbara harbor, and 2), Goleta Beach due to the construction of the Santa Barbara airport and the loss of tidal prism at Goleta Slough. The greatest widening of beach widths occurred immediately updrift

of the harbor (>200m) as a result of sand impoundment and sand bypassing, with a groin field widening beach widths by >100m.

The combination of beach width envelops and changes in shoreline orientation demonstrated that the west facing beaches of Ellwood 255°-240° were naturally the most stable with beach widths between 25 and 75 meters, while the east facing beaches 120°-105° were naturally the most variable ranging from 0 to 150m.

Shoreline change rates were evaluated at both the wet/dry shoreline and back beach reference feature in conjunction with the beach width changes. Average shoreline change rates for the 70km study area show mild accretion of the back beach and a slightly larger erosion rate at the wet/dry shoreline. This is consistent with the placement loss of armoring ~60% of the study area with a variety of structures.

The construction of the harbor breakwater and sand impoundment created an erosion wave resulted in narrowing of Carpinteria and other beaches down drift. The beach width analyses revealed that this erosion wave narrowed the beaches by nearly 150m in places, but served to reorient the coast and resulted in moderate downcoast accretion along the same segment of beach. Long-term shoreline change rates of the wet/dry shoreline show a similar trend of beach rotations.

The beach width response to the 1997-98 and 1982-83 El Niño match a long-term reorientation pattern measured in the wet/dry shoreline and beach width changes with erosion at the west end and accretion at the east end. This provides some evidence that extreme El Niños events play an important role in long-term coastal evolution.

The evaluation of beach widths provides additional information to inform shoreline change analyses and can provide coastal managers with additional information on shoreline orientations and quantitative information to assess cumulative impacts.

REFERENCES

Bailard, J., and Jenkins, S.A. (1982). City of Carpinteria Beach Erosion and Pier Study. Final Report to the City of Carpinteria. Bailard/Jenkins Consultants. April 1982. 292 pgs.

Boak, E. H. and Turner, I. L. (2005). Shoreline Definition and Detection: A Review. *Journal of Coastal Research* 21(4), 668-703.

Crowell, P.J., and Leatherman, S.P. (editors) (1999). Coastal Erosion Mapping and Management. Journal of Coastal Research Special Issue #28. Coastal Education & Research Foundation, Inc.

Graham, N.E. (2003). Variability in the Wave Climate of the North Pacific – Links to Inter-Annual and Inter-Decadal Variability. Proceedings of OCEANS 2003. Vol.2: 969-972.

Griggs, G.B., Patsch, K., Savoy, L. (2005). Living with the Changing California Coast. *University of California Press.* Berkeley, CA. 539p

Hapke, C.J, and Reid, D., Richmond, B.M., Ruggiero, P., List, J. (2006) National

Assessment of Shoreline Change Part 3. Historical Shoreline Change and Coastal Land Loss Along Sandy Shorelines of the California Coast. USGS Open File Report 2006-1219.

Hubbard, D., and Dugan, J.E. (2003). Shorebird use of an exposed sandy beach in southern California. *Estuarine, Coastal and Shelf Science* 58S (2003) 41-54.

Inman, D.L. and Jenkins, S.A. (1999). Climate Change and the Episodicity of Sediment Flux of Small California Rivers. *Journal of Geology*, 107:251-270.

King, P. and Symes, D. (2004). Potential loss in GNP and GSP from a failure to maintain California's beaches. *Shore and Beach* 72(1):3-8.

Mantua, N.J., Hare, S.R., Zhang, Y., Wallace, J.M., Francis, R.C. (1997). A Pacific interdecadal climate oscillation with impacts on salmon production. *Bulletin of the American Meteorological Society* Vol. 78 pp. 1069-1079.

Morton, R.A. and Speed, F.M. (1998). Evaluation of shorelines and legal boundaries controlled by water levels on sandy beaches. *Journal of Coastal Research,* 18(2), 329-337.

Moore, L.J. (2000). Shoreline Mapping Techniques. *Journal of Coastal Research*, 16(1), 111-124.

Moore, L.J., Ruggiero, P., List, J.H. (2005). Comparing Mean High Water and High Water Line Shorelines: Should Proxy-Datum Offsets be Incorporated in Shoreline Change Analysis? *Journal of Coastal Research* May 2005.

Ranasinghe, R., McLoughlin, R., Short, A., Symonds, G. (2004). The Southern Oscillation Index, wave climate, & beach rotation. *Marine Geology* 204:273-287.

Revell, D.L., Komar, P.D., and Sallenger , A.H.,(2002). An Application of Lidar to analyses of El Niño erosion in the Netarts littoral cell. *Journal of Coastal Research* 18(4):792-801.

Revell, D. L., and Griggs, G.B. (2006). Beach Width and Climate Oscillations Along Isla Vista, Santa Barbara, California. *Shore and Beach* 74(3)8-16.

Runyan, K.B., and Griggs, G.B. (2002). Implications of harbor dredging for the Santa Barbara littoral cell. *Proceedings California and the World Oceans 2002*, Santa Barbara, CA. ASCE.

Runyan, K.B., and Griggs, G.B. (2003). The Effects of Armoring Seacliffs on the Natural Sand Supply to the Beaches of California. *Journal of Coastal Research* 19(2) 336-347.

Sallenger A.H., Krabill, W., Swift, R., Brock, J., List, J., Jansen, M., Holman, R.A., Manizade, S., Sontag, S., Meredith, A., Morgan, K.,. Yunkel, J.K., Frederick, E.B. and Stockdon, H.F. (2003). Evaluation of airborne topographic lidar for quantifying beach changes. *Journal of Coastal Research*, 19(1), 125-133.

Thieler, E.R., Martin, D., and Ergul, A. (2003). Digital Shoreline Analysis System, Version 2.0: Shoreline change measurement software for ArcView. USGS Open File Report 03-076.

Weigel, R. L. (2002). Seawalls, Seacliffs, Beachrock: What Beach Effects? Part 2. *Shore and Beach*. 70(2)13-22.

Willis, C.W. and Griggs, G.B. (2003). Reductions in fluvial sediment discharge by coastal dams in California and implications for beach sustainability. *Journal of Geology* 111:167-182.

ENGINEERING ACTIVITIES INFLUENCING HISTORICAL SEDIMENT TRANSPORT PATHWAYS AT THE COLUMBIA RIVER MOUTH, WA/OR

Mark R. Byrnes[1], Sarah F. Griffee[1], and Hans R. Moritz[2]

1. Applied Coastal Research and Engineering, Inc., 766 Falmouth Road, Suite A-1, Mashpee, MA 02649, USA. mbyrnes@appliedcoastal.com.

2. US Army Corps of Engineers, Portland District, P.O Box 2946, Portland, Oregon 97208, USA. Hans.R.Moritz@nwp01.usace.army.mil.

Abstract: Regional sediment transport dynamics at and adjacent to the MCR were quantified using historical shoreline and bathymetry surveys. Four distinct depositional trends were identified: 1) the modern ebb shoal was deposited approximately 2-mi seaward of the natural shoal in about 90- to 130-ft water depth as a result of jetty construction; 2) the primary area of sedimentation on the ebb shoal is north of the entrance, and it continues to migrate north with time; 3) northward-directed sediment transport from the entrance has resulted in net accretion along the shoreline and on the continental shelf seaward of Long Beach Peninsula; and 4) continual shoreface erosion south of the MCR is the result of sediment diversion by the south jetty to the west and north of the entrance toward the ebb shoal and onto the continental shelf. The long-term sediment budget indicates that approximately 4.4 Mcy of sediment is transported to the continental shelf north of the MCR on an annual basis.

INTRODUCTION

The Columbia River is the largest on the west coast of the U.S., draining about 259,000 mi^2 and extending some 1,200 mi from British Columbia to the coasts of Oregon and Washington (McManus, 1972; Gailani et al., 2003). Average annual discharge is approximately 200,000 cubic feet per second (cfs), more than twice the combined discharges of all other rivers in California, Oregon, and Washington (Barnes et al., 1972; Komar and Li, 1991). Peak discharges of 740,000 cfs occur in May and June as the result of snowmelt, whereas minimum flows (106,000 cfs) occur in August and September (Neal, 1972; USACE, 1999). It is the major source of sediment to the northwest continental shelf (Sternberg, 1986). Suspended sediment discharge from the river is about 1 to 2 x 10^{13} g/yr (5 to 10 x 10^6 yd^3/yr), and bedload discharge is estimated

to be on the order of 10^{12} g/yr (10^6 tons) (Karlin, 1980). Gross and Nelson (1966) estimate that the Columbia River discharges 10^4 times more sediment to the northwest continental shelf than all other sources combined.

The continental shelf seaward and north of Tillamook Head, Oregon to the entrance of Willapa Bay, Washington is characterized as relatively narrow (about 25 mi) and steep (21 ft/mi) (McManus, 1972). South of the Columbia River, ocean beaches, backed by substantial dunes along a stretch of coast referred to as Clatsop Plains, extend for 20 mi to Tillamook Head (Fig. 1). This rocky headland extends seaward to deep water, effectively interrupting any further movement of sand south along the coast by littoral processes (Clemens and Komar, 1988). North of the Columbia River mouth, Long Beach Peninsula extends about 25 mi north from Cape Disappointment (North Head) to Leadbetter Point at the entrance to Willapa Bay. Three prominent sediment texture trends have been identified by McManus (1972) as characteristic of the continental shelf seaward and adjacent to the Columbia River entrance: 1) an inner-shelf sand wedge extends south of the Columbia River to Tillamook Head and offshore to about 230 ft water depth; 2) north of the Columbia River and seaward to a depth of about 165 ft is a blanket of fine sandy nearshore sediment, not forming a pronounced wedge; and 3) a dominant mid-shelf silt deposit extending from the mouth of the river in a north-northwest direction.

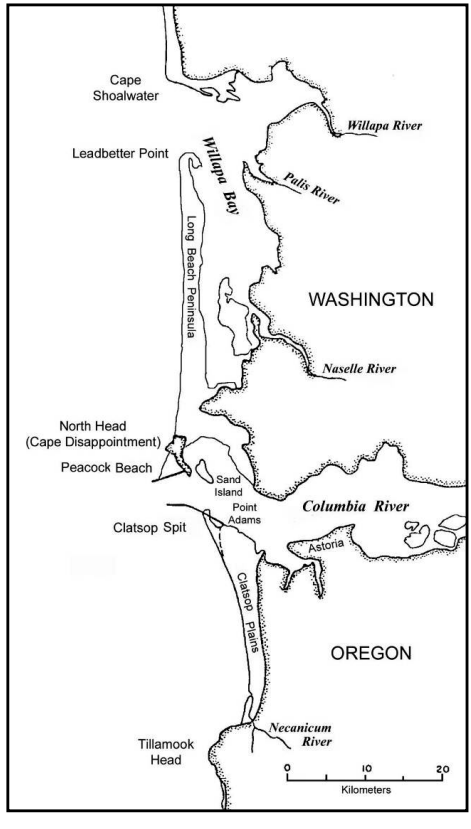

Fig. 1. Washington and Oregon coast north and south of the Columbia River.

Regional sediment transport pathways and rates of change adjacent to the Mouth of the Columbia River (MCR) were documented through geomorphic analysis of historical shoreline and bathymetry data for the period 1868 to 2003. Thirteen digital bathymetric and shoreline surveys of the entrance area and ebb shoal were compared to quantify sediment transport magnitudes and pathways. The U.S. Army Corps of Engineers

(USACE) Sediment Budget Analysis System (SBAS; Rosati and Kraus 2001) was used to calculate and display transport pathways and analyze sediment volume fluxes for the period 1958 to 2003. In addition, USACE, Portland District, channel dredging and placement volumes were included in a sediment budget to accurately reflect dredging activities for the analysis period. Regional sediment transport trends documented throughout the Columbia River Littoral Cell (CRLC) by Buijsman et al. (2003) provided background and information on oceanic boundary conditions for the MCR and vicinity.

HISTORY AND ENGINEERING ACTIVITIES

In the late 1780s, the Boston Fur Company was formed to engage the Pacific Northwest natives in the trading of sea otter furs. On 7 May 1792, Captain Robert Gray, a New England native, sailed his ship, the Columbia, into Bullfinch Harbor (later renamed Grays Harbor). Searching for still more trading partners, Gray sailed into the mouth of the Columbia River, advancing some 15 miles by 10 May 1792, just 3 days after he had sailed into Grays Harbor. To commemorate the event, the river was named Columbia in honor of the ship (Bohlander, 1984).

A chart prepared by Captain George Vancouver, dated 1798, illustrates many of the same major features and shapes in the estuary that exist today (Fig. 2). The first extensive mapping of the harbor was completed in 1839 by Sir Edward Belcher, but the first survey quality map was produced about 30 years later in 1868/77 by the U.S Coast and Geodetic Survey (USC&GS). The most significant geomorphic changes are those associated with construction of jetties at the entrance and the response of the shoreline and shoals to engineering activities (CREDEP, 1983; Byrnes and Li, 2001; USACE, 1999; Buijsman et al., 2003).

Continual adjustments in channel configuration and shoaling patterns at the MCR have caused navigation problems since its discovery in 1792. Ships often had trouble traversing the Columbia River bar, and the natural channels often shifted widely within the course of several tidal cycles. As such, it was decided that structural control of the MCR was needed to maintain safe navigation through the entrance area, so in April 1885, construction on the south jetty began. Nearly 10 years later (October 1895), a 4.5-mi jetty was completed from Point Adams in a northwesterly direction. Although a general improvement in navigation was achieved, shoals began to form along both sides of the jetty causing renewed shoaling problems at the entrance. Extension and rehabilitation of the south jetty were completed in 1913, giving the structure a total length of 7 mi. Construction of the north jetty began in 1913 as a component of the 40-ft entrance project. When completed in 1917, the structure extended about 2 mi in a southwesterly direction from Cape Disappointment (Lockett, 1967; USACE, 1999).

Since 1883, the Portland District has been surveying the harbor and entrance area to monitor shoreline position and changes in shoal and channel morphology. Structures imposed substantial influence on estuarine hydrography and channel characteristics, creating a self-scouring inlet that has moved the crest of the offshore bar seaward into deeper water and significant sand deposition along beaches north and south of the harbor.

Table 1 presents a summary of the construction and rehabilitation history for the entrance jetties since authorization for reference with long-term changes in sediment erosion and deposition at and adjacent to the entrance.

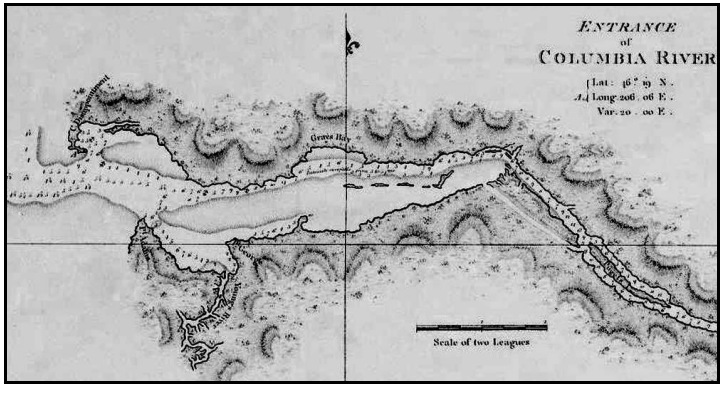

Fig. 2. Map of the Columbia River entrance prepared by Vancouver in 1798 (modified from Washington State Archives).

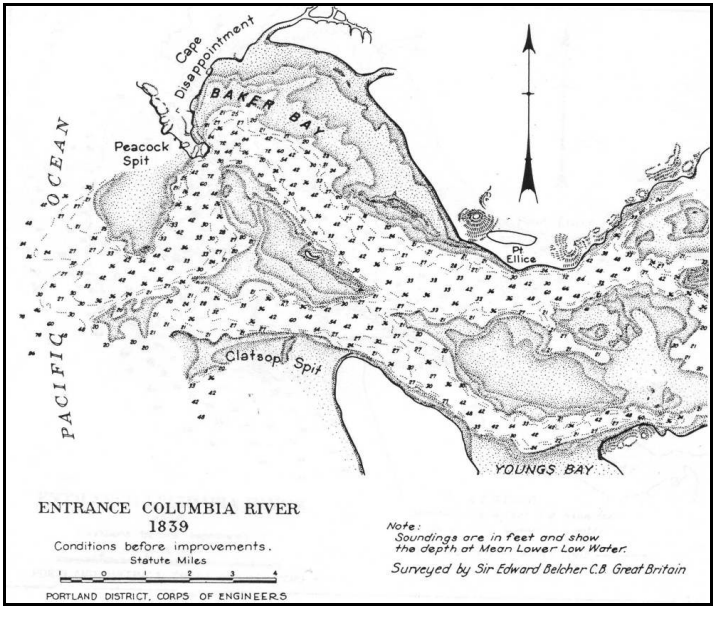

Fig. 3. First extensive mapping of the Columbia River entrance by Belcher in 1839.

Table 1. Engineering Events Affecting the Evolution of the Mouth of the Columbia River

1882	Congress recommends construction of a jetty along the south side of the Mouth of the Columbia River and approves a 30 ft deep entrance channel.
1885	Construction of the south jetty began but proceeded slowly.
1889	Rapid construction of the south jetty commenced; 20 ft. controlling depth in the entrance channel.
1895	South jetty completed to a distance of 4.5 miles from shore with four groins constructed along the north side of the jetty; 31 ft. controlling depth in the entrance channel.
1903	Congress approves extending the south jetty 2.5 miles west of the existing structure, construction of a north jetty extending about 2 miles from Cape Disappointment, a channel controlling depth of 40 ft., and channel dredging.
1904	Initiation of hopper dredging at the MCR.
1913	South Jetty extension completed; North Jetty construction began.
1917	North Jetty completed; channel controlling depth on the bar increased to 37 ft.
1918	Entrance channel controlling depth of 40 ft.
1927	Entrance channel controlling depth of 47 ft.
1931	South Jetty rehabilitation began.
1936	Reconstruction of the South Jetty completed; disintegration of the outer end of the structure continued due to winter waves.
1938	North Jetty rehabilitation began.
1939	North Jetty rehabilitation completed and asphalt added; concrete terminal structure placed at the end of the jetty; Jetty A completed.
1939 to 1955	Dredging at entrance confined to Clatsop Spit.
1942	South Jetty rehabilitated with asphalt mastic, and a concrete terminal structure was completed about 3,900 ft shoreward of the end of the jetty as completed in 1913.
1945	Regular annual dredging of the out bar channel initiated.
1954	Entrance channel controlling depth of 48 ft approved by Congress.
1956	Dredging of the entrance channel to 48 ft began.
1958	Dredged material disposal Sites A and C abandoned; Site B used extensively.
1961	South Jetty and Jetty A rehabilitated.
1977	52 ft. entrance channel project initiated; EPA provides interim designation for MCR ocean dredged material disposal sites.
1984	Entrance channel controlling depth of 55 ft.
1986	Final designation of MCR ocean dredged material disposal sites.
1997	Temporary expansion of dredged material disposal sites B and E.

Sources: Hickson and Rodolf, 1951; Simenstad et al., 1984; USACE, 1999

Channel dredging was initiated in 1904 to maintain a 30-ft navigation channel across the entrance bar. Intermittent shoals formed by sand transport from Clatsop and Peacock spits created navigation hazards that required periodic maintenance (USACE, 1999). Between 1904 and 1940, approximately 8.3 million cubic yards (Mcy) had been dredged from the MCR entrance bar and placed in open water disposal sites. During this time, channel shoaling was tolerated to a certain degree; however, by 1945, consistent annual maintenance dredging at the MCR was required. Between 1945 and 1955, annual maintenance dredging averaged about 1.2 Mcy/yr (USACE, 1999). Quantities increased to an average of about 4.2 Mcy/yr from 1956 to present, most of which was deposited offshore in ocean disposal sites.

DATA SOURCES

Two primary data sources were used to compile shoreline and bathymetry data for this study. U.S. Coast and Geodetic Survey (USC&GS, predecessor to NOS) topographic and hydrographic surveys (T-and H-sheets) and U.S. Army Corps of Engineers (USACE) field surveys provided superior coverage of inlet and nearshore morphodynamics at the Columbia River Entrance. Surveys of the offshore bar and entrance area have been completed annually since construction began on the south jetty in 1885. In addition, shoreline positions interpreted from aerial photography by the Washington Department of Ecology (DOE) and the Oregon Department of Geology and Mineral Industries (DOGAMI) were used in analyzing more recent changes. Time series of change associated with construction and rehabilitation of the jetties isolates sediment transport trends that reflect the performance of navigation structures. A detailed presentation of data sources is described in Byrnes and Griffee (2006). Methods used for compiling and analyzing historical bathymetric and shoreline data sets are described in Byrnes and Hiland (1994), Byrnes and Hiland (1995), and Baker and Byrnes (2004).

INLET MORPHODYNAMICS

Hydrographic surveys of regional nearshore morphology provide a direct source of information for quantifying changes in seabed elevation. This type of analysis is used to document trends in regional-scale coastal evolution, and to evaluate the impact of natural processes and engineering activities on coastal sediment dynamics. The primary feature affecting coastal sediment erosion and accretion throughout the study area is the Columbia River entrance. Seafloor elevations to approximately 200 ft water depth were compiled and analyzed to identify patterns of erosion and deposition associated with the MCR and adjacent nearshore environs.

Prior to jetty construction, the entrance and shoal system appeared typical of fluvial-dominated estuarine entrances (Hayes and Kana, 1976; Reinson, 1992). Regional characteristics of inlet and nearshore morphology for the entrance to the Columbia River estuary and adjacent shelf environs (1868/77) are illustrated in Fig. 4. All significant bathymetric features are associated with the lower estuary and entrance shoal/channel deposits. First, the braided channel features of the lower estuary give way to a single primary channel exiting the coast in a south-southwest direction. Substantial shoal deposits exist in the lower estuary and entrance area as a result of sediment input from

the river and nearshore marine environments (Lockett, 1967; McManus, 1972). A large sand shoal is present along the south margin of the entrance (Clatsop Shoal), extending in a northwest direction off Point Adams. It is about 2.5-mi long and controls channel position and orientation in the entrance area. To the north, seaward of Cape Disappointment, a smaller shoal extends southwestward from the rocky headland along the north margin of the entrance. In between, Sand Island and adjacent shoals and deposits associated with the ebb-tidal delta seaward of the entrance made navigation during peak flows and high-energy events quite challenging. The shield of the Columbia River ebb shoal is defined by the 50-ft depth contour. Continual shifting of these shoals and channels prompted the USACE to propose jetties to control sedimentation processes in the entrance area (Lockett, 1967).

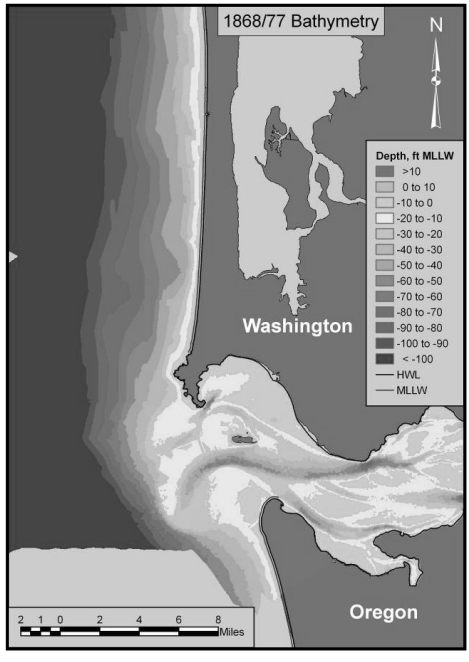

Fig. 4. Nearshore bathymetry (1868/77) at and adjacent to the MCR, WA/OR.

Between 1868/77 and 1926, large adjustments in sediment volume occurred at the entrance where the ebb-tidal shoal moved seaward about 2 mi, depositing approximately 252 Mcy of sediment in 90-ft water depth (Fig. 5). Approximately 70% of this deposition occurred between 1899 and 1926, after the entrance jetties were constructed (Byrnes and Griffee, 2006). The ebb-shoal that formed was skewed to the north, even though the channel exits the coast to the south-southwest. Deposition of northward directed sand from the ebb-shoal created Benson Beach, just north of the north jetty and south of Cape Disappointment. Clatsop Spit evolved in association with construction of the south jetty, creating a 3.5-mi long beach and filling the 1868 entrance channel as the new channel shifted north and displaced Sand Island. Net sediment deposition north of the channel and adjacent to the southern part of Baker Bay (158 Mcy), east of Cape Disappointment, appears to be the result of decreased flow in the area resulting from jetty placement and channel realignment. Conversely, seafloor erosion south of the south jetty is the result of decreased sediment supply to the area when the entrance channel shifted to the north, jetting much of its sediment load seaward to the ebb shoal. Net sediment erosion associated with channel realignment and erosion south of the south jetty (543 Mcy) controlled the sediment budget in the entrance area.

Bathymetric changes recorded for the period 1926 to 1958 illustrate net northward transport of sediment to and northwest of the north-oriented ebb shoal. The shoal depocenter has again moved seaward in response to flow from the increasingly-deeper channel (-40 to -48 ft during this time period; Fig. 6); net sediment deposition on the ebb shoal during this time was 182 Mcy. A substantial zone of erosion exists just landward of the ebb shoal, marking the position of the 1926 ebb-tidal delta. The magnitude of erosion for this feature (81.4 Mcy) is a little less than half of the deposition recorded for the ebb shoal. Another indication of northward sand transport is the apparent streaming of sand north from the ebb-tidal delta to the beaches along the coast of Long Beach Peninsula (Fig. 1). About 94 Mcy of sand deposited along the coast during this period.

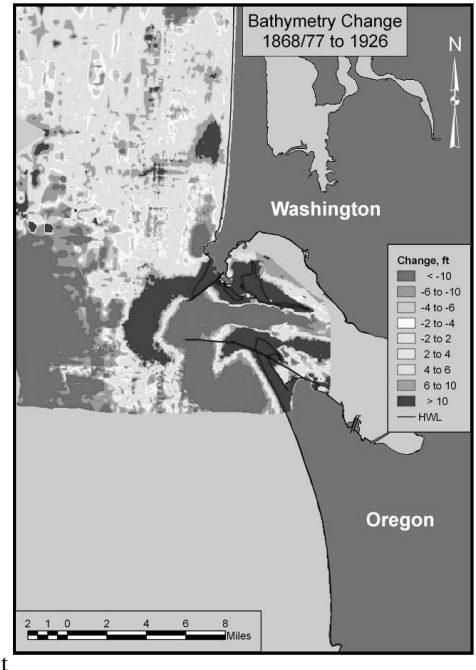

Fig. 5. Bathymetric change surface, 1868/77 to 1926. Bright red reflects maximum erosion, and dark blue reflects maximum deposition.

For the period 1958 to 2003, seafloor changes illustrate the same general trends as those presented for the 1926 to 1958 comparison, except the magnitude of accretion and erosion has increased. The centroid of deposition on the ebb shoal (minus the impact of dredged material placement offshore) shifted to the north (Fig. 7). Sediment accretion north of the entrance along Long Beach Peninsula continued as the shoreline moved seaward. In addition, erosion associated with the 1926 ebb-tidal delta increased, and the magnitude of sediment deficit south of the south jetty was enhanced.

SEDIMENT BUDGET AND TRANSPORT PATHWAYS

Regional sediment transport patterns for the Columbia River entrance and adjacent environs are consistent for all analysis time intervals (Byrnes and Griffee, 2006). Although coastal process measurements identify two distinct seasonal circulation trends, net sediment deposition and erosion in the study area is relatively steady and predictable. Changes in subaqueous spit formation and entrance shoal migration at the MCR since the mid-1800s indicate that net sediment transport in this area is from south to north. Prior to jetty construction, sand shoal accretion north and west of Point Adams (northern Clatsop Plains) would detach from the coast, migrate to the north and force the channel

to the north side of the entrance, thereby supplying large quantities of sand to the north side of the entrance area and eventually onto the ebb shoal. Jetty placement enhanced net northward directed transport by restricting sand movement within the entrance, effectively eliminating sand supply from the MCR to the offshore areas south and west of the Clatsop Spit. Although sand supplied to the shoreface south of the south jetty was blocked once the south jetty was constructed, the erosive power of waves and currents continued to rework the shelf surface in this area, creating a large area of seafloor erosion that persists today (see Figs. 6 and 7). Most eroded sand from this area is transported north to the ebb shoal, eventually making its way to beaches and/or the shelf surface north of the MCR. Sediment deposition to the northwest off the ebb shoal is documented since 1926, and this result supports the findings of previous studies (e.g., Sternberg, 1986). Although south-directed transport has been associated with summer conditions, all regional geomorphic response data suggest that high-energy, northward-directed flow, characteristic of the winter season, controls net transport direction in the study area.

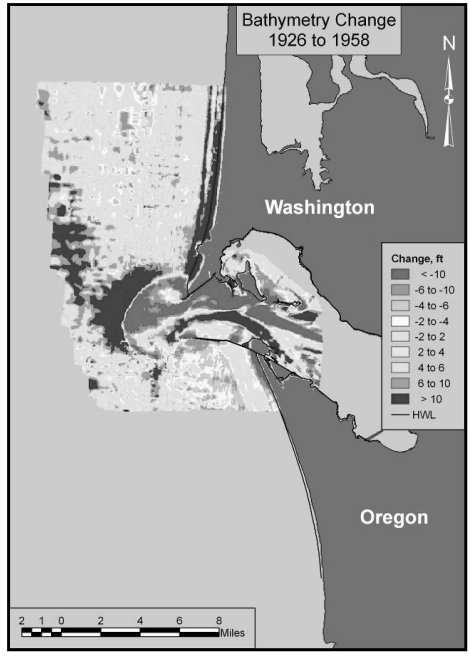

Fig. 6. Bathymetric change surface, 1926 to 1958. Bright red reflects maximum erosion, and dark blue reflects maximum deposition.

The period 1958 to 2003 was evaluated for estimating the net sediment budget and long-term sediment movement at and adjacent to the MCR. Channel dredging and offshore disposal of sediment were included in the analysis. Sediment input to the MCR from the estuary (4.0 Mcy/yr; about 30% sand and 70% fines) was estimated based on USACE dredging records for the lower estuary provided by Kaminsky et al. (2000) and Bisson et al. (2000). This quantity also is consistent with Columbia River sediment supply estimates provided by Sherwood et al., 1990; Gelfenbaum et al., 2001; and Buijsman et al., 2003 for the period 1958 to 1997. Furthermore, long-term bathymetric change from 1868/77 to 2003 indicates a sediment surplus of about 3.5 Mcy/yr. Longshore transport rate estimates for Clatsop Plains (1.0 Mcy/yr) and Long Beach Peninsula (1.5 Mcy/yr) were derived from Kaminsky et al. (2000) and through personal communications (Kaminsky, 2006). However, seasonal shifts in longshore transport do provide sand to beaches south of the entrance (Clatsop Plains) via south-directed transport. Onshore transport of sand via aeolian processes was estimated at 40,000 to 50,000 cy/yr based on the presence of extensive dune deposits along accreting beaches.

Fig. 8 illustrates the net sediment budget for the period 1958 to 2003. Polygon boundaries were based on erosion/accretion areas illustrated in Fig. 7. Volume change quantities shown in parentheses represent net annual change values as derived from erosion/accretion estimates based on bathymetric data comparisons. Sediment dredging (R) and placement (P) are documented for each change polygon. Sediment fluxes are associated with arrows and represent the estimated net quantity of sediment transported from one geomorphic area to another on an annualized basis (Mcy/yr).

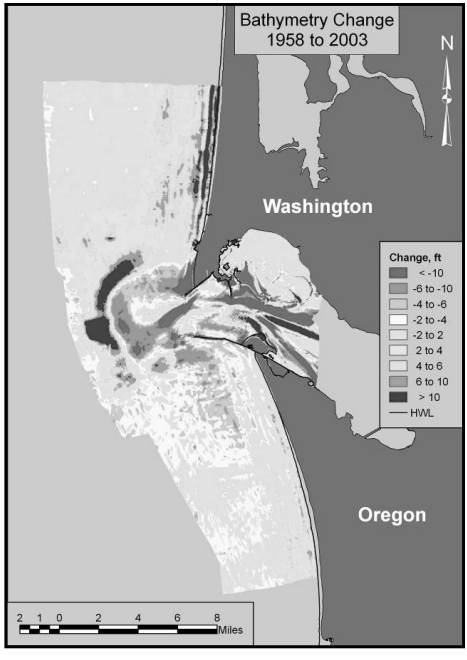

Fig. 7. Bathymetric change surface, 1958 to 2003. Bright red reflects maximum erosion, and dark blue reflects maximum deposition.

Substantial erosion took place in the entrance channel and offshore region seaward of Clatsop Spit over this 45 year period. Conversely, net deposition occurred in all areas north of the entrance channel area, again illustrating the net northward drift of sediment from the MCR (Fig. 8). Bakers Bay and the littoral zone of Clatsop Plains recorded minor amounts of net deposition. Significant quantities of sediment were transported from the channel, across the ebb shoal, and to the northwest onto the offshore shelf fronting Long Beach Peninsula. Sediment deposition along southern Clatsop Plains beaches indicates that seasonal south-directed and onshore transport may contribute to net deposition in this region. Net depositional trends throughout the study area are consistent with geomorphic changes recorded for the 1926 to 1958 period (Fig. 6), and with the findings of Barnes et al. (1972), Healy (1983), Nittrouer et al. (1979), Sternberg (1986), and Buijsman et al. (2003). Sediment flux to the northwest on the continental shelf was estimated at 2.2 Mcy/yr.

CONCLUSIONS

A regional analysis of shoreline and bathymetry change was completed to evaluate sediment transport dynamics associated with natural processes and engineering activities at the Columbia River entrance since 1868. Volume change estimates were derived to relate grouped cut and fill relationships with natural processes and engineering activities.

Four distinct depositional trends were identified. One, the modern ebb-tidal delta developed as a result of jetty construction. Currently, it resides approximately 2-mi seaward of the original shoal in about 90- to 130-ft water depth. The deposit contains about 411 Mcy of sediment, approximately half of which comes from the old ebb shoal. Two, the depocenter for sedimentation on the ebb shoal is to the north of the entrance centerline, and it migrates to the north with time. Three, northward-directed sediment transport from the entrance has resulted in net accretion along the shoreline and on the continental shelf seaward of Long Beach Peninsula. Four, erosion south of the south jetty is the result of sediment blocking by the jetty and subsequent transport toward the ebb shoal and onto the continental shelf.

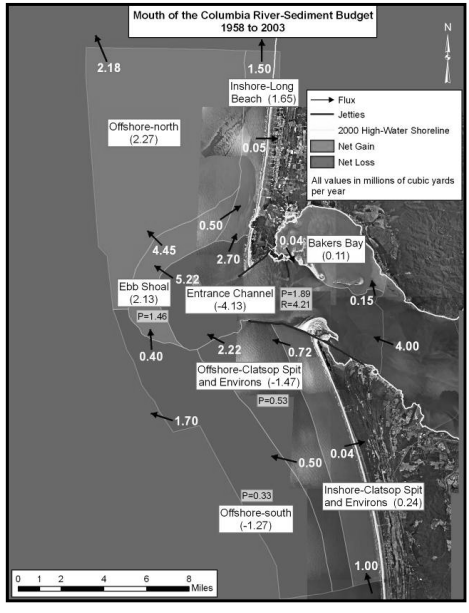

Fig. 8. Long-term sediment budget and net transport pathways for the MCR, 1958 to 2003.

The 1958 to 2003 sediment budget for the MCR reflects sediment movement from the entrance and along the continental shelf after construction and rehabilitation of the jetties. Although seasonal reversal in sediment transport are present, seafloor elevation differences between the 1958 and 2003 surfaces document a long-term flux of sediment from south to north from the MCR, the continental shelf, and coastal environments. Large quantities of sediment have been eroded from the entrance channel (about 4.13 Mcy/yr), transported in a north-northwest direction, and deposited along the beaches (1.65 Mcy/yr) and on the continental shelf (4.4 Mcy/yr). This pattern of change is similar for all time periods after jetty construction was completed.

ACKNOWLEDGEMENTS

Funding for this project was provided by the USACE Portland District under the Regional Sediment Management Demonstration Program. Special thanks to Ms. Doris McKillip (NWP) for RSM guidance early on in the project, to Ms. Jessica Baker for data compilation and analysis assistance, and to Ms. Liz Hunt (Applied Coastal) for technical and editorial assistance.

REFERENCES

Baker, J.L. and M.R. Byrnes, 2004. "Appendix F: Shoreline and Bathymetry Data," *In: Kraus, N.C. and H.T. Arden (editors), North Jetty Performance and Entrance Channel Maintenance, Grays Harbor, Washington,* Technical Report ERDC/CHL TR-03-12, US Army Engineer Research and Development Center, Vicksburg, MS.

Barnes, C. A., A. C. Duxbury, and B. A. Morse, 1972. "Circulation and selected properties of Columbia River effluent at sea," *In: A. T. Pruter and D. L. Alverson (eds.), The Columbia River Estuary and Adjacent Waters, Bioenvironmental Studies*, University of Washington Press, Seattle, WA, p. 41-80.

Bisson, P.A., C.C. Coutant, D. Goodman, R. Gramling, D. Lettermaier, J. Lichatowich, E. Loudenslager, W. Liss, L. McDonald, D. Philipp, and B. Riddell, 2000. "The Columbia River Estuary and the Columbia River Basin Fish and Wildlife Program," Independent Scientific Advisory Board Report 2000-5, Northwest Power Planning Council, National Marine Fisheries Service, Portland, OR, 35 p.

Bohlander, R. E., editor, 1984. "World Explorers and Discoverers," Macmillan Publishing Company, New York, NY.

Buijsman, M.C., C.R. Sherwood, A.E. Gibbs, G. Gelfenbaum, G. Kaminsky, P. Ruggiero, and J. Franklin, 2003. "Regional Sediment Budget of the Columbia River Littoral Cell, USA, Analysis of Bathymetric- and Topographic-Volume Change," Open-File Report 02-281, U.S. Geological Survey, Menlo Park, CA.

Byrnes, M.R. and S.F. Griffee, 2006. "Regional Sediment Transport Patterns Relative to Engineering Activities at the Mouth of the Columbia River, Washington/Oregon," Final Report to the U.S. Army Corps of Engineers, Portland District, Portland, OR., 45 p. + Appendices.

Byrnes, M.R. and M.W. Hiland, 1994. "Compilation and analysis of shoreline and bathymetry data (Appendix B)," *In: N.C. Kraus, L.T. Gorman, and J. Pope (editors), Kings Bay Coastal and Estuarine Monitoring and Evaluation Program: Coastal Studies,* Technical Report CERC-94-09, Coastal Engineering Research Center, Vicksburg, MS, p. B1-B89.

Byrnes, M.R. and M.W. Hiland, 1995. "Large-scale sediment transport patterns on the continental shelf and influence on shoreline response: St. Andrew Sound, Georgia to Nassau Sound, Florida, U.S.A," *In: J.H. List and J.H.J. Terwindt (editors), Large-Scale Coastal Behavior, Marine Geology,* 126: 19-43.

Byrnes, M.R. and F. Li, 2001. "Regional Analysis of Sediment Transport and Dredged Material Dispersal Patterns, Columbia River Mouth, Washington/Oregon, and Adjacent Shores," Final Report to the USACE, Coastal and Hydraulics Laboratory, Vicksburg, MS, 49 p.

Clemens, K. E. and P. D. Komar, 1988. "Oregon beach-sand compositions produced by the mixing of sediments under a transgressing sea," *Journal of Sedimentary Petrology,* 58 (3): 519-529.

CREDDP, 1983. "Bathymetric Atlas of the Columbia River Estuary. Columbia River Estuary Data Development Program, Columbia River Estuary Study Taskforce (CREST)," Astoria, OR.

Gailani, J.Z., J.W. Smith, N.C. Kraus, D.D. McGee, E.B. Hands, C.J. Mayers, H.R. Moritz, H.P. Moritz, M.D. Siipola, D.B. Slocum, M.R. Byrnes, F. Li, T.L. Dibble, W.H. Hollings, C.R. Lund, C.K. Sollitt, and D.R. Standley, 2003. "Monitoring Dredged Material Disposal at Mouth of Columbia River, Washington/Oregon, USA," Technical Report ERDC/CHL TR-03-5, US Army Engineer Research and Development Center, Vicksburg, MS, 237 p.

Gelfenbaum, G., M.C. Buijsman, C.R. Sherwood, H.R. Moritz, and A. Gibbs, 2001. "Coastal evolution and sediment budget at the Mouth of the Columbia River, USA," *Proceedings of Coastal Dynamics '01*, pp. 818-827.

Gross, M. G. and J. L. Nelson, 1966. "Sediment movement on the continental shelf near Washington and Oregon," *Science,* 154: 879-880.

Hayes, M.O. and T.W. Kana, 1976. "Terrigenous Clastic Depositional Environment," Technical Report CRD-11, Department of Geology, University of South Carolina, Columbia, SC, 364 pp.

Healy, M.J., 1983. "Dispersal of Mount St. Helens Ash Across the Washington Continental Shelf," M.Sc. Thesis, Lehigh University, Bethlehem, PA.

Hickson, R.E. and F.W. Rodolf, 1951. "History of the Columbia River jetties," *Proceedings of the 1st Conference on Coastal Engineering,* Chapter 32, p. 283-298.

Kaminsky, G.M., 2006. "Personal Communication with Mark Byrnes regarding estimates of net longshore sand transport rates north and south of the MCR."

Kaminsky, G.M., M.C. Buijsman, and P. Ruggiero, 2000. "Predicting shoreline change at decadal scale in the Pacific Northwest, USA," *Proceedings of the International Conference on Coastal Engineering 2000,* pp. 2400-2413.

Karlin, R., 1980. "Sediment sources and clay mineral distribution off the Oregon Coast," *Journal of Sedimentary Petrology,* 50(2): 543-560.

Komar, P. D. and M. Z. Li, 1991. "Beach placers at the mouth of the Columbia River, Oregon and Washington," *Marine Mining,* 10 (2): 171-187.

Lockett, J. B., 1967. "Sediment transport and diffusion: Columbia River estuary and entrance," *Proceedings of the American Society of Civil Engineers, Journal of Waterways and Harbors Division*, 93(WW4), 167-175.

McManus, D. A., 1972. "Bottom topography and sediment texture near the Columbia River mouth," *In: A. T. Pruter and D. L. Alverson (eds.), The Columbia River Estuary and Adjacent Waters, Bioenvironmental Studies,* University of Washington Press, Seattle, WA, p. 241-253.

Neal, V. T., 1972. "Physical aspects of the Columbia River and its estuary," *In: A. T. Pruter and D. L. Alverson (eds.), The Columbia River Estuary and Adjacent Waters, Bioenvironmental Studies,* University of Washington Press, Seattle, WA, p. 19-40.

Nittrouer, C.A., R.W. Sternberg, R. Carpenter, and J.T. Bennett, 1979. "The use of Pb-210 geochronology as a sedimentological tool: application to the Washington shelf," *Marine Geology,* 31: 297-316.

Reinson, G. E., 1992. "Transgressive barrier islands and estuarine systems," *In: R. G. Walker and N. P. James (eds.), Facies Models: Response to Sea Level Change,* Geological Association of Canada, p. 179-194.

Rosati, J.D., and Kraus, N.C. 2001. "Sediment Budget Analysis System (SBAS): Upgrade for Regional Applications," Coastal and Hydraulics Engineering Technical Note ERDC/CHL CHETN-XIV-3, US Army Engineer Research and Development Center, Vicksburg, MS.

Sherwood, C.R., D.A. Jay, R.B. Harvey, P. Hamilton, and C.A. Simenstad, 1990. "Historical changes in the Columbia River Estuary," *Progress in Oceanography,* 25: 299-352.

Simenstad, C., D. Jay, C.D. McIntire, W. Nehlsen, C. Sherwood, and L. Small, 1984. "The Dynamics of the Columbia River Estuarine Ecosystem," *Columbia River Estuary Data Development Program (CREDDP), Columbia River Estuary Study Taskforce (CREST),* Astoria, OR.

Sternberg, R. W., 1986. "Transport and accumulation of river-derived sediment on the Washington continental shelf, USA," *Journal of the Geological Society of London,* 143 (6): 945-956.

USACE, 1999. "Integrated Feasibility Report for Channel Improvements and Environmental Impact Statement: Columbia and Willamette River Federal Navigation Channel, Appendix H, Exhibit B, Physical Processes and Geological Resources," U.S. Army Corps or Engineers, Portland District, Portland, OR,160 p.

IMPLEMENTING REGIONAL SEDIMENT MANAGEMENT TO SUSTAIN NAVIGATION AT AN ENERGETIC TIDAL INLET

Hans R. Moritz[1], Guy R. Gelfenbaum[2], George M. Kaminsky[3], Peter Ruggiero[4], Joan Oltman-Shay[5], and Doris J Mckillip[1]

1. U.S. Army Corps of Engineers, Portland District, POB 2946, Portland, Oregon, 97208, USA hans.r.moritz@usace.army.mil. and doris.j.mckillip@usace.army.mil
2. U.S. Geological Survey, Coastal and Marine Geology Program, Menlo Park, CA, USA. ggelfenbaum@usgs.gov .
3. Washington Department of Ecology, Coastal Monitoring & Analysis Program, Olympia, WA, USA. gkam461@ecy.wa.gov.
4. Oregon State University, Dept of Geosciences, ruggierp@science.oregonstate.edu
5. Northwest Research Associates, Bellevue, WA joan@nwra.com.

Abstract: Regional Sediment Management (RSM) is a systems-based approach for managing multiple projects involving sediment. RSM fosters balance between infrastructure and natural system processes, resulting in reduced project costs and achievement of greater benefits. This paper introduces the RSM concept and describes how RSM is being implemented at the Mouth of the Columbia River to sustain the inlet's 100-year old navigation infrastructure and adjacent shore lands. Implementing RSM at this energetic inlet involves feeding the inlet's morphology using dredged material, and letting nature do the work of dispersing the placed dredged material to supplement the inlet's sediment budget, without compromising the reliability of the navigation channel. The paper discusses the types of data that are being collected and analyzed to understand the environmental forcing affecting the inlet's morphology. The paper also addresses how dredged material disposal is being conducted to implement RSM.

INTRODUCTION

This paper summarizes the application of Regional Sediment Management (RSM) at the Mouth of the Columbia River and is composed of three parts. The Mouth of the Columbia River (MCR) is located on the Pacific Northwest Coast of the USA, at Long-Lat 124 W-45 N, between the states of Oregon and Washington (Figure 1). The forces of

nature can be very energetic at MCR, motivating significant yet complex trends in sediment transport. The MCR is also "energetic" in terms of the convergence of political-socio-economic forces that emerge when initiatives are proposed to improve the management of a critical non-renewable resource at the inlet – sand. This paper describes how RSM is being implemented to reconcile the "energies" of the inlet by leveraging management of the MCR maintenance dredging program to sustain the inlet's morphology and jetties; thereby ensuring stability of the MCR navigation channel.

Due to the intrinsic relevance of RSM for many types of water resource projects, the first part of this paper is devoted to describing the RSM concept. The physical attributes of Mouth of the Columbia River are also described, as the evolution of this deep-draft navigation project is related to the present sediment processes and management challenges. The second part of this paper describes recent pilot projects for dredged material placement and initiatives for collection/analysis, in context of the RSM demonstration program at MCR. Lessons learned from the RSM demonstration project at the Mouth of the Columbia River are outlined in the third part of the paper. http://www.nwp.usace.army.mil/op/n/projects/mcr/regionalsediment.asp

Regional Sediment Management

RSM is a programmatic approach employed to reduce the life-cycle costs of infrastructure affected by water-borne sediment transport. The RSM imperative is to adaptively manage infrastructure (projects) in terms of the extended time and space scales as defined by natural sediment processes. By broadening the "planning horizon" for projects and broadening the number of project proponents and funding partners, greater benefits and cost savings can be accrued. In other words, RSM seeks to manage project(s) in a two-way context of how the sediment processes and infrastructure interact within a given region. The "region" is defined by the spatial extent over which a continuum of sediment processes is applicable and may include multiple unrelated projects. Projects may include harbors, navigation channels, dredging actions, in-water structures (jetties, breakwaters, revetments), shoreline preservation, dams, flood control works, biological resources, habitat management, etc. The motivation for employing RSM is to collectively manage groups of possibly disparate projects by linking the projects to regionally continuous sediment processes affecting each project. Projects are linked to address a common sediment process so that the overall cost of managing a group of projects can be reduced or the costs shared among a larger group of beneficiaries, producing greater collective benefits for the region. Consider an example (hypothetical) case where a navigation channel requires annual dredging to maintain depth and the dredged material is normally placed in a disposal site which provides no benefit. An RSM initiative, brokered by an environmental advocacy group and partially funded by the property owner or resource organization, provides an opportunity to utilize the dredged sediment to create riparian habitat. The example RSM initiative provides added benefits of stabilizing an eroding river bank, preventing river channel migration, decreasing channel dredging, increasing biological productivity, and fostering a higher level of collaboration among resource stake-holders, property owners, and project proponents. In this example, consideration of the collective benefits associated with

riparian habitat creation provided the political motivation and financial resources to implement the RSM project.

The objective of implementing RSM is to reduce collective project costs, minimize environmental impacts, and achieve greater overall benefits within the affected region. On a technical basis, successful RSM implementation requires a firm understanding of the processes that drive the transport of sediment within a given region, the related morphological response due to such processes, and effects on infrastructure and the environment. Technical information serves as the basis for rational decision making regarding the proposition and assessment of RSM initiatives. As part of the RSM collaborative framework, technical information should be objectively vetted by peer review with results clearly communicated to project participants, managers, and decision makers. A challenging issue which may impede many RSM projects deals with demonstrating how RSM initiatives will not adversely affect the environment, especially living resources. Since it can be problematic to conclusively demonstrate no impact (i.e., to prove a negative), RSM initiatives may need to be considered/advocated using an adaptive management framework to minimize perceived risk to natural resources. On a socio-economic and political basis, RSM can not be successfully initiated without the active involvement of project proponents, participating levels of government, and stakeholders. The inclusion of project participants during all phases of RSM implementation can not be overemphasized. RSM takes place within the public realm, and all interested/affected parties must be consulted throughout the RSM planning and execution process. RSM is as much about building trust among project participants as it is about understanding the sediment processes affecting the projects of interest. Continual collaboration is an essential ingredient for successful RSM implementation. RSM fosters a balance between infrastructure, sedimentation processes, natural resources affected by sedimentation, and political-socio-economic constraints. Implementation of RSM at the Mouth of the Columbia River is an example where balance between these competing "forces" is being addressed to sustain deep draft navigation.

The Mouth of the Columbia River (MCR)

The MCR is a regionally critical coastal inlet located on the ecologically sensitive Pacific Northwest Coast of the US and is the ocean terminus for one of the largest rivers on the West Coast of North America. A system of convergent seacoast jetties was constructed during 1885-1939 to establish and retain the 8-km long MCR deep draft navigation channel, which passes between the states of Oregon and Washington (figure 1-2). The central project feature at MCR is the navigation channel. The MCR jetties now function in concert with the large tidal shoals to maintain the stability of the navigation channel. At present, more than 12,000 commercial vessels and 100,000 recreational or charter vessels navigate through the MCR annually, transporting $14 billion of U.S. products (48 million tons of cargo) to world markets. The existing authorized deep-draft navigation project at MCR provides for a 905-m wide channel across the Columbia River bar. The northerly 610 m of the channel is maintained at –17 m MLLW (plus 1.5 m for over dredging), and the southerly 195 m of the channel is maintained at –15 ft MLLW (plus 1.5 m for over dredging). Over-dredging is needed to

ensure that the deep-draft channel is passable during winter, when dredging is not possible. Due to its regional importance, the MCR channel must be fully maintained. The MCR plays an important role in the ecology and fisheries of the lower Columbia River and Pacific Northwest. Many of the salmon species that pass through the MCR are listed as endangered or threatened, while the bounty of other fish and shellfish species supports a regional economy based on the heritage of fishing. The regional economy associated with the MCR Dungeness crab fishery alone is estimated at $20 million annually, and there are numerous other commercial and recreational fisheries. Most crab fishing occurs north of the Columbia River mouth at depths ranging from 7 to 76 m. Management of MCR sediment (dredged material disposal activities) must address ecological and other impacts that may be associated with proposed actions.

http://www.nwp.usace.army.mil/op/n/projects/mcr/documents.asp

Dredging and Dredged Material Disposal at MCR

The MCR navigation channel has required periodic dredging to maintain the channel's authorized depth, since 1904. A programmatic approach for dredging the MCR channel began in the mid 1950s, after the channel was deepened to 15 m below MLLW. Presently, the U.S. Army Corps of Engineers (USACE) dredges 2.3 to 3.8 million cubic meters (Mm^3) of sediment per year at MCR to maintain the 8-km long deep draft navigation channel. The total unit cost of dredging the MCR channel normally ranges $2.00-$3.00 per m^3 dredged. Due to the severe wave conditions of fall-spring, maintenance dredging at MCR can only be performed by hopper dredges during the relative calm of summer (June- September, when waves at MCR are typically less than 3 m). Two hopper dredges are used at the MCR, operating 24 hr/day. The per load capacity of each hopper dredge varies between 1,900 to 4,200 m^3, requiring more than 1,000 load cycles to maintain the channel. The dredged material is classified as fine-medium marine sand (0.15-0.27 mm); fine-grained material content is less than 4%. The sand dredged from the MCR channel is placed within designated/permitted open water disposal sites by the hopper dredges. Since 1945, approximately 152 Mm^3 of sand have been dredged from the MCR channel; 60% has been placed in water depths less than 18 m. Placement of MCR dredged material normally occurs during dump-runs that cover a lineal distance of 300-1,000 m. Deposition of dredged material on the seabed, resulting from an individual dump, occurs as the negatively buoyant plume of material is released from the hopper dredge and encounters the seabed. The depositional thickness of an individual dump along the centroid axis can range 4 to 20 cm, for dredged material is placed in water depth of 15-20 m. MCR dredged material disposal sites are located within a finite distance from the dredging area to allow completion of maintenance dredging during a 3 month operational window. Typically, each hopper dredge will spend 0.75-1.5 hr to fill its hopper (actively dredge), 0.5 to 1.5 hr to transit to and return from the disposal site, and 3-12 min placing each load of dredged material within the disposal site. The minimum working depth for the hopper dredges used at MCR is about 10 m. There is little flexibility to significantly modify the disposal sequence of the hopper dredges, due to the scale and schedule constraints of the dredging-disposal operation at MCR. Even modest modifications to the dredging operation can impair completion of the project. For example, increasing the unit cost of MCR dredging disposal by $0.75/$m^3$ can cost the project an additional $2 million/year; funding that may

not be available. Increasing the time (30-60 min) to place each hopper load cycle to facilitate a "special" placement alternative could prevent completion of the annual MCR maintenance dredging program.

Existing MCR dredged material disposal sites are shown in Figure 2. Approximately 65% of all sand currently dredged at MCR is placed within the SWS area, 10% is placed within the NJS area, and 25% is placed within the DWS area. Dredged material placed within the NJS area is intended to protect the south side of the north jetty from severe foundation scour/undermining. Use of the SWS is intended to augment the littoral budget of Peacock Spit; to feed the littoral zone north of MCR and reduce the recession rate affecting the morphology along the north side of the inlet. Use of the DWS area is considered a wasting operation. The DWS is used as "a last resort," after the SWS and NJS have been used to their annual working capacity. Dredged sand placed within the DWS is rendered littorally inert, due to the water depth at the site (> 60 m). A primary goal for RSM at MCR is eliminate use of the DWS, by obtaining additional disposal sites (at locations acceptable to stakeholders) which can be used to place dredged material within the littoral zone north and south MCR. The BB site was used for a pilot study in 2002, when 33,000 m^3 was pumped ashore directly from a hopper dredge (USACE 2002) to evaluate the feasibility of inter-tidal disposal of MCR dredged material. The SJ Experimental Site was used in 2005 to assess the bottom deposition of dredged material placed using hopper dredges (6 loads totaling 23,000 m^3), in context of evaluating the placement of dredged material south of the MCR. Refer to the following document: http://www.nwp.usace.army.mil/op/n/projects/mcr/docs/reports/MCRSiteUsagePlan2006.pdf

The activity of placing 2.3 to 3.8 M m^3 of dredged sand within open water disposal sites at MCR has the potential to affect the environment or interfere with other uses of the inlet's coastal waters. Two primary issues of concern include dredged material harming benthic biota during dredged material disposal (as the placed sand impacts the seabed), and multiple placed loads dredged material coalescing into large mounds which may cause waves to shoal (amplify) or break. Placement of dredged material within the DWS (>60 m) or pump-ashore (inter-tidal disposal) options are favored by the fisheries resource stakeholders as opposed to nearshore disposal. The MCR project proponent (USACE) and state shoreline resource agencies normally advocate nearshore disposal due to the benefit derived from placing large quantities of dredged sand within the littoral zone to augment the coastal sediment budget. Tensions can arise between fisheries-resource stakeholders and the MCR project proponent when modifications or improvements for dredging disposal actions are proposed and evaluated. This means that dredged material "disposal" initiatives at MCR are subject to scrutiny and financial hardship; thus providing a motivating framework to employ RSM.

MCR PHYSICAL ENVIRONMENT - RELAVANCE TO RSM

The ocean entrance at MCR is characterized by large waves and strong currents interacting with spatially variable bathymetry. The Columbia River estuary is the largest fluvially dominated estuary in the Pacific Northwest and its tidal prism is about 1,140 km^2-m. Riverine discharge from the Columbia River is marked by a high seasonal

variability, typically ranging from summer-fall flows of 2,800 m^3/sec to spring freshets of 11,000 m^3/sec (under regulated flow conditions). Astronomical tides at MCR are mixed semi-diurnal with a diurnal range of 2.3 m. The average water depth through the throat of the MCR entrance is about 15 m, with local excursions to 34 m. During the peak of ebb tide, the combination of riverine and estuarine flow through the 3.3 km-wide wide entrance of MCR can produce surface and mid-depth currents greater than 3 m/sec and instantaneous flowrate that exceeds 51,000 m^3/sec; instantaneous flowrate during flood tide exceeds 28,000 m^3/sec. Sustained bottom current through the MCR channel can approach 1.5 m/sec. In coastal waters immediately adjacent to the MCR, the dynamics of the Columbia River plume exerts its influence, tending to draw (denser, 32 o/oo) bottom marine waters into the estuary while discharging low salinity (10 o/oo) estuarine/riverine plume waters at the surface. Between 80-90% of the total sediment through flow at MCR is composed of suspended sediment (silt and clay) and is transported throughout the continental shelf. Sand moving through the MCR is usually transported as bed load; sometimes as transient suspended sediment. The processes governing suspended sediment and bedload transport are based on completely different hydraulic regimes. Suspended sediment is subject to the whims of highly stratified circulation within MCR, while the bedload is governed by bottom current. If the bottom current regime can be reliably modeled, sand transport and morphological evolution within MCR and the nearshore coastal areas can be estimated; a goal of RSM at the MCR. Much of the sediment annually dredged from the MCR navigation channel is believed to originate from the morphology adjacent to the MCR channel. At present, approximately 10-25% of the sand sized sediment deposited within the MCR channel (and subsequently dredged) is believed to originate from the Columbia River estuary (USACE 1999).

The continental shelf break (300 m depth) lies within 30 km from the MCR. As waves propagate shoreward toward the MCR, the waves are modified (waves begin to shoal and refract) by the asymmetry of the MCR's underwater morphology. These modified currents interact with the shoaling waves to produce a complex and agitated wave environment within the MCR. The asymmetric configuration of the MCR and its morphology are characterized by the significant offshore extent of Peacock Spit on the north side of the North Jetty, southwesterly alignment of the north and south jetties and channel, and the absence of a large shoal on the south side of the MCR. Approximately 70% of all storm waves approaching the MCR are from the west-northwest (Moritz 2004). During winter storm conditions, the ocean offshore of the jettied river entrance is characterized by high swells approaching from the north-northwest to southwest combined with locally generated wind waves from the south to southwest. From October to April, average offshore wave height and period are 3 m and 12 sec. During the winter storm season, nearshore wave heights can range between 4 to 10 m with wave period of 12-22 sec. During storms, the nearshore waters at MCR can be subject to significant "stirring" to water depths of 35 m: Wind stress can produce sheet flow conditions where the current throughout the water column exceeds 80 cm/sec; storm waves can produce seabed orbital motion that exceeds 2 m/sec; and shoaling wave groups can produce infra-gravity motions resulting in a transient bottom current having amplitude exceeding 20 cm/sec (Moritz et al 2000, 2001, and 2006). These observations indicate that

significant annual littoral transport occurs deeper than 20 m along the coastal margin of MCR, and that dredged material placed inshore of 20-m depth will be littorally beneficial. From May to September, average offshore wave height and period are 1.5 m and 9 sec, and waves approach mostly from the west-northwest. Occasional summer storms produce waves approaching MCR from the south-southwest with wave heights of 2 to 4 m and wave periods of 7 to 12 sec.

Pre-Jetty Morphology: Baseline Condition

Historically, the Columbia River has been a major source of sediment to the NE Oregon and SW Washington state coasts (Gelfenbaum et al 2001). Estimates for the average annual rate of sand delivered through the MCR to the coast, prior to jetty construction, range from 1.4 to 2.6 Mm^3/year. Prior to jetty construction (1885), a broad system of unstable flood and ebb tidal shoals dominated the 8 km wide inlet at MCR. The seaward extent of the ebb tidal shoal (denoted by the 1885 12-m depth contour in Figure 3) was symmetric across the inlet, indicating that littoral transport was balanced in the north and south direction at MCR. Woxell (1999) had analyzed the evolution of shore lands 30 km north and south of the MCR inlet for the period of 3000 YBP-1800 AD and determined that the shoreline accretion rate of the coast north and south of MCR was approximately equal at 0.6 m/year (Figure 4). Figures 3 and 4 indicate that prior to jetty construction, sand discharged from the MCR was transported by littoral processes in equal proportion to adjacent coastal areas north and south sides of MCR. Given that the pre-jetty littoral transport rate of sand from MCR was distributed equally north and south of the inlet, there would have been 0.7 to 1.3 Mm^3/year of sand moving in both alongshore directions away from the MCR. This is an important pre-jetty baseline condition to acknowledge, especially if the goal of RSM at MCR is to emulate the longterm littoral trend at MCR. Consideration of this baseline condition fosters the RSM concept of "sustainability through balance."

Navigation Development at MCR and Morphological Response

During 1885-1939, three rubble mound jetties were constructed on massive tidal shoals of the MCR to stabilize the inlet, confine flow within a 3.3 km-wide entrance, and prevent encroachment of shoals into the engineered navigation channel. The initial 7.4-km section of the South Jetty was constructed to secure a 12-m channel across the MCR during 1885-1896, with a 3.9-km extension completed in 1914. The 4.1-km long North Jetty was constructed during 1914-1917 to reduce shoaling within the MCR channel. The 1.8 km long Jetty-A was constructed in 1939 to prevent migration of the navigation channel toward the North Jetty foundation. The phased construction of the MCR jetties resulted in a radical realignment of the inlet's tidal shoals, shifting the pre-jetty morphology of the MCR from a symmetric orientation to a highly asymmetric condition (Figure 3). MCR jetty construction facilitated the discharge of 300-600 Mm^3 of sand from the estuary to areas offshore MCR. The displaced sand was dispersed by waves/currents onto nearshore areas north and south of MCR. This huge pulse of sediment resulted in rapid landform accretion, as exhibited by the shore land response shown in figures 3-5. Figures 4-5 show that the post-jetty accretion rate of shoreland for area north and south of MCR was equivalent (at 2-4 m/year), and 4-5 times greater than

the pre-jetty accretion rate. Figure 5 shows that the shoreland accretion rate of the north side lagged the south side accretion rate by about 20 years (due to phased jetty construction). Collectively, these results indicate that littoral transport of sediment displaced by the jetties was similar (symmetric) for the north and south sides of MCR.

Between 1885 and 1919, the 12-m depth contour had migrated 3 km seaward on the north side of the inlet (forming Peacock Spit) while the opposite occurred along the inlet's south side. This north-south offset effect was due to the phased jetty construction (recall that the south jetty was constructed 20 years before the north jetty). Phased jetty construction enabled the ebb tidal shoal north of the south jetty to be discharged offshore and forced the opposite trend south of the south jetty, due in part to the south jetty cutting off the sediment supply to areas south of the MCR. The presence of the very long south jetty acts as a littoral boundary and has created a gyre-like circulation pattern which appears to have forced the ebb tidal shoal south of the jetty to migrate shoreward, as exhibited by the pronounced shoreland accretion (>5 km) of shoreland south of the south jetty.

After 1919, the 12-m depth contour on the north side of MCR began to recede landward as the newly formed morphology (Peacock Spit) was beginning to diffuse its sediment northward and westward, in response to the morphology's protruding orientation within the regional wave and local circulation patterns. The landward recession of the 12-m depth contour south of MCR has continued since completion of the south jetty; as described above (shown in figure 3). The present seabed south of MCR (at water depths of 10-18 m) is at an elevation several meters lower than the pre-jetty seabed as discussed in Kaminksy (2005), indicating that the present sediment budget south of MCR is deficient. The post-jetty sediment flux and circulation patterns differ significantly from north to south across the MCR (due to the post-jetty morphological orientation of the inlet). What may appear as a dominant south to north transport regime (or an apparent down drift offset) at MCR is really an inlet thrown out of equilibrium by a lagged response in post-jetty morphology development; motivated by phased jetty construction. The present northerly flux of sediment emanating from Peacock Spit has been estimated to be 2.3 – 3.8 Mm^3/year, which is 3 times the estimated pre-jetty northerly flux from MCR. The present southerly sediment flux from the MCR inlet appears to be close to zero, based on results from Gelfenbaum et al (2001) and Kaminsky (2005). Most of the sediment presently being supplied to the coastal area south of MCR (to Tillamook Head) appears to be sourced from cross-shore feeding. This implies that the south side of MCR is in a sediment deficit of 0.7 - 1.3 Mm^3/year, as compared to pre-jetty conditions.

Equilibrium Adjustments: Morphology Accretion Turns to Recession

MCR jetty construction produced a huge "pulse" of sediment which was discharged to the adjacent coastal areas; equivalent to several hundred years of "natural" deposition. This sediment pulse and the attendant morphology shift had thrown the littoral system of MCR out of balance. Now, the surplus of sand is beginning to run its course; the surplus is turning to deficit and energetic coastal processes are bringing the system back to equilibrium. Figures 6 and 7 illustrate the effect of recent morphology changes upon the

jetties and the region. The MCR post-jetty ebb tidal shoals have been a source of sediment to the coastal areas north and south of MCR. As sediment continues to be transported off the MCR tidal shoals, the shoals will continue to be diminished in size and the volume of sediment supplied to the littoral areas north & south of MCR will decrease. The shoreline in close proximity to MCR that was rapidly accreting immediately after jetty construction had begun to recede in the 1930s for areas south of the south jetty and in 1950s for area north of the north jetty. As the ebb tidal shoals change shape, nearshore waves and currents will change; adding to the rate and extent of sediment pulse diffusion and shoreline adjustment (recession). The 100-year old MCR rubblemound jetties were built on the inlet's flood and ebb tidal shoals. The shoals have protected the jetties from the full brunt of waves and currents, and the jetties-shoal composites have acted to confine ebb-flood currents within the active inlet and prevent encroachment of shoals in the navigation channel. Due to the present de-evolution of tidal shoals at MCR, the sand foundation of each jetty is receding. As the tidal shoals recede, the water depth near the jetties gets deeper, more vigorous waves batter the jetties, the foundation of jetties is scoured, and the jetties become unstable and unravel (Figure 6). The deterioration or sudden failure of a jetty can significantly impact the inlet's navigation function and the stability of adjacent shorelands.

MCR bathymetry change for 1958-2003 is shown in Figure 7 (Byrnes et al 2006). Note the changes occurring on Peacock Spit (north side of MCR), where a significant volume of sediment was transported northward and made available to the littoral budget of Washington; thus maintaining the accretionary condition north of North Head. However, Benson Beach (located just north of the North Jetty) experienced erosion as did the foundation of the north jetty along the seaward on-third of the structure. Augmentation of the littoral sediment budget immediately north of the north jetty is presently needed. The sediment budget along the south side of the north jetty has been sustained by dredged material placed at the NJS disposal area. Assuming that the north side of MCR may reach equilibrium after 60% of the present volume within Peacock Spit has been dispersed, it is estimated that the north side of MCR may sustain a decreasing accretionary condition for Washington shorelands for 20-40 years from present; by which time the MCR north jetty will have been seriously imperiled. Along the south side of MCR, there is no large accetionary feature to feed the nearshore. It appears that the nearshore south of MCR is feeding on itself, providing cross-shore transport to the shore lands south of MCR. The shorelands immediately adjacent to the south jetty are presently eroding as is the jetty foundation. Augmentation of the littoral sediment budget north and south of the south jetty is presently needed.

IMPLEMENTING RSM at MCR

The MCR is an energetic coastal inlet exhibiting very high potential rates for littoral sediment dispersal at nearshore areas north and south of the inlet (out to water depth of 20 m). Due to recent evolution of the morphology at the MCR inlet, the 100-year old MCR jetties are now susceptible to serious negative consequences arising from erosion of the ebb tidal shoals on which the jetties were built. As the morphology devolves, the supply of sediment to adjacent shorelands is reduced. RSM is being implemented to feed

the inlet's morphology using dredged material, and letting nature do the work of dispersing the placed dredged material to supplement the sediment budget of the inlet and adjacent nearshore coast, without compromising the reliability of the navigation channel or environmental resources. To do this, we need to understand the context of sediment flux for which we should target the RSM. This means that at a minimum we should emulate pre-jetty sediment delivery to coast south of MCR, to the extent possible emulate the present sediment delivery to the coast north of MCR; and to collectively do so with emphasis on supplementing present morphology essential for jetty stability.

In 2002, the MCR was selected by HQ USACE as a location to apply RSM in terms of a demonstration site. HQ provided limited funding, as "seed" money, to initiate a collaborative process with MCR stakeholders to plan and ultimately execute RSM actions. Additional funding and in-kind services from the Portland District and stakeholders provided the budget needed to implement several RSM pilot projects at MCR. There was also Congressional interest in RSM and funding was provided for studies on SW Washington Littoral Drift Restoration (BB) and Clatsop Spit (SJRS), South Jetty, Oregon. All of these pilot projects are discussed below. RSM Demo activities focused on: A) Hosting a series of mentored workshops to instruct MCR stakeholders on Collaborative Learning concepts, B) Collecting data to increase our understanding of how sand is transported at MCR and adjacent nearshore areas, and C) Initiating pilot scale disposal and monitoring actions to assess viability of alternative disposal sites for using MCR dredged material to augment the littoral sediment budget. An essential element of the RSM Demo at MCR was creation of multiple Cooperative Agreements between the Portland District and contributing RSM team members, allowing USACE to work efficiently/collaboratively with diverse groups. Nine RSM pilot projects, completed during 2002-2006, are summarized below and at: http://www.nwp.usace.army.mil/op/n/projects/mcr/docs/MortRSMupdate06.pdf

Bathymetry Data Collection: Collection and analysis of bathymetry data allows one to assess nearshore morphology change and infer littoral sediment transport, which is essential for implementing RSM at an energetic coastal inlet. Since 2002, the USGS and WDOE have been supporting USACE in monitoring the coastal nearshore areas north and south of the MCR inlet to document morphology change and related impacts (Ruggiero 2006). Results from this collaborative monitoring program have been very useful. A multi-beam bathymetric survey of the MCR inlet and adjacent nearshore areas (including the DWS and the SJ Exp. Site) was conducted concurrently with the Aug 2005 mega-transect experiment to provide detailed data for correlating bedform features with process measurements. Backscatter data from the multibeam survey was used to delineate the different sediment materials present on the bed, and allowed for the identification of dredged material in context of ambient seabed materials. Additional MB surveys were performed by Portland District during Aug 2006 to assess the foundation of the MCR jetties and evaluate bedform change within and outside the SWS disposal area.

GIS & Spatial Analysis: During 2003-2005, Applied Coastal Research and Engineering, Inc compiled shoreline and bathymetry data for the Portland District. Some 20 USACE

shoreline and bathymetric surveys of the MCR to be used for analyzing morphologic response to the jetties, channel migration and dredging, and dredged-material maintenance activities. The survey data are compiled in digital format (ArcGIS), for analyzing variations in sediment transport patterns at the Columbia River entrance (Byrnes and Griffee 2006). The compiled data provides valuable historical information on sediment transport pathways and quantities for addressing RSM.

Sediment Cores: A vibracoring project was implemented in September 2003, as supported by a cooperative agreement between the U.S. Army Corps of Engineers-Portland District and the Washington Department of Ecology (WDOE). The field work and core analyses were performed by WDOE to assess the suitability of the existing subsurface for supporting the jetties, and provide greater insights into the severity of erosion problems and the existing habitat that could be affected by dredged material placement operations. Results from the 11 vibracores (from the 7 sites) collected and analyzed under the RSM Demo were combined with previous coring studies to provide vital seafloor surface and subsurface sediment data used for estimating the sediment budget at MCR (Kaminsky and Ferland 2005). Each core was approximately 6 m long and was sufficient to make the assessments required.

ARGUS: As part of the RSM Demo at MCR, the Portland District deployed an ARGUS beach monitoring system (ABMS) to monitor shoreline changes in Peacock Spit response to various dredged material placement scenarios. The Portland District teamed Northwest Research Associated, Inc to install the ABMS within the North Head lighthouse in Feb 2004, where the system has been operational since. Successful ABMS installation was made possible by assistance from the US Coast Guard, WA State Parks, WDOE, ERDC-CHL, and Evans Hamilton, Inc. The ABMS is a video-based remote sensing metric system to monitor the evolution of submerged and emergent morphology on open-coast beaches (Oltman-Shay 2006). The purpose of the MCR ABMS is to cost-effectively monitor shoreline change at Benson Beach (3 km of shoreline between the North Jetty and North Head), and wave shoaling over the SWS dredged material disposal area, with high spatial and temporal resolution and quantify shoreline change with a high degree of accuracy. The ABMS deployment at North Head lighthouse needed to be flexible in terms of adding additional analysis capability and allowing for adjustments to the physical deployment of hardware. http://www.planetargus.com/north_head/

Mega-Transect: A data collection campaign to acquire prototype data describing the three-dimensional circulation within MCR was conducted by the Corps of Engineers, Moffatt-Nichol, Inc, Evans-Hamilton, Inc, US Geological Survey, and PI Engineering, LLP during August-September 2005. The "mega-transect" experiment was intended to improve the hydrodynamic understanding of the processes affecting sediment transport through the MCR and enhance our ability to manage the sediment resources within the inlet/estuary. Data collection consisted of detailed measurements for current profile, water level in terms of sub-surface pressure (short-and long-waves), near-bed suspended sediment, bottom current, and near-bed water conductivity-temperature. Acquisition of vertical profile data for water conductivity-temperature was also made. Data were

recorded concurrently at 5 locations spanning a 3-km transect across the MCR, during 6 Aug – 10 Sept 2005. The data are being used to describe the lateral and vertical variation in water circulation and sand transport through the MCR for the purpose of verifying conceptual (and computer) models for the flux of water and sand through the MCR. A report documenting the "mega-transect" data collection is in preparation.

Crab Burial Study: The USACE Portland District engaged with the Marine Sciences Laboratory of the U.S. Department of Energy's Pacific Northwest National Laboratory to investigate impacts on Dungeness crabs (Cancer Magister) resulting from impacts of dredged material disposal. Preliminary results based on numerical modeling and lab studies indicate that for burial greater than 10 cm, Dungeness crabs were unable to recover the respiratory pathway and switched to moving up through the sediment, a process that occurred over 24 hours. The observation that crabs can take some hours to emerge after burial suggests that multiple dumps over the same area would increase vulnerability. In most cases, the standard disposal practice is to not dump sequentially at the same location but to systematically spread the dumps over the whole of the disposal site (Pearson 2006).

Modeling: Having the ability to simulate/predict sediment transport and morphology change at MCR is an essential element for developing rational RSM-based decisions at the inlet. Portland District has supported a significant body of modeling work at MCR. Much progress has been accomplished by a host of collaborating groups using many types of models (ADCIRC, DELFT-3D, M2D/3D, MDFATE, STWAVE, SWAN, Bouss-2D). Applying multiple models aids in "comparative improvement" of each model and increases understanding of the processes affecting waves, circulation, and sediment transport. Participants included Portland District, NOAA's-Coastal Storm Initiative, ERDC-CHL, USGS, WDOE, OSU, and other. Recent results applying DELFT-3D to simulate the fate of dredged material placed at the SWS area appear most promising (Gelfenbaum et al 2005). Applicable models have benefited greatly from calibration studies using the "Mega-transect" data and will continue to be refined.

Benson Beach Pump-Ashore: Constraints dealing with disposal site capacity and potential impacts of using nearshore disposal sites have led to the perception that placing dredged material on Benson Beach may ameliorate dredged material disposal issues at MCR. As requested by Congress, the Portland District undertook efforts to examine the impacts/benefits of placing dredged material on Benson Beach; located on the southern-most shoreline of the State of Washington, adjacent to the MCR (BB in Figures 2,6,7). During July 2002, 33,000 m^3 of MCR dredged sand was placed on the inter-tidal area of Benson Beach using a hopper dredge (pumped ashore from the dredge at a unit cost of \$22/m^3, or 10 times greater than normal disposal practices). Monitoring activities were undertaken (by USACE, USGS, and WDOE) to assess operational, environmental, and economic effects of dredged material placement. After placement on Benson Beach, the placed dredged material was transported toward the North Jetty. Future placement of dredged material on Benson Beach may be warranted to protect the North Jetty from foundation scour, but the scale-economies of the operation must be further evaluated. More work is needed to evaluate the regional littoral benefit of Benson Beach dredged

material placement. For additional information Refer to: http://www.nwp.usace.army.mil/op/n/projects/mcr/docs/reports/bbreport.pdf

South Jetty Research Site (SJRS): In August 2003, Portland District tasked ERDC-CHL and Evans-Hamilton, Inc to measure oceanographic data 1.5 km south of the MCR south jetty in water depth of 16 m, in anticipation of assessing the viability of dredged material disposal at a location south of the south jetty (Moritz 2006). The data record spanned September –December 2003; included current profile, bottom current, short/long waves, and OBS-CTD; and was used to help motivate a Phase I of the South Jetty Research Sit (SJRS). SJRS-Phase I involved placing 6 discrete loads (each 3,800 m^3/load) of dredged material within the SJRS during 25 September 2005, to assess the physical "effect" of dredged material deposition on the seabed. Stakeholder and state regulatory interests were concerned about potential negative effects of placing dredged material within the nearshore south of MCR; a deposition threshold of 10 cm was selected as defining a minimal impact level for epibenthic fauna. A significant effort was expended by the Port of Astoria, Lower Columbia Solutions Group, and EPA to issue a research permit for the SJRS as a "research disposal site". Monitoring was performed using Sediment Profile Imaging, sediment sampling, and a multibeam survey (backscatter) to measure the thickness and areal extent of each disposal foot print. MDFATE model results had indicated that the maximum foot print thickness would be 10-15 cm (in 16 m water depth). Only the backscatter data from the SJRS multibeam survey could detect the rough areal extend of each deposited load. It was generally accepted by all stakeholders that the maximum thickness deposited on the SJRS seabed was less than 10 cm. SJRS-Phase II was conducted as a series of collaborative modeling tasks during 2006 to determine the feasibility of using MCR dredged material, deposited to form a large accretion feature (LAF), to protect the south jetty from storm wave action and augment the littoral budget south of the south jetty. Various "berm" geometries were evaluated using wave models for wave attenuation/impacts and several circulation models were applied to assess sediment transport off the LAF. Phase II was a highly successful collaboration between Oregon State University, USGS, ERDC-CHL, WDOE, nearshore stakeholders, and federal/state regulatory agencies. Phase II results are pending final reporting. The SJRS is of strategic importance to bring balance back to the MCR regional sediment budget. SJRS - Phase I results are described in: http://www.nwp.usace.army.mil/op/n/projects/mcr/regionalsediment.asp

Although proposals to increase the amount of dredged material placed within the nearshore (littoral zone, where depth is less than 60 ft depth) offer increased littoral benefit and add little burden to the dredging project, nearshore disposal of dredged material at MCR carries the liability of "potential impact" upon living resources within the nearshore benthos. Potential benthos impacts are related to the deposition dredged material on the seabed; burial or disruption of benthic infauna/epifauna. The challenge is to rationally align RSM objectives with the constraints governing maintenance dredging at MCR and the need to address potential environmental impacts associated nearshore dredged material disposal. The pilot projects executed through this RSM Demo program have significantly enhanced our understanding of sediment transport processes and effects associated with littoral dredged material disposal at MCR, and the RSM Demo has greatly improved working relationships between the Corps and various stakeholder

groups. The legacy of the RSM Demo at MCR is that the RSM approach will continue to thrive at MCR and will grow geographically to address wider regional issues dealing with sediment, infrastructure, and environmental resources.

CONCLUSIONS

Long term sustainability of navigation at MCR may be maintained, if dredged material can be used to supplement the sediment budget of the affected tidal shoals. This requires that MCR be viewed as a system of structural features and transient morphology that interact with the environmental forcing at the inlet to attain an ever changing "dynamic equilibrium". The imperative for sustainability at MCR is to employ RSM to manage the inlet in terms of extended time-space scales as defined by natural sediment processes. The key to successfully managing dredged material for effective augmentation of MCR morphology requires a reliable and detailed understanding littoral the sediment budget at the MCR.

The present morphological orientation and sediment transport at MCR is imbalanced, in terms of north and south sediment flux emanating from the inlet. The north side of MCR has a large, yet depleting source of littoral sediment contained in Peacock Spit while the south side of MCR has no appreciable sediment source. The asymmetry of the present post-jetty morphology at MCR does not serve as a good indicator of the net regional littoral transport direction. Based on the results presented herein, it appears that the potential littoral transport is equivalent for nearshore areas north and south of MCR

Existing MCR nearshore (littoral) disposal sites do not have the capacity to accept all disposal of the sand annually dredged from MCR, and there is no nearshore disposal site located south of the inlet. At present 0.6 to 1.1 Mm^3/yr of sand dredged from MCR is placed within the DWS, and represents lost opportunity for augmenting the littoral budget at MCR. As a region it is imperative that alternative disposal areas be located within the MCR littoral zone (north and south of the inlet) and fully utilized, to avoid placing any MCR dredged material within the DWS. If all MCR dredged material (2.3 to 3 Mm^3/yr) were to be placed within the nearshore areas north and south of MCR, the nearshore area south of MCR should receive a minimum of 0.7 to 1.3 Mm^3/yr, and the nearshore area north of MCR should receive 2.3 – 3.8 Mm^3/yr. Additional work is needed to resolve the optimal locations for RSM-based nearshore dredged material disposal sites.

Lessons Learned

When starting an RSM project, define clear objectives and do not over scope the region of interest. When an RSM study is first initiated, minimize the geographical limits of the region, and then expand outward as success grows the project. Strive to determine how the sediment system works within a given region and how infrastructure interacts with sediment. It is best to express known quantities in terms of statistical uncertainty. Visualization of data and concepts is paramount. Well prepared pictorial and graphical explanations for analyses and proposals significantly improve the communication of

RSM initiatives and increase likelihood of a forward progress. Some proactive RSM precepts include: Learn by doing; Sustainability thru balance; Understanding through collaborative learning.

Producing good science and engineering will not guarantee a successful RSM initiative. Collaborative learning by project proponents, stakeholders, regulators, and environmental constituencies is required through every phase of an RSM project to achieve a productive outcome. The "team" has to work together to gain an understanding of how the regional sediment system works, and work together to formulate RSM initiatives. Clear and open communication is paramount. A well crafted and executed monitoring plan (with follow-up contingency actions) can help reduce risks associated with implementing RSM initiatives. Resources and funding should be pooled and leveraged at every opportunity, to combat budgetary restrictions. Formalized cooperative agreements between various levels of government provide an excellent means to build positive working relationships, share resources, and provide contributing services toward RSM implementation. Opportunities should be sought to elicit the support of local universities/colleges on RSM activities.

Integration of all data relevant to a given RSM initiative is essential to gain balanced perspective on the many factors affecting sediment movement, infrastructure, and environmental response within a region. Collaborative learning can be achieved by a thoughtful review of exiting data; by performing a shared literature review. Fully exploit field data collection activities as team building and advertise the data to others in the region. Sharing resources to collect field data builds trust and elevates the outcome and utility of field data collection. In many cases, data are collected and analyzed for a specific purpose; whereas much more can be learned by "mining" the newly collected data for derivative information.

ACKNOWLEDGEMENTS

The authors are grateful for the support and contributions of resources made by their respective participating organizations. The authors thank Charley Chessnutt and Lynn Martin of the Corps of Engineers' Institute for Water Resources for their creative vision and sponsorship of the RSM Demo at MCR. RSM Demo program managers Julie Rosati, Ty Wamsley, Jack Davis, and Jeff Waters, of the Engineering Research and Development Center-Coastal and Hydraulics Lab, provided flexible and effective leadership.

REFERENCES

Byrnes, M.R. and Griffee, S. (2006). "Regional Sediment Transport Patterns Relative to Engineering Activities at the Mouth of the Columbia River, Washington/Oregon-Final Report". Prepared for USACE-Portland District by Applied Coastal Research and Engineering, Inc, Mashpee, MA.

Gelfenbaum, G., Buijsman, M.C., Sherwood, C.R., Moritz, H.R., and Gibbs, A.E. (2001). Coastal evolution and sediment budget at the mouth of the Columbia River, USA, Proceedings of the 4th Conference on Coastal Dynamics, pp. 818-827.

Gelfenbaum, G.R. and Lesser, G. (2005). "Progress toward a Verified Sediment Transport Model

for the Columbia River Estuary". Prepared for USACE-Portland District and WDOE by USGS Menlo Park, CA

Hericks, D.B. and Osborne, P. (2005). "Roving 3D Current Measurements across Mouth of Columbia River - Oceanographic Data Collection Mega Transect across MCR Regional Sediment Management at MCR". Prepared for USACE-Portland District by PI Engineering, LLP, Edmonds, WA.

Kaminsky, G. M. and Ferland, M.A. (2005). "Vibracores at the Mouth of the Columbia River-Final Report". Prepared for USACE-Portland District by Washington Department of Ecology, Olympia, WA

Moritz, H.R., Smith, J.W., Kraus, N.C., and Gailani, J.Z. (2000). "Bottom Sediment Suspension due to Wave-Current Effects at the Mouth of the Columbia River, USA", 27th International Conference on Coastal Engineering, September 2000, Sydney, Australia

Moritz, H. R. (2001). Observing Large Waves Using Bottom-Mounted Pressure and Current Meters, Waves 2001 Conference, ASCE, San Francisco.

Moritz, H.R., Moritz, H.P., Hays, J.R., and Sumerell, H.R. (2003). 100-years of shoal evolution at the Mouth of the Columbia River: Impacts on channel, structures, and shorelines, Proceedings of Coastal Sediments '03, East Meets West productions, CD-ROM, 14 p.

Moritz, H.R. , Moritz, H.P., Hays, J.R. , and Sumerell, H.P. (2003). "Holistic Framework for Assessing the Functional Integrity of Navigation Structures at the Mouth of the Columbia River", Proceedings International Conference on Coastal Structures, Portland, OR

Moritz, H. P. and Moritz, H.R. (2004). "Regional Analysis of Extremal Wave Height Variability Oregon Coast, USA". Proceedings 8th International Workshop in Wave Hindcasting and Forecasting, Oahu, HI

Moritz, H.R., Gelfenbaum, G.R., and Kraus, N.C. (2006). "Observations of Cross Shore Infragravity Energy and Related Pulsating Bottom Currents", 30th International Conference on Coastal Engineering, September 2006, San Diego, CA

Oltman-Shay, J. (2006). "The Argus Beach Monitoring Station at the Mouth of the Columbia River - North Head, WA – Report 3 of a Series". Prepared for USACE-Portland District by Northwest Research Associates, Inc. Bellevue, WA.

Ruggiero, P., Kaminsky, G.M., Gelfenbaum, G.R., and Moritz, H.R. (2006). "Beach Monitoring of Benson Beach 1997 – 2006: Quantifying Nearshore Morphological Change In Support of Regional Sediment Management". Draft Data Series Report 06- USGS-Menlo Park, CA.

Pearson, W.H., Miller M.C., Williams G. D., Kohn N. P., Skalski J. R. (2006). "Preliminary Assessment of Potential Impacts to Dungeness Crabs from Disposal of Dredged Materials from the Columbia River". Prepared for the U.S. Army Corps of Engineers, Portland District Portland, Oregon by Pacific Northwest National Laboratory.

U.S. Army Engineer District, Portland (1999). "Integrated Feasibility Report for Channel Improvements and EIS: Appendix H, Volume I, Exhibit B". Portland District – US Army Corps of Engineers.

U.S. Army Engineer District, Portland (2002). "Evaluation of Alternative Dredged Material Disposal Methods for Maintenance Dredging at the Mouth of the Columbia River, OR and WA – Placement of Dredged Material on Benson Beach", A Progress Report to Congress, Appropriations Committee. Portland District- US Army Corps of Engineers.

Woxell, L.K. (1998). "Prehistoric Beach Accretion Rates and Long-Term Response to Sediment Depletion in the Columbia River Littoral System, USA". A thesis submitted in partial fulfillment of the requirements for the degree of Master of Science in Geology, Portland State University1998.

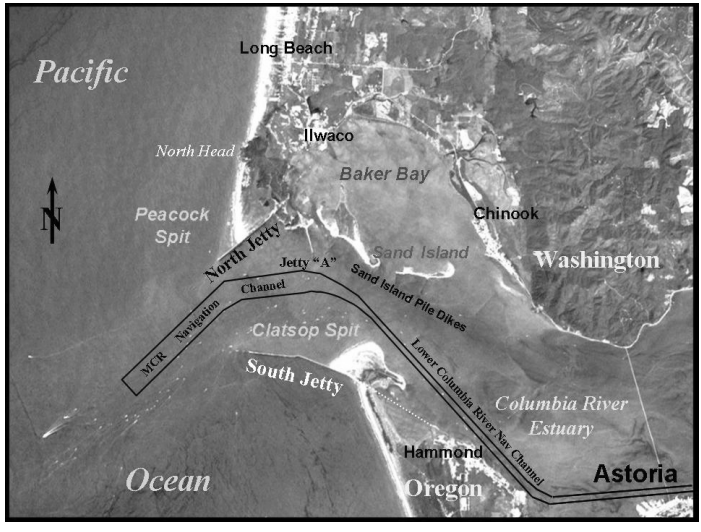

Figure 1. Mouth of the Columbia River (MCR), Oregon and Washington USA. The 8 km long MCR deep-draft navigation channel extends inland to Jetty "A". Minimum distance between North and South Jetties is 3 km.

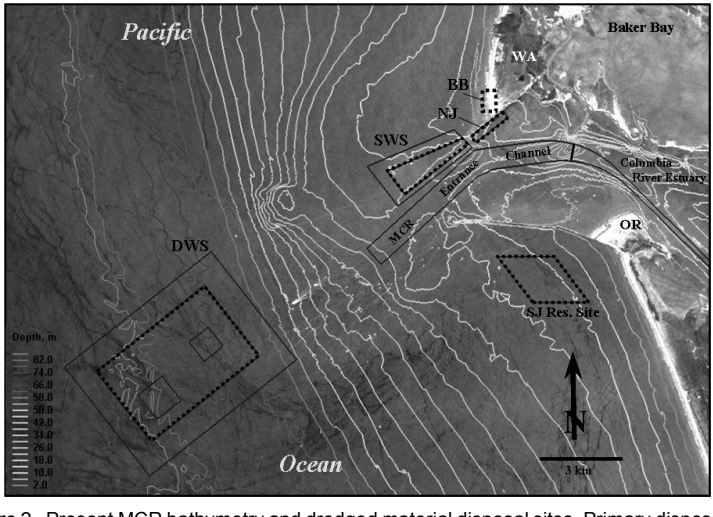

Figure 2. Present MCR bathymetry and dredged material disposal sites. Primary disposal sites are SWS, NJS, and DWS. Site BB is a shore placement area used in 2002 and requires that the hopper dredge to be "pumped ashore". The SJ Research Site is an area that may be used to enable littoral placement of dredged material south of the MCR inlet.

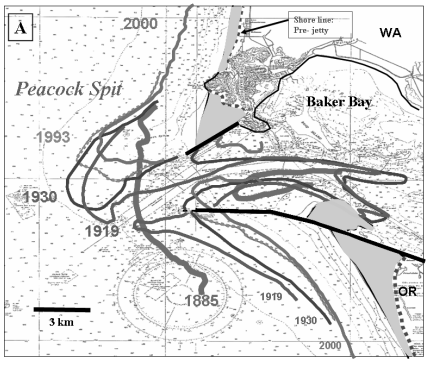

Figure 3. Evolution of the 40-ft depth contour at MCR during 1885 (pre-jetty) to 2000. Note the symmetric orientation of the 40 ft (12 m) contour prior to jetty construction indicating a balanced system of littoral transport north and south of the inlet. The shaded shoreline areas resulted in response to jetty construction. Refer to text concerning asymmetric alignment of the inlet in response to phased jetty construction.

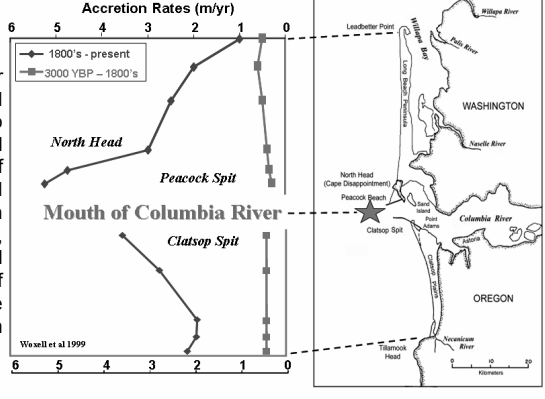

Figure 4. Accretion rates for pre-historical record and recent historical response to jetty construction (Woxell 1998). Note the symmetry of accretion rates north and south of the MCR for both time periods shown, indicating equal littoral transport north and south of the MCR. Alongshore distance shown is for 30 km north and south of MCR.

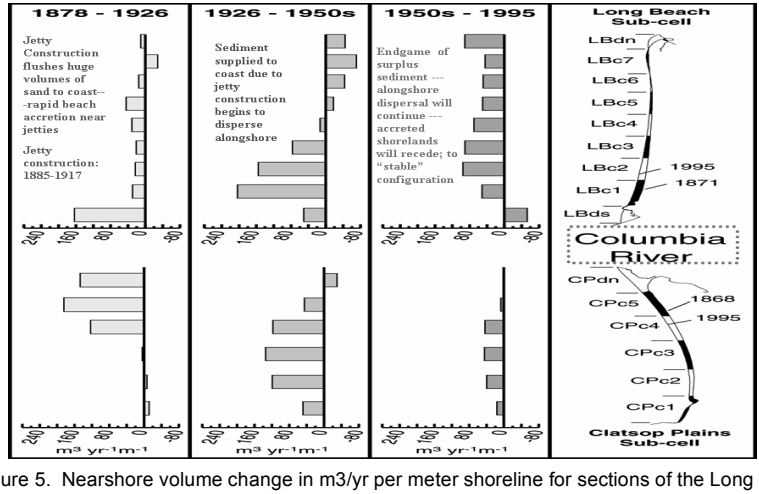

Figure 5. Nearshore volume change in m3/yr per meter shoreline for sections of the Long Beach Peninsula and Clatsop Plains. The alongshore lengths of the boxes are approximately 5 km (Gelfenbaum et al 2001).

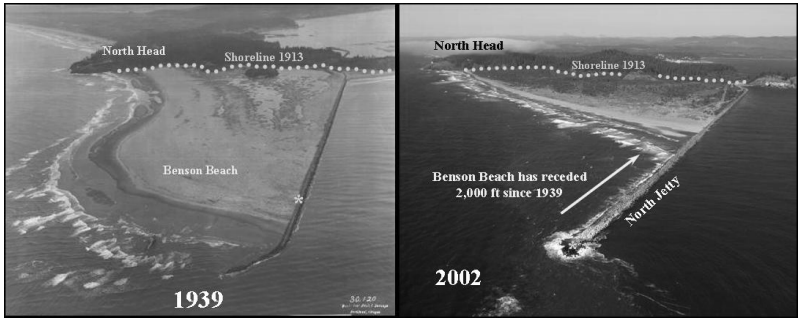

Figure 6. Left panel shows accretion of Benson Beach in 1939 in response to north jetty construction during 1914-1917. Note pre-jetty shoreline location. Right panel shows de-evolution of Benson Beach as of 2002. Benson Beach had receded 2,000 ft (660 m) landward from 1939 affecting the north jetty stability. North jetty has receded landward by 460 m. An Argus BMS has been installed within the North Head light house to monitor the morphodynamics of Benson Beach and its nearshore area.

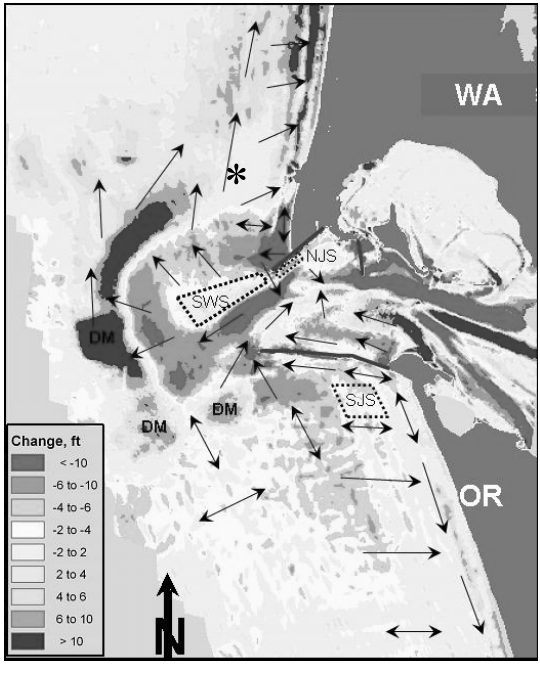

The arrows indicate present sediment transport direction. Deposition is shown within the NJS. Use of the SWS appears to have significantly reduced the erosion rate on Peacock Spit. The material placed at SWS is moving to the north-northwest onto the spit and ultimately into the littoral zone of WA.

Figure 7. MCR bathymetry change during 1958-2003 (Byrnes and Griffee 2006), indicating the present day trend of bathy change and related sediment flux. Reds indicate erosion, blue deposition. The north side of MCR is dominated by bathymetry change on Peacock Spit. The nearshore area along Benson Beach has experienced significant erosion as manifest in figure 6. Excluding the SWS, the top of Peacock Spit has been eroding, with the eroded sediment being transported toward the west and north. Sediment transported to the seaward base of Peacock Spit is being fluxed along the base of the spit toward the nearshore of WA. Areas marked by DM indicate where dredged material had been previously placed. The area marked by (*) is believed to have large quantities of sediment fluxed

DECADAL EVOLUTION OF SHOREFACE GEOMETRY IN SOUTH CAROLINA, USA

Reynolds, B. M.[1], Wren, P.A.[2] and Gayes, P.T.[3]

1. Center for Mar. & Wetland Studies, Coastal Carolina Univ. Conway, SC 29526 bmreynol@coastal.edu
2. Center for Marine & Wetland Studies, Coastal Carolina Univ. Conway, SC 29526 awren@coastal.edu
3. Center for Marine & Wetland Studies, Coastal Carolina Univ. Conway, SC 29526 ptgayes@coastal.edu

Abstract: A long-term statewide beach surveying program in South Carolina has compiled a substantial record of beach and shoreface geometry across a region of diverse hydrodynamic and geologic framework. Initiated to support statewide beachfront regulatory obligations, the accumulated time-series has also afforded long-term monitoring of several beach nourishment projects and record of evolution of profile geometry in areas progressively interfacing with coastal development as well as relatively undisturbed systems on a decadal scale.

Work to date has focused on the influence of underlying geologic framework on profile geometry and variability. In sediment starved areas of South Carolina's Grand Strand, profile geometry is often better defined as a series of linear segments rather than a smooth concave up form. The breaks in slope frequently reflect stratigraphic changes observed in nearshore geophysical records and cores collected in the lower beachface. The time series documents 13+ years of behavior, revealing decadal-scale changes across the full active shoreface. These changes are relevant to consideration of long term coastal evolution.

Estimates of shoreline change have traditionally been defined by change in subaerial features or datums such as the wet-dry line defined on aerial photos or Mean High Water (MHW) contour. Across the state, and much of the nation's shoreline, these features are progressively encroaching on development and are being influenced by "hard" and "soft" erosion protection strategies. In practice, some sections of the South Carolina coast have been defined as stable (zero long term erosion rates) as the subaerial shoreline features have been artificially stabilized. These same areas continue to require beach nourishment and other engineering efforts to maintain beach volume and function. Profiles across the shoreface over the past 13 years in several such locations show evidence of continued migration of the lower shoreface. The resulting steepening of the

beachface may be expected to modify prevailing hydrodynamics and sediment dispersal and demonstrate change in profile geometry on annual –decadal scales.

Efforts to predict long term coastal behavior are traditionally been based on some variation of the Bruun Rule, which presumes migration of persistent profile geometry in the face of rising sea level. Any approximation of persistent profile geometry requires the subaerial and shoreface systems to migrate uniformly at all depths. The decoupling of the upper beach system by modifications such as groins, seawalls, and beach nourishment from the mid-to lower-shoreface suggests that profile geometry for a site may evolve not only on annual time scales, but on decadal time scales as well. Additionally, at one location experiencing substantial expansion of coastal dune fields over the past 20 years, the shoreface has continued migrating landward also resulting in a net steepening of the nearshore.

Within the time series of shoreface profiles are glimpses of the incremental development of the marine unconformity surface characteristic of transgressing shorelines. The composite envelop of profile minima is locally expressed as a series of scarps into older underlying substrate with limited expression on the fair-weather sea floor. In some areas relief on the order of 0.5 meters exists which may become emergent during storm events and also influences processes and sediment dispersal.

Recent efforts towards modeling morphological behavior in predicting longer term coastal evolution have shown substrate slope influences transgression rates (Stolper et al, 2005). The growing database of actual behavior across the shoreface on decadal scales may provide important verification to developing models and investigating coastal behavior on time periods longer than single "events" but shorter than "geologic time scales" evidence on the inner shelf.

INTRODUCTION

Estimates of shoreline change are traditionally defined by change in subaerial features or datums such as the wet-dry line interpreted from aerial photos and MHW contour. Across South Carolina and much of the nation, the shoreline is progressively encroaching development and is being influenced by "hard" and "soft" erosion protection strategies. In practice, some sections of the South Carolina coast have been defined as stable (zero long term erosion rates) due to artificial stabilization of subaerial shoreline features. These same areas continue to require beach nourishment and other engineering efforts to maintain beach volume and function. The Beach Erosion Research and Monitoring program (BERM) at Coastal Carolina University was initiated in 1993 through support of government agencies to collect cross-shore beach profiles for the entire populated coast of South Carolina. The growing database of shore-perpendicular profiles that extend across the entire active shoreface system provide a better understanding of nearshore dynamics. In addition, the database is used to delineate the setback line for coastal property management (Bernstein et al. 2003, Gayes et. al. 2001). The 13 year time series of profile changes can now be utilized to understand coastal behavior over annual to decadal periods. Profile analysis may provide important verification to developing models.

Slope analysis of several locations demonstrates that uniform profile migration is not occurring. Persistent profile geometry requires uniform migration of the subaerial and shoreface systems at all depths. Instead, profiles show evidence of continued migration of the lower shoreface at several beach locations, despite management practices to stabilize the subaerial beach. This behavior results in decoupling of the upper and lower shoreface and can cause steepening of the beachface. Decoupling of upper and lower beach systems can occur due to 1) differential erosion/accretion of upper and lower shoreface systems, 2) stabilization of upper or lower systems through natural phenomena such as impedance by rocky substrate, and 3) stabilization of upper or lower systems through anthropogenic interactions such as the construction of a seawall or nourishment project. The apparent decoupling of the upper and lower beach systems suggest that profile geometry for a site evolves not only on annual time scales, but on decadal time scales as well.

STUDY AREA

Profiles from several South Carolina beaches were selected for this study. Sites selected include Waites Island, Surfside/Myrtle Beach, DeBordieu Island, and Folly Beach (Fig.1). Although each of these locations differs with respect to coastline orientation, sediment availability, coastal development, and coastal management practices, the long-term profiles at each location reveal similar shoreface behavior over the past decade.

DeBordieu Island, Surfside Beach and Waites Island are all located along the shores of Long Bay in northern South Carolina. Long Bay is bounded by Cape Fear, NC and Cape Romaine, SC and is classified as a sediment starved region due to the lack of local sediment supply (Gayes 2003). The Grand Strand, within Long Bay, is roughly 60 miles long and contains some of the longest uninterrupted stretches of beach along the US Atlantic coast (South Carolina Department of Parks, Recreation, & Tourism, 2004). South Carolina's Office of Coastal Resource Management (OCRM) calculated the 40 year annual erosion rates for Waites Island and DeBordieu Island to be 3.05m/yr and 3.29m/yr, respectively. Surfside Beach is described as stable, with yearly erosion rates close to 0 (OCRM 2006).

Waites Island, the northern most of the study areas, is located at the North Carolina – South Carolina border between Little River and Hog Inlets. Little River Inlet was stabilized by a jetty system in the early 1980's. Over the past 20 years, Waites Island has experienced substantial expansion of its coastal dune fields (OCRM 2006). Expansion of the upper shoreface due to natural causes is unique among the four beaches selected in this study. Prior to the construction of the jetty system, the established shoreline change rates for Waites Island were erosional between 4 and 10 ft yr^{-1}.

DeBordieu Island is a private beach located at the southern end of Long Bay between Pawleys Inlet and North Inlet. The central portion of the island is protected by a seawall which extends roughly from benchmarks 4130 to 4140 (Fig.1). South of this region the calculated long term erosion rates of the upper shoreface range from -8 to -12 ft yr^{-1}.

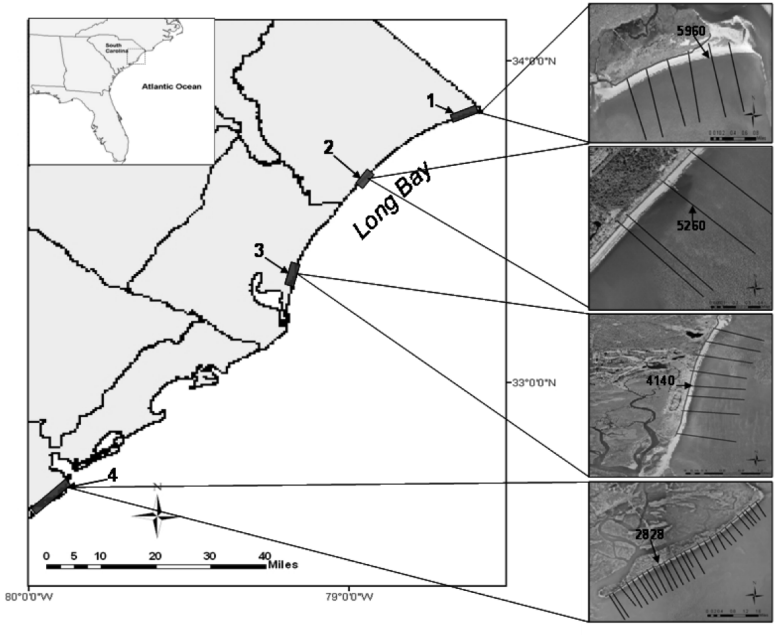

Fig. 1. Study Areas. 1) Waites Island 2) Myrtle Beach 3) DeBordieu Island 4) Folly Beach. Areas 1-3 are located on a stretch of beach known as the Grand Strand.

Benchmarks 4150-4180 are located north of the seawall in an area that is mostly undeveloped with extensive dune fields. This stretch of beach is said to be nearly stable with slight accretion possibly occurring (OCRM 2006). Extensive nourishment projects took place at DeBordieu in 1990, 1998 and 2006. In all three cases, the upper beach was nourished between benchmarks 4125 and 4160 where the majority of the development in the area is located. Due to DeBrodieu's nourishment history, shoreline change rates for the MHW contour were calculated between 1998 and present.

The section of beach between Surfside and Myrtle Beach State Park is one of the only areas in the Grand Strand that has not been nourished. Some sands from nourishment projects to the north and south, however, may have reached this area. Overall, this section of beach is considered stable (OCRM 2006).

Folly Beach is located just south of Charleston Harbor. Folly is characterized by many engineered structures including seawalls, groins, rock revetments, nearby jetties and several substantial nourishment projects. Two nourishment projects were captured by BERM surveys. The first of these large-scale projects took place between 1992 and 1993 and the second in the summer of 2005. Thus, shoreline

change rates were calculated between the1993 and 2005 nourishments. Variability of regional morphology and engineering structures, contributes to variable rates of shoreline change ranging from 8m yr^{-1} erosional to 0.35 m yr^{-1} accretion (Anders et al. 1990). The area known as "The Washout" is one of the most rapidly eroding areas on the Island. The localized, rapid erosion has been linked to the presence of an old paleo-channel (Gayes et al. 1998, Thieler et al. 1999). Therefore, elevated levels of erosion would be expected in this area. Folly is the only populated beach in South Carolina that does not have a jurisdictional setback line. South Carolina's OCRM determined that the jetties leading into Charleston Harbor have severely limited the sediment supply to the region.

METHODS

Profile Collection

Since in 1988, shore-perpendicular beach profiles extending seaward have been collected annually at approximately 400 benchmarks along the entire populated coast of South Carolina. Profiles extend from benchmarks to a pre-determined distance offshore, beyond the predicted depth of closure. Geographic coordinates of benchmarks are precisely known and provide consistent reference points for beach profile surveys. Throughout BERM, survey methods have evolved from the traditional rod-level and sled-based profilers to a GPS orientated system. Starting in 2001, Real Time Kinematic GPS surveys are preformed with sub-decimeter vertical accuracy. Survey methods from 1993 to present use the BERM system described in more detail in Bernstein et al. 2003 and Gayes et al. 2001. The BERM system consists of a boat mounted with an integrated fathometer and GPS system for offshore portions of profiles, and a backpack/ATV mounted GPS system for the subaerial portions of the survey.

Contours

Lack of persistence in profile geometry can be quantified by measuring changes in contour locations at a given benchmark through time. The MHW and a lower contour (LC) were selected as the two standard contours for shoreface migration rate assessment. The MHW contour is a function of the local tide range and mean tide level, and is often used to define shoreline location (List 2006, USGS 2005, Sallenger et al. 2003, Stockdon et al. 2002). MHW contour locations were calculated throughout the study area from National Oceanic and Atmospheric Administration (NOAA) tide station data. Calculated values for each of the four regions was found to be approximately 1.50 ft relative to the NAVD 88 tidal datum.

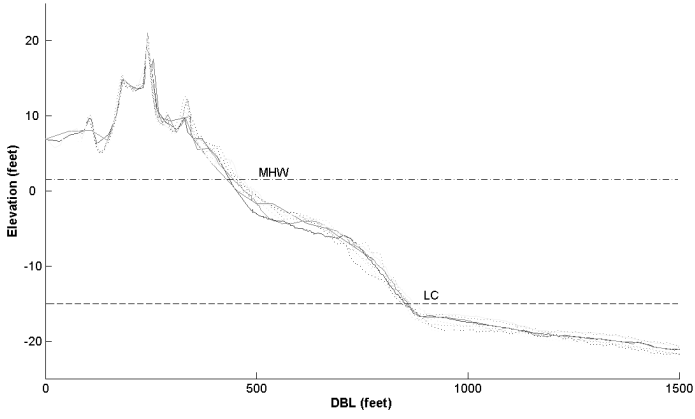

Fig. 2. Example of selected elevation contours

A second contour elevation was picked in order to determine migration rates on the lower shoreface. A contour elevation was selected where non-breaking wave energy prevails (Larson 1999). The LC was selected by visual inspection of profiles at each benchmark. An elevation below the apparent seasonal variations and immediately above the inflection point marking the transition onto the inner-shelf was selected for each benchmark (Fig. 2). The LC is assumed to be unaffected by daily and seasonal wave-driven bar activity. Similarly, the 7ft contour line was used to calculate dune migration rates at Waites Island. This contour intersects the face of the primary dune at all benchmarks throughout the study period.

At each benchmark, the migration rates of the MHW contour and the LC were calculated. Regression analysis was used to get a linear trend-line for each contour over the appropriate sampling interval. A positive value denotes seaward migration, and a landward migration rate is denoted by negative values. The determined migration rates of the subaerial and lower shoreface systems indicate whether a uniform migration of the profile is occurring. If decoupling of the MHW contour and the LC occur, a change in shoreface slope will result.

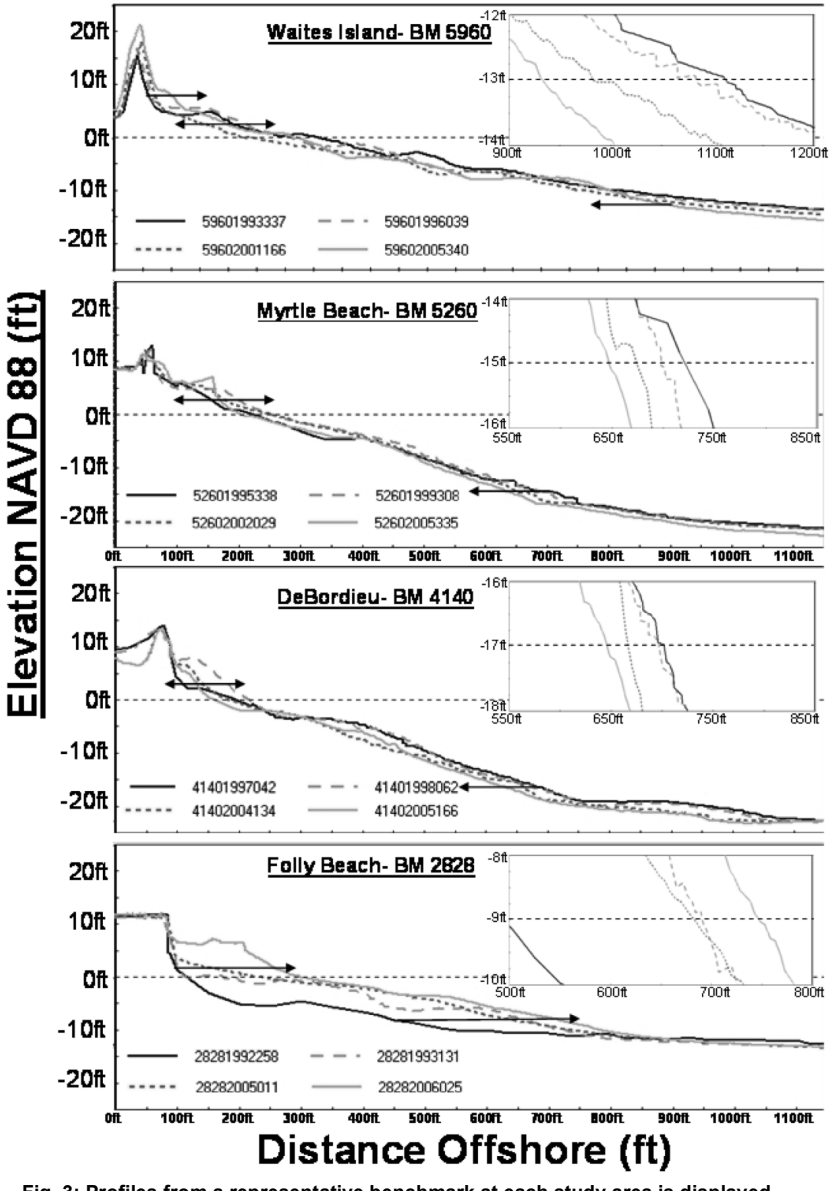

Fig. 3: Profiles from a representative benchmark at each study area is displayed. Insets show migration of the LC. Scales for each cross-section are equivalent.

RESULTS

Waites Island

MHW contours at benchmarks 5945, 5930 and 5915 are migrating seaward at a rate of 5.73-11.22 ft yr^{-1} while the MHW contour at benchmark 5960 is migrating landward at a rate of 2.98 ft yr^{-1}. Surveys at all benchmarks indicate that the coastal dune field has accreted at a rate of 3.00-12.79 ft yr^{-1}, while the LC has been retreating landward at a rate of 3.00-16.60 ft yr^{-1} (Table 1). The data indicate that steepening is in fact occurring at Waites Island which suggest that a non-uniform profile migration may occur naturally as well as due to anthropogenic influences.

Table 1: Waites Island Summary

Waites Island				
Benchmark	**5915**	**5930**	**5945**	**5960**
Lower contour (LC)	-15	-15	-14	-13
LC rate of Δ (ft yr-1)	-3.5	-3	-5.03	-16.6
LC R^2	0.843	0.812	0.841	0.742
MHW rate of Δ (ft yr-1)	11.22	8.65	5.73	-2.98
MHW R^2	0.875	0.713	0.424	0.369
Dune Elevation	7	7	7	7
Dune rate of Δ (ft yr-1)	12.79	8.08	9.74	3
Dune R^2	0.823	0.812	0.841	0.742

Myrtle Beach State Park

MHW contours at benchmarks 5250, 5260 and 5270 are migrating seaward at a rate of 1.56-1.95 ft yr^{-1}. The LC for each of the benchmarks is migrating landward at a rate of 2.45-4.50 ft yr^{-1}. The R^2 values for the MHW contours are rather low and range from .124-.172 while the R^2 values for the LC range from .682-.733 (Table 2). All three benchmarks from this beach demonstrate the same general trend of the lower shoreface eroding while the upper shoreface appears to be rather stable.

Table 2: Myrtle Beach State Park Summary

Myrtle Beach State Park			
Benchmark	**5250**	**5260**	**5270**
Lower contour (LC)	-17	-15	-15
LC rate of Δ (ft yr-1)	-2.45	-4.50	-3.87
LC R^2	0.682	0.733	0.722
MHW rate of Δ (ft yr-1)	1.95	1.56	1.68
MHW R^2	0.172	0.143	0.124

DeBordieu Island

MHW contours at benchmarks 4125, 4130, 4140 and 4150 are migrating landward at a rate of 4.76-17.87 ft yr^{-1}, while the MHW contour at benchmark 4160 is migrating seaward at a rate of 1.91 ft yr^{-1}. The LC at benchmarks 4125, 4130, 4140 and 4160 are migrating landward at a rate of 1.16-24.45 ft yr^{-1} while benchmark 5960 is migrating seaward at a rate of .82 ft yr^{-1} (Table 3). Benchmark 4140 is located at the

northern end of a seawall and is described as being the pivot point of the island. To the south, the upper shoreface is eroding, and to the north, the upper shoreface is stable or accreting (table 3) (OCRM 2006). Benchmark 4130, located at the southern end of the seawall, exhibits the highest rates of landward migration for both the LC and MHW contours of the selected profiles. Benchmark 4125, located just down the beach to the south of benchmark 4130, has "the next highest" rates of erosion.

Table 3: DeBordieu Island Summary

DeBordieu Island					
Benchmark	**4125**	**4130**	**4140**	**4150**	**4160**
Lower contour (LC)	-12	-12	-17	-14	-15
LC rate of Δ (ft yr-1)	-12.21	-24.45	-4.50	0.82	-1.16
LC R^2	0.897	0.823	0.607	0.009	0.156
MHW rate of Δ (ft yr-1)	-16.85	-17.87	-9.58	-4.76	1.91
MHW R^2	0.893	0.490	0.853	0.419	0.144

Folly Beach

MHW contours at benchmarks 2828 and 2830 are migrating seaward at rates of 1.83 and 1.45 ft yr^{-1}, respectively. However, MHW contours at benchmarks 2843 and 2863 are migrating landward at rates of 1.72 and 3.82 ft yr^{-1}, respectively. LCs at benchmarks 2828, 2843 and 2863 are migrating landward at a rate of 0.76-7.01 ft yr^{-1} while benchmark 2830 is migrating seaward at a rate of 0.78 ft yr^{-1} (Table 4).

Table 4: Folly Beach Summary

Folly Beach				
Benchmark	**2828**	**2830**	**2843**	**2863**
Lower contour (LC)	-9	-9	-9	-10
LC rate of Δ (ft yr-1)	-0.76	0.78	-1.97	-7.01
LC R^2	0.008	0.006	0.056	0.568
MHW rate of Δ (ft yr-1)	1.83	1.45	-1.72	-3.82
MHW R^2	0.075	0.101	0.087	0.222

DISCUSSION

Although none of the beaches monitored by BERM are truly pristine and free from the affects of human modification, Waites Island is close to a natural state. The rate of seaward dune migration relative to the lower shoreface is quite substantial at benchmarks 5945, 5930 and 5915. This process alone leads to an increased slope in profile geometry. At benchmark 5960, the MHW and dune contours are migrating at -2.98 and +3.00 ft yr^{-1}, respectively. This trend is quite different from the trend seen at the other three benchmarks, and is likely a result of closer proximity to the Little River jetties. Despite the lack of significant seaward accretion taking place at benchmark 5960 in the upper shoreface, the LC is moving landward at a rate much higher than is seen at the other three benchmarks. Accretion of aeolian-deposited subaerial features suggests an abundant sediment supply at this location, which is atypical along the Grand Strand and is most likely to inlet dynamics as well. The processes occurring at all benchmarks result in a net steepening of the shoreface.

Benchmarks located in the area of Myrtle Beach State Park demonstrate a continued shoreward migration of the lower shoreface. The seafloor in this region has been characterized as hard-ground based on side-scan sonar records (Gayes, P.T. and Donovan Ealy, et al., 1996). Differential rates of erosion are expected for the different types of substrates (i.e. loose sand or compacted-sand/hard-bottoms). Loose sands erode more easily than compacted or lithified sands; however, this is not what is observed. The lower shoreface, composed of compacted sediments is migrating shoreward while the upper shoreface, composed of loose sediments, is holding stable. Sands from adjacent nourishment projects in nearby Myrtle Beach and Surfside Beach have likely bled into this region and may influence the irregular trend at the MHW contour (Table 2).

DeBordieu Island, the southern most of the three study sites selected within Long Bay, also demonstrates a lower shoreface erosion rate exceeding those of the upper shoreface. Historic shorelines from 1872 to 1962 indicate that North Inlet is migrating to the south. Processes associated with the southward migration of North Inlet are likely contributing to elevated levels of erosion at the southern end of DeBordieu Island. Historic shorelines indicate North Inlet was located approximately one mile north of its present location.

Folly Beach, located just south of Charleston Harbor, is complicated by an extensive nourishment history, inlets, and engineered structures. Profile evolution at benchmark 2828 suggests that the system has been "flooded" with sand and remains stable between nourishment projects (Fig. 3). Benchmark 2830, .320m north along the seawall shows the same trend as benchmark 2828. The seaward migration of both the LC and MHW contours is consistent through the seawall area (benchmarks 2828 and 2830) (Fig. 3). Benchmark 2863, located in a paleo-channel (Gayes et al. 1998, Thieler et al. 1999), shows LC retreat at a higher rate than the surrounding benchmarks. It is, however, consistent with migration rates at the other study sites. Large and rapid changes in contour locations in this area may be influenced by excessive use of engineered structures.

CONCLUSION

Measurements of MHW and LC locations through time demonstrate that uniform profile migration is not occurring. Traditionally, engineering design and coastal zone management strategies for protecting our nation's shorelines have focused extensively on the upper shoreface and subaerial beach. Despite efforts to preserve South Carolina's beaches through stabilization and nourishment of the upper shoreface, the natural rate of shoreline migration still occurs which can result in an overall net steepening of the shoreface. Implications of a steepened shoreface include modification of prevailing hydrodynamic and sediment dispersal patterns. Future nourishment and hard structure efforts may be limited due to lack of funds and shoreline management policies. Accelerated levels of erosion will then occur as the steepened shoreface returns to an equilibrium shape. While these results strongly suggest changes in profile geometry on annual to decadal time scales, methodology must continually be refined to better understand and quantify shoreface migration.

ACKNOWLEDGEMENTS
This is a contribution of the SC Coastal Erosion Study. Funding for BERM program was provided through the US Geological Survey, the South Carolina Sea Grant Consortium, the South Carolina Department of Health and Environmental Control-Office of Ocean and Coastal Resource Management, the US Army Corp. of Engineers-Charleston District, Horry County and the City of North Myrtle Beach. We also like to thank Dr. Rich Viso for his scrupulous review of this manuscript.

REFERENCES

Anders, F.J., Reed, D.W., and Meisbuger, E.P., 1990. Shoreline movements: Report 2--Tybee Island, Georgia to Cape Fear, North Carolina 1851-1983. U.S. Army Corps of Engineers, Technical Report CERC-83-1, 152 p.

GAYES, P.T. AND DONOVAN EALY, ET AL., 1996, Myrtle Beach Renourishment Project Pre-nourishment nearshore physical survey: Interim report, prepared by the South Carolina Marine Resources Research Institute, South Carolina Marine Resources Division, Charleston, South Carolina for the U.S. Army Corps of Engineers, Charleston District. 32 pp.

Gayes, P.T., Donovan-Ealy, P., Harris, M.S. and Baldwin, W., 1998. Assessment of Beach Renourishment Resources on the Inner Shelf Off Folly Beach and Edisto Island, South Carolina. Final Report of the South Carolina Task Force on Offshore Resources and Critical Habitats to the Minerals Management Service Office of International Activities and Mineral Resources 43 p.

Gayes, P.T., Baldwin, W., Van Dolah, R.F., Jutte, P., Eiser, W.C., and Hansen, M., 2001. Systematic coastal monitoring: The South Carolina Coast. Proceedings – Coastal Dynamics 2001, p. 868-877. (0,2;cme,sc)

Gayes, P.T., Schwab, W.C., Driscoll, N.W., Morton, R.A., Baldwin, W.E., Denny, J.J., Wright, E.E., Harris, M.S., Katuna, M.P. and Putney, T.R, 2003, Sediment Dispersal pathways and conceptual sediment budget for a sediment starved embayment: Long Bay: in Davis, R. Sallenger, A. and Howd, P., Coastal Sediments, American Society of Civil Engineers, St. Petersburg, FL

List, J.H., Farris, A.S., and Sullivan, C., 2006, Reversing storm hotspots on sandy beaches: spatial and temporal characteristics: Marine Geology, v. 226, p. 261-279.

NOAA, 1998. National Oceanic and Atmospheric Administration National Data Buoy Center NWS/NOAA Data Archives: station 41004. Stennis Space center online data: http://seaboard.ndbc.noaa.gov/index.html. September 2003

Sallenger, A.H. Jr., Krabill, W.B., Swift, R.N., Brock, J., List, J., Hansen, M., Holman, R.A., Manizade, S., Sontag, J., Meredith, A., Morgan, K., Yunkel, J.K., Frederick, E.B., and Stockdon, H., 2003, Evaluation of airborne topographic lidar

for quantifying beach changes: Journal of Coastal Research, v. 19, no. 1, p. 125-133.

South Carolina Department of Parks, Recreation & Tourism, 2004, Official tourism Website of South Carolina: accessed November 7, 2006, at http://www.discoversouthcarolina.com/scfacts.

South Carolina-Office of Ocean and Coastal Resource Management (SC-OCRM), 2000, Surveyors Packages; Grand Strand Area. SC-OCRM

Stockdon, H.F., Sallenger, A.H., List, J.H., and Holman, R.A., 2002, Estimation of shoreline position and change using airborne topographic lidar data: Journal of Coastal Research, v. 18, no. 3, p. 502-513.

Stolper, D., List, J. H. and Thieler, E. R., 2005. Simulating the evolution of coastal morphology and stratigraphy with a new morphological-behavior model (GEOMBEST). Marine Geology 218, 17-36.

Thieler, E. R., P. T. Gayes, W. C. Schwab, M. S. Harris, N. C. Kraus, and W. G. McDougal, 1999, Tracing sediment dispersal on nourished beaches; two case studies: Coastal sediments '99: 4th international symposium on Coastal engineering and science of coastal sediment processes; Scales of coastal sediment motion and geomorphic change, v. 4, Vol. 3, p. 2118-2136.

USGS Open-File Report 2005-1027, An Operational Mean High Water Datum for Determination of Shoreline Position from Topographic Lidar Data.

IMPROVING STATISTICAL VALIDITY IN CALCULATING EROSION HAZARDS FROM HISTORICAL SHORELINES

Ayesha S. Genz[1], L. Neil Frazer[2], Charles H. Fletcher[3]

1. Department of Geology and Geophysics, University of Hawaii, 1680 East West Road, Honolulu, HI 96822, U.S.A. agenz@hawaii.edu.
2. Department of Geology and Geophysics, University of Hawaii, 1680 East West Road, Honolulu, HI 96822, U.S.A. neil@hawaii.edu.
3. Department of Geology and Geophysics, University of Hawaii, 1680 East West Road, Honolulu, HI 96822, U.S.A. fletcher@soest.hawaii.edu.

Abstract: We evaluate three classes of shoreline change rate methods on all sandy beaches of Maui: 1) methods that estimate shoreline change transect by transect, 2) methods that combine data from all transects to estimate shoreline change, and 3) extensions of (2) that include acceleration. Using these, we compare 50 yr hazard zones from beaches exposed to different conditions, natural beaches versus altered beaches, and well-defined littoral cells versus open systems. Acceleration methods fit the data well, but don't predict the erosion hazard zone well. Altered beaches and open system beaches are better fit by methods with acceleration at a higher proportion than natural or pocket beaches. The traditional transect by transect method that calculates shoreline change at discrete points along a beach never qualifies as the best fit model.

INTRODUCTION

Historical shorelines are commonly extracted from aerial photographs and NOAA topographic surveys (T-sheets). They are generally limited and spaced unevenly through time. Currently the most common shoreline change method is the single-transect (S-T) method. S-T uses data from individual shore-normal transects to calculate shoreline change rates. As there are only 5-10 shorelines at each transect, the resulting rates are often uncertain. The equation for S-T at each transect is:

$$y_j - \bar{y} = (t_j - \bar{t})r + n_j \quad (1)$$

where y_j is the shoreline position at time t_j, $\bar{y}$ is the baseline, $\bar{t}$ is the time origin, r is the change rate, and n_j is the noise. As the baseline has been chosen to give a zero intercept, there are effectively two model parameters for each transect. For a beach with I transects, the S-T method requires $2I$ parameters.

Genz et *al*. (in press) recently introduced binning (hereinafter, T-binning) as a new method that improves the significance of fit and lowers uncertainties. T-binning combines transects with rates that are insignificantly different and calculates one rate for each bin. Grouping transects requires heavy user input that can bias results. Frazer et *al*. (in review) improve on T-binning by removing user input. Called A-binning, transects are binned using the corrected Akaike Information Criterion (AICc) to identify best groupings. However, computation-time increases rapidly with the number of bins. In both T-binning and A-binning, change rate is discontinuous at bin boundaries.

Frazer et *al*. (in review) also introduced the PX method (think: polynomial in x), an alternative to binning and single-transect that makes change rate continuous along a beach. The PX method fits transect measurements to the following equation,

$$y_{ij} - \bar{y}_i = \sum_{k_0=0}^{K_0} \alpha_{k_0}^{(0)} P_{k_0}(z(x_i)) + (t_j - \bar{t}) \sum_{k_1=0}^{K_1} \alpha_{k_1}^{(1)} P_{k_1}(z(x_i)) + n_{ij} \quad (2)$$

in which $\bar{y}_i$ is the baseline at transect i, the x_i are the transect locations, $z(x)$ is a mapping from alongshore distance to the interval [-1,1], the $P_k(z)$ are basis functions (e.g., Legendre polynomials), the α_k are coefficients, and n_{ij} is noise. A well chosen baseline causes all the coefficients in the first sum to vanish, hence the number of parameters in the model is $I + K_1$, where I is the number of transects.

After the coefficients have been found, the second sum on the right hand side of equation (2) gives the change rate of the beach at time $\bar{t}$. Frazer et *al*. (in review) suggested three types of basis functions for use in PX, denoting PX by LX when Legendre polynomials are used, by RX when trigonometric functions are used, and by EX when empirical orthogonal functions of the beach data are used (Table 1). The motivation for EX is that, if the beach physics can be represented by a linear system, the beach at any instant in time must be a linear sum of the eigenfunctions of a linear operator.

To allow for a rate that changes with time, the right hand side of equation (2) can be augmented with an acceleration term,

$$\frac{(t_j - \bar{t})^2}{2} \sum_{k_2=0}^{K_2} \alpha_{k_2}^{(2)} P_{k_2}(z(x_i)) \quad . \quad (3)$$

If the acceleration term is present, the PX method is referred to as PXT, since the rate is changing with time. Similar to PX, PXT is divided into three methods according to their basis functions – LXT, RXT, and EXT (Table 1). Genz et *al*. (in review) compared PXT to other methods and found PXT to be more erratic in predicting known positions.

Table 1. Description of Methods

Method	Basis Functions	Acceleration?
S-T	---	no
LX	Legendre polynomial	no
RX	Trigonometric functions	no
EX	Eigenvector of beach data	no
LXT	Legendre polynomial	yes
RXT	Trigonometric functions	yes
EXT	Eigenvector of beach data	yes

In the expressions above, the upper limits K_1 and K_2 can be as large as the number of transects I, so there are I possible PX models and I^2 possible PXT models. Of interest here is the fact that if lower order basis functions are selectively included or omitted, the number of possible PX models increases to 2^I, and the number of possible PXT models increases to 2^{2I}. By testing all combinations, a better-fit model may be obtained. In this paper we use synthetic data to investigate the omission of lower-order terms.

Fletcher et *al*. (2003) calculated shoreline change using S-T for all sandy beaches of Maui. They used Reweighted Least Squares (RLS) to determine shoreline change at each transect. We also calculate shoreline change on all sandy beaches of Maui by predicting the 50-yr hazard zone. We compare S-T, LX, RX, EX, LXT, RXT, and EXT. Our study is motivated by the assumption that when different models predict similar hazard zones, the predicted hazard zones are more reliable.

EXCLUSION OF LOWER-ORDER TERMS IN PX AND PXT

If lower order terms in equations (2) and (3) can be selectively omitted, comparing the AICc score of all possible PX and PXT models is impractical. For example, if there are 25 transects on a beach, all possible PX models would equal 2^{25}, or 33,554,432. All possible PXT models would equal $2^{(2*25)}$, or 1.13×10^{15}. At present, computers are too slow to calculate every possible combination in a timely manner, so usually we do not calculate all possible combinations for PX and PXT; we include all lower-order terms basis functions when calculating higher order polynomials. However, Genz et *al*. (in review) show inconsistent hazard predictions using PXT. This leads us to investigate whether the exclusion of lower-order terms might improve the 50 yr hazard prediction. One way to test a large number of models is by using genetic algorithms (GA). Goldberg (1989) has an excellent explanation of GAs, which we briefly summarize: As the name indicates, genetic algorithms are based on biological ideas of natural selection. Any GA begins with a population of models, coded as strings; each string can be thought of as an individual organism with a single chromosome, and each parameter in the model can be thought of as a gene. Each string has a "fitness" based on how well it fits the data. Fitter strings are passed on to the next generation; thus, each generation evolves from the previous generation, and the best-fit string(s) are found after many generations. In our

application, each string is a binary number with number of bits equal to the number of possible basis functions in the model. Each bit corresponds to a particular basis function. If the first bit is a zero (one) the lowest order basis function is excluded (included) in the model, and so forth. The fitness value of a string is the fitness of the best-fit model with the permitted basis functions.

Each generation is produced by *selection*, *crossover*, and *mutation* of the previous population. Selection is based on the fitness function; a string with higher fitness function has a better chance of being selected. Crossover occurs between pairs of strings that have undergone selection. Each pair is cut at the same location and string segments are swapped to make a new pair. The final, and less important, operation is mutation, whereby the value at each location on a string has a very low probability of being switched from zero to one or vice-versa.

In the shoreline scenario of a beach with 25 transects, we use a Matlab GA to determine the optimal combination of terms for both PX and PXT. In an initial generation with a population size of 100, there are 100 strings, each with a different combination of coefficient terms. The fitness function is the negated AICc score. By specifying the number of generations and acceptable tolerance limits, we can efficiently identify the combination of coefficient terms. Figure 1 is an example of output from a GA in MATLAB.

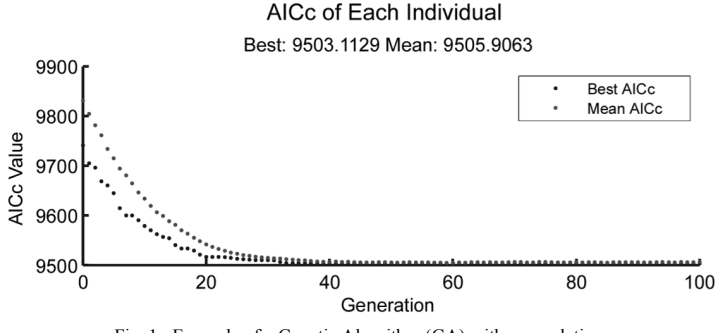

Fig. 1. Example of a Genetic Algorithm (GA) with a population size=100 and a limit of 100 generations.

MAUI SETTING

The sandy beaches of Maui Island form three regions: Kihei, West Maui, and North Shore (Figure 2). Each region is exposed to different wind and wave regimes (Fletcher et *al.,* 2003; Rooney et *al.,* 2003). Kihei is protected by the islands of Molokai, Lanai, Kahoolawe and is subjected to refracted North Pacific swell, south swell, and Kona storm waves (Rooney and Fletcher 2005). Kona is a low-pressure system that creates winds and waves from the south. West Maui is affected by North Pacific swell, Kona storms and south swell (Eversole and Fletcher 2003). The North Shore is strongly affected by

the north swell, and tradewind waves (Fletcher et *al.,* 2003; Makai Ocean Engineering and Sea Engineering 1991; Rooney et *al.,* 2003).

Each beach is classified into one of five categories, based on whether the beach has hardened structures (Table 2). The first classification includes beaches with hardened structures where no backshore fronts the structures. These beaches are severely impacted. If enough shoreline data exists, then only post-hardened shorelines are used to predict the 50 yr hazard zone. If shoreline data are sparse, then pre-hardened shorelines are used to identify beach change without predicting the 50-year hazard zone. Including both pre- and post-hardened shorelines in an analysis violates the underlying assumption of the change rate methods, which is that beach physics are constant.

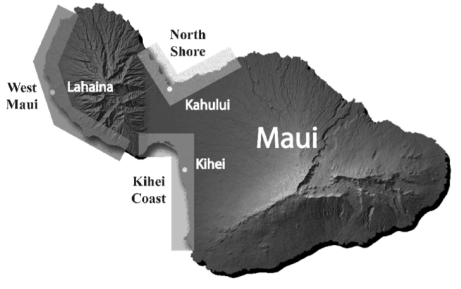

Fig. 2. Three regions of Maui

If a backshore exists in front of hardened structures, we assume the beach is not impacted and all shorelines are used for the analyses. If a beach experienced direct impact (e.g., beach nourishment), then a 50 yr hazard zone is not predicted. If the beach appears to be unaltered by hardened structures (natural), then a 50 yr hazard zone is predicted using all shorelines.

Using the classification scheme, there are 30 natural beaches and 46 hardened beach segments on Maui (Table 3). The 50 yr hazard zone is not calculated for two beaches (classified as category #2 and #4). We do not include these two beaches in our analysis.

Table 2. Beach Classification

Category	Hardened Shoreline?	backshore present?	Hazard Zone Predicted?
1	yes	no	yes
2*	yes	no	no
3	yes	yes	yes
4**	yes	yes	no
5	no	--	yes

* not enough post-hardened data
** excessive human interference

Of the 74 beaches, 27 have well-defined borders (pocket beaches), and 17 have ill-defined borders (open system beaches). Fourteen beaches are actually segments of longer beaches since hardened structures (i.e., groins) serve as borders for these areas. These beaches are not included in the definition of pocket or open system beaches.

Table 3. Maui Beach Breakdown

Category	Kihei	West Maui	North Shore	Total
1	4	13	5	22
2	1	0	0	1
3	5	2	15	22
4	0	0	1	1
5	11	13	6	30
Total	21	28	27	76

METHODS

Our methodology includes two distinct procedures. The first is to test the exclusion of lower-order terms with GAs. The second is to calculate the 50 yr hazard zone for all sandy beaches on Maui.

Using the genetic algorithm

Synthetic data are used to compare the GA process (testing randomly up to 2^{2I}) with the limited iterative process (testing up to I^2) by predicting a known 50 yr hazard line. We calculate the hazard line for the PX methods (LX and RX) and the PXT methods (LXT and RXT). EX and EXT are excluded from this analysis because the number of possible models is limited by the number of shoreline years (Frazer et *al.,* in review). The synthetic data has 100 transects, a 3 m intercept, an alongshore rate modeled by a quadratic polynomial, and a constant acceleration that equals 0.01 m/yr/yr. The noise is sampled from a Gaussian distribution with zero mean. We repeat experiments using noise processes with different standard deviations. The first experiment has a standard deviation of 1.95 m, which is based on the root mean squared error of a PX fit at an actual beach in Maui. Successive experiments have noise processes with standard deviation equal to 5, 10, 25, 50, 100, and 250 m.

50 yr Hazard Zone

For the 74 beaches, we calculate a 50 yr hazard position using S-T, LX, RX, EX, LXT, RXT, and EXT. We omit the binning methods, as Genz et *al*. (in review), found that results from A-binning and T-binning were insignificantly different from LX, RX, and EX on these beaches. All methods utilize Weighted Least Squares (WLS) to calculate misfit. The 50 yr hazard zone is the 50 yr position with a 2σ (95%) uncertainty band. We calculate the AICc score for each beach to determine which method best fits that beach. We also apply an ANOVA test on the 50-yr hazard prediction to determine whether the resulting predictions from all methods are significantly different or not.

RESULTS

Within Maui beaches, 9 of 22 beaches with hardened structures have only 3 shorelines (category 1, Table 2). Although there are more shorelines at these beaches, hardened structures dominate the beaches starting in 1975. Because 3 shorelines are not enough to

make sizeable predictions (such as the 50 yr hazard position), we remove these beaches and report the results of the remaining 65 beaches.

Genetic algorithms

For all noise processes, predictions using GA and predictions using the limited iterative process were similar (Figures 3 and 4). Figure 3 illustrates the GA 50 yr hazard predictions compared to the 'true' hazard line determined using synthetic data. Figure 4 illustrates the limited iterative process hazard predictions compared to the 'true' hazard line. LXT identifies acceleration in all but one experiment (LXT does not identify acceleration in the limited iterative process when the noise has a standard deviation of 500). RXT never identifies acceleration and equals RX in both the GA and limited iterative process. RX/RXT is more variable than LX and LXT. For both sets of predictions, LXT is closest to the 'true' position when the standard deviation of the noise is less than 100. As noise increases, LX is more consistent than LXT.

Allowing lower-order basis functions to be excluded does not reduce the variability associated with the PXT methods, as the results are consistent between GA and the limited iterative process. However, the AICc values of all methods are slightly lower with the GA.

Maui Hazard Zones

Based on the AICc scores, acceleration methods were the best methods for 48 beaches (Table 4). AICc identified EX, LX or RX as the best method for 17 beaches. For all 17 beaches, EXT, LXT, and RXT did not identify acceleration (i.e., EXT, LXT, and RXT equaled EX, LX, and RX, respectively). AICc did not identify S-T as the best method for any beach. Of the 65 beaches, 83.1% of the beaches had insignificant S-T rates.

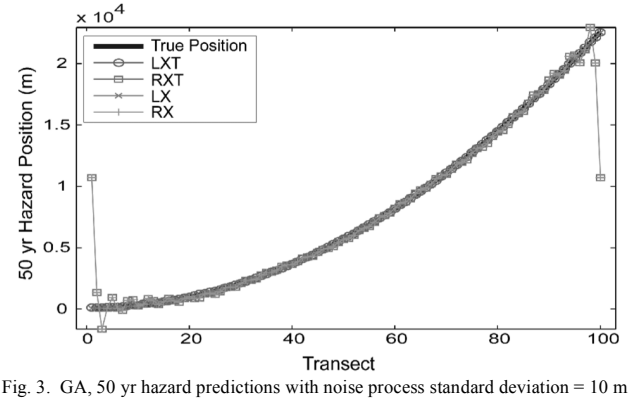

Fig. 3. GA, 50 yr hazard predictions with noise process standard deviation = 10 m.

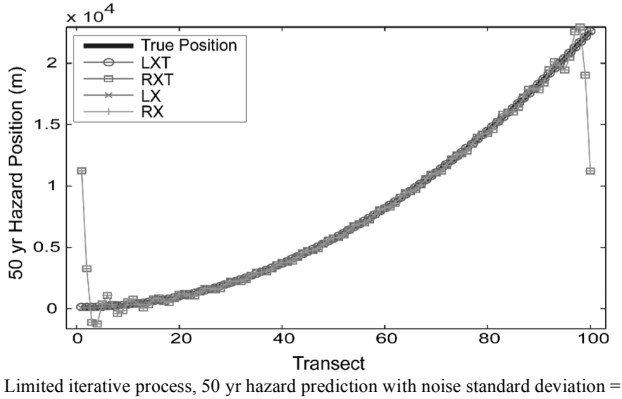

Fig. 4. Limited iterative process, 50 yr hazard prediction with noise standard deviation = 10 m.

Table 4. Number of Beaches Identified by AICc

	Method	Kihei	West Maui	North Shore	Total
Acceleration Methods	EXT	13	11	14	58.5%
	LXT	2	3	1	9.2%
	RXT	2	1	0	4.6%
	LXT ≈ RXT	1	0	0	1.5%
Non-Acceleration Methods	LX ≈ RX	1	2	1	6.2%
	EX	1	3	6	15.4%
	LX ≈ RX ≈ EX	0	1	2	4.6%
	S-T	0	0	0	0.0%

Table 5 reports AICc results of natural beaches and hardened beaches. Hardened beaches tend to identify acceleration more than natural beaches (77.1% hardened beaches vs. 70.0% natural beaches); while natural beaches tend to identify non-acceleration methods more than hardened beaches (30.0% natural beaches vs. 22.9% hardened beaches).

Table 5. Number of Beaches Identified by AICc

	Method	Natural Beaches	Hardened Beaches
Acceleration Methods	EXT	14	24
	LXT	5	1
	RXT	2	1
	LXT ≈ RXT	0	1
	Total	70.0%	77.1%
Non-Acceleration Methods	LX ≈ RX	4	0
	EX	4	6
	LX ≈ RX ≈ EX	1	2
	S-T	0	0
	Total	30.0%	22.9%

Acceleration is recognized in 63.0% of pocket beaches, while 37.0% have no acceleration (Table 6). Open systems tend to pick acceleration methods at a much higher percentage (94.1%) than pocket beaches. S-T is not identified as the best method in any of these beach systems.

Table 6. Number of Beaches Identified by AICc

	Method	Pocket Beaches	Open System Beaches
Acceleration Methods	EXT	13	11
	LXT	2	3
	RXT	1	2
	LXT ≈ RXT	1	0
	Total	63.0%	94.1%
Non-Acceleration Methods	LX ≈ RX	4	0
	EX	5	1
	LX ≈ RX ≈ EX	1	0
	S-T	0	0
	Total	37.0%	5.9%

An ANOVA test is calculated to identify whether the means of 50 yr hazard positions are significantly different. Three main categories emerge as dominant groupings of methods (Table 7). Predictions from all methods are insignificantly different from each other in 36.9% of the beaches. Seven of these beaches have deceptive results because LXT, RXT, and EXT have extreme erosional/accretional predictions that cancel out when the mean is calculated (e.g., Figure 5). S-T was not distinguishable from LX, RX and EX in 24.6% of the beaches. S-T, the PX methods and the PXT methods were significantly different from each other in 18.5% of the beaches.

The hazard zone is composed of the 50 yr hazard position plus an uncertainty band at the 95% confidence interval. Looking at the uncertainty associated with the hazard position, S-T has the highest uncertainties for 31 beaches (Table 8). LXT, RXT, and EXT also have high uncertainties. EX has the lowest uncertainties for 48 beaches.

TABLE 7. ANOVA Results of Hazard Positions

		# of Beaches			
	Method Groupings	Kihei	West Maui	North Shore	Total
1	All Methods	5	6	13	36.9%
2	S-T LX ≈ RX ≈ EX LXT ≈ RXT ≈ EXT	3	5	4	18.5%
3	S-T ≈ LX ≈ RX ≈ EX LXT ≈ RXT ≈ EXT	9	3	4	24.6%

LX and RX also have low uncertainties. LXT, RXT, and EXT have the lowest uncertainties for 25 beaches (highlighted in Table 8). None of these 25 beaches identify

acceleration, hence, in this case LXT, RXT, and EXT equal LX, RX, and EX, respectively.

Table 8. Mean Hazard Uncertainty

Method	# Beaches with Lowest Uncertainty	# Beaches with Highest Uncertainty
S-T	2	31
LX	15	0
RX	13	0
LXT	8	12
RXT	6	21
EX	48	1
EXT	11	6

DISCUSSION

In all beaches, hazard predictions with LX, RX, and EX are always in agreement. These methods also have the lowest hazard position uncertainties. Genz et *al*. (in review) showed that these methods, along with binning, predict known positions more accurately than other methods. With that in mind, and with the consistency shown with these methods in all beaches of Maui, we currently advocate the use of these methods.

Although AICc identifies acceleration in 73.8% of the beaches, Genz et *al*. (in review) showed that predictions of known positions with these methods are inconsistent. AICc finds the best fit model so it is possible that acceleration models fit the data better, but do not enhance predictions. As shown by the GA results, excluding polynomials with lower-order terms did not significantly improve predictions; this is fortunate, as calculations with GA have significantly longer run times than those with the limited iterative process. More research on acceleration methods may be necessary for better predictions.

Beach Comparisons

LX, RX, and EX are identified by the AICc in pocket beaches at a higher proportion than in open system beaches. Compared to open system beaches, pocket beaches are smaller, with defined borders, such as headlands, that restrict sediment movement (Woodroffe 2002). Thus, open system beaches are more influenced by changes, such as interruptions to longshore sediment transport. Acceleration methods better account for the influx and outflow of sediment in open systems; hence 94.1% of these types of beaches show acceleration.

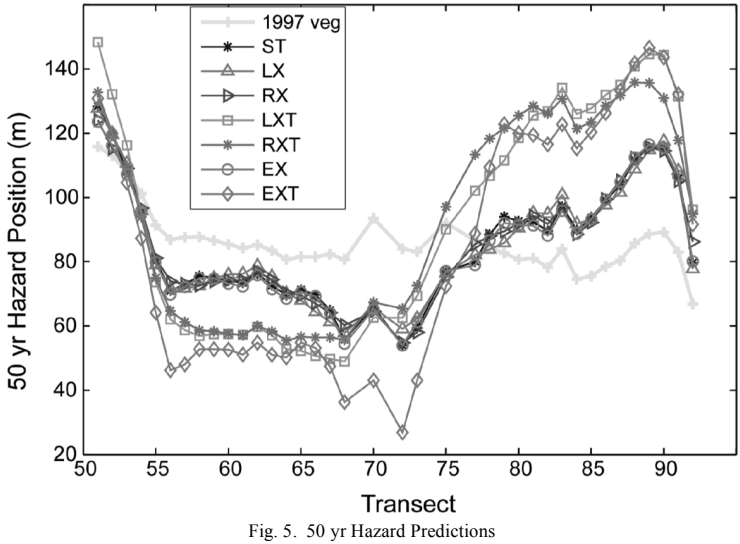

Fig. 5. 50 yr Hazard Predictions

Hardened shorelines fit a slightly higher percentage of acceleration methods than natural shorelines. Although it is a minimal difference, acceleration might be favored in hardened shorelines due to structures causing rates to vary with time. Other factors, such as storms, could influence the high frequency of acceleration found in natural beaches.

Hardened Shorelines

An important assumption of all shoreline change methods is that beach physics remain stable through the time period of interest (Fenster et *al.,* 1993; Morton 1991). Hardened structures and storms are common influences on beaches that violate this assumption. Fenster et *al*. (1993) recognized the impracticality of the change-rate methods on beaches that have undergone structural changes and introduced the Minimum Description Length (MDL) method to minimize violations of this assumption. They proposed fitting higher-order polynomials at each transect to determine the erosional trend shift and using data after the trend shift to predict future hazard positions. However, there might not be enough data to fit a higher-order polynomial at each transect.

It is important to have as long a temporal span as possible to reduce the effects of noise on the long-term trend (Crowell et *al.,* 1993). However, changes such as hardened structures and storms affect the resulting trends of a beach. Many have argued that removing storm-influenced shorelines from long-term rate analysis is valid because post-storm shorelines eventually recover to their pre-storm positions and therefore do not affect the long-term rate (e.g., Crowell et *al.,* 1993; Douglas and Crowell 2000; Galgano et *al.,* 1998; Zhang et *al.,* 2002). Unlike storms, the addition of hardened structures does affect the long-term trend. Removal of post-hardened shorelines in change-rate analysis

would only give predictions based on natural beaches. However, removal of pre-hardened shorelines would result in predictions based on beach behavior with the involvement of structures.

We addressed hardened structures in the following way: If hardened structures were present, and no backshore existed in front of the beach, we removed pre-hardened shorelines (Category 1, Table 2). However, where a backshore persisted in front of a hardened structure, we interpreted the structure as having little influence on beach dynamics, and we included the hardened beaches in our analysis (Category 3, Table 2).

AICc

Nine beaches have three shorelines and are all classified as category 1, which signifies hardened shorelines (Table 2). Only 3 shorelines are utilized in all 9 cases, with RXT identified as the best method for 3 beaches, LXT identified as the best method for 4 beaches, and S-T identified as the best method for 2 beaches. RXT, LXT, and S-T have the lowest AICc scores in these situations because the equation for AICc fails. Burnham and Anderson (2002) present the AICc equation as:

$$AICc = N\log(RSS/N) + \frac{2KN}{(N-K-1)} \quad (4)$$

Where *RSS* is the residual sum of squares, *N* is the sample size, and *K* is the number of parameters. The value of the first half of equation (4) decreases as RSS decreases. The second half of equation (4) is a correction factor that increases as the number of parameters increase. This factor should always be positive in order to penalize the use of extra parameters. Thus, AICc is a tradeoff between the goodness of fit and the number of parameters, preventing over- or under-fitting of the data. However, if $K \geq N$, the correction factor in equation (4) is a large negative number. As the best-fit model is the lowest AICc score, a large negative number leads to nonsense results. This situation occurs for LXT, RXT, and S-T when ≤ 3 shorelines exist. LX, RX, EX, and EXT are not affected by this issue because *K* is never greater than or equal to *N*.

If the beach has ≤ 3 shorelines, LXT, RXT, and EXT should not be used. These methods identify whether rates are changing with time at each transect (Figure 6). Fitting a quadratic model on 3 points is over-fitting, so non-acceleration methods should be used if only 3 shorelines exist.

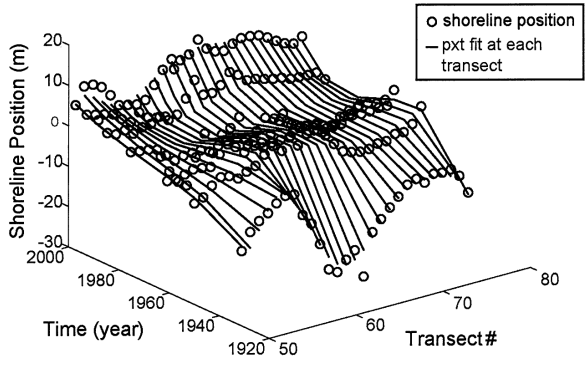

Fig. 6. Rates Changing With Time at Each Transect (PXT)

CONCLUSIONS

Overall, predictions from RX, LX, and EX are insignificantly different from each other and are recommended for use in hazard zone predictions. Predictions using polynomials without lower-order terms are consistent with predictions using all lower-order terms. LXT, RXT, and EXT appear to need more research. Ideally, the more shorelines that are available, the better the hazard predictions are. If, however, beaches have hardened structures without any backshore present in front of the structures, then only post-hardened shorelines should be used to predict future hazard zones. If there are ≤ 3 shorelines, the AICc equation does not function properly for LXT, RXT, EXT, and S-T. Both pocket beaches and open-system beaches identify acceleration methods at a higher percentage than non-acceleration methods. Still, pocket beaches identify non-acceleration methods at a higher proportion than open-system beaches possibly due to less variability in sediment transport in pocket beaches.

ACKNOWLEDGEMENTS

Funding for this research was provided by the U.S. Geological Survey, the University of Hawaii Sea Grant College of the National Oceanographic and Atmospheric Administration, Maui County Planning Department, Kauai County Planning Department, and the City and County of Honolulu. We thank members of the University of Hawaii Coastal Geology Group for their assistance.

REFERENCES

Burnham, K. P., and Anderson, D. R. (2002). *Model Selection and Multimodel Inference*, Springer-Verlag, New York.

Crowell, M., Leatherman, S. P., and Buckley, M. K. (1993). "Shoreline Change Rate Analysis: Long Term Versus Short Term Data." *Shore and Beach*, 61(2), 13-20.

Douglas, B. C., and Crowell, M. (2000). "Long-term Shoreline Position Prediction and Error Propagation." *Journal of Coastal Research*, 16(1), 145-152.

Eversole, D., and Fletcher, C. H. (2003). "Longshore Sediment Transport Rates on a Reef-Fronted Beach: Field Data and Empirical Models Kaanapali Beach, Hawaii." *Journal of Coastal Research*, 19(3), 649-663.

Fenster, M. S., Dolan, R., and Elder, J. F. (1993). "A New Method for Predicting Shoreline Positions from Historical Data." *Journal of Coastal Research*, 9(1), 147-171.

Fletcher, C. H., Rooney, J. J. B., Barbee, M., Lim, S.-C., and Richmond, B. M. (2003). "Mapping Shoreline Change Using Digital Orthophotogrammetry on Maui, Hawaii." *Journal of Coastal Research*, Special Issue 38, 106-124.

Frazer, L. N., Genz, A. S., and Fletcher, C. H. (in review). "Toward Parsimony in Shoreline Change Prediction (I): New Methods." *Journal of Coastal Research*.

Galgano, F. A., Douglas, B. C., and Leatherman, S. P. (1998). "Trends and Variability of Shoreline Position." *Journal of Coastal Research*, Special Issue 26, 282-291.

Genz, A. S., Fletcher, C. H., Dunn, R. A., Frazer, L. N., and Rooney, J. J. (in press). "The Predictive Accuracy of Shoreline Change Rate Methods and Alongshore Beach Variation on Maui, Hawaii." *Journal of Coastal Research*, 23.

Genz, A. S., Frazer, L. N., and Fletcher, C. H. (in review). "Toward Parsimony in Shoreline Change Prediction (II): Applying Statistical Methods to Real and Synthetic Data." *Journal of Coastal Research*.

Goldberg, D. E. (1989). *Genetic Algorithms in Search, Optimization, and Machine Learning*, Addison-Wesley Publishing Company, Reading.

Makai Ocean Engineering and Sea Engineering. (1991). *Aerial Photograph Analysis of Coastal Erosion on the Islands of Kauai, Molokai, Lanai, Maui and Hawaii*, Office of State Planning Coastal Zone Management Program, Honolulu, HI.

Morton, R. A. (1991). "Accurate Shoreline Mapping: Past, Present, and Future." Coastal Sediments '91, 997-1010.

Rooney, J. J. B., and Fletcher, C. H. (2005). "Shoreline Change and Pacific Climatic Oscillations in Kihei, Maui, Hawaii." *Journal of Coastal Research*, 21(3), 535-547.

Rooney, J. J. B., Fletcher, C. H., Barbee, M., Eversole, D., Lim, S.-C., Richmond, B. M., and Gibbs, A. "Dynamics of Sandy Shorelines in Maui, Hawaii: Consequences and Causes." *Coastal Sediments '03 Proceedings*, Clearwater Beach, Florida.

Woodroffe, C. D. (2002). *Coasts Form, processes and evolution*, Cambridge University Press, Cambridge, UK.

Zhang, K., Douglas, B., and Leatherman, S. (2002). "Do Storms Cause Long-Term Beach Erosion along the U.S. East Barrier Coast?" *Journal of Geology*, 110(4).

LINKING COASTAL EVOLUTION AND SUPER STORM DUNE EROSION FORECASTS

L.M. van der Burgh[1,5], K.M. Wijnberg[1,5], S.J.M.H. Hulscher[1,5], J.P.M. Mulder[1,2,5], M.van Koningsveld[3,4,5]

1. University of Twente, P.O. Box 217, 7500 AE Enschede, The Netherlands. L.m.vanderburgh@ctw.utwente.nl, K.m.wijnberg@ctw.utwente.nl S.j.m.h.hulscher@ctw.utwente.nl, J.p.m.mulder@ctw.utwente.nl
2. Rijkswaterstaat, National Institute for Coastal and Marine Management, P.O. Box 20907, 2500 EX The Hague, The Netherlands. j.p.m.mulder@rikz.minvenw.nl
3. WL|Delft Hydraulics, Marine and Coastal Management, P.O. Box 177, 2600 MH Delft, The Netherlands mark.vankoningsveld@wldelft.nl
4. Delft University of Technology, Department of Civil Engineering, P.O. Box 5048, 2600 GA Delft, The Netherlands m.vankoningsveld@tudelft.nl
5. NCK, National Centre for Coastal Research, P.O. Box 177, 2600 MH Delft, The Netherlands

Abstract: To assess the long-term safety of a dune-protected coastal area, models are needed for forecasting both long-term coastal evolution and dune erosion due to the occurrence of a super storm. In long-term model forecasts, however, information on dune shape is lost. Explorative calculations show that the output of the event-scale dune erosion model is quite sensitive to the dune height. For a given super storm, a higher dune leads to a larger forecasted erosion volume, but to a less land inward position of the erosion line (the line that indicates how far erosion is expected to reach land inward). Clearly, a solution should be found for adding information on realistic dune shapes to the long-term coastal evolution forecast. EOF decomposition of observed dune profiles provides simple but realistic dune shape functions that could be used to redistribute forecasted dune volumes into realistic dune shapes.

INTRODUCTION

Dunes are part of the coastal system which need to be considered in the scope of

coastal management and engineering practices (Saye et al. 2005), since they form an important link in the coastal sediment budget (Arens & Wiersma 1994). Arens & Wiersma (1994) show that, for the Dutch coast, on a yearly basis, an average of 3 – 3.5 m^3/m to a maximum of $25m^3/m$ sediment is transported into the dunes. In addition, in the Netherlands, dunes protect large parts of the coast during storms (see figure 1, 'soft defenses'). However, dunes are often neglected in (long-term) coastal modeling exercises.

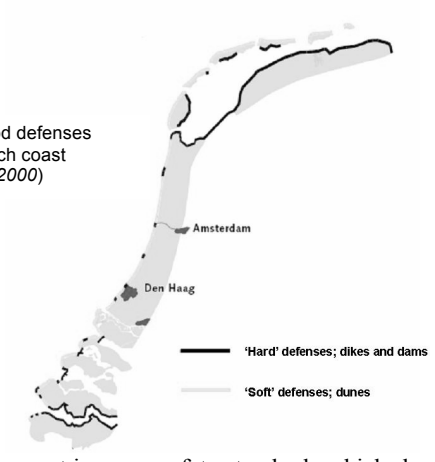

Figure 1. Flood defenses along the Dutch coast *(From: CPD, 2000)*

The Dutch government imposes safety standards which should be met by all sea defenses. Along the Holland coast, flood defenses should be able to withstand a 1:10.000 storm, i.e. conditions corresponding to a storm with a probability of occurrence of once per 10.000 years. In the future however, rising sea-level and more frequent and severe storm conditions might jeopardize the safety provided by the flood defenses.

In 1984, the Technical Advisory Committee for Flood Defenses (TAW 1995) published a guideline on how to test safety of the Dutch dune areas. To assess the current 'strength' provided by the dunes, a method was designed to calculate dune erosion as a result of a storm event. This method is based on the DUROS (DUne eROSion) model. From the dune erosion calculations, the position of erosion lines are determined (figure 2). Erosion lines indicate how far erosion might reach land inward as a result of occurrence of an extreme storm event. Figure 2 illustrates that if a 1:10.000 super storm were to occur today, the land seaward of the solid line would be eroded.

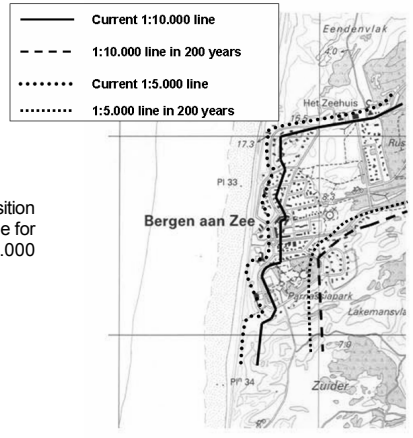

Figure 2. Present and expected future position of erosion lines for a Dutch sea-side village for super storms with a 1:10.000 and 1:5.000 probability of occurrence
(From: RIKZ, 2005)

However, sustainable coastal zone management not only asks for the current dune strength to be known, but also how this dune strength evolves through time, in order to anticipate to future developments. Until recently, long-term safety forecasts involved running the DUROS model with an unchanged beach and dune configuration, but with a higher mean sea level. The dashed line in figure 2 illustrates how the erosion line might shift landward according to this approach. However, evolving morphology might affect the position of erosion lines in the future as well. Therefore, it is of importance to include morphological behavior in long-term safety assessment.

In Dutch coastal management practice, a behavior oriented model called PONTOS is currently used to forecast long-term evolution of the Holland coast (figure 7). In this model, dune morphology is highly schematized, and therefore does not provide the spatially detailed information required for a DUROS calculation.

Apparently, there is a 'gap' between the model that calculates the effects of low-frequency, high-magnitude events (DUROS) and the model that is designed to forecast long-term coastal evolution due to high-frequency, low magnitude processes (PONTOS).

In this paper, we will explore how the 'lost morphological information' can be reintroduced into the PONTOS forecast, in order to make the long-term model forecast suitable for DUROS calculations to obtain erosion line positions (see figure 3).

In order to determine the effect of extreme events 50 to 200 years from now, we need to take into account the temporal and spatial evolution of morphological characteristics of the coastal cross-shore profile. More specifically, we need to consider that part of the profile which is needed for DUROS, i.e. from ca. -2m Dutch Ordnance Level to the dune area.

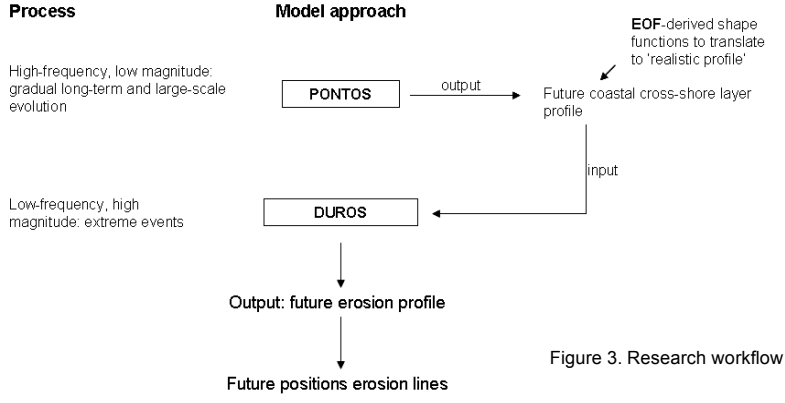

Figure 3. Research workflow

This paper is organized as follows: The next two sections explain the concepts of the DUROS model and the PONTOS model, followed by a section which describes the study area. In the following section, we examine the sensitivity of dune erosion volumes and erosion line positions to the shape of the dune area. Thereafter, we focus on Empirical Orthogonal Function (EOF) decomposition of dune topography measurements. EOF provides realistic shape characterizations for the dunes. The shape functions obtained from EOF may be used to translate the PONTOS dune schematizations to a realistic set of dune profiles.
The gained knowledge might aid in determining the 'optimal' dune configuration to reduce the effects of super storms.

PRESENT SAFETY ASSESSMENT OF DUTCH DUNES: THE DUROS MODEL

DUROS is a cross-shore model that, for pre-defined conditions, calculates the amount of dune erosion as a result of the occurrence of an extreme storm (Van de Graaff 1984; TAW 1995). The DUROS model is used in safety assessment of the Dutch dune area (figure 1 and 7). To determine the amount of erosion, it is required to know the position of the cross-shore profile right *before* a storm, since this will determine the extent of erosion of the dune as a result of the storm, and, hence, the safety provided by the dune as a natural defense against flooding of the hinterland, which in the case of the Netherlands is located largely below MSL.

In DUROS, the amount (volume) of dune erosion is a function of (1) the location (position) of the initial cross-shore profile, (2) the maximum wave height and sediment characteristics and (3) the maximum storm surge level. With these parameters, a sediment balance is calculated, which results in the position of the erosion profile. The shape of the erosion profile is assumed to be known, and is a function of the significant wave height and the fall velocity of the dune sand in standing water (see figure 4).

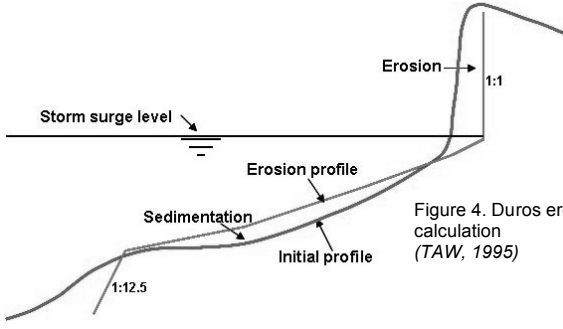

Figure 4. Duros erosion profile calculation *(TAW, 1995)*

The position of the initial profile, rather than the shape of the initial profile, is considered to determine to a large extent the amount of dune erosion (Van de Graaff 1984; TAW 1995). This is because a closed sediment balance in cross-shore direction is assumed. By shifting the erosion profile with respect to the initial profile in such a way that the amount of erosion equals the amount of sedimentation, a closed sediment balance is obtained.

LONG-TERM COASTAL EVOLUTION: THE PONTOS MODEL

The long-term and large-scale evolution of the Holland coast can be simulated by the behavior-oriented PONTOS model (Steetzel & Wang 2003). PONTOS is a physical-mathematical coastline model, in which the coastal cross-section is schematized into five horizontal layers each representing a sediment volume (figure 5). Erosion or sedimentation, modeled per layer, is caused by gradients in the longshore and cross shore sediment transport. PONTOS provides a crude schematization of the cross-shore profile from which a position of erosion lines cannot be obtained. The dune area in PONTOS is represented by one sediment volume layer. This layer is positioned from +3 m with respect to the Dutch Ordnance Level (NAP) to the top of the first dune row.

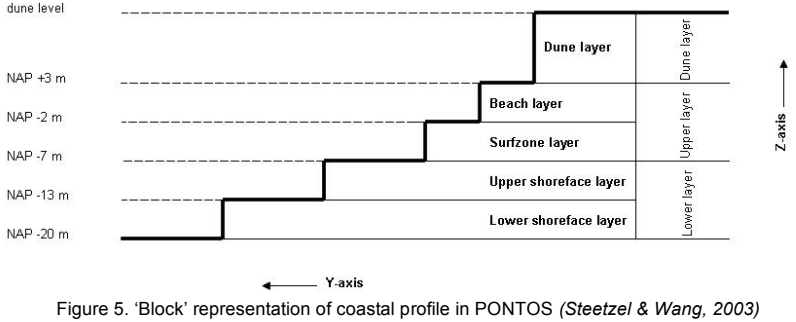

Figure 5. 'Block' representation of coastal profile in PONTOS *(Steetzel & Wang, 2003)*

In order to forecast the amount of dune erosion under extreme storm conditions, we need a cross-shore distribution of sediment as input for DUROS, rather than the layer representation of PONTOS. Recent developments to obtain a cross-shore profile from the PONTOS-layers are made by Wang et al. (2006) who transform the layer representation to a smooth profile as follows (see dotted line in figure 6):

1. The cross-shore profile of each layer is replaced by a straight line according to: $y=a_i z+b_i$, for $z_{i+1} \le z \le z_i$ (1)
2. In each layer, mass conservation is guaranteed in accordance with the principles of the PONTOS model.

This profile is then used to perform a dune erosion calculation. This profile is however still highly schematized and does not reflect a 'real' profile shape (compare in figure 6 the dotted line with the smooth line based on Jarkus measurements (Yearly Coastal Surveys).

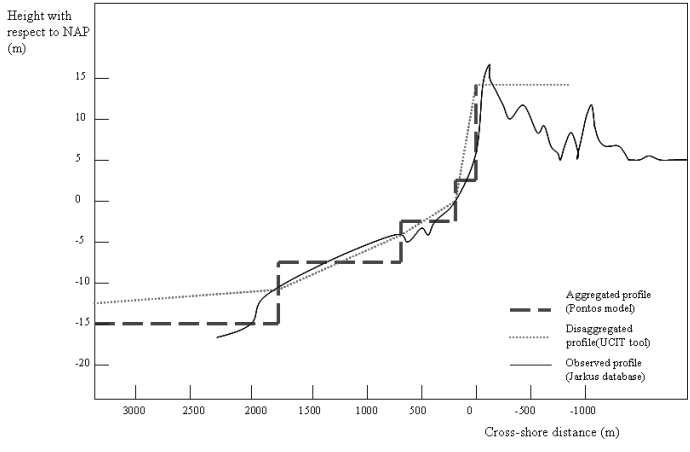

Figure 6. Aggregated profile generated by PONTOS, disaggregated smooth profile and an observed coastal profile by Jarkus data *(Wang et al., 2006)*

DESCRIPTION OF THE STUDY AREA

We use coastal cross-shore data from the coast of Noord-Holland, the Netherlands (figure 7) as input to DUROS to explore the sensitivity of dune erosion to different input profiles. The coastal cross-shore data are obtained from the Jarkus database, which provides year to year measurements of coastal profiles extending from the foredune to app. 1000 m seaward. The distance between the profiles is 200-250 m and there is a total number of about 3000 profiles along the Dutch coast (Guillen et al. 1999). Two Jarkus profiles for the year 2004, viz. transect number 3325 and 4475 (figures 7 and 8) were selected as a first exploration in examining the role of the dune shape on the amount of erosion and position of the erosion line. Transect 3325 is situated close to the coastal town of Bergen aan Zee, whereas transect 4474 is situated near Castricum aan Zee. Hereafter, the transect numbers will be referred

to as the Bergen and Castricum transects. For EOF analysis, 87 profiles from Noord-Holland (also for the year 2004) were used.

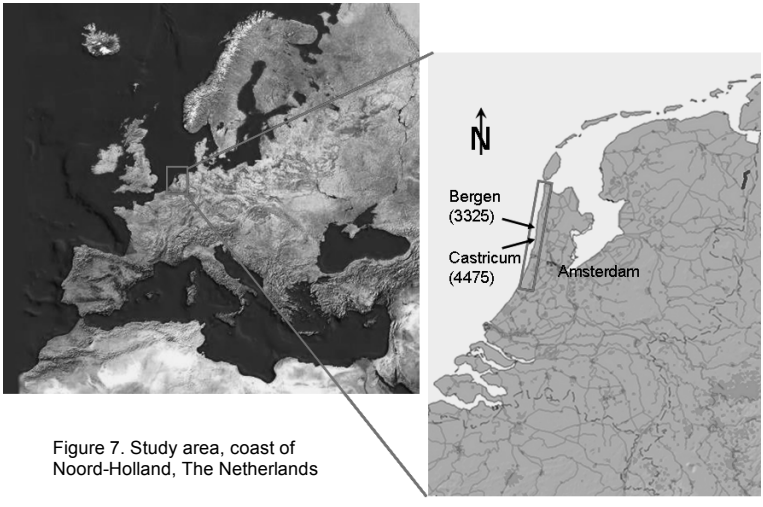

Figure 7. Study area, coast of Noord-Holland, The Netherlands

EFFECT OF DUNE SHAPE ON EROSION VOLUME AND EROSION LINE POSITION

Both the DUROS calculation method and the Jarkus database are embedded in a model environment called UCIT (Universal Coastal Intelligence Toolkit) (Van Koningsveld et al. 2005). For each selected Jarkus transect we can perform a dune erosion calculation, thereby taking into account different forecasting periods, different sea-level rise scenarios as well as user-defined hydraulic conditions, such as storm peak periods and significant wave heights. The selected transects of Bergen and Castricum have different foreshore slopes and the foredunes differ in both transects as well (figure 8). The foredune of the Bergen transect has a height of app. 8 meters, whereas the foredune of the Castricum transect has a height of about 16 meters. This part of the coast of Noord-Holland is intensely used for recreational activities and since most parts of the coast of Noord-Holland are subject to erosion, beach and foreshore nourishments are frequently carried out with positive effects on beach width. The Bergen transect is highly altered by human activity and can be considered an 'artificial' dune (Arens 1994).

Castricum is situated 11.5 kilometers south of Bergen. This transect is in a 'semi-natural' state; sand fences have been placed and marram grass has been planted in order to stabilize the dunes in this area (Arens 1994).

There are no seawalls or groins situated close to the transects which might influence sedimentation or erosion in this area.

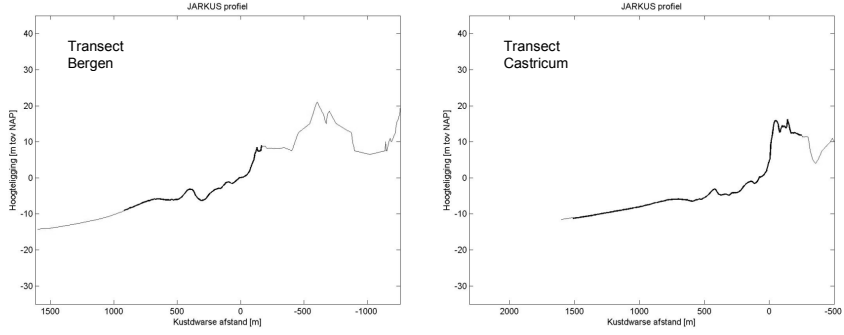

Figure 8. Transects Bergen (3325) and Castricum(4475)

In order to examine the role of dune geometry on the amount and extent of erosion, we performed a model experiment in the UCIT environment for the Bergen and Castricum transects. Each profile was transformed into different hypothetical profiles, varying in height and width, based on a fixed, hypothetical added volume. Figure 9 illustrates two hypothetical profiles for the Bergen transect. We took the +3 m NAP (Dutch Ordnance Level) as the dunefoot position. According to Ruessink & Jeuken (2002), this level roughly corresponds to the break in slope between the beach and the foredune. From this level, we added the artificial dune volume, which we set at 4000 m^3/m, based on expert judgement. We defined the minimum dune width to be 100 m and the maximum dune width to be 500 m. Dune width will be varied in steps of 20 m. According to Volume = width * height, the dune height takes a height belonging to a certain width.

When we plot the different erosion volumes and positions of the erosion lines against the different dune heights (fixed dune volume of 4000 m3/m), we observe in figures 9 and 10 that for the Bergen transect a decreasing dune height leads to a smaller erosion volume, but to a more landward shift of the erosion point position (denoted by R in figure 9). This is because the shape of the erosion profile is fixed, so in order to maintain a closed sediment balance when the shape of the beach and foreshore remain the same, leads to a more landward position of the erosion point if dune height decreases. For the Castricum transect with the same height-width ratios for the dune area as the Bergen transect, similar results are obtained: a decrease in dune height leads to a smaller erosion volume, but to a more landward position of the erosion point. Apparently, the *shape* (height) of the initial dune profile seems to affect to a large extent the dune erosion volume and erosion line position, since a higher dune leads to a higher erosion volume and to a more seaward erosion line position.

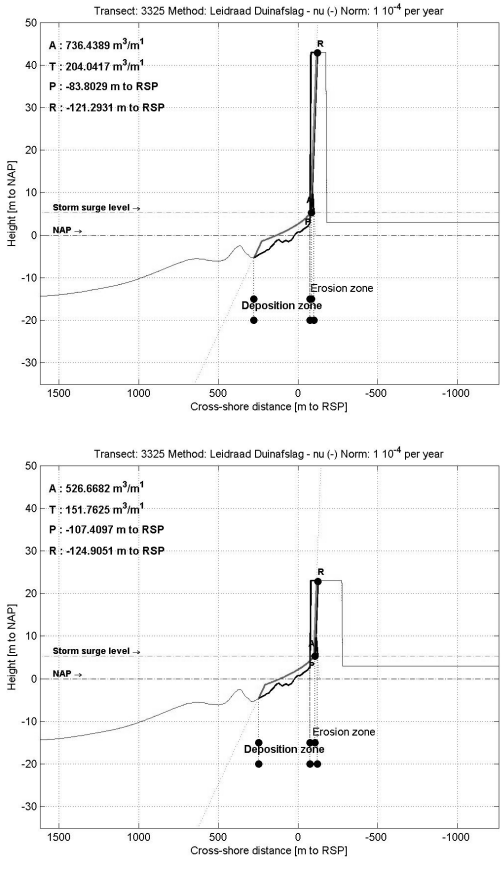

Figure 9. Different erosion volumes and erosion point positions for two hypothetical dune configurations for the Bergen transect
A is the erosion volume
T is an 'extra' erosion volume to account for uncertainties
P is the intersection between the 'new' dunefoot position and the storm surge level
R is the erosion point at the surface

Besides the dune shape, the foreshore configuration also plays a role in the amount of erosion and the position of the erosion point. Figure 10 and table 1 show that although the dune configurations and volumes are identical for both transects, different erosion volumes and erosion line positions arise. A steep foreshore slope 'demands' more sediment from the dunes in order to obtain a closed sediment balance needed for the erosion profile (figure 4).

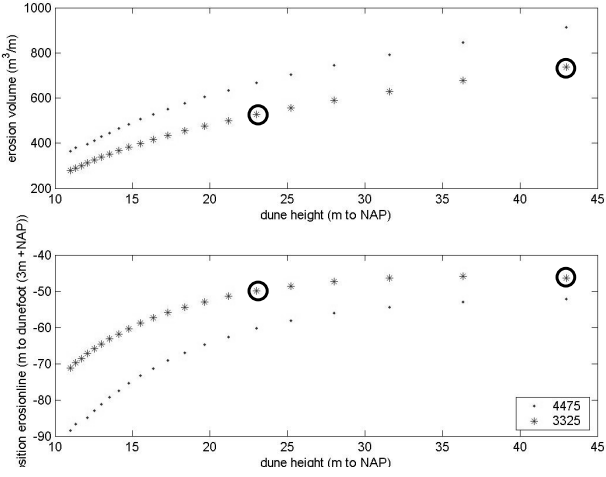

Figure 10. Varying dune heights versus erosion volumes and erosion point positions for Bergen (transect number 3325) and Castricum (transect number 4475). Circles indicate the values of figure 9

Table 1. Erosion volumes and erosion line positions at different hypothetical dune heights for Bergen (3325) and Castricum (4475)

DUNE HEIGHT (M TO NAP)	EROSION VOLUME 4475 (IN M^3/M)	EROSION LINE POSITION 4475 (M TO DUNEFOOT)	EROSION VOLUME 3325 (IN M^3/M)	EROSION LINE POSITION 3325 (M TO DUNEFOOT)
43	912.82	-52.20	736.44	-46.29
36.333	845.89	-53.06	677.01	-45.89
31.571	790.95	-54.48	629.61	-46.37
28	744.29	-56.12	590.31	-47.37
25.222	703.69	-58.19	556.445	-48.59
23	667.52	-60.32	526.67	-49.91
21.182	634.84	-62.59	500.26	-51.41
19.667	604.93	-64.81	476.30	-52.93
18.385	577.33	-67.05	454.32	-54.47
17.286	551.67	-69.05	434.07	-55.82
16.333	527.87	-71.39	415.38	-57.30
15.5	505.51	-73.30	397.87	-58.87
14.765	484.46	-75.33	381.52	-60.33
14.111	464.62	-77.47	366.13	-61.92
13.526	445.87	-79.25	351.64	-63.18
13	428.04	-81.16	337.95	-64.60
12.524	411.12	-83.00	324.96	-65.96
12.091	395.00	-84.97	312.63	-67.22
11.696	379.62	-86.65	300.92	-68.67
11.333	364.97	-88.48	289.68	-69.8
11	-	-	279.05	-71.20

Since profile shape affects the amount of erosion and the position of erosion lines, the question arises whether we can find a simple but realistic representation of profile shape to be implemented into long-term morphological model forecasts (PONTOS). To investigate this, we first concentrate on characterization of the dune profile. We propose to use Empirical Orthogonal Function (EOF) to extract shape functions which characterize dune shape.

EMPIRICAL ORTHOGONAL FUNCTION (EOF) ANALYSIS

EOF analysis provides a method to reduce the number of data variables required to represent our data set (Aubrey 1979). With EOF we attempt to reveal a simple spatial structure that is present within the dune profiles.

If we consider the dune profiles – which extend from the dunefoot position (origin) towards a 200 m landward position - along a 22 km long stretch of the coast of Noord-Holland , we obtain a mean profile shape indicated figure 11 (upper panel). This part of the coastal cross-shore profile corresponds to the dune layer in the PONTOS model, viz. from NAP + 3 m to the dune top. The mean dune top is situated at about NAP + 16 meters, but there is a standard deviation of approximately 4 meters (lower panel figure 11).

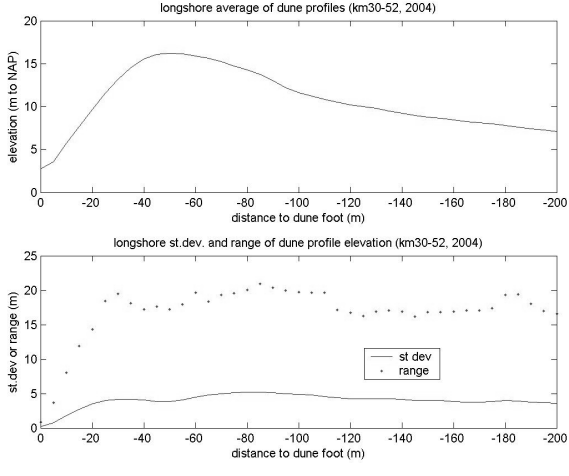

Figure 11. Mean cross-shore dune profile of Noord-Holland and standard deviation and range of the mean profile

The standard deviation does not provide information on how actual deviations from the mean profile are related in space. EOF's describe how the dune profiles differ from the mean profile in terms of orthogonal shape functions (for instance the sine and cosine functions). Since we consider 87 profiles along the coast, each cross-shore position (with respect to distance in meters to the dunefoot) has different heights in longshore direction. Therefore, each cross-shore position has a variation

around the mean profile, which can be expressed in terms of variance (or standard deviation, lower panel in figure 11). The first EOF (upper panel, figure 12) explains 43% of this observed variance. The second eigenfunction explains 24% of the observed variance.

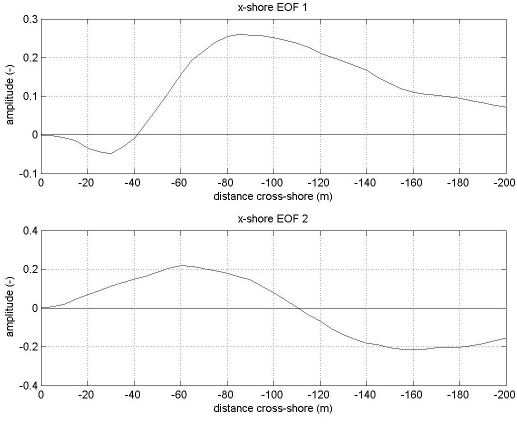

Figure 12. First and second shape functions of the selected profiles from transect 3000 to 5200

Thus, the first two shape functions explain two-third of the observed variance, which means that the shape functions describe to a large extent the variation we observe in the mean profile.

Potentially, the shape functions can be used to remodel the PONTOS dune layer into a (more) natural shape, on which a dune erosion calculation can be performed in DUROS.

It is still premature to assign a physical explanation for these observed variations, but variations are possibly related to the absence or presence of vegetation, sediment supply and management practices (Saye et al. 2005).

DISCUSSION

This research shows the first steps towards examining the importance of the dune/beach configuration in calculating erosion volumes and position of erosion lines. We want to stress the fact that the dune volumes we considered are highly schematized, without accounting for a width-height-slope relationship (Hesp & Hastings 1998). In reality, dune height cannot continue to grow without a corresponding increase in width, although it appears that especially dune height is important in the DUROS calculations. Different dune slopes will also affect the amount of erosion and position of erosion lines, since it will affect the closed sediment balance needed for DUROS. Also, dune slope affects dune stability, which implies that certain dunes might be more prone to erosion than other dunes.

Since the foreshore configuration also plays a role in the erosion calculations, examining a beach-dune morphological relationship might provide additional insight with regard to the state of the dune and a possible trend in dune evolution, i.e. eroding or accreting (Saye et al. 2005).

For the EOF analysis, we have considered all transects within a 22 km long coastal stretch irrespective of differences in dune type such as (1) the developmental stage of the dune, (2) aeolian processes at work (erosion or deposition) and (3) effects of dune management (human-altered vs. natural dunes) (Arens & Wiersma 1994). Whether more refinement in dune shape functions is actually needed is not clear yet. Applying EOF analysis to subsets of dune profiles grouped by dune type, will reveal whether these differences are reflected in differently shaped dune shape-functions or not.

CONCLUSIONS

This research illustrates the importance of dune configuration in dune erosion calculations. For a given storm, dune configuration determines to a large extent the erosion volume and position of erosion lines. Higher dunes result in a more seaward position of erosion lines, but result in higher erosion volumes compared to a lower dune. In addition, it also appeared that foreshore configuration matters in the erosion calculations.

We have proposed EOF analysis as a tool to characterize the dune shape in order to reintroduce the 'small scale information' to long-term forecasts such that a dune erosion calculation in DUROS is possible. It is thus a method to bridge the cap between a small scale, event-based model and a long-term, large scale model.

ACKNOWLEDGEMENTS

The Delft Cluster project DC 05.20 North Sea and Coast is acknowledged for facilitating the exchange of Van der Burgh with WL|Delft Hydraulics.
This research is financed by the Earth and Life Sciences Council (ALW) of the Netherlands Organisation for Scientific Research (NWO) through the LOICZ research program.

REFERENCES

Arens, S.M., and Wiersma, J. (1994). "The Dutch Foredunes: Inventory and Classification," *Journal of Coastal Research*, 10, 189-202

Aubrey, D.G. (1979). "Seasonal Patterns of Onshore/Offshore Sediment Movement," *Journal of Geophysical Research* 84(10), 6347-6354

CPD. (1990). "Kustverdediging na 1990, 1st Coastal Policy Document," Ministerie van Verkeer en Waterstaat, 65 p.

CPD. (2000). "Traditie, Trends en Toekomst, 3rd Coastal Policy Document," Ministerie van Verkeer en Waterstaat, 122 p.

Guillen, J, Stive, M.J.F., Capobianco, M. (1999). "Shoreline evolution of the Holland coast on a decadal scale," *Earth Surface Processes and Landforms* 24,

517-536

Hesp, P.A., and Hastings, K. (1998). "Width, height and slope relationships and aerodynamic maintenance of barchans," *Geomorphology* 22, 193-204

RIKZ. (2005). "Hoofdrichtingen voor risicobeheersing in kustplaatsen," Tech. Rep. RIKZ/2005.021, Ministerie van Verkeer en Waterstaat, 80 p.

Ruessink, B.G., and Jeuken, M.C.J.L. (2002). "Dunefoot dynamics along the Dutch coast," *Earth Surface Processes and Landforms* 27, 1043-1056

Saye, S.E., van der Wal, D., Pye, K., Blott, S.J. (2005). "Beach-dune morphological relationships and erosion/accretion: An investigation at five sites in England and Wales using LIDAR data," *Geomorphology* 72, 128-155

Steetzel, H., and Wang, Z.B. (2003). "Development and application of a large-scale morphological model of the Dutch coast, phase 2: Formulation and application of the PONTOS-model version 1.4," Tech. Rep. Alkyon and WL|delft hydraulics, prepared for the National Institute for Coastal and Marine Management/Rijkswaterstaat-RIKZ

TAW. (1995). *"Basisrapport Zandige Kust,"* Technische Adviescommissie voor de Waterkeringen, 507 p.

Van de Graaff, J. (1984). "Probabilistische methoden bij het duinontwerp, Achtergronden van de TAW-Leidraad 'Duinafslag'," Tech. Rep. Delft University of Technology, 83 p.

Van Koningsveld, M., Stive, M.J.F., and Mulder J.P.M. (2005). "Balancing Research Efforts and Management Needs. A Challenge to Coastal Engineering", *Proceedings of the 29th Conf. of Coast. Eng.* Lisbon, Portugal, 2004, 3136-3148

Wang, Z.B., Steetzel, H., van Koningsveld, M. (2006). "Effecten van verschillende scenario's van kustonderhoud, Resultaten lange-termijn simulaties morfologische ontwikkeling Nederlandse Noordzeekust," Tech. Rep. WL|Delft Hydraulics & Alkyon, 102 p.

CHARTS-ENABLED DATA FUSION FOR COASTAL ZONE CHARACTERIZATION

Jennifer M. Wozencraft[1], Christopher L. Macon[2], W. Jeff Lillycrop[3]

1. Joint Airborne Lidar Bathymetry Technical Center of Expertise, U.S. Army Corps of Engineers Mobile District, 7225 Stennis Airport Road, Suite 100, Kiln, MS 39556, USA. jennifer.m.wozencraft@usace.army.mil.
2. Joint Airborne Lidar Bathymetry Technical Center of Expertise, U.S. Army Corps of Engineers Mobile District, 7225 Stennis Airport Road, Suite 100, Kiln, MS 39556, USA. christopher.l.macon@usace.army.mil.
3. Joint Airborne Lidar Bathymetry Technical Center of Expertise, U.S. Army Corps of Engineers Engineer Research and Development Center, 7225 Stennis Airport Road, Suite 100, Kiln, MS 39556, USA. jeff.lillycrop@usace.army.mil.

Abstract: The Compact Hydrographic Airborne Rapid Total Survey (CHARTS) system collects lidar and hyperspectral data for the U.S. Army Corps of Engineers (USACE) National Coastal Mapping Program. CHARTS is owned by the U.S. Naval Oceanographic Office and operated jointly with the USACE through the Joint Airborne Lidar Bathymetry Technical Center of Expertise. Simultaneous collection and shared geo-referencing enables fusion of the two data types into high-level information products that are used to support decision-making at USACE coastal projects. New products resulting from data fusion research currently coming online are bathymetric laser bottom reflectance images, atmospherically-corrected image mosaics, and hyperspectral final bottom images. All of these products are input for automated classification algorithms that generate physical and environmental characterizations of the coastal zone.

INTRODUCTION

Airborne laser and imagery data collected by the Compact Hydrographic Airborne Rapid Total Survey (CHARTS) system are the foundation of the U.S. Army Corps of Engineers (USACE) National Coastal Mapping Program (NCMP). USACE Headquarters funds the NCMP to support planning, engineering, construction, operation and maintenance activities in the coastal zone, like navigation and flood protection projects, and to support

regional sediment management practices. The NCMP is designed to provide high-resolution lidar and imagery data for U.S. shorelines on a recurring basis. At the current level of funding, one survey cycle, including the U.S. Gulf, Atlantic, and Pacific Coasts, the U.S. shorelines of the Great Lakes, and the shorelines of the five largest Hawaiian Islands, is projected to take 8 years. Since its inception in spring 2004, NCMP has completed mapping on the Gulf and Atlantic Coasts, from Mississippi to Maine, and initiated work in the Great Lakes.

The CHARTS sensor suite includes an Optech SHOALS-3000T20 and an Itres CASI-1500 (Wozencraft and Millar 2005). The SHOALS-3000T20 is itself an integrated sensor containing a 3,000 pulse-per-second (pps) bathymetric laser, a 20,000 pps topographic laser, and a digital RGB camera that records one frame every second. The CASI-1500 is a programmable pushbroom hyperspectral imager capable of collecting from 4 to 288 spectral bands over the spectral range from 375 to 1050 nm, at pixel sizes ranging from 20 cm to 5 m depending on system configuration (Wozencraft and Lillycrop 2006). Either laser can be operated simultaneously with the RGB camera and hyperspectral imager, but the lasers are operated separately. CHARTS is owned by the U.S. Naval Oceanographic Office (NAVOCEANO) and operated jointly with the USACE through the Joint Airborne Lidar Bathymetry Technical Center of Expertise (JALBTCX).

CHARTS collects all four data types for the NCMP. Bathymetric lidar is collected from the shoreline to 1 km offshore, or to extinction, whichever occurs first. Bottom determination using bathymetric lidar is limited by water clarity. The lidar can discriminate depths 2-3 times the visible depth of the water column. Topographic lidar is collected from the shoreline to 0.5 km onshore. RGB imagery is collected automatically whenever the lasers fire. Hyperspectral imagery is collected concurrently with both the bathymetric and topographic laser data, but the sensor is operated independently of the laser system from its own operator console.

At the JALBTCX, the high-resolution lidar and imagery data collected for NCMP are analyzed and processed to higher-level information products in GIS format. The products are designed to facilitate the use of the large regional datasets in coastal studies and decision-making processes at USACE projects. The current product line includes bathymetric/topographic Digital Elevation Models (DEMs), RGB orthomosaics, NAVD88 shorelines, building footprints, and bare earth grids. New products coming online in the current year include reflectance images from the bathymetric laser, atmospherically-corrected hyperspectral orthomosaics, and final bottom images from the hyperspectral data. These products are the result of years of research and development efforts in data fusion at the JALBTCX.

JALBTCX activities in data fusion began in the mid-1990's during the field trials of the original SHOALS system (Lillycrop and Estep 1995; Estep et al. 1994). CASI overflights of the SHOALS field test area provided lidar elevation and hyperspectral data for researchers to use in generating a bottom type image in Sarasota Bay, Florida. Work

continued in this area with pilot studies in Laguna Madre, Texas (Estep 1998), Biscayne Bay, Florida (Wozencraft et al. 2002), and Kaneohe Bay, Hawaii (Wozencraft et al. 2003). In 2005, JALBTCX specified an upgrade to the CHARTS sensor that included integration of a hyperspectral sensor with the SHOALS instrument and foundation data fusion software. Currently, JALBTCX is co-sponsoring a 3 year contract with NOAA through the National Ocean Partnership Program (NOPP) to further develop the foundation software for improved bottom classification and to move data fusion techniques onto the land. JALBTCX is in the second year of development on a new lidar and imaging sensor suite called the Coastal Zone Mapping and Imaging Lidar (CZMIL). The goal of the CZMIL project is to produce a state-of-the-art optical system designed for accurate elevation measurement and environmental characterization. The current NCMP product line was developed from a system designed for depth discrimination. CZMIL provides an opportunity to design a system and processing software suite optimized for generation of all the NCMP data products.

This paper will outline CHARTS characteristics that make it an ideal platform for sensor fusion work, describe products coming online for the next field season of the NCMP in spring and summer 2007, and introduce ongoing development efforts focusing on fusing the aforementioned products at the pixel and image level to achieve high-accuracy classifications of the coastal zone.

CHARTS AND DATA FUSION

Data fusion in the context of CHARTS surveys is any combination of data from the active laser system and passive RGB and hyperspectral image systems. Three aspects of the CHARTS system enable advances in data fusion work that have been unattainable in the past. First, simultaneous operation of the laser and image systems eliminates assumptions regarding any temporal disparity between the data collections. Elevations, water column properties, and bottom reflectance derived from the laser measurements coincide nearly simultaneously with collection of the passive image data. The pointing angles of the individual instruments result in a small temporal shift in the data collection of laser and image data at each geographic location (Tuell et al. 2005a). The CASI-1500 looks directly nadir, while both lasers point 22 degrees forward of nadir. This design aspect improves water surface and target detection capability of the bathymetric laser, and reduces the dynamic range of the signal returning to the bathymetric receivers (Guenther et al. 2000). The bathymetric laser pulses are positioned on the water surface using two scanning mirrors to maintain a constant incidence angle on the water surface. The action of the dual mirrors results in a semi-circular pattern of laser spots on the water surface. When the topographic laser is firing, one mirror remains fixed, resulting in a saw-tooth pattern of the laser spots on the ground.

Second, the sensors have similar, very high spatial resolutions. The bathymetric laser is programmable from a 2- to 5-meter grid and the topographic laser from a 1- to 2-meter grid. For the topographic laser the spot spacing is largely determined by flying height. The hyperspectral imager is also programmable, with a trade-off between spectral and spatial resolution (Wozencraft and Lillycrop 2006). For bathymetric data collection, or

collection over water, the hyperspectral imager is set for an integration time of 30 milliseconds, which results in on-ground pixel size near 2 m. For topographic laser collections, the CASI-1500 is set for 16 millisecond integration time, which results in on-ground pixel size near 1 m. The similarity in spatial resolution reduces the generalization, or sometimes oversampling that occurs to bring one dataset to the resolution of the other. The high spatial resolution of both datasets enables characterization at the shoreline, where large pixel sizes often preclude analysis because land corrupts analysis of water pixels and vice-versa.

Third, the laser and hyperspectral instruments both sit on a rigid optical plate above the view window of the aircraft. As such, the hyperspectral data are georeferenced using the same positioning and orientation data stream used to position the laser data. There is no ambiguity regarding datum or projection of the two datasets. Figure 1 shows a view of the installation from immediately outside the aircraft door (a), and from underneath the aircraft (b). The rigid optical plate is labeled in both views, while the sensors are shown in Figure 1(a) and their view windows through the plate in Figure 1(b).

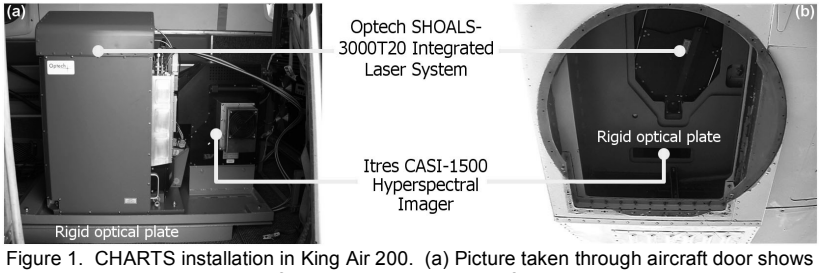

Figure 1. CHARTS installation in King Air 200. (a) Picture taken through aircraft door shows sensors. (b) Picture taken from underneath the aircraft shows sensor view windows.

OPERATIONAL PRODUCTS

Products moving from research and development to operations this year are bathymetric laser bottom reflectance images, atmospherically-corrected hyperspectral image mosaics, and hyperspectral final bottom images. Bathymetric laser bottom reflectance images, or SHOALS bottom reflectance images, are derived solely from the lidar waveform. Atmospherically-corrected hyperspectral image mosaics are a data fusion product in that the mosaicking process uses a DEM created from concurrently collected lidar data to position the pixels in projected map space. Both of these data products, and some intermediate products not designed for release, are inputs for the formation of a data fusion product called hyperspectral final bottom images.

Bathymetric laser bottom reflectance images at 532 nanometers, which is the wavelength of the SHOALS bathymetric laser, are derived from the bathymetric lidar waveform, or the digitized electrical signal generated by photons returning to receivers in the aircraft. These images are similar to topographic lidar intensity images and SHOALS psuedoreflectance images, with one important distinction. To generate bathymetric laser bottom reflectance images, the two receivers in the SHOALS system must be

radiometrically calibrated (Kopilevich et al. 2005). The calibration relates digital counts output from the receivers to input optical power from the target. Reflectance of a target is derived through the lidar equation. Reflectance is an inherent optical property of an object not subject to ambient light conditions, output laser power, laser incidence angle, or other measurement parameters. Topographic lidar intensity images, and SHOALS pseudoreflectance images (Tuell and Park 2004) do not utilize radiometrically-calibrated receivers, so intensity and pseudoreflectance of an object may vary from flightline to flightline and day to day. Intermediate products derived from the lidar data and waveforms as part of this process are SHOALS depth images, images of $a+b_b$, a measure of absorption and backscattering in the water column, at 532 nanometers, and images of water column reflectance at 532 nanometers. Bathymetric laser bottom reflectance images are generated using the Optech, Incorporated, SHOALS Ground Control System and the Optech International Rapid Environmental Assessment (REA) processor. Descriptions of SHOALS radiometric calibration and estimation of bottom reflectance from bathymetric lidar waveforms, see Tuell et al. (2005b).

An example of a bathymetric laser bottom reflectance image is shown in Figure 2. The bathymetric lidar data were collected as a demonstration of capability at Portsmouth Harbor, New Hampshire, in October 2005. Figure 2 (a) shows a true color image, or the red, green and blue bands, extracted from 36 bands of hyperspectral imagery collected concurrently with the lidar data. The overlay in Figure 2(b) is the bottom reflectance image. The range of reflectance values represented by the overlay is 0 to 0.2, where brighter colors have the highest reflectance. The gap in the bottom reflectance image at the shore is caused by an inability of the algorithms to estimate $a+b_b$, and therefore bottom reflectance, in shallow waters. This is an area of ongoing research.

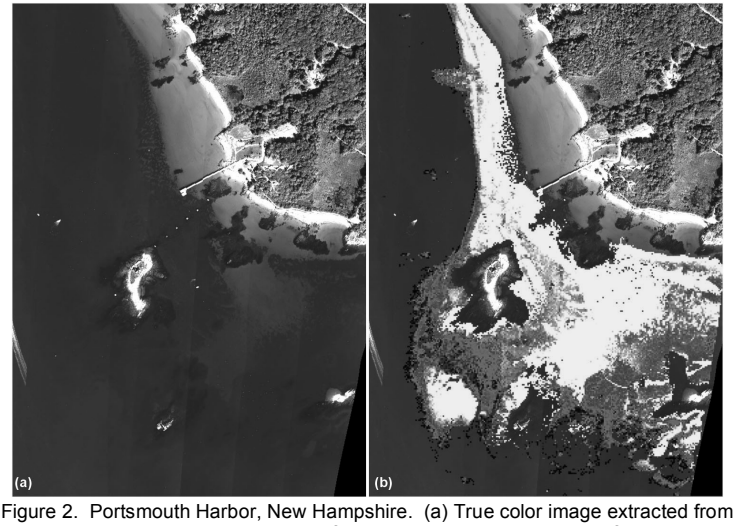

Figure 2. Portsmouth Harbor, New Hampshire. (a) True color image extracted from hyperspectral imagery. (b) Bottom reflectance overlay. Values range from 0 to 0.2.

Atmospherically-corrected hyperspectral image mosaics are created using raw CASI-1500 imagery, navigation data from SHOALS data processing, a lidar DEM, and some ancillary information about the weather and flight parameters, like visibility, flight direction, and collection time. The raw CASI imagery is first corrected to at-sensor radiance using a laboratory radiometric calibration and Itres standard processing software. The at-sensor radiance image strips are processed in two ways depending on whether the flight is over land or water. CASI imagery collected over land is atmospherically corrected using the Tafkaa6s atmospheric correction model developed at the U.S. Naval Research Laboratory (Gao et al. 1993). This model converts at-sensor radiance to reflectance by removing the effect of the atmosphere on light traveling from the sun to the image scene, and from the image scene to the aircraft. Like the bathymetric laser bottom reflectance images, the values of atmospherically-corrected hyperspectral image pixels are reflectance of the objects in the scene, regardless of ambient light conditions or image viewing geometry. Itres standard processing routines are used to combine the atmospherically-corrected image strips, the navigation file generated from the SHOALS system and ground station raw GPS data, and the lidar elevation DEM into an orthomosaicked image product.

Figure 3 shows three stages in the process to create an atmospherically-corrected hyperspectral image mosaic over land at Wells Harbor, Maine. Figure 3(a) are radiometrically corrected CASI image strips, shown as they were flown in flightlines with opposing directions. Figure 3(b) shows a color-scaled DEM created from concurrently collected lidar elevation data. Figure 3(c) shows the final atmospherically-corrected hyperspectral image mosaic. Figure 4 shows an example of at-sensor radiance (a) and reflectance (b) images from Seabrook Harbor, New Hampshire. These image data were collected over three days. Some data were collected in the late afternoon when light conditions change rapidly. In Figure 4(a) the differences in illumination from day to day and during a single flight are visible as differences in brightness across the image. In the atmospherically-corrected, or reflectance image (Figure 4b) these differences have been removed. Based on the inundation of the channels through the wetland, it is evident that the left side of the image was also collected at a different stage of tide than the right.

Path length radiance bias is removed from CASI imagery collected over water using the Optech International REA processor prior to atmospheric correction. Atmospheric correction for images over water is accomplished using Tafkaa_tabular (Montes et al. 2001), because Tafkaa6s cannot correct for the specular reflection of the air-water interface (Montes et al. 2004). Following atmospheric correction, the Optech REA processor removes sun glint from the water surface. Itres standard processing software is used to geocorrect the CASI imagery in a method similar to that described for the hyperspectral mosaic product, but each flight line is placed into its own image and a constant elevation is used in place of the lidar DEM. Finally, the Optech REA processor Color Balancing and Mosaicking (CBM) routine combines the lines into a single image. CBM uses surface reflectance derived from the bathymetric laser bottom reflectance, $a+b_b$, water column reflectance, and depth images to normalize the surface reflectance at all wavelengths of the hyperspectral imagery (personal communication, J.Y. Park).

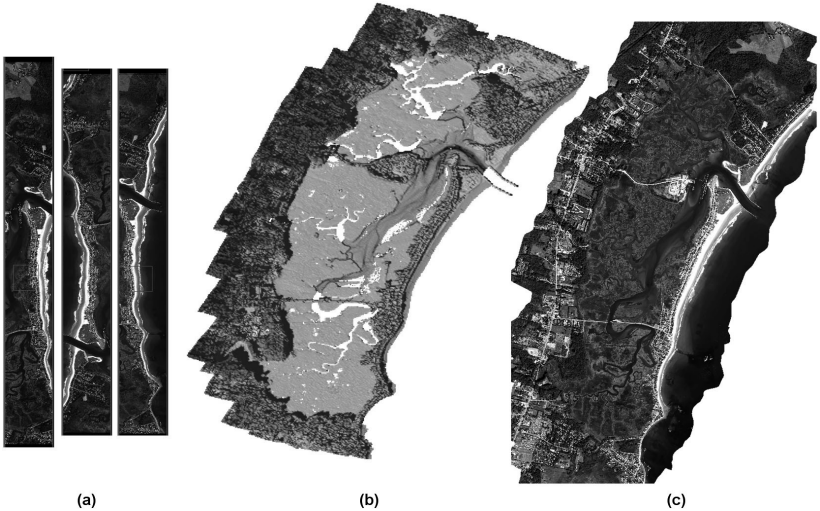

Figure 3. Steps to create an atmospherically-corrected hyperspectral image mosaic, Wells Harbor, Maine. (a) Radiometrically-corrected image strips. (b) Lidar DEM. (c) Final mosaic.

The final bottom image is bottom reflectance at all wavelengths of the hyperspectral imagery. It is created solely in the Optech REA processor. First, homogeneous areas are selected based on the bathymetric laser bottom reflectance image and an approximate bottom image. The approximate bottom image is calculated from the CBM surface reflectance image, SHOALS depth, and an estimate of water column attenuation that is constant across the image. In the homogeneous areas, with known water depth and the same bottom type in every pixel, $a+b_b$, water column reflectance, and bottom reflectance can be calculated for each wavelength of the hyperspectral data. Offsets are calculated between these values and SHOALS derived values for these parameters at the laser wavelength of 532 nanometers. The offsets scale the SHOALS images for these parameters, providing spatially varying values of $a+b_b$ and water column reflectance at every wavelength of the hyperspectral data. These values and SHOALS depth allow for the solution of the radiative transfer equation for bottom reflectance at each hyperspectral wavelength over the entire image area. For details on calculating the final bottom image, see Tuell et al. (2005a).

PRODUCTS IN DEVELOPMENT

Products currently in development at the JALBTCX are coastal zone classifications generated from the current suite of NCMP data products. Work is underway to identify a basic set of coastal thematic classes that can be identified using a combination of lidar elevation and hyperspectral imagery data, and classification algorithms in commercial-off-the-shelf software. One example is shown in Figure 5, where the Spectral Angle Mapper algorithm in ENVI was used to classify hyperspectral imagery at Portsmouth

Harbor, New Hampshire. This classification algorithm, and others like the Maximum Likelihood Classifier, can be used on final bottom images and bathymetric laser bottom reflectance images to create classifications of bottom type. Development in the Optech International REA processor includes some higher-level data fusion techniques that seek to reconcile the differences in bottom classifications from different sources to achieve a classification with higher accuracy. Work for the NOPP contract includes automatic attribution of the shoreline vector extracted from lidar elevation data using classification techniques. In this work, homogeneous areas in the hyperspectral imagery on land are automatically delineated and attributed with information extracted from the lidar data. The homogeneous areas are identified based on these attributes as coastal data features like sand, rock, buildings, roads, etc. Once this identification is made, the shoreline vector is segmented and attributed based on its intersection with the coastal data features.

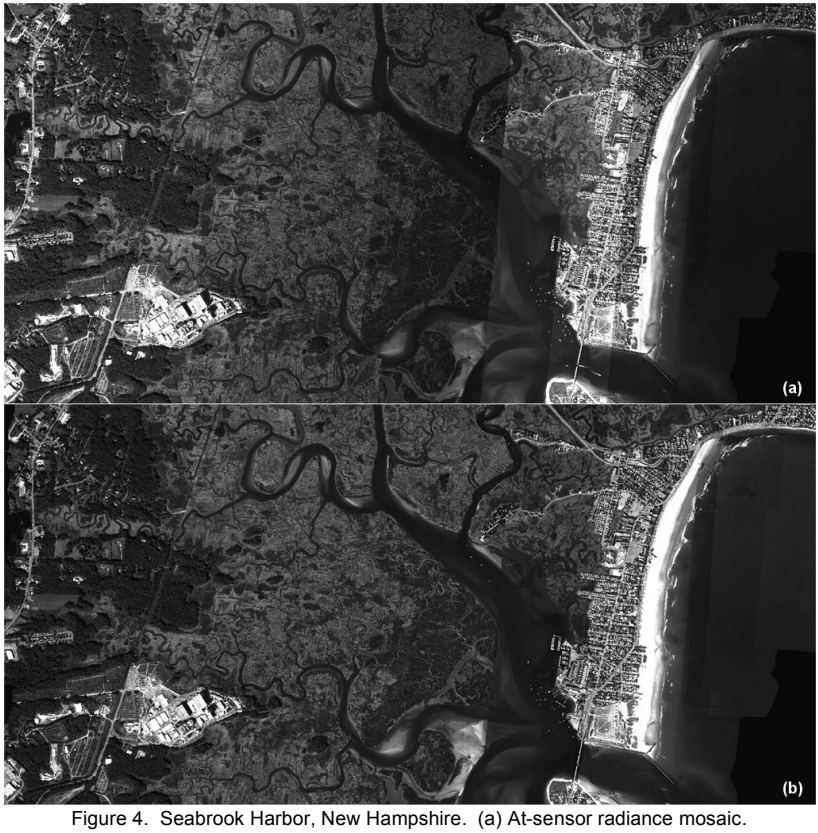

Figure 4. Seabrook Harbor, New Hampshire. (a) At-sensor radiance mosaic. (b) Atmospherically-corrected image mosaic.

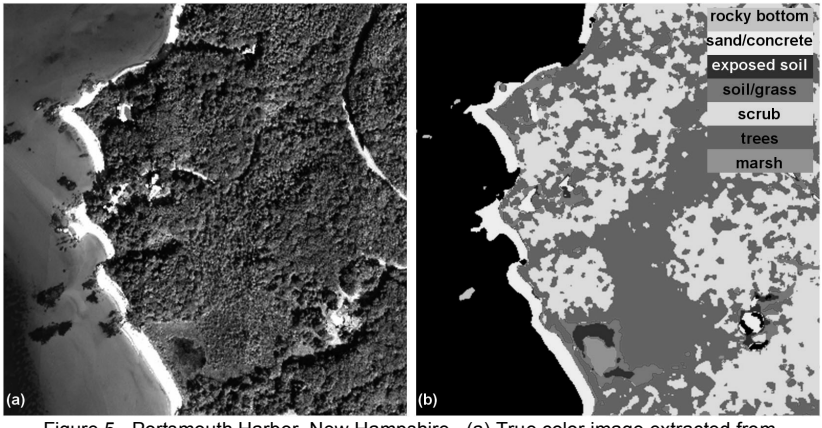

Figure 5. Portsmouth Harbor, New Hampshire. (a) True color image extracted from hyperspectral mosaic. (b) Basic image classification.

CONCLUSION

Data collected by the CHARTS system for the NCMP provide the basis for a rich set of data products to be used in support of planning, engineering, construction, operation and maintenance activities in the coastal zone, and to support regional sediment management practices. These include bathy/topo DEMs, RGB and hyperspectral image mosaics, building footprints, and bare earth grids. New data fusion products are the bathymetric laser bottom reflectance image, atmospherically-corrected hyperspectral image mosaics, and hyperspectral final bottom images. New product development uses each of these either singly or in conjunction to generate accurate land cover and bottom type classifications to characterize the coastal zone. New JALBTCX sensor development effort, CZMIL, will create a hardware and software system optimized to produce accurate elevation measurements and environmental characterizations in the coastal zone.

ACKNOWLEDGEMENTS

The author would like to thank Vinod Ramnath (Optech International) for his assistance in generating the bathymetric laser bottom reflectance images. Information presented herein, unless otherwise noted, is based on work funded by Headquarters, USACE, Operations, Construction, and Readiness Division. Permission to publish this paper was granted by the Chief of Engineers.

REFERENCES

Estep, L.L. (1998). *Depth measurement and bottom classification of Laguna Madre, Texas,* Report prepared for USACE Galveston District, Joint Airborne Lidar Bathymetry Technical Center of Expertise, Mobile, AL.

Estep, L.L., Lillycrop, W.J., and Parson, L.E. (1994). "Sensor Fusion for Hydrographic Applications," *Proceedings, USACE 1994 Training Symposium, Surveying and Mapping, Remote Sensing/GIS*, New Orleans, LA, SM:2B 1-7.

Gao, B.-C., Heidebrecht, K. H., and Goetz, A. F. H. (1993). "Derivation of scaled surface reflectances from AVIRIS data," *Remote Sens. Env.*, 44, 165-178.

Guenther G.C., Cunningham, A.G., LaRocque, P.E., and Reid, D.J. (2000). "Meeting the accuracy challenge in airborne LIDAR bathymetry," *Proc. 20th EARSeL Symposium: Workshop on LIDAR Remote Sensing of Land and Sea*, CD-ROM Published by European Association of Remote Sensing Laboratories, Paris, France ISBN:2-908885-50-6, 28 p.

Kopilevich, Y.I., Feygels, V.I., Tuell, G.H., and Surkov, A. (2005). "Measurement of ocean water optical properties and seafloor reflectance with Scanning Hydrographic Operational Airborne Lidar Survey (SHOALS): I. Theoretical Background," *Proc. SPIE Vol. 5885, Algorithms and Technologies for Multispectral, Hyperspectral, and Ultraspectral Imagery XI*, S. Chen and P. Lewis Ed., 9 p.

Lillycrop, W.J., and Estep, L.L. (1995). "Generational Advancements in Coastal Surveying, Mapping," *Sea Technology*, 36(6), 10-16.

M. J. Montes, Gao, B.-C., and Davis, C. O. (2004). *NRL Atmospheric Correction Algorithms for Oceans: Tafkaa Users' Guide*, Coastal and Ocean Remote Sensing Branch, Remote Sensing Division, Naval Research Laboratory, March 22 ed.

M. J. Montes, and Gao, B.-C. (2001). "A new algorithm for atmospheric correction of hyperspectral remote sensing data," *Proc. SPIE Volume 4383, Geo-Spatial Image and Data Exploitation II*, William E. Roper Ed., 23-30.

Tuell, G.H., Feygels, V.I., Kopilevich, Y.I., Weidemann, A.D., Cunningham, A.G., Mani, R., Podoba, V., Ramnath, V., Park, J. Y., and Aitken, J. (2005b). "Measurement of ocean water optical properties and seafloor reflectance with Scanning Hydrographic Operational Airborne Lidar Survey (SHOALS): II. Practical results and comparison with independent data," *Proc. SPIE Vol. 5885, Algorithms and Technologies for Multispectral, Hyperspectral, and Ultraspectral Imagery XI*, S. Chen and P. Lewis Ed., 13 p.

Tuell, G., and Park, J.Y. (2004). "Use of SHOALS Bottom Reflectance Images to Constrain the Inversion of a Hyperspectral Radiative Transfer Model," *Proc. SPIE Vol. 5412, Laser Radar Technology Applications IX*, G. Kammerman Ed., 185-193.

Tuell, G.H., Park, J.Y., Aitken, J., Ramnath, V., Feygels, V.I., Guenther, G.C., and Kopilevich,Y.I. (2005a). "SHOALS-enabled 3-d benthic mapping," *Proc. SPIE Vol. 5806, Algorithms and Technologies for Multispectral, Hyperspectral, and Ultraspectral Imagery XI*, S. Chen and P. Lewis Ed., 816-826.

Wozencraft, J.M., Hardegree, L.C., Tuell, G.H., and Lee, M. (2002). "Merging airborne lidar bathymetry and spectral imagery for more complete coastal mapping," *Proceedings, Seventh International Conference on Remote Sensing for Marine and Coastal Environments*.

Wozencraft, J.M., Lee, M., Tuell, G.T. and Philpot, W. (2003). "Use of SHOALS data to produce spectrally-derived depths in Kaneohe Bay, Hawaii," *Proceedings, Hydro '03,* Biloxi, Mississippi, USA.

Wozencraft, J.M. and Lillycrop, W.J. (2006). "JALBTCX Coastal Mapping for the USACE," *International Hydrographic Review* 7(2), 28-37.

Wozencraft, J.M. and Millar, D. (2005). "Airborne lidar and integrated technologies for coastal mapping and charting," *Marine Technology Society Journal* 39(3), 27-35.

USING TOPOGRAPHIC LIDAR DATA TO DELINEATE THE NORTH CAROLINA SHORELINE

Patrick W. Limber[1], Jeffrey H. List[2], Jeffrey D. Warren[3], Amy S. Farris[4], and Kathryn M. Weber[5]

1. North Carolina Division of Coastal Management, 1638 Mail Service Center, Raleigh, NC, 27699-1638, USA. patrick.limber@ncmail.net
2. United States Geological Survey, Woods Hole Science Center, 384 Woods Hole Rd., Woods Hole, MA, 02543, USA. jlist@usgs.gov
3. North Carolina Division of Coastal Management, 1638 Mail Service Center, Raleigh, NC, 27699-1638, USA. jeff.warren@ncmail.net
4. United States Geological Survey, Woods Hole Science Center, 384 Woods Hole Rd., Woods Hole, MA, 02543, USA. afarris@usgs.gov
5. United States Geological Survey, Woods Hole Science Center, 384 Woods Hole Rd., Woods Hole, MA, 02543, USA. kkonicki@usgs.gov

Abstract: In North Carolina, shoreline change rates are an important component of the state's coastal management program. To enhance methods of measuring shoreline change, the NC Division of Coastal Management (DCM) is considering using mean high water (MHW) shorelines extracted from lidar data together with traditional wet/dry shorelines digitized from aerial photography. To test their compatibility, a wet/dry line and MHW shoreline derived from a concurrent 2004 oceanfront photography and lidar dataset were compared along a distance of 244 km. Results show that the MHW shoreline was seaward of the wet/dry shoreline by 2.82 m on average, and that this offset biased shoreline change rates by an average of 0.05 m/yr. The offset was greatest on low-sloping beaches experiencing higher water levels at the time of photography, but overall was small enough to suggest that the MHW shoreline can be a reliable substitute for the wet/dry shoreline.

INTRODUCTION

Coastal policy and shoreline change rates in North Carolina

Every five to six years, the North Carolina Division of Coastal Management (DCM) updates the state's shoreline change rates, which have been required for the establishment of oceanfront building setbacks since 1979 under the North Carolina Coastal Area Management Act (CAMA). CAMA rules require that any new

oceanfront structure must meet a specified setback distance measured landward from the first line of stable, natural vegetation surveyed on the beach. In general, the setback distance is a multiplier of the long-term (42 to 71 years) average annual erosion rate. With few exceptions, oceanfront development intended for single-family use must meet a setback distance of 30 times the average annual erosion rate or a minimum of 60 feet (~18 m). Commercial and multi-family development greater than or equal to 5,000 ft^2 (465 m^2) must meet more stringent setbacks, often based on a 60-year multiplier. It follows that the accuracy of shoreline change rates must be high so that setbacks ultimately reflect actual conditions and coastal development can be sited at reduced risk.

In 1999, the North Carolina Coastal Resources Commission's (CRC) Science Panel on Coastal Hazards, a technical committee primarily composed of geologists and engineers that provides scientific and technical guidance to the CRC, recommended that DCM: 1) begin moving towards using linear regression-based erosion rates instead of end-point rates for calculating oceanfront setbacks and 2) explore the use of short-term erosion rates as a complement to long-term rates. However, switching to linear regression rates would necessitate the use of several statewide shoreline positions, and calculating short-term shoreline change rates (<10 years) may require a shoreline indicator of higher accuracy than what DCM traditionally has used (the wet/dry line, see next section). DCM is currently performing a statewide erosion rate update using a concurrent 2004 aerial photo and lidar dataset, and multiple shoreline indicators are being considered for inclusion. A better knowledge of how these different shoreline types compare and contrast to each another (and why) will not only create a better, more accurate understanding of North Carolina's dynamic coastal processes, but will also increase the effectiveness of many coastal management and coastal policies that rely upon shoreline analysis.

The wet/dry line

Traditionally, the wet/dry line interpreted from aerial photography (e.g. Dolan et al. 1980; Martin 1997; Overton et al. 1999; Overton and Fisher 2003) has been used to delineate the shoreline and to calculate shoreline change rates in North Carolina. Acting as a visual proxy for shoreline position, the wet/dry line is defined simply as the boundary observed on the beach between wet and dry sand (Figure 1) and is affected by factors such as tides, wave run-up, sediment characteristics (e.g. grain size and porosity), and groundwater levels (Martin 1997).

Although the wet/dry line can sometimes be considered a surrogate for the high water line (HWL; Boak and Turner 2005), it is important to note the differences between them. The HWL has received thorough consideration (e.g. Shalowitz 1964; Stafford 1971; Pajak and Leatherman 2002; Ruggiero et al. 2003; Moore et al. 2006), and is interpreted as the landward extent of the previous high tide (Shalowitz 1964). Even though it was at one time a wet/dry boundary, it is not necessarily a clearly saturated boundary at the time of photography. Rather than actively migrating seaward and landward during a tidal cycle similar to the wet/dry line (Dolan et al. 1980), the HWL is a more static boundary that can be identified by other visual cues besides saturation such as sand discoloration or debris left by the last high tide (Shalowitz 1964). For the

purposes of this study, "HWL" will refer to this definition. The HWL as so defined is often located higher on the beach face than the wet/dry line, and has been quantitatively defined as the elevation exceeded by 2% of wave run-up maxima (Ruggiero et al. 2003). The wet/dry line, on the other hand, has been approximated in North Carolina as the elevation exceeded by 33% of wave run-up (Martin 1997).

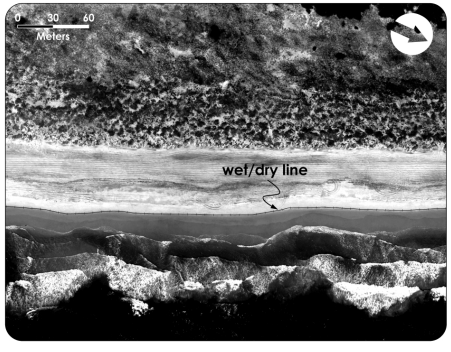

Figure 1. An example of the wet/dry line near Nags Head, NC.

An assessment of lateral short-term wet/dry line instability due to wave run-up and tides in North Carolina showed that the wet/dry line varied by up to 5.8 m during a single tidal cycle (Dolan et al. 1980) and 10.3 m during a single day (Martin 1997). Similarly, the HWL has been shown to vary on the order of 10 m during a month in North Carolina (Pajak and Leatherman 2002). This potential instability can introduce uncertainty into shoreline change rates, as a given rate may be an expression of short-term water level variability rather than a true indicator of shoreline movement (Ruggiero et al. 2003).

Interpretation of the wet/dry line from aerial photography, as with other visual shoreline proxies such as the HWL, can vary (Daniels et al. 2000; Ruggiero et al. 2003) due to the different skill or knowledge levels of the digitizers. Daniels et al. (2000) found, for instance, that two interpretations of the HWL on the same set of photography differed on average by 12.44 m. This, along with short-term variability and the possible positional inaccuracies of aerial photography (Ruggiero et al. 2003), can introduce uncertainty into shoreline change rates and in turn affect the accuracy oceanfront structure setbacks or other coastal policy decisions.

Lidar-derived datum-based shorelines

Recently, topographic lidar surveys have been used to generate shorelines based on the elevation of a tidal datum, such as mean high water (MHW), calculated over an 18.6-year tidal epoch (e.g. Judge et al. 2001; Stockdon et al. 2002; Moore et al. 2006). Such datum-based shoreline positions may offer noteworthy advantages over photo-interpreted shorelines such as the wet/dry line. First, datum-based lidar shorelines can shift only in response to sediment transport, and any short-term variation due to wave run-up and/or tides is eliminated (List et al. 2006). Second, there is no interpretation

necessary and the shoreline extraction procedure is therefore objective and repeatable. MHW is the most common tidal datum used to extract a shoreline from lidar data because its position on a given beach is thought to be analogous to other shoreline indicators such as the HWL and those derived from National Ocean Service T-sheets (Shalowitz 1964).

Before a lidar-derived MHW shoreline can be included in a long-term shoreline change analysis in North Carolina, the degree of consistency between it and the wet/dry line must first be tested so that any bias to shoreline change rates introduced by using two different shoreline indicators can be quantified. Several studies have addressed the relationship between the HWL and MHW, and the HWL has been found to be landward of MHW by approximately 50 m in Washington (Ruggiero et al. 2003), 18.8 m on Assateague Island (Maryland and Virginia; Moore et al. 2006), and 13.4 m in North Carolina (Pajak and Leatherman 2002). Because the wet/dry line falls somewhat lower on the beach than the HWL, we would expect the offset and possible bias to shoreline change rates found in this study to be less than indicated in previous studies.

In August and September of 2004, a concurrent set of orthophotography and lidar was obtained for the entire North Carolina coast that allows for direct comparison between the wet/dry shoreline and the lidar-derived MHW shoreline. Using this dataset, the goals of this study are to assess 1) the degree of interchangeability between the wet/dry and MHW shorelines over a large and morphologically diverse oceanfront shoreline study area (~244 km) and 2) the feasibility of using MHW shorelines to calculate long-term shoreline change rates in North Carolina.

STUDY AREA, DESCRIPTION OF DATASET, AND METHODOLOGY

The Atlantic barrier island coastline of North Carolina (Figure 2) is a wave-dominated, microtidal environment. Mean annual significant wave heights (H_{sig}) are 0.7 – 1.6 m (NOAA 2006), and semidiurnal tides range, on average, from ~1 m along the northern coast to ~1.5 m near the South Carolina border (NOAA 2006). Because "hard" shoreline stabilization structures such as seawalls and groynes have been banned since 1985, the North Carolina coast is largely unaffected by engineered structures.

Between 27 August and 3 September 2004, MD Atlantic Technologies (Huntsville, AL), co-contracted by the US Army Corps of Engineers (USACE) and DCM, collected a dataset of concurrent lidar and aerial photography covering the entire 516 km-long ocean coastline of North Carolina. Figure 3 shows the dates and times of the surveys, as well as the tidal stage and approximate H_{sig} values. Lidar was collected with an Optech ALTM 3100 sensor mounted on a Cessna 206. Vertical accuracy is generally expected to be ±0.15 m (Sallenger et al. 2003), which includes all known sources of error. Digital elevation models (DEMs) gridded from the lidar returns were tested and found to be within this range (MD Atlantic 2005). However, subsequent comparisons between the returns of two lidar passes separated by about an hour over the same 40 km-long area showed a significantly greater amount of vertical error – about 0.3 m – which caused MHW shorelines generated from each pass to be offset

by, on average, 2.45 m. This error is likely due to the potential for the GPS data to drift vertically over time (Sallenger et al. 2003). The GPS error is not well understood, so it is difficult to estimate the appropriate error for each data point within a data set. Although the level of vertical drift error present in some of this lidar data might be much higher than what is normally expected, with only limited data demonstrating this we cannot determine a general increased error term to apply to all the data; therefore, we used the standard vertical error estimate of ±0.15 m.

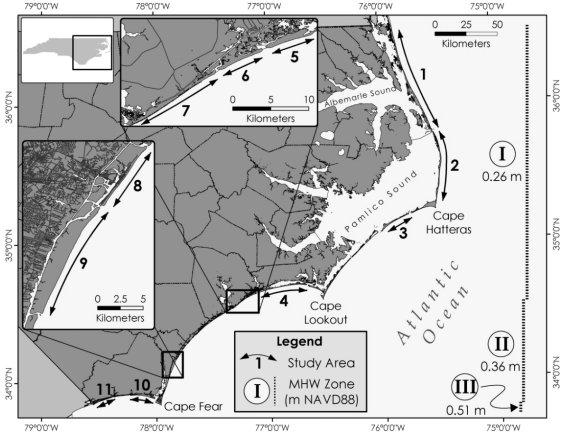

Figure 2. North Carolina location map showing study areas and MHW zones.

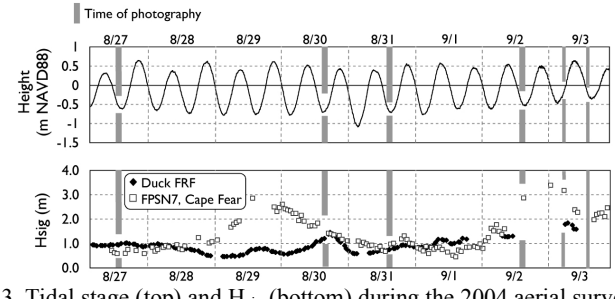

Figure 3. Tidal stage (top) and H_{sig} (bottom) during the 2004 aerial survey dates. Tidal data are from the USACE Field Research Facility (FRF) at Duck, NC; H_{sig} values are from the FRF waverider buoy at Duck and NOAA buoy FPSN7 near Cape Fear.

A method similar to that presented by Stockdon et al. (2002) was used to extract a MHW shoreline from the North Carolina lidar data. Every 20 m alongshore, beach profiles of scattered lidar data were extracted and a linear regression through a selected set of foreshore data points was used to locate the intercept of a MHW elevation with the beach profile. Operational MHW elevation zones as mapped by

Weber et al. (2005) were used to determine the elevation of MHW. Three such zones exist in North Carolina (Figure 2; relative to NAVD88): Virginia to Cape Lookout (0.26 m), Cape Lookout to Cape Fear (0.36 m), and Cape Fear to South Carolina (0.51 m). Given a vertical accuracy of ±0.15 m for all data points and using beach slopes measured at each cross-shore transect, the vertical error was converted into a horizontal error. This term was added in quadrature, i.e. the square root of the sum of the squares, to the 95% confidence interval of the MHW intercept on the regression line and resulted in a composite horizontal error estimate for each MHW data point. There were many areas for which a MHW shoreline position could not be produced due to problems encountered in the lidar data, and as a result, the MHW shoreline contains recurrent data gaps.

Digital aerial photography was collected simultaneously with the lidar survey. Using lidar-generated DEMs, the photography was orthorectified and subsequently tested to have a total root mean square (RMS) error of ±1 m (MD Atlantic 2005). The resulting orthophotos have a ground cell resolution of 0.15 m and are at scale of 1:2400. The wet/dry line was digitized from the orthophotography for use in comparing to the MHW shoreline, and three DCM staff members inspected the shoreline to ensure that the wet/dry interpretation was as consistent as possible.

Eleven study areas totaling a distance of 244 km were chosen in which to compare the wet/dry shoreline with the MHW shoreline (Figure 2). We excluded areas where the photos and lidar were asynchronous, large data gaps existed in the MHW shoreline, and consistent wet/dry interpretation was problematic. Comparisons were made using ArcGIS 9 equipped with the Digital Shoreline Analysis System (DSAS; Thieler et al. 2005) at transects spaced every 20 m alongshore.

MHW AND WET/DRY LINE INTERCHANGEABILITY

Observed proxy-datum offsets

To test the interchangeability of the MHW and wet/dry shorelines, we measured horizontal and vertical offsets between them (i.e. proxy-datum offsets) for all study areas. Vertical proxy-datum offset is defined as the elevation difference between the wet/dry line and MHW, and the elevation of the wet/dry line was measured by intersecting it with the lidar data. The elevation of the wet/dry is assumed to be a relative indicator of water level (i.e. tidal stage and wave run-up) on the beach profile, although other physical variables such as groundwater seepage and sediment permeability can control wet/dry line location (Martin 1997). Figure 4 and Table 1 summarize all observed offsets as well as other results that will be discussed in subsequent sections. On average, the wet/dry line was landward of the MHW shoreline by 2.82 m ($\sigma = 5.31$) and higher on the beach profile by 0.18 m ($\sigma = 0.29$). The position of the wet/dry line varied horizontally from 35.87 m landward to 12.30 m seaward of the MHW shoreline, and vertically from –0.73 m to 2.4 m. Table 1 shows the mean horizontal proxy-datum offsets for each study area, which range from 0.05 m (Oak Island) to 15.61 m (Ocracoke Island). Positive numbers indicate that the wet/dry line is landward of the MHW shoreline.

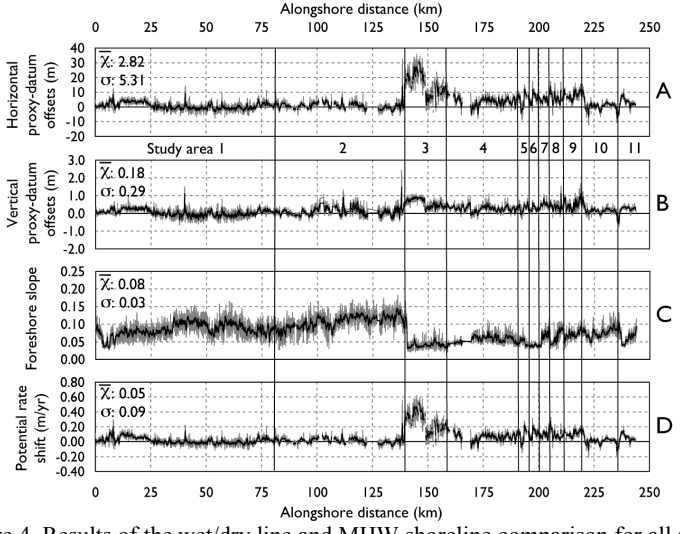

Figure 4. Results of the wet/dry line and MHW shoreline comparison for all study areas. Positive numbers on plots A and B indicate that wet/dry line is landward and higher in elevation than MHW, respectively. Positive rate shift values on plot D indicate an erosion rate decrease. The gray line represents per-transect values, and the black line is a smoothed 340-m average.

Table 1. Shoreline position and comparison data for all study areas

Study Area	ID	Length (km)	Mean Offset (m)	σ Offset	Mean Rate Shift (m/yr)	σ Rate Shift	Mean Slope	2004 Survey Date
Nags Head	1	81	0.65	2.57	0.01	0.05	0.085	8/27
Cape Hatteras	2	59	0.87	2.66	0.02	0.05	0.107	8/27
Ocracoke	3	19	15.61	8.49	0.27	0.15	0.041	9/03
Bogue Banks	4	35	3.68	3.51	0.06	0.06	0.057	8/30
Bear Island	5	4	5.75	4.17	0.10	0.08	0.038	8/30
Brown's Island	6	3	7.34	2.65	0.13	0.05	0.039	8/30
Onslow Beach	7	5	6.19	3.43	0.12	0.07	0.063	8/30
Wrightsville Beach	8	5	4.97	3.28	0.07	0.05	0.072	9/02
Masonboro Island	9	10	7.94	2.99	0.11	0.04	0.072	9/02
Oak Island	10	16	0.05	2.70	0.00	0.05	0.075	8/31
Ocean Isle Beach	11	7	3.68	2.70	0.06	0.04	0.059	8/31
TOTAL		**244**	**2.82**	**5.31**	**0.05**			

Previous studies have shown the HWL interpreted from aerial photography to be landward of the elevation of MHW by approximately 50 m (Ruggiero et al. 2003), 18.8 m (Moore et al. 2006), and 13.4 m (Pajak and Leatherman 2002). As expected, because the wet/dry line falls consistently lower on the beach face than the HWL, the horizontal proxy-datum offsets measured here are comparatively small. This suggests that a lidar-derived MHW shoreline can be used as a reliable substitute for the

wet/dry line and that bias to shoreline change rates will be minimal, especially over the long-term (>50 years).

Causes of observed proxy-datum offsets

Causes of the trends and magnitudes in offset between the shorelines can depend on variables such as beach slope, short-term variability of the wet/dry line due to water level changes, and consistency of wet/dry line interpretation. Ruggiero et al. (2003) and Moore et al. (2006) found that horizontal proxy-datum offsets are larger on low-sloping, high-energy beaches, and that beach slope may be a good general predictor of offset magnitude. Figure 4A shows horizontal proxy-datum offsets aligned with beach slope measurements alongshore, and many regional and local trends in shoreline offset are inversely proportional to beach slope. For example, the increase in horizontal offset beyond ~140 km alongshore (study areas 3-11, Figure 2) is accompanied by a flattening of the foreshore beach profile, and the small shoreline differences in study areas 1 and 2 are accompanied by the steepest overall slopes in North Carolina. It is interesting to compare the variation of vertical proxy-datum offsets (Figure 4B) with horizontal offsets, as they are linked together by beach slope (Figure 4C). Between roughly 100 and 125 km in study area 2 (Figure 4), for example, the vertical offset approaches 1 m, but due to a steep beach the horizontal offsets are minimal (<5 m). Conversely, on Ocracoke Island (study area 3), vertical offset approaches 1 m, but there a low-sloping beach produces horizontal offsets over 30 m.

The position of the wet/dry line can be variable depending on tidal stage and wave run-up (Martin 1997). All photography used in this study was taken during or near low tide (Figure 3); however tidal stage still varied from a maximum of approximately –0.1 m (9/3, Ocracoke Island) to a minimum of –0.7 m (8/31, Oak Island and Ocean Isle). H_{sig}, measured at the USACE FRF waverider buoy near Duck, NC and at NOAA buoy FPSN7 offshore of Cape Fear (NOAA 2006; Figure 3), also potentially varied between surveys. Both buoys indicate that H_{sig} was generally lowest during the surveys on 8/27 and 8/31, higher on 8/30 and 9/2 (although data points are sparse), and highest on 9/3. Consequently, the wet/dry line should not be at a consistent elevation on the beach profile for each survey. Mean horizontal and vertical offsets were lowest on 8/27 and 8/31, higher on 8/30 and 9/2, and highest on 9/3. This suggests, as proposed by Ruggiero et al. (2003), that higher wave energy pushes the wet/dry line higher on the beach profile and increases the horizontal offset at a magnitude inversely proportional to beach slope, while lesser wave energy allows the wet/dry line to be lower on the beach profile and decreases horizontal offsets. On 9/3, in addition to the high H_{sig}, the tidal stage was also the highest observed, and that in combination with a low-sloping beach produced the large mean 15.61 m horizontal offset measured on Ocracoke Island. The majority of the total study area, however, was surveyed on 8/27 and 8/31 when H_{sig} was moderate (0.6-1.3 m). In North Carolina, mean annual H_{sig} is 0.7–1.6 m, and so these dates can be taken as representing average, fair-weather conditions. Horizontal offset between the wet/dry and MHW shorelines on 8/27 and 8/31 averaged 0.80 m, indicating that during low tide and fair-weather wave conditions, the shorelines are nearly equivalent. It is

important to note that for study areas at a large distance from both wave buoys (e.g. Bogue Banks, Onslow Beach), H_{sig} values should be taken as approximations only.

Assuming a relatively constant water level, beach slope alone could theoretically be a good general predictor of horizontal proxy-datum offsets. As discussed above, tides and H_{sig} varied between survey dates, and wave run-up (and therefore the elevation of the wet/dry line and vertical proxy-datum offsets) should be expected to vary alongshore within study areas as a function of beach slope (Holman 1986; Stockdon 2006). The magnitude of horizontal offsets throughout all study areas is therefore dependent on both beach slope and water level and we can test this relationship using a simple equation:

$$X_0 = \frac{H_{proxy} - H_{datum}}{m} \quad (1)$$

where X_0 is the horizontal proxy-datum offset (Moore et al. 2006); H_{proxy} and H_{datum} are the heights of the wet/dry line and MHW, respectively; and m is beach slope (note that the numerator is the vertical proxy-datum offset shown in Figure 4B). Figure 5 (left) shows the correlation between horizontal proxy-datum offset (X_0) and beach slope along 857 cross-shore transects chosen at random throughout all study areas. Even though the trend is significant at the 95% confidence level, the overall relationship is indistinct. A conspicuous subset of points with high values of X_0 from Ocracoke Island is labeled on the graph where the beach is relatively flat but X_0 was exaggerated as a result of the high water levels observed on that particular survey date (9/3). Along the same 857 transects, the elevation of the wet/dry line, assumed to be a relative indicator of water level, was measured and equation (1) was applied to predict X_0. Results were compared with the observed X_0 and are shown in Figure 5 (right). The correlation is very strong and illustrates that X_0 will be larger on low-sloping and/or higher energy beaches. This relationship can explain the mean X_0 magnitudes for all study areas and survey dates, including the high X_0 measured on Ocracoke Island on 9/3 and the low X_0 measured in study areas 1 and 2 on 8/27 wherein the beach profile was relatively steep and H_{sig} was moderate. Plugging the mean beach slope (0.08) and mean vertical proxy-datum offset (0.18 m) for all study areas into equation (1) yields a predicted mean X_0 of 2.25 m, which is close to the observed total mean of 2.82 m. In some cases, the assumption of a linear beach slope between the wet/dry line and MHW shoreline may not hold true, and fluctuations in vertical proxy-datum offset may reflect inconsistencies in digitizing the wet/dry line rather than actual water level changes. These factors can account for the discrepancies between observed and predicted offset values.

Rate shifts

If the horizontal offset between the wet/dry line and MHW shoreline is large enough, (i.e. if water level is high and/or beach slope is low) it may begin to bias, or shift, change rates when one shoreline indicator is used as a substitute for the other. If the proxy-datum offset and the time elapsed between shoreline positions is known,

however, this rate shift is predictable when using end-point rates and can be determined as follows (Moore et al. 2006):

$$R_{Se} = \frac{X_0}{t} \tag{2}$$

where R_{Se} is the end-point rate shift; X_0 is the measured horizontal offset between the wet/dry and MHW shorelines (also defined in equation 1 as $[H_{proxy} - H_{datum}/m]$); and t is the temporal span between the recent and historic shorelines used to calculate the shoreline change rate. The effects of the horizontal proxy-datum offset, X_0, will thus be greater at short time intervals (Moore et al. 2006).

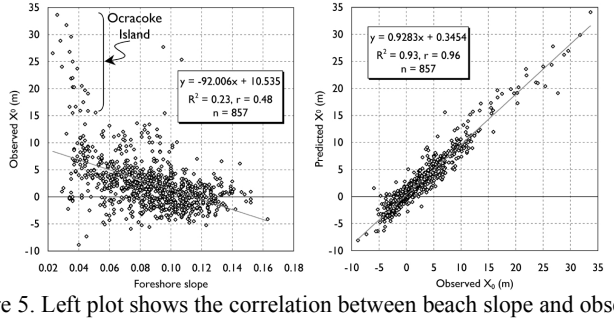

Figure 5. Left plot shows the correlation between beach slope and observed horizontal proxy-datum offset. Right plot shows the correlation between observed horizontal offsets and horizontal offsets predicted using equation (1).

DCM uses a composite statewide historical shoreline for calculating long-term end-point shoreline change rates that dates between 1933 and 1962; with the 2004 shoreline, t in equation (2) varies from 42 to 71 years. Figure 4D shows the per-transect rate shifts that are possible if the 2004 MHW shoreline is used instead of the 2004 wet/dry line to calculate change rates with the historical baseline shoreline, and Table 1 lists the mean rate shifts for each study area. The total mean rate shift is 0.05 m/yr (positive number indicates erosion rate will be reduced and accretion rate will be increased) for all study areas and ranges for individual study areas between 0 (Oak Island, t = 60 years) and 0.27 m/yr (Ocracoke Island, t = 58 years). If the rate of shoreline change is rapid or the temporal span between shoreline positions is sufficiently long, the rate shift will only be a small fraction of the total change rate and may be small enough to completely disregard (Moore et al., 2006). Since horizontal proxy-datum offsets are relatively small in North Carolina and the time spans used are typically >50 years, much of the offset will produce negligible rate shifts. On the other hand, if the rate of change is slow and/or the proxy-datum offset is large, the rate shift may be a much greater fraction of the total rate. In this case, equation (2) can be used to correct for the shift if the mean horizontal offset is known or approximated.

Relative shoreline uncertainties

Some horizontal differences between the MHW and wet/dry shorelines may not be significantly different than zero due to the inherent positional uncertainties of the shorelines. To understand this, we must first assemble an approximate uncertainty budget for the wet/dry shoreline. As discussed above, there are three main sources of wet/dry line uncertainty: interpretation, short-term variability due to water level changes, and source error (Daniels et al. 2000; Ruggiero et al. 2003). Source error of the orthophotos used in this study was determined to be ±1 m (MD Atlantic 2005) after comparing locations on the photos with ground control points. To assess the uncertainty associated with interpretation, two wet/dry lines digitized by DCM staff were compared over a distance of 85 km. The first shoreline was checked for accuracy and consistency by DCM staff to act as a baseline for comparison, and specific visual cues were defined so that shoreline identification would remain consistent for the second iteration. Comparisons of the two shorelines revealed that the second shoreline was seaward of the original by 0.6 m with a total root mean square (RMS) uncertainty of ±2.6 m.

It was not possible to determine the short-term variability of the wet/dry due to water level changes because we lack the necessary frequent observations. In areas where 2004 photography from two different dates was available, the wet/dry line was seen to migrate landward approximately 10 m over a 12-hour period (Ocracoke Island), seaward 20 m over 3 days (Bogue Banks), and around 20 m landward over a month (near Cape Hatteras). Pajak and Leatherman (2002) assessed the variability of the HWL in North Carolina during July, August, and September from 1994-1996 over hourly, daily, and monthly time periods. Excluding storm events, they established a generalized estimate on the order of ±10 m. In addition, field measurements of the wet/dry line in North Carolina by Martin (1997) indicated a variability of ±10.3 m during a single day. These measurements agree with our cursory observations and provide a useful estimate of wet/dry variability in North Carolina, acknowledging that further work needs to be completed to assess its true variability.

Summing the source error (±1 m), interpretation uncertainty (±2.6 m), and potential short-term variability (±10 m) in quadrature yields a total wet/dry line uncertainty of ±10.4 m. Other similar uncertainty budgets for HWL shorelines total ±20 m (straight sum of ±3 source error, ±2 interpretation, ±15 short-term variability; Daniels et al. 2000) and 51-150 m (quadrature sum of ±4 source error, ±11 interpretation, ±50-150 m short-term variability; Ruggiero et al. 2003). Mean uncertainty of the MHW shoreline for all study areas is ±2.22 m (σ = 0.92). Taking the total uncertainty estimate for both shorelines into account, only 6% (694 out of 11,159) of measured horizontal proxy-datum offsets are significant, most of which are located on Ocracoke Island. This suggests a high degree of interchangeability between shorelines.

DISCUSSION

Lidar-derived, datum-based shorelines can offer an increase in accuracy over the wet/dry line for use in end-point rates and can also be used as a supplement to existing wet/dry lines in linear regression models. Short-term change rates (<10 years) that may be difficult to resolve using wet/dry lines are possible using MHW

shorelines, and DCM is considering using them for areas where long-term change rates are heavily biased by beach fill projects (e.g. Wrightsville Beach, Bogue Banks, Oak Island) so that the change rate can be more accurately measured between beach fill episodes. Results presented here suggest that a lidar-derived MHW shoreline is interchangeable with DCM's traditional shoreline proxy, the wet/dry line, given a steep sloping beach and/or low water levels at the time of photography. Under these circumstances, a MHW shoreline will introduce minimal bias to long-term end-point shoreline change rates in North Carolina. However, during times of high water level and on low-sloping beaches, as demonstrated at Ocracoke Island, the proxy-datum offset is much greater and the interchangeability between the wet/dry line and MHW shoreline is decreased. Here, rate shifts will be a larger fraction of the total change rate, and it is therefore difficult to determine categorically that the shoreline indicators are equivalent because it depends on the conditions at the time of photography as well as beach morphology. On average, though, the observed rate shifts and proxy-datum offsets were small enough that the shorelines can be considered compatible. In future studies, the height of the wet/dry line can potentially be estimated using numerical wave run-up models as discussed in Martin (1997). This could allow proxy-datum offsets and rate shifts to be estimated without a rigorous proxy-datum comparison as described herein, and could also facilitate an assessment of the short-term variability of the wet/dry line.

Horizontal and vertical proxy-datum offsets, based on beach slope and the elevation of the wet/dry line, and the effect of resultant rate shifts on shoreline change rates can be connected through a simple equation using variables from equations (1) and (2) (after Moore et al. 2006):

$$R_A = \left(\frac{\left(\frac{H_{proxy} - H_{datum}}{m} \right)}{t} \right) + R_0 \qquad (3)$$

where R_0 is the original shoreline change rate and R_A is the adjusted shoreline change rate after the incorporation of the rate shift. H_{proxy}-H_{datum} is the vertical proxy-datum offset, the vertical proxy-datum offset divided by slope (m) is the horizontal proxy-datum offset (or X_0), and the horizontal proxy-datum offset divided by time span (t) is the rate shift. Because horizontal and vertical offsets are relatively small in North Carolina and shoreline change rates are calculated over sufficiently long time spans, the R_0 and R_A values should be very similar and the wet/dry line and MHW shoreline can be considered generally interchangeable. The overall mean difference between R_0 and R_A values for our study was 0.05 m/yr.

CONCLUSIONS

The 2004 photo-derived wet/dry shoreline presented here, measured over a distance of 244 km in North Carolina, is on average 2.82 m (σ = 5.31) landward of the 2004 lidar-derived MHW shoreline (Figure 4A) and 0.18 m (σ = 0.29) higher on the beach profile (Figure 4B). The magnitude of mean horizontal proxy-datum offset varies by

study area and ranges from 0.05 to 15.61 m (Table 1). Considering the uncertainty of the wet/dry line and MHW shoreline, 6% of measured offsets were significantly different than zero. Given a low tide and fair-weather wave conditions at the time of photography and/or a steep-sloping beach, these results suggest that the MHW shoreline can be used as a reliable substitute for the wet/dry line in regional shoreline change analyses. Rate shifts caused by using the MHW shoreline instead of the wet/dry line average 0.05 m/yr for all study areas (Figure 4D) and vary between zero and 0.27 m/yr for individual study areas (Table 1). Rate shifts either a) are a small percentage of the overall change rate and can potentially be disregarded or b) can be corrected using equation (2) providing that the mean proxy-datum offset is known or approximated through equation (1).

ACKNOWLEDGMENTS

We would like to thank Ken Richardson, Guy Stefanski, and the rest of the DCM staff for providing valuable technical and administrative support; Rob Thieler and S. Jeffress Williams of the US Geological Survey for contributing comments that greatly enhanced this manuscript; the NOAA Coastal Management Fellowship program and the Environmental Careers Organization for providing key financial assistance; the US Army Corps of Engineers Field Research Facility in Duck, NC for wave and tide data; and John Fisher, Margery Overton, and the rest of the Coastal Resource Commission's Science Panel on Coastal Hazards for developing the initial concepts, ideas, and recommendations regarding shoreline datum comparisons and calibrations.

REFERENCES

Boak, E.H. and Turner, I.L., 2005. Shoreline definition and detection: a review. *Journal of Coastal Research,* 21(4), 688-703.

Daniels, R.C., Ruggiero, P., and McCandless, D., 2000. Interpretation of the average high water line from aerial photography: variability and repeatability. In: *Southwest Washington Coastal Erosion Workshop Report 1999*. Eds. G. Gelfenbaum and G. Kaminsky. USGS Open-File Report 00-439, 58-74.

Dolan, R., Hayden, B.P., May, P., and May, S.K., 1980. The reliability of shoreline change measurements from aerial photographs. *Shore and Beach,* 48(4), 22-29.

Holman, R.A., 1986. Extreme value statistics for wave runup on a natural beach. *Coastal Engineering,* 9(6), 527-544.

Judge, E.K., Overton, M.F., and Fisher, J.S., 2001. Long-term erosion rates and shoreline position databases: merging two and three-dimensional data sets. *Proceedings for the Conference on Coastal Zone Management*, July 2001.

List, J.H., Farris, A.S., and Sullivan, C., 2006. Reversing storm hotspots on sandy beaches: Spatial and temporal characteristics. *Marine Geology,* 226, 261-279.

Moore, L.J., Ruggiero, P., and List, J.H., 2006. Comparing mean high water and high water shorelines: should proxy-datum offsets be incorporated into shoreline change analysis? *Journal of Coastal Research*, 22(4), 894-905.

Martin, J., 1997. Analysis of the wet/dry line as an indicator of shoreline position on a sand beach. Masters Thesis, North Carolina State University, 71p.

MD Atlantic Technologies, 2005. *North Carolina Division of Coastal Management*

Digitial Orthophotography and Raw LiDAR Survey, North Carolina Coastline: Reports. Huntsville, AL, 46p plus appendices.

National Oceanic and Atmospheric Administration (NOAA), 2006. National Data Buoy Center: Silver Spring, Maryland. Available online: <http://www.ndbc.noaa.gov>

Overton, M.F., Grenier, R.R., Judge, E.K., and Fisher, J.S., 1999. Identification and analysis of coastal erosion hazard areas: Dare and Brunswick Counties, North Carolina. *Journal of Coastal Research Special Issue No. 28*, 69-84.

Overton, M.F. and Fisher, J.S., 2003. *The 1998 Long-term Erosion Rate Update for the North Carolina Shoreline.* NC Department of Environment and Natural Resources, Division of Coastal Management, Raleigh, NC, 17p.

Pajak, M.J. and Letherman, S., 2002. The high water line as a shoreline indicator. *Journal of Coastal Research*, 18(2), 329-337.

Ruggiero, P., Kaminsky, G.M., and Gelfenbaum, G., 2003. Linking proxy-based and datum-based shorelines on a high-energy coastline: implications for shoreline change analyses. *Journal of Coastal Research Special Issue No. 38*, 57-82.

Sallenger, A. H., Krabill, W., Swift, R., Brock, J., List, J., Hansen, M., Holman, R.A., Manizade, S., Sontag, J., Meredith, A., Morgan, K., Yunkel, J.K., Frederick, E. and Stockdon, H., 2003. Evaluation of airborne scanning lidar for coastal change applications. *Journal of Coastal Research*, 19(1), 125-133.

Shalowitz, A.L., 1964. *Shore and Sea Boundaries with Special Reference to the Interpretation and Use of Coast and Geodetic Survey Data.* Washington, D.C.: U.S. Government Printing Office, Department of Commerce, Coast and Geodetic Survey, 484p.

Stafford, D.B., 1971. An aerial photographic technique for beach erosion surveys in North Carolina. *Technical Memorandum No. 36,* U.S. Army Corps of Engineers, 115p.

Stockdon, H., Sallenger, A., Holman, R. and List, J., 2002. Estimation of shoreline position and change using airborne topographic lidar data. *Journal of Coastal Research*, 18(3), 502-513.

Stockdon, H.F., Holman, R.A., Howd, P.A., and Sallenger, A.H. Jr., 2006. Empirical parameterization of setup, swash, and runup. *Coastal Engineering,* 53, 573-588.

Thieler, E.R., Himmelstoss, E.A., Zichichi, J.L., and Miller, T.L., 2005. *Digital Shoreline Analysis System (DSAS) version 3.0: An ArcGIS© extension for calculating shoreline change*. USGS Open-File Report 2005-1304. Available online: <http://woodshole.er.usgs.gov/project-pages/DSAS/version3/>

Weber, K.M., List, J.H., and Morgan, K.L.M., 2005. *An operational mean high water datum for determination of shoreline position from topographic lidar data*. USGS Open-File Report 2005-1027. Available online: <http://pubs.usgs.gov/of/2005/1027/>

EXPLORING RIPPLED SCOUR DEPRESSIONS OFFSHORE HUNTINGTON BEACH, CA

Eleyne L. Phillips[1]; Curt D. Storlazzi[2]; Peter Dartnell;[3] Brian D. Edwards[4]

1. Earth & Planetary Sciences, UC Santa Cruz 1156 High St., Santa Cruz, CA 95064. ephillips@pmc.ucsc.edu
2. US Geological Survey, Coastal and Marine Geology 400 Natural Bridges, Santa Cruz, CA 95060. cstorlazzi@usgs.gov
3. US Geological Survey, Coastal and Marine Geology 345 Middlefield Rd., Mail Stop 999, Menlo Park, CA 94025. pdartnell@usgs.gov
4. US Geological Survey, Coastal and Marine Geology 345 Middlefield Rd., Mail Stop 999, Menlo Park, CA 94025. bedwards@usgs.gov

ABSTRACT: U.S. Geological Survey (USGS) scientists used 1999 multibeam data, and 2002 lidar data collected on the inner shelf off southern California to investigate a field of (<1 m) features, termed "Rippled Scour Depressions" (RSDs). RSDs are elongate, shore-normal, and bathymetrically depressed features; their morphology was determined from multibeam and lidar bathymetry. Wavelengths of ripples seen within RSDs and on the surrounding seafloor were calculated from photography and video collected in 2004 and related to sediment samples collected in the same year. The RSDs were divided into two areas: Region I RSDs contained large (~80 cm wavelength), straight-crested ripples with coarse-grained lag, and decreased in area between 1999 and 2002; Region II RSDs were smaller, in shallower water, closer to shore, and contained shorter (~30 cm wavelength) ripples, and increased in area from 1999-2002. The RSDs did not display marked alongshore asymmetry.

INTRODUCTION:

Active continental margins, such as off of California's coast, tend to be narrow with deep, steep shelf breaks, all of which significantly affect cross-shelf circulation and transport (Nittrouer and Wright 1994). Sediment deposits on the inner shelf are impermanent features that can be deposited or eroded rapidly and episodically (Nittrouer and Wright 1994; Storlazzi and Jaffe 2002), even after long periods of apparent stasis. Many datasets gathered in shelf sedimentary environments represent a transitory condition. Modern marine research often utilizes temporally repeated datasets (e.g., Goff et al. 2005) not only to document changes within the dynamic inner shelf environments, but also to identify the likelihood for perturbation. As coastal research increasingly focuses on erosion, benthic habitats, and the impact of hard structures, improved understanding of inner-shelf dynamics will enable managers to more effectively monitor and manage the coastal zone.

Multibeam backscatter and bathymetric data collected in 1999 from the inner San Pedro shelf seaward of Long Beach, CA (Dartnell et al. 2004) show a relatively flat shelf pitted by a series of high-backscatter elongate features near Huntington Beach (Fig. 1). These shore-normal features, defined by Cacchione et al. (1984) as Rippled Scour Depressions (RSDs), are approximately one meter lower than the surrounding seafloor. Typically RSDs are hundreds of meters wide, and up to kilometers in length. Often they are characterized by large, shore-parallel ripples, which are composed of coarser sediment than that on the surrounding seafloor. While a number of recent studies have identified RSDs in diverse coastal environments (Green et al. 2004; Murray and Thieler 2004; Garnaud et al. 2004; Goff et al. 2005), the origins of these features are not well understood.

RSDs were originally noted to be roughly symmetric in transverse bathymetric profile, although RSDs have since been described in other regions as having marked asymmetry (Murray and Thieler 2004; Goff et al. 2005). Hydraulic roughness created by the large bedforms within the RSDs has been proposed to increase local turbulence, inhibiting settlement of finer-grained sediment, explaining their persistence during periods of low wave energy (Goff et al. 2005). Cacchione et al. (1984) proposed initiation of individual RSDs through scour induced by storm-driven downwelling that removes finer-grained surficial sediment typically seen on the seafloor adjacent to RSDs. Local steep seafloor gradients associated with rocky outcrops and high current-induced bed stress were originally proposed to concentrate downwelling flows with localized intensification leading to preferential scour. A lack of correlation between rock outcrops and RSD along-coast spacing, however, as well as the occurrence of RSDs in regions without rocky outcrops indicate that other causes are locally important (Murray and Thieler 2004). Recent work in South Carolina and Massachusetts indicate that strong along-shore currents can also influence the formation and migration of RSDs, causing them to be asymmetrical in transverse bathymetric profile (e.g., Fig. 2 of Murray and Thieler 2004; Goff et al. 2005). Murray and Thieler (2004) also suggest that these alongshore currents could lead to differential sand transport of coarse and fine fractions, resulting in self-organization of RSDs in some cases.

This paper investigates RSDs offshore of Huntington Beach, CA. High-resolution bathymetry data, gathered in 1999 and 2002, show changes in the spatial extents of these features. These data in conjunction with seafloor photographs and video of small-scale bedforms collected in 2004, shed light on the dynamics affecting these features.

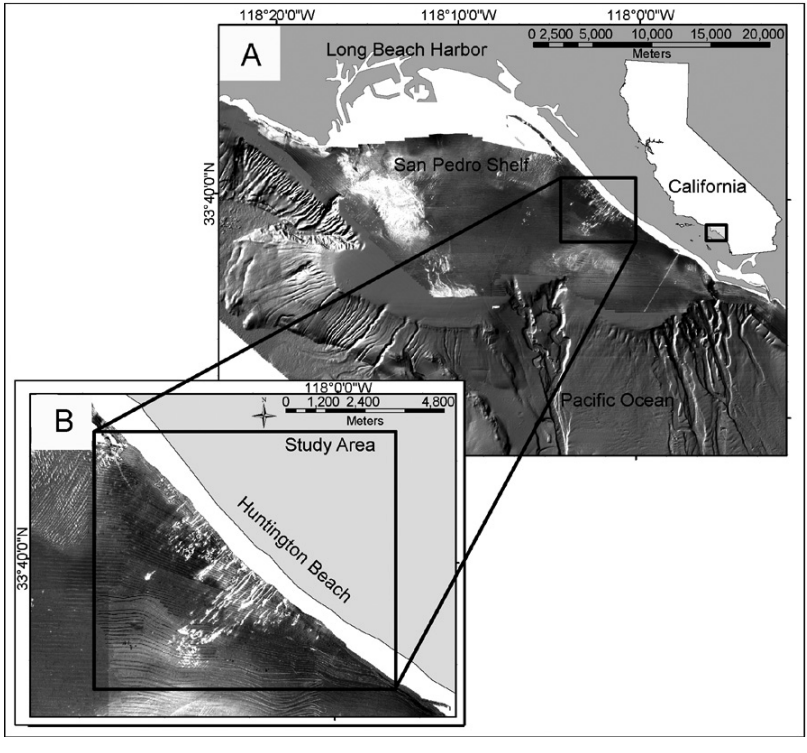

Figure 1. A) Multibeam backscatter mosaic overlain on shaded relief bathymetry of San Pedro Shelf and slope offshore of Long Beach, CA. B) Enlarged view of the study area located immediately offshore of Huntington Beach, CA, showing the location of the highly reflective (bright), elongate, shore-normal rippled scour depressions (RSDs), which contrast sharply with the adjacent, less-reflective (darker) seafloor.

STUDY AREA

The study area is located from one to six km offshore of Huntington Beach, CA on the San Pedro Shelf, the widest section of continental shelf in southern California; this area is part of the Southern California Borderland. The seafloor is characterized by unconsolidated to poorly consolidated Quaternary sediments that blanket the shelf (Karl et al. 1980; Fisher et al. 2004; Bohannon et al. 2004). Extensive urbanization in the region has had a major impact on the sediment budget. While anthropogenic

affects such as flood-control by the damming and channelization of rivers and bluff armoring are mostly offset by nourishments, there is an estimated loss to the inner shelf of ~90 m^3/yr (~120 yds^3/yr) of sand (Slagel 2005; Patsch and Griggs 2006).

The Southern California Borderland is characterized by submarine canyons, banks, and offshore islands, which shadow the shelf from wave directions other than the west and the south (Emery 1960; O'Reilly 1993; O'Reilly and Guza 1997; Noble et al. 2003; Xu 2005). Midshelf significant wave heights for the area are typically 0.5 m to 0.7 m from April to October and 1.0 m with storm peaks at 2.5 m from November to March (Drake et al. 1985). The Southern California Eddy, a poleward recirculating limb of the south-flowing California Current (Hickey 1992), dominates currents on the shelf during the summer months. A recent study shows the presence of strong downcoast flows to the southeast during the summer months as well (Noble et al. 2003; Xu 2005) with the subtidal currents on the order of 5 cm/s to 10 cm/s dominating innershelf currents (Xu 2005).

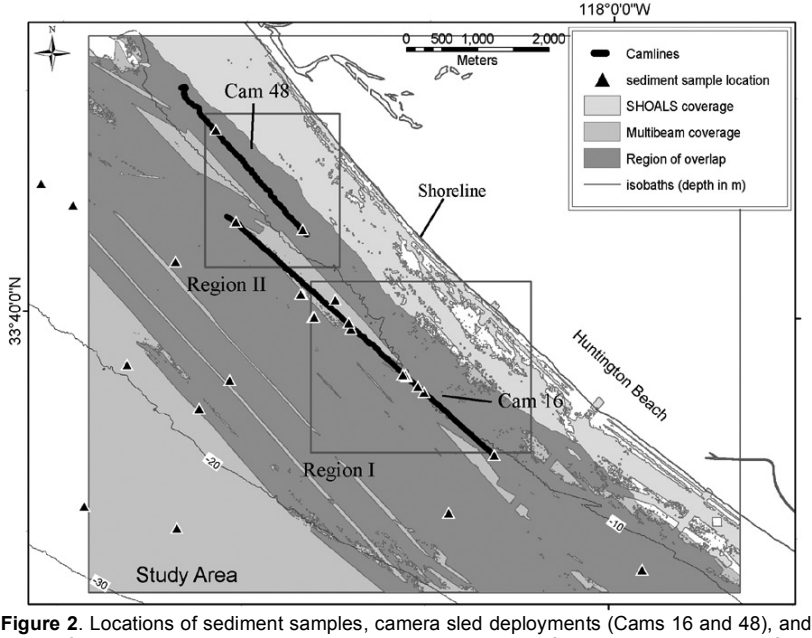

Figure 2. Locations of sediment samples, camera sled deployments (Cams 16 and 48), and areas of multibeam and lidar coverage. A dark grey region defines where the extents of the multibeam (medium grey) and the lidar (light grey) data overlap. All subsequent areal coverage calculations for the RSDs were restricted to the zone of overlap. Also shown are the extents of RSD Regions I and II discussed in the text.

METHODS

USGS researchers collected multibeam data in 1999 from the San Pedro shelf as part of a regional mapping project (Gardner and Dartnell 2002). Subsequently, in

conjunction with scientists from the Los Angeles County Sanitation District (LACSD) and Orange County Sanitation District (OSCD), USGS researchers collected seafloor video and still photography and sediment samples in 2004 to map the dominant seafloor facies and benthic habitats on San Pedro Shelf, including our study area (Dartnell et al. 2004; Edwards et al. 2006). The 1999 multibeam data were compared with existing SHOALS bathymetric lidar data collected in a narrow alongshore strip from the beach to 20 m water depth by the U.S. Army Corps of Engineers (USACOE) in 2002 (Fig. 2). Data pertaining to the study area were loaded into a Geographical Information System (GIS) database using ESRI ArcInfo™ and analyzed to quantify changes in the RSD field during the five-year period.

Sediment Samples

Thirty-eight seafloor sediment samples were collected in December 2004 within the study area (Fig. 2). The samples were analyzed for grain size using a coulter counter and settling tubes. These data were added to the GIS database, and ancillary data—depth, backscatter intensity and closest seafloor photograph—were assigned to each data point.

Digital Video and Photography

Ten hours and 7.3 line-kilometers of seafloor video data were collected within the study area in 2004. Two video camcorders recorded oblique and vertical-looking video of the same field of view, in which two dots from the laser beams provided scale. RedHen™ Systems' proprietary hardware/software package recorded navigational GPS data onto the videotapes. Layback, the offset incurred by towing a sled, was calculated and applied to the navigation data. The resulting navigation data were associated with the video and photographs and loaded into the GIS dataset. Three-minute segments of video were also mosaicked into jpegs, as described in Rzhanov et al. (2002) and added to the GIS dataset (Fig. 4A).

Onboard scientists used a remote switch to capture seafloor images with a 6 mega-pixel digital camera approximately every 30 seconds during the sled deployment (termed a "Cam"). The Huntington Beach region of interest contains Cam 16 and Cam 48 (Fig. 2), which traverse two sections of the RSD field. Cam 16 was run shore-parallel along the 11 m isobath; Cam 48, located northwest of Cam 16, was run shore-parallel along the 9 m isobath. Over 750 photographs were collected during those deployments. Measurements of the ripple wavelengths, determined by measuring from one ripple crest to the next, were made for all images that have one or both sets of lasers and identifiable ripple crests. Because the limited field-of-view (~1 m^2) resulted in an inability to identify two lasers (for scale) and/or two complete ripple crests, the size of large ripples (wavelength >50 cm) typically could not be quantified in still photographs (Fig. 4B). When the ripples were too large to measure on photographs, ripple wavelengths were determined from the video, again using laser dots to determine scale, with measurements taken approximately every 30 s. The resulting measurements and associated depth values, taken from the multibeam bathymetry data, were added to the GIS dataset.

Multibeam Data

Regional multibeam bathymetry and acoustic backscatter data for water depths between 8 m and 900 m were collected in 1999 with a Kongsberg Simrad EM3000D multibeam echosounder (Fig. 2; Gardner and Dartnell 2002). Mosaics of these data gridded to 4 m pixels (Dartnell et al. 2004) were used in this study. Polygons were visually identified and hand-drawn in the GIS dataset, identifying elongate bathymetric depressions with continuous, distinct contours. A co-registered backscatter intensity mosaic was inspected to distinguish RSDs from small bathymetric data artifacts. Where RSDs extended to the limits of the dataset, the perimeter of the polygon coverage was defined as the edge of the dataset. To avoid false positive identification, only regions of high backscatter that ran shore-normal and had smooth, depressed bathymetric profiles were identified as RSDs (Fig. 3). The resulting polygons were used to make areal comparisons of RSDs identified in both bathymetric datasets, and were compared to the photography, sediment samples, and video collected in 2004.

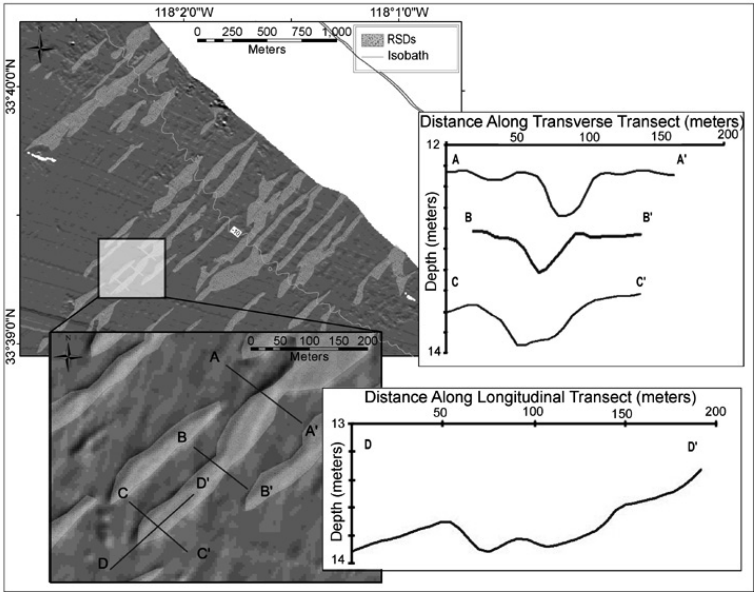

Figure 3. Shaded relief multibeam bathymetry of the study area with RSDs identified in light grey. Enlarged region shows bathymetric profiles of transects across selected RSDs, showing both transverse transects (A-A', B-B', C-C') and a longitudinal one over the offshore edge (D-D'). Transverse transects are run over progressively deeper locations on the RSD; each transect displays a region of bathymetric depression with a relatively symmetrical profile. The offshore extent of the RSD is also characterized by a distinct bathymetric gradient boundary, as shown in D-D'.

SHOALS Lidar

In 2002, the USACOE gathered SHOALS bathymetric lidar data from the shoreline to depths of 20 m offshore of the Los Angeles region. Areal coverage is complete except for limited regions of missing data due to breaking waves and other visibility issues (Fig. 3). The raw SHOALS data were gridded to 4 m pixel resolution to match the resolution of the multibeam data. The two datasets were aligned and registered using Orange County Sanitation District sewer outflow pipes, located outside of the Study Area, and rock outcroppings north of Huntington Beach, visible in both the lidar and the multibeam data. Few data artifacts were present within the SHOALS data, and the boundaries of the RSDs were easily determined. RSDs were identified in the GIS using the methodology previously described for the multibeam dataset. A polygon defining the region of overlap of multibeam and lidar datasets was created, and the RSD polygons identified in multibeam and lidar datasets were restricted (clipped) to the region of overlap. Two areas, Regions I and II (Fig. 2), were identified to maximize coverage of RSDs within the area being analyzed, and percent coverage and areal change between 1999 and 2002 were calculated for RSDs both within the entire study area and in the two subregions.

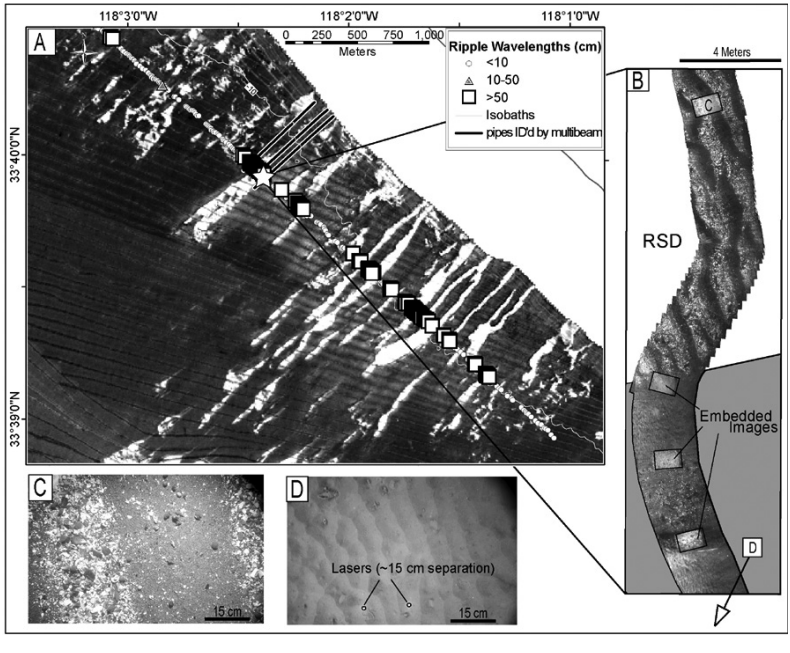

Figure 4. A) Multibeam backscatter mosaic of Region I displaying a section of ripple wavelength measurements, as well as the pipes that were identified through backscatter intensity and bathymetry data. The large ripples (>50 cm) identified on the map do not correlate exactly with the multibeam background image, indicating migration of the RSDs. A star indicates the location of a section of B) a videostrip from Cam 16 with embedded photographs. This section of video imaged the boundary of a RSD, and displays the location

of C) a photograph of large ~70 cm wavelength shore-parallel ripples with shell debris and gravel in the troughs. D) A photograph of small ripples with a measured wavelength of 6.6 cm, located ~5 meters from the edge of the videostrip.

RESULTS

The backscatter mosaic offshore of Huntington Beach is predominantly characterized by low-backscatter (dark) returns, with isolated well-defined elongate, shore-normal regions of high (bright) backscatter returns. Co-registered bathymetric data were used to identify these acoustically bright features (RSDs) as depressed approximately ~0.5 m below the surrounding seafloor.

The main RSDs identified in our dataset extend offshore 2.5 km to the 14 m isobath from the nearshore boundary of the overlap region (~1.0 km offshore at 8 m water depth). Nearby, additional RSD fields occur outside of our study area up to 5.5 km offshore (18 m to 23 m water depth). Video and photography taken of and sediment samples recovered from the RSDs in 2004 indicate that the majority of RSDs identified offshore of Huntington Beach contain sediment coarser than that of the surrounding seafloor with shore-parallel sand ripples (λ = 40 cm to 120 cm), that have gravel and shell debris in the troughs. These RSDs are up to 1.5 km long, and are often greater than 100 m wide. They are sharply defined by both strong acoustic backscatter returns and clearly identifiable, continuous margins in the bathymetry data that delineate the 0.3 m to 0.5 m depressions. Interspersed between these RSDs are rock outcrops that outcrops, which protrude0.5 m to 1.0 m from the seafloor 0.5 m to 1.0 m, and are typically surrounded by slight depressions. The RSDs do not have an alongshore rhythmic spacing, and rock outcrops do not appear related to the alongshore spacing of the RSDs.

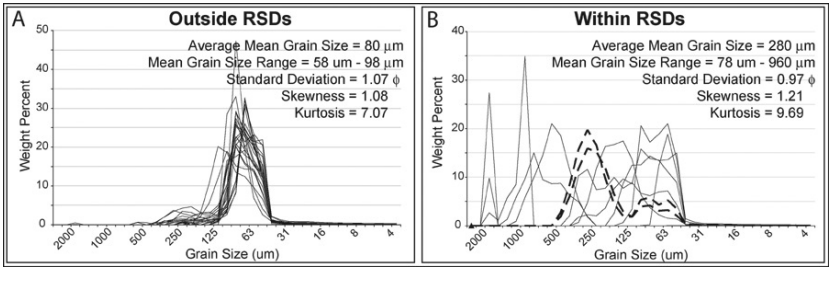

Figure 5. Grain size distributions of sediment samples collected A) on the seafloor surrounding the RSDs with a moderately-sorted very fine sand and B) within RSDs with a poorly-sorted medium sand. Bold dashed lines in B represent sediment samples collected within Region II; solid lines in B represent samples in Region I.

Sediment Size

The sediment outside of the RSDs was characterized by moderately sorted (average σ = 0.97 φ) very fine sand (average mean = 80 μm) (Fig. 5A). Ripple wavelengths were less than 10 cm. The sediment in the RSDs was characterized by poorly sorted (average σ = 1.07 φ) medium sand (average mean = 280 μm). Coarse sediment

samples do not show a trend based on depth or subregions: two coarse sediment samples, recovered in a single sampling location in Region II (bold dashed lines in Fig. 5B), fall well within the range of grain size distributions of sediment samples collected from within Region I (solid lines in Fig. 5B).

While the sediment samples correlate well with the video and photographic data gathered in the same year (2004), they do not always correlate positively with the multibeam and lidar data (collected in 1999 and 2002, respectively) (Fig. 4A).

Ripple sizes

Region I (Cam 16) was characterized by large wavelength, straight-crested ripples with shell debris and gravel in the troughs (Fig. 6A-1). Region II (Cam 48) was characterized by smaller, less orderly ripples, and lacked visible coarse lag deposits within the RSDs. Large ripples located in both Region I and II do not exactly correlate with either the 1999 multibeam-identified RSDs or the 2002 lidar-identified RSDs, and offsets between these data are irregular.

The ripples can be separated into three distinct groups. Within the RSDs in Region I, ripple wavelengths were 72±25 cm. Within the RSDs in Region II, ripple wavelengths were 29±9 cm. Small, well-organized ripples with wavelengths of 7±1 cm occur outside of the RSDs in the fine-grained sediment of Regions I and II (Fig 6 B-E).

RSD Coverage

The combined multibeam and lidar overlap datasets cover 25.3 km^2, and the statistics for Regions I and II are summarized below in Table 1. Between 1999 and 2002, RSD coverage decreased by 0.7 km^2 with variability within the Regions. In Region I, most RSDs whose shoreward extent lay closer than 1 km to shore in 1999 disappeared or decreased in area by 2002 (Fig. 8A), and total coverage decreased from 0.9 km^2 to 0.7 km^2. In Region II, the RSDs grew from 0.2 km^2 to 0.3 km^2, primarily in the shoreward (northeast) direction (Fig. 7B).

Table 1. RSD Coverage by Region and Year

	Total Coverage	RSDs - 1999 multibeam	RSDs - 2002 lidar
Study Area	25.0 km^2	11.3 km^2 (45%)	10.6 km^2 (42%)
Region I	4.6 km^2	0.9 km^2 (20%)	0.7 km^2 (15%)
Region II	2.3 km^2	0.2 km^2 (9%)	0.3 km^2 (13%)

DISCUSSION

Both lidar and multibeam datasets contain regions that do not overlap, and those regions were not treated in the quantitative analyses. There are, however, some general trends that appear when inspecting the entire datasets. Many Region I RSDs appear to have migrated offshore or decreased in areal coverage from 1999 to 2002

(Table 1). Examination of the 2002 lidar data shoreward of the 1999 multibeam data extent does not show more identifiable RSDs in Region I. In Region II, the RSDs, appear to have expanded shoreward and become more extensive, and examination of the 2002 lidar shows continuation of the RSD field shoreward of the 1999 multibeam data extent. The smaller RSDs seen in Region II extend further inshore to shallower water (8 m as opposed to 11 m in Region I) in both 1999 and 2002, and are likely to thus more frequently become mobilized.

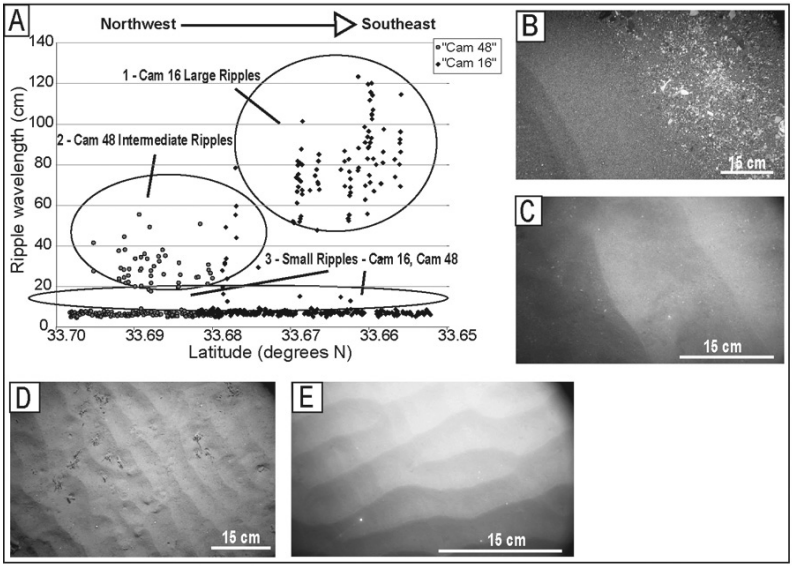

Figure 6. A) Ripple wavelengths (in cm) identified by video and still photography plotted versus latitude. B-E) Photographs, taken from northwest to southeast, of typical ripple morphologies for each size class. Data for Cam16 are shown as black triangles and for Cam 48 as grey circles. Ellipses identify three size class clusters: 1) the largest ripples with λ = 40 cm - 120 cm, located in Cam 16, 2) intermediate ripples with λ = 18 cm – 55 cm, located in Cam 48, and 3) short ripple wavelengths withλ = 5 cm – 10 cm, characterizing the seafloor outside of the RSDs for both Cams 16 and 48.

All of the ripples in the study area are symmetric with sharp, narrow crests and flat, broad troughs. In other ways, however, the ripples differ between the RSDs in Regions I and II. Within Region I, the median ripple wavelength in the RSDs is 75 cm with 84% of the measurements falling above 50 cm. The median RSD ripple wavelength in Region II is 28 cm. The larger ripples in Region I RSDs were straight crested with gravel or shell hash in the troughs. On the other hand, the larger ripples in Region II RSDs were short-crested without gravel or shell debris in the troughs.

The depth of a RSD does not appear to be a function of its size, and RSDs from both Regions I and II have approximately the same amount of bathymetric depression.

The interfaces between the RSDs and the surrounding seafloor, which is characterized by very fine sand and small ripples, are sharp. Areas with the largest ripples tended to have the straightest and the most continuous ripple crests, and the most gravel exposed in the ripple troughs. Medium ripples (~10 cm to 50 cm) within Region I were also generally less organized, suggesting an intermediate stage in RSD development, for instance a transition after recent mobilization and reorganization under different flows than those that initially formed the RSDs.

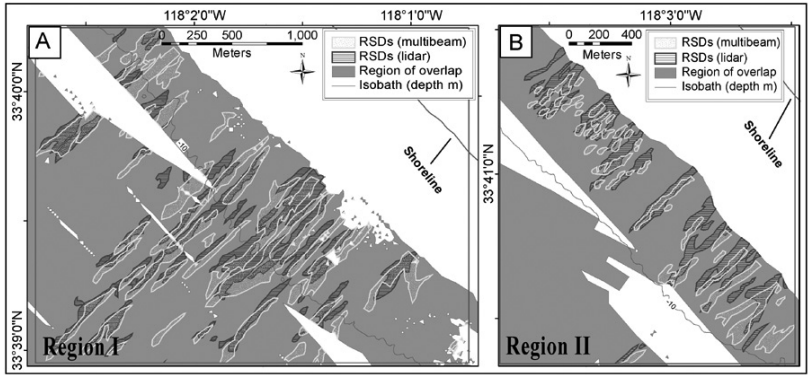

Figure 7. RSD locations in1999 (light grey) and 2002 (dark grey) for A) Region I and B) Region II.

Gravel, shell debris, and coarse sand are major constituents of the RSD floor; however, the RSD sediment samples show that there is not one grain size class, or grain size distribution, that dominates the system (Fig 5B), and there is no significant difference between Region I and II RSD sediment samples. Fine sediment is largely absent from some, but not all, of the RSD sediment samples. The homogeneity of the fine-grained sediment cover outside of the RSDs extends far outside of the study area. The heterogeneity of the RSD samples, which likely represents a coarse-grained basal lag, is similar to the coarse-grained intertidal lags exposed on many southern Californian Borderland beaches during the winter when much of the sediment has been stripped off the beaches. The heterogeneous nature of this lag reflects the mode of its emplacement, likely by stream action during the previous sea level lowstand (Drake et al. 1985).

RSDs most likely form and expand under high-energy conditions. Storms produce downwelling currents capable of removing the overlying fine-grained material that is suspended by storm waves, thus exposing the underlying coarser-grained lag (Cacchione et al. 1984; Garnaud et al. 2004). Within our study area, large, extensive RSDs typically contain well-organized, straight-crested, shore-parallel ripples with shell hash and gravel in the troughs that end abruptly at the edges of the RSDs. These RSDs decreased in coverage from 1999 to 2002. Smaller, less extensive RSDs contained intermediate, short-crested ripples lacking gravel and shell debris in the

trough. These smaller RSDs were also distinct from the surrounding seafloor, and increased in coverage between 1999 and 2002. Unlike the RSDs reported elsewhere (Murray and Thieler 2004, Green et al. 2004, and Goff et al. 2005), the lack of asymmetry in the RSDs' bathymetric profiles and their irregular alongshore spacing in both Regions, as well as the presence of shore-parallel ripple crests within the RSDs, does not support longshore currents as a dominant causal factor offshore of Huntington Beach. The relatively minor change in spatial extent and form of the RSDs likely reflects the quiescent nature of the inner shelf in the years between the surveys. The wave climate of the Southern California coast has been well documented as being strongly affected by ENSOs (El Niño-Southern Oscillation), (e.g. Storlazzi and Griggs 2000, Xu and Noble 2007). ENSO events have been documented to produce mean significant wave heights 50-100% higher than normal along the Southern California coast for the same months in non-ENSO years (Xu and Noble 2007) and these storm waves arrive more frequently out of the west and southwest (Storlazzi and Wingfield, 2005). 1998 was a strong ENSO event year, (Storlazzi and Griggs 2000), and as such the study area was impacted by larger, more southerly waves that directly impacted the southeast-trending shoreline, causing less energy loss to refraction and resulting in greater wave-driven set-up; this increased set-up likely drove the offshore-directed near-bed flows that either formed or help maintain the RSDs. Between 1998 and 2004 no new large regions of RSDs formed in the study area. A lack of large storms between the 1999 multibeam and 2002 lidar surveys, however, has not resulted in the burial of the RSDs or even a large reduction in their extent, suggesting that self-maintenance due to hydraulic roughness (Murray and Thieler 2004) is a likely characteristic of the dynamics of this system. The frequency of sampling and a lack of data before 1998, however, does not support definitive conclusions on the evolution or maintenance of these features.

CONCLUSIONS

The symmetrical RSDs offshore of Huntington Beach fall into two distinct categories: those observed in Region I, a collection of 1 km to 2 km long, greater than 100 m wide features containing large wavelength (>70 cm), straight-crested ripples with gravel and shell debris in the troughs, and those observed in Region II to the northeast, a grouping of shallower, smaller, shorter RSDs containing short-crested ripples with wavelengths less than 30 cm. The RSDs within Regions I and II showed differential areal change between 1999 and 2002 with those in Region I shrinking, and those in Region II becoming more extensive during the same time period. No trends were recognized in grain size between groups of RSDs, as there were limited sediment samples recovered, and the grain size distributions of sediment samples from RSDs were highly variable. However, there was a distinct difference in grain-size distribution between the sediment surrounding the RSDs and the coarser material within them.

ACKNOWLEDGMENTS

We wish to thank Jingping Xu and John Dingler for their critical reviews of the draft manuscript as well as Dave Cacchione and Greg Gable for valuable discussion. The officers and crews of the Los Angeles County Sanitations District (LACSD) R/V Ocean Sentinel and the Orange Country Sanitation Districts (OCSD) contract vessel,

the R/V Early Bird II and Hank Chezar, Kevin O'Toole and Gerry Hatcher provided able support for the data collection phase of the study. Funding for the study was provided by the LACSD and the USGS Coastal and Marine Program. We thank Joe Meistrell (LACSD) and George Robertson (OCSD) for providing ship time, and acknowledge the scientific contributions of the science staff of both LACDS and OCSD. We particularly appreciate the insight and encouragement provided by Joe Meistrell, Dave Montagne, and Don Cadien of LACSD. Unpublished SHOALS bathymetric lidar data were provided courtesy of Art Shak (USACOE). Any use of trade, product, or firm names in this publication is for descriptive purposes only and does not imply endorsement of the U.S. Government.

BIBLIOGRAPHY

Bohannon, R.G., Gardner, J.V., and Sliter, R.W., 2004. "Holocene to Pliocene Tectonic Evolution of the Region Offshore of the Los Angeles Urban Corridor, Southern California." Tectonics, v.23, #1:TC1016, 34p.

Cacchione, D.A., Drake, D.E., Grant, and W.D., Tate, G.B., 1984. "Rippled Scour Depressions of the Inner Continental Shelf off Central California." Journal of Sedimentary Petrology, v.54, #4:1280-1291.

Dartnell, P., Gardner. J.V., Mayer, L.A., Hughes Clark, J.E., 2004. "Los Angeles and San Diego Margin High-Resolution Multibeam Bathymetry and Backscatter Data." U.S. Geological Survey Open-File Report, 04-1221.

Drake, D.E., Cacchione, and D.A., Karl. H.A., 1985. "Bottom Currents and Sediment Transport on San Pedro Shelf, California." Journal of Sedimentary Petrology, v. 55, #1:15-28.

Edwards, B.D., Dartnell, P., Phillips, E., Cadien, D.B., Montagne, D.E., Walther, S.M., and Robertson, G.L., 2006. "Mapping mid- and upper slope benthic habitats offshore of San Pedro, CA". ASLO/Ocean Sciences Meeting, Honolulu, HI, CD Abstract - OS12B-01.

Emery, K.O., 1960. The Sea off Southern California: A modern habitat of petroleum. John Wiley and Sons, New York, 366pp.

Fisher, M.A., Normark, W.R., Langenheim, V.E., Calvert, A.J., and Sliter, R.W., 2004. "Marine Geology and Earthquake Hazards of the San Pedro Shelf Region, Southern California". U.S. Geological Survey Professional Paper 1687, Reston, Va., 33pp.

Gardner, J.V. and Dartnell, P., 2002. "Multibeam Mapping of the Los Angeles, California Margin". Open-File Report 02-162, U.S. Geological Survey, 2002.

Garnaud, S., Leseur, P., Garlan, T., 2004. "Origin of rippled scour depressions associated with cohesive sediments in a shoreface setting (eastern Bay of Seine, France)." Geo-Marine Letters, 25:34-42.

Goff, J.A., Mayer, L.A., Traykovski, P., Buynevich, I., Wilkens, R., Raymond, R., Glang, G., Evans, R., Olson, H., and Jenkins, C., 2005. "Detailed Investigation of Sorted Bedforms, or "Rippled Scour Depressions" within the Martha's Vineyard Coastal Observatory, Massachusetts." Continental Shelf Research, 25 (2005) 461-484.

Green, M.O., Vincent, C.E., and Trembanis, A.C., 2004. "Suspension of Coarse and Fine Sand on a Wave-Dominated Shoreface, with Implications for the

Development of Rippled Scour Depressions", Continental Shelf Research, 24 (2004) 317-335.

Hickey, B.M., 1992. "Circulation over the Santa Monica-San Pedro basin and shelf." Proceedings of Oceanography, v.30, 37-115.

Karl, H.A., Cacchione, D.A., Drake, D.E., 1980. "Erosion and transport of sediments and pollutants in the benthic boundary layer on the San Pedro shelf, southern California." Open-File Report 80-386, US Geological Survey (54pp).

Murray, A.B. and Thieler, E.R., 2004. "A New Hypothesis and Exploratory Model for the Formation of Large-Scale Inner-Shelf Sediment Sorting and 'Rippled Scour Depressions'". Continental Shelf Research, 24 (2004) 295-315.

Nittrouer, C.A., and Wright, D.L., 1994. "Transport of Particles Across Continental Shelves." Review of Geophysics, v.31 #1:85-113.

Noble, M., Xu, J.P., Rosenfeld, L., Largier, J., Hamilton, P., Jones, B., Robertson, G., 2003. "Huntington Beach shoreline contamination investigation, phase III." U.S. Geological Survey Open-File Report, OF 03-0062.

O'Reilly, W.C. 1993. "The Southern California Wave Climate: Effects of Islands and Bathymetry." Shore and Beach, July 1993.

O'Reilly, W.C., and Guza, R.T., 1998. "Assimilating Coastal Wave Observations in Regional Swell Predictions. Part I: Inverse Methods." Journal of Physical Oceanography, 28 pp. 679-691.

Patsch, K., and Griggs, G., 2006. Littoral Cells, Sand Budgets, and Beaches: Understanding California's Shoreline. Institute of Marine Science, UC Santa Cruz, California.

Rzhanov, Y., Huff, L., Cutter, G.R., 2002. "Seafloor video mapping: modeling, algorithms, apparatus." International Conference on Image processing: Proceedings, 2002 volume 1, pp. 868–871.

Slagel, M. 2005. Unpublished Master's Thesis, UC Santa Cruz.

Storlazzi and Griggs, 2000. "Influence of El Niño-Southern Ocsillation (ENSO) events on the evolution of central California's shoreline." Geological Society of America Bulletin, February 2000 v.112 #2:236-249.

Storlazzi, C.D., and Jaffe, B.E., 2002. "Flow and Sediment Suspension Events on the Inner Shelf of Central California." Marine Geology, 181 (2002) 195-213.

Storlazzi, C.D. and Wingfield, D.K., 2005. "The Spatial and Temporal Variability in Oceanographic and Meteorologic Forcing along Central California: 1980-2002." *U.S. Geological Survey Scientific Investigations Report 2005-5085*, 39 pg.

Xu, J.P., 2005. "Observations of Plan-View Sandripple Behavior and Spectral Wave Climate on the Inner Shelf of San Pedro Bay, CA." Continental Shelf Research, 25 (2005) 373-396.

Xu, J.P., and Noble, M.A., 2007. "Variability of the southern California wave climate and associated implication for sediment transport." Earth Science in the Urban Ocean: the Southern California Borderland. Lee, H., Normark, B., eds. Geological Society of America, 2007, *in publication.*

A STUDY OF INTERTIDAL BAR DYNAMICS USING THE ARGUS VIDEO SYSTEM

Amaia Ruiz de Alegria Arzaburu[1], Suzana Ilic[1], Yohama Gunawardena[1]

1. Department of Geography, Lancaster University, Lancaster, LA1 4YB, UK. a.r.alegria@lancaster.ac.uk; s.ilic@lancaster.ac.uk; y.gunawardena@lancaster.ac.uk.

Abstract: The following paper describes the cross-shore and longshore seasonal intertidal beach dynamics along the macro-tidal beach of Cleveleys (UK). The studied beach is characterised by the presence of shore-parallel runnel (channels) and ridges (tabular bodies), and intersecting drainage channels. Argus video images and *in-situ* field measurements have been used in order to quantify the spatial and temporal variability of the complex and dynamic runnel-ridge system. In the short-term, the impact of a major storm has been analysed and correlated to the changes in intertidal bathymetry. The long-term ridge position has been determined using the Argus image contouring technique and existing beach surveys since 1991. It has been demonstrated that the frequent cross-shore ridge migration mainly occurs during high energy conditions and is governed by surf zone processes. The longshore ridges' migration occurs at larger time scales and is associated with the dynamics of intersecting or mini rip channels.

INTRODUCTION

Many macro-tidal beaches, such as those around the British Isles, have complex topography as a result of the strong interaction between tide, waves, currents, groundwater and sediments. These beaches are often intersected with runnels (channels parallel to the shore) and drainage and/or rip channels (transverse channels) resulting in a difference in elevations across the beach. A runnel and ridge beach is a special case. The ridges are

formed as shore-parallel intertidal bars and separated from each other by shore-parallel runnels. Often, the ridges are also transversely cut by drainage channels, which usually follow irregular patterns and have high depth variability from several centimetres to several tenths of centimetres.

Although the intertidal bars have been studied since the 1940's (King and Williams, 1949), little is still known about their generation, evolution and decay (Wijnberg and Kroon, 2002). Most studies in the past used large numbers of beach surveys, (King and Williams, 1949, Masselink and Anthony, 2001) and cross-shore hydrodynamic measurements (Voulgaris *et al*. 1998) in order to determine the offshore/onshore beach dynamics and the bar formation and position. A recent study of intertidal bars dynamics using aerial photography and Lidar images (Van Houwelingen *et al*., 2006) showed that the intertidal bars not only migrate across-shore but also in the alongshore direction. Not much is known about transverse channel formation and their impact on the intertidal bars. It is still unknown whether these channels are rip channels formed due to surf zone processes during high tide, or drainage channels developed due to the tidally-induced ebb flow. They might also be formed due to a combination of wave induced, tidal and groundwater flow.

The beach volumes seem to be strongly related to the presence and deconstruction of ridges as well as their volume (Parker, 1975, Ilic and Ruiz de Alegria, 2006). Hence, it is necessary to get a better understanding of the intertidal morphodynamics in order to be able to predict the risk of future flooding and undertake proper shoreline management plans. The aim of this study is to investigate the cross-shore and longshore intertidal beach dynamics and the channels formation and migration by using long-term beach survey data, Argus video images and *in-situ* measurements.

STUDY AREA AND DATA COLLECTION

The study is conducted on the macro-tidal beach in Cleveleys at the eastern edge of the Irish Sea (Fig.1), several kilometres north from Blackpool, where the first investigations of intertidal bars were conducted and the "ridge" and "runnel" terms come from. The researched area is a macro-tidal beach with a mean tidal range of about 8m during spring tide and exposed to waves of limited fetch. Coastal defences such as groynes and a seawall have been built at Cleveleys to prevent beach erosion and protect the area from future flooding.

The Fylde coast where Cleveleys is located is an almost straight stretch of coastline, and is orientated NNW-N-NNE. However the shoreline at Cleveleys is slightly concave. The intertidal zone, which is 400-450m wide is characterised by the presence of two ridges (Fig.2.1 and 2.2). This area is also intersected by shore-normal, rip/drainage channels and shore-parallel runnels. The crest of the upper ridge is currently located between 110-160m and the crest of the lower ridge around 220-260m from the shoreline.

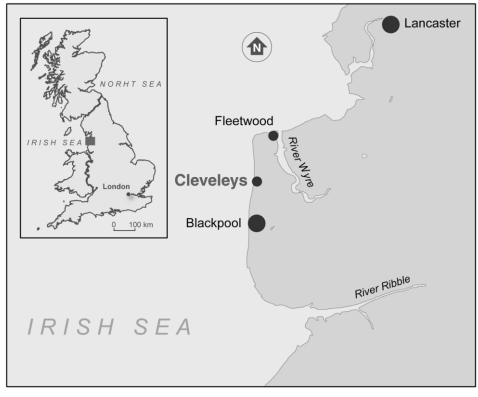

Fig.1. Site location map.

The Wyre Borough Council undertakes beach surveys between Fleetwood and Cleveleys at irregular intervals, but mostly twice per year since 1991. In addition, the Council deployed the ARGUS video imagery system (Holman *et al*., 1993, Aarninkhof *et al*., 2003) to monitor the beach changes due to the replaced seawall on the top of the beach. Two Argus stations are about 700m apart and cover the area up to 700m offshore. Argus video images have been collected from both stations every 30 minutes. On several occasions, a 5 minute continuous image collection has been set up in order to get a better resolution of beach profiles derived from the images.

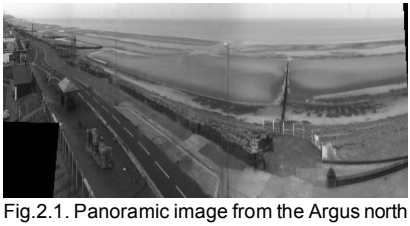

Fig.2.1. Panoramic image from the Argus north station (August 2005)

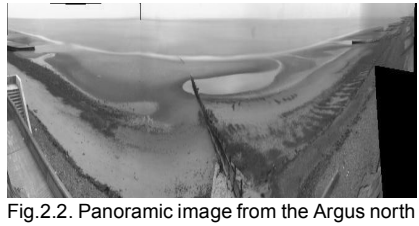

Fig.2.2. Panoramic image from the Argus north south (August 2005)

In-situ field measurements were conducted between 23rd September and 15th October 2006 in the area in front of the Argus north station. Hydrodynamics measurements were taken at two self-logging instrument rigs placed on the top of the outer ridge, (see X2 in Fig.3) and at the bottom of the runnel, (see X1 in Fig.3). Each rig contained an Acoustic Doppler Velocitymeter (ADV), an external pressure transducers (PT), and an optical backscatter sensor (OBS).Data were collected at 4Hz for about 6-7h when the instruments were submerged. The tidal elevation data from Heysham (north of the site), and wave data from two offshore buoys in Irish Sea are used to complement the field measurements. Also, wind velocities and directions were measured at the Argus Northern Station.



Fig.3. Location of the study area. The yellow rings indicate the location of the Argus video stations at Cleveleys. X1 is the location of the instrument rig in the channel and X2 shows the location of the second instrument rig on the top of the ridge.

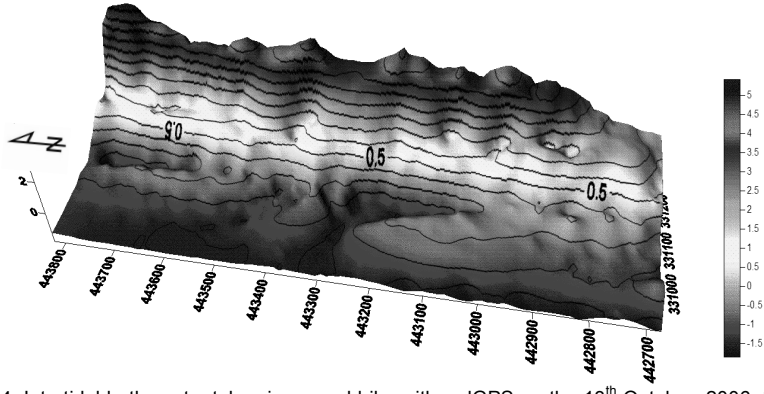

Fig.4. Intertidal bathymetry taken in a quad bike with a dGPS on the 13th October, 2006; the cross-shore and longshore distances are Ordnance Survey's Easting and Northing respectively. The colour scale indicates the elevation in metres.

Morphological measurements of intertidal bathymetry were conducted from 19th September until 15th October 2006 using a Trimble differential GPS (dGPS). A shore-normal profile through the instrument locations and two adjacent profiles were surveyed each day. These surveys were validated with surveys obtained with a total station in the first week of fieldwork. Additional profiles were surveyed as time allowed. At two occasions (6th and 13th October), the whole beach between two Argus stations was surveyed using a quad-bike and dGPS. The overall bathymetry of the intertidal area between two Argus stations derived from a dGPS survey is presented in Fig.4, which nicely shows the location of the runnel and ridges and the intersecting channels. Analysis of sediments collected on the outer ridge and runnel in the first week of fieldwork did not reveal much difference between the ridge and runnel sediment size (D_{50}=0.18 and 0.21mm respectively).

RESULTS

The intertidal area between the Argus north and south stations (Fig.3) has been analysed.

Long-term dynamics from beach surveys

Figure 5 shows beach profiles for Profiles 1, 2 and 3 (see Fig.3 for their locations) surveyed during or immediately after winter months. Unlike stationary ridges on the neighbouring Blackpool beach (Masselink and Antony, 2001; King and William, 1949) the ridges on the Cleveleys beach are highly dynamic. Most of the time two ridges are present, one immediately below the upper steeper shingle beach (inner ridge) and one on the lower beach (outer ridge). Both are located between mean low water neap and high water neap elevations. Inner ridges move onshore for about 120m over a period of approximately 3 years while outer ridges can move for about 160m in a shorter period of time. Inner ridges are more persistent and there are no outer ridges when the inner ridges are at their most offshore location.

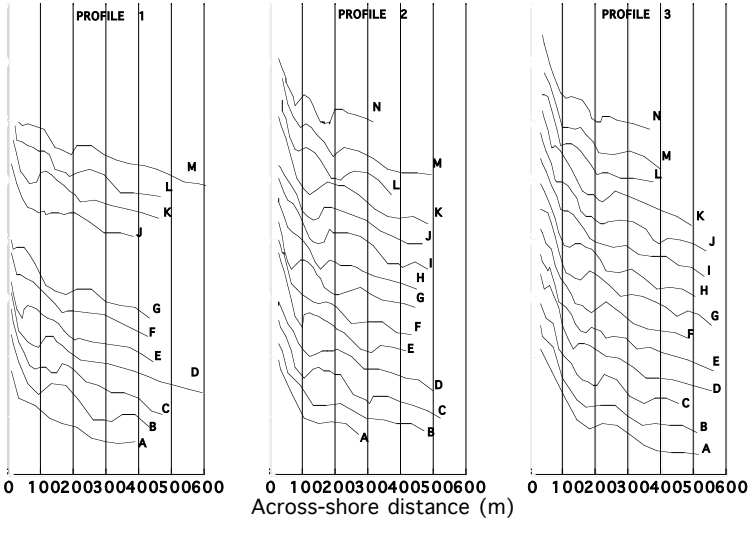

Fig.5. Intertidal beach profiles measured over the period 1991-2006 (data from the Wyre Borough Council, UK). The profiles have been vertically offset by 1m. The surveys were taken on: A=Oct 91, B=Sep 92, C=Sep 93, D=Sep 94, E=Sep 95, F=Sep 96, G=Sep 97, H=Sep 98, I=Sep 99, J=Nov 00, K=Mar 01, L=Oct 04, M=Oct 05 and N=Nov 06.

Figure 5 also illustrates the difference in the longshore position of ridges and runnels indicating their longshore migration. However, it is difficult to distinguish longshore and cross-shore migrations from beach profiles only. Particularly, the longshore dynamics is characterized by the movement of the intersecting drainage and mini rip channels. This is clearly seen from aerial photographs but it is difficult to track a position of a particular bar or a channel due to irregular and infrequent sampling (van Houwelingen *et al*.,

2006). The Argus video images taken at regular and more frequent intervals enable to track migrations of a particular ridge or channel.

Seasonal dynamics from Argus video images

The outer ridge contours, at a constant but arbitrary tidal level, approximately -1.7 m below ordnance datum Newlyn, UK, have been derived from the plan view Argus images from northern station for several days in 2005 and 2006. Figure 6 shows the variation in the length, width and shape of the outer ridge and the high mobility of the intersected channels. There were two ridges, separated by a rip channel, present in May 2005. In August 2005, the southern ridge advanced to the north, and a new intersecting channel was formed further north. After the winter, the southern ridge became flattened and the northern ridge expanded further south. In August 2006, the northern ridge became shorter but more pronounced while in October 2006 the ridge became flattened again. The intersecting channels moved north and south in this period. The northern ridge also moved onshore between May 2005 and May 2006 but expanded again offshore in August 2006. From August until October 2006, the ridge had moved again slightly towards onshore. Figure 6 clearly shows cross-shore and longshore dynamics of ridges and associated channels through winter/summer seasons.

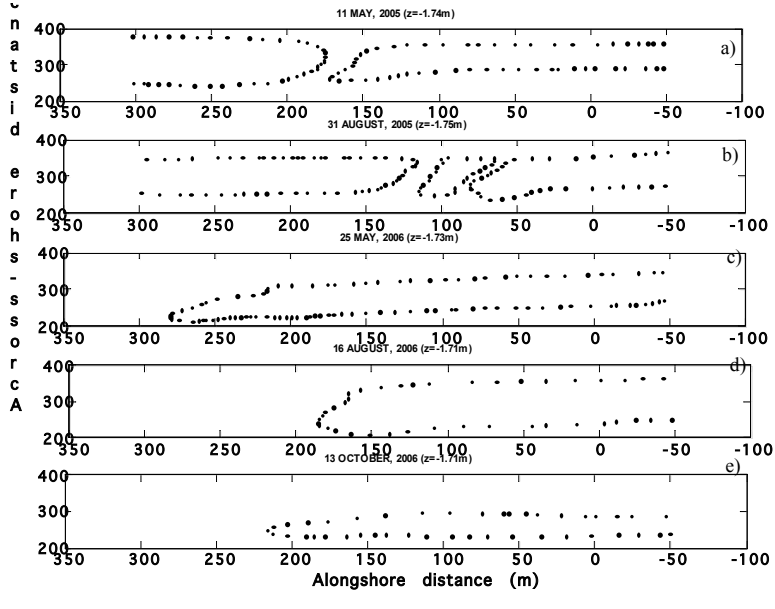

Fig. 6. Outer ridge contours derived from the Argus plan-view images at an approximate depth of -1.7m below ordnance datum, Newlyn, UK, for: a) 11th May 2005, b) 31st August 2005, c) 25th May 2006, d)16th August 2006, and e) 13th October 2006.

Short-term dynamics from *in-situ* measurements

The tidal elevation at Heysham, significant wave height and nearshore currents measured on the outer ridge between 24th September and 15th October are shown in Figure 7. Each of the dots represents measurements over 17min. Almost two complete spring-neap tidal cycles are covered. The second spring tide on 9th October was the second largest spring tide in the year and a total tidal range of 10.44m was recorded. Calm and more energetic periods were recorded, with significant wave heights between 0.03 and 0.87m. During spring tides, the high water level reaches the seawall and some wave energy is reflected back increasing the nearshore wave height. The mean wave period is 5.53s, which is also associated with more energetic waves. The wave direction varied from south-west up to north-west with westerly direction being more frequent. However the waves are mostly refracted by the time they reach the intertidal zone. The most energetic periods were on 27th September, between 2nd and 5th October and on 12th October. A severe storm (Hs=3.4m in Liverpool Bay) coincided with large spring tidal ranges of 9.25m and 10.16m on 6th and 7th October respectively. Unfortunately the equipment had to be rescued and there is no field record for this storm.

Time-averaged cross-shore and longshore currents plotted in Figure 7 show a presence of tidal modulation. During low wave activity, cross-shore and longshore currents are nearly symmetrical in respect to the high water. Both maximum cross-shore and longshore currents occur mid way between low and high and high and low tide and there are slack conditions during high tide. Maximum recorded longshore velocity of 0.32 m/s during spring tide and 0.19m/s during neap tide was recorded during low wave activity. They are northward directed during flood and southward directed during ebb. Cross-shore currents are onshore directed during flood and offshore during ebb with a maximum velocity of 0.12m/s during spring tide. During larger wave activity, the presence of wave-induced currents increased northward longshore currents and decreased southward directed longshore currents, but this is highly dependant of the wave direction. Cross-shore currents were mostly offshore directed through whole tidal cycle.

Several beach profiles were surveyed daily using the dGPS through the duration of field campaign. The beach profile through instrument location, starting on the 19th of September, (bottom) and finishing on the 15th of October, (top) is shown in Figure 8. The figure shows clearly the onshore migration of inner runnel and ridge, narrowing of the outer runnel and flattening of the outer ridge throughout the observation period. Also, the landward and seaward slopes of the outer runnel became less steep and the runnel became shallower. The main changes in profile occur after the storms on 27th September, 2nd/3rd October and 6th/7th October.

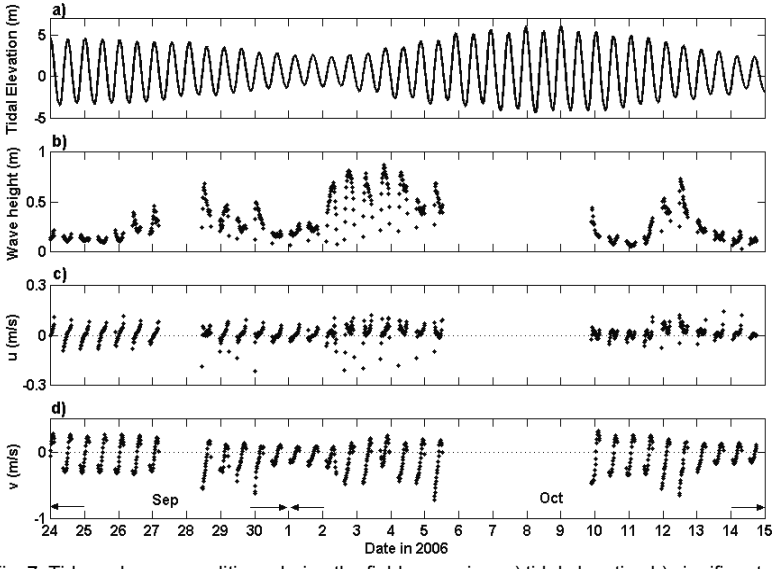

Fig. 7. Tide and wave conditions during the field campaign: a) tidal elevation b) significant wave height, c) cross-shore current velocity, d) longshore current velocity. Positive cross-shore and longshore currents are toward offshore and the south, respectively.

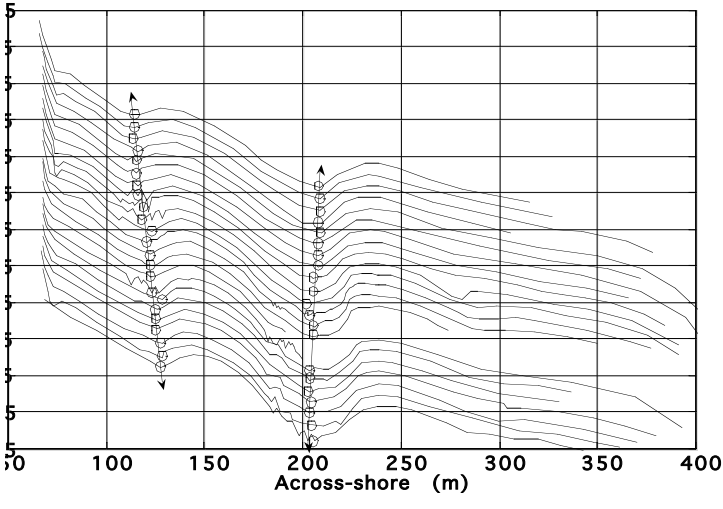

Fig. 8. Beach profiles collected from the 19th September till the 15th October 2006 (except 23rd, 24th, 29th and 30th September) respectively from the bottom to the top of the figure. All the profiles were collected *in-situ* with the differential GPS.

Figure 9 shows more clearly the changes in the profile given in Figure 8, after two storms in October ($6^{th}/7^{th}$ and 12th October). The crest of the upper ridge has migrated inshore, whereas the crest of the lower ridge remained fairly stationary. The runnels have narrowed and the seaward slope of runnels and ridges decreased. The seaward slope of the upper ridge through the lower runnel was calculated for these three profiles (m1.1, m2.1, m3.1). It decreased from 1/27 to 1/34 during the first storm, and then further to 1/37 during the second storm. The landward slopes of the outer ridge, (m1.2, m2.2, m3.2) changed uniformly from 1/33 to 1/39 and then to 1/45. The seaward slopes (m1.3, m2.3, m3.3) of the outer ridge changed again uniformly from 1/64 to 1/67 and then to 1/70. Finally, the areas of the lower ridge reduced from A1=36.1 m^2 to A2=28.3m^2 during the first storm and then to A3=25.9m^2 during the second storm. These results indicate that the onshore migration of the inner ridge and erosion of the outer ridge was mainly caused due to larger wave activity during the storms.

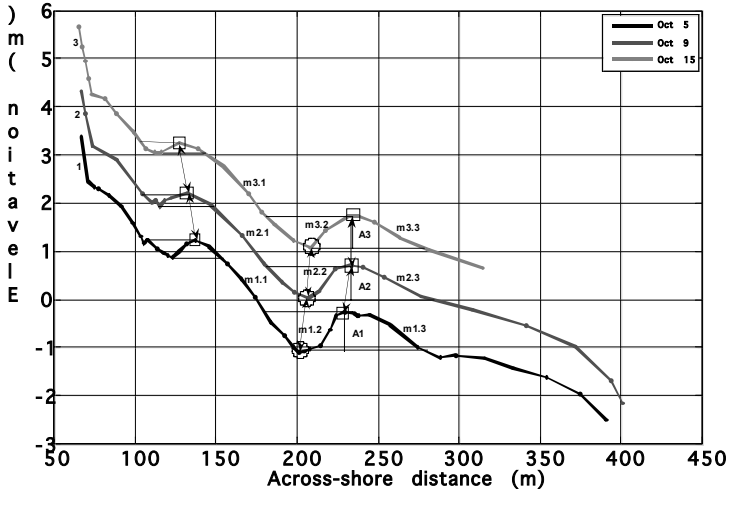

Fig.9. Differential GPS beach profiles for the 5th, 9th and 15th of October 2006.

In addition, a presence of different bedforms was observed during storm and calm conditions. Large mega-ripples, dune like forms of width about 40cm, could be observed in both runnels after the large wave activity. They are also apparent in surveyed profiles in Figure 8. Those bedforms have been covered with smaller ripples. In these conditions the material deposited in runnels was mainly sand and no bedforms were observed on the top of ridges. During calmer conditions ripples were observed on the ridges and runnels and silty material was deposited between ripples crests in the runnels.

DISCUSSION

The analysis of existing beach profiles since 1991, Argus images since 2005, and short term field measurements of beach morphology showed spatial and temporal variability of the ridges and runnels. Although the observed changes during the field campaign have been small in comparison with inter-annual changes, the same trend of onshore ridges migrations was present. The cross-shore sediment transport from the ridge to the runnel, which moves ridges slowly onshore, occurred mainly during energetic conditions during neap and spring cycles. This onshore sediment transport is associated with bore propagation after the wave breaking on the ridge (Kroon and Masselink, 2002). Cross-shore currents measured on the top of the ridge were mainly shoreward orientated during energetic wave conditions causing offshore sediment transport on the seaward side of the ridge filling adjacent runnels and changing the size of the ridges and their seaward slope. These findings are in agreement with those of Kroon and Masselink (2002) confirming that the onshore bar migration is mainly due to surf zone processes.

The intersecting channels have been stationary during the field campaign but there is an evidence of their movement, within a year, from the Argus images. It is not clear yet how these channels are formed and deconstructed and beach structures such as groynes might influence their formation (Short, 1993). However, the sediment transported from ridges into runnels is then moved by the longshore tidal and wave-induced currents in the runnels and through intersecting channels. Also, sediment that is transported longshore on the ridge gets trapped in intersecting channels. Parker (1975) put forward a conceptual model for a multi-barred foreshore, which includes surf zone processes on ridges as well as processes due to a combination of tidal and wave-induced currents in runnels and intersecting channels which need to be verified.

So far Argus images have been used here for qualitative study of beach changes. Quantitative analyses have not been possible mainly due to poor spatial coverage of waterlines derived from images taken every 30min. As the beach slope is quite gentle and the tide range is large, the tide is progressing rapidly over the intertidal area and hence a reduced number of waterlines can be derived from the images. A more frequent setting of 5min gave much better resolution and better coverage of a complex bathymetry. Figure 9 compares the beach profiles derived from Argus images, with 30 and 5min settings, with beach profiles surveyed with dGPS on 23rd June 2006. A very good match can be clearly seen between a profile derived from Argus images collected every 5 min and dGPS in Figure 9a. Hence, there is a possibility that with this setting, the detailed study of cross-shore and longshore beach dynamic can be conducted.

Future work will include further analysis of data collected in the runnel and Argus video images to clarify the importance of nearshore circulation on morphology and their mutual feedback.

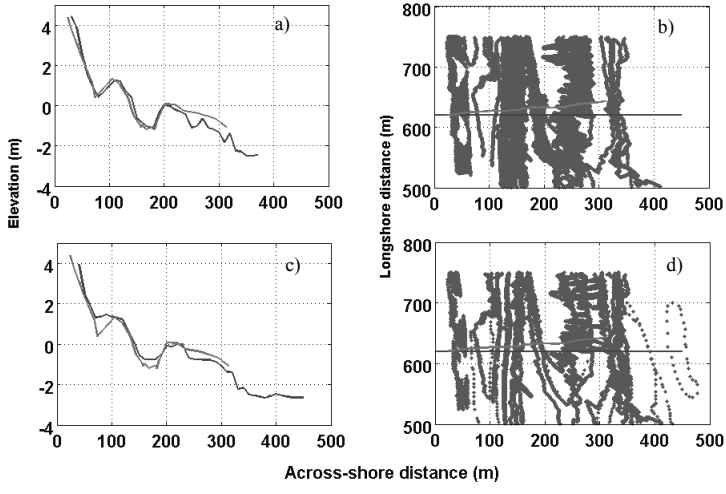

Fig. 9. Argus image analysis for the 23rd of June 2006. The blue profile is the Argus derived profile for a certain location in the Argus south station area. The red profile is a dGPS-collected beach profile for the same location as the Argus one but with a slight rotational angle. a) and b) have been processed using a 5 minute image collection lag whereas c) and d) have been derived from a 30 minute image derived waterlines. The blue profile in a) and c) is derived from the previously plotted waterlines and the black lines in b) and d) are the waterlines derived from the plan-view images.

CONCLUSION

This study demonstrates the spatial and temporal variability of a runnel and ridge system on the Cleveleys beach. Cross-shore migration is governed by surf zone processes during energetic wave conditions equally during the spring and neap tidal cycle. Longshore ridge migration is a seasonal and long-term feature governed by longshore sediment transport due to tidal and wave-induced currents. Argus video images with appropriate time setting are potentially useful for getting comprehensive information of 3D intertidal bathymetry over different time scales.

ACKNOWLEDGEMENTS

We would like to thank to the Wyre Borough Council for funding this project and in particular, to Mr Carl Green, Paul Long and Chris Atherton for their help with maintaining cameras and the field surveys. We are also thankful to Dr Stefan Aarninkhof, Mr Irv Elshoff and Ms Anna Cohen from the Delft Hydraulics for setting up and calibrating the cameras, and for setting up the analysis software. Our thanks also go to Peter Ganderton from University of Plymouth for his help with the field equipment, and to our 'field helpers', Igor Ruzic, Richard Peters and Dr Howard Southgate.

REFERENCES

Aarninkhof, S.G.J., Turner, I.L., Dronkers, T.D.T., Caljouw, M. and Nipius, L. 2003. "A video-based technique for mapping intertidal beach bathymetry". *Coastal Engineering*, 49, 275-285.

Holman, R.A., Sallenger, JR. A.H., Lippmann,T.C. and Haines, J. 1993. "The application of video image processing to the study of nearshore processes". *Oceanography*, 6(3), 78-85.

Ilic, S.,and Ruiz de Alegria, A. 2006. "Study of the impact of a seawall during storm events using Argus video images: Cleveleys, UK," Proceedings 2nd International Short Course and Workshop in Coastal Processes and Engineering, ASCE, *to appear*

King, C.A.M., and Williams, W.E. 1949. "The formation and movement of sand bars by wave action." *Geographical Journal*, 113, pp 70-85.

Kroon, A. and Masselink, G. 2002. Morphodyanmics of intertidal bar morphology on a mactrotidal beach under low wave energy conditions, north Lincolnshire, England. *Marine Geology*, 190, pp 591-608.

Masselink, G., and Anthony, E.J. 2001. "Location and height of intertidal bars on macrotidal ridge and runnel beaches". *Earth Surface Processes and Landforms,* 26, pp 759-774.

Parker, W.R. 1975. "Sediment mobility and erosion on a multibarred foreshore (southwest Lancashire, UK). *In Nearshore Sediment Dynamics and Sedimentation*, Hails J, Carr A (eds.) Wiley and Sons, London, 151-179.

Short, A.D. 1992. "Beach systems of the central Netherlands coast – processes, morphology and structural impacts in a storm driven multibar system". *Marine Geology*, 107 (1-2), pp 103-137.

Van Houwelingen, S. Masselink, G and Bullard, J. 2006. "Characteristics and Dynamics of Multiple Intertidal Bars, North Lincolnshire, England". *Earth Surface Processes and Landforms*, 31, pp 428-443.

Voulgaris, G., Simmonds, D., Michel, D., Howa, H., Collins, M.B., Huntley, D.A. 1998. "Measuring and Modelling Sediment Transport on a Macrotidal Ridge and Runnel Beach: An Intercomparison". *Journal of Coastal Research*, 14(1), pp 315-330.

Wijnberg, K.M., and Kroon, A. 2002." Barred beaches". *Geomorphology*, 48, pp 103-120.

DEPTH OF CLOSURE DERIVED FROM AIRBORNE LASER BATHYMETRY

William Robertson V[1,2], Keqi Zhang[1,3], Dean Whitman[2]

1. International Hurricane Research Center, FIU UP Campus MARC 360, 11200 SW 8th St., Miami, FL 33199, USA. wrober01@fiu.edu.
2. Department of Earth Sciences, Florida International University, Miami, FL 33199, USA. whitmand@fiu.edu.
3. Department of Environmental Studies, Florida International University, Miami, FL 33199, USA. zhangk@fiu.edu.

Abstract: This study develops a method to identify the depth of closure using airborne laser bathymetric data, and compares the measured depth of closure with estimated depth of closures. Airborne laser data sets were collected before and after the 2004 hurricane season in southeast Florida. Estimated depth of closures in terms of wave data is compatible to the measured depth of closures. However, the estimated depth of closure is on average larger than was measured, especially in the southern end of the study area, which could be due to geologic influence. Further research is needed to determine if geology plays a critical role in the depth of closure at this study's location.

INTRODUCTION

Soft stabilization (beach nourishment) has become the principal coastal defense from the encroaching ocean (Finkl et al. 2005). It is essential to mine the sediments from an offshore area that does not have significant sediment exchange with the active sediment movement zone in the nearshore. The locations for beach sediment extraction often rely on the determination of the depth of closure (DOC). The DOC is the location at which repetitive cross-shore profile surveys show little change (Hallermeier 1978). Cost limitation in profile measurement, especially for underwater portions, has motivated researchers to develop methods to estimate the DOC based on the sediment movement induced by waves.

By using linear wave theory, Hallermeier (1978) proposed an equation for estimating

DOC:

$$DOC_e = aH - b\left(\frac{H^2}{gT^2}\right) \quad (1)$$

where DOC_e is the estimated DOC, H is deep wave height, g is gravity, and T is the deep wave period. DOC_e for any specific location changes as the wave condition varies. Wave climates for most U.S. coasts undergo seasonal variation. Sediments are transported offshore to form sandbars when storm or winter waves dominate, while sediments move toward the shore to form berms when the swell or summer waves dominate (Komar 1998). In order to determine the offshore limit of an active zone where yearly onshore and offshore cycle of sediment movement occurs, Hallermeier (1977) proposed to use an extreme wave height, which exceeds 12 hours per year from the distribution for cumulative wave heights, and corresponding wave period. Coefficients a and b are 2.28 and 68.5, respectively, when the extreme wave height and period are used. However, other research has shown that the coefficients can vary (Table 1). In fact, Birkemeier found a reasonable fit to Duck, North Carolina data by applying only wave height with the equation:

$$DOC_w = cH \quad (2)$$

where c is 1.57. Further research is needed at other beach types in order to test the effectiveness of each set of coefficients.

Table 1. DOC Coefficients*

Data Source	Wave Condition	a	b
Hallermeier	12 hr. Wave	2.28	68.5
Birkemeier	12 hr. Wave	1.75	57.9
Nicholls	12 hr. Wave	1.70	82.3
	Peak Wave	1.33	43.9
This Study	Peak Wave	2.49	192.8

*Coefficients obtained from Hallermeier (1977), Birkemeier (1985), and Nicholls (1998).

Large scale bathymetric measurements are required to locate the DOC and adequately test DOC models. Advances in remote sensing techniques have improved our ability to measure large scale coastal change, and airborne laser bathymetry (ALB) provides unprecedented resolution of bathymetric measurements at relatively high accuracies (Irish et al. 2000). Multiple ALB data measuring the same areas over time yield 3-dimensional spatial change and can be used to determine the DOC location.

Southeast Florida is an ideal location for comparing measured DOC with calculated DOC due to an extensive ALB data collection. Two ALB flights were flown before and after the 2004 hurricane season, thus providing a data set for measuring onshore and offshore sediment movement. The main objective of this study is to develop a method for extracting DOC information from multiple ALB data sets, and to compare the measured DOC with estimated DOC based on wave data.

STUDY AREA

The peninsula of Florida is located on the southeastern tip of the United States. This study focuses on southeast Florida, including Palm Beach, Broward, and Miami-Dade Counties (Figure 1). The study area is determined by the extent of overlapping ALB data, covering almost 2 km north of South Lake Worth Inlet (south-central Palm Beach County) to the southern point of Miami Beach (Government Cut) and approximately 600 m offshore. The total length of coastline is over 100 km with 6 inlets.



Figure 1. Map showing southern Florida with hurricane tracks and southeastern Florida. Black polygon along coastline shows the extent of the November 2004 CHARTS data.

DATA

The U.S. National Oceanographic and Atmospheric Administration's (NOAA) Coastal Services Center (CSC) houses many airborne laser data sets measuring coastal environments. This study utilizes the Joint Airborne Lidar Bathymetry Technical Center of Expertise's (JALBTCX) compact hydrographic airborne rapid total survey (CHARTS) ALB data collected on the southeastern coast of Florida in June and November 2004. The CHARTS system produced a nominal 8 m point spacing for the bathymetry and a 2 m point spacing for the topography for each flight line. Due to multiple flight lines, the resulting point density for each airborne laser data collection is slightly higher.

Airborne laser data processing involved interpolating the irregularly spaced laser measurements onto a regularly spaced grid to produce a set of digital elevation models (DEMs). The data were gridded at 4 m resolution using kriging interpolation with a linear variogram. DEMs for each flight were produced with a common origin and cell size for overlaying analysis. The DEMs were then analyzed in a ESRI's ArcGIS to produce elevation contours and transects.

In order to compare the measured DOC with estimated DOC using Equations 1 and 2, wave heights and periods from various locations along the shore are required. Unfortunately, there are no measured alongshore wave data available in the study area. The closest NOAA wave buoy to our study area is located off Cape Canaveral, approximately 200 km north. Therefore, we used offshore wave heights and periods estimated by NOAA's Wavewatch III model for 19 locations along the study area spaced approximately 5 km apart. Peak conditions during Hurricane Frances were tabulated. Although Hurricane Jeanne (Category 3) was one category larger than Hurricane Frances (Category 2) on the Saffir-Simpson scale, the relatively slow moving Frances produced wave heights in excess of 9 m, while Jeanne produced wave heights less than 5 m (Beven 2004; Lawrence and Cobb 2005). This study only analyzes Hurricane Frances data. Hurricane Frances estimated wave heights ranged from 9.4 to 6.4 m, with a period from 10 to 9 seconds. The higher values were found to the north and steadily decreased to the south.

METHODS

DOC_m Extraction

Identification of the DOC is a multi-step process that requires an understanding of measurement limitations. The first step is to produce a difference grid by subtracting the DEM derived after the hurricane season from the DEM derived before the hurricane season. The resulting raster image contains pixels that represent change in volume. Theoretically, locations of zero change should represent the location of the DOC. However, the resolving ability of the CHARTS sensor is limited by noise in the measurements. An in-depth accuracy assessment for the CHARTS system was carried out prior to the June 2004 data collect (Optech 2004). Mean offsets between CHARTS measurements and known elevations ranged between -0.18 to 0.23 m, but most measurements were within ±0.15 m. The noise in the measurements ranged between

0.05 to 0.28 m, which suggests that changes within this range would yield unreliable results.

The three dimensional change can be represented two dimensionally by contouring the change grid. We contoured the change surface at 5 cm steps to empirically determine the level of change that yielded a contour that can be relatively consistent and measurable. We found that changes with absolute values greater than ±0.3 m can be detected reliably in the difference grid. Therefore, the difference grid was contoured at 0.3 and -0.3, and the most seaward intersection of either contour with a transect represented the location of the DOC at this transect.

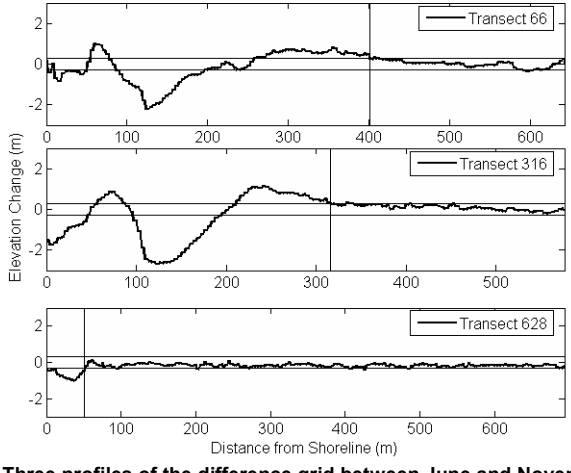

Figure 2. Three profiles of the difference grid between June and November CHARTS data. Thin horizontal lines are the ±0.3 m change. Vertical thin lines are the location of the DOC_m.

Analysis of change greater than ±0.3 m is confirmed by analyzing the profiles in the difference grid. Three representative transects were extracted to explain the profile of the change grid. Transects 66, 316, and 628 represent the change profile offshore of Palm Beach, Boca Raton, and Fort Lauderdale, respectively (Figure 2). Each profile sustained large change near the shoreline, but the change diminished to low level fluctuations further offshore. The low level fluctuations correspond to locations of hard grounds or sand flats that sustain little change if any during storm conditions, thus it is reasonable to assume that these fluctuations are partly due to instrument noise (Finkl and Warner 2005). The low level fluctuations are effectively filtered out when only analyzing change that occurs landward of the most seaward change greater than 0.3 m or less than −0.3 m. When confirming Equation 1 with field data, Hallermeier (1977) determined that change less than ±0.3 m was negligible due to limitations in fathometer measurement resolution.

Comparison of DOC_m and DOC_e

The relative positions of DOC_m were measured using an ArcGIS based shoreline and beach volume mapping system (Robertson et al. 2005; Zhang et al. 2005). This system generates a set of transects perpendicular to the coastline and calculates distance to the intersection of each transect with other linear features. One thousand and forty-six transects spaced 100 m were analyzed over the 104 km length of shoreline. Intersections between transects and the DOC_m contour are converted to points using ESRI's Intersect command. Depths are assigned to each point with ESRI's Extract Values to Points tool based on the CHARTS November DEM. Since DOC_m exhibits considerable changes alongshore, a moving average filter with a window size of 5 (500 m) was employed to reduce possible outliers.

To compare the DOC_e and DOC_m, DOC_e was estimated using Equations 1 and 2 at 19 locations along the shore using wave data from NOAA's Wavewatch III model and were converted into ArcGIS point Shapefiles. As a result, DOC_e can be directly compared to DOC_m alongshore using spatial overlaying.

RESULTS

All data are presented as distance along the coastline, from north to south. Each successive transect represents an alongshore position 100 m south of the previous position. Since we are trying to locate the DOC of typical beaches, we removed data that contain transects surrounding inlets.

Table 2. Measured DOC Values*

Location	DOC Dist.	DOC_m				Sign Count	
	Mean	Mean	Min	Max	St.D.	Positive	Negative
North limit to South Lake Worth	266	-7.8	-4.5	-10.3	0.93	97	66
South Lake Worth to Boca Raton	259	-6.7	-4.3	-9.0	0.74	161	61
Boca Raton to Hillsboro	163	-4.7	-2.6	-6.7	1.00	39	35
Hillsboro to Port Everglades	54	-2.2	-0.3	-6.8	1.00	24	133
Port Everglades to Haulover	124	-2.9	-0.3	-6.3	0.93	76	123
Haulover to Government Cut	116	-3.0	-0.1	-6.5	1.30	48	98

*Measured DOC values split by inlets, from north to south. DOC Dist. is the distance from the shoreline to the DOC_m. DOC_m is the depth, in meters. Sign count is the number of positive or negative contours that are most seaward and represent the DOC_m.

The DOC_m measured from the difference between two ALB data sets appears to be highly variable alongshore, but there is a clear progression of reducing depth from north to south. DOC_m ranges from −10.3 m north of South Lake Worth Inlet to only −0.1 m located off of Miami Beach (Table 2). The −10.3 m represents localized areas of change in Palm Beach County, and the −0.1 m is an unusual location of almost no change offshore of Miami Beach. When separating the results by inlet location, the average DOC_m reduces from −7.8 m in the north to −3.0 m in the south. The reduction in DOC_m depth appears to stop south of Hillsboro Inlet, and the Pompano Beach to Fort Lauderdale section of coastline (Hillsboro Inlet to Port Everglades Inlet) shows a relatively shallow DOC_m average of −2.2 m. The same signal is found when analyzing the distance of DOC_m from the shoreline. DOC_m is on average located 266 m from the

shoreline in the north and 116 m offshore in the south, with the Pompano Beach to Fort Lauderdale section averaging only 54 m offshore.

Table 3. DOC_m vs. DOC_e*

Coefficients	Data	dMean	dMin	dMax	dSt.D.
Hallermeier	raw	-8.4	-5.2	-10.9	1.6
	filtered	-8.0	-6.1	-10.9	1.4
Birkemeier	raw	-4.9	-2.3	-7.5	1.7
	filtered	-4.6	-2.5	-7.6	1.5
Birkemeier Wave Only	raw	-7.8	-4.3	-10.7	1.8
	filtered	-7.4	-5.5	-10.6	1.5
Nicholls	raw	-2.7	0.0	-5.2	1.8
	filtered	-2.4	-0.2	-5.3	1.6
Nicholls Peak Wave	raw	-2.6	0.1	-5.3	1.8
	filtered	-2.2	-0.1	-5.4	1.6
This Study	raw	-0.9	0.1	-3.4	1.8
	filtered	-0.6	-0.1	-3.3	1.8

*Vertical difference between measured and estimated DOC, in meters. Data were filtered by a 5 point (500 m) moving average.

Similarities between the DOC_m and DOC_e suggest that the DOC is physically linked to wave dynamics. Since both Hurricanes Frances and Jeanne made landfall immediately north the study area limits (Figure 1), the increased wave activity to the north should contribute to deeper northern DOC values. For coefficients used to estimate DOC during Hurricane Francis, Nicholls' peak wave coefficients of 1.33 and 43.9 for *a* and *b* in Equation 1, respectively, best matched DOC_m being 2.6 m deeper, on average (Figure 3, Table 3). The average difference between filtered DOC_m and DOC_e is about 2.2 m. Although the mean differences for Hurricane Frances are large, each estimated DOC curve matched the general trend of the measured DOC where the DOC is reduced from north to south.

DISCUSSION AND CONCLUSIONS

The DOC_m is extremely variable alongshore. Depending on which transect is observed, the DOC_m ranges from −10 m to just below the water surface. Since extreme values at various alongshore sections differ from the mean by as much as 3 m (Table 2), the alongshore variability in the DOC indicates that a single transect cannot explain the DOC for the immediate area. The use of ALB data appears to be an effective method for measuring the DOC in relatively clear waters like south Florida.

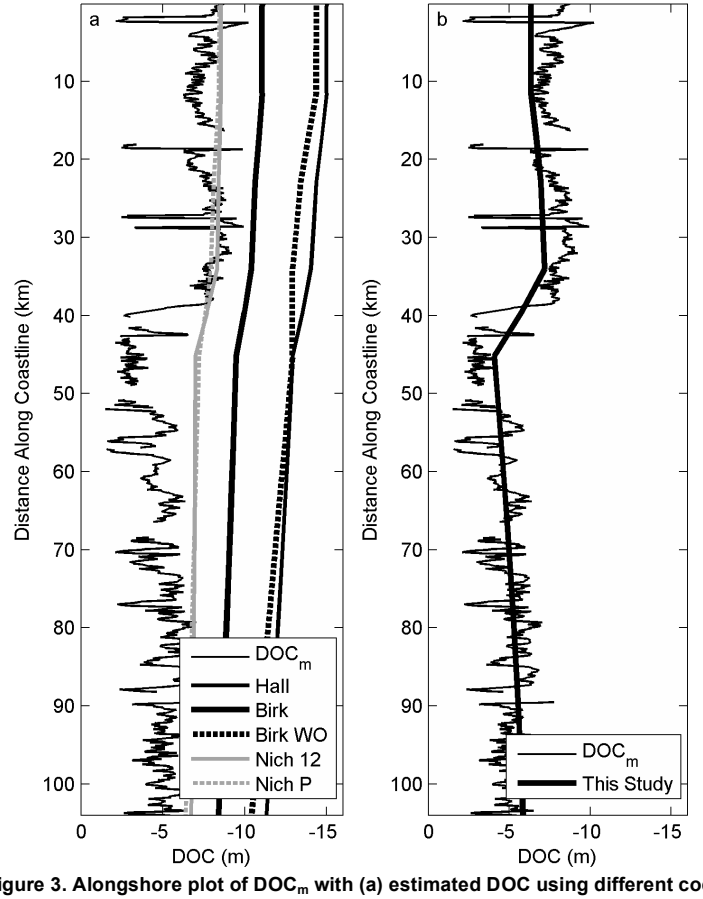

Figure 3. Alongshore plot of DOC_m with (a) estimated DOC using different coefficients and (b) coefficients calculated using this study's data. Estimated DOC include Hallermeier, Birkemeier, Birkemeier wave only (Eq. 2), Nicholls 12 hour waves, Nicholls peak waves.

Hallermeier's estimate of the depth of closure is determined by an average annual wave condition. Hurricanes often induce storm waves with large heights and long periods; therefore the depth of closure for a storm wave condition should be larger than those from a typical annual wave condition. The estimated DOC in Table 3 that used peak wave heights caused by the hurricanes are larger than the measured DOC. Two explanations could account for this difference. Since the airborne laser bathymetry was not collected immediately following the hurricanes, the survey may not completely capture the change caused by only the hurricanes. In addition, previous studies from this area suggest that the active profiles consist of more than only loose sands. There are hardgrounds comprised of exposed bedrock and reefs landward of the DOC, especially

south of Hillsboro Inlet (Brown 1998; Finkl and Warner 2005). Further research is needed to compare the extracted DOC with local geologic units to gain a perspective on the level of local geologic control.

ACKNOWLEDGEMENTS

We would like to thank Jeff Lillycrop and the Joint Airborne Lidar Bathymetry Technical Center of Expertise's (JALBTCX) team for providing the CHARTS data. NOAA's Florida Hurricane Alliance supported Mr. Robertson.

REFERENCES

Beven, J.L. (2004). "Tropical cyclone report: Hurricane Frances", In: *Tropical Cyclone Report*, National Hurricane Center, p. 28.

Birkemeier, W.A. (1985). "Field data on the seaward limit of profile change", *Journal of Waterway, Port, Coastal and Ocean Engineering*, 111(3), 598-602.

Brown, K.E. (1998). "Morphological analysis of beach profiles in relation to shoreline change", In: *Department of Geography and Geology*, Florida Atlantic University, p. 144.

Finkl, C.W., Benedet, L. and Campbell, T.J. (2005). "Beach nourishment experience in the United States: status and trends in the 20th Century", *Shore & Beach*, 74(2), 8-16.

Finkl, C.W. and Warner, M.T. (2005). "Morphologic features and morphodynamic zones along the inner continental shelf of Southeastern Florida: An example of form and process controlled by lithology", *Journal of Coastal Research*, 79-96.

Hallermeier, R.J. (1977). "Calculating a yearly limit depth to the active beach profile", In: *Technical Paper 77-9*, Army Corps of Engineers, p. 28.

Hallermeier, R.J. (1978). "Uses for a calculated limit depth to beach erosion", In: *Sixteenth Conference on Coastal Engineering*, ASCE, pp. 1493-1512.

Irish, J.L., McClung, J.K. and Lillycrop, W.J. (2000). "Airborne lidar bathymetry: the SHOALS system", *PIANC Bulletin*, 103, 43-53.

Lawrence, M.B. and Cobb, H.D. (2005). "Tropical cyclone report: Hurricane Jeanne", In: *Tropical Cyclone Report*, National Hurricane Center, p. 20.

Nicholls, R.J., Birkemeier, W.A. and Lee, G.H. (1998). "Evaluation of depth of closure using data from Duck, NC, USA", *Marine Geology*, 148(3-4), 179-201.

Optech (2004). "Field Test Report for CHARTS", Optech Inc., p. 76.

Robertson, W., Zhang, K., Whitman, D. and Leatherman, S.P. (2005). "Shoreline and beach volume change before and after the 2004 hurricane season, Palm Beach County, Florida", *Shore & Beach*, 73(2-3), 79-84.

Zhang, K.Q., Whitman, D., Leatherman, S. and Robertson, W. (2005). "Quantification of beach changes caused by Hurricane Floyd along Florida's Atlantic coast using airborne laser surveys", *Journal of Coastal Research*, 21(1), 123-134.

ASSESSING NEARSHORE BAR MOVEMENTS DURING STORMS USING TIME-AVERAGED X-BAND RADAR IMAGES

Luciana S. Esteves[1], Jon J. Williams[1], Paul S. Bell[2]

1. School of Geography, University of Plymouth, Drake Circus, Plymouth, PL4 8AA, UK. luciana.esteves@plymouth.ac.uk or jon.j.williams@plymouth.ac.uk
2. Proudman Oceanographic Laboratory, Joseph Proudman Building, 6 Brownlow Street, Liverpool, L3 5DA, UK. pbs@pol.ac.uk

Abstract: The study examines temporal and spatial changes in nearshore morphology using time-averaged images obtained by X-band radar along a 3-km long section of Cassino beach, southern Brazil. A GIS platform has been used to quantify the mean position and magnitudes of cross-shore movements of the three nearshore bars identified on the radar images in a time period between April 15 and May 31, 2005. Analysis of the time-averaged images show that increasing wave energy results in straight bars while reducing wave energy gives rise to crescentic features. The first bar responds rapidly to changes in wave energy while the two other bars respond only to extended periods of hydrodynamic forcing and generally exhibit a lagged response time in relation to the first bar. A storm with significant wave height of 1.1 m, period of 8 s and currents reaching 1.5 m/s resulted in migration rates of about 30 m/day for the first bar and 13 m/day for the second and third bars that lasted two to four days.

INTRODUCTION

This study presents results from a standard marine X-band radar deployed at Cassino Beach, southern Brazil between April and July 2005 during an international project studying wave attenuation over muddy sediments[1]. In the past, X-band radars have been used to obtain two-dimensional directional wave spectra, estimates of near surface currents, and bathymetry over a relatively large area in offshore and coastal waters (e.g. Young et al. 1985, Reichter et al. 1998, Bell 1999). Deployed from a relatively low vantage point, the X-band radar offers a relatively low-cost and reliable technology able

1 http://cassino.log.furg.br

to monitor a radial area of approximately 3 km, 24 hours a day, irrespective of the weather conditions (Bell et al. 2005). It provides an undistorted plan view of the area, making complex image rectification unnecessary. This paper presents preliminary results of an ongoing study that aims to analyze cross-shore and alongshore changes in the position and the morphology of nearshore bars using sequences of time-averaged radar images in a Geographical Information System (GIS) platform. Specifically, this study focuses on the temporal and spatial changes in bar location before, during, and after storms that occurred from April 15 to May 31, 2005. Estimates of mean bar positions and rates of change for specific time intervals are provided, as well as a description of the longshore variations in bars dynamics.

STUDY AREA

Cassino Beach is the only major coastal urban area found in the southernmost 490 km of the Brazilian coastline. It is located about 215 km north of the Uruguayan border, in the municipality of Rio Grande, state of Rio Grande do Sul (Figure 1). The field site was situated 3 km south of the main urban area and 9 km south of the Patos lagoon mouth. The X-band radar was installed in the grounds of the Aquaculture Marine Station (FURG), at 32°14'56"S; 052°9'36"W (Figure 1). Here, the beach is composed of fine to very fine quartzose sands (median grain size, D_{50} = 0.150 mm). The beach has a slope of 1/30, and usually three nearshore bars are present. The area is subject to a microtidal regime with semidiurnal mean tidal range not exceeding 0.5 m (Tomazelli et al. 1998). The most important water level changes are caused by meteorological forcing, with storm surge elevations reaching 1m (Calliari et al. 1998a, Saraiva et al. 2003). Waves are the main hydrodynamic agent with mean significant height (H_s) of 1.4 m and peak period (T_p) of 7 s to 9 s that can exceed 3 m and 12 s, respectively during the passage of extra-tropical cyclones (Almeida and Toldo 1997).

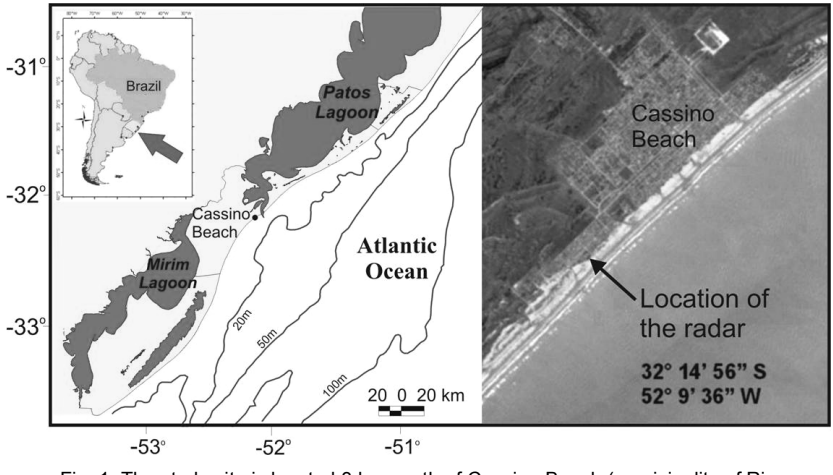

Fig. 1. The study site is located 3 km south of Cassino Beach (municipality of Rio Grande) at the southern coast of Brazil.

The beach at Cassino has an orientation of 240º (NE-SW) and the angle of waves approach at the breaker line is generally 5º to 15º. It is usually more than 100 m-wide with the waterline position changing with the same magnitude and frequently reaching the base of the dunes during storms (Esteves et al. 2006). The beach width changes seasonally, accreting in the summer (December to March) as a result of the dominant fair weather conditions, and eroding in the winter (June to August) due to the more energetic conditions (Calliari and Klein 1993, Esteves et al. 2006). Several studies have shown that this part of the coast is accreting in the short and long-term (Calliari et al. 1998b, Dillenburg et al. 2000, Esteves et al. 2006). Probably this is a result of longshore gradient of wave energy that favors deposition in large-scale coastal embayments resulting in positive sediment budget (Dillenburg et al. 2004).

Although field observations show that longshore currents are bi-directional, flows to the south dominante (Esteves et al. 2007) due the north-easterly and easterly waves generated by the dominant north-easterly winds. However, coastal geomorphic features (Tomazelli and Villwock 1992) and modeling results (Williams and Esteves 2005) indicate a net northward sediment transport driven by larger storm-associated waves approaching from the south. Although modeling results show that longshore sediment transport can explain the majority of measured shoreline changes in the area (Williams and Esteves 2005), the presence of offshore bars suggests that complex cross-shore sediment transport is also important.

METHODS

The nearshore sandbar morphology can be assessed indirectly through the visualization of waves breaking over the bar. This was first applied in studies of surf zone morphology by examining time-averaged images from digital video cameras (e.g. Lippmann and Holman 1989, Holland et al. 1997), and later to X-band radar images (Ruessink et al. 2002). In the present study, sequences of 256 radar images spanning approximately 10 minutes were recorded digitally every hour and resultant time-averaged images were used to quantify temporal and spatial changes in the surf zone morphology. During moderate to high wave conditions three bars were visible in most of the images. Hereafter these will be referred to as first (closest to the shoreline), second (at a mid-position in the surf zone), and third (furthest offshore). During acquisition of radar images, high wave energy events occurred around April 22 to 26, May 8 and 23, June 16 and 21, and July 5, 2005 (Figure 2). During May, waves and water levels were measured by pressure sensors (installed by Naval Postgraduate School/USA) and beach profiles were measured daily during fair-weather conditions (FURG/Brazil).

The X-Band Radar Data Collection

A standard marine X-band radar operating at 9.41 GHz (approximately 3 cm wavelength) was installed behind the dunes in Cassino Beach, about 300 m from the waterline, on top of a 6-m high scaffold tower (Figure 3). The X-band radar was installed from April 8 to July 30, 2005 and collected more than 400 h of data. The main

field experiment occurred in May when other instruments were simultaneously installed at the site, including a 4-camera Argus system (Naval Research Laboratory, USA); PUVs and OBSs in different elevations and positions across the surf zone (Naval Postgraduate School, USA); ADVs and ADCPs at 9m and 12m depths (UNIVALI and UFRJ, Brazil); one waverider placed offshore (UFSC, Brazil), and tidal gauges placed in three different locations along the coast.

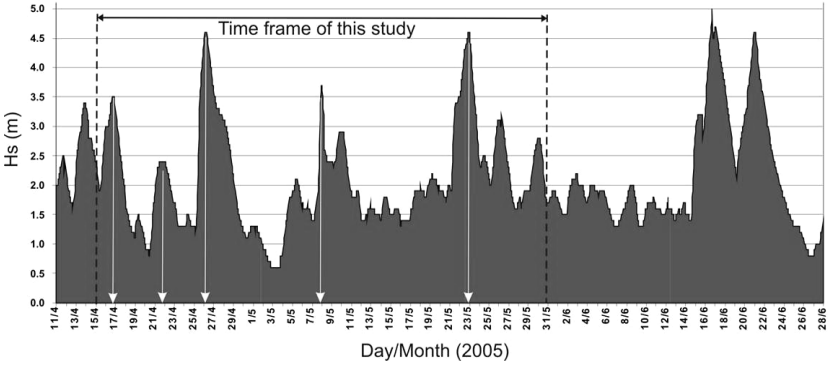

Fig. 2. Prediction of significant wave heights (H_s) for deep waters offshore of Rio Grande (32º00S, 48º75W). Vertical arrows point to dates of high-energy waves. Source of data: NOAA/NCEP WaveWatch III model (http://polar.ncep.noaa.gov/waves/main_table.html).

The 1.8-m long antenna provided a horizontal beamwidth of 1.2º and presented a rotation rate of 2.4 s. The returned echo of each pulse was digitally recorded at 20MHz corresponding to a radial resolution of 7.5 m. For the Cassino Experiment, the X-band radar was set to record 256 images in a 10-minute interval every hour, starting to record at the beginning of the hour. The snapshot radar images collected information of waves in a 4-km range, as is presented in Figure 3 for calm wave and storm conditions, respectively. The bright areas correspond to regions of high radar backscatter from the front face of the waves with respect to the radar. The very large signals in the lower part of the image relate to regions of breaking waves. The radar position is indicated by the zero mark at the bottom middle part of the images.

The time-averaged X-band radar images can be used to identify areas where waves are breaking on submerged sand bars (e.g. Lippmann and Holman 1989, Ruessink et al. 2002). Using sequences of these images it is possible to followed through time the movement and morphological evolution of the sand bars. According to Lippmann and Holman (1989), the bar crest location can be identified using the maximum video intensity. Ruessink et al. (2002) showed that the same applies when using radar images, although their results suggested that the maximum radar reflection could be displaced $O(10)$ m from the actual bar crest position due to variations in water level. The authors consider that changes in depth over the bar crest have to be at least $O(0.5)$ m to affect the position of maximum reflection in relation to the location of the bar crest. Although

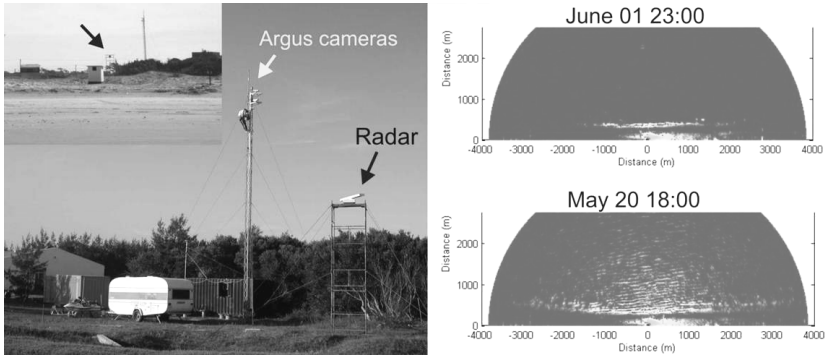

Fig. 3. The X-band radar was installed at the top of 6-m high scaffold tower at the grounds of a Marine Station belonging to the Fundação Universidade Federal do Rio Grande about 300m from the shoreline. At the right, examples of snapshot images obtained during calm (top) and stormy wave conditions (bottom). The X and Y axis show alongshore and cross-shore distances, respectively, from the radar position.

assessment of the effect of water levels on the position of bars has not yet been conducted in the present study, the position of digitized features is assumed here to be subject to an error of 10 m. Hourly time-averaged images were produced to give sufficient contrast to allow identification of the main nearshore morphological features along 2 or 3 km of the coastline.

Mapping the Position of the Shoreline and Nearshore Bars

The processing of the time-averaged images was conducted on ArcGis© 9.0 and consisted in three phases:

(1) *Referencing the images to a local coordinate system*. Local coordinates of fixed objects clearly identifiable on the time-average X-band images were used as control points. Since the *x,y* origin of the local coordinate system is the starting point of the transect of the beach profiles, all figures and distances presented hereafter will be referenced to it. In some cases the exact location of the control points was difficult to find in images with low contrast (i.e. during high water levels) resulting in errors that were always submetric.

(2) *Digitizing the position of the shoreline and the crest of the bars.* These features were always visible on the images and associated with the pixels showing the strongest reflection. Here 18 time-averaged images were used to digitize the position of the bars, covering a time interval of 46 days from April 14 to May 31. The date and time of the radar images analyzed were chosen based on the availability of beach profile data, *in situ* measurements of waves and currents, and the occurrence of storms and fair weather conditions. Five images were chosen to represent the changes observed from April 15-30, six images represent the period May 01-19, and seven images illustrate the changes from May 20-31. The reflection of the third bar was very faint in several images causing a greater inaccuracy on the location of the crest. The first and second bars were always easier to map.

(3) *Spatial analysis to determine cross-shore movement of the bars*. The distance between the digitized features, and the envelope of each one of the feature groups (i.e. shoreline and the three bars), were measured using shore-normal transects from a baseline drawn parallel to the shoreline at the position of the radar. Measurements were obtained at 250 m intervals along the shore to identify alongshore differences in the behavior of the bars. Measured distances between identified features were used to quantify changes in bar positions. These were then corrected to the local coordinate system.

RESULTS AND DISCUSSION

Visual analysis of 82 images (a set of about two time-averaged images per day) from April 15 to May 31 obtained at Cassino Beach shows rhythmic bars forming when there is a reduction in wave energy and straight bars forming as wave energy increases. The first and second bars were crescentic in 50% of the images, and straight in the other 50%. The analysis of the third bar was more difficult as it was very faint in 22% of the images and there was not enough contrast to define the position of the crest in another 20% of the images. For the remaining images, the third bar was identified as straight in most cases (87%) and crescentic in only 13% of the images. Based on the digitized images, figure 4 shows the changes in the cross-shore mean position of the three bars within a band representing the minimum and maximum values through time. It shows also when the morphology of the bars was straight (S) or rhythmic (R). The mean position of the shoreline is around 205 m (standard deviation, std = 17.1 m), with maximum and minimum distances of 264 m and 152 m (variation of 112 m), respectively (not illustrated). The first bar has a mean position around 239 m (std = 8.3 m), with maximum variation *O*(130)m (maximum and minimum values of 322 m and

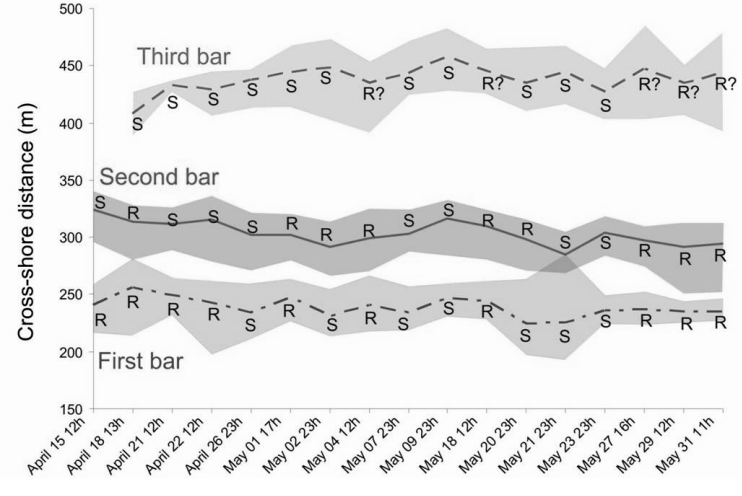

Fig. 4. Mean position of the bars crest through time based on the digitized images. The shading bands around the mean position lines represent maximum and minimum positions observed in each day. Straight bars are indicated with 'S' and rhythmic bars with 'R'

193 m, respectively. The mean position of the second bar is around 303 m (std = 10.5 m), with maximum variation *O*(90) m (maximum and minimum values of 340 m and 250 m, respectively). The mean position of the third bar is around 438 m (std = 11.21 m), with maximum variation *O*(100) m and maximum and minimum values of 485 m and 386 m, respectively). Thus the distances from shoreline to the first bar and between successive bars are 34 m, 64 m, and 135 m. It is noted that the distance between the shoreline and the second bar and the third bar are approximately twice and four times the distance between the shoreline and the first bar.

The response of bars to changing wave conditions is difficult to visualize in figure 4 as bar positions are not represented equidistantly through time. However, it is evident that the response of the three bars is not always in phase. The first bar responds rapidly to increasing wave energy with a retreat *O*(15) m, as can be observed after the storms of April 17 and 26, and May 8 and 21. Reducing wave energy results in a landward movement of the bar *O*(20) m which can eventually weld to the shore. The response of the bars seems to depend also on the frequency and magnitude of the events that represent changes in wave conditions. The second bar appears to respond only to changes that are more consistent in time, instead of moving according to oscillations within longer lasting trends. The major landward changes were *O*(20-30) m and occurred from April 15 to May 02 (not taking notice of the April 17 and 26 events), May 09 to 21 and from May 23 to 29 (only the last two time intervals clearly represented reducing wave energy). Retreat of this bar *O*(20) m resulted from well defined events of increasing wave energy from May 02 to 09, and May 21 to 23. The third bar behaves the in opposition of the second bar from April 18 to May 02 showing a retreat *O*(40) m. During the May events, the third bar responds similarly (in direction and magnitudes) to the second bar but with a time lag of two days. Generally, the features associated with crescentic bars migrate alongshore and landward during calm wave conditions. This adds to the complexity of analyzing changes in bar morphology and position using mean statistical parameters. There are also alongshore differences on the way bars respond both on the amount and direction of change. Details on the measured changes and bar behavior will be provided below for the three analyzed time intervals.

Bars Migration and Morphology – April 15 to 30, 2005

The radar mean images clearly show three straight bars at April 13 with the first bar changing into a rhythmic well developed 3D morphology at April 18 (Figure 4), returning to a 2D morphology at April 24. For the same time, the second bar shows a 3D morphology with a three-day delay that has a much shorter duration than at the first bar. As a result of reducing wave energy, the first bar starts to show a 3D morphology after April 27 while the second bar only show similar changes two days later. It was described previously that the second bar did not retreated as a result of the higher wave energy events of late April, it rather responded changing its shape and remaining as a 2D feature for the entire period. Figure 5 presents digitized positions of the three bars for April 18 and 26, and May 01 to illustrate cross-shore movements and alongshore variations. The third bar migrated seaward showing a mean displacement *O*(50) m (std=10 m), with the biggest changes occurring from April 18 to 21, when it moved 8 m/day in average (std=4 m), slowing gradually to 1.5 m/day (std=1.9 m) from April 26

to May 01. In contrary, the second bar moved mainly landward showing less cross-shore movement and greater alongshore differences in the magnitude and direction of changes (Figure 5). The mean displacement was 11.5 m (std=13.6 m), with reducing net changes

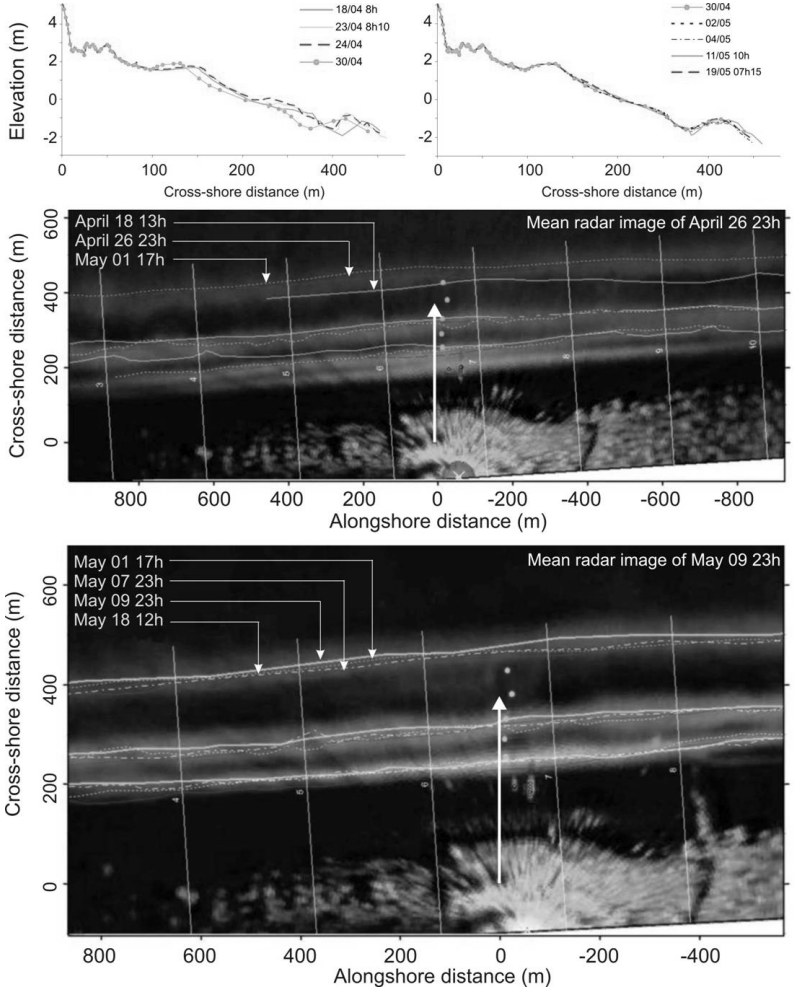

Fig. 5. Mean radar images and digitized position of bars crest for periods from April 18 to May 01, and May 01 to 18. White arrow represents the location of the beach profiles shown at the top. Green dots in the surf zone show position of in situ measurements (PUV1, PUV2, tower, PUV3, and PUV4, from the closest to shore to the most offshore). Thin white lines perpendicular to the shore represent transects of measured distances between the bars and origin of the beach profiles (zero, *x,y* position).

towards the south. Bar migration occurred with rates *O*(3.5) m/day from April 15 to 18 and April 21 to 26, and insignificant mean changes were from April 26 to May 01 that resulted mainly from the 3D bar morphology in May 01. The second bar presents the greatest variability of the three, showing stability or small seaward migration in the south (transects 7 to 10) and landward migration in the north (Figure 5). The largest changes occurred from April 15 to 18 when the bar retreated across the area with mean *O*(5) m/day (std=7 m) and April 21 to 22 with a landward migration *O*(18) m/day from transects 5 to 12 and a seaward migration *O*(12) m/day at the north. Although the displacement of bars is highly variable alongshore, the measurements obtained at the central part of the image where the beach profiles were taken (represented by the white arrow in Figure 5) agree well with the profile measurements. At the central transect, the first and second bar moved landward around 32m and 9m from April 18 to 26. Beach profiles show that the first and second bars moved onshore 38 m and 18 m, and became shallower 0.7 m and 0.2 m, respectively, from April 18 to 24. The April 30 profile shows a berm retreat of about 20 m and bar morphology indicating migration seawards (although the position of the second bar is still landward of the previous profiles indicating that it continued to move landward after April 24). This is associated with increasing wave heights around April 27 (Figure 2).

Bars Migration and Morphology –May 01 to 19 2005

This period is characterized by calm wave conditions with increasing wave energy from May 05 to 08 and reducing wave energy from May 09 to 11 (Figure 2). Changes shown in beach profiles are not significant either vertically or cross-shore (Figure 5) but analysis of mean radar images show a significant retreat of the three bars from May 07 to 09 (during and after a storm when profiles are not available) while landward movements dominate at other times. Note also that at the position of the profiles (white arrow at the bottom of figure 5), net changes in the position of the second bar are smaller compared to other areas alongshore. The mean images show 3D bars for most of this period, except around May 07-09. The third bar was not visible in many of the mean X-band images during lower energy conditions probably because local winds are too low to generate capillary waves and waves are too small to break at that location. The available data show small displacement values (around 10m) that were landward for most of the time except from May 07 to 09 (Figure 5). The overall net displacement of the third bar for the period is *O*(7) m landward from transects 2 to 6 and seaward from transects 7 to 12. The largest changes occurred from May 07 to 09 as a result of increasing wave energy with a mean seaward migration *O*(7) m/day (std =7 m), although magnitudes of changes were highly variable alongshore. The second bar presents the characteristic alternating seaward and landward movements in adjacent transects as a result of a 3D bar migrating alongshore, except between May 07 and 09 when the bar migrated seawards *O*(6.5) m/day (Figure 5). From May 09 to 18 mean values of change are relatively insignificant *O*(0.7) m/day. The first bar presents the greatest alongshore variability and the greatest changes also occurring from May 07 to 09 *O*(6) m/day and less changes from May 09 to 18 *O*(0.5) m/day similarly to the other bars. The first bar shows a behavior indicating a more 2D morphology (as can be also seen at the images), as it does not show the

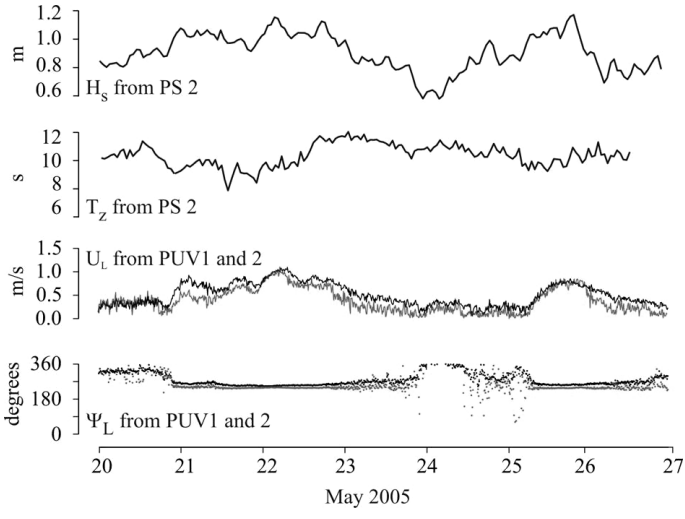

Fig. 6. Data from PUV1 and PUV2 measurements for the period of May 20 to 27 showing changes in significant wave height (H_s), zero-crossing period (T_z), current speed (U_L)and direction (ψ_L).

alternating seaward and landward movements in adjacent transects. It seems that here, a more well defined increase in wave energy after an extended period of reducing wave energy results in similar behavior in the three bars.

Bars Migration and Morphology –May 20 to 31 2005

At this period, there were three consecutive peaks of wave energy at May 22-23, 26, and 29 with short times of reducing wave energy in between (Figure 2). Figure 6 shows in situ measurements from PUV1 and PUV2 (the two instruments located between the first and second bars in Figures 5 and 7) of waves and currents from May 20 to 27. Significant wave heights (H_s) vary from 0.6 m to 1.1 m, zero-crossing period (T_z) reduces from 12 s to 8 s with increasing H_s and longshore current speed (U_L) increase from less than 0.5 m/s to 1.0 m/s and usually flow to the north (ψ_L=360º). Although this was not a particular strong storm it caused considerable bar movements (Figure 7) probably because it followed an extended period of relatively lower wave conditions. Figure 7 shows that the bars did not presented a significant net movement in the period, especially for the second bar and at the southern section of the third bar; however, the largest migrations have occurred in between the illustrated dates as described next. Most of the retreat measured at the third bar actually occurred from May 25 to 27 with mean O(13)m/day reaching up to 36m/day in the northern sector. The following two days accounted for a landward bar migration in proportions similar to that described previously, resulting in the bar returning to a position similar to May 23 in the southern part of the study area. Net changes for the second bar result mainly from the 3D bars presented at the beginning and end of the period being out of phase (Figure 7).

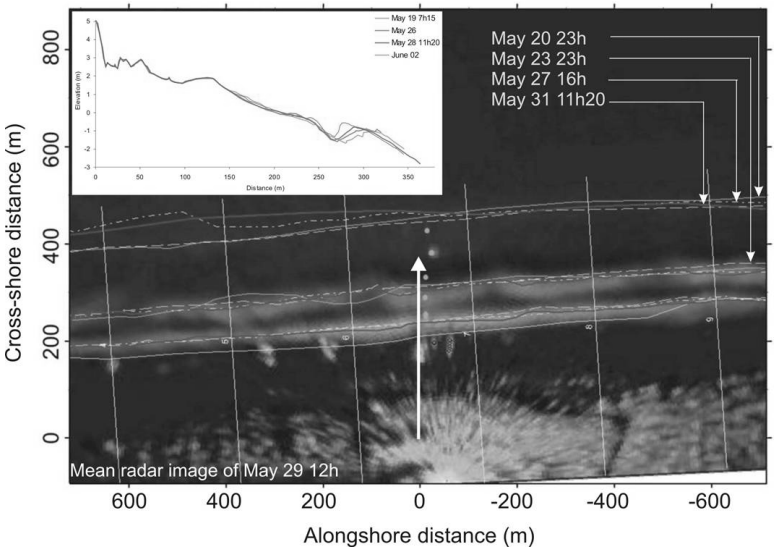

Fig. 7. Mean radar image and digitized position of bars crest for the period from May 20 to 31. White arrow represents the location of the beach profiles shown at the top. Green dots in the surf zone show position of in situ measurements (PUV1, PUV2, tower, PUV3, and PUV4, from the closest to shore to the most offshore). Thin white lines perpendicular to the shore represent transects of measured distances between the bars and origin of the beach profiles (zero, *x,y* position).

Measurements show that the largest displacement of the second bar occurred from May 20 to 21 when it migrated landward *O*(13) m/day (std =13 m) and from May 21 to 23 when the average movement was *O*(19) m seawards (std = 8 m) or about 9 m/day. After that there was a slower landward migration *O*(13) m (std = 13 m) from May 25 to 29. At the center of the image, where the beach profile is taken, a continuous landward migration of the second bar is observed, with magnitudes matching with the measured profiles (Figure 7). The first bar retreated *O*(40) m from May 21 to 23 (in opposition to the second bar that was already moving landward) and continue to retreat from May 23 to 25 with even higher rates, reaching a mean *O*(32) m/day. Such retreat was balanced by a fast landward migration *O*(40) m/day from May 25 to 27 that continued in much slower rates afterwards. A simple calculation using the shape of the beach profiles measured in May 19 and June 02 (Figure 7) indicated that there was a gain in sediment volume of approximately 135 m^3/m of beach width in that sector of the beach and that the migration of the second bar involved about 38 m^3/m. However, as beach profiles are not existent for the time of greatest bar movements (during the storm) there is no assessment of the volume changes during high energy events.

CONCLUSIONS

Time-averaged images generated by X-band radar provide a valuable data set to quantify temporal and spatial evolution of nearshore bars independently of weather conditions. The approach of high-energy waves changes the inner bar from a crescentic shape (which dominates during fair weather conditions) to a more continuous and straight configuration. Generally, the features associated with crescentic bars migrate alongshore and landward during calm wave conditions while during storm conditions the bar becomes straight and migrates offshore. However, the first bar responds rapidly to changes in wave conditions while the second and third bars respond only to the major trend of longer-lasting events and usually with a time lag in relation to the first bar. This will result in bars moving to opposite directions in certain times. There are also alongshore differences on the way bars respond both on the amount and direction of change. A storm presenting significant wave height of 1.1m, period of 8s and currents reaching 1.5m/s (that is not considered a major storm for the area) resulted in migration rates of about 30m/day for the first bar and 13m/day for the second and third bars. In that storm, bars were rapidly migrating seaward for two days followed also by a rapid migration landward in the next two days. After the storm faded, most of the migration occurred alongshore with cross-shore movements resulting from alongshore migration of crescentic bars without resulting in net changes in the bars position.

ACKNOWLEDGEMENTS

The authors want to thank Ed Thorton and Mark Orzek from Naval Postgraduate School (USA) for providing the wave and current data from the in situ measurements, Todd Holland from Naval Research Laboratory (USA) for providing the coordinates of the instruments and control points to reference the images, Rafael Guedes and Pedro Pereira from FURG (Brazil) for providing the beach profiles data, and all the students (especially Maria Aline Lisniowski and Heitor Perotto) and technical people (especially Milico and Marco) that helped making sure the radar was working properly after the many power cut offs.

REFERENCES

Almeida, L. E. S. B. and Toldo Jr., E. E. (1997). "Estudos Ambientais em Áreas Costeiras e Oceânicas na Região Sul do País – Região de Osório, RS," Instituto de Pesquisas Hidráulicas,Universidade Federal do Rio Grande do Sul (Porto Alegre, Brazil), Relatório técnico, 110p.

Bell, P. S. (1999). "Shallow water bathymetry derived from an analysis of X-band marine radar images of waves," *Coastal Engineering* 37(3-4), 513-527.

Bell, P. S. (2001). "Determination of bathymetry using marine radar images of waves," *Proceedings of the 4th International Symposium on Ocean Wave Measurement and Analysis* (San Francisco, California) vol. 1, 251-257.

Bell, P. S., Williams, J. J., Clark, S., Morris, B. D., and Vila-Concejo, A. (2003). "Nested Radar Systems for Remote Coastal Observations," *Journal of Coastal Research SI 39(Proceedings of the 8th International Coastal Symposium, Itajaí, Brazil)* in press.

Borge, R.-C. N., Reichert, K., and Dittmer, J. (1999). "Use of marine radar as a wave monitoring instrument," *Coastal Engineering* 37(3-4), 331-342.

Calliari, L. J., Tozzi, H. A. M., and Klein, A. H. F. (1998a). "Beach morphology and coastline erosion associated with storm surges in southern Brazil – Rio Grande to Chuí," *Anais da Academia Brasileira de Ciências* 70(2), 231-247.

Calliari L. J., Speranski, N. and Boukareva, I. (1998b). "Stable focus of wave rays as a reason of local erosion at the southern Brazilian coast," *Journal of Coastal Research* SI 26, 19-23.

Dillenburg, S. R., Esteves, L. S., and Tomazelli, L. J. (2004). "A critical evaluation of coastal erosion in Rio Grande do Sul, southern Brazil," *Annals of the Brazilian Academy of Science* 76(3), 611-623.

Dillenburg, S. R., Roy, P. S., Cowell, P. J., and Tomazelli, L. J. (2000). "Influence of antecedent topography on coastal evolution as tested by the Shorface Translation-Barrier Model (STM)," *Journal of Coastal Research* 16, 71-81.

Esteves, L. S., Williams, J. J., and Dillenburg, S. R. (2006). "Seasonal and interannual influences on the patterns of shoreline changes in Rio Grande do Sul, southern Brazil," *Journal of Coastal Research* 22(5), 1076-1093.

Esteves, L. S., Williams, J. J., Lisniowski, M. A., and Perotto, H. (2007). "Measured cross-shore and vertical variations in grain size, sorting and composition in suspended sediments transported by longshore currents," *Journal of Coastal Research* SI 50, *Proceedings of the International Coastal Sediments 2007* (in press).

Holland, K. T., Holman, R. A., Lippmann, T. C., Stanley, J., and Plant, N. (1997). Practical use of video imagery in nearshore oceanographic field studies. *Journal of Oceanic Engineering* 22, 81– 92.

Lippmann, T. C., and Holman, R. A. (1989). "Quantification of sand bar morphology: a video technique based on wave dissipation," *Journal of Geophysical Research* 94, 995–1011.

Reichert, K., Nieto, J.C.N., and Dittmer, J. (1998). "WaMoS II: an operational wave monitoring system," *Proceedings of the Oceanology '98* (Brighton, England) vol. 3, 455–462.

Ruessink, B. G., Bell, P. S., van Enckevort, I. M. J., and Aarninkhof, S. G. J. (2002). "Nearshore bar crest location quantified from time-averaged X-band radar images," *Coastal Engineering* 45(1), 19-32.

Saraiva, J. M. B., Bedran, C., and Carneiro, C. (2003). "Monitoring of storm surges on Cassino Beach, RS, Brazil," Journal of Coastal Research SI 35, 323-331.

Thieler, E. R., Himmelstoss, E. A., Zichichi, J. L., and Miller, T. L. (2005). "Digital Shoreline Analysis System (DSAS) version 3.0: An ArcGIS© extension for calculating shoreline change," U.S. Geological Survey Open-File Report 2005-1304.

Tomazelli, L. J. and Villwock, J. A. (1992). "Considerações sobre o ambiente praial e a deriva litorânea de sedimentos ao longo do litoral norte do Rio Grande do Sul, Brasil," Pesquisas 19, 3-12.

Tomazelli, L. J., Villwock, J. A., Dillenburg, S. R., Bachi, F. A., and Dehnhardt, B. A. (1998). "Significance of present-day coastal erosion and marine transgression, Rio Grande do Sul, southern Brazil," Annals of the Brazilian Academy of Science 70(2), 221-229.

Young, I. R., Rosenthal, W., and Ziemer, F. (1985). "A three-dimensional analysis of marine radar images for the determination of ocean wave directionality and surface currents," *Journal of Geophysical Research* 90(C1), 1049–1059.

Williams, J. J. and Esteves, L. S. (2005). "Predicting shoreline changes: A case study in Rio Grande do Sul, Brazil," *Geophysical Research Letters* 32(11), L11602, doi:10.1029/2005GL022979.

Wolf, J. and Bell, P. S. (2001). "Waves at Holderness from X-band radar," *Coastal Engineering* 43, 247-263.

LONGSHORE MIGRATION OF COASTAL FEATURES OBSERVED WITH X-BAND RADAR

Satoshi Takewaka[1], El Sayed Galal[2], Ryosuke Matsumoto[3], Shinya Sasakura[4]

1. Department of Engineering Mechanics and Energy, University of Tsukuba, Tsukuba, Ibaraki, 305-8573, Japan. takewaka@kz.tsukuba.ac.jp.
2. Graduate School of Systems and Information Engineering, University of Tsukuba, Tsukuba, Ibaraki, 305-8573, Japan. sayed@surface.kz.tsukuba.ac.jp.
3. West Japan Railway Company. Former graduate student.
4. Graduate School of Systems and Information Engineering, University of Tsukuba, Tsukuba, Ibaraki, 305-8573, Japan. sasakura@surface.kz.tsukuba.ac.jp.

Abstract: Intertidal morphology was monitored continuously with an X-band radar at research pier HORS located in Hasaki, Japan facing Pacific Ocean. The horizontal extent of a radar image is approximately 5.6 km and hourly averaged radar images were processed to observe longshore distributions of shoreline and bar positions. Longshore mean shoreline and bar positions and their variation showed a seasonal change, which follows so-called beach-cycle. Wavy features with wavelength of several hundred meters were observed in shoreline locations at low energy periods, which migrated to the down-wave. Migration speeds show high correlation with the longshore current velocities measured at the pier. Wavy appearances were also observed in bar locations and their migrations are also correlated with the longshore velocities.

INTRODUCTION

Longshore migrations of coastal features, like shoreline, foreshore morphology, rip channels, bar system etc are observed at coasts in the world, which are fascinating for scientists and annoying for engineers (e.g. Van Enckevort et al. 2004; Holman et al. 2006; Turner et al. 2007). Reported mean migration speeds of the features vary from order of several meters to several tens of meters per day, and no generally accepted explanations are given for migration mechanisms. There are also reports in Japan, which describe unidirectional longshore migrations of eroded areas and try to

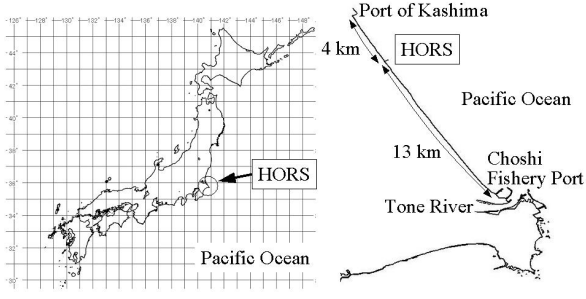

Fig. 1. Research Pier HORS

predict arrival time of erosion at downstream areas on the coast (e.g. Itabashi and Uda 1999; Tsuchiya 1997). From engineering viewpoint, if a better understanding on the migration mechanism and speeds is available, coastal prevention works may be planned more adequately.

This work displays the results of continuous X-band radar observations of shoreline and bar features for years at Hasaki Coast, Japan facing Pacific Ocean. Seasonal changes of the coastal area and down-wave, longshore migrations of shoreline and bar features are described in respect to their speeds and correlations with measured longshore current velocities.

FIELD EXPERIMENT

X-band radar measurements were conducted at the research pier HORS of the Port and Airport Research Institute (PARI), located in Hasaki, Japan (Fig. 1). The main facilities are a 400 m length pier extending into the Pacific Ocean and a research building located nearly 110 m backward from the mean shoreline position. HORS is on an almost straight sandy coast approximately 17 km long with Choshi Fishery Port at the south end and Kashima Port at the north end of the coast. The pier is located approximately 4 km from Kashima Port. Bottom profile and longshore velocities along the pier are surveyed on weekdays.

The radar system employed in this study is a conventional marine X-band radar, usually installed on fishing or recreational boats. The radar antenna is installed on the roof of the research building 17 m above the mean sea level. The antenna rotates with a period of approximately 2.5 s and transmits with a beam width of 0.8° horizontally and 25.0° vertically. The echo signals from the sea surface, generally called sea clutter, are captured with a specially designed A/D board installed on a computer.

Individual echo images sampled at every 2 seconds are averaged yielding a "time-averaged image" or so-called "time exposure". Figure 2 shows images averaged over 17 minutes for complicated shoreline and bar system for calm sea state and straightened situation during stormy condition. The horizontal extent of an image is

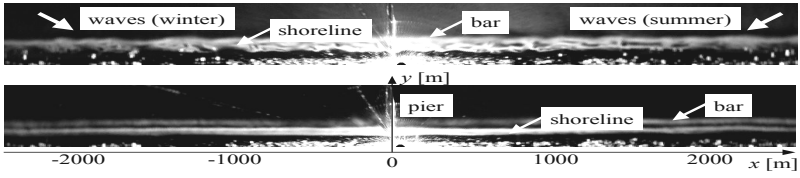

Fig. 2. Time averaged echo images and coordinate system.
Upper panel: calm condition (2005/April/28).
Lower panel: stormy condition (2005/July/28).
Length of the pier is approximately 400 m.

5556 m (3.0 nautical miles). Individual waves disappear in the time-averaged image and an edge extending in the long-shore direction becomes visible. Several features such as the breaker zone, shoreline position, near-shore bar crest locations etc can be estimated using the averaged image. The accuracy of intertidal morphology mapping with averaged images has been examined with survey results (Takewaka 2005). The x-axis corresponds to the long-shore extent and positive towards Choshi Fishery Port and the y-axis coinciding with the pier and oriented in the offshore direction.

Time-averaged images are processed hourly and accumulated from year 2004 to the present almost continuously. There are several missing periods due to system trouble; however, these don't affect the following analyses.

The offshore waves are measured by the Nationwide Ocean Wave Information Network for Ports and Harbors (NOWPHAS) station at Kashima Port where the mean water depth is approximately 24 m. Tide level is measured by Japanese Meteorological Agency at Choshi Fishery Port.

RESULTS AND DISCUSSION

The results of the observations of year 2005 are shown here to demonstrate the unique ability of radar measurements and to discuss the morphological behaviors of the site.

Longshore Mean: Shoreline and Bar Locations and Their Variability

Shoreline positions $Y_S(t, x)$ at longshore position x were digitized at time t when tide levels were between 0.75 m and 0.8m (local Datum Level), which are the most frequent tide levels observed at the site. Then the longshore mean shoreline position $\overline{Y}_S(t)$ at t

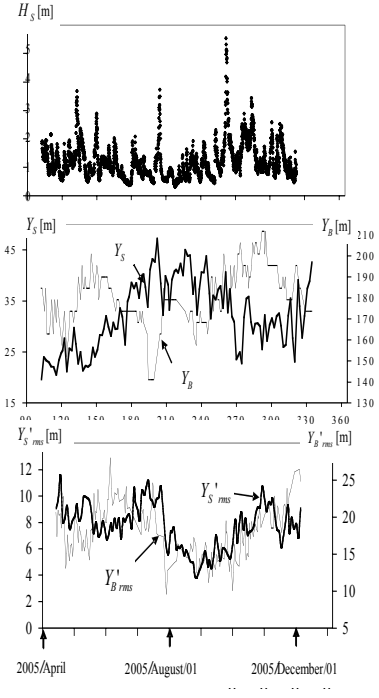

Fig. 3. Variation of longshore mean shoreline and bar locations and their variability

$$\overline{Y}_S(t) = \frac{1}{x_1 - x_0}\int_{x_0}^{x_1} Y_S(t,x)dx \tag{1}$$

and intensity of the fluctuation $Y_{S'rms}(t)$ at t

$$Y_{S'rms}(t) = \sqrt{\frac{1}{x_1 - x_0}\int_{x_0}^{x_1}(Y_S(t,x) - \overline{Y}_S(t))^2 dx} \tag{2}$$

are estimated, where x_0 = -2727 m and x_1 = 2829 m are the starting and ending locations of the imaging extent. In a similar manner, bar positions $Y_B(t, x)$, its mean $\overline{Y}_B(t)$ and fluctuation intensity $Y_{B'rms}(t)$ are estimated.

Figure 3 displays seasonal variations of significant wave height measured by NOWPHAS, longshore mean shoreline and bar positions and their fluctuation intensities observed in year 2005.

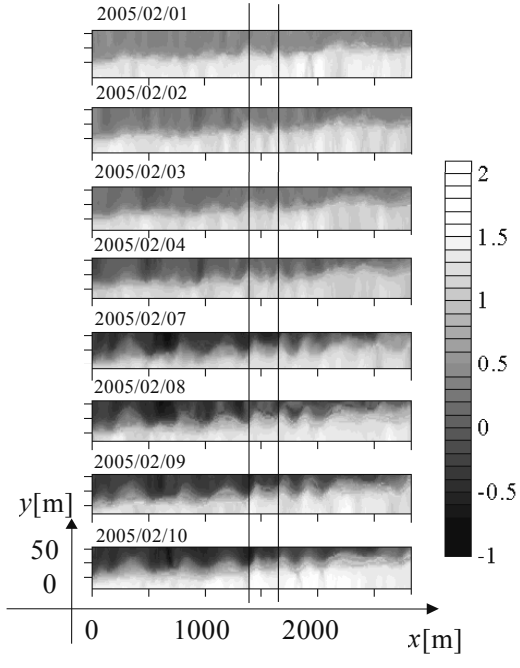

Fig. 4. Intertidal morphology mapping
Wavy features (wave length ~ 350 m) in the foreshore are migrating in +*x* direction with a speed of 16 m/day. Bottom elevations (local D.L., [m]) are displayed in gray scale.

Macroscopic movements of mean shoreline position $\overline{Y}_S(t)$ are seawards shift during the period from April to September, and landwards shift during the following period. Several high waves attacked the shore and mean shoreline position $\overline{Y}_S(t)$ showed quick recessions and fluctuation intensity $Y_S{}'_{rms}(t)$ decreased suddenly.

Mean bar position $\overline{Y}_B(t)$ shifted landwards during the period from May to July keeping relatively large fluctuation intensity $Y_B{}'_{rms}(t)$. After the high waves attacked the shore in the end of July 2005, mean bar position $\overline{Y}_B(t)$ shifted seawards and fluctuation intensity $Y_B{}'_{rms}(t)$ decreased.

The features observed in mean shoreline and bar positions are almost consistent with the result reported by Kuriyama and Lee (2001) who analyzed the daily bathymetric data measured along the pier and described the seasonal behavior of the beach. The changes observed here are parts of the so-called beach-cycle (Wright and Short 1984).

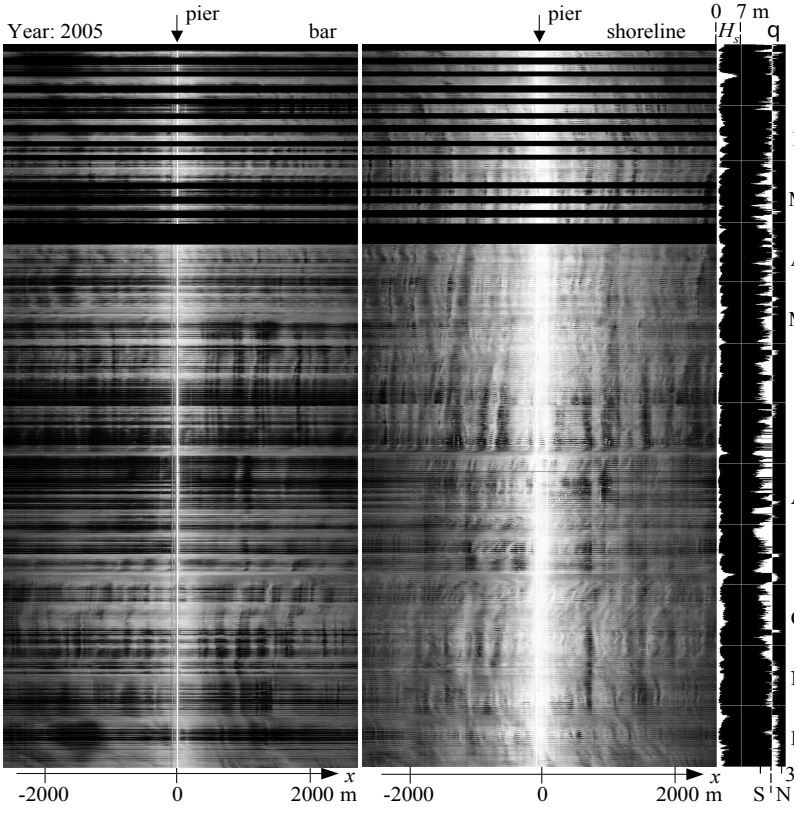

Fig. 5. Longshore migrations of wavy features in shoreline and bar locations observed in year 2005

Time-stack images whose horizontal extent is the longshore extent and vertical is the elapsed time from January to December 2005.

H_S: significant wave height, full scale = 7 m.
θ: significant wave angle, S = southern incidence, N = northern incidence.

Oblique streaks correspond to longshore migration of wavy features of shoreline and bar. During winter seasons (mostly January, February and December, and waves are incident from northern), the streaks are extending from upper left to lower right, implying migration is directed to +*x*. During the other months, like June and July, migration is directed to -*x*. The propagations of the features are almost headed for the down-wave.

During energetic sea state (e.g., end of July), the streaks become blurred due to regularization of the shoreline and bar, or so-called coastal reset.

Longshore Migration of Coastal Features

Figure 4 shows an example of intertidal morphology mappings processed from time averaged radar images and tidal record (Takewaka 2005). Wavy patterns with wavelengths of approximately 350 m are moving to positive x direction with a speed of approximately 16 m/day. The movements are directing to the down-wave and follow the longshore current observed at the pier.

This kind of migration in the intertidal region was observed through the year, especially during low energy periods. To visualize the temporal and spatial situation of the migration, time-stack image was processed: longshore pixel intensities are extracted from time averaged images for every hour close to the waterline. The cross-shore locations of the extractions have been shifted in accordance with the observed tide level. The result of this processing is shown in the right panel of Fig. 5 with the observed significant wave height and wave angle by NOWPHAS. The horizontal extent of the diagram is the longshore extent and the vertical is the elapsed time from January to December 2005.

Black-white pattern in the diagram shows the locations of waterlines and dried area: seawater exists at bright areas and dried shore appears dark. The vertical and bright streak in the diagram is the pier.

Oblique patterns or streaks are observed in the diagram: they are extending to the lower right mostly in January, February and December, the winter months, and to the lower left in the other months. These indicating that wavy features observed in the intertidal morphologies are migrating to the directions of the streaks and with speeds proportional to the slope of the streaks.

Oblique patterns become blurred when high waves attack the shore, for example at the end of July. The coast is straightened at stormy periods as shown in Fig. 2, the longshore variation of pixel intensities become small and it appears as uniform parts in the time-stack image.

The migrations speeds V_S (t) of wavy shoreline patterns were estimated by analyzing the slopes of the streak patterns in the time-stack image. Figure 6 depicts the variation of migration speed V_S (t) displayed with the longshore current speed V_L (t) observed at the pier (y = 115 m), showing a fairly high correlation between V_S and V_L. The maximum absolute V_S (t) observed in the study is approximately 25 m/day, which is in the same order compared to the results reported by Turner et al. (2007), but larger than the annual mean value reported by Itabashi and Uda (1999).

The movements of the bar are analyzed in a similar manner as described above. Time-stack image to visualize the bar migration is depicted in the left panel of Fig. 5. The oblique patterns appearing in the diagram resemble to those in the time-stack of the shoreline positions, although the overall appearance is somewhat unclear. Figure 7 compares the migration speed of the bar V_B (t) and longshore current speed V_L (t)

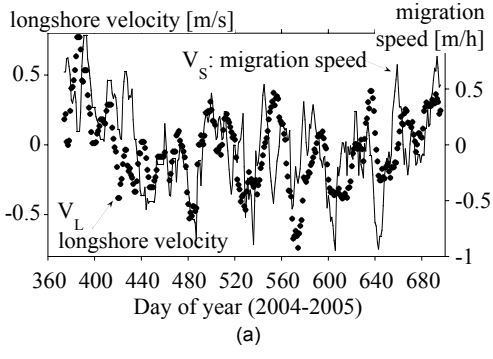

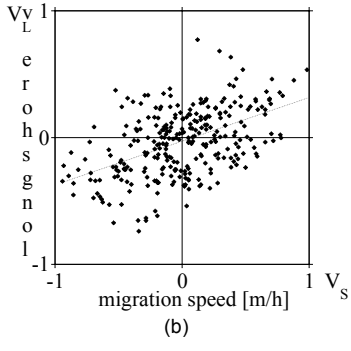

Fig. 6. Variation of shoreline migration speed V_S and longshore current velocity V_L.

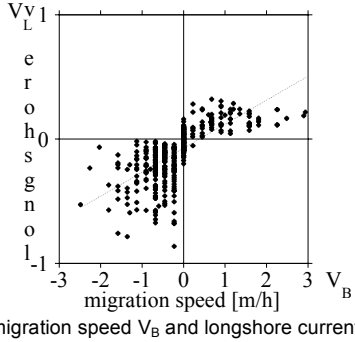

Fig. 7. Bar migration speed V_B and longshore current velocity V_L.

observed at the pier. Migration speeds of the bar are higher compared to those of shorelines at certain conditions, which is not specified yet.

Wavy migrating patterns of shoreline and bar locations, and variations of V_S and V_B showed organized appearances for certain periods. This suggests that sediment

motion between shoreline and bar should have certain organized structure to maintain the migration, which is not well understood at the present.

CONCLUDING REMARKS

Intertidal morphology was monitored continuously with an X-band radar at research pier HORS. The horizontal extent of a radar image is approximately 5.6 km and hourly averaged radar images were processed to digitize longshore distributions of shoreline and bar positions.

Longshore mean shoreline and bar positions and their variation showed a seasonal change which follow the so-called beach-cycle proposed by Wright and Short (1984): Shoreline position shifted seawards in spring-summer months and landwards during the following period. During this seasonal variation, several high waves attacked the shore and mean shoreline position showed quick recessions and sudden decreases in its longshore fluctuation intensity. Bar position shifted landwards in spring months keeping relatively high fluctuation intensity. So-called coastal resets are observed if high waves attack the shore, in which mean bar position shifted seawards and its fluctuation intensity decreased instantly.

Wavy features with wavelength of several hundred meters were observed in shoreline and bar locations at low energy periods, which migrated to the down-wave. Migration speeds showed a high correlation with the longshore current velocities measured at the pier.

ACKNOWLEDGEMENTS

The authors are grateful to the members of the Littoral Drift Division, PARI, who provided assistance in radar measurements and results of the depth surveys, wave and current measurements. Part of this study was financially supported by the Grants-in-Aid of the Japan Society for the Promotion of Science (JSPS).

REFERENCES

Holman R. A., G. Symonds, E. B. Thornton, R. Ranasinghe (2006). “Rip spacing and persistence on an embayed beach,” *Journal of Geophysical Research* 111, C01006, doi:10.1029/2005JC002965.

Itabashi N. and Uda T. (1999). “Field observation of erosion and accretion waves on Shizuoka and Shimizu Coasts in Suruga Bay in Japan,” *Coastal Engineering* 1998, (*Proceedings of* 26*th International Conference on Coastal Engineering*), 3178-3191.

Kuriyama Y. and Lee J. H. (2001). “Medium-term beach profile change on a bar-trough region at Hasaki, Japan, investigated with complex principal component analysis,” *Proceedings of Coastal Dynamics* '01, 959-968.

Takewaka S. (2005). “Measurements of shoreline positions and intertidal foreshore slopes with X-band marine radar system,” *Coastal Engineering Journal* 47, 91-107.

Turner I. L., Whyte D., Ruessink B. G. and Ranasinghe R. (2007). "Observations of rip spacing, persistence and mobility at a long, straight coastline," *Marine Geology* 236, 209-221.

Tsuchiya Y. (1997). "Erosive waves in shoreline change due to the reduction of a river delta," *Coastal Engineering* 1996 (*Proceedings of* 25*th International Conference on Coastal Engineering*), 4038-4051.

Van Enckevort I. M. J., Ruessink B. G., Coco G., Suzuki K., Turner I. L., Plant N. G. and Holman R. A. (2004). "Observations of nearshore crescentic sandbars," *Journal of Geophysical Research* 109, C06028, doi:10.1029/2003JC002214.

Wright, L.D. and Short A.D. (1984). "Morphodynamic variability of surf zones and beaches," *Marine Geology* 56, 93-118.

DETAILED 3-D MODELS OF NEW ZEALAND BARRIER STRATIGRAPHY PROVIDE INSIGHT INTO COASTAL EVOLUTION IN VARIOUS SPATIAL AND TEMPORAL SETTINGS

Amy J. Dougherty[1] and Scott L. Nichol[1]

1) School of Geography, Geology and Environmental Science, University of Auckland, Private Bag 92019, Auckland, New Zealand. a.dougherty@auckland.ac.nz and s.nichol@auckland.ac.nz

Abstract: The application of ground-penetrating radar (GPR) to five prograding barriers around northern New Zealand has produced detailed three-dimensional morphostratigraphic models. These barriers exist within a variety of geologic settings ranging from the high-energy, sediment rich west coast to the lower-energy, sediment starved east coast. Additionally, a composite Pleistocene-Holocene barrier exists along the east coast providing the unique opportunity to study barrier evolution not only through space but time. Nearshore, beach and dune facies delineated within each barrier lithosome form regressive facies successions with differences in shoreface geometry between sites. These differences detected within the stratigraphy are reflected in the contrasting depositional settings of the west coast dissipative morphodynamic state versus the east coast intermediate morphodynamic state. The replication of this stratigraphic form along shore and over successive sea-level stands indicates that the present day barrier evolution and depositional setting is similar over various spatial and temporal settings.

INTRODUCTION

Barriers exist along every heavily populated continent, spanning a range of geologic settings and time scales. Research over the past few decades has focused on deciphering how barriers have evolved in order to predict their response to physical influences such as accelerated sea-level rise. Progradational barriers maintain the highest preservation potential for recording past nearshore, beach and dune sedimentary processes within their accreting layers. Previous studies of coastal evolution on both Holocene and Pleistocene barriers around the world have produced generalized stratigraphic models that lack facies detail due to their construction from point source data (Figure 1).

Recently, Ground-Penetrating Radar (GPR) has been utilized to remotely sense a continuous cross-sectional view of the subsurface stratigraphy within sandy barriers, revealing large-scale features and facies boundaries previously undetected by coring alone (Jol et al., 1996). This technology enables detailed three-dimensional models of barrier stratigraphy to be constructed providing greater insight into the influences sea-level, sediment supply and accommodation space on their evolution.

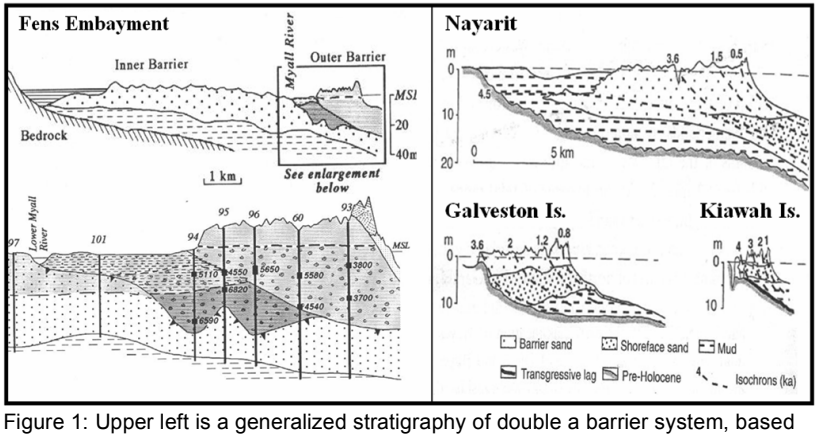

Figure 1: Upper left is a generalized stratigraphy of double a barrier system, based on core and dating techniques shown lower left (modified from Thom et al., 1992). Right are examples of general models of prograding barrier stratigraphy found in textbooks (modified from Woodroffe, 2002 and Davis and Fitzgerald, 2004).

Sea-level, sediment supply and accommodation space have long been recognized as the primary variables controlling barrier evolution, but singling out the role of any one is difficult due to their complex interactions during progradation. The northern coast of New Zealand offers an opportunity to achieve this due to spatial variability in sediment supply regimes and antecedent geology as well as temporal fluctuations in sea-level over the last two successive highstands. The influences of sediment supply and wave energy are inter-coastal variables created between the high-energy, sediment rich west coast and the lower-energy, sediment starved east coast and the influence of accommodation space is an intra-coastal variability determined by varied preservation of Pleistocene depositional sequences and irregular bedrock topography. Ultimately, by comparing barrier stratigraphy along and across shore, a comprehensive study of evolution from a spectrum of sediment-rich with poor accommodation space to sediment starved with good accommodation space has been completed. Additionally, by studying a composite Quaternary barrier system that formed during two highstand configurations, it is possible to look at the influence of sea-level in barrier evolution.

This study augments existing coring and dating techniques with digital GPR to produce detailed 3-D stratigraphic models of five prograding barriers which span the east and west coast of New Zealand and incorporate deposits laid down during oxygen isotope

stage 5e and stage 1. The aim of this paper is two fold: 1) present detailed 3-dimensional morphostratigraphic models of prograding barriers in a range of coastal settings, 2) compare differences in barrier architecture to decipher the influence of sea-level, sediment supply and/or accommodation space in barrier evolution. This information will not only fill a gap in knowledge about New Zealand barriers, but because of their diverse nature they are representative of prograding landforms the world over.

NORTHERN NEW ZEALAND

Barriers are a common landform throughout New Zealand's long and varied coastline (Healy and Kirk, 1992), yet despite being frequently regarded as a 'world class natural laboratory of coastal geomorphology', remarkably little is known about them (Hesp et al., 1999). Approximately 12 % of New Zealand's 18,200 km of coast is fronted by barriers (Rouse and Goff, 2003; Shepard and Hesp, 2003). Due to the distinctive geology of New Zealand, barriers have evolved in a variety of settings ranging from the high-energy, sediment rich west coast to the lower-energy, sediment starved east coast. The stark contrast between the east and west coasts is particularly pronounced in the sub tropical northern portion of the North Island, which unlike its southern counterpart has no active tectonism or volcanism eliminating these evolutionary complications.

In Northland the supply of sediments from local fluvial inputs is negligible due to small stream drainage basins within the hinterlands. The majority of the sand in this northern region originates from central north island and delivered to the coast by the Waikato River, where it is then distributed northward by longshore currents. The Waikato River has switched its course between the two coastlines and has been discharging its load on the west coast since ca. 18 ka creating a sediment-rich littoral system (Figure 2). In contrast the east coast sediment budget is limited to offshore sands deposits from when the Waikato flowed through the Firth of Thames (Figure 2). The west coast littoral drift system is driven by open ocean swells from the Tasman Sea resulting in high-energy conditions, while the leeward east coast maintains a more benign wave climate of low to moderate wind and wave regime, disturbed only occasionally by extra-tropical cyclones (Brander, et al., 2003). The tides in New Zealand are classified for the most part as meso-tidal and are strongly semi-diurnal (de Lang et al., 2003).

Over the last 140 ka years sea-level has only been close to present levels twice on the New Zealand Coast, about 120-125 ka (oxygen isotope stage 5e) and mid-late Holocene (stage 1), having risen from glacial levels of 120 meters below present to roughly present-day level some 5 000 to 7 000 years ago. Studies of sea-level change over the remaining part of the Holocene vary between a still stand and up to a two meter fall (Chappell and Shackleton, 1986 and Gibbs, 1986). Presently, sea-level is rising in New Zealand at a rate of 1.6mm/yr ± 0.2mm (Hannah, 2004), which is similar to global estimations of 0.15 m per century (Gornitz and Lebedeff, 1987).

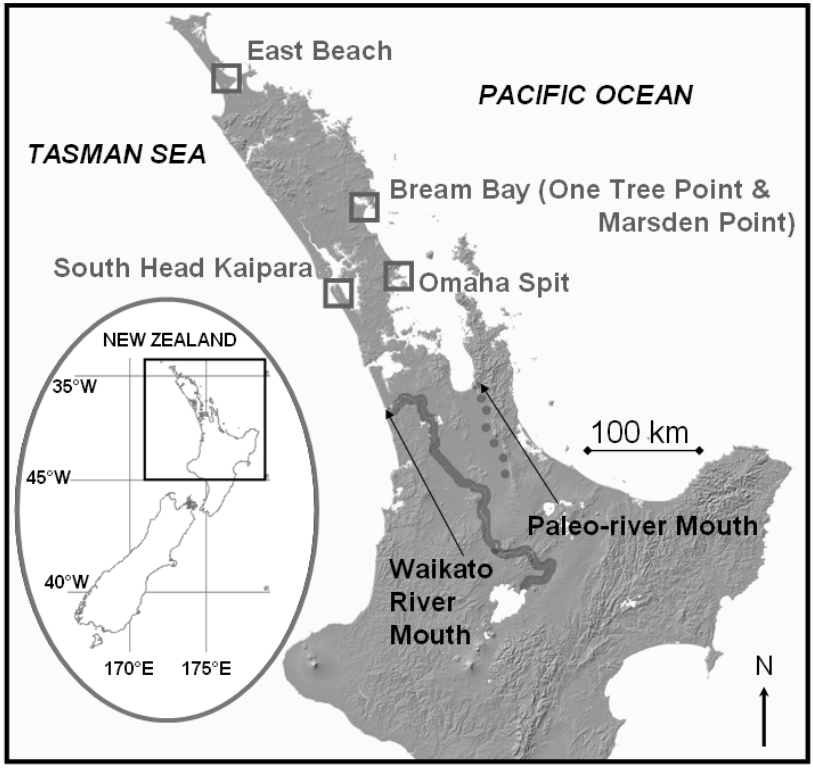

Figure 2: Location map of study sites throughout the Northland region of the North Island, New Zealand. Note the alternate route of the Waikato River.

As a result of contrasting geologic and oceanographic settings, with variable accommodation space and sporadic sediment supply, the coastal landforms differ widely with close proximity. East Coast Holocene barriers in Northland began to form at the cessation of sea-level rise around 6,000 years ago (Shepard and Hesp, 2003). During the ensuing relative stillstand offshore sediment was reworked onshore by wave action. Sand accumulated within embayments to form progradational barriers confined to coastal compartments disconnected by a predominantly rocky indented coastline. These headland-attached barriers and spits display characteristic foredune / beach ridges with beaches comprised of white quartzo-feldspathic sands and are intermediate to reflective in nature (Figure 3). The West Coast barriers began forming around the same time as the East Coast, but the added influence of longshore sediment supply from the Waikato River resulted in a long continuous coastline where barrier spits form in front of large harbors. These large Pleistocene-Holocene composite barriers contain black

titanomagnetite sand, with wide dissipative beaches and inland dunes over 100m in places. These embayment barriers are separated by dune-capped coastal cliffs (Figure 2).

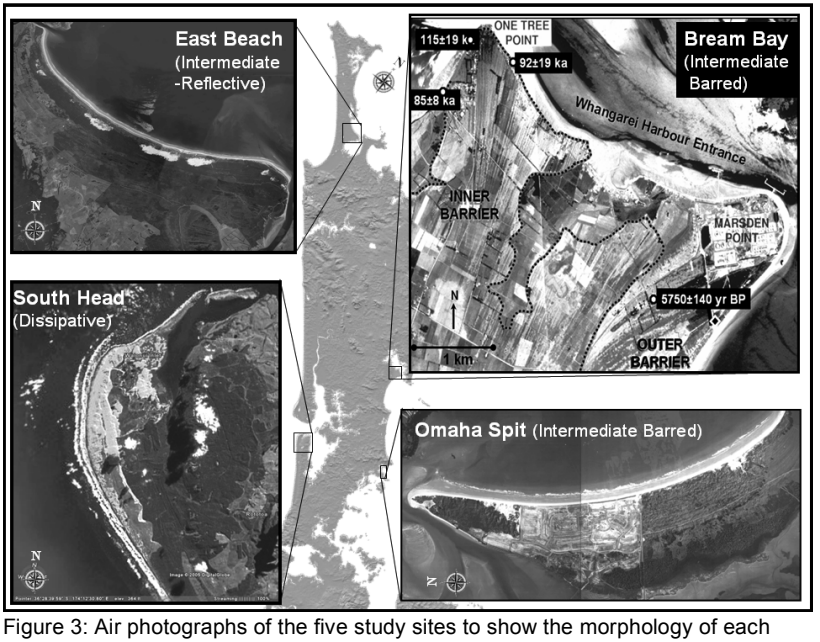

Figure 3: Air photographs of the five study sites to show the morphology of each barrier.

To represent these various barrier types four Holocene barriers and one Pleistocene barrier were selected for field investigations. Work on New Zealand barriers lacks stratigraphic and chronological detail, resulting in classification based on morphology. Therefore, the five study sites are classified using barrier types compiled by Shepard and Hesp (2003) as follows; One Tree Point is a Pleistocene Beach Ridge Barrier, Marsden Point and East Beach are Holocene Foredune Barriers, Omaha Spit is a Holocene Beach Ridge Barrier and South Head Kaipara is a Transgressive Dunefield Barrier (Figure 4).

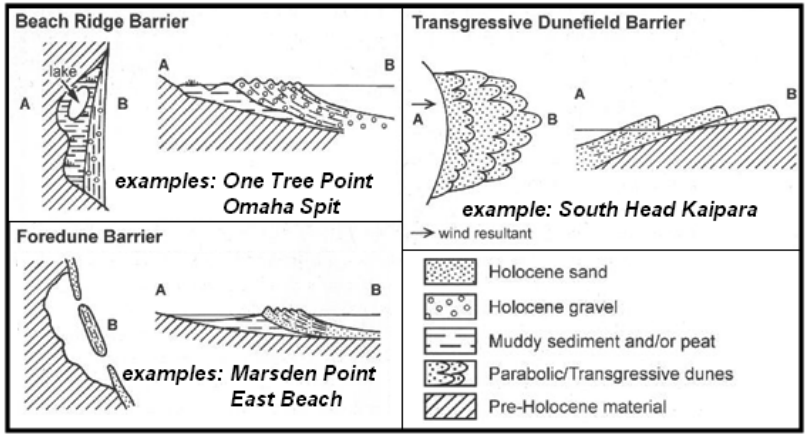

Figure 4: Characteristics of New Zealand barrier types relevant to this study (modified from Shepard and Hesp, 2003).

METHODS & DATABASE

This investigation is a combination of five individual studies involving an integrated high-resolution geophysical and sedimentological approach. The internal stratification of each barrier was investigated using a GSSI SIR-2000 ground-penetrating radar (GPR) system with a 200 MHz transceiver. Initial large-scale shore parallel and perpendicular GPR transects were collected on the order of several hundred meters in length at each site. Topographic corrections were applied using a Sokkia Electronic Total Station on profiles that had over 0.5 m variation in elevation. A representative subsection of each barrier was then selected to acquire a dense grid network optimal for constructing a 3-D model (Grasmueck et al., 2005). Finally, the nature of the reflectors in the geophysical data was ground-truthed using scarp exposures and core data. GPR analysis was performed using Radan 6.5 Software and interpretations of the recorded facies are described following the terminology of van Heteren et al. (1998). Textural and compositional characteristics of sediment samples were examined using Malvern particle analyzer for grain size, in addition to standard sedimentological techniques to provide a basis for interpreting barrier facies.

RESULTS

Geophysical data delineate three barrier facies (nearshore, shoreface and dune) within the lithosome of each study site. The geometry of the sedimentary layers was documented to sub-meter scale in the digital record, as demonstrated by replicating the stratigraphy exposed along an outcrop at One Tree Point (Figure 5). These remotely sensed continuous cross-sectional views of the barrier subsurface stratigraphy are described in two and three dimensions below.

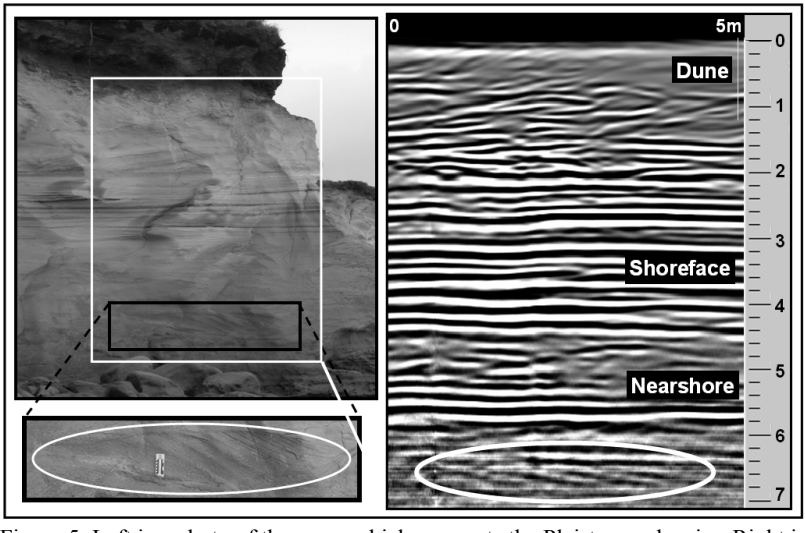

Figure 5: Left is a photo of the scarp which crosscuts the Pleistocene barrier. Right is a GPR record collected from along the top of this outcrop.

East Beach

The uppermost radar facies is characterized by generally weak / reflector free areas with faint steeply dipping reflectors mainly in the seaward direction (Figure 6, AI). The capping dune facies averages about 3 meters thick and consists of well-sorted, fine-grained quartz sand. The middle radar facies is dominated by a series of stacked high amplitude reflectors that dip gently in a seaward direction (Figure 6, AII). These sediments contain moderate- to well-sorted quartz with coarse grains and shell hash within the beachface. The basal radar displays overall flat-lying geometry with some small-scale, landward-dipping trough and planar cross-beds detected within the nearshore facies (Figure 6, AIII). The corresponding lowermost sedimentary facies consists of moderately-sorted, fine-to medium grained quartz sand with small amounts of broken shell.

One Tree Point

The topmost radar facies is characterized by generally weak / reflector free areas separated by distinct steeply dipping reflectors mainly in the seaward direction (Figure 6, BI). This dune facies comprises a massive 2 meter bed of well-sorted, fine-grained quartz sand with heavy mineral layers. The middle radar facies consists of a series of high amplitude reflectors that dip slightly in a seaward direction with a measured strike slope of about 1° (Figure 6, BII). These beachfaces are highlighted by stark contrast of alternating laminated beds of moderate- to well-sorted quartz and heavy minerals. The basal radar facies displays overall flat-lying geometry with some small-scale, landward-dipping trough and planner cross-beds (Figure 6, BIII). The corresponding lowermost

sedimentary facies consists of moderately-sorted, fine-to medium grained quartz sand with some gravel and heavy minerals.

Marsden Point

The capping radar facies is characterized by an opaque, reflector-free record with faint structures including indistinct medium to large-scale trough cross-bedding and high angle planner cross bedding (Figure 6, CI). This dune facies consists of well-sorted, fine-grained, quartz-rich sand to a depth of 5 meters. The middle radar facies is displays multiple closely spaces high amplitude, tangential-oblique to curvilinear reflectors (Figure 6, CII). These beachfaces consist mainly of medium-sized quartz sand with shells, often forming a sharp contact at the top of the facies and contain very little heavy mineral sands. The lowermost facies displays overall flat-lying geometry (Figure 6, CIII). The overlying beachfaces grades into silt with increased shell and organic matter to around a depth of 10 meters.

Omaha

The uppermost radar facies is characterized by generally weak / reflector free areas with faint steeply dipping reflectors mainly in the seaward direction (Figure 6, DI & Figure 7, BI). The capping dune facies averages about 2.5 meters thick and consists of well-sorted, fine-grained quartz sand. The middle radar facies is dominated by a series of evenly space reflectors that dip gently in a seaward direction (Figure 6, DII & Figure 7, BII). The corresponding sediments consist of moderate- to well-sorted quartz with coarse grains and shell hash the beachface. The lowermost facies displays overall flat-lying geometry (Figure 6, DIII & Figure 7, BIII). The overlying beachfaces grades into silt with increased shell and organic matter to around a depth of 10 meters.

South Head Kaipara

The uppermost radar facies is opaque towards the top but grades into more prominent with medium- to large-scale trough cross bedding and high angle planner cross-bedding dipping in both a seaward and landward directions (Figure 7, AI). This capping dune facies consisted of well-sorted, fine-grained sand with a higher heavy mineral content than the east coast barriers. This dune sequence is about 2.5 meters thick in the swale of the large dunes where the GPR was collected. The middle radar facies has three or four stacked high amplitude flat-lying reflectors that dip gently in a seaward direction (Figure 7, AII). The basal radar displays overall flat-lying geometry with some small-scale, landward-dipping trough and planar cross-beds detected within the nearshore facies (Figure 7, AIII). The corresponding lowermost sedimentary facies consists of moderately-sorted, fine grained sand with a high percentage of heavy minerals.

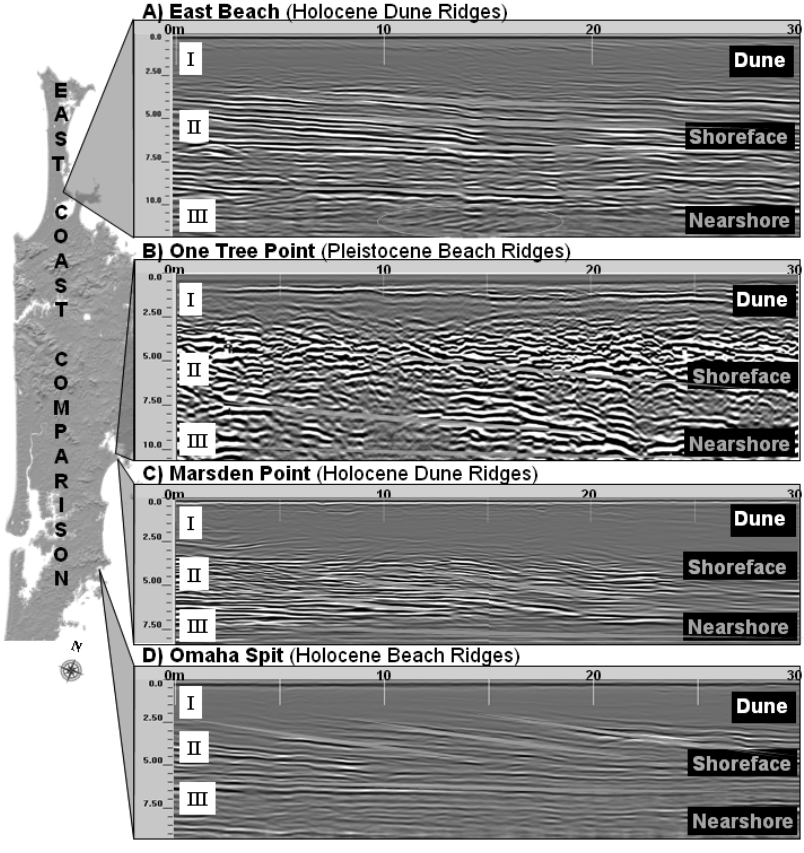

Figure 6: GPR transects from each of the east coast barriers set to same scale for comparison of internal stratigraphy. Reflectors within the shoreface and nearshore have been digitally highlighted to accentuate bedding geometry within these facies. Note dune facies are represented by diffuse or opaque as a lack of contrast with well sorted sand produces no strong reflectors.

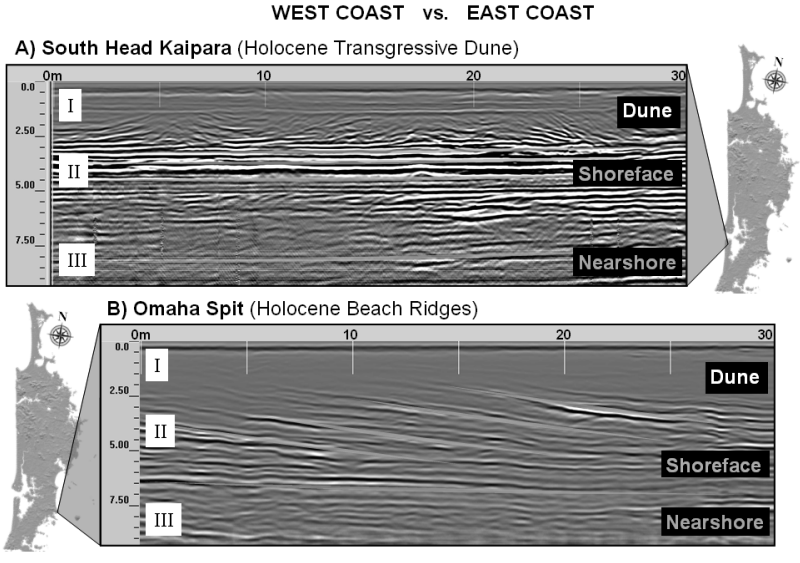

Figure 7: GPR transects from the west coast barrier compared to its longitudinal east coast component. Again reflectors within the shoreface and nearshore have been digitally highlighted accentuating the flattened, stacked geometry within the west coast shoreface as compared the evenly spaced curvilinear geometry within the east coast.

DISCUSSION

Nearshore, beach and dune facies were delineated within each barrier lithosome, but the geometry and spacing of the paleo-beachfaces varies between sites. The overall internal stratigraphy of barriers along the east coast is similar for each site. The stratigraphy is dominated by uniform, curvilinear, seaward-dipping reflectors that represent paleo beachfaces. Despite their similar geometry, the slight differences in spacing appear to be related to morphology in that barriers with beach ridges displayed evenly spaced beachfaces that are directly related to individual overlying beach ridges; where foredune barriers maintained closely spaced beachfaces that do not appear to correlate directly with surface morphology. The result is that GPR transects from the east coast barriers show similar stratigraphy for the two beach ridge barriers (One Tree Point and Omaha Spit) regardless of age difference, and the stratigraphy of the two Holocene dune ridge barriers (Marsden Point and East beach) are alike.

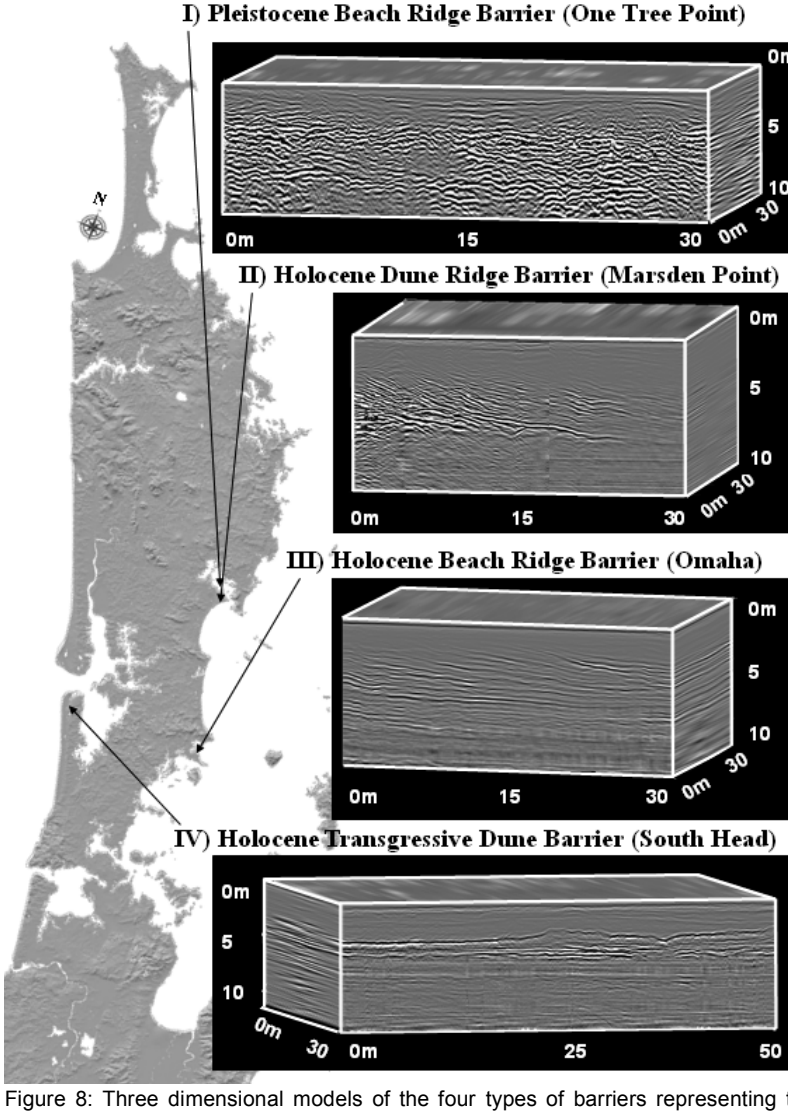

Figure 8: Three dimensional models of the four types of barriers representing the Northland Region. Note the lateral continuity of the nearshore, shoreface and dune stratigraphy as evidenced by the flat lying bedding planes alongshore in the Z-direction.

The beachfaces of the South Head Kaipara are completely different to all of the east coast sites exhibiting a more flattened, low-gradient, stacked configuration. The differences in beachface stratigraphy between the two coasts can be explained by considering the depositional setting in which the barrier formed, with the high-energy west characterized by a dissipative morphodynamic state while the lower-energy east coast maintains a more intermediate morphodynamic state. The replication of stratigraphic form along the east coast shoreline and over successive sea-level stands indicates that the depositional setting is similar throughout space and time on the east coast.

Three dimensional stratigraphic models were constructed for the four various barrier types identified in this study: Pleistocene Beach Ridge Barrier, Holocene Dune Ridge Barrier, Holocene Beach Ridge Barrier and Holocene Transgressive Dunefield Barrier (Figure 8). The representative three-dimensional stratigraphic models highlight the subsurface architecture of the beach and dune facies recorded in the geophysical record. These models show that the barrier stratigraphy is laterally continuous along shore as indicated by the flat lying shore parallel bedding planes in the Z-direction. To show the correlation of these laterally continuous stratigraphic beds with the overlying dunes, detailed morphostratigraphic models were constructed (Figure 9). To create these models large scale shore perpendicular GPR transects were used in conjunction with the topographic profiles.

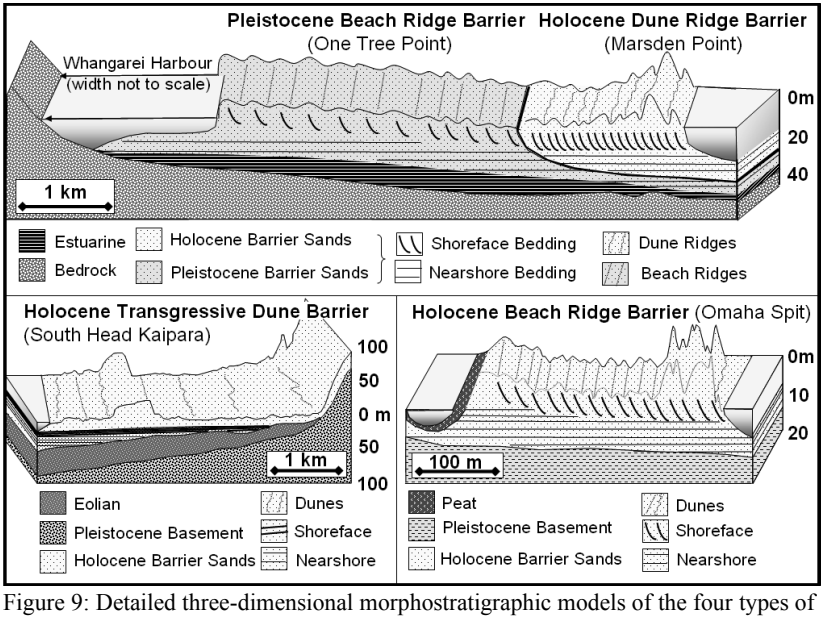

Figure 9: Detailed three-dimensional morphostratigraphic models of the four types of prograding barriers in Northland.

CONCLUSIONS

- High-resolution geophysical and sedimentological data has produced detailed three-dimensional morphostratigraphic models for prograding barrier around the coastline of northern New Zealand.

- The internal architecture of the morphostratigraphic models presented in this paper differs slightly from existing general models of prograding barrier stratigraphy.

- The difference in shoreface geometry between the east to west coast can be explained by the depositional setting in which they formed, with the high-energy west characterized by a dissipative morphodynamic state while the lower-energy east coast maintains a more intermediate morphodynamic state.

- The replication of this stratigraphic form along the Holocene shoreline and over successive sea-level stands indicates that the present day barrier evolution and depositional setting is similar throughout space and time.

- Due to the variation of barrier types along the lower energy east coast, wave energy is not considered a factor in determining if progradation style results in beach or dune ridge barriers. This makes intuitive sense in that dunes are formed by wind, but interesting when considering that the beachface is linked directly with over lying morphology. Even though prevailing wave energy does not appear to be a defining factor, intermittent / dominant conditions such as storms could play a key role.

- Sea-level does not appear to be a determining factor in the construction of a beach ridge barrier as One Tree Point has formed during the rapidly dropping sea-level during oxygen isotope stage 5e and Omaha during stage 1.

- The difference in sediment supply, relative to accommodation space, plays a major role in the contrasting inter-coastal prograding barrier types. The west coast has a steady supply of sediment moving along shore creating barrier spits in front of large embayment. Once the spits formed sand remains offshore in the littoral system that runs along the straightened coastline or is stored onshore in large dune complexes. In comparison east coast barriers have formed by the reworking of limited offshore sand deposit that has accumulated in embayments along this rocky indented coastline.

ACKNOWLEDGEMENTS

This work was partially funded through a University of Auckland International Doctoral Scholarship and The School of Geography and Environmental Science Internal Postgraduate Research Fund awarded to A. Dougherty.

REFERENCES

Brander, R. W., Osborne, P.D. and Parnell, K., 2003, High-energy beach and nearshore processes, *in* Goff, J. R., Nichol, S.L. and Rouse, H.L., editor, The New Zealand Coast: Palmerston North, Dunmore Press.

Chappell, J., and Shackleton, N.J., 1986, Oxygen isotopes and sea level: Nature, v.324, p.137-140

Davis, R., A., JR., and Fitzgerald, Duncan, M., 2004, Beaches and Coasts, Blackwell Publishing Company, 419 p.

de Lang, W. P. a. H., T.R., 1986, New Zealand tsunamis 1840-1982: New Zealand Journal of Geology and Geophysics, v. 29, p. 115-134.

Gibb, J. G., 1986, A New Zealand regional Holocene eustatic sea-level curve and its application to determination of vertical tectonic movements. Royal Society of New Zealand, Bulletin, v. 24, p. 377-395.

Gornitz, V. a. L., S., 1987, Global sea-level changes during the past century, *in* Nummedal, D., Pilkey, O. H. and Howard, J., editor, Sea-level fluctuation and coastal evolution, Special Publication - Society of Economic Paleontologists and Mineralogists, p. 3-16.

Grasmueck, M., Weger, Ralf, and Horstmeyer, Heinrich, 2005, Three-dimensional ground-penetrating radar imaging of sedimentary structures, fractures, and archaeological features at submeter resolution. Geology, v. 32, p. 933-936.

Hannah, J., 2004 An updated analysis of long-term sea level change in New Zealand. Geophysical Research Letters, v. 31, L03307, p.4

Hesp, P. A., Sheperd, M.J., and Parnell, K., 1999, Coastal geomorphology in New Zealand 1989-1999.: Progress in Physical Geography, v. 23, p. 501-524.

Jol, H. M., Smith, D.G., and Meyers, R.A., 1996, Digital ground penetrating radar (GPR): a new geophysical tool for coastal barrier research (examples for the Atlantic, Gulf and Pacific coasts, U.S.A.): Journal of Coastal Research, v. 12, p. 960-968.

Healy, T. R. and Kirk, R.M., 1992, Coasts, *in* Selby, J. M. S. a. M. J., editor, Landforms of New Zealand: Auckland, Longman Paul, p. 161-186.

Rouse, H. a. Goff., J., 2003, Te Tai O Aotearoa: The future of New Zealand's Coast, *in* Goff, J. R., Nichol, S.L. and Rouse, H.L., editor, The New Zealand Coast: Palmerston North, Dunmore Press.

Shepard, M. a. Hesp., Patrick, 2003, Sandy barriers and coastal dunes, *in* Goff, J. R., Nichol, Scott, L., Rouse, Helen, L., editor, The New Zealand Coast (TE TAI O AOTEAROA): Palmerston North and Wellington, Dunmore Press and Whitireia Publishing, p. 163-189.

Thom, B. G., Shepard, M., Ly, C.K., Roy, P.S., Bowman, G.M. and Hesp, P.A., 1992, Coastal Geomorphology and Quaternary Geology of the Port Stephens-Myall Lakes Area: Canberra, The University of Sydney Printing Services.

van Heteren, S., FitzGerald, D.M., McKinlay, P.A., and Buynevich, I.V., 1998, Radar facies of paraglacial barrier systems: coastal New England, USA. Sedimentology, v. 45, p. 181-200.

Woodroffe, 2002, Coasts: form, process, and evolution: Cambridge, University Press.

A FORMULA FOR LONGSHORE SEDIMENT TRANSPORT IN THE SWASH

Magnus Larson[1] and Ty V. Wamsley[2]

1. Lund University, Department of Water Resources Engineering, Box 118, 221 00 Lund, Sweden. Magnus.Larson@tvrl.lth.se
2. U.S. Army Engineer Research and Development Center, Coastal and Hydraulics Laboratory, 3909 Halls Ferry Road, Vicksburg, MS 39180-6199, USA. Ty.V.Wamsley@erdc.usace.army.mil

Abstract: A formula is proposed for the longshore sediment transport in the swash based on the study by Larson *et al.* (2004) on swash-zone transport and foreshore evolution. Hydrodynamics needed to predict the local transport rate were derived from ballistics theory, where both the cases with and without friction were investigated. The formula was validated with data from two experiments carried out in the Large-scale Sediment Transport Facility (LSTF) of the Coastal and Hydraulics Laboratory. In total five experimental cases were reproduced using a typical value on the transport rate coefficient from Larson *et al.* A simple exponential decay with distance offshore was employed to model the transition between the swash zone and the inner part of the surf zone. The LSTF data on transport rates measured in this region supported such a simplified model.

INTRODUCTION

The swash zone constitutes the area of the beach where the waves run up and down, dissipating or reflecting their remaining energy after traveling towards shore. Propagation of waves up the beach is typically referred to as uprush, whereas the return of the water is denoted as backwash (thus, uprush and backwash together encompass a swash cycle). The morphologically active part of the beach corresponding to the swash zone is often called the foreshore (or beach face), that is, the part of the beach that is shaped by the hydrodynamic forces in the swash. Although the swash zone is a very narrow strip, it is of great importance for the sediment exchange between land and sea, which in turn affects both the subaerial and subaqueous evolution of the beach.

Morphological processes such as erosion during severe storms, post-storm recovery, seasonal variation in foreshore shape, subaerial accumulation updrift of structures (e.g., jetties), and evolution of rhythmic features are all related to this exchange.

Hydrodynamic and sediment transport conditions are highly complex in the swash zone involving, for example, rapidly varying flow (in time and space), nonlinear wave transformation, wave-wave interaction, and multiphase flow with possible infiltration and exfiltration effects. In spite of these difficulties, significant progress has been made in the last decade concerning the hydrodynamics and sediment transport conditions in the swash zone and the associated response of the foreshore (see Elfrink and Baldock 2002; Larson *et al*. 2004). However, most previous studies have focused on the water and sediment transport in the cross-shore direction (i.e., perpendicular to the main orientation of the contour lines on the foreshore), and only limited work has been carried out on the transport in the longshore direction.

The main objectives of the present investigation were to develop a formula for the longshore sediment transport rate in the swash and to validate it towards high-quality data from laboratory experiments carried out in the Large-scale Sediment Transport Facility (LSTF) at the Coastal and Hydraulics Laboratory in Vicksburg, MS. The swash-zone sediment transport formula proposed by Larson *et al.* (2004) was generalized to describe the longshore transport rate. Hydrodynamic quantities needed in the formula were derived from ballistics theory and assuming self-similarity in the flow variation along the foreshore. Theoretical expressions were obtained both for the cases with and without friction. Measurements of the longshore sediment transport rate in the swash-zone carried out in the LSTF were employed to validate the new formula. Good agreement was achieved using coefficient values from Larson *et al.* determined when modeling cross-shore sediment transport in the swash.

THEORETICAL DEVELOPMENTS

Swash-Zone Sediment Transport

Madsen (1991, 1993) proposed the following formula for calculating the instantaneous bed load transport rate (q_b),

$$\frac{q_b(t)}{\sqrt{(s-1)gd}\,d} = \frac{8}{1+\dfrac{\tan\beta(t)}{\tan\phi_m}}\left(|\psi(t)|-\psi_{cr,\beta}\right)^{3/2}\frac{\tau_b(t)}{|\tau_b(t)|} \qquad (1)$$

where s is the specific weight of the sediment ($s=\rho_s/\rho$ in which ρ_s and ρ is the density of sediment and water, respectively), g the acceleration of gravity, d the sediment diameter, β the local beach slope ($=\mathrm{d}h/\mathrm{d}x$, where h is the bottom elevation and x a cross-shore coordinate), ϕ_m the friction angle for a moving grain (about 30 deg), t time, τ_b the instantaneous bed shear stress, and $\psi=\tau_b/(\rho_s-\rho)gd$ (Shields parameter). The subscript cr,β refers to incipient conditions for sediment movement at the slope β. Although Eq. 1 was obtained for bedload transport under waves and currents in a homogenous fluid,

Larson *et al.* (2004) assumed that the general relationship is also valid in the swash when a particular location x is subject to a flow (during time periods when there is no flow, the transport is set to zero). At x, the transport is onshore during the uprush phase and offshore during the backwash phase.

Integrating the transport rate over a swash cycle at x gives a mean transport $q_{b,net}$,

$$\frac{q_{b,net}}{\sqrt{(s-1)gd}\,d} = \frac{8\tan\phi_m}{\tan^2\phi_m - (dh/dx)^2}\left(I_U + I_B\right)\left(\frac{dh}{dx} - \tan\beta_e\right) \tag{2}$$

where I_U and I_B are integrals of the Shields parameter (*i.e.*, shear stress) over the uprush and backwash phase, respectively. The condition for the local equilibrium slope $\tan\beta_e=(I_U-I_B)/(I_U+I_B)$ was used to derive Eq. 2 (see Larson *et al.*, 2004). In order to compute the net transport, the time history of τ_b at x during a swash cycle must be known. If the shear stress is assumed proportional to the local velocity (u) squared, the problem reduces to estimate the variation in u at x. Larson *et al*. (2004) assumed that properly scaled, the velocity variation in time is approximately similar across the swash zone, that is, $u/u_o = \Gamma\left((t-t_s)/t_o\right)$, where u_o and t_o is a scaling velocity and time, respectively, and Γ a function that characterizes the non-dimensional velocity variation in time at all locations in the swash zone (cf., Masselink and Hughes, 1998; Waddell, 1973). The velocity u_o is taken as the wave front velocity at uprush and t_o as the duration of the swash at the particular location, determined as discussed in the following sections.

Developing Eq. 2 by solving the integrals I_U and I_B using the self-similar velocity variation (employing a quadratic dependence of τ_b on u and neglecting the critical shear stress), and absorbing the various non-dimensional coefficients (including friction factors and the integral of the function Γ) into one coefficient K_c, gives for the cross-shore transport rate:

$$q_{bc,net} = K_c \frac{\tan\phi_m}{\tan^2\phi_m - (dh/dx)^2}\frac{u_o^3}{g}\left(\frac{dh}{dx} - \tan\beta_e\right)\frac{t_o}{T} \tag{3}$$

Eq. 3 describes the net transport in the cross-shore direction, whereas the transport in the longshore direction may be estimated as,

$$q_{bl,net} = K_l \frac{\tan\phi_m}{\tan^2\phi_m - (dh/dx)^2}\frac{u_o^2 v_o}{g}\frac{t_o}{T} \tag{4}$$

where K_l is an empirical coefficient, possibly with a different value from K_c. Eq. 4 was heuristically derived by looking at Eq. 3 and assuming that the mobilization of the sediment is proportional to u_o^2 and the transporting velocity to v_o (compare with general sediment transport formula by Camenen and Larson 2004). Eq. 3 implies that the net cross-shore sediment transport rate is zero in the swash when the foreshore slope is in equilibrium, whereas longshore transport may still occur if the waves approach at an angle. The cross-shore velocity will still affect $q_{bl,net}$ at equilibrium since the mobilization of sediment is a function of u_o^2.

Swash-Zone Hydrodynamics without Friction

The transformation of the waves as they travel up and down the foreshore is quite complex and many existing models have limited predictive capability concerning details of the flow during a swash cycle. However, it has been shown that the speed of the wave front as it propagates up the foreshore may be reasonably well described using simple theory in which the front is regarded as a slug of water moving under the action of gravity (and possibly friction). The solution to the wave front propagation is analogous to the so called ballistic theory in mechanics. Thus, the movement of the front is governed by the following equation,

$$\frac{d^2 x_o}{dt^2} = -g \sin\beta \tag{5}$$

where x_o is the position of the wave front as it travels along the foreshore (positive in the onshore direction and x_o is taken along the foreshore), β is the foreshore slope taken as a constant and t is time ($u_o = dx_o / dt$). Eq. 5 is easily integrated to yield the velocity and position of the wave front as a function of time as $u_o = u_s - g \sin\beta t$ and $x_o = x_s - g \sin\beta t / 2 + u_s t$, respectively, where u_s is the wave front speed at the start of the uprush and x_s the location at the start of the swash zone where u_o=u_s (x_s taken to be zero at the still-water shoreline; SWS). These equations are applicable for both the uprush and backwash phase, making the variation in u_o and x_o symmetric with respect to the two phases.

The time (t_{max}) when the maximum runup height is attained, implying that u_o=0, is given by $t_{\max} = u_s / (g \sin\beta)$ and the corresponding location is $x_{\max} = u_s^2 / (2g \sin\beta)$. Transforming x_{max} into a vertical distance and denoting this distance as the runup height (R) yield $R = u_s^2 / (2g)$. The value of u_s may be difficult to estimate and this velocity can instead be substituted with R for which there is a wide range of predictive equations to choose from (e.g., Hunt, 1959; Mase, 1988; Mayer and Kriebel, 1994). Based on the equations governing the movement of the wave front one can derive the duration (t_o) any location on the foreshore will be submerged according to,

$$\frac{t_o}{T} = \sqrt{1 - \frac{z_o}{R}} \tag{6}$$

where z_o is the vertical distance from the reference level to x_o and R was introduced instead of u_s. It was assumed that the duration of the swash cycle is similar to the incident wave period (T), which is appropriate for values approximately larger than one

on the surf similarity parameter (ξ_o) defined based on deepwater conditions (Holman 1986). For smaller values on ξ_o the swash period is longer than the incident wave period and marked interaction between consecutive waves is expected in the swash (Erikson *et al.* (2005). The following expression may be derived for the wave front speed:

$$\frac{u_o}{u_s} = \sqrt{1 - \frac{z_o}{R}} \tag{7}$$

Eqs. 6 and 7 were employed to scale the local velocity variation at a point x on the foreshore when further developing Eq. 2 to calculate sediment transport in the swash zone (Eq. 3).

If the waves approach the foreshore at an angle, the wave front speed will have both a cross-shore and a longshore component. Employing simple theory again, Eq. 5 has to be supplemented with the equation $d^2 y_o / dt^2 = 0$ to describe the complete movement of the front, where y_o is the longshore position of the front (the foreshore is uniform alongshore so there are no gravitational effects in this direction). Assuming a velocity U_s at the start of the uprush oriented at an angle α with respect to the y-axis, with the cross-shore and longshore components $u_s = U_s \sin\alpha$ and $v_s = U_s \cos\alpha$, respectively, yields the solution for the longshore direction $v_o = v_s$ and $y_o = y_s + v_s t$, whereas the solution for the cross-shore direction is given by the previously discussed equations.

Swash Hydrodynamics with Friction

Some previous studies have included friction in the simple theory used to describe the swash motion (e.g., Kirkgöz, 1981; Hughes, 1995; Erikson *et al.*, 2005). Typically, a frictional force is added in the governing equation, where the force is taken to be proportional to the velocity square,

$$\frac{du_o}{dt} = -g\sin\beta - Ku_o^2 \tag{8}$$

where K is an empirical coefficient. Hughes (1995) expressed this coefficient as $K = f / 8h_o$, in which f is a friction factor and h_o a representative water depth (assumed to be a constant). Eq. 8 has the solution,

$$u_o = \frac{u_s - \frac{1}{\sqrt{\varepsilon}}\tan\left(\sqrt{\varepsilon} g \sin\beta t\right)}{1 + u_s\sqrt{\varepsilon}\tan\left(\sqrt{\varepsilon} g \sin\beta t\right)} \tag{9}$$

where $\varepsilon = K / g\sin\beta$ and u_o=u_s when t=0. Integrating Eq. 9 ($u_o = dx_o / dt$) with respect to t yields the position of the wave front during uprush:

$$x = \frac{1}{\varepsilon g \sin\beta}\ln\left(\frac{\cos\left(\arctan(u_s\sqrt{\varepsilon}) - \sqrt{\varepsilon} g \sin\beta t\right)}{\cos\left(\arctan(u_s\sqrt{\varepsilon})\right)}\right) \tag{10}$$

Setting u_o=0 in Eq. 9 yields the time when the runup height is obtained:

$$t_{\max} = \frac{1}{\sqrt{\varepsilon} g \sin\beta} \arctan\left(\sqrt{\varepsilon} u_s\right) \tag{11}$$

Combining Eqs. 10 and 11 gives the runup height including friction:

$$R = \frac{1}{\varepsilon g} \ln\left(\frac{1}{\cos\left(\arctan(\sqrt{\varepsilon} u_s)\right)}\right) \tag{12}$$

For the limiting case of no friction ($\varepsilon \to 0$) Eq. 12 reverts back to $R = u_s^2/(2g)$.

Eq. 8 is valid for the uprush case, whereas during the backwash the frictional force is acting in the opposite direction and the following equation should be solved:

$$\frac{du_o}{dt} = -g\sin\beta + Ku_o^2 \tag{13}$$

Using the initial condition that u_o=0 for τ=t-t_{max}=0 gives the solution:

$$u_o = -\frac{1}{\sqrt{\varepsilon}} \frac{1-\exp\left(-2\sqrt{\varepsilon} g \sin\beta\tau\right)}{1+\exp\left(-2\sqrt{\varepsilon} g \sin\beta\tau\right)} = -\frac{1}{\sqrt{\varepsilon}} \tanh\left(\sqrt{\varepsilon} g \sin\beta\tau\right) \tag{14}$$

For $\tau \to \infty$, Eq. 14 has the limit $u_o = \sqrt{g\sin\beta / K}$, which is the steady-state solution to Eq. 13. The position of the wave front during backwash is obtained by integrating Eq. 14 yielding,

$$x_o = x_{\max} - \frac{1}{\varepsilon g \sin\beta} \ln\left(\cosh\left(\sqrt{\varepsilon} g \sin\beta\tau\right)\right) \tag{15}$$

where the initial condition that x_o=x_{max} at τ=0 was used.

In order to describe 2D runup with friction, the alongshore equation of motion should be modified to,

$$\frac{dv_o}{dt} = -Kv_o^2 \tag{16}$$

bearing in mind that $v_o = dy_o / dt$. The solution to this equation, applying the initial condition v_o=v_s when t=0, yields:

$$v_o = \frac{v_s}{1 + Kv_s t} \tag{17}$$

Integrating Eq. 17 with respect to time gives the longshore position of the wave front,

$$y_o = \frac{1}{K} \ln\left(\exp\left(Ky_s\right)\left(1 + Kv_s t\right)\right) \tag{18}$$

assuming that y_o=y_s when t=0. Replacing t in Eq. 17 with x by using Eq. 10 will illustrate how the longshore front speed varies with position on the foreshore during the uprush. Similarly, employing Eq. 15 to substitute t with x, the variation during the backwash phase is obtained.

Similar to the runup height, the swash duration is affected by friction and the uprush phase has a different duration than the backwash phase. The uprush lasts until the wave front speed u_o becomes zero, which yields the following duration T_{uf} (from Eq. 9):

$$T_{uf} = \frac{\arctan\left(\sqrt{\varepsilon} u_s\right)}{\sqrt{\varepsilon} g \sin\beta} \tag{19}$$

The backwash ends when the wave front has returned to the starting point of the swash (*i.e.*, the SWS), which corresponds to x_o=0. During the backwash the wave front location is given by Eq. 15, and applying the condition that x_o=0 yields the backwash duration T_{bf} (after some manipulation),

$$T_{bf} = \frac{1}{\sqrt{\varepsilon} g \sin\beta} \ln\left(A + \sqrt{A^2 - 1}\right) \tag{20}$$

where:

$$A = \frac{1}{\cos\left(\arctan\left(\sqrt{\varepsilon} u_s\right)\right)} \tag{21}$$

Thus, the swash duration with friction is given by T_f=T_{uf}+T_{bf}, whereas the duration neglecting friction (T_s) is obtained as $T_s = 2u_s / (g \sin\beta)$. It is convenient to present the influence of the friction on the swash properties, such as the runup height and swash duration, by introducing the non-dimensional parameter $\delta = Ku_s^2 / (g \sin\beta)$ $(= \varepsilon u_o^2)$. This parameter expresses the ratio between the friction force and the gravitation force. Fig. 1 illustrates the influence of friction on the runup height (R_f) and the swash duration (T_f, T_{uf}, and T_{bf}), where the corresponding values for no friction was used as normalizing

quantities. The figure shows that the swash duration is always shorter if friction is included, and that the duration of the backwash is always longer than the uprush. In the following comparisons with the experimental data, friction was not included to avoid introducing another calibration parameter. However, when applying Eqs. 3 and 4 in the general case, u_o, v_o, and t_o should be estimated based on the solution with friction,

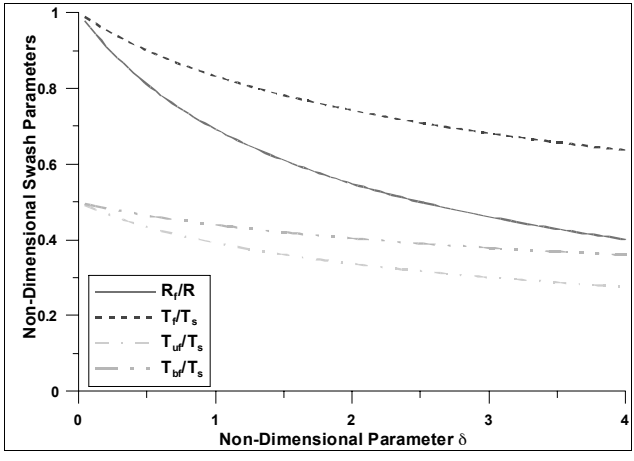

Fig. 1. Influence of friction on runup height and swash duration.

COMPARISON WITH EXPERIMENTAL DATA

The proposed formula for the longshore sediment transport rate in the swash (Eq. 4) was validated with data from movable-bed experiments carried out in the LSTF (Wang *et al.*, 2002; Gravens and Wang, 2007). Previously the cross-shore transport formula (Eq. 3) was validated using field data from Japan (Larson *et al.*, 2004), where appropriate values on the transport coefficient (K_c) were determined through calibration against measured data on the profile response on the foreshore. It will be assumed that the transport coefficient for the longshore direction (K_l) has a similar value to K_c. Data on the longshore sediment transport in the swash zone is available from LSTF experiments, including the spilling/plunging wave experiment conducted by Wang *et al.* (2002) and the detached breakwater experiment by Gravens and Wang (2007; base cases performed before any structure was put in). Results from comparison between predictions with the formula and the data for these two experiments are reported in the following.

The general experimental setup and measurement procedure were similar for the two LSTF experiments. Measurements of the longshore sediment transport rate in the swash zone encompassed only two locations on the foreshore using traps at a distance of -0.3 m and -0.9 m from the initial still-water shoreline (negative values refer to a distance shoreward of this shoreline). However, this still gave a basis for assessing how appropriate the formula is and for a rough estimate of suitable coefficient values. More

detailed measurements were available for the surf zone and the region where it is expected that the swash and surf zone would significantly interact. In order to describe the latter region, as a first approach, sediment from the swash zone is assumed to diffuse out into the surf zone in manner that may be described by an exponential decay. The measured transport rate in the inner part of the surf zone was relatively constant, which was a result of the beach profile being in equilibrium with similar rate of energy dissipation for sediment mobilization and similar longshore current for transport alongshore. Thus, the decay in the transport rate from the swash zone was made to approach this constant value (estimated from the data) defining the value of the rate coefficient in the exponential decay.

In order to compute the transport rate in the swash, several input quantities and coefficients are necessary, including the runup height (used to estimate initial velocity of runup waves in the ballistics model), the wave angle prior to runup, the transport rate coefficient, and the foreshore slope. For general validation of the formula a typical coefficient value of $K_c=10^{-3}$, which was a typical value obtained by Larson *et al*. (2004) when modeling the cross-shore sediment transport in the swash for field data, was employed for the coefficient (K_l) in the longshore sediment transport formula. The runup height was computed with the Hunt (1959) formula and the wave angle in a water depth of about 0.05 m was used as input to the swash calculations using Snells law to estimate the wave angle in shallow water. This water depth is somewhat arbitrarily chosen, but approximately corresponds to the limit of the backwash.

Experiments by Wang *et al.*

Wang *et al*. (2002) performed movable-bed experiments in the LSTF to study the spatial and temporal variations in the surf-zone currents and sediment transport rates due to obliquely incident breaking waves. The beach and wave conditions were uniform alongshore (water was recirculated to simulate an infinite beach) and two main cases were investigated where spilling and plunging breakers were predominant, respectively. The sand had a median grain size of 0.15 mm and the waves were allowed to act a sufficiently long time to ensure near-equilibrium conditions (the foreshore slope was approximately linear with $\tan\beta_e=0.18$). The (calculated) deepwater wave conditions for the spilling and plunging case were H_{mo}=0.27 m, T_p=1.5 s, ϕ=10.4 deg, and H_{mo}=0.24 m, T_p=3.0 s, ϕ=16.3 deg, respectively, where H_{mo} is the significant wave height, T_p the peak wave period, and ϕ the wave angle. The transport rates measured by sediment traps at the downdrift end of the LSTF were used for the comparison in the present study (rates were converted to include porosity and correspond to a yearly amount).

Figures 2 and 3 display the results for the spilling and plunging case carried out by Wang *et al*. (2002), respectively, indicating good agreement between the predictions by the proposed formula and the measurements. Although the measurement points in the swash zone are only two, the transport magnitude seems to be well predicted with the typical transport coefficient value as well as the extent of the swash zone and the distribution of the transport rate. The results presented in the figures give rise to the following observations: (1) The simple Hunt formula seems to give a reasonable

estimate of the runup height (using the foreshore slope and the significant wave height). Since the runup height basically depends on the surf similarity parameter the predictions are quite different for the spilling and plunging case, in agreement with observations; (2) The value on the cross-shore transport coefficient obtained from the Japanese field data seems to yield good quantitative predictions and to be applicable for the longshore transport coefficient as well; and (3) The simple decay formulation applied seaward of the swash zone produces reasonable results, although for a case where the longshore transport in the inner part of the surf zone is not nearly constant (*i.e.*, equilibrium conditions prevail) some modifications are needed.

The decay coefficient was set to 1.0, although it should scale with the wave properties in the general case, and the equilibrium longshore transport rate in the inner part of the surf zone was given as 150 and 200 m^3/m/yr for the spilling and plunging case, respectively. When applied in simulations of beach topography change some procedure is probably needed to smooth the distinct peak at the still-water shoreline, which is a result of switching from the transport formula in the swash to the exponential decay.

Experiments by Gravens and Wang

Further testing of the swash-zone sediment transport formula was carried out by comparing with data on the longshore transport rate from the experiment by Gravens and Wang (2007) on beach topography evolution in the vicinity of detached breakwaters. In this experiment, four base cases were conducted on a natural beach without any structure present. Three of the experimental cases included waves (BC1, BC2, and BC4) and data

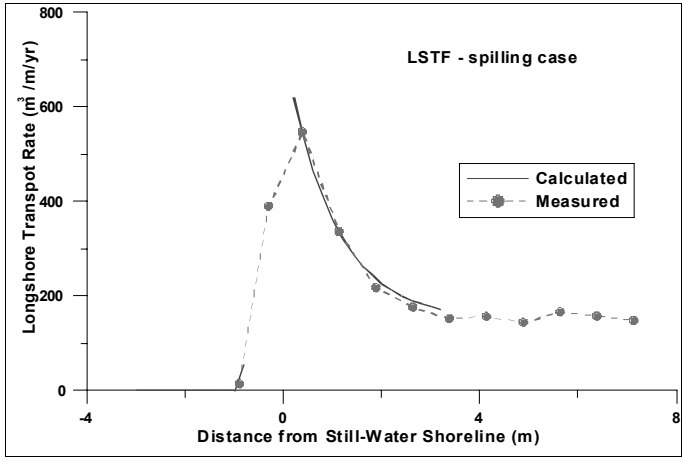

Fig. 2. Comparison between calculated and measured longshore transport rate in the swash and inner part of the surf zone for the spilling case from Wang *et al.* (2002).

from these cases were employed in the present study. All cases had the same offshore wave conditions (H_{mo}=0.32 m, T_p=1.5 s, and ϕ=8.5 deg), whereas Case BC1 had a recirculating current in the basin corresponding to the wave-generated current (simulating the current induced by the breaking waves on an infinitely long beach). Cases BC2 and BC4 encompassed recirculating currents corresponding to 2 and 1.5 times the wave-generated current, respectively, in order to simulate an external current (e.g., generated by tide or wind) superimposed on the wave-generated current.

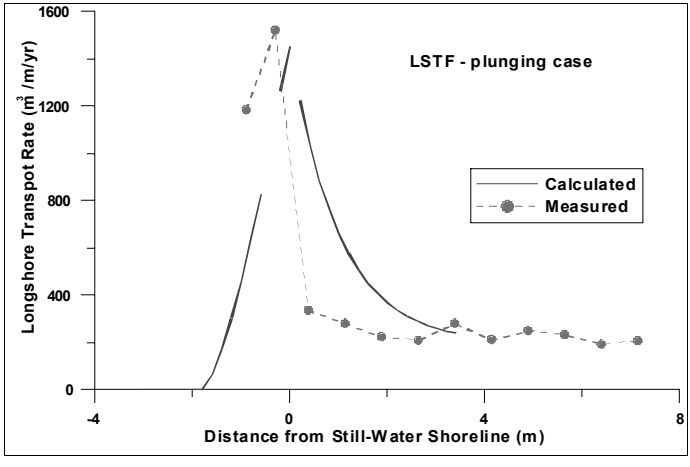

Fig. 3. Comparison between calculated and measured longshore transport rate in the swash and inner part of the surf zone for the plunging case from Wang *et al*. (2002).

The sediment was the same as in the experiment performed by Wang *et al*. (2002), and the foreshore profile was similar. Wave conditions recorded at the break point were used to derive input wave data (the waves were backed out to deep water from the break point, and the runup height was computed with the Hunt formula using deepwater wave conditions). Since the breaking wave conditions reported by Gravens and Wang (2007) were the same for all experimental case, the calculated runup height was the same, as well as the transport rate distribution in the swash zone. However, the equilibrium longshore transport in the inner part of the surf zone that the calculated transport rate was set to decay towards was different for the three cases studied, namely 130, 270, and 200 m^3/m/yr for Cases BC1, BC2, and BC4, respectively (approximate estimates from the measurements). This estimate scales well with the magnitude of the current employed in the various cases.

The same procedure and coefficient values were employed as for the Wang *et al*. (2002) comparisons without any additional tuning. Figures 4, 5, and 6 show the results for Cases BC1, BC2, and BC4, respectively. For Cases BC1 and BC4 there is some overestimation, but the result for BC2 is in good agreement.

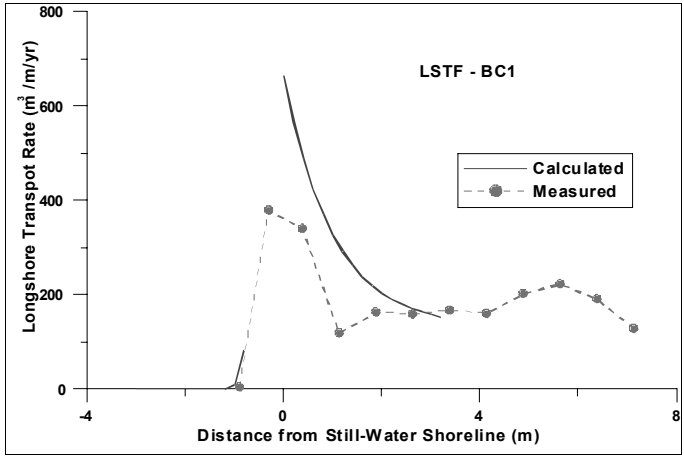

Fig. 4. Comparison between calculated and measured longshore transport rate in the swash and inner part of the surf zone for Case BC1 from Gravens and Wang (2007).

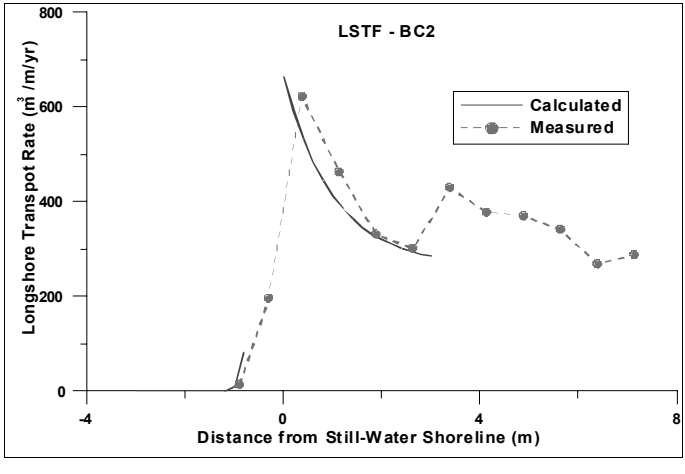

Fig. 5. Comparison between calculated and measured longshore transport rate in the swash and inner part of the surf zone for Case BC2 from Gravens and Wang (2007).

CONCLUSION

A formula for the longshore sediment transport rate in the swash zone was proposed based on the work by Larson *et al.* (2004) on cross-shore sediment transport in the swash. Needed hydrodynamic input on the wave front speed and swash duration was

derived from ballistics theory, where both the cases of no friction and friction were studied. Comparisons between calculated and measured transport rates were performed based on previous movable-bed experiments in the LSTF encompassing in total five cases. These comparisons indicated that the typical value on the transport rate coefficient determined by Larson *et al.* for cross-shore transport in the swash using field data from Japan provided a good estimate for the LSTF data as well.

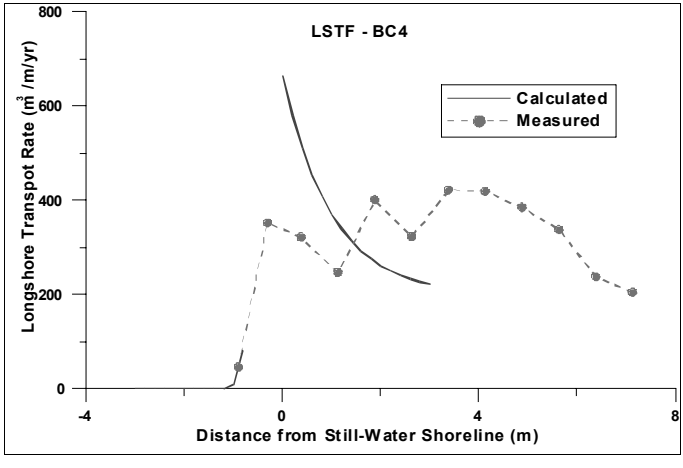

Fig. 6. Comparison between calculated and measured longshore transport rate in the swash and inner part of the surf zone for Case BC4 from Gravens and Wang (2007).

The transition from the swash zone to the surf zone was described through a simple exponential decay from the peak in the swash zone transport rate at the still-water shoreline to the rate observed in the seaward portion of the inner surf zone, where the transport seemed to take on a fairly constant value. The value on the decay coefficient employed was on the order of one for the experiments, but this value should scale with some hydrodynamic quantity in the general case (e.g., wave height). In the present study the foreshore slope was taken as constant. If the slope is more complex, the presented solutions may be applied for piecewise sections of the foreshore where the slope is approximately constant. Although the present study indicated the potential applicability of the proposed formula, more comparisons with data are needed to validate the formula and to obtained appropriate transport coefficient values.

ACKNOWLEDGEMENTS

This work was conducted under the Inlet Modeling System Work Unit of the Coastal Inlets Research Program, U.S. Army Corps of Engineers. The experimental data from the LSTF provided by Dr. Ping Wang, University of South Florida, and Mr. Mark Gravens, Coastal and Hydraulics Laboratory are greatly appreciated.

REFERENCES

Camenen, B., and Larson, M. (2003). "A bedload sediment transport formula for the nearshore," *Estuarine, Coastal, and Shelf Science,* 63, 249-260.

Elfrink, B. and Baldock, T. (2002). "Hydrodynamics and sediment transport in the swash zone: a review and perspectives," *Coastal Engineering*, 45, 149-167.

Erikson, L., Larson, M., and Hanson, H. (2005). "Prediction of swash motion and run-up including the effects of swash interaction," *Coastal Engineering*, 52, 285-302.

Gravens, M.B., and Wang, P. (2007). "Data report: LSTF experiments - transport by waves and currents, and tombolo development behind headland structures," Draft Technical Report, ERDC/CHL TR, Coastal and Hydraulics Lab., US Army Engineer Research and Development Center, Vicksburg, MS.

Holman, R.A. (1986). "Extreme value statistics for wave runup on a natural beach," *Coastal Engineering*, 9, 527-544.

Hughes, M.G. (1995). "Friction factors for wave uprush," *Journal of Coastal Research*, 13, 1089-1098.

Hunt, I.A. (1959). "Design of seawalls and breakwaters," *Journal of Waterways and Harbors Division*, 85, 123-152.

Kirkgöz, M.S. (1981). "A theoretical study of plunging breakers and their runup," *Coastal Engineering*, 5, 353-370.

Larson, Kubota, S., and Erikson, L. (2004). "Swash zone sediment transport and foreshore evolution: Field experiment and mathematical modeling," *Marine Geology*, 212, 61-79.

Madsen, O.S. (1991). "Mechanics of cohesionless sediment transport in coastal waters," *Proceedings Coastal Sediments '91*, ASCE, 15-27.

Madsen, O.S. (1993). "Sediment transport on the shelf," *Proceedings Sediment Transport Workshop DRP TA1*, 8-9 June, CERC, Vicksburg, Miss.

Mase, H. (1988). "Spectral characteristics of random wave run-up," *Coastal Engineering*, 12, 175-189.

Masselink, G., and Hughes, M. (1998). "Field investigation of sediment transport in the swash zone," *Continental Shelf Research*, 18, 1179-1199.

Mayer, R.H., and Kriebel, D.L. (1994). "Wave runup on composite-slope and concave beaches," *Proceedings 24th Coastal Engineering Conference*, ASCE, 2325-2339.

Waddell, E. (1973). "A field investigation of swash characteristics," *Coastal Engineering in Japan*, 16, 61-71.

Wang, P., Ebersole, B.A., Smith, E.R., and Johnson, B.D. (2002). "Temporal and spatial variations of surf-zone currents and suspended-sediment concentration," *Coastal Engineering*, 46, 175-211.

IMPORTANCE OF THE SWASH LONGSHORE SEDIMENT TRANSPORT IN MORPHODYNAMIC MODELS

Yasuyuki Baba[1] and Benoît Camenen[2]

1. Disaster Prevention Research Institute, Kyoto University, Yoko-oji, Fushimi, Kyoto, 612-8235, JAPAN
   baba@uh31.dpri.kyoto-u.ac.jp
2. Cemagref Lyon, 3 bis quai Chauveau CP 220, 69336 LYON cedex 09, FRANCE
   camenen@lyon.cemagref.fr

Abstract: This paper discusses the effect of the longshore sediment transport in the swash zone on the evolution of the shore line. The beach evolution model presented here is based on an N-line approach including a local estimation of the sediment transport function of the local current and wave characteristics. A simple model for the longshore sediment transport in the swash zone is implemented to the beach evolution model. The erosion and the accumulation of sediments around a groin appear to be significantly influenced by the introduction of the swash sediment transport.

INTRODUCTION

2-DH and N-line models were developed in order to take into account both longshore and cross-shore beach topography changes and allow short and mid-term modeling (including storm effects etc...). Hanson & Larson (2000) argued that realistic predictions for the cross-shore distribution of the longshore and cross-shore sediment transport are the fundamental part for these types of models. To use a local sediment transport formula which includes current and wave interaction seems to be the most adequate method to correctly estimate the beach topography changes. However, these formulas are generally not valid on the swash zone as the sediment processes are different in this zone (effect of the equilibrium slope, infiltration...). In the cross-shore direction, to neglect the swash zone dynamic does not affect significantly the formation of the longshore bar and the beach profile equilibrium in general, although this zone is very dynamic in a short term period. On the other hand, in the longshore

direction, it seems that the role of the longshore sediment transport in the swash zone is much more significant and does strongly affect the evolution of the shoreline (Van Wellen et al, 2000; Elfrink & Baldock, 2002). Indeed, Uda & Kawano (1996) proposed a N-line model with a typical cross-shore distribution of the longshore sediment transport which basically corresponds to the swash zone transport only, and obtained interesting results for the evolution of the shoreline. The purpose of this paper is thus to quantify the effects of the swash zone on the evolution of the shoreline.

MODEL THEORY

The numerical model presented here is made up of four main components with the following objectives:

1) wave propagation

2) calculation of the depth-averaged current in the longshore direction and cross-shore direction (mean undertow)

3) sediment transport simulation

4) beach profile change using an N-line approach

Most of the hydrodynamic and sediment transport calculations are performed along individual profile lines, and the coupling between the lines occurs through a semi-empirical model to take into account the effects of a structure on the currents and waves and the sediment volume conservation equation. The details concerning these components were illustrated by Baba et al (2004) and Baba et al (2006).

As the model does not include the hydrodynamic and morphodynamic swash zone, a simple model is proposed to estimate the cross-shore profile of the total longshore transport in the swash zone. The swash zone is particularly complex, involving rapidly varying flow (in time and space), nonlinear waves transformation, and possible infiltration and exfiltration effects (Elfrink and Baldock, 2002; Larson *et al.*, 2004). To be taken into account in an N-line model, which is depth and time averaged, many simplifications on the swash dynamic are necessary.

Hydrodynamic model in the swash zone

The swash zone may be delimited around the still water level (SWL) from an estimation of the run-up R_{up} and run-down R_{down} heights. The classic formulation by Hunt was used:

$$R_{up} = A_R \tan\beta_f \sqrt{H_\infty L_\infty} \quad (1)$$

where $\tan\beta_f$ is the foreshore slope, H_∞ and L_∞ the wave height and length, respectively, in deep water, and A_R a calibration coefficient ($A_R=2.0$ using the data from LSTF). R_{down} has been chosen as a fraction of R_{up} ($R_{down} = R_{up}/4$). Then, the "mean" water depth in the swash zone is estimated assuming a linear law from both edges of the swash zone (*cf.* Fig 1).

Using the mean water level (MWL) and the Snell law, the wave direction may be estimated at x=0 (limit of the SWL). Then, following Shen and Meyer, 1963, and Larson *et al.*, 2004, the trajectory of the bore front follows a parabolic movement.

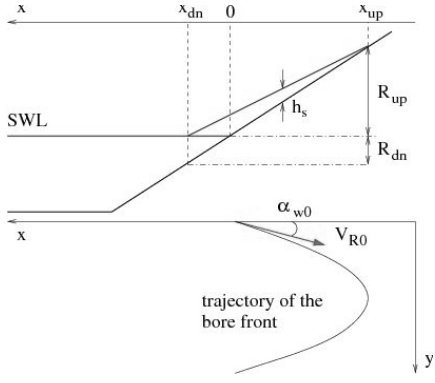

Fig. 1. Schematic view of the swash zone

The celerity of the bore at the foot of the swash zone and the swash period are then found respectively:

$$V_{R0} = \sqrt{2gR_{up}} \tag{2}$$

$$T_s = \frac{2V_{R0}}{g \sin \beta_f} \tag{3}$$

From this system, the longshore component V_{ry} of the bore velocity is presumed constant whereas its cross-shore component V_{rx} decreases linearly in the swash to be null at $x=x_{up}$. In the same way, the effective swash duration T_{sx} decreases linearly from T_s at $x=0$ to 0 at $x=x_{up}$. Thus, the temporal variation of the cross-shore velocity in the swash may be simulated by a saw-tooth shaped velocity profile with a period T_{sx} and a maximum velocity V_{rx}.

Sediment transport model in the swash zone

The model proposed by Camenen and Larson (2005, 2007; i.e. the "Lund-CIRP" formula) may be used to estimate both bed load and suspended load in the swash zone using the hydrodynamic conditions presented above. The bottom shear stress is estimated assuming a linear interaction between a cross-shore oscillatory flow and a longshore steady flow. As Camenen and Larson (2005, 2007) used a mean value of the shear stress (or its dimensionless value, the Shields parameter), it is found for the a saw-tooth shaped velocity profile:

$$\theta_{cw,m} = \frac{1/6\left(V_{rx}^{\ 2} + V_{ry}^{\ 2}\right)}{(s-1)gd_{50}} \tag{4}$$

where $_s$ is the relative sediment density and d_{50} the median grain size.

This model was compared with the experimental data obtained by Wang *et al.* (2002) at the LSTF (Vicksburg, Mississippi, USA). In Fig. 2, the longshore sediment transport is plotted on a cross-shore section for two different experiments. The first

one (test1) corresponds to a spilling breaking case whereas the second one (test3) corresponds to a plunging breaking case. The proposed model yields correct results for the longshore sediment transport in the swash zone (dashed line). It significantly improves the results for the estimation of the cross-shore profile of the longshore sediment transport compared to the model with the swash zone excluded. There are however some uncertainties on the position of the maximum (assumed to be at *x=0*, edge of the SWL) and on the maximum which is highly function on the estimation of the run-up height.

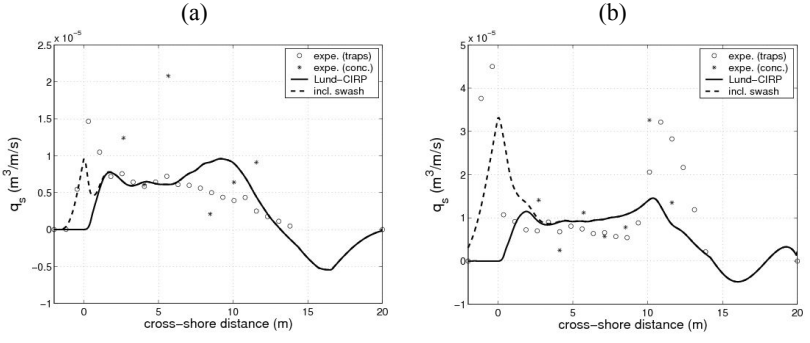

Fig. 2. Cross-shore profile of the longshore sediment transport for the LSTF experiments (a: spilling case; b: plunging case)

In the swash zone, the bed load appeared to prevail whereas the suspended load is prevailing in the surf zone, which is in agreement with the experimental observations (Wang *et al.*, 2002; Larson *et al.*, 2002).

MODEL TESTS AND RESULTS

Fig 3 displays the schematized computational domain for tests of the model. The computational domain is 15000m wide and 5000m long in longshore and cross-shore directions, respectively. The initial bottom slope is 1/100, and a groin (L=2000m) is set in the middle of the calculating area. Each cell of the N-line model is 50m wide and 0.5m deep.

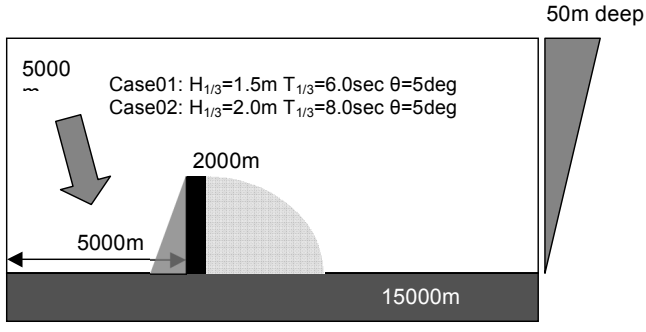

Fig. 3. Schematized computational domain

The sediment transport rate in shadowed area in Fig 3 is assumed to be affected by the groin. In the calculation here, sediment transport rate around the groin is depressed according to the inverse of the distance from the groin without the effects of diffraction and the existence of counter flow and so on.

Fig 4 shows cross-shore profile of the longshore sediment transport in both Case01 and Case02. The offshore boundary conditions in those cases are as follows;

Case 01: $H_{1/3}$=1.5m $T_{1/3}$=6.0sec θ=5.0deg
Case 02: $H_{1/3}$=2.0m $T_{1/3}$=8.0sec θ=5.0deg

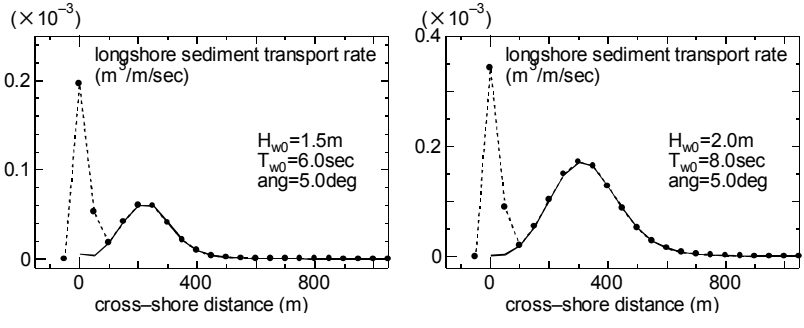

Fig. 4. Cross-shore profile of the longshore sediment transport
(solid: without swash model, dash & dots: include swash model)

In both profiles in Fig 4, longshore sediment transport rates in swash zone are calculated relatively higher than those under sea water, and these profiles have similar characteristics with the experimental results in Fig 2. Though this sediment transport model in swash zone have need of further quantitative verification, the

longshore sediment transport model in swash zone presented here is applied the following model tests.

Fig 5 shows the plane views of bottom contours around the groin after 10 days exposure to the continuous wave conditions for the case 01. The bold line in the figure is the shore line, and the black thin rectangle is the groin. In each figure, the accumulation in the left hand side of the groin is generated. As the total longshore sediment transport in a cross-shore line is larger when longshore sediment transport in swash zone is included, the magnitude of the accumulation is also larger. The inclusion of the swash longshore transport also yields a modification of the shoreline whereas the shoreline does not move when the longshore sediment transport in swash zone is not included. Moreover, some erosion downdrift of the groin occurs in the case with longshore sediment transport in swash zone. On the contrary, in the case without longshore sediment transport in swash zone, the shoreline (bold lines in the figures) downdrift of the groin still keeps the initial profile. It is thus observed that the erosion and the accumulation around the groin appear more clearly due to the introduction of the longshore sediment transport in swash zone.

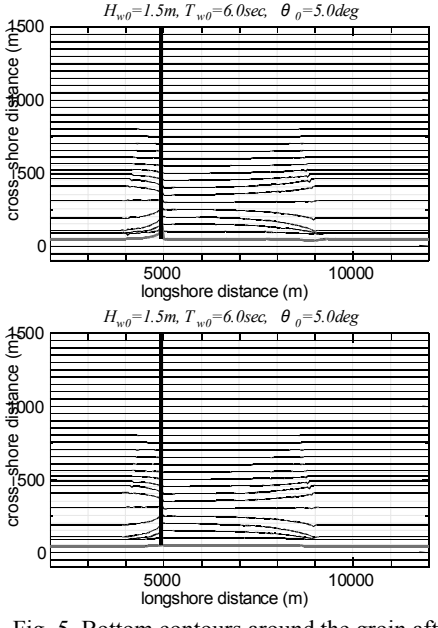

Case 01
With longshore sediment transport in swash zone
(bold line: shore line SWL=0)

Case 01
Without longshore sediment transport in swash zone
(bold line: shore line SWL=0)

Fig. 5. Bottom contours around the groin after 10 days exposure for the Case 01

In Fig. 6, similar calculations are presented for the case 02 which is more energetic. Again, if the longshore sediment transport in the swash zone is not included, no movements of the shoreline are observed. On the contrary, when the longshore

sediment transport in the swash zone is included, a significant movement of the shoreline (with a larger magnitude as for the case 01) is observed in both side of the groin (accumulation close to the groin and erosion downdrift to the groin). From these computations, no real differences are observed in the surf zone close to the groin although an influence of the shoreline movement on this part of the domain was expected.

In both Fig 5 and Fig 6, some of the perturbations on the contour lines are observed in both side of the groin. These perturbations occur around the boundary between affected and no-affected areas by the groin. Some modifications of sediment transport around the groin are required to simulate appropriate profile change.

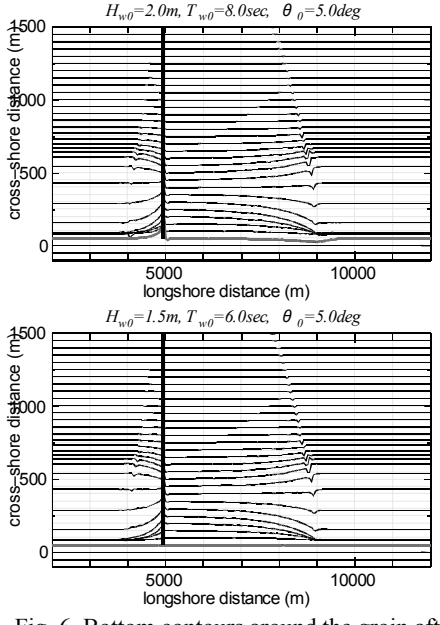

Case 02
With longshore sediment transport in swash zone
(bold line: shore line SWL=0)

Case 02
Without longshore sediment transport in swash zone
(bold line: shore line SWL=0)

Fig. 6. Bottom contours around the groin after 10 days exposure for the Case 02

Fig 7 shows the temporal variations of contour line at SWL=0 in the case with longshore sediment transport in swash zone. As time passes, the erosion and the accumulation proceed around the groin. The magnitude of the erosion around x=9000m reaches more than 20m, and the eroded area have the tendency to expand to downward region. The accumulation updrift to the groin develops more rapidly than the erosion downdrift of the groin. This erosion appeared however on a longer domain. This kind of beach erosion is not generated without longshore sediment transport in swash zone.

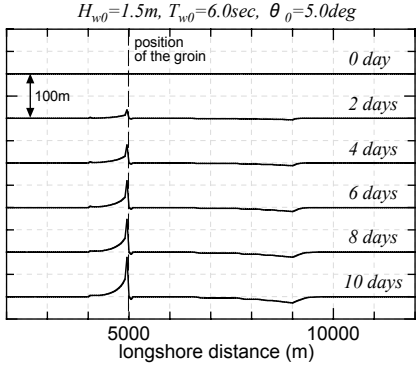

(a) Case01

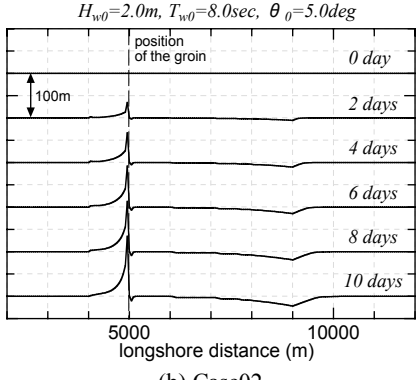

(b) Case02

Fig. 7. Temporal variations of contour line at SWL=0

CONCLUSIONS

In this study, a longshore sediment transport model for the swash zone is implemented to a beach evolution model based on N-line approach. The influence of the introduction of the longshore sediment transport in the swash zone on the evolution of the shore line is discussed. The erosion and the accumulation around the shore line are clearly represented by the introduction of sediment transport in swash zone, especially for the shoreline change. The sediment transport model in the swash zone needs however some further considerations and validations. It is found from the results that sediment transport in swash zone has an important role for the beach evolution and could be one of the main contributors for the erosion/accumulation processes close to the shore line.

REFERENCES

Baba, Y., M. Larson, H. Hanson, and T. Yamashita (2004). Simulation of coastal evolution using a n-line model including wind-induced current. 29th ICCE, pp. 2436-2448. ASCE.

Baba, Y., B. Camenen and T. Yamashita (2006). Development and Application of an N-line Model on the Joetsu-Ogata Coast, Japan, 30th ICCE, ASCE.

Camenen, B. and Larson, M., (2005). "A bedload sediment transport formula for the nearshore" Estuarine, Coastal and Shelf Sciences 63, 249– 260.

Camenen, B. and Larson, M., (2007). "A suspended load sediment transport formula for the nearshore" Accepted in J. Coastal Research.

Camenen, B. and Larson, M., (2007). "A total load formula for the nearshore" Proceeding of the conference Coastal Sediment'07, New Orleans, Louisiana, USA.

Elfrink, B. and Baldock, T., 2002. "Hydrodynamics and sediment transport in the swash zone: a review and perspectives." Coastal Engineering 45, 149– 167.

Larson, M., Kubota, S. and Erikson, L. (2002). "Swash-zone sediment transport and foreshore evolution: field experiments and mathematical modeling" Marine Geology 212, 61-79.

Shen, M.C., and Meyer, R.E., (1963). Climb of a bore on a beach: Part 3. Run-up. J. of Fluid Mechanics 16, 113–125.

Wang P., Ebersole B.A. and Smith E.R. (2002) "Longshore sand transport - Initial results from large-scale sediment transport facility", CHETN-II-46, Coastal and Hydraulics Laboratory, U.S. Army Corps of Engineers, Vicksburg, Mississippi, USA

DIRECT BED SHEAR STRESS MEASUREMENTS IN BORE-DRIVEN SWASH AND SWASH INTERACTIONS

Matthew P. Barnes[1], Tom E. Baldock[1]

1. University of Queensland, Department of Civil Engineering, Brisbane, Queensland, 4072, Australia. mbarnes@uq.edu.au; t.baldock@uq.edu.au

Abstract: Bore-driven swash and swash interactions are investigated experimentally. Direct bed shear stress measurements suggest bore/swash backwash interactions act to interrupt backwash (seaward) sediment transport. Catch up and absorption causes landward directed bed shear force (enhanced by impact forces onto the bed) of a short duration that does not follow the measured flow velocity trend. A single swash interaction is likely to restrict seaward direct transport and/or suspend sediment in large volumes but not directly contribute to the landward advection of sediment. Bore-driven swash hydrodynamics for a single swash event were predicted well using a non-linear shallow water wave equation model. In the mid-swash region measured uprush bed shear stress was predicted well using the drag law estimate with constant friction factor $C_f \approx 0.02$. A smaller or time-varying C_f is required to accurately predict measured backwash bed shear stress.

INTRODUCTION

In simplified terms, the swash zone is characterised by fluid uprushes and subsequent backwashes on the beachface. The uprushes and backwashes transport sediment in higher concentrations than elsewhere in the nearshore zone and largely dictate beachface morphology. Swash zone hydrodynamics are primarily controlled by the inner surf zone and beach face gradient (Elfrink and Baldock, 2002). In terms of sediment transport, the backwash is not simply a mirror of the uprush. A common finding in many field investigations of swash hydrodynamics is that, for a given velocity, the uprush transports more sediment than the backwash (e.g. Hughes *et al*., 1997; Masselink and Hughes, 1998; Puleo *et al*., 2000). The asymmetrical nature of swash transport is a requirement for beach equilibrium. If the uprush and backwash sediment transport rates were equal, the longer backwashes would gradually erode more sediment than the uprushes could contribute (Masselink *et al*., 2005).

It is generally accepted that turbulence due to bore collapse is a contributor to the sediment advected into the swash zone; however a greater knowledge of the process is required to allow its inclusion in swash models. Boundary shear stress and bore turbulence are unlikely to operate independently and therefore the interaction of the two processes requires attention.

As a fully developed bore travels landward through the surf zone, where the water depth h_o is sufficiently large relative to the bore height H ($h_o/H > 0.75$) turbulent motions produced at the bore front are unlikely to significantly influence sediment suspension. As a bore continues to propagate through the inner surf zone towards the swash zone, h_o generally reduces and the incident bore typically encounters:

a) No impeding flow and collapses onto the intermittently wet/dry beach (i.e. the initial stage of swash uprush) referred to herein as 'true bore collapse';
b) A thin accelerating seaward directed flow (i.e. a preceding swash backwash; generally supercritical flow conditions) referred to herein as a 'collision'; or
c) A decelerating landward directed flow (i.e. a preceding swash uprush; generally subcritical flow conditions) referred to herein as 'catch up and absorption'.

For these three cases the flow depths may be sufficiently small for the bore turbulence to affect the seabed and/or beachface.

A 'true bore collapse' drives a single swash event with the location of bore collapse defining the seaward swash boundary. Providing the bore period T_b is larger than the swash period T_s, the uprush and subsequent backwash are not impeded by preceding nor subsequent swashes and large run-up distances generally occur. The energetic bore collapse is expected to play a significant role in suspending sediment in the early stages of the uprush (Jackson *et al*., 2004) and may in fact counterbalance erosive processes in the swash. Pritchard and Hogg (2005) developed an analytical description of sediment transport by a single swash event following bore collapse, proposing a relationship between sediment entrained by the initial bore collapse and the net transport direction. During the decelerating uprush stages, sediment is transported predominantly by sheet flow with some sediment settling on the beachface. The subsequent stronger backwash that follows transports any sediment still in suspension seaward. In a laboratory investigation, Kobayashi and Lawrence (2004) reported sediment being transported in backwash flow beyond the seaward swash boundary (note that Kobayashi and Lawrence referred to bores described by (a) as "positive solitary waves").

'Collisions' and 'catch up and absorption' are often referred to as swash interactions. A swash flow interacting with an incident bore may be a sediment transport mechanism. Remaining largely unknown, however, is the direction and magnitude of these forces during the passage of the bore front as it propagates with or against swash flow.

Kobayashi and Lawrence (2004) found collisions (referred to by Kobayashi and Lawrence as 'negative solitary waves') to suspend less sediment in comparison to true bore collapse. Wave run-up against the impeding seaward flow was much smaller. The weak backwash that followed the small run-up deposited sediment only on the beachface and not seaward of the run-down. No beach face erosion by the backwash was observed. Van Wallen *et al*. (2000) presented a nearshore sediment transport model that included swash interactions and associated transport rates. However the study was limited by available data sets to test the model. More recently Erikson *et al*. (2005) presented modifications to a hydrodynamics model describing swash motions (Baldock and Holmes, 1999) by including swash interactions. Model comparisons with laboratory data suggested the modifications improved swash duration prediction for a mild sloping beach ($\tan\beta = 0.07$). While Erikson *et al*. (2005) included the process of catch up and absorption in their swash duration model, to the authors' knowledge the process is yet to be investigated experimentally. Of particular interest in the present investigation is the role catch up and absorption may play in enhancing sediment suspension process.

Kobayashi and Lawrence's (2004) laboratory results imply that the presence of collisions may play an important role in maintaining beach equilibrium. This theory was originally proposed by Kemp (1975). Models presented by Van Wellen *et al*. (2000) and Holland and Puleo (2001) suggest that when the incident bore period T_b exceeds the duration required for a swash event to be completed, no collisions will occur and the accelerating backwash will be able to entrain and transport sediment seaward of the point of the initial bore collapse. Under such erosive conditions, the beach profile is likely to flatten and in turn gradually lengthen the swash duration. In contrast, swash interactions can be expected when the incident bore period T_b is less than the swash period T_s. Collisions between the swash flow and subsequent uprush may cause sediment to be stranded landward of the initial uprush position (i.e. the point of the initial bore collapse). Shorter swash periods will lead to accretion and steepening of the beach profile. For each case, the beach profile is adjusting towards equilibrium and conditions where T_s and T_b are approximately equal.

The aim of the present work is to investigate how an incident bore affects the bottom boundary in experimental flow conditions replicating swash interactions. Particular focus has been given to forces felt at the bed at the locations of bore/backwash collision, and the incident bore's ability to retard and/or reverse the direction of flow and shearing stress. Furthermore, in an effort to simulate catch up and absorption, the measured effects at the bottom boundary when a bore engulfs a stationary bore (hydraulic jump) are also reported. Finally, bore-driven swash and the variation of bed shear stress over the swash cycle are investigated experimentally and compared to a finite volume shallow water wave equation model.

EXPERIMENTS

Swash interactions

Considering a bore propagating toward the true swash zone to be analogous to a fully-developed positive surge (or a *quasi-steady* hydraulic jump), the flow conditions can be

solved using the continuity and momentum principles. With a control volume across the front of the bore (refer to Figure 1) travelling at celerity C the continuity equation yields,

$$q = (U_o + C)h_o = (U_{conj} + C)h_{conj} \tag{1}$$

where q is the discharge per unit width, U is the horizontal flow velocity and h is the depth. Subscripts o and $conj$ refer to conditions in front of and behind the bore respectively. Flow conditions behind the bore are often referred to as 'conjugate'.

Neglecting friction, the momentum equation sums all the forces acting on the same control volume, yielding

$$\frac{1}{2}\rho g h_o^2 - \frac{1}{2}\rho g h_{conj}^2 = \rho q\left(U_{conj} - U_o\right) \tag{2}$$

where ρ is the fluid density and g is acceleration due to gravity. The relationship between flow depth before and after the passage of the bore is provided by

$$\frac{h_{conj}}{h_o} = \frac{1}{2}\left(\sqrt{1 + 8Fr_1^2} - 1\right) \tag{3}$$

where Fr_1 is the surge Froude number before the passage of the bore:

$$Fr_1 = (U_o + C)/\sqrt{g h_o} \tag{4}$$

Similarly, the momentum equation can be used to describe the relationship between Froude numbers before and after the passage of the bore

$$\frac{Fr_{conj}}{Fr_1} = \frac{2^{\frac{3}{2}}}{\left(\sqrt{1 + 8Fr_1^2} - 1\right)^{\frac{3}{2}}} \tag{5}$$

where Fr_{conj} is the surge Froude number after the passage of the bore:

$$Fr_{conj} = (U_{conj} + C)/\sqrt{g h_{conj}} \tag{6}$$

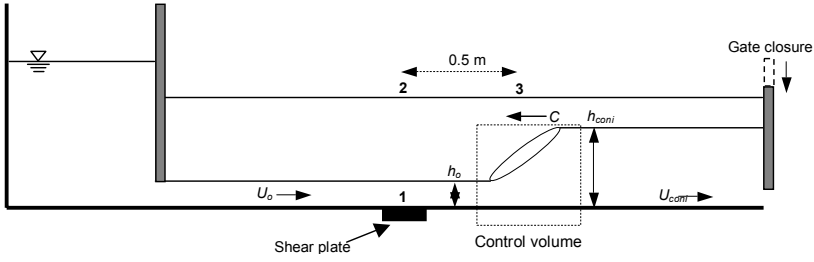

Fig. 1. Propagating bore with control volume experiment sketch

Experiments were conducted in a rectangular open channel (3.2 m long, 0.5 m wide and 0.3 m deep) with a smooth PVC bed (slope = 0º) at the University of Queensland Hydraulics Laboratory (Figure 1). The initial flow depth d_o was controlled by a 'rounded gate' and flow rate measured via venturi meter.

Instantaneous velocities were recorded using a SonTek micro Acoustic Doppler Velocimeter (ADV) 16 MHz at sampling rate of 50 Hz. The ADV probe had a two-dimensional side-looking head positioned at the bed with a horizontal distance to sample volume of 5 cm. The micro-ADV sample volume is cylindrical in shape with a diameter of 4.2 mm and a height of 6.2 mm. The U_x velocity component was aligned longitudinally with the flow direction, and U_y component orientated normal to the channel side wall. Recorded velocities were < 1.7 ms^{-1} within a 1% accuracy of the measured velocity. However, air entrainment (small bubbles) in turbulent flows can lead to signal dropout and may also influence absolute velocities. ADV data was acquired using HorizonADV v1.04 software. Velocity data was post-processed using WinADV v2.010.

Free surface elevation was recorded at two locations (0.5 m spacing) along the channel centreline using non-intrusive Microsonic Mic+35/IU/TC acoustic displacement meters (ADM) with an accuracy of 0.18 mm and a response time of 70 ms (Microsonic, 2005). Koch and Chanson (2005) compared Microsonic ADM measurements to pointer gauge measurements in steady open channel flow and against digital images for non-horizontal free-surface profiles and found comparisons to be within the stated accuracy of the systems. Spacing of the ADMs allowed bore front development to be examined and the bore celerity to be estimated.

Direct measurements of bed shear stress were performed using a shear plate (SP). Prior calibrations of the SP force/displacement relationship were performed *in-situ*. During operation the shear cell below the SP is filled with water. The pressure that exists in the gap at each longitudinal plate edge is measured via two Druck PMP 317-2780 pressure transducers with ±0.15% accuracy (GE Druck, 2006). The pressure in the gaps is a secondary force capable of producing work on the small area of the plate's edge (i.e. plate width × thickness). The additional force in the gaps must be removed from the total

force measured by the shear plate in order to resolve the shear stress. More detail on the SP may be obtained in Barnes and Baldock (2007).

Velocity components close to the bed, surface elevation, and bed shear stress as a bore propagates against supercritical flow, simulating typical swash collisions, were recorded for various initial steady flow conditions. Weak ($1.7 < Fr < 2.5$) and oscillating ($2.5 < Fr < 4.5$) bores were generated by the abrupt closure of a tainter gate located at the downstream end of the channel. Bore propagation distance from the gate to instrumentation was 2 m, a similar distance to that used by Yeh and Ghazali (1988) and Yeh *et al*. (1989) in their experimental studies of bore run-up. It should be noted that the bores in the present investigation differ from most previous studies due to the presence of an initial inflow velocity thus simulating a bore/swash backwash interaction.

The effects at the boundary following catch up and absorption were investigated using a propagating bore engulfing a stationary hydraulic jump. In nature catch up and absorption is likely to occur when the bore period T_b is significantly smaller than the swash period T_s. Repeated experiments were conducted with a hydraulic jump positioned approximately 0.1 m seaward of the SP centreline. A single bore was generated following the abrupt closure of a tainter gate. The bore propagated across the subcritical region behind the hydraulic jump. A plunging collapse onto the supercritical inflow and impacting onto the bed was observed immediately following the bore engulfing the hydraulic jump.

Bore-driven swash

Separate experiments investigating a single swash cycle driven by "true bore collapse" were conducted at the University of Aberdeen (UA) Fluids Mechanics Laboratory. The UA swash facility (Figure 2) is built into an existing flume 20 m long, 0.45 m wide and 0.9 m deep. A reservoir of water of depth D is held by a dam gate at one end of the flume. In front of the gate is a quiescent body of water of depth d. Adopting the dam-break concept, a single fully-developed bore is generated following the high-speed vertical removal of the dam gate. The bore travels for approximately 4 m before collapsing at the still water shore line (SWL) and initiating the swash cycle. The flume has an impermeable Perspex bed with a 1/10 beach slope. Care was taken to reproduce the experimental conditions reported by Honderbrink (2006) and O'Donoghue *et al*. (2006) who obtained high detail fluid velocity measurements using Particle Image Velocimetry (PIV) for a highly repeatable swash event.

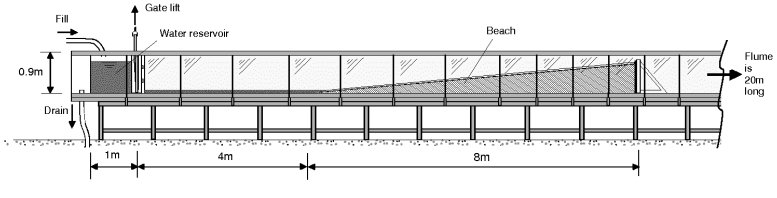

Fig. 2. The University of Aberdeen swash facility (O'Donoghue *et al*., 2006).

In this paper measurements obtained at an offshore location (x = -1.8 m), at the SWL (x = 0 m), and at two positions on the beachface (x = 2 m and 3 m) are presented. Swash depth h and bed shear stress τ were measured using ADMs and SP previously described. Depth average velocity time-series at x = 2 m and 3 m obtained by Honderbrink (2006) and presented by O'Donoghue *et al*. (2006) are used.

Bore-driven swash measurements are compared to the ANUGA (Australian National University and Geoscience Australia) hydrodynamic modelling tool. ANUGA is a two dimensional finite volume Non-Linear Shallow Water wave Equation (NLSWE) solver. The model is useful for wetting and drying scenarios including a swash event on a beachface. Frictional resistance is implemented using Manning's formula (represented by n) with the present work offering a validation with regard to bottom friction. More details of ANUGA may be obtained in Nielsen (2005).

RESULTS

Swash interactions

In a fully developed bore, flow conditions immediately upstream and downstream of the bore front must satisfy the continuity and momentum principles. This may be investigated through the comparison of the measured conjugate depths ratio (h_{conj}/h_o) and the relationship given by (3). Figure 3 shows results for the present investigation. Water depths were resolved using ADM measurements at single location before and after the passage of the bore. Conjugate depth was obtained by averaging approximately 1s of the recorded samples immediately behind the bore front. An averaged value for h_{conj} was considered necessary since free surface oscillations immediately behind the bore front can lead to a misleading measured depth if a single instantaneous measurement is used. The surge Froude number given by (4) was calculated using ADV measured inflow
velocity and bore celerity deduced from ADM measurements at two locations.

The experimental data in Figure 3 show a very good agreement with classical theory. Small discrepancies may be due to the bore not being fully developed and/or difficulty in accurately defining h_c. For breaking bores, Koch and Chanson (2005) cited possible small errors in determining water depths using ADM. Air entrainment and turbulence may affect water depth measurements in front and immediately behind the bore front. Discrepancy between experiments and theory may also be due to the measured velocity being affected by the presence of the bed. Figure 3 suggests that the bores in the present investigation are a good approximation to a steady bore and gives confidence in the experimental method and instrumentation.

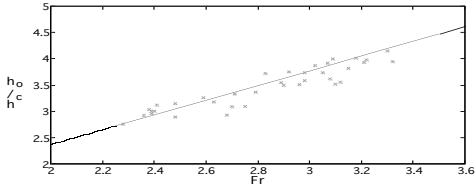

Fig. 3. Comparison of measured conjugate depths ratio (crosses) and momentum principle (dot-dash line).

Measured ensemble average "bore collision" flow characteristics for two initial inflow conditions are presented in Figure 4. Inflow velocity U_o = -1.29 ms^{-1} and -0.86 ms^{-1} for bores with surge Froude number Fr_1 = 2.7 and Fr = 2.1 respectively. Taking a typical inner surf/swash zone approach, negative values are seaward or offshore directed and positive values are landward or onshore directed. For both bores the initial inflow depth h_o = 0.04 m. Time t = 0 s was determined as the time the bore arrived at x = -0.5 m measured from the shear plate centre line. Bore celerities were C = 0.4ms^{-1} (Fr = 2.7) and 0.43 ms^{-1} (Fr = 2.1).

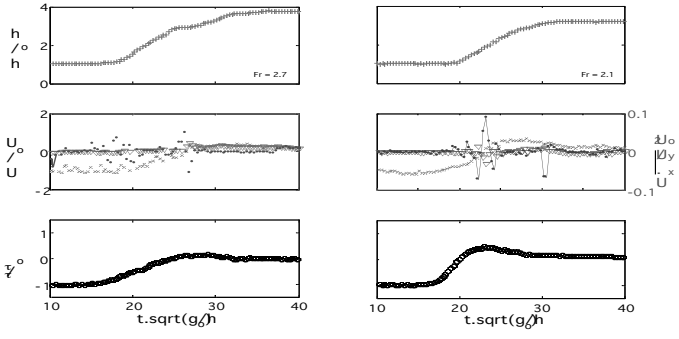

Fig.4. Bore collision; ensemble average non-dimensional depth h/h_o (pluses), velocity U/U_o (U_x crosses; U_y triangles), Reynolds stress $\rho\overline{U_x U_y}/U_o^2$ (solid line), and bed shear stress τ/τ_o (circles) as a function of dimensionless time $t\sqrt{g/h_o}$. Fr_1 = 2.7 left; Fr_1 = 2.1 right.

Reasonably steady velocity components were measured in the inflow region. The decrease in seaward directed velocity coincides with the arrival of the bore toe. U_x continues to decrease as the flow depth increases during the passage of the bore front, thus satisfying continuity. Flow reversal close to the bed was measured in the region of the turbulent roller for the bore collision with the weaker inflow velocity (Fr_1 = 2.1). In contrast, little (virtually zero) flow reversal was detected for the higher inflow velocity collision (Fr_1 = 2.7) despite the stronger bore. Maximum instantaneous Reynolds stresses and bed shear stress were measured close the mid point within the turbulent roller region. A more prominent landward directed stress for a longer duration was measured for the weaker inflow velocity. Measured longitudinal velocity U_x close to the

bed and bed shear stress followed a similar trend for both bore collision conditions. Measurements suggest backwash velocity is important in controlling the effect of swash interaction on sediment transport.

Measured ensemble average "catch up and absorption" flow characteristics are presented in Figure 5. Inflow velocity U_o = -1.31 ms^{-1} with an initial inflow depth h_o = 0.035 m. The bore generated following the sudden closure of the gate propagated relatively quickly (C = 0.58 ms^{-1}) across the subcritical region seaward of the hydraulic jump. Non-dimensional depth measurements indicate a steep, plunging bore front following absorption. A rapid decrease in seaward directed velocity combined with sharp peaks in instantaneous Reynolds stresses were measured at the early stage of the plunging collapse. Weak flow reversal close to the bed was measured throughout the roller region and for a short period behind the bore front. The peak in measured landward directed bed shear stress enhanced by roller turbulence reaching the bed was approximately equal in magnitude to the seaward directed bed shear stress. In contrast to the bore collisions, within the bore roller region the bed shear stress displayed a notably different trend to the longitudinal velocity component.

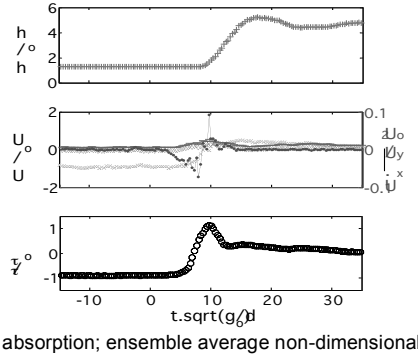

Fig.5. Catch up and absorption; ensemble average non-dimensional depth h/h_o (pluses), velocity U/U_o (U_x crosses; U_y triangles), Reynolds stress $\rho\overline{U_x U_y}/U_o^2$ (solid line), and bed shear stress τ/τ_o (circles) as a function of dimensionless time $t\sqrt{g/h_o}$.

The measured peak in shear stress following catch up and absorption is likely to be a sediment suspension mechanism and is more likely to occur when $T_b << T_s$. Field observations indicate shorter inner surf zone [bore] periods occur during quiescent intervals when infragravity energy is low (e.g. Holland and Puleo, 2001). During such time the beachface may steepen due to accretion.

Bore-driven swash

Measured and ANUGA predicted depth h time series at offshore location x = -1.8m and at the SWL x = 0m is given in Figure 6. Following the abrupt removal of the reservoir gate, the dam water plunges into quiescent water and forms a bore. The early stages of bore development are not predicted accurately due to the two-dimensional nature of

ANUGA. The model cannot resolve vertical convection such as wave breaking or three-dimensional turbulence. Nevertheless Figure 6 shows reasonable depth comparison at the offshore location for $t < 5$ s and excellent agreement for the remaining time. Good agreement between the measured and predicted h was obtained at the SWL.

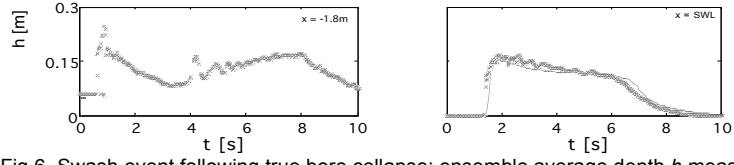

Fig.6. Swash event following true bore collapse; ensemble average depth h measured (crosses) and modelled (dash line) at x = -1.8 and x = 0m (SWL).

Figure 7 presents measured ensemble depth h, longitudinal velocity U_x, and bed shear stress τ at x = 2 m and 3 m for a swash event with maximum runup $R_{max} \approx 5.8$ m measured along the slope. ANUGA predicted depth and velocity with a Manning's n = 0.01 are given by the dash-line. The additional lines in the shear stress subplot are predicted shear stresses using the drag law estimate

$$\tau = C_f \frac{1}{2} \rho U |U| \tag{7}$$

where C_f is a constant friction factor (Darcy friction factor $f = 4C_f$). Solid line, dash line, and dash-dot line are calculated using (7) and $C_f = 0.005$, 0.01, and 0.02 respectively.

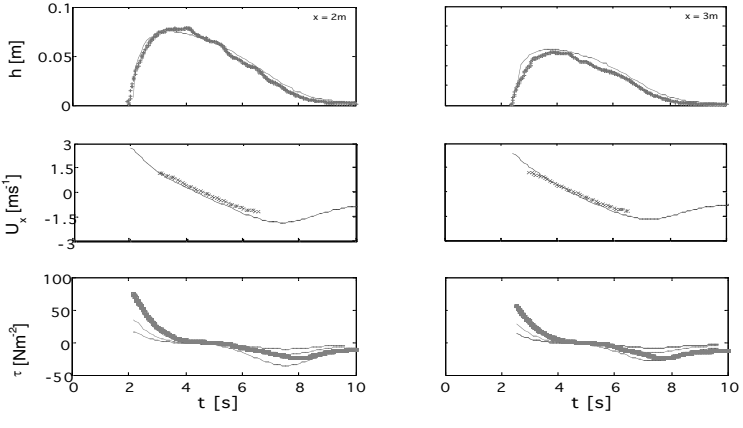

Fig.7. Swash event following true bore collapse; ensemble average depth h (pluses), longitudinal velocity U_x (PIV) (crosses), and bed shear stress (circles) τ as a function of time at x = 2 m and 3 m; model results (dash line); predicted bed shear stress using constant C_f = 0.005 (solid line), 0.01 (dash line), 0.02 (dash-dot line).

Good agreement between measured and modelled depth was obtained at both locations. PIV measurements were difficult to resolve during the arrival of the uprush at the measurement location and late in the backwash when flow depths became sufficiently small. Nevertheless, velocity measurement presented show reasonable agreement with the modelled velocity. Shear stress time series show a maximum positive (landward directed) shear stress at the fluid tip followed by a rapid decay throughout the decelerating uprush interior. Following flow reversal (approximately t = 4.5 s) the maximum negative (seaward directed) shear stress occurs late in the accelerating backwash phase. The measured shear stress tends to zero as the backwash flow depth decreases, the relative roughness increases, and flow velocity is reduces due to friction. Predicted shear stress using a constant friction factor and ANUGA predicted velocity suggest C_f = 0.02 gives excellent agreement with the measured shear stress throughout the uprush phase and a slightly over predicted shear stress throughout the backwash.

DISCUSSION

The present bore/backwash interaction experiments suggest the process acts to interrupt seaward direct transport rather than significantly contributing to the landward advection of sediment. Measurements may support Puleo *et al*. (2000) who observed sediment suspended by bores to quickly settle out behind the bore. Following simulated catch up and absorption the peak in shear stress was of short duration with the hydrodynamics behind the engulfed bore only weakly landward directed. Similar to bore collisions, the role of a single catch up and absorption event may contribute to the suspension of sediment but not necessarily to the landward advection of sediment. Considering that bore collisions and catch and absorption are more frequent when the incident bore period T_b is less than the swash period T_s it is likely suspended sediment will be encountered by a subsequent propagating bore. It remains unknown whether a propagating bore encountering sediment in suspension is an efficient transport mechanism however measurements (Kobayashi and Lawrence, 2004) and observations (Holland and Puleo, 2001) suggest that small incident bore periods (in the absence of high infragravity energy) may promote accretive conditions.

The present work supports Van Wellen *et al*. (2000) who argued that the interactions between waves [bores] and swash flow and the resulting sediment transport rate was not a monotonic relationship. Their simplistic Swash TRansport and Nearshore Dynamics (STRAND) model treats interaction by replacing swash flow hydrodynamics and associated transport with that of the incident bore. STRAND sensitivity testing suggested transport rate and direction was strongly related to the ratio T_b /T_s. While it was not possible to measure swash period in the present bore collision experiments, the relative T_b/T_s ratio can be assumed by considering the initial inflow velocity. For example, a weaker inflow (backwash) velocity simulates a collision that occurs early in the backwash phase prior to the seaward directed flow reaching its maximum velocity as it accelerates down the beachface. For a collision to occur early in the backwash phase one would expect T_b to be smaller than, maybe close to half, T_s. A stronger inflow velocity is simulating a collision that occurs late in the backwash phase and therefore T_b is only slightly smaller than T_s. Catch up and absorption would be indicative of T_b being

significantly smaller than T_s. It should be noted that random waves experienced in nature makes T_b difficult to quantify. STRAND predicts that landward transport rates decrease with increasing T_b/T_s ratio until the ratio reaches 1 (greater than 1 indicates no collisions are occurring), perhaps consistent with the bed shear stress measurements in the present study where largest landward directed forcing close to the bed was measured following catch up and absorption ($T_b << T_s$) and a decrease in landward directed forcing with increasing backwash velocity following a bore collision. It would appear the potential for swash interactions and the T_b/T_s ratio are important components of beach morphological prediction. However, further work is required since low amplitude long period swell, giving $T_s < T_b$, would be expected to also result in beach accretion.

Measured bore height, swash flow depth, and velocity compared well with a NLSWE solver (ANUGA). Comparative results support the use of two-dimensional NLSWE models tuned with an appropriate friction coefficient for inner surf and swash hydrodynamics despite the simplification of the true processes (in particular vertical convection and turbulence due to wave [bore] breaking). The optimal Manning's coefficient for the present experiments was $n \approx 0.01$, consistent with appropriate n values for smooth beds suggested in the literature.

Directly measured uprush bed shear stress in the mid swash region was predicted well following (7) and a constant friction factor $C_f = 0.02$. A similar C_f value closely predicted the measured peak shear stress for dam break flows (analogous to swash uprush) presented by Barnes and Baldock (2007). However, in their study prediction throughout the flow interior was less favourable when using a constant friction factor. It should be noted the dam break measurements presented by Barnes and Baldock (2007) were lower in the "swash" region and on a horizontal bed. In the present investigation backwash shear stress prediction using $C_f = 0.02$ was less favourable at $x = 2$m, however was more reasonably predicted at $x = 3$m. A time varying friction factor may be more appropriate in the backwash, particularly late in the phase as flow depths become small and the relative roughness increases. Eulerian measurements in the present investigation suggest that swash bed shear stress may closely follow conventional theory at higher cross shore positions on the beach where pressure gradients and the effects of bore induce turbulence are smallest. Future work will investigate this further.

CONCLUSION

Inferences from the present investigation are based on simplified experimental inner surf and swash processes. Processes likely to influence sediment transport rates in nature not accounted for include longshore currents, beach face permeability, groundwater/beachface interactions, and the effects of sediment suspension on swash hydrodynamics. Further experimental work for a wider set of initial conditions will allow simplified swash processes to be understood and described. It is inappropriate to attempt to predict sediment transport rates on beaches when a complete understanding of simplified experiments is lacking. Significant findings supported by the experimental data presented include:

- For bore collisions bed shear stress and longitudinal velocity follow a similar trend.
- The effect of bore turbulence at the bed is strongly related to backwash depth and velocity.
- Experimental inner surf zone bores colliding with a strong seaward directed flow (analogous to swash backwash) interrupt seaward directed bed shear stress but don't significantly contribute to landward directed sediment transport.
- Catch up and absorption causes landward directed shear forces (possibly enhanced by impact forces into the bed) for a short duration. This is likely to be a process causing sediment suspension.
- Bore propagation, bore collapse at the SWL, swash depths, and fluid velocity is predicted reasonably well using a two-dimensional NLSWE solver.
- For swash uprush directly measured shear stress in the mid swash region compares well with predicted shear stress using modelled velocity and conventional constant friction factor ($C_f \approx 0.02$); a smaller or time-varying friction factor is required to reasonably predict backwash bed shear stress.

ACKNOWLEDGEMENTS

The authors acknowledge support from the UQ Graduate School and Sustainable Tourism CRC in the form of research scholarships and travel grant for MB. Assistance with bore-driven swash experiments from Dr Tom O'Donoghue and the University of Aberdeen Fluids Group is greatly appreciated.

REFERENCES

Baldock, T. E., A. J. Baird, Horn, D. P. and Mason, T. E. (2001). "Measurements and modelling of swash induced pressure gradients in the surface layers of a sand beach," *Journal of Geophysical Research (Oceans)* 106(C2): 2653-2666.

Barnes, M. P. and Baldock, T. E. (2007). "Direct bed shear stress measurements in laboratory swash," *Proceedings International Coastal Symposium '07*, *in review*.

Butt, T., P. Russell, et al. (2004). "The influence of bore turbulence on sediment transport in the swash and inner surf zones," *Continental Shelf Research* 24(7-8): 757-771.

Chanson, H. (2004). "Environmental Hydraulics of Open Channel Flows," Elsevier-Butterworth-Heinemann Oxford, UK: 483 pp.

Elfrink, B. and Baldock, T. (2002). "Hydrodynamics and sediment transport in the swash zone: a review and perspectives," *Coastal Engineering* 45(3-4): 149-167.

Erikson, L., Larson, M. and Hanson, H. (2005). "Prediction of swash motion and run-up including the effects of swash interaction," *Coastal Engineering* 52(3): 285-302.

GE Druck (2006). "Automotive Pressure Transducers – PMP 317," website:http://www.gesensing.com/products/pmp_317.htm?bc=bc_ps+bc_druc

Holland, K. T. and Puleo, J. A. (2001). "Variable swash motions associated with foreshore profile change," *Journal of Geophysical Research* 106(C3): 4613-4623.

Honderbrink, L. J. (2006). "Numerical and experimental study of bore-driven swash on impermeable slopes," University of Aberdeen PhD thesis.

Hughes, M. G., Masselink, G. and Brander, R. W. (1997). "Flow velocity and sediment transport in the swash zone of a steep beach," *Marine Geology* 138: 91-103.

Jackson, N. L., Masselink, G. and Nordstorm, K.F. (2004). "The role of bore collapse and local shear stresses on the spatial distribution of sediment load in the uprush of an intermediate-state beach," *Marine Geology* 203: 109-118.

Kemp, P. H. (1975). "Wave asymmetry in the nearshore zone and breaker area," *Nearshore Sediment Dynamics and Sedimentation*, ed. by J. Hails and A. Carr, Wiley-Interscience, New York, 47–67.

Kobayashi, N. and Lawrence A. R. (2004). "Cross-shore sediment transport under breaking solitary waves," *Journal of Geophysical Research (Oceans)* 109(C3): C03047.

Koch, C. and H. Chanson (2005). "An Experimental Study of Tidal Bores and Positive Surges: Hydrodynamics and Turbulence of the Bore Front," Report No. CH 55/05 Department of Civil Engineering, The University of Queensland, 68 pp.

Masselink, G. and Hughes, M. G. (1998). "Field investigation of sediment transport in the swash zone," *Continental Shelf Research* 18(10): 1179-1199.

Masselink, G., Evans, D., Hughes, M. G., and Russell, P. (2005). "Suspended sediment transport in the swash zone of a dissipative beach," *Marine Geology* 216: 169–189.

Nielsen, O., Roberts, S., Grey, D., McPherson, A., and Hitchmen, A. (2005). International Congress on Modelling and Simulation. *Proceedings Modelling and Simulation Society of Australia and New Zealand '05*: 518-523.

O'Donoghue, T., Honderbrink, L. J. and Pokrajac, D. (2006). "Bore-driven swash on beaches – numerical modelling and large scale experiments," *Proceedings Coastal Engineering '06, in press*.

Pritchard, D. and Hogg, A. J. (2005). "On the transport of suspended sediment by a swash event on a plane beach," *Coastal Engineering* 52(1): 1-23.

Puleo, J. A., Beach, R., Holman, R. and Allen, J. (2000). "Swash zone sediment suspension and transport and the importance of bore-generated turbulence," *Journal of Geophysical Research (Oceans)* 105: 17021-17044.

Van Wellen, E., Baldock, T., Chadwick, A. and Simmonds, D. (2000). "STRAND – a Model for Longshore Sediment Transport in the Swash Zone," *Proceedings Coastal Engineering '00*: 3139-3150.

Yeh, H. H. and Ghazali, A. (1988). "On bore collapse," *Journal of Geophysical Research* 93(C6): 6930-6936.

Yeh, H. H., Ghazali, A. and Marton, I. (1989). "Experimental study of bore run-up," *Journal of Fluid Mechanics* 206: 563-578.

LIMITS OF BEACH AND DUNE EROSION IN RESPONSE TO WAVE RUNUP ELUCIDATED FROM SUPERTANK

Tiffany M. Roberts[1], Ping Wang[1], Nicholas C. Kraus[2]

1. Department of Geology, University of South Florida, 4202 E. Fowler Ave., Tampa, FL 33620, USA. tmrobert@cas.usf.edu
2. U.S. Army Engineer Research and Development Center, Coastal and Hydraulics Laboratory, 3909 Halls Ferry Road, Vicksburg, MS 39180-6199, USA. Nicholas.C.Kraus@erdc.usace.army.mil.

Abstract: The unique dataset from SUPERTANK is analyzed to examine the upper limit of beach change in response to elevated water level caused by wave runup. Thirty SUPERTANK runs are investigated, including both erosional and accretionary wave conditions under random and monochromatic waves. The upper limit of beach change approximately equals the maximum vertical excursion of swash runup. Exceptions to this direct relationship are those with beach or dune scarps. The vertical extent of wave runup above mean water level on a non-scarped beach is approximately equal to the significant breaking wave height. Scarps substantially limit the uprush of swash motion, resulting in a much reduced maximum runup. Predictions of wave runup are not improved by including a slope-dependent surf-similarity parameter. The limit of wave runup is substantially less for monochromatic waves than for random waves, attributed to absence of low-frequency motion for monochromatic waves.

INTRODUCTION

Quantification of wave runup and its relationship to the upper limit of beach-profile change are required for understanding and predicting beach and dune erosion, especially during storms. Wave runup is composed of wave setup, defined as a super-elevation of the mean water level, and swash runup, or fluctuations about that mean (Holman and Sallenger 1985; Nielsen 1988; Yamamoto et al. 1994; Holland et al. 1995). Numerous studies on the limits of wave runup have been conducted, resulting in the development of several predictive models, from three approaches.

The earliest physics-based approach is developed upon a theoretical derivation for monochromatic waves. Bowen et al. (1968) derived a wave setup slope inside the surf zone for monochromatic (sinusoidal) waves as:

$$\frac{\partial \bar{\eta}}{\partial x} = -K\frac{\partial h}{\partial x} \qquad K = (1 + 2.67\gamma^{-2})^{-1} \tag{1}$$

where h = still-water depth, $\bar{\eta}$ = wave setup, x = cross-shore coordinate, $\gamma = H/(\bar{\eta} + h)$ and H = wave height. Based on both theory and laboratory measurements, the maximum set-up under a monochromatic wave, $\overline{\eta_M}$, was found to occur at the shoreline:

$$\frac{\overline{\eta_M}}{H_b} = 0.3\gamma \tag{2}$$

where H_b = breaking wave height (Battjes 1974). The above equations concern only the wave setup portion of the runup.

The second approach is based mainly on field measurements made on dissipative beaches. Guza and Thornton (1981) suggested that the setup at the shoreline, $\overline{\eta_{sl}}$, is linearly proportional to the significant deepwater wave height H_o:

$$\overline{\eta_{sl}} = 0.17H_o \tag{3}$$

In a following study, Guza and Thornton (1982) found that the significant wave runup, R_s, (including both wave setup and swash runup) is also linearly proportional to the significant deepwater wave height:

$$R_s = 3.48 + 0.71H_o \qquad \text{(units of centimeters)} \tag{4}$$

Comparing Eqs. (3) and (4), the entire wave runup is approximately 4 times the wave setup, i.e., swash runup constitutes a significant portion of the total elevated water level. According to Huntley et al. (1993), Eq.(4) is the best choice for predicting wave runup on dissipative beaches. Based on field measurements on highly dissipative beaches, Ruessink et al (1998) and Ruggiero (2004) also found linear relationships, but with different empirical coefficients.

The third and more recent approach, proposed by Holman (1986) and several similar studies (Holman and Sallenger 1985; Ruggiero et al. 2004; Stockdon et al. 2006), argued that more accurate predictions can be obtained by including the surf similarity parameter, ξ:

$$\xi = \frac{\beta}{(H_o / L_o)^{1/2}} \tag{5}$$

where L_o is the deepwater wavelength, and β is the beach slope. Holman (1986) found a dependence of the 2% exceedence of runup R_2 on the deepwater significant wave height and the surf similarity parameter:

$$R_2 = (0.83\xi_o + 0.2)H_o \tag{6}$$

Stockdon et al. (2006) expanded upon the Holman (1986) analysis and developed the empirical equation:

$$R_2 = 1.1\left(0.35\beta_f (H_o L_o)^{\frac{1}{2}} + \frac{\left[H_o L_o (0.563\beta_f{}^2 + 0.004)\right]^{\frac{1}{2}}}{2}\right) \quad (7)$$

Realizing the variability of beach slope in terms of both definition and measurement, Stockdon et al. (2006) define the foreshore beach slope as the average slope over a region of two times the standard deviation of continuous water level record.

Most field studies were conducted on gentle sloping dissipative beach and found wave runup within the swash zone to be dominated by infragravity frequency components, or surf beat. Mechanisms for generating low-frequency motion at the shoreline include 1) obliquely incident wave groups (Gallagher 1971; Bowen and Guza 1978), 2) time-varying wave breaking (Symonds et al. 1982; List 1992), and 3) bound long wave generated by periodical variations of mean water level due to wave groupiness outside the surf zone (Longuet-Higgins and Stewart 1962). In contrast to numerous studies on wave runup, little data are available relating the limit of wave runup with that of the beach-profile change.

In this paper, data from the prototype-scale SUPERTANK experiment (Kraus et al 1992; Kraus and Smith 1994) are examined to study the limit of wave runup and corresponding limit of beach dune erosion. Specifically, this study examines 1) the level of swash run-up and wave setup; 2) time-series beach-profile changes under erosional and accretionary waves; 3) the relationship between the above two phenomena; and 4) the accuracy of existing wave runup prediction methods. A new empirical formula predicting the limits of wave runup and that of beach change is proposed based on the SUPERTANK data.

SUPERTANK EXPERIMENTS

One of the largest and most densely instrumented laboratory movable-bed studies to date is the SUPERTANK experiment. This multi-institutional effort sponsored by the Corps of Engineers was conducted at the O.H. Hinsdale Wave Research Laboratory at Oregon State University from July 29 to September 20, 1991 (Fig. 1). This facility is the largest wave channel in the United States that can contain a sandy beach through which experiments comparable to the magnitude of naturally occurring waves can be conducted (Kraus et al. 1992).

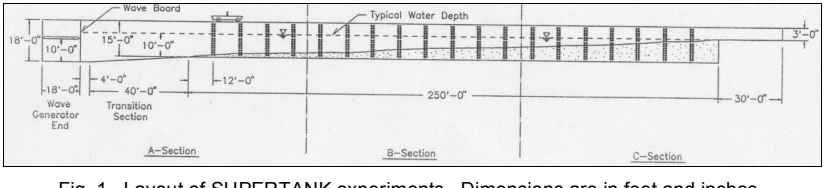

Fig. 1. Layout of SUPERTANK experiments. Dimensions are in feet and inches.

The SUPERTANK experiment measured total-channel hydrodynamics and sediment transport along with the resulting beach-profile changes. The wave channel was 104 m

long, 3.7 m wide, and 4.6 m deep (the still water level was typically 1.5 m below the top) with a constructed sandy beach extending 76 m offshore (Fig. 1). The beach was composed of 600 m^3 of fine, well-sorted quartz sand with a median size of 0.22 mm and a fall speed of 3.3 cm/s. The wave generator and wave channel were equipped with a sensor to absorb the energy of reflected waves. The water-level fluctuations were measured with 16 resistance and 10 capacitance gauges. These 26 gauges, spaced 3.7 m apart, provided detailed wave propagation patterns, especially in the swash zone. The beach profile was surveyed following each wave run. The initial profile was constructed based on the equilibrium beach profile developed by Dean (1977) and Bruun (1954) as:

$$h(x) = Ax^{\frac{2}{3}} \tag{8}$$

where h = still-water depth, x = horizontal distance from the shoreline, and A = a shape parameter corresponding to a mean grain size of 0.30 mm. The initial beach was built steeper with a greater A-value to ensure adequate water depth in the offshore area (Wang and Kraus 2005). For efficiency, most SUPERTANK tests were initiated with the final profile of the previous run. Approximately 350 surveys were conducted using an auto-tracking, infrared Geodimeter targeting prism attached to a survey rod mounted on a carriage pushed by researchers. Although three lines, two along the wave-channel wall and one in the center, were surveyed, only the center line is examined in this study. Wave-processing procedures are discussed in Kraus and Smith (1994). To separate incident-band wave motion from low-frequency motion, a non-recursive, low-pass filter was applied. The period cutoff for the filter was set to twice the peak period of the incident waves.

After inspection of all 20 SUPERTANK tests, 5 tests with 30 wave runs were selected for analysis in the present study. The selection was based on the particular purpose of the wave run, the trend of net sediment transport, and measured beach change. Time-series beach-profile changes and cross-shore distribution of wave height and mean water level were analyzed. The breaker point is defined at the location with a sharp decrease in wave height (Wang et al. 2002). The maximum runup is defined by the location and beach elevation of the swash gauge that contained a value larger than zero wave height, i.e., water reached that particular gauge. There may be some differences in the runup measured in this study as compared to the video method (e.g., Holland et al. 1995) and horizontally elevated wires (e.g., Guza and Thornton 1982). The differences are not expected to be significant.

RESULTS AND DISCUSSION

The subject 30 wave runs are summarized in Table 1. The thirty cases are composed of 12 erosional random wave runs (ER), 3 erosional monochromatic wave runs (EM), 7 accretionary random wave runs (AR), 3 accretionary monochromatic wave runs (AM), and 5 dune erosion random wave runs (DE). The first two numbers in the Wave Run ID "10A_60ER" indicate the major data collection test, the letter "A" indicates a particular wave condition, and "60" describes the minutes of wave action. The erosional and accretionary cases are designed based on the Dean number N,

$$N = \frac{H_b}{wT} \tag{9}$$

where w = fall speed of the sediment, and T = wave period.

Table 1. Summary of Selected Wave Runs and Input Wave and Beach Conditions (Notation is explained at the bottom of the table).

Wave Run ID	H_o m	T_p s	L_o m	n	N	H_b m	β_s	ξ	H_{b_h} M	H_{b_l} m	H_{sl_h} m	H_{sl_l} m
10A_60ER	0.78	3.0	14.0	20	6.4	0.68	0.10	0.42	0.66	0.15	0.13	0.24
10A_130ER	0.78	3.0	14.0	20	6.8	0.68	0.09	0.38	0.67	0.15	0.10	0.23
10A_270ER	0.78	3.0	14.0	20	6.9	0.68	0.10	0.42	0.65	0.16	0.10	0.24
10B_20ER	0.71	3.0	14.0	3.3	6.6	0.65	0.14	0.58	0.63	0.17	0.10	0.23
10B_60ER	0.73	3.0	14.0	3.3	6.8	0.67	0.11	0.44	0.65	0.17	0.11	0.24
10B_130ER	0.72	3.0	14.0	3.3	7.0	0.69	0.09	0.36	0.67	0.18	0.12	0.25
10E_130ER	0.69	4.5	31.6	20	4.9	0.72	0.11	0.69	0.71	0.15	0.15	0.16
10E_200ER	0.69	4.5	31.6	20	5.0	0.74	0.12	0.77	0.72	0.15	0.15	0.18
10E_270ER	0.69	4.5	31.6	20	5.1	0.76	0.09	0.58	0.74	0.15	0.16	0.20
10F_110ER	0.66	4.5	31.6	3.3	5.1	0.75	0.09	0.58	0.72	0.18	0.15	0.26
10F_130ER	0.68	4.5	31.6	3.3	5.1	0.76	0.08	0.48	0.74	0.18	0.13	0.21
10F_170ER	0.69	4.5	31.6	3.3	5.1	0.76	0.08	0.50	0.73	0.20	0.12	0.24
G0_60EM	1.05	3.0	14.0	M	10.0	1.18	0.10	0.43	1.18	0.01	0.11	0.03
G0_140EM	1.04	3.0	14.0	M	10.5	1.04	0.10	0.41	1.04	0.04	0.08	0.10
G0_210EM	1.15	3.0	14.0	M	10.8	1.07	0.09	0.39	1.07	0.04	0.11	0.02
30A_60AR	0.34	8.0	99.9	3.3	1.6	0.41	0.14	2.24	0.40	0.06	0.24	0.08
30A_130AR	0.33	8.0	99.9	3.3	1.6	0.39	0.13	2.09	0.38	0.06	0.24	0.09
30A_200AR	0.34	8.0	99.9	3.3	1.6	0.41	0.13	2.02	0.40	0.06	0.25	0.10
30C_130AR	0.31	9.0	126.4	20	1.4	0.40	0.13	2.36	0.40	0.04	0.18	0.05
30C_200AR	0.31	9.0	126.4	20	1.4	0.39	0.15	2.31	0.38	0.04	0.19	0.06
30C_270AR	0.31	9.0	126.4	20	1.4	0.39	0.15	2.60	0.38	0.04	0.20	0.06
30D_40AR	0.37	9.0	126.4	20	1.4	0.41	0.13	2.00	0.42	0.05	0.17	0.07
I0_80AM	0.60	8.0	99.9	M	2.9	0.76	0.20	2.78	0.76	0.01	0.38	0.03
I0_290AM	0.63	8.0	99.9	M	3.1	0.81	0.17	2.35	0.81	0.01	0.34	0.02
I0_590AM	0.60	8.0	99.9	M	2.7	0.72	0.12	1.64	0.73	0.01	0.25	0.03
60A_40DE	0.69	3.0	14.0	3.3	6.2	0.61	0.12	0.55	0.58	0.14	0.16	0.24
60A_60DE	0.69	3.0	14.0	3.3	6.2	0.61	0.10	0.46	0.60	0.14	0.12	0.24
60B_20DE	0.64	4.5	31.6	3.3	4.4	0.66	0.11	0.74	0.63	0.15	0.18	0.24
60B_40DE	0.63	4.5	31.6	3.3	4.4	0.66	0.11	0.76	0.62	0.16	0.18	0.25
60B_60DE	0.65	4.5	31.6	3.3	4.4	0.66	0.12	0.79	0.63	0.17	0.18	0.30

n = spectral peakedness; β_s. = beach slope defined as the slope of the section approximately 1 m landward and 1 m seaward of the shoreline; H_{b_h} = incident band wave height at the breaker line; H_{b_l} = low frequency band wave height at the breaker line; H_{sl_h} = incident band wave height at the shoreline; H_{sl_l} = low-frequency band wave height at the shoreline.

Beach Profile Change

Typically, erosion is defined as a net offshore transport of sand resulting in a loss of beach volume above the mean water line. Accretion is defined as a total net onshore transport of sand, building the beach above mean water level. As expected, a larger Dean number N resulted in erosion, and a smaller N induced accretion (Table 1).

Significant profile change occurred during the first erosional wave run case, 10A, over the monotonic initial profile (Eq. 8). Substantial shoreline recession occurred along with the development of an offshore bar (Fig. 2A). Initially, the foreshore exhibited a convex shape while the end profile was concave. The 270-min profile was substantially steeper near the shoreline than the initial profile. A bar formed after 60 min of wave action.

After 270 min, the bar moved 4 m further offshore. The maximum beach-face recession occurred at the +0.37 m contour line. The subsequent wave runs were conducted over the barred beach. The beach-profile changes are detectable, but much more subtle. Fig. 2B shows an example of shoreline accretion and onshore bar movement.

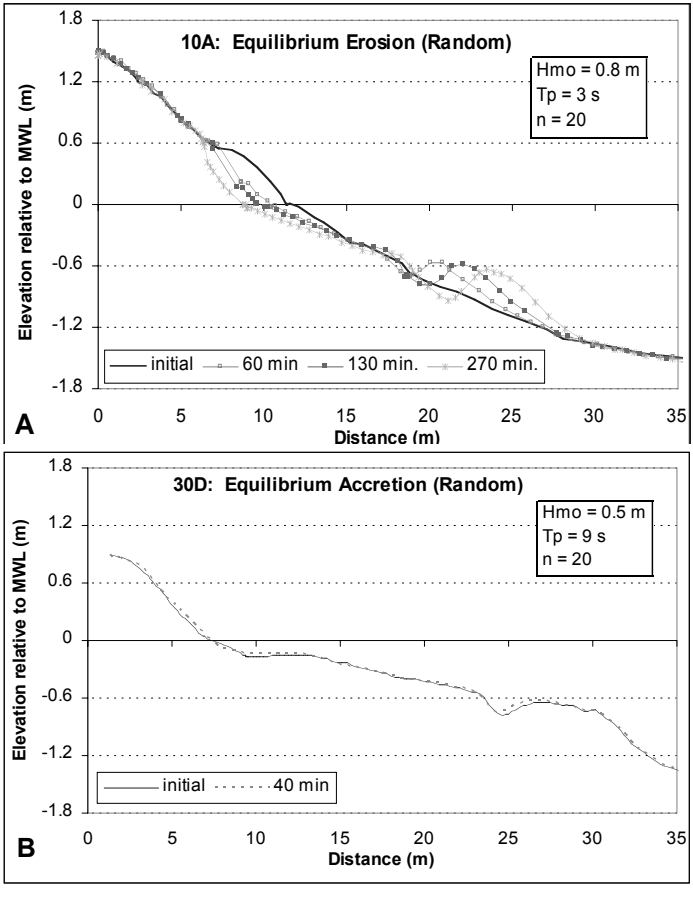

Fig. 2. (A) Bar development over monotonic equilibrium beach-profile, and (B) profile developed under accretionary random waves

In some of the erosional wave runs, a scarp developed (Fig 3A). Beach slope immediately seaward of the scarp tends to be steeper than on a non-scarped beach. The nearly vertical scarp had significant influence on the wave runup, limiting the swash uprush abruptly. Monochromatic waves tend to create erratic and undulating profiles (Fig 3B), in contrast to the smooth profiles under random waves, likely because of wave

reflection. The erratic profile evolution did not seem to approach a stable equilibrium shape. In addition, the profile shape developed under monochromatic waves does not represent profiles typically measured in the field (Wang and Davis 1998).

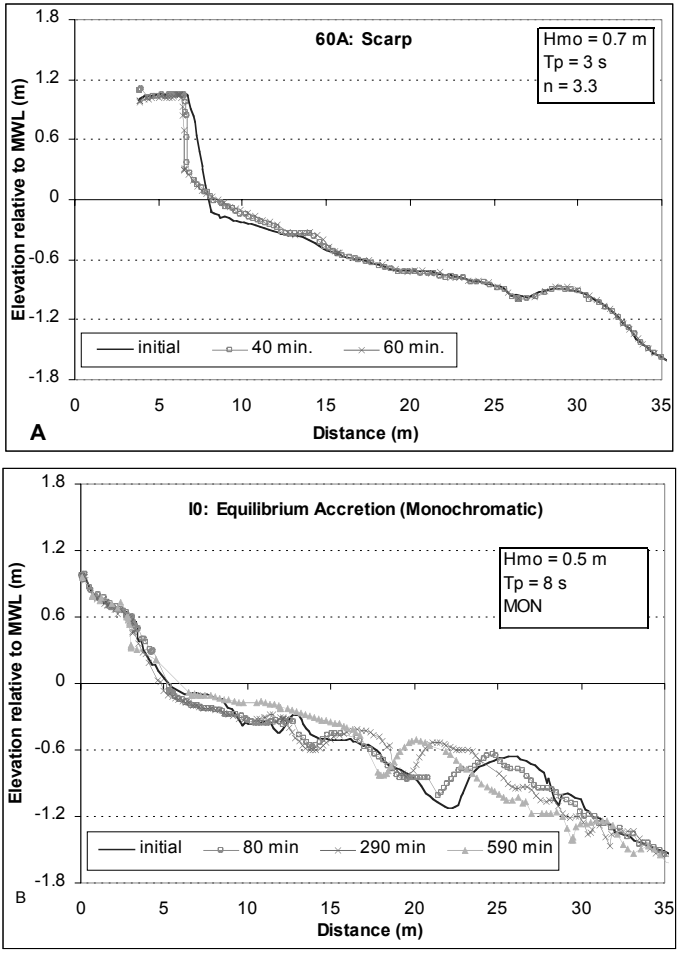

Fig. 3. (A) Scarp development, and (B) beach profiles under monochromatic waves.

The time-series of beach profiles (e.g., Figs. 2 and 3) were examined to determine the trend of erosion or accretion, and the upper and lower limits of change during each wave run (Table 2). Table 2 also summarizes the measured and predicted limits of wave runup, discussed in the following section. For the scarped cases, the upper limit of profile change was at the top of the scarp. Thus, it is controlled by the height of the

beach berm or dune, and does not directly represent the extent of wave action. In Table 2, the listed upper limit used for the scarped cases was the elevation of the scarp toe. The purpose is to link toe erosion or accretion to the wave condition.

For the studied 30 wave runs, the incident breaking wave height ranged from 0.39 to 1.18 m (Table 2). The measured upper limit of profile change, including the scarped cases, ranged from 0.27 to 0.70 m. The lower limit of beach change ranged from 0.65 to 1.61 m. Relationship between the profile change and wave condition is discussed in the following sections.

Table 2. Summary of Upper and Lower Limit of Beach Changes and Measured and Predicted Wave Runup Equations.

Wave Run ID	H_b m	R_{max} m	UL m	LL *m*	Scarp	Eq 4 m	Eq 6 M	Eq 7 m	Eq 10 m
10A_60ER	0.68	0.60	0.66	1.29	No	0.59	0.43	0.31	0.68
10A_130ER	0.68	0.60	0.66	1.29	No	0.59	0.40	0.29	0.68
10A_270ER	0.68	0.70	0.66	1.29	No	0.59	0.43	0.31	0.68
10B_20ER	0.65	0.33	0.67	1.35	No	0.54	0.49	0.38	0.65
10B_60ER	0.67	0.70	0.67	1.35	No	0.55	0.42	0.31	0.67
10B_130ER	0.69	0.64	0.67	1.35	No	0.55	0.36	0.26	0.69
10E_130ER	0.72	0.77	0.74	1.52	No	0.52	0.53	0.46	0.72
10E_200ER	0.74	0.78	0.84	1.52	No	0.52	0.58	0.51	0.74
10E_270ER	0.76	0.45	0.84	1.52	No	0.52	0.47	0.41	0.76
10F_110ER	0.75	0.40	0.43	1.52	Yes	0.50	0.45	0.40	0.75
10F_130ER	0.76	0.38	0.42	1.52	Yes	0.52	0.41	0.36	0.76
10F_170ER	0.76	0.45	0.48	1.52	Yes	0.52	0.42	0.36	0.76
G0_60EM	1.18	0.28	0.38	1.61	No	0.78	0.58	0.36	1.18
G0_140EM	1.04	0.18	0.25	1.61	Yes	0.77	0.56	0.35	1.04
G0_210EM	1.07	0.32	0.27	1.61	Yes	0.85	0.60	0.35	1.07
30A_60AR	0.41	0.41	0.31	1.36	No	0.28	0.70	0.72	0.41
30A_130AR	0.39	0.43	0.31	1.36	No	0.27	0.64	0.66	0.39
30A_200AR	0.41	0.42	0.31	1.36	No	0.28	0.64	0.66	0.41
30C_130AR	0.40	0.40	0.39	1.01	No	0.25	0.67	0.73	0.40
30C_200AR	0.39	0.42	0.42	1.01	No	0.25	0.73	0.79	0.39
30C_270AR	0.39	0.42	0.42	1.01	No	0.25	0.73	0.79	0.39
30D_40AR	0.41	0.23	0.43	0.65	No	0.30	0.69	0.76	0.42
I0_80AM	0.76	0.27	0.46	1.82	No	0.46	1.51	1.27	0.76
I0_290AM	0.81	0.16	0.53	1.82	No	0.48	1.35	1.12	0.81
I0_590AM	0.72	0.35	0.53	1.82	Yes	0.46	0.94	0.80	0.72
60A_40DE	0.61	0.17	0.28	1.16	Yes	0.52	0.45	0.34	0.61
60A_60DE	0.61	0.17	0.28	1.16	Yes	0.52	0.40	0.29	0.61
60B_20DE	0.66	0.16	0.38	0.99	Yes	0.49	0.52	0.45	0.66
60B_40DE	0.66	0.16	0.38	0.99	Yes	0.48	0.52	0.45	0.66
60B_60DE	0.66	0.17	0.38	0.99	yes	0.5	0.56	0.48	0.66

R_{max} = measured maximum wave runup; **UL, LL** = upper and lower limit of beach change, respectively.

Wave Runup

Measured and predicted wave runup is summarized in Table 2. Three examples, a random wave run without scarp (Fig. 4A), a random case with scarp (Fig. 4B), and a monochromatic case (Fig. 4C), are given. The non-scarp random wave cases are most compatible with existing field studies. The measured wave runup for the scarp cases are much lower than that for the non-scarp cases, apparently limited by the steep scarp. Wave runup generated by monochromatic waves is also much smaller than that by random waves with similar statistical wave height and period.

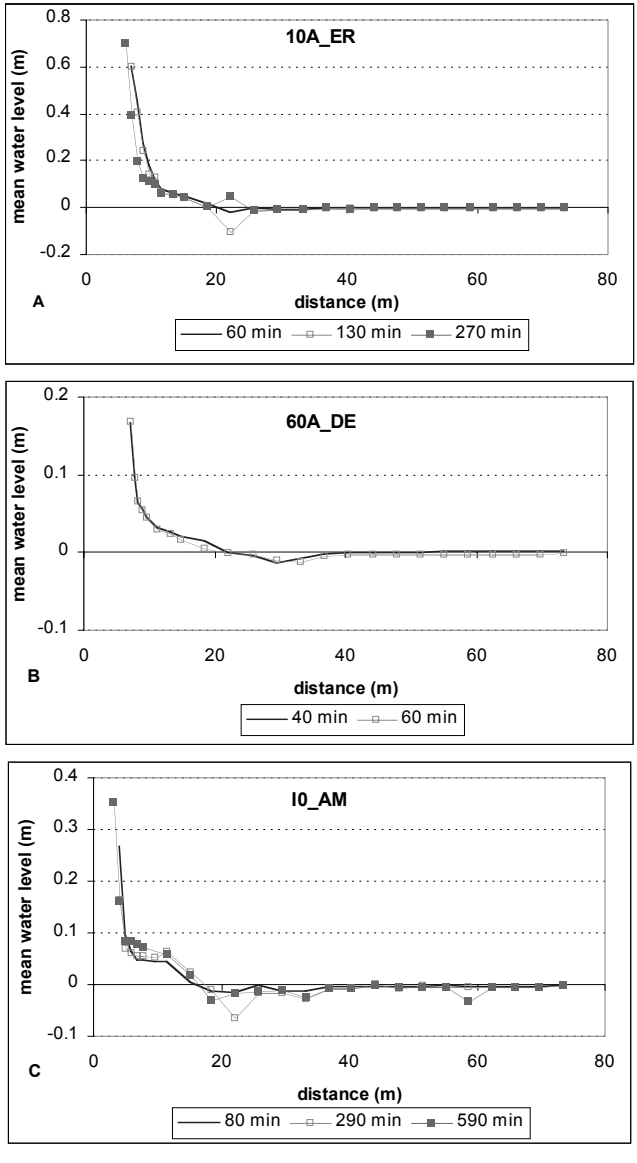

Fig. 4. Examples of wave runup under random wave (A), over a scarped beach, and (B) under monochromatic waves (C).

A direct relationship between the measured runup height on non-scarp beach and breaker height as developed with the SUPERTANK data is:

$$R_{max} = 1.0\ H_b \tag{10}$$

Compared to the various existing empirical formulas, Eq. (10) adopts the approach introduced by Guza and Thornton (1982) and is simple, involving only the breaking wave height. Except for three wave runs, the observed wave runup equals the breaking wave height. Eq. (10) reproduced the measured values closely (Fig. 5). Agreement between measured and predicted values was reduced by including the surf similarity parameter, ξ. Eqs. (6) and (7) under-predicted the measured wave runup significantly for the erosional cases with steep waves, while over-predicted for accretionary cases. Loss of predictive capability is caused by the substantially greater ξ for the gentle long-period accretionary waves than the steep short-period erosional waves (Table 1).

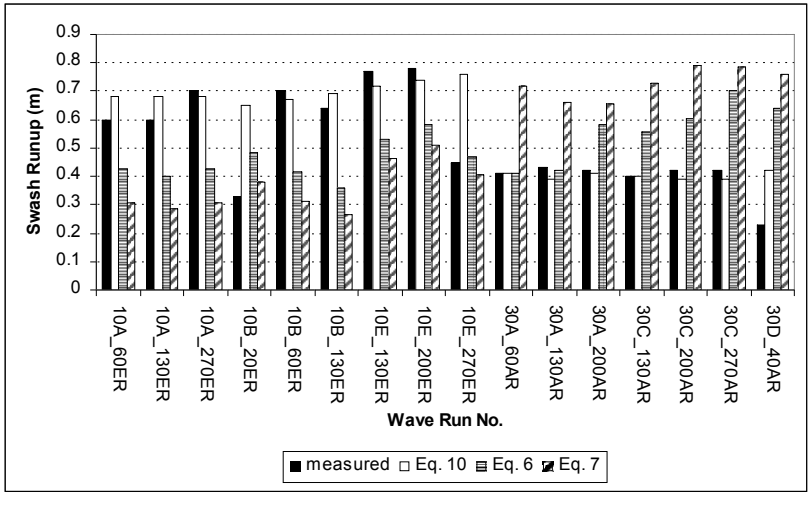

Fig. 5. Comparison of measured and predicted wave runup by three equations.

Douglass (1992) re-analyzed the Holman (1986) data set and found no correlation between runup and beach-face slope. He further argued that beach slope is a dependent variable that is free to respond to the incident wave energy and should not be included in a runup prediction. In practice, beach face slope is a difficult parameter to define and determine. Except for Stockdon et al. (2006), a clear definition of beach slope is not given in most studies. However, the Stockdon et al. definition of beach slope is difficult to utilize. In the present paper, the slope is defined over that portion of the beach extending roughly 1 m landward and seaward from the shoreline. The accretionary cases tend to have greater slope, 0.13 to 0.20, whereas the erosional case have slopes of 0.08 to 0.14 (Table 1). Examination of Fig. 3 indicates that the beach face is curved instead of planar. Therefore, substantially different beach slopes can be obtained by imposing different definitions. Including the beach slope thus adds ambiguity in applying the

empirical formulas. Determining offshore wave height may also cause uncertainty. In most field studies, the offshore wave height was taken to be that measured at a wave gage in the study area. Similarly, here it is taken as that from the offshore-most gauge. Under extreme storm conditions, estimating the offshore wave height may not be straightforward (Wang et al. 2006).

One of the first empirical formulas (Eq. 4) predicting the significant runup height R was developed by Guza and Thornton (1982) based on field measurements. As discussed previously, wave runup height measured here is expected to approximate the maximum runup R_{max}. If a Raleigh distribution of wave height is assumed, the maximum wave height should be 1.4 times the significant height. Multiplying the proportional constant of 0.71 in Eq. (4) by 1.4 yields approximately 1, which is the empirical coefficient obtained here. Therefore, the simple formula found in this study agrees with the form found by Guza and Thornton (1982).

It has been documented in many field studies performed on gently sloping beach that the swash motion and, therefore runup, is dominated by low-frequency wave energy. Typically, the low-frequency energy is defined as that carried by the wave components exceeding twice the incident peak period. The magnitudes of the incident and low-frequency energy are compared at the breaker line, H_{b_h} and H_{b_l}, and at shoreline, H_{sl_h} and H_{sl_l} (Table 1). For monochromatic waves, little low-frequency energy was measured at the breaker line and the shoreline. Lack of low-frequency modulation may explain the relatively low swash runup measured during the regular wave cases (Table 2).

For the random wave cases, energy from the incident band dominates at the breaker line (Table 1). The incident-band energy decreased significantly at the shoreline, whereas the low-frequency energy increased. This is readily apparent for the short-period steep erosional waves, where low-frequency energy dominated at the shoreline. The wave spectral peakedness n does not seem to have great influence on this trend. For the longer period gentle accretionary waves, the decrease of incident-band energy was not as rapid and low-frequency energy did not become the dominant band at the shoreline (Table 1). The low-frequency component is defined dynamically here as exceeding twice the incident peak period. For the erosional waves, the low-frequency component starts at 6 or 9 s, whereas for the longer accretionary waves, it starts at 16 or 18 s.

Relationship between Wave Runup and Limit of Beach-Profile Change

A major goal of studying the maximum wave runup is to predict the upper limit of beach changes. Knowledge of the maximum runup is valuable in evaluating the limit of storm-induced beach or dune erosion. For the random wave runs without scarps, the measured upper limit of beach-profile change roughly equals the measured wave runup (Fig. 6). Thus, the wave runup, predictable using significant breaking wave height, can be directly used to calculate the upper limit of beach erosion. For cases with beach or dune scarps, the upper limit of the beach change is controlled by the elevation of the back-beach berm or dune (Fig. 3A). Once a scarp forms, the overlying sediment will eventually collapse under gravity and cause significant change above the upward limit of water excursion.

The measured wave runup is subdued by the nearly vertical scarp and the steep beach slope directly seaward of the scarp; and it cannot be predicted by known empirical formulas.
Beach-profile change under monochromatic waves differs greatly from that under the more realistic random waves. Both wave runup and upper limit of beach-profile change are significantly smaller than those under random waves with similar statistical wave height and period. Findings from laboratory monochromatic movable-bed studies are not directly applicable to field conditions, as also discussed by Wang and Kraus (2005).

Although not a focus of this study, the lower limit of beach changes was also measured and is listed in Table 2. Typically, the lower limit of beach-profile change is 1.5 to 3 times the significant breaking wave height. Longer period waves seem to influence beach change in deeper water (~ 3 times H_s), as compared to shorted period waves (~ 2 times H_s). It was beyond the scope of this paper to examine factors controlling the lower limit of the beach change.

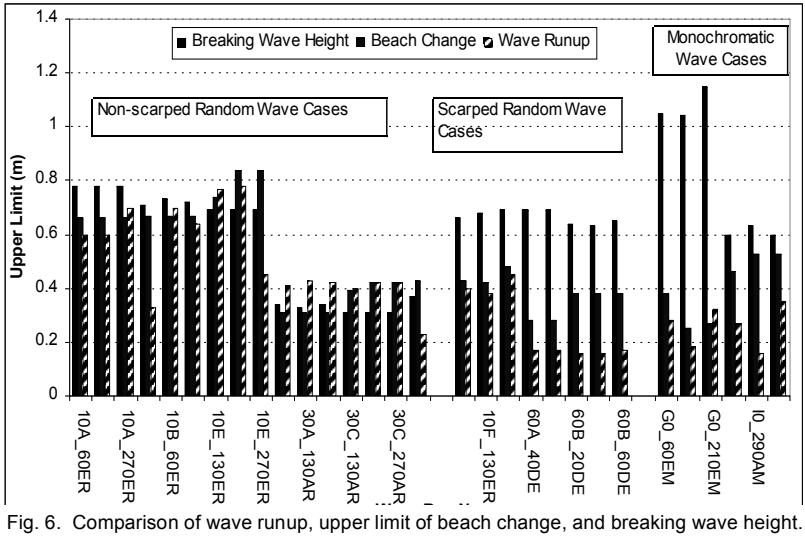

Fig. 6. Comparison of wave runup, upper limit of beach change, and breaking wave height.

CONCLUDING DISCUSSION

SUPERTANK's unique dataset was analyzed to examine the effects of elevated water level caused by wave setup and swash runup on the upper limit of beach and dune change. Thirty SUPERTANK wave runs were investigated. The investigated runs demonstrate that the Dean Number is a reliable indicator for predicting the general trend of beach erosion and accretion. In fact, the SUPERTANK experiments were designed in this way (Kraus and Smith 1992).

The SUPERTANK data indicate that the vertical extent of wave runup above mean water

level on a non-scarped beach is approximately equal to the significant breaking wave height. A simple empirical formula for predicting the maximum wave runup, *Rmax*: $R_{\max} = 1.0\, H_b$, is therefore developed. This formula agrees with the original runup formula concept of Guza and Thornton (1982). The reliability of the calculated wave runup decreased, as compared to measured values, by including the surf similarity parameter. An exception to the direct relationship between breaking wave height and runup concerns dune or beach scarping. The steep scarp substantially limits the uprush of swash motion, resulting in a much reduced maximum level, as compared with the non-scarping situation. For monochromatic waves, the measured wave runup is much smaller than the breaking wave height. The lack of low-frequency modulation limits the wave runup for monochromatic waves.

Based on the SUPERTANK experiments, the upper limit of beach-profile change was found to be approximately equal to the maximum vertical excursion of swash runup. Therefore, the limit of swash runup can serve as an estimate of the landward limit of beach change. Physical situations that are exceptions to this direct relationship are those with beach or dune scarping. For the scarping cases, the upper limit of beach change is much higher than the maximum swash runup and is controlled by the elevation of backbeach/berm or dune.

ACKNOWLEDGEMENTS

This study was jointly funded by the Coastal Inlets Research Program (CIRP) conducted by the U.S Army Corps of Engineers (USACE), and by the University of South Florida. Permission was granted by Headquarters, USACE, to publish this information.

REFERENCES

Battjes, J.A. 1974. Computations of set-up, longshore currents, run-up overtopping due to wind-generated waves. *Rep. 74-2*, Delft Univ. Technol., Delft, The Netherlands.

Bowen, A.J., Inman, D.L., and Simmons, V.P. 1968. Wave "set-down" and "set-up." *J. Geophys. Res.*, 73(8), 2569-2577.

Bowen, A.J., and Guza, R.T. 1978. Edge waves and surf beat. *J. Geophys. Res.*, 83(4), 1913-1920.

Bruun, P. 1954. Coastal erosion and the development of beach profiles. *Tech. Memo. No. 44*, Beach Erosion Board, U.S. Army Corps of Engineers.

Dean, R.G. 1977. Equilibrium beach profiles: U.S. Atlantic and Gulf coasts. *Ocean Engineering Rep. No. 12*, Dept. of Civil Eng., Univ. of Delaware, Newark, DE.

Douglass, S.L. 1992. Estimating extreme values of run-up on beaches. *J. Waterway, Port, Coastal and Ocean Eng.*, 118, 220-224.

Gallagher, B. 1971. Generation of surf beat by non-linear wave interactions. *J. Fluid Mech.*, 49(1), 1-20.

Guza, R.T., and Thornton, E.B. 1981. Wave set-up on a natural beach. *J. Geophys. Res.*, 86(C5), 4133-4137.

Guza, R.T., and Thornton, E.B. 1982. Swash oscillations on a natural beach. *J. Geophys. Res.* 87(C1), 483-490.

Holland, K.T., Raubenheimer, B., Guza, R.T., and Holman, R.A. 1995. Runup kinematics on a natural beach. *J. Geophys. Res.*, 100(C3), 4985-4993.

Holman, R.A. 1986. Extreme value statistics for wave run-up on a natural beach. *Coastal Eng.*, 9, 527-544.

Holman, R.A., and Sallenger, A.H. 1985. Setup and swash on a natural beach. *J. Geophys. Res.*, 90(C1), 945-953.

Huntley, D.A., Davidson, M., Russell, P., Foote, Y., and Hardisty, J. 1993. Long waves and sediment movement on beaches: Recent observations and implications for modeling. *J. Coastal Res.*, 15, 215-229.

Kraus, N.C., and Smith, J.M., (Eds.) 1994. SUPERTANK Laboratory Data Collection project, Volume 1: Main text. *Tech. Rep. CERC-94-3*, U.S. Army Eng. Waterways Experiment Station, Coastal Eng.. Res. Center, Vicksburg, MS.

Kraus, N.C., Smith, J.M., and Sollitt, C.K. 1992. SUPERTANK Laboratory data collection project. *Proc.23rd Coastal Eng. Conf*, ASCE, 2191-2204.

List, J.H. 1992. A model for the generation of two-dimensional surf beat. *J. Geophys. Res.*, 97(C4), 5623-5635.

Longuet-Higgins, M.S., Stewart, R.W. 1962. Radiation stress and mass transport in gravity waves, with application to "Surf Beat". *J.Fluid Mech.*, 13, 481-504.

Nielsen, P. 1988. Wave setup: A field study. *J. Geophys. Res.*, 93(C12), 15,643-652.

Ruesslink, B.G., Kleinhans, M.G., and van den Beukel, P.G.L. 1998. Observations of swash under highly dissipative conditions, *J. Geophys. Res.*, *103*, 3111–3118.

Ruggiero, P., Holman, R.A., and Beach, R.A. 2004. Wave run-up on a high-energy dissipative beach. *J. Geophys. Res.*, 109(C06025), 1-12.

Stockdon, H.F., Holman, R.A., Howd, P.A., and Sallenger, A.H. 2006. Empirical parameterization of setup, swash, and runup. *Coastal Eng.*, 53, 573-588.

Symonds, G., Huntley, D.A., and Bowen, A.J. 1982. Two-dimensional surf beat: long wave generation by a time-varying breakpoint. *J. Geophys. Res.*, 87(C1), 492-498.

Wang, P., Ebersole, B.A., Smith, E.R., and Johnson, B.D. 2002. Temporal and special variations of surf-zone currents and suspended-sediment concentration. *Coastal Eng.*, 46, 175-211.

Wang, P., and Davis, R.A., Jr. 1998. A beach profile model for a barred coast – case study from Sand Key, west-central Florida. *J. Coastal Res.*, 14, 981-991.

Wang, P., and Kraus, N.C. 2005. Beach profile equilibrium and patterns of wave decay and energy dissipation across the surf zone elucidated in a large-scale laboratory experiment. *J. Coastal Res.*, 21, 522-534.

Wang, P., Kirby, J.H., Haber, J.D., Horwitz, M.H., Knorr, P.O., and Krock, J.R., 2006. Morphological and sedimentological impacts of Hurricane Ivan and immediate post-storm beach recovery along the northwestern Florida barrier-island coasts, *J. Coastal Res.*, 22(6), 1,382-1,402.

Yamamoto, Y., Tanimoto, K., and Harshinie, K.G. 1994. Run-up of irregular waves on gently sloping beach. *Proc.23rd Coastal Eng. Conf*, ASCE, 689-703.

INTERACTION OF DUNE FACE AND SWASH ZONE

Jaap S.M. van Thiel de Vries[1,2], Linden B. Clarke[3], Stefan G.J. Aarninkhof[4], E. Martijn Coeveld[5], Rob A. Holman[3], Meg L. Palmsten[3], Ad J.H.M. Reniers[1], Marcel J.F. Stive[1], Wim S. J. Uijttewaal[1]

1. Delft University of Technology, Faculty of Civil Engineering and Geosciences, Section of Hydraulic Engineering, Stevinweg 1, 2628 CN, Delft, The Netherlands. j.s.m.vanthieldevries@tudelft.nl, a.j.h.m.reniers@tudelft.nl, m.j.f.stive@tudelft.nl, w.s.j.uijttewaal@tudelft.nl.
2. Delft Hydraulics, Rotterdamseweg 185, 2629 HD, Delft, The Netherlands.
3. Oregon State University, College of Oceanic and Atmospheric Sciences, Marine Geology and Geophysics Faculty, 104 COAS admin bldg, Corvallis OR, 97331-5503, USA. lclarke@coas.oregonstate.edu, holman@coas.oregonstate.edu, mpalmsten@oregonstate.edu.
4. Delft Hydraulics, Rotterdamseweg 185, 2629 HD, Delft, The Netherlands (now. Royal Boskalis Westminster nv, Hydronamic bv, Rosmolenweg 20, 3350 AA Papendrecht, The Netherlands). S.G.Aarninkhof@boskalis.nl
5. Obrechtstraat 92, 2517 VX Den Haag, The Netherlands (private adress) martijn.coeveld@gmail.com

Abstract: The objective is to develop a physical based wave impact driven erosion model for the dune face and fore shore morphology under extreme conditions. Both (stereo) video and in-situ measurements from a large scale dune erosion experiment are available to develop this model. Visual observations during the experiments and image intensity time stacks are used to make a first analysis of dune face slumping characteristics. Three-dimensional dune and beach morphology are reconstructed from stereo video imagery to quantify morphodynamic response. Also a preliminary investigation of the relationship between wave impact and dune face erosion is presented.

INTRODUCTION

During severe storms a significant surge can flood the beach causing large storm waves to impact the sandy dunes. These wave impacts cause episodical slumping of sand from the dune face onto the active beach. In turn, inner surf and swash zone processes redistribute this sand over the foreshore resulting in a beach profile evolving toward equilibrium with the extreme hydraulic conditions. The system is characterized by a feedback between the evolving beach profile and inner surf and swash zone processes eroding the dune (Figure 1).

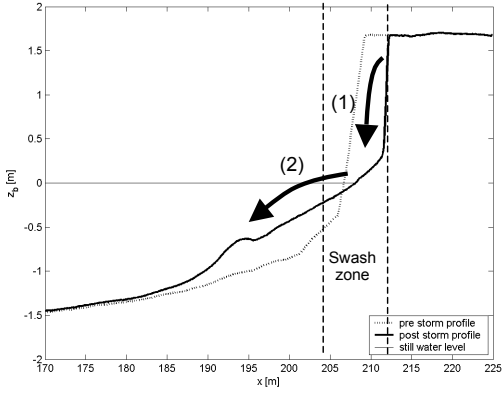

Figure 1: Dune erosion during severe storms. Sand slumps from the dune face onto the active beach (1) where it is transported further offshore by inner surf and swash zone processes (2).

Progress in understanding and modeling dune erosion during extreme storm surges requires better knowledge of inner surf and swash zone processes and the interaction of these processes with the dune face and fore shore. Hydrodynamics of inner surf and swash zones are complex due to limited water depth, non linear interactions, and high turbulence rates. Furthermore the addition of sediment from the collapsing dune face is irregular in time and significantly influences near shore hydrodynamics and sediment transports.

Several approaches have been proposed to describe sediment fluxes over the dry dune face and swash zone. A first approach relates dune face erosion and swash zone sediment transports to the capacity of the near shore flows to transport sediment offshore (Steetzel 1993; Steetzel 1994). Sediment transports are computed with a physical based model up to a critical water depth. Then, the sediment transport at the critical water depth is empirically extrapolated over the swash and dune face till a computed run-up level. In the model waves do not necessarily have to impact the dune face in order for it to retreat and the geotechnical properties of the dune face are not considered in the model.

Another approach is to directly decouple inner surf and swash zone sediment transports from dune face erosion by relating dune face wave impacts to dune face erosion as proposed by Fisher et al. (1986). In addition a wave impact driven dune face erosion model may be coupled with a process based morphodynamic model for the fore shore to model dune erosion. In this model the beach morphology in front of the dune foot does not evolve from an empirical sediment transport function but is free to be shaped by the near shore hydrodynamics. This allows for a physical feedback between near shore hydrodynamics, dune face erosion and the evolution of the fore shore from that erosion.

The objective is to develop a process-based dune erosion model driven by wave impact. To that end this paper examines the relation between wave impact and dune face retreat using data from a large scale dune erosion experiment in the Delta flume, a WL|Delft Hydraulics research facility. Characteristics of dune face slumping such as slump volume, frequency and failure mode are investigated using visual observations and image intensity time stacks derived from video. Detailed analysis of the morphological response of the dune face is obtained stereo video images. Preliminary conclusions arising from the observations are also presented.

DUNE EROSION EXPERIMENT

Eight large scale dune erosion experiments were conducted in the WL|Delft Hydraulics Delta flume (length width and depth respectively 225 m, 5m, 7m) from November 2005 through February 2006 (Van Gent et al. 2006). The total duration of each test varied, but was at least six hours. Tests were temporarily interrupted to carry out bed profile measurements. Other measurements were obtained using both in-situ instruments and video cameras.

In-situ hydrodynamic measurements were obtained from a cluster of instruments deployed on the flume wall. Ten pressure sensors spaced along the flume measured wave transformation over the foreshore, three resistance wires and a combined pressure and current velocity sensor were used to distinguish between incoming and shore line reflected waves, and two electromagnetic current velocity sensors measured the inner surf and swash zones hydrodynamics (Figure 2). The collocated pressure and current velocity sensors deployed at 205 meters from the wave board may best be used to obtain further insight into wave impacts on the dune face.

Two synchronized video cameras (referred to as camera C1 and C2) were deployed to obtain stereo video data with the objective of three-dimensional reconstruction of the dune face, inner surf and swash zone. Images were collected from video streams with a sample frequency of 2 Hz or 4 Hz depending on the experiment and the two cameras were synchronized using an 11 volt trigger signal. Video data were synchronized with in-situ measurements using a small led light visible in camera C2 that illuminated at the start of in-situ measurements.

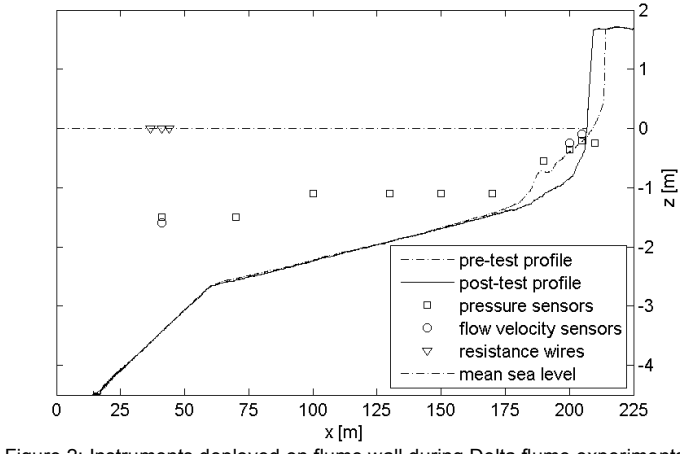

Figure 2: Instruments deployed on flume wall during Delta flume experiments

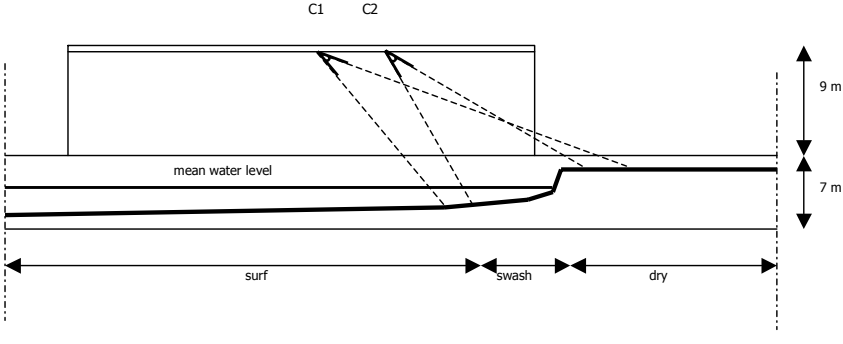

Figure 3: Camera configuration C1 and C2 during Delta flume experiments

Cameras C1 and C2 were fixed to the roof of the flume's enclosure approximately above the flume centre line (see Figure 3). Both cameras were pointed in the direction of wave propagation and resolve bathymetries in an area covering about twelve meters in along flume direction and six meters in cross flume direction. Camera positions and orientation are listed in Table 1. The coordinate system originates at the wave board ($x = 0$), the flume centre line ($y = 0$) and the top of the flume wall ($z = 0$).

Table 1: camera geometries

Camera	*x* (m)	*y* (m)	*z* (m)	*fov* (°)	Tilt (°)	Roll (°)	Azimuth(°)
C1	190.474	0.032	8.331	30.3496	55.06	-87.62	89.49
C2	196.811	0.022	8.312	38.2679	45.98	-90.58	91.40

VISUAL OBSERVATIONS

A first analysis of in-situ profile measurements during the experiments show that after one hour waves, time averaged, spatial sediment transport gradients on the newly formed fore shore are relatively small (Figure 4). It seems the vertical elevation of the fore shore is close to equilibrium if a longer period of time is considered. However, observations on a shorter time scale indicate that the beach in front of the dune face is frequently far away from equilibrium elevation due to slumping sand deposited on the beach. Near shore hydrodynamics constantly reshape the beach and on average sediment is transported in seaward direction where the sand settles and extends the fore shore. Developing a physical based dune erosion model requires that the shorter time scale slumping and its interaction with the fore shore hydrodynamics has to be simulated correctly in order to predict the behavior on a longer time scale.

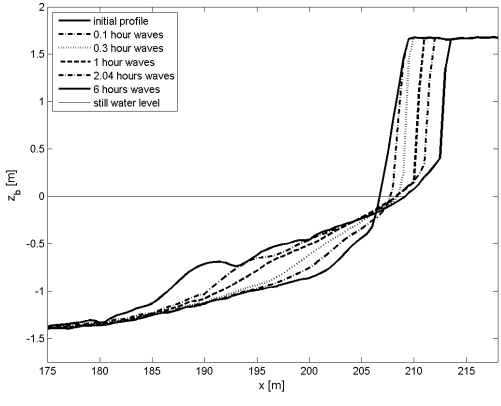

Figure 4: Profile development during the first six hours in the seventh test of the dune erosion experiment. The vertical elevation of the fore shore remains approximately the same on a longer time scale meaning time averaged spatial sediment transport gradients are small.

Visual observations during the experiments revealed that the dune face will retreat as long as incoming waves run-up the beach and hit the dune face. Considering this it is hypothesized that the rate of dune face retreat should be related to the wave impact frequency. However a direct relation between wave impact and dune face erosion was not observed. Collapsing of the dune face also occurred after an experiment in the absence of waves. In general, the dune face is overhanging slightly before slumping suggesting the dune face becomes unstable reaching a critical slope. The apparent decorrelation between discrete wave impacts and dune face retreat suggests examining a relation between dune face retreat and the accumulated dune face wave impacts between two slumps.

At the beginning of an experiment the dune foot is just below mean water level, the

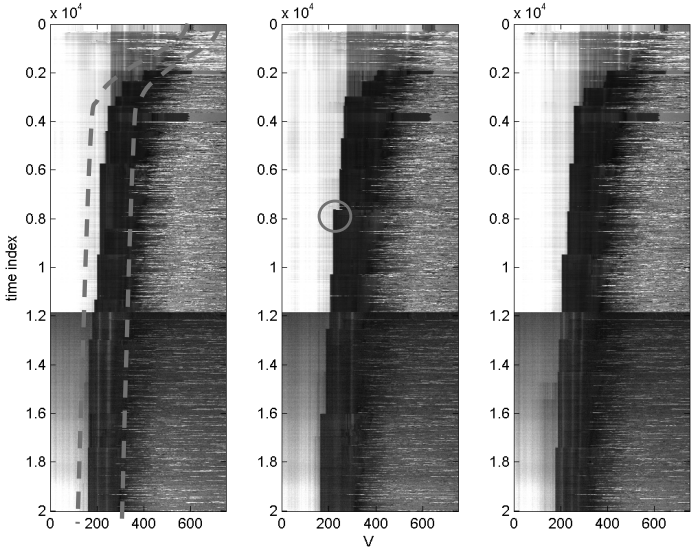

Figure 5: Time stacks for three transects in cross tank direction comprising the first two hours of the seventh test (Figure 6 left panel). The dune crest (lying between the dashed lines in left panel) is indicated by the transition from light to dark, where light is the top of the dune. Slumps are indicated by a discontinuity of the dune crest in time (i.e. circle middle time stack)

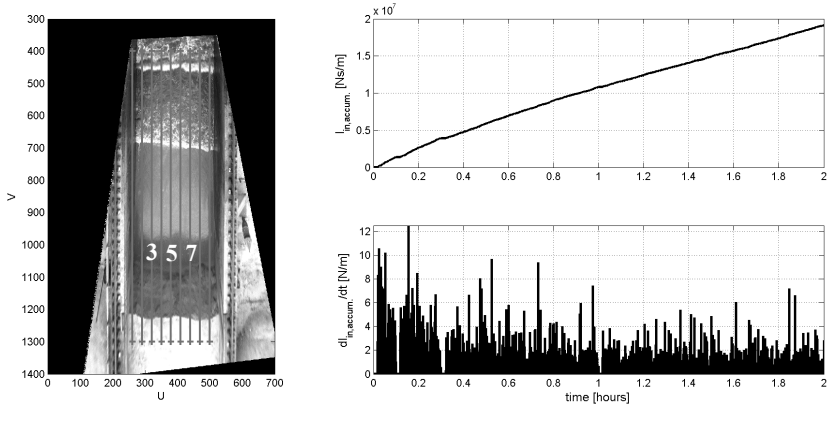

Figure 6:(left): Rectified image with transects used to generate time stacks. Transect 3,5 and 7 are used in elaborating Figure 5. (right upper): Accumulated shore ward directed momentum at the collocated pressure and current velocity sensor at 205 meter from the wave board. (right lower): Ten minutes averaged gradient of shore ward directed momentum at the same location.

erosion rates are large and so is the number of waves reaching the dune face. Due to continuing dune erosion the fore shore starts to develop causing waves to dissipate more energy further offshore. In addition the retreating dune foot becomes located above the still water level and waves have to run-up the newly formed beach before the dune can be impacted. Consequently, the number of waves reaching the dune face and the wave impact intensity are expected to decrease as the experiment progresses The resulting decrease in dune erosion rate with time is confirmed by the dune crest position in time stacks for three transects along the flume axis (Figure 5). The rate of dune face retreat decreases whereas the time interval between successive slumps becomes larger as the experiment continues. Time stacks from the various transects illustrate that a slumping event does not necessarily extend over the full width of the flume.

At the start of the experiment the dune face is rapidly eroded and steepened as waves run up the dune face instead of impacting it (Figure 5). It is hypothesized that erosion mechanisms during the transient steepening of the dune face are different and are also due to shear stress driven sediment transports exerted by the flow.

Accumulated on-shore directed momentum obtained from the collocated pressure and current velocity sensors at 205 meters from the wave board decreases with time and illustrates the reduction in wave energy reaching the dune face as the result of fore shore development and dissipation of incoming wave energy further offshore (Figure 6, upper panel).

DETAILED ANALYSIS

To examine a relation between wave impact and dune face erosion a linear relation ship is assumed between the change in momentum of waves impacting the dune face (a force F) and the weight of the sediment volume eroded from the dune (ΔW) (Fisher et al. 1986; Overton et al. 1987; Nishi and Kraus 1996; Larson et al. 2004;):

$$\Delta W = C_E F \tag{1}$$

In this expression C_E is an empirical coefficient to be obtained from data and ΔW is computed from the eroded sediment volume from the dune (ΔV) (Figure 7 left panel):

$$\Delta W = \Delta V \rho_s (1 - p) g \tag{2}$$

where ρ_s is sediment density, p is porosity and g is the gravitational acceleration.

Coefficient C_E in relation (1) is calibrated for the Delta flume experiments by computing the change in dune face volume (ΔV) for a slump event using stereo video data to reconstruct the dune face just before and after a slump event. The average wave impact (F) is derived from in-situ data.

Slump events in the available video data are detected using time stacks of nine uniformly

spaced transects in cross flume direction (Figure 6 left panel and Figure 8). The real world distance between transects is about half a meter which is close enough to detect most slump events. Since retreat of the dune face does usually not extend over the full width of the flume, slump events are not necessarily visible in all time stacks. Consequently, accumulated wave impacts between successive slumps (assumed to be uniform in cross flume direction) are related to the cross flume integrated volume change of the dune.

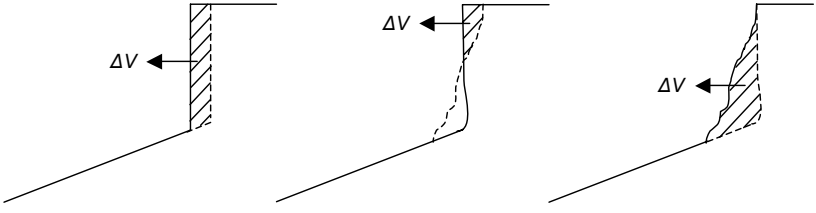

Figure 7: (left): Sketch of eroded sediment volume from the dune as computed in the wave impact model. (middle): Sketch of morphological response of the dune dune face over a slump. (right): Sketch of morphological response of beach and dune face between two slumps.

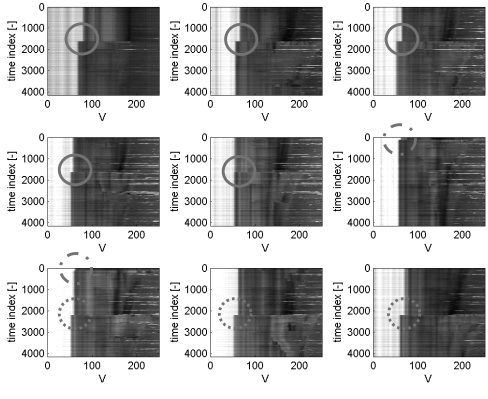

Figure 8: Time stacks for nine transects at January 13th 2006. Three slumps are observed indicated by the solid, dashed-dotted and dotted circles. Successive slumps are not necessarily in the same transect.

Near shore morphodynamic response

Three dimensional reconstructions of the dune face and near shore are obtained from a single image pair (for example Figure 9). The image required camera geometries including camera orientation, position and focal length (as described in Table 1) were computed following Holland et al. (1997).

Synchronous images from C1 and C2 are preprocessed to enhance contrast and remove

lens distortion. Features in images from C1 are mapped to corresponding features in images from C2 using an automated algorithm (Clarke et al. 2007, in preparation). The three-dimensional coordinates (XYZ) of imaged features are computed using the differences in feature pixel coordinates from the two views in conjunction with camera geometries. Computed XYZ may be obtained for any point in the image providing there is a significant local gradient in pixel intensity to uniquely identify the point in both images. Computed XYZ are interpolated on a grid to reduce noise, reduce the number of data points and simplify further analysis.

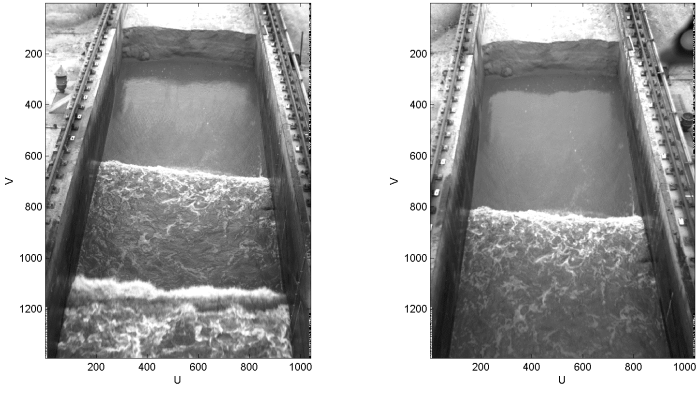

Figure 9: (left): Raw image camera C1 (right): Raw image camera C2

For the dune experiments there are some areas in the flume where features appear as reflections on either the water surface or the wet sand surface during shallow swash up rush or down rush. Computed coordinates for reflected features are erroneous compared to the coordinates in the absence of such reflections. To guard against spurious feature matches the water surface, dry beach and reflection areas are identified using a series of empirical image processing algorithms prior to the feature matching process (Figure 10). The water line is detected using the contrast between wave breaking induced foam and the dry beach. Using intensity variance images, large variance areas are identified as wet whereas small variance areas are marked as dry. In addition, the most shoreward bore edge (indicated by the white arrow in the right panel of Figure 10) is detected as the continuous line maximizing the sum of variance across the flume. If the resulting bore edge is within a user specified number of pixels from the water line the bore edge is marked as being the water line. When the bore edge marks the boundary between water and dry beach it is used as a strong feature to generate high confidence coordinates along contour lines on an otherwise poorly featured beach. Areas in the image containing reflected features are marked and excluded from further analysis (Figure 10 right panel).

Computed XYZ are interpolated onto a regular grid with spacing 1cmx1cm. Since the dune face is nearly vertical, this feature is resolved in the interpolation by first rotating computed XYZ to a new coordinate system, XYZ', where the plane XY' represents a

best fit through XYZ. Transformed points XYZ' are interpolated onto a regular grid in XY'. Interpolated grid points are then transformed back to the unrotated reference frame (Figure 11).

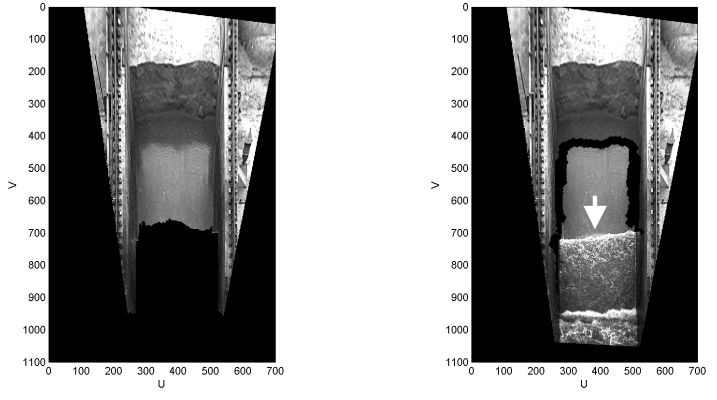

Figure 10: (left): Distinguish between water surface and dry beach. Here the water surface is masked. (right): Masking of edges reflection area. The white arrow points to the most shoreward bore

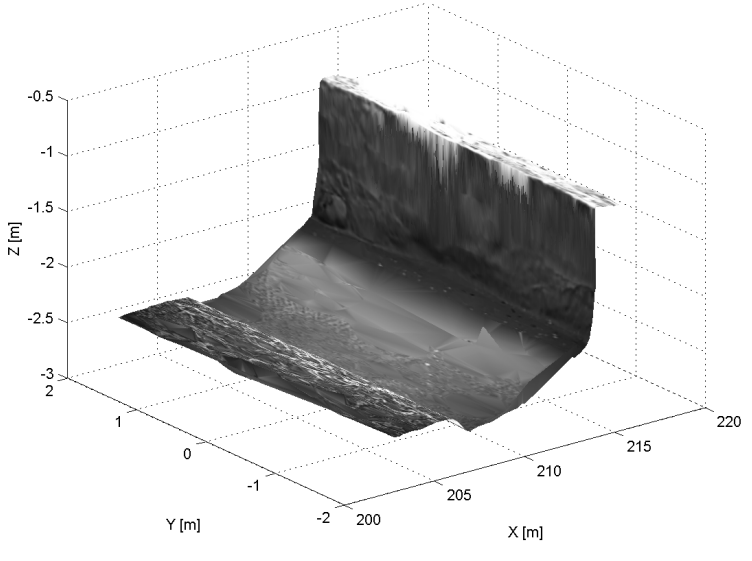

Figure 11: Three dimensional reconstruction of near shore area using two images.

Reconstructed dune and beach morphology immediately before and after an slump event (Figure 12, upper panels) are differenced to determine volume changes of the dune face (Figure 12, lower panels). From this quantified morphodynamic response an erosion volume has to be specified in order to relate wave impact to dune face erosion. In the wave impact model this volume is expressed as the sediment volume eroded from the dune (see Figure 7 left panel). However obtaining the relevant volume from the measured morphological response over a slump is not straight forward since it is not obvious from this response what sand is active and behaves like a sediment source to the swash zone (Figure 7 middle panel). Taking the eroded sediment volume from the dune, as proposed in the model, probably results in an underestimation of dune face erosion since a significantly larger volume of sand is redistributed by the near shore hydrodynamics in the interval between successive slumps. From a physical point of view it might be better to compute the wave impact related sediment erosion volume from the combined volume change of the beach and dune between two slumps (Figure 7 right panel) instead of computing it from the volume change of the dune alone for a single slump (Figure 7 middle panel).

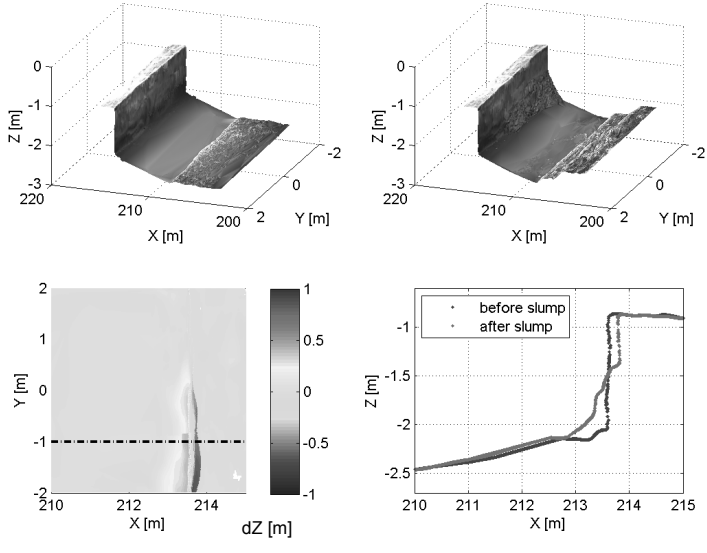

Figure 12: Morphodynamic response during dune face slump. Upper panels show the three dimensional reconstruction of the near shore area just before and after the slump. The lower panels show the morphodynamic response of the dry beach and dune. The profiles in the lower right panel are obtained from interpolated grid data with Y values between -1.05 [m] and -0.95 [m]. The still water level is at -2.5 [m]

Wave impacts

To examine relation (1), in addition to slump volumes also wave impacts are needed. Wave impacts are derived from measurements from the most shoreward located (205 [m] from the wave board) pressure and current velocity sensor. Using shallow water linear wave theory pressure time series are translated into water surface elevations. Current velocity time series are de-spiked such that velocity peaks with a minimum amplitude of 0.25 [m/s] and a maximum width of 1 second are removed. Both pressure and current velocity time series are used to distinguish between incoming and shoreline reflected waves assuming shallow water (Guza et al. 1984):

$$\eta_{in} = \frac{\eta + u\sqrt{h/g}}{2} \text{ and } \eta_{out} = \frac{\eta - u\sqrt{h/g}}{2}, \tag{3}$$

where η_{in} and η_{out} are respectively the water surface elevation associated with the incoming waves and outgoing waves, η (= η_{in+} η_{out}) is the measured water surface elevation, u is the measured velocity, h is water depth and g is the gravitational acceleration.

Only the incoming wave signal is considered in elaborating wave impacts. The amount of incoming wave momentum is separated into two contributions, respectively a term representing advection of momentum by the flow and a term taking in account the dynamic water pressure:

$$I = \rho u_{in}(t)^2 h_{in}(t) + 0.5\rho g \eta_{in}(t)^2, \tag{4}$$

where u_{in} is the current velocity associated with the incoming waves and h_{in} the water depth associated with the incoming waves ($h_{in} = h_{mean} + \eta_{in}$).

The incoming momentum is absorbed in the swash zone and by the dune face. Since the dune face retreats during the experiment, the distance between the most shoreward located sensors and dune face will increase. In addition the momentum absorbed over this distance is expected also to increase. To include this effect requires the modeling of intra wave forces that act on the fluid in the swash zone.

CONCLUSIONS

Initial review of some of the video imagery and hydrodynamic measurements from the series of large-scale dune erosion experiments confirm a complex relationship between waves and morphodynamic response of the fore shore and dune face. Dune retreat may be characterized by two stages. In the initial stage the dune face evolves to a vertical face and sediment transport from dune to near shore environment is affected by wave up-rush over the full dune height. In the later stage sediment is delivered in bulk to the upper swash zone by intermittent failure of the vertical dune face where it is subsequently transported offshore by swash and near shore flow.

Accumulated wave momentum at the most shoreward sensor indicates a non-linear decrease in energy available for dune erosion as the newly formed fore shore evolves progressively into deeper water. Bar formation and increased dissipation of wave energy further offshore characterizes the later stage of the experiment.

Time stacks and morphology reconstruction from stereo provide high resolution measurements in time and space with demonstrated capability of resolving dune and foreshore response to waves. Integrating over an extended sequence of slump events and associated wave impacts will allow calibration of the dune erosion model cited in this paper. A detailed analysis of video and hydrodynamic data is required to fully exploit existing measurements but they represent a valuable suite of observations with which to formulate and quantitatively test improved models for dune response to extreme wave conditions.

ACKNOWLEDGEMENTS

The Dr.ir Cornelis Lely Foundation and Delft Cluster are thanked for financing this work as part of a PhD study on dune erosion. Also we thank RWS RIKZ for their contribution to the large scale dune erosion experiments in the Delta flume.

REFERENCES

Fisher, J.S., M.F. Overton, and T.Chisholm. (1986). Field Measurements of dune erosion, *Coastal engineering conference, ASCE,*

Guza, R.T., E.B. Thornton, and R.A. Holman. (1984). Swash on steep and shallow beaches, *Coastal engineering conference*, ASCE 1, 708-723.

Holland, K.T., R.A. Holman, C. Lippmann, J. Stanley, and N. Plant. (1997). Practical use of video imagery in nearshore oceanographic field studies, *IEEE journal of oceanic engineering*, 22, 81-92.

Larson, M., L. Erikson, and H. Hanson. (2004). An analytical model to predict dune erosion due to wave impact, *Coastal engineering* (51), 675-696.

Nishi, R., and N.C. Kraus. (1996). Mechanism and and calculation of sand dune erosion by storms, *Coastal engineering conference, ASCE*, 3034-3047.

Overton, M.F., J.S. Fisher, and T.A. Fenaish. (1987). Numerical analysis of swash forces on dunes, *Coastal engineering conferenc, ASCE*, 632-641.

Steetzel, H.J. (1994). Sophistication DUROSTA-model, Delft Hydraulics, Marknesse, Netherlands (In Dutch).

Steetzel, H.J. (1993). Cross-shore transport during storm surges, Ph.D. Thesis thesis, Delft University of Technology, Delft, Netherlands.

Van Gent, M.R.A., E.M. Coeveld, D.J. Walstra, J. Van de Graaff, H.J. Steetzel, and M. Boers. (2006). Dune erosion tests to study the influence of wave periods on dune erosion, *Coastal engineering conference, ASCE,* San Diego

CRITICAL WIDTH OF BARRIER ISLANDS AND IMPLICATIONS FOR ENGINEERING DESIGN

Julie Dean Rosati[1], Gregory W. Stone[2]

1. U.S. Army Engineer Research and Development Center, Coastal and Hydraulics Laboratory, 109 St. Joseph Street, Mobile, AL 36602 USA. Julie.D.Rosati@erdc.usace.army.mil.
2. Louisiana State University, Coastal Studies Institute and Department of Oceanography and Coastal Sciences, 316 Howe-Russell, Baton Rouge, LA 70803, USA. gagreg@lsu.edu.

Abstract: The critical width of a barrier island is defined as the smallest cross-shore dimension that minimizes net loss of sediment from the island over periods from decades to centuries. This concept is of importance for large-scale restoration of barrier islands which involves rebuilding these islands to a specified geometry. Within constraints of coastal forcing and geologic and regional characteristics at the site, islands having critical width will capture deposition of washover sediment onto the subaerial beach over the project lifetime. This study reviews previous investigations of barrier island critical width and applies a newly-developed model of barrier island migration, consolidation, and overwash to assist engineering design.

INTRODUCTION

The term "critical width" has been discussed with reference to barrier islands, overwash, and washover deposits since the 1970s (e.g., Leatherman 1976, 1979; Jiménez and Sánchez-Arcilla 2004). Critical barrier width is defined herein as the smallest cross-shore dimension that minimizes net loss of sediment from the barrier island over periods from decades to centuries. The magnitude of critical width is related to availability and volume of littoral sediment in addition to that in the dune system. In addition, the influx of sediment via longshore sediment transport is important, for example during post-storm recovery. To illustrate the definition and introduce terminology, Figure 1 shows a barrier island and sediment transport pathways. If the barrier width equals or exceeds the critical value, transport of washover sediment from the ocean beach, Q_{wo} , is deposited

entirely on the bay beach, and residual loss of this washover into the bay, Q_{bwo}, equals zero. For barrier widths less than the critical value, $Q_{bwo} > 0$.

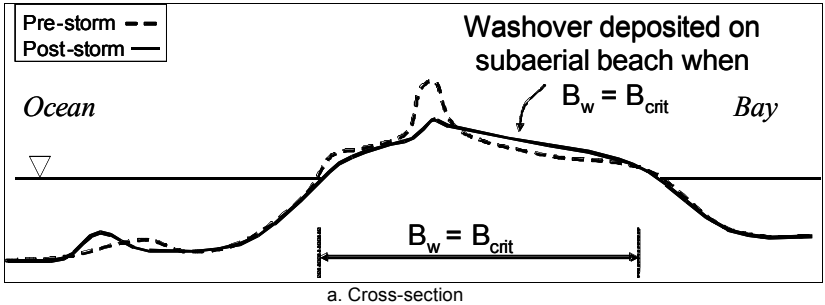

a. Cross-section

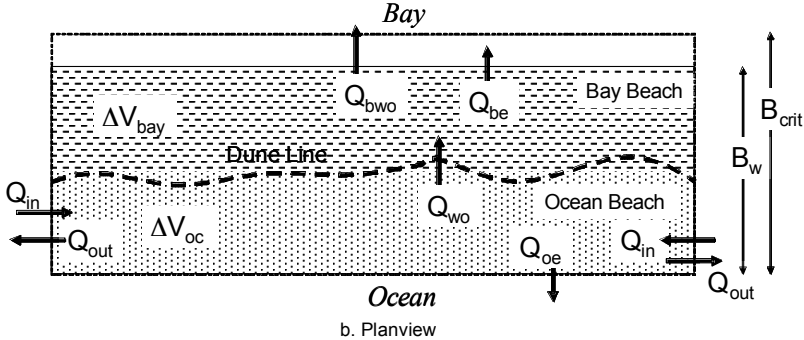

b. Planview

Legend

Q_{in} = longshore transport rate into barrier system	Q_{oe} = rate transported offshore
Q_{out} = longshore transport rate out of barrier system	Q_{be} = rate transported into bay
ΔV_{oc} = volume change rate on ocean beach	Q_{wo} = washover rate from ocean beach
ΔV_{bay} = volume change rate on bay beach	Q_{bwo} = washover rate lost into bay
B_w = barrier width	B_{crit} = critical barrier width

Fig. 1. Definition of terminology

Application of this concept is important for the large-scale restoration of barrier islands such as is being considered for degraded islands along the Northern Gulf of Mexico, particularly in Louisiana. These barrier islands have lost subaerial volume through time due to a combination of factors, including a lack of littoral sediment in the regional system, wave erosion due to tropical cyclones and winter storms on both the Gulf and Bay shores, and rapid relative sea level rise. Large-scale restoration involves

reconstruction of the island to specified height, width, length, and spacing (for multiple islands) using sediment derived from an external source. The goal in large-scale restoration is to maximize the lifetime of the island in protecting the bay, estuary, and mainland shores, while minimizing the cost of the project. In the North-Central Gulf of Mexico, loading of the compressible substrate with additional sediments increases consolidation. Thus, the volume of sediment used to restore a barrier becomes critical in that a larger restoration project will incur more losses due to consolidation when compared to a smaller volume (Rosati et al 2006, 2007).

In this study, we applied a migration, consolidation, and overwash model to determine the critical barrier island width given forcing and geologic parameters. Storm characteristics and consolidation characteristics of the underlying substrate were varied. The study concludes with preliminary recommendations for critical design width for large-scale restoration of barrier island systems that overlie a compressible substrate.

PREVIOUS STUDIES

Leatherman (1976, 1979) investigated overwash and washover along the northern end of Assateague Island, Maryland, and found that overwash processes were effective in migration of the barrier "…only where the barrier width is less than a critical value (122 to 213 m)." The island did not narrow below these values because overwash processes were effective at transporting sediment to the bayshore, therefore keeping pace with the rate of ocean shoreline migration. Sections of the island with greater widths experienced washover deposits that did not reach the bayshore, and the island narrowed due to ocean shoreline migration until it reached the critical width. The only process that widened the barrier beyond the critical width was breaching, formation of a partially subaerial flood shoal, and subsequent inlet closure (Leatherman 1976).

Eitner (1996) discussed potential response of the East Frisian barrier islands due to a 1-m rise in sea level occurring over approximately 170 years. Although critical width is not discussed, the most likely future outcome proposed is one in which the barrier islands maintain width while increasing in height and migrating landward. This stability of barrier cross-section implies that a critical width is maintained over the long term.

Jiménez and Sánchez-Arcilla (2004) applied the concept of critical width in a decadal-scale barrier evolution model to determine when overwash processes would contribute to bayshore accretion. They developed the model for the Ebro Delta, Spain, and estimated the critical width of the barrier spit as 225 m. When the barrier island was wider than the critical width, washover deposition on the bayshore was zero. When the barrier width was less than or equal to the critical width, washover deposition was estimated as:

$$Q_{bwo} = Q_{wo}\left(\frac{B_{crit}}{B_w}\right)^{\alpha} \quad or \quad B_{crit} = B_w\left(\frac{Q_{bwo}}{Q_{wo}}\right)^{1/\alpha} \tag{1}$$

where Q_{bwo} is the volumetric washover rate of deposition to the bayshore, Q_{wo} is the volumetric washover rate on the oceanside of the barrier, B_{crit} is the critical barrier width,

B_w is the barrier width at any time, and α is a parameter greater than or equal to 1 to incorporate sediment eroded from the subaerial barrier during overwash events (notation has changed slightly from original reference for consistency herein). Jimenez and Sanchez-Arcilla evaluated the influence of α values ranging from 1 to 2; greater α values increased the rate at which the barrier reaches an equilibrium condition, but did not change the final equilibrium state. For α values greater than 1, volumetric overwash into the bay will be greater than that transported from the ocean for all values of barrier width less than the critical width.

A sediment budget approach can be applied to estimate the critical width (Figure 1). Applying the requirement that Q_{wo} remain on the subaerial beach at critical width (i.e., $Q_{bwo} = 0$ when $B_w = B_{crit}$), and assuming that transport of the washover sediment into the bay, Q_{bwo}, is linearly related to the critical width, then:

$$B_{crit} = B_w \left(\frac{Q_{wo}}{Q_{wo} - Q_{bwo}} \right), \quad or$$
$$B_{crit} = B_w \left(\frac{Q_{in} - Q_{out} - Q_{oe} - \Delta V_{oc}}{Q_{be} + \Delta V_{bay}} \right) \tag{2}$$

Stone et al. (2004) compiled total volumes for four barrier sub-environments at Santa Rosa Island, Florida (Gulf, Berm, Dune, Bay Beach, and Bay Platform) over a 6.5-year period which can be used in Eq. 2 to determine the critical width. Considering volumetric change from February 1996 to 2002, a sediment budget can be formulated as shown in Figure 2. In formulating this budget, it was assumed that all volumetric change was due to cross-shore transport, and the gradient in longshore transport was zero. Applying Eq. 2 with a barrier width B_w = 220 m, Q_{in} - Q_{out} = 0 cu m/yr, Q_{oe} = 12.8 cu m/yr, ΔV_{oc} = -40.8 cu m/yr, Q_{be} = 0 cu m/yr, and ΔV_{bay} = 24.5 cu m/yr, the critical width can be estimated as B_{crit} = 220* (0-12.8+40.8)/(0+24.5) ~ 250 m.

MCO MODEL

The Migration, Consolidation, and Overwash (MCO) model (Rosati et al. 2006, 2007) was applied to develop guidance for barrier island critical width. This model simulates cross-shore evolution of a barrier island over periods extending from years to centuries, with given substrate and storm characteristics. Methodology underlying the model is briefly reviewed in this section.

Overwash

Overwash is any wave uprush which passes over the crown or crest of the barrier beach, and the feature created by the overwash is the washover deposit (Leatherman 1980). Overwash and the associated washover are one of the mechanisms through which the barrier island migrates towards the bay, in the cross-shore direction.

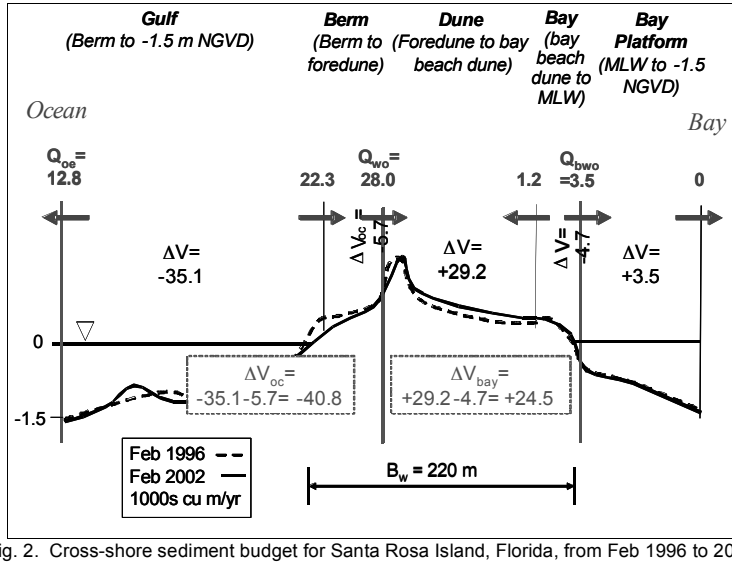

Fig. 2. Cross-shore sediment budget for Santa Rosa Island, Florida, from Feb 1996 to 2002 (data from Stone et al. 2004)

The overwash transport rate over the beach crest due to runup overwash per unit length of beach, $q_{DR}(t)$, can be described as (Donnelly et al. 2006):

$$q_{DR}(t) = 2K_R\sqrt{2g}\,\frac{z_R(t)^2}{R(t)}, \quad 0 < z_R(t) \text{ and } S(t) < b_h(t) \tag{3}$$

where K_R is a calibration coefficient that accounts for sediment stirring and properties of the wave bore; g is the acceleration due to gravity; $z_R(t)$ is the elevation of the runup, $R(t)$, relative to the dune crest elevation, $b_h(t)$, and S(t) is the total water depth (including storm surge). For calculations herein, K_R was set equal to 0.005 (Donnelly et al. 2006).

The two-percent runup, $R_{u2\%}(t)$, is calculated as (Hughes 2004):

$$R_{u2\%}(t) = 4.4\,S(t)\tan\beta(t)^{0.70}\left[\frac{M_F(t)}{\rho g S(t)^2}\right]^{1/2} \quad \text{for } \frac{1}{30} \le \tan\beta(t) \le \frac{1}{5} \tag{4}$$

in which $\tan\beta(t)$ is the beach slope, ρ is the density of water, and the maximum dimensionless depth-integrated wave momentum flux per unit width is:

$$\left[\frac{M_F(t)}{\rho g S(t)^2}\right]_{\max} = A_0(t)\left[\frac{S(t)}{gT_p(t)^2}\right]^{-A_1(t)}$$

$$\text{where} \quad A_0(t) = 0.6392\left(\frac{H_{mo}(t)}{S(t)}\right)^{2.0256} \tag{5}$$

$$\text{and} \quad A_1(t) = 0.1804\left(\frac{H_{mo}(t)}{S(t)}\right)^{-0.391}$$

The zeroth-moment deep water wave height is $H_{mo}(t)$, with associated peak period, $T_p(t)$. In applications described herein, these were randomly generated about a user-specified mean.

If the barrier island is submerged, the transport rate over the beach crest per unit width of beach, $q_{DI}(t)$, is given by (Donnelly et al. 2006) as:

$$q_{DI}(t) = (K_I + K_R)\, 2\sqrt{2g}\; z_R(t)^{3/2}, \quad 0 < z_R(t) \text{ and } S(t) \geq b_h(t) \tag{6}$$

in which K_I is an empirical coefficient, and $z_R(t)$ is as defined previously. For calculations, K_I was set to 0.001 (Donnelly et al. 2006).

The rate of washover deposition q_f varies as a function of distance over the dune crest (Larson et al. 2004):

$$q_f = \frac{q}{1 + \mu s / B_D} \tag{7}$$

where q is the transport rate over the dune crest as calculated in Eq. (1) or (4), s is a coordinate originating at the dune crest and increasing with distance over the dune, μ is an empirical coefficient, and B_D is the width of flow over the dune crest. For calculations, μ/B_D=0.12 (Larson et al. 2004).

Erosion

If the storm surge plus wave runup do not exceed the barrier island elevation, the time-dependent berm erosion, $E(t)$, is calculated using the Convolution Storm Erosion Method (Kriebel and Dean 1993):

$$E(t) = \frac{E_\infty}{2}\left\{1 - \frac{\beta_t^2}{1+\beta_t^2}\exp\left(-\frac{2\sigma t}{\beta_t}\right) - \frac{1}{1+\beta_t^2}\left[\cos 2\sigma t + \beta_t \sin 2\sigma t\right]\right\} \tag{8a}$$

in which the maximum potential erosion retreat distance is given by:

$$E_\infty = S(t)\left(\frac{W_b(t) - \dfrac{h_b(t)}{\tan\beta(t)}}{B + h_b(t) - \dfrac{S(t)}{2}}\right) \tag{8b}$$

and β_t is the ratio of the erosion time scale to the storm duration,

$$\beta_t = \frac{2\pi T_s}{T_D} \tag{8c}$$

In Eq. (8a), the term $\sigma = \pi/T_D$, where T_D is the total storm duration. The characteristic erosion time scale of the system is given by:

$$T_s = 320 \frac{H_b(t)^{1.5}}{g^{0.5} A^3} \left(1 + \frac{h_b(t)}{B} + \frac{\tan\beta(t) W_b(t)}{h_b(t)} \right)^{-1} \tag{8d}$$

in which $H_b(t)$ is the breaking wave height, $h_b(t)$ is the breaking depth, B is the berm elevation, and $W_b(t)$ is the distance to the wave breaker line calculated as:

$$W_b(t) = \left(\frac{h_b(t)}{A} \right)^{1.5} \tag{8e}$$

in which A is the equilibrium beach profile scade parameter, set to 0.063 $m^{1/3}$ representing 0.1 mm sand typical of Louisiana barrier islands.

Consolidation

Sediment has the potential to compress significantly under load due to factors such as reduction in void space, biochemical decay of organic materials, and grain shifting and breakage. Pore pressure increases if a load is applied to a saturated soil. For sands, the excess pore pressure is dissipated quickly due to their high permeability. However, clays, organic soils, and silts have much smaller permeability; thus, the excess pressure dissipates much more slowly, and consolidation continues for a much longer time.

Coastal substrates that have the potential for significant consolidation include fine-grained sediment that have not been previously loaded, for example, clays and silts deposited by river systems, organic peaty sediment, and sediment with interlaying organic strata. Sediment loaded at an earlier time in its geologic history, e.g., due to glacial loading or construction of infrastructure, will rebound slightly once the load is removed. If reloaded with a greater weight, they will continue the consolidation process. Terzaghi (1943) derived a relationship for primary consolidation based upon hydraulic principles. For one-dimensional vertical flow, the final consolidation, z_c, for a given increase in loading, $\Delta W(t)$, can be calculated as:

$$z_c = z_0 \left(\frac{C_c}{1 + e_0} \log_{10} \frac{W_0 + \Delta W(t)}{W_0} \right) \tag{9}$$

where z_0 is the initial thickness of compressible sediment; C_c is the compression index, which can be determined experimentally from a consolidation test; e_0 is the initial void ratio, equal to the volume of voids divided by the volume of solids, and averaged over z_0; and W_0 is the initial loading on the sediment. In a study of the consolidation potential for Louisiana sediment, Kuecher (1994) found values of $C_c = 4.7$ to 5 for peat and organic mud; 1 to 3 for prodelta mud; 0.86 for bay sediment; 0.123 for natural levee sands and

silts, and 0.063 for point bar sands. Larger C_c values indicate a greater potential for consolidation. For calculations presented herein, C_c was 0.86. The depth of undisturbed sediments, z_0, was determined to be 4.7 m through iteration with the model by reproducing the rate of relative sea level rise measured at Grand Isle, Louisiana (9.9 mm/year) given the eustatic rate in the region (2.4 mm/year, Stone and Morgan 1993).

Terzaghi's (1943) time-dependent relationship for consolidation is:

$$\frac{\partial u}{\partial t} = c_v \frac{\partial^2 u}{\partial z^2} \tag{10}$$

where u is pore water pressure in excess of hydrostatic pressure, t is elapsed time, c_v is a property of the compressible sediment, referred to as the coefficient of consolidation, and z is the vertical coordinate with the origin at the initial sediment surface. The proportion of the initial pore water pressure remaining at any time, $M(t)$, can be expressed as:

$$M(t) = \frac{1}{z_0}\int_0^{z_0} \frac{u}{u_0} dz = \frac{e(t) - e_f}{e_0 - e_f} \tag{11}$$

in which u_0 is the initial pore water pressure, $e(t)$ is the average void ratio at any time, and e_f is the final average void ratio. The variable $M(t)$ varies from 1 and 0, at time $t = 0$ and infinity, respectively. The proportion of vertical consolidation that occurs at any time can also be expressed as:

$$z(t) = z_c \left(\frac{e_0 - e(t)}{e_0 - e_f} \right) \tag{12}$$

Combining Eqs. (11) and (12) gives,

$$z(t) = z_c (1 - M(t)) \tag{13}$$

where $M(t)$ can be expressed as (Dean 2002, p. 119)

$$M(t) = 8 \sum_{n=1}^{\infty} \frac{e^{-\left[(2n-1)\pi\right]^2 c_v t / 4 z_0^2}}{(2n-1)^2 \pi^2} \tag{14}$$

APPLICATION

To determine the influence of barrier island width on migration, barrier island evolution was simulated with a storm surge and wave climate randomly generated about a mean value that ranged from 0.5 to 2 m relative to Mean Sea Level (MSL) (Figure 3). Dune elevations for the barrier islands were independently varied from 0.75 to 2 m MSL, with and without consolidation of the underlying substrate. All simulations ran for 100 years, and results from the MCO model are shown in Figures 4 through 8.

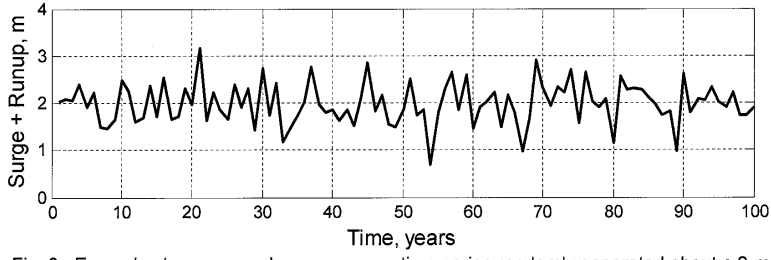

Fig. 3. Example storm surge plus wave runup time series randomly generated about a 2-m MSL mean

For each simulation, the minimum width at which migration does not change has been noted as the critical width. Results from these simulations can be summarized as:

(1) The magnitude of critical width increases for decreasing dune height. This finding implies that there is a critical cross-section required for minimum migration.

(2) The critical width increases with magnitude of storm surge plus wave runup.

(3) Figures 4 through 6 (storm surge plus wave runup from 0.5 to 1.5 m) show that barrier islands with greater consolidation of the substrate (dashed lines) result in greater migration distances and larger values of critical width as compared to barrier islands with lower consolidation substrates (solid lines). This is logical, because islands with greater consolidation reduce elevation as compared to lower consolidation substrates, and thus migrate more rapidly. However, Figures 7 and 8 (storm surge plus wave runup from 2 to

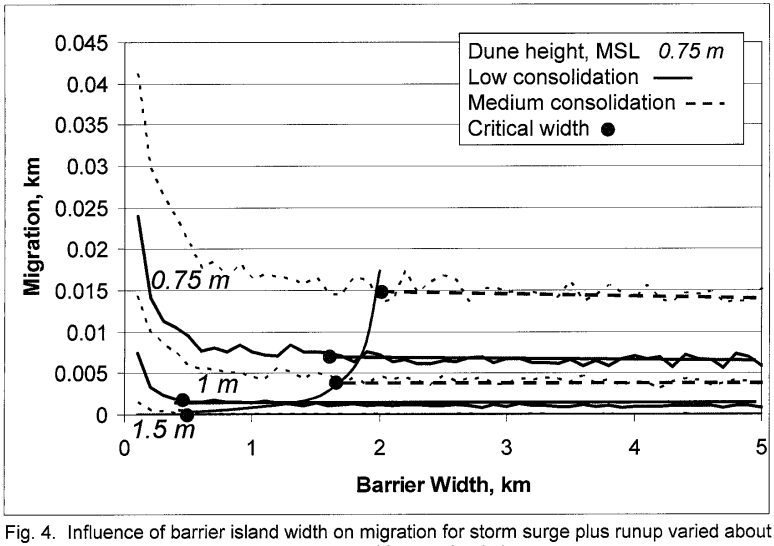

Fig. 4. Influence of barrier island width on migration for storm surge plus runup varied about 0.5-m mean, 100-year simulation

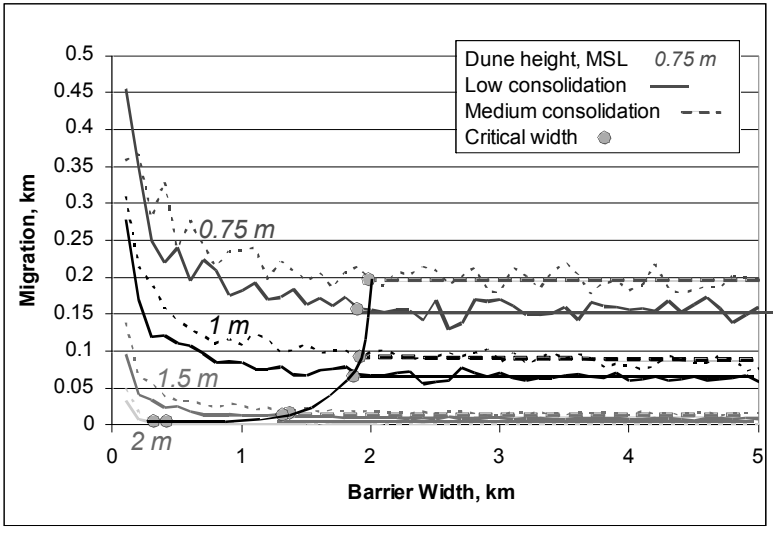

Fig. 5. Influence of barrier island width on migration for storm surge plus runup varied about 1-m mean, 100-year simulation

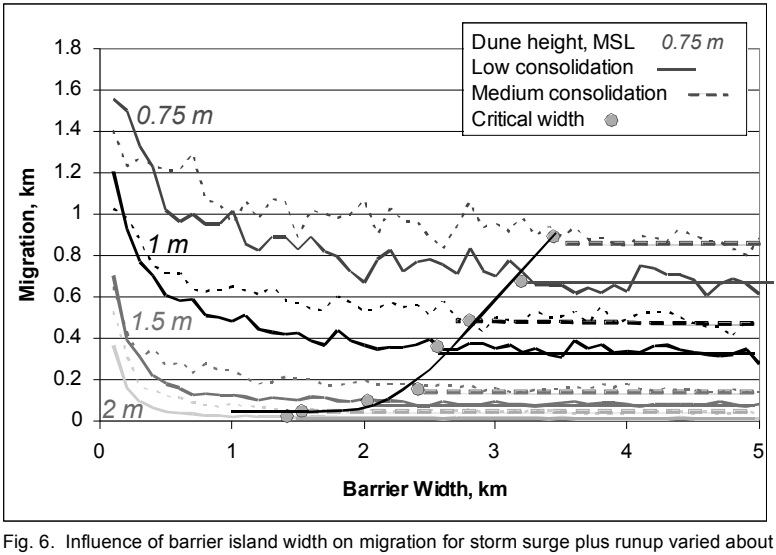

Fig. 6. Influence of barrier island width on migration for storm surge plus runup varied about 1.5-m mean, 100-year simulation

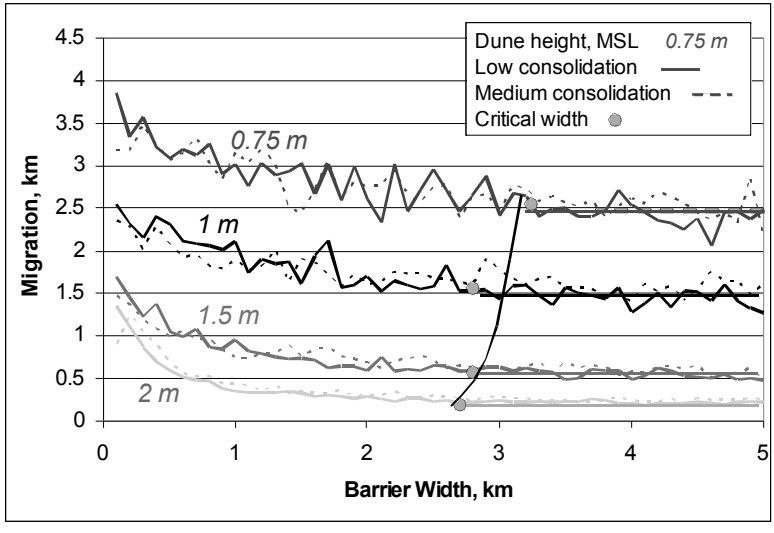

Fig. 7. Influence of barrier island width on migration for storm surge plus runup varied about 2-m mean, 100-year simulation

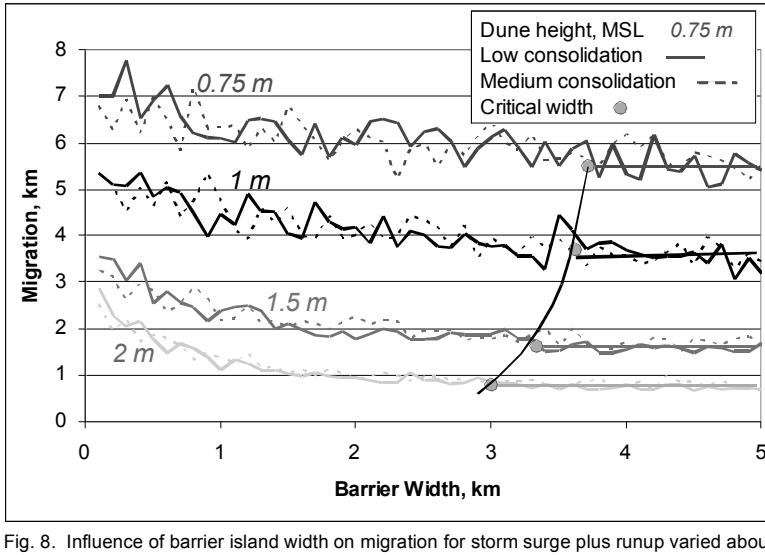

Fig. 8. Influence of barrier island width on migration for storm surge plus runup varied about 2.5-m mean, 100-year simulation

2.5 m) show that both types of substrates have similar migration and critical width values. The explanation for this result is that the barrier loading does not overlay the substrate for sufficient time for consolidation to be significant.

For each simulation with small consolidation, values of critical width and initial dune elevation were correlated with the storm surge plus wave runup. Figure 9 shows that the critical cross-sectional area, A_*, is slightly better correlated (R^2=0.72) to the storm surge plus runup, S, as compared to the critical width, W_* (R^2=0.64). These results indicate that, for barrier islands with small rates of consolidation of the underlying substrate, the critical cross-sectional area and width to reduce migration of the barrier island are 1,420 and 880 times the long-term (100-year) average surge plus wave runup, respectively.

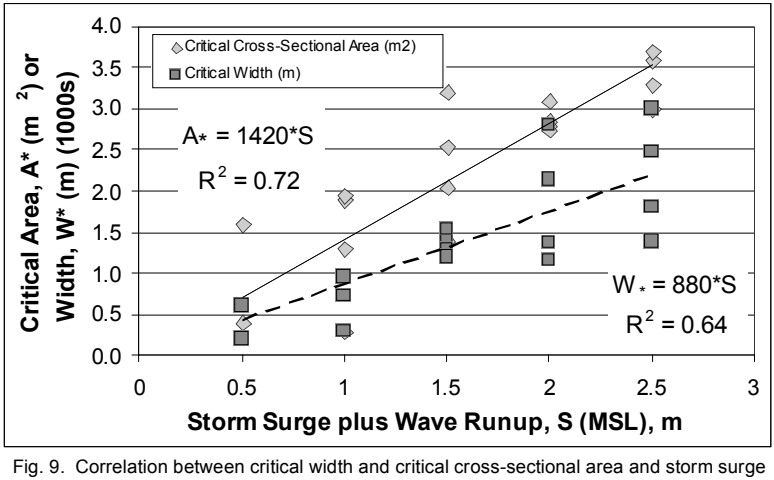

Fig. 9. Correlation between critical width and critical cross-sectional area and storm surge plus wave runup, low consolidation

SUMMARY AND CONCLUDING DISCUSSION

Critical width is the smallest cross-shore dimension that minimizes net loss of sediment from a barrier island and thus reduces migration of the island over periods of decades to centuries. The concept of critical width is important for large-scale barrier island restoration, in which islands are reconstructed to optimum height, width, and length for providing protection for estuaries, bays, marshes and mainland beaches. In this study, a recently Migration, Consolidation, and Overwash (MCO) model was applied to evaluate the dependence of barrier island width on migration rates and longevity of the island. Storm surge and wave forcing were randomly generated about mean values ranging from 0.5 to 2.5 m MSL, and barrier widths ranged from 100 m to 5 km and dune heights from 0.5 to 2 m. Low and medium values of consolidation were applied. Each MCO run simulated 100 years of hydrodynamic forcing and barrier island response.

Results indicated that there is a minimum width, the critical width, at which barrier island migration reaches a relatively constant value, regardless of increasing initial width. However, the barrier island critical cross-sectional area is better correlated to average long-term storm surge plus wave runup as compared to critical width. Preliminary recommendations from this study suggest that the critical cross-sectional area (with initial dune height and width, in square meters) to minimize long-term migration of a barrier island is 1,420 times the average surge plus wave runup (m), relative to a common datum. A slightly weaker correlation was obtained for the critical width, which is recommended as 880 times the average surge plus wave runup (m).

The above findings are based on hypothetical simulations for wave transformation over and sediment transport of non-cohesive sediment. For coastal settings such as in Louisiana, numerical predictions have been shown to overestimate measurements of wave energy during storms as waves are transformed over muddy seabeds (e.g., Sheremet and Stone 2003). Thus, actual storm waves for sandy barrier islands in a muddy environment may be less than predicted here, and this preliminary guidance may be slightly conservative. Also, barrier islands in Louisiana consist both of sand and a partially consolidated core of clay and silt sediments (Stone et al. 1995), which will respond differently to storms than these hypothetical simulations. During erosional wav and water level conditions, the sand surface sand may be eroded from these islands, leaving partially consolidated core clay and silt sediments that are more readily eroded during typical wave and water-level conditions as compared to non-cohesive sediment. Future research will compare these preliminary recommendations to field estimates of critical width.

ACKNOWLEDGEMENTS

This research was partially supported by the System-Wide Water Resources Program at the Engineer Research and Development Center's Coastal and Hydraulics Laboratory, U.S. Army Corps of Engineers. Permission was granted by the Chief, U.S. Army Corps of Engineers to publish this information. We thank Drs. R.G. Dean, N.C. Kraus, and H.H. Roberts for integral contributions to this research. We also thank Dr. Kraus for excellent review of the paper.

REFERENCES

Dean, R.G. (2002). "*Beach Nourishment Theory and Practice*," Advanced Series on Ocean Engineering – Vol. 18, World Scientific Press, River Edge, NJ.

Donnelly, C., Ranasinghe, R., and Larson, M. (2006). "Numerical modeling of beach profile change caused by overwash," *Proceeding, Coastal Dynamics 05*, CD-ROM.

Eitner, V. (1996). "Geomorphological response of the East Frisian barrier islands to sea-level rise: an investigation of past and future evolution," *Geomorphology* 15, 57-65.

Hughes, S.A. (2004). "Estimation of wave run-up on smooth, impermeable slopes using the wave momentum flux parameter," *Coastal Engineering* 51, 1085-1104.

Jiménez, J. A., and Sánchez-Arcilla, A. (2004). "A long-term (decadal scale) evolution model for microtidal barrier systems," *Coastal Engineering* 51, 749-764.

Kriebel, D.L., and Dean, R.G. (1993). "Convolution method for time-dependent beach-profile response," *Journal of Waterway, Port, Coastal and Ocean Engineering* 119(2), 204-227.

Kuecher, G.J. (1994). "Geologic framework and consolidation settlement potential of the Lafourche Delta, topstratum valley fill sequence; implications for wetland loss in Terrebonne and Lafourche parishes, Louisiana," Dissertation submitted to Louisiana State University and Agricultural and Mechanical College, Baton Rouge, LA.

Larson, M., Wise, R.A., and Kraus, N.C. (2004). "Coastal Overwash, Part 2: Upgrade to SBEACH," ERDC/RSM-TN-15, U..S. Army Engineer Research and Development Center, Vicksburg, MS, 43 p.

Leatherman, S. P. (1976). "Barrier island migration: an assessment of the overwash process," Geological Society of America Abstracts with Programs 8, p. 215.

Leatherman, S. P. (1979)."Migration of Assateague Island, Maryland, by inlet and overwash processes," *Geology*, 7, 104-107.

Leatherman, S.P. (1980). "*Overwash Processes*," Benchmark Papers in Geology Vol. 58, Hutchinson Ross Publishing Company, Stroudsburg, PA, 376 p.

Rosati, J.D., Stone, G.W., Dean, R.G., and Kraus, N.C. (2006). "Restoration of barrier islands overlying poorly-consolidated sediments, south-central Louisiana," Gulf Coast Association of Geological Societies Transactions, v. 56, 727-740.

Rosati, J.D., Dean, R.G., Kraus, N.C., and Stone, G.W. (2007). "Morphologic evolution of subsiding barrier island systems," *Proceedings 30th International Coastal Engineering Conference*, World Scientific Press, in press.

Sheremet, A., and Stone, G.W. (2003). "Wave dissipation due to heterogeneous sediments on the inner Louisiana shelf," *Proceedings Coastal Sediments '03*, CD-ROM Published by East Meets West Productions, Corpus Christi, TX, 120-121 (www.wavcis.lsu.edu).

Stone, G.W., Xu, J.P., Zhang, X. (1995). "Estimation of the wave field during Hurricane Andrew and morphological change along the Louisiana coast." *Journal of Coastal Research* 21, 234-253. (Special Issue).

Stone, G. W., Liu, B., Pepper, D. A., and Wang, P. (2004). "The importance of extratropical and tropical cyclones on the short-term evolution of barrier islands along the northern Gulf of Mexico, USA," *Marine Geology*, 210, 63-78.

Stone, G.W., and Morgan, J.P. (1993). "Implications for a constant rate of relative sea-level rise during the last millennium along the northern Gulf of Mexico: Santa Rosa Island, Florida," *Shore & Beach* 61(4), 24-27.

Terzaghi, K. (1943). "*Theoretical Soil Mechanics*," John Wiley and Sons, NY, 510 p.

BARRIER ISLAND VULNERABILITY TO BREACHING: A CASE STUDY ON DAUPHIN ISLAND, ALABAMA

Mark Hansen[1] and Asbury H. Sallenger[2]

1. U.S. Geological Survey, Florida Integrated Science Center, Coastal and Watershed Studies, 600 4th Street South, St. Petersburg, FL 33701-4846, USA. mhansen@usgs.gov
2. U.S. Geological Survey, Florida Integrated Science Center, Coastal and Watershed Studies, 600 4th Street South, St. Petersburg, FL 33701-4846, USA. asallenger@usgs.gov

Abstract: Breaching of barrier islands can adversely impact society by severing infrastructure, destroying private properties, and altering water quality in back bays and estuaries. This study provides a scheme that assesses the relative vulnerability of a barrier island to breach during storms. Dauphin Island, Alabama was selected for this study because it has a well documented history of island breaches and extensive geological and geomorphic data. To assess the vulnerability of the island, we defined several variables contributing to the risk of breaching: island geology, breaching history, and island topography and geomorphology. These variables were combined to form a breaching index (BI) value for cross island computational bins, each bin every 50 m in the alongshore direction. Results suggest the eastern section of Dauphin Island has the lowest risk of breaching with the remaining portion of the island having a moderate to high risk of breaching. Two reaches in the western section of the island were found to be particularly vulnerable due primarily to their minimal cross-sectional dimensions.

INTRODUCTION

The recent trend of numerous major hurricanes has significantly increased awareness of coastal impacts in terms of geomorphic changes and the vulnerability of society to storms. Even with improved data sets, such as lidar, and better numerical models, the magnitude and geographic extent of significant impacts and the prediction of vulnerability is still difficult. Island breaching is one impact that forces coastal changes on a local scale but also can affect a large portion of society by cutting off vital transportation routes for evacuation, rescue, and post-storm recovery. Costs to

repair a breach are significant. In addition to societal impacts, coastal breaching can adversely impact the environment by degradation of estuarine water quality and loss of sensitive habitats, exposure of bay waters to increased waves and currents, and accelerated destabilization of jetties (Kraus and Wamsley, 2003).

Barrier island breaches created during hurricanes form a conduit that allows water to flow between ocean and bay/lagoon water bodies at all stages of the tide. They typically occur in narrow areas of barrier islands or barrier spits. During storms in the Atlantic Ocean and Gulf of Mexico, seaward side breaching typically occurs because of a gradient in water level across the island caused by wave setup and storm surge. Bay side breaching is initiated by long periods of higher than normal water levels in the bay relative to the ocean. Inundation allows seepage into porous island sediments creating a liquefied condition (Kraus and Wamsley, 2003). Once the breach occurs, large volumes of sediment can be quickly transported as the sediments are already in a liquefied state. The underlying geological framework, geomorphology, and topography influence the location and evolution of coastal breaches. This study analyzes these basic parameters in order to create an index that ranks all stretches of a barrier island for their relative potential to breach. Island breaching history, if know, can also be used to indicate weaknesses in the island's internal and external structure, and indirectly measure critical physical processes that cannot be currently assessed or are otherwise unknown. The intent is not to predict exact breaching locations, but to provide guidance on barrier island vulnerability and to assist numerical modeling studies focus their domain boundaries.

Dauphin Island, Alabama (Fig. 1) was chosen for this study as it has a history of island breaching, a well documented geological framework, and high resolution topographic lidar surveys that cover the entire island. We anticipate applying techniques and results developed for Dauphin Island to the remaining Gulf of Mexico and Atlantic barrier islands as part of the U.S. Geological Survey's Hurricane and Extreme Storm Impact Studies. Our preliminary efforts and results are summarized below.

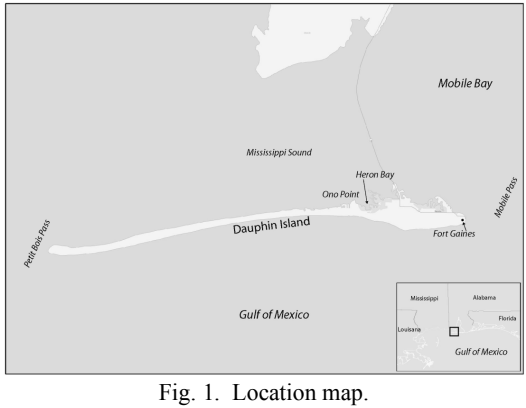

Fig. 1. Location map.

RISK VARIABLES
Geology

Dauphin Island is bounded by Mobile Pass to the east and Petit Bois Pass to the west, and protects Mississippi Sound and the Alabama mainland from direct wave attack. The eastern 5.5 km of the present island is composed of a Pleistocene (10,000 to 2 million years bf) core (Fig. 2) that was once a coastal ridge on the mainland (Otvos, 2005). As sea level rose, the former mainland was flooded leaving the peaks of the ridges emergent. Holocene (modern) sediments moving westward across the Mobile Bay ebb-tidal delta were deposited on the topographic highs forming beaches and dune fields. Juxtaposed on the Pleistocene core, the eastern end of Dauphin Island has active dune fields and is heavily forested with oaks and pines. Active sand dunes rise 14 m above sea level near Fort Gaines (Canis, et al., 1985). Sediments transported further westward formed a low lying (near sea-level) sand spit that now extends 22 km from Dauphin Island's eastern tip. The sand spit is typical of an active barrier island in that it lacks well developed continuous dunes, vegetation cover, and is backed by a marsh on the bay side. Since 1882, the length of Dauphin Island has varied from 16 to 25 km (Otvos, 1997). Petit Bois Island was once part of western Dauphin Island spit until a hurricane 150 ybp cleaved it and formed Petit Bois Pass.

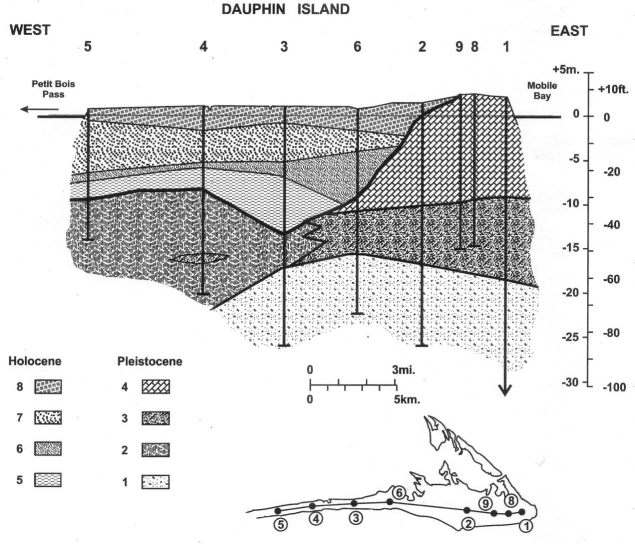

Fig. 2. W-E geologic cross-section across eastern Dauphin Island (Otvos, 2004).

Island Breaching History

The impacts of hurricanes have been documented on Dauphin Island for the past 150 years. An 1863 Civil War map of Alabama (Fig. 3) identifies an extensive breach in the central section of Dauphin Island. This breach had filled as revealed by the 1892 U.S. Coast and Geodetic Survey Chart #188. Chart #188 indicates Dauphin Island was a contiguous island, narrow through the center section, widening to the west, with a bulbous end on the western end. In 1916, a hurricane breached the island immediately west of the Pleistocene core near Oro Point creating an 8 km-wide shallow inlet (Canis, et al., 1985). The 1933 U.S. Coast and Geodetic Survey chart #1267 documents the breach, comparable in size to the one shown on the 1863 map. In 1947, another hurricane breached the island in the same central location. Hurricane Frederic impacted the island in 1979, creating multiple breaches west of Oro Point and formed continuous overwash deposits along the entire sand spit portion of the island. The 1981 National Oceanographic and Atmospheric Administration (NOAA) chart #11376 reveals the breach from Hurricane Frederic had filled in, leaving a thin band of sand backed by marsh. Prior to Hurricane Ivan in 2004, numerous roads and residential homes had been constructed along most of Dauphin Island. Hurricanes Ivan in 2004 (Fig. 4) and Katrina in 2005 created significant breaches and overwash deposits from Heron Bayou to the western end of the island.

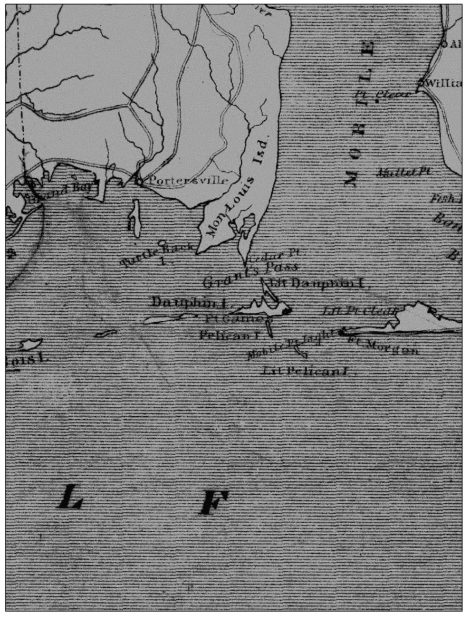

Fig. 3. Civil War era (1864) map indicating an island breach on Dauphin Island (NOAA archives).

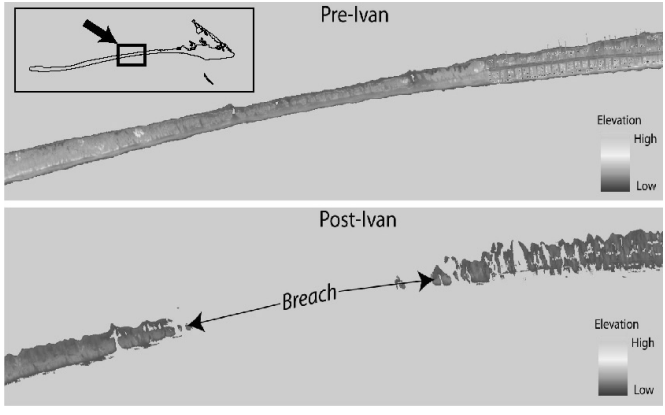

Fig 4. Dauphin Island, Alabama topography before and after Hurricane Ivan indicating multiple island breaches. Darker colors represent lower elevations and lighter colors represent higher elevations (USGS, 2007).

Topography

The topography of a barrier island greatly influences the response of an island to storms. We know that island width and height control the hydrodynamics of water flow across an island, e.g. areas with low elevation and narrow island width are more susceptible to overwash and breaching. Topographic information for Dauphin Island was derived from post Hurricane Katrina data acquired with the National Atmospheric and Space Administration (NASA) Experimental Advanced Airborne Research Lidar (EAARL) aircraft lidar system. Lidar data was processed to XYZ coordinates, and a surface grid was produced using an inverse distance weighting technique. To best model the true land surface, a structure and vegetation removal technique was applied to the surface grid. Grid values within the footprint of structures and vegetation were set to null or NaN.

Computational bins, 50 m in width, were generated normal to a shoreline parallel baseline along the entire length of the island, for a total of 510 bins for the entire island. Two measurements were computed for each bin, island width and a height.

Measuring island width is straightforward; however, assessing island height is complex due to beach, dune, and inland topographic features with an unlimited number of combinations. Island width was computed for each bin along a transect that bisected each bin. Width was computed as the distance from the shoreline (0 m NAVD88) on the ocean side to the shoreline on the bay side. When marsh islands or low-lying sand flats were present on the bay side, their bay fronting shorelines were considered the bay shoreline. Island height was derived in the following manner. Transects were generated normal to the shoreline parallel baseline at 2 m spacing, thus 25 transects were created for each computational bin. The maximum elevation along each transect was then identified. Island height for each bin was defined by the

minimum value of the maximum elevations. We believe this measurement of height best represents the inundation potential within each bin.

BREACHING INDEX

A breaching index (BI) was calculated for each bin. The breaching index used in this study was based upon the following categories: geology, island width, and island height. These categories were selected because of prior knowledge that each greatly influences island breaching (Kraus, 2003). The last category, breaching history, is included as an indicator of unknown structural weaknesses and physical processes. We believe there are numerous other categories that contribute to breaching, and our plan is to investigate these in future studies. For each category, a scaling value from 1 to 3 was assigned to each bin with 1 defined as the least risk and 3 the greatest risk.

For the geology category, bins where manmade structures (seawalls, revetments) are located contribute the lowest risk and were assigned a value of 1. Those located where resistive sediments (Pleistocene core) outcrop at the surface where given a value of 2. Bins in which Holocene sands are located contribute the greatest risk, thus were assigned a value of 3.

Island width was subdivided based upon standard deviations from the mean value. A scaling value of 1 represents values that are between the mean plus one standard deviation to the max, a scaling value of 2 represents values between plus and minus one standard deviation from the mean, and a scaling factor of 3 represents values that are between zero to the mean minus one standard deviation.

Island height was subdivided based upon the computed height relative to the maximum of the maximum (MOM) hurricane surge levels for Dauphin Island, derived from NOAA's SLOSH (Sea, Lake and Overland Surges from Hurricanes) numerical model. The SLOSH model estimates storm surge heights at specific locales based upon hurricane pressure, size, forward speed, track and winds. MOM estimates were calculated at the center of Dauphin Island for Category 1, 3, and 5 (Saffir-Simpson Scale) hurricanes. Estimated surges levels for the three hurricane categories was 1.55 m, 3.47 m, and 5.12 m NAVD88, respectively. Computational bins that had island heights between 0 and 3.47 m (Category 3) were assigned a scaling value of 3, those between 3.47 m and 5.12 m (Category 5) assigned a value of 2, and bin heights greater than 5.12 m given a scaling value of 1.

Zones that have not experienced breaching in the documented past have a value of 1, a single breach event is assigned a value of 2, and multiple breach events are assigned a scaling value of 3.

The breaching index calculation developed for this study is similar to that of Thieler and Hammar-Klose (2000) and Gornitz, et al. (1994). The contribution of each of the four categories to island breaching is unknown, thus each category has equal weighting when calculating the breaching index for each bin. This method clearly identifies those bins where all categories have either a minimum or maximum value;

however, it can artificially group bins having a mixed range of values. The index does not correlate directly with physical processes; however, each category is a result of geologic and coastal processes acting on the barrier island. Thus, the index implies the relative likelihood of where a breach may occur on the barrier island.

For each bin, a breaching index (see Eq. 1) is computed based upon assigned values from each category (Table 1). BI values have a potential range of 0.5 to 4.5. The breaching index is calculated as

$$BI = \sqrt{((a*b*c*d)/4)} \quad (1)$$

where: a = geology ; b = island width; c = island height; and d = breaching history.

Quartile BI divisions were created within this range: 0.5 to 1.5, low; 1.5 to 2.5, medium; 2.5 to 3.5, high; and 3.5 to 4.5, very high. Low values are considered to have a minimal risk of island breaching with high values a relatively greater risk of breaching. The calculated BI values for Dauphin Island (Fig. 6) range from 0.7 to 4.5.

Table 1. Ranking for each Breach Index (BI) category.

Ranking of Breaching Index Categories			
	Low	**Medium**	**High**
Variable	1	2	3
Geology/ Geomorphology	Hardened shore	Resistive core	Holocene sands
Island Width	(μ + δ) to max	(μ - δ) to (μ + δ)	0 to (μ - δ)
Island Height	< 3.47 m	> 3.47 m to < 5.12 m	> 5.12 m
Breaching History/Events	0	1	>1

DISCUSSION

The eastern section of the island from Mobile Pass to Heron Bay, is located on top of a Pleistocene core, has high relief and is significantly wider than other sections of the island. Here, the geological framework of Dauphin Island is expressed in the present day geomorphology and topography. As a result, the BI for this section is relatively low with values in the 0.7 to 1.5 range (Fig. 6). Since the 1850's, there have been no documented breaches from Heron Bay east to Mobile Bay. Results here suggest this section has a low risk of breaching.

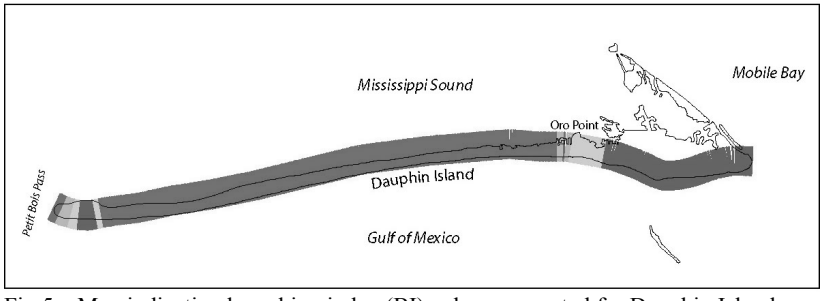

Fig 5. Map indicating breaching index (BI) values computed for Dauphin Island, Alabama. Color explanation: dark blue indicates low risk, light blue moderate risk, orange high risk, and red very high risk. (USGS, 2007)

A transition section in the region of Oro Point has moderate BI values in the range from 1.5 to 2.5. The section is characterized on the gulf side by absent or low lying dunes backed by a rather extensive marsh system on the bay. Extensive overwash deposits have been created in this region as a result of repeated hurricanes, most recently hurricanes Ivan and Katrina. These deposits in addition to marshes and islands near the bay shoreline widen the island relative to western sections, thus the width category strongly influences the BI values computed here.

Unlike the eastern section, the section of Dauphin Island from Oro Point to the western end is a sandy spit composed of coastal sands. Over the past 150 years, island breaches have been document numerous times in this section. It has no antecedent core and being relative young in age, has a relief of 0.5 to 2.0 m above MSL and is relatively narrow. Non-contiguous, low relief dunes are the only coastal protection. Significant overwash deposits are located here indicating total inundation of the island during recent storms. The bay side of this section is composed of coastal marshes and overwash fans. Low elevation and narrow width contribute significantly to the high BI values in this section. The BI values range from 3.5 to 4.5 suggesting this section has a high risk of breaching.

The bulbous, western end of Dauphin Island is composed of substantial dunes with a maximum relief of 3.5 m and is relatively wide. These factors contribute to low BI values ranging from 0.7 to 2.5. From this stretch to the western tip of the island, the BI values are high (2.5 to 4.5) due to low topography and narrow island width.

CONCLUSIONS

The breach index (BI) developed for Dauphin Island is a methodology for assessing the relative risk of island breaching during storms. It is based upon a limited number of known variables that control coastal processes or indicate physical weaknesses. For this study, each variable is assigned an equal weight or influence. An improvement would be a proportional weighting scheme with additional variables considered, such as bay volume and tidal prism.

We have documented the geological framework and geomorphologic anomalies of Dauphin Island, AL and found a correlation to documented breach locations. Hurricane induced inland breaches have occurred in the same general zones many times in the past 100 years. These breach zones are composed of island spit sediments, and are topographically low and narrow compared to other stretches. The BI values computed for these zones suggest they are at higher risk for future island breaching. Conversely, zones that are structurally more resistant to erosion and are relatively dimensionally larger have no documented island breaches. The BI values for these reaches are relatively low, suggesting a low risk for island breaching.

This study on Dauphin Island suggests potential hurricane induced coastal breach locations can be identified by applying existing knowledge of barrier island framework combined with detailed topographic and geomorphic information. Numerical modeling studies on island breaching could use these results to help focus domain boundaries. This information would be beneficial to coastal planners and emergency management teams for preparing evacuation routes and planning post-storm infrastructure recovery and repair. Coastal engineers may also benefit from such studies by redirecting dredge disposal locations to minimize the coastal breach potential, and thus reduce construction cost of post-event breach mitigation.

ACKNOWLEDGEMENTS

The lidar data used for this study was acquired through a joint agreement between the USGS, NASA, and the US Army Corps of Engineers. We would like to thank H. Stockton, P. Howd, L. Fauver, D. Thompson, E. Otvos, and R. Morton for their technical assistance and advice. This work was funded by the USGS Coastal and Marine Program's *Hurricane and Extreme Storm Impact Studies* Project.

REFERENCES

Canis, W. F, Neal, W. J., Pilkey, Jr., O. H., Pilkey, Sr., O. H. (1985). Living with the Alabama-Mississippi shore, Duke University Press, Durham, NC, 215 p.

Gornitz, V. M., Daniels, R. C., White, T. W., and Birdwell, K. R. (1994). The development of a coastal risk assessment database: Vulnerability to sea-level rise in the U.S. southeast, *J. Coastal Research*, Special Issue No. 12, 327-338.

Kraus, N.C. (2003). Analytical model of incipient breaching of coastal barriers, *Coastal Engineering Journal*, Vol. 45, No. 4, 511-531.

Kraus, N.C. and Wamsley, T.V. (2003). Coastal Barrier Breaching, Part 1: Overview of Breaching Processes, U.S Army Corps of Engineers, ERDC/CHL CHETN-IV-56, 14 p.

Otvos, E. G. (1997). Northeastern Gulf Coastal Plain Revisited Neogene and Quaternary Units and Events – Old and New, *Guidebook, Louisiana to Northwest Florida Field Trip*, Pub. New Orleans Geological Society, 73-121.

Otvos, E. G. (2005). Gulf Coast Geology, Field Trip 4, Geological Society of America, 54th Annual Meeting of the Southeastern Section, 64-88.

Thieler, E.R., Hammar-Klose, E.S. (2000). National assessment of coastal vulnerability to sea-level rise, Preliminary results for the U.S. Gulf of Mexico Coast: U.S. Geological Survey Open-File Report 00-179.

MORPHOLOGIC MODELING OF MULTIPLE BARRIER ISLAND BREACHES FOR REGIONAL APPLICATION

Kenneth J. Connell[1], Magnus Larson[2], Nicholas C. Kraus [1]

1. U.S. Army Engineer Research and Development Center, Coastal and Hydraulics Laboratory, 3909 Halls Ferry Road, Vicksburg, MS 39180-6199, USA. Kenneth.J.Connell@erdc.usace.army.mil; Nicholas.C.Kraus@erdc.usace.army.mil.
2. Department of Water Resources Engineering, Lund University, Box 118, S-221 00 Lund, Sweden. Magnus.Larson@tvrl.lth.se.

Abstract: This paper introduces a time-dependent model of regional barrier island breaching for multiple openings, whether as permanent inlets or as new breaches to the same bay. The model allows an arbitrary number of breaches and is forced by tide, storm surge, and wave set up. Limitations on the hydrodynamics, hence calculated breach evolution, are those associated with the Keulegan inlet model. The model includes possible closure or limited breaching by shoaling of the breach channel by longshore transport. Capabilities of the multiple breaching model are examined through eight sensitivity tests.

INTRODUCTION

A breach in a barrier island occurs if inundation with strong flow develops a channel through the barrier. The inundation may be forced from the ocean side or the bay side. During a breach, the initial channel typically expands vertically and horizontally in exponential manner (Kraus 2003) to dynamic equilibrium dimensions. Forcing of the water flow in the breach is caused by a difference between bay and ocean water levels, influenced by wave runup and overwash.

High ocean water surface elevations and large waves associated with severe storms can produce multiple breaches along a coastal barrier island complex at regional spatial scales. Occurrences of multiple breach channels cut by storms has been reported (e.g., Price 1947; Terchunian and Merkert 1995; Wamsley and Hathaway 2004; Wutkowski 2004; Freeman et al. 2004), but there remains a paucity of quantitative barrier island

breach field data. Reviews of coastal barrier island breaching causes, processes, and remediation are given by Kraus and Wamsley (2003) and Wamsley and Kraus (2005).

Kraus and Hayashi (2005) developed a process-based numerical model to simulate morphologic evolution of coastal barrier island breaching for engineering use. The objective of the present study is to extend the capabilities of the Kraus and Hayashi model to include development and evolution of multiple breaches in areas along a barrier island, which may include presence of permanent inlets. This multiple-breach morphological model is applied on regional spatial scales by integration with the Cascade model of regional sediment transport and shoreline change (Larson et al. 2002; Larson and Kraus 2003; Larson et al. 2006; Connell and Kraus 2006; Larson et al. 2007).

COASTAL BREACH MODEL

The morphologic breaching model is based on analytical models for inlet stability and inlet channel cross-sectional area (Kraus 1998, 2003), and it has been extended to include morphologic evolution of a rectangular barrier island (Kraus 2003) and a stacked rectangle pyramidal barrier island (Kraus and Hayashi 2005). Studies have examined predictions of the coastal breach morphology model by comparison to field and laboratory breaches (Kraus and Hayashi 2005; Wamsley et al. 2006; Wamsley et al. 2007). The coastal breaching model simulates breaching by iteratively solving the 1-D Keulegan (1967) equations for inlet hydrodynamics to determine breach current velocity and bay elevation through time based on breach channel cross-sectional area and area of the bay. The coastal breaching model calculates under the assumptions that the bay must accommodate uniform water surface deviation, the bay is composed of vertical walls so that volume and surface area are directly correlated, and the breaches do not overlap.

If multiple breach channels are calculated to occur in the simulation, the Keulegan equations become:

$$\frac{\partial U_i}{\partial t} + \frac{g}{L_i}\left(\eta_B - \eta_O\right) + \left(K_{en,i} + K_{ex,i} + \frac{2c_{f,i}L_i}{R_{h,i}} \right) \frac{|U_i| U_i}{2L_i} = 0 \tag{1}$$

for momentum, and:

$$\sum_{i=1}^{N} (A_c)_i U_i = A_{Bay} \frac{d\eta_B}{dt} \tag{2}$$

for conservation of water volume, where U_i = depth-averaged and inlet-length integrated current velocity at breach or inlet i of N openings; t = time; g = gravitational acceleration; L = width of breach through the barrier island; η_O = water surface deviations from Mean Sea Level (MSL) in the ocean; K_{en} and K_{ex} = entrance and exit losses, respectively (non-dimensional); R_H = hydraulic radius of the breach or inlet (m); A_C = breach or inlet channel cross-sectional area below MSL (m^2); A_{Bay} = surface area of the bay (m^2). The bottom friction coefficient c_f is represented by Mannings formula,

$$c_f = g n^2 / h^{1/3} \tag{3}$$

in which n = Mannings coefficient typically set as 0.025 s/m$^{1/3}$; and h = water depth.

Sediment transport through the breach is calculated employing the Watanabe et al. (1991) total load formula:

$$q_B = \alpha \frac{(\tau_m - \tau_c)}{\rho g} U \tag{4}$$

in which α = empirical coefficient typically of order 0.1 to 10 (non-dimensional); $\tau_m = c_f \rho \langle |U| U \rangle$, the time-averaged bottom shear stress for waves and current; $\tau_c = (\rho_s - \rho) g d_{50} \Psi_c$, the critical shear for sediment motion, where ρ_s is the density of sand (kg/m^3), ρ is the density of water (kg/m^3), d_{50} = median grain size diameter (m); and Ψ_c = critical Shields parameter, set to 0.05 for fine to medium sand.

If waves are not included in the breaching simulation, Eq. 4 becomes:

$$q_B = \alpha \left[\frac{n^2}{h^{1/3}} U^3 - \left(\frac{\rho_S}{\rho} - 1 \right) d_{50} \Psi_c U \right] \tag{5}$$

Sediment transport along the walls of the channel is calculated as a fraction of the transport along the breach floor. A typical value for side transport is approximately 70% of the transport along the channel.

$$q_S = \beta q_B \tag{6}$$

where β is the calibration factor for the channel wall fraction (e.g., 0.7).

The wave setup contribution to mean water level at the shoreline is calculated following Stockdon et al. (2006):

$$\eta_{setup} = 0.35 \beta_f \sqrt{H_0 L_0} \tag{7}$$

where β_f = beach foreshore slope; H_0 = deep-water wave height (m); L_0 = deep-water wavelength (m). Kraus and Hayashi 2005; Wamsley et al. (2006) discuss calculation of channel infilling and shoaling due to longshore transport estimates calculated from wave input data. Longshore transport is implemented in the coastal breaching model with the CERC formula in the *Coastal Engineering Manual* (Headquarters, U.S. Army Corps of Engineers 2002):

$$Q_l = K\left(\frac{\rho\sqrt{g}}{16\kappa^{\frac{1}{2}}(\rho_s-\rho)(1-n)}\right)H_{b\,rms}^{\frac{5}{2}}\sin(2\alpha_b) \quad (8)$$

where K = dimensionless sediment transport coefficient based on wave energy, κ =breaker index (non-dimensional ~ 0.8), n = sediment porosity, $H_{b\,\mathrm{rms}}$ = root-mean-square wave height at breaking point (m), and α_b = wave breaking angle.

The present study extends the capabilities of the morphologic breaching model by implementing multiple breaches with variable (in time and space) breach forcing. Furthermore, breaching model connectivity with the Cascade model is now possible by employing a subset of the wave and water surface elevation data used as inputs to Cascade, and spatially and temporally variable longshore sediment transport. Cascade output can control breach infilling and shoaling rates by longshore transport in place of Eq. 8 in the breaching model, subject of a planned future paper.

METHOD

An idealized alongshore barrier dune-crest topography (Fig. 1) was developed to simulate breaching at topographic lows in the dunes. This topography can be arbitrary, and the topographic lows function as potential pilot channels for the breaching model. Pilot channels of different elevations may exist, providing selective inundation for different water levels at various times in a storm and thereafter. Morphologic evolution of breach channels occurs only if the pilot channel is inundated. Local forcing, including longshore transport, waves, water level, and shoreline position for the breaches is provided at regional scale by the Cascade model. Sensitivity tests are conducted to isolate some of the complex processes that force change in breach morphology and to evaluate the functionality of the model under hypothetical forcing.

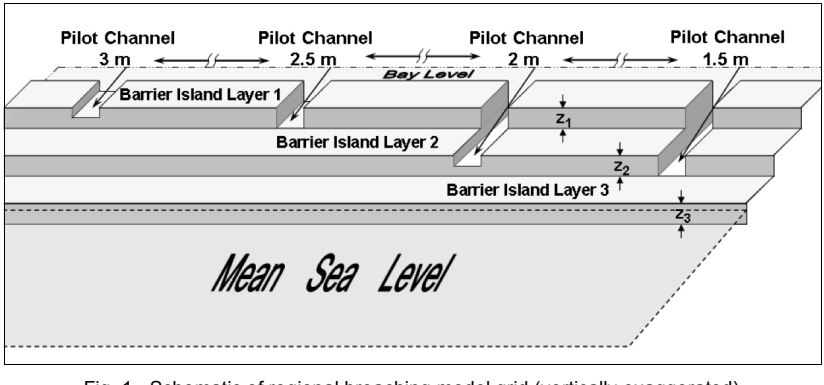

Fig. 1. Schematic of regional breaching model grid (vertically exaggerated)

Eight 14-day simulations of the evolution of multiple breach channels were conducted (Table 1) with the idealized barrier alongshore topography. Dune crest elevation was 3.5 m, and four different pilot channels 10 m wide by 50 m long were cut with elevations of 3, 2.5, 2, and 1.5 m. The location of the pilot channels along the barrier island is arbitrary and influenced only where input forcing is (optionally) extracted from Cascade. It is assumed that the breaches cannot converge, and therefore, pilot channels cannot be located at points along the barrier where the potential exists for two or more breaches to merge into one. Bay surface area was held constant at 5×10^8 m^2. The time-step for the simulations was set at 10 s. Empirical coefficients for sediment transport along the bottom and along the side of the breach were set to 0.5 and 0.7, respectively. Sediment porosity was 0.4, and the *K*-coefficient of the CERC formula was set to 0.39 (based on significant wave height). Finally, water (sediment) density was set to 1,025 kg/m^3 (2,650 kg/m^3).

The first sensitivity test (Case HD) held a constant 0.2-m head difference along the entire length of the barrier generated by a constant ocean water surface elevation at 3-m above MSL and a constant bay water surface elevation at 2.8-m above MSL. Two other cases were conducted employing the same constant head difference water level forcing between ocean and bay, added wave forcing to simulate wave setup forcing and sediment infilling due to longshore transport. Case HD-H1_T8_D0 includes waves with constant $H_0 = 1$ m, $T_0 = 8$ s, and $б_0 = 0$ deg, and Case HD-H1_T8_D30 includes waves with constant $H_0 = 1$ m, $T_0 = 8$ s, and $б_0 = 30$ deg.

Three sensitivity tests were conducted forced with a 1-m amplitude M_2 (12.42-hr period) tidal wave with 90-deg phase lag between the ocean and bay levels, applied along the entire length of the barrier with a vertical datum shift of 2-m above MSL. These cases are listed in Table 1 as Case M2, Case M2-H1_T8_D0, and Case M2-H1_T8_D30. Two cases also included wave forcing to estimate wave setup and sediment infilling due to longshore transport. Case M2-H1_T8_D0 includes waves with constant $H_0 = 1$ m, $T_0 = 8$ s, and $\alpha_0 = 0$ deg, and Case M2-H1_T8_D30 includes waves with constant $H_0 = 1$ m, $T_0 = 8$ s, and $б_0 = 30$ deg.

The two remaining sensitivity tests examined response of the model to a synthetic storm surge. The first of the storm surge simulations (Case Surge in Table 1) was forced with a constant water level 1 m above MSL until day 5, after which a 2 m simulated parabolic storm surge extending over 2 days was added to initiate breach inundation (Fig. 2). This surge was set out of phase for each breach channel so that each breach would be initiated 6 hr after the previous breach. The second surge case (Case Surge+M2 in Table 1) consisted of the same synthetic surge as Case Surge, but the surge arrival was equal for all breaches, and a simple 1-m M_2 tide with 90-deg phase lag between the ocean and bay levels was added to the surge (Fig. 3). This M_2 tide differed from Case M2 in that it did not reach 2 m above MSL to prevent breach inundation prior to the surge arrival.

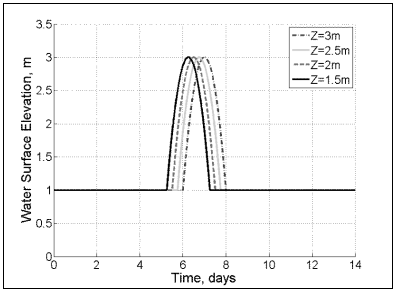

Fig. 2. Ocean and bay water level – Case Surge

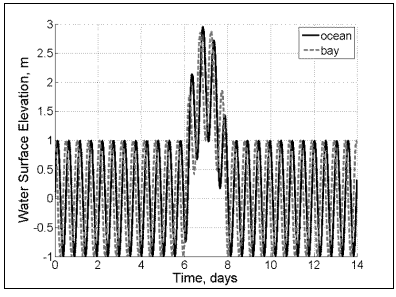

Fig. 3. Ocean and bay water level – Case Surge+M2

Table 1. Regional Breach Model Sensitivity Test Cases

Case Name	Water level forcing	Deep Water Wave Height (H_0), m	Deep Water Wave Period (T_0), s	Deep Water Wave Deg (α_0), deg
HD	Constant ocean = 3 m constant bay = 2.8 m	N/A	N/A	N/A
HD-H1_T8_D0	Constant ocean = 3 m constant bay = 2.8 m	1	8	0
HD-H1_T8_D30	Constant ocean = 3 m constant bay = 2.8 m	1	8	30
M2	M_2-tide amp: 1 m phase: ocean = 0° phase: bay = 90°	N/A	N/A	N/A
M2-H1_T8_D0	M_2-tide amp: 1 m phase: ocean = 0° phase: bay = 90°	1	8	0
M2-H1_T8_D30	M_2-tide amp: 1 m phase: ocean = 0° phase: bay = 90°	1	8	30
Surge	2-m storm surge w/6-min arrival delay for consecutive breach	N/A	N/A	N/A
Surge+M2	2-m storm surge + M_2-tide amp: 1-m phase:ocean = 0° phase: bay = 90°	N/A	N/A	N/A

RESULTS

Calculated evolution of breach channel depth, width, total transport through the four breaches, and cross-sectional area are shown in Figs. 4-7. Breaches that started in pilot channels at lower elevation (e.g., elevation $z = 1.5$ m, $z = 2$ m) were cut deeper (Fig. 4) and at a faster rate than those that developed in pilot channels at higher elevations (e.g., $z = 2.5$ m, $z = 3$ m). Conversely, the lateral growth of higher elevation channels in Fig. 5 is greater than the deeper, low-elevation channels. The greater lateral growth is explained by increased shear stresses by bottom friction in the sediment transport and hydrodynamic models. Breaching is not induced at the pilot channel stating at $z = 3$ m, because this elevation is the same as the ocean water surface elevation. Stair-shaped behavior observed in Fig. 6 is an artifact of the layered pyramidal barrier island, corresponding to the transport rates being reduced as a result of channel cuts into incrementally longer (in cross-shore orientation) barrier island layers. As breach channel depth increases, the transport can increase in magnitude and duration.

Figure 7 shows the breach cross-sectional area over the simulation period for Case HD. Breach channel cross-sectional area is a representation of the channel dimensions and serves as a good indicator of channel stability and channel evolution morphology. A delayed and extended incipient breaching stage occurs in the breach channel initially at $z = 2.5$ m relative to the channels at $z = 2$ and $z = 1.5$ m. This is, again, explained by the increased shear stress associated with shallow water over the channel bottom. A shallower channel is forced to grow laterally if sediment transport rates (Fig. 6) increase due to greater shear stress applied over a larger channel bottom surface area than generated in deeper breach channels.

Figures 8 and 9 compare breach channel cross-sectional area for Cases HD-H1_T8_D0 and HD-H1_T8_D30, respectively. Figure 8 retains many of the same patterns observed in the cross-sectional area plots of Case HD (Fig. 7). However, because of the presence of waves and the associated wave setup, a shorter incipient breaching stage is observed at the breach of $z = 2.5$ m, and the channel cross-sectional area for each breach in Fig. 8 at the end of the simulation is greater than those observed in Fig. 7. Figure 9 shows an entirely different pattern. In fact, due to the large incident wave angle relative to shoreline, significant longshore transport causes most of the channels to shoal. Breach closure does not occur for the breach at $z = 1.5$ m because this breach pilot channel is sufficiently deep to avoid closure during the incipient phase of the breach.

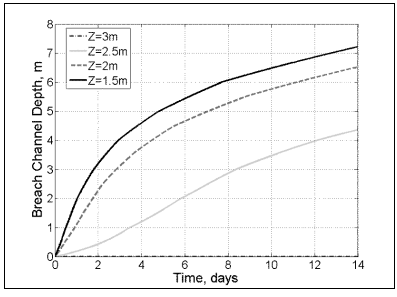

Fig. 4. Calculated breach depth , Case HD

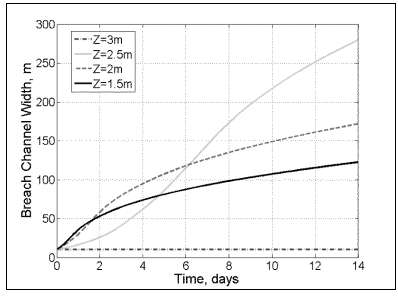

Fig. 5. Calculated breach width, Case HD

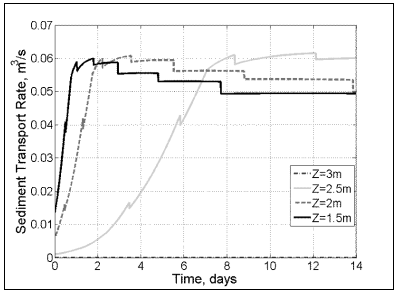

Fig. 6. Calculated sediment transport rate through the four breaches, Case HD

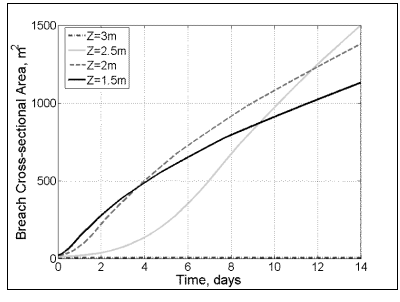

Fig. 7. Calculated Breach channel cross-sectional area evolution, Case HD

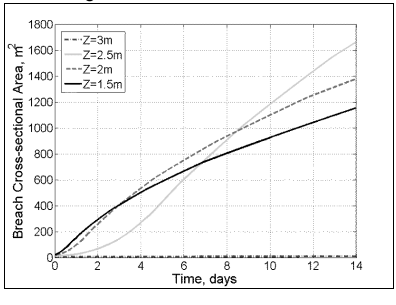

Fig. 8. Calculated Breach channel cross-sectional area evolution, HD_H1_T8_D0

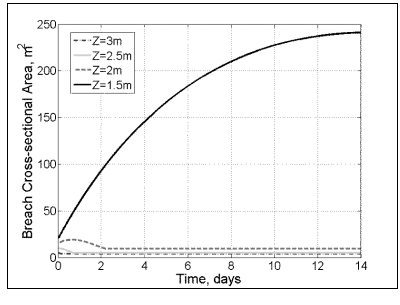

Fig. 9. Calculated Breach channel cross-sectional area evolution, HD_H1_T8_D30

Figures 10-13 illustrate breach transport and cross-sectional area for the M2, M2-H1_T8_D0, and M2-H1_T8_D30 cases. Figure 10 demonstrates the periodicity of sediment transport associated with the M_2 water elevation forcing. Depending on level of the breach channel relative to the forcing water level, transport rates may never approach zero, whereas sometimes the breach channel may be completely depleted of water as seen in Fig. 10 (z = 2.5 m). This switching on and off of transport rates

significantly reduces total transport through the breach as shown by the relative difference in cross-sectional area plots (Fig. 11) between $z = 2.5$ m and the much greater cross-sectional area represented in the $z = 1.5$ m and $z = 2$ m pilot channels. Case M2-H1_T8_D0 (Fig. 12) also demonstrates similar morphologic response as Case M2 (Fig. 11), but with slightly greater cross-sectional area and shorter incipient breach phase times. It appears that, in this case, the addition of wave setup has increased flow through the breaches, thereby increasing the channel area. Significant differences in cross-sectional area are achieved in Case M2-H1_T8_D30 with waves approaching at an incident angle (Fig. 13). This case suggests that a breach channel can be overwhelmed by longshore sediment transport, and infilling occurs to the point of closure such that the breach cross section remains constant, and the channel is no longer inundated.

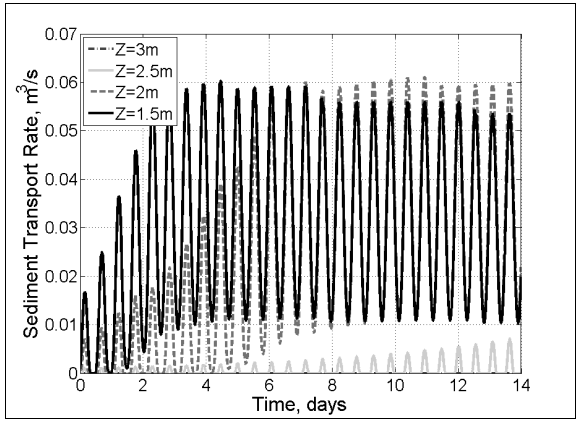

Fig. 10. Calculated sediment transport rate through the four breaches, Case M2

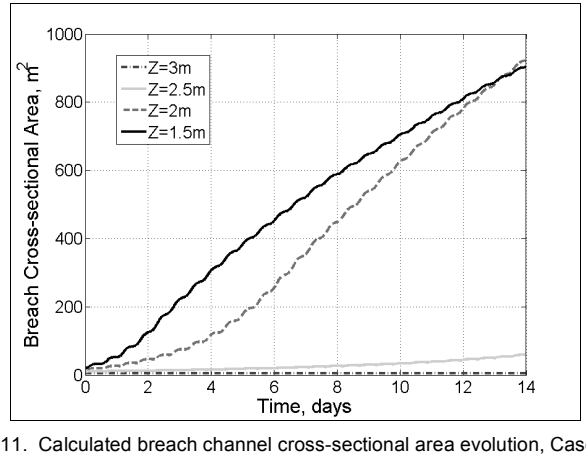

Fig. 11. Calculated breach channel cross-sectional area evolution, Case M2

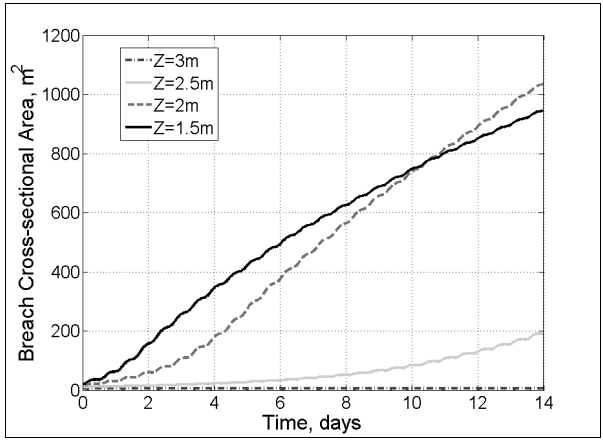

Fig. 12. Breach channel cross-sectional area evolution, Case M2-H1_T8_D0

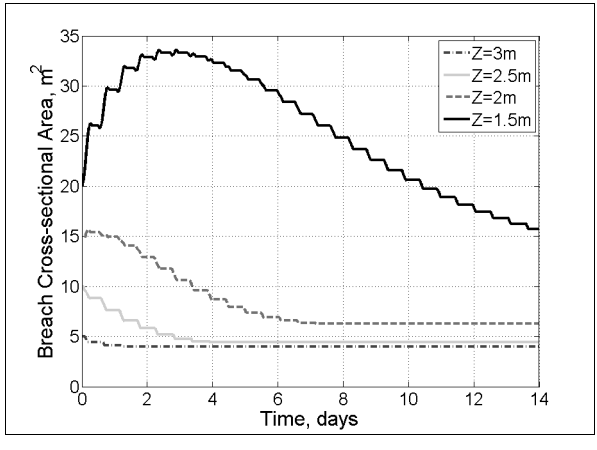

Fig. 13. Breach channel cross-sectional area evolution, Case M2-H1_T8_D30

Figures 14-17 illustrate breach transport and cross-sectional area for the Surge and the Surge+M2 cases. Because of the rapid increase in water level fromr the simulated storm surge, peaks in sediment transport (Fig. 14) are present immediately after inundation. These peaks grow progressively as pilot channels of initial elevations z = 1.5 m, z = 2 m, and z = 2.5 m are separately inundated and expanded. The growth of the peaks corresponds to the increase in incipient transport according to the depth of water in the breach channel. Shallow channels can transport more sediment because of larger bottom shear stress. Figure 15 indicates a rapid increase in cross-sectional area associated with the time of the storm surge.

Figure 16 illustrates the difference caused by addition of a tide to the storm surge. Because of the higher frequency M_2 tide relative to the surge, sediment transport (Fig. 16) goes to zero at periods of low tide during the surge. After the surge, transport rates for breaches at z = 1.5 m and z = 2 m continue to oscillate at the tidal frequency, indicating an open breach remains. Intermittent drying of the inlet causes a much reduced transport for the breach channels that had high pilot channels (z = 3 m, z = 2.5 m) where little to no inundation is present. Because of the reduced transport, the higher elevation channels remain closed after the surge, and cross-sectional area is constant (Fig. 17).

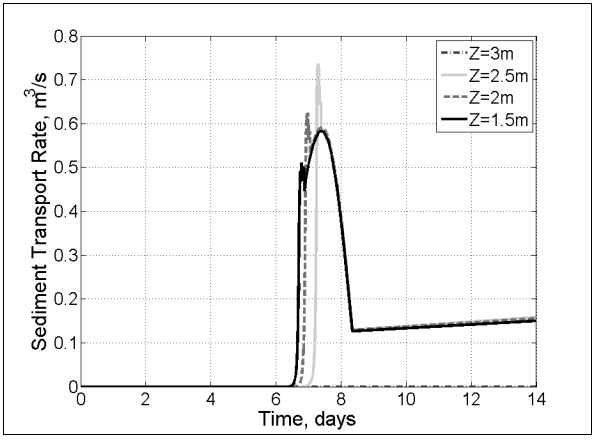

Fig. 14. Calculated sediment transport rate through the four breaches, Case Surge

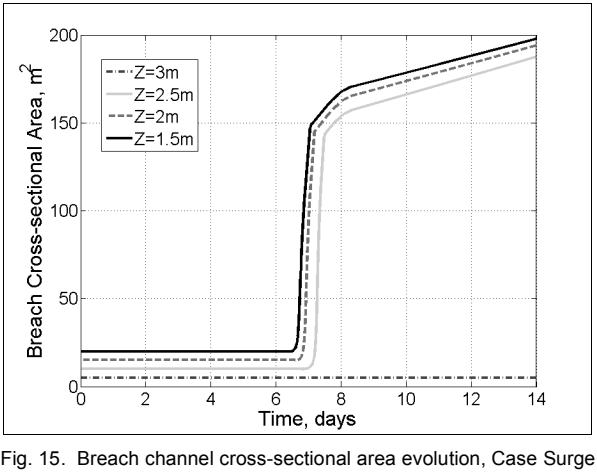

Fig. 15. Breach channel cross-sectional area evolution, Case Surge

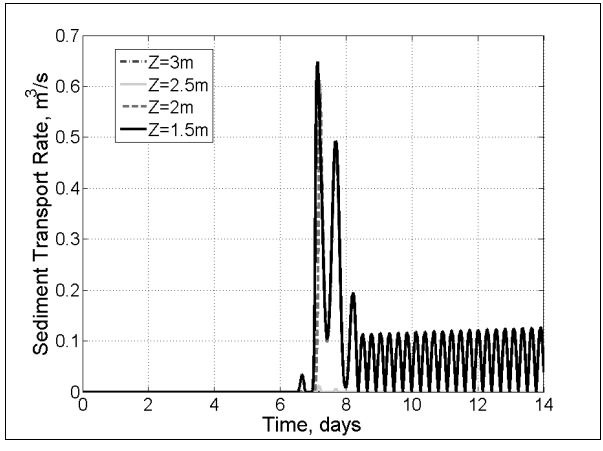

Fig. 16. Calculated sediment transport rate through the four breaches, Case Surge+M2

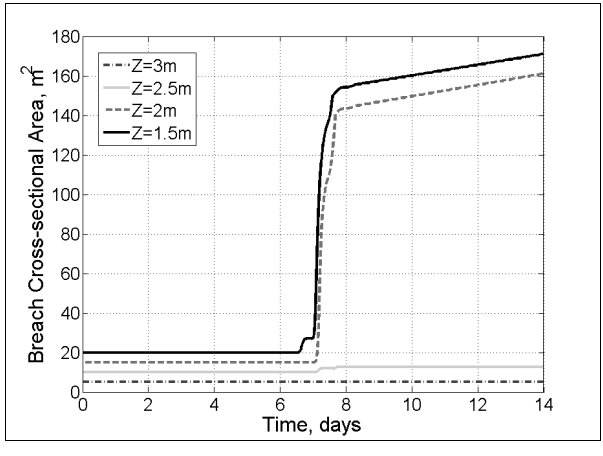

Fig. 17. Breach channel cross-sectional area evolution, Case Surge+M2

CONCLUDING DISCUSSION

This study investigated predictions of a new numerical model of multiple coastal barrier breaches at a regional scale allowing, for example, investigation of processes associated with independent evolution of each breach. Numerical simulations of coastal breaches at regional scale improve understanding of the physical processes by isolating forcing mechanisms and comparing responses of breach channels of varying dimensions. Enhancements to the morphologic breaching model add the capability to simulate multiple breach development at the regional scale with boundary condition forcing interaction with Cascade.

Calculation results indicate that slow, shallow inundation of breach pilot channels tends to produce breach width expanding at a greater rate than breach depth. This is likely due to the increased shear stress applied over a wider breach channel surface area in the model. A shallow breach also promotes a longer incipient breach phase and longer time before developing a tidally efficient channel. Fast and large inundation appears to promote rapid increase in depth as well as a more rapid incipient breach phase, where the cross-sectional area quickly changes.

Future research will examine model performance by comparison of predictions with observations of multiple breaches serving the same bay. Developments of the regional breaching model are expected to continue with an embedded form in Cascade for fully automated forcing and interaction. Finally, interaction between breaches serving the same bay will need to be represented for examining multiple inlet stability for a nearly fixed available tidal prism.

ACKNOWLEDGEMENTS

This study was conducted as an activity of the Coastal Morphology Modeling and Management (Cascade) work unit of the System-Wide Water Resources Program (SWWRP) with support from the Coastal Inlets Research Program (CIRP) conducted at the U.S. Army Engineer Research and Development Center. Permission was granted by Headquarters, U.S. Army Corps of Engineers, to publish this information.

REFERENCES

Connell, K.J., and Kraus, N.C. (2006). "Cascade Version 1: User's guide," ERDC TNSWWRP-06-5, U.S. Army Engineer Research and Development Center, Vicksburg, MS, (https://swwrp.usace.army.mil/).

Freeman, C.W., Bernstein, D.J., and Mitasova, H. (2004). "Rapid response 3D survey techniques for seamless topo/bathy modeling: 2003 Hatteras Breach, North Carolina," *Shore & Beach* 72(2), 3-7.

Hayes, M.O. (1967). "Hurricanes as geological agents, south Texas coast," *American Assoc. Petroleum Geologists Bull.* 51, 937-942.

Headquarters, U.S. Army Corps of Engineers. (2002). *Coastal Engineering Manual*, EM 1110-2-1100, Washington, DC.

Keulegan, G.H. (1967). "Tidal flow in entrances: Water level fluctuations of basins in communication with the seas," Committee on Tidal Hydraulics Technical Bulletin No. 14, U.S. Army Engineer Waterways Experiment Station, Vicksburg, MS.

Komar, P.D. (1998). "*Beach processes and sedimentation*," 2nd edition, Prentice-Hall, NJ, 544 p.

Kraus, N.C. (1998). "Inlet cross-sectional area calculated by process-based model," *Proc. 29th Coastal Eng. Conf*, ASCE, 3,265- 3,278.

Kraus, N.C. (2003). "Analytical model of incipient breaching of coastal barriers," *Coastal Eng. Journal*, 45(4), 511-531.

Kraus, N.C., and Hayashi, K. (2005). "Numerical morphological model of barrier island breaching," *Proc. 29th Coastal Eng. Conf.*, World Scientific Press, 2,120-2,132.

Kraus, N.C., and Wamsley, T.V. (2003). "Coastal barrier breaching. Part 1: Overview of breaching processes," Coastal and Hydraulics Laboratory Technical Note ERDC/CHL CHETN IV-56, U.S. Army Engineer Research and Development Center, Vicksburg, MS, (http://chl.wes.army.mil/library/publications/chetn).

Larson, M., and Kraus, N.C. (2003). "Modeling regional sediment transport and coastal evolution along the Delmarva Peninsula, USA," *Proc. Coastal Sediments '03*, World Sci. Press., CD-ROM, East Meets West Productions, ISBN-981-238-422-7, 14 p.

Larson, M., Kraus, N.C., and Hanson, H. (2003). "Simulation of regional longshore sediment transport and coastal evolution - the 'Cascade' model," *Proc. 28th Coastal Eng. Conf.*, World Sci. Press, 2,612-2,624.

Larson, M., Kraus, N.C. and Connell, K.J. (2006). "Cascade Version 1: Theory and model formulation," ERDC TN-SWWRP-06-7, U.S. Army Engineer Research and Development Center, Vicksburg, MS, (https://swwrp.usace.army.mil/).

Larson, M., Kraus, N.C., Connell, K.J. (2007). "Modeling sediment storage and transfer in large-scale coastal evolution models," *Proc. 30th Coastal Eng. Conf.*, in press.

Price, W.A. (1947). "Equilibrium of form and forces in tidal basins of coast of Texas and Louisiana," *American Assoc. Petroleum Geologists Bull.* 31, 1,619-1,663.

Stockdon, H.F., Holman, R.A., Howd, P.A., and Sallenger, A. H. (2006). "Empirical parameterization of setup, swash, and runup," *Coastal Eng.* 53(7), 573-588.

Terchunian, A.V., and Merkert, C.L. (1995). "Little Pikes Inlet, Westhampton, New York," *J. Coastal Research* 11(3), 697-703.

Wamsley, T.V., and Hathaway, K.K. (2004). "Monitoring morphology and currents at the Hatteras Breach," *Shore & Beach* 72(2), 9-14.

Wamsley, T.V., and Kraus, N.C. (2005). "Coastal barrier island breaching, Part 2: Mechanical breaching and breach closure," Coastal and Hydraulic Laboratory Technical Note ERDC/CHL CHETN IV-65, U.S. Army Engineer Research and Development Center, Vicksburg, MS, 21 p, (http://chl.wes.army.mil/ library/ publications/chetn).

Wamsley,T.V., Kraus, N.C., Larson, M., Hanson, H., Connell, K.J. (2007). "Coastal barrier breaching: Comparison of numerical and physical models," *Proc. 30th Coastal Eng. Conf.*, World Sci. Press, in press.

Wamsley, T.V., Cialone, M.A., Connell, K.J., Kraus, N.C. (2006). "Breach history and susceptibility study, south jetty and navigation project, Grays Harbor, Washington," Coastal and Hydraulics Laboratory Technical Report ERDC/CHL TR-04-2, U.S. U.S. Army Engineer Research and Development Center, Vicksburg, MS.

Watanabe, A., Shimuzu, T., and Kondo, K. (1991). "Field application of a numerical model of beach topography response," *Proc. Coastal Sediments '91*, ASCE Press, 1,814-1,928.

Wutkowski, M. (2004). "Hatteras Breach closure," *Shore & Beach* 72(2), 20 -24.

BREACH STABILITY AND GROWTH ANALYSIS USING A MORPHOLOGICAL MODEL

Santiago R. Alfageme[1], Masood Khondker[2], Rafael Canizares[3]

1. Moffatt & Nichol, 104 West 40th Street, 14th Floor, New York, NY 10018, USA. salfageme@moffattnichol.com.
2. Moffatt & Nichol, 104 West 40th Street, 14th Floor, New York, NY 10018, USA bkhondker@moffattnichol.com.
3. Moffatt & Nichol, 104 West 40th Street, 14th Floor, New York, NY 10018, USA rcanizares@moffattnichol.com.

Abstract: The formation of a new breach through coastal barrier islands is relatively common occurrence during extreme storm events. In fact, breaching has a significant role in the development and long-term morphological evolution of natural barrier islands by providing the backbarrier with sediments that accommodate both barrier island migration and the establishment of new intertidal and subtidal habitats. However, breaches also have the potential to adversely affect adjacent bays and inlets with conditions including increased water levels, damages to buildings and infrastructure on the barrier island, and impacts to existing inlets which may experience increased shoaling or even closure in the event of a breach. This paper examines the analytical/empirical tools presently used to assess breach stability and long-term growth, and it presents preliminary results from an initial attempt to simulate these processes using a numerical morphological model.

INTRODUCTION

Due to some or all of the impacts related to breaching listed above, there is generally an interest in the part of local stakeholders to close a new breach as soon as possible typically by means of placing sand from an available borrow source. In fact, in places like Long Island, New York, contingency plans have been developed to respond quickly to any barrier island breaches that may occur (USACE, 1996). Design, economic justification, and even environmental mitigation measures associated with such contingency plans require knowledge of the likelihood that a new breach will remain

open at a specific location (i.e., breach stability) and its long-term growth potential, including sediment accumulation in the ebb and flood shoals.

Until very recently, the only tools available to coastal engineers to analyze these processes consisted of simplified analytical models of breach/inlet stability based on the Escoffier closure curve concept (van de Kreeke, 1984) and analytical breach cross-sectional growth functions fitted to available empirical data (USACE, 1996). Although these tools are still considered indispensable, recent developments in numerical modeling have allowed scientists and engineers to explore in more detail the hydrodynamic, sediment transport, and morphologic processes associated with breach stability and growth.

This presents the results of an initial attempt to model breach stability and long-term breach growth using the Delft3D morphological modeling system. The advantage of this numerical, process-based approach is that it does not require schematization of the inlet/bay system and it specifically accounts for all of the relevant coastal processes (i.e., tides, currents, waves, and sediment transport). The analytical approach to determine breach and inlet stability based on the Escoffier inlet closure curve concept requires significant schematization of the hydrodynamic and sediment transport processes, which leads to results that are extremely sensitive to input assumptions regarding controlling inlet cross-sectional area and inlet length, friction losses, and equilibrium shear stress/flow velocity. Needless to say, the reliability of breach growth estimates based on empirical data is a direct function of the amount and quality of the data, as well as its applicability to the area of interest. For most coastal areas this type of data is non-existent.

ANALYTICAL/EMPIRICAL TOOLS

The following paragraphs provide a brief summary of the analytical and empirical tools commonly used by coastal engineers to study breach and inlet processes and some of the drawbacks associated with these techniques. An application example and results are also presented below. In the following section, these examples will be used as a benchmark to evaluate the performance of the morphological models.

Breach/Inlet Stability

Escoffier (1940), O'Brien and Dean (1972), Bruun (1978) and many others have developed methodologies which can be used to assess the stability of a tidal inlet against closure. Each of these authors advance the argument that inlet stability depends on the balance between tidal flows which tend to keep the channel open and littoral drift which tends to close the inlet. The O'Brien and Dean (1972) theory has been applied to both Moriches and Shinnecock Inlets by the New York District (1983, 1987) to assess the overall stability of those inlets. Van de Kreeke (1984, 1990a, 1990b) extended tidal inlet stability theory to address the matter of multiple inlets connected to a single bay. The analysis provides a means for determining whether: (1) the bays can support more than one inlet, and (2) if not, which opening, i.e. the breach or existing inlet, is most likely to remain open.

Inlet stability analyses focuses on the equilibrium between inlet cross-sectional area and inlet hydrodynamics. The controlling variables are the actual tidal maximum velocity (or shear stress) in the tidal inlet, and the equilibrium tidal velocity (or shear stress) that is required to flush sediments carried into the inlet by longshore currents. According to Bruun (1978), Van de Kreeke (1990), and others, the equilibrium velocity for most inlets is 1 meter per second (3.28 feet per second). This velocity corresponds to an equilibrium shear stress of about 4.5 Newton per meter squared (N/m^2). When the actual velocity equals the equilibrium velocity the inlet is in equilibrium. When the actual velocity exceeds the equilibrium velocity then the inlet is in a scouring or erosional mode, and conversely, when the actual velocity is lower than the equilibrium velocity the inlet is in a shoaling or depositional mode. The equilibrium velocity, among other factors, depends on the magnitude and direction of longshore sediment transport rates. Specifically, the equilibrium velocity increases with littoral transport rate.

Escoffier (1940) was the first to present the concept of a closure curve which is a plot of inlet cross-section (abscissa) versus inlet velocity or shear stress (ordinate axis). An illustrative example is presented in Figure 1 which shows that shear stress (and velocity) initially increases with inlet area, reaches a maximum value, and then steadily decreases with increasing area. The first portion of the curve (i.e., $A < Au$) pertains to flow conditions that are dictated by frictional forces, i.e., flow is restricted by friction in the inlet. On the right hand side of the curve, flow velocities and attendant shear stress ($A > As$) are controlled by continuity considerations where the discharge remains constant and velocity decreases with an increase in flow area. The equilibrium flow velocity is normally plotted on the closure curve in order to make judgments about the inlet stability, see Figure 1.

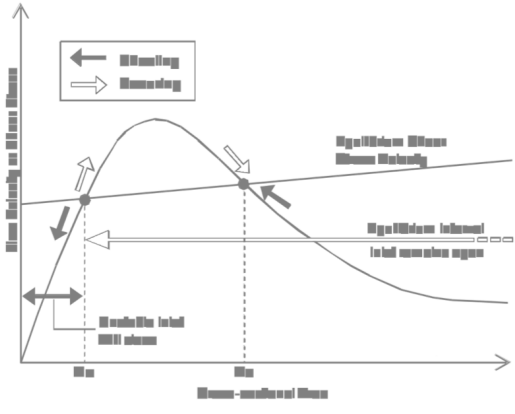

Fig. 1. Escoffier's Inlet Stability Diagram

Referring to Figure 1, *Au* represents an unstable inlet cross-sectional area, while *As* represents a stable cross-sectional area. An inlet is considered stable when the cross-section area is in the equilibrium interval which is defined as the portion of the closure curve which has cross-sectional area characteristics of $A > Au$. For $A < Au$, inlet velocities are incapable of clearing the inlet of shoaled sediment and will eventually close. Similarly, for $A > As$, inlet velocities are insufficient to keep the inlet from shoaling and the inlet cross section will eventually return to an area within the equilibrium interval. The actual area of the inlet will tend to vary over time depending on the continuous balance between scouring potential and longshore sediment transport. Stable inlets will have areas which remain in the equilibrium interval. An inlet can close, however, if a severe storm deposits a large amount of sediment in the inlet resulting in a cross-section lower than *Au*. Inlets which are marginally stable or those which remain open through dredging are most vulnerable to closure.

The stability analysis of a two-inlet bay system has been the subject of studies of Van de Kreeke (1985; 1988; 1990a; 1990b). Generally, for both inlets to have a stable cross-section, the enhanced parts of the equilibrium flow curves must intersect. This situation does not often occur in nature. Therefore, where two inlets connect the same bay to the ocean it is more likely that, at best, one inlet will remain open.

One drawback with this stability curve methods is that the analysis is typically based on a more or less schematized description of the inlet/bay hydrodynamics that allows for analytical computations or relatively simple numerical methods (Seabergh and Kraus, 1997). This makes the choice of input parameters such representative inlet and dimensions, representative tide levels, and friction energy losses a very sensitive task. Conversely, however, these methods allow for rapid evaluation of multiple scenarios and are simple to use and calibrate.

Application to FIMP

As part of the U.S. Army Corps of Engineers' (USACE) Fire Island to Montauk Point (FIMP) Reformulation Study (http://www.nan.usace.army.mil/fimp/reform.htm) multiple inlet stability analyses were carried out for the inlets and bays within the study area. (Figure 2). The work concluded that all three bays are vulnerable to breach formation. In the case of Great South Bay, results suggest that the existing Fire Island Inlet would shoal and maybe even close, while the breach would remain open. In the case of Moriches and Shinnecock Bays, the analyses also concluded that one of the openings would tend towards closure in the long-term, however which opening (the existing inlet or the breach) would depend on the exact location of the breach (Headland et al, 1999).

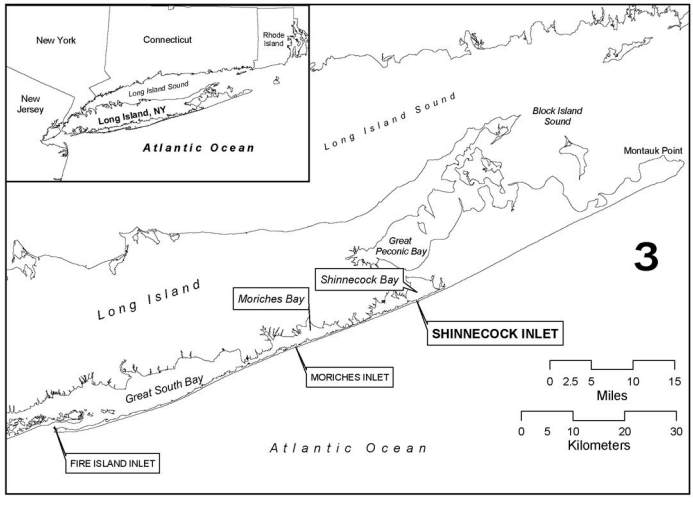

Fig. 2. FIMP Study Area

Long-term Breach Growth

As part of the FIMP study, a Breach Contingency Plan (BCP) was developed to determine what measures can be taken by Federal, State and local governments to react quickly to breach conditions along the FIMP study area (USACE, 1996). The BCP examined historic breach data to determine long-term growth characteristics and sediment transport processes. Of the breaches that have occurred within the FIMP study area during and after 1938, three remained open for long periods (i.e., several months or more). Shinnecock Inlet opened on September 21, 1938 and was subsequently stabilized. The January 14, 1980 northeaster opened a breach adjacent to Moriches Inlet. A fill project completed on February 25, 1981 closed this breach. The northeaster that struck Westhampton on December 10, 1992, created two breaches. One of the breaches was closed mechanically using dredged material from the Intracoastal Waterway (ICW) within a month of opening. The one that remained open expanded to an average width of 1,800 feet before being closed mechanically in October, 1993. Based on the growth of these three breaches the BCP presented a method for estimating breach along-shore cross-sectional area versus time according to the following exponential breach growth equation:

$$A(t) = A_0\left(1 - e^{-kt}\right) \tag{1}$$

Where t is the time in months from breach initiation, A_0 is the maximum breach cross sectional area, and k is the breach growth coefficient which varies from 0.15 to 0.30 month^{-1}. These parameters vary depending on the bay where the breach occurs and were obtained as part of the breach inlet stability analysis (USACE, 1996). Specifically, the maximum breach cross sectional area is based on long-term stable values corresponding

to existing tidal inlet areas. As such, breach growth would be attended by a reduction of tidal inlet area, although the trade-off between inlet and breaches areas may not be absolute. This behavior was observed during the breach at Moriches Inlet in 1980 when cross-sectional surveys of the breach and inlet indicated that the total area of both inlets was constant at approximately 2,000 m^2. Estimated growth parameter values are summarized for Great South Bay, Moriches Bay, and Shinnecock Bay in Table 1. These breach growth equation and selected parameter values compare favorably with survey data for the 1980 and 1992 breaches at Cupsogue and Pikes Beach, respectively (USACE, 1996).

Table 1. Breach Growth Parameters

Project Reach	A_0 *(sq. m.)*	k *(month)*$^{-1}$
GSB	3,350	0.15-0.3 (0.2 average)
MB	1,500	0.15-0.4 (0.3 average)
SB	1,640	0.15-0.4 (0.3 average)

Estimated potential breach cross-sectional areas are shown in Figure 3, assuming probable breach closure scenarios based on the experience at Westhampton Beach and recommendations of (i.e., 1 to 12 months).

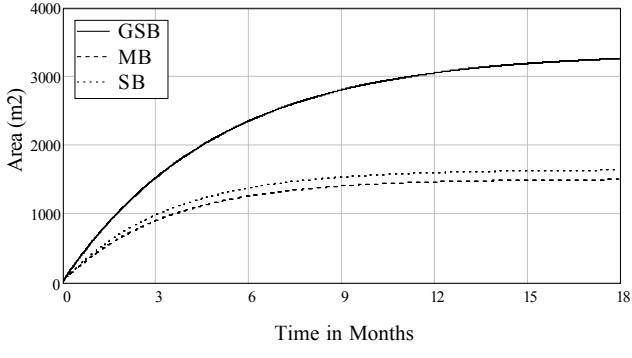

Fig. 3. Breach Growth Curves

MORPHOLOGICAL MODELING

Generic bay-inlet-breach morphological models were developed using the Delft3D modeling system. Geometry and dimensions of the bay and inlet are roughly representative of bay-inlet systems within the FIMP area. Specifically, a rectangular grid was built covering an area roughly equal to Great South Bay and with an inlet similar in geometry and dimensions to Fire Island Inlet. A second, also rectangular, grid representative of Moriches and Shinnecock bays was also built. The geometry was kept very simple to minimize required grid resolution and computational expense.

Delft3D Modeling System

Delft3D is a surface water modeling system which allows for flexible integration of hydrodynamic, wave, sediment transport, and morphology update models (WL | Delft Hydraulics, 2001). The model solves the coupled equations for shallow water flow and sediment transport including bed load using the Van Rijn (1993) formulations. Hydrodynamic, sediment transport and bottom update computations are performed simultaneously (or "online"). A detailed description of the approach, including results of several validation tests is included in Lesser et al. (2004). By using an "online" approach changes in bathymetry are immediately fed back to the hydrodynamic calculations and data exchange between each module (which requires large data files when using a decoupled modeling approach) is relatively simple and efficient.

In the "online" version of Delft3D, sediment (up to five sand and/or mud fractions) is treated as any other constituent and added modeled using an advection-diffusion transport solver. Additional formulations generally following the approach described by van Rijn (1993) are included to describe relevant sediment processes such settling, bed sediment exchange, and bed load transport.

The elevation of the bed is dynamically updated at each computational time-step. This is one of the distinct advantages over an "offline" morphological computation as it means that the hydrodynamic flow calculations are always carried out using the correct bathymetry. At each time-step, the change in the mass of bottom sediment that has occurred as a result of the sediment sink and source terms is calculated. This change in mass is then translated into a change in thickness of the bottom sediment layer using the density of the bed material. This change in thickness is equivalent to a change in bed elevation, which is applied to the depth values stored at computational points.

Erosion of Dry Cells (Lateral Breach Growth)

Initial efforts to simulate the morphological evolution of a new inlet (Roelvink et al., 1994) were hampered by the model's inability to erode existing "dry" points and allow for alongshore widening and migration of the inlet mouth. Nonetheless, these preliminary efforts demonstrated that the model could at least reproduce the initial morphodynamic response observed in a similar physical model. Erosion of dry points and "avalanching" of steep slopes is very difficult to solve using a process-based approach because it requires an extremely fine numerical grid that would make model application impractical. To solve this problem the version of the Delft3D model used in this study includes a mechanism by which a fraction of the sediment eroded from a wet cell is withdrawn from adjacent dry cells, if present (Roelvink et al., 2003). This fraction is user-specified and can be calibrated to available data. Comparison of this model to the Zwin breach growth experiment (as reported by Visser, 1998) suggests that a fraction on the order 0.9 yields a good comparison between model results and prototype breaching data.

Morphological Acceleration Factor

Analysis of medium- to long-term breach stability requires long morphological simulations over periods ranging from a few weeks to several months. On the other

hand, hydrodynamic and sediment transport processes have a much shorter time scale and require modeling time steps of minutes or even seconds depending on spatial resolution. Accommodating both short and long time-scales requires use of so-called "morphological updating" strategies that allow for significantly faster simulation times. These techniques include "tide-averaging", "continuity corrections", and "morphological acceleration factors" (Roelvink, 2006).

In the "online" version of Delft3D the bottom is updated at the same time intervals as the flow and sediment transport but the morphological change rates can be multiplied by "morphological (acceleration) factor" which effectively extends the morphological time step (Lesser et al, 2004). Work by Roelvink (2006) and Lesser at al (2004) suggest that for tidal and wave-driven situations "morphological factor" values in the order of 50-100 do not significantly alter the solution and are therefore feasible. Nonetheless, sensitivity to morphological factor selection should always be carefully tested.

Model results

Figures 4 through 8 show results for a new breach into a bay roughly the size of Great South Bay an with the existing Fire Island Inlet open. This particular simulation was made over a 1 month period including two spring-neap cycles. A morphological factor of 12 was applied to simulate a total of 12 months of morphological evolution. Initial breach width was 300 meters. As shown in the figures, the model seems capable of simulating long term breach growth as well as the accumulation of sediment in ebb and flood shoals. Note that waves were not included in the simulation, and therefore lateral growth is fairly symmetrical.

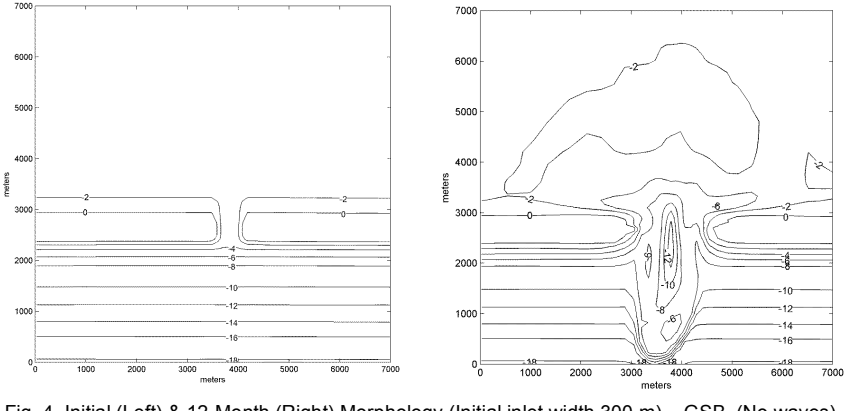

Fig. 4. Initial (Left) & 12-Month (Right) Morphology (Initial inlet width 300 m) – GSB (No waves)

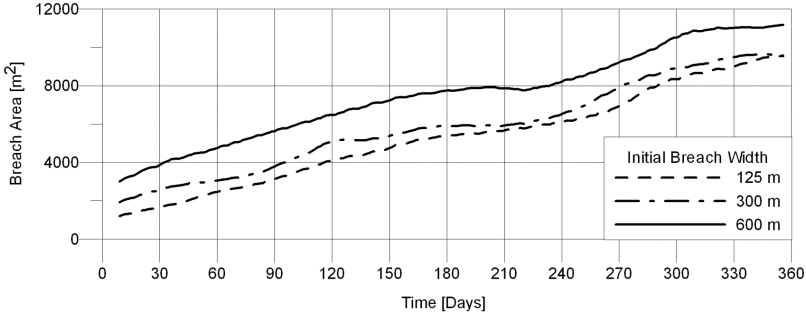

Fig. 5. Breach Area Evolution – GSB (No waves)

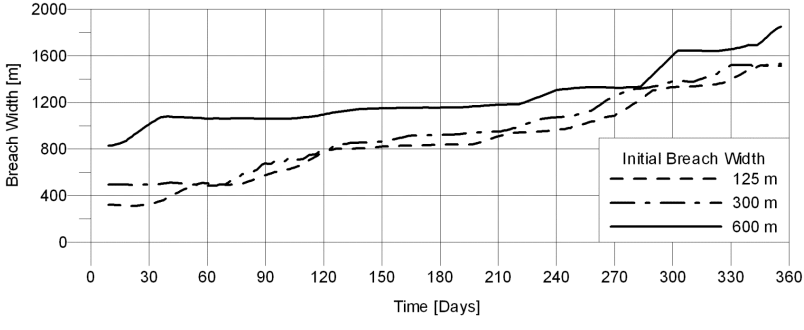

Fig. 6. Breach Width Evolution – GSB (No waves)

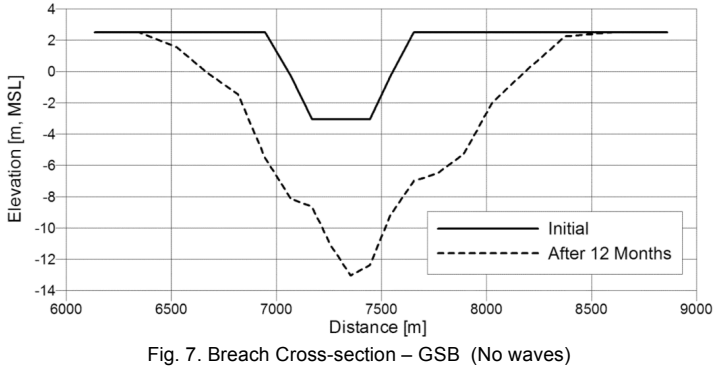

Fig. 7. Breach Cross-section – GSB (No waves)

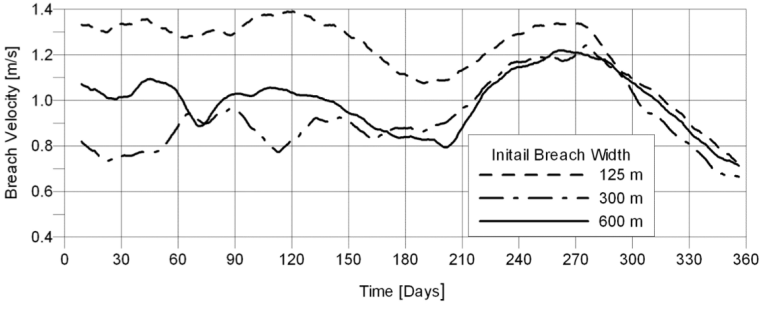

Fig. 8. Max. Velocity at Breach - GSB (No waves)

The time scale of the observed morphological evolution also appears to be reasonable as cross-sectional area and especially maximum flow velocities through the breach appear to taper off after 10 months suggesting that the breach is reaching a more stable condition.

However, when compared to the analytical/empirical estimates of potential breach growth in Great South Bay, model results suggest a significantly larger cross-sectional area (10 to 11,000 m^2 vs. 3,400 m^2) after 12 months. Recall, however, that the maximum breach cross sectional area in the analytical model is based on long-term stable values corresponding to existing tidal inlet areas and these may not be representative of the maximum possible area at the breach location. This is particularly true in the case of Great South Bay where the existing Fire Island Inlet has a very different (and much less hydraulically efficient) geometry than a new breach would. More importantly, this simulation does not include the effect of the waves and longshore sediment transport, which would tend to place sand in the inlet and reduce its cross-section.

Figure 9 shows the results for a breach in Shinnecock Bay, this time including the effects of waves (Hs=1.5 m, Tp=7 sec and θ=26 degrees offshore) and staring from a much narrower initial breach (30 m width). As shown on the figure, longshore sediment transport generated by the waves forces the channel to move alongshore causing increased erosion of the downdrift shoreline. In this case, the cross-sectional area predicted by the model after 6 moths (1,500 m^2) is very similar to the analytical/empirical estimate (1,200 m^2).

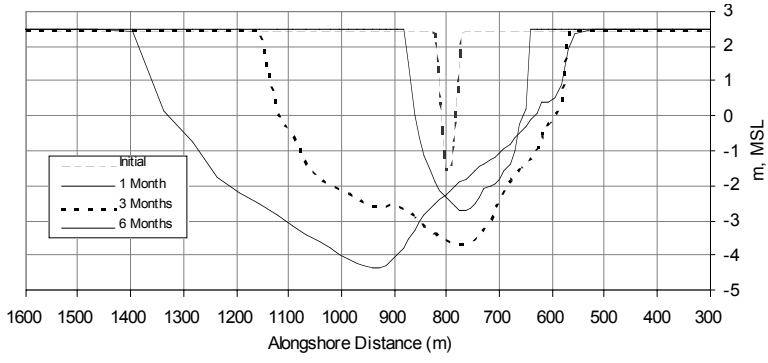

Fig. 9. Breach Cross-section Evolution – Shinnecock Bay (with waves)

One interesting finding from this simulation was that in this case the results were very sensitive to the choice of a morphological acceleration factor. Initial runs with factor of 12 resulted in rapid closure of the breach due accumulation of sediment transported by the waves. However, close inspection of the results suggested that changes were too rapid to use a morphological factor and therefore a hybrid approach was used. The first month was run with a factor of 1 (i.e., no acceleration), months 2 and 3 were run with a factor of 2, and months 4, 5, and 6 were run with a factor of 3. This approach of slowly increasing the morphological factor proved to be stable and to yield results very similar to those obtained with no morphological acceleration included in the model.

Nonetheless, not being able to use a larger morphological factor, particularly at the beginning, makes simulating initial breach stability (i.e., when the beach is relatively small) very difficult and computationally expensive. This problem is compounded by the fact that both empirical data and simulations suggest that the initial stability of the breach and its growth rate in the case of a stable one is very dependent on water level and wave climate conditions. Therefore, a proper analysis of the risk of a breach in particular location would require simulation of not just typical conditions but various storm and tide conditions. The statistical probability of each result would then need to be combined to provide for a representative estimate of the risk the breach would grow.

SUMMARY

An initial attempt to simulate breach stability and long-term growth using an "online" morphological model suggests that important processes (lateral growth, alongshore migration, and shoal accumulation) can be represented with the model and that results that compare reasonably well with the limited available empirical data can be obtained.

However, this preliminary work suggests that the results are very sensitive to the choice of "morphological acceleration factor", particularly during the initial evolution of small, recently opened breaches. Under those conditions it seems like using anything higher than a factor of 1 (i.e., no acceleration) may lead to erroneous results (e.g., breach

closing instead of opening). This constraint leads to longer simulation times and may significantly reduce the practicability of using these models to assess breach stability and long-term growth, particularly when compared to the more efficient analytical/empirical tools.

On the other hand, a process-based morphological model allows for a detailed description of the water levels and wave climate which drive the morphological processes. Relatively small differences in these environmental conditions following the storm that opened the breach (e.g., a spring tide combined with an average nor'easter storm vs. a neap tide during calm wave conditions) may mean the difference between a breach that closes quickly and one that "explodes". Therefore, both process-based morphological models combined with more conceptual analytical tools are likely required for comprehensive studies in which probability-based results are needed.

REFERENCES

Headland, J. R., Rasmussen, C., Bocamazo, L., Smith, W. G., and Herrman, M. (1999). "Tidal inlet stability at Fire Island, Moriches and Shinnecock Inlets, Long Island, New York," Proceedings of Coastal Sediments '99, ASCE.

Lesser, G., J. van Kester and J.A. Roelvink 2000. Online Sediment Transport within Delft3D-FLOW. WL | Delft Hydraulics report, October 2000.

Lesser, G.J., J.A. Roelvink, J. van Kester and G.S. Stelling (2003). Development and Validation of a Three-dimensional Morphological Model. Coastal Engineering, Volume 51, Issue 8-9, 1 October 2004, Pages 883-915

van de Kreeke, J. (1984). "Stability of Tidal Inlets," Hydrodynamics and Sediment Dynamics of Tidal Inlets , D.G. Aubrey, editor, Springer Verlag, pp. 1-23

van de Kreeke, J. (1988). "Hydrodynamics of tidal inlets," Hydrodynamics and Sediment Dynamics of Tidal Inlets, D.G. Aubrey, editor, Springer Verlag, pp. 1-23.

van de Kreeke, J. (1990a). "Can multiple inlets be stable?, "Estuarine, Coastal and Shelf Science, 30, pp.

van de Kreeke, J. (1990b). "Stability of a two-inlet bay system," Coastal Engineering, Elsevier Scientific Publishing, March, 1990.

van Rijn, L.C., 1993. Principles of Sediment Transport in Rivers, Estuaries and Coastal Seas. Aqua Publications, Amsterdam.

Seabergh, W. C., and Kraus, N. C. (1997). "PC program for coastal inlet stability analysis using Escoffier method," Coastal Engineering Technical Note CETN IV-11, U.S. Army Engineer Research and Development Center, Vicksburg, MS, 7 pp.

Stive, M. J. F. (2003). "Morphologic modeling of tidal basins and coastal inlets," Proceedings Coastal Sediments '03, CD-ROM Published by East Meets West Productions, Corpus Christi, TX ISBN-981-238-422-7, 14 p.

USACE (1996). "Breach Contingency Plan, Fire Island Inlet to Montauk Point, Long Island, New York, Reformulation Study," New York District, New York.

Visser, P.J. 1998. Breach growth in sand dikes. Ph.D.-thesis Delft University of Technology, the Netherlands.

WL | Delft Hydraulics 2001. User Manual Delft3D-FLOW. Delft, the Netherlands

SPATIAL DISTRIBUTION OF CROSS-SHORE SEDIMENT TRANSPORT RATE FOR BERM FORMATION AND EROSION

Takayuki Suzuki[1], Maiko Takeuchi[2], Naoki Tomoda[3], Satomi Yamaguchi[4], Yoshiaki Kuriyama[5]

1. Researcher, Littoral Drift Division, Port and Airport Research Institute (PARI), Nagase 3-1-1, Yokosuka, Kanagawa 239-0826, Japan. suzuki-t@pari.go.jp
2. Graduate Student, Toyohashi University of Technology, Department of Architecture and Civil Engineering, Tempaku-cho 1-1, Toyohashi, Aichi 441-8580, Japan. m-takeuchi@mail.goo.ne.jp
3. Researcher, Littoral Drift Division, Port and Airport Research Institute, Nagase 3-1-1, Yokosuka, Kanagawa 239-0826, Japan. tomoda-n84w6@pari.go.jp
4. Researcher, Graduate School of Engineering, Hokkaido University, Nishi 8, Kita 13, Sapporo, Hokkaido 060-8628, Japan. s-kawamr@eng.hokudai.ac.jp
5. Head of Littoral Drift Division, Port and Airport Research Institute, Nagase 3-1-1, Yokosuka, Kanagawa 239-0826, Japan. kuriyama@pari.go.jp

Abstract: A 2.5-year data set of beach profiles was used to examine the characteristics of berm shape and the spatial distributions of the cross-shore sediment transport rate for berm formation and erosion. The seaward distance, x, is normalized by the distance of the investigation area, X, which is from the maximum wave run-up position, $x/X = 0.0$, to the position where the standard deviation of the beach profile takes the lowest value seaward of the mean shoreline position, $x/X = 1.0$. Analysis of the data reveals that the landward sediment transport rate for the berm formation increases from $x/X = 0.0$ to 0.4 and reaches a constant value toward $x/X = 1.0$. As for berm erosion, the landward sediment transport rate peaks at $x/X = 0.10$ and the sediment transport rate changes in the seaward direction at $x/X = 0.20$. From this position, the rate decreases until $x/X = 0.60$.

INTRODUCTION

Beach topography in the swash zone responds to wave run-up and run-down. In the swash zone, sediments are transported by both bed load transport and suspended load transport owing to very shallow water with high velocity. The sediment transport

above the mean sea level is caused by swash, which is strongly asymmetric (e.g. Hughes *et al.*, 1997; Osborne and Rooker, 1999). Thus, a beach profile in the swash zone is formed by the imbalance between uprush and backrush sediment transport on the beach face.

Berms are commonly formed between the mean sea level and the maximum wave run-up level. During mild wave conditions, berms form on the foreshores (e.g., Thomas and Baba, 1986; Katoh and Yanagishima, 1992). In contrast, during severe wave conditions, the enhanced wave run-up washes sediment over the berm crest which is transported seaward with the backwash, and berm erosion occurs (e.g., Eliot and Clarke, 1986; Katoh and Yanagishima, 1993). In order to understand the berm topography change, we need to investigate the sediment transport rate for both berm formation and erosion. The sediment transport rates in the swash zone have been studied by a number of researchers. Horn and Mason (1994) investigated the relative proportions of bed load and suspended load by carrying out field experiments at four beaches in the United Kingdom. The bed load transport was found to dominate the backwash, and more sediment was transported on the flood tide than on the ebb. Masselink and Hughes (1998) measured swash flow velocity and sediment transport on a natural beach and observed strong correlation between the sediment load and the velocity cubed. Puleo *et al.* (2000) studied the swash zone sediment transport using field data. They found that vertical profiles of backwash differed from that of the uprush and that bore-derived turbulence may affect local sediment transport. Also, Puleo *et al.* (2003) reported that suspended sediment transport rates obtained from the sediment concentration and the velocity measurements showed the best comparisons with a modified sediment transport model that includes a physical mechanism for enhancing transport rates due to flow acceleration. Austin and Masselink (2006) observed the morphological change and swash sediment load at a steep gravel beach. They found that the morphological change is directly related to the maxima in shoreline elevation and identified four modes of berm adjustment. However, sediment transport rates during berm formation and berm erosion have not been fully investigated.

The main objective of this study was to investigate the spatial distributions of the cross-shore sediment transport rate for berm formation and erosion on the basis of a 2.5-year data set of beach profiles obtained at a stable dissipative beach.

DATA DESCRIPTION

Beach Profile Data

Beach profile data were obtained from August 1987 to January 1990 at Hazaki Oceanographical Research Station (HORS), a research facility for field measurements of various phenomena in the nearshore zone on the Hasaki coast of Japan facing the Pacific Ocean (Fig. 1). HORS has a 427-m-long pier, which is located perpendicularly to the shore. The cross-shore distance along the pier is defined relative to the reference point of HORS, located near the entrance of the pier, and the seaward direction is set as being positive.

The Hasaki coast is stable, and the bathymetry around HORS is almost uniform alongshore. The beach profiles along the pier were measured at 5-m intervals everyday, except for weekends and holidays, with a 3-kg lead from the pier and with a level and a staff shoreward of the pier. The median sediment diameter is approximately 0.18 mm and almost uniform along the pier. Based on the data, the sea levels at the Hasaki coast (Tokyo Peil -0.687 m) show high, mean and low water levels of 1.252 m, 0.651 m, and -0.196 m, respectively.

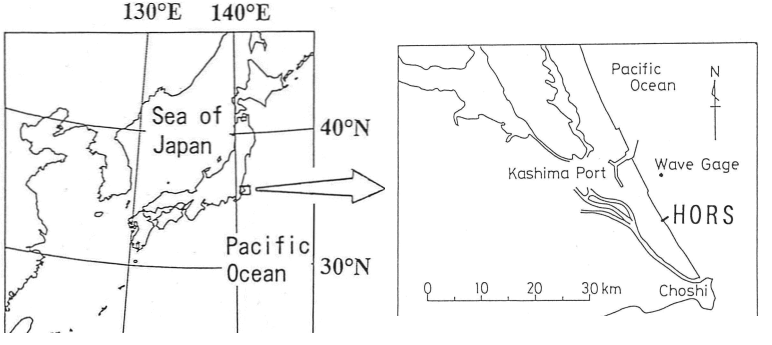

Fig. 1. Location of Hazaki Oceanographical Research Station (HORS)

Figure 2 shows the mean beach profile and its standard deviation in the offshore, the surf zone, the inner surf zone, foreshore and backshore. The beach slope around the shoreline, where the seaward distance is -4 m, is about 0.024. From the figure, several peaks can be seen in the distribution of the standard deviation. The relatively high values around the seaward distance of -10 m are due to berm formation and berm erosion, and the high values from the seaward distance 200 m to 350 m are due to bar movement.

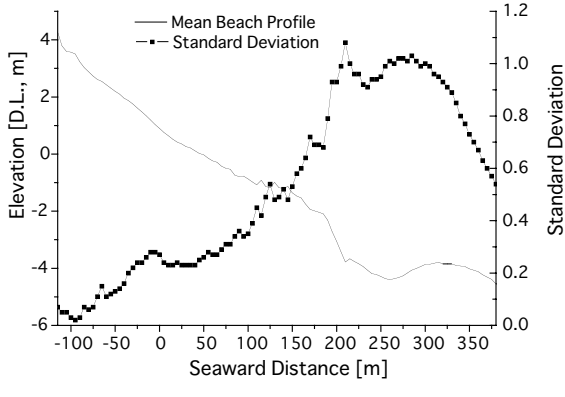

Fig. 2. Mean beach profile and its standard deviation.

Offshore Wave Data

Offshore waves have been observed at the mean water depth of 23.4 m offshore the Port of Kashima, which is about 8 km north from HORS, by using a current meter type wave directional gage (CWD) sensor for 20 minutes every 2 hours. During the investigation period, the offshore significant wave height and the offshore significant wave period varied from 0.37 m to 5.66 m and from 4.88 s to 14.98 s, respectively.

The offshore wave energy flux is calculated from the offshore wave height and the celerity.

$$E_f = \frac{1}{16}\rho g \left(H_{1/3}\right)_0 C_{g0}, \tag{1}$$

where ρ is the sea water density, g is the gravity acceleration, $H_{1/3}$ is the significant wave height and C_{g0} is the celerity. In this analysis, the daily wave energy flux is used.

Wave Run-up Position

The shoreline position varies predominantly owing to beach topography, tide and wave set-up near the shoreline. In this study, the wave run-up level is defined as the total sum of mean sea level, run-up level of infragravity waves and that of incident wind waves. Katoh and Yanagishima (1993) proposed an equation for estimating the wave run-up level $R_{\max}$, which had been empirically derived from field observation data obtained at HORS.

$$R_{\max} = \overline{\eta}_0 + 0.96H_L + 0.31 \ \ [\mathrm{m}], \tag{2}$$

where $\overline{\eta}_0$ is the mean sea level and H_L is the height of the infragravity waves at the shoreline. The second term and the third constant term are considered to present the run-up heights caused by the effect of infragravity waves and incident wind waves, respectively. The wave run-up level is based on the datum line.

BERM FORMATION AND BERM EROSION

Beach Topography Change

The space-time map of the variation from the mean beach profile at HORS and the wave energy flux from August 1987 to January 1990 are shown in Figs. 3(a) and 3(b), respectively. For Fig. 3(a), the elevation above and below the mean beach profile is shown by warm and cold colors, respectively. The solid line indicates the mean wave run-up position, which is averaged from the wave run-up positions calculated from the beach profile obtained once a day and the wave run-up level estimated every 2 hours.

From the figure, the shoreline position and the beach topography changed greatly in 1987. However, their fluctuations become small after 1988. Berm formation mostly occurs above the mean wave run-up position, and the cross-shore scale of the berm

which is the cross-shore distance area above the mean beach profile is nearly the same scale, 25 m. Berms are generally formed during non-storm conditions, e.g., February 1988 and July 1989, and are eroded during storm conditions. Therefore, it can be considered that the berms are formed when a low wave energy flux continues and disappear in the presence of a relatively large wave energy flux.

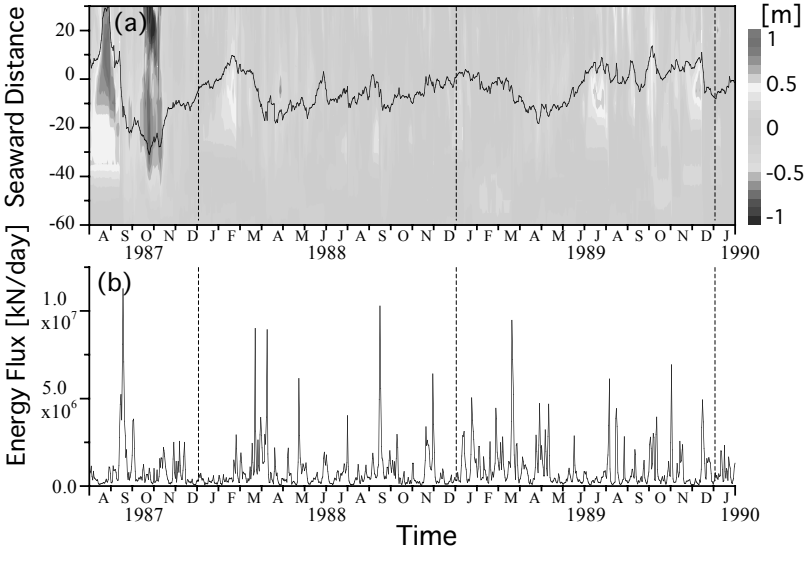

Fig. 3. (a) Variation from the mean beach profile at HORS. Elevations above and below the mean beach profile are shown by warm and cold colors, respectively. (b) Wave energy flux

Characteristics of Berm Shape

Based on the daily beach profile data, the topography changes of berm formation and berm erosion were selected. Katoh and Yanagishima (1992) identified 219 cases of berm formation and 58 cases of berm erosion from the 2.5-year (August 1987 to January 1990) beach profile data set obtained at HORS. This data was used to investigate the characteristics of the berm shape and the cross-shore variations of the cross-shore sediment transport rate for berm formation and erosion.

As mentioned above, berm formation occurred during calm wave conditions, and the berm crest grew up to the maximum wave run-up level (Katoh and Yanagishima, 1992). Berm erosion occurred when the enhanced wave run-up passed through the berm crest. Thus, the maximum wave run-up position is important for examining berm formation and erosion. Figure 4 shows the histogram of the maximum wave run-up position, where the maximum daily wave run-up position, for berm formation and erosion. The maximum wave run-up position changes from x = -58.0 m to -0.5 m for berm formation and from x = -78.3 m to -23.2 m for berm erosion, and the averaged wave run-up positions are x = -29.7 m and x = -49.9 m, respectively.

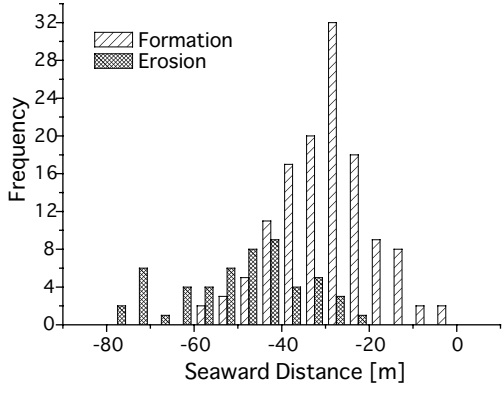

Fig. 4. Histogram of maximum wave run-up position for berm formation and erosion.

In this analysis, the investigation area is set from the maximum wave run-up position, which is defined as the onshore boundary, to x = 25 m, where the standard deviation takes the lowest value seaward of the high peak of the standard deviation x = -10 m (see Fig. 2) and is defined as the offshore boundary. Since the maximum wave run-up position varies owing to the beach profile and the wave run-up level, the investigation area is normalized by using the distance from the onshore boundary to the offshore boundary. Namely, the onshore boundary is set as x/X = 0.0 and the offshore boundary is set as x/X = 1.0.

Let us first examine the cross-shore position of the berm crest. Figure 5 shows the histogram of the berm crest position, which is defined as the place where the vertical distance between the beach profile and a straight line, which begins at the maximum wave run-up position and extends to the intersection point between the onshore boundary and the beach profile, is the largest. The positions are decided on the basis of the beach profile of the day before berm erosion occurs. The histogram of the berm crest position is observed from x/X = 0.0 to 0.6, and the averaged berm crest position is located at x/X = 0.29. This indicates that during the berm formation, although the wave reaches the maximum wave run-up position, the sediments mainly settle at around x/X = 0.29.

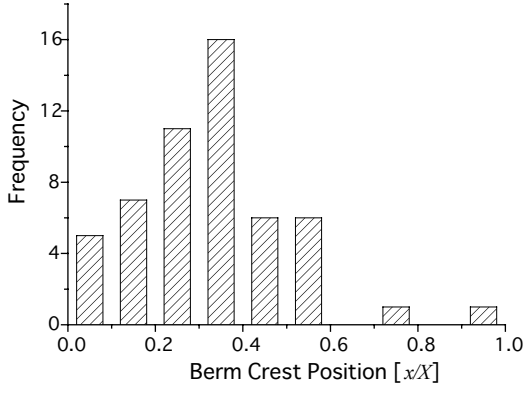

Fig. 5. Histogram of berm crest position.

In spite of the various berm crest heights, the beach profile becomes mild after berm erosion. Figure 6 shows a comparison of berm slope before and after berm erosion. Although the spread of the berm slopes before the erosion reach 0.0385, it becomes small after the erosion, and the data plots gather around 0.0242, which is approximately the same as the mean beach slope around the shoreline, 0.024.

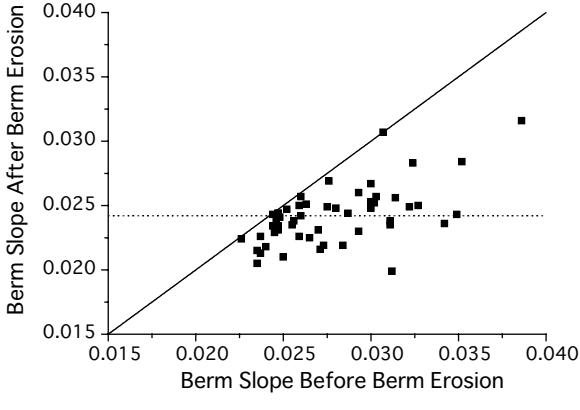

Fig. 6. Comparison of berm slopes of before and after beach erosion

Cross-shore Distribution of Cross-shore Sediment Transport Rate

The sediment transport volume of each cross-shore section is estimated from beach profile changes on the basis of a mass conservation equation, which is expressed as Eq. 3.

$$\frac{\Delta Q}{\Delta x} = \gamma \frac{\Delta z}{\Delta t}, \tag{3}$$

where Q is the cross-shore component of sediment transport rate per unit length in the alongshore direction, Δx is the spacing interval in the cross-shore direction, γ is the volume of sediment in a unit volume of the bed (= 0.7, Nielsen, 1992), z is the elevation, and t is the time.

The estimation of the cross-shore sediment transport rate with Eq. 3 is based on the assumption that the beach profile changes were induced by the cross-shore gradient of the cross-shore sediment transport, and the alongshore gradient of longshore sediment transport rate is ignored due to the alongshore uniformity of the topography around HORS (Kuriyama, 1991). This method has been applied to estimations of the cross-shore sediment transport rates in the surf zone (e.g., Kuriyama, 2002). Equation 3 becomes Eq. 4.

$$\left[Q(i,t) - Q(i-1,t)\right] = \gamma \frac{dz}{dt}\Delta x = \gamma \left[z(i,t) - z(i,t-1)\right]\frac{\Delta x}{\Delta t}, \tag{4}$$

where i is the number of the point where the cross-shore sediment transport rate is defined. The sediment transport rate for each position from the foot of the foredune, x = -115 m, to the offshore boundary is estimated using Eq. 4. The positive and negative values indicate the landward and the seaward sediment transport rate, respectively.

In order to consider the characteristics of the sediment transport rate for berm formation and erosion, the spatial distributions of sediment transport rate are calculated using Eq. 4. Figure 7 shows the spatial distribution of sediment transport rate for berm formation. Each line indicates the distribution of the sediment transport rate, and the berm formation cases total 219. The horizontal axis is the seaward position, x, normalized by the distance from the onshore boundary to the offshore boundary, X. The onshore boundary is set at the intersection point of the beach profile and the maximum wave run-up level. Therefore, the sediment transport rate at x/X = 0.0 should be zero or an extremely small amount. However, the rate at x/X = 0.0 has some value. Since the maximum wave run-up level is calculated using the statistical values derived from 20-minute data, which is observed every hour, the calculated maximum wave run-up level is not equivalent to the run-up level of the largest wave during the time. This may affect the variation of the sediment transport rate at x/X = 0.0.

The value of the sediment transport rate increased until approximately x/X = 0.40, and the variation of the sediment transport rate was relatively small between x/X = 0.0 and x/X = 0.4.

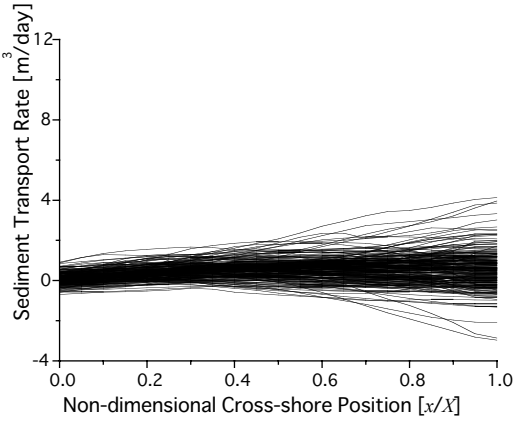

Fig. 7. Spatial distributions of sediment transport rate for berm formation (219 cases).

Figure 8 shows the spatial distribution of sediment transport rate for berm erosion. Each line indicates the distribution of the sediment transport rate, and the berm erosion cases total 58. For the same reason as the berm formation, the value of the sediment transport rate at $x/X = 0.0$ varies. The variation of the sediment transport rate is larger than that of the berm formation.

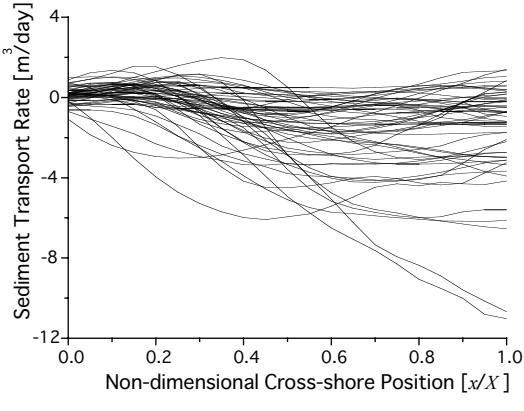

Fig. 8. Spatial distributions of sediment transport rate for berm erosion (58 cases).

The spatial distributions of the averaged sediment transport rate for berm formation and erosion are shown in Fig. 9. The bars indicate the standard error of the mean.

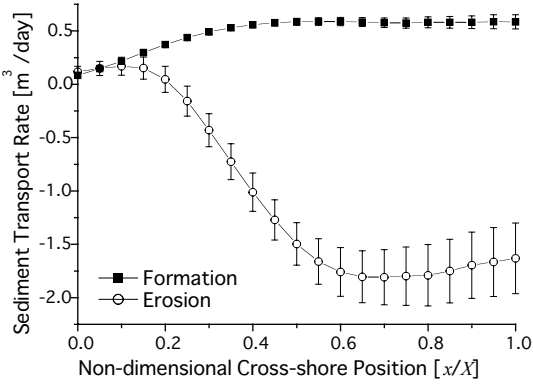

Fig. 9. Spatial distributions of averaged sediment transport rate for berm formation and erosion.

For berm formation, the landward sediment transport rate gradually increases until $x/X = 0.4$ and takes a steady value seaward of $x/X = 0.4$. This finding indicates that sediments mainly accumulate from $x/X = 0.0$ to 0.4 and a berm will be formed in this area. This can be inferred from the histogram of the berm crest position (Fig. 5). As for berm erosion, initially, the run-up wave washes sediment over the berm crest and sediments are transported landward. For this reason, the landward sediment transport rate has a high peak at $x/X = 0.10$ and sediment accumulation occur from $x/X = 0.0$ to 0.1. Next, the run-up water moves seaward with sediments washing over the berm. Therefore, after the peak of the landward sediment transport rate, the rate decreases until around $x/X = 0.6$. From $x/X = 0.6$, the rate becomes steady. Considering the distribution of the histogram of the berm crest position (Fig. 5), the peak seaward sediment transport rate occurs at nearly the same position as the berm crest position, $x/X = 0.29$.

Since the spatial scales of the berms is considered to be of nearly the same scale (see Fig. 3) and the berm slope becomes constant after berm erosion (see Fig. 6), the mass of the sediment transport volume due to berm erosion may be proportional to the berm height. Figure 10 shows the comparison of the berm height and the area of the berm, which is estimated by integrating the area above the straight line which begins at the maximum wave run-up position and extends to the intersection point between the onshore boundary and the beach profile.

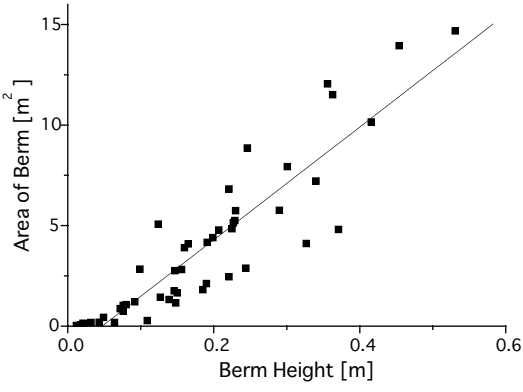

Fig. 10. Comparison of berm height and area.

The figure shows a linear correlation between the two (R^2 = 0.81). Thus, it can be assumed that the sediment transport rate for berm erosion can be estimated by using the berm height.

From Fig. 9, the spatial position at x/X = 0.4 for berm formation and at x/X = 0.1 and x/X = 0.6 for berm erosion are particular points of the spatial distributions of the sediment transport rate. Once the sediment transport rates of these points are formulated by using the wave energy flux, the berm height or any other parameters, the spatial distributions of the cross-shore sediment transport rate for berm formation and erosion can be estimated.

CONCLUSIONS

Beach profile data were obtained at HORS every weekday for the two and a half years, and the data set was used in order to investigate the characteristics of berm shape and the spatial distributions of the cross-shore sediment transport rate for berm formation and berm erosion. The investigation area is normalized by the distance from the onshore boundary, at the intersection point of the maximum wave run-up level and the beach profile, to the offshore boundary, where the standard deviation of beach profile takes the lowest value seaward of the mean shoreline position. Namely, the onshore boundary is set as x/X = 0.0 and the offshore boundary is set as x/X = 1.0. The conclusions obtained in the present study are as follows:

(1) The landward sediment transport rate for berm formation increases from x/X = 0.0 to x/X = 0.4 and becomes steady toward x/X = 1.0.
(2) The landward sediment transport rate for berm erosion peaks at x/X = 0.10, and the sediment transport rate changes in the seaward direction at x/X = 0.20. From that point, the rate decreases until x/X = 0.60.
(3) The averaged berm crest position just before berm erosion occurs is located at x/X = 0.29. During berm erosion, the peak seaward sediment transport occurs at nearly the same position as the berm crest position.

ACKNOWLEDGEMENTS

The authors would like to express our appreciation to the Kashima Port and Airport Construction Office, Ministry of Land Infrastructure and Transport and the Marine Information Division, Port and Airport Research Institute for allowing us to utilize the wave data of the Port of Kashima. We also thank all the staff members at HORS for conducting the field surveys.

REFERENCES

Austin M.J. and Masselink, G. (2006). "Observation of morphological change and sediment transport on a steep gravel beach", *Marine Geology*, Vol. 229, 59-77.

Eliot, I.G. and Clarke, D.J. (1986). "Minor storm impact on the beachface of a sheltered sandy beach", *Marine Geology*, Vol. 73, pp. 61-83.

Horn, D.P. and Mason, T. (1994). "Swash zone sediment transport modes", *Marine Geology*, Vol. 120, pp. 309-325.

Hughes, M.G., Masselink, G., Hanslow, D. and Mitchell, D. (1997). "Toward a better understanding of swash zone sediment transport", *Proc. Coastal Dynamics '97*, ASCE, pp. 804-813.

Katoh, K. and Yanagishima, S. (1992). "Berm formation and berm erosion", *Proc. 23rd Int. Conf. Coastal Eng.*, ASCE, pp. 2136-2149.

Katoh, K. and Yanagishima, S. (1993). "Beach erosion in a storm due to infragravity waves", *Rep. of PHRI*, Vol. 31, 5, pp. 73-102.

Kuriyama, Y. (1991), "Investigation of cross-shore sediment transport rates and flow parameters in the surf zone using field data", Report of the Port and Harbour Research Institute, Vol. 30, No. 2, pp. 3-58.

Kuriyama, Y. (2002), "Medium-term bar behavior and associated sediment transport at Hasaki, Japan", *J. Geophys. Res.*, Vol. 107, C9, 3132, doi:10.1029/ 2001JC000899.

Masselink, G. and Hughes, M. (1998). "Field investigation of sediment transport in the swash zone", *Continental Shelf Res.*, Vol. 18, 10, pp. 1179-1199.

Nielsen, P. (1992). "Coastal bottom boundary layers and sediment transport", World Scientific, River Edge, N. J., 324 pp.

Osborne, P.D. and Rooker, G.A. (1999). "Sand re-suspension Events in a high infragravity swash zone", *J. Coastal Res.*, Vol. 15, 1, pp. 74-86.

Puleo, J.A., Beach, R.A., Holman, R.A. and Allen, J.S. (2000). "Swash zone sediment suspension and transport and the importance of bore-generated turbulence", *J. Geophys. Res.*, Vol. 105, C7, pp. 17021-17044.

Puleo, J.A., Holland, K.T., Plant, N.G., Slinn, D.N. and Hanes, D.M. (2003). "Fluid acceleration on suspended sediment transport in the swash", *J. Geophys. Res.*, Vol. 108, C11, 3350, doi:10.1029/2003JC001943, 2003.

Thomas, K.V. and Baba, M. (1986). "Berm development on a monsoon-influenced microtidal beach", *Sedimentology*, Vol. 33, 4, pp. 537-546

SEDIMENT TRANSPORT PATTERNS DURING OVERWASH

Ana Matias[1], Ana Vila-Concejo[2], Óscar Ferreira[3],Brad Morris[4], João A. Dias[3]

1. CIACOMAR – Universidade do Algarve, Avenida 16 Junho, s/n, 8700-311 Olhão, Portugal. ammatias@ualg.pt.
2. Coastal Studies Unit, School of Geosciences F09, University of Sydney, Sydney NSW 2006, Australia. aconcejo@geosci.usyd.edu.au.
3. F.C.M.A./C.I.M.A. – Universidade do Algarve, Campus de Gambelas, 8005-139Faro, Portugal. oferreir@ualg.pt, jdias@ualg.pt
4. W.R.L., School of Civil and Environmental Engineering, University of New South Wales, King St, Manly Vale, Sydney NSW 2093, Australia. b.morris@wrl.undw.edu.au.

Abstract: Overwash is an important process in the evolution of barrier systems. The main aim of this paper is to present short-term measurements on sediment transport induced by overwash processes. For that purpose fieldwork campaigns were performed including measurements of oceanographic conditions, overwash flows, overwash-induced morphology variations, and sediment transport patterns. The sediment dynamics induced by overwash varied according to the washover morphology even though the tidal levels or incident energy were similar. The sediment movement inside the washover plain during an overwash event can be divided into three main stages: Stage 1 – Crest Accretion, Stage 2 – Onshore Transport, and Stage 3 – Dynamic Equilibrium. The sediment transport inside the washover lobe can be characterized by one onshore flow stage, but with variations in magnitude related to the tidal levels and breaking wave height.

INTRODUCTION

Overwash corresponds to a seawater intrusion over the frontal dune or, when absent, over the washover seaward limit. The main types of washover morphologies are: (1) washover plain, and (2) washover lobe (Matias, 2006). The washover plain is a wide and low-lying denuded area where overwash is frequent, and have been named also as washover ramp (Fisher and Simpson 1979), washover sheet (e.g. Ritchie and Penland 1988), washover flat (e.g. Holland *et al.* 1991), and washover terrace (e.g. Bray and

Carter 1992). The washover lobe is a laterally confined feature that cut the dune field in specific places, and has also been named as hurricane channel (e.g. Hayes 1967), washover breach (e.g. Hosier and Cleary 1977), overwash features (e.g. Armon and McCann 1979), washovers (e.g. Fisher and Simpson 1979), washover fan (e.g. Kochel and Wampfler 1989), individual washovers (e.g. Bray and Carter 1992), and perched fans (Morton and Sallenger 2003).

The evaluation of sediment transport induced by overwash constitutes a major issue in coastal processes, predominantly moving sand from the beach face to the washovers and backbarrier environments (e.g. Hayes 1967; Schwartz, 1975). The sediment transport during overwash events has been measured through surveys performed before and after a storm (e.g. Fisher *et al.* 1974; Stone *et al.* 2004), and also by measuring the washover dimensions and deposit thickness (e.g. Schwartz 1975; FitzGerald *et al.* 1994). The overwash sediment transport has also been semi-quantitatively evaluated with ground photographs and aerial vertical or oblique photographs by measurements of overwash intrusion, normally identified by the contact between fresh sand and marsh/dune vegetation (e.g. Cleary *et al.* 2001; Morton and Sallenger 2003), or by the existence of a debris-line, particularly noticeable in developed coasts (e.g. Nordstrom and Jackson 1995; Webb *et al.* 1997).

Despite the variety of studies related to overwash processes, there is still a lack of detailed knowledge about short-term overwash sediment transport at washover plains and lobes. In situ measurements of overwash sediment transport are scarce, and no application of tracers was found in the literature. Sediment transport studies using fluorescent tracers (FT) have been very important in the development of coastal theories and were used for diverse purposes like the quantification of sediment transport on swash platforms (Oertel 1972), on submarine sand banks (Collins *et al.* 1995), on tidal inlet margins (Vila-Concejo *et al.* 2004), longshore sediment transport (Komar and Inman 1970), and harbour infilling processes (Ferreira *et al.* 2002). The objective of this work is the definition of sediment transport stages and patterns under confined and unconfined overwash flows, using detailed field studies.

STUDY AREA

The study area is the western part of Barreta Island, located on the Ria Formosa barrier island system, Algarve, Portugal (Figure 1). The system is composed of five islands and two peninsulas that extend over 55 km.

The western part of Barreta Island is on the downdrift margin of the Ancão Inlet (Figure 1). This inlet undergoes eastwards migration cycles, and the study area is located inside the inlet migration path. In June 1997 Ancão Inlet was artificially opened, and reached its dynamic equilibrium as a "mature migrating inlet" in May-July 1999 (Vila-Concejo *et al.* 2003).

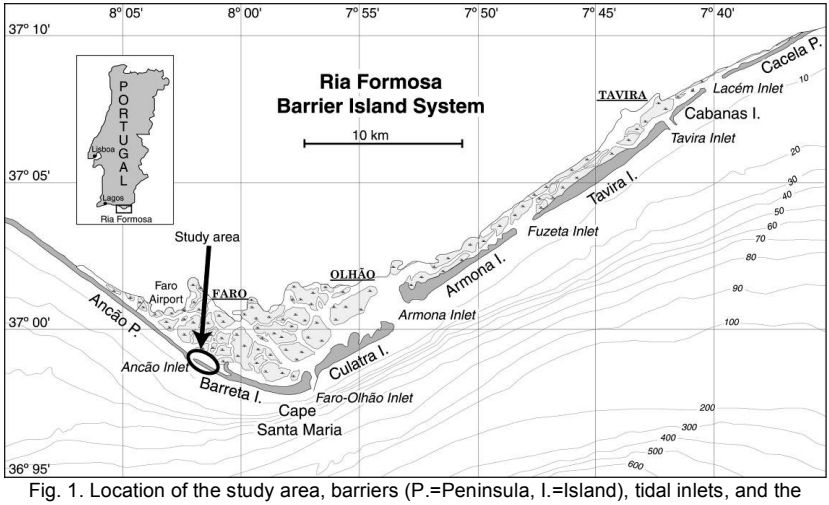

Fig. 1. Location of the study area, barriers (P.=Peninsula, I.=Island), tidal inlets, and the bathymetry of the adjacent continental shelf (in meters).

Whilst Ancão Inlet was evolving towards dynamic equilibrium, it was acting as a sediment trap, and therefore Barreta Island was undergoing sediment starvation that caused dune erosion and shoreline retreat. Due to the erosion of the dunes, overwash processes were frequent forming washover lobes and an extensive washover plain.

The Ria Formosa barrier island system is mesotidal, with mean tidal range of about 2 m that can reach up to 3.5 m during spring tides. Offshore wave climate is dominated by west-southwest waves (71% of occurrences; Costa *et al.* 2001). SE waves that consist of short period waves generated by regional winds (locally called "Levante") are also frequent (about 23%; Costa *et al.* 2001). Wave energy is moderate with an average annual significant offshore wave height (H_{SO}) of 1.0 m and average peak period (Tp) of 8.2 s (Costa *et al.* 2001). Between 1986 and 1993, storm conditions (defined as $H_{SO} > 3$m) corresponded to 1% of the offshore wave climate (Costa 1994). The western part of Barreta Island has a northwest-southeast orientation, therefore directly exposed to the W-SW longer fetch waves, but sheltered with respect to SE waves.

METHODS

Fieldwork data collection

Two fieldwork campaigns were made: GO.1 (February 9-10, 2001) and GO.3 (February 18-19, 2003). Fieldwork was undertaken on a washover plain during GO.1 and on a washover lobe during GO.3 (Figure 2).

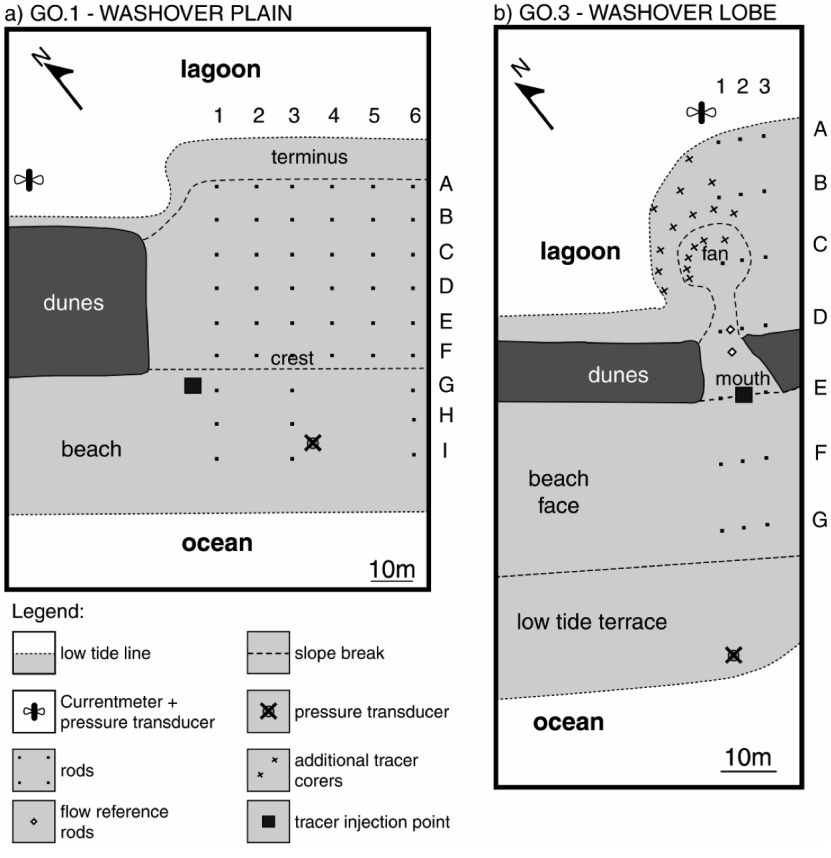

Fig. 2. Setting of the GO.1 and GO.3 fieldwork campaigns.

Pressure transducers were deployed on the beach (at a sample rate of 4 Hz), and on the lagoon side (at a sample rate of 0.1 Hz) for both campaigns. During GO.3 the overwash velocity was measured by timing the passage of the overwash water front between rods located at the washover channel (Figure 2b).

For GO.1, a 10×10 m grid of rods was established over the beach and washover plain (Figure 2a), covering an area of about 4,000 m^2. For GO.3, an irregular grid was established that was composed of three cross-shore profiles (1 to 3 in Figure 2b), 4 m apart, seven longshore profiles (A to G in Figure 2b), 10-12 m apart, and two additional rods on the central lobe (diamonds in Figure 2b) and 17 on the fan (crosses in Figure 2b). Surveys were made using a total station (GO.1) and a real-time kinematic DGPS (GO.3). During both fieldwork campaigns surveys were conducted before and after

overwash, and the rod heights were measured every 30 minutes, during the overwash events.

During GO.1, 40 kg of FT were placed at the top of the beach face, 1 m from the washover crest; and during GO.3, 42 kg of FT were dropped into the flow at the washover mouth. Shallow cores were taken manually after the overwash event, next to each rod. The obtained cores (41 for GO.1 and 31 for GO.3) were sub-sampled every 5 cm. Figure 2 shows detailed sketches of set up for the fieldwork campaigns.

Data processing and laboratory procedures

The PT data was used for wave and tide computations (sensor location in Figure 2). The PT on the lagoon side was also used for tidal computations. The procedures to determine the tidal elevation can be found in Matias (2006). The wave parameters (significant wave height at breaking, H_{sb} and peak period, Tp) were calculated using the methods of moments (described in USACE, 2002).

For all topographic surveys, the cross-shore profiles were obtained and the volume computations were made, using the kriging interpolation method with a linear variogram to make the upper surface and using the mean sea level (MSL) as base line.

From the sub-samples of the cores an aliquot of 20 g was obtained, the number of FT grains was counted under UV light and the counting was used to generate maps of FT distribution for each 5 cm layer. The definition of FT mass centroids was obtained by applying the Spatial Integration Method (Komar and Inman 1970; Madsen 1987) that is an average location of the FT cloud weighted by the mass of FT at each position of the grid. The percentage of remaining tracer (i.e. the relation between the FT injected and the FT sampled; named percentage of recovery in Madsen 1987 and Ciavola *et al.* 1998) was estimated using the method developed by Vila-Concejo *et al.* (2004). This method consists in determining the mass of FT remaining in the study area (the sum of all FT in each layer) by obtaining an estimation of FT mass in the volume represented by each sample, through a density relation.

RESULTS

Both campaigns were made during equinoctial spring tides, with a maximum oceanic tidal level of 1.71 m above MSL for GO.1 and 1.69 m above MSL for GO.3. For the lagoon side, approximately the same maximum tidal levels were reached for both campaigns (1.67 m above MSL).

Average H_{sb} for GO.1 was 1.28 m and average Tp was 11.1 s. For GO.3, the average H_{sb} was 1.21 m and average Tp was 16.0 s. For both campaigns, H_{sb} was somewhat variable during fieldwork (GO.1: 0.57-1.39 m, GO.3: 0.62-1.25 m) because the instruments were located inside the beach system, and therefore the recorded waves were greatly influenced by the nearshore topography.

The overwash event during GO.1 fieldwork started at 01:27 and finished at 06:02, February 10th 2001, with complete overwash occurring between 02:10 and 04:54. The overwash event during the GO.3 fieldwork started at 01:59 and finished at 05:27, February 19th 2003, with complete overwash occurring between 02:44 and 04:39. The overwash flow velocities measured between rods during GO.3 fieldwork varied between 0.9 m/s and 5.7 m/s; however the most frequent velocities range between 2.5 and 3.0 m/s.

The six cross-shore profiles measured before and after the overwash event of GO.1 fieldwork, showed relatively similar morphologic variations. The greatest variation occurred on the washover crest, where an overall accretion of about 16 cm of sand occurred (Figure 3).

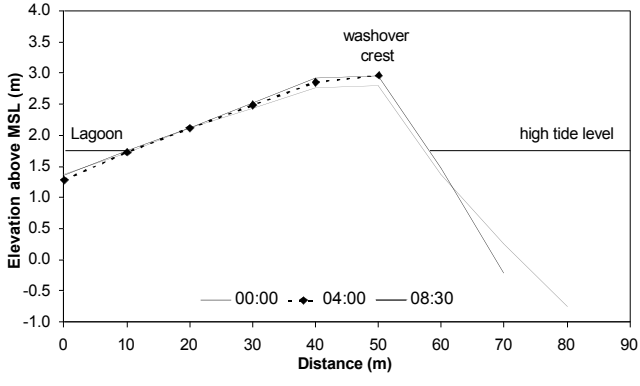

Fig. 3. Washover plain morphologic variations for an average cross-shore profile (profiles 1 to 6 of Figure 2), during GO.1 fieldwork campaign.

The accretion was wedge shaped, with a null point located above lagoon high tide level, below which the small variations (generally less than 10 cm) can be attributed to the lagoon currents. The accretion mostly occurred until 04:00; after which time small morphologic variations were noticed. The average volume variation in the study area was approximately +3.4 m^3/m.

During GO.3 fieldwork, the washover lobe central profile showed erosion on the mouth and channel, and accretion on the fan (Figure 4). On the contrary to the washover plain, some morphological changes were noticed, after 04:00. The volume variation of the central lobe profile was +4.7 m^3/m.

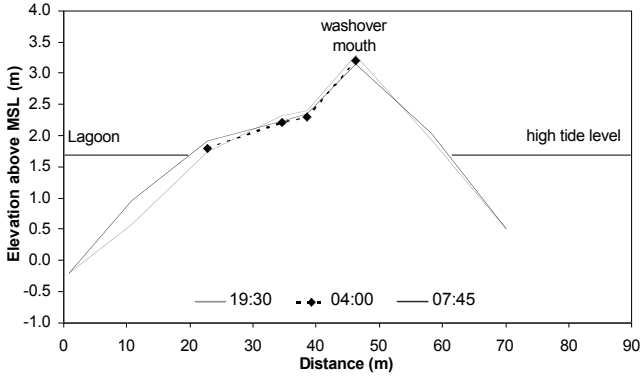

Fig. 4. Morphologic variations during GO.3 fieldwork for the washover lobe central profile.

The transport of the 40 kg of tracer during GO.1 began at 00:43 on February 10th 2001. The FT distribution map of GO.1 point to two main areas of sand transport, one landward of the injection point and another near the SE end of the sampling grid (Figure 5). However, the higher FT counting was next to or at less than 10 m landward from the injection point.

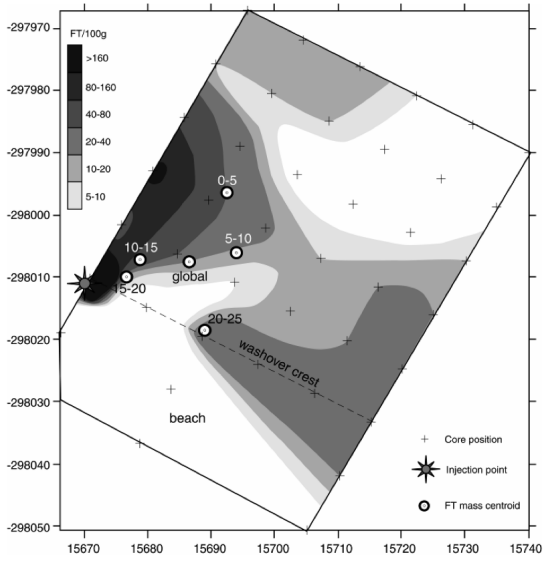

Fig. 5. FT distribution map integrating all sampled layers (0 to 25 cm depth), for GO.1 fieldwork. Mass centroids location is also represented.

About 57% of the FT counted in the laboratory was in the layers 10-15 cm and 15-20 cm, and only about 4% were in the deepest layer (20-25 cm). The mass centroid positions constitute an estimate of the average transport distance for each of the layers. The deepest layer (20-25 cm) shows a displacement in relation to the injection point that is dominated by the longshore downdrift component, yet in the superficial layer (0-5 cm) the average FT transport is dominated by the cross-shore landward component (Figure 5). The remaining percentage of FT on the sampled area after overwash was about 68%.

The FT distribution maps of GO.3 showed a progressive displacement of the FT cloud and mass centroids landward, from the deepest layers (20-25 cm, Figure 6e) to the superficial layer (0-5 cm, Figure 6a). In some layers (0-5 cm and 10-15 cm) there was FT transport to an adjacent eastwards washover; however the highest concentrations were located on the top of the washover fan belonging to the washover lobe (Figure 6). The layer that had the highest count was the deepest (20-25 cm), with the two superficial layers (0-5 cm and 5-10 cm) accounting for only 18% of the count. The remaining percentage of FT on the sampled area after overwash was about 77%.

DISCUSSION

The two fieldwork campaigns recorded non-storm overwash events that resulted from average winter waves ($H_{sb} \approx 1.2$ m) coupled with equinoctial spring tides (tidal level ≈ 1.7 m above MSL). However, the measured overwash flow velocities are in the same magnitude (around 2 m/s) as the ones found in the literature for storm overwash. Leatherman (1977) obtained a mean overwash flow velocity of 1.95 m/s, with an electromagnetic current meter, in Assateague Island (U.S.A); Leatherman and Zaremba (1987) measured 0.5 m/s to 2.0 m/s overwash flow velocities, with an electromagnetic current meter at Nauset Spit-Eastham (U.S.A); mean velocities of 2.0 m/s, measured with a video recording system, were obtained by Holland *et al.* (1991) at the Isles Dernieres (U.S.A.); Bray and Carter (1992) measured by timing wooden floats between markers, overwash flow velocities between 1 and 3 m/s at a barrier in Lake Erie (U.S.A); and a maximum of 1.5 m/s was the overwash flow measured with a flow meter through the Trabucador Bar, Spain (Guillén *et al.* 1994).

The two fieldwork campaigns recorded overwash events under similar oceanographic conditions, therefore the differences in sediment transport were mostly related to the morphologic characteristics of the washovers.

The shape of the washover plain was of a convex featureless surface, gently dipping landward (Figure 3). The washover crest marks the transition between the top of the beach and the washover, and had an asymmetrical cross-sectional profile with a steep side facing seaward (slope of about 0.14) and a gentle slope side facing landward (slope of about 0.03). During the early stages of overwash, when the intrusion was relatively small, the upper beach face and the washover crest were in sedimentary connection. The sediment transport in this stage had an important longshore component (mass centroid of layer 20-25 cm, Figure 5). The washover crest was the most dynamic part (Figure 3),

with accretion taking place as a consequence of the drop in flow capacity as the overwash overcomes the crest and flows over a gently landward dipping surface. Therefore, the convex crest shape was a very significant factor in retarding the flow progression.

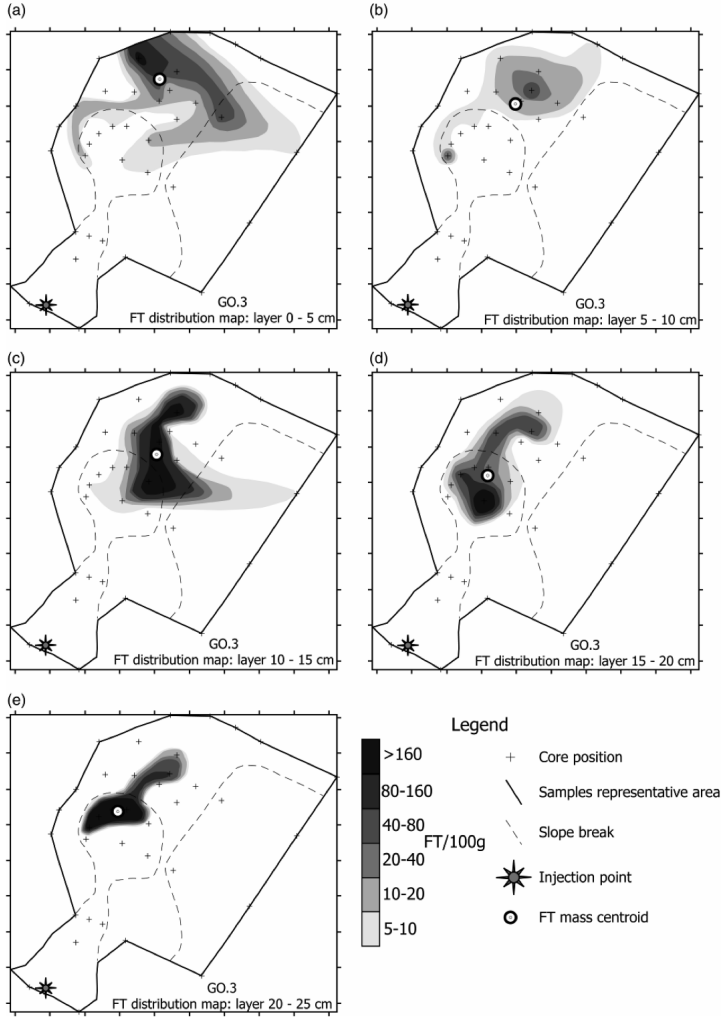

Fig. 6. FT distribution map for all sampled layers, for GO.3 fieldwork: (a) 0-5 cm, (b) 5-10 cm, (c) 10-15 cm, (d) 15-20 cm, and (e) 20-25 cm depth. Mass centroids are also represented.

As overwash frequency increased the onshore sediment transport became more significant. The patterns show that there was very small longshore transport of the tracer, thus suggesting that the overwash flow induced transport was dominantly cross-shore. It was found that the overwash flows on washover plains were constructive, generating a wedge-like layer of sand (Figure 3), denoting a decrease in flow capacity as it progresses through the washover surface. The sediment movement on the washover plain during an overwash event can be divided into three main stages: Stage 1 – Crest Accretion, Stage 2 – Onshore Transport, and Stage 3 – Dynamic Equilibrium. Stage 1 is characterized by the early overwash flows, where the crest is overtopped but the progression of the flow is inhibited by the friction and infiltration on a gentle landward angle crest. Stage 2 corresponds to a higher tidal level that induces an increase in overwash frequency and intrusion, and the occurrence of complete overwash. Once the tide starts to drop Stage 3 begins, inducing almost negligible morphological changes even though overwash continues to occur.

The washover lobe was distinct from the washover plain, not only in plan-view (Figure 2) with a distinct teardrop shape, but also in cross-shore profile (Figure 4). The mouth was very sharp and well defined (Figure 4), marking the transition between the steep beach face (slope of about 0.11) and the steep washover channel (slope of about 0.11). Landward of the channel, the gently dipping slope of the washover fan ended in the prograding steep distal fan. During the overwash event, the cross-shore profile had significant morphological changes, especially erosion of the seaward washover morphologies (mouth and channel) and accretion of the landward morphology (washover fan distal surface, Figure 4). Dune erosion, due to wave-generated run up impingement, caused the deepening and enlargement of the washover mouth. Once the mouth was overwashed, the lateral restriction of the flow in the channel together with the steeper landward slope induced the increase of the flow velocity and subsequent erosion. The bottom friction and infiltration on the surface, together with a lateral spreading due to the absence of dunes on the lagoon side of the barrier, induced a deceleration of the flow and the consequent sand deposition. During the early stages of overwash the deposition was closer to the washover channel (deepest layers, Figures 6d and 6e) and at later stages the deposition was displaced towards the lagoon (superficial layers, Figures 6a and 6b).

CONCLUSION

An innovative set of data was acquired for non-storm overwash occurring on a low barrier island. The overwash flow velocities under these non-storm events had the same order of magnitude as reported by other studies of storm overwash. The same magnitude of waves and similar tidal amplitudes induced different sediment transport patterns according to the washover morphology. Sediment transport inside washover plains and lobes was supported by the sequence of processes that occurred during the overwash events and that were noticeable by the integration of measurements of topography and tracers. The different types of sediment transport stages and patterns were interpreted as a result of distinct interactions between the overwash flow and the three-dimensional morphology of the washovers.

ACKNOWLEDGEMENTS

The authors gratefully acknowledge the people that made fieldwork under very difficult and demanding conditions. The work was partially funded by the project PRIMO (POCTI/CTA/39849/2001). Ana Matias was supported by CIMA-Universidade do Algarve grant CIMA/GT1-01/2005 and FCT grant SFRH/BPD/18476/2004.

REFERENCES

Armon, J.W., and McCann, S.B. (1979). "Morphology and landward sediment transfer in a transgressive barrier island system, southern Gulf of St. Lawrence, Canada," *Marine Geology* 31, 333-344.

Bray, T.F., and Carter, C.H. (1992). "Physical processes and sedimentary record of a modern, transgressive, lacustrine barrier island," *Marine Geology* 105, 155-168.

Ciavola, P., Dias, N., Ferreira, Ó., Taborda, R., Dias, J.A. (1998). "Fluorescent sands for measurement of longshore transport rates: a case study from Praia de Faro in southern Portugal," *Geo-Marine Letters* 18, 49-57.

Cleary, W.J., McLeod, M.A., Rauscher, M.A., Johnston, M.K., Riggs, S.R. (2001). "Beach nourishment on hurricane impacted barriers in Southeastern North Carolina, USA: targeting shoreface and tidal inlet sand resources," *Journal of Coastal Research* (SI) 34, 232-255.

Collins, M.B., Simwell, S.J., Gao, S.S., Powell, H., Hewitson, C., Taylor, J.A. (1995). "Water and sediment movement in the vicinity of linear sandbanks: the Norfolk Banks, southern North Sea," *Marine Geology* 123, 125-142.

Costa, C. (1994). "Final Report of Sub-Project A. Wind Wave Climatology of the Portuguese Coast," Report PO-WAVES 6/94-A, IH/LNEC, 80 p.

Costa, M., Silva, R., Vitorino, J. (2001). "Contribuição para o estudo do clima de agitação marítima na costa portuguesa". *Proceedings of 2as Jornadas Portuguesas de Engenharia Costeira e Portuária*, International Navigation Association PIANC, Sines, Portugal (in Portuguese).

Ferreira, Ó., Fachin, S., Coli, A., Taborda, R., Dias, J.A., Lontra, G. (2002). "Study of a harbour infilling using sand tracer experiments," *Journal of Coastal Research* SI (36), 283-289.

Fisher, J.J., and Simpson, E.J. (1979). "Washover and tidal sedimentation rates as environmental factors in development of a transgressive barrier shoreline", In: *Barrier Islands – From the Gulf of St. Lawrence to the Gulf of Mexico* (ed. S. P. Leatherman), Academic Press, 127-148.

Fisher, J.S., Leatherman, S.P., Perry, F.C. (1974). "Overwash processes on Assateague Island," *Proceedings of 14th Conference on Coastal Engineering*, ASCE, 1194-1211.

FitzGerald, D.M., Van-Heteren, S., Montello, T.M. (1994). "Shoreline processes and damage resulting from the Halloween Eve storm of 1991 along the north and south shores of Massachusetts Bay, USA," *Journal of Coastal Research* 10 (1), 113-132.

Guillén, J., Camp, J., Palanques, A. (1994). "Short-time evolution of a microtidal barrier-lagoon system affected by storm and overwashing: the Trabucador Bar (Ebro Delta, NW Mediterranean)," *Zeitschrift für Geomorphologie* 38 (3), 267-281.

Hayes, M.O. (1967)." Hurricanes as geological agents: Case sudies of Hurricane Carla, 1961, and Cindy, 1963," Report of Investigations no. 61, Bureau of Economic Geology, University of Texas, Austin, 54 p.

Holland, K.T., Holman, R.A., Sallenger, A.H. (1991). "Estimation of overwash bore velocities using video techniques," *Proceedings of the International Conference on Coastal Sediments '91*, ASCE, 489-497.

Hosier, P.E., and Cleary, W.J. (1977). "Cyclic geomorphic patterns of washover on a barrier island in southeastern North Carolina," *Environmental Geology* 2, 23-31.

Kochel, R.C., and Wampfler, L.A. (1989). "Relative role of overwash and aeolian processes on washover fans, Assateague Island, Virginia-Maryland," *Journal of Coastal Research* 5 (3), 453-475.

Komar, P.D., and Inman, D.L. (1970). "Longshore sand transport on beaches," *Journal of Geophysical Research* 75, 5514-5527.

Leatherman, S.P. (1977). "Overwash hydraulics and sediment transport," *Proceedings of Coastal Sediments '77*, ASCE, 135-148.

Leatherman, S.P., and Zaremba, R.E. (1987). "Overwash and Aeolian Processes on a US Northeast Coast Barrier," *Sedimentary Geology* 52 (3-4), 183-206.

Madsen, O.S. (1987). "Use of tracers in sediment transport studies," *Proceedings of the International Conference on Coastal Sediments '87*, ASCE, 424-435.

Matias, A. (2006). "Overwash sedimentary dynamics in the Ria Formosa barrier islands," PhD thesis, Universidade do Algarve, 253 p.

Morton, R.A., and Sallenger, A.H. (2003). "Morphological impacts of extreme storms on sandy beaches and barriers," *Journal of Coastal Research* 19 (3), 560-573.

Nordstrom, K.F., and Jackson, N.L. (1995). "Temporal scales of landscape change following storms on a human-altered coast, New Jersey, USA," *Journal of Coastal Conservation* 1 (1), 51-62.

Oertel, G.F. (1972). "Sediment transport of estuary entrance shoals and the formation of swash platforms," *Journal of Sedimentary Petrology* 42 (4), 857-863.

Orford, J.D., and Carter, R.W.G. (1982). "Crestal overtop and washover sedimentation on a fringing sandy gravel coast, Carnsore Point, Southeast Ireland," *Journal of Sedimentary Petrology* 1, 265-278.

Ritchie, W., and Penland, S. (1988). "Rapid dune changes associated with overwash processes on the deltaic coast of South Louisiana," *Marine Geology* 81, 97-122.

Schwartz, R.K. (1975). "Nature and genesis of some storm washover deposits," Technical memorandum, Coastal Engineering Research Center, 61, 69 pp.

Stone, G., Liu, B., Pepper, D.A., Wang, P. (2004). "The importance of extratropical and tropical cyclones on the short-term evolution of barrier islands along the northern Gulf of Mexico, USA," *Marine Geology* 210, 63-78.

USACE (2002). "Coastal Engineering Manual – Part II," U.S. Army Corp of Engineers Report no. EM1110-2-1100-PartII, 121p.

Vila-Concejo, A., Ferreira, Ó., Matias, A., Dias, J.A. (2003). "The first two years of an inlet: sedimentary dynamics," *Continental Shelf Research* 23, 1425-1445.

Vila-Concejo, A., Ferreira, Ó., Ciavola, P., Matias, A., Dias, J.A. (2004). "Tracer studies on the updrift margin of a complex inlet system," *Marine Geology* 208, 43-72.

Webb, C.A., Bush, D.M., Young, R.S. (1997). "Property damage lessons from Hurricane Opal: The Florida panhandle coast, October 4, 1995," *Journal of Coastal Research* 13 (1), 246-252.

CHARACTERISATION AND MODELLING OF WASHOVER FANS

Chantal Donnelly[1], Asbury H. Sallenger.[2]

1. Department of Water Resources Engineering, Lund University, Box 118, S-221 00 Lund, SWEDEN
   Chantal.Donnelly@tvrl.lth.se
2. USGS, Center for Coastal and Watershed Studies, 600 4th. Street S., St. Petersburg, FL 33701, U.S.A.
   asallenger@usgs.gov

Abstract: Pre- and post-storm topography and aerial photography, collected in regions where new washover fans were formed, were studied to determine the extent of morphologic, vegetative and anthropogenic control on washover shape and extent. When overwash is funnelled through a gap in a dune ridge and then spreads laterally on the back barrier, decelerating and depositing sediment, it forms washover fans. Fans were shown to primarily occur at pre-existing gaps in the foredune. During overwash, these gaps, or overwash throats, widened and deepened. The shape and extent of the fan was shown to depend on not only the pre-storm topography, but also the existence of beach tracks, roads and other anthropogenic influences and vegetation. The cross-shore overwash profile change model by Larson et al. (2005) and Donnelly et al. (2005) was modified to include pre-storm throat widths and a lateral spreading angle estimated from the pre-storm topography as inputs and tested using cross-shore profiles through the fan centres. These new inputs make the model more generalised, such that the calibrated model is applicable to a wider range of cross-shore profiles.

INTRODUCTION

Recent increases in frequency and intensity of tropical storms highlight the importance of understanding physical storm phenomena such as overwash. Overwash is the transport of water and sand landward of the beach crest by elevated wave and water levels, sometimes as far as the back barrier bay or lagoon (in the case of barrier island overwash). The sediment deposited by overwash is usually described as washover.

Washover contributes to the sediment budget of barrier islands and is thought to maintain the width of barrier islands as they migrate landward. It can also provide specific habitat for endangered species such as the piping plover. Overwash can also be a hazard, particularly on developed coasts where water and sand intrusion, scour (of coastal roads for example), and even structural damage by debris entrained in the overwashing flow cause problems. The ability to predict the occurrence, magnitude and shape of overwash deposits is therefore of importance to coastal managers, authorities and residents alike. The causes of overwash and overwash processes are well documented (e.g. Hayes 1967, Leatherman 1976, Donnelly et al. 2006), and the ability to predict overwash occurrence (Sallenger et al. 2000) and model beach profile change due to overwash (Wise et al. 1996 , Larson et al. 2005, Donnelly et al. 2005) is just beginning to emerge.

Washover fans are formed when overwash is focused through a local gap in the dune ridge. This gap is known as an overwash throat. Behind the dune ridge the overwashing flow spreads laterally. At the same time the flow decelerates due to the combined effects of lateral spreading, friction and infiltration. Local topography changes may also decelerate (or accelerate) flow. As the flow decelerates, entrained sediment is deposited, forming a washover fan. Such features are commonly identified on the US Gulf and Atlantic coasts following major hurricanes and northeasterly storms.

Data consisting of high resolution, three-dimensional, pre-and post-storm topography collected by lidar, and oblique aerial photography, were collated for several washover fans. The data showed washover fans on Hatteras Island, NC, following Hurricane Isabel, 2003. This high quality data provided the unique opportunity to, for a number of deposits, analyse washover fan shapes and morphologies, measure pre- and post-storm washover throat widths, identify topographical and surface texture restraints on lateral spreading, and in some cases, estimate a potential lateral spreading angle.

Using measurements of the throat width, B_{pre}, and the potential lateral spreading angle, β, an existing algorithm for overwash flow behind the crest of a mainland or barrier beach by Donnelly et al. (2005) and Larson et al. (2005) was tested with these new inputs. Previously these dimensions have been included in the model through coefficients which were calibrated to the post-storm data. The inclusion of these new inputs makes the model more generalised, and hence a calibrated model should be applicable to a wider range of profiles.

DATA EMPLOYED

Hatteras Island is an 80 km long barrier island located in North Carolina, on the Atlantic Coast of the U.S.A. The island has a distinct bend at Cape Hatteras such that the southern portion of the island is facing south-southeast while the northern portion of the island faces east-southeast (Figure 1). The island is relatively undeveloped, with a population of just 4000. A paved road extends parallel to the shore along the island. Hurricane Isabel made landfall as a category 2 hurricane on September 18, 2003 near Cape Hatteras causing numerous washover deposits along the coast. Maximum

sustained winds of 128 km/hr were measured near the cape, and maximum deepwater wave heights were estimated to exceed 15 m offshore of the cape. Along the Hatteras coast, the storm surge exceeded 2m (Fauver 2005).

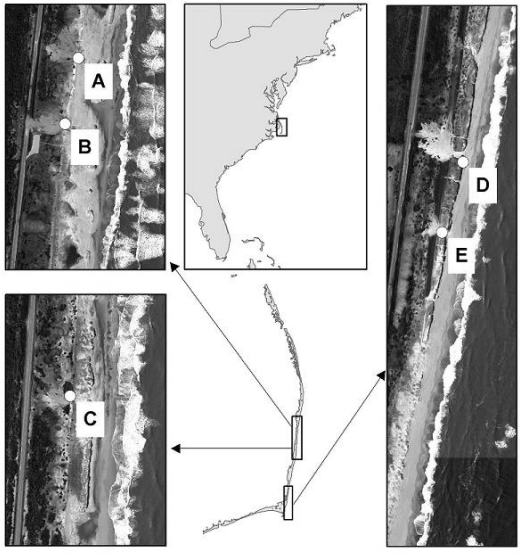

Figure 1. Location map showing U.S. Atlantic Coast, Hatteras Island, and aerial photographs showing locations of the studied fan deposits.

Airborne topographic lidar (light detection and ranging) surveys were used to collect topographical data along the Hatteras Island shoreline immediately prior to and after the landfall of Hurricane Isabel. The pre-storm survey was made September 16, 2003, immediately prior to the first storm wave impacts on the shoreline (Fauver 2005) and the post-storm survey was made on September 21, 2003. The topographic survey data analyzed in this study was collected approximately 45 km northeast of the point of landfall. Oblique and geo-rectified aerial photographs of the Hatteras coastline were also taken on September 21, and these may be compared with pre-storm oblique aerial photographs taken after the previous major storm in 1999.

Lidar surveys allow the rapid collection of large regions of topographic data. Further information about the lidar survey technique and its application in the coastal environment can be found in Brock et al. (2002). In a study statistically comparing data collected using lidar with three traditional ground survey techniques, the accuracy of the individual lidar elevation measurements was deemed to be approximately 15 cm (Sallenger et al. 2003). This level of accuracy is generally suitable for studying changes due to overwash. Large deposit regions with thicknesses of the order of 10-15 cm are observed; however if the measurement error is not systematic, the existence of these

deposits is true, even if the accuracy of the deposit thickness may vary from that measured.

Three regions of pre- and post-storm topographic lidar data in which washover fans occurred were selected (Figure 1). All data is from the section of shoreline north of Cape Hatteras. Each region encompassed a stretch of coastline approximately 650 m long and 250 – 300 m wide from the shoreline landwards. The survey data was linearly triangulated onto a 2 x 2 m grid and plotted on contour maps to evaluate the pre- and post- storm topography. A difference grid, showing the differences in elevation between the pre-storm and the post-storm grids was also calculated and plotted as a contour map, the topography differences map. Cross-sections and alongshore sections were extracted from the grid data for regions of interest.

Hydrodynamic data was also available. A 3-hourly time-series of significant wave-height and peak wave period was extracted from NOAA's WAVEWATCH III model (Tolman 1997, 1999) for a period spanning the pre- and post-storm surveys. The data was extracted at the pre-storm location of the Diamond Shoals wave buoy (41025, depth 54.9 m), which stopped recording some hours prior to storm landfall, hence the use of hindcast wave characteristics. The nearest NOAA tidal gauge, Hatteras Fishing Pier, also failed during the peak of the storm; however, water level data is available from the NOAA Duck Field Research Facility tidal gauge (8651370) which was shown to correlate well with the Hatteras gauge prior to failure (Fauver 2005).

The combination of pre- and post storm topographic data and aerial photography taken immediately prior to and following a hurricane landfall, the sections plotted from the data, and the associated hydrodynamic data, allowed the opportunity to study the morphologic, anthropogenic and surface texture controls on washover fan formation, and model cross-shore profile change caused by overwash using knowledge of these controls.

DATA ANALYSIS

The post-storm changes on the island can be evaluated by examining the topography differences map (the difference between the post-storm and pre-storm elevations) and the post-storm aerial photography. Figure 2 shows an example of a topography differences map (left) beside the pre-storm topography map (right). Positive values of topography difference indicate deposition, and negative values indicate erosion. A general inspection of these maps indicates erosion of the dune face and crest and isolated deposits behind the pre-storm dune location. These are washover fan deposits (dashed outline, Figure 2).

Five distinct washover fans were observed in the three regions. These are labelled *Fan A* to *Fan E* from north to south, as shown in Figure 1. Immediately seaward of the washover fans the rear dune slope is also eroded and a region of higher erosion rates exists through the dune. This is the overwash throat (solid outline, Figure 2). During overwash, overtopping flow is channelled through pre-existing gaps in the foredune and

then spreads laterally behind the dune where the topographical restraints on the flow are more limited. Sheet overwash can occur when the entire dune ridge is overwashed, but this study is limited to confined overwash.

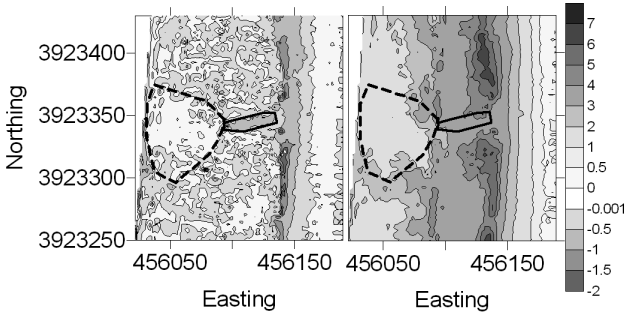

Figure 2 – Pre- and post-storm Topography Differences Map (left) and Pre-storm topography map (right), showing the region of deposition in the washover fan (dotted line) and the region of erosion in the overwash throat (solid line) for Fan C.

Overwash Throats

Comparison of the post-storm throat locations with the pre-storm topography indicates that the location of the overwash throats is primarily determined by pre-existing gaps in the foredune ridge, as can be seen on Figure 2, for Fan C. This has been recognised in overwash literature (e.g. Cleary and Hosier 1979, Dolan and Hayden 1981). The pre-storm photography indicated a pre-existing washover fan at this location.

In the regions where Fans C, D and E occurred, prominent foredune ridges, up to 7 m in height existed. No pre-existing washover fans were observed at the locations of Fans D and E, but the pre-storm topography indicates gaps in the foredune at these locations.

Fans A and B occurred behind a secondary dune ridge. The pre-storm topography does not indicate pre-existing gaps in this dune ridge; however, there were gaps in the foredune ridge directly in front of the fan locations. Additionally, the aerial photography indicates a beach access path passing through the rear dune ridge at the location of Fan B. The pre- and post-storm topography maps for Fan B are shown in Figure 3. The post-storm topography shows that most of the foredune was destroyed. It is suggested that the overwashing flow channelled in the foredune overwash throat had sufficient velocity to overwash the rear-dune, forming an overwash throat through which subsequent overwash was channelled. Along most of this coastal section, the pre-existing foredune throats widened, until eventually they merged. Rapid widening of washover throats was observed in experiments conducted by Donnelly et al. (2005) and Tuan et al. (2006). Sheet overwash of the beach crest would then have been possible. Note that there is some remnant of the foredune remaining directly in front of the rear dune throat, indicating that channelling during the entire storm contributed to the fan formation through the rear dune at this location.

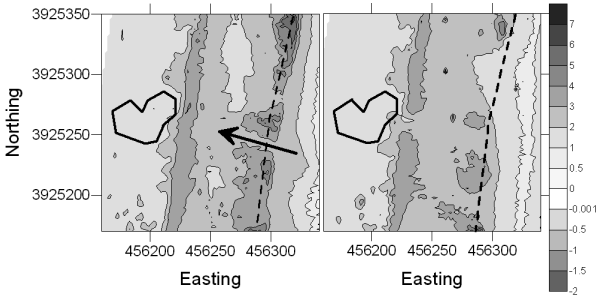

Figure 3 –Pre-storm topography map (left), and Post-storm topography map (right) for Fan B, showing the region of deposition in the washover fan (solid line) and the location of the pre-storm foredune ridge (dashed line).

Alongshore sections taken along the foredune show the deepening and widening of overwash throats during overwash (Figure 4). Pre- and post- storm overwash throat widths were measured from the long sections. The throat width, B, was defined as width at the top of the throat (Fig. 4), because observations during laboratory experiments indicated that during overwash, the sides of the throat collapsed into the channel due to notching, such that the sides of the throat were vertical (Donnelly et al. 2007). Pre and post-storm throat widths are listed in Table 1. Note that in some cases widening is not observed when comparing B_{pre} and B_{post}; however widening is observed at the sides and bottom of the throat. At Fan C, for example, vegetation is observed to hinder the widening of the top of the overwash throat.

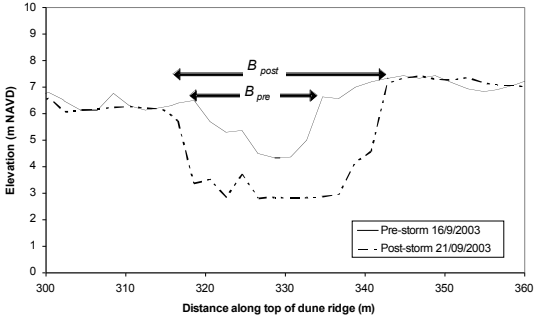

Figure 4- Long-section taken along the foredune at Fan D, defining B_{pre} and B_{post}.

Washover Fans

Table 1 summarises the observed geometry and characteristics of the 5 fans. An outline of the accreted region observed on the topography differences map was compared with the outline of bare sand on the geo-rectified aerial photography taken after the storm

(Figure 5). The outlining of this region was made subjectively due to noise in the data. As expected the two regions are very similar; however, the bare sand region extends seaward through the overwash throat where erosion is observed on the topography differences map. Other small differences in extent are probably due to the resolution of the lidar data. Using the overwash throat and the region of deposited sediment, the lateral spreading angle of the washover throat was measured. In most cases the fans were not symmetrical, so a north, a south, and an average lateral spreading angle was calculated. Additionally, the lengths, *L*, and widths, *W*, of the longest and widest dimensions of the fans were measured, assuming a fan axis parallel to the overwash throat.

Table 1 – Summary of Fan Characteristics

Fan	Shape	β_{north}	β_{south}	β_{ave}	*L* (m)	*W* (m)	*L/W*	B_{pre} (m)	B_{post} (m)
A	Assymetric	64°	14°	39°	67	82	0.8	na**	26
B	Long Diamond	25°	18°	22°	93	42	2.2	28	30
C	Diamond	30°	30°	30°	55	52	1.1	62	66
D	Wide Diamond	25°	42°	33°	28	57	2.0	16	29
E	Wide Triangle	na	45°	na	90	109	0.8	36	34

**There was no pre-existing gap in the rear dune at this location

In the absence of lateral or landward topographic constraints, the overwashing flow is directed landwards, perpendicular to the dune ridge, but spreads laterally as it leaves the confinement of the overwash throat. The fan develops a diamond shape, as velocities are highest in the centre of the fan, thus transporting sediment furthest inland along the fan axis. In reality, topographic constraints, vegetation and anthropogenic development all influence the eventual shape of the fan. Morton (1979) also showed how wind can influence the washover fan shape development. The results shown in Table 1 indicate that the fans can be long and narrow, short and wide or entirely asymmetric. The pre-storm topography and aerial photography were used to examine how the pre-storm morphology and surface texture control the overwash throat and washover fan shape development.

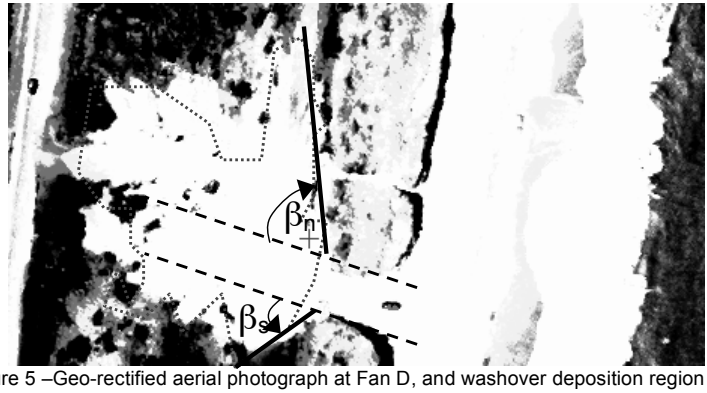

Figure 5 –Geo-rectified aerial photograph at Fan D, and washover deposition region from lidar for Fan D (dotted blue line), and definition of lateral spreading angles, β.

The pre-existing Fan C was extended both landwards and laterally; however, dense vegetation impeded the widening of the overwash throat on the northern side. At Fan C, the lateral spreading angle can be estimated from the pre-storm topography. Lines were drawn from the pre-existing throat to areas of topography at the same elevation as the throat. The angle of these lines to the overwash throat axis, 30°, was similar to that measured on the topography differences maps and geo-rectified photography.

The pre-storm topography indicated that Fans A, B, and D are all relatively unconfined laterally by topography on the back barrier, so it was not possible to use topographical influences to quantitatively predict the fan shape. The fans show a large variation in shape and lateral spreading angle, so factors other than lateral topography must also have a strong influence. Figure 6 shows aerial photographs of Fans A, B, C and E (Fan D is shown in Figure 5).

Fan A is actually two fans merged together. Close inspection of the post-storm photography indicates a smaller throat to the north of the main throat. Additionally, overwashing flow in the main throat appears to have occurred in two directions, perpendicular to the dune ridge and along the northern edge of the dune. There is a small portion of a remnant foredune remaining in front of the overwash throat, and division of flow around this may have lead to two different streams of overwashing flow.

At Fan B, an unpaved beach access track perpendicular to the dune ridge facilitated the development of a long, thin washover fan. Flow along the fan axis, therefore penetrated a lot further landward than would otherwise have been seen. Although not seen in the topography, the track was probably at slightly lower elevation than the surrounding back barrier, and the surrounding barrier is vegetated, indicating less frictional restraint in the track.

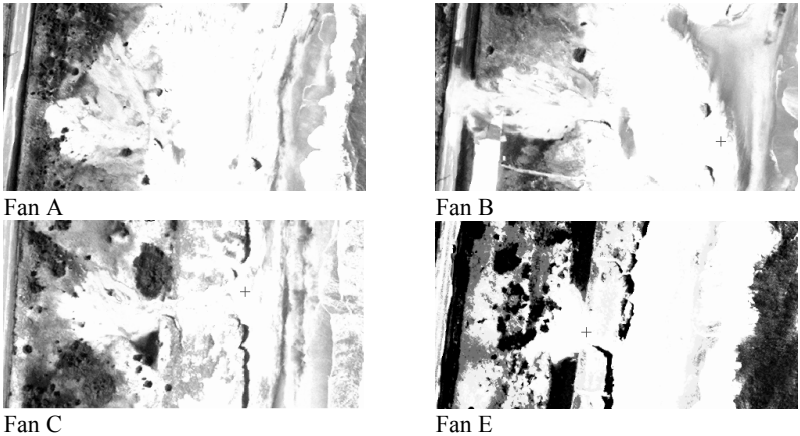

Figure 6 - Post-Storm geo-rectified aerial photography (Fan D is shown in Figure 5)

The shape of Fan D is also affected by an unpaved beach access track perpendicular to the dune ridge, in addition to a paved road located immediately behind and parallel to the foredune ridge. The overwash throat is located 50 m to the south of the track, but the fan extends further inland along the track, and hence is asymmetric. The fan has also extended substantially to the north along the paved road. Finally, Fan E is much wider than it is long due to lateral spreading in both directions along the same paved road and confinement by topography and vegetation on the landward side of the road.

To summarise, washover fans were diamond shaped but varied substantially in length to width ratio. Lateral spreading angles varied from as low as 15° up to 65° but ranged mostly between 20° and 45°. In most cases complicated back barrier topography, dense vegetation, tracks and roads, multiple overwash throats and complicated topography on the foreshore all contributed to the shape development of the washover fans; however, for a simple case, such as at Fan C, topographical confinement alone may be used to quantitatively predict fan shape development. Influences such as tracks and roads can be used to qualitatively predict where overwash will spread. It was seen that overwash flow penetrates further along tracks and roads where friction is reduced.

MODELLING

Larson et al. (2005) and Donnelly et al. (2005) developed an algorithm to calculate beach profile change due to overwash taking into account two different flow regimes over the beach crest, namely runup and inundation overwash, respectively. Ballistics theory was used to calculate the hydrodynamics in the swash zone and the flow rate over the beach crest during runup overwash, whereas weir overflow theory was used to calculate the flow rate over the beach crest during inundation overwash. The concentration of sediment in the overwashing flow was assumed constant following Kobayashi *et al.* (1996). The water flow on the back barrier slope was calculated by considering the continuity of a block of water at steady-state, including lateral spreading and infiltration, and the sediment transport rate was assumed proportional to the velocity cubed. The model was implemented within the SBEACH numerical model for simulating storm-induced beach profile change (Larson and Kraus, 1989).

Donnelly et al. (submitted) calibrated and verified the model for 2-D profiles. Initial overwash throat width, lateral spreading angles and infiltration rates were included together in three overwash coefficients which were calibrated for each location. These coefficients took into account 1) the proportion of sediment in the overtopping flow along with a bore front/weir coefficient for the runup overwash/inundation overwash modules, respectively, (2) the initial throat width and lateral spreading angle, and (3) the infiltration rate. Donnelly et al. (submitted) showed that the model could be verified using calibrated parameters for similarly shaped profiles in the same region, but not for profiles in different regions. This new, 3-D data, allowed the opportunity to input actual overwash throat widths and lateral spreading angles, in order to produce a more generalised cross-shore overwash profile change model. The algorithm was reformulated

such that the initial overwash throat width and a potential lateral spreading angle could be entered. For simplicity, infiltration was assumed to be negligible. A single calibration coefficient remains in the algorithm to represent the proportion of sediment in the overtopping flow along with a bore front/ weir coefficient for the runup overwash /inundation overwash modules, respectively.

Figure 8 shows the results of cross-shore profile modelling at Fans B and C. Initial overwash throat widths, B_{pre}, of 28 m and 62 m were identified for Fans B and C, respectively, using an alongshore section of the dune ridge crest. It is acknowledged that the throat width varies during overwash, but in a predictive mode, the pre-storm throat width is specified. This value is kept constant during the simulation. At Fan C, a potential lateral spreading angle, β_{ave}, of 30° was identified using the pre-storm topography confinement. At Fan B, there was no pre-storm topography confinement and the shape development was affected by anthropogenic influences, so the measured post-storm angle of 17° was used instead to verify the model. In a predictive mode, lateral spreading angles may be derived, where possible, using pre-storm topography confinement, but note that anthropogenic influences and vegetation affect lateral spreading significantly. Where a previous fan exists, the lateral spreading angle of the old fan may provide a good initial estimate. In the absence of a better estimate, an angle of 30 degrees represents the average lateral spreading angle of the measured fans. The model was calibrated at Fan C and verified at Fan B using the overwash coefficient value determined during calibration. The model was run using the aforementioned time-series for wave characteristics and water level during Hurricane Isabel.

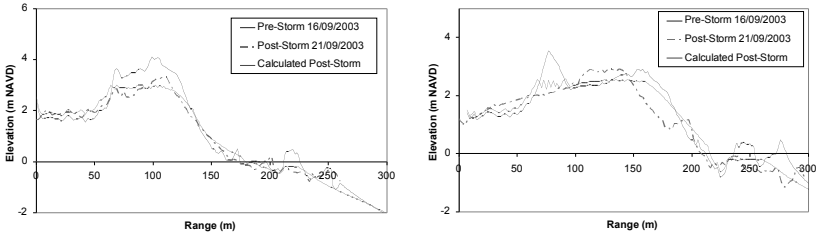

Figure 7 – Cross-shore profiles showing results of overwash model simulations (a) Calibration Run: Fan C, and (b) Verification run: Fan B

The results indicate the model's capability to predict the subaerial barrier evolution, including destruction of dunes, lowering of the beach crest and the landwards deposition of sediment. Optimal root-mean-square (RMS) error values were reached for the same overwash coefficient, indicating the general applicability of the model for similar locations in a predictive mode. The subaerial RMS value for Fan C was 0.231 and for Fan B was 0.397.

CONCLUSIONS

Several washover fans deposited during Hurricane Isabel, 2003, on Hatteras Island, NC, were studied to determine the controls on washover fan development. Fans were shown to typically form at pre-existing gaps in the dune ridge. Two fans were shown to form behind the rear dune ridge, where a gap pre-existed in the fore dune ridge, indicating that flow channelling in the foredune enabled breaching and subsequent overwashing of the rear dune. Overwash throats were shown to both widen and deepen during overwash.

The washover fans were mostly diamond shaped, with landward penetration maximum along the fan axis. Topography, vegetation and anthropogenic influences such as roads and tracks, however, were shown to obstruct this natural fan development and the fans varied substantially in length to width ratio. Lateral spreading angles varied from as low as 15° up to 65° but ranged mostly between 20° and 45°. It could be seen that washover spread laterally over a wider region where shore parallel roads and tracks existed, and penetrated further inshore along shore perpendicular tracks. Vegetation was seen to impede both throat widening and lateral spreading. Qualitatively, the shape development of a fan can be predicted using these observations. The quantitative lateral spreading angle was able to be predicted for one fan where vegetative and anthropogenic obstructions were negligible and where the pre-storm topography clearly varied in height on the back-barrier.

Initial throat widths and lateral spreading angles (both predicted and measured) were used as inputs to a generalized version of the overwash model by Larson et al. (2005) and Donnelly et al. (2005). The results indicated the model's capability to predict the subaerial barrier evolution. This more generalized cross-shore overwash profile change model can be applied to cross-shore profiles at which overwash is identified as a potential hazard, ie. at pre-existing gaps in the dune ridge using a measured throat width and a potential lateral spreading angle, if a potential lateral spreading can be predicted from the back barrier topography, vegetation, roads or pre-existing fans. It is otherwise suggested that an angle of 30° be used, as this is near to the average angle for the studied fans.

ACKNOWLEDGMENTS

The study was partly conducted as an activity of the Coastal Morphology Modeling and Management (Cascade) work unit of the System-Wide Water Resources Program (SWWRP) and partly as part of the European Commission research project FLOODsite (Contract Number: GOCE-CT-2004-505420).

Sincere thanks are expressed to Laura Fauver and Karen Morgan, USGS Center for Coastal and Watershed Studies, who took time to help select and extract the lidar data and provide helpful reviews, to Karin Larsson, Lund University GIS Centre for her assistance with Figure 1, and to Magnus Larson for advice regarding modelling and a helpful review of the article.

REFERENCES

Brock, J.C., Wright, C.W., Sallenger, A.H., Krabill, W.B., and Swift, R.N. (2002). "Basis and methods of NASA airborne topographic mapper lidar surveys for coastal studies", *Journal of Coastal Research,* 18(1), 1-13.

Cleary, W.J., and Hosier, P.E., (1979). "Geomorphology, washover history, and inlet zonation: Cape Lookout, N.C. to Bird Island, N.C." *In* Leatherman, S.P ed. *Barrier Islands, from the Gulf of St. Lawrence to the Gulf of Mexico*. Academic Press, NY, 237-271.

Dolan, R., and Hayden, B., 1981. "Storms and shoreline configuration". *Journal of Sedimentary Petrology*, 51 (3), 737-744.

Donnelly, C., Ranasinghe, R., and Larson, M., (2005). "Numerical modeling of beach profile change caused by overwash", *Proceedings Coastal Dynamics '05*, CD-ROM, ASCE, 14 pp.

Donnelly, C., Kraus, N.C., and Larson, M. (2006). "State of knowledge on measurement and modeling of coastal overwash", *Journal of Coastal Research*, 22 (4), 965-991.

Donnelly, C., Hanson, H. and Larson, M. (submitted). A numerical model of coastal overwash", *Proceedings of ICE Maritime Engineering.*

Fauver, L. (2005) *Toward predicting barrier island vulnerability: Simple models for dune erosion.* M.S. Thesis, College of Marine Science, University of South Florida, St. Petersburg, FL, 159 pp.

Hayes, M. O. (1967). "Hurricanes as geological agents, south Texas coast", *American Association Petroleum Geologists Bulletin,* 51, 937-942.

Kobayashi, N., Tega, Y., and Hancock, M.W. (1996). "Wave reflection and overwash of dunes", *Journal of Waterway, Port, Coastal, and Ocean Engineering,* 122(3), 150-153.

Larson, M., and Kraus, N.C., 1989. *SBEACH. Numerical Model for Simulating Storm-induced Beach Change; Report 1. Empirical Foundation and Model Development.* Technical Report CERC-89-9, U.S. Army Engineer Waterways Experiment Station, Coastal Engineering Research Center, Vicksburg, MS, 267 pp.

Larson, M., Wise, R. A., and Kraus, N. C. (2005). "Modeling dune response due to overwash transport", *Proceedings 29th Coastal Engineering Conference*, World Scientific Press, 2133-2145.

Leatherman, S. P. (1976). *Quantification of overwash processes,* Ph.D. Dissertation, Department of Environmental Sciences, University of Virginia, Charlottesville, VA, 245 pp.

Morton, R. A. (1979). "Subaerial storm deposits formed on barrier flats by wind-driven currents", *Sedimentary Geology*, 24, 105-122.

Sallenger, A.H. Jr., 2000. "Storm impact scale for barrier islands", *Journal of Coastal Research*, 16(3), 890-895.

Sallenger, A.H., Krabill, W.B., Swift, R.N., Brock, J.C., List, J., Hansen M., Holman, R.A., Manizade, S., Sontag, J., Meredith, A., Morgan K., Yunkel, J.K., Frederick, E.B., and Stockdon, H. (2003), "Evaluation of airborne topographic lidar for quantifying beach changes," *Journal of Coastal Research*, 19(1), 125-133.

Tolman, H.L. (1997). "User manual and system documentation of WAVEWATCH-III

version 1.15. NOAA / NWS / NCEP / OMB Technical Note 151, 97 pp.

Tolman, H.L. (1999). "User manual and system documentation of WAVEWATCH-III version 1.18. NOAA / NWS / NCEP / OMB Technical Note 166, 110 pp.

Tuan, T.Q., Verhagen, H.J., Visser, P., and Stive, M. (in press) "Numerical modeling of wave overwash on low-crested sand barriers." *Proceedings 30th Coastal Engineering Conference*, World Scientific Press, 13pp.

Wise, R. A., Smith, S.J., and Larson, M. 1996. "SBEACH: Numerical model for simulating storm-induced beach change. Report 4. Cross-shore transport under random waves and model validation with SUPERTANK and field data", *Technical Report CERC-89-9*, U.S. Army Engineer Waterways Experiment Station, Coastal Engineering Research Center, Vicksburg, MS.

EXPERIMENTAL STUDY OF OVERWASH

Billy L. Edge[1], Young Hyun Park[2], Margery Overton[3]

1. Coastal and Ocean Engineering Division, Department of Civil Engineering, Texas A&M University, College Station, TX 77840, USA. bedge@civil.tamu.edu.
2. Coastal and Ocean Engineering Division, Department of Civil Engineering, Texas A&M University, College Station, TX 77840, USA. tomypark@hotmail.com.
3. Department of Civil, Construction and Environmental Engineering, North Carolina State University, Raleigh, NC 27695, USA. overton@ncsu.edu

Abstract: Overwash induced by storm conditions is one mechanism causing coastline change with cross-shore erosion and deposition. Many field studies have been conducted but laboratory experiments are few. This experimental study was conducted for estimation of eroded sand volume by overwash. The experiments were conducted at two different wave heights and four different wave periods in two different slopes of beach face for regular and irregular waves. The experiments were done in a 2D wave tank on mid-scale at Texas A&M University. The measured data from 32 different tests were used to analyze the characteristics of overwash.

INTRODUCTION

The understanding of interaction between waves and the beach is necessary for understanding erosion caused from severe wave action. Storms accompanied by large waves and sea level rise cause overtopping and overwash over the berm. During an overtopping event, a huge amount of sand is eroded and transported landward by overwash. Available field data are very difficult to obtain during severe weather conditions on the beach, so laboratory data are convenient to analyze overwash. Williams (1978) conducted a small-scale experiment and found that sediment transport of much greater distance was produced from a steep slope beach face than a flatter slope. Hancock (1994) conducted an experiment for simulation of overwash. He measured beach profiles and the amount of eroded sand by overwash for different beach slopes and irregular wave conditions. Kobayashi et at. (1996) developed an

empirical equation for rate of sand overwash and wave reflection based on the work of Hancock (1994).

In this study experiments were conducted with overwash by tropical storm conditions. The offshore slope was 1:10 and two different nearshore beach slopes were used in a two dimensional tank. Different wave heights and wave periods were used for regular and irregular waves at the different slopes of beach faces. The experimental results were used for developing empirical formulas to describe the process for the different conditions tested.

EXPERIMENTAL SETUP

The experiment was conducted in a 2D wave tank that was 28.0 m long, 1.5 m wide, and 3.0 m high as shown in Fig. 1. A flap type of wave generator was located at the end of the channel 1.1 m above the bottom and it generated regular and irregular waves in this experiment. A false bottom was constructed from the bottom of the wave paddle to the toe of the beach slope. This was constructed to prevent energy losses from the wave generator and minimize the amount of sand used to build the artificial beach. A berm was constructed on the top of the structure. Its measured median grain size and specific gravity were 0.15 mm and 2.65, respectively. Each experiment was conducted for 327 seconds and the sampling rate for waves was 50 Hz.

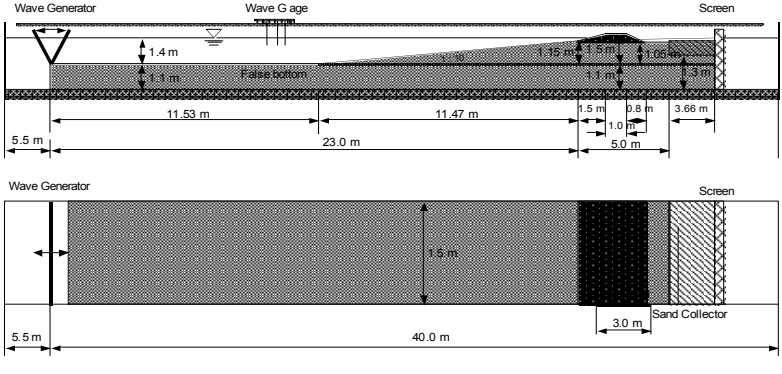

Fig. 1. Side and plan view of experimental facilities.

The experiments were conducted with two wave heights of 0.14 and 0.17 m and four wave periods of 1.4, 1.6, 1.8, 2.0 for regular waves and two H_{mo} of 0.10 and 0.15 m and four peak wave periods (T_p) of 1.4, 1.6, 1.8, 2.0 for irregular waves using TMA spectrum in Table 1. Three wave gages for the separations of incident and reflected waves were installed in the middle of tank and the data were analyzed by the method of three wave gages (Sub et al., 2001). A false bottom was extended on a slope of 1:10 to the beachface and the experiments included two different slopes of beach face (1:4 and 1:5) in the berm. When the slope of beach was milder than 1:5, overwash

could not be generated. About 2.5 m^3 fine sand (d_{50} of 0.15mm) was used to build a laboratory berm on a false bottom and the top of berm was 0.1 m higher than still water level. The initial shape of sand berm is shown in Fig 2.

Table 1. Wave Heights and Periods for Regular and Irregular waves.

Slopes of beach face	Regular waves		Irregular waves	
	Wave Height (m)	Wave Period (sec)	H_{mo} (m)	T_p (sec)
1:4	0.14	1.4	0.10	1.4
		1.6		1.6
		1.8		1.8
		2.0		2.0
	0.17	1.4	0.15	1.4
		1.6		1.6
		1.8		1.8
		2.0		2.0
1:5	0.14	1.4	0.10	1.4
		1.6		1.6
		1.8		1.8
		2.0		2.0
	0.17	1.4	0.15	1.4
		1.6		1.6
		1.8		1.8
		2.0		2.0

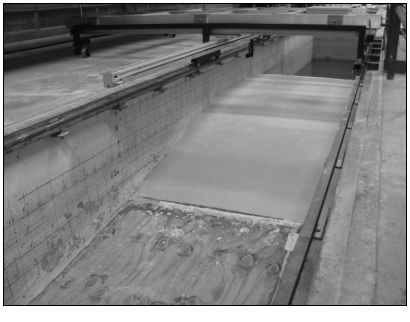

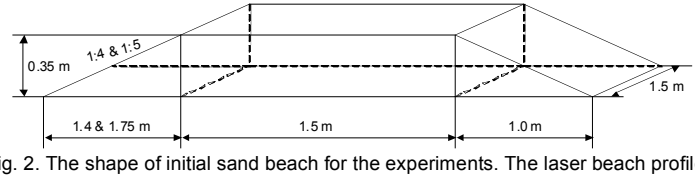

Fig. 2. The shape of initial sand beach for the experiments. The laser beach profiler is installed above the sand berm.

The speed of bores was measured with two wave gages located on the top of berm. The heights of bore proved difficult to measure during overwash events using capacitance wave probes. Typically, it was almost 3 or 4 cm, when it was checked by direct measurement. The speeds of bores were computed by Eq. (1). The speed of bore changed during the experiment with the change of beach profiles. The speeds of bores were measured for first 60 seconds and it was averaged by the number of overwash events. For example, the bore speed was 0.896 m/s, when the wave height was 0.14 m and the wave period was 1.4 sec. The speeds of bores for irregular waves were not measured due to its irregularity.

$$\text{Speed of bore} = \frac{\text{Distance between two gages}}{\text{Time to reach from } 1^{st} \text{ gage to } 2^{nd} \text{ gage}} \quad (1)$$

A laser profiling system was constructed to measure the change of profiles during and after the experiments. It is shown schematically in Fig. 3. The measurements were controlled by a personal computer. The user defined the first and last corner of the measurement field. Then the measurements were conducted automatically. Beach profiles were measured by a laser with 0.5 mm accuracy every 5 mm in x (cross-shore) and 20 mm in y directions. It took about 15 minutes to measure the whole area which was 5.0 m in x and 1.0 m in y directions. Each measurement was conducted at a location 0.25 m away from both walls to eliminate the impact of wall effects. The laser measurement system provided an opportunity to conduct measurements without touching the target. It was also used to measure the beach changes during the experiments. The time series of profile changes were measured within a limited range during the experiments, because the laser beam was reflected by the suspend sediment or foam on the water surface. This laser profiling system improved the accuracy and automation in measurements.

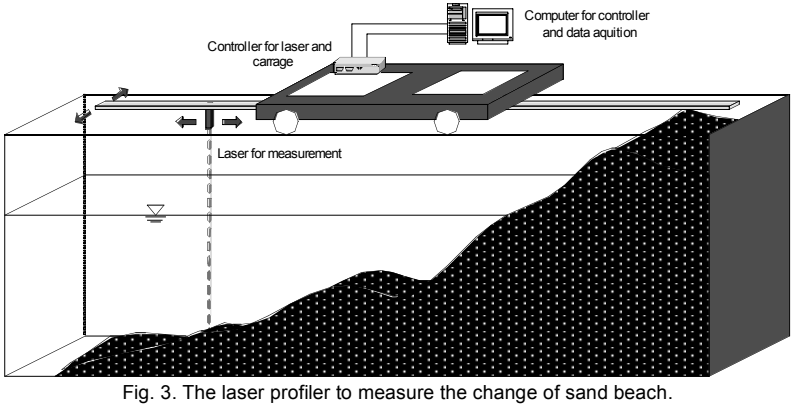

Fig. 3. The laser profiler to measure the change of sand beach.

An example of the measured final beach profile is displayed in Fig. 4. The image was produced by Surfer from the data in x, y and vertical elevation.

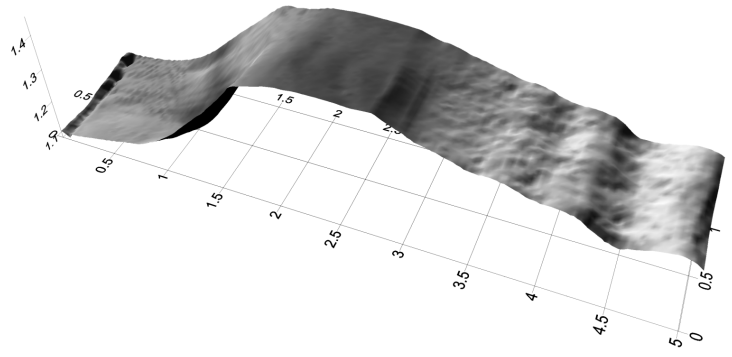

Fig. 4. The plot of sand profile by a laser profile after a beach erosion test.

EXPERIMENTAL RESULTS

The profile data measured every 20 mm in longshore direction were averaged and a representative line from the averaged result was produced in the cross shore direction as shown in Fig. 5. The initial sand profiles were measured at each test. The final beach profiles were measured after running waves for 327 seconds. The measurements of profiles were conducted after all suspended sand was deposited completely and it usually took 10 minutes. Because the maximum range of the laser profiler was 5.0 m in cross-shore direction, the measurements beyond the range were conducted by moving of the laser system. The laser profiler is installed on the top of rails along the wave tank and it can be moved to an interesting location manually.

The creation of a sand bar helped to reduce and stop the impact of overwash by energy dissipation of wave breaking. The larger and longer waves showed more erosion of sand over the berm by overwash. Typical results are shown in Fig. 5 for two wave heights (0.14 and 0.17 m) and four wave periods (1.4, 1.6, 1.8 and 2.0 sec). The sand berm was installed from about 1.0 m to 5.0 m and the bottom outside this area was made by plywood. Therefore there was no erosion below this elevation.

The location of offshore bar was related to the reflection coefficient. The changes of reflection coefficient at each wave period and slope of beach face are shown in Fig. 6. As the reflection coefficient was increased, the bar was located much further offshore. At the longest wave period (2.0 sec), the sediment transport over the berm was increased with lowering of the berm height and the bar moved shoreward. For this wave period, the reflection coefficient also decreased.

The transportation of eroded sand by overwash reduced to nearly zero beyond the 7.0 m mark shown in Fig. 5 for all cases. Sediment transport over the berm was also weak in most of tests for 1.4 and 1.6 sec wave periods. The sediment transport distances landward were not measured in this study but they also correlated with

wave period. Much sand was transported and deposited behind the berm as shown in Fig. 5. The collected volume of sand was almost zero in the test of short wave period and the maximum was 0.0058 m^3 at 0.17 m of wave height and 2.0 sec of wave period. The eroded sand out of this measurement range was collected to calculate the transport rate by the volume.

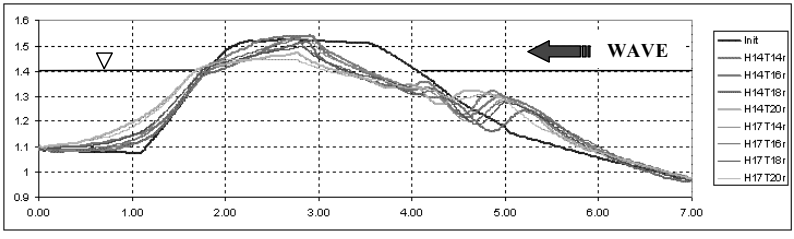

Fig. 5. Beach profiles for regular waves at 1:4 slope of beach. In the legend, Init represents Initial shape of beach and H14T14r means the test result at 1.4 m of wave height, 1.4 sec of wave period and regular waves.

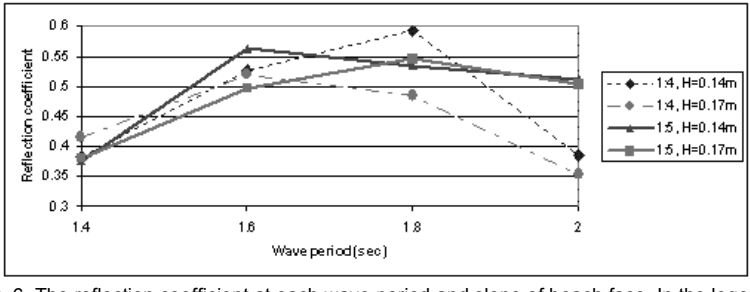

Fig. 6. The reflection coefficient at each wave period and slope of beach face. In the legend, the first and second numbers mean slope of beach face and wave height, respectively.

The experimental results by irregular waves are shown in Fig. 7. The differences between each test were not apparent over 327 seconds. The offshore bars were located at the same location in each test. The test duration (327 seconds) was selected the same as the tests for regular waves for comparison but it was considered that this duration was not enough time to analyze for irregular waves.

Overwash events continued occurring as long as the slope of beach face became steeper than about 1:6 for irregular waves. The erosion rate suddenly reduced after reaching this slope and the beach face retreated while maintaining this slope as shown in Fig. 11. However, erosion and sediment transport behind the berm were different at each wave period for irregular waves in Fig. 7. Longer and higher wave also produced much erosion behind the berm like the results by regular waves. Because irregular waves are composed of different wave heights and periods, their intensity of erosion and transport was weaker than the results by regular waves.

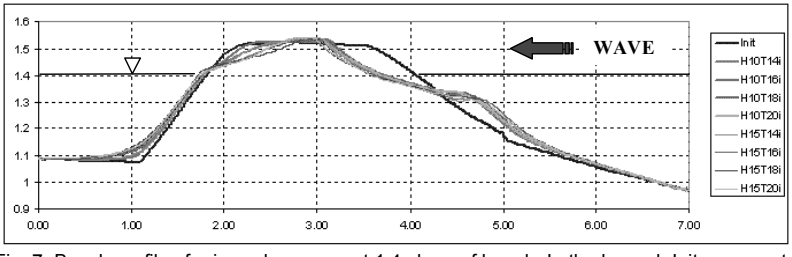

Fig. 7. Beach profiles for irregular waves at 1:4 slope of beach. In the legend, Init represents Initial shape of beach and H14T14i means the test result at 1.4 m of wave height, 1.4 sec of wave period and irregular waves.

The time series of profile changes measured by the laser profiler was used to find the correlation between overwash, erosion rate and time. One of test results is shown in Fig. 8. The time series of profile changes were recorded every 60 seconds. The sand profiles below the water were not measured, because the beam of the laser profiler was reflected on the surface of water with suspend sediment. Most of beach profile changes occurred at the beginning of the experiment and nearly ceased before the end of the test results.

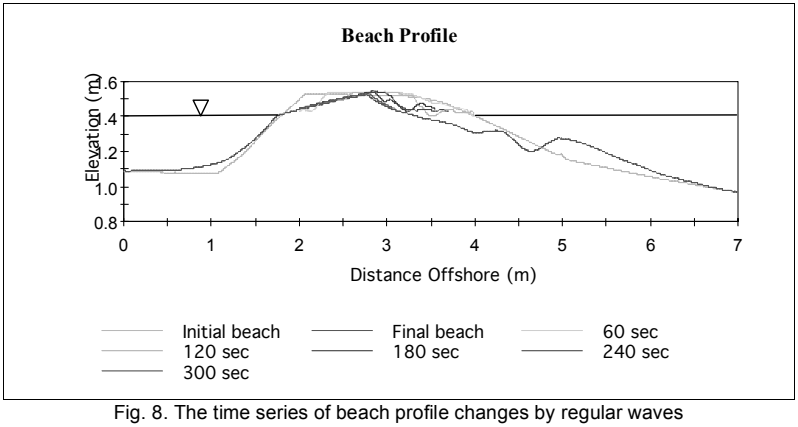

Fig. 8. The time series of beach profile changes by regular waves (height = 0.17 m, period = 1.6 sec, slope = 1:4).

The comparison by different wave height is shown in Fig. 9. Only two different wave heights were used for this study; the higher wave height produced much more erosion as would be expected. It also showed the same results in different slopes of beach face (Fig. 10).

A comparison was made by different beach slopes at the same wave height and period and is shown in Fig. 9 and Fig. 10. Erosion by overwash was much stronger at

a slope of 1:4 than at 1:5 as might be expected. Much sand was transported over the berm and deposited at a steeper slope.

Erosion by overwash was increased according to increasing of wave periods. The differences by different wave heights and periods are shown in Fig. 5. In summary erosion and sand transport were strongest at higher wave height, longer wave period and steeper beach face.

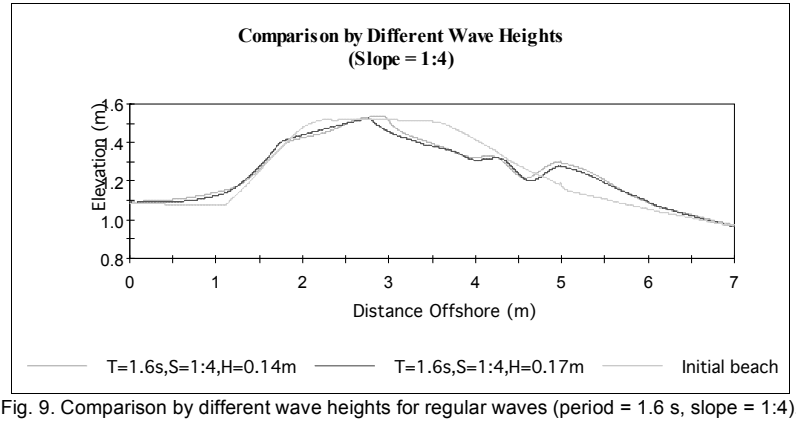

Fig. 9. Comparison by different wave heights for regular waves (period = 1.6 s, slope = 1:4).

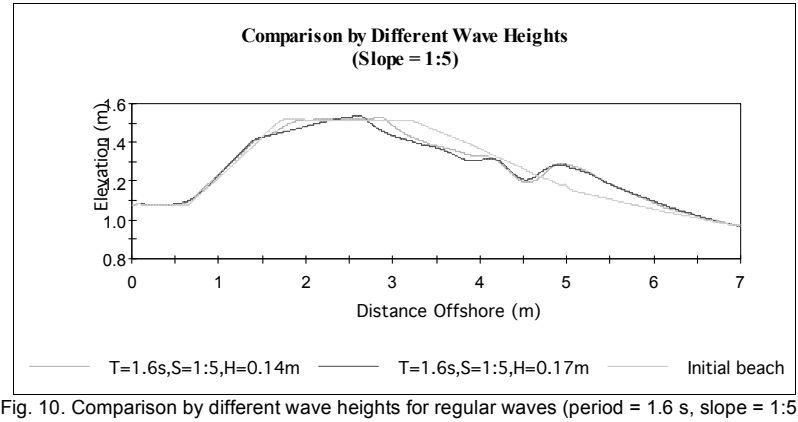

Fig. 10. Comparison by different wave heights for regular waves (period = 1.6 s, slope = 1:5).

The changes of profiles over a longer period are shown in Fig. 11. Each profile was measured at every 327 seconds. The rates of retreat were 51.85 %, 22.22 %, 9.26 %, 9.26 % and 7.41 % at every 327 seconds and it is shown in Fig. 12. The rate of retreat in beach face was reduced and became constant after 981 seconds. About 50 % of retreat was conduct in first 327 seconds.

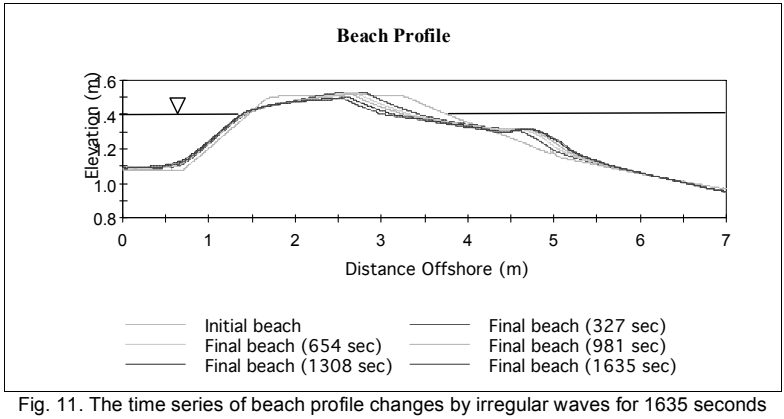

Fig. 11. The time series of beach profile changes by irregular waves for 1635 seconds (H_{mo} = 0.15 m, T_p = 2.0 sec, slope = 1:5). The profiles were measured at every 327 seconds.

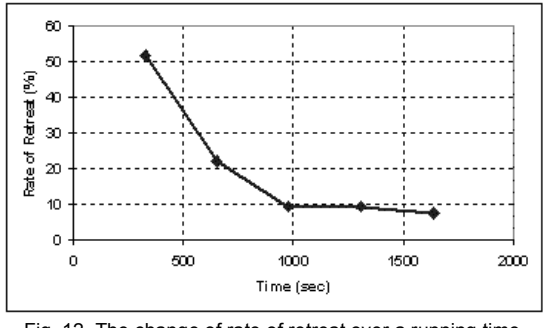

Fig. 12. The change of rate of retreat over a running time.

CONCLUSION

The mid-scale laboratory experiment was designed and conducted to reduce scale effects in this type of laboratory testing of sediment transport. This study presents a set of laboratory experiments by regular and irregular waves for analysis of overwash. The movement and location of the offshore bar has a major effect on the reflection coefficient. The increase of transmission rate by overwash over the berm reduced the eroded sand which was transported offshore. When the wave period was 2.0 sec, othe ffshore bar was generated near to the beach face. The erosion rate was highest at higher wave heights, longer wave periods and steeper beach slopes. About 50 percent of erosion by overwash occurred at the first 327 seconds in the long-term test and the subsequently the erosion rate was decreased and became essentially constant thereafter with time.

These characteristics of overwash by wave height, wave period and slope of beach face had the same trend at each test and they can be used for developing empirical

formulas and analytical methods for continued study of these interesting and important processes.

REFERENCES

Hancock, M. W. (1994). "Experiments on irregular wave overtopping and overwash of dunes," Master of Civil Engineering, University of Delaware, Newark, DE.

Kobayashi, N., Tega, Y., and Handcock, M.W. (1996). "Wave reflection and overwashof dunes," *Journal of Waterway, Port, Coastal, and Ocean Engineering*, ASCE, Vol. 122, No. 3, 150-153.

Suh, K. D., Park, W. S., and Park, B. S. (2001). "Separation of Incident and Reflected Waves in Wave-Current Flumes," *Coastal Engineering*, 43, 149-159.

Williams, P. (1978). "Laboratory development of a predictive relationship for washover volume on barrier island coastlines," Master of Civil Engineering, University of Delaware, Newark, DE.

BACKBARRIER EVOLUTION AND COMPLETE OVERWASH OCCURRENCE

Ana R. Carrasco[1], Óscar Ferreira[2], Ana Matias[1], João A. Dias[2]

1. CIACOMAR/CIMA, Universidade do Algarve, Av. 16 de Junho s/n, 8700-311, Olhão, Portual. azarcos@ualg.pt, ammatias@ualg.pt
2. FCMA/CIACOMAR/CIMA, Universidade do Algarve, Campus Gambelas, 8005-139, Faro, Portugal. oferreir@ualg.pt, jdias@ualg.pt

Abstract: The shoreline changes along the backbarrier of a barrier system are extremely variable and critically dependent upon geographic location and the inherent interaction with hydrodynamic processes. There are only a few studies describing the backbarrier morphodynamic evolution and inherent implications to the entire barrier system. In the present study it is performed the classification of the major evolution and maturation trends observed at Ria Formosa backbarrier, evaluating in particular the role of the complete washover occurrence. Besides the direct influence of inlets displacement, complete overwashes were considered to be one of the main events responsible for sediment availability at the backbarrier, and consequently interfered with the obtained evolution/maturation. Complete washover were assumed to contribute both to immature and mature backbarriers, at different time scales observation.

INTRODUCTION

Beaches identified as low energy occur in a wide range of coastal environments, including those in ocean bays and sounds, gulfs, seas, straits, estuaries, lagoons protected by coastal barriers, amongst others environments (Jackson et al. 2002a).The term low energy has been applied to beaches in environments that range from narrow, shallow lagoons, where onshore winds can generate wave heights <0.10 m on the foreshore (Jackson et al. 2002a), to beaches in the lee of reefs, where significant breaker height is up to 1.0 m (Hegge et al. 1996). Low energy environments are usually fetch-limited and sheltered at the same time and experience a mixture of local and non-local

wave (Jackson et al. 2002b). In fetch-limited environments, like the bayside of barrier islands, wave heights generated by local winds mainly depended on wind conditions and basin dimensions (width, length and depth) and have generally short periods (Nordstrom 1992; Jackson et al. 2002b).

Main controls and shoreline characteristics differ over short distances due to differences in fetch length, exposure to winds, and distance to inlets (Nordstrom 1992). Moreover, beach morphology may also be inherited from overwash events. This type of events is usually related with beach and dune erosion, and can cause major sediment input to the backbarrier area (e.g. Dillon 1970; Leatherman 1976; Dingler et al. 1993). As a consequence, the shorelines occurring along the backside of barrier islands are extremely diverse and variable with respect to morphologies and evolution.

The backbarrier of the Ria Formosa barrier system is an example of a restricted fetch system. The main objective of this paper is to recognize different states of backbarrier evolution and maturation through the application of a Backbarrier Development Classification, evaluating the role of complete washover occurrence in the main evolutionary trends of the backbarrier.

BACKBARRIER DEVELOPMENT CLASSIFICATION

The following sections synthesize the Backbarrier Development Classification, in particular the indexes formulation and it application.

General definitions

The Backbarrier Development Classification is based on the determination of the backbarrier evolution for a giving period of analysis. After performing aerial photograph georectification and interpretation, backbarrier evolution is obtained by the determination of the backbarrier longshore changes through time. The period of analysis must be at least of 10 years, and can be extended to several decades, depending on the available aerial photographs sets.

The longshore evaluation includes the identification and quantification of the longshore extension of the main present morphologies: inner beach next to a barrier (IBB), salt marsh (SM), and inner beach next to inlet (IBI) (Figure 1). The total backbarrier coastline extend (BC) is obtained by the sum of the coastline extend of salt marsh (SMC) and inner beach (TIBC = IBB+IBI coastlines). BC accounts with prominent and embayed parts of the coastline. Longshore changes (in meters) maybe of decreasing or increasing in extend. Longshore analysis also accounts with the measurement of the rectilinear length of each island/peninsula (coastal length - CL) (Figure 1).

Description of the classification

The backbarrier classification is composed of two types of indexes: backbarrier evolution (Bevol) and backbarrier maturation (Bmatur). Bevol gives an overview of the backbarrier evolution and Bmatur indicates the maturation state and observed trend. Bevol is obtained by the relation between backbarrier coastline extend variation (ΔBC)

and the coastal length variation (ΔCL) for a given period (Figure 2A).

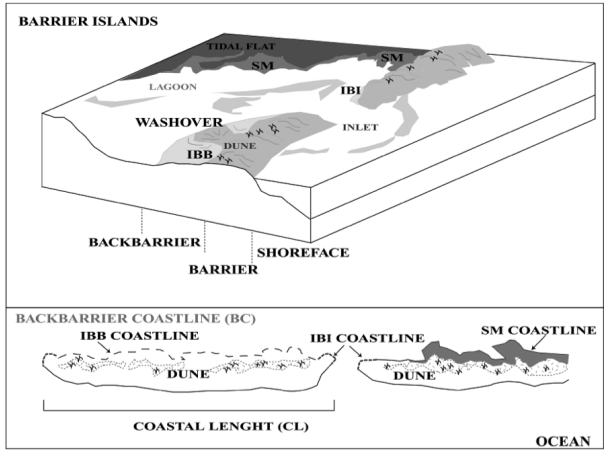

Fig. 1. Schematic representation of the main morphological units existent at backbarriers. IBB, inner beach next to a barrier; SM, salt marsh; and IBI inner beach next to inlet

The backbarrier coastline extend variation (ΔBC) is given by:

$$\triangle BC(\%) = (BCfinal\text{-}BCinitial)*100/(BCinitial) \quad (1)$$

The coastal length variation (ΔCL) is giving by:

$$\triangle CL(\%) = (CLfinal\text{-}CLinitial)*100/(CLinitial) \quad (2)$$

A Backbarrier Growth is defined by a *BC* increase simultaneously to an enlarging of *CL* (Figure 2A). On the contrary, a Backbarrier Reduction exhibits a BC decrease simultaneously to a CL shortening (Figure 2A). Intermediate states, Backbarrier Ramification and Smoothing Backbarrier, represent opposite evolutions of BC and CL (Figure 2A).

Bmatur is given by the relation between the backbarrier maturation state (*Bmat*) and the backbarrier maturation change ($\Delta Bmat$; Figure 2B). Bmat is given by:

$$Bmat = (SMCfinal/TIBCfinal) \quad (3)$$

Higher levels of backbarrier maturation (Bmat) are promoted by higher extension of salt marshes (*SMC*) in relation to sandy beaches (*TIBC*).ΔBmat will give an indication of the maturation process between the initial and final year of analysis:

$$\triangle Bmat = [(SMCfinal/TIBCfinal)/(SMCinitial/(TIBCinitial)] \quad (4)$$

Backbarrier classification using the obtained Δ*Bmat* is related with local hydrodynamic conditions: decrease in hydrodynamic conditions results in salt marsh construction/maintenance (Maturating Backbarrier) and thus ΔBmat>1 (Figure 2B), while increase in hydrodynamic conditions results in salt marsh destruction (Rejuvenating Backbarrier) and thus ΔBmat<1 (Figure 2B).

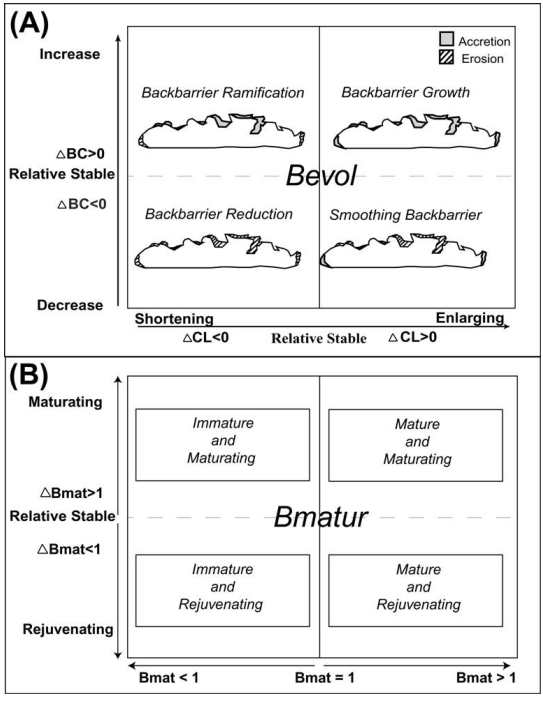

Fig. 2. Conceptual scheme defining the different states of backbarrier classification in terms of evolution (A), and maturation (B)

COMPLETE WASHOVER OCCURRENCE

Complete washover identification is based on the aerial photograph georectification/interpretation, using the same periods of analysis defined for the backbarrier evolution. Implications of complete washover events are inferred by the determination of the number of occurrences and by the quantification of BC affected by complete washovers in a giving period. Therefore, it is possible to quantify the total number of complete washovers and the longshore washover extend (in meters and percentage) for the entire system per period of observation. In addition, cross-shore transects located in complete washover areas are used to quantify its influence in the backbarrier landward/shoreward displacement. The join analysis of the washover parameters and the backbarrier evolution allows the identification of the relative role of

overwashes on the evolution of backbarrier coastlines.

APPLICATION OF THE BACKBARRIER DEVELOPMENT CLASSIFICATION

Study Area

The Ria Formosa is a multi-inlet barrier island system located in southern Portugal (Figure 3). Its present configuration consists of two peninsulas and five islands that extend over 56 km. The entire backbarrier covers an area of 8.4×10^7 m^2 (Andrade 1990), characterized by: i) large salt marsh areas with a high density of shallow meanders, largely composed by silt and fine sand (Bettencourt 1984); ii) large sand flats partially flooded and reworked during spring tides (Pilkey et al. 1989); and iii) a complex net of natural and partially-dredged channels, which narrow and shoal in upper regions of the system (Salles 2001). The inner shoreline, along the backbarrier islands and peninsulas is characterized by low, narrow sandy beaches alternating with portions of salt marsh, and washover plains (Andrade 1998).

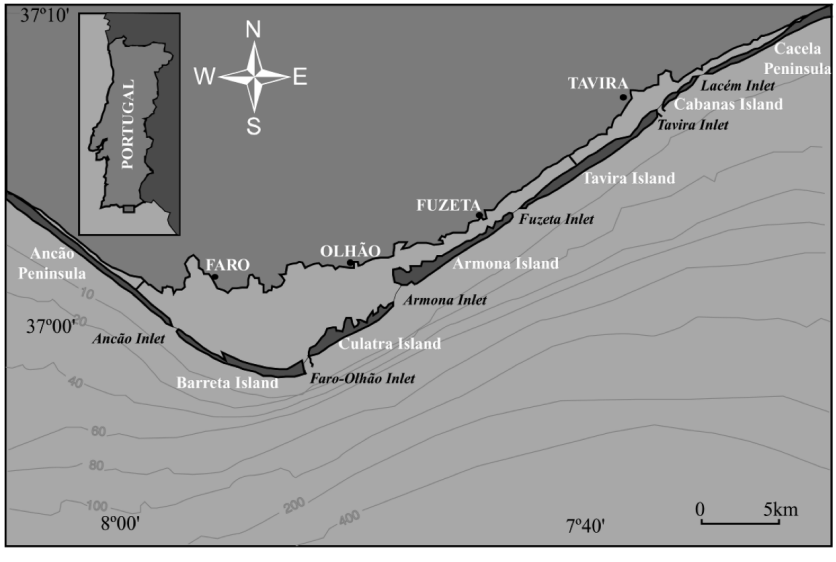

Fig. 3. Study area location

Tides in the area are semi-diurnal, average ranges are 2.8 m for spring tides and 1.3 m during neap tides, however, maximum ranges of 3.5 m can be reached. Wave climate in the area is moderate to high (Ciavola et al. 1997). Incident waves are normally from the W-SW, representing 71% of the total, although SE conditions represent 23% of the total (Costa et al. 2001). The cuspate shape of the Ria Formosa system produces two different areas in terms of exposure to wave action. The west flank is more energetic, being under the direct influence of the dominant wave conditions (W-SW), while the east flank is only directly exposed to the "Levante" conditions (E-SE wind and waves).

Recent evolution of the Ria Formosa barrier system is strongly dominated by physical alterations conduced by inlets position displacement/stabilization (see inlets location at Figure 3). With exception of Armona Inlet, considered to be the only naturally stable inlet of the system (Wheinholtz 1964), the other non-stabilized inlets, Ancão, Fuzeta and Lacém inlets, presents a cyclic easterly migration. Both Ancão and Fuzeta inlets have been relocated in the late 90's into a western position (Vila-Concejo et al. 2002). Faro-Olhão and Tavira inlets are the two stabilized inlets present at the system.

Backbarrier Development Classification

The backbarrier development classification was applied to the Ria Formosa system for the period comprised between 1947 and 2001 (Table 1 and Figure 4). Table 2 presents the main observed characteristics present in the backbarrier of each island/peninsula, as well as a qualitative measure of overwash occurrence and inlets influence, in order to facilitate indexes application discussion.

Table 1. Period of analysis considered for each island/peninsula

Barrier	Period
Ancão Peninsula	1947-2001
Barreta Island	1947-2001
Culatra Island	1947-2001
Armona Island	1969-2001
Tavira Island	1947-2001
Cabanas Island	1989-2001
Cacela Peninsula	1976-2001

In what concerns to the backbarrier evolution (Bevol) barriers are mainly distributed between Backbarrier growth and Backbarrier reduction categories (Figure 4A); an intermediate state was only observed at Armona Island, Smoothing backbarrier. The irregularly in the barriers evolutionary trends, does not allow to define a linear pattern to the overall system, it is however possible to observe a backbarrier reduction trend in the extremes of the system together with a dominant enlarging at the central part.

The backbarrier maturation (Bmatur) was obtained through the determination of ΔBmat for the same period of analysis (Table 1), while Bmat was determined for 2001. Almost all analyzed backbarrier presented ΔBmat>1 (Maturating backbarriers) or stability behavior between 1947 and 2001 (Figure 4B). The western part of the system can be considered as immature but facing maturation; the central part of the system tends to maturation, and the eastern part of the system is formed by two backbarriers subject to opposite levels and trends of maturation (Cabanas Island is mature and under maturation while Cacela Peninsula is immature and rejuvenating).

Table 2. Main characteristics of the Ria Formosa backbarrier, qualitative measure of overwash occurrence and inlets influence.

Barrier	Backbarrier main characteristics	Complete washover occurrence	Inlets influence
Ancão Peninsula	Western: salt marsh Central: with human occupation	Moderate	
	Eastern: sandy beach	Low	Ancão Inlet migration
Barreta Island	Western: sandy beach Eastern: salt marsh	Extreme	Ancão Inlet migration
Culatra Island	Western: human occupation and engineering structures Central: human occupation, salt marsh and sandy beach Eastern: sandy beach as recurved spits	Low	Armona Inlet narrowing
Armona Island	Western: human occupation and salt marsh; Central: salt marsh	Moderate	
	Eastern: sandy beach and salt marsh	Moderate	Fuzeta inlet migration
Tavira Island	Western: sandy beach; Central: salt marsh in the central part Eastern: human occupation and engineering structures		Fuzeta Inlet migration
Cabanas Island	Western: sandy beach and salt marsh and engineering structures	Low	
	Eastern: sandy beach	High	Lacém Inlet migration
Cacela Peninsula	Western: sandy beach Eastern: salt marsh	Moderate	Lacém Inlet migration

Complete washover occurrence

A total of 62 complete washovers were observed at Ria Formosa between 1947 and 2001 (Figure 5). These washovers represented a total longshore extend > 4 000 m for the Ria Formosa backbarrier, 3615 m in the west flank, and >288 m in the east flank (Table 3). The percentage of backbarrier coastline with complete washovers was more significant before 1947 and between 1989 and 1996 due to the washover longshore extent in these periods (Matias 2006). Cabanas Island included the higher number of

occurrences, 21 complete washovers, with major expression between 1976 and 1989. Aerial photograph coverage/quality only allowed quantifying landward/shoreward displacement, as a result of complete washover, at Ancão and Cacela peninsulas and Barreta Island. Results showed a landward displacement of 1myr^{-1} and 2 myr^{-1} at Ancão and Cacela peninsulas, while the western sector at Barreta Island verified a shoreward displacement of 4 myr^{-1}. Table 3 relates the observed maturation trend and the complete washover occurrence between the overall period 1947-2001.

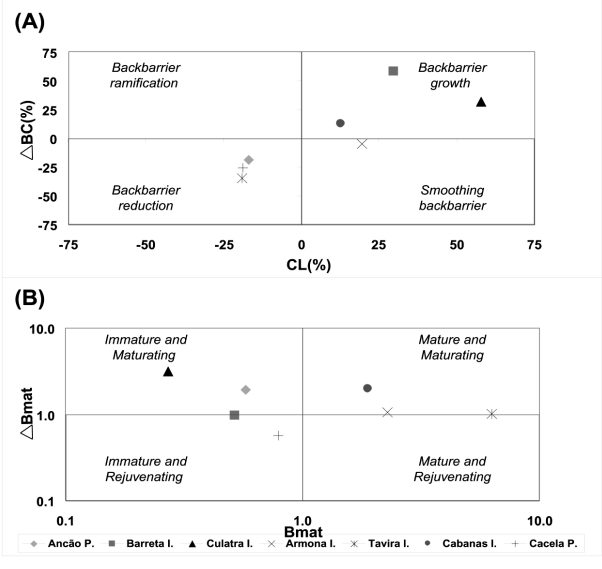

Fig. 4. Classification of the backbarrier development in terms of evolution (A), and in terms of maturation (B)

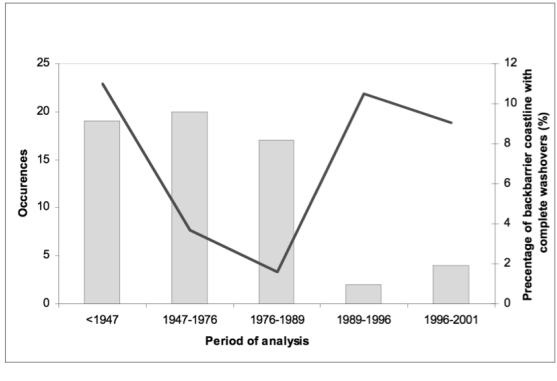

Fig. 5. Occurrences of complete washovers at Ria Formosa in 1947-2001. The number of occurrences is represented by columns and the percentage of BC with washovers by the line

Table 3. Maturation trend and complete overwash occurrence between 1947 and 2001

Barrier	ΔBmat	Nº of complete washovers	Washover longshore extend, m
Ancão Peninsula	Maturating (1.9)	10	368
Barreta Island	Stability (1.0)	11	3247
Culatra Island	Maturating (3.2)	2	44
Armona Island	Stability (1.0)	13	*
Tavira Island	Stability (1.0)	-	-
Cabanas Island	Maturating (2.0)	21	244
Cacela Peninsula	Rejuvenating (0.6)	5	*
Total		62	>4000

* Was not possible to determine washover longshore extend.

DISCUSSION

The definition of different trends of evolution/maturation of backbarriers relies in the application of two types of indexes: Bevol and Bmatur. Bevol provides an overview of the backbarrier evolution through time, while Bmatur provides an overview of the maturation state and its recent evolutionary trend. Both indexes were applied to the Ria Formosa backbarrier. Application of the Bevol showed that most of the barriers are mainly included in the Backbarrier growth and Backbarrier reduction classifications, and presented a maturating/stability trend between 1947 and 2001 (Figure 4A and 4B).

The obtained classification is intrinsically dependent in the recent evolution of the study area. Recent evolution of Ria Formosa barriers is conditioned by several coastal processes, including inlet dynamics (Vila-Concejo et al. 2006) and overwash occurrence (Matias 2006). Changes in inlets position promoted dramatic changes in barriers length and therefore changes in BC and CL, and interfered with local hydrodynamic conditions (Esaguy 1984; 1985; 1986a; 1986b; Andrade 1990; Salles 2001; Vila-Concejo 2003). For instance, Ancão Peninsula and Barreta Island evolutionary classifications are dependent on the chosen period for indexes application and its timings in relation to Ancão Inlet migration cycle (Vila-Concejo et al. 2002). Enlargement of CL and BC in Barreta Island occurred simultaneously to shortening of CL and BC at Ancão Peninsula (backbarrier growth and backbarrier reduction). Likewise, the evolutionary classification (Bevol) of Armona, Tavira, Cabanas and Cacela barriers are also dependent on the respective non-stabilized inlets migration cycle (Table 2).

Besides the influence in Bevol, inlets migration may induce also different backbarrier maturation trends. Alteration in the inlets patterns can promote areas of predominant salt marsh construction by a decrease in hydrodynamic conditions, but can also be responsible by the destruction of salt marsh areas, by an increase in hydrodynamic conditions. For example, the progressive growth of Culatra Island due to Armona Inlet narrowing created areas of lower energy conditions as they became more distant from the inlet channel, which in turn allowed the development of new salt marsh areas (maturating backbarrier). In other cases, for instance Cacela Peninsula, the areas downdrift of the inlet had an increase in hydrodynamic conditions that promoted backbarrier reduction encompassed by a decrease in the salt marsh areas (rejuvenating backbarrier, Figure 4 and Table 2).

Whether overwash plays or not a significant role in a barrier island dynamics depends on numerous factors such as the elevation of islands, presence of vegetation, sediment supply to the beach, and frequency and strength of storms (Leatherman 1976). Increases in BC and variations in Bmatur may be promoted by complete overwash occurrence. The main role of these events to backbarrier sedimentary dynamics is an increase of sand availability. Consequently, complete overwash occurrence is generally associated with cross-shore landward displacement of backbarrier coastline, as observed at Ancão and Cacela peninsulas. In these barriers it was observed after complete washover occurrence a landward displacement of the backbarrier limits ($1myr^{-1}$ and $2\ myr^{-1}$, respectively), by a transference of sediments into the lagoon. The scale of occurrence of complete overwash is thus extremely important when evaluating the medium- long-term barrier evolution. Barreta Island shoreward displacement is mostly justified by the Ancão Inlet migration (Andrade 1990; Vila-Concejo 2003), where overwash events plays a secondary role.

Two different overwash influence can be expected at different time scales: (1) shortly after overwash, the proportion of sandy beach increases (by destruction of SMC or increase of TIBC) and therefore the backbarrier is rejuvenating, and became immature (Figure 6A); and (2) at a later stage, considering that these same complete washovers are not reworked by overwash, salt marsh develop over the washover deposits, therefore the barrier became maturating, and eventually becomes a mature barrier (Figure 6B). Marsh progradation over backbarrier is interpreted as a result of abundant sediment, which permitted marsh expansion (French et al. 1993; Pethick 1998). Example of type 1 influence is the case of Cacela Peninsula that presents a rejuvenating and immature backbarrier (Table 3) in the presence of complete washovers. The classification of the maturity state of a barrier may be related with the timing of overwash. As in the case of Cacela Peninsula, where the overwash influence is relatively recent and therefore its backbarrier is presently immature (Figure 6A), but may in the future turn to a type 2 overwash influence as it maturates. Barreta Island is also an immature backbarrier but in stability, however this barrier is very heterogeneous in terms of backbarrier morphologies (Table 2). The western part is almost permanently overwashed (more than 3 000 m of washover longshore extend) and fully composed of sandy beach, while the eastern part is composed of salt marsh. The classification of stability obtained for this barrier results from an average estimative, but is not representative of any of the two

parts. The Barreta western part is another example of type 1 overwash influence, where a high washover longshore extend (Table 3) was responsible for rejuvenating and immature backbarrier.

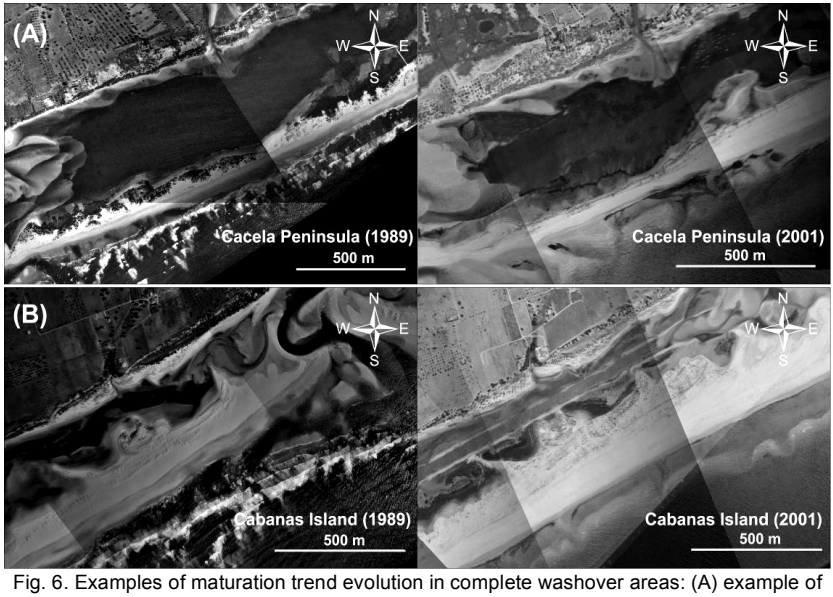

Fig. 6. Examples of maturation trend evolution in complete washover areas: (A) example of type 1 evolution; and (B) example of type 2 evolution

An example of type 2 overwash influence is Cabanas Island (about 240 m of washover longshore extend), that was until recently growing (Table 2) and frequently affected by overwash occurrence (Table 3). This events lead to the existence of a sandy flat that later allowed the development of salt marsh, and consequently a maturating process, which lead to the classification as mature backbarrier (Figure 6B). Armona Island is another example of type 2 overwash influence, providing sediments for salt marsh development (mature backbarrier). Like described for Barreta Island, Armona backbarrier stability resulted from the existence of opposite trends in the backbarrier evolution. The central part of the island was subjected to moderate complete overwash occurrence (Table 2), that afterwards developed salt marsh and initiated a maturating process.

CONCLUSION

The available studies evaluating backbarrier environments evolution are scarce. The main objective of the present study was the application of a Backbarrier Development Classification to the Ria Formosa barrier system, Algarve, Portugal, between 1947 and 2001, and to identify the implications of the complete overwash processes to the definition of such classification and the evolution processes of backbarriers. This classification evaluates the backbarrier evolution and maturation through time.

Results of the evolutionary indexes shows that most of the islands/peninsulas are mainly included in the Backbarrier growth and Backbarrier reduction classifications. In the same analyzed period, most of the barriers presented maturating and stability backbarriers. The obtained classification was shown to be related with the direct influence of inlets displacement, while complete overwashes were also considered to be one of the main events responsible for such classification. Events promoting an increase in sediment availability at the backbarrier, like complete washover, were assumed to have two different influences at the backbarrier evolution according to different time scales: (1) at short-term overwash leads to rejuvenating and immature backbarriers; and (2) at a later stage (medium- to long-term) washover deposits may allow a barrier maturation process.

In cases of backbarrier environments it is extremely important to develop coastal management practices based on predict behaviors of evolution. Application of the Backbarrier Development Classification reveals to be a good approach in the classification of Ria Formosa backbarrier evolutionary trend and likely of being related with the main constrains affecting the system.

ACKNOWLEDGEMENTS

This work was partially funded by the BERNA project (*Beach Evolution in Areas of Restricted Fetch: Experimental and Numerical Analysis*), funded by the Fundação para a Ciência e Tecnologia (POCTI/CTA/45431/2002). A. Matias was supported by CIMA – Universidade do Algarve, grant CIMA/GT1-01/2005, and by FCT grant SFRH/BPD/18476/2004.

REFERENCES

Andrade, C. (1990). "*O ambiente barreira da Ria Formosa, Algarve-Portugal,*" Ph.D. Thesis, University of Lisbon, 626 p. (in Portuguese).

Andrade, C., Barata, A., Teles, M. (1998). "An analysis of the vulnerability to overwash of the Ria Formosa barrier island system (Portugal) using a simple multi-attribute technique (SMART) approach," *Proceedings of Littoral98 Conference*, 511-519.

Bettencourt, P. (1994). "*Les Environements Sédimentaires de la Côte Sotavento (Algarve, Sud Portugal) et leur Évolution Holocéne et Actuelle,*" PhD thesis, Université de Bordeaux I, 568 p. (in French).

Ciavola, P., Taborda, R., Ferreira, Ó., Dias, J. A. (1997). "Fied measurements of longshore sand transport and control processes on a steep meso-tidal beach in Portugal," *Journal of Coastal Research* 13 (4), 1119-1129.

Costa, M., Silva, R., Vitorino, J. (2001). "Contribuição para o estudo do clima de agitação marítima na costa portuguesa," *Proceedings of 2as Jornadas Portuguesas de Engenharia Costeira e Portuária*, CD-ROM, PIANC (in Portuguese).

Dillon, W. P. (1970). "Submergence effects on a Rhone Island Barrier and lagoon and inferences on migration Barriers," *Geology* 78, 94-106.

Dingler, J. R., and Reiss, T. E. (1990). "Cold-Front Driven Storm Erosion and Overwash in the Central Part of the Isles Dernieres, a Lousiana Barrier-Island Arco," *Marine Geology* 91, 195-206.

Esaguy, A. S. (1984). "*Ria de Faro, Barra da Armona. Evolução 1873-1983"* Direcção Geral de Portos, Internal Report, 5 p. (in Portuguese).

Esaguy, A. S. (1985). "*Ria de Faro, Barra da Fuseta. Evolução 1944-1984"* Direcção Geral de Portos, Internal Report, 11 p. (in Portuguese).

Esaguy, A. S. (1986a). "*Ria de Faro, Barra de Faro-Olhão. Evolução 1955-1985"* Direcção Geral de Portos, Internal Report, 10 p. (in Portuguese).

Esaguy, A. S. (1986b). "*Ria de Faro, Ilha de Tavira. Evolução 1950-1985"* Direcção Geral de Portos, Internal Report, 13 p. (in Portuguese).

French, J., and Spencer, T. (1993). "Dynamics of sedimentation in a tide-dominated backbarrier salt marsh, Norfolk, UK," *Marine Geology* 110, 315-331.

Hegge, B., Eliot, I., Hsu, J. (1996). "Sheltered Sandy Beaches of Southwestern Australia," *Journal of Coastal Research*, 12 (3), 748-760.

Jackson, N., Nordstrom, K., Eliot, E., Masselink, G. (2002a). "'Low energy' sandy beaches in marine and estuarine environments: a review," *Geomorphlogy* 48, 147-162.

Jackson, N., Nordstrom, K., Smith, D. (2002b). "Geomorphic – Biotic Interations on Beach Foreshores in estuaries," *Journal of Coastal Research* SI 36, 414-424.

Leatherman, S. (1976). "Barrier islands dynamics: overwash processes and aeolian transport," *Proceedings of Coastal Engineering Conference,* ASCE, 1958-1973.

Nordstrom K. (1992). "*Estuarine Beaches: An Introduction to Physical and human Factors Affecting Use and Management of Beaches in Estuaries, Lagoons, Bays and Fjords,"* Elsevier Applied Science, 217 p.

Matias, A. (2006). *"Overwash Morphodynamic on Ria Formosa Barrier Island System(Algarve, Portugal),"* Ph.D. Thesis University of Algarve, 253 p.

Pethick, J. (1998). "*An Introduction to Coastal Geomorphology,"* John Wiley & Sons Inc., 260 p.

Pilkey Jr, O. H., Neal, W. J., Monteiro, J. H., Dias, J. A., 1989. Algarve barrier islands: a non coastal-plain system in Portugal. *Journal of Coastal Research*, 5 (2), 239-261.

Salles, P. (2001). "*Hydrodynamic Controls on Multiple Tidal Inlet Persistence,"* Ph.D. Thesis, Massachusetts Institute of Technology and Woods Hole Oceanographic Institution, 266 p.

Vila-Concejo, A. (2003). "*Sediment Dynamics and Tidal Inlet Relocation in Mixed-Energy Settings: the case of Ancão Inlet (Algarve-Portugal),"* Ph.D. Thesis, University of Algarve, 197 p.

Vila-Concejo, A., Matias, A., Ferreira, Ó., Duarte, C., Dias, J .A. (2002). Recent Evolution of the Natural Inlets of a Barrier Island System in Southern Portugal. *Journal of Coastal Research* SI 36, 741-752.

Vila-Concejo, A., Matias, A., Ferreira, Ó., Pacheco, A., Dias, J. A. (2006). "Quantification of inlet-related hazards in barrier island systems. An example from Ria Formosa (Portugal)," *Continental Shelf Research* 26 (9), 1045-1060.

Wheinholtz, M. (1964). "O cordão litoral da Ria de Faro e a sua utilização para fins turísticos e balneares. Contribuição para o estudo da evolução das flechas de areia na costa sotavento do Algarve", *Boletim Trimestral de Informação da Direcção Geral dos Serviços de Hidráulica*, 14 p. (in Portuguese).

GEOMORPHIC FEATURES SHAPED BY CROSSING WAVES

Robert B. Nairn[1] and Mohammad Dibajnia[2]

1. Baird & Associates, 627 Lyons Lane, Suite 200, Oakville, Ontario, L6J 5Z7, Canada. rnairn@baird.com.
2. Baird & Associates, 627 Lyons Lane, Suite 200, Oakville, Ontario, L6J 5Z7, Canada. mdibajnia@baird.com.

Abstract: Ridge-like shoal topography is well developed on the continental shelves of the Mid-Atlantic Bight and the northeastern Gulf of Mexico. In both cases, these linear sand ridges are oriented parallel to the predominant wave approach direction, suggesting common processes for their evolution and maintenance. Along the coasts of tropical islands surrounded by coral reefs, spur-like features are sometimes found. The spurs consist of coral rubble made available by the die-off or destruction of coral through natural processes or anthropogenic factors. The spur features emanate from rubble fields and are aligned parallel to the predominant direction of wave attack. These features, from disparate environmental settings, owe their maintenance and evolution to crossing wave patterns that form through refraction of waves up either side of the shoal or spur features. This paper presents examples of these geomorphic forms in both settings. Existing capabilities for simulating crossing wave processes are discussed.

INTRODUCTION

Improvements to the understanding of physical processes are often driven by the desire and need to explain observations in nature. These observations may consist of direct measurements or the presence and evolution of geomorphic features. The advantage of geomorphic features is that they represent the integrated effects of all forcing functions in the coastal and marine environment over large areas and over long periods of time. This paper investigates the role of crossing waves in the development of two geomorphic forms in very different settings.

Along the continental shelves of the Atlantic and Gulf coasts of the US ridge-like shoal topography is widespread. These linear sand ridges are oriented parallel to the direction

of predominant storm wave attack, suggesting that common wave-related processes are responsible for their evolution and maintenance. The first part of the paper reviews the current state of knowledge on these features and the role of crossing waves in their maintenance.

The second type of geomorphic feature that will be investigated as part of this paper consists of coral rubble spurs that are oriented parallel to the direction of wave attack close to shore at a location in Barbados. Being nearshore features, their orientation is usually close to shore perpendicular. Similar features have been observed along the coast of the Hawaiian Islands. There is clear evidence that these features are created through crossing wave patterns.

Following the review of these two distinct features a general discussion of other examples of the role of crossing waves on the development of geomorphic features is presented. Also, a summary of our ability to predict the hydrodynamic, sediment transport and morphodynamic processes associated with crossing waves is provided.

RIDGE-LIKE SHOALS

The Minerals Management Service (MMS) of the U.S. Department of the Interior is responsible for the management of all mineral resources in federal waters along the Outer Continental Shelf of the US. MMS has the authority to convey, on a noncompetitive basis, the rights to OCS sand, gravel or shell resources for shore protection, beach or wetlands restoration projects, or for use in construction projects funded or authorized by the US Federal Government. One of the key targets of OCS sand are offshore ridge-like shoals. Key questions associated with removing sand from these shoals are: how much can be removed while still maintaining the geomorphic integrity of the features and where is the best location to remove sand to preserve the geomorphic form?

Hayes and Nairn (2004) in an investigation for MMS, completed a literature review of the understanding of the distribution, genesis, maintenance and characteristics of linear ridge and shoal features. Ridge and swale topography is exceptionally well developed on the continental shelves of the Mid-Atlantic Bight (see Figure 1) and the northeastern Gulf of Mexico (see Figure 2). In both cases, these linear ridges are oriented parallel to the predominant wave approach direction, suggesting common processes for their evolution and maintenance. Most researchers have concluded that ridges were derived from shorefaces of barrier islands as they retreated across the shelf in response to rising sea level and that tides or storm-driven currents maintain them.

The widely cited ridge formation theory of Huthnance (1982) developed originally for linear sand banks offshore the Norfolk coast of England requires a sufficient sand source, currents to move the sand, and an irregularity on the sea floor around which the ridges are initiated. Trowbridge (1995) developed a shoal preservation theory for linear shoals located close to the US Atlantic coast that was based on southerly currents created by northeasterly wave attack during storm events. McBride and Moslow (1991) postulated that one of the initial irregularities is a segment of an ebb-tidal delta abandoned by inlet

migration. These theories of origin and initial preservation provide little information on how these features maintain their form once they are detached from the shore yet remain in a zone of active wave attack (i.e. in depths less than 20 m). Snedden et al. (1999) indicate that shoals in water depths less than approximately 20 m are migrating shoreward through the influence of Stokes Drift under fair-weather waves based on the work of McHone (1973). However, this model does not explain the maintenance of the form of linear shoal and ridge features.

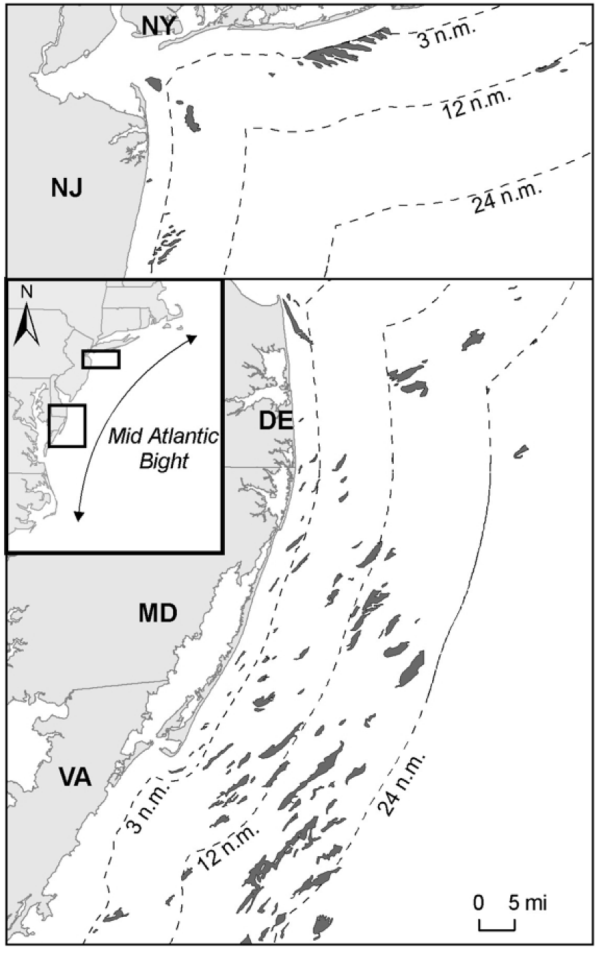

Fig. 1. Map Showing Ridge-Like Shoal Features for part of the US Atlantic Coast

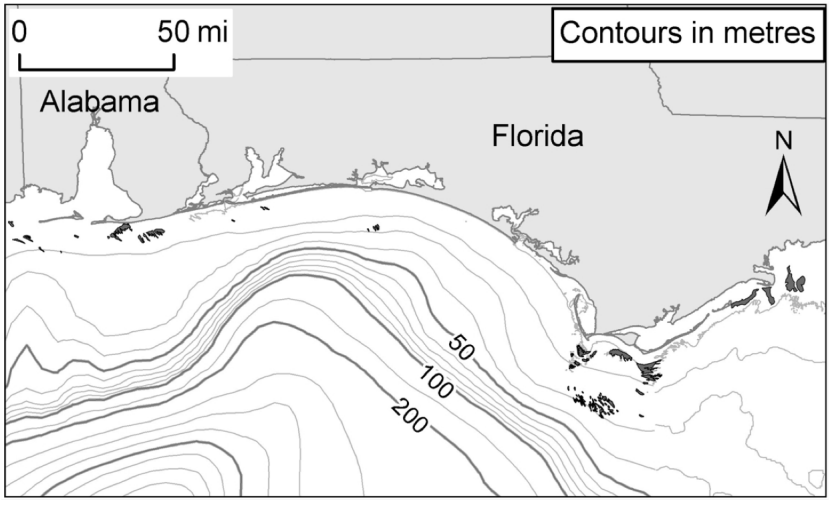

Fig. 2. Map Showing Ridge-Like Shoal Features on the Northeast US Gulf Coast

Hayes and Nairn (2004) present a new conceptual model for the preservation of the linear ridge-like shoal features of the Atlantic and Gulf coasts of the U.S. This model recognizes that the main axis of these shoals is aligned with the dominant direction of storm wave attack. For example, along most of the Atlantic coast of the U.S. the shoals point northeast into the predominant Nor'easters. As an exception, in the lee of Long Island, which provides shelter from the Nor'easters, the shoals have a more east-west orientation. Along the northeast coast of the Gulf of Mexico offshore Alabama the shoals point southeast into the predominant direction of wave attack. The direct influence of wave action on the preservation and evolution of ridge and shoal features has received little attention in the literature on this subject.

A review of the morphology of typical ridge-like features revealed depositional signatures in the form of steep slopes on both the shoreward and seaward side of southerly half of the shoals on the Atlantic coast. This coupled with the observation that these shoals located on the OCS migrate in a southerly or southwesterly direction provide evidence pointing to the importance of wave action and particularly crossing waves. Several articles report on the migration of ridge-like shoal features in the direction of the steep edge of the shoal including Hoogendoorn and Dalrymple (1986) for shoals off Sable Island offshore Nova Scotia, Byrnes et. al. (1999) for shoals offshore Alabama, and Duane et. al. (1972) for shoals offshore Virginia and Delaware. Mariners have often noted the confused sea state over the crest of these offshore shoals, again suggesting wave attack from more than one direction.

Hayes and Nairn (2004) describe the application of a Boussinesq wave model to describe the way in which northeasterly waves interact with a typical group of shoals (Fenwick,

Weaver and Isle of Wight) offshore the Maryland – Delaware border on the OCS (see Figure 3 for the location of these shoals). The MIKE21 Boussinesq Wave (BW) model was applied to simulate waves with a significant wave height of 3 m and a peak period of 16 s from the ENE direction representing a Nor'easter event. A snapshot of an animation of the simulation of wave conditions over the shoals for this condition is shown in Figure 4. The crossing wave pattern over the crest of Fenwick and Weaver Shoals is clearly evident. As waves approach the shoal they split into sets propagating southwest along either side of the shoal and refract towards the crest of the shoal, intersecting or crossing over the crest. The hydrodynamics predicted by the MIKE21 BW model were input to a sediment transport model that considers the influence of non-linear orbital velocity and steady currents based on the work of Dibajnia et. al. (2001). While this approach was able to show there is a convergence of sediment transport over the crest of the shoal (helping to preserve the shape of the shoal against forces tending to flatten and smear the form of the feature), it cannot fully simulate the two components of transport over the crest. Only a single resultant sediment transport vector is predicted (see Figure 5). As explained in the Discussion section of this paper, there are some cases where this will provide a reasonable representation of reality. In general, however, this remains a shortcoming of our capabilities to predict sediment transport under crossing waves.

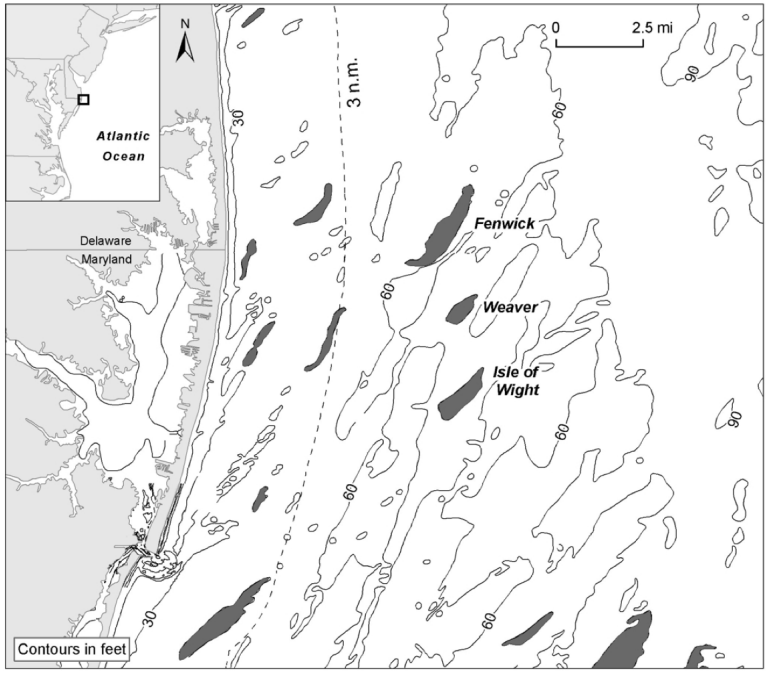

Fig. 3. Location of the Fenwick, Weaver and Isle of Wight Shoals Offshore Maryland/Delaware Border

Based on the wave model, and an interpretation of the sedimentology and geomorphology, a conceptual model of the processes that preserve the form of the ridge-like shoals and cause the features to migrate is shown in the schematic Figure 6. The conceptual model is based on Fenwick Shoal shown in Figures 3 and 4. The steep southeast side of the shoal (bottom right in Figure 6) is the accreting edge of the feature, it is slowly migrating in this direction. From Figures 4 and 5 it is evident that wave heights and associated sediment transport are greater on the northwest side of the feature, perhaps explaining the net deposition and steep slope on the southeast edge. The appearance of crossing sediment transport vectors in Figure 5 is an artifact of the vector lengths representing sediment transport being larger than the model grid spacing. Baird & Associates are currently completing an investigation consisting of field monitoring of waves and currents and numerical modeling to develop a better understanding of the evolution of these features to develop guidelines for dredging shoals for MMS.

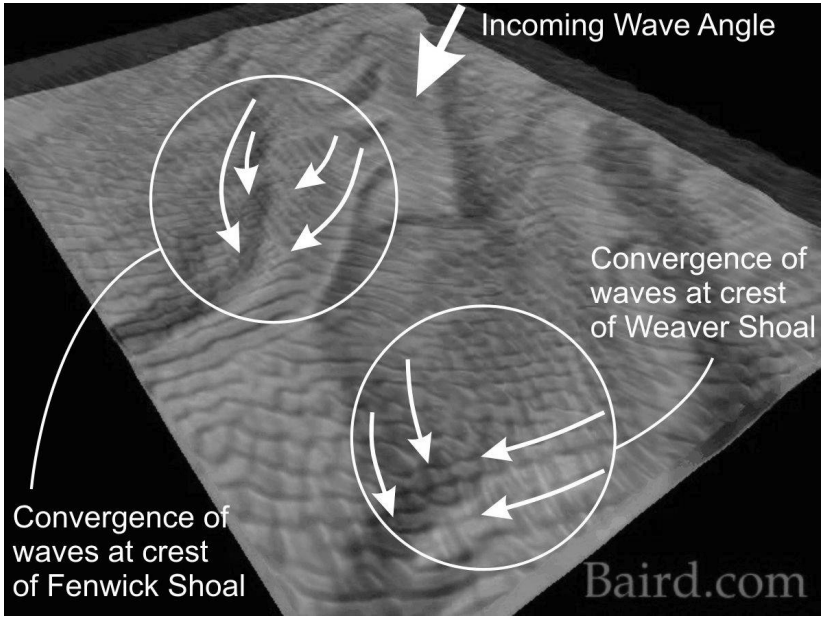

Fig. 4. Snapshot of the Animation of Boussinesq Wave Model Simulation Showing Crossing Waves over the Crest of Fenwick and Weaver Shoals Offshore Maryland/Delaware Border (Wave Condition: H_s = 3 m, T_p = 16 s, ENE direction)

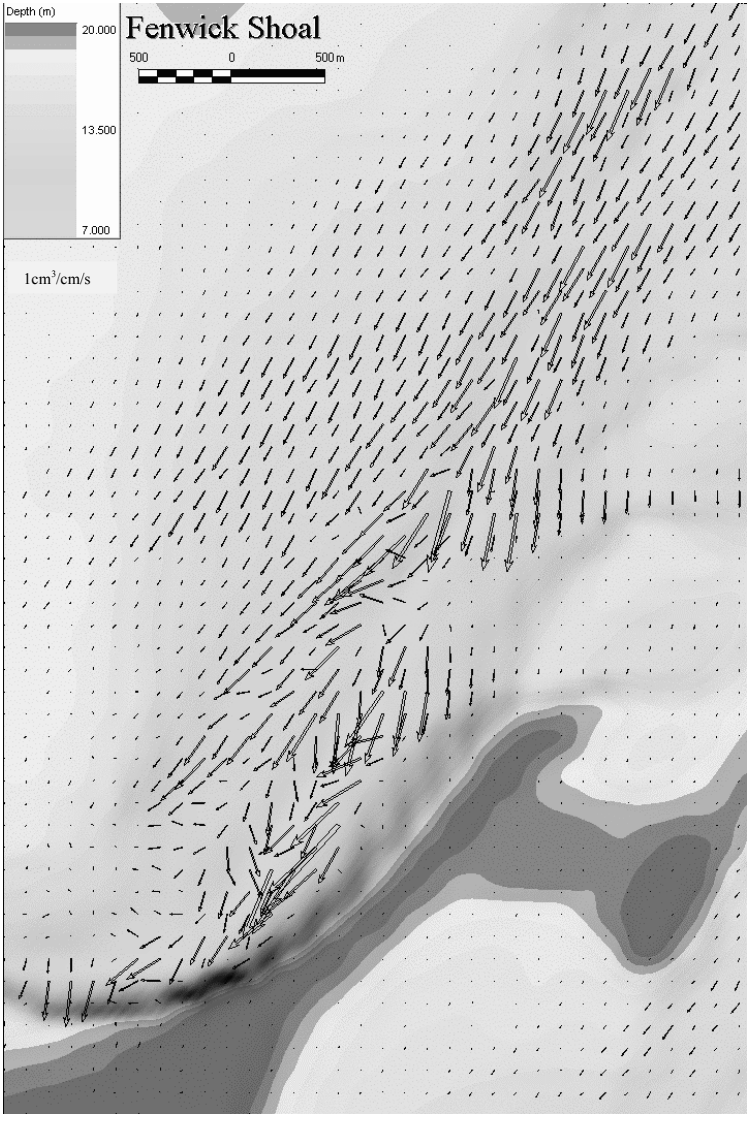

Fig. 5. Sediment Transport Prediction for the Boussineq Wave Simulation Shown in Figure 4 for Fenwick Shoal

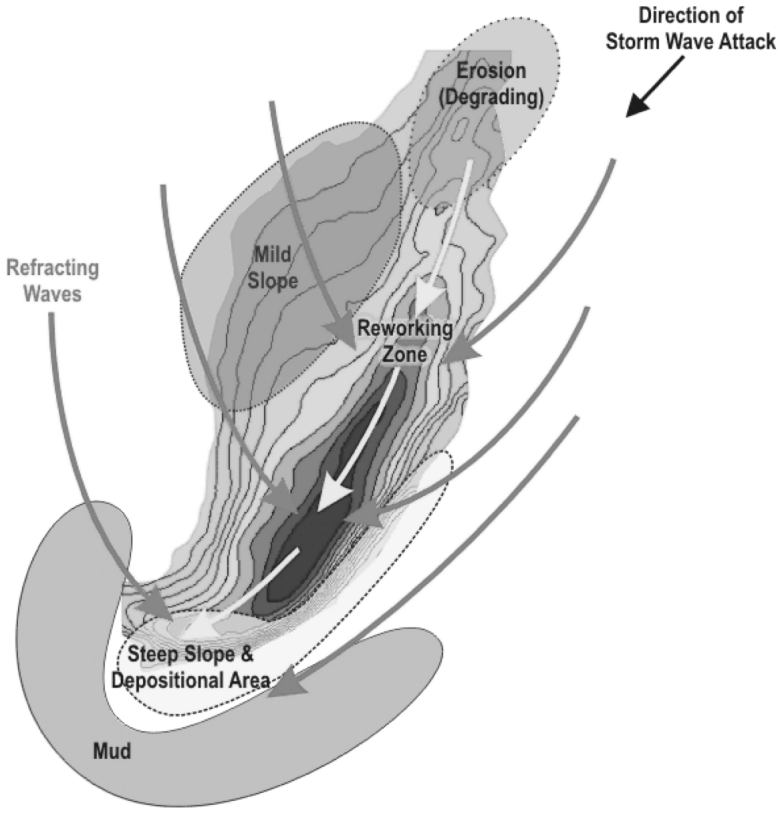

Fig. 6. Conceptual Model of the Role of Crossing Waves in the Geomorphic Evolution of Ridge-Like Shoals (based on Fenwick Shoal, north is straight up). Note: the depth contours are every meter and the crest of the shoal is 6 m below datum.

CORAL RUBBLE SPUR FEATURES

Baird & Associates recently completed a two-year investigation of the physical and biological processes associated with the beaches, lagoon and reef system at Worthing or Sandy Beach on the south coast of Barbados. The beach at Worthing is anchored by three coral rubble spur features as shown in Figure 7. These spur features have an important role in changes to the beach dynamics at Worthing in addition to the water quality and related coral reef health in the lagoon formed by the central and east spurs. Test pits on the spurs revealed that the spurs are composed of pieces of *Accropora palamata* with diameters ranging from 100 to 300 mm covering a wider range of broken coral sizes mixed with sand.

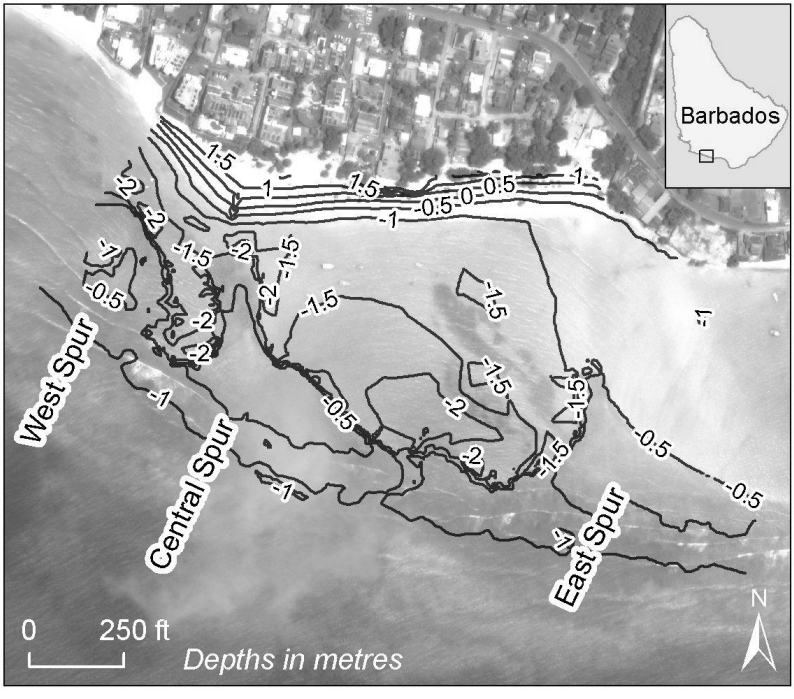

Fig. 7. Three Coral Rubble Spurs Offshore Worthing Beach
on the Southwest Coast of Barbados (on 2005 satellite image)

A historical comparison of the inshore edge of the reef is shown in Figure 8. The three spurs that extend from the reef toward the shoreline are clearly visible. Although there has been little change in the plan form of the east and central spurs, the west spur has extended approximately 55 m toward the shore between 1964 and 2000 with most of the growth occurring between 1973 and 1983. The passage of Hurricane Ivan in September 2004 caused considerable damage to the south coast of Barbados, the most since Hurricane Allen in 1980. The west spur was shifted to the west, the central spur was reduced in length (a crest height reduction) and the east spur was pushed further inshore.

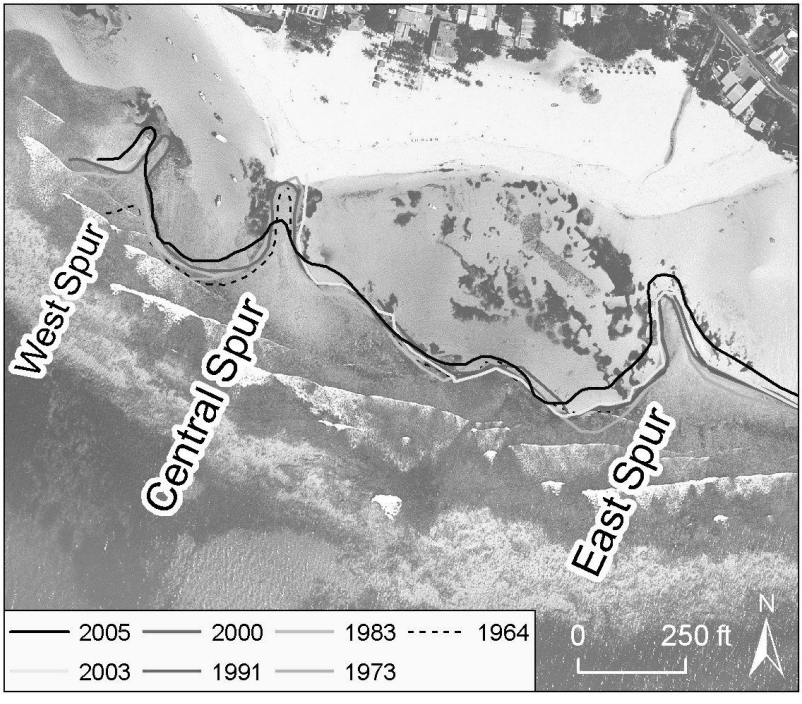

Fig. 8. Historical Change in the Coral Rubble Spur Form at Worthing Based on Air Photo Analysis in GIS (on 2000 air photo)

The predominant wave attack at Worthing is from the south and SSE. The coral rubble spurs have a significant influence on wave transformation which in turn influences the beach stability at Worthing. Also, the waves themselves influence the slow evolution of the spurs. A spectral wave model was applied to describe the wave pattern associated with typical wave attack. The results in the form of wave vectors for the wave condition associated with the 1973 air photo are shown in Figure 9. It is evident from the air photo that both the east and central spurs cause the waves to cross as they propagate inshore on either side of the features refracting towards the crest. Similar to the ridge-like shoal features described in the previous section, this wave transformation process both preserves and develops the form of the spur feature and elongates it slowly in a shoreward direction. The wave direction from the spectral wave model is the result vector direction wherever there are two crossing wave trains – this is particularly evident along the east and central spurs. In the presentation of the vector addition of wave direction from the spectral model, the crossing wave pattern can be inferred from the convergence of wave directions and the abrupt change in direction from one side of the spur to the other. It is possible to output the full 2D directional-frequency spectra from the spectral wave model and this would preserve the two independent waves directions.

The generation and evolution of the coral rubble spurs is initiated by one or more events that lead to the death of coral including: disease, bleaching and hurricane wave attack. At Worthing Beach in Barbados, the initial coral rubble field was created by the death of the *Accropora palmata* likely due to widespread disease in the late 1970's and the damage of Hurricane Allen in 1980. Three rubble spurs were created at Worthing due to the ability of waves to penetrate a relatively long linear and shore-parallel rubble field at two places allowing for three lines of wave convergence – one for each of the three spurs.

Coral rubble spur features are likely created wherever there is an abundant supply of coral rubble generated relatively rapidly due to widespread die off or damage. Another example of coral rubble spurs is shown in Figure 10 located offshore Kihei on Maui in the Pacific Ocean. Several spur features extend from a linear coral rubble field (with breaks between spurs) to shore over a distance of about 100 m. Based on a review of air photos from 1960, 1975, 1988 and 1997 it was determined that the coral rubble field first appeared in 1975 and the spurs have developed in form since that time (personal communication, John Rooney, U. of Hawaii). Rooney postulates the coral rubble was generated through three possible mechanisms: 1) major storms in the 1960s; 2) the tsunami of 1946; or 3) blasting from the combat demolition team in WWII.



Fig. 9. Spectral Wave Model Application for the Waves
that Existed During the 1973 Air Photo at Worthing, Barbados (H_o=1m, T=8s)



Fig. 10. Coral Rubble Spurs at Kihei Offshore Maui, Hawaiian Islands

DISCUSSION OF CROSSING WAVES AND GEOMORPHIC FEATURES

This paper has reviewed examples of two types of geomorphic forms created by crossing wave patterns. Other common examples where crossing waves contribute to the evolution of geomorphic features include: salients in the lee of breakwaters, small islands and the shoreward limbs of ebb shoals at river or inlet mouths. Crossing waves are also a persistent feature of wave attack at many locations in the world that are exposed to two dominant sources of wave generation. This is often the case at mid-latitude sites that are exposed to open ocean swells at the same time as more locally generated waves from trade winds or extra-tropical storms. At these locations the crossing waves influence entire beaches and not just localized areas such as coral rubble spurs or ridge-like shoals. Regardless, the coastal engineer or scientist is faced with the same problem of how to consider the influence of crossing waves on sand transport and the evolution of geomorphic features.

From the two examples presented, it was evident that the phase-resolving Boussinesq wave model was able to reproduce the crossing wave pattern, while the spectral wave model could not, at least not based on the summary parameters that are typically output (versus the full 2D spectra). The Boussinesq model also predicts the bi-directionality of the orbital velocities at the bed for the example of the offshore shoals. However, to the authors' knowledge there are no commonly available sediment transport predictors or numerical models with such predictors to consider the influence of two crossing wave

trains on sediment transport. So the question arises, is the resultant wave vector and/or orbital velocity speed and direction sufficient to predict the direction and rate of sediment transport under crossing wave conditions?

If two progressive and crossing wave trains with the same period are in phase, the orbital path will be a straight line with its length equal to the orbital amplitude of the combined waves. If the difference in wave approach direction is 90 degrees between two crossing waves with the same period, and the waves are 90 degrees out of phase without any non-linearity due to shoaling, theoretically the orbital path would be circular in plan. Therefore, it is likely that the orbital path for most conditions with crossing waves is somewhere in between and elliptical in planform. Net transport occurs through three possible conditions or mechanisms related to orbital velocity: 1) under non-linear shoaling waves where the onshore velocity under the wave crest is much larger resulting in net shoreward transport; 2) where condition (1) is more pronounced because the offshore component of the orbital velocity is less than the threshold for motion of the sediment grains; and 3) where the peak in suspended sediment concentration is in phase with either the offshore or onshore component of the orbital velocity (either of which may occur under rippled conditions leading to net offshore or onshore transport). Where there is a strong steady current and the waves are only important for entrainment of sediment with the currents being responsible for advection, simply using the resultant vector of crossing waves is likely appropriate. The challenge of considering crossing waves is probably most important under conditions (1) and (2) when there is not a strong current present. Such conditions may also influence the ripple pattern on the sea bed, which in turn could influence the phasing and intensity of sediment re-suspension over ripple crests. While it may not be possible to systematically predict sand transport under crossing wave trains in these conditions, it would be possible to check whether a resultant vector might result in misleading predictions.

CONCLUSIONS

Crossing waves can lead to the development of unique geomorphic forms including offshore shoals, coral rubble spurs and salients under a wide variety of conditions. Crossing waves are also a common feature along coastlines at mid-latitudes exposed to both ocean swell generated at long distances and locally generated sea waves. There are no commonly accepted or standard practices for predicting sand transport and morphologic evolution under crossing waves. In some cases the estimation of the resultant wave condition through the vector addition of two crossing wave trains may be sufficient to predict sediment transport with an acceptable level of accuracy. Nevertheless, this will often not be the case and the validity of using vector addition of either the two wave directions for crossing waves or the associated orbital velocity components should be checked by evaluating the form of the orbital pathway and the speed of water particles along this path together with a consideration of the threshold of motion for the sediment.

ACKNOWLEDGEMENTS

The authors wish to thank Dr. Mike Risk of McMaster University in Canada for his guidance on coral disease and generation of coral rubble, Dr. John Rooney of the University of Hawaii for sharing his air-photo analysis of the coral rubble spurs on Maui, and Bill Curtis and Joan Pope of the US Army Corps of Engineers for the information they provided concerning the coral rubble spurs in Maui. The authors also wish to thank the Coastal Zone Management Unit of Barbados and the US Minerals Management Service for sponsoring Baird's investigations of the coral rubble spurs and offshore ridge-like shoals, respectively.

REFERENCES

Byrnes, M.R., Hammer, R.M., Vittor, B.A., Ramsey, J.S., Snyder, D.B., Bosma, K.F., Wood, J.D., Thibaut, T.D., and Phillips, N.W. (1999). *Environmental Survey of Identified Sand Resource Areas Offshore Alabama: Volume I: Main Text, Volume II: Appendices*, Herndon, Virginia: Minerals Management Service OCS Report MMS 99-0052, 326 pp. + 132 pp. appendices.

Dibajnia, M., Moriya, T., and Watanabe, A. (2001). "A Representative Wave Model for Estimation of Nearshore Local Transport Rate." *Coastal Engineering*, 43(1), 1-38.

Duane, D.B., Field, M.E., Meisburger, E.P., Swift , D.J.P. and Williams, S.J. (1972). "Linear shoals on the Atlantic inner continental shelf, Florida to Long Island." *In:* Swift, D.J.P., Duane, D.B. and Pilkey, O.H. (eds.), *Shelf Sediment Transport: Process and Pattern*, Stroudsburg, Pennsylvania: Dowden, Hutchinson and Ross, pp. 447-498.

Hayes, M.O. and Nairn, R.B. (2004). "Natural Maintenance of Sand Ridges and Linear Shoals on the US Gulf and Atlantic Coast Shelves and the Potential Impacts of Dredging". *Journal of Coastal Research*, Vol. 20, pp. 138-148.

Hoogendoorn, E.L. and Dalrymple, R.W. (1986). "Morphology, lateral migration and internal structures of shoreface-connected sand ridges, Sable Island Bank, Nova Scotia, Canada." *Geology* 14, 400-403.

Huthnance, J.M. (1982). "On one mechanism forming linear sand banks." *Estuarine and Marine Coastal Science*, 14, 79-99.

Mcbride, R.A. and Moslow, T.F. (1991). Origin, evolution, and distribution of shoreface sand ridges, Atlantic inner shelf, U.S.A. Marine Geology, 97, 57-85.

Mchone, J.F., Jr. (1973). "Morphological time series from a submarine sand ridge on the southern Virginia coast." Norfolk, Virginia: Old Dominion University, M.S. thesis, 55 p.

Snedden, J.H., Kreisa, R.P., Tillman, R.K., Culver, S.J. and Schweller, W.J. (1999). "An expanded model for modern shelf sand ridge genesis and evolution on the New Jersey Atlantic shelf. *In:* Bergman, K.M. and Snedden, J.W. (eds.) *Isolated Shallow Marine Sand Bodies: Sequence Stratigraphic Analysis and Sedimentologic Interpretation*. Tulsa, Oklahoma: SEPM (Society for Sedimentary Geologists) Special Publication no. 64, pp. 147-164.

Trowbridge, J. H. (1995). "A mechanism for the formation and maintenance of shore-oblique sand ridges on storm-dominated shelves." *Journal of Geophysical Research*, 15 August 1995, 16,071-16,086.

OBSERVATION AND MODELING OF CRESCENTIC BARS IN BARCELONA EMBAYED BEACHES

F. Ribas[1], R. Garnier[2], E. Ojeda[1], A. Falqués[2], J. Guillén[1], D. Calvete[2].

1. Institut de Ciències del Mar, CSIC, Passeig Marítim de la Barceloneta 37-49, 08003 Barcelona, Spain. ribas@cmima.csic.es, jorge@cmima.csic.es, eojeda@cmima.csic.es
2. Universitat Politècnica de Catalunya, Applied Physics Dept., Jordi Girona 1-3, 08034 Barcelona, Spain. rgarnier@fa.upc.edu, falques@fa.upc.edu, calvete@fa.upc.edu

Abstract: Two events of crescentic bar formation in La Barceloneta beach are analyzed (Mediterranean coast of Spain). They occurred on October 2003 and on December 2005, during Eastern storms with offshore root-mean-square heights between 1.5 m and 2 m, peak periods of about 9 s and angles of incidence relative to shore-normal between 15° and 30°. The final alongshore spacings are about 300 m in the first event and about 100-200 m in the second. A nonlinear morphodynamic model is then applied to La Barceloneta conditions to reproduce these two events. The model is able to simulate the final shape of the crescentic bars, reproducing the observed spacings.

INTRODUCTION

Field observations of crescentic bars

Shore-parallel sand bars can display a number of different shapes, the most simple being rectilinear (linear shore-parallel bars). Under certain wave conditions, these bars can develop alongshore inhomogeneities that consist of shallower and deeper areas alternating along the bar (Wright and Short, 1984). When this occurs, a prominent circulation pattern characterized by the presence of rip currents is also established. These strong and narrow offshore-flowing currents are part of a larger circulation cell, which includes an onshore-flowing component as well as feeder currents taking the water alongshore into the rip. The rip currents flow offshore in the channels that breach the bar and the onshore flow takes place over the shoals.

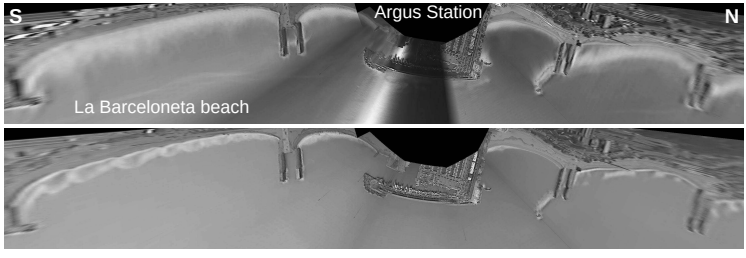

Fig. 1. Planview images of Barcelona city beaches. Upper panel: Linear shore-parallel bar in La Barceloneta on the 10 of December of 2005 at 9h. Lower panel: Well-developed crescentic bar with shoreline attachments (megacusps) on the 13 of December of 2005 at 8h.

This results in a wavy shape of the bar in planview, thus called crescentic bar (see the lower panel of Fig. 1). These alongshore undulations and the corresponding circulation cells frequently occur at regular or quasi-regular intervals. Crescentic bars have been observed on many beaches (up to 33 references are listed in Table 1 of van Enckevort et al., 2004) but systematic field studies are scarce, especially in the case of embayed beaches.

Most of the knowledge of mid-term dynamics of crescentic bars relates to bar state models (Wright and Short, 1984). During the peak of a storm, a shore-parallel bar is developed or enlarged and migrates offshore (longshore bar and trough state). Under the subsequent lower energetic conditions, the bar becomes crescentic and migrates slowly onshore (rhythmic bar and beach state) until the horns occasionally weld to the shore (transverse bar and rip state). The following stormy period destroys the rhythmicity and rebuilds the shore-parallel bar.

Previous modeling of crescentic bars

Although the formation of crescentic bars has been often attributed to the hydrodynamic forcing by infragravity edge waves, it is nowadays well accepted that the most plausible cause is a positive feedback between breaking waves, currents and the evolving morphology (self-organization processes). Small random perturbations are always present in the bottom of any alongshore-uniform beach. The existence of such bottom perturbations will cause changes in both the currents and the wave properties (such as their height and angle of incidence). Their joint interaction will produce small perturbations in the net sediment transport that in turn will modify the bottom of the beach. If there is a positive feedback between a certain developing perturbation (like a crescentic bar) and the associated sediment transport, the former will grow and dominate the beach bathymetry.

The existing modeling studies based on self-organization describe the generating mechanism and predict the order of magnitude of the wavelength and the migration rate (Deigaard et al., 1999; Falqués et al., 2000; Caballeria et al., 2002;

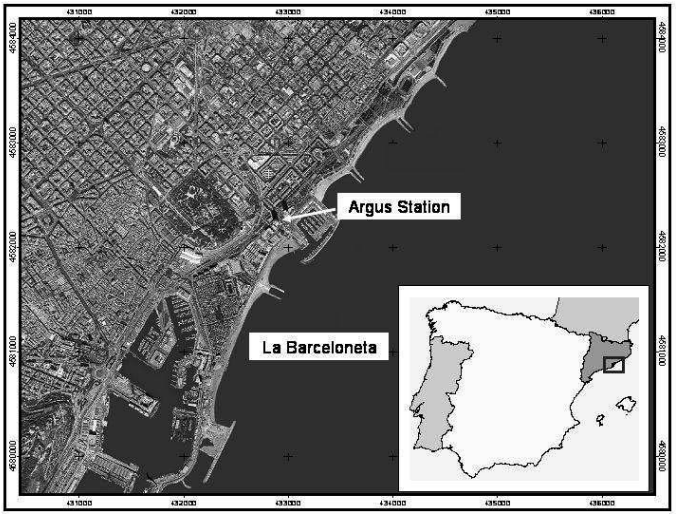

Fig. 2. Study region including the location of the Argus video station.

Damgaard et al., 2002; Reniers et al., 2004; Calvete et al., 2005). However, a serious limitation of our present knowledge on crescentic bars is the lack of quantitative comparisons between field observations and model results. A pioneer study is that of van Enckevort et al. (2004), where observations of crescentic bars in four open beaches were qualitatively compared with existing model results.

Present study

The embayed beaches on the waterfront of Barcelona have been monitored with an Argus video system since November 2001 (Ojeda and Guillén, 2006). In one of these beaches, La Barceloneta, a single shore-parallel bar is usually present, which often exhibits a crescentic shape (see Fig. 1). This system is therefore an ideal lab to test models for crescentic bar formation. The aim of the present research is to investigate the formation and evolution of crescentic bars in La Barceloneta, comparing field observations with the predictions of the nonlinear morphodynamic model proposed by Garnier et al. (2006).

The field site is presented in the next section and two events of crescentic bar formation observed in La Barceloneta are reported in the third section. The model, presented in the fourth section, is then applied to La Barceloneta conditions and the corresponding results are described in the subsequent section. The sixth section contains a discussion of the model results and a comparison with the observations.

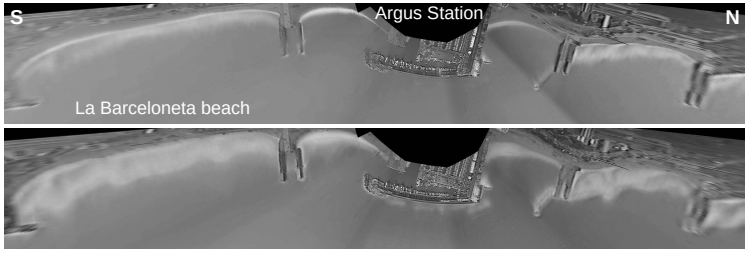

Fig. 3. Planviews of Barcelona city beaches. Upper panel: Linear bar in La Barceloneta on the 15 of October of 2003 at 8h. Lower panel: Crescentic bar on the 18 of October of 2003 at 16h.

FIELD SITE

The field site is located in La Barceloneta beach, at the seafront of Barcelona city (Spain). This artificial beach has an orientation N18^{o}E, a length of 1100 m and it is confined between two groins, the southern one showing an L-shape (see Fig. 2). In the nearshore domain (water depth <5 m), the sediment has a mean grain size of 0.40 mm and the mean slope is 0.033.

Being a microtidal region (water level fluctuations <0.20 m), the winter storms are the major hydrodynamic forcing in Barcelona city beaches. Due to the shoreline orientation, the most important ones are those coming from the East, which are frequently associated to the cyclonic activity in the Western Mediterranean Sea. Their typical duration is of a few days and their main occurrence is from October to April. The significant wave height, H_s, can increase up to 6 m during winter storms but the mean annual H_s is lower than 1 m. Before 2004, only one virtual buoy was providing directional wave information every three hours (WANA2066051 point). These data are computed by the Spanish National Institute of Meteorology using the numerical models HIRLAM and WAM. Since 2004, direct hourly measurements of a directional buoy located at 69 m depth are also available (COST-BARCELONA buoy). Bathymetries of La Barceloneta beach collected on the 6 of October of 2003, the 5 of November of 2003 and the 26 of October of 2005 revealed the existence of two types of profiles: constant sloping beaches during summer (before the arrival of winter storms) and profiles with one bar after the occurrence of significant storms.

An Argus video system (Holman and Stanley, 2006), composed of five full color cameras, was located on November 2001 atop a building close to the Olympic Marina, at 142 m high (see Fig. 2). They span a 180° view and allow full coverage of the four beaches surrounding the marina (Ojeda and Guillén, 2006). Nearshore bars are seen as white stripes (high intensity values) in the time exposure images (averaged over 10 minutes). These images from the five cameras are rectified and merged to a single planview image (see Fig. 1).

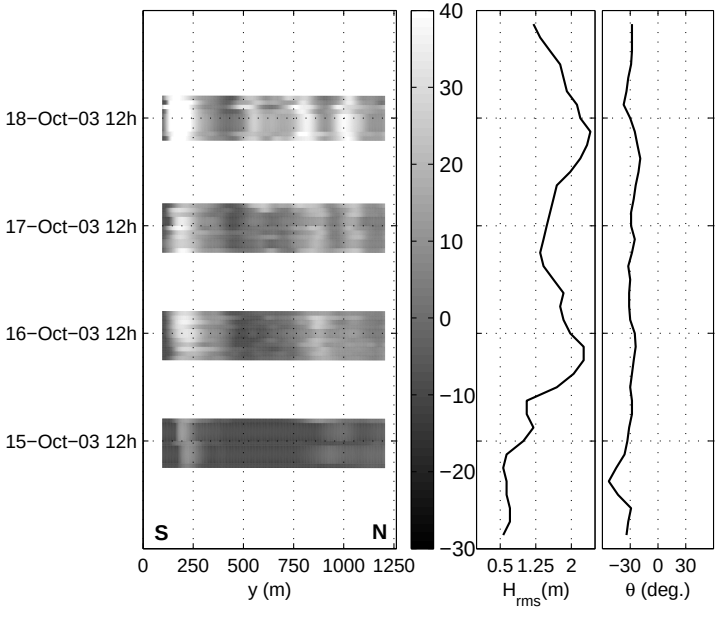

Fig. 4. Crescentic bar event in La Barceloneta during October 2003. Time series of (from left to right) the bar crest lines, $\hat{x}(t, y)$, the root-mean-square wave height, H_{rms}, and the angle of wave incidence, θ, relative to shore-normal. In the first panel, $y{=}0$ corresponds to the southern edge of the beach. Wave conditions were obtained from the WANA2066051 point.

FIELD OBSERVATIONS

Methodology

The characteristics and dynamics of the nearshore bar in La Barceloneta beach have been studied using the planview images obtained from the Argus station. A detailed description of the methodology can be found in van Enckevort et al. (2004) and Ojeda et al. (2007). Bar detection capability of this system is restricted to a range of wave conditions ($0.9 < H_s < 3.5$ m), when wave breaking patterns can be identified. The lines of maximum intensity are extracted from the images using the BLIM program developed by the University of Utrecht. Three preprocessing steps are then applied in order to remove (1) the pixel induced noise, (2) the large-scale shoreline curvature and (3) the bar crest obliquity. The obtained quantity, $\hat{x}(t, y)$, is assumed to be representative of the perturbations of the bar crests with respect to an averaged position. The overall behavior of the bar crest lines from November 2001 to December 2004 was described in Ojeda et al. (2007), including their response to storms and the coupling with the shoreline dynamics. The present contribution focuses on the two most clear events of crescentic bars formation found from November 2001 to December 2005.

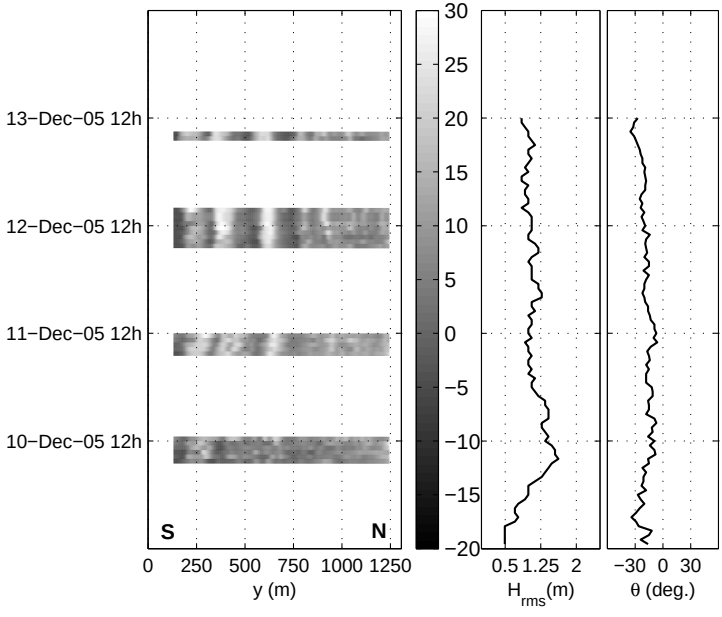

Fig. 5. Crescentic bar event in La Barceloneta during December 2005. Graph description can be found in the caption of Fig. 4. Wave conditions were obtained from the COST-BARCELONA buoy at 69 m depth.

Detected crescentic bar events

The first event of crescentic bar formation of the studied period occurred during a major Eastern storm in October 2003. A crescentic bar emerged (see the lower panel of Fig. 3) and prevailed during the entire 2004 (Ojeda et al., 2007). A space-time diagram (timestack) of the bar line perturbations $\hat{x}(t, y)$ corresponding to this event is shown in Fig. 4, together with the wave conditions. In the first panel, $y = 0$ m corresponds to the southern edge of the beach. Only one seaward perturbation around $y = 250$ m was present on October 15th. As described in Ojeda et al. (2007), this seaward perturbation was present near the southern tip of La Barceloneta from November 2001 to December 2004, probably formed during a period of extreme wave conditions in October 2001. On October 18th, the last day of the storm, four perturbations could be detected along the 1100 m alongshore length, giving an alongshore spacing of about 300 m. The averaged offshore wave conditions during the storm were a root-mean-square height of $H_{rms} = 1.9$ m, a peak period of $T_p = 9.9$ s and an angle of wave incidence of $\theta = 28^o$, relative to shore-normal. The averages were taken from October 16th at 3h to October 19th at 3h ($H_{rms} > 1.25$ m), using the data from the WANA2066051 point.

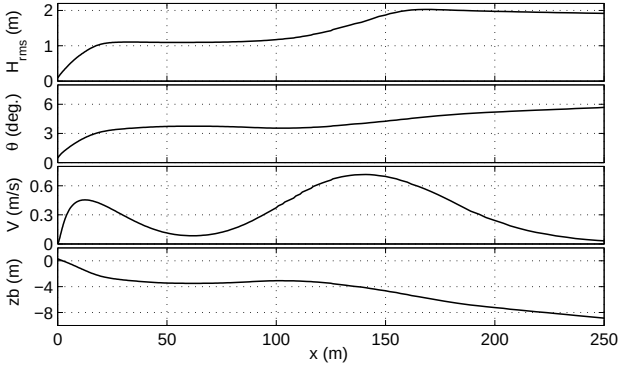

Fig. 6. Initial reference state used in the simulation of the first event of crescentic bar formation in La Barceloneta. The cross-shore distribution of (from top to bottom) wave height, angle of wave incidence, longshore current and beach profile are shown. The x-axis is the cross-shore direction. The profile is taken from a bathymetry measured on the 5 of November of 2003.

The second event of formation of a crescentic bar in La Barceloneta occurred during a less energetic Eastern storm in December 2005. The planviews corresponding to this event have been shown in Fig. 1. A well-developed crescentic bar with at least six undulations is visible on December 13th at 8h, displayed in the lower panel. This can also be seen in the corresponding timestack, shown in Fig. 5. Only the seaward perturbation at $y = 250$ m was detected on December 10th, whereas six seaward perturbations were visible on December 13th. They were spaced every 200 m in the southern half of the beach and every 100 m in the northern half. The storm-averaged offshore wave conditions corresponding to this event were $H_{rms} = 1.1$ m, $T_p = 8.7$ s and $\theta = 17^o$. The averages were taken from December 10th at 4h to December 13th at 12h ($H_{rms} > 0.75$ m), using the data of the COST-BARCELONA buoy.

MODEL FORMULATION

A nonlinear 2DH morphodynamic model (Garnier et al., 2006) is used to describe the initial formation and further evolution of crescentic bars in La Barceloneta. The model describes the feedbacks between depth-averaged mean currents, waves and an erodible bed in a nearshore zone bounded by a straight and infinite coastline (no groin effects are included). The hydrodynamics is modeled with the wave- and depth-averaged shallow water equations for water momentum balance, water mass conservation and wave energy and phase conservation. Waves are assumed to have a narrow spectrum in frequency and wave vector whilst their heights are assumed to be random and to follow the Rayleigh distribution, characterized by H_{rms}. Bed level evolution is described with a sediment mass conservation equation, where the sediment transport is modeled with the Soulsby/van Rijn formula (Soulsby, 1997).

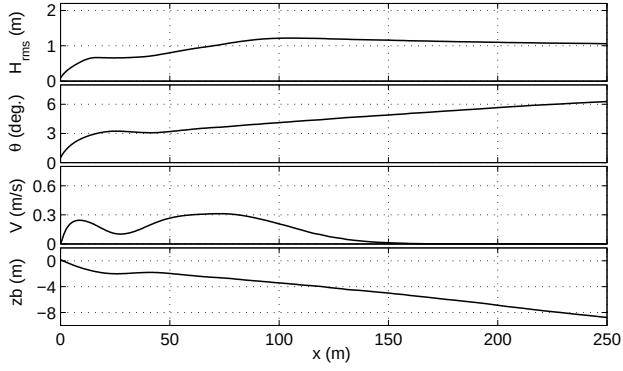

Fig. 7. Initial reference state used in the simulation of the second event of crescentic bar formation in La Barceloneta. Graph description can be found in the caption of Fig. 6. The profile is taken from a bathymetry measured on the 26 of October of 2005.

The model solves the full set of nonlinear equations and provides information about the mid-term behavior of the system O(weeks). The solution procedure starts by selecting an initial alongshore uniform reference state that is in equilibrium (i.e. steady). In this study, the chosen reference profiles $z_b^o(x)$ are obtained from the available bathymetries measured in La Barceloneta (on the 5 of November of 2003 for the first event and on the 26 of October of 2005 for the second). Then, the offshore wave conditions are imposed at 69 m depth and the cross-shore distribution of the equilibrium hydrodynamic quantities is computed: H_{rms}, θ, the longshore current, V, and the elevation of the mean free surface, z_s. Figures 6 and 7 show the initial reference state used in events 1 and 2, respectively. The lower panels display the reference beach profiles, $z_b^o(x)$. As can be seen, on the bathymetry measured on the 5 of November of 2003, the bar was located at about 100 m from the shoreline, whereas this distance was approximately 40 m in the bathymetry of the 26 of October of 2005. Table 1 summarizes the parameter setting used to simulate the two events, including the wave conditions imposed at 69 m depth. The reason why the angle of wave incidence used is smaller than the measured ones (described in the third section) will be explained in the next section.

Once the reference state has been solved, small random perturbations O(cm) are superimposed to it and direct numerical time-integration of the full set of equations (including bed evolution) is performed. The computational domain is a rectangle of 250 m in the cross-shore direction and 2000 m in the alongshore direction. The solution is assumed to be periodic in the lateral boundaries and constant wave conditions are imposed on the offshore boundary. This latter assumption is in agreement with the measured wave conditions leading to crescentic bar formation in La Barceloneta (see Figs. 4 and 5).

Table 1. Parameter setting used in the model of this study.

Wave conditions event 1			Wave conditions event 2			Other parameters	
$H_{rms}(m)$	T_p (s)	θ	$H_{rms}(m)$	T_p (s)	θ	d_{50} (mm)	z_0 (m)
1.9	9.9	10°	1.1	8.7	10°	0.4	0.01

MODEL RESULTS

Model runs were performed to simulate the two events of crescentic bar formation of La Barceloneta in October 2003 and December 2005. The existing literature shows that formation of crescentic bars is favored by shore-normal wave incidence (for instance, see Calvete et al., 2005) and this was also verified in La Barceloneta. When running the model with the angle of wave incidence measured in the offshore buoys (28° in event 1 and 17° in event 2), unreasonably large values for the growth times and the wavelengths were obtained. The offshore wave angle had to be reduced to 10° to obtain more realistic results. The results presented in the rest of this paper are those corresponding to $\theta = 10^o$ and the measured values of H_{rms} and T_p. They are shown in Table 1, together with the values used for the grain size, d_{50}, and the roughness length, z_0).

Figure 8 shows the result of the model for the conditions of the first event. The upper panel is a time series of the bottom perturbation with respect to the initial beach for a longshore transect located at $x = 50$ m. During the first four days the bathymetry developed what would be the final dominant wavelength, with a spacing between channels of about 400 m. This is best shown in the lower panel of Fig. 8, which displays the Fourier transform of the signal shown in the upper panel. During the subsequent two days the crescentic topography evolved without changing the dominant spacing, the pattern growing in amplitude with nearly no migration. During the seventh day of numerical evolution, before growth saturation had been reached, the model blew up.

Figure 9 displays a planview of the topographic and hydrodynamic results obtained on day 7 (just before the model blew up). Three undulations can be detected in the alongshore length of 1200 m that is shown, corresponding to the dominant wavelength of 400 m. Resembling the observed systems of crescentic bars and rip currents in natural beaches, the shape of the undulations is alongshore variable. The flow field has two main components: the initial longshore current flowing from left to right (waves arrive from the bottom left corner of the planview) and a rip-current system with the alternation of offshore and onshore flowing. This results in a meandering of the longshore current with some strong rips (for instance at $y = 1250$ m).

The results obtained when using the conditions corresponding to the second event are shown in Figs. 10 and 11. The planview with the topographic and hydrody-

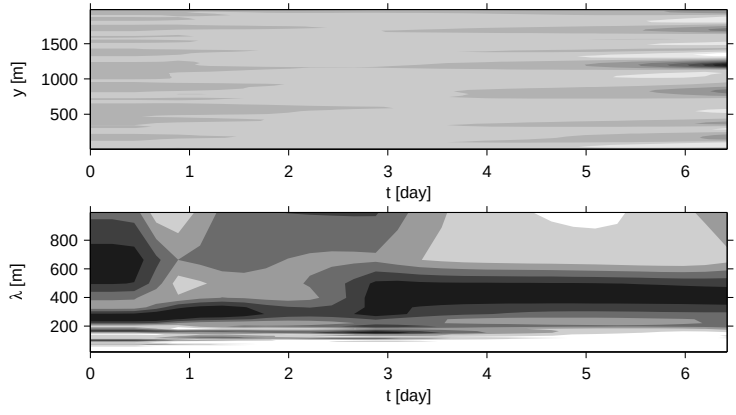

Fig. 8. Model simulation of the first event of crescentic bar formation in La Barceloneta beach. Time series of the bottom perturbation with respect to the initial beach for the longshore transect located at $x=50$ m (upper panel) and the corresponding Fourier transform (lower panel), which is indicative of the dominant wavelengths. In the upper panel, light (dark) gray corresponds to shallow (deeper) sections. In the lower panel, dark gray indicates larger spectral density.

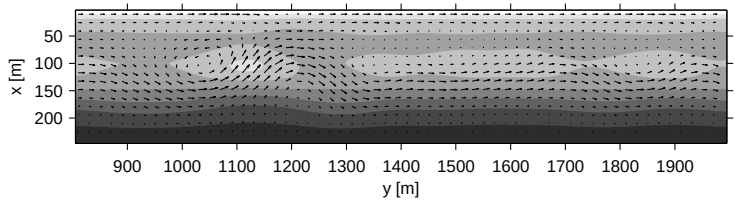

Fig. 9. Planview of the final state obtained for the first event. Colors represent the bottom level (deeper sections are darker) and the small arrows correspond to the 2DH flow field coupled with the emerging morphology. The x-axis is the cross-shore direction ($x=0$ being the shoreline) and the y-axis stands for the longshore direction (an alongshore length of 1200 m is shown).

namic results obtained by the model before it blew up shows similarities with that of event 1. It consists of a crescentic bar with alongshore variable undulations and the longshore current is meandering due to the presence of rip currents. The most significant difference is a reduction of the length scales by a factor of 2, the dominant wavelength being now 200 m (three undulations in an alongshore length of 600 m). The time series of Fig. 11 shows that the model needed about four days to reach the final dominant wavelength of 200 m. However, in this case there was another detectable (but weaker) wavelength of 100 m. During the subsequent five days the crescentic feature grew in amplitude with nearly no migration, until the model blew up at the end of the eighth day, before saturation had been reached.

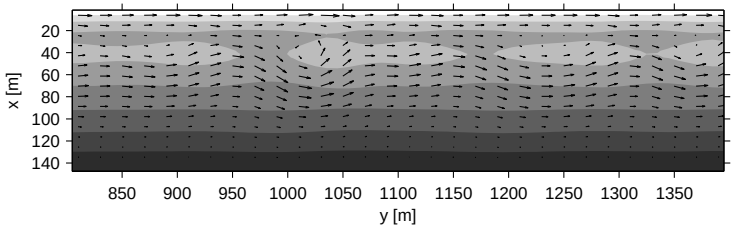

Fig. 10. Planview of the final state obtained for the second event. Graph description can be found in the caption of Fig. 9, but the scaling of the axis is different in the present figure (an alongshore length of 600 m is shown).

DISCUSSION AND MODEL-DATA COMPARISON

The crescentic bars observed in La Barceloneta beach showed a wavelength of about 300 m in October 2003 and of 100-200 m in December 2005. Previous models have predicted that the wavelength of crescentic bars increases roughly linearly with the distance from the shoreline to the crest of the initial bar (Deigaard et al., 1999; Damgaard et al., 2002; Calvete et al., 2005). This is consistent with our observations, the bar being further offshore in the first event, as can be seen in the corresponding planviews (lower panels of Figs. 1 and 3). This is also confirmed by the available bathymetries, the 5 of November of 2003 the bar was located at 100 m from the shore whilst the 26 of October of 2005 the distance was 40 m (see Figs. 6 and 7). In qualitative agreement with what was observed in La Barceloneta, the model used in the present contribution predicted a wavelength of 400 m in the first event and a combination of 200 m and 100 m in the second event. Therefore, the physical processes responsible for crescentic bar formation that are included in the model by Garnier et al. (2006) could explain some of the properties of the bars detected in La Barceloneta.

However, the model was not able to describe appropriately some other characteristics of the detected crescentic bar events. In particular the angles of wave incidence used in the simulations were smaller than those that were measured in the field. It should be pointed out that the existing models (including the one by Garnier et al., 2006) have some properties that limit the comparison of their results with the field observations in La Barceloneta. Firstly, the geometry used in the models is highly idealized: a rectilinear shoreline with periodic boundary conditions (rather than groin simulation) and initial alongshore uniform conditions in the bathymetry. The geometry of La Barceloneta beach is significantly different, since it is limited by groins, it has a curvilinear shoreline and it displays significant alongshore inhomogeneities in all the available bathymetries.

Future work should include the development of the model, prioritizing the description of groin effects. Moreover, events of crescentic bar formation in other

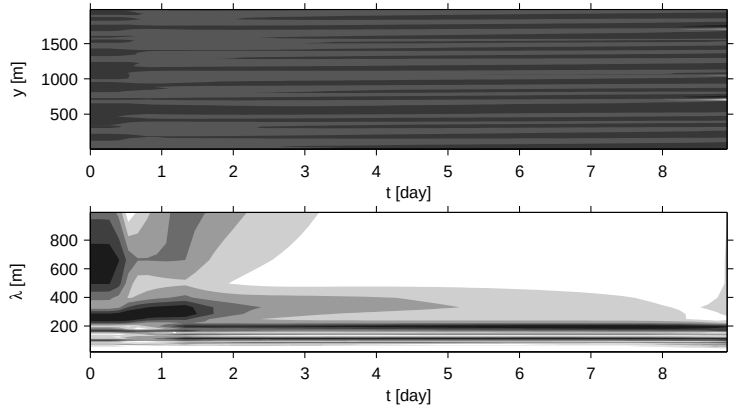

Fig. 11. Model simulation of the second event of crescentic bar formation in La Barceloneta beach. Graph description can be found in the caption of Fig. 8.

beaches should be analyzed to better fit with model results in case of θ larger that 15°. Finally, the model blew up before saturation of the growth of crescentic bars was reached. This is the case in all the nonlinear models for crescentic bar formation that are available (e.g., Caballeria et al., 2002; Damgaard et al., 2002; Reniers et al., 2004). However, the model used in the present study was able to reproduce the growth and saturation of transverse/oblique shore-attached bars in initially plane beaches (Garnier et al., 2006). More research is needed to obtain growth saturation of crescentic bars in initially barred beaches.

CONCLUSIONS

The characteristic wave conditions leading to formation of crescentic bars in La Barceloneta beach, on the Spanish Mediterranean coast, have been determined. Crescentic bars emerge during Eastern storms with offshore root-mean-square heights between 1.5 and 2 m, peak periods of 9 s and angles of incidence between 15° and 30°, relative to shore-normal. The observations are coherent with the theoretical prediction that the wavelength of crescentic features increases when the distance from the bar crest to the shoreline is larger.

Two events of crescentic bar formation detected in La Barceloneta have been reasonably reproduced with a nonlinear morphodynamic model, the predicted and the detected wavelengths being in qualitative agreement (from 100 m to 400 m). Future improvements of the model should be to include groin effects and to consider larger angles of wave incidence for crescentic bar formation.

ACKNOWLEDGMENTS

This research is part of the PUDEM project which is funded by the Spanish

government under contract REN2003-06637-C02-01/MAR. The work of F. Ribas, E. Ojeda and D. Calvete is supported by the Spanish government through the programs 'Juan de la Cierva', 'Becas FPU' and 'Ramon y Cajal', respectively. R. Garnier is funded by the Catalan government through the program 'Beques IQUC'. Wave conditions nearby Barcelona are provided by the Spanish institution 'Puertos del Estado'. Thanks to Dr. G.Ruessink for providing the program BLIM.

REFERENCES

Caballeria, M., G. Coco, A. Falqués, and D. A. Huntley (2002), Self-organization mechanisms for the formation of nearshore crescentic and transverse sand bars, *J. Fluid Mech.*, 465, 379–410.

Calvete, D., Dodd, N., Falqués, A., and van Leeuwen, S. M. (2005), Morphological development of rip channel systems: normal and near normal wave incidence, *J. Geophys. Res.* C, in press.

Damgaard, J., Dodd, N., Hall, L., and Chesher, T. (2002). Morphodynamic modelling of rip channel growth, *Coastal Eng.*, 45, 199–221.

Deigaard, R., N. Drønen, J. Fredsoe, J. H. Jensen, and M. P. Jørgesen (1999), A morphological stability analysis for a long straight barred coast, *Coastal Eng.*, 36(3), 171–195.

Falqués, A., Coco, G. and Huntley, D. A. (2000), A mechanism for the generation of wave-driven rhythmic patterns in the surf zone, *J. Geophys. Res.*, 105(C10), 24071–24088.

Garnier, R., D. Calvete, A. Falqués, and M. Caballeria (2006), Generation and nonlinear evolution of shore-oblique/transverse sand bars, *J. Fluid Mech.*, 567, 327–360.

Holman, R. A., and J. Stanley (2006), The history, capabilities and future of Argus, *Coastal Eng.*, accepted for publication.

Ojeda, E., and J. Guillén (2006), Monitoring beach nourishment based on detailed observations with video measurements, *J. Coastal Res.*, SI 48, 100–106.

Ojeda, E., J. Guillén, and F. Ribas (2007), Bar and shoreline coupling in artificial embayed beaches, *Coast. Eng. 2006*, in press.

Reniers, A. J. H. M., J. A. Roelvink, and E. B. Thornton (2004), Morphodynamic modeling of an embayed beach under wave group forcing, *J. Geophys. Res.*, 109(C01030), doi:10.1029/2002JC001,586.

Soulsby, R. L. (1997), *Dynamics of Marine Sands*, Thomas Telford, London, U.K.

van Enckevort, I. M. J., Ruessink, B. G., Coco, G., Suzuki, K., Turner, I. L., Plant, N. G. and Holman, R. A. (2004), Observations of nearshore crescentic sandbars, *J. Geophys. Res.*, 109, C06028, doi:10.1029/2003JC002214.

Wright, L. D. and A. D. Short (1984), Morphodynamic variability of surf zones and beaches: A synthesis, *Mar. Geo.*, 70, 251–285.

MESOSCALE BEHAVIOUR OF LONGSHORE BARS – NET ONSHORE OR NET OFFSHORE MIGRATION

Troels Aagaard[1] and Aart Kroon[2]

1. Department of Geography, University of Copenhagen, Oster Voldgade 10, DK-1350 Copenhagen K., Denmark. taa@geogr.ku.dk
2. Department of Geography, University of Copenhagen, Oster Voldgade 10, DK-1350 Copenhagen K., Denmark. ak@geogr.ku.dk

Abstract: The aim of this study is to compare long-term (30 yr) bar migration characteristics at two field sites on the Danish North Sea coast. One site displays systematically onshore migrating bars (Skallingen) while the bar migration at the other site (Vejers) is systematically offshore. Using cross-shore profile data and a sediment transport model, the paper discusses the mechanisms that cause divergent longshore bar behaviour at the two sites. The main reason for the difference appears to be larger undertow speeds at Vejers, caused by a steeper outer shoreface and a larger bar relief, leading to breaking wave reformation between bars.

INTRODUCTION

With the emergence of data sets on long-term profile change in e.g. the Netherlands and on the East coast of the US, it has been realized that multiple bar systems often display a tendency towards a systematic offshore migration of individual bars. Observations of such systematic seaward bar displacements were reported by Kroon (1990) and Wijnberg and Terwindt (1995) off the Dutch coast. Similar offshore migration tendencies were observed at Duck, N.C. (Plant et al., 1999) and in New Zealand (Shand and Bailey, 1999). The characteristics of the offshore bar migration cycle are similar at most sites. Longshore bars are formed close to the shoreline, they oscillate back and forth in the inner surf zone for a few years and then they begin to migrate consistently offshore. In water depths of 4-7 m, the migration cycle slows down and stops, subsequent to which the bars decay and eventually disappear. The return period for the bar migration cycle ranges between 1-13 years for the different study sites (Ruessink and Terwindt, 2000; Ruessink et al., 2003).

The onset of offshore bar migration is probably related to the decay of the outermost bar in the system. When the outer bar decays, larger wave heights are allowed further into the surf zone. This causes increased speeds of the undertow under breaking waves across the inner bars and hence increased rates of offshore sediment transport on those bars.

However, the reasons for the offshore bar decay are not known and the relationships between the bar migration cycle and coastal sediment budgets are poorly understood. The offshore bar migration cycle should lead to a sediment loss from the beach and an erosion of the shoreline. This does not appear to be the case. Consequently, it has been suggested that there may be a recycling of the sediment within the bar system such that the sand from the outermost decaying bar is transported landward during the decay process (Ruessink and Terwindt, 2000). Alternatively, the bar migration may be only a translation of the form with no sediment transport involved.

Not all multiple bar systems display a net offshore migration. Net onshore migrating bars were observed within a multiple-barred system at Skallingen, Denmark (Aagaard et al., 2004a). At this site, longhore bars originate in water depths of 3.5-4 m, migrate onshore through the surf zone and finally weld with the beach face. The onshore bar migration is consistent with measurements of sediment transport which is onshore directed across the bars during storm conditions (Aagaard et al., 2002).

A short distance north of Skallingen, at Vejers on the exposed Danish North Sea coast, the longshore bars migrate offshore in the long term. The aim of this paper is to conduct a comparative study of the two sites at Skallingen and Vejers using long-term profile data and a recently proposed sediment transport model (Aagaard et al., 2002) in order to analyze the mechanisms that cause divergent longshore bar behaviour at the two sites. Additionally, the relationships between the bar migration cycles and the sediment budget at the two sites will be addressed.

FIELD SITES

The two sites are both located on the Danish North Sea coast at either side of the submerged shoal of Horns Rev which is a Saalian terminal moraine and the two sites are separated by a distance of approximately 25 km (Figure 1). Horns Rev is attached to the cuspate foreland of Blaavands Huk which acts as a natural groyne to the southerly littoral drift along the North Sea coast.

The Horns Rev shoal significantly affects the two sites. Vejers is located updrift of the shoal and there is a large influx of sand from more northerly sources through the southerly directed littoral drift. According to the Danish Coastal Authority (DCA, 2001), the annual supply of sand to the beaches around Vejers is on the order of 2.3 million cubic meters per year (Table 1) due to a negative littoral drift gradient north of the shoal. Even though there is no doubt that the cuspate foreland at Blaavands Huk has been built up by the littoral drift, the shoreline at Vejers is currently almost stable. In contrast, Skallingen is located to the south of the shoal with a positive littoral drift gradient and the shoreline is receding by about 4-5.5 m/yr on average.

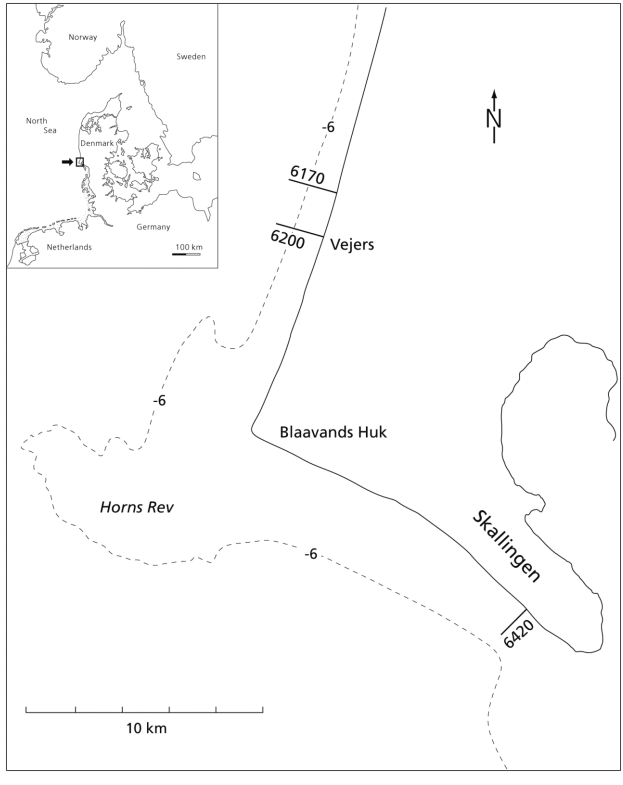

Figure 1. Map of the study area at the Danish North Sea coast. The two field sites at Vejers and Skallingen are separated by the submerged shoal of Horns Rev.

The annual (southerly directed) net littoral drift at the southern end of Skallingen has been estimated at about 0.6 million cubic meters per year, which is approximately similar to the annual sediment loss from the barrier (Table 1). There is no or very little sediment moving across the Horns Rev (DHI, 2002) because the shoal acts as a wave guide.

Because of the shoreline exposure and the location of the shoal, the two sites are also exposed to different hydrodynamic boundary conditions. The mean annual significant offshore wave height is 1.2 m at Vejers, and 1.0 m at Skallingen and the mean spring tidal range is 1.2 and 1.8 m, respectively (Table 1). Low swell frequently occurs at Vejers whereas that is not the case at Skallingen.

Table 1. Environmental boundary conditions and morphological characteristics at Vejers and Skallingen

	Vejers	Skallingen
Mean annual H_s, m	1.2	1.0
Mean spring tidal range, m	1.2	1.8
Net annual littoral drift*, $m^3 \times 10^6$	2.3	0.6
Mean slope, upper shoreface	0.006	0.006
Modal beach state	Intermediate	Dissipative

*The net littoral drift is directed towards the south. Numbers are based on DCA (2001) for Vejers and Aagaard et al. (2004b) for Skallingen.

As Skallingen is located at the head of the bight formed by Horns Rev and the Wadden Sea barriers further south, it often experiences severe storm surges during which the mean water level may reach approximately 4 m DNN (Danish Ordnance Datum). Surges at the more exposed site at Vejers are considerably smaller.

Figure 2 illustrates the cross-shore profiles and mean sediment grain sizes at the two sites. Both profiles are typically triple-barred. The mean grain size on the upper shoreface at Vejers is about 180 microns with sediments at bar crests being slightly coarser. The mean grain size is finer at the lower shoreface, about 110 microns. At the crest at the outermost bar, at $x \approx 1200$ m, the grain size is much coarser, 520 microns, suggesting a local winnowing of the sediment. Similar grain sizes occur at Skallingen even though bar crest sediments are slightly finer than at Vejers and there is no evidence of winnowing. As a result, the mean upper shoreface slope is similar at both sites, $\beta = 0.006$ and the seaward slopes of the bars are also similar, $\beta \approx 0.025$. However, the bars are much larger at Vejers where the bar relief is often up to 3 m whereas it is < 1 m at Skallingen. As a consequence of the deeper troughs at Vejers, waves tend to break through plunging at bars and reform between the bars and the modal beach state is intermediate, while it is dissipative at Skallingen where continuously spilling breakers tend to occur across a wide surf zone.

LONGSHORE BAR BEHAVIOUR

Figure 3 illustrates the profile evolution at DCA Line 6170 at Vejers during the period 2002-2006. Four bars appear in the profile: A small inner bar very close to the shoreline, a larger middle bar at $x = 1400$-1500 m, a very large outer bar at $x = 1700$-1800 m and a broad, low-relief fourth bar in a water depth of about 5 m. In the course of one year (2005-2006), the middle and outer bars both migrated about 60 m offshore and increased in size whereas the fourth bar decreased in size as the crest and landward slope eroded.

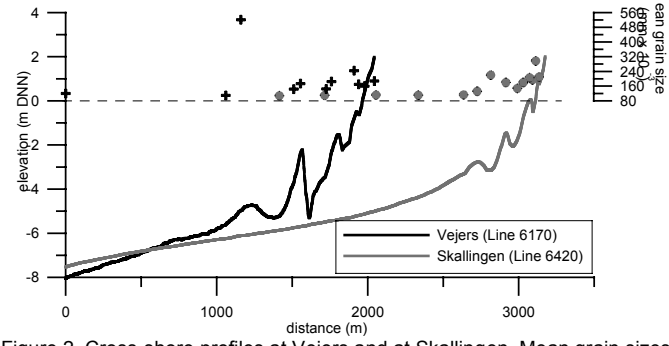

Figure 2. Cross-shore profiles at Vejers and at Skallingen. Mean grain sizes across the shoreface are plotted.

It is likely that this bar had entered the state of decay which is consistent with the indication of winnowing of the sediment (Figure 2).

A similar plot for DCA Line 6420 at Skallingen is shown in Figure 4 for the years 1994, 1995 and 1996. In 1994, the shoreface was double-barred with longshore bars at $x = 150$ m and $x = 300$ m. Within the following year, a trough was eroded at $x = 400$ m with a new bar forming further seaward. The two existing bars remained stable in position. During the period 1995 to 1996, all three bars migrated between 50-100 m onshore.

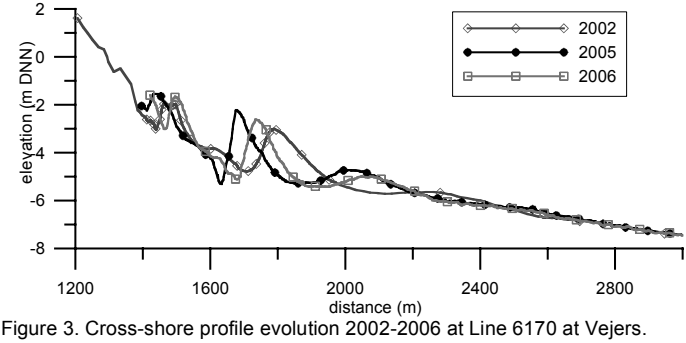

Figure 3. Cross-shore profile evolution 2002-2006 at Line 6170 at Vejers.

To provide a longer-term perspective, bar crest positions in Lines 6200 and 6420 are plotted in Figure 5 for the periods 1969-2002 and 1969-1998, respectively. At Vejers, the bars originate at the shoreline and subsequently migrate offshore at average speeds of 45-55 m/yr and they decay approximately 800-900 m from the shoreline in water depths of 5.5-6 m. In 2006, the outermost bar in the profile (Figure 3) had almost reached this position. The duration of the bar migration cycle is in the order of 15 years. If the

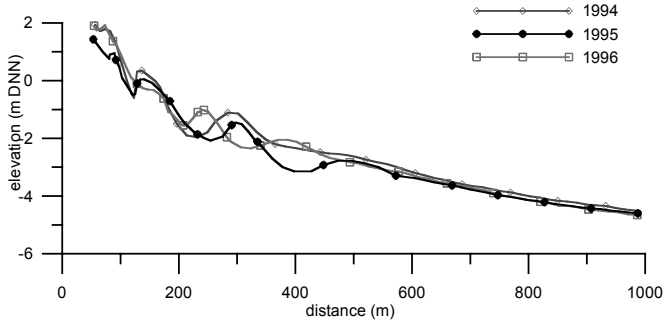

Figure 4. Cross-shore profile evolution 1994-1996 at Line 6420 at Skallingen.

seaward migration of the bars at Vejers involves a net cross-shore transport of sediment, the bar size and the migration speed correspond to a mean annual loss of about 50 m^3/m from the beach. However, the surveys indicate that the shoreline and the dunes are weakly accreting by about 6-7 m^3/m/yr and the 8 m depth contour, representing the limit of the outer shoreface is moving slightly landward, ≈ 3 m/yr (Figure 5). Thus, there is no evidence for any significant sediment loss from the beach to the shoreface.

At Skallingen, longshore bars originate in water depths of 3-4 m and they migrate onshore with speeds of 20-30 m/yr (Figure 5). When the bars enter the intertidal zone, they become dissected by rip channels which initiate cell circulations with onshore directed mean currents across the bars and rip currents in the channels (Aagaard et al., 2004a). This circulation forces the bars further onshore and they finally weld to the beach face. The bar cycle return period is in the order of 8 years, corresponding to a net onshore directed sediment supply of 6-7.5 m^3/m/yr. The 5 m depth contour is translating landward at an average rate of 8-17 m/yr, probably in response to a loss of sand from the

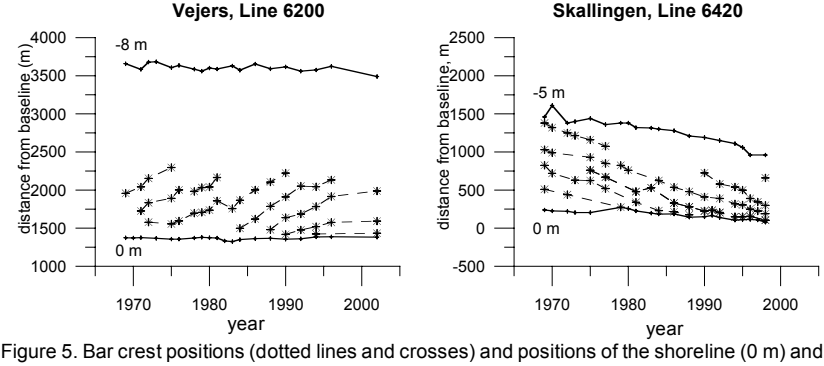

Figure 5. Bar crest positions (dotted lines and crosses) and positions of the shoreline (0 m) and upper/lower shoreface boundary at DCA Lines 6200 and 6420. Distances are given relative to the DCA baseline.

shoreface, associated with the onshore migrating bar forms. However, there is again a mismatch between the inferred direction of sediment transport and the movement of the shoreline. The mean rate of shoreline recession is 4-5.5 m/yr with brief interruptions to the long-term trend when longshore bars are welding (Figure 5). The main reason for the shoreline recession is the longshore sediment loss which currently far exceeds the onshore supply of sand (Aagaard et al., 2004b).

WAVES, CURRENTS AND SEDIMENT TRANSPORT

The causes for the different profile response were investigated by running a wave transformation model across representative shoreface profiles at the two sites. The model selected is the well-validated Battjes-Janssen model (Battjes and Janssen, 1978) which was recently assessed in detail for field conditions by Grasmeijer and Ruessink (2003). The selected profiles are depicted in Figure 2: Line 6170 in 2005 at Vejers, and Line 6420 in 1995 at Skallingen. The model is run for two representative (high energy) wave conditions; a westerly storm and a northwesterly gale.

The storm event was large but not extreme and it occurred on January 8-9, 2005. The mean significant wave height in deep water was 3.5 m and 3.3 m at Vejers and Skallingen, respectively and zero-crossing wave periods were 7.3 s and 7.6 s. The angle of deep-water wave incidence was 18^0 and 28^0, respectively. Mean surge heights were 0.5 m at Vejers and 1.5 m at Skallingen.

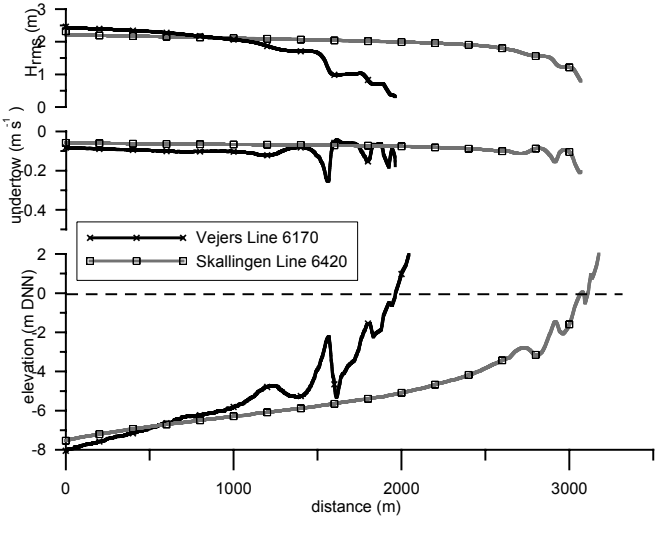

Figure 6. Wave height transformation and undertow speeds across the shoreface at Vejers and Skallingen during storm events..

Model outputs of rms wave height and undertow speed across the shoreface are plotted in Figure 6. Due to the steeper outer shoreface at Vejers, wave energy dissipation across the bars is more intense, particularly across the large outer bar. The wave transformation model predicts reformation of the breaking waves between bars. At Skallingen, the gently sloping outer shoreface results in much more gradual wave height decay and the waves lose energy across a wide surf zone with no reformation between bars, in accordance with visual observations.

The different patterns of wave transformation result in different speeds of the offshore directed mean currents at the two sites. The predicted undertow is up to −0.25 m s^{-1} on the upper shoreface at Vejers (at the outer bar) whereas maximum undertow speeds on the shoreface at Skallingen are only up to −0.15 m s^{-1} at the inner (intertidal) bar. In addition, it is unlikely that an undertow does occur at the inner bar at Skallingen as cell circulations tend to dominate in the shallow water depths at this position.

Figure 7 depicts the model predictions from more moderate wave conditions. The event selected occurred on November 12-13, 2004. The offshore H_s was 2.1 and 1.6 m at Vejers and Skallingen and wave periods were 5.8 and 5.0 s. The angle of wave incidence was close to zero at Vejers and 44^0 at Skallingen. Mean surge heights were 0 and 0.5 m.

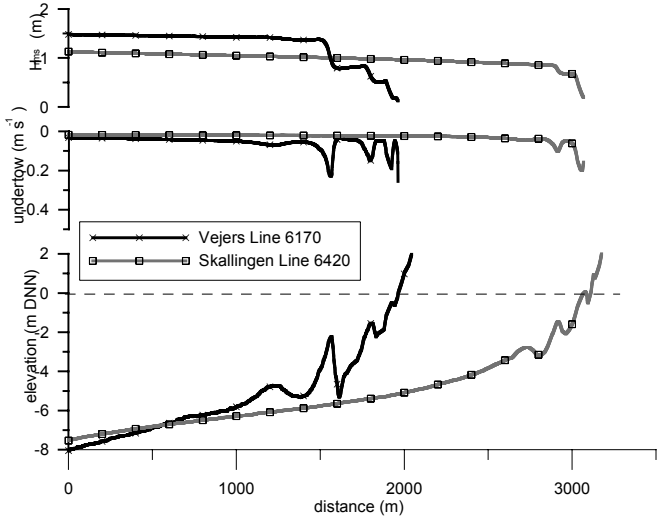

Figure 7. Wave height transformation and undertow speeds across the shoreface at Vejers and Skallingen during gale events.

The predicted wave height and mean current characteristics are qualitatively similar to the storm case. Wave dissipation is strong across the large bars at Vejers and much more gradual at Skallingen. Waves reform between the bars at Vejers whereas that is not the

case at Skallingen. Maximum undertow speeds are almost identical to those occurring during storms conditions.

Most numerical models for cross-shore sediment transport predict net offshore transport under breaking waves (e.g. Gallagher et al., 1998; van Rijn et al., 2003) and therefore they cannot be used to assess the differences in sediment transport characteristics at these two sites, because the transport and the bar movement is onshore under breaking waves at Skallingen. Instead, the empirical sediment transport model proposed by Aagaard et al. (2002) is used to evaluate the processes that result in seaward bar migration at Vejers and landward migration at Skallingen. In this model, a non-dimensional sediment transport index, Q_d, takes the values between −1 and +1 such that landward sediment transport occurs for positive values of Q_d and seaward transport occurs for negative values. If $Q_d = +1$, the suspended sediment transport is completely dominated by the incident waves and hence directed onshore; if $Q_d = -1$, the transport is accomplished completely by the undertow. Q_d does not predict the magnitude of the transport, only the directional tendencies of this transport.

Q_d depends on the non-dimensional parameter, D:

$$D = \frac{psu_{rms}}{|U|} \tag{1}$$

(Aagaard et al., 2002) where p is the cross correlation between instantaneous (cross-shore) velocity and sediment concentration, s is (cross-shore) velocity skewness, u_{rms} is orbital velocity magnitude and U is the mean cross-shore current (undertow) speed. As s and particularly p currently cannot be predicted from any numerical model, D was reformulated in terms of more easily predictable parameters and is denoted Γ:

$$\Gamma = \frac{\theta_{\max}(H_s / h_b)u_{rms}}{\gamma_s^{\,2} \tan\beta} \tag{2}$$

where θ_{max} is the wave-current Shields parameter, computed according to Soulsby (1997), H_s is the local (significant) wave height, h_b is the depth of initial wave breaking, γ is the local relative wave height (H_s/h) and β is the local slope. Based on field observations the empirical relationship

$$Q_d = 0.026\Gamma - 0.752 \tag{3}$$

was obtained (Aagaard et al., 2002). Eq.(2) contains parameters which are all predicted from the wave transformation model, or that can be obtained from the beach profile. Consequently, Eqs.(2) and (3) were calculated across the profiles at Vejers and Skallingen. The model is only applicable for locally breaking waves ($\gamma_s > 0.40$) and positive (*i.e.* seaward facing) slopes. For the computation of the Shields-parameter, a

grain size of 200 microns has been used for Vejers, which represents the average grain size on the three bar crests, whereas 180 microns has been used at Skallingen.

Outputs from the sediment transport model for storm conditions are illustrated in Figure 8. The model predicts $Q_d < 0$ across all bars (except at the outermost decaying bar) and hence offshore migrating bar forms at Vejers, whereas $Q_d > 0$ consistently for Skallingen, except for the innermost intertidal bar where cell circulation tends to replace undertow. Hence, the model is in qualitative agreement with longshore bar migration tendencies at both locations.

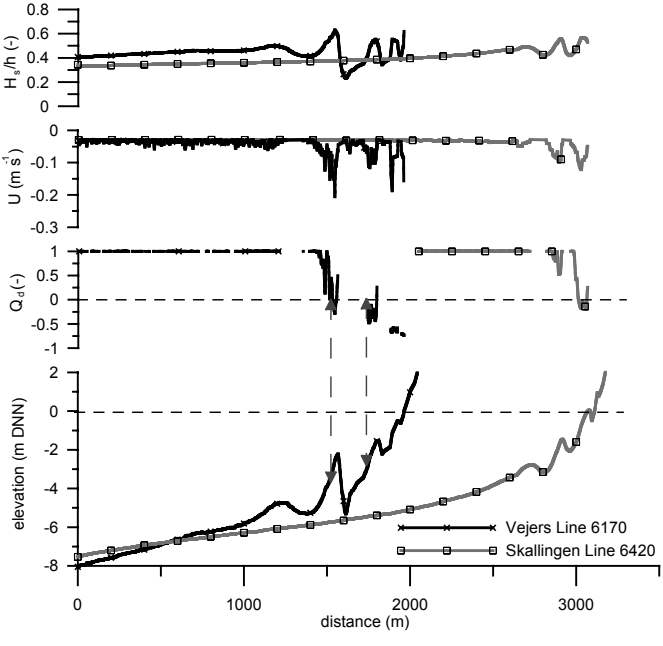

Figure 8. Model predictions of non-dimensional sediment transport (Q_d), undertow speed (U) and relative wave height across the shoreface at Vejers and Skallingen during storm events.

The model predicts two zones of sediment transport convergence at Vejers (at $x \sim 1500$ m and 1730 m), both located 65-70 m seaward of the existing bar crests. These convergence zones correspond to positions towards which bar crests should tend to migrate. No sediment transport convergence zones are predicted for Skallingen (except in the intertidal zone) and the bars are predicted to migrate consistently onshore during storms, in agreement with observations.

The reason for the different (predicted) behaviour at the two sites during storms is mainly due to larger undertow speeds at Vejers (Figure 8). Model predicted undertow speeds are slightly smaller than predictions from the Battjes-Janssen model (Figure 6), $U = -0.21$ m s^{-1} at Vejers and $U \sim -0.10$ m s^{-1} across the bar crests at Skallingen. Undertow speeds are larger at Vejers because of larger relative wave heights across bars, which are caused by 1) the smaller energy dissipation across the relatively steep outer shoreface, and 2) the reformation of breaking waves in troughs between bars.

Figure 9 depicts the model predictions for the moderate gale case. The sediment transport tendencies are identical to the storm case, but the zone of active wave breaking has narrowed and the model is applicable only to the inner parts of the profiles. The predicted points of sediment transport convergence on the bars at Vejers have moved slightly onshore because of the smaller wave heights but they are still located on the seaward slopes of the bars and the bars should still tend to migrate offshore at this site.

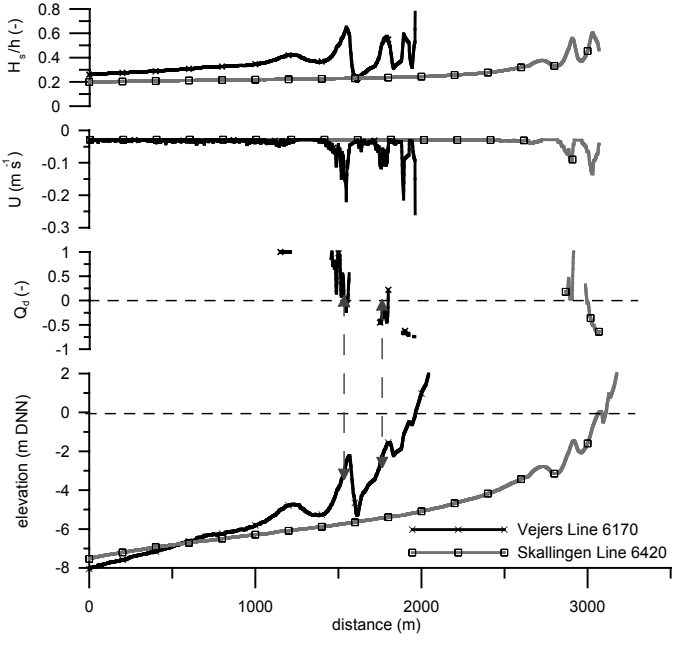

Figure 9. Model predictions of non-dimensional sediment transport (Q_d), undertow speed (U) and relative wave height across the shoreface at Vejers and Skallingen during gale events.

DISCUSSION AND CONCLUSIONS

The long-term behaviour of longshore bars is very different at Vejers and Skallingen. At Vejers, longshore bars move offshore in the long term, whereas the opposite is the case

at Skallingen where longshore bars move onshore under breaking waves. The empirical sediment transport model used here suggests that the main reason for this difference is the larger undertow speeds at Vejers during breaking wave conditions. During storms, the offshore sediment transport caused by the undertow exceeds the onshore sediment transport due to incident wave skewness while the reverse situation occurs at Skallingen.

The larger undertow speeds at Vejers occur because a): The lower shoreface is steeper which allows larger waves to reach the upper shoreface and, in particular, b): The bars are much higher and larger at the intermediate beach at Vejers than they are at the dissipative site at Skallingen. This causes significantly larger wave energy and hence radiation stress gradients across the bars at Vejers, as well as larger relative wave heights due to delayed wave breaking.

The reasons for the larger bar relief at Vejers so far remain speculative because sediment grain sizes are approximately identical at the two sites. There are two factors that are likely to contribute. One is the difference in tidal range. Tidal ranges are larger at Skallingen and tides tend to smear the morphology, producing smaller bars, because of the divergent sediment transport directions within the surf zone over a tidal cycle (Aagaard, 2002). The other likely explanation is the effect of the littoral drift. Vejers receives a large longshore supply of sediment due to the negative littoral drift gradient updrift of the Horns Rev. Longshore sediment transport occurs primarily on bars which then intuitively should accrete as a consequence of the sediment deposition. At Skallingen, the situation is the opposite. Because of the positive littoral drift gradient south of the Horns Rev, the beach erodes and the bars are starved of sediment, leading to smaller-relief features.

The littoral drift gradients are also the likely explanation for the mismatch between the cross-shore sediment transport direction and the long-term profile behaviour at the two sites. The beach at Skallingen recedes even though longshore bar migration (and sediment transport during storms) is landward directed. This is because the longshore loss of sediment far exceeds the onshore supply through the onshore migrating bars (Aagaard et al., 2004b). At Vejers, the beach and dunes are accreting even though bar migration is offshore. It is likely that the longshore supply of sand is an essential factor in this behaviour.

The sediment transport model predicts onshore directed transport across the outermost decaying bar at Vejers (Figure 8) and the lower shoreface is not accreting (Figure 5). Hence, it does not appear that the sand supplied through the offshore migrating bar forms is permanently deposited in the profile at Vejers. Research is ongoing in order to close the sediment budget and to ascertain whether the offshore bar migration at Vejers indeed does involve a net transport of sand.

ACKNOWLEDGEMENTS

This work was funded by the Danish Research Council, grant no 272-05-0415. We gratefully acknowledge permission to use the Danish Coastal Authority profile data.

REFERENCES

Aagaard, T., 2002. Modulation of surf zone processes on a barred beach due to changing water levels. *Journal of Coastal Research*, 17, 25-38.

Aagaard, T., Black, K.P. and Greenwood, 2002. Cross-shore suspended sediment transport in the surf zone: a field-based parameterization. *Marine Geology*, 185, 283-302.

Aagaard, T., Davidson-Arnott, R.G.D., Greenwood, B. and Nielsen, J., 2004a. Sediment supply from shoreface to dunes: linking sediment transport measurements and long-term morphological evolution. *Geomorphology,* 60, 205-224.

Aagaard, T., Nielsen, J., Jensen, S.G. and Friderichsen, 2004b. Longshore sediment transport and coastal erosion at Skallingen. *Danish Journal of Geography,* 104, 5-14.

Battjes, J.A. and Janssen, J.P.F.M., 1978. Energy loss and set-up due to breaking of random waves. *Proc.16th Int. Conf. on Coastal Eng.*, ASCE, New York, pp.570-587.

DCA, 2001. Sedimentbudget – Vestkysten. Report, Danish Coastal Authority, Lemvig, 54pp.

Gallagher, E.L., Elgar, S. and Guza, R.T., 1998. Observations of sand bar evolution on a natural beach. *Journal of Geophysical Research*, 103, 3203-3215.

Grasmeijer, B.T. and Ruessink, B.G., 2003. Modeling of waves and currents in the nearshore parametric vs. probabilistic approach. *Coastal Engineering*, 49, 185-207.

Kroon, A., 1990. Three-dimensional morphological changes of a nearshore bar system along the Dutch coast near Egmond aan Zee. *Journal of Coastal Research* Special Issue 9, 430-451.

Plant, N.G., Holman, R.A., Freilich, M.H. and Birkemeier, W.A., 1999. A simple model for interannual sandbar behaviour. *Journal of Geophysical Research,* 104, 15755-15776.

Ruessink, B.G. and Terwindt, J.H.J., 2000. The behaviour of nearshore bars on the time scale of years: a conceptual model. *Marine Geology,* 163, 289-301.

Ruessink, B.G., Wijnberg, K.M., Holman, R.A., Kuriyama, Y. and van Enckevort, I.M.J., 2003. Intersite comparison of interannual nearshore bar behaviour. *Journal of Geophysical Research,* 108(C8), 3249.

Shand, R.D. and Bailey, D.G., 1999. A review of net offshore bar migration with photographic illustrations from Wanganui, New Zealand. *Journal of Coastal Research,* 15, 365-378.

Soulsby, R., 1997. *Dynamics of Marine Sands.* Thomas Telford, London, 249pp.

Van Rijn, L.C., Walstra, D.J.R., Grasmeijer, B., Sutherland, J., Pan, S. and Sierra, J.P., 2003. The predictability of cross-shore bed evolution on sandy beaches at the time scale of storms and seasons using process-based profile models. *Coastal Engineering,* 47, 295-327.

Wijnberg, K.M. and Terwindt, J.H.J., 1995. Extracting decadal morphological behaviour from high-resolution, long-term bathymetric surveys along the Holland coast using eigenfunction analysis. *Marine Geology,* 126, 301-330.

MORPHOLOGICAL CHARASTERISTICS OF RIP CURRENT EMBAYMENTS ON THE OREGON COAST

Matthew M. Dalon[1], Merrick Haller[1], Jonathan Allan[2]

1. Department of Civil, Construction, and Environmental Engineering, Oregon State University, 220 Owen Hall, Corvallis, OR 97331, USA. dalonm@engr.orst.edu, hallerm@engr.orst.edu.
2. Oregon Department of Geology and Mineral Industries, 313 SW 2nd, Suite D, Newport, OR, 97365, USA. Jonathan.Allan@dogami.state.or.us.

Abstract: A methodology is presented to identify possible rip current embayments from lidar-derived shorelines along the U.S. Oregon coast. Analyses of these features include their location and their representative length scales in an effort to determine a desired orientation of the features. A total of 99 embayments were analyzed having an average length and amplitude of 575 meters and 17 meters. During the major El Niño event of 1997/1998 there is an increase in size; however, the total number of embayments remained unchanged. The locations of rip embayments in the respective surveys does not show any significant correlation and appears to be random.

INTRODUCTION

Natural shoreline morphologies are complex and often exhibit various types of cuspate and rhythmic features at both small and large scales. Recent advances in rapid, large scale surveying technologies such as lidar have provided the comprehensive topographic data necessary to quantify the occurrence and evolution of these shoreline features. Rip embayments are spatially localized areas of erosion, sometimes called an erosional "hotspot" (Komar 1998; Kraus and Galgano 2001), and are an example of a cuspate-type feature that is common on the winter shorelines of the Pacific Northwest. These embayments can occur as either rhythmic or independent forms and they generally have a longshore length scale on the order of hundreds of meters, similar to sand waves, arrhythmic giant cusps, or rhythmic giant cusps (Dolan 1971). Their cross-shore length

scale (amplitude) can be as large as 50 meters and essentially represents their erosional impact. Rip embayments, as their name implies, are generally assumed to be the result of the hydrodynamics associated with rip currents. However, as with beach cusps and many other shoreline features, their hydrodynamic origin is not always certain.

The presence of rip embayments creates vulnerability within the natural beach defense system. Storm waves will preferentially attack the beach through the deeper areas along the rip channels leading to the embayments. This means they are also better able to reach backing dunes and cliffs, which are the last defense for most coastal developments. Extreme events such as these have been well documented in Oregon, at times accounting for up to 30 meters of dune erosion in 3 weeks and causing houses and property to succumb to the ocean (Komar and Rea 1976).

Observations have established that a rip current that persists and is reasonably stationary will carve out a channel along the main flow axis where the currents are the strongest. The rip current or "rip cell" is supplied by longshore feeder currents and the net result is often a net offshore transport of sand. As sand along the beachface is removed by these currents, a localized erosional feature termed a rip embayment is created (Komar 1971). Swash processes also play a role in the erosion leading to the formation of embayments; however, their exact contribution is not well understood. Nonetheless, much of the sediment is likely carried offshore within the rip current and can often be seen as a large plume of suspended sediment extending beyond the break point (Shepard et al 1941).

Field observations of rip current embayments are limited and mainly derived from the shorelines of the Pacific Northwest (e.g. Komar and Rea 1976; Komar et al 1989; Revell et al 2002). The frequent, long period swell found here is conducive to rip generation and hence, is the likely culprit. However, rip embayments have been noted in California (Shepard et al, 1941), the East coast of the United States (Dolan 1971; List et al 2006), New Zealand (Stephens et al. 1999; Shand et al, 2004) and Australia (Wright and Short 1984; Short and Hesp 1982). Though, it should be noted that those were mainly qualitative measurements that focused on the amount of dune erosion, while detailed measurements of the rip embayment morphologies were not undertaken. The observed length scales ranged from 300-800 meters and their amplitude was described in terms of the associated dune erosion (O(10) meters).

In the following sections we present a methodology for identifying rip embayments (or at least features with the characteristics of rip embayments, though their actual origin remains unknown). The developed methodology is then applied to a representative shoreline contour, in this case the Mean High Water (MHW) contour extracted from lidar surveys undertaken along Oregon coast in 1997, 1998, and 2002. From these data we examine the morphological and spatial characteristics of rip embayments and their frequency of

occurrence on the Oregon coast. The analysis will also consider whether embayments form at preferential locations and whether the 1997-1998 El Niño played a role in increasing the frequency of embayments or contributed to their migration.

STUDY SITE

The Oregon coast can be divided into approximately 18 "pocket beach" littoral cells that are headland bounded. These cells can further be subdivided into sub-cells by the presence of inlets, jetties, and rocky promontories. In the present work we identify populations of shoreline features that are characteristic of rip current embayments from lidar surveys of four separate sub-cells. However, to be clear, we are unable to definitively establish the physics of embayment formation. Nevertheless, henceforth we will refer to them as rip current embayments and quantify their physical scales.

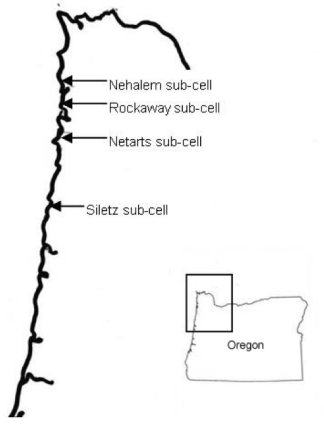

Figure 1 – Locations of the sub-cells used in this study.

The lidar data utilized herein are from portions of the Netarts, Siltetz, Nehalem, and Rockaway littoral cells. The Netarts sub-cell encompasses Cape Lookout State Park and extends ~9 km north to the Netarts Bay inlet. The Siletz sub-cell extends ~10 km from Government Point north to the inlet to Siletz Bay. The Rockaway sub-cell extends ~9 km north from the Tillamook Bay to Nehalem Bay, while the Nehalem sub-cell extends ~8 km north of Nehalem Bay to Neahkahnie Mountain. The morphodynamic characteristics of three of the sub-cells, Netarts, Rockaway, and Netarts, are similar and typified by wide, gently sloping (~2.3°) fine sand beaches, making them fully dissipative in the

morphodynamic classification of Wright and Short (1984). In contrast, beaches along the Siletz littoral cell are characterized by coarse sand, and steeper beach slopes so they are classified as intermediate to reflective.

Wave conditions on the central to northern Oregon coast are much the same. During the winter, the wave regime is characterized by long period high energy waves (~3 meters wave height, ~12 second wave period) from the southwest accompanied with elevated water levels. The summer months have relatively calmer conditions with waves (~1 meter height and 8 second period) arriving from the northwest on lower water levels (Ruggiero et al, 2005). Rip embayments are thought to be less prevalent in the summer months (Komar et al 1989), whether they remain throughout the year has not been documented.

DATA

Anticipating the 1997-1998 El Niño event, the USGS conducted lidar surveys along the Washington, Oregon and California coastline in the fall of 1997 and again in the spring of 1998 (Revell et al 2002). Specific flights within our area of interest were carried out on 17 October, 1997 and on 28 April, 1998. Lidar data from a flight on 20 September 2002 are also examined as part of this study.

The most prevalent source of error in lidar data arises from reflections off the water surface, which creates a noisy topographic signal. These points are eliminated by establishing the tidal elevation during the flight time and removing data points taken from areas below this elevation (Stockton et al 2002). To establish the water elevation, data from nearby tide gages during the approximate times of the lidar flights were used.

As noted by Revell et al (2002), the 1997 surveys were conducted during mid-tide. This tidal elevation is less than a meter from our desired datum, which caused noise similar to that found in Stockdon et al (2002). Due to this effect only the shoreline from the Netarts sub-cell was resolved. The 1998 and 2002 surveys were flown during low tide where tidal elevations were at least a meter below our shoreline datum. Thus a shoreline was able to be extracted from all locations.

The presence of rip current embayments (as with most morphologic features) is dependant in some fashion on the antecedent wave conditions. As context for the lidar determined shorelines from 1997, 1998, and 2002, the antecedent wave conditions for Oregon are shown in Figure 2. Continuous wave height and period data were collected from the National Data Buoy Center station 46002 located 275NM West of Coos Bay, OR. As can be seen in Figure 2, the October 1997 LIDAR was preceded by two major storms, characterized by significant wave heights that exceed 8 m with the capability of transporting large quantities of sediment. A period of nearly five months of low energy conditions preceded the September 2002 survey.

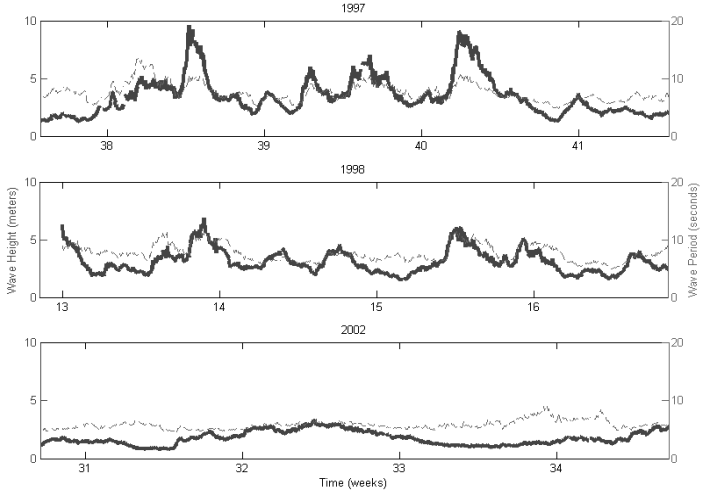

Figure 2 – Antecedent wave conditions prior to lidar surveys, wave height (solid blue line), wave period (dotted green line), x-axis represents weeks (lidar surveys took place at the end of each respective record).

METHODOLOGY

As a representative shoreline contour, we utilize the MHW level. Using a datum based shoreline provides unbiased repeatability whereas proxy shorelines based on visual cues are highly subjective. The study sites have a constant value for MHW that has been established at 2.1 meters NGVD88 (Weber et al 2005).

The raw lidar data was obtained from the NOAA Coastal Services Center (http://maps.csc.noaa.gov/TCM/). In post-processing NOAA has modified the data into a 5 meter grid within the Oregon State Plane North projection oriented in Northings and Eastings. This provides a series of beach profiles along the Eastings and with a profile located every 5 meters in the Northings direction. On average, the beaches were oriented with a six degree offset from true north and thus an Easting cross-shore profile closely resembled a true profile oriented normal to shore. For each profile, the cross-shore location of the most seaward MHW elevation is found through simple interpolation. Through these cross shore profiles a beach face slope is calculated for the portion within on meter of the MHW elevation. Once the location of MHW is found for each profile the MHW shoreline contour can be determined.

In order to establish the rip embayment locations we must identify local areas of erosion relative to the overall mean shoreline (baseline). The baseline is established by lowpass filtering the raw MHW contour. This filter consists of a running average filter applied twice with a window size of 1500 m and then demeaning the signal. Applying the filter twice results in a sharp cutoff, whereby only features with length scales larger than 1500 m remain. A second signal is then created with short scale features such as beach cusps (and remnant noise), removed from the raw shoreline by another lowpass filtering operation (100 m window size, applied twice) and again demeaned. The first signal is subtracted from the second, resulting in a bandpassed signal with bandpass limits of 100 m and 1500 m. An example of the bandpassed MHW shoreline contour that results from this method is shown in the middle of Figure 3 (bold line) where positive values are indicative of erosion.

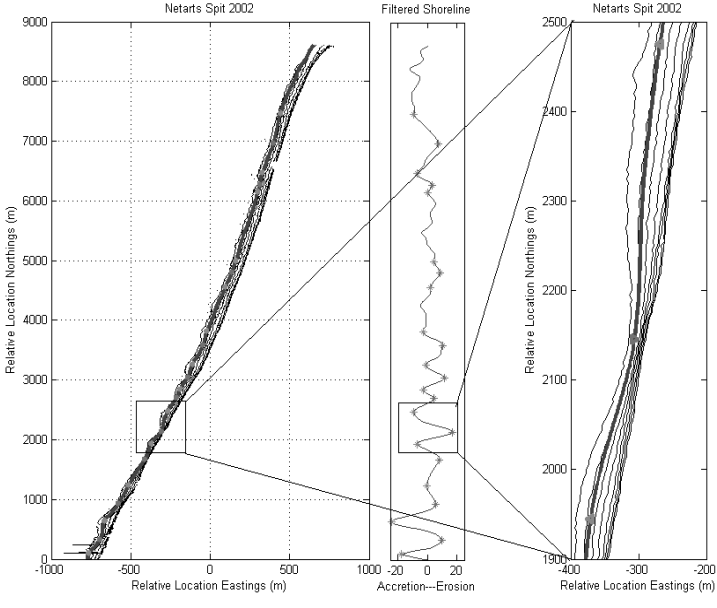

Figure 3 – (left panel) Elevation contours from lidar data, filtered MHW shoreline shown in bold, contour interval is 0.5 meters; (middle panel) filtered MHW shoreline (right panel) expanded view of a single rip embayment. In all panels, stars represent the locations of embayments and horns.

Individual embayments and horns are identified by applying a local maximum-minimum method (Koptenko 2003) on the bandpassed shoreline with a threshold that ignores small scale features less than 100 meters in length and less than 5 meters in amplitude (marked in the center panel of figure 3).

Using a datum based shoreline allows consistent and repeatable measurements of the features. A simple diagram of the scale definitions we have employed for rip embayments is shown in Figure 4. The length of the embayment is measured as the linear distance between adjacent horns located on the bandpassed shoreline (bold line in right and left panel figure 3. The amplitude of the embayment is the perpendicular distance from the maximum point of erosion within the embayment to the line of length.

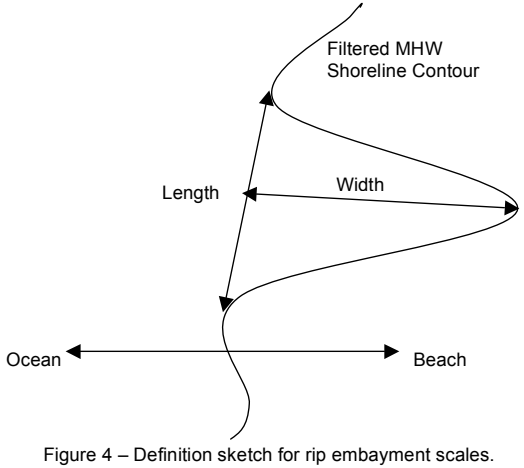

Figure 4 – Definition sketch for rip embayment scales.

Measurements of the rip embayments are dependant upon the chosen datum used for the analysis. As an example, a more complete topographic survey of a rip embayment, obtained from a land-based technique May 2005 (see e.g. http://www.oregongeology.com/sub/Nanoos1/index.htm) is shown in Figure 5. This feature was surveyed using a Trimble 5700/5800 RTK-DGPS surveying system mounted on an ATV and extends further offshore than the lidar survey. This feature remained through July 2005 but was erased by October 2005. It is evident from Figure 5 the survey that estimated embayment amplitudes would effectively increase if lower contours were used for the analysis, and at the upper levels of the beach face there is very little signal of the embayment. However, the longshore scale of the embayment appears less dependent on the chosen contour. The filtering process applied

to the lidar data also inherently reduces the amplitude of the embayments. However, for comparison, using the MHW contour for the data in Figure 5, the observed embayment is approximately 450 meters in length with an amplitude of about 25 meters, which compares favorably with the scales estimated from the lidar data in this sub-cell.

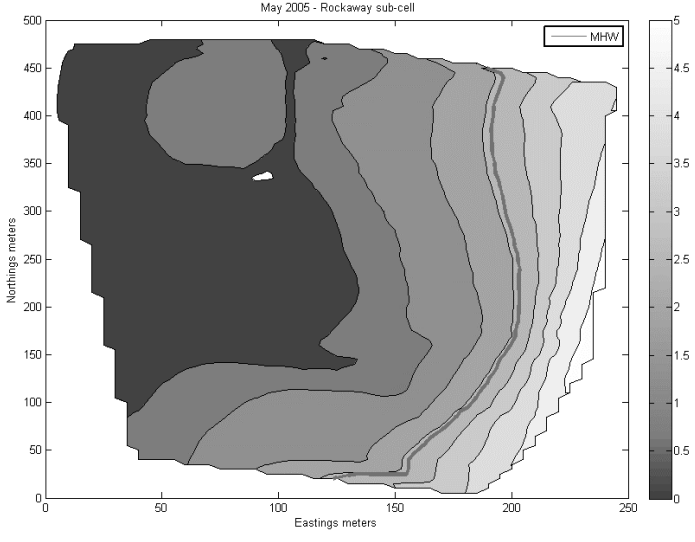

Figure 5 – Land-based survey of rip current embayment, located at 2231500 X 224910 Y in Oregon State Plane North.

RESULTS

Following the method described above plausible rip current embayment length, amplitude, slope, and spatial location were analyzed for four sections of coast for the three years in which lidar data is available. A summary of all features is first provided, followed by an examination of the temporal relationships and particularly the response pf the embayments to the 1997-1998 El Niño in the Netarts sub-cell.

A total of 99 rip current embayments were detected and measured along sandy shorelines totaling approximately 90 km, with an average of eleven embayments per year, per study site. Table 1 provides a summary of the results for each sub-cell throughout the study period. As defined, the embayments exhibit a mean length and amplitude of 575 meters and 17 meters respectively. These values are located near the center of the expected range;

however, the scales have a large standard deviation. Nonetheless, the majority of the features had a length and amplitude less than 1000 meters and 30 meters.

The center of erosion of the embayments in not often located equidistant from its horns. For each study period there is no predisposition to be skewed to the north or the south. This asymmetric nature may be the result of some form of minor migration of the embayment. Another possibility is that the rip current channel is directed at an oblique angle to the shoreline causing a preferred side of erosion.

Examining the embayments from a given site, it is evident that under the same offshore wave conditions individual embayment response was not consistent. Some embayments were characterized by an increase in both their length and amplitude, while other embayments exhibited a decrease in their morphological dimensions; still others experienced an increase in their length and a decrease in amplitude.

Table 1 – Numerical summary of rip current embayment measurements

	Embayment Count	Mean Length [m]	Std Length [m]	Mean Amplitude [m]	Std Amplitude [m]	Mean Space [m]	Std Space [m]
Netarts Spit							
1997	10	556	112	9	5	662	334
1998	10	641	207	14	6	814	438
2002	10	557	195	15	7	738	367
Siletz Spit							
1998	14	542	195	21	16	533	202
2002	10	467	135	16	7	686	393
Nehalem Spit							
1998	10	564	121	18	8	667	336
2002	12	621	257	22	12	651	289
Rockaway Beach							
1998	11	596	254	20	16	745	300
2002	12	630	203	22	15	654	226

It is expected that rip current size scales with rip current strength and, correspondingly, rip embayment amplitude would scale with length. Indeed, there is an apparent linear relationship between the length and amplitude of the embayments as shown in Figure 6. At the Siletz sub-cell, the embayments are relatively shorter than those at other sites (or equivalently, the Siletz embayments are of larger amplitude). It is possible this is due to the coarser grained sediments and steeper beach face found at this site

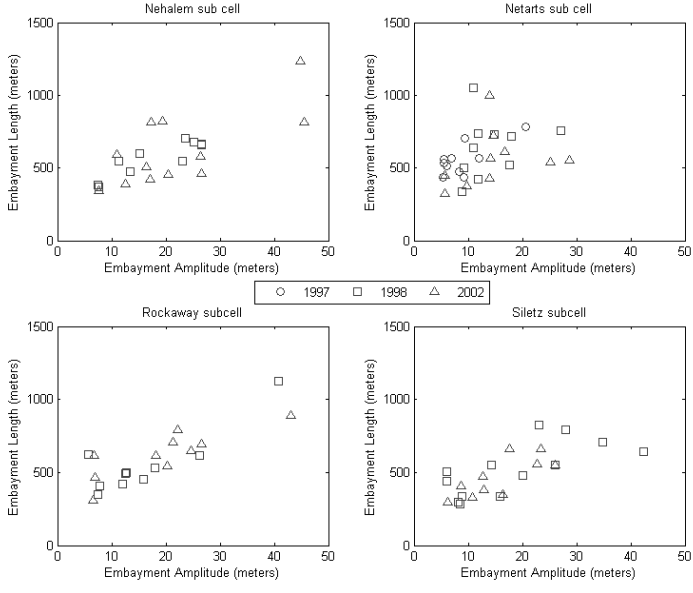

Figure 6 – Summary of Observed Embayments

Although the number of embayments at each site did not vary significantly between the different years, there was some change in the characteristic dimensions of the features. For example, in the Netarts sub-cell data that spans the major 1997-98 El Niño, there is a general increase in the spatial scale of the embayments. The embayment length scale increased 15% and the amplitude of the embayments increased by 55%.

The data also indicate a correlation between beach slope and the location of the rip embayments. Figure 7 shows the bandpassed MHW shorelines along with the local cross-shore beach slope at the MHW contour. It is evident from the figure that within most of the embayments the slope increases to a maximum at the center of the embayment. This appears to be a characteristic of rip embayments, and may possibly be used as an additional criterion for distinguishing erosive embayment features from other shoreline variability.

The spacing and location of embayments on a given shoreline is shown in Figure 8 and appears to be random. A few embayments are found directly adjacent to one another

creating localized rhythmic behavior, while at other locations a single embayment is isolated in a long stretch of straight beach. Due to the differences in the locations of the embayments from year to year, it is likely that embayments are not preferentially occurring at a given location. Even in the 1998 survey, which took place only 6 months after the 1997, there does not appear to be any correlation with the embayment locations from the 1997 survey. It is likely that the largest storms that occurred that winter wiped clean the shoreline embayment signals. Although there may be evidence of preferential dune erosion at the site of rip embayments that remains in the 1998 data. As yet, we have not examined this hypothesis.

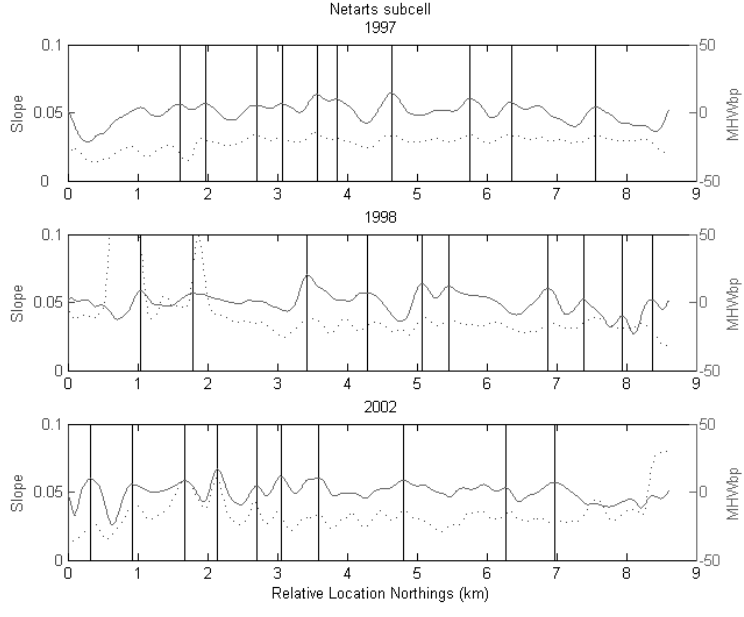

Figure 7 – Correlation between embayments and slope. The solid line represents the filtered MHW shoreline. The dotted line represents the slope. The vertical lines represent the center of the embayments.

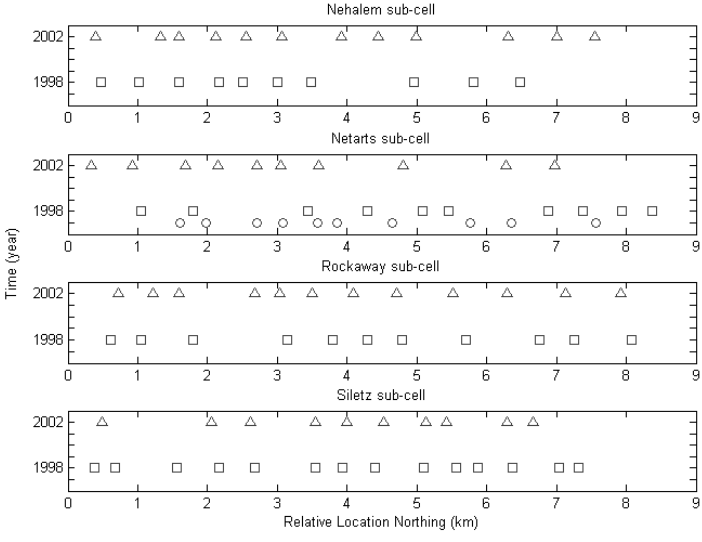

Figure 8 – Locations of embayment center versus survey time.

It is not clear yet if the antecedent wave conditions (Figure 2) for each survey has played a significant role in the embayment results. The wave data show that prior to the October 1997 survey there were two significant storm events with offshore wave heights of nearly 10 meters. Prior to the April 1998 survey there were two moderate storm events with wave heights around 5 meters. Prior to the September 2002 survey wave conditions there were five months of low energy conditions. Given these differences in the antecedent wave conditions, the only significant difference we have discerned in the rip embayments is the aforementioned general increase in embayment scales at the Netarts site for the 1998 data. Clearly further work is necessary to better understand the link between the wave conditions and the creation of rip embayments.

CONCLUSIONS

Using a bandpass filtered, datum based shoreline, morphologic features characteristic of rip current embayments with longshore length scales in the range of 100—1500 meters were extracted and analyzed. These erosional features are fairly common along the Oregon coast. In total, 99 embayments were found in shoreline data from four sites and three different years (9 shorelines total, ~90 km of sandy coastline). Consistent measurements of embayment length and amplitude made along the filtered shoreline had a mean length and

amplitude of 500-700 meters and 10-20 meters respectively. The features appear to be distributed randomly along the coastline with no correlation in the locations from year to year. However, there does appear to be a correlation between the location of the embayments and the local slope in the cross-shore profile, with the slope tending to reach a maximum at the centers of the embayments.

FUTURE WORK

In order to better establish the hydrodynamic origin of rip embayments and their relationship to the prevailing wave conditions, our plan is to simulate the hydrodynamics of these morphologies with a sophisticated wave-driven circulation model. However, a prerequisite to this modeling effort will be to first obtain comprehensive bathymetric surveys (full surf zone coverage) of representative rip current embayments. We are presently developing a bathymetric survey system based on a personal watercraft in order to achieve this. Once obtained, the nearshore circulation field induced by these representative embayments will be simulated numerically. Finally, we will establish which wave conditions are necessary for rip circulations to develop.

REFERENCES

Dolan, R. (1971), 'Coastal Landforms: Crescentic and Rhythmic', *Geological Society of America Bulletin* **82**, 177-180.

Komar, P.D. (1971), 'Nearshore Cell Circulation and the Formation of Giant Cusps', *Geological Society of America Bulletin* **82**, 2643-2650.

Komar, P.D. & Rea, C.C. (1976), 'Erosion of Siletz Spit, Oregon', *Shore and Beach* **44**, 9-16.

Komar, P.D. Good, J.W. & Shih, S. (1989), 'Erosion of Netarts Spit, Oregon: Continued Impacts of the 1982-83 El Nino', *Shore and Beach* **56**, 11-19.

Komar, P.D. (1998), *Beach Processes and Sedimentation*, Prentice Hall, Inc., Englewood Cliffs, NJ.

Koptenko, Sergei (2003) http://www.mathworks.com/matlabcentral/fileexchange/loadFile.do?objectId=3170

Kraus, N.C. and Galgano, F.A. (2001),'Beach Erosional Hot Spots: Types, causes and solutions', US Army Corps of Engineers.

List, J.H., Farris, A.S. & Sullivan, C. (2006), 'Reversing storm hotspots on sandy beaches: Spatial and temporal characteristics', *Marine Geology* **226**, 261-279.

Revell, D.L., Komar, P.D. & Jr., A.H.S. (2002), 'An Application of Lidar to Analyses of El Nino Erosion in the Netarts Littoral Cell, Oregon', *Journal of Coastal Research* **18**(3), 792-801.

Ruggiero, P., Kaminsky, G.M., Gelfenbaum, G. & Voigt, G. (2005), 'Seasonal to Interannual Morphodynamics along a High-Energy Dissipative Littoral Cell', *Journal of Coastal Research* **21**, 553-578.

Shand, R., Hesp, P. & Shepherd, M. (2004), 'Beach cut in relation to net offshore bar migration', *Journal of Coastal Research* **Special Issue 39**.

Shepard, F., Emery, K. & Fond, E.L. (1941), 'Rip Currents: A process of geological importance', *The Journal of Geology* **49, No. 4**, 337-369.

Short, A. and Hesp, P. (1982), 'Wave, Beach and Dune Interactions in southeastern Australia', *Marine Geology* **48**, 259-284.

Stephens, S., Healy, T., Black, K. & Lange, W. (1999), 'Arcuate Duneline Embayments, Infragravity Signals, Rip Currents and Wave Refraction at Waihi Beach, New Zealand', *Journal of Coastal Research* **Vol. 15, No. 3**, 823-829.

Stockdon, H.F., Jr., A.H.S., List, J.H. & Holman, R.A. (2002), 'Estimation of Shoreline Position and Change using Airborne Topographic Lidar Data', *Journal of Coastal Research* **18**(3), 502-513.

Weber, K.M., List, J.H. & Morgan, K.L.M. (2005), 'An Operational Mean High Water Datum for Determination of Shoreline Position from Topographic Lidar', *U.S. Gelogical Survey Open-File Report 2005-1027*.

Wright, L.D. (1980),'Beach Cut in Relation to Surf Zone Morhpodynamics' 'Conference Proceedings Coastal Engineering'.

Wright, L. & Short, A. (1984), 'Morphodynamic variability of surf zones and beaches: a synthesis', *Marine Geology* **56**, 93-118.

GEOLOGIC FRAMEWORK OF THE LONG BAY INNER SHELF: IMPLICATIONS FOR COASTAL EVOLUTION IN SOUTH CAROLINA

Walter Barnhardt[1], Jane Denny[1], Wayne Baldwin[1], William Schwab[1], Robert Morton[2], Paul Gayes[3], and Neal Driscoll[4]

1. U.S. Geological Survey, 384 Woods Hole Rd, Woods Hole, MA 02543, USA. wbarnhardt@usgs.gov, jdenny@usgs.gov, wbaldwin@usgs.gov, bschwab@usgs.gov
2. U.S. Geological Survey, 600 4th Street South, St. Petersburg, FL 33701, USA. rmorton@usgs.gov
3. Coastal Carolina University, 1270 Atlantic Avenue, Conway, SC 29526, USA. ptgayes@coastal.edu
4. Scripps Institution of Oceanography, La Jolla, CA 92093, USA. ndriscoll@ucsd.edu

Abstract: The inner continental shelf off northern South Carolina is a sediment-limited environment characterized by extensive hardground areas, where coastal plain strata and ancient channel-fill deposits are exposed at the sea floor. Holocene sand is concentrated in large shoals associated with active tidal inlets, an isolated shore-detached sand body, and a widespread series of low-relief sand ridges. The regional geologic framework is a strong control on the production, movement and deposition of sediment. High-resolution geologic mapping of the sea floor supports conceptual models indicative of net southwestward sediment transport along the coast.

INTRODUCTION

The U.S. Geological Survey is working in cooperation with the state of South Carolina, the National Oceanic and Atmospheric Administration's South Carolina Sea Grant Consortium, several universities, and the U.S. Army Corps of Engineers to better understand the factors that control beach erosion, marine habitat distribution, and vulnerability of coastal communities to storms and sea-level rise. The primary objective is to determine the influence of the regional geologic framework on coastal evolution through the interpretation of high-resolution geophysical data and bottom samples. This report is largely based on the work of Baldwin et al. (2004, 2006), Putney et al. (2004) and Denny et al. (2006) which used geologic mapping to provide insight into the processes that have shaped the South Carolina coast and inner shelf.

GEOLOGIC SETTING

The study area is located on the inner continental shelf of Long Bay along the northeastern coast of South Carolina (Figure 1). This area lies on the passive, trailing-edge, U.S. Atlantic continental margin. Although the region experiences little tectonic activity today, its long-term evolution has been heavily influenced by crustal deformation that occurred during the early rifting stages of the Atlantic Ocean (Klitgord et al., 1988). The most prominent structural component underlying the coast is the Carolina Platform, a broad area of crust that is slightly uplifted relative to the flanking marginal basins and embayments. Together, these features form an undulating, subsurface paleotopography that has heavily influenced regional patterns of deposition and erosion since the Cretaceous (Gohn, 1988; Riggs and Belknap, 1988). Repetitive sea-level fluctuations during the Tertiary and Quaternary periods interacted with this underlying paleotopography to further modify the morphology of the coastal plain and inner shelf.

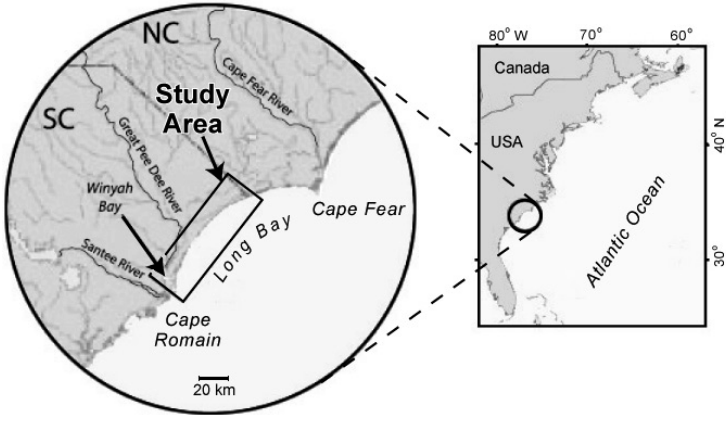

Figure 1. Map showing the location of the study area. The black rectangle indicates the extent of maps in Figures 2 and 7.

The Grand Strand coast consists of a nearly continuous series of sandy beaches that extend about 100 km (62 mi) along the central and southern portions of Long Bay between Little River Inlet and the tidal estuary of Winyah Bay (Figure 2). This arcuate stretch of coast encompasses a central, mainland-attached beach that is bounded by two sets of barrier islands and spits at the northern and southern ends of the littoral cell. Shoreline-change studies show that the coastline has remained relatively stable ($< \pm 1$ m/yr) since 1872, except near tidal inlets (Morton and Miller, 2005). The Grand Strand lies in the transition zone between the wave-dominated, microtidal barrier islands of North Carolina and the tide-dominated, mesotidal barrier islands of the Georgia Bight (Hayes, 1994). The region is periodically impacted by hurricanes and northeasters, causing extensive erosion and damage to coastal infrastructure. Sediment supply is limited by the lack of major rivers entering the central part of Grand Strand coast. Most sediment carried by the Pee Dee River

system, which reaches the coast at the southern margin of the littoral cell, is trapped behind dams or in the estuarine section of Winyah Bay (Patchineelam et al., 1999).

GEOLOGIC FRAMEWORK OF THE INNER SHELF

The inner shelf of Long Bay is low relief and gently slopes from the shoreface to the seaward extent of the study area about 10 km offshore. Water depths in the survey area range from 4-14 m (Figure 2A). Six geophysical surveys were conducted from 1999-2003 to map the geologic framework of the inner shelf and shoreface. Approximately 700 km² of the inner shelf were mapped using interferometric sonar (swath bathymetry), sidescan sonar, high-resolution seismic-reflection profiles, cores and grab samples. Full descriptions of the data acquisition and processing are presented in Baldwin et al. (2004) and Denny et al. (2006).

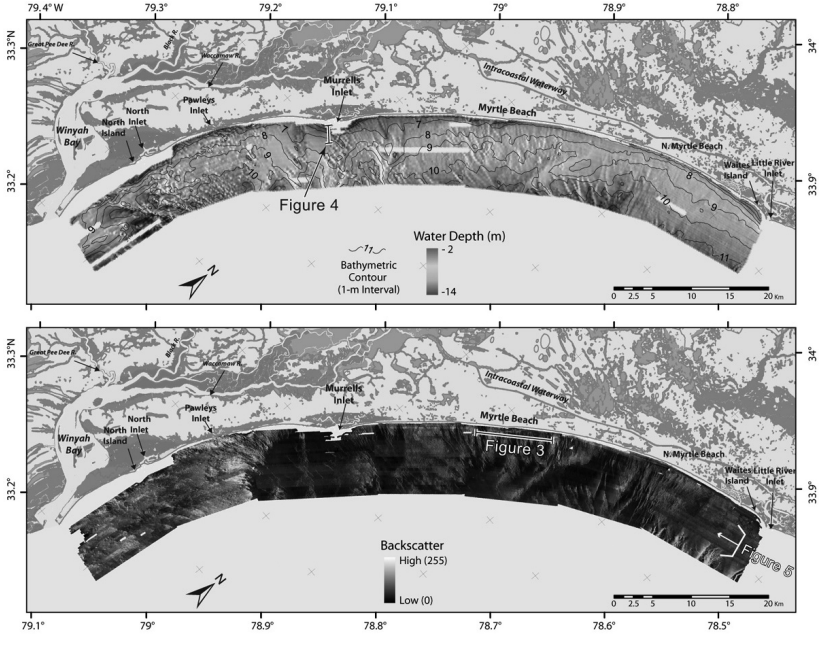

Figure 2. TOP: Map of bathymetry on the Long Bay inner shelf. BOTTOM: Sidescan-sonar image of the Long Bay inner shelf. High backscatter is represented by light tones; low-backscatter is represented by dark tones. *Modified from Denny et al. (2006)*.

The geologic framework of the Long Bay inner shelf consists of four primary components: 1) Cretaceous and Tertiary sedimentary rocks, 2) incised paleochannel deposits, 3) a regional transgressive unconformity, and 4) Holocene inner shelf sand bodies The following sections provide a summary of each component and examine their significance in the context of a dynamic, evolving coast.

Sedimentary Rocks

The sandy mudstones and siltstones underlying the Grand Strand coastal system range in age from Cretaceous to Tertiary. These coastal plain strata were originally deposited in shelf environments similar to what exists today off South Carolina (Colquhoun et al., 1991; Gohn, 1988). The stratigraphic section representing this time is thin due to its location on the flank of the relatively uplifted Mid-Carolina Platform High, or Cape Fear Arch (Snyder et al., 1982; Riggs and Belknap, 1988). Younger units are generally absent along the axis of this subsurface structural high due to erosion or non-deposition resulting from repeated shoreline transgression/regression.

Exposures of coastal plain strata on the inner shelf are represented by high-backscatter within the sidescan-sonar imagery (Figure 2B). The sedimentary rocks are slightly deformed and gently dip down towards the south-southeast, away from the Mid-Carolina Platform High. Erosion has truncated the dipping beds and exposed layers of different composition and physical competence. More resistant units locally crop out on the sea floor, forming low-relief ledges and hardgrounds that are important habitat for benthic-dwelling organisms (Figure 3; Ojeda et al., 2004). When eroded by waves and currents, the older sedimentary rocks supply much-needed new sediment to the coastal system (Riggs et al., 1995; Gayes et al., 2003). Differential erosion of the tilted, coastal plain strata has also influenced the location of river systems, as evidenced by a complex network of incised paleochannels that record relict drainage across the region (Baldwin et al., 2006).

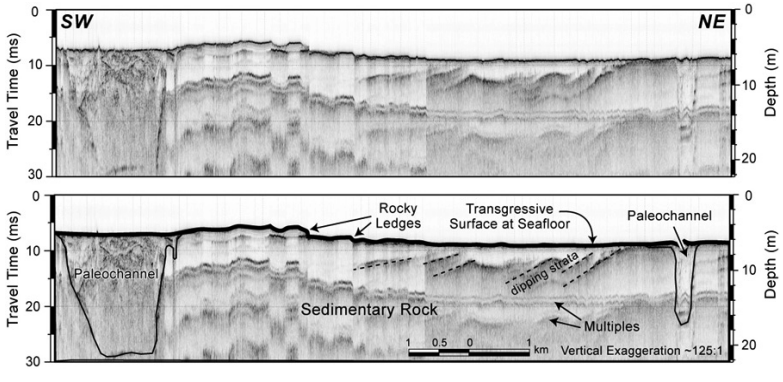

Figure 3. Subbottom profile and interpreted section showing paleochannel deposits incised into sedimentary rock. Both are commonly exposed at the sea floor as hardgrounds. Holocene sediment is thin to absent and the transgressive unconformity is at the sea floor. See Figure 2 for location. *Modified from Baldwin et al. (2004).*

Paleochannel Deposits

A review of previously published studies and interpretation of seismic-reflection profiles and boreholes indicate that the mouth of the Pee Dee River has migrated in a southerly direction over approximately the last 2 million years (Baldwin et al., 2006). Seven groups of sediment-filled channels cross beneath the lower coastal plain and

inner shelf of the Grand Strand. The paleochannels are incised 6-24 m deep into the underlying sedimentary rocks and range in width from 1-12 km. During Pleistocene highstands of sea level, the formation of barrier islands on the lower coastal plain caused the river to progressively shift southward from the center of Long Bay near the NC/SC border to its present position at Winyah Bay.

Erosion during multiple episodes of Quaternary sea-level change has heavily truncated the paleochannel deposits on the inner shelf. Their eroded upper surfaces are typically exposed at the sea floor as high-backscatter hardgrounds, except locally where they are buried by thin, discontinuous deposits of relatively low-backscatter Holocene sediment**.** Subbottom profiles across the paleochannels exhibit seismic signatures that range from transparent, homogeneous fill to intricate cut-and-fill geometries that represent multiple episodes of incision and deposition (Figure 3). Evidence from boreholes collected onshore confirms that the channel-fill sediments were deposited within fluvial, estuarine, open-bay, back-barrier, and nearshore-marine settings.

Transgressive Unconformity

A regional surface of erosion is deeply etched into the coastal plain strata and paleochannel deposits that underlie the shelf. This transgressive unconformity is a major bounding surface that formed in part during the most recent marine transgression (Baldwin et al., 2004, 2006). The unconformity probably represents a much longer period of geologic history, including successive phases of sea-level change during the glacial-interglacial periods of the Pleistocene epoch.

The transgressive unconformity is a low-relief surface that dips gently seaward at very low slopes (< 1°). It separates underlying, geologically older strata from overlying, Holocene sedimentary deposits. In many areas that lack Holocene sediment cover, the transgressive unconformity is exposed at the sea floor as rocky ledges and high-backscatter hardgrounds (Figure 3).

Holocene Sand Bodies

Deposits of Holocene sand lie above the low-relief transgressive unconformity and are expressed as minor bathymetric highs. Denny et al. (2006) identified three principal types of sand bodies that occur in the study area: 1] shoals associated with tidal inlets, 2] an isolated, shore-detached shoal, and 3] small-scale, low-relief ridges.

Inlet-associated shoals contain the largest accumulations of sediment on the inner shelf. The thickest deposits (> 4 m) are within low to moderate backscatter, shore-normal ridges that extend offshore from modern tidal inlets. These deposits generally thin in a seaward direction (Figure 4) and extend seaward beyond the boundary of the study area. Well-defined sand ridges are superimposed on the inlet shoals in the southern part of the littoral cell and are oriented at angles of 35-50° to the coast. The largest ridges near Winyah Bay measure 2-6 m high from crest to trough; smaller features along Pawleys and Debidue islands are 1-2 m high. Older sedimentary rock

and paleochannel deposits are commonly exposed in the troughs, creating complex patterns of high- and low-backscatter within the sidescan-sonar imagery (Figure 2).

Subbottom profiles across the shoal offshore of Murrells Inlet revealed several small, shallow channels lying *above* the transgressive unconformity (Figure 4). These channels are much younger than the large paleochannels that incise the coastal plain strata (Baldwin et al., 2006), and measure less than 100-m wide and 2-m deep in cross section. A second unconformity within the Holocene section truncates the top of the small channels, which are discontinuous in a cross-shelf direction. The channels probably represent a former drainage system, such as tidal creeks and/or local swashes that developed early in the ongoing transgression, when sea-level was lower than present.

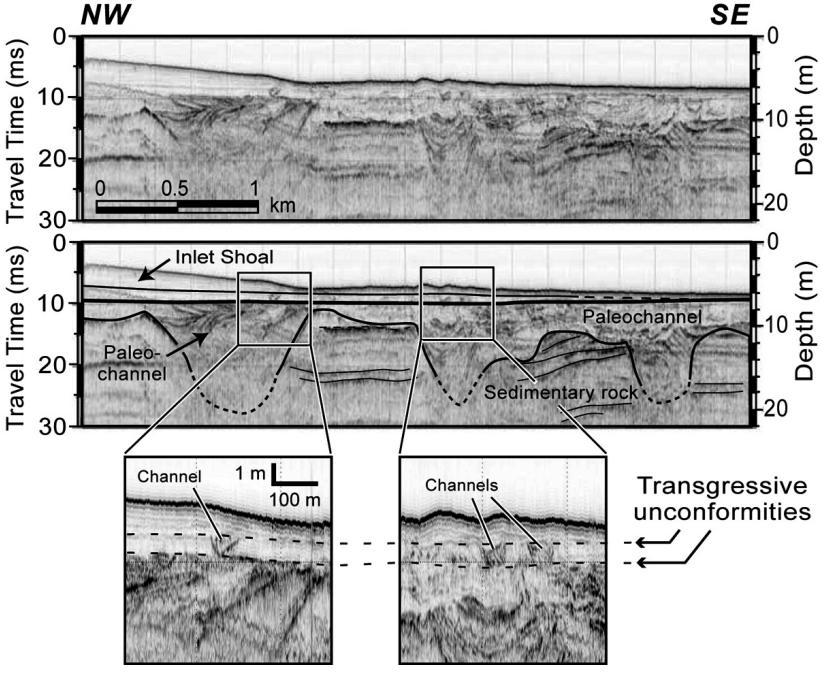

Figure 4. Subbottom profile and interpreted section showing seaward-thinning deposits of the inlet-associated shoal off Murrells Inlet and two transgressive unconformities. See Figure 2 for location. *Modified from Baldwin et al. (2004)*.

The isolated, shore-detached sand shoal that lies 3 km off Myrtle Beach is anomalous because it is not associated with an active tidal inlet. This lobate deposit extends from the shoreface to the offshore margin of the study area in water depths of approximately 7-12 m (Figure 5). The shoal measures about 3-km wide and 11-km along its NE-SW trending axis, and is about 2-m high where it rises above the

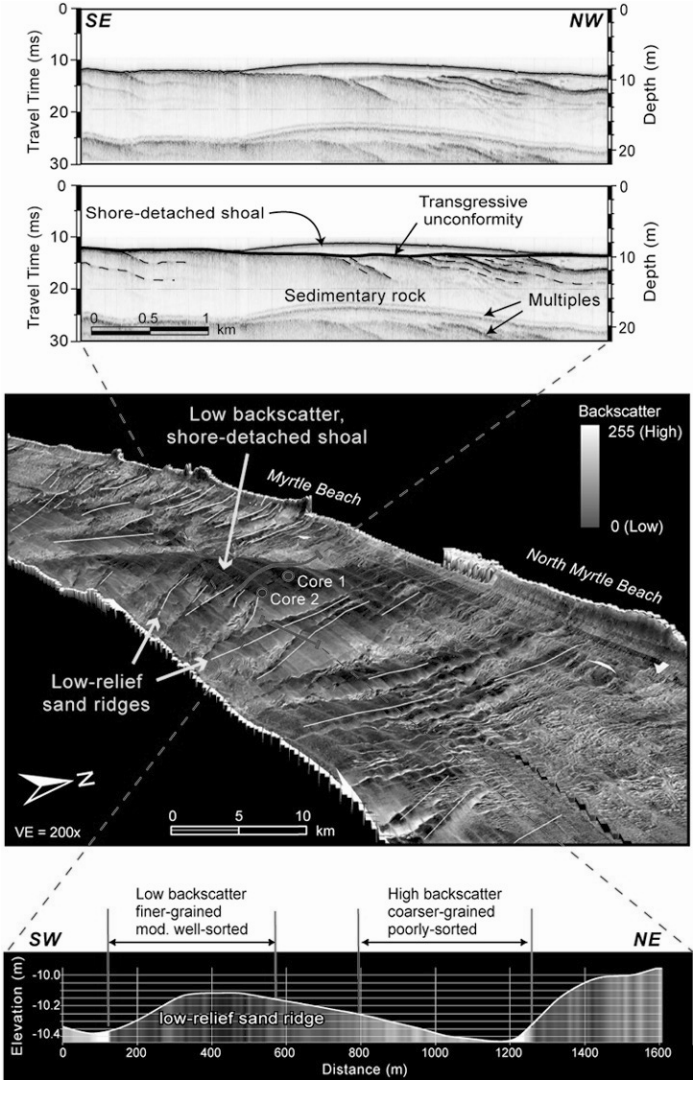

Figure 5. TOP: Subbottom profile across shore-detached shoal off Myrtle Beach. MIDDLE: Perspective view of sidescan-sonar imagery draped over bathymetry, looking toward the southwest. High backscatter is represented by light tones; low-backscatter by dark tones. BOTTOM: Bathymetric profile across a low-relief sand ridge showing asymmetry with steeper slope facing to the southwest. High-backscatter, coarser-grained sediment covers the trough and NE-facing side of the ridge. Low backscatter, finer-grained sediment covers the crest and SW-facing side. See Figure 2 for location. *Modified from Denny et al. (2006)*.

otherwise flat sea floor. It contains an estimated volume of 26 million m^3 of sediment, largely consisting of medium-grained quartz sand with a gravelly lag at the base that coincides with the transgressive surface. In cross section, the feature exhibits no asymmetry that would indicate a direction of net sediment transport.

No internal stratification was observed in subbottom profiles across the shoal, suggesting that the sediment is generally uniform. Cores through the shoal contained up to 1.5 m of fine-medium, shelly sand overlying an erosional surface at the base (Figure 6). The maximum age of the sand body is constrained by two radiocarbon-

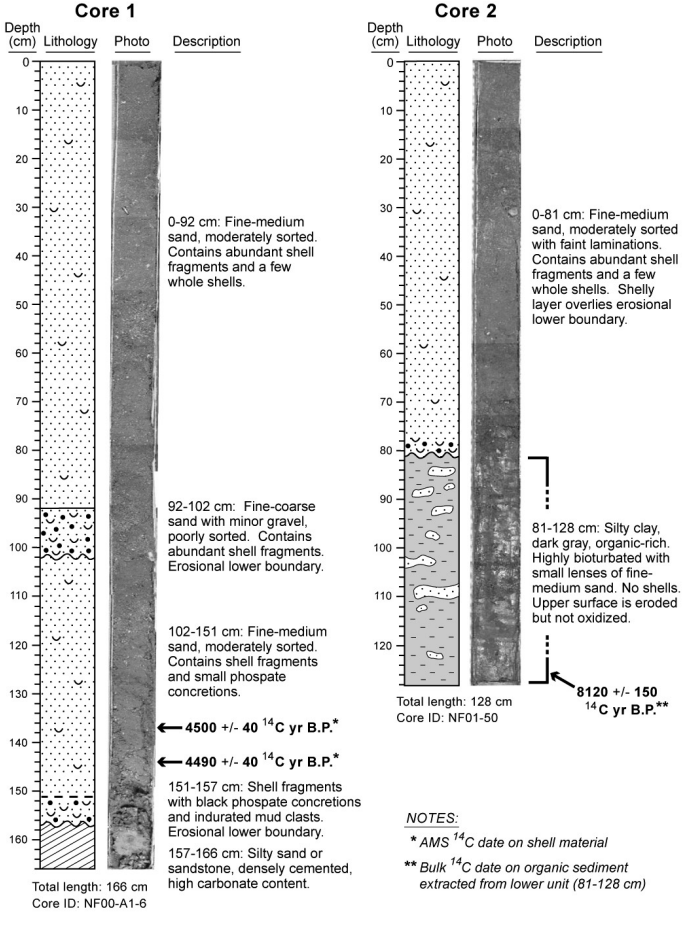

Figure 6. Descriptive logs and photographs of cores collected from the shore-detached shoal off Myrtle Beach. See Figure 5 for locations. *Descriptions by E. Karabanov (pers. comm., 2001).*

dated shells that returned ages of 4810-4540 cal. yr BP. An organic-rich sample from muddy deposits at the base of the sand body, at or just above the transgressive surface, returned an age of 9470-8600 cal. yr BP. Small channel-fill deposits of Holocene age (i.e., overlying the transgressive unconformity) were imaged beneath the shoreface just inshore of the shoal.

Low-relief sand ridges occur over large areas from the shoreface to the offshore edge of the study area, and are present within or adjacent to the inlet shoal complexes. These subtle features are generally less than 1-m high, about 1-km wide, and up to 3-km long. The ridge crests are roughly linear, vary in orientation from shore-perpendicular to shore-oblique, and are covered with low-backscatter, fine sand (Figure 5). In cross section, the sand ridges are slightly asymmetric with a steeper slope generally facing toward the southwest.

IMPLICATIONS FOR COASTAL EVOLUTION

Geological framework studies reveal the sediment-limited nature of the Grand Strand coastal system. A general, structurally-driven lack of accommodation space and long-term reduction in sediment supply are the major factors responsible for sediment limitation. The region's central position on the Mid-Carolina Platform restricts space for sediment to accumulate and exposes very old Cretaceous and Tertiary strata at or near the sea floor. The relatively gentle slope of the shallow margin also maximizes the potential for erosion across a broad area.

Large sand shoals on the Long Bay shelf experienced modification during marine transgression, and were partially preserved as sea level rose to the present-day position. Waves and currents continue to rework the Holocene deposits, as evidenced by the low-relief ridges within and adjacent to the shoal deposits. Except for locally thick shoal deposits, sediment cover is thin and discontinuous over the majority of the Long Bay inner shelf (Figure 7). The relative lack of mobile sediment suggests that

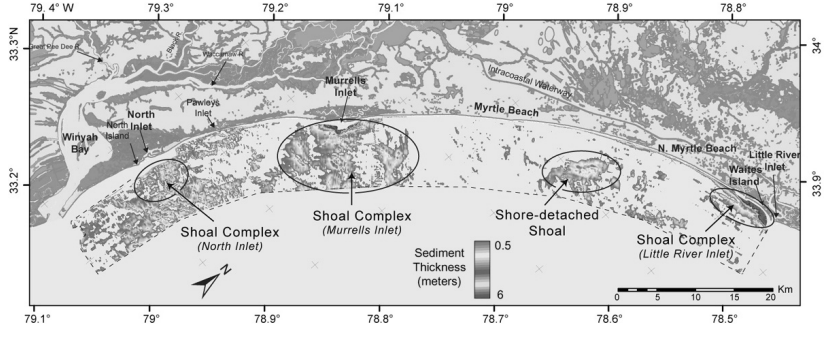

Figure 7. Isopach map showing the thickness of modern sediment accumulation above the transgressive unconformity. Extensive areas of the inner shelf lack modern sediment that is thicker than approximately 0.5 m. *Modified from Denny et al. (2006).*

the ongoing transgression has been very efficient in recycling sediment and conserving it as the coast has migrated landward. Preservation is generally low for coastal deposits that existed on the inner shelf during earlier parts of the transgression. However, deposits of early-middle Holocene age are preserved in at least two locations: the inlet-shoal complex off Murrells Inlet and the shore-detached shoal off Myrtle Beach.

The inlet-shoal complex off Murrells Inlet contains buried channel-fill deposits of probable estuarine or backbarrier origin (Figure 4). The preserved section is 1-2 m thick and bounded above and below by a pair of flat-lying transgressive unconformities. The lower surface is interpreted as the *tidal ravinement unconformity*, an erosional surface that formed relatively early in the transgression at the base of tidal inlets or channels (Allen and Posamentier, 1993). Preservation of this unconformity is low; it is generally destroyed by passage of the shoreface as the transgression proceeds. The upper surface is interpreted as the *shoreface ravinement unconformity*, a major erosional surface that formed beneath the transgressive shoreface (Swift, 1968). This wave-cut surface generates a strong, flat reflection that truncates older sedimentary rock and paleochannel deposits in most parts of the study area. The two surfaces merge offshore in water depths of 6-8 m. In an alternative interpretation, the younger channels could represent tidal distributaries that built out during a slight stillstand of sea level; thus the upper unconformity would be a *flooding surface*. Coring and dating of these surfaces is required to determine their origins and place them in the correct sequence-stratigraphic context.

The shore-detached shoal off Myrtle Beach does not resemble the inlet-shoal complex described above and is not associated with an active tidal inlet. The origin of the shoal is uncertain, but radiocarbon-dated shells from just above the transgressive unconformity constrain its maximum age to the middle Holocene (Figure 6). Muddy deposits at the base of the shoal might represent "freshwater lagoon deposits" that accumulated in the early Holocene (E. Karabanov, personal communication, 2001). Although subbottom profiles show no evidence of small Holocene channels within the shoal itself, several of these younger channels are preserved above the transgressive unconformity in areas located just inshore of the shoal. Based on overall sand-body geometry and setting, the shore-detached shoal is interpreted as a reworked inlet deposit. The shoal is probably the remnant of a tidal delta or a large sand body that was originally confined to the throat of a former inlet. The small channels above the transgressive unconformity probably represent tidal channels or swashes that existed landward of the inlet throat. Similar deposits were described from transitional inlets along the flank of the Georgia Bight (Hubbard et al., 1979; see their figure 10). In this transition zone, which includes the Grand Strand, the shape and orientation of sand bodies reflect the relatively equal importance of wave and tidal action. Geomorphic evidence onshore also suggests that the shoal originated as an inlet deposit. A series of small lakes and swashes on the mainland, possibly remnants of a larger lagoon, line up with the margins of the proposed inlet. Lennon et al. (1996, p. 79) suggested that the lakes "... mark a back-barrier lagoon that filled in when a barrier island welded onto the mainland." As the

barrier migrated landward in this hypothetical scenario, a relatively high topographic gradient onshore prevented the landward expansion of the lagoon. The lagoon decreased in area and presumably the inlet closed due to loss of tidal prism.

Geologic mapping supports conceptual models of sediment generally moving from northeast to southwest along the coast. Baldwin et al. (2004, 2006) showed that the Pee Dee River has migrated in a southerly direction for millions of years, thereby shifting the major supply of fluvial sediment away from the center of the Grand Strand. Consequently, the central and northern parts of the Grand Strand now depend primarily on the reworking of relict shoreline and inner shelf deposits to provide new sediment. This long-term reduction in sediment supply and the interaction of coastal processes with the underlying geologic structure has produced extensive hardbottom areas. Over shorter time scales (i.e., the late Holocene), the southerly direction of net sediment transport is inferred from bedform asymmetry and textural variations observed on the inner shelf (Figure 5, bottom panel). These characteristic patterns are indicative of sediment-transport pathways and are being used to guide process-oriented studies.

After the geologic mapping was completed, a series of instruments were deployed on and near the shore-detached shoal to measure winds, currents, wave characteristics, and suspended sediment concentrations. Data were collected at eight sites from October, 2003 to April, 2004 (Sullivan et al., 2005). Preliminary results show that different storm systems influence the direction and magnitude of net sediment transport over the shoal (Sullivan et al., 2006). Cold fronts and warm fronts generally drive sediment transport toward the northeast; tropical storms and hurricanes generally drive it to the southwest. If transport is roughly equal in each direction, it provides a potential mechanism for partially preserving the shore-detached shoal off Myrtle Beach. Over the last 5000 years or so since the shoal was formed, storm waves have shifted sediment back and forth across the shelf rather than fully eroding the deposit.

ACKNOWLEDGEMENTS

A cooperative partnership between the U.S. Geological Survey and the South Carolina Sea Grant Consortium provided funding for this study. The success of this project depended on the hard work of many people, including William Danforth, Tom O'Brien, Dave Nichols, Charles Worley, Barry Irwin, Shawn Dadisman, Jenna Hill, Ilya Buynevich, Paul Byham, Richard Goldberg, Elizabeth Johnston, Neil Gielstra, German Ojeda, and Jamie Phillips. Excellent ship support was provided by the captains and crews of the *R/V Atlantic Surveyor*, *R/V Megan Miller*, and the *R/V Coastal II*. We thank Jeff List and Larry Poppe for thorough reviews of this manuscript.

REFERENCES

Allen, G.P. and Posamentier, H.W. (1993). "Sequence stratigraphy and facies model of an incised valley fill: the Gironde Estuary, France," *Journal of Sedimentary Petrology*, 63, 378-391.

Baldwin, W., Morton, R., Denny, J., Dadisman, S., Schwab, W., Gayes, P. and Driscoll, N. (2004). "Maps showing the stratigraphic framework of South Carolina's Long Bay from Little River to Winyah Bay," *U.S. Geological Survey Open-File Report 2004-1013*. Available online at pubs.usgs.gov/of/2004/1013/

Baldwin, W., Morton, R., Putney, T., Katuna, M., Harris, M., Gayes, P., Driscoll, N., Denny, J. and Schwab, W. (2006). "Migration of the Pee Dee River system inferred from ancestral paleochannels underlying the South Carolina Grand Strand and Long Bay inner shelf," *Geological Society America Bulletin*, 118, 533-549.

Colquhoun, D.J., Johnson, G.H., Peebles, P.C., Huddlestun, P.F., and Scott, T. (1991). "Quaternary geology of the Atlantic Coastal Plain", *in* Morrison, R.B. (ed.), *Quaternary Nonglacial Geology: Conterminous U.S.*, The Geology of North America, v. K-2, Geological Society of America, : Boulder, Colorado, 629-650.

Denny, J.F., Baldwin, W.E., Schwab, W.C., Gayes, P.T., Morton, R.A., and Driscoll, N. (2006). "Modern sediment distribution on the inner shelf of South Carolina's Long Bay from Little River Inlet to Winyah Bay". *U.S. Geological Survey Open-File Report 2005-1035*. Available online at pubs.usgs.gov/of/2005/1035/

Gayes, P., Schwab, W., Driscoll, N., Morton, R., Baldwin, W., Denny, J., Wright, E., Harris, M., Katuna, M., Putney, T. and Johnstone, E. (2003). "Sediment dispersal pathways and conceptual sediment budget for a sediment starved embayment; Long Bay, South Carolina," *Proceedings of Coastal Sediments '03*, CD-ROM Published by East Meets West Productions, Corpus Christi, TX, 14 p.

Gohn, G.S. (1988). "Late Mesozoic and early Cenozoic geology of the Atlantic Coastal Plain: North Carolina to Florida," *in* Sheridan, R.E., and Grow, J.A. (eds.), *The Atlantic Continental Margin: U.S.*, The Geology of North America, v. 1-2, Geological Society of America, Boulder, CO, 107-130.

Hayes, M.O. (1994). "The Georgia Bight barrier system," *in* Davis, R., (ed.) *Geology of Holocene Barrier Island Systems*, Springer-Verlag, New York, 233-304.

Hubbard, D.K., Oertel, G., and Nummedal, D. (1979). "The role of waves and tidal currents in the development of tidal-inlet sedimentary structures and sand body geometry: Examples from North Carolina, South Carolina, and Georgia," *Journal of Sedimentary Petrology*, 49, 1073-1092.

Klitgord, K.D., Hutchinson, D.R., and Schouten, H. (1988). "U.S. Atlantic continental margin; structural and tectonic framework," *in* Sheridan, R.E., and Grow, J.A. (eds.), *The Atlantic Continental Margin: U.S.*, The Geology of North America, v. 1-2, Geological Society of America, Boulder, CO, 19-55.

Lennon, G., Neal, W.J., Bush, D.M., Pilkey, O.H., Jr., Stutz, M., and Bullock, J. (1996). *"Living with the Coast of South Carolina,"* Duke University Press, Durham, NC, 241 p.

Morton, R. A., and Miller, T. L., (2005). "National assessment of shoreline change: Part 2: Historical shoreline changes and associated coastal land loss along the U.S. Southeast Atlantic coast," *U.S. Geological Survey Open-File Report 2005-1401*. Available online at pubs.usgs.gov/of/2005/1401/

Ojeda, G.Y., Gayes, P.T., Van Dolah, R.F. and Schwab, W.C. (2004). "Spatially quantitative sea floor habitat mapping: Example from the northern South Carolina inner continental shelf," *Estuarine Coastal and Shelf Science*, 59, 399-416

Patchineelam, S., Kjerfve B. and Gardner, L. (1999). "A preliminary sediment budget for the Winyah Bay estuary, South Carolina," *Marine Geology*, 162, 133-144.

Putney, T.R., Katuna, M.P., and Harris, M.S. (2004). "Subsurface stratigraphy and geomorphology of the Grand Strand, Georgetown and Horry Counties, South Carolina," *Southeastern Geology*, 42(4), 217-236.

Riggs, S.R., and Belknap, D.F. (1988). "Upper Cenozoic processes and environments of continental margin sedimentation: eastern United States," *in* Sheridan, R.E., and Grow, J.A. (eds.), *The Atlantic Continental Margin: U.S.*, The Geology of North America, v. 1-2, Geological Society of America, Boulder, CO, 131-176.

Riggs, S.R., Cleary, W.J., and Snyder, S.W. (1995). "Influence of inherited geologic framework on barrier shoreface morphology and dynamics," *Marine Geology*, 126, 213-234.

Snyder, S.W., Hine, A.C., and Riggs, S.R. (1982). "Miocene seismic stratigraphy, structural framework, and sea level cyclicity: North Carolina continental shelf," *Southeastern Geology*, 23, 247-266.

Sullivan, C.M., Warner, J.C., Martini, M.A., Voulgaris, G., Work, P.A., Haas, K.A., and Hanes, D.H. (2005). "South Carolina Coastal Erosion Study Data Report for Observations October 2003 - April 2004" *U.S. Geological Survey Open-File Report 2005-1429*. Available online at pubs.usgs.gov/of/2005/1429/

Sullivan, C.M., Warner, J.C., and Voulgaris, G. (2006). "The influence of storms on circulation and sediment transport in Long Bay, South Carolina, USA," *Eos Trans. AGU,* 87(36), Ocean Sci. Meet. Suppl., Abstract OS35E-08.

Swift, D.J.P. (1968). "Coastal erosion and transgressive stratigraphy," *Journal of Geology*, 76, 444-456.

A RELIC SAND WAVE FIELD IN A TIDAL CHANNEL

Shelley J. Whitmeyer[1], Duncan FitzGerald[2]

1. Boston University, Dept. of Earth Sciences, 685 Commonwealth Ave., Boston, MA, 02215, USA, shelleyj@bu.edu.
2. Boston University, Dept. of Earth Sciences, 685 Commonwealth Ave., Boston, MA, 02215, USA, dunc@bu.edu.

Abstract: A sand wave field in the eastern flood channel of Moriches Inlet was monitored for eight weeks during the summer of 2005. Bathymetric data show sand waves which are 15 m long and 39 cm tall with shallow slip faces. These sand waves remained stationary over the eight week study. Analysis based on work by van Rijn (1984) and Yalin (1964) suggests that these sand waves were created when the current velocity reaches 80 cm/s. However, the peak current speeds recorded during this study are less than 60 cm/s. Infrequent, high-energy events are believed to have created these sand waves. A hypothetical event creating these sand waves is described based on a linear analysis of tidal range and peak tidal currents. Water level data from Sandy Hook, NJ and Shinnecock Inlet, NY are used to identify this event. This study demonstrates that episodic events may control sand wave morphology and that once emplaced the sand waves become autonomous.

INTRODUCTION

Sand waves are potential hazards in navigation channels. As they develop within the channel or migrate into the channel from adjacent areas, they reduce the project depth. In the Panama City Entrance Channel and in the Columbia River sand waves reduce the navigation depth by half. In addition to causing channel shoaling, sand waves also decrease the depth-averaged flow velocity and increase turbulence. To efficiently manage tidal navigation channels and model sediment transport it is necessary to understand and predict the geometry, distribution, and migration rates of sand waves.

The conditions under which sand waves develop have been well defined through flume experiments. Under these controlled conditions variations in grain size, water depth, and flow velocity create predictable changes in bedform morphology. However, these

predictive relationships are less reliable to natural settings, especially in tidal channels. Complications arise because:

1. water depth, flow velocity, and grain size are not independent of one another,
2. channel morphology and flow conditions typically are not in equilibrium,
3. sand supply may be limited, and
4. wave-current interaction may change flow conditions.

Moriches Inlet, which is located along the South Shore of Long Island, New York, USA, is a wave-dominated, micro-tidal inlet (Figure 1). It is a sand rich-inlet that connects Moriches Bay directly to the Atlantic Ocean. The focus of this study is the sand wave field in the eastern flood channel (2-4 m) of Moriches Bay. The sand wave field is on a shallow bank (~2-3 m deep) between two relatively deep channels; the west is ebb dominated and the east is flood dominated. Data collected at the inlet include eight weekly bathymetric surveys, sediment samples (d_{50}=0.43 mm), current measurements (peak tidal currents 60 cm/s), and water level data (spring range=1 m, neap range=60 cm). The field study was designed to measure the geometry of the sand waves, document any morphological change, track sand wave migration, and record the hydraulic conditions.

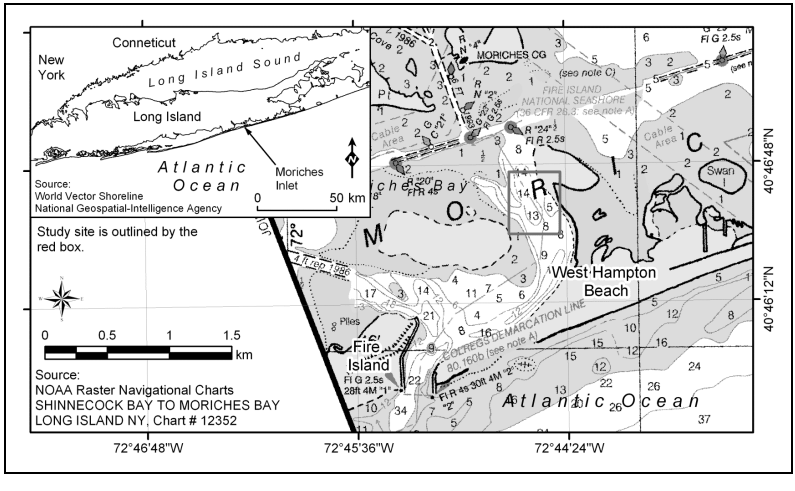

Figure 1. Location of the study area within Moriches Bay. Study site is delineated by the red box.

SAND WAVE MOPHOLOGY

Weekly bathymetric surveys were collected using an Innerspace Model 455 single-beam depth sounder (200 kHz and 8°). The location of the boat was tracked with a Trimble AgGPS 132 GPS (sub-meter accuracy). Two surveys were taken over the first 24 hours to capture sand wave response to a spring tide. Thereafter, the surveys were collected

weekly (29 July, 5 August, 12 August, 19 August, 26 August, and 2 September). Sand waves in this area can generally be divided into two groups- well-defined, flood-orientated sand waves on the bank and smaller, ebb-orientated sand waves in the ebb channel.

Bathymetric surfaces were modeled using ArcGIS ™. A Triangulated Irregular Network (TIN) was created from the individual soundings for each survey. The TINs were converted to grids in order to run more efficiently in ArcMap™ (Figure 2). The error of the bathymetric interpolation is ±12 cm. The sand wave location, height, wavelength, and orientation were identified on each of the eight surveys. Cross-sectional profiles were extracted from the bathymetric grid along each of the survey lines running northwest-southeast and then imported into MatLab for analysis with a script written by the author. The crests and troughs of the sand waves were identified by calculating the approximate derivative of each cross section (Figure 3). The wavelength, height, and slope of the sand waves calculated from the crests and troughs. This information was then imported back into ArcMap™. In ArcMap™, the sand wave crests were delineated along those crests points imported from MatLab.

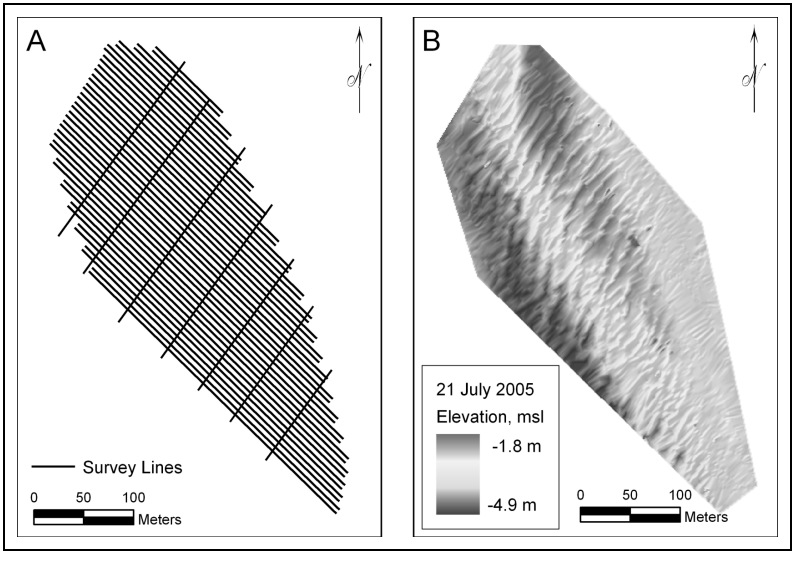

Figure 2. a) Survey track lines along which bathymetric data were collected. b) Bathymetric map of the study area on 21 July 2005. The map is a one meter grid.

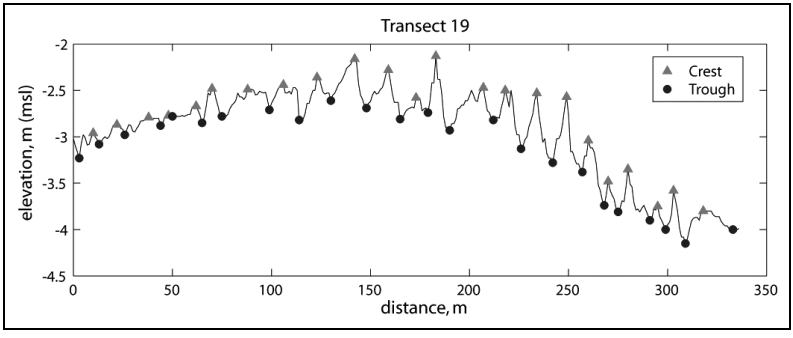

Figure 3. Cross Section from transect 19 which runs through the center of the study area. Crests are shown as triangles and the troughs are shown as circles.

Bathymetric surveys within the 0.07 km^2 study area show two unique morphologies. There are larger, better-defined flood-dominate sand waves on the shallow bank, and smaller ebb-dominate sand waves in the ebb channel. The mean height was 39 cm and the wave length was 15 m over the entire study area. The average spacing of the ebb- and flood-orientated sand waves was the same, but their heights varied. The ebb-orientated sand wave height was 23 cm compared to the larger flood-orientated sand wave height which was 46 cm. The slip face slopes are shallow. The slopes are sub-horizontal, varying from 3.6˚ to 4.4˚. There was little variation in these dimensions during the study period. Morphological changes between the spring and neap tide cycles were not documented.

The location of the sand wave crests were tracked over the seven week study period (Figure 4). Considering the horizontal uncertainty of the depth soundings (±1 m), an uncertainty of ±2 m should be assumed when comparing surveys. These data indicate a lack of systematic migration of the sand waves over the study period. Realignment, flexing, and some bifurcation of the crests occurred. However, bifurcating crests usually returned to their previous continuous configuration, and therefore, may be the result of variations in interpolation due differences in the location of the soundings between surveys rather than changes in the morphology.

PREDICTED SAND WAVE HEIGHT

Laboratory studies (Southard 1971; Southard, et al. 1990) and field studies (Aliotta, et al. 1987; Boothroyd, et al. 1975; Dalrymple, et al. 1978; Dalrymple, et al. 1995; Gabel 1993; Mazumder 2003; McCave 1971; Yalin 1964; Zarillo 1982) have demonstrated that bedform morphology is a function of flow depth, grain size, and flow velocity or shear stress. Yalin (1964) and van Rijn (1984) have estimated the dimensions (height and spacing) of sand waves based on the shear stress. Yalin's derivation for sand wave spacing begins with non-dimensional parameters for the "relative roughness" and "grain-size Reynolds number," i.e., the particle Reynolds number. The Reynolds number

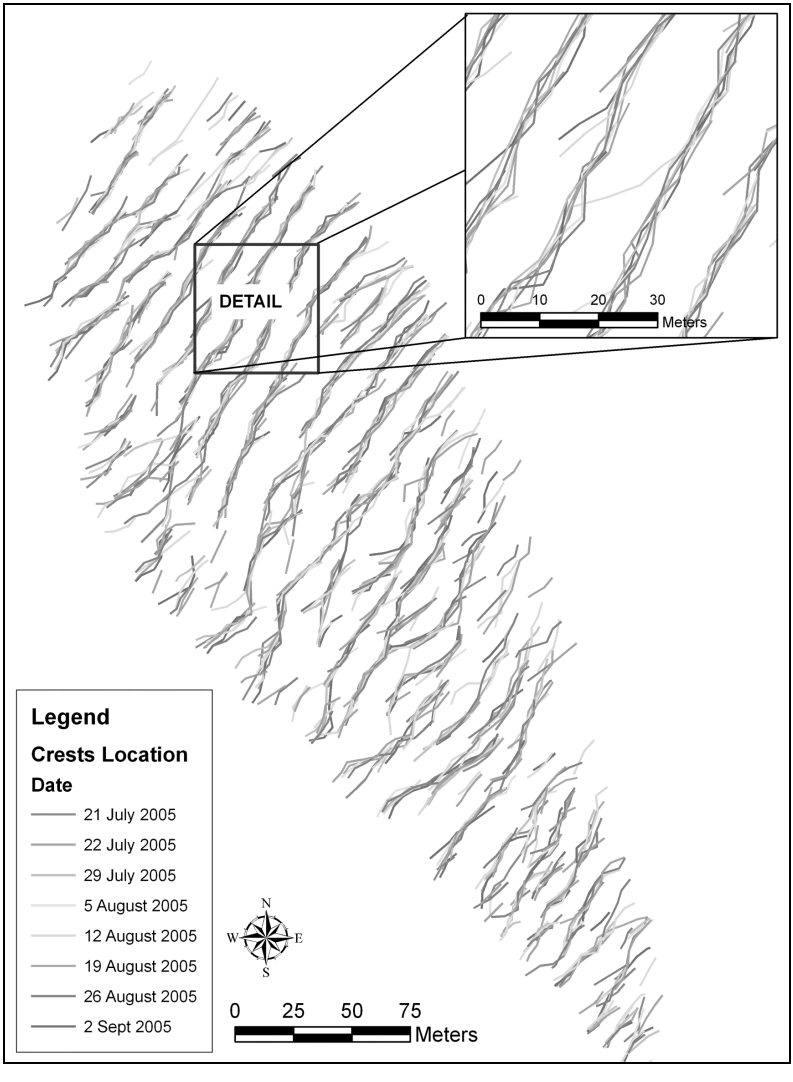

Figure 4. Lines show location of sand wave crests from 21 July to 2 September 2005. There is some movement due to reworking of the sand waves and uncertainty in the surveys but there is no systematic movement of the sand waves indicating migration.

incorporates viscosity, grain size, water depth, and flow velocity. The relative roughness is flow depth over the grain size. Assuming the sand waves develop under rough flow conditions, where the turbulence is not related to the grain size, the equation simplifies, and the wavelength remains dependant only on the flow depth. Yalin goes on to support his equations empirically. Yalin's prediction of sand wave height is based on shear stress, which implicitly includes viscosity, flow density, grain size, and flow velocity. The equation for height is also derived empirically from flume and river data.
Yalin's relationships are:

$$\eta = 0 \qquad \tau < \tau_{cr} \qquad \text{Equation 1}$$

$$\eta = \frac{h}{6}\left(1 - \frac{\tau_{cr}}{\tau}\right) \qquad \tau_{cr} < \tau < 17.6\tau_{cr} \qquad \text{Equation 2}$$

$$\eta = 0 \qquad \tau \geq 17.6\tau_{cr} \qquad \text{Equation 3}$$

$$\lambda = 2\pi h \qquad \text{Equation 4}$$

where η is the sand wave height, τ is the shear stress, τ_{cr} is the critical shear stress, λ is the sand wave spacing, and h is the water depth. Van Rijn's sand wave height prediction also incorporates grain size, but his wavelength equation is still based only on water depth. Van Rijn's relationships are:

$$\eta = 0 \qquad \tau < \tau_{cr} \qquad \text{Equation 5}$$

$$\eta = 0.11h\left(\frac{d_{50}}{h}\right)^{0.3}\left(1 - e^{-0.5T_s}\right)\left(25 - T_s\right) \qquad \tau_{cr} < \tau < 26\tau_{cr} \qquad \text{Equation 6}$$

$$\eta = 0 \qquad \tau \geq 26\tau_{cr} \qquad \text{Equation 7}$$

$$\lambda = 7.3h \qquad \text{Equation 8}$$

$$\text{where } T_s = \frac{\tau - \tau_{cr}}{\tau_{cr}} \qquad \text{Equation 9}$$

and d_{50} is the median grain size. Both models predict no transport if the shear stress is less than the critical value, $\tau < \tau_{cr}$, and, therefore, no sand waves are predicted to develop if that condition is met. They also acknowledge a maximum shear stress beyond which bedforms are 'washed out.' Using values representative of the Moriches Inlet field site (d_{50}=0.48 mm and h=3 m) the height and length of the sand waves can be estimated. The shear stress was evaluated for a current velocity of 0.4 m/s, 0.5 m/s, and 0.6 m/s, and the associated shear stress values were 0.28 N/m^2, 0.43 N/m^2, and 0.62 N/m^2, respectively. The wavelength predictions are larger than observations, 19-22 m compared to an observed average wavelength of 15 m (Table 1). The standard deviation of the observed wave lengths is 4 m, so the prediction and observations agree. Sand wave height is consistently under-predicted, 2-29 cm compared to observations of 39 cm. The standard deviation of the sand wave heights measured at Moriches Inlet is 13 cm. Again, the predicted and observed values agree, albeit ~~just~~ barely.

Table 1. Predicted Sand Wave Heights and Wavelength

	$\overline{U}$ = 0.4 m/s	$\overline{U}$ = 0.5 m/s	$\overline{U}$ = 0.6 m/s
Yalin Height (m)	0.04	0.20	0.29
Yalin Wavelength (m)		19	
van Rijn Height (m)	0.02	0.17	0.29
van Rijn Wavelength (m)		22	

$\overline{U}$ is the depth-averaged velocity

MOBILIZATION OF THE SAND WAVE FIELD

The sand wave field at Moriches Inlet is a persistent feature which has been observed on aerial photographs from 2001 and 2004, and bathymetric surveys from 2004 and 2005, however, the conditions responsible for creating them was not observed during this study. Predictions of sand wave height based on flow velocity measured at Moriches Inlet (Yalin, Equation 2; van Rijn, Equation 6) under predict the height of the sand waves, suggesting that a stronger current velocity was responsible for building these features. Assuming these predictions are accurate, the flow conditions responsible for creating these features were likely not observed during this study.

Evidence for sand wave development under conditions different than those seen during this study is also evident in the slope of the slip face and the steepness of the sand waves. The sand waves display an asymmetrical profile, but the slip face is gently sloped and does not approach the angle of repose. This indicated that the sand waves are not actively migrating. These sand waves were likely actively migrating during their developing phase, but are now stationary because the net sediment transport is not sufficient to cause migration. The weak current and negligible sediment transport have modified the morphology of the sand waves but not erode them or reversed their orientation.

Given the reasons described above, it is concluded that the sand wave field at Moriches Inlet developed when flow conditions where stronger than those observed during this study, possibly during a storm surge or other meteorological event that increased the tidal current velocity. Since then, the typical flow conditions have gently reworked the sand waves, relocating the crests to a more central location, and flattening the slip face while the sand waves remain stationary.

The hypothetical event creating the sand waves can be reconstructed using the empirical equations for sand wave height published by van Rijn (1984) and Yalin (1964) and the physical relationship between tidal range and current speed. The observed sand wave height is 39 cm. To achieve this height, according to the relationships published by Yalin (1964) and van Rijn (1984), the current speed should reach 80 cm/s. Therefore, it can be assumed that the event creating these sand waves caused current velocity in the study area to increase to 80 cm/s.

The velocity of the tidal current is a function of the tidal prism. Because the tidal period remains constant, as the tidal prism increases, the water must flow faster in order to accommodate the larger flux. As long as the area of the bay is constant as the water level rises, tidal range is a valid proxy for tidal prism. In a bay with steep sides and few tidal flats, such as Moriches Bay, the area of the bay remains fairly constant throughout the tidal cycle and, therefore, the relation between tidal prism and current speed can be extrapolated to tidal range and current speed. The current data collected during this study also suggests the bay area remains constant as the water elevation nears high tide. The velocity gradually decreases near high tide; if there were large changes in the bay area as the tide rose, the velocity record would show an acceleration near high tide but it does not.

An increase in tidal range will increase the current speed. Changes in the tidal range are generally periodic and caused by lunar and solar forcing. However, there is also a stochastic component to the tides which is forced by metrological conditions such as wind and/or barometric pressure. For example, during a storm, low barometric pressure, wave setup, and wind forcing may increase or decrease the elevation of the water's surface. This change may increase the tidal range and, therefore, the current velocity.

The water level and current data collected at Moriches Inlet were used to calculate the tidal range and the peak current speeds so that a relationship between these two parameters could be defined. The linear regression between peak current speed and tidal range was calculated for four records. Other current records were disregarded because of the poor data quality (high signal-to-noise ratio or invalid velocities because the meter tipped over) or the length of the record (at least four days of measurements were needed). In addition to being a function of tidal prism, current velocity also depends on the bathymetry; therefore, the relationship between peak tidal current and tidal range is spatially dependent. Because of the spatial dependence, each record was analyzed separately (each record was collected from a slightly different location within the study area). These data were further separated by flow direction. In areas with an asymmetrical tidal signal, the relationship between the peak flood velocity and the tidal range is different than relation between the peak ebb velocity and the tidal range. The study area is generally flood-dominate, so the flood and ebb velocities were analyzed separately. The flood velocities were stronger and showed a better correlation to tidal range than did the ebb velocities. After the analysis was completed, one additional record was disregarded because it had a strong diurnal inequality which resulted in a poor correlation between the current velocity and the tidal range. The R-squared values for the individual stations were 0.73, 0.94, and 0.94. An overall relation between tide range and peak current velocity for the study area was obtained for these three stations (Figure 5):

$$U_{peak} = 0.12 + 0.41(\text{Tidal Range}) \qquad \text{Equation 10}$$

where U_{peak} is the peak tidal current in m/s. For this equation, the R-squared value dropped to 0.51, but the inclusion of all the data makes it a more robust predictor for the

general study area. Based on the regression, the peak current velocity will be 80 cm/s when the tidal range is 1.66 m.

Water level data from Sandy Hook, NJ[1] and Shinnecock Bay[2] were used to evaluate the frequency of events with a tidal range exceeding 1.66 m. Shinnecock Inlet is 30 km east of Moriches Inlet, and the tide gauge was just inside the inlet (Figure 6). Sandy Hook is the National Oceanic and Atmospheric Administration (NOAA) reference station for Moriches Inlet. The correction for low water is 0.60, and the correction for high water is 0.62. These corrections were applied to the observed water levels measured at Sandy Hook to approximate the tidal range at Moriches Inlet (Figure 7). Between May 1998 and December 2005, the tidal range exceeded 1.66 m only once, on 12 December 2000. This tidal range could have increased the tidal velocity and created the sand wave field at Moriches Inlet. This large tidal range was caused by strong winds and a drop in atmospheric pressure. During that day, the wind velocity increased from 2 m/s to 19 m/s, and the wind turned from the north (Figure 8). In addition, the barometric pressure dropped below 1,000 pHa. The drop in atmospheric pressure raised the elevation of the high tide and wind amplified the ebb flow out of the bay and created an extra low low-tide. The result was an extremely large tidal range of 1.95 m.

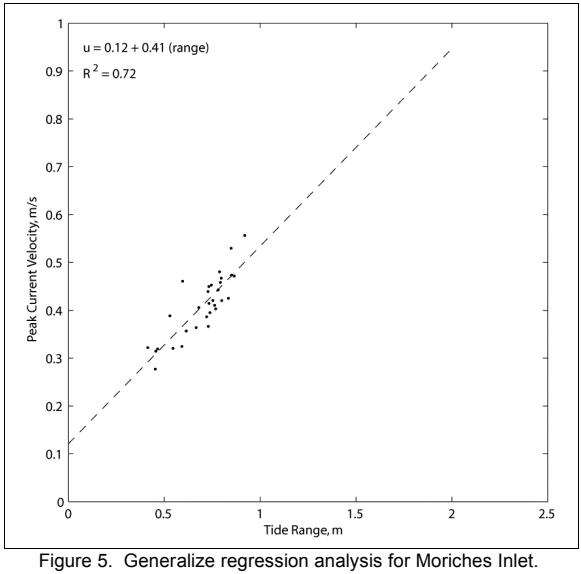

Figure 5. Generalize regression analysis for Moriches Inlet.

1 NOAA Tide Station 8531680 (40° 28.0' N, 74° 0.6' W)

2 The Shinnecock Bay tide gauge was maintained by the LIShore program under the direction of the USACE, Coastal Inlets Research Program.

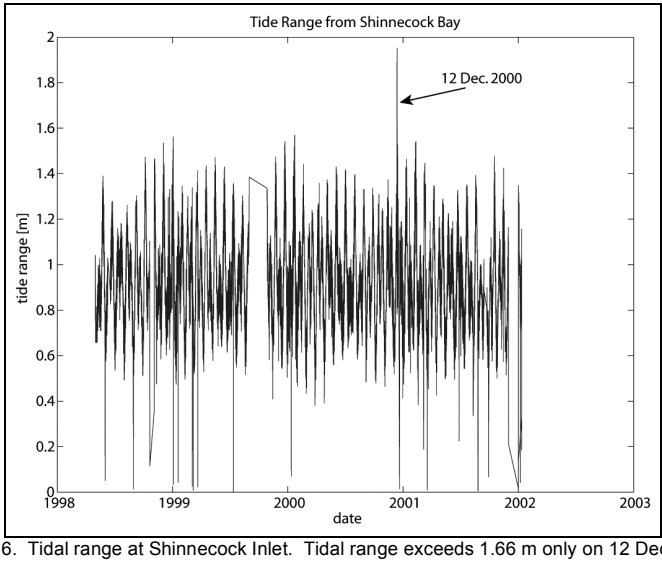

Figure 6. Tidal range at Shinnecock Inlet. Tidal range exceeds 1.66 m only on 12 December 2000, when it reached 1.95 m.

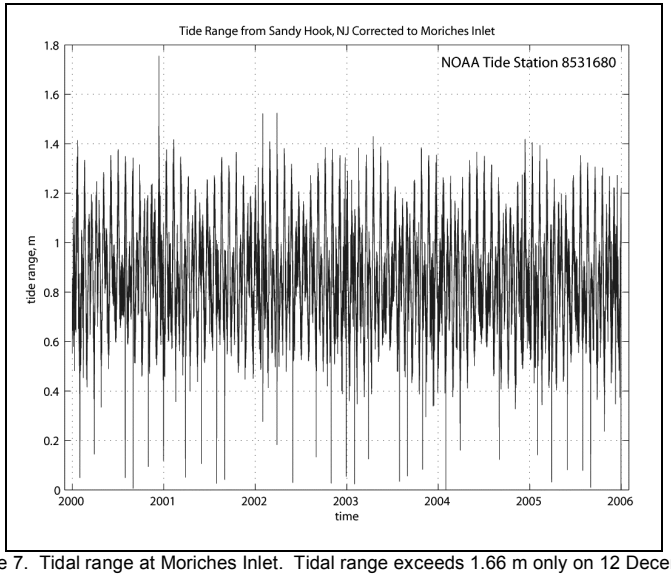

Figure 7. Tidal range at Moriches Inlet. Tidal range exceeds 1.66 m only on 12 December 2000.

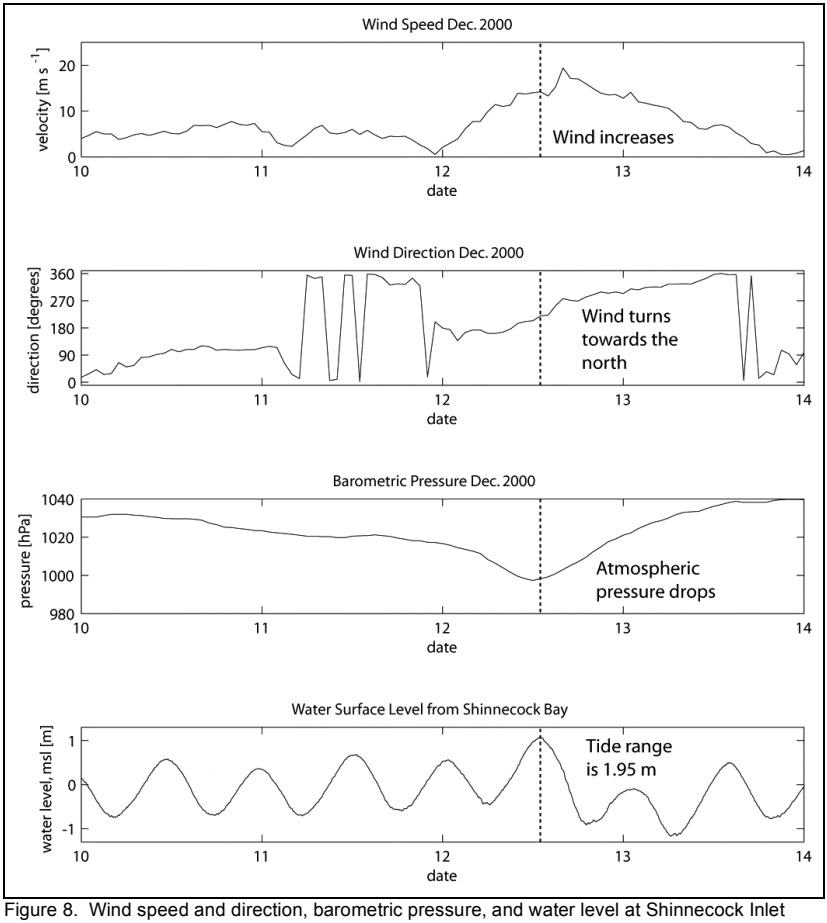

Figure 8. Wind speed and direction, barometric pressure, and water level at Shinnecock Inlet 10 December-14 December 2000. Wind data are from the National Data Buoy Center (Station 44025) and the water level data are from the LIShore Shinnecock Bay tide gauge.

CONCLUSION

The sand waves at Moriches were compared to predictive models of sand wave height presented by Yalin (1964) and van Rijn (1984). Both models are based on shear stress. Yalin's and van Rijn's equations under predicted the sand wave height by 10 cm. Their model both predict a sand wave height of 29 cm compared to 39 cm as measured at Moriches. Although the sand waves are asymmetrical, the slip face angle is very shallow. The average slope ranges from 3.8˚ to 4.7˚. The steepest slip faces are 5.9˚-6.2˚.

It is unlikely that the observed flow conditions are responsible for the development of this sand wave field. According to Yalin's and van Rijn's predictions, the current velocities are too weak to build these features. Episodic storms events could increase the tidal currents, which could produce these features. After the passage of the storm the typical tidal currents continue to rework the sand waves. Slowly the sand wave crest is eroded and the slip face angle is flattened. Typical current conditions do not completely erode the sand wave but active migration is not observed during these conditions.

The observation of this moribund, or relic sand wave field at Moriches Inlet suggests that sand waves may persist long after the conditions responsible for their development have subsided. Once sand waves are present on the seabed, the bathymetric irregularities caused by these features help maintain the sand waves during extended periods of low flow conditions. During typical hydrodynamic conditions sand waves become autonomous or self maintaining. This conclusion suggests that infrequent high-energy flow events should be taken into account when trying to predict the development of sand waves.

ACKNOWLEDGEMENTS

The authors would like to thank the following organizations and individuals for their financial and technical support of this study:

- Office of Naval Research for graduate funding through the National Defense Sciences and Engineering Fellowship.
- Coastal Inlets Research Program, U.S. Army Corps of Engineers for their financial support of the field work.
- Geological Society of America for financial support of the field work through their Graduate Student Research Grant.
- Steven Borgeld, from Humboldt State University, for supplying the grain size data for the Humboldt Entrance Channel.

REFERENCES

Aliotta, S. and Perillo, G. M. E. (1987). "A sand wave field in the entrance to Bahia Blanca estuary, Argentina," *Marine Geology* 76, 1-14.

Boothroyd, J. C. and Hubbard, D. K. (1975), "Genesis of bedforms in mesotidal estuaries," *in* L. E. Cronin, ed., Estuarine Research, Vol. II: New York, New York, Academic Press, Inc., p. 217-234.

Dalrymple, R. W., Knight, J. R. and Lambiase, J. J. (1978). "Bedforms and their hydraulic stability relationships in a tidal environment, Bay of Fundy, Canada," *Nature* 275, 100-104.

Dalrymple, R. W. and Rhodes, R. N. (1995), "Esturine dunes and barforms," *in* G. M. E. Perillo, ed., Geomorphology and Sedimentology of Estuaries, Elsevier Science, p. 359-422.

Gabel, S. L. (1993). "Geometry and kinematics of dunes during steady and unsteady flows in the Calamus River, Nebraska, U.S.A.," *Sedimentology* 40, 237-269.

Mazumder, R. (2003). "Sediment transport, aqueous bedform stability and

morphodynamics under unidirectional current: a brief overview," *Journal of African Earth Sciences* 36, 1-14.
McCave, I. N. (1971). "Sand waves in the North Sea off the coast of Holland," *Marine Geology* 10, 199-125.
Southard, J. B. (1971). "Presentation of bed configurations in depth-velocity-size diagrams," *Journal of Sedimentary Petrology* 41(4), 903-915.
Southard, J. B. and Boguchwal, L. A. (1990). "Bedform configurations in steady unidirectional water flows. Part 2: synthesis of flume data," *Journal of Sedimentary Petrology* 60(5), 658-679.
van Rijn, L. C. (1984). "Sediment transport, part III: bed forms and alluvial roughness," *Journal of Hydraulic Engineering* 110(12), 1733-1754.
Yalin, S. M. (1964). "Geometric properties of sand waves," *Journal of the Hydraulics Division* 90(HY5), 105-120.
Zarillo, G. A. (1982). "Stability of bedforms in a tidal environment," *Marine Geology* 48, 337-351.

GEOMETRIC AND STATISTICAL CHARACTERISTICS OF BED FORMS IN THE LOWER MISSISSIPPI RIVER

K. Kheiashy [1], J. McCorquodale [2], I. Georgiou [3], E. Meselhe [4]

1. Doctoral Candidate, Civil and Environmental Engineering Department ,University of New Orleans, Hydraulic Modeler, C.H. Fenstermaker and Associates Inc. 135 Regency Square, Lafayette, LA 70518, e-mail:karim@fenstermaker.com
2. Professor, Civil and Environmental Engineering Department ,University of New Orleans, New Orleans, LA 70148, e-mail:jmccorqu@uno.edu
3. Assistant Professor, Earth and Environmental Sciences Department, University of New Orleans, New Orleans, LA 70148 e-mail:igeorgiou@uno.edu
4. Professor, Civil Engineering Department, University of Louisiana at Lafayette, Senior Hydraulic Engineer, C.H. Fenstermaker and Associates Inc. 135 Regency Square, Lafayette, LA 70518, e-mail:ehab@fenstermaker.com

Abstract: Bed forms in alluvial systems are three dimensional. The most common bed forms are: ripples, dunes and bars. Under certain flows, different bed forms may be superimposed on each other, e.g. dunes superimposed on bars or ripples superimposed on dunes. The irregularity in the bed of alluvial streams caused by the existence of bed forms produces additional flow resistance, which affects the hydrodynamics and sediment transport properties of the system. The geometry of bed forms in large alluvial rivers such as the Lower Mississippi River exhibits both coherent and random characteristics. Average wave lengths and heights alone cannot adequately describe these bed forms. A spectral approach was used in this study to capture the periodicity and frequency distributions of the observed bed forms along a study reach in the Lower Mississippi River extending from river mile zero (Head of Passes) to river mile 234 (near Baton Rouge, LA).

INTRODUCTION

An alluvial river like the Mississippi River is defined as a stream that transports gravel, sands or/and clays. Alluvial rivers normally have an aspect ratio (width to depth) of 10 or greater (Yalin and da Silva, 2001).

One of the major characteristics of alluvial rivers is that their channel geometry is not only affected by the magnitude of the discharge, but also by the amount of sediment being transported. The river discharge causes a change in the river sediment transport and in turn, the channel bed geometry responds to this change. This causes a change in the water level elevation and thus another change in the sediment transport. The resulting bed forms appear in two flow regimes, lower-flow regime and upper-flow regime.

Bed forms in the lower-flow regimes, with Froude number ($Fr = \frac{U}{\sqrt{gh}}$, where U is the mean velocity; g is the acceleration of gravity; h is the mean flow depth) generally less than 1, are as follows: ripples, dunes, washed out dunes (also called transition dunes). With higher velocities, the lower-flow regime transitions into the upper flow regime (Froude number near or greater than 1), which has the following bed forms: plane bed, antidunes, and chutes and pools (Simons and Richardson, 1966).

Once bed forms appear, streamlines near the bed may not conform to the bed surface, especially in the case of ripples and dunes where the flow separates at the crest of the bed form so that there is a pressure gradient between the downstream and upstream faces of the bed form. The net force thus produced is the form resistance of the bed form. As a major component of resistance, form resistance changes as the flow conditions change. Hence, the effective 'friction' factor in an alluvial river varies with flow conditions.

During the transformation of a sand bed from a flat bed to ripples, and subsequently to dunes, the resistance to flow tends to increase. Then resistance decreases as the dunes are washed out at higher discharges. At even higher velocities, nearly symmetrical sand waves (antidunes) form with little or no flow separation at the crests. Therefore, the form resistance is smaller than that for dunes. The energy loss is more than that for a plane bed, because the breaking of the sand waves generates a strong local turbulence that dissipates part of the flow energy. Energy must also be expended to transport the increased bed material load.

The geometric characteristics of bed forms are irregular and random in nature and therefore the notion of average bed form wave length and average bed form wave amplitude is not sufficient to describe the geometry of the bed forms; alternative statistical indicators are introduced in this study.

PROBLEM DEFINITION

Extensive research has been conducted on the flow and sediment transport over bed forms in alluvial rivers (e.g. mean flow field, turbulence, shear partitioning, bed load transport, bed form geometry). Much of this work was either laboratory studies or small scale field investigations. Recently (1990s) advances in technology have improved the way data are collected and analyzed, e.g. flow data, velocity data and detailed bathymetric information providing greater knowledge about the bed form geometry.

Kennedy and Karim (1990) stated the following *"this finding suggests that models that are significantly more accurate than those that have already been developed, including those presented herein, likely will not be forthcoming until more accurate and more comprehensive field and laboratory data are available"*.

American Society of Civil Engineers (ASCE) Task Committee on Flow and Transport over Dunes (2002) reported the following conclusions "*Field studies with detailed measurements of not only dune characteristics but also flow and transport are valuable and daunting for the same reason: they indicate the complexity of the real problem, which together with practical constrains on field measurements, make more difficult the analysis and interpretation of the data"*.

Recent technological advances in river bottom mapping and data collection devices such as multi-dimensional surveys of the riverbed (also called Multibeam Bathymetric Surveys) represent an opportunity for researchers to overcome some of these hurdles, as they can provide information that could have never been acquired with older technology.

Bathymetry surveys use sound navigation and ranging (sonar) systems to collect depth information. Single-beam sounders collect discrete data points along survey track lines, while multibeam sounders collect continuous high-resolution bathymetry data with complete overlap throughout the survey area. This study uses bathymetry from Multibeam Surveys to characterize the bed forms in the Lower Mississippi River.

METHODOLOGY

The approach in this study was to apply spectral analysis to multibeam bathymetric survey data of the Lower Mississippi River to examine the periodicity in the bed form sequences. Spectral analysis belongs to a family of time series analytic techniques whose aim is to uncover trends or patterns in a sequence of data over time. By extending the temporal methods and substituting space for time, one dimensional spatial data can also be analyzed by these techniques (Granger, 1969; Bennet 1979; Richards, 1981).

Examples of this application are the determination of objective wavelengths in meanders (Speight, 1965, 1967; Chang and Toebes, 1970; Ferguson, 1975; Hokke, 1984), pools and riffles (Richards, 1976), bed forms (Naden 1987, Nordin 1971), and pools caused by coarse woody debris (Nakamura and Swanson, 1996). These successful applications suggest that spectral analysis may be a useful tool for detecting the periodicity in bed forms in the Lower Mississippi River.

Spectral analysis partitions the variation in a time (or spatial) series into components according to the duration or length of the intervals within which the variation occurs (Rayner, 1971). Spectral analysis was applied in this study to the Multibeam bathymetric survey data collected by the Army Corps of Engineer in the Lower

Mississippi River during the period from June 2003 to August 2003. These data were provided to the authors as a part of a hydrodynamic and ecological modeling study of the lower Mississippi River. Meselhe et al (2005) presents more detailed explanation of the study. Multibeam data were collected from River Mile (RM) Zero (Head of Passes) up to RM 234 (near the city of Baton Rouge). Figure 1 shows the extent of the reach where of the Multibeam data were collected.

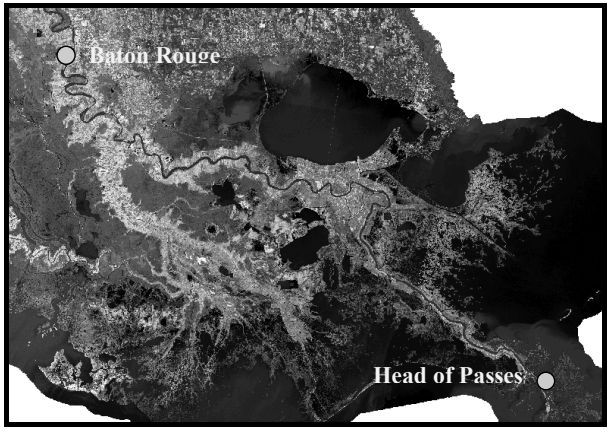

Figure 1: Range of Multibeam bathymetric data collected by USACE

A sample three dimensional view of a Multibeam dataset collected at RM 223 is shown in Figure 2.

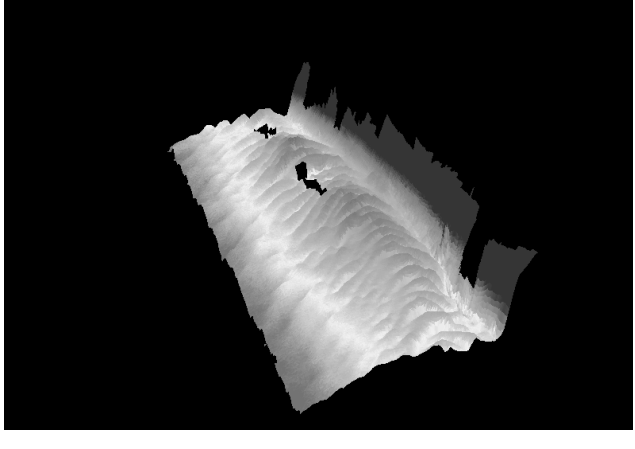

Figure 2: 3D view of a Multibeam data collected in RM 223

A total of 31 Multibeam datasets were acquired and several longitudinal profiles were extracted from each data set. The profile locations were selected such that they cover

the total width of each dataset. To ensure the capture of the bed forms variation in size, sections both parallel and perpendicular to the main flow direction were extracted. Spectral analysis was then applied to the extracted profiles.

RESULTS

A sample extracted profile from Multibeam dataset at RM 223 (Figure 3) is shown in Figure 4, while spectral analysis results of the same profile is shown in Figure 5.



Figure 3: Plan view of Multibeam dataset at RM 223

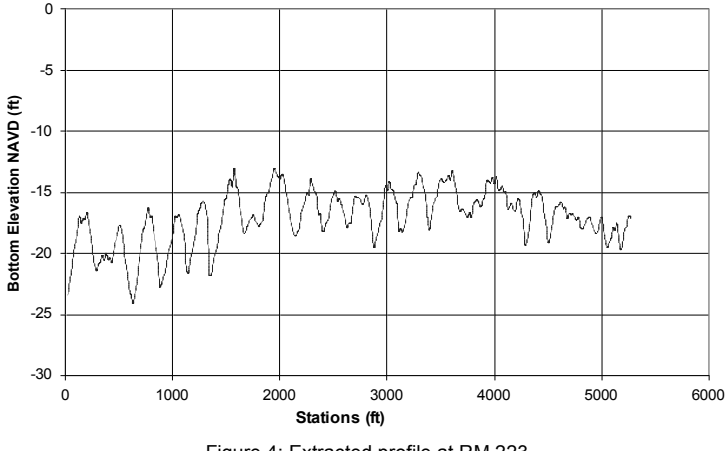

Figure 4: Extracted profile at RM 223

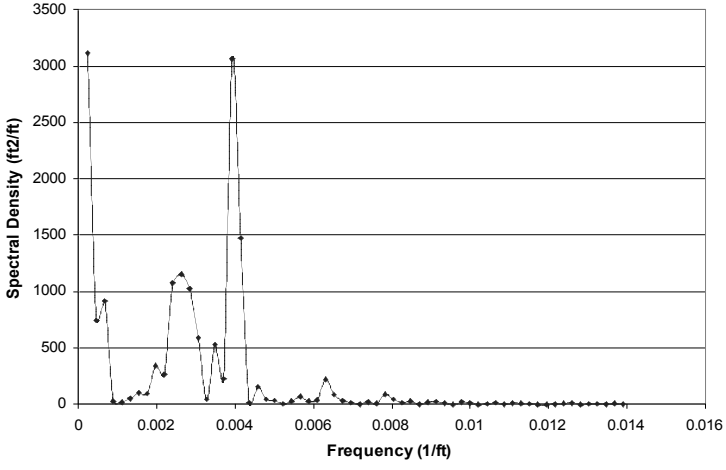

Figure 5: Spectral analysis results at RM 223

Results of the spectral analysis show a distinct periodic character in the longitudinal bed profiles in the sampled datasets. Statistically significant spectral peaks were detected in almost all of the datasets; several reaches exhibit more than one significant peak as shown in Figure 5. At least three significant peaks were noted for each profile and then the corresponding bed form wave lengths, heights and steepness (height/wavelength) were calculated. The calculated wave lengths, heights and steepness for the entire length of the studied reach are shown in Figure 6, 7 and 8.

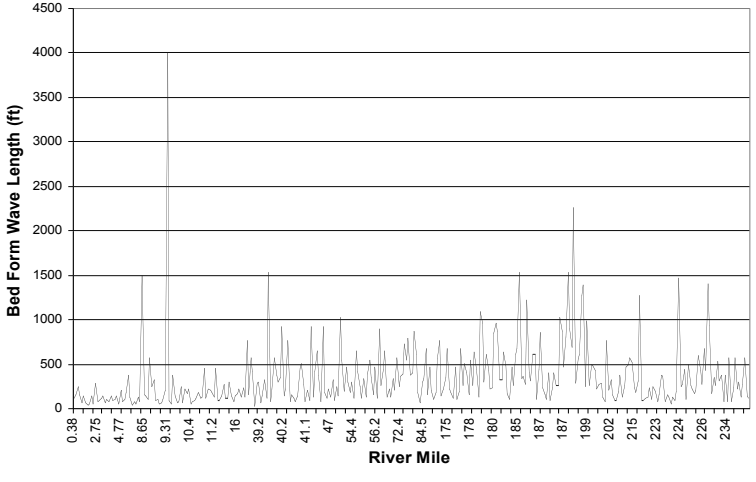

Figure 6: Time series of bed form wave length

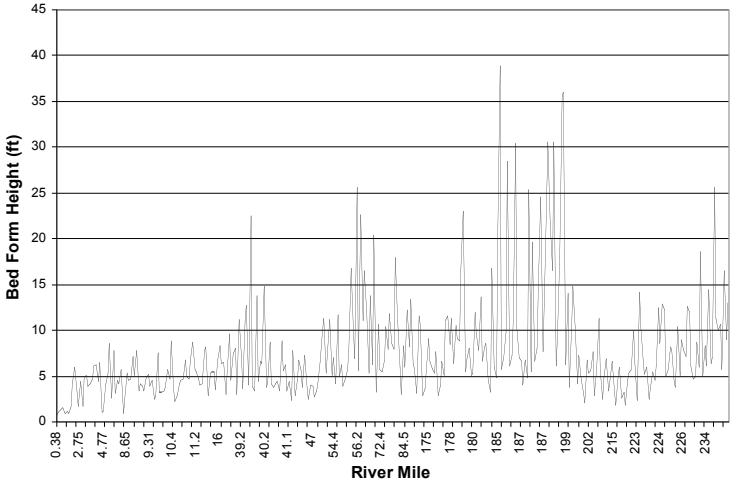

Figure 7: Time series of bed form height

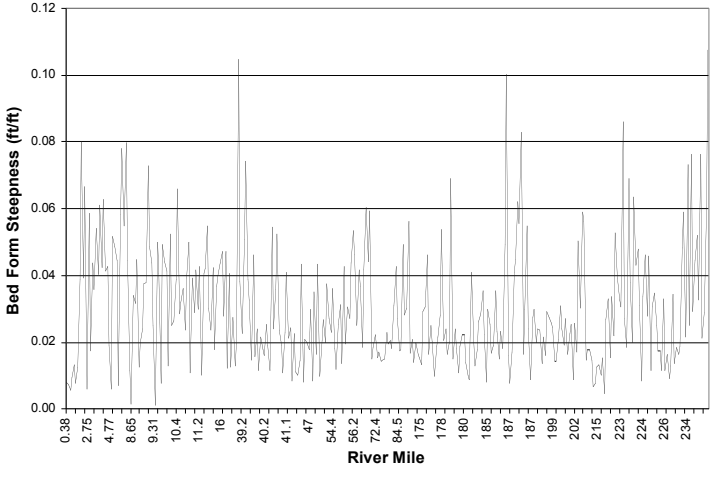

Figure 8: Time series of bed form steepness

Figure 6 shows that the dominant bed form wave lengths on average ranged from 50ft to 500ft in the upstream section of the studied reach while an increase in the wave length was observed in the downstream section of the reach where the bed form wave length on average ranged from 250 – 1000ft. The same pattern was also observed in the bed form height (Figure 7) where the heights on average ranged from 1ft to 7ft in the upstream reaches of the River, while in the downstream reaches they ranged from 4ft to 15ft. Although figures 6 to 8 reveal some valuable information about the bed

form geometry in the studied reach of the Lower Mississippi River, they also clearly show that presenting the spectral results only as spatial series plots is not adequate to represent the results. Table 1 summarizes additional statistical analysis performed on the spectral results obtained from the survey.

Table 1 One variable summary of the spectral results

One Variable Summary			
	Bed form length (ft)	**Bed form Height (ft)**	**Steepness (ft/ft)**
Mean	354.58	7.717	0.03011
Variance	135659.49	34.134	0.00033
Std. Dev.	368.32	5.842	0.01821
Median	242.71	6.000	0.02520
Minimum	29.44	0.850	0.00100
Maximum	4026.00	38.860	0.10742
Range	3970.56	38.010	0.10642

The statistical measures summarized in Table 1 reveal the high variability present in this natural system; the bed form standard deviation is the same order of magnitude as the mean suggesting that the bed form data are following a skewed probability density function. To quantify the degree of skewenesses present in the bed form data, frequency histograms for the bed form wave lengths, heights and steepness were constructed (Figure 9, 10 and 11). These frequency plots list the numbers of observation of each variable (length, height and steepness) in different classes.

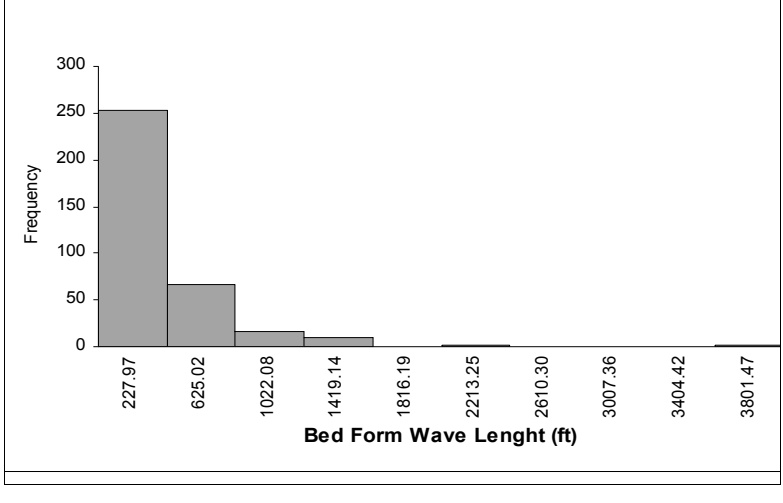

Figure 9 Histogram of the bed form wave length

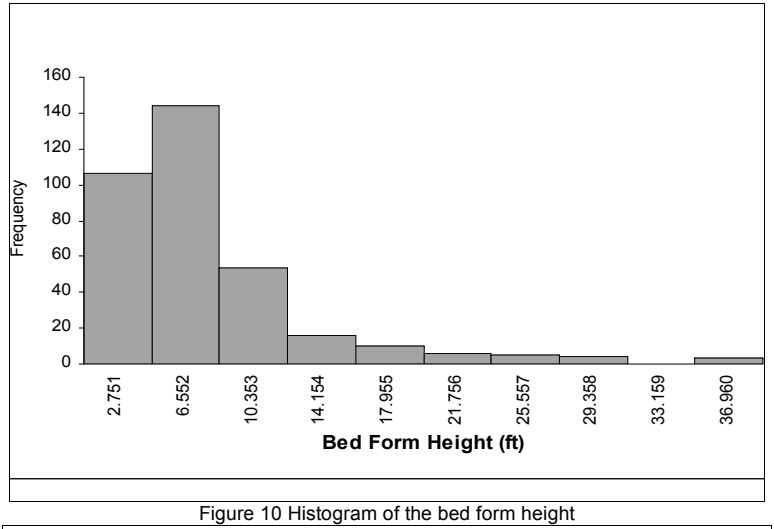

Figure 10 Histogram of the bed form height

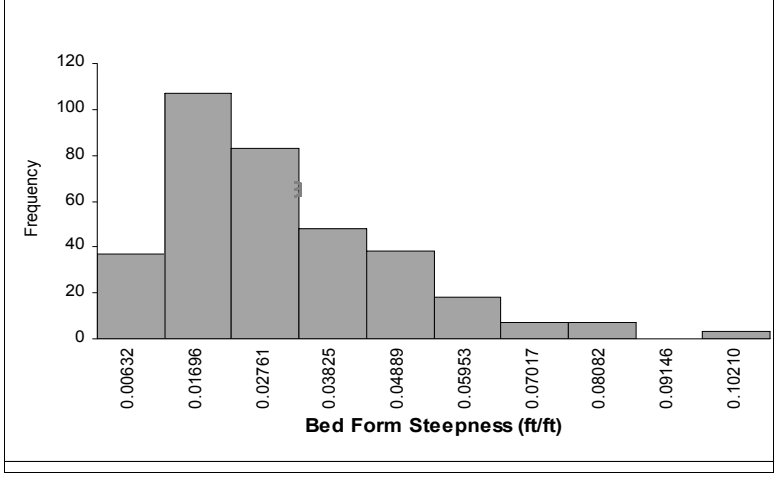

Figure 11 Histogram of the bed form steepness

The histogram shapes confirm the skeweness observed in the one variable summary presented in Table 1. The histograms plots showed skeweness to the right with a single peak. For bed form wave lengths (Figure 9), the majority of the calculated wave lengths are in the 250 -500ft range, while for bed form height (Figure 10), the majority of the values are in the range of 6 - 8 ft; the steepness was in the range of 0.01 to 0.03.

FLOW- RESISTANCE RELATION

The bed form statistical geometry findings presented above were then correlated with some hydrodynamic features that resulted from an undergoing hydrodynamic modeling study of the Lower Mississippi River described in Meselhe et al (2005). This process is ongoing; however, a sample of the preliminary results is presented here.

Hydrodynamic model results for the period between June 2003 and August 2003 (same period when the multibeam data were collected) were obtained from a calibrated one-dimensional model for the Lower Mississippi River, the model extends from Tarbert Landing RM 306, MS to the Head of Passes RM Zero, LA (Meselhe et al 2005). Model data that were used included: Average velocity (U), Total Average Hydraulic Radius (R_h), Energy Slope (S) values at several points along the study reach and utilized to calculate the bed form shear stress as follows:

$$\tau''_0 = \frac{1}{2}\rho C_d \frac{H_d}{\lambda} U^2 \tag{2}$$

where τ_0" is the bed form shear stress; ρ is the density; C_d is the drag coefficient = 0.25; H_d is the bed form height; λ is the bed form wave length; U is the average cross sectional velocity.

Different values for C_d have been obtained from the literature ranging from 0.21 (Smith and McLean, 1977) to 0.23 (Wilberg and Nelson, 1992) to 0.25 (Nelson and others, 1993). The value of C_d was found to have a direct effect on the shear computations.

The bed form shear velocity (u_*") was then calculated as follows:

$$u_*'' = \sqrt{\frac{\tau_0''}{\rho}} \tag{3}$$

The flow parameter ψ_{35} was then calculated as follows:

$$\psi_{35} = \frac{\rho_s - \rho}{\rho} x \frac{d_{35}}{R'_h S} \tag{4}$$

where ρ_s is the bed material density, d_{35} is the sieve size in the bed material of which 35 percent is finer (ranged from 0.2 to 0.3 mm in the studies reach with a trend to gets finer in the downstream direction), and plotted versus U/ u_*" as shown in Figure 12.

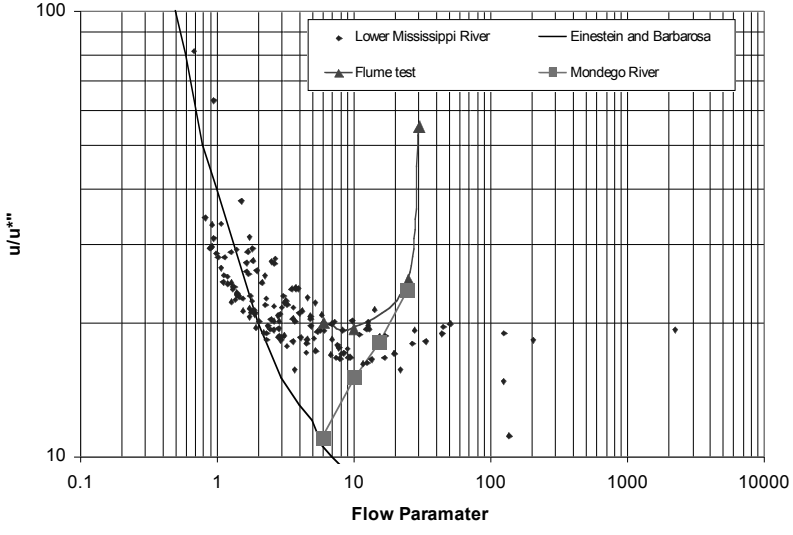

Figure 12 Preliminary Bed Form Resistance versus flow parameter for the Lower Mississippi River

The results shown in Figure 12 follow the general trend established by Einstein and Barbarossa (1952); however the data in the lower section of the plot are in better agreement with a curve based on later flume tests by Einstein and another curve for the Mondego River in Portugal by Cunha (1967). However both of these experiments included coarser sand (coarser than 0.6 mm) than that in this study (0.2 to 0.3 mm).

Previous research on bed forms was primarily laboratory studies or small scale field investigations. This study extends the range of bed form dimensions beyond those that have been considered in the current literature. Future analysis and ongoing acquisition of more detailed sediment size distribution of the Lower Mississippi River will help improve the accuracy of Figure 12.

SUMMARY AND CONCLUSIONS

Spectral analysis process was performed to 31 Multibeam datasets covering approximately 234 miles of the Lower Mississippi River for the purpose of quantifying the periodicity of bed form geometry in the river. The spectral results indicated that the dominant wave lengths varied from 50 to 500 ft at the downstream part of the study reach and 250 to 1000 ft in the upper part of the study reach. Similarly the bed forms heights increased in the upstream direction from 1 – 7 ft to 4 -15 ft. These changes were consistent with an increase in the bed shear stress in the upstream direction. Statistical characterization of the results was also performed for the purpose of testing the variability in the data. Results from histogram plots and

spatial series plots indicated the existence of wide variability in the data and the existence of a strong right skeweness phenomenon in the data.

Preliminary correlations between the resulted bed form geometry and some hydrodynamic features of the river were also performed. The results show a distinct relation between the bed form resistance and the flow characteristics. The wide range of bed form dimensions presented in this study produced a wider range of bed form resistance than has been previously included in the published literature.

All the analysis presented in this study was based on data extracted from a large alluvial river (Lower Mississippi River), with a very low energy gradient (less than 0.002 %), covered with a fine sediment bed (0.2 – 0.3 mm) and carrying a wash load in the range of 100-200 mg/L and should not be generalized to different natural river systems.

There has been much theoretical research and applications of bed form mechanics. Bed forms are primary contributors to resistance in alluvial rivers; their varying dimensions and migration from one regime to another (e.g., flat to dune to antidune) produce continuing change in the energy gradient. The work presented in this study was aimed at developing resistance relationships based on field data and computational procedures. Ultimately this research is intended to provide a better representation of flow resistance in hydrodynamic and sediment transport modeling codes.

REFERENCES AND BIBLIOGRAPHY

ASCE Task Force on Flow and Transport over Dunes, 2002, Flow and Transport over Dunes, Forum paper, Journal of Hydraulic Engineering, Volume 128, No. 8, pp 726-728 ASCE Task Force on Bed Forms in Alluvial Channels, Committee on Sedimentation, 1966, Nomenclature for bed forms in alluvial channels, Journal of the Hydraulics Division, Vol. 92, No. 3, pp 51-64

Bennett, R. J., 1979, Spatial time series: London, Pion, Ltd., 674 p.

Bennett, J.P., 1995, Algorithm for resistance to flow and transport in sand-bed channels, Journal of Hydraulic Engineering, Vol. 121, No. 8, pp 578-590.

Bennett, S.J. and Best, J.L., 1995, Mean flow and turbulence structure over fixed, two dimensional dunes: implications for sediment transport and bedform stability, Sedimentology, Vol. 42, pp 491-513

Chang, T. P., and Toebes, G. H., 1970, A statistical comparison of meander planforms in the Wabash Basin: Water Resources Research, v. 6, p. 557–577. 165 of step-pool mountain streams

Chow, V.T., 1959, Open-Channel Hydraulics, MaGraw-Hill, New York, 680 p. Coleman, S.E. and Fenton, J.D., 1996, Potential flow instability theory and bed forms, Proceedings North America Water and Environment Congress '96, American Society of Civil Engineers, Anaheim, CA, 6 pages

Cunha, L.V..Da, "About the Roughness in Alluvial Channels with Comparatively Coarse Bed Materials." Proceedings, 12th Cong. Intern. Assoc. Hyd.Res., Vol 1, 1967, pp. 76-84

Davis, J. C., 1986, Statistics and data analysis in geology (second edition): New York, John Wiley, 550 p.

Einstein, H.A., 1942, Formulas for the transportation of bed load, Transactions of American Society of Civil Engineers, Vol. 107, pp 561-573

Einstein, H.A., 1950, The bed load function for sediment transportation in open channels, Technical Bulletin 1026, U.S. Department of Agriculture, Soil Conservation Service, Washington, D.C.

Einstein, H.A., and Barbarossa, N.L., 1952, River channel roughness, Transactions of the American Society of Civil Engineers, vol. 117, pp1121-1146.

Einstein, H.A., and Chien, Ning, 1954, Second approximation to the solution of the suspended load theory: University of California Institute Engineering Research/U.S. Army Corps of Engineers Missouri River Division Sediment Series 8, 75 p.

Einstein, H.A., and Chien, Ning, 1955, Effects of heavy sediment concentration near the bed on velocity and sediment distribution, Report 8, University of California-Berkley and Missouri River Division Corps of Engineers, 96 p.

Ferguson, R. I., 1975, Meander irregularity and wavelength estimation: Journal of Hydrology, v. 26,

p. 315–333.

Garcia, M.H., 1999, Sedimentation and erosion hydraulics, in Hydraulic Design Handbook, L.W. Mays, Ed., McGraw-Hill, New York, pp 6.1-6.113,

Garcia, M.H., 1989, Depositing and eroding sediment-driven flows: turbidity currents, PhD dissertation University of Minnesota

Granger, C. W. J., 1969, Spatial data and time series analysis, in Scott, A.J., editor, Studies in regional science:London, Pion, 217 p.

Granger, C. W. J., and Hatanaka, M., 1964, Spectral analysis of economic time series: Princeton, New Jersey,

Hooke, J. M., 1984, Changes in river meanders: a review of techniques and results of analyses: Progress in Physical Geography, v. 8, p. 473–508.

Karim, Fazle, 1995, Bed configuration and hydraulic resistance in alluvial channel flows, Journal of Hydraulic Engineering, Vol. 121, No. 1, pp 15-25

Karim, Fazle, 1999, Bed-form geometry in sand-bed flows, Journal of Hydraulic Engineering, Vol. 125, No. 12, pp 1253-1261.

Karim, Fazle and Kennedy, J.F., 1990, A menu of coupled velocity and sediment discharge relations for rivers, Journal of Hydraulic Engineering, Vol. 116, pp978-996

Kennedy, J.F., 1963, The mechanics of dunes and antidunes in erodible-bed channels, Journal of Fluid Mechanics, Vol. 16, No. 4, pp 521-544

Kennedy, J.F., 1969, The formation of sediment ripples, dunes, and anti-dunes, Annual Review Fluid Mechanics, Vol. 1, pp 147-168

Kennedy, J.F. and Odgaard, A.J., 1991, Informal monograph on riverine sand dunes, U.S. Army Coastal Engineering Research Center Contract Report CERC-91-2, 192 p.

Meselhe E.., Mader C., McCorquodale A., Habib E., Georgiou I. 2005, Hydro-Ecological Modeling of the Lower Mississippi River: Proceedings of the 14th Biennial Coastal Zone Conference, New Orleans, LA.

Naden, P. S., 1987, Modelling gravel-bed topography from sediment transport: Earth Surface Processes and Landforms, v. 12, p. 353–367.

Naden, P. S., and Brayshaw, A. C., 1987, Small- and medium-scale bedforms in gravel-bed rivers, in Richards, K., editor, River channels: environment and process: Oxford, United Kingdom, Basil Blackwell, 391 p.

Nordin, Jr., C.F., 1964, Aspects of flow resistance and sediment transport: Rio Grande near Bernalillo, New Mexico, U.S. Geological Survey Water Supply Paper 1498H, 41 p.

Nordin, Jr., C.F., and Dempster, G.R., 1963, Vertical distribution of velocity and suspended sediment, Middle Rio Grande, New Mexico, U.S. Geological Survey Professional Paper 462-B, 20 p.

Nordin, Jr., C.F. and Algert, J.A., 1965, Geometrical properties of sand waves, Discussion, Journal of Hydraulics Division, Vol. 91, No. HY5,

Nordin, Jr., C.F. and Algert, J.A.,1966, Spectral analysis of sand waves, Transactions of the American Society of Civil Engineers, Vol. 92, No. HY5, pp 95-114 1819-J, 35 p.

Rayner, J. N., 1971, An introduction to spectral analysis: London, Pion, Ltd., 174 p.

Richards, K. S., 1976, The morphology of riffle-pool sequences: Earth Surface Processes, v. 1, p. 71–88.

Richards, K., and Clifford, N., 1991, Fluvial Geomorphology: structured beds in gravelly rivers: Progress in Physical Geography, v. 15, no. 4, p. 407–422.

Shen, H.W., 1962, Development of bed roughness in alluvial channels, Journal of the Hydraulics Division, Vol. 88, No. HY3, pp 45-58

Shen, H.W., Mellema, W.J., and Harrison, A.S., 1978, Temperature and Missouri River stages near Omaha, Journal of the Hydraulics Division, Vol. 104, No. HY1, pp 1-20

Simons, D.B., Richardson, E.V., and Nordin,C.F., 1965A, Sedimentary structures generated by flow in alluvial channels, American Association of Petroleum Geologists, Special Publication No. 12

Simons, D.B., and Richardson, E.V., 1966, Resistance to flow in alluvial channels, U.S. Geological Survey Professional Paper 422-J, 61 p.

Speight, J. G., 1965, Meander spectra of the Angabunga River: Journal of Hydrology, v. 3, p. 1–15.

Yalin, M.S., 1992, River Mechanics, Pergamon Press, Oxford, 220 p.

Yalin, M.S. and da Silva, A.M.F., 2001, Fluvial Processes, International Association of Hydraulic Engineering and Research Monograph, Delft, The Netherlands, 197 p

Yalin, M.S. and Karahan, E., 1979, Steepness of sedimentary dunes, Journal of Hydraulics Division, Vol. 105, No. HY4, pp 381-392.

BATHYMETRIC EVOLUTION OF A SANDY BED UNDER TRANSIENT PROGRESSIVE WAVES

Blake J. Landry[1], Marcelo H. Garcia[2]

1. Ven Te Chow Hydrosystems Laboratory, Department of Civil and Environmental Engineering, University of Illinois at Urbana-Champaign, 205 North Mathews Avenue, Urbana, IL 61801-2352, USA. blandry2@uiuc.edu
2. Ven Te Chow Hydrosystems Laboratory, Department of Civil and Environmental Engineering University of Illinois at Urbana-Champaign, 205 North Mathews Avenue, Urbana, IL 61801-2352, USA. mhgarcia@uiuc.edu

Abstract: Laboratory experiments were conducted in a large wave flume to study the effects transient wave conditions on ripple geometry. Two primary experiments of nine hours each were performed in which the order of two wave conditions (4m and 6m waves) was altered. Bed measurements over the region were acquired using acoustic equipment, and results of ripple equilibrium characteristics were compared.

INTRODUCTION

Sand ripples play a vital role in a variety of coastal engineering topics such as bottom boundary layer flow, sediment transport, friction factor estimates for wave attenuation, and, a relatively new area, acoustic interaction with sonar signals. It is no wonder, that ripples have long held the interest of numerous researchers worldwide, throughout the years. A great amount of investigation has been conducted on the mechanism of ripple formation and equilibrium ripple characteristics under constant oscillatory flow conditions. Studies have lead to numerous equilibrium ripple predictors under constant forcing with the current most widely accepted by Wiberg and Harris (1994). However, in coastal environments, flow conditions seldom remain constant. Therefore, it becomes critical to investigate the resulting ripple geometries under these transient conditions. Only recently have laboratory studies begun to focus on this area. However, most experiments utilized small oscillatory sediment trays (i.e. Smith and Sleath 2005) or oscillatory flow tunnels (i.e Doucette and O'Donoghue 2006) in which many researchers

always tend to question the validity of results when extrapolating towards ripples generated in the field environment. With this in mind, it is the aim of this study to provide results on ripple formation under transient wave conditions within a large-scale wave flume in which flow conditions are thought to be more representative of the natural coastal region, and to serve in expanding the knowledge base from other wave flumes experiments such as Faraci and Foti (2001) and Testik et al. (2005).

EXPERIMENTAL SETUP

Experiments were conducted in the large tilting wave flume (49m long x 1.83m wide x 1.20m high) located in the Ven Te Chow Hydrosystems Laboratory.

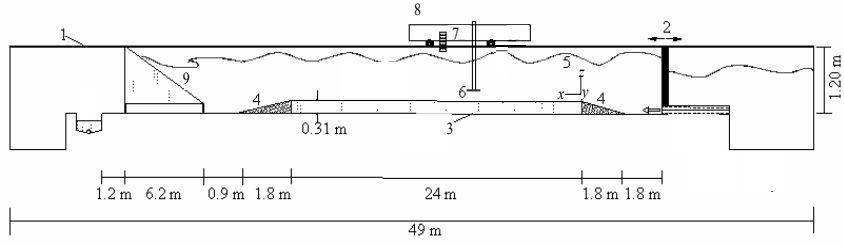

Figure 1: Schematic of Experimental Facility: 1. wave flume; 2. wavemaker paddle; 3. sand bed; 4. wooden ramp; 5. waves; 6. Seatek sensors; 7. water surface acoustic sensor; 8. movable carriage 9. beach; (Modified from Cataño 2005)

The sidewalls of the flume were composed of 1.22m (4ft) long sections of plexiglas to allow for optical visualizations and measurements, while the floor was composed of steel plating. A sand bed (approximately 30cm thick) composed of 0.25mm mean grain size diameter was located over the entire lateral span of the middle 24m of the flume. Two wooden ramps were present at either end of the bed to provide a gradual transition and retain the sand. Waves were generated in water depth of 60cm over the sand bed by a piston-type wavemaker located 3.6m from the beginning of the sand bed. Bathymetric measurements were obtained from a 32 element SeaTek sensor array (accuracy of ± 2mm in the vertical) having 4cm sensor offsets oriented about the centerline of the tank spanning the lateral dimension of the flume. A STI acoustic probe (model SU7110) was used to measure the wave amplitude at various positions along the tank (vertical accuracy of ±0.8mm). Sampling rates of the water surface probe were adjusted to ensure an integer number of waves were measured to reduce the energy leakage when performing FFT analysis on the wave data. Sensors were affixed to a wheeled frame containing an internal moveable cart controlled by linear-screw drives which allowed for the accurate positioning of the sensors over a 130cm length section, while the wheeled frame allowed for the movement/repositioning along the entire length of the tank. Wave reflection was minimized by implementing a specially modified beach composed of fibrous horse-hair matted material at a 1 on 6 slope, which resulted in approximately less than 5% reflection depending on the wave characteristics. Thus, for all practical purposes, the waves in theses experiments were considered to be progressive waves. Lastly, a Logitech 1.3 mega-pixel camera was used to provide a visual record of the ripple evolution.

EXPERIMENTAL PROCEDURE

In order to perform preliminary study on the transition of ripples under progressive waves, two exemplary experiments, experiment "A" and experiment "B", were conducted. Each experiment was run with a specified wave condition for an initial 3-hour block which was sufficient for the ripples to reach two-dimensional (2-D) quasi-equilibrium state. For the subsequent 3-hour block, the wave conditions were changed and the rippled bed was allowed to respond to the newly induced wave forcing. In order to ensure ripples had reached their ultimate 2-D quasi-equilibrium due to the second wave forcing, an additional 3-hour block was conducted. Thus, each experiment consisted of a total of nine hours composed of three 3-hour intermittent blocks, with a specific wave condition for the first 3-hours and different condition for the remaining six hours. Experiment "A" was initialized with a wave of 5.1cm amplitude and 2.63sec period for the first 3-hour block and then changed to a shorter 1.87sec wave of 5.9cm amplitude for the remaining two 3-hour blocks. Oppositely, experiment "B" was started with a 1.87sec wave then switched to the 2.63sec wave. Wave periods, *T,* of 2.63sec and 1.87sec were selected in order to achieve integer number wavelengths of 6m and 4m, respectively, with the 60cm water depth used in the experiments (based on dispersion relationship). Wave amplitudes, *a,* of 5.9cm and 5.1cm were selected to provide comparable estimates of the Shields stress parameters of 0.8 and 0.6 respectively, based on computations assuming linear water waves.

Prior to each experiment, the sand bed was smoothed and initiator ripples were created across the width of the bed at 1.22m intervals along the length of the entire sand bed, to provide uniform perturbations from which ripples can readily generate (providing the condition for incipient motion is meet) (Rosengaus 1987). The influence of tank-end effects and variations in wave conditions were minimized by studying only the middle 6m of the flume. During the initial hour of each 3-hour block, wave measurements were conducted at 0.5m intervals over the 6m span. Immediately after each 3-hour block, waves were stopped and bathymetric measured were performed at 1cm intervals along the longitudinal direction over the 6m region. Ripple wavelength and height were computed for each sensor array along the 6m region by averaging ripple crest to crest and crest to trough distances around each ripple crest, respectively. Finally, since the implementation of the SeaTek in these experiments was limited to providing a detailed three-dimensional "snapshot" of the bed at every 3-hour interval, a 1.3 mega-pixel camera was setup to view the 1064cm to 1186cm region from the wavemaker and record pictures at 2-minute intervals to qualitatively capture the transition of the sand bed, due to the change in wave forcing.

EXPERIMENTAL RESULTS & ANALYSIS

Resulting data from the experiments "A" and "B" can be seen in figures 2 and 3, respectively. In each figure, the results for the first 3-hour block are shown in the left column while the results for the subsequent 3-hour block are presented in the right column of the figure. Subplots 1a) and 1b) in each figure depict the resolved first and second harmonic water wave amplitudes which were present over the test region for that 3-hour duration. Based on the first harmonics, reflection coefficients were computed to

be about 4.5% (essentially progressive waves, as previously mentioned). However, it is important to note that the long scale variation in the second harmonic amplitudes are due to the presence of a free second harmonic in the tank as discussed in Madsen (1971).

Subplots 2(a&b) and 3(a&b) illustrate the ensemble of the ripple wavelengths and heights from each SeaTek sensor array along the 6m region, respectively. Due to minor small scale variations in the rippled bed, there exists some scatter in the results; however the dominant characteristics can be seen. After the initial 3-hours, both experiment "A" and "B" exhibited variations in the ripple wavelength which where out of phase with the first harmonic of the water wave which is as expected from wave theory. One would anticipate a similar trend in the ripple heights; however the data appears too scattered to distinguish an unmistakable coherent pattern.

In the subsequent 3-hour block (3 to 6 hours) the newly imposed wave forcing clearly resulted in modified ripple wavelengths and heights. In the case of experiment "A", ripple wavelengths decreased (on average) from ~10.5cm to ~8cm, while ripple heights experienced a slighter decrease from ~1.75cm to ~1.25cm. Experiment "B" resulted in a similar change with ripple wavelengths and heights increasing from ~8cm to ~10.5cm and ~1.25cm to ~1.75cm, respectively. As a result of the transition, data scatter is increased, which is to be expected as the bed evolves from a previously rippled state to a new equilibrium state. However, despite the scatter, the prevalent results of the subsequent 3-hour blocks of one experiment are consistent with the initial 3-hour block results of the other experiment. Thus, it seems that despite the bed being previously rippled, 3 hours seems to be an adequate amount of time for the bed to display dominant ripple characteristics of that wave forcing. It should be noted that experiment data agreed well with the current ripple predictor by Wiberg and Harris (1994). Extending the experiments an additional 3 hours (6 to 9 hours) resulted in similar ripple characteristics to that of the previous time block (3 to 6 hours).

Results from the camera were utilized to achieve greater qualitative temporal resolution of the bed transition. Select camera images can be seen in figure 4. Within the first 3 hours of the experiments the bed resulted in nice uniform 2-D ripples. After approximately 40 minutes into the new waves conditions (time=3:40), experiment "A" (having the 1.87sec waves) had exhibited a rapid response in ripple lengths nearly approaching the new equilibrium ripple length. Since the water wavelength in experiment "B" was increased, the bed underwent a more gradual transition in which existing ripple lengths slowly increased toward new equilibrium, instead of the more abrupt change of new ripple forming between existing ripples as predominate in experiment "A". By the 6hr and 9hr marks, the bed appeared to lack the 2-D uniformity as was present at the initial 3hr time of the experiments. However, the newly resulting bed was two-dimensional enough to exhibit the general associated ripple equilibrium characteristics.

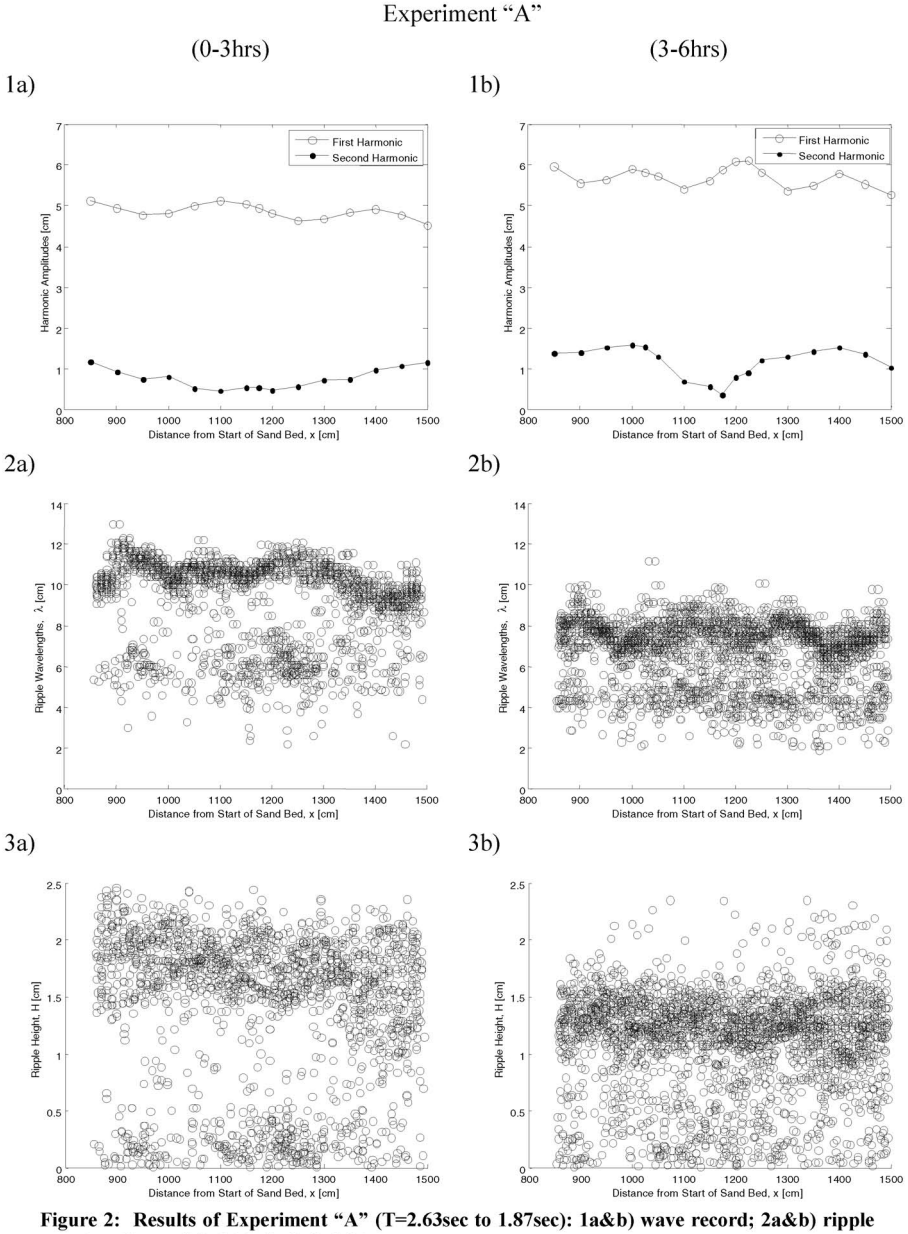

Figure 2: Results of Experiment "A" (T=2.63sec to 1.87sec): 1a&b) wave record; 2a&b) ripple wavelengths; and 3a&b) ripple height.

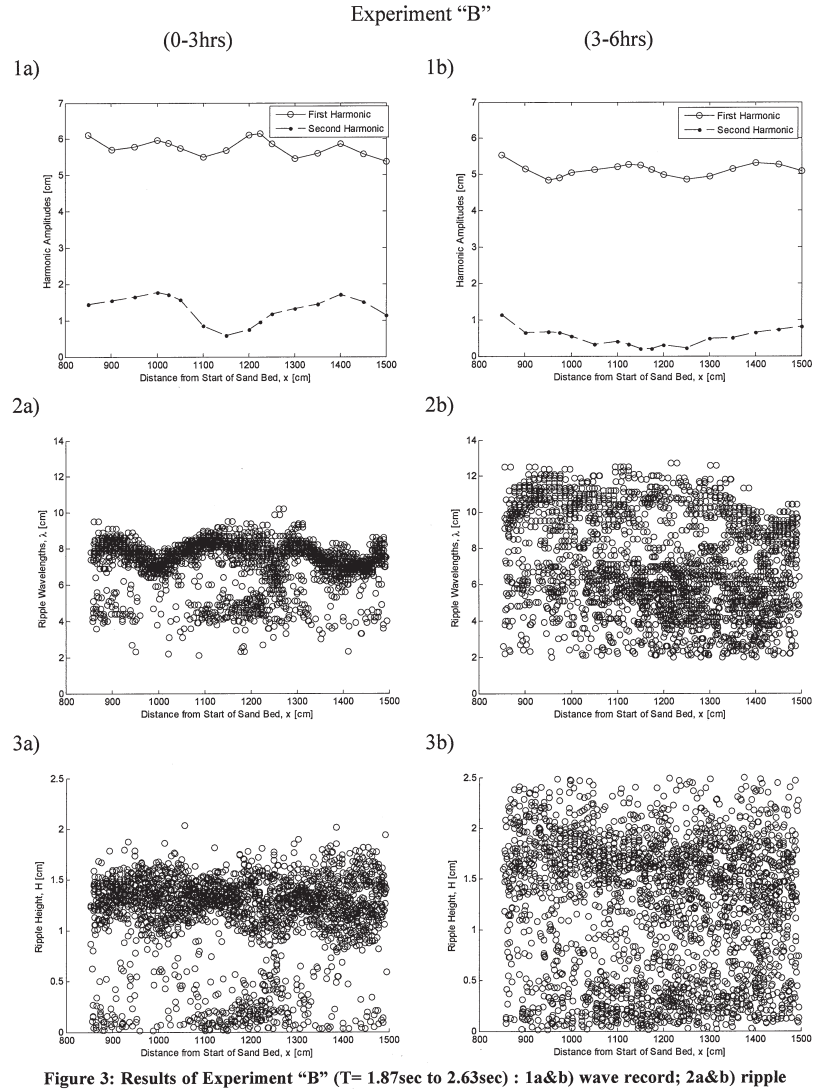

Figure 3: Results of Experiment "B" (T= 1.87sec to 2.63sec) : 1a&b) wave record; 2a&b) ripple wavelengths; and 3a&b) ripple height..

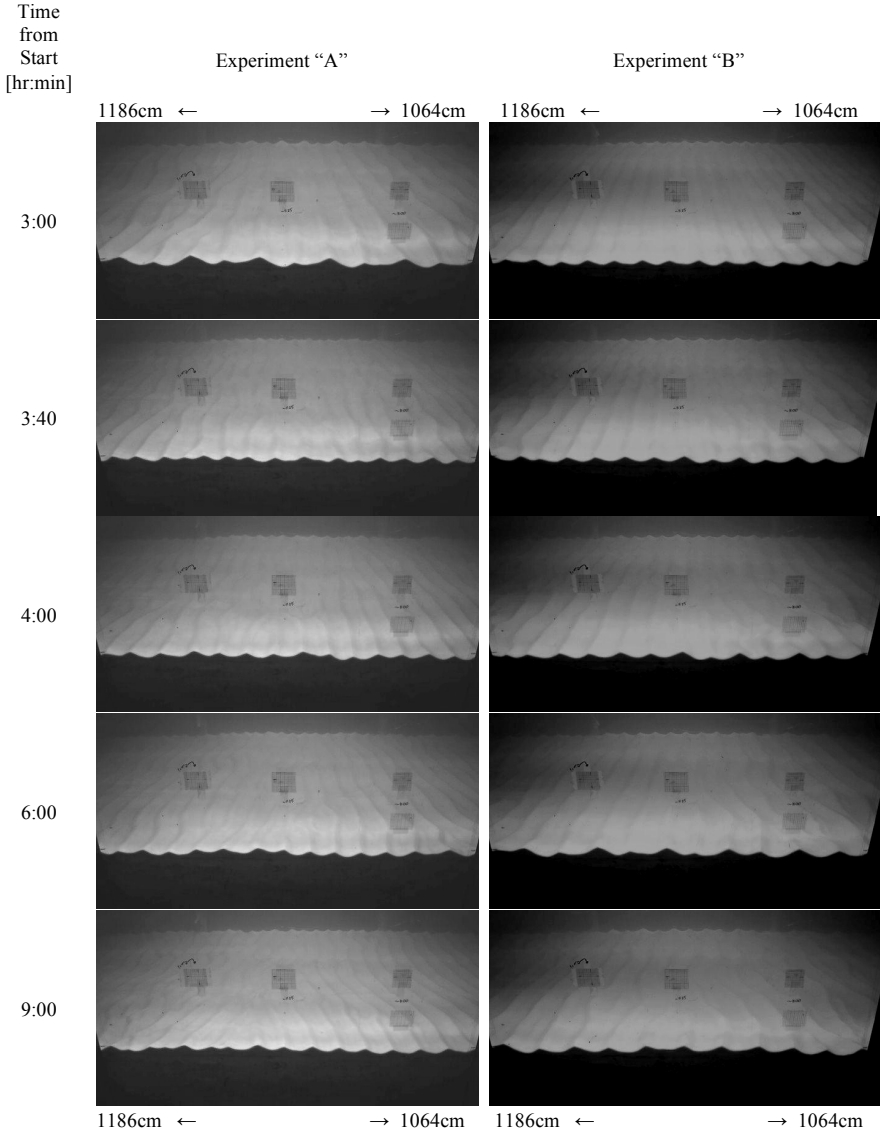

Figure 4: Sample results from the camera positioned over 1064cm to 1186cm from start of sand bed. (note: hr – hours and min – minutes)

CONCLUSIONS

The ripple measurements presented herein show that ripples under transient wave conditions achieve the ripple equilibrium for that specified wave condition provided there is adequate forcing time. For the wave conditions used in this study, 3 hours was ample time to reach the equilibrium conditions from an initially flat bed (with initiator ripples). The subsequent 3-hour block under the new wave forcing resulted in a sand bed which was not entirely uniformly 2-D; however dominant ripple equilibrium characteristics were apparent. The slight variations in 2-D ripples persisted even after an additional 3 hours.

FUTURE WORK

Future research will involve canceling the second harmonic using the method discussed by Madsen (1971). In order to allow total control of the waves, the wavemaker will be controlled via a personal computer rather than the current built-in function generator. Also, the internal screw drive on cart will be automated to allow the SeaTek to rapidly scan the bed, enabling additional three-dimensional scans at much shorter time intervals.

ACKNOWLEDGEMENTS

The authors wish to thank the US Office of Naval Research for financial support under Grant N00014-05-1-0083. Also, we wish to thank Francisco Pedocchi and other laboratory researchers for many valuable discussions. Finally, we would like to acknowledge Brett Zitny for his help with our laboratory experiments.

REFERENCES

Cataño Y, (2005) "Burial of short cylinders induced by local scour and bedform migration under waves plus current" Ph.D. thesis UIUC .

Doucette and O'Donoghue (2006). "Response of sand ripples to change in oscillatory flow," *Sedimentology* 53, 581–596

Faraci, C. and Foti, E. (2001) "Evolution of small scale regular patterns generated by waves propagating over a sandy bottom," *Physics of Fluids* Vol. 13, Num. 6

Madsen, O. S. (1971). "On the generation of long waves," *Journal of Geophysical Research*. 76, 8672–8683.

Rosengaus, M. M. (1987). "Experimental study on wave generated bedforms and resulting wave attenuation," Sc.D. thesis. M.I.T.

Smith, D. and Sleath, J. F. A. (2005). "Transient ripples in oscillatory flows," *Continental Shelf Research* 25 p.485–501

Testik, F. Y., Voropayev, S. I., and Fernando, H. J. S. (2005). "Adjustment of sand ripples under changing water waves," *Physics of Fluids* Vol. 17, Iss. 7, pp. 072104-072104-8.

Wiberg, P. L., and C. K. Harris (1994) Ripple geometry in wave-dominated environments. *Journal of Geophysical Research*, 99(C1):775-789.

ANALYSIS OF SEBASTIAN INLET, FL MORPHOLOGIC CHANGES USING COMPLEX EMPIRICAL ORTHOGONAL FUNCTIONS (CEOF)

Florian G. A. Brehin[1], Jo-Ann Rosario-Llantin[2], and Gary A. Zarillo[3]

1. Department of Marine and Environmental Systems 150 West University Blvd.
   Florida Institute of Technology Melbourne, FL 32901
   fbrehin@fit.edu
2. Department of Marine and Environmental Systems 150 West University Blvd.
   Florida Institute of Technology Melbourne, FL 32901
   jrosario@fit.edu
3. Department of Marine and Environmental Systems 150 West University Blvd.
   Florida Institute of Technology Melbourne, FL 32901
   zarillo@fit.edu

Abstract: Complex empirical orthogonal function (CEOF) analysis is applied to investigate the medium-term morphologic evolution of the ebb shoal at Sebastian Inlet, using a high resolution decadal dataset of hydrographic surveys. Results indicate that most of the variance (98.2%) is found in the first complex function (SM-1) interpreted as the average bathymetry, showing no significant time-dependent fluctuation. The second function (SM-2) accounts for 0.8% of the total variance and is dominated by a cross-shore transfer between the shoreward and leeward flanks of the shoal, as well as deposition from the ebb-jet and natural bypassing around the shoal. The temporal dependence (TM-2) showed large random changes that may correspond to bypassing activities in the inlet vicinity. The CEOF technique is successful in reproducing propagating sedimentation patterns not recognized by regular EOF, such as bypassing around the leeward flanks of the shoal, and cross-shore transfer around the terminal lobe and availability for bypassing.

INTRODUCTION

The long-term prediction of sediment transport and inlet/beach morphological changes is a difficult task since there is insufficient knowledge of the governing processes and how these processes are described in equation form (Larson *et al.*, 2003). Coupled with this limitation are nonlinear processes found within coastal systems that create chaotic behavior and restrict the effectiveness of physically based models. The alternative is modeling based directly on analysis of the sampled data for a particular study area such that one might capture the essential properties of beach morphology in time and space. The strength of data-based models is the replication of morphologic behavior without requiring insights into the physical processes. Although this causes concern when applying a model to different study areas, this can be alleviated by continuing efforts to link data-analysis results with knowledge of physical forcing (Larson *et al*., 2003).

As a first step toward data-based modeling, the application of principal components analysis (PCA) is utilized whereby the data are examined to identify and quantify (1) dominant patterns as they evolve in time and space and (2) how these patterns relate to one another. The added benefit of PCA in reducing large data sets to a few basic patterns is the ability to separate the signal (long-term morphological processes) from the noise (smaller scale processes and inaccuracies in measurement) within the data.

One particular form of PCA is Empirical Orthogonal Function (EOF) analysis, which projects the observed data onto a set of shape functions (the spatial EOFs) that are derived from the data itself. These functions are empirical in that they are defined by the covariant nature of the measured, long-term data set. They are orthogonal in that no two functions describe the same variance. The limitation of traditional EOF analysis to detect standing oscillations only, makes it difficult to accurately represent patterns that propagate with time. In order to determine characteristics of wave-like motions within the data (e.g. wavelength and wave speed of bedforms), complex EOF (CEOF) analysis must be performed where the phase information is retained for comparison to the amplitude. A few studies to date have been performed that employ CEOF analysis. Since CEOF captures both amplitude and phase information, the analysis performed by Liang and Seymour (1991) on nearshore bathymetric data efficiently described the fast moving sand wave and other propagating features in their study area.

Sebastian Inlet (Figure 1) is well documented in terms of wave climate and morphologic evolution. Hydrographic surveys of the inlet system and surrounding beaches were conducted on a semiannual basis since 1991. Although the data coverage (Figure 1) includes the entire inlet system (ebb shoal, throat, sand trap and flood shoal), and the adjacent beaches to the north and to the south, the present study focuses only on the ebb shoal complex. Volumetric analysis of the ebb shoal by Zarillo, *et al.* (2003) have shown that the inlet is in state of quasi-equilibrium, with impoundment of sand on the north beaches and the ebb shoal and a sand deficit on the beach immediately to the south of the inlet

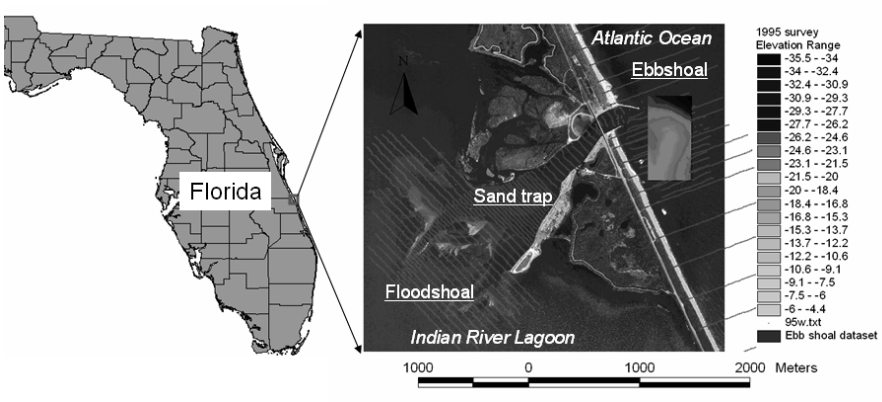

Figure 1 Study area. A TIN created from a mask to delineate the ebb shoal and generate different elevations on the grid from data (xyz) imported into ArcView® GIS.

Management strategies for sand budgets have included dredging, bypassing from an interior sand trap at the edge of inlet channel, and beach nourishment on the downdrift beaches. Net longshore sediment transport rates are directed southerly and estimates range from 120,000 to 230,000 m^3 per year (Dombrowski, 1993). This is mostly due to Northeasters occurring in the winter months creating strong southerly drifts, whereas tropical systems from the south tend to reverse longshore sediment transport to the north. In recent years, due fewer winter extratropical storms, the net drift has been from south to north therefore reducing the rate of ebb shoal growth and enhancing accretion of the south fillet. A previous study of inlet morphodynamics conducted by Goshow (2000) using regular EOF analysis determined standing sedimentation patterns and suggested a relationship with wave climate and engineering activities in the inlet vicinity.

The present study is the first attempt to apply CEOF analysis at a stabilized inlet to investigate ebb shoal morphodynamics and gain insight into the natural bypassing mechanisms. The study aimed at 1) identifying the main sedimentation patterns represented by each complex eigenmode, 2) determining possible seasonal variation in the patterns, and 3) evaluating the use of the complex EOF technique versus regular EOF technique in capturing the propagating sedimentation patterns of a very dynamic morphologic feature.

COMPLEX EMPIRICAL ORTHOGONAL FUNCTIONS

Preprocessing of data for CEOF analysis begins with obtaining a complex time series after applying a Hilbert transform on the scalar variable of interest. This approach, described in Equation (1), allows the amplitudes obtained to remain unchanged and extract information about the temporal phase of each component. In other words, the real part of this new complex time series retains the original data array information $z(x,t)$ whereas the imaginary part $\tilde{z}(x,t)$ (described as the Hilbert transform of the

original data set) provides the corresponding temporal phase information within the set.

$$Z(x,t) = z(x,t) + i\tilde{z}(x,t) \qquad (1)$$

The next step in the preprocessing of data for the CEOF method is to compute the complex covariance matrix of the newly formed complex bathymetry data set. Normally, the equation form of this step can be written as:

$$C = \frac{1}{N_x N_t} \sum_{n=1}^{N_x} Z_{jn}^* Z_{kn} \qquad (2)$$

That is, Equation (2) expresses the covariance relationship between the complex bathymetry matrix and its complex conjugate for the jth and k^{th} terms for the total of surveyed points N_x and the surveyed times N_t.

It is from the complex covariance matrix (C) that the eigenfunctions (eigenvectors (ϕ_n) and eigenvalues (λ_n)) are determined. Since the complex covariance matrix (C) is Hermitian combining the eigenvalues and the trace of the matrix will provide a direct measure of the variance (σ_n^2) that is comprised in each function (or mode) according to:

$$\sigma_n^2 = \frac{\lambda_n}{T_r(C)} \qquad (3)$$

The determination of the variance allows to establish which are the principal eigenfunctions that can be used to reduce (or compress) the information in the original data into fewer modes. Usually, most of the variance is expressed in three or five modes and therefore considered sufficient to reconstruct the original data. In this study only the first four modes are of interest.

Different approaches in the reconstruction of data from the CEOF modes exist and result from variations in the weights used in the computation of the complex empirical orthogonal functions. Although more rigorous approaches to the determination of the temporal and spatial weights exist the technique employed here yields similar results in a mathematically simpler and straightforward method.

The temporal modes (φ_n) are obtained from an equation of the form:

$$\varphi_n = \tilde{z}(x,t) - \bar{\tilde{z}}_x(x,t) \qquad (4)$$

The complex empirical orthogonal functions that describe the general shape of the data variability are termed spatial modes. To obtain these spatial modes (A_n),

$$A_n = \varphi_n \times \phi_n \qquad (5)$$

Usually, the first spatial mode describes the mean bathymetry featured in the data, the second and subsequent spatial modes describe the changes that occur to the mean bathymetry during the time span of the data series.

In order to have a better understanding of the magnitude in which the spatial and temporal modes affect the interpretation, scaling is performed on each of the temporal

and the spatial components. When using a covariance matrix, as was done in this analysis, every temporal function is scaled by the average of its absolute values. For the spatial functions, each is normalized by multiplying its temporal scale factor. With this procedure, every spatial function is then considered to represent average change (Goshow, 2000).

When reconstructing the bathymetry data from the selected principal modes, only the real part can be considered and it can be expressed in the form:

$$z(x,t) = \left[\sum_{n} real\left\{ A_n(x) \cdot \phi_n(t)' \right\} \right] + real\left\{ \overline{\tilde{z}}_x(x,t) \right\} \quad (6)$$

As previously discussed, the advantage of EOF and CEOF analysis is that most all of the variance is described by the first few modes allowing for data reduction. It is the analysis of these first few spatial modes that provides insight about the behavior of the physical processes captured within the data sets. When combined with the information described by the temporal weights (*i.e.* the temporal modes), a better understanding of the evolution of the bathymetric features can be obtained and their connection to natural and anthropogenic effects can be facilitated.

MEAN AND RECONSTRUCTED BATHYMETRIES

The mean bathymetry of the entire time series is shown in Figure 2-a. The bathymetry contours range from z = -10ft. at the top of the bypass bar (shallow region) to approximately z = -18ft. at the outer edge of the bar. There is a sharp drop in the elevation (z = -28ft.) to the NE of the bypass bar. The orientation of the bypass bar is clearly shown as being 45° to the shoreline and attaches to the downdrift beach as an attachment bar (SW corner of Figure 2-a).

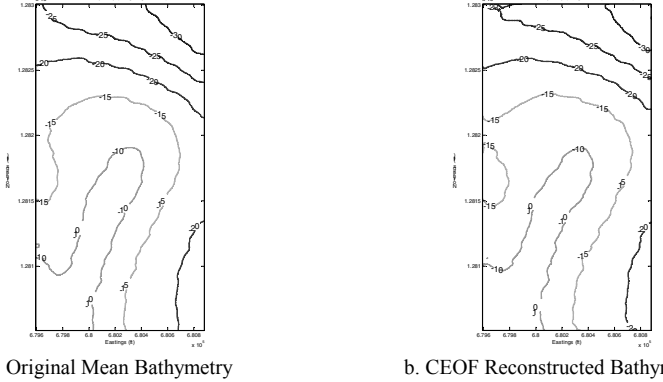

a. Original Mean Bathymetry b. CEOF Reconstructed Bathymetry

Figure 2. The mean bathymetry values of the original data set (a) and reconstructed bathymetry (b). Units are in feet for depth values and coordinates (Eastings and Northings).

As shown in Table 1, CEOF analysis on the morphological evolution of the bypass bar reveals that most of the variance is comprised into mode 1 (98.2%) which

represents the mean bathymetry. The subsequent modes reflect the other dynamic variations within the data and are interpreted according to the physical processes of the particular study area. In order to reconstruct the original data of any time series, the inclusion of at least the four most dominant modes is considered standard practice. The inclusion of these four modes represents 99.4% of the total variance.

Table 1. Percentage of variance represented by each mode.

MODE #	% of Total Variance	MODE #	% of Total Variance
1	98.153	11	0.032176
2	0.80106	12	0.026667
3	0.27903	13	0.021687
4	0.17225	14	0.020218
5	0.12497	15	0.016627
6	0.10314	16	0.013964
7	0.066099	17	0.011502
8	0.053469	18	0.010531
9	0.044016	19	0.0088727

In order to interpret the results correctly, values associated with the first complex eigenmode were directly added to the corresponding mean bathymetry in that year, whereas for higher eigenmodes these values were subtracted from the mean bathymetry. This allows for a more realistic description of the dynamics occurring at the study area. Thus, notice that in Figures 3-b to 3-d and Figure 4 lighter gray contour lines indicate erosion patterns, whereas darker gray contour lines correspond to accretion patterns.

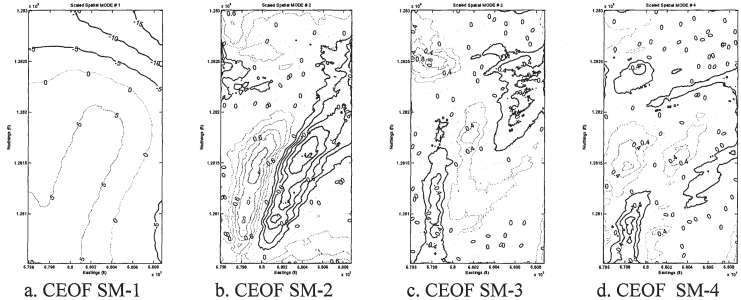

a. CEOF SM-1 b. CEOF SM-2 c. CEOF SM-3 d. CEOF SM-4

Figure 3. CEOF Spatial Modes 1-4. Gray indicate positive values (erosion); Black indicate negative values (deposition) except for SM-1 where the sign indicates deviations from the mean.

First Complex Eigenmode

The 10:1 ratio in scaling of spatial mode 1 (SM-1) versus the other three modes (Figure 3-a) reflects the predominance of the pseudo-mean bathymetry of the bypass bar. It is termed "pseudo-" because it is a result of the CEOF analysis and is called "-

mean" because the contours resemble the original data. Further, the variability in the first temporal mode shows no time-dependent fluctuation (Figure 4-a), which is in agreement with the minimal time-dependence characteristics of the mean-beach function. The temporal mode 1 (TM-1) showed an increasing trend until 1995, then decreased until late 1998, and increased again until 2000. This is in agreement with the phase shifts observed in late 1994 and late 1998. Positive jumps in the amplitude were observed in 1993, 1994, 1997 and 1999 and may correspond to sand inputs from mechanical bypassing projects. The amplitude and phase curves follow the same trend over the time period.

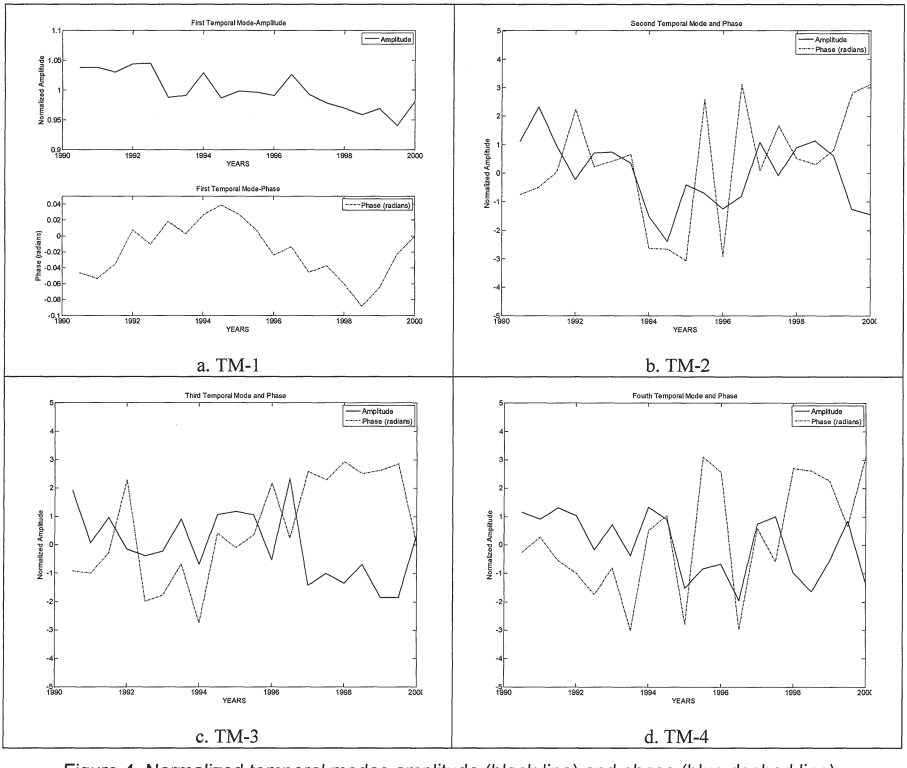

Figure 4. Normalized temporal modes amplitude (black line) and phase (blue dashed line).

Second Complex Eigenmode

Contour results for the second spatial function (SM-2) are presented in Figure 3-b. A significant cross-shore exchange of sediment is observed between the leeward and shoreward edge of the shoal. Maximum values of positive contours reach 0.6 ft, whereas negative contours attain values of -1.2 feet. Negative contours represent the tendency to decrease in depth therefore representing deposition. Further, the patterns

of the negative contours were found to extend much more to the Northeast of the study site, following the bathymetric contours. This would suggest an input from natural bypassing and a longshore component in the dominant patterns as well. Even though the majority of changes occur in the southern part of the domain, a smaller area with deposition pattern (negative contours) is observed in the NW corner of the contour plot, with values around -0.5 ft. This area corresponds to the terminal lobe of the ebb shoal, at the edge of the ebb jet.

To further investigate the evolution of the sedimentation patterns and the propagation of geomorphic features of the ebb shoal, a sequential representation of the fluctuating second, third and fourth complex eigenmodes is presented in Figure 5. The spatial evolution of mode 2 indicated two main patterns corresponding to a shift in the shoal's ridge position (Figure 5-a). During the first three years of the study, patterns were dominated by the erosion of the shoreward flanks of the shoal and deposition on the leeward flanks. At the same time, a deposition area was observed on the ebb shoal. From Fall/Winter 1994 to Spring/Summer 1997, a shift in the patterns was observed, with accretion on the shoreward flanks while the leeward flanks were eroding. At the same time, the deposition area from the ebb-jet was less pronounced, exhibiting no appreciable change tending to erode at a now reduced area closer to the inlet mouth. Finally, patterns were reversed again until the end of the study period. Changes in these patterns were represented by sharp reversals rather than smooth shift from erosion to accretion. To some degree, it appears as if the patterns of leeward accretion/shoreward erosion occurred right after the bypassing projects.

The second temporal mode (TM-2) of the ebb shoal presented in (Figures 4-b) showed large random changes, with no noticeable seasonal patterns. However, shorter trends within the time period consisted in a decrease in the normalized amplitude from summer 1991 to summer 1994, increasing again until 1999, toward equilibrium. A longer trend of approximately 20 months is revealed in the occurrence of consecutive positive as well as negative peak values. Although no explanation for this apparent cycle is offered, further investigation of this oscillation will be later explored. A closer look at the curves of normalized amplitude and phase revealed that they follow pretty much the same trends over the time period, with a positive peak in winter 1991 and negative peak in summer 1994. The positive jumps in TM-2 occurred subsequent to bypassing activities with a lag time of approximately a year. The noticeable peak in winter of 1991 occurs before the extreme storm season affecting the area, responsible for the subsequent decreasing trend in the amplitude. Events like the Halloween Storm of 1991, with wave heights of over 3m and periods of 20 seconds, lasted for several days later in Fall is therefore responsible for creating that major drop observable in the temporal amplitude of mode 2. The 3 year cycle was found to last until 1994 and was related to an active season for storms. The same area was nourished in 1992-93, but with half the volume and is associated with the peak at this time being less pronounced (Figure 4-b). Another major peak in the temporal variability of mode 2 occurred during the 1998-99 mechanical bypass project.

Third Complex Eigenmode

As indicated by Table 1, the third complex eigenfunction accounts for 0.27 % of the total variance, which is about three times less than the second eigenfunction. Spatial pattern fluctuations for the third complex eigenmode (SM-3) are shown in Figure 5-c. Unlike the SM-2, cross-shore patterns for SM-3 in the southwest part of the area were found to be reversed. Negative contours corresponding to sand deposition were identified on the shoreward flank of the shoal and positive (erosion) on the leeward flank. The linear shape of the contours was interpreted to describe a pattern of seasonal bar migration. In addition, the deposition area to the northwest corner of the domain previously identified for the SM-2 as a deposition zone, it is now related to erosion patterns for the SM-3.

Deposition was also observed farther offshore on the terminal lobe, suggesting a cross-shore exchange between the ebb shoal and terminal lobe. The spatial propagation patterns recognized in the third eigenmode showed a linked trend between the terminal lobe in northeast part of shoal to the shoreward flanks to the southwest, as well as a link between the leeward flank (southeast part) and the ebb shoal (northwest part), suggesting a complex transverse sediment flux involving several morphologic features.

The response of the third temporal eigenmode (TM-3) presented in Figure 4-c was found to exhibit a slightly decreasing trend over the time period, as well as an increased seasonality in the signal. Positive jumps in the normalized amplitude were observed mostly in summer; this is further discussed in the seasonal variability section. A noticeable phase shift was observed in Fall/Winter 1992 dataset, as well as in Fall/Winter of 1994. The amplitude and phase curves follow the same trends, with a slight phase lag until 1995 and then become out of phase, especially from 1996 to 2000.

Fourth Complex Eigenmode

The fourth complex eigenmode accounted for less than 0.2% of the total variance and the spatial patterns are represented in Figure 3-d. Patterns consisted of patches of deposition/erosion on the shoreward flanks of the shoal, as well as deposition around the outer area. There appears to be scouring at the edge of the main ebb channel from the ebb jet and at the reef rock outcrops (black, Figure 5-d). Again, cross-shore fluxes along the banks of the bypass bar are evident in the fourth spatial eigenmode (SM-4). A noticeable erosion area is located in the middle of the shoreward flank of the shoal. The temporal function (TM-4, in Figure 4-d) continues to emphasize the seasonality of the changes as discussed for mode 3. Clearly, these more variable patterns (mode 3 and 4) were associated with summer and winter changes in the physical forcing and seasonal comparison in the spatial patterns was performed between these modes to recognize any characteristics pattern of each season.



Figure 5. Spatial Modes 2 to 4. Lighter grays indicate positive values (accretion). Dark grays to black indicate negative values (erosion). White indicates zero change.

Seasonal variations in spatial eigenmodes

The CEOF analysis was performed on Spring/Summer and Fall/Winter data sets independently and contour plots for the third and fourth mode are presented in Figure 6. The two first modes are not shown since no significant seasonal differences in the

patterns were observed. However, significant changes in patterns were observed in the third and fourth modes, especially reversals in cross shore shoal motion. For the spatial mode 3 (SM-3 in Figure 6-a and 6-d), extended deposition along the shoreward flanks of the shoal (Figure 6-a southwest region) was observed during the Spring/Summer months whereas the opposite occurred during the Fall/Winter, including deposition on leeward side of the shoal. The deposition basin which corresponds to the other significant exchange feature is located father off the inlet mouth in Spring/Summer.

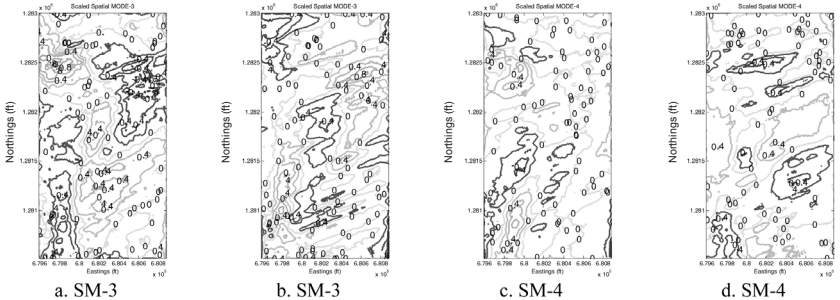

a. SM-3 Spring/Summer | b. SM-3 Fall/Winter | c. SM-4 Spring/Summer | d. SM-4 Fall/Winter

Figure 6. Spatial Modes for Spring/Summer (a, c) and Fall/Winter (b, d). Lighter grays indicate erosion; Darker grays indicate deposition.

This last observation could be related to seasonal differences in wave climate. Winter months are usually dominated by Nor'easters, and more deposition could be expected toward the inlet mouth and channel since sediment is being pushed by waves into that region. In summer, gentler wave climate and fewer high energy events occur so that the ebb jet extends the shoals farther offshore on to the terminal edge so that sand is available for bypassing to the south beaches in winter. The sand bar formation in the

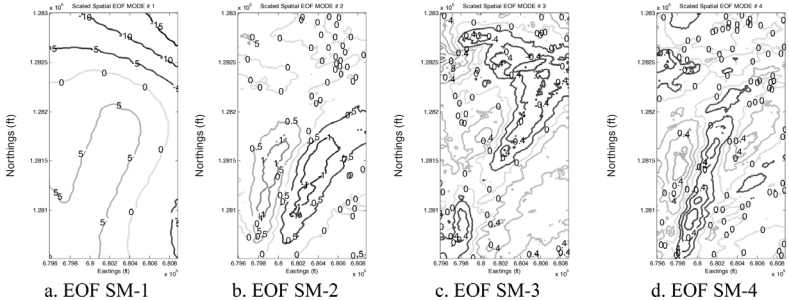

a. EOF SM-1 | b. EOF SM-2 | c. EOF SM-3 | d. EOF SM-4

Figure 7. Spatial Modes from regular EOF analysis. Grays are positive values (erosion); dark grays to black are negative values (deposition).

third eigenmode, in the south-west part of the area was located shoreward and had a very linear shape. However, patterns for Fall/Winter indicated a more discontinuous bar, located farther offshore and characterized by significant erosion towards the shoreward flanks of the bar as indicated by the light grey contour lines.

In addition to the CEOF analysis, regular EOF was performed on the same data sets for comparison of resulting patterns (Figure 7). Differences were notable in each of the higher order modes (SM-2, SM-3, and SM-4). For the second eigenmode (SM-2), the main difference is in the shape of the negative contours. It also seems that the second and fourth regular EOF modes (EOF SM-2 and SM-4) are described by the second complex eigenmode (CEOF SM-2), indicating that regular EOF is not as effective as CEOF in separating higher order modes. The elongated form of the pattern was not fully described by the regular EOF technique. Under Complex EOF analysis, sediment bypassing is more evident and clearly reproduced whereas the regular EOF technique did not fully recognized the propagating pattern.

SUMMARY AND DISCUSSION

The ebb shoal at Sebastian Inlet has a complex bathymetry, and the area experiences complex waves refraction patterns that create unique sedimentation patterns. In addition, these complex wave interactions may create localized reversals in the drift direction, meaning that under storm conditions (Northeasters) sediment pathways would be to the north, filling in the South fillet and inlet channel.

Several reversals in the patterns were observed in the second eigenmode (SM-2), and northward transport and channel infilling and impoundment of the south jetty seemed to occur when the shoreward flanks of the shoal are accreting. This very dynamic area often experiences a return of the longshore current that has been interrupted by jetties, wave induced currents, and by the rip currents that are enhanced by the reef outcrops. The predominance of the cross ridge exchange on ebb shoal morphodynamics suggested by Mode 2 may also be related to wave breaking and induced currents, suggesting that the bypass bar shares the morphodynamic characteristics of a shoreface rather than a shoal. The elongated shape of the deposition patterns of the second eigenmode (SM-2) also suggested the natural bypassing mechanisms and sand transfer from updrift to downdrift beaches, as well as from the swash bars and terminal lobe (from ebb-jet) to the bypassing and attachment bars. The deposition area at the mouth of the inlet is located farther offshore in Spring/Summer, which is consistent with the gentler wave climate in summer and dominance of ebb-jet sedimentation pattern rather than wave reshaping. This observation agrees with previous studies on natural bypassing at inlets which found that under normal or non-storm conditions, sand in the channel was moved in a net seaward direction and deposited on the terminal lobe (FitzGerald et al., 2000). The deposition area observed in Mode 2 at the end of the inlet mouth corresponds to the deposition basin of the ebb shoal, where sand is being deposited and available for being moved toward the terminal lobe and bypassed. This includes sediment being transferred directly from the updrift beach to the ebb shoal/bypass bar complex and from the main ebb channel.

The observation of the spatial evolution in the second and third eigenmodes also indicated that an important transfer mechanism was occurring between the ebb shoal deposition basin at the edge of the main ebb channel and the terminal lobe. The longshore influence is not evident and appears more clearly in Modes 3 and 4. The third and higher modes were associated with increased variability (chaos) of the area. Spatially this was represented by alternating patterns of accretion/erosion along the shoreward flanks of the shoal. The formation of a consequent sand bar suggested by the third eigenmode (SM-3) may be interpreted as the classic mean bar function. The bar was found to be more linear bar and located more shoreward in summer compared to a discontinuous bar located farther offshore in winter. This resembles the seasonal bar formation and beach profile evolution along the seasons.

CONCLUSIONS AND RECOMMENDATIONS

The morphologic evolution of the ebb shoal at Sebastian Inlet was analyzed using Complex EOF technique, from 1990 to 2000. The technique successfully identified the dominant sedimentation patterns and bypassing mechanisms occurring on the ebb shoal of a stabilized inlet. Patterns recognized by the second complex eigenmode included a cross-ridge sand transfer between the leeward and shoreward flanks of the shoal, deposition along the bypass bar and on the ebb shoal at the end of the main ebb channel. Reversals in the patterns were observed and temporal patterns indicated that the morphologic evolution of the shoal is a function of bypassing activities and irregular forcing mechanisms such as the number and intensity of storms, as well as changes in the drift direction. The third complex eigenmode represented the sand bar position and shape in the southwest area, as well as deposition on the terminal lobe. The seasonal comparison for the third and fourth complex eigenmodes was primarily a function of the wave climate. The ebb shoal morphodynamics in summer were controlled by tidally driven currents of the ebb-jet feature whereas wave induced transport dominates in winter.

The CEOF is a powerful technique which recognized more sedimentation patterns in each mode than the regular EOF, emphasizing the bypassing component identified in the second eigenmode, the deposition on the terminal lobe. CEOF was also more effective in describing the seasonal migration pattern of the bar in SM-3, as well as the propagating behavior of the terminal lobe which was being pushed away from the inlet mouth and made available for bypassing to the south beaches.

Although, the temporal modes are useful in relating the spatial patterns to possible forcings or management activities, some of the drastic changes accompanied with opposing temporal phase trends make it difficult to properly characterize the processes acting on the study area. Therefore, care must be taken in the interpretation of the data without prior knowledge of the basic dynamics of the study area.

This type of analysis can be useful in supporting the calibration of numerical models for morphology change. That is, considering that enough data is available, shorter model runs can be completed and still “catch” all the pattern changes described in the eigenfunctions of the hydrodynamic regime.

Additional accompanying analysis techniques and further investigation are required to provide a wholistic view of the dynamics around the Sebastian Inlet ebb shoal. It is suggested that a Canonical Correlation Analysis (CCA) should be performed to complement the CEOF analysis and to detect the possible correlations between morphological changes and the wave forcings. Although CCA is a powerful analytical tool in explaining the correlation between two different sets of data, the results are often difficult to interpret because of the multiple sets of new variables generated as its product. An effort to apply CCA to the present study data will be attempted by implementing the technique to a smaller (resampled) bathymetry data set. It is expected that this approach will yield faster computational times, but information on the higher order variability will be lost. It is therefore recommended that other techniques be attempted such as 3-Way EOF or Non-Linear EOF.

ACKNOWLEDGEMENTS

The authors would like to thank the Sebastian Inlet Tax District for providing the data. In addition we acknowledge Pamela J. Christian for her feedback and Dr. Eric Thosteson for his insight on coding CEOF and for instilling the motivation to publish the findings of what started as a class project.

REFERENCES

Dombrowski, M. R., 1993. Inlet and management practices: southeast coast of Florida. *Journal of Coastal Research,* Special Issue 18, 29-57.

FitzGerald, D. M., Kraus, N. C., and Hands, E. B., 2000. *Natural Mechanisms of Sediment Bypassing at Tidal Inlets. models, Technical Note*. ERDC/CHL CHETN-IV-30, Coastal Engineering Research Center, U.S. Army Engineer Waterways Experiment Station, Vicksburg, MS.

Goshow, C.K., 2000: Inlet morphodynamics determined by empirical orthogonal function. *Master's Theses, Division of Marine and Environmental Systems, Florida Tech,* Melbourne, FL.

Hoeke, R.K., 2001. Decadal time scale where morphodynamics determined from remotely sensed shoreline positions. *Master's Theses, Division of Marine and Environmental Systems, Florida Tech,* Melbourne, FL.

Larson, M., Capobianco, M., Jansen, H., Rozynski, G., Southgate, H.N., Stive, M., Wjinberg, K.M., and Hulscher, S., 2003. Analysis and modeling of field data on coastal morphological evolution over yearly and decadal time scales. Part 1: Background and linear techniques. *Journal of Coastal Research,* 19, 4, 760-775.

Liang, G., and Seymour, R.J. 1991.Complex Principal Component Analysis of Wave-Like Sand Motions". Proceedings of Coastal Sediments '91, Seattle, WA, pp. 2175-2186.

Ruessink, B.G., van Enckevort, I.M.J., Kingston, K.S., and Davidson, M.A., 2000. Analysis of observed two- and three-dimensional nearshore bar behaviour. *Marine Geology,* 169, 161-183.

Zarillo, G. A., Kraus, N. C., and Hoecke, R. K., 2003. Morphologic analysis of Sebastian Inlet, Florida: enhancements to the tidal inlet reservoir model. *Proceedings Coastal Sediments '03*.

INVESTIGATING SHIP INDUCED SCOUR IN A CONFINED SHIPPING CHANNEL

David Taylor[1], Kevin Hall[2], Neil MacDonald[3]

1. Cardno Lawson Treloar, Gordon, NSW, Australia. david.taylor@cardno.com.au
2. Queen's University, Kingston, ON, Canada. hallk@civil.queensu.ca
3. Pacific International Engineering, Ottawa, ON, Canada. nmacdonald@piengr.com

Abstract: Deep draft ships transiting through confined channels can significantly alter surrounding hydrodynamic conditions. The Burlington Shipping Channel is a confined channel on Lake Ontario which has experienced significant scour due to ship drawdown. A range of investigations including the development of an *SGH* model of the Burlington Channel have been undertaken to understand the processes leading to scouring near the channel walls. It is proposed the direction of ship motion is fundamental to the depth of scour observed at the entrances to the channel. The *SGH* model achieved a good level of hydrodynamic calibration and an assessment of modeled scour based on spatial variation in critical sediment size is consistent with observed scour patterns. The critical sediment diameter along the channel is an order of magnitude greater than the native bed material. In the mid-sections of the channel, scour potential is generally independent of direction of ship motion and consecutive ship movements in opposite directions appear to cause minimal net sediment transport. The development of design criteria curves for channel protection using the *SGH* model is presented.

INTRODUCTION

Deep draft ships transiting through confined, shallow water bodies can significantly alter the ambient hydrodynamic conditions. These impacts are observed through two main processes; wake and drawdown. Wake is the term given to the stern and bow waves generated by a moving ship. The waves propagate away from the ship and generally have periods of less than 10s. The character of wake waves is influenced by the vessel profile and ship speed.

Drawdown is the observed decrease in water level surrounding the ship as it moves through the channel and is primarily caused by the ship's displacement of the channel cross-section (Herbich and Schiller 1984). A feature of drawdown is the long period nature of the waveform in shallow, confined water bodies (surge wave). Although the amplitude of the surge wave may not be large, the period of this wave can be between 30 to 100 seconds. The orbital motion associated with the drawdown wave is relatively uniform through the water column and current speeds near the sea bed can be large. The surge wave generated by drawdown in confined channels is a function of ship speed, depth under the ship, drawdown height and blockage ratio (Maynord 2004). The blockage ratio is the wetted cross-section of the ship relative to the channel.

Wake and drawdown can interact with the surrounding shoreline and bed material, and shoreline erosion and bed scour due to ship movements has been observed at numerous sites.

BURLINGTON SHIPPING CHANNEL

Hamilton Harbour is a 2,150 ha protected body of water located on the western shoreline of Lake Ontario. It is located approximately 60 km southwest of Toronto and is a major industrial centre of Canada. Hamilton Harbour is the busiest Canadian Port on the Great Lakes. It handles over 700 ship passages and 12 million tonnes of cargo each year. The port is situated in a naturally enclosed basin separated from Lake Ontario by a narrow channel, the Burlington Shipping Channel. Recent studies have shown that sections of the Burlington Shipping Channel have been significantly scoured. In response, a series of data collection, engineering and numerical modeling investigations have been undertaken to investigate; the causes of scour, magnitude and spatial variation in the physical forcing causing scour and potential stabilization techniques.

Hamilton Harbour evolved with Lake Ontario during the glacial retreat approximately 9,500 to 12,500 years ago (Gilbert, 1994). Prior to 1823, a sand spit separated Hamilton Harbour and Lake Ontario with a shallow channel to the north of the present channel (O'Connor, 2002). The Burlington Shipping Channel was constructed in 1823 and is 88m wide with a design depth of approximately 9.5m to chart datum (CD). The channel is constructed with vertical sheet piles. The bed material within the channel and surrounding areas is generally a medium grain sand. Figure 1 is an aerial photo of the Burlington Channel.

A variety of different bulk carrier ships frequent Hamilton Harbor. The size of ships in the Great Lakes is limited by the capacity of the structures which facilitate vessel movement between the lakes and the Atlantic Ocean. In general, the ship specifications are relatively uniform due to the size constraints of the St Lawrence Seaway.



Fig. 1. Aerial view of the Burlington Shipping Channel

The most common ship type is the SeawayMax class which is the maximum sized vessel allowed in the St Lawrence Seaway. The maximum dimensions of ships in the St Lawrence Seaway are:-

- Length: 225.5m,
- Beam: 23.7m, and
- Draft: 8.1m.

Certain sections of the seaway can accommodate larger ships however these ships are unable to pass into the Atlantic Ocean. Depending on water levels, ships can move through some inner sections of the Great Lakes (including Hamilton Harbour) with a draft up to 9.5m.

SHIP DRAWDOWN IN CONFINED CHANNELS

Drawdown caused by deep draft ships in confined channels has been widely observed and studied. Schif (1949) developed the concept of the limiting speed in confined channels. This concept results in a self-propelled ship not being able to exceed a speed where the flow velocity (ship speed plus return flow speed under the ship) is equal to the celerity of a gravity wave.

A number of analytical methods have been developed from the initial work of Schif (1949) to estimate peak long period currents due to ship movements including PIANC (1987) and Maynord (1996). These methods have been shown to provide reasonable estimates of velocities and drawdown height away from the ship when applied to channels with simple cross-sections, for example rectangles or trapeziums. In these cases, the decay of the surge wave can be neglected. The analytical methods are unable to evaluate ship effects near channel transitions (Maynord, 2004)

In recent years, considerable efforts have been applied to develop numerical tools to investigate ship effects on spatial scale. Stockstill and Berger (1999) documented an extension of the finite element model HIVEL2D to investigate ship effects. The 2D

shallow water equations were modified to include the ship hull as a pressure source. The depth-averaged approximation can be made because the wavelength of the surge wave is in the same order of magnitude as the ship length, which is much greater than the depth in most navigation channels. The HIVEL2D drawdown model has been shown to produce good estimates of current speeds and surge wave heights in a number of studies (Stockstill and Berger 1999; Stockstill and Berger 2001; Maynord 2004).

STUDY APPROACH

A number of investigations were undertaken in 2005 and 2006 to study ship hydrodynamics and associated scour along the Burlington Shipping Channel. Those relevant to this study are briefly described below.

Site Data Collection

Bathymetric and hydrodynamic data was collected to examine the extent of scour and the physical forcing contributing to it. Figure 2 is produced from bathymetric survey conducted in May, 2005. Areas in dark blue indicate depths up to 14mCD, which is significantly greater than the design depth of the channel. The areas of scour are most pronounced across the eastern (Lake Ontario) entrance to the channel. There is also a smaller extent of scour observed surrounding the western (Hamilton Harbor) entrance and along the channel centerline.

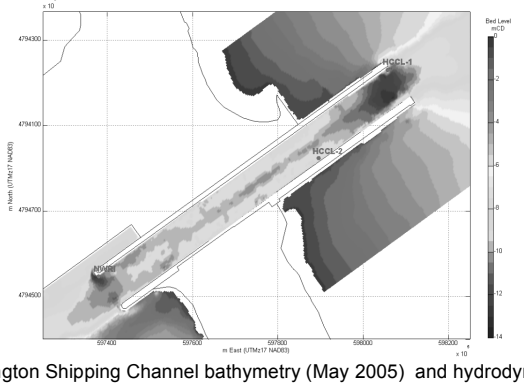

Fig. 2. Burlington Shipping Channel bathymetry (May 2005) and hydrodynamic data collection sites (scour areas are shown in dark blue).

In response to the scour observed in Figure 2, a field data collection exercise was undertaken in August to September 2005, to collect hydrodynamic data from a series of three locations in the channel during the transit of deep draft ships (HCCL, 2005). Acoustic Doppler Current Profiler (ADCP) instruments were deployed at a total of three locations for seven ship movements. The locations are indicated on Figure 2 (HCCL-1, HCCL-2 and NWRI). The ADCP instruments were configured to record currents in 0.3m bins through the water column every 0.5s. Ensembles were averaged every 5s. The dimensions (length, beam and draft) and approximate transit velocity were recorded for each ship movement.

Numerical Model Investigations – *SGH*

Following the field data and desktop engineering studies, an applied research study was undertaken to investigate the ship induced hydrodynamics and scour along the whole channel. The field data provided snapshot information on ship induced forces at particular locations. A suitability calibrated numerical model is able to investigate these forces along the whole channel.

SGH (Ship-Generated Hydrodynamics) is a sophisticated ship wake and drawdown model which is capable of efficiently investigating ship induced hydrodynamics over a large model domain with complex bathymetry. It is a 2D depth-averaged, finite difference model which can simultaneously simulate wake and drawdown processes due to deep draft ships. The motivation behind its development was the need to investigate the combined impacts of drawdown and wake along the St Lawrence River. *SGH* is a proprietary software product of Pacific International Engineering and was developed as part of the sediment transport software SedSim (Davies and Macdonald, 2001). The investigations at Burlington Channel have applied the drawdown module of *SGH* only. Wake is of only secondary importance at the Burlington Channel due to the sheet pile edge treatment of the channel.

SGH uses the same technique as the US Army Corp of Engineers' model HIVEL2D to model a vessel as a moving pressure field (Stockstill and Berger 1999). A spatial representation of the vessel hull is specified. *SGH* consists of two computational domains. The first is a temporally varying domain which propagates along with the ship. This domain features high resolution to resolve the steep gradients around the vessel. The results from this grid are superimposed on the overall model domain and all parameters are solved at each location on the grid.

Open or closed boundaries can be specified, and ambient hydrodynamic conditions, for example currents, can be specified along model boundaries. Energy absorption can be specified within the model to minimize reflections along boundaries. The model is sensitive to the shape of the vessel hull.

A full description of the development of *SGH* including model source terms is contained in Macdonald (2003).

RESULTS

Hydrodynamic Data

A full discussion of the hydrodynamic data collected at the Burlington Channel is contained in Taylor *et al* (2007). Maximum near-bed currents recorded during the ship movements were:-

- HCCL-1: 1.6m/s
- HCCL-2: 1.1m/s
- NWRI: 0.8m/s

Figure 3 is a plot of the current profile through the water column at Location HCCl-1 during a ship movement. Bin 1 refers to near-bed current speeds and Bin 48 near the water surface. The current profile is relatively uniform.

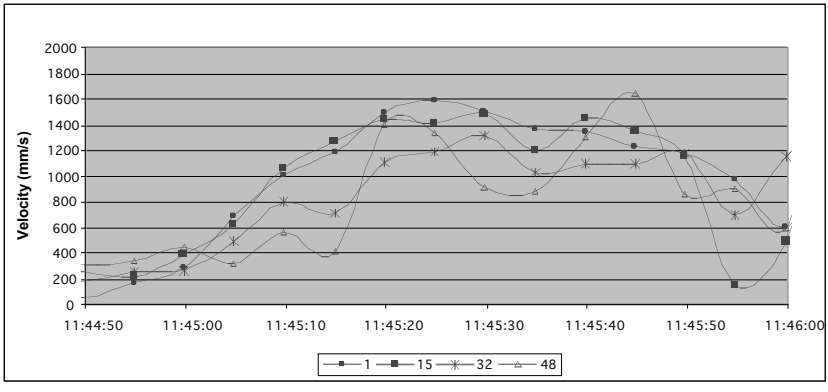

Fig. 3. Vertical velocity profile at Location HCCL-1 during an east bound ship movement.

Conceptual Scour Model

Based on the observed hydrodynamic conditions described in Taylor *et al* (2007) and the bathymetric survey of the channel, a conceptual scour model of the Burlington Channel has been developed.

A number of studies have been undertaken into the properties of the surge wave generated by large ships in confined channels including Herbich and Schiller (1984). In general, ships passing through a confined channel generally causes a significant drop in initial water level in front of the ship, and a resulting surge as the ship proceeds along the channel. The surge wave propagates in the opposite direction to ship motion.

The ADCP current data collected at Burlington Channel was found to be consistent with Herbich and Schiller (1984). In all cases, the direction of the peak near-bed current was in the opposite direction to the motion of the ship. The direction of ship motion is significant on the magnitude of observed currents near the entrances. At Location NWRI, largest currents were observed during the west bound movement of ships, and at Location HCCL-1 the largest currents were observed during east bound ship movements. At Location HCCL-2, a large difference in current magnitude between east and west bound ships was not observed.

Following the initial review of the field data and available literature, two key outcomes were evident; sediment transport potentially occurs along the whole channel, not only at

the entrances, and that the scour pattern observed at the entrance is similar in nature to that observed at channel constrictions.

Of the scour areas identified in Figure 2, the most significant are near the channel walls at the western and eastern entrances. There is evidence of scour in the order of 0.5m up to 300m east of the western entrance (Fig. 2). The scouring of the channel centerline is a result of the jet induced by the ship propellers and does not impact on any of the surrounding structures. The conceptual sediment transport model focuses on the physical processes that lead to the scour at each entrance and along the channel piers.

The observed currents in the mid-section of the Burlington Channel are large enough to initiate motion of medium grain sand material. Therefore sediment transport is expected to occur along most of the Burlington Channel. The absence of scour in the middle sections of the channel is the result of no net sediment transport occurring over a longer period of time. Ships have to enter and leave Hamilton Harbor through the Burlington Channel. As a result there is an equal number of ship movements in each direction. In the mid-sections of the channel the sediment transport induced by a ship moving in a particular direction is counteracted by ship movement in the opposite direction. As a result, over the long term little net sediment transport occurs.

The Burlington Channel acts as a flow constriction to ship induced flow at both the Hamilton Harbor (western) entrance and the Lake Ontario (eastern) entrance. Investigations undertaken by Gill (1981) illustrate the general scour processes near a confined channel. Importantly, the scour at the entrance to the confinement is significantly larger than in downstream sections of the channel. The physics behind this outcome can be explained by the behavior of shear stress surrounding an obstruction. Investigations undertaken by Molinas *et al* (1998) quantified the shear stress concentrations surrounding a vertical wall obstruction in a channel. This work showed that bed shear stress concentrates near the upstream toe of an obstruction.

A consequence of this constriction effect is that bed shear stresses are highest when flow is being directed towards the entrances of the Burlington Channel from outside the channel. The field data indicated that current speeds at both entrances were highest when the ship induced flow was heading into the channel. The larger currents and scour observed at the eastern entrance is the result of a larger confinement ratio between the channel and adjoining water body. Bed shear stress investigations by Gill (1981) indicated that the bed shear stress near a contraction was a function of the confinement ratio between the upstream and downstream sections of the constriction. At the Burlington Channel, the confinement ratio at the eastern entrance which adjoins Lake Ontario is significantly larger than for the western entrance. As a result the scour magnitude and extent is larger at the eastern entrance. It is proposed that the scour pattern observed at the entrances to the channel are an imprint of the bed shear stress during ship movements causing flow into the channel. That is, east bound ship movements cause the greatest scour at the eastern entrance when currents caused by the

drawdown are directed into the channel, and similarly west bound ships produce the greatest scour at the western entrance.

Numerical Model Investigations – *SGH*

Model Calibration

Simulations were undertaken for each of the seven observed ship movements. Figure 4 is a time series plot of model (solid red) and measured (dashed blue) current speed, current direction and water level during the west-bound movement of a SeawayMax vessel (*Canadian Transport*) at Location HCCL-2 (mid-channel). Calibration in the mid sections of the channel was better than at the entrances where three-dimensional processes associated with the flow acceleration are more significant (Taylor *et al*, 2007).

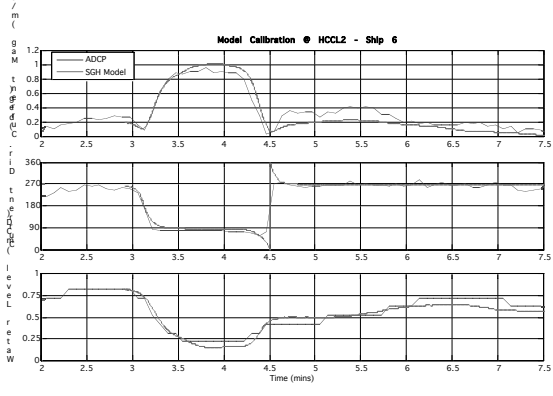

Fig. 4. Calibration of the *SGH* model at Location HCCL-2.

Overall the model calibrated well to the available field data; however, it must be noted that due to the two-dimensional assumption of the model, the magnitude of currents in the immediate vicinity of the western entrance, and to a larger extent the eastern entrance, will generally be underestimated within the model. In the application at the Burlington Channel, 'slip' boundary conditions were employed along the channel walls to achieve a good level of calibration. A full description of the calibration of the *SGH* model of Burlington Channel is described in Taylor *et al* (2007).

Critical Sediment Diameter and Scour Potential

A general formula to estimate potential scour due to ship induced scour (due to drawdown) in and near confined channels is not available. In order to investigate the potential spatial variation in scour depths along the Burlington Channel, the spatial variation in critical sediment diameters has been determined from the peak currents determined by the *SGH* model during a theoretical ship movement. As highlighted in Figure 3, the velocity profile through the water column during the peak of the surge

wave does not observe a logarithmic profile. Therefore, instead of using Shields formula to estimate critical sediment diameter of bed material in the channel, the Isbash formula was adopted. This method does not assume a velocity profile and the calculated peak velocity from the *SGH* model (depth-averaged) was adopted as the near-bed velocity. The form of the Isbash equation used in this study is shown in Equation 1.

$$D = b\frac{v^2}{2g\Delta} \tag{1}$$

where D = sediment diameter (critical), v = peak velocity (near-bed), g = acceleration due to gravity ($9.81 m^2/s$), Δ = relative density (1.65), and b = turbulence coefficient. A value of 0.7 was adopted for b which is typical of normal turbulent flow.

SeawayMax ship specifications and a speed of 3.5m/s were adopted for these investigations. East and west bound ship movements were simulated to quantify the influence of ship direction on forcing contributing to the observed scour. As the *SGH* model is not designed to resolve the hydrodynamics within the immediate vicinity of the ship and under the ship, areas within 10m of the ship path have been neglected from this study.

Figures 5 and 6 present the critical sediment diameter (mm) for east and west bound ships respectively. Comparing the two results, at the western end of the channel, the model predicts significantly larger critical sediment diameters in the western section during east bound ship movements. This is consistent with the observed scour pattern (Fig. 2) where some degree of scour occurs up to 200m east of the western entrance. At the western entrance itself, the model predicts larger critical sediment diameters during west bound ship movements.

At the eastern entrance, east bound ships produce larger critical sediment diameters. The model predicts the largest critical sediment diameters approximately 250 to 350m from the western entrance along the northern pier. However, the magnitude of the critical sediment diameter in this region is generally similar for east and west bound ships. As the direction of sediment transport varies with ship direction, assuming equal numbers of ship movements in each direction the model is consistent with the observation of minimal net scour over time in this region (Fig.2). Overall, along the channel piers the model predicts critical sediment diameters in the order of 30mm to 60mm.

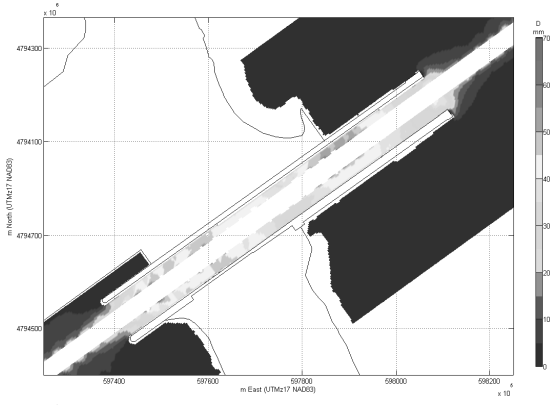

Fig. 5. Critical sediment diameter (m) during east bound movement.

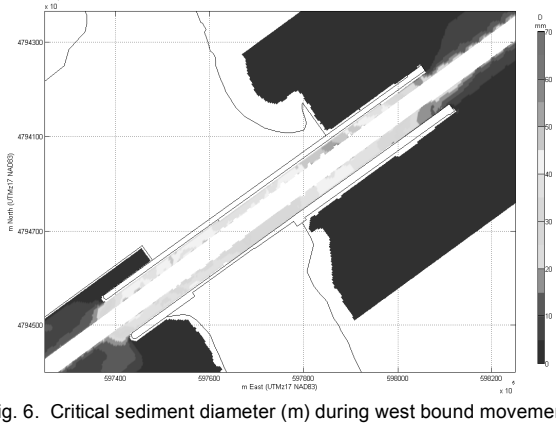

Fig. 6. Critical sediment diameter (m) during west bound movement.

DISCUSSION

The *SGH* model of the Burlington Channel demonstrated a good degree of hydrodynamic calibration, particularly in the mid-sections of the channel. At the channel entrances, the two-dimensional assumption of the model appears to underestimate potential currents near the entrances (Taylor *et al* 2007). Investigations into critical sediment sizes throughout the channel using the *SGH* model indicate that net scour is concentrated at the channel entrances. There is significant variation in scour potential at each entrance depending on the direction of ship motion. Greater scour is observed at the eastern entrance due to the larger confinement ratio.

Investigating potential scour within the channel using the variation in critical sediment size between east and west bound ship movements is a simplified approach. Scour within the Burlington Channel and near the entrances will be influenced by a range of

additional factors including the upstream (relative to the current direction) supply of sediment. Figure 7 presents a relative comparison of observed scour (left) and modeled potential scour (right). Areas in red indicate scour areas. It is evident that the model is consistent with the observation that bed levels within the mid-sections of the channel over time are relatively stable despite the hydrodynamic forces being sufficient to move the native bed material. Over time, the equal numbers of ship movements in the each direction appear to cancel out potential scour. Overall, the extent of scoured areas near the entrances is smaller for the model compared to the observed extent.



Fig. 7. Measured (left) and modeled scour areas (right)

Numerical models such as *SGH* are particularly suited to engineering applications. Theoretical design criteria for peak current speed and wave height associated with the surge wave have been determined throughout the Burlington Channel to further investigate the physical processes which cause scour. A series of simulations with a range of ship draft and speed combinations have been undertaken to determine design criteria curves for bed protection at the locations in Figure 8. The following parameters have been adopted for these simulations:-

- Ship speeds: 2m/s, 2.7m/s, 3.5m/s and 4.0m/s
- Ship draft: 7.75m, 8.5m and 9.25m

These parameters encompass the full range of ship speed and draft specifications which may be expected. SeawayMax specifications for ship length and beam were adopted. A water level of 0.5mCD (74.7mIGLD85) was adopted and this value is reflective of the mean water level in Lake Ontario.

The peak current speed, current direction and surge wave magnitude for each location have been obtained from each simulation. Design plots for surge wave amplitude and peak current speed based on ship speed and draft have been prepared. The plots are presented in a dimensionless form.

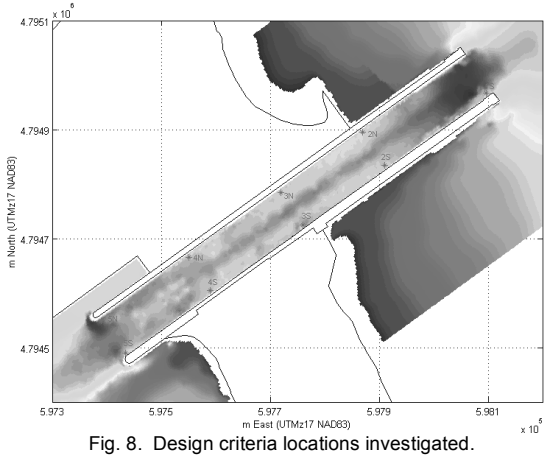

Fig. 8. Design criteria locations investigated.

The x-axis quantity is the ship Froude number as described by Herbich and Schiller (1984). The ship Froude number is described by Equation 2.

$$Fr_{ship} = \frac{v_{ship}}{\sqrt{gd}} \tag{2}$$

where v_{ship} is the ship velocity and d is the ship draft.

The surge wave plots have a y-axis of described by Equation 3.

$$\frac{H_{surge}}{d} \tag{3}$$

where H_{surge} is the amplitude of the surge wave and d is the ship draft.

The peak current speed plots have a modified Froude number for the y-axis described by Equation 4.

$$Fr_{Upeak} = \frac{u_{peak}}{\sqrt{gd}} \tag{4}$$

where u_{peak} is the peak current speed of the surge wave and d is the ship draft.

Figures 9 to 13 present dimensionless design criteria plots for peak current speed and surge wave height at Locations 1N, 2N, 3N, 4N and 5N respectively. The plots for the corresponding locations along the southern wall have been omitted because they show the same general trend as the northern locations. In these plots, west bound ship

conditions are shown in red and east bound ship conditions are shown in blue. Least squares fitted quadratic curves are shown in solid lines and 95% confidence intervals are enclosed by the dashed lines.

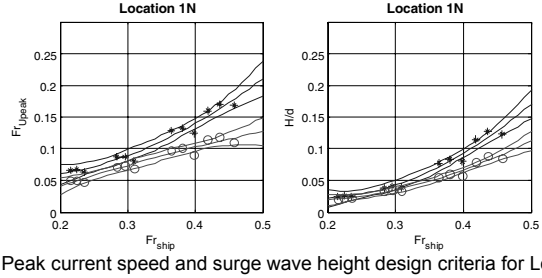

Fig. 9. Peak current speed and surge wave height design criteria for Location 1N (West bound (o), East bound (*))

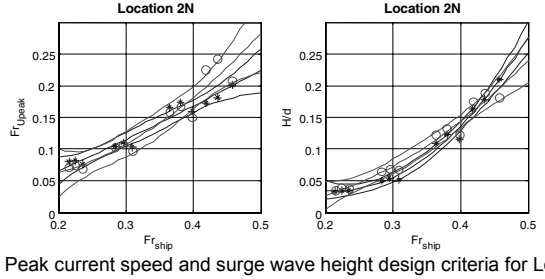

Fig. 10. Peak current speed and surge wave height design criteria for Location 2N (West bound (o), East bound (*))

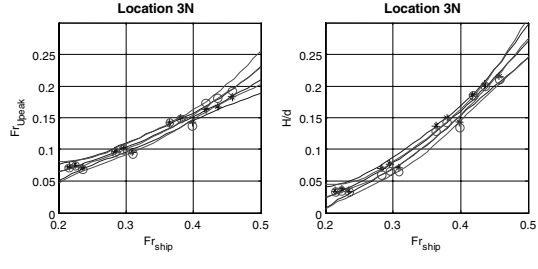

Fig. 11. Peak current speed and surge wave height design criteria for Location 3N (West bound (o), East bound (*))

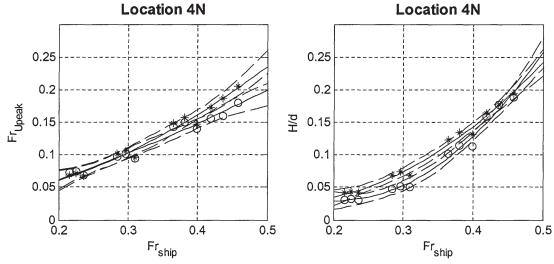

Fig. 12. Peak current speed and surge wave height design criteria for Location 4N (West bound (o), East bound (*))

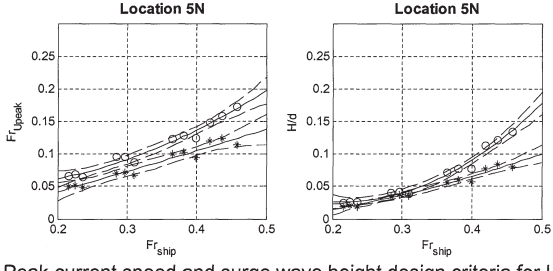

Fig. 13. Peak current speed and surge wave height design criteria for Location 5N (West bound (o), East bound (*))

East bound ship movements produce critical design conditions at Location 1N and west bound movements produce critical design conditions at Location 1S. This is consistent with observed conditions at Burlington Channel and the conceptual scour model where east-bound ship movements produce peak currents which are directed into the channel. Similarly, at Location 5N, west bound ship produce the critical design conditions. In the middle section of the channel east and west bound ship movements produce similar design conditions.

CONCLUSIONS

Investigations into ship induced scour in a confined channel, the Burlington Shipping Channel, have been undertaken. Measured hydrodynamic data together with bed survey data highlighted the significance of contracting flow at the channel entrance on observed scour patterns. An *SGH* numerical model used to simulate the surge wave generated by ships moving through the Burlington Channel has been developed. This model achieved a good degree of hydrodynamic calibration, particularly in the mid-sections of the channel. The model generally underestimated potential current speeds near the eastern entrance channel where the confinement induced by the channel causes significant flow acceleration.

The critical sediment size investigations with the *SGH* model indicate that the model can identify areas with significant scour potential. The model has been used to produce theoretical design criteria relationships for bed protection along the channel. Models such as *SGH* can provide significant value to engineering investigations associated with channel scour. Ship induced scour investigations near major hydraulic controls, for example strongly confined entrances, require comprehensive hydrodynamic data collected at the site.

ACKNOWLEDGEMENTS

The authors wish to thank Riggs Engineering and HCCL, Canada for allowing their data to be utilized in these investigations. Pacific International Engineering, Ottawa generously provided *SGH* and technical assistance for this project. The work at Queen's University was made possible through funding by Cardno Lawson Treloar, Sydney.

REFERENCES

DAVIES M.H., and MACDONALD N.J., (2001). *SedSim2001 – Transport Modelling Tools.* Prepared for the Canadian Hydraulics Centre, Ottawa. HYD-TR-063 Engineering, Ottawa.

GILBERT R., (1994). A field guide to the glacial and postglacial landscape of southeastern Ontario A field guide to the glacial and postglacial landscape of southeastern Ontario. Geological Survey of Canada. Bulletin 453 pp 74.

GILL M. A. (1981). "Bed Erosion in Rectangular Long Contraction". *Journal of Hydraulic Engineering*. Vol 107 (HY3).

HCCL. , (2005). Burlington Channel Ship Movement and Channel Scour Investigation. HCCL, Kingston, Canada.

HERBICH J.B., and SCHILLER R.E., (1984). Surges and Waves Generated by Ships in a Constricted Channel". *In* EDGE B.L. (ed.) *Coastal Engineering – 1984*. New York, USA. ACSE, pp. 3213-3226.

MACDONALD N.J., (2003). Numerical Modelling of Coupled Drawdown and Wake. *Proc Canadian Coastal Conf*. 2003, Kingston, ON. 16 pp.

MAYNORD, S.T., (1996). *Return velocity and drawdown in navigation channels.* US Army Engineer Waterways Experiment Station, Vicksburg, Mississippi, 1996, Technical Report HL-96-7.

MAYNORD, S.T., 2004. Ship effects at the bankline of navigation channels. *Maritime Engineering*, 157(MA2), 93-100.

MOLINAS A., KHEIREDLIN K., and WU B., (1998). "Shear Stress around Vertical Wall Abutments". *Journal of Hydraulic Engineering*. Vol 124(8), pp 828-830.

O'CONNNOR K.M., (2002). *Remedial action plan for Hamilton Harbour: Stage 2 Update 2002.* Prepared for Hamilton Harbour RAP Stakeholder Forum. ISBN 0-9733779-0.

PERMANENT INTERNATIONAL ASSOCIATION OF SSOCIATION NAVIGATION CONGRESSES (PIANC). Guidelines for the Design and Construction of Flexible Revetments Incorporating Geotextiles for Inland Waterways. Brussels, Supplement to Bulletin No. 57, 1987.

SCHIJF J.B., (1949). *Proceedings of the 17th International Navigation Congress.* (Lisbon, Portugal 1949). Section 1 Subject 2, pp. 67-78.

STOCKSTILL R.L., and BERGER R.C., (1999). *A two -dimensional flow model for vessel-generated currents.* Prepared for the U.S. Army Engineer District, Rock Island, U.S. Army District, St Louis and U.S. Army District, St Paul. ENV report 10.

STOCKSTILL R.L. , and BERGER R.C., (2001). Simulating barge drawdown and currents in channel and backwater areas. *Journal of Waterway, Port, Coastal and Ocean Engineering*. Vol 127(5), pp290-298.

STRAUB L.G., (1934). "Effect of Channel Contraction Works upon Regimen of Moveable Bed Streams". Transactions, American Geophysical Union.

TAYLOR D.R., HALL, K., AND MACDONALD N., (2007). "Investigations into ship induced hydrodynamics and scour in confined shipping channels". Proceedings of the 9th International Coastal Symposium, Gold Coast, Australia. Abstract accepted for publication.

EVOLUTION OF GRAIN-SIZE DISTRIBUTION ON BOGUE BANKS: IMPLICATIONS FOR SELECTION OF BORROW MATERIAL

Timothy W Kana

Coastal Science & Engineering, PO Box 8056, Columbia, SC 29202-8056 USA. tkana@coastalscience.com

Abstract: Bogue Banks, North Carolina is 40 kilometers (km) long and has received 6.6 million cubic meters of nourishment in the past five years. Six borrow areas of varying quality have been used ranging from fine, muddy sand in a federal dredge disposal area to coarse, shelly sand in an offshore borrow area. Composite sediment samples representing the native beach (foredune to low-tide terrace) were sampled before nourishment in June 1999 and after nourishment in November 2006. Profiles have been surveyed along the beach and combined by reach to form composite sections before and after nourishment. This paper provides representative pre/postnourishment grain-size distributions (GSDs) and composite profiles to illustrate similarities and (mostly subtle) differences between the native and nourished beaches. Despite some wide differences in GSDs, the nourished beaches and inshore morphology were generally maintained in the postnourishment profile. Additional sediment sampling and profiling are being conducted to quantify differences among the Bogue Banks projects.

INTRODUCTION

A widely accepted tenet of beach nourishment design is that the borrow source should attempt to match the native grain-size distribution (NRC 1995). It is presumed that if the nourishment material is similar to the native beach sediment, the project will perform as a natural beach (ie, erode at approximately the same rate), and environmental impacts will be minimized. Because discrete sediment samples tend to have a unique size distribution, common practice is to pool results of many samples in such a way as to define a composite size distribution both for the native beach and for a prospective borrow area. These composite grain-size distributions can then be compared to judge how closely the borrow source matches the beach. The analysis is even further reduced when applying accepted sediment compatibility models, such as the James (1975) overfill factor (R_A), which require only four measures: mean size and sorting parameter of the native and borrow sediment.

Using data from North and South Carolina nourishment projects, we find that traditional compatibility analyses work acceptably where there is little variation in sediment size distribution over the littoral profile (eg, South Carolina fine-sand beaches). Composite native size distributions in these cases tend to consist of well-sorted (poorly graded) sediments with a distinctive mode and an easily computed mean (cf, Kana and Mohan 1998). South Carolina beaches tend to maintain simple profiles with a narrow dry beach, wide wet beach, and little offshore topography. Given the relative homogeneity of sediments across most South Carolina beaches, finding and identifying matching sediments for nourishment is fairly straightforward.

Many North Carolina beaches, by contrast, consist of poorly sorted sediments (in the composite). Large variations in grain size occur across the profile, which in turn, probably accounts for the complexity of topography and persistence of an offshore bar. Commonly, North Carolina beaches have relatively wide, dry-sand berms, narrow wet-sand beach faces, and a nearshore platform on which a breakpoint bar forms. Mean grain size tends to go from fine sand in the dunes to coarse sand in the inner surf zone, then back to fine sand over the bar. This multi-modal size distribution does not lend itself to simple classification based on a single mean grain size. Selection of borrow sources, in these cases, should seek the broadest range of sizes possible. If the full spectrum of sizes is placed on the beach via hydraulic fills, the presumption is that waves will sort the sediments and better reproduce the cross-profile grain-size variations observed on the natural beach.

Bogue Banks, North Carolina (Fig 1), provides an example of a beach that has received multiple nourishments in the past five years in discrete segments using six borrow sources. This paper compares the prenourishment and postnourishment beach in terms of the changes (or similarity) of sediment grain-size distribution and profile development. Sediment comparisons are limited to the visible beach (dune to low-tide terrace), because that zone served as the initial baseline condition for selection of borrow areas for the majority of the shoreline (CSE–Stroud 2001).

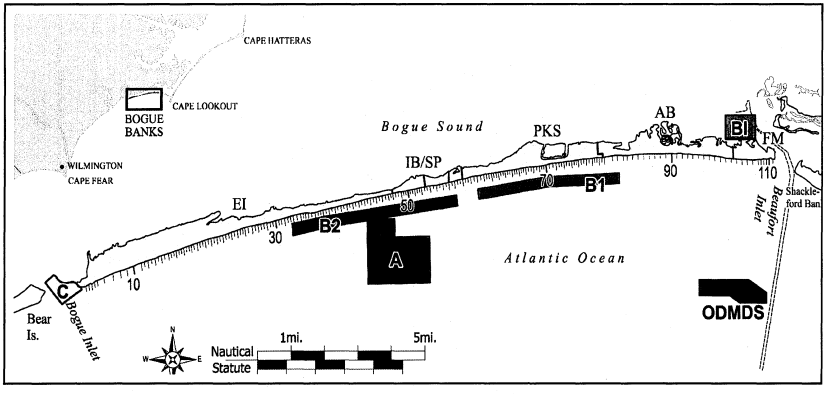

Fig 1. Bogue Banks, North Carolina. Communities: AB – Atlantic Beach; PKS – Pine Knoll Shores; IBSP – Indian Beach/Salter Path; EI – Emerald Isle. Borrow areas utilized for nourishment 2002–2005.

SETTING

Bogue Banks is a 40-kilometer-long (25 miles) barrier island trending east-west and bounded by large tidal inlets: Beaufort Inlet to the east and Bogue Inlet to the west. Situated about 25 km from Cape Lookout, Bogue Banks is sheltered from northeast storm waves but exposed to seas and swell from the southeast and southwest. Tide range is approximately 1.1 meters (m) (3.6 feet), average significant wave height is of the order 1.2 m (3.9 ft) (Roessler 1998) and **net** sediment transport is indeterminate based on available hindcast data and erosion rate information, but is likely to be of the order 50,000 cubic meters per year (m^3/yr) or less (CSE–Stroud 2001). Beach sediments typically vary across the profile with fine sand (~0.25 mm diameter) in the foredune, medium to coarse sand on the berm (0.35-0.6 mm), and fine sand on the outer bar (~0.2 mm diameter). Estimated profile closure depth in this setting is in the depth range –15 to –20 ft mean sea level (Bodge et al 2006, CSE 2006).

Four municipalities and one state park form the political boundaries along the island (east to west): Fort Macon State Park, Atlantic Beach (AB), Pine Knoll Shores (PKS), Indian Beach/Salter Path (IBSP), Emerald Isle (EI).

The beach has been relatively stable over the past 50 years with erosion rates averaging ~0.6 meters per year (m/yr) (2 ft/yr) (NCDENR 2004 – http://dcm2.enr.state.nc.us/Maps/ER_1998/SB_Factor.htm). The island contains well-developed dunes with over 5 m (16.5 ft) relief in the foredune (typical). Serious erosion first impacted Atlantic Beach in 1954 (Hurricane *Hazel*), because it was the center of development along the island. Seawalls built in response to storms and erosion eliminated much of the dry beach in this locality by the 1970s (Pilkey et al 1975).

NOURISHMENT PROJECTS

Prior to 1999 only Atlantic Beach and Fort Macon State Park had been nourished. These are sites of federal dredge-disposal projects with large inputs in 1986 and 1994 (USACE 1993). Much of this material was obtained from a US Army Corps of Engineers dredge disposal area – Brandt Island (Fig 1, labeled BI). Maintenance dredging of the Beaufort Inlet navigation channel and Morehead City Harbor uses Brandt Island for disposal. This diked containment area is periodically pumped out to Atlantic Beach so it can be reused. Anecdotal information indicates the 1986 and 1994 pump-outs introduced large quantities of fine sand and mud with much of the material moving offshore. The sediments remaining on Atlantic Beach by 1999 were well-sorted fine sand (CSE–Stroud 2001).

Several hurricanes impacted Bogue Banks in quick succession between 1996 and 1999 with *Floyd* (September 1999) causing extensive property damage along PKS, IBSP, and EI. Atlantic Beach sustained almost no dune recession and served as a model for other communities considering nourishment. By 2001, the remaining towns along Bogue Banks had initiated nourishment projects using several different sand sources.

Between 2001 and 2005, 6.6 million cubic meters (8.6 million cubic yards) were added to the beach, advancing the shoreline an average of ~23 m (75 ft). Virtually the entire length of Bogue Banks received new sand during this period (Fig 2). Of the total volume placed since 2001, 70 percent has been retained between the base of the foredune and the outer bar [measured to –11 ft NGVD 1929 vertical datum which approximates –3 m (–10 ft) mean sea level]. The remainder is accounted for between the outer bar and depths of –6 m (–20 ft) (CSE 2006). The principal storm events since nourishment were Hurricane *Isabel* (September 2003) and *Ophelia* (September 2005), both of which made landfall as Category 1 storms in this locality. Hurricane *Ophelia* caused upward of 1.2 million cubic meters of erosion (~17 percent of the nourishment volume) along the subaerial beach to the outer bar and accounts for much of the visible sand losses and profile adjustment.

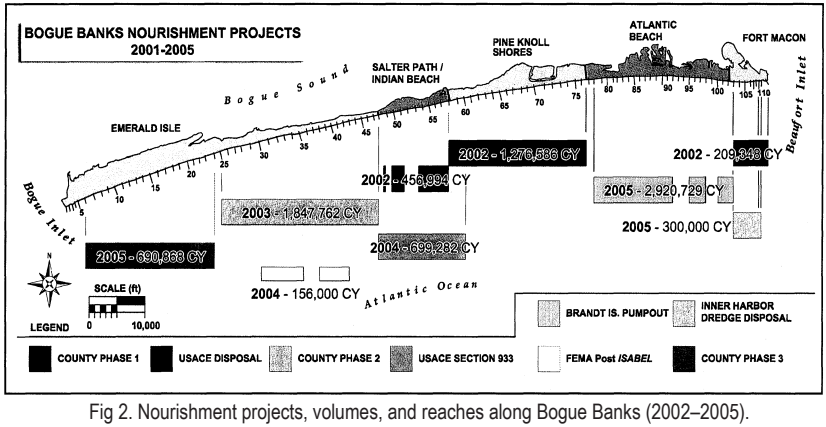

Fig 2. Nourishment projects, volumes, and reaches along Bogue Banks (2002–2005).

BORROW SOURCES

Six sand sources have been used for nourishment along Bogue Banks with estimated percentages of the aggregate volume placed.

BI – Brandt Island (33 percent) – Federal dredge spoil containment basin which was pumped out and deposited along Atlantic Beach and Fort Macon State Park in 1986, 1994, and winter 2005.

Offshore Area A and B1 (20 percent) – Used for PKS and IBSP in 2002.

Offshore Area A and B2 (23 percent) – Used for EI in 2003.

ODMDS (10 percent) (Ocean Dredge Material Disposal Site) – Utilized for federal Section 933 projects to IB/SP and eastern EI in 2004 (Fig 2).

Bogue Inlet (Area C) (8 percent) – used for western EI in 2005.

Outer Harbor Channel (6 percent) – Beaufort Inlet used for Fort Macon State Park in 2002 and 2005.

Geotechnical studies by CSE–Stroud (2001) sampled the native beach (subaerial portion to the low-tide terrace), Brandt Island, Bogue Inlet, and offshore areas A, B1, and B2. Later sampling was performed in the ODMDS. Composite samples (pooling groups of beach samples and groups of offshore borings) were used to determine sediment compatibility of potential borrow sources. The beach was resampled in 2006 at the same localities for comparison after nourishment and profile adjustment. In some localities, the fill has had four years to adjust while in most areas there has only been 1–2 years of adjustment. All localities were impacted by Hurricane *Ophelia* after nourishment, but before the 2006 samples were collected.

PRENOURISHMENT TO POSTNOURISHMENT SEDIMENT GRAIN SIZES

Figures 3–7 show representative composite grain-size distributions for prenourishment conditions (June 1999), postnourishment (November 2006), and the respective borrow area used. (Note: Where more than one area has been used, the dominant one is compared.)

Atlantic Beach (Fig 3) is the only section of Bogue Banks with fine sand. It was nourished in 1986 and 1994 using Brandt Island spoil sediments, so the "native" grain-size distribution (GSD) differed from the rest of the island. Its 2005 nourishment also utilized Brandt Island. Borrow material tested finer (mean = 0.203 mm), but the postnourishment result on the subaerial beach is incrementally coarser than the prenourishment condition (mean before = 0.237 mm, mean after = 0.256 mm). (Note the near-uniformity of the 1999 and 2006 size frequency curves.) CSE (2006) estimated ~0.8 million cubic meters (~35 percent) of the nourishment volume were eroded during placement and shifted seaward of the outer bar. The portion lost and

portion retained within the subaerial beach are reflected in the difference between borrow frequency curve and the native beach. The fine fraction in this case shifted offshore, leaving the coarser fractions along the berm and swash zone where all sampling took place.

Pine Knoll Shores and Indian Beach/Salter Path were nourished in 2002 (Phase 1 of a three-phase project), and eastern Emerald Isle was nourished in 2003 (Phase 2) using sand from offshore Area A (~50 percent), Area B1 (~25 percent), and B2 (~25 percent). Figure 4 shows pre/postnourishment composite GSDs (1999 versus 2006). Figure 5 compares the offshore borrow areas with the 2006 composite, and Figure 6 compares the ODMDS (used for a limited reach) with the 2006 beach. In this case, two offshore borrow areas (B1 mean = 0.276 mm, and B2 mean = 0.313 mm) had a significant fine-sand fraction, but they also contained an admixture of coarser sediments making the deposits poorly sorted and strongly coarse-skewed (CSE–Stroud 2001). Borrow Area A (mean = 0.525 mm) was the coarsest of the three offshore sites with the flattest GSD frequency curves.

These deposits were selected for use in the Phase 1 and Phase 2 projects because of their proximity to nourishment areas and their lower overfill ratios. The coarse material consisted largely of crushed shell which became controversial in this jurisdiction. Prenourishment shell content on the subaerial beach averaged ~15 percent, whereas borrow Areas A, B1, and B2 averaged ~40 percent. The result after profile adjustment shows a good match of the modal grain size (~0.30 mm) but retention of a significant coarse fraction in the gravel range (>2 mm diameter). Retention of coarse material is believed to account for reduced sand losses compared with Atlantic Beach (CSE–Stroud 2001). By 2006, the percent shell ($CaCO_3$) had reduced to ~21 percent along the Phase 1 and Phase 2 reaches.

Western Emerald Isle (Phase 3) was nourished using sediment from Bogue Inlet (Area C mean = 0.313 mm). The pre/postnourishment composites (Fig 7) yield an excellent match with the borrow composite (prenourishment mean = 0.341 mm, postnourishment mean = 0.332 mm). In this case, the means, modes, and shape of the frequency curves are nearly identical after 1.5 years of fill adjustment.

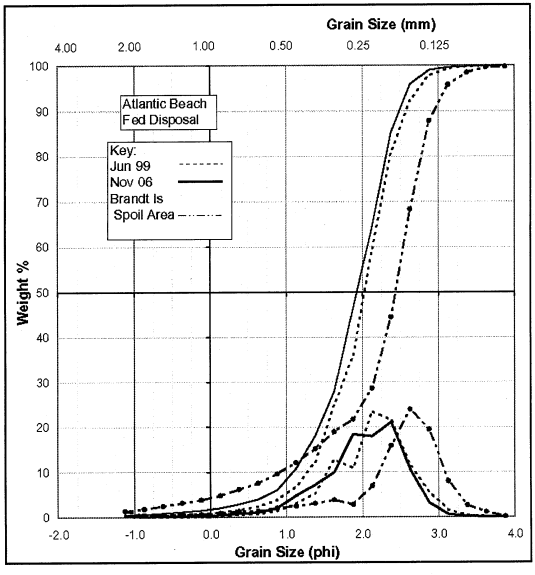

Fig 3. Atlantic Beach composite sediment GSD: Toe of Dune to Low Tide Terrace, before and after nourishment. Brandt Island (BI) was the borrow area.

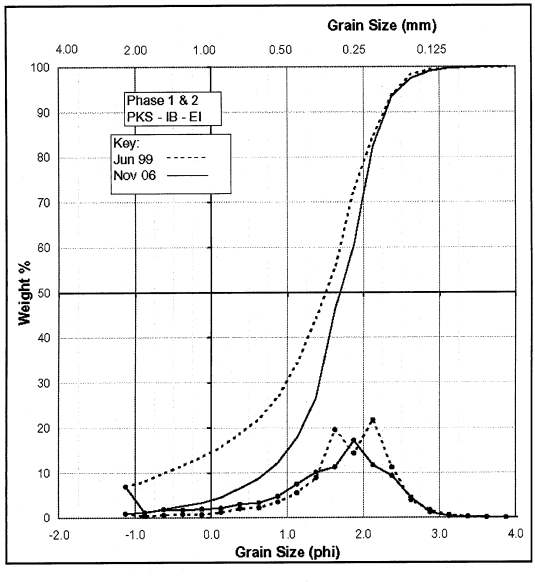

Fig 4. Phases 1 and 2 (PKS, IBSP, and eastern EI) composite sediment GSD before and after nourishment.

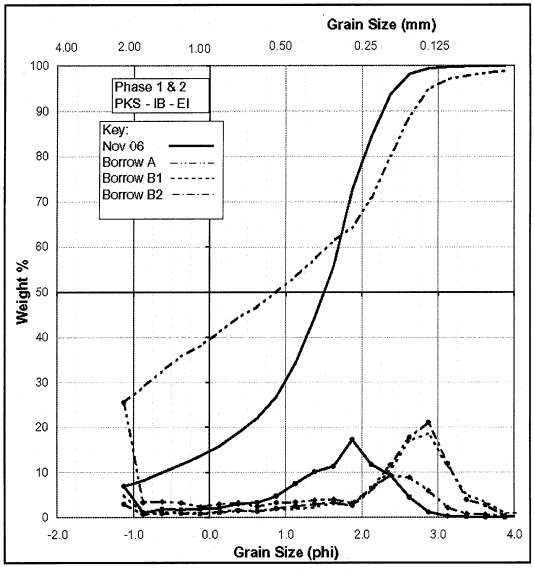

Fig 5. Phases 1 & 2 composite GSD for PKS, IBSP, and eastern EI after nourishment versus offshore borrow Areas A, B1, and B2 used for ~85 percent of the nourishment along this reach.

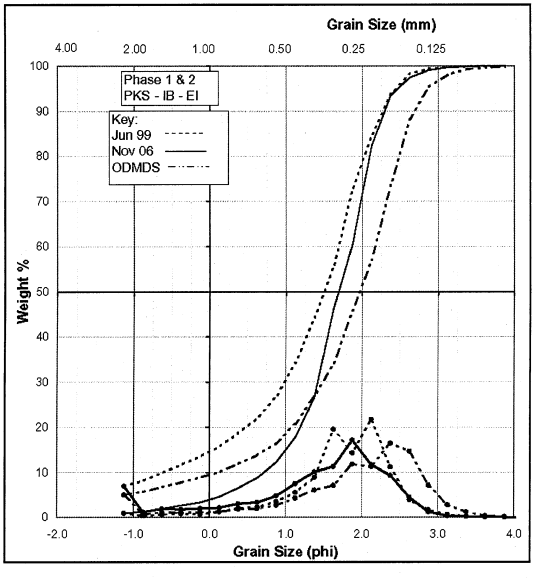

Fig 6. Phases 1 & 2 composite GSD for PKS, IBSP, and eastern EI versus the ODMDS borrow area used for ~15 percent of the nourishment along three communities.

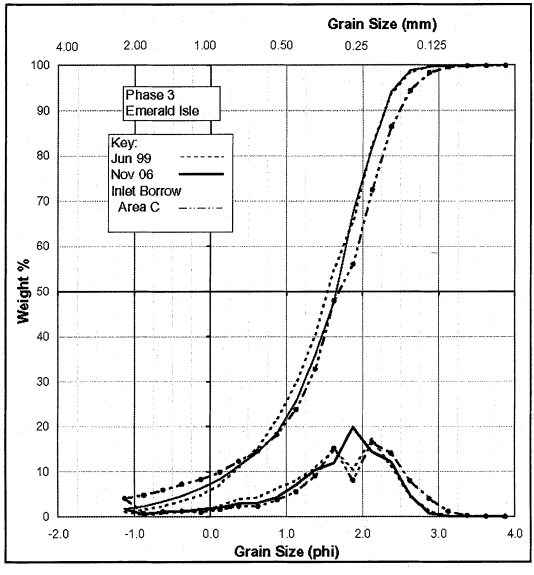

Fig 7. Phase 3 (western EI) composite sediment GSD before and after nourishment. Bogue Inlet Area C was the borrow area.

PROFILE EVOLUTION

Island-wide surveys are available for several years between 1999 and 2006. Figures 8 and 9 illustrate the typical evolution of the profile for portions of Atlantic Beach and Indian Beach/Salter Path since nourishment [see CSE (2006) for a comprehensive data set]. The profiles before and after nourishment have been matched at the mean high water contour to illustrate changes or similarities in shape and position of the active surf zone.

Profile shape in the surf zone reflects the mixing and sorting of nourishment sediments. The degree of similarity of shapes, therefore, reflects the match of borrow and native sediments on the beach. In both examples, the postnourishment shape closely matches the prenourishment shape in the principal breaker/swash zone [+5 ft to –7 ft NGVD; equals (~)+1.2 m to –2.5 m MSL]. The Atlantic Beach profile generally lacked a distinctive offshore bar prior to nourishment—instead demonstrating a series of inflections in the offshore profile. The general morphology was retained after nourishment, although the underwater inflection points varied. Note how closely the beach face slopes match (average is 0.032 between the +5 and –7 ft NGVD contour).

Indian Beach was nourished with much coarser sediment (similar to its native). The postnourishment profile retains the steeper inshore slope (~0.042) and topography of the offshore bar. Relief of the trough-bar system is greater, but the width of the trough and height of the outer bar are similar to prenourishment conditions.

One might expect such similarities in profile shape if the nourishment (section) volumes were small. But in both examples, the nourishment was substantial, displacing the shoreline 20–40 m. As a result, the native sediments remain largely buried under the nourishment sands.

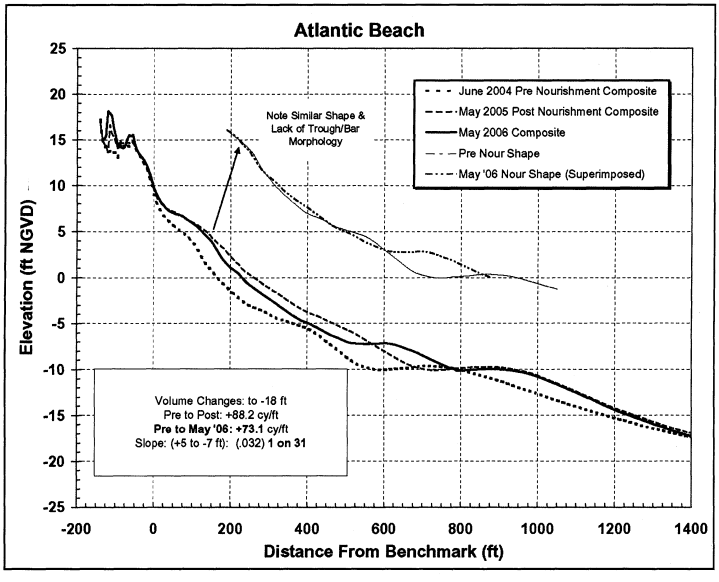

Fig 8. Pre/postnourishment profiles (composites) for Atlantic Beach. Surf zone to outer bar section has been displaced and overlain to illustrate similarity of postnourishment shape and slope.

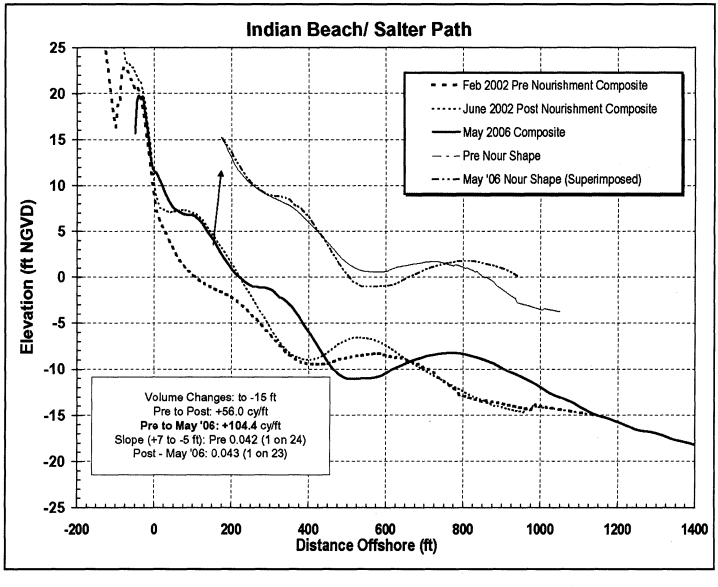

Fig 9. Pre/post nourishment profiles for IBSP. Note retention of shape, morphology, and general dimensions.

IMPLICATION FOR DESIGN

These preliminary results suggest that the inner surf zone and profile of a nourished beach can adopt a similar slope and morphology as the native beach if the borrow area matches the native beach closely (ie, Bogue Inlet – Area C), or if the mean grain size of a poorly sorted deposit matches the native beach (ie, Phases 1 and 2 areas using offshore Areas A, B1, and B2). The result for Atlantic Beach suggested that the sediments in the Brandt Island borrow area would not have produced a similar profile as native along PKS, IBSP, and EI because they were much finer. The resulting beach-face slope for AB was ~1 on 32 versus ~1 on 24 along the Phase 1 and Phase 2 communities. AB's borrow material resulted in a good match with that native beach segment largely because it had been nourished previously in 1986 and 1994 using similar fine-grained sediment.

The NC Coastal Resources Commission has recently adopted sediment grain-size standards for the state to insure that excess fines or excess gravel and shell are not placed on state beaches by nourishment projects (cf, http://www.nccoastalmanagement.net/sediment.htm). While such regulations are a step forward, mean sediment grain size should also be matched wherever possible to avoid changes in beach slopes and morphology. Placing 0.2-mm sediment along all of Bogue Banks, in effect, would flatten the beach face slope and reduce or eliminate bar-trough morphology. Conversely, placing much coarser material on the beach may result in a persistent lag deposit and produce steeper-than-native slopes. Additional sampling is needed to quantify these effects.

ACKNOWLEDGMENTS

This work was conducted as part of the design services contracts between the towns of Emerald Isle, Pine Knoll Shores, and Indian Beach (NC) and the author's company. Philip McKee, Trey Hair, Diana Sangster, and Kim Baker assisted with data collection, laboratory testing, and preparation of the manuscript.

REFERENCES

Bodge, KR, SC Howard, and EJ Olsen. 2006. Regional sand transport study: Morehead City Harbor federal navigation project. Summary Report to Carteret County Board of Commissioners; Olsen Associates Inc, Jacksonville (FL), 108 pp.

CSE. 2004. Survey report 2004, Bogue Banks, North Carolina. Monitoring Report for Carteret County Shore Protection Office (CCSPO), Emerald Isle, North Carolina; Coastal Science & Engineering (CSE), Columbia (SC) and Morehead City (NC), 82 pp + 4 appendices.

CSE. 2006. Survey report 2006, Bogue Banks, North Carolina. Monitoring Report for CCSPO, Emerald Isle, North Carolina; CSE, Columbia (SC), 95 pp + 4 appendices.

CSE–Stroud. 2001. Environmental Impact Statement, Bogue Banks beach restoration plan. EIS for NC Department of Environment and Natural Resources, Division of Coastal Management; submitted by Carteret County (NC); prepared by CSE and Stroud, Sections 1–6 and Apps A–G.

James, WR. 1975. Techniques in evaluating suitability of borrow material for beach nourishment. Rept No TM-60, CERC, US Army Waterways Experiment Station, Vicksburg (MS).

Kana, TW, and RK Mohan. 1998. Analysis of nourished profile stability following the fifth Hunting Island (SC) beach nourishment project. Jour Coastal Engineering, Vol 33, pp 117-136.

NRC. 1995. *Beach Nourishment and Protection.* Committee on Beach Nourishment and Protection, Marine Board, Commission on Engineering and Technical Systems, National Research Council; National Academy Press, National Academy of Sciences, Washington (DC), 334 pp.

Pilkey, Jr, OH, OH Pilkey Sr, and R Turner. 1975. How to live with an island: a handbook to Bogue Banks, North Carolina. NC Dept Nat and Econ Resources, Raleigh (NC), 119 pp.

Roessler, TS. 1998. Effects of offshore geology and the Morehead City harbor project on eastern Bogue Banks, North Carolina. MS Thesis, Univ North Carolina, Chapel Hill, 112 pp.

USACE. 1993. Environmental assessment and finding of no significant impact. Disposal of dredged material on the ocean beach of Bogue Banks from combined maintenance dredging and deepening of Morehead City harbor and pumpout of Brandt Island upland diked disposal site, Carteret County, NC. Wilmington Dist, US Army Corps of Engineers, 12 pp + app.

NEW FINDINGS IN EQUILIBRIUM GRAIN SIZE DISTRIBUTION

Jordi Galofre[1], Raúl Medina[2], Gabriela Medellin[3], César Vidal[4]

1. Tarragona Coastal Service, Coastal Directorate, Ministry of Environment, Pl. Imperial Tarraco 4-4fl., 43005 Tarragona, Spain. jgalofre@mma.es.
2. Ocean and Coastal Research Group, University of Cantabria, Avda. de los Castros s/n. 39005 Santander, Spain. medinar@unican.es.
3. Ocean and Coastal Research Group, University of Cantabria, Avda. de los Castros s/n. 39005 Santander, Spain. gabriela.medellin@alumnos.unican.es.
4. Ocean and Coastal Research Group, University of Cantabria, Avda. de los Castros s/n. 39005 Santander, Spain. vidalc@unican.es.

Abstract: One of the key elements in predicting beach fill performance is the evaluation of the "compatibility" of beach sands. Several formulations have been proposed to estimate the "compatibility" or "overfill" ratio. Most of them assume that both native and borrow sand has a log-normal grain size distribution. Log-normal distribution has long been accepted as the most adequate distribution for characterizing marine sediment samples. Furthermore, Galofre and Medina (2000) showed that for specific conditions of the marine dynamics a log-normal grain size distribution is achieved as the final equilibrium distribution of a sediment deposit. However other distributions, such as weibull or hyperbolic distributions, have also been proposed to represent sediment samples. In this paper, new field data are analyzed in order to further explore Galofre and Medina (2000) equilibrium grain size distribution hypothesis and to identify those situations in which sediment samples do not fit a log-normal distribution.

INTRODUCTION

The equilibrium beach profile concept suggests that beaches respond to wave forcing by adjusting their form to an equilibrium or constant shape attributable to a given type of incident waves. Since profile shape is just a consequence of sediment reallocation, the equilibrium concept should be also valid for cross-shore grain size distribution. The existence of an equilibrium grain size distribution was theoretically showed by Galofre

and Medina (2000). These authors showed that for specific conditions of the acting dynamics and of the sediment characteristics, a log-normal grain size distribution is achieved as the final equilibrium distribution. Furthermore, some relation between the wave dynamics characteristics and the grain size distribution was also found (Galofre and Medina 2000; Galofre and Medina 2001)

Several authors had previously suggested that log-normal distribution can be used as a good estimation of the grain size distribution, (e.g. Krumbein 1938; Inman 1953; Moutzouris 1988; Moutzouris 1991; Medina et al 1994). However, other authors had suggested that log-normal is not the most appropriate distribution to characterize the grain size distribution. These authors claim that in some cases, log-normal distribution doesn't provide an adequate adjustment of extreme points of distribution. Furthermore, other authors have showed that bimodal samples can be fit using overlapping log-normal distributions.

Log-hyperbolic distribution has also been used on sediment grain size distribution characterization as an option to traditional log-normal. Log-hyperbolic distribution is defined by four parameters and is shown in log-normal scale like a hyperbola. The parameters can be related to mean, standard deviation, symmetry, and kurtosis. The domain variation in the last two parameters are a triangle, hyperbolic triangle shape, in those can be found the samples according the distribution shape, hyperbolic or other limit shape (Normal or Gaussian) and they are related to erosion or accretion. The comparison between log-normal and log-hyperbolic distributions (Wyrwoll and Smith 1985) has been made in desert dunes. The log-normal distribution can be seen as the limit case of a log-hyperbolic distribution.

Fredlund et al. (2000), developed an equation defined by five parameters for one-modal samples that fits better in well graded samples than log-normal with two parameters, specifically in mud and clay materials. The obtained values for R^2 were of 0.999, a reasonable number considering that many parameters were used to ensure a better adjustment. Other authors used Weibull's distribution functions in order to fit multi-modal samples. This author concluded that log-normal distribution performs equal or better for fluvial or lake sediment samples while Weibull distribution fits better for multi-modal samples.

From the above paragraphs it can be concluded that a general consensus on the distribution to be used or the reason why one distribution fits better or which distribution should be used in a particular marine environment, does not exist.

It is worth noting that the analytical method proposed by Galofre and Medina (2000) stated that if a turbulent dynamic acts on a sediment deposit no matter what grain size distribution, the eroded material has a log-normal distribution. The non eroded sediment deposit will have the initial distribution minus the log-normal eroded part. Note that the sediment deposit that is found at a particular time in a specific marine location could be the eroded part or the non-eroded part of a previous sediment deposit. For instance, the

beach bar is the eroded sediment part during the bar formation (eroded from the berm) and it is the non-eroded part during the beach recovering stage.

The above mentioned statement is illustrated in figure 1. In this example, an initial uniform distribution, P_0, is forced by 20 events of turbulent dynamics. After these 20 events, the initial volume, (V_0) is partially eroded and becomes (V_N), as some volume (V_E) has been eroded. V_E has a log-normal grain size distribution.

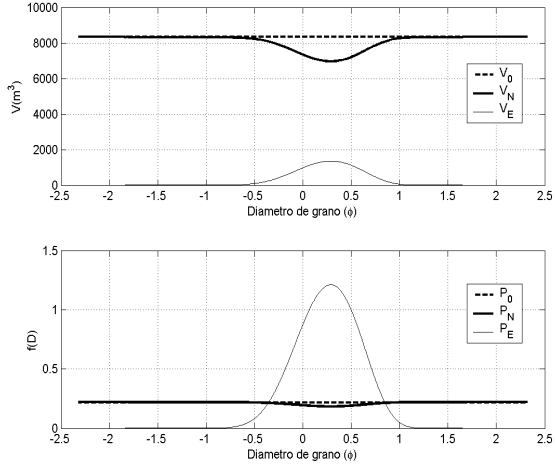

Fig. 1. An initially uniform grain size distribution generates a log-normal grain size distribution. Upper panel in volume, lower panel in probability density function.

The eroded volume will become a sediment deposit somewhere. If this new deposit, that now has a log-normal distribution, is then subjected to 20 new turbulent events, it will be further eroded. The eroded part of the deposit will have a log-normal distribution while the remaining sediment will have a log-normal minus a log-normal distribution (bi-modal). See example in figures 2 and 3.

Beach restoration and periodic nourishment maintenance is probably the most attractive method of beach erosion control. It is one of the most direct methods for maintaining and improving recreational benefits in shore protection projects and it is also used for emergency storm protection. One of the key elements in predicting beach fill performance is the evaluation of the "compatibility" of beach sands, that is, the determination of the amount of required borrow material needed to yield one unit that is consistent with the native material.

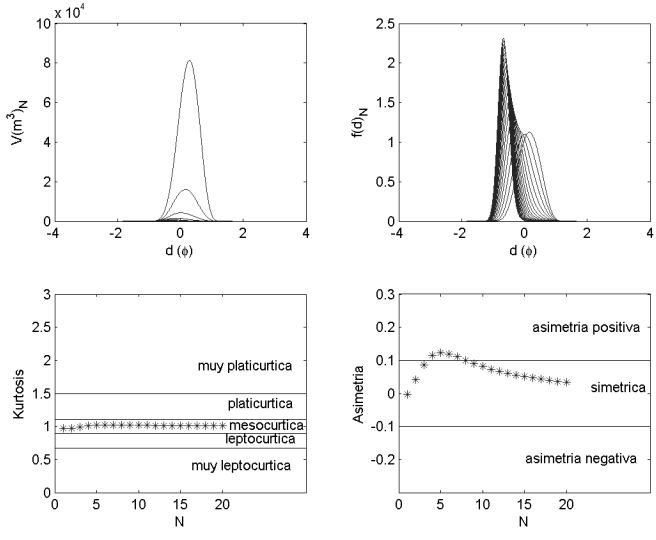

Fig. 2. Initial log-normal distribution. Upper left graphic in volume, upper right graphic in probability density functions, lower panel shows asymmetry and kurtosis.

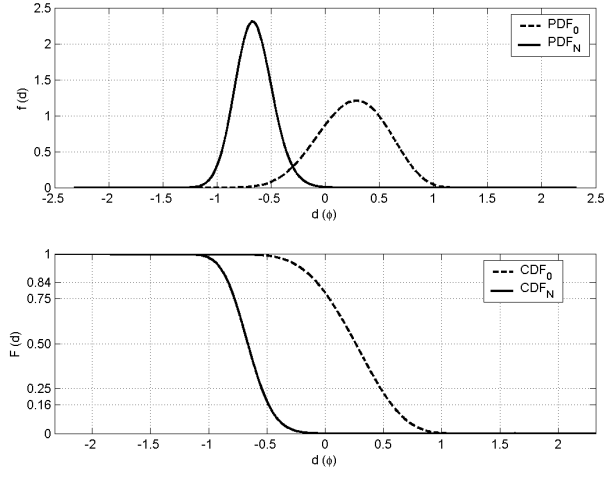

Fig. 3. Final log-normal distribution, after N=20 actions, from initial log-normal distribution. Upper panel in volume, lower panel in probability density function.

Taking advantage of the log-normal equilibrium distribution, Galofre and Medina (2001) and Galofre (2001) developed a simple method for estimating the relative compatibility of borrow material. However, several circumstances may invalidate the hypothesis of a log-normal native and borrow sand, namely:

- Wave climate that changes in time (seasonally, periodically, and randomly) and induces temporal variation of turbulent dynamics.
- Borrow sand sources with non log-normal distribution.
- Morphological changes that may affect sediment characterization and local wave climate.

In this paper, new field data are analyzed in order to further explore Galofre and Medina (2000) equilibrium grain size distribution hypothesis and to identify those situations in which sediment samples do not fit a log-normal distribution.

NEW DATA BASE ANALYSIS

More than 5.000 samples have been used to further explore Galofre and Medina (2000) equilibrium grain size distribution hypothesis. The samples were collected in 31 Spanish beaches. These beaches are classified into three groups: Cantabric Sea (13), South Atlantic (11), and Mediterranean Sea (7).

All the samples were best fitted to a log-normal distribution. The statistical parameters evaluated were: mean (first momentum) and standard deviation (second momentum), using phi units ($\phi = -\log_2 d$, d in mm.), avoiding the extreme values from the distribution as follow:

$$\bar{\phi} = \frac{\phi_{75} + \phi_{50} + \phi_{25}}{3} \tag{1}$$

$$\sigma_{\phi_{7525}} = 0.75 \cdot \left(\phi_{75} - \phi_{25}\right) \tag{2}$$

where $\bar{\phi}$ is the mean grain diameter in phi units, ϕ_n represents the sieve diameter in phi units that retains n percent of granulometric sediment sample weight, and $\sigma_{\phi_{7525}}$ is the standard deviation using percentages 75 y 25.

In a log-normal distribution, the Standard deviation ($\sigma_{\phi_{7525}}$) is evaluated using the percentages 16 y 84, $\sigma_{\phi_{8416}}$, as a result of taking into account all the data, σ_ϕ,

$$\sigma_\phi = \sigma_{\phi_{8416}} = \sigma_{\phi_{7525}} \tag{3}$$

evaluated from,

$$\sigma_{\phi_{8416}} = 0.5 \cdot (\phi_{84} - \phi_{16}) \tag{4}$$

$$\sigma_{\phi} = \sqrt{\frac{1}{n-1}\sum_{i=1}^{n} p_i (\phi_i - \bar{\phi})^2}, \quad \bar{\phi} = \sum p_i \phi_i \tag{5}$$

p_i is the probability of occurrence of ϕ_i, diameter on phi units of grain size *i*.

The asymmetry (third momentum) and kurtosis (fourth momentum) are the parameters that can show information about whether the analysed grain size samples are log-normal or not. These parameters are evaluated in phi units.

$$\text{Asymmetry} = \frac{(\phi_{84} - \phi_{50})}{(\phi_{84} - \phi_{16})} - \frac{(\phi_{50} - \phi_{10})}{(\phi_{90} - \phi_{10})} \tag{6}$$

$$\text{Kurtosis} = \frac{(\phi_{90} - \phi_{10})}{1.9 \cdot (\phi_{75} - \phi_{25})} \tag{7}$$

Negative asymmetry means that the finest grain sizes have been washed by the waves. On the other hand, positive asymmetry shows accumulation of fine sand compared with log-normal distribution. This parameter can be used to fix the limits of which fractions of the samples can be considered log-normal.

Some plots comparing the different ways of calculating standard deviation are presented in figure 4 for the Cantabrian Sea case. If the distribution were a perfect log-normal, results obtained from the three different procedures would be the same. The correlation coefficient shows the similarity of the computed values. The samples that show a greatest disagreement are those collected at El Puntal beach.

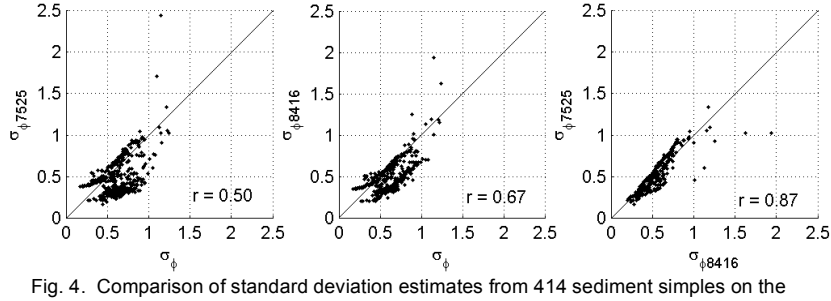

Fig. 4. Comparison of standard deviation estimates from 414 sediment simples on the Cantabrian Coast.

An example of the ability of the log-normal grain size distribution to fit the most non-log-normal sediment samples of El Puntal Beach is shown, figure 5. Note that the larger

disagreements between data and log-normal distribution always appear in the coarser fraction of the sample. The larger disagreements are encountered in the sediment samples located around the bar location (-5 m.) that usually appear on this beach.

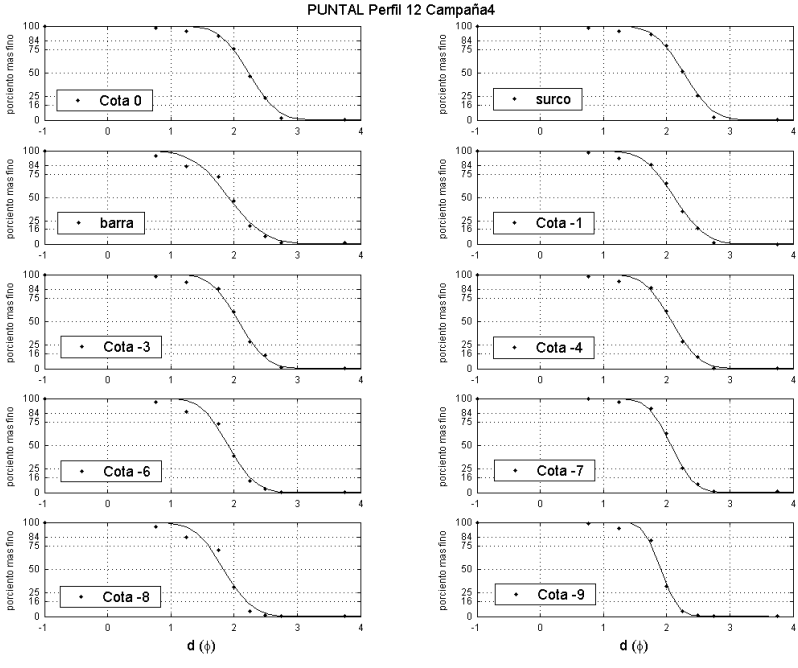

Fig. 5. Log-normal best fit distributions for El Puntal sediment samples.

The agreement between log-normal distribution and field data is also represented in figure 6. From this figure it can be concluded, that samples with negative asymmetry shows a lower R^2 than those with null asymmetry. Likewise, when the standard deviation is greater and when the distribution is leptokurtics, R^2 decreases.

Note that the worst fit corresponds to the negative asymmetry, in other words, to those places in which the fine sediment has eroded. These samples are located mainly on the bar during the accreting period of the beach. It is also worth noting that even though the discrepancy from the log-normal distribution is significant in the coarse fractions, it is negligible from the volume point of view since it only affects less than 10% of the sample.

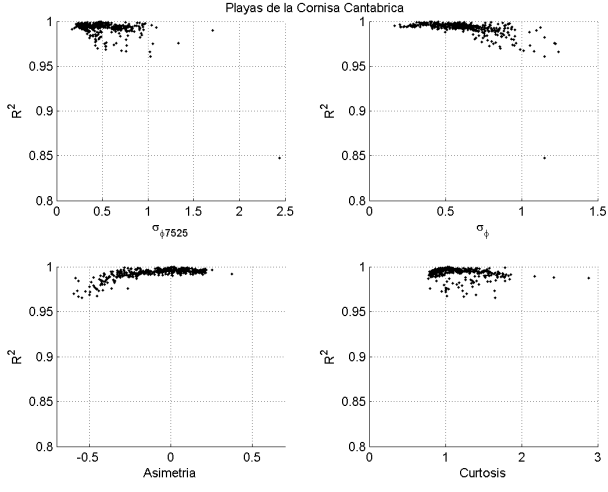

Fig. 6. Correlation coefficient, R, for sediment simples of the Cantabrian coast.

LOG-NORMAL APPLICATIONS

According to Galofre and Medina (2000) and Galofre and Medina (2001), log-normal distribution is the equilibrium grain size distribution of a sediment deposit generated by the accumulation of sediment eroded from an existing sediment source.

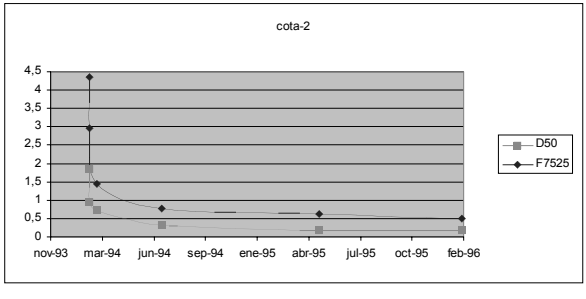

Fig. 7. Altafulla, Tarragona, profile 3. D_{50} and F_{7525} temporal evolution.

If this equilibrium distribution is changed, for example by nourishment works, the new material will not be in equilibrium with the existing dynamics, and a new equilibrium gain size distribution will be reached. Figure 7 shows the results from a monitoring survey after a beach nourishment project at Altafulla. We can see that the sediment grain size distribution reached the log-normal equilibrium distribution one year after the

nourishment works. The log-normal grain size distribution parameters are the mean and standard deviation. Mean is represented by D_{50}, and standard deviation, σ, by $F_{7525} = (\phi_{75} - \phi_{25})/2$. ϕ_x represents the sieve size, in units $\phi = -\log_2 d(mm)$, that retains x% of material.

It seems reasonable to acknowledge that there is a relationship between some parameter of wave climate and the grain size distribution. Galofre and Medina (2000), Galofre and Medina (2001) and Galofre (2001) found a relationship between H_{S12}, significant wave height that exceeded 12 hours a year, and F_{7525}. The relation between a wave parameter, H_{S12}, and log-normal grain size distribution parameter, F_{7525}, is shown in figure 8.

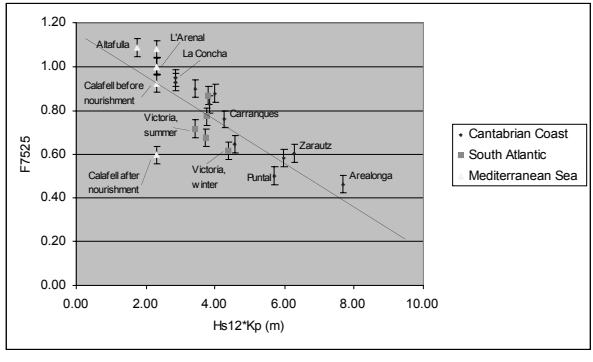

Fig. 8.- Relation between H_{S12} and F_{7525}

$$F_{7525} = -0{,}1.\ H_{S12}(buoy).K_p + 1{,}16 = -0{,}1.\ H_{S12}(local).K_p + 1{,}16 \qquad (8)$$

The overfilling ratio in beach nourishment works is necessary in order to predict beach fill effectiveness. Overfilling ratio measures the amount of required borrow sand needed to yield one unit that is consistent with the native material. Several attempts have been made to develop a procedure for evaluating the compatibility of borrow material compared to the native material (Krumbein and James 1965; Dean 1974; Guillen and Hoekstra 1996). Their basic assumption is that the borrow material will reach a final log-normal grain size distribution and that the mean and standard deviation of this final distribution $N(\phi_{50n}, \sigma_{\phi n})$ are related to those of the native distribution $N(\phi_{50n}, \sigma_{\phi n})$, where sub-index 'n' and 'b' are related to native and borrow sand.

An exhaustive analysis based on the compatibility of grain size distribution samples from borrow sand to equilibrium distribution was made using the principles shown in figure 9. New overfilling factors, R_A and S, were proposed (Galofre and Medina 2001; Galofre 2001).

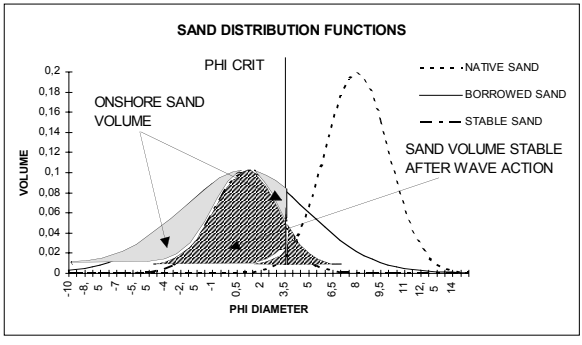

Fig. 9. Native, borrow and stable sand distribution functions in nourishment works.

This method assumes that native, borrow and final equilibrium grain size distribution are log-normal. This is useful for obtaining analytical expressions of overfilling ratios. It can be evaluated also by assuming that grain size distribution of native and final equilibrium sand are log-normal.

For analytical analysis one must assume that all grain size distribution is log-normal. In this method, the part of borrow sand that has a log-normal distribution is considered to be stable with the mean of borrow material and the standard deviation of native sand, $N(\phi_{50b}, \sigma_{\phi n})$.

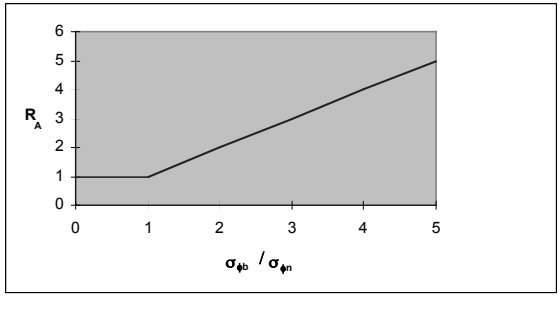

Fig. 10. Evolution of R_A versus $\sigma_{\phi b}/\sigma_{\phi n}$.

According to these assumptions, R_A, overfilling ratio of the stable sand, can be calculated based on the principles exposed previously:

a) If $\sigma_{\phi b} < \sigma_{\phi n}$, then $R_A = 1$

b) If $\sigma_{\phi b} > \sigma_{\phi n}$, then $R_A = \sigma_{\phi b}/\sigma_{\phi n}$ .In this case $R_A > 1$

Figure 10 shows the evolution of R_A with $\sigma_{\phi a}/ \sigma_{\phi n}$. R_A is related to the quotient $\sigma_{\phi b}/ \sigma_{\phi n}$. Therefore, this parameter provides the following information: if $\sigma_{\phi b} < \sigma_{\phi n}$ all borrow material is stable and if $\sigma_{\phi b} > \sigma_{\phi n}$ only the material which has a D_{50} of the borrow sand and a σ of the native or equilibrium material is stable.

The remaining sand is not only made up of stable sand, but also of 'coarse' material, still present in the nourished area. ϕ critical, ϕ_{crit}, is defined as that which differentiates the material remaining on the beach from that which has been washed away. ϕ_{crit} is defined by a parameter, Dalrymple (1992), dividuing the material that goes onshore from that which goes offshore. According to this principle, S can be calculated. the overfilling ratio of remaining sand, as the addition of stable and coarse material:

a) If $\sigma_{\phi b} < \sigma_{\phi n}$, then $S = R_A$.
b) If $\sigma_{\phi n} < \sigma_{\phi b}$, then $S = R_A/(1+\alpha.R_A)$, where α is a factor depending on native and borrow sand parameters. In this case, as a result, $S < R_A$.

From this analysis some conclusions were found:

a) If borrow material is well sorted, than the native equilibrium sand has a distribution with standard deviation of borrow sand. If it is assumed log-normal, grain size distribution after nourishment works will be $N(\phi_{50b}, \sigma_{\phi b})$.
b) If coarser material remains in the filled area, the grain size distribution is not log-normal. It is a distribution divided into stable sand, log-normal, and the coarser material.
c) Poorly sorted material is heavily resistant to wave action.
d) All existing methods for calculating overfilling ratio assume that native, borrow and equilibrium or stable sand have a log-normal distribution.

CONCLUSION

The log-normal distribution function adjusts the granulometric beach samples. The analytical method suggested by Galofre and Medina (2000) and the field data (Galofre and Medina 2001; Galofre 2001) show that any granulometric sample subjected to a turbulent action reaches a log-normal distribution. Over time, this distribution will reach equilibrium.

When the beach sample is subjected to turbulence dynamic and the process is slow, the parameters of the log-normal distribution D_{50} and σ are respectively related to the source of the sediment and the marine dynamics.

Taking into account that the equilibrium distribution is log-normal in the beach nourishment cases, and assuming that the borrow sand is log-normal, a new formula to calculate the over-fill factors R_A and S is presented.

REFERENCES

Dean, R.G. (1974). "Compatibility of Borrow Material for Beach Fills". *14th International Conference on Coastal Engineering*, Chapter 77, pp.1319-1333.

Fredlund, M.D., Fredlund, D.G., and Wilson, G.W. (2000). "An equation to represent grain size distribution". *Canadian Geotechnical Journal*, Vol 37, pp. 817-827.

Galofre, J., and Medina, R. (2000). "An equilibrium grain size distribution model for beaches". *27th International Conference on Coastal Engineering*, pp. 2509-2521.

Galofre, J. (2001). "Desarrollo y validación de un modelo de distribución granulométrica de sedimentos en playas". Ph.D. University of Cantabria.

Galofre, J., and Medina, R. (2001). "Compatibility of borrow material for beach fills: a revised formulation". *4th International Conference on Coastal Dynamics*, pp. 858-867.

Guillen, J., and Hoekstra P. (1996). " The Equilibrium Distribution of Grain Size Fractions and its Implications for Cross - Shore Sediment Transport: a Conceptual Model". *Marine Geology*, Vol. 135, pp. 15 -33.

Inman, D.L. (1953). "Areal and Seasonal Variations in Beach and Nearshore Sediments al La Jolla, California". Technical Memories, 39, Beach Erosion Board, Washington D.C.

Krumbein, W.C. (1938). "Size Frequency Distribution of Sediments and the Normal Phi Curve". *Journal of Sedimentary Petrology*, Vol. 18, pp. 84-90.

Krumbein, W.C., and James, W.R. (1965). "A log-normal Size Distribution Model for Stimating Stability of Beach Fill Material". Technical Memorandum Nº16, U.S. Army. Coastal Engineering Research Center, Washington D.C.

Medina, R., Losada, M.A., Losada I.J., and Vidal, C. (1994). "Temporal and Spatial Relationship Between Sediment Grain Size and Beach Profile". *Marine Geology*, Vol. 118, pp. 195-206.

Moutzouris, C.I. (1988). "Longshore Sediment Transport Rate vs. Cross - Shore Distribution of Sediment Grain Sizes". *21th International Conference on Coastal Engineering*, pp. 1959-1973.

Moutzouris, C.I. (1991). "Beach Profiles vs. Cross-Shore Distributions of Sediment Granin Sizes". *International Conference on Coastal Sediments*, pp. 860-975.

Wyrwoll, K.-H., and Smyth, G.K. (1985). On using the log-hyperbolic distribution to describe the textural characteristics of eolian sediments. *Journal of Sedimentary Petrology*, Vol. 55, pp. 471-478.

DETERMINATION OF OVERFILL FACTOR FOR OFFSHORE SAND IN BARRIER ISLAND RESTORATION ON THE LOUISIANA COAST

Daniel L. Bolinger, P.E.[1], Dominic Izzo, P.E., F.ASCE[2], Edward J. Schmeltz, P.E.[3]

1. Bolinger Engineering Consultants, L.L.C., 1912 Dublin Street, New Orleans, LA 70118, USA. BolingerDaniel@Bellsouth.net.
2. Exponent, Inc., 10988 Kinghurst Drive, Houston, TX 77099, USA. Dizzo@Exponent.com.
3. DMJM Harris, Inc., 605 New York, NY 10158, USA. Edward.Schmeltz@dmjmharris.com

Abstract: The Louisiana Department of Natural Resources (LDNR), along with the other Coastal Wetlands Planning, Protection, and Restoration Act (Public Law 101-646, Title III)(CWPPRA) agencies, authorized a team led by DMJM Harris to design the restoration of the West Flank of Whiskey Island. Significant among the overall project objectives are:

- Demonstrate the feasibility of using Ship Shoal sands for restoration projects.
- Restoring the integrity of the West Flank of Whiskey Island.
- Adding offshore sediment to Whiskey Island to increase sediment supply.

A key design factor was the determination of the overfill requirements, which would determine how much material had to be removed from Ship Shoal to achieve the appropriate quantity and quality of material on the West Flank of Whiskey Island after the project had been completed and conditions stabilized. There are two primary approaches to determining the overfill factor, which are described in the United States Army Corps of Engineers (USACE) 2002 Coastal Engineering Manual (CEM), (USACE, 2002). This manuscript discusses the design analysis, the decision on which approach to use, and associated results on the overfill factor chosen for this project.

INTRODUCTION

The Isles Dernieres barrier island chain, which includes Whiskey Island, is considered one of the most rapidly deteriorating barrier shorelines in the United States. The islands are not rolling over and preserving area as would be predicted by conventional coastal engineering theory. Higher retreats and loss rates are observed in the middle of the island chain including Whiskey and Trinity Islands, as compared to the ends of the chain system, which includes Raccoon and East Islands. This would indicate that the two interior islands are acting as feeders for the two exterior islands in this chain. The Isles Dernieres chain is losing its structural integrity and the capability to perform its function in the coastal and estuarine ecosystem. Chief among these is the chain's storm buffering capacity and the protection it provides to population centers, oil and gas infrastructure, inland bays, estuaries, and wetlands.

To address the potential loss of Whiskey Island, the Coastal Wetlands Planning, Protection, and Restoration Act (Public Law 101-646, Title III) (CWPPRA) authorized the Ship Shoal-Whiskey Island West Flank Restoration Project (TE-47) for funding. The federal sponsor, the Environmental Protection Agency – Region 6 and the local sponsor, the Louisiana Department of Natural Resources (LDNR), authorized a team led by DMJM Harris to design the restoration of the West Flank of Whiskey Island. The Ship Shoal-Whiskey Island West Flank Restoration Project (TE-47) is located on the West Flank of Whiskey Island 17.5 miles southwest from Cocodrie, Louisiana in Terrebonne Parish. It is bounded by Coupe Colin and Raccoon Island to the west, Whiskey Pass and Trinity Island to the east, Lake Pelto to the northeast, Caillou Boco to the north, Caillou Bay to the northwest, and the Gulf of Mexico to the south. The proposed borrow site is located entirely within Block 88 of Ship Shoal approximately 10.1 miles south-southwest of Whiskey Island in the Gulf of Mexico. The project site and the proposed borrow site are shown in Figure 1.

Significant among the overall project objectives are to:

- demonstrate the feasibility of using Ship Shoal sands for restoration projects.
- restore the integrity of the West Flank of Whiskey Island
- add offshore sediment to Whiskey Island to increase sediment supply.

This paper is a summary of the design efforts that resulted in the DMJM Harris Final Design Report (DMJM Harris, 2005) which includes the Moffatt & Nichol Final Coastal Engineering & Modeling Report (Moffatt & Nichol, 2004a), Moffatt & Nichol Sediment Suitability Assessment (Moffat & Nichol, 2004b), Soil Testing Engineers Report of Sampling Investigation, Whiskey Island (Soil Testing Engineers, 2004a), Soil Testing Engineers Report of Sampling Investigation, Ship Shoal-Block 88 (Soil Testing Engineers, 2004b).

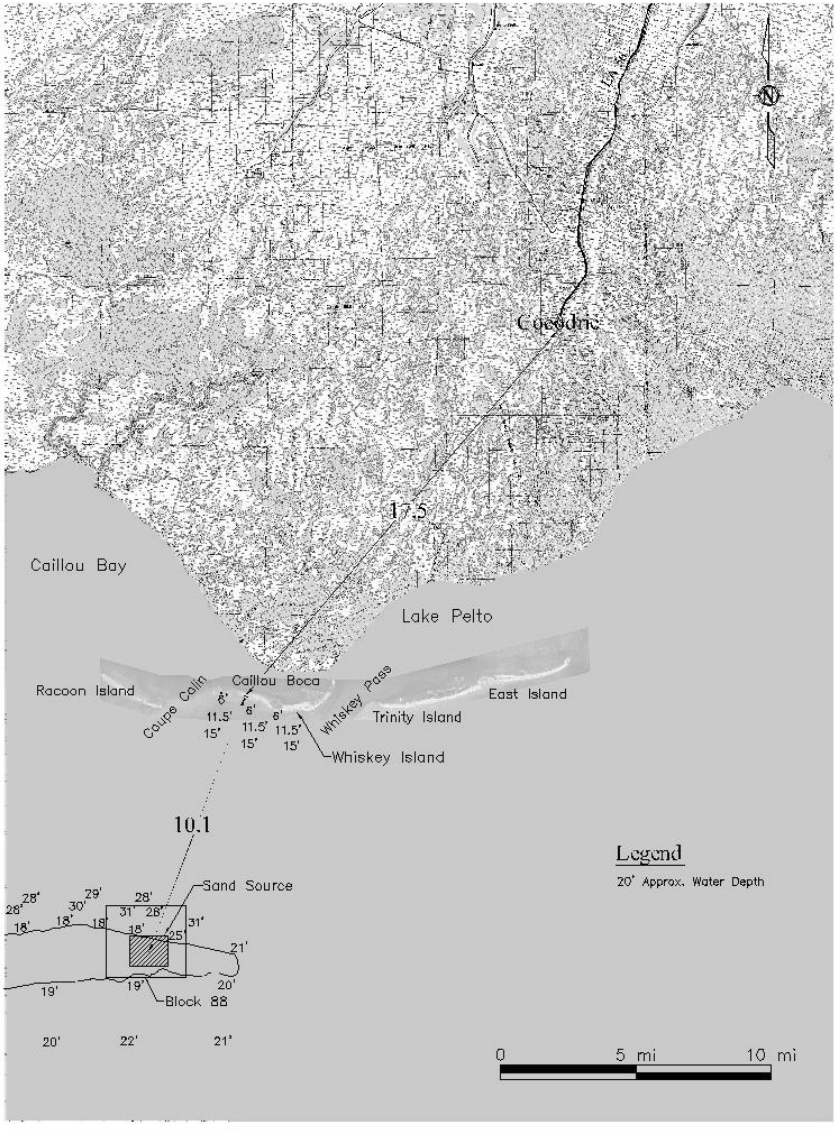

Figure 1: Whiskey Island and Ship Shoal Location

SEDIMENT INVESTIGATIONS

The Project Team concluded, based on the data presented in C&C Technologies, 2003 and Kulp et al., 2001, that the most suitable sand materials for island replenishment with Block 88 appeared to exist near the middle to southern half of the block. The Project Team developed a sediment investigation plan based on this data provided by LDNR after producing the requisite *Quality Assurance Project Plan***.** They conducted the investigation on Ship Shoal and Whiskey Island and prepared *Sand Source Maps* of potential Ship Shoal Borrow Areas showing viable sand thicknesses.

The proposed borrow site is entirely within Minerals Management Service's (MMS) designated Block 88 of Ship Shoal. In order to develop detailed information on the borrow site surroundings and soil characteristics a geophysical survey of the proposed borrow site was performed in August of 2003. The geophysical survey including 35 vibracores was completed to depths of approximately 15 to 20 feet below the mudline. The potential borrow area within Block 88 is approximately 30 million square feet in size. The hydrographic conditions across most of the borrow area site are relatively flat, with the controlling depths at approximately minus 18-feet mean lower low water (MLLW) datum. Based on the vibracores performed as part of the geophysical survey, the top nine to fifteen feet of the borrow area were determined to be a fine-grained sand, which is similar to the sand on Whiskey Island.

On Whiskey Island, the Team used intertidal and subaerial beach samples to characterize the beach and nearshore environment. Although USACE recommends a composite containing the mean high water, mid-tide, and mean low water to give the best representation of the foreshore beach, the Team determined to use samples at or above MLW and samples along the shallow crest of the West Flank to develop composite values for a more appropriate comparison of native beach materials with the Ship Shoal borrow area materials. Analysis of the Whiskey Island samples resulted in a determination that it was a moderately sorted fine sand not radically different from the Ship Shoal sand.

In performing the Ship Shoal Sediment Investigation the Project Team also determined there were no known active pipelines, fixed platforms, caissons, wellheads, or other structures within the proposed borrow area in Block 88. A sonar survey of the site did pick up eleven sonar contacts, which were mostly debris. Many additional unidentified magnetic anomalies were located by the sonar survey, all of which were assumed to be debris.

Various Grain Size Diameters

Different statistical measures are used in various models and designs to describe the sand grain distribution on barrier islands. It is useful to review the differences between

reported average median and average mean values along with what sediment data was used to compute or determine these values.

The ***mean grain size diameter*** for a sediment sample is the value estimated using the three sediment size diameters of $\mathbf{D_{16}}$, $\mathbf{D_{50}}$, and $\mathbf{D_{84}}$. The ***average mean grain size diameter*** $\boldsymbol{D_{50}}$ is computed based on the average of the mean grain size diameters for all the samples included in the sample set.

The ***median grain size diameter*** is the value in the sediment sample that has an equal number of values above and below this median value. The ***average median grain size diameter*** would be computed based on the average of the median grain size diameters for all the samples included in the sample set.

The Team developed models using the Delft3D computer modeling system for the project. Delft3D computer modeling for sediment transport and morphology requires an ***average median grain size diameter*** for the project area including supratidal and subtidal sediment characteristics. The average median grain size diameter for Whiskey Island was computed to be $D_{50} = 0.15$ mm.

DETERMINATION OF OVERFILL REQUIREMENTS

Ideally, the borrow sediment used in restoration projects should be texturally similar to the native sediment of the coastal area to be restored (Louisiana Gulf Shoreline Restoration Report, 2003). While the average mean and average median grain sizes of the Whiskey Island and Ship Shoal borrow material are close, of course, the grain size distribution of the borrow material does not exactly match the grain size distribution of the native material at Whiskey Island. Therefore, an analysis was required to assess the compatibility of the two materials from a functional perspective. Borrow material placed on the beach will undergo sorting as a result of the coastal processes; and given enough time, will approach the native grain-size distribution. The portion of borrow material that does not match the native sediment grain-size distribution is assumed to be lost to the offshore.

Included in the design were a ***Sediment Suitability Assessment*** and ***Basis of Design Determination***. The Project Team sampled sediment on Whiskey Island and Block 88 of Ship Shoal and developed composite statistics for the beach material at Whiskey Island and compared them to composite statistics for each potential borrow area to assess the materials' compatibility.

A key design factor was the determination of the overfill requirements, which would determine how much material had to be removed from Ship Shoal to achieve the appropriate quantity and quality of material on the West Flank of Whiskey Island after the project had been completed and conditions had stabilized. The CEM describes two primary approaches to determining the overfill factor (USACE, 2002).

One method is based on the equilibrium beach profile concept, an assessment of storm-induced erosion, and an assessment of wave-driven longshore transport losses. The equilibrium beach profile concept is based on a single grain size parameter, the ***average median grain size diameter*** and does not consider the natural variations in grain size that occur in natural and nourished beaches.

The other method, which we will call the CEM method for computing the overfill requirement, consists of calculating relationships between the mean and standard deviations of the φ (phi)-scale grain size distributions of the native beach and the borrow site and then computing an overfill factor. Borrow material placed on the beach will undergo sorting as a result of the coastal processes and, with time, approach the native grain-size distribution. The portion of borrow material that does not match the native sediment grain-size distribution is assumed to be lost to the offshore (USACE, 2002). The CEM has adopted this concept and recommends the use of an overfill factor (R_A) as "*the volume of borrow material required to produce a stable unit of usable fill material with the same grain size characteristics as the native beach sand.*" Conceptually the overfill material is the estimated quantity of material that does not fit the native beach and will be washed away.

The overfill factor is a way of computing the fill volume when the borrow and native sediments have different gradation characteristics. The overfill factor method is based on the assumption that sorting processes will selectively remove borrow material from the various size classes until a stable grain size distribution results. The closer the overfill factor is to 1.0, the more appropriate is the borrow site selected.

It should be noted that the overfill factor is different from the cut-to-fill factor, which accounts for losses in the dredging and placement process, not for differences in the grain-size distribution of the material. The cut-to-fill factor was considered in the design process to determine the volume of materials required to be removed from the borrow area. Most beach fill projects assume that dredging payment will be based on gross fill volumes as opposed to measured cut volume at the borrow site. Dredging contractors typically estimate this and other dredging process inefficiencies and account for them in their cost estimates and bids. A conservative cut-to-fill ratio factor of 1.7 was considered in the design process for sizing and permitting the limits of the borrow area. The Sand Source Borrow Area was delineated to use those portions of the borrow material that would yield lower overfill factors.

The total dredgeable material available within the specificed limits of the Sand Source Borrow Area is 6.61 million cubic yards. The estimated quantity to be placed on the project site for bidding purposes is 3.85 million cubic yards.

Design Results

Sediment compatibility was analyzed between sediment from Ship Shoal to be placed on Whiskey Island and the native material of Whiskey Island. The Project Team analyzed

the sediment compatibility using the two methods to determine sediment compatibility and the overfill factor for the design of the project fill volume.

The first method, the equilibrium beach profile concept, compares the ***average median grain size diameter*** for the samples at or above Mean Low Water (MLW) with samples taken along the shallow crest of the present West Flank of Whiskey Island to the average median grain size diameter of the sand from Ship Shoal. The average median grain size diameter for the West Flank of Whiskey Island is a D_{50}= 0.20 mm. The average median grain size diameter from the proposed borrow area of Ship Shoal is a D_{50}= 0.20 mm. Using this method the overfill requirement would be equal 1.0. This methodology suggests that additional borrow material would not be required and no additional overfill would be placed on the island during construction.

The second method for determining the overfill factor, the CEM Method correlates the ***average mean grain size diameter*** for Whiskey Island (a D_{50} = 0.19mm) with the ***average mean grain size diameter*** from all the vibracore locations in the investigated borrow area on Ship Shoal.

Overfill factors were computed using data from each of the borrow area vibracores. For each vibracore, composite characteristics in phi (φ) units including the mean (M_φ) and standard deviation (σ_φ) were developed for the upper sand layer within the Ship Shoal borrow area. These characteristics were used as input to the Coastal Engineering Design and Analysis System (CEDAS) software package developed by the USACE to compute the overfill factors for each vibracore. The values are presented in Table 1.

This method produced an average overfill factor of **1.2** to be used for the design of the project fill volume required. This average overfill factor provided 1.2 units of borrow material to create 1.0 units of stable native Whiskey Island material

Since the first methodology is based on a single grain size parameter and produced a placement factor of 1.0 and the CEM Method considered the distribution of grain sizes spread around the mean and produced a more conservative overfill factor, the Project Team determined that the CEM method was the more prudent method for this project. The entire design process underwent detailed reviews by LDNR that included a thorough vetting with concerned state and Federal agencies.

The methodologies are based on variable data. The 35 vibracores on Ship Shoal on an individual basis yielded overfill factors from 1.00 to 1.50. The average overfill factor of 1.2 will be used for the project. Several poorly sorted (well graded) samples with relatively coarse mean grain sizes have overfill factors near or equal to 1.0. All samples had overfill factors less than 1.53, with the majority close to the average value of 1.2.

This means that there will be variability in the performance of the fill over time as dredged material differs depending on the specific location within the source area. The Project Team used this information to design the borrow area so as to remove the most

consistent material first and increase the probability of the long term volume retention of the material placed on Whiskey Island and improve the degree of successful restoration.

The mean sediment diameters (M_φ) and standard deviations (σ_φ) for the native (*n*) and borrow materials (*b*), were computed as follows:

$$M_\phi = \left(\frac{\phi_{16} + \phi_{50} + \phi_{84}}{3} \right) \quad (1)$$

and

$$\sigma_\phi = \left[\left(\frac{\phi_{84} - \phi_{16}}{4} \right) + \left(\frac{\phi_{95} - \phi_5}{6} \right) \right] \quad (2)$$

where:

$\sigma_{\varphi n}$ = standard deviation or measure of sorting for native material.
$\sigma_{\varphi b}$ = standard deviation or measure of sorting for borrow material.
$M_{\varphi n}$ = mean sediment diameter for native material.
$M_{\varphi b}$ = mean sediment diameter for borrow material.

TABLE 1

Composite Characteristics and Overfill Factors for Ship Shoal-Block 88 Vibracores

Sample	Composite M_φ	Composite σ_φ	$(M_{\varphi b}-M_{\varphi n})/\sigma_{\varphi n}$	$\sigma_{\varphi b}/\sigma_{\varphi n}$	Overfill Factor
VIBRACORE 04-SS88-01(P)	2.40	0.58	0.01	0.76	1.26
VIBRACORE 04-SS88-02(P)	2.28	0.43	-0.15	0.56	1.50
VIBRACORE 04-SS88-03(P)	2.30	0.85	-0.12	1.11	1.01
VIBRACORE 04-SS88-04(P)	2.30	0.54	-0.12	0.70	1.16
VIBRACORE 04-SS88-01(S)	2.33	0.68	-0.08	0.88	1.02
VIBRACORE 04-SS88-02(S)	2.39	0.55	-0.01	0.72	1.32
VIBRACORE 04-SS88-03(S)	2.37	0.59	-0.04	0.77	1.18
VIBRACORE 04-SS88-04(S)	2.42	0.64	0.04	0.83	1.18
VIBRACORE 04-SS88-05(S)	2.35	0.60	-0.06	0.78	1.13
VIBRACORE 04-SS88-06(S)	2.38	0.63	-0.02	0.82	1.12
VIBRACORE 04-SS88-07(S)	2.34	0.61	-0.08	0.79	1.10
VIBRACORE 04-SS88-08(S)	2.46	0.72	0.08	0.94	1.14
VIBRACORE 04-SS88-09(S)	2.38	0.67	-0.03	0.88	1.07
VIBRACORE 04-SS88-10(S)	2.39	0.88	-0.01	1.14	1.06
VIBRACORE 04-SS88-11(S)	2.51	0.65	0.16	0.84	1.37
VIBRACORE 04-SS88-12(S)	2.75	0.62	0.46	0.81	1.53
VIBRACORE 04-SS88-13(S)	2.21	0.67	-0.24	0.87	1.00
VIBRACORE 04-SS88-14(S)	2.40	0.64	0.00	0.83	1.14
VIBRACORE 04-SS88-15(S)	2.40	0.72	0.01	0.94	1.04
VIBRACORE 04-SS88-16(S)	2.30	0.53	-0.12	0.69	1.18
VIBRACORE 04-SS88-17(S)	2.28	0.78	-0.14	1.01	1.00
VIBRACORE 04-SS88-18(S)	2.35	0.59	-0.06	0.77	1.14
VIBRACORE 04-SS88-19(S)	2.39	0.56	0.00	0.72	1.29
VIBRACORE 04-SS88-20(S)	2.41	0.63	0.02	0.82	1.17
VIBRACORE 04-SS88-21(S)	2.36	0.57	-0.04	0.75	1.20
VIBRACORE 04-SS88-22(S)	2.42	0.61	0.03	0.79	1.24
VIBRACORE 04-SS88-23(S)	2.33	0.59	-0.08	0.76	1.11
VIBRACORE 04-SS88-24(S)	2.37	0.64	-0.04	0.84	1.10
VIBRACORE 04-SS88-25(S)	2.35	0.81	-0.06	1.06	1.01
VIBRACORE 04-SS88-26(S)	2.43	0.66	0.04	0.86	1.16
VIBRACORE 04-SS88-27(S)	2.35	0.50	-0.05	0.66	1.39
VIBRACORE 04-SS88-28(S)	2.30	0.47	-0.12	0.62	1.36
VIBRACORE 04-SS88-29(S)	2.37	0.52	-0.03	0.68	1.37
VIBRACORE 04-SS88-30(S)	2.33	0.47	-0.08	0.61	1.46
VIBRACORE 04-SS88-31(S)	2.35	0.48	-0.06	0.63	1.49
				Minimum	**1.00**
				Maximum	**1.53**
				Average	**1.20**

CONCLUSION:

It is feasible to use Ship Shoal sands for restoration projects in the Isles Dernieres. Projects using the sediments available on Ship Shoal can be used in barrier island restoration with the proper design. In this case, the project will restore the integrity of Whiskey Island in the near-term. Replacing lost sediment without changing the regional hydrogeomorphology probably means the island will erode again over the long-term. On the other hand, adding approximately 4 million CY of offshore sediment to Whiskey Island will increase the overall sediment supply in the coastal zone of the Isles Dernieres.

In reviewing the two methods to determine the appropriate volume to be placed on Whiskey Island, the Design Team recommended that the method that provided an overfill factor of 1.2 be used. LDNR has approved this design recommendation, which will increase the probability of the long-term volume retention of the material placed on Whiskey Island and improve the degree of successful restoration.

The project specifications require that pre and post topographic and bathymetric surveys will be taken along the Plan transects. These surveys will be used to calculate the volume of fill placed on the project site.

It is also recommended that periodic continued topographic and bathymetric surveys be conducted in order to measure the movement and performance of the island. These subsequent surveys could be used to also estimate the rate at which material is lost from the island during its post restoration life and verify the accuracy of the overfill factor, which was selected.

ACKNOWLEDGEMENTS

The authors appreciate the cooperation of LDNR and the other CWPPRA agencies for their efforts that encouraged the whole design process to undergo their thorough review. The authors acknowledge and thank all the design team members for their design contributions especially Moffatt & Nichol Engineers. Finally the authors thank DMJM Harris for their permission to present this manuscript.

REFERENCES

C&C Technologies, 2003. High Resolution Geophysical and Archeological Survey of Portions of Blocks 87, 88, 89, 94 and 95 Ship Shoal Area – Whiskey Island West Flank Restoration Project Using Ship Shoal Sediment Coastal Terrebonne Parish, Louisiana.

DMJM Harris (2005). Ship Shoal-Whiskey Island West Flank Restoration (TE-47) Final Design Report.

Kulp, M., Penland, S., and Ramsey, K. 2001. Ship Shoal Sand Resource Synthesis Report, Coastal Research Laboratory, Department of Geology and Geophysics, University of New Orleans, New Orleans, Louisiana.

Louisiana Gulf Shoreline Restoration Report, 2003. Louisiana Coastal Area, LA – Ecosystem Restoration. Comprehensive Coastwide Ecosystem Restoration Study.

Moffatt & Nichol, 2004a. Final Coastal Engineering & Modeling Report. Prepared for DMJM Harris for the LDNR Ship-Shoal-Whiskey Island West Flank (TE-47) Restoration Project, Terrebonne Parish, Louisiana.

Moffatt & Nichol, 2004b. Technical Memorandum: Sediment Suitability Assessment for Ship Shoal: Whiskey Island West Flank Restoration Project. Prepared for DMJM Harris for the LDNR Ship-Shoal-Whiskey Island West Flank (TE-47) Restoration Project, Terrebonne Parish, Louisiana.

Soil Testing Engineers, 2004a. Report of Sampling Investigation, Whiskey Island – East & West Flanks. Prepared for DMJM Harris for the LDNR Ship-Shoal-Whiskey Island West Flank (TE-47) Restoration Project, Terrebonne Parish, Louisiana.

Soil Testing Engineers, 2004b. Report of Borrow Site Investigation, Ship Shoal-Block 88. Prepared for DMJM Harris for the LDNR Ship-Shoal-Whiskey Island West Flank (TE-47) Restoration Project, Terrebonne Parish, Louisiana.

U.S. Army Corps of Engineers (2002). Coastal Engineering Manual (CEM) – Engineering Manual 1110-2-1100, Washington, D.C.

BROWARD COUNTY BEACH DEMONSTRATION PROJECT: FROM BEERS TO BEACHES

Christopher Makowski[1], Gordon Thomson, P.E.[2], Peter Foye[3], Stephen Higgins[4]

1. Coastal Planning & Engineering, Inc. 2481 NW Boca Raton Blvd, Boca Raton, FL 33431, USA. cmakowski@coastalplanning.net.
2. Coastal Planning & Engineering, Inc. 2481 NW Boca Raton Blvd, Boca Raton, FL 33431, USA. gthomson@coastalplanning.net.
3. Broward County Commission, Office of Waste & Recycling Services, 1N University Drive, Suite 400-B, Plantation, FL 33324, USA pfoye@broward.org
4. Broward County Department of Environmental Protection, 1N University Drive, Suite 300, Plantation, FL 33324, USA shiggins@broward.org.

Abstract: Broward County relies on its beaches to attract tourists but 21 of the 24 miles of Broward beaches are defined as critically eroded. The Broward County Office of Waste and Recycling Services processed approximately 15,000 tons of glass each year and is searching for beneficial use of this material. The Broward County Beach Demonstration Project is investigating the feasibility of using recycled glass to augment the shore protection program needs, specifically in areas of higher relative erosion (hotspots). The addition of glass cullet as emergency beach fill may extend the life of the shore protection project by nourishing these areas with smaller volumes of fill. This paper details investigations performed to date including a literature review, geotechnical investigation, biological analyses, public perception research, and abiotic testing and shows that glass cullet is a viable beach compatible material.

INTRODUCTION

Broward County has conducted numerous beach nourishment programs since the early 1960's because its beaches are in a chronic state of erosion. Significantly, 21 of the 24 miles of Broward beaches are defined as critically eroded (Florida Department of Environmental Protection, 2000). Broward County has several potential sources of beach compatible sand including offshore inter-reef sedimentary infills, upland dune, inland sources, and aragonite sand from the Bahama Banks to provide fill for these

projects. However, the Broward County Office of Waste and Recycling Services processed 15,840 tons of glass in 2004 at cost of $145,000 (Austin, 2004) and is searching for a beneficial use of this material. Broward County is implementing a demonstration project to determine the feasibility of using recycled glass as beach-compatible material. This material could supply, on an emergency basis, some of the volumetric needs of the County's shore protection program while providing another market for recycled glass.

It is proposed to use glass cullet as a potential alternative source material for beach fill. Glass cullet has physical properties similar to natural silica sands, making it a viable alternative beach fill material along critically eroded shorelines (Finkl and Kerwin, 1997; Kerwin, 1997). Recycled glass cullet has many advantages as a potential alternative beach fill material including:

1. The ability to mechanically select grain sizes comparable to the native beach characteristics;
2. Chemical, mechanical, geologic, and engineering properties of appropriately sized glass cullet are similar to natural sand;
3. The ability to utilize a readily available recycled product;
4. Proactive implementation of a comprehensive recycling program;
5. Utilization of an environmentally safe, inert material.

Despite the potential advantages of glass cullet, additional investigations were necessary prior to placing this material on the beach. The Broward County Beach Demonstration Project has completed a literature review (Thomson *et al.*, 2004a), geotechnical investigation (Thomson *et al.*, 2004b), public perception research (MARS Research, 2004), biological analyses (Makowski *et al*., 2005), and abiotic testing (Makowski *et al*., 2006). This paper outlines the findings from these investigations.

LITERATURE REVIEW

Due to the limited secondary materials market and increasing cost of recycling glass, the Broward County Commission, Office of Waste and Recycling Services conducted a pre-feasibility study on using recycled glass as beach fill material (Malcolm Pirnie, 2003). This study concluded that using glass cullet as beach fill material was a viable concept and recommended that further studies be conducted. A feasibility study for Moonlight Beach, California, conducted by Woodward-Clyde (1993), also showed that glass cullet was a viable beach compatible material.

Studies conducted at Texas A&M University compared the performance characteristics of recycled glass to natural sand (Edge, 2002) in physical model experiments where a 3-D wave tank generated regular waves. The tank was divided into two channels: one for a glass beach and the other for native beach sand. Six tests measured beach profile change due to wave action in the tank. At the end of the test, glass cullet and native beach sands were found to have the same performance characteristics for the conditions tested. The wave reflection coefficient for glass cullet was less than native beach sand, suggesting that glass cullet absorbs energy better than sand.

Also investigated was the rate of abrasion and loss of mass through abrasion (Edge, 2002). A tumbler machine was used to simulate wave action, current, and wind. This experiment measured mass loss for two samples: one was glass only and the other was a mixture of glass plus sand. The latter combination was an attempt to simulate real world effects where the glass cullet and sand are mixed. The glass and sand/glass samples were placed in the tumbler machine with water. After several days of tumbling, the samples were sieved and dried. Grain sizes less than sieve #200 were removed from the sample. Masses were measured after 7, 14, and 36 days of tumbling. These tests showed that the glass-only sample had a very high initial rate of abrasion, but the rate eventually stabilized and was comparable to the glass/sand mixture.

Glass cullet has been placed on two beaches on the Caribbean island of Curaçao, at the Hilton Hotel on Piscadera Bay (southern coast near downtown Willemstad) and at Zanzibar Park (also on the southern coast). Grain sizes of the cullet placed on these beaches ranged from 0.20 mm to 0.60 mm (Paardekooper, 2004).

The volume of glass cullet placed at the Hilton Hotel is unknown, but approximately 110 cubic yards of glass cullet was mixed with native beach sand in a 1,000 square foot area at Zanzibar Park (Paardekooper, 2004) along with a control section of 100% cullet. According to Paardekooper (2004), beachgoers preferred the beach sand - glass cullet mixture compared to the control plot with only glass cullet. This study noted, however, that visitors did not distinguish between sections of the beach that had varying ratios of natural sand to glass cullet. Turtle nesting occurred at both sites but there is no official data available from the local government agency regarding nesting or hatching success (Paardekooper, 2004).

A glass cullet beach was also constructed in the Town of Lake Hood, New Zealand. The Town created a beach using recycled glass cullet to encourage recycling and to increase environmental awareness (Temple, 2004). The lake is man-made, and WasteBusters Trust Canterbury constructed a beach for a festival in January 2003. The "Crystal Beach," composed entirely of glass cullet, is reported to look and feel like natural sand (WasteBusters, 2004).

Literature on two other "glass beaches" was also found. The one in Fort Bragg, California was the site of an old dumpsite. This practice was halted and large items such as cars and refrigerators were removed. Eventually, wave action washed out many of the paper products leaving glass that has become rounded over time. Near the Town of Port Allen on the island of Kauai, Hawaii, there is a beach composed of winnowed glass fragments. The site was a former dumping ground for glass bottles. Reworked by wave action, the glass has been comminuted and reduced to pebble size. However, neither of these beaches is representative of the type of material that is proposed for use on Broward County's beaches.

GEOTECHNICAL INVESTIGATIONS

Geotechnical investigations were conducted to determine grain-size distribution, Munsell color, carbonate content, grain angularity, and chemical analyses for potential contaminants in beach sand and glass cullet. Six samples of beach sand were collected from a back dune area at the southern end of the broad walk on Hollywood Beach, City of Hollywood Beach, Broward County, Florida (following the Broward County Segment III Shore Protection Project). Beach samples, collected as part of the Broward County Shore Protection Project General Reevaluation Report (Coastal Planning & Engineering / Olsen Associates Joint Venture, 2003) were also included in the comparison. Samples of glass cullet were obtained from three manufacturers including: Andela Products Ltd., Richfield Springs, NY; Glass Aggregate Systems, Faribault, MN; Recycle America Alliance, New Haven, CT.

The manufacturers were requested to provide pulverized glass samples that were similar to the grain size distribution of the natural sand along the Hollywood, Florida beaches. The results of the grain size analysis are summarized in the Table 1 below.

Table 1. Summary of Grain Size Analyses.

Sample	Mean Grain Size (mm)	Sorting	Percent Fines [2]
Beach Samples			
Sample #1 (surface)	0.50	0.74	1.7
Sample #2 (-1.5 ft)	0.47	0.76	1.1
Sample #3 (-3ft)	0.46	0.86	0.7
Sample #4 (surface)	0.54	0.77	1.6
Sample #5 (-1.5ft)	0.48	0.67	1.1
Sample #6 (-3ft)	0.51	0.82	0.7
Average	0.49	0.77	1.2
GRR Beach Samples [1]			
R-114 (dune)	0.65	0.97	0.0
R-114 (mid berm)	0.44	0.82	0.4
R-117 (dune)	0.38	0.61	0.3
R-117 (mid berm)	0.43	0.50	0.1
R-117 (mean high water)	0.71	0.58	0.0
R-117 (mean tide level)	0.83	0.64	0.0
Glass Cullet Samples			
Andela Products	0.89	1.12	3.7
Glass Aggregate Systems	0.40	0.84	2.7
Recycle America Alliance	0.33	0.95	7.5

1. CPE/Olsen J-V, 2003
2. Percent material passing the #230 sieve.

Table 1 shows that there was a range of mean grain sizes produced by the glass cullet manufacturers that bracketed the grain size values observed for the beach samples. Equally important is that the percent fines was low. The Florida Department of Environmental Protection (FDEP) requires that beach fill sediments contain no more than 5% fines (silt plus clay).

Public perception and FDEP requirements require that glass cullet looks like beach sand. A Munsell Color analysis was performed and the results are summarized in Table 2.

Table 2. Summary of Munsell Color Analysis.

Sample	Munsell Color Value		Munsell Color Description	
	Dry	Wet	Dry	Wet
Beach Samples				
Sample #1 (surface)	10YR 7/1	10YR 6/2	Light gray	Light brownish gray
Sample #2 (1.5 ft)	10YR 7/2	10YR 6/3	Light gray	Pale brown
Sample #3 (3ft)	10YR 7/2	10YR 6/3	Light gray	Pale brown
Sample #4 (surface)	10YR 7/1	10YR 6/2	Light gray	Light brownish gray
Sample #5 (1.5ft)	10YR 7/2	10YR 6/2	Light gray	Light brownish gray
Sample #6 (3ft)	10YR 7/2	10YR 6/3	Light gray	Pale brown
Glass Cullet Samples				
Andela Products	5Y 3/2	5Y 5/2	Olive gray	Dark olive gray
Glass Aggregate Systems	2.5Y 8/3	5Y 6/4	Pale yellow	Pale olive
Recycle America Alliance	10Y 8/1	5Y 6/3	Light greenish gray	Pale olive

Beach sands can be broadly categorized by their chemical composition into either carbonate beaches ($CaCO_3$) or siliciclastic/quartz (SiO_2) beaches. The beaches in Broward County are a mixture of bioclastic carbonate sands (coquina shell fragments, reef fragments, and skeletal fragments of marine organisms) and silica sands in the form of quartz (Coastal Planning & Engineering / Olsen Associates Joint Venture, 2003). The carbonate content is important because carbonate sands perform differently than silica sands due to different intraparticle porosities, density, bulk density, and structural integrity of carbonate grains (Halley, 2000). In Miami-Dade County, weathering of carbonate sands produces sediments with higher concentrations of silt and clay sized material, which results in elevated turbidity levels in the nearshore zone (USFWS, 2002). Glass cullet avoids these issues because it is composed primarily of silica-based compounds and fines can be controlled prior to placement on the beach.

The average carbonate content of the beach samples was 70%, but ranged from 61% to 84%. The glass cullet samples were not tested for carbonate content because they are chemically 100% silica.

The angularity, or roundness, of individual grains affects sediment settling and motion initiation. It can also be important as a public perception issue. Sample grains of the beach sand and glass cullet were placed under a microscope and visually examined to determine grain angularity using Power's visual classification (Powers, 1953). The existing beach sand is rounded to sub-angular with both high and low sphericity values while the glass cullet was very angular with low sphericity. Edge (2002) showed that glass cullet abrades but that the rate of abrasion decreases and stabilizes with time. Therefore, the angularity of the glass cullet can be expected to decrease over time. Angularity is not expected to have a significant impact on the performance of the glass cullet as beach fill.

FDEP requires that for fill material to be considered beach-compatible that it must not contain toxic material, as specified in Section 62B-41.007 (2)(j)(4) of the Florida Administrative Code. Glass cullet and beach sands were tested for contaminants as part of the geotechnical investigations. Beach sands were used as a control or guide to general background contaminant levels to which the glass cullet would be compared. Tests were performed to detect the presence of lead (Pb), mercury (Hg), total coliform, fecal coliform, enterococci bacteria, 85 semi volatile organics (8270C test), petroleum hydrocarbons (FL-PRO test), and total salt content. Only 5 of the semi-volatile organics registered and these were all below the FDEP (2001) level for direct residential exposure.

PUBLIC PERCEPTION

A public perception investigation was performed by MARS Research (2004) to determine whether the concept of using glass cullet would be accepted by the public. The analysis was broken into three parts: a focus group meeting with beach professionals; a focus group meeting with tourism representatives; and a random phone survey of over 400 Broward County representatives.

The beach professionals were most skeptical about the concept. Most of their concerns did not appear to be with the concept of using recycled glass but of the likelihood that it could be permitted. Interestingly, once the beach professionals were shown a sample of the glass cullet, they adopted a more positive attitude. The beach professionals had several questions regarding the performance of the glass cullet that could not be answered at the time, as most of the investigations presented in this report had not been performed yet. These questions included the similarity of glass cullet to natural beach sand with respect to abiotic and environmental factors.

Overall, the tourism professional focus group was supportive of the concept. Their primary concern was erosion of the beaches, which is obviously one of the key reasons that tourist visit Broward County.

The phone surveys showed that there was support from the public with 89% approving of the concept (45% completely approved, 35% somewhat approved, while 9% disapproved). Overall, the findings were that using glass cullet for beach nourishment is appealing, interesting, and relevant to the public.

BIOLOGICAL ANALYSES

In response to a directive from the Florida Fish and Wildlife Conservation Commission (FFWCC) and FDEP, the CPE team developed a phased scientific investigative program to evaluate material effects on invertebrate and vertebrate (fish) biotic community assemblage. Other studies have demonstrated that experimental bioassays can accurately detect either adverse or benign effects on marine organisms (Peters *et al.*, 2002; Ringwood and Keppler, 2002). In addition, State resource protection agency representatives have suggested that the habitation and colonization of lower invertebrates may serve as a good indicator of the effect recycled glass cullet will have on higher vertebrates. These investigations were undertaken to validate the hypothesis that recycled glass cullet is a viable beach fill alternative to more traditional sand sources. A complete record of this study and the data found are presented in Makowski & Rusenko (in press).

The objective of the biological investigation was to monitor the colonization and survivability of lower invertebrates and fish, through experimental bioassays, in various cullet mixtures. A saltwater flow system was utilized to simulate natural beach conditions within each test matrix. Direct observations and supplemental chemical analyses were conducted to determine whether recycled glass cullet has an affect on biological communities.

Five combinations of glass cullet and beach sand were investigated: 100% beach sand, 75% beach sand/25% glass cullet, 50% beach sand/50% glass cullet, 25% beach sand/ 75% glass cullet, and 100% glass cullet. Saltwater, obtained through the Gumbo Limbo Nature Center oceanic intake system, was delivered through a network of PVC pipes to each test container and provided a constant supply of fresh saltwater (approximately nine water changes over a 24 hr period) to the marine organisms and sediments. Each combination of sand/cullet had three replicate containers. Photo 1 shows three of the containers used to perform the bioassays.

Species introduced into each test matrix were collected or supplied by the Gumbo Limbo Nature Center of Boca Raton, Florida, and included local representative microfauna (i.e., copepods, ostracods, nematodes) and macrofauna organisms (i.e., crustaceans, mollusks, fish). All testing and recorded observations were conducted from May to July, 2005, at the Gumbo Limbo Nature Center.

Macrofaunal organisms were allowed a 24-hour acclimation period before monitoring was initiated. Live marine shrimp were added weekly as a source of food, and uneaten material was not allowed to accumulate in the containers. Biological monitoring of macrofaunal test organisms were conducted through direct visual observations performed at least twice per week for the duration of the study. Macrofauna success rate was calculated by taking the proportion of survived individuals over the total number of individuals introduced to a specific sediment matrix. A complete census of all individuals was taken on a weekly basis.

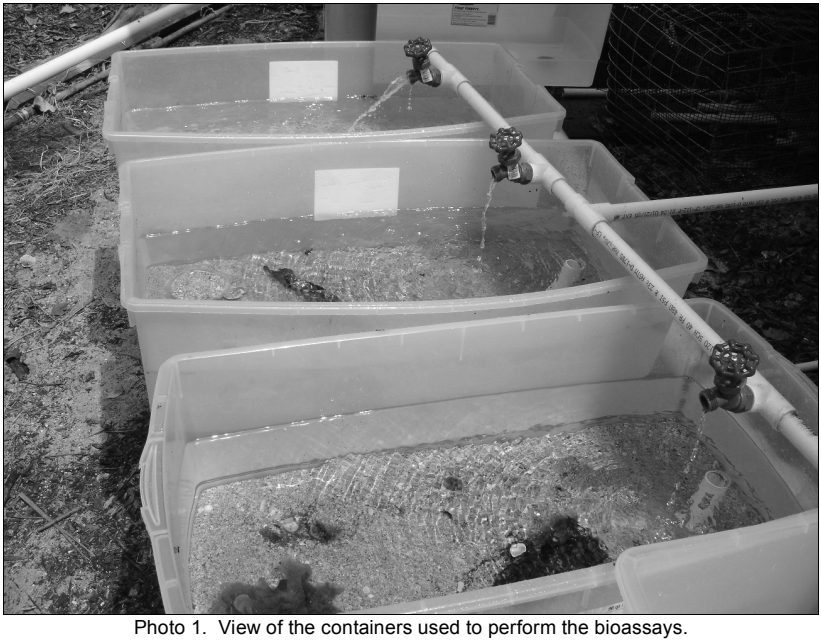

Photo 1. View of the containers used to perform the bioassays.

Microfauna organisms were introduced to each test container by taking a five pound sample of 'live' sand from established (nitrogen cycled) reef display tanks located at the Gumbo Limbo Nature Center. A one-week acclimation and colonization period was allowed before monitoring was initiated.

Biological monitoring of microfauna test organisms was conducted through interstitial core analysis. A 50.1 g interstitial core sample was extracted from each test matrix using a 0.5m long piece of ½ inch PVC pipe and a stopcock. Core samples were taken on a weekly basis and analyzed for the presence/absence of microfauna under a trinocular video microscopy system at a total magnification of 400x. Identification of microorganisms was through external characterization, and active status of individuals was digitally documented.

An important and unexpected observation during the study was the formation of a blackish film that began to develop on the different cullet sediment mixtures after three weeks of testing, first starting on the 100% cullet and then appearing on all the other experimental series, including the controls near the end of the testing period. Further analysis determined that the black film was a precipitation of hydrogen sulfide. This anaerobic sulfide-reducing process has been documented in stagnant coastal waterway systems that lack influential wave action (Carlson *et al.*, 1994). However, when

sediments containing the cullet were mixed and allowed to aerate by directing water movement into the substrate (wave simulation), the visible hydrogen sulfide accumulations disappeared, and no microbial zonation was detected. Hydrogen sulfide test readings also showed that levels were decreased after the wave simulation and aeration was initiated.

After a two-month exposure to glass cullet sediments, it was determined that the artificial cullet substrate did not adversely affect macro-organism habitation or micro-organism colonization. This was evident with the uniform lack of mortality observed in the introduced individuals and the active presence of interstitial microfauna.

Individuals displayed normal active behavior within the cullet matrices and showed no adverse signs of physical stress. Of particular note, was the use of the cullet as defensive camouflage by the test crustaceans and mollusks. In order to shield themselves from predators or direct UV light, the sargassum and blue crabs would thrust their carapaces backward into the cullet until they were completely covered. This behavior was shown repeatedly over the testing period with no harm to the crabs. Similarly, whelks would burrow deep into the cullet as a protective measure, and would do so with no observed injury to their foot or mantle.

Microscopic analyses revealed that colonization of interstitial microorganisms were successful within the cullet mixtures. All the same classes of microorganisms were observed in the control as well as the experimental replicates. Interstitial movements were documented and showed that microorganisms were able to actively transport without adverse effects. Uniform colonization of the sediment mixtures was also reaffirmed by the consistent organic content readings in all the test series.

ABIOTIC ANALYSES

Supplemental testing of abiotic factors was deemed necessary by the FFWCC and FDEP to document the acceptability of glass cullet as an alternative beach fill material. The abiotic factors of temperature, humidity, and gas exchange are considered the most important abiotic variables affecting the survival of reptilian embryos (Ackerman, 1980, 1991; Miller, 1985; Packard and Packard, 1988; Maloney *et al.*, 1990; Mortimer, 1990). In this case, sea turtles were identified as the species of concern. Florida serves as one of the most important nesting environments for sea turtles in the United States, with more than 50,000 nests annually. When an alternative sediment type is introduced to the system, the main concern is that a foreign incubation environment may be produced. Sand acts as a barrier through which water vapor, carbon dioxide (CO_2), and oxygen (O_2) diffuse and dissipate heat. For incubation to be successful and produce hatchlings onto the beach surface, the nest environment must facilitate embryonic development (Georges *et al.*, 1993). Minute differences in temperature, moisture, and gas exchange have the potential of dramatically affecting the sex ratios and survivability of sea turtles during their developmental stages (Mrosovsky and Yntema, 1980; Standora and Spotila, 1985; Mrosovsky, 1988).

The purpose of this *in situ* study was to determine if glass cullet mixtures exhibit the same abiotic characteristics (temperature, moisture content, and respiratory gas exchange) when compared to the current beach sediments. Within the glass cullet, the synergism between moisture, temperature, and gas exchange must be similar to natural beach conditions in order to avoid impacts to the development of embryos during incubation. A complete record of this study and the data found are presented in Makowski *et al.* (in review).

A test plot was constructed on a beach in the City of Hollywood Beach, Broward County, Florida in March 2006. The test plot was 12 m (40 feet) long, 3 m (10 feet) wide, and 1 m (3 feet) deep. Sixteen individual test sections (4 sections for each of the 4 natural beach/glass cullet mixtures) were constructed within the test plot. Each section was 1.5 m (5 feet) by 1.5 m square and 1 m (3 feet) deep. The four natural beach/glass cullet mixtures tested were 100% beach sand, 75% beach sand/25% glass cullet, 50% beach sand/50% glass cullet, and 25% beach sand/75% glass cullet. Photo 2 shows the test plot with each individual section roped and labeled.



Photo 2. A view of the test plot with the rope demarking varying mixture sections.

Using three programmed data loggers placed in each of 16 simulated nests within the native sand/glass cullet matrix, measurements are obtained at the bottom, center, and near the top of each monitoring section. The data loggers collected specific

measurements on temperature and relative humidity every half hour. In addition to the temperature and humidity measurements, gas probe samples are analyzed weekly for O_2 partial pressures (gas exchange) using an oxygen gas analyzer.

After a 171 day testing period (March to August 2006), it was determined that all glass cullet test sections offered a suitable nesting environment for incubating sea turtle embryos based on the measured abiotic factors . Temperature in the glass cullet sections was found to be insignificantly different from the native beach sand controls. All sections, experimental glass cullet and control, logged similar dew point temperatures and relative humidity readings that would allow sea turtle eggs the necessary moisture during incubation. And gas probe samples taken from all the experimental cullet test section recorded high concentrations of oxygen, with no significant variations from the beach sand controls.

UPCOMING WORK

The next step of the project is to place glass cullet along the beach and determine how it performs. A proposal to place and monitor approximately 765 m^3 (1,000 cubic yards) along the beach in The City of Hollywood, Broward County is currently being reviewed by Regulatory Agencies.

CONCLUSION

The analyses conducted to date show that glass cullet is a viable, beach compatible, fill material. The geotechnical analyses suggest that the grain size, color, percent fines, and angularity of glass cullet are sufficient to characterize the material as beach compatible. Contaminant analyses show that the material is clean. The public perception research suggested that the public is amenable to the concept of using glass cullet as a source of beach fill. Biological and abiotic testing both suggest that there will be no impact to microfauna or macrofauna communities, and that sea turtle embryo development will not be impacted due to the use of this material upon the beach.

ACKNOWLEDGEMENTS

We would like to acknowledge the Broward County Commission Office of Waste and Recycling Services and the Florida Department of Environmental Protection for their funding and support of this project. The Broward County Environmental Protection Department has provided valuable assistance in the development of the program and technical contributions. We would also like to acknowledge Malcolm Pirnie, Inc for leading this project. Gumbo Limbo Nature Center has provided facilities to conduct several of these investigations and Dr. Kirt Rusenko has provided time and insight into the biological aspects of the work.

REFERENCES

Ackerman, R.A., 1980. "Physiological and ecological aspects of gas exchange by sea turtle eggs," American *Zoologist*, 20, 575-583.

Austin, N., December 2004. Personal communication (e-mail correspondence). Broward County Commission, Office of Integrated Waste Management, Fort

Lauderdale, Florida.

Carlson Jr., P.R., Yarboro, L.A., and Barber, T.R. 1994. "Relationship of sediment sulfide to mortality of Thalassia testudinum in Florida Bay," *Bulletin of Marine Science* 54, 733-746.

Coastal Planning & Engineering, Inc., and Olsen Associates, Inc. (J-V), 2003. "*Broward County, Florida, Shore Protection Project, Segments II and III, General Reevaluation Report*," Boca Raton, Florida: Coastal Planning & Engineering, Inc., and Olsen and Associates, 2 Volumes.

Edge, B.L.; Cruz-Castro, O., and Magoon, O.T., 2002. "Recycled Glass for Beach Nourishment," *Proceedings of the 28th International Conference on Coastal Engineering*, World Scientific, Vol. 3, pp. 3630-3641.

Finkl, C.W. and Kerwin, L., 1997. "Emergency beach fill from glass cullet: An environmentally green management technique for mitigating erosional 'hot spots' in Florida," *Proceedings 10th Annual National Conference on Beach Preservation Technology* (St. Petersburg, Florida), pp. 304-319.

Florida Department of Environmental Protection, 2000. "*State of Florida Strategic Beach Management Plan*," Florida Department of Environmental Protection, Tallahassee, Florida.

Florida Department of Environmental Protection, 2001. Guidance for Disturbance and Use of Old Closed Landfills or Waste Disposal Areas in Florida. Tallahassee, Florida: Florida Department of Environmental Protection, Solid Waste Section.

Halley, R.B., 2000. "11 Things A Geologist Thinks an Engineer Should Know About Carbonate Beaches," *Carbonate Beaches 2000*. ASCE, pp 1-14.

Kerwin, L., 1997. "*Potential Applications for Recycled Glass in Beach Management: Emergency Stabilization of "Hot Spots" in Broward County, Florida*," Boca Raton: Florida Atlantic University, Master's thesis.

Makowski, C., and Rusenko, K., in press. "*Recycled Glass Cullet as an Alternative Beach Fill Material: Results of Biological and Chemical Analyses*," *Journal of Coastal Research*.

Makowski, C., Rusenko, K., Thomson, G.G., and Kruempel, C.J., 2005. "*Broward County Beach Demonstration Project: Biological Analysis of Recycled Glass Cullet*," Boca Raton, Florida: Coastal Planning & Engineering, Inc., (Prepared for Malcolm Pirnie, Inc., Fort Lauderdale, Florida) 24p.

Makowski, C., Rusenko, K., Thomson, G.G., and Kruempel, C.J., 2006. "*Broward County Beach Demonstration Project: Abiotic Analysis of Recycled Glass Cullet*," Boca Raton, Florida: Coastal Planning & Engineering, Inc., (Prepared for Malcolm Pirnie, Inc., Fort Lauderdale, Florida) 22p.

Makowski, C., Rusenko, K., Thomson, G.G., and Kruempel, C.J., in review. "*Abiotic suitability of Recycled Glass Cullet as an Alternative Sea Turtle Nesting Substrate*," *Endangered Species Research*.

Malcolm Pirnie, Inc, 2003. "*Beach Renourishment Pre-Feasibility Study,"* Fort Lauderdale, Florida: Malcolm Pirnie, Inc.

Maloney, J.E.; Darian-Smith, C.; Takahashi, Y., and Limpus, C.J., 1990. "The environment for development of the embryonic loggerhead turtle (Caretta caretta) in Queensland," *Copeia*, 1990(2), 378-387.

MARS Research, Inc., 2004. "*Broward County Beach Demonstration Project: Public Perception Phase, Initial Findings Report*," Plantation, Florida. (Prepared for Malcolm Pirnie, Inc., Fort Lauderdale, Florida) 14p

Miller, J.D., 1985. "Embryology of marine turtles," in: Gans C.; Billett F., and Maderson P.F.A. (eds.), *Biology Of The Reptilia*. New York: Wiley-Interscience, Vol. 14a, 269-328.

Mortimer, J.A., 1990. "The influence of beach sand characteristics on the nesting behavior and clutch survival of green turtles (Chelonia mydas)," *Copeia*, 1990, 802-817.

Mrosovsky, N., 1988. "Pivotal temperatures for loggerhead turtles (Caretta caretta) from northern and southern nesting beaches," *Canadian Journal Zoology*, 66, 661-669.

Mrosovsky, N., and Yntema, C.L., 1980. "Temperature dependence of sexual differentiation in sea turtles: Implications for conservation practices," *Biology Conservation*, 18, 271-280.

Paardekooper, Williem-Jan, November 2004. Personal correspondence with Gordon Thomson (e-mail correspondence). Curexglass Sales, Curaçao, Dutch Antilles.

Packard, G.C., and Packard, M.J., 1988. "The physiology ecology reptilian eggs and embryos," in: Gans C., and Huey R.B. (eds.), *Biology Of The Reptilia*. New York: Alan R. Liss, Vol. 16, pp. 523-605.

Peters, C., Becker, S., Noack, U., Pfitzner, S., Bulow, W., Barz, K., Ahlf, W., and Berghahn, R. 2002. "A Marine Bioassay Test Set To Assess Marine Water and Sediment Quality – Its need, the approach, and first results," *Ecotoxicology* 11, 379-383.

Powers, M.C., 1953. "A New Roundness Scale for Sedimentary Particles," *Journal of Sediment Petrology*, 23, 117-119.

Ringwood, A.H., and Keppler, C.J. 2002. "Comparative in situ and laboratory sediment bioassays using juvenile clams, Mercenaria mercenaria," Environ. *Toxicol*. Chem. 21: 1651-1657.

Scientific Environmental Applications, Inc., 1999. "*Sediment and Carbonate Analysis Report, Broward County Segments II & III Sand Samples*," Melbourne Village, FL: Scientific Environmental Applications, Inc. Book 2 of 2.

Standora, E.A., and Spotila, J.R., 1985. "Temperature dependent sex determination in sea turtles," *Copeia*, 3, 711-722.

Temple, I., November 2004. Personal communication with Gordon Thomson (e-mail correspondence). Event Management Services. Auckland, New Zealand.

Thomson, G.G.; Finkl, C.W.; Kruempel, C., and Krause, K., 2004a. "*Broward County Beach Demonstration Project: Literature Review*," Boca Raton, Florida: Coastal Planning & Engineering, Inc., (Prepared for Malcolm Pirnie, Inc., Fort Lauderdale, Florida) 14p.

Thomson, G.G.; Finkl, C.W., and Kruempel, C., 2004b. "*Broward County Beach Demonstration Project Geotechnical Investigation Report: Technical Memorandum,*" Boca Raton, Florida: Coastal Planning & Engineering, Inc., (Prepared for Malcolm Pirnie, Inc., Fort Lauderdale, Florida) 12p.

U.S. Fish and Wildlife Service, 2002. "*Fish and Wildlife Coordination Report, Broward County Beach Erosion Control Project*". U.S. Fish and Wildlife Service, Vero Beach, FL, pp28.

WasteBusters Trust Canterbury, 2004.
http://www.wastebusters.orcon.net.nz/crystalbeach.html.
Woodward-Clyde Consultants, 1993. "*Feasibility Study of Recycled Ground Glass Beach Sand for the City of Encinitas*," San Diego, California.

BEACH NOURISHMENT EVOLUTION IN THE CANCÚN BEACH, QUINTANA ROO, MÉXICO

Diana K. Morán[1], Paulo Salles. A de A[2], José C. Sánchez[3], Juan C. Espinal[4]

1. Universidad Nacional Autónoma de México, Instituto de Ingeniería, Ciudad Universitaria, Coyoacán, México D. F., 04510, México. dmorang@iingen.unam.mx
2. Universidad Nacional Autónoma de México, Instituto de Ingeniería, Ciudad Universitaria, Coyoacán, México D. F., 04510, México. psallesa@iingen.unam.mx.
3. Comisión Federal de Electricidad, Gerencia de Estudios de Ingeniería Civil, Gerencia de Oceanografía. Torre Hemicor, Av. Insurgentes Sur 826, 5° piso, México D. F. csanchezl@cfe.gob.mx.
4. Universidad Nacional Autónoma de México, Instituto de Ingeniería, Ciudad Universitaria, Coyoacán, México D. F., 04510, México. jespinalg@iingen.unam.mx.

Abstract: This paper presents the analysis of the evolution of the Cancun Beach Nourishment, in Quintana Roo, México. The nourishment project was based on the analysis of four beach profile sets (1985, 1989, 2000, and 11/2005, after hurricane Wilma), high resolution satellite images, wave data and native sediment samples from Cancun Beach. After Wilma the remaining sand volume was approximately 0.5x106 m3, with beachwidth of only 10 to 17 m. Although the nourishment sediment volume ($2.7x10^6$ m^3) was limited by the available federal budget, the design dry beach width was estimated to be between 22 and 28 meters. After nourishment, three beach profile sets were analyzed (April, August and November 2006), as well as the associated morphodynamic state. At present, the beach profile tends to a pre-Wilma natural slope. This process is however decreasing the dry beach width to find a stable state along the beachface.

INTRODUCTION

The beach of Cancún as most of the Mexican beaches are dominated by erosion processes, associated with world climate change, form of the beachface, sediment characteristics and the occasional but not less important the effects of strong hurricanes striking the region like Gilbert in 1988 and Wilma in .2005.

Previous studies have determined that under normal wave conditions Cancún beach is dissipative, according to the morphodynamic state classification proposed by Wright and

Short (1984). This morphodynamic state changes when a meteorological extreme event like a cold front or hurricane occurs. The beach response to these events is strong but not uniform. In fact, the erosion is stronger in the Northern zone of Cancún beach, near Punta Cancún, than in the south near to Punta Nizuc (see Fig. 5). This erosion process, translates in the sediment being transported toward the lower areas of beach profile (offshore) forming longshore bars wich in turn play an important role protecting the beachface and keeping the sand within the closure depth. These events change the beach from "dissipative" to a "dissipative and lonsghore bar-trough". See Fig. 1 and Fig. 2.



Fig. 1 Cancún Beach before nourishment



Fig. 2 Cancún Beach after Nourishment

During the storm, waves are larger and the closure depth shifts offshore to deeper areas. After the storm, the longshore bar-trough state evolves to the initial state (dissipative), and the original closure depth is also reestablished. However, these are inevitably some loss of sand because one part of the material was transported beyond this original closure depth during the storm.

This process has been observed through the last 20 years. During this period the two most important hurricanes on record ocurred: Gilbert in 1988 and Wilma in 2005. Both hurricanes were classified as category five in the Saffir-Simpson scale. Particularly, after Wilma in October 2005, the beachface (from Punta Cancun to Punta Nizuc, a 12 km long) lost approximately 5.5 millions m^3 of sand with zones showing only with a 10 to 17 meters dry beach widths (Fig. 3). and zones without dry beach, as shown in Fig. 4.



Fig. 3 Cancún Beachface with a 17 meters of Dry Beach. After Wilma



Fig. 4 Beachface without Dry Beach. After Wilma

Due to the beach condition after hurricane Wilma, and the importance of this resort to México (the most important tourist destination), an emergency project of nourishment was implemented. The objective was to rehabilitate the beach profile with to produce a dry beach width between 22 and 28 meters along to the coastal front from Punta Cancun to Punta Nizuc. The final project and supervision contract was assigned to CFE ("Comisión Federal de Electricidad"). CFE gathered and analyzed beach morphodynamics studies during the last 20 years, as well as the most recent bathymetric surveys, to evaluate the dynamics of the processes responsible of the beach behavior and its response to an extreme wave climate occurrence. Furthermore, the aim of the project

surveys, to evaluate the dynamics of the processes responsible of the beach behavior and its response to an extreme wave climate occurrence. Furthermore, the aim of the project was to identify the evolution of the morphodynamic states by means of Benedet´s (2004) procedure implementation to identify boundary conditions which characterize the beach in terms of these morphodynamic states. Finally, the observation and analysis of the beach profiles, contributed to determine the morphodynamic evolution after the nourishment works and to find possible long-term solutions to the erosion problem.

STUDY AREA

Cancún beach is located in the Mexican southeastern state of Quintana Roo, and it belongs to the Municipio Benito Juarez (Fig. 5). It is a headland beach, confined to the North by Punta Cancun (21°,07',08''N, 86°,44',25''W) and to the South by Punta Nizuc (21°,02',07N, 86°,46',38''W). It is bounded to the North by Bahia de Mujeres, to the East by the Caribean Sea and to the West by Nichupté Lagoon.

The study zone is a littoral barrier beach, and it has a 12 kilometer beachface. Its native beach sediment is mainly of biogenic origin, with mean grain size between 0.22 and 0.55 mm. Due to the erosion processes, the beachface is not in dynamic equilibrium. Historically, several hurricanes have hit the project area, accelerating the erosion processes considerably, such as Hurricanes Gilbert in 1988 and Wilma in 2005.

Before Hurricane Gilbert Punta Nizuc Punta Nizuc showed a 57 meters beach width with a sand volume of 10.5×10^6 m^3 (CFE, 2006), as shown in Fig. 6. After hurricane Gilbert occurrence the mean beachwidth decreased to 35 meters, with a sand volume of 6.0×10^6 m^3 (i.e., 4.5×10^6 m^3 were lost). Seventeen years later Hurricane Wilma hit Cancun beach again increasing considerably the erosion problem along the project area, so the sand loss was estimated in additional 5.5×10^6 m^3, therefore the remaining sand volume in the beachfront was approximately 0.5×10^6 m^3. The mean grain diameter (d_{50}) was 0.24 to 0.32 mm.

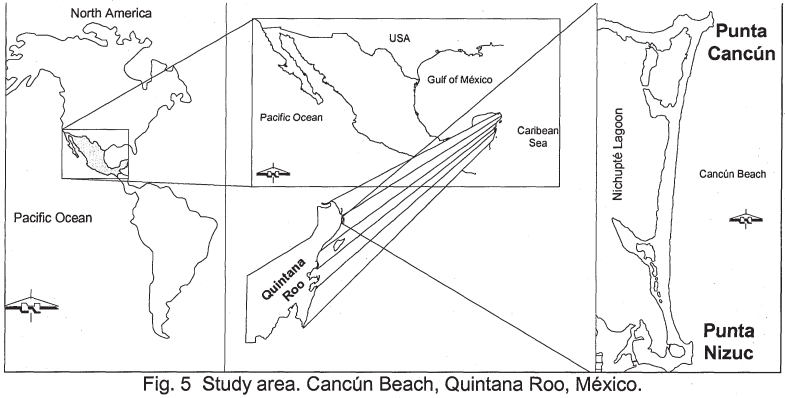

Fig. 5 Study area. Cancún Beach, Quintana Roo, México.



Fig. 6 Punta Nizuc in 1985, before Hurricane Gilbert.

Preliminary Studies (Coast Line Evolution)

The erosion process caused by hurricane Wilma along the project area was analyzed by CFE using high resolution satellite images. In Fig. 7 to 12 the red line shows the coastline before hurricane Wilma and the blue one shows the coastline after Wilma. Fig. 7 to 12 show the beach width loss which varies between 7 (South zone) and 32 m (central zone). Table 1 summarizes the beach width loss with 21.68 m as a mean value.



Fig. 7 Beachfacewidth loss (1+700)

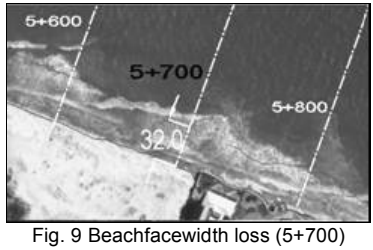

Fig. 9 Beachfacewidth loss (5+700)

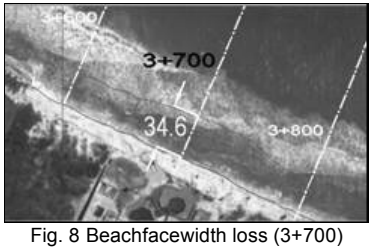

Fig. 8 Beachfacewidth loss (3+700)

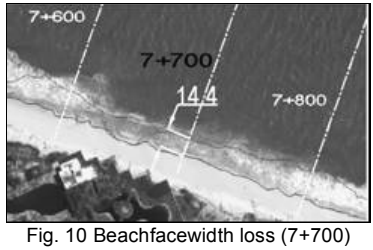

Fig. 10 Beachfacewidth loss (7+700)

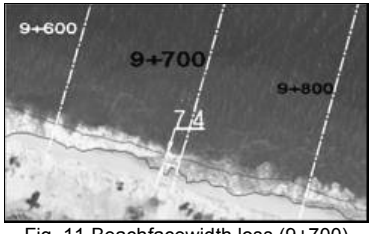

Fig. 11 Beachfacewidth loss (9+700)

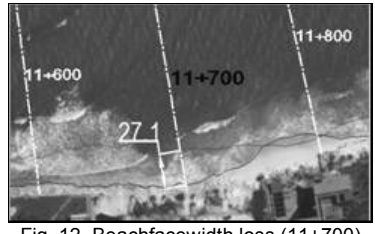

Fig. 12 Beachfacewidth loss (11+700)

Table 1 Beachwidth Loss in Cancún By Hurricane Wilma, 2005

Section	Loss of Dry Beach m	Section	Loss of Dry Beach m
1+700	20.2	7+700	14.4
2+700	20.0	8+700	18.5
3+700	34.6	9+700	7.4
4+700	21.3	10+700	16.3
5+700	32.0	11+700	27.1
6+700	26.7		
		Mean value	**21.68**

Emergency Beach Nourishment Project

The emergency beach nourishment project was performed by the CFE Oceanography Department. The main objective was to restore the beach profile along the 11.6 kilometers of Cancún Beach. According to CFE's preliminary design and the first bathymetric survey after Wilma, the design width was estimated to be between 22 and 28 meters, with a construction width of 60 meters.

The sand volume estimate for the Cancun beach nourishment was the result of assessing the sediment transport rate by waves and currents, as well the native and fill sediment characteristics. The nourishment volume of sediment was unfortunately restricted by the available federal budget (U.S. $ 20 Million) which corresponded to only $2.7x10^6$ m^3 of sand. The borrow area was located 30 kilometer NE of the project area with a 30 m mean depth.

Post Construction Monitoring Cancun Beach

For the nourishment Project CFE analyzed the coastline evolution from bathymetries surveyed in 1985, 1989, 2000 and 2005. In addition three more detailed bathymetries were performed by CFE on April, August and November 2006, after the nourishment.

The detailed beach profile analysis was made every 100 m, with a starting point on 0+600 m and a final point on 12+100 m, on Punta Nizuc. In order to save space 6 beach profiles were selected to show the applied methodology, and they are shown in Fig. 13.

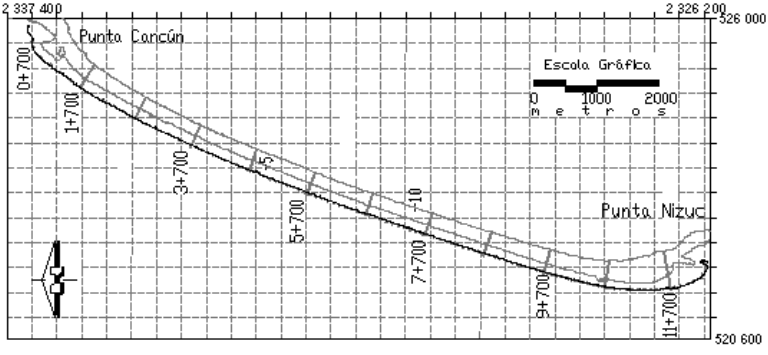

Fig. 13 Selected beach profiles.

The wave climate was determined by jeans of a wave-current-temperature measurement instrument (InterOcean S4) deployed at 20 m depth in front of Punta Cancún. The measurement period presented here starts on January 25th and ends on August 17th, 2006.

Fig. 14 shows the wave rose, observing that during the measurement period the dominant direction comes from the range 100 to 135° (SE). The wave heights vary from 0.27 to 2.2 m.

Table 2 shows the statistical treatment to the whole sample. The mean value for the wave height varies from 0.6 to 1.2 m, meanwhile the wave periods vary from 5 to 6.5 seconds.

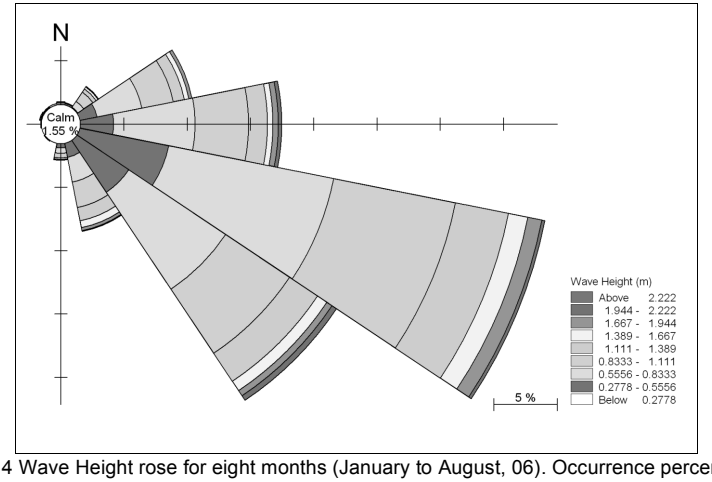

Fig. 14 Wave Height rose for eight months (January to August, 06). Occurrence percentage to wave height and its direction.

Table 2 Wave Climate Statistics, January to August 2006, Cancún Beach.

Wave Climate	Time Period	Wave Height	Wave Period
		m	s
1	January 25 -March 25	0.8-1.2	6-6.5
2	March 26 - May 25	0.6-0.8	5-5.5
3	May 26 - July 25	0.4-0.6	6-6.5
4	July 26 - August 17	0.6-0.8	6-6.5

The fill sediment characterization along the 11.6 km was determined through the analysis of 100 sand samples evenly spaced distribution. The results indicate that the grain size distribution varies between 0.27 and 0.53 mm. The mean grain size for the nourishment sand was 0.39 mm, meanwhile the mean grain size for the native sand is 0.32 mm

BACKGROUND

The morphodynamic state of a beach can be represented by Wright & Short's classification (1984) which is based on the dimensionless fall velocity (Ω) given by

$$\Omega = H_b / \omega T \tag{1}$$

where H is the breaker wave height, T the period and ω the fall velocity. Based on experiments and observations Wright and Short (1984) found that the dimensionless fall velocity is a prediction equation which helps to identify the beach state according to the wave characteristics and the beach grain size. When $\Omega > 6$ the beach tends to be dissipative, and when $\Omega < 1$ it tends to be a reflective. The intermediate beaches have values of dimensionless fall velocity between 1 and 6.

Bennedet, et. al., 2004, proposed the calculation of boundary conditions, via. mean grain size of a beach fill that will generate mostly dissipative or reflective beach conditions, given by

$$\Omega = K d_f^{-b} \tag{2}$$

where K is a specific value function of the H_b / T and df^{-b} is the fill composite sand grain size. Finally, with the fitted of Ω the morphodynamic boundary conditions can be obtained.

ANALYSIS RESULTS

Previous studies have determinates that close to Punta Cancun Northern zone, the beach profiles are more vulnerable than the Southern one. As a result of that behavior three-dimensional post-storm longshore bars form to protect the beachface from Punta Cancún to the section 7+700 (Morán, et. al., 2006).

During the hurricane occurrence, three-dimensional post-storm longshore bars formed as far as the 7+700 section (Fig. 13), and their geometric characteristics and position along to the profile are linked to the degree erosion on that area.

From the post-Wilma profiles we can see that the distance from shoreline to the shoreward side of bar is smaller in the sections where larger dry beach erosion occurred (Table 1). This suggests that the sand lost during hurricanes is able to return to the active profile (dry beach), depending to the wave climate conditions.

Besides, from the 7+800 profile to Punta Nizuc it a soft longshore sand bar is observed, given the stabilization of zone. As the zone is more stable than Punta Cancún, the lost of sand is so much smaller that the natural cover can be possible.

In turn, from the post beach fill profiles we can see that the profile evolution obeys a tendency to recover a pre-Wilma equilibrium state. In all of cases it is observed that changes in the low profile (between the oceanward end of the bar and closure depth) are small, suggesting a state close to equilibrium in that zone of the profile.

On section 1+700 we can see that after nourishment the sand fill and the longshore bar migrated first offshore, and later the bar redistributed along the active profile, suggesting in turn a tendency to reach the equilibrium slope.

On section 3+700 the longshore bar also migrated offshore and disappeared, but apparently in this area it did not redistribute along the profile, suggesting the deposited san volume was sufficient to reach an equilibrium state.

The behavior on sections 5+700 and 7+700 is similar. In both sections the longshore bar evolution is slightly shoreward (26 to 30 m.). The longshore bar indeed returned to its pre-Wilma position.

For section 9+700 the erosion effects only were significant in the first 100 meters, favoring a relatively small dry beach loss of only 10 meters, as well as faster profile stabilization.

Finally, the large loss of dry beach (27m) in section 11+700 was caused by the presence of protection structures close to the section (11+800 and 11+900).

On another hand, Fig. 15 show the coast line evolution in the area corresponding to the same profiles observed before. The black line is the coast line position before nourishment, the red line represents the coastline position on August 2006 (soon after the end of the fill process) and the green line represents the coastline position on November 2006. It can be seen first that the beach profile changes is companied by important changes in the coastline. For instance, sections 3+700 to 5+700 present a coastline retreat of 8-11 m, which, as shown before, is related to the development of a new equilibrium profile. It is important to keep in mind that volume fill is not enough to the beachface reach the stability state.

Finally, Fig. 16 shows the morphodynamic state of the beach as a function of the sand

fill and the wave climate reported on the Table 2. For all wave climate conditions the state of the beach is intermediate with dimensionless fall velocity varying from 5.7 to 1.47. Also fitting curves for morphodynamic bounded conditions area presented. The grain size necessary to reach dissipative states varies from 0.155 to 0.265 mm. For the Cancún beach to represent a state close to reflective the wave climate has to be similar to "wave climate 3" (Table 2), with grain size of 0.58 mm. Although the rest of the wave climate states also decrease as the grain size increases, they do not reach the reflective state for the grain size encountered in the area.

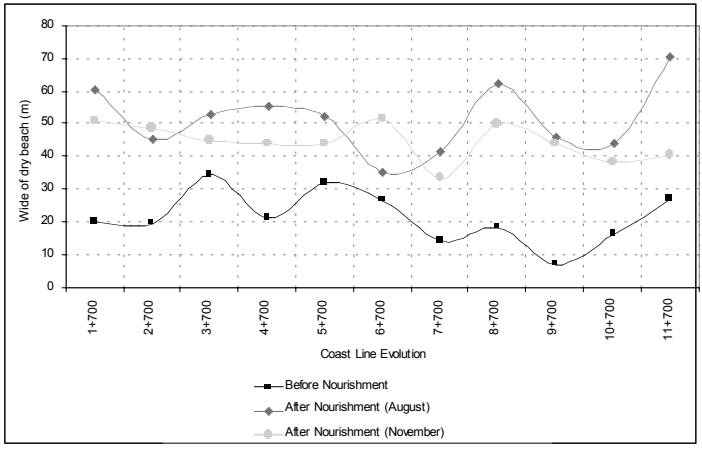

Fig. 15 Coast line evolution at Cancún beach after nourishment.

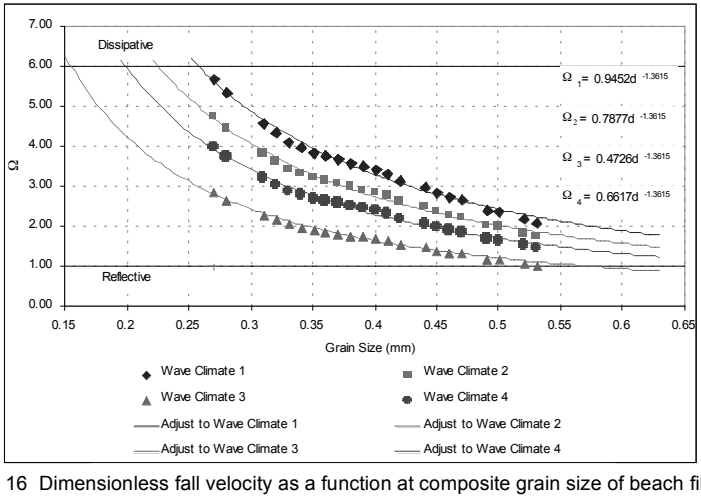

Fig. 16 Dimensionless fall velocity as a function at composite grain size of beach fill for Cancún Beach.

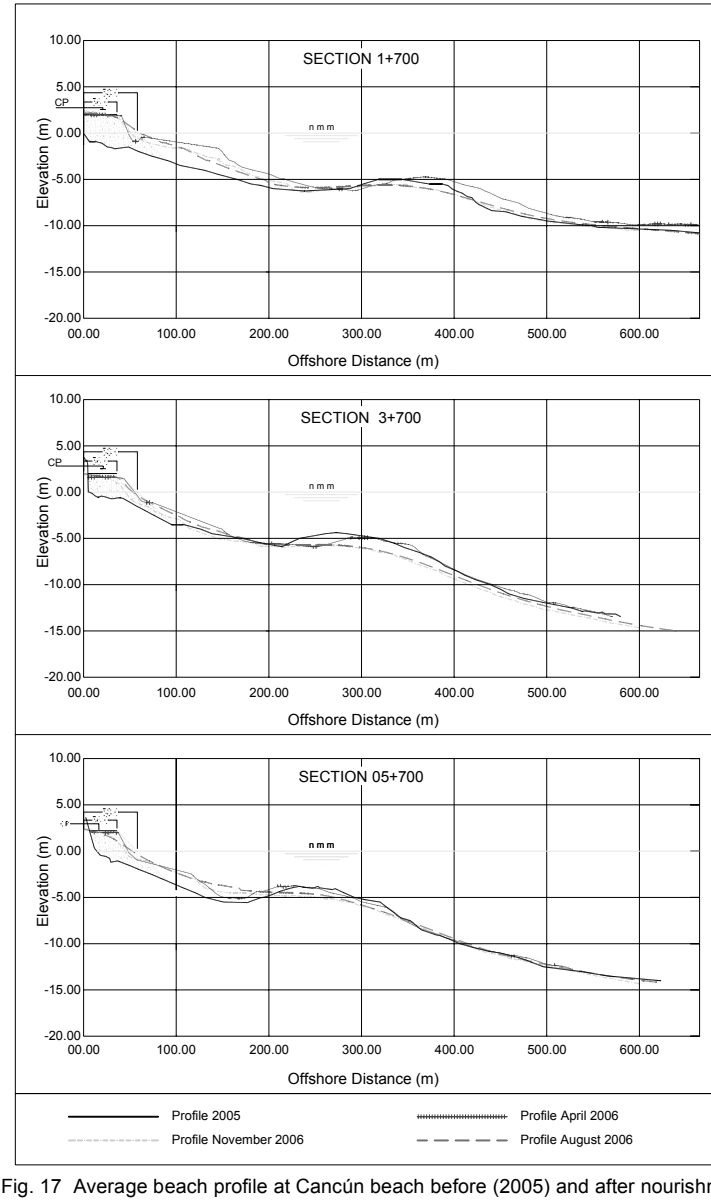

Fig. 17 Average beach profile at Cancún beach before (2005) and after nourishment sections 1+700, 3+700 and 5+700.

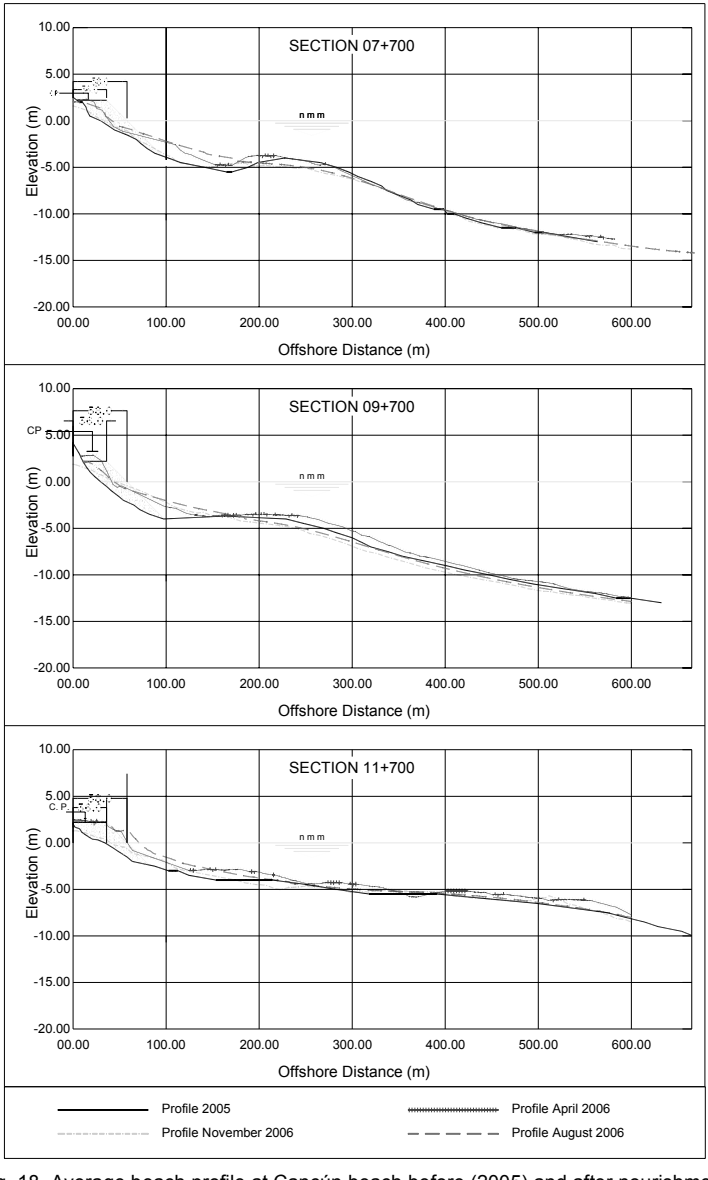

Fig. 18 Average beach profile at Cancún beach before (2005) and after nourishment, sections 7+700, 9+700 and 11+700.

CONCLUSION

The beach profiles analysis presented here suggest that the beach, after nourishment, is evolving towards a new equilibrium state beach. The coastline is retreating, but this is not necessarily associated with instability. Instead, it should be regarded as the evolution to a new equilibrium condition, in which unfortunately the sand fill volume was not sufficient.

This study also shows that the main damage of hurricane Wilma was not on the dry beach, but on the low and offshore part of profile. After the hurricane, the upper part of the profile eroded in order to provide sand to the lower and (through the formation and migraton of a longshore bar), and thus reach the equilibrium slope and profile. The Cancún beach tends today to be a stable system again, until the impact of another hurricane.

REFERENCES

Benedet, Lindino, Charles W. Finkl, Thomas Campbell, Antonio Klein., (2004). "Predicting the effect of beach nourishment and cross-shore sediment variation on beach morphodynamic assessment," Coastal Engineering 51 (2004). pp. 839-861

CFE, 2006. "Proyecto Ejecutivo de Restauración y Recuperación de las playas de Cancún, Quintana Roo," Gerencia de estudios de Ingeniería Civil (GEIC) de la Comisión Federal de Electricidad.

Morán, Salles, Adame, Sánchez, Espinal, 2006. "Análisis Morfológico de las playas de Cancún," XXII Congreso Latinoamericano de Hidráulica, Ciudad Guayana, Venezuela, octubre 2006.

Wright, L. D., Short, A. D., (1984). "Morphodynamic variability or surf zones and beaches: a synthesis," Marine Geology 56, 93-118.

GEOMORPHIC RESPONSE AND ELEMENTS OF SEDIMENT BUDGET AT ST. JOSEPH HARBOR, SOUTHEAST LAKE MICHIGAN

Mohammad Dibajnia[1], Robert B. Nairn[2], James P. Selegean[3]

1. Baird & Associates, 627 Lyons Lane, Suite 200, Oakville, Ontario, L6J 5Z7, Canada. mdibajnia@baird.com.
2. Baird & Associates, 627 Lyons Lane, Suite 200, Oakville, Ontario, L6J 5Z7, Canada. rnairn@baird.com.
3. U.S. Army Corps of Engineers, 477 Michigan Avenue, Detroit, MI 48226, USA. James.P.Selegean@lre02.usace.army.mil.

Abstract: This paper describes a series of geomorphic investigations conducted to establish a long-term sediment budget and quantify sources and sinks of sediment contributing to the growth of fillet beaches and erosion of adjacent shorelines at the St. Joseph Harbor area on southeast Lake Michigan. Long-term bluff recession and lakebed erosion rates are determined for the study area. The impact of the harbor and its operations on the sediment budget are discussed.

INTRODUCTION

The city of St. Joseph is located on southeast Lake Michigan (Figure 1). The jetties of St. Joseph Harbor were initially constructed between 1837 and 1839. There were several extensions to the north and south jetties. The final extensions to the present day length were completed in 1903. The north jetty is approximately 2,740 ft (835 m) long; the south jetty is about 175 ft (53 m) shorter than the north jetty. Figure 2 summarizes the history of St. Joseph Harbor construction. Following the construction, sand was trapped in the fillet beaches, which grew on both sides of the harbor, and later in the navigation channel. The loss of sand from the littoral system is likely to have exacerbated the natural erosion over some time periods at certain locations south of the harbor. Starting in 1970, the US Army Corps of Engineers (USACE) has placed a quantity of sand approximately equal to the amount of sand intercepted by and dredged from the outer navigation channel back into the littoral system on the south side of the harbor. Prior to 1970, the dredged material was dumped offshore.

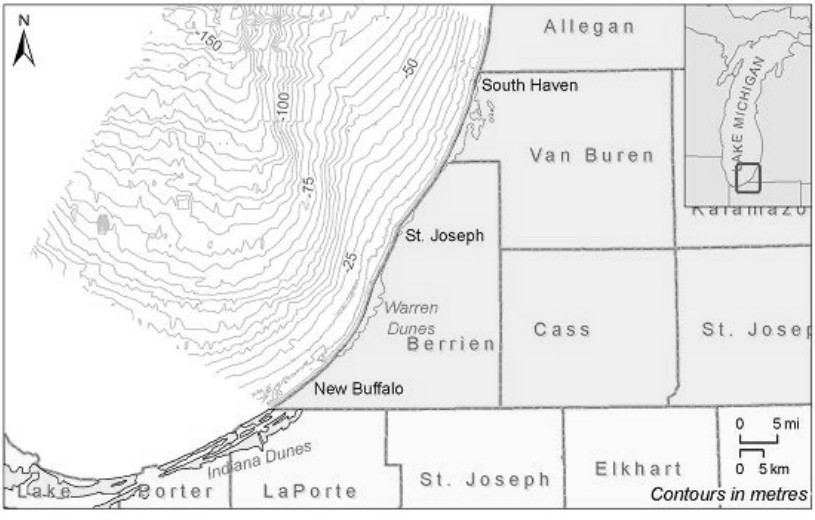

Fig. 1. Southeast Lake Michigan and the study area



Fig. 2. Harbor construction history

The present study was to evaluate the environmental, topographic/hydrographic and geologic conditions of an area extending from approximately 10 miles (16 km) north of the St. Joseph Harbor to 10 miles (16 km) south of the harbor and quantify sources and sinks of sediment to establish a long-term sediment budget. Morphological developments resulting from construction of the harbor and related activities will be discussed.

GEOLOGIC SETTING

The Indiana Dunes complex at the south end of Lake Michigan and the Grand Mere and Warren Dunes deposits south of the harbor (see Figure 1) have formed through the deposition of sand carried along the shore from the north over the last several thousand years, as described by Thompson and Baedke (1995). Thompson and Baedke (1995), Baedke and Thompson (2000) and Baedke et al. (2004) used the successive depositional ridges in the Indiana Dunes complex and found that a beach ridge is formed approximately once every 33 years in response to quasi-periodic high lake levels. The continuous record of deposition of these ridges up to the early 1800's indicates that the supply of sand has remained relatively constant through the last 100's of years (Thompson et al. 2004). The sand that is deposited in the Indiana Dunes may be conclusively related to littoral transport from the northeast (due to the form of the ridges) through natural erosion of the southeast shores of Lake Michigan (Thompson and Baedke, 1995). The end moraines that formed at the toe of glacial ice lobes moving south down the long axis of Lake Michigan (Larson, 2006) have been eroded over the last several thousand years, most likely by wave action as there were no subsequent glacial advances (Larson and Schaetzl 2001; Larson 2006), and supplied the sand to create the dunes in the Grand Mere Lakes (Tague, 1942) and Warren Dunes area and the Indiana Dunes to the south.

The geology around St. Joseph Harbor varies from glacially consolidated bluffs (with 10 to 80% clay/silt content) to sand dune deposits. This variability in geology distinguishes the erosion processes along these shorelines from the well-studied fully sandy coasts. Larson (2006) has produced a map view of the surficial geology together with stratigraphic sections for the study area north and south of the harbor based on information collected and interpreted over the past 20 years (see Figure 3). Below is a description of the geology south of the harbor where shoreline erosion has been an ongoing concern.

There is a 3 miles (5 kilometers) long reach immediately south of the harbor that consists of three primary stratigraphic units; lacustrine sand, sandwiched between an upper till at the surface and a lower till at and below the lake level. The bluff height is about 90 ft (27 m) through most of this reach, but diminishes to 70 ft (21 m) towards the south end. With the exception of the south fillet beach, this is a cohesive shore zone with exposed till in the nearshore zone.

Further to the south there is a zone of about 2.3 miles (3.7 km) long where the upper till layer no longer exists and the lower till layer initially is discontinuous and then

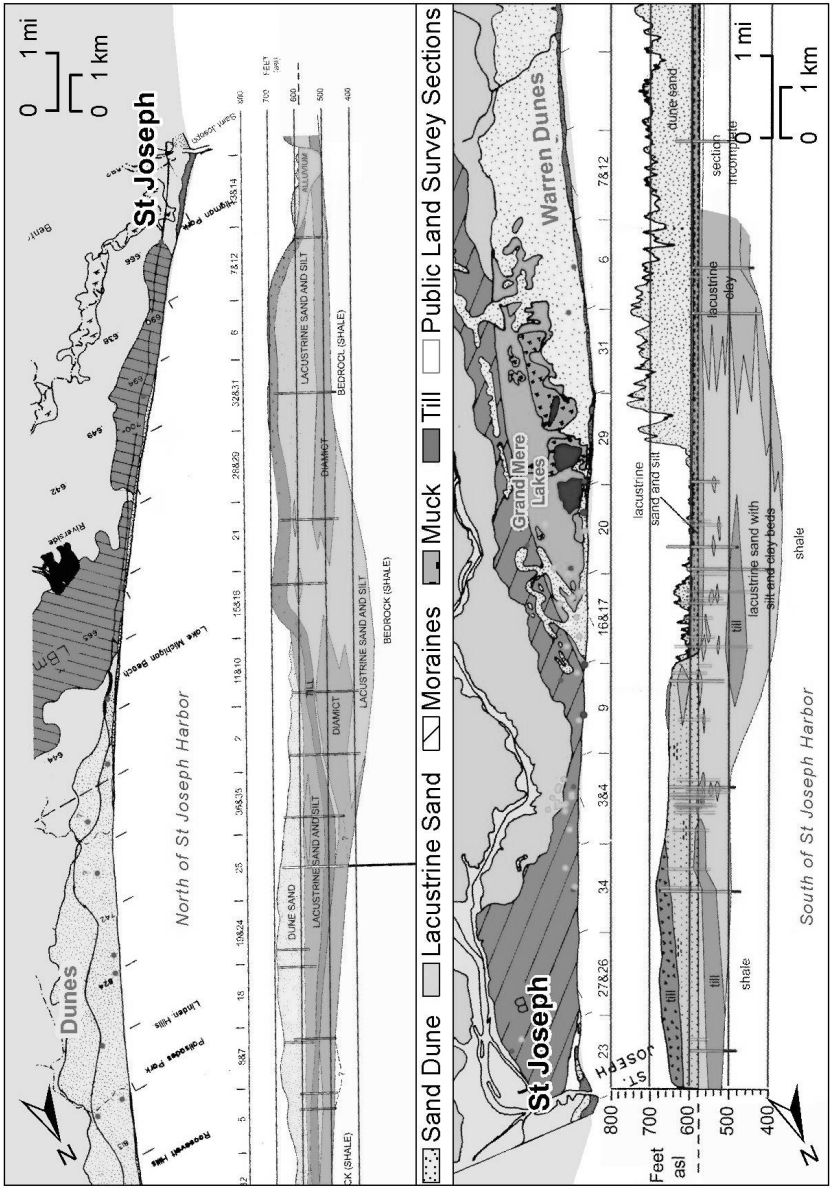

Fig. 3. Geology of the study area

disappears entirely and only lenses of clay appear below lake level within a "Lacustrine Sand" body. The cohesive shore gradually changes to a sandy shore over this zone. The average bluff height is about 60 ft (18 m). Most of the sediment eroded from this area is lacustrine sand. The Lacustrine Sand unit both north and south of St. Joseph is a mix of stratified sand, silt, and clay with some thin gravel layers (Larson, 2006). The dominant lithology, however, is sand (sand proportion varies along the shore from locations with almost 100% sand to places with only 50% sand).

South of the above zone there is a "Lacustrine Sand and Silt" layer with less pronounced bluffs. This layer consists chiefly of fine-to-coarse sand, which likely was deposited in an open near-shore environment in less than about 30 ft (9 m) of water during transgression of the Nipissing I high lake level (Larson 2006). This zone extends for about 2.5 miles (4 km) followed by Grand Mere dunes and then Warren dunes. Grand Mere dunes range from 20 to 40 ft (6 to 12 m) in height and sit over top of the lacustrine sand and silt unit. In summary, the shoreline south of the harbor changes from dominantly cohesive to dominantly sandy from a location about 3 miles (5 km) south of the harbor over a short section of shoreline.

BLUFF RECESSION AND LAKEBED EROSION (SEDIMENT SOURCES)

Historic erosion rates of the shorelines and bluffs, both north and south of the harbor, were determined through comparisons of snapshots of the shoreline and bluff conditions from maps, air photos and a satellite image. The primary reference years were based on:

- Michigan General Land Office (GLO) mapping from 1829/1830;
- Map of the bathymetry of the harbor area from 1871;
- Air photographs from 1938, 1960, and 2002.

All the images and historic charts were georegistered in GIS and both the shorelines and top of bluff lines were digitized. A recession analysis was then completed for both shorelines and top of bluff lines using a tool that measures transects between a historic and recent line at 20 m intervals. The Average Annual Recession Rate (AARR) was determined by taking the mean of all transects over the area of interest and then dividing by the number of years in the comparison period. This result is the Average Annual Recession Rate for that particular time period.

Bluff Recession Rates

Bluff recession rates were calculated for the periods in between four pairs of snapshots from the years: 1830, 1871, 1938, 1960 and 2002. Figures 4 and shows sample results of bluff line comparison from 1830 to 1871. From this figure, it is evident that between 1830 and 1871 the natural (pre-harbor) erosion increased over a 3 mile (4.8 km) reach south of the harbor. Bluff recession rates in this zone ranged between 2.5 to 9.0 ft/yr (0.75 and 2.7 m/yr) with an average of 5.2 ft/yr (1.6 m/yr). Further to the south of this zone of harbor influence, however, the bluff recession rates in Zone 2 were in the range of 0.7 to 2.6 ft/yr (0.2 to 0.8 m/yr) with an average of 1.7 ft/yr (0.5 m/yr). This rate may be considered to be the natural background erosion rate for this zone, at least for the wave conditions and water levels associated with this period.

North of the harbor in Benton Harbor Township, the two maps provided a limited comparison of bluff lines, resulting in an average recession rate of 0.75 ft/yr (0.2 m/yr), which may be considered as the natural background erosion rate for north of the harbor again, for the conditions of this period. The explanation of the difference in background AARR is attributed to an increase in wave energy south of the harbor due to existence of a rise in the lakebed centered on a point directly northwest of the harbor. Numerical modeling of wave transformation using spectral wave models showed that this lakebed high (Figure 1) acts as a lens to focus waves from the north and northwest, thus creating a high wave energy zone over an approximately 10-mile (16 km) long reach south of the harbor. The average bluff recession rate in Zone 3 for the 1830-1871 period was 1.08 ft/yr (0.3 m/yr). Moving from Zone 2 to Zone 3, the geological composition changes from a mixture of cohesive and sandy bluffs to a sandier environment, and the bluff/dune height decreases, while the percentage of sand content increases. Zone 4 consists mostly of sand dunes, and a bluff/dune line was difficult to define. Similarly, bluff recession rates were defined for 1871-1938, 1938-1960 and 1960-2002 as shown in Table 1.

Table 1. Bluff Recession Rates (m/yr)

	North of the harbor	Zone 1	Zone 2	Zone 3
1830 to 1871	0.23 (0.16)	1.60 (0.71)*	0.53 (0.28)	0.33 (0.18)
1871 to 1938	0.40 (0.15)	0.45 (0.16)	0.71 (0.16)	0.53 (0.21)
1938 to 1960	0.28 (0.23)	0.34 (0.22)	0.59 (0.36)	0.26 (0.17)
1960 to 2002	0.23 (0.02)	0.23 (0.24)	0.82 (0.46)	0.35 (0.20)

* Values inside the parentheses show the standard deviation associated with the spatial averaging of the estimates of recession rate made every 20 m within each zone.

The period from 1871 and 1938 includes gradual extension of the jetties until 1903 to their present length. In this period the erosion in Zone 1 was reduced to an average of 1.5 ft/yr (0.45 m/yr). This reduction in recession rate is mostly due to the implementation of shore protection (along the coastal railway and highway) toward the end of this period. The area of highest erosion shifted to Zone 2, which had an average recession of 2.33 ft/yr (0.7 m/yr). The recession rate in Zone 3 also increased to 1.7 ft/yr (0.5 m/yr). The 1938 to 1960 period corresponds to the introduction of even more shore protection structures in Zone 1. Recession rate in Zone 1 was further reduced to 1.1 ft/yr (0.3 m/yr) as a result of shore protection measures. Spatially averaged erosion rates for Zones 2 and 3 were 0.85 and 1.9 ft/yr (0.25 and 0.6 m/yr), respectively. The area of highest recession was again found in Zone 2 for this period. Between 1920 and 1938, lake levels were well below average, resulting in creation of wide beaches that could have protected the bluffs during early 1938-1960 period. The average bluff recession rate north of the harbor for this period was 0.92 ft/yr (0.3 m/yr).

Construction of shore protection structures continued in the most recent period of 1960 to 2002. Although historic low lake levels were recorded in 1965, lake levels were well above average during the 1970's, 1980's, and 1990's, resulting in extensive bluff erosion. The average recession rate in Zone 1 was reduced further to 0.75 ft/yr (0.23 m/yr), probably as a result of shore protection measures. Average erosion rates in Zones 2 and 3 were 2.7 ft/yr (0.83 m/yr) and 1.1 ft/yr (0.35 m/yr), respectively. The area of peak erosion remained within Zone 2 during this period.

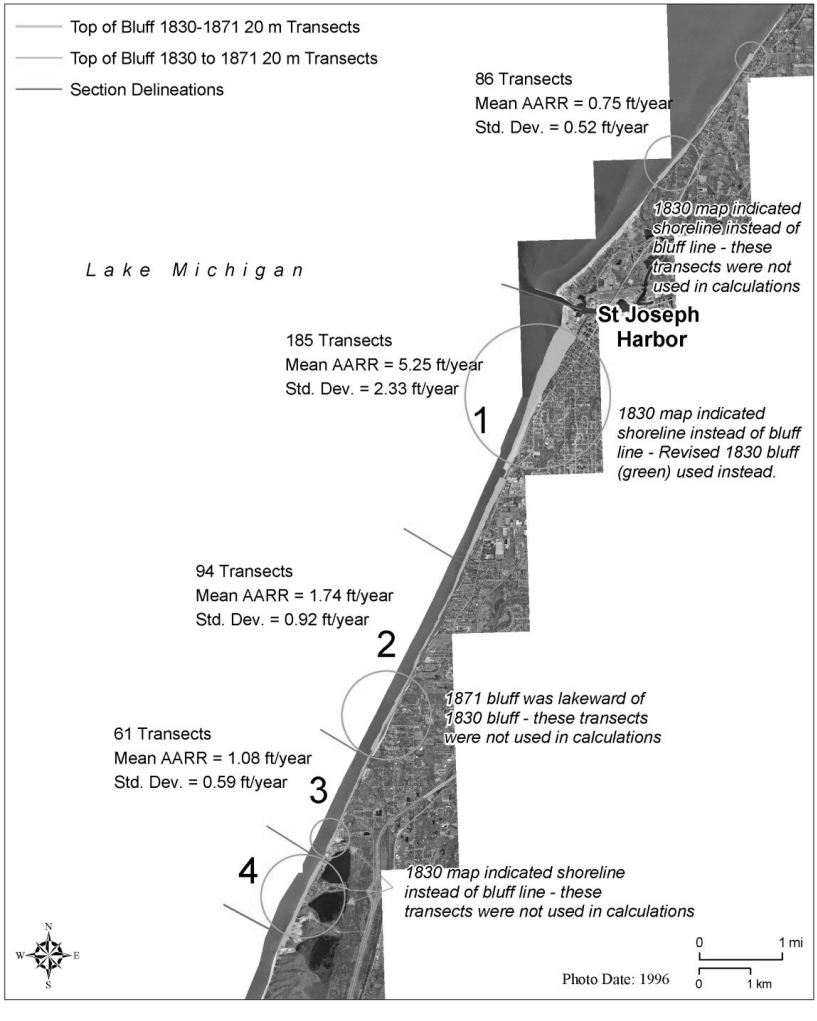

Fig. 4. AARR summary for 1830-1871 period

Lakebed Erosion

Lakebed erosion volumes south of the harbor were determined through comparisons of marine-based hydrographic surveys of 1871, 1954, 1965, and the airborne Light Detection and Ranging (LIDAR) survey of 1999. The 1954 and 1965 charts together provided a complete coverage of the full study area. Figure 5 shows the bathymetry comparison between 1871 and 1954/65. Lakebed erosion is observed in Zones 1, 2, 3, and part of Zone 4. Most of Zone 4, however, experienced accretion in this period. Accretion is also observed along the deeper part of Zone 1 that corresponds to establishment of a bypassing shoal. The average erosion rate in Zones 1, 2 and 3 was relatively uniform; ranging from 0.016 $yd^3/yd^2/yr$ (0.015 $m^3/m^2/yr$) in Zone 1 near the harbor to 0.015 $yd^3/yd^2/yr$ (0.014 $m^3/m^2/yr$) in Zone 3. The unit $yd^3/yd^2/yr$ may be considered as an average rate of lakebed lowering in yards per year or yd/yr. Erosion and accretion volumes in Zone 4 are almost equivalent.

Similar bathymetry comparison between 1954/65 and 1999 showed that erosion rate in Zone 1 increased to 0.041 $yd^3/yd^2/yr$ (0.038 $m^3/m^2/yr$) as a result of construction of more shore protection structures. Zone 4 also experienced erosion in this period. Compared to the earlier period, the average erosion rate was 0.01 $yd^3/yd^2/yr$ (0.001 $m^3/m^2/yr$) at the southern end of Zone 1 and in Zone 2. The erosion rate reduced to 0.013 $yd^3/yd^2/yr$ (0.012 $m^3/m^2/yr$) in Zone 2 and 0.012 $yd^3/yd^2/yr$ (0.011 $m^3/m^2/yr$) in Zone 3. The reduction in lakebed erosion during this period compared to the previous period may be attributed to the USACE nourishment activities that started in 1970.

Combined Bluff and Lake Bed Erosion Rates

Based on the bluff recession rates and the lakebed erosion rates discussed above, total erosion quantities (i.e. including lakebed and bluff components) were calculated for four snapshots between 1871, 1938, 1960, and 2002. Also, using the percentage sand content information, the corresponding sand volumes eroded from the bluffs and lakebed were estimated. In addition, the eroded sand volume prior to the construction of the jetties before 1836 was estimated by removing the distinctive harbor erosion influence (Zone 1 in Figure 5). The total (lakebed and bluff) average annual sand volume eroded from the area for different periods was thus estimated as follows:

Before 1836: 131,000 yd^3/yr (100,000 m^3/yr)
1871 to 1938: 191,000 yd^3/yr (146,000 m^3/yr)
1938 to 1960: 209,000 yd^3/yr (159,800 m^3/yr)
1960 to 2002: 216,000 yd^3/yr (165,100 m^3/yr)

It may be seen that the erosion volume has increased over the time. It should be noted, however, that the above values are long-term averaged numbers and actual erosion volumes during shorter periods may considerably deviate from these numbers depending on the supply rate from updrift, river and nourishment activities as well as the outgoing longshore transport rate that are discussed below.

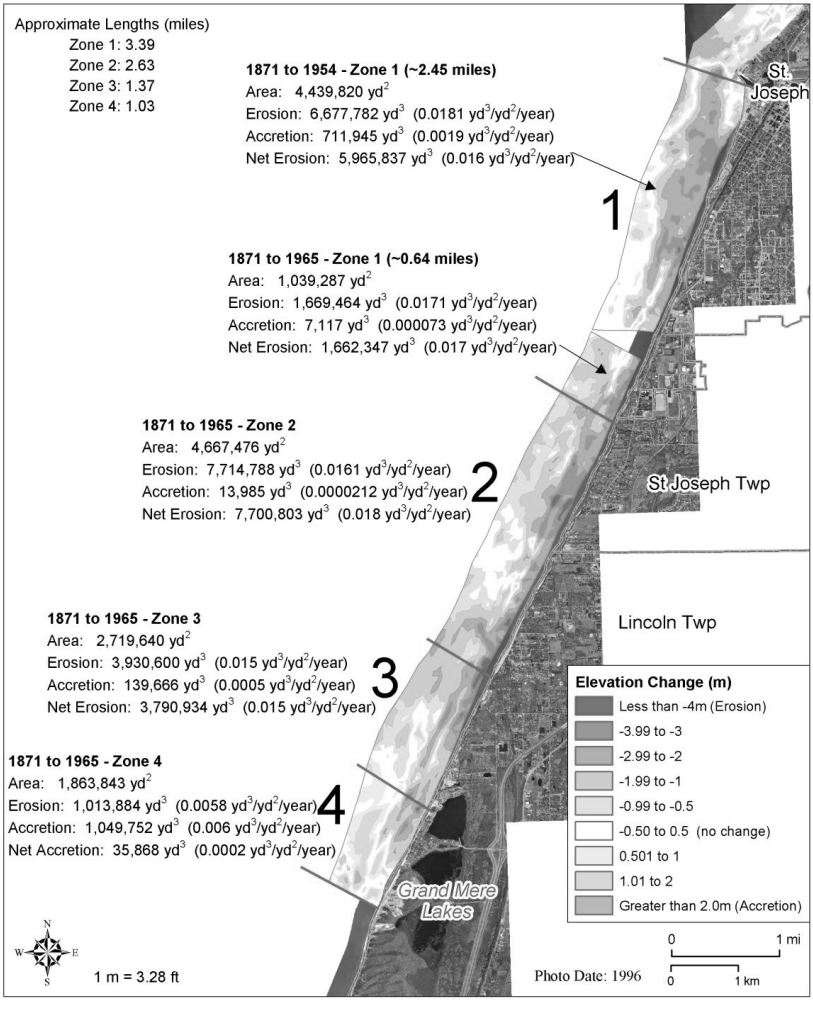

Fig. 5. 1871 to 1954/65 lakebed comparison

HARBOR INFLUENCE (SEDIMENT SINKS)

There are three key forms of sinks to the littoral sediment budget associated with harbors:

1. Accumulation of sediment in fillet beaches;
2. Dredging and disposal of sediment dredged from navigation channels;
3. Loss of sediment to the creation of bypass shoals.

Each of these three possible sinks is evaluated in this section.

Fillet Beach Accumulation

The jetties at St. Joseph Harbor started to trap sand since their construction until they reached their trapping capacity. The history of the growth of the north fillet beach area derived from historic shorelines since 1834 is shown in Figure 7. The variability in fillet beach size is related to natural factors and in particular to changing water levels. The water level effect was therefore removed by adjusting the fillet beach area based on the difference between the water level at the time of the survey and a common reference level. The solid lines represent an estimate of fillet beach area growth with the water level effect removed. The lines represent two different beach/nearshore slopes required for the adjustment (representative of the range of average beach slopes at the site). It may be seen that the north fillet beach has three periods of response: 1) Between 1836 when the jetties were first constructed and around 1870 when they were first extended, 2) Between 1870 and 1893 to 1903, when the last lengthening of the jetties was completed in a series of stepwise extensions as shown in Figure 2, and 3) The period from 1903 to the present. The three periods feature an asymptotic trend that is consistent with rapid initial growth followed by increasingly slower growth toward the end of each period (i.e. as more sand moves past the fillet beach into the navigation channel). In particular, the north fillet beach has had a slow growth over the last 30 to 40 years, indicating that the fillet beach area is no longer expanding.

Sand was similarly lost into the south fillet beach; however, the south fillet is much smaller because the north waves, being larger than south waves, are able to remove much more sand from the south side of the south jetty (Dibajnia et al. 2004). Comparison of pre-harbor and post-harbor charts also suggests that the south fillet was mostly formed by redistribution of the sediment that once formed the old river mouth bar prior to construction of the jetties. The St. Joseph south fillet beach grew between 1836 and 1938 and has been relatively stable since then.

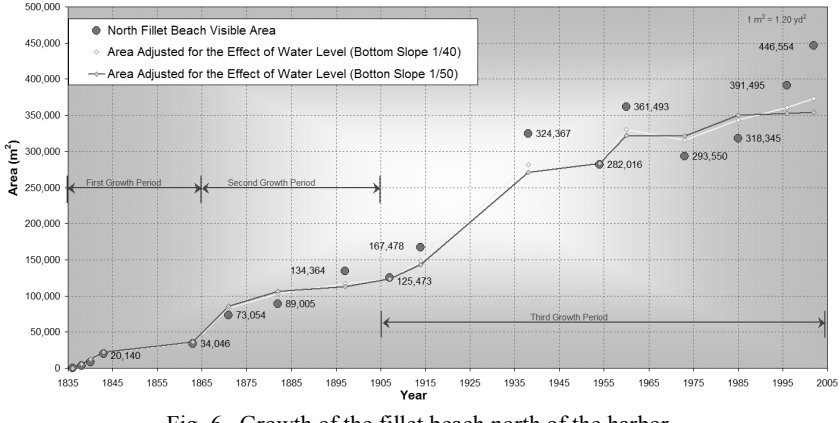

Fig. 6. Growth of the fillet beach north of the harbor

Dredging

For St. Joseph Harbor, deposition in the navigation channel is generally divided into two areas: the inner and outer channels. Deposition in the outer channel is mostly related to littoral sand transport, whereas sediment deposited in the inner channel is mostly derived from the river and watershed. There is likely some amount of deposition in the outer channel related to sediment supplied by the river. The inner channel often includes a significant quantity of fine sediment (i.e. grain size less than about 0.125 mm) that would not remain in the littoral zone even if it were to make it to the lake. Dredging records dating back to 1879 were obtained and reviewed to determine the amount of maintenance dredging associated with the inner and outer channel areas, and this information is presented in Figure 7. The red dots represent the total maintenance dredging and, where sufficient information is provided, the inner and outer channel components are indicated (blue squares and green diamonds respectively). There is considerable variability in year-to-year dredging due to inter-annual variability in trapping or sediment deposition in channels, as well as decisions on when to dredge due to economic and other factors (the navigation channel depth has varied through time as shown in Figure 7). The total maintenance dredging reached a peak in the mid-1900's, and is now decreasing. There has been a trend for increasing outer channel dredging between 1900 and the present. This corresponds to the slowing of fillet beach growth as it approaches maturity and the corresponding increase in transport of sand past the fillet beach and into the navigation channel. The entrance channel depth is now supposed to be maintained to 24 ft (7.3 m) below low water datum, across a width of 300 ft (90 m) or more. It is clear that a limited amount of sediment is able to bypass this channel without being deposited in it. From the data available since about 1960, the rate of outer channel dredging has averaged about 30,000 yd^3/yr (22,900 m^3/yr).

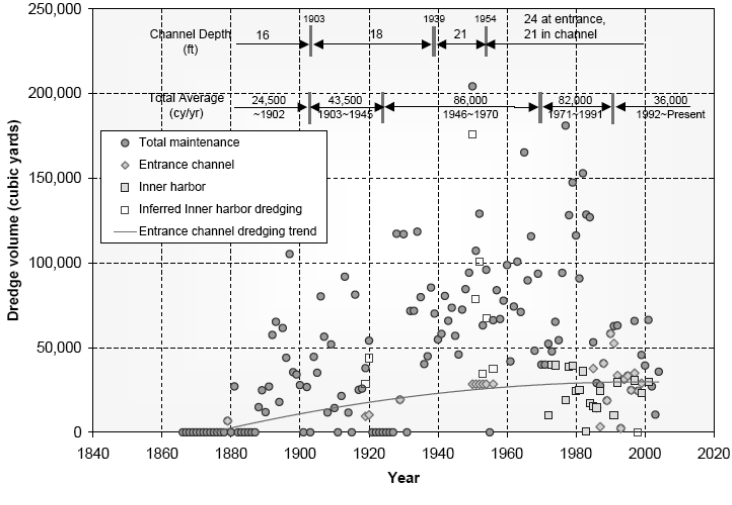

Fig. 7. Dredging History at St. Joseph Harbor (from USACE Detroit District)

The inner channel dredging would appear to have been responsible for the peak in total maintenance dredging in the 1950's and 1960's, and this peak is consistent with observations by others that this period corresponded to the highest erosion of agricultural land (due to extensive agriculture and poor soil conservation practices; see Trimble and Crosson 2000). More recently, it is believed that loads were reduced through urbanization of previously agricultural land and through improved agricultural practices relating to soil conservation. Similarly, prior to European settlement (i.e. prior to logging and then agriculture), there would have been little sediment delivered from the river and watershed. This topic of watershed sediment will be discussed in a separate paper.

Deposition in Bypassing Shoals

As fillet beaches approach maturity in terms of growth, bypassing of the harbor commences, whereby sand moves around the harbor. Sand transported along the shore by waves and wave-driven currents will attempt to reinstate the net rate of longshore transport by creating a bypassing shoal. As the bypass shoal builds, inevitably it disrupts the main purpose of the jetties by providing the pathway for sand to fill in the navigation channel and results in the need to dredge.

An assessment of possible bypassing shoals has been completed through lakebed surface comparisons to describe areas of net erosion/sedimentation between 1907, 1954, and 2001 (these data represent snapshots when the required data was available). The results for the 1907-1954 period are shown in Figure 8. This figure shows three zones of deposition (most apparent in Figure 10). Starting from offshore, Zone 3 is a large zone stretching across the length of both fillet beaches and generally extends between water depths of 12 and 16 m (40 and 50 ft); Zone 2 consists of two lobes (2a and 2b) of sediment that appear to emanate from the outer navigation channel towards the north and south in depths of 6 to 11 m (20 to 36 ft); and Zone 1 corresponds to the underwater part of the north and south fillet beaches (and was accounted for under the discussion of the fillet beach accumulation).

The deposition rate in Zone 3 was approximately 39,000 yd^3/yr (29,800 m^3/yr) (including both clay/silt and sand fractions) prior to 1954 and 37,000 yd^3/yr (28,200 m^3/yr) between 1954 and 2001, and 109,000 yd^3/yr (83,300 m^3/yr) up to 1970 (considering that offshore dumping was stopped in 1970). Based on the numerical modeling results (completed for the river flows with and without the influence of wave action), and location data of offshore dumping, it appears that most of the deposition in Zone 3 must have been a result of offshore dumping.

The volume of sediment accumulation in Zone 2 corresponds to annualized deposition rates of approximately 65,000 and 3,900 yd^3/yr (49,700 and 3,000 m^3/yr) of sand for the periods 1907-1954 and 1954-2001, respectively. Since approximately 1970, there has been some minor erosion of the Zone 2a deposits, and accumulation has recently occurred in Zone 2b only, which indicates that part of the updrift supply is also deposited in Zone 2b (i.e. between the 6 and 11 m contours below low water datum). From the numerical model results it was found that when south and north waves interact with river

flows, sediment is carried and, in some instances deposited in the two Zone 2 lobes. One reason for the reduction in the growth of the Zone 2 shoals is the increase in the navigation channel depth over the 1900's (see Figure 9 for the change in channel depth). Also, it should be considered that the Zone 2 lobes effectively represent a bypass shoal for river sediment to make its way back to the shore. It took many years for the bypass shoals to build and now they have effectively reached maturity. The Zone 2 shoals likely consist of a mix of sandy and silty sediments owing to the important role of river sediments in building these deposits.

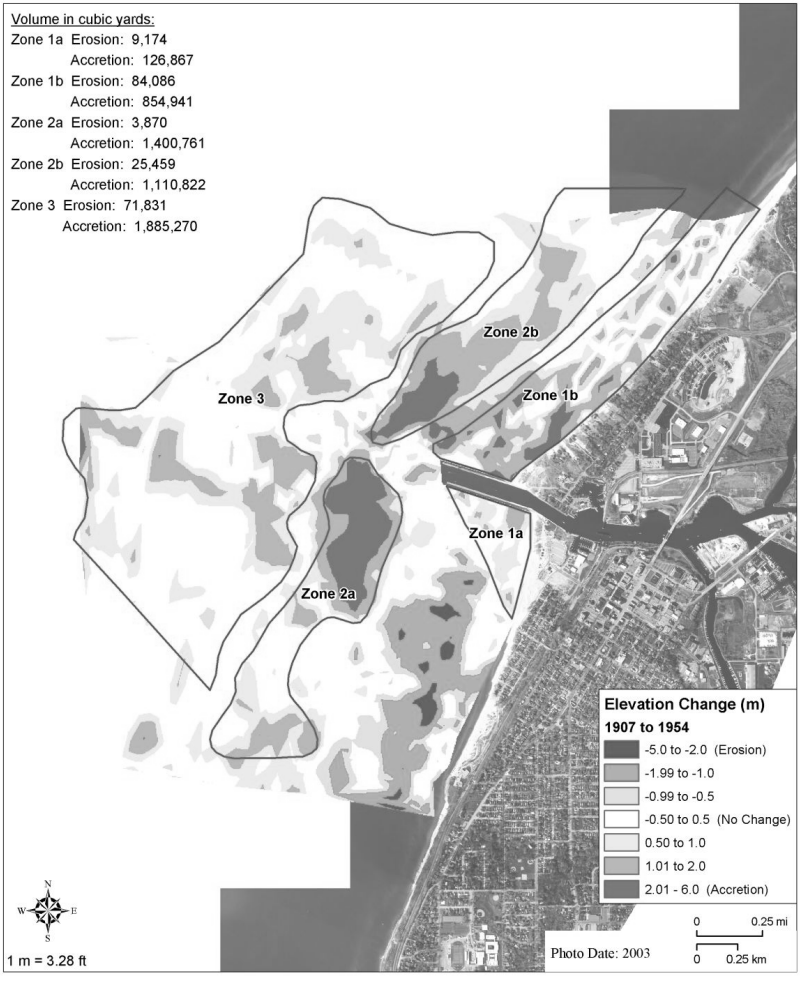

Fig. 8. Lakebed change between 1907 and 1954 around the harbor

Numerical modeling of sediment bypassing showed that presently about 45,000 yd^3/yr (34,400 m^3/yr) can bypass the north jetty of which more than 35,000 yd^3/yr (26,700 m^3/yr) is trapped by the navigation channel, and there is minimal bypassing (less than 10,000 yd^3/yr (7,600 m^3/yr) of the harbor mouth for longshore sand transport on an annual basis to south downdrift of the harbor (i.e. almost all the sand is trapped in the navigation channel). Sand is transported from the south into the navigation channel on a very infrequent basis. Details of the numerical modeling work will be presented in a future paper.

CONCLUSION

Factors contributing to the long-term sediment budget at St. Joseph Harbor were quantified. These were divided into sediment source factors including bluff recession and lakebed erosion rates as well as river sediment load, and sediment sink factors including accumulation in fillet beaches and bypassing shoals and dredging from the navigation channel.

ACKNOWLEDGEMENTS

The authors would like to thank the USACE, Detroit District, for supporting this study.

REFERENCES

Baedke, S.J. and Thompson, T.A. (2000). "A 4,700-year record of Lake level and Isostacy for Lake Michigan", *Journal of Great Lakes Research* 26(4), 416-426.

Baedke, S.J., Thompson, T.A., Johnston, J.W., and Wilcox, D.A. (2004). "Reconstructing paleo lake levels from relict shorelines along the Upper Great Lakes", *Aquatic Ecosystems Health & Management*, Special Issue: Emerging Issues in Lake Superior Research, 7(4), 435-449.

Dibajnia, M., R.B. Nairn and Ross P. (2004). "Analysis of long-term sand accumulation at a harbor using 2DH numerical simulation", *Coastal Engineering*, Elsevier Science, 51, 863-882.

Larson, G.J. and Schaetzl, R. (2001). "Origin and Evolution of the Great Lakes", *J. Great Lakes Res.* 27, 518-546.

Larson, G.J. (2006). "Geology and Lake-Shore Evolution of the St. Joseph Area, Southeastern Lake Michigan", Report to the Dept. of Justice for Banks et al. vs. USA.

Tague, G. C. (1942). "The Post-Glacial Geology of the Grand Marais Embayment, Berrien County, Michigan", PhD dissertation, University of Michigan. 79 p.

Thompson, T.A. and Baedke, S.J. (1995). "Beach ridge development in Lake Michigan: shoreline behavior in response to quasi-periodic lake-level events", *Marine Geology* 129, 163-174.

Thompson, T.A., Baedke, S.J., and Johnston, J.W. (2004). "Geomorphic expression of late Holocene lake levels and paleowinds in the upper Great Lakes", In Hansen, E.C., ed., *The Geology and Geomorphology of Lake Michigan's Coast.* Michigan Academician, 35(4), 355-371.

Trimble, S.W. and Crosson, P. (2000). "U.S. Soil Erosion Rates - Myth or Reality", *Science* 289, 248-250.

CHESAPEAKE BAY: HEADLAND CONTROL SYSTEMS PERFORMANCE INCLUDING HURRICANE ISABEL

C. Scott Hardaway, Jr.[1], James R. Gunn[2]

1. Virginia Institute of Marine Science, College of William and Mary, P.O. Box 1346, Gloucester Point, VA 23062, USA. hardaway@vims.edu.
2. Coastal Design and Construction, P.O Box 650, Gloucester, VA 23061

Abstract: Headland Control is a unique shoreline management technique whereby existing geomorphic features (*i.e.* headlands) are enhanced with large stone breakwaters and/or the breakwaters are strategically placed alongshore to create headlands. These enhanced or created shore headlands are widely spaced for economy, and the adjacent coasts are allowed to continue to erode toward an equilibrium shore position where a wide, stable, and protective sand beach becomes vegetated and forms a low dune. The final equilibrium planform is a large pocket beach whose dimensions will depend on the amount of sand that will come to reside in the evolving embayment. Headland Control is applicable to long reaches of agricultural or unmanaged shore land since protecting the entire property is very expensive per linear foot. Three sites where this method of shore management was implemented are discussed in terms of shore planform prediction, overall shore change, and storm response.

INTRODUCTION

Headland Control is a unique shoreline management technique whereby existing geomorphic features (*i.e.* headlands) are enhanced with large stone breakwaters and/or large stone breakwaters are strategically place alongshore to create headlands. These enhanced or created shore headlands are widely spaced for economy, and the adjacent coasts erode toward an equilibrium shore position or planform. The final equilibrium planform is a large pocket beach whose dimensions will depend on the amount of sand that will come to reside in the evolving embayment. Sand is usually only placed directly behind the created headland during construction, and vegetation is planted along the backshore to assist in the dune creation process. Headland control generally is applied to long reaches of agricultural or unmanaged shore land

to begin the process of shore stabilization by pocket beach creation.

This paper discusses three headland control sites, two of which are located along the Potomac River in Virginia and one on the St. Mary's River in Maryland (Figure 1). They include: 1) Summerille/Staples, Northumberland County, Virginia, 2) Murphy, Westmoreland County, Virginia, and 3) St. Inigoes Neck, St. Mary's County, Maryland. The Summerille/Staples project was initially installed in 1978 while Murphy (installed in 1997) and St. Inigoes (installed in 2001) are newer installations. All three of these sites are included in the Chesapeake Bay Breakwater Database currently being developed by the Virginia Institute of Marine Science (VIMS) for the U.S. Army Corps of Engineers, Section 227 Program. In predicting the final shore planform, we utilized the Static Equilibrium Bay (SEB) formula by Hsu and Silvester (1989) and Silvester and Hsu (1993). The net direction of wave approach was ascertained from an analysis of historical shoreline change using aerial imagery as well as wind/wave modeling.

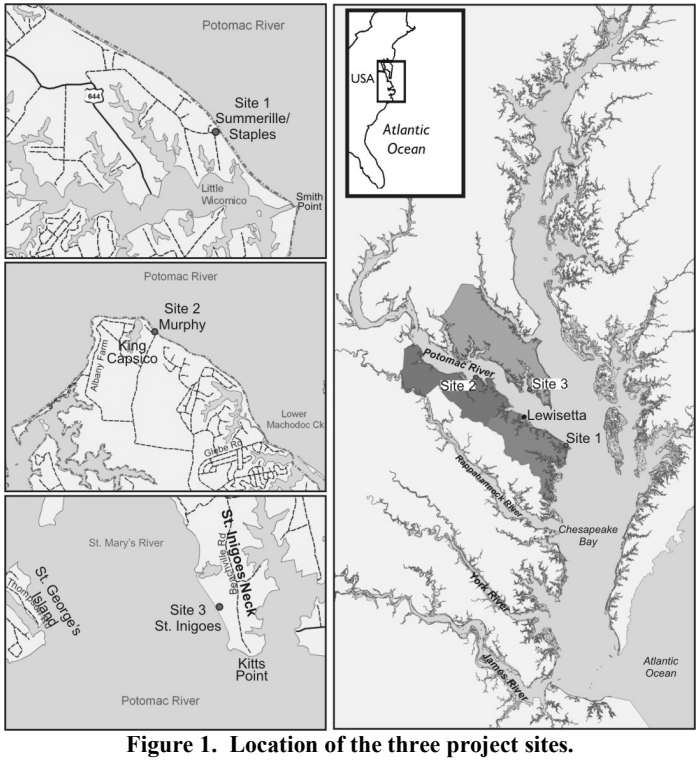

Figure 1. Location of the three project sites.

EQUILIBRIUM

Determining the shape or shore planform of crenulate/spiral and pocket beaches or embayments has been the subject of numerous research efforts. This procedure was first developed by Silvester (1970) and later refined by Hsu *et al*. (1989) and Silvester and Hsu (1993). The method is referred to as the Static Equilibrium Bay (SEB) method (Figure 2). This is an empirical model developed by analyzing hundreds of pocket and embayed beaches around the world. Hardaway *et al.* (1991) introduced this to Chesapeake Bay in order to better design headland breakwater systems for shore protection. Since then, many headland breakwater sites have been installed, analyzed, and reported on (Hardaway and Gunn 1991; Hardaway *et al*. 1993; Hardaway *et al*. 1995; Hardaway and Gunn 1999a; Hardaway and Gunn 1999b; Hardaway and Gunn 2000; and Hardaway and Gunn 2003). These reports often utilized a combination of RCPWAVE, a wave refraction computer model, and SMB, a wind/wave generation computer model, to characterize the impinging wave climate on headland breakwater sites.

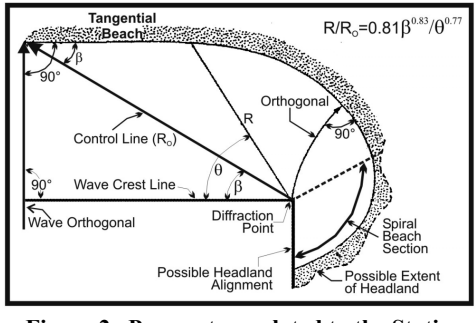

Figure 2. Parameters related to the Static Equilibrium Bay Model (Hsu *et al.* 1989).

The SEB method was initially developed along open ocean coasts for "natural" coastal embayments. A certain degree of common sense is required to utilize the model since it was originally developed to assess if a given embayment is in "equilibrium". Therefore, one needs a bay to apply the SEB model. If sand is moving along an embayed coast, it may be considered in "dynamic equilibrium" until such time as sand supply is cut off and the shore planform further evolves to a more static condition. This is the condition often found along sand starved Bay coasts.

Determining both the direction of wave approach and the control line (Ro) are important. The updrift headland is usually easy to define in a natural setting, but the downcoast headland can cause complications especially if it protrudes into the bay (Silvester and Hsu 1993) (Figure 3). In Chesapeake Bay, this is usually the case for headland breakwater design, and therefore the transition point occurs at the water line or contour which will be used for the bay shape calculations, usually mean high water (MHW). It is not an exact calculation, and the method should be used only to get a good approximation of bay shape. The tangential section turns into the impinging

wave climate, and then the spiral section adjusts to it.

Ultimately, the embayed beach is the primary element for shore protection. The design of the embayed or pocket beach's shore planform must account for sand supply and wave climate. Along open coasts, a dominant direction of wave approach with only minor short-lived reversals is assumed. In Chesapeake Bay, this may or not be the case. Many shore reaches will have an annual and storm direction of wind/wave approach from different directions. The more oblique the impinging wave crest to the coast (*i.e.* as β becomes bigger), the deeper or more indented the pocket bay. Headland Control requires allowing the shoreline between breakwater units to erode. Storms, Hurricane Isabel in particular, have hastened and more clearly defined the future of this shoreline management strategy.

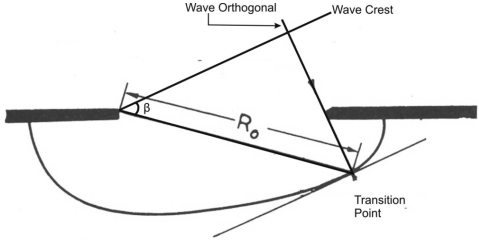

Figure 3. Diffraction due to protruding downcoast headland (Sylvester and Hsu 1993).

SHORE EVOLUTION

Shore change assessment is a very useful tool in understanding how a given reach of coast has evolved over time, particularly around the fetch-limited and depth-limited sheltered coasts of Chesapeake Bay. The use of orthorectified historical aerial imagery provides information not only on the position of the shoreline but also types of land use, infrastructure, shoreline structures and offshore bar systems that exist in a moment in time. Aerial archive data sets are not very complete so a certain amount of interpolation and interpretation is necessary. The open coasts of the Bay and rivers have undergone some dramatic changes and understanding shore evolution is necessary when assessing the hydrodynamic forces acting on the coast.

Most of the Bay shoreline is receding as a result of rising sea level and the local impinging wave climate. The wave climate is a function of wind-driven waves often in combination with tidal currents. The greatest wave energy is generated during storm events. In the Bay region, this is during northeasters and the occasional hurricane where elevated water levels (storm surge) and large wind-driven waves combine to impact the Bay shores at higher than normal elevations, cutting into upland banks, and producing large quantities of bank sediments for the littoral system. Shore erosion, particularly along the upland banks, is greatest during storm events which must be accounted for in developing shoreline protection strategies for a given shore reach.

Shore evolution is the response to the process. The longer the temporal record, the more hydrodynamic forcing has occurred. The geomorphic evolution of the upland banks provides insight into how larger storms have formed that coastal reach over time. Movement of sand features such as spits also provide evidence of the direction of wave attack and, consequently, sediment transport. One can ascertain net sediment movement and if it is somewhat balanced or bidirectional. Assessing the sand supply also is critical to beach development in pocket bay evaluations.

Hurricane Isabel impacted the Chesapeake Bay on September 18, 2003 with record high storm surge and high winds. Virtually all shorelines were impacted to one degree or another especially those with open fetch exposures to the north, northeast, east, southeast and south as Isabel's winds rotated north to south through her passage. Hundreds, if not thousands, of shore protection systems were damaged or destroyed. Many open shorelines with no protection incurred erosion rates of 10 to 30 ft (3 to 9 m) depending on location to the storm surge and wind/wave climate. Sites with headland control systems experienced varying degrees of shoreline recession as they eroded toward equilibrium.

In the fall of 2006, three coastal storms, including Tropical Storm Ernesto, impacted the Bay coast of Virginia and Maryland. Although water levels were less than Isabel, they had high water and winds that significantly impacted the estuarine shorelines. Of the three sites, Murphy was most impacted by these storms.

Table 1. Recent storm statistics for Lewisetta, Virginia on the Potomac River.

Storm	Maximum Tide Level Relative to MLLW (feet)	(meters)	Maximum Sustained Winds (mph)	(m/s)	Peak Gust (mph)	(m/s)	Max Wind Direction (°TN)
Hurricane Isabel	6.5	2.0	52	23	69	31	95
Hurricane Ernesto	5.6	1.7	43	19	63	28	90
Northeast Storm 10-6-2006	3.1	0.9	38	17	46	21	85
Northeast Storm 11-2-2006	2.5	0.8	21	9	29	13	2

HEADLAND SITES

Site 1: Summerille/Staples, Northumberland County, Virginia

Site 1 is located along the Potomac River near Smith Point (Figure 1). The shoreline is oriented northwest/southeast with fetch exposures to the north, northeast, and east of 25 n.m., 16 n.m., and 13 n.m. (46 km, 30 km, 24 km), respectively. Until 1937, the shoreline was relatively straight with a continuous beach along most of the reach. Alongshore transport was mostly uninterrupted except for areas of overwash into small coastal ponds on either side of the Site 1 shore (Figure 4). The upland banks along the Site 1 are about +12 ft MLW (+3.6 m MLW) and composed of fine sands. Bank geology varies along the Potomac River coasts and as the banks erode they provide the sediments for the shore and nearshore regions. The sand and gravel

fractions accumulate on the beach and offshore bars while the silts and clays tend to be carried offshore into deeper waters of the River and Bay.

A crenulate embayment was created at Site 1 due to the Summerille groinfield and the shore hardening that defines the downriver boundary of that embayment. The upriver tidal pond embayment also had become well developed. This area had been known as the Summerille site and was the subject of scrutiny in the 1978. The downriver offset created by the Summerille groinfield increased steadily since its installation in the 1960s. By 1978, the shore at the site had eroded more than 100 ft (30 m). The solution was to install a spur to abate the immediate problem (Anderson *et al*. 1983) (Figure 4). Since then, the spur has been lengthened and additional spurs were added to the downriver revetment in the late 1990s that clearly defined the boundaries of the Site 1 embayment (Figure 4). The embayment had taken on the classic log spiral/crenulate shape.

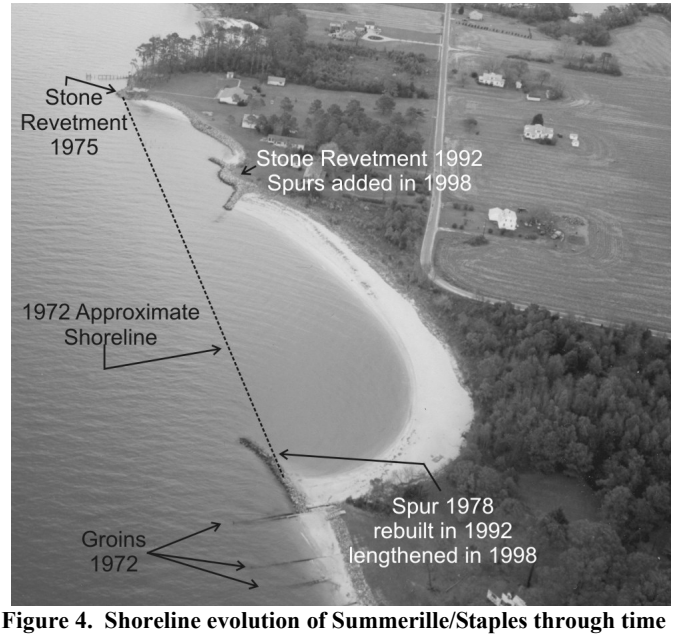

Figure 4. Shoreline evolution of Summerille/Staples through time shown on a post-Hurricane Isabel photo (2003).

The upland banks within the embayment continued to erode and evolve toward an equilibrium planform as seen in 1994. The tangential section of the bay was used to portray the net direction of wave approach. Using this reverse method to establish the incident wave condition, the SEB model was applied during a 1991 VIMS study

to predict where the spiral section of the bay would evolve. This study predicted the resulting line *i.e*. whether it was the shoreline, the base of bank or top of bank (Hardaway *et al*. 1991). Figure 5 shows the predicted bay shape on 1994 imagery.

The 2002 imagery shows a shore advance as result of the added spur on the downriver boundary which perched the tangential section thereby helping the bay to equilibrate. It is important to understand that this is a sand rich system and the input of sand into the bay was essential to beach expansion. Once the sand reached the limit of the downriver boundary it began to bypass. The spiral section of the bay finally eroded/evolved to where the beach as wide enough to attenuate storm waves against the adjacent upland banks. The average beach width is 65 ft (20 m) from MLW to the base of the bank, and the elevation is +6 ft MHW (+1.8 m) at the base of the bank.

Hurricane Isabel brought a large amount of sand into the embayment to the point that the established dune grasses along the backshore were almost completely covered. Recent northeast storm events brought even more sand into the bay. The bay is now in dynamic equilibrium.

Site 2: Tayloe Murphy, Westmoreland County, Virginia

Site 2 resides further up the Potomac River at King Capsico (Figure 1). The Site 2 shoreline occurs on the downriver side of King Capsico Point and faces northeast with fetch exposures to the north, northeast, and east of 9 n.m., 5 n.m., and 6 n.m. (17 km, 9 km, and 11 km), respectively. In 1937, the shorelines adjacent to and including Site 2 had beaches along the coast. The land use was almost all agricultural. The eroding banks were +15 to +20 ft MLW (+4.5 to +6 m MLW) and composed of a variety of sands and gravels.

By 1969, significant shore development had occurred on King Capsico Point with subsequent shore hardening and installation of groins. The Site 2 shore was still mostly undeveloped except for the main Murphy house on the point. Two large spits resided in front of the Murphy home at that time. The nearshore was paved with cobble eroded from the adjacent bank which reinforced the base of bank such that a natural headland was created. This headland eroded much slower than the adjacent downriver coast. In 1987, two large groins were installed in front of the Murphy home, further enhancing that point. The downriver reach shore continued to erode, and, by 1994, had become a concern of Mr. Murphy. A revetment was installed along the north shore to protect the house but the downriver reach continued to recede. The offset had evolved into an open ended embayment pinned on the upriver end by the point.

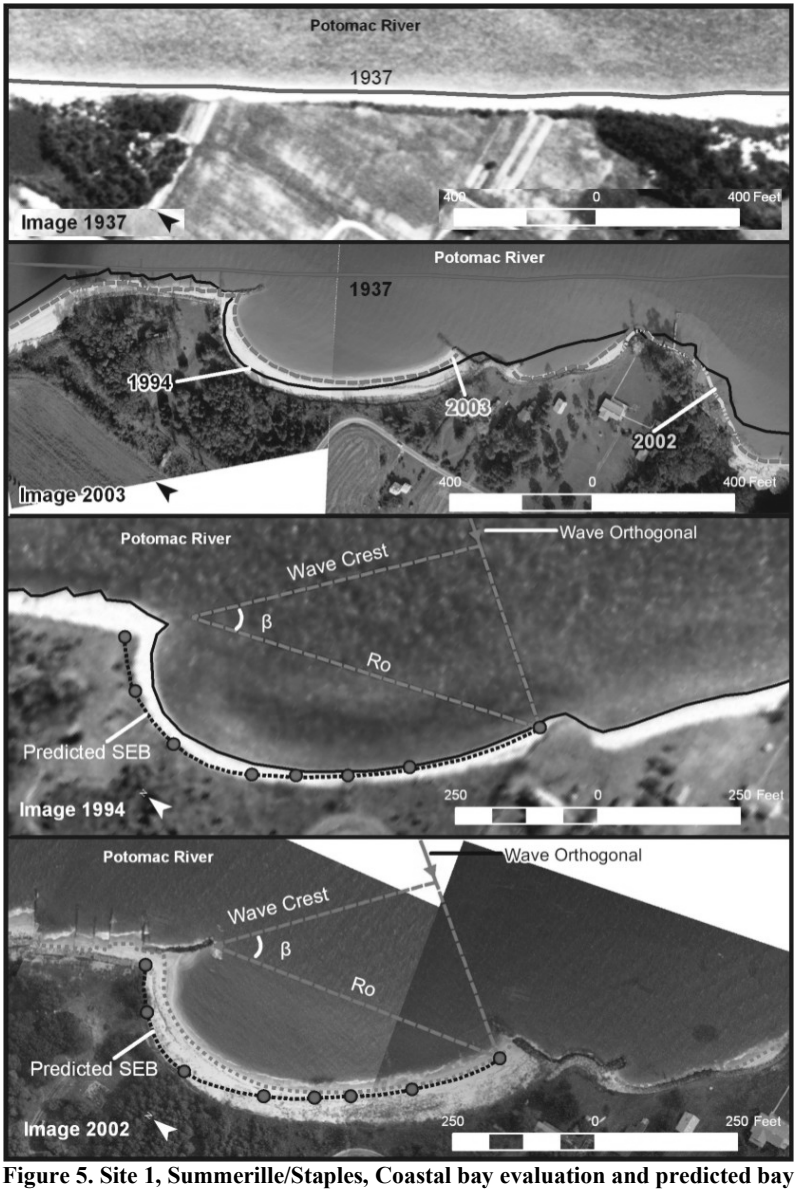

Figure 5. Site 1, Summerille/Staples, Coastal bay evaluation and predicted bay shoreline using SEB. Dots are values of R for a given θ (see Figure 2).

Mr. Murphy contacted Coastal Design and Construction, Inc., and it was decided that

a series of widely spaced headland breakwaters could be cost effectively installed along the embayed coast and allow the adjacent shorelines to evolve toward equilibrium (Figure 6). If this became unacceptable then additional breakwaters or a revetment could be installed. A wave climate analysis indicated the net direction of impinging waves for annual northerly conditions and the occasional northeast storm attack.

The result was the installation of a large headland spur and three headland breakwaters with beach fill to create the tombolos in 1997 (Figure 6). The design was based partly on the impinging wave climate, shore morphology, and cost. The spur, which is BW1, is about 200 ft (60 m) long and shelters the embayment from the northwest. Breakwaters 2 and 3 are 150 ft (45 m) each at +4 ft MLW (+1.2 m MLW) while breakwater 4 is shorter and lower to allow a smoother transition onto the adjacent unprotected shore (Hardaway *et al*. 1993). A bulkhead further downriver acts as a boundary for the embayment.

Figure 6 shows the site in 1999 with Bay B still actively eroding. A change in the geology of the bank sediments occurred over time. Initially, a relatively thick 5 to 8 ft (1.5 to 2.4 m) sand layer existed along the base which would "feed" the embayments with sand even as the banks between structures continued to erode. However, with time the strata facies changed to a siltier substrate. Hurricane Isabel caused a significant retreat of the unprotected banks (Figure 6). However, the headland breakwaters and tombolos remained intact. Recent northeasters have continued the erosion, and although "equilibrium" is not far off, Mr. Murphy opted for a revetment along the backshore. The low, stone revetment is small and is perched at the back of a wide beach berm.

Site 3: St. Inigoes, St. Mary's County, Maryland

Site 3 occurs on the west shore of St. Inigoes Neck in St. Mary's County, Maryland (Figure 1). The land is very low with little or no sand in the banks which were eroding at an average of -4 ft/yr (-1.2 m/yr) with the greatest erosion occurring adjacent to the south headland at over -6 ft/yr (-1.8 m/yr) (Figure 7). The land use is agricultural such that Headland Control seemed an appropriate, cost-effective strategy for this coast.

The project site is over 4,800 ft (1,460 m) long and is defined by a headland on the south boundary that has been hardened with a stone revetment which runs along the south shore of Kitts Point and turns north up the St. Mary's river. The north boundary is defined by a small tidal pond (Sage Pond), marsh and inlet complex which has been a headland feature since 1853 (and before) and defines the south boundary of another embayed coast up the St. Mary's River. The upland bank along the project site is about +5 ft to +8 ft MLW (+1.5 m to 2.5 m MLW) and composed of silts and fine sands. The nearshore is shallow tidal flats, and a very narrow beach existed along the pre-project coast.

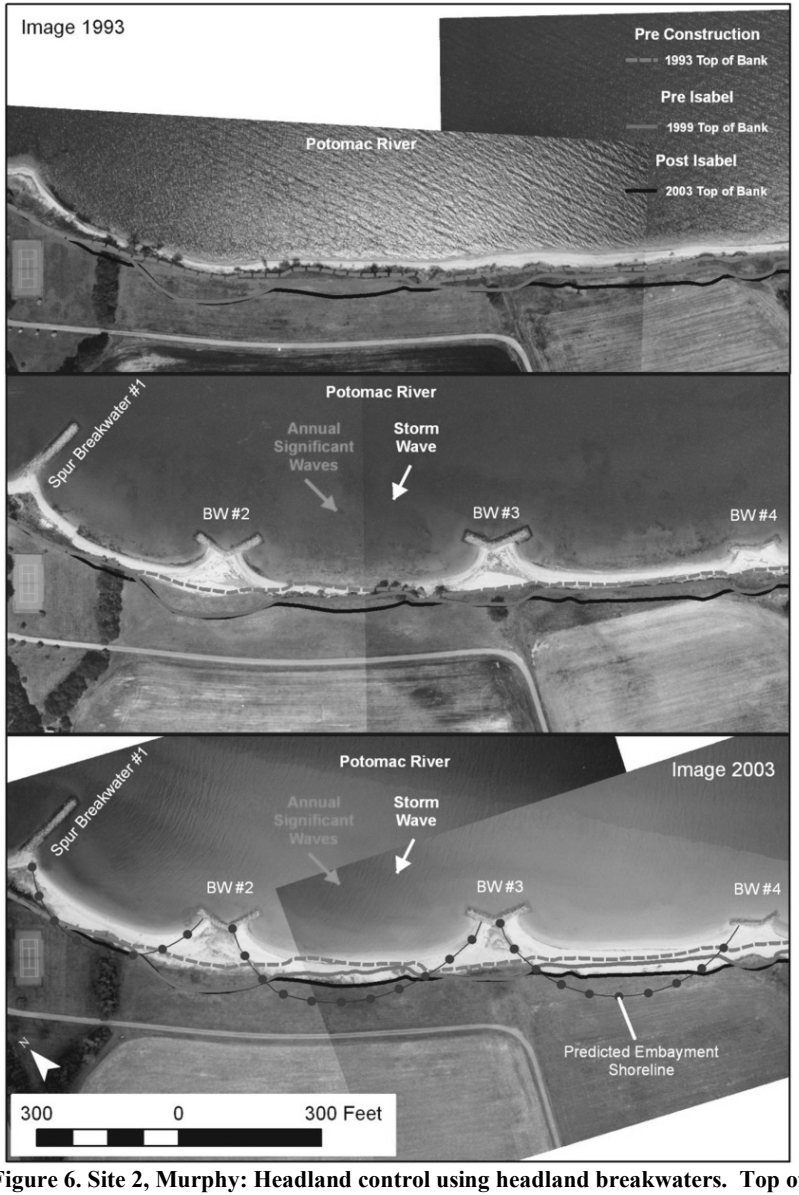

Figure 6. Site 2, Murphy: Headland control using headland breakwaters. Top of bank in the embayments eroded over 7 m during H. Isabel. A revetment has been installed along the base of bank and a wide beach resides in the bays.

Fetch exposures to the northwest, west, and southwest are 3 n.m., 2.5 n.m., and 7

n.m.(3 km, 2.5 km, and 7 km), respectively. Evidence of a "Bay" wave, which can travel up the St. Mary's River from the south and southeast, exists. This long-period swell was observed on one site visit and might be injurious to the shore over time. The evolution and shape of the natural embayments along Site 3 indicates the dominate direction of wave approach is from the south and southwest. Although northwesters can be furious during the winter months, the shorter fetch and nearshore flats reduce their influence on this coast. However, some wave energy can turn up the St. Mary's River around St. George's Island from the northwest wind/wave train coming down the Potomac River. This wave approaches the project coast from the southwest but dissipates as it goes north up the St. Mary's.

The project design began where the worst erosion occurred along the southern part of the site, the spiral section of the larger bay. The first breakwater (BW1) was placed near the end of the revetment while BW2 and BW3 were placed in front of a farm road where a tree line intersected the shore. These three units are closer together so equilibrium might be attained sooner to minimize land loss. Other subtle features included a small patch of trees for BW5, a small point for BW6, a drainage ditch for BW7, and on the south side of the inlet to Sage Pond for BW8, the terminal structure. BW4 was sited at the upriver limit of construction for the southern four units. This left a relatively wide gap between BW4 and BW5 which the landowner understood might require an additional structure.

Nearby borrow pit sands were used to build the tombolos and provide construction access. Each unit is 180 ft (55 m) along its crest and the center inflection point is approximately about 80 ft (24 m) from MLW with the ends of each unit about 100 ft (30 m) from MLW. These structures were built relatively close to shore with large tombolos to insure long-term headland attachment. The embayed coasts began adjusting soon after installation. Although the approximate net direction of wave approach was gleaned from the pattern of shore change, once the tombolos were set then the equilibrium bay could more easily be plotted. Hurricane Isabel revealed the true nature on the impinging wave climate as the spiral section of each bay eroded significantly and the tangent sections were set. The "equilibrium" shore planform is plotted in white and represents approximate MHW (Figure 8). Like Site 2, the long-term options were to add sand and/or breakwaters as funds and conditions dictate.

After Hurricane Isabel additional sands were placed in Bay B, C and D. Each received about 1000 cubic yards (765 cubic meters) each to supplement the bay beaches. It is evident that additional sands are needed to enhance the bay beaches, but the bay coasts needed to evolve to a point where the sands would reside more comfortably in the bay spiral or pocket. Bay E, the widest, will receive an additional breakwater unit with sand tombolo.

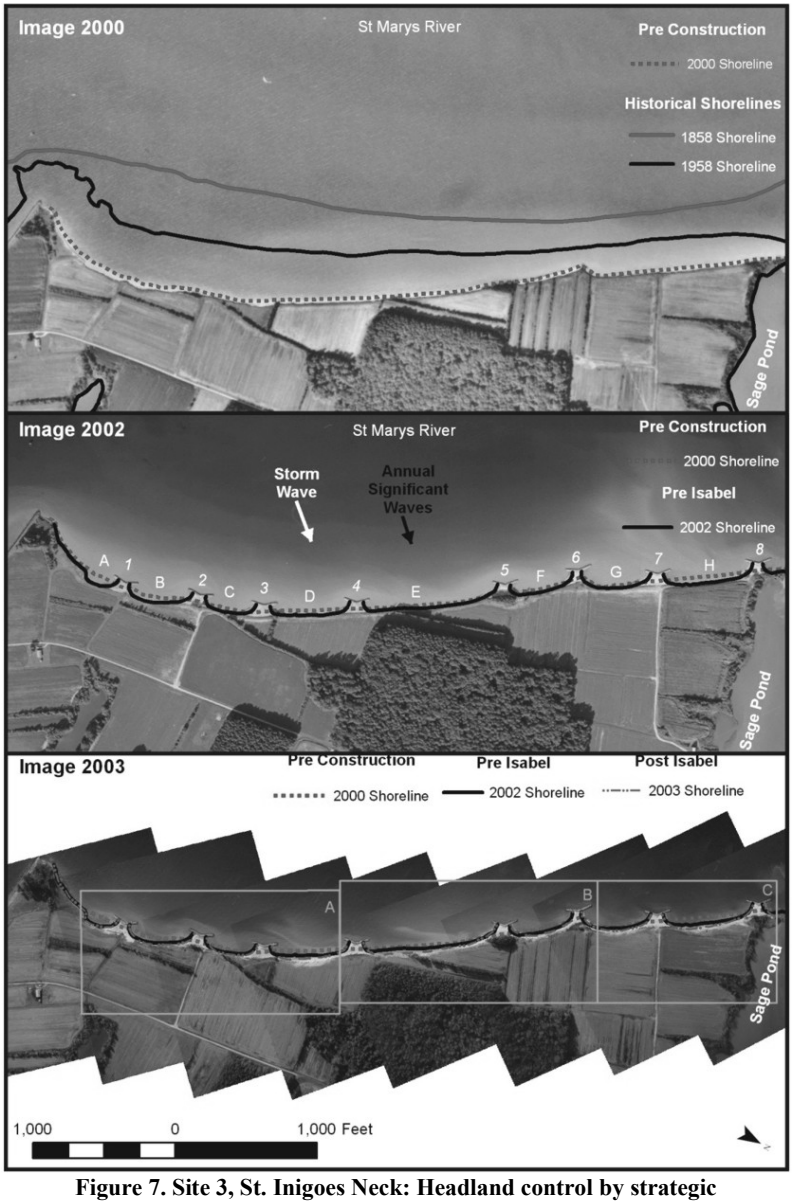

Figure 7. Site 3, St. Inigoes Neck: Headland control by strategic placement of headland breakwaters.

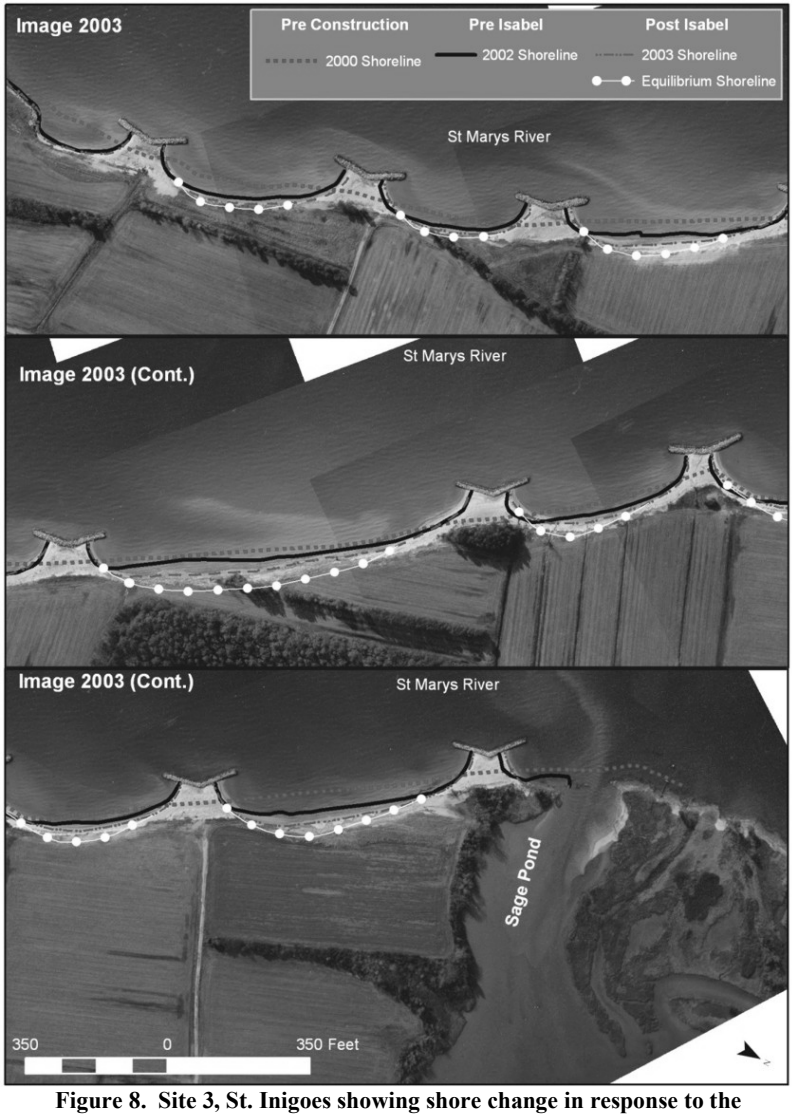

Figure 8. Site 3, St. Inigoes showing shore change in response to the breakwaters. Beach erosion in the predicted bay shape still requires additional sand for a protective beach.

CONCLUSION

The use of Headland Control can be a cost-effective method of reach management. This is done by placing widely spaced breakwaters and/or enhancing existing shore features and allowing the adjacent embankments to erode and evolve into equilibrium embayments. The "final" equilibrium planform is dependent on the impinging wave climate and the amount of sand in the system.

The three sites discussed in the paper have different physical settings and relative amounts of sand in the littoral system. It is important that the property owner understands potential issues when Headland Control is recommended for shoreline managment; these include 1) time, 2) added sand, 3) added structures and 4) cost. The SEB model helps predict ultimate equilibrium but not necessarily how long it will take. Projected erosion rates based on the shore history is probably the most reasonable, but, as we have seen, severe storms may hasten issues 2 and 3. Costs are always an issue, and sand sources can be the most critical in terms of availability and proximity to the site.

Severe storms may be good for headland control systems. They erode the unprotected upland banks in the embayments toward the design planform. Equilibrium is reached with a wide, stable and protective sand beach that becomes vegetated and forms a low dune. Along many undeveloped reaches of Chesapeake Bay, shore erosion is significant and protecting the entire property is very expensive per linear foot. However, by establishing headlands, the shoreline will eventually reach equilibrium. Since initial cost is only for the headlands and a small volume of sand for construction access, the cost per linear foot is greatly reduced. Ongoing monitoring is required in order to determine when another structure or sand is needed.

ACKNOWLEDGEMENTS

The authors would like to thank Donna Milligan for her help in revising, editing and formatting this paper as well as creating some of the figures. Thanks to George Thomas for obtaining the low-level aerial photography. Christine Wilcox did an excellent job rectifying the historic and recent images in GIS as well creating the figures. Finally, thanks to Kevin O'Brien for his help in summarizing storm data as well as reviewing the report.

REFERENCES

Anderson, G.L., Hardaway, C.S., and Gunn, J.R., (1983). "Beach response to spurs and groins," *Proceedings Coastal Structures '83*, American Society of Civil Engineers, p. 727-739.

Hardaway, C.S., Thomas, G. R., and Li, J. –H., (1991), "Chesapeake Bay shoreline study: headland breakwaters and pocket beaches for shoreline erosion control. Special Report in Applied Marine Science and Ocean Engineering No. 313, Virginia Institute of Marine Science, College of William & Mary, Gloucester Point, Virginia.

Hardaway, C.S. and Gunn, J.R., (1991), "Headland breakwaters in the Chesapeake Bay," *Proceedings, Coastal Zone '91,* ASCE, 2, 1267-1281.

Hardaway, C.S., Gunn, J.R., and Reynolds, R.N., (1993), "Breakwater design in the Chesapeake Bay: dealing with the end effects." *Coastal Engineering Considerations in Coastal Zone Management, Proceedings Coastal Zone '93,* American Shore and Beach Preservation Association/ASCE, 27-41.

Hardaway, C.S., Gunn, J.R., and Reynolds, R.N., (1995), "Headland Breakwater Performance in Chesapeake Bay," *Proceedings of the 1995 National Conference on Beach Preservation and Technology*, St. Petersburg FL, 365-382.

Hardaway, C.S., and Gunn, J.R., (1999a), "Chesapeake Bay: design, installation, and early performance of four (4) new headland breakwater/composite systems," *Beach Preservation Technology 1998,* Florida Shore and Beach Preservation Assoc., 1-18.

Hardaway, C.S., and Gunn, J.R., (1999b), "Chesapeake Bay: design and early performance of three headland breakwater systems." *Coastal Sediments '99.* ASCE, 828-843.

Hardaway, C.S., and Gunn, J.R., (2000), "Shoreline Protection: Design Guidelines for Pocket Beaches in Chesapeake Bay, USA," *Proceedings Carbonate Beach 2000,* ASCE, December 5-8, 2002, Key Largo, FL. p. 126-139.

Hardaway, C.S., and Gunn, J.R., (2003), "Chesapeake Bay: The prudent use of banks sands and revetments in headland breakwater systems," *Proceedings Coastal Sediment '03*, CD-ROM Published by East Meets West Productions, Corpus Christi, TX ISBN-981-238-422-7.

Hsu, J.R.C., Silvester, R., and Xia, Y.M., (1989), "Static equilibrium bays: new relationships," *Journal of Waterway, Port, Coastal, and Ocean Engineering* 115(3).

Silvester, R., (1970), Growth of crenulate shaped bays to equilibrium, Journal of Waterways Harbors Div., American Society of Civil Engineers 1, 550-563 p.

Silvester, R., and Hsu, J.R.C. , (1993), "*Coastal Stabilization: Innovative Concepts*," Prentice-Hall, Englewood Cliffs, New Jersey. 578 p.

COASTAL PROTECTION AGAINST WIND-WAVE INDUCED EROSION USING SOFT AND POROUS STRUCTURES: A CASE STUDY AT LAKE BIEL, SWITZERLAND

Selim M. Sayah[1] and Stephan Mai[2]

1. Swiss Federal Institute of Technology - Lausanne, now at Lombardi SA, Via F. Simen 19, CH-6648 Minusio, Switzerland. selim.sayah@lombardi.ch
2. University of Hannover, now at German Federal Institute of Hydrology, Koblenz, Germany, mai@bafg.de

Abstract: At the southern shore of Lake Biel in Mörigen, Switzerland, the sandy beach covered with reed plantations suffers strong erosion although a protection project was realized in the late 20th century. The design of this protection project included the construction of segmented porous structures (brushwood fences) parallel to the shoreline. Their purpose was to damp the incoming energy of wind-generated waves and to protect the shoreline against additional erosion. In order to enhance the shoreline protection, an additional study, based on in situ analysis of wind, waves and bathymetric evolution and numerical modeling of wave field and nearshore wave generated current responsible of sediment transport on the other hand, was carried out. The results revealed that by an adaptation of the existing system an enhancement can be achieved in order to thwart any further erosion and to promote sediment deposition at the leeside of the fences.

INTRODUCTION

Brushwood fences (see Fig. 1a-b) are most commonly used in lakes to provide reliable, soft, and cheap shore protection (Sayah et al. 2004). They are especially effective in shallow regions where hydrodynamic forces, generated by wind and currents, are not very significant. The fences are mainly composed of two elements (see Fig. 1b). The first one, related to the structural stability, is composed of two parallel rows of wooden piles (average spacing of piles equals 0.6 m). Between the two rows, wooden branches, often called "fascines", are inserted in a cylindrical bundled manner. This porous middle

element is responsible for the dissipation of incident waves. The average porosity of fascines varies between 10% and 80%.

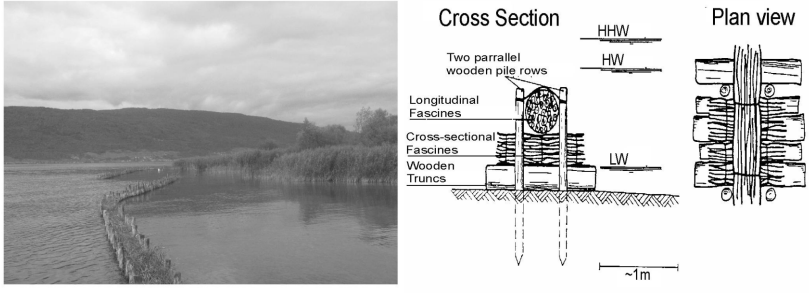

(a) (b)

Fig. 1. (a) Brushwood fences in Lake Biel (Switzerland) used to protect reed plantation; (b) Typical design concept of the brushwood fences

The site selected for the case study where multiple brushwood fences are constructed is located at the South-Eastern shore of Lake Biel (see Fig. 2) at almost 6 km South of Biel city. The location is called Mörigen. The selection of this site was based on three main reasons:

1. Many field surveys were carried out in this site: wind, waves, and bathymetric measurements
2. This site is located almost at the middle of the shore side of Lake Biel where erosion is most active
3. More than ten brushwood fences segments are located at this site used for wave damping

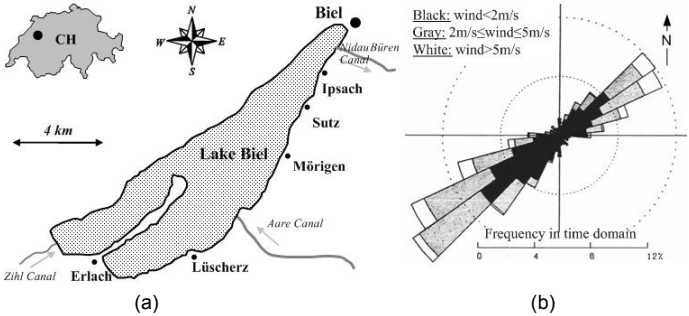

(a) (b)

Fig. 2. (a) Lake Biel in Switzerland and localities where in situ measurements are undertaken; (b) Wind rose based on statistical analysis at Payerne wind station situated at 30km south-west of Lake Biel (MeteoSuisse 1990)

The segmented brushwood fences in Mörigen are shown in Fig. 3. Each extremity of a single structure was located using GPS technique that provided the Swiss coordinates X

and Y. The altitude Z for each segment was measured locally. In addition to the positions of brushwood fences, wind velocities over water are measured at almost 2 m above the water level together with wave characteristics and the transmission coefficient of one single segment of brushwood fences at the upper part.

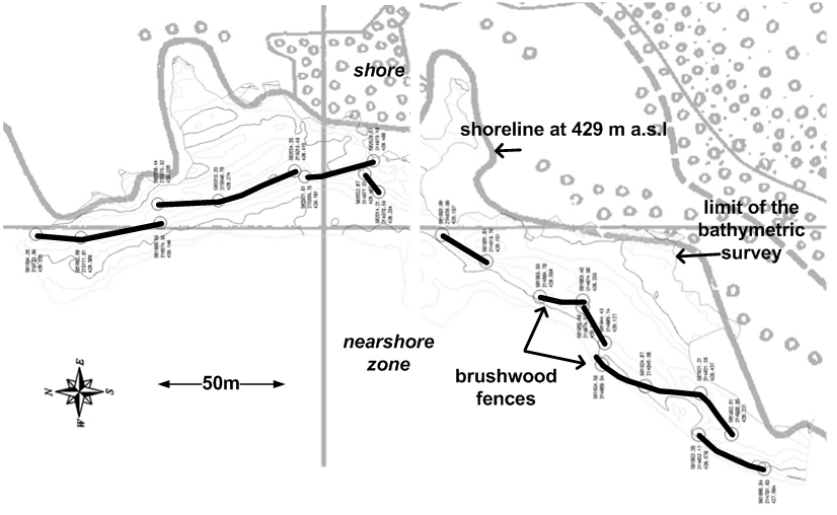

Fig. 3. Segmented brushwood fences at Mörigen in Lake Biel

FIELD MEASUREMENTS OF WIND AT MORIGEN

In situ wind measurements at Lake Biel have been realized in several other localities. However, the measurements of wind at the site of Mörigen selected for the present case study, show substantial results concerning wind velocities for the two major regimes over Lake Biel (see Fig. 1b). Instant over water wind velocities U_W and directions are measured during 6 months period (from first of October 2004 until the end of March 2005) with a Young anemometer Velocities and directions are averaged at 10 minutes intervals. Furthermore, the wind is measured at Payerne ANETZ wind station (wind over land) for the same period of time (wind rose of the fixed wind station is at Fig. 1b).

The comparison of over water and over land wind speeds and events shows relevant similarities. The events are selected when wind speed is significantly higher than 2.5 m/s and lasting at least 1 hour. The events at Payerne occur at the same period and almost for the same direction trends as at Mörigen. However, the measured wind speeds are at both station shows little discrepancy.

Fig. 4 highlights the effect of wind speed variation due to transition from land to water. The data shown corresponds to wind speeds for the South-western wind events during the period [Dec. 2004 - Mar 2005]. It includes measurement during more than 10 wind

events. Thus, wind speed tends to increase after a transition from a land surface. However, due to the behavior of water roughness as a function of wind speed, the ratio of over water wind speed at a fixed level to over land wind speeds (U_W/U_L) is not constant, but varies nonlinearly. Fig. 4 provides the trend for the form of such variation. The exact magnitude and characteristics of the transition depend on the roughness properties of the terrain and vegetation on one hand, and on the stability of the air flow on the other hand. Resio and Vincent (1982) presented a simple approximation of this wind speed variation based on a logarithmic fitting curve to the asymptotic over land and over water wind speed values.

Furthermore, trends in Fig. 4 indicate, as expected, that wind speeds over water follow a power law. The ratio (U_W/U_L) tends to infinity when U_L tends to zero and to almost 1 when U_L tends to infinity. The latter fitting depends mostly on the location of on water measurement station and on the wind regime. For "mean" wind speeds (roughly varies between 6 and 10 m/s in Switzerland), corresponding to recurrent wind events, such fitting provides a rough ratio of (U_W/U_L) equal to 1.35. Thus, wind over water is 35% stronger than wind over land for average wind events. This rough estimation strongly depends on the nature of vegetation beside the lake and the local topographic conditions. Therefore it could be not used for general applications.

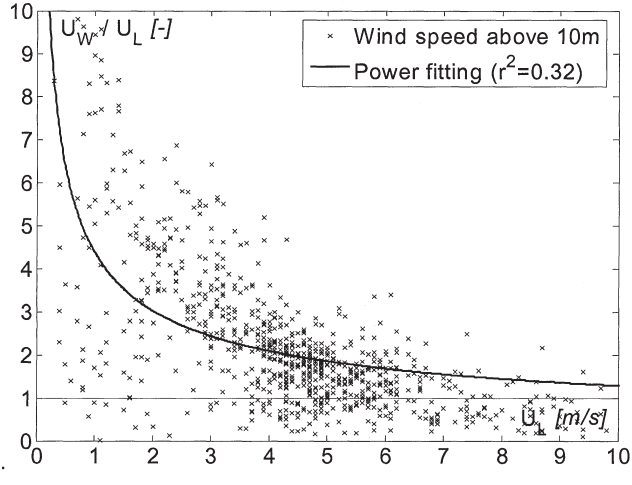

Fig. 4. Ratio of wind speed over water U_W at Mörigen to wind speed over land U_L at Neuchâtel according to U_L for a wind sector [210°-240°] during [Dec. 2004 - Mar 2005]

IN SITU WAVE TRANSMISSION

The field measurements of waves were carried out at the upper part of the brushwood fences field in Mörigen. Waves were measured before and behind a typical segment of brushwood fences during the same period as the wind measurements. The waves selected for the analysis correspond to significant waves heights H_s greater than 0.15 m.

Results of K_T according to the dimensionless freeboard R_c/H_s are provided in Fig. 5. During field measurements, the lake water level was always lower than the top of the brushwood fences. Therefore, the structure was always emerging and the transmission coefficient calculated is considered as average. The mean K_T value could be estimated during such conditions is equal to $K_{T,mean}$=0.32.

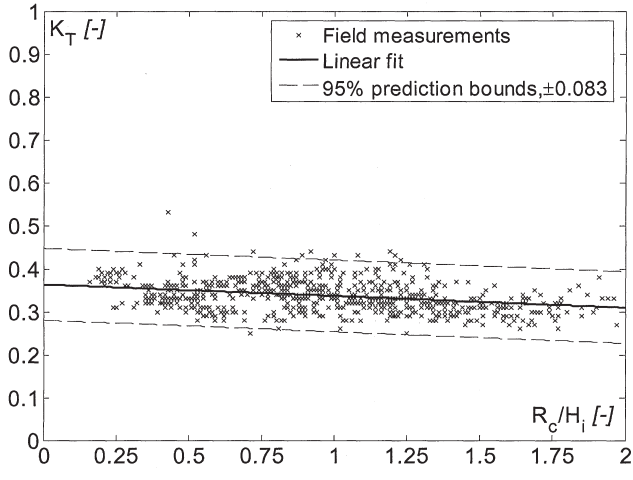

Fig. 5. Transmission coefficient K_T of typical brushwood fences at Mörigen according the relative freeboard R_c/H_s for a structure height h=1.12 m

ANEMOMETRIC AND LIMNIMETRIC BOUNDARY CONDITIONS

For the present case study, it is proposed to calculate incoming wave in the region of Mörigen using the numerical analysis by Swan model (Booij et al. 1996) .Since the duration of wave measurements in the nearshore region of Mörigen is too short, a long term analysis of incoming waves could not be carried out. Therefore, it was proposed to calculated wind-waves based of the statistics of wind measured off shore (at Payerne) after applying on wind velocities the correction coefficient as described before in order to obtain calibrated data.

Three main wind regimes are considered for Mörigen as following:

1. South-Western wind (sector [210°-240°]) "Le Vent": fetch=7000 m
2. North-Eastern wind (sector [30°-60°]) "La Bise": fetch=4500 m
3. North-Western wind (sector [300°-330°]) "Le Joran": fetch=3500 m

By using the long term statistical analysis for the three regimes, a calculation of wind velocities for every wind sector and return period could be made. Afterwards, the calculation of waves is carried out in Swan, using as input wind velocities and

directions. Since waves are refracting near Mörigen, incoming wave directions are different than wind directions. Therefore special attention should be given to wave direction used afterwards when calculating wave field in the brushwood fences location.

By calculating wave heights, periods and directions in Swan, it is possible to introduce these values as boundary conditions for the modeling of the wave field at Mörigen. Fig. 6 provides an example of wave characteristics for the stronger and more frequent wind regime (le Vent). The wind duration does not play a major role since the condition for the selection of wind velocities is defined when the duration is long enough to produce a fetch limited condition (Kamphuis 2000) Furthermore, the wind speed depends mainly on the selected return period T_r.

The return periods of waves are the same as the return periods of winds. Only three return periods are selected as follows: T_r= 1, 5, and 20 years. For each return period, three water levels of the Lake Biel are selected: MHWL= 429.60 m, MWL=429.20 and MLWL=428.8 m.

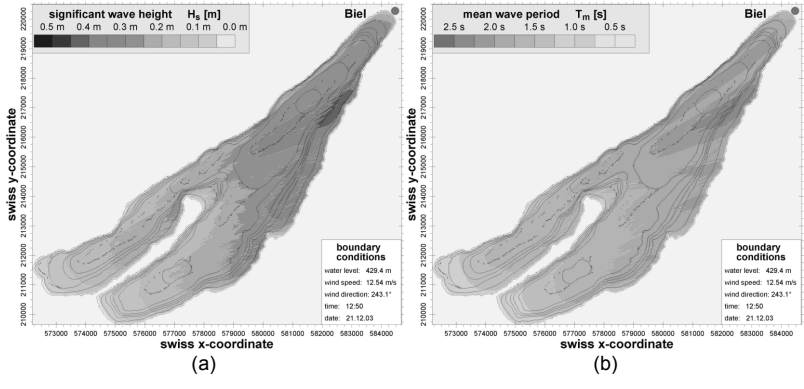

Fig. 6. Wave field in Lake Biel during a South-Eastern wind regime for the MHWL: (a) significant wave heights; (b) mean wave periods

EFFECT OF THE LAKE WATER LEVEL VARIATION

This section highlights the effect of the present nearshore brushwood fences field at Mörigen on the incoming waves when the lake water level changes. They are based on numerical modeling carried out by an elliptic mild slope solver as described by Madsen and Larsen (1987). It was proposed to calculate first the wave field without introducing any structures. In a next step, the wave field is calculated with the presence of the protection system as described before. This allows an accurate description of the effect of the protection system on the nearshore hydrodynamics and constitutes the basis of any protection enhancement proposals.

The variation of the water level influences significantly the shoreline position (see Fig. 7). Therefore, for the MHWL the shoreline moves in the landward direction and for MLWL, it moves in the seaward direction. At some shallow places, for a water level variation of 0.80 m, the shoreline displacement could reach 25 m. Furthermore, for shallower regions the shoreline displacement is almost 75 m. Such high values bring out the effect of the distance of brushwood fences from the shoreline. This distance should be long enough in order to enable a good performance of the structure during low water regimes. The results show that this criterion is practically fulfilled in almost all the cases. Even for the MLWL, all brushwood fences structures are still in water and able to damp efficiently the incoming waves.

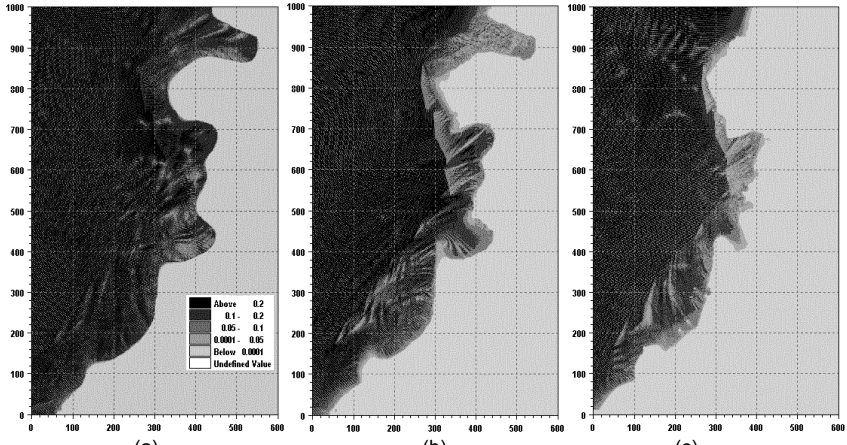

Fig. 7. Wave heights at Mörigen during a Western wind regime with the presence of the protection structures and T_r= 5 years (a) MHWL (B) MWL (c) MLWL

Additionally, the wave damping effect decreases significantly for all the modeled wind regimes when the water level is high. Therefore, when comparing in wave heights behind the brushwood fences field for the three modeled water levels of the lake, it is apparent that during a MHWL period, the incoming waves are almost equal before and behind the protection structures. It has to be noted that during this water level regime, the structures are totally submerged.

For the MWL, waves in the protected area at the leeside of the brushwood fences are much smaller than waves corresponding to the MHWL. However, when compared to waves during the MLWL, they do not appear to be much higher, although the water level variation is the same. This is probably due to the fact that for both water level regimes, the structure in emerging. For this condition, its efficiency is almost constant. Concerning the wave field width at the leeside of the protection structure, the results

show that for MWL, the protected region is much wider than the one corresponding to MLWL.

EFFECT OF THE WIND REGIME VARIATION

The wind regime has a clear effect on the nearshore wave field at Mörigen. When comparing results in Fig. 8 it appears that waves tend to be higher for the South-Western regime. This could be clearly seen for the return period T_r= 5 years. Such high waves are essentially due to the fact that the fetch of this wind regime is almost twice as large as the fetches of the two other main wind regimes. Moreover, wind speeds for South-Western wind are the highest.

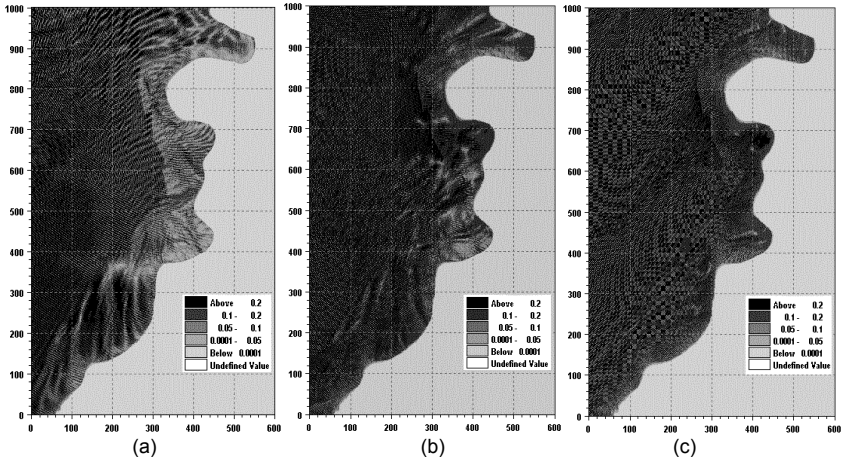

Fig. 8. Wave heights at Mörigen during a three different wind regimes with the presence of the protection structures at the MHWL and T_r= 5 years (a) South-Western (b) Western (c) North-Eastern

With the presence of the brushwood fences (see Fig. 8), wind regimes influences significantly the wave field at the leeside of the protection structures. Therefore, when comparing wave fields for MHWL, it appears clearly that for both North-Eastern and Western wind regimes, waves reach more easily the shore by diffraction through the wide gaps in the brushwood fences field. However, during a South-Western wind regime, although waves are higher, it seems that the present geometrical disposition of the structures protects the shoreline very efficiently.

Furthermore, the efficacy of the brushwood fences geometrical disposition during a South-Western wind regime is clearly shown for the MHWL. When comparing the wave field in Fig. 8, it appears that the average wave heights in the lee of the structures are almost twice smaller for the South-Western wind.

NEARSHORE CURRENT GENERATION

For the most significant cases, radiation stresses (Copeland 1985) were calculated in order to generate current maps in the nearshore region of Mörigen. This has been carried out using a hydrodynamic model.

The main conclusions of current simulations were as follows (see Fig. 9):

1. The nearshore wave generated bed currents are significantly reduced for the MHWL. However, for the MLWL, strong currents are more frequent and could easily reach values up to 0.5 m/s.
2. Without the presence of the protection structures, the currents could be easily "canalized" parallel to the shore. Their presence enhances current disturbance and damping.

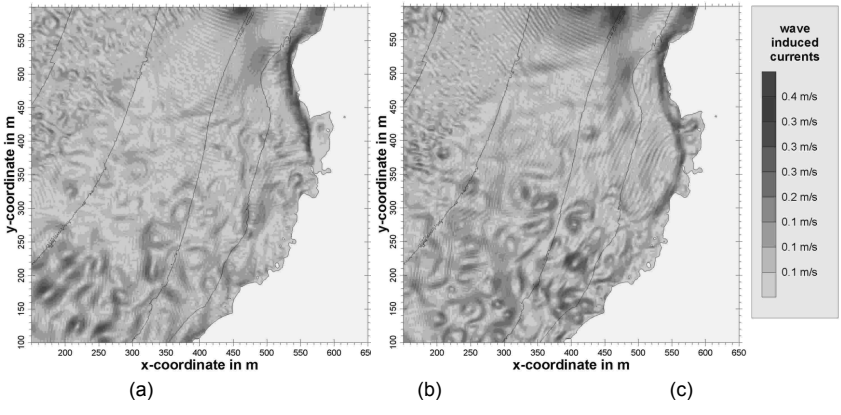

Fig. 9. Wave generated currents based on the calculation of the radiation stresses for the MWL and T_r= 5 years (a) with the protection system (b) without the protection system

CONCLUSIONS AND RECOMMENDATIONS

The brushwood fences field at Mörigen in Lake Biel has been modeled using the elliptic mild slope equation. The wave field at the leeside of the fences is obtained for the three main lake water levels, and for the three main wind regimes. The statistical analysis of in-situ over-land wind measurements permitted the identification of three main wind directions, North-East, North-West and South-West. After adjustment of wind velocities based on the ratio of over-water and over-land wind speeds (equal to 1.35), waves statistics for each regime were determined using the numerical model of the entire lake based on Swan application. In average, for a wind return period of T_r= 20 years, corresponding to an average wind velocity of 12 m/s , the waves at Mörigen are almost 0.4 m height and 2.2 s period. The introduction of the transmission values of the brushwood fences and bottom characteristics into the numerical model of the nearshore

region of Mörigen are provided through in-situ measurements and depend on water level variation.

For each wind regime, eighteen cases have been investigated. In order to evaluate the effectiveness of the brushwood fences field related mainly to their geometrical distributions, nine cases are considered without the presence of the structures and nine cases with the presence of the structures. They correspond to the three selected return periods, T_r= 1, 5 and 20 years, for each, three selected water levels, MHWL,MWL and MLWL are considered.

The comparison of the results permitted the following conclusions:

1. When the water level of the lake is MHWL, the effectiveness of the brushwood fences field is very low. The transmission of the incoming waves is almost 100%
2. Although during the South-Western wind regime, incoming waves reaches their highest values, they are efficiently damped by the particularly adapted geometrical configuration of the brushwood fences field. For the two other wind regimes, waves are able to reach the shore through wide gaps between the fences

The present study demonstrated the effectiveness of the use of elliptic mild slope equation to model real cases, where porous structures are built. The input of the results obtained by the Swan model for wind-wave data appeared to be very relevant and adequate. Further detailed numerical analysis of currents and bedload sediment transport is crucial, and should reveal significant nearshore phenomenon that contributes to a better understanding of the hydrodynamics of the brushwood fences field in order to suggest resolute enhancement of the protection system.

REFERENCES

Booij, N., L. H. Holthuijsen, et al. (1996). “The SWAN Wave Model for Shallow Water,” *15th International Conference on Coastal Engineering*, Orlando, Florida, USA.

Copeland, G. J. M. (1985). “Practical radiation stress calculations connected with equations of wave propagation,” *Coastal Engineering* 9: 195-219.

Kamphuis, J. W. (2000). *“Introduction to Coastal Engineering and Management,”* World Scientific.

Madsen, P. A. and J. Larsen (1987). “An efficient Finite-Difference Approach to the Mild-Slope Equation,” Danish Hydraulic Institute, Denmark: 329-351.

Resio, D. T. and C. L. Vincent (1982). “A comparison of various numerical wave prediction techniques,” *11th Annual offshore technology conference*, Houston, USA.

Sayah, S. M., J.-L. Boillat, et al. (2004). “The Use of Soft Shore Protection Measures in Shallow Lakes: Research Methodology and Case Study," *Limnologica* 34(1-2): 65-74.

PHYSICAL PROCESSES STUDY OF GOLDSMITH INLET, NEW YORK

Michael J. Morgan[1], Nicholas C. Kraus[2]

1. U.S. Army Engineer District, New York, 26 Federal Plaza, New York, NY 10278. Michael.J.Morgan@usace.army.mil.
2. U.S. Army Engineer Research and Development Center, Coastal and Hydraulics Laboratory, 3909 Halls Ferry Road, Vicksburg, MS 39180-6199, USA. Nicholas.C.Kraus@erdc.usace.army.mil.

Abstract: Goldsmith Inlet is a small semi-natural and non-navigable inlet located on the northeast shore of Long Island, NY, and it connects Goldsmith Pond to Long Island Sound. The coast is gravelly, waves relatively small because of limited fetch, and tide range relatively large at 2 m as compared to the south shore of Long Island. The inlet has been in existence since at least the 1700's, but is apparently prone to closure in recent times. Field data collection, GIS analysis of morphology, and numerical modeling of the inlet current were performed. The inlet is found to be highly flood dominant, with two natural sills restricting ebb flow. As a result, gravel remains at the inlet mouth, with the flood shoal composed of fine sand. No ebb shoal is found, probably a result of the limited ebb-tidal discharge. It is concluded that an easterly orientation promotes channel stability and is to be preferred to re-alignment of the inlet to run straight out to Long Island Sound.

INTRODUCTION

Goldsmith Inlet (Fig.1 and Fig. 2) is a small, semi-natural inlet located on the northeast shore of Long Island, NY, and connects Goldsmith Pond to Long Island Sound (Leatherman et al. 1997). The inlet is not navigable, and it is protected on the up-drift side by a structure called a jetty that should be considered as a groin in retaining sand on its up-drift (west) side. Goldsmith Inlet is of interest in that it is a gravelly inlet, migrates down drift, has no ebb shoal, is strongly flood dominant, and is relatively stable. This paper abstracts information contained in a comprehensive study by Morgan et al. (2005).

In contrast to the south shore of Long Island, inlets on the north shore have received little study. Many are small and serve small and isolated water bodies. North shore inlets appear to be more stable in location than the south shore inlets. The sediment along the south shore consists predominantly of fine to medium sand, with a median grain size of 0.3 mm being typical. In contrast to the sandy beaches backed by dunes found along the south shore, high bluffs and a wide range in grain size characterize the north shore of Long Island. The tide range along the north shore is about double that of the south shore and the waves along the north shore are smaller and steeper. Longshore sediment transport is an order of magnitude less on the north shore as compared to the south shore.

This paper discusses coastal processes at Goldsmith Inlet. Field data collection conducted in Oct 2002, during a spring tide, included surveys of the adjacent nearshore, inlet, and Goldsmith Pond; measurements of water level in Long Island Sound and in the pond; short-term measurement of the current; and sediment sampling. Available aerial photographs were obtained, starting in 1938, and aerial photographs of the study area were taken on 15 Apr 2003 and 16 Apr 2004. A GIS analysis of inlet morphology and morphology change was conducted. A tidal inlet hydrodynamics model DYNLET (Amein and Kraus 1991) was established to calculate the inlet current and water level.



Fig. 1. Goldsmith Inlet, 16 Apr 2003

Goldsmith Inlet has been in existence since at least the 1700s. Historically, a strong tidal current at Goldsmith Inlet is indicated by the presence of a tidal mill on Goldsmith Pond from about 1840 to the early 1890s. The sediment on the neighboring beaches is coarse sand to gravel, and the sediment in the inlet is primarily gravel and cobble.

Goldsmith Inlet has a depth of 0.3-0.6 m, and inlet width ranges from about 3 to 30 m. The mean width is about 15 m (Fig. 2), and it is approximately 360 m long. Goldsmith Pond has a mean depth of 0.5 m and a surface area of approximately 88,000 sq m. The

tide range in this area is about 2 m, and spring tide range is 2.3 m. The tidal prism of Goldsmith Inlet and Goldsmith Pond is calculated to be 8.5×10^4 m^3, based on measured bay area and half the spring tide range.



Fig. 2. Goldsmith Inlet entrance with view of east beach, 28 Mar 2003

Construction of the jetty was completed in 1964. Since 1964, the jetty has gradually deteriorated. Degradation and complete impoundment of sediment on the jetty's west side have led to greater sediment intrusion. The inlet has been occasionally dredged as a source of sand and gravel for upland activities and to provide sediment for renourishment of Kenneys Road Beach, located east and down drift of the inlet. More recently, Goldsmith Inlet has been dredged on an emergency basis, when the inlet has experienced closure, with the dredged material placed on the adjacent down-drift beach. Since the bathymetric survey of Oct 2002, the mouth of Goldsmith Inlet migrated to the east. In the winter of 2003-2004, a west-oriented spit accreted at the inlet mouth, redirecting the mouth slightly toward the west. The presence of ice directly east of the inlet may have been partially responsible for buildup of this west-oriented spit as well as the redirecting of the inlet mouth to the west. The Town of Southold has discussed the future of Goldsmith Inlet and the Goldsmith Inlet jetty. Beyond the creation of a deeper channel, an option being considered is shortening of the jetty, which may mitigate erosion east of the jetty yet still preserve a portion of the beach fillet west of it.

DATA COLLECTION

A bathymetric survey of the offshore adjacent to Goldsmith Inlet was conducted by boat on 6-8 Oct 2002. Goldsmith Inlet and Pond, the beaches adjacent to the inlet, and the area from the shoreline to wading depth were surveyed with a total survey station and surveying rod. The survey of Goldsmith Inlet and Goldsmith Pond was conducted on 8 Oct 2002. A water level gauge was deployed from 19 Sep to 8 Oct 2002. Flood current velocity was measured in the inlet from 1323 to 1643 GMT, 8 Oct 2002 by

means of a hand-held current meter mounted on a pole that was sunk into the bed. Sediment samples were also taken.

Bathymetry

The coast west of Goldsmith Inlet is characterized by a relatively uniform shoreline and a large number of glacial erratics. The shoreline east of Goldsmith Inlet is less uniform. The area offshore on both sides of Goldsmith Inlet has a steep gradient, with a slope of approximately 1:10 from the beach to a depth of approximately 6 m NAVD88. A depression that is oriented parallel to the shoreline is located from 200 to 600 m offshore, where the depth reaches 7 m NAVD88. The entrance to Goldsmith Inlet is narrow and shallow. Depths range between 0.3 and 1.3 m NAVD88, and a large in-channel bar formation in the center of the channel becomes exposed during low tide. The channel has been observed to contain running water at all times during numerous field visits. At the time of the 6-8 Oct 2002 survey, the channel was 4 m wide at the entrance to the Long Island Sound and expanded to 35 m at the entrance to Goldsmith Pond.

An interesting finding of the survey is that Goldsmith Inlet lacks an ebb shoal. To the west of the inlet, an elevated formation (shoal) is located 300 to 600 m offshore. Because of this distance, this formation is not considered a consequence of either the modern or the historic inlet. Although the maximum ebb-current velocity at Goldsmith Inlet exceeds 1 m/sec and is comparable to that at other inlets that have formed ebb-tidal shoals, the volume of water flow or discharge is evidently too small to construct an ebb shoal. Sediment transported by the ebb current to the mouth of Goldsmith Inlet is transported from the entrance by waves and the wave-induced longshore current. This conclusion implies that bypassing from west to east occurs around the jetty, onto the spit, and back to the shore on the east side along a bypassing bar.

In contrast to lack of an ebb shoal, Goldsmith Inlet possesses a well-developed flood shoal consisting of three lobes. The lobes are located on the east bank, center channel, and west bank, where Goldsmith Inlet enters Goldsmith Pond (Fig. 3). Because of the mild elevation relief in the pond, the east and west lobes of the flood shoal are exposed during low water. The west lobe of the flood shoal is located approximately 250 m into the inlet. Sediment entering the inlet during flood tide is inferred to have formed this feature. This attachment on the west bank may redirect the ebb and flood tidal current and decrease the flushing capacity of the inlet. Sediment also approaches the inlet entrance from the spit that forms adjacent to the jetty. The entrance channel tends to align to the east, a characteristic that has become more pronounced with growth of the attachment shoal and the build-up of sediment along the jetty.

Water level

A tide gauge was placed near the southern bank of Goldsmith Pond and secured to the pond bottom. Water level at Goldsmith Pond is plotted in Fig. 4, together with that in Long Island Sound measured at the nearby Mattituck Inlet jetty (a Federal inlet located 8.4 km west of Goldsmith Inlet). In Goldsmith Pond, the average water level of the record was 0.28 m above NAVD88. This means that the pond does not completely empty to mean sea level (MSL), because the water flow is retarded by a sill in the area of

the flood shoal, as indicated in Fig. 6 and, to a lesser extent, by a sill in the inlet located near the shoreline.

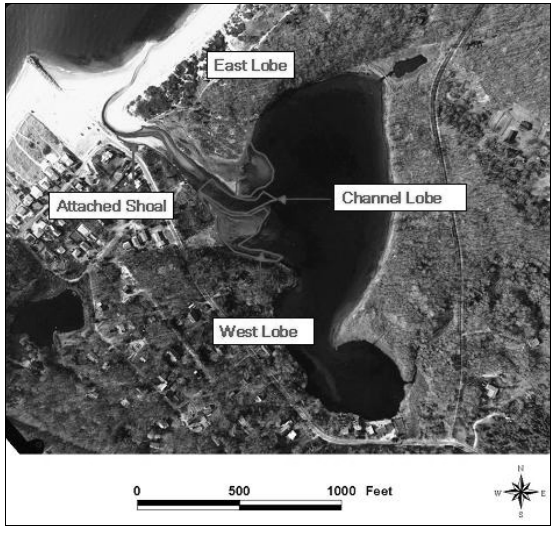

Fig. 3. Goldsmith Pond flood shoal. 16 Apr 2003

The measured tidal range within Goldsmith Pond varied from 0.37 to 1 m NAVD88. The mean tidal range for the deployment was calculated to be 0.66 m, with a spring tidal range of approximately 0.9 m for the period of record. The reduction in tide at Goldsmith Pond is, therefore, about 1 m or half the tidal range in Long Island Sound. Fig. 4 plots water level at Mattituck Inlet and Goldsmith Inlet for 5–7 Oct 2002. Because the tidal wave travels from east to west in Long Island Sound, the phase of the tide at Goldsmith Inlet will slightly lead that outside of Mattituck Inlet.

The bottom of the mouth of Goldsmith Inlet is located approximately at the elevation of the NAVD88 datum, near the visually observed mean shoreline position. Therefore, flow into the inlet and pond can only occur when the water level in the Sound is above MSL. The relation between NAVD88 and MSL at the mouth of the inlet is not known with confidence. Flow into the inlet and pond can only occur if the water level in the Sound is above the NAVD88 or MSL datums, according to the modeling results. When high tide is reached in the Sound, high tide in the pond occurs about 29 min later (median lag) and is 0.8 m lower. In contrast, the median phase lag for the low waters is 195 min (3.24 hr).

The long-term average water level in Goldsmith Pond is expected to be constant. The time duration of the high water is much shorter than the duration of the low water about the mean water level. Because the same amount of water must enter on flood as leaves at ebb to maintain the average water level in the pond, but in a shorter time, the average of the inlet channel cross-sectional current velocity on flood must be much greater than on

ebb. Such an inlet is called flood dominant, referring to the greater magnitude, but shorter duration of the flood tide.

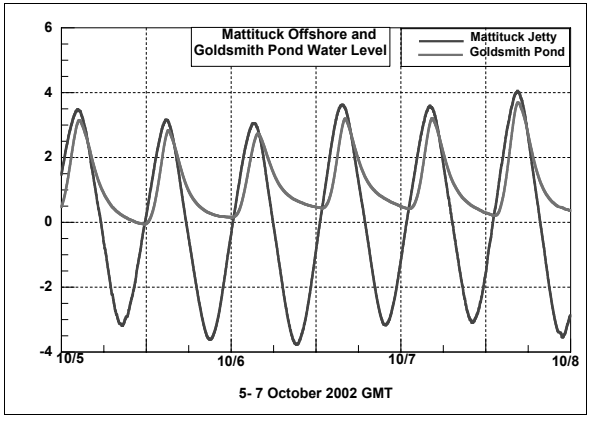

Fig. 4. Goldsmith Inlet water level, 5–7 Oct 2002

Current

The flood current velocity at mid depth and flood tide reached 1.3m/sec, after which the meter had to be removed because of concerns over the rising water level and strong current on. Corresponding to discussion of water level, there must be a strong asymmetry in current velocity at Goldsmith Inlet, with flood current being significantly stronger than ebb current. Sediment transport is proportional to a power of water velocity, typically the third power. Therefore, the flood-dominance will tend to transport sediment into Goldsmith Pond.

Sediment

Fourteen sediment grab samples were collected from Goldsmith Inlet on 8 Oct 2002, supplemented by 17 samples collected on 31 Jul 2003. The surficial sediment at the inlet entrance is predominantly composed of gravel (-6 to -2 ϕ). A transitional area is located around the shoal attached to the west bank where smaller gravel (-4 to -2 ϕ) dominates sand. The area of the inlet south of this region, which includes the flood shoal and the bottom of the pond is composed primarily of fine gravel and very coarse to coarse sand (-1 to 1 ϕ).

Figure 5 is a plan-view distribution of sediment grain size at Goldsmith Inlet. The plan view clearly shows fining of sediment with distance into the inlet and pond from the entrance. Current velocity magnitude plays a major role in determining the distribution of grain size within an inlet, resulting in a graded deposit and sorting within the channel. The greater velocity magnitude at the inlet mouth entrains and transports increasingly larger grain sizes. As the current velocity magnitude decreases, the larger grain size fractions are deposited, whereas finer sediments are transported further into the inlet.



Fig. 5 Goldsmith Inlet median grain size distribution of surface samples

CALCULATION OF CURRENT

Water-surface elevation and current velocity at Goldsmith Inlet and Goldsmith Pond were calculated with the DYNLET model. DYNLET is a 1-D plus model in that it solves for current velocity at specified stations along each cross section. Water level at the nodes and velocity at the stations are calculated, with the velocity apportioned at the stations according to the bottom friction or conveyance of the channel. A uniform rectilinear bathymetry grid for Goldsmith Inlet and Goldsmith Pond was created by importing the Oct 2002 bathymetry survey data into DYNLET. Thirty-one nodes with cross sections of varying length were then generated (Fig. 6).

The model was forced at Node 1 with water level measurements adapted from the Mattituck Inlet jetty gauge, and a no-discharge boundary condition (current velocity of zero) was specified at Node 31 located at the back of the pond. The distance between nodes was determined so as to represent significant changes in morphology through consideration of channel or pond width, depth, and roughness of the bottom. The DYNLET grid of Goldsmith Inlet originates approximately 200 m offshore. The distance between nodes within the channel and pond is approximately 20 m.

Water level measurements obtained offshore of Mattituck Inlet from 19 Sep to 8 Oct 2002 drove the model. The relation between MSL and NAVD88 at Goldsmith Inlet and Pond is not known. It was found by numerical experimentation that raising the water surface elevation by 0.25 m produced a successful model simulation that accurately

represented the tidal signature recorded at Goldsmith Pond, while not drying the channel. The authors have never observed the inlet channel to dry, even during low tide. A shift upward in the driving water level is functionally equivalent to shifting the entire bathymetry grid down by the same amount.

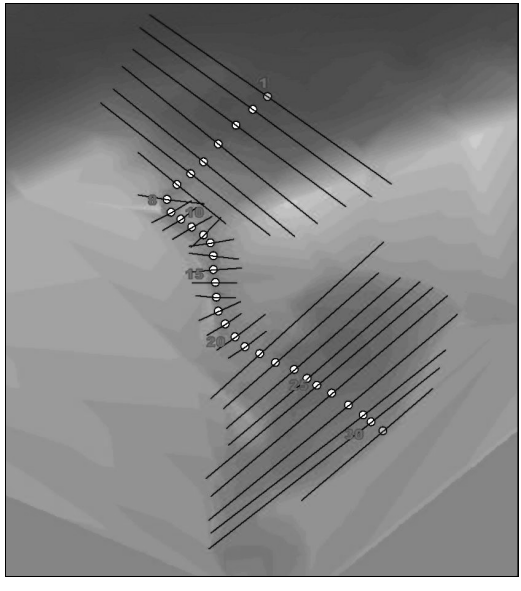

Fig. 6. DYNLET grid of Goldsmith Inlet, with nodes and extents of nodal cross-sections

DYNLET was calibrated by specifying larger values of the bottom friction coefficient in the Goldsmith Inlet channel, where small rocks are present and can protrude above the water surface, some of which may be remnants from jetty construction. The default value of Mannings n of 0.025 m/sec$^{1/3}$ was maintained at most nodes, but in the channel where rocks and roiling water are observed, the value was increased to 0.03 to 0.04. The time step in the model was set as 30 sec. The tidal record offshore of Mattituck Inlet was therefore adjusted forward 36 min to account for the time of tidal wave travel. This adjustment implies that the tidal wave moves westward at about 0.23 m/sec along the shallow water of this portion of the north shore of Long Island.

Figure 7 compares measured and calculated water level for 5-8 Oct 2002, a period of spring tide. Current velocity measurements taken for a short interval on 8 Oct 2002 are compared to corresponding DYNLET current velocity calculations (Nodes 13 and 14) in Fig. 8. The calculations well reproduce the limited length of the measurements. The current velocity is strong, exceeding 1 m/sec, and the calculated current is flood dominant.

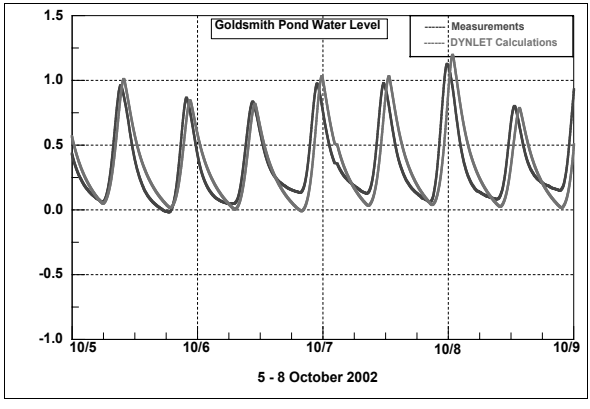

Fig. 7. Water level measurement and calculations (Node 30) off shore of Goldsmith Inlet 5-8 Oct 2002

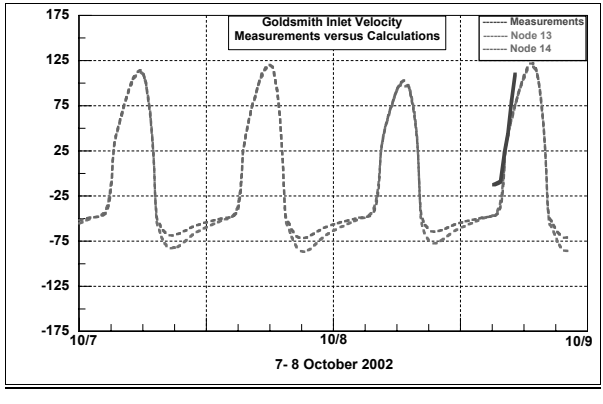

Fig. 8. Measured and calculated current velocity at Nodes 13 and 14, 7-8 Oct 2002

MORPHOLOGY CHANGE AND CHANNEL MIGRATION

Our analysis indicates that the greatest rates of erosion on the down-drift beach occurred between 1972 and 1978. Effective natural sediment bypassing was not established until the spit directly east of the jetty had reached a certain volume and areal extent. The impoundment fillet directly west of the jetty was the apparent primary sediment sink in this area prior to 1972. After this, the formation of the spit directly east of the jetty became the primary sediment sink for the local sand-sharing system. This period may have also been characterized by greater rates of sediment intrusion within the inlet.

Construction of the jetty apparently stabilized the inlet for 17 years by blocking eastward-moving material, because the first dredging of record occurred in 1977. Goldsmith Inlet was dredged seven times until 1990, and several times in the early 1990s. The inlet apparently maintained a degree of stability from the mid 1990s to 2002. The relatively large tidal range and large sediment grain size contribute to inlet stability. The instability observed in recent times may owe to continued degradation of the jetty, which allows sediment to enter the inlet.

Because Goldsmith Inlet is free to migrate to the east and away from the jetty, the location of its entrance channel is dynamic. The orientation of the channel, sediment impoundment west of the jetty, and the formation of a fillet east of the jetty were analyzed for times available from aerial photographs. The reorientation indicates that the inlet is presently an ephemeral inlet, in contrast to the preceding century when it was apparently more stable and open.

Figure 9 shows selected orientations of the inlet entrance from 1993 to 2004. Change in location and morphology of the Goldsmith Inlet channel entrance between 6-8 Oct 2002 and 16 Apr 2003 is substantial. Sediment accumulation extended the beach 18-25 m for the 150 m directly east of the jetty, and the entrance channel mouth migrated 107 m to the east. The effective greater length of the channel reduces the ebb flow and contributes to closure. The acute angle of the inlet relative to the shoreline however allows for more effective sediment bypassing.

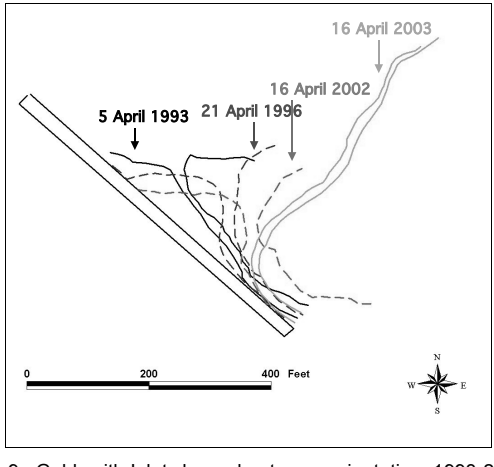

Fig. 9. Goldsmith Inlet channel entrance orientation, 1993-2003

TIDAL ASYMMETRY

The times series of water level in Goldsmith Pond exhibits three remarkable properties: (1) low tide usually does not reach 0 NAVD88, which is approximately MSL at the site, (2) the tide range in the pond is less than half that in Long Island Sound, and (3) water

level rises much more rapidly than it falls, and the duration of ebb is much longer than flood. Properties (1) and (2) are related. In Goldsmith Pond, the duration of the average ebb tide (peak to trough) of record was 8 hr, 56 min, and the duration of the average flood tide (trough to peak) was 3 hr, 28 min.

Tidal asymmetry of coastal inlets has been well studied and is summarized by Walton (2002). For example, shoaling channels truncate the lowest portion of the tide, resulting in a longer falling tide and weaker ebb current as compared to the flood current. Such a truncation is a hypsometric effect, the control of water surface elevation by the geometry of the bathymetry or depths. At the inlet, the elevation of the entrance is near MSL. At the lower water levels of ebb tide, the sills at the flood shoal and shoreline become more effective in retarding flow. In addition, water enters the fringing marsh of Goldsmith Pond on flood tide more rapidly than when it exits on ebb. The effective friction of the marsh, creating storage capacity, will release water slowly as compared to its entrance at flood tide.

The tidal water levels calculated in DYNLET levels exhibit strong asymmetric behavior for Goldsmith Inlet. Figure 10 plots water level at selected nodes along the inlet channel for 5-8 Oct 2002. At nodes located near the forcing in Long Island Sound, the water level signal is sinusoidal. With distance into the inlet, the water level signal becomes more asymmetric, achieving a greater maximum on flood than on ebb, and with a shorter time of flood than ebb. There are three possible causes for the asymmetry. The first and likely dominant cause is the presence of sills in the inlet. The higher water of flood can enter the inlet rapidly, because the tide wave celerity is given by the square root of the product of gravitational acceleration and depth. On the lower water of ebb, the depth has decreased, and the water that can ebb slows. Connected with this hypsometric change in wave speed, bottom friction will retard flow more strongly for shallower water.

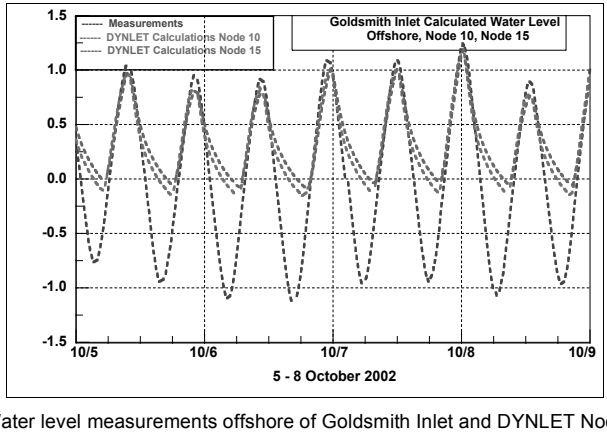

Fig. 10. Water level measurements offshore of Goldsmith Inlet and DYNLET Nodes 15 and 20 calculations, 5-8 October 2002

A second cause for the asymmetry in water level and current signals in the inlet and pond is the preferential drainage in the wetland surrounding Goldsmith Pond. It is expected that flooding water will enter the wetland more rapidly than the draining water on ebb. A third reason for the asymmetry is the non-linear interactions of flow components introduced by the bottom friction terms and advective terms in the equations of motion.

Figure 11 plots the maximum calculated velocity at each node for a spring flood tide and the subsequent ebb tide on 7 Oct 2002, together with the bottom elevation. The flood current had maximum velocity of 1.43 m/sec for this time interval. Strong flood-tidal currents persist to the exit of the channel into Goldsmith Pond. The ebb current at the mouth exceeds 1 m/sec.

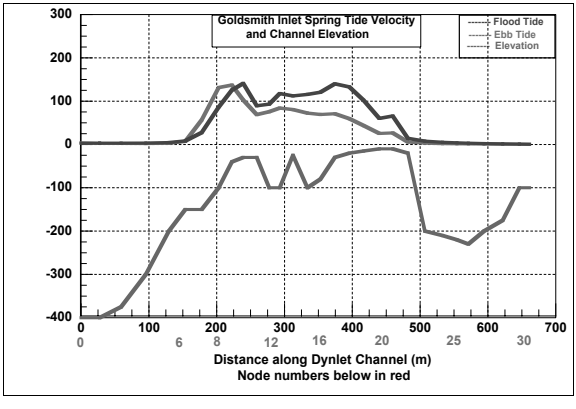

Fig. 11. Maximum calculated flood and ebb spring tide current speed and water elevation 7 Oct 2002

Figures12 and 13 display composite surfaces of maximum calculated flood and ebb velocity within the channel for hours 400 to 450 of the model run. A strong flood current persists over the entire channel and into the pond, whereas the ebb current is weak over much of the channel and pond, except at the mouth of the inlet. Such behavior would tend to transport sediment, particular sand, toward Goldsmith Pond, promoting flood shoal development and growth. The strong ebb current at the entrance would tend to maintain the inlet by sweeping finer sediments away from the mouth. However, sediment brought into the inlet on flood will not be flushed on ebb, promoting closure by constriction inside the inlet and not necessarily at the mouth.

CONCLUDING DISCUSSION

The presence of a tidal mill at Goldsmith Inlet in the 18th and 19th centuries indicates stability of the channel and strong tidal flow prior to the partial modifications of 1963-1964. The construction of the west jetty and the new-work dredging (1964) promoted stability of the inlet by substantially interrupting longshore transport of sediment to the east for approximately 14 years. In 1978, the jetty at Goldsmith Inlet appears to have

reached impoundment capacity. Thereafter, sediment intrusion into the Inlet increased, promoting dynamic morphological evolution within Goldsmith Inlet, partially mitigated by dredging. The increased rates of sediment intrusion resulted in the creation of an attachment fillet directly east of the inlet, the eventual maturation of the flood shoal, and a subsequent increase in the rate of channel infilling.

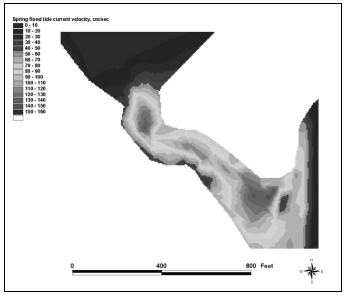

Fig. 12. Goldsmith Inlet spring flood tide maximum current velocity, inlet channel

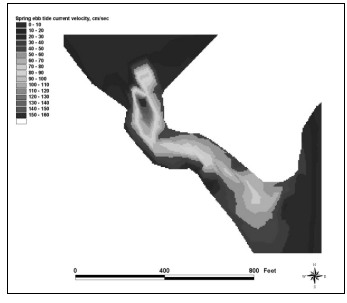

Fig. 13. Goldsmith Inlet spring ebb tide maximum current velocity, inlet channel

Re-establishment of an effective natural longshore sediment bypassing system appears to have taken place sometime in the early 1980s, when an attached fillet located directly east of the jetty reached an areal extent that promotes bypassing. Partial dredging from 1980 to 2000 apparently mitigated the continued growth and maturation of this attached fillet, and the eastward migration of the inlet entrance. The lack of dredging in recent years (in addition to continued degradation of the jetty) has allowed for rapid growth of this feature and resulting eastward migration of the inlet entrance (2001-2002). Re-establishment of a natural system of sediment bypassing has occurred, where sediment is transferred from this attached fillet via a bypassing bar located near the swash zone and eventually to the beach east of Goldsmith Inlet.

The current through Goldsmith Inlet is strongly flood dominant, determined in main part by the shallow sills in the channel. Because sediment transport is proportional to a power of water velocity, net sediment transport is directed into Goldsmith Pond. The greater velocity magnitude at the inlet mouth entrains and transports larger grain sizes. As the current velocity magnitude decreases with distance into the inlet, gradational deposition occurs, with the larger grain size fractions deposited and finer sediments transported further into the inlet.

The elevation of the entrance to Goldsmith Inlet is located near MSL. At the lower water levels of ebb tide, the sills at the flood shoal and shore become more effective in retarding flow. In addition, water enters the fringing marsh of Goldsmith Pond on flood tide more rapidly than when it exits on ebb. The effective friction of the marsh, creating storage capacity, releases water slowly as compared to its entrance at flood tide.

The mouth of Goldsmith Inlet appears to be at or near locational and cross-sectional equilibrium if it is oriented to the east, as shown in Fig. 1. Past dredging practice has realigned the channel parallel to the jetty. It is concluded that an orientation with the mouth directed to the east is the optimum for sediment bypassing and maintenance of inlet stability. The accretion fillet to the east, between the jetty and the inlet mouth, now functions to bypass sediment via transport by wave-induced current in the swash zone and by the ebb current issuing from an easterly orientation. If the accretion fillet to the west were mined substantially, impoundment at the jetty would reduce the sediment bypassing volume, turning back the processes in time.

ACKNOWLEDGEMENTS

Field data collection led by Mr. William Grosskopf of OCTI, East Coast, and discussions with Mr. William Seabergh of the Coastal and Hydraulics Laboratory, U.S. Army Engineer Research and Development Center (ERDC) are appreciated. This study was supported by the Coastal Inlets Research Program conducted at the ERDC, Vicksburg, MS. Permission was granted by Headquarters, U.S. Army Corps of Engineers, to publish this information.

REFERENCES

Amein, M., and Kraus, N.C. (1991). "DYNLET1: Dynamic implicit numerical model of one-dimensional tidal flow through inlets," TR CERC 91-10, U.S. Army Engineer Waterways Experiment Station, Vicksburg, MS.

Leatherman, S.P., Dean, R.G., Kana, T., and Anders, F.J. (1997). "Goldsmith Inlet and adjacent areas, north shore of Long Island, New York: Erosion problems and suggested modifications," *Shore and Beach* 65(3), 13-16.

Morgan, M.J., Kraus, N.C., and McDonald, J. 2005. "Geomorphic analysis of Mattituck Inlet and Goldsmith Inlet, Long Island, New York," ERDC/CHL TR-05-2 U.S. Army Engineer Research and Development Center, Coastal and Hydraulics Laboratory, Vicksburg, MS, 332 p.

Walton, T. L., Jr. (2002). "Tidal velocity asymmetry at inlets," ERDC/CHL CHETN IV-47, U.S. Army Engineer Research and Development Center, Coastal and Hydraulics Laboratory, Vicksburg, MS.

DESIGN OF NAVIGATION CHANNEL DEEPENING WORKS USING A MORPHOLOGICAL MODEL IN BARRANQUILLA, COLOMBIA

Rafael Cañizares[1], Santiago Alfageme[2], Tucker Mahoney[3]

1. Moffatt & Nichol, 104 West 40th Street, New York, NY 10018, rcanizares@moffattnichol.com.
2. Moffatt & Nichol, 104 West 40th Street, New York, NY 10018, salfageme@moffattnichol.com
3. Moffatt & Nichol, 104 West 40th Street, New York, NY 10018, tmahoney@moffattnichol.com

Abstract: The Port of Barranquilla is one of the two main Colombian Ports on the Caribbean coast. Shoaling in the Port's access channel from the mouth of the Magdalena River to the terminal of the Regional Port Society of Barranquilla has historically restricted navigation for vessels with drafts as shallow as 30 feet. The existing harbor facilities in Barranquilla will require a 40-foot deep access channel in order to allow permanent access for larger ships without navigation restrictions. A feasibility study proposed several flow training structures to scour the channel and maintain navigable access to the Port. In this study, a hydrodynamic and morphological model was constructed using the Delft3D system to test the validity of the solution defined in the feasibility study. The model was further applied to improve that solution in order to guarantee a stable navigation channel with a depth of 40 feet and a width of 150 feet as required for safe navigation. The model prediction suggests that the improved solution will create and maintain the design navigation channel within 3-4 years after construction.

INTRODUCTION

The Port of Barranquilla is one of the two main Colombian Ports on the Caribbean coast. The Port's access channel from the mouth of the Magdalena River to the terminal of the Regional Port Society of Barranquilla has historically presented navigation restrictions

even for 30-foot draft ships. The Ministry of Transportation of Colombia has contracted a number of technical studies over the last decade with the goal of developing a plan that could ensure the required channel depth in the last 22 kilometers of the Magdalena River that guarantees access to the main terminals of the Port of Barranquilla from the mouth of the River. These studies concluded that the depth of the channel constitutes the limiting factor in increasing the competitiveness of the Port. The existing harbor facilities in Barranquilla will require a 40-foot deep access channel in order to allow permanent access for ships of 35000 TPM without restriction. An initial feasibility study (Universidad del Norte, 1999) identified two critical shoaling locations, near the river mouth and at Isla 1972 (see Figure 1), which is in a straight sector of the river situated between two bends. These areas have required a significant amount of dredging in the past.

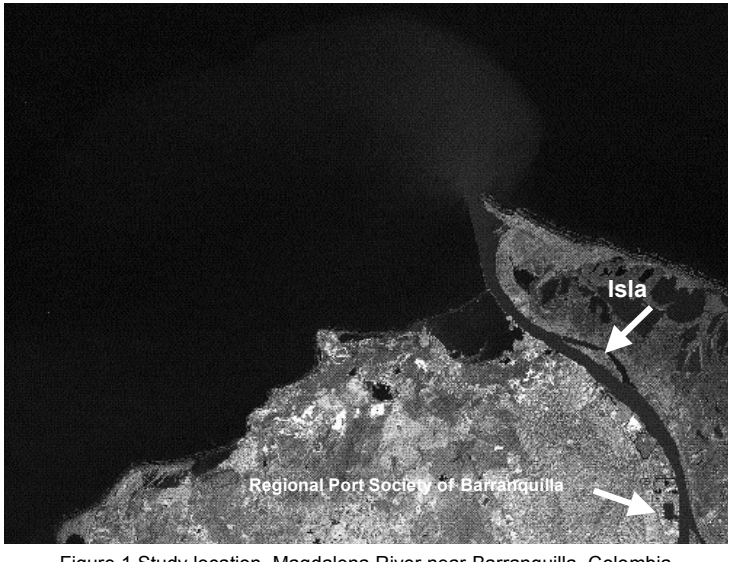

Figure 1 Study location. Magdalena River near Barranquilla, Colombia

To permanently improve the navigation conditions the feasibility study proposed a solution that consisted of a number of groin-type structures to create contractions of the river's cross section. It is predicted that the contractions would increase flow velocity and thereby scour the river bottom to the depth required for safe navigation.

This paper presents the development and application of a 3D morphological model of the last 22 kilometers of the Magdalena River to study the performance of the proposed solution and to define an alternative solution if the proposed one fails to ensure safe navigation. The following paragraphs describe the model development, model predictions and the final solution which is under construction at this time.

MORPHOLOGICAL MODEL SETUP

The morphological model was developed using the Delft3D modeling system (WL | Delft Hydraulics, 2006). The orthogonal curvilinear grid extends 20 km upstream of the river mouth to approximately 2 km offshore from the tip of the existing breakwaters. Grid resolution is approximately 100 m along the river and 30 m across. This grid resolution was selected to accurately simulate the hydrodynamics along the main navigation channel and the morphological changes generated by the groin-like structures while keeping the simulation time required for long term morphological simulations within manageable limits. The selected grid resolution does not allow for an accurate simulation of the flow patterns at the tips of the structures and therefore local scour for the design of the structures was calculated analytically.

.

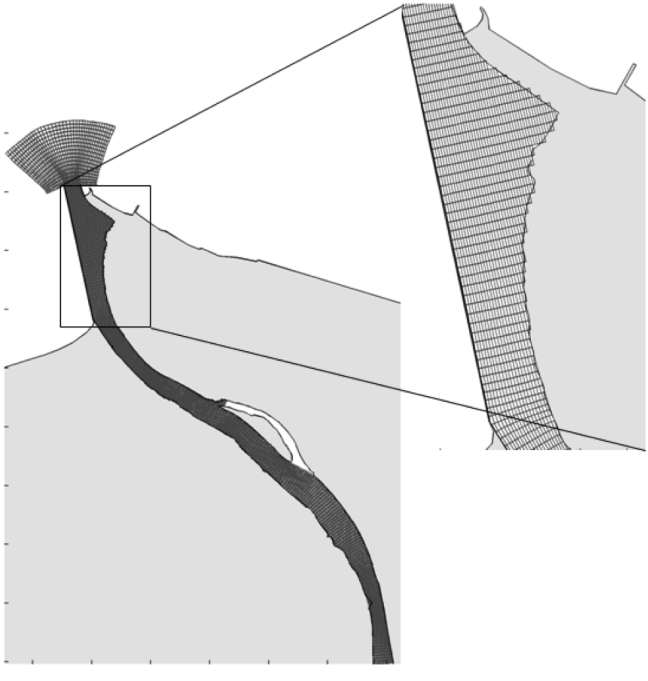

Figure 2 Numerical Model Grid

Where the river mouth opens to Caribbean Sea, the depth abruptly changes to 60 meters from the 12 to 14 meters typical of the navigation channel. This is a persistent feature observed in all available historical bathymetries. Figure 3 presents the bathymetry of the study area in November 2005 where the two critical shoaling locations can be observed near the river mouth and at Isla 1972. These areas have required a significant amount of dredging in the past and are the sections of the river where the flow training structures should have the largest impact.

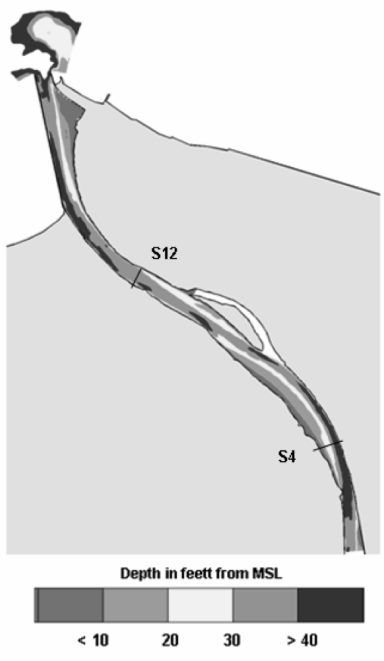

Figure 3 Model Bathymetry for November 2005 conditions. Depths are in feet in order to show areas below 40 feet, which is the require depth for the design channel.

Since the river mouth is one of the areas where sedimentation in the navigation channel is regularly observed, a three-dimensional model was used to simulate the interaction between the river fresh water and the denser water of the Caribbean Sea at the mouth. The vertical grid was defined using sigma coordinates which are bottom fitted with a free surface. The model has a total of 7 vertical layers. In addition the model also used the κ-ε turbulence closure scheme. Model boundary conditions were prescribed at the upstream and downstream boundaries. Since the tidal variability was not included in the model, the downstream boundary water level was constant and equal to the mean sea level, independently of the river discharge. The upstream boundary is a discharge boundary and has been defined using available rating curves from records since 1967 to present. In every simulation a salinity boundary condition of 30 ppt was used at the offshore boundary and 0 ppt at the upstream boundary.

The hydrodynamic model was calibrated to historical and recently measured data. In particular, the hydrodynamic model was calibrated to reproduce the observed variation in water levels in the last 20 kilometers of the river and also the observed averaged velocities under different flow conditions. Most of the data used for calibration were

provided by the Las Flores Hydraulic Engineering Laboratory of Universidad del Norte, in Barranquilla, Colombia.

Three flow conditions were considered for calibration: 9,800 m^3/s, 8,000 m^3/s and 3,900 m^3/s. These conditions are representative of high, average and low flow conditions, respectively, in the Magdalena River. Figure 4 presents the simulated water levels for these three discharges versus the observed range of levels.

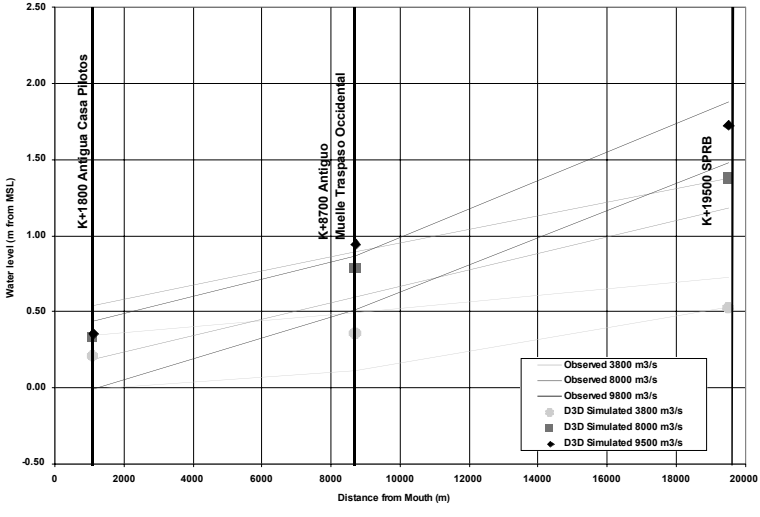

Figure 4 Simulated and observed range of water levels along the last 20 kilometers of the river for three different flows (after Universidad del Norte, 2005).

Velocities were also compared to observations at two sections of the river corresponding to kilometers 17 (S4) and 8 (S12) from the river mouth (see Figure 3). Simulated depth average velocity values across the section for a discharge of 9,500 m^3/s are 1.42 and 1.49 m/s for S4 and S12 respectively, which are very similar to the observed values at the same sections (1.42 and 1.49 m/s respectively). In addition Figure 5 shows the simulated distribution of velocities in cross sections S4 and S12. The distribution of velocities across the channel and in the vertical in these two sections is comparable to those observed in the field.

During the calibration phase it was observed that the model was able to reproduce the secondary flow at the river bends, simulating surface and bottom transversal currents in opposite directions; however, a quantitative comparison could not be made since data was not available for this purpose. Figure 6 presents simulated salinity and velocities in a vertical profile along the navigation channel for the last 2 kilometers of the river and offshore of the river mouth. Results are shown for a simulation with average river discharge. The model simulates the flow of the river fresh water above the denser ocean

water. It has been observed in the field that due to high river discharge, the penetration of the denser saline water layer upstream is limited to the first couple of kilometers from the river mouth.

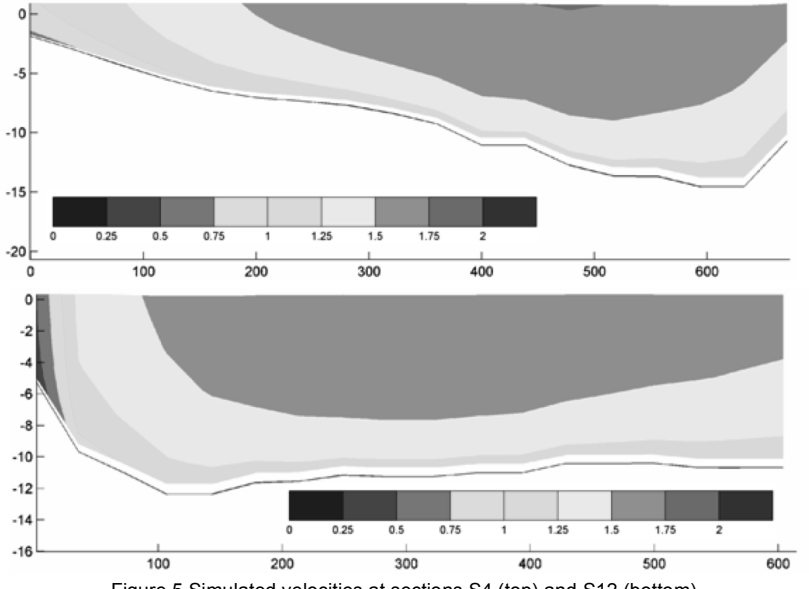

Figure 5 Simulated velocities at sections S4 (top) and S12 (bottom)

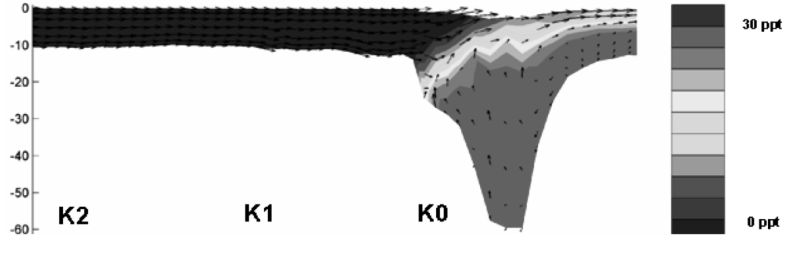

Figure 6 Simulated salinity distribution at the river mouth. Depths are in m from MSL. K0, K1 and K2 are kilometric points from the river mouth.

The river carries a large amount of suspended sediment most of which is in the form of washload consisting of very fine sand and mud. Bottom sediment samples were collected throughout the study area and it was observed that very fine sand and mud only accumulate in a few locations near the river banks. The D50 value for the non-cohesive sediment in suspension has a value between 0.08 and 0.09 mm, and D90 between 0.1 and 0.125 mm. This material is more fine than that found on the river bottom. The navigation channel river bottom consists of fine sand with a D50 in the order of 0.2 mm. Since the washload is carried by the river offshore, mud transport has not been simulated in the numerical model. Bed load and suspended load was simulated for sand with a D50 of 0.2 mm. Upstream sediment transport model boundary conditions use the equilibrium profile concentration. The equilibrium profile is computed by the model so that the suspended sediment load entering the model through the upstream boundary is adapted to the local flow conditions.

The Delft3D morphological model applied in this study follows Lesser and Roelvink (2004) with the sediment transport formulation of Van Rijn (1984) which considers separately bed load and suspended transport and is well suited to simulate sediment transport in rivers. Morphological changes in the study area that are calculated at one hydrodynamic model time step tend to be very small. Therefore, it is possible to apply a morphological multiplication factor since the model simulates quasi-steady state conditions based on the prescribed flow at the upstream boundary condition and does not consider the effect of waves and tides,. This factor speeds up the morphological changes in such a way that those calculated from a specific period of time will be equivalent to that period multiply by the morphological factor. Results from a sensitivity study indicated that for this particular model setup a morphological factor of up to 365 produce very similar results to a simulation using a factor of 1. A factor of 365 was used in this study, and therefore changes obtained during a one day of hydrodynamic simulation represent morphological changes during one year.

There are some limitations regarding data availability and simplifications made in the model setup that could have an effect on the results and the calibration of the morphological model: the model does not simulate the erosion of the banks which could have an influence in long term changes; the model does not consider flood plains which inundate during periods of high flow; the model does not consider dredging events in the navigation channel that take place regularly; and the available bathymetric data are not complete from bank to bank.

MORPHOLOGICAL MODEL CALIBRATION

The model was calibrated for the periods 1998-2003 and 2003-2004 and then validated for April 2004 to November 2005. Figure 7 shows the initial cross sections in April 2004 and the simulated and observed cross sections in November 2005 at the two standard sections S4 and S12. As it can be observed the model reproduces the deepening of the channel that was generally observed in the two control sections. In addition Figure 8 shows the measured and simulated deepest value at each kilometer for the last 13 kilometers, which is the river segment to be primarily affected by the river training

structures. The model predicts the general morphological trends in the navigation channel during this period and in particular replicates the erosion of the navigation channel between kilometers 2 and 4 and the accumulation between kilometers 11 and 13. The latter is an area of concern and requires regular maintenance dredging.

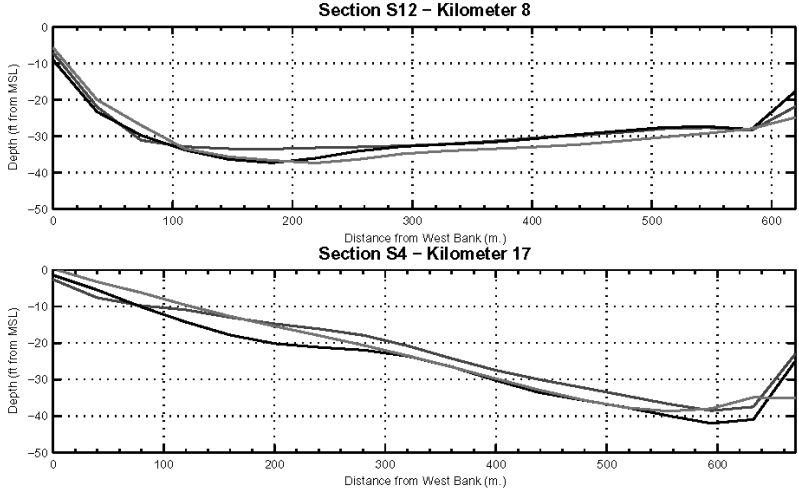

Figure 7 Measured cross sections in April 2004 (Blue) and November 2005 (Black) and model simulated for November 2005 (Red).

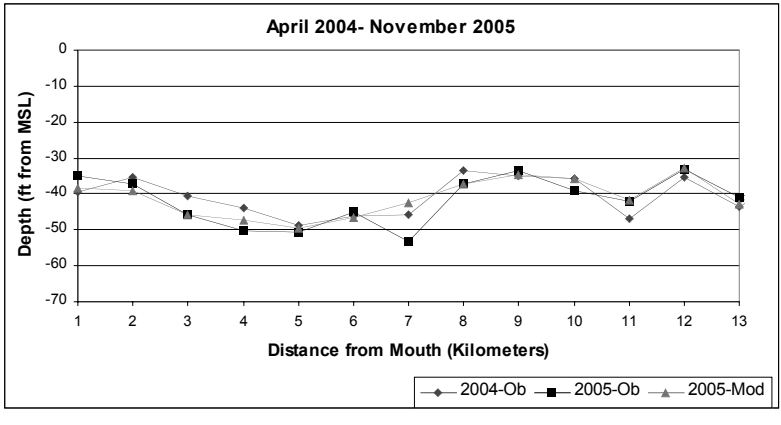

Figure 8 Maximum cross section depth measured in April 2004 (Blue) and November 2005 (Black) and model simulated for November 2005 (Red).

MORPHOLOGICAL FLOW

Daily river flows have been estimated for the 1967-2005 period from existing rating curves. In order to compute the sediment transport associated to a river flow, the average velocity associated to this flow has to be known. Available velocity data was used to develop a relation between average velocity in the project area and the river flow. Daily sediment transport for the 1967-2005 period was calculated using the estimated average velocities, at a depth of 12 m (average existing navigation channel depth) using the sediment transport formulation of Van Rijn 1984. The flow representative of the average sediment transport, or morphological flow, for the 1967-2005 period, is approximately 7,500 m^3/s, while the average flow is in the order of 6,400 m^3/s. Figure 9 shows the annual average sediment transport as a percentage of the sediment transport associated to the morphological flow. Years represented in blue indicate years in which the annual sediment transport was higher than the one associted to the morphological flow while years in red represents years with an average flow lower than the morphological flow. It has to be noted that there is a strong relation between the annual river flows in the Magdalena River and the occurrence of El Niño or La Niña events in the Tropical Pacific. Figure 9 shows the strong signature of the last El Niño event of the 20th Century in 1997-98.

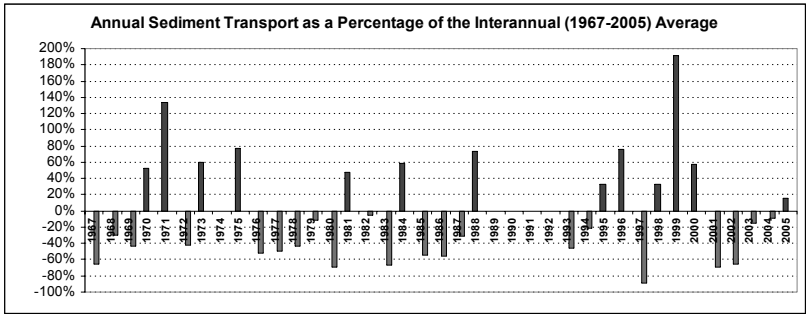

Figure 9 Annual sediment transport as a percentage of the sediment transport associated to the morphological flow

MORPHOLOGICAL MODEL APPLICATION

The morphological model was used to predict morphological changes up to 6 years after the construction of the training works. The previously defined morphological flow was applied at the upstream boundary for all the simulation period. Sensitivity tests were performed to confirm that considering monthly or seasonal variability in the morphological flow produced similar long term results to using an average annual value. The model was initially used to test the validity of the alternative defined in the feasibility study (Universidad del Norte, 1999). Results from this alternative did not produce a navigation channel with a depth of 40 feet and a width of 150 feet to allow navigation of the design vessel continuously from the river mouth to the port terminals.

The length, number and location of each groin (called espolones in Spanish) were modified for each defined alternative and simulated with the morphological model in order to optimize the solution. Nearly 20 plans were simulated in order to reach to the final alternative presented in Figure 10. This final solution included some modification of the structures defined in the feasibility study and the inclusion of three new short groins. Groin 0 was added to extent the influence of the structures further upstream particularly in the area near kilometer 12 where dredging is regularly required under existing conditions. Additionally, groins 5 and 7 were added to the external curve to provided continuity to the navigation channel during the first years after construction. Simulations predicted that without these groins the stable channel at the external curve will be disrupted by the sediment eroded from the channel in the upstream sections. The model also predicts that the channel will tend to form again in the same location within 4 to 5 years after construction.

Figure 11 shows the evolution of the navigation channel width as predicted by the model every year up to 4 years after construction of the final selected alternative. It can be observed that the model predicts an uninterrupted 40 ft channel wider than 150 meters along the area influenced by the structures, between the river mouth and kilometer 12.

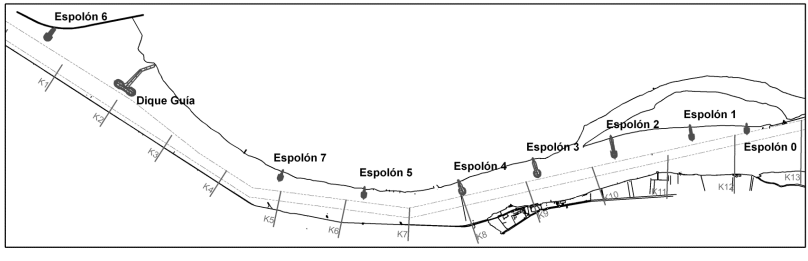

Figure 10 Final alternative

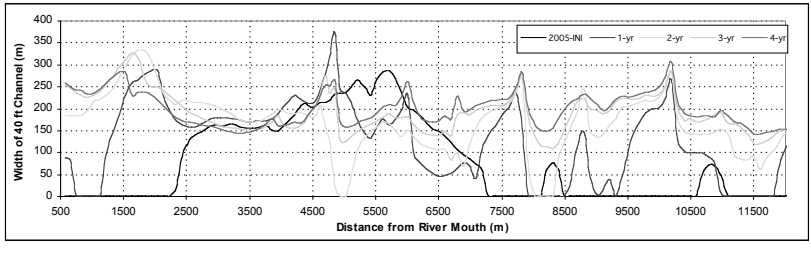

Figure 11 Simulated evolution of the width of a 40 ft deep navigation channel in the area of influence of the structures. (Required with is 150 m)

Figure 12 shows the initial bathymetry and the simulated bathymetry after 5 years in three sections of the river for the final alternative. It can be observed from the Figure how the navigation channel is completely formed and stable after 5 years.

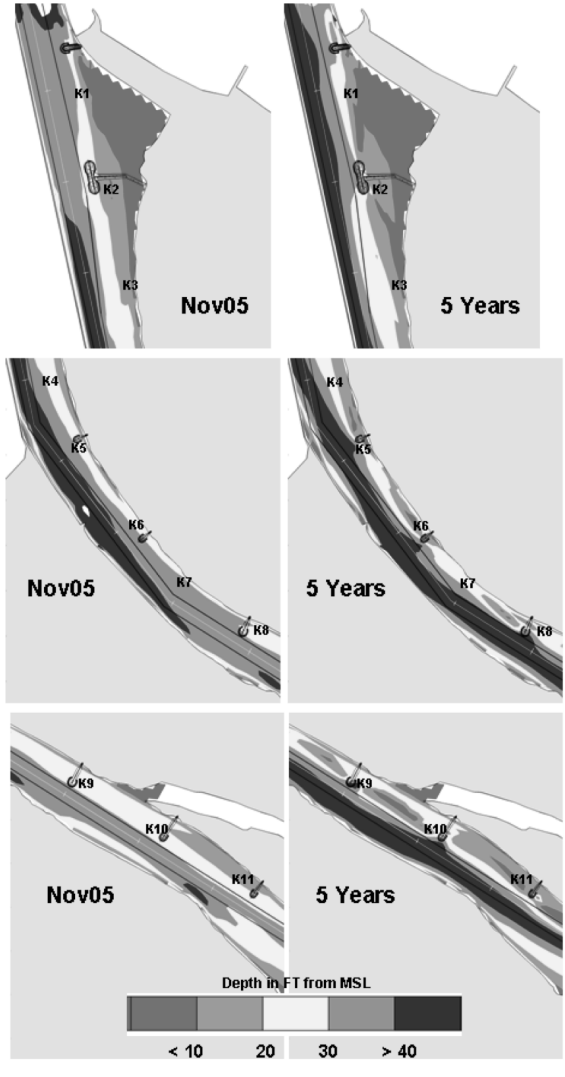

Figure 12 Model initial and 5-year simulated bathymetries for the final alternative

Figure 13 presents the maximum depth average velocities along the navigation channel under pre and post-constructions conditions. The structures could produce an increase on the maximum velocities in the channel in the order of 0.2-0.3 m/s. These results were used to study the effect that this increase on velocities will have on navigability along the channel.

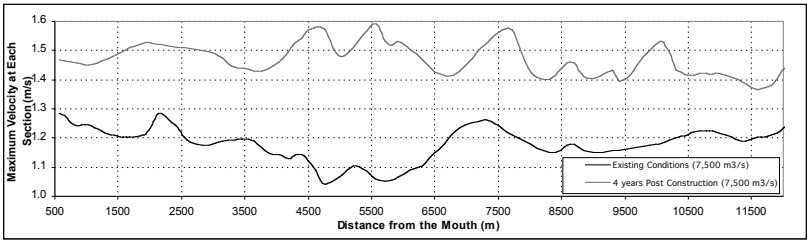

Figure 13 Simulated maximum depth average velocities along the navigation channel for pre and post-contruction conditions

CONCLUSION

A state of the art morphological model has been applied in Barranquilla, Colombia to design navigation channel deepening works. A hydrodynamic and morphological model was calibrated and validated to available recent and historical data. The model was able to reproduce the primary historical morphological trends observed in the study area.

The calibrated model was then used as a tool to test several deepening works alternatives with goal of producing a navigation channel 150 meters wide and 40 feet deep. Although not explicitly discussed here, model predictions have also been used as inputs to a navigation model to study the navigation conditions for the design vessel in the predicted channel.

Construction of the final alternative is under way. Figure 14 shows a picture of groin 1 (Espolón 1) after construction. Recent post-construction surveys indicate that the constructed structures are already deepening the navigation channel as predicted by the model. Comparison of model predictions and observed post-constructions bathymetries will be considered in future studies in order to asses the prediction capabilities of this type of morphological model.



Figure 14 Groin 1 after construction

ACKNOWLEDGEMENTS

The Authors would like to thank the Las Flores Hydraulic Engineering Laboratory (LEH-LF) of Universidad del Norte for the data provided for this study.

REFERENCES

Lesser, G., Roelvink, J.A., van Kester, J.A.T.M. and Stelling, G.S., 2004. Development and validation of a three-dimensional morphological model, *Coastal Engineering*, 51, 883-915.

Universidad del Norte, 1999. Diseño de las Obras Fluviales para la Profundización del Canal de Acceso a los Terminales Portuarios de Barranquilla – Rio Magdalena.. Universidad del Norte – Haskoning B.V. 1999

Universidad del Norte, 2005. Estudios e Investigaciones en el Canal Navegable de Acceso al Puerto de Barranquilla entre Bocas de Ceniza (K0) y Puente Pumarejo (K22), Barranquilla. Report E-004-039-05

Van Rijn, L.C.; 1984. Sediment Transport, Part I: Bed Load Transport. Journal of Hydraulic Engineering, ASCE Vol. 110, No 10. and Part II: Suspended Load Transport. Journal of Hydraulic Engineering, ASCE Vol. 110, No 11.

WL | Delft Hydraulics, 2006. User Manual Delft3D-FLOW. Delft, The Netherlands.

BEACH RENOURISHMENT THROUGH SPOIL DISPOSAL DOWNDRIFT OF A DREDGED ENTRANCE CHANNEL

Kyle C. Spiers[1], Terry R. Healy[2]

1. Coastal Marine Group, Dept. of Earth and Ocean Science, University of Waikato, 3240 Hamilton, New Zealand. kspiers@mail2kyle.com

2. Coastal Marine Group, Dept. of Earth and Ocean Science, University of Waikato, 3240 Hamilton, New Zealand. trh@waikato.ac.nz

Abstract: The offset configuration of Tauranga tidal inlet delta system, in combination with the dredged entrance channel, hinders sediment supply to the down-drift beaches. Maintenance dredging of the entrance channel provides suitable sediment to be deposited as a nearshore berm, downdrift of the entrance channel, as a means to artificially bypass the tidal inlet and renourish the beaches of Mt Maunganui. During April and May of 2004, ~112,000 m³ of dredged medium sand was deposited between two nearshore dump grounds (Sites B and C), under the assumption that onshore transport would occur and act to renourish the beaches shoreward of these sites. Bathymetric and side-scan sonar monitoring showed erosion of the mounds at both sites and significant onshore dispersal at Site B clearly evident after disposal. Sub-aerial beach profile monitoring from 1999 to 2005 shows continued accretion of the sub-aerial beach from 2001 to 2005, partially in response to ongoing beach nourishment. This suggests that any reduction in sediment supply to the down-drift beaches is being successfully alleviated.

INTRODUCTION

Capital and maintenance dredging of Tauranga Harbour entrance channel has been undertaken since 1968, with the spoil mainly used for reclamation projects (Sulphur Point), deposited in approved dump grounds (Healy *et al.,* 1998), or used for commercial purposes. However, the dredged entrance channel acts as a sink for the littoral drift, partially cutting off sediment supply to the downdrift beaches of Mount Maunganui. To remedy any possible sediment deficit, the Port of Tauranga Ltd uses the dredged sediment from the tidal inlet delta system to renourish the adjacent downdrift beaches.

Previous studies of an inner shelf dump ground in 8 m water depth off Mt Maunganui beach have been carried out by Foster (1991), and reported in Foster *et al.* (1994, 1996). That disposal campaign was carried out in 1991-1992, where some 80,000 m³ of coarse sandy sediment from the entrance channel was deposited in ~8 m water depth off Mt Maunganui Beach (Site A, Figure 1). This material was subsequently monitored for 16 months and, as predicted, shoreward migration was observed (Foster *et al.,* 1994, 1996).

From the beginning of April through to the 24th of May 2004, maintenance dredging of the entrance channel to Tauranga Harbour was undertaken using the trailer suction dredge *Pelican*. To mitigate any potential reduction in sediment supply to the downdrift beaches, 112,000 m³ of the dredge spoil was deposited ~3.5 km east of the entrance channel, in ~4-17 m water depth (Sites B and C, Figure 1). The dredge spoil was deposited under the assumption that onshore sediment movement would occur and act to renourish the beach. Of the 112,000 m³ deposited at Sites B and C, 83,225 m³ of sediment was deposited at Site B and 28,696 m³ at Site C.

To date no investigations of dredge spoil dispersal have been carried out at Sites B or C (Figure 1).

The aims of this paper are to characterize the natural dump ground sediment facies and identify any changes resulting from the subsequent dredge spoil disposal; and investigate the fate of, and account for, the material dumped in disposal sites B and C.

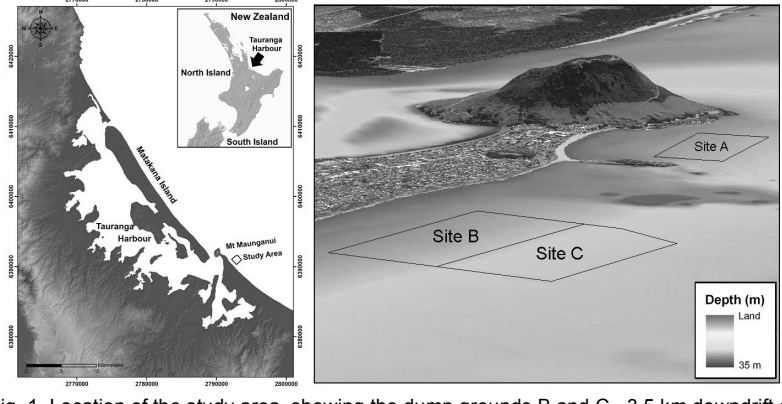

Fig. 1. Location of the study area, showing the dump grounds B and C ~3.5 km downdrift of the entrance channel.

STUDY SITE

Tauranga Harbour is a mesotidal estuarine lagoon (851 km^2) located on the northeastern coast of New Zealand (Figure 1)(de Lange and Healy, 1990; Healy, Cole and de Lange, 1996). The Port of Tauranga maintains ~8.2 km of navigation channels (Healy *et al.*, 1998), including the dredged entrance channel, which is maintained at 14.1 m (C.D).

Hume and Herdendorf (1992) categorise the Bay of Plenty coastline (which includes the disposal ground on the beach adjacent to Tauranga Harbour) as a wave exposed, open sediment system, comprising sandy beaches developed by the littoral drift. Healy *et al.* (1977) suggests that the orientation of Tauranga entrance and the depth of the tidal gorge act as a partial barrier to the net southeasterly directed littoral drift. This can lead to accretion at Matakana (updrift) and erosion at Mt Maunganui (downdrift) (Healy *et al.,* 1977). The limited bypassing of the littoral drift is further exacerbated through deepening the entrance channel by dredging (Healy, 1980).

DATA COLLECTION AND ANALYSIS

Side-Scan Sonar Surveys

In order to assess any changes to the nature of the dump ground sediments and bedforms after dredge spoil disposal, a series of side-scan sonar surveys were undertaken for Sites B and C. These comprised one pre-disposal survey (April-04) and three post disposal surveys (June-04, October-04 and January-05). All of the surveys (aside from October-04) were undertaken in conjunction with surficial sediment sampling, providing ground truthing to aid in the sonograph interpretation. Side-scan sonar surveys were carried out using a dual frequency Klein 595 side-scan system. The surveys consisted of 8 run lines from 3-18 m depth, overlapped to gain full coverage of the dump ground area. A swath width of ~150 m was used. To allow better reflection of wave generated bedforms, survey lines were carried out parallel to the shore, similar to those conducted at Mt Maunganui by Harms (1989) and Foster (1991), and at Mangawhai-Parkiri by Healy *et al.,* (1996). A geo-referenced mosaic of the survey data (processed to 0.5 m resolution) was generated in post-processing, and overlaid on aerial photographs.

Sediment Sample Collection and Analysis

In order to provide ground truthing for the side-scan sonar surveys, two cross-shore transects were created through the dump grounds. Samples were collected at 100 m intervals along each transect using a Van Veen sediment grab sampler. All samples were collected on the same day as the side-scan surveys were undertaken. Sediment textural analyses were then carried out using the University of Waikato Rapid Sediment Analyser (RSA). The RSA is a fall tube apparatus which is thoroughly discussed in Darlan (1991).

Bathymetric Surveys

In order to identify and to monitor the dispersal of the deposited sediments within the active nearshore profile, repeated singlebeam and multibeam bathymetric surveys of the dump grounds were undertaken. Surveys were carried out on 4 occasions, viz., November 2003 (pre-disposal), 9th June (~17-20 days after disposal), August 2004 and April 2005.

The November-03 and June-04 surveys were undertaken by the Port of Tauranga Ltd, using a 200 kHz Knudsen singlebeam echosounder. Positional information was recorded by Real Time Kinematic GPS accurate to ±0.05 m (Owen Maynard, pers.comm.). The surveys consisted of 24 runlines, spaced at 50 m intervals, perpendicular to the shore. The August 2004 and April 2005 dump ground soundings were acquired with an

EM3000 shallow water multibeam system. The surveys consisted of shore parallel run lines which were overlapped to obtained full ensonification. The surveys encompassed the entire dump ground areas and an area ~200 m shoreward of the dump ground. All depth measurements are relative to local chart datum.

Data from each survey was gridded in SURFER®. Volumetric and morphological variation due to dredge spoil dumping and dispersal was obtained by subtracting the gridded surface of each survey from the preceding one. However volumetric comparisons between the multibeam survey (undertaken on August 2004 and obtaining close to full coverage) and the interpolated grid of the single beam survey (June 2004), must be viewed with caution, taking into account the obvious limitations when comparing an interpolated surface with an actual surface.

Sub-Aerial Beach Surveys

To assess the possible changes to the sub-aerial and inter tidal beaches (shoreward of Sites B and C) as a result of dredge spoil dispersal, 6 shore normal survey lines were established. Surveys were conducted every 2-3 months (April-04 to May-05) at low tide, using standard staff and level techniques. The survey lines were spaced at 100-150 m intervals. The accuracy of this type of survey method and those similar to it i.e. the "Emery method" is suggested to be in the order of ±0.01-0.05 m (Gable and Wanetick, 1984).

To quantify the temporal and spatial change between surveys, the raw profile data was converted to XYZ coordinates and gridded. This allowed estimates of volume change between each survey to be undertaken. Volumetric calculations based on grids where the data is widely spaced are unable resolve any variations that occur between any two survey lines; thus they only provide an estimate of the change in volume.

RESULTS AND DISCUSSION

Side-Scan Sonar and Textural Analysis

The pre dumping sonograph for both sites B and C demonstrates that the dump grounds are primarily dominated by the fine featureless sonograph facies (FFS). Textural analyses from this study and previous studies by Foster (1991) suggest that this featureless pattern coincides with moderately to moderately well sorted fine sands. Two areas, ~ 90 x 90 m of the medium to coarse grained, rippled sediments (termed CGR's) are observed in the middle of Site B (Figure 2). Some confined patches of coarse grained ripples (CGR's) are also distributed through Site C. Comparisons with the side-scan sonar surveys undertaken in the same area in 2002 suggest that these areas may be residual deposits of coarse sediments corresponding to previous dredge spoil disposal campaigns.

The first post dumping side-scan survey (June-04) is again dominated by the FFS sonograph facies at Site B (Figure 2). A number of small areas of CGR's can be identified through the middle of Site B. These areas correspond to the primary disposal areas at this site and thus may represent areas where the finer proportion of the dredge sediments has been selectively removed, leaving a concentration of the coarser dredge

spoil. Alternatively, as CGR facies were also apparent in these areas prior to dumping, it may indicate that higher turbulence over these areas inhibits the deposition of fine sediments (Green *et al.,* 2004). Although the area corresponding to spoil disposal also appears to exhibit a slightly darker return (higher acoustic response) on the sonograph than the April-04 survey, surficial sediment samples show no significant change in grain size and only a slight increase in shell content. The October-04 and January-05 surveys exhibit a similar pattern to the June-04, whereby the Site B dump ground is dominated by FFS sonograph facies (Figure 2). The small areas of CGR facies are still present, but have reduced in size. Overall at Site B little obvious change as a result of dredge spoil disposal can be identified.

Contrary to Site B, at Site C the areas of dredge spoil deposition are clearly identifiable (Figures 2 and 3). One month after disposal (June-04) the dump mounds (~10-14 m water depth) are distinguished by areas of the CGR's facies, characterized by dark coloured and rough textured sonograph facies (Healy 1985, Harms, 1989, Bradshaw *et al.,* 1994). Surficial sediment samples from these areas consist of medium to coarse sediments with a high shell content. These areas are dominated by rippled bedforms, aligned parallel to the shore, with wave-lengths of 0.7-1 m. Surrounding these areas are the combined CGR/FFS facies (coarse grained ripples with sand dunes and "ribbons" of fine sediment overlayed). The formation of concentrated areas of CGR on dredge spoil mounds has previously been reported by Dahm and Healy (1980). They conclude that the reworking of the dredge spoil by wave focusing leads to the selective removal of the fine constituent of the spoil, resulting in the formation of this facies (CGR), which is also typically observed to occur naturally on the inner shelf (cf. Spiers, 2005).

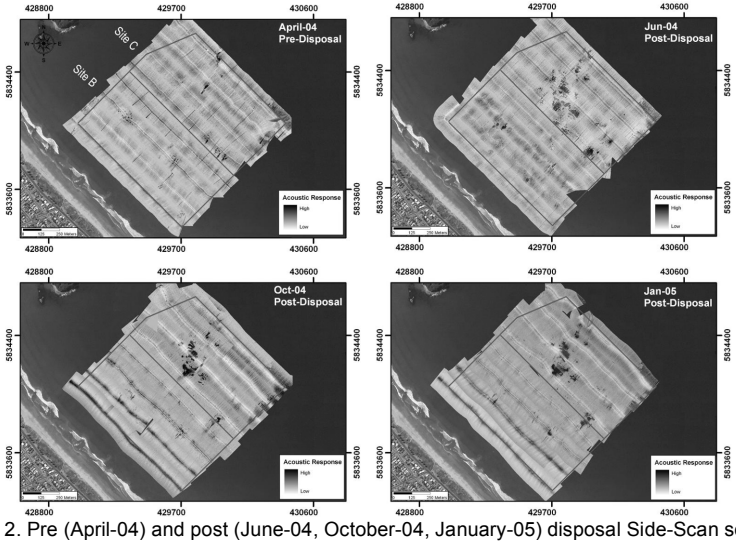

Fig. 2. Pre (April-04) and post (June-04, October-04, January-05) disposal Side-Scan sonar mosaics for dump grounds at Sites B and C. Photograph courtesy of the Eastern Bay of Plenty Regional Council.

The October-04 and January-05 surveys display a reduction (since June-04) of the area of CGR's at Site C. The two largest areas of CGR's are still evident and are generally unchanged between June-04 to January-05. However, the smaller areas have been replaced by the combination facies CGR/FFS or, in many cases have been completely enveloped by fine featureless sand (FFS). Interestingly, the most significant change at Site C is the reduction in the CGR/FFS facies between June-04 and January-05. The pronounced 'ribbons' of fine sand (Bradshaw *et al.,* 1994) transgressing the underlying coarse dredged sediments are only found in close proximity to the large CGR's facies, being replaced by the FFS over the rest of the dump ground. Aside from the large areas of CGR's, the rest of the dump ground appears to have rapidly reverted back to its pre-disposal state. As suggested by the significant reduction in the size of the coarse lag deposits between 2002 and 2004, it is anticipated that the large areas of CGR's will degrade and revert to FFS over time.

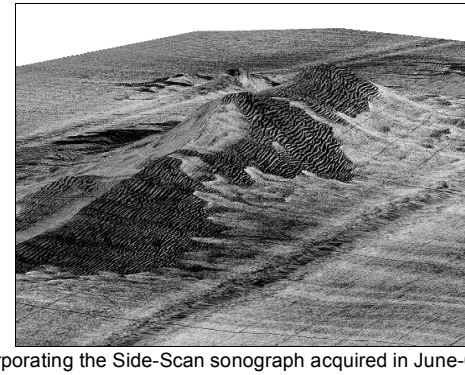

Fig. 3. Image incorporating the Side-Scan sonograph acquired in June-04 with dump ground bathymetry from the same time to allow a 3D view of the sonograph. This figure represents a view of the seaward side of the main Site C dump mound from a side-on perspective (from the east). Dump mound relief has been vertically exaggerated to emphasize the main features.

Dump Mound Formation and Nearshore Dispersal

The residual difference between the Nov-03 (pre-dumping) and Jun-04 (1st post dumping) surveys reveals the extent of the deposited dredge spoil (Figure 4). Dredge spoil appears to have been deposited in a line through the centre of Site B at ~5-8 m water depth (relative to chart datum). The line of spoil is characterized by three dominant mound features, with peaks of up to ~0.7 m and cross-shore widths ranging from 50-250 m. Volume calculations suggest that sediment accretion of ~52,500 m³ has occurred at Site B since the pre-dumping survey, the majority of which is clearly attributed to the 83,000 m³ of spoil deposited at this site.

The volume of sediment accounted for at Site B is ~30,500 m³ less than the dredge recorded volume deposited at this site. The timing of the pre- and post-disposal surveys may provide one explanation for the observed difference. As the pre-disposal survey was undertaken 4 months prior to the start of disposal, any changes occurring over this

time period (i.e. erosion and accretion) are also incorporated into the volume calculations between the pre and post disposal surveys. Therefore, any reduction in bed level occurring prior to disposal, but corresponding to the disposal areas, would lead to a reduction in the volume of sediment accounted for. Spiers (2005) reports that natural variation in the nearshore is commonly observed along Mt Maunganui beach and can result in large volume changes over short periods of time (3-4.5 months). Also, as the post-disposal survey was not undertaken until ~17-20 days after all of the dredge spoil had been deposited (and ~3 months since dumping began), it could be postulated that the dredge spoil had already undergone significant migration out of the dump ground by this time. This idea seems plausible given the likely influence of shoreward mass transport in this area (Harms, 1989; Healy *et al.,* 1991) and frequency of time that sediment is entrained at these depths (80 % of the time in 8 m depth, Spiers (2005)).

The main area of deposition at Site C occurs as one primary mound feature, located slightly seaward of the boundary between Sites B and C (Figure 4). This area contains peaks of up to ~0.85 m and occurs between the 10 and 14 m contours. The main mound has an extent of 450 m in the alongshore direction and 270 m in the cross-shore direction. A number of smaller mounds can be observed surrounding this area and slightly seaward of the main mound area. Volume computations show deposition of ~32,000 m³ at Site C between Nov-03 and Jun-04. Unlike Site B, the 28,700 m³ of dredge spoil deposited at Site C can be completely accounted for, indicating that little or no dispersal of the deposited sediments has taken place by the post-disposal survey (~17-20 days after disposal). This is likely to be a result of the slower dispersive nature of this site (Healy *et al.,* 1998) and the lower incidence of sediment entrainment with increased depth.

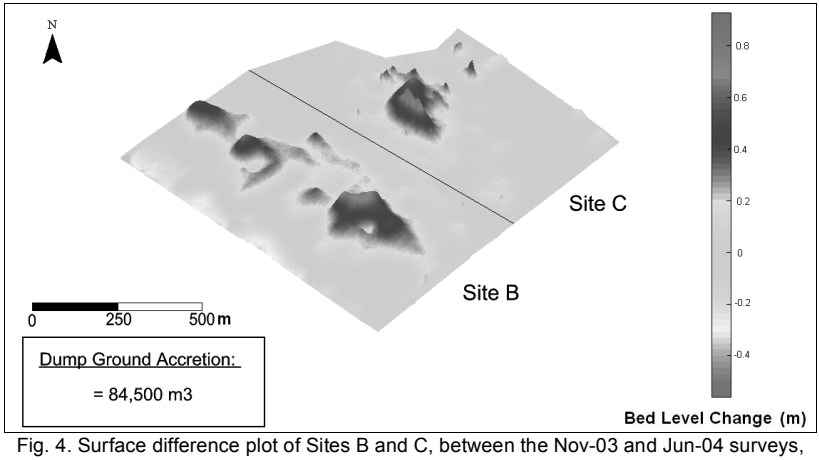

Fig. 4. Surface difference plot of Sites B and C, between the Nov-03 and Jun-04 surveys, revealing the areas of dredge spoil disposal.

In order to monitor any dispersal from the dump mounds since disposal, the Jun-04, Aug-04 and April-05 surveys have been compared. Residual differences between the Jun-04 and Aug-04 (Figure 5a) surveys indicate that the primary areas of erosion within the dump grounds occur around the peaks of the main spoil mounds. At Site B erosion of the dump mounds is primarily in the range of 0.1-0.2 m with a maximum bed level reduction of 0.4 m from the highest peaks. This suggests a significant reduction in the height of the main dump mounds (> 50% in places), which initially showed elevations of up to 0.7 m in the Jun-04 survey. Other isolated pockets of erosion are also observed at various regions throughout the dump ground, where erosion is generally between 0-0.15 m. Volume computations show that ~14,200 m³ of sediment has eroded at Site B between Jun-04 and Aug-04. Most of this eroded volume appears to be a result of dredge spoil dispersal from the 3 or 4 main dump mounds (Figure 5a).

The main area of accretion observed at Site B, from Jun-04 to Aug-04, forms an elongated trail on the western side of the dump ground and is located directly shoreward of the eroded dump mounds (Figure 5a). This elongated trail of accretion has a cross shore length of ~250 m, with a maximum alongshore width of ~100 m and a vertical extent of up to ~0.2 m. Clearly this feature is indicative of onshore diabathic transport from the nearby eroded dump mounds. Further to the west of this elongated trail are a number of other areas of accretion which appear to result from onshore migration of the deposited dredge spoil. These areas have also accreted by up to 0.2m and extend 30-60 m shoreward of the eroded dump mounds. A number of smaller more localized areas of accretion are also observed throughout Site B. Between Jun-04 and Aug-04 approximately 9,500 m³ of accretion is identified at Site B, of which a considerable proportion can be attributed to the shoreward dispersal of sediment from the eroded dump mounds. A "cut and fill" comparison (the accreted volume minus eroded volume) indicates a loss of 4,700 m³ of sediment from Site B. The elongated areas of accretion, identified shoreward of the eroded dump mounds, provide evidence to suggest that this loss has occurred as a result of onshore transport of the deposited dredge spoil.

As observed for Site B, between Jun-04 and Aug-04 the main areas of erosion at Site C correspond to the peaks and inner areas of the main spoil mounds (Figure 5a). The dump mounds appear to have eroded by up to 0.5 m in places, which corresponds to > 50% of the observed height as at Jun-04 (~0.85 m). A number of other areas of erosion, generally ranging from 0.1-0.3 m are also observed throughout the dump ground area. Volume computations suggest that ~8,900 m³ of sediment has eroded at Site C, a large proportion of which can be attributed to erosion of the deposited dredge spoil.

As anticipated, the slower dispersive nature of Site C (due to the deeper water depth and lower incidence of sediment entrainment) confined the primary areas of accretion to a small radius around the main mound areas. The observed accretion occurs mainly within small areas of 30-50 m in both the cross and alongshore extent and up to 0.3 m in the vertical. The areas of accretion tend to be distributed both shoreward and seaward of the main spoil mounds and in some areas occur between the main peaks of the mound, which may indicate transport of sediment from the main peaks into these areas.

However, it must be noted that a number of the observed accretional areas are located between the run lines of the June singlebeam survey. It is possible that some of these areas may correspond to areas of dredge spoil disposal that were not resolved by this survey, possibly leading to a false indication of accretion between the Jun-04 and Aug-04 surveys. Therefore the volumetric computations for Site C, between Jun-04 and Aug-04, should be viewed with caution. Volume computations suggest that ~10,000 m^3 of accretion occurred at Site C (Jun-04 to Aug-04), indicating a net gain of ~1,100 m^3 of sediment at this site. As expected, this value suggests that most of sediment eroded from the spoil mounds is likely to have been redistributed within the dump ground area. The 1,100 m^3 gain may be a result of either diabathic or parabathic transport into this site or potentially represents areas of accretion that were under-sampled by the June singlebeam survey.

The residual contour plot for the period Aug-04 to April-05 indicates that Sites B and C have accreted significantly over this 7 month period (Figure 5b). Accretion at Site B dominates the majority of the site and is characterized by an increase in bed level of ~0.2-0.4 m. Erosion occurring at Site B between Aug-04 and April-05 is confined to a small number of areas, corresponding to the original dump mound locations. These areas are small in extent (maximum of 40 m) and show a reduction in bed level of 0.1-0.4 m. A "cut and fill" comparison for Site B indicates that 69,450 m^3 of accretion and 1000 m^3 of erosion have occurred between Aug-04 and April-05. This equates to a residual gain of 68,450 m^3 over Site B. The volume of sediment entering the site makes any dispersal of the deposited sediments impossible to detect.

Accretion at Site C between Aug-04 and April-05 appears to encompass the majority of the site (Figure 5b). The average bed level change at this site ranges from 0.3-0.4 m. By April-05, the areas of observable erosion at Site C are limited to two small patches (maximum of 15 m in width) which correspond to the position of the main dump mound (as at Jun-04). Volume computations indicate that Site C showed accretion of ~100,000 m^3 and erosion of ~160 m^3 between Aug-04 and April-05. This corresponds to a net gain of ~99,840 m^3 over the dump ground or +0.2 m of vertical change (accretion) per m^2 of the surveyed area. As with Site B, due to the large increase in the volume of sediment entering the site, it is not possible to detect dredge spoil dispersal.

The area shoreward of the dump ground has also accreted considerably between the two surveys (Figure 5b). By April-05 the formation of longshore bar system with a vertical extent of up to 1.6 m is clearly apparent. Two areas of erosion (up to 1m) are observed directly shoreward of the bar, indicating a well developed trough and bar system. These features may have formed in response to erosion of the berm and beach face area, after periods of high storm activity (Komar, 1998). This would seem logical, given the high levels of accretion observed throughout the rest of the dump ground area at this time.

The findings from the residual contour plot indicate that any dredge spoil dispersal that has taken place between Aug and April is concealed by a significant amount of natural variation in the nearshore and therefore can not be detected. As the total net gain over

Sites B and C (~169,300 m³) between Aug-04 and April-05 is larger than the volume of dredge spoil deposited, its dispersal is increasingly difficult to separate or even detect from the natural variation.

The morphological variation observed between the surveys is likely to result from sediment exchange between the dune-beach-nearshore components of the beach system in response to short term and seasonal variations in wave climate (Healy *et al.,* 1977), in particular by the number of storms events occurring over that period. During calmer periods or those dominated by long period swell waves and offshore winds (Spiers, 2005), the sediment deposited in the nearshore tends to migrate shoreward, accreting the beach and building out the berm (Healy *et al.,* 1977).

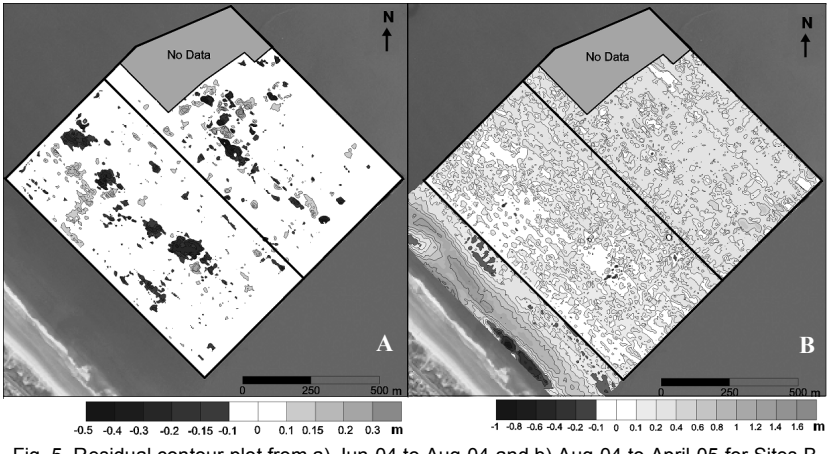

Fig. 5. Residual contour plot from a) Jun-04 to Aug-04 and b) Aug-04 to April-05 for Sites B and C.

Sub Aerial Beach Surveys

A comparison between the April-04 and Jun-04 beach profiles indicates that the beach shoreward of Sites B and C had accreted by ~9,000 m³ (Figure 6). This equates to ~0.14 m of accretion per m² of beach. Accretion was widespread over most of the beach and especially notable at the eastern extent of the surveyed area, with an increase in beach level ranging from 0.05 to 0.6 m. The April-04 survey was completed directly after a large erosive event, which suggests that the accretion observed at this site is likely to be indicative of the post storm recovery phase i.e. sediment is redistributed from the nearshore to build up the sub-aerial beach. Bathymetric analysis from the nearshore zone between Nov-03 and Jun-04 (1st post disposal survey) indicates that > 30,500 m³ of dredge spoil could not be accounted for. Several possible explanations for this have been presented in the preceeding sections, including the suggestion that significant migration of the deposited dredge spoil had already occurred prior to the June-04 survey. The

accretion noted between Apr-04 and Jun-04 further supports the idea that a proportion of the material accreting onto the beach by Jun-04, may have resulted from shoreward dispersal of the dredge spoil.

By September-04 further progradation is apparent, with ~5,600 m³ (0.087 m/m^2 of beach) of sediment accumulating on the beach (Figure 6). It is suggested that the observed accretion is partially due to the onshore dispersal of the deposited dredge spoil. This is consistent with nearshore bathymetric analysis undertaken between Jun-04 and Aug-04, where it was established that shoreward migration of the dredge spoil deposited at Site B had occurred.

Between Dec-04 and Feb-05 the beach shoreward of Sites B and C had undergone considerable erosion of ~12,800 m³ (-0.198 m/m^2 of beach). The observed erosion appears to have been caused by a large storm event (associated with strong onshore winds) several days prior to surveying. As previously mentioned, it is likely that a storm such as this would result in a significant amount of deposition in the nearshore, similar to that noted in the April-05 bathymetric surveys (Figure 5b). Between Feb-05 and May-05 the beach had accreted by 21,630 m³ (0.33 m/m^2 of beach), with approximately one third more sediment accreted than had been eroded by the Feb-04 storm. During the May-05 survey it was evident that the beach had noticeably accreted just prior to surveying. Sizable amounts of pumice (likely originating from the inner shelf) and large accumulations of the Gastropod whelk *Struthiolaria papulosa* were evident at the high tide mark throughout survey site. Accumulations of *Struthiolaria papulosa* are often observed after large wave events which coincide with offshore winds and are suggestive of diabathic transport (Healy pers.comm).

Volumetric computations from the entire period April-04 to May-05 indicate that the beach has accreted by ~24,200 m³ (0.37 m/m^2 of beach). As explained in the preceding section, the residual volume gain or loss over the entire survey period appears to be dependant on which phase of the cut and fill cycle is occurring at each survey time. The April-04 survey was undertaken after a large erosive event, whereas the May-05 survey occurred during a period of recovery, albeit apparently rapid recovery; therefore the gain between these two surveys was as anticipated.

Historical beach profile data for this site, dating back to 1999 (Figure 7), indicates that the sub-aerial beach and inter-tidal zones have continually accreted from 2001 to 2005. The ENSO signal is evident in the data, with erosion of the beach from 1999 to 2001 attributed to a La Nina period. The June-05 profile represents the most seaward position of the upper beach face and berm between Oct-99 and 2005. This suggests that potential for the entrance channel to reduce sediment supply to the downdrift beaches has been countered by dredge spoil disposal or by natural processes.

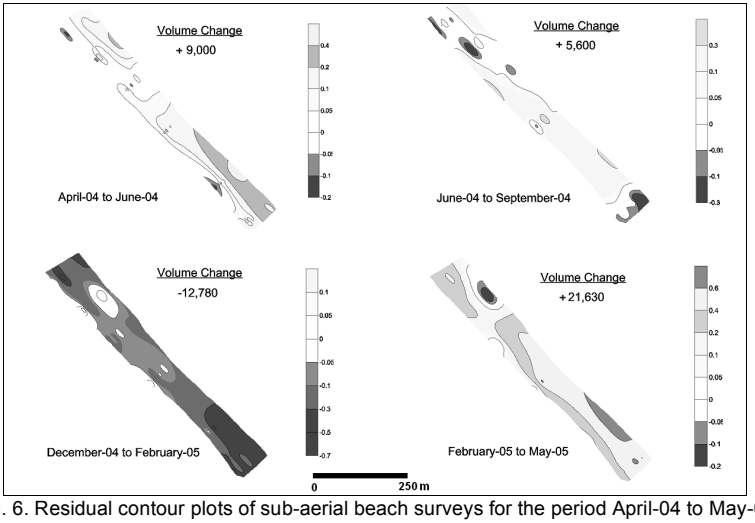

Fig. 6. Residual contour plots of sub-aerial beach surveys for the period April-04 to May-05 for Sites B and C.

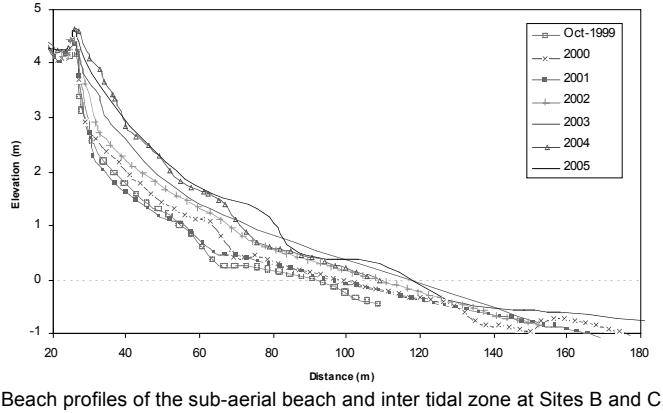

Fig. 7. Beach profiles of the sub-aerial beach and inter tidal zone at Sites B and C, for the period Oct-1999 to June-2005. Note that all profiles are taken from the month of June or July unless otherwise stated in the legend (data supplied by Environment Bay of Plenty).

CONCLUSIONS

Side-Scan sonar surveys of Site C confirm the presence of coarse grained ripples surrounded by ribbons of fine featureless sonograph facies, which correspond to the areas of dredge spoil dumping (as indicated by textural analysis). However, the extent of these areas (the combination facies CGR/FFS in particular) is significantly reduced over the monitoring period, suggesting that the dump ground is reverting back to its pre-

disposal state. Conversely, at Site B there is little variation in pre and post disposal surveys, which is consistent with textural analysis results.

Repeat bathymetric surveys (multibeam hydrographic and single beam echosounding) and beach profiles, were used to account for and investigate the fate of the deposited dredge spoil. The deposited dump mounds were clearly identified by the Jun-04 survey. Erosion of the dump mounds was evident at all sites and significant shoreward migration clearly identifiable at Site B. Dispersal at Site C was also evident, however only in a localized radius around the main dump mound, consistent with the findings of Healy *et al.* (1998), who argued that dispersal from this site would occur at a slower rate. However, analysis of the surveys conducted between August-04 and April-05 indicates that natural variation over the dump ground can be significant, making dispersal difficult to detect.

Changes to the sub-aerial beach and inter-tidal zones were dominated by a cycle of rapid storm-induced "cut", followed by persistent recovery (fill). Post storm progradation of the sub-aerial beaches and inter-tidal zone was exhibited at between Apr-04 and Dec-04. Observed shoreward dispersal from the dump mounds (Site B) during this period, suggests that this accretion can be partially attributed to the shoreward migration of the deposited dredge spoil. Over the monitoring period, the sub-aerial beach and inter-tidal zones showed an estimated volume gain of ~24,200 m^3 at Sites B and C. The observed gain is related to inputs into the system (i.e. beach nourishment induced from dredge spoil disposal) and the phase of the "cut" and "fill" cycle that the profiles were in when compared.

Historical beach profiles indicate that any reduction in sediment supply to the downdrift beaches of Mt Maunganui (as a result of the entrance channel) is being successfully mitigated. However, the effects of the ENSO cycle are evident, and clearly play an important role in the determining the beach state over time. Progradation of the sub-aerial beaches, which is partially attributed to ongoing beach renourishment, is construed as a "positive impact", enhancing the amenity value of the beach and providing stability against erosive events.

ACKNOWLEDGMENTS

The Port of Tauranga Ltd are acknowledged for providing monetary support for this research. Dirk Immenga and Brad Scarfe are thanked for assisting with data collection and processing. E.Rogers is thanked for reviewing this manuscript.

REFERENCES

Bradshaw, B.E., Healy, T.R., Nelson, C.S., Dell, P.M., de Lange, W.P. (1994). "Holocene sediment lithofacies and dispersal systems on a storm-dominated, back-arc shelf margin: the east Coromandel coast, New Zealand," *Marine Geology* 119, 75-98.

Dahm, J., Healy, T.R. (1980). "A study of dredge spoil dispersion off the entrance to Tauranga Harbour," Report for the Bay of Plenty Harbour Board. 64 p.

Darlan, Y. (1991). "Comparative study of the RSA and sieving methods for particle size

analysis," University of Waikato, MSc Thesis, 145 p.
de Lange, W.P., Healy, T. R. (1990). "Renourishment of a flood-tidal delta adjacent beach, Tauranga Harbour, New Zealand," *Journal of Coastal Research* 6(3), 627-640.
Foster, G.A. (1991). "Beach nourishment from a nearshore dredge spoil dump at Mount Maunganui Beach," University of Waikato, MSc Thesis, 156 p.
Foster, G.A., Healy, T.R., de Lange, W.P. (1994). "Sediment budget and equilibrium beach profiles applied to renourishment of an ebb tidal delta adjacent beach, Mt. Maunganui, New Zealand," *Journal of Coastal Research* 10(3), 564-575.
Foster, G.A., Healy, T.R., de Lange, W.P. (1996). "Presaging beach renourishment from a nearshore dredge dump mound, Mt. Maunganui Beach, New Zealand," *Journal of Coastal Research* 12(2), 395-405.
Gable, C.G., Wanetick, J.R. (1984). "Survey techniques used to measure nearshore profiles," *Proc. 19th Conference on Coastal Engineering*, ASCE, pp. 1879-1895.
Green, M.O., Vincent, C.E., Trembanis, A.C. (2004). "Suspension of coarse and fine sand on a wave-dominated shoreface, with implications for the development of rippled scour depressions," *Continental Shelf Research* 24, 317-335.
Harms, C. (1989). "Dredge spoil dispersion from an inner shelf dump-mound," University of Waikato, M(Phil) Thesis, 177 p.
Healy, T.R. (1980). "Erosion and sediment drift on the Bay of Plenty coast," *Soil and Water*. August 1980, pp. 12-14.
Healy, T.R. (1985). "Tauranga Harbour study: Parts II and V. Field collection programme and morphological study," A report for the Bay of Plenty Harbour Board. 25 p.
Healy, T.R., Harray, K.G., Richmond, B. (1977). "The Bay of Plenty coastal erosion survey," Occasional report 3, University of Waikato. 64 p.
Healy, T., Harms, C., de Lange, W. (1991). "Dredge spoil and inner shelf investigations off Tauranga Harbour, Bay of Plenty, New Zealand," *Coastal Sediments '91*, ASCE. pp. 2037-2051.
Healy, T.R., Cole, R., and de Lange, W.P. (1996). "Geomorphology and ecology of New Zealand shallow estuaries and shorelines," *In:* Nordstrom, K.F., and Roman, C.T. (ed.), *Estuarine shores: Evolution, environments and human alterations.* John Wiley and Sons Ltd, pp. 115-154.
Healy, T.R., Nichol, S., Hume, T., Immenga, D., Mathew, J. (1996). "The Mangawhai-Pakiri sand study, module 2: technical report marine sands," Report prepared for the Auckland Regional Council. 111 p.
Healy, T., Thompson, G., Mathew, J., Pildtich, C., Tian, F. (1998). "Assessment of environmental effects: maintenance dredging and disposal," Unpublished report for the Port of Tauranga Ltd. 170 p.
Hume, T.M., Herdendorf, C.E. (1992). "Factors controlling tidal inlet characteristics on low drift coasts*," Journal of Coastal Research* 8(2), 355-375.
Komar, P.D. (1998). "*Beach Processes and Sedimentation,*" Second Edition, Prentice Hall Inc, New Jersey. 544 p.
Spiers, K.C. (2005). "Continued beach renourishment for dredge spoil disposal," University of Waikato, MSc thesis, 241 p.

DESKTOP METHODOLOGY FOR ESTIMATING MAINTENANCE DREDGING REQUIREMENTS FOR WIDENED AND DEEPENED NAVIGATION CHANNELS

Larry A. Wise[1], Oleg Mouraenko[2]

1. Moffatt & Nichol, 11011 Richmond Ave. Suite 200, Houston, TX 77042, USA. lwise@moffattnichol.com.
2. Moffatt & Nichol, 11011 Richmond Ave. Suite 200, Houston, TX 77042, USA. omouraenko@moffattnichol.com.

Abstract: Estimates of maintenance dredging quantities were needed for a proposed widening and deepening of a navigation channel. However, detailed numerical modeling of sediment transport was not desired at the time. Channel sedimentation rates were estimated based on a new semi-empirical methodology. The methodology is based on a simplification of the sediment deposition equations (Krone 1962 and DuBoys 1879). Basic inputs to these equations include water velocities, total suspended sediment concentration (TSS), critical bottom shear stresses for erosion and deposition, Manning friction coefficient, bulk density of settled muds, and settling velocity for sediment particles (flocs). These equations are solved at discrete locations along the channel and integrated over time to give an overall sedimentation rate. The desktop methodology is applied to the Matagorda Ship Channel (Texas) widening and deepening project. The methodology offers a relatively simple way to estimate changes in maintenance dredging quantities for modifications to existing projects.

INTRODUCTION

The Matagorda Ship Channel (MSC) is a deep-draft navigation channel on the central Texas coast which serves the Calhoun County Navigation District's Port of Port Lavaca-Point Comfort. The channel transits from the open Gulf of Mexico through Matagorda and Lavaca Bays, both shallow estuaries. A map of the area is shown in Figure 1.

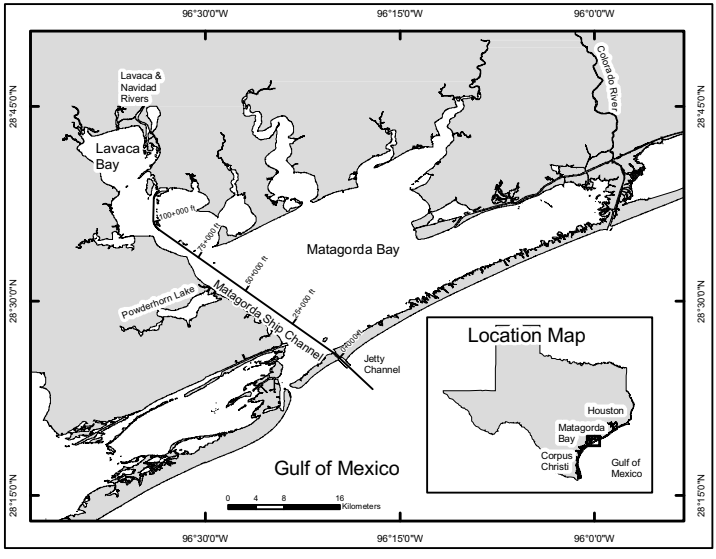

Fig. 1. Area Map

Presently, the channel has a depth of 36 ft mean low tide (MLT) with a 200 ft toe-to-toe width inside of Matagorda Bay. (MLT is a local tidal datum used by the U.S. Army Corps of Engineers Galveston District and is roughly equivalent to an annual low tide event.) Proposed improvements to the channel include widening the channel to a width of 400 ft toe-to-toe and deepening the channel to 44 ft MLT in the Matagorda and Lavaca Bay segments. The deepening would also include 2 ft of advanced maintenance and 2 ft of allowable overdepth dredging for a total depth of up to 48 ft MLT. The offshore portion of the channel would also be widened and deepened; however, it is not treated in this paper. A separate, but related, project would also widen the jetty channel at the entrance to Matagorda Bay.

As with many Gulf Coast navigation channels, the MSC has relatively high rates of sedimentation. Based on 40 years of dredging records the present vertical accumulation rates for the channel are approximately 1.3 ft/yr in the Matagorda Bay segment and 2.1 ft/yr in the Lavaca Bay segment. Sedimentation rates have been very consistent over time for much of the channel, with the exception of the upper channel near the port where there has been a notable trend toward increased sedimentation. The majority of material settling in the channel is clay and silt, with only minor portions of sand in most areas. The source of sediment shoaling in the channel is believed to be primarily from sediments suspended in the water column that settle out in the channel. The sources of suspended sediment include riverine input through the Colorado River, Lavaca River,

Navidad River, and several other smaller river inputs to the Bays (although the navigation channel is not a riverine channel) along with sediments resuspended from the shallow bay surrounding the channel by waves and currents and sediment eroded from the clay bluffs which surround much of the Bays.

For planning and cost estimating purposes, estimates of maintenance dredging quantities were needed for the proposed widening and deepening. However, detailed numerical modeling of sediment transport was not desired at the time. The existing methods of estimation of maintenance dredging quantities are generally based on gross geometric assumptions or extrapolation of trends from past widening and deepening project (Trawle, 1981). In the case of the Matagorda Ship Channel no prior widening and deepening projects have been performed making extrapolation of such trends impossible.

Therefore a simplified semi-empirical methodology was developed for estimation of changes in maintenance dredging quantities for the new project geometry. The methodology is based on historic dredging records and can be based on either numerical model output of water velocities in the channel or simple assumptions on the changes in water velocities due to the modifications. Since a hydrodynamic and salinity model was created for assessment of salinity impacts in the estuary, the results of the numerical model were available for use.

SEDIMENTATION ESTIMATE METHODOLOGY

The methodology is based on a simplification of sediment deposition equations with a few basic assumptions. The primary process of sedimentation considered is due to the suspended sediment transport, and does not include bedload or fluid mud processes. The rate of change in bed elevation due to deposition is proportional to the sediment flux near the bottom surface

$$\frac{dh}{dt} = \frac{1}{\rho_f} p W_s C \tag{1}$$

where h is the local water depth, ρ_f is the bulk density of sediments, p is the probability of deposition, W_s is the sediment settling velocity, and C is the representative mass concentration of suspended sediments.

The probability of deposition can be approximated as (Krone, 1962)

$$p = \begin{cases} 1 - \dfrac{\tau}{\tau_s}, & \tau < \tau_s \\ 0, & \tau \geq \tau_s \end{cases} \tag{2}$$

where τ_s is the critical shear stress for deposition, and τ is the bed shear stress. Using DuBoys' approximation (1879), the bottom shear stress can be determined as

$$\tau = \gamma R S \tag{3}$$

where γ is the unit weight of water equal to water density multiplied by the gravity, R is the hydraulic radius of the channel, S is the slope of water surface relative to the channel bottom. The hydraulic radius is found as a ratio of the cross-section area (A) and the wet perimeter (P), which are determined from geometry of the channel.

According to Manning's equation, the velocity in the channel can be approximated as

$$u = \frac{1}{n} S^{\frac{1}{2}} R^{\frac{2}{3}} \tag{4}$$

where n is the Manning's roughness coefficient.

Finally, the relationship between the shear stress and current velocity becomes

$$\tau = \gamma\, n^2 u^2 R^{-\frac{1}{3}} \tag{5}$$

If time series of velocity data is available for a period of time (T) then the average accumulation rates (r) can be found by integrating of equation (1) such as

$$r(x) = \frac{1}{\rho_f} \overline{p}(x) W_s(x) C(x) \text{ with } \overline{p}(x) = \frac{1}{T} \int_0^T p(\tau, x) d\tau \tag{6}$$

in which the probability p is a function of time, while other variables are assumed to be constant with time and only vary with location along the channel (x).

Representative suspended sediment concentration can be found by inversion of equation (6) with some expected values for settling velocity and bulk density of sediments. Assuming no change in concentration for the modified channel, the new accumulation rates then can be calculated if the change in velocities is somehow known or can be estimated.

The primary sources for suspended sediments are river inflows and redistribution of sediment within the bay by action of waves and currents. Resuspension of sediments within the channel is assumed to be a minor source. By changing configuration of the channel, it is assumed that the primary sources are not affected and, therefore, the representative concentration is assumed to remain constant.

The methodology does not include the effects of local erosion and redeposition in the channel. When erosion occurs it resuspends some of the recently deposited sediments; thus, the calculated representative suspended sediment concentration may be lower than the actual concentrations within the channel. When deposition is the prevailing condition the difference between the representative suspended sediment concentration and actual measured long-term average concentration (if available) would represent the

amount of material resuspended. Explicit inclusion of erosion would necessitate solving the time varying mass balance equations for sediment transport in and near the channel.

By increasing channel dimensions (width and depth) changes in all major hydraulic parameters can be expected. Due to increase in hydraulic radius, resistance of the channel decreases. This may result in increase of total flow through the channel. However, since the channel is not restricted from sides, slope of water surface will not necessarily remain the same. Therefore, combined changes in slope and hydraulic radius may result in either increase or decrease of flow velocity.

With a deeper channel, intensity of density currents is expected to increase as they depend on a cube of water depth (Ward et al, 1980). A deeper channel is expected to be more vertically stratified with larger volumes of sea water entering the bay during each tidal cycle. Presence of the density currents can increase flood and decrease ebb tidal currents within the channel. The effects of density currents with proposed changes to the channel geometry were not explicitly integrated into the sedimentation model; however, the model simulations from which the velocities were extracted account for such density currents.

It is also assumed that density of settled sediments and critical shear stress for deposition remain constant and water column salinity and changes in salinity do not affect sedimentation rates.

APPLICATION TO MATAGORDA SHIP CHANNEL WIDENING AND DEEPENING

For application to the MSC, dredging records for the period of 1963–1998 were analyzed to find long-term average sedimentation rates for each 5,000 ft channel segment. (Note that all distances for the MSC are given as along channel distance north of the Gulf entrance.) The velocities in the existing and modified channel were estimated with a three-dimensional numerical model (Moffatt & Nichol, 2006), and available as a time series for a six month period (April through September, 2003). In general, velocities for the proposed channel are on average approximately 20% higher in the lower channel and approximately 10% lower in the upper channel (see Figure 2) primarily as a result of the widened jetties (Moffatt & Nichol, 2006). The widened jetty channel decreases friction losses through the entrance to the bay and results in an increased tidal prism. The settling velocities were assumed to be a constant value along upper part of the channel and linearly increasing closer to the channel entrance. The increase in settling velocity is due to increasing content of fine sand in suspension.

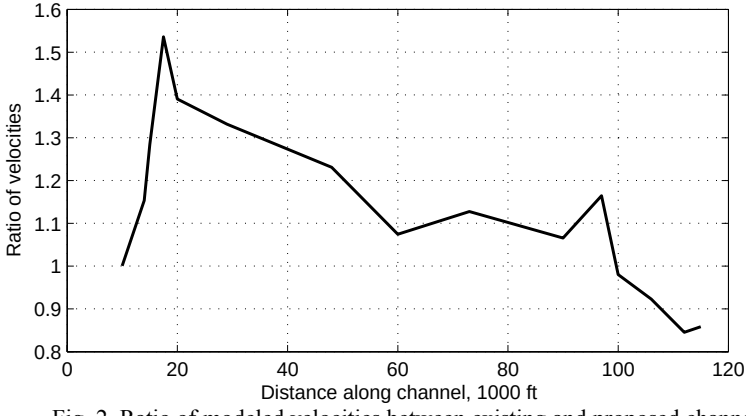

Fig. 2. Ratio of modeled velocities between existing and proposed channel

Values for critical shear stresses were taken from laboratory measurement and were estimated to be: for deposition—0.03 Pa; for erosion—0.10 Pa (ALCOA, 1998). The accumulation rates were calculated neglecting erosion. This approximation seems to be valid because for the most part of the channel the applied shear stress exceeds the critical stress for erosion during less than 40% of time (see Figure 3). And even though erosion can occur at some stages of tidal cycle the eroded sediments are assumed to remain within the channel. Therefore, one of the underlying assumptions of this model is deemed reasonable for a desktop analysis. Since velocities are, in general, increased, the assumption of neglecting erosion also leads to more conservative (i.e., larger volume) results.

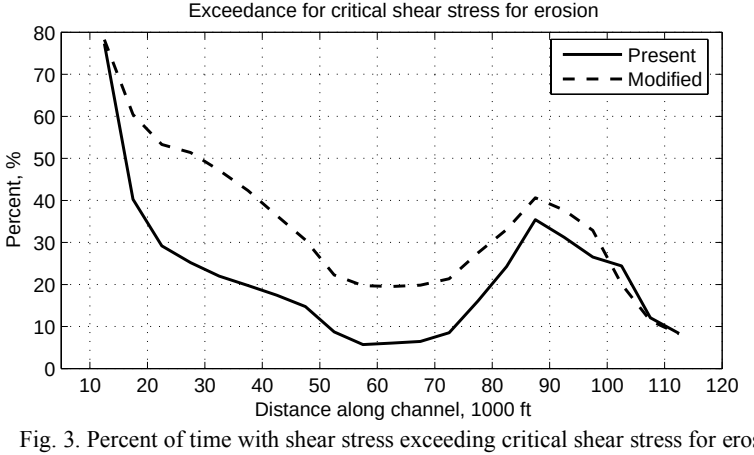

Fig. 3. Percent of time with shear stress exceeding critical shear stress for erosion

Long-term averages of suspended sediment concentrations vary along the channel. Data from the Texas Commission on Environmental Quality's (TCEQ's) water quality database are shown in Figure 4. The average concentrations were interpolated along the channel according to distance from the monitoring stations. It is noted that the various sample locations had different numbers of samples collected at different time periods; however, the average for each station was used for the analysis without further analysis of data spread, seasonality, or other factors. Average measured TSS was 40 mg/l. TSS levels estimated from historic dredging records are shown in Figure 4 along with the average and range of measured data and were used in the model as a calibration parameter. There is a good agreement with measured TSS data; however, the concentrations were underestimated in the lower portion of the channel mainly due to increasing erosion which is neglected in the model.

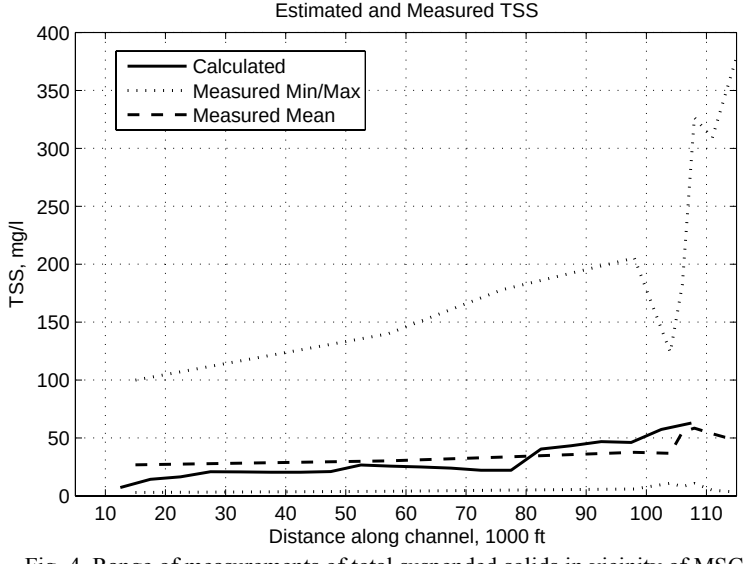

Fig. 4. Range of measurements of total suspended solids in vicinity of MSC with estimated TSS levels within the channel

Assuming that the suspended sediment concentrations do not change after the channel modification, average dredging volumes were estimated. Results of the calculations are presented in Figures 5 through 7. The total vertical accumulation rates are presented in Figure 8. The sedimentation rates (ft/year) were based on the approximate top width of the channel where the dredge cut intersects the natural bay bottom as this was is the effective width for sediment trapping. Table 1 gives an overview of the total sedimentation rates. It can be seen that the increase in channel dimensions has the largest effect on the total volumes. The sedimentation rate increases 67% due to the change in channel geometry. The effect of changes in hydrodynamics is much smaller.

It results in an approximately 5% overall decrease in vertical accumulation rate. However, there is a shift in areas of sedimentation with higher vertical accumulation rates after project expected in the upper channel.

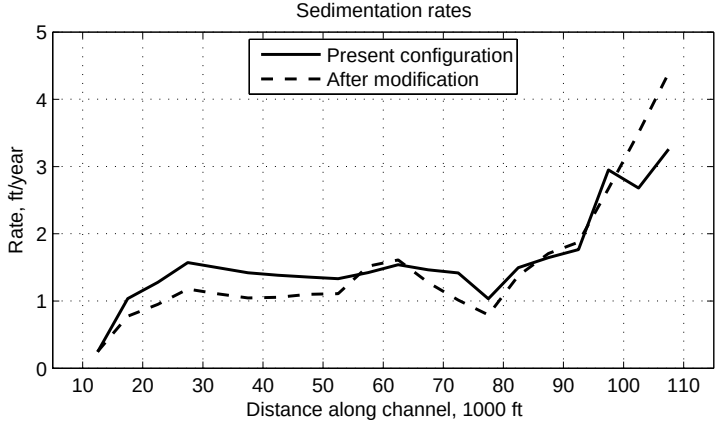

Fig. 5. Estimation of sedimentation rates

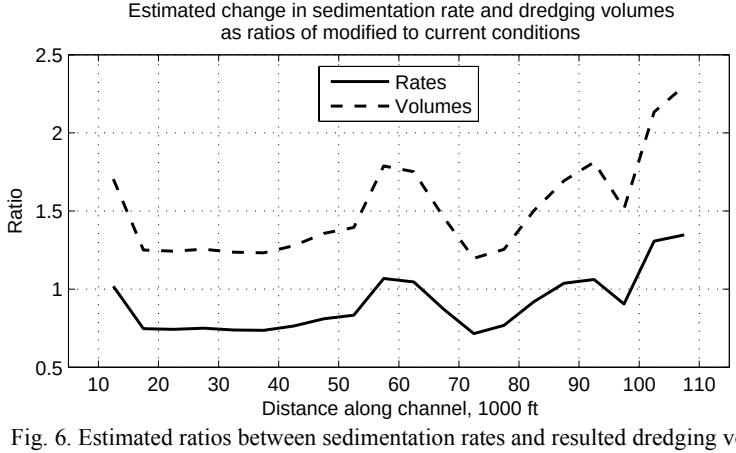

Fig. 6. Estimated ratios between sedimentation rates and resulted dredging volumes

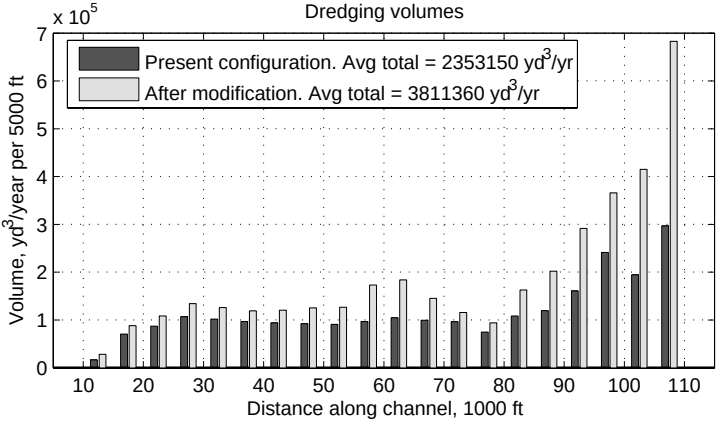

Fig. 7. Averaged dredging volumes in present configuration and after proposed modification

Table 1. Total dredged volumes calculated

Case	Total dredged volume, yd3/year	Ratio	Change in vertical accumulation rate, %
Present configuration	2,353,150	–	–
Due to increased dimensions	3,933,802	1.67	–
Combined effect of increased dimensions and accumulation rate	3,811,360	1.62	–5%

CONCLUSION

A methodology for estimating sedimentation for navigation channel widening and deepening was developed. The methodology is relatively simple and is suitable for desktop type analysis where a full, detailed numerical sedimentation model is not desired or feasible. The methodology is based on a simplification of the sediment deposition equations (Krone 1962 and DuBoys 1879). Basic inputs to these equations include water velocities, critical bottom shear stresses for deposition, Manning friction coefficient, bulk density of settled mud, and settling velocity for sediment particles (flocs) with total suspended sediment concentration (TSS) used as a calibration parameter. These equations are solved at discrete locations along the channel and integrated over time to give an overall sedimentation rate. The equations can be solved either based on assumed changes in velocities or using velocities from a numerical model.

The methodology was applied to the MSC widening and deepening to develop estimates of future maintenance dredging needs. Existing sedimentation rates based on long-term dredging records were used to estimate TSS as a calibration parameter. The TSS values calculated agree reasonably well with measurements in the vicinity. For the proposed channel modifications, including widening of the jetty channel which allows for a greater

tidal prism, the velocities in the channel were found to generally increase except in the upper end of the channel. This in turn leads to estimation of slightly decreased vertical accumulation rates for most of the channel, but with increased vertical accumulation rates in the upper channel. Overall the sedimentation rates are estimated to increase approximately 62% over present sedimentation rates, mostly due to the increased channel plan area.

ACKNOWLEDGEMENTS

Work described in this paper was done under contract for the Calhoun County Navigation District. Review and input on the work was received from URS Corporation staff including Chris Reed and U.S. Army Corps of Engineer staff including Ishaq Syed at the Galveston District and Nick Kraus and Lihwa Lin at the Engineer Research and Development Center.

REFERENCES

ALCOA (1998) "Development and application of a modeling framework to evaluate hurricane impacts on surficial mercury concentrations in Lavaca Bay", Technical Report, Project No ACOA0020.

DuBoys, M.P. (1879). "Le Rhone et les rivieres a lit affouillable. Mem. Doc.", *Ann. Pint* et Chaussees, 18(5).

Krone, R.B. (1962). "Flume studies of the transport of sediment in estuarial processes, Final report," Hydraulic Engineering Laboratory and Sanitary Engineering Research Laboratory, University of California, Berkeley.

Moffatt & Nichol (2006) "Matagorda Ship Channel Improvement Project, Hydrodynamic and Salinity Model," Draft Report (Rev. A) dated October 30, 2006.

Texas Coastal Ocean Observation Network (TCOON) (2006), retrieved from http://lighthouse.tamucc.edu/TCOON/HomePage

Texas Commission on Environmental Quality (TCEQ), retrieved from http://www.tceq.state.tx.us/

Trawle, M.J. (1981). "Methods of estuarine shoaling analysis," WES Technical Report H-78-5, U.S. Army Corps of Engineers Waterways Experiment Station, Vicksburg, MS

Ward, G.H, Jr., N.E. Armstrong, and the Matagorda Bay Project Teams (1980) "Matagorda Bay, Texas: its hydrography, ecology and fishery resources", US Fish and Wildlife Service, Biological Services Program, FWS/OBS-81/52, Washington, D.C.

A MASS-BALANCE, CONTROL-VOLUME APPROACH FOR ESTIMATING VERTICAL SEDIMENT FLUX AND SETTLING VELOCITY WITHIN DREDGE PLUMES

S. Jarrell Smith[1], Carl T. Friedrichs[2]

1. U.S. Army Engineer Research and Development Center, Coastal and Hydraulics Laboratory, 3909 Halls Ferry Road, Vicksburg, MS 39180-6199, USA. Jarrell.Smith@erdc.usace.army.mil.
2. Virginia Institute of Marine Science, College of William and Mary, P.O. Box 1346, 1208 Greate Rd., Gloucester Point, VA 23062-1346, USA. cfried@vims.edu.

Abstract: A mass-balance, control-volume approach is presented for estimating vertical sediment fluxes and mass-averaged settling velocities in dredge plumes. The method requires detailed measurements of velocity and suspended sediment concentration along the control volume boundaries. An example application is presented in which horizontal fluxes at the control volume boundaries are derived from Acoustic Doppler Current Profiler data. Results of the analysis demonstrate good qualitative agreement with the general understanding of sediments at the site. The control-volume method is suitable for application to other types of dredge plumes and general sediment transport research related to vertical fluxes and settling of suspended sediments.

INTRODUCTION

Navigation dredging is a vital activity for national economic security, enabling access to ports by commercial, deep-draft, ocean-going vessels (USACE, 1983). During dredging operations, sediments are removed from the channel bottom and transported by pipeline or vessel to approved dredged material placement sites. However, a portion of the sediments removed from the bed are suspended into the water column, transported from the dredging and placement sites by ambient currents, and returned to the bed through particle settling and deposition. The transport and fate of sediments suspended by dredging operations is a primary concern due to potential impacts to natural resources (USACE, 1983; Wilber and Clarke, 2001).

Elevated suspended sediment concentration (SSC) and turbidity may impose a range of environmental impacts such as gill abrasion and clogging; increased light attenuation and reduced photic depth (impacts to micro-algae, macro-algae, and submerged aquatic vegetation); burial, smothering, and abrasion of demersal eggs; reduced growth rate of larval and juvenile organisms (leading to increased mortality and reduced recruitment); blockage of fish migration routes; degradation of spawning habitat; and dispersion of sediment-adsorbed contaminants (Newcombe and Jensen, 1996; Wilber and Clarke, 2001). Newcombe and Jensen (1996) propose that impacts to fish are a function of SSC, duration of exposure, species, and life stage. In the United States, natural resource agencies (state departments of environmental quality; state, regional, and federal fisheries agencies; and federal environmental protection) require dredging proponents (such as port authorities and the U.S. Army Corps of Engineers) to demonstrate that proposed dredging activities meet regulatory requirements established by under Section 404 of the Clean Water Act, Section 103 of the Marine Protection, Research, and Sanctuaries Act, National Environmental Policy Act of 1969, and state water quality standards.

Numerical models are among the primary tools through which dredging proponents demonstrate that proposed dredging activities are likely to meet regulatory requirements. These models represent the processes of sediment suspension, advection, diffusion, settling, and deposition through a collection of both empirical- and physics-based equations to predict transport and fate of sediments suspended by dredging operations (Koh and Chang, 1973; Johnson, 1990; Johnson et al. 2000). Wide variations in dredging equipment and sediment characteristics and limited knowledge of the rates of suspension and characteristics of suspended material lead to large uncertainties in model estimates of sediment transport and fate (Germano and Cary, 2005). Milligan and Hill (1998) suggest that time-variant flocculation effects must be included in sediment transport models for assessing environmental impacts in the coastal zone. Similarly, advancement of the predictive capabilities of dredged material transport, fate, and impacts are not expected until better understanding is gained of the influences of dredge and sediment types on sediment suspension and sediment dynamics.

To present, limited progress has been made in quantifying the rate of sediment suspension from various dredge types and even less progress has been made in describing suspended sediment characteristics and settling processes in dredge plumes. Limitations in present knowledge of suspension and settling in dredge plumes are largely attributable to past limitations in sampling technology. Until the early 1990s, field measurements were limited to physical pump and bottle samples analyzed for total suspended solids (McLellan et al. 1989). Limited spatial and temporal resolution available with physical sampling in dredge plumes characterized by high spatial and temporal gradients made quantifying suspension rates and settling extremely challenging. Advances in the fields of optical, acoustic, and photographic instrumentation permit corresponding advances in the ability to collect information about dredge plume dynamics (Puckette, 1998; Tubman and Corson, 2000; Reine et al., 2002). These recent advances in suspended sediment sampling technologies have opened new possibilities in research directed toward understanding of suspended sediment characteristics and settling dynamics in dredge plumes. Better understanding of settling dynamics in dredge plumes will lead to improved predictive methods, better informed dredging operation planning, reduced impacts to natural resources, and increased efficiency of dredged material management.

The purpose of this paper is to describe a method developed for estimating vertical flux and mass-averaged settling velocities within dredge plumes. The method presented is dependent upon high-resolution velocity and suspended sediment measurements within dredge plumes. Recent advances in Acoustic Doppler Current Profiler (ADCP) technology permit both velocities and concentrations to be quantified from a moving platform.

CONTROL VOLUME APPROACH

For a dredge plume, a control volume of size $\Delta x \times \Delta y \times \Delta z$ can be defined (Figure 1) such that time variations of the mean suspended sediment concentration within the control volume are given by differences in spatially averaged sediment fluxes across the bounding surfaces as follows:

$$\frac{\Delta C}{\Delta t}\Delta x\,\Delta y\,\Delta z = \Delta y\Delta z\left(F_{x1} - F_{x2}\right) + \Delta x\Delta z\left(F_{y1} - F_{y2}\right) + \Delta x\Delta y\left(F_{z1} - F_{z2}\right) \qquad (1)$$

where C = suspended sediment concentration (M L^{-3}), t = time, x,y,z = Cartesian coordinates, F = suspended sediment flux (M L^{-2} T^{-1}) averaged over each boundary.

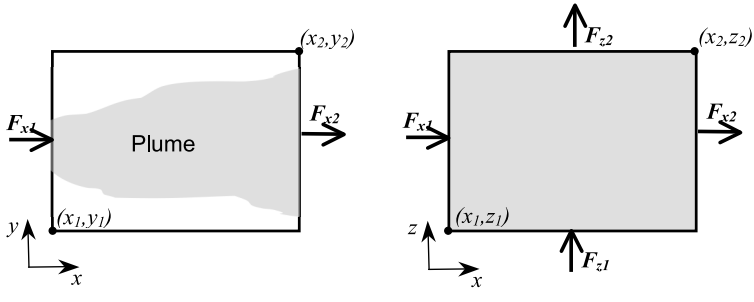

Fig. 1. Control volume for flux balance of dredge plumes.

Assuming that the plume traveling through the control volume has reached steady state (dC/dt = 0), that the lateral control-volume boundaries are outside the plume ($F_{y1} = F_{y2} = 0$), and that there is no sediment flux through the top of the control volume at the water surface ($F_{z2} = 0$), the spatially averaged vertical flux across the bottom surface of the control volume reduces to:

$$F_{z1} = \frac{\left(F_{x2} - F_{x1}\right)\Delta z}{\Delta x} \qquad (2)$$

To estimate vertical flux to the seabed within the defined control volume, measurements of cross-sectionally averaged horizontal fluxes at *x1* and *x2* are required. Neglecting horizontal turbulent diffusion, sediment flux at a point on the boundary is given by $F=uC$, where u = boundary-orthogonal velocity component. ADCPs are capable of providing both velocity and suspended sediment concentration (SSC) necessary to compute sediment flux across control volume boundaries. Acoustic backscatter has been shown to

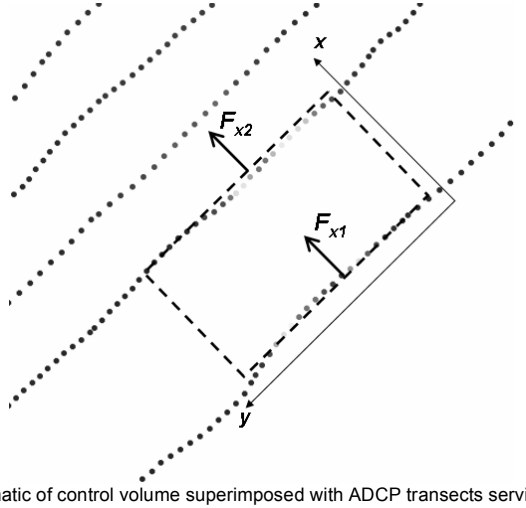

Fig. 2. Schematic of control volume superimposed with ADCP transects serving as control-volume boundaries in the *x* direction.

be a reliable, unobtrusive estimator of SSC (Thorne et al., 1991; Land and Bray, 2000), including measurements of dredge plumes (Battisto and Friedrichs, 2003; Reine et al. 2002; Clarke, et al. 2005). Figure 2 presents ADCP transects taken orthogonal to the prevailing current through a dredge plume. These transect lines define control-volume boundaries, with the velocity and SSC data providing basis for horizontal suspended sediment fluxes. Neglecting horizontal turbulent diffusion, the cross-sectionally averaged horizontal fluxes at *x1* and *x2* can each be calculated from a subsection of the ADCP transect data that includes the suspended sediment plume as follows:

$$\overline{F_x} = \frac{\sum_{i=1}^{NY}\sum_{k=1}^{NZ} u_{i,k} C_{i,k} \Delta z_k \Delta y_i}{\sum_{i=1}^{NY}\sum_{k=1}^{NZ} \Delta z_k \Delta y_i} \tag{3}$$

where the *i.k*, subscripts associated with $u_{i,k}$, $C_{i,k}$, Δy_i and Δz_k in Eq. 3 refer to ADCP bins, not the control volume.

Assuming mean vertical fluid velocities to be negligible, there are two contributions to the average vertical flux at the base of the control volume, namely gravitational settling and vertical turbulent diffusion:

$$F_{z1} = w_s C_1 - K_{z1} \frac{dC_1}{dz} \tag{4}$$

where the vertical eddy diffusivity, K_z, sediment concentration, and vertical concentration gradient are all evaluated at the height of the base of the control volume, z_1, and are all

averaged across the width of the control volume, Δy. By rearranging the terms, an expression for the settling velocity at height z_1 is obtained:

$$w_s = \frac{F_{z1} + K_{z1}\dfrac{dC_1}{dz}}{C_1} \tag{5}$$

which requires estimation of vertical flux, vertical diffusion, and vertical concentration distribution. Note that in Eq. 5, w_s and F_{z1} are expected to be negative with the adopted positive upward convention. In the typical situation of negative vertical concentration gradient, gradient diffusion (represented by $K_z\ dC/dz$) hinders settling by exchanging lower-concentration sediment-water mixture from above with higher-concentration mixture from below. For constant vertical flux and near-bed concentration, if gradient diffusion increases, still-water settling velocity must also increase.

MEASUREMENTS

The U.S. Army Engineer Research and Development Center, Environmental Laboratory (ERDC-EL) conducted vessel-mounted ADCP surveys near a hydraulic dredging outfall to monitor dredged material plumes in the vicinity of seagrass beds in St. Andrew Bay near Panama City, Florida (Figure 3). A hydraulic cutterhead dredge removed sediments classified as predominantly fine sand from Port Panama City and transported the slurry through a pipeline to a spill barge (located at the "S" in "Spill Barge" in Figure 3) within the permitted placement area. The end of the pipeline was directed vertically downward, 3 m beneath the water surface in 12-m depth. During the study, numerous surveys were

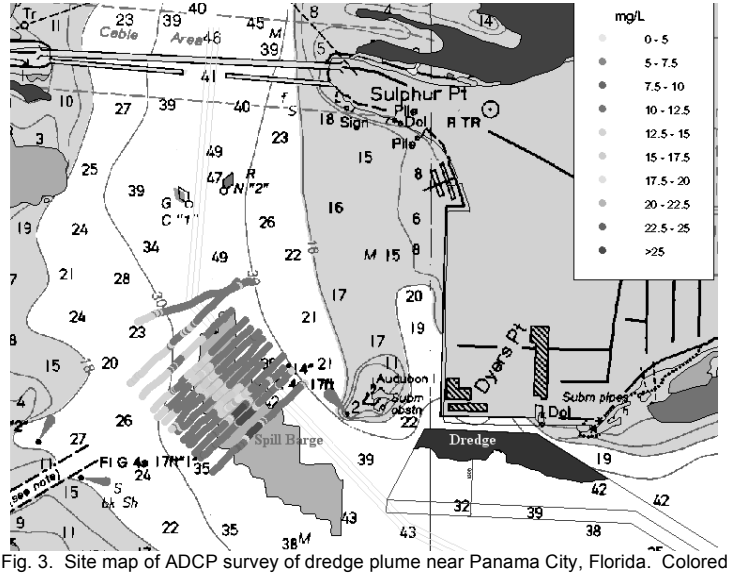

Fig. 3. Site map of ADCP survey of dredge plume near Panama City, Florida. Colored shading along transect lines indicates depth-averaged concentration.

conducted during various stages of the tidal cycle, each consisting of 10 or more transects oriented perpendicular to the tidal current. The data presented in this paper are from a survey conducted during flood tide immediately down current of the placement location as shown by the transect lines in Figure 3. Spacing between transects ranges from 30 to 80 m, with median spacing of 40 m, and spacing between individual soundings along each transect averages 4-5 m.. Each transect took less than 5 minutes to complete, and the 10 transects used in this analysis were completed in less than 45 minutes, ensuring a relatively small change in the tidal hydrodynamics. Velocity and SSC data were collected with a 600 kHz ADCP. Data collection and calibration methods were performed in accordance with Land and Bray (2000) and Reine et al. (2002).

Examples of concentration and velocity data from Transect 2 (the 2nd transect north-west of the spill barge) are presented in Figure 4. The concentration data indicate rational trends of variation associated with the high-concentration plume down current of the discharge point. However, the velocity signal is dominated by random noise. (Mean velocity perpendicular to Transect 2 is 0.08 m s^{-1}, but the standard deviation is 0.34 m s^{-1}.) Because the investigators collecting these data were interested primarily in monitoring suspended sediment concentrations, bin spacing of the ADCP was set at 0.25 m to maximize resolution of the suspended sediment plume at the expense of velocity data quality. For a study dedicated to assessing settling dynamics of a dredge plume, bin spacing must be optimized to provide adequate vertical resolution of SSC while maintaining good quality velocity data.

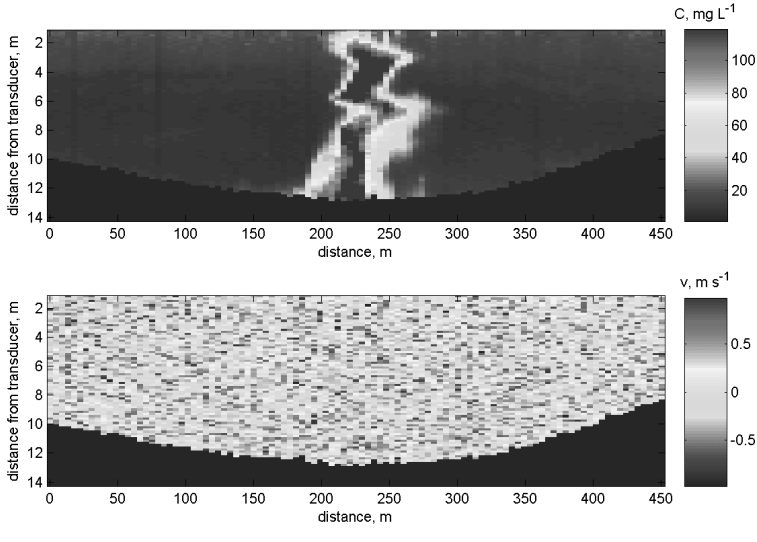

Fig. 4. Raw concentration and velocity data from Transect 2. Velocity data represent magnitude perpendicular to the transect. (+u = NW, -u = SE).

A significant observation from the concentration data is the distinct signature of sediment settling from the plume with distance from the discharge point as shown in Figure 5. Sediment concentrations within the plume at Transect 1 are large, but progressively decrease to near-ambient levels at Transect 5. Transect 1 passes within 10 meters of the spill barge, through the high-concentration effluent of the discharge pipe. Common slurry content of hydraulic dredge effluent is approximately 15-20 percent (by volume) or 400-500 g L^{-1}. At these large concentrations, significant acoustic energy is absorbed by suspended sediment (Thorne et al., 1991; Wren et al. 2000), resulting in lower acoustic backscatter and consequently lower inferred SSC. This effect of high sediment concentration on acoustic backscatter is shown as a zone of lower inferred concentration within the plume between 6-10 m below the transducer in Transect 1. As SSC is likely underestimated within this region, Transect 1 is omitted from later analysis.

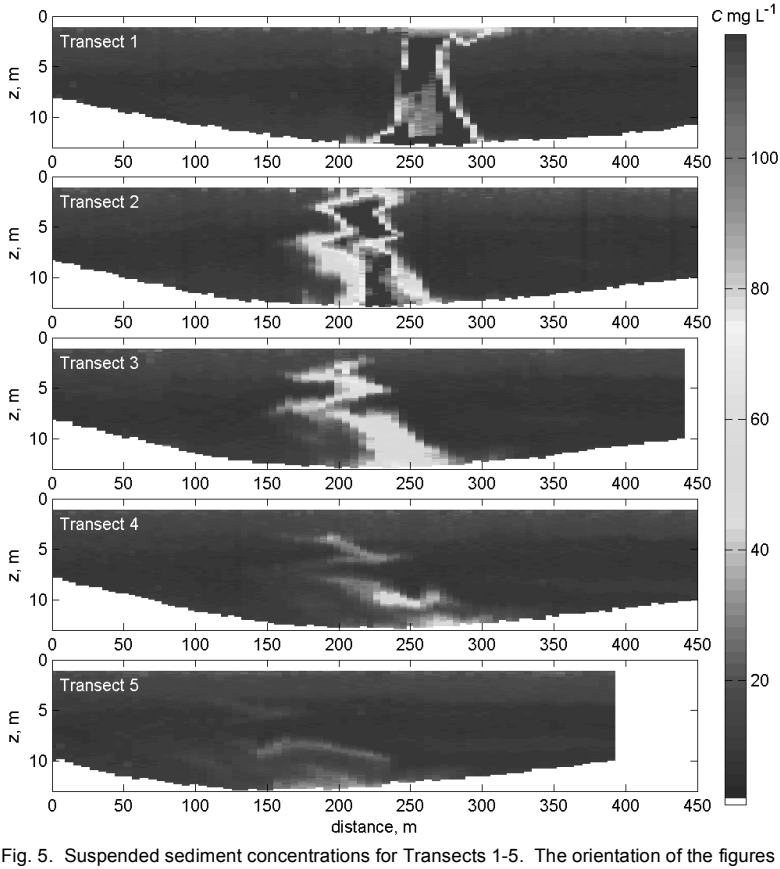

Fig. 5. Suspended sediment concentrations for Transects 1-5. The orientation of the figures is such that flow is into the page.

RESULTS

Horizontal suspended sediment flux is estimated from the data collected along Transects 2 through 6. Transect 1 was omitted as previously explained due to assumed acoustic attenuation in the concentration signal resulting from large SSC. At and beyond Transect 6, the dredge plume is barely distinguished from ambient sediment concentrations. The lateral range of data used to compute horizontal fluxes was determined visually and limited to the portion of data clearly identified as a plume. As discussed previously, quality of velocity data was poor due to the small bin height selected for data collection. Due to the noisy signal, average velocities were determined for each transect and applied to the horizontal flux calculations of Eqn. 3 which are presented in Figure 6. Note that the cross-sectionally averaged horizontal fluxes decrease from 3 to 1.3 g m^{-2} s^{-1} over a 120 m distance, with the horizontal flux gradient decreasing with distance from the pipeline outfall.

Vertical flux for each control volume is estimated by Eq. 2 from the computed horizontal fluxes at each transect, distance between transects, Δx, and mean water depth (substituted for Δz), with the width of each control volume limited to the maximum width of the two bounding transects containing the dredge plume. Mean vertical sediment fluxes are plotted in Figure 6 at the central position of each of the four control volumes. Mean vertical flux magnitude is greatest between Transects 2 and 3 at -0.4 g m^{-2} s^{-1} and decreases by roughly an order of magnitude to -0.03 g m^{-2} s^{-1} 100 m away between Transects 5 and 6. The marked reduction in horizontal and vertical fluxes within such a short distance from the pipeline outfall suggests that much of the suspended sediment in the dredge plume deposits near the placement site.

With estimates of vertical sediment flux, near-bed sediment concentration, near-bed vertical concentration gradient, and an estimate of vertical diffusivity, Eq. 5 permits an

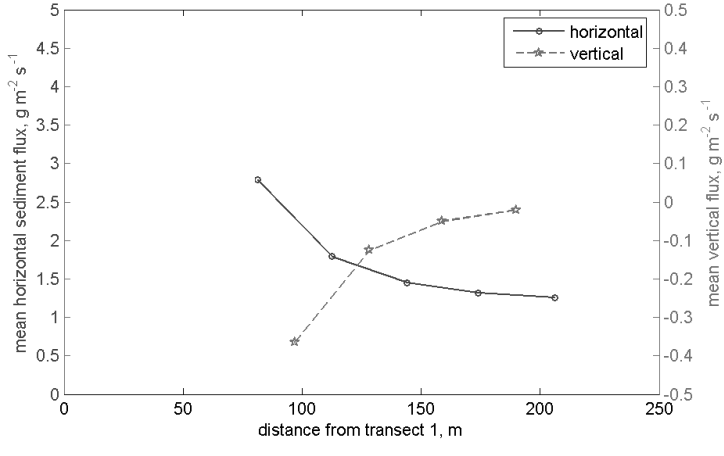

Fig. 6. Cross-sectionally averaged horizontal and vertical fluxes for Transects 2-6.

estimate of mass-averaged sediment settling velocity. For this application, mean suspended sediment concentration and vertical concentration gradient were averaged for bins within 3 m of the bed and between the bounding transects. Velocity measurements were not of acceptable quality to directly estimate K_z from the vertical velocity profile, so an alternate, first-order approximation was estimated assuming logarithmic distribution of velocities in the benthic boundary layer, parabolic distribution of vertical eddy diffusivity, sandy bed with hydraulic roughness, $z_0 = 0.006$ m, and the transect-averaged velocity. Average value of K_z for the four control volumes is 0.005 m^2s^{-1}. The resulting estimates of settling velocity for the four control volumes is presented in Figure 7. The first two control volumes, for which horizontal fluxes rapidly decrease have an estimated settling velocity on the order of 0.02 m s^{-1}, and settling velocity decreases to 0.012 and 0.005 m s^{-1} in the final two control volumes.

As the dredged material in this example is predominantly fine sand and settling velocities estimated in Figure 7 fall in the range of expected fall velocities of fine sand, an estimate of the equivalent sand diameters can be made using an empirical estimate of sand settling velocity (Soulsby 1997):

$$w_s = \frac{\nu}{d}\left[\left(10.36^2 + 1.049D_*^3\right)^{1/2} - 10.36\right] \tag{6}$$

where ν = kinematic viscosity of water, d = sediment diameter, $D_* = \left[\frac{g(s-1)}{\nu^2}\right]^{1/3} d$, $s = \frac{\rho_p}{\rho}$, ρ = water density, and ρ_p = particle density. Given settling velocity and water properties, Eq. 6 is solved for d. Estimated equivalent sand diameters are presented in Figure 7. The trends in d follow those of w_s, decreasing with distance from the plume

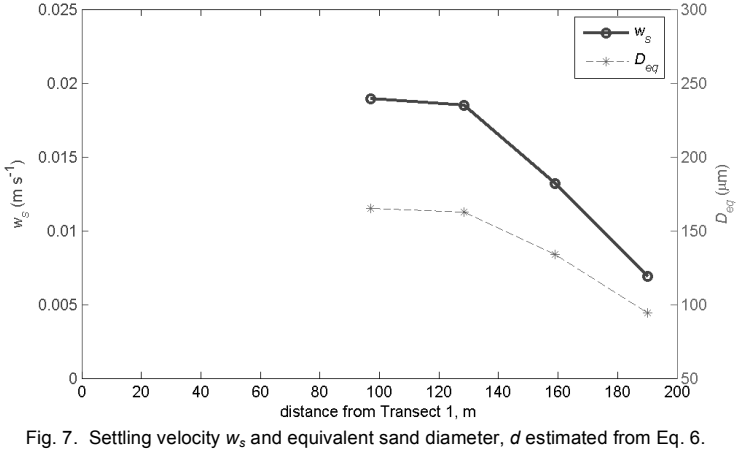

Fig. 7. Settling velocity w_s and equivalent sand diameter, d estimated from Eq. 6.

source, ranging from 160 μm for the first control volume down to approximately 100 μm for the last control volume. The equivalent diameters are not verifiable from the data collected for this example, but are consistent with the general classification of sediments from the dredging site. Decreasing settling velocities and inferred equivalent diameters with distance from the plume source suggest that coarser sediments deposit near the pipeline outfall and progressively finer sediments remain in suspension longer to be transported and deposited farther from the source.

Given the relatively weak currents at the site and the relatively large settling velocities of the suspended fine sand, gradient diffusion plays a minor role in opposing settling and deposition of the plume sediments. Comparing the relative strength of the settling flux ($w_s C$) to the gradient diffusion flux ($K_z \, dC/dz$) indicates that the magnitude of the diffusive flux is between 5 to 15 percent of the settling flux.

DISCUSSION

The control-volume approach is shown to provide reasonable results in estimating vertical fluxes to the seabed in dredging plumes, with ADCP data (velocity and concentration) providing the necessary data to estimate horizontal fluxes across longitudinal control volume surfaces. Additionally, if details of near-bed vertical diffusion and concentrations are available, a mass-averaged settling velocity estimate is possible.

Significant attention must be given to instrument configuration and experimental procedures for reliable estimates from the analysis. ADCP bin spacing must be optimized to produce good resolution of suspended sediment concentration without degrading the quality of Doppler-estimated velocities. For the example application presented in this paper (which was performed to estimate SSC only), the ADCP was configured to provide maximum resolution of SSC which caused significant errors in the velocity record. Even with the problems in the velocity data, the method was shown to provide reasonable estimates of vertical flux and settling velocity. The robustness of the method for the example application is attributed to the strong settling signature of the sandy sediments in suspension. For applications involving sediments with smaller settling velocities (such as clay and silt), the method is likely to be less forgiving regarding quality of the velocity data.

One of the founding assumptions in the method presented is steady-state nature of the plume. While plumes resulting from hydraulic pipeline placement (such as shown in the example) are characteristically steady state, other dredging operations are not. For instance, mechanical dredging with a clamshell, backhoe, or bucket dredge is characterized by discrete pulses of suspended sediment. For this case, transects should be conducted repeatedly at fixed distances from the dredging operation to obtain mean fluxes across the control volume boundaries. Data collection becomes even more complicated for hopper dredges, in which transect lines must be run relative to a moving source. In this case, two ADCP systems transecting the dredge plume at fixed relative distances must operate in tandem.

While the control volume approach presented here has been developed with dredging applications in mind, the method is suitable for other suspended sediment research topics in a wide range of environments. Research of vertical sediment flux and deposition at river mouths, estuaries, and the inner shelf could apply the control-volume approach with sediment flux defined by ADCP transects. As with dredging applications, careful attention to spatial and temporal scales of variation in fluxes, assumptions of the analysis method, and limits in instrumentation and data collection would need to be considered.

CONCLUSION

A mass-balance control volume approach to horizontal sediment fluxes in dredge plumes is shown to provide reasonable estimates of vertical flux and mass-averaged settling velocity. The method relies on ADCP or similar instrumentation to provide suspended sediment flux at the control volume boundaries. Estimating vertical flux within the control volume requires estimates of velocity and SSC along the control volume boundaries. Further analysis of near-bed concentrations, vertical concentration gradients, and near-bed vertical diffusion allows estimation of mass-averaged settling velocity. The method presented is applicable to non-steady dredging plumes or other sources of suspended sediment with appropriate modification to data collection methods.

ACKNOWLEDGEMENTS

Funding for this work was provided by the U.S. Army Corps of Engineers Dredging Operations and Environmental Research (DOER) Program. Program Manager for DOER is Dr. Todd Bridges. Permission was granted by the Chief of Engineers to publish this information. Data for the example application were provided to the authors by Dr. Douglas Clarke, Kevin Reine, and Chuck Dickerson (U.S. Army Engineer Research and Development Center – Environmental Laboratory). The development and presentation of the control volume technique benefited from discussions with Dr. Courtney Harris (Virginia Institute of Marine Science) and Dr. Larry Sanford (University of Maryland, Horn Point Laboratory).

REFERENCES

Battisto, G.M and Friedrichs, C.T. (2003). "Monitoring suspended sediment plume formed during dredging using ADCP, OBS, and bottle samples," *Proceedings Coastal Sediments 2003*, CD-ROM Published by East Meets West Productions, Corpus Christi, TX ISBN-981-238-422-7, 14p.

Clarke, D.; Martin, A.; Dickerson, C.; Moore, D. (2005). "Suspended sediment plumes associated with mechanical dredging at the Port of Oakland, California,". Proceedings of the Western Dredging Association Twenty-fifth Technical Conference & Thirty-Seventh Texas A&M Dredging Seminar, Western Dredging Association, 187-202.

Germano, J. D., and Cary, D. (2005). "Rates and effects of sedimentation in the context of dredging and dredged material placement," DOER Technical Notes Collection (ERDC TN-DOER-E19), U.S. Army Engineer Research and Development Center, Vicksburg, MS. http://el.erdc.usace.army.mil/dots/doer/doer.html

Johnson, B. H. (1990). "User's Guide for Models of Dredged Material Disposed in Open Water," Technical Report D-90-5, U.S. Army Engineer Waterways Experiment Station, Vicksburg, MS.

Johnson, B.H.; Andersen, E.; Isaji, T.; Teeter, A.M.; Clarke, D.G. (2000). "Description of the

SSFATE numerical modeling system," ERDC TN-DOER-E10. U.S. Army Engineer Research and Development Center, Vicksburg, MS.

Koh, R. C. Y., and Chang, Y. C. (1973). "Mathematical Model for Barged Ocean Disposal of Waste," Environmental Protection Technology Series EPA 660/2-73-029, U.S. Environmental Protection Agency, Washington, DC.

Land, J.M. and Bray, R.N. (2000). "Acoustic measurement of suspended solids for monitoring of dredging and dredged material disposal," *Journal of Dredging Engineering* 2(3), 1-17.

McLellan, T.N, Havis, R.N., Hayes, D.F., and Raymond, G.L. (1989). "Field studies of sediment resuspension characteristics of selected dredges," Technical Report HL-89-9. U.S. Army Engineer Waterways Experiment Station, Vicksburg, Mississippi.

Milligan, T.G. and Hill, P.S. (1998). "A laboratory assessment of the relative importance of turbulence, particle composition, and concentration in limiting maximal floc size and settling behavior," *Journal of Sea Research*, 39:227-241.

Newcombe, C.P. and Jensen, J.O.T. (1996). "Channel suspended sediment and fisheries: a synthesis for quantitative assessment of risk and impact," *North American Journal of Fisheries Management*, 16: 693-727.

Puckette, T.P. (1998). "Evaluation of dredged material plumes: physical monitoring techniques," DOER Technical Notes Collection (ERDC-TN-DOER-E5), U.S. Army Engineer Research and Development Center, Vicksburg, Mississippi.

Reine, K.J. Clarke, D.G., and Dickerson, C. (2002). "Acoustic characterization of suspended sediment plumes resulting from barge overflow," *DOER Technical Notes Collection* (ERDC-TN-DOER-E15), U.S. Army Engineer Research and Development Center, Vicksburg, MS. http://el.erdc.usace.army.mil/elpubs/pdf/doere15.pdf

Soulsby, R.L. (1997). *Dynamics of marine sands*. Thomas Telford, London. p. 134

Thorne, P.D., Vincent, C.E., Hardcastle, P.J., Rehman, S., and Pearson, N. (1991). "Measuring suspended sediment concentrations using acoustic backscatter devices," *Marine Geology*, 98: 7-16.

Tubman, M.W. and Corson, W.D. (2000). "Acoustic monitoring of dredging-related suspended-sediment plumes," DOER Technical Notes Collection (ERDC-TN-DOER-E7), U.S. Army Engineer Research and Development Center, Vicksburg, Mississippi.

U.S. Army Corps of Engineers (USACE) (1983). "Dredging and Dredged Material Disposal," Engineering Manual 1110-2-5025.

Wilber, D.H. and Clarke, D.G. (2001). "Biological effects of suspended sediments: a review of suspended sediment impacts on fish and shellfish with relation to dredging activities in estuaries," *North American Journal of Fisheries Management*, 21: 855-875.

Wren, D.G., Barkdoll, B.D., Kuhnle, R.A., and Derrow, R.W. (2000). "Field techniques for suspended-sediment measurement," *Journal of Hydraulic Engineering*, 126(2), 97-104.

WHAT DOES "PHYSICAL REGENERATION" OF MARINE AGGREGATE DREDGING SITES MEAN?

Markus Diesing[1, 2]

1. Institute of Geosciences, Christian-Albrechts-University, Olshausenstr. 40-60, D-24098 Kiel, Germany.
2. Centre for Environment, Fisheries and Aquaculture Science, Burnham Laboratory, Remembrance Avenue, Burnham-on-Crouch, Essex, CM0 8HA, United Kingdom. Markus.Diesing@cefas.co.uk.

Abstract: The impact of dredging and the physical regeneration of a sand-dredging site were monitored over a period of almost seven years with side-scan sonar and multi-beam echo sounder. The seabed physically regenerated from the dredging impact within a few years, except for a limited area where multiple dredging caused a pronounced impact and the seabed remained in an altered state. Based on the observed results, questions arise regarding the meaning of the term "physical regeneration". Here I intend to propose working definitions of physical regeneration, which are dependant on the nature of the particular of investigation.

INTRODUCTION

In recent years, marine aggregates (sand and gravel) have evolved as an important resource for the construction industry and for coastal protection issues. In the near future, demand is expected to grow due to an increasing urbanization of the coastal zone and large-scale construction projects. Furthermore, a large percentage of the global coastlines are receding. This problem might become even more important due to a rising sea level, caused by global warming (Church et al. 2001). Preferred "soft" coastal protection schemes will therefore possibly cause an increasing demand for marine sand. Despite several advantages of marine aggregates, when compared to those of terrestrial origin, including quality, availability and ease of transport, possible negative impacts have to be considered:

1. **Coastal engineering-related impacts**: Marine aggregate dredging often causes significant changes in seabed elevation, which in turn may alter inner shelf and shoreface wave and current fields, thereby indirectly affecting sediment transport patterns. Direct negative impacts on coastal sediment budgets and finally coastal erosion are expected, when aggregates are extracted within the active beach-shoreface sediment system (Demir et al. 2003).

2. **Benthic biology-related impacts**: Mining of marine sand and gravel directly leads to degradation or even destruction of benthic biotopes (ICES 2001). A major pre-requisite for the recovery of benthic biotopes is the naturally induced physical regeneration of the seabed. The natural regeneration of such areas following cessation of dredging is dependant on several factors such as the hydrodynamic conditions, the type of the extracted resources, the benthic life within the dredging site and the intensity and depth of dredging.

Here I present results from repeated seabed surveys performed at a dredging site in the western Baltic Sea, a practically non-tidal epicontinental shelf sea in northern Europe. The site is located approximately 2 nautical miles west of the village Wustrow, Germany off the coast of the Fischland peninsula (Fig. 1) in water depths between 10 and 12 m below mean sea level (msl). This stretch of coastline can be described as wave-dominated according to the classification of Davis and Hayes (1984).

The dredging site Wustrow II is 1,100,000 m^2 in size. According to the map of Tauber and Lemke (1995), the upper layer of the seabed is composed of moderately sorted fine sands. The mean grain size of surface sediments ranges from 210 to 250 µm, while the average thickness of the deposit amounts to 1.9 m.

In autumn 1997, approximately 320,000 m^3 of sand were extracted by trailer-suction hopper dredging (Krause 2002). This method normally leads to the production of shallow linear or curved furrows on the seabed (Fig. 2A). The extracted sands were used for a beach replenishment scheme at a nearby coastal strip of the Fischland peninsula. The morphological evolution of the site was monitored during the following seven years. The obtained results raise questions, which lead to working definitions of physical regeneration. A second extraction took place some time between May 2000 and March 2005 (according to the gathered data), but this has not been considered in the frame of this study.

METHODS

Data from side-scan sonar surveys were collected in March 1998, September 1998, May 2000, October 2004 and March 2005. The equipment consisted of a towed Klein 595 dual-frequency (100/384 kHz) side-scan sonar during the first four surveys and a towed EG&G 272TD dual-frequency (105/390 kHz) side-scan sonar during the last survey. Data acquisition was performed in digital format from May 2000 onwards (with Isis Sonar, Triton-Elics), while during the initial two surveys paper printouts were produced. During the last survey, the dredging site was also surveyed with an L3-Communications/Elac Nautik Seabeam 1185 multi-beam echo sounder with a working

frequency of 180 kHz. Data were digitally recorded with the software Hydrostar (L3-Communications/Elac Nautik Seabeam 1185).

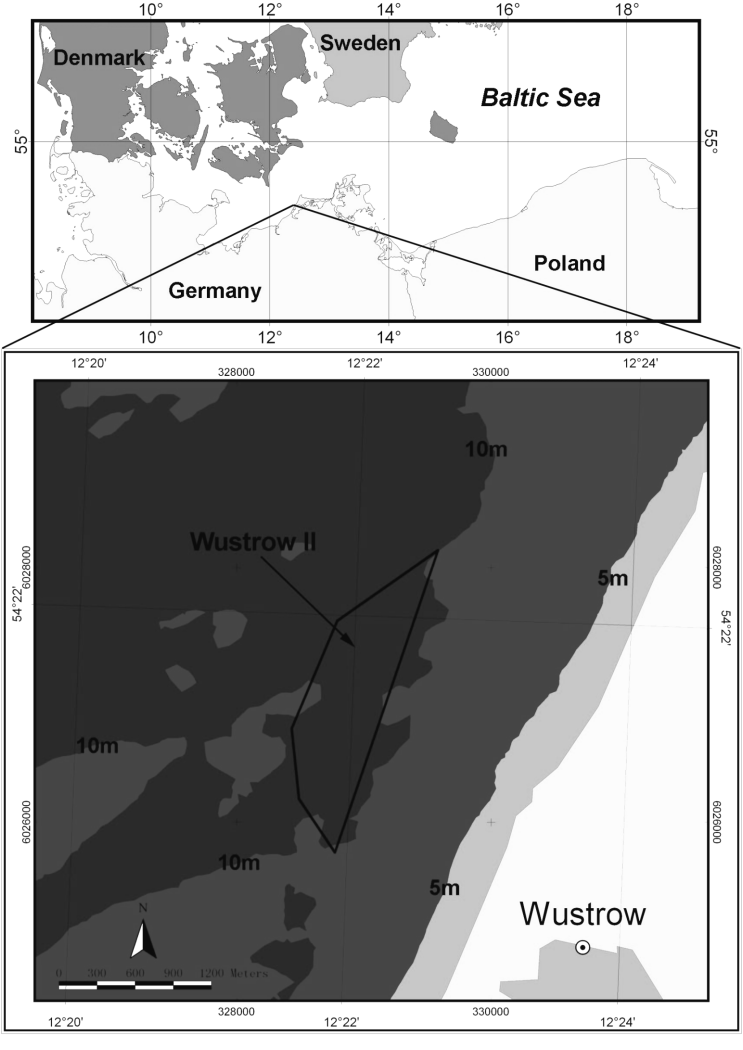

Fig. 1. Location of the dredging site "Wustrow II" in the western Baltic Sea.

During all surveys, the ship's track lines were chosen to allow full coverage of the seabed. Positioning was achieved by differential GPS, providing an accuracy of the vessel's

(and therefore also of the multi-beam's) position better than 5 m. The side-scan sonar was towed behind the vessel with about 10 m of cable out. This offset was accounted for by a constant value for each profile, when calculating the position of the tow-fish. The positioning error of the side-scan sonar is thus greater compared to the multi-beam.

The digital side-scan sonar data were processed and geo-referenced using the Isis Sonar and Delphmap software packages (Triton-Elics) in order to create mosaics of the study area. The analog data were digitized and geo-referenced according to a procedure outlined in Kubicki and Diesing (2006), which was successfully applied by Diesing et al. (2006). The geo-referenced side-scan sonar data were projected in Universal Transverse Mercator (UTM) projection and displayed in a geographical information system. Blocks of 100 m by 100 m size were defined according to the UTM grid. The number of identifiable tracks per block was visually counted for each survey. As a result, maps displaying the number of dredge tracks per 100 m by 100 m block were created. Tracks produced during a second extraction were not taken into consideration. The post-processing of the raw multi-beam data was conducted using the software packages HDPpost and HDPedit (L3-Communication/Elac Nautik).

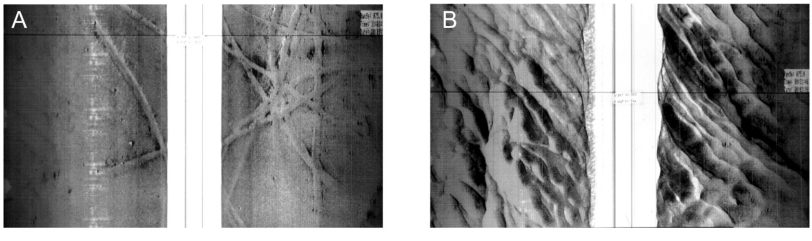

Fig. 2. Impact of dredging four months post-dredging using side-scan sonar: A – Individual dredge tracks; B – Multiple dredge tracks causing a significant depression on the seabed.

RESULTS

An initial survey four months post-dredging revealed that vast areas of the dredging site were affected by approximately 2 m wide and 0.5 m deep dredging furrows caused by trailer-suction hopper dredging (Figs. 2A, 3A). The highest impact was recorded in the southwest of the dredging site, where multiple dredge tracks created a depression of more than 5 meters below the surrounding seabed (Figs. 2B, 3A). Six months later (September 1998), the less intense impacted areas showed a reduction in the number of dredge tracks, but the impact in the heavily dredged site was still clearly visible (Fig. 3B). In May 2000 (30 months post-dredging) the situation was significantly different (Fig. 3C): Detectable dredge tracks were limited to the high-impact site and had a weathered appearance. The number of tracks had decreased significantly. Instead tracks had gained in width, thus indicating a merging of individual dredge tracks. During the two final surveys in October 2004 (82 months post-dredging) and March 2005 (87 months post-dredging), only a few heavily weathered dredge tracks were discernable in the high-impact site (Fig. 3D).

The side-scan sonar data indicated that the dredging site appeared to be completely re-generated outside the high-impact area, as no dredge tracks were recognizable. In the high-impact area, backscatter was slightly lower indicating the presence of finer or less compacted sediments or a combination of both. Additionally, the multi-beam bathymetric survey from March 2005 showed the presence of a depression with a size of 450 m in length, 130 m in width and up to 4 m in depth below the surrounding seabed in the high-impact site (Fig. 4).

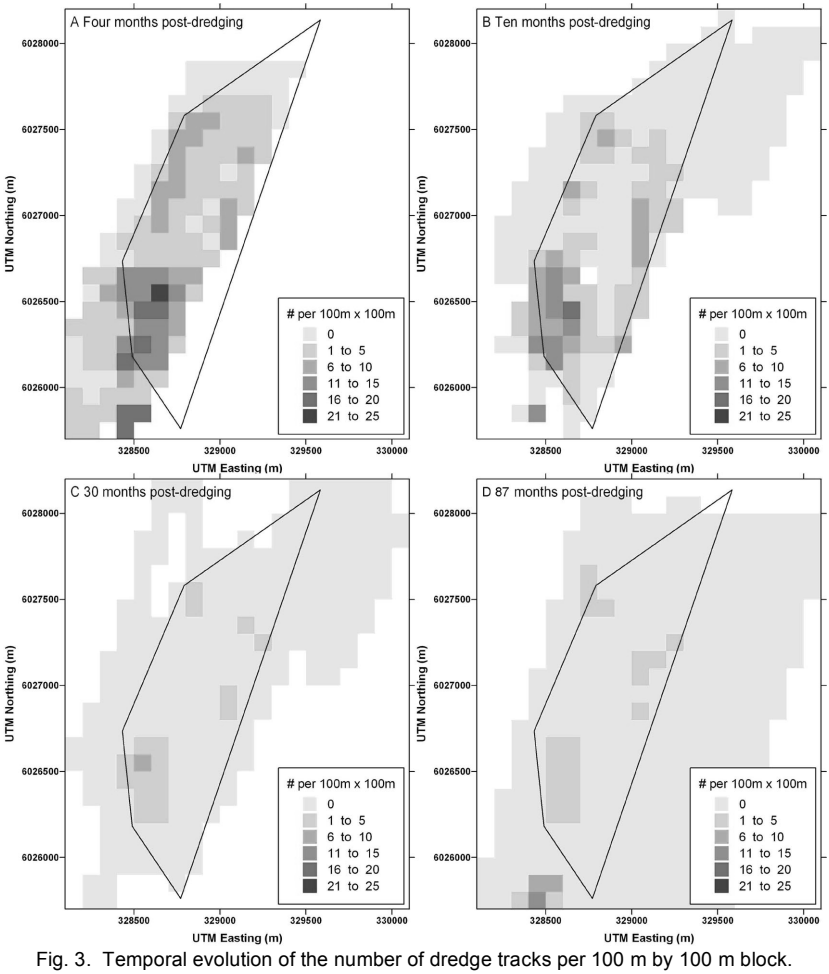

Fig. 3. Temporal evolution of the number of dredge tracks per 100 m by 100 m block.

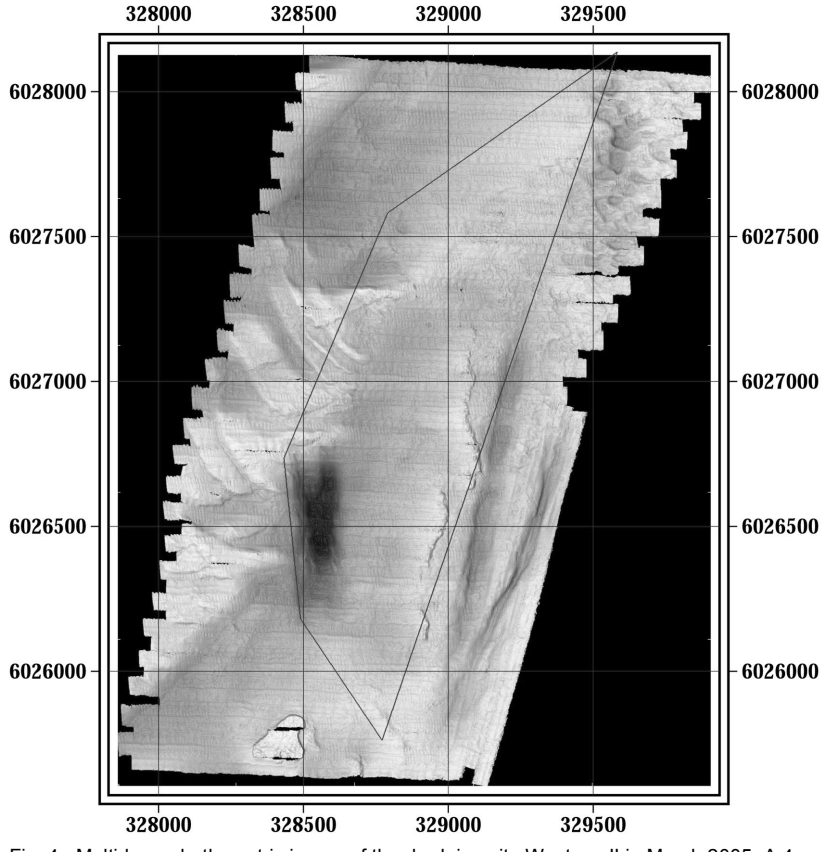

Fig. 4. Multi-beam bathymetric image of the dredging site Wustrow II in March 2005. A 4 m deep depression in the high-impact site is clearly visible.

DISCUSSION

When do we consider a dredging site to be physically regenerated? And how do we measure this regeneration? These are questions, which arise from the above-mentioned observations. As outlined below, the definition of "physical regeneration" depends on the aims of the study and whether it is dealing with coastal engineering-related or benthic biology-related impacts of dredging.

Although the pre-dredging status of the dredging site Wustrow II is unknown, which prevents the calculation of volume change, it is fairly clear that the sediment budget is far from being balanced. In this sense, the dredging site cannot be judged as being physically regenerated. The remaining depression on the seabed might therefore have an impact on wave and current fields and ultimately on sediment transport patterns. It is,

however, unlikely that direct negative effects, such as infilling from beach sediments (Demir et al. 2003), arise from the dredging impact, as the depression lies beyond the active zone of the shoreface-beach profile, which is located in approximately 10 m below msl (Dette et al. 2001).

In the high-impact area, lower backscatter values indicate different sediment properties when compared to the surrounding areas. In fact, Krause et al. (in review) show that during the initial ten months post-dredging, fine sands enriched in organic carbon content replaced the medium sands of low organic carbon content, which were present prior to dredging. However, this area is relatively limited in size when compared to the whole dredging site. Moreover, dredge tracks were practically not discernable using side-scan sonar outside the high-impact area, which indicates that the small-scale morphology induced by dredging is leveled out and the seabed sediments in this area do not significantly differ from the non-impacted surrounding seabed. Such conditions might be sufficient for the initiation of the biological recovery of the seabed, which can be defined as the establishment of a benthic community that is statistically indistinguishable from surrounding non-impacted sites, assuming the surrounding sites were similar to the dredged area prior to dredging (Cooper et al. 2005).

The definition of physical regeneration is therefore dependant on the nature of the particular investigation: If we are interested in sediment budgets and the alteration of sediment transport patterns than a dredging site might be considered to be physically regenerated when the sediment balance is zero. This is a very robust and quantitative definition, however, it does not account for alterations in the quality of sediments, e.g. grain-size, sorting, compaction, etc., which have a profound influence on the benthic communities they support. On the other hand, if we are investigating the physical regeneration as a major pre-requisite for the biological recovery of the seabed and the restoration of benthic biotopes, than it might be sufficient that the small-scale topography induced by dredging is leveled out and the physical properties of the seabed sediments are comparable to the status prior to dredging even if the sediment balance is still (slightly) negative. Such investigations can be best performed with high-resolution side-scan sonar, while the determination of the sediment budget implies the utilization of multi-beam echo sounders.

CONCLUSION

The definition of the term “physical regeneration” is dependant on the studied subject and the nature of the particular investigation. In this contribution, definitions are given for coastal engineering purposes and investigations dealing with the recovery of benthic biotopes after dredging. Other definitions are likely to emerge, depending on the aim of the study. It is therefore recommended that for every study the term “physical regeneration” should be clarified before using it.

ACKNOWLEDGEMENTS

The fieldwork was assisted by the Captain and crew of R/V Littorina of the Leibniz Institute of Marine Science at Kiel University. My colleagues Dave Limpenny and Keith

Cooper (both Cefas, Burnham) critically reviewed the draft document. Jochen Krause (German Federal Agency of Nature Conservation, Isle of Vilm) helped me to understand the biological aspects of recovery. I would like to thank all persons and institutions mentioned above.

REFERENCES

Church, J. A., Gregory, J. M., Huybrechts, P., Kuhn, M., Lambeck, K., Nhuan, M. T., Qin, D., and Woodworth, P. L. (2001). "Changes in sea level." Climate change 2001: the scientific basis. Contribution of Working Group 1 to the Third Assessment Report of the Intergovernmental Panel on Climate Change, J. T. Houghton, Y. Ding, D. J. Griggs, M. Noguer, P. J. van der Linden, X. Dai, K. Maskell, and C. A. Johnson, eds., Cambridge University Press, Cambridge, New York, 639-693.

Cooper, K. M., Eggleton, J. D., Vize, S. J., Vanstaen, K., Smith, R., Boyd, S., Ware, S., Morris, C. D., Curtis, M., Limpenny, D. S., and Meadows, W. J. (2005). "Assessment of the Rehabilitation of the seabed following marine aggregate extraction - part II." Science Series Technical Report, Cefas Lowestoft, 130, 82p.

Davis, R. A., and Hayes, M. O. (1984). "What is a wave-dominated coast?" *Marine Geology*, 60, 313-329.

Demir, H., Otay, E. N., Work, P. A., and Börekci, O. S. "Effects of dredge holes on the shoreline change in the Black Sea." *Proceedings Coastal Sediments '03, CD-ROM Published by East Meets West Productions*, Corpus Christi, TX ISBN-981-238-422-7, 14p.

Dette, H.-H., Raudkivi, A. J., and Oumeraci, H. (2001). "Morphologische Änderungen des Unterwasserstrandes an der Westküste des Fischlandes." *Die Küste*, 64, 201-234.

Diesing, M., Kubicki, A., Winter, C., and Schwarzer, K. (2006). "Decadal scale stability of sorted bedforms, German Bight, southeastern North Sea." *Continental Shelf Research*, 26(8), 902-916.

ICES. (2001). *Effects of extraction of marine sediments on the marine ecosystem*, ICES Cooperative Research Report, 247, 80p.

Krause, J. C. (2002). "The effects of marine sediment extraction on sensitive macrozoobenthic populations in the southern Baltic Sea," Ph.D. Thesis Universität Rostock, Rostock.

Krause, J. C., Diesing, M., and Arlt, G. (in review). "The physical and biological impact of sand extraction: a case study of a dredging site in the western Baltic Sea." *Journal of Coastal Research*.

Kubicki, A., and Diesing, M. (2006). "Can old analogue sidescan sonar data still be useful? An example of a sonograph mosaic geo-coded by the DECCA navigation system." *Continental Shelf Research*, 26(16), 1858-1867.

Tauber, F., and Lemke, W. (1995). "Map of sediment distribution in the western Baltic Sea (1:100,000), Sheet "Darß"." *Deutsche Hydrographische Zeitschrift*, 47(3), 171-178.

PERFORMANCE OF BEACH FILL AND NEARSHORE BREAKWATERS AT EAST OCEAN VIEW BEACH, NORFOLK, VA

Peter Elkan[1], Laurel Krynock[2], Nicole Vanderbeke[3]
James White[4], Lee Rosenberg[5]

1. Moffatt & Nichol, 1616 East Millbrook Rd, Suite 160, Raleigh, NC 27609, USA pelkan@moffattnichol.com.
2. Moffatt & Nichol, 1616 East Millbrook Rd, Suite 160, Raleigh, NC 27609, USA. lkrynock@moffattnichol.com.
3. Moffatt & Nichol, 1616 East Millbrook Rd, Suite 160, Raleigh, NC 27609, USA. nvanderbeke@moffattnichol.com.
4. City of Norfolk, 810 Union Street, 7th Floor, Norfolk, VA 23510, USA. james.d.white@norfolk.gov.
5. City of Norfolk, 810 Union Street, 7th Floor, Norfolk, VA 23510, USA. lee.rosenberg@norfolk.gov

Abstract: Over the past decade, the City of Norfolk, USA has financed design and construction of multiple nearshore breakwater fields and numerous beach fill projects. In 2005, an assessment of historical shoreline conditions was performed to evaluate the need for an extension of an existing breakwater field in conjunction with periodic nourishment. Based on the shoreline assessment, it was recommended that the breakwater field be extended.

Three additional breakwaters at East Ocean View were designed and constructed in June 2006. Since construction, salients have formed under the local wave climate and have been maintained since construction. Periodic monitoring surveys are used to evaluate shoreline response in the vicinity of the structures and along East Ocean View beach. Monitoring will serve as the basis of design guidelines for future detached breakwater and fill placement design.

INTRODUCTION

Detached breakwaters have been used in low energy environments to increase the longevity of beach nourishment at several sites within the Chesapeake Bay. Over the past decade, the City of Norfolk, Virginia, USA has financed design and construction of multiple nearshore breakwater fields and numerous beach fill projects.

The City of Norfolk's shoreline is located on the Chesapeake Bay. The shoreline extends approximately 7.3 miles, from Little Creek Inlet to Willoughby Spit (Figure 1). East Ocean View Beach section of the Norfolk shoreline extends from Little Creek approximately 5300 feet northwest towards Willoughby Spit.

East Ocean View Beach has historically experienced long-term shoreline recession since stabilization of the inlet at Little Creek in 1929. In the past 10 years, northeast storms (noreasters) and hurricanes have significantly impacted this shoreline, resulting in erosion and loss of the frontal dune system, increasing the risk of damage to beachfront properties. The East Ocean View Beach area is experiencing residential and commercial development. It has become an increasing concern to maintaining adequate protection of existing and proposed structures and improving the quality of the shoreline.

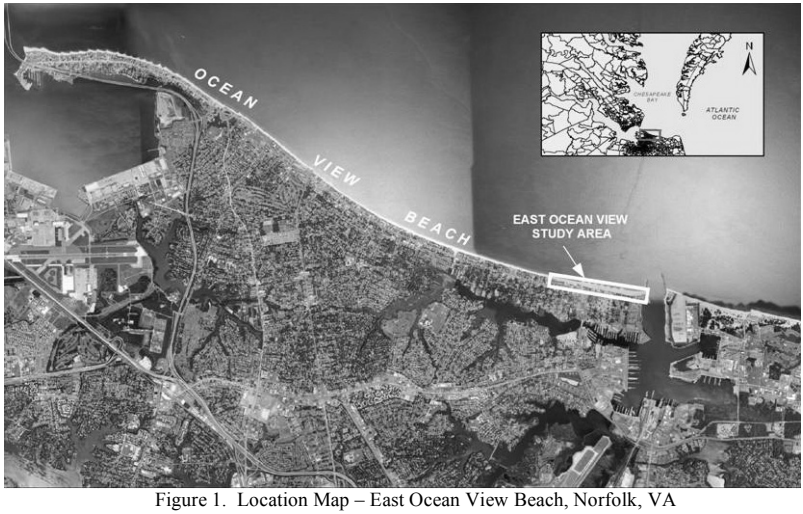

Figure 1. Location Map – East Ocean View Beach, Norfolk, VA

In an effort to mitigate erosion along the East Ocean View Beach shoreline, numerous beach nourishment projects have been undertaken during the past fifty years (1953, 1960, 1984, 1989, and 2003). The source, quality and performance of the sand fill material have varied. In addition to the beach nourishment efforts, concrete rubble has been placed by the City as an emergency measure in an effort to stabilize the shoreline at sites with severe erosion.

A study conducted in 1995 for the City of Norfolk by Andrews Miller & Assoc. (1993), designated the shoreline along East Ocean from 17th Street to the west jetty at Little Creek inlet as a critically eroding area and recommended construction of a nearshore breakwater field. In an effort to increase the longevity of the sand fill, seven nearshore breakwaters along East View shoreline were constructed in August 2000 and November 2001. A beach nourishment project was subsequently completed in December 2003.

In 2005, an assessment of historical shoreline conditions was performed to evaluate the need for an extension of the existing breakwater field in conjunction with periodic nourishment. Based on the historical assessment, it was recommended that the breakwater field be extended.

Three additional breakwaters at East Ocean View were designed and constructed to meet project objectives. Project construction of the new breakwaters was completed in January 2006. Periodic monitoring surveys were used to evaluate shoreline response in the vicinity of the structures and along Ocean View beach.

The objectives of this paper are to: (a) summarize the historical shoreline analysis performed in 2005, (b) present an overview of the breakwater design and (c) document shoreline response along East Ocean View.

HISTORICAL SHORELINE ASSESSMENT

An evaluation of shoreline change within the project area was performed using historical shoreline data available from 1929 to 2004 and recent beach and nearshore profiles surveyed in 2003 and 2005.

Shoreline Change 1929 to 2004

Shoreline data was derived from a combination of sources. Several data sets were compiled as part of the shoreline analysis completed for the City of Norfolk (Beach Consultants, January 2004). Shorelines were digitized and placed in an AutoCAD format. A baseline for measuring shoreline positions was digitized approximately along Ocean View Avenue at East Ocean View Beach. Transects running perpendicular to the baseline were placed every 180 feet across the shoreline. The distance from the baseline to the shoreline was measured along each transect. In the event that digital aerial photography was not georectified, the hard-copy aerial photographs were scanned and georeferenced using ArcGIS software tools and other available georeferenced images for the study area.

Shoreline change is estimated for three distinct reaches (Figure 2):

(1) Western portion of the study area (Station 50+35 to 37+33)
(2) Nearshore breakwater field – (Breakwaters #1 through 7) which were constructed in August 2000 and November 2001 (Station 12+55 to 37+33)
(3) Planned nearshore breakwater zone (Breakwaters #8, 9, 10) (Station 0 to 12+55)

Table 1 summarizes the historical shoreline change within East Ocean View project area from 1929 to 2004. Table 2 identifies the engineering activity along the East Ocean View Shoreline since stabilization at Little Creek Inlet.

From 1929 to 1942, Reaches 2 and 3 experienced a shoreline erosion rate of 9 to 10 feet/year. Shoreline instability within the project area may in part be attributable to stabilization of the inlet. Net longshore transport of sediment in the project area is from east to the west. Therefore, the inlet may act as a sediment sink, interrupting the natural bypassing of sediment to Reach 1 at East Ocean View.

Table 1. Average Historical Shoreline Change Statistics (ft) at East Ocean View, Norfolk, VA

Location	Stat	1929-1942	1942-1970	1970-1980	1980-1995	1995-1999	1999-2002	2002-2004
Reach 1	average	-3.0	-0.1	-2.8	0.1	-9.2	-12.6	43.7
Reach 2	average	-8.9	2.2	-4.5	-0.3	-9.9	0.0	78.8
Reach 3	average	-10.8	3.9	-4.6	-0.9	-9.7	-7.0	81.2
Total	Min	-0.3	4.6	1.3	0.8	-0.8	25.1	127.5
	Max	-11.8	-1.9	-9.0	-1.8	-23.5	-28.7	12.6
	average	-6.9	1.4	-3.9	-0.2	-9.7	-4.3	66.5

Table 2. Engineering Activity at East Ocean View

Date	Project Type
1926-1928	Jetty Construction at Little Creek Inlet
1953	Beach Nourishment
1953	Beach Nourishment
1960	Beach Nourishment
1982	Beach Nourishment
1984	Beach Nourishment
1989	Beach Nourishment
Aug-00	Breakwater Construction (2,3,4)
Nov-01	Breakwater Construction (1,5,6,7)
Oct-03	Beach Nourishment
Nov-03	Beach Nourishment
Jan-06	Breakwater Construction - 8,9,10

In an effort to mitigate erosion, beneficial use of dredged material was initiated at Ocean View as early as 1953. During the past 53 years (from 1953 to present) a total of 3.6 million cubic yards (Mcy) of sand has been placed on the East Ocean View shoreline. The placement of sand on the beach accounts for the shoreline advancement during the period from 1942 to 1970.

There are few periods within the past 50 years during which the shoreline change rate was not directly influenced by nourishment. The periods from 1929 to 1942, 1970 to 1980 and 1995 to 1999 provide an indication of shoreline change, without direct sand placement. The average rates of shoreline change during 1970 to 1980 and 1995 to 1999, within Reach 3, were -4.6 ft/year and -9.7 ft/year respectively. During the period from 1995 to 1999 (prior to breakwater construction), the rate of erosion along the shoreline at Reach 2 was estimated to be -9.9 ft/year.

Nearshore Breakwaters & Beach Fill

Most recent efforts to stabilize the shoreline at East Ocean View include construction of seven nearshore breakwaters (Reach 2) and placement of beach fill (Reach 1,2,3) undertaken in December of 2003 (Figure 2). The nearshore breakwaters were constructed during August 2000 and November 2001. Each structure extends an average length (Ls) of 240 feet, with a distance between breakwaters (Lg) of 120 feet.

The December 2003 beach nourishment project consisted of a placement of a total of 366,000 cy of material along East Ocean View shoreline, an average of approximately 66 cy/linear foot. The median sediment grain size by profile ranged from 0.4 to 0.5 mm (Moffatt & Nichol, 2004).

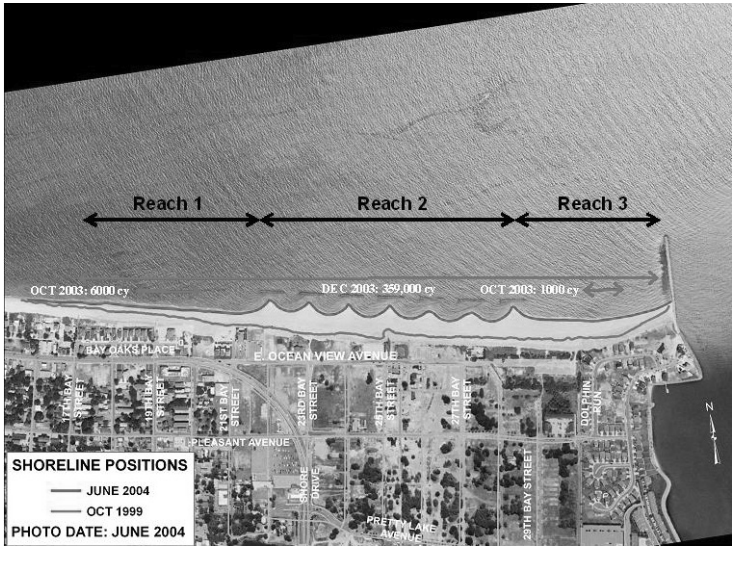

Figure 2. Shoreline Response to Nearshore Breakwater Construction & Beach Fill

Comparison of the post construction December 2003 to the September 2005 beach fill profiles was performed. Table 3 summarizes the shoreline change by Reach. Figures 3 and 4 illustrate the shoreline response and volumetric change to a depth of -10 ft NAVD.

Table 3. Average Shoreline Change from December 2003 to September 2005

Location	Shoreline Change (ft)	Volumetric Change (cy/ft)	Total Volumetric Change (cy)
Reach 1	-60.6	-28.8	-55,646
Reach 2	-24	-8.1	-20,364
Reach 3	-72	-17.1	-19,609

Shoreline response at East Ocean View is influenced by a multitude of factors including: (a) magnitude and direction of wave energy, (b) sediment characteristics of the beach fill material, (c) beach fill placement template, (d) presence of hard structures including nearshore breakwaters and west jetty at Little Creek Inlet and (e) relative location within the regional littoral cell.

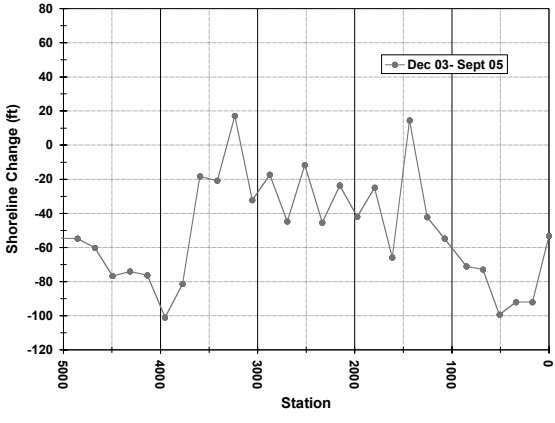

Figure 3. Shoreline Change December 2003 to September 2005

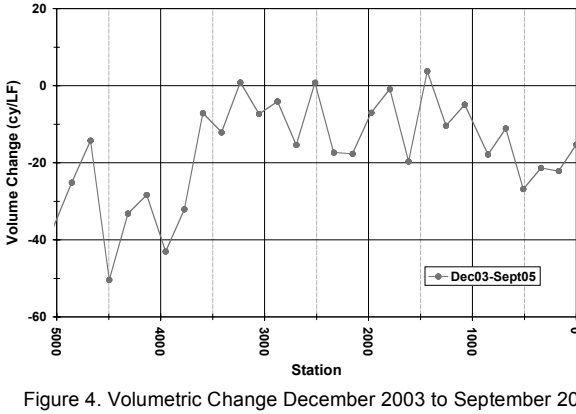

Figure 4. Volumetric Change December 2003 to September 2005

Since construction of the beach fill project in 2003, salients have formed in the landward of the nearshore breakwaters (Figure 3). During the period from December 2003 to September 2005, within Reach 2 there was an average shoreline recession of -24 ft, eroding at an average rate of -8 cubic yards/linear foot (cy/lf). Comparing the rate of shoreline change to the adjacent areas (Reaches 1 and 3), the breakwaters appear to have

been effective at reducing local erosion of the shoreline. Performance of the breakwaters indirectly has an effect on the rate of erosion at the downdrift beach; the downdrift shoreline (Reach 1) had eroded at a rate of -28.8 cy/lf.

During the 21 month period, the average shoreline recession over Reach 3 was -72 ft, eroding at -17 cy/lf. The cumulative erosion along Reach 3 was approximately 19,600 cy. Although, adjustment of the shoreline was anticipated after placement of beach fill, the shoreline is exhibiting an accelerated rate of erosion compared to Reach 2. Given the rate of erosion and risk of property damage along Reach 3, the City elected to pursue extension of the breakwater field in this region

NEASHORE BREAKWATER DESIGN

Breakwaters are designed to reduce wave energy by protecting the shoreline from wave attack and transforming incoming waves. When a wave interacts with a permeable structure, a portion of the energy is (a) dissipated on the structure, (b) reflected (depending on the geometry of the structure), (c) diffracted through the gaps, (d) transmitted through the structure and (e) transmitted over the structure (depending on the elevation of the structure).

Design considerations for the extension of the nearshore breakwaters at East Ocean View are discussed below.

Planform Geometry

Detached breakwaters have been used in low energy environments to increase the longevity of beach nourishment at several sites within the Chesapeake Bay, Gulf of Mexico and in the Great Lakes. Although detailed performance assessments are not available, general observations regarding the shoreline response have been used to develop guidelines.

Empirical relationships have been developed that predict the nearshore response based on three dimensionless ratios, Y/ds, Ls/Lg and Ls/Y. Where: (Y) Distance of breakwater from nourished shoreline; (Ls) Length of breakwater structure; (Lg) Gap distance between adjacent breakwater segments; (Ds) Depth (average) at breakwater structure below mean water level.

The ratio Ls/Y is most commonly used as an indicator of shoreline response. Several references cite tombolo formation under conditions where Ls/Y is greater than 1.5 (USACE, draft 2002). Ahrens and Cox (1990) assessment of nearshore breakwaters in the Chesapeake Bay documents salient formation at L_S/Y of 1.5 and subdued salient formation where Ls/Y = 0.8 to 1.5.

Salients are most likely to form in environments where breakwaters are sufficiently offshore, short relative to incident wavelength, and transmissible either by being low

crested or having large gaps between structures.

Existing breakwaters at Ocean View beach serve as a design analog. The seven existing breakwaters along Ocean View from 21st Bay Street to Little Creek Inlet extend an average length (Ls) of 240 feet, with a distance between breakwaters (Lg) of approximately 120 feet. Distance from the pre-nourished shoreline to breakwater (Y) varies from approximately 180 to 220 feet. The resulting Ls/Y is estimated to be 1.09 to 1.33, within the limits identified for salient formation. The ratio Ls/Lg for the existing breakwaters is 2.0 with the ratio Y/ds ranging from 23 to 32.

Figure 5 depicts the response of the shoreline landward of the existing structures. Salients have formed under the local wave climate and have been maintained since construction of the nourishment project in 2003. Based on initial observations since construction, all else being equal, the ratio of Ls/Y used for the initial breakwater design is appropriate to create salient formation for the local conditions.



Figure 5. Salient formation along existing breakwaters at East Ocean View (Photo taken in September 2005)

Three additional breakwaters at East Ocean View were designed with Ls = 260 ft and Lg =130 ft (Ls/Lg = 2). Although the jetties at Little Creek Inlet create a shadowing effect that causes reduction in incident wave energy along the shoreline, the proposed additional breakwaters were conservatively sited to within a 150 ft distance of the west jetty. The orientation of the breakwater closest to the Little Creek Inlet is set approximately parallel to the 6 ft contour, normal to predominant incident wave energy. Based on the pre-nourishment surveys, the ratio Ls/Y was estimated to be 1.2 to 1.3 and Yavg/ds = 33 to 37.

Physical Design Parameters

Design procedures were employed to evaluate the integrity of existing breakwaters and

design additional breakwaters. Methods were used to evaluate the cross-sectional geometry of the breakwater, sizing the armor stone and the performance of the breakwaters in terms of wave transmission.

Table 4 identifies the tidal range at the NOAA gage data at the Chesapeake Bridge.

Table 4. Water levels at the Chesapeake Bridge - NOAA gage 8638863

Datum/Event	ft NAVD	m NAVD
Mean High High Water (MHHW)	1.29	0.39
Mean High Water (MHW)	0.98	0.30
Mean Low Water (MLW)	-1.57	-0.48
Mean Low Low Water (MLLW)	-1.61	-0.49
Historical High occurring 2/5/98	4.97	1.51
Historical Low occurring 1/11/78	-4.54	-1.38

A range of storm surge and significant wave height design conditions were considered. Design storm surge elevations were characterized based on available data and prior investigations by the Virginia Institute of Marine Sciences (VIMS) in Boon et. al. (1978). Breakwaters were designed for a range of surge elevations up to 4 ft NAVD (approximately a 10-year recurrence interval event) and a design breaking wave height under a maximum surge of 7.5 feet.

General guidelines for the sizing of armor stone of nearshore breakwaters do not exist. Methods developed for sizing stone of conventional offshore breakwaters was applied, with consideration of the basis of empirical methods. Cross-section geometry and stone size were evaluated using empirical methods identified in the CEM. Selection of an appropriate armor stone for design storm conditions was performed using Hudson's formula and Van De Meer's approach. The crest elevation of the breakwaters was established at +2 ft NAVD, approximately 1 ft above MHW (+0.98 ft NAVD).

Figure 6 illustrates the design cross-section for the nearshore breakwaters.

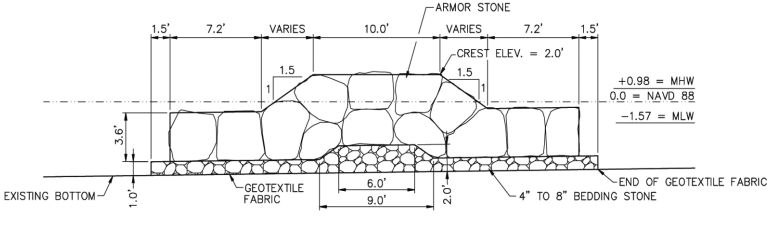

Figure 6. Nearshore breakwater design cross-section

An empirical method developed by Ahrens (2001) was employed for estimating the total

wave transmission for nearshore breakwaters. The breakwater was determined effective in reducing the transmission of wave energy during frequent storm conditions. With the surge elevation at 0.0 ft NAVD and wave heights ranging from 2 ft to 4 ft, the wave height was estimated to be reduced by an average of 23%. During low frequency events with surge elevation at 3.8 ft NAVD and wave heights ranging from 5 to 6 ft, the incident wave energy was estimated to be reduced by 10%.

MONITORING NEARSHORE BREAKWATER FIELD AND BEACH FILL (SEPTEMBER 2005 TO OCTOBER 2006)

Wave Climate

As identified above, shoreline response at East Ocean View is directly influenced by magnitude and direction of wave energy. In March 2006 a wave gage was installed as part of the City of Norfolk comprehensive shoreline management program. The wave gage was placed in 23 feet of water approximately 6400 ft offshore of the beach at Norfolk; it is located approximately 2000 ft west of the project area. Summary statistics for the period from March 2006 through August 2006 are identified in Table 5.

Table 5. Summary statistics for the period from March 2006 to August 2006

Wave Statistic	Mar	Apr	May	Jun	Jul	Aug
Average Significant Wave Height, H_s (ft)	1.3	1.3	1.2	1.0	0.8	1.0
Average Wave Period, T_m (s)	2.5	2.6	2.5	2.5	2.4	2.4
Average Peak Wave Period, T_p (s)	5	5.4	4.8	5.9	5.6	5
Max Observed Significant Wave (ft)	3.9	4.6	5.2	4.4	2.2	4.4
Maximum Observed Height, H_{max} (ft)	6.2	8.3	8.4	7.3	3.8	6.6

The largest wave heights recorded were during tropical storm Ernesto. During this storm on September 1, 2006, maximum wave heights of 13 feet were recorded and significant wave heights of up to 7.7 feet. Based on the NOAA gage 8638160, the maximum recorded surge elevation was +3.87 ft NAVD, approximately 2.9 ft above MHW. Figure 7 illustrates the growth in wave height during the Ernesto.

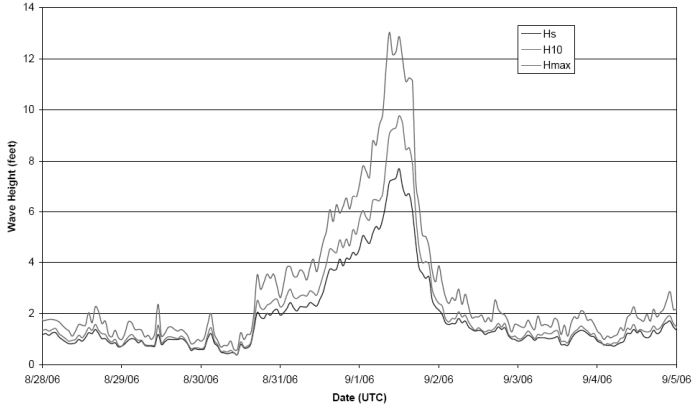

Figure 7. Wave Height recorded during Tropical Storm Ernesto

Performance of Breakwater Field & Beach Fill

Project construction of the three additional breakwaters was completed in January 2006. Periodic monitoring surveys (September 2005, March 2006 and October 2006) were used to evaluate shoreline response in the vicinity of the structures and along Ocean View beach shoreline. Figure 8 illustrates the post-construction monitoring conditions and shoreline change between 2004 and 2006.

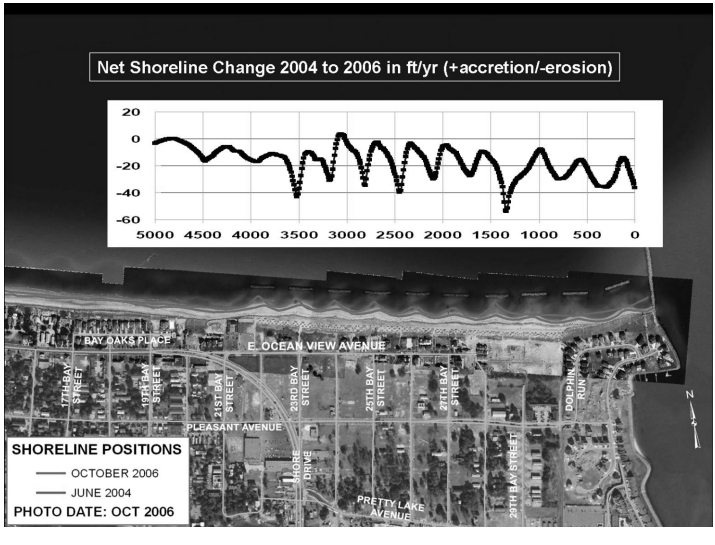

Figure 8. Shoreline Change from June 2004 to October 2006

During the period from June 2004 to October 2006 the majority of shoreline experienced recession (Figure 8). Salients formed behind the constructed nearshore breakwaters within Reach 3; along the existing breakwater field salients are less pronounced than they were during the prior shoreline characterization in June 2004.

A summary of shoreline change based on beach and nearshore profiles is compiled in Tables 6, 7 and 8.

Table 6. Average Shoreline Change at MHW (ft)

Location	Sept 05-Oct 06 (ft)	March 06-Oct 06 (ft)
Reach 1	-9.4	-4.6
Reach 2	-20.5	-27.0
Reach 3	-20.0	-24.0
Total	-16.8	-19.0

Table 7. Average Volumetric Change Rate March 2006 - October 2006

Location	Above 0 ft NAVD (cy/lf)	Above -15 ft NAVD (cy/lf)
Reach 1	-4.57	-9.55
Reach 2	-3.47	-4.83
Reach 3	-3.18	-3.28
Total	-3.76	-6.00

Table 8. Cumulative Volumetric Change March 2006 - October 2006 (cy)

Location	Above 0 ft NAVD	Above -15 ft NAVD
Reach 1	-8,169	-18,100
Reach 2	-8,739	-12,157
Reach 3	-2,847	-2,874
Total	-19,755	-33,131

During the period from September 2005 to March 2006 there was an average accretion of approximately 2.9 cy/lf/period along Reach 1; cumulative volume change over this reach was approximately 8,000 cy of material. From September 2005 to March 2006, the average volumetric change (above -15 ft NAVD) for Reach 2 and 3 was estimated to be +1 cy/lf/period and -1 cy/lf/period, respectively.

The Reach 1 shoreline at MHW, during the period from March 2006 to October 2006, realized an average rate of recession of less than 5 ft/year. Although there was little change in the shoreline at MHW, the total erosion (above -15 ft NAVD) was -9.6 cy/lf. This reach experienced an average erosion rate of -4.6 cy/lf above 0.0 ft NAVD from March 2006 to October 2006 (Figure 9).

Reaches 2 and 3 experienced similar trends during the monitoring period from March 2006 to October 2006. The average shoreline recession at MHW along Reaches 2 and 3

was estimated to be -24 ft/year and -27 ft/year. Average erosion (above -15 ft NAVD) was estimated to be -4.8 cy/lf and -3.3 cy/lf for Reach 2 and 3, respectively. As illustrated in Figure 9, the majority of the net erosion along both Reaches 2 and 3 appeared to be above 0.0 ft NAVD. The portion of erosion occurring above 0.0 ft NAVD is estimated to account for greater than 70% of the total erosion occurring at Reaches 2 and approximately 95% of the net total erosion occurring at Reach 3; this is most likely attributable to Ernesto.

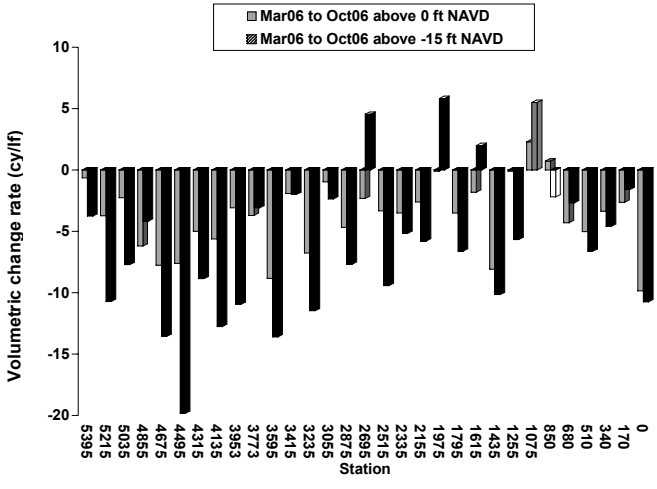

Figure 9. Volumetric Change March 2006 to October 2006 in cy/lf/period

Figure 10 illustrates the cross-section profile change that occurred from December 2003 to October 2006 at the gaps between breakwaters. Station 510 is located in the gap between breakwaters 9 and 10. Erosion of the beach fill material placed in December of 2003 is evident. From March 2006 to October 2006, there was continued erosion of the dune (-5.7 cy/ft/period). Below the MHW water level, the profile experienced accretion at some locations with a net change of -1.6 cy/lf/period.

An example of a cross-section adjacent to a breakwater is illustrated in Figure 11. Station 340 is located at the midpoint of the eastern most breakwater (adjacent to the west jetty at Little Creek Inlet). From March 2006 to October 2006, the shoreline was relatively stable; the salient feature is evident in the cross-section surveys.

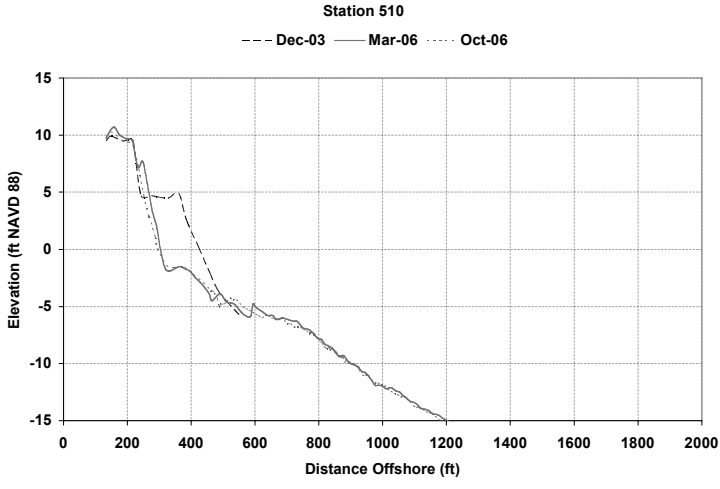

Figure 10. Monitoring beach profiles at Station 510

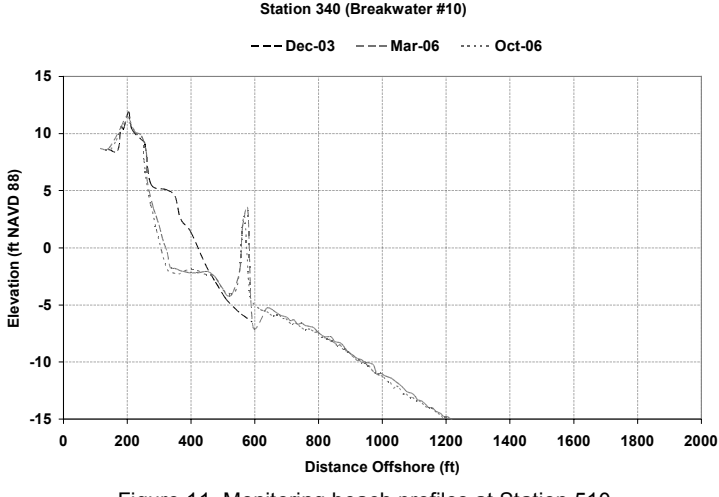

Figure 11. Monitoring beach profiles at Station 510

CONCLUSION

During the monitoring period, the East Ocean View shoreline experienced a maximum storm surge of (+3.9 ft NAVD) and significant wave height (7.7 feet). Although the shoreline realized extensive dune and berm erosion at several locations, there was no

evidence of structural damage to the breakwaters. The shoreline landward of the breakwater field has responded in plan form as designed. Salients have formed in landward of the constructed breakwaters; no tombolos have been established.

The nearshore breakwater field has reduced the relative rate of beach erosion along the landward shoreline and indirectly affected the downdrift beaches. Based on monitoring from December 2003 to September 2005, of the approximately 66 cy/lf of beach fill, an average of 8 cy/lf of material eroded landward of the breakwater field during the initial 21 months. The downdrift shoreline eroded at an average rate of -28.8 cy/lf.

Trends in shoreline change from March 2006 to October 2006, provide additional indication of the effectiveness of the nearshore breakwaters. The average berm and dune erosion landward of the breakwater field was estimated to be on average approximately 33% less than that calculated for downdrift beaches. The total rate of erosion experienced along the shorefront landward of the breakwater field was approximately 45% of that calculated for the downdrift shoreline.

As part of a comprehensive monitoring program the City of Norfolk plans to continue to collect data including: wave gage measurements, beach and nearshore profiles, and aerial photographs. Additional data will allow for further assessment of the performance of nearshore breakwaters and will aid in the cost effective design and planning.

REFERENCES

Andrews Miller & Associates, Inc. “Beach Management Pan, City of Norfolk Virginia”, January 1993.

Ahrens, J. P., and Cox, J. 1990. "Design and Performance of Reef Breakwaters," Journal of Coastal Research," Vol 6, No.1 pp 61-75

Basco, D.R. “ Chesapeake Bay Shoreline Study: City of Norfolk, Virginia”, Beach Consultants Inc, Norfolk, Virginia, January, 2004.

Boone, J.D. C.S Welch, H.S Chen, R.J. Lunkens, C.S. Fang, and J.M. Zeigler. June 1978.“A Storm Surge Model Study, Volume 1: Storm Surge Height-Frequency. Analysis and Model Prediction for Chesapeake Bay”, Virginia Institute of Marine Science.

Dally, W. R., and Pope, J. 1986. "Detached Breakwaters for Shore Protection," Technical Report CERC-86-1, U.S. Army Engineer Waterways Experiment Station, Vicksburg, MS.

Goda, Y. 2002. “Random Seas and Design of Maritime Structures”.

Moffatt & Nichol, 2004. “East Ocean View Beach Nourishment Project”. Prepared for City of Norfolk.

Moffatt & Nichol, June 2006. Norfolk Wave Climate Monitoring. Prepared for the City of Norfolk. First Deployment Period.

Moffatt & Nichol, October 2006. Norfolk Wave Climate Monitoring. Prepared for the City of Norfolk. Second Deployment Period.

Rosati, J.D. September 1990. "Functional Design of Breakwaters for Shore Protection: Empirical Methods". Miscellaneous Paper CERC-90-15. U.S. Army Engineer Waterways Experiment Station, Vicksburg, MS.

US Army Corps of Engineers. 2002. "Coastal Engineering Manual".

CONVERSION TO SI UNITS

1 foot = 0.3048 m
1 cubic yard = 0.7064 cubic meters

ASSESSING BEACH FILL COMPATIBILITY THROUGH PROJECT PERFORMANCE EVALUATION

Donald K. Stauble[1]

1. U.S. Army Engineer Research and Development Center, Coastal and Hydraulics Laboratory, 3909 Halls Ferry Road, Vicksburg, MS 39180-6199, USA. Donald.K.Stauble@erdc.usace.army.mil.

Abstract: Part of the design processes in beach nourishment projects is to determine the suitability of the borrow material for placement on the native beach. Ideally the sediment would be of similar grain size distribution, shape and color. Often the borrow source is a different environment and therefore a different size distribution and predicting the amount of borrow that will remain on the profile once it is placed is problematic. Case studies on past projects indicate that fill compatibility is complex and not well predicted by using the standard suitability methods. Use of the entire grain size distribution is needed to better predict performance. Borrow material similar to the native sediment will return to a native distribution within one year, while finer or coarser distributions take longer to equilibrate. Coarser borrow material seems to provide a more stable fill. Fill volume is also important along with grain size in project success.

INTRODUCTION

The correct analysis of sediment data is important to the design engineer and regulatory official in obtaining the following information about a beach nourishment project:

1) The suitability of borrow area sand for erosion control projects
2) The volume of sand needed to obtain the desired level of storm protection
3) Assessment of long-term sediment characteristics, fill stability and the timing of renourishment.

Two basic approaches are commonly used that apply grain size parameters to characterize the native (pre-nourished beach) and borrow area sediment: 1) calculation of the overfill ratio and 2) application of the equilibrium beach profile in determining needed fill volumes (CEM 2003). These methods are used in design of almost every

nourishment project to assess fill suitability, but little follow up has been reported on how well these methods have predict actual project performance. Both methods use the basic sediment statistics of mean and sorting to characterize the native beach and borrow area. These simple statistics are limited in characterizing the beach and do not do well in predicting actual behavior of the fill over time. A method that uses the entire grain size distribution is needed to better cover the resorting of borrow material placed on a beach. The evolution of the entire grain size distribution on the case study beaches have shown that the sediment response is complex and further research is needed to come up with a more reliable method to predict fill suitability and renourishment requirements. Long-term monitoring is also needed on select projects to evaluate fill evolution and relate that to project performance. Case Studies are used here to examine actual project sediment behavior from initial beach and borrow area characterization to post-fill long-term redistribution.

SEDIMENT CHARACTERIZATION

Sediment distributions are three dimensional both on the beach and in the borrow area. A good sampling scheme is required to document the variability in both the cross-shore and alongshore direction on the native beach and in the horizontal and vertical limits of the borrow area.

Native Beach

Spatial variations may be present due to variations in the underlying geology, transient morphology (i.e. beach cusps, bar features), influences of shore protection structures (i.e. groins, breakwaters, jetties) and hot spots (areas of increased erosion). Characterization of the native beach can be divided into two interrelated tasks on collection and analysis of: 1) the native beach grain size distribution and 2) the beach profile morphology (Stauble 1991a; 1991b). Beaches are made up of a variety of mineral components and contain a wide range of grain sizes that vary in both the cross-shore and alongshore directions. While the main component of most beach nourishment project sediment is quartz sand, many beaches may contain components such as carbonate material (i.e. shell, coral fragments, aragonite), rock fragments (i.e. volcanic basalts, plagioclase, chert), and heavy minerals. The grain size distribution at any given point on the beach is a function of the energy of the cumulative coastal processes (i.e. wind, waves and currents) and mineralogy of the available sediment. In addition, color, shape and roundness, and sediment bulk density also play a roll in the choice of borrow sediment makeup and aesthetics of beach fill material.

Differences in the cross-shore grain size distribution have been documented on natural beaches, with the coarsest grains found in an area between the backwash/surf interaction zone and the highly turbulent shore break plunge point (Bascom 1959; Zarillo, et al 1985; Stauble 1992). The berm crest area also contains significant coarse material due to runup sediment transport dynamics. Finer, better-sorted material is found in the dune area owing to predominantly wind transport processes. Seaward of the surf zone, sediments become consistently finer and better sorted, at least out to depth of closure. A long-term sediment study of the Ocean City, MD beach fill project (Stauble and Bass

1999) also exhibited this cross-shore sediment distribution. The pattern was found in the native pre-fill beach; within six months after fill placement and in the long-term (ten year) fill resorting. A typical adequate cross-shore sample scheme will collect sediment at the dune base, berm crest, mid tide, low tide terrace (trough) and several samples in the nearshore from bar crest out to closure. A plot of mean grain size versus cross-shore location of all profiles at the Ocean City MD beach fill project shows a consistent distribution of coarsest sediment in the low tide/trough area, with fining in the inshore and offshore direction based on a ten year span of sediment data (Figure 1).

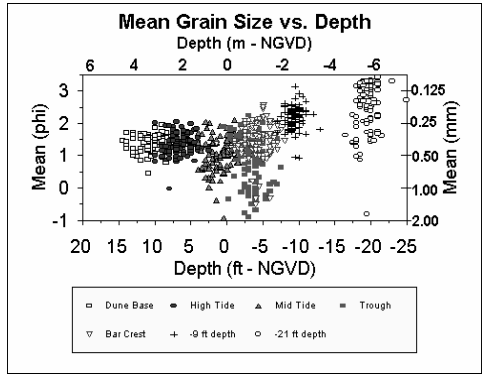

Composite Samples

To reduce variability in the cross-shore grain size distributions, composite samples are usually constructed combining several samples into a new single distribution, where either the sieve classes are mathematically averaged or the samples are mixing together before sieving. Several types of composite samples were examined (Stauble and Hoel 1986) to determine which combination of beach samples eliminated spatial variability and provided the best comparison of actual behavior over time from various beach fill projects. Two basic types of composites were chosen after an examination of various combinations of samples available from each project:

1) The typical method uses a ***profile composite*** of all the samples collected across a profile to approximately the depth of closure. This composite was usually skewed to the finer grain sizes due to the more uniform nearshore samples, which often exhibited a good match to finer borrow material but over time more fill loss was measured on these projects.
2) The ***intertidal composite*** uses samples from the intertidal zone (between mean high water and mean low water). This composite gave the best representation of the beach-fill behavior over time since this is the location of typical fill placement and of subsequent fill reworking on most projects. Intertidal composites were usually coarser by excluding the finer nearshore samples. This resulted in a higher overfill ratio, but long-term project performance was more favorable.

Based on the comparison of composite samples and analysis of project fill behavior over at least one year, the intertidal composite is recommended as it better represent the native beach and provide more accurate input to the overfill calculations. The resulting higher overfill factors required more fill volume to be placed but in general, those projects retained more fill volume within the first year than projects that used the profile composite (Stauble and Hoel 1986).

Borrow Area Samples

Borrow area sediments need to be adequately characterized to determine suitability. To characterize the variation in sediment distribution in the borrow area, several representative surface samples and cores are needed to adequately describe the three-dimensional nature of most borrow sources. Sediment samples are collected from representative sediment layers within each core. *Core composite samples* are made by combining sample data from within each core and *borrow area composite* samples are made by combining sample data from cores collected over the entire borrow area.

Fill material for beach nourishment can come from a variety of sources, such as upland stock piles, inlet ebb and flood shoal mining, navigation channel dredging, sand trap mining or sand bypassing, estuarine sands and nearshore shelf sands (Stauble and Hoel, 1986).. Because the environment of deposition of a borrow area can be different from the beach, variations in the makeup of borrow sands cause design challenges for determining what is stable fill material and what is environmentally suitable for placement.

PROJECT PERFORMANCE EVALUATION

To evaluate how well the borrow material performed; a review of several projects was done to measure the performance of fill sand over time. The overfill factor is defined as the volume of borrow material required to produce a unit volume of stable fill material (CEM 2003). Thus a overfill factor of 2 means that ½ of the borrow material is unstable and twice the design volume of borrow area sediment would have to be placed on the beach to provide the desired protection. A review of the three overfill calculation methods are given in Stauble (2005). A few beach nourishment projects had well designed monitoring programs that collected adequate samples of the native beach, the pre-dredge borrow area and a systematic set of post-fill placement samples ranging from one to up to ten years of project life. Analysis of the sediment grain size data has allowed an assessment of the pre-placement native beach and borrow sediment by applying the overfill and equilibrium profile methods. This process was used to identify suitability of borrow material, based on the existing models. It also allowed for evaluation of how grain distributions of fill material actually behaved over a given periods of project life. Sediment samples and profiles collected on a quarterly, semi-annual and annual bases allow for long term study of fill resorting and change due to seasonal, storm and renourishment cycles. Many beach nourishment projects exhibit hot spots of higher erosion (Stauble and Gravens 2004). The combination of sediment and profile response at hot spots relative to the background project response has provided insight into causes and possible remedial actions. Use of coarser grain size fills and extra fill volume placed specifically in hot spot areas can reduce overall renourishment requirements in the long term life of the project.

To assess how well suitability predictions work on actual projects, four projects are presented to evaluate sediment grain size distributions and volumes retained over at least one year after fill placement. Two of the example projects cover a post placement period

of one year, with one covering an eight year period and one covering a ten year period. The investigation examines the pre-fill native beach, a representative sample of the borrow area and the distribution of the post-fill sediment on the four projects. The percentage of fill volume lost over time was measured from profile change. A comparison of what actually happened to the fill with what the model predicted provided an idea of how the models actually worked.

The Ocean City, New Jersey beach fill project is located on a barrier island along the southern New Jersey coast, where 918,000 cu m was placed along a 3.6 km section of beach south of Great Egg Harbor Inlet in 1982 (Figure 2). Sediment samples from the Ocean City, NJ project consisted of intertidal samples only collected at the high tide (HT), mid tide (MT) and low tide (LT) areas of the profile (Stauble and Hoel 1986). The native-borrow comparison (Figure 3a), shows that both the native and borrow had similar distributions of very well sorted sands with the borrow material having a slightly lower percentage in the 0.177 to 0.125 mm (2.5 to 3.0 phi) range and excess sand in the 0.105 to 0.044 mm (3.25 to 4.5 phi) range. The slightly finer fill material was due to its Great Egg Harbor Inlet flood shoal origin which was placed on the ocean beach by pipeline dredge. The native mean was 0.171 mm (2.55 phi) and a sorting of 0.58 phi as compared to the borrow mean of 0.149 mm (2.75 phi) and sorting of 0.50 phi. Some of this excess fine material was immediately transported offshore during placement by hydraulic dredge. The fill factor was calculated at 1.75. One year later the fill material had returned to a native-like grain size distribution as shown by the grain size distribution curve in Figure 3b. Some fine

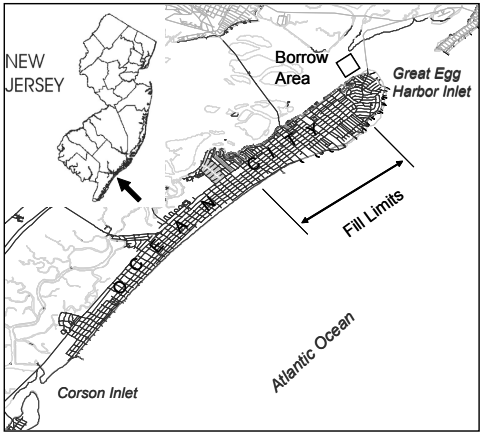

Figure 2. Location of Ocean City NJ project.

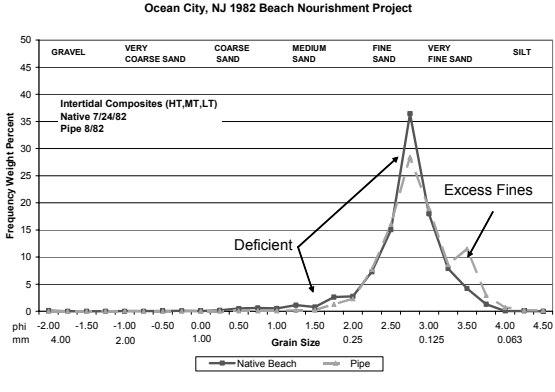

Figure 3a. Pre and Borrow grain size distributions at 1982 Ocean City, NJ. project.

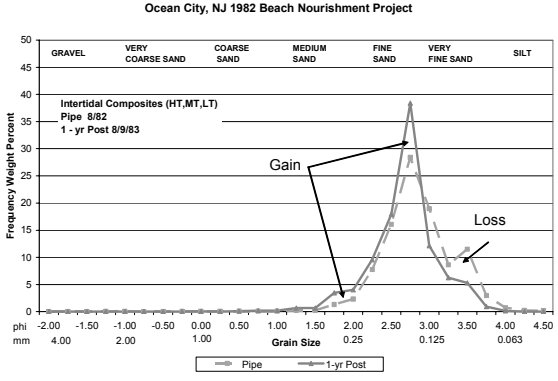

Figure 3b. Borrow and 1-yr post fill grain size distributions at 1982 Ocean City, NJ. project.

material was lost from the intertidal area and a small amount of coarser grain material was deposited on this flat slopping beach. An estimate of 69% of the fine grained fill was remaining after one year but the profiles did not reach to closure (Stauble and Hoel 1986)

The Indialantic/ Melbourne Beach Florida beach nourishment project is located along a 3.38 km stretch of barrier island in the central Atlantic coast of Florida (Figure 4). In 1981, 195,000 cu m of sand was trucked to the site from an upland stockpile created after dredging of the Port Canaveral navigation channel and turning basin. Borrow material for the project contained excess coarse shell material (4.0 to 0.5 mm, -2.0 to 1.0 phi), excess fine-grained material (0.18 to 0.04 mm, 2.5 to 4.5 phi) but was deficient in the 0.5 to 0.18 mm (1.0 to 2.5 phi) medium sand range found on the native beach (Stauble and Hoel 1986). Figure 5a compares the intertidal composite (HT, MT, LT) with the borrow material showing the coarser more poorly sorted borrow as compared with the native sand. The native mean was 0.32 mm (1.62 phi) and exhibited a sorting of 0.72 phi, while the borrow mean was 0.33 mm (1.59 phi) with a sorting of 1.61 phi. Though the mean grain-size was similar, the borrow material was more poorly sorted with a fill factor of 1.38. This example emphasizes the importance of looking at the entire grain size distribution when determining the suitability of a borrow material for a beach, and not just using the mean and sorting values alone. One year later, the fill had mixed with the underlying native sands and had resorted itself back to close to the native distribution with a loss of the fine material and a slight loss of coarse shell hash (Figure 5b). Only 45% of the fill remained within the study area after one year but the profiles did not reach closure depth so volume could not be adequately

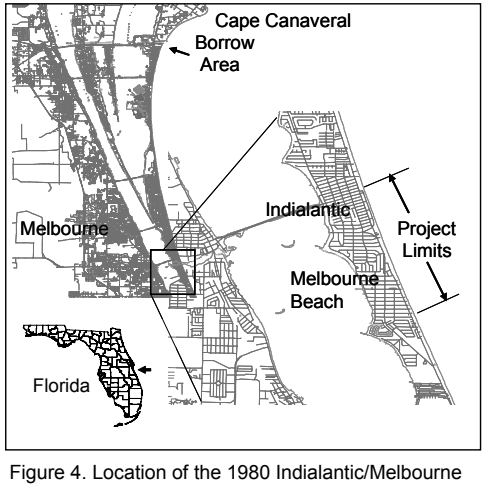

Figure 4. Location of the 1980 Indialantic/Melbourne Beach, FL project.

measured (Stauble and Hoel 1986).

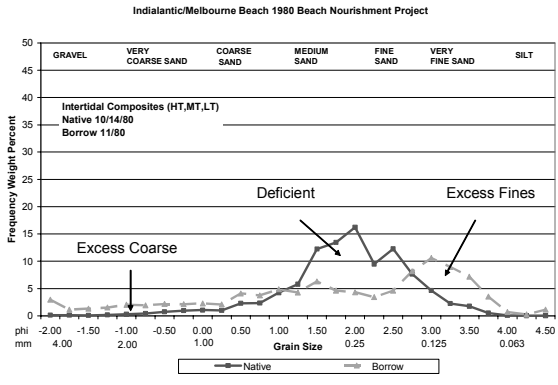

Figure 5a. Native and borrow grain size distributions at the 1980 Indialantic/Melbourne Beach project.

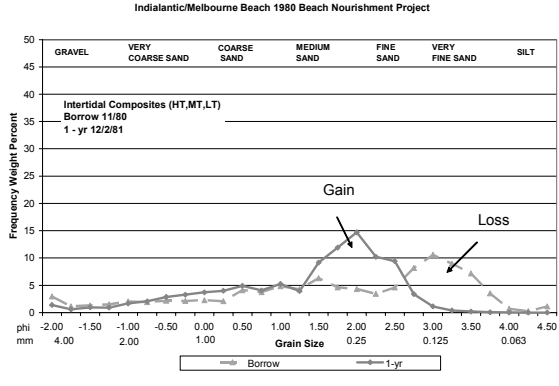

Figure 5b. Borrow and 1-year post fill grain size distributions at the 1980 Indialantic/Melbourne Beach project

Delray Beach, Florida is located on the southeast Florida Atlantic coast. At this particular fill event a volume of 1.25 mill cu m was pumped from an offshore source and placed along 3.05 km of barrier island shoreline (Figure 6). The Delray Beach fill project of 1974 was a example of placement of much finer offshore borrow material on a relatively coarse native beach (a somewhat worst case scenario of incompatibility of borrow material). The offshore borrow source area sediment contained a large excess of fine-grained material 0.25 to 0.044 mm (2.0 to 4.5 phi) and is deficient in the larger sand-sized fractions 2.0 to 0.25 mm (-1.0 to 2.0 phi). The native beach (profile composite only data available) had a mean and sorting of 0.49 mm (1.02 phi) and 0.57 phi respectively. The borrow material had a mean and sorting of 0.21 mm (2.27 phi) and 0.67 phi respectively. This is an extremely large difference in mean grain-size, but the sorting was similar (Figure 7a). The fill factor was greater than 10. Large losses of the fine-grained sediments were seen initially and eight years later the sediment was still finer than the native beach (Figure 7b). This project is an example of the borrow area sediment distribution permanently changing the distribution of the beach after placement with the long-term (8-year) grain size distribution falling in between the original native and finer borrow. Limited profile and sediment data on this project made detailed analysis difficult, but there was some indication of large loss of this fine fill material from the beach, with much of the material residing in the nearshore. A second fill was placed in 1978 and the only available post-

placement data was in 1980. A rough estimate of 26% of fill remaining in the profiles within the 8 year study period suggests that the fine material was not adequate for the project (Stauble and Hoel 1986).

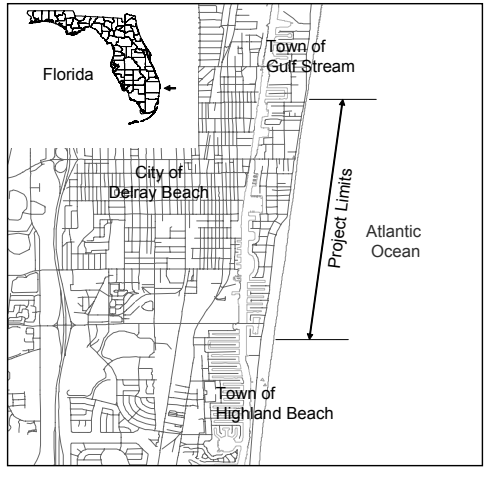

Figure 6. Location of the Delray Beach, FL 1973 Project.

Ocean City, Maryland is located on Fenwick Island, a barrier Island in the middle of the Delaware-Maryland-Virginia (Delmarva) Peninsula (Figure 8). The beach fill project covers 14.7 km of open Atlantic beachfront and was constructed in two phases. Phase I started in 1988 with a State of Maryland sponsored recreational fill that placed 2.0 mill cu m of sand. The Federal Fill added an additional 2.8 mill cu m of sand for hurricane and storm protection in 1989-90. Due to high storm activity the project added an additional 1.2 million cu m in 1992 and 917,520 cu m in 1994. Sand was pumped from several offshore borrow sites over the 5 year period. Native sediment data was collected just prior to Phase I placement in July 1988 and after the project was completely constructed from May 1995 to April 1998, just before the first renourishment (Stauble and Bass 1999). It was difficult to assess the borrow sediment makeup, due to the multiple offshore sites used over the multiple placements from 1988 to 1994. The first sediment collected after project completion in May 1994 was used as a proxy to represent a mixture of all the borrow areas used. This project also had several hot spots where the erosion exceeded the average project wide erosion (most related to shore-attached shoals). As a corollary, there were also cold spots where accretion was above the amount of fill placed, indicating the three-dimensional nature of sediment transport and profile readjustment on this project. Analysis of

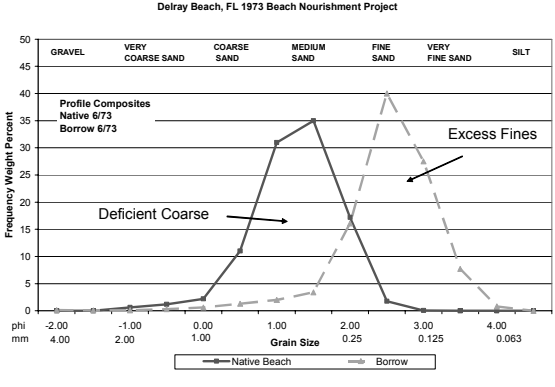

Figure 7a. Native and borrow grain size distributions at the Delray Beach, FL project

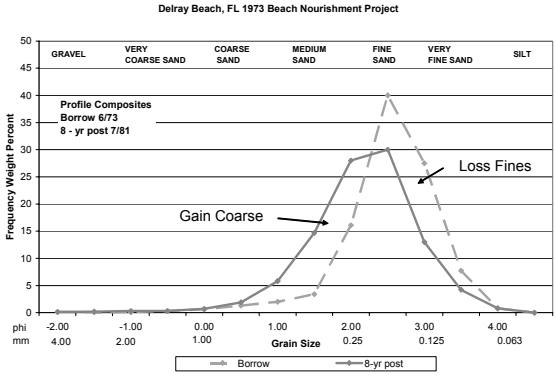

Figure 7b. Borrow and 8-year post fill grain size distributions at Delray Beach, FL.

sediment and profiles provided a picture of project performance. The overfill factor was around 1.0 based on calculations using samples form cores of several offshore borrow areas (James Snyder, USACE Baltimore District, personal communications). The native beach intertidal composite (July 1988), was compared with the May 1994 post-fill proxy of the borrow area mix at a cold spot at 45th Street (Figure 9a) and a hot spot at 81st Street (Figure 9b). This proxy borrow composite of intertidal sand at 45th Street (south) matched up well with the native intertidal composite. Excess coarse material in the 1.41 to 0.35 mm (-0.5 to 1.5 phi) sizes was found at 81st Street (north), due to two different borrow areas used for the north and south sections of fill placement. At 45th Street, the native mean was 0.36 mm (1.48 phi) and sorting of 0.57 phi and the borrow composite had a mean of 0.44 mm (1.18 phi) with a less well sorting of 0.67 phi. At 81st Street, the native intertidal composite had a mean of 0.32 mm (1.65 phi) and a sorting of 0.74 phi, while the proxy borrow had a coarser mean of 0.46 mm (1.11 phi) and a less well sorting of 0.81 phi. A comparison of the proxy borrow composite with the intertidal composite collected in April 1998 (10-year post Phase I fill) indicated that the beach had become coarser at both sites. The long-term intertidal composite mean at 45th Street had a coarser mean of 0.49 mm (1.03 phi) and a better sorting of 0.44 phi (Figure 10a).

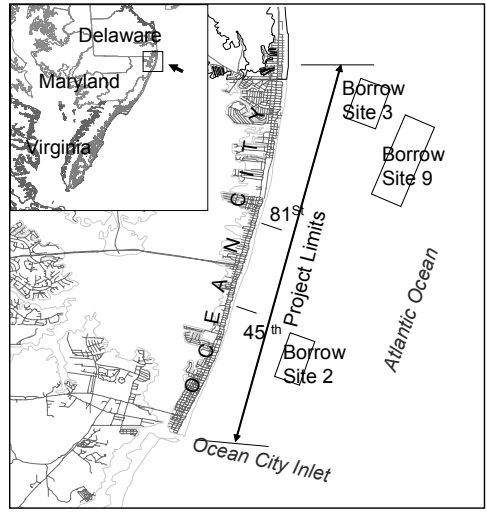

Figure 8. Location of the Ocean City, MD project.

At 81st Street the long-term intertidal composite had a mean of 0.74 mm (0.43 phi) and a poor sorting of

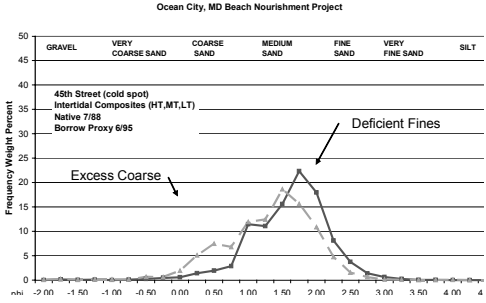

Figure 9a. Native beach and borrow grain size distributions placed at 45th St Ocean City, MD project.

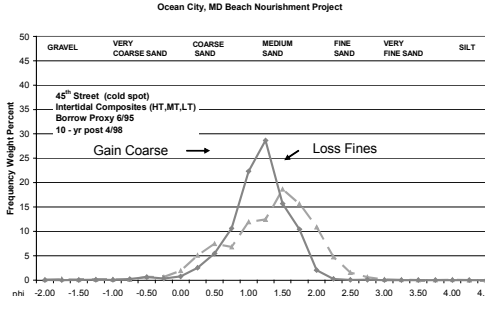

Figure 9b. Borrow and 10-year post fill grain size distributions at 45th Street, Ocean City, MD project.

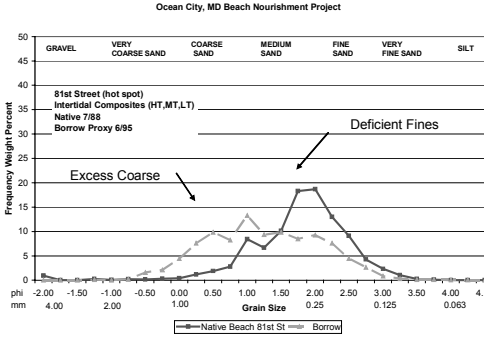

Figure 10a. Native Beach and borrow grain size distributions at 81st Street, Ocean City, MD project

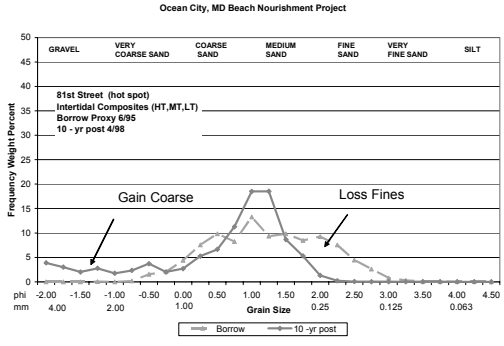

1.03 phi. The hot spot has increased shell hash and pea gravel size material of between 4 and 2 mm (-2 to -1 phi) (Figure 10b). This coarsening may be from winnowing of the fine sand (0.25 to 1.25 m or 2 to 3 phi) over time. This 10 year long-term monitoring through a period of 65 intense storms showed that the volume of sand has remained within the project with the least amount of loss at the cold spots (45th street measures a total loss of around 10 cu m/m or about 89% of fill remains) and the largest loss at the hot spots (81st Street measures a loss of around 148 cu m/m or about 74% of fill remains) (Stauble and Bass 1999). The coarse borrow has provided the protection needed with little over all loss to the project but there is still a three-dimensional resorting on this project.

These four projects provide a verity of borrow to native sediment compatibilities. The Ocean City, NJ project had a borrow sediment that was similar to the native beach with an overfill factor of 1.75. The Indialantic/Melbourne Beach project had a dissimilar borrow which was bi-modal (containing both coarser and finer material than the native beach and had an overfill factor of 1.38. The Delray Beach project had a much finer borrow than the native with an overfill factor greater than 10. The Ocean City MD project had a borrow that was coarser but was about the same distribution as the native and had an overfill factor of around 1.0. The performance of each project (as measured by the percent of fill remaining) did not directly reflect the overfill factor or the grain size distribution change over time.

FILL DENSITY

The amount of fill placed also appears to be important in how well a project performs. Fill density is defined as the amount of fill placed per length of beach. Fill volumes of greater than 175 cu m/m (70 cu yd/ft) of beach were found to provide greater than 70% retention of fill after one year based on review of several projects (Stauble and Hoel 1986). Fill volumes less than the above resulted in projects with high fill losses in the first year. Table 1 shows the fill density of the four projects related to the other characteristics. The fill volume rule seems to hold except for the Delray Beach project. Here, even though the volume was high to compensate for the high overfill factor, the borrow grain size distribution was so fine that the fill was unstable and eroded easily. In project design both overfill factor calculations and design of fill volumes are needed to provide for a successful project. In the Delray Beach case, it appears that if the borrow is drastically different from the native sediment distribution, high overfills did not

Table 1. Project Characteristics

Project	Overfill Factor	Borrow to Native Sed. Distribution	Borrow to Out year Distribution	Fill Remaining %	Fill Density m^3/m
Ocean City, NJ	1.75	Similar match	Return to Native	69 (1 yr)	260
Indialantic/ Melbourne Beach, FL	1.38	Poorer Sorting	Return to Native	45 (1 yr)	75
Delray Beach, FL	> 10	Much Finer	Middle of both dist.	26 (8 yrs)	120 - 300
Ocean City, MD	1.00	Coarser	Coarser	74-89 (10 yrs)	270 - 440

overcompensate for such fine borrow material and changed the long-term sand distribution to become finer than the native.

Q MODE ANALYSIS

Analysis of a suite of sediment samples using just the mean and standard deviation or median values as in the overfill factor method or calculating an equilibrium profile using a single A value for fill profile design is somewhat limiting. As seen in these four case studies, the frequency curve comparisons show how specific grain sizes are either winnowed away or remain on the beach. A newer approach of Q-mode analysis of native and borrow area sediment distributions is suggested for a possible tool to assess suitability. The Q-mode analysis uses the entire sediment distribution instead of the more limiting mean and sorting statistics used in the existing methods and gives a more complete picture of sediment resorting over time. One of the main advantages of Q-mode factor analysis is that the entire grain-size distribution is considered in the analysis, providing a way to differentiate sediments based on the entire distribution. Using an analytical method to determine statistical relationships is more objective because it does not require arbitrary statistical descriptors or a-priori knowledge of the environment and location of samples (Klovan, 1966). A large number of samples can be objectively ordered by shape of a frequency curve to determine interrelationships between beach and borrow area samples. This method has not been used with beach fills, but it has been used to characterize the depositional patterns of a suite of samples at inlets and infer sediment pathways (Stauble and Cialone, 1997) and a study to couple the beach profile evolution, sediment deposition patterns and their resulting grain size distributions with the physical processes active at a native pre- and post-storm beach (Stauble and Cialone, 1996). This method may provide a way to use the entire sediment grain size distribution of a native beach and borrow area to identify fill suitability and some indication of fill behavior. More research is needed to apply this method to beach fill projects to improve suitability and stability determination.

CONCLUSION

Little work has been done on how a beach fill project actually performs relative to the sand suitability and design techniques commonly used. Four projects with good monitoring data have been presented to assess performance. On projects where native and borrow sediment grain size distributions are similar, the fill response over time very similar to the native beach. More uncertainty is introduced in the design process when the native and borrow sediments have different grain size characteristics as is the case in three of the four studies. The overfill factor and equilibrium profile methods have been commonly used to determine borrow area suitability and the volume of fill needed to produce a desired level of shore protection. Each method requires grain size analysis of both native beach and borrow area by standard sieve analysis.

The Overfill Factor Method using only the mean and sorting values of the native and borrows sediment, gives the best estimate of fill material to predict the volume of borrow material needed to produce a unit volume of stable fill material with the same general grain size as the native beach. This method does not take into account any coastal processes or profile changes. The CEM (2003) states that it should be used only to determine if the borrow material will be suitable to be placed on the beach, and give a ballpark value of a multiplier of how much borrow material will be needed to produce a stable fill. Overlaying a frequency curve of the representative native and borrow material will show the overlapping grain sizes and the excess or deficient grain sizes of the borrow material as compared to the native beach. The use of the foreshore composite in calculating the native beach and post-fill borrow sediment grain size data gave the best fit to actual fill project behavior and long-term resorting evaluation.

The CEM (2003) suggests methods for computing fill volumes and the shape of a design profile when the borrow material is of a different grain size distribution than the native beach. Based on the case histories, borrow material finer than the native beach winnowed out of the intertidal area. Some coarse material was also removed, possibly by burial of the coarse material under the finer fill. Post-placement fill distributions take on the characteristics of the native beach except in areas where the borrow sediment is either finer or coarser. The large volume of disparate borrow sands changes the filled beach distribution to that of the borrow material. Fill density also seems to play a part where greater than 175 cu m/m (70 cu yd/ft) of fill placed appears top play an important role in fill stability. More research is needed to improve the suitability determination of a borrow material. New Q-mode analysis suggest using the entire grain size distribution to quantify the suitability and stability of a borrow area as compared with native sediment.

ACKNOWLEDGEMENTS

This paper was based on research conducted under the Quantifying Vulnerabilities in Coastal Flood Damage Reduction work unit in the Technologies and Operational Innovations for Urban Watershed Networks (TOWNS) Program. Additional data was based on work originally funded by the Florida Sea Grant Program. Case study support

provided by the respective USACE Districts. Permission to publish has been granted by the Chief of Engineers.

REFERENCES

Bascom, W. N. (1959). "The relationship between sand size and beach face slope," *American Geophysical Union Transactions*, 32(6), 866-874.

CEM, (2003). *"Coastal Engineering Manual,"* U.S. Army Engineer Research and Development Center, Coastal and Hydraulics Laboratory, Vicksburg, MS.

Klovan, J. E. (1966). "The use of factor analysis in determining depositional environments from grain-size distributions. *Journal of Sedimentary Petrology*, 36 (1), 115-125.

Stauble, D. K. (1992). "Long-Term Profile and Sediment Morphodynamics: FRF Case History," Tech. Rep. CERC-92-7, US Army Engineer Coastal Engineering Research Center, Coastal and Hydraulics Laboratory, Vicksburg, MS.

Stauble, D. K. (1991a). "Recommended Physical Data Collection Program for Beach Nourishment Projects," CETN II-26, U.S. Army Engineer Research and Development Center, Coastal and Hydraulics Laboratory, Vicksburg, MS., 14 p.

Stauble, D. K. (1991b). "Native Beach Assessment Techniques for Beach Fill Design," CETN II-29, U.S. Army Engineer Research and Development Center, Coastal and Hydraulics Laboratory, Vicksburg, MS., 10 p.

Stauble, D. K. (2005). "A review of the role of grain size in beach nourishment projects," 2005 *Proceedings National Conference on Beach Nourishment Technology*, Published by Florida Shore and Beach Preservation Association, Tallahassee FL, http://www.fsbpa.com/2005%20Proceedings.htm

Stauble, D. K. and Hoel, J. (1986). "Guidelines for Beach Restoration Projects, Part II – Engineering," SGR-77, Florida Sea Grant College, Gainesville, FL, 100 p.

Stauble, D. K. and Cialone, M. A. (1996). "Sediment dynamics and profile interactions: DUCK94," *Proceedings of the 25th International Conference on Coastal Engineering*, ASCE, New York, NY, 3921-3934.

Stauble, D. K. and Cialone, M. A. (1997). "The tale of three inlets: sediment management techniques," *Proceedings of the 10th National Conference on Beach Preservation Technology*, FSBPA, Tallahassee, FL, 199-214.

Stauble, D. K. and Bass, G. P. (1999). "Sediment dynamics and profile interactions of a beach nourishment project," *Coastal Sediments '99*, ASCE, Reston VA, 2566-2581.

Stauble, D. K. and Gravens, M.B. (2004). "Identification of and remedial approaches to hot spots," ERDC/CHL CHETN-II-47, U.S. Army Engineer Research and Development Center, Coastal and Hydraulics Laboratory, Vicksburg, MS., 30 p.

Zarillo, G. A., Liu, J. and Tsien, H. S. (1985). "A New Method for Effective Beach-Fill Design" *Coastal Zone '85*, ASCE, 985-1001.

COASTAL STRUCTURE DESIGN FOR BEACH PROTECTION ANDSAND RETENTION: PRACTICAL ASPECTS

John R. Headland[1], Santiago Alfageme[2], Eric Smith[3], Peter Kotulak[4]

1. Moffatt & Nichol, 104 West 40th St., 14th Floor, NY, NY 10018, USA jheadland@moffattnichol.com
2. Moffatt & Nichol, 104 West 40th St., 14th Floor, NY, NY 10018, USA salfagemel@moffattnichol.com
3. Moffatt & Nichol, 2700 Lighthouse Point East, Suite 501, Baltimore, MD, USA esmith@moffattnichol.com
4. Moffatt & Nichol, 2700 Lighthouse Point East, Suite 501, Baltimore, MD, USA. pkotulak@moffattnichol.com

Abstract: After more than a century of development in the field of coastal engineering and science, serious practical questions remain concerning the optimal design of coastal protection works including detached breakwaters, groins and seawalls. This paper reviews current technology applicable to coastal structure design with a critical assessment of existing and needed tools for practical applications involving sediment-structure interaction. This paper considers both functional and structural design issues and addresses the relative merits of these technologies. In this regard, it should be noted that sophisticated modeling technologies, with all of their advantages, have not yet obviated the use of empirical equations and rules of thumb in engineering practice. This is true both for design of structure plan-form arrangements (e.g., number, spacing and length of structures) as well as structure cross-section geometry (e.g., toe design, use of sacrificial toes, merits of armoring landward of a structure crest.)

INTRODUCTION

Coastal structures must be designed with a view towards functional and structural performance. With regard to functional design, the goal is to establish an efficacious structure plan-form which retains sand and considers both the near and far-field impacts of the proposed works recognizing that damaging far-field impacts will normally eliminate structure application as a feasible alternative. Structural design stems directly

from the beach profile bottom elevation that fronts the structure during storm wave attack. This bottom elevation, combined with the water level, establishes depth fronting the structure which, in turn, dictates the maximum wave that can reach the structure. Three technologies commonly bear on functional design: (1) rules of thumb and analytical/empirical equations, (2) physical model tests, and (3) numerical models. This paper discusses the tools available, the limitations of these tools, and the desirability of additional technology (preferably on the basis of full scale model tests and/or evaluation of existing prototype installations) to better determine design conditions. It is emphasized that many successful coastal structure installations have been constructed and serve their purposes well (be it sand retention or shore protection.) The discussions here are not a criticism of coastal engineering practice which, by and large, is diligently exercised using existing technology. The point here is that there are opportunities to further quantify important design issues that presently rely on empirical rules of thumb (e.g. sizing of a sacrificial toe, spacing/geometry of T-groins.) The most expedient means for extending design rules appears to be large- or full scale physical model tests (for seawalls & revetments) and/or monitored field investigations (for sand retention structures). Such investments would be small compared to the savings that could be saved on constructed installations.

DEPENDENCY OF STRUCTURAL DESIGN ON SEDIMENTARY CONDITIONS

Structural design focuses on the development of stable structure cross section for a range of wave, water level, and morphological conditions. Most coastal stabilization structures are subject to depth-limited design wave conditions. The principle design determinant is therefore the bottom depth that fronts the structure toe as these depths dictate the wave heights that reach the structure. The controlling depth normally consists, *a posteriori*, of: (1) the long-term equilibrium shoreline position and profile shape, (2) the general scour /deposition fronting the structure due to storm-induced cross-shore sediment transport and (3) localized scour owing to the complex interaction of waves/currents and sediments at the structure toe. These determinants are illustrated in Figure 1.

The geometry in Figure 1 pertains to design of a buried seawall (i.e., item (5)) at Dam Neck Virginia (Headland, 1992; Basco et al (1998)) but is relevant to any coastal structure placed on an active beach profile subject to breaking waves. Item (1) denotes the "normal" beach profile prior to any long-term or storm-induced erosion. If the shoreline in question is subject to long-term erosion, it is customary to assume that the profile will retreat without a change in geometry as indicated in Item (2). The eroded profile should be translated a distance equal to the product of the average annual long-term shoreline recession rate and period of time equal to the project life (e.g. 20-50 years) factoring in the desirability of using beach nourishment to ameliorate long-term erosion. It should be noted that the translated profile brings deep water closer to the structure toe.

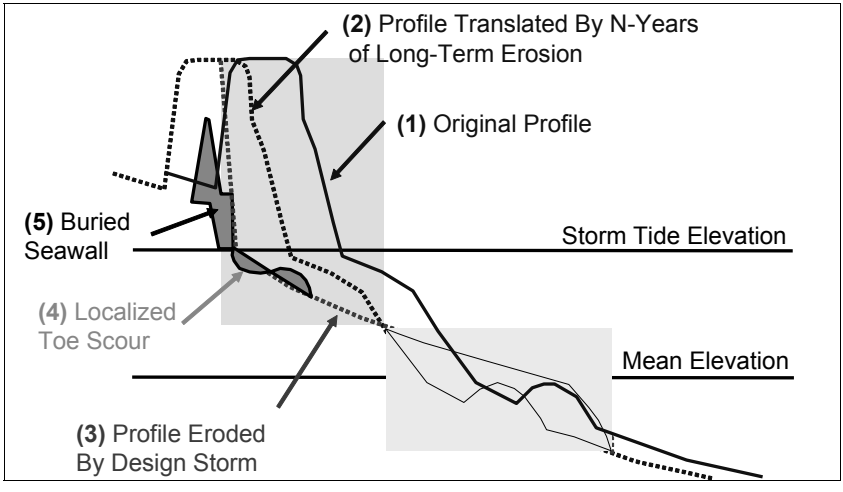

Fig. 1. Definition Sketch for Determining Design Toe Elevation at Foot of a Coastal Structure

Once item (2) geometry has been established, it is necessary to compute the storm-induced erosion profile, Item (3). The authors normally compute this profile using a beach/dune erosion model such as SBEACH. The difficulty here is that most beach/dune erosion models cannot simulate a typical sloping rubble mound structure. This is true of the beach profile areas both seaward and landward of the structure. Accordingly, approximations are necessary for practical applications. Normally, the authors will use the seawall feature in SBEACH (or similar model) and place the seawall at the horizontal centerline of the sloping structure with a height equal to the actual structure. This approach is judged to produce an exaggerated (i.e., conservative) amount of profile lowering in front of the actual sloping coastal structure as indicated in Figure 1. This subject would benefit dramatically from further, full scale, physical model tests of sloping rubble mound structures. The costs of such tests would be small in comparison the savings, both in initial construction and/or in avoided damages, that would be realized over a large range of applications. Furthermore, there are further opportunities to optimize the buried seawall concept.

Finally, it is necessary to estimate the local scour that immediately fronts the structure toe as indicated by item (4). While this scour is not separable from the storm profile estimated from cross-shore erosion models, the additional/accelerated local scour is not included in such models. It may be a conservative approach to add the local scour to the overall profile scour, but a necessary one in the absence of definitive design criteria. It should also be mentioned that sacrificial toe protection geometries are normally used to protect against local scour. While such measures are generally successful, the overall dimensions of such features are poorly understood as are stone sizes and gradations. Again, investments in physical model tests are recommended.

There are several means for estimating localized toe scour, nearly all of which are based on scaled, movable bed, physical model tests dating to the 1960s. Four methods are considered here: (1) SPM rule of thumb, (2) Hughes and Fowler, (3) MacDougal et al, and (4) Sumer and Fredsoe. The first method is quoted below from the 1973 version of the Shore Protection manual to emphasize the longevity of this guidance.

"*As a general rule, the maximum depth of a scour trough below the natural bed is about equal to the height of the maximum unbroken wave that can be supported by the original depth of water at the toe of the structure*."

The above approach has likely been applied with ubiquity and turns out to be a reasonable, if simple, approach. For example, Steetzel (1988) concluded from model tests that the depth of the scour trough at the seawall toe to be about 0.75 of the original depth at the toe (i.e. on the order of the breaking wave height of 0.78 of the same original depth.) Methods 2 and 3 pertain to vertical seawalls. Method 4 was developed for sloping structures exposed to non-breaking waves and is included only for comparison purposes. Figure 2 presents example results for each of the four methods. Local wave conditions at the toe of the structure were computed using Goda's surf zone model.

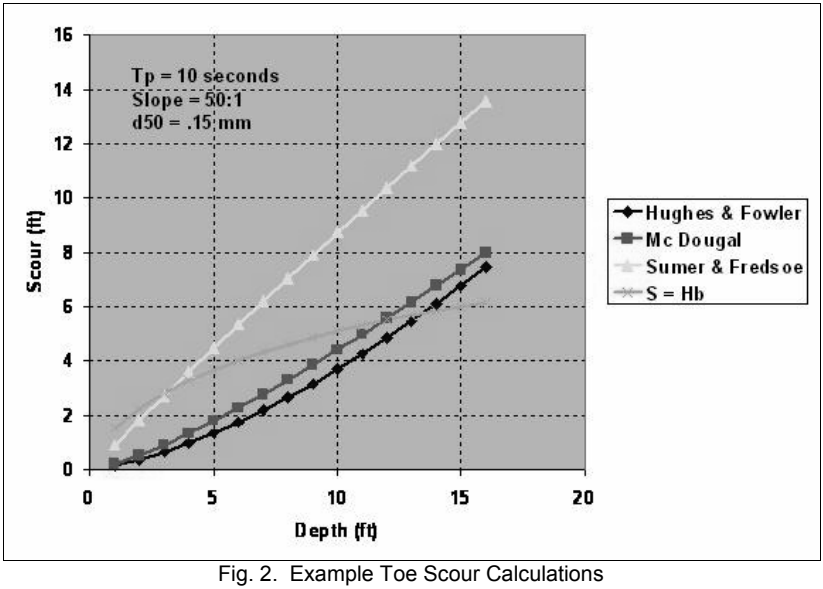

Fig. 2. Example Toe Scour Calculations

Interestingly, Figure 2 shows that the SPM guidance (S=Hb) gives reasonably similar results to both Hughes and Fowler as well as McDougal et al. The results also show how critically the original depth at the toe of the structure bears on the level of scour. As emphasized previously, the resulting depth dictates all of the additional variables that

govern design of a rubble mound structure. This is shown in Figure 3 for a typical 2:1 (H:V) sloping rubble mound seawall exposed to waves having a peak spectral period of 10 seconds. Calculations were made using Van der Meer's equations for wave runup, overtopping, and stone size. Figure 3 shows that the required crest elevation for the specified allowable overtopping and the required armor stone size are both a very strong function of the predicted bottom elevation at the toe of the structure.

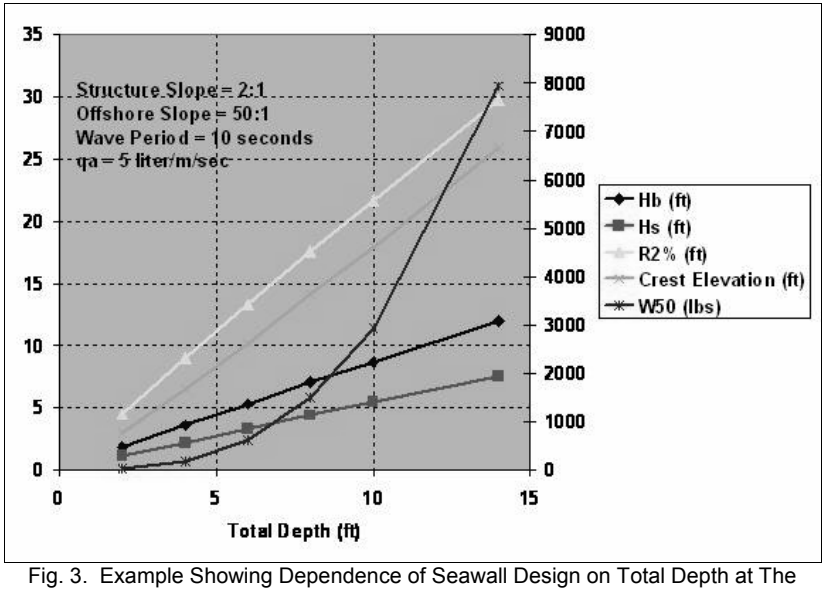

Fig. 3. Example Showing Dependence of Seawall Design on Total Depth at The Structure Toe.

Designs for the previously mentioned seawall at Dam Neck, Virginia were developed using procedures similar to those presented above as presented by Headland (1992) and Basco et al (1998.) Results of the design procedure and performance during Hurricane Isabel (an event within 0.8 feet of the design 100-year storm) are summarized below.

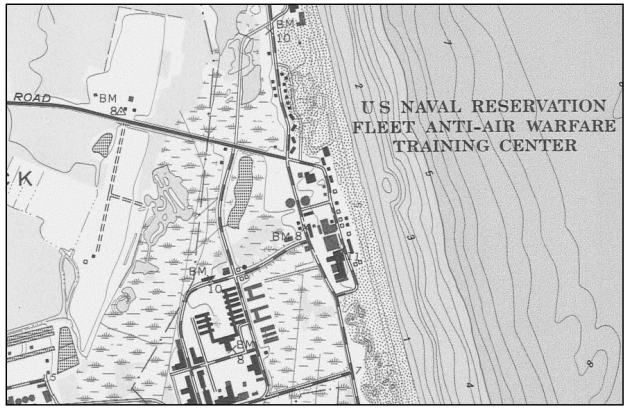

Fig. 4. Project Location, Dam Neck, Virginia

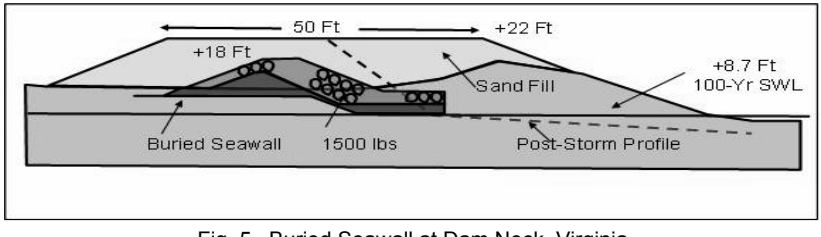

Fig. 5. Buried Seawall at Dam Neck, Virginia

Storm conditions during hurricane Isabel resulted in erosion of the beach face to the seaward edge of the seawall sacrificial toe as suggested in Figure 7 and much as predicted in Figure 5. Overall, the performance is judged to corroborate the approach outlined in Figure 1. The Dam Neck examples and others like it demonstrate that reasonable design guidelines are available for practitioners. Numerous difficulties remain, however, as regards a generalized procedure for designing coastal structures fronted by beaches, namely: (1) there are no generalized full scale model tests to quantify the separation of general profile change from localized scour, (2) there are no available means for evaluating the influence of structure slope, roughness or crest elevation on eroded profile shape, and (3) there is no means for quantifying the dimensions/elevations of a sacrificial toes other than rules of thumb. Although present practices have been demonstrated to be safe, there is much fundamental knowledge to be gained in sediment/structure interaction to improve design methods.

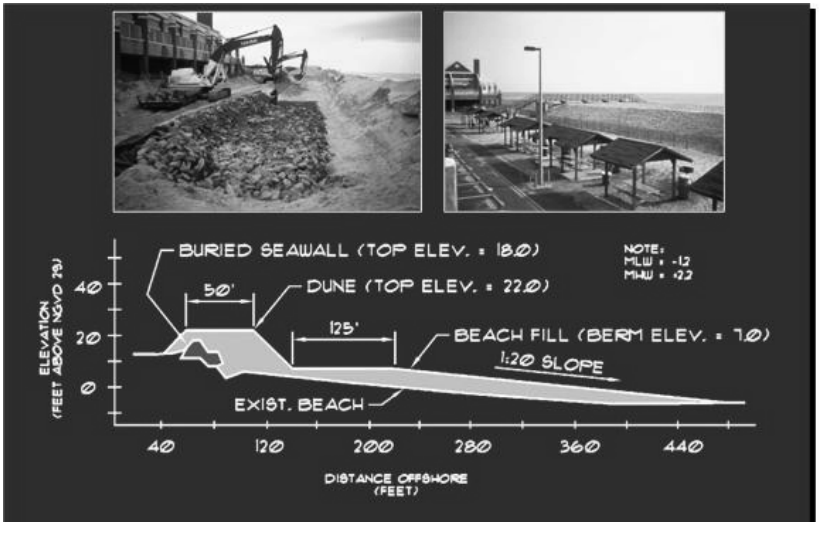

Fig. 6. Buried Seawall under Construction



Fig. 7. Dam Neck Buried Seawall- Post Isabel (provided by D. Basco)

LINKAGE BETWEEN OVERTOPPING DISCHARGE OR VELOCITY AND STRUCTURAL/SEDIMENTARY CONDITIONS

It has become commonplace to establish seawall/revetment crest elevations on the basis of allowable overtopping discharges, q_a (liters/s/m). Typical limits are summarized in terms of qualitative descriptions. The Coastal Engineering Manual (CEM) q_a guidance

for "revetments" ranges from 50 to 1000 depending on whether the "promenade" is paved or not. Similarly, q_a for "embankment seawalls" ranges from 2 to 1000 depending on whether the "crest is not protected", the "backslope is not protected," or the seawall is "fully protected." While this appears, *prima facie*, to be sufficiently quantitative, many questions remain. For example, what is the difference between a "revetment" and a "seawall?" As best as the authors can tell, the difference is that a revetment does not have an armored back slope. Similarly, what pavement cross section is needed to prevent damage? What size armor is needed on the structure crest? Can the upper slope of a structure be protected with vegetation? Unfortunately, these questions are fundamental from a practitioner's point of view and have a large bearing on selected crest elevations and costs of typical coastal structures. While it may not seem so, the issue is very much an issue of sediment/structure interaction inasmuch as most damage experience by heavily overtopped coastal structures involves erosion of the crest and back-slope areas comprised of earthen or partially armored slopes (i.e., armored with rock, pavement, blocks, or vegetation.)

Figure 8 presents a system of coastal dikes located at Poplar Island in the Chesapeake Bay exposed to hurricane wave conditions. The original structure was designed for 30 to 40-year conditions based on economic optimization techniques. The site is designed to serve as a clean dredged material placement site which will eventually be a restoration project comprised of upland and inter-tidal habitat. The economic optimization analysis of the protection works made it clear that it was preferable to repair the protection works after a major storm rather than design for an event more severe that 30- to 40 years. Furthermore, physical model tests indicated that the seaward rock portions of the containment dikes would remain intact in a 100-year storm although the structure would be heavily overtopped. The total length of armored dikes for the project is over 7 miles.

The structure was exposed to a 100-year water level and roughly 20-year storm waves during hurricane Isabel in September, 2003. All but 300 feet of structure stood up without any damage whatsoever. The rock portion of the damaged section remained fully intact as predicted by physical model test. The areas landward of the rock crest, however, were damaged. Specifically, portions of a gravel roadway and the sand back slope were washed out. The project sponsors were very pleased with the performance of Poplar Island during the 100-year event and the minor repairs were expeditiously carried out with equipment on site. Still, it is instructive to examine the nature of the limited damage that was experienced.

Figure 9 shows a cross section of the original dike section. Figure 10 shows a photo of the damaged area. An analysis of the dike system is presented in Figure 11. The structure was originally design using a Van der Meer et al (1995) method (Old); the New method is taken from Van der Meer (2002). The q_a used for design was the difference in required crest elevation is about 2 feet (higher with the new method), which is of concern. The originally required crest elevation was 10 feet (lowered to 9.5 feet for other reasons in the damaged area; the higher adjacent areas were undamaged). The required

crest elevation for the Hurricane Isabel event (shown as 100-year return period for convenience) was computed as 12 feet (old) to 14 feet (new).



Fig. 8. Poplar Island Dike System; Damaged Area Shaded upper Right

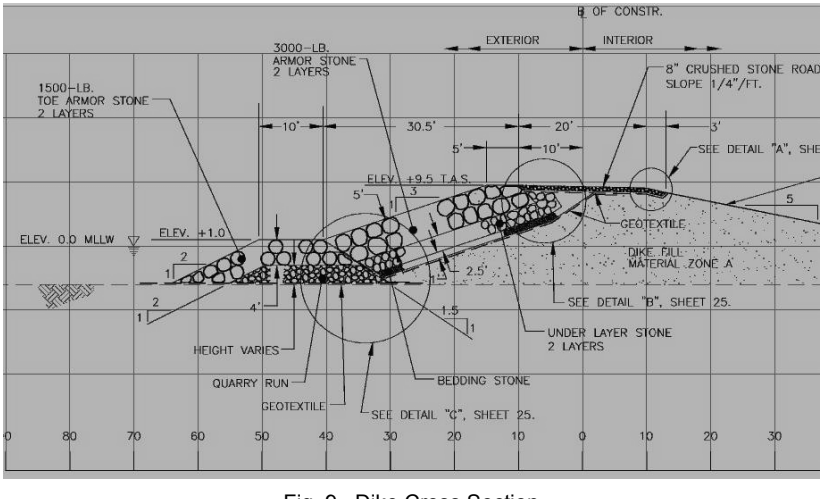

Fig. 9. Dike Cross Section



Fig. 10. Erosion of Sediment on Lee Side of Dike

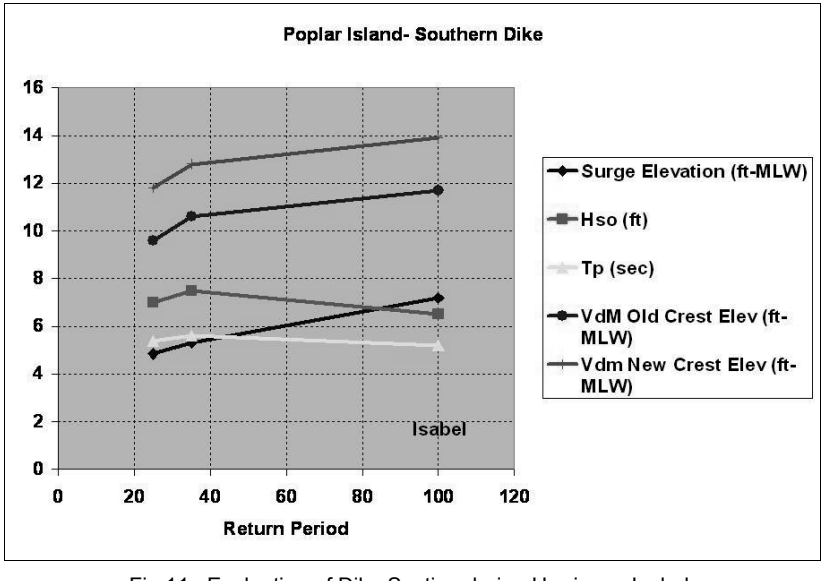

Fig.11. Evaluation of Dike Section during Hurricane Isabel.

Accordingly, the dike was heavily overtopped and eroded despite the presence of a crushed rock roadway that remained largely in place (Figure 10.) The difficulty here, as

mentioned above, is that there is no connection between the sedimentary damage experienced landward of the rock dike and the overtopping discharges. In this regard, the consequence of excessive overtopping is poorly understood for most coastal structures backed by earthen and/or vegetated slopes. As stated above for the Dam Neck case, the practicing profession would be greatly served by systematic model tests (preferably at full scale) to examine the consequence of excessive overtopping for a variety of surfaces (e.g., armored, unarmored, vegetated, sloped, flat, etc.) Additionally, it would be desirable to correlate damages (or percent damages) with overtopping velocity per Schuttrumpf et al (2002), rather than the more nebulous overtopping discharge.

ALTERNATIVE METHODS FOR FUNCTIONAL DESIGN OF T-GROINS

A new system of T-groins is envisaged for the western end of Coney Island in New York City, see Figure 12. Detailed planning, modeling and engineering task have been carried out to layout and prepare design documents for the proposed works. The work offers an opportunity to compare various functional methods including: (1) empirical design, (2) designs based on physical modeling techniques, (3) numerical modeling based on Delft 3D morphological simulation technology and (4) GENSIS modeling tools. Observations regarding the efficacy of each method are described below. Details surrounding each of the functional design methods are described in further detail in Smith et al (2006.)



Fig. 12. Coney Island Project Area

The project has been designed for a 50-year life, the need to maintain a shoreline that is seaward of the 1988 historical shoreline, structure crests no higher than +6 feet NGVD for aesthetic reasons, and a 10-year re-nourishment cycle. Empirical modeling techniques were based on equilibrium shoreline concepts. Moveable bed physical model

tests were conducted at the Canadian Hydraulics Laboratory. The resulting shorelines are presented in Figure 13. Figure 14 presents projected shorelines from Delft3D modeling, while Figure 15 presents results from GENESIS modeling. The empirical methods cannot be dismissed despite the lack of sophistication owing to the fact that they are grounded in experience at other successful T-groin installations. The physical model tests, though subject to interpretation owing to scale effects issue, served two purposes, namely, they served to evaluate the structural integrity of the T-groins and they served as a check on equilibrium shoreline shapes under the joint action of both waves and tidal currents. The DELFT3D results provided a similar role relative to wave and current forcing of the shoreline but do not fully represent the physics of wave diffraction and recommend a shorter period of simulation than GENESIS simulation. Finally, the GENESIS results further corroborate the basic findings of the other tools but extend over a longer period of time albeit only as a one-line model when strong two dimensional effects are apparent from both the model tests and the DEFLT3D model. Each functional design technique has its shortcomings and final selection of system structural geometry necessarily involved engineering judgment. This particular design exercise, though thorough, demonstrate some of the short comings of existing technology to solve the most fundamental sediment-structure interactions facing engineer, scientists and other decision makers.



Fig. 13. Shoreline Derived from Empirical Methods and Physical Model Tests

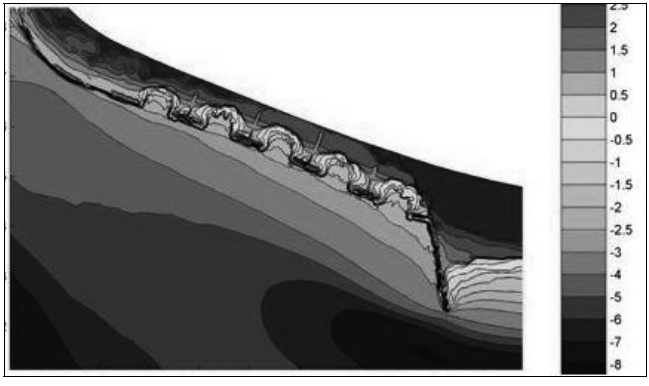

Fig. 14. DELFT3D Morphological Modeling Results for Equilibrium Conditions



Fig. 15. Shoreline Conditions Based on GENESIS Modeling

CONCLUSIONS

Existing methods for evaluating the structural and function design of coastal protection works located on dynamic sandy shoreline are reasonable useful in many applications. Many fundamental issues remain, however, and have been examined in this paper. These include the need to more accurately evaluate: (1) the beach profile geometry fronting a

vertical and/or sloping rubble mound structure, and (2) the connection between overtopping wave conditions and the structural/sedimentary features leeward of a coastal structure. Both of these problems should be addressed through systematic full scale physical model tests. An additional area requiring further research includes functional design of sediment retaining structures such as groins, t-groins and headlands. Empirical design methods remain very useful and physical and numerical models can serve to corroborate the empirical methods. Advancing knowledge regarding functional design of these systems will require further field installations with detailed measurements and monitoring. It is hoped that practitioner's observations advanced in this paper will help to provide impetus for further, focused, research in the highlighted areas.

REFERENCES

Basco, D., (1998). "The Economic Analysis of "Soft" Versus "Hard" Solutions for Shore Protection: An Example," *Proc. 27th ICCE*, Copenhagen.

Headland, J.R. (1992), "Design of Protective Dunes at Dam Neck, Virginia," *Proc. ASCE Coastal Engineering Practice Conference*, Long Beach, CA.

Hughes S. . and Fowler J.E. (1991). "Wave-induced scour prediction at vertical walls," *Proc. Coastal Sediments '91*; ASCE Press, 1886-1900.

McDougal, W.G., Kraus, N., and Ajiwibowo H. (1996). "The effects of seawalls on the beach: Part 2, Numerical modeling of SUPERTANK seawall tests." *Journal of Coastal Research*, vol.12, n 3; 702-713.

Meer, J.W. van der, (2002). "Technical Report, Wave Run-up and Overtopping at Dikes," Technical Advisory Committee for Water Retaining Structures.

Meer, J.W. van der,. and Janssen, J.P.F.M. (1995) "Wave run-up and wave overtopping at dikes," *Wave Forces on Inclined and Vertical wall Structures*, pp 1-26, ed. Kobayashi N. & Demirbilek Z., ISBN 0-7844-0080-6, ASCE, NY.

Schuttrumpf, H., Moller, J, and Oumeraci, H. (2002), "Overtopping Flow Parameters on the Inner Slope of Seadikes," *Proc. 28th ICCE,* Cardiff.

Smith, E., Rahoy, D., Yang, D., Cornett, A., Headland, J., (2006), "Design of T-Groin Shore Protection System for Recreational Beach, Coney Island, New York" *Proc. 30th ICCE*, San Diego.

Steetzel, H.J., (1985). "Model Tests of Scour near the Toe of Dune Revetments," (in Dutch). Report M 2051-II, Delft Hydraulics Laboratory, Delft, The Netherlands.

Stive, M.J.F. (2003). "Morphologic modeling of tidal basins and coastal inlets," *Proc. Coastal Sediments '03*, CD-ROM Published by East Meets West Productions, Corpus Christi, TX ISBN-981-238-422-7, 14 p.

Sumer, B.M., and Fredsoe, J. (2000). "Experimental study of 2D scour and its protection at a. rubble-mound breakwater," *Coastal Engineering*, 40(1), pp 59-87.

QUANTITATIVE EVALUATION OF CONTROLLING EFFECT OF HEADLAND ON LONGSHORE SAND TRANSPORT USING MODEL FOR PREDICTING CHANGES IN CONTOUR LINES AND GRAIN SIZE

Takayuki KUMADA[1], Takaaki UDA[2] and Masumi SERIZAWA[3]

1. Ph. D., Laboratory of Aquatic Science Consultant Co., Ltd., Meishin Building, 1-14-1 Kami-ikedai, Ota, Tokyo 145-0064, Japan. kumada@lasc.co.jp.
2. Dr. Eng., Executive Director, Public Works Research Center, 1-6-4 Taito, Taito, Tokyo 110-0016, Japan. uda@pwrc.or.jp.
3. Coastal Engineering Laboratory Co., Ltd., 1-22-301 Wakaba, Shinjuku, Tokyo 160-0011, Japan. coastseri@nifty.com.

Abstract: On Oharai Beach, a large amount of sand has accumulated owing to the formation of a wave shelter zone of the port breakwater, causing excess deposition in the navigation channel, whereas severe beach erosion has occurred south of Oharai Port. With these large-scale beach changes, the grain size of the seabed materials has significantly changed, and the area covered with coarse sand has been expanding. Simultaneously, the catch of Japanese hard clams, the habitat of which lies in a seabed composed of fine sand, has decreased. A model for predicting the changes in contour lines and grain size was applied to Oharai Beach; the controlling effect on longshore sand transport of an artificial headland was quantitatively evaluated in terms of beach and grain size changes, and the optimum depth of the headland was determined.

INTRODUCTION

On Oharai Beach on the Kashimanada coast, facing the Pacific Ocean, a large amount of sand has accumulated in the port since the 1980s owing to the formation of a wave shelter zone associated with the construction of the port breakwater, resulting in sand deposition in the navigation channel. Simultaneously, severe erosion has occurred on the coast outside the wave shelter zone (Uda *et al.*, 1986). The grain size of the seabed materials has also changed with these beach changes, resulting in a

rapid decrease in the catch of Japanese hard clams, *Mertrix lamarckii*, which are a local speciality of the Kashimanada coast and live on sand beds covered with fine sand. These bathymetric and grain size changes are closely related to the preservation of a sound coastal environment. However, such changes have not yet been sufficiently studied. Here, the model for predicting the changes in contour lines and grain size proposed by Kumada *et al.* (2006) is applied to Oharai Beach to solve these problems. The controlling effect on longshore sand transport of an artificial headland under construction is quantitatively evaluated, and the optimum depth of the headland is determined.

CHARACTERISTICS OF BEACH CHANGES IN STUDY AREA

2.1 Analysis of shoreline changes using aerial photographs

To investigate the beach changes around Oharai Port, shoreline changes were measured using aerial photographs in the study area of a 39-km-long stretch of the Kashimanada coast between Oharai and Kashima Ports. **Figure 1** shows the shoreline changes in the study area with reference to the shoreline in 1964 with the names of the local coasts. The pulse-like shoreline changes in 2002 mean that the shoreline changes are caused by the construction of artificial headlands. The shoreline markedly advanced in the wave shelter zones owing to the breakwaters of Oharai and Kashima Ports, resulting in a maximum shoreline advance of 700 m in the vicinity of Oharai Port, whereas the shoreline receded as a whole in the central part of the coast.

Figure 2 shows an aerial photograph of the vicinity of Oharai Port taken in 2002. An offshore breakwater extends east of the port, and a triangular beach had formed in the wave shelter zone because of this offshore breakwater. There is a navigation channel between the north breakwater and the beach south of the port. Therefore, longshore sand transport, having originally been supplied from the Naka River located 3 km north of the port and flowing south, can no longer reach the south beach. In terms of the mass conservation of sand, it is suggested that all the sand accumulated in the wave shelter zone of the port breakwater must have been supplied from the south coast. This resulted in erosion in an extensive area south of Oharai

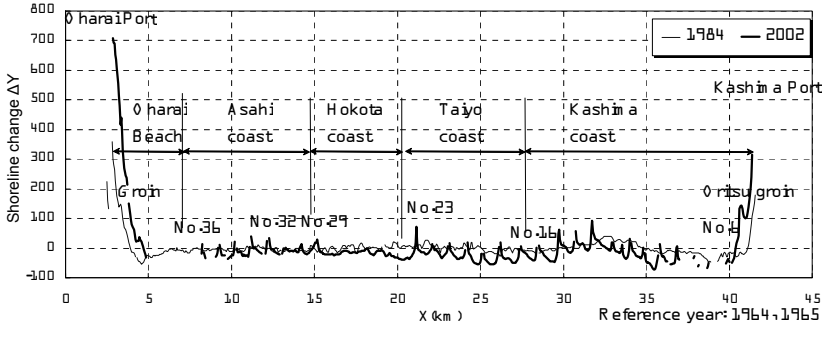

Fig. 1. Longshore distribution of shoreline changes with reference to shoreline in 1964

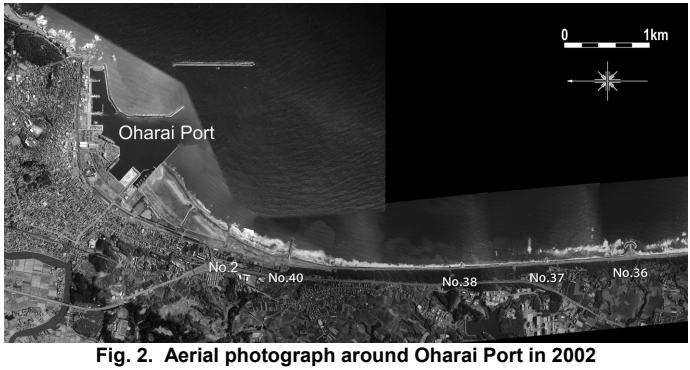

Fig. 2. Aerial photograph around Oharai Port in 2002

Port. **Figure 2** clearly shows that the foreshore in front of the seawall had completely disappeared for a distance of 3.5 km in the south part of Oharai Port.

Shoreline changes with the same pattern as those in the vicinity of Oharai Port occurred in the north part of Kashima Port, as shown in **Fig. 1**; the foreshore was markedly extended on the adjacent beach, whereas the beach north of the port was eroded. In other words, longshore sand transport from outside to inside the wave shelter zone of the port breakwater had been induced, resulting in shoreline advance inside the port and shoreline recession north of the accretion zone.

2.2 Analysis of beach changes using bathymetric survey data

To investigate the beach changes in the offshore zone, the bathymetric survey data were analyzed. **Figure 3** shows the bathymetry in 2004 and the planar distribution of the changes in depth between 1984 and 2004 calculated from the bathymetric survey data. A large amount of sand was deposited at both ends of the coastline; in contrast, the other areas eroded. **Figure 4** shows the changes in sand volume with time around Oharai Port (A), on the Hokota coast (B) and around Kashima Port (C). In the twenty-year period between 1984 and 2005, volumes of sand of 5.0×10^6 m^3 and 3.0×10^6 m^3 accumulated in the vicinity of Oharai and Kashima Ports, respectively, whereas 1.0×10^6 m^3 of sand was lost from the Hokota coast, although there were variations to some extent. In conclusion, it is clear that accretion occurred over an extensive area including the offshore zone around the port area, and in contrast, erosion occurred on the neighboring coast.

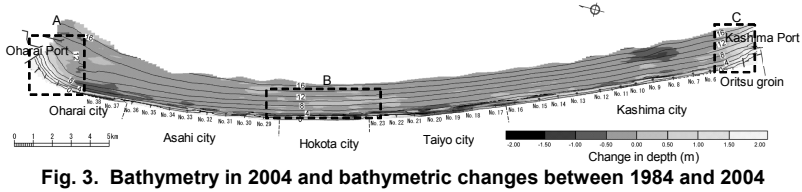

Fig. 3. Bathymetry in 2004 and bathymetric changes between 1984 and 2004

2.3 Grain size analysis of foreshore materials

Grain size analysis of the foreshore materials was carried out in July 2005 between Oharai and Kashima Ports. **Figure 5** shows the longshore distribution of the median diameter d_{50}. Sand accumulated in the wave shelter zone is composed of fine sand with a grain size of 0.1 mm, and the grain size tends to become large in the erosion zone. When longshore sand transport is induced from outside to inside the wave shelter zone of the offshore breakwater, fine sand is selectively transported from the surrounding coast toward the wave shelter zone and deposited in the port area, resulting in the accumulation of fine sand in the port and leaving the seabed covered with coarse sand in the surrounding area. Accordingly, the occurrence of longshore sand transport from the surrounding coasts toward the port is also inferred from the longshore distribution of the grain size of the foreshore materials. The phenomenon in which the composition of seabed materials of the surrounding coast becomes coarser is assumed to be the main factor devastating the habitat of Japanese hard clams, which prefer fine sand of 0.106-0.16 mm grain size (Higano *et al.*, 1993).

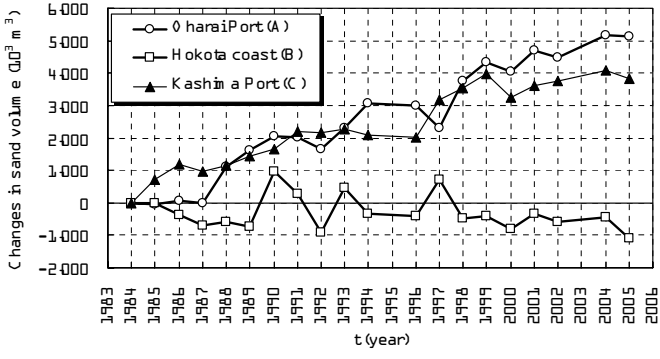

Fig. 4. Changes in sand volume with time around Oharai Port (A), on Hokota coast (B) and around Kashima Port (C)

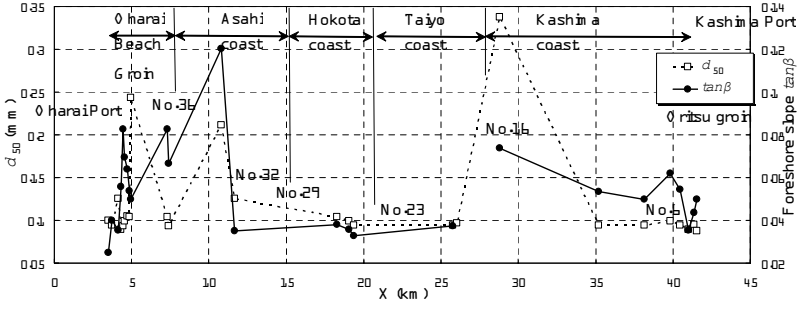

Fig. 5. Longshore distribution of median diameter of foreshore materials and foreshore slope measured in 2005

PREDICTION OF CHANGES IN CONTOUR LINES AND GRAIN SIZE

3.1 Calculation conditions

On the basis of the field data, the model for predicting topographic changes and grain size change developed by Kumada *et al.* (2006) was applied to Oharai Port and the Hokota coast, and the effects of extending the headland on the beach topography and grain size were evaluated to determine the optimum countermeasure against beach erosion. The calculation domain is from Oharai Port to the Hokota coast south of headland No. 29, where the effect of the wave shelter zone of the breakwater of Oharai Port may diminish, as shown in **Fig. 1**.

Calculations for four cases were carried out. In case 1, the bathymetry in 2004 was reproduced given the initial topography in 1964 under the natural conditions before the construction of Oharai Port. The initial topography had straight, parallel contours deformed by the wave-sheltering effect of Cape Oharai. The point depth of the artificial headland is assumed to be 7 m in case 2, and the effect of changing the point depth was investigated in cases 3 and 4 with point depths of 6 m and 8 m, respectively. In all cases, the bathymetry in 2024 was predicted given the reproduced topography and grain size distribution in 2004 as the initial conditions.

For the incident wave conditions, rough waves occurring several times a year were assumed; the breaker height and wave period were H_b= 4 m and T=9 s, respectively. The wave direction was set to be from the east, which is approximately normal to the coastline and the most frequent incident direction. The depth range where the beach changes occur is between the berm height of h_R=3 m and the depth of closure of h_c=12 m, which sufficiently covers the depth range, characterized by the occurrence of small bathymetric changes in the offshore zone composed of fine materials such as silt, as determined by comparing longitudinal profiles (Mimura and Kato, 1991). The south boundary of the calculation domain is a free boundary, through which longshore sand transport can freely occur. The equilibrium slopes were set to be 1/65 in the depth zone shallower than 5 m and 1/100 in the depth zone between 5 m and 12 m, since the longitudinal slopes in each depth zone have been stably expressed by combining these two slopes on the basis of the comparison of the measured profiles.

The initial content rates of the grains in the zone shallower than 5 m with a longitudinal slope of 1/65 were assumed to be the average of all the sampling data of the sand grains measured at the foreshore in July 2005 in the study area. For the initial content rates of the grains in the zone deeper than 5 m with a longitudinal slope of 1/100, the content rate for each grain size in the offshore zone was adjusted so that the equilibrium slope was 1/100, using the method proposed by Noshi *et al.* (2006), in which the equilibrium slope corresponding to the grain size is given, assuming that the range of grain sizes in the offshore zone is the same as that measured on the shoreline but that there is a difference in the content rates. Finally, the content rates of fine sand and silt, medium sand and coarse sand were assumed to be 59.4, 40.3 and 0.3%, respectively, at depths less than 5 m, and 85, 15 and 0%, respectively, at depths greater than 5 m.

3.2 Reproduction of bathymetry and grain size (case 1)

Figures 6(a) and **6(b)** show the reproduced bathymetry in 2004 and the changes in depth since 1964. Because longshore sand transport from outside to inside the wave shelter zone of the breakwater of Oharai Port was triggered by the extension of the long breakwater, sand accumulated inside the port and erosion occurred on the surrounding coast far from the port. The contour lines retreated particularly rapidly around headlands No.38-No.36 at X=4-7 km, respectively, and this is in good agreement with the severe erosion at these sites.

Figure 7 shows the comparison between the measured and calculated shoreline changes between 1964 and 2004. The shoreline advance ΔY of 700 m in the wave shelter zone of the port and the shoreline recession of 65 m on the surrounding coast outside the wave shelter zone are accurately reproduced, although the eroded and accreted areas are slightly overestimated. In the calculation, the shoreline changes in the wave shelter zone due to the headland were not reproduced, because the headland was regarded as a short groin without a wave-sheltering effect.

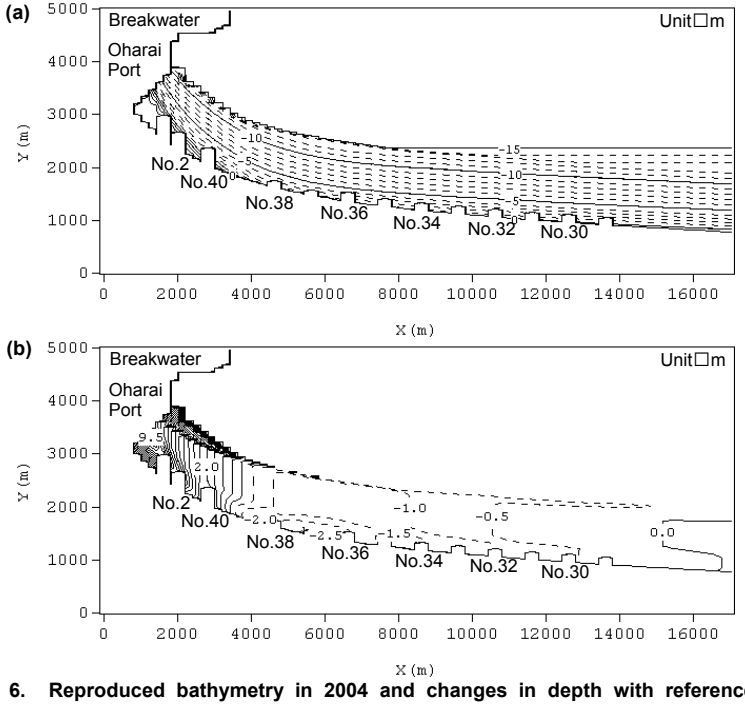

Fig. 6. Reproduced bathymetry in 2004 and changes in depth with reference to bathymetry in 1964 (case 1)

Figure 8 shows the predicted mean diameter of the bed materials in 2004. The grain size of the bed materials became fine with an average size of 0.09 mm in the wave shelter zone. In contrast, outside the wave shelter zone, comparatively coarse materials of 0.11 mm and 0.16 mm size were left in the offshore zone and near the shoreline, respectively. In particular, the grain size increased in both shoreward and offshore zones of the area between X=3.5 km and 8.0 km, where severe erosion occurred. This is because fine sand was selectively transported from outside the wave shelter zone, resulting in the coverage of the seabed surface with coarse sand, whereas fine sand accumulated in the wave shelter zone, when longshore sand transport from outside to inside the wave shelter zone took place.

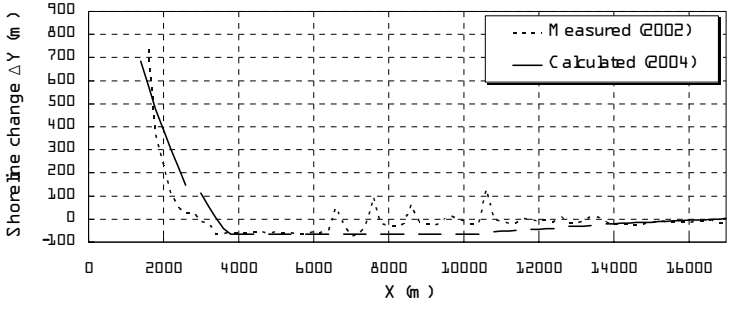

Fig. 7. Measured and calculated shoreline changes between 1964 and 2004 in case 1

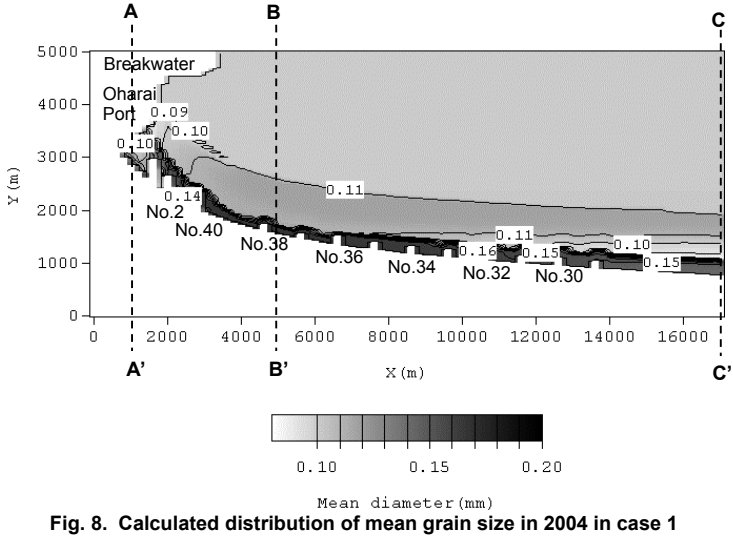

Fig. 8. Calculated distribution of mean grain size in 2004 in case 1

Figure 9 shows the calculated and measured content rates by percentage of sand along survey lines AA' in an accretion zone, BB' in an erosion zone and CC' crossing the free boundary of the south end of the calculation domain, as shown in **Fig. 8**. Both results were in good agreement, in that the content rate of fine sand is higher than 80% at survey line AA' and as low as 50% at survey line BB'. Moreover, there is no significant difference between the measured and calculated content rates at survey line CC', further showing the good agreement of both results.

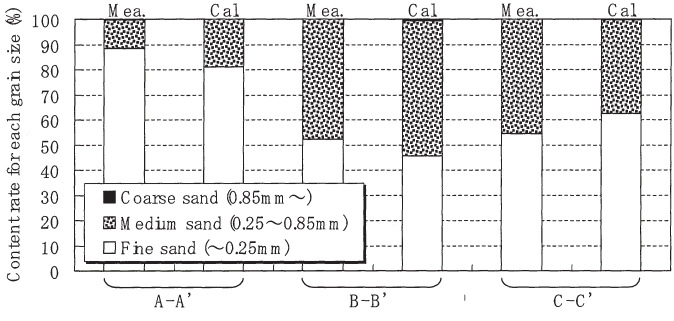

Fig. 9. Calculated and measured content rates by percentage of sand along survey lines AA', BB' and CC'

3.3 Prediction of bathymetry and grain size (cases 2, 3 and 4)

Figure 10 shows the predicted bathymetric changes for case 2 in 2024, in which the point depth of headland No. 40 was extended to a depth of 7 m, given the reproduced topography in 2004 as the initial conditions. The change in depth is measured with reference to that in 2004. If the headland is extended, a large amount of sand accumulates south of the headland, because northward longshore sand transport is more obstructed by the headland. In contrast, erosion occurred between the short groin No. 2 and headland No. 40, implying the occurrence of the secondary damage associated with the extension of the headland. Furthermore, beach erosion is still in progress in the zone between X=6 km and 14 km.

Figure 11 shows the predicted distribution of the mean diameter of bed materials for case 2 in 2024. When compared with the results in case 1, as shown in **Fig. 8**, the mean grain size becomes fine with sand accumulation south of headland No. 40, but the mean grain size is still larger than that in the offshore zone. In contrast, the grain size increases along with erosion north of the headland, and a zone with a large change in mean grain size reaches the port. Since many young Japanese hard clams live there, their habitat will be significantly damaged. In the offshore zone north of headland No. 40, the zone covered with fine sand expands compared with the present condition. This implies that the extension of headland No. 40 increases wave calmness, resulting in the accumulation of fine sand in this area. This area seems to

have an appropriate environment for full-grown Japanese hard clams in terms of the distribution of fine sand, but in the calculation, the mud content rate becomes too high in this area, resulting in the formation of an inappropriate environment for full-grown Japanese hard clams.

Figure 12 shows the bathymetric changes for case 3 in 2024, in which the point depth of headland No. 40 was extended to a depth of 6 m. Comparing this result with that in case 2, as shown in **Fig. 10**, erosion does not occur north of the headland, although there is no change in the accreted volume of sand south of headland No. 40. This is because more sand can pass the tip of the headland in case 3, resulting in an increase in sand supply north of the headland, since the point depth of the headland was 1 m lower. Conversely, it can be said that the trapping effect of longshore sand transport in case 3 is slightly smaller than that in case 2 with the point depth of 7 m,

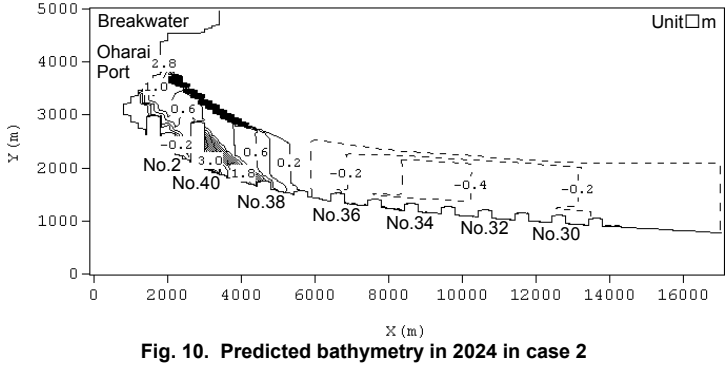

Fig. 10. Predicted bathymetry in 2024 in case 2

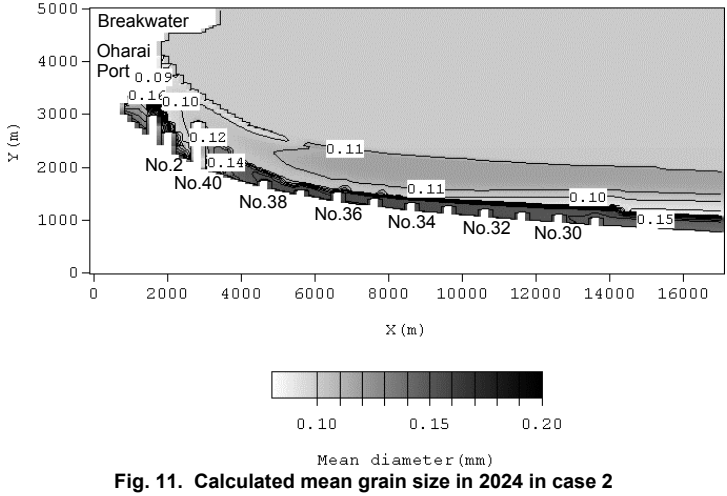

Fig. 11. Calculated mean grain size in 2024 in case 2

inferring a trade-off relationship between the trapping and erosion effects of the headland.

Figure 13 shows the predicted distribution of the mean diameter of bed materials for case 3 in 2024, in which the point depth of the headland was extended to the depth of 6 m. Comparing this result with that in case 2, as shown in **Fig. 11**, the area covered with coarse sand north of headland No. 40 disappeared owing to the reduction in beach erosion, inferring less damage to the habitat of young Japanese hard clams. However, in the offshore zone north of headland No. 40, fine sand still accumulates, resulting in a severe environment for full-grown Japanese hard clams.

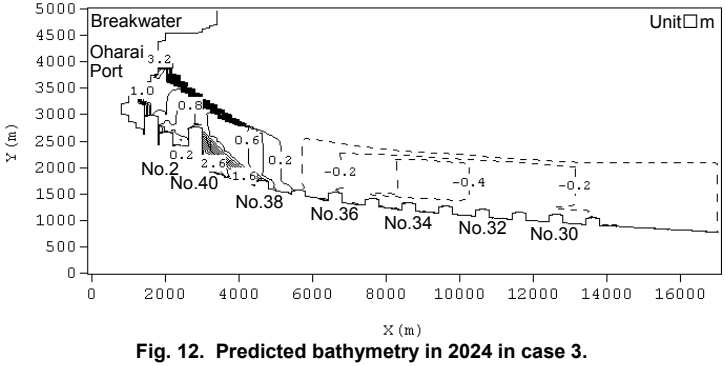

Fig. 12. Predicted bathymetry in 2024 in case 3.

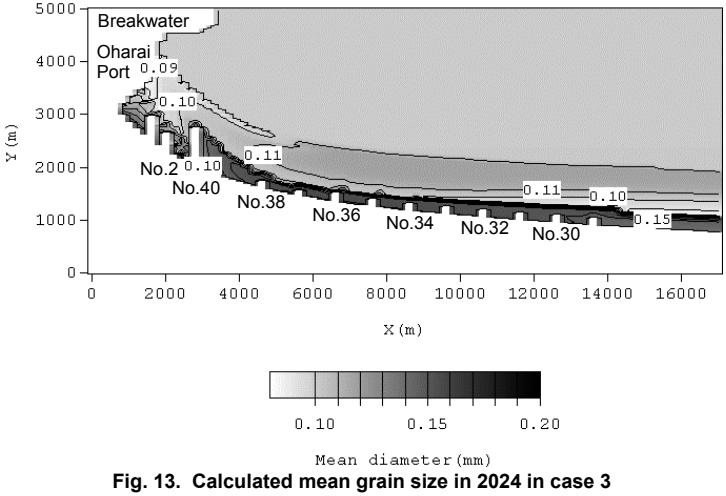

Fig. 13. Calculated mean grain size in 2024 in case 3

Figure 14 shows the bathymetric changes for case 4 in 2024, in which the point depth of headland No. 40 was extended to a depth of 8 m. Comparing this result with that in case 2, as shown in **Fig. 10**, sand accumulation south of the headland does not change, but erosion occurs between headland No. 40 and the short groin No. 2, inferring the possibility of secondary coastal damage associated with the extension of the headland.

Figure 15 shows the predicted distribution of the mean diameter of bed materials of case 4 in 2024. Comparing this result with that in case 2, as shown in **Fig. 11**, the seabed area covered with coarse sand north of headland No. 40 further expands. The increase in the effect of obstructing longshore sand transport caused by the extension of the headland significantly affects the beach changes and erosion accelerates. Accordingly, in this case, the most severe changes on the habitat of young Japanese

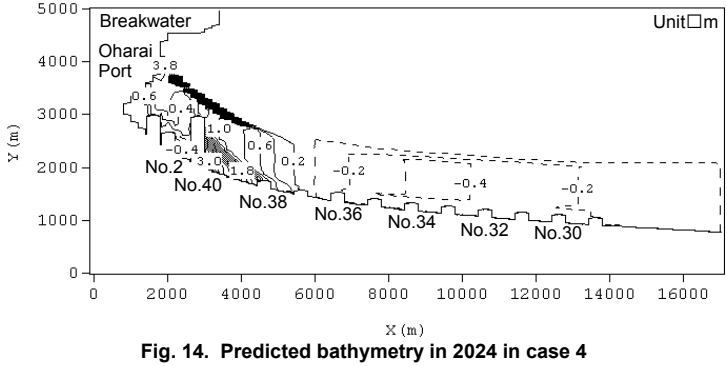

Fig. 14. Predicted bathymetry in 2024 in case 4

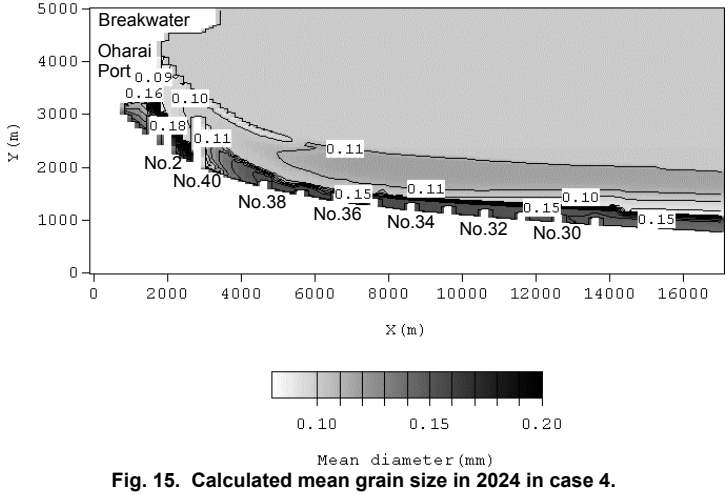

Fig. 15. Calculated mean grain size in 2024 in case 4.

hard clams will be induced.

Figure 16 shows the shoreline changes for cases 2, 3 and 4 in 2024 with reference to the shoreline in 2004, in which the point depth of headland No. 40 is extended to 7, 6 and 8 m, respectively. With the extension of the headland, the shoreline advances south of the headland, and the maximum shoreline advance approaches a constant value of approximately 200 m in the case of the point depths of 7 and 8 m. In contrast, the shoreline recedes north of the headland and the maximum shoreline recession tends to approach approximately 50 m as in the case of the point depths of 7 and 8 m. Considering the aim of preventing erosion between headlands No. 38 and No. 40, the effect of the trapping of longshore sand transport caused by headland No.40, as a measure against deposition in the navigation channel, and the resulting erosion north of headland No. 40, it is difficult to select the cases of the point depths of 7 and 8 m.

This conclusion is obtained only from the comparison of the shoreline changes in 2024, but the bathymetry had not yet reached a stable form in 2004. Therefore, the shoreline changes with time on both sides of headland No. 40 were investigated. **Figure 17** shows the time sequences of the shoreline position on both sides of the headland between 2004 and 2044. The volume of sand trapped on the south side of the headland increases with the point depth of the headland, whereas on the north side, the shoreline recedes 50 m until 2014 independent of the point depth of the groin, and then it advances. This is because sand can pass the tip of the headland, resulting in sand supply from south to north and accretion north of the headland.

Note that the time when the shoreline alteration north of the headland changes from erosive to accretive is delayed with the increase in the point depth. Although the proportion of longshore sand transport obstructed is increased with the extension of the headland, there is no change in the maximum shoreline recession of approximately 50 m, and instead, the time until accretion starts is delayed. Since a shore width of approximately 100 m still remains at the foot of headland No. 40 at

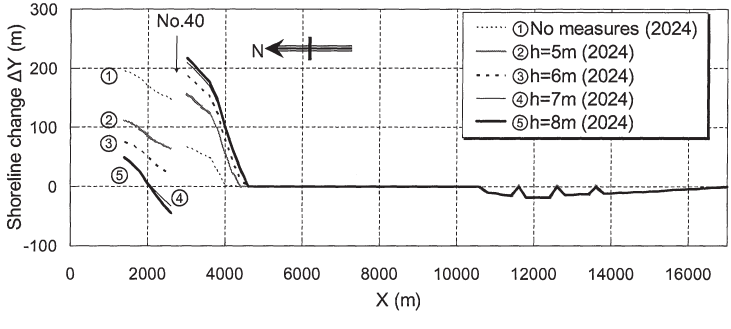

Fig. 16. Shoreline changes in 2024 in cases 2, 3 and 4 with reference to that in 2004

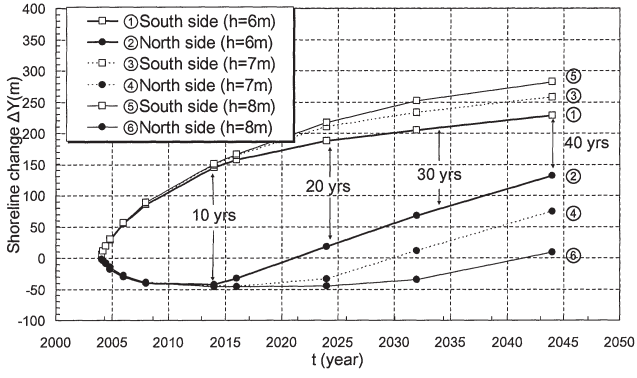

Fig. 17. Changes in shoreline position with time on both sides of headland No. 40

present, the selection of the time that erosion can occur in the future becomes important, even if a shoreline recession of approximately 50 m is permitted.

In the technological sense, a 20-year period is assumed to be an appropriate duration for determining the effect of the extension of the headland. In this case, the most appropriate measure is considered to be case 3 with the point depth of 6 m, in which the time of erosion is shortest. The longshore sand transport passing through off the tip of the headland after its completion causes deposition in the navigation channel, and therefore, 'sand back pass' in which sand is removed from the area south of the headland and deposited further south along the coast, becomes one of the valuable measures of preventing erosion, as in the case of the southern Kashimanada coast (Sumiya *et al.*, 2006). A shore width of 50 m is considered to be sufficient to prevent wave overtopping disasters, but there is a possibility of the expansion of the seabed area covered with coarse sand owing to the temporary erosion. Accordingly, further discussion is required for the evaluation of measures to preserve the habitat of Japanese hard clams.

CONCLUSIONS

A model predicting changes in bathymetry and the grain size of seabed materials was applied to the quantitative evaluation of the depth of an artificial headland as a measure against beach erosion associated with the formation of a wave shelter zone around Oharai Port. The point depth of 6 m was selected to be optimum in terms of accretion on the updrift side of the headland, prevention of the shoaling of the port navigation channel, preservation of the habitat of Japanese hard clams and the reduction in erosion downcoast of the headland. It is clear that the present model is a useful tool for predicting not only beach changes, but also grain size changes.

REFERENCES

Higano, J., K. Kimoto and Y. Yasunaga (1993). Influence on the relation between burrowing behavior and physical environment regarding the distribution of sandy beach bivalves *Mertrix lamarckii* and *Gomphina melanaegis*, Bull. N. R. I. F. E., No. 14, pp. 65-87. (in Japanese)

Kumada, T., T. Uda and M. Serizawa (2006). Model for predicting composition changes of grain size of bed materials, Proc. 30th ICCE, ASCE. (in press)

Mimura, N. and H. Kato (1991). Topographic responses to the construction of large port structure on Oarai Coast, Coastal Sediments 91, ASCE, pp. 2292-2306.

Noshi, Y., A. Kobayashi, T. Uda, T. Kumada and M. Serizawa (2006). Relationship between local seabed slope and grain size composition of bed materials, Proc. 30th ICCE, ASCE. (in press)

Sumiya, M., T. Uda, T. Kumada and M. Serizawa (2006). Simultaneous prediction of beach changes and grain size distribution on coast with artificial headlands, Proc. 30th ICCE, ASCE. (in press)

Uda, T., M. Sumiya and Y. Kobayashi (1986). Analysis of beach erosion around large-scale coastal structures, Proc. 20th ICCE, ASCE, pp. 2329-2343.

EVALUATION OF CONTROLLING EFFECT OF SAND TRANSPORT BY DETACHED BREAKWATERS BUILT ON DYNAMICALLY STABLE BEACH

Takaaki UDA[1], Masumi SERIZAWA[2] and Toshinori ISHIKAWA[3]

1. Dr. Eng., Executive Director, Public Works Research Center, 1-6-4 Taito, Taito, Tokyo 110-0016, Japan. uda@pwrc.or.jp.
2. Coastal Engineering Laboratory Co., Ltd., 1-22-301 Wakaba, Shinjuku, Tokyo 160-0011, Japan. coastseri@nifty.com.
3. Public Works Research Center, 1-6-4 Taito, Taito, Tokyo 110-0016, Japan. ishikawa@pwrc.or.jp.

Abstract: The contour-line-change model was applied for predicting the beach changes around headlands on the Shimizu coast, which were built using pairs of detached breakwaters. Before constructing the headlands, there was a dynamically stable beach, at which longshore sand transport of 1.3×10^5 m^3/yr flowed continuously alongshore, but it was altered to a new equilibrium state, in which longshore sand transport was reduced to 7×10^4 m^3/yr owing to the construction of the headlands. The effect of countermeasures against beach erosion was also predicted using this model. It was found that the extension of the present detached breakwaters by 50 m in the updrift and downdrift directions to narrow the interval between the detached breakwaters is effective for reducing the necessary amount of sand nourishment by (0.5-1.0) $\times 10^4$ m^3/yr.

INTRODUCTION

The Shizuoka and Shimizu coasts have a 17-km-long coastline extending from the mouth of the Abe River along the outer margin of the Mihono-Matsubara sand spit. On these coasts, 1.3×10^5 m^3/yr of sand was continuously transported by northeastward longshore sand transport before extensive riverbed mining, and sand was deposited at the north end of the sand spit, as well as being discharged into the deep ocean through a submarine canyon (Uda, 1997). The fluvial sand supply from the mouth of the Abe River markedly decreased owing to the extensive riverbed mining before 1967 (Uda and Yamamoto, 1994; Itabashi and Uda, 1998), and

simultaneously, its impact started to propagate downcoast as a wave of erosion. Then, a wave of accretion, which was generated in 1983 by large floods in the Abe River, started to propagate from the Shizuoka coast to the Shimizu coast because of the prohibition of riverbed mining.

By 1983, the wave of erosion had reached the tip of the Mihono-Matsubara sand spit on the Shimizu coast. As a measure against beach erosion, a group of headlands each consisting of a couple of detached breakwaters have been built since 1983 to stabilize the shoreline. Five sets of headlands have now been built. After their construction, the shoreline downcoast of the detached breakwaters retreated, forming a hook-shaped bay, and resulted in the exposure of the foot of the seawall at the eroded sites, increasing the probability of collapse of the seawall.

As another measure, beach nourishment, using 3.5×10^4 m^3 of sand, has been carried out annually to compensate the shortage of sand supply, but its effect has been very limited and the sand has been quickly lost. Therefore, whether the reduction in beach nourishment is possible without increasing the severity of beach erosion is one of the present issues. In this study, a dynamically stable beach of the Shimizu coast is reproduced using the contour-line-change model, in which a large amount of sediment is continuously transported alongshore, and then the possibility of reducing the annual amount of beach nourishment necessary is investigated by altering the configuration of the detached breakwaters.

CHARACTERISTICS OF SHIMIZU COAST

The study area is the area between No. 54 and No. 68 of the Shimizu coast, as shown in **Fig. 1**, located at the outer margin of the Mihono-Matsubara sand spit. Off the coastline in the vicinity of the study area, a continental shelf with a gentle slope has developed, whereas in the vicinity of No. 30, a steep submarine canyon has developed. The beach changes associated with the construction of headlands built as a set of two detached breakwaters on the Shimizu coast have been described in detail in Uda (1997).

Figure 2 shows the results of this paper. In 1988, the offshore contours extended parallel to the gradually curved shoreline, and a steep slope of 1/10 had formed between the foreshore and a depth of 5 m, whereas in the zone deeper than 5 m, the seabed slope became as gentle as 1/50. At this stage, 1.3×10^5 m^3/yr of sand was continuously transported by the northeastward longshore sand transport on the Shimizu coast (Itabashi and Uda, 1998); this was a dynamically stable state, in which the same amount of sand flows in and out from both ends of the study area, as shown in **Fig. 2**.

On this coast, headlands composed of a set of two detached breakwaters had been built at two locations by 1992, and a straight shoreline remained west of detached breakwaters･and ･, as shown in **Fig. 2(b)**, whereas the shoreline had significantly retreated east of the detached breakwaters.

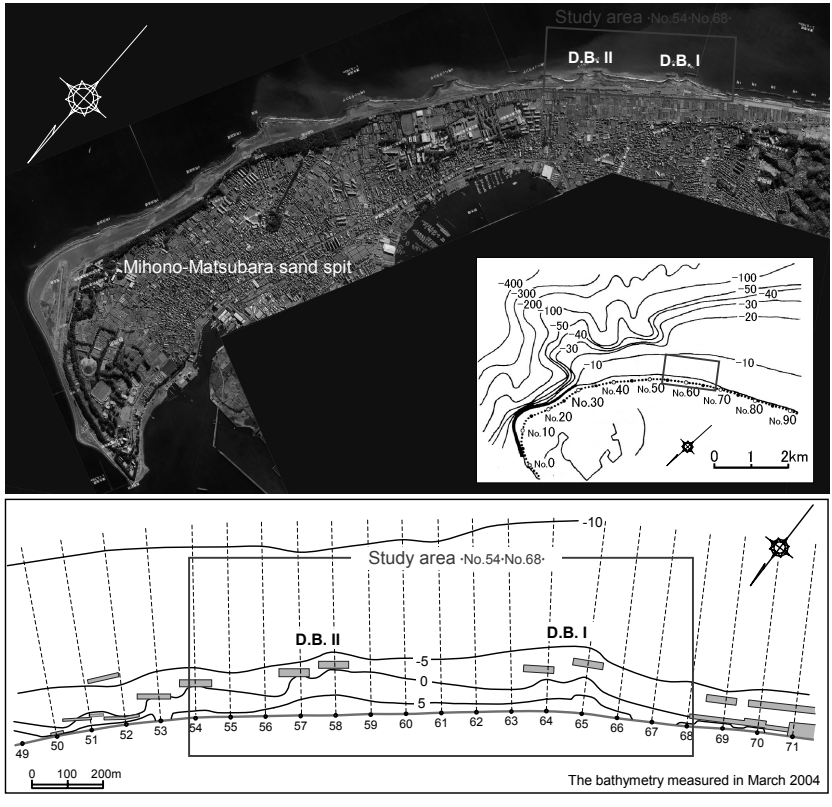

Fig. 1. Study area along Shimizu coast

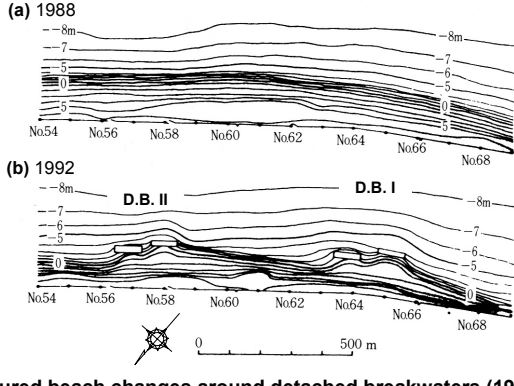

Fig. 2. Measured beach changes around detached breakwaters (1988 vs. 1992)

For example, **Fig. 3** shows the shoreline near detached breakwaters I on October 14, 2005. A new berm had formed owing to the accumulation of gravel from the concrete armor units shown at the right corner of the figure, and a generally concave shoreline had formed, allowing the approach of the berm to the foot of the seawall downcoast. In this area, severe wave overtopping has taken place, and the foreshore in front of the seawall has eroded away in recent years, resulting in the exposure of the foot of the seawall. To prevent seawall damage and reduce wave overtopping, 3.5×10^4 m^3 of sand has been nourished every year, but the effect of the beach nourishment has been regarded as questionable, since the same amount of sand is discharged immediately after the nourishment.



Fig. 3. Beach around detached breakwaters I taken on October 14, 2005

The detached breakwaters must have contributed to the reduction in longshore sand transport relative to that in the natural condition, 1.3×10^5 m^3/yr, but its effect has not yet been evaluated. The meandering of the contours offshore the detached breakwaters implies that part of the longshore sand transport may pass offshore of the detached breakwaters, but its quantitative evaluation is difficult using only **Fig. 2**.

REPRODUCTION OF DYNAMICALLY STABLE BEACH

A dynamically stable beach of the Shimizu coast is reproduced using a numerical model, and the controlling effect of longshore sand transport due to the detached breakwaters is investigated. **Figure 1** shows the bathymetry measured in March 2004. This figure is very similar to **Fig. 2(b)**, implying that the topography of the coast has reached an approximately dynamically stable state after the construction of the detached breakwaters. From this reason, a 1.4-km-long and 500-m-wide rectangular domain, as shown in **Fig. 1**, was selected, and beach changes in this study area were predicted. In this case, to reproduce the phenomenon that part of the longshore sand transport is diverted by the detached breakwaters and is carried downcoast, the contour-line-change model (Serizawa *et al.*, 2003) is applied, in which the effects of cross-shore sand transport depending on the balance between the local slope and the equilibrium slope, and the effect of longshore sand transport are taken into account, and the prediction of three-dimensional beach changes is possible. **Table 1** shows the calculation conditions for the model.

Table 1. Calculation conditions

Initial topography	Straight parallel contours (shoreline in 1989) Uniform slope of $tan\beta$ =1/10 Detached breakwaters (K_t=0.6)
Wave conditions	Breaker height: H_0'=3 m, T=9 s Breaker angle: α_b=17 deg. Tide level: mean sea level
Depth of closure	h_c=7 m
Berm height	h_R=3 m
Coefficients of sand transport	K_1=0.0042 K_2=0.2K_1 K_2=1.62K_1
Depth distribution of sand transport rate	Cubic equation given by Uda *et al.* (1996)
Equilibrium slope	$tan\beta_c$ =1/10
Critical slope	1/2 on land and 1/2 on seabed
Calculation domain	z=+3.5 to -7.5 m
Mesh size	Δx =10 m and Δz=1 m
Time interval	Δt=2 hrs
Total time of calculation	t = 5 years (21,900 steps)
Boundary conditions	Right boundary : Q_{in} =1.3x10^5 m^3/yr Left boundary : Free boundary Landward and offshore boundaries : q_z=0
Calculation method	Explicit finite difference method

An initial topography with straight parallel contours is set using an expanded coordinate system, to which the curvilinear coordinates fixed along the shoreline in 1989 are assigned, in accordance with the method of Uda *et al.* (1998a). The x-axis is taken to be alongshore and the y-axis is perpendicular to the x-axis. The initial beach slope is 1/10 on the basis of the measured bathymetry, and the detached breakwaters are set in this coordinate system. The reproduced period of beach change is 15 years between 1989 and 2004, and the beach change five years from the present is predicted, after confirming the applicability of the model for this calculation. The selection of a prediction period of five years is due to the fact that urgent measures are required because of severe beach erosion on the Shimizu coast.

For the wave conditions, rough waves with a 5% probability of occurrence are selected on the basis of the results of wave observation off the Shimizu coast, and considering that beach changes are more significantly affected by rough waves than normal waves. The selected equivalent wave height H_0' and the wave period are 3 m and 9 s, respectively. The predominant wave direction of this coast is south, and under oblique wave incidence, Snell's law gives a breaker angle of α_b=17 deg.

For the other important factors, the depth of closure h_c and berm height h_R are 7 and 3 m, respectively, on the basis of the analysis of bathymetric survey data (Itabashi and Uda, 1998; Uda *et al.*, 1998b), and the equilibrium slope is assumed to be 1/10 in the model. For the calculation in the vertical direction, the depth range between z=-7.5 m and z=3.5 m was divided into cells with Δz=1 m. Since the seabed slope in the offshore zone is as gentle as 1/50, there is no sinking of sand to a deeper zone. As a boundary condition, a longshore sand transport Q_{in} of 1.3×10^5 m^3/yr is introduced at the right boundary of the calculation domain, and longshore sand transport is distributed over depth in accordance with the depth distribution reported by Uda *et al.* (1996).

At the left boundary, a free boundary permitting the passage of longshore sand transport is set; longshore sand transport along each contour line invariant. The coefficient of longshore sand transport is adjusted so that Q at any point along the initial shoreline is equal to Q_{in}, satisfying the condition that the same amount of longshore sand transport as the inflow flows out from the left boundary. For this purpose, the coefficient of longshore sand transport K_1 was selected as 0.0042, which is two orders of magnitude smaller than the ordinary value. This is because the continuous action of rough waves with a small probability of occurrence over a year is assumed.

If we assume the ordinary value of the coefficient, excess longshore sand transport may be generated, and a dynamically stable beach cannot be reproduced. Under these conditions, a dynamically stable beach under the natural conditions before the construction of the detached breakwaters was reproduced using the model. Then, the detached breakwaters were placed on this dynamically stable beach, and the above-mentioned rough waves were generated for 15 years using the coefficient of longshore sand transport.

Figure 4(a) shows the initial and predicted topographies after 10 years; both results completely coincide with each other. **Figures 4(b)** and **4(c)** show the bathymetry after the detached breakwaters were built and show a comparison of the measured and predicted shoreline changes ΔY, respectively. In the calculation, the contour lines around the detached breakwaters approach this stable form within several years, and a dynamically stable beach is obtained in about ten years. Note that if only the present sand supply of 3.5×10^4 m^3/yr is given from upcoast, erosion gradually proceeds from upcoast, and the real shoreline changes cannot be reproduced. Sand supply from upcoast was increased by the trial-and-error method, and finally, it was found that if a sand supply of 7.0×10^4 m^3/yr is given, the present shoreline remains dynamically stable.

Figure 4(b) shows the dynamically stable beach topography predicted when the detached breakwaters were built, which corresponds well to the measured beach topography in 1992, as shown in **Fig. 2**. The contour line changes upcoast and downcoast of the detached breakwaters were accurately reproduced, as well as the

prediction of the meandering of contour lines offshore of the detached breakwaters, which corresponds to the passage of part of the longshore sand transport offshore of the detached breakwaters. **Figure 4(c)** shows the comparison between measured and predicted shoreline changes. The measured shoreline changes are accurately reproduced by the numerical simulation.

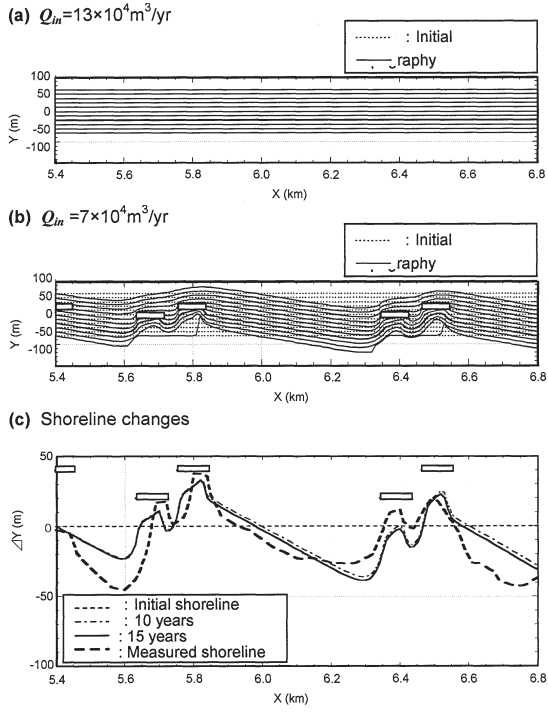

Fig. 4. Dynamically stable beach topography predicted when detached breakwaters were built and comparison of shoreline changes

IMPROVEMENT OF SHAPE OF DETACHED BREAKWATERS AND BEACH NOURISHMENT AS MEASURE AGAINST EROSION

4.1 Effect of beach nourishment on surrounding coast

Since the Shimizu coast is currently in dynamical equilibrium, the hasty construction of various facilities is feared to cause a rapid expansion of the eroded zone. Therefore, the effect of beach nourishment on the surrounding coast was investigated by varying the volume and location of the beach nourishment. **Figure 5(a)** shows the shoreline changes in the case that the annual nourishment volume from upcoast is reduced by 1.0x10^4 m^3/yr. In this case, the shoreline significantly receded in an extensive area updrift of detached breakwaters I, and the maximum shoreline recession reached as large as 20 m on the updrift boundary at X=6.8 km. This means

that the reduction of the present nourishment volume to reduce cost will cause severe erosion.

An additional supply of sand of 1.0×10^4 m^3/yr was considered at the eroded location immediately downcoast of detached breakwaters I, instead of the nourishment upcoast of the detached breakwaters, although this is slightly aside from the original aim of determining whether the reduction in nourishment volume is possible. The results are shown in **Fig. 5(b)**. This method is effective in reducing the shoreline recession immediately downcoast of the detached breakwaters to some extent, as shown in the figure, but the continuation of sand nourishment every year aggravate the problem.

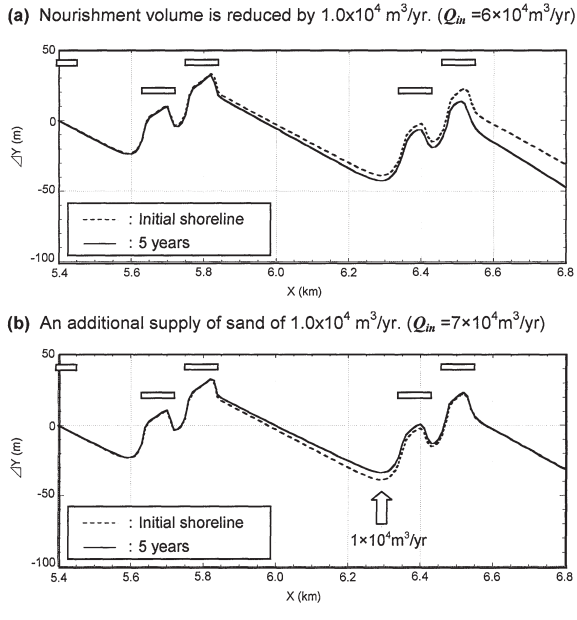

Fig. 5. Comparison of shoreline changes when changing volume of beach nourishment

4.2 Comparison of beach changes around detached breakwaters and T-shaped groin

In the case of the headlands using the detached breakwaters, longshore sand transport may pass between the breakwaters and the shoreline during storm wave conditions, resulting in a reduction in the obstruction effect of longshore sand transport due to detached breakwaters, and nourished sand may be transported away downcoast. Because of this, the alteration of the detached breakwaters to T-shaped groins has been proposed locally. To investigate this point, beach changes were predicted in

cases that longshore sand transport passing through behind the detached breakwaters was totally obstructed owing to the alteration of the detached breakwaters to T-shaped groins, while maintaining the present volume of nourishment.

Figure 6(a) shows the bathymetry in a dynamically stable condition in the case when one of detached breakwaters I, located on the updrift side of the detached breakwaters, was altered to a T-shaped groin, and **Fig. 6(b)** shows the shoreline changes. In this case, the salient formed behind the detached breakwaters was significantly eroded and then disappeared, because longshore sand transport was blocked by the T-shaped groin. It is clear that the alteration of the detached breakwater to a T-shaped groin is ineffective in maintaining a dynamically stable beach and in conserving the beach without large changes.

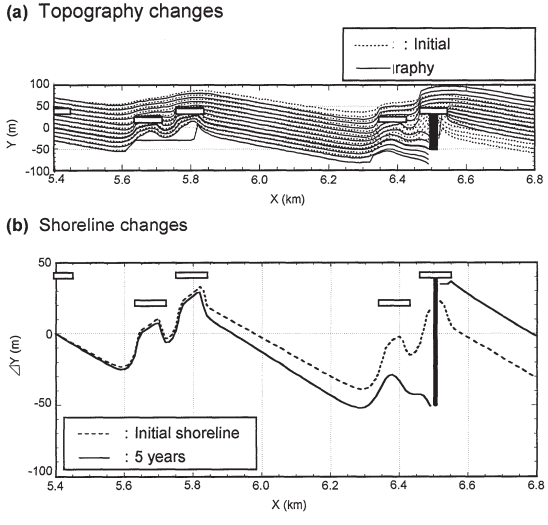

Fig. 6. Dynamically stable beach topography when one of detached breakwaters was altered to T-shaped groin and comparison of shoreline changes

4.3 Beach changes associated with extension in length of detached breakwaters

The dynamically equilibrium condition was predicted in the case that the length of each detached breakwater was extended by 50 m alongshore without changing the present volume of nourishment. The results of the shoreline changes are shown in **Fig. 7**. In the case that detached breakwater I-1 was extended in the updrift direction, the shoreline upcoast of detached breakwaters I gradually advanced, as shown in **Fig. 7(a)**, whereas the shoreline recession increased by 5 m downcoast of detached breakwaters I, as an adverse effect.

In the case that detached breakwater I-2 was extended in the downdrift direction, the location of the maximum shoreline recession downcoast of detached breakwaters I

shifted by 50 m, as shown in **Fig. 7(b)**, but the shoreline recession did not change compared with the present. In the case that detached breakwater II-1 was extended in the updrift direction, the shoreline advanced in an extensive area upcoast, as shown in **Fig. 7(c)**, but the change was ineffective in reducing the shoreline recession immediately downcoast of detached breakwaters I, because the distance between the detached breakwaters was is too long.

In the case that detached breakwaters I-2 and II-1 were extended simultaneously, the location where the shoreline retreated most severely downcoast of detached breakwaters I was shifted by 50 m downdriftward, and shoreline recession was reduced, as shown in **Fig. 7(d)**. It is clear that narrowing the distance between the detached breakwaters is effective in preventing beach erosion. In the case that both of detached breakwaters I were simultaneously extended, the shoreline on the updrift side advanced significantly, because the effect of obstructing longshore sand transport due to detached breakwaters I was increased, but the shoreline recession immediately downcoast increased by 5 m.

4.4 Reduction in beach nourishment volume by extension of detached breakwaters

In the previous sections, to reduce the beach nourishment volume, the case in which beach nourishment volume is simply reduced and the case using T-shaped groins were investigated, but no effective results were obtained. On the other hand, the extension of the detached breakwaters was found to be effective in reducing the shoreline recession to some extent. Therefore, the possibility of the reduction in beach nourishment volume was investigated here under the condition that the distance between the detached breakwaters is shortened by extending the length of each detached breakwater by 50 m.

First, the shoreline advance was investigated in the case that the same beach nourishment volume as present was supplied to beaches after the extension of the detached breakwaters. The bathymetry and shoreline changes are shown in **Figs. 8(a)** and **8(b)**. In this case, the location where the shoreline markedly receded immediately downcoast of detached breakwaters I shifted by 50 m, the shoreline upcoast of detached breakwaters I advanced significantly, and the maximum shoreline recession was reduced. Thus, it was found that this method is very effective.

Furthermore, the annual sand supply rate was reduced to 6.0×10^5 and 6.5×10^5 m^3/yr, which means reductions in sand supply by 0.5×10^4 and 1.0×10^4 m^3/yr, respectively, compared with the present nourishment volume, to investigate the possibility of a reduction in beach nourishment volume. **Figure 8(c)** shows the results of the case in which nourishment volume was reduced by 1.0×10^4 m^3/yr. Although the shoreline receded both upcoast and downcoast of the detached breakwater owing to the reduction in nourishment volume, the shoreline recession downcoast of the detached breakwaters was insignificant compared with that in the case shown in **Fig. 8(a)**.

Thus, extending detached breakwaters is effective in reducing the annual sand supply from 3.5×10^4 to 2.5×10^4 m^3/yr.

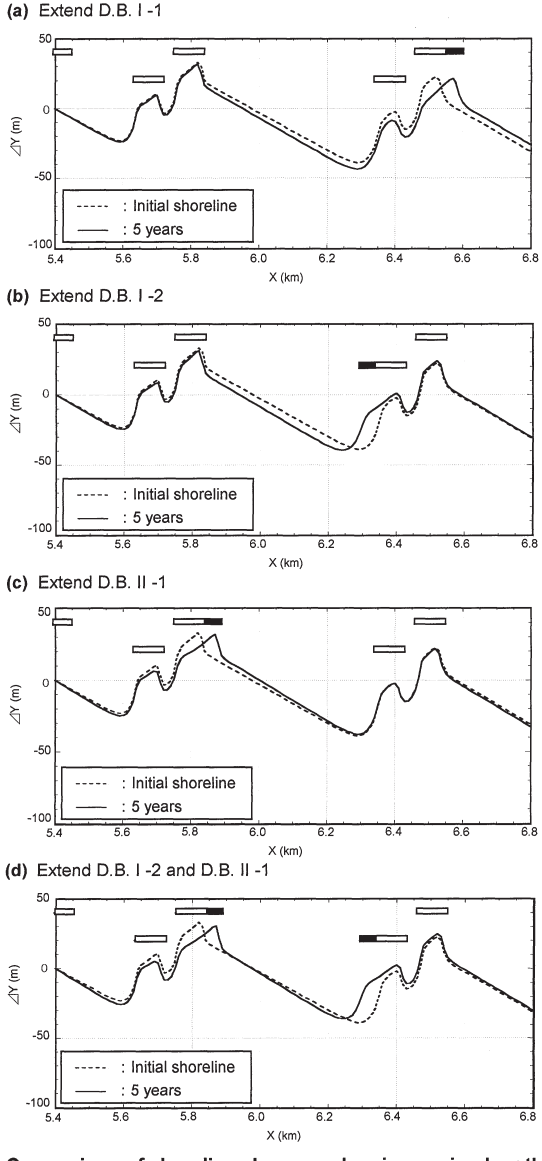

Fig. 6. Comparison of shoreline changes when increasing length of detached breakwaters.

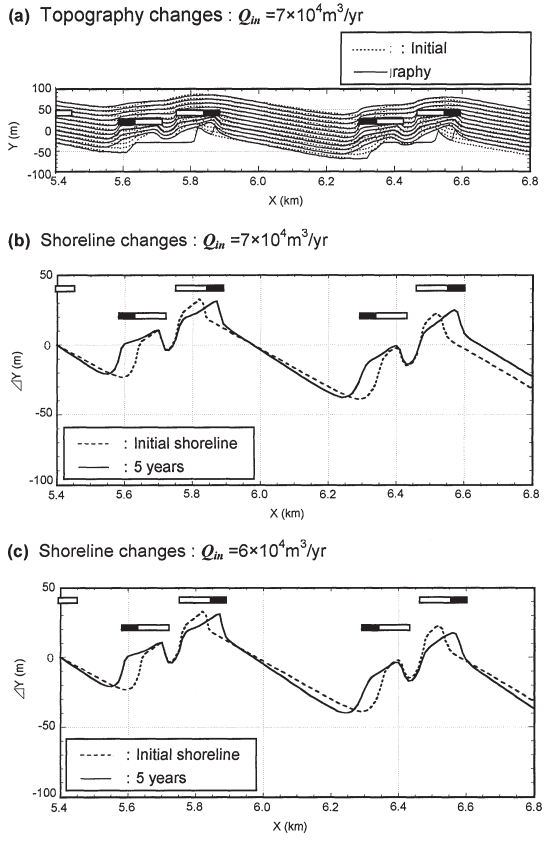

Fig. 8. Dynamically stable beach topography when detached breakwaters were extended and comparison of shoreline changes when reducing beach nourishment

CONCLUSIONS

(1) On the Shimizu coast, 1.3x10^5 m^3/yr of sand had been continuously transported by northeastward longshore sand transport before the construction of the detached breakwaters, while maintaining a dynamically stable state. After the construction of the detached breakwaters, the longshore sand transport rate was reduced to 7.0x10^4 m^3/yr, resulting in a new dynamically stable state.

(2) Because the longshore sand transport rate in the new dynamically stable state is larger than the annual amount of beach nourishment of 3.5x10^4 m^3/yr, the beach has eroded. Erosion downcoast of the detached breakwaters has occurred, increasing the probability of seawall damage.

(3) As a measure to ease beach erosion and to reduce longshore sand transport, reshaping the detached breakwater into a T-shaped groin was studied, but this was ineffective because of the occurrence of severe downcoast erosion.
(4) Extending the existing detached breakwaters by 50 m to narrow the distance between them is effective in mitigating erosion and in reducing the annual amount of beach nourishment necessary.

REFERENCES

Itabashi, N. and T. Uda (1998). Field observation of erosion and accretion waves on Shizuoka and Shimizu coasts in Suruga Bay in Japan, Proc. 26th ICCE, pp. 3178-3191.

Serizawa, M., T. Uda, T. San-nami, K. Furuike and T. Kumada (2003). Improvement of contour line change model in terms of stabilization mechanism of longitudinal profile, Coastal Sediments '03, pp. 1-15.

Uda, T. and K. Yamamoto (1994). Beach erosion around a sand spit - an example of Mihono-Matsubara sand spit, Proc. 24th ICCE, pp. 2726-2740.

Uda, T., Y. Yamamoto, N. Itabashi and K. Yamaji (1996). Field observation of movement of sand body due to waves and verification of its mechanism by numerical model, Proc. 25th ICCE, pp. 137-150.

Uda, T. (1997). *Beach erosion in Japan*, Sankaido Press, Tokyo, p. 442. (in Japanese)

Uda, T., M. Sumiya, H. Yazawa, Y. Ohtani and Y. Atsusaka (1998a). Prediction of beach changes around Oyazawa-bana sand spit using expanded coordinate system, Annual Jour. of Coastal Eng., JSCE, Vol. 45, pp. 541-545. (in Japanese)

Uda, T., H. Yamagata, K. Katoh and N. Akamatsu (1998b). Predictive model of three-dimensional development and deformation of a river mouth delta by applying contour line change model, Proc. 26th ICCE, pp. 3138-3150.

GEOLOGIC CHARACTERIZATION of SHELF AREAS USING usSEABED for GIS MAPPING, MODELING PROCESSES and ASSESSING MARINE SAND and GRAVEL RESOURCES

S. Jeffress Williams[1], James D. Bliss[2], Matthew A. Arsenault[3], Chris J. Jenkins[4], John A. Goff[5]

1. U.S. Geological Survey, Woods Hole Science Center, Woods Hole, MA 02543, USA. jwilliams@usgs.gov.
2. U.S. Geological Survey, 520 North Park Ave, Tucson, AZ 85719, USA. jbliss@usgs.gov.
3. U.S. Geological Survey, Woods Hole Science Center, Woods Hole, MA 02543, USA. marsenault@usgs.gov.
4. INSTAAR, University of Colorado, Boulder, CO 80309, USA. chris.jenkins@colorado.edu.
5. Institute for Geophysics, Jackson School of Geosciences, University of Texas, Austin, TX 78759, USA. goff@utig.ig.utexas.edu.

Abstract: Geologic maps depicting offshore sedimentary features serve many scientific and applied purposes. Such maps have been lacking, but recent computer technology and software offer promise in the capture and display of diverse marine data. Continental margins contain landforms which provide a variety of important functions and contain important sedimentary records. Some shelf areas also contain deposits regarded as potential aggregate resources. Because proper management of coastal and offshore areas is increasingly important, knowledge of the framework geology and marine processes is critical. Especially valuable are comprehensive and integrated digital databases based on high-quality information from original sources. Products of interest are GIS maps containing thematic information, such as sediment character and texture. These products are useful to scientists modeling nearshore and shelf processes as well as planners and managers. The U.S. Geological Survey is leading a national program to gather a variety of extant marine geologic data into the usSEABED database system. This provides centralized, integrated marine geologic data collected over the past 50 years. To date, over 340,000 sediment data points from the U.S. reside in usSEABED,

which combines an array of physical data and analytical and descriptive information about the sea floor and are available to the marine community through three USGS data reports for the Atlantic, Gulf of Mexico, and Pacific published in 2006, and the project web sites: (http://woodshole.er.usgs.gov/project-pages/aggregates/ and http://walrus.wr.usgs.gov/usseabed/)

INTRODUCTION

Rapid population growth and development in the coastal zone continues and demographic projections suggest that people will continue moving to the coast to live and recreate, placing more people and development at risk. With climate change likely causing accelerating global sea-level rise and increased storminess, coastal regions may become even more dynamic, experiencing greater vulnerability to erosion, inundation, and more frequent storm-surge flooding.

Beach nourishment is increasingly viewed as the preferred soft-engineering method for use on developed coasts to mitigate erosion, reduce storm and flooding risk and enhance recreation. Over the past 80 years more than 650 million cubic meters of sand have been used throughout the U.S. for beach nourishment, mostly from offshore dredging. For beach nourishment to be viable, however, large volumes of high-quality sand are necessary. Also, the sand deposits must be located reasonably close to the beaches being nourished and in water depths ranging typically from approximately about -10 m, an approximate "depth of closure" for sediment transport, to -40 m, an approximate current limit of U.S. commercial dredging (Williams, 1992).

Continental shelf regions adjacent to the mainland are products of a complex geologic history and dynamic oceanographic processes, dominated by the Holocene marine transgression (>100 m sea-level rise) during the past 20,000 years. The area of the Exclusive Economic Zone, extending 200 nautical miles seaward of the coast, is larger than the continental U.S. This area contains submerged landforms that provide a variety of natural functions and societal benefits, such as: critical habitats for fisheries, ship navigation and home-land security, and engineering activities (i.e., oil and gas platforms, pipeline and cable routes, potentially wind energy generation). Some parts of the continental margins also contain unconsolidated hard-mineral deposits, such as sand and gravel, regarded as potential aggregate resources to augment needs not met by onshore deposits.

A broad and diverse range of sedimentary deposits (Figure 1) on the inner continental shelf, considered the best quality sand sources for beach nourishment, are not random in occurrence, but instead are well defined in terms of their stratigraphic framework, sediment texture and character, and geologic origins. Some of the sand bodies are relict landforms, some are associated with modern shelf processes, while others are relict but highly modified by the late Holocene marine transgression and modern processes.

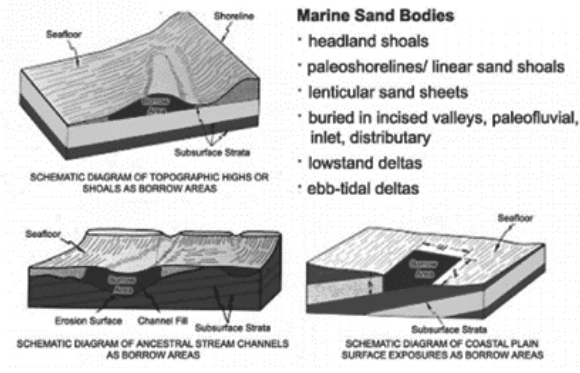

Figure 1. Schematic of the variety of surface and buried marine sand bodies on the shelf.

Onshore aggregate shortages in some parts of the country might be met using marine aggregates. However offshore aggregate resources are sparse or mostly unknown for many regions, and sand volumes needed to meet beach nourishment requirements and sustain long-term (50 yr projects) beach nourishment are uncertain (Williams et al., 2003). For example, projects planned for Long Island, New York, and the Mississippi-Alabama coast will each require an estimated 40 million cubic meters of suitable sand. Coastal restoration of Louisiana, following Hurricanes Katrina and Rita in 2005, is projected to require more than 100 million cubic meters of assorted sediment types including sand for barrier nourishment, clay for levees, and sandy muds for wetlands restoration.

Because offshore aggregate areas are increasingly important for a variety of purposes, knowledge of the geological framework and processes is critical. Further comprehensive, up-to-date, and integrated computer databases are needed by a variety of users. Products of greatest value are Geographic Information System (GIS) compatible base maps displaying thematic information such as sea floor physiography, geology, sediment character and texture, sea floor roughness, and geotechnical engineering properties. Digital geologic maps, based on unified national datasets showing the sedimentary character of continental margins, are critical for scientists to better understand and interpret the geologic history and sedimentary processes that formed and continue to modify the sea floor. These map products are useful to planners and managers for regulating and managing coastal and offshore areas. This paper presents examples of usSEABED data use and application for two regions, New York Bight and Louisiana.

Assessing Marine Aggregate Resources

The U.S.Geological Survey (USGS), in collaboration with other Federal agencies (e.g., Office of Naval Research, Minerals Management Service, U.S. Army Corps of

Engineers, National Oceanic and Atmospheric Administration) and a number of universities (e.g., University of Colorado, University of Texas, University of New Orleans), is leading a nationwide effort to assemble legacy marine geologic data shown in Figure 2 into a unified database system called usSEABED, as a task of the Marine Aggregate Resources and Processes (MARP) project.

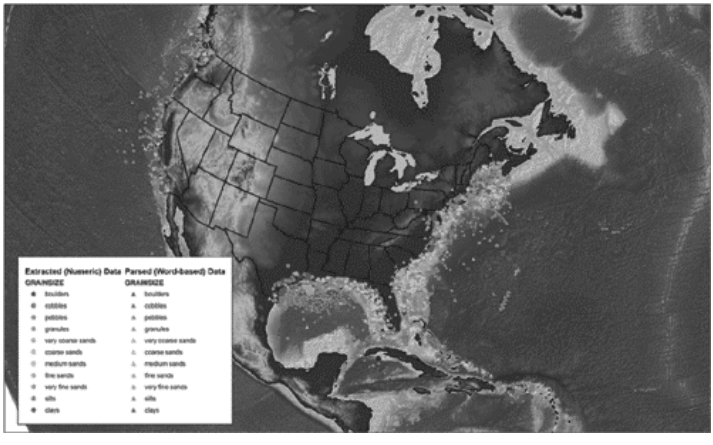

Figure 2. Map of current usSEABED data coverage and sediment grain size.

The objectives of MARP are to produce a series of new geologic maps and reports of the sea floor that will provide scientific insights into the character and geologic development of U.S. continental margins. These maps and information are used to assess the potential availability of offshore sand and gravel resources using stochastic techniques such as resource modeling and Monte Carlo simulations in combination with GIS maps. The mapping and aggregate resource assessments are being conducted on a national scale using the usSEABED database as described in Williams et al. (2006a; 2006b). Potential uses for these data include: (1) defining the geological variability of the sea floor, in relation to benthic habitat diversity; (2) improving our understanding of the processes that control the distribution and transport of bottom sediments and benthic habitats; (3) locating aggregate resources for beach nourishment and industrial applications; and (4) providing a detailed geospatial framework for future marine science research, monitoring, and management activities. The initial assessments are in progress for the New York Bight and the Louisiana offshore deltaic plain.

The first three of the usSEABED data releases: Atlantic Coast Offshore Surficial Data Release, version 1.0 (Reid et al., 2005) was published as USGS Data Series 118. Its sister publication, Gulf of Mexico and Caribbean Offshore Surficial Data Release, version 1.0 (Buczkowski et al., 2006), is available as USGS Data Series 146. A third data release, covering the Pacific Coast (Reid et al., 2006), was published in late

2006. Other data series reports for Hawaii and Alaska will be published in 2007. Altogether, the database currently includes over 340,000 locations of sea floor data and sediment characteristics (Figure 2). Although the majority of these samples are surficial samples, additional sampling devices include piston and vibracores and dredge samples. The data supplied in these reports are made available with geographic coordinates to allow the data to be incorporated into any GIS system. Federal Geographic Data Committee compliant metadata are included with the data layers.

In an effort to make the data more accessible to the public, geographically relevant subsets of data are being posted to coastal state GIS clearinghouse websites. Many of these sites serve as the primary source of GIS information for state and local researchers and agencies. The majority of the holdings on these sites are on-land features and the addition of usSEABED data constitutes a substantial expansion of their coverage for offshore areas. As an added bonus, many of the clearinghouses have helped the USGS establish additional connections with local agencies and their data collections.

METHODS and RESULTS

usSEABED Sediment Database and dbSEABED Processing System

The usSEABED database is based on the dbSEABED system for integrating sea floor datasets. The approach differs from traditional relational databases in that processing seeks the parts of each dataset that conform to standards or can be brought to conformance (Jenkins, 1997; Jenkins, 2002; Reid et al., 2001). The result is an information rich, quality assured, GIS-ready point dataset.

In addition to the usual forms of numeric analytical sediment data, estimates of seabed characteristics are produced from word-based descriptions. The ability to handle word-based data greatly extends the power of the system to map seabed, where on a global average greater than 85 percent of the data characterizing the seabed are word-based (Jenkins, 1997). Also, it extends to information to biogenic, very coarse and rock terrains that are hard to sample or analyze. The handling of word-based descriptive data is based on a parser that divides the descriptions into linear equations around objects, quantifiers and modifiers (Jenkins, 1997), a thesaurus that attaches meanings and memberships, and a linear weighted assembly of the numerical totals. Term meanings and memberships are defined with using Fuzzy Set Theory.

The dbSEABED's expanded capability to extract data increases the overall spatial coverage of the data, but also requires users to understand a clearly defined distinction between the variations in output data. Altogether, five output files are written, each classified by its processing history and content (Extracted, Parsed, Calculated, Component and Facies). Extracted data, those data from strictly performed, lab-based, numeric analyses, are written to a data file with the _EXT tag. Most data in this file are listed as reported by the source data report, and are based on rigorous lab-determined values. These data are the most precise, but used alone may

cause a lack of representation since they refer mainly to finer sediments. Alternatively, outputs obtained from deck and lab descriptions (including core descriptions), video or photographic descriptions, or geophysical mapping are held in the parsed data set. Together, these two types of output represent the actual values from the original survey and laboratory materials/reports.

Additional values that can be calculated or estimated from the extracted and parsed results using documented empirical or theoretical relationships are reported in the calculated outputs. Although the calculated data could be combined with the extracted and the parsed, they are kept separate and are the least reliable of the three data file types and should be used with caution.

The final two file types, Component and Facies have similar in content. The Component file contains component abundance and feature intensity information. The abundances intensities are evaluated solely on major the synonyms of the specific terms within the original descriptions. On the other hand, the facies file identifies how strongly a sample expresses groups of components and features.

Uncertainty and variability of marine sediments

Sea floor sediments comprising the continental shelf are spatially heterogeneous on many scales: from regional-scale variations, such as those associated with depocenters or the shoreline, to micro-scale variations, such as those associated with ripple bedforms. Between these extremes, are variations associated with different bedforms, or patchiness caused by factors such as localized erosion, biologic processes, or glacial deposits (Goff et al., 2004; 2006). Because spatial sediment variability is related to geological framework and processes, Goff et al., (in prep) are using usSEABED and statistical tools to achieve basic understanding of the geologic response to the oceanographic forcing at the sea floor. The next step will be to use these data as a predictive tool. Although usSEABED coverage is far from uniform, it provides, in many continental shelf and estuarine regions, data sets that are sufficient in quantity and coverage to robustly estimate spatial variability functions such as the semi-variogram. Such a predictive capability would have important scientific and engineering applications in ocean acoustics, where seabed variability strongly affects signal detection. Understanding sediment variability is also important for interpolation and GIS map making using kriging and other similar mapping methods.

Sand and Gravel Resources on the Continental Shelf

A wide variety of sedimentary sand bodies or deposits, such as cape-associated and linear shoals (Figure 1) develop, and are preserved on storm dominated shelves. They are particularly notable on the mid-Atlantic shelf from Long Island to South Carolina. Other sand bodies, such as those off the Louisiana delta plain, are remnants of older deltas and transgressed barrier islands. These marine sand deposits are recognized as containing desirable sand suitable for beach nourishment and related activities. There is now a need to provide a quantitative assessment of these sand resources that permits a probabilistic estimate of how much sand may be present as a potential resource. To carry out such assessments, a statistical approach extensively used for quantitative mineral resource assessment is being used in the MARP project

(Bliss and Bolm, in review). Assessments are underway for the New York Bight region and offshore Louisiana and will be reported in 2007.

Mineral-resource assessments may be considered a form of regional mineral-deposit planning that is highly formalized and are conducted by an assessment team. Such assessments have also found application in land planning, land exchanges, and in the evaluation of possible management and development situations. Application of the approach calls for a number of new models that are a simplification of information and data about marine deposit systems, such as cape-associated and linear shoals. One type of model is descriptive in that it is a narrative that allows for a consistent recognition of marine sand deposits. Also needed are a number of quantitative models that are statistical or empirical distributions that describe quantitative characteristics to help recognize known sand deposits. This model also includes helping to recognize targets for deposits that have not been characterized.

Variables of deposits considered for quantitative modeling include: area, thickness, bathymetry, mean sand grain size, volume, portions of the deposit that are sand-dominated facies, and spatial density. The last variable, spatial density is particularly helpful in estimating the number of undiscovered deposits within permissive tracts on the shelf. Two of the models being used in Monte Carlo simulations include the volume model and sand facies model. These models, together with estimates of number of undiscovered deposits, allow a probabilistic prediction of how much sand may be present within each tract (Bliss and Bolm, in review).

New York Bight Region

Broad regions of the continental shelf, such as the New York Bight, are the product of a complex geologic history and dynamic oceanographic processes, dominated by the Holocene marine transgression (>100 m sea-level rise) following the last Pleistocene ice sheet advance about 20,000 years ago. The present distribution of surficial sediment off the northeastern U.S. is shaped from the deposits left by the last glaciation and reflects the cumulative effects of erosion, transport, sorting, and deposition by storm and tidal processes during the Holocene rise in sea level. As a result, the sediments on the sea floor represent both an historical record of former conditions and an indication of present oceanographic processes (Williams et al., 2006a).

Figures 3, 4 and 5, from Williams et al. (2006a) based on data in Reid et al. (2005), are example GIS products that are possible using usSEABED. These figures present the distribution of sediment size (mean grain size in phi units), the percent composition of sea floor samples (gravel, sand and mud), sorting ratios, and percentages of sand (often used to identify high quality sand for beach nourishment). Figure 4 shows potential borrow areas.

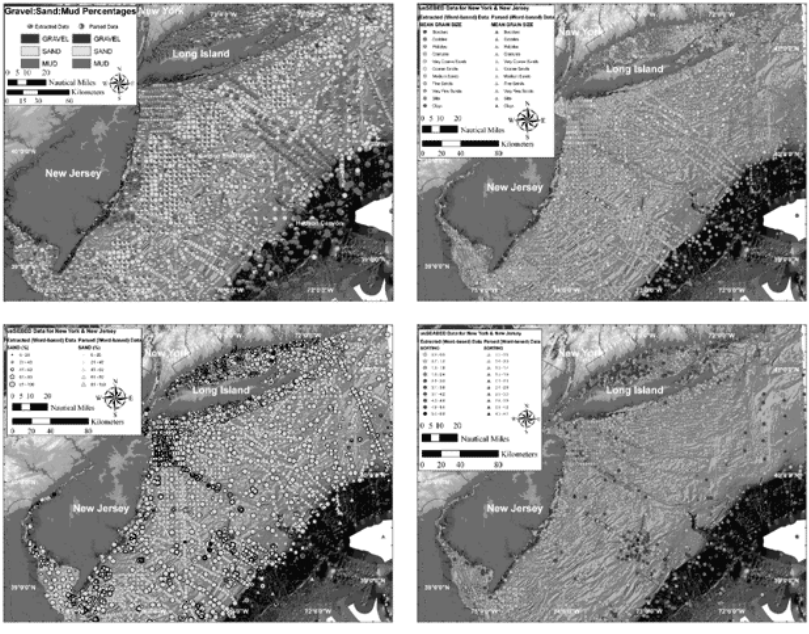

Figure 3. Maps of sediment character in the New York Bight offshore region. While sand predominates across the region, muddy sediments are associated with the Hudson shelf valley and deeper regions. Gravelly sands are common in erosional areas.
(From Williams et al. 2006a).

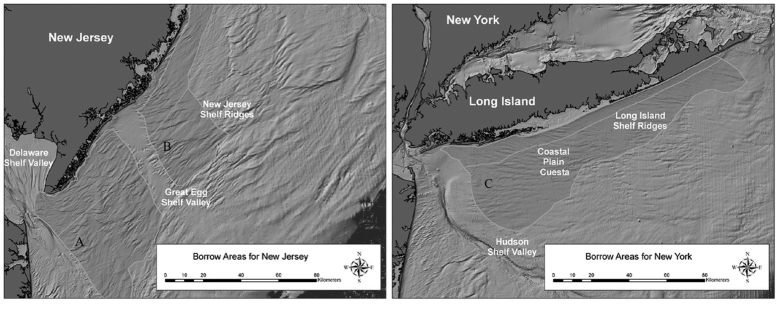

Figure 4. Map of three potential sand and gravel borrow areas in New York Bight being considered in the sand and gravel assessment study.

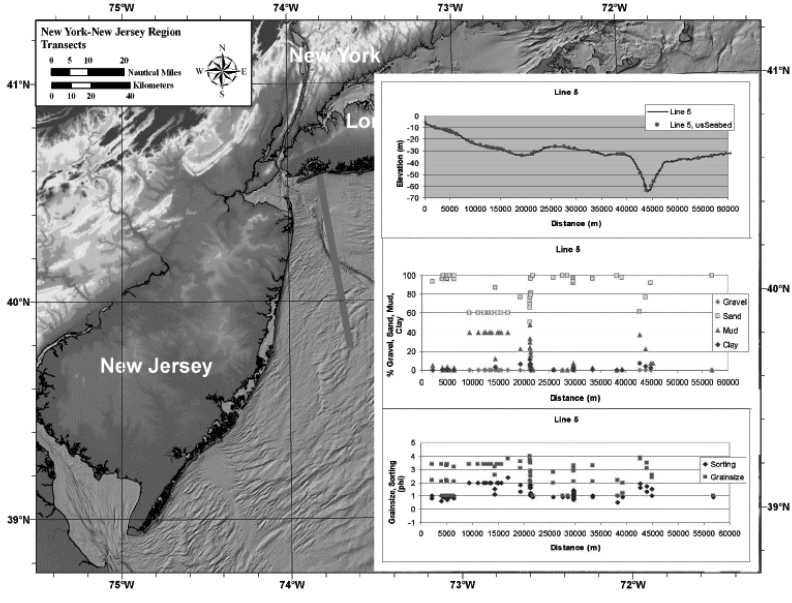

Figure 5. North-south shelf transect from Rockaway Beach, NY across the Hudson shelf valley with associated plots of seabed sediment grain size and sorting.
(From Williams, 2006a).

Louisiana Delta Plain Region

The Louisiana coastal zone, comprising the Mississippi River delta plain and stretching nearly 400 km from Sabine Pass at the Texas border east to the Chandeleur Islands at the Mississippi border, represents one of North America's most important coastal ecosystems in terms of natural resources, human infrastructure, and cultural heritage (Figure 6). At the same time, this region has the highest rates of coastal erosion and wetland loss in the Nation due to the complex interaction of natural processes and anthropogenic actions over the past century. Comparison of historical maps dating back to 1855 and recent aerial photography and Lidar surveys show the Louisiana coast undergoing net erosion at highly variable rates. These rates have increased significantly during the past several decades. (Williams et al. in press).

Earlier published rates of statewide average shoreline erosion were >6 m/yr; rates have increased to more than 10 m/yr. The increase is attributable to the collective actions of storms (e.g., Hurricanes Katrina and Rita), rapid natural and hydrocarbon-removal induced subsidence, and pervasive man-made alterations of the rivers, wetlands and the coast. In response to the dramatic landloss, regional-scale restoration plans are being developed by a partnership of federal and state agencies for the delta plain that have the objectives of maintaining the barrier islands, reducing

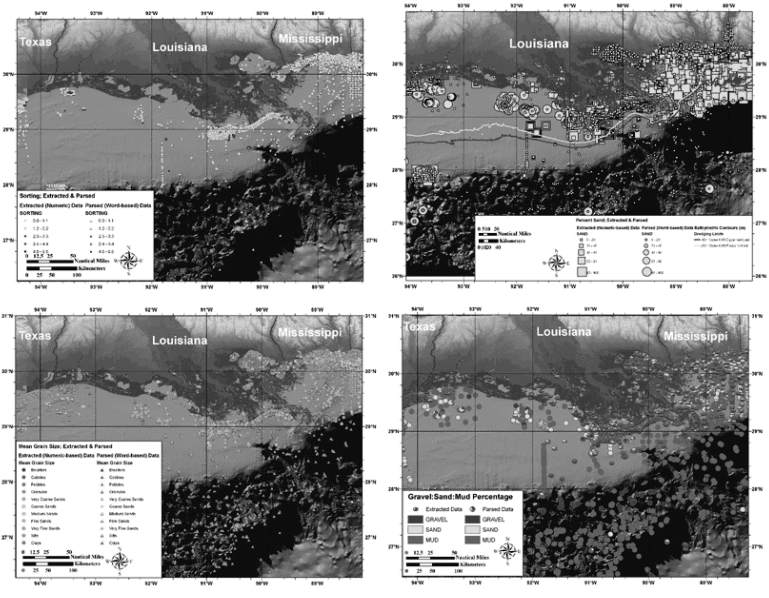

Figure 6. Maps of sediment character of the Louisiana offshore. While muddy sediments predominate due to the Mississippi River, sands are present in nearshore deposits and relict submerged sand bodies on the shelf. (From Williams et al. 2006b).

wetland loss, and enhancing the natural sediment delivery processes. There is growing awareness that the sustainability of Louisiana's coastal features and human infrastructure depends on the successful restoration of natural geologic processes. Critical to the long term success of restoration is scientific understanding of the geologic history and processes of the coastal zone region, including interactions between the rivers, wetlands, coast, and inner shelf.

A variety of geophysical studies and mapping of Late Quaternary sedimentary framework and coastal processes by USGS and other scientists have documented that the Louisiana delta plain is the product of a complex history of cyclic delta switching by the Mississippi River and its distributaries over the past approximately 10,000 years, resulting in laterally overlapping deltaic depocenters (Williams, et al., 2006b). The interactions among riverine, coastal, and inner shelf processes have been superimposed on the Holocene transgression resulting in distinctive landforms and sedimentary sequences.

Four Holocene shelf-phase delta complexes have been identified using seismic-reflection data and vibracores. Each delta complex is bounded by transgressive surfaces. Following each cycle of deposition and abandonment, the delta lobes

undergo regional subsidence and marine reworking that forms transgressive coastal systems and barrier islands. Ultimately, the distal end of each of the abandoned delta lobes is marked by submerged marine sand bodies representing drowned barriers. These five sand bodies, shown in Figures 7 and 8 (e.g., Ship Shoal, Outer Shoal, Trinity Shoal, Tiger Shoal, Cat Island Ebb Shoal, St. Bernard Shoal), offer the largest volumes and highest quality sand offshore Louisiana for beach nourishment and wetlands restoration (Kulp et al., 2005; Williams et al., 2006b).

The four large sand shoals on the inner shelf, representing the reworked remnants of former prograded deltaic headlands that existed on the continental shelf at lower sea level, were generated in the retreat path of the Mississippi River delta plain during the Holocene transgression. Kulp et al. (2005) and Williams et al. (in press) describe how these sand bodies represent former shoreline positions associated with lower stands of sea level. Cat Island Ebb Shoal is a modern feature. Short periods of rapid relative sea-level rise led to the transgressive submergence of the shorelines which today can be recognized at the -10 m to -20 m isobaths on the Louisiana continental shelf. Trinity Shoal and Ship Shoal represent the -10 m middle-to-late Holocene shoreline trend, whereas Outer Shoal and the St. Bernard Shoals define the -20 m middle Holocene shoreline trend. Collectively, these sand shoals constitute a large volume of high quality sandy sediment potentially suitable for barrier island nourishment and coastal restoration.

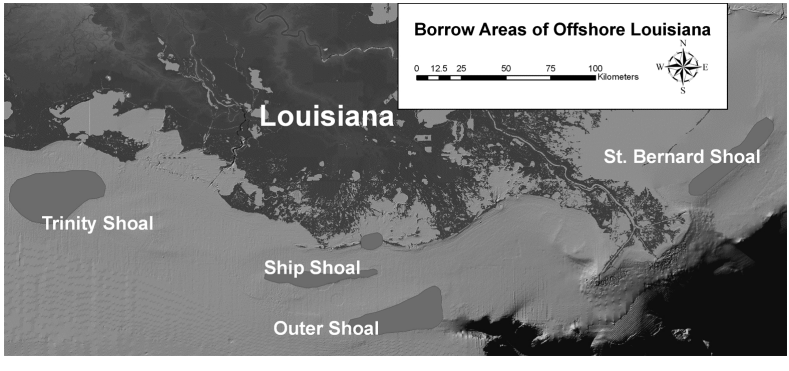

Figure 7. Map of five major sand bodies and potential borrow areas offshore Louisiana being considered in the sand and gravel assessment study. Cat Island Ebb Shoal is the central unlabeled feature.

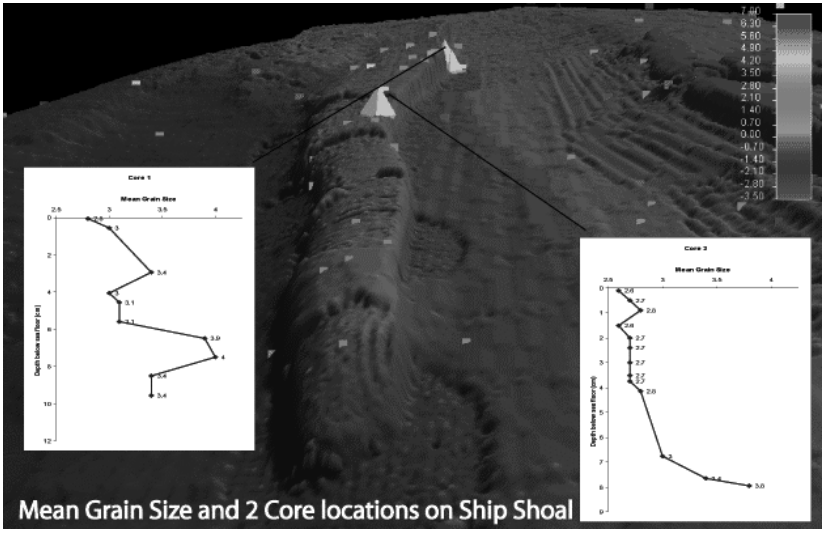

Figure 8. Diagram of Ship Shoal, Louisiana showing the elongate and asymmetric morphology of the feature, 50km in length and 3- 5m in height, and internal grain size based on representative cores. Ship Shoal, a drowned barrier island, is a premier marine sand body on the Louisiana shelf.

CONCLUSIONS

A national program led by the USGS is gathering a variety of extant marine geologic data into the usSEABED system. The data in this system are being used to generate new geologic maps of offshore areas and assessing potential marine aggregate resources. The usSEABED system provides a centralized, fully integrated digital database of marine geologic data collected by USGS, other federal and state agencies, universities and private companies. The usSEABED, which combines a broad array of physical data and information about the sea floor, including sediment textural, statistical, geochemical, geophysical, and compositional information, is available to the marine community through USGS Data Series publications. The use of usSEABED and derivative GIS map products is part of ongoing USGS efforts to conduct regional assessments of potential marine sand and gravel resources, map benthic habitats, and support research in understanding sea floor character and sediment transport processes.

ACKNOWLEDGEMENTS

This study, supported by the USGS Coastal and Marine Geology Program, represents a partnership with the University of Colorado and University of Texas, as well as other federal and state agencies. In particular, ONR supports the studies on sediment uncertainty and variability. The support of these partners in moving this study along

is appreciated. Constructive reviews of this paper by L.J. Poppe and E. Pendleton, both USGS, are appreciated.

ADDITIONAL INFORMATION

The opportunities for multidisciplinary studies of offshore areas using the usSEABED database are significant and the marine science community is encouraged to learn more about the Marine Aggregates Assessment project and usSEABED. In addition, the community is encouraged to contribute additional datasets to continue building this marine sediment archive. Questions about the Marine Aggregate Resources and Processes project may be addressed to S.J. Williams; inquiries for adding data to usSEABED may be addressed to M.A. Arsenault.

REFERENCES

Bliss, J.D., and Bolm, K.S., in review, Modeling and assessing marine sand resources for cape- and ridge-associated marine sand deposit types, in review, chapter contribution to Contributions to Industrial-Minerals Research, USGS Bulletin 2209, 47p.

Buczkowski, B., Reid, J.M., Jenkins, C., Reid, J.A., Williams, S.J., and Flocks, J.G., 2006. usSEABED, Gulf of Mexico and Caribbean (Puerto Rico and U.S. Virgin Islands) Offshore Surficial Data Release, version 1.0, U.S.Geological Survey Data Series 146, CD-ROM.

Goff, J.A., Kraft, B.J., Mayer, L.A., Schock, S.G., Sommerfield, C.K.,Olson, H.C., Gulick, S.P.S., and Nordfjord, S., 2004, Seabed characterization on the New Jersey middle and outer shelf: Correlability and spatial variability of sea floor sediment properties, *Marine Geology*, 209, 147-172.

Goff, J. A., Jenkins, C., and Calder, B., 2006, Maximum likelihood resampling of noisy, spatially correlated data, *Geochem. Geophys. Geosys*, doi:10.1029/2006GC001297, 2006.

Goff, J.A., Jenkins, C., and Williams, S.J., in preparation, Characterization of seabed sediment variability using the usSEABED data base, 35 p.

Jenkins, C.J., 1997, Building Offshore Soils Databases. *Sea Technology*, 38, 25-28.

Jenkins, C.J., 2002, Automated digital mapping of sediment colour descriptions, *Geo-Marine Letters* , 22, 181-187.

Kulp, M., Penland, P.S., Williams, S.J., Jenkins, C., Flocks, J.G., and Kindinger, J.L., 2005. Geologic Framework, Evolution, and Sediment Resources for Restoration of the Louisiana Coastal Zone: *Journal of Coastal Research*, SI44, 56-71.

Reid, J.A., Jenkins, C., Field, M. E., Gardner, J. V., and Box, C. E. 2001, usSEABED: Defining the Surficial Geology of the Continental Shelf Through Data Integration and Fuzzy Set Theory. 2001. GSA Annual Meeting Program Abstracts, A-106.

Reid, J.M., Reid, J.A, Jenkins, C. J., Hastings, M. E., Williams, S. J., and Poppe, L. J., 2005. usSEABED: Atlantic coast offshore surficial sediment data release, v 1.0, USGS DS 118, online and CD_ROM.

Reid, J.A., Reid, J.M., Jenkins, C.J., Zimmermann, M., Williams, S.J., and Field, M.E., 2006. usSEABED: Pacific Coast (California, Oregon, Washington) Offshore Surficial-Sediment Data Release: U.S. Geological Survey Data Series 182, version 1.0., online at http://pubs.usgs.gov/ds/2006/182.

Williams, S. J. 1992. Sand and Gravel Resources—An Enormous Offshore Resource Within the U.S. Exclusive Economic Zone, U.S. Geological Survey Bulletin 1877, H1-H10.

Williams, S.J., Reid, J.R., and Manheim, F.T., 2003. A bibliography of selected references to U.S marine sand and gravel mineral resources: U.S. Geological Survey Open-File Report 03-300, CD-ROM.

Williams, S.J., Arsenault, M.A., Poppe, L.J., Reid, J.A., Reid, J.M. and Jenkins, C.J., 2006a. Surficial sediment character of the New York-New Jersey offshore continental shelf region: a GIS Compilation, online at http://pubs.usgs.gov/ofr/2006/1046.

Williams, S.J., Arsenault, M.A., Buczkowski, B.J., Reid, J.A., Flocks, J., Kulp, M.A., Penland, S., and Jenkins, C.J., 2006b. Surficial sediment character of the Louisiana offshore continental shelf region: a GIS Compilation, U.S. Geological Survey Open-File Report 2006-1195, online at http://pubs.usgs.gov/of/2006/1195.

Williams, S.J., Kulp, M., Penland, S., Kindinger, J.L., and Flocks, J.G., in press, Mississippi River Delta Plain, Louisiana coast and inner shelf: Holocene geologic framework and processes, chapter in Holmes, C. (ed.), The Gulf of Mexico- Its Origin History, Archaeology and Geology, *Texas A&M Press*.

USGS ADVANCES IN INTEGRATED, HIGH-RESOLUTION SEA-FLOOR MAPPING: INNER CONTINENTAL SHELF TO ESTUARIES

Jane F. Denny[1], William C. Schwab[1], David C. Twichell[1], Thomas F. O'Brien[1], William W. Danforth[1], David S. Foster[1], Emile Bergeron[1], Charles W. Worley[1], Barry J. Irwin[1], Bradford Butman[1], Page C. Valentine[1], Wayne E. Baldwin[1], Robert A. Morton[2], E. Robert Thieler[1], David R. Nichols[1], and Brian D. Andrews[1]

1. U.S. Geological Survey, 384 Woods Hole Road, Woods Hole, MA 02543, USA. jdenny@usgs.gov, bschwab@usgs.gov, dtwichell@usgs.gov, tobrien@usgs.gov, bdanforth@usgs.gov, dfoster@usgs.gov, ebergeron@usgs.gov, cworley@usgs.gov, birwin@usgs.gov, bbutman@usgs.gov, pvalentine@usgs.gov, wbaldwin@usgs.gov, rthieler@usgs.gov, drnkhols@usgs.gov, bandrews@usgs.gov.

2. U.S. Geological Survey, 600 4th Street South, St. Petersburg, FL 33701, USA. rmorton@usgs.gov.

Abstract: The U.S. Geological Survey (USGS) has been involved in geological mapping of the sea floor for the past thirty years. Early geophysical and acoustic mapping efforts using GLORIA (Geologic LOng Range Inclined ASDIC) a long-range sidescan-sonar system, provided broad-scale imagery of deep waters within the U.S. Exclusive Economic Zone (EEZ). In the early 1990's, research emphasis shifted from deep- to shallow-water environments to address pertinent coastal research and resource management issues. Use of shallow-water, high-resolution geophysical systems has enhanced our understanding of the processes shaping shallow marine environments. However, research within these shallow-water environments continues to present technological challenges.

INTRODUCTION

The U.S. Geological Survey (USGS) has been heavily involved in geological mapping of the sea floor since the 1960's; fulfilling its mission to provide objective scientific information to the research community, federal and state governments, and the public. Over the past thirty years, USGS sea-floor mapping programs have migrated from low-resolution reconnaissance mapping of the deep ocean to detailed, high-resolution mapping of the inner continental shelf and estuarine settings. This migration from deep-

to shallow-water research evolved in order to address pertinent coastal issues such as erosion, sediment availability, sediment transport, geologic controls on shoreline evolution, vulnerability of coastal areas to natural and anthropogenic hazards, and habitat and resource management. Coupled with this shift in scientific focus were technological advances in acoustic, positioning and computing systems that enabled efficient operation within the shallow coastal ocean (Hughes Clarke, 1996; Driscoll, 1999; Lurton, 2002; Mayer, 2006).

Development and use of the high-resolution geophysical systems designed for shallow-water operation has improved our understanding of the processes shaping marine and coastal environments. However, research in the shallow inner shelf continues to present technological challenges due to the dynamics of the environment, high volume of data collected, and the geophysical limitations of operating in shallow water. This paper describes the evolution of the sea-floor mapping operation at the USGS. Examples of deep-water and inner-shelf studies are presented to illustrate the evolution and integration of emerging technology and demonstrate the contribution to advancements in coastal geoscience.

DEEP-WATER MAPPING: THE EEZ (1980's)

In 1984, the USGS began an eight-year program to conduct the world's first reconnaissance mapping of the sea floor within the Exclusive Economic Zone (EEZ), an area extending from 3 to 200 nautical miles off the coast of United States territories. The United States claimed sovereign rights and jurisdiction to all natural resources within the EEZ in 1983. With the formation of the EEZ, the USGS mandate to map territorial lands extended to the newly claimed submarine lands. The objective of the USGS 'EEZ-SCAN' mapping effort was to identify and define the natural resources, physiography and geologic processes acting within the EEZ in order to assess the resource potential and consequences of exploration to the sea-floor environment. Ultimately, the results from these extensive mapping efforts would also provide a base for future site-specific geologic and oceanographic studies (Gardner and others, 1996).

Mapping the vast territories of the EEZ presented technological challenges. Many sonar systems of the early 1980's were not practical for use in deep-water reconnaissance mapping due to their limited swath width and bottom coverage (Gardner and others, 1996; Mayer, 2006). The most economical use of time and funds was to utilize a wide-swath sonar that could efficiently map the sea floor within the deep waters (> 200 m) of the EEZ (Gardner and others, 1998). Thus, the United Kingdom's Institute of Oceanographic Sciences (IOS), GLORIA II (Geologic LOng Range Inclined ASDIC) sidescan-sonar system was selected because of its wide-swath reconnaissance mapping capabilities. GLORIA II was a long-range, low-frequency (6.5 kHz), digital sidescan-sonar capable of achieving swath widths on the order of 10's of kilometers and resolving features on the order of 50 - 100 meters. By June 1991, the USGS and IOS scientists had successfully mapped over six million square kilometers of the deep-waters of the EEZ at close to 100% bottom coverage. Seismic-reflection profiling, gravity, magnetic and ground-truth surveys were also conducted in order to define the geologic framework

within the deeper regions of the EEZ (Gardner and others, 1996).

GLORIA II demonstrated that systematic, reconnaissance mapping of the sea floor was possible (Figure 1). Interpretation of these and other geophysical data provided insight into geologic processes that contribute to the formation and development of continental margins, tectonics, earthquake and volcanic activity, and sedimentary processes acting within the EEZ (Gardner and others, 1996). Additionally, the challenge of maintaining and operating GLORIA II and managing digital data led to the development of new methodologies and computing software for data acquisition and processing; specifically in development of digital sidescan-sonar mosaicking techniques (Chavez, 1986; Gardner and others, 1996).

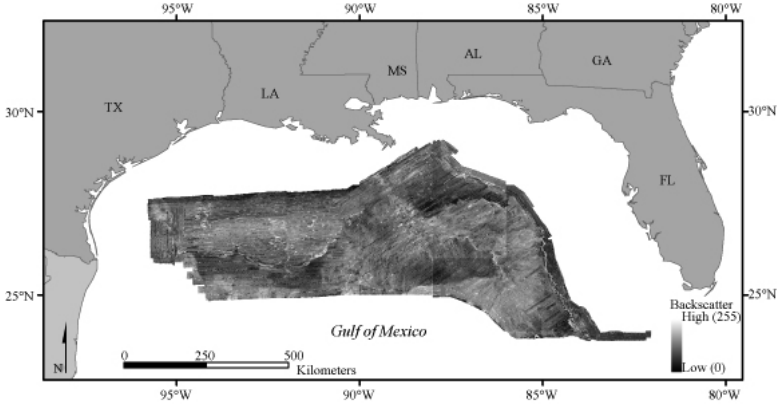

Figure 1: GLORIA II imagery collected within the Gulf of Mexico, 1982 – 1991. High backscatter is represented by light tones within the imagery and low backscatter is represented by dark tones.

SHALLOW-WATER MAPPING, PART I: THE INNER SHELF (1990's)

GLORIA II proved an effective reconnaissance mapping tool for deep-water, however it was not designed for surveying the relatively shallow waters of the inner-continental shelf; leaving the most heavily used portion of the sea floor unmapped. The migration from low-resolution (10's of meters) reconnaissance mapping of the deep-waters of the EEZ to high-resolution (meters), regionally-focused mapping in the shallow-waters (< 50 m) of the inner continental shelf was ultimately spurred by technological advances in sonar, navigation, ancillary systems and computing power of the late-1980's and early 1990's (Gardner and others, 1998; Pickrill and Todd, 2003; Mayer, 2006). Advancements in frequency-modulated (chirp) technology allowed for improved range and resolution in sidescan-sonar, and increased vertical resolution in seismic-reflection systems (Parent, 1993). Additionally, developments in positioning systems improved data accuracy. The USGS implemented these latest technologies to initiate inner shelf

studies designed to provide detailed, geologic framework (surficial and sub-surface) information to guide marine and coastal resource management and to support additional site-specific studies.

The use of improved mapping systems required the collection of large volumes of data due to high repetition and sample rates. Data volumes climbed from 10's of megabytes per day during early sea-floor mapping operations, to 100's of gigabytes per day by the end of the 1990's. Data management and processing software modifications were necessary in order to accommodate the higher data volumes and extract additional information contained within the higher bandwidth (Danforth and others, 1991; Cohen and Stockwell, 2001; Paskevich, 1992; Henkart, 2005). Also, continued development of data visualization and data integration software began to alter the way in which geophysical data were analyzed and presented (Lurton, 2002; Mayer, 2006). During this time, the USGS looked to streamline sea-floor mapping operations and refine data acquisition and processing techniques in order to build on these developments. By the mid- to late- 1990's, equipment was in place to accomplish these goals on a routine basis; systematic, high-resolution mapping of the inner shelf became a core component to USGS shallow-marine geologic studies.

In 1995, the USGS began a five-year collaborative research effort with the U.S. Army Corps of Engineers (USACE) New York District to map the surficial geology and shallow stratigraphy of the inner shelf offshore of New York-New Jersey. This mapping effort integrated high-resolution geophysical and sampling techniques (Figure 2) to define sea-floor physiography, the structure and geometry of underlying strata and its role in the evolution of this coastal region, and assess sand resource availability (Schwab and others, 1997; 2000; 2003). By achieving 100% sea-floor coverage, acquired primarily with chirp sidescan-sonar along with a dense grid of chirp seismic-reflection profiles, this study provided detailed views of the small-scale heterogeneity of the sea floor within a ~200 km long by 10 – 30 km wide area (Figure 3). This new view of the sea floor and its variability highlighted the variety of processes shaping the inner shelf and the importance of the underlying geologic framework in controlling the sea-floor geology. The data proved essential for assessing anthropogenic impacts to the sea-floor environment and addressing marine and coastal resource management issues (Schwab and others, 1997; 2003; Butman and others, 2002).

Although, the sidescan-sonar imagery and closely spaced high-resolution seismic-reflection profiles greatly improved our understanding of the sea-floor geology, the ability to map the geomorphology of the sea floor was limited. Traditionally, as part of any sea-floor mapping effort, the USGS acquired bathymetry with single-beam echosounders to define the gross morphology of the sea floor; bathymetric systems were supplemental to sidescan-sonar and seismic-reflection systems due to their low resolution and limited bottom coverage. However, the advent of high-resolution multibeam echosounders enabled mapping of sea-floor morphology at sub-meter scales; defining the complexity and heterogeneities of the sea bed in new detail (Hughes Clark and others, 1996; Locat and Sanfaçon, 2002; Pickrill and Todd, 2003; Mayer, 2006).

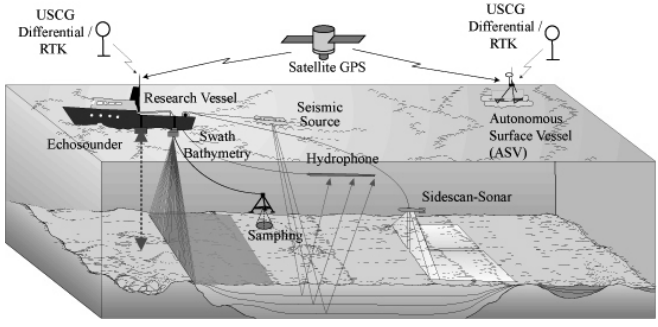

Figure 2: Illustration of the systems used to define the surficial sediment distribution, sea-floor topography, and underlying geologic structure.

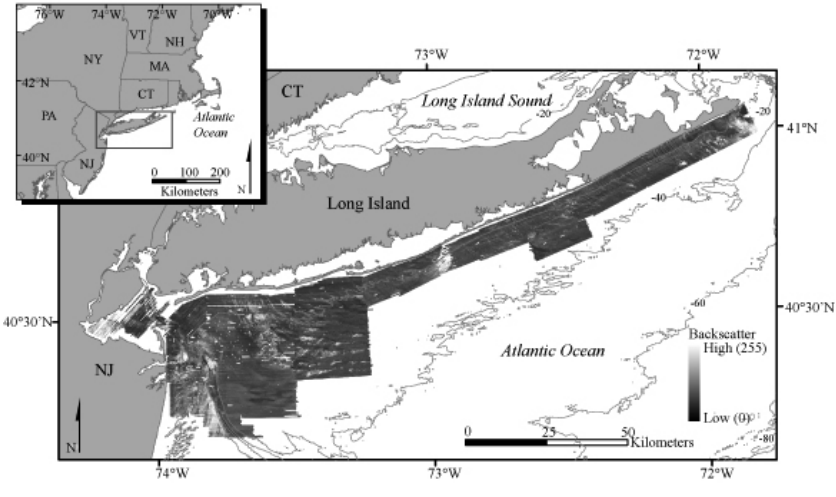

Figure 3: Sidescan-sonar mosaic collected within the New York Bight, 1995 - 1998. High-backscatter is displayed as light tones within the imagery, low-backscatter as dark tones. Bathymetric contours are in meters. Inset shows regional location.

Concurrent with the start of the New York-New Jersey mapping effort, was a collaborate research effort off the coast of New England involving the USGS, University of New Brunswick (UNB), Canadian Hydrographic Service (CHS), and National Oceanic and

Atmospheric Administration (NOAA) to map the Stellwagen Bank National Marine Sanctuary (SBNMS) and western Massachusetts Bay using multibeam echosounder technology (Figure 4). These mapping efforts defined the distribution of surficial sediment, sea-floor morphology and biological habitats in order to: 1) foster successful management of natural resources within SBNMS, and 2) to assess sediment and pollutant transport within Massachusetts Bay (Valentine and others, 1998; Butman and others, 2004; Valentine, 2005).

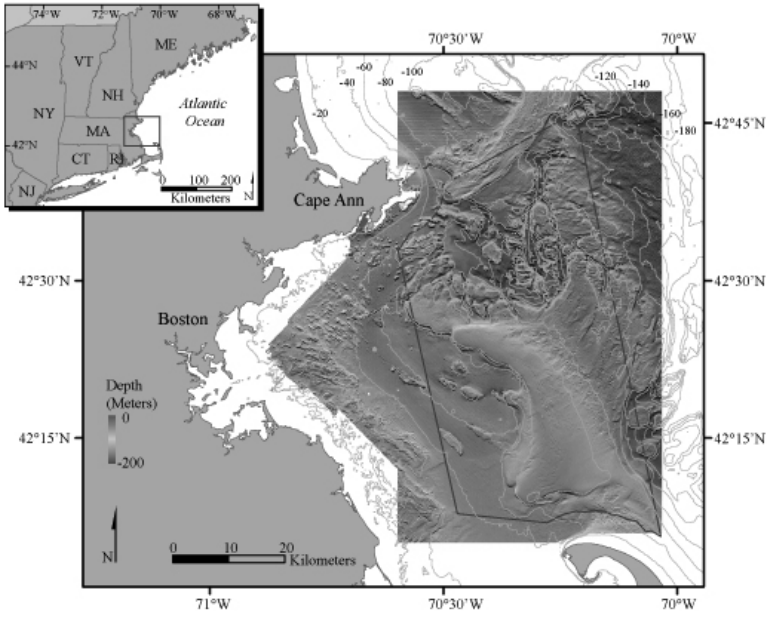

Figure 4: Shaded-relief bathymetry collected with a multibeam echosounder off the coast of Massachusetts, 1994 – 1999. Red box indicates area of Stellwagen Bank National Marine Sanctuary (SBNMS). Inset shows regional location.

An interesting by-product of the multibeam echosounder surveys off the New England coast was its large impact on the broader oceanographic research and management communities. Interpretive maps generated from these high-resolution data and subsequent sampling programs within SBNMS and western Massachusetts Bay, provided insight into the distribution of benthic habitats, the relationship between biologic communities and physiography of the sea floor, and geologic, oceanographic and biologic processes modifying the sea floor (Butman and others, 2004;Valentine, 2005). Additionally, these data have provided critical information for fisheries research, and environmental and resource management (Auster and others, 2001; Valentine, 2005).

SHALLOW-WATER MAPPING, PART II: THE COASTAL ZONE (1999 – 2004)

The introduction of multibeam echosounders into sea-floor mapping operations enhanced interpretations of sea-floor geology by providing highly detailed images of sea bed topography and acoustic backscatter (Gardner and others, 1998; Butman and others, 2002; 2004; Schwab and others, 2003; Pickrill and Todd, 2003; Valentine, 2005). Use of multibeam echosounders in USGS research continued, primarily through collaborative efforts with universities, other Federal agencies and the private sector (Butman and others, 2003; 2006). However, as USGS research interests moved into coastal and estuarine environments (water depths ranging from 2 to 30 meters), the use of multibeam echosounders for 100% coverage of the sea floor became impractical due to their limited bottom coverage in shallow water (swath widths on the order of 3-5 times water depth). In order to efficiently and economically map sea-floor topography within the nearshore environment, the USGS looked to incorporate a bathymetric system that could achieve wide swath widths in shallow water and be easily configured to run concurrently with existing geophysical systems (Figure 2). In the late 1990's, interferometric sonars had developed into viable shallow-water, wide-swath bathymetric surveying systems, generally achieving swath widths on the order of 7-10 times water depth (Geen, 1999). These systems have multiple (two or more), parallel receiving elements in the sonar transducers. A comparison of the phase of the return signal between the receive elements is used to determine depth to the sea floor (Geen, 1999). Acoustic backscatter data similar to data collected with traditional sidescan-sonar systems are also acquired (Geen, 1999; Lurton, 2002). In 1999, the USGS took delivery of an interferometric sonar to augment inner shelf geophysical studies. Additionally, further advancements in chirp seismic-reflection systems at this time allowed for increased vertical resolution of the subsurface and enabled high-resolution mapping of the shallow stratigraphy (Driscoll, 1999; Baldwin and others, 2004). Fine-scale (sub-meter to meter) geomorphology of the sea floor could now be defined through integrated use of these surficial and sub-surface mapping systems.

The first use of interferometric sonar and improved chirp seismic-reflection systems was along the northern coast of South Carolina as part of a regional coastal erosion study. In 1999, the USGS in partnership with the NOAA South Carolina Sea Grant Consortium (SCSGC) began a study to investigate inner continental shelf and shoreface processes offshore of the Grand Strand, SC (Figure 5). The objectives of the USGS/SCSGC cooperative program were to define the shallow geologic framework and its role in coastal evolution; to identify and model the physical processes affecting coastal ocean circulation and sediment transport; and to identify sediment sources and transport pathways (Gayes, 2003; Baldwin and others, 2004; Sullivan and others, 2006; Denny and others, 2007). Incorporation of the new technologies provided highly-detailed imagery of the region, identifying a complex, condensed stratigraphy capped by an extremely sediment-limited, modern coastal system (Figure 6). These data improved our understanding of long-term changes in sea level, sediment supply and coastal geomorphology, allowing for reconstruction of an extensive paleofluvial system and identification of several relict, inner-shelf sediment bodies (Baldwin and others, 2006;

Denny and others, 2007; Barnhardt and others, 2007 (this volume)). See Barnhardt and others, 2007 (this volume) for a more detailed description of the scientific findings.

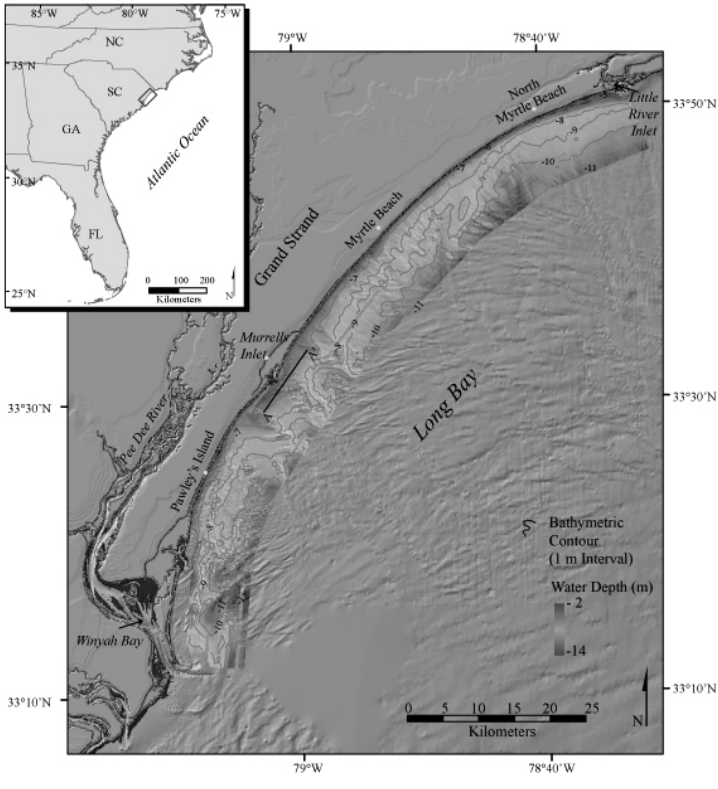

Figure 5: Swath bathymetric data collected offshore of the Grand Strand, SC, 1999 – 2004. Line A-A' indicates location of subbottom profile in Figure 6. Inset shows regional location.

VERY SHALLOW-WATER MAPPING: ESTUARIES (2004 - 2006)

High-resolution geophysical and sampling systems were routinely used in all inner shelf mapping studies by the end of the 1990's. By early 2000, USGS research interests began migrating farther inshore. Studies were focused on addressing the spatial and temporal variability of nearshore sedimentary processes and shallow geologic framework on a variety of time scales, and their implications for coastal evolution. The dynamics of operating within nearshore environments due to shallow depths, high-energy conditions, and high data volumes posed new challenges to geophysical surveying.

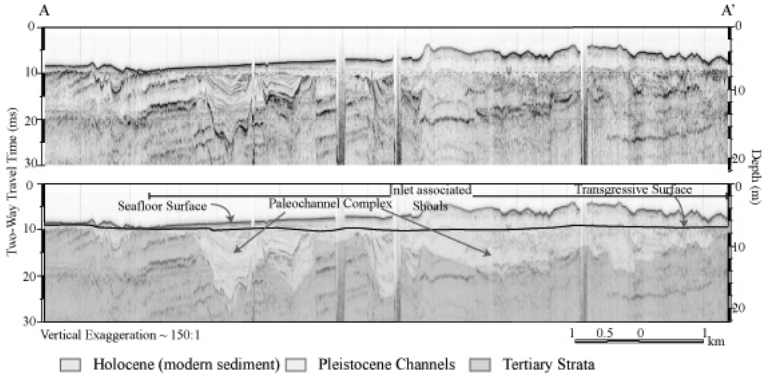

Figure 6: Example of chirp seismic-reflection profile collected offshore of the Grand Strand, South Carolina showing the thickness of modern sediment above the transgressive unconformity and structure of underlying strata. See Figure 5 for location.

In 2004, the USGS, in cooperation with NOAA Coastal Services Center and the Apalachicola National Estuarine Research Reserve, began a study to define the distribution of oyster resources within Apalachicola Bay, Florida. The bay is located in the northern Gulf of Mexico along the Florida panhandle (Figure 7) and is the largest oyster fishery in Florida and the third largest within the United States. Potential changes to the influx of fresh water due to dam placement on the Apalachicola River system and coastal development may prove harmful to the oyster fishery. The USGS/NOAA collaborative effort was designed to map the present distribution of oyster beds and the shallow geologic framework, in order to provide baseline information on the benthic resources within the bay.

Geophysical mapping within Apalachicola Bay presented technological challenges that required modification of standard surveying techniques. The bay is very shallow, ranging from 0.5 to 5 m water depth, with oyster beds concentrated in water depths < 2 m. Additionally, the waters are very turbid, precluding the use of aerial mapping technologies such as bathymetric LIDAR (Light Detection and Ranging). The deeper waters of the bay (> 2 m) were successfully mapped with sidescan-sonar, chirp seismic-reflection, and interferometric sonar systems deployed from a 25-foot, shallow-draft research vessel. However, the oyster beds remained inaccessible due to their location in shallow depths. In order to operate in such extremely shallow waters, the USGS collaborated with engineers in the private sector to develop a shallow-draft Autonomous Surface Vessel (ASV) configured with chirp sidescan-sonar and seismic-reflection systems, and a single-beam echosounder (Figure 8). The ASV was first deployed in June, 2006 and acquired imagery of the sea bed and underlying strata in shallow, previously inaccessible areas that enhanced interpretations of the shallow geologic framework within the bay. Operation and testing of the ASV is on-going. Modifications

to acquisition and processing methodologies will continue in order to maximize data quality and functionality of the vehicle.

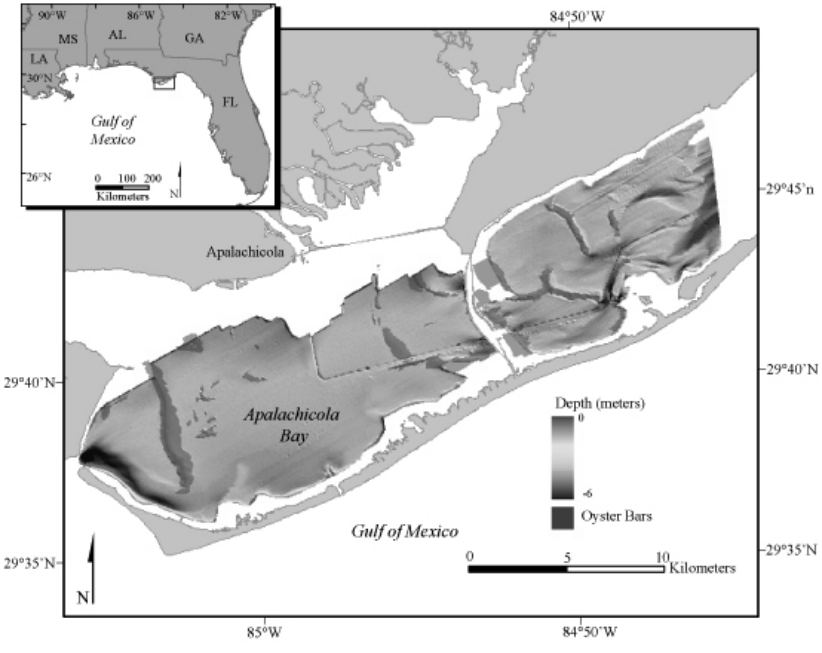

Figure 7: Map showing bathymetry collected within Apalachicola Bay, Florida. Inset shows regional location.



Figure 8: Picture of the ASV surveying within Apalachicola Bay, Florida in June 2006. Pontoons are ~2-m in length.

FUTURE DIRECTIONS

The interplay of science and technology will continue to enhance research within the broader oceanographic community. Further advancements in sonar and positioning technology will allow for finer spatial and temporal resolution; defining sea-floor geology in ever greater detail. Continued improvements in visualization and data integration will further alter the way in which marine geophysical data are analyzed and presented. And, new developments with surface vessels such as the ASV will enable more efficient operation within the shallow-marine environment to bridge the gap between marine and onshore geology.

CONCLUSION

Sea-floor mapping has evolved from reconnaissance, wide-swath mapping in the deep ocean areas to high-resolution mapping of the inner continental shelf to the very shallow estuarine settings. Significant technologic advances have enabled changing research directions that increasingly focus on the shallow coastal ocean. Advances in sonar design, positioning, and computing power have produced systems for mapping and visualization of the sea floor and subsurface in unprecedented detail. Integrated use of surficial, sub-bottom, and sampling instruments within inner shelf geologic studies has contributed to enhancing our understanding of modern sedimentary processes, sea bed dynamics and the evolution of coastal systems.

ACKNOWLEDGEMENTS

We would like to thank all of our colleagues who have contributed to the growth and success of the USGS mapping efforts, specifically Dave Russ, John Haines, Debbie Hutchinson, Jeff Williams, John Hughes Clarke, Larry Mayer, Neal Driscoll, Larry Kooker, Mike Boyle, VeeAnn Cross, Ken Parolski, Valerie Paskevich, Dann Blackwood, Chris Polloni, Shawn Dadisman, Kathy Scanlon, Larry Popppe, Uri ten Brink, Ann McKinney and Paul Gayes. We would also like to thank Walter Barnhardt and John Warner for the reviews of this manuscript.

REFERENCES

Auster, P.J., Joy, K., and Valentine, P.C., (2001), "Fish species and community distributions as proxies for seafloor habitat distributions: The Stellwagen Bank National Marine Sanctuary examples (Northwest Atlantic, Gulf of Maine)," *Environmental Biology of Fishes*, 60, 331-346.

Baldwin, W.E., Morton, R.A., Denny, J.F., Dadisman, S.V., Schwab, W.C., Gayes, P.T., and Driscoll, N.W., (2004), "Maps showing the stratigraphic framework of South Carolina's Long Bay from Little River to Winyah Bay," *U.S. Geological Survey Open-File Report 2004-1013*, Woods Hole, MA.

Baldwin, W.E., Morton, R.A., Putney, T.R., Katuna, M.P., Harris, M.S., Driscoll, N.W., Denny, J.F., and Schwab, W.C., (2006), "Migration of the Pee Dee River system inferred from ancestral paleochannels underlying the South Carolina Grand Strand and Long Bay inner shelf," *Geological Society of America Bulletin*, 118(5/6), 533-549.

Barnhardt, W., Denny, J.F., Baldwin, W.E., Schwab, W.C., Morton, R.A., Gayes, P.T., and Driscoll, N., (2007), "Geologic framework of the Long Bay inner shelf: Implications for coastal evolution in South Carolina," *Proceedings Coastal Sediments '07*, May 2007 (this volume).

Butman, B., Danforth, W.W., May, B., Knowles, S.C., and Serrett, L., (2002), "Sea floor topography and backscatter intensity of the historic area remediation side (HARS), offshore of New York, based on multibeam surveys conducted in 1996, 1998, 2000," *U.S. Geological Survey Open-File Report 00-503*, DVD-ROM, Woods Hole, MA.

Butman, B., Middleton, T.J., Thieler, E.R., Schwab, W.C., (2003), "Topography, shaded relief and backscatter intensity of the Hudson Shelf Valley, Offshore of New York," *U.S. Geological survey Open-File Report 03-372*, CD-ROM, Woods Hole, MA.

Butman, B., Valentine, P.C., Danforth, W.W., Hayes, L., Serrett, L.A., and Middleton, T.J., (2004), "Shaded relief, backscatter intensity and sea floor topography of Massachusetts Bay and the Stellwagen Bank region, offshore of Boston, Massachusetts," *U.S. Geological Survey Geologic Investigation Map I-2734*, scale 1:125,000, CD-ROM, Woods Hole, MA.

Butman, B., Twichell, D.C., Rona, P.A., Tucholke, B.E., Middleton, T.J., and Robb, J.R., (2006), "Sea floor topography and backscatter intensity of the Hudson Canyon region offshore of New York," *U.S. Geological Survey Open-File Report 2004-1441*, CD-ROM, Woods Hole, MA.

Chavez, P.S., Jr., (1986), "Processing techniques for digital sonar images from GLORIA," *Journal of Photogrammetric Engineering and Remote Sensing*, 52(8), 1133-1145.

Cohen, J.K., and Stockwell, J.W., Jr., (2001), "CWP/SU: Seismic Unix Release 35: a free package for seismic research and processing," *Center for Wave Phenomena, Colorado School of Mines, http://www.cwp.mines.edu/cwpcodes*.

Danforth,W.W., O'Brien, T.F., Schwab, W.C., (1991), "Near-real time mosaics from high-resolution side-scan sonar," *Sea Technology*, 32(1), 54-59.

Denny, J.F., Baldwin, W.E., Schwab, W.C., Gayes, P.T., Morton, R.A., and Driscoll, N.W., (2007), "Morphology and Textures of Modern Sediments on the inner shelf of South Carolina's Long Bay from Little River Inlet to Winyah Bay," *U.S. Geological Survey Open-File Report 2005-1345*, Woods Hole, MA.

Driscoll, N.W., (1999), "New geophysical tool for imaging shallow water environments," *MARGINS Newsletter*, no. 3, 12 – 14.

Gardner, J.V., Field, M.E., and Twichell, D.C., (1996), ed. "*Geology of the United States' Seafloor; The View from GLORIA*," Cambridge University Press, 364 p.

Gardner, J.V., Butman, P.B., and Hughes Clarke, J., (1998), "Mapping U.S. Continental Shelves," *Sea Technology*, 39(6), 10-16.

Gayes, P.T., Schwab, W.C., Driscoll, N.W., Morton, R.A., Baldwin, W.E., Denny, J.F., Wright, E.E., Harris, M.S., Katuna, M.P., Putney, T.R., and Johnstone, E., (2003), "Sediment dispersal pathways and conceptual sediment budget for a sediment starved embayment; Long Bay, South Carolina," *Coastal Sediments '03*, 5th Annual Symposium on Coastal Engineering and Science of Coastal Sediment Processes, Clearwater Beach, Florida, May 18-23, 2003, Proceedings, 14 p.

Geen, M., (1999), "Applications of Interferometric Swath Bathymetry," *Sea Technology*,

40(6), 25 – 30.
Henkart, P., (2005) "SIOSEIS, Scripps Institution of Oceanography seismic processing software package," *http://sioseis.ucsd.edu*.
Hughes Clarke, J.E., Mayer, L.A., and Wells, D.E., (1996), "Shallow-water imaging multibeam sonars: A new tool for investigating seafloor processes in the coastal zone and on the continental shelf," *Marine Geophysical Researches*, 18, 607-629.
Locat, J., and Sanfaçon, R., (2002), "Multibeam Surveys – a major tool for geosciences," *Sea Technology*, 43(6), 35-38.
Lurton, X., (2002), "*An Introduction to Underwater Acoustics Principles and Applications*," Praxis Publishing, 347 p.
Mayer, L.A, (2006), "Frontiers in seafloor mapping and visualization," *Marine Geophysical Researches*, 27, 7-17.
Parent, M.D., Fang, C., O'Brien, T.F., and Danforth, W.W., (1993), "First results of a deep tow chirp sonar seafloor imaging system," *Offshore Technology Conference Proceedings*, Houston, Texas, 3-6 May, 1993, 19 p.
Paskevich, V., (1992), "Digital processing of side-scan sonar data with the Woods Hole image processing system software," *U.S. Geological Survey Open-File Report 92-204*, 87 p.
Pickrill, R.A. and Todd, B.J., (2003), "The multiple roles of acoustic mapping in integrated ocean management, Canadian Atlantic continental margin," *Ocean & Coastal Management*, 46, 601-614.
Schwab, W.C., Allison, M.A., Corso, W., Lotto, L.L., Butman, P.B., Buchholtz ten Brink, M., Denny, J.F., Danforth, W.W., and Foster, D.S., (1997), "Initial Results of high-resolution sea-floor mapping offshore of the New York-New Jersey metropolitan area using sidescan sonar," *Northeastern Geology & Environmental Sciences*, 19(4), 243-262.
Schwab, W.C., Thieler, E.R., Allen, J.R., Foster, D.S., Swift, B.A., and Denny, J.F., (2000), "Influence of inner-continental shelf geologic framework on the evolution and behavior of the barrier-island system between Fire Island Inlet and Shinnecock Inlet, Long Island, New York," *Journal of Coastal Research*, 16(2), 408-422.
Schwab, W.C., Denny, J.F., Foster, D.S., Lotto, L.L, Allison, M.A., Uchupi, E., Danforth, W.W., Swift, B.A., Thieler, E.R., and Butman, B., (2003), "High-resolution Quaternary seismic stratigraphy of the New York Bight continental shelf," *U.S. Geological Survey Open-File Report 02-152*, DVD-ROM Published by USGS, Woods Hole, MA ISBN-0-607-90067-9.
Sullivan, C.M, Warner, J.C., Voulgaris, G., (2006), "The influence of storms on circulation and sediment transport in Long Bay, South Carolina, USA.," *EOS, Transactions, AGU*, 87(36), Ocean Science Meeting Supplement., Abstract OS35E-08.
Valentine, P.C., Baker, J.F., Unger, T.S., Evans, J., and Polloni, C., (1998), "Sea floor topographic, backscatter, and interpretative maps and bottom photos of the Massachusetts Bay disposal site region off Boston, Massachusetts," *U.S. Geological Survey Open-File Report 98-344*, CD-ROM, Published by USGS, Woods Hole, MA.
Valentine, P.C., (2005), "Sea floor image maps showing topography, sun-illuminated topography, backscatter intensity, ruggedness, slope, and the distribution of boulder

ridges and bedrock outcrops in the Stellwagen Bank National Marine Sanctuary Region off Boston, Massachusetts," *U.S. Geological Survey Scientific Investigations Map 2840*, Woods Hole, MA.

A RAPID COMPATIBILITY ANALYSIS OF POTENTIAL OFFSHORE SAND SOURCES FOR BEACHES OF THE SANTA BARBARA LITTORAL CELL

Neomi Mustain[1], Gary Griggs[1], Patrick L. Barnard[2]

1. Department of Earth and Planetary Sciences, University of California, Santa Cruz, 1156 High Street, Santa Cruz, CA 95060, USA. nmustain@pmc.ucsc.edu, griggs@pmc.ucsc.edu
2. United States Geological Survey, Pacific Science Center, 400 Natural Bridges Drive, Santa Cruz, CA 95060, USA. pbarnard@usgs.gov

Abstract: The beaches of the Santa Barbara Littoral Cell, which are narrow as a result of either natural and/or anthropogenic factors, may benefit from nourishment. Sand compatibility is fundamental to beach nourishment success and grain size is the parameter often used to evaluate equivalence. Only after understanding which sand sizes naturally compose beaches in a specific cell, especially the smallest size that remains on the beach, can the potential compatibility of source areas, such as offshore borrow sites, be accurately assessed. This study examines sediments on the beach and in the nearshore (5-20m depth) for the entire Santa Barbara Littoral Cell east of Point Conception. A digital bed sediment camera, the Eyeball©, and spatial autocorrelation technique were used to determine sediment grain size. Here we report on whether nearshore sediments are comparable and compatible with beach sands of the Santa Barbara Littoral Cell.

INTRODUCTION

Beaches are extremely important in California: they provide a large recreational area for an ever increasing tourist and coastal population, they offer invaluable protection to bluffs, cliffs and back beach development from direct wave attack, and they provide unique habitats supporting many diverse species. In addition, the beaches of California benefit not only the economy of local communities and the state, but also the entire United States (King 2002; King and Symes 2003). Most of the beaches of the eastern Santa Barbara Littoral Cell (from Point Conception to Point Mugu) are naturally narrow (Flick 1993; Wiegel 1994). Although beach widths fluctuate in response to seasonal and

climatic cycles (e.g. PDO, ENSO), there is data suggesting that the beaches of this cell are also narrowing in response to human activities (Runyan and Griggs 2003; Willis and Griggs 2003; Revell and Griggs 2006). Because the beaches of California are a valuable natural resource, it is important to consider approaches to expand the existing beaches to a healthy width that will allow the surrounding coastal communities to maintain beaches that are safe and appealing for recreation, suitable for existing biological diversity, and are economically productive.

One possible way to widen a beach is through nourishment, or the addition of sediment to the beach. For a nourishment project to be successful, however, suitable sediment-sand with a grain size equivalent to or slightly coarser than sand found naturally on the beach-must be used (National Research Council 1995; Dean 2002; U.S. Army Corps of Engineers 2002). In this study we have surveyed the Santa Barbara Littoral Cell beaches and nearshore inner shelf to inventory natural grain size distributions and determine whether suitable material for nourishment exists offshore. Traditional methods of grain size analysis require considerable time to process samples, whether through sieving or settling. As an alternative, we used a relatively new method, the USGS-developed digital bed sediment Eyeball© camera and autocorrelation algorithms, to rapidly collect and process over 400 sediment samples (Rubin 2004; 2006). The speed and efficiency of both the collection process and the grain size determination technique have allowed for an unprecedented amount of data to be gathered quickly (within a summer) for the study area, thus allowing us to quickly assess the broad compatibility of inner shelf and onshore sediments throughout a very large area-about 149 km (~93 miles) of coastline.

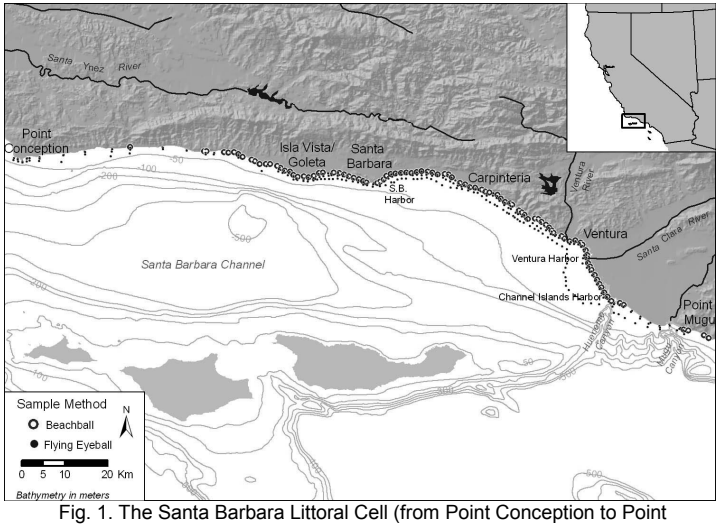

Fig. 1. The Santa Barbara Littoral Cell (from Point Conception to Point Mugu), with beach (Beachball) and nearshore (Flying Eyeball) sampling locations.

BACKGROUND

The Santa Barbara Littoral Cell, east of Point Conception, extends 149 km southeast, terminating at the Hueneme and Mugu Submarine Canyons (Fig. 1). In the west, the majority of the south facing coastline consists of thin, narrow beaches backed by vertical sedimentary cliffs. South of the Ventura River, the coast opens up into a large, populated alluvial plain, fronted by wider beaches and coastal dunes. Sediment is supplied to the cell from north of Point Conception, coastal cliffs and small coastal streams along the northern Santa Barbara Channel, and two large rivers (the Ventura and Santa Clara) in the eastern portion of the cell (Patsch and Griggs 2005). Sediment is transported through the cell primarily by longshore currents, which flow dominantly from west to east due to the common oblique wave approach. Although waves drive the longshore current, the wave climate is generally mild along most of the south-facing coast. This is a result of the coastal orientation which limits wave exposure: waves must enter the Channel directly from the west, bend around Point Conception from the north, or pass between the Channel Islands from the south. From Isla Vista to the Mugu Naval Air Base human development dominates the coast. In addition to building coastal protection structures directly on the beach, people have also extensively developed atop coastal dunes, bluffs and reclaimed wetland areas.

Nourishment may be a solution to the problem of narrow beaches, although many concerns still exist (Griggs 2006; Patsch and Griggs 2006). One issue along this coast is that a very large volume of sediment would be needed for a successful project, as the rates of littoral drift are very high throughout the cell; rates are estimated to be ~300,000 yds^3/yr at the Santa Barbara Harbor, ~600,000 yds^3/yr at the Ventura Harbor and ~1,000,000 yds^3/yr at the Channel Islands Harbor (Patsch and Griggs 2005). As a result of the large volume of sediment needed for nourishment, offshore sediment sources, as opposed to inland sources, may be the more economical option (Patsch and Griggs 2006). When initially locating a suitable offshore source, or potential borrow area, sediment characteristics, environmental impacts and dredging feasibility, both technological and economical, must be considered (National Research Council 1995; McLellan and Hopman 2000; Dean 2002).

Sediment characteristics, such as grain size, sorting, and thickness, in the potential borrow area are very important. Sediment that is too fine-grained is not suitable nourishment material: fine sediment will not remain on the beach, is undesirable by the user population and may also store contaminants (National Research Council 1995). Previously, the sand-silt cutoff diameter, 0.0625 mm, has been used to determine what could be placed on the beach. However, recent studies have shown that on some of California's high-energy beaches very fine-grained sand, or in some cases, even fine-grained sand, is not stable (Limber et al. in press). As a result d_{10}, or the finest 10% of a sample's sediment distribution, has been used to define the littoral cutoff diameter (LCD), or the smallest size of grains that are present or stable on any particular beach (Best and Griggs 1991; Runyan and Griggs 2003; Limber et al. in press).

Offshore California, there is generally a gradation from coarser to finer sediments

moving offshore and typically coarser sediments (consistent with a transgressive shoreline) in the subsurface. Processes that operate along the coast-wind, wave and current driven-control the ultimate site of sediment deposition. Coarse sediments can be deposited in high-energy environments, while fine sediments are kept in suspension until they are transported into calmer environments where they can settle out. The California coast is dominated by very fine sands and mud; however, the Offshore Surficial Geology Map of California also indicates that there may be medium and coarse sands, suitable deposits for beach nourishment, offshore (Welday and Williams 1975). Deposits of coarse sediment may be found in localized, present-day high-energy environments, or as relict beach or channel deposits trapped within tectonically controlled structural highs and lows which were deposited when sea level was lower (Welday and Williams 1975; Fischer 1983).

Recently, the USGS has compiled data on seafloor sediment characteristics, including surficial grain size from cores, into a comprehensive database, usSEABED (Reid et al. 2006). Some nearshore cores reported in usSEABED are inconsistent with the Offshore Surficial Geology Map of California: instead of coarse and medium-grained sand, cores contain very fine sand or silt (Welday and Williams 1975; Reid et al. 2006). While these differences may represent natural changes within a dynamic environment, the change may alternately result from limitations of the Welday and Williams map. The Offshore Surficial Geology Map was compiled from various sources which were collected between 1855 and 1975. Currently there is no detailed information about data density, data quality or the original data collection methods or classification schemes. In addition, fine sands and very fine sands were mapped together as one unit, and if the specific class of sand was undefined in the original data set, it was mapped as medium sand by Welday and Williams. The present study will rework and update this surface sediment map for the innershelf.

Previous studies have surveyed the continental shelf, with geophysical profiling and coring, to assess offshore sand sources in various locations of the Santa Barbara Littoral Cell (Noble Consultants 1989). This study takes a different approach to locate additional suitable sand deposits; we examine and map mean surface grain size over a wide area of the inner shelf using the Eyeball© camera and spatial autocorrelation algorithm. The major shortcoming of this method is that only surface grain size is captured. However, this bias can be limited by testing Eyeball© images with grab samples that penetrate several centimeters beneath the surface. The major advantages of this method are the extensive amount of area that can be covered as a result of the speed of the collection method, the number of samples that can be processed as a result of the rapid grain size determination method, and that samples can be taken in very shallow depths-as shallow and close to shore as small coastal research vessels can safely transit.

METHODS

The field survey was designed to collect samples along a cross-shore profile, from the beach and the nearshore at 5, 10 and 20 m water depth, with transects spaced at least every kilometer alongshore, throughout the entire Santa Barbara Littoral Cell (Fig. 1). To

compare seasonal grain size variations, beach samples were also collected in March and October (winter and summer samples) at Isla Vista/Goleta, Carpinteria, and Ventura at a higher spatial resolution.

Two different Eyeball© camera systems were used to collect digital samples. Swash samples were collected with the Beachball© camera, a 5-megapixel digital camera encased in a waterproof housing (Rubin 2006). To sample the beach, the camera is placed flush against the sediment, which is illuminated by a ring of LED lights. Camera settings such as aperture, shutter speed, zoom, focus, and pixel resolution of the image are held constant. Nearshore samples were collected with the underwater Eyeball© version, the Flying Eyeball©, which is a video camera illuminated by LED lights encased in a wrecking ball (Rubin 2006). Live video is reviewed on deck while the instrument is repeatedly raised and lowered to the seafloor to collect digital video samples. The clearest frames of video are then captured as still images and processed for grain size. For both systems, multiple images are taken at each location and later averaged into one grain size result.

Images are processed by running a Matlab© script that uses a spatial autocorrelation algorithm developed by Rubin (2004). This algorithm determines the correlation (as measured by pixel intensities) between a pixel and subsequent pixels at increasing distances. Grain size of an image is then interpolated by comparing the spatial autocorrelation result to a calibration matrix. The calibration matrix contains spatial autocorrelation results of calibrated sample images and was produced by imaging ¼ phi interval sieved sediment collected from throughout the study area with the same equipment and camera settings as used in the field. The calculated calibration matrices are valid only for sediment of similar size, shape and mineralogy as the sediment initially sieved and imaged. Figure 2 shows the mean grain size determined from the autocorrelation method compared to mean grain size from both processing samples in a settling tube (Fig. 2b) and from point counting, or calculating the mean of an image by hand-measuring the size of 100 grains in the image (Fig. 2a).

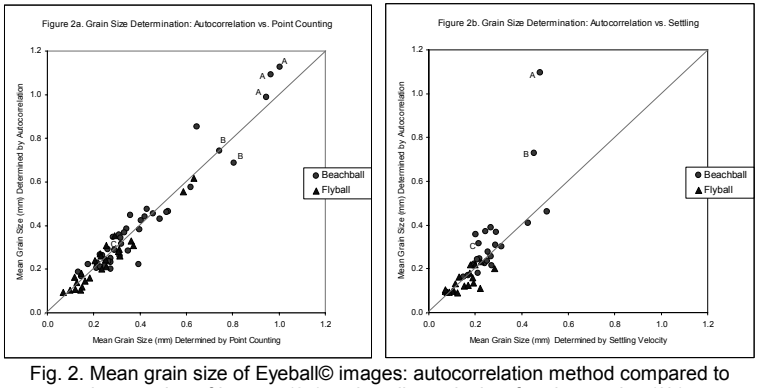

Fig. 2. Mean grain size of Eyeball© images: autocorrelation method compared to point counting of images (2a) and settling velocity of grab samples (2b). Samples A, B, and C are labeled in both 2a and 2b.

On the beach, there is a potential bias for sampling coarser surficial sediments (Fig. 2b). This may occur if fine sediments have been winnowed away or if a coarsening-upward sequence has developed. Beach samples that fall off the 1:1 line of correlation in Figure 2b may be a result of either of these two processes. However, the autocorrelation method is still valid-samples off the 1:1 line in 2b, appear near the 1:1 line in 2a-since point counting determines whether the algorithm accurately determines grain size of the image. In the nearshore, there is a potential bias for surface sediments to be finer than the immediate subsurface layer (Fig. 2). Consistent with rising sea level, this may be a result of recent fine sediment deposition. Alternately, fine sediments could have been winnowed or washed while bringing the grab sampler to the surface, resulting in grab samples appearing coarser than they actually were.

The autocorrelation method, especially when using the Flying Eyeball©, is limited by pixel resolution: once grains become very small (as small as or smaller than two or three pixels) clusters or flocs of small grains begin to look (in terms of correlation) like larger grains. As a result, when nearshore grain size is less than 0.09 or 0.10 mm, the ability to accurately determine grain size by the autocorrelation method is diminished. However, this is not a significant problem for this study because the aim of offshore sampling is to determine if beach compatible material exists, and from the following conclusions, an acceptable grain size cutoff for the Santa Barbara Littoral Cell beaches is 0.125 mm, making the Flying Eyeball© results adequate and this study applicable.

RESULTS

The mean grain size of 93 swash zone samples from throughout the Santa Barbara Littoral Cell ranged from 0.15 mm to 0.43 mm (fine to medium sand; Fig. 3). The mean of one sample just north of the Port Hueneme Harbor was 0.60 mm, or coarse sand. The average of all (94) samples was 0.27 mm. Grab samples were well sorted: in most cases, 80% of a sample's grain size was distributed across only one phi interval. The finest sediment on the beach (d_{10}) varied from location to location, but followed the mean well (when the mean increased so did d_{10}). Very fine-grained sand did not remain on the beach in any significant amount anywhere throughout the cell (Fig. 3). Mean grain sizes of summer swash samples were smaller than winter swash samples throughout the beaches of Isla Vista/Goleta, Carpinteria, and Ventura. Grain size in the southeast decreased seasonally more than in the northwest: Ventura beaches seasonally fined an average of 0.15 mm, Carpinteria beaches fined an average of 0.08 mm, while Isla Vista/Goleta beaches fined an average of only 0.05 mm.

Throughout the cell, 319 nearshore locations were examined, although some areas were cobble or bedrock reefs, which did not allow for grain size determination. Mean grain size was determined for about 100 samples at each water depth (5, 10, and 20 m). Grain size fined moving from the beach offshore (Fig. 4). Only 2% of all samples were medium

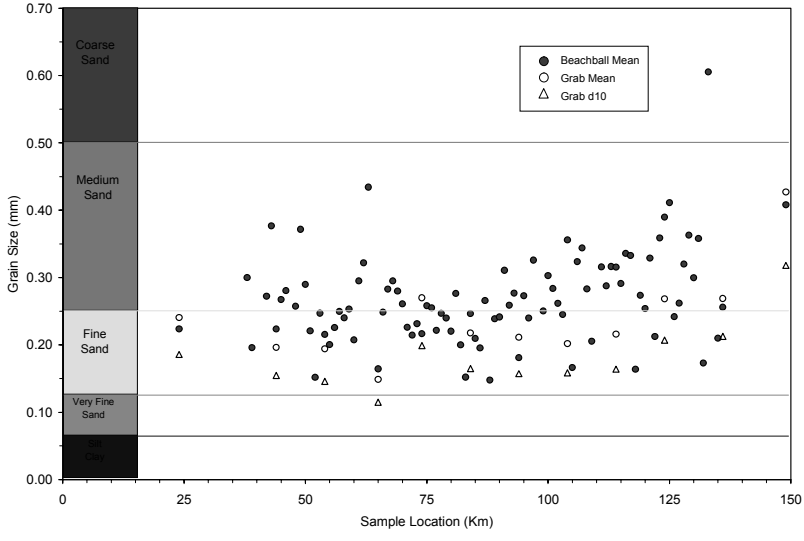

Fig. 3. Mean grain size and d_{10} of beach samples. Horizontal axis is distance east of Pt. Conception.

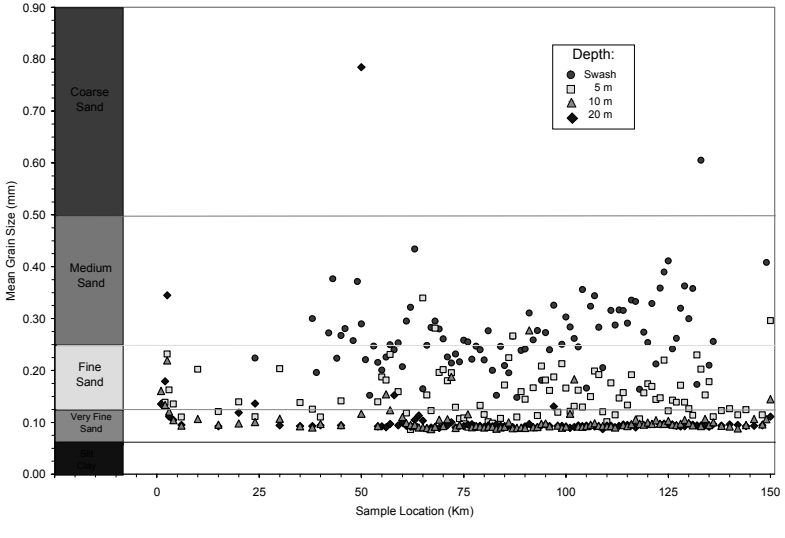

Fig. 4. Mean grain size of beach and nearshore samples. Horizontal axis is distance east of Pt. Conception.

sand, 24% were fine sand and 74% were very fine sand or smaller. The coarsest samples were found in shallow depths: 82% of all samples coarser than very fine sand were located in 5 m water depth. Only 5% of all Flying Eyeball© (15 samples) found in 10 or 20 m water depth were coarser than very fine sand. Some of these coarser, deep samples were located near major headlands, such as Point Conception and Point Mugu, near offshore reefs, such as west of Coal Oil Point in Isla Vista and Sand Point in Carpinteria, or offshore rivers and streams, such as Gaviota Creek and Rincon Creek. Samples coarser than very fine sand not located near headlands, were likely to be fine sand (75%) rather than medium or coarse sand (25%).

DISCUSSION

The majority of Santa Barbara Littoral Cell beach sediment is fine to medium-grained sand (Fig. 5). When the cell is divided based on physical setting by the Ventura River (location #117), beach sand in the western portion of the study area is finer grained than in the eastern portion. This is likely a result of regional differences in both sediment inputs and coastal processes. For example, if the Ventura and Santa Clara rivers in the southeast deliver a coarse load, and if the fine-grained bluffs of the west contribute fine sediments to the beach, than the resulting beach grain size could be a result of sediment source grain size. Differences in wave energy and nearshore current velocities are also important in determining what sediment grain sizes compose the beach. Coarser beaches in the east are more exposed to high wave energy as compared to finer beaches in the west/central, which are more sheltered from the dominant wave energy. (Beaches at the westernmost end of the Channel would also be exposed to greater wave energies and may also be comparatively coarser, but these beaches were not sampled.) Seasonal alongshore variation, as measured by the magnitude of grain size change, may be a result of alongshore differences in both sources and processes acting on each particular beach.

Summer grain size distributions represent the finest sediment that remains on the beach. An examination of the grain size distribution of summer grab samples indicates that nowhere in the cell does the sand/silt break define what grain sizes compose the beach. Runyan and Griggs (2003) previously determined that the average Santa Barbara LCD was about 0.125 mm. However, results from this study indicate that a single value cannot accurately define what remains on the beaches throughout the entire cell. When nourishing a beach, the appropriate cutoff diameter, specific to that beach, should be used. In general terms, when assessing potential offshore sources for the cell, the boundary between fine sand and very fine sand (i.e. 0.125 mm), can be used as a general LCD because this value will not underestimate what will remain on the beach. However, in some cases-possibly more in the eastern portion of the study area-this value may be an extreme overestimation.

As expected, finer sediments are found offshore. Coarser sediments are not transported into deeper waters since they are not easily kept in suspension; instead they settle nearshore. Overall, the coarsest offshore sediments exist in an extremely narrow zone close to shore, probably within the depth of closure. These fine and medium-grained sands are likely an active part of the littoral drift system and anchor the submarine beach

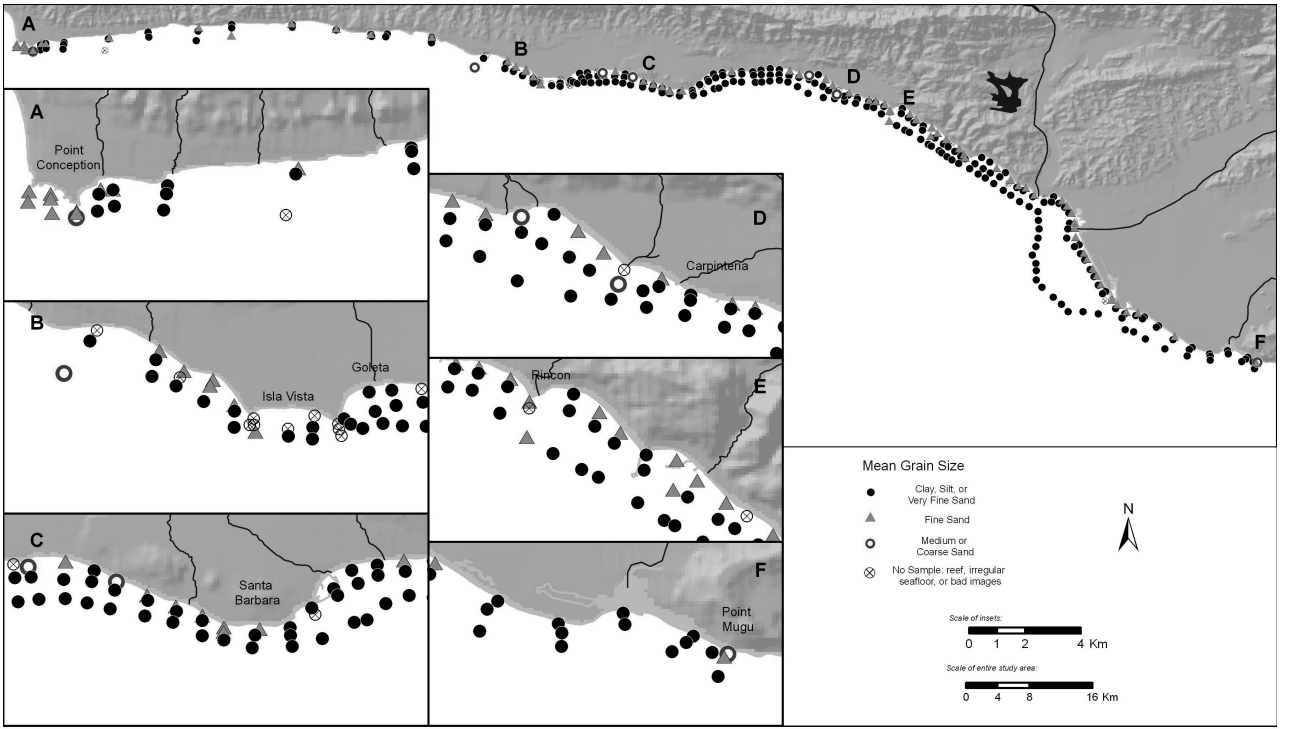

Fig. 5. Mean grain size of nearshore (5, 10, 20 m)
Flying Eyeball Samples, eastern Santa Barbara Littoral Cell.

profile. As a result these coarser, shallow sediments should only be considered sources for beach nourishment with a thorough evaluation of the coastal impact. This includes sediment within 5 m and other deeper areas affected by higher energy.

The coarsest offshore sediments deeper than 5 m are found at only a few locations throughout the cell (Fig. 6 and 7). Coarser sediments are commonly found near major headlands, such as Point Conception and Point Mugu, as a result of the steeper nearshore slopes and/or higher energy environment. As a result of additional energy focused onto the headland and because these sediments are located close to shore, within ¾ of a km at Point Conception, these deep, coarser sediments may still be part of the active littoral drift system, within the depth of closure. However, more information is needed. If it is confirmed that these deposits are part of the active littoral system, then they should not be dredged. However, if they are not, then thickness of the deposit and the economics of dredging these areas should be evaluated-keeping in mind that these sediments are located far from populated beaches needing nourishment.

If Point Conception is not considered too far to serve as a potential borrow area, then one other site should be examined: an offshore geology map indicates a large sand deposit just offshore of Point Conception (Greene and Kennedy 1989). The sediment here could be a final sink for the Santa Maria Littoral Cell (a debated cell extending from the Santa Maria River to Point Conception), or if there is a single continuous cell around the point, then this deposit could be a partial sink within the Santa Barbara Littoral Cell (Patsch and Griggs 2005). Either way the deposit is likely to have accumulated as a result of the longshore current deflecting sediments offshore as it encounters the headland. Further investigation of the area is recommended; both sediment thickness and grain size data should be obtained.

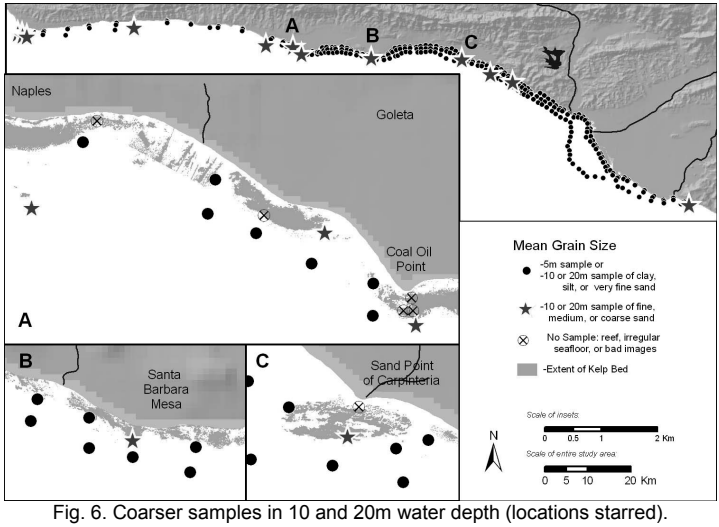

Fig. 6. Coarser samples in 10 and 20m water depth (locations starred). Insets show coarser samples and proximity to kelp beds.

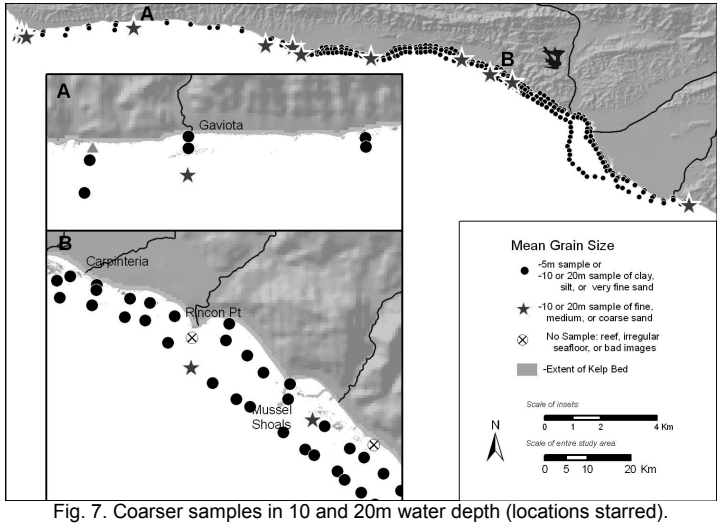

Fig. 7. Coarser samples in 10 and 20m water depth (locations starred). Insets show coarser samples and proximity to kelp beds and streams.

Sample locations of coarser sediment found deeper than 5 m, were examined with respect to distance from kelp beds, a proxy for exposed bedrock outcrops on the seafloor (Fischer 1983; California Department of Fish and Game 2006). Sediments found near rocky reefs are likely to be composed of coarser broken reef fragments which have accumulated in reef pockets. These deposits are presumably very thin and therefore not viable for dredging. The samples west of Coal Oil Point and offshore of Sand Point in Carpinteria are in very close proximity to the mapped kelp beds (Fig. 6). In addition it was noted in the cruise field notes that the Flying Eyeball© had to be navigated through kelp to reach the seafloor at these locations. As a result, these coarser deposits are most likely only thin deposits within reef pockets and are therefore not considered suitable borrow areas for beach nourishment. For a few locations, south of Coal Oil Point, Naples, and the Santa Barbara Mesa, it is not clear whether coarser samples are related to the nearby reefs (Fig. 6). All three of these samples were in close proximity to kelp; however, the isopach maps of Fischer et al (1983) indicate that the unconsolidated sediment is at least 4 m thick at each of these locations.

Coarser samples deeper than 5 m are sometimes found offshore rivers and streams (Fig. 7). If these deposits are not relict beaches, than they may be associated with the stream as either part of a paleostream deposit or as a result of a more recent hyperpycnal flow (Fischer 1983; Warrick and Milliman 2003). If the deposit is related to an old stream channel from an earlier sea level, it would be expected to contain coarser sands and gravels, which may or may not be suitable for nourishment. Grain parameters such as shape and roundness, and characteristics such as sorting and layering of grain sizes within the deposit, should be thoroughly examined to determine if sediments are compatible with the beach. In addition, it should be confirmed whether sediment

thickness is sufficient in these areas. The isopach maps of Fischer et al (1983) indicate adequately thick unconsolidated sediments at Gaviota, Rincon Point, and Mussel Shoals. However, while these samples are not located within the present-day kelp cover, they are located within the historic kelp extent as mapped by Fischer et al. (1983).

In addition, because the Flying Eyeball© only samples surface sediments and coarser deposits may exist beneath the surface, it is recommended that complete grain size distribution be obtained offshore Goleta, the Santa Barbara Mesa and Harbor, and the Ventura/Oxnard area (Fig. 8). However, since greater wave energy is received in the eastern portion of the study area, if compatible sediments are found at 10 m water depth in the Ventura/Oxnard area, it needs to be determined whether these sediments reside within the depth of closure before a borrow area is considered.

It is difficult to evaluate how well the results of this study compare to the offshore surficial deposits map, since an overwhelming 98% of the offshore samples observed were very fine sand or fine sand which was mapped as one unit by Welday and Williams (1975). However, some of the smaller pockets of medium and coarse sand delineated by Welday and Williams were found in this study to be composed of fine sand or very fine sand. It is not known however, if this is a result of the original data collection and processing methods, the mapping scheme of Welday and Williams (for example, undefined sand was mapped as medium sand), or as a result of sampling only the very surface with the Eyeball©. Alternately, the observed change may be legitimate and simply the consequence of sediment transport and deposition in a dynamic environment for over 100 years.

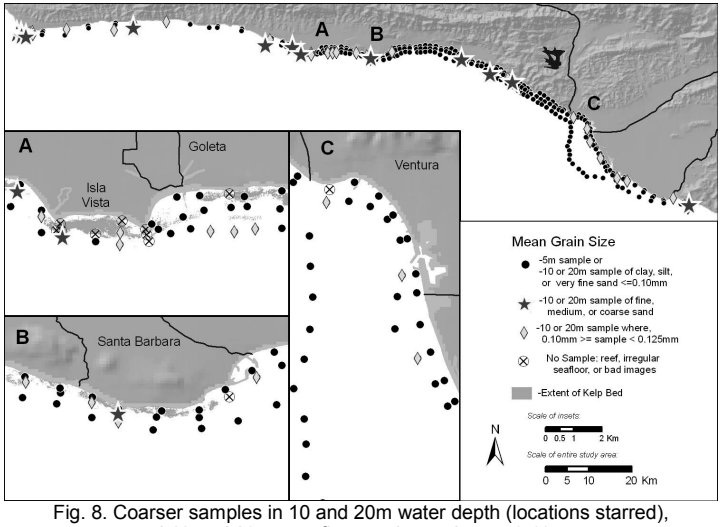

Fig. 8. Coarser samples in 10 and 20m water depth (locations starred), and 10 and 20m very fine sand samples >= 0.10mm.

CONCLUSION

The Eyeball© cameras provide a rapid way to determine the grain size of many surface sediments throughout a very large beach and offshore area. Overall, compatibility is poor between beach and nearshore surface sediments in the Santa Barbara Littoral Cell. The coarsest offshore sediments are found at 5 m, most likely within the depth of closure. Some coarser deposits exist deeper, for example at Naples, Coal Oil Point, the Santa Barbara Mesa, and Rincon Point, but it is unclear whether they are part of a thick deposit of suitable nourishment material, or simply a thin, coarser deposit within reef pockets. Further grain size analysis of cores is recommended to resolve this question. In addition, cores should also be taken at Goleta, the Santa Barbara Harbor, and the Ventura/Oxnard area; surface sediments at these locations were not coarser than very fine sand, but complete grain size distribution should be completed as they showed more promising results of coarser surface sediments and sufficient sediment thickness than most other locations.

ACKNOWLEDGEMENTS

We would like to thank the USGS, California Department of Boating and Waterways, Beach Erosion Authority for Clean Oceans and Nourishment (BEACON), and the City Carpinteria for funding this study. In addition, this study could not have been accomplished without the help of Hank Chezar (with the Flying Eyeball©), Shane Anderson and Dave Farrar of UCSB (for driving the R/V Connell as well as assisting the sample collection process), and also the many volunteers who helped sample the beach and nearshore. Thanks also to the UCSC Coastal Lab who read and greatly improved this manuscript.

REFERENCES

Best, T.C. and Griggs, G. B. (1991). "A sediment budget for the Santa Cruz Littoral Cell California." *Society for Sedimentary Geology Special Pub.* 46: 35-50.

California Department of Fish and Game (2006). California Coastal Kelp Survey. GIS shapefile. http://www.dfg.ca.gov/itbweb/gis/mr_nat_res.htm.

Dean, R.G. (2002). Beach Nourishment: Theory and Practice. World Scientific, New Jersey. 399 p.

Fischer, P.J. et al. (1983). Study on Quaternary shelf deposits (sand and gravel) of southern California. State of California, Department of Boating and Waterways. FR82-11. 75 p.

Flick, R.E. (1993). "The myth and reality of Southern California Beaches." *Shore & Beach* 61(3): 3-13.

Greene, H.G. and Kennedy, P.K. (1989). California continental margin geologic map series, south-central California continental margin, map no. 4a. California Division of Mines and Geology.

Griggs, G.B. (2006). Considerations for beach nourishment in California. California and the World Ocean Conference, Long Beach, California.

King, P.G. (2002). Economic analysis of beach spending and the recreation benefits of beaches in the city of Carpinteria. Prepared for the City of Carpinteria.

King, P.G. and Symes, D. (2003). "Potential loss in GNP and GSP from a failure to maintain California's beaches." *Shore & Beach* 72(1): 3-8.

Limber, P.W., Patsch, K. and Griggs, G.B. (in press). "Coastal sediment budgets and the littoral cut-off diameter: a grain size threshold for quantifying active sediment inputs."

McLellan, T.N. and Hopman, R.J. (2000). Innovations in Dredging Technology: Equipment, Operations, and Management. U.S. Army Engineer Research and Development Center, Waterways. ERDC-TR-DOER-5. http://el.erdc.usace.army.mil/dots/doer/pdf/trdoer5.pdf.

National Research Council (1995). Beach Nourishment and Protection. National Academy Press, Washington, D.C. 334 p.

Noble Consultants (1989). Coastal Sand Management Plan Santa Barbara / Ventura Couny Coastline, Appendix B Offshore Sand Sources. BEACON.

Patsch, K. and Griggs, G.B. (2005). Development of sand budgets for California's major littoral cells. California Department of Boating and Waterways, California Coastal Sediment Management Workgroup.

Patsch, K. and Griggs, G.B. (2006). Littoral cells, sand budgets, and beaches: understanding California's shoreline. California Department of Boating and Waterways, California Coastal Sediment Management Workgroup.

Reid, J.A., et al. (2006). usSEABED: Pacific Coast (California, Oregon, Washington) offshore surficial-sediment data release: U.S. Geological Survey Data Series 182. http://pubs.usgs.gov/ds/2006/182/.

Revell, D. L. and Griggs, G. B. (2006). "Beach Width and Climate Oscillations along Isla Vista, Santa Barbara, California." *Shore & Beach* 74(3): 8-16.

Rubin, D. M. (2004). "A simple autocorrelation algorithm for determining grain size from digital images of sediment." *Journal of Sed. Research* 74(1): 160-165.

Rubin, D. M. et al. (2006). Underwater microscope for measuring spatial and temporal changes in bed-sediment grain size. U.S. Geological Survey. Open-file report 2006-1360. 15 p.

Runyan, K.B. and Griggs, G.B. (2003). "The effects of armoring seacliffs on the natural sand supply to the beaches of California." *Journal of Coastal Research* 19(2): 336-347.

U.S. Army Corps of Engineers (2002). *Coastal Engineering Manual-Part V*. Chapter 4: Beach Fill Design. Vicksburg, Mississippi: EM 1110-1-1100, 113 p.

Warrick, J.A. and Milliman, J.D. (2003). "Hyperpycnal sediment discharge from semiarid southern California rivers: implications for coastal sediment budgests." *Journal of Geology* 31(9): 781-784.

Welday, E.E. and Williams, J.W. (1975). Offshore surficial geology of California, Map sheet 26. California Division of Mines and Geology.

Wiegel, R.L. (1994). "Ocean beach nourishment on the USA Pacific coast." *Shore & Beach* 62(1): 11-36.

Willis, C.W. and Griggs, G.B. (2003). "Reductions in fluvial sediment discharge by coastal dams in California and implications for beach sustainability." *Journal of Geology* 111(2): 167-182.

Presence of Beach-Compatible Sediments in Offshore Borrows: New Challenges and Trade Offs in Developing Codifications

Charles W. Finkl[1], Jeffrey L. Andrews[1], and Lindino Benedet[1]

1. Coastal Planning & Engineering, Inc., 2481 NW Boca Raton Boulevard, Boca Raton, FL 33431, USA. cfinkl@coastalplanning.net; jandrews@coastalplanning.net; lbebedet@coastalplanning.net

Abstract Appropriate protocols are required for selection of beach-compatible sediments from offshore borrows. Determination of what constitutes 'native' beach sand can be problematic where prior renourishment modifies true native beach sediments. Because borrow sands must at some level approximate 'native beach sediments,' offshore exploration methodologies need to efficiently differentiate bottom sediments into usable and non-usable categories. Sand search models (SSMs) are one approach where exploration protocols are based on literature searches and geophysical-geotechnical techniques that are conditioned by regional geomorphology, sediment dynamics, sedimentary properties, seismostratigraphy (calibrated with vibracores), and deposit morphologies (including facies recognition). Engineering-environmental performance guides attempts to 'match' borrow sediments with existing beach sands, but exact matches always may not be found in offshore materials. This guidance is, in large part, a balancing act that attempts to replicate beach stability and biological beach performance where trade offs are inevitable.

INTRODUCTION

Over the last few decades, beach nourishment has become the method of choice for shore protection (Finkl and Walker, 2002). Most commonly, sediments are dredged from offshore areas, referred to as borrows, and placed onshore as sand-water slurries pumped from the dredge. In the early stages of nourishment when sand was pumped onshore from offshore borrows, the deposited sediment was regarded as 'fill' that met volumetric needs to supply wide subaerial beaches for shore protection and recreation. Over time, as some undesirable materials were inadvertently pumped onshore to produce unsightly beaches or beaches that performed poorly from an engineering or environmental point of view, it became apparent

that more effort was required to characterize the nature of offshore sediments (Finkl, 1981). Eventually, it became apparent that grain size was an important determining factor of the engineering performance of beaches (*e.g.* Dean, 2002). Most recently, environmental concerns not only focused on grain size but also other parameters such as sand color and mineralogical composition of borrow materials as well as properties of the placed materials such as modes of grain packing (voids), aeration (oxygen levels), and moisture because these properties were important to sea turtle nesting sites (Maloney *et al*., 1990; Wood and Bjorndal, 2000). Thus, the list of do's and don'ts for beach nourishment grew over time until some states such as Florida and North Carolina codified in administrative codes what can and can not be placed on the beach. These guidelines attempt to define 'native beach sediments,' types of borrow materials, and identify degrees of agreement between the two. That is, how well borrow materials match native beach sediments. Implicit in these codifications are levels of uncertainty and risk of assessment, factors that are considered in different ways.

The purpose of rules and regulations regarding the kinds of materials that can be placed on the beach (or in dunes) is to ensure that only appropriate sediments comprise beach fills. The development of guidelines is a complicated task that has to account for numerous variables, be specific and yet broad enough to be practical, while at the same time conforming to engineering-environmental requirements. The process is not only driven by advances in increased understanding of coastal morphodynamics, such as relationships between grain size and beach state, but also by negative impacts to beaches that have accrued over time due to unknown materials occurring in borrows or below intended cuts (when dredges cut too deep into undesirable materials). Some of these processes are discussed below as exemplars of problematic situations, especially the so-called "compatibility problem." The procedure here will be to discuss perceptions of materials that constitute 'native beach' sediments, processes for evaluating the nature and properties of offshore sediments, and methodologies for estimating the 'match' between the two. Explicit to these discussions are considerations of various risk factors, temporal and spatial accuracy of parameter measurement, and levels of risk or variance that are acceptable.

CHARACTERIZATION OF NATIVE BEACH SEDIMENTS

The term 'native beach sediment' is deceptively complex for numerous reasons but mainly because concepts of 'native' are time-dependent variables that are conditioned by pre-existing geology and ambient conditions such as wave climate, morphodynamic beach state, whether a beach is accreting or eroding, and local biology (*e.g.* presence of nearshore shell deposits, coral reefs). Because beaches are among the most dynamic geomorphic features on earth, the timing of sampling and location of samples is extremely important. In many locations such as occur in Florida, beaches have been renourished several times and it is difficult to determine what is 'native' because the original sediments (determined at some start point in time) have been modified by fill admixtures. Natural modification during severe storms (hurricanes) by storm surge erosion and deposition is an additional factor that complicates determination of what constitutes native beach sediments.

CONCEPTS OF NATIVE BEACH SAND

Perceptions of materials that constitute native beach sand are conditioned by educational backgrounds (*e.g.* geology vs. engineering vs. environmental science) as each discipline will have a different 'take' on the situation. Managerial needs influence the decision-making process, often accepting extent conditions as 'native' when in fact they might represent an end point in a natural cycle as would be observed, for example, on an eroded beach. What sediments remain on a severely eroded beach that is perched on top of bedrock, as variously occurs in Palm Beach County where lags are superposed on top of the Anastasia Formation,

should not be considered as representing normal conditions. Concepts of native beach sand are temporal perceptions that are tied to an arbitrary point in time, which may not be a good representation of conditions during beach half-life. Beach sand samples may be highly representative of existing conditions, but ranges of variability vary within themselves depending on what particular parameter is addressed (Smith, 1992). Perceptions of native beach sands are thus largely spatio-temporal compromises that are conditioned by numerous variables, some of which are discussed below.

Spatio-Temporal Variability of Beach Grain Size

Collection of representative beach samples is no easy task because beaches are dynamic morphosedimentary bodies in a constant state of flux due to changing energy conditions (Komar, 1998). Of the few examples of regional beach sediment sampling programs, efforts in Florida (Charles, Malakar and Dean, 1994) and North Carolina (Rice, 2003) are notable. Beach sand data collected along the east coast of Florida, from mean sea level to -3.6 m (NGVD), was later used by Benedet, Finkl and Klein (2004) to determine site-specific (beach profile) grain sizes for the same region. In attempts to determine the degree of variation in sedimentary characteristics for different areas, these examinations summarized a wide range of parameters that were believed to be important: location (geographic coordinates), station, sample number, elevation, distance from benchmark, geomorphic position, carbonate content, collection date, grain size distribution, data source, *etc*. In the example of North Carolina, Rice (2003) reports average sedimentary characteristics for oceanfront beaches where the statewide average beach sediment is predominantly medium to fine sand with ~2.9% gravel (<2 mm by weight), ~2% fines (silt plus clay), and ~5.8% shell material (based on the Wentworth Classification). Carbonate contents were highly variable (ranging from 0 to 99%) but showed a mean statewide content of ~5.8% and a median content of 2%. Beaches of the northern Outer Banks (north of Cape Hatteras) are slightly coarser than the statewide average whereas Brunswick County beaches are finer grained. The average beach sediments of Onslow Bay and the southern Outer Banks (Cape Hatteras to Cape Lookout) are similar to statewide averages.

These kinds of efforts (*i.e*. Florida and North Carolina beach sediment studies) help establish baseline data that can be used for comparative purposes when evaluating compatibility of borrow sediments. The main points to consider when working with these data is that they are variable and dynamic. That is, beach sediments are prone to change in time and space depending on weather systems and interference by human activities (*e.g*. coastal construction, beach nourishment).

It is impossible in the space allotted here to adequately discuss all of the problems associated with sediment sampling and characterization of beaches by grain size. Some of the overriding problems include bias in sample selection and variation in grain size caused by cross-shore selective sorting of bimodal sediments (*e.g*. admixtures of biogenic carbonate fragments and silicate grains), temporal changes in beach grain size, seasonal wave patterns, and inputs of new sediments to the littoral system, as discussed by Benedet, Finkl and Klein (2004) for the Florida Atlantic coast. Grain sizes of beaches are known, for example, to show high-frequency event-related variability (Komar, 1998; Wright and Short, 1984), especially after significant wave events that sort beach grains. Just as timing of sampling is critical to characterization of native sediment status, so are spatial considerations of exactly where samples are collected alongshore, cross-shore, and at what depth (surface sample vs. depth of sampling). Beach sediments are normally collected from toe of the dune (beach back berm area) to the theoretical depth of closure (DoC). This morphodynamic zone typically incorporates numerous sediment collection sub-zones viz. back berm, middle berm, mean

high water line, mean tide line, bar and trough systems, and at specified intervals on the upper shoreface to a defined depth (such as the DoC). Even on a single morphodynamic unit such as the beachface there can be considerable variability in grain size both alongshore and cross shore. This situation becomes poignantly evident where the beachface is decorated by beach cusps where coarser grains tend to accumulate in the horns and finer grains in the bays. Sediment sampling without regard for process-from relationships evident in beach systems can bias results that are then used to determine native beach sediment grain-size distribution patterns. Low frequency sampling in time and space provides a weak database upon which to base assumptions of native beach sediments. Additionally, small changes in grain size may be statistically insignificant (see discussion below).

Sampling Limitations

The brief discussion above points to limitations in sampling and emphasizes sample location and timing of collection as important parameters that need to be considered in the determination or characterization of 'native' beach sand. Samples obtained within a day's difference, or within the same day, for example, can return different mean grain size values depending on sample location and sampler bias. Significant in this respect also is cognizance of wave conditions, and beach-surfzone morphology conditions that cause varying trends in beach state (whether transitioning from dissipative storm beach to intermediate fair weather beach). The value of grain-size data are thus of limited use unless morphodynamic parameters and other locational data are carefully noted at the time of collection. If this kind of collateral data does not accompany beach sediment sampling regimes, the data should be cautiously adjudicated in attempts to determine the status of native beach sediment or for comparison with other datasets. There are additional complications when beaches are artificially renourished and offshore sediments are introduced to the beach system. Artificial beach renourishments typically equilibrate to ambient conditions in distinct phases that lead to morphodynamic stability, and sometimes to instability, before the next renourishment cycle begins. These sediments are admixed with native beach sediments to produce a new 'native' beach sediment over time. Native beach sediments are thus not a constant but a variable or moving target.

Significance of Grain Size Differences to Beach Nourishment Design

Because of spatial and temporal variability of beach sediment, mean value estimates for grain size populations often vary widely for different sampling periods or sampling schemes. Beach nourishment often introduces new sands that have different textural characteristics than the "native" material. The equilibrium beach profile theory (EBP) (Dean, 1991, 2002) is often used to quantify the effects of nourishing a beach with a specified grain size diameter. The EBP is described by the relation

$$h = Ay^{2/3}$$

where h is depth, y is distance and A is the so called "profile scaling parameter". Appropriate values for A as a function of grain size are often estimated (Dean, 2002; USACE, 2002) but the overall premise is that finer-than-native grain sizes produce flatter beaches (less subaerial beach area per unit volume of beach fill) whereas coarser-than-native grain sizes produce steeper beaches (more subaerial beach area per unit volume of beach fill). Dean (2002) developed a simplified method for determining the value of additional beach width by calculating the ratio between the profiling scale parameter of the fill to the native beach.

As an example, consider application of the EBP, as described by Dean (2003), by assuming a native beach grain size of 0.2 mm (A factor = 0.15) and two potential borrow sites, one with a

mean grain size of 0.18 mm (A factor = 0.14) and another with a mean grain size of 0.22 mm (A factor = 0.159). A volume of 250 m^3/m is proposed for placement on a beach where the berm height is 1.8 m and the closure depth is 4.9 m. If the borrow sand had the same grain size as the native beach, an equilibrated dry beach width of 37.5 m would result.

Calculating A-factor ratios between the native beach and proposed fill volumes gives equilibrated additional dry beach widths for the smaller and larger grain sizes as 7.6 m and 56 m. These values compare to 37.5 m when borrow sediments are similar to native beach sediments, as described in Dean's (2002, 2003) procedure. It is thus seen that different predictions in equilibrated beach widths can result from minor differences in mean grain size.

Differences in predicted equilibrated beach widths between native and finer grains, for example, range more than 100% for a grain size variation of 0.02 mm, or less than 10% of the native grain estimate of 0.2 mm. Concern thus naturally arises over consideration of small difference in grain size. The problem boils down to predictions that are based on a mean grain size estimate that can be in error or biased by spatio-temporal variability, low sampling resolution, and statistical distributions (*e.g.* Benedet *et al*., 2004). In a Gaussian distribution, the mean has a standard deviation of ± 34%, thus a 10% difference in grain size will fall within the standard deviation. If native beach and borrow sands have the exact same statistical distribution, then variability about the mean would be minimal. Spatio-temporal and sampling density variability still exist, however.

Simply put, an estimated equilibrated beach width becomes less than meaningful unless variability of input data is comprehended. Although the EPB method is a useful complement to beach nourishment design, it is necessary to include probabilistic distributions in final design estimates, as suggested by Capobianco *et al.* (2002). Design estimates thus should ideally indicate equilibrated beach widths for mean grain sizes as well as for a number of possibilities around the mean with respective probabilities. This realization becomes ever more important when it is understood that mean grain size estimates used in common design procedures are not absolute numbers but highly uncertain estimates that variable.

DETERMINATION OF BORROW SEDIMENT PROPERTIES

Recognizing problems associated with the determination of native beach sediments and efforts to approximate them with offshore borrow materials, governmental agencies and proprietary organizations have adopted quality assurance (QA) and quality control (QC) measures to ensure placement of acceptable fill materials on the beach. Working with researchers and consulting groups, the Bureau of Beaches and Coastal Systems (BBCS, Florida Department of Environmental Protection) has codified QA/QC plans for beach nourishment projects that qualify sand searches and fill materials. Louisiana has established sand search protocols (Khalil, 2004; Finkl and Khalil, 2005a,b) and North Carolina is in the process of approving technical standards for beach fill projects. Efforts in these three states provide guidance for the middle and south Atlantic coasts (Carolinas and Florida east coast) and the Gulf of Mexico (Florida west coast and Louisiana). Extracts from state administrative codes and guidelines provide the basis for the discussion that follows, particularly the definition of native beach sediments, qualification of borrow materials, and the degree of correspondence between the two.

Initial determinations of sediments on the continental shelf of the southeast United States were provided, for example, by Gorsline (1963), Giles and Pilkey (1965), Duane and Meisburger (1969), Meisburger and Duane (1971), Field and Duane (1974), and Meisbureger

(1977), among others. In addition to these seminal large-scale studies, modern sediment surveys are conducted by university researchers and consultants.
Relational databases, generally supported or maintained by government agencies, collate much information on the character of seabed sediments viz. ROSS (Reconnaissance Offshore Sand Search in Florida), usSEABED (U.S. Geological Survey Data Series 118, usSEABED: Atlantic Coast Offshore Surficial Sediment Data; U.S. Geological Survey Data Series 146: usSEABED: Gulf of Mexico and Caribbean (Puerto Rico and U.S. Virgin Islands) Offshore Surficial Sediment Data) and LASARD (Louisiana Sand Resources Database) (Khalil, 2005). A recent summary for the North Carolina inner shelf, prepared by Boss and Hoffman (2000), investigates offshore resources but did not consider the issue of compatibility with beach sediments.

QA/QC PROCEDURES IN SAND SEARCHES

Methodologies for marine sand searches are specialized applications of geotechnical and geophysical procedures that have developed with experience over time in a range of seafloor conditions. Organization of techniques for sand exploration as a strategic approach has advantage over blanket exploratory surveys that do not target areas of interest prior to going to sea. The purpose of exploration protocols is to methodically narrow potential sand targets to those that are compatible with native beach sediments. To this end, QA/QC procedures help to comprehend natural variability in sedimentary deposits, reduce placement of unwanted materials on the beach, and better define borrow materials that will approximate desired environmental and engineering performance.

Exploration Protocols

There are no universal or comprehensive guidelines regarding the best possible way to conduct an offshore sand search, but several models for specific geographic regions have been developed (*e.g.* Finkl, Khalil and Andrews, 1997; Finkl, Khalil, and Spadoni, 2002; Finkl, Andrews, and Benedet, 2003; Khalil, 2004; Finkl and Khalil, 2005a,b). The lack of comprehensive guidelines occurs because sand searches are site specific and they must be geared to specific geographic environments that retain similar shelf histories. Continental shelves are drowned coastal plains and the characteristics of those plains are largely fashioned by terrestrial regimes of the hinterlands that reach the coast. Of particular note here are fluvial (incl. estuarine) systems that flowed across the coastal plains to the sea. The specificity of coastal marine environments is such an overwhelming problem that it militates against development of a comprehensive set of guidelines that cover all situations. Efforts thus tend to be localized and concentrate on coastal marine environments that are germane to jurisdictional boundaries. The Coastal Engineering Research Center (CERC) [now part of the Coastal and Hydraulics Laboratory, CHL], which developed some general guidelines for conducting sand searches, now includes them in the electronic version of the *Coastal Engineering Manual* (CEM) (USACE, 2002). Other works related to procedural methods for sand searches include the recommendations of Finkl, Benedet and Andrews (2003), Finkl, Khalil and Andrews, (2002), and Meisburger (1990).

Because sand searches must be geared or tailored to geological conditions in the area of the study, approaches to conducting the search must be compatible with the specific geographic parameters of that region. This means that exploration methodologies must be capable of resolving required detection limits that are determined by deposit configuration in different geographic areas. The same search techniques would not, by way of an extreme example, be deployed in the search for large sedimentary blanket or shoal deposits as would be required for the detection of fluvial valley infills that are buried by muddy overburden. Even though marine sand searches must be oriented to the detection of specific geologic

features, there are, however, broadly accepted procedures for conducting a geotechnical investigation for the purpose of identifying potential offshore borrow sites.

These general procedures consist of sequential tasks that are conducted in a phase-wise manner, as enumerated in Figure 1. The sequence of investigation boils down to ten essential steps that involve: (1) literature reviews and analyses of prior data, (2) development of action plans that incorporate digital databases of prior data, (3) reconnaissance geological (geotechnical) and geophysical surveys, (4) identification of target area, (5) detailed geophysical surveys, (6) detailed geotechnical surveys, (7) evaluation of geophysical and geotechnical data, (8) hazard and archaeological assessment survey, (9) selection of borrow area and depths of cut, and (10) preparation of reports. There are ranges of sub-tasks within each of these main phases of work, the whole process taking several months to complete depending on project size, location, amount of previous work completed (assuming that the data collected is adequate, appropriate, accurate, and relevant), available funding, weather conditions (especially sea state), *etc*. Ideally, all of these steps can be completed in a couple of months provided enough personnel are put on the job and sufficient funds are immediately available. Ideal conditions are seldom encountered in the real world, however, and completion times can lag significantly behind anticipated job closure. Weather conditions are an important variable where rough seas can delay marine surveys for days to weeks at a time, as in the case where there is passage of successive closely-spaced cold fronts or development of northeasters.

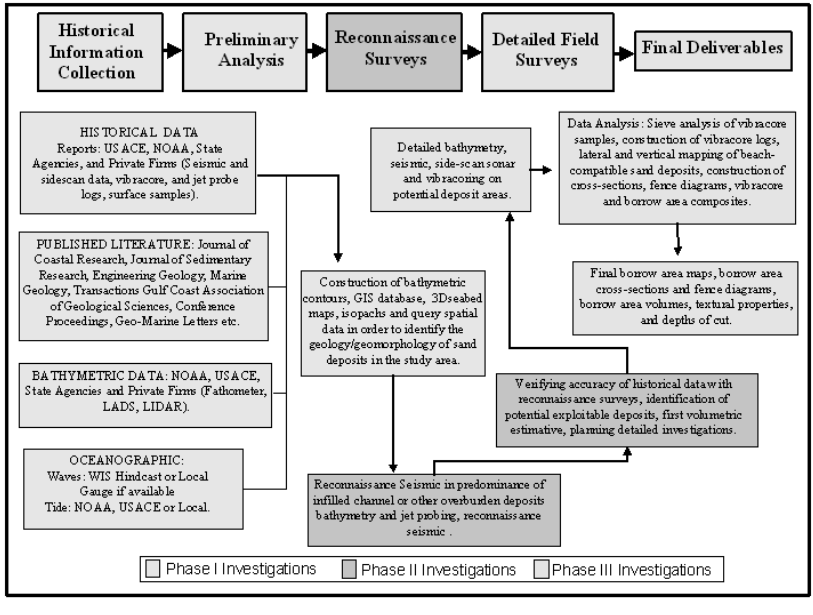

Fig 1. Generalized sequential steps in offshore sand searches, showing phases of marine investigation that lead to designation of specified deposits for borrow development.

These guidelines are briefly summarized in terms of tasks to be completed within ten main phases. The descriptions, which are here not meant to be definitive or binding, indicate general strategies that logically work toward completion of phases so that future work can build on prior accomplishments that, to a certain degree, direct the course of subsequent actions. Capstones occur at the end of Phases II and III where results and plans are reviewed and evaluated for the purpose of modifying or redirecting future search techniques. These capstone reviews may require that previous steps be revisited if there are problems with the resulting data that could adversely impact utilization or interpretation of the data.

This kind of methodological approach to marine sand searches should be adapted to sand search investigations by assimilating good quality legacy data so that existing information does not have to be duplicated. In comprehensive marine sand searches, comprehensive sequential survey procedures are employed to maximize resources and effectively characterize offshore sand deposits. These sequential surveys collect preliminary data over relatively large expanses of seafloor in the form of surface grab samples, jet probes, and reconnaissance bathymetry prior to the collection of remotely sensed data (*i.e*. seismic reflection profiles, side-scan characterization of the seafloor, and magnetometer surveys) and vibracores in smaller target areas. Reconnaissance-level surveys that cover large areas of the seafloor provide useful information that helps define smaller targets (areas with higher potential for containing materials that are suitable for beach nourishment) where more intensive (and more expensive) sand and cultural resource investigations are conducted.

Sand Search Models

Sand search methodologies presently deployed by CPE (*e.g*. Florida SSM (Panhandle, west coast, east coast), Delta SSM (Mississippi River deltaic area), Texas SSM, Carolinas SSM, New England SSM) are based on knowledge of prior work, coastal geological conditions, and advanced geophysical/geotechnical survey methods. Other useful tools for assessing sand quality on the seabed include the ROSS (Reconnaissance Offshore Sand Search) surficial sediment database and gINT®. ROSS allows the identification and assessment of potential offshore sand resources that are suitable for beach nourishment projects. The tool consists of a corporate database that can be addressed, searched, and manipulated through an online query builder as well as with existing ArcIMS® Geographic Information System (GIS) routines that provide access over the Internet (Web). The gINT® geotechnical and geoenvironmental software is used for fully customizable borehole/boring and well logs, cross sections, geotechnical testing, and other professional engineering reports. Based on a powerful relational database system, the user has full control over the design of database structures, report formats, and symbol libraries.

Risk and Variability

Spatial distributions of seafloor sediment and rock types, usually shown in maps and based on results of samplings or inspections of the seabed at numerous sites, leads to consideration of degrees of uncertainty. Information is gained about the seabed from direct sampling (e.g. vibracore, jet probe, grab sample), remote sensing (*e.g*. bathymetric-fathometer survey, sidescan sonar, seismic reflection profiling, multibeam survey, magnetic survey), diver inspections (*e.g*. by digital camera, videography), and from instrumented probes. These types of mapping are generally grouped as 'geological' but they are widely practiced in engineering as well. Uncertainties in geological seabed mapping are partly related to disturbed or incompletely recovered cores, variable levels of assurance in interpretation of remotely sensed data, extreme patchiness (variability) of seabed of materials, poor analyses by some laboratories, and validations that produce unexpected results. These problems relate to the

reliability of seabed mappings based on point-site data and often beg the question as to how these uncertainties should be quantified and displayed. Attempts to approach a rational understanding of deficiencies in geological point-site datasets focus attention on how they can best be overcome.

Risk comes from a variety of sources and avoidance must be multi-pronged. Rarely is risk eliminated altogether as it is too pervasive and costly to attempt elimination. So, from a practical point of view, risk is mitigated by attempting to reduce uncertainty as much as practical. Two major sources of risk are natural sediment variability within a deposit or borrow area and completeness of geological information. Variation within a deposit depends on numerous factors such as provenance, coastal geomorphic environment (quiescent vs. high-energy, transgressive-regressive sequences), spatio-temporal scales of depositional cyclicity, mode of deposition, syndepositional inclusions (facies changes), reworking by organisms (bioturbation), postdepositional compaction, and so on. Homogeneous borrows containing compatible materials thus have less risk than a borrow area known to contain strata of noncompatible material.

Point site data such as that obtained from vibracores is normally assumed to represent a volume greater than what was sampled in a 10-cm (4-inch) diameter core. The 'sphere of influence' of a vibracore depends on deposit architecture; homogeneous laminated deposits extend the zone of confidence a specified distance from the sample site. Conversely, the sphere of influence of a vibracore in a more heterogeneous deposit is restricted by a higher degree of uncertainty. Seismic reflection profiles often can extend the zone of confidence (decrease uncertainty). In a best-case scenario in a homogeneous deposit, based on 300 m centers for vibracore site sampling, extrapolation of deposit continuity from the vibracore would be a 150 m radius. That gives a potential seabed surface area of about 70,700 m^2 and a total sediment volume of about 495,000 m^3 per 7-m vibracore. Characterization of a sphere of influence for a sediment volume of nearly 500,000 m^3 from a 10-cm core (7 m long) is an industry standard but there is clearly room for concern as it seems clear that heterogeneous deposits offer greater scope for uncertainty. Closer spacing of vibracores in borrow areas with known variability is facilitated by dynamic vibracoring plans where spacing can be adjusted on the fly as cores are retrieved and inspected aboard ship. Risk of pumping undesirable material onshore is thus reduced by decreasing the representative sphere of influence, that is, by decreasing reliance of interpolated data between vibracores.

COMPATIBILITY OF BORROW AREA WITH NATIVE BEACH MATERIAL

The BBCS, for example, has codified geological information requirements in Rules 62B-41.007(2)(j) and 62B-41.008(1)(k)4, Florida Administrative Code (FAC) for determining the nature of proposed beach fill material and its compatibility with naturally occurring beach sediment when applying for a Joint Coastal Permit. The purpose of these standards and guidelines is to minimize risk by reducing uncertainty in the exploration process so that beach fill materials maintain the general character and functionality of the material occurring on the beach and adjacent dune in the coastal system. Guidelines are thus provided for sediment properties such as grain-size distribution, color, mineralogical composition (quartz vs. carbonate), and bulk properties of cementation and compaction. The term 'functionality' in the FAC refers to the suitability of the material as nesting substrate for marine turtles as well as maintenance of water quality standards (turbidity) and littoral transport performance. As an example, the rules provide specific grain size parameters that may not be exceed so that *compatible* beach fill material must not contain: (1) >5% (by weight) silt, clay, or colloids passing the #230 sieve (4.0φ), (2) >5% (by weight) fine gravel retained on the #4 sieve (-2.25 φ), and (3) coarse gravel, cobbles or material retained on the ¾ inch sieve in a percentage or

size greater than found on the native beach. After an identified sand deposit is determined not to exceed grain-size parameters specified in the rule, then similarity in color and grain-size distribution (sand grain frequency, mean and median grain size and sorting value) to the material in the existing coastal system at the disposal site becomes the determining factor in the acceptability of the borrow sediments. It should be noted that the character of the material within the dry beach berm is used to define the material within the existing coastal system. This is true because suitability is keyed to marine turtle nesting as the primary consideration of environmental functionality of the beach sediment.

Particle-size analyses may be conducted according to numerous procedures viz. hydrometer, pipette, sedimentation, and sieving methods. Although not specified in the state codes, grain size analyses are normally conducted for sand samples in accordance with the American Society for Testing and Materials (ASTM), Standard Material Designation D422-63 for partial-size analysis of soils. Mechanical sieving is accomplished using calibrated sieves, with a gradation of half phi intervals, per U.S. Army Corps of Engineers standards. Grain-size distribution curves are typically prepared and raw sedimentological data are developed into a GIS database that is available for electronic transfer. Sediment-size analysis of vibracore mud and clay samples can be conducted, for example, using a Coulter LS200 particle-size analyzer, which employs laser diffraction to measure the size distribution of sedimentary particles. The LS200 utilizes size-dependent optical characteristics of particles to determine the population of particle sizes within a sediment sample (see discussion in Finkl and Khalil, 2005a,b).

According to the NCAC Rule, compatibility of borrow sediments with those on the beach is determined by strict criteria that include, for example (in terms of average percentage by weight): (1) limits on fine-grained sediment (<0.0625 mm) in the borrow not to exceed fine-grained sediment of the recipient beach characterization plus 5%; (2) sediments in a navigation channel are compatible if the average of fine-grained (<0.0625 mm) sediment is less than 10%, (3) material other than natural sediment and shell is not considered compatible [which eliminates glass cullet as a possible new alternative sediment source that is being developed in other regions (Finkl, 1996; Thompson, Finkl and Kruempel, 2004)], (4) granular sediment (≥2 mm and <4.76 mm) or gravel (≥4.76 mm) can not exceed occurrence in the recipient beach by more than 5%, and (5) calcium carbonate content in a borrow can not exceed that of the recipient beach by more than 15%, *etc*.

CODIFICATION: RULES AND REGULATIONS FOR BEACH FILL PROJECTS

Beach renourishment projects require oversight to ensure proper placement of compatible materials. Although there are many caveats in the process, the State of Florida (BBCS) initiated codification of principles and practices to regulate offshore sand searches for compatible beach sediments in the early 1990s with subsequent amendments as, for example, Specific Authority 161.041, 370.021(1) FS (formerly 16B-41.007, amended 10-23-01). Guidelines for offshore sand searches in Louisiana (Khalil, 2004) provide a basis for codification as the Louisiana Department of Natural Resources moves towards strategic assessment of seabed sand resources in various types of deposits. The State of North Carolina is in the process of approving rules and regulations for beach nourishment projects. Both state efforts provide guidelines for offshore sand searches, borrow development, and onshore placement.

In the state of Florida, quality standards and QA/QC procedures for projects differ. Larger beach restoration projects, for example, must follow a comprehensive set of guidelines (as indicated above) whereas permits for individual residents and similar small projects are governed by a different permit program that has a broader sand quality standard. Smaller projects such as coastal buildings generally fall under the Coastal Construction Control Line Program (CCCL) (Chapter 62B-26-54 FAC, parts effective 1997), an essential element of Florida's coastal management program, which allows a wider range of acceptable standards for sand color and composition as specified in Chapter 62B-36 (Beach Management Assistance Program, effective 2003). Some communities such as Panama City Beach, Florida, for example, set their own standards for specific sand characteristics that meet local conditions. Given the prevalence of white sand in Florida Panhandle, Panama City Beach adopted ordnance that renourishment sand must have a Munsell Color value of 7 or greater. The state standard allows darker colored sand to be placed on the beach. Rules as occur in the FAC provide minimum standards for borrow materials that must approximate native beach sands. Local standards may be more restrictive as conditions necessitate.

Channel sediments in Florida are suitable for placement on the beach when they meet certain standards. Pursuant to subsection 62B-41.005(15) FAC, for example, sandy sediments with up to 10% fine material (-230 sieve sediments) by weight from the maintenance of coastal navigation channels can be used for beach placement, provided they meet other sediment and water quality standards.

DISCUSSION

Strict compliance with similarity criterion is rarely achieved because sediments in offshore borrows are typically poorly sorted or have a bimodal grain-size distribution compared to well-sorted berm sediments. Most offshore deposits in Florida, for example, contain admixtures of carbonate sand or shell fragments with a mean and median grain size greater than the beach sediments. Compliance with similarity criteria involves avoidance of borrow area sediments that contain a high percentage of fine-grained carbonate sands and/or shell fragments because they may cause post-placement compaction and cementation. To this end, compaction is limited to values less than 500 psi (700 kg m^{-2}) to protect marine turtles. Cementation is not allowed under any circumstances because it prevents nesting by sea turtles, reduces habitat for shorebirds, restricts groundwater flow in beach sediments, and causes a range of other environmental concerns as well as presenting safety issues for beach users. This limit is, however, an implied goal without definitive standing in the rules. Beach fills with a measured strength greater than 500 psi have to be tilled, but are not directly prevented from being built. Some unstated higher value of compaction would be against the rules, although this value is not mentioned in the rules directly.

The resulting mixtures of autochthanous (native) and allochthonous (introduced) sediments by default become a new ‘native beach sand’ that must be approximated by borrow sediments. The evolving beach sands on renourished beaches thus acquire new characteristics with each renourishment cycle producing a ‘moving target’ of what officially constitutes ‘native beach sand.’ Before conducting a marine sand search, it is thus necessary to ascertain what constitutes that so-called ‘native beach’, which in fact is a temporal perception. Comparison of pre-nourishment beach sands, in Florida for example, with beach sediments that have resulted from several renourishment cycles can be quite different, as seen for example at Captiva Island, Longboat Key, Delray Beach, *etc*.

Other problems that are associated with the development of borrow sand is determining exactly what is meant by the term ‘beach compatible.’ Although the term clearly has different

meanings, the one that counts is that adopted by the permitting agency, especially those that have been codified as in Florida and nearly so in North Carolina. Again, this can be largely perceptual and not definitively defined in sedimentological terms. Particularly troublesome, for example, are mixed sediment beaches where there are naturally variable amounts of siliciclastics and carbonates as occur on the central to southern east and west coasts of Florida. As a general rule, the percentage of siliciclastics decreases from north to south and the percentage of carbonate decreases from south to north. In northern Broward County on the southeast coast of Florida, for example, the siliciclastic-carbonate contents are about 50-50. Matching existing beach sands with 'beach compatible' sediments in borrows may be controversial because borrows typically do not exist as exact analogs to present combinations of beach sediments. On the east coast of Florida, borrows are developed in inter-reefal flats where sands are mostly siliceous whereas on the west coast borrows are often developed in carbonate-rich sand ridges. There thus occurs a trade off where borrow sediments are not exactly compositionally similar to existing beach sediments (quartz vs. carbonate, shell content) but they may be very similar in terms of the average silicate grain size expressed as D_{50}. In Louisiana, for example, restoration of barrier islands finds that there is not much compositional variation between beach and borrow sediments, both being derived from Mississippi River alluvium, but there can be difficulty finding deposits of appropriate quartz grain size along a muddy coast environment. Similarly, but this time in a glacial coastal environment along the coast of Nantucket in New England, location of suitable offshore borrows can be challenging in a marine-modified drowned pro-glacial landscape (sandur plain) where there is extreme spatial variation in sediment quality over short distances (*e.g.* moraine vs. outwash plain).

Efforts in the field, laboratory, and office combine to focus on the most advanced methodologies possible and yet the marine environment demands better understanding, more precise measurement, and better appreciation of complexity introduced by drowning of coastal plain terrestrial and coastal/marine deposits to become continental shelves and their subsequent modification by marine processes. Better matching of sedimentary deposits in borrows with beach sediments for proposed renourishment is a goal that should be approached judiciously and cautiously because there are no short cuts nor has the methodology been codified in most instances. Even though offshore materials may never achieve full compatibility, partial compatibility may be the best of all reasonable options that are sufficient and better than alternatives such as seawalls or shoreline retreat.

CONCLUSIONS

The determination of what constitutes beach-compatible sediments in offshore borrows is sometimes confounded by efforts to ascertain the true nature of 'native beaches.' The definition of 'native' sand along eroded or renourished coasts is an evolving paradigm because increased awareness (by governmental agencies, consultants, and environmental groups) is now achieving better focus on spatio-temporal problems of sediment sampling. Bias in sediment sampling on beaches is intrinsically problematical to characterization of 'native' beach sediments. Compatibility of borrow sediments with native beach sands posits new questions as the scope for onshore placement of unwanted materials is ever present in deposits of variable composition. Risk of dredging undesirable sediments in borrows can be reduced by increasing the number of vibracores (decreasing the vibracore sphere of influence) and achieving better understanding of coastal geological (incl. geomorphological and morphodynamic conditions) frameworks and environments of deposition. Florida's Bureau of Beaches and Coastal Systems is leading coastal states in the codification of sedimentary properties that are useful in beach renourishment activities, including development of offshore borrows. Rules and regulations will soon be in place in North Carolina

while Louisiana follows guidelines for offshore sand searches and characterization of marine sand resources.

ACKNOWLEDGEMENTS

For critical comments and general review of the paper, we thank Gregory Rudolph (Carteret County Shore Protection Office, Emerald Isle, North Carolina) and Syed Khalil (Louisiana Department of Natural Resources, Coastal Engineering Division, Baton Rouge, Louisiana).

REFERENCES

Benedet, L.; Finkl, C.W. and Klein, A.H.F. (2004). "Morphodynamic classification of beaches on the Atlantic coast of Florida: Geographical variability of beach types, beach safety and coastal hazards," *Journal of Coastal Research* SI 39, 360-365.

Benedet, L.; Finkl, C.W.; Campbell, T., and Klein, A. (2004). "Predicting the effect of beach nourishment and cross-shore sediment variation on beach morphodynamic assessment," *Coastal Engineering* 51(2004), 839-861.

Boss, S.K., and Hoffman, C.W. (2000). *Final Report: Sand Resources of the North Carolina Outer Banks*, Prepared for the Outer Banks Task Force and the North Carolina Department of Transportation, 87p. (www.obtf.org/NC12/REPORTS/NC12PDF/COMP.PDF)

Charles, L.; Malakar, S.B., and Dean, R.G. (1994). "Sediment Data for Florida's East Coast," Gainesville: University of Florida, Report No. UFL/COEL-94/014, v.p.

Capobianco, M.; Hanson, H.; Larson, M.; Steetzel, H.; Stive, M.J.F.; Chatelus, Y.; Aarnikhof, S., and Karambas, T. (2002). "Nourishment design and evaluation: applicability of model concepts," *Coastal Engineering* 47(2), 113-137.

Dean, R. G. (1991). Equilibrium beach profiles: Characteristics and applications, *Journal of Coastal Research* 7(1), 53-84.

Dean, R. G. (2002). "Beach Nourishment: Theory and Practice," World Scientific, 397 p.

Dean, R. G., 2003. "Beach Nourishment," *Short-Course Material*, Coastal Sediments 2003 (St. Petersburg, Florida).

Duane, D.B. and Meisburger, E.P. (1969). "Geomorphology and Sediment on the Nearshore Continental Shelf, Miami to Palm Beach, Florida," U.S. Army Corps of Engineers, Technical Manual No. 29, Vicksburg, Mississippi.

Field, M.E. and Duane, D.B. (1974). "Geomorphology and Sediments of the Inner Continental Shelf, Cape Canaveral, Florida," U.S. Army Corps of Engineers, Technical Manual No. 42, Vicksburg, Mississippi.

Finkl, C.W. (1981). "Beach nourishment, a practical method of erosion control," *Geo-Marine Letters* 1(2), 155-161.

Finkl, C.W. (1996). "Beach fill from recycled glass: A new technology for mitigation of localized erosional 'hot spots' in Florida", *9th Annual Conference on Beach Preservation Technology, Conference Proceedings*. Tallahassee: Florida Shore & Beach Preservation Association, pp. 174-175.

Finkl, C.W. and Khalil, S.M. (2005a). "Offshore exploration for sand sources: General guidelines and procedural strategies along deltaic coasts," *Journal of Coastal Research* SI 44, 198-228.

Finkl, C.W. and Khalil, S.M. (2005b). "Offshore exploration for sand sources: General guidelines and procedural strategies along deltaic coasts," *In*: Finkl, C.W. and Khalil, S.M., (eds.), Saving America's Wetland: Strategies for Restoration of Louisiana's Coastal Wetlands and Barrier Islands. *Journal of Coastal Research* Special Issue No. 44, pp. 203-233.

Finkl, C.W. and Walker, H.J. (2002). "Beach nourishment," *In*: J. Chen, K. Hotta., D. Eisma, and J. Walker (eds.), *Engineered Coasts*. Dordrecht, Netherlands: Kluwer, pp. 1-22.

Finkl, C.W.; Andrews, J., and Benedet, L. (2003). "Shelf sand searches for beach renourishment along Florida Gulf and Atlantic coasts based on geological, geomorphological, and geotechnical principles and practices," *Proceedings Coastal Sediments'03* CD-ROM Published by East Meets West Productions, Corpus Christi, TX USBN 981-238-422-7.

Finkl, C.W.; Khalil, S.M., and Andews, J.L. (1997). "Offshore sand sources for beach replenishment: potential borrows on the continental shelf of the eastern Gulf of Mexico," *Marine Resources & Geotechnology* 15, 155-173.

Finkl, C.W.; Khalil, S.M., and Spadoni, R.H. (2002). "Carbonate sand for beach re-nourishment along the inner continental shelf off southeast Florida: A geomorphological approach to sand searches," *Carbonate Beaches 2000* (Key Largo, Florida). [Arlington, Virginia: American Society of Civil Engineers], pp. 53-66.

Giles, R.T. and Pilkey, O.H. (1965). "Atlantic beach and dune sediments of the southeastern United States," *Journal of Sedimentary Petrology* 35(4), 900-914.

Gorsline, D.S. (1963). "Bottom sediments of the Atlantic shelf and slope off the southeastern United States," *Journal of Geology* 71(4), 422-440.

Khalil, S.M. (2003). "General Guidelines – Exploration for Offshore Sand Searches," Baton Rouge: Louisiana Department of Natural Resources, Coastal Engineering Division, Coastal Protection Systems Design Guidelines, 200p.

Khalil, S.M. (2005). "Louisiana sand resource database (LASARD) - a concept for geo-scientific data management for offshore sand sources in coastal Louisiana," *Geological Society of America Abstracts with Programs* 37(2), 48.

Komar, P.D., 1998. "Beach Processes and Sedimentation," Prentice Hall, 544p.

Maloney, J.E.; Darian-Smith, C.; Takahashi, Y., and Limpus, C.J. (1990). "The environment for development of the embryonic loggerhead turtle (*Caretta caretta*) in Queensland," *Copeia* 2, 378-387

Meisburger, E.P. (1977). "Sand Resources on the Inner Continental Shelf of the Cape Fear Region," U.S. Army Corps of Engineers Miscl. Rep, 77-11, Vicksburg, Mississippi.

Meisburger, D., 1990. "Exploration and Sampling Techniques for Borrow Areas," U.S. Army Engineer Waterways Experiment Station, Coastal Engineering Research Center, Tech, Rep. CERC-90-18. Vicksburg, Mississippi

Meisburger, E.P. and Duane, D.B. (1971). "Geomorphology and Sediments of the Inner Continental Shelf, Palm Beach to Cape Kennedy, Florida," U.S. Army Corps of Engineers, Tech. Man. No. 34, Vicksburg, Mississippi.

Rice, T.M. (2003). "Native Sediment Characteristics of North Carolina Beaches," U.S. Fish & Wildlife Service, Raleigh, North Carolina.

Smith, A.W. (1992). "Description of beach sands," *Shore and Beach* 60, 3, 23-30.

Thomson, G.G.; Finkl, C.W., and Kruempel, C.J. (2004). "Broward County Beach Demonstration Project Geotechnical Investigation Report: Technical Memorandum," Coastal Planning & Engineering, Inc., Boca Raton, Florida, (Prepared for Malcolm Pirnie, Inc., Fort Lauderdale, Florida), 12p.

USACE (2002). "Coastal Engineering Manual," U.S. Army Corps of Engineers, EM 1110-2-1100, 6 vols, Washington, DC.

Wood, D.W. and Bjorndal, K.A. (2000). "Relation of temperature, moisture, salinity and slope to nest site selection in loggerhead sea turtles," *Copeia* 2000, 1, 119-128.

Wright, L.D. and Short, A.D. (1984). "Morphodynamic variability of surf zones and beaches: A synthesis," *Marine Geology* 56, 93-118.

Subject Index

Page number refers to the first page of paper

Aggregates, 2394
Alabama, 1047, 2002
Alaska, 463
Australia, 1033, 1417

Backwashing, 1947
Barrier beaches, 492
Barrier islands, 647, 671, 685, 699, 976, 1153, 1179, 1722, 1988, 2002, 2011, 2254
Barriers, 434, 814, 935, 1731, 1910, 2084
Bars, 2111, 2124
Bathymetry, 1877, 2191
Bays, 341, 463, 814, 856, 1311, 2137, 2151
Beach erosion, 1142, 1311, 1601
Beach nourishment, 776, 2279, 2358, 2418, 2501, 2515
Beaches, 300, 314, 378, 406, 420, 463, 477, 506, 520, 531, 545, 584, 626, 935, 1019, 1227, 1269, 1455, 1696, 1708, 1740, 1787, 1851, 1865, 1947, 1661, 2111, 2241, 2265, 2402, 2460
Bed load, 56
Belgium, 1431
Berms, 449
Brazil, 1455
Breaking waves, 42, 2124
Breakwaters, 2402, 2460
Bulkheads, 561

California, 1696, 1740, 1851, 2501
Canada, 351
Caribbean, 572
Case reports, 1391
Channels, 1431, 1571, 1678, 2164, 2213, 2345, 2358, 2372
Chesapeake Bay, 2306
Cliffs, 1696
Climatic changes, 963, 1214
Closed form solutions, 15
Coastal engineering, 434, 1241, 1405
Coastal environment, 179, 207, 449, 828, 842, 1117, 1129, 1283, 1475, 1647, 1669, 1813, 1827, 1900, 1910, 1924, 2084, 2151, 2321
Coastal morphology, 1, 137, 272, 364, 492, 671, 736, 814, 828, 842, 986, 1019, 1033, 1165, 1200, 1297, 1354, 1363, 1417, 1455, 1529, 1571, 1582, 1589, 1635, 1938, 2011, 2025, 2137, 2199, 2345
Coastal structures, 2432
Colorado River, 1502
Currents, 42
Cyclones, 935

Damage, 1008
Deep water, 1, 341
Deltas, 207, 736, 749, 828, 882
Design, 420, 785, 1988
Dikes, 392, 785, 1008
Dredge spoil, 2358
Dredging, 2372, 2382, 2394
Dunes, 612, 897, 951, 1033, 1089, 1241, 1283, 1813, 1961, 1975
Dynamics, 584

Empirical equations, 1431
Environmental issues, 1827
Equilibrium, 897, 2241
Erosion, 96, 612, 1722, 1799, 1813, 1961, 2037, 2074, 2265, 2321
Esthetics, 420
Estimation, 1008, 2372, 2382
Estuaries, 531, 1200, 1609, 1623, 1669, 2487
Evaluation, 626

Failures, 392, 1008
Field investigations, 661
Fills, 2402, 2418

Florida, 151, 378, 1047, 1297, 1326, 1377, 1582, 1589, 1877, 2199, 2265
Flumes, 124
Forecasting, 1813
Forests, 1117
France, 531

Geology, 2151, 2473, 2487
Geometry, 1787, 2002, 2177
Geomorphology, 165, 762, 2097, 2292, 2306
Grain size, 259, 314, 1255, 1623, 2229, 2241, 2446
Gravel, 477, 492, 520, 572, 584, 2473
Gravity waves, 1, 235
Great Lakes, 392
Ground water, 506
Gulf of Mexico, 935, 1515

Harbors, 1431, 2292
Hawaii, 1227
Hazards, 1799
Heterogeneity, 921
History, 364, 867
Hurricanes, 151, 882, 888, 911, 976, 986, 996, 1047, 1466, 2306
Hydrodynamics, 221, 1297, 1489, 1557, 1582, 1787, 1924
Hydrographs, 1827
Hydrologic models, 1669

Ice formation, 798
Imaging techniques, 1886
Indonesia, 1019
Infiltration, 506
Inlets, waterways, 1165, 1297, 1326, 1354, 1363, 1377, 1391, 1475, 1489, 1502, 1515, 1529, 1543, 1557, 1589, 1468, 2199, 2331
Integrals, 286
Islands, 1340, 1708, 1722, 1865

Japan, 1269, 1354, 1900, 2460

Laboratory tests, 68, 235, 248
Lagoons, 1708
Land reclamation, 598
Latin America, 2345
Littoral currents, 1405
Littoral drift, 165, 179
Louisiana, 647, 661, 671, 685, 699, 762, 785, 888, 911, 921, 1165, 1179, 2254

Mapping, 2487
Marshes, 785, 1571
Maryland, 1340
Massachusetts, 814, 856, 1142
Mathematical models, 1075
Measurement, 221, 561, 1609, 1678, 1947
Mexico, 996, 2279
Michigan, 392, 2292
Mississippi, 1466
Mississippi River, 699, 712, 722, 749, 882, 2177
Models, 300, 406, 897
Monitoring, 406
Morphology, 235, 1391, 1557, 1900, 2199
Mud, 1660, 1669, 1690

Navigation, 1431, 1502, 1678, 1768, 2345, 2372
Nearshore, 1, 56, 584, 951, 1886
Netherlands, 1129, 1363
New England, 798
New York, 1722, 2331
New Zealand, 1441, 1910
North Carolina, 327, 963, 1153, 1543, 1837, 2229
North Sea, 2124
Numerical analysis, 1089
Numerical models, 341, 671, 736, 749

Oregon, 449, 1754, 2137
Outwash, 2049, 2074, 2084

Parameters, 124, 626
Permeability, 520
Plumes, 736, 2382
Porous media, 2321
Portugal, 545, 1557
Predictions, 314, 612, 1103
Probability, 272
Progressive waves, 2191

Radar, 1900
Reefs, 572, 1647

Remedial action, 1601
Restoration, 647, 685, 699, 776, 785
River basins, 1647
River beds, 2177
Rivers, 842

Salts, 798
Sand, 42, 68, 96, 193, 248, 259, 314, 477, 492, 506, 520, 545, 584, 685, 699, 1255, 1269, 1340, 1405, 1609, 1708, 2164, 2191, 2254, 2432, 2446, 2460, 2473, 2501
Sandbars, 28
Scour, 598, 1609, 1851, 2213
Sea floor, 598, 1635, 1660, 2487
Sea level, 1153, 1179, 1193, 1200, 1214
Sediment, 15, 28, 207, 300, 463, 531, 633, 661, 671, 712, 722, 736, 749, 776, 867, 951, 1047, 1075, 1103, 1283, 1326, 1635, 1647, 1768, 1877, 1988, 2229, 2292, 2382, 2473, 2515
Sediment transport, 42, 56, 68, 82, 96, 110, 124, 137, 151, 179, 193, 221, 286, 351, 911, 996, 1117, 1241, 1405, 1441, 1669, 1678, 1754, 1924, 1938, 2037, 2049, 2446, 2460
Sedimentation, 798, 1377
Seismic effects, 856
Shear stress, 193, 1947
Sheet flow, 286
Ship motion, 110
Ships, 685, 2213
Shoaling, 921, 1311
Shoreline changes, 327, 364, 378, 392, 888, 1129, 1142, 1214, 1227, 1417, 1601, 1740, 1754, 1799, 1837, 2306
Shores, 561, 633
Simulation, 259, 2097
Simulation models, 1623
Skewness, 137
Slopes, 137, 165
South Carolina, 1787, 2151
Spatial distribution, 2037
Spits, coastal, 351
Sri Lanka, 842, 1061
Statistics, 1799, 2177
Stones, 531
Storm surges, 996, 1466
Storms, 951, 963, 1813, 1886, 2061
Stratification, 1635
Structural design, 2432
Subsurface environment, 82
Subsurface investigations, 785
Surf zone, 82, 151, 1455, 1865
Surface waters, 1690
Suspended sediments, 221, 248
Switzerland, 2321

Texas, 1475, 1502, 1515, 1529
Tides, 1129, 1179, 1354, 1417, 1543, 1589, 1731, 1768, 2164
Time dependence, 193, 867, 1690
Topography, 867, 1623, 1837, 1865, 1938, 2061, 2097
Tracers, 449
Transport rate, 179
Tropical regions, 1731, 2061
Tsunamis, 842, 1008, 1019, 1033, 1061, 1075, 1089, 1103, 1117
Turbulence, 15

United Kingdom, 434, 1200

Vegetation, 1571
Velocity, 15, 28, 2382
Virginia, 364, 2402

Washington, 561, 1311, 1754
Water circulation, 327
Water levels, 963
Wave groups, 110
Wave runup, 272, 1075, 1089, 1924, 1938, 1947, 1961, 1975
Wave tanks, 259
Waves, 661, 1660, 1690, 1731
Wetlands, 722, 1179, 1193
Wind, 1255

This page intentionally left blank

Author Index

Page number refers to the first page of paper

Aagaard, Troels, 951, 2124
Aarninkhof, Stefan G. J., 598, 1975
Abbe, Tim, 561
Adams, Mark B., 1142
Adams, Peter N., 463
Alfageme, Santiago R., 2345, 2432, 2025
Allan, Jonathan C., 449, 2137
Allison, Mead A., 661, 882
Alonso, Ignacio, 1283
Alsina, J. M., 272
Amaro, Venerando E., 1731
Anderson, Carl M., 1529
Andrews, Brian D., 2487
Andrews, Jeffrey L., 685, 699, 2515
Andrus, T. Mitchell, 722, 785
Argow, Brittina A., 798
Arsenault, Matthew A., 2473
Asano, Go, 1623
Ashton, Andrew D., 327, 341, 351, 1214
Austin, Martin J., 584

Baba, Yasuyuki, 1938
Baig, Stephen, 1466
Baldock, Tom E., 272, 286, 506, 1947
Baldwin, Wayne E., 2151, 2487
Barcak, Ronnie G., 1502
Barlett, William, 749
Barnard, Patrick L., 2501
Barnes, Matthew P., 272, 1947
Barnhardt, Walter A., 856, 2151
Barthélemy, Eric, 235
Bass, Gregory P., 1340
Batten, Brian K., 1515
Beck, Tanya M., 1377, 1582
Bell, Paul S., 1886
Bell, Robert G., 1441
Bender, Christopher, 151
Benedet, Lindino, 671, 699, 2515
Benoit, Jeff, 1601
Bentley, Samuel J., 722, 1441
Bergeron, Emile, 2487
Bliss, James D., 2473
Boer, Sander, 598
Bokuniewicz, Henry, 1722
Bolinger, Daniel L., 2254
Bradbury, Andrew P., 492
Brehin, Florian G. A., 1297, 2199
Briére, C., 137
Brocchini, M., 1635
Brown, J. M., 1609
Buonaiuto, Frank, 1722
Buschman, Frans, 1647
Buscombe, Daniel, 584
Butman, Bradford, 2487
Byrnes, Mark R., 762, 1754

Calliari, Lauro J., 1455
Calvete, D., 2111
Camenen, Benoît, 15, 56, 1938
Campbell, T., 671
Cañizares, Rafael, 2025, 2345
Canning, Paul, 520
Carrasco, Ana R., 2084
Carrasquero, José, 561
Carter, Joshua, 1489
Clarke, Linden B., 1975
Cleary, William J., 1543
Cleveringa, Jelmer, 1129
Coates, Tom C., 406
Coeveld, E. Matrijn, 612, 1975
Conley, D. C., 1635
Connell, Kenneth J., 2011
Cowell, P. J., 633
Cox, Andrew, 1466
Crowley, Tom, 1214
Curoy, J., 531

Dalon, Matthew M., 2137
Dan, Sebastian, 207
Danchuk, Samantha, 749
Danforth, William W., 2487
Darnell, Joel T., 776

Dartez, Dane, 911
Dartnell, Peter, 1851
Das, Himangshu, 1466
Davies, A. G., 1609
Davis, Richard A., 1582
de Alegria Arzaburu, Amaia Ruiz, 996, 1865, 2279
de Sonneville, B., 671
de Vroeg, Hans, 612
Dean, Robert G., 626
Dekker, Frank, 1117
Dellapenna, Timothy M., 882
Denny, Jane F., 2151, 2487
Dias, Alveirinho, 1557
Dias, João A., 2049, 2084
Dibajnia, Mohammad, 392, 2097, 2292
Diesing, Markus, 2394
Dill, Nathan, 749
Dohmen-Janssen, C. Marjolein, 1019
Donnelly, Chantal, 2061
Dornbusch, U., 531
Dougherty, Amy J., 1910
Driscoll, Neal, 2151
Durham, William McKinney, 82

Edge, Billy L., 2074
Edwards, Brian D., 1851
Elias, Edwin P. L., 598, 1363
Elkan, Peter, 2402
Elko, Nicole A., 378
Espinal, Juan C., 996, 2279
Esteves, Luciana S., 221, 1886

Falchetti, S., 1635
Falqués, A., 2111
Farris, Amy S., 1837
Fauver, Laura A., 897
Ferland, M. A., 633
Ferreira, Óscar, 1557, 2049, 2084
Finkl, Charles W., 671, 685, 699, 2515
FitzGerald, Duncan M., 798, 856, 1165, 1179, 2164
Fitzpatrick, Kathy, 1326
Fletcher, Charles H., 1227, 1799
Foster, David S., 2487
Foye, Peter, 2265
Frazer, L. Neil, 1799
Friedrichs, Carl T., 2382

Fujii, Hiroyuki, 1008
Fukuhama, Masaya, 259, 1008, 1623
Furuike, Kou, 314

Galal, El Sayed, 1900
Galofre, Jordi, 2241
Garcia, Marcelo H., 2191
Garnier, R., 2111
Gayes, Paul T., 1787, 2151
Gelfenbaum, Guy R., 1103, 1117, 1768
Genz, Ayesha S., 1799
Georgiou, I., 2177
Georgiou, Ioannis, 1179
Gibeaut, James C., 1193
Giese, Graham S., 1142
Giosan, Liviu, 828
Goff, James R., 1033, 1061
Goff, John A., 2473
Goñi, Miguel A., 882
Gonzalez, Mauricio, 300
Grandy, Greg M., 647
Granja, Helena, 545
Grasmeijer, Bart, 1
Grasso, Florent, 235
Griffee, Sarah F., 1754
Griggs, Gary B., 1740, 2501
Grosskopf, William G., 1340
Grüne, Joachim, 248
Guannel, Gregory, 28
Guard, P., 286
Guedes, Rafael M. C., 1455
Guidroz, Walter S., 911
Guillén, J., 2111
Gunawardena, Yohama, 1865
Gunn, James R., 2306

Haghshenas, S. Abbas, 1690
Hall, Kevin, 1660, 2213
Haller, Merrick, 28, 2137
Hamilton, Stuart, 986
Hansen, Mark, 2002
Hanson, Hans, 15
Hapke, Cheryl J., 1696
Harcourt, Jenny S., 406
Hardaway, C. Scott, Jr., 2306
Harikai, Souichi, 1269
Hart, Roger, 449
Hashimoto, Koji, 1354

Hatchett, Lyle, 1466
Hayashi, Kentaro, 1354
Head, Richard, 406
Headland, John R., 2432
Healy, Terry R., 165, 2358
Heilman, Daniel J., 776, 1502
Hein, Christopher J., 856
Higgins, Stephen, 2265
Higman, Bretwood, 1103
Hoekstra, Piet, 1647
Hoitink, Ton, 1647
Holland, K. Todd, 1455
Holman, Rob A., 1975
Honma, Akihiro, 1354
Hopf, Frank, 1241
Horn, Diane P., 520, 506
Horwitz, Mark H., 1047
Hotta, Shintaro, 1255, 1269
Houghton, Jon, 477
Houser, Chris, 986
Howes, Nick, 1179
Hsu, Tian-Jian, 1669
Hughes, Michael G., 1417
Hughes, Zoe J., 798, 1179
Hulscher, Suzanne J. M. H., 1019, 1813

Ilic, Suzana, 1865
Inukai, Takushi, 1623
Irwin, Barry J., 2487
Ishii, Toshimasa, 96
Ishikawa, Toshinori, 259, 314, 2460
Ishino, Kazuo, 842
Izzo, Dominic, 2254

Jaffe, Bruce, 1103, 1117
Jaffe, David A., 867
Jaramillo, Sergio, 661
Jenkins, Chris J., 2473
Jennings, Simon C., 434
Jiménez, José, 1283
Joffrion, Russ, 785
Jose, Felix, 921, 935

Kaminsky, George M., 633, 1768
Kana, Timothy W., 2229
Kato, Fuminori, 1008
Kemp, Jonathan A., 406
Keon, Theodore, 814
Khalil, Syed M., 685, 699
Kheiashy, K., 2177
Khondker, Masood, 2025
Kirby, James T., 28
Kirwan, Matthew L., 1571
Klekotka, John, 477
Knaapen, Michiel A. F., 1200
Knotts, Christopher P., 685
Kobashi, Daijiro, 921
Kolberg, Mark O., 1708
Komar, Paul D., 420
Kos'yan, Ruben, 248
Kotulak, Peter, 2432
Kozuka, Masayuki, 96
Kraus, Nicholas C., 193, 1377, 1475, 1502, 1515, 1529, 1961, 2011, 2331
Krecic, Michael, 151
Kremkau, Kevin, 1326
Kroon, Aart, 951, 2124
Krynock, Laural, 2402
Kubota, Susum, 1255, 1269
Kumada, Takayuki, 314, 2446
Kuriyama, Yoshiaki, 179, 2037

Landry, Blake J., 2191
Larson, Magnus, 56, 1924, 2011
Li, Ling, 506
Lillycrop, W. Jeff, 888, 1827
Limber, Patrick W., 1837
Lin, Lihwa, 1502, 1515
Lisniowski, M. A., 221
List, Jeffrey H., 221, 327, 1837
Littlewood, Ryan, 341, 351
Liu, Baozhu, 935
Long, Bernard F., 124
Lorente, Paloma, 1283
Loureiro, Eduardo, 545
Lovelock, Catherine, 1441
Lynett, Patrick, 1103

Maathuis, Ben H. P., 1019
MacDonald, Neil J., 110, 2213
Macon, Christopher L., 1827
Madsen, Ole Secher, 82, 96
Mahoney, Tucker, 2345
Mai, Stephan, 2321
Makowski, Christopher, 2265
Mann, Douglass W., 1405

Manoonvoravong, P., 272
Mark, David J., 1311
Masselink, Gerhard, 584
Matias, Ana, 2049, 2084
Matsumoto, Hideo, 1678
Matsumoto, Ryosuke, 1900
Matsura, Seizo, 1354
McBride, Randolph A., 364, 762
McCorquodale, J., 2177
McKillip, Doris J., 1768
Medellin, Gabriela, 2241
Medina, Raúl, 300, 2241
Meilianda, Ella, 1019
Merrifield, Mark A., 1227
Meselhe, E., 2177
Meyer-Arendt, Klaus, 986
Michallet, Hervé, 235
Mimura, Nobuo, 96
Miner, Michael D., 1165, 1179
Momose, Kazuo, 96
Montreuil, Stéphane, 124
Moore, Andrew, 1103
Morán, Diana K., 996, 2279
Morang, Andrew, 1311
Morgan, Michael J., 2331
Moritz, Hans R., 633, 1754, 1768
Morris, Brad, 2049
Morrison, Steve, 561
Morton, Robert A., 572, 1061, 2151, 2487
Moses, C. A., 531
Mouraenko, Oleg, 2372
Mulder, Jan P. M., 1813, 1019
Murray, A. Brad, 341, 351, 1214, 1571
Mustain, Neomi, 2501

Nairn, Robert B., 392, 1708, 2097, 2292
Nakagawa, Hajime, 842
Nakagawa, Yasuyuki, 1678
Nakamura, Nagatomo, 1255
Nawarathna, Bandara, 842
Neto, Francisco Santos, 1731
Nichol, Scott L., 1061, 1910
Nicholls, Robert J., 1200
Nichols, David R., 2487
Niedoroda, Alan W., 1466
Nielsen, P., 286

Özkan-Haller, H. Tuba, 28

O'Brien, Thomas F., 2487
O'Donoghue, Tom, 42
Odroniec, Kristen, 151
Ojeda, E., 2111
Oltman-Shay, Joan, 1768
Oravetz, Jonathan, 986
Orford, Julian D., 434, 492
Osborne, Philip D., 110
Oumeraci, Hocine, 248
Oveisy, Ali, 1660
Overton, Margery, 2074

Pacheco, André, 1557
Palmsten, Meg L., 1975
Park, Young Hyun, 2074
Parkinson, Shaun, 110
Pawlak, Geno, 1227
Penland, Shea, 1179
Pereira, Pedro S., 1455
Perotto, H. L. S., 221
Perry, M. Cameron, 776
Phillips, Eleyne L., 1851
Placido Jr., Jose S., 1731
Podymov, Igor, 248
Poff, Michael, 785
Pope, Joan, 963

Quartel, Susanne, 951

Ramsey, John, 1326
Ranasinghe, Roshan Suminda, 68
Ranasinghe, Roshanka, 1417
Reid, Dave, 1696
Reniers, Ad J. H. M., 1975
Requejo, Soledad, 300
Revell, David L., 1740
Reynolds, B. M., 1787
Ribas, F., 2111
Ribberink, Jan S., 1, 42
Richardson, Trent M., 364
Richmond, Bruce M., 572
Risk, Michael J., 1708
Roberts, Susan, 1601
Roberts, Tiffany M., 1961
Robertson, William, V., 1877
Robinson, D. A., 531
Roblin, Rachel R., 392
Rodríguez-Herrerías, Manuel, 1283

Roelvink, Dano (J.) A., 598, 736
Rosario-Llantin, Jo-Ann, 2199
Rosati, Julie Dean, 1988
Rosenberg, Lee, 2402
Rossington, Kate, 1200
Ruessink, Gerben, 1
Ruffman, Alan, 1075
Ruggiero, Peter, 463, 633, 1768
Ruthven, Trey, 1326

Sánchez, José C., 2279
Sabatier, François, 207
Saifee, Shabbar, 1466
Sakagami, Takeharu, 96
Sakamoto, Hikari, 179
Sallenger, Asbury H., 179, 888, 897, 976, 2061
Salles, Paulo, 996, 2279
San-nami, Toshiro, 314
Santo, Renato E., 1455
Sasaki, Takayuki, 1354
Sasakura, Shinya, 1900
Sato, Shinji, 68, 1089
Sayah, Selim M., 2321
Schmeltz, Edward J., 2254
Schmidt-Koppenhagen, Reinold, 248
Schupp, Courtney A., 1340
Schwab, William C., 2151, 2487
Seabergh, William C., 1391
Seaver, Kathryn, 1722
Selegean, James P., 392, 2292
Serizawa, Masumi, 259, 314, 2446, 2460
She, Kaiming, 520
Shepsis, Vladimir, 1489
Sheremet, Alex, 661, 882
Sherman, Douglas J., 1241
Shibayama, Tomoya, 1690
Shimozono, Takenori, 1089
Short, Andrew D., 1417
Simpson, David, 477
Slott, Jordan, 1214
Smith, David E., 1075
Smith, Eric, 2432
Smith, Ernest R., 193, 1502
Smith, Jane M., 1311
Smith, S. Jarrell, 2382
Soltanpour, Mohsen, 1690
Son, Minwoo, 1669
Son, P. Kim, 272
Soulsby, Richard L., 1075
Spiers, Kyle C., 2358
Stauble, Donald K., 814, 2418
Stive, Marcel J. F., 207, 736, 1363, 1589, 1975
Stockdon, Hilary F., 976
Stolper, David, 1153
Stone, Gregory W., 911, 921, 935, 1988
Storlazzi, Curt D., 1227, 1851
Storms, Joep E. A., 736
Suzuki, Takayuki, 2037
Swales, Andrew, 1441
Sweeney, Rachel, 647

Tajima, Yoshimitsu, 96, 1089
Takagi, Toshimitsu, 1008, 1623
Takeuchi, Maiko, 2037
Takewaka, Satoshi, 1900
Talmon, A. M., 137
Tanaka, Hitoshi, 842
Tarya, Ayi, 1647
Taylor, David, 2213
Taylor, Matthew J., 762
Teakle, I., 286
Thieler, E. Robert, 2487
Thomas, Robert C., 1502
Thompson, David M., 897, 976
Thomson, Gordon G., 647, 2265
Tidwell, David K., 1377
Tomoda, Naoki, 2037
Tonkin, Susan P., 561
Trim, Louise, 520
Tsuru, Masahito, 96
Tung, Tran Thanh, 1589
Twichell, David C., 2487

Uda, Takaaki, 259, 314, 2446, 2460
Uijttewaal, Wim S. J., 1975

Valdemoro, Herminia I., 1283
Valentine, Page C., 2487
Valvo, Lisa, 1214
van de Graaff, Jan, 612, 1589
van den Bergh, Gert, 1647
van der Burgh, L. M., 1813
van der Spek, Ad J. F., 1129
van der Werf, Jebbe J., 1, 42

van Gent, Marcel R. A., 612
van Heteren, Sytze, 1129
van Koningsveld, M., 1813
van Ormondt, M., 137
van Rijn, Leo V., 1, 137
van Thiel de Vries, Jaap S. M., 1975
Vanderbeke, Nicole, 2402
Vatvani, Deepak, 1117
Vellinga, Tiedo, 598
Verwaest, Toon, 1431
Vidal, César, 2241
Vila-Concejo, Ana, 1417, 1557, 2049
Vincent, Chris E., 248
Vital, Helenice, 1731
Vitousek, Sean, 1227

Waldron, Ryan, 749
Walstra, Dirk Jan R., 137, 207, 671, 736, 1589
Wamsley, Ty V., 1924
Wang, Ping, 378, 1047, 1377, 1582, 1961
Wang, Zhanxian, 626
Warren, Jeffrey D., 1837
Warrick, Jonathan A., 463
Weaver, Robert, 1466
Weber, Kathryn M., 1837
Weishar, Lee L., 814
Welsh, John M., 1543
White, James, 2402
Whitman, Dean, 1877
Whitmeyer, Shelley J., 2164
Wijnberg, K. M., 1813
Williams, Deidre D., 1529
Williams, Jon J., 221, 1886
Williams, R. B. G., 531
Williams, S. Jeffress, 1153, 2473
Willson, Clinton S., 749
Winer, Harley S., 712
Wise, Larry A., 2372
Worley, Charles W., 2487
Wozencraft, Jennifer M., 1827
Wray, Michael, 477
Wren, P. A., 1787
Wright, C. Wayne, 888

Yamaguchi, Satomi, 2037
Yano, Shinichiro, 842

Zarillo, Gary A., 1297, 2199
Zhang, Keqi, 1877